

ارائه به روزترین منابع، کتابها و جزوات مهندسی عمران
به زبان فارسی و انگلیسی به صورت کاملاً رایگان

www.TheSetosa.com

ASM Handbook®

Volume 4A Steel Heat Treating Fundamentals and Processes

Prepared under the direction of the
ASM International Handbook Committee

Volume Editors

Jon. L. Dossett, FASM, Consultant
George E. Totten, FASM, Portland State University

Editorial Committee and Advisors

Madhu Chatterjee, Bodycote
Rafael Colás, Universidad Autónoma De Nuevo León
Edward (Derry) Doyle, RMIT University
Kiyoshi Funatani, IMST Institute (Consultant)
Robert J. Gaster, Deere & Company
Peter Hodgson, Institute for Frontier Materials, Deakin University
Franz Hoffmann, IWT Bremen
D. Scott MacKenzie, Houghton International
Michael J. Schneider, The Timken Company

ASM International Staff

Steve Lampman, Content Developer
Vicki Burt, Content Developer
Amy Nolan, Content Developer
Susan Sellers, Editorial Assistant
Madrid Tramble, Manager of Production
Kate Fornadel, Senior Production Coordinator
Patty Conti, Production Coordinator
Diane Whitelaw, Production Coordinator
Karen Marken, Senior Managing Editor
Scott D. Henry, Senior Manager, Content Development

Editorial Assistance

Elizabeth Marquard
Jo Hannah Leyda
Buz Riley



Copyright © 2013
by
ASM International®
All rights reserved

No part of this book may be reproduced, stored in a retrieval system, or transmitted, in any form or by any means, electronic, mechanical, photocopying, recording, or otherwise, without the written permission of the copyright owner.

First printing, November 2013

This Volume is a collective effort involving hundreds of technical specialists. It brings together a wealth of information from worldwide sources to help scientists, engineers, and technicians solve current and long-range problems.

Great care is taken in the compilation and production of this Volume, but it should be made clear that NO WARRANTIES, EXPRESS OR IMPLIED, INCLUDING, WITHOUT LIMITATION, WARRANTIES OF MERCHANTABILITY OR FITNESS FOR A PARTICULAR PURPOSE, ARE GIVEN IN CONNECTION WITH THIS PUBLICATION. Although this information is believed to be accurate by ASM, ASM cannot guarantee that favorable results will be obtained from the use of this publication alone. This publication is intended for use by persons having technical skill, at their sole discretion and risk. Since the conditions of product or material use are outside of ASM's control, ASM assumes no liability or obligation in connection with any use of this information. No claim of any kind, whether as to products or information in this publication, and whether or not based on negligence, shall be greater in amount than the purchase price of this product or publication in respect of which damages are claimed. THE REMEDY HEREBY PROVIDED SHALL BE THE EXCLUSIVE AND SOLE REMEDY OF BUYER, AND IN NO EVENT SHALL EITHER PARTY BE LIABLE FOR SPECIAL, INDIRECT OR CONSEQUENTIAL DAMAGES WHETHER OR NOT CAUSED BY OR RESULTING FROM THE NEGLIGENCE OF SUCH PARTY. As with any material, evaluation of the material under end-use conditions prior to specification is essential. Therefore, specific testing under actual conditions is recommended.

Nothing contained in this Volume shall be construed as a grant of any right of manufacture, sale, use, or reproduction, in connection with any method, process, apparatus, product, composition, or system, whether or not covered by letters patent, copyright, or trademark, and nothing contained in this Volume shall be construed as a defense against any alleged infringement of letters patent, copyright, or trademark, or as a defense against liability for such infringement.

Comments, criticisms, and suggestions are invited, and should be forwarded to ASM International.

Library of Congress Cataloging-in-Publication Data

ASM International

ASM Handbook

Includes bibliographical references and indexes

Contents: v.1. Properties and selection—irons, steels, and high-performance alloys—v.2. Properties and selection—nonferrous alloys and special-purpose materials—[etc.]—v.23. Materials for Medical Devices

1. Metals—Handbooks, manuals, etc. 2. Metal-work—Handbooks, manuals, etc. I. ASM International. Handbook Committee. II. Metals Handbook.

TA459.M43 1990 620.1'6 90-115
SAN: 204-7586

ISBN-13: 978-1-62708-011-8
ISBN-10: 1-62708-011-2

ASM International®
Materials Park, OH 44073-0002
www.asminternational.org

Printed in the United States of America

Foreword

In this 100th anniversary year of ASM International, it is especially fitting to release *ASM Handbook*, Volume 4A, *Steel Heat Treating Fundamentals and Processes*. Since its 1913 origin as the Steel Treating Club, formed by Detroit blacksmith William Park Woodside, ASM International has grown in scope; yet steel heat treating remains a core subject of the Society. Woodside's vision and recognition of the need to exchange information on steel heat treating are further recognized by many successful publications including the renowned *Metals Handbook*.

The *ASM Handbook* (formerly *Metals Handbook*) series is being expanded into several volumes on heat treatment. This reflects the roots of ASM International, as well as the Heat Treating Society (An Affiliate Society of ASM International) with its ongoing member contributions in the field of heat treating. ASM International and the Heat Treating Society extend a very special thanks to George E. Totten and Jon Dossett as Volume Editors. Their initiatives and contributions were instrumental in the development of this Volume. We are indebted to them and to the subject editors, authors, and reviewers for this publication.

Thomas E. Clements
President, Heat Treating Society

Gernant E. Maurer
President, ASM International

Thomas S. Passek
Managing Director, ASM International

Policy on Units of Measure

By a resolution of its Board of Trustees, ASM International has adopted the practice of publishing data in both metric and customary U.S. units of measure. In preparing this Handbook, the editors have attempted to present data in metric units based primarily on *Système International d'Unités* (SI), with secondary mention of the corresponding values in customary U.S. units. The decision to use SI as the primary system of units was based on the aforementioned resolution of the Board of Trustees and the widespread use of metric units throughout the world.

For the most part, numerical engineering data in the text and in tables are presented in SI-based units with the customary U.S. equivalents in parentheses (text) or adjoining columns (tables). For example, pressure, stress, and strength are shown both in SI units, which are pascals (Pa) with a suitable prefix, and in customary U.S. units, which are pounds per square inch (psi). To save space, large values of psi have been converted to kips per square inch (ksi), where 1 ksi = 1000 psi. The metric tonne ($\text{kg} \times 10^3$) has sometimes been shown in megagrams (Mg). Some strictly scientific data are presented in SI units only.

To clarify some illustrations, only one set of units is presented on artwork. References in the accompanying text to data in the illustrations are presented in both SI-based and customary U.S. units. On graphs and charts, grids corresponding to SI-based units usually appear along the left and bottom edges. Where appropriate, corresponding customary U.S. units appear along the top and right edges.

Data pertaining to a specification published by a specification-writing group may be given in only the units used in that specification or in dual units, depending on the nature of the data. For example, the typical yield strength of steel sheet made to a specification written in customary U.S.

units would be presented in dual units, but the sheet thickness specified in that specification might be presented only in inches.

Data obtained according to standardized test methods for which the standard recommends a particular system of units are presented in the units of that system. Wherever feasible, equivalent units are also presented. Some statistical data may also be presented in only the original units used in the analysis.

Conversions and rounding have been done in accordance with IEEE/ASTM SI-10, with attention given to the number of significant digits in the original data. For example, an annealing temperature of 1570 °F contains three significant digits. In this case, the equivalent temperature would be given as 855 °C; the exact conversion to 854.44 °C would not be appropriate. For an invariant physical phenomenon that occurs at a precise temperature (such as the melting of pure silver), it would be appropriate to report the temperature as 961.93 °C or 1763.5 °F. In some instances (especially in tables and data compilations), temperature values in °C and °F are alternatives rather than conversions.

The policy of units of measure in this Handbook contains several exceptions to strict conformance to IEEE/ASTM SI-10; in each instance, the exception has been made in an effort to improve the clarity of the Handbook. The most notable exception is the use of g/cm^3 rather than kg/m^3 as the unit of measure for density (mass per unit volume).

SI practice requires that only one virgule (diagonal) appear in units formed by combination of several basic units. Therefore, all of the units preceding the virgule are in the numerator and all units following the virgule are in the denominator of the expression; no parentheses are required to prevent ambiguity.

Officers and Trustees of ASM International (2012–2013)

Gernant E. Maurer

President
Carpenter Technology Corporation

C. Ravi Ravindran

Vice President
Ryerson University

Christopher C. Berndt

Immediate Past President
Swinburne University of Technology

Thomas Passek

Managing Director
ASM International

Robert Fulton

Treasurer
Hoeganaes Corporation (Retired)

Iver Anderson

Ames Laboratory

Mitchell Dorfman

Sulzer Metco (US), Inc.

Diana Essock

Metamark Inc.

James C. Foley

Los Alamos National Laboratory

David U. Furrer

Pratt & Whitney

Jeffrey A. Hawk

National Energy Technology
Laboratory

William J. Lenling

Thermal Spray Technologies Inc.

Vilupanur A. Ravi

California State Polytechnic University

Linda S. Schadler

Rensselaer Polytechnic Institute

Student Board Members

Jennifer L. Breidenich

Georgia Institute of Technology

Gregory A. Vetterick

Drexel University

Blake Whitley

The University of Alabama

Members of the ASM Handbook Committee (2012–2013)

Joseph W. Newkirk

Chair 2012–
Member 2005–
Missouri University of Science & Technology

George Vander Voort

Vice Chair 2012–
Member 1997–
Vander Voort Consulting

Craig D. Clauser

Immediate Past Chair Member 2005–
Craig Clauser Engineering Consulting

Jeffrey A. Hawk

Board Liaison and Member
Member 1997–
U.S. Department of Energy

David E. Alman (2011–)

National Energy Technology Laboratory

Scott W. Beckwith (2010–)

BTG Composites Inc.

Rodney R. Boyer (2010–)

Sarup K. Chopra (2007–)

Consultant

Narenra B. Dahotre (2012–)

University of North Texas

Craig V. Darragh (1989–)

The Timken Company (Retired)

Jon L. Dossett (2006–)

Consultant

Alan P. Druschitz (2009–)

Virginia Tech

Donald E. Duvall (2010–)

Engineering Systems Inc.

Gerald S. Frankel (2010–)

Ohio State University

Larry D. Hanke (1994–)

Materials Evaluation and Engineering Inc.

Paul D. Jablonski (2011–)

U.S. Department of Energy

Kent L. Johnson (1999–)

Applied Materials Technology Inc.

Kang N. Lee (2010–)

Rolls Royce Corporation

Brett A. Miller (2011–)

IMR Metallurgical Services

Dale Newbury (2010–)

National Institute of Standards

Toby V. Padfield (2004–)

ZF Sachs Automotive of America

Thomas E. Prucha (2010–)

American Foundry Society

Elwin L. Rooy (2010–)

Elwin Rooy & Associates

Prasan K. Samal (2010–)

North American Höganäs

Roch J. Shipley (2012–)

Professional Analysis Consulting Inc.

Jeffery S. Smith (2009–)

Material Processing Technology

Jaimie S. Tiley (2012–)

US Air Force Research Lab

George E. Totten (2012–)

G.E. Totten & Associates

Michael K. West (2008–)

South Dakota School of Mines

And Technology

Charles V. White (2011–)

Kettering University

Chairs of the ASM Handbook Committee

J.F. Harper

(1923–1926) (Member 1923–1926)

W.J. Merten

(1927–1930) (Member 1923–1933)

L.B. Case

(1931–1933) (Member 1927–1933)

C.H. Hertzy, Jr.

(1934–1936) (Member 1930–1936)

J.P. Gill

(1937) (Member 1934–1937)

R.L. Dowdell

(1938–1939) (Member 1935–1939)

G.V. Luerssen

(1943–1947) (Member 1942–1947)

J.B. Johnson

(1948–1951) (Member 1944–1951)

E.O. Dixon

(1952–1954) (Member 1947–1955)

N.E. Promisel

(1955–1961) (Member 1954–1963)

R.W.E. Leiter

(1962–1963) (Member 1955–1958, 1960–1964)

D.J. Wright

(1964–1965) (Member 1959–1967)

J.D. Graham

(1966–1968) (Member 1961–1970)

W.A. Stadler

(1969–1972) (Member 1962–1972)

G.J. Shubat

(1973–1975) (Member 1966–1975)

R. Ward

(1976–1978) (Member 1972–1978)

G.N. Maniar

(1979–1980) (Member 1974–1980)

M.G.H. Wells

(1981) (Member 1976–1981)

J.L. McCall

(1982) (Member 1977–1982)

L.J. Korb

(1983) (Member 1978–1983)

T.D. Cooper

(1984–1986) (Member 1981–1986)

D.D. Huffman

(1986–1990) (Member 1982–2005)

D.L. Olson

(1990–1992) (Member 1982–1988, 1989–1992)

R.J. Austin

(1992–1994) (Member 1984–1985)

W.L. Mankins

(1994–1997) (Member 1989–)

M.M. Gauthier

(1997–1998) (Member 1990–2000)

C.V. Darragh

(1999–2002) (Member 1989–)

Henry E. Fairman

(2002–2004) (Member 1993–2005)

Jeffrey A. Hawk

(2004–2006) (Member 1997–)

Larry D. Hanke

(2006–2008) (Member 1994–)

Kent L. Johnson

(2008–2010) (Member 1999–)

Craig D. Clauser

(2010–2012) (Member 2005–)

Joseph W. Newkirk

(2012–) (Member 2005–)

Preface

The *ASM Handbook*, Volume 4A, *Steel Heat Treating Fundamentals and Processes*, represents the first of several Volumes to be published on heat treating. As indicated in the title, Volume 4A focuses on the fundamental aspects of steel heat treating and the many processes of steel heat treating. The Volume 4B, planned for future publication, will cover the heat treating and behavior of the many types of steels and cast irons.

As with the last edition of this Volume, the Volume Editors recognized that the researchers, engineers, technicians and students that will use this Volume 4A have different needs with regard to their level of understanding. Articles on the fundamentals provide in-depth background on the scientific principles associated with steel heat treatment, while articles on the various heat treating processes take a more practical approach. The Volume Editors have also tried to present a comprehensive reference that can be of use to the diverse heat treating community.

All sections of this Volume have been reviewed to be sure that they reflect the current status of the technology. Many sections have been expanded, such as the sections on fundamentals and processing methods for carburizing and nitriding of steels. Coverage on the hardenability of steels is expanded, and several new articles have been added on quenching fundamentals and processes. Updates have been done as appropriate, and efforts were taken to include charts, examples, and reference information from the substantive archives of the Society—and its predecessors—the American Society for Metals, and the American Society for Steel Treating. This Volume is especially fitting in the 100th anniversary year of ASM International.

We wish to thank our many colleagues who served as editors and authors of the individual articles. In particular, the editors also are indebted to the Heat Treating Society (An Affiliate Society of ASM International) and its members, which give the foundation for this publication and other events, conferences, and educational programs. This Volume would not have been possible without their efforts.

Jon Dossett
George Totten

List of Contributors and Reviewers

- A.B. Ahmed**
McMaster University
- Toru (Tohru) Arai**
Consultant
- Michael A. Aronov**
IQ Technologies, Inc
- Manfred Behnke**
NÜSSE GmbH & Co.KG
- William J. Bernard, III**
Surface Combustion, Inc.
- Volker Block**
Saarstahl AG, Germany
- Rainer Braun**
NÜSSE GmbH & Co.KG
- Anja Buchwalder**
Technical University Bergakademie Freiberg
- Eckhard H. Burgdorf**
NÜSSE GmbH & Co.KG
- Lauralice de C. F. Canale**
University of São Paulo
- Charles Caristan**
Airliquide
- Madhu Chatterjee**
Bodycote
- Brigitte Clausen**
Stiftung Institut für Werkstofftechnik,
Bremen
- Rafael Colás**
Universidad Autónoma De Nuevo León
- James Conybear**
Metlab
- Narendra B. Dahotre**
University of North Texas
- Craig Darragh**
The Timken Company (Retired)
- S. Dilip**
Fluidtherm
- Jon Dossett**
Consultant
- Edward (Derry) Doyle**
RMIT University
- Kevin M. Duffy**
The Duffy Co.
- Bernd Edenhofer**
Ipsen Industries International GmbH (retired)
- Jan Elwart**
Bodycote European Holdings GmbH
- Imre Felde**
University of Óbuda
- Allen J. Fuller**
Jr. Amsted Rail Company, Inc.
- Kiyoshi Funatani**
IMST Institute (Consultant)
- Weimin Gao**
Institute for Frontier Materials, Deakin
University
- Winfried Gräfen**
Hanomag Härtol Gommern Lohnhärtere
i GmbH, Germany
- Robert J. Gaster**
Deere & Company
- Jianfeng Gu**
Shanghai Jiao Tong University
- David Guisbert**
QA Metallurgical Services LLC
- M.S. Hamed**
McMaster University
- Larry Hanke**
Materials Evaluation and Engineering, Inc.
- Volker Heuer**
ALD Vacuum Technologies GmbH
- Peter Hodgson**
Institute for Frontier Materials, Deakin
University
- Franz Hoffmann**
IWT Bremen
- Ralph Hunger**
Bodycote European Holdings GmbH
- Peter Hushek**
Phoenix Heat Treating
- Michael Ives**
Park Metallurgical Corporation
- Scott Johnston**
Caterpillar
- J. Kalucki**
Nitrex Metal Inc
- Guldem Kartal**
Istanbul Technical University
- Gary D. Keil**
Caterpillar Inc.
- John R. Keough**
Applied Process Inc.
- Matthew T. Kiser**
Caterpillar Inc
- Nikolai Kobasko**
IQ Technologies, Inc
- Lingxue Kong**
Institute for Frontier Materials, Deakin
University
- Maciej Korecki**
SECO/WARWICK Corporation
- Jim Laird**
Consultant
- B. Liščić**
University of Zagreb
- Thomas Luebben**
IWT Bremen
- Xinmin Luo**
Jiangsu University
- D. Scott MacKenzie**
Houghton International
- Jim Malloy**
Kolene Corp.
- Mohammed Maniruzzaman**
Caterpillar Inc
- Božidar Matijević**
Quenching Research Centre
- Dan McCurdy**
Bodycote
- L.L. Meekisho**
Portland State University
- E.J. Mittemeijer**
Max Planck Institute for Intelligent Systems
(formerly Max Planck Institute for Metals
Research)
- B. Hernández-Morales**
Universidad Nacional Autónoma de México
- Aaron Muhlenkamp**
The Timken Company

Fahrettin Ozturk
Nigde University

George Pantazopoulos
ELKEME Hellenic Research Centre
for Metals S.A.

Renata Neves Penha
Universidade de São Paulo

Joseph A. Powell
IQ Technologies, Inc

Narayan Prabhu
National Institute of Technology, India

Mark Ratliff
Avion Manufacturing

Arthur Reardon
The Gleason Works

Thomas Risbeck
The Timken Company

Barbara Rivolta
Politecnico di Milano (Polytechnic
Institute Milan)

Olga K. Rowan
Caterpillar Inc.

Valery Rudnev
Inductoheat Incorporated

Satyam S. Sahay
John Deere Asia Technology Innovation Center

S. Santhanakrishnan
Indian Institute of Technology Madras

Peter Schiefer
Ford-Werke GmbH

Michael J. Schneider
The Timken Company

Juyan Shi
Taiyuan University of Technology

Mark Surrine
Flame Treating Systems

Saša Singer
University of Zagreb

Richard D. Sisson Jr.
Worcester Polytechnic Institute

Marcel Somers
Technical University of Denmark

John G. Speer
Advanced Steel Processing and Products
Research Center, Colorado School of Mines

Heinz-Joachim Spies
Technical University Bergakademie Freiberg

Bill Stofey
National Polymer Laboratories and
Development Co.

George E. Totten
Portland State University

Eva Troell
Swerea IVF AB

André Tschiptschin
Universidade de São Paulo

David Van Aken
Missouri State Univ.

Jan Vatavuk
Presbyterian University Mackenzie

Li Wang
Automotive Steel Research Institute,
R&D Center

Dale Weires
Boeing

K.M. Winter
Process-Electronic GmbH

Roger Wright
Rensselaer Polytechnic
Institute (retired)

Rolf Zenker
Technical University Bergakademie
Freiberg

Craig Zimmerman
Bluewater Thermal Solutions

Tim Zwirlein
Caterpillar

Contents

Introduction to Steel Heat Treating	1	Molten Metal Quenchants	125
Introduction to Steel Heat Treatment	3	Molten Salt and Hot Oil Quenchants.	126
Introduction	3	Oil Quenchants.	129
Constitution of Iron.	4	Quench Oil Bath Maintenance	139
Phases of Heat Treated Steel	7	Oil Quench System Monitoring	144
Transformation Diagrams	16	Safe Use of Petroleum Quench Oils	144
Isothermal Transformation Diagrams	16	Polymer Quenchants	146
Continuous Cooling Transformation Diagrams	20	Fixtures	151
Thermal and Residual Stresses.	21	Characterization of Heat Transfer during Quenching	
Hardness and Hardenability of Steels	26	<i>B. Hernández-Morales</i>	158
Introduction	26	Heat-Transfer Basics	159
Jominy End-Quench Testing	26	Heat Generated by Microstructural Evolution.	162
Quench Severity in Hardenability Evaluation.	30	Liquid Quenching Heat Transfer	162
Ideal Critical Diameter	33	Active Heat-Transfer Boundary Condition.	167
Hardenability Correlation Curves	33	Large Probes for Characterization of Industrial Quenching Processes	
Other Hardenability Tests	35	<i>Božidar Liščić and Saša Singer</i>	176
Jominy Equivalence Charts	40	Laboratory Tests to Evaluate the Cooling Intensity of	
Determining Hardenability Requirements	41	Liquid Quenchants	176
Factors Affecting Hardenability	45	Differences between Laboratory Tests and Characterization of	
Variability in Jominy Data Sets	46	Industrial Quenching Processes.	179
Calculation of Steel Hardenability	47	Critical Heat-Flux Densities of Liquid Quenchants	179
Steel Selection for Hardenability	48	Temperature Gradient Method for Evaluation of	
Hardenability Limits and H-Steels	50	Cooling Intensity in Workshop Conditions.	180
H-Steels Classified by Hardness at End-Quench Positions.	51	The Liščić/Petrofer Probe	181
Hardenability Calculation of Carbon and Low-Alloy Steels		Prediction of Hardness Distribution after Quenching Axially	
with Low or Medium Carbon	60	Symmetrical Workpieces of Any Shape.	183
Introduction	60	Numerical Solution of the Inverse Heat-Conduction	
Principles of Computational Hardenability.	60	Problem	184
Modeling Approaches to Hardenability of Steels	62	Smoothing of Measured Temperatures	188
Caterpillar Hardenability Calculator (1E0024)	64	Simulation Examples.	189
Estimation of Jominy Curves from Compositions.	69	Quench Process Sensors	
Calculation Example for 8645 Steel	70	<i>G.E. Totten</i>	192
Calculation Example for Boron Steel (86B45)	71	Fluid Flow in Quenching.	192
Regression Analysis of Hardenability in Europe.	71	Fluid Flow Measurement.	192
Calculation of Hardenability in High-Carbon Steels	80	Intensive Quenching of Steel Parts	
Background	80	<i>Michael A. Aronov, Nikolai I. Kobasko, Joseph A. Powell,</i>	
Derivation of Multiplying Factors.	83	<i>and George E. Totten</i>	198
Multiplying Factors.	83	Mechanical Properties and Cooling Rate of Quenching.	198
Use of the Multiplying Factors.	86	Intensive Quenching and Other Quench Methods	199
Limitations of the Multiplying Factors	87	Heat Transfer during Quenching.	200
Steel Quenching Fundamentals and Processes	89	Batch Intensive Quenching (IQ-2)	201
Quenching of Steel		Single-Part IQ Process (IQ-3).	203
<i>G.E. Totten, J.L. Dossett, and N.I. Kobasko</i>	91	Improvement of Steel Microstructure, Mechanical Properties,	
Mechanism of Quenching	91	and Stress Conditions	204
Quenching Process Variables	94	IQ Process and Part Distortion	207
Metallurgical Aspects	95	Design of Production IQ Systems.	207
Quench Severity	100	Practical Applications of IQ Processes	210
Tests and Evaluation of Quenching Media.	103	Inverse Hardening	
Cooling Curve Test.	104	<i>B. Liščić and George E. Totten</i>	213
Heat-Transfer Coefficient Calculations	110	Heat-Extraction Dynamics	213
Common Quenching Process Variables	113	Metallurgical Aspects	215
Quenching Systems.	118	Quenchants Enabling Controllable Delayed Quenching.	218
Water- and Air-Quenching Media.	122	Properties	218
Aqueous Salt (Brine) Solutions	122	Summary	219
		Gas Quenching	
		<i>Volker Heuer</i>	221
		Introduction	221

Physical Principles	221	Castings.	287
Equipment for Gas Quenching	222	Sheet and Strip.	287
Gas Types	223	Annealing of Steel	
Cooling Curves	224	<i>Satyam S. Sahay</i>	289
Prediction of Core Hardness	225	Metallurgical Principles	289
Gas-Flow Reversing	227	Annealing Cycles	290
Dynamic Gas Quenching	228	Guidelines for Annealing	291
Fixtures for Gas Quenching	229	Annealing Temperatures	291
Control of Distortion with HPGQ	230	Spheroidizing	291
Salt Quenching		Process Annealing	294
<i>J.R. Keough</i>	232	Annealed Structures for Machining	294
Equipment for Salt Quenching	233	Industrial Annealing	295
Time and Temperature Considerations	233	Annealing of Steel Sheet and Strip	297
Critical Characteristics for the Operation of Salt Quenching		Annealing of Steel Forgings	301
Systems	234	Annealing of Bar, Rod, and Wire	302
Environmental and Safety Considerations in		Annealing of Plate and Tubular Products	303
Salt Quenching	236	Accelerated Cycling Annealing	303
Fluidized-Bed Quenching		Subcritical Annealing and Normalizing	
<i>Weimin Gao, Lingxue Kong, and Peter Hodgson</i>	238	<i>Roger N. Wright</i>	305
Design of Quenching Fluidized Beds	238	Subcritical Temperatures	305
Quenching Power	239	Temperature-Time Relations	306
Application of Fluidized-Bed Quenching	242	Normalizing	307
Spray Quenching	245	Induction Thread Softening	307
Introduction	245	Austenitizing in Steels	
Water Quenching Heat Transfer	247	<i>John G. Speer and Robert J. Gaster</i>	309
Immersion Quenching	247	Introduction	309
Spray Quenching	247	Purposes and Overview of Austenitization	309
Jet Quenching	248	Thermodynamics and Kinetics of Austenite Formation	309
Summary	250	Austenite Grain Growth	314
Press Quenching		Control of Solute Concentrations in Austenite	315
<i>Arthur Reardon</i>	252	Quenching and Partitioning Steel Heat Treatment	
Equipment	252	<i>Li Wang and John G. Speer</i>	317
Factors in Distortion Control	255	Chemical Composition and Annealing Process	318
Wire Patenting		Microstructure and Mechanical Properties	318
<i>Xinmin Luo and George E. Totten</i>	257	Mechanical Behavior and Stability of	
Wire Patenting Processes	257	Retained Austenite	320
Cooling Behavior Experiment Materials and Procedures	257	Welding Properties	322
Cooling Curves and Cooling-Rate Curves Results		Tempering of Steels	
and Analysis	257	<i>Renata Neves Penha, Lauralice C.F. Canale, Jan Vatavik,</i>	
Concentration-Fog Flux Effect	260	and <i>Steven Lampman</i>	327
Controlled Fog-Cooling Patenting with CMC Additive	261	Introduction	327
Conclusion	261	Principal Variables	327
Steel Heat Treatment Processes	263	Tempering Temperatures and Stages	327
Cleaning of Steel for Heat Treatment		Tempering Time and Temperature	332
<i>Mohammed Maniruzzaman, Xiaolan Wang, and Richard</i>		Effect of Composition	334
<i>D. Sisson</i>	265	Dimensional Change during Tempering	336
Surface Contaminants on Heat Treated Parts	266	Tensile Properties and Hardness	338
Cleaning Methods	267	Toughness and Embrittlement	339
Cleanliness Measurement	271	Equipment for Tempering	344
How Clean Is Clean?	272	Special Tempering Procedures	345
Case Studies	272	Induction Tempering	347
Pollution Control and Resource Recovery	273	Austempered Steel	
Safety	273	<i>John R. Keough</i>	352
Summary	274	Steels for Austempering	353
Stress-Relief Heat Treating of Steel	275	Section Thickness Limitations	354
Sources of Residual Stress	275	Applications	354
Thermal Stress-Relief Methods	275	Dimensional Control	357
Stress Relief of Springs	277	Modified Austempering	357
Normalizing of Steel	280	Austempering Problems and Solutions	359
Introduction	280	Martempering of Steels	
Heating and Cooling	281	<i>Lauralice de C.F. Canale, Jan Vatavik, and George E. Totten</i>	362
Applications of Normalizing Based on Steel		Introduction	362
Classification	282	Advantages	364
Forgings	284	Martempering Media	364
Bar and Tubular Products	286	Safety Precautions	367
		Suitability of Steels for Martempering	368
		Control of Process Variables	371

Dimensional Control	373	Application Tips and Troubleshooting	459
Applications	376	Electron Beam Surface Hardening	
Selection of Austenitizing Equipment	377	<i>Rolf Zenker and Anja Buchwalder</i>	462
Selection of Martempering Equipment	377	Electron Beam Generation and Interaction with Material	462
Martempering Bath Maintenance	378	Processing Techniques	464
Racking and Handling	380	Electron Beam Hardening Technologies	466
Washing the Work	380	Electron Beam Facilities and Manufacturing Systems	
Cold and Cryogenic Treatment of Steel	382	with Integrated EB Facilities	469
Cold Treatment of Steel	382	Applications	471
Cryogenic Treatment of Steels	383	Laser Surface Hardening	
Case Hardening of Steels	387	<i>Soundarapandian Santhanakrishnan and Narendra B. Dahotre</i>	476
Introduction to Surface Hardening of Steels		Conventional Surface-Hardening Techniques	476
<i>Michael J. Schneider and Madhu S. Chatterjee</i>	389	Laser Surface Hardening	478
Diffusion Methods of Surface Hardening	389	Absorptivity	479
Carburizing and Carbonitriding	390	Laser Scanning Technology	480
Nitriding and Nitrocarburizing	393	Laser Annealing	481
Applied Energy Methods	395	Laser Cladding	481
Other Methods	396	Laser Shock Peening	483
Process Selection	397	Laser Heat Treatment	483
Stop-Off Technologies for Heat Treatment		Thermokinetic Phase Transformations	485
<i>Eckhard H. Burgdorf, Manfred Behnke, Rainer Braun,</i>		Challenges in Obtaining the Specified Hardness	487
<i>and Kevin M. Duffy</i>	399	Influence of Cooling Rate	488
Mechanical Masking	399	Effect of Processing Parameters on Temperature,	
Copper Plating	399	Microstructure, and Case Depth Hardness	488
Stop-off Paints	400	Laser Surface Hardening of Nonferrous Alloys	491
Methods of Measuring Case Depth in Steels		Carburizing and Carbonitriding of Steels	503
<i>William J. Bernard III.</i>	405	Introduction to Carburizing and Carbonitriding	
Introduction	405	<i>Allen J. Fuller, Jr.</i>	505
Measurement Specifications	405	Introduction	505
Chemical Method	406	History	505
Mechanical Methods	407	General Process Description	506
Visual Methods	411	How to Carburize	509
Nondestructive Methods	413	Basic Carburizing Reactions	510
Applied-Energy Case Hardening of Steels	417	Advantages and Limitations	512
Flame Hardening of Steels		Carburizing Steels	514
<i>B. Rivolta</i>	419	Quality Assurance	514
Methods of Flame Hardening	419	Possible Complications	516
Fuel Gases	421	Methods of Carburizing and Carbonitriding	518
Burners and Related Equipment	423	Evaluation of Carbon Control in Carburized Parts	
Operating Procedures and Control	426	<i>Gary D. Keil and Olga K. Rowan.</i>	522
Preheating	427	Hardness Testing	522
Depth and Pattern of Hardness	427	Microscopic Examination	522
Maintenance of Equipment	428	Analysis of Consecutive Cuts	523
Preventive Maintenance	431	Analysis of Shim Stock	524
Safety Precautions	431	Analysis of Rolled Wire	526
Quenching Methods and Equipment	431	Spectrographic Analysis	526
Quenching Media	432	Electromagnetic Testing	527
Flame-Hardening Problems and Their Causes	432	Gas Carburizing	
Tempering of Flame-Hardened Parts	433	<i>Olga K. Rowan and Gary D. Keil.</i>	528
Surface Conditions	433	Thermodynamics and Kinetics	528
Dimensional Control	433	Carbon Sources and Atmosphere Types	532
Selection of Process	433	Carbon-Transfer Mechanism	535
Selection of Material	435	Carburizing Modeling and Case Depth Prediction	536
Flame Annealing	436	Carburizing Equipment	538
Induction Surface Hardening of Steels		Furnace Temperature and Atmosphere Control	540
<i>Valery Rudnev and Jon Dossett</i>	438	Carburizing Cycle Development	544
Principles of Induction Heating	438	Process Planning	547
High-Temperature Electrical, Magnetic, and		Dimensional Control	555
Thermal Properties	440	Case Depth Evaluation	556
Eddy-Current Distribution	443	Pack Carburizing	560
Induction Hardening and Tempering	446	Introduction	560
General Equipment and Process Factors	451	Advantages and Disadvantages	560
Surface-Hardening Parameters	456	Carburizing Medium and Compounds	561
		Process Control	562
		Furnaces for Pack Carburizing	562

Carburizing Containers	563	9. Microstructural Development of the Compound Layer	628
Packing	564	10. Kinetics of Compound-Layer Growth	633
Liquid Carburizing and Cyaniding of Steels		11. Microstructural Development of the Diffusion Zone	635
<i>Jon Dossett</i>	565	12. Kinetics of Diffusion-Zone Growth	639
Cyanide-Containing Liquid Carburizing Baths	565	Epilogue	641
Cyaniding (Liquid Carbonitriding)	566	Gas Nitriding and Gas Nitrocarburizing of Steels	
Noncyanide Liquid Carburizing	567	<i>K.-M. Winter and J. Kalucki</i>	647
Carbon Gradients	571	Introduction	647
Hardness Gradients	571	Terminology for Gas Reactions	648
Process Control	571	Low-Temperature Nitriding and Nitrocarburizing	649
Control of Case Depth	572	Nitriding	651
Dimensional Changes	574	Ferritic and Austenitic Nitrocarburizing	656
Quenching Media	574	Other High-Temperature Processes	657
Salt Removal (Washing)	575	Nitriding Processing	659
Typical Applications	576	Atmosphere Control	661
Precautions in the Use of Cyanide Salts	577	Measuring the Potentials	665
Disposal of Cyanide Wastes	578	Temperature Control	668
Low-Pressure Carburizing		Impact of Measuring Errors	669
<i>Volker Heuer</i>	581	Simulation of Nitriding Processes	669
Process	581	Inspection and Quality Control	669
Physical Principles	582	Lab Equipment and Sample Preparation	670
Equipment for Low-Pressure Carburizing	583	Selective Nitriding	673
Carburizing Strategies	584	Common Problems	673
Prediction of Carbon Profiles	585	Rules of Thumb	674
Applications	586	Safety Precautions	674
Quality Control of the LPC Process in Mass Production	587	Equipment	675
High-Temperature LPC	587	Liquid Nitriding of Steels	
Plasma Carburizing		<i>D. George Pantazopoulos</i>	680
<i>Brigitte Clausen and Winfried Gräfen</i>	591	Liquid Nitriding Applications	680
Principles of Plasma Carburizing	591	Liquid Nitriding Systems	680
Carburizing Reaction in Plasma Carburizing	593	Liquid Pressure Nitriding	681
Advantages and Disadvantages	594	Aerated Bath Nitriding	681
Production Equipment	595	Case Depth and Case Hardness	683
Application Example	596	Operating Procedures	683
Carbonitriding of Steels		Equipment	684
<i>John Dossett</i>	599	Maintenance Schedules	684
Process Description	600	Safety Precautions	685
Case Composition	601	Liquid Nitrocarburizing	685
Depth of Case	603	Nontoxic Salt Bath Nitrocarburizing Treatments	686
Case-Depth Uniformity	603	Wear and Antiscuffing Characteristics of the Compound	
Hardenability of Case	604	Zone Produced in Salt Baths	687
Hardness Gradients	605	Appendix 1—Liquid Salt Bath Nitriding Noncyanide	
Void Formation	605	Baths	688
Control of Retained Austenite	605	Appendix 2—Liquid Salt Bath Nitriding	689
Furnace Atmospheres	606	Plasma (Ion) Nitriding and Nitrocarburizing of Steels	
Temperature Selection	609	<i>Jan Elwart and Ralph Hunger</i>	690
Quenching Media and Practices	610	Introduction	690
Tempering	611	Process History and Developments	690
Hardness Testing	612	Glow-Discharge Process	693
Applications	613	Plasma Nitriding Furnaces	695
Carbonitriding of Powder Metallurgy Parts	614	Process Control	696
Ammonia Guidelines	614	Case Structures and Formation	698
Nitriding and Nitrocarburizing of Steels	617	Workpiece Factors	699
Fundamentals of Nitriding and Nitrocarburizing		Ion Nitriding Applications	700
<i>E.J. Mittemeijer</i>	619	Plasma Nitrocarburizing	701
Introduction	619	Diffusion Coatings	705
1. Advent of Nitriding	619	Pack Cementation Processes	707
2. Nitrided/Nitrocarburized Microstructure, Thermodynamics, and Kinetics	620	Aluminizing	707
3. The Iron-Nitrogen Phase Diagram	621	Siliconizing	708
4. Nitriding Potential and the Lehrer Diagram	622	Chromizing	708
5. Controlled Nitriding	623	Boriding (Boronizing) of Metals	
6. Carburizing Potential and Controlled Carburizing	624	<i>Craig Zimmerman</i>	709
7. Controlled Nitrocarburizing	625	Characteristic Features of Boride Layers	709
8. Local Equilibria and Stationary States	626	Boriding of Ferrous Materials	713
		Boriding of Nonferrous Materials	716

Thermochemical Boriding Techniques	717	Controlling Coating Reagent Conditions	732
Applications of Thermochemical Boriding	721	High-Temperature Salt Bath Carbide Coating	733
Chemical Vapor Deposition	722	High-Temperature Fluidized-Bed Carbide Coating	735
Thermoreactive Deposition/Diffusion Process for Surface		Low-Temperature Salt Bath Nitride Coating	736
<i>Toru (Tohru) Arai</i>	725	Properties of Coated Parts	737
Hardening of Steels	725	Practical Applications	738
Introduction	725	Supercarburizing	
Coating Mechanism and Types	726	<i>J.Y. Shi</i>	741
Carbide Coating Nucleation and Growth	727	Supercarburizing with Conventional	
Nitride Coating Nucleation and Growth	728	Carburizing Steel	741
Factors Controlling the Growth Rate of Coatings	729	Steels for Supercarburizing	744
Coating Processes	730	Index	745

Introduction to Steel Heat Treating

Introduction to Steel Heat Treatment	3	Steel Selection for Hardenability	48
Introduction	3	Hardenability Limits and H-Steels	50
Constitution of Iron.	4	H-Steels Classified by Hardness at End-Quench Positions	51
Phases of Heat Treated Steel (Ref 14).	7		
Transformation Diagrams	16	Hardenability Calculation of Carbon and Low-Alloy Steels	
Isothermal Transformation Diagrams (Ref 36, 59)	16	with Low or Medium Carbon	60
Continuous Cooling Transformation Diagrams (Ref 71)	20	Introduction	60
Thermal and Residual Stresses (Ref 59)	21	Principles of Computational Hardenability.	60
		Modeling Approaches to Hardenability of Steels	62
Hardness and Hardenability of Steels	26	Caterpillar Hardenability Calculator (1E0024)	64
Introduction	26	Estimation of Jominy Curves from Compositions	69
Jominy End-Quench Testing	26	Calculation Example for 8645 Steel	70
Quench Severity in Hardenability Evaluation.	30	Calculation Example for Boron Steel (86B45)	71
Ideal Critical Diameter	33	Regression Analysis of Hardenability in Europe.	71
Hardenability Correlation Curves	33		
Other Hardenability Tests	35	Calculation of Hardenability in High-Carbon Steels	80
Jominy Equivalence Charts	40	Background	80
Determining Hardenability Requirements	41	Derivation of Multiplying Factors.	83
Factors Affecting Hardenability	45	Multiplying Factors.	83
Variability in Jominy Data Sets (Ref 33).	46	Use of the Multiplying Factors.	86
Calculation of Steel Hardenability	47	Limitations of the Multiplying Factors	87

Introduction to Steel Heat Treatment*

Introduction

Heat treatment is roughly defined as controlled heating and cooling of a solid material, so as to change the microstructure and obtain specific properties. Almost all metals and alloys respond to some form of heat treatment in the broadest sense of this definition, but individual metals and alloys may respond differently. Almost any metal can be softened by annealing after cold working, while fewer alloy systems can be strengthened or hardened by heat treatment. Steel is very notable, because it is very responsive to hardening and strengthening by heat treatment.

The responsiveness of steel from heat treatment is due to some important properties of iron and the metallurgical effects of carbon in iron. Fundamentally, all steels are mixtures or, more properly, alloys of iron with a small amount of carbon (along with varying amounts of other alloying elements such as manganese, chromium, nickel, and molybdenum). One important effect is the size of carbon atoms relative to that of iron atoms. The carbon atom is only $1/30$ the size of the iron atom, and carbon atoms are sufficiently small to fit between the interstices of the larger iron atoms. Other atoms small enough to fit in the interstitial regions of solid iron are hydrogen, nitrogen, and boron. In general, interstitial atoms can easily diffuse—jumping from one interstitial site to another—unlike larger atoms (which can only jump by “substitution” into the vacancies within a crystal lattice). This, along with the effect of temperature on diffusion, makes the mobility of carbon responsive during solid-state heating.

Another important metallurgical phenomenon is the allotropy of iron, which means that the iron atoms can arrange themselves into more than one crystalline form or phase. At room temperature, for example, iron atoms arrange themselves into a body-centered cubic (bcc) crystal structure—called ferrite or alpha (α) iron. At higher temperatures, the iron atoms form a face-centered (fcc) crystal structure—called austenite or gamma (γ) iron. The existence of these two phases, along with carbon alloying, are fundamental in the heat treatment of steel.

One important difference between iron ferrite and austenite is the spacing of iron atoms. The iron atoms in austenite are more widely spaced than in ferrite (Fig. 1). This allows austenite to accommodate more carbon atoms in the interstitial regions of the crystal lattice. Solid solubility is a measure of how much solute can be dissolved (or incorporated) into the host lattice. Temperature influences the extent of solubility, because higher temperatures expand the host lattice and thus provide a better opportunity for the solute to fit in the lattice. However, carbon is almost insoluble in α iron—ranging from only 0.008 wt% near room temperature to a maximum solubility limit of 0.02 wt% at 727 °C (1340 °F) (Fig. 2).

When the solubility of carbon in either austenite or ferrite is exceeded, not all the carbon atoms can be accommodated within the interstitial sites between the iron atoms. In this case, the excess carbon atoms may combine to form graphite or, more typical for steels, an iron-carbide compound (Fe_3C) referred to as cementite or θ -carbide. Cementite has an orthorhombic crystal that can accommodate more

carbon atoms in its crystal structure. For each atom of carbon in the compound, there are three atoms of iron, giving an atomic composition of 25 at.% C. The corresponding weight percent carbon in cementite turns out to be 6.7.

The orthorhombic lattice of cementite is a bit more complex than either the bcc structure of ferrite or the fcc structure of austenite. Cementite also is not completely stable, because carbon ultimately decomposes into graphite over time. However, cementite is sufficiently stable to be considered as a near-equilibrium phase that occurs when carbon levels exceed the solubility limit in iron. The morphology and distribution of cementite also can be manipulated by heat treatment. The compound cementite has higher strength and lower ductility than either ferrite or austenite and, depending on its morphology and distribution, contributes in a variety of ways to the strengthening, deformation, and fracture of steels.

Cementite is hard, ranging in hardness from 800 to 1400 HV, depending on the substitution of elements for iron. Heat treatment also can alter the amount, shape, and distribution of the hard cementite particles in the microstructure of steel. For example, the hard cementite phase can be dissolved into a single iron-carbon phase when the iron phase becomes austenitic. This process, known as austenitizing, dissolves cementite, because carbon is much more soluble in austenite, with a maximum solubility of approximately 2 wt% at 1150 °C (2100 °F). This is 2 orders of magnitude greater than the maximum solubility of carbon in alpha ferrite. Thus, austenitizing is often used as the starting point to create a single-phase solid solution. Then, by cooling from the austenite region, a two-phase formation of ferrite and cementite can be controlled for strengthening. This allows plain carbon steel to obtain a wide range of properties after heat treatment.

Carbon also has two other important effects on the constitution of iron during heat treatment. Carbon lowers the temperature for complete austenitization (Fig. 2). This allows for complete dissolution of cementite at lower temperatures and the subsequent manipulation of carbide formation during cooling. Moreover,

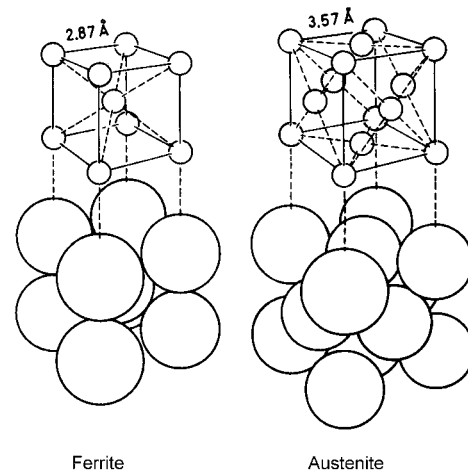


Fig. 1 Crystal structure and lattice spacing of iron atoms with (a) body-centered cubic and (b) face-centered cubic crystal structures. Source: Ref 1

* Portions adapted from G. Krauss, *Physical Metallurgy and Steel Heat Treatment, Metals Handbook Desk Edition*, American Society for Metals, 1985; T. Ericsson, *Principles of Heat Treating of Steels, Heat Treating, Vol 4, ASM Handbook*, ASM International, 1991; and J. Dossett and H. Boyer, *Practical Heat Treating*, 2nd ed., ASM International, 2006

4 / Introduction to Steel Heat Treating

when austenitized steel is rapidly cooled (quenched), a different mechanism of phase transformation occurs. During rapid quenching from austenite to ferrite, there is not enough time for the excess carbon atoms to diffuse and form cementite along with the bcc ferrite. Therefore, some (or all) of the carbon atoms become trapped in the ferrite lattice, causing the composition to rise well above the 0.02% solubility limit of carbon in ferrite. This causes lattice distortion, so much so that the distorted bcc lattice rapidly transforms into a new metastable phase called martensite. Martensite does not appear as a phase on the iron-carbon equilibrium phase diagram because it is a metastable (nonequilibrium) phase that occurs from rapid cooling.

The unit cell of the martensite crystal is a body-centered tetragonal (bct) crystal structure, which is similar to the bcc unit cell, except that one of its edges (called the *c*-axis) is longer than the other two axes (Fig. 3). The distorted form of the bct is a supersaturated condition that accommodates the excess carbon. The bct structure also occupies a larger atomic volume than ferrite and austenite, as summarized in Table 1 for different microstructural components as a function of carbon content. The density of martensite thus is lower than ferrite (and also austenite, which is denser than ferrite). The resulting expansion gives martensite its high

hardness and is the basis for strengthening steels by heat treatment.

Constitution of Iron

The atoms in solids typically arrange themselves into a unique crystal structure under equilibrium conditions, but some elements and compounds have polymorphic (multishaped) crystal structures. That is, their structure transforms from one crystal structure to another with changes in temperature and pressure, where each crystal structure is a distinctively separate solid-state phase. Heat spurs the movement of atoms through diffusion, and the heating can cause atoms to rearrange themselves into different types of crystal lattices.

The solid-state change of crystal structure is referred to as an allotropy (existing in another form). For example, both iron and carbon have a number of allotropic forms. Carbon can exist as diamond, soot, graphite, and the more recently discovered form of fullerenes. However, the allotropy of carbon is not a significant variable as an alloying element in iron. In contrast, the allotropy of iron is of fundamental importance in the heat treating of steel. Iron is an allotropic element that changes its structure at several temperatures known as transformation temperatures (Fig. 4).

The process by which iron (or any material) changes from one atomic arrangement to another when heated or cooled is called a phase transformation. Figure 4 illustrates changes in the phases of pure iron during very slow (near-equilibrium) heating or cooling. During a phase transformation, the temperature stays constant during heating (or cooling) until the phase transformation of iron is complete. This is the same behavior as the temperature plateau during the phase changes of pure metal during melting or solidification. The so-called critical temperatures of the iron phase transformation are assigned the letter “A,” derived from the French word *arrêt*, which stands for the arrest in temperature during heating or cooling through the transformation temperature. The letter “A” also is followed by either the letter “c” or “r” to indicate transformation by either heating or cooling, respectively. The use of the letter “c” for heating is derived from the French word *chauffant*, meaning warming. If cooling conditions apply, the critical temperature is designated as “Ar,” with the letter “r” being derived from the French word *refroidissant* for cooling.

Below the melting point of 1540 °C (2800 °F), there are three temperature plateaus when solid iron undergoes a phase change. Consider first the process of solidification as liquid iron cools from its melting point of 1540 °C (2800 °F). It begins to freeze, with no further drop in temperature until it transforms itself completely into a solid form of iron referred to as delta iron or delta ferrite. Ferrite has a bcc crystal structure. Delta ferrite is the high-temperature bcc phase of iron. After solidification is complete, the temperature drops at a uniform rate until the temperature of 1394 °C (2541 °F) is reached.

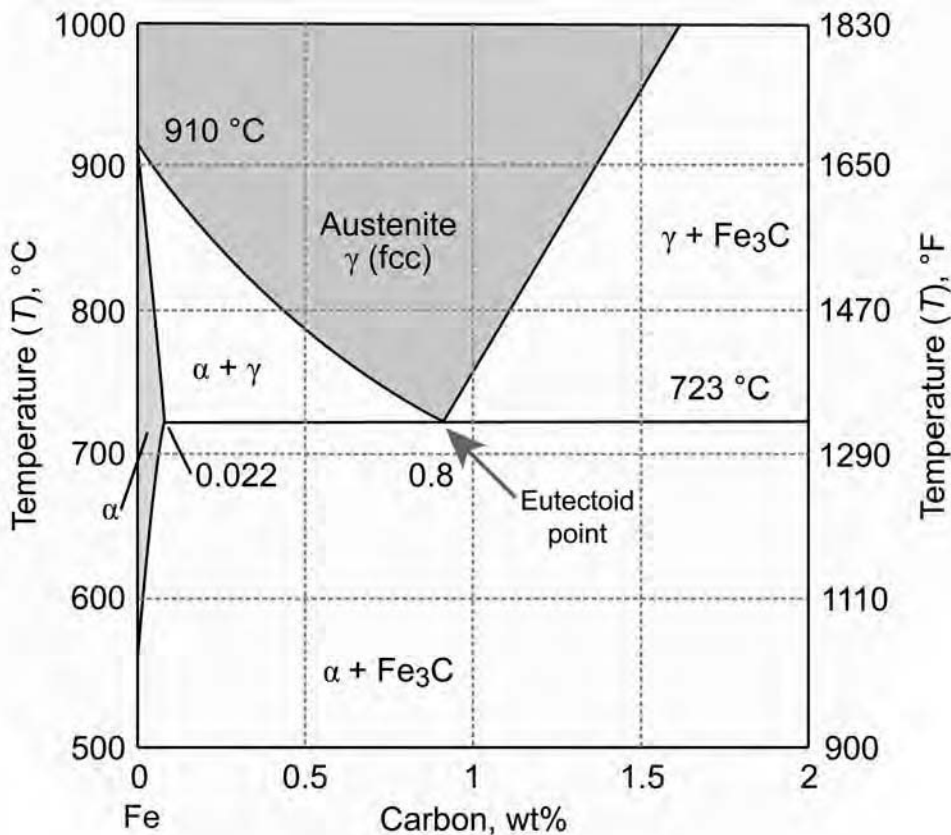


Fig. 2 Portion of the Fe-Fe₃C phase diagram of carbon steel. fcc, face-centered cubic

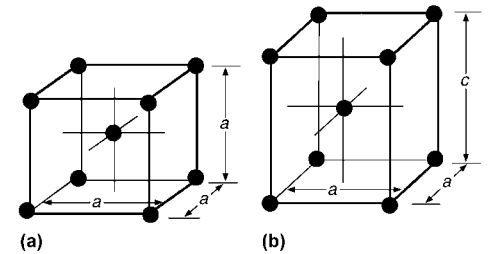


Fig. 3 Structure of (a) ferrite (body-centered cubic) and (b) martensite (body-centered tetragonal)

Table 1 Atomic volumes of selected microstructural constituents of ferrous alloys

Phase	Apparent atomic volume, Å ³
Ferrite	11.789
Cementite	12.769
Ferrite + carbides	11.786 + 0.163 C(a)
Pearlite	11.916
Austenite	11.401 + 0.329 C(a)
Martensite	11.789 + 0.370 C(a)

(a) C = % carbon. Source: Ref 2

This temperature marks the beginning of a transformation of the bcc delta iron into an fcc crystal phase, called austenite or gamma (γ) iron. The temperature stays constant until the transformation is complete, that is, until all of the iron has an austenitic (fcc) phase structure.

Further cooling of the gamma (fcc) iron continues at a uniform rate until the temperature reaches 912 °C (1674 °F). This is the transformation temperature when gamma iron begins the transformation into a nonmagnetic form of iron with a bcc crystal lattice. The temperature holds steady during cooling until all the iron atoms are completely transformed into a bcc crystal lattice. This low-temperature bcc phase of iron is referred to as alpha (α) iron or alpha ferrite. Finally, a similar cooling plateau occurs at 769 °C (1416 °F), which is the transformation temperature when the nonmagnetic form of alpha iron changes into a magnetic form of alpha iron. This is the Curie temperature. In ferromagnetic materials that are below their Curie temperature, the magnetic moments of adjacent atoms are parallel to each other, such that all of the individual magnetic moments are aligned in one direction.

These phase changes, which can be done very slowly, are called equilibrium transformations, meaning that sufficient time is needed for the metal to reach equilibrium during a given phase change. Enough energy, referred to as latent heat, must be added or released to complete an equilibrium transformation. Experimental latent-heat values at the transformation temperatures of pure iron are given in Table 2 for the phase transformations. In the case of the Curie temperature (T_C), the additional energy needed to disorient the magnetic dipoles in iron is described by a sharp increase in specific heat (Fig. 5)

During an equilibrium transformation, the temperature remains constant until the phase change is complete for the entire material. This temperature plateau or arrest is roughly indicated by the small steps at the transformation temperatures indicated in Fig. 5. All equilibrium transformations are based on the movement of atoms by diffusion, which occurs by pronounced thermal agitation of atoms or molecules. Thus, all equilibrium transformations are classified as thermal or diffusive (reconstructive) transformations, because phase growth or decomposition is activated by the thermal (kinetic) energy of the atoms in the solid. Slow changes under near-equilibrium conditions are also reversible; the very same changes can take place in reverse order. That is, when iron or steel is subjected to slow heating from room temperature, alpha iron first becomes nonmagnetic alpha iron and then becomes gamma iron on further heating.

Hysteresis in Heating and Cooling. Under conditions of very slow heating or cooling under near-equilibrium conditions, the transformation temperatures for heating and cooling are the same. However, heating rates in

commercial practice usually exceed those in controlled laboratory experiments, and a higher rate of heating or cooling can change the transformation temperature. For example, when the heating rate is high, the Ac transformation temperatures will be higher than those in Fig. 5. Likewise, on slow cooling in commercial practice, transformation changes occur at temperatures a few degrees below the Ar transformation temperatures in Fig. 5. Also, the faster the heating or cooling rate, the greater the gap between the Ac and Ar points. Going one step further, transformation temperatures during cooling can be suppressed several hundreds of degrees by rapid cooling or quenching. The rate of cooling and heating can be a key factor in many heat treatments.

Ferrite and Austenite in Pure Iron. Ferrite and austenite are the two crystal structures of solid iron under equilibrium conditions. Ferrite has atoms at each of the four corners of the unit cell (Fig. 1) with one atom in the center. The edge length (or lattice parameter) of alpha ferrite is approximately 2.87 Å at 20 °C (70 °F) increasing to approximately 2.9 Å at 910 °C (1670 °F) (Table 3). In contrast, the lattice parameter of the austenitic unit cell is on the order of approximately 3.57 Å at the transformation temperature of 912 °C (1674 °F). This provides greater interatomic space for the greater solubility of carbon in austenite, as compared to ferrite.

An fcc crystal also is a close-packed structure, which means that the atoms are packed together with a minimum total volume.

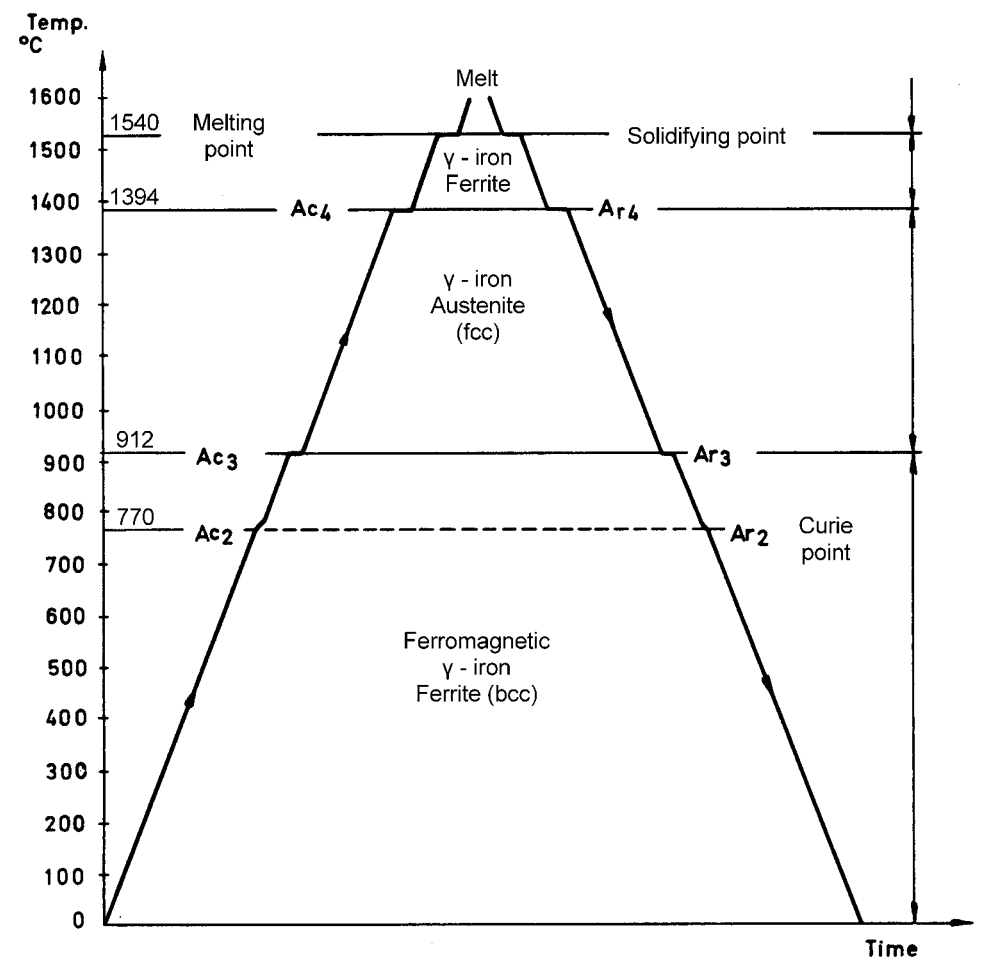


Fig. 4 Equilibrium transformation temperatures of pure iron. fcc, face-centered cubic; bcc, body-centered cubic

Table 2 Latent heats of phase transformations for pure iron

Transformation	Temperature, K	Temperature, °C	Latent heat, kJ/kg
Alpha ferrite (α) to austenite (γ)	1185	912	16
Austenite (γ) to delta ferrite (δ)	1667	1394	15
Fusion (liquid to solid)	1881	1538	247 ± 7

Source: Ref 3

6 / Introduction to Steel Heat Treating

Therefore, austenite can pack more atoms into a given volume than ferrite. One unit cell of the bcc structure consists of two complete atoms, calculated from the one atom in the center of the cell, plus the four corners with one-quarter of each corner atom within the cube of the unit cell. Like ferrite, austenite also has atoms at the four corners of the unit cell. However, the fcc lattice also has six additional atoms of each face of the unit cell (Fig. 1), where one-half of each face-centered atom is within the cube of the unit cell. Thus, the fcc unit cell is equivalent to four complete atoms (1/2 of each atom on the six faces, plus 1/4 of each atom on the

four corners). The packing results in a higher density of fcc compared to that of a bcc lattice (Table 4). A plot of volume per atoms also indicates a sharp contraction when alpha ferrite transforms into austenite (Fig. 6).

Diffusion Coefficient of Carbon in Iron.

As noted, carbon readily diffuses as an interstitial atom. The activation energy for diffusion of carbon in iron is small (Table 5), and the diffusion coefficient is larger than that of typical substitutional elements (Fig. 7), where the diffusion coefficient (D) is a function of temperature according to an Arrhenius equation, such that:

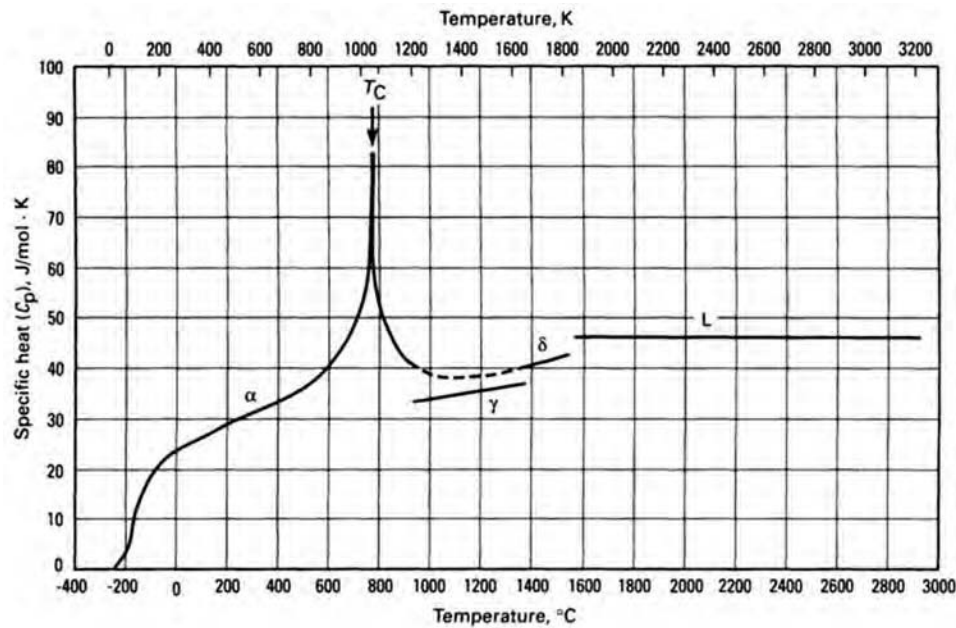


Fig. 5 Specific heat of iron from 0 to 3200 K. T_C , Curie temperature. Source: Ref 4, 5

Table 4 Density of austenite, alpha ferrite, and delta ferrite at selected temperatures

Phase	Temperature		Density, g/cm ³
	°C	°F	
Alpha ferrite	20	68	7.870(a)
Alpha ferrite	910	1670	7.47(b)(c)
Austenite	912	1673	7.694(a)
Austenite	1390	2534	7.66(b)(d)
Delta ferrite	1394	2541	7.406(a)

(a) Source: Ref 7. (b) Source: Ref 8. (c) Computed from the following relation for alpha iron (to 912 °C, or 1673 °F): $K \text{ (Kelvin)} \times \Delta\rho/\rho_0 \times 10^5 = 4.3$. (d) Computed from the following relation for gamma iron (912 to 1394 °C, or 1673 to 2541 °F): $K \text{ (Kelvin)} \times \Delta\rho/\rho_0 \times 10^5 = 6.7$

Table 5 Activation energies for diffusion of selected elements in iron

Diffusing element	Diffusing through	Diffusion activation energy (Q), cal/mol	Diffusion frequency factor (D_0), cm ² /s
Carbon	Ferrite (α iron)	18,100	0.0079
Carbon	Austenite (γ iron)	33,800	0.21
Nickel	Austenite (γ iron)	66,000	0.5
Manganese	Austenite (γ iron)	67,000	0.35
Chromium	Ferrite (α iron)	82,000	30,000
Chromium	Austenite (γ iron)	97,000	18,000

Source: Ref 1

Table 3 Effect of temperature on lattice parameters of ferrite and austenite in pure iron

Temperature,		Lattice parameter, nm
°C	°F	
20	68	0.28665 α -Fe
53	127	0.28676
154	309	0.28708
248	478	0.28750
315	599	0.28775
378	712	0.28806
451	844	0.28840
523	973	0.28879
563	1045	0.28882
588	1090	0.28890
642	1188	0.28922
660	1220	0.28920
706	1303	0.28923
730	1346	0.28935
754	1389	0.28940
764	1407	0.28940
772	1422	0.28943
799	1470	0.28946
862	1584	0.28988
898	1648	0.29012
907	1665	0.29005
950	1742	0.36508 γ -Fe
1003	1837	0.36535
1076	1969	0.36599
1167	2133	0.36660
1249	2280	0.36720
1361	2482	0.36810
1390	2534	0.29315 δ -Fe
1439	2622	0.29346
1480	2696	0.29378
1508	2746	0.29396

Source: Ref 6

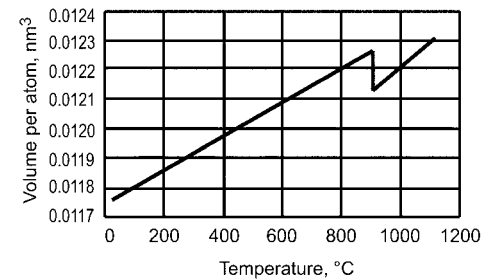


Fig. 6 Volume per atom for iron. Source: Ref 9

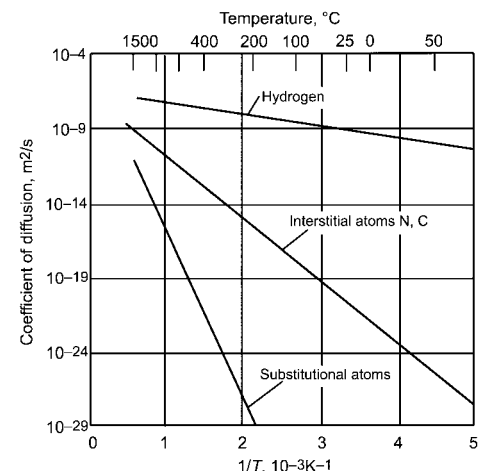


Fig. 7 Diffusion coefficients (D) of interstitial elements (hydrogen, carbon, nitrogen) compared with substitutional elements in alpha iron. Adapted from Ref 10

Table 6 Representative data for diffusion of carbon in ferrite and austenite

Diffusing species	Solvent metal	D_0 , m ² /s	Activation energy, kJ/mol	Calculated values		
				Temperature		D , m ² /s
				°C	°F	
Fe	α -Fe (body-centered cubic)	2.8×10^{-4}	251	500	930	3.0×10^{-21}
Fe	γ -Fe (face-centered cubic)	5.0×10^{-5}	284	900	1650	1.8×10^{-15}
				1100	2010	7.7×10^{-16}
C	α -Fe	6.2×10^{-7}	80	500	930	2.4×10^{-12}
				900	1650	1.7×10^{-10}
C	γ -Fe	2.3×10^{-5}	148	900	1650	5.9×10^{-12}
				1100	2010	5.3×10^{-11}

Source: Ref 11

$$D = D_0 \exp \left[-\frac{Q}{RT} \right]$$

where D_0 is the frequency factor (in units of cm²/s), Q is the activation energy (kJ/mol), T is absolute temperature (K), and R is the gas constant (8.31 J/mol · K).

Typical values for D_0 are given in Table 6, and the temperature dependence of D is shown for a number of material systems in Fig. 8. The change of the diffusion coefficient of carbon as the concentration of carbon changes in iron at 930 °C (1700 °F) is shown in Fig. 9. The activation energy, Q , reflects the energy required to move an atom over a barrier from one lattice site to another; the barrier is associated with the requirement that the atom must vibrate with a sufficient amplitude to break the nearest neighboring bonds to move to a new location.

Phases of Heat Treated Steel (Ref 14)

The heat treatment of steel is based on the physical metallurgical principles that relate processing, properties, and structure. In heat treatment, the processing is most often entirely thermal and modifies only structure. Thermo-mechanical treatments, which modify component shape and structure, and thermochemical treatments, which modify surface chemistry and structure, are also important processing approaches that fall into the domain of heat treatment. Scientific principles link the processing parameters to structure and properties and are increasingly necessary for proper application of the equipment and instrumentation now available for control of heat treatment processes. Examples of scientific efforts that directly support the technology of heat treatment include characterization of mechanisms of phase transformations that produce desired structures and properties of heat treated parts; determination of phase transformation and annealing kinetics that establish processing times, temperatures, and cooling rates for heat treatments; and evaluation of mechanisms of deformation and fracture of the structures produced by heat treatment.

In view of the importance of structure and its formation to heat treatment, the purpose of this section is to describe the various microstructures that form in steels, the various factors that determine the formation of microstructures during heat treatment processing of steel, and some of the characteristic properties of each of the microstructures. Structure-sensitive properties such as strength, ductility, and toughness establish the ease of manufacturing, service performance, and limitations to service conditions of heat treated steels. The descriptions of the microstructures and principles presented here should be considered only introductory.

The Iron-Carbon Phase Diagram

The microstructures that result from heat treatment of steel are composed of one or more phases in which the atoms of iron, carbon, and other elements in steel are associated. Figure 10 shows a portion of the iron-carbon phase diagram from pure iron through the carbon concentration of cementite, 6.67 wt%. The temperature and composition ranges in which the various phases exist are shown on the diagram. Alloys containing up to 2 wt% C are classified as steels; alloys containing more than 2 wt% C are classified as cast irons. The solid lines represent conditions where carbon, when it exceeds its solubility in ferrite and austenite, is present in the form of cementite (Fig. 10). This is invariably the case in steels. The dashed lines represent the conditions where carbon is present as graphite rather than as cementite, a situation much more common in cast irons than in steels.

As noted, the temperatures that are the boundaries of the various phase fields are frequently referred to as critical temperatures. Because the critical temperatures are often identified by changes in slope or thermal arrests in heating and cooling curves, they are given the designation "A." If equilibrium conditions are applicable, the designations Ae_1 , Ae_3 , and Ae_{cm} , or simply A_1 , A_3 , and A_{cm} , are used, as shown in Fig. 10. If heating conditions (which raise the critical temperatures relative to equilibrium) apply, Ac_1 , Ac_2 , and Ac_{cm} are used, the subscript "c" being derived from the French

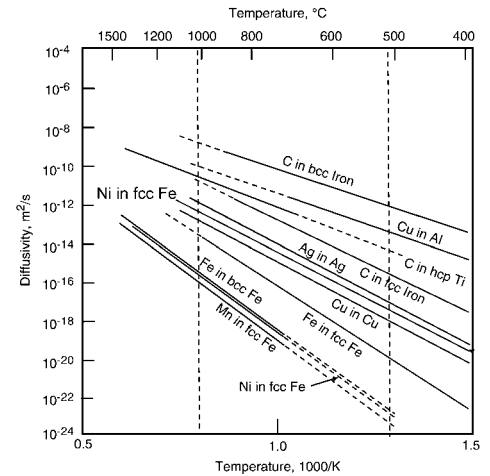


Fig. 8 Arrhenius plot of diffusivity of various metal systems. bcc, body-centered cubic; hcp, hexagonal close-packed; fcc, face-centered cubic. Adapted from Ref 12

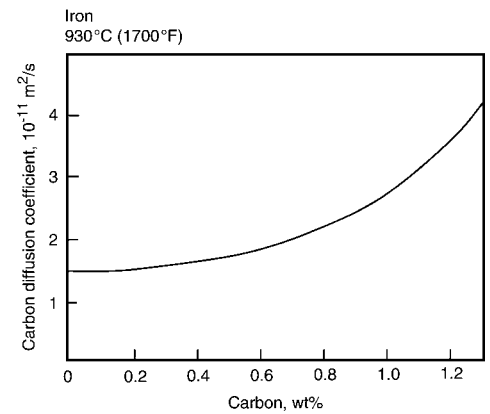


Fig. 9 Variation of diffusion coefficient with carbon concentration. Source: Ref 13

word *chauffant*. If cooling conditions (which lower the critical temperature relative to equilibrium) apply, the designations Ar_1 , Ar_3 , and Ar_{cm} are used, the subscript "r" being derived from the French word *refroidissant*. There is hysteresis in the transformation temperatures because continuous heating and cooling leave insufficient time to accomplish the diffusion-controlled phase transformations at the true equilibrium temperatures.

The symbols used to designate the different critical temperatures are summarized in Table 7. The A_1 transformation temperature (whether Ae_1 , Ac_1 , or Ar_1) is referred to as the *lower critical temperature*, while the A_3 transformation temperature (whether Ae_3 , Ac_3 , or Ar_3) is referred to as the *upper critical temperature*. As noted, carbon lowers the A_3 transformation temperature. Carbon also lowers the freezing point of iron (which is important for cast irons). Steels and cast irons contain, in addition to iron

8 / Introduction to Steel Heat Treating

and carbon, many other elements that shift the boundaries of the phase fields in the iron-carbon diagram. Some alloying elements such as manganese and nickel are austenite stabilizers and extend the temperature range over

which austenite is stable. Elements such as chromium and molybdenum are ferrite stabilizers and restrict the ranges of austenite stability. Therefore, care must be taken in the direct use of the iron-carbon diagram to predict

phase relationships in commercial alloys that contain elements in addition to iron and carbon. Nevertheless, the iron-carbon diagram is the most important reference for understanding the relationships between structure and heat treatment of steels and, subject to the aforementioned limitations, is used in this article to illustrate the basis for microstructural formation in steels as well as iron-carbon alloys.

The phase diagram shown in Fig. 10 assumes equilibrium, that is, that the carbon and iron have had sufficient time to distribute themselves in the various phases as shown. Sometimes, equilibrium is difficult to achieve, especially in steels that contain elements which diffuse only sluggishly, and, in fact, certain heat treatments such as hardening are designed to prevent formation of equilibrium structures. Thus, the fact that equilibrium may not be achieved, together with the shift of the phase-field boundaries by alloying elements, place limitations on the direct use of the iron-carbon phase diagram.

Austenite, also referred to as γ -iron, is the fcc crystal form or phase of iron that is stable at high temperatures. Figure 10 shows that carbon in iron-carbon alloys is soluble in austenite up to just over 2 wt%, and that the single-phase austenite field dominates the iron-carbon diagram at high temperatures. In all low-alloy steels, therefore, it is possible to produce a single-phase austenite microstructure. This characteristic is perhaps the most important feature of steels in that it enables steels to be hot worked or wrought. Also, cooling from the single-phase austenite field makes possible a wide variety of heat treatments based on transformation of the austenite.

The single-phase austenite, without the obstacles that second phases present to dislocation motion and without the sites for fracture initiation that second-phase particles offer, deforms and recrystallizes readily so that substantial reductions in section size by hot rolling or forging may be accomplished. Traditionally, hot deformation is performed in the upper temperature range of the austenite field. Hot deformation of austenite at lower temperatures or even in the two-phase ferrite-austenite field (controlled rolling) and the addition of small amounts of alloying elements (microalloying)

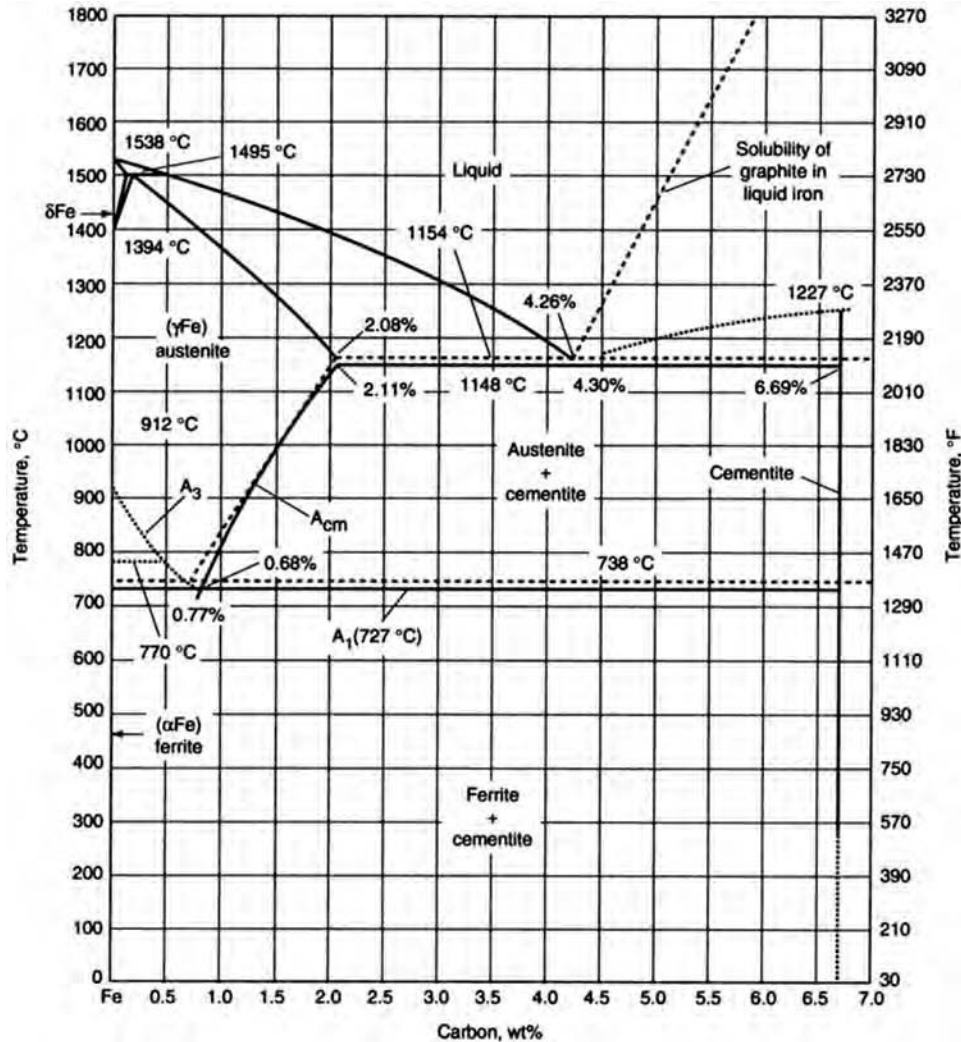


Fig. 10 Expanded iron-carbon phase diagram showing both the eutectoid (0.77 wt% C) and the region of the eutectic (at 4.26% C). Dotted lines represent iron-graphite equilibrium conditions, and solid lines represent iron-cementite equilibrium conditions. The solid lines at the eutectic are important to white cast irons, and the dotted lines are important to gray cast irons.

Table 7 Definitions of critical transformation temperatures in steel

A _{e1}	The critical temperature when some austenite begins to form under conditions of thermal equilibrium (i.e., constant temperature)
A _{C1}	The critical temperature when some austenite begins to form during heating, with the "c" being derived from the French <i>chauffant</i>
A _{r1}	The temperature when all austenite has decomposed into ferrite or a ferrite-cementite mix during cooling, with the "r" being derived from the French <i>refroidissant</i>
A _{e3}	The upper critical temperatures when all the ferrite phase has completely transformed into austenite under equilibrium conditions
A _{C3}	The temperature at which transformation of ferrite to austenite is completed during heating
A _{r3}	The upper critical temperatures when a fully austenitic microstructure begins to transform to ferrite during cooling
A _{e_{cm}}	In hypereutectoid steel, the critical temperature under equilibrium conditions between the phase region of an austenite-carbon solid solution and the two-phase region of austenite with some cementite (Fe ₃ C)
A _{C_{cm}}	In hypereutectoid steel, the temperature during heating when all cementite decomposes and all the carbon is dissolved in the austenitic lattice
A _{r_{cm}}	In hypereutectoid steel, the temperature when cementite begins to form (precipitate) during cooling of an austenite-carbon solid solution
A _r	The temperature at which delta ferrite transforms to austenite during cooling
M _s	The temperature at which transformation of austenite to martensite starts during cooling
M _f	The temperature at which martensite formation finishes during cooling

Note: All of these changes, except the formation of martensite, occur at lower temperatures during cooling than during heating and depend on the rate of change of temperature.

such as niobium and vanadium, which precipitate as fine alloy carbonitrides at low temperatures, are new approaches to processing of steels (Ref 15, 16). The low-temperature deformation and/or precipitation retard or prevent austenite recrystallization and grain growth and therefore produce finer austenite grains and subsequently fine austenite transformation products during cooling after hot deformation.

Ferrite, also referred to as α -iron, is the bcc form or phase of iron that is stable at low temperatures. Microstructures in low-carbon steels that consist largely of polycrystalline ferrite are highly formable at room temperature; dislocations move readily on the many slip systems of the bcc structure (Ref 17). However, at low temperatures, dislocation motion in the bcc structure is severely restricted (Ref 18, 19). As a result, ferrite grains fracture in a brittle manner with little plastic deformation at low temperatures. This well-known effect of all bcc metals is described by the ductile-to-brittle transition temperature, which refers to the region in which the toughness drops and the fracture mechanisms and features change from ductile to brittle (Fig. 11).

As noted, carbon is dissolved in the octahedral interstitial sites between iron atoms in ferrite and austenite and forms cementite when the carbon is above its solubility limit. Moreover,

the interstitial sites for carbon in ferrite are much smaller than those in austenite; therefore, the solubility of carbon in ferrite is significantly lower than in austenite. Figure 12 shows an expanded portion of the iron-rich side of the iron-carbon diagram. The maximum solubility of carbon in ferrite is only about 0.02 wt% and with decreasing temperature becomes almost negligible. As a result of the decreasing solid solubility with decreasing temperature, on slow cooling, cementite forms on ferrite grain boundaries.

If, for some reason, cooling is too rapid for cementite formation, the carbon is trapped in the interstitial sites and contributes to various aging phenomena unique to ferrite steels (Ref 18, 20). The one process is associated with segregation of carbon atoms to dislocations and grain boundaries and is referred to as strain aging. The other process is associated with precipitation of fine carbide particles either on dislocations or in the ferrite matrix and is referred to as quench aging. Figure 13 shows an example of fine dendritic cementite particles that have formed by quench aging on dislocations in the ferrite of a low-carbon steel. Both strain aging and quench aging effectively pin dislocations and are responsible for the discontinuous yielding of low-carbon steels with largely ferritic microstructures.

Pearlite and Bainite

An iron-carbon alloy containing 0.77 wt% C is the eutectoid composition, where three equilibrium phases (austenite with dissolved carbon, ferrite with dissolved carbon, and cementite) can coexist at a temperature of 727 °C (1340 °F). The eutectoid region of the iron-carbon equilibrium diagram is shown in Fig. 14. If austenite in an iron-carbon alloy containing 0.77 wt% C is cooled below 727 °C (1340 °F), then it must transform to ferrite and cementite. This type of solid-state reaction, in which one phase transforms to two other phases, is referred to as a eutectoid reaction. In iron-carbon alloys and steels, a unique parallel array of ferrite and cementite lamellae, termed pearlite, develops as a result of the eutectoid reaction. Figure 15 shows pearlite that has formed in a eutectoid steel; here, the cementite appears dark and the ferrite light.

Pearlite in a eutectoid steel is nucleated at austenite grain boundaries and grows as spherical-shaped colonies or nodules into the austenite. Carbon must diffuse to the growing cementite lamellae of the pearlite. Also, iron atoms must rearrange themselves by short-range diffusion from the fcc structure of austenite to their arrangements in the crystal structures of ferrite and cementite at the interface of the growing pearlite colonies. The rate of transport of carbon and iron atoms is temperature dependent and increases exponentially with increasing temperature.

At temperatures just below the 727 °C (1340 °F) eutectoid temperature (Fig. 14), the thermodynamic driving force for the eutectoid reaction (the decrease in free energy per unit volume when austenite is replaced by pearlite) available to offset the increase in energy associated with pearlite colony/austenite interfaces and the ferrite-cementite interfaces within the pearlite colonies is low. As a result, the nucleation rate of colonies is low and the spacing of cementite lamellae within the colonies is

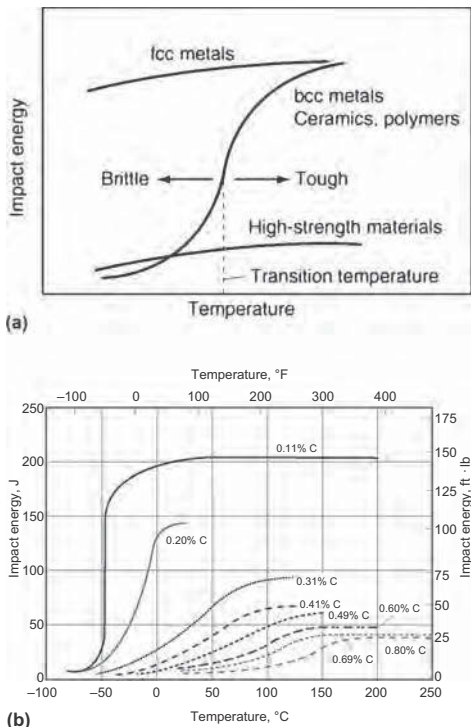


Fig. 11 Ductile-to-brittle transition temperature. (a) General behavior of body-centered cubic (bcc) and face-centered cubic (fcc) metals. (b) Effect of carbon content in ferrite-pearlite steels on Charpy V-notch transition temperature and shelf energy

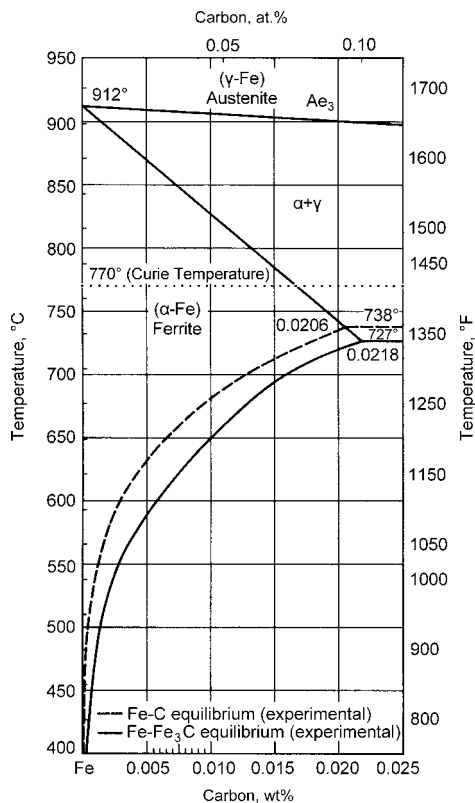


Fig. 12 Iron-rich side of iron-carbon diagram, showing extent of ferrite phase field and decrease of carbon solubility with decreasing temperature



Fig. 13 Transmission electron micrograph showing cementite precipitated on dislocations in an 0.08C-0.63Mn steel aged 115 h at 97 °C (207 °F). Courtesy of J.E. Indacochea (Ref 21)

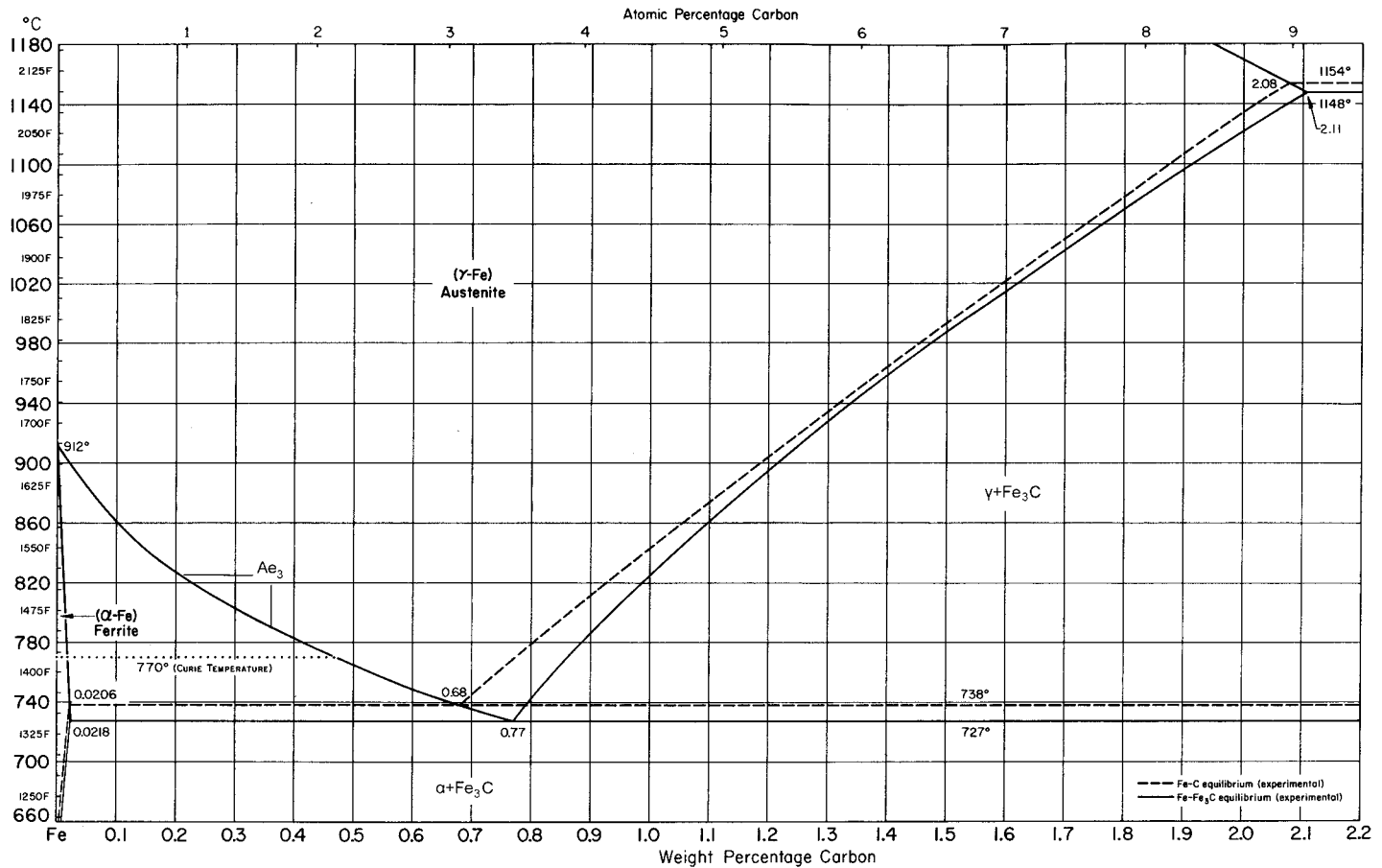


Fig. 14 Eutectoid region of the iron-carbon phase diagram

large. The coarse interlamellar spacing increases the diffusion distance for carbon and causes a low rate of growth for those colonies that manage to nucleate. Thus, pearlite transformation at temperatures close to the eutectoid temperatures is sluggish, and the pearlite microstructure that forms is relatively coarse. With increased undercooling, the thermodynamic driving force increases, the nucleation rate of pearlite colonies increases, interlamellar spacings decrease, and the growth rate of colonies increases. As a result of the latter changes, the transformation of austenite to pearlite accelerates with decreasing temperature.

Figure 16 shows an isothermal transformation diagram for a eutectoid steel. The diagram shows the beginning and end of the eutectoid transformation of austenite to pearlite for specimens cooled from the single-phase austenite field and held isothermally at temperatures between A_1 and 540°C (1000°F). The acceleration of the transformation with decreasing temperature is apparent.

At temperatures below 540°C (1000°F), the diffusion of iron atoms is reduced to the extent that they can no longer be readily transferred even the very short distance across the pearlite-austenite interface. Therefore, the mechanism

for the change in crystal structure from austenite to ferrite changes from diffusion to shear. Instead of an atom-by-atom transfer across an interface, large numbers of iron atoms shear or move cooperatively to form lath- or plate-shaped crystals of ferrite. Carbon diffusion and cementite formation must still occur because of the low solubility of carbon in the bcc ferrite, but the cementite forms as separate particles rather than as continuous lamellae, as in pearlite. The microstructure produced by both shear and diffusion is termed bainite, after Edgar C. Bain, who did much pioneering work in the characterization of austenite transformation and hardenability of steels (Ref 24).

Two forms of bainite develop in steels. One is termed upper bainite because it forms at relatively high temperatures, just below the range of pearlite formation. Upper bainite forms in patches containing many parallel laths of ferrite. Carbon is rejected from the ferrite and concentrates to form relatively coarse cementite particles between the ferrite laths. Figures 17(a) and (c) are light optical micrographs of upper bainite in two steels. Figure 18(a) is a micrograph from 4150 steel with patches of upper bainite formed by partial transformation of the austenite at 460°C (860°F). The

austenite that did not transform at 460°C (860°F) formed martensite (light background phase) on quenching to room temperature. The general morphology of upper bainite is shown in Fig. 18(a), but the ferrite laths and cementite particles are too fine to be resolvable in the light micrograph.

The other type of bainite is termed lower bainite because it forms at lower temperatures than does upper bainite. The ferrite takes a plate morphology, and the cementite is present as very fine particles within the ferrite plates (Fig. 17b, d). Figure 18(b) shows lower bainite that has formed in a 4150 steel. The bainite plates are at angles with respect to each other, giving an acicular or needlelike appearance to the microstructure rather than the blocky or feathery appearance of upper bainite. Again, the very fine carbide particles in the bainite plates are not resolvable in the light micrograph.

Proeutectoid Ferrite and Cementite

Figure 14 shows that alloys which contain either less carbon (hypoeutectoid steels) or more carbon (hypereutectoid steels) than the

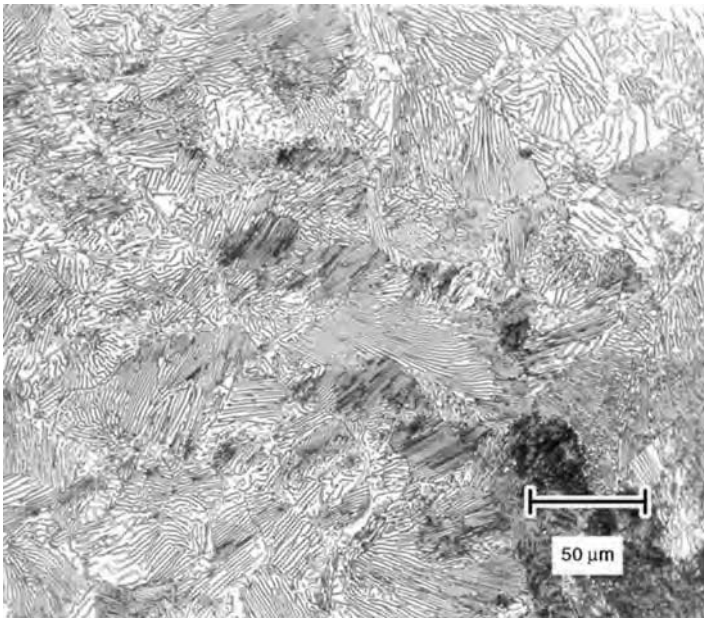


Fig. 15 Pearlite colonies of a plain carbon UNS G10800 steel showing colonies of pearlite. 4% picral etch. Original magnification: 200 \times . Source: Ref 22

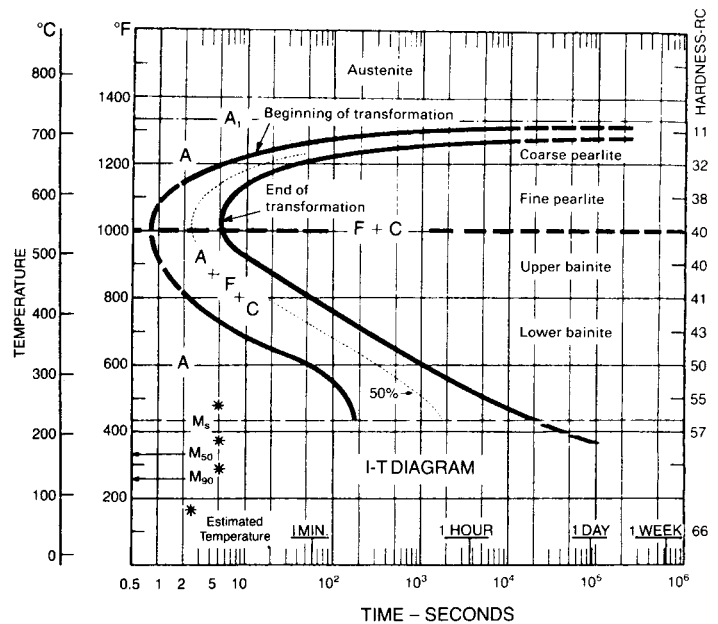


Fig. 16 Isothermal transformation diagram for 1080 steel containing 0.79% C and 0.76% Mn. Austenitized at 900 °C (1650 °F); ASTM grain size No. 6. Source: Ref 23

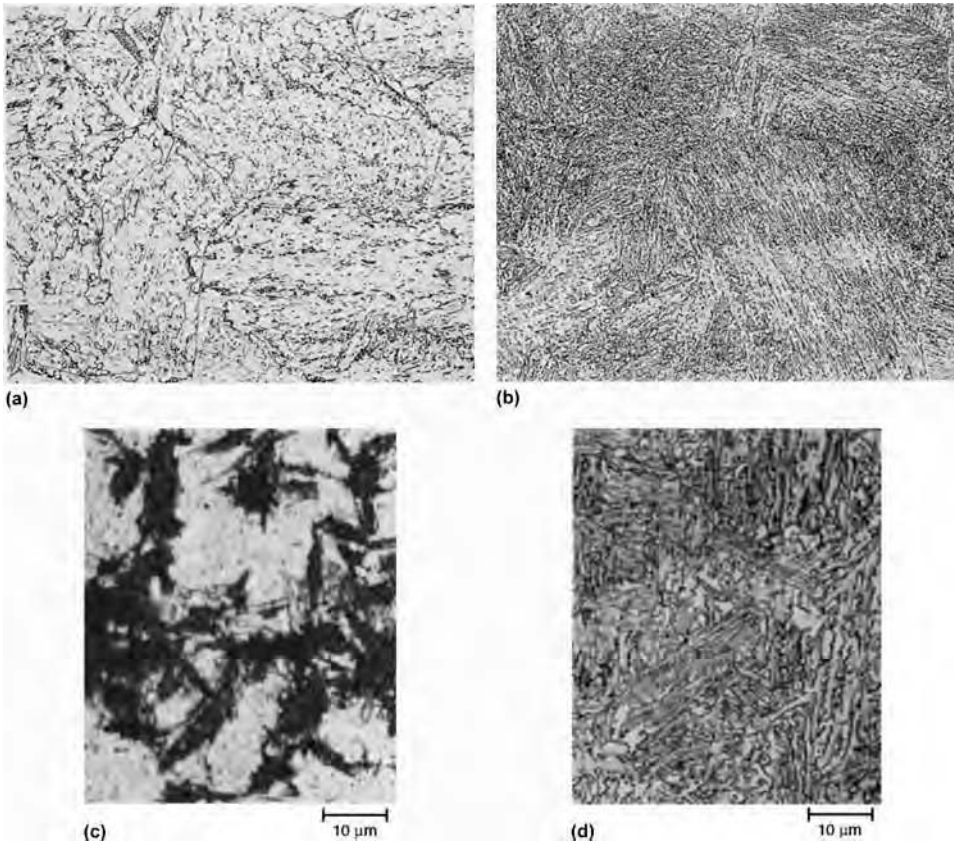


Fig. 17 Microstructure of (a) upper bainite and (b) lower bainite in a Cr-Mo-V rotor steel. 2% nital + 4% picral etch. Original magnification: 500 \times . (c) S5 tool steel austenitized, isothermally transformed (partially) at 540 °C (1000 °F) for 8 h, and water quenched to form upper bainite (dark); balance of austenite formed martensite. 4% picral + 2% nital. Original magnification: 1000 \times . (d) S5 tool steel austenitized, isothermally transformed at 400 °C (750 °F) for 1 h, and air cooled to form lower bainite. 37 to 38 HRC. 4% picral + 2% nital. Original magnification: 1000 \times

eutectoid composition must first form either ferrite or cementite when slowly cooled from the single-phase austenite field. In hypoeutectoid steels, the ferrite that forms before the eutectoid reaction is termed proeutectoid ferrite (Fig. 19a), while the cementite that forms before the eutectoid reaction in hypereutectoid steels is termed proeutectoid cementite (Fig. 19b).

When hypoeutectoid steel is austenitized and then slowly cooled below the A_3 critical temperature, proeutectoid ferrite nucleate in the austenite grain boundaries. As the ferrite grains grow, carbon is rejected into the austenite grain. Eventually, the carbon concentration is sufficient for pearlite formation, and the balance of the microstructure is transformed to pearlite. The microstructures of two hypoeutectoid steels are shown in Fig. 20. They have a mixed ferrite-pearlite microstructure, with the amount of pearlite (dark) depending on the carbon content. Most of the pearlite colonies appear uniformly black because the light is scattered by the lamellar structures, which are too closely spaced to be resolvable in the light micrograph. Ferritic-pearlitic steels are common for a host of structural applications. These steels are relatively inexpensive and are produced in large tonnages with a wide range of properties. In most ferrite-pearlite steels, the carbon content and the grain size determine the microstructure and resulting properties.

The growth of proeutectoid ferrite is dependent on the rejection of carbon atoms into the austenite and the transfer of iron atoms across the ferrite/austenite interface from the fcc to the bcc structure. The latter process is dependent on the degree

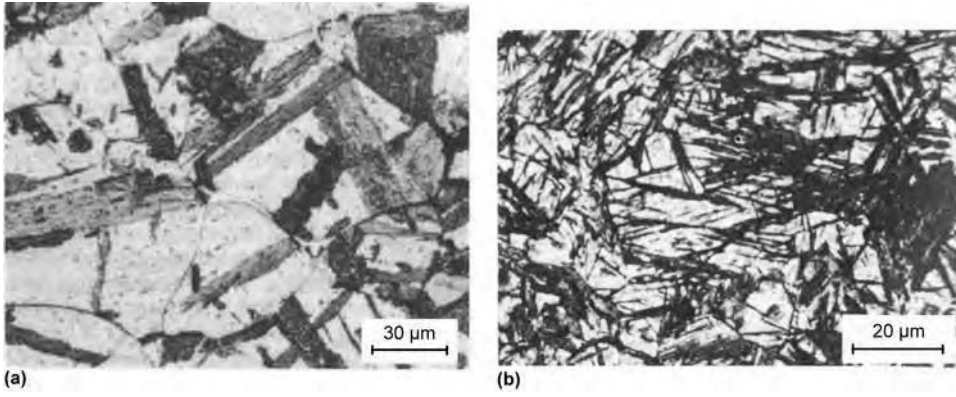


Fig. 18 Light micrograph showing patches of (a) upper bainite formed in 4150 steel partially transformed at 460 °C (860 °F) and (b) lower bainite (dark plates) in 4150 steel (nital etch). Courtesy of F.A. Jacobs (Ref 25)

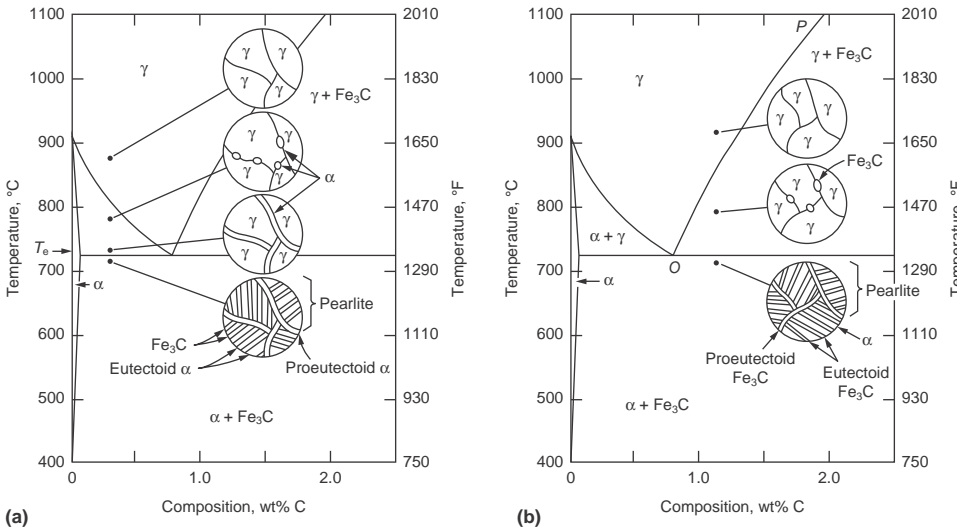


Fig. 19 Formation of (a) proeutectoid ferrite in hypoeutectoid steel and (b) proeutectoid cementite in hypereutectoid steel

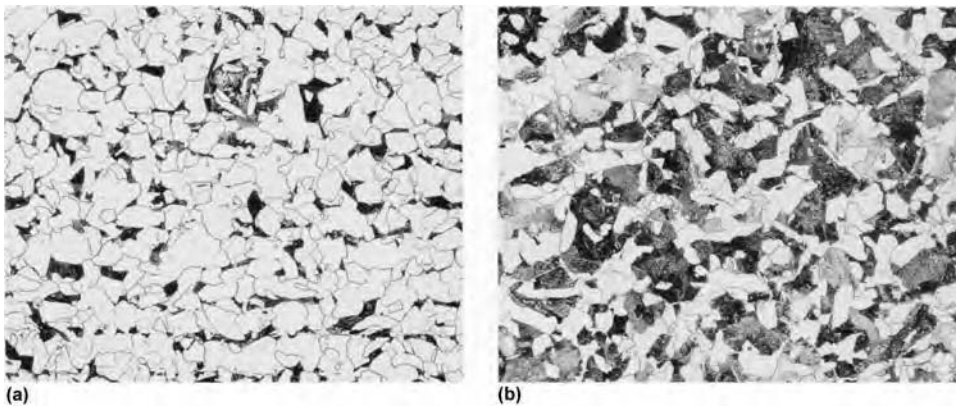


Fig. 20 Microstructure of typical ferrite-pearlite structural steels at two different carbon contents. (a) 0.10% C. (b) 0.25% C. 2% nital + 4% picral etch. Original magnification: 200x. Source: Ref 26

of coherency or disorder in atom arrangement at the interface. Also under some conditions, substitutional alloying elements must be incorporated into the ferrite structure if they are ferrite stabilizers or rejected from the ferrite if they are austenite stabilizers. Experimental and theoretical work on the effects of alloy element partitioning and interface structure on the formation of proeutectoid ferrite is reviewed in Ref 27.

Generally under conditions of slow cooling, the proeutectoid ferrite grows uniformly into austenite and an equiaxed ferrite grain structure. However, if the austenite in hypereutectoid steels is rapidly cooled, the transfer of iron atoms across ferrite/austenite interfaces is restricted, and the diffusion-controlled growth of ferrite is replaced by a shear mechanism. As a result, a plate-shaped morphology of ferrite, frequently referred to as acicular or Widmanstätten ferrite, develops in rapidly cooled low-carbon steels. Substitutional alloying elements such as manganese tend to retard the formation of equiaxed ferrite grains and promote acicular ferrite formation.

In hypereutectoid steels, proeutectoid cementite nucleates and grows on austenite grain boundaries during cooling from the austenite phase field (Fig. 19b). Figure 21 shows a network of proeutectoid cementite that has formed on austenite grain boundaries of a hypereutectoid steel. Initial proeutectoid cementite growth appears to depend only on diffusion of carbon and therefore can proceed very rapidly. In alloy steels, later stages of cementite growth require partitioning of substitutional alloying elements (such as chromium) and therefore are very sluggish (Ref 28). The very rapid initial growth of proeutectoid cementite may occur even during oil quenching for hardening and is associated with the intergranular fracture often observed in high-carbon steel quenched from temperatures above A_{cm} (e.g., Ref 29, 30).

In view of the brittleness that continuous networks of proeutectoid cementite impart, hypereutectoid steels are reheated intercritically into the austenite/cementite two-phase field for annealing (if maximum ductility and machinability are desired) or for hardening (if wear and fatigue resistance are required). During the intercritical heating, proeutectoid cementite networks as well as the lamellae of cementite in pearlite partially dissolve and spheroidize. For example, consider a 1095 steel (0.95 wt% C) received from a steel mill. If this steel is heated to 760 °C (1400 °F), the temperature-composition point is shown in Fig. 22 as an open circle with the horizontal arrowed line passing through it. Because the temperature-composition point lies in the shaded two-phase region labeled $\gamma + C_m$, this steel must consist of a mixture of austenite having composition O (0.85% C) and cementite of composition P (6.7% C). The schematic diagram illustrates what the microstructure would look like in the two-phase (intercritical) region of the phase diagram. The cementite appears as small, spherically-

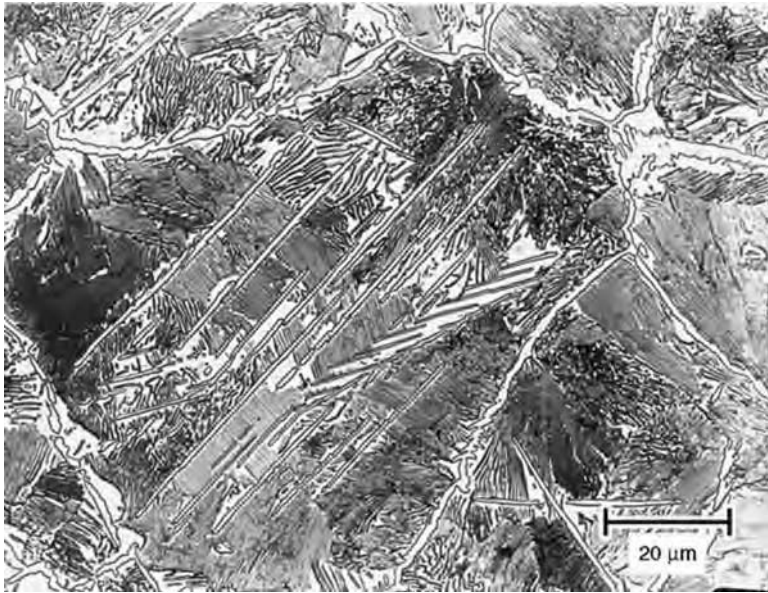


Fig. 21 Microstructure of 1.2% C-Fe alloy showing cementite outlining the prior-austenite grain boundaries and cementite needles in the grains of pearlite. The grain-boundary cementite is called proeutectoid cementite. This microstructure represents a hypereutectoid steel. 4% picral etch. Original magnification: 200×. Source: Ref 22

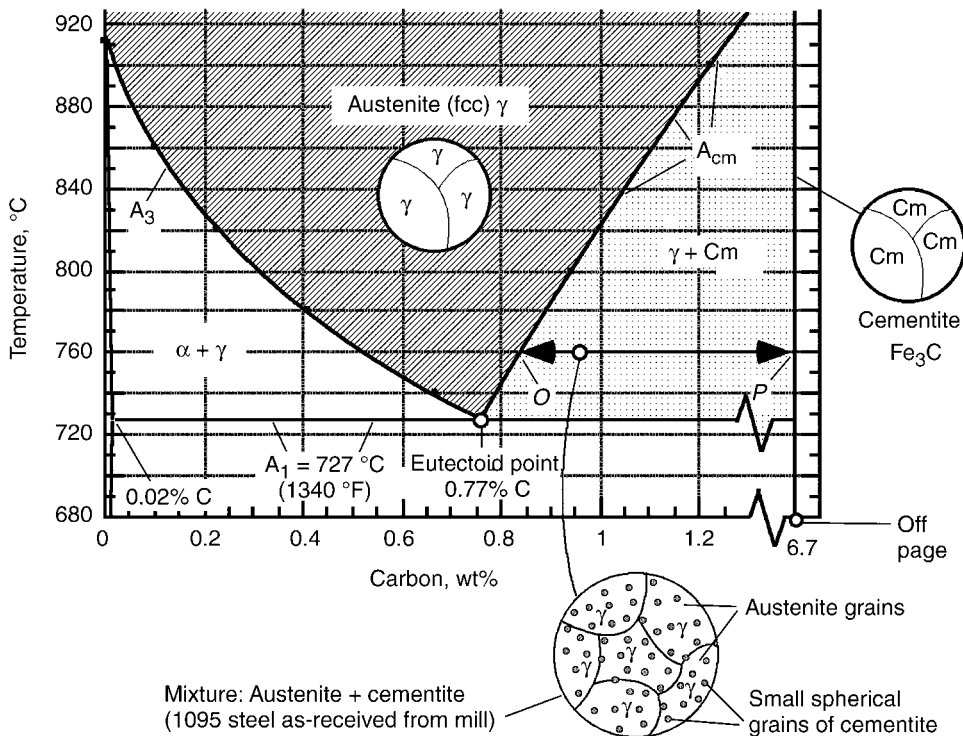


Fig. 22 Extension of the iron-carbon phase diagram to alloys illustrating intercritical heating to spheroidized cementite in a hypereutectoid steel. Source: Ref 31

shaped grains distributed fairly randomly over the austenite grains. After quenching, the spheroidized cementite particles are then dispersed in a matrix of martensite. This improves toughness, because fracture is

initiated at the fine spherical carbide particles, thus promoting a transgranular fracture morphology (rather than by intergranular fracture due to proeutectoid cementite along prior-austenite grain boundaries. With spheroidized cementite particles

in hypereutectoid steels, toughness is related to spacing of the particles (Ref 32).

Martensite

Martensite is the phase formed in steels by a diffusionless, shear transformation of austenite and is the base structure for hardened steels. Martensite is not shown on the iron-carbon diagram because it does not form under equilibrium conditions; generally rapid cooling to temperatures well below A_1 is required to form martensite. As expected from the iron-carbon diagram, martensite eventually decomposes to a mixture of ferrite and cementite if heated below A_1 .

Shear or the displacive, cooperative movement of many atoms has already been mentioned as a mechanism by which bainite and acicular proeutectoid ferrite form. The formation of the latter structures, however, occurs under conditions such that carbon diffusion accompanies the formation of bcc ferrite. When martensite forms, even the carbon atoms cannot diffuse. Thus, the carbon atoms are trapped in the octahedral interstitial sites, creating a supersaturated ferrite with a bct crystal structure. The higher the concentration of carbon atoms, the greater the tetragonality (Ref 33).

Figure 23 shows schematically a martensite plate that has formed in austenite adjacent to a free surface. The martensite surface is tilted by the shear transformation, and the austenite plane along which the martensite forms is termed the habit plane. To accomplish the shape deformation shown, not only must the fcc austenite lattice transform to the bct lattice of martensite, but the martensite crystal once formed must accommodate itself to the constraints of the surrounding bulk austenite and the restrictions imposed by the plane-strain deformation shown, as a result, martensite in steels contains a high residual density of dislocations and/or fine twins.

The martensitic transformation is characterized by athermal kinetics; that is, the amount of martensite formed is independent of time and is a function only of the amount of undercooling below the martensite-start temperature (M_s), the temperature at which martensite starts to form on cooling in a given steel. The following equation has been developed (Ref 35) for estimating the volume fraction of martensite, f , formed by quenching to any temperature, T_q :

$$f = 1 - \exp \left[-0.011(M_s - T_q) \right]$$

Thus, if the M_s of a given steel is known, the amount of martensite formed on quenching to any temperature below M_s can be established. A plot of martensite percentage versus the amount of undercooling below the M_s is in Fig. 24.

The M_s temperature is a function of the carbon and alloying-element content of a steel,

and a number of relationships have been developed to relate M_s to composition. Table 8 is a summary of typically used calculations for critical temperatures and martensite-start temperatures, although various martensite-start formulas have been developed over the years (Table 9, Ref 36). Figure 25 shows M_s as a function of carbon content. The decrease in M_s with increasing carbon content is related to the increased shear resistance produced by increasing amounts of carbon in solid solution in the austenite. An important consequence of low M_s temperature, according to the aforementioned equation, is the reduced amount of martensite that forms on cooling to room temperature. Therefore, large volume fractions

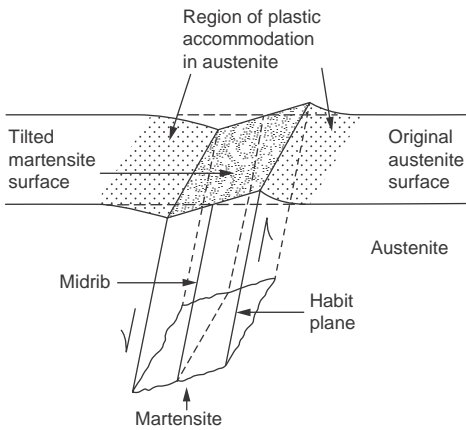


Fig. 23 Diagram of martensite crystal, showing shear and surface tilting. Courtesy of M.D. Geib (adapted from Ref 34)

of austenite may be retained in high-carbon steels.

Figure 25 indicates that two types of martensite form in carbon steels. The two categories are based on morphology and microstructural characteristics of the martensite (Ref 36, 41). The lath morphology forms in low- and medium-carbon steels and consists of regions or packets where many fine laths or board-shaped crystals are arranged parallel to one another. The habit plane of the laths is close to but not exactly {111}. The width of most of the laths is less than 0.5 μm , that is, below the resolution of the light microscope, and therefore the microstructure appears very uniform, with only the largest laths resolvable. Figure 26(a) is a micrograph of lath martensite in a low-alloy steel. Electron microscopy is required to show that the fine structure of lath martensite consists of a high density of tangled dislocations and that retained austenite is present as thin films between the martensite laths (Ref 43).

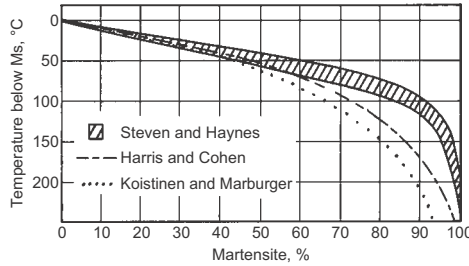


Fig. 24 Extent of martensite formation as a function of undercooling below the martensite-start temperature. Source: Ref 36

The plate morphology of martensite (Fig. 26b) forms in high-carbon steels and consists of martensite plates that form at angles with respect to each other on either $\{225\}_\gamma$ or $\{259\}_\gamma$ habit planes. Consistent with the low M_s of this alloy, a large amount of retained austenite is present. The fine structure of plate martensite consists of thin twins, approximately 10 nm thick, and/or dislocation arrays typical of low-temperature plastic deformation. The impingement of nonparallel plates during development of a martensite microstructure sometimes causes microcracks to form in the martensite (Ref 44). Examples of microcracks are shown in the large plate of Fig. 27. The density of microcracks in plate martensite is reduced by formation of martensite in fine-grained austenite, by lowering the carbon concentration of the austenite by intercritical austenitizing (thereby developing a more parallel martensite morphology and less impingement), and by tempering.

The carbon range in which a mixed morphology of lath and plate martensite forms is sensitive to alloy content and is not well known. Even in the range of carbon contents where lath martensite forms, there is a gradual decrease in the definition of packets with increasing carbon content (Ref 46).

Martensite Hardness and Hardenability. As-quenched martensite is very hard and brittle, typically requiring tempering for some degree of softening. The hardness of martensite depends solely on the carbon content (Fig. 28). Its hardness increases monotonically with carbon content up to approximately 0.7 wt%. At the higher levels of carbon, some of the softer austenitic phase remains stable after quenching, and so the effect of hardening due to martensite becomes limited (Fig. 28). Alloying does not change the hardnesses of martensite. However, alloying can slow the kinetics of pearlite formation and thus promote the formation of martensite at slower cooling rates. If martensite can form at slower cooling rates, then the depth of hardening is increased. The ability of steel to be hardened to greater depths during quenching is referred to as hardenability (see also the article “Hardness and Hardenability of Steels” in this Volume).

Hardenability of steel is usually determined by the Jominy end-quench test, where a bar of standard dimension is austenitized and quenched at one end. This results in different

Table 8 Typical formulas for calculating transformation temperatures of low-alloy steels

Formula	Reference
Ae_1 ($^{\circ}\text{F}$) $\sim 1333 - 25 \times \text{Mn} + 40 \times \text{Si} + 42 \times \text{Cr} - 26 \times \text{Ni}$	37
Ae_3 ($^{\circ}\text{F}$) $\sim 1570 - 323 \times \text{C} - 25 \times \text{Mn} + 80 \times \text{Si} - 3 \times \text{Cr} - 32 \times \text{Ni}$	37
Ac_1 ($^{\circ}\text{C}$) $\sim 723 - 10.7 \times \text{Mn} + 29.1 \times \text{Si} + 16.9 \times \text{Cr} - 16.9 \times \text{Ni} + 290 \times \text{As} + 6.38 \times \text{W}$	38
Ac_3 ($^{\circ}\text{C}$) $\sim 910 - 203 \times \sqrt{\text{C}} + 44.7 \times \text{Si} - 15.2 \times \text{Ni} + 31.5 \times \text{Mo} + 104 \times \text{V} + 13.1 \times \text{W}$	38
M_s ($^{\circ}\text{F}$) $\sim 930 - 600 \times \text{C} - 60 \times \text{Mn} - 20 \times \text{Si} - 50 \times \text{Cr} - 30 \times \text{Ni} - 20 \times \text{Mo} - 20 \times \text{W}$	39
M_{10} ($^{\circ}\text{F}$) $\sim M_s - 18$	40
M_{50} ($^{\circ}\text{F}$) $\sim M_s - 85$	40
M_{90} ($^{\circ}\text{F}$) $\sim M_s - 185$	40
M_f ($^{\circ}\text{F}$) $\sim M_s - 387$	40
B_s ($^{\circ}\text{F}$) $\sim 1526 - 486 \times \text{C} - 162 \times \text{Mn} - 126 \times \text{Cr} - 67 \times \text{Ni} - 149 \times \text{Mo}$	40
B_{50} ($^{\circ}\text{F}$) $\sim B_s - 108$	40
B_f ($^{\circ}\text{F}$) $\sim B_s - 216$	40

Table 9 Formulas used for calculating martensite-start temperatures

Investigators	Date	Equation
Payson and Savage	1944	M_s ($^{\circ}\text{F}$) = $930 - 570\text{C} - 60\text{Mn} - 50\text{Cr} - 30\text{Ni} - 20\text{Si} - 20\text{Mo} - 20\text{W}$
Carapella	1944	M_s ($^{\circ}\text{F}$) = $925 \times (1 - 0.620\text{C})(1 - 0.092\text{Mn})(1 - 0.033\text{Si})(1 - 0.045\text{Ni})(1 - 0.070\text{Cr})(1 - 0.029\text{Mo})(1 - 0.018\text{W})(1 + 0.120\text{Co})$
Rowland and Lyle	1946	M_s ($^{\circ}\text{F}$) = $930 - 600\text{C} - 60\text{Mn} - 50\text{Cr} - 30\text{Ni} - 20\text{Si} - 20\text{Mo} - 20\text{W}$
Grange and Stewart	1946	M_s ($^{\circ}\text{F}$) = $1000 - 650\text{C} - 70\text{Mn} - 70\text{Cr} - 35\text{Ni} - 50\text{Mo}$
Nehrenberg	1946	M_s ($^{\circ}\text{F}$) = $930 - 540\text{C} - 60\text{Mn} - 40\text{Cr} - 30\text{Ni} - 20\text{Si} - 20\text{Mo}$
Steven and Haynes	1956	M_s ($^{\circ}\text{C}$) = $561 - 474\text{C} - 33\text{Mn} - 17\text{Cr} - 17\text{Ni} - 21\text{Mo}$
Andrews (linear)	1965	M_s ($^{\circ}\text{C}$) = $539 - 423\text{C} - 30.4\text{Mn} - 12.1\text{Cr} - 17.7\text{Ni} - 7.5\text{Mo}$
Andrews (product)	1965	M_s ($^{\circ}\text{C}$) = $512 - 453\text{C} - 16.9\text{Ni} + 15\text{Cr} - 9.5\text{Mo} + 217(\text{C})^2 - 71.5(\text{C})(\text{Mn}) - 67.6(\text{C})(\text{Cr})$

Source: Ref 36

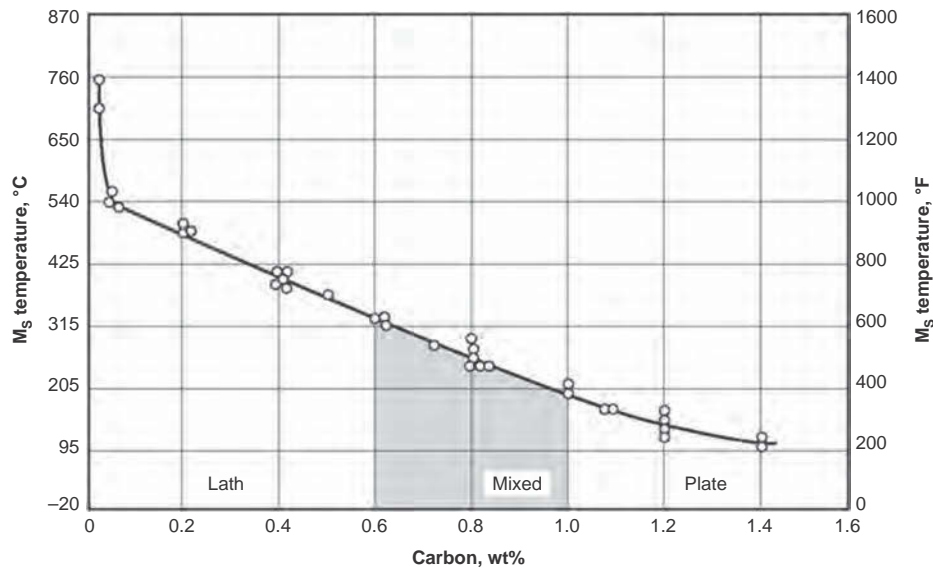


Fig. 25 Effect of carbon content on martensite-start (M_s) temperature in steels. Composition ranges of lath and plate martensite in iron-carbon alloys are also shown. Source: Ref 15

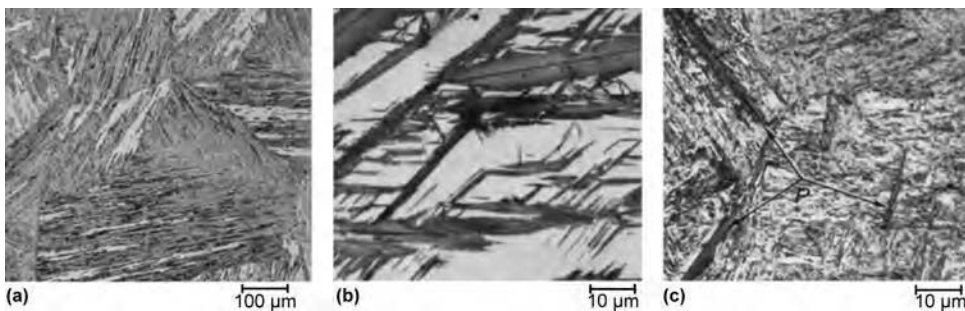


Fig. 26 Light micrographs of morphologies of martensite. (a) Lath martensite in low-carbon steel (0.03C-2.0Mn, wt%) at original magnification: 100 \times . (b) Plate martensite in matrix of retained austenite in a high-carbon (1.2 wt% C) steel at 1000 \times . (c) Mixed morphology of lath martensite with some plate martensite (P) in a medium-carbon (0.57 wt% C) steel at original magnification: 1000 \times . All 2% nital etch. Source: Ref 42

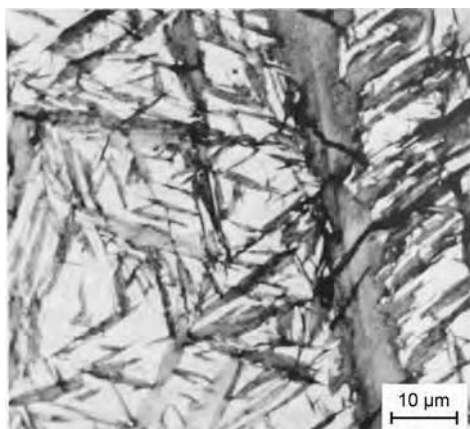


Fig. 27 Light micrograph (aqueous 10% sodium bisulfide etch) showing plate martensite and retained austenite in an Fe-1.39C alloy. Source: Ref 45

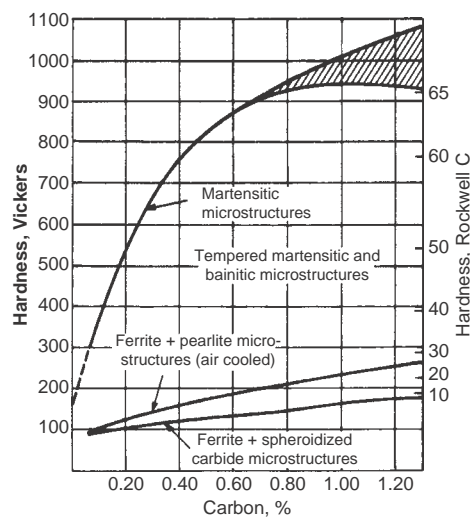


Fig. 28 Martensite hardness as a function of carbon content for various microstructures in steels. Cross-hatched area shows effect of retained austenite. Source: Ref 47

cooling rates along the length of the bar and thus different hardnesses and percentages of martensite along the bar (see the article “Hardness and Hardenability of Steels”). Positions along the Jominy bar are equivalent to cooling rates. Positions on the Jominy bar also can be equated to an equivalent bar diameter (see the article “Hardness and Hardenability of Steels”).

Tempered Martensite

As-quenched martensite is supersaturated with carbon, has a very high interfacial energy per unit volume associated with the fine laths or plates of the martensitic microstructure, contains a high density of dislocations that store considerable strain energy, and may coexist with retained austenite. As a result of these characteristics, martensitic microstructures are quite unstable and decompose when heated. A practical benefit of the decomposition is increased toughness, and for this reason, almost all hardened steels are heated to some temperature below A_c , a heat treatment process that is referred to as tempering.

A wide range of microstructures may be produced by tempering of martensite. Carbon atoms rearrange themselves into various configurations and structures within the martensite crystals even at temperatures well below 100 °C (212 °F) (Ref 48). Tempering between 100 °C and A_{c1} produces various types of carbide-particle dispersions as well as major changes in the matrix martensite. The reactions that produce the carbides have long been recognized and are classified as stages of tempering: T_1 , T_2 , and so on. The reactions that depend on very short-range rearrangement of carbon atoms in the as-quenched martensite prior to carbide formation have only recently been studied, and to distinguish those reactions from the carbide-forming reactions, it has been suggested that they be classified as aging reactions: A_1 , A_2 , and so on (Ref 49, 50).

Table 10 lists the various reactions and microstructural changes that may be developed by tempering steel (Ref 50). The aging and tempering classifications serve primarily to mark microstructures that form on the way to equilibrium, ultimately a microstructure that consists of spheroidized carbide particles dispersed in a matrix of equiaxed ferrite grains. Many of the reactions or microstructural states require further characterization, some occur concurrently, and others may yet be discovered. The reactions are controlled by diffusion of carbon, iron, and/or alloying elements, and therefore, steel composition, time, and temperature determine where a given tempering treatment stops in the sequence of structural changes indicated in Table 10.

Significant increases in toughness are achieved by tempering at temperatures above 150 °C (300 °F). In general, subject to the development of various embrittlement phenomena,

Table 10 Tempering reactions in steel

Temperature range		Reaction and symbol (if designated)	Comments
°C	°F		
-40 to 100	-40 to 212	Clustering of 2 to 4 carbon atoms on octahedral sites of martensite (A_1); segregation of carbon atoms to dislocations and boundaries	Clustering is associated with diffuse spikes around fundamental electron diffraction spots of martensite.
20 to 100	70 to 212	Modulated clusters of carbon atoms on (102) martensite planes (A_2)	Identified by satellite spots around electron diffraction spots of martensite
60 to 80	140 to 175	Long-period ordered phase with ordered carbon atoms (A_3)	Identified by superstructure spots in electron diffraction patterns
100 to 200	212 to 390	Precipitation of transition carbide as aligned 2 nm diameter particles (T_1)	Recent work identifies carbides as eta (orthorhombic, Fe_2C); earlier studies identified the carbides as epsilon (hexagonal, $Fe_{2.4}C$).
200 to 350	390 to 660	Transformation of retained austenite to ferrite and cementite (T_2)	Associated with tempered-martensite embrittlement in low- and medium-carbon steels
250 to 700	480 to 1290	Formation of ferrite and cementite; eventual development of well-spheroidized carbides in a matrix of equiaxed ferrite grains (T_3)	This stage now appears to be initiated by chi-carbide formation in high-carbon Fe-C alloys.
500 to 700	930 to 1290	Formation of alloy carbides in Cr-, Mo-, V-, and W-containing steels. The mix and composition of the carbides may change significantly with time (T_4)	The alloy carbides produce secondary hardening and pronounced retardation of softening during tempering or long-time service exposure at approximately 500 °C (930 °F).
350 to 550	660 to 1020	Segregation and cosegregation of impurity and substitutional alloying elements	Responsible for temper embrittlement

as tempering temperature increases, toughness increases and hardness decreases. Therefore, in applications where high hardness must be retained, tempering is performed at relatively low temperatures, usually between 150 and 200 °C (300 and 390 °F). Very fine carbide particles precipitate from the supersaturated martensite as a result of low-temperature tempering (Ref 51). The carbides are not cementite but rather transition carbides. Transition carbides include epsilon-carbide with a hexagonal structure as identified by x-ray diffraction (Ref 52), and another designated eta-carbide with an orthorhombic structure as identified by electron diffraction (Ref 53). Both the epsilon-carbide and eta-carbide have carbon contents substantially higher than that of cementite.

Steels tempered to develop the fine transition carbides show a modest but significant increase in toughness. The hardness, however, remains high because of the extremely fine carbide dispersion and the retention of much of the dislocation substructure introduced by the martensitic transformation.

In steels tempered between 200 and 350 °C (390 and 660 °F), the transition carbide is replaced by cementite or chi (χ)-carbide, and retained austenite transforms to ferrite and cementite. The χ -carbide is a complex carbide with a monoclinic structure that forms in tempered high-carbon martensites and is eventually replaced by cementite. Chi-carbides are coarser than the transition carbides present at the interfaces of the martensite plates as well as within the plates (Ref 54). Tempering between 200 and 350 °C (390 and 660 °F) also leads to transformation of retained austenite (see the article "Tempering of Steels" in this Volume). The retained austenite is stable throughout the tempering temperature range in which the transition carbide forms but begins to transform at temperatures above 200 °C (390 °F) (Ref 55). Austenite in medium-carbon steels is retained between martensite laths and, when it transforms on tempering, produces relatively coarse plates of interlath cementite (Ref 43).

The coarse carbides produced by replacement of the transition carbides and

transformation of the retained austenite, together with a limited recovery of the dislocation substructure of the martensite, reduce impact toughness. This decrease in impact toughness produced by tempering in the range of 250 to 400 °C (480 to 750 °F) is referred to as tempered martensite embrittlement (see the article "Tempering of Steels" in this Volume).

Tempering at temperatures above 400 °C (750 °F) produces substantial coarsening of the microstructure. Not only do the cementite particles coarsen and spheroidize but also the martensitic matrix is significantly altered. The laths are almost dislocation-free and are now ferrite because all carbon has completely precipitated as carbides. The reduction in dislocation density is driven by the reduction of the strain energy that accompanies the elimination of the dislocations and is accomplished by various recovery mechanisms.

As tempering temperature increases above 400 °C (750 °F), hardness and strength drop rapidly and toughness improves significantly. In alloy steels, the development of fine alloy carbide dispersions offsets the softening that accompanies the changing dislocation substructure and coarsening of the lath and cementite structure. In fact, if the alloy carbide dispersions are sufficiently fine and dense, an increase in hardness may develop. This increase in hardness due to alloy carbide precipitation high in the tempering-temperature range is referred to as secondary hardening.

As noted, toughness increases significantly with increasing tempering temperature. However, if impurities such as phosphorus, antimony, and tin are present in a steel, these elements may segregate to grain boundaries and/or carbide-matrix interfaces and cause large reductions in impact toughness (Ref 56). This phenomenon develops during tempering in, or slow cooling through, the temperature range 350 to 550 °C (660 to 1020 °F) and is referred to as temper embrittlement. The impurity atom segregation may be accompanied by the cosegregation of the substitutional alloying elements present in steels (Ref 57).

Transformation Diagrams

The previous sections have shown that the decomposition of austenite produces a wide variety of microstructures in response to such factors as steel composition, temperature of transformation, and cooling rate. Several factors determine the rates of austenite decomposition into pearlite, bainite, primary ferrite, primary cementite, or martensite. The rates depend strongly on temperatures and whether cooling is rapid or slow, because nonequilibrium conditions can have marked effects on the nucleation and growth rates of the constituents created during austenite decomposition and the resultant microstructure.

To characterize the conditions that produce the various microstructures, two types of transformation diagrams have been developed. Isothermal transformation (IT) diagrams are based on the austenite decomposition at constant temperatures, while continuous transformation diagrams follow microstructural development as a function of cooling rate. As an example, Fig. 29 compares an IT diagram with a continuous cooling transformation (CCT) diagram of steels with approximate eutectoid compositions. The main difference between IT and CCT diagrams is that the transformation boundaries are shifted due to hysteresis with continuous cooling (Fig. 29). Most heat treatments are performed by continuous cooling, and therefore CCT diagrams are commonly encountered in commercial practice.

Isothermal Transformation Diagrams (Ref 36, 59)

Isothermal transformation diagrams, also referred to as time-temperature transformation diagrams, are used to describe either the decomposition of austenite upon cooling or the isothermal heating for the formation of austenite. The latter is often referred to as an isothermal heating transformation (IHT) diagram. Isothermal transformation curves can be found in standard graphs obtainable

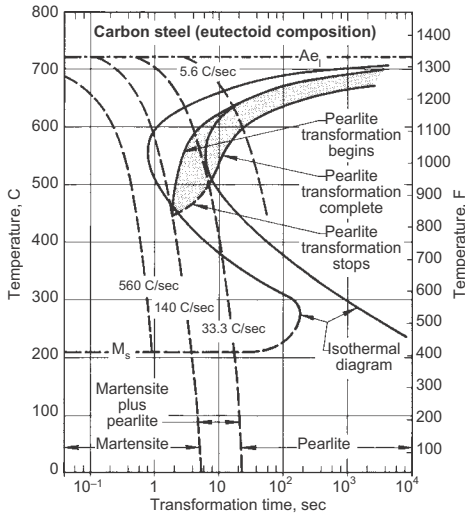


Fig. 29 Continuous cooling transformation diagram (shaded) and isothermal transformation diagram of a carbon steel with a eutectoid composition. Source: Ref 58

from the International Organization for Standardization (ISO), the Metallurgical Society of AIME, and ASM International (Ref 60). There is also a well-known German reference (Ref 61) that includes a large collection of IHT diagrams.

The IHT diagram is not as common as the isothermal cooling diagrams, although heating diagrams are useful in short-time heat treatments such as induction and laser hardening. The original microstructure also plays a great role in heating. A finely distributed structure such as tempered martensite is more rapidly transformed to austenite than, for instance, a ferritic-pearlitic structure. This is particularly true for alloyed steels with carbide-forming alloying elements such as chromium and molybdenum. It is important that the heating rate to the hold temperature be very high if a true isothermal diagram is to be obtained.

Isothermal decomposition of austenite is determined by quenching small specimens in a lead or salt bath at a proscribed temperature. Specimens are held at temperature for different holding times and then quenched to room temperature (Fig. 30). The amount of phases formed in the microstructure is then determined metallographically. An alternative method involves using a single specimen and a dilatometer that records the elongation of the specimen as a function of time. The basis for the dilatometer method is that the microconstituents undergo different volumetric changes (Table 11). A thorough description of the dilatometric method can be found in Ref 65.

From this, a series of curves plot the volume fraction of phases. The C-shaped curve is typical for transformation curves. The transformation-start curve provides an estimate for

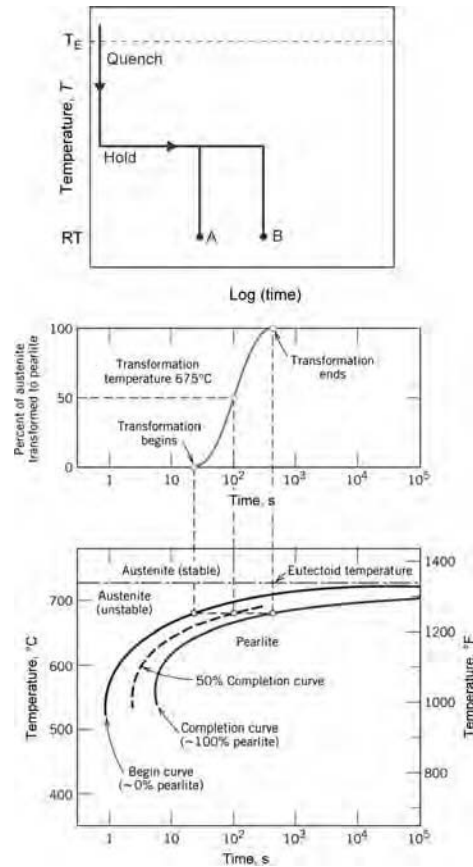


Fig. 30 Generation of an isothermal transformation diagram

the upper-limit time (in seconds) for nucleation time, τ . Nucleation time, τ_x , for a volume fraction (x) can be estimated semiempirically by a relation of the type (Ref 66):

$$\tau_x = \frac{\exp(Q/RT)}{2^{N/8} \cdot \Delta T^3} f \cdot I(x)$$

where x is the volume fraction of the transformed phase; Q is an activation energy related to the boundary diffusion activation energies for the alloying elements; N is the ASTM International grain size number for austenite; T is the temperature (in Kelvin); ΔT is the undercooling ($A_3 - T$) for ferrite, ($A_1 - T$) for pearlite, and an empirical value for bainite; f is a linear function of the volume fractions of carbon and alloying elements; and I is the volume fraction integral giving the dependence of the transformed phase on the volume fraction.

The combined effect of the $I/\Delta T^3$ factor, which increases with decreasing undercooling (that is, increasing temperature), and the $\exp(Q/RT)$ factor, which increases with decreasing temperature, results in long nucleation times, τ_x , for high and low temperatures and short nucleation times for intermediate temperatures. The C-shape can thus be obtained and understood. The factor $2^{N/8}$ is included

to take into consideration the fact that the transformation rate is larger for smaller austenite grain sizes.

Time-Temperature Effects of Eutectoid Transformation. At constant temperature, growth of pearlite nodules in carbon steels proceeds by the edgewise advance of the ferrite and cementite lamellae at a constant rate. However, the overall transformation rate, which is defined as the rate of increase of the volume percentage of pearlite, is not constant. In the early stages of the transformation, only a few small pearlite nodules are formed. As the transformation proceeds, new nodules form and grow, and this growth is accompanied by the continued growth of the nodules already present.

Because the overall transformation rate is proportional to the area of the pearlite-austenite interface that exists at any time, this rate is relatively low initially and increases as long as growth of the nodules is unimpeded. Impingement occurs at a time that depends on the ratio of the austenite grain size to the rate of nodule growth. From this time on, the overall rate decreases until transformation is complete.

The rate of nucleation of colonies and the rate of growth vary with temperature, as shown in Fig. 31. These rates are typical of commercial steels, which usually contain 0.3 to 1% Mn and smaller amounts of other elements. For a high-purity iron-carbon alloy (0.78% C and approximately 0.01% total phosphorus, manganese, silicon), the rate of growth is 6.5×10^{-2} mm/s at 600 °C (1110 °F), which is approximately seven times the value shown at that temperature in Fig. 31. The times required for the isothermal transformation to begin and be completed at any temperature are summarized in Fig. 16.

Interlamellar Spacing. The apparent variation of interlamellar spacing from colony to colony can be explained by differences in lamellar orientation with respect to the polished surface, but true spacing is approximately the same in all colonies, at a given temperature of transformation. This spacing changes from approximately 0.7 μ m in pearlite formed at 700 °C (1290 °F) to 0.15 μ m in pearlite formed at 600 °C (1110 °F). Figure 32, which depicts the effect of suddenly lowering the temperature of transformation from 700 to 674 °C (1290 to 1245 °F), suggests that there is a unique spacing at each transformation temperature. The variation in spacing with temperature of transformation is summarized graphically in Fig. 33.

When measuring spacing with a light microscope, one should be wary of results that approach the limit of optical resolution (approximately 0.3 μ m), because regions of finer spacing will be overlooked. Electron microscopy, which has higher resolution, should then be used. Replica techniques are subject to uncertainty of measurement due to variation of lamellar orientation, whereas both thin-foil and scanning techniques allow

Table 11 Volume and size changes due to different transformations

Reaction	Volume change, %	Dimensional change(a), in./in.
Spheroidite (spheroidized pearlite) to austenite (contraction)	2.21 (%C)-4.64	0.0074 (%C)-0.0155
Austenite → martensite	4.64-0.53 (%C)	0.0155-0.00118 (%C)
Spheroidized pearlite to martensite	1.68 (%C)	0.0056 (%C)
Austenite → lower bainite(b)	4.64-1.43 (%C)	0.0156-0.0048 (%C)
Spheroidized pearlite to lower bainite(b)	0.78 (%C)	0.0026 (%C)
Austenite → aggregate of ferrite and cementite(b)	4.64-2.21 (%C)	0.0155-0.0074 (%C)
Spheroidized pearlite to aggregate of ferrite and cementite(c)	0	0

(a) Linear changes are approximately one-third the volume changes. Lower bainite is assumed to be a mixture of ferrite and epsilon-carbide. Upper bainite and pearlite are assumed to be mixtures of ferrite and cementite. Source: Ref 62, 63-64

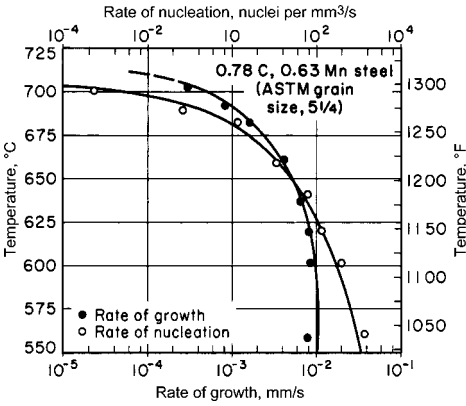


Fig. 31 Temperature versus rates of nucleation and growth of pearlite colonies in a steel with eutectoid composition



Fig. 32 Pearlite that was formed isothermally in steel by partial transformation at 700 °C (1290 °F) and by further partial transformation at 674 °C (1245 °F). The pearlite at left was formed when the specimen was at the higher temperature and is coarser than the pearlite at center, which was formed when the specimen was at the lower temperature. Composition of steel: 0.87 C, 0.44 Mn, 0.17 Si, 0.21 Cr, 0.39 Ni

selection of lamellae that are normal to the surface.

Transformation Times. The times required for initiation and completion of the pearlite transformation in a carbon steel of eutectoid composition, under conditions of continuous cooling at various rates, have been derived from the IT diagram of this steel and are shown in a CCT diagram in Fig. 29. The CCT diagram is usually determined experimentally. At low cooling rates, there is often little microstructural difference between isothermally and continuously cooled specimens because, as Fig. 29 shows, the pearlite reaction occurs over a temperature range as narrow as 30 °C (55 °F). At high cooling rates, the range increases and moves to lower temperatures, until the pearlite reaction is arrested and increasing amounts of martensite are formed. Thus, it is not possible by continuous cooling to form pearlitic structures at temperatures below the line so indicated in Fig. 29.

Effects of Alloying. Steels with carbon content above or below the eutectoid composition and alloy steels have more complex transformation diagrams. Figure 34 shows schematic IT diagrams for eutectoid steel and a hypoeutectoid plain carbon steel containing nominally 0.5% C. Also shown is their relationship to the iron-carbon diagram. The beginning and ending curves for pearlite formation approach

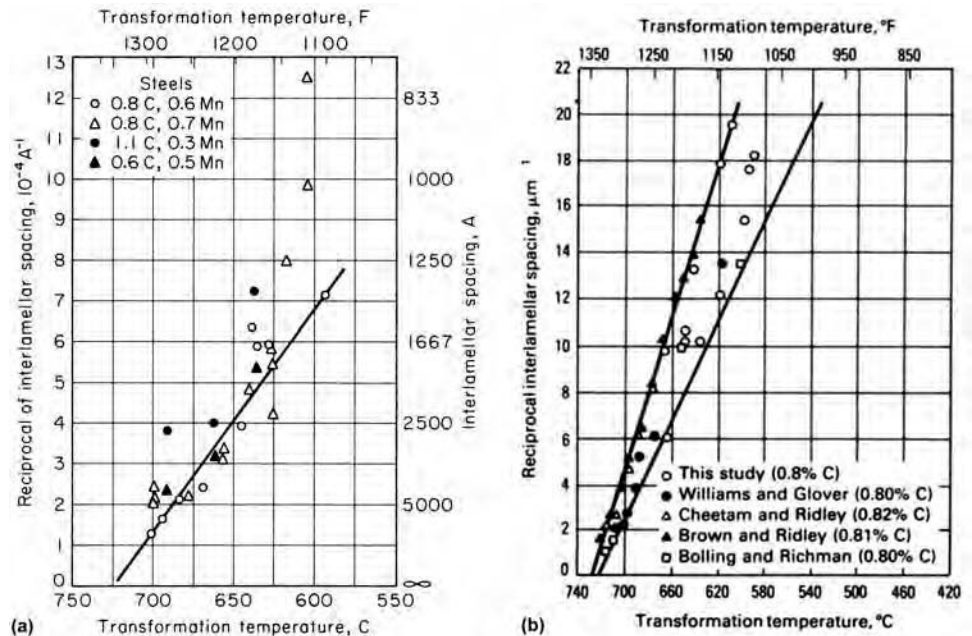


Fig. 33 Two plots of pearlite interlamellar spacing versus transformation temperature. (a) Source: Ref 67. (b) Source: Ref 68

the Ae_1 temperature at very long transformation times and move to shorter times with decreasing transformation temperature. The IT diagram for the hypoeutectoid steel has an extra curve to mark the beginning of proeutectoid ferrite formation. As indicated in Fig. 34, the latter curve approaches the Ae_3 temperature for the 0.5% C steel with increasing transformation time. Hypoeutectoid steels with lower carbon contents would have higher Ac_3 temperatures and therefore expanded regions of proeutectoid ferrite coexistence with austenite. Similarly, hypereutectoid steels would have IT diagrams with curves for the beginning of proeutectoid cementite formation.

Figure 34 shows other differences between the IT diagrams for eutectoid and hypoeutectoid steels. One difference is in M_s temperatures: the lower the carbon content, the higher the M_s temperature. Another difference is the acceleration of austenite transformation to proeutectoid ferrite with decreasing carbon content, as shown by the position of the nose of the hypoeutectoid steel at shorter times relative to that of the eutectoid steel. The dotted lines in Fig. 34(b) and (c) reflect experimental uncertainty in the exact positions of the beginning of transformation curves.

Slow cooling of a carbon steel with carbon content other than 0.8 wt% from a temperature in the austenite region of the phase diagram yields a proeutectoid constituent, either ferrite or cementite, until 727°C (1341°F) is reached. The austenite of eutectoid carbon content will then transform to pearlite. Figure 35(a) shows the ferrite-and-pearlite mixture in commercially processed bar after cooling in still air from 805°C (1480°F); most of the ferrite has a rounded or blocky form. Figure 35(b) shows the same material after forced-air cooling from 805 to 410°C (1480 to 770°F); here the proeutectoid ferrite delineates the prior-austenite grain boundaries and forms a thin envelope around the pearlite. In both specimens, Widmanstätten side plates of ferrite grew into the prior-austenite grains, but to a greater extent at the higher cooling rate. A point-count analysis showed that the steel in Fig. 35(a) had a pearlite volume fraction of 73%, whereas the specimen shown in Fig. 35(b) had a volume fraction of 83%. An equilibrium diagram constructed to reflect the alloy content of this steel shows that the eutectoid composition of the steel was 0.67% C. Hence, one would predict that the final structure would contain 40% ferrite and 60% pearlite. The larger amounts of pearlite, which were actually measured, are examples of suppression of the proeutectoid reaction with increasing cooling rates.

Substitutional alloying elements affect the eutectoid reaction in several ways. The resulting values of eutectoid temperature and eutectoid carbon content are shown, respectively, in Fig. 36(a) and (b). These curves do not indicate the carbon or alloy content in either the ferrite or carbide phase. The strong effects of alloying on the kinetics of the pearlite reaction result in the increased hardenability of alloy steels

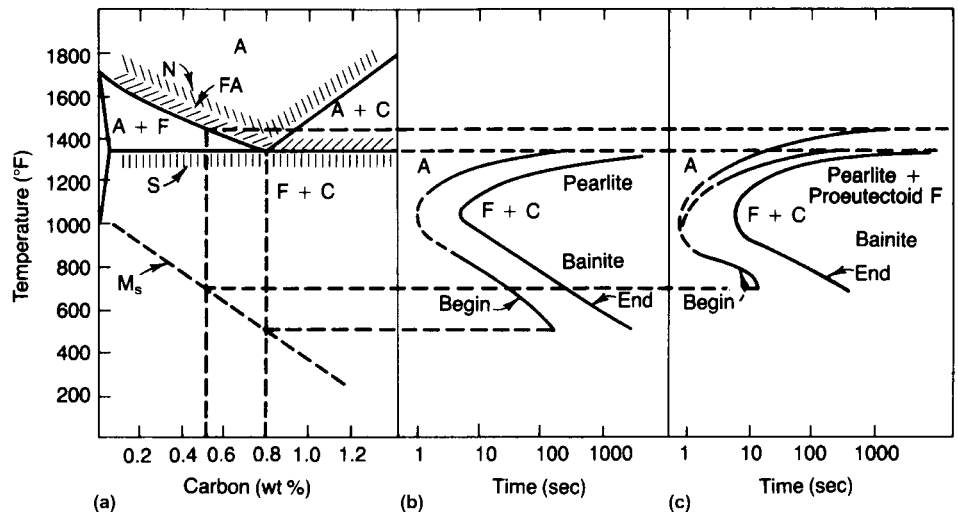


Fig. 34 Relationship to (a) iron-carbon diagram of isothermal transformation diagrams of (b) eutectoid steel and (c) steel containing 0.5% C. The regions identified as "N," "FA," and "S" in (a) are temperature ranges for normalizing, full annealing, and spheroidizing heat treatments, respectively.

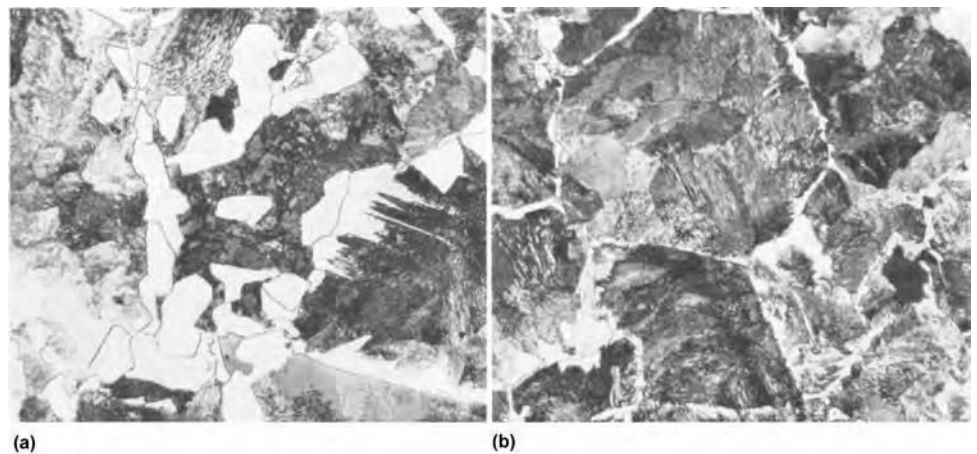


Fig. 35 Pearlite and proeutectoid ferrite (light areas) in commercially processed bar of a hypoeutectoid steel that was water quenched from 1050 to 805°C (1920 to 1480°F) and then air cooled. (a) Cooled from 805°C (1480°F) to room temperature in still air, which resulted in most of the ferrite having a rounded or blocky form. (b) Cooled from 805 to 410°C (1480 to 770°F) in forced air, then to room temperature in still air, which resulted in the presence of less ferrite than in (a), the ferrite forming only a thin envelope around the pearlite. Composition of steel: 0.40 C, 1.44 Mn, and 0.22 Si. Nital etch. Original magnification: $500\times$

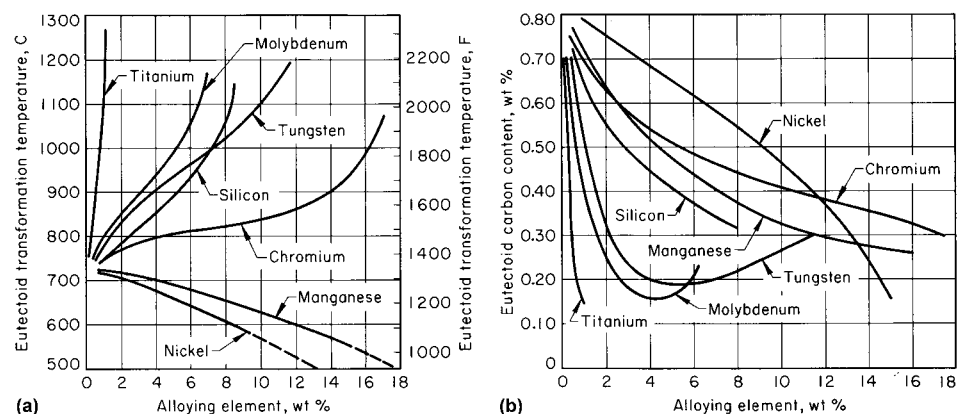


Fig. 36 Effect of percentage of substitutional alloying on (a) temperature and (b) carbon content of the eutectoid transformation point. Source: Ref 69

compared with that of carbon steels. Such a shift of time scale is easily observed metallographically. Comparative shifts in isothermal transformation times for different alloying elements are illustrated in Fig. 37. The appearance of other low-temperature transformation products on continuous cooling is a major effect of alloying. Significant departures from the usual appearance of pearlite have been observed in highly alloyed steels.

Continuous Cooling Transformation Diagrams (Ref 71)

Most heat treatments are performed by continuous cooling, and therefore, CCT diagrams are commonly encountered in commercial practice. Few heat treatment processes involve step-wise cooling. If cooling rates are slow, the structures correspond more closely to the upper regions of the IT diagram. Faster cooling rates have considerable effect on the starting temperature and progress of the transformation. It follows that some kind of continuous cooling curve is needed.

In addition, the CCT diagram can be a tool in evaluating hardenability if one knows the required cooling rate at the minimum depth (or an equivalent bar diameter) for hardening. The CCT diagrams constructed by Atkins (Ref 71) or Thelning (Ref 72) are particularly suitable. For example, two diagrams from Atkins are in Fig. 38. In these charts, the CCT curves are plotted with cooling rates and equivalent bar diameters with different quenchants. This provides a comparison for the depth of martensite formation. For example, 100% martensite is formed in bar diameters less than 0.18 mm (0.007 in.) with air cooling of the 1038 carbon steel (Fig. 38a), while the alloy steel (Fig. 38b) would have 100% martensite in bar diameter up to approximately 1 mm (0.04 in.) with air cooling. Hardenability is thus apparent in CCT diagrams and related to the

cooling rates on Jominy end-quench test specimens (Fig. 39). Positions along the Jominy bar are equivalent to cooling rates and can be expressed as equivalent bar diameters (see the article "Hardness and Hardenability of Steels" in this Volume).

The difficulty with CCT diagrams is the time and effort required in developing them for alloys of heat-to-heat analysis of hardenability. Care also should be taken in using CCT diagrams. Both the austenitizing temperature and soaking time affect the grain size of the austenite, thus modifying the subsequent transformation characteristics on cooling. The austenitizing temperature also affects the

composition of the austenite if the steel contains strong carbide-forming elements, and consequently, undissolved carbides may be present. Therefore, care should be taken when adapting the diagrams for austenitizing conditions different from those indicated. For this reason, the diagrams are not readily adapted to surface hardening by induction or flame heating, because rapid heating and short thermal cycle times have a drastic effect on the condition of the austenite.

Another major factor, which cannot be illustrated in the diagram, is the effect of agitation in the quenching medium, whether it be air, oil, or water. Agitation is obviously dependent

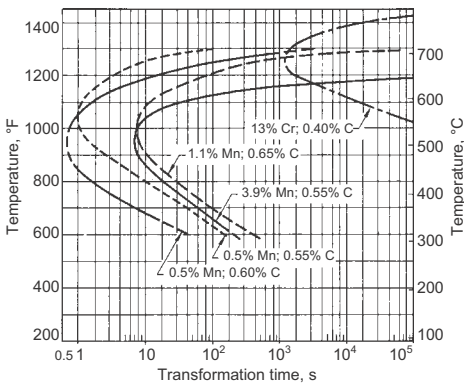


Fig. 37 Comparative time intervals for 50% isothermal transformation in steels containing different amounts of alloying elements. Source: Ref 70

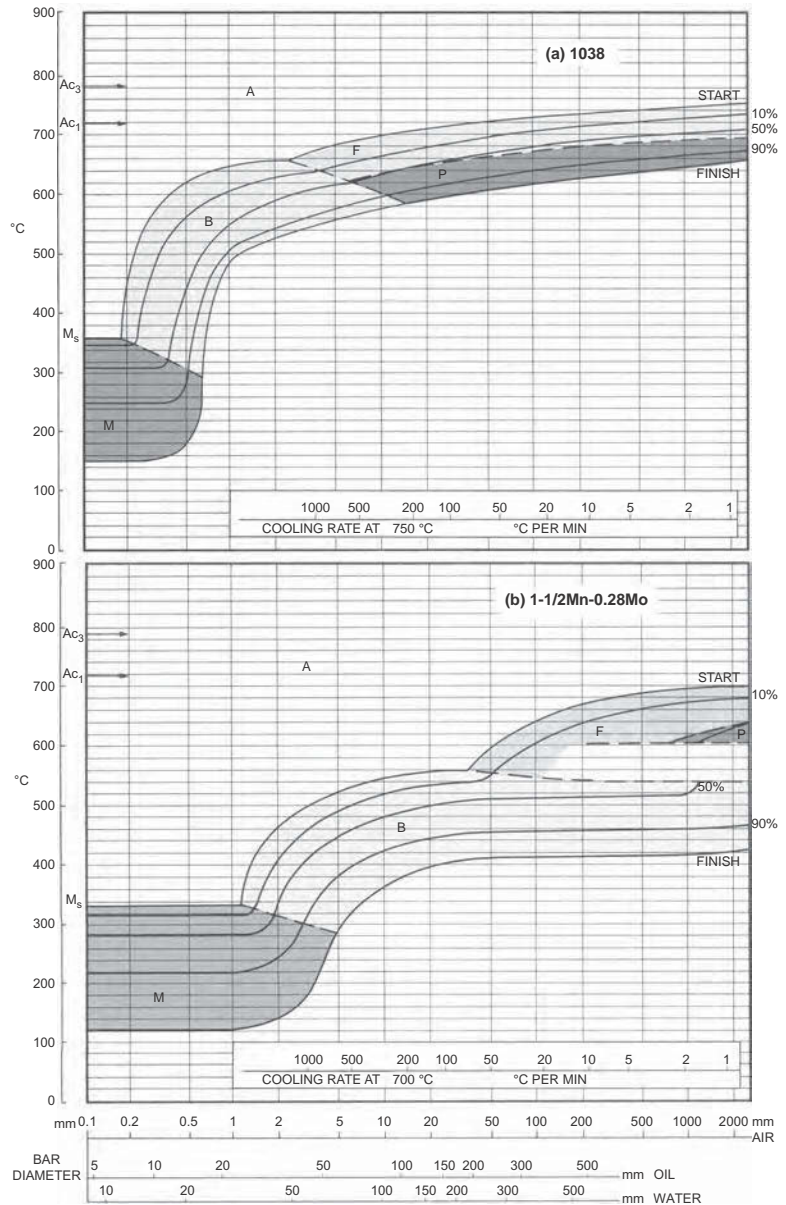


Fig. 38 Comparison of continuous cooling transformation diagrams for two steels. (a) 1038 steel (0.38 C, 0.20 Si, 0.70 Mn, 0.020 P, 0.020 S) rolled, austenitized at 860 °C (1580 °F), with as-quenched austenite grain size of 8 to 10. (b) Alloy steel (0.35 C, 0.28 Mo, 1.55 Mn, 0.20 Si, 0.025 P, 0.025 S) rolled, austenitized at 845 °C (1555 °F), with as-quenched austenite grain size of 7 to 8

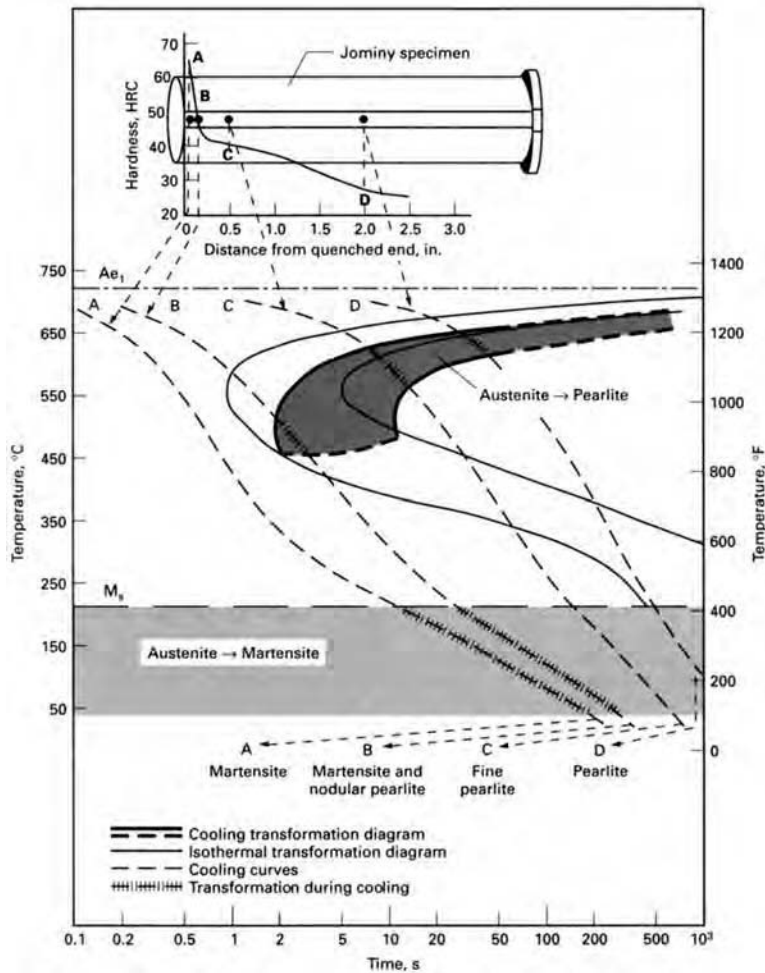


Fig. 39 Relationship of continuous cooling transformation (CCT) (shaded area) and isothermal transformation (light lines) diagrams of eutectoid (0.8 wt% C) steel. Four cooling rates from different positions on a Jominy end-quench specimen are superimposed on the CCT diagram.

on such practical features as bath size and component size and shape. These effects can only be examined experimentally. If, however, actual cooling curves can be obtained for a particular combination of operating conditions, they can then be converted into the corresponding bar diameters by use of the charts for equivalent diameters for equal cooling rates in the article “Bar Cooling Correlations” in a companion Volume (Ref 73) of this Handbook.

Thermal and Residual Stresses (Ref 59)

Given the fact that martensite causes expansion, transformation hardening of steel is usually accompanied by the evolution of large residual stresses, that is, stresses that exist without any external load on the part considered. Causes for such stresses include:

- Thermal expansion or contraction of a homogeneous material in a temperature gradient field
- Different thermal expansion coefficients of the various phases in a multiphase material
- Density changes due to phase transformations in the metal
- Growth stresses of reaction products formed on the surface or as precipitates, for example, external and internal oxidation

Residual stresses can be divided into three categories. A macroscale residual stress is the average of the residual stress in many adjacent grains of the material. If a workpiece is cut or material is removed, the presence of macroscale residual stress will cause a distortion. The introduction of macroscale residual stresses into a workpiece by heat treatment or plastic deformation may also cause a distortion of the part. The pseudo-macroscale residual stress is the average of the residual stress in many grains of one phase in a multiphase material minus the

macroscale residual stress. The macroscale residual stress in a part is the total residual stress minus the macroscale residual and the pseudo-macroscale residual stress. The residual stresses considered in this section are of the macro type. Stresses that exist during the entire heat treatment process are also discussed in the following paragraphs.

Residual stresses after heat treatment of steel is a subject of extensive interest and fundamental import. A brief introduction, the principle for the creation of thermal stresses on cooling, is shown in Fig. 40 for a 100 mm (4 in.) diameter bar that was water quenched from the austenitizing temperature of 850 °C (1560 °F). The surface temperature (S) decreases more rapidly than the core temperature (C), and at time w , the temperature difference between the surface and core is at a maximum of approximately 550 °C (1020 °F). This means that the specific volume is greater in the core than in the surface. The volume contraction in the surface is prevented by the higher specific volume in the core. The thermal stress is approximately proportional to the temperature difference and is tensile in the surface and compressive in the core. Large thermal stresses are favored by low thermal conductivity, high heat capacity, and high thermal expansion coefficient. Other factors increasing the temperature difference and thermal stresses are large thickness dimensions and high cooling intensity of the cooling medium. A large yield stress at elevated temperatures will decrease the degree of plastic flow and thus the residual stress, while the yield stress at the ambient temperature puts an upper limit on the residual stress.

The added effect of transformation of austenite to martensite in steel is demonstrated in Fig. 41. At time t_1 , the surface temperature falls below the M_s temperature, and the surface starts to transform. The surface expands and the thermal tensile stresses are counteracted. The stress reversal takes place earlier than when transformation stresses are not taken into consideration. At time t_2 , the core transforms, causing another stress reversal. After cooling, transformation-induced tensile stresses at the surface dominate over the thermally induced compressive stresses.

To predict hardening stresses quantitatively, it is necessary to consider interactions among various factors. As shown in Fig. 42, these include: (1) phase transformations, (2) latent heat, (3) thermal stress, (4) transformation stress and plasticity, (5) heat generation due to deformation, and (6) mechanically induced transformation. The most important of these are interactions 1, 3, and 5. Interaction 6, however, is also a very important factor. When discussing mechanically induced transformation, at least three different effects should be mentioned (Ref 77). The first is that the M_s temperature is decreased by hydrostatic pressure and raised by tensile stress (see Fig. 43, which shows an increase of ~ 15 °C, or ~ 27 °F, for a high-carbon steel). The second effect is the

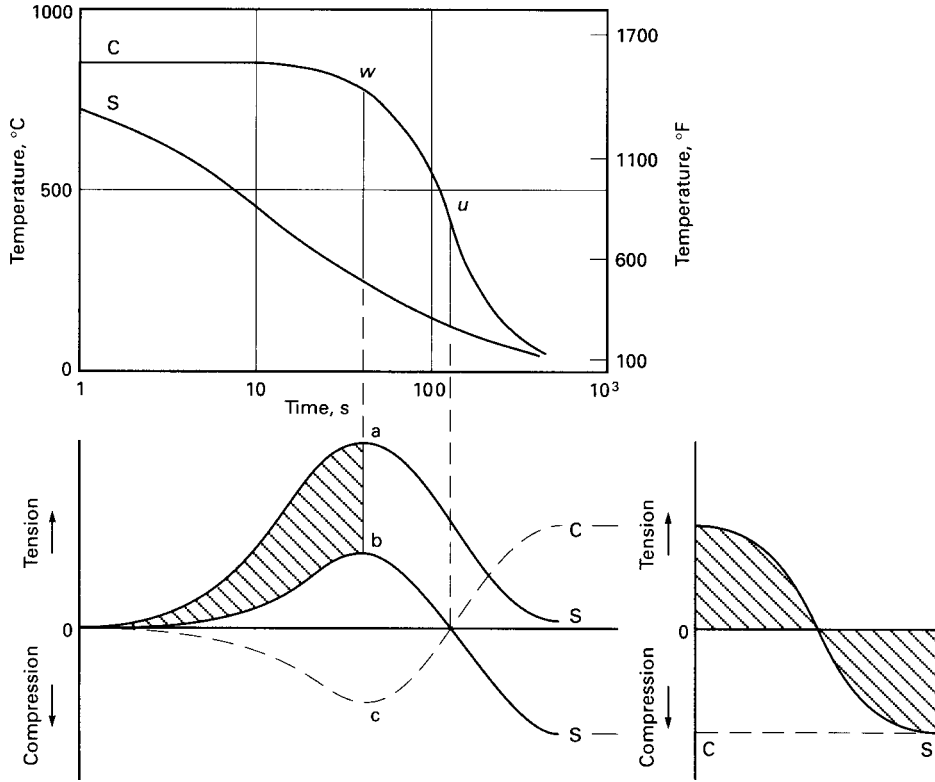


Fig. 40 Formation of thermal stresses on cooling in a 100 mm (4 in.) steel specimen. C designates the core, S the surface, u the stress reversal time instant, and w the time instant of maximum temperature difference. The top graph shows the temperature variation with time at the surface and in the core; the graph below shows the hypothetical thermal stress, a, which is proportional to the temperature difference between the surface and the core; the actual stress at the surface, b, which can never exceed the yield stress; and the actual stress in the core, c. To the right is shown the residual-stress distribution after completed cooling as a function of the specimen radius. Source: Ref 74

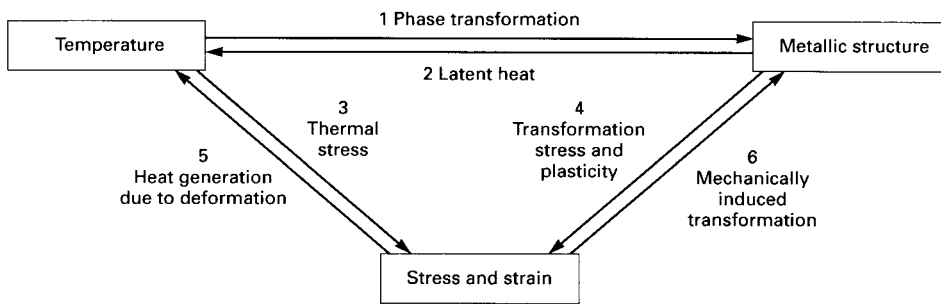


Fig. 42 Interactions between various factors of importance for residual-stress generation. Source: Ref 76

transformation plasticity, which is a permanent strain that occurs during an ongoing phase transformation under applied stress lower than the yield stress. It is displayed in Fig. 43 as an increase in the elongation from approximately 1% under an applied stress of 18 MPa (2.6 ksi) to 3% under 285 MPa (41 ksi) applied stress. The third effect is the incubation time of the nonmartensitic transformations, which is prolonged by hydrostatic pressure (Ref 78) and shortened by tensile stress (Ref 79). This

is particularly important for large dimensions. It has also been shown that a separate steel sample that is inserted into a cylinder of the same hardenable steel (Carney-type test) has a higher hardness value than the material in the same position in a homogeneous steel cylinder. The inserted steel specimen has the same temperature history but is not exposed to hardening stresses.

Cracking and Distortion due to Hardening. Hardening is usually accompanied by

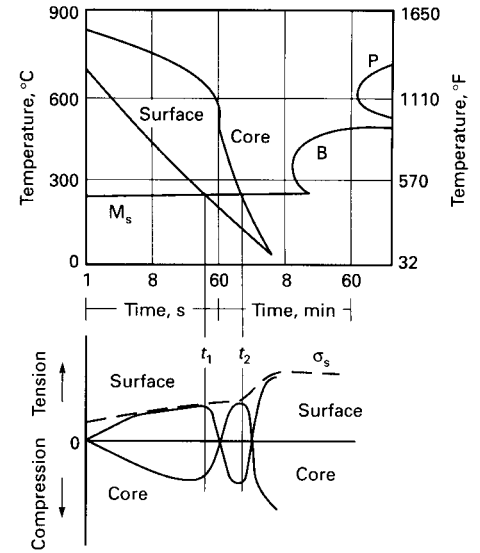


Fig. 41 Formation of residual stress on cooling, considering thermal expansion and the austenite-to-martensite transformation. The dashed line is the yield stress, σ_s , at the surface. See text for details. Source: Ref 75

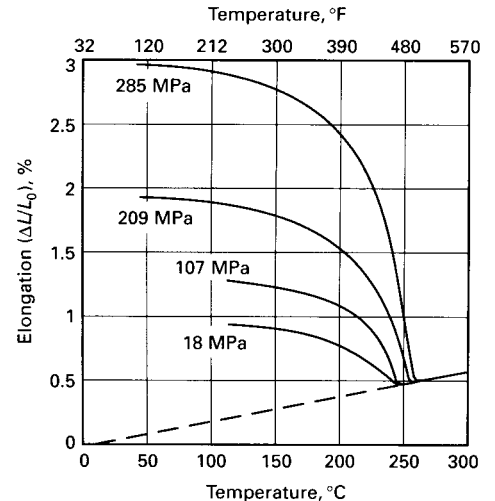


Fig. 43 Dilatometer curves for a steel with 0.6 wt% C for different applied tensile stresses. Source: Ref 77

distortion of a workpiece. The degree of distortion depends on the magnitude of the residual stresses. Hardening procedures that minimize transient and residual stresses are beneficial, as well as the use of fixtures (press hardening). Distortion can also occur during tempering or annealing due to release of residual stresses or phase transformations during tempering.

There also is a risk for cracking of a workpiece if large tensile stresses, transient or residual, are combined with the presence of a brittle

microstructure (particularly martensite). Quench cracking is a particular issue (see the article "Quench Cracking" in the upcoming companion Volume, Ref 73). Thermal stresses during cooling generally increase with the size of a workpiece. For phase-transformation-induced stresses, geometric dimension, hardenability of the steel, and quench intensity interact in a complicated manner, as has been described in earlier paragraphs. However, as a general rule, it holds that the use of a more efficient cooling medium, for example, water as compared to oil, will lead to larger stresses, as demonstrated in Fig. 44 to 46. The presence of geometric stress raisers increases the risk of cracking.

Figure 41 indicates that tensile stresses are present at the surface when the surface transformation to martensite is complete and the core transformation is in progress. As such, there is the risk of surface cracking. However, it is shown in Fig. 44 and 45 that through hardening does not necessarily lead to tensile stresses at the surface. Large tensile stresses in the core at lower temperatures may lead to center cracks even if the microstructure is not martensitic. Figure 46 shows that such a situation exists

for larger-diameter cylinders with a martensitic surface and a ferritic-pearlitic core. Case hardening may also lead to core cracking.

REFERENCES

1. K. Thelning, *Steel and Its Heat Treatment*, Butterworths, 1967
2. A. Bavaro, Heat Treatments and Deformation, *Trait. Therm.*, Vol 240, 1990, p 37-41
3. Y.S. Touloukian, *Thermodynamic Properties of High Temperature Solid Materials*, Vol 1, MacMillan, 1967, p 604
4. R.L. Orr and J. Chipman, *Trans. AIME*, Vol 239, 1967, p 630
5. *Properties and Selection of Metals*, Vol 1, *Metals Handbook*, 8th ed., American Society for Metals, 1961, p 1206
6. M.B. Peterson, J.J. Florek, and R.E. Lee, *ASLE Trans.*, Vol 3, 1960, p 101
7. L. Zwell, G.R. Speich, and W.C. Leslie, *Metall. Trans.*, Vol 4, 1973, p 1990
8. W. Hume-Rothery, Z.S. Basinski, and A.L. Sutton, *Proc. R. Soc. (London) A*, Vol 229, 1955, p 459

9. H. Stuart and N. Ridley, *J. Iron Steel Inst.*, Vol 204, 1966, p 711
10. E. Hornbogen, *Werkstoffe*, 2nd ed., Springer-Verlag, Berlin, 1979
11. E.A. Brandes and G.B. Brook, *Smithell's Metal Reference Book*, 7th ed., Butterworth-Heinemann, 1992
12. L.H. Van Vlack, *Elements of Materials Science and Engineering*, 4th ed., Addison-Wesley Publishing Company, 1980
13. A.G. Guy, *Elements of Physical Metallurgy*, 2nd ed., Addison-Wesley Publishing Company, 1959
14. G. Krauss, Physical Metallurgy and Steel Heat Treatment, *Metals Handbook Desk Edition*, American Society for Metals, 1985, p 28-1 to 28-10
15. A.J. DeArdo, G.A. Ratz, and P.J. Wray, Ed., *Thermomechanical Processing of Microalloyed Austenite*, TMS-AIME, Warrendale, PA, 1982
16. G. Krauss, Ed., *Deformation, Processing, and Structure*, American Society for Metals, Metals Park, OH, 1984
17. J.P. Hirth and J. Loll, *Theory of Dislocations*, McGraw-Hill, New York, 1968
18. W.C. Leslie, *The Physical Metallurgy of Steels*, McGraw-Hill, New York, 1981
19. M. Meshii, Ed., *Mechanical Properties of bcc Metals*, TMS-AIME, Warrendale, PA, 1982
20. W.C. Leslie, The Quench-Aging of Low-Carbon Iron and Iron-Manganese Alloys: An Electron Transmission Study, *Acta Metall.*, Vol 9, 1961, p 1004-1022
21. J.E. Indacochea, "Dual Phase Behavior and Aging of a Renitrogenized Steel," M.S.

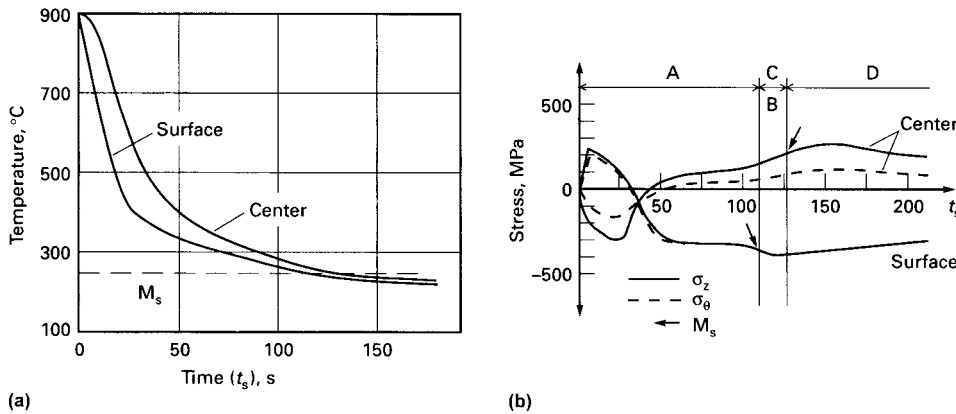


Fig. 44 (a) Temperatures and (b) calculated stresses in a long 0.6 wt% C low-alloy steel cylinder with 50 mm (2 in.) diameter quenched in 20 °C (70 °F) oil. In region A, the temperature is above martensite start (M_s); in region D, it is below M_s . In region C and B, the temperature is above M_s at the center but below M_s at the surface. σ_z , axial stress; σ_θ , tangential stress. Source: Ref 80

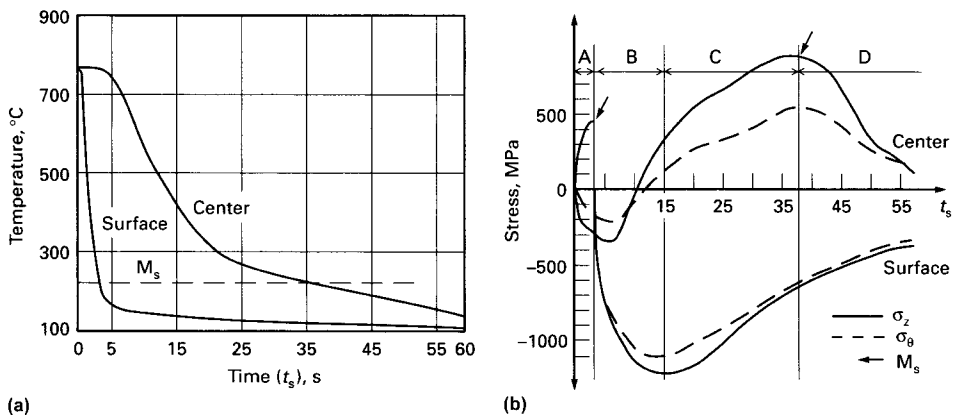


Fig. 45 Same type of diagram for the same steel and cylinder as in Fig. 44, but the specimen is quenched in 20 °C (70 °F) water. The final microstructure is completely martensitic. Source: Ref 80

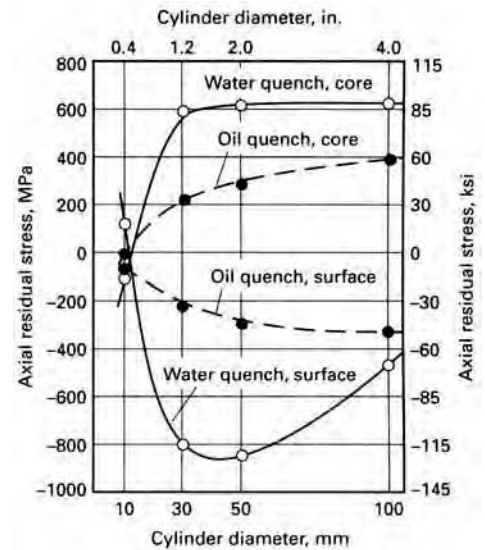


Fig. 46 Dependence of axial residual stresses on cylinder diameter. AISI 1045 steel cylinder diameters quenched from 850 °C (1560 °F) in 20 °C (70 °F) water. The core is martensitic for 10 mm (0.4 in.) diameter but ferritic-pearlitic for larger diameters. Source: Ref 81

- thesis, Colorado School of Mines, Golden, CO, 1978
22. B.L. Bramfitt and S.J. Lawrence, Metallography and Microstructures of Carbon and Low-Alloy Steels, *Metallography and Microstructures*, Vol 9, *ASM Handbook*, ASM International, 2004, p 608–626
 23. *Isothermal Transformation and Cooling Transformation Diagrams*, American Society for Metals, 1977, p 28
 24. H.W. Paxton and J.B. Austin, Historical Account of the Contribution of E.C. Bain, *Metall. Trans.*, Vol 13, 1972, p 1035–1042
 25. F.A. Jacobs, “The Combined Effects of Phosphorus and Carbon on Hardenability and Phase Transformation Kinetics in 41xx Steels,” M.S. thesis, Colorado School of Mines, Golden, CO, 1982
 26. B.L. Bramfitt, Effects of Composition, Processing, and Structure on Properties of Irons and Steels, *Materials Selection and Design*, Volume 20, *ASM Handbook*, ASM International, 1997
 27. H.I. Aaronson, D.E. Laughlin, R.F. Sekerko, and C.M. Wayman, Ed., *Solid-Solid Phase Transformations*, TMS-AIME, Warrendale, PA, 1982
 28. T. Ando and G. Krauss, Development and Application of Growth Models for Grain Boundary Allotriomorphs of a Stoichiometric Compound in Ternary Systems, *Metall. Trans. A*, Vol 14, 1983, p 1261–1269
 29. K. Nakazawa and G. Krauss, Microstructure and Fracture of 52100 Steel, *Metall. Trans. A*, Vol 9, 1978, p 681–689
 30. T. Ando and G. Krauss, The Effect of Phosphorus Content on Grain Boundary Cementite Formation in AISI 52100 Steel, *Metall. Trans. A*, Vol 12, 1981, p 1283–1290
 31. J.D. Verhoeven, *Steel Metallurgy for the Non-Metallurgist*, ASM International, 2007
 32. G. Krauss, The Relationship of Microstructure to Fracture Morphology and Toughness of Hardened Hypereutectoid Steels, *Microstructure and Residual Stress Effects on the Properties of Case Hardened Steels*, TMS-AIME, Warrendale, PA, 1984
 33. C.S. Roberts, Effect of Carbon on the Volume Fractions and Lattice Parameters of Retained Austenite and Martensite, *Trans. AIME*, Vol 197, 1953, p 203–204
 34. B.A. Bibby and J.W. Christian, The Crystallography of Martensite Transformations, *JISI*, Vol 197, 1961, p 122–131
 35. D.P. Koistinen and R.E. Marburger, A General Equation Prescribing the Extent of the Austenite-Martensite Transformation in Pure Iron-Carbon Alloys and Plain Carbon Steels, *Acta Metall.*, Vol 7, 1959, p 59–60
 36. G. Krauss, *Principles of Heat Treatment of Steel*, American Society for Metals, Metals Park, OH, 1980
 37. R.A. Grange, *Met. Prog.*, Vol 79, April 1961, p 73
 38. K.W. Andrews, *JISI*, Vol 203, 1965, p 721
 39. E.S. Rowland and S.R. Lyle, *Trans. ASM*, Vol 37, 1946, p 27
 40. W. Steven and A.G. Haynes, *JISI*, Vol 183, 1956, p 349
 41. A.R. Marder and G. Krauss, The Morphology of Martensite in Iron-Carbon Alloys, *Trans. ASM*, Vol 60, 1967, p 651–660
 42. D. Aliya and S. Lampman, Physical Metallurgy Concepts in Interpretation of Microstructures, *Metallography and Microstructures*, Vol 9, *ASM Handbook*, ASM International, 2004, p 44–70
 43. G. Thomas, Retained Austenite and Tempered Martensite Embrittlement, *Metall. Trans. A*, Vol 9, 1978, p 439–450
 44. A.R. Marder and A.O. Benschoter, Microcracking in Fe-C Acicular Martensite, *Trans. ASM*, Vol 61, 1968, p 293–299
 45. A.R. Marder, A.O. Benschoter, and G. Krauss, Microcracking Sensitivity in Fe-C Plate Martensite, *Metall. Trans.*, Vol 1, 1970, p 1545–1549
 46. T. Maki, K. Tsuzaki, and I. Tamura, The Morphology of Microstructure Composed of Lath Martensite in Steels, *Trans. Iron Steel Inst. Jpn.*, Vol 20, 1980, p 207–214
 47. E.C. Bain and H.W. Paxton, *Alloying Elements in Steel*, 2nd ed., American Society for Metals, Metals Park, OH, 1961
 48. Winchell Symposium on Tempering of Steel, *Metall. Trans. A*, Vol 14, 1983, p 985–1146
 49. G.B. Olson and M. Cohen, Early Stages of Aging and Tempering of Ferrous Martensites, *Metall. Trans. A*, Vol 14, 1983, p 1057–1065
 50. G. Krauss, Tempering and Structural Change in Ferrous Martensites, *Phase Transformations in Ferrous Alloys*, TMS-AIME, Warrendale, PA, 1984
 51. D.L. Williamson, K. Nakazawa, and G. Krauss, A Study of the Early Stages of Tempering in an Fe-1.22%C Alloy, *Metall. Trans. A*, Vol 10, 1979, p 1351–1363
 52. K.H. Jack, Structural Transformations in the Tempering of High Carbon Martensitic Steel, *ISIJ*, Vol 169, 1951, p 26–36
 53. Y. Hirotsu and S. Nagakura, Crystal Structure and Morphology of the Carbide Precipitated for Martensitic High Carbon Steel during the First Stage of Tempering, *Acta Metall.*, Vol 20, 1972, p 645–655
 54. C.-B. Ma, T. Ando, D.L. Williamson, and G. Krauss, Chi-Carbide in Tempered High Carbon Martensite, *Metall. Trans. A*, Vol 14, 1983, p 1033–1045
 55. D.L. Williamson, R.G. Schupmann, J.P. Materkowski, and G. Krauss, Determination of Small Amounts of Austenite and Carbide in a Hardened Medium Carbon Steel by Mossbauer Spectroscopy, *Metall. Trans. A*, Vol 10, 1979, p 379–382
 56. C.J. McMahon, Jr., Temper Brittleness—An Interpretive Review, *Temper Embrittlement in Steel*, STP 407, ASTM, 1968, p 127–167
 57. M. Guttman, P. Dumonlin, and M. Wayman, The Thermodynamics of Interactive Co-Segregation of Phosphorus and Alloying Elements in Iron and Temper-Brittle Steels, *Metall. Trans. A*, Vol 13, 1982, p 1693–1711
 58. *ASM Trans.*, Vol 29, 1941, p 85
 59. T. Ericsson, Principles of Heat Treating of Steels, *Heat Treating*, Vol 4, *ASM Handbook*, ASM International, 1991, p 3–19
 60. *Atlas of Isothermal Transformation and Cooling Transformation Diagrams*, American Society for Metals, 1977
 61. *Atlas zur Wärmebehandlung der Stähle*, Vol 1–4, Max Planck Institut für Eisenforschung, with the Verein Deutscher Eisenhütteleute, Verlag Stahleisen, Düsseldorf, 1954–1976
 62. B. Hildenthal and T. Ericsson, Prediction of Residual Stresses in Case Hardening Steels, *Hardenability Concepts with Application to Steel*, TMS-AIME, 1978
 63. F. Legat, Why Does Steel Crack during Quenching, *Kovine Zlitine Technol.*, Vol 32 (No. 3–4), 1998, p 273–276
 64. W. Bohl, Difficulties and Imperfections Associated with Heat Treated Steel, Lesson 13, Heat Treatment of Steel, Materials Engineering Institute Course 10, ASM International, 1978
 65. G.T. Eldis, A Critical Review of Data Sources for Isothermal Transformation, *Hardenability Concepts with Application to Steel*, D.V. Doane and J.S. Kirkaldy, Ed., TMS-AIME, 1978, p 126–157
 66. J.S. Kirkaldy, Diffusion-Controlled Phase Transformations in Steels: Theory and Applications, *Scand. J. Metall.*, Vol 20 (No. 1), 1991
 67. G.E. Pellissier et al., *ASM Trans.*, Vol 30, 1942, p 1049
 68. A.R. Marder and B.L. Bramfitt, *Metall. Trans. A*, Vol 6, 1975, p 2009–2014
 69. E.C. Bain, *Functions of the Alloying Elements in Steel*, American Society for Metals, 1939
 70. M. Grossmann and E. Bain, Principles of Heat Treatment, American Society for Metals, 1964
 71. M. Atkins, *Atlas of Continuous Transformation Diagrams for Engineering Steels*, British Steel Corporation, Sheffield, 1977; U.S. edition, American Society for Metals, 1980
 72. K.-E. Thelning, *Steel and Its Heat Treatment*, 2nd ed., Butterworths, 1984
 73. *Heat Treating of Irons and Steels*, Vol 4B, *ASM Handbook*, ASM International, to be published in 2004
 74. A. Rose and H.P. Hougardy, Transformation Characteristics and Hardenability of

- Carburizing Steels, *Transformation and Hardenability in Steels*, Climax Molybdenum, 1967
75. R. Chatterjee-Fischer, Beispiele für durch Wärmebehandlung bedingte Eigenspannungen und ihre Auswirkungen, *Härt.-Tech. Mitt.*, Vol 28, 1973, p 276–288
76. A.M. Habraken, M. Bourdouxhe, S. Denis, and A. Simon, Generating of Internal and Residual Stresses in Steel Workpieces during Cooling, *International Conference on Residual Stress, ICRS2*, Elsevier Applied Science, 1989
77. S. Denis, E. Gautier, A. Simon, and G. Beck, Stress-Phase Transformation Interactions—Basic Principles, Modelling and Calculation of Internal Stresses, *Mater. Sci. Technol.*, Vol 1, 1985, p 805–814
78. S. Denis, E. Gautier, S. Sjöström, and A. Simon, Influence of Stresses on the Kinetics of Pearlitic Transformation during Continuous Cooling, *Acta Metall.*, Vol 35, 1987, p 1621–1632
79. E. Gautier, A. Simon, and G. Beck, Plasticité de Transformation durant la Perlitique d'un Acier Eutectoïde, *Acta Metall.*, Vol 35, 1987, p 1367–1 375
80. S. Denis, "Influence du Comportement Plastique d'un Acier Pendant la Transformation Martensitique sur la Genèse des Contraintes au Cours de la Trempe," Thesis, Inst. Nat. Polytechnique de Lorraine, Nancy, 1980
81. H.J. Yu, U. Wolfstieg, and E. Macherauch, Zum durch Messereinfluss auf die Eigenspannungen in öl- und Wasserabgeschreckten Stahlzylindern, *Arch. Eisenhüttenwes.*, Vol 51, 1980, p 195

Hardness and Hardenability of Steels*

Introduction

Hardenability refers to the ability of steel to obtain satisfactory hardening to some desired depth when cooled under prescribed conditions. Hardening is achieved by transformation of austenite to martensite, and the extent of martensite formation depends on the necessary cooling rate to rapidly cool austenitized steel below the martensite-start temperature without significant transformation of austenite into pearlite or other transformation products (see the preceding article, "Introduction to Steel Heat Treatment," in this Volume). Thus, steels that exhibit deep hardening (martensite formation) are considered to have high hardenability, while those that exhibit shallow martensitic hardening are of low hardenability.

Hardenability, as an empirical measure of hardening ability, should not be confused with hardness or with maximum hardness of martensite after quenching. Hardness depends on carbon level and the extent of martensite formation, as illustrated in Fig. 1 and Table 1 for different levels of carbon in steels with varying amount of martensite. At a given carbon level, the maximum attainable hardness is with 100% martensite, which may only be possible at the surface or within the section of a small steel specimen. Cooling rates within larger sections may not be rapid enough to result in 100% martensite formation, thus reducing the depth of martensite formation and hardening in the part.

Unlike the effect of carbon on the hardness of martensite, other alloying elements do not increase the hardness of as-quenched steel (Fig. 2). The hardness of martensite depends only on carbon content. Nonetheless, other alloying elements of steel can increase the hardenability of steel. Alloying can slow carbon diffusion (needed for pearlite formation), thus increasing hardenability by promoting martensite formation at slower cooling rates (and thus greater hardening depths). For example, rapidly cooling a steel with 1% C after austenitizing will cause it to develop much higher hardness than a 3% Ni steel containing only 0.3% C, but the nickel steel will have greater hardenability because it will harden fully through a larger section.

Figures 3 and 4 are examples. Figure 3 is a qualitative example where steel A is of lower carbon content but higher alloy content than steel B. Suppose that several different-sized bars of each of these steels are quenched under identical conditions, transversely sectioned, and tested for hardness from the surface to the axis. If the hardness of each bar is then plotted in the form of a curve of hardness values versus distance from the axis, two sets of hardness-transverse curves are obtained, such as those shown in Fig. 3. It is noted that the 0.5 and 1 in. diameter bars of steel A have hardened completely, whereas the 2 in. diameter bar has only partially hardened, and the 3 in. diameter bar has not hardened to any extent. On the other hand, the 0.5 in. diameter bar of steel B has hardened fully, but the 1 in. diameter bar has only partially hardened, and neither the 2 nor 3 in. diameter bars have hardened appreciably. Thus, the rate at which a 1 in. diameter bar cools in the particular quenching medium adopted has been sufficient to fully harden steel A but not steel B. The higher-alloy steel A, despite its lower maximum hardness, is therefore said to have greater hardenability than steel B, because under similar quenching conditions, it will harden in greater diameters, although steel B is capable of developing the greater maximum hardness.

Figure 4 (Ref 4) is a quantitative example of carbon steel (1045) and chromium-vanadium alloy steel (6140) hardened sections after water quenching (Fig. 4a, b) and oil quenching (Fig. 4c, d). Both are of similar carbon content, but the alloy steel is through hardened with both water and oil quenching a section with diameter of 13 mm ($\frac{1}{2}$ in.). In contrast, the carbon steel is only fully hardened at the surface of the 25 and the 13 mm (the 1 and the $\frac{1}{2}$ in.) sections after water quenching. The interior of the carbon steel is not fully hardened even with the rapid cooling of a water quench. In this way, hardenability is a key characteristic steel response to heat treatment.

The hardenability of steel is governed almost entirely by the chemical composition (carbon and alloy content) at the austenitizing temperature and the austenite grain size at the moment of quenching. In addition to composition, the

hardening response of steel also can depend on other variables, such as austenitizing temperature, time at temperature, and prior microstructure. This article introduces the methods to evaluate hardenability and the factors that influence steel hardenability and selection. Hardenability of steel is also the subject of many publications, with some examples being Ref 5 through 9 as well as more recent reviews in Ref 10 and 11.

Jominy End-Quench Testing

The hardenability of a steel is governed by the cooling rates at which austenite decomposes to ferrite, pearlite, bainite, and martensite during quenching. Consequently, hardenability is best assessed by determining the hardening response in a way that determines hardness for a variety of cooling rates in a reproducible fashion. Several test methods have been used, but the Jominy end-quench test is a relatively simple test that has been almost universally adopted in evaluating hardenability (see the section "Other Hardenability Tests" in this article for other methods).

The Jominy-end quench test, first developed by Jominy and Boegehold for carburized steels (Ref 12), was soon applied by Jominy to evaluate the hardenability of medium-carbon steels (Ref 13). The method has since been standardized in ISO 642, ASTM A255, and SAE J406. Although variations are sometimes made to accommodate specific requirements, the test bars for the end-quench test are normally 25 mm (1 in.) in diameter by 100 mm (4 in.) long with a collar on one end to hold it in a quenching jig (Fig. 5a). The test involves heating the test specimen to the proper austenitizing temperature and then transferring it to the quenching fixture, so designed that the specimen is held vertically 13 mm (0.5 in.) above an opening through which a column of water can be directed against the bottom face of the specimen (Fig. 5a). While the bottom end is being quenched by the column of water, the opposite end is cooling slowly in air, and intermediate positions along the specimen are cooling at intermediate rates. After the specimen has been quenched, parallel flats 180° apart

* H. Burrier, Hardenability of Carbon and Low-Alloy Steels, *Properties and Selection: Irons, Steels, and High-Performance Alloys*, Vol 1, ASM Handbook, ASM International, 1990, p 464-484

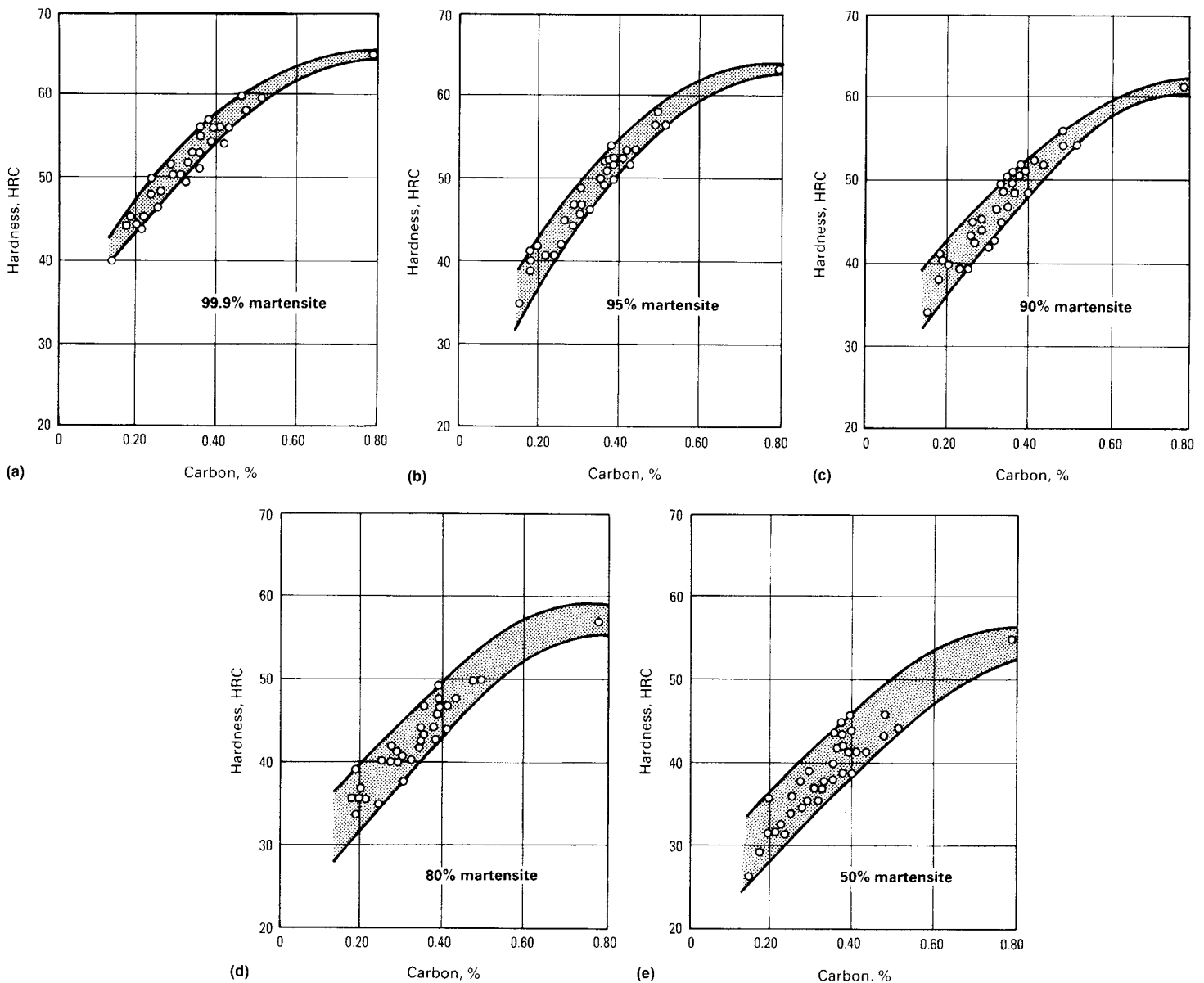


Fig. 1 Effect of carbon on the hardness of martensite structures

are ground 0.38 mm (0.015 in.) deep on the cylindrical surface. Hardness (typically Rockwell C) is measured at intervals of 1.6 mm ($1/16$ in.) for alloy steels and 0.8 mm ($1/32$ in.) for carbon steels, starting from the water-quenched end.

A typical plot of these hardness values and their positions on the test bar is shown in Fig. 5(b). In effect, this plots the depth of hardening (or hardenability) of the steel in a consistent way. The figure also identifies approximate cooling rates for the designated test positions on the Jominy bar. The positions correlate directly with surface cooling rates at each position, because the cooling rate is essentially independent of steel composition. Thus, the Jominy positions can provide a useful cor-

relation between hardness and cooling rate with some provisos.

The approximate cooling rates in a Jominy specimen are given in Table 2 as a function of distance from the quenched end. However, cooling rates, as a function of distance from the quenched end, are approximate and vary with the conductivity and transformation products of the particular alloy being quenched (Fig. 6). Cooling rates at 705 °C (1300 °F) cannot reliably be used to predict hardness in carbon and low-alloy steels because the critical temperature range moves to higher or lower temperatures as the concentration of alloy elements changes between the different grades (Ref 15). Correlation of end-quench specimen positions with cooling rates is discussed in

more detail in the section "Hardenability Correlation Curves" in this article.

Relative hardenability of steels can be easily discerned by comparing the curves resulting from end-quench tests (Fig. 7). Steels with higher hardenability will be harder at a given distance from the quenched end of the specimen than steels with lower hardenability. Thus, the flatter the curve is, the greater the hardenability will be. On the end-quench curves, hardness usually is not measured beyond approximately 50 mm (2 in.), because hardness measurements beyond this distance are seldom of any significance. At approximately 50 mm (2 in.) from the quenched end, the effect of water on the quenched end has deteriorated, and the effect of cooling from the surrounding

Table 1 Effect of carbon concentration and martensite content on the as-quenched hardness of steel

Carbon, %	Hardness, HRC, with extent of martensite (M) content				
	99% M	95% M	90% M	80% M	50% M
0.10	38.5	32.9	30.7	27.8	26.2
0.12	39.5	34.5	32.3	29.3	27.3
0.14	40.6	36.1	33.9	30.8	28.4
0.16	41.8	37.6	35.3	32.3	29.5
0.18	42.9	39.1	36.8	33.7	30.7
0.20	44.2	40.5	38.2	35.0	31.8
0.22	45.4	41.9	39.6	36.3	33.0
0.23	46	42	40.5	37.5	34
0.24	46.6	43.2	40.9	37.6	34.2
0.26	47.9	44.5	42.2	38.8	35.3
0.28	49.1	45.8	43.4	40.0	36.4
0.30	50.3	47.0	44.6	41.2	37.5
0.32	51.5	48.2	45.8	42.3	38.5
0.33	52	48.5	46.5	43	39
0.34	52.7	49.3	46.9	43.4	39.5
0.36	53.9	50.4	47.9	44.4	40.5
0.38	55.0	51.4	49.0	45.4	41.5
0.40	56.1	52.4	50.0	46.4	42.4
0.42	57.1	53.4	50.9	47.3	43.4
0.43	57.2	53.5	51	48	44
0.44	58.1	54.3	51.8	48.2	44.3
0.46	59.1	55.2	52.7	49.0	45.1
0.48	60.0	56.0	53.5	49.8	46.0
0.50	60.9	56.8	54.3	50.6	46.8
0.52	61.7	57.5	55.0	51.3	47.7
0.54	62.5	58.2	55.7	52.0	48.5
0.56	63.2	58.9	56.3	52.6	49.3
0.58	63.8	59.5	57.0	53.2	50.0
0.60	64.3	60.0	57.5	53.8	50.7

Source: Ref 1, 2

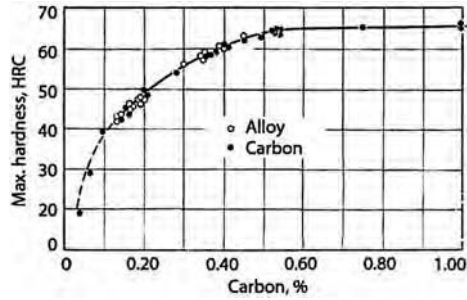


Fig. 2 Maximum hardness as a function of carbon for carbon and alloy steels. Source: Ref 3

air has become significant. An absolutely flat curve demonstrates conditions of very high hardenability, which characterize air-hardening steel, such as some highly alloyed steels.

The standard end-quench procedure employs $24 \pm 3 \text{ }^\circ\text{C}$ ($75 \pm 5 \text{ }^\circ\text{F}$) water. The effect of water temperature (Fig. 8) is slight up to approximately $40 \text{ }^\circ\text{C}$ ($100 \text{ }^\circ\text{F}$). Some investigators employ oils or polymers to perform the end quench and then compare the results obtained with the alternate quenchant with the results produced by water. The Jominy end-quench test is not a generally acceptable method for use with aqueous polymer quenchants, because the

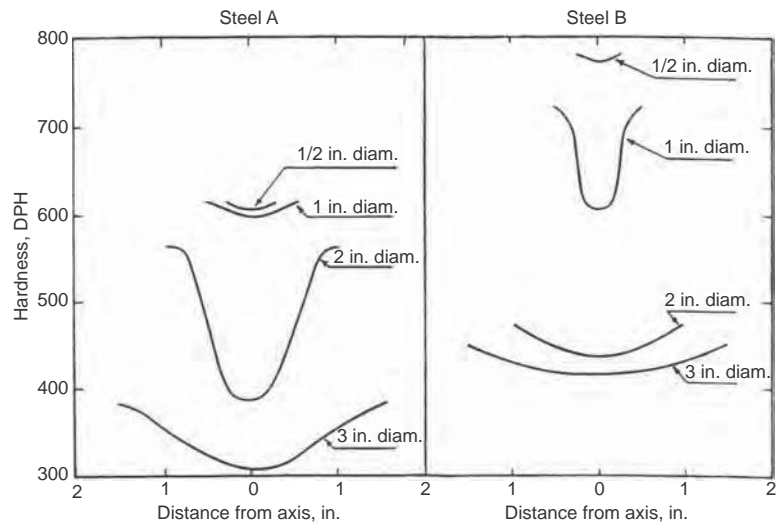


Fig. 3 Hardness traverse to illustrate difference between hardenability and maximum hardness. Steel A has greater hardenability than steel B, but the maximum hardness of steel B is higher than steel A

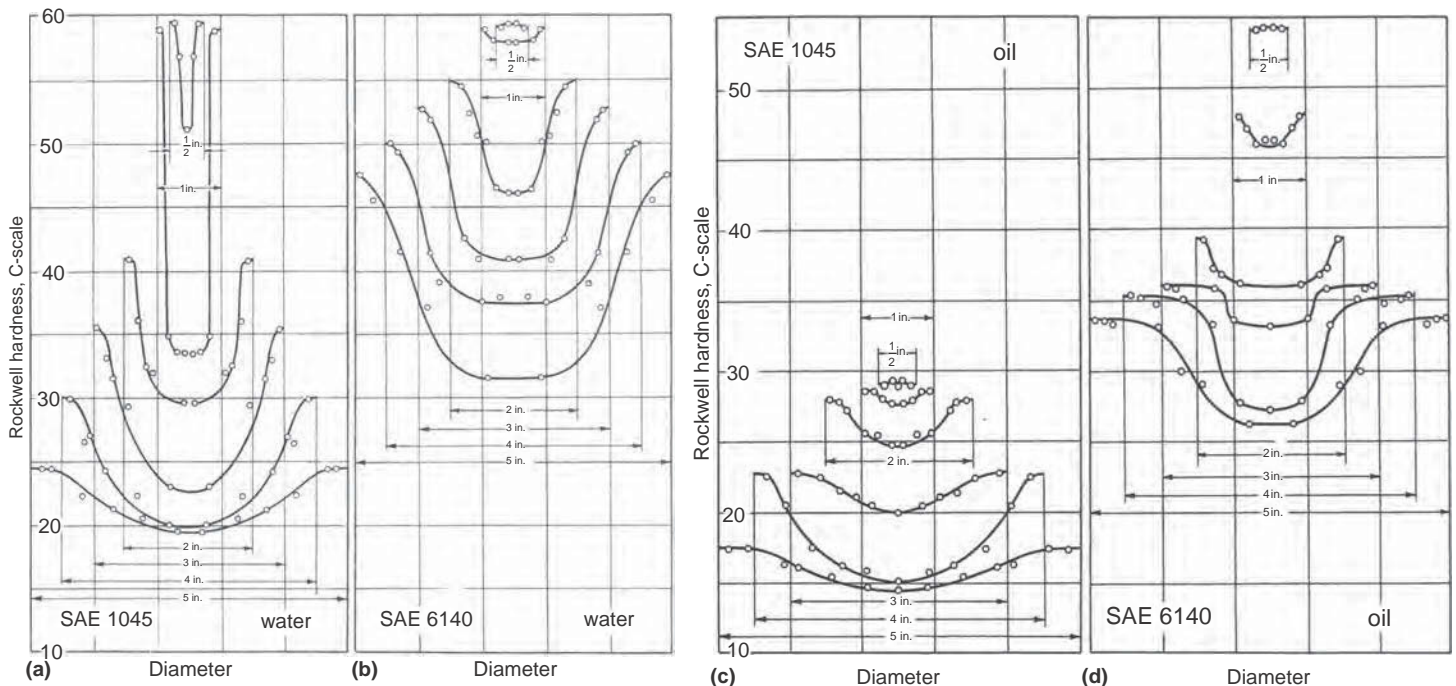


Fig. 4 Hardness distribution of carbon steel (1045) and alloy steels (6140) in various section sizes with water quench (a, b) and oil quench (c, d). Source: Ref 4

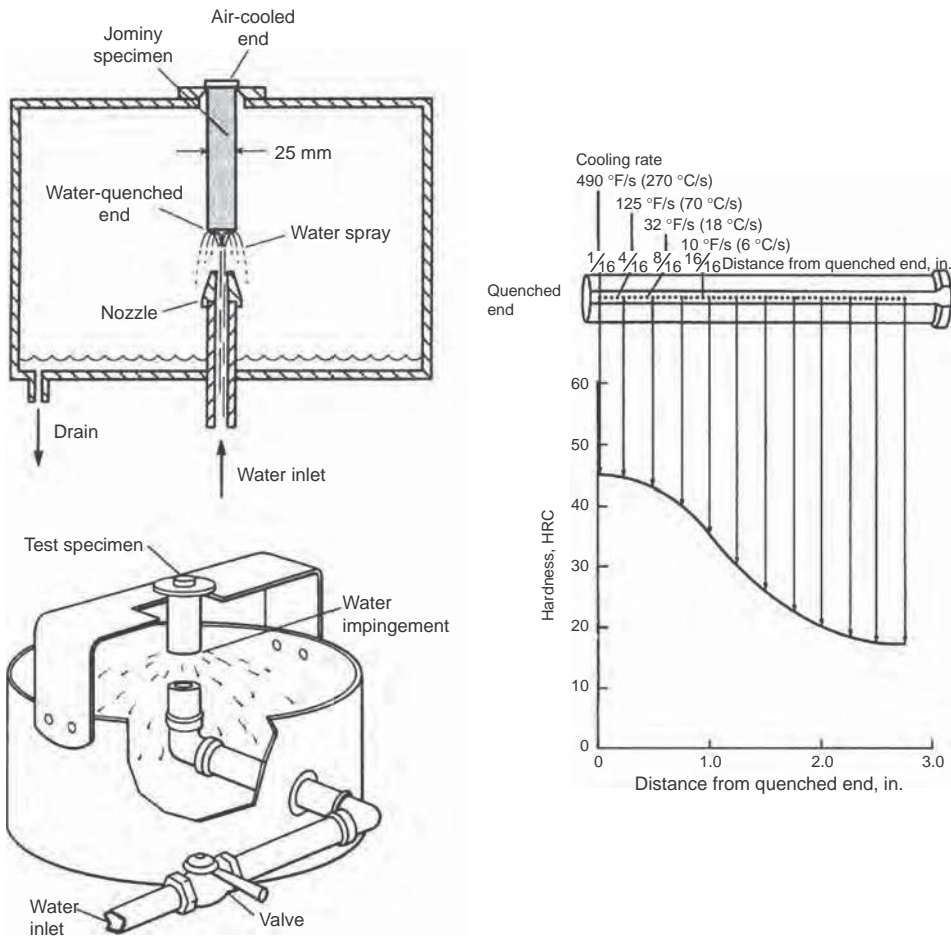


Fig. 5 Jominy end-quench hardenability test. (a) Standard end-quench test specimen and in a quenching jig. (b) Hardness plot and cooling rate as a function of distance from the quenched end

pressure of the flood quench at the end of the test specimen often disrupts film-forming properties of the polymer at the hot metal interface.

Given an alloy and its Jominy curve, there is no ambiguity concerning the end hardness value, which corresponds to fully hardened martensite of the given composition. The hardness for different martensite fractions depends on carbon content (Table 1), and data such as in Table 1 can be used to choose reference points during the formulation of specifications of hardenability for steels of different carbon contents. With such relations of hardness to martensite, several things can be discerned from the Jominy curve of a steel. Points on the Jominy curve also can be related to a continuous cooling diagram (Fig. 9).

The inflection point (Fig. 10) represents the region of a very abrupt change in the amount

Table 2 Typical cooling rates at 705 °C (1300 °F) in a Jominy specimen as a function of distance from the quenched end

Distance from water-quenched end, 1.6 mm (1/16 in.)	Cooling rate	
	°C/s	°F/s
1	270	490
2	170	305
3	110	195
4	70	125
5	43	77
6	31	56
7	23	42
8	18	33
9	14	26
10	11.9	21.4
12	9.1	16.3
14	6.9	12.4
16	5.6	10.0
18	4.6	8.3
20	3.9	7.0

Source: Ref 14

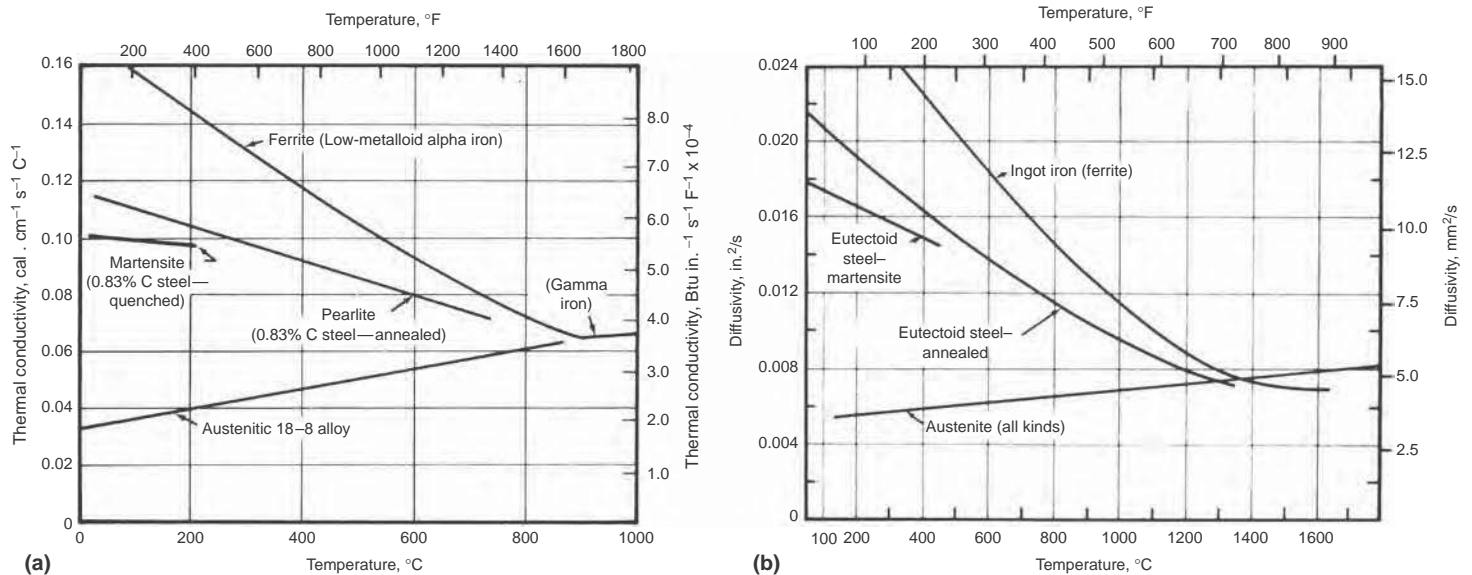


Fig. 6 Effect of temperature on (a) thermal conductivity and (b) phases in steel

of martensite in the as-quenched transformation product (Ref 16), and it represents the point of approximately 50% martensite. The steepness of a Jominy curve at the inflection point is also of interest, because it relates to the intensity of internal stresses and to distortion, together with the inflection point or mean depth of hardening. However, it should be appreciated that the actual observed or predicted values of the hardness value at the inflection point are of very little intrinsic interest to the quality-control officer or the heat treater. Rather, it is the upper or lower limits of surface (J1) and core (J32) hardness, the half-hardness location, and the slope of the hardness curve at this location that represent valuable information.

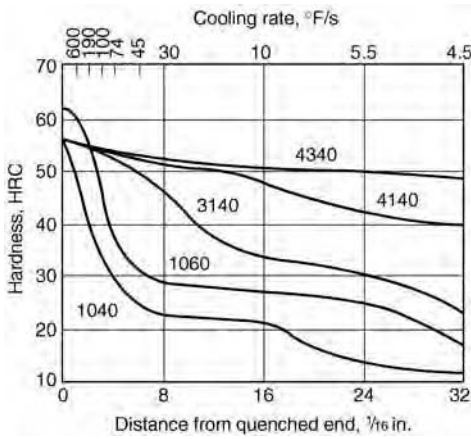


Fig. 7 Plot of end-quench test results for five different steels

The Jominy test is acceptably, if not ideally, reproducible (Ref 17) under controlled conditions, and because it is informative and relatively economical, it is not surprising that the Jominy test has become the standard of the industry. However, a main objectionable feature of the test lies in its impractical shape and quench configuration. Radially quenched bars are by far the most common configuration. Therefore, it is helpful if Jominy data can be related to variations in quench severity and

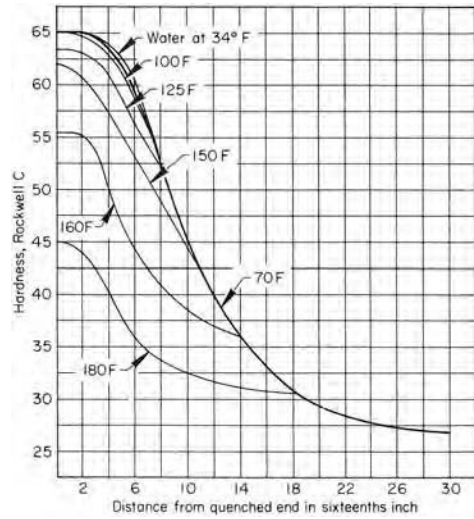


Fig. 8 Effects of quenchant temperature on cooling power in end-quench test. Effect is slight up to 38 °C (100 °F), impaired at 52 °C (125 °F), and greatly impaired above 71 °C (160 °F)

cooling rates within different bar sizes, shapes, and positions within a bar. This has been effectively done with the Lamont transformations (Ref 14). From heat-transfer models developed by T.F. Russell (Ref 18) and by Grossmann et al. (Ref 19), the Lamont transformations are an important tool in relating Jominy hardenability data to practical variations in quench severity and cooling rates within parts (see the section “Hardenability Correlation Curves” in this article). The method is based on the Grossmann method of characterizing steel hardenability in terms of an ideal critical diameter, as described in the next section.

Quench Severity in Hardenability Evaluation

Depth of hardening depends not only on the hardenability of the steels but also on the cooling capacity (or quench severity) of the quenchant

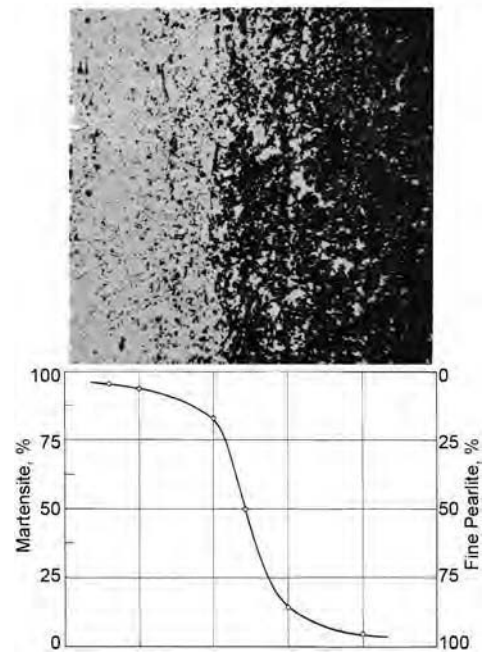
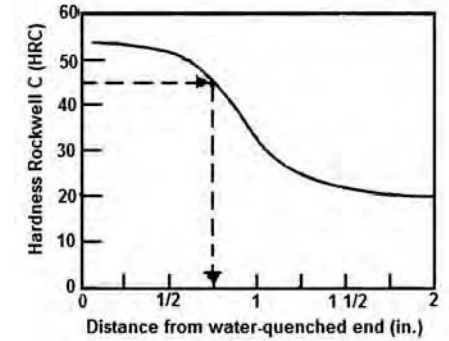


Fig. 10 Transition to 50% martensite occurs at approximately the inflection point on Jominy curve (a), because the transition from martensite to fine pearlite is abrupt (b)

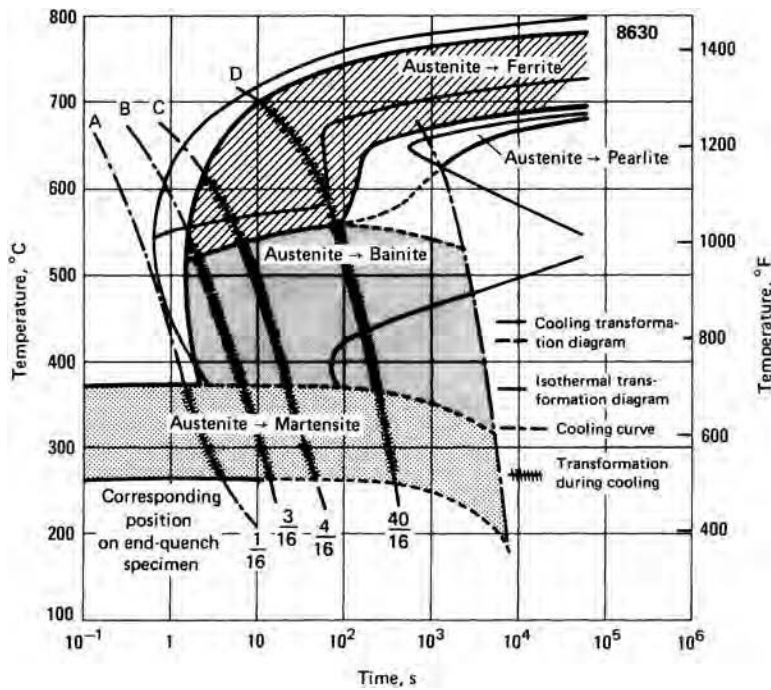


Fig. 9 Transformation diagrams and cooling curves for 8630 steel, indicating the transformation of austenite to other constituents as a function of cooling rate

and the size and shape of the parts being quenched. Therefore, methods have been developed to relate hardenability in terms of quench severity and cooling rates within parts.

Quench severity is defined as the ability of a quenching medium to extract heat from a hot steel workpiece. Heat removal from the workpieces during quenching can be quantitatively described by Newton's law of cooling in terms of the interfacial heat-transfer coefficient (h), such that:

$$h = \frac{Q}{A(T_s - T_1)} \quad (\text{Eq 1})$$

where Q is the heat flow from the workpiece to the quenchant, A is the surface area of the part, T_s is the surface temperature of the steel, and T_1 is the quenchant temperature. The interfacial heat-transfer coefficient (h) is also known as the film coefficient. The rate of heat transfer at the surface is thus:

$$\left(\frac{dQ}{dt}\right)_s = h(T_s - T_1)$$

such that T_s is time dependent. The greatest conceivable quench severity would be when the surface is cooled instantaneously to that of the quenchant. A less severe quench leads to less rapid temperature reduction. Within the steel part itself, the flux of heat is related to temperature gradient, such that:

$$\frac{dQ}{dt} = k\left(\frac{dT}{dx}\right)$$

where k is the thermal conductivity of steel. At the surface, the temperature gradient is:

$$\left(\frac{dQ}{dt}\right)_s = k\left(\frac{dT}{dx}\right)_s$$

So that at the surface, then:

$$\left(\frac{dT}{dx}\right)_s = \frac{h}{k}(T_s - T_1)$$

To obtain the temperature distribution and gradients with a steel part over time requires the use of Fourier's second law of heat conduction, which, in simplified form for one dimension, is:

$$\frac{dT}{dt} = \alpha\left(\frac{d^2T}{dx^2}\right)$$

where α is the thermal diffusivity of steel, which is related to steel density (ρ), specific heat (C_p), and thermal conductivity as: $k = \alpha \rho C_p$. Solution of the differential equations for Fourier's second law under appropriate boundary conditions (e.g., surface temperature, part shape, part size) requires numerical integration of the differential equations for heat transfer. This was done by Russell (Ref 18), so that is possible to estimate the time required for any position in a round bar, square, flat, or plate to be cooled to a given temperature during quenching. Russell assumed a constant value for the thermal diffusivity of steel ($\alpha = 0.009 \text{ in.}^2/\text{s}$).

Grossmann Number. Although it is possible to determine quench severity from the cooling rate, Grossmann et al. (Ref 19) developed a method that is based on the measurement for the depth of hardening of round bars of different diameters. In this method, the depth of hardening is measured as a ratio of unhardened diameters (D_U) to the total diameter (D) of a bar. The diameter of the unhardened core (D_U), defined as the diameter with a microstructure of 50% martensite, is measured in terms of microstructure or, more conveniently, as

hardness. If the carbon content is known, then the depth of 50% martensite can be determined from hardness measurements and a chart such as that in Fig. 11. With 50% martensite, hardness of the other 50% is influenced by hardness effects of other alloying.

The unhardened core diameters (D_U) are plotted versus bar diameters (D) for different quenching conditions (Fig. 12). As expected, the unhardened diameter becomes greater when quenching larger-diameter bars. For each of the two different quench conditions in Fig. 12, there is a critical diameter (D_0) when $D_U = 0$. Moreover, Grossmann et al. also showed that two steels, A and B, with high and low hardenability, respectively, could have the same critical size, D_0 ($D_U = 0$) as differently quenched (A in oil, B in water), but that their respective depths of hardening at all other equal sizes for comparison would be different; that is, their D_U versus D or characteristic curves would always differ. Also, the authors found that the form of these characteristic curves was identical for a series of specimens and quenches under one set of circumstances, covering the range from high-velocity quenching of small sizes of low-hardenability steels to mild quenching of large specimens of deep-hardening steels. The identity in form existed when the product of the heat-transfer factor, H , and the critical diameter, D , was a constant. So long as HD is constant, all D_U/D curves are the same if the scale of plotting is correctly chosen. Thus, one characteristic curve represents an entire family when HD_U is plotted against HD instead of D_U versus D . Then, all steels and all quenches may be covered in a family of HD_U versus HD curves (detailed characteristic curves), as in Fig. 13. Constant values of D_U/D are shown as dashed lines appropriately marked.

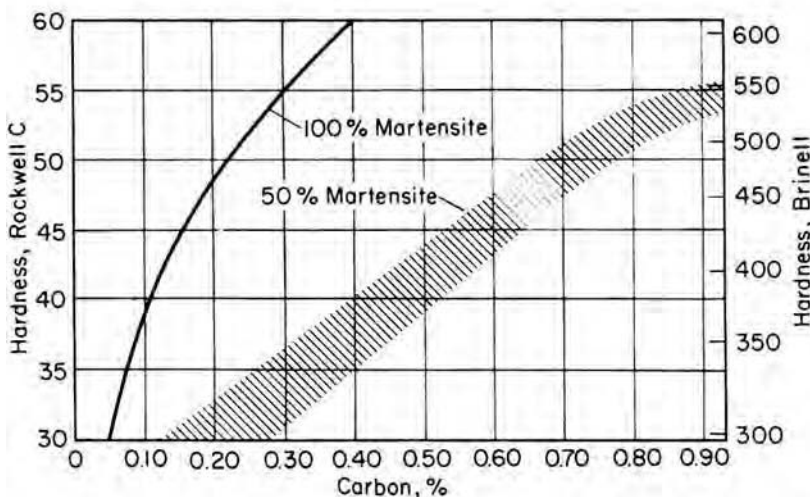


Fig. 11 Hardness values for 50% martensite and 100% martensite conditions in quenched carbon steels as a function of carbon. With 50% martensite, the hardness depends on the structure of the other 50% and residual or alloying. Steel with more alloying would be at the top of the band. Source: Ref 20

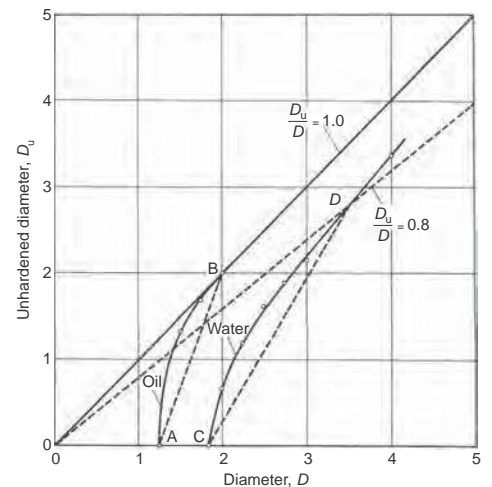


Fig. 12 Plot of unhardened core diameter (<50% martensite) as a function of bar diameter with water and oil quench. Source: Ref 19

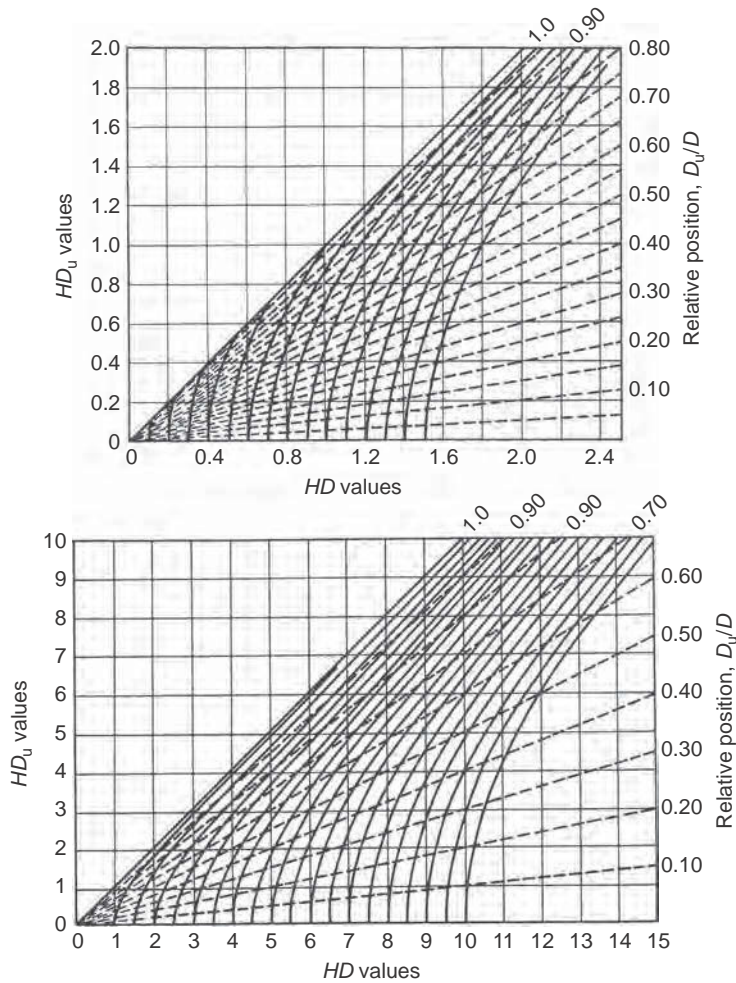


Fig. 13 Characteristic curves of HD_u and HD for two ranges of HD values. Source: Ref 19

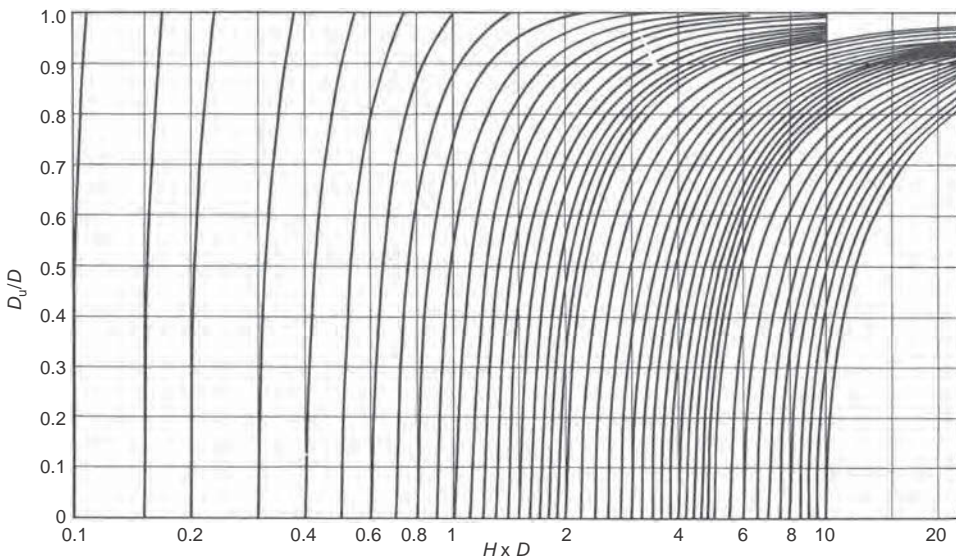


Fig. 14 Chart for determining HD and hence H versus the ratio of unhardened diameters (D_u) and bar diameter (D). Source: Ref 19

Thus, with a characteristic curve such as those if Fig. 12, it is only necessary to match its form to one of the curves of Fig. 13 to find the HD_0 and hence the H -value. Two short methods are introduced for this purpose involving the inclination of certain D_u/D value so that finally the knowledge of the depth of hardening in two suitable sizes serves to identify in a unique manner both the hardenability of the steel (D_u/D) and the severity of quench (heat-transfer factor, H). This can be accomplished by a second shortcut, the logarithmic chart in Fig. 14.

In heat-transfer terms, the Grossmann number (H) is:

$$H = h/2k$$

where k is the thermal conductivity, and h is the interfacial heat-transfer coefficient, or the film coefficient (Eq 1). Many variables influence quench severity and Grossmann H -values. Nonetheless, the charts and methods of Grossmann and his co-workers have important practical value, even though the method assumes that the H -value is constant during the quench. The calculation and methods are not rigorous with respect to different steels in different sizes (see, for example, the section "Carney Empirical Correlations" in this article). However, the method clearly accounts for the general phenomenon that as the size of the quenched bar is increased, the proportion of unhardened core increases more rapidly with a mild quench than when the quench is more severe. It also clarifies other circumstances, such as the persistence of a shallow-hardened zone in exceedingly large rounds, even of moderately low hardenability, when the quench is very severe, and the little change of its thickness ($D - D_u$) with change in diameter. Similarly, the abrupt disappearance of a hardened rim in specimens of fairly small size in steels quenched in mild media is clarified. In turn, these data show how soft spots are almost inevitable under certain conditions. Surface conditions of the steel that influence heat abstraction (scale thickness and texture), as well as thermal diffusivities, are comprehended in the H -factor. Further, the influence of agitation in removing vapor films, which retard quenching, is also reflected in the numerical value of H .

It is also useful to note that the product $H \times D$ corresponds to the Biot number (Ref 21), which is a well-known dimensionless factor in heat transfer. The Biot number compares the relative magnitudes of surface heat transfer and internal conduction resistance to heat transfer. A very low value of the Biot number means that internal-conduction resistance is negligible compared with surface heat-transfer resistance. This in turn implies that the temperature will be nearly uniform throughout the workpiece. Therefore, the magnitude of the Biot number shows the nonuniformity of temperature distribution throughout the body of the workpiece during quenching.

The Grossmann numbers cover a range for different quench conditions:

Mode of quench	H-value
Cooling in still air	0.02
Moderate motion in oil	0.4-0.5
No motion in water	1.0
High-velocity oil	1.5
Moderate motion in warm brine	2.0
Moderate motion in water	3.0-4.0
High-velocity water	5.0 and up

These values can provide some practical guidance, even though the quench velocities are not well defined. From Fig. 15, it is noted that there is very little practical difference between $H = 5$ and an ideal quench ($H = \infty$).

Ideal Critical Diameter

The Grossman H -factor provides a method to quantify steel hardenability independently of quench conditions. This is done by mathematically

relating the critical diameter (D_0) to a theoretically ideal quench, when the surface of the test bar is immediately cooled to ambient temperature.

The Grossmann ideal critical diameter is the diameter of a bar that can be quenched to 50% martensite in the center when the surface is cooled at an ideal (infinite) rate. Although ideal cooling cannot be carried out in practice, one can mathematically extrapolate the situation for an ideal quench ($H = \infty$), when the quench is able to reduce the temperature of the steel to the bath temperature in zero time and hold it at this temperature during cooling of the interior. In effect, ideal cooling is when the quench is sufficiently severe that the heat-removal rate is controlled by the thermal diffusivity of the metal and not by the surface heat-transfer rate.

Ideal critical diameters can provide a quantitative measure of steel hardenability. Charts by Grossmann and his co-workers also provide a way of relating ideal diameters and critical diameters under various levels of quench severities (Fig. 15). As an example, consider the two curves in Fig. 16 with hardness of

approximately 53 HRC at the 50% martensite zone. In the Grossmann methods, first determine HD and H from Fig. 14, and then read D_1 from Fig. 15. The H -value is approximately 2.3, and the critical diameter for this quench is 0.86 in., with a D_1 of approximately 1.22 in.

The method has practical significance, because both D_1 values and H -values essentially represent cooling rates that can be correlated with positions on Jominy end-quench specimens (Fig. 17). The Grossman H -number is a measure of heat-extraction capability at the surface and thus can be correlated with positions along an as-quenched Jominy bar. The ideal critical diameter also is a measure of the required cooling rate at the center of a bar to achieve 50% martensite transformation with ideal cooling ($H = \infty$) at the surface. Thus, D_1 values also correlate with Jominy distances (J_d) (Fig. 17c). The original correlation by Grossmann and his co-workers was refined by Carney, as indicated.

Hardenability Correlation Curves

The ability to correlate distance from the quenched end in a Jominy bar with a unique cooling rate extends the versatility of both Jominy and Grossmann measures of hardenability. Thus, for example, the Jominy distance should be capable of being related to the D_1 because both are measures of the cooling rate to produce a specific structure (50% martensite). Knowing J_d for a steel and the H -value of the quenching medium, one can predict the depth of hardening in any sized bar. Measuring cooling rates is obviously impractical or, in many cases, impossible, and so the unique correlation of Jominy distance with cooling rates provides a method of relating Jominy hardness values to equivalent cooling rates and depth of hardening within various section sizes and shapes.

The basic assumption is that equivalent cooling rates at two positions in a steel bar will exhibit the same hardness. For example, Fig. 18 illustrates the inflection point (which often corresponds to 50% martensite) on the Jominy curve

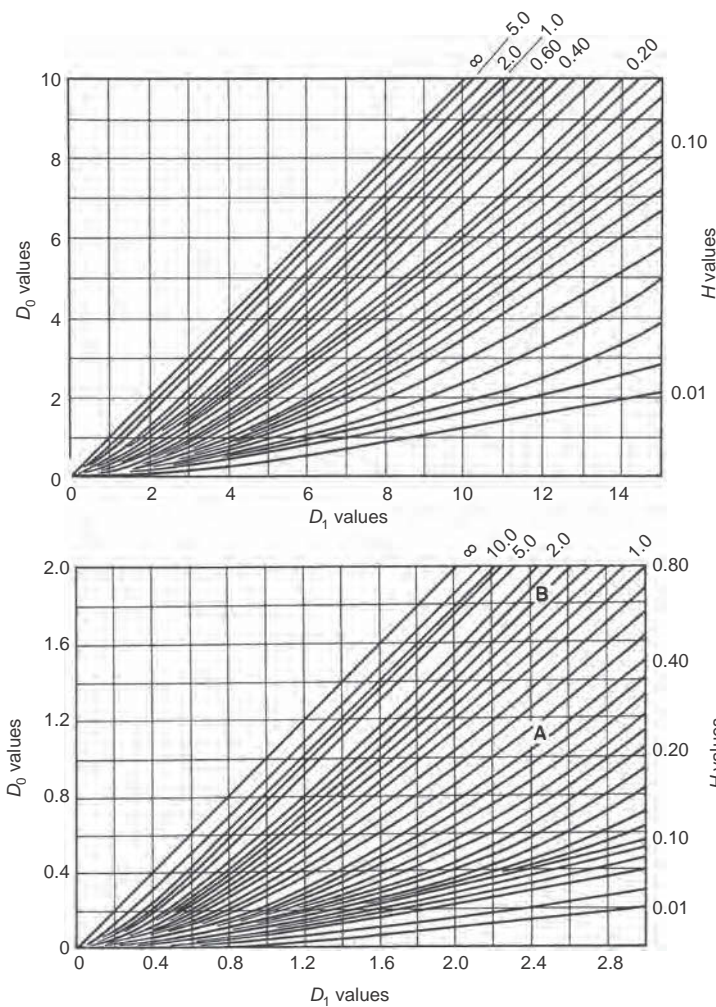


Fig. 15 Relationship between ideal critical diameters (D_1) and critical diameters (D_0) with different quench severities (H -values)

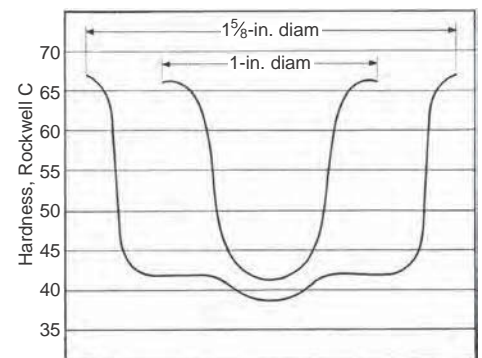


Fig. 16 Example hardness distribution in eutectoid steel with average hardenability using a warm brine quench. Source: Ref 20

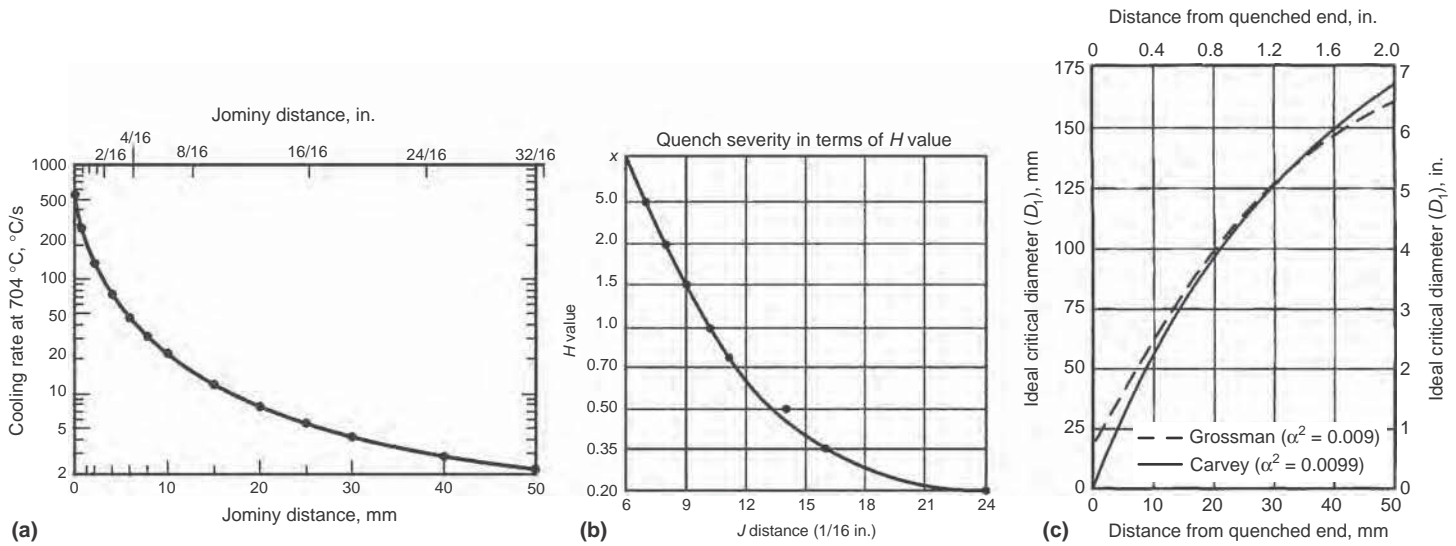


Fig. 17 Equivalent expression of cooling rate as a function of Jominy end-quench positions. Source: Ref 14, 22, 23

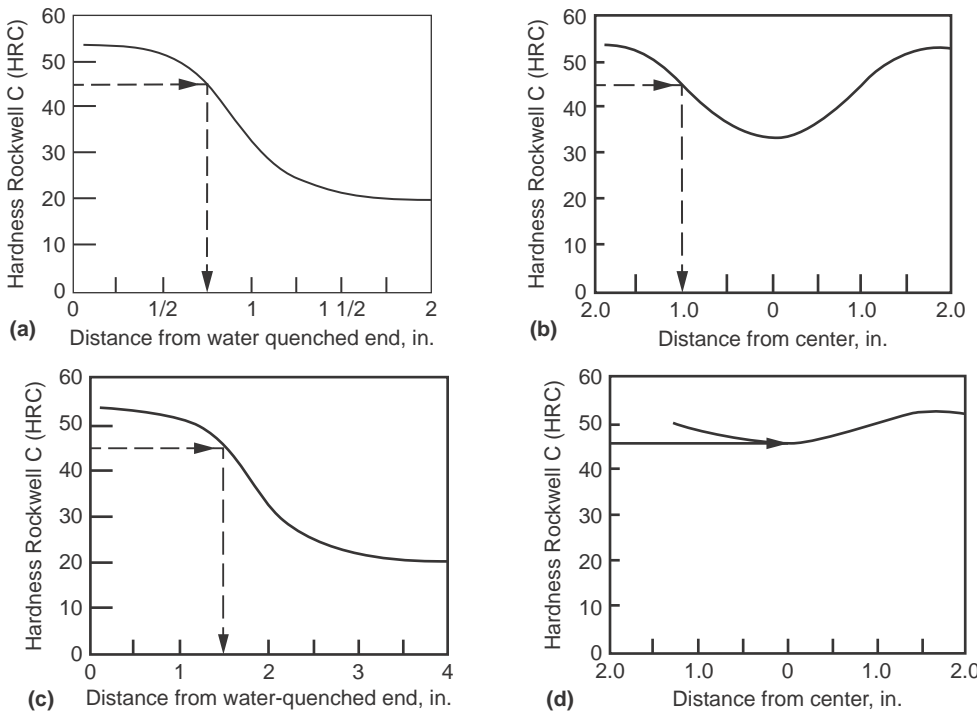


Fig. 18 Jominy hardenability curves of two steels with different hardenabilities and cross-sectional hardness curve for a 100 mm (4 in.) diameter quenched round bar of the same steel

for two steels with different hardenability. The Jominy curve of the steel with lower hardenability (top) has an inflection point at 45 HRC. The cooling rate at this point corresponds to a cooling rate hardening to the half-radius position ($D_U/D = 0.5$) in a 100 mm (4 in.) diameter bar (Fig. 18b). The steel with higher hardenability (bottom) also has an inflection point of 45 HRC, but the Jominy distance (J_d) of the inflection point is greater (at the 24/16 in. position). This corresponds to lower cooling rate for hardening,

and through hardening can be achieved in a 100 mm (4 in.) diameter bar with a quench severity (H -value) shown in Fig. 18(d).

This process can be extended to develop the Jominy equivalent cooling (J_{ec}) rate chart in Fig. 19. The practical use of this chart is to correlate hardness values on an end-quench bar to equivalent positions within round bars of various sizes with different quench severities (H -values). For example, the hardening of the two different steels in Fig. 18 can illustrate the use of the chart

in Fig. 19. First consider the steel in Fig. 18(a), which needs to be hardened to a half-radius depth within a 100 mm (4 in.) diameter bar (Fig. 18b). The required quench severity to achieve this depth of hardening can be determined from Fig. 19 in conjunction with the Jominy curve of the steel (Fig. 18a). The inflection on the Jominy curve is at the Jominy distance of 12/16 in. Then, reading up from the 12/16 position on the bottom graph in Fig. 19 (for bars with 4 in. diameters), the required quench severity is approximately $H = 1.5$ for hardening this steel to a half-radius depth.

Through hardening (50% martensite at the center) of a 100 mm (4 in.) diameter bar is not possible with the hardenability of the steel in Fig. 18(a). Repeating the previous process in Fig. 19 for full hardening, the required quench severity would have to exceed that of ideal cooling ($H = \infty$) at the surface. However, the higher-hardenability steel (Fig. 18c) can be hardened at the center of a 100 mm (4 in.) bar (Fig. 18d) with quench severity just a little under $H = 0.5$. The inflection point of the higher-hardenability steel is at a Jominy bar position of 1.75 in., which (using the bottom graph in Fig. 19) is equivalent to hardening the center of a 100 mm (4 in.) diameter bar with cooling intensity of just under $H = 0.5$.

Figures 19 and 20, for larger bar sections, provide a practical way of relating end-quench to equivalent hardness within different-sized bars and quench severities. Thus, with an end quench for a given steel, the distribution of hardness throughout the cross section can be estimated for all of the given section sizes and severities. The charts are especially useful for estimating through-section strength, because the entire hardness profile of the prospective steel (and, to a degree, microstructure as well) can be predicted for rounds with different diameters from one set of end-quench data. Instructions for the procedure are given in the caption.

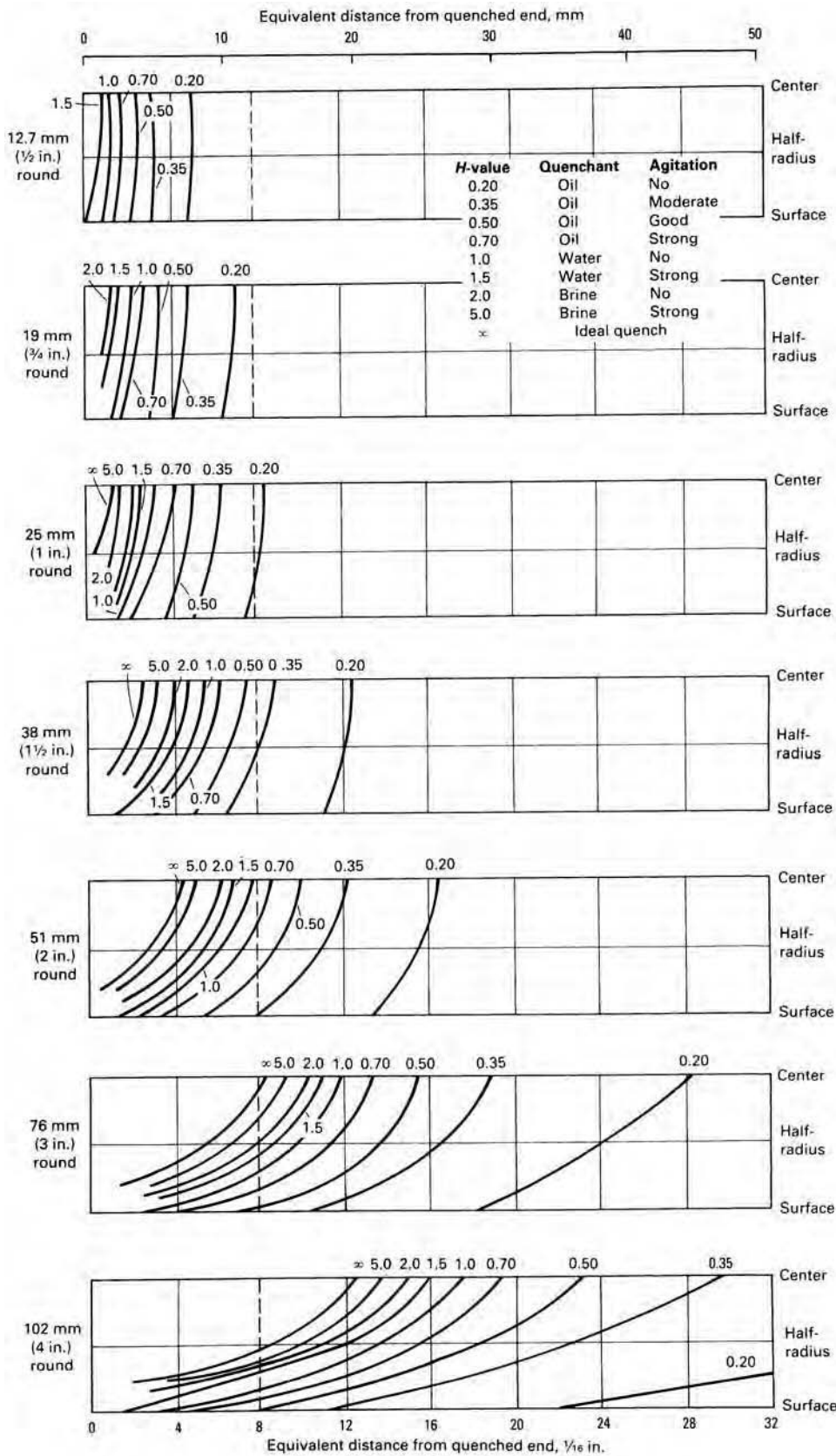


Fig. 19 Correlation of Jominy equivalent hardness positions in end-quenched hardenability specimen for equivalent cooling rates within various locations in round bars quenched in oil, water, and brine. The dashed line shows the various positions in 12.7 to 102 mm (1/2 to 4 in.) diameter rounds that are equivalent to the J8 (8/16 in.) position on the end-quench bar. To determine cross-sectional hardnesses from results of end-quench tests, pick out the end-quench hardness at an appropriate point on the bottom line and extend an imaginary line upward to the curved line that corresponds to the quenching severity needed to obtain that hardness for the given diameter of round. See text for examples.

With the Grossmann charts (Fig. 15, 17c) as a basis, Lamont (Ref 14) used the basic principle of equivalent cooling as a function of Jominy position (Table 2) to develop plots for the fractional depth of hardening of sections with different H -values. Figure 21 is an example for through hardening and hardening to a half-radius depth for bars of different diameters. Similar charts were done by Lamont for other hardening depths, as shown in Fig. 22 and 23 for round bars. Similar charts are described in more detail in the section "Jominy Equivalence Charts" in this article. It should be noted that the Lamont diagrams were based on the Grossmann plot of J_d versus D_1 (Fig. 17c), which was subsequently refined by Carney.

Carney Empirical Correlations (Ref 23). D.J. Carney developed an improved curve for correlating ideal critical diameter with Jominy end-quench position (Fig. 17c). The Carney corrections account for the variation of H with different sizes and positions. From an analysis of cooling rates and hardening characteristics of round bars and end-quench specimens, more reliable correlation curves based on 50, 80, and 95% martensite positions (instead of cooling rates) were obtained for rounds and end-quench specimens using moderate-to-good quenches in oil and water. For example, Fig. 24 summarizes the changes in H -value for positions with more than 50% martensite.

Correlation curves of equal cooling times in end-quench bars and in rounds are shown in Fig. 25 for water- and oil-quenched specimens. These curves do not agree with the calculated curves of Lamont. Hardenability correlation curves of Lamont are based on an assumption of constant H by Grossmann and his co-workers. The data from the Carney empirical correlations are summarized in Table 3 and Fig. 26 and 27. For the steels investigated, equivalent positions with more than 50% martensite cooled at approximately the same rates. For positions of greater than 50% martensite, a thermal diffusivity value of $6.4 \text{ mm}^2/\text{s}$ ($9.9 \times 10^{-3} \text{ in.}^2/\text{s}$) proved to be satisfactory. For positions of less than 50% martensite, the cooling rates were affected by the variable diffusivity of pearlite, ferrite, bainite, and martensite.

It is common practice to use published average H -values for a given quenchant and method of quenching, such as severe, good, poor, or still, rather than to actually measure the H -value. By doing this and ignoring the variation of H with size and position for a given quenching procedure, it is probable that the predicted depth of hardening will be less than that actually obtained in the smaller-sized rounds and will be much greater than that actually obtained in the larger-sized rounds. When this has happened, it has meant that some heat treaters using a given quenchant could have used a leaner alloy steel for the smaller sections and should have used a deeper-hardening alloy for the larger sections.

Other Hardenability Tests

The Jominy test has become the standard of the industry, because it is informative,

relatively economical, and has good reproducibility (Fig. 28). The Jominy test is considered to provide valid data on steels having an ideal critical diameter (D_1) in the range of from approximately 25 to 150 mm (1 to 6 in.). The D_1 can be less than 25 mm (1 in.), but this normally requires that Vickers hardness readings be taken closer to the quenched end of the bar and closer together than is possible using

standard Rockwell hardness measuring equipment. Other hardenability tests are also used.

Carburized Hardenability Test. It is often necessary to determine the hardenability of the high-carbon case regions of carburized steels. Such information is important in controlling carburizing and quenching practice and in determining the ability of a specific steel to meet the microstructural and case depth requirements

of the carburized component manufactured from the steel. Reference 25 contains Jominy curves of several grades of carburized steels, such as that illustrated in Fig. 29.

As a general rule, adequate core hardenability does not ensure adequate case hardenability, especially when it is required to reheat for hardening after carburizing rather than to quench directly from the carburizing furnace. Two factors are responsible for this fact. The first is that equal alloying additions do not have the same effect on the hardenability of all carbon levels of alloyed steels. The second factor (as noted earlier) is that the high-carbon case regions do not always achieve full solution of alloy and carbides, as is normally achieved in the austenite of the low-carbon core region, prior to quenching. Accordingly, direct measurements of case hardenability are very important whenever a carburizing steel must be selected for a specific application.

Measurements of case hardenability are performed as follows. A standard end-quench bar is pack carburized for 9 h at 925 °C (1700 °F) and end quenched in the usual manner. A comparison bar is simultaneously carburized in the same pack to determine carbon penetration. Successive layers are removed from it and analyzed chemically to determine the carbon content at various depths. When a carbon-penetration curve is established, depths to various carbon levels can be determined in the Jominy bar, assuming that the distribution of carbon in the end-quench specimen is the same as in the carbon gradient bar. Longitudinal flats are then carefully ground to various depths on the end-quench bar (usually to carbon concentrations of 1.1, 1.0, 0.9, or 0.8%, and, in some cases, to as low as 0.6%), and hardenability is determined at these carbon levels by hardness traverses.

In grinding, care must be exercised to avoid overheating and tempering, and in conducting

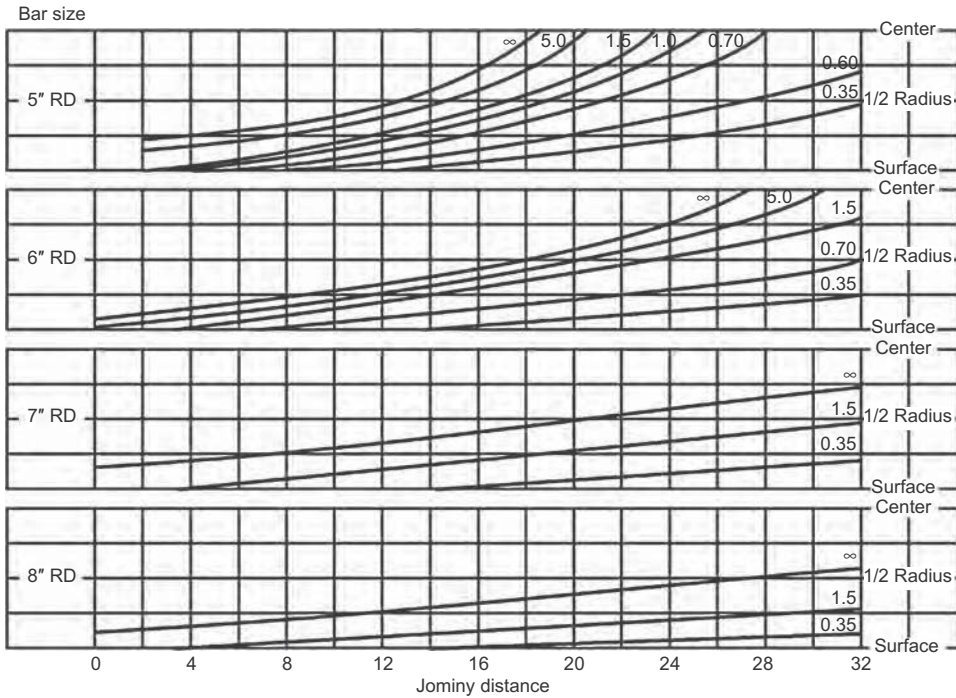


Fig. 20 Continuation of Fig. 19 with correlation of Jominy equivalent hardness (J_{eh}) positions for 125 to 200 mm (5 to 8 in.) rounds. Source: Ref 24

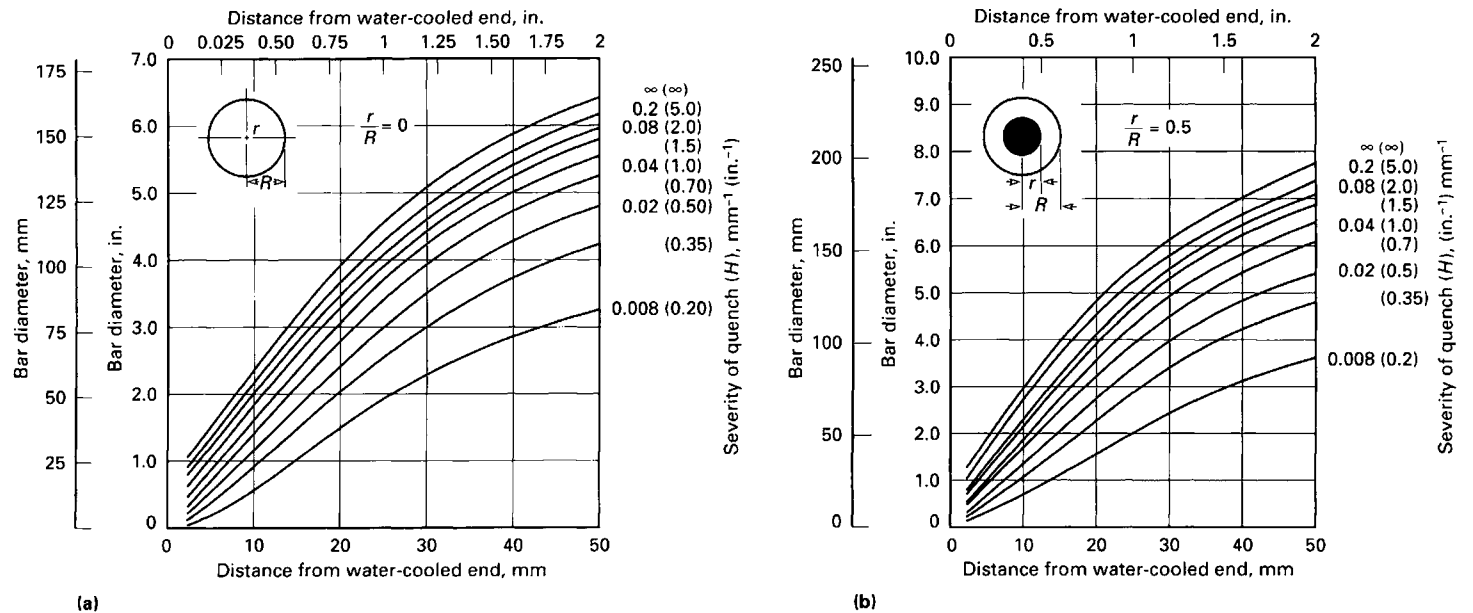


Fig. 21 Lamont diagrams of equivalent end-quenched Jominy positions with different quench severities and round bar diameters for hardening with 50% martensite at (a) center position and (b) half-radius position of bar. Source: Ref 14

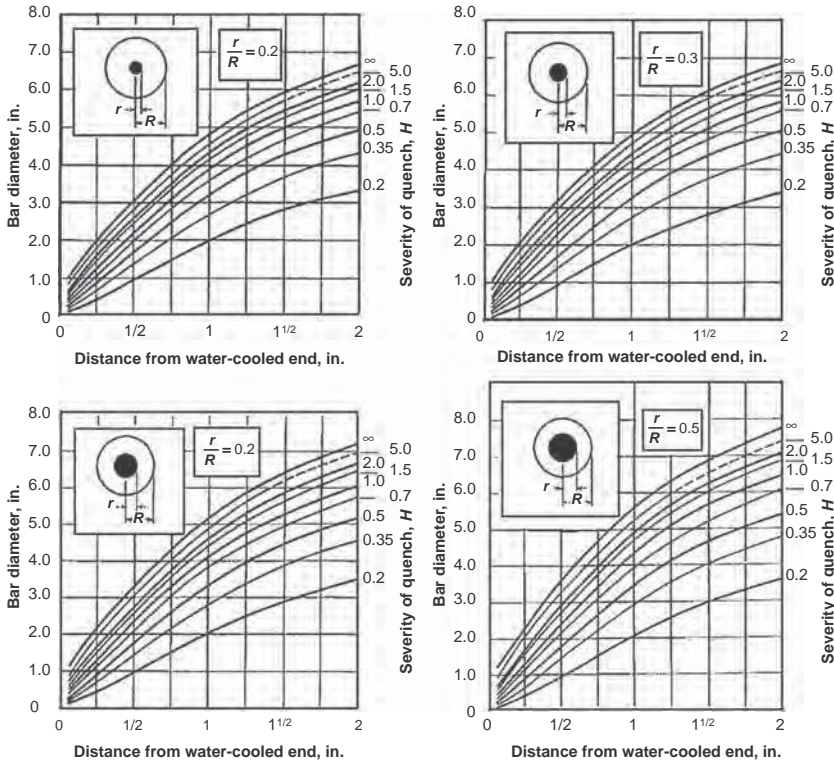


Fig. 22 Continuation of Fig. 21 with Lamont diagrams for equivalent end-quenched Jominy positions with round bar diameters for fractional hardening from $r/R = 0.2$ to 0.5 . Source: Ref 14

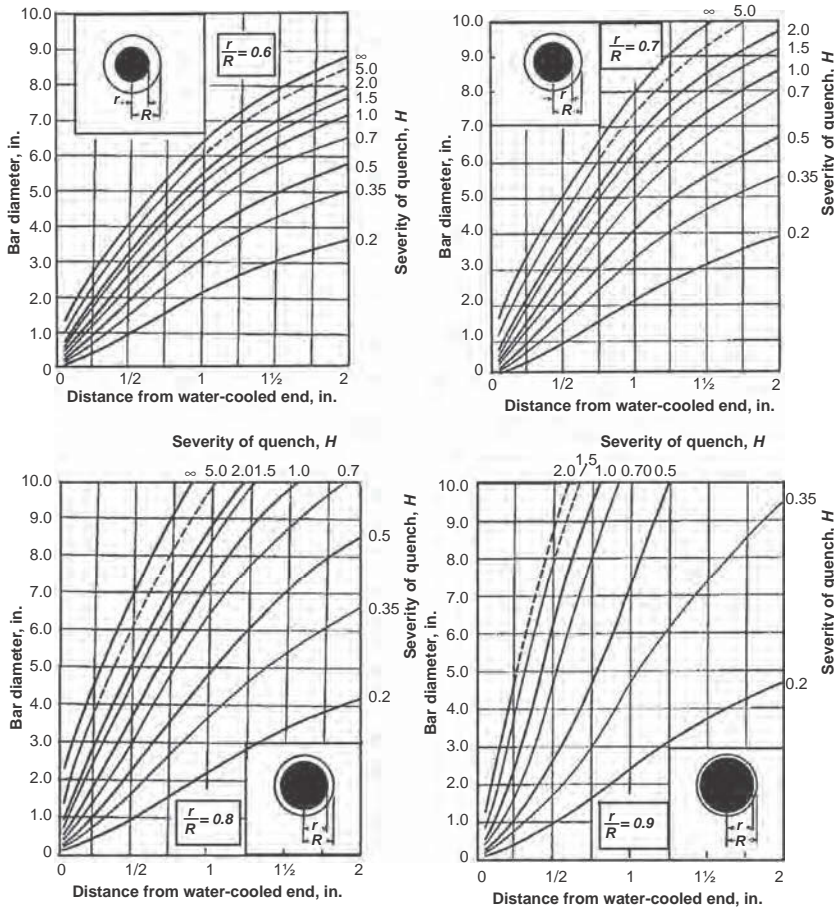


Fig. 23 Continuation of Fig. 21 with Lamont diagrams for equivalent end-quenched Jominy positions with round bar diameters for fractional hardening from $r/R = 0.6$ to 0.9 . Source: Ref 14

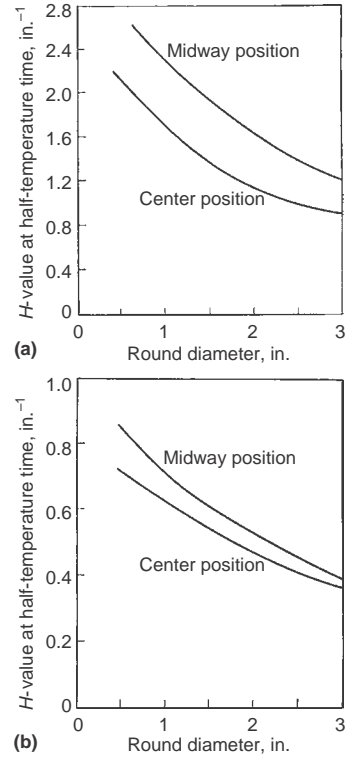


Fig. 24 Variation in H -value with half-temperature time in rounds (a) water quenched and (b) oil quenched from $845\text{ }^{\circ}\text{C}$ ($1550\text{ }^{\circ}\text{F}$). Source: Ref 23

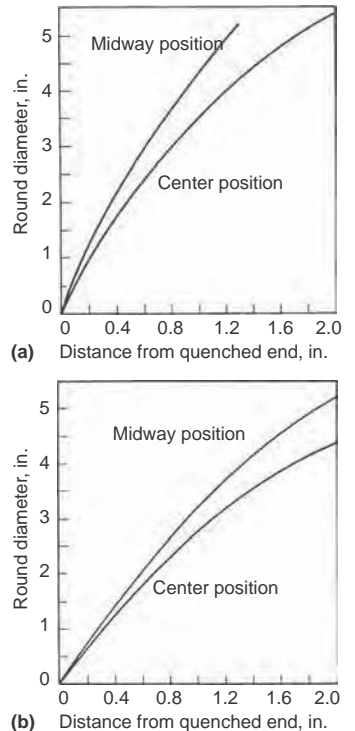


Fig. 25 Equivalent Jominy positions for equal half-temperature with bar positions (a) water quenched and (b) oil quenched from $845\text{ }^{\circ}\text{C}$ ($1550\text{ }^{\circ}\text{F}$). Source: Ref 23

hardness surveys, similar concern must be shown to ensure that the hardness level corresponds to a single carbon level by remaining in the exact center of the flat. Rockwell A hardness readings are preferable to Rockwell C readings

because they minimize the depth of indenter penetration into softer subsurface layers. Rockwell A values are converted into Rockwell C values for plotting. In the higher-carbon layers of carburized specimens, the hardness will be

influenced by the presence of retained austenite. Therefore, it is often useful to evaluate the microstructure/depth relationship by metallographically polishing and etching the ground flats. The Jominy distance to some chosen level of nonmartensitic transformation product can then be used as a measure of hardenability.

The case hardenability of steels that are carburized and then reheated for hardening at temperatures below 925 °C (1700 °F), such as 8620, 4817, and 9310, can also be determined by using a modification of this technique. The carburized end-quench specimens and companion gradient bars are oil quenched together from carburizing but are then reheated in an atmosphere furnace to the desired austenitizing temperature for a total of 55 to 60 min, which should ensure at least 30 to 35 min at temperature. The hardenability specimen is then end quenched, and the carbon gradient bar is oil quenched and tempered to facilitate machining for carbon gradient determination, as described previously. It is recommended that case hardenability tests be performed on no fewer than two test specimens. A more detailed description of the case hardenability measurement technique appears in SAE J406.

Table 3 Observed correlation of end-quench bar with center positions of rounds quenched in oil and water

End-quench distance, 1/16 in.	Ideal diameter, in.	Round size, equal microstructures, in.							
		Round size, equal half-temperature time, in.		Round size, equal microstructures, in.					
		Water	Oil	95% martensite		80% martensite		50% martensite	
1	0.60
2	1.00	0.70	0.40	0.40	0.25	0.40	0.25	0.55	0.25
4	1.75	1.25	0.80	0.75	0.45	0.75	0.50	1.0	0.50
8	2.75	2.05	1.50	1.45	0.80	1.60	0.95	1.65	1.0
12	3.65	2.80	2.15	1.95	1.15	2.05	1.35	2.10	1.45
16	4.50	3.50	2.80	2.30	1.50	2.40	1.75	2.60	1.85
24	5.75	4.60	3.45	2.75	2.05	2.90	2.40	3.10	2.45
32	6.70	5.40	4.30	2.90	...	2.95

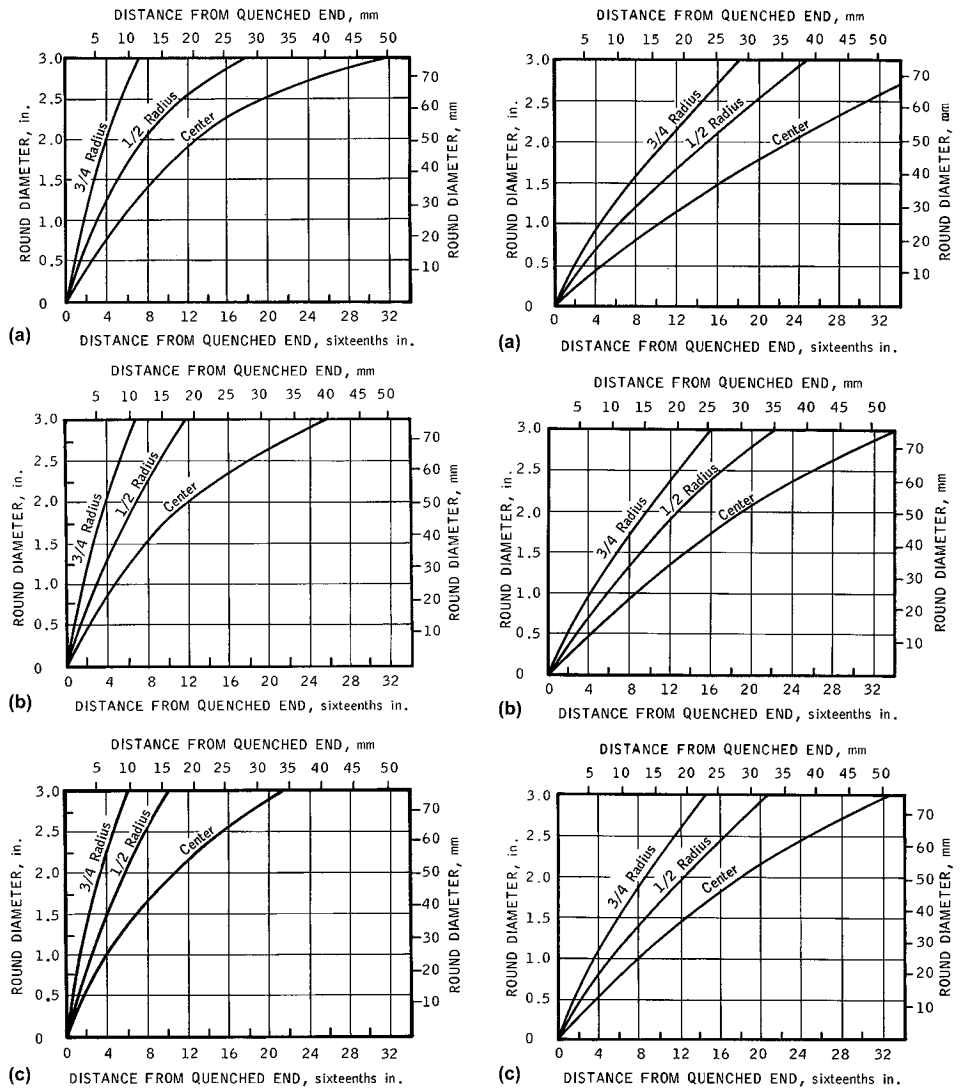


Fig. 26 Equivalent Jominy positions with round bars water quenched from 845 °C (1550 °F). (a) 95% martensite. (b) 80% martensite. (c) 50% martensite. Source: Ref 23

Fig. 27 Equivalent Jominy positions with round bars oil quenched from 845 °C (1550 °F). (a) 95% martensite. (b) 80% martensite. (c) 50% martensite. Source: Ref 23

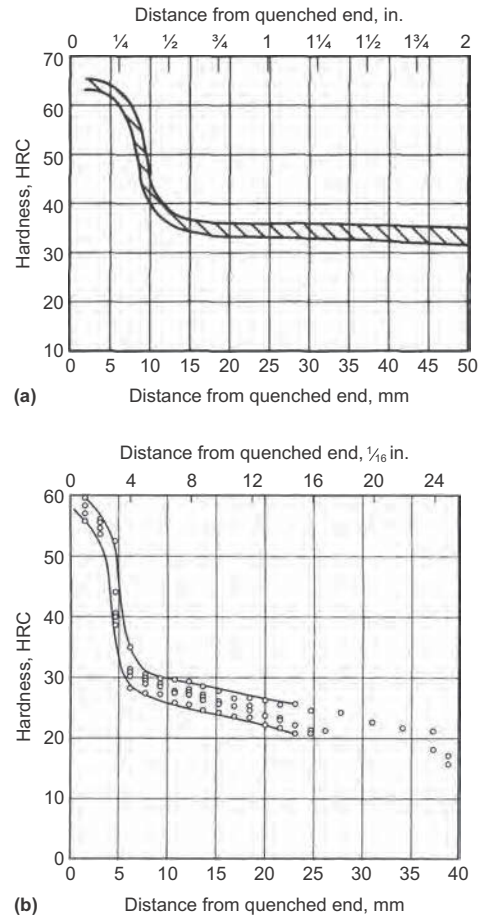


Fig. 28 (a) Jominy test reproducibility results from tests by nine laboratories on one heat of 4068 steel. (b) Reproducibility between different organizations using standard Jominy system. Source: Ref 12, 17

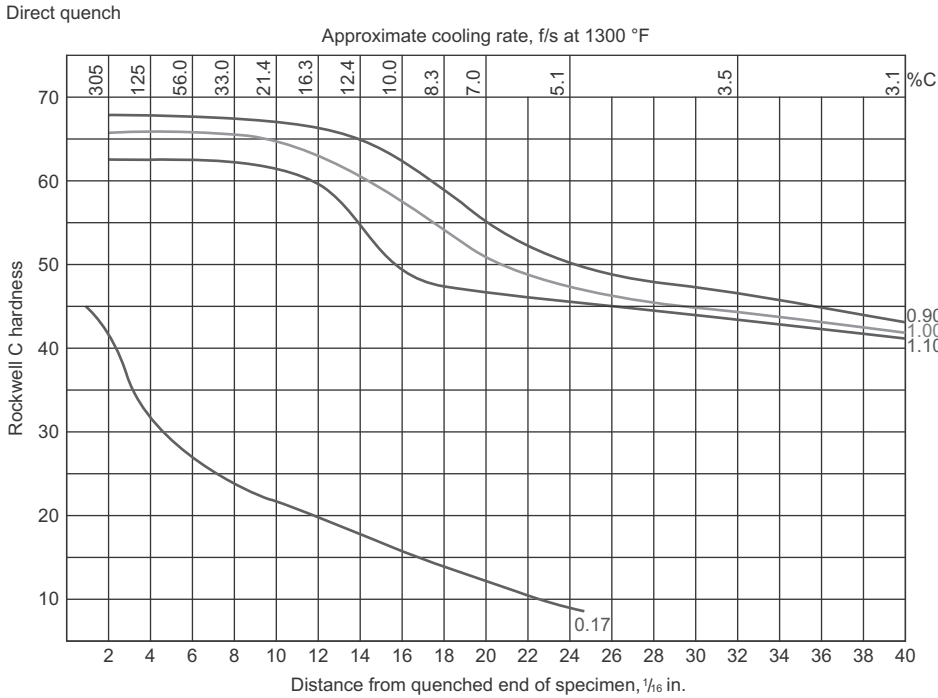


Fig. 29 Jominy curve of carburized 5120 steel (0.17 C, 0.81 Mn, 0.29 Si, 0.18 Ni, 0.72 Cr, 0.05 Mo). Normalized bar austenitized 20 min at 925 °C (1700 °F), pack carburized 9 h at 925 °C (1700 °F), direct quenched. Austenite grain size 6 to 8 (McQuaid-Ehen). Source: Ref 25

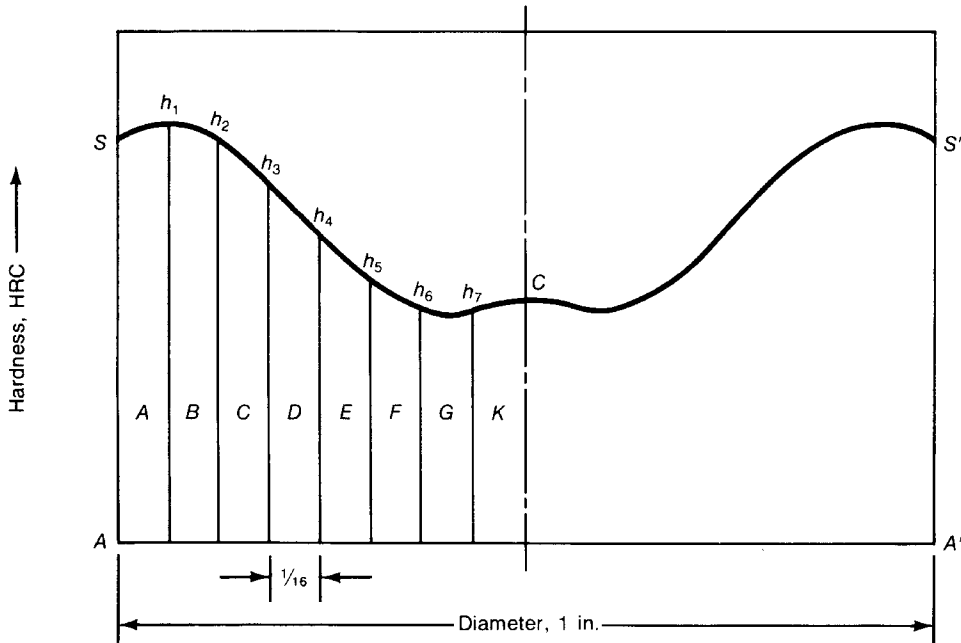


Fig. 31 Surface-area-center estimation of area

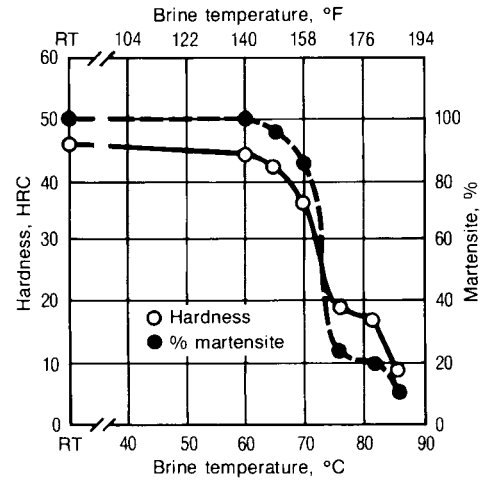


Fig. 30 Typical results of the hot-brine hardenability test. Steel composition: 0.18% C, 0.81% Mn, 0.17% Si, and 1.08% Ni. Austenitized at 845 °C (1550 °F). Grain size: 5 to 7. RT, room temperature. Source: Ref 27

Air Hardenability Test. An air hardenability test method is described in Ref 26. This test is used to evaluate hardening performance when either a steel is cooled at a rate slower than that applied to the end-quench bar or when steels with very high hardenability are being evaluated. A 25.4 mm (1.00 in.) test bar is placed in a fixture with 100 mm (4 in.) length of the test bar length exposed for exposure to still air during cooling. The assembly is heated to the proper austenitizing temperature, after which it is transferred to a convenient location for cooling in still air. This cooling procedure results in very slow and ever decreasing cooling rates along the length of the test bars. Hardness is then measured at discrete intervals along each test bar and plotted against distance from the exposed end on charts specifically designed for this purpose.

Low-Hardenability Steels. In plain carbon and very low-alloy steels, the cooling rate at even the 1.6 mm (1/16 in.) position on a standard Jominy bar may not be fast enough to produce full hardening. Therefore, this test lacks discrimination between these steels. Tests that are more suited to very low-hardenability steels include the hot-brine test and the surface-area-center (SAC) test.

In the hot-brine test proposed by Grange (Ref 27), test coupons are quenched in brine maintained at a series of different temperatures. As shown in Fig. 30, the resulting hardnesses provide a very sensitive test of hardenability.

In the SAC test, a 25.4 mm (1.00 in.) round bar is normalized by cooling in air and then is re-austenitized for water quenching. Hardnesses are measured on a specimen cut from the center of the 100 mm (4 in.) length. Hardness is determined on the surface, the center, and at 1.6 mm (1/16 in.) intervals from surface to center. An area hardness is then computed as the sum of the average hardness in each interval $\times \frac{1}{16}$ (Fig. 31). The resulting set of three-digit numbers, for example, SAC No. 63-52-42,

indicates a surface hardness of 63 HRC, a Rockwell-inch area of 52, and a center hardness of 42 HRC. Testing details are given in SAE J406.

Jominy Equivalence Charts

Once the Jominy curve has been determined, the cooling rate in critical areas of quenched parts must be estimated. The true measure of applicability of any steel to a part requiring heat treatment is the relation of its hardenability to the critical cross section of the part at the time it is heat treated. The term *critical cross section* refers to that section of the part where service stresses are highest and therefore where the highest mechanical properties are required. For example, if the part is a rough forging 64 mm (2½ in.) in diameter at the critical cross section, which is later machined to 50 mm (2 in.) in diameter, and the finished part must be hardened to three-quarter-radius (that is, 6.4 mm, or ¼ in., deep), then the hardenability of the steel must be such that the rough forging will harden 13 mm (½ in.) deep.

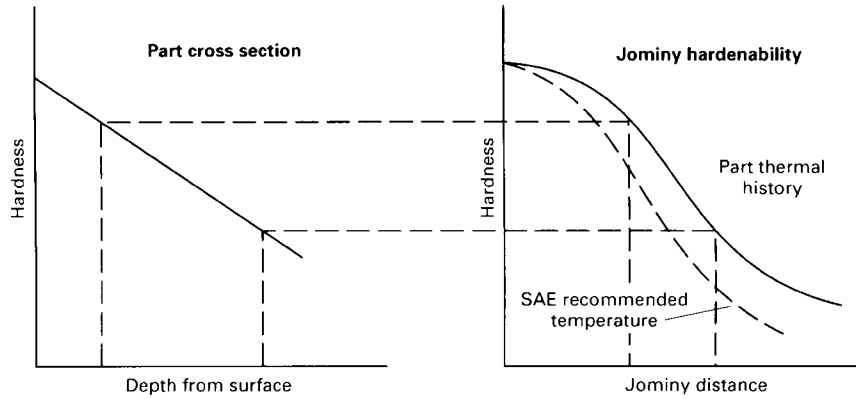
Several kinds of charts are used to determine the Jominy equivalence of cooling rates within a part of a given size and configuration. The Lamont diagrams (Fig. 21, 22 to 23) and the previously described charts in Fig. 19 and 20 are types of Jominy equivalence charts for round bars. Basically, there are two methods of determining Jominy equivalence:

- **Method 1:** The correlation of end-quench hardness data with equivalent hardness (J_{eh}) locations in variously quenched shapes
- **Method 2:** The correlation of end-quench cooling rate data (J_{ec}) with equivalent cooling rate locations in variously quenched production shapes.

Method 1 is the more accurate and preferred method, because in practice it has been found that, when cooling at the same rates, large sections produce somewhat lower hardnesses than smaller sections, including end-quench and air hardenability bars. This difference has been attributed to two factors (Ref 23):

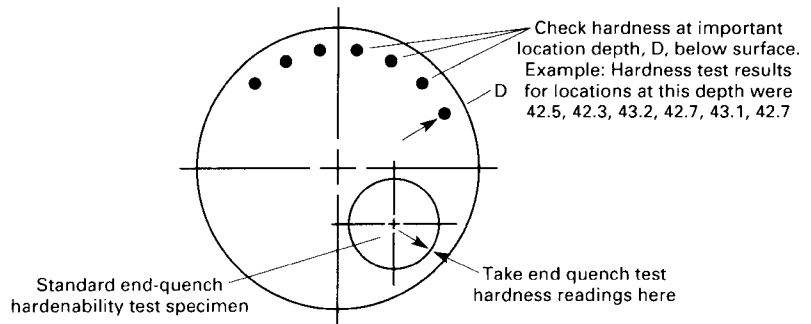
- Higher contraction stresses in large parts accentuate the transformation of austenite.
- Quenching severity, H , decreases with an increase in section size.

Also, in using the cooling rate method (method 2), it is difficult to determine cooling rates with a high degree of accuracy. Nevertheless, correlations that equate cooling conditions along the end-quench bar (J_{ec}) with those in production shapes quenched in various liquid media are also extremely useful when attempting to establish the required hardenability and/or quenching conditions for a production part. One method of establishing the cooling rate is to determine the Jominy equivalent distance, which is outlined in Fig. 32.



Procedure to determine quench cooling rates at important locations in a workpiece:

- **Step 1:** Obtain at least two test parts (a) made from the same heat of steel and manufactured as close as possible to the proposed production method. Castings will do if forging dies are not available
- **Step 2:** Machine parts to condition in which they will be hardened. Copper plate or otherwise protect parts from any carburizing or decarburizing action. Process parts through heat-treating operations for times estimated to be approximately that for the production part. Quench part No. 1 in a manner as close to production as possible (no temper)
- **Step 3:** Cut, grind, and polish hardened sections from part No. 1 so hardness readings may be taken as shown on example below:



- **Step 4:** Machine end-quench hardenability test specimens from part No. 2 test location on hardenability specimens to correspond to depth D, below surface. Harden end-quench specimens from same temperature as part No. 1. Example test results as follows:

Distance from quenched end, 1/16 in.	1	2	3	4	5	6	8
Hardness, HRC	56	55	55	54	52	48	43

- **Step 5:** By comparing hardness results obtained at reference location of step 3 (HRC 42.7) to end-quench results (step 4), it can be seen that this hardness occurs at 1/16 in. on end-quench curve. Quench cooling rate at reference point is approximately equal to 1/16 in. in end-quench test
- **Step 6:** Confirm cooling rate subsequently on a number of different heats of production parts and adjust material or heat treatment or both to obtain the engineering requirements more precisely

(a) Can be used on gear teeth, roots of splines, and other part shapes. If section in which cooling rate must be determined (such as a gear tooth) is too small for an end-quench hardenability specimen, test results from a separate test may be used. An attempt should be made to make end-quench hardness tests on metal of same location in cross section as gear tooth.

Fig. 32 Determination of Jominy equivalent condition (J_{eq})

Jominy Equivalent Hardness Method. The Jominy equivalent hardness (J_{eh}) method is summarized in Fig. 33. The basic method is as follows:

1. Select hardening and quenching conditions that the production hardening equipment can easily fulfill.
2. Select a low-hardenability steel, such as 8620, 4023, or 1040, and manufacture a quantity of finished components: gears, bearings, shafts.

3. Quench a number of these components (in the uncarburized condition) in the production facility.
4. Measure the hardnesses obtained at all critical locations from the surface to the core.
5. Compare the measured hardness values at these locations with equivalent hardness values produced at some end-quench (J_{eh}) location on a Jominy bar made from the same heat and end quenched from the same thermal conditions.

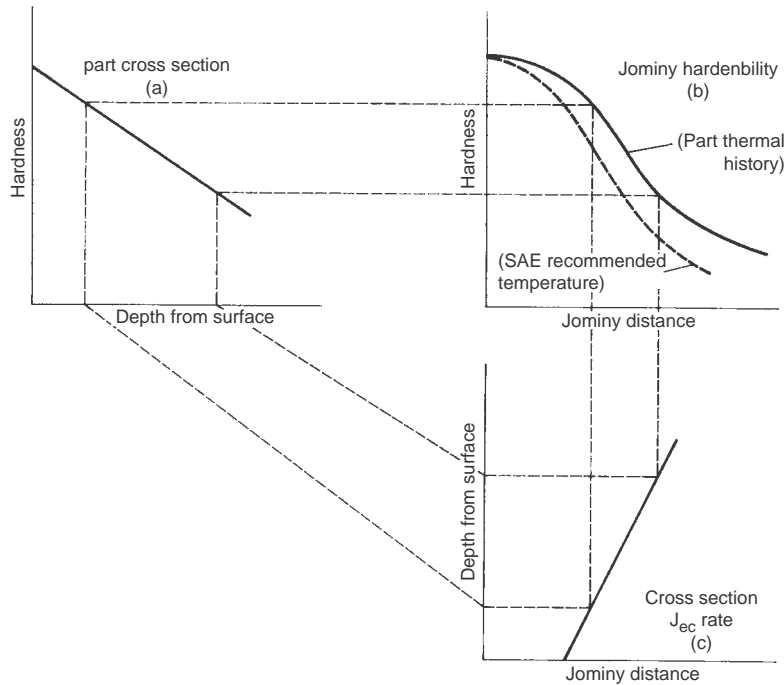


Fig. 33 Jominy equivalent hardness (J_{eh}) criterion. Hardenability evaluation by Jominy equivalent hardness (J_{eh}) rates is done by comparing the hardnesses of (a) cross sections of parts receiving the established production heat treatment to the hardnesses obtained on (b) end-quenched bars of the same steel. The equivalent Jominy cooling rate (J_{ec}) of the cross section also maps (in part c) to the Jominy distance (J_d), which is directly related to cooling rate. See text

6. The J_{eh} values obtained in this fashion define the equal hardness cooling conditions for each location in the production-quenched component.
7. Finally, select from available end-quench data a steel that will produce the hardnesses required at each critical J_{eh} location in the finished production part. If end-quench data are not available, calculate a suitable composition by one of the standard methods.

The chart in Fig. 19 (as previously described in the section "Hardenability Correlation Curves") is another example of the equivalent hardness criterion for round bars. Instructions for the procedure are given in the caption. Similar charts apply for other product shapes.

Rectangular or Hexagonal Bars and Plate. Except in critical or borderline applications, size relationships for rounds can be applied without correction to square or hexagonal sections. The charts for round bars (Fig. 19, 20) and also Fig. 34 and 35 can be used for rectangular bars in which the ratio of width to thickness (W/T) is less than 4, but the value 1.4 times the thickness should be used as the equivalent round. Large plates cool considerably more slowly than bars. The cooling-rate relationships shown in Fig. 36 and 37 apply to these shapes.

Tubular Parts. The application of end-quenched hardenability data to the selection of steel for hollow cylindrical sections is based largely on production experience with similar parts. There has been some progress in equating tubular sections to round bars and in developing

dimensionless temperature-time charts for long, hollow cylinders. Hollomon and Zener (Ref 28) determined by calculation the diameter of solid steel cylinders that, when quenched in a given medium, could be expected to have the same hardness at the center as the minimum hardness in the wall of hollow cylinders when quenched in the same medium. The rule of thumb of doubling the tube wall thickness to obtain the diameter of an equivalent solid bar is a useful first approximation.

Equivalent Cooling Rates. The cooling rate can be determined based on knowledge of the quenchant and the cross section of the part. Figure 38 shows the correlation between cooling rates along the end-quench hardenability specimen and at four locations in round bars up to 100 mm (4 in.) in diameter for both oil and water quenching at 60 m/min (200 sfm). The charts provide for various bar diameters ranging from approximately 13 to 100 mm ($1/2$ to 4 in.). The cooling rates at the surface, three-quarter-radius, half-radius, and center are related to the cooling rates at an equivalent distance from the end of a quenched Jominy bar. Thus, the cooling rate at the center of a 50 mm (2 in.) diameter bar quenched in water has a cooling rate equivalent to the value at a distance of approximately $6/16$ in. from the end of the Jominy bar. The cooling rate at the center of a 50 mm (2 in.) diameter bar quenched in oil has a cooling rate comparable to a point $10/16$ in. from the water-quenched end of a Jominy bar. Relationships

between bar diameter and other simple part geometries such as squares and plates are shown in Fig. 39.

Determining Hardenability Requirements

The basic information needed to specify steel with adequate hardenability includes:

- The as-quenched hardness required prior to tempering to final hardness that will produce the best stress-resisting microstructure
- The depth below the surface to which this hardness must extend
- The quenching medium that should be used to achieve hardening depth

For a specific application, the first decision is to determine the carbon levels for the required hardness. The desired as-quenched hardness is a function of the hardness desired after tempering (Fig. 40a). It is possible, as shown in Fig. 40(b), to select steels that will produce these hardnesses with less than 90% martensite. To ensure optimum properties, common practice is to select the steel with the lowest carbon content that will produce the indicated as-quenched hardness using the quenching medium available (or one that can be made available). Following this procedure, the structures possessing the indicated hardnesses would be fully hardened; that is, they would contain more than 90% martensite, which is a common and practical definition of full hardening and the one employed by the SAE committee. For components subjected to bending in service, it is considered adequate to have 90% martensite at the three-quarter-radius location. To ensure this, hardness levels are specified at half-radius.

Depth of Hardening. The depth and percentage of martensite to which parts are hardened may affect their serviceability, but it always affects the hardenability required and therefore the cost. In parts less highly stressed in bending, hardening to 80% martensite at three-quarter-radius of the part as finished may be sufficient; in other parts, even less depth may be required. The latter include principally those parts designed for low deflection under load, in which even the exterior regions are only moderately stressed. In contrast, some parts loaded principally in tension and others operating at high hardness levels, such as springs of all types, are usually hardened more nearly through the section. In automobile leaf springs, the leaves are designed with a low section modulus in the direction of loading. The allowable deflection is large, and most of the cross section is highly stressed.

In general, hardening need be no deeper than is required to provide the strength to sustain the load at a given depth below the surface. Therefore, parts designed to resist only surface wear,

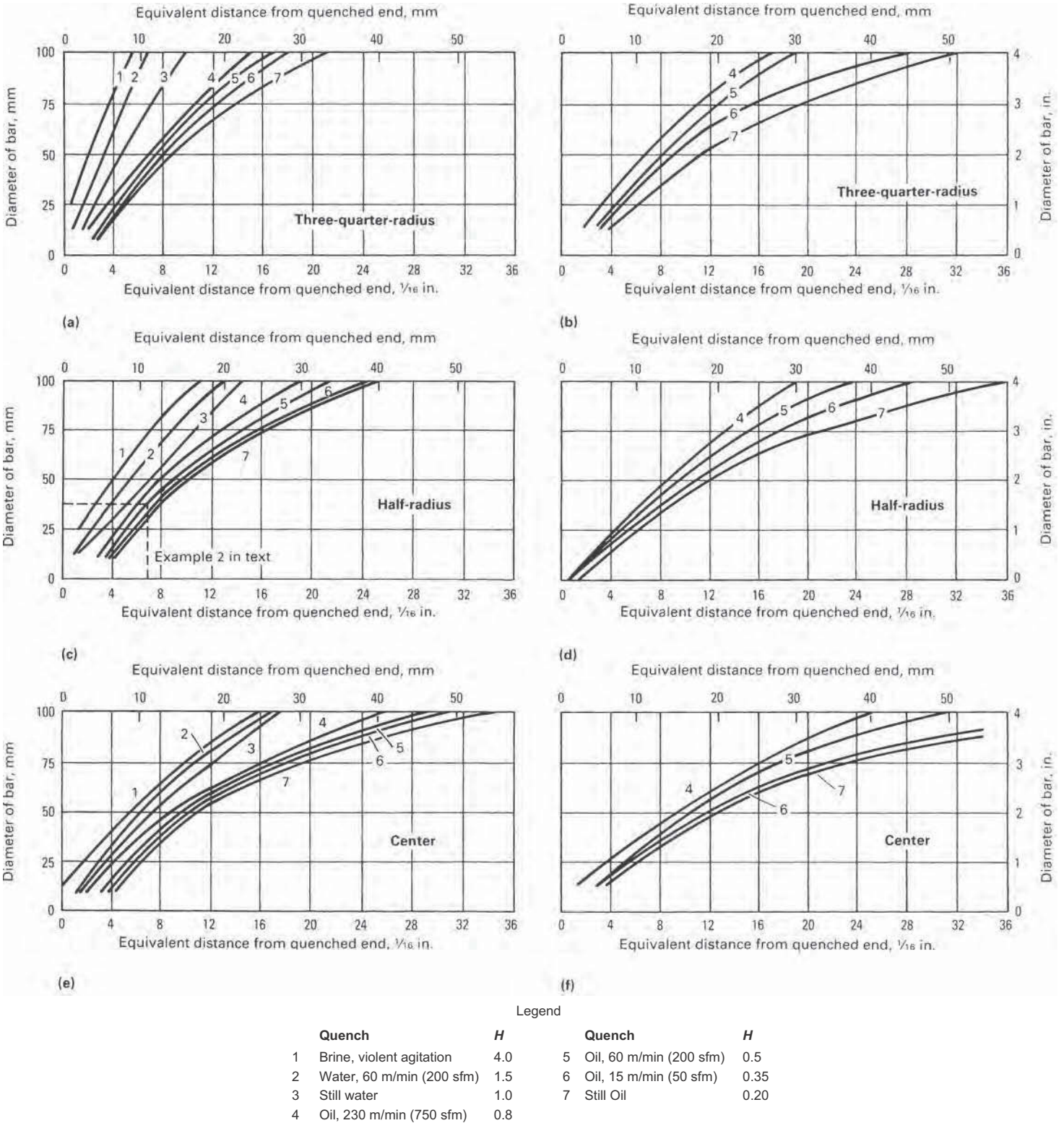


Fig. 34 Correlation of Jominy equivalent cooling rates (J_{eq}) of the end-quenched specimen with round bars quenched in oil, water, and brine. (a), (c), and (e) nonscaling austenitizing atmosphere. (b), (d), and (f) austenitized in air

pure bending, or rolling contact often do not justify the cost of providing the hardenability required for hardening through the entire cross section.

When service requirements mandate that hardening must produce more than 80% martensite, the section size that can be hardened to a prescribed depth decreases rapidly as the

percentage of martensite required increases. For example, let us assume that 95% martensite (51 HRC minimum hardness) is required in 8640H steel. Then the largest section size that

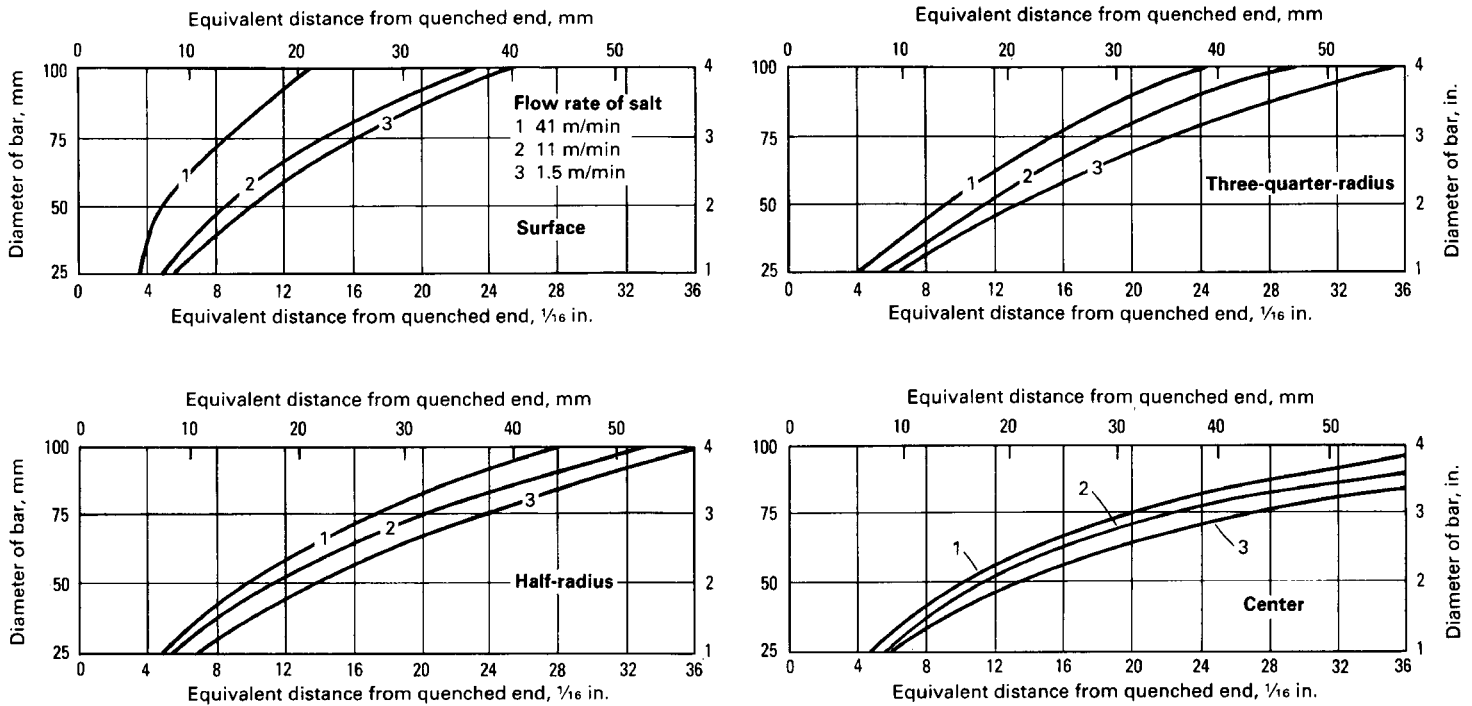


Fig. 35 Correlation of Jominy equivalent cooling rates (J_{ec}) of the end-quenched hardenability specimen and round bars quenched in salt at 200 °C (400 °F)

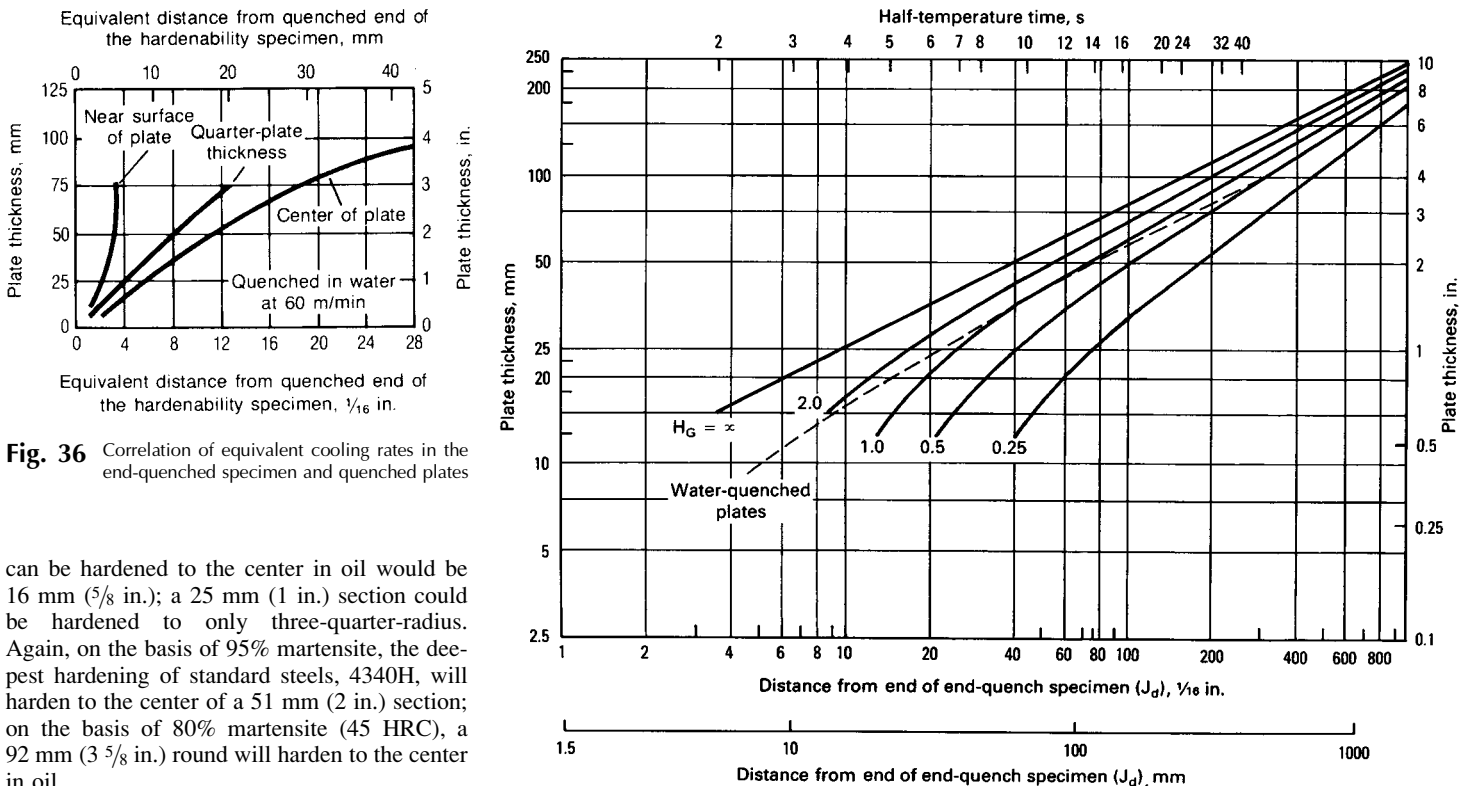


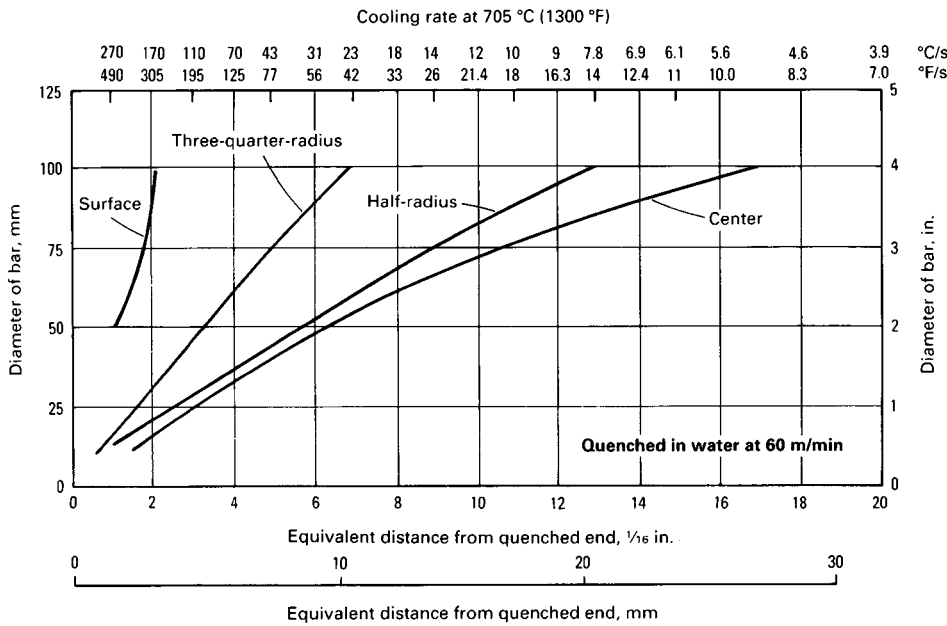
Fig. 36 Correlation of equivalent cooling rates in the end-quenched specimen and quenched plates

can be hardened to the center in oil would be 16 mm ($5/8$ in.); a 25 mm (1 in.) section could be hardened to only three-quarter-radius. Again, on the basis of 95% martensite, the deepest hardening of standard steels, 4340H, will harden to the center of a 51 mm (2 in.) section; on the basis of 80% martensite (45 HRC), a 92 mm ($3\ 5/8$ in.) round will harden to the center in oil.

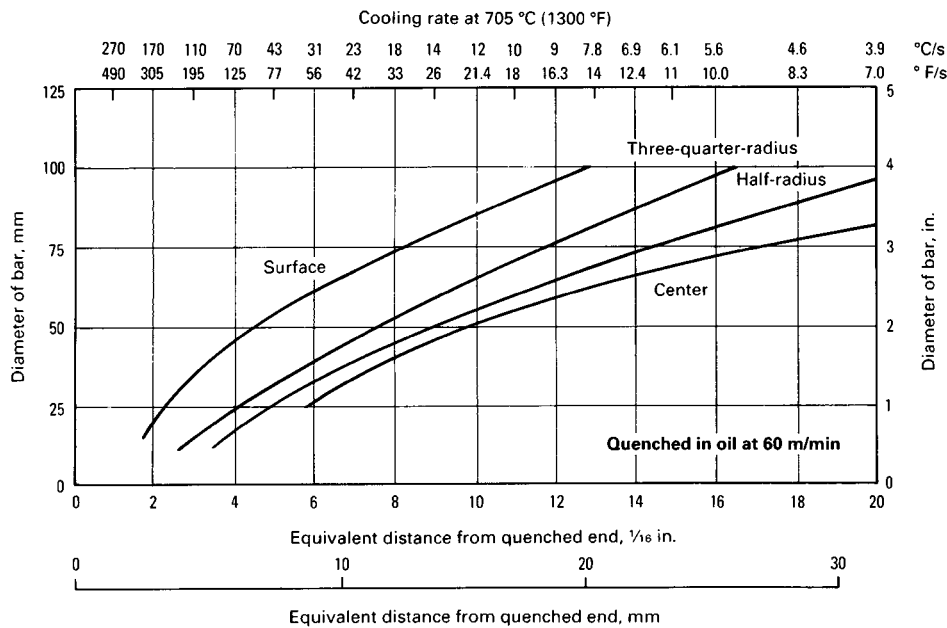
The aforementioned examples emphasize the need for engineering judgment in requiring very deep hardening or unusually high percentages of martensite. When these requirements are not wholly justified, the results are overspecification of steel at higher cost and greater likelihood of distortion and quench cracking.

Fig. 37 Correlation between J_{ec} and center cooling rates in plates quenched at various severities

Quenching Media. The cooling potential of quenching media is a critical factor in heat treating processes because of its contribution to attaining the minimum hardenability requirement of the part or section being heat treated. The cooling potential, a measure of quenching severity, can be varied over a rather wide range by:



(a)



(b)

Fig. 38 Equivalent cooling rates for round bars quenched in (a) water and (b) oil. Correlation of equivalent cooling rates in the end-quenched hardenability specimen and quenched round bars free from scale. Data for surface hardness are for mild agitation; other data are for 60 m/min (200 sfm).

- Selection of a particular quenching medium
- Control of agitation
- Additives that improve the cooling capability of the quenchant
- Optimize the properties of the steel selected
- Permit the use of less expensive quenching media
- Improve productivity and achieve cost reductions as a result of shorter cycle times and higher production rates

Any or all of these variables can be employed to increase quenching severity and provide the following advantages:

- Permit the use of less expensive (lower-alloy) steels of lower hardenability

In practice, however, two other considerations modify the selection of quenching medium and quenching severity: the amount

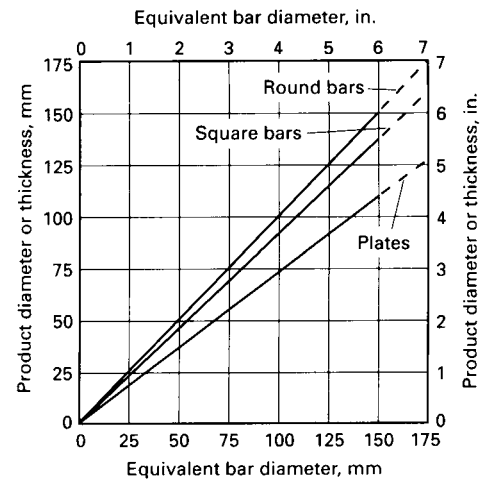


Fig. 39 Relation between through-quenched bar diameter and the through-quenched thickness of plates and square bars

of distortion that can be tolerated and the susceptibility to quench cracking.

In general, the more severe the quenchant and the less symmetrical the part being quenched, the greater the size and shape changes that result from quenching and the greater the risk of quench cracking. Consequently, although water quenching is less costly than oil quenching, and water-quenched steels are less expensive than those requiring oil quenching, it is important that the parts to be hardened be carefully reviewed to determine whether the amount of distortion and the possibility of cracking as a result of water quenching will permit taking advantage of the lower cost of water quenching. Oil, salt, and synthetic water-polymer quenchants are alternatives, but their use often requires steels of higher alloy content to satisfy hardenability requirements.

A rule regarding selection of a steel and quenching medium for a given part is that the steel should have a minimum hardenability not exceeding that required by the quenching severity of the medium selected. The steel should also contain the lowest carbon content compatible with the required hardness and strength properties. This rule is based on the fact that the quench cracking susceptibility of steels increases with a decrease in M_s temperature and/or an increase in carbon content.

Table 4 lists typical quenching severity, or H_v values for the common quenching media and conditions. The data in Table 4 are media containing no additives. Considerable improvement in the cooling capability of quenchants can be obtained by such additions as water to hot salt, proprietary additives to oil, and polyalkylene glycol (polymer) to water. The polymer-water mixtures polyacrylamide gel, polyvinyl pyrrolidone, and polyvinyl alcohol can be made to span the quenching severity range from oil to water by simple variation of the glycol (polymer) concentration in water. Also, because they are

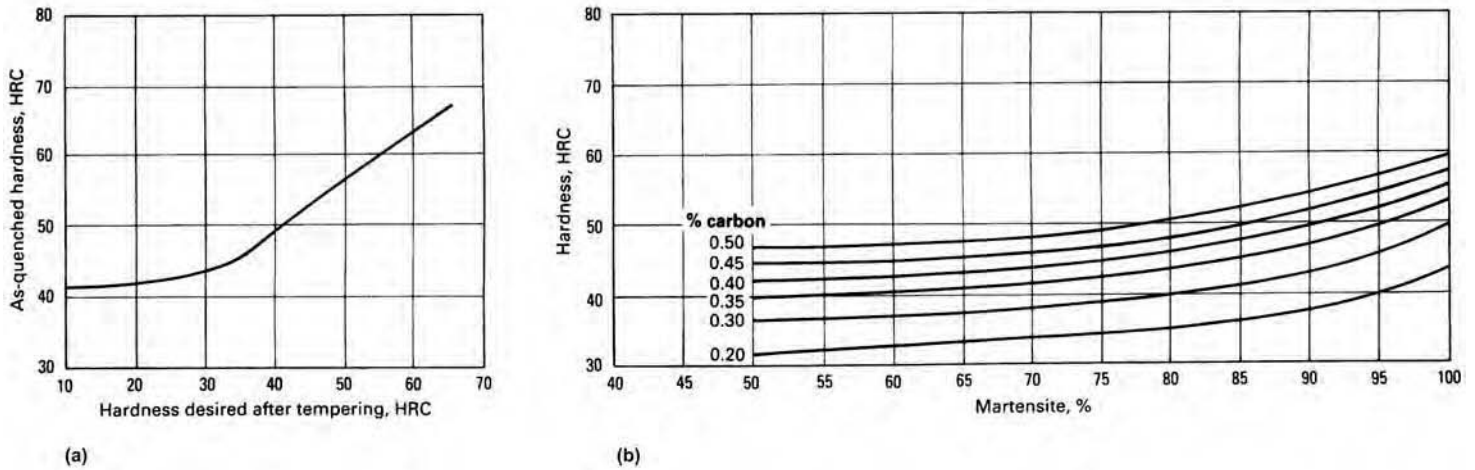


Fig. 40 Curves for steel selection based on hardness. (a) Minimum as-quenched hardness to produce various final hardnesses after tempering. (b) Dependence of as-quenched hardness on percentages of martensite and carbon

free of fire hazards and obnoxious environmental pollution agents, they have no adverse effect on working conditions. The quenching severity of these media should be tested at frequent intervals because dragout and thermal breakdown may affect their quenching efficiency.

Factors Affecting Hardenability

As noted, the hardenability of steel is governed almost entirely by the chemical composition (carbon and alloy content) at the austenitizing temperature, the austenite grain size, and other variables such as austenitizing temperature, time at temperature, and prior microstructure. Carbon affects the hardness and also has an effect on hardenability by decreasing the critical cooling rate for martensite formation (Fig. 41). However, the hardenability of carbon steel increases with an increase in austenite grain size, where the effect becomes more pronounced if the carbon content is increased at the same time (Fig. 42). There are limits to increasing grain size, because toughness is degraded with larger grain size. Increases in grain size also increase the possibility of quench cracking. When the danger of quench cracking is remote (no abrupt changes in section thickness) and engineering considerations permit, it may sometimes appear to be more practical to use a coarser-grained steel rather than a fine-grained or more expensive alloy steel to obtain hardenability. However, the use of coarser-grained steels usually involves a serious sacrifice in notch toughness.

In terms of alloying, any dissolved element in austenite (except for cobalt, Ref 20) retards the nucleation or growth of diffusion-controlled products during austenite decomposition. The exception is when the chemical composition of the austenite at the moment of quenching may not be the same as that determined by chemical analysis. For example, if carbides are not dissolved at the austenitizing temperature,

Table 4 Quenching severities (*H*) for various media and quenching conditions

Quenchant agitation	Typical flow rates		Typical <i>H</i> -values			
	m/min	sfm	Air	Mineral oil	Water	Brine
None	0	0	0.02	0.20-0.30	0.9-1.0	2.0
Mild	15	50	...	0.20-0.35	1.0-1.1	2.1
Moderate	30	100	...	0.35-0.40	1.2-1.3	...
Good	61	200	0.05	0.40-0.60	1.4-2.0	...
Strong	230	750	...	0.60-0.80	1.6-2.0	4.0

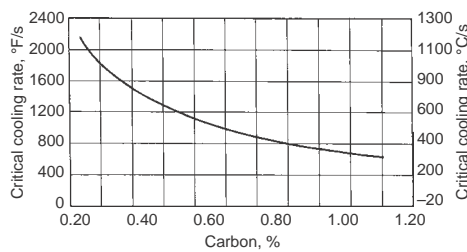


Fig. 41 Effect of carbon content on critical quenching rate of pure iron-carbon austenite. Source: Ref 20

then some carbon remains tied up in the carbides and is not available for martensitic hardening. Thus, undissolved carbides can actively decrease hardenability. This is especially important in high-carbon (0.50 to 1.10%) and alloy carburizing steels, which may contain excess carbides at the austenitizing temperature. Casting and hot reduction practices may also develop localized or periodic inhomogeneities within a given heat, further complicating hardenability measurements.

In general, alloying elements can be separated according to whether they are austenite stabilizers, such as manganese, nickel, and copper, or ferrite stabilizers (for example, γ -loop formers), such as molybdenum, silicon, titanium, vanadium, zirconium, tungsten, and

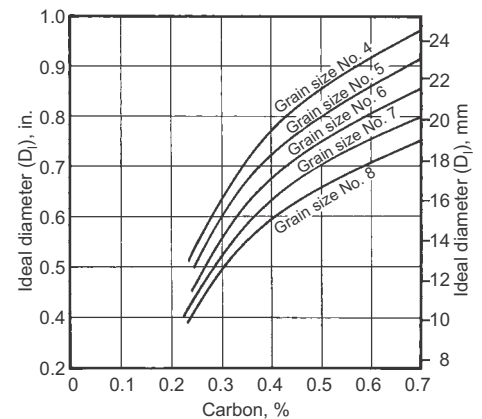


Fig. 42 Hardenability of pure iron-carbon alloys as a function of carbon and austenite grain size. Source: Ref 29

niobium (Ref 30). Ferrite stabilizers require a much lower alloying addition than the austenite stabilizers for an equivalent increase in hardenability. However, with many of these ferrite stabilizers, the competing process of carbide precipitation in the austenite depletes the austenite of both carbon and alloy addition, thus lowering hardenability. The precipitates also produce grain refinement, which further decreases hardenability.

In terms of alloying, usually the least expensive means of increasing hardenability at a given carbon content is by increasing the manganese content. Chromium and molybdenum also increase hardenability and are also among the most economical elements per unit of increased hardenability. Nickel is the most expensive per unit but is warranted when toughness is a primary consideration.

Boron can considerably improve hardenability, the effect varying notably with the carbon content of the steel. The full effect of boron on hardenability is obtained only in fully deoxidized (aluminum-killed) steels. The effects of boron on hardenability are unique in several respects:

- A very small amount of boron (approximately 0.001%) has a powerful effect on hardenability.
- The effect of boron on hardenability is much less in high-carbon than in low-carbon steels.
- Nitrogen and deoxidizers influence the effectiveness of boron.
- High-temperature treatment reduces the hardenability effect of boron.

In carburizing steels, the effect of boron on case hardenability may be completely lost if nitrogen is abundant in the carburizing atmosphere.

The cost of boron is usually much less than that of other alloying elements having approximately the same hardenability effect.

Hardenability also varies with interactions between alloying elements. Important synergistic effects can also occur when combinations of alloying elements are used in place of single elements. Some examples of known synergistic combinations are nickel plus manganese, molybdenum plus nickel, and silicon plus manganese. Table 5 summarizes some general effects of alloying on hardenability (along with alloying effects on tempering, because most hardened steels are tempered). More information on the effects of alloying is in the companion publication, *Heat Treating of Irons and Steels*, Volume 4B of the *ASM Handbook* (Ref 32).

Variability in Jominy Data Sets (Ref 33)

Under controlled conditions, the Jominy test can provide acceptable, if not ideal, reproducibility (Fig. 28). However, even with controlled conditions with the shown experimental

reproducibility, hardness at a fixed Jominy depth near the inflection point of an H-steel in controlled tests can typically be ± 6 HRC. However, it is important to recognize the inherent limitations of even well-established empirical data such as Jominy end-quench hardenability curves. For example, Fig. 43 shows sets of Jominy curves selected from a large international set for 8620 carburizing steels and deep-hardening 4140 automotive steels of almost the same nominal composition and grain size. Such discrepancies could be attributed to incorrectly reported chemistry, careless test procedures, and/or unreported or uncontrolled process variables. Likewise, continuous cooling transformation curves also conceal comparable empirical errors, because fractions transformed and cooling histories are incompletely determined or ambiguous, and these deficiencies can be expressed alternatively as an uncertainty in the time scale of the superposed cooling curves of factors reaching as high as four (Ref 35, 36).

The foregoing comments pertain mainly to shallow- and medium-hardening steels. Focusing on deeper-hardening steels such as 4340 (Fig. 44), the idea of a Jominy depth of hardening becomes rather indefinite. Even though

Table 5 Effects of alloy elements on hardenability and tempering of steels

Effect of alloy on hardenability during quenching	Effect of alloy on tempering
Manganese contributes markedly to hardenability, especially in amounts greater than 0.8%. The effect of manganese up to 1.0% is stronger in low- and high-carbon steels than in medium-carbon steels.	Manganese increases the hardness of tempered martensite by retarding the coalescence of carbides, which prevent grain growth in the ferrite matrix. These effects cause a substantial increase in the hardness of tempered martensite as the percentage of manganese in the steel increases.
Nickel is similar to manganese at low alloy additions but is less potent at the high alloy levels. Nickel is also affected by carbon content, with the medium-carbon steels having the greatest effect. There is an alloy interaction between manganese and nickel that must be taken into account at lower austenitizing temperatures.	Nickel has a relatively small effect on the hardness of tempered martensite, which is essentially the same at all tempering temperatures. Because nickel is not a carbide former, its influence is considered to be due to a weak solid-solution strengthening.
Copper is usually added to alloy steels for its contribution to atmospheric-corrosion resistance and at higher levels for precipitation hardening. The effect of copper on hardenability is similar to that of nickel, and in hardenability calculations it has been suggested that the sum of copper plus nickel be used with the appropriate multiplying factor of nickel.	Copper is precipitated out when steel is heated to approximately 425–650 °C (800–1200 °F) and thus can provide a degree of precipitation hardening.
Silicon is more effective than manganese at low alloy levels and has a strengthening effect on low-alloy steels. However, at levels greater than 1%, this element is much less effective than manganese. The effect of silicon also varies considerably with carbon content and other alloys present. Silicon is relatively ineffective in low-carbon steel but is very effective in high-carbon steels.	Silicon increases the hardness of tempered martensite at all tempering temperatures. Silicon also has a substantial retarding effect on softening at 316 °C (600 °F) and has been attributed to the inhibiting effect of silicon on the conversion of ϵ -carbide to cementite.
Molybdenum is most effective in improving hardenability. Molybdenum has a much greater effect in high-carbon steels than in medium-carbon steels. The presence of chromium decreases the multiplying factor, whereas the presence of nickel enhances the hardenability effect of molybdenum.	Molybdenum retards the softening of martensite at all tempering temperatures. Above 540 °C (1000 °F), molybdenum partitions to the carbide phase and thus keeps the carbide particles small and numerous. In addition, molybdenum reduces susceptibility to tempering embrittlement.
Chromium behaves much like molybdenum and has its greatest effect in medium-carbon steels. In low-carbon steel and carburized steel, the effect is less than in medium-carbon steels but is still significant. As a result of the stability of chromium carbide at lower austenitizing temperatures, chromium becomes less effective.	Chromium, like molybdenum, is a strong carbide-forming element that can be expected to retard the softening of martensite at all temperatures. Also, by substituting chromium for some of the iron in cementite, the coalescence of carbides is retarded.
Vanadium is usually not added for hardenability in quenched and tempered structural steels (such as ASTM A678, grade D) but is added to provide secondary hardening during tempering. Vanadium is a strong carbide former, and the steel must be austenitized at a sufficiently high temperature and for a sufficient length of time to ensure that the vanadium is in solution and thus able to contribute to hardenability. Moreover, solution is possible only if small amounts of vanadium are added.	Vanadium is a stronger carbide former than molybdenum and chromium and can therefore be expected to have a much more potent effect at equivalent alloy levels. The strong effect of vanadium is probably due to the formation of an alloy carbide that replaces cementite-type carbides at high tempering temperatures and persists as a fine dispersion up to the A_1 temperature.
Tungsten has been found to be more effective in high-carbon steels than in steels of low carbon content (less than 0.5%). Alloy interaction is important in tungsten-containing steels, with Mn-Mo-Cr having a greater effect on the multiplying factors than silicon or nickel additions.	Tungsten is also a carbide former and behaves like molybdenum in simple steels. Tungsten has been proposed as a substitute for molybdenum in reduced-activation ferritic steels for nuclear applications.
Titanium, niobium, and zirconium are all strong carbide formers and are usually not added to enhance hardenability for the same reasons given for vanadium. In addition, titanium and zirconium are strong nitride formers, a characteristic that affects their solubility in austenite and hence their contribution to hardenability.	Titanium, niobium, and zirconium should behave like vanadium because they are strong carbide formers.
Boron can considerably improve hardenability, the effect varying notably with the carbon content of the steel. The full effect of boron on hardenability is obtained only in fully deoxidized (aluminum-killed) steels.	Boron has no effect on the tempering characteristics of martensite, but a detrimental effect on toughness can result from the transformation to nonmartensitic products.

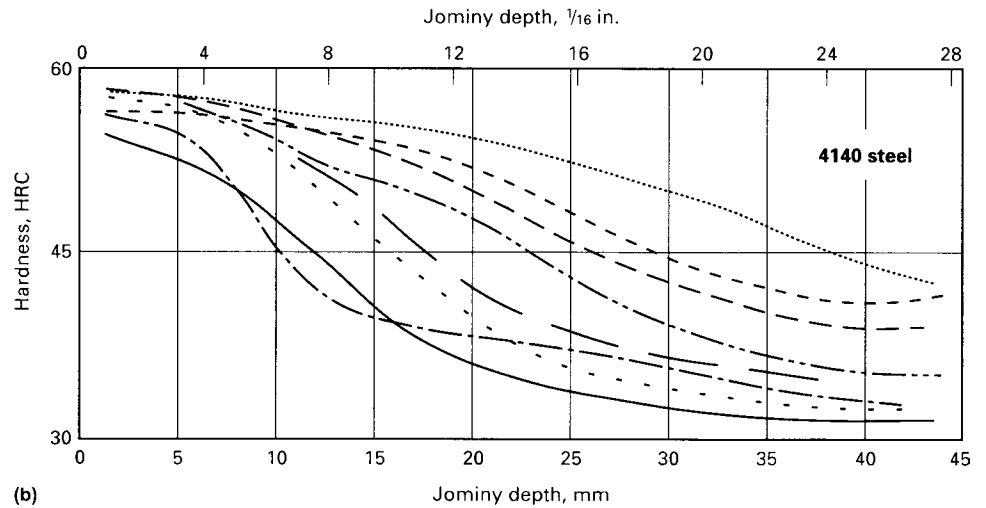
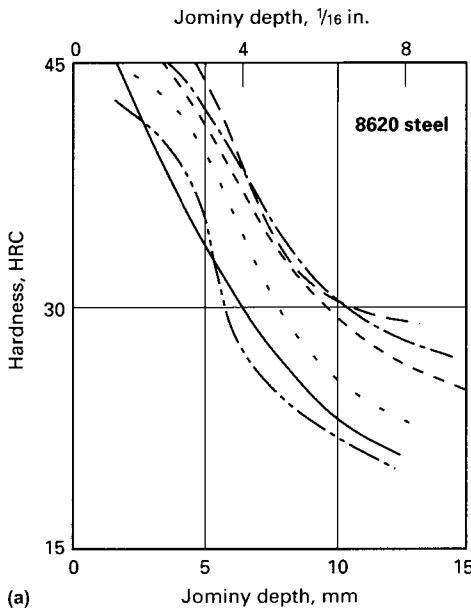


Fig. 43 Summary of reported Jominy tests by several laboratories on an (a) SAE 8620 steel and a (b) 4140 steel of approximately the same composition and grain size. Source: Ref 34

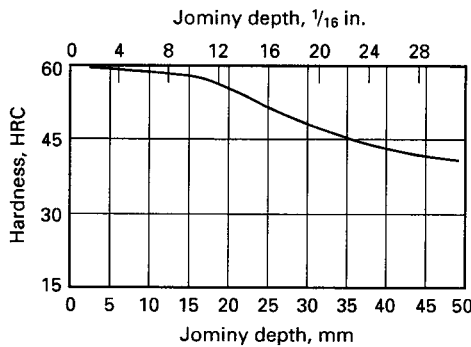


Fig. 44 Typical Jominy curve for a high-hardenability (4340) steel

determination of D_I from an experimental set of critical diameters (D_0) remains a valid concept, this test option for deep-hardening steels is not considered for cost reasons. The specification and interpretation problem in this case is not strongly associated with the shape of the curve but with the extreme sensitivity of the hardnesses to the austenitizing temperature and time actually used in the Jominy test. To a lesser extent, this is also true for low-alloy steels. This problem arises from the fact that the higher-carbon hardenable steels are invariably hypereutectoid and therefore possess a substantial volume fraction of very unstable, undissolved carbides in the as-rolled condition. The quality-control officer and heat treater should be critical of both the hardenability specifications and the experimental Jominy curves received for such grades. On the positive side, the heat treater should be cognizant of the flexibility afforded by minor variations in the austenitizing temperature.

Calculation of Steel Hardenability

The hardenability of steel is primarily a function of the composition (carbon, alloying elements, and residuals) and the grain size of the austenite at the instant of quenching. If this relationship can be determined quantitatively, it should be possible to calculate the hardenability of steel from composition and grain size. Such a technique was published by Grossmann in 1942, based on his observation that hardenability could be expressed as the product of a series of composition-related multiplying factors (Ref 37). The result of the calculation is an estimate of the ideal Grossmann diameter (D_I) as a measure of inherent steel hardenability. The equations most often are based on multiplicative factors.

The set of Grossmann factors, offered annually for many years in the June issue of *Metal Progress*, are now included in the Appendixes to ASTM Code A255-89 and SAE Standard J406. Other methods are based on regression equations and on calculation from thermodynamic and kinetic first principles. To date, no one prediction method has proved to be universally applicable to all steel types; that is, different predictors are more suited to steels of given alloying systems, carbon contents, and hardenability levels. In addition, it is often necessary to fine-tune the predictions based on the characteristics (residuals, melt practice, and so on) of a particular steel producer.

In the Grossmann method, ideal critical diameter (based on a definition of 50% martensite at the center of the specimen, with $H = \infty$) is calculated from steel composition and austenite grain sizes. The following

equation is one expression for calculating the ideal critical diameter:

$$D_I = D_{I\text{base}} \cdot f_{\text{Mn}} \cdot f_{\text{Si}} \cdot f_{\text{Cr}} \cdot f_{\text{Mo}} \cdot f_{\text{V}} \cdot f_{\text{Cu}} \quad (\text{Eq 2})$$

where f_x is the multiplicative factor for the particular alloying element. One set of D_I and alloy factors is presented in Table 6. These alloy factors were developed based on data from medium-carbon steels of medium hardenability. The general procedure for calculating the hardenability of a steel from the composition includes the following steps:

1. Determine the ASTM International grain size
2. Obtain a chemical composition
3. Determine $D_{I\text{base}}$ from the carbon content and the grain size (Table 6)
4. Determine alloy factors (Table 6)
5. Multiply the factors according to Eq 2 to provide the calculated ideal critical diameter

In Eq 2, the base D_I ($D_{I\text{base}}$) is a function of carbon content and grain size, with the multiplying factors (f) being independent of each other (which is not always true). Kramer et al. (Ref 29) subsequently determined carbon factors that were as much as three times larger than those of Grossmann, while the manganese factors were lower by approximately the same ratio. Why this discrepancy?

Grossmann had to use end-quench bars of carbon steels containing some manganese so that he could measure the base hardenability reproducibly. In the analysis, therefore, he had to separate the effects of manganese and carbon in these

Table 6 Tabulated hardenability factors of steels as a function of carbon content, carbon grain size, and selected alloying elements

Carbon, %	Base ideal diameter (D_{base}) at following carbon grain size			Alloying factor (f_x) where element, x, is				
	No. 6	No. 7	No. 8	Mn	Si	Ni	Cr	Mo
0.05	0.0814	0.0750	0.0697	1.167	1.035	1.018	1.1080	1.15
0.10	0.1153	0.1065	0.0995	1.333	1.070	1.036	1.2160	1.30
0.15	0.1413	0.1315	0.1212	1.500	1.105	1.055	1.3240	1.45
0.20	0.1623	0.1509	0.1400	1.667	1.140	1.073	1.4320	1.60
0.25	0.1820	0.1678	0.1560	1.833	1.175	1.091	1.54	1.75
0.30	0.1991	0.1849	0.1700	2.000	1.210	1.109	1.6480	1.90
0.35	0.2154	0.2000	0.1842	2.167	1.245	1.128	1.7560	2.05
0.40	0.2300	0.2130	0.1976	2.333	1.280	1.146	1.8640	2.20
0.45	0.2440	0.2259	0.2090	2.500	1.315	1.164	1.9720	2.35
0.50	0.2580	0.2380	0.2200	2.667	1.350	1.182	2.0800	2.50
0.55	0.273	0.251	0.231	2.833	1.385	1.201	2.1880	2.65
0.60	0.284	0.262	0.241	3.000	1.420	1.219	2.2960	2.80
0.65	0.295	0.273	0.251	3.167	1.455	1.237	2.4040	2.95
0.70	0.306	0.283	0.260	3.333	1.490	1.255	2.5120	3.10
0.75	0.316	0.293	0.270	3.500	1.525	1.273	2.62	3.25
0.80	0.326	0.303	0.278	3.667	1.560	1.291	2.7280	3.40
0.85	0.336	0.312	0.287	3.833	1.595	1.309	2.8360	3.55
0.90	0.346	0.321	0.296	4.000	1.630	1.321	2.9440	3.70
0.95	4.167	1.665	1.345	3.0520	...
1.00	4.333	1.700	1.364	3.1600	...

compositions, and this was done incorrectly. Because Kramer and his group used pure iron-carbon alloys as base compositions, they were able to measure the low hardenabilities very sensitively by quenching a series of small rounds.

As an interesting point, ideal critical diameters to 50% martensite calculated by Grossmann agree very well with those factors determined by Kramer for most practical compositions. However, to calculate hardenabilities of low- and medium-carbon steels in which complete solution of carbon and alloy can be readily obtained, the Kramer factors are recommended (Fig. 45, 46). Calculations with these factors are accurate within $\pm 15\%$ at D_1 values up to 114 mm (4.5 in.).

For steels with D_1 values greater than 114 mm (4.5 in.), the Kramer factors (as well as all others) are not accurate enough for practical use for three reasons.

First, steels of high hardenability are primarily bainitic, and the hardenability effects of several elements (such as molybdenum) are very different when bainite is the first transformation product.

Second, when some solution and carbide-forming elements (such as nickel and molybdenum) are used together, they produce synergistic hardenability effects; that is, the specific effect of each alloying element is larger than its effect when by itself in a composition.

Third, steels of high hardenability usually contain large quantities of strong carbide-forming elements that are often not completely dissolved.

Several hardenability-calculation techniques have been based on the multiplying-factor principle. One early example was a United States Steel calculator in the 1970s (Ref 38). A Climax Molybdenum calculator (Ref 39) was reported to more accurately predict the hardenability in low- to medium-carbon steels. Methods for determining the ideal critical diameter of an alloy from the composition and grain size also have been compared for a large number of

steels (Ref 9). Properly used, hardenability calculations can provide a valuable tool for designing cost-effective alternative steels, for deciding the disposition of heats in the mill prior to rolling, and possibly for replacing the costly and time-consuming measurement of hardenability. For more details, see the article "Hardenability Calculation of Carbon and Low-Alloy Steels with Low or Medium Carbon" in this Volume.

Steel with High Carbon (Ref 40). High-carbon (hypereutectoid) steels normally contain large quantities of undissolved carbides when hardened by commercial austenitizing procedures. If these conditions were not strictly controlled, it would not be possible to derive a single factor for the hardenability effect of an alloying element, because the quantity of alloy and carbon in solution would vary. Thus, prior structure; prior carbide size, shape, and distribution; and austenitizing time and temperature will influence the specific hardenability effect of a given quantity of alloy. Although also influential, grain size is of less importance because it does not vary greatly from ASTM 6 to 8 when excess carbides are present.

In high-carbon steels, prior structure of normalized steels range from 100% martensite to 100% lamellar carbides, two microstructures that transform to austenite easily during reheating. Microstructures of annealed material, however, usually contain large spheroidal carbides that are difficult to dissolve when the steel is reheated for hardening. If the prior structure, grain size, and temperature and time of austenitizing are controlled very closely, the specific hardenability effect of a given amount of alloying element can be reproduced enough to derive multiplying factors for many elements at high carbon levels.

For more information, see the article "Calculation of Hardenability in High-Carbon Steels" in this Volume.

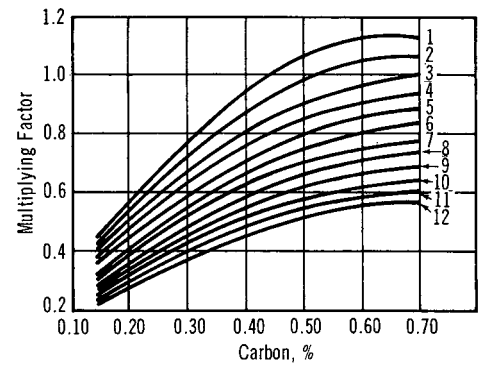


Fig. 45 Kramer factors for carbon and ASTM International grain size numbers are used with Fig. 46 for calculating hardenabilities of low- and medium-carbon steels, aluminum-killed. Source: Ref 29

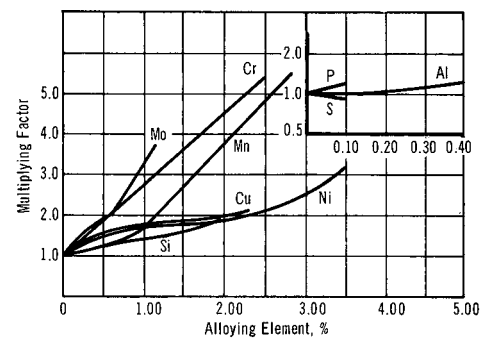


Fig. 46 Alloy multiplying factors to be used with Fig. 45

Calculation of Jominy Curves (Ref 33).

The development of linear regression formulas to a set of hardnesses corresponding to selected Jominy depths has been widely explored. This can be fairly effective for a single grade, provided the data set densely covers the chemistry limits and hardness bands. Such formulas, however, cannot be used outside of this single-grade context, so comprehensive information or expert systems based on such procedures are inherently inflexible and exaggerated. However, producers or users of a limited number of grades may find this appropriate as an alternative to grade-selected Grossmann factors.

A comprehensive, if relatively crude, system has been given for the HRC distribution in a Jominy bar by Just (Ref 41), who developed a universal Jominy curve shape in terms of penetration "E" in sixteenths of an inch and linearly regressed the coefficients for the weight percent of all of the constituents except carbon. A more recent example is the section "Caterpillar Hardenability Calculator (1E0024)" in the article "Hardenability Calculation of Carbon and Low-Alloy Steels with Low or Medium Carbon" in this Volume.

Steel Selection for Hardenability

To select the proper steel, one should first check the maximum attainable hardness chart,

such as Table 1, using the carbon range that will give the required surface hardness, from the 95 or 99.9 % martensite column. The commercially accepted range for surface hardness after tempering is 5 HRC points or 40 HB points (with Brinell numbers corresponding to indent diameters in 0.05 mm, or 0.002 in., increments) (Ref 42).

The maximum attainable (as-quenched) surface hardness depends on steel carbon content and the hardenability of the steel. The maximum section size that will harden through to the maximum surface hardness in oil is as follows:

Steel grade	Maximum section size	
	mm	in.
1045	6.35	0.250
5140	19.0	0.750
4140	38.1	1.5
4340	76.1	3.0

Determining the expected core hardness range can be determined by using the Jominy equivalent chart in Fig. 19 and the hardenability band for the steel being used (for example, Fig. 47 for 4140H steel). The Jominy equivalent chart shows that a 50 mm (2 in.) round hardened with a strong oil quench would create a cooling rate at the surface that is equivalent to the J4 (4/16 in.) position on a Jominy bar. The equivalent cooling rates at the core would be equivalent to the J8.5 Jominy distance. With a 4140H steel, the hardenability curve (Fig. 47) corresponds to a surface hardness range of 51 to 59 HRC with a core hardness of 46 to 57 HRC. The actual hardness of a given heat of steel would depend strictly on the specific

hardenability of that heat. To reduce the variation in hardening response and thus narrow the surface and core hardness values that result after heat treatment, the hardenability of the steel chosen can be narrowed by either using an H-steel or using a restricted hardenability specification of an H-steel.

Most of the hardenable 1xxx-series carbon steels have 0.60 to 0.90% Mn, although several grades have higher and others have lower manganese contents. Manganese has a marked effect on hardenability. Even a difference of 0.25% makes a significant difference on the end-quench hardenability of 0.50% C steel (Fig. 48).

Considering the range of manganese that is available in carbon steels, it follows that a wide range of hardenability can exist (Fig. 49). For example, 1541 steel frequently shows end-quench hardenability values higher than the minimum of the hardenability band for 1340 steel (Fig. 50). Thus, there is a gradual transition in hardenability from carbon grades to alloy grades. Because many carbon steels are produced from recycled scrap, residual elements in standard grades may vary.

There also are many applications for which minimum, rather than maximum, hardenability is needed, which accounts for the many low-manganese grades melted. For example, it is often desirable to produce thin layers of maximum hardness on shaft bearings or cam contours. This is usually accomplished by induction or flame hardening; however, if the hardened zone is too deep, an unfavorable pattern of residual stresses will be established, with resultant cracking in quenching or premature failure in service. In one instance, cams were made from standard 1050 steel

(0.60 to 0.90% Mn) and induction hardened to 60 HRC to a depth of approximately 1.6 mm (1/16 in.). If the hardened zone became as deep as 3.2 mm (1/8 in.), a significant number of parts cracked. Cracking was eliminated by using a modified grade of 1050 steel (0.30 to 0.60% Mn), which resulted in a shallower hardened zone after induction hardening.

Alloy Steels. Because the sections treated are often relatively large and because the alloying elements have the general effect of lowering the temperature range at which martensite is formed, the thermal and transformational stresses set up during quenching tend to be greater in alloy steel parts than those encountered in quenching the necessarily smaller sections of plain carbon steels. In general, the greater stresses result in distortion and risk of cracking.

Alloying elements, however, have two functions that tend to offset these disadvantages. First, and probably most important, is the

Hardness limits for specification purposes

J distance, 1/16 in.	Hardness, HRC	
	Max	Min
1	60	53
2	60	53
3	60	52
4	59	51
5	59	51
6	58	50
7	58	48
8	57	47
9	57	44
10	56	42
11	56	40
12	55	39
13	55	38
14	54	37
15	54	36
16	53	35
18	52	34
20	51	33
22	49	33
24	48	32
26	47	32
28	46	31
30	45	31
32	44	30

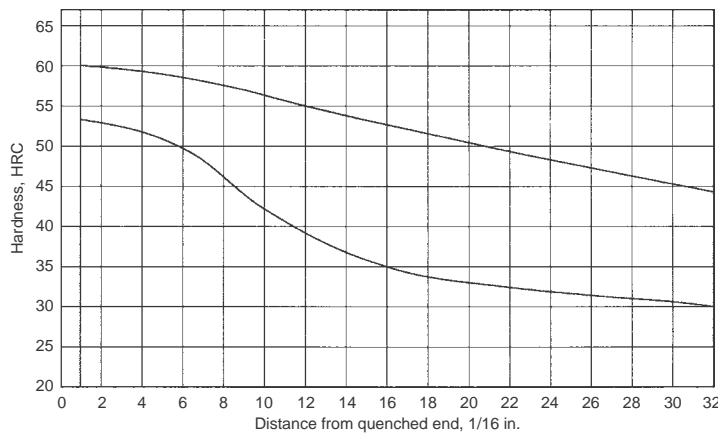


Fig. 47 Hardenability band for 4140H (UNS H41400) steel. Heat treating temperatures recommended by SAE. Normalize (for forged or rolled specimens only): 870 °C (1600 °F); austenitize: 845 °C (1550 °F)

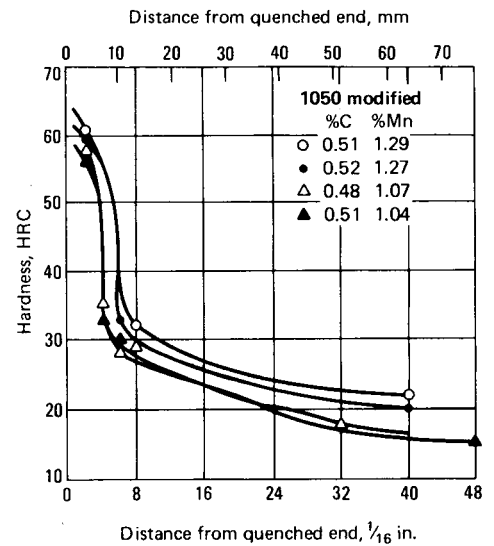


Fig. 48 Effect of carbon and manganese on end-quench hardenability of 1050 steel. The steels with 1.29 and 1.27% Mn contained 0.06% residual chromium. Steels with 1.07 and 1.04% Mn contained 0.06 and 0.08% residual chromium, respectively. No other residual elements were reported.

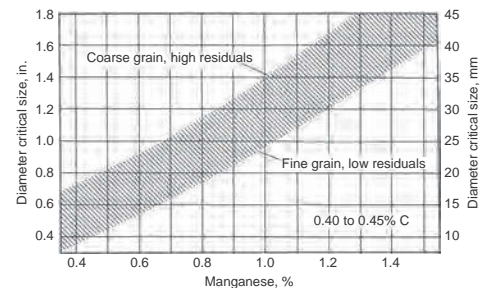


Fig. 49 Variation in critical diameter size (D_c , 50% martensite in center) with water quench (H approximately 5) from manganese contents and the band of variation due to residuals and austenite grain size. Source: Ref 20

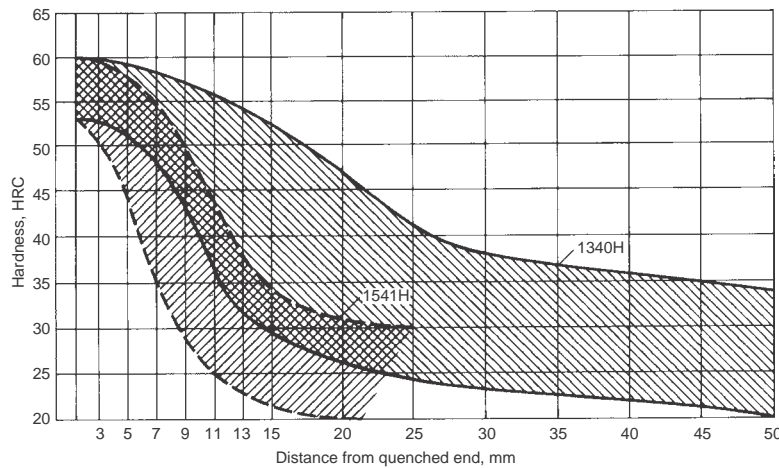


Fig. 50 Comparison of 1340H and 1541H hardenability ranges

capacity to permit the use of a lower carbon content for a given application. The decrease in hardenability accompanying the decrease in carbon content may be readily offset by the hardenability effect of the added alloying elements, and the lower carbon steel will exhibit a much lower susceptibility to quench cracking. This lower susceptibility results from the greater plasticity of the lower-carbon martensite and from the generally higher temperature range at which martensite is formed in the lower-carbon materials. Quench cracking is seldom encountered in steel containing 0.25% C or less, and the susceptibility to cracking increases progressively with increasing carbon content.

The second function of the alloying elements in quenching is to permit slower rates of cooling for a given section because of increased hardenability, thereby generally decreasing the thermal gradient and, in turn, the cooling stress. It should be noted, however, that this is not altogether advantageous, because the direction, as well as the magnitude, of the stress existing after the quench is important in relation to cracking. To prevent cracking, surface stresses after quenching should be either compressive or at a relatively low tensile level. In general, the use of a less drastic quench suited to the hardenability of the steel will result in lower distortion and greater freedom from cracking.

Furthermore, the increased hardenability of these alloy steels may permit heat treatment by austempering or martempering, and therefore, the level of adverse residual stress before tempering may be held to a minimum. In austempering, the workpiece is cooled rapidly to a temperature in the lower bainite region and is held at that temperature so that the section transforms completely to bainite. Because transformation occurs at a relatively high temperature and proceeds rather slowly, the stress level after transformation is quite low, and distortion is minimal.

In martempering, the workpiece is cooled rapidly to a temperature just above M_s , held there until the piece attains a uniform temperature throughout, and then is cooled slowly (usually by air cooling) through the martensite range. This procedure causes martensite to form more or less simultaneously throughout the entire section, thereby holding transformational stresses at a very low level, which minimizes distortion and the danger of cracking.

Example 1: Use of Hardenability Charts to Verify that 4140H Steel Will Fulfill Hardness Specifications for a 44.45 mm (1.75 in.) Diameter Shaft. A shaft 44.45 mm (1.75 in.) in diameter and 1.1 m (3½ ft) long is required in a machine. The engineering analysis indicates that the torsion requirements will approach a maximum of 170 MPa (25 ksi) and that the bending stresses will reach a maximum of 550 MPa (80 ksi). Because several other parts in production in the same plant are being made from 4140H steel, it is desired to know whether 4140H has enough hardenability for this shaft.

Because the shear stress in torsion is approximately one-half that in bending, the latter will be the primary consideration. In bending, stresses approach zero in the neutral axis; therefore, the steel need not be hardened completely to the center. This is helpful because the distribution of stress in quenching will decrease the danger of quench cracking and, after tempering, should leave the exterior portion of the shaft in compression.

To withstand a fatigue load of 550 MPa (80 ksi) in bending, a minimum hardness of 35 HRC is required. For this example, it will be assumed that 35 HRC should be obtained by tempering a structure that, as-quenched, contains at least 80% martensite. From experience with similar parts, it is known that the 80% martensite structure should be present down to the three-quarter-radius position in the shaft.

Because 4140H has a minimum carbon content of 0.37%, the first operation on the charts (Fig. 51) is to find the as-quenched hardness that corresponds to 0.37% C in an 80%

martensite structure. As shown in the top chart of Fig. 51—the same data as in Fig. 1(d)—this as-quenched hardness is 45 HRC.

The original question (whether 4140H is appropriate for this part) can now be rephrased to read: Will 4140H provide the required minimum as-quenched hardness of 45 HRC at three-quarter-radius in the 44.45 mm (1.75 in.) diameter shaft? To determine the answer to this question, enter the middle chart of Fig. 51 (this is the same as Fig. 38b) at the diameter level of 44.45 mm (1.75 in.) and move horizontally to an intersection with the $\frac{3}{4}$ -radius curve. This intersection occurs at the $\frac{6.5}{16}$ position on the specimen. Then, move down vertically into the bottom chart to an intersection with the curve for minimum hardenability of 4140H. The intersection occurs at 49 HRC. Because no more than 45 HRC is required, 4140H has more than enough hardenability for this part.

Hardenability Limits and H-Steels

Hardenability bands are Jominy curves (based on much historical data) that describe the range of hardenability for many grades of carbon and alloy steels. Hardenability bands also are used for the specification of H-steels, which are steels produced to a specific hardenability band. These steels are designated by the letter “H” following the composition code or preceding the UNS designation.

The H-steels are guaranteed by the supplier to meet these hardenability limits for a specified range of chemical composition. The tighter hardenability bands of four H-steels are compared in Fig. 52 with the wider hardenability bands of similar steel grades based on composition. The end-quench hardenability bands of H-steels are summarized in Table 7.

When an H-steel is specified, the steel producer shows on the shipping papers or by some other acceptable means the hardenability characteristics of the heat involved. The heat hardenability is shown either by hardness values at specified reference points or at the specified distances from the quenched end of the test specimen. No reading is reported below 20 HRC. The heat hardenability is determined from either a cast or a forged end-quench test bar.

Figure 53 shows the differences between minimum hardenability curves for six series of steels. In each series, alloy content is essentially constant, and the effect of carbon content on hardenability can be observed over a range from 0.15 to 0.60%. The hardness effect is shown by the vertical distance between the curves at any position on the end-quench specimen, that is, for any cooling rate. This effect varies significantly, depending on the type and amounts of alloying elements. For example, referring to Fig. 53(d), (e) to (f), an increase in carbon content from 0.35 to 0.50% in each of the three series of steels causes hardness increases (in Rockwell C

Result
80% martensite structure of 0.37% C has as-quenched hardness of 45 HRC

Required
45 HRC min at 3/4 radius in a 44.45 mm (1.75 in.) diam shaft, oil quenched

To determine whether 4140H will meet requirement, start with 44.45 mm (1.75 in.) diameter

49 HRC
Minimum hardenability of 4140H meets the requirement

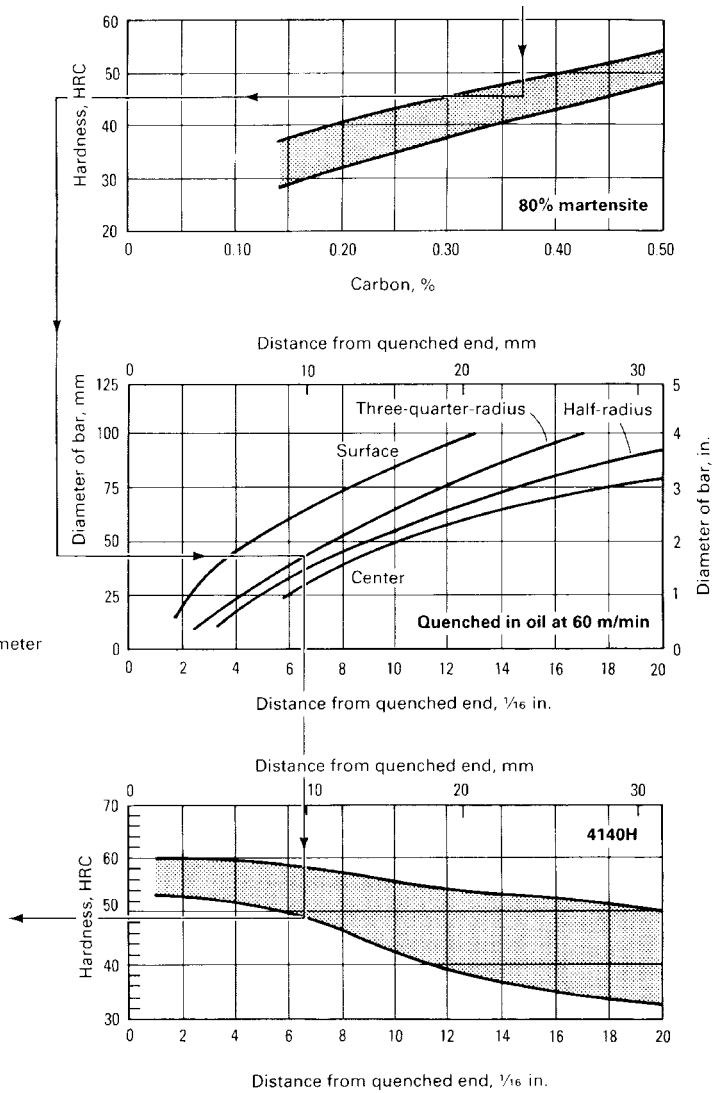


Fig. 51 Illustration of the use of hardenability data in steel selection. See text

points) at four different end-quench positions, as shown subsequently:

Series	Distance from quenched surface, in.			
	1/16	4/16	9/16	12/16
41xxH	8	10	17	20
51xxH	8	13	9	8
86xxH	8	12	18	12

The hardenability effect of carbon content is read on the horizontal axis in Fig. 53. If the inflection points of the curves are used to approximate the position of 50% martensite transformation, the effect of carbon content on hardenability in 8650 versus 8630 steel can be expressed as + 4/16; that is, the inflection point is moved from the 5/16 position to the 9/16 position. Similarly, with nominal carbon contents of 0.35 and 0.50%, the hardenability effect of carbon is seen to be less (2/16) in 51xx-series steels and more (6/16) in 41xx steels.

Considering the combined hardening and hardenability effects in terms of quenching speed, the cooling rate (or quenching speed) required to produce 45 HRC is affected more by 0.15% C with certain combinations of alloying elements than it is by other combinations. For example, in a steel containing 0.75 Cr and 0.15 Mo (a 41xxH-series steel, for example), increasing the carbon content by 0.15% lowers the required or critical cooling rate to obtain 45 HRC from 25 to 4.6 °C (45 to 8.3 °F) per second, while in a steel containing 0.75% Cr and no molybdenum (51xxH series), the same increase in carbon content lowers the cooling rate from 47 to 21 °C (85 to 37 °F) per second.

The practical significance of the effect of carbon and alloy contents on cooling rate is considerable. In a 50 mm (2 in.) diameter bar of 4150 steel, a hardness of 45 HRC can be obtained at half-radius using an oil quench

without agitation. In a 4135 steel bar of the same diameter, to obtain the same hardness at half-radius would require a strongly agitated water quench. Comparing 32 mm (1¼ in.) diameter bars of 5135 and 5150 steel, an agitated water quench will produce a hardness of 45 HRC at half-radius in the 5135 bar; the identical condition can be obtained in the 5150 bar using an oil quench with moderate agitation. Thus, an increase or decrease in carbon content or an alloying addition, such as 0.15% Mo, affects the results obtained both in terms of the quenching severity required and the section size in which the desired results can be obtained.

Figure 54 shows how steels are rated on the basis of ideal critical diameter by expressing the effect of carbon and alloy content on the section size that will harden to 50% martensite at the center, assuming an ideal quench. An ideal quench is defined as one that removes heat from the surface of the steel as fast as it is delivered to the surface. In general, the relation between hardness and carbon content that is important in practice is obscured in this rating method because the steel is rated to a constant microstructure. Hardness decreases continuously with lower carbon contents.

H-Steels Classified by Hardness at End-Quench Positions

Table 8 shows the location on the end-quenched specimen of the low limit of the H-band for six different hardness levels that may be specified for as-quenched hardness: 55, 50, 45, 40, 35, and 30 HRC. The last two levels apply primarily to the core hardness of carburized parts. This table, which includes most of the steels for which H-bands have been established, has been devised to work with the charts in Fig. 34 and 35 and reduces the amount of chart-hopping that has been needed in the past to examine all the available steels for the purpose of selecting one. The use of Fig. 34 and Table 8 is described in the following example.

Example 2: Selection of a Steel with 38 mm (1½ in.) Diameter Section Equivalent Having 45 HRC at Half-Radius. This example traces the steps needed to select a steel that will harden to 45 HRC at half-radius in a part having a significant section equivalent to a 38 mm (1½ in.) diameter bar. First, it is assumed that, to prevent distortion, the quench will be in oil at 60 m/min (200 sfm) ($H = 0.5$) and that a nonscaling atmosphere will be used for heating to the austenitizing temperature. Therefore, the chart for half-radius in Fig. 34 (c) is applicable.

The following steps will then lead to the selection of a steel. First, trace horizontally at the level of 1½ in. diameter to the curve for oil quench at 60 m/min (200 sfm)

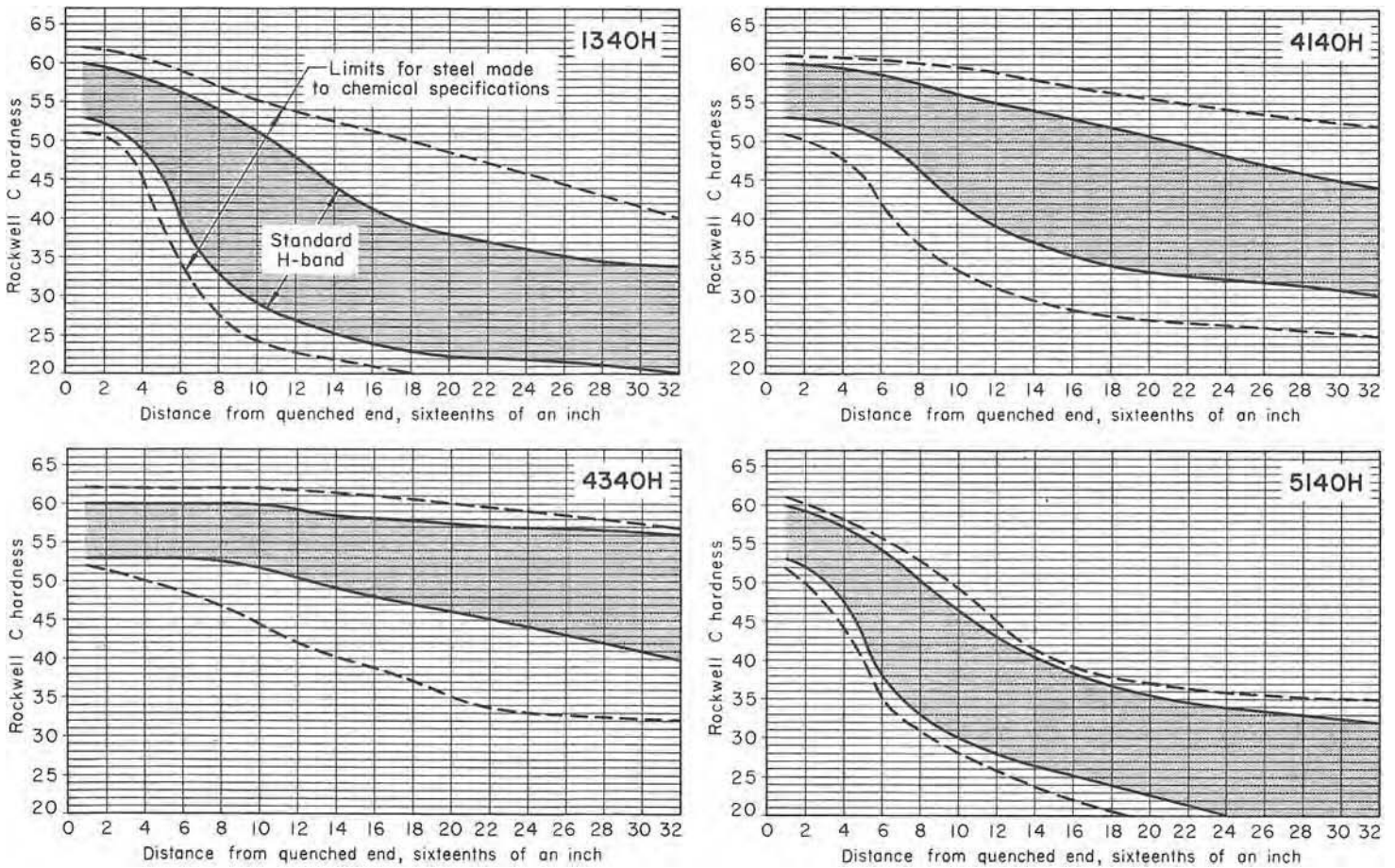


Fig. 52 Examples of hardenability bands of H-steels compared to the wider bands for similar steels made to chemical specification only

Table 7 End-quench hardenability bands for H-steels

Steel	Jominy position, 1/16 in.																																
	1	2	3	4	5	6	7	8	9	10	11	12	13	14	15	16	17	18	19	20	21	22	23	24	25	26	27	28	29	30	31	32	
1038H max	58	55	49	37	30	28	27	26	25	25	...	24	...	23	...	21
1038H min	51	34	26	23	22	21
1045H max	62	59	52	38	33	32	31	30	29	29	...	28	...	27	...	26	...	25	...	23	...	22	...	21	
1045H min	55	42	31	28	26	25	25	24	23	22	...	21	...	20	
1522H max	50	47	45	39	34	30	27	
1522H min	41	32	22	20	
1524H max	51	48	45	39	35	32	29	27	26	25	...	23	...	22	...	20	
1524H min	42	38	29	22	
1526H max	53	49	46	39	33	30	27	26	24	24	...	23	...	22	...	21	...	20	
1526H min	44	38	26	21	
1541H max	60	59	57	55	52	48	44	39	35	33	...	32	...	31	...	30	...	30	...	29	...	28	...	26		
1541H min	53	50	44	38	32	27	25	23	23	22	...	21	...	20	
15B21H max	48	47	46	44	40	35	27	20	
15B21H min	41	40	38	30	20	
15B28H max	53	53	52	51	51	50	49	48	46	43	40	37	34	31	30	...	27	...	25	...	25	...	24	...	23	...	22	...	21	...	20		
15B28H min	47	47	46	45	42	32	25	21	20	
15B30H max	55	53	52	51	50	48	43	38	33	29	27	26	25	24	23	22	...	20	
15B30H min	48	47	46	44	32	22	20	
15B35H max	58	56	55	54	53	51	47	41	...	30	...	27	...	26	...	25	24	22	20		
15B35H min	51	50	49	48	39	28	24	22	...	20	
15B37H max	58	56	55	54	53	52	51	50	...	45	...	40	...	33	...	29	27	25	23	21		
15B37H min	50	50	49	48	43	37	33	26	...	22	...	21	...	20	
15B41H max	60	59	59	58	58	57	57	56	55	55	54	53	52	51	50	49	...	46	...	42	...	39	...	36	...	34	...	33	...	31	...	31	
15B41H min	53	52	52	51	51	50	49	48	44	37	32	28	26	25	25	24	...	23	...	22	...	21	...	21	...	20	...	20	
15B48H max	63	62	62	61	60	59	58	57	56	55	53	51	48	45	41	38	...	34	...	32	...	31	...	30	...	29	...	29	...	28	...	28	
15B48H min	56	56	55	54	53	52	42	34	31	30	29	28	27	27	26	26	...	25	...	24	...	23	...	22	...	21	...	20	
15B62H max	65	65	64	64	64	63	63	63	62	61	60	...	58	...	54	...	48	...	43	...	40	...	37	...	35	...	34		
15B62H min	60	60	60	60	59	58	57	52	43	39	37	35	35	34	33	33	...	32	...	31	...	30	...	30	...	29	...	28	...	27	...	26	
1330H max	56	56	55	53	52	50	48	45	43	42	40	39	38	37	36	35	...	34	...	33	...	32	...	31	...	31	...	31	...	30	...	30	
1330H min	49	47	44	40	35	31	28	26	25	23	22	21	20	
1340H max	60	60	59	58	57	56	55	54	52	51	50	48	46	44	42	41	...	39	...	38	...	37	...	36	...	35	...	35	...	34	...	34	

(continued)

(a) Formerly standard steels

Table 7 (Continued)

Table with 32 columns (Steel, 1-32) and 32 rows. Columns 1-32 represent Jominy position in 1/16 in. units. The table lists various steel grades and their corresponding hardness values at different positions.

(continued)

(a) Formerly standard steels

Table 7 (Continued)

Steel	Jominy position, 1/16 in.																															
	1	2	3	4	5	6	7	8	9	10	11	12	13	14	15	16	17	18	19	20	21	22	23	24	25	26	27	28	29	30	31	32
4145RH min	57	57	56	56	55	55	54	53	52	52	51	50	49	48	47	46	...	44	...	43	...	42	...	40	...	40	...	39	...	38	...	37
4161RH max	65	65	65	65	65	65	65	65	65	65	65	64	64	64	63	63	...	62	...	62	...	61	...	60	...	59	...	58	...	57	...	57
4161RH min	60	60	60	60	60	60	60	60	60	60	60	59	59	59	58	57	...	56	...	54	...	53	...	51	...	49	...	47	...	46	...	45
4320RH max	47	46	44	41	39	36	34	32	31	29	28	26	25	24	24	23	...	22	...	22	...	21	...	21	...	21	...	21	...	21	...	21
4320RH min	42	40	37	34	31	29	27	25	24	23	22	21	20
4620RH max	47	44	40	37	32	29	27	25	24	23	22	21	20
4620RH min	42	37	30	27	24	21	20
4820RH max	47	47	46	45	43	41	40	38	36	35	34	33	32	31	30	29	...	28	...	27	...	26	...	25	...	25	...	25	...	24	...	23
4820RH min	42	42	41	40	36	33	32	30	28	27	26	25	24	24	23	23	...	22	...	22	...	21	...	20	...	20
50B40RH max	59	59	58	58	57	56	55	54	52	50	49	47	45	44	41	38	...	36	...	34	...	33	...	32	...	31	...	30	...	29	...	28
50B40RH min	54	54	53	53	52	50	47	43	38	35	33	32	31	30	29	28	...	26	...	24	...	23	...	22	...	21	...	20
5130RH max	55	53	51	49	46	44	42	39	37	35	34	33	32	31	30	29	...	28	...	27	...	26	...	25	...	24	...	23	...	22	...	21
5130RH min	50	47	44	41	37	35	33	31	29	27	26	25	24	23	22	21	...	20
5140RH max	59	58	57	55	53	51	48	46	44	43	41	40	39	37	36	35	...	34	...	33	...	32	...	31	...	30	...	30	...	29	...	29
5140RH min	54	53	51	49	45	41	38	36	34	33	32	31	30	29	28	27	...	26	...	25	...	24	...	23	...	22	...	21	...	20
5160RH max	65	65	65	65	64	63	62	60	58	56	55	53	51	50	48	47	...	44	...	43	...	42	...	41	...	40	...	39	...	39	...	38
5160RH min	60	60	60	59	58	57	54	50	45	42	40	39	38	37	36	36	...	35	...	34	...	33	...	32	...	31	...	30	...	29	...	29
8620RH max	47	45	41	38	34	31	29	28	26	25	24	23	23	22	22	21	...	20
8620RH min	42	39	35	30	26	24	22	21	20
8622RH max	49	47	45	41	38	35	32	30	29	28	27	26	25	24	24	23	...	23	...	22	...	22	...	22	...	22	...	22	...	22	...	22
8622RH min	44	41	37	32	29	27	24	22	21	20
8720RH max	47	45	43	40	36	33	31	29	28	27	26	25	24	24	23	...	23	...	22	...	22	...	22	...	21	...	20
8720RH min	42	39	37	32	28	26	24	23	22	21	20
8822RH max	49	48	47	43	40	37	35	33	32	31	30	30	29	28	28	27	...	27	...	26	...	26	...	26	...	26	...	25	...	25	...	25
8822RH min	44	43	40	35	31	29	27	26	25	25	24	23	23	22	22	21	...	21	...	20
9310RH max	42	42	42	41	41	40	40	39	38	37	37	36	35	34	34	33	...	33	...	32	...	32	...	32	...	32	...	32	...	31	...	31
9310RH min	37	36	36	35	34	33	32	31	30	29	29	28	28	28	28	27	...	27	...	26	...	26	...	26	...	26	...	26	...	25	...	25

(a) Formerly standard steels

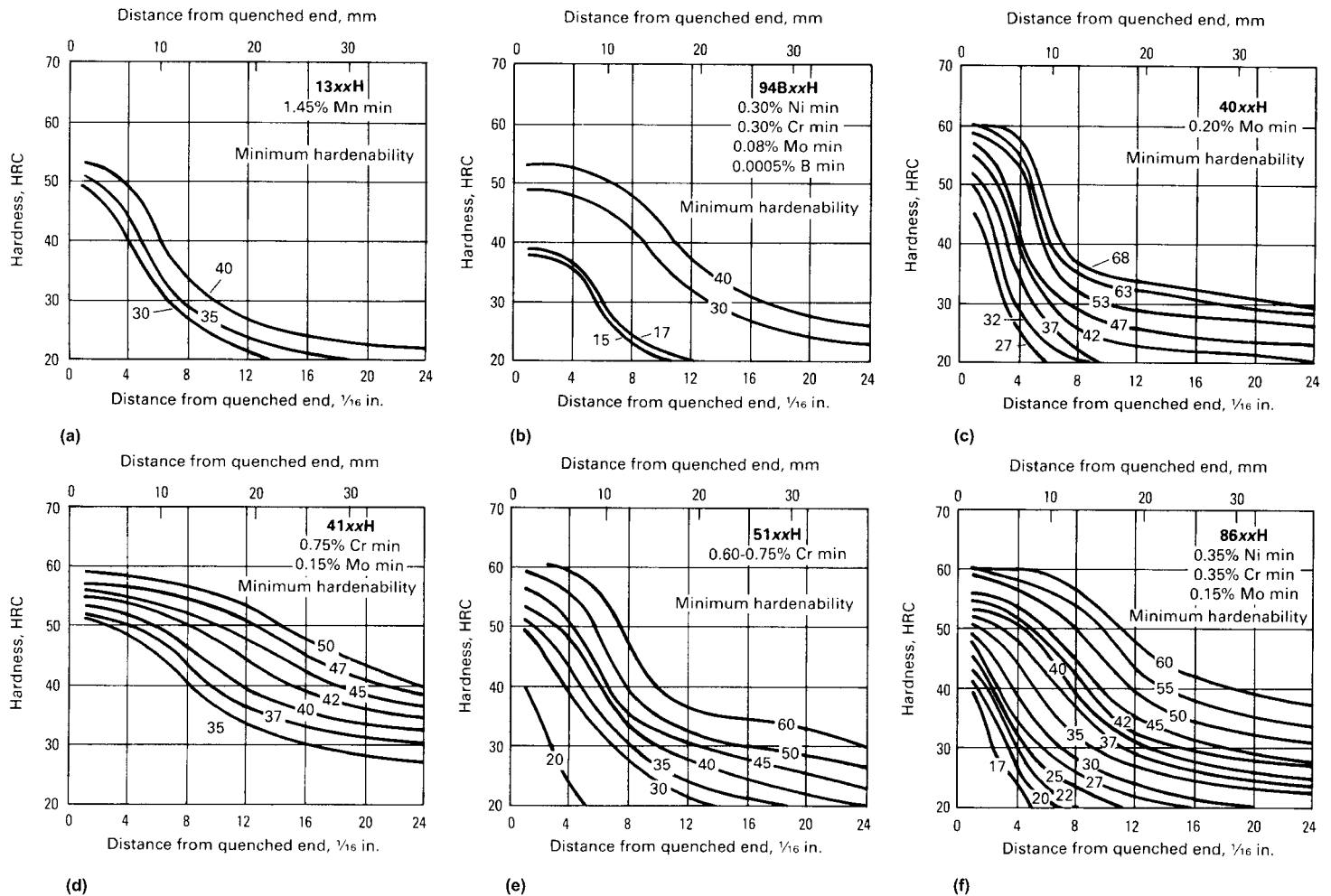


Fig. 53 Effect of carbon content on the minimum end-quench hardenability of six series of alloy H-steels. The number adjacent to each curve indicates the carbon content of the steel, to be inserted in place of xx in alloy designation.

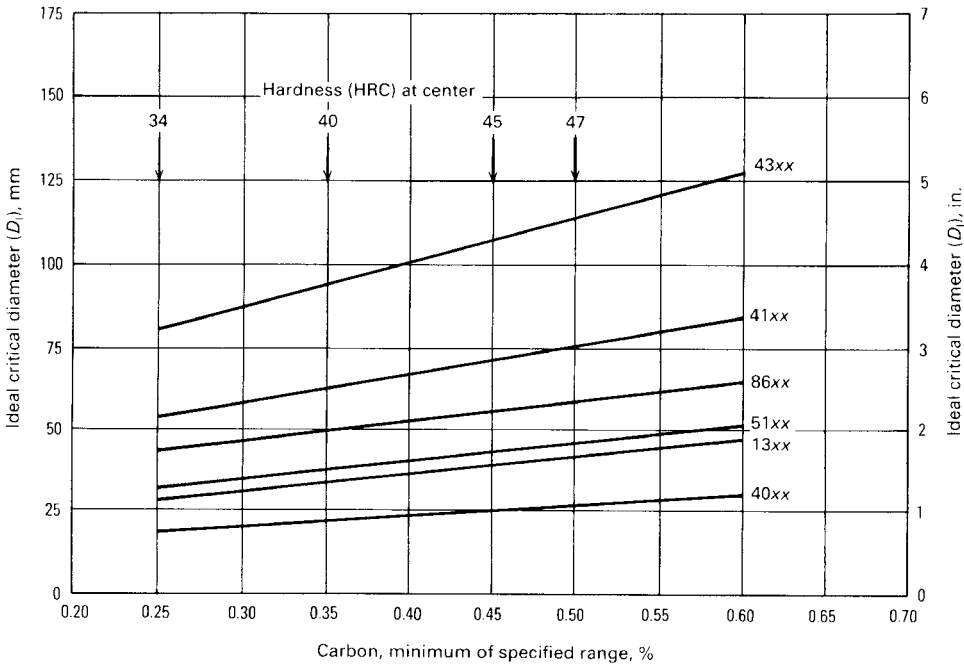


Fig. 54 Effect of carbon content on ideal critical diameter, calculated for the minimum chemical composition of each grade

(curve 5). From the point of intersection with this curve, trace vertically to the x-axis to determine the location on the end-quenched bar that has the same cooling rate as the point at half-radius in the 1½ in. round. This location is 6.5/16 from the quenched end of the bar. Then turn to the section of Table 8 that gives the location of 45 HRC on the end-quenched bar for the various H-steels. Here it is found that four steels will produce 45 HRC at 6.5/16 from the end of the bar: 8640, 8740, 5150, and 94B30. If some additional hardenability is not undesirable, steels that will produce 45 HRC at 7/16 can be included—4137, 8642, 6145, and 50B40. Steel 9261 is also in the same category, but it would not be applicable, because it is a spring steel used only when the as-quenched hardness must be as high as 50 to 55 HRC. Therefore, eight steels are available that will meet the hardenability requirements of the stipulated specification. From knowledge of other characteristics of these steels, including machinability, forgeability, crackability, distortion, availability, and cost, the selector can decide which of these eight will be the most desirable for the part in question.

Table 8 Classification of H-steels according to minimum hardness at various distances from quenched end

Distance from quenched end, 1/16 in.	H-steels with a minimum hardenability curve that intersects the specified hardness at the indicated distance from the quenched end of the hardenability specimen	Typical values(a) obtained by the use of Fig. 34 bar diameter (in.) for equivalent cooling rate at:					
		Three-quarter-radius		Half-radius		Center	
		Oil at 200 sfm; H = 0.5	Water at 200 sfm; H = 1.5	Oil at 200 sfm; H = 0.5	Water at 200 sfm; H = 1.5	Oil at 200 sfm; H = 0.5	Water at 200 sfm; H = 1.5
30 HRC							
2½	8617, 4118, 4620, 5120, 1038, 1522, 4419	0.4	1.5	...	1.1	...	0.8
3	4812, 4027, 1042, 1045, 1146, 1050, 1524, 1526, 4028, 6118	0.6	1.8	...	1.2	0.3	0.95
3½	4720, 6120, 8620, 4032	0.7	2.05	0.5	1.4	0.45	1.1
4	4815, 8720, 4621, 8622, 1050(b)	0.9	2.35	0.7	1.5	0.6	1.3
4½	46B12, 4817, 4320, 8625, 5046	1.05	2.6	0.8	1.6	0.7	1.45
5	4037, 1541, 4718, 8822	1.2	2.9	0.9	1.8	0.85	1.6
5½	94B15, 8627, 4042, 1541, 15B35	1.4	3.2	1.1	1.9	1.0	1.7
6	94B17
6½	4820, 1330, 4130, 8630, 1141	1.7	3.8	1.4	2.2	1.25	2.0
7	9130, 5130, 5132, 4047	1.85	...	1.5	2.4	1.35	2.1
7½	1335, 50B46, 15B37	2.0	...	1.7	2.5	1.5	2.2
8	5135	2.1	...	1.8	2.7	1.6	2.35
9½	1340	2.5	...	2.2	3.3	1.9	2.7
10	8635, 5140, 4053, 50B40	2.6	...	2.3	3.4	2.0	2.8
11	4640	2.8	...	2.4	3.7	2.15	3.0
12	8637, 1345, 50B44, 5145, 94B30	3.05	...	2.6	3.9	2.3	3.2
14	50B50
16	4135, 5147, 8645, 8740	3.85	...	3.3	...	2.8	3.85
20	4063	3.6
22	4068, 50B60, 5155, 86B30, 9260	3.7
24	4137, 5160, 6150, 81B45, 51B60, 8650	3.85
32	4140
35 HRC							
1½	8617	...	0.9	...	0.8	...	0.45
2	4812, 4118, 4620, 5120, 1038, 1522, 4419, 6118	...	1.2	...	0.9	...	0.65
2½	4028, 4720, 8620, 4027, 1042, 1045, 1146, 1050, 1524, 1526	0.4	1.5	...	1.1	...	0.8
3	9310, 46B12, 4320, 6120, 8720, 4621, 8622, 8625, 4032, 4815	0.6	1.8	...	1.2	0.3	0.95
3½	4815, 4817, 94B17, 5046, 1050(b), 4781, 8822	0.7	2.05	0.5	1.4	0.45	1.1

(continued)

(a) If based on equivalent hardness, actual bar diameter will be less. (b) High residual alloy

Table 8 (Continued)

Distance from quenched end, 1/16 in.	H-steels with a minimum hardenability curve that intersects the specified hardness at the indicated distance from the quenched end of the hardenability specimen	Typical values(a) obtained by the use of Fig. 34 bar diameter (in.) for equivalent cooling rate at:					
		Three-quarter-radius		Half-radius		Center	
		Oil at 200 sfm; H = 0.5	Water at 200 sfm; H = 1.5	Oil at 200 sfm; H = 0.5	Water at 200 sfm; H = 1.5	Oil at 200 sfm; H = 0.5	Water at 200 sfm; H = 1.5
4	8627, 4037	0.9	2.35	0.7	1.5	0.6	1.3
4½	94B15, 4042, 1541	1.05	2.6	0.8	1.6	0.7	1.45
5	4820, 1330, 4130, 5130, 8630, 5132, 1141, 50B46, 4047, 15B35, 94B17	1.2	2.9	0.9	1.8	0.85	1.6
5½	1335	1.4	3.2	1.1	1.9	1.0	1.7
6	5135	1.55	3.5	1.2	2.1	1.1	1.85
6½	15B37
7	8635, 1340, 5140, 4053	1.85	...	1.5	2.4	1.35	2.1
8	4063, 1345, 5145	2.1	...	1.8	2.7	1.6	2.35
8½	8637	2.2	...	1.9	2.9	1.7	2.45
9	4640, 4068, 50B40	2.35	...	2.0	3.1	1.8	2.6
9½	8640, 50B44, 5150	2.5	...	2.2	3.3	1.9	2.7
10	8740, 9260
10½	4135, 50B50	2.7	...	2.35	3.5	2.1	2.9
13	4137	3.25	...	2.8	...	2.45	3.4
16	4140, 6150, 81B45, 86B30	3.85	...	3.3	...	2.8	3.85
40 HRC							
1	5120, 6120	...	0.65	...	0.6	...	0.3
1½	4118, 4620, 4320, 4720, 8620, 8720, 1038, 1522, 1526, 4621	...	0.9	...	0.8	...	0.45
2	8622, 8625, 4027, 1045, 1524, 4028, 4718	...	1.2	...	0.9	...	0.65
2¼	1146	0.3	1.3	...	1.0	...	0.7
2½	4820, 8627, 4032, 1042, 1050	0.4	1.5	...	1.1	...	0.8
3	4037, 8822	0.6	1.8	...	1.2	0.3	0.95
3½	4130, 5130, 8630, 5046, 1050(b), 1541	0.7	2.05	0.5	1.4	0.45	1.1
4	1330, 5132, 4042	0.9	2.35	0.7	1.5	0.6	1.3
4½	5135, 1141, 4047	1.05	2.6	0.8	1.6	0.7	1.45
5	1335, 50B46, 15B35	1.2	2.9	0.9	1.8	0.85	1.6
5½	8635, 5140, 4053, 15B37	1.4	3.2	1.1	1.9	1.0	1.7
6	1340, 9260, 4063	1.55	3.5	1.2	2.1	1.1	1.85
6½	8637, 5145, 1345	1.7	3.8	1.4	2.2	1.25	2.0
7	4640, 4068	1.85	...	1.5	2.4	1.35	2.1
7½	8640, 5150	2.0	...	1.7	2.5	1.5	2.2
8	4135, 8740, 50B40	2.1	...	1.8	2.7	1.6	2.35
8½	6145, 9261, 50B44, 5155	2.2	...	1.9	2.9	1.7	2.45
9	4137, 8642, 5147, 50B50, 94B30	2.35	...	2.0	3.1	1.8	2.6
9½	8742, 8645, 5160, 9262	2.5	...	2.2	3.3	1.9	2.7
10½	6150, 50B60	2.7	...	2.35	3.5	2.1	2.9
11	4140	2.8	...	2.4	3.7	2.15	3.0
11½	81B45, 8650, 5152	2.9	...	2.5	3.8	2.25	3.1
12	86B30
13	51B60	3.25	...	2.8	...	2.45	3.4
14	8655	3.45	...	2.95	...	2.6	3.55
15	4142	3.65	...	3.1	...	2.7	3.7
15½	8750	3.75	...	3.2	...	2.75	3.8
18	4145, 8653, 8660	3.45
19	9840, 86B45	3.45
20	4147	3.6
24	4337, 4150	3.85
32	4340
36+	E4340, 9850
45 HRC							
1	4027, 4028, 8625
1½	8627, 1038	...	0.9	...	0.8	...	0.45
2	4032, 1042, 1146, 1045	...	1.2	...	0.9	...	0.65
2½	4130, 5130, 8630, 4037, 1050, 5132	0.4	1.5	...	1.1	...	0.8
3	1330, 5046, 1541	0.6	1.8	...	1.2	0.3	0.95
3¼	1050(b)	0.65	1.9	...	1.3	0.4	1.05
3½	1335, 5135, 4042, 4047	0.7	2.05	0.5	1.4	0.45	1.1
4	8635, 1141	0.9	2.35	0.7	1.5	0.6	1.3
5	8637, 1340, 5140, 50B46, 4053, 9260, 15B37	1.2	2.9	0.9	1.8	0.85	1.6
5½	5145, 4063	1.4	3.2	1.1	1.9	1.0	1.7
6	4135, 4640, 4068, 1345	1.55	3.5	1.2	2.1	1.1	1.85
6½	8640, 8740, 5150, 94B30	1.7	3.8	1.4	2.2	1.25	2.0
7	4137, 8642, 6145, 9261, 50B40	1.85	...	1.5	2.4	1.35	2.1
7½	8742, 50B44, 5155	2.0	...	1.7	2.5	1.5	2.2
8	8645, 5147	2.1	...	1.8	2.7	1.6	2.35
8½	4140, 6150, 5160, 9262, 50B50	2.2	...	1.9	2.9	1.7	2.45
9	50B60	2.35	...	2.0	3.1	1.8	2.6
9½	81B45, 8650, 86B30	2.5	...	2.2	3.3	1.9	2.7
10	5152	2.6	...	2.3	3.4	2.0	2.8
11	51B60, 8655	2.8	...	2.4	3.7	2.15	3.0

(continued)

(a) If based on equivalent hardness, actual bar diameter will be less. (b) High residual alloy

Table 8 (Continued)

Distance from quenched end, $\frac{1}{16}$ in.	H-steels with a minimum hardenability curve that intersects the specified hardness at the indicated distance from the quenched end of the hardenability specimen	Typical values(a) obtained by the use of Fig. 34 bar diameter (in.) for equivalent cooling rate at:					
		Three-quarter-radius		Half-radius		Center	
		Oil at 200 sfm; $H = 0.5$	Water at 200 sfm; $H = 1.5$	Oil at 200 sfm; $H = 0.5$	Water at 200 sfm; $H = 1.5$	Oil at 200 sfm; $H = 0.5$	Water at 200 sfm; $H = 1.5$
11½	4142	2.9	...	2.5	3.8	2.25	3.1
12	8750	3.05	...	2.6	3.9	2.3	3.2
13	8653, 8660	3.25	...	2.8	...	2.45	3.4
14	9840, 4145	3.45	...	2.95	...	2.6	3.55
16	86B45, 4147	3.85	...	3.3	...	2.8	3.85
17	4337	3.35
18	4150	3.45
22	4340	3.7
26	4161
30	E4340
36	9850
50 HRC							
1	4032, 5132, 1038	...	0.65	...	0.6	...	0.3
1½	1335, 5135, 8635, 4037, 1042, 1146, 1045	...	0.9	...	0.8	...	0.45
2	4135, 1541, 15B35, 15B37	...	1.2	...	0.9	...	0.65
2¼	1050(b)	0.3	1.3	...	1.0	...	0.7
2½	4042	0.4	1.5	...	1.1	...	0.8
3	8637, 5140, 5046, 4047	0.6	1.8	...	1.2	0.3	0.95
3½	4137, 1141, 1340	0.7	2.05	0.5	1.4	0.45	1.1
4	4640, 5145, 50B46	0.9	2.35	0.7	1.5	0.6	1.3
4½	8640, 8740, 4053, 9260	1.05	2.6	0.8	1.6	0.7	1.45
5	8642, 4063, 1345, 50B40	1.2	2.9	0.9	1.8	0.85	1.6
5½	8742, 6145, 5150, 4068	1.4	3.2	1.1	1.9	1.0	1.7
6	4140, 8645	1.55	3.5	1.2	2.1	1.1	1.85
6½	9261, 50B44, 5155	1.7	3.8	1.4	2.2	1.25	2.0
7	5147, 6150	1.85	...	1.5	2.4	1.35	2.1
7½	5160, 9262, 50B50	2.0	...	1.7	2.5	1.5	2.2
8	4142, 81B45, 8650	2.1	...	1.8	2.7	1.6	2.35
8½	5152, 50B60	2.2	...	1.9	2.9	1.7	2.45
9½	4337, 8750, 8655	2.5	...	2.2	3.3	1.9	2.7
10	4145, 51B60	2.6	...	2.3	3.4	2.0	2.8
10½	9840	2.7	...	2.35	3.5	2.1	2.9
11	8653, 8660	2.8	...	2.4	3.7	2.15	3.0
11½	8645	2.9	...	2.5	3.8	2.25	3.1
12	86B45
13	4340, 4147	3.25	...	2.8	...	2.45	3.4
14	4150	3.45	...	2.95	...	2.6	3.55
20	E4340	3.6
22	9850, 4161	3.7
55 HRC							
1	1141, 1042, 4042, 4142, 1045, 1146, 1050 (b), 8642	...	0.65	...	0.6	...	0.3
1½	50B46	...	0.9	...	0.8	...	0.45
2	8742, 5046, 4047, 5145	...	1.2	...	0.9	...	0.65
2½	6145	0.4	1.5	...	1.1	...	0.8
3	4145, 8645, 1345	0.6	1.8	...	1.2	0.3	0.95
3½	86B45, 5147, 4053, 9260	0.7	2.05	0.5	1.4	0.45	1.1
4½	5150, 4063	1.05	2.6	0.8	1.6	0.7	1.45
5	81B45, 6150, 9261, 5155	1.2	2.9	0.9	1.8	0.85	1.6
5½	8650, 5152, 4068	1.4	3.2	1.1	1.9	1.0	1.7
6	50B50	1.55	3.5	1.2	2.1	1.1	1.85
6½	5160, 9262	1.7	3.8	1.4	2.2	1.25	2.0
7	4147, 8750, 8655	1.85	...	1.5	2.4	1.35	2.1
7½	50B60	2.0	...	1.7	2.5	1.5	2.2
9	8653, 51B60, 8660	2.35	...	2.0	3.1	1.8	2.6
9½	4150	2.5	...	2.2	3.3	1.9	2.7
17	9850	3.35

(a) If based on equivalent hardness, actual bar diameter will be less. (b) High residual alloy

REFERENCES

1. *Metals Handbook*, American Society for Metals, 1948
2. G. Totten and C. Bates, *Heat Treating*, Vol 4, *ASM Handbook*, ASM International, 1991
3. J.L. Burns, T.L. Moore, and R.S. Archer, Quantitative Hardenability, *Trans. ASM*, Vol 26, 1938, p 1
4. M.A. Grossmann and E.C. Bain, *Principles of Heat Treatment*, 5th ed., American Society for Metals, 1964
5. *Hardenability of Steels*, American Society for Metals, 1939
6. W. Craft and J.L. Lamont, *Hardenability and Steel Selection*, Pitman Publishing, 1949
7. M.A. Grossmann, *Elements of Hardenability*, American Society for Metals, 1952
8. C.A. Siebert, D.V. Doane, and D.H. Breen, *The Hardenability of Steels: Concepts, Metallurgical Influences, and Industrial Applications*, American Society for Metals, 1977
9. D.V. Doane and J.S. Kirkaldy, Ed., *Hardenability Concepts with Applications to Steel*, American Institute of Mining, Metallurgical, and Petroleum Engineers, 1978

10. B. Liščić, Hardenability, *Steel Heat Treatment: Metallurgy and Technologies*, G.E. Totten, Ed., CRC Press, 2007, p 213–276
11. L.C.F. Canale, L. Albano, G.E. Totten, and L. Meekisho, Hardenability of Steel, *Comprehensive Materials Processing*, G. Krauss, Ed., Elsevier Ltd., Kidlington, U.K., 2013, p 1–63
12. W.E. Jominy and A.L. Boegehold, A Hardenability Test for Carburizing Steels, *Trans. ASM*, Vol 26, 1938, p 574–606
13. W.E. Jominy, Hardenability Tests, *Hardenability of Alloy Steels (Medium- and Low-Alloy Steels up to 5% Alloy)*, The American Society for Metals, 1939, p 66–94
14. J.L. Lamont, How to Estimate Hardening Depth in Bars, *Iron Age*, Vol 152, Oct 14, 1943, p 64–70
15. C.E. Bates, *J. Heat Treat.*, Vol 6, 1988, p 27–45
16. M.A. Grossmann et al., Hardenability of Steel, *Metals Handbook*, American Society for Metals, 1948, p 494
17. G.T. Brown and B.A. James, The Accurate Measurement, Calculation and Control of Steel Hardenability, *Metall. Trans.*, Vol 4, 1973, p 2245–2256
18. T.F. Russell, “Some Mathematical Considerations on the Heating and Cooling of Steels,” Special Report 14, Iron and Steel Institute, U.K., 1936, p 149–187
19. M.A. Grossmann, M.A. Asimov, and S.F. Urban, Hardenability, Its Relationship to Quenching and Some Quantitative Data, *Hardenability of Alloy Steels*, American Society for Metals, 1939, p 237–249
20. H.W. Paxton and E.C. Bain, *Alloying Elements in Steel*, American Society for Metals, 1964
21. J.P. Holman, *Heat Transfer*, McGraw-Hill Kogakusha, Ltd., Tokyo, 1976, p 114–115
22. R. Kern, Distortion and Cracking, II: Distortion from Quenching, *Heat Treat.*, March 1985, p 41–45
23. D.J. Carney, Another Look at Quenchants, Cooling Rates and Hardenability, *Trans. ASM*, Vol 46, 1954, p 882–927
24. *Practical Data for Metallurgists*, 17th ed., Timken
25. *Atlas: Hardenability of Carburized Steels*, Climax Molybdenum, 1960
26. C.F. Jatzak, Effect of Microstructure and Cooling Rate on Secondary Hardening of Cr-Mo-V Steels, *Trans. ASM*, Vol 58, 1965, p 195
27. R.A. Grange, Estimating the Hardenability of Carbon Steels, *Metall. Trans.*, Vol 4, Oct 1973, p 2231
28. J.H. Hollomon and C. Zener, Quenching and Hardenability of Hollow Cylinders, *Trans. ASM*, Vol 33, 1944, p 1
29. I.R. Kramer, S. Siegel, and J.G. Brooks, Factors for the Calculation of Hardenability, *Trans. AIME*, Vol 167, 1946, p 670
30. A.R. Marder, Heat-Treated Alloy Steels, *Encyclopedia of Materials Science and Engineering*, Vol 3, M.B. Bever, Ed., Pergamon Press and MIT Press, 1986, p 2111–2116
31. R.W.K. Honeycombe, *Steels—Microstructure and Properties*, Edward Arnold, London, 1982
32. *Heat Treating of Irons and Steels*, Vol 4B, *ASM Handbook*, ASM International, to be published in 2014
33. J.S. Kirkaldy, Quantitative Prediction of Transformation Hardening in Steels, *Heat Treating*, Vol 4, *ASM Handbook*, ASM International, 1991, p 20–32
34. J.S. Kirkaldy and S.E. Feldman, Optimization of Steel Hardenability Control, *J. Heat Treat.*, Vol 1, 1989, p 57–64
35. G.T. Eldis, A Critical Review of Data Sources for Isothermal and Continuous Cooling Transformation Diagrams, *Hardenability Concepts with Applications to Steel*, D.V. Doane and J.S. Kirkaldy, Ed., Metallurgical Society of AIME, 1978, p 126–157
36. P. Maynier, J. Dollet, and P. Bastien, Prediction of Microstructure via Empirical Formulae Based on CCT Diagrams, *Hardenability Concepts with Applications to Steel*, D.V. Doane and J.S. Kirkaldy, Ed., Metallurgical Society of AIME, 1978, p 163–178
37. M.A. Grossmann, Hardenability Calculated from Chemical Composition, *Trans. AIME*, Vol 150, 1942, p 227
38. “Hardenability Slide Rule,” U.S. Steel Corp., 1970
39. “Hardenability Index Slide Rule,” Climax Molybdenum Company
40. C.F. Jatzak, Determining Hardenability from Composition, *Met. Prog.*, Vol 100 (No. 3), Sept 1971, p 60
41. E. Just, *Met. Prog.*, Nov 1969, p 87–88
42. J.L. Dossett, Make Sure Your Specified Heat Treatment Is Achievable, *Heat Treat. Prog.*, March/April 2007, p 23

Hardenability Calculation of Carbon and Low-Alloy Steels with Low or Medium Carbon

Introduction

Hardenability of steel is the property that determines the depth and distribution of hardness induced by quenching. The extent and depth of hardening of steel parts are critically important material and process design parameters, and thus, hardenability is usually the single most important factor in the selection of steel for heat treated parts. It describes the ability of steel to harden by martensite formation and is related to parameters such as austenitizing temperature, cooling rates after austenitizing, and part size and shape. Hardenability also is often referred to as the inverse measure of the required quench severity, allowing production of a martensitic structure from quenching of austenitized steel to avoid diffusion-controlled transformation products such as pearlite and bainite.

Hardenability is a composition-dependent property of steel, and it depends on carbon content and other alloying elements as well as the grain size of the austenite phase. As such, methods have been developed to calculate hardenability from the composition of steels. The relative importance and influence of the various alloying elements is calculated by determining the equivalent carbon content of the steel. One benefit of computational hardenability is the ability to use a finite amount of experimentally measured data (based on the Jominy procedure along with grain size and chemistry data) to predict the hardenability behavior of a wide variety of steels. The more practical advantage of computational hardenability is its potential in customizing a heat treatment process to suit specific customer demands of desired hardness profiles in a finished heat.

This article provides an overview of predictive procedures to determine hardenability of shallow-hardening, low-carbon steels, plain carbon, and low-alloy medium-carbon steels. Discussion of the hardenability of carburized steels is covered in a separate article. Hardenability of high-carbon (carburized) steels has some unique hardenability features that warrant a specialized treatment (see the article "Calculation of Hardenability in High-Carbon Steels" in this Volume). Sufficient background, detail, and references are provided in this article to enable

the reader to adequately understand and practice the methods discussed.

This article also provides background on the subject of hardenability and its practice from an experimental measurement and quantification point of view. An overview is given on a wide range of testing procedures used to determine and quantify steel hardenability, ranging from classical fracture and etching, Grossmann hardenability, and Jominy end-quench testing to manual and computerized computational methods. It then uses this as a backdrop for the implementation of the core concepts of hardenability in a variety of predictive tools for calculating hardenability.

Principles of Computational Hardenability

L.L. Meekisho, Portland State University

Continuous cooling transformations (CCTs) are at the heart of understanding and quantifying steel heat treatment. Hardenability is one of the common targets of heat treatment practice. It is defined as the ability of a ferrous material to acquire hardness after austenitization followed by quenching. Most heat treatment processes involve heating steel into the austenite temperature range, then cooling it through a predetermined path to achieve target transformation products. Phase-transformation products and their corresponding mechanical and metallurgical properties are dependent on the cooling rate. By way of illustration, consider a eutectoid steel subjected to two different cooling rates, as shown in Fig. 1. In the figure, it is noteworthy that the time scale is based on a logarithmic scale, with which it enables the tracking of cooling times in the order of hours. It is noteworthy as well that the nearly C-shaped dashed curves denote the start and finish loci of the pearlite phase transformation under isothermal conditions. The solid curves represent the start and

finish loci under continuous cooling conditions. With CCTs, pearlite transformations take place at lower temperatures and delayed times compared to isothermal transformations.

The ability of a material to reach a certain hardness is associated with the highest hardness attainable by that material, which in turn depends on the carbon content of the material. Strictly, *carbon content* here refers to the carbon dissolved in the austenite phase following the austenitization process, because this is the carbon that plays the dominant role in the austenite-to-martensite transformation. The term *hardenability* is attributed to the definition by Krauss (Ref 2) as the relative ability of a ferrous alloy to form martensite when quenched from a temperature above the upper critical temperature (A_{c3}), the austenitizing temperature.

During quenching, cooling rates at the surface are expected to be naturally higher than rates in the core of steel parts of appreciable size. These cooling rates are also proportional to the quench severity or the rate of the cooling process, which in turn determine the phase-transformation products. Figure 2 shows different cooling rates associated with a eutectoid steel depicting common heat treating trajectories and associated transformation products. The cooling path depicted by the dashed line corresponds to the so-called critical cooling rate. Any cooling faster rate than the critical cooling rate (i.e., to the left of the dashed line) produces a martensitic structure, while slower rates produce structures that contain some pearlite.

The theoretical concepts and practical implications of critical cooling rates and critical bar diameters have been studied experimentally and documented extensively by numerous studies, including Ref 1 to 3. These are complicated interdisciplinary phenomena, which make them natural candidates for the implementation of predictive/modeling methods discussed in later sections of this article. Such investigations involve determining the depth profile of a structure comprised of 50% martensite and 50% pearlite results, which in turn is influenced by several factors, including steel chemistry, austenite grain size, quench bath severity, and the diameter of the bar. In the illustration shown in Fig. 3,

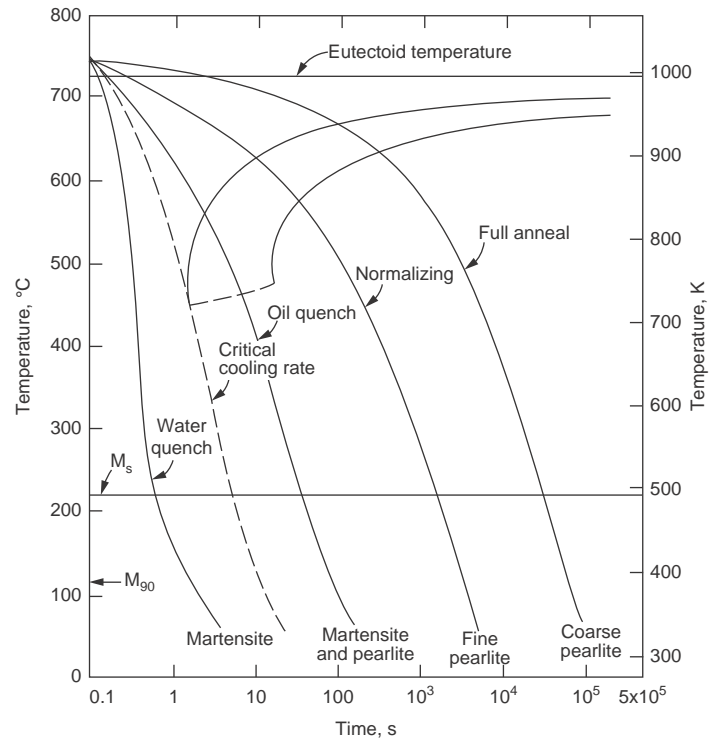
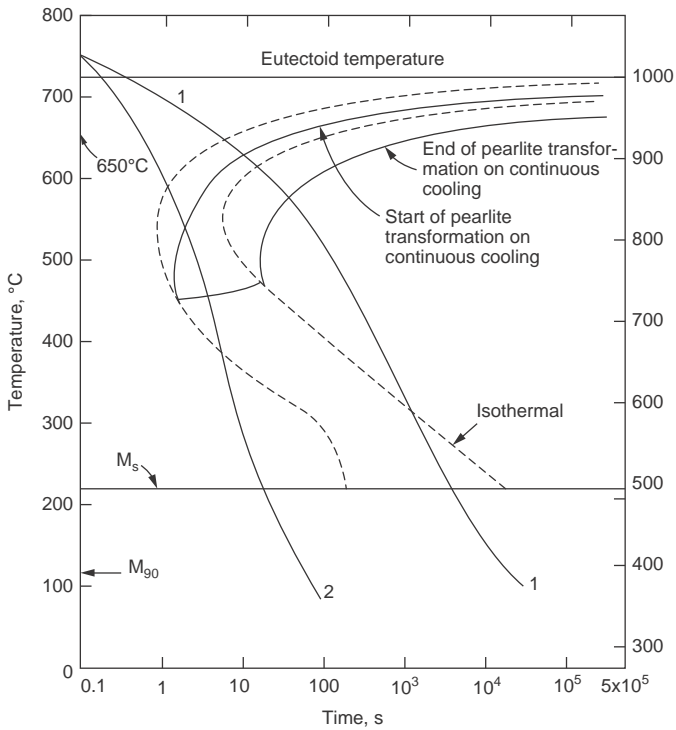


Fig. 1 Relationship of continuous cooling diagram to the isothermal diagram for a eutectoid steel. Adapted from Ref 1

Fig. 2 Trajectories for microstructures as a function of cooling rate for a eutectoid steel. Source: Ref 1

the 25 mm (1 in.) diameter bar has the unique distribution of the 50%-50% martensite-pearlite structure only in the middle of the bar, with higher martensite content toward the surface. This diameter is termed the critical diameter. Smaller-diameter bars of the same steel material subjected to the same quenching conditions will exhibit through-thickness high-hardness martensitic structure, while bars of larger diameters treated similarly will have soft core centers consisting of pearlite and a hard martensite shell. It can be surmised that the steel represented by Fig. 3 has a moderate hardenability because its critical diameter is 25 mm (1 in.). If alloying elements are added to the steel in reference, it would increase its hardenability level and, correspondingly, its critical diameter.

The critical diameter, D , of steel gives a measure of the hardenability of the steel; however, this in turn is influenced by the rate of heat removal, which is embedded in the type of quench system used. To have a uniform reference basis with regard to types of quenching, general heat treatment practice adopted the use of a standard cooling medium in hardenability measurements. This standard is commonly referred to as the ideal quench, because it uses a hypothetical quench medium that has the assumed ability to cool the surface temperature of the steel to and maintain it at the temperature of the quench bath. The critical diameter of quenched steel bars subjected to ideal quench conditions is accordingly referred to as the ideal critical diameter (referred to as D_I or DI in other sections of this article). A summary of critical diameter (D), ideal critical diameters (D_I), and associated rates of cooling (H) is represented in Table 1 and Fig. 4 as good

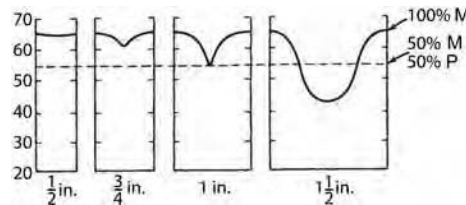


Fig. 3 Schematic of hardness (Rockwell C) test traverses made on a series of steel bars of the same composition but with different diameters. Adapted from Ref 1

Table 1 Severity of quench (H) values for typical quench conditions

H -value	Quenching condition
0.20	Poor oil quench, no agitation
0.35	Good oil quench, moderate agitation
0.50	Very good oil quench, good agitation
0.70	Strong oil quench, violent agitation
1.00	Poor water quench, no agitation
1.50	Very good water quench, strong agitation
2.00	Brine quench, no agitation
5.00	Brine quench, violent agitation
∞	Ideal quench

Source: Ref 1

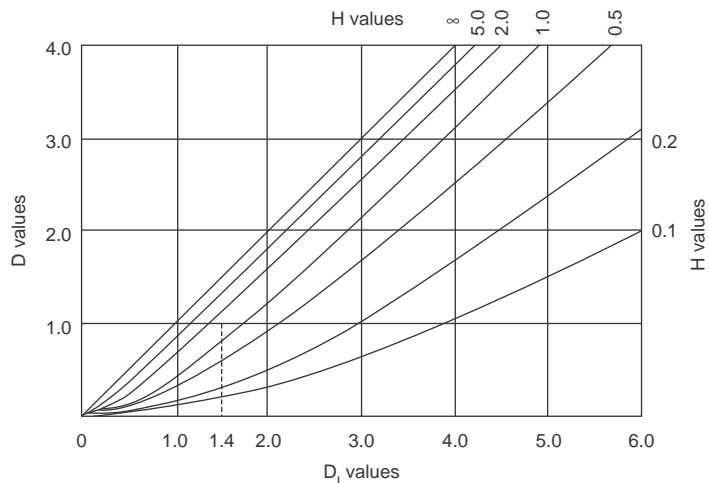


Fig. 4 Relationship of the critical diameter, D , to the ideal critical diameter, D_i , for several rates of cooling, H . Adapted from Ref 4

benchmarks for the computational hardenability modeling community.

Modeling Approaches to Hardenability of Steels

The hardenability of steels is a function of the carbon content and other alloying elements as well as the grain size of the austenite phase. The relative importance and influence of the various alloying elements is calculated by determining the equivalent carbon content of the steel. In general, the higher the carbon content, the higher the hardenability. Alloying elements such as nickel, manganese, chromium, and molybdenum tend to increase the depth of hardening.

As noted, hardenability is also often referred to as the inverse measure of the required quench severity. Therefore, hardenability (and thus the chemical composition of steel) plays a key role in determining critical cooling rates to produce a martensitic structure. The fluid used to quench the material directly influences the cooling rate, because the thermal conductivities and specific heats are dependent on the carbon content and other alloying elements. Liquids such as brine (salt solution in water) and water have a much higher cooling rate capability than air and oil. Additionally, when the fluid is agitated, its cooling rate capability increases quite significantly. The geometry of the part being quenched also affects the cooling rate; specifically, given two samples of equal volume, the one with higher surface area will cool faster. This concept can be extended to a load of components being quenched at the same time, for which it can be surmised that the smaller the load, the higher the likelihood of even quenching for the load (Ref 5, 6).

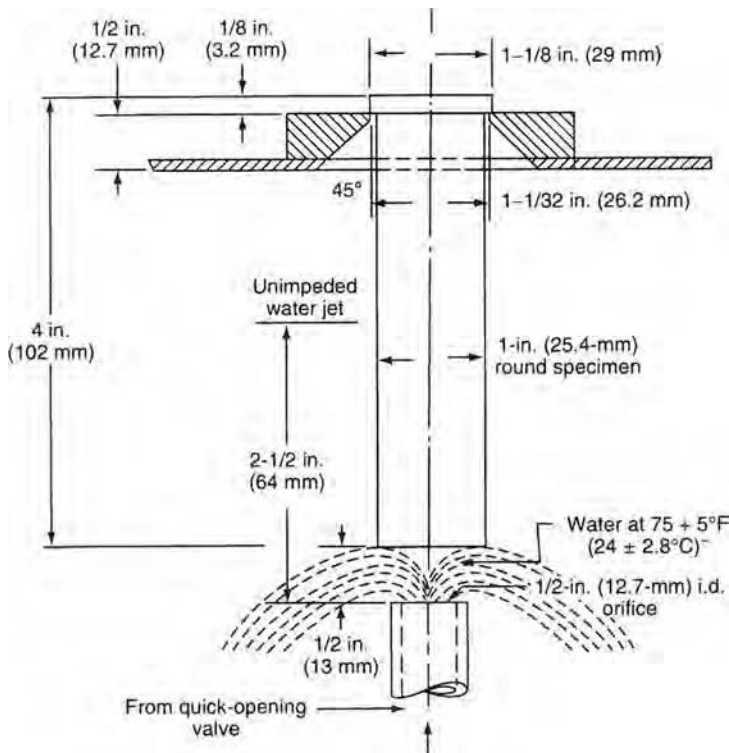


Fig. 5 Typical Jominy specimen specifications quench test setup

The hardenability of ferrous alloys is usually measured by the Jominy test: a round metal bar of standard size (ASTM A255) is heated in a furnace until it is transformed to 100% austenite, then quickly transferred to a Jominy quench tank where it is quenched on one end with room-temperature water. A typical physical setup of the Jominy hardenability measurements is shown in Fig. 5. Necessarily, the cooling rate will be highest at the quenched end and will decrease with distance toward the end exposed to room-temperature air. Hardenability is then determined by measuring the hardness along the bar in 1.6 mm ($1/16$ in.) steps, and it can be surmised that the farther away from the quenched end the hardness extends, the higher the hardenability for the alloy under study. The literature is rich with documentation of hardenability studies, both experimentally as well as with computational modeling.

Considerations of quantitative prediction of hardenability of steels must take into account the fact that even though the Jominy testing procedure and data extraction is well established by an ASTM International standard, there is significant spread of hardness versus depth. Figure 6 shows the Jominy hardenability results for SAE 8620 steel samples of the same grain size, conducted in different laboratory testing conditions. Differences in test equipment, ambient conditions, and operator effectiveness in transferring specimens from the furnace to the test stand could have played a role in the data scatter.

Similar trends were reported for 4140 steel (Ref 8, 9). Such discrepancies, which are widely reported in the literature, may be attributed to several things, including errors in reporting the correct steel chemistry, careless and erroneous test procedures, or process control.

Hardenability data extracted from Jominy test curves are closely related to CCT curves and isothermal transformation (IT) curves. The CCT and IT curves are at the core knowledge of metallurgy. Hardness profiles of a Jominy test specimen, which are determined by microstructures that evolve from the differential cooling rates, can be constructed from CCT and IT curves superimposed on the same set of axes, as shown in Fig. 7 (Ref 10). This type of construction gives good insight on ways to develop mechanisms for predicting mechanical properties of arbitrarily shaped components.

Prediction of hardenability in steels is a complicated process. It involves an interdisciplinary approach to quantifying fairly complex transient thermal fields that drive microstructure developments, and mechanical response and transformation behavior, as indicated by Fig. 8 (Ref 7, 9).

Several works can be cited in the literature that represent varying degrees of success in implementing models that predict steel alloy hardenability. The hardenability factors attributed to the work of Grossman (Ref 11) were, for a long time, the de facto standard. Subsequent work by Kirkaldy (Ref 12) addressed several shortcomings of Grossman's models and, to date, serves as the benchmark against which hardenability models are compared.

Finite-element analysis (FEA) techniques have been embraced by many investigators as a tool for tackling the challenges of modeling hardenability of alloy steels. Li et al. (Ref 13)

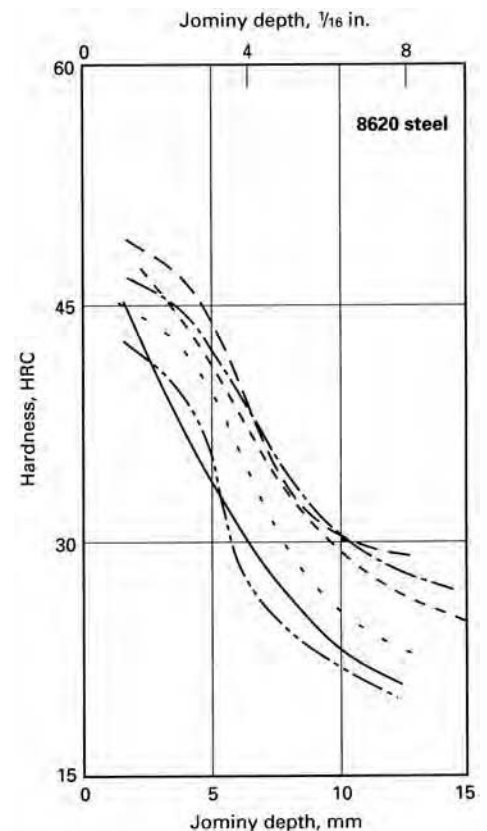


Fig. 6 Summary of reported Jominy tests by several laboratories on SAE 8620 steel of approximately the same chemical composition and grain size. Source: Ref 7

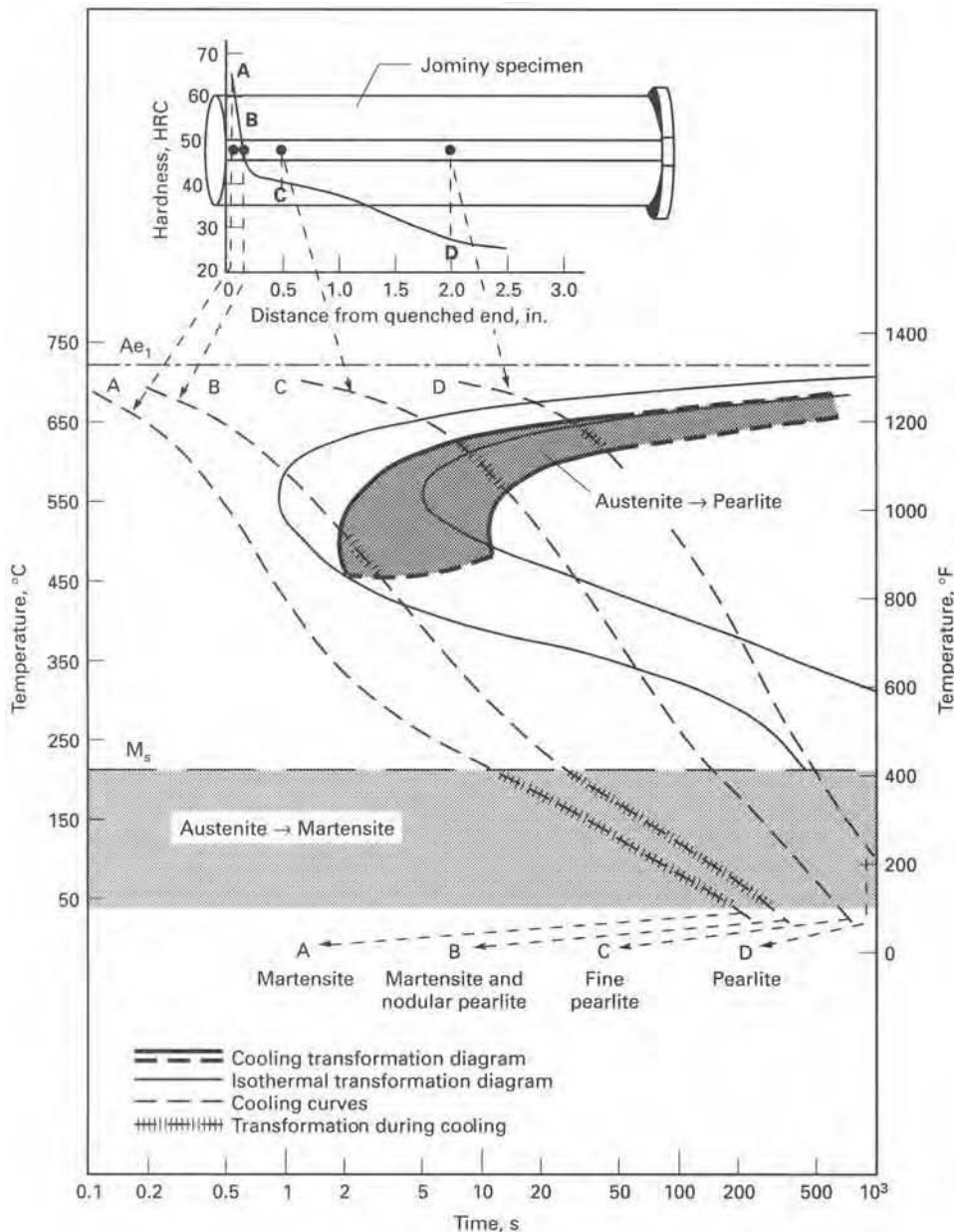


Fig. 7 Relationship of continuous cooling transformation and isothermal transformation curves of a eutectoid steel showing four cooling paths—A, B, C, and D—and corresponding transformation products. Source: Ref 10

developed a computational model for predicting steel hardenability. This model was formulated to predict the hardness distribution in end-quenched bars of heat treatable steels by incorporating a thermodynamics model to compute phase equilibria in multicomponent Fe-C-M systems, a finite-element model to simulate the heat transfer induced by end quenching of Jominy bars, and a reaction kinetics model for austenite decomposition. This effort required the development of several subroutines that were incorporated into a commercial FEA program, ABAQUS. This study concluded that the model in reference was in good agreement with, and added some improvement and reliability to, the work of Kirkaldy (Ref 12).

Malikizadi (Ref 14) used an FEA program alongside the commercial computing software MATLAB to simulate the cooling behavior

and microstructure development of powder metallurgy steels. A significant effort of this work focused on the comparison of predicted hardenability behavior to well-established experimental-based benchmarks.

Just (Ref 15) used the correlation of average carbon and alloy steel compositions to develop equations for computing hardenability profiles. To accomplish this predictive modeling tool, Just used multiple regression analysis to determine the effect of changing an individual alloying element at a time while keeping all the other variables constant. Necessarily, this method is not reliable in predicting steel hardenability with good precision. The author recommends that this method is good largely for assisting the alloy designer in determining the steel to select for a particular application and for assisting the metallurgist in ways to tweak

the melt. Examples of hardnesses on the Rockwell C scale predicted by this method are:

$$J_1 = 52(\%C) + 1.4(\%Cr) + 1.9(\%Mn) + \text{HRC } 33$$

$$J_6 = 89(\%C) + 23(\%Cr) + 7.4(\%Ni) + 24(\%Mn) + 34(\%Mo) + 4.5(\%Si) - \text{HRC } 30$$

$$J_{22} = 74(\%C) + 18(\%Cr) + 5.2(\%Ni) + 16(\%Mn) + 21(\%V) + 4.5(\%Si) - \text{HRC } 29$$

where subscripts 1, 6, and 22 in the previous equations represent the distances of $\frac{1}{16}$, $\frac{6}{16}$, and $\frac{22}{16}$ in. from the quenched end. In a follow-up study, Just modified to accommodate nonlinear behavior of the chemical composition of steels, for which experiments indicated that as alloying element content increased, their effect on hardenability decreased.

Results of Just's hardenability predictions were in good agreement with measurements for a wide variety of standard SAE-grade steels. Implementation of multiple regression algorithms was conducted by other investigators. Siebert et al. (Ref 16) proposed a procedure for first establishing cooling rates at various locations along the Jominy bar, then transforming the time axis such that time zero corresponds to the Ae_3 temperature. Corresponding cooling rate curves were then related to proper CCT start curves. The critical cooling rate was taken to be the point at which hardness began to drop. The pearlite volume fraction associated with each cooling rate was converted to a percent martensite and then to a corresponding hardness. The results of this study involving an SAE 4068 steel are shown in Fig. 9, from which it is noteworthy that experimental results (dashed curve) compared very favorably with predicted results in the range of 0 to 50% martensite for the ASTM grain size range of 4 to 12.

Sarmiento et al. (Ref 17) applied several numerical prediction tools to improve the SAE J 406 (Ref 18) hardenability predictor. To accomplish their hardenability prediction improvements, Sarmiento et al. used numerical codes IN-PHATRAN and INDUCTER-B, which were developed for modeling of heat treatment processes, duly modified to predict the spatial distribution of hardness in steel hardenability samples. Hardness prediction results initially did not fare well with other established predictors, such as CAT, STECAL, AMAX, and Minitch. Upon applying least-squares fitting procedures on their predicted data, the result was a significant improvement of the SAE J 406 hardenability predictor. Effectively, the improved SAE J 406 predictor resulted in J-curves that tracked right between the J 406-predicted results and experimentally determined results for a variety of steels.

The use of computer technology, such as data-acquisition systems and software, has greatly enhanced the ease and reliability of computing the predicted hardenability of steels. Commercial software products such as Minitch Predictor (Ref 7) are available in the public domain. Typical input data for Minitch are the Jominy hardness, chemical composition,

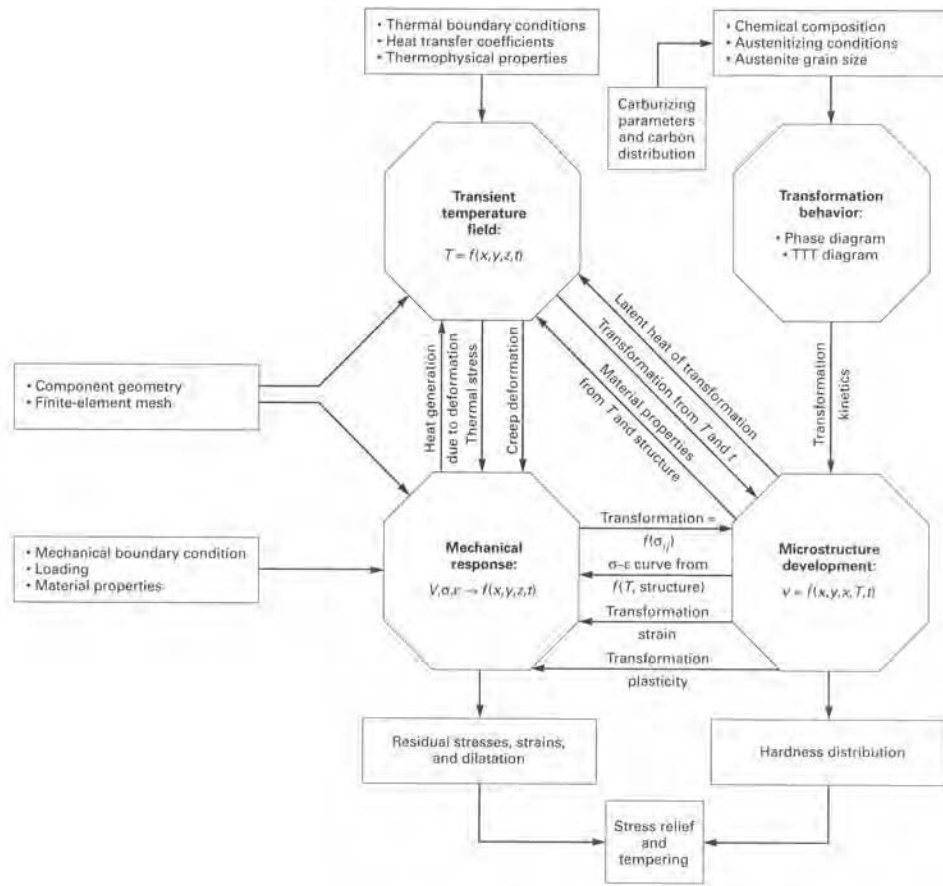


Fig. 8 General system overview of a program for predicting the thermomechanical behavior of low-alloy steels. TTT, time-temperature transformation. Source: Ref 9

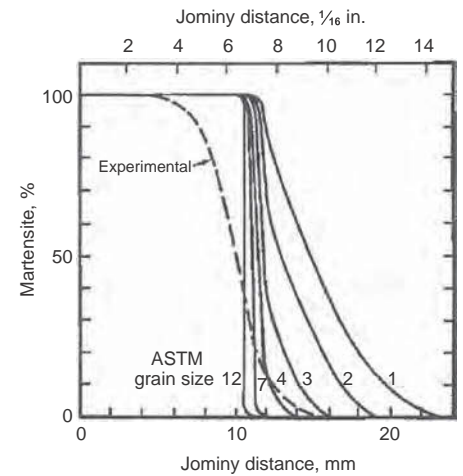


Fig. 9 Predicted Jominy curves for SAE 4068 steel as a function of grain size. Source: Ref 16

Minitech, the customer's specifications are refined to the final heat, as shown in Fig. 11(b).

Brooks (Ref 20) conducted an analysis similar to that of Siebert et al. (Ref 16), which amounted to a refinement of Just's (Ref 15) original regression analysis. Brooks' equations for computing hardness at various Jominy distances as a function of steel chemical composition are summarized in Table 2. The numbers beside the element symbols represent the amount of that element in weight percent. Grain size was not included in Brooks' regression analysis, but it was in the range of ASTM 8 to 12; ranges of chemistries in this work are summarized in Table 3.

Neural networks application for the simulation of hardenability in steels is another modeling tool that has seen a fair amount of activity in the computational hardenability research literature. Dobranski et al. (Ref 21) developed a modeling technique for predicting the hardenability of steels based on the chemical composition of steels. Their work was based on multilayer feed-forward neural networks whose learning rule was based on the error propagation algorithm. Their technique employed more than 500 neural networks, with various numbers of hidden layers and hidden neurons. They used a large number of iterations (100 to 10,000), resulting in a robust modeling tool that was used successfully to predict the hardenability of a wide range of steel chemistries as well as a large variation of heats of carburization.

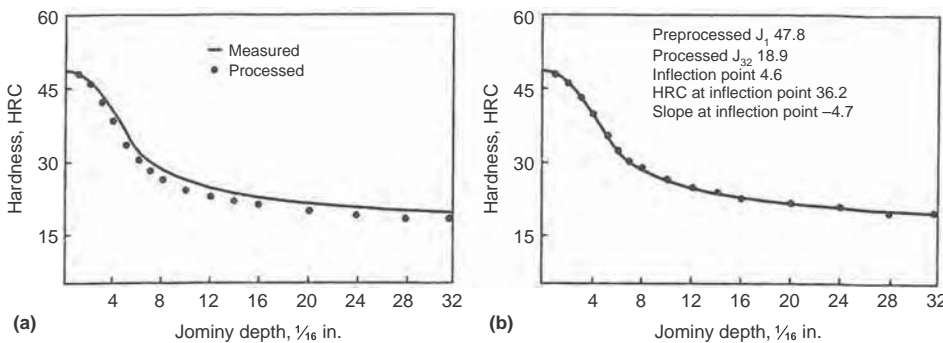


Fig. 10 Outputs from Minitech Predictor data processing for best fit to measured Jominy data. (a) Initial trial. (b) Final trial. Source: Ref 7

and estimated grain size. A typical initial curve of hardness versus distance predicted by Minitech, along with the initial computed data points, is shown in Fig. 10(a) (Ref 7). This clearly indicates a significant separation between measured and predicted results. To improve the reliability of the numerically processed data, effective carbon content and grain size were adjusted in an iterative manner to minimize the weighted root mean square deviation from the experimental data. The final best-fit data points are shown plotted alongside experimental data in Fig. 10(b) (Ref 7).

With the aid of computer-aided Minitech computations, computed Jominy hardness curves can be used confidently in place of experimentally measured Jominy hardness curves. This is a particularly potent tool when dealing with steels that are difficult or nearly impossible to test, for example, SAE 8620H.

Practical applications of the reliable prediction of hardenability in refining steelmaking processes abound. As an example, a steel customer has a desired Jominy hardness trajectory of steel by specifying three points within an H-band for SAE 8620H, as shown in Fig. 11(a). With

Caterpillar Hardenability Calculator (1E0024)

Mohammed Maniruzzaman and Matthew T. Kiser, Caterpillar Inc.

Hardenability of a steel alloy refers to the relative ability of the alloy to transform to martensite when quenched from the austenite phase

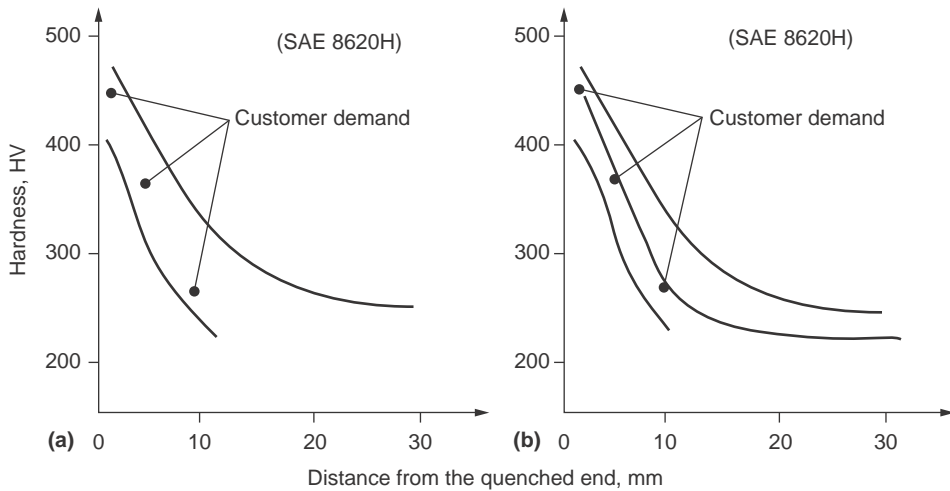


Fig. 11 (a) Customer specifications of hardenability within an H-band for SAE 8620H. (b) Jominy curve for finished heat. Source: Ref 19

Table 2 Brooks' equations for hardness prediction

See Table 3 for composition ranges for these equations.

Jominy distance, 1/16 in.	Hardness, HRC
1	204C + 4.3Si + 8.32Cu - 241.3C ² B + 11.03
2	207.9C + 7.06Cu - 246.3C ² + 400MnB + 9.94
3	226.3C + 2.28Mn + 6.15Cu - 281.7C ² + 7.43 × 10 ³ C ³ B + 4.176
4	7.02Ni - 13.07 + 23.9 × 10 ³ CB - 9.01 × 10 ⁶ CB ² + 47.76
5	17.88Ni - 11.76Cr + 33.8 × 10 ³ CB - 19 × 10 ⁶ CB ² + 5.29 × 10 ³ MnB + 39.8
6	41.73Ni - 80.32MnS + 23.5 × 10 ³ CB - 23.1 × 10 ⁶ CB ² + 10.27 × 10 ³ MnB + 32.9
7	8.46Mn - 115.6S + 64.4Ni + 26.7Cr - 17.4 × 10 ⁶ CB ² + 12.47 × 10 ³ Mn ² B + 18.1
8	14.34Mn - 80.34S + 68.77Ni + 36.84Cr - 16.13 × 10 ⁶ CB ² + 9.89 × 10 ³ Mn ² B + 7.7
9	27.15 Mn + 136.9P + 69.06Ni + 33.6Cr + 1.715Mn ² B - 9.329
12	14.01Mn + 87.59P + 31.33.Ni + 21.17Cr + 70.76Mo + 5.49
16	22.93C + 9.173Mn + 50.54P + 16.36Ni + 13.29Cr + 57.44 + 1.696
20	29.11C + 10.41Mn + 1.02Ni + 12.71Cr + 50.43Mo - 2.93

Source: Ref 20

field. It is commonly measured as a depth below the surface at which steel of a given composition can be quenched to attain a specified hardness, as, for example, 50 HRC, or to yield a specific microstructure, such as 50% martensite and 50% other transformation products. Hardenability is influenced by the austenite grain size, carbon content, and alloy content.

The Caterpillar 1E0024 Hardenability Calculator is a personal computer-based program that calculates the Jominy curve based on the steel composition. The method used in the calculator is based on the ideal critical diameter (*DI*) estimation as a function of steel chemistry, using Grossmann's method for characterizing hardenability. The *DI* represents the diameter of a round steel bar that will harden at the center to 50% martensite when subjected to an ideal quench (i.e., Grossmann quench intensity $H = \infty$). $H = \infty$ is a hypothetical quench intensity at which the surface temperature of the quenched bar reduces to the quenchant temperature instantaneously.

Caterpillar refined the carbon multiplying factors used in Grossmann's method by using many years of steel mill heat data. It uses a boron factor that is a function of both carbon and alloy content to provide increased accuracy of the calculated *DI*

and separate dividing factors for boron and nonboron steels to account for the inherent shape difference of Jominy hardenability curves. This increased accuracy was the result of the analysis of thousands of heats of both boron and nonboron AISI 15xx-, 41xx-, 50xx-, and 86xx-series steels. The resulting calculator is valid for *DI* ranges from 25 to 177.5 mm (1.0 to 7.0 in.), with alloy factors for boron steel up to 26, and the composition ranges shown in Table 4.

The predicted results of 1E0024 are applicable to low- and medium-carbon steel. It assumes the austenite grain size of 7 (ASTM number), because a high percentage of steel mill heats conform to this size. For design purposes, the calculated *DI* and Jominy hardenability curves are valid only within the *DI*, alloy factor, and chemical composition ranges stated earlier. For estimating purposes for higher-alloy steels, hardenability multiplying factors have been included for calculating the *DI* within the chemical composition ranges shown in Table 5.

The method used to calculate the *DI* and Jominy curve in the Caterpillar Hardenability Calculator is similar to the procedure described in SAE J406 and ASTM A 255-10. The Caterpillar Hardenability Calculator also permits comparison of the predicted hardenability of two

Table 3 Composition ranges for Brooks' equations

Element	Composition range, %
Carbon	0.28-0.46
Manganese	0.8-1.4
Silicon	0.13-0.39
Nickel	0.00-0.28
Chromium	0.05-0.25
Molybdenum	0.01-0.06
Copper	0.08-0.22
Boron	0.0001-0.0019

Table 4 Limiting values of chemical composition used in the Caterpillar Hardenability Calculator

Element	Range, wt%
Carbon	0.10-0.70
Manganese	0.50-1.65
Silicon	0.15-0.60
Chromium	1.35 max
Nickel	1.50 max
Molybdenum	0.55 max
Vanadium	0.20 max

Table 5 Maximum composition ranges in the Caterpillar Hardenability Calculator (for melting process)

Element	Range, wt%
Carbon	0.00-0.90
Manganese	0.00-1.95
Silicon	0.00-2.40
Chromium	0.00-2.50
Nickel	0.00-3.50
Molybdenum	0.00-0.55
Copper	0.00-0.55
Vanadium	0.00-0.20
Zirconium	0.00-0.25

compositions, displaying and/or printing both the calculated results and plotted Jominy hardenability curves. Screenshots of the program input and output are shown in Fig. 12.

The following sections describe the method for boron and nonboron steels, with calculation examples for 8645 steel and 86B45 steel. In addition to the *DI*, alloy factor, and boron factor, it also calculates the carbon equivalent (C_{eq}) by using the following equation, which is an important indicator factor for the weldability of steel:

$$C_{eq} = w_C + \frac{w_{Mn}}{6} + \frac{(w_{Cr} + w_{Mo} + w_V)}{5} + \frac{(w_{Ni} + w_{Cu})}{15}$$

where w_i is the weight percent of alloying element *i*.

A copy of the Caterpillar Hardenability Calculator (version 1.1a) is available upon written request to A518 Design Control, Caterpillar Inc., Advanced Materials Technology, Bldg. MM2, 901 Washington St., East Peoria, IL 61630. This program can also be obtained from the Society of Automotive Engineers (as the EA406 Hardenability Prediction Calculator) by contacting the Society of Automotive Engineers, Customer Service Department, 400 Commonwealth Dr., Warrendale, PA 15096-0001.

DI Calculation for Nonboron Steels

Grossmann first introduced a detailed method to calculate *DI* for a steel of known chemistry and austenite grain size by considering the effect of carbon and other alloying elements. He determined the effect of individual alloying elements and expressed the effect as a factor depending upon the amount of alloying elements. The *DI* of alloy steel was then predicted by multiplying the *DI* of plain carbon steel with the factors for each alloying element. A detailed review of the method is discussed in Ref 20.

In the Caterpillar Hardenability Calculator, factors of all alloying elements except carbon are combined into a single factor as an alloy factor (AF) defined as:

$$AF = f_{Mn} \times f_{Si} \times f_{Ni} \times f_{Cr} \times f_{Mo} \times f_{Cu} \times f_{V} \times f_{Zr} \quad (\text{Eq 1})$$

where f_x is associated with the individual alloying element denoted by the subscript “x.”

The *DI* of the alloy steel, expressed in inches, is calculated by using the following equation:

$$DI = f_c \times AF \quad (\text{Eq 2})$$

where f_c is the factor associated with carbon level.

The equations in the following lists are used to estimate the multiplying factor of individual alloying elements used in alloy steel as a function of weight percent of corresponding alloying elements (where w_i is the weight percent of alloying element i). Multiplying factors for carbon (f_c) at levels of weight percent carbon (w_c) are:

Hardenability factors for carbon (Eq 3)

Carbon level	Carbon multiplying factor
$w_c \leq 0.39$	$f_c = 0.54 \times w_c$
$0.39 < w_c \leq 0.55$	$f_c = 0.171 + 0.001 w_c + 0.265 w_c^2$
$0.55 < w_c \leq 0.65$	$f_c = 0.115 + 0.268 w_c - 0.038 w_c^2$
$0.65 < w_c \leq 0.75$	$f_c = 0.143 + 0.2 w_c$
$0.75 < w_c \leq 0.9$	$f_c = 0.062 + 0.409 w_c - 0.135 w_c^2$

Multiplying factors for alloying elements are:

Hardenability factors of alloying elements (Eq 4)

Alloy level	Alloy multiplying factor
$w_{Mn} \leq 1.20$	$f_{Mn} = 3.3333 w_{Mn} + 1.0$ (Eq 4a)
$1.20 < w_{Mn} \leq 1.95$	$f_{Mn} = 5.1 w_{Mn} - 1.12$ (Eq 4b)
$w_{Si} \leq 2.40$	$f_{Si} = 0.7 w_{Si} + 1.0$ (Eq 5)
$w_{Ni} \leq 1.50$	$f_{Ni} = 0.363 w_{Ni} + 1.0$ (Eq 6a)
$1.50 < w_{Ni} \leq 3.50$	$f_{Ni} = 0.32111 + 1.4501 w_{Ni} - 0.6119 w_{Ni}^2 + 0.1253 w_{Ni}^3$ (Eq 6b)
$w_{Cr} \leq 2.50$	$f_{Cr} = 2.16 w_{Cr} + 1.0$ (Eq 7)
$w_{Mo} \leq 0.55$	$f_{Mo} = 3.0 w_{Mo} + 1.0$ (Eq 8)
$w_{Cu} \leq 0.55$	$f_{Cu} = 0.365 w_{Cu} + 1.0$ (Eq 9)
$w_V \leq 0.2$	$f_V = 1.73 w_V + 1.0$ (Eq 10)
$w_{Zr} \leq 0.25$	$f_{Zr} = 2.53 w_{Zr} + 1.0$ (Eq 11)

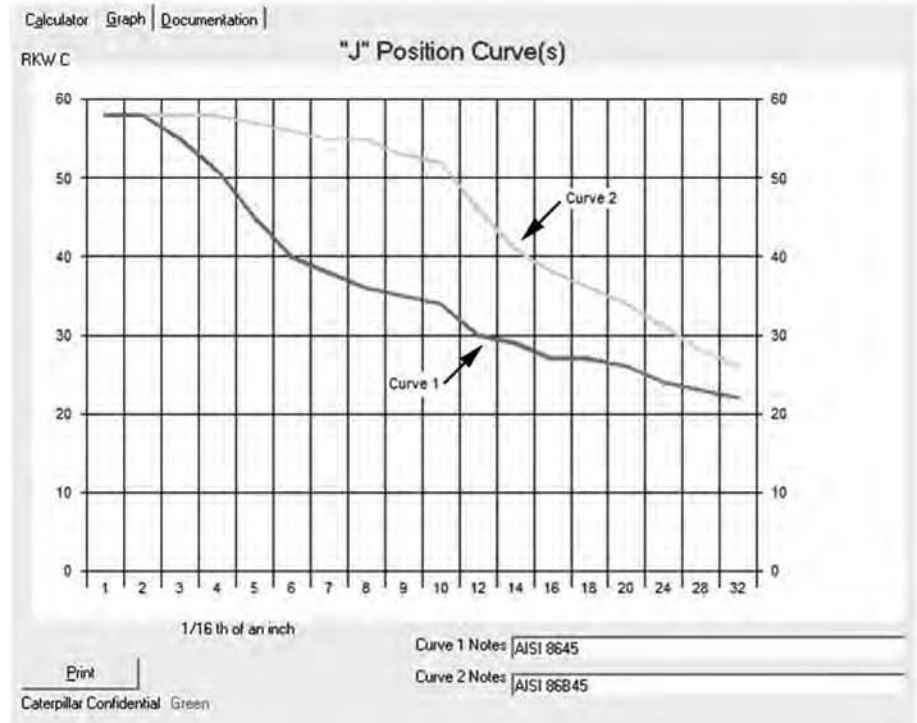
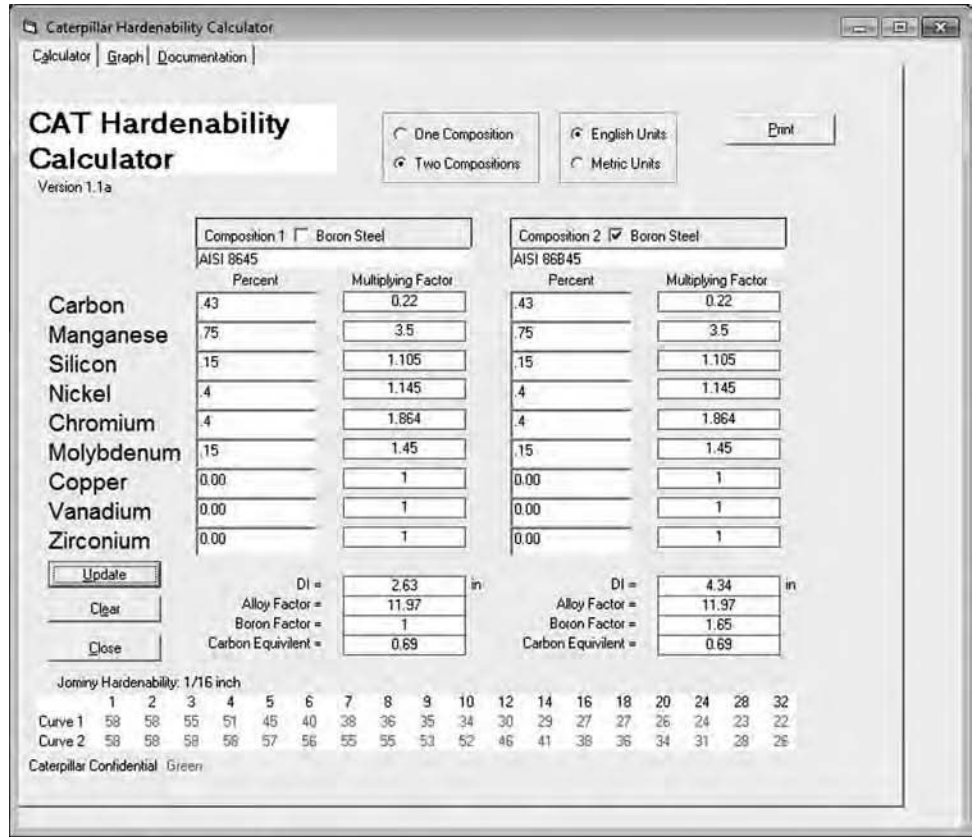


Fig. 12 Screenshots of Caterpillar Hardenability Calculator showing data input and results of a typical calculation

The multiplying factors for both vanadium and zirconium were taken from Ref 22, but they are known to be less precise for vanadium as a result of variations in the

solubility of vanadium carbides. A data table of alloy multiplying factors as a function of weight percent alloy content is presented in Table 6.

Table 6 (Continued)

Alloy, wt%	C (grain size 7)	Mn	Ni	Si	Cr	Mo	Cu	V	Zr	Alloy, wt%	C (grain size 7)	Mn	Ni	Si	Cr	Mo	Cu	V	Zr
3.05	2.607	3.28	2.916
3.06	2.619	3.29	2.931
3.07	2.631	3.3	2.946
3.08	2.644	3.31	2.961
3.09	2.656	3.32	2.976
3.1	2.669	3.33	2.991
3.11	2.682	3.34	3.007
3.12	2.694	3.35	3.023
3.13	2.707	3.36	3.038
3.14	2.721	3.37	3.054
3.15	2.734	3.38	3.070
3.16	2.747	3.39	3.086
3.17	2.760	3.4	3.103
3.18	2.774	3.41	3.119
3.19	2.788	3.42	3.136
3.2	2.801	3.43	3.152
3.21	2.815	3.44	3.169
3.22	2.829	3.45	3.186
3.23	2.843	3.46	3.203
3.24	2.858	3.47	3.220
3.25	2.872	3.48	3.238
3.26	2.887	3.49	3.255
3.27	2.901	3.5	3.273

DI Calculation for Boron Steels

The presence of boron in a very small concentration, such as 0.001 wt%, in low-carbon steel retards the formation of primary ferrite and pearlite and thereby influences the hardenability of alloy steel (Ref 23). The carbon level and amount of alloy influence the boron effect, with the effectiveness of boron decreasing with increasing carbon and alloy content.

The boron factor is usually defined as:

$$f_B = \frac{DI_{\text{Measured from Jominy data and carbon content}}}{DI_{\text{Calculated from composition excluding boron}}} \quad (\text{Eq 12})$$

In 1E0024, boron factors are defined as a function of alloy factor and carbon level. Alloy factor is defined as a product of the multiplying factors of all alloying elements in the steel, excluding boron, as shown in Eq 1. A set of fifth-degree polynomial equations is developed from nonlinear regression analysis of Jominy data of numerous boron steels and nonboron steels of similar compositions and is presented in Table 7. Linear interpolation is used to calculate the boron factor when the estimated alloy factor of a given alloy chemistry falls between two listed alloy factors. The critical ideal diameter of boron steel, DI_B , is calculated as:

$$DI_B = DI_{\text{Calculated without boron}} \times f_B \quad (\text{Eq 13})$$

A data table of boron factors as a function of percent carbon and alloy factor is also presented in Table 8.

Estimation of Jominy Curves from Compositions

Jominy curves for alloy steel can be calculated from the DI . Based on the experimentally

Table 7 Equations for boron factor calculation

Alloy factor	Carbon level, wt%	Equations
5	$w_C > 0.85$	$f_B = 1$
	$w_C \leq 0.85$	$f_B = 13.121 - 101.16 w_C + 383.76 w_C^2 - 729.9 w_C^3 + 675.13 w_C^4 - 242.44 w_C^5$
7	$w_C > 0.81$	$f_B = 1$
	$w_C \leq 0.81$	$f_B = 10.318 - 70.135 w_C + 248.92 w_C^2 - 454.75 w_C^3 + 411.02 w_C^4 - 146.47 w_C^5$
9	$w_C > 0.77$	$f_B = 1$
	$w_C \leq 0.77$	$f_B = 10.542 - 80.631 w_C + 320.36 w_C^2 - 653.01 w_C^3 + 655.52 w_C^4 - 257.51 w_C^5$
11	$w_C > 0.73$	$f_B = 1$
	$w_C \leq 0.73$	$f_B = 9.034 - 64.879 w_C + 252.92 w_C^2 - 515.53 w_C^3 + 522.33 w_C^4 - 208.46 w_C^5$
13	$w_C > 0.67$	$f_B = 1$
	$w_C \leq 0.67$	$f_B = 8.0941 - 55.906 w_C + 219.38 w_C^2 - 466.23 w_C^3 + 504.97 w_C^4 - 219.45 w_C^5$
15	$w_C > 0.63$	$f_B = 1$
	$w_C \leq 0.63$	$f_B = 9.0484 - 77.438 w_C + 362.81 w_C^2 - 895.73 w_C^3 + 1101.9 w_C^4 - 532.49 w_C^5$
18	$w_C > 0.59$	$f_B = 1$
	$w_C \leq 0.59$	$f_B = 6.9212 - 48.238 w_C + 207.29 w_C^2 - 507.17 w_C^3 + 644.04 w_C^4 - 328.39 w_C^5$
22	$w_C > 0.55$	$f_B = 1$
	$w_C \leq 0.55$	$f_B = 7.24 - 55.334 w_C + 254.54 w_C^2 - 655.33 w_C^3 + 867.43 w_C^4 - 459.59 w_C^5$
26	$w_C > 0.53$	$f_B = 1$
	$w_C \leq 0.53$	$f_B = 7.1116 - 56.58 w_C + 273.26 w_C^2 - 740.01 w_C^3 + 1021.5 w_C^4 - 559.45 w_C^5$

determined Jominy curve, a correlation has been developed between the initial hardness (IH), the hardness at various distances from the quenched end of the Jominy bar (expressed as distance hardness, DH), and the ideal critical diameter (DI).

Initial hardness, IH , corresponds to hardness at the location of 1.6 mm ($1/16$ in.) from the quenched end of the Jominy bar, where the microstructure is assumed to be 100% martensite and is estimated as a function of carbon by using the following polynomial equation:

$$IH(\text{HRC}) = 33.087 + 50.723 w_C + 33.662 w_C^2 - 2.7048 w_C^3 - 107.02 w_C^4 + 43.523 w_C^5 \quad (\text{Eq 14})$$

Hardness corresponding to 50% martensite (MH) is estimated using the following equation:

$$MH(\text{HRC}) = 21.93 + 27.153 w_C + 226.89 w_C^2 - 717.17 w_C^3 + 958.62 w_C^4 - 491.25 w_C^5 \quad (\text{Eq 15})$$

Tabulated data of IH (100% martensite) and MH (50% martensite) as a function of percent carbon are presented in Table 9.

The relationship between Jominy distance for 50% martensite and DI can be expressed by the following equations:

$$DI(\text{inch}) = 0.0156 + 0.54358 x - 0.0292133 x^2 + 0.001186 x^3 - 2.696E - 0.5 x^4 + 2.49 E - 0.7 x^5 \quad (\text{Eq 16})$$

$$DI(\text{mm}) = 0.5203 + 8.7522 x - 0.3003 x^2 + 0.00778 x^3 - 0.0001123 x^4 + 6.5978 E - 0.7 x^5 \quad (\text{Eq 17})$$

Table 9 Initial (100%) and 50% martensite hardness as a function of percent carbon

%C	50% martensite hardness, HRC		%C	50% martensite hardness, HRC	
	Initial hardness, HRC	50% martensite hardness, HRC		Initial hardness, HRC	50% martensite hardness, HRC
0.1	38	26	0.51	62	48
0.11	39	27	0.52	62	48
0.12	40	27	0.53	62	48
0.13	40	28	0.54	63	49
0.14	41	29	0.55	63	49
0.15	41	29	0.56	63	50
0.16	42	30	0.57	64	50
0.17	43	30	0.58	64	50
0.18	43	31	0.59	64	51
0.19	44	31	0.6	65	51
0.2	44	32	0.61	65	51
0.21	45	33	0.62	65	52
0.22	46	33	0.63	65	52
0.23	46	34	0.64	65	52
0.24	47	34	0.65	65	53
0.25	47	35	0.66	66	53
0.26	48	36	0.67	66	53
0.27	49	36	0.68	66	53
0.28	49	37	0.69	66	54
0.29	50	37	0.7	66	54
0.3	50	38	0.71	66	54
0.31	51	38	0.72	66	54
0.32	52	39	0.73	66	54
0.33	52	39	0.74	66	54
0.34	53	40	0.75	65	54
0.35	53	40	0.76	65	54
0.36	54	41	0.77	65	54
0.37	55	41	0.78	65	54
0.38	55	42	0.79	65	54
0.39	56	42	0.8	64	53
0.4	56	43	0.81	64	53
0.41	57	43	0.82	64	53
0.42	57	44	0.83	63	52
0.43	58	44	0.84	63	52
0.44	58	45	0.85	62	51
0.45	59	45	0.86	62	50
0.46	59	45	0.87	61	49
0.47	60	46	0.88	61	48
0.48	60	46	0.89	60	47
0.49	61	47	0.9	60	46
0.5	61	47

Calculation Example for Boron Steel (86B45)

For boron steel 86B45, the *DI* and hardenability curve calculations are different than that of the previous example for 8645 steel. For the *DI* calculation, multiplying factors from Table 6 are as follows for 86B45:

Element	wt%	Multiplying factors (from Table 6)
Carbon	0.43	0.22
Manganese	0.75	3.5
Silicon	0.15	1.105
Nickel	0.40	1.145
Chromium	0.40	1.864
Molybdenum	0.15	1.45
Copper	0	...
Vanadium	0	...
Zirconium	0	...
Boron	Yes	...

Thus:

$$DI_{\text{Without boron}} = 0.22 \times 3.5 \times 1.105 \times 1.145 \times 1.865 \times 1.45$$

Table 10 Dividing factor (DF) for distance hardness of nonboron steel in English units

J-distance, 1/16 in.	Ideal critical diameter (DI), in.	DF or initial hardness/distance hardness (IH/DH) ratio
2	DI > 2.1	1
	DI ≤ 2.1	4.68956 – 11.0081 DI + 13.8329 DI ² – 8.80266 DI ³ + 2.78692 DI ⁴ – 0.348793 DI ⁵
3	DI > 3.1	1
	DI ≤ 3.1	2.34904 – 0.282541 DI – 1.42995 DI ² + 1.16697 DI ³ – 0.33813 DI ⁴ + 0.0340258 DI ⁵
4	DI > 4.1	1
	DI ≤ 4.1	5.66795 – 6.14648 DI + 3.52874 DI ² – 1.06026 DI ³ + 0.163013 DI ⁴ – 0.0101538 DI ⁵
5	DI > 4.4	1
	DI ≤ 4.4	4.52902 – 2.90739 DI + 0.986608 DI ² – 0.163588 DI ³ + 0.012095 DI ⁴ – 0.000257202 DI ⁵
6	DI > 5.0	1
	DI ≤ 5.0	4.39435 – 2.16072 DI + 0.560273 DI ² – 0.0814472 DI ³ + 0.00840098 DI ⁴ – 0.000530827 DI ⁵
7	DI > 5.3	1
	DI ≤ 5.3	4.15002 – 1.43154 DI + 0.00235893 DI ² + 0.112947 DI ³ – 0.0237546 DI ⁴ + 0.00150903 DI ⁵
8	DI > 5.6	1
	DI ≤ 5.6	4.44473 – 1.79085 DI + 0.246168 DI ² + 0.0337785 DI ³ – 0.0118874 DI ⁴ + 0.000841843 DI ⁵
9	DI > 5.6	1
	DI ≤ 5.6	4.95421 – 2.43521 DI + 0.629832 DI ² – 0.0791415 DI ³ + 0.00399154 DI ⁴ – 0.0000120363 DI ⁵
10	DI > 6.1	1
	DI ≤ 6.1	5.3161 – 2.80977 DI + 0.841834 DI ² – 0.141781 DI ³ + 0.0130138 DI ⁴ – 0.000512388 DI ⁵
12	DI > 6.6	1
	DI ≤ 6.6	5.63649 – 2.89264 DI + 0.903086 DI ² – 0.17297 DI ³ + 0.0188104 DI ⁴ – 0.00086593 DI ⁵
14	...	5.83176 – 2.99646 DI + 0.940882 DI ² – 0.17734 DI ³ + 0.0183885 DI ⁴ – 0.0007900148 DI ⁵
16	...	6.06952 – 3.15198 DI + 0.992968 DI ² – 0.180096 DI ³ + 0.0172029 DI ⁴ – 0.000664079 DI ⁵
18	...	7.32018 – 4.60605 DI + 1.68442 DI ² – 0.338443 DI ³ + 0.0345114 DI ⁴ – 0.00138927 DI ⁵
20	...	7.81382 – 5.10022 DI + 1.92141 DI ² – 0.394591 DI ³ + 0.040784 DI ⁴ – 0.00165327 DI ⁵
24	...	9.18138 – 6.69048 DI + 2.75891 DI ² – 0.611613 DI ³ + 0.0677165 DI ⁴ – 0.00293074 DI ⁵
28	...	9.27904 – 6.21461 DI + 2.33158 DI ² – 0.469723 DI ³ + 0.0472664 DI ⁴ – 0.00186035 DI ⁵
32	...	8.62857 – 5.16125 DI + 1.81214 DI ² – 0.35489 DI ³ + 0.035687 DI ⁴ – 0.001434 DI ⁵

$$DI_{\text{Without boron}} = 2.639 \text{ in. (67.03 mm)}$$

The alloy factor (AF) is:

$$AF = 3.5 \times 1.105 \times 1.145 \times 1.3864 \times 1.45$$

$$AF = 12$$

With an alloy factor of 12, the boron factor (*f_B*) of 1.65 is determined from Table 8 by linear interpolation of the boron factors of 1.71 and 1.59 for, respectively, AF = 11 and AF = 13 with 0.43 wt% C as follows:

$$f_B(\text{AF} = 12, 0.43\text{wt}\%C) = 1.59 + \frac{(1.71 - 1.59)}{2} = 1.65$$

The ideal critical diameter is thus:

$$DI_B = DI \times f_B = 2.639 \times 1.65$$

$$DI_B = 4.35 \text{ in. (110.5 mm)} \approx 4.4 \text{ in. (110 mm)}$$

For estimating the hardenability curve, the initial hardness (*IH*) at *J* = 1/16 in. (or 1.6 mm) is (similar to 8645) 58 HRC from Table 9 for steel with 0.43 wt% C. Hardness for other Jominy positions (or distance hardness, *DH*) is determined by dividing *IH* by the corresponding *IH/DH* or dividing factors from Table 16 (inches) or Table 17 (millimeters) for boron steel. It should be noted that the *DI* should be rounded to the nearest 0.1 in. (or 2.5 mm) to use the data from the table. For *DI* = 4.4 in. (110.0 mm) with *IH* = 58 HRC

J-distance, 1/16 in.	IH/DH ratio or dividing factor for 4.4 in. DI	Distance hardness (DH), HRC
1	...	58
2	1	58
3	1	58
4	1	58
5	1.01	57
12	1.26	46
32	2.17	27

J-distance, mm	IH/DH ratio or dividing factor for 110.0 mm DI	Distance hardness (DH), HRC
1.5	...	58
3	1	58
5	1	58
7	1	58
9	1.06	55
20	1.45	40
50	2.48	23

Regression Analysis of Hardenability in Europe

Volker Block, Saarstahl AG, Völklingen, Germany

As noted, the calculation of hardenability can save time and money in predicting hardenability from a production heat. Calculated

Table 11 Dividing factor (DF_B) for distance hardness of boron steel in English units

J -distance, 1/16 in.	Ideal critical diameter of boron (DI_B), in.	DF_B or initial hardness/distance hardness (IH/DH) ratio
2	$DI_B > 2.5$ $DI_B \leq 2.5$	1 $26.3659 - 63.9376 DI_B + 64.5141 DI_B^2 - 32.4046 DI_B^3 + 8.08566 DI_B^4 - 0.801282 DI_B^5$
3	$DI_B > 2.9$ $DI_B \leq 2.9$	1 $11.1118 - 23.185 DI_B + 21.5865 DI_B^2 - 10.0461 DI_B^3 + 2.32282 DI_B^4 - 0.212967 DI_B^5$
4	$DI_B > 3.5$ $DI_B \leq 3.5$	1 $28.5063 - 46.7047 DI_B + 31.9047 DI_B^2 - 10.9128 DI_B^3 + 1.86573 DI_B^4 - 0.127476 DI_B^5$
5	$DI_B > 4.4$ $DI_B \leq 4.4$	1 $24.5637 - 33.7061 DI_B + 19.3462 DI_B^2 - 5.52133 DI_B^3 + 0.780889 DI_B^4 - 0.0437473 DI_B^5$
6	$DI_B > 4.9$ $DI_B \leq 4.9$	1 $5.32872 + 1.00334 DI_B - 3.67571 DI_B^2 + 1.70752 DI_B^3 - 0.310244 DI_B^4 + 0.0201755 DI_B^5$
7	$DI_B > 5.2$ $DI_B \leq 5.2$	1 $5.34598 + 0.988092 DI_B - 3.15067 DI_B^2 + 1.33727 DI_B^3 - 0.222853 DI_B^4 + 0.0133182 DI_B^5$
8	$DI_B > 5.6$ $DI_B \leq 5.6$	1 $2.61398 + 4.69071 DI_B - 4.71552 DI_B^2 + 1.58031 DI_B^3 - 0.228445 DI_B^4 + 0.012192 DI_B^5$
9	$DI_B > 5.8$ $DI_B \leq 5.8$	1 $3.8094 + 2.96446 DI_B - 3.58846 DI_B^2 + 1.22906 DI_B^3 - 0.177306 DI_B^4 + 0.00938121 DI_B^5$
10	$DI_B > 6.1$ $DI_B \leq 6.1$	1 $11.7514 - 8.15904 DI_B + 2.57305 DI_B^2 - 0.42384 DI_B^3 + 0.0367906 DI_B^4 - 0.00135613 DI_B^5$
12	$DI_B > 6.6$ $DI_B \leq 6.6$	1 $10.9458 - 6.42904 DI_B + 1.729 DI_B^2 - 0.241867 DI_B^3 + 0.0176917 DI_B^4 - 0.000547832 DI_B^5$
14	$DI_B > 6.9$ $DI_B \leq 6.9$	1 $14.8683 - 10.1637 DI_B + 3.327 DI_B^2 - 0.594795 DI_B^3 + 0.0563926 DI_B^4 - 0.00221015 DI_B^5$
16	...	$14.1027 - 7.94906 DI_B + 1.93841 DI_B^2 - 0.223573 DI_B^3 + 0.0108383 DI_B^4 - 0.00010342 DI_B^5$
18	...	$11.2953 - 4.46248 DI_B + 0.412863 DI_B^2 + 0.0909664 DI_B^3 - 0.020345 DI_B^4 + 0.00109529 DI_B^5$
20	...	$7.14753 + 0.354995 DI_B - 1.61359 DI_B^2 + 0.49403 DI_B^3 - 0.0587857 DI_B^4 + 0.00250946 DI_B^5$
24	...	$12.4479 - 4.7358 DI_B + 0.442135 DI_B^2 + 0.0815263 DI_B^3 - 0.018158 DI_B^4 + 0.000938336 DI_B^5$
28	...	$27.5099 - 20.4594 DI_B + 6.97578 DI_B^2 - 1.25184 DI_B^3 + 0.115427 DI_B^4 - 0.00432751 DI_B^5$
32	...	$43.3562 - 35.3425 DI_B + 12.5823 DI_B^2 - 2.2982 DI_B^3 + 0.211959 DI_B^4 - 0.00785122 DI_B^5$

Table 12 Dividing factor (DF) for distance hardness of nonboron steel in SI units

J -distance, mm	Ideal critical diameter (DI), mm	DF or initial hardness/distance hardness (IH/DH) ratio
3	$DI > 52.5$ $DI \leq 52.5$	1 $0.170547 + 0.173925 DI - 0.0109291 DI^2 + 0.000313863 DI^3 - 0.00000432086 DI^4 + 0.0000000231674 DI^5$
5	$DI > 105$ $DI \leq 105$	1 $3.03987 - 0.0855161 DI - 0.00138048 DI^2 - 0.00000998717 DI^3 + 0.0000000264963 DI^4 + 5.46044 \times 10^{-12} DI^5$
7	$DI > 125$ $DI \leq 125$	1 $4.32366 - 0.134451 DI + 0.00228151 DI^2 - 0.000019625 DI^3 + 0.0000000835338 DI^4 - 0.000000000138456 DI^5$
9	$DI > 135$ $DI \leq 135$	1 $4.46324 - 0.0992003 DI + 0.00119387 DI^2 - 0.00000740686 DI^3 + 0.0000000226087 DI^4 - 2.46815 \times 10^{-11} DI^5$
11	$DI > 140$ $DI \leq 140$	1 $4.40915 - 0.0792024 DI + 0.000674319 DI^2 - 0.00000197223 DI^3 - 0.00000000321758 DI^4 + 2.08025 \times 10^{-11} DI^5$
13	$DI > 150$ $DI \leq 150$	1 $4.60261 - 0.0820023 DI + 0.000718416 DI^2 - 0.000002528 DI^3 + 0.000000000230089 DI^4 + 1.25368 \times 10^{-11} DI^5$
15	$DI > 155$ $DI \leq 155$	1 $5.01595 - 0.0957695 DI + 0.00095624 DI^2 - 0.00000462213 DI^3 + 0.0000000892787 DI^4 - 8.74859 \times 10^{-13} DI^5$
20	...	$5.51133 - 0.10431 DI + 0.00115299 DI^2 - 0.00000751801 DI^3 + 0.0000000275126 DI^4 - 4.31101 \times 10^{-11} DI^5$
25	...	$6.15369 - 0.127486 DI + 0.00157885 DI^2 - 0.0000112233 DI^3 + 0.0000000421359 DI^4 - 0.00000000064246 DI^5$
30	...	$7.16001 - 0.171328 DI + 0.0024282 DI^2 - 0.0000191259 DI^3 + 0.000000076732 DI^4 - 0.000000000121571 DI^5$
35	...	$8.46964 - 0.229424 DI + 0.00354915 DI^2 - 0.0000297166 DI^3 + 0.000000124831 DI^4 - 0.000000000205434 DI^5$
40	...	$9.13657 - 0.252296 DI + 0.00394419 DI^2 - 0.0000333383 DI^3 + 0.000000141462 DI^4 - 0.000000000235541 DI^5$
45	...	$8.84696 - 0.223317 DI + 0.00325787 DI^2 - 0.000026293 DI^3 + 0.00000010819 DI^4 - 0.000000000176244 DI^5$
50	...	$8.10202 - 0.171039 DI + 0.00212643 DI^2 - 0.0000152754 DI^3 + 0.0000000578179 DI^4 - 0.000000000087989 DI^5$

hardenability also helps to reduce the scatter-band of results from the measurement of hardenability (Fig. 13). Various test parameters affect the dispersions of results from the Jominy end-quench test, and replacement (or supplementing) hardness measurement with calculation of hardenability based on chemical composition allows the reduction of dispersions due to test conditions.

This section describes a program within the Steel Institute VDEh working group to derive the formulas for the calculation of hardenability and how cooperative formulas, valid for several steel producers, are received. In the early 1980s, many methods and formulas for the calculation of hardenability existed in Europe. All steel producers had their own formulas, so that the acceptance of calculated values by the

customers was low. In 1986, a working group of four German steel producers within the Steel Institute VDEh was founded to develop calculations of hardenability based on chemical composition. Within this working group, several methods for the calculation of hardenability were tested. Among these methods, the multiple linear regression method revealed the best potential. Although it is a very simple

Table 13 Dividing factor (DF_B) for distance hardness of boron steel in SI units

J -distance, mm	Ideal critical diameter of boron (DI_B), mm	DF_B or initial hardness/distance hardness (HH/DH) ratio
3	$DI_B > 70$	1
	$DI_B \leq 70$	$- 7.44914 + 0.865852 DI_B - 0.0344068 DI_B^2 + 0.000671203 DI_B^3 - 0.00000646154 DI_B^4 + 0.0000000246154 DI_B^5$
5	$DI_B > 80$	1
	$DI_B \leq 80$	$- 0.0786286 + 0.192924 DI_B - 0.00833546 DI_B^2 + 0.000155518 DI_B^3 - 0.00000135556 DI_B^4 + 0.00000000454711 DI_B^5$
7	$DI_B > 100$	1
	$DI_B \leq 100$	$17.3759 - 0.917265 DI_B + 0.0207515 DI_B^2 - 0.00023599 DI_B^3 + 0.00000134895 DI_B^4 - 0.00000000310646 DI_B^5$
9	$DI_B > 135$	1
	$DI_B \leq 135$	$12.401 - 0.468682 DI_B + 0.00767674 DI_B^2 - 0.0000619712 DI_B^3 + 0.000000245123 DI_B^4 - 0.000000000378588 DI_B^5$
11	$DI_B > 150$	1
	$DI_B \leq 150$	$11.6875 - 0.36703 DI_B + 0.00494941 DI_B^2 - 0.0000323202 DI_B^3 + 0.000000100462 DI_B^4 - 0.000000000115393 DI_B^5$
13	$DI_B > 160$	1
	$DI_B \leq 160$	$10.509 - 0.275509 DI_B + 0.00296424 DI_B^2 - 0.0000136307 DI_B^3 + 0.0000000197461 DI_B^4 + 0.000000000014985 DI_B^5$
15	$DI_B > 165$	1
	$DI_B \leq 165$	$10.227 - 0.238757 DI_B + 0.00217091 DI_B^2 - 0.00000649911 DI_B^3 - 0.0000000102394 DI_B^4 + 6.42594 \times 10^{-11} DI_B^5$
20	$DI_B > 170$	1
	$DI_B \leq 170$	$12.0019 - 0.289503 DI_B + 0.00321898 DI_B^2 - 0.0000187998 DI_B^3 + 0.0000000573608 DI_B^4 - 7.29343 \times 10^{-11} DI_B^5$
25	...	$12.7759 - 0.267261 DI_B + 0.00240278 DI_B^2 - 0.0000100713 DI_B^3 + 0.0000000172914 DI_B^4 - 4.94824 \times 10^{-12} DI_B^5$
30	...	$11.4394 - 0.175773 DI_B + 0.000641712 DI_B^2 + 0.00000514585 DI_B^3 - 0.000000044737 DI_B^4 + 9.20061 \times 10^{-11} DI_B^5$
35	...	$10.0009 - 0.099856 DI_B - 0.000621697 DI_B^2 + 0.000014892 DI_B^3 - 0.0000000807801 DI_B^4 + 0.00000000014357 DI_B^5$
40	...	$21.5687 - 0.57096 DI_B + 0.00707779 DI_B^2 - 0.0000471456 DI_B^3 + 0.000000164959 DI_B^4 - 0.000000000239499 DI_B^5$
45	...	$43.7678 - 1.47943 DI_B + 0.0218008 DI_B^2 - 0.000164441 DI_B^3 + 0.000000624269 DI_B^4 - 0.000000000947543 DI_B^5$
50	...	$47.0305 - 1.565 DI_B + 0.0226057 DI_B^2 - 0.00016697 DI_B^3 + 0.000000621257 DI_B^4 - 0.000000000926214 DI_B^5$

method, the calculation results showed good significance. The derived equations can be used with any calculation software and any calculator.

Derivation of Formulas. To ensure a uniform procedure for the derivation of the formulas, the working group defined several guidelines. These guidelines are published in the SEP1664 (06/2004), which has nearly the status of a DIN specification. To obtain the best results using the multiple linear regression method, steel grades are divided into steel families, such as MnCr-alloyed case-hardening steels or NiCrMo-alloyed case-hardening steels. The universe of data for the regression analysis consists of a database of measured hardness values (Rockwell C) in the Jominy end-quench test (according to ISO 642) and the chemical compositions of the heats.

The hardness at a given distance (d , in millimeters) from the quenched end of a Jominy specimen is the target value of the multiple linear regression model. An equation is derived for the calculation of the hardness for each Jominy distance (J_d), such that:

$$J_d \text{ [HRC]} = \text{Function (chemical composition)} \\ = \text{Constant} + a_1x(\text{wt\% C}) + a_2x(\text{wt\% Si}) + \dots$$

In populating the database for regression analysis, the SEP1664 (Ref 24) gives the following recommendations:

- The elements carbon, silicon, manganese, phosphorus, sulfur, chromium, molybdenum,

nickel, aluminum, and nitrogen must be considered.

- Any other element that influences hardenability must also be considered.
- The minimum amount of heats for a sufficient significance of the derived formulas should be equal to the square of number of elements in the regression universe.

Experience has shown that 200 heats are sufficient for a good significance of calculation results. Normally, a higher number of heats will not bring a significant improvement of calculation results.

To obtain cooperative formulas for a steel family, 50 heats from each steel producer, including measured hardness and chemical composition, are taken to fill up the regression universe. As a control universe, another 20 heats are used. Due to the derivation of these cooperative formulas, the specific formulas of the different steel producers for a steel family have been replaced by one set of equations that is valid for all the steel producers (Ref 24–36). This led to a good acceptance of the formulas by the customers. So, an increasing number of customers in Europe accept calculated hardness values on the basis of the cooperative formulas.

Assessment of the Formulas. For assessment of the formulas, three residual dispersions are defined in the SEP1664:

- Residual dispersion S_A is built for each Jominy distance and all heats.
- Residual dispersion S_S is built for each heat.

- Residual dispersion S_G is built for all distances and all heats.

The dispersion S_A reveals the quality of the equations for each Jominy distance, the dispersion S_S helps to find heats with strange measured hardness values, and S_G allows assessment of the complete set of equations.

To guarantee trustworthy results concerning the calculated hardness values, these dispersions must meet the following requirements:

- S_A should be smaller or comparable to the standard deviation of measurement.
- The percentage of heats with $S_S > 4$ HRC should be smaller than 5%.
- S_G should be smaller than 2 HRC for steels without steep decline in hardness.

These dispersions are calculated for the regression universe and a control universe. The control universe is built up with melts, which were not in the regression universe. If one of these universes hurts the requirements for the three types of dispersion, the derivation for the considered steel family must be repeated with a new arranged regression universe.

To describe this method of assessment, the set of equations for CrNiMo case-hardening steels is given as an example. The results for the three dispersions are shown in Fig. 14. The residual dispersions S_A for all Jominy distances of both regression and control universes lie below 2 HRC, that is, below the

Table 17 Initial hardness/distance hardness (IH/DH) ratio as a function of ideal critical diameter (DI) in millimeters for boron steel

DI , mm	Jominy end-quench distance, mm													
	3	5	7	9	11	13	15	20	25	30	35	40	45	50
40.0	1.07	1.25	1.92	2.56
42.5	1.06	1.21	1.73	2.34
45.0	1.05	1.18	1.57	2.14	2.64	2.96
47.5	1.04	1.14	1.45	1.97	2.44	2.75
50.0	1.03	1.12	1.35	1.83	2.26	2.57
52.5	1.03	1.09	1.28	1.7	2.1	2.4	2.68
55.0	1.02	1.08	1.22	1.59	1.96	2.24	2.52	3.18
57.5	1.02	1.06	1.17	1.49	1.83	2.1	2.37	3.01
60.0	1.02	1.05	1.14	1.41	1.71	1.97	2.23	2.85
62.5	1.01	1.04	1.11	1.35	1.61	1.86	2.1	2.7	3.26
65.0	1.01	1.03	1.09	1.29	1.53	1.75	1.99	2.56	3.09	3.45	3.7
67.5	1.01	1.03	1.08	1.24	1.45	1.66	1.88	2.43	2.94	3.28	3.53	3.87	4.29	...
70.0	1.02	1.02	1.07	1.2	1.38	1.57	1.78	2.32	2.79	3.13	3.37	3.67	4.02	...
72.5	1	1.02	1.06	1.17	1.32	1.5	1.7	2.21	2.66	2.98	3.22	3.49	3.78	4.07
75.0	1	1.01	1.06	1.14	1.27	1.43	1.62	2.11	2.53	2.84	3.08	3.32	3.57	3.83
77.5	1	1.01	1.05	1.12	1.23	1.37	1.55	2.01	2.42	2.71	2.95	3.17	3.38	3.62
80.0	1	1.01	1.05	1.11	1.19	1.32	1.48	1.93	2.31	2.59	2.82	3.02	3.21	3.43
82.5	1	1	1.05	1.1	1.16	1.27	1.43	1.85	2.21	2.47	2.7	2.89	3.06	3.26
85.0	1	1	1.04	1.09	1.13	1.23	1.38	1.78	2.11	2.37	2.59	2.77	2.92	3.11
87.5	1	1	1.04	1.08	1.11	1.2	1.33	1.71	2.03	2.27	2.48	2.66	2.8	2.98
90.0	1	1	1.03	1.07	1.09	1.17	1.29	1.65	1.95	2.18	2.38	2.55	2.69	2.86
92.5	1	1	1.03	1.07	1.08	1.15	1.26	1.59	1.87	2.09	2.29	2.46	2.59	2.75
95.0	1	1	1.02	1.06	1.07	1.13	1.23	1.54	1.81	2.01	2.2	2.37	2.5	2.65
97.5	1	1	1.01	1.06	1.06	1.11	1.2	1.49	1.74	1.94	2.12	2.28	2.42	2.56
100.0	1	1	1	1.06	1.05	1.09	1.18	1.45	1.69	1.87	2.05	2.21	2.34	2.48
102.5	1	1	1	1.05	1.04	1.08	1.16	1.41	1.63	1.81	1.98	2.13	2.27	2.41
105.0	1	1	1	1.05	1.04	1.07	1.14	1.37	1.58	1.75	1.91	2.07	2.21	2.34
107.5	1	1	1	1.05	1.04	1.07	1.13	1.34	1.54	1.7	1.86	2.01	2.15	2.27
110.0	1	1	1	1.04	1.03	1.06	1.12	1.31	1.5	1.65	1.8	1.95	2.09	2.21
112.5	1	1	1	1.04	1.03	1.06	1.11	1.28	1.46	1.61	1.75	1.89	2.03	2.16
115.0	1	1	1	1.03	1.03	1.05	1.1	1.25	1.43	1.56	1.7	1.84	1.98	2.1
117.5	1	1	1	1.03	1.03	1.05	1.09	1.23	1.39	1.53	1.66	1.8	1.93	2.05
120.0	1	1	1	1.03	1.03	1.05	1.08	1.21	1.36	1.49	1.62	1.75	1.88	2.01
122.5	1	1	1	1.02	1.02	1.04	1.08	1.19	1.34	1.46	1.58	1.71	1.84	1.96
125.0	1	1	1	1.02	1.02	1.04	1.07	1.17	1.31	1.43	1.55	1.67	1.8	1.91
127.5	1	1	1	1.01	1.02	1.04	1.07	1.15	1.29	1.4	1.52	1.64	1.75	1.87
130.0	1	1	1	1.01	1.02	1.04	1.06	1.14	1.27	1.38	1.49	1.6	1.71	1.83
132.5	1	1	1	1.01	1.02	1.04	1.05	1.13	1.25	1.35	1.46	1.57	1.68	1.79
135.0	1	1	1	1.01	1.02	1.03	1.05	1.11	1.23	1.33	1.44	1.54	1.64	1.75
137.5	1	1	1	1	1.01	1.03	1.04	1.1	1.21	1.31	1.41	1.51	1.61	1.72
140.0	1	1	1	1	1.01	1.03	1.04	1.09	1.19	1.29	1.39	1.48	1.58	1.68
142.5	1	1	1	1	1.01	1.02	1.03	1.08	1.18	1.27	1.37	1.45	1.55	1.65
145.0	1	1	1	1	1.01	1.02	1.03	1.07	1.16	1.25	1.34	1.43	1.52	1.62
147.5	1	1	1	1	1.01	1.01	1.02	1.06	1.15	1.24	1.32	1.41	1.49	1.59
150.0	1	1	1	1	1.01	1.01	1.02	1.05	1.14	1.22	1.3	1.38	1.47	1.56
152.5	1	1	1	1	1	1	1.02	1.05	1.12	1.2	1.28	1.36	1.44	1.53
155.0	1	1	1	1	1	1	1.01	1.04	1.11	1.18	1.26	1.34	1.42	1.51
157.5	1	1	1	1	1	1	1.01	1.03	1.1	1.17	1.24	1.31	1.4	1.48
160.0	1	1	1	1	1	1	1.01	1.03	1.09	1.15	1.22	1.29	1.37	1.45
162.5	1	1	1	1	1	1	1.01	1.02	1.07	1.13	1.2	1.27	1.35	1.43
165.0	1	1	1	1	1	1	1.01	1.02	1.06	1.12	1.18	1.25	1.32	1.4
167.5	1	1	1	1	1	1	1	1.01	1.05	1.1	1.16	1.22	1.3	1.37
170.0	1	1	1	1	1	1	1	1	1.04	1.08	1.14	1.2	1.27	1.33
172.5	1	1	1	1	1	1	1	1	1.03	1.07	1.12	1.17	1.23	1.29
175.0	1	1	1	1	1	1	1	1	1.02	1.05	1.1	1.14	1.19	1.25
177.5	1	1	1	1	1	1	1	1	1.01	1.04	1.08	1.11	1.14	1.2

10. G. Krauss, *Steels: Heat Treatment and Processing Principles*, ASM International, 1990, p 94
11. M.A. Grossman and E.C. Bain, *Principles of Heat Treatment*, 5th ed., American Society for Metals, 1964
12. J.S. Kirkaldy, Prediction of Alloy Hardenability from Thermodynamic and Kinetic Data, *Metall. Trans.*, Vol 4, 1973, p 2333
13. M.V. Li, D.V. Niebuhr, L.L. Meekisho, and D.G. Atteridge, A Computational Model for the Prediction of Steel Hardenability, *Metall. Mater. Trans. B*, Vol 29, 1998, p 627
14. A. Malikizadi, "Simulation of Cooling Behavior and Microstructure Development of Powder Metallurgy Steels," M.S. Diploma, Department of Materials and Manufacturing, Chalmers University of Technology, Gothenburg, Sweden, 2010
15. E. Just, New Formulas for Calculating Hardenability Curves, *Met. Prog.*, Nov 1969
16. C.A. Siebert, D.V. Doane, and D.H. Breen, Recent Contributions to Hardenability Predictions, *The Hardenability of Steels—Concepts, Metallurgical Influences and Industrial Applications*, American Society for Metals, 1977
17. G. Sanchez Sarmiento, M.A. Morelli, and J. Vega, Improvements to the SAE J406 Hardenability Predictor, *First International Automotive Heat Treating Conference*, R. Colas, K. Funatani, and C.A. Stickels, Ed., ASM International, 1998, p 401–414

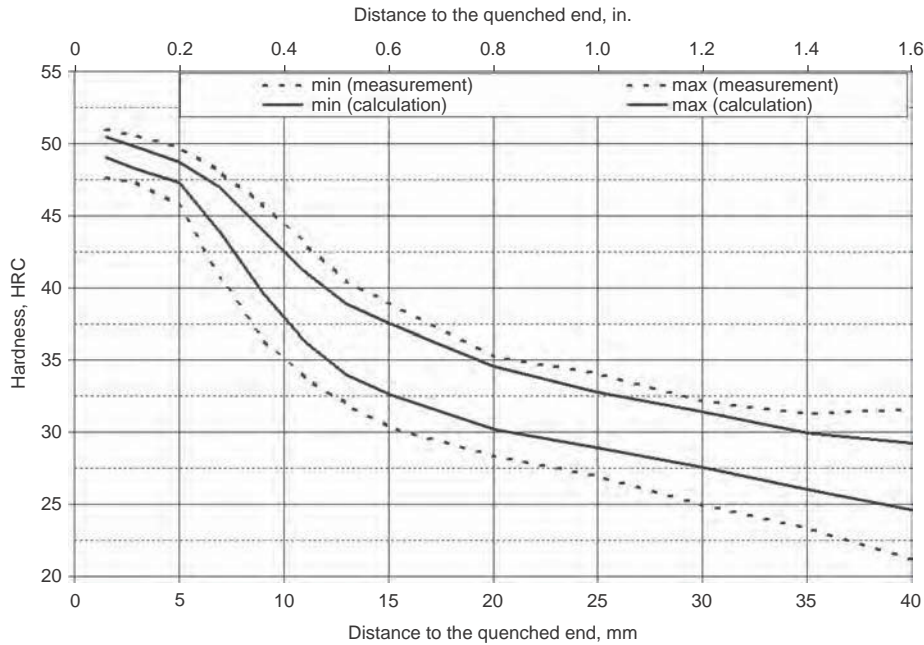


Fig. 13 Scattering bands of calculated and measured hardness values for manganese-chromium case-hardening steel

		Distance to the quenched end, mm											
Regression universe		1.5	3	5	7	9	11	13	15	20	25	30	40
S_{A_1} , HRC		0.83	0.75	0.89	1.35	1.60	1.67	1.66	1.69	1.55	1.49	1.43	1.38
S_{G_1} , HRC	1.39	$S_s > 4$ HRC: 1.4%											
max S_s , HRC	5.02												
		Distance to the quenched end, mm											
Control universe		1.5	3	5	7	9	11	13	15	20	25	30	40
S_{A_1} , HRC		0.90	0.78	0.77	1.28	1.65	1.70	1.66	1.52	1.25	1.10	1.43	0.99
S_{G_1} , HRC	1.25	$S_s > 4$ HRC: 0%											
max S_s , HRC	3.34												

Fig. 14 Residual dispersions for regression and control universe of Cr-Ni-Mo case-hardening steels

Table 18 Regression analysis coefficients for Cr-Ni-Mo-alloyed case-hardening steels

J_s , mm	Coefficients of elements											
	Constant	C	Si	Mn	P	S	Cr	Mo	Ni	Al	Cu	N
1.5	31.326	65.799	0.000	0.000	0.000	0.000	0.988	0.000	0.000	0.000	0.000	0.000
3	30.373	60.416	2.484	0.000	0.000	0.000	0.843	0.000	0.655	0.000	2.451	0.000
5	20.405	67.366	2.121	1.713	0.000	26.459	2.268	0.000	3.939	0.000	1.778	0.000
7	2.542	91.732	0.000	4.445	0.000	52.466	5.644	0.000	8.286	0.000	0.000	0.000
9	-12.350	113.634	2.742	5.996	0.000	44.306	8.558	0.000	11.000	0.000	3.794	0.000
11	-20.891	123.811	5.381	7.346	0.000	26.830	10.670	0.000	11.837	0.000	6.370	0.000
13	-24.844	130.575	5.046	7.350	0.000	0.000	11.832	0.000	12.159	0.000	6.947	0.000
15	-26.523	122.742	6.361	9.120	0.000	0.000	12.838	8.416	9.861	0.000	8.454	0.000
20	-26.257	105.032	6.550	9.953	61.729	0.000	13.378	16.103	7.311	0.000	9.540	0.000
25	-23.850	92.430	6.809	9.575	55.798	0.000	13.253	16.460	6.278	0.000	10.173	0.000
30	-22.970	82.291	6.691	10.027	51.676	0.000	13.081	15.763	6.358	0.000	9.623	0.000
40	-21.156	74.165	6.587	9.909	0.000	0.000	12.621	10.106	7.345	0.000	7.956	0.000

18. SAE Iron and Steel Division, "Methods of Determining Hardenability of Steels," SAE J 406, revised by the Iron and Steel Technical Committee, Division 8, Hardenability of Carbon and Alloy Steels, last rev., June 1993, p 1.23-1.48
19. T. Lund, "Carburizing Steels: Hardenability Prediction and Hardenability Control in Steel Making," SKF Steel Technical Report 3, 1984
20. C.R. Brooks, *Principles of the Heat Treatment of Plain Carbon and Low-Alloy Steels*, ASM International, 1996
21. L.A. Dobranski and W. Sitek, "Computer Simulation of Heat Treatable Steel," International Conference on Heat Treatment and Surface Engineering (IFHTSE) of Tools and Dies, June 8-11, 2005 (Pula Croatia)
22. W. Crafts and J. Lamont, The Effects of Some Elements on Hardenability, *Trans. AIME*, Vol 158, 1944, p 162
23. C.T. Kunze and G. Keil, "A New Look at Boron Effectiveness in Heat Treated Steels," Symposium on Boron Steels, Sept 18, 1979 (Milwaukee, WI), TMS-AIME
24. "Derivation of Equations by Multiple Regression for the Calculation of Hardenability in the Jominy End Quench Test on the Basis of the Chemical Composition of Steels," SEP1664 and supplementary sheet to SEP1664, June 2004, Verlag Stahleisen
25. P.G. Dressel, S.J. Engineer, A. Lübben, and H. Rohloff, *Streuungen der Härbarkeit im Stirnabschreckversuch bedingt durch Prüflabors und Vorbehandlungszustände*, Proceedings, VDEh, 1986-1987 (in German)
26. H. Gulden and P. Schüler, *Härbarkeitsrechnung*, Proceedings, VDEh, March 1990 (in German)
27. H. Stelzenmüller, *Einflüsse auf die Streuungen der Härbarkeit im Stirnabschreckversuch*, FB6.012, VDEh, March 1990
28. H. Gulden, K. Krieger, D. Lepper, A. Lübben, H. Rohloff, P. Schüler, V. Schuler, and H.J. Wieland, Errechnung der Härbarkeit im Stirnabschreckversuch bei Einsatz und Vergütungsstählen, *Stahl Eisen*, Vol 111 (No. 7), 1991, p 103-110 (in German)
29. P. Schüler, Calculation of Hardenability in the Jominy End Quench Test on the Basis of the Chemical Composition of Steels, *Rev. Metall.*, Jan 1992
30. R. Caspari, H. Gulden, K. Krieger, D. Lepper, A. Lübben, H. Rohloff, P. Schüler, V. Schüler, and H.J. Wieland, Errechnung der Härbarkeit bei Einsatz und Vergütungsstählen, *HTM*, Vol 47 (No. 3), 1992, p 183-188 (in German)
31. S.J. Engineer, H. Rohloff, and H.-J. Wieland, Härbarkeit von borlegierten Edellaustählen, *Stahl Eisen*, Vol 114 (No. 11), 1994, p 121-124 (in German)
32. R. Caspari, H. Gulden, B. Kontiokari, K. Krieger, A. Lübben, H. Rohloff, P.

Table 19 Limiting values of chemical composition in regression analysis of steel hardenability in the SEP 1664

Steel	Type		C	Si	Mn	P	S	Cr	Ni	Mo	Cu	Al	N	Ti	B	V
Chromium alloyed	Quenched and tempered	min	0.220	0.02	0.59	0.005	0.003	0.800	0.010	0.005	0.0170	0.012	0.0060
		max	0.468	0.36	0.97	0.037	0.038	1.240	0.280	0.090	0.3200	0.062	0.0148
Chromium-molybdenum alloyed	Quenched and tempered	min	0.160	0.100	0.580	0.0050	0.0030	0.809	0.050	0.120	0.0500	0.006	0.0050
		max	0.457	0.350	0.920	0.0280	0.0590	1.222	0.340	0.284	0.4900	0.052	0.0208
Unalloyed carbon	Quenched and tempered	min	0.320	0.11	0.50	0.004	0.005	0.030	0.030	0.005	0.0290	0.015	0.0050
		max	0.560	0.32	0.90	0.033	0.042	0.290	0.200	0.090	0.3400	0.052	0.0156
Manganese-chromium-boron alloyed	Quenched and tempered	min	0.277	0.18	1.02	0.008	0.003	0.260	0.020	0.006	0.0100	0.021	0.0025	0.010	0.0016	...
		max	0.420	0.44	1.66	0.037	0.038	0.620	0.220	0.080	0.2500	0.080	0.0108	0.060	0.0044	...
Alloyed chain steels	Quenched and tempered	min	0.168	0.14	0.80	0.006	0.001	0.480	0.450	0.170	0.0110	0.021	0.0046
		max	0.280	0.26	1.40	0.017	0.016	0.870	1.110	0.605	0.2100	0.045	0.0147
Chromium-vanadium alloyed	Quenched and tempered	min	0.480	0.147	0.818	0.0038	0.0010	0.950	0.018	0.002	0.0100	0.001	0.0035	0.085
		max	0.564	0.350	1.065	0.0220	0.0320	1.140	0.242	0.093	0.2400	0.042	0.0140	0.159
Manganese-chromium alloyed	Case hardening	min	0.130	0.02	1.02	0.006	0.002	0.820	0.020	0.010	0.0400	0.012	0.0060
		max	0.231	0.38	1.48	0.033	0.044	1.290	0.300	0.090	0.3500	0.063	0.0180
Chromium-nickel alloyed	Case hardening	min	0.100	0.15	0.41	0.004	0.001	0.740	0.800	0.004	0.0100	0.018	0.0049
		max	0.230	0.35	1.09	0.025	0.060	2.030	2.010	0.100	0.4000	0.058	0.0160
Chromium-nickel-molybdenum alloyed	Case hardening	min	0.110	0.030	0.450	0.0050	0.0010	0.460	0.800	0.070	0.0070	0.009	0.0060
		max	0.240	0.579	1.100	0.0340	0.0520	1.920	1.790	0.440	0.2700	0.051	0.0170
Molybdenum-chromium alloyed	Case hardening	min	0.170	0.06	0.68	0.005	0.002	0.400	0.015	0.160	0.0075	0.013	0.0040
		max	0.263	0.40	0.97	0.023	0.039	1.010	0.648	0.467	0.3200	0.054	0.0161
Manganese-chromium alloyed (high hardenability)	Case hardening	min	0.197	0.14	1.07	0.006	0.010	1.005	0.020	0.004	0.0110	0.014	0.0071
		max	0.280	0.37	1.40	0.028	0.042	1.400	0.265	0.097	0.3170	0.040	0.0172
Manganese-chromium-boron alloyed	Case hardening	min	0.120	0.15	1.01	0.005	0.014	0.929	0.020	0.000	0.0100	0.012	0.0036	...	0.0010	...
		max	0.200	0.39	1.30	0.033	0.037	1.291	0.300	0.120	0.3100	0.059	0.0246	0.005	0.005	...

Schüler, H.-J. Wieland, Berechnung der Härtebarkeit aus der chemischen Zusammensetzung bei Einsatz und Vergütungsstählen, *Stahl Eisen*, Vol 115 (No. 9), 1995, p 101–108 (in German)

33. K. Krieger, R. Caspari, H. Gulden, Jung, B. Kontiokari, H. Rohloff, Schmitz, and H.-J. Wieland, *Neuere Ergebnisse der Ermittlung von Rechenformeln für die Berechnung der Härtebarkeit im Stirnabschreckversuch aus der chemischen Zusammensetzung von Stählen*, Conference proceedings, Nov 7, 1996 (Düsseldorf), VDEh (in German)

34. K. Krieger, Stand der Entwicklung der Härtebarkeitsrechnung, *HTM*, Vol 54 (No. 5), 1999, p 301–306 (in German)

35. V. Block, Neuer Formelsatz zur Berechnung der Stirnabschreckhärtekurve für CrNiMo-Einsatzstähle, *Stahl Eisen*, Vol 124 (No. 9), 2004, p 85–87 (in German)

36. *Errechnung der Härtebarkeit aus der chemischen Zusammensetzung von Edelbaustählen*, Conference proceedings, April 30, 2004 (Düsseldorf), Stahl Eisen Verlag (in German)

Calculation of Hardenability in High-Carbon Steels

Adapted from the work of C.F. Jatzcak*

HARDENABILITY of steel depends on carbon content and other alloying elements, as well as the grain size of the austenite phase. As such, methods have been developed to calculate hardenability from the composition of steels. Calculation of hardenability is expressed in terms of the ideal critical diameter (D_1), which is very relatable to the heat treating response of a given component/application being produced from a given or proposed type and/or heat of steel (see also the article “Hardness and Hardenability of Steels” in this Volume).

This article describes the calculation of high-carbon (carburized) steel hardenability. The methodology described in this article is based on the work of C.F. Jatzcak (Ref 1–5) for high-carbon steels. Jatzcak’s work on high-carbon hardenability uses a D_1 value based the criterion of a 10% nonmartensitic transformation—meaning that the D_1 value is equated with the diameter of bar that will achieve 90% martensite at its center when quenched in an “ideal” medium (i.e., a medium that could instantly cool the surface temperature of the bar to the temperature of the medium). This criterion for defining D_1 values of high-carbon hardenability differs from that of D_1 values for low- and medium-carbon steels (where D_1 values are based on criterion of 50% martensitic transformation at the bar center). The different D_1 criteria thus are sometimes noted as $D_{1-50\%}$ values or $D_{1-90\%}$. Hardenability calculation of low- and medium-carbon steels is described in the preceding article “Hardenability Calculation of Carbon and Low-Alloy Steels with Low or Medium Carbon” in this Volume.

The system uses the following empirical equation from Grossmann (Ref 6) to predict hardenability from composition:

$$D_1 = (\text{Base } D_1) \cdot f_{\text{Mn}} \cdot f_{\text{Si}} \cdot f_{\text{Cr}} \cdot f_{\text{Ni}} \dots \text{ and so forth} \quad (\text{Eq 1})$$

Multiplying factors (MF) for the hardenability effects of manganese, silicon, chromium, nickel, molybdenum, aluminum, and boron at high carbon levels were derived for a pure iron or alloy-free base for austenitizing conditions ranging from 800 to 925 °C (1475 to 1700 °F). Base factors were also determined for carbon in the range of 0.60 to 1.10%.

The MFs are presented in both tabular (Tables 1A, 1B, 2) and graphical form and can be used to predict hardenability from composition for homogeneous high-carbon steels as well as the case hardenability of high-carbon regions in carburizing grades. Case hardenability can be calculated for both the single-quench practice, wherein the steel is hardened by direct or delay quenching from carburizing, and the double-quench practice, wherein the steel is reheated for hardening to some lower temperature after a prior air cooling (normalizing) or quenching from the carburizing treatment. The accuracy of hardenability prediction using these factors has been found to be within $\pm 10\%$ of the measure hardenability at ideal critical diameters as high as 660 mm (26 in.).

Background

This writing was adapted directly from the work of C.F. Jatzcak described in Ref 1 to 5, which was aimed at the calculation and control of hardenability at high carbon levels. In all instances, the Grossmann (Ref 6) system for characterizing hardenability in terms of D_1 was employed to establish the specific hardenability effects of manganese, silicon, chromium, nickel, molybdenum, and boron at carbon levels ranging from roughly 0.75 to 1.10% in singly and multiply alloyed compositions quenched from 800, 830, 855, and 925 °C (1475, 1525, 1575, and 1700 °F). These austenitizing temperatures encompass the range

of commercial hardening conditions to which such hypereutectoid compositions as tool steels, 1.0% C bearing steels, and the case regions of carburizing grades are normally subjected.

When quenched from such temperatures, all of these materials normally contain excess or undissolved carbide particles, which means that the quantity of alloy and carbon in solution could vary with the condition of treatment and prior structure. Thus, prior carbide size, shape, and distribution as well as austenitizing time and temperature would be expected to influence the hardenability effect of a given quantity of alloy and carbon. Grain size could also be influential but to a lesser degree, because it does not vary greatly from ASTM 6 to 9 when excess carbides are present, and its effect is generally small, particularly if bainite rather than pearlite limits the hardenability (Ref 7).

As a rule, homogeneous high-carbon alloy steels are usually spheroidize annealed for machining prior to hardening, whereas carburizing grades are either normalized (i.e., air cooled) or quenched in oil directly from carburizing before reheating for hardening. The initial quench from the carburizer may also be the final hardening treatment itself. The latter three conditions produce case microstructures in which the austenite transformation product may range from 100% martensite (with excess carbides and retained austenite) to 100% lamellar carbide of variable interlamellar spacing. All of these prior transformation products transform to austenite rather easily during reheating for hardening (Ref 8). During cooling, however, the undissolved carbides will nucleate pearlite prematurely and act to reduce hardenability, but they do not affect the bainite reaction significantly.

By contrast, the spheroidize-annealed prior structures also contain carbides, but these are present as large spheroids that are much more difficult to dissolve when the steel is reheated

*Adapted from several publications (Ref 1 to 5) by C.F. Jatzcak.

Table 1A Multiplying factors for the calculation of case hardenability of carburizing steels and the hardenability of high-carbon steels hardened after a prior normalize or quench treatment

See also Table 1B

Percent	Mn*(a)				Si*(a)				Cr*(a)				Chromium carburized steels(b)
	800 °C (1475 °F)	830 °C (1525 °F)	855 °C (1575 °F)	925 °C (1700 °F)	800 °C (1475 °F)	830 °C (1525 °F)	855 °C (1575 °F)	925 °C (1700 °F)	800 °C (1475 °F)	830 °C (1525 °F)	855 °C (1575 °F)	925 °C (1700 °F)	925 °C (1700 °F)
0.05	1.02	1.04	1.04	1.04	1.02	1.04	1.04	1.04	1.02	1.04	1.04	1.04	1.04
0.10	1.06	1.06	1.06	1.06	1.06	1.06	1.06	1.06	1.06	1.06	1.06	1.06	1.06
0.15	1.10	1.10	1.10	1.10	1.10	1.10	1.10	1.10	1.10	1.10	1.10	1.10	1.10
0.20	1.14	1.14	1.14	1.14	1.14	1.14	1.14	1.14	1.14	1.14	1.14	1.14	1.14
0.25	1.18	1.18	1.18	1.18	1.18	1.18	1.18	1.18	1.18	1.18	1.18	1.18	1.18
0.30	1.26	1.26	1.27	1.26	1.19	1.19	1.20	1.24	1.22	1.22	1.24	1.23	1.30
0.35	1.31	1.32	1.33	1.33	1.20	1.20	1.21	1.33	1.26	1.27	1.28	1.31	1.41
0.40	1.35	1.38	1.39	1.39	1.21	1.21	1.21	1.40	1.28	1.32	1.33	1.39	1.49
0.45	1.41	1.44	1.45	1.44	1.22	1.22	1.22	1.48	1.31	1.35	1.36	1.44	1.59
0.50	1.45	1.47	1.48	1.47	1.23	1.23	1.24	1.54	1.33	1.38	1.39	1.47	1.67
0.55	1.48	1.53	1.53	1.53	1.24	1.24	1.25	1.61	1.34	1.41	1.41	1.52	1.75
0.60	1.52	1.58	1.58	1.56	1.25	1.25	1.26	1.67	1.35	1.43	1.44	1.56	1.84
0.65	1.55	1.61	1.62	1.59	1.26	1.26	1.27	1.72	1.36	1.46	1.46	1.61	1.89
0.70	1.59	1.65	1.67	1.61	1.27	1.27	1.28	1.78	1.38	1.47	1.47	1.66	1.95
0.75	1.62	1.69	1.72	1.66	1.28	1.28	1.29	1.84	1.39	1.49	1.48	1.73	2.00
0.80	1.65	1.73	1.76	1.71	1.29	1.29	1.30	1.88	1.39	1.51	1.50	1.76	2.05
0.85	1.67	1.76	1.81	1.75	1.31	1.31	1.31	1.93	1.40	1.51	1.51	1.81	2.09
0.90	1.69	1.81	1.86	1.81	1.32	1.32	1.32	1.96	1.41	1.52	1.52	1.86	2.12
0.95	1.73	1.85	1.89	1.91	1.33	1.33	1.32	1.99	1.41	1.53	1.53	1.92	2.15
1.00	1.75	1.88	1.93	2.00	1.34	1.34	1.33	2.00	1.41	1.54	1.54	1.96	2.18
1.05	1.78	1.92	1.98	2.09	1.35	1.34	1.34	2.01	1.41	1.55	1.54	2.00	2.21
1.10	1.80	1.96	2.00	2.19	1.35	1.35	1.34	2.01	1.41	1.56	1.55	2.06	2.24
1.15	1.82	2.02	2.04	2.28	1.36	1.36	1.35	2.04	1.41	1.56	1.56	2.08	2.27
1.20	...	2.07	2.09	2.33	1.36	1.37	1.35	2.05	1.41	1.58	1.57	2.12	2.29
1.25	...	2.14	2.16	2.40	1.38	1.38	1.36	2.06	1.41	1.59	1.58	2.15	2.32
1.30	...	2.21	2.23	2.45	1.39	1.39	1.38	2.07	1.41	1.59	1.58	2.18	2.35
1.35	...	2.29	2.33	2.49	1.40	1.40	1.39	2.08	1.41	1.59	1.59	2.21	2.39
1.40	...	2.37	2.42	2.55	1.41	1.41	1.40	2.09	1.42	1.61	1.59	2.23	2.44
1.45	...	2.50	2.54	2.59	1.42	1.43	1.41	2.10	1.43	1.61	1.59	2.24	2.47
1.50	...	2.58	2.62	2.62	1.43	1.45	1.43	2.11	1.44	1.61	1.59	2.25	2.50
1.55	2.66	1.45	1.46	1.45	...	1.45	1.62	1.60	2.26	2.53
1.60	2.69	1.47	1.47	1.46	...	1.45	1.62	1.61	2.27	2.55
1.65	2.72	1.48	1.49	1.48	...	1.46	1.63	1.62	...	2.57
1.70	2.75	1.50	1.51	1.51	...	1.47	1.64	1.64	...	2.60
1.75	2.79	1.52	1.53	1.53	...	1.47	1.65	1.65
1.80	2.82	1.54	1.55	1.55	...	1.48	1.67	1.67
1.85	2.86	1.57	1.58	1.58	...	1.49	1.68	1.69
1.90	2.89	1.60	1.60	1.60	...	1.52	1.69	1.70
1.95	2.93	1.62	1.62	1.62	...	1.54	1.72	1.72
2.00	2.95	1.66	1.66	1.65	...	1.56	1.74	1.74

(a) These are factors applicable to single-alloy compositions and to ALL multiple-alloy steels when quenching from 925 °C (1700 °F); however, when heat treating from 800-855 °C (1475-1575 °F), use only for those multi-alloy compositions that do not have a combined Ni and Mo content above 1.0 and 0.15%, respectively. For example, a steel with 1.5 Mn, 2.0 Ni, but 0 Mo conforms to this rule. (b) When hardening directly from carburizing, use the chromium carburized steels factor in place of Cr*.

Table 1B Multiplying factors for the calculation of case hardenability of carburizing steels and the hardenability of high-carbon steels hardened after a prior normalize or quench treatment

See also Table 1A

Percent	Ni*(a)				Mo*(a)				Al	Multialloy Si(b)			
	800 °C (1475 °F)	830 °C (1525 °F)	855 °C (1575 °F)	925 °C (1700 °F)	800 °C (1475 °F)	830 °C (1525 °F)	855 °C (1575 °F)	925 °C (1700 °F)	800 → 925 °C (1475 → 1700 °F)	800 °C (1475 °F)	830 °C (1525 °F)	855 °C (1575 °F)	925 °C (1700 °F)
0.05	1.00	1.00	1.00	1.00	1.05	1.05	1.05	1.13	1.02	1.01	1.04	1.04	1.04
0.10	1.01	1.01	1.01	1.01	1.10	1.10	1.10	1.27	1.05	1.06	1.06	1.06	1.06
0.15	1.03	1.03	1.02	1.03	1.15	1.15	1.17	1.42	1.08	1.10	1.10	1.10	1.10
0.20	1.04	1.04	1.04	1.04	1.20	1.20	1.26	1.56	1.12	1.14	1.14	1.14	1.14
0.25	1.05	1.05	1.05	1.05	1.24	1.24	1.35	1.73	1.15	1.18	1.18	1.18	1.18
0.30	1.07	1.07	1.07	1.07	1.29	1.29	1.45	1.90	1.18	1.26	1.26	1.27	1.27
0.35	1.09	1.09	1.09	1.11	1.34	1.34	1.55	2.09	1.22	1.31	1.32	1.33	1.36
0.40	1.11	1.11	1.11	1.14	1.39	1.39	1.65	2.27	1.27	1.35	1.36	1.36	1.46
0.45	1.12	1.13	1.12	1.16	1.44	1.44	1.75	2.45	1.31	1.41	1.40	1.40	1.54
0.50	1.13	1.14	1.13	1.18	1.49	1.49	1.86	2.64	1.35	1.45	1.45	1.45	1.67
0.55	1.14	1.15	1.14	1.20	1.54	1.54	1.97	2.82	1.40	1.47	1.48	1.47	1.80
0.60	1.15	1.16	1.15	1.22	1.60	1.60	2.09	3.03	1.45	1.49	1.50	1.49	1.92
0.65	1.16	1.17	1.16	1.24	1.66	1.66	2.21	3.26	1.48	1.52	1.53	1.52	2.06
0.70	1.16	1.18	1.17	1.25	1.72	1.72	2.32	3.52	1.53	1.54	1.55	1.54	2.21

(continued)

(a) These are factors applicable to single-alloy compositions and to ALL multiple-alloy steels when quenching from 925 °C (1700 °F); however, when heat treating from 800-855 °C (1475-1575 °F), use only for those multialloy compositions that do not have a combined Ni and Mo content above 1.0 and 0.15%, respectively. For example, a steel with 1.5 Mn, 2.0 Ni, but 0 Mo conforms to this rule. (b) When the Ni and Mo contents exceed 1.0 and 0.15% together, use these multialloy factors for Ni, Mn, and Si with Cr*, Mo, and Al.

Table 1B (Continued)

Percent	Ni*(a)				Mo*(a)				Al	Multialloy Si(b)			
	800 °C (1475 °F)	830 °C (1525 °F)	855 °C (1575 °F)	925 °C (1700 °F)	800 °C (1475 °F)	830 °C (1525 °F)	855 °C (1575 °F)	925 °C (1700 °F)	800 → 925 °C (1475 → 1700 °F)	800 °C (1475 °F)	830 °C (1525 °F)	855 °C (1575 °F)	925 °C (1700 °F)
0.75	1.17	1.18	1.18	1.26	1.80	1.80	2.44	3.80	1.57	1.56	1.56	1.56	2.35
0.80	1.18	1.19	1.19	1.27	1.87	1.87	2.55	4.08	1.61	1.58	1.58	1.58	2.51
0.85	1.19	1.19	1.20	1.29	1.92	1.92	2.67	4.40	1.65	1.59	1.59	1.59	2.68
0.90	1.20	1.20	1.21	1.31	2.07	2.07	2.78	4.80	1.70
0.95	1.21	1.21	1.22	1.34	2.18	2.18	2.91	5.20	1.73
1.00	1.22	1.23	1.23	1.35	2.33	2.33	3.03	5.50	1.77
1.05	1.22	1.24	1.23	1.36	1.80
1.10	1.23	1.24	1.24	1.37	1.84
1.15	1.24	1.25	1.25	1.39	1.87
1.20	1.25	1.26	1.25	1.41	1.90
1.25	1.26	1.27	1.26	1.43	1.93
1.30	1.26	1.28	1.26	1.45	1.95
1.35	1.27	1.29	1.27	1.48	1.97
1.40	1.28	1.30	1.28	1.52	1.99
1.45	1.29	1.31	1.29	1.56	2.00
1.50	1.31	1.32	1.31	1.58	2.00
1.55	1.32	1.33	1.32	1.62
1.60	1.33	1.34	1.33	1.66
1.65	1.34	1.35	1.35
1.70	1.35	1.36	1.36
1.75	1.37	1.37	1.37
1.80	1.38	1.39
1.85	...	1.41
1.90	...	1.43
1.95	...	1.45
2.00	...	1.49

(a) These are factors applicable to single-alloy compositions and to ALL multiple-alloy steels when quenching from 925 °C (1700 °F); however, when heat treating from 800–855 °C (1475–1575 °F), use only for those multi-alloy compositions that do not have a combined Ni and Mo content above 1.0 and 0.15%, respectively. For example, a steel with 1.5 Mn, 2.0 Ni, but 0 Mo conforms to this rule. (b) When the Ni and Mo contents exceed 1.0 and 0.15% together, use these multialloy factors for Ni, Mn, and Si with Cr*, Mo, and Al.

Table 2 Multiplying factors for carbon (ASTM 5 to 9 grain size range)

Percent	800 °C (1475 °F)	830 °C (1525 °F)	855 °C (1575 °F)	925 °C (1700 °F)
0.60	0.77	0.79	0.79	0.79
0.65	0.795	0.81	0.82	0.82
0.70	0.82	0.83	0.85	0.85
0.75	0.83	0.845	0.875	0.875
0.80	0.83	0.86	0.90	0.90
0.85	0.80	0.85	0.91	0.93
0.90	0.73	0.81	0.90	0.935
0.91	0.715	0.785	0.89	0.935
0.92	0.70	0.765	0.88	0.93
0.93	0.685	0.745	0.87	0.92
0.94	0.675	0.73	0.86	0.91
0.95	0.66	0.71	0.85	0.90
0.96	0.65	0.70	0.835	0.89
0.97	0.64	0.69	0.825	0.875
0.98	0.625	0.675	0.81	0.86
0.99	0.62	0.665	0.795	0.845
1.00	0.61	0.655	0.78	0.83
1.01	0.60	0.645	0.76	0.815
1.02	0.595	0.64	0.74	0.80
1.03	0.59	0.63	0.725	0.79
1.04	0.58	0.625	0.71	0.78
1.05	0.575	0.62	0.695	0.77
1.06	0.57	0.61	0.68	0.76
1.07	0.565	0.605	0.67	0.75
1.08	0.56	0.60	0.655	0.74
1.09	0.557	0.595	0.645	0.735
1.10	0.555	0.59	0.64	0.73
Avg grain size	8–9	7–8	6–7	5–7

for hardening. It is therefore obvious that for any fixed austenitizing condition of temperature and time (plus grain size), the amount of alloy and carbon dissolved would be less when starting with a spheroidized rather than a

normalized or quenched prior structure. It has been demonstrated, however, that despite this handicap, a spheroidized prior structure will actually yield higher hardenability than a prior normalized structure, at least for austenitizing conditions up to roughly 855 °C (1575 °F). The reasons commonly noted are:

- The larger carbides are not efficient nuclei for early pearlite formation upon cooling as are fine and lamellar carbides.
- They are present in a lower numerical concentration.

It would appear then that the task of developing singular multiplying factors for a given quantity of alloy and carbon would be impossible under such conditions of nonhomogeneous solution at temperature and/or erratic nucleation upon cooling.

Fortunately, with strict control of austenitizing temperature and time, the solution of carbon and alloy can be reproduced with sufficient consistency to permit derivation of multiplying factors with satisfactory precision for either prior structure condition.

The hardenability effects of manganese, silicon, chromium, nickel, molybdenum, and boron were studied in 1.0% C compositions austenitized at 800, 830, 855, and 925 °C (1475, 1525, 1575, and 1700 °F) for 40 min at temperature. Multiplying factors were derived for both prior structure states: spheroidize annealed and normalized. In the process, a number of low-carbon counterparts of many of the 1.0% C analyses were also prepared, then

carburized for up to 8 h at 925 °C (1700 °F), oil quenched, and fully assessed for case hardenability at the 1.0% C level at all of the aforementioned reheat conditions. Very good agreement was obtained between the case hardenability results of the carburized steels and the basic hardenability of the 1.0% C counterparts when quenched from the normalized prior structure. It was thus confirmed that all multiplying factor data obtained with prior normalized 1.0% C steels could be used to calculate the hardenability of all carburizing grades that are reheated for hardening following carburizing.

To account for those steels that are hardened by direct quenching from carburizing and in which better solution of alloy and carbon could be expected because of the longer carburizing or soak times, additional low-carbon specimens were carburized at 925 °C (1700 °F) for 16 h, then end quenched directly and again compared to their 1.0% C counterparts austenitized for 40 min at 925 °C (1700 °F). In all singly and multiply alloyed series, the agreement was more than satisfactory, except for the steels containing significant amounts of chromium. It was later observed (Ref 3) that the solution of chromium and carbon in steels quenched directly from the carburizer was greater than in similar steels reheated for 40 min at 925 °C (1700 °F); consequently, factors for chromium were developed for use with direct-quenched carburizing grades.

Although multiplying factors were also determined for steels that are spheroidize annealed prior to hardening, a different

empirical method for calculation of hardenability from composition was devised and adopted (Ref 1). This method involves the use of multiplying factors derived for the prior normalized condition and the further use of a statistically determined conversion curve for converting the normalized D_1 value so obtained to an annealed D_1 value (Fig. 1).

The calculation methodology uses the basic D_1 calculation format from Grossmann (Eq 1). As noted, Jatzcak's experimental work (Ref 1-5) describing the generation of the elemental multiplying factors uses the criterion of a 10% nonmartensitic transformation D_1 (the diameter of a bar that will achieve 90% martensite at its center when quenched in an ideal medium, i.e., one that could hypothetically lower instantaneously the surface temperature of the bar to that of the medium). This is denoted as D_{1-90} . This is in contrast to the common system for calculating the D_1 at low- and medium-carbon steels, that is, D_{1-50} , which employs a 50% transformation criterion.

The relationship between D_1 and J -distance in a Jominy bar is shown in Fig. 2. This curve was developed by Carney (Ref 9) and modified slightly by Jatzcak to better represent the heat-transfer parameters of a microstructure of 90% martensite with 10% untransformed product. For purposes of reference, experimental Jominy curves are shown in Fig. 3 to 6 for some carburized steels.

Derivation of Multiplying Factors

Although D_1 values were generated to three different structure criteria of 1, 10, and 50% transformed product, multiplying factors were determined using only the criterion of 10% nonmartensitic transformation (90% martensite

and austenite). This criterion was adopted for this purpose in preference to the other two structure criteria for the following reasons:

1. A 10% transformation can be more precisely measured than the more desirable but hard-to-measure 1% or full-hard condition.
2. It is more practical for high-carbon steels than a 50% or half-hard structure because it correlates closely to a desired hardness of 60 to 62 HRC (Ref 1, 11).
3. It can clearly define whether pearlite or bainite limits the hardenability.
4. Should synergistic effects occur between elements in multiple-alloyed steels, the specific reasons for their occurrence can be more easily deduced because of the reason 3.

The latter could not be readily accomplished if instead a mixture of pearlite and bainite were present, such as may occur if a 50% transformation were the selected criterion. Although only the 10% criterion was used, an empirical relationship between the three criteria is given in Fig. 7. It should be noted that a different relationship applies when bainite rather than pearlite limits the hardenability. This was also recognized by Hollomon (Ref 7).

Multiplying Factors

Multiplying factors for manganese, silicon, chromium, nickel, molybdenum, and aluminum are presented in Tables 1A and 1B with carbon factors in Table 2. Factors to be used for boron in high-carbon steels are shown in Fig. 8 (Ref 2, 12, 13).

Graphical presentations of the multiplying factors for manganese, silicon, chromium,

nickel, molybdenum, and aluminum for the 830 and 925 °C (1525 and 1700 °F) quench conditions are given in Fig. 9 and 10. Similar data for the 800 and 855 °C (1475 and 1575 °F) conditions may be observed in Fig. 11 to 13, where the MFs are plotted individually by element to show the influence of austenitizing temperature on the specific hardenability effect. Additionally, a graphical display of the carbon factors for all quench conditions is given in Fig. 14. Here, the data have been plotted against a background of similar data derived by Kramer (Ref 14) in medium-carbon steels. Kramer's data have similarly been inscribed for the other elements in Fig. 11 to 13.

As a rule, the MFs disclosed in Fig. 9 through 13 were principally determined in compositions to which only singular-alloy additions were made and which were generally pearlitic in initial transformation behavior. Consequently, these MFs may certainly be applied to the calculation of hardenability of all singly alloyed high-carbon compositions as well as to those multialloyed compositions that remain pearlitic when quenched from these austenitizing conditions. To illustrate, the single- and multialloyed compositions that are satisfactorily covered by this rule are all analyses containing less than 0.15% Mo and/or less than 2% total of nickel plus manganese and also less than 2% Mn, Cr, or Ni when present individually. All of the factors in Fig. 9 through 13 and Tables 1A, 1B, and 2 also apply to the calculation of case hardenability of similar carburizing compositions that are rehardened from these temperatures following air cooling or quenching from the carburizer.

For steels containing more molybdenum, nickel, manganese, and chromium than the aforementioned percentages, the measured

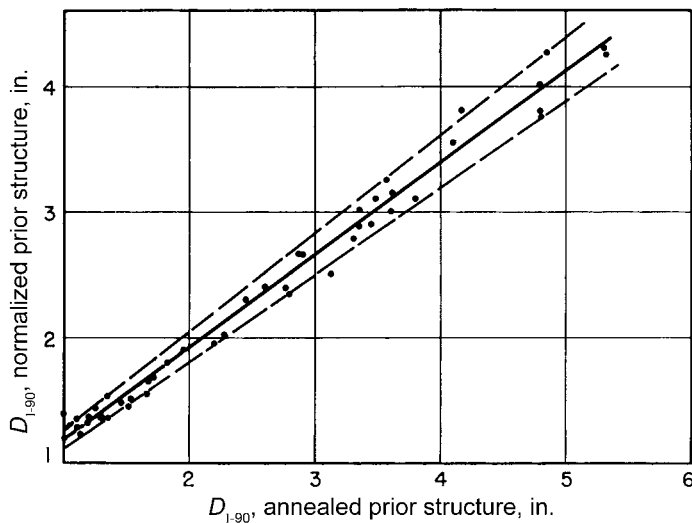


Fig. 1 Correlation between hardenability based on normalized and spheroidized-annealed prior structures in alloyed 1.0% C steels. Source: Ref 1

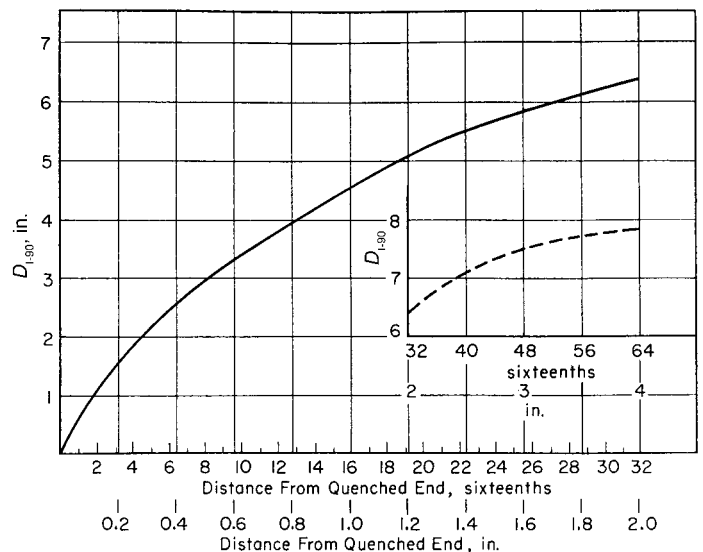


Fig. 2 Relationship between Jominy distance and ideal critical diameter, D_1 . Source: Ref 3

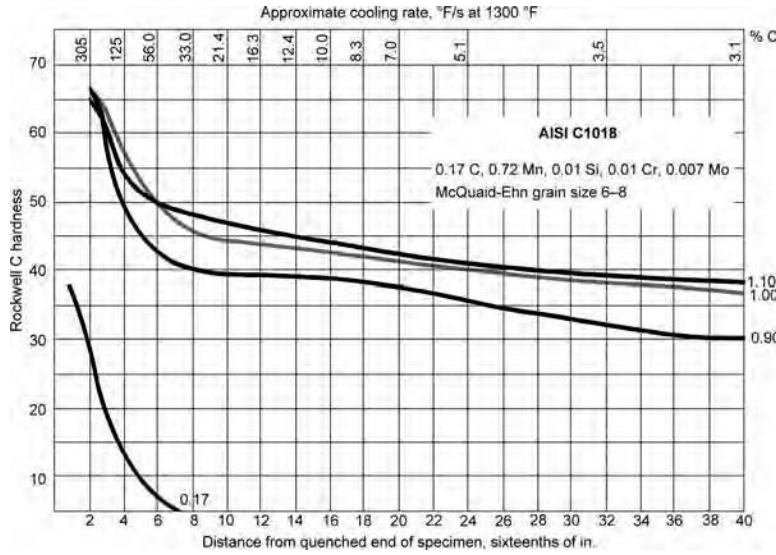


Fig. 3 Jominy hardenability of carburized carbon steel. All bars normalized at 925 °C (1700 °F). Core: austenitized 20 min at 925 °C (1700 °F). Case: pack carburized 9 h at 925 °C (1700 °F), direct quenched. Source: Ref 10

hardenability was always higher than calculations made using the single-alloy MFs (except at the 925 °C, or 1700 °F, condition). This was due to two causes:

1. Such steels became bainitic rather than pearlitic.
2. Synergistic hardenability effects were found to occur between certain elements when present together.

The second effect was specifically noted between nickel and manganese at quenching conditions between 800 and 855 °C (1475 and 1575 °F) and especially in steels that were made bainitic with 0.15% or more molybdenum and contained more than 1.0% Ni.

Nickel acts to increase the activity of carbon, which tended to produce greater-than-normal solution of carbon and carbide-forming elements when excess carbides were present. Later, silicon was also noted to have a similar effect in molybdenum (bainitic) steels (Ref 4, 11).

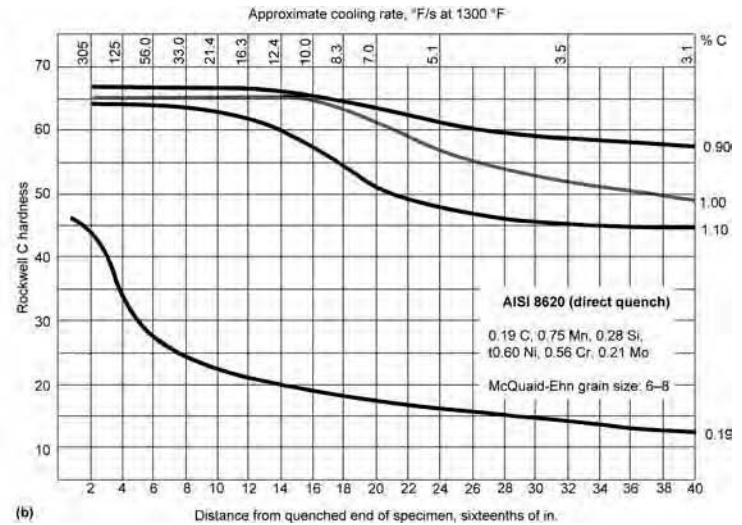
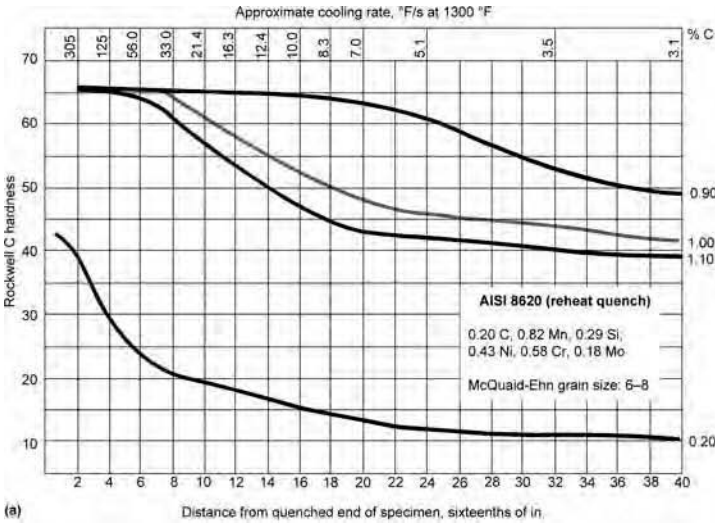


Fig. 4 Jominy hardenability of carburized 8620 steel. (a) Reheat quench. All bars normalized at 925 °C (1700 °F). Core: austenitized 20 min at 845 °C (1550 °F). Case: pack carburized 9 h at 925 °C (1700 °F), box cool; reheated 20 min at 845 °C (1550 °F), quenched. (b) Direct quench. All bars normalized at 925 °C (1700 °F). Core: austenitized 20 min at 925 °C (1700 °F). Case: pack carburized 9 h at 925 °C (1700 °F), direct quenched. Source: Ref 10

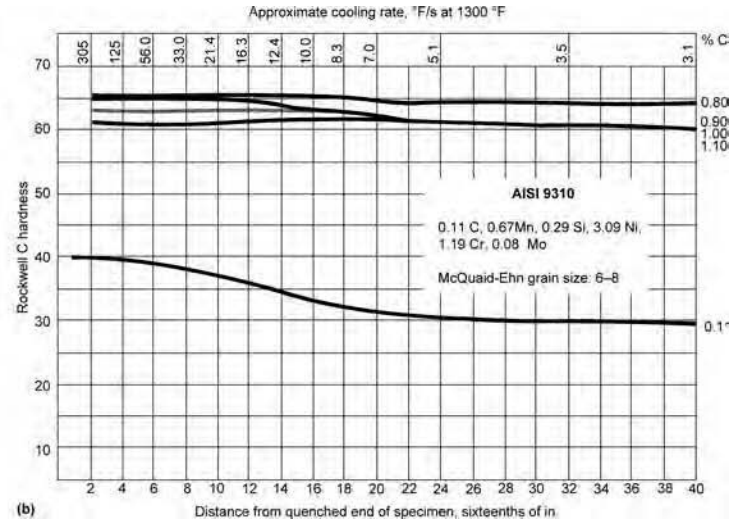
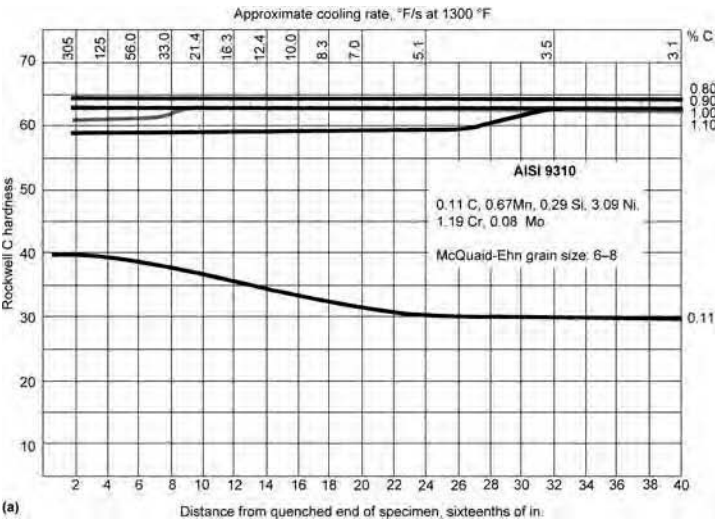


Fig. 5 Hardenability of carburized 9310 from two Jominy specimens. (a) All bars normalized at 925 °C (1700 °F). Core: austenitized 20 min at 845 °C (1550 °F). Case: pack carburized 16 h at 925 °C (1700 °F), air cooled; reheated 40 min at 845 °C (1550 °F). (b) Reheat quench. All bars normalized at 925 °C (1700 °F). Core: austenitized 20 min at 845 °C (1550 °F). Case: pack carburized 9 h at 925 °C (1700 °F), air cooled; reheated 40 min at 800 °C (1475 °F), quenched. Source: Ref 10

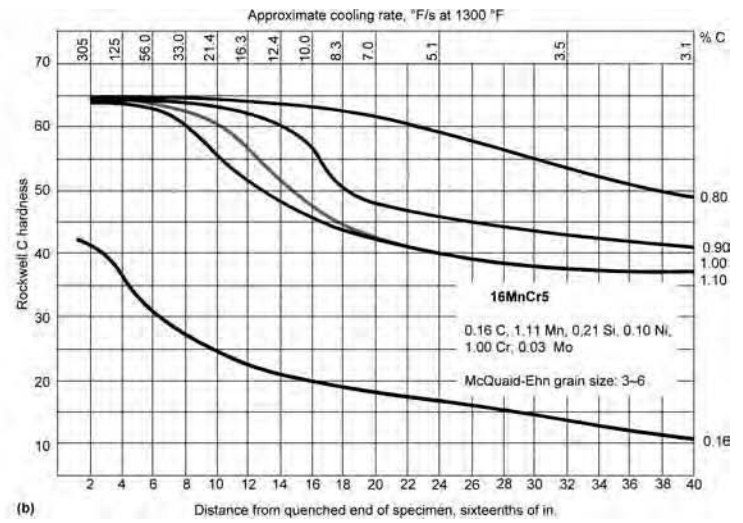
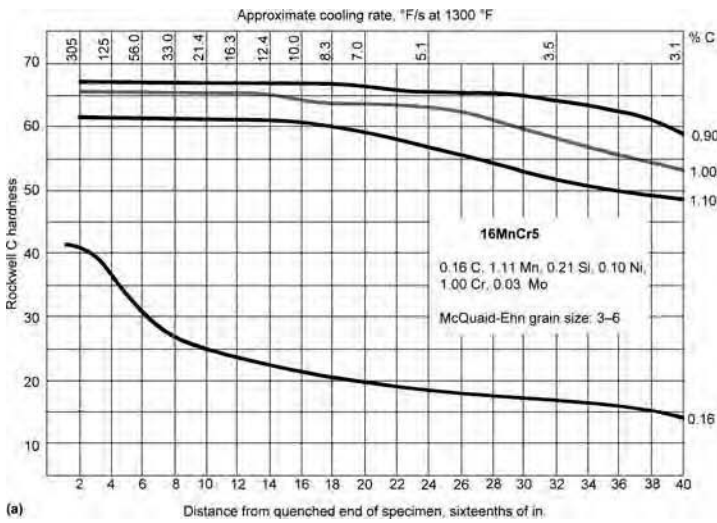


Fig. 6 Jominy hardenability of carburized 16MnCr5 German steel. (a) Direct quench. All bars normalized at 925 °C (1700 °F). Core: austenitized 20 min at 920 °C (1690 °F). Case: pack carburized 9 h at 920 °C (1690 °F), direct quench. (b) All bars normalized at 925 °C (1700 °F). Core: austenitized 20 min at 860 °C (1580 °F). Case: pack carburized (Goerig CMD 12) 9 h at 900 °C (1850 °F), box cooled; reheated in compound to 860 °C (1580 °F), quenched. Source: Ref 10

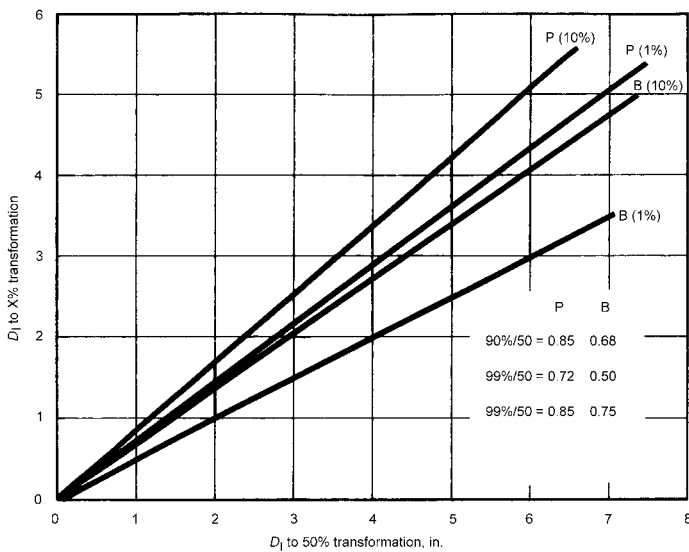


Fig. 7 Ideal critical diameter (D_1) relationship between 1, 10, and 50% structure criteria. P, pearlite; B, bainite. Source: Ref 5

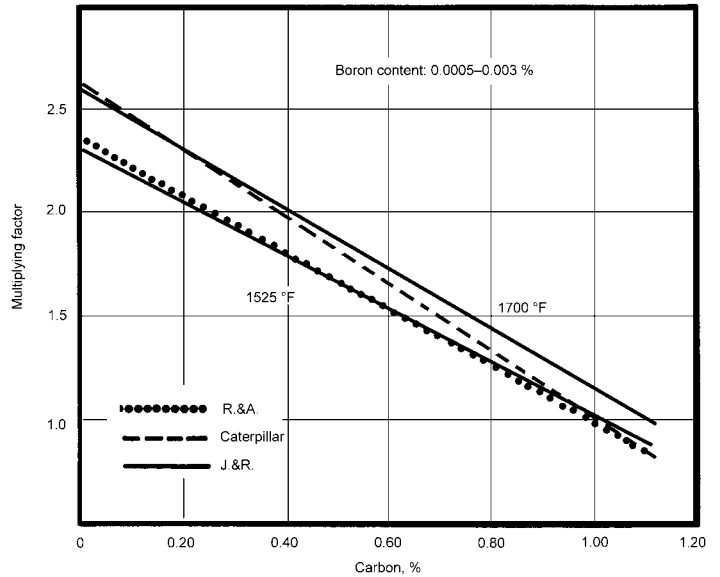


Fig. 8 Multiplying factors for boron at 830 and 925 °C (1525 and 1700 °F) when hardenability criterion is 10% transformation. Source: Ref 5

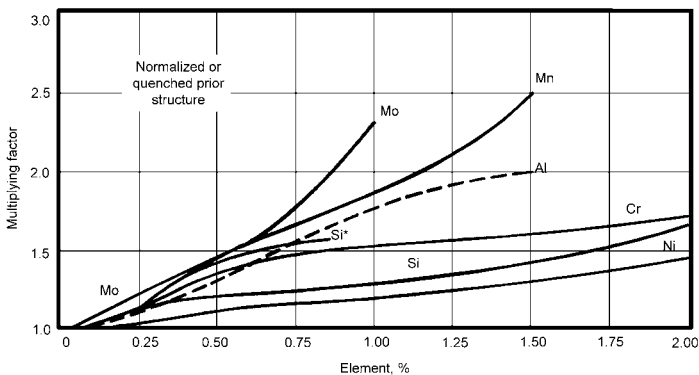


Fig. 9 Multiplying factors for calculation of hardenability at high carbon levels when quenched from 830 °C (1525 °F) when composition contains more than 1% Ni and 0.15% Mo. Source: Ref 5

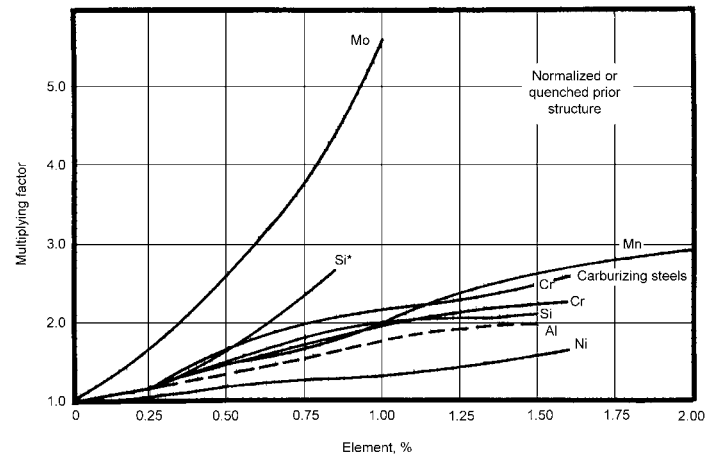


Fig. 10 Multiplying factors for calculation of hardenability at high carbon levels when quenched from 925 °C (1700 °F). Source: Ref 5

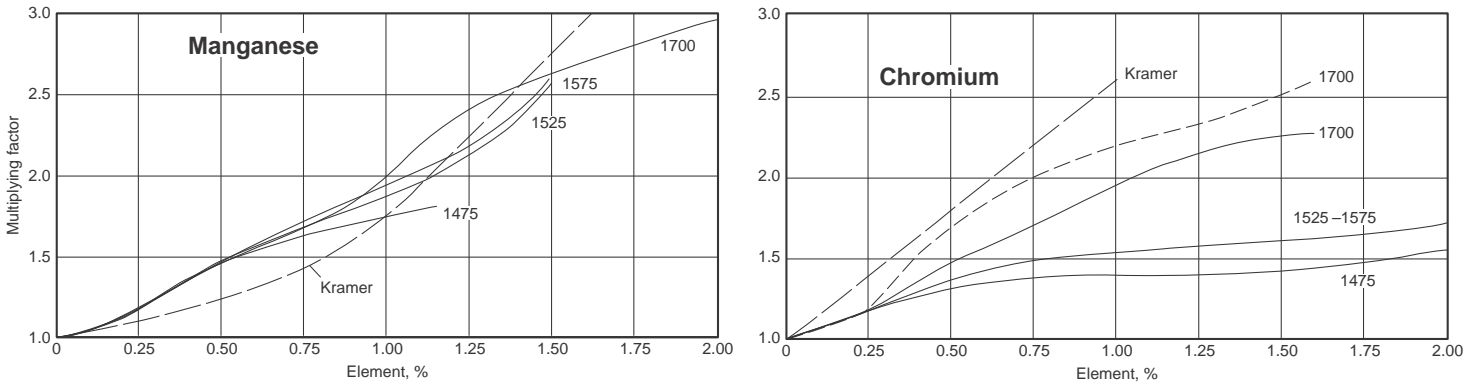


Fig. 11 Effect of austenitizing temperature on multiplying factors for manganese and chromium at high carbon levels. (Note Kramer data, Ref 14, for medium-carbon steels.) Source: Ref 5

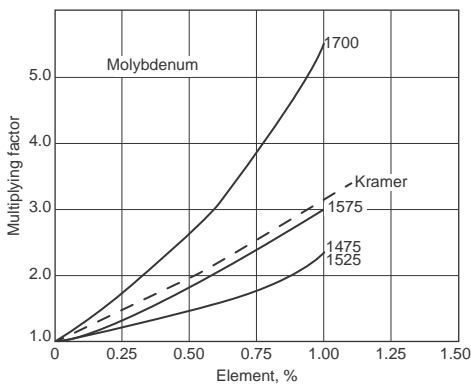


Fig. 12 Effect of austenitizing temperature on multiplying factors for molybdenum at high carbon levels. Source: Ref 5

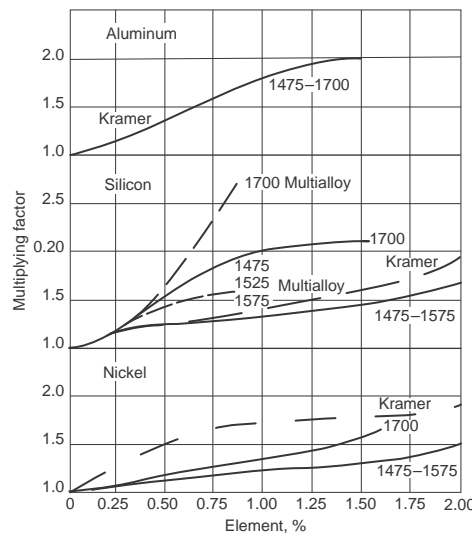


Fig. 13 Effect of austenitizing temperature on multiplying factors for aluminum, silicon, and nickel at high carbon levels. (Arrow on aluminum curve denotes maximum percentage studied by Kramer.) Source: Ref 5

The sum total of these interactions was that the combined effects for manganese and nickel were always much larger than indicated from consideration of their individual effects.

The presence of synergistic effects precludes the use of individual MFs for manganese and nickel, because independence of alloying-element effects is implicit in the Grossmann multiplying factor approach. This difficulty, however, is successfully surmounted by the expedient of computing combined nickel and manganese factors for use in conjunction with the other individual factors. The revised values for the nickel and manganese factors to be used for steels containing more than 1.0% Ni and 0.15% Mo and quenched between 800 and 855 °C (1475 and 1575 °F) are given in Fig. 15.

By contrast, many of the single- and almost all of the multialloyed high-carbon compositions are initially bainitic (at 10% transformation) when either quenched directly from carburizing or requenched from 925 °C (1700 °F). They also contain much less undissolved carbide. Consequently, synergistic effects are not as readily apparent. Instead, each individual element shows a higher hardenability effect (except for aluminum) than noted at the lower temperatures for any given amount of alloy—in particular, note silicon in Fig. 13. Thus, all

925 °C (1700 °F) factors listed in Tables 1A, 1B, and 2 and Fig. 10 apply to all single- and multialloyed high-carbon steels within the limits of alloy content shown. In addition, they also apply to the calculation of case hardenability in carburizing grades quenched from 925 °C (1700 °F), with one precaution: that the chromium factor labeled “carburizing steels” be used when quenching directly from carburizing.

The factors in Tables 1A, 1B, and 2, and Fig. 8 through 15 can also be used for high-carbon steels that are spheroidize annealed prior to hardening. However, the calculated D_I value will have to be converted to an *annealed* D_I using Fig. 1.

Use of the Multiplying Factors

Procedure 1. For the calculation of case hardenability of carburizing steels hardened by direct quenching from the carburizer (925 °C,

or 1700 °F), use the factors in Tables 1A, 1B, and 2 as follows:

1. If composition is pearlitic, that is, contains less than 1.0% Ni and 0.15% Mo, use the factors Mn*, Si*, Ni*, Mo*, and Al with the chromium carburized steels factor from Tables 1A and 1B. Multiply these together with proper factors for carbon and boron chosen from Table 2 and Fig. 8.
2. If composition is bainitic, that is, contains more than 1.0% Ni and 0.15% Mo, again use the factors Mn*, Ni*, Mo*, Al, and chromium carburized steels, but use the multialloyed silicon factor in Tables 1A and 1B. Use the proper carbon and boron factors from Table 2 and Fig. 8.

Procedure 2. For the calculation of case hardenability of carburizing steels that are normalized or quenched from carburizing and then reheated to 925 °C (1700 °F) for hardening, and for the hardenability of hypereutectoid steels that are to be normalized prior to rehardening from 925 °C (1700 °F), follow procedure 1 but use the regular Cr* factor listed in Table 1A. This is a seldom-used practice.

Procedure 3. For the calculation of case hardenability of carburizing steels and/or high-carbon steels that are normalized or quenched prior to rehardening from 800 to 855 °C (1475 to 1575 °F), use the following factors:

1. If composition is pearlitic, use the factors labeled Mn*, Si*, Cr*, Ni*, Mo*, and Al in Tables 1A and 1B with the appropriate carbon and boron factors in Table 2 and Fig. 8.
2. If bainitic, use the factors Cr*, Mo*, and Al with the multialloyed silicon factor in Tables 1A and 1B, the appropriate combined factors for nickel and manganese from Fig. 15, and carbon factors (Table 2) and boron factors (Fig. 8).

Procedure 4. For the calculation of hardenability of high-carbon steels hardened from a spheroidize-annealed prior structure, use procedure 3 and then convert the D_I value obtained to the annealed D_I value using Fig. 1.

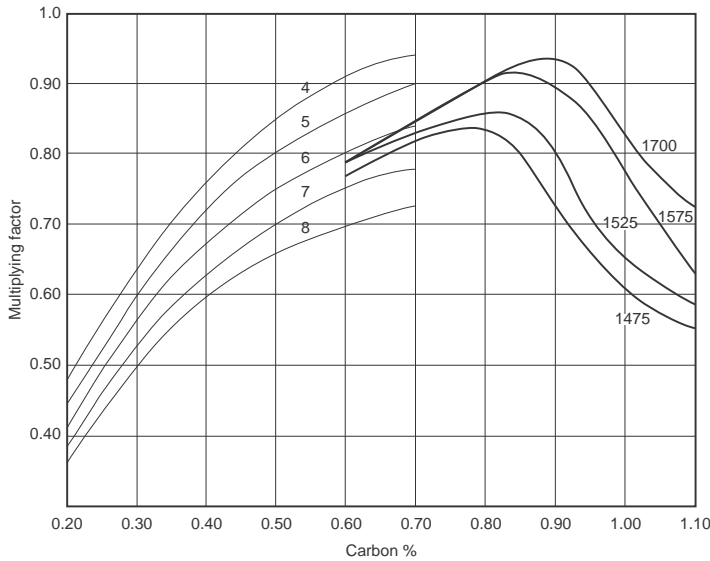


Fig. 14 Multiplying factors for carbon at each austenitizing condition. Data plotted on background of original Kramer (Ref 14) data for medium-carbon steels with grain-size variation from ASTM 4 to 8. Source: Ref 5

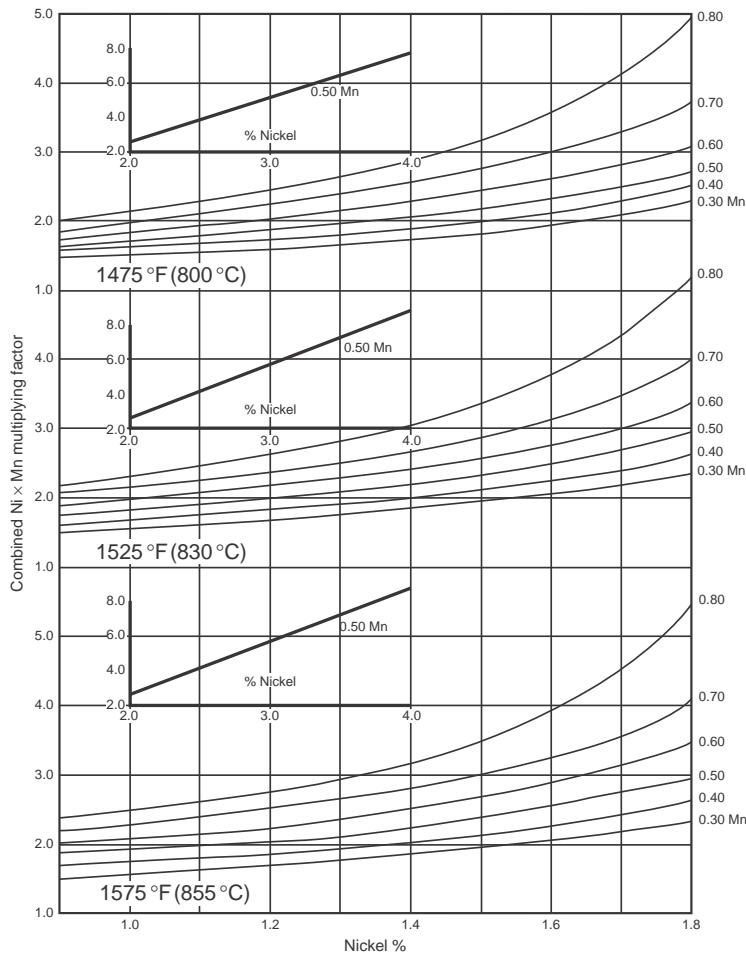


Fig. 15 Combined multiplying factor for nickel and manganese in bainitic high-carbon steels quenched from 800 to 855 °C (1475 to 1575 °F). Use in place of standard factors in Fig. 14 when composition contains more than 1.0% Ni and 0.15% Mo. Source: Ref 5

Limitations of the Multiplying Factors

Limitations of the multiplying factors include:

1. The reheat time at the austenitizing temperature during rehardening of prior normalized or spheroidize-annealed high-carbon steels and carburizing steels should be reasonably close to the 35 to 40 min used here.
2. Although grain-size variations need not be taken into consideration with these factors, it is recognized that slight variations in hardenability due to variation in grain size may exist, particularly in pearlitic steels.
3. The boron factors in Fig. 8 apply for boron additions protected with titanium, aluminum, and zirconium. A lower effect will likely result if other boron alloys are used (Ref 15).

ACKNOWLEDGMENTS

The information in this article is largely adapted from:

- C.F. Jatzcak and R.W. Devine, Jr., *Trans. ASM*, Vol 47, 1955, p 748
- C.F. Jatzcak and E.S. Rowland, *Trans. ASM*, Vol 45, 1953, p 771
- C.F. Jatzcak and D.J. Girardi, *Trans. ASM*, Vol 51, 1959, p 335
- C.F. Jatzcak, *Met. Prog.*, Sept 1971, p 60
- C.F. Jatzcak, *Met. Trans.*, Vol 4, Oct 1973, p 2267
- W. Crafts and J. Lamont, *Trans. TMS-AIME*, Vol 154, 1943, p 386
- W. Crafts and J. Lamont, *Trans. TMS-AIME*, Vol 158, 1944, p 157
- M. Grossman, M. Asimow and S.F. Urban, *Trans. ASM*, Vol 27, 1939, p 125
- R.V. Fostini and F.J. Schoen, *Transformation and Hardenability in Steels Symposium*, Climax Molybdenum Company, 1967, p 195

REFERENCES

1. C.F. Jatzcak and R.W. Devine, Jr., *Trans. ASM*, Vol 47, 1955, p 748
2. C.F. Jatzcak and E.S. Rowland, *Trans. ASM*, Vol 45, 1953, p 771
3. C.F. Jatzcak and D.J. Girardi, *Trans. ASM*, Vol 51, 1959, p 335
4. C.F. Jatzcak, *Met. Prog.*, Sept 1971, p 60
5. C.F. Jatzcak, *Met. Trans.*, Vol 4, Oct 1973, p 2267
6. M.A. Grossmann, *Trans. TMS-AIME*, Vol 150, 1942, p 227
7. J.H. Hollomon and L.D. Jaffee, *Trans. TMS-AIME*, Vol 167, 1946, p 643
8. E.S. Rowland, J. Welchner, and R.H. Marshall, *Trans. TMS-AIME*, Vol 158, 1944, p 168
9. D.J. Carney, *Trans. ASM*, Vol 46, 1954, p 882
10. *Atlas: Hardenability of Carburized Steels*, Climax Molybdenum Co., 1960

88 / Introduction to Steel Heat Treating

11. E.J. Whittenberger, R.R. Burt, and D.J. Carney, *Trans. TMS-AIME*, Vol 206, 1957, p 1008
12. G.O. Rahrer and C.D. Armstrong, *Trans. ASM*, Vol 40, 1948, p 1099
13. J.R. Sloan, Caterpillar Tractor Co., Peoria, IL, personal communication
14. I.R. Kramer, S. Siegel, and J.G. Brooks, *Trans. TMS-AIME*, Vol 67, 1946, p 670
15. G. Melloy and J.R. Russ, *Met. Prog.*, Nov 1966, p 83

SELECTED REFERENCES

- W. Crafts and J. Lamont, *Trans. TMS-AIME*, Vol 158, 1944, p 157
- M. Grossman, M. Asimow and S.F. Urban, *Trans. ASM*, Vol 27, 1939, p 125
- R.V. Fostini and F.J. Schoen, *Transformation and Hardenability in Steels Symposium* Climax Molybdenum Company, 1967, p 195

Steel Quenching Fundamentals and Processes

Quenching of Steel	91	Intensive Quenching and Other Quench Methods	199
Mechanism of Quenching	91	Heat Transfer during Quenching	200
Quenching Process Variables	94	Batch Intensive Quenching (IQ-2)	201
Metallurgical Aspects	95	Single-Part IQ Process (IQ-3)	203
Quench Severity	100	Improvement of Steel Microstructure, Mechanical Properties, and Stress Conditions	204
Tests and Evaluation of Quenching Media	103	IQ Process and Part Distortion	207
Cooling Curve Test	104	Design of Production IQ Systems	207
Heat-Transfer Coefficient Calculations	110	Practical Applications of IQ Processes	210
Common Quenching Process Variables	113		
Quenching Systems	118	Inverse Hardening	213
Water- and Air-Quenching Media	122	Heat-Extraction Dynamics	213
Aqueous Salt (Brine) Solutions	122	Metallurgical Aspects	215
Molten Metal Quenchants	125	Quenchants Enabling Controllable Delayed Quenching	218
Molten Salt and Hot Oil Quenchants	126	Properties	218
Oil Quenchants	129	Summary	219
Quench Oil Bath Maintenance	139		
Oil Quench System Monitoring	144	Gas Quenching	221
Safe Use of Petroleum Quench Oils (Ref 253)	144	Introduction	221
Polymer Quenchants	146	Physical Principles	221
Fixtures	151	Equipment for Gas Quenching	222
		Gas Types	223
Characterization of Heat Transfer during Quenching	158	Cooling Curves	224
Heat-Transfer Basics	159	Prediction of Core Hardness	225
Heat Generated by Microstructural Evolution	162	Gas-Flow Reversing	227
Liquid Quenching Heat Transfer	162	Dynamic Gas Quenching	228
Active Heat-Transfer Boundary Condition	167	Fixtures for Gas Quenching	229
		Control of Distortion with HPGQ	230
Large Probes for Characterization of Industrial Quenching Processes	176	Salt Quenching	232
Laboratory Tests to Evaluate the Cooling Intensity of Liquid Quenchants	176	Equipment for Salt Quenching	233
Differences between Laboratory Tests and Characterization of Industrial Quenching Processes	179	Time and Temperature Considerations	233
Critical Heat-Flux Densities of Liquid Quenchants	179	Critical Characteristics for the Operation of Salt Quenching Systems	234
Temperature Gradient Method for Evaluation of Cooling Intensity in Workshop Conditions	180	Environmental and Safety Considerations in Salt Quenching	236
The Liščić/Petrofer Probe	181		
Prediction of Hardness Distribution after Quenching Axially Symmetrical Workpieces of Any Shape	183	Fluidized-Bed Quenching	238
Numerical Solution of the Inverse Heat-Conduction Problem	184	Design of Quenching Fluidized Beds	238
Smoothing of Measured Temperatures	188	Quenching Power	239
Simulation Examples	189	Application of Fluidized-Bed Quenching	242
Quench Process Sensors	192	Spray Quenching	245
Fluid Flow in Quenching	192	Introduction	245
Fluid Flow Measurement	192	Water Quenching Heat Transfer	247
		Immersion Quenching	247
Intensive Quenching of Steel Parts	198	Spray Quenching	247
Mechanical Properties and Cooling Rate of Quenching	198	Jet Quenching	248
		Summary	250

Press Quenching	252	Cooling Behavior Experiment Materials and Procedures	257
Equipment	252	Cooling Curves and Cooling-Rate Curves Results	
Factors in Distortion Control	255	and Analysis	257
Wire Patenting	257	Concentration-Fog Flux Effect	260
Wire Patenting Processes	257	Controlled Fog-Cooling Patenting with CMC Additive	261
		Conclusion.	261

Quenching of Steel

G.E. Totten, Portland State University
J.L. Dossett, Consultant
N.I. Kobasko IQ Technologies, Inc.

QUENCHING OF STEEL is the rapid cooling of steel from a suitable elevated temperature. This generally is accomplished by immersion of the hot steel into a vaporizable fluid such as water; petroleum, vegetable, or animal oil; aqueous polymer solution; or an aqueous (salt) solution. Other quenching media include molten salt, fluidized bed, or gas, although forced air is sometimes used. As a result of the quenching process, production parts must develop an acceptable as-quenched microstructure and, in critical areas, mechanical properties that will meet minimum specifications after the parts are tempered.

The effectiveness of the quenching process depends on the cooling characteristics of the quenching medium relative to the hardenability of the steel. Thus, results may be varied by varying the steel composition or the agitation, quenchant temperature, or the quenching medium. The design of the quenching system and the thoroughness with which the system is maintained contribute to the success of the process. Part design also contributes to the mechanical properties and distortion that will result from a particular quenchant and process.

The rate of heat extraction attributable to a quenching medium is greatly modified by the manner or condition in which the quenching medium is used. These modifications have resulted in the assignment of specific names to various quenching methods, such as direct, time, selective, spray, fog, and interrupted quenching:

- **Direct quenching:** This is the most widely used method of treating steel. When carburized work is quenched from the carburizing temperature or from a slightly lower temperature, the term *direct quenching* is used to distinguish this method from the more indirect practice of carburizing, slow cooling, reheating, and quenching. Direct quenching practice is relatively simple and economical, and distortion of carburized parts is usually less frequent with direct quenching than with reheating and quenching, particularly on smaller parts.
- **Time quenching:** This form of quenching is used when the cooling rate of the part being quenched is changed abruptly at some time

during the cooling cycle. The change in cooling rate may comprise either an increase or a decrease, depending on which is needed to attain desired results. The usual practice is to lower the temperature of the part by quenching in a medium (for instance, water) for a short time until the part has cooled below the nose of the time-temperature transformation curve, and then to remove the part for quenching in a second medium (for instance, oil), so that it cools more slowly through the martensite transformation range. In many applications, the second medium is still-air. Time quenching is most often used for minimizing distortion, cracking, and dimensional change. It should be used with caution because successful application depends greatly on the skill of the operator.

- **Selective quenching:** This process is used when areas of a part are selected to remain relatively unaffected by the quenching medium. This can be accomplished by insulating the area to be protected or by allowing the quenchant to contact only those areas of the part that are to be quenched.
- **Spray quenching:** Streams of quenching liquid are directed at high pressure, up to 825 kPa (120 psi), to local areas of the workpiece in spray quenching practice. The cooling rate is fast and uniform over the entire temperature range of the quenching cycle because of the large volume of coolant used and because all of the coolant makes direct contact with the part being quenched. The velocity of the stream removes any vapor bubbles and creates spray droplets, which are available for heat transfer. However, low-pressure spraying, in effect a flood-type flow, is preferred with certain polymer quenchants.
- **Fog quenching:** This procedure uses a fine fog or mist of liquid droplets and a carrier gas as the cooling agents. Although similar to spray quenching, fog quenching is less effective, because the quenching mist or fog is not readily adapted to rapid removal or replacement by the cooler fog or mist once it has been heated by contact with the part being quenched.

Quenching systems have two components: the quenching medium and the equipment used to perform the hardening operation. In this article, an overview of common quenching media and process variables encountered in the heat treating plant is provided, including quenchant evaluation, classification, selection, and maintenance.

Mechanism of Quenching

Several factors are involved in the mechanism of quenching:

- Internal conditions of the workpiece that affect the diffusion of heat to the surface
- Surface and other external conditions that affect the removal of heat
- Heat-extracting potential of the quenching fluid at the fluid temperatures and pressures being used
- Changes in the heat-extracting potential of the fluid caused by variation in agitation, temperature, or pressure

An unagitated quenchant experiences unavoidable movement as a result of immersion of the hot work into the fluid, turbulence surrounding the hot steel surface due to nucleate boiling of the fluid, and convection currents. Although this relatively minimal degree of agitation of the fluid eventually dissipates the accumulated heat to the surrounding liquid, localized volumes of liquid may be heated excessively, or may even vaporize, which may affect the uniformity of the quenching process.

The inherent nonuniformity of the surface rewetting process that occurs when quenching into a vaporizable fluid without the use of additives is shown when hot steel is quenched into water. Figure 1 shows that water does not effectively wet the surface of steel during the quenching process (Ref 1). In fact, at least three distinctly different cooling regimes, with dramatically different heat-transfer characteristics, are present on the surface simultaneously, which will produce thermal gradients potentially sufficient to increase distortion.



Fig. 1 Quench of a 25 mm diameter \times 100 mm (1.0 in. diameter \times 4 in.) cylinder of a CrNi steel into water at 30 °C (85 °F) with an agitation rate of 0.3 m/s (1 ft/s). Courtesy of H.M. Tensi, Technical University of Munich

Cooling Curves. The most useful way of accurately describing the complex mechanism of quenching is to develop a time-temperature cooling curve for the quenching fluid under controlled conditions. The cooling curve is desirable because it is sensitive to many of the factors that may affect the cooling ability of the quenchant.

Time-temperature cooling curves, such as those shown in Fig. 2, may be obtained by quenching a hot testpiece of the same steel of which the parts are made, into a sample of the quenching fluid. Alternatively, an austenitic stainless steel or Inconel test specimen is used to avoid soaking or the necessity for a protective atmosphere. The test specimen is typically a round bar where the length is at least four times the diameter (a so-called infinite cylinder that minimizes end-cooling effects). Cooling curves are generated by inserting thermocouples into the desired locations of the test specimens. Two common thermocouple configurations are test probes with thermocouples inserted into the geometric center or alternatively with thermocouples located at the center and surface (or within 1 to 2 mm, or 0.04 to 0.08 in., under the surface) at midlength. The time-temperature behavior of the cooling process is measured using a high-speed recorder, data logger, or by use of a computer equipped with an analog/digital board. The resulting time-temperature curve indicates the heat-transfer characteristics of the quenching fluid.

Steel hardening requires preheating of steel to an alloy-specific austenitizing temperature in the range of 750 to 1100 °C (1380 to 2010 °F), at which point the steel is quenched (cooled) in a defined way to obtain the desired mechanical properties, such as hardness and tensile strength. Most vaporizable quenchants used for this process exhibit boiling temperatures between 100 and 300 °C (212 and 570 °F) at atmospheric pressure. When steel is quenched at these temperatures, the rewetting of the surface is usually time-dependent, which influences the cooling process and achievable hardness.

G.J. Leidenfrost described the rewetting process approximately 250 years ago (Ref 2). The Leidenfrost temperature is defined as the surface temperature where the vapor film (full-film boiling) collapses and the surface is wetted by

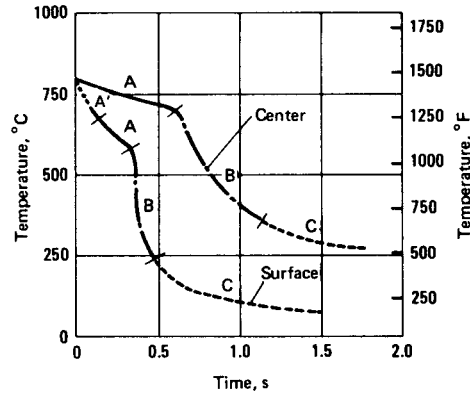


Fig. 2 Typical surface and center cooling curves indicating the different heat-transfer mechanisms (stages) from the hot metal to the cooler vaporizable liquid quenchant

the liquid (nucleate boiling). Literature reports water temperatures for this event to be 150 to 300 °C (300 to 570 °F) (Ref 3–6). It is apparent that the Leidenfrost temperature is influenced by a variety of factors, some of which cannot be quantified precisely even today (2013) (Ref 7).

An example of a typical surface and center cooling curve for a quenchant is shown in Fig. 2. Four stages of heat transfer from the surface of the hot probe into the cooler vaporizable liquid are evident.

Stage A' in Fig. 2 illustrates the first effects of immersion. Sometimes called the initial liquid contact stage, this stage is characterized by the explosive or sudden formation of vapor bubbles (shock-film boiling), which is due to the very large temperature difference between the hot metal surface and the much cooler quenchant. Initially, small vapor bubbles are formed that grow in size until they detach from the steel surface and form a vapor blanket (full-film boiling) that surrounds the hot metal surface (Ref 8). The duration of stage A' is typically approximately 0.1 s and is relatively unimportant in the evaluation of heat-transfer characteristics due to the relatively large amount of heat removed over such a short time. Shock-film boiling is detectable only when extremely sensitive equipment is used, and it cannot be detected when the liquid is viscous, contains entrained gases, or when the quenchant bath temperature approaches the boiling point of the liquid. Thus, this important cooling process is typically not observed in most cooling curve analyses.

Stage A, called the vapor blanket cooling stage, is characterized by the Leidenfrost phenomenon, namely, the formation of an unbroken vapor blanket that surrounds the testpiece. It occurs when the supply of heat from the surface of the testpiece exceeds the amount of heat needed to form the maximum vapor per unit area of the piece. This stage is one of slow cooling, because the vapor envelope acts as an insulator, and cooling occurs principally by radiation through the vapor film. However, as Fig. 1 shows, for a non-steady-state cooling

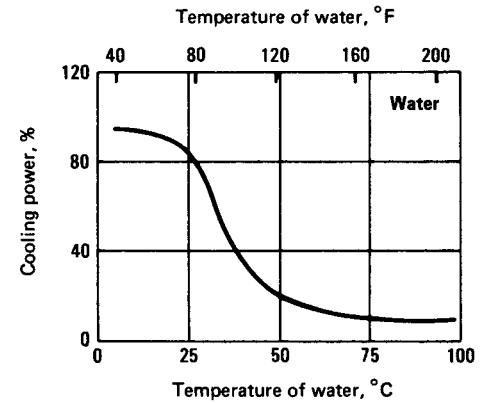


Fig. 3 Relationship between the surface cooling power of water with mild agitation and water temperature

process, the surface temperature for all portions of the surface area of the part are not equal to the Leidenfrost temperature. When the vapor blanket (full-film boiling) collapses, wetting begins by nucleate boiling due to the influence of lateral heat conduction relative to the surface (Ref 2). This is due to the simultaneous presence of various heat-transfer conditions during vapor blanket cooling (or film boiling, FB), nucleate boiling (NB), and convective cooling (conv) with significantly varying heat-transfer coefficients: α_{FB} (100 to 250 $\text{W/m}^2 \cdot \text{K}$), α_{NB} (10 to 20 $\text{kW/m}^2 \cdot \text{K}$), and α_{conv} (approximately 700 $\text{W/m}^2 \cdot \text{K}$) (Ref 1).

In quenchants such as plain water or conventional (slow) petroleum oil with minimal agitation, the film-boiling (vapor blanket) stage may be prolonged. This prolongation, which varies with the degree to which the complexity of the part being quenched encourages vapor entrapment and with the temperature of the quench water, results in uneven hardness and unfavorable distribution of stress. This may cause distortion, cracking, or soft spots. To obtain reproducible results, especially with water quenching, the temperature, agitation, and contamination must be controlled. Water at a temperature of 15 to 25 °C (55 to 75 °F) may provide uniform quenching speed and reproducible results. However, as illustrated in Fig. 3, the surface cooling power of water decreases rapidly as water temperature increases. (This behavior also is demonstrated in Fig. 4.)

Hot water may be used because it is traditionally believed that decreased quench severity will result in decreased distortion. The opposite effect may be obtained because cooling power decreases as the boiling point is approached, especially in the critical region where distortion is facilitated due to the formation of the relatively unstable vapor blanket of approximately 30 to 60 °C (85 to 140 °F). As the temperature is further increased, the vapor blanket becomes more stable, and surface cooling resembles that of steam. In addition, however, film boiling is stabilized and may be present over the metal surface intermittently, leading to substantially

increased thermal gradients and increased distortion and cracking potential. For this reason, agitation is especially important in water quenching, because it ruptures the vapor blanket that is formed, disperses vapor bubbles from the surface of the parts, and directs cooler water against the workpiece. It has been shown that intensive cooling of the steel surface will eliminate vapor blanket formation, resulting in increased hardness, improved fatigue, and substantially reduced distortion

Stage A is not detectable in aqueous solutions of nonvolatile solutes (at approximately 5% concentration), such as potassium chloride, lithium chloride, sodium hydroxide, or sulfuric acid. Cooling curves for these solutions start immediately with stage B. When saturated solutions of barium hydroxide, calcium hydroxide, or other slightly soluble materials; solutions containing finely dispersed solids; or colloidal solutions in water are used, films are deposited on the testpiece during the A-stage, and typically a prolongation of both the A- and C-stages results. This condition usually causes a more violent action in stage B. Solutions of some colloids or gels, including water-soluble polymers such as polyvinyl alcohol, gelatin, soap, and starch, form a gelatinous envelope outside the vapor blanket formed in stage A. The presence of this gel envelope prolongs the A-stage and succeeding stages.

Stage B, the vapor transport cooling stage (nucleate boiling) produces the highest rate of heat transfer and begins when the temperature of the surface metal has been sufficiently reduced to allow the continuous vapor film to collapse; violent boiling of the quenching liquid then occurs and heat is removed from the metal at a very rapid rate, largely as heat of vaporization. The transition temperature between A- and B-stage cooling is the Leidenfrost temperature. The boiling point of the quenchant determines the conclusion of this stage. Size and shape of the vapor bubbles are important in controlling duration of stage B, as well as the cooling rate developed within it.

Stage C is called the liquid cooling stage (convective cooling); the cooling rate in this stage is slower than that developed in stage B. Stage C begins when the temperature of the metal surface is reduced to the boiling point (or boiling range) of the quenching liquid. Below this temperature, boiling stops and slow cooling occurs by conduction and convection. The difference in temperature between the boiling point of the liquid and the bath temperature is a major factor influencing the rate of heat transfer. Viscosity also affects cooling rate in stage C.

Tensi Classification of Surface-Cooling Modes of Heat Transfer. Tensi studied the rewetting behavior of a broad range of quenching media by combining time-temperature cooling curves to characterize surface heat transfer with time-conductance curves to characterize rewetting behavior. Typically, as the steel surface is wetted by the quenchant after vapor blanket collapse, conductance will increase. In

the laboratory, conductance is measured by heating the probe to 850 °C (1560 °F) and then immersing it into the quenching medium of interest (Ref 9, 10). When the metal is covered by a vapor film, the resistance between the metal surface and the quenching fluid is high.

When the vapor film breaks, the surface conductance increases in proportion to the relative amount of the surface that is wetted. The variation of probe conductance with respect to total immersion time is measured. Typical time-conductance curves are shown in Fig. 5 along

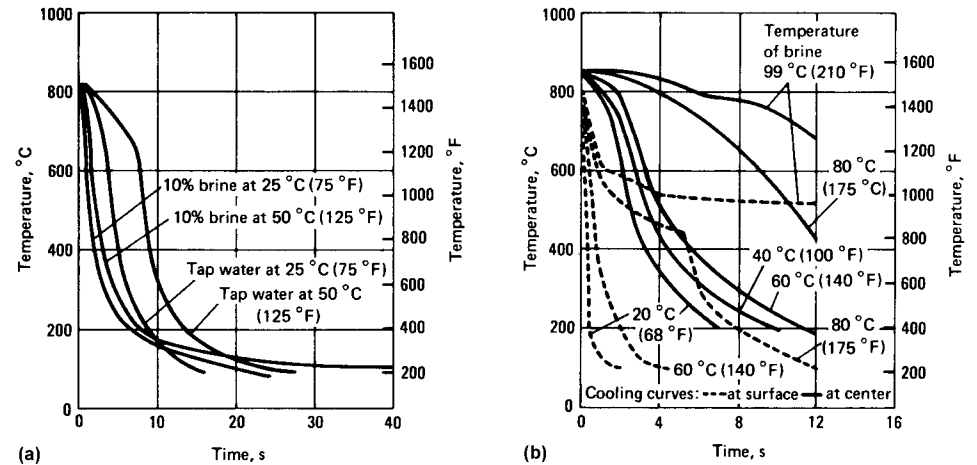


Fig. 4 Cooling curves illustrating the effect of temperature and quench severity (cooling power)

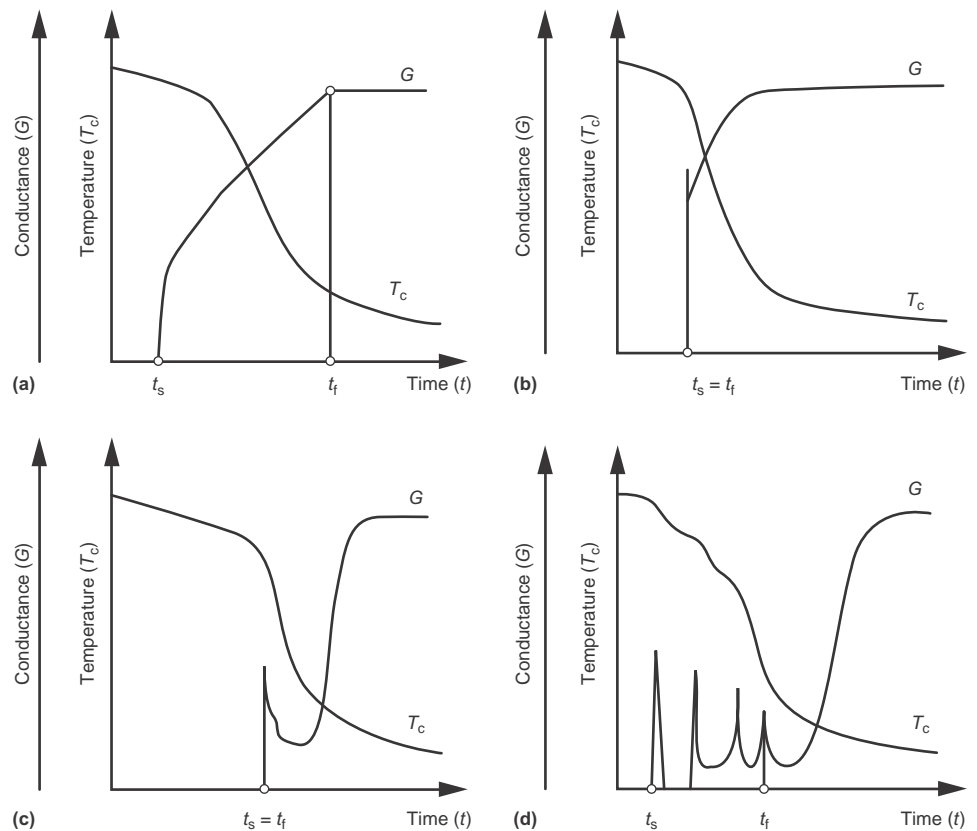


Fig. 5 Illustration of four common rewetting profiles when quenching steel from the austenitization temperature. (a) Slow wetting typically encountered during a water quench. (b) Explosive wetting with rapidly ascending bubbles, and metal surface permanently wetted by the fluid (polymer quenchant 1). (c) Explosive wetting with large bubbles remaining on the surface, with polymer depositions remaining on the metal surface (polymer quenchant 2 at lower concentration). (d) Repeated explosive wetting, with large bubbles remaining on the surface (polymer quenchant 2 at higher concentration)

with corresponding time-temperature cooling curves for the same probe quenched in the same manner (Ref 9–11).

Four modes of heat transfer were found to characterize the different quenching media studied by Tensi, which are illustrated in Fig. 5 and are characterized as (Ref 9):

- **First heat-transfer mode:** Where full-film boiling and nucleate boiling are present at the same time on the probe surface (Fig. 5a). The rewetting front accompanying the transition from full-film (vapor-film) boiling, which occurs during the cooling process, typically moves axially along the metal surface during cooling (Ref 12).
- **Second heat-transfer mode:** Where the first step is characterized by film boiling occurring over the entire metal surface (Fig. 5b). At a certain point in time, nucleate boiling instantaneously replaces film boiling. When boiling ceases, convection heat transfer occurs (Ref 12).
- **Third heat-transfer mode:** In Fig. 5(c), some localized areas of the metal surface are covered by the vapor film (blanket), while at the same time, other areas experience nucleate boiling (Ref 12).
- **Fourth heat-transfer mode:** Film boiling and nucleate boiling periodically replace each other during quenching of a steel part in liquid medium, as shown in Fig. 5(d) (Ref 12, 13).

Each heat-transfer mode possesses a specific boundary condition when analyzing the heat transfer that is occurring computationally. For this reason, it is impossible to determine which heat-transfer mode is occurring at the surface of a test probe when the probe that is used to study this process contains only one thermocouple at the center, as is characteristic of most commercially available equipment at the present time. To properly solve this problem, the test probe should be instrumented with multiple thermocouples located on the surface or preferably near the surface and at positions below the surface (Ref 12–15). For evaluation of heat flux densities and heat-transfer coefficients, numerous methods of solving inverse problems have been developed, although they mostly refer to the second type of heat-transfer mode. Computational methodology is discussed subsequently.

Quenching Process Variables

Thus far, the mechanism of quench cooling has been discussed. Quench processes, however, are affected by a number of variables, including the quenchant, agitation, bath temperature, and workpiece temperature. Additional coverage on quenchants and quenching system

design is provided in *Heat Treating of Irons and Steels*, Volume 4B of *ASM Handbook* (Ref 16). Other prominent variables are briefly discussed here.

Agitation is externally produced movement of the quenching liquid relative to the part, which is achieved either by agitation of the liquid by propeller, pump, vibration, and so on (Ref 17, 18), or moving the part, or both in combination (Ref 19). This activity has an extremely important influence on the heat-transfer characteristics of the quenching liquid. It causes an earlier mechanical disruption of the vapor blanket in stage A and produces smaller, more frequently detached vapor bubbles during the vapor transport cooling stage (stage B). It mechanically disrupts or dislodges gels and solids, whether they are on the surface of the testpiece or suspended at the edge of the vapor blanket, thus producing faster heat transfer in liquid cooling (stage C). In addition to the aforementioned effects, agitation also brings cool liquid to replace heat-laden liquid.

Temperature of Quenchant. The temperature of the liquid may markedly affect its ability to extract heat (Ref 1, 11, 12). As an example, water temperature is very important because it loses its cooling power as it approaches its boiling point (Ref 11, 20). In oil, this effect is not

as pronounced, because oil becomes less viscous as the temperature is increased. This thinning of the oil offsets the temperature rise by a substantial amount (Ref 20).

Workpiece Temperature. Increasing the temperature of the testpiece has relatively little effect on its ability to transfer heat to the quenchant. Typically, the rate of heat transfer may increase because a greater temperature difference exists. Heat transfer may be affected due to more rapid surface oxidation of the steel at higher temperatures, especially when carbon steel and alloy steels are heated in air (Ref 21–23). Initially, an increase in the cooling rate may be observed due to an increase in surface roughness and therefore an increase in surface area. This increased surface area creates more nucleation sites for bubble formation, thus facilitating nucleate boiling and more rapid heat transfer, as shown in Fig. 6 (Ref 23). However, Fig. 6 also shows that increases in the thickness of the oxide layer due to increased austenitization temperatures or increased residence times, or both, may result in the creation of an insulating effect due to poorer thermal transport properties, reducing the overall heat-transfer rate from the cooling steel surface (Ref 22).

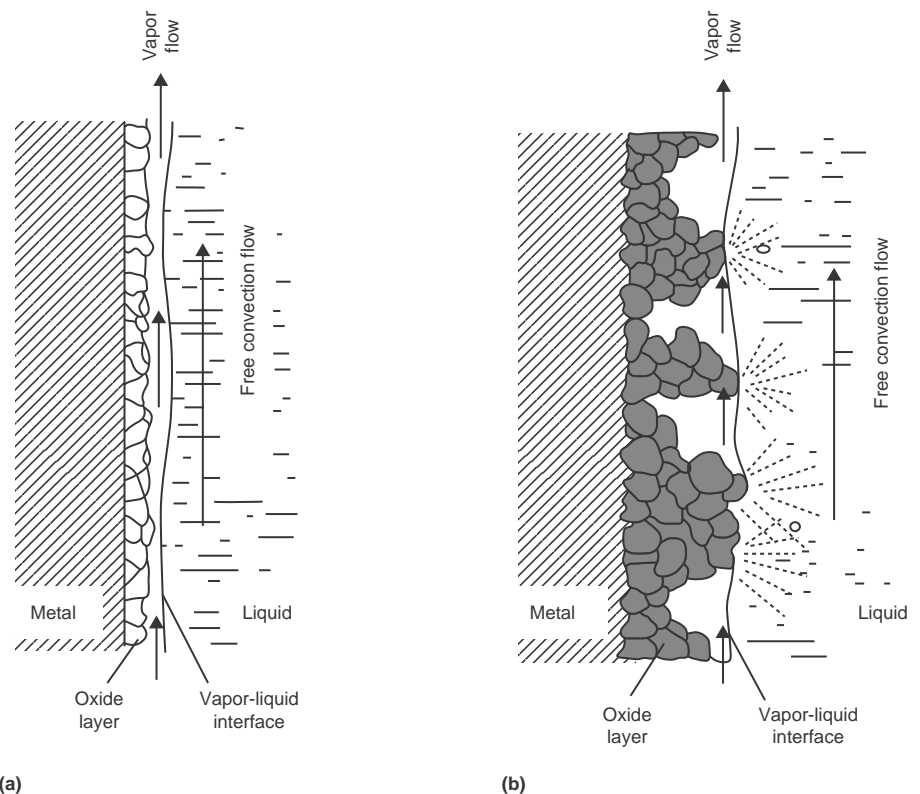


Fig. 6 Illustration of the formation of (a) a cooling rate accelerating light oxide scale on the surface of steel and (b) a sufficiently thick insulating oxide layer that results in decreased (and often nonuniform) cooling rate reduction. Source: Ref 23

Metallurgical Aspects

The testing of quenching media can be classified into two categories: tests of hardening power (metallurgical response) and tests of cooling power (thermal response). The two properties are not the same, because hardening power also is related to the size, microstructure, and composition of the steel being quenched. This section provides a selected overview of common metallurgical response tests to determine the ability to achieve the desired as-quenched microstructure.

Steel is quenched to control the transformation of austenite to the desired microconstituents. Two types of transformation diagrams are typically used to illustrate transformation products

formed upon cooling. One type is the time-temperature transformation (TTT) diagram, which is also called an isothermal transformation diagram (Ref 24, 25). It is developed by heating small samples of steel to the austenitizing temperature and then rapidly cooling to a temperature intermediate between the austenitizing and martensite start (M_s) temperatures, followed by holding for a fixed period of time (holding time) until the transformation is complete, at which point the transformation products—ferrite, pearlite, bainite, and martensite—are determined (see also the article “Introduction to Steel Heat Treatment” in this Volume).

This is done repeatedly until a TTT diagram is constructed. The TTT diagrams can only be read along the isotherms shown, and these

diagrams strictly apply only to those transformations conducted at constant temperature. One of the critically important parameters for which TTT diagrams are used is in determining the cooling rate necessary to completely through harden steel. Furthermore, TTT diagrams provide some insight into the effect of alloying elements on phase transformation upon quenching. This is illustrated by comparing the TTT diagrams for AISI 1045 carbon steel with AISI 5140, 4140, and 4340 low/medium-alloy steels shown in Fig. 7. Based on the position of the pearlite transformation, it is evident that the increasing order of hardenability of the steel alloys shown is:

$$1045 < 5140 < 4140 < 4340$$

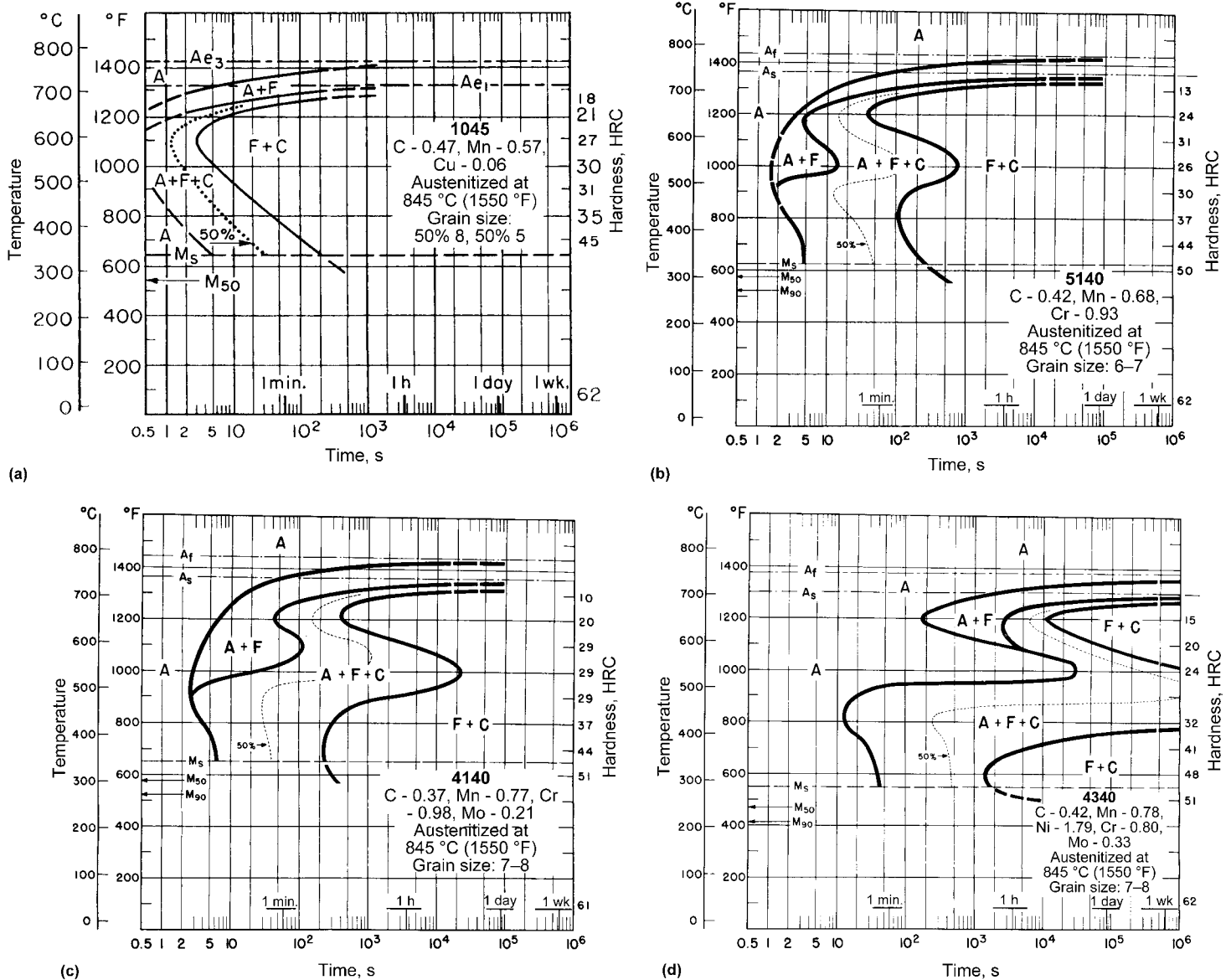


Fig. 7 Comparison of time-temperature transformation diagrams for AISI (a) 1045, (b) 5140, (c) 4140, and (d) 4340 steels

When a heat treatment process is not conducted isothermally, the second type of transformation diagram is formed, which involves heating steel test specimens to the austenitizing temperature for the alloy of interest and then continuously cooling the test specimen in a quenching bath at a temperature and cooling rate suitable for the alloy and section size being treated. Steel test specimens may be cooled at different specified rates, and the proportion of transformation products formed after cooling to various temperatures intermediate between the austenitizing and M_s temperatures are determined; a continuous-cooling transformation (CCT) diagram is then constructed. Note that bainite transformations are not shown in CCT diagrams. The CCT diagrams provide data on the temperatures for each phase transformation, the amount of phase transformation product obtained for each cooling rate with respect to time, and the cooling rate necessary to obtain martensite. The CCT diagrams can only be read along the isotherms for different cooling rates.

The CCT diagrams are used to predict the microstructural transformation products obtained after quenching. These curves also provide cooling rate information for the surface and core of a section of the steel alloy being quenched. The CCT diagrams may be obtained by various methods (including from Jominy data obtained with a Jominy bar instrumented with surface thermocouples, so that as-quenched microstructures are then correlated with cooling rates calculated from the thermocouple data). This is an example of how steel hardenability can be used with CCT curves to predict steel transformation using different quenching media.

As Fig. 8 shows, the relative effects of composition on steel hardenability can be observed directly from the CCT diagram. For example, low-hardenability steels such as AISI 1045 transform very quickly to ferrite and pearlite or bainite. As steel hardenability increases, such as from AISI 5140 to 4140 to 4340, the transformation curves occur at lower temperatures and are displaced further to the right as hardenability increases. Typically, high-hardenability steels transform from austenite to predominantly martensite over a wide range of part thicknesses and quenching cooling rates.

As described in the article "Introduction to Steel Heat Treatment" in this Volume, CCT and TTT diagrams differ in that longer times are required for transformation to begin. Often this delay in transformation shown in CCT curves displaces the bainitic transformation regions, making it more difficult to observe relative to TTT curves. It is also important to note that CCT and TTT curves are different representations. Transformation products are shown in CCT curves at the bottom of the diagram and at the right side of the TTT diagram. Phase changes are indicated by CCT diagrams, but TTT diagrams illustrate the actual transformation phase (Ref 26).

Both TTT and CCT diagrams are characterized by the presence of a nose (also commonly referred to as a shoulder or knee) that represents the point where pearlite first starts to form. The cooling rate at the nose of the transformation curve is defined as the critical cooling rate of a steel, which is "the slowest cooling rate at which the steel can be cooled and yet completely harden" (Ref 27), or the slowest

cooling rate that will produce 100% martensite. Martensite is often the desired as-quenched microstructure. To obtain the maximum amount of martensite, the cooling rate must be sufficiently fast to avoid the nose of the TTT or CCT curve of the steel being quenched. If the cooling rate is too slow to miss the nose of the curve, some transformation to bainite, pearlite, or ferrite will occur, with a corresponding decrease in the amount of martensite formed and the hardness developed. The pearlite nose is typically shifted down and to the right in a CCT diagram, relative to the depiction in a TTT diagram, which indicates that more time is available for martensite transformation than is shown on the corresponding TTT diagram. In fact, one error of TTT diagrams relative to CCT diagrams is that they typically indicate a faster cooling rate than is actually necessary to form 100% martensite on quenching (Ref 26). Therefore, because TTT or CCT diagrams represent very different cooling processes, the corresponding critical cooling rates will also be different, which explains why the procedure by which the critical cooling rate is calculated must also be provided.

Typical microstructures that may be obtained are depicted by the four curves in Fig. 9. Curve 1 (water quench) illustrates a relatively rapid cooling rate. The nose of the pearlite transformation curve is largely avoided, resulting in essentially 100% martensite formation. Curve 2 (oil quench) illustrates a relatively moderate cooling rate. Part of the cooling process occurs within the pearlite transformation region, resulting in the formation of mixed microstructures, in this case, approximately 50% martensite and 50% pearlite. Such

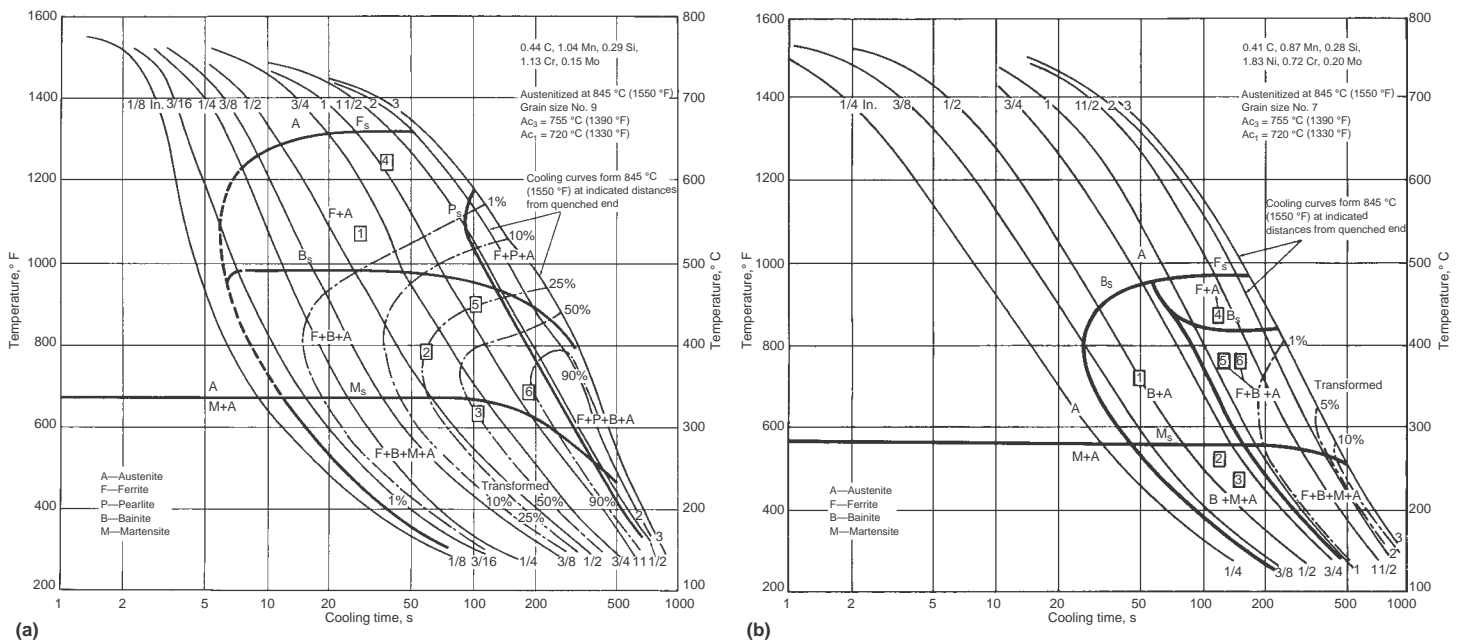


Fig. 8 Continuous-cooling transformation diagrams for AISI (a) 4140 and (b) 4340 steels

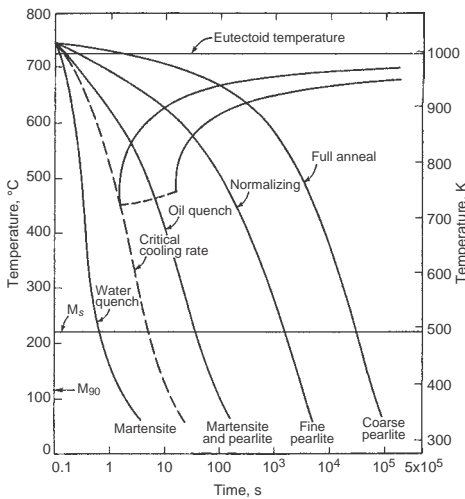


Fig. 9 Effect of cooling times on steel transformation product formation for a eutectoid steel

processes are conventionally referred to as split transformations. The relatively slower cooling rate depicted by curve 3 (normalizing) results in the formation of fine pearlite, while the fourth curve (full anneal) represents even slower cooling, resulting in the formation of coarse pearlite.

Figure 10 shows the use of a CCT diagram in conjunction with cooling curves for a water, petroleum oil, and an aqueous polymer quenchant to quench a low-hardenability AISI 1045 steel (Ref 28). These data show that quenching into water occurs sufficiently fast that no diffusional transformation occurs and only martensite is formed. However, quenching into a petroleum oil produces cooling rates that are inadequate to form martensite and austenite is transformed into ferrite and pearlite. The exotherm (temperature increase) observed with oil quenching occurs because of the latent heat released during phase transformation. The intermediate cooling rate obtained with the aqueous polymer quenchant resulted in the formation of approximately 85% martensite with the remaining 15% being retained austenite. These predictions were validated experimentally and this work illustrates the value of the use of steel transformation diagrams with cooling time-temperature behavior of the quenchant being used.

Carbon Content and Hardenability. The maximum hardness obtainable in a steel quenched at a sufficient rate to avoid the nose of the TTT curve depends only on the carbon content. Steels must contain greater than approximately 0.3% C to be hardenable by heat treatment to form martensitic structures. The relation of carbon content and percentage of martensite formed to as-quenched hardness is shown in Table 1 (Ref 29).

The cooling rate (quenching efficiency) necessary to obtain a fully martensitic structure depends on the hardenability of the steel and the thickness and shape of the part. The term

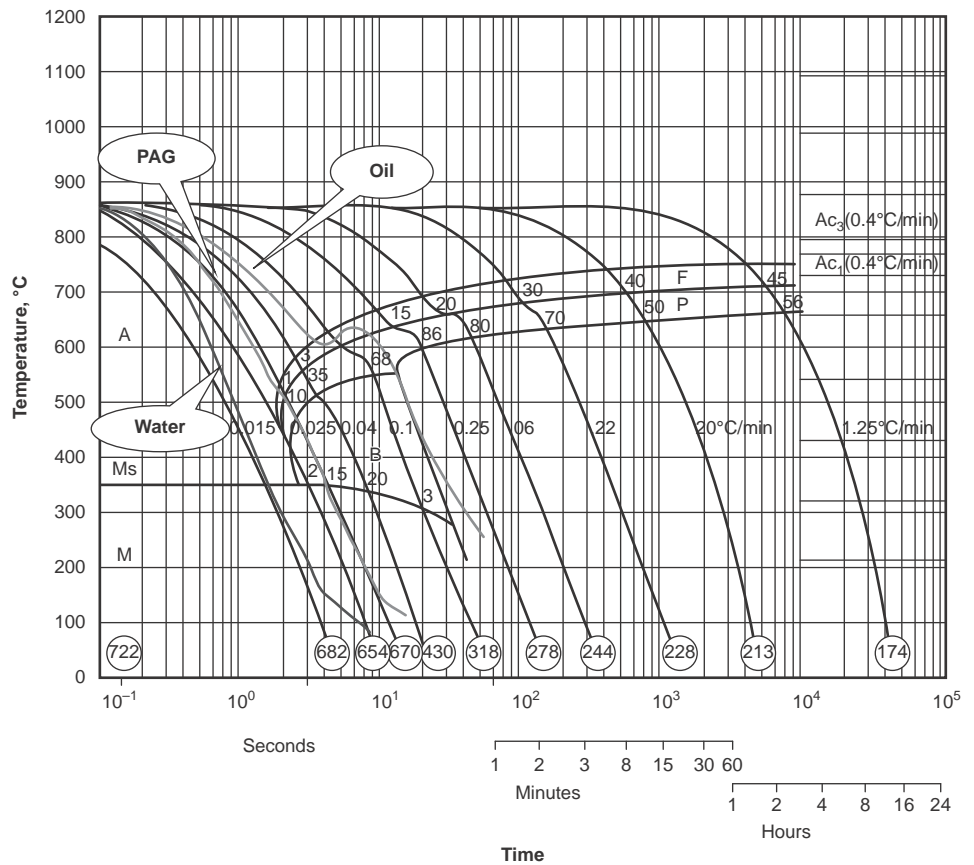


Fig. 10 Cooling time-temperature curves for water, petroleum oil, and an aqueous polymer (PAG, polyalkylene glycol) quenchant superimposed on the continuous-cooling transformation curve for AISI 1045 steel

Table 1 Effect of carbon concentration and martensite content on the as-quenched hardness of steel

Carbon, %	Hardness, HRC				
	99% martensite	95% martensite	90% martensite	80% martensite	50% martensite
0.10	38.5	32.9	30.7	27.8	26.2
0.12	39.5	34.5	32.3	29.3	27.3
0.14	40.6	36.1	33.9	30.8	28.4
0.16	41.8	37.6	35.3	32.3	29.5
0.18	42.9	39.1	36.8	33.7	30.7
0.20	44.2	40.5	38.2	35.0	31.8
0.22	45.4	41.9	39.6	36.3	33.0
0.24	46.6	43.2	40.9	37.6	34.2
0.26	47.9	44.5	42.2	38.8	35.3
0.28	49.1	44.8	43.4	40.0	36.4
0.30	50.3	47.0	44.6	41.2	37.5
0.32	51.5	48.2	45.8	42.3	38.5
0.34	52.7	49.3	46.9	43.4	39.5
0.36	53.9	50.4	47.9	44.4	40.5
0.38	55.0	51.4	49.0	45.4	41.5
0.40	56.1	52.4	50.0	46.4	42.4
0.42	57.1	53.4	50.9	47.3	43.4
0.44	58.1	54.3	51.8	48.2	44.3
0.46	59.1	55.2	52.7	49.0	45.1
0.48	60.0	56.0	53.5	49.8	46.0
0.50	60.9	56.8	54.3	50.6	46.8
0.52	61.7	57.5	55.0	51.3	47.7
0.54	62.5	58.2	55.7	52.0	48.5
0.56	63.2	58.9	56.3	52.6	49.3
0.58	63.8	59.5	57.0	53.2	50.0
0.60	64.3	60.0	57.5	53.8	50.7

Source: Ref 29

hardenability should not be confused with hardness, which is a material property that is proportional to strength. Hardness is dependent only on the carbon content of the steel, whereas *hardenability* refers to the ability to achieve a certain hardness at a certain depth, which depends on both the carbon content and the presence and amount of alloying elements. The actual depth of hardness depends on:

- Size and shape of the cross section
- Hardenability of the material
- Quenching conditions

Dossett has shown that the maximum section size that will through harden to the maximum attainable surface hardness is dependent on both carbon content and *hardenability*. Table 2 shows the variation of the maximum section size that is through hardened for four different steel alloys with increasing *hardenability*: 1045 < 5140 < 4140 < 4340 (Ref 30).

Depending on the carbon content and *hardenability* of the steel, the cooling rate should be fast enough so that a high percentage of martensite will be produced in critically stressed areas of the part. Lower percentages of martensite are often acceptable in areas subject to lower stresses in service. Higher percentages of martensite in the as-quenched structure will produce higher fatigue and impact properties after tempering.

The effect of quenching conditions on the depth of hardening is not only dependent on the quenchant being used and its physical and chemical properties but also on process parameters such as bath temperature and agitation, which was discussed previously.

Table 3 shows *hardenability* data for a number of through-hardened gear steels made to the minimum composition range for that grade (Ref 31). For comparison, the critical cooling rate in this example was taken as the cooling rate at 705 °C (1300 °F). In addition, the hardness at 60% martensite and the maximum diameter that will through harden in a so-called mild quench are also summarized for these steels. Mild agitation has been traditionally defined using Grossmann quench severity (*H*-values). A mildly agitated oil is reported to exhibit *H*-values of 0.30 to 0.35, and mildly agitated water exhibits *H*-values of 1.0 to 1.1. A still-water quench at 30 °C (85 °F) is defined as *H* = 1.0 (Ref 32). As discussed earlier, the critical cooling rate was defined in this example as

Table 2 Effect of hardenability on maximum section size through hardened to maximum attainable surface hardness

Steel grade	Maximum section size	
	mm	in.
1045	6.35	0.250
5140	19.0	0.750
4140	38.1	1.5
4340	76.1	3.0

that cooling rate that is just sufficient to produce a fully martensitic structure for the steel alloy composition under consideration.

As-quenched hardness not only depends on section size but also on shape. Round bars, square bars, and plates exhibit different depths of hardening, which is dependent on the total surface area exposed to the quenchant. The total surface area significantly affects heat extraction during quenching and therefore the depth of hardening. This is why rectangular-shaped bars achieve a relatively lower depth of hardening than round bars of the same cross-sectional size (Ref 33). Figure 11 can be used to convert the diameter or thickness of square bars and plates to the equivalent diameter of the circular cross-sectional size (Ref 11). The equivalent diameter is considered to be the diameter of a circle that can be transcribed in the section of interest.

Alternatively, Aerospace Standard AS 1260 (Ref 34) can be used to convert the diameter or thickness of square bars and plates to the equivalent diameter of a round bar. However, it is important to note that while it is possible to use these charts to approximate the size of a cross section that will provide equivalent hardness to another shape when quenched into a medium of known quench severity, the difference decreases as the quench severity increases. Therefore, it is important to validate these approximations experimentally. Validation is also important because the effective *H*-value may vary somewhat with different-sized bars, steel compositional differences, in cases where very low depths of hardening are anticipated, if there may be scale on the bars, or if the thermal diffusivity varies significantly due to alloy content (Ref 35).

A third method involving the use of Kondratjev form (shape) factors is discussed subsequently (Ref 36).

Steel *hardenability* is dependent on grain size and steel composition and may be defined in terms of the ideal critical diameter (*D_I*), which

is the largest bar diameter that can be quenched to produce 50% martensite at the center after quenching in an ideal quench, that is, under infinite quenching severity. This is a microstructural definition, and there is no reference to hardness (Ref 37). An ideal quench reduces the surface temperature of the austenitized steel to the quenching bath temperature instantaneously (Ref 38). Under these conditions, the cooling rate at the center of a round bar depends only on the thermal diffusivity of the steel. However, it is important to note the limitation of the use of hardness measurements to determine the position where 50% martensite occurs, because this does not account for non-martensitic structures that may be formed, such as pearlite or bainite, with each contributing differently to the overall as-quenched hardness.

It is typically difficult to quantitatively assess martensite content microscopically as 100% martensite content is approached. However, traditionally it has been known that it was possible

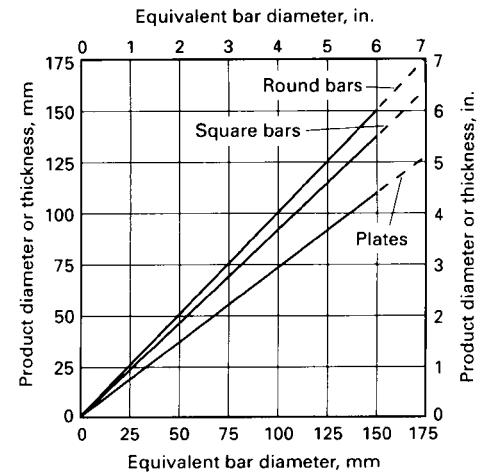


Fig. 11 Relationship between through-quenched round bar diameter and through-quenched thickness of plates and square bars. Source: Ref 11

Table 3 Typical gear steel hardenability data(a)

Steel alloy, AISI	Hardness at 60% martensite, HRC	Critical cooling rate at 705 °C (1300 °F)		Maximum diameter of round that will through harden		Mildly agitated quenching medium(b)
		°C/s	°F/s	mm	in.	
1045	50.5	220(c)	400(c)	13(d)	0.5(d)	Water
1060	54	70(c)	125(c)	30(d)	1.2(d)	Water
1335	46	110	195	25	1.0	Water
2340	49	70	125	15	0.6	Oil
3140	49	70	125	15	0.6	Oil
4047	52	110	195	25	1.0	Water
				10	0.4	Oil
4130	44	170	305	18	0.7	Water
4140	49	31	56	25	1.0	Oil
4340	49	5.5	10	71	2.8	Oil
5145	51	70	125	15	0.6	Oil
5210	60	17	30	33	1.3	Oil
6150	53	43	77	20	0.8	Oil

(a) Each steel grade was made to the minimum composition range. (b) Mild agitation has been traditionally defined using Grossmann quench severity (*H*-values). Mildly agitated oil is reported to exhibit *H*-values of 0.30-0.35, and mildly agitated water exhibits *H*-values of 1.0-1.1. A still-water quench at 30 °C (85 °F) is defined as *H* = 1.0. (c) Estimated values. (d) Data obtained from a nominal composition instead of the minimum specification range. Source: Ref 32

to identify 50% martensite (also known as half-hardening, Ref 39) with reasonable precision etching because the hardness gradient is typically sharp in this region, and therefore, it may be well correlated with the position where the dark martensitic microstructure begins (Ref 40). Grossmann et al. further refined this criterion by stating that the reference point for hardening was 50% martensite when subjected to an infinite quench (Ref 41).

It is important to know the actual D_I of the steel being heat treated and quenched, because it provides an important process limitation. It is impossible to obtain hardness greater than the D_I of the steel, regardless of the quenchant being used. The D_I values for many steels may be determined experimentally using several cylindrical bars of different diameters (Ref 42, 43). The length is typically 4 to 5 times the diameter of the bars, to minimize end-cooling effects. The objective is to determine the bar diameter with 50% martensite, which is the critical diameter (D_{crit}). However, the value of D_{crit} is quenchant-dependent and will vary as the quench severity is varied. Therefore, the Grossmann quench severity value (H) is used. Values of H that have been traditionally used are shown in Table 4. Conventionally, $H = 1.0 \text{ in.}^{-1}$ for a still-water quench at room temperature is used as the reference. For most commonly used traditional commercial quenching systems, H -values vary between 0.2 and 5.0 in.^{-1} (except for intensive quenching, which is considerably greater, >7 to 8 in.^{-1}).

Using the H -values shown in Table 4 and Fig. 12 (Ref 43), it is possible to determine the ideal critical diameter, D_I , where 50% martensite is formed at the center of the steel bar when subjected to an ideal quench. An ideal quench refers to cooling the surface of the steel at an infinitely rapid rate, which assumes $H = \infty$ where $D_{crit} = D_I$. Refer to the line for $H = \infty$ in Fig. 12. If one assumes a value of H for the quenching system that may be selected from Table 4, and D_0 is measured, then Fig. 12 may be used to determine the D_I for the steel independent of the quenching medium used.

The D_I values for many steels are also readily calculated manually or by using simple-to-use software available from various steel producers (Ref 46). Ranges of D_I values for common steels are provided in Table 5 (Ref 45).

Hardenability Bands (H-Steels). As discussed previously, steel hardenability is

dependent on composition, which varies within specified limits for each steel grade. However, there is a normal variation in hardenability that may be encountered for any grade of steel within its compositional specification limits, and, in some cases, tighter control of the composition is necessary for an application where that steel may be used. To reduce the variability in hardening response and thus narrow the surface and core hardness values after heat treatment, the hardenability of the steel alloy selected can be narrowed by either using an H-steel or by using a restricted (R-steel) hardenability specification of an H-steel (Ref 30). Therefore, many steels are also available as an H-grade that possesses tighter compositional control, and the control is specified by the maximum and minimum allowable hardenability (see the article "Hardness and Hardenability of Steels" in this Volume for more details on H-steels).

One method of establishing the allowable hardenability variation for each steel grade is to provide minimum and maximum D_I values for each grade of steel, such as those shown in Table 5. Alternatively, the most common method used to establish the allowable hardenability variation for a range of steels is based on Jominy end-quench curve data. For each H-grade steel composition, there exists a maximum and minimum Jominy curve. Specifications such as SAE J1268 provide for the maximum and minimum Jominy curves corresponding to these compositional limits (Ref 47). Therefore, for each grade of steel, there exists an acceptable range of hardenabilities exemplified by a so-called hardenability (H) band. Typically, the H -bands become broader as the steel hardenability increases.

It is important to note that for the same composition, the Jominy H -bands for as-cast and wrought steel will be the same. However, the

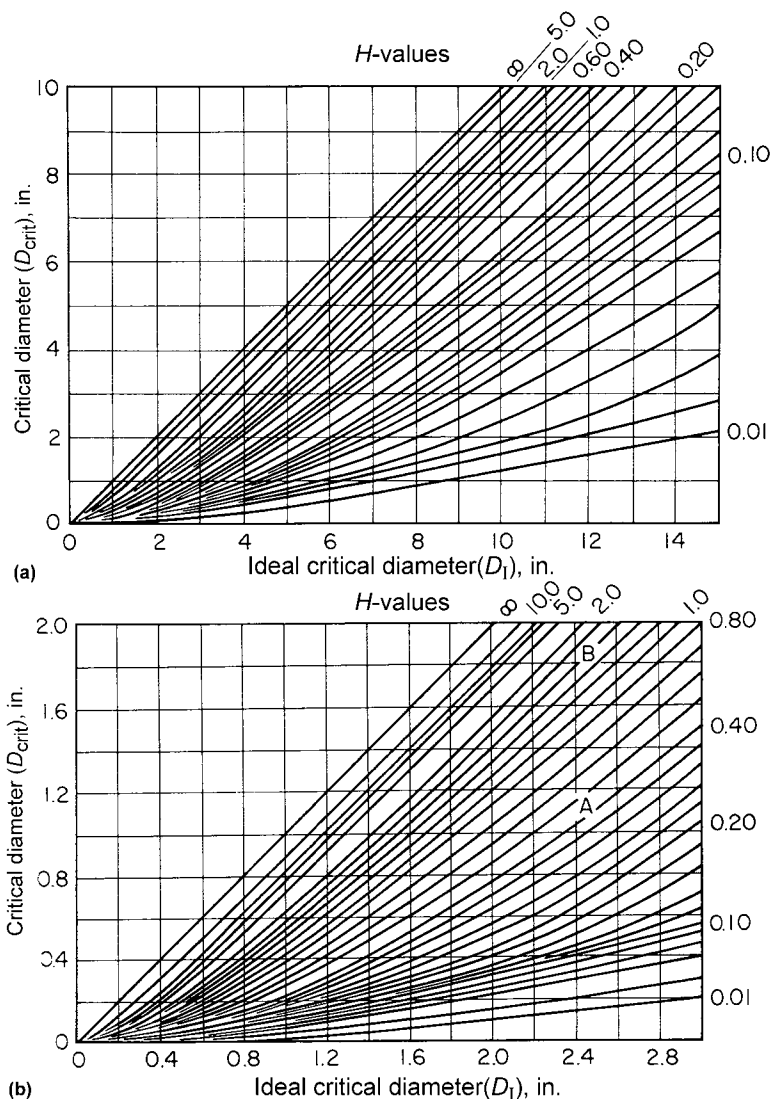


Fig. 12 Charts for the interconversion of critical diameter and ideal critical diameter if the Grossmann hardenability (H) value is known. (a) For small bars. (b) For large bars. Source: Ref 45

Table 4 Grossmann H -values for different quenching media

Quenching conditions	Air	Oil	Water	Brine
No circulation	0.02	0.25–0.30	0.9–1.0	2
Mild circulation	...	0.30–0.35	1.0–1.1	2–2.2
Moderate circulation	...	0.35–0.40	1.2–1.3	...
Good circulation	...	0.40–0.50	1.4–1.5	...
Strong circulation	0.05	0.5–0.8	1.6–2.0	...
Violent circulation	...	0.8–1.1	4	5

Source: Ref 44

Table 5 Ideal critical diameter (D_i) ranges for various steel alloys

Steel	D_i range	Steel	D_i range	Steel	D_i range
1045	0.9–1.3	4135H	2.5–3.3	8625H	1.6–2.4
1090	1.2–1.6	4140H	3.1–4.7	8627H	1.7–2.7
1320H	1.4–2.5	4317H	1.7–2.4	8630H	2.1–2.8
1330H	1.9–2.7	4320H	1.8–2.6	9632H	2.2–2.9
1335H	2.0–2.8	4340H	4.6–6.0	8635H	2.4–3.4
1340H	2.3–3.2	X4620H	1.4–2.2	8637H	2.6–3.6
2330H	2.3–3.2	4620H	1.5–2.2	8640H	2.7–3.7
2345	2.5–3.2	4621H	1.9–2.6	8641H	2.7–3.7
2512H	1.5–2.5	4640H	2.6–3.4	8642H	2.8–3.9
2515H	1.8–2.9	4812H	1.7–2.7	8645H	3.1–4.1
2517H	2.0–3.0	4815H	1.8–2.8	8647H	3.0–4.1
3120H	1.5–2.3	4817H	2.2–2.9	8650H	3.3–4.5
3130H	2.0–2.8	4820H	2.2–3.2	8720H	1.8–2.4
3135H	2.2–3.1	5120H	1.2–1.9	8735H	2.7–3.6
3140H	2.6–3.4	5130H	2.1–2.9	8740H	2.7–3.7
3340	8.0–10.0	5132H	2.2–2.9	8742H	3.0–4.0
4032H	1.6–2.2	5135H	2.2–2.9	8745H	3.2–4.3
4037H	1.7–2.4	5140H	2.2–3.1	8747H	3.5–4.6
4042H	1.7–2.4	5145H	2.3–3.5	8750H	3.8–4.9
4042H	1.8–2.7	5150H	2.5–3.7	9260H	2.0–3.3
4047H	1.7–2.4	5152H	3.3–4.7	9261H	2.6–3.7
4053H	1.7–2.4	5160H	2.8–4.0	9262H	2.8–4.2
4063H	1.8–2.7	6150H	2.8–3.9	9437H	2.4–3.7
4068H	1.7–2.4	8617H	1.3–2.3	9440H	2.4–3.8
4130H	1.8–2.6	8620H	1.6–2.3	9442H	2.8–4.2
4132H	1.8–2.5	8622H	1.6–2.3	9445H	2.8–4.4

Source: Ref 43, 45

presence of residual elements that exhibit substantial effects on hardenability, such as chromium, may cause a significant broadening in the H-band, and therefore, the potential presence of such residual elements must be monitored carefully.

When even greater hardenability control is required beyond that afforded by the H-grade, to provide more controlled heat treatment response and dimensional control, then a special grade of steel with restricted hardenability (RH-grade) is typically specified (Ref 48). Generally, the hardness range for RH-grade steels will not exceed 5 HRC at the initial position on the end-quench hardenability bar ($J = 0$) and not greater than 65% of the hardness range for standard H-band steels according to SAE J1268 (Ref 47) in the inflection region. The RH hardenability band usually follows the middle of the corresponding standard H-band (Ref 48).

Quench Severity

Quench severity refers to the ability to extract heat from hot steel and is expressed in terms of a dimensionless Grossmann (HD) value. Grossmann developed the term HD , which was a quantitative representation of quench severity and which was correlated to heat transfer by (Ref 49):

$$HD = hR = Bi = \left(\frac{\alpha}{\lambda}\right)R$$

where:

- H is the heat-transfer equivalent (Grossmann H -value) consisting of the ratio of the heat-

transfer coefficient ($h/2$) to thermal conductivity, indicating the heat dissipation rate from the hot steel to the quenching medium (in.^{-1}).

- D is the bar diameter (in.).
- R is the radius to any point in the cross section of a cylindrical bar (in.).
- Bi is the Biot number, which is a dimensionless number that represents the ratio of the resistance to heat transfer from the inside of the body to the surface of the body (Ref 50).

For simplification, it is usually assumed that the thermal conductivity is temperature independent. In this case, the H -value depends only on the heat-transfer coefficient at the surface of the body (h) and therefore on the cooling properties of the quenchant.

Instead of the Biot number, Grossmann et al. used the term HD , a dimensionless number, to indicate quench severity, and H as a heat-transfer factor. By combining terms, the simple form of this equation that is encountered most often is:

$$H = \frac{h}{2\lambda}$$

These calculations presume that the heat-transfer coefficient is constant throughout the entire cooling process, which is usually not the case, especially for vaporizable quenchants such as water and oil, where the cooling mechanism changes as the steel cools from full-film boiling (vapor blanket cooling) to nucleate boiling to convective cooling, with each cooling process characterized by a very different heat-transfer coefficient. However, the Grossmann description of quenching continues to be used today (2013), approximately 75 years later (Ref 49). Table 4 provides a summary of

H -values for different quenching media and degrees of agitation reported previously by Grossmann (Ref 44). Aronov et al. (Ref 50) came to the conclusion that Grossman factor H is generalized Biot number Bi_v .

One practical method of determining the quench severity in the heat treatment shop is to quench so-called H -bars. This is a method developed by Grossmann that was based on the observation that as the bar diameter (D) is increased, the diameter of the unhardened core (D_U) increases more rapidly with increasing quench severity (Ref 51, 52). While the method can be used with a single H -bar, it is recommended that at least two (or more) steel bars of increasing diameter be quenched. As noted earlier, the length of the round bars should be at least 4 to 5 times the length.

The H -bars are austenitized, quenched, and sectioned to determine the unhardened diameter (D_U) by hardness measurements or microstructure. The unhardened core contains 50% martensite (or less), and this diameter is the critical diameter D_U . A plot of D_U/D is prepared for several bar diameters. The D_U/D curve is superimposed on Fig. 13 to determine the best fit. The HD value is obtained from the plot and divided by the bar diameter (in.) to obtain the value of H (in.^{-1}) for the quenching system used, which includes quenchant, agitation system, and so on.

Although it is possible to determine H -values by quenching steel bars, it is often inconvenient because the procedure is time-consuming and requires sacrificing the steel test bars of different diameters. Unless substantial quantities of steel bars with different diameters and with the required composition and grain size are available, it is difficult to compare H -value variations over time, because normal lot-to-lot variations in steel composition necessarily produce data scatter. Furthermore, several steels with different hardenabilities are required to obtain test precision when evaluating quenchant ranging from agitated water and brines to poorly agitated oils. Therefore, an alternative method for determining the H -value that does not require sacrificing and metallographic characterization of steel test specimens is desirable.

One method for easily obtaining experimental Grossmann H -values was originally reported by Monroe and Bates, who described the use of cooling curve analysis using a type 304 stainless steel probe to estimate H -values based on a finite-difference heat-transfer program (Ref 54). Cooling curves were collected for the cylindrical type 304 stainless steel test bars, where the length was at least four times the diameter, with a type K thermocouple inserted into the geometric center of the probe. The probe diameters were 13, 25, 38, and 50 mm (0.5, 1.0, 1.5, and 2.0 in.). The calculated time-temperature profiles were analyzed to determine the cooling rate at 705 °C (1300 °F) as a function of imposed quench severity and bar diameter. These data were

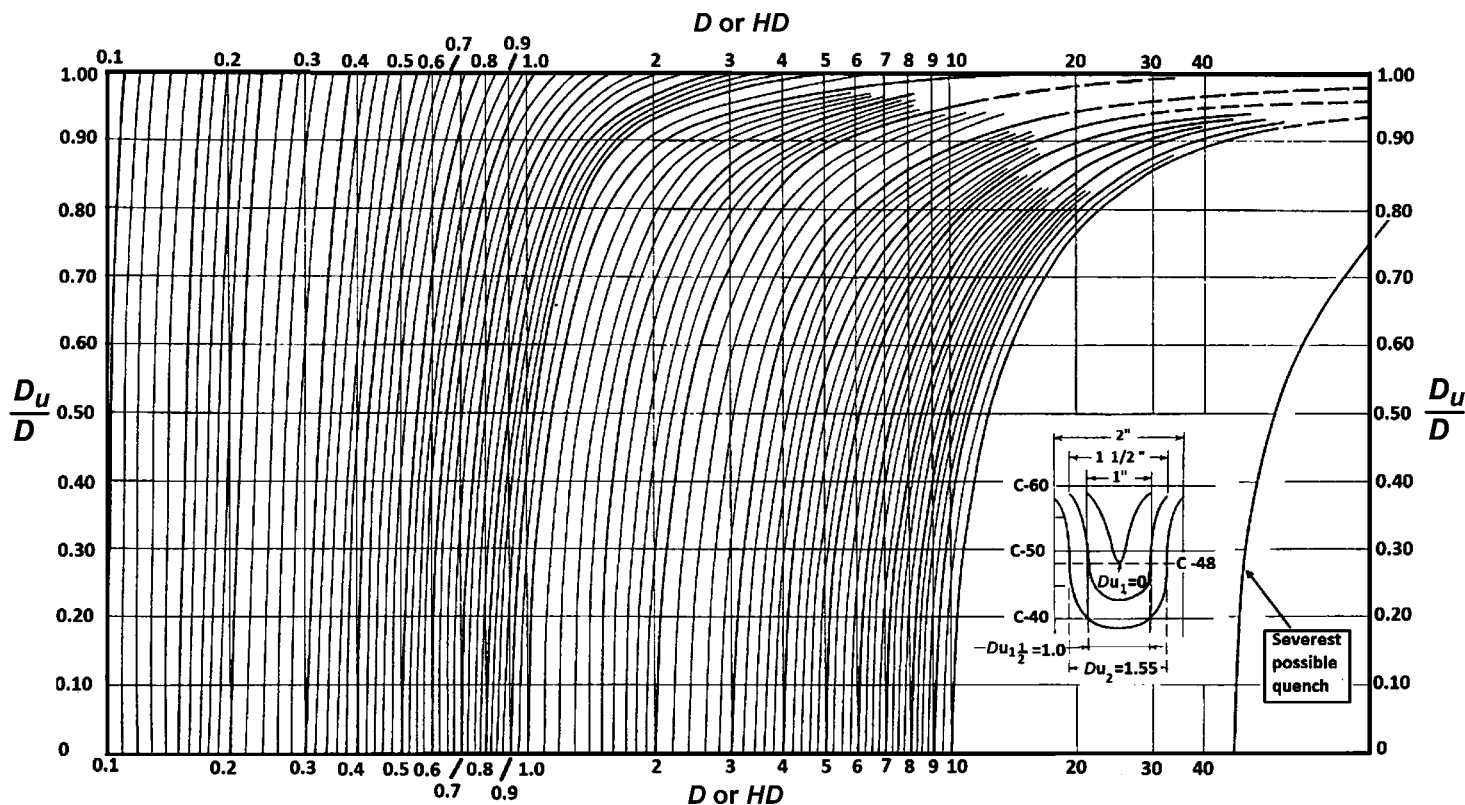


Fig. 13 Grossmann's interrelationship between quench severity (HD), bar diameter (D), and depth of hardening (D_u/D). Source: Ref 53

analyzed statistically to fit the cooling rate data obtained for the different probe diameters, and the following equation was developed (Ref 55):

$$H = AX^C \exp(BX^C)$$

where H is the Grossmann H -value (heat-transfer equivalent as defined previously), X is the cooling rate in $^{\circ}F/s$ at $705^{\circ}C$ ($1300^{\circ}F$), and A , B , C , and D are statistical modeling parameters summarized in Table 6 (Ref 55).

The use of this model and type 304 stainless steel probes and the cooling rate curves obtained from the experimental time-temperature cooling curve data provides a nondestructive and reproducible determination of H -values provided by various quenchant media.

In addition to experimental methods for determining H -values, it is also possible to calculate them based on heat-transfer properties by various methods, such as those described in Ref 50, 54, and 56.

Jominy End-Quench Test (ASTM A255). This Jominy end-quench test was developed by Jominy and Boegehold and first reported in 1938 (Ref 57). The end-quench test is still in common use today (2013) and is the basis of many national standards, including ASTM A255 (Ref 58), SAE J406 (Ref 59), JIS G 0561 (Ref 60), DIN 50191 (Ref 61), and ISO 642:1999 (Ref 62).

Table 6 Statistical modeling parameters for Grossmann H -value determination using instrumented type 304 stainless steel probes(a)

Cylindrical probe diameter(b)		Curve-fitting parameters			
mm	in.	A	B	C	D
13	0.5	0.002802	0.1857×10^{-7}	1.201	2.846
25	1.0	0.002348	0.2564×10^{-9}	1.508	4.448
38	1.5	0.002309	0.5742×10^{-9}	1.749	5.076
50	2.0	0.003706	0.03456×10^{-10}	1.847	6.631

(a) A type K thermocouple is press-fitted or soldered to the geometric center of the probe. (b) Infinite probe dimensions, where the length of the bar is at least four times the diameter to minimize end-cooling effects. Source: Ref 55

The Jominy end-quench consists of heating a 25 mm (1 in.) round by 100 mm (4 in.) long bar to the desired hardening temperature and then withdrawing heat from one end of the bar by the use of a water-jet quench. The bar is then ground along its length to 0.4 mm (0.015 in.) below the surface, and hardness readings along the flat are taken 1.6 mm ($1/16$ in.) apart. Most carbon and low-alloy steels are heated in the range of 870 to $900^{\circ}C$ (1600 to $1650^{\circ}F$). It is important that precautions be taken to prevent decarburizing and scaling during the time the Jominy test bar is heated. Hardenability is expressed in terms of the distance from the quenched end to a given hardness (Ref 63, 64). Further details relating to the development and different uses of the Jominy tests are provided in the article "Hardness and Hardenability of Steels" in this Volume.

The Jominy end-quench test provides valid data for steels with an ideal diameter (D_i) of approximately 25 to 160 mm (1 to 6 in.). The D_i may be less than 25 mm, although this requires Vickers hardness measurements closer to the quenched end and closer together than is typically possible with Rockwell hardness-measuring equipment. Also, Weinman et al. have reported that Jominy end-quench cooling curves do not correlate well with oil-quenched round bar results when appreciable amounts of pearlite and ferrite are formed (Ref 65).

From each Jominy curve, it is possible to determine the so-called Jominy equivalent cooling rate, which is the cooling rate at $704^{\circ}C$ ($1300^{\circ}F$) for each Jominy position (Ref 66, 67). The $704^{\circ}C$ temperature is used because the Jominy equivalent cooling rate is approximately independent of the steel composition,

because the thermophysical properties of carbon and low-alloy steels are very similar at this temperature, although not identical (Ref 68). It should be noted that although the cooling rate at 704 °C is traditionally used, there are reports that the cooling rate over the temperature interval of 700 to 500 °C (1290 to 930 °F) is more preferred (Ref 66). Jominy equivalent cooling rates are often shown along with hardness and Jominy position correlations, or, alternatively, if the hardness and Jominy position are known, the corresponding Jominy equivalent cooling rate can be determined from Fig. 14. However, the Jominy equivalent cooling rate corresponds to the distance from the quenched end at the surface. The cooling rate in the center of the bar is dependent on the bar diameter. Nevertheless, the amount of martensite formed dictates steel hardness, and hardness is a function of the cooling rate. Thus, if the hardness is known at any position, the Jominy equivalent cooling rate can be determined.

Boegehold used Jominy bar test data with a series of curves to construct a Jominy equivalent cooling rate chart, such as that shown in Fig. 15, that interrelates bar diameter and Grossmann quench severity (*H*-value) to predict the hardness of round bars at the surface, midradius (1/2*R*) and center (*R*) (Ref 63, 64). This is done by using Fig. 15 and the following procedure (Ref 69):

1. Select the family of curves for the size of the round bar to be quenched.
2. The curve most representative of the *H*-value of the quenching medium to be used is then identified.
3. From these data, the Jominy distance from the curve of the desired position on the selected round bar size is determined.
4. From the Jominy distance, the hardness is determined from the Jominy curve.

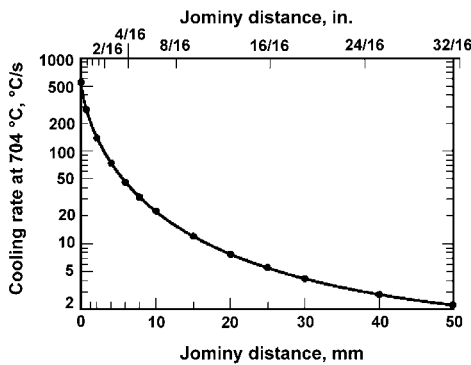


Fig. 14 Correlation of Jominy equivalent cooling rate and Jominy distance. Cooling rates are surface cooling rates at each position where hardness is measured on the Jominy bar. Because the cooling rate is essentially independent of steel composition, this curve can be used for any carbon or low-alloy steel.

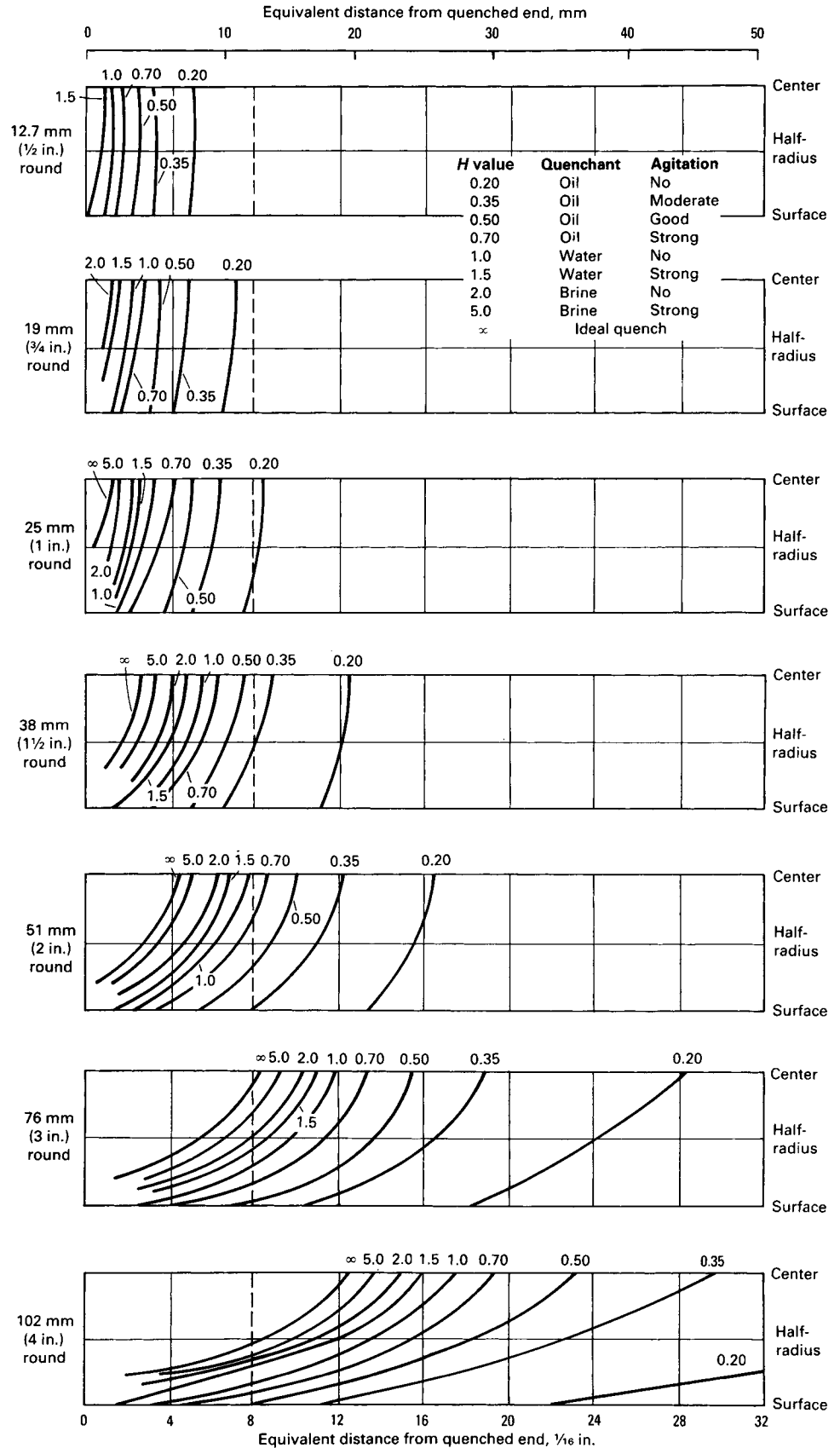


Fig. 15 Jominy equivalent cooling rate by round (RD) bar size and quench severity. Source: Ref 69

Jominy Hardenability to Round Bar Hardness Transformation—Rushman Approach.

Rushman developed an approach to predict the as-quenched hardness of a steel bar of known hardenability by using the Jominy diagram for the steel of interest, a two-diameter test bar shown in Fig. 16 and a modified Grossmann chart shown in Fig. 17 (Ref 70). The two-diameter test bar is used to evaluate the quenchant under actual production conditions. The test bar is austenitized with the production load of parts, typically in the same basket with the parts being heat treated, and then quenched. Although the test bar may be machined from the same alloy as the parts being produced, more typically, to keep the size of the test bar small, it is machined from a low-hardenability steel. The largest diameter of the test bar is selected so that the as-quenched hardness will fall on the sloping portion of the Jominy curve for that steel. After austenitizing and quenching, the two-diameter bar is sectioned and the hardnesses at the center are determined at three points: at the center of each diameter and at the common point. These hardness values are used with Fig. 17.

The Grossmann diagram relates the D_1 value to Jominy distances (Ref 70). This well-known diagram may be modified by extending the lines indicating quench severity (H -values) to a common point, as shown in Fig. 17 (Ref 71). This common point may be used to define specific quench severities of a quenchant in a tank in the heat treating shop. The use of this approach to evaluate the quench severity is now illustrated.

For the Rushman approach, the Jominy curve (hardenability) for the steel and the bar diameter are known. For example, assume that the hardness of the steel at $5/16$ in. from the quenched end of a Jominy bar is HRC = 45. If a 25 mm (1 in.) bar were quenched into the tank and the resulting hardness was HRC = 45, then $H = 0.5$. Because all of the H -value lines on the Grossmann chart converge at a common point, the measured hardness and the common point determine the line on the modified Grossmann chart. Figure 17 illustrates the use of this approach to determine the quench severities of three commercial quench systems: still water, oil, and salt at 840 °C (450 °F) (Ref 71).

In practice, it was found that for some steel alloys, the two-step bar proposed by Rushman (Ref 71) became too long to be useful. Therefore, a test variant was developed that involved the use of two test bars keeping the

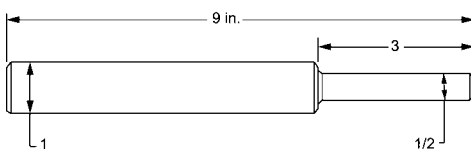


Fig. 16 Two-diameter test bar recommended by Rushman. Source: Ref 71

length/diameter ratio at 6. In addition, when AISI 1141 was used, it was found that center segregation was encountered. However, after changing to AISI 1040, no problems were encountered. Determination of H -values is most useful on new or unknown quench systems. More often, instead of Rushman bars, test pins were used to assure that the quench systems were in proper control. (Refer to the section “Maintenance of Quenching Installations” in this article for the use of test pins.)

There are many cases when it is necessary to characterize quenchant and quench systems in the heat treating shop where the various available laboratory tests are inadequate. In such cases, the Rushman test or some variant provides a satisfactory alternative. Relatively recently, Guisbert described the successful use of the Rushman test as a control procedure for quenching systems used for the production of gears (Ref 72).

Tests and Evaluation of Quenching Media

In the previous section, various tests that have been successfully used for quenchant and quenchant system characterization were discussed. In this section, an overview of quenchant characterization using cooling-power (thermal response) tests is provided. These tests are classified as either hardening-power or cooling-power tests.

Hardening-Power Tests. The final criterion for selection of a quenchant is its hardening power, that is, its ability to develop a specified hardness in a given material/section size combination, under certain conditions of the quenchant selection, agitation, and bath temperature. Major factors influencing hardness obtained on quenching include:

- Type (water, salt solutions, oil, aqueous polymer, and concentration, if applicable) of quenchant
- Quenchant bath temperature
- Agitation and mass flow of quenchant
- Material composition, structure, and thermal history of the metal component
- Section size, geometry, and surface condition of the metal component

Cooling-Power Tests. Because hardening-power tests are time-consuming and relatively difficult to perform, the heat treating industry has developed simple, reproducible cooling-power tests for the evaluation of quenching media. Four tests that have been used for this purpose include:

- Interval method, or 5 s test
- Magnetic test
- Hot wire test
- Cooling curve test (or basic thermocouple test)

Interval Test. This method, also known as the 5 s test, is a rapid method of comparing the cooling power of quenchant. In this test, a 2 L (0.5 gal) sample of an oil is placed in an insulated container, and the oil temperature is noted. A bar of metal (usually stainless steel) weighing approximately 250 g (8.8 oz) is heated to 815 °C (1500 °F) and quenched for 5 s. The oil sample is then stirred to ensure temperature equalization throughout the bath, and the temperature rise is noted to the nearest tenth of a degree Celsius. This process is repeated for a series of test bars. Finally, a bar of the same metal and size is fully quenched in a second 2 L sample of oil, and the rise in temperature is noted. Quenching power of the oil is computed according to the following equation:

$$\frac{A}{B} \times 100 = \% \text{ quench speed}$$

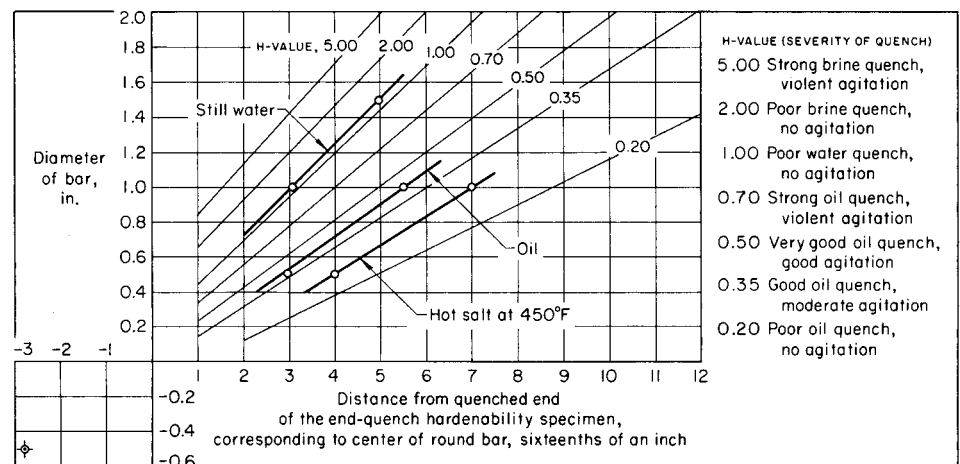


Fig. 17 Modified Grossmann diagram to be used in conjunction with Rushman’s two-diameter test bar illustrated in Fig. 16. Source: Ref 71

where A represents the average rise in oil temperature for the 5 s quench bars, and B represents the maximum temperature rise of the oil sample for the fully quenched specimen.

The 5 s test is used for determining gross changes in quenching oil, because it is expedient and requires no special equipment. A duration of 5 s in quenching, however, constitutes only a comparison in the higher-temperature region of the quench, and this may be misleading because it encompasses only a portion of the cooling curve, namely, the vapor blanket and vapor transport stages.

Magnetic Test (Also Known as the GM Quenchothermometer Test). This test makes use of the properties of metals that lose their magnetism when heated above the Curie temperature (historically designated as the magnetic limit) and regain their magnetism when cooled below this temperature. The magnetic test was devised to provide a means of comparing the heat-extraction rates of oil, molten salt, water, or other quenching media. The test method involves the heating of a 22 mm ($7/8$ in.) diameter pure nickel ball, weighing approximately 50 g (1.8 oz), to 835 °C (1625 °F) in either air or a controlled atmosphere (Ref 73, 74). The Curie temperature of nickel is 354 °C (670 °F). This test was developed into ASTM D3520 (Ref 75), which specifically uses a chromium-diffused nickel ball to eliminate the need for a protective atmosphere, to avoid marked alteration of surface finish due to oxidation (Ref 76). However, similar tests have been reported using various iron-nickel alloy balls as well (Ref 77). After uniformity of temperature is attained, the heated ball is quenched in a 200 mL sample of quenchant located within a magnetic field. As the nickel ball cools through the Curie temperature, it becomes magnetic and is attracted to the magnetic field. The time required for the nickel ball to cool from 835 °C (1625 °F) to the Curie temperature, which is 354 °C (670 °F), is a measure of the cooling power of the quenching medium. The Curie temperature of nickel is below the nose of the isothermal transformation diagrams for most steels. Thus, with this method, quenching media can be compared for steels as well as for other metals. The faster the cooling power of the medium, the shorter the time required for the nickel to regain its magnetism.

A modification of the magnetic quench test has been used to study the influence of circulation and heat on the cooling power of quenching oils. A device known as the electronic quenchothermometer is installed directly in the quenching system so that results are obtained from the actual quenching process conditions of media, temperature, and agitation (Ref 76). Figure 18 provides an illustration of a GM Quenchothermometer typically used for laboratory testing (Ref 78).

The GM Quenchothermometer times obtained according to ASTM D3520 have long been used throughout the heat treating industry in the United States to classify petroleum oil-based quenchant as slow, medium, and fast. These classifications are summarized in Table 7 (Ref

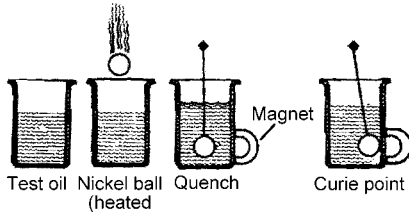
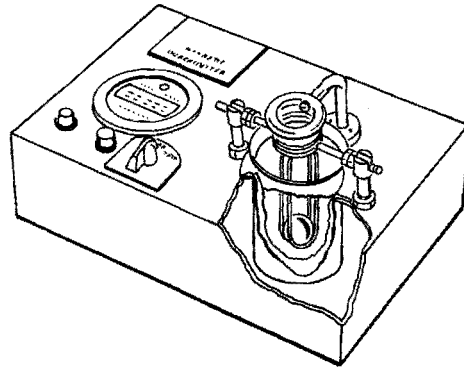


Fig. 18 Illustration of a GM Quenchothermometer typically used for quench oil testing

Table 7 Classification of quenchant by GM Quenchothermometer times

Quenchant	GM Quenchothermometer time, s
Fast oil	8–10
Medium oil	11–14
Slow oil	15–20
Martempering oil	18–25
Deionized water	2.0
9% aqueous solution of NaCl	1.5

78). Although the GM Quenchothermometer test has been a common test for evaluating and classifying quench oils, it is occasionally difficult to obtain reproducible test results. In addition, the GM Quenchothermometer times, which are based on a relatively limited portion of the total time-temperature cooling process, often cannot be related to as-quenched hardness or cracking properties. The test is limited to defining the heat-removal rate over the high-temperature portion of the time-temperature cooling curve (Ref 79, 80).

The deficiencies of the use of GM Quenchothermometer data were illustrated by a study conducted on three so-called 10 s petroleum oil quenchant. An attempt was made to correlate these cooling times with cooling curve analysis data performed with a 13 mm (0.5 in.) diameter by 127 mm (5.0 in.) cylindrical type 304 stainless steel probe with a type K thermocouple inserted to a depth of 76 mm (3.0 in.) at the geometric center. The study was conducted with a proprietary agitation system that was capable of providing linear flow rates past the cooling probe of 38 and 61 m/min (125 and 200 ft/min). The probe was heated to 845 °C (1550 °F), at which time it was immersed into the petroleum quench oil bath maintained at 65 °C (150 °F) with a cooling coil. The cooling rate data obtained are summarized in Table 8 (Ref 81).

Table 8 Comparison of quench cooling rates for three fast oils having a GM Quenchothermometer value of approximately 10 s

Quench oil sample No.	Agitation rate		Cooling rate, °F/s, at:		
	m/min	ft/min	705 °C (1300 °F)	345 °C (650 °F)	205 °C (400 °F)
1	38	125	207	44.2	18.4
2	38	125	129.8	55.8	19.2
3	38	125	175.5	75.2	20.6
4	38	125	195.5	85.3	22.6
1	61	200	230	58.9	24.6
2	61	200	155.8	64.9	24.6
3	61	200	217	74.5	20.6
4	61	200	231.3	78	17.3

Note: The 13 × 127 mm (0.5 × 5 in.) type 304 stainless steel probe was heated to 845 °C (1550 °F) and then immersed into the petroleum quench oil shown at a bath temperature of 65 °C (150 °F) with the flow rate shown. Source: Ref 81

These data show that the cooling rates throughout the cooling process varied considerably, especially at the higher probe temperatures of 705 and 345 °C (1300 and 650 °F), which means that although the GM Quenchothermometer times were approximately the same, the overall cooling properties afforded by these three quench oils were very different. Similar results were obtained in other studies that showed poor or no correlation between GM Quenchothermometer times and cooling curve behavior (Ref 79, 80). This indicates that cooling curves provide much more reliable and insightful data.

Hot Wire Test. This method of quenchant evaluation consists of heating a nichrome or cupron wire (of standard gage and electrical resistance) by means of an electrical current in a small quantity (100 to 200 mL) of quenchant. The quenchant tested usually is at quenching temperature, and the wire is supported by two copper or brass electrodes. Heating of the wire is accomplished by steadily increasing the current by means of a rheostat. The cooling power of the quenchant is indicated by the maximum current reading, as measured by an ammeter. Quenchant capable of extracting heat faster permit the passage of higher currents through the wire and thus register higher current values (Ref 82). A correlation between the hot wire test and the GM Quenchothermometer test results (times) is shown in Fig. 19 (Ref 83).

Cooling Curve Test

As has been shown thus far, the primary function of a quenchant is to control heat-transfer rates from parts during the quenching process and to produce the desired microstructure and mechanical properties, including hardness, tensile and fatigue strength, and toughness. Simultaneously, the quenching process should control residual stresses and minimize distortion and cracking potential. As the heat treating industry becomes more competitive, monitoring of the quenching process becomes increasingly important. Consistency checks are vitally important to identify variations in quench severity and to qualify new quenchant and quench processes.

Quench severity can be quantified by hardening-power tests, such as determination of cross-sectional hardness surveys (U-curves) and Jominy end-quench tests using procedures such as the Rushman test and other variations. However, these traditional tests are time-consuming and relatively expensive. Furthermore, metallurgical response tests vary with normal variations in the chemistry of the steel test specimens. As a consequence, development of alternative test procedures has been, and continues to be, of considerable interest.

A quenchant may be characterized by methods other than direct hardness measurements on test specimens or parts. A common alternative procedure is to measure the cooling power of quenchants. Although various methods have been developed and continue to be used, such as the hot wire test and the GM Quenchometer (nickel) ball test, as a group, these methods are rather limited, and great care must be taken with respect to data interpretation. Of the various test procedures developed thus far, cooling curve analysis has generally been accepted as the most useful means of quenchant characterization (Ref 84, 85–87). Cooling curves are particularly sensitive to factors that affect the ability of quenchants to extract heat and include the effects of bath temperature, agitation, and concentration, where relevant.

The next section covers the methodology involved in obtaining cooling curves, the currently accepted standardized methods of testing, and the use of newer methods of cooling curve data interpretation that more properly reflect the quenching process. In the latter case, various calculation examples are provided.

Cooling Curves. A cooling curve is a time-temperature diagram of the cooling process, which involves interfacial heat transfer from

the surface of the hot metal into the cooler quenching medium. The shape of the cooling curve is indicative of the various cooling mechanisms involved when cooling a metal test specimen preheated to the steel austenitization temperature in the quenching medium. Figure 20

illustrates three stages of cooling upon immersion of a hot probe into a vaporizable quenchant, including full-film boiling (vapor blanket or A-stage cooling), nucleate boiling (B-stage cooling), and convective (C-stage) cooling. Shock-film boiling (A'-stage cooling) is not observed in this case due to the very short duration and relative insensitivity of the probe used to acquire the data shown (Ref 88). Each of these boiling processes involves very different overall cooling mechanisms, which were discussed previously.

The transition from film boiling to nucleate boiling is classically known as the Leidenfrost temperature and is independent of the initial temperature of the metal being quenched, as shown in Fig. 21 (Ref 89).

From the measured cooling curve, it is possible to calculate the cooling rate curve as a function of time or temperature. The time required to cool to any temperature, the temperature at any time, and the time to cool over any temperature range can be readily calculated also. Often these calculations are performed using readily available spreadsheet software and the initial time-temperature data obtained from the analysis. Figure 22 illustrates various common representations of cooling curve data (Ref 89).

Cooling Curve Data Acquisition. Traditionally, high-speed recorders were used to obtain time-temperature data. More recently, data loggers or computer desktop or laptop computers equipped with an analog/digital device to convert the experimental analog signal coming from the thermocouple (millivolts) into a digital signal for subsequent numerical processing have been used (Ref 90). For most cooling curve analysis work, common data-acquisition rates

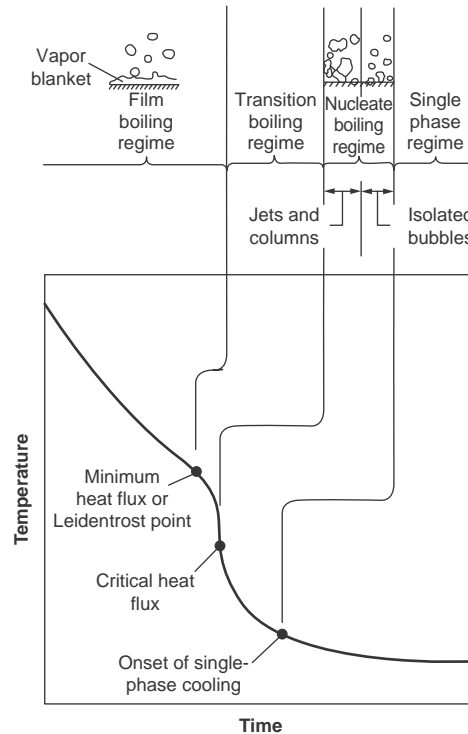


Fig. 20 Cooling curve illustration of three cooling mechanisms encountered when quenching into a vaporizable quenchant. Source: Ref 88

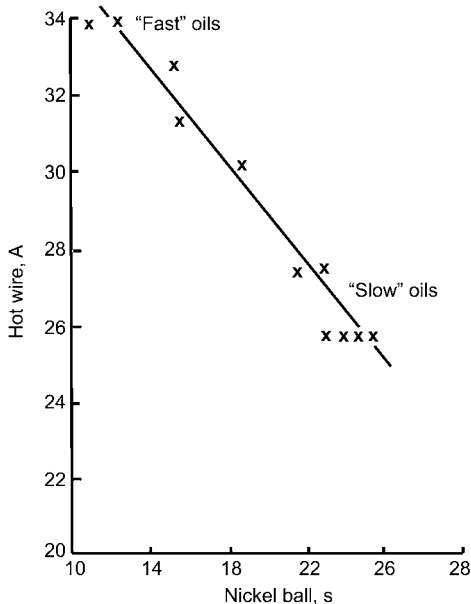


Fig. 19 Correlation of hot wire test times with GM Quenchometer times for various petroleum-based quench oils

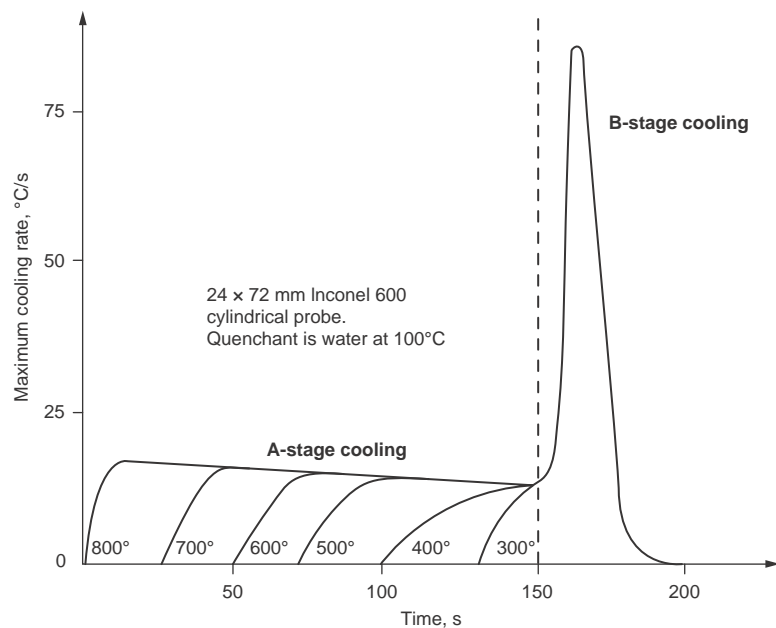


Fig. 21 Cooling rate as a function of time for an Inconel 600 probe quenched into water. The vertical dashed line indicates the Leidenfrost temperature.

vary between 5 and 20 Hz (datapoints/second). The data-acquisition rate is selected to provide a smooth, unclipped cooling rate curve (Fig. 23). Excessive data-acquisition rates may produce unnecessarily noisy data.

The Probe. The earliest reference to the use of cooling curve analysis of quenchant cooling behavior was first published by Le Chatelier in 1904 (Ref 91) and followed by Haedicke in the same year (Ref 92). Many variations of cooling curve analyses, most of which involve a variety of probe sizes and designs, have been successfully used since the

publications by Le Chatelier and Haedicke. Details of a number of these procedures are described in Ref 93.

A wide range of probe shapes and materials have been used since Le Chatelier's 18 by 18 mm (0.7 by 0.7 in.) square iron bar with a thermocouple at the geometric center (Ref 91), including spheres, plates, rings, coils, round disks, and production parts (Ref 89). Probes have been constructed of various materials, including steel alloys, stainless steel, Inconel 600, and silver. Currently, the most common probe materials for standardized cooling curve analysis procedures include Inconel 600 and silver. Type 304 stainless steel is used to a lesser extent. Actual steel alloy probes are not used for routine cooling curve analyses, because they are not reusable due to surface oxidation, corrosion, or cracking. Table 9 provides a comparison of the thermal conductivity and thermal diffusivity of various materials at room temperature (Ref 94). Such data are necessary when calculating heat-transfer coefficients.

Currently, the most common probe in use worldwide is the so-called Wolfson probe, which is a 12.5 mm (0.5 in.) diameter by 60 mm (2.4 in.) cylindrical Inconel 600 probe with a type K thermocouple inserted to the geometric center, as illustrated in Fig. 24 (Ref 95). This probe is the basis of international standards, including ISO 9950 (Ref 92), ASTM D6200 (Ref 96), ASTM D6482 (Ref 97), ASTM D6549 (Ref 98), and the Chinese National Standard JB/T 7951-2004 (Ref 99). The temperature-dependent thermophysical properties for Inconel 600 are shown in Table 10 (Ref 100). Inconel 600 was selected as the probe material for these international and national standards because:

- The thermal conductivity is much closer to steel than silver.
- Small probe size is suited to routine use for quality-control monitoring of quenchants with limited quantities of quenching fluid (approximately 2 L or less).
- There are no phase transformations with Inconel during quenching.
- An Inconel 600 probe, while less sensitive than silver to cooling curve transitions, provides a more stable thermocouple signal with less noise.

However, some in the industry strongly favor the use of silver as the probe material. A standard 10 mm (0.4 in.) diameter by 30 mm (1.2 in.) cylindrical silver probe with a surface thermocouple located at 15 mm (0.6 in.) from the end is used for JIS K 2242:1980 (Ref 101). However, more recently, this silver probe standard was replaced by JIS 2242:2012 (Ref 102), where the surface thermocouple design was replaced by a center thermocouple placement, as shown in Fig. 25. This is the same probe used for ASTM D7646 (Ref 103).

Note the following changes:

- The title of the new JIS K 2242 was changed from "Heat Treating Oils" to "Heat Treating Fluids" to accommodate both petroleum oils and aqueous polymer quenchants.
- The reference oils for the new JIS K 2242 include both the traditional dioctyl phthalate and a petroleum oil. The specifications for the new reference oil in JIS K 2242 are: kinematic viscosity at 40 °C (105 °F): 19.8 to 24.2 mm²/s (0.031 to 0.038 in.²/s); viscosity index: 95 to 105; Cleveland open-cup flash point: 211 to 219 °C (412 to 426 °F). The required cooling curve parameters for the JIS K 2242 reference oil are: characteristic temperature: 500 ± 10 °C (930 ± 18 °F); cooling time from 800 to 400 °C (1470 to 750 °F): 5.2 ± 0.3 s.

Other silver probes are equipped with thermocouples within the probe and located at the geometric center. These probes include the cylindrical 10 mm (0.4 in.) diameter by 30 mm (1.2 in.) probe with the thermocouple at the geometric center specified in both ASTM D7646 (Ref 103) and the Chinese SH/T0220-92 standard (Ref 104), as well as the AFNOR NFT 60178 cylindrical 12.5 mm (0.5 in.) diameter by 50 mm (2.0 in.) silver probe (Ref 105). Temperature-dependent thermal conductivity values for silver (W/m · K) may be calculated over the temperature range of 100 to 1234 K using the following multiple linear regression equation (Ref 106):

$$K = aT^b e^{ct} e^{d/t}$$

where a = 230.9532, b = 0.113561, c × 10⁴ = -3.19146, d = 17.17667, and temperature (T)

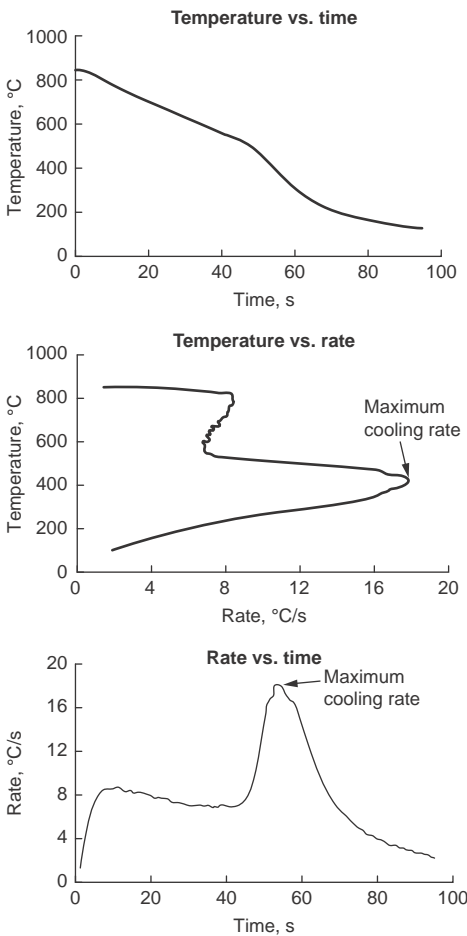


Fig. 22 Illustration of various common representations of cooling curve data

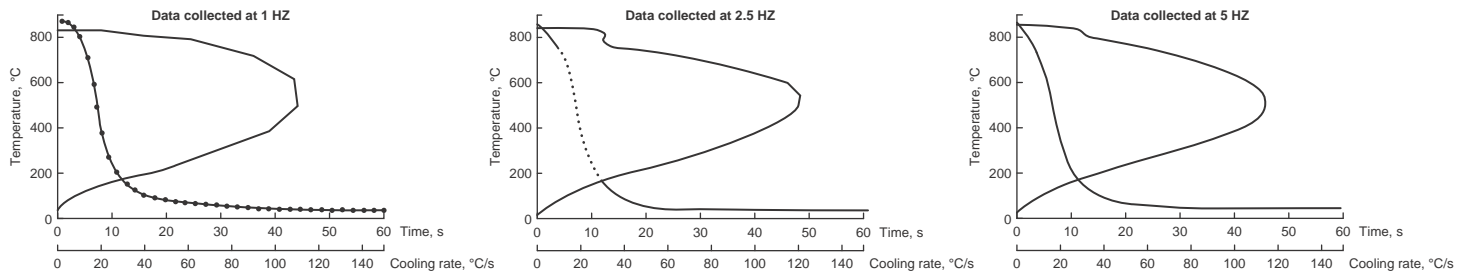


Fig. 23 Effect of data-acquisition rate on the smoothness of cooling rate curves

Table 9 Approximate thermal conductivity and thermal diffusivity of various materials at room temperature

Material	Thermal conductivity(a), J/s · cm · K	Thermal diffusivity(b), 10 ⁶ m ² /s
Silver	407	165
Inconel 600	14.9	3.4
Austenitic steel	15	3.8
Ferritic steel	19	5.1
AISI 1040 steel	55	14.3
Iron	75	21

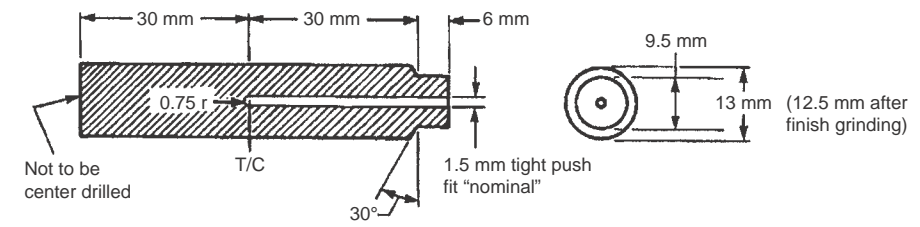
(a) Thermal conductivity is a measure of the ability of a material to conduct heat. (b) Thermal diffusivity is the thermal conductivity of a material divided by its density and specific heat capacity at constant pressure and is a measure of thermal inertia (rate at which heat is conducted through a material).

Table 10 Temperature-dependent thermophysical values for Inconel 600

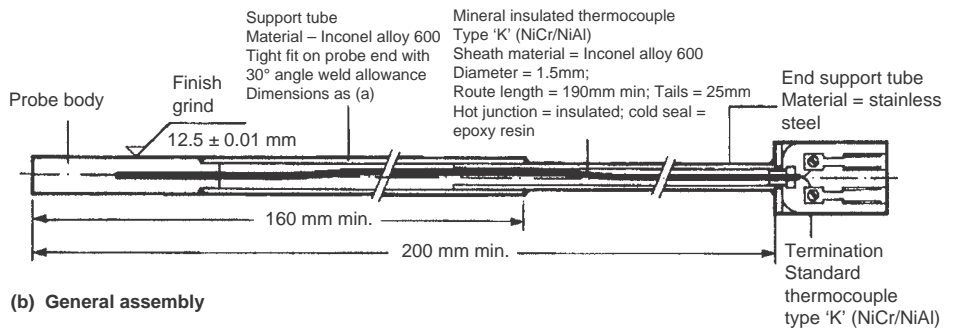
Thermal conductivity		Specific heat		Density	
Temperature, °C	K, W/m·K	Temperature, °C	C, J/kg·K	Temperature, °C	ρ, kg/m ³
50	13.4	50	451	20	8400
100	14.2	100	467	100	8370
150	15.1	200	491	200	8340
200	16.0	300	509	300	8300
250	16.9	400	522	400	8270
300	17.8	500	533	500	8230
350	18.7	600	591	600	8190
400	19.7	700	597	700	8150
450	20.7	800	602	800	8100
500	21.7	900	611	900	8060
700	25.9
900	30.1

is absolute in Kelvin. The specific heat capacity of silver (cal/g · K) as a function of temperature may also be calculated by a multiple linear regression equation of the same form, where $a = 0.475069$, $b = -0.35933$, $c = 0.000571$, and $d = -77.0249$ (Ref 107). The thermal diffusivity for silver metal at 22 °C (72 °F) has been reported to be 1.61 cm²/s (0.25 in.²/s) (Ref 108). A tabulation of the temperature-dependent thermophysical properties for silver has been reported by Narazaki et al. and is shown in Table 11 (Ref 109).

One of the problems encountered with the relatively small Inconel 600 probe shown in Fig. 24 and the silver probe shown in Fig. 25 is that it is very difficult to obtain good interlaboratory repeatability and reproducibility. One of the reasons for this problem, especially when quenching into vaporizable quenchants, is that vapor may become entrapped at the bottom of the probe upon immersion, which does not transition to nucleate boiling at the same time as boiling transitions over the remainder of the probe surface. Another observed potential difficulty is that the sharp edge at the bottom of the probe may also contribute to nonuniform vapor film breakage, which Narazaki called the edge effect, which was most pronounced when quenching in water (Ref 110).



(a) Probe details



(b) General assembly

Fig. 24 Schematic illustration of the probe originally reported for cooling curve analysis in ISO 9950 (Ref 95) and ASTM D6200 (Ref 96) and which is used in a number of other national standards

This problem has been studied in considerable detail. For example, Narazaki et al. studied the effect of probe shape on the instabilities of full-film boiling and transition boiling, including a hemispherical probe tip (Ref 110) as well as a spherical probe (Ref 111). Neither alternative to the flat-tipped probe design produced the same problem of entrapment of vapor at the probe tip as did the flat probe tip. Zhang performed a wide range of fundamental studies and also demonstrated the problems of vapor entrapment at the bottom of flat surfaces during quenching, in addition to confirming the edge effect on vapor film rupture reported by Narazaki (Ref 112, 113). Luebben et al. (Ref 114, 115) and Hernandez-Morales et al. (Ref 116, 117) also demonstrated this problem and recommended alternative probe designs to substantially alleviate or eliminate this problem, which leads to variability of cooling curve results. Partially, as a result of this study, Frerich and Luebben recommended a chamfered probe tip to minimize vapor pocket entrapment at the probe tip during quenching (Ref 118).

Currently, there is increased emphasis on the calculation of heat-transfer coefficients and heat flux to better and more fully characterize the overall heat-transfer process involved in quenching. This has led to the increased use of small probes with near-surface thermocouples, such as that shown in Fig. 26 (Ref 116). It has also been shown that when quenching into vaporizable liquids, there is a movement of the rewetting front of the surface as the steel cools, as can be seen in Fig. 1. By locating thermocouples along the probe body, the movement of the wetting front can be measured by

determining the rewetting time (Ref 119, 120). Rewetting times may be determined by using multiple thermocouple probes and is an important parameter for characterizing hardness (Ref 120) and distortion and cracking potential (Ref 121). Furthermore, the time-temperature data collected can be used to calculate surface heat-transfer coefficients and critical heat flux densities. Recently, an Inconel 600 probe using the design as recommended by Tensi, shown in Fig. 27, was used to calculate heat transfer and critical heat flux densities for vegetable and petroleum oil quenchants, with excellent results (Ref 122). (It is noteworthy that vegetable oils typically exhibit little or no film boiling relative to petroleum oils.)

Although there is increasing recognition of the importance of the use of near-surface thermocouples to accurately predict surface temperatures during quenching, there is not a consensus on the design of the probe tip, because the shape of the probe tip can affect the stability of the initial surface vapor film. To address this problem, Hernández-Morales et al. studied the effect of probe tip design on fluid flow and stability of vapor film formation and breakage on the probe surface and concluded that the conical shape provided the least perturbation of fluid flow during quenching (Ref 117). Figure 28 provides an illustration of this optimized probe design.

Using video analysis of the quenching process occurring on the probe surface, Luebben et al. were also concerned with the problems of the flat surface of the probe tip, and they developed a probe with a chamfered tip design, depicted in Fig. 29 (Ref 123).

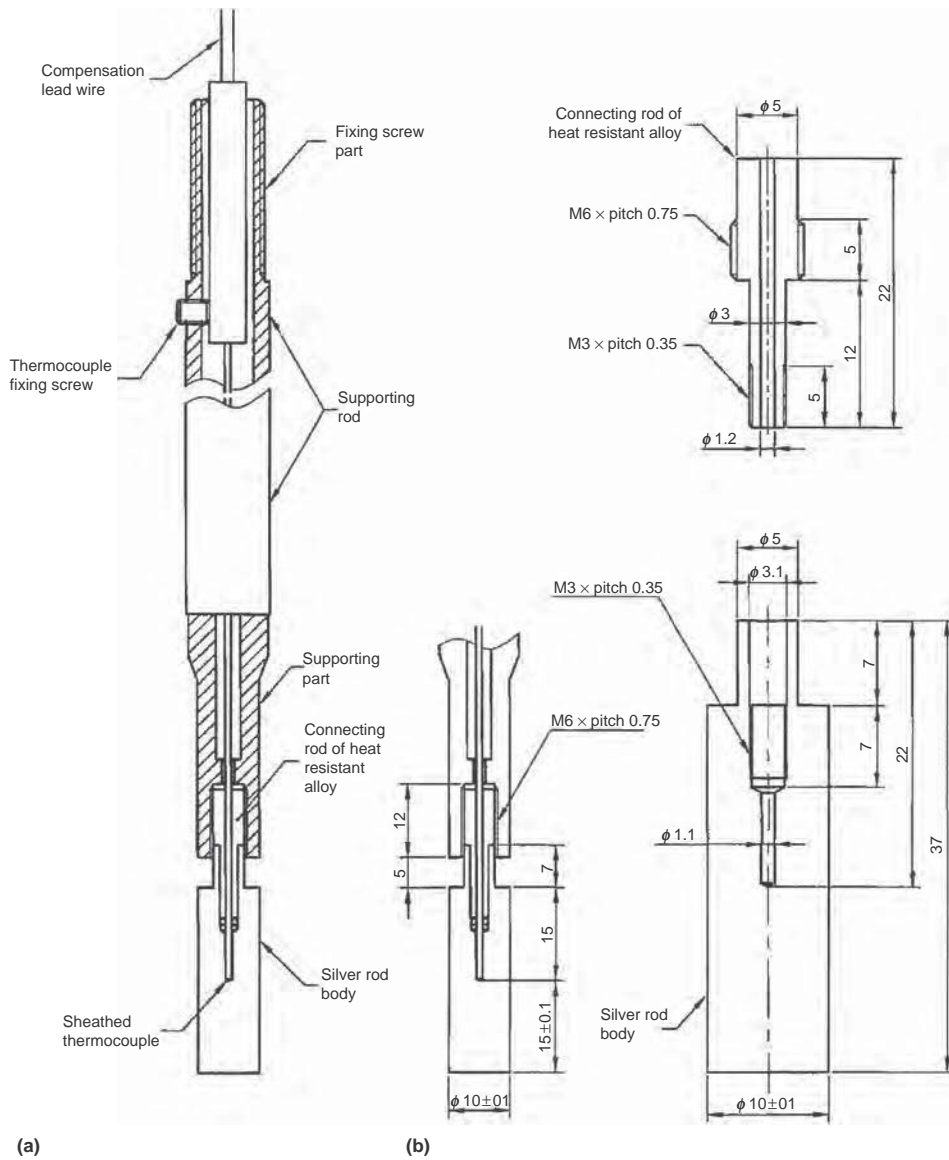


Fig. 25 Schematic illustration of the silver probe used in ASTM D7646 (a) general assembly, (b) probe details. All dimensions are in millimeters. Source: Ref 103

Table 11 Narazaki's thermophysical properties of silver

Temperature, K	Thermal conductivity, W/m·K	Specific heat, kJ/kg·K	Density, kg/m ³	Heat capacity, kJ/m ³ ·K	Thermal diffusivity, mm ² /s
150	432	0.214	10,570	2261	192
250	428	0.232	10,510	2438	176
300	427	0.237	10,490	2486	174
600	405	0.248	10,300	2554	161
800	389	0.258	10,160	2621	149
1000	374	0.272	10,010	2722	137
1200	358	124

Source: Ref 109

Whatever probe material is used, it is essential to assure thermocouple contact throughout the temperature range where data are being acquired. Data derived from the resulting cooling curves are used to calculate heat-transfer coefficients and temperature distributions

throughout the quenching process (Ref 124, 125). Accurate calculations require accurate time-temperature data. This means that the actual temperature must be measured with minimal time lag. The most significant contributors to time-lag delay in temperature measurement

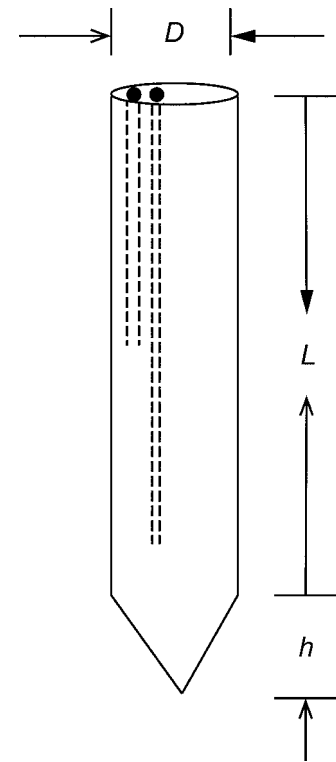


Fig. 26 A 13 mm (0.5 in.) diameter type 304 cylindrical stainless steel probe with a conical end. The dimensions for length (L) = 57 mm (2.3 in.) and height (h) = 10 mm (0.4 in.), reported by Hernández-Morales and López-Valdéz. One thermocouple is inserted to a depth of 40 mm (1.6 in.), and the second thermocouple is inserted to a depth of 50 mm (2.0 in.). The thermocouple holes are 1.58 mm (0.06 in.) in diameter, and they are located 2.38 mm (0.094 in.) from the probe surface. Source: Ref 116

are thermocouple size, materials of construction, and thermocouple contact with the probe body throughout the quenching process (Ref 124).

The sheathed thermocouple, where a metal sheath protects a thermocouple wire, is the most widely used today (2013). Sheathed thermocouple variables include dimensions, junction design, and sheath and insulating materials. Most thermocouples used for steel heat treating may be used over the temperature range of -200 to 1200 °C (-330 to 2190 °F) (Ref 124). The best thermocouple response is typically obtained when the measuring junction is welded to the probe material. Tensi et al. reported that the least time-lag and temperature distortion was obtained with the following:

- Optimal contact between the probe body and the thermocouple is assured.
- The size of thermocouple holes is minimized. The smaller the hole, the better the thermocouple contact.
- The probe materials and materials used to construct the thermocouple should possess similar thermal properties.

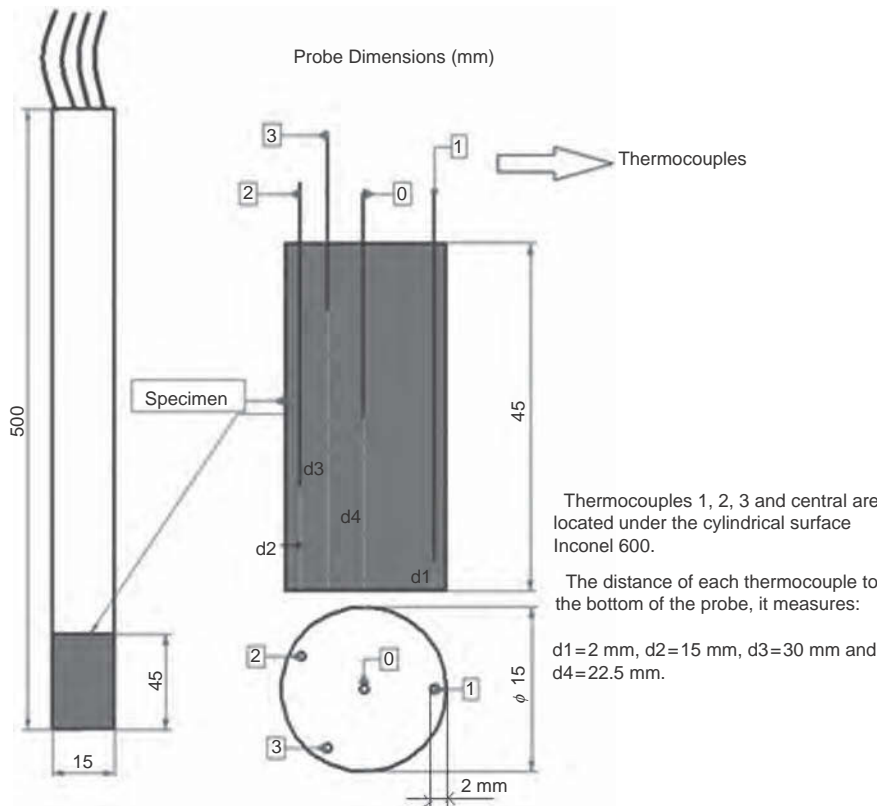


Fig. 27 Tensi design of Inconel 600 multiple-thermocouple probe. Source: Ref 122

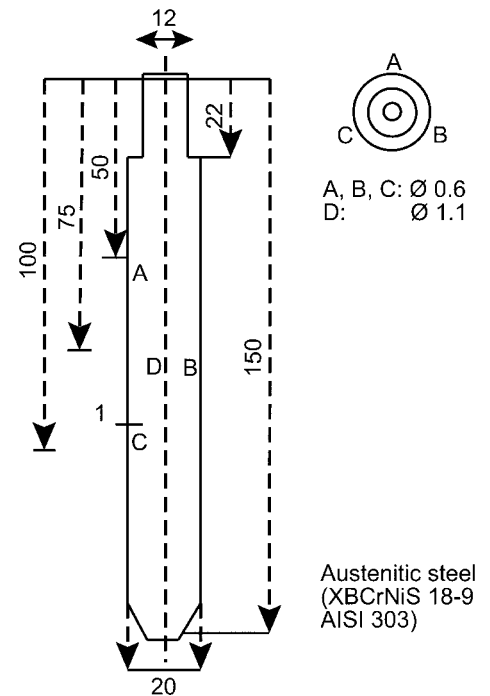


Fig. 29 Luebben et al. type 303 austenitic stainless steel probe with chamfered tip. All dimensions are in millimeters. Source: Ref 123

on the surface. The next step is cooling curve analysis.

Cooling Curve Analysis. Initially, cooling curve analysis involved a visual comparison of time-temperature curves run under the same laboratory conditions. The visual inspection primarily involves the time required to complete the different characteristic cooling transitions and the temperatures where these occur. Various quenchants and quenching conditions may be comparatively evaluated by superimposing the cooling time-temperature curves of interest (Ref 126, 127).

There are numerous methods of comparatively analyzing cooling curve data. However, two methods are currently the most commonly encountered. The first of these is cooling curve parameterization, and the parameters suggested by Tensi include (Ref 128):

1. Film-boiling to nucleate-boiling transition time(s) (t_{A-B})
2. Temperature of film-boiling to nucleate-boiling transition ($^{\circ}\text{C}$) (T_{A-B})
3. Film-boiling to nucleate-boiling transition cooling rate ($^{\circ}\text{C/s}$) (CR_{DHmin})
4. Cooling rate at 700°C (CR_{700})
5. Maximum cooling rate ($^{\circ}\text{C/s}$) (CR_{max})
6. Temperature of the maximum cooling rate ($^{\circ}\text{C}$) (T_{CRmax})
7. Cooling rate at 300°C (CR_{300})
8. Time to cool to 300°C (t_{300})
9. Cooling rate at 200°C (CR_{200})
10. Time to cool to 200°C (t_{200})

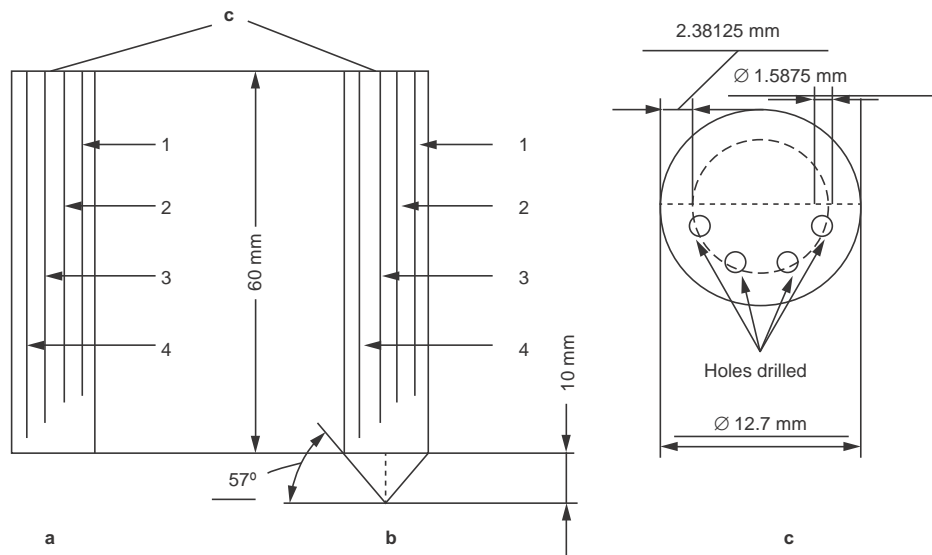


Fig. 28 Multiple-thermocouple cylindrical type 304 stainless steel test probe developed by Hernández-Morales et al. Source: Ref 117

- Minimum temperature lag can be assured by welding the thermocouple wires to the body of the probe. The use of a sheathed thermocouple with a 0.5 mm (0.02 in.) outer diameter is recommended.
- The use of heat-conducting pastes on the measuring junction welded to the sheath does not improve sensitivity.

Once the data-acquisition system and the probe design and material are selected, the probe is heated to the appropriate temperature and immersed into the quenching medium being studied. Temperature-time data are collected, and a time-temperature cooling curve is obtained that is illustrative of the different cooling mechanisms occurring

Parameters 1 to 3 are related to the full-film-boiling (vapor blanket cooling) to nucleate-boiling transition time and temperature and the cooling rate at critical temperatures. Cooling rate at 700 °C, parameter 4, is measured because it is usually desirable to maximize this cooling rate to avoid the steel pearlite transformation region. Parameters 5 and 6 are the maximum rate of cooling and the temperature where this occurs. Generally, it would be desirable to maximize CR_{max} and minimize T_{CRmax} . Rate of cooling at temperatures such as 200 and 300 °C, parameters 7 to 10, are also determined because they are related to the potential for steel cracking and distortion. To minimize these problems, it is desirable to minimize cooling rates in this region. Parameters 7 to 10 are related to the region of martensite transformation. It is generally desirable to minimize these parameters. These are illustrated in Fig. 30 and are most often used with steel, stainless steel, and Inconel 600 probes. These are parameters cited in ASTM D6200 (Ref 96), D6482 (Ref 97), and D6549 (Ref 98).

For cooling curves obtained by using a silver probe, there are various cooling parameters used as well, but often they involve two or more of the following (Ref 129):

- Leidenfrost temperature and cooling rate
- Transition temperature from nucleate boiling to convective cooling
- Time for cooling to 600, 400, and 300 °C (1110, 750, and 570 °F)
- Maximum cooling rate and cooling rate at 300 °C (570 °F)
- Critical heat flux densities which can be evaluated from cooling curves (Ref 14, 139)

It is important to understand the inherent variability of cooling curve analysis data. When specific statistical data are not available, a useful limitation of the precision of the data being reported is ± 8 to 10%. While complete statistical analysis results are not generally available, the precision results for ASTM D6200, which is a test procedure using the Inconel 600 probe

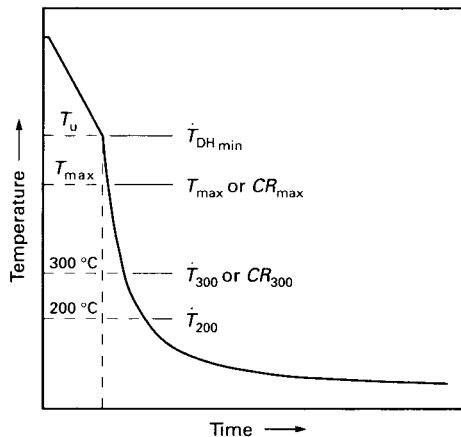


Fig. 30 Illustration of common cooling curve characterization parameters

shown in Fig. 24 for unagitated petroleum oil quenchants, are available (Ref 96). There are many reasons for such variability, some of which include thermocouple size, contact and response times, precision of the thermocouple hole placement in the body of the probe, triggering mechanism and temperature where time-temperature data collection begins, data-acquisition rate, probe surface condition and cleaning procedure, probe placement in the quenchant, volume of the quenchant, and other factors. Considering the number of laboratories reporting cooling curve data, the variability in probe suppliers and test equipment, and so on, it is surprising that the variability is not even greater.

Heat-Transfer Coefficient Calculations

In this section, an overview of the fundamentals involved in heat-transfer coefficient and heat flux of quenching processes is provided. This discussion is followed by various actual examples of applications of these methods using simplified equations. For example, simplified methods of cooling time and cooling rate calculations are considered, which may be used when analyzing heat transfer occurring when quenching simple shapes of steel parts in vaporizable liquid quenchants. Simplified methods are discussed of calculation of heat-transfer coefficients (HTCs) by solving an appropriate inverse problem when the exact mathematical model of the quenching process and surface temperature or temperature below the surface, which are obtained by experiment. Average HTCs are discussed that are evaluated on the basis of regular thermal condition theory, which is used for cooling time and cooling rate determination.

The symbols used in this discussion include:

- HTC = heat-transfer coefficient
- T = temperature (K or °C)
- T_m = medium temperature (K or °C)
- T_s = saturation temperature (K or °C)
- T_{Sf} = surface temperature (K or °C)
- τ = time (s)
- α = heat-transfer coefficient ($W/m^2 \cdot K^{-1}$)
- λ = thermal conductivity ($W/m^{-1} \cdot K^{-1}$)
- v = cooling rate (K/s^{-1} or $^{\circ}C/s^{-1}$)
- a = thermal diffusivity (m^2/s^{-1})
- ρ = material density (kg/m^{-3})
- C_p = heat capacity ($kJ/kg^{-1} \cdot K^{-1}$)
- q = heat flux density (MW/m^{-2})
- σ = surface tension (N/m^{-1})
- r^* = latent heat of evaporation (J/kg^{-1})
- ρ'' = vapor density (kg/m^{-3})
- $\Delta T = T_{Sf} - T_s$ = wall overheat (K)
- q_{cr1} = first critical heat flux density (MW/m^{-2})
- q_{cr2} = second critical heat flux density (MW/m^{-2})
- R = radius (m)

- Z = height of cylinder (m)
- K = Kondratjev form factor (m^2)
- S = surface area (m^2)
- V = volume (m^3)
- Bi_V = generalized Biot number (dimensionless)
- Kn = Kondratjev number (dimensionless)
- $\Omega = 0.24k$; $k = 1, 2, 3$ for plate, cylindrical, and spherical forms

Inverse Method

The field of inverse problems was first discovered and introduced by Soviet-Armenian physicist Viktor Ambartsumian. Inverse modeling in heat transfer involves the estimation of boundary conditions, such as a specified temperature or heat flux, inside of a conducting body using experimentally obtained thermal data. Inverse problems of heat conduction rely on temperature measurements for the estimation of unknown quantities appearing in the mathematical formulation of physical problems, including boundary heat flux, heat source, thermal properties, and boundary shape and size. Noise, which is present in any measurement of temperature, can cause instabilities in the predicted heat fluxes. However, the prediction can be greatly improved by measuring temperature at two locations. Because solutions are sensitive to random errors in the experimentally measured data, solution of these so-called ill-posed problems requires the use of a regularization technique.

Tikhonov Regularization Method. A successful solution of an inverse heat-transfer problem often involves a reformulation into an approximate well-posed problem, often a least-squares method. There are various regularization methods, including Tikhonov's regularization method that involves the addition of smoothing terms to a least-squares equation to reduce the instability effects due to measurement errors (Ref 130). Using this procedure, Tikhonov proved theoretically that inverse problems could be solved correctly (Ref 131). Because thermal processes during quenching are complicated, additional investigations were needed to develop further improvements in solving inverse heat-conduction problems (Ref 132, 133).

Green Function Method for Solving Inverse Problems. Guseynov also used the Green function method for solving linear and nonlinear inverse problems (Ref 132, 133). This approach is used for solving nonlinear inverse problems for the hyperbolic heat-conductivity equation, where some parameters of the mathematical model cannot be derived from the experiment but are determined from exact calculations.

Statistical Regularization Method. Kri-voshey used a stochastic approach of solving inverse problems that assumes a stochastic nature of all parameters of the mathematical model (Ref 13). It was used for solving inverse problems for the fourth heat-transfer mode.

General Approach of Solving Inverse Heat-Conduction and Mass Transfer Problems. Krukovskiy used the Newton-Gauss and Tikhonov methods (Ref 134, 135). A method for solving inverse problems, proposed by Beck et al., is widely used in the United States (Ref 136). The Tikhonov method is well known in Europe. Results of solving inverse problems for the second type of heat-transfer mode are usually presented as HTC versus surface temperature, as shown in Fig. 31. The HTCs are used to calculate quenching processes that include cooling time and cooling rate values, which are responsible for phase transformations in steel.

Regular thermal condition theory is used to calculate average HTCs, cooling time, and cooling rate for any forms of steel parts (Ref 138).

In Fig. 31, average HTCs are shown that were calculated using the regular thermal condition theory of Kondratjev (Ref 138). The Kondratjev theory has been used to calculate average effective HTCs during nucleate boiling (Ref 137). In this case, HTCs can be used only for cooling time and cooling rate calculations at the core of steel parts (Ref 137). Simplified methods for the calculation of nucleate-boiling process duration, cooling time, and cooling rate calculations are discussed subsequently.

Simplified Methods

Mathematical Models of Second Heat-Transfer Mode. The equation of nonstationary thermal conductivity is given as (Ref 14, 137):

$$C\rho \frac{\partial T}{\partial t} - \text{div}(\lambda \text{grad}T) = 0 \tag{Eq 1}$$

with corresponding boundary conditions at film boiling:

$$\left[\frac{\partial T}{\partial r} + \frac{\alpha_f}{\lambda}(T - T_s) \right]_{r=R} = 0 \tag{Eq 2}$$

and initial conditions:

$$T(r, 0) = T_0 \tag{Eq 3}$$

The transition from film boiling to nucleate takes place when:

$$q_{cr2} = \alpha_f(T_{Sf} - T_s) \tag{Eq 4}$$

The second critical heat flux density, q_{cr2} , can be evaluated from (Ref 139):

$$\frac{q_{cr2}}{q_{cr1}} = 0.2 \tag{Eq 5}$$

To provide minimum distortion of steel parts after quenching, localized film boiling should be eliminated completely (Ref 140). Film boiling can be eliminated if q_{cr1} is maximized (Fig. 32, 33). It has been established (Ref 14,

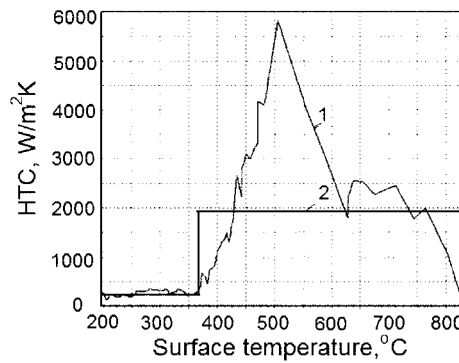


Fig. 31 Heat-transfer coefficient (HTC) versus surface temperature for MZM-16 oil at 61 °C (142 °F) with a cylindrical test specimen of 19.9 mm (0.78 in.) diameter and 80 mm (3.2 in.) height. 1, by solving inverse problem; 2, by regular thermal condition theory. Source: Ref 137

137) that there is an optimal concentration of water-salt solution and an optimal temperature of quench oils where the first critical heat flux density, q_{cr1} , is maximum, as shown in Fig. 32 and 33 (Ref 141).

Thus, quenching processes can be optimized by optimizing critical heat flux densities, which should be maximum to eliminate local film boiling. Elimination of local film boiling decreases distortion significantly (Ref 140).

When full-film boiling is finished and local film boiling is absent, the boundary conditions at nucleate boiling can be written as:

$$\left[\frac{\partial T}{\partial r} + \frac{\beta^m}{\lambda}(T - T_s)^m \right]_{r=R} = 0 \tag{Eq 6}$$

Note that during boiling processes it is necessary to consider the difference $\Delta T = T_{Sf} - T_s$, instead of $\Delta T = T_{Sf} - T_m$, because formation of nucleating critical centers, R_{cr} , depends only on overheating of a boundary layer, which is determined by:

$$R_{cr} \cong \frac{2\sigma T_s}{r^* \rho'' \Delta T} \tag{Eq 7}$$

where R_{cr} is the critical size of a bubble that is capable of growth and function.

Active nucleating centers are the basic carriers of heat that remove heat from a surface and transfer it to a cold liquid.

During convection, the boundary condition is similar to the boundary condition during film boiling:

$$\left[\frac{\partial T}{\partial r} + \frac{\alpha_{conv}}{\lambda}(T - T_m) \right]_{r=R} = 0 \tag{Eq 8}$$

$$T(r, \tau_{nb}) = \psi(r) \tag{Eq 9}$$

The transition from nucleate boiling to convection is given as $q_{nb} = q_{conv}$.

As seen from Fig. 34, during quenching of steel in a water-NaOH solution, film boiling

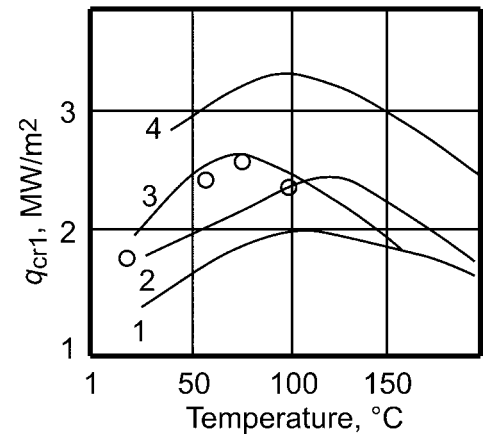


Fig. 32 First critical heat flux density, q_{cr1} , versus petroleum oil temperature (T). 1 is MZM-120; 2 is MS-20; 3 is a petroleum quenching oil named Effectol; 4 is MZM-16. Source: Ref 14

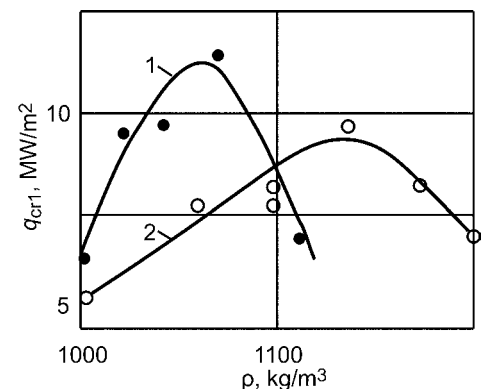


Fig. 33 First critical heat flux, q_{cr1} , versus density (ρ) of water-salt solutions. 1, NaCl-water solution; 2, LiCl-water solution. Source: Ref 14

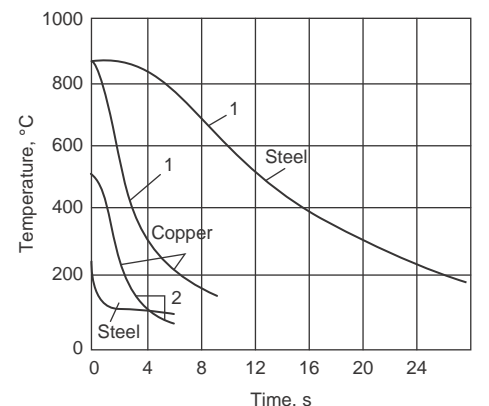


Fig. 34 Temperature vs. time plotted during quenching of a sphere 38.1 mm (1.5 in.) in diameter in a 5% water solution of NaOH. Source: Ref 142

is absent. The transient nucleate-boiling process is the primary heat-transfer mode here, and its duration can be calculated by Eq 10 (Ref 14, 137).

Duration of the transient nucleate-boiling process can be evaluated by solving Eq 1 with the boundary condition (Eq 6). The boiling process duration can be calculated by Kobasko's equations (Eq 5):

$$\tau_{nb} = \left[\Omega + b \ln \frac{\vartheta_1}{\vartheta_{II}} \right] \frac{K}{a} \tag{Eq 10}$$

where $b = 3.21$:

$$\vartheta_1 = \frac{1}{\beta} \left[\frac{2\lambda(\vartheta_0 - \vartheta_1)}{R} \right]^{0.3} \tag{Eq 11}$$

$$\vartheta_{II} = \frac{1}{\beta} [\alpha_{conv}(\vartheta_{II} + \vartheta_{uh})]^{0.3} \tag{Eq 12}$$

To make calculations correctly, it is necessary to know the β -value (Eq 11, 12). For water and water solutions, it can be considered as $\beta = 3.45$ (Ref 14, 137, 143, 144).

Cooling-Time Calculation. The following generalized equation for cooling-time calculation of any shape of a steel part was obtained (Ref 14):

$$\tau = \left[\frac{kBi_V}{2.095 + 3.867Bi_V} + \ln \left(\frac{T_0 - T_m}{T - T_m} \right) \right] \frac{K}{aKn} \tag{Eq 13}$$

The primary parameters in this equation are the Kondratjev form factor, K (Table 12) (Ref 36), Kondratjev number, Kn , and generalized Biot number, Bi_V . Average thermal diffusivity, a , is characteristic of a material.

Equation 13 includes the Kondratjev number, Kn , which is a function of the generalized Biot number, Bi_V (Ref 138):

$$Kn = \frac{Bi_V}{\sqrt{Bi_V^2 + 1.437Bi_V + 1}} \tag{Eq 14}$$

$$Bi_V = \frac{\alpha}{\lambda} K \frac{S}{V} \tag{Eq 15}$$

Cooling Rate Calculation. Cooling rate at the core of a steel part of any shape can be calculated from (Ref 14, 137):

$$v = \frac{aKn}{K} (T - T_m) \tag{Eq 16}$$

Table 12 Kondratjev form factor, K , $\frac{S}{V}$, and K for steel parts of different shapes

Shape	K, m^2	$\frac{S}{V}, m^{-1}$	$K \frac{S}{V}, m$
Slab with thickness L	$\frac{L^2}{\pi^2}$	$\frac{2}{L}$	$\frac{2L}{\pi^2}$
Cylinder of radius R	$\frac{R^2}{5.784}$	$\frac{2}{R}$	$0.346R$
Cylinder of radius R and height Z	$\frac{1}{\frac{5.784 + \pi^2 Z^2}{R^2}}$	$\left(\frac{2}{R} + \frac{2}{Z} \right)$	$\frac{2RZ(R+Z)}{5.784Z^2 + \pi^2 R^2}$
Cube with sides of L	$\frac{L^2}{3\pi^2}$	$\frac{6}{L}$	$0.203L$
Sphere	$\frac{R^2}{\pi^2}$	$\frac{3}{R}$	$0.304R$

Source: Ref 36

where v is the cooling rate ($^{\circ}C/s$), a is the thermal diffusivity, Kn is the Kondratjev number (dimensionless value), T is the temperature ($^{\circ}C$), T_m is the bath temperature ($^{\circ}C$), and K is the Kondratjev form factor. For an infinite cylinder:

$$K = \frac{R^2}{5.784}$$

Some useful data for cooling-time calculation of steel parts are presented in Table 12. Thermal properties of Inconel 600 and austenite are presented in Table 13.

Examples of Heat-Transfer Calculations

Simplified calculation methods for determining cooling time, cooling rate calculations, and heat-transfer coefficients are demonstrated in this section through the use of actual real-world examples. These examples illustrate how these simplified methods may be used for quenching process optimization.

Example 1. Quenching is performed in a tank where film boiling is absent and only nucleate boiling occurs. Surface temperature during immersion of steel parts into the quenchant decreases almost instantly to the saturation temperature and then is held at the boiling point, which decreases slightly throughout the different boiling processes. In this case, Eq 10 can be used to calculate the duration of boiling. For example, fasteners 20 mm (0.8 in.) in diameter and 120 mm (4.7 in.) long, made of AISI 5140 steel, are cooled in agitated water where the HTC during convection is $1200 \text{ W/m}^2 \cdot \text{K}$. Evaluate the duration of the transient nucleate-boiling process if fasteners are cooled from an initial temperature of $850 \text{ }^{\circ}C$ ($1560 \text{ }^{\circ}F$) in agitated water at $20 \text{ }^{\circ}C$ ($70 \text{ }^{\circ}F$). To evaluate the duration of the transient nucleate-boiling process, the values of ϑ_1 and ϑ_{II} should be calculated using Eq 11 and 12:

$$\begin{aligned} \vartheta_1 &= \frac{1}{\beta} \left[\frac{2\lambda(\vartheta_0 - \vartheta_1)}{R} \right]^{0.3} \\ &= \frac{1}{3.45} \left[\frac{2 \times 22(750 - 25.9)}{0.01} \right]^{0.3} = 25.9^{\circ}C \end{aligned}$$

$$\begin{aligned} \vartheta_{II} &= \frac{1}{\beta} [\alpha_{conv}(\vartheta_{II} + \vartheta_{uh})]^{0.3} \\ &= \frac{1}{3.45} [1200 \times (9.35 + 80)]^{0.3} = 9.35^{\circ}C \end{aligned}$$

Using these data, the duration of nucleate boiling can be calculated by Eq 10:

$$\begin{aligned} \tau &= \left[\Omega + b \ln \frac{\vartheta_1}{\vartheta_{II}} \right] \frac{K}{a} \\ &= \left[0.48 + 3.21 \ln \frac{25.9}{9.35} \right] \frac{17.2 \times 10^{-6} m^2}{5.4 \times 10^{-6} m^2/s} \\ &= 1.95 \text{ s} \approx 12 \text{ s} \end{aligned}$$

Example 2. Calculate the conveyor speed for a continuous fastener quenching line if length L of the conveyor submerged into the quenchant is 1.5 m (4.9 ft) and the duration of nucleate boiling is 12 s (see example 1). At the end of the nucleate-boiling process, the fasteners should be out of the quenchant to prevent crack formation and allow self-tempering. The conveyor speed of w is calculated as:

$$w = \frac{L}{\tau} = \frac{1.5 \text{ m}}{12 \text{ s}} = 0.125 \frac{\text{m}}{\text{s}} \text{ or } 450 \text{ m/h}$$

Example 3. Semitruck axles are made of AISI 1045 steel. Their thickness is 60 mm, or 0.06 m (2.4 in., or 0.2 ft). Calculate the core cooling time of semitruck axles from an initial temperature of $860 \text{ }^{\circ}C$ ($1580 \text{ }^{\circ}F$) to the martensite start temperature of $350 \text{ }^{\circ}C$ ($660 \text{ }^{\circ}F$) when quenching in water flowing at 10 m/s (33 ft/s). It is known that a water flow of 10 m/s provides a generalized Biot number of $Bi_V = 7$ or a Grossmann factor of $H = 7$. Because semitruck axles are long ($L \gg D$), calculate the Kondratjev form factor from:

$$K = \frac{R^2}{5.784} = \frac{(0.03 \text{ m})^2}{5.784} = 155.6 \times 10^{-6} m^2$$

The Kondratjev number, Kn , is calculated from Eq 14:

$$Kn = \frac{Bi_V}{\sqrt{Bi_V^2 + 1.437Bi_V + 1}} = \frac{7}{\sqrt{49 + 1.437 \times 7 + 1}} = 0.903$$

The average thermal diffusivity for AISI 1045 steel is $a = 5.5 \times 10^{-6} \text{ m}^2/s$. Using these data, calculate the cooling time for semitruck axles using Eq 13:

$$\begin{aligned} \tau &= \left[0.48 + \ln \frac{T_0 - T_m}{T - T_m} \right] \frac{K}{aKn} \\ &= \left[2.095 + 3.867 \times 7 + \ln \left(\frac{860 - 20}{350 - 20} \right) \right] \\ &\quad \frac{155.6 \times 10^{-6} m^2}{5.5 \times 10^{-6} m^2/s \times 0.903} = 44.2 \text{ s} \end{aligned}$$

Table 13 Temperature-dependent thermal diffusivity and heat conductivity of Inconel 600 and stainless steel (another material often used for probe construction)

Temperature		Inconel 600		Stainless steel 304	
$^{\circ}C$	$^{\circ}F$	$a \times 10^{-6}, m^2/s$	$\lambda, W/m \cdot K$	$a \times 10^{-6}, m^2/s$	$\lambda, W/m \cdot K$
100	212	3.7	14.2	4.55	17.5
150	300	3.9	15.1	4.59	17.75
200	390	4.1	16	4.63	18
250	480	4.3	16.9	4.66	18.8
300	570	4.5	17.8	4.7	19.6
400	750	4.8	19.7	4.95	21
500	930	5.1	21.7	5.34	23
600	1110	5.4	23.7	5.65	24.8
700	1290	5.6	25.9	5.83	26.3
800	1470	5.8	26.8	6.19	27.8
900	1650	6.0	28.4	6.55	29.3

The value of 0.48 in the previous equation was determined from:

$$\frac{kBi_V}{2.095 + 3.867Bi_V} = \frac{2 \times 7}{2.095 + 3.867 \times 7} = 0.48$$

Intensive cooling of semitruck axles in water flowing at 10 m/s (33 ft/s) should be interrupted in 44 s to provide self-tempering and higher surface residual stresses.

Example 4. Calculate the average HTC of a hot oil at 100 °C (212 °F) if the cooling rate at the center of a standard probe (shown in Fig. 24) at 600 °C (1110 °F) is equal to 75 °C/s (135 °F/s). The standard probe is made of Inconel 600 material, and its diameter is 12.5 mm (0.5 in.). To calculate the HTC, Eq 15 is used. From Eq 15, the Kondratjev number, Kn , can be evaluated if the cooling rate is known:

$$Kn = \frac{Kv}{a(T - T_m)} = \frac{6.7 \times 10^{-6} \text{ m}^2 \times 75 \text{ °C/s}}{5.1 \times 10^{-6} \text{ m}^2/\text{s} \times (600 \text{ °C} - 100 \text{ °C})} = 0.197$$

Here:

$$K = \frac{(0.00625)^2}{5.784} = 6.7 \times 10^{-6} \text{ m}^2; a = 5.1 \times 10^{-6} \text{ m}^2/\text{s}$$

From Eq 14, it follows that $Bi_V = 0.23$ if $Kn = 0.197$. Using Eq 15, the average heat-transfer coefficient is:

$$\alpha = \frac{\lambda Bi_V V}{KS} = \frac{20 \text{ W/mK} \times 0.23 \times 0.00625 \text{ m}}{6.7 \times 10^{-6} \text{ m}^2 \times 2} = 2145 \frac{\text{W}}{\text{m}^2 \text{ K}}$$

Here:

$$\frac{V}{S} = \frac{R}{2} = \frac{0.00625 \text{ m}}{2}$$

Example 5. Rings made of AISI 52100 steel are quenched into hot oil at 100 °C (212 °F) to increase hardness and decrease distortion. The thickness of the ring is 8 mm (0.3 in.) and its height is 20 mm (0.8 in.). The outside diameter of the ring is 200 mm (8 in.). Rings can be considered as a prism with sides 8 and 20 mm (0.3 and 0.8 in.). The rings are heated to 860 °C (1580 °F) and after quenching in hot oil, they are cryogenically treated. Calculate the cooling time required to cool the core of the rings from 860 to 250 °C (1580 to 480 °F) if the HTC of the hot oil is 2145 W/m² · K (see example 4). The average thermal diffusivity of AISI 52100 steel is 5.3 × 10⁻⁶ m²/s and the thermal conductivity is 22 W/m · K. The Kondratjev form factor, K , is calculated as (Ref 138):

$$K = \frac{1}{\frac{9.87}{L_1^2} + \frac{9.87}{L_2^2}} = \frac{1}{\frac{9.87}{(0.008 \text{ m})^2} + \frac{9.87}{(0.02 \text{ m})^2}} = 5.5 \times 10^{-6} \text{ m}^2$$

For a long prism:

$$\frac{S}{V} = \frac{(0.016 + 0.04) \text{ mZ}}{0.008 \text{ m} \times 0.02 \text{ m} \times Z} = 350 \text{ m}^{-1}$$

The generalized Biot number is calculated from Eq 15:

$$Bi_V = \frac{\alpha K S}{\lambda V} = \frac{2145}{22} \times 5.5 \times 10^{-6} \times 350 = 0.188$$

$$Kn = \frac{Bi_V}{\sqrt{Bi_V^2 + 1.437Bi_V + 1}} = \frac{0.188}{\sqrt{0.0353 + 0.27 + 1}} = 0.165$$

$$\frac{kBi_V}{2.095 + 3.867Bi_V} = \frac{0.188}{2.095 + 0.727} = 0.067$$

The cooling time of the rings is:

$$\tau = \left[\frac{kBi_V}{2.095 + 3.867Bi_V} + \ln \frac{T_0 - T_m}{T - T_m} \right] \frac{K}{aKn} = \left[0.067 + \ln \left(\frac{860 - 100}{250 - 100} \right) \right] \frac{5.3 \times 10^{-6}}{5.3 \times 10^{-6} \times 0.165} = 10.63 \text{ s}$$

The rings quenched into hot oil should be cooled approximately 11 s to obtain a core temperature of 250 °C (480 °F).

Common Quenching Process Variables

The most important influences on the cooling rate of steel in various quenching media are:

- Surface condition of the workpiece
- Mass and section size of the workpiece
- Agitation (flow rate) of the quenching liquid

Surface Condition

Surface oxidation, texture, and roughness exhibit substantial effects on the quenching process and therefore can potentially exhibit large effects on residual stresses and distortion. This is even a potential problem for heat-resistant and corrosion-resistant materials, such as those used for probes for cooling curve analyses (Ref 145). These factors are also very important for quench cracking in the following circumstances (Ref 146):

- Surface roughness increases the tendency for quench cracking of steel if the surface roughness (maximum height of irregularities) is larger than approximately 1 μm.
- Surface texture made by lapping tends to cause greater occurrence of quench cracking than by grinding or emery polishing. This phenomenon is caused mainly by stress concentration at the surface of the steel workpieces. Geometric shapes on the surface, such as polishing, lapping, and grinding marks, tool cutting marks, micronotches,

and so on, act as stress raisers and triggers for inducing quench cracking.

- Surface texture of a probe has no effect on the cooling characteristics during the vapor blanket (full-film boiling) stage of the cooling process (Ref 110).
- However, increasing surface roughness increases the Leidenfrost temperature (the lower temperature limit of film-boiling) (Ref 110).

Figures 35 and 36 illustrate the effect of surface oxidation on cooling of silver, Inconel, stainless steel, and pure iron during quenching in unagitated water at room temperature. These figures show that surface oxidation has no effect on the cooling characteristics during vapor blanket cooling (full-film boiling). However, surface oxidation increases the Leidenfrost temperature, and this effect is more pronounced as the water quenchant temperature is decreased. This is due to the presence of the porous surface oxide layer, which possesses low thermal conductivity and increased surface roughness (Ref 110, 146). Figure 35 illustrates the effect of the thickness of the surface oxide layer on cooling.

Figure 36 shows that surface oxidation leads to unstable cooling (Ref 110). Murata and Nishio reported that the variation in cooling properties was due to the coexistence of simultaneous film and transition boiling processes occurring on the cooling, oxidized steel surface. The instability of the onset of film boiling is dependent on the cavities on the steel surface (surface roughness) when air may become entrapped. These instabilities may also be caused by geometry and wettability of the cavity wall (Ref 147).

One of the reasons for vapor film instability in the presence of surface oxides is the flaking off of the oxide layer from the surface during the quench, as shown in Fig. 37. The degree to which the scale begins to flake off is dependent on the nature of the subsequent surface, which determines the nature of the vapor film and the entire quenching process (Ref 148).

However, it is also known that the presence of thin oxide surface coatings may both promote heat-transfer rates and provide more uniform heat transfer. Ma reported that the oxide thickness of an AISI 4140 steel heated for 1 h at 850 °C (1560 °F) was approximately 78 μm and after heating for 4 h, the oxide thickness had increased to 104 μm, which is still less than the critical insulation thickness of 200 μm. In this case, the increased surface roughness would be expected to increase heat-transfer rates by destabilizing the vapor film formed on the surface during the initial stages of the quench. Table 14 illustrates the effect of surface oxidation on quench cracking when quenching S45C and SK4 steel in water (Ref 146).

A different study examined the effects of the presence of oxide scale on quenching characteristics. Figure 38 shows the effect of an oxide scale on cooling curves that were obtained by still quenching in a fast oil. A scale not more than 0.08 mm (0.003 in.) deep increases the rate of cooling of 1095 steel as

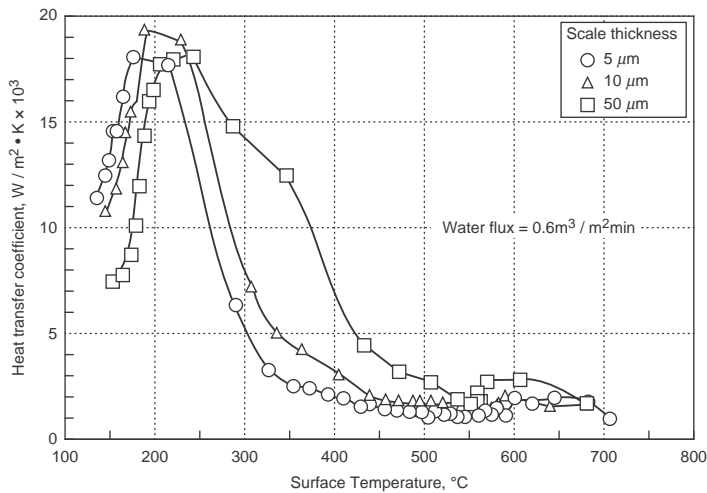


Fig. 35 Effect of thickness of surface oxide scale on the heat-transfer coefficient during spray cooling of hot steel plate. Source: Ref 110

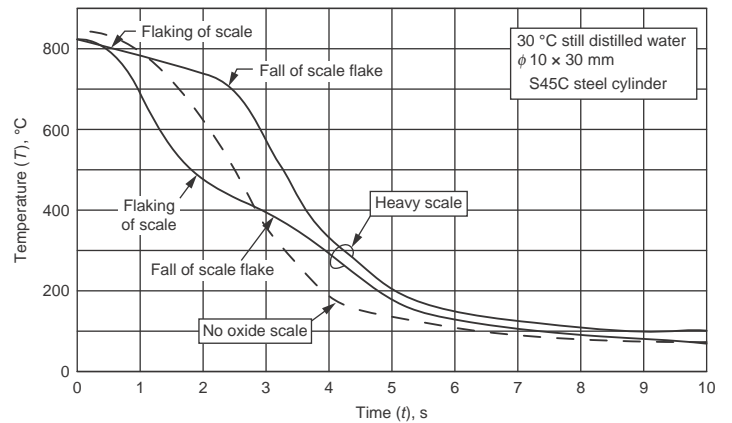


Fig. 36 Unstable cooling due to surface oxidation during water quenching of S45C carbon steel. Water temperature is 30 °C (85 °F). Test specimen is a solid cylinder 10 mm (0.4 in.) in diameter by 30 mm (1.2 in.) in length.

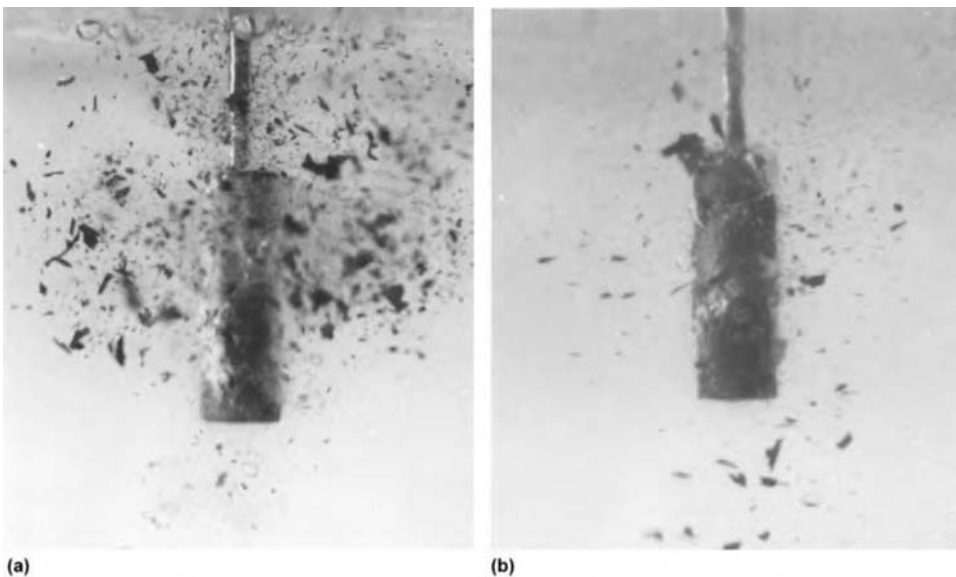


Fig. 37 Flaking of oxide scale during water quenching of S45C carbon steel. Water temperature is 30 °C (85 °F). Test specimen is a solid cylinder 10 mm (0.4 in.) in diameter by 30 mm (1.2 in.) in length. (a) Light oxide coating after heating for 3 min at 860 °C (1580 °F) in air in argon gas. (b) Heavy oxide coating after heating for 20 min at 860 °C (1580 °F) in air. These illustrations show that oxide film spatters as small flakes immediately after immersion in (a). The oxide film falls off as larger and thicker flakes during cooling, and some flakes remain on the metal surface. In this case, vapor between the metal surface and oxide flake inhibit cooling. After the flakes drop off, the cooling rate increases. Courtesy of M. Narazaki, Utsunomia University, Utsunomia, Japan

compared to the rate obtained on a specimen without scale. However, a heavy scale, 0.13 mm (0.005 in.) deep, retards the cooling rate. A very light scale, 0.013 mm (0.0005 in.) deep, is also shown to increase the cooling rate of an 18-8 stainless steel over that obtained on a steel test specimen without scale.

In a study on the effect of surface oxidation of AISI 4140 steel, it was reported that after heating at 850 °C (1560 °F) in air for 1 h, an oxide scale that was approximately 78 μm was formed, and after heating for 4 h, the scale thickness was 104 μm. However, in this study, a critical insulation thickness of approximately 200 μm was required

to observe a 10% decrease in the cooling rate upon immersion quenching into a petroleum oil (Ref 22). If the critical insulation thickness is less than 200 μm, cooling rate increases will result because of the increased surface roughness caused by oxide scale formation.

Mass and Section Size Effects

The effect of section size on cooling time-temperature and cooling rate behavior is illustrated in Fig. 39, which shows that quench sensitivity increases as section size decreases

Table 14 Effect of surface oxidation on quench cracking in water quenching of steel disks

S45C (0.45% C, 0.67% Mn)		SK4 (0.98% C, 0.77% Mn)	
Surface condition (heating condition)	Frequency of occurrence (%) quench cracking	Surface condition	Frequency of occurrence (%) quench cracking
No scale, heated in argon	30	No scale, heated in argon	20, flat surface 80, hole surface
Light scale, heated in air 30 min	0	Light scale, heated in air 30 min	80, flat surface 20, hole surface
Heavy scale, heated in air 20 min	0	Heavy scale, heated in air 20 min	0

Note: Quenched in water at 30 °C (85 °F); agitation by upward nozzle jet (1 m/s, or 3 ft/s). Disks are 20 mm (0.8 in.) diameter × 60 mm (2.4 in.) long. Source: Ref 146

(Ref 89). This is one reason why probes with such relatively small diameters (10 to 12.5 mm, or 0.4 to 0.5 in.) are used for quenchant and quenching studies. However, diameters of less than this are not typically used because of the difficulty of temperature control during transfer from the furnace to the quench bath. The cooling curves in Fig. 40 and 41 demonstrate the effect of mass and section size on the cooling curves of carbon steel in water and in oil, respectively. Figure 42 is a summary of data for quenching with still air, for the center positions of the bars of various diameters. The combined effects of mass and quenching medium for cooling small sections are shown in Fig. 43 and 44.

Agitation

Of all of the various actions that the heat treater may take to affect quench severity, many of which have dramatic effects, the only

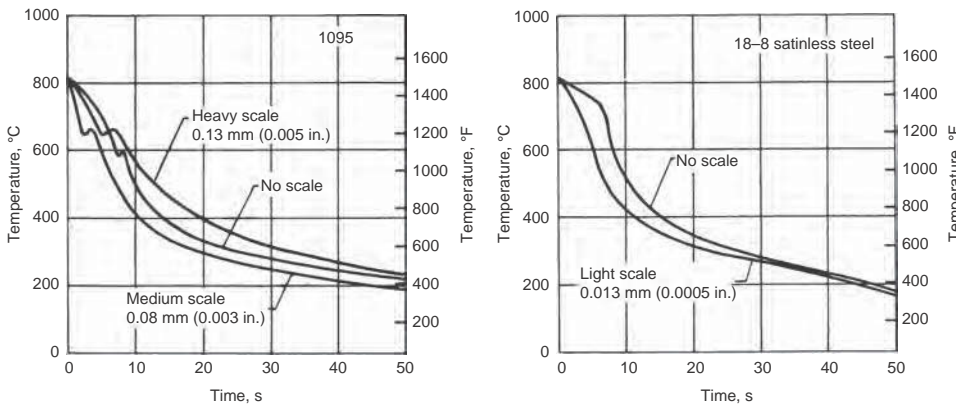


Fig. 38 Center cooling curves showing the effect of scale on cooling curves for 1095 carbon steel and 18-8 stainless steel quenched without agitation in fast oil. Oil was at 50 °C (125 °F) for the 1095 steel and 25 °C (75 °F) for the 18-8. Specimens were 13 mm (0.5 in.) diameter by 64 mm (2.5 in.) long.

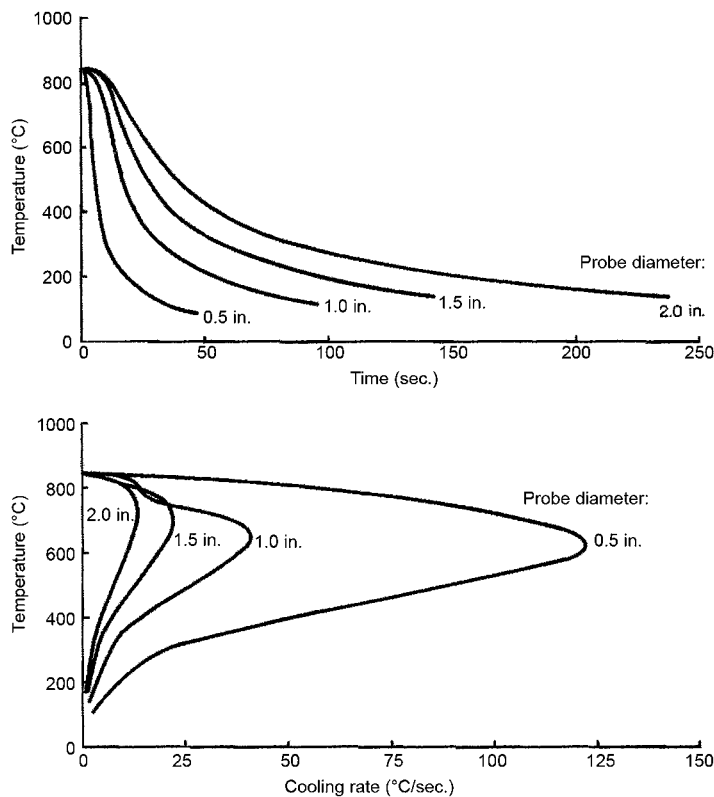


Fig. 39 Cooling curves for a typical accelerated quenching oil as a function of probe size. Probe is type 304 stainless steel with a type K thermocouple at the geometric center. Bath temperature = 65.5 °C (149.9 °F). Flow rate past the probe surface = 15 m/min (50 ft/min).

variable that can be effectively changed after immersion of the hot steel is agitation. An understanding of these factors is particularly important when quenching into vaporizable quenchants, such as water, brine, petroleum oil, and aqueous polymer solutions. With these quenchants, a vapor blanket is formed around the hot steel upon immersion. This is important because the vapor film thickness and its stability is one of the most common contributors to nonuniform quenching, leading to increased

distortion and cracking potential (Fig. 45). However, effectively increasing the uniformity and flow rate of the fluid past the hot steel at rates of approximately 50 to 60 m/min (160 to 200 ft/min) can mechanically rupture the vapor blanket, thus providing the desired more-uniform heat transfer. In this section, an overview of the factors affecting agitation during quenching is provided.

Factors Controlling Agitation. In all agitated quenching baths, the degree and character

of agitation vary from point to point within the bath; these variations are even more pronounced in spray quenching. Although accurate description or measurement of agitation is difficult, the principal factors that control agitation are well known. These include the general shape of the bath, location of the work, direction of flow currents, type of agitator, flow rate, and power consumed. In spray or jet quenching, additional factors are encountered, such as the shape, arrangement, and placement of the spray head in relation to the work; the pressure, velocity, and size of the jets; and the total volume of quenching fluid used per unit of time.

Quenching velocities depend primarily on the mode of agitation. Very low velocities, not exceeding 0.9 m/s (3 ft/s), are encountered in immersion by gravity. Intermediate velocities, ranging from 1.1 to 1.8 m/s (3.5 to 6.0 ft/s), are achieved in hand quenching with an up-and-down, circular, or figure-eight movement over 510 mm (20 in.) of travel. Spray quench rings are usually operated between 4.6 and 30 m/s (15 and 100 ft/s); special applications sometimes use velocities as high as 150 m/s (500 ft/s).

Turbulent agitation in a quenching bath takes the form of a multitude of swirling eddy currents. This action is usually accompanied by a systematic gross movement within the quench tank caused by the position of the propeller or jet source of agitation and by the shape of the tank. Turbulent agitation is desirable for uniform cooling of those shapes that do not lend themselves to a complete washing of all surfaces with a lamellar, or streamline, flow. A multitude of turbulent eddy currents often will cause sufficiently uniform average movement over all surfaces of an irregular shape to produce adequate quenching.

Agitation Equipment

The agitation of a quenchant can be obtained in several ways. In conventional quench tanks, circulation of the quenching medium is usually provided by:

- Pumps
- Passage of the workpiece through the quenching medium (gravity fall)
- Manual or mechanical movement of the workpiece
- Mechanical propellers

The selection of any type of agitation method is dependent on the tank design, type of quenchant, volume of quenchant, the part design, and the severity of quench required.

Pumps are commonly employed because they provide a controllable means for directing the quenchant. Also, the flow of the quenchant can be readily divided to provide circulation to more than one location in the tank. When the quenching medium is oil and a cooling system is employed, the pump used to recirculate oil to the cooling system also may be used to

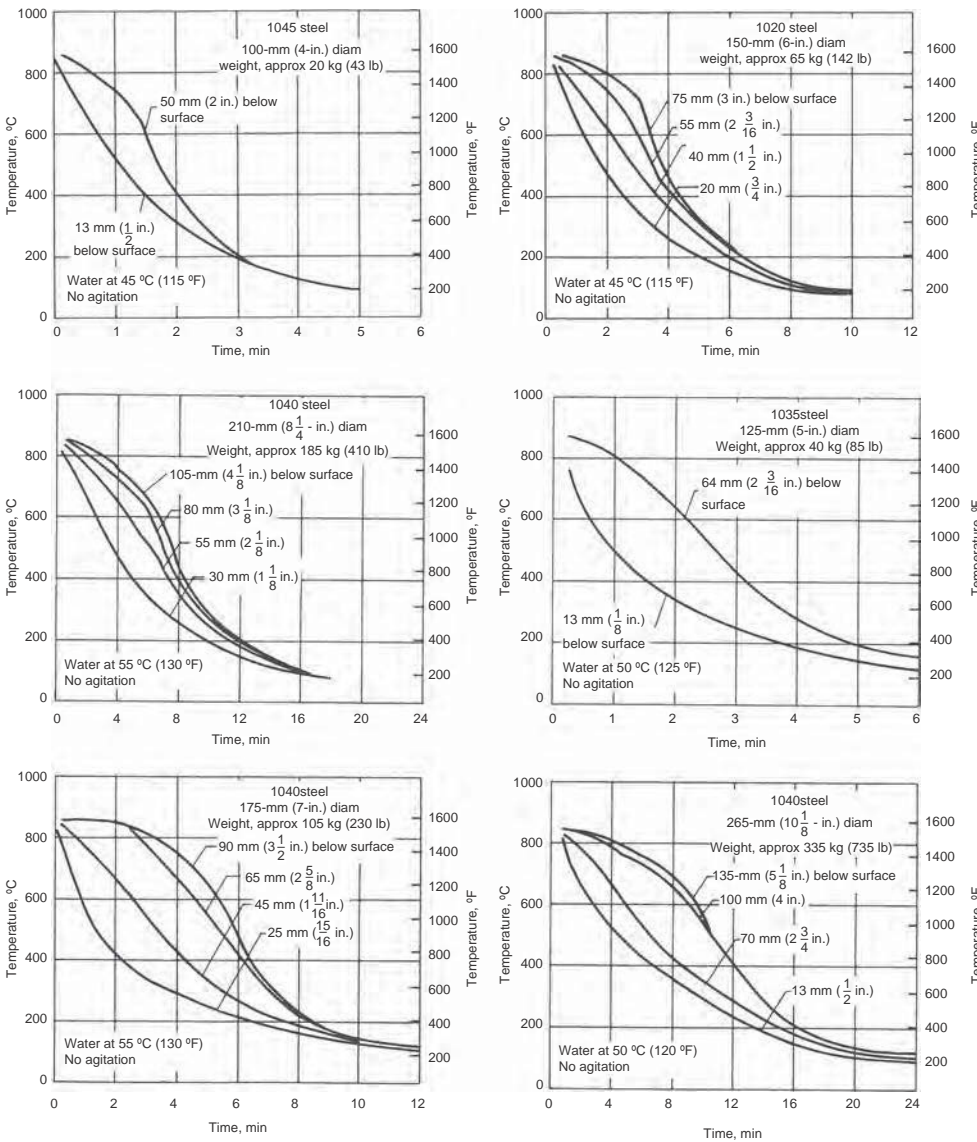


Fig. 40 Effect of mass and section size on cooling curves in water quenching

provide agitation. Recirculating pumps may be preferred for use in a floating fountain quench that is capable of removing heat quickly from an internal cavity of a workpiece.

Gravity fall of the hot workpiece through the quenchant usually is employed for quenching lightweight parts that have a large ratio of area to unit weight. If pumps or mechanical agitators were used, such workpieces probably would drift in the tank, and it would be difficult to handle the load with a conventional elevator-conveyor discharging quench tank.

Movement of the Workpiece. During the quenching of steel, it usually is desirable to obtain the most rapid cooling when the steel temperature is above approximately 540 °C (1000 °F). In this temperature range, the part is usually enveloped in the vapor blanket, and the cooling rate is slowest. To accelerate cooling in this temperature range and to remove undesirable scale, rapid

relative motion of the part in the quenchant is necessary. On small, low-production items, this can be accomplished by moving the part, or a small basket or tray of parts, through the quenchant by hand, in a figure-eight motion. Workpieces may also be driven mechanically with respect to the quenching medium. For example, shafts are sometimes rotated in the quenching medium to produce the effect of agitation.

Propellers. Where a variety of shapes and sizes are to be quenched, however, propeller agitation is most desirable, because it produces a turbulent motion. Aside from providing effective agitation, propellers, which are self-contained mechanical agitators, are compact, require no piping, and can be easily removed for maintenance. Propellers must be properly located in the quench tank in order to function effectively.

Propellers are usually placed near the bottom of the quench tank to produce the most

desirable agitation. A liquid accelerated by a propeller flows in a helical motion, in the same direction as the rotation of the propeller blades. This high-velocity stream moves across the bottom of the tank and spreads out as it moves away from the propeller. Upon striking the opposite wall, the stream is diverted upward and in the direction of rotation of the propeller. This produces a general rotation of the liquid, which is partially disrupted by the return cycle of the liquid to the propeller. The general motion of the quenchant in the tank is therefore a swirling motion and an up-and-down motion.

Propeller agitators may be either top-entry or side-entry units, as indicated in Fig. 46 and 47. Side-entry units are usually placed below the floor level, to conserve floor space. Top-entry units require more floor space but less excavation for installation. An alternative procedure for determining the flow speed of an oil quenchant through the workload for integral quench furnaces using Michigan marine propellers ($P/D = 1$) is discussed here.

Many older oil quenching systems for both integral quench batch and continuous pusher carburizer furnaces came equipped with marine propellers for oil agitation, with shrouding to direct the oil flow from the bottom of the quench tank up through the load to provide the highly agitated quenching system. It has also been shown that oil flow rates of up to 60 m/min (200 ft/min) past the work can be beneficial in creating the best quenching for the most predictable metallurgical results. (Uniform surface and core hardnesses, as well as predictable and uniform part distortion and size change, are provided by mechanically rupturing the vapor film surrounding the hot steel upon initial immersion.)

The nomograph shown in Fig. 48 can be used to measure the flow rate for existing systems as well as adjustments that can be made to the system to achieve the desired flow rate. The following discussion provides a procedure for using the nomogram, with an accompanying example.

Measurement of the existing oil flow rate includes the following:

- **Agitation system:** Requires the revolutions per minute (rpm) speed of the marine propeller agitators (generally, there are one or two). This can be determined by using a tachometer on the propeller shaft or by using the drive motor nameplate rpm multiplied by the diameter of the motor pulley divided by the diameter of the propeller pulley.
- **Propeller diameters:** These can usually be found on the original quench tank prints, but they may need to be determined by actual inspection, if system modifications have been made.
- **Projected area through which the oil must flow (shrouded):** This is generally a few centimeters (inches) larger around on all sides of the load being quenched. For example, for a 76 by 122 cm (30 by 48 in.) fixtured tray, the projected oil flow area may be 91 by 137 cm (36 by 54 in.).

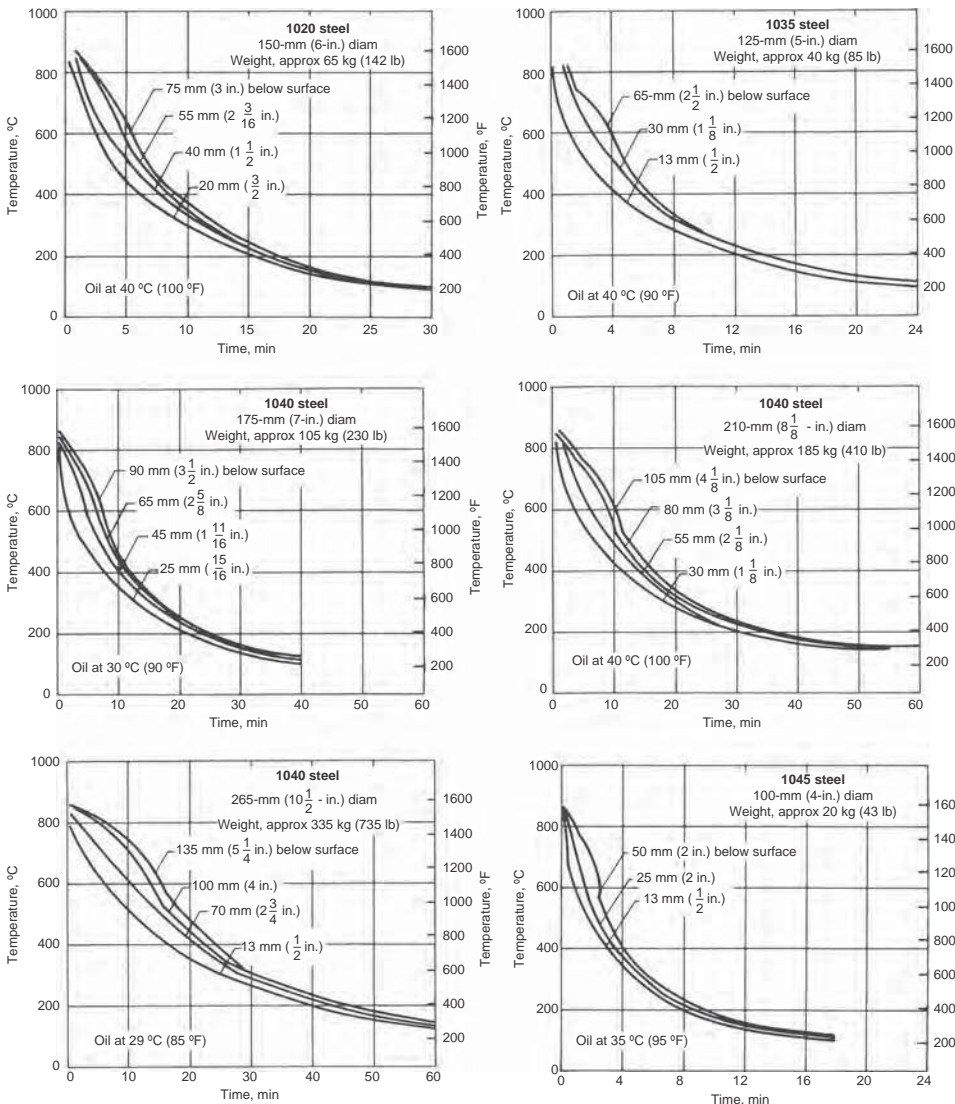


Fig. 41 Effect of mass and section size on cooling curves in oil quenching

- **Corrections to the nomograph readings:** These may need to be made as noted, but for 100 SUS (Saybolt universal seconds) fast oils, the values may be used directly from the nomogram.

Example. There are two propeller agitators with a 20 in. propeller diameter. The rpm speed of each propeller shaft is 390. Fitting a straight line through 390 as the rpm speed on the right and 20 in. propeller diameter gives a value of approximately 6000 gallons per minute (gpm) and a 5 hp motor for each propeller, for a total of 12,000 gpm.

Given that there are 231 in.³/gal, and the projected area is 36 by 54 in., or 1944 in.²:

$$12,000 \text{ gpm} \times 231 \text{ in.}^3/\text{gal.} = 2,772,000 \text{ in.}^3/\text{min}$$

$$2,772,000 \text{ in.}^3/\text{min} \div 1944 \text{ in.}^2 = 1426 \text{ in.}/\text{min}, \text{ or } 119 \text{ ft}/\text{min} \text{ flow through the work}$$

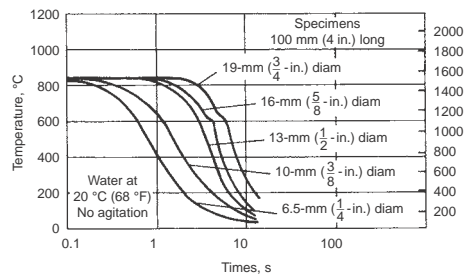


Fig. 43 Cooling curves for 100 mm (4 in.) long drill rod cylinders of various diameters

To increase the flow to approximately 200 ft/min, a flow of approximately 20,000 gpm would be required (10,000 gpm from each propeller). To achieve that flow would require

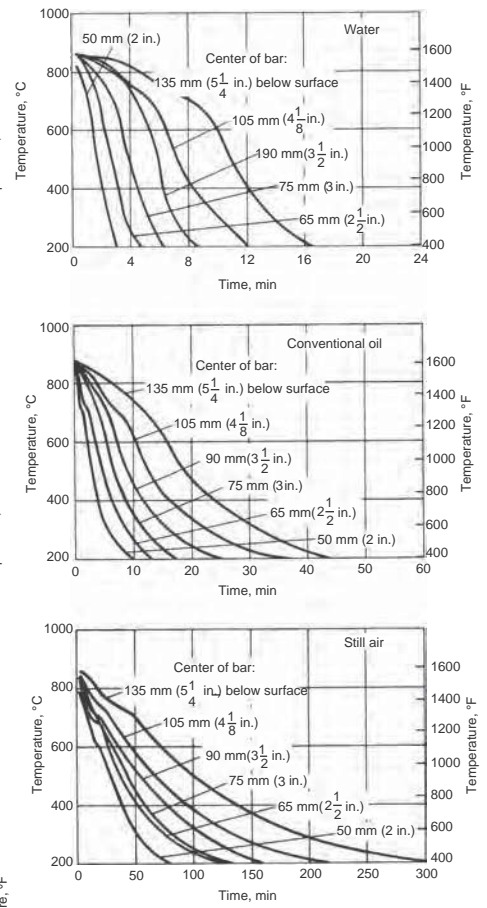


Fig. 42 Summary of data on still-air quenching

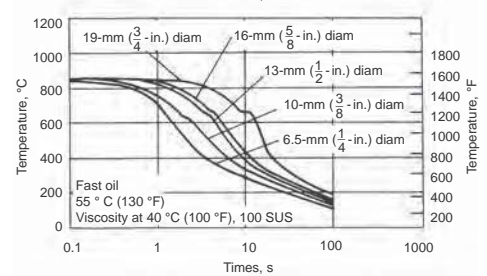
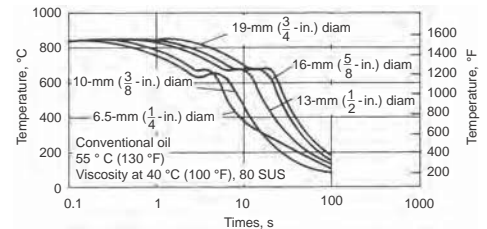


Fig. 44 Effect of mass and section size on center cooling curves in still quenching 100 mm (4 in.) long commercial drill rod cylinders of various diameters in water

15 hp motors and a new set of drive sheaves to give a speed of 600 rpm per propeller. **Draft Tubes.** Directional agitation can be provided by pumps, propellers, and mechanical



Fig. 45 Quenching a 25 mm (1 in.) square bar of austenitized steel into room-temperature water. This clearly illustrates immediate vapor blanket formation. This photo was taken only 0.0001 s after immersion. Courtesy of E.J. Cox, Pittsburgh Commercial Heat Treating Co.

movement of the parts, or even with moving submerged and open spray assemblies. Another common method of efficiently obtaining directional flow in a quench tank is to use draft-tube pumps (which use propellers encased in a tube), such as the example shown in Fig. 49. The following characteristics maximize performance of a draft tube (Ref 149, 150):

- A down-pumping flow path to take advantage of the bottom of the tank
- An angle of 30° on the entrance flare to minimize head loss and to establish a uniform velocity profile at the inlet
- Liquid coverage over the top of the draft tube of at least one-half of the tube diameter to avoid flow restriction and flow disruption of the inlet velocity profile
- Anticavitation or internal flow-straightening vanes to prevent fluid swirl
- Proper propeller positioning with respect to insertion and depth into the draft tube of a distance equal to at least one-half of the tube diameter, as required by the inlet velocity profile, and a diameter fitting tight enough to prevent fluid flow along the sides of the draft tube
- Antideflection capability to account for occasional high deflection

Measurement of Flow Velocity

There are a variety of methods for determining fluid flow speeds. However, two of the more common methods are discussed here: Mead turbine velocimeter and the use of a Pitot tube.

Mead Turbine Velocimeter. One of the simplest and most straightforward instruments used for measuring flow is the Mead turbine velocimeter, shown in Fig. 50 (Ref 151). This instrument is a mechanical flow device that uses a turbine blade attached to a handle and is simply immersed at the point of interest. A turbine (also described as an axial turbine) flow meter translates the mechanical rotational motion of the turbine in the liquid into a user-

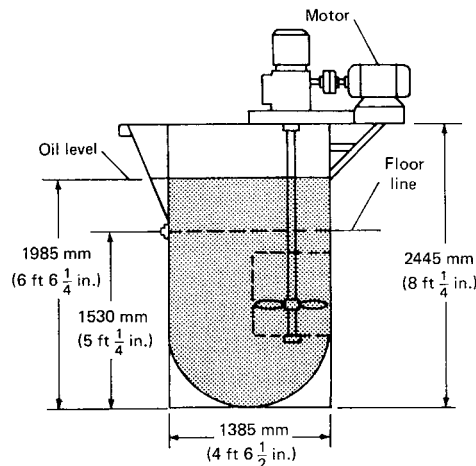


Fig. 46 Oil quenching tank with four top-entry propeller-type agitators used for quenching bar stock

readable rate of flow (gallons per minute, liters per minute, etc.). The turbine wheel, shown at the end of the handle in Fig. 50, is placed in the path of the fluid stream to be measured, which impinges on the turbine blade, setting the rotor in motion. When a steady rotation speed has been achieved, the recorded rotational speed is proportional to fluid velocity.

If the fluid viscosity and density are known, the Reynolds number can easily be calculated, because the cross-sectional area of the measurement head is known. The linear flow rate is determined directly from the measurement.

The Reynolds number (Re) is a dimensionless number that is used to quantitatively characterize different flow regimes, such as laminar or turbulent flow. Laminar flow occurs at low Reynolds numbers (<2300) and is characterized by smooth, constant fluid motion. Turbulent flow occurs at high Reynolds numbers (>4000) and produces a turbulent flow. Reynolds numbers in the range of 2300 to 4000 are referred to as transition flow. One equation used to calculate Reynolds numbers is:

$$Re = \frac{\rho v L}{\mu} = \frac{v L}{\nu}$$

where v is the mean velocity of the fluid (m/s), L is the traveled length of the fluid (m), μ is the dynamic viscosity of the fluid (Pa · s, or $N \cdot s/m^2$, or $kg/(m \cdot s)$), ν is the kinematic viscosity ($\nu = \mu/\rho$) (m^2/s), and ρ is the density of the fluid (kg/m^3).

The Pitot tube is useful for measuring unidirectional velocity, such as that of a lamellar or jet stream, although it is not suitable for measuring turbulent (multidirectional) flow. A schematic illustration of a Pitot tube is provided in Fig. 51.

The tube can be constructed by drawing 6.5 mm ($1/4$ in.) glass tubing to an inside diameter of approximately 0.4 mm ($1/64$ in.) and grinding the drawn end flat and square with the tube axis. It may also be made of metal, provided the tube opening is knife-sharp and

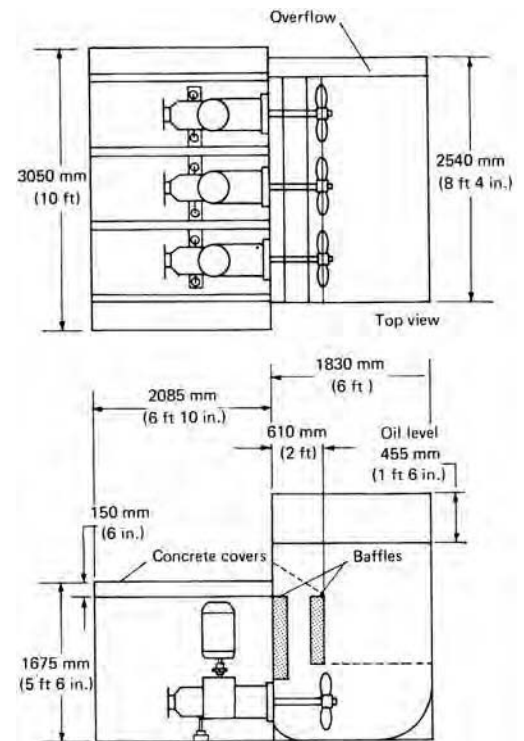


Fig. 47 Quench tank of 10,000 L (2600 gal) capacity with three propeller-type agitators entering from the side

square with the axis of the tube. A suitable bourdon gage or a manometer is connected by rubber or transparent plastic hose to the tube. If precise measurements are required, a correction must be made for any quenchant column height in excess of the level of the upper opening of the Pitot tube.

The axis of the Pitot tube must be accurately aligned parallel to, and in the center of, the stream being measured. Alignment is obtained by exploring the stream with the tube, searching for the highest pressure reading.

The velocity of the fluid as it strikes the tube is converted to a pressure head that is measured by the pressure gage. The pressure head (h), in feet of water, is converted into velocity (v), in feet per second, by the equation:

$$v = K\sqrt{2gh}$$

where K is the Pitot tube constant (most often 1.0, or close to unity), and g is the acceleration of gravity (980 cm/s^2 , or 32.2 ft/s^2). The relationships are shown in the Pitot tube calibration charts in Fig. 52.

Quenching Systems

Quenching systems have two components: the quenching medium and the equipment used to perform the hardening operation. In this section, an overview is provided on quenchant selection, while subsequent sections describe

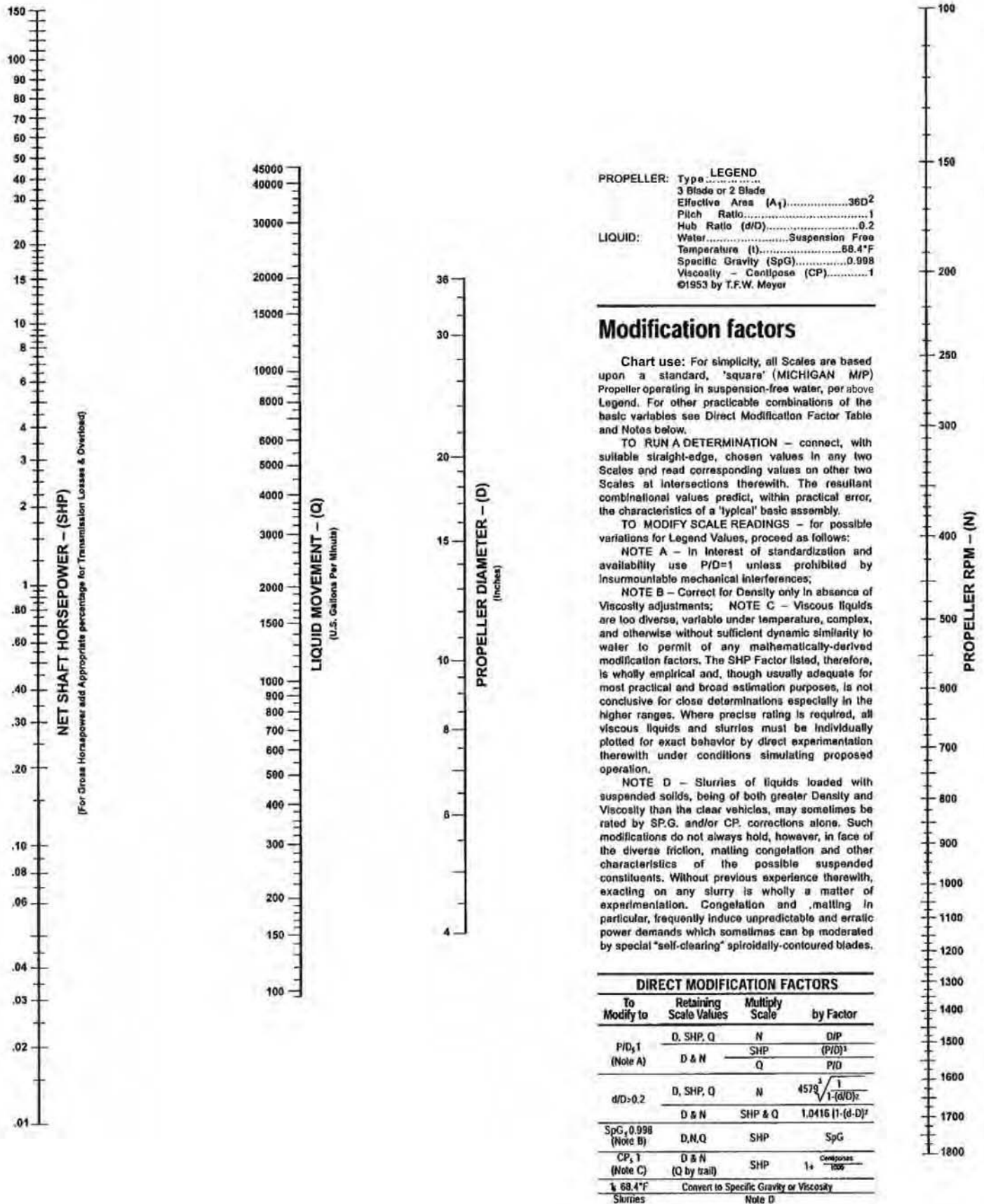


Fig. 48 Nomograph to approximate liquid movement (Q) with the power and other characteristics of a standard square industrial propeller (two- or three-blade, Michigan M/P Propeller) when used in the agitation of water (see legend for details). Solutions are more typical than specific. This is particularly true of liquid movement (Q), which, in practice, may register from +20% to -30% of the scale values (with or without effect on SHP or N factors, as indicated). Nevertheless, it is a reliable index (excluding abnormalities) to the powering and rating of such propellers when used strictly for stirring or agitation within the confine of a single vessel. It does not extend to, and must not be used on, directional movements through pipe orifices, filters, and so on, or other condition of specific resistance requiring a definite pressure or head. Courtesy of Michigan Wheel Company

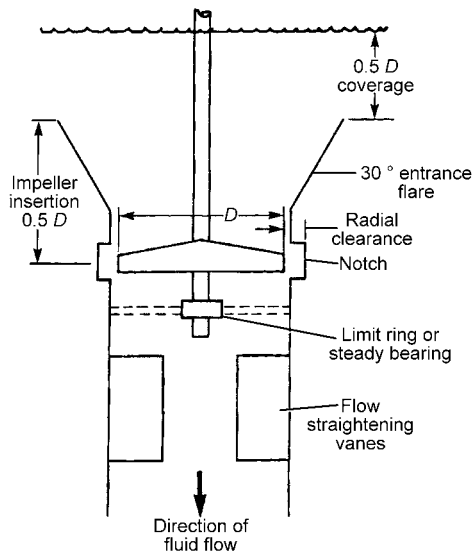


Fig. 49 Characteristics of a draft-tube propeller pump. Draft-tube systems such as this may be designed to uniformly control the direction of fluid flow, for example, up through a load from bottom to top of the tank. Source: Ref 149

common quenching media encountered in the heat treating plant, with discussions on quenchant classification, selection, and maintenance.

In terms of equipment, requirements may vary widely for different quenching operations. Each day, a small plant making machine parts may require the hardening of only a few simple carbon steel parts weighing approximately 1.4 kg (3 lb) apiece. For such an application, the quenching system would comprise a barrel of water, with piping to the water supply and a drain to the sewer. Handling equipment would consist simply of a pair of tongs. As the quantity of work to be quenched and the complexity of workpieces increase, however, various other items of equipment must, of course, be added to the quenching system.

For a complete quenching system, the following functional equipment usually is required and installed:

- Work tank or machines
- Facilities for handling the quenched parts
- Quenching medium
- Equipment for agitation
- Coolers
- Heaters
- Pumps and strainers or filters
- Quenchant supply tank
- Equipment for ventilation and for protection against hazards
- Equipment for automatic removal of scale from tanks

Quenchant Selection and Quench Severity

The classification of a quenchant based on its relative ability to remove heat from steel during



Fig. 50 Mead turbine velocimeter. Courtesy of Mead Instruments Corporation

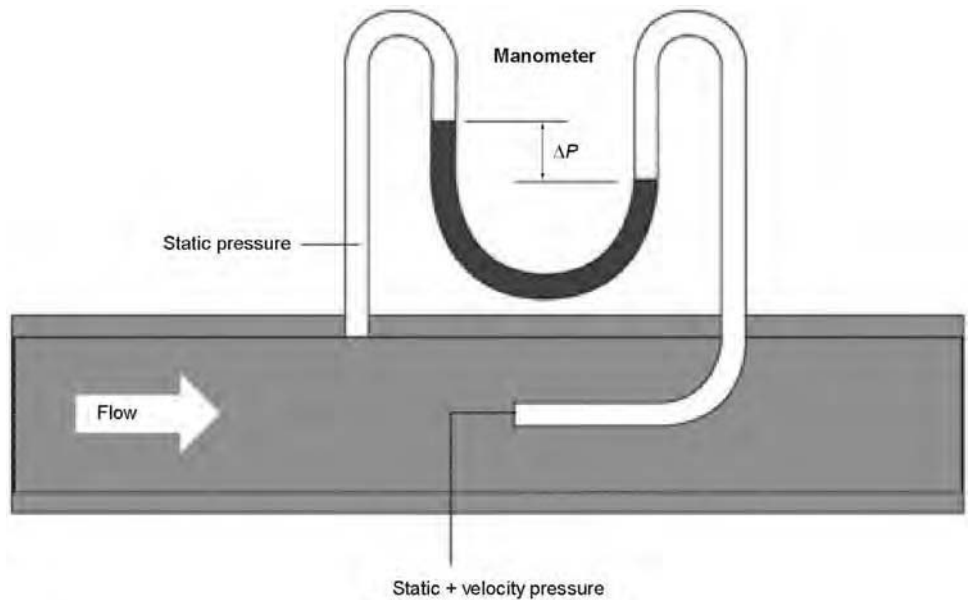


Fig. 51 Schematic illustration of a Pitot tube used to measure fluid flow

the cooling process is critical for determining its applicability for a particular hardening operation. Over the years, various methods have been used to characterize the heat-removal efficiency of a quenchant, including the Jominy end-quench test, cross-sectional hardness survey, cooling curve analysis, and Grossmann hardenability (H) value. Of these, the Grossmann H -value continues to be one of the most widely used to quantify the quench severity of quenchant. Figure 53 illustrates the range of H -values characteristic of various quenchant. Figure 53 illustrates the range of H -values characteristic of various quenchant. Figure 53 illustrates the range of H -values characteristic of various quenchant.

Figure 53 provides one type of illustration of quenchant selection based on Grossmann H -values. Alternatively, a tabular summary of Grossmann H -values for quenching media of interest may be used, such as that shown in Table 15 (Ref 146). The utility of data such as that shown in Table 15 is limited because the actual flow rates for “good,” “moderate,” “strong,” and “violent” agitation are unknown. Alternatively, measured values of heat-transfer coefficients (as shown in Table 16, Ref 146)

and heat fluxes do provide a quantitative meaning, but specific data relative to the quenchant and quench systems of interest must be developed and would be user-specific, in most cases.

Typically, with the exception of intensive quenching processes (described in the article “Intensive Quenching of Steel Parts” in this Volume), the greater the quench severity, the greater the propensity of a given quenching medium to cause increased distortion and cracking. This is usually the result of increased thermal stress, not transformational stress. Specific, or required, options for quench media selection are provided in various national and international specifications as well as industry- and company-specific specifications. Some additional general comments regarding quenchant selection include (Ref 146):

- Most machine parts made from alloy steels are oil quenched to minimize distortion.
- Most small parts, or finish-ground larger parts, are free quenched. Larger gears, typically those larger than 205 mm (8 in.), are

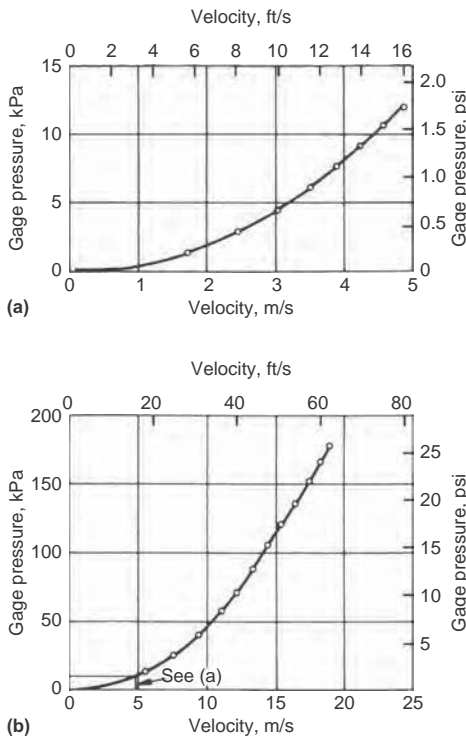


Fig. 52 Chart for calibration of Pitot tube, assuming a Pitot tube factor, K , of 1.0. Velocity equals $K\sqrt{64.4h}$, where h is the pressure head, in feet of water. (a) Low velocity. (b) Full range

- die quenched to control distortion. Similar gears and parts such as bushings are typically plug quenched on a splined plug usually constructed from AISI 8620 steel.
- Although a reduction of quench severity leads to reduced distortion, it may also be accompanied by undesirable microstructures, such as the formation of upper bainite (quenched pearlite) with carburized parts.
- Quench speed may be reduced by quenching in hot (150 to 205 °C, or 300 to 400 °F) oils. When hot oil is used for carburized steels, lower bainite, which exhibits properties similar to martensite, is formed.
- Excellent distortion is typically obtained with austempering, quenching into a medium just above the M_s temperature. The formation of retained austenite is a significant problem and is most pronounced where manganese and nickel are major components of the steel. The best steels for austempering are plain carbon, chromium, and molybdenum alloy steels.
- Aqueous polymer quenchant may often be used to replace petroleum oils, but quench severity is still of primary importance.
- Gas or air quenching will provide the least distortion and may be used if the steel has sufficient hardenability to provide the desired properties.
- Low-hardenability steels are quenched into brine or vigorously agitated oil. However, even with a severe quench, undesirable microstructures such as ferrite, pearlite, or bainite can form.

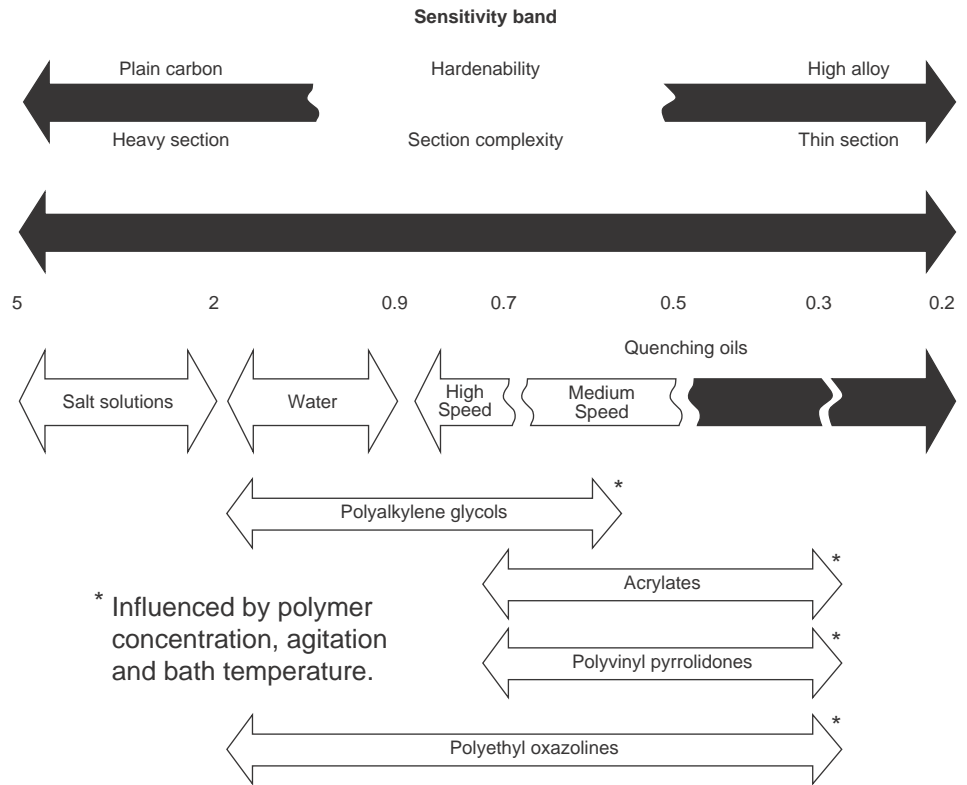


Fig. 53 Graphical illustration of Grossmann hardenability value classification of quenching media. Note the assessment of the potential suitability of a quenchant for use with low-hardenability carbon steels and high-hardenability alloy steels, in addition to thick or thin section size. Source: Ref 153

Table 15 Typical quenching conditions and Grossmann H -values

Quenching medium	Grossmann H -value, in.^{-1}
Poor (slow) oil quench, no agitation	0.2
Good oil quench, moderate agitation	0.35
Very good oil quench, good agitation	0.5
Strong oil quench, violent agitation	0.7
Poor water quench, no agitation	1.0
Very good water quench, strong agitation	1.5
Brine quench, no agitation	2
Brine quench, violent agitation	5

Note: It is possible, especially with high-pressure impingement, to achieve H -values > 5.0. Source: Ref 146

Table 16 Comparison of typical heat-transfer rates for various quench media

Quenching medium	Heat-transfer rate, $\text{W/m}^2 \cdot \text{K}$
Still air	50–80
Nitrogen (1 bar)	100–150
Salt bath or fluidized bed	350–500
Nitrogen (10 bar)	400–500
Helium (10 bar)	550–600
Helium (20 bar)	900–1000
Still (unagitated) petroleum oil)	1000–1500
Hydrogen (20 bar)	1250–1350
Circulated petroleum oil	1800–2200
Hydrogen (40 bar)	2100–2300
Circulated water	3000–3500

Source: Ref 146

Maintenance of Quenching Installations

Because quenching baths vary widely in design, shape, size, and method of operation, it is not feasible to establish standard procedures for maintenance. However, typical schedules for maintaining large quenching installations are described in the following.

For oil quenching, the following schedule applies:

- Daily:
- Check oil level in quench tanks.
 - Check oil temperature.
 - Check oil filter pressure.
 - Check oil pumps and oil flow.

- Run test pin in each oil quench system to verify quench effectiveness (see the section “Oil Quench System Monitoring” in this article).

Weekly:

- Check quenching rate of oil in production system.
- If oil filters are not included in oil system, check for solids in oil.
- Check oil temperature controller and control setting.

Monthly:

- Drain quench tanks and remove sludge (if indicated by bottom sludge sampling).

Semiannually:

- Check heat exchanger coils, pipes, and pumps.
- Replace oil filters when necessary.
- Check screens ahead of oil filter.
- Check oil storage tank for sludge, water leaks, and general condition.
- Calibrate oil-temperature gage.
- Check the viscosity at least semiannually. (In one specific example where this was found to be critical, problems were being encountered with an accelerated oil that had thickened from 95 to 110 SUS at 38 °C, or 100 °F, which was causing helical gears to be off lead after carburizing. The problem was solved by burning 19,000 L, or 5000 gal, of used fluid in the quench in in-house boilers and replacing it with new oil.)
- Check oil for contamination.

For water quenching, the following schedule applies:

Daily:

- Check water temperature.
- Check water pressure.
- Check water circulation.

Weekly:

- Drain quench tanks and remove sludge.
- If water is recirculated, make necessary chemical addition to prevent calcium compounds from building up in tubes.

For brine quenching, the following schedule applies:

Daily:

- Check brine temperature.
- Check brine concentration and adjust as required.

Weekly:

- Drain tanks and remove sludge.
- Check pumps and tank condition.
- Check quenching fixtures for signs of deterioration.

Water- and Air-Quenching Media

Air. The oldest, most common, and certainly least expensive quenching medium is air. Air, being a gas, cools the hot steel by a film-boiling mechanism. The relative quench severity of still air, compared to other quenching media, is shown in Table 16. As with other quenching media, the heat-transfer rates of air cooling are dependent on the flow rate of air past the steel surface (Fig. 54). Although air is commonly available and inexpensive, air quenching typically does not provide sufficient quench severity to adequately harden most steels.

Water. Other than air, the oldest and most common quenching medium is water. Cold

water is one of the most severe quenchants. However, the quench severity of water can be highly variable. For example, distilled water (soft water) exhibits substantially increased film-boiling behavior relative to tap water or hard water, which may contain variable quantities of hard metal salts. The hard metal salts present in hard water adsorb to the surface of steel, creating nucleation sites that facilitate bubble formation and nucleate boiling, thus decreasing the duration of the film-boiling step.

Metal components of hard water include carbonates and bicarbonates of calcium and magnesium in addition to salts of other polyvalent metals. Differences in cooling performance of tap water and distilled water are shown in Fig. 55 (Ref 154). Effects of quench bath temperature and agitation on cooling rates exhibited by water are shown in Fig. 56 (Ref 154).

Some important conclusions regarding the effect of bath temperature and agitation on water quenching include (Ref 154):

- Cooling times increase with increasing water temperature.
- The maximum cooling rate decreases with increasing water temperature.
- The temperature where the maximum cooling rate occurs decreases with increasing water temperature.
- The cooling rate at 343 °C (649 °F) decreases only slightly with increasing water temperature.
- The cooling rate at 232 °C (450 °F) is only minimally affected by water temperature.
- When quenching in cold water at 20 °C (68 °F), nonuniform cooling results because of the simultaneous presence of all three boiling mechanisms during the quenching process. However, at 60 °C (140 °F) (hot water), the vapor blanket was more stable and required mechanical agitation for film breakage.
- Cold water quenching with increasing agitation rates produced lower residual stresses than attainable with unagitated hot water.

The effect of component design on distortion and cracking is covered elsewhere. However, the following quenchant-specific component design recommendations have been made (Ref 146):

- Parts that are long (L) with a thin cross section (d) should be quenched as follows. Long and thin parts are defined as greater than $L = 5d$ and may be quenched in water; if $L = 8d$, parts should be oil quenched, and if $L = 10d$, parts should be austempered.
- Parts that possess a large cross-sectional area (A) and are thin (t) are defined as $A = 50t$. Parts that exceed these dimensions must be straightened or press quenched to maintain dimensional stability. If possible, materials with sufficient hardenability should be oil or molten salt quenched.

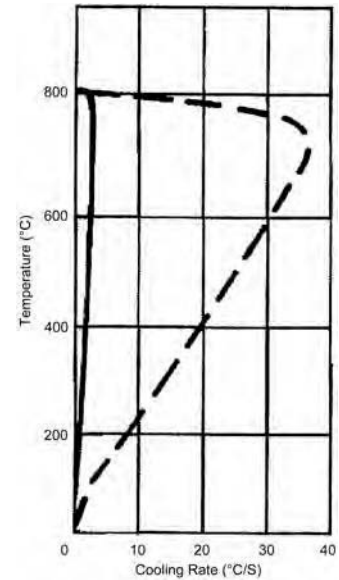


Fig. 54 Comparison of the cooling capacity of still air at atmospheric pressure (solid line) and compressed air at 1 kg/cm² cooling (dashed line) of steel. The heat transfer was measured using a 20 mm (0.8 in.) diameter silver sphere with a center thermocouple.

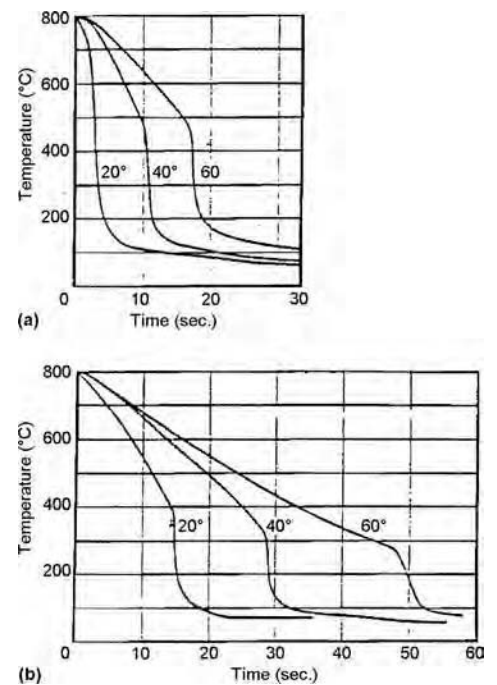


Fig. 55 Effect of hard metal ions on the cooling rate of water. Cooling curves were obtained using a spherical silver probe with a center thermocouple. (a) Hard water. (b) Distilled water

Aqueous Salt (Brine) Solutions

The term *brine* refers to aqueous solutions containing various concentrations of salts, such as sodium or calcium chloride. Cooling rates provided by a brine are higher than those

obtained with distilled water at the same agitation rate. The presence of salts will decrease the propensity for vapor blanket formation, which leads to nonuniform cooling, increased distortion, cracking, and soft spot formation. While many types of salt solutions may be used, the two types most commonly used in the heat treating industry are:

- Sodium chloride, typically at concentrations of approximately 10%

- Sodium hydroxide (also designated as caustic), typically at concentrations of approximately 3%

Petrash studied the effects of NaCl and NaOH addition on the vapor blanket stability of water. The addition of as little as 5% NaCl almost totally eliminated vapor blanket cooling, as shown in Fig. 57(a) (Ref 155). Optimal cooling rate increases with the addition of 15% NaCl to water. Although increasing brine

temperatures produce the expected decrease in quench severity, Fig. 57(b) shows that this decrease is not accompanied with the extended vapor blanket cooling observed for water (Ref 155).

The most common alternative to aqueous NaCl solutions is aqueous caustic (NaOH) solutions. The addition of NaOH produces cooling rate increases similar to those obtained with NaCl at higher cooling temperatures. However, slower cooling rates than obtained with NaCl are obtained in the martensitic transformation temperature region for many steels (<350 °C, or 660 °F), which would be expected to reduce cracking susceptibility. Figure 58 shows the effect of NaOH concentration on cooling rate (Ref 155).

Cui et al. studied the effect on heat transfer during spray cooling by the addition of 0.06 mol/L of NaCl, Na₂SO₄, and MgSO₄ to water (Ref 156). They reported that while the addition of NaCl and Na₂SO₄ accelerated heat transfer during nucleate boiling, neither salt significantly impacted transition boiling. Of these salts, NaCl exhibited the least effect at this concentration, while MgSO₄ exhibited the greatest effect. Increasing the MgSO₄ concentration increased the effect up to 0.2 mol/L and exhibited the greatest increase in the heat flux during both transition boiling and nucleate boiling. In addition, it was also reported that MgSO₄ was found to adhere to the metal surface during transition boiling and increased both surface roughness and heat transfer.

Recently, Arai and Furuya studied the film-boiling process with a 30 mm (1.2 in.) diameter type 304 spherical stainless steel probe with a type K thermocouple inserted into the sphere and tungsten inert gas welded at a position of 2 mm (0.08 in.) from the bottom surface (Ref 157). After austenitizing, the probe was

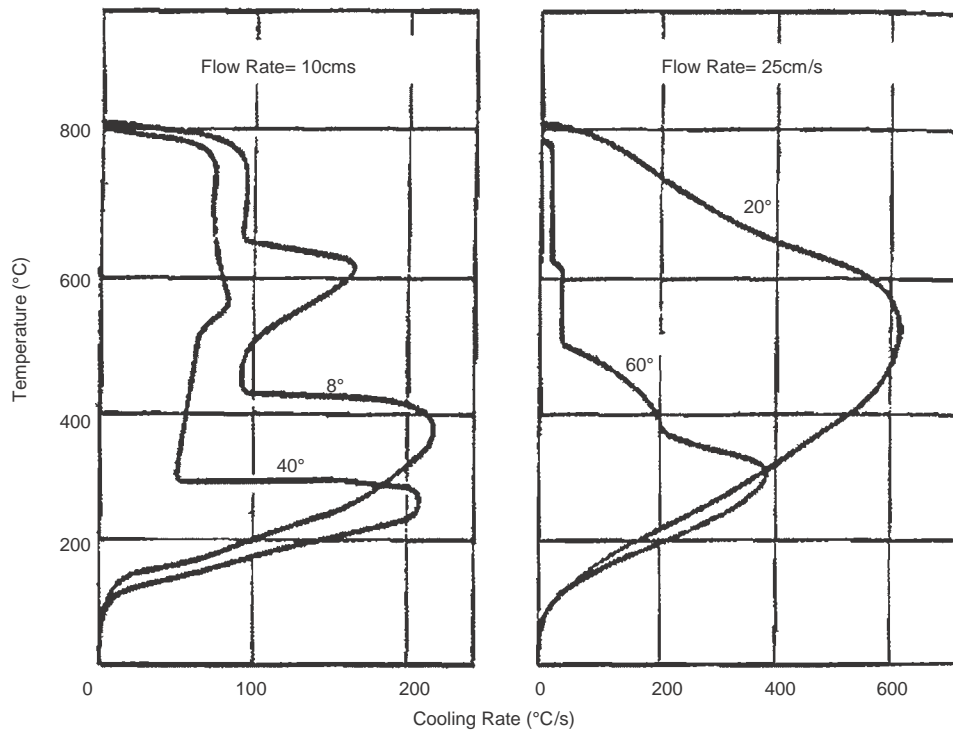


Fig. 56 Effect of bath temperature and agitation on the cooling rates of water. Cooling curves were obtained using a spherical silver probe with a center thermocouple.

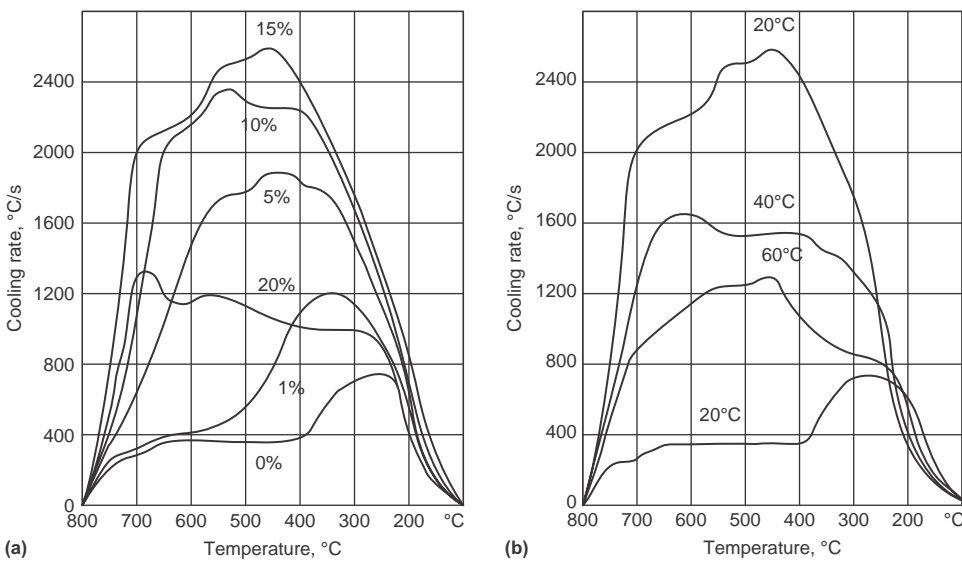


Fig. 57 (a) Effect of NaCl concentration on cooling rate. (b) Effect of NaCl bath temperature on cooling rate. Source: Ref 155

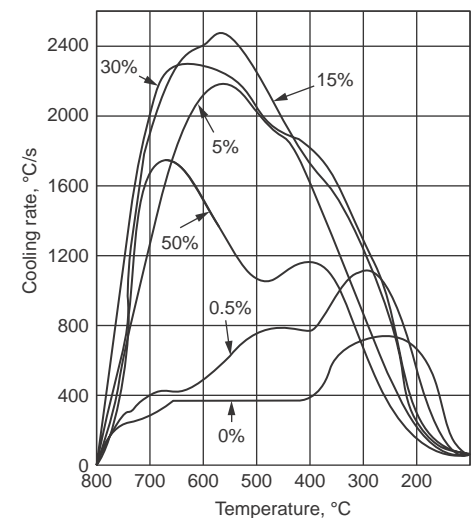


Fig. 58 Effect of NaOH concentration on cooling rate. Bath temperature: 20 °C (70 °F). Source: Ref 155

124 / Steel Quenching Fundamentals and Processes

immersed one-half of the diameter (15 mm, or 0.6 in.) into the quenchant, either pure water or an aqueous solution of CaCl_2 . The quenchant temperature was 80 °C (175 °F). When the near-surface temperature was 800 °C (1470 °F), that was taken as 0.0 s. A new probe was used for each experiment. The boiling behavior was observed using a digital video camera with a frame rate of 30 frames/second and a shutter speed of $1/8000$ s. Therefore, both a cooling time-temperature curve and a video of the cooling process were obtained for each experiment. Figure 59 shows the cooling curve obtained, and Fig. 60 shows selected high-speed images illustrating the effect of CaCl_2 on the cooling process.

The positions marked as “A,” “B,” “C,” “D,” and “E” on the cooling curve for pure water in Fig. 59 indicate:

- Position “A” was taken at 0.0 s and indicates the formation of a stable vapor film.
- The vapor film still exists at position “B,” confirming that it is stable.
- The vapor film begins to collapse at position “C.”
- At position “D,” the vapor film is collapsing across the sphere, and numerous vapor bubbles form.

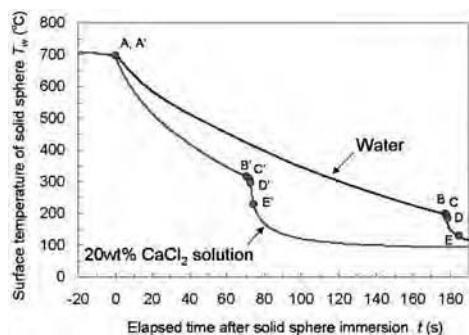


Fig. 59 Effect of the presence of a hydrated salt on the cooling time-temperature curve. Source: Ref 157

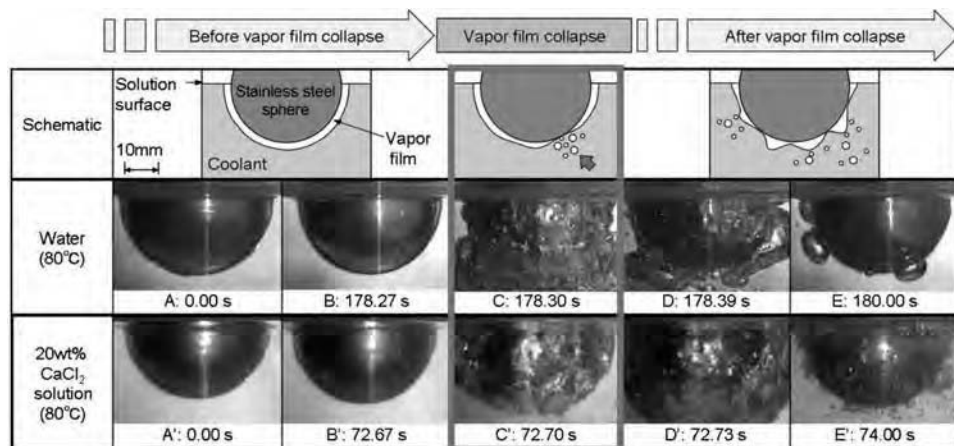


Fig. 60 Effect of 20% CaCl_2 on vapor film collapse. Source: Ref 157

- There is nucleate boiling around the sphere at position “E.”
- The corresponding cooling processes for the 20% aqueous solution of CaCl_2 are also shown in Fig. 59. However, there were a number of differences in interfacial cooling behavior compared to pure water. For example, the vapor film was thinner and collapsed much faster than that which occurred in pure water. When film boiling transitioned to nucleate boiling, position “D,” small vapor bubbles separated from the surface, and the CaCl_2 solution became cloudy.

Taken together, these data show that the presence of CaCl_2 improves film-boiling heat transfer and effectively destabilizes the vapor film. In the case of pure water, the vapor film thickness was approximately 0.5 mm (0.02 in.), the maximum vapor film thickness occurs at position “A,” and the vapor film propagated toward the water surface. In the case of the CaCl_2 solution, the film thickness of the vapor film was substantially less. In both cases, film boiling occurred in the superheat range of 500 K and greater. Surface heat flux decreased as the amount of superheating decreased, and the transition to nucleate boiling occurred when the surface heat flux was at a minimum. Relative to pure water, the CaCl_2 solution exhibited similar trends, but the surface heat flux during film boiling and the maximum heat flux were greater than with pure water (Ref 157).

Mukhina et al. evaluated the use of concentrated solutions of calcium chloride (CaCl_2) at 10 to 12% and magnesium chloride (MgCl_2), also called bischofite, at 14%. They found that in combination with intense agitation, medium-carbon steels formed high surface-compressive stresses that prevented crack formation by elimination of film boiling at the steel surface during quenching (Ref 158). In addition, the mechanical properties were 20 to 30% greater than those achievable with oil quenching. In a more recent study, Kobasko

et al. extended Mukhina’s earlier work by evaluating the use of additional salt solutions, including NaNO_3 , Na_2CO_3 , NaCl , CaCl_2 , and $\text{Ca}(\text{OH})_2$ (Ref 141). However, in all cases, not only must the optimal solution concentration of the salt be used, but it must be used in combination with intensively agitated water. (Note: An optimal concentration is that concentration of salt that produces the least amount of film boiling.)

The carbon content of steel is one of the determining factors for quenchant selection, especially because cracking potential increases with increasing carbon content. Table 17 provides a summary of the mean carbon content limits for conventional water, brine, and caustic quenching of some steels (Ref 146, 159). These guidelines do not apply for intensive quenching processes.

The concentration of a salt solution is usually quantified by specific gravity or density. Typical values for various concentrations of NaCl and NaOH are shown in Table 18 (Ref 153).

Relative cooling rates of water and different aqueous salt solutions to other media are compared in Table 19 (Ref 160). As expected, the salt solutions exhibited the greatest relative cooling rates of those shown. Also, increasing water temperature resulted in progressively slower relative cooling rates. Importantly, and a factor to be discussed subsequently, relative cooling rates of oils (in particular petroleum oils) may vary widely. Hot water, air, and

Table 17 Suggested carbon content limits for water, brine, and caustic quenching

Hardening method/shapes	Maximum carbon, %
Furnace hardening	
General usage	0.30
Simple shapes	0.35
Very simple shapes, e.g., bars	0.40
Induction hardening	
Simple shapes	0.50
Complex shapes	0.33

Table 18 Relationship of brine concentration and brine density

Salt, %	Direct reading by hydrometer	°Be(a)	Salt concentration	
			g/L	lb/gal
NaCl solutions				
4	1.0268	3.8	41.1	0.343
6	1.0413	5.8	62.4	0.521
8	1.0559	7.7	84.5	0.705
9	1.0633	8.7	95.9	0.800
10	1.0707	9.6	107.1	0.894
12	1.0857	11.5	130.3	1.087
NaOH solutions				
1	1.0095	1.4	10.1	0.0842
2	1.0207	2.9	20.4	0.1704
3	1.0318	4.5	31.0	0.2583
4	1.0428	6.0	41.7	0.3481
5	1.0538	7.4	52.7	0.4397

(a) Be = Baume, the specific gravity for liquids that are heavier than water, is $145/(145 - n)$ where n is the reading on the Be scale as °Be.

vacuum are the slowest cooling media of those evaluated.

Molten Metal Quenchants

One of the most common metals that has been used historically for quenching is lead. Lead exhibits a melting point of 327 °C (621 °F) and is typically used at 343 to 927 °C (649 to 1701 °F). Below 343 °C (649 °F), lead is too “mushy” to be effectively used as a quenchant. The thermophysical properties of molten lead are summarized in Table 20 (Ref 161). Although lead is toxic and possesses disposal problems, it continues to be used for patenting of steel wire and for some austempering operations. Because molten lead possesses a high thermal

conductivity and exhibits no film-boiling cooling phase, it provides relatively rapid cooling rates in a high-temperature range not easily achievable with other quenching media.

The cooling process during lead bath patenting is influenced by the thermophysical properties of the molten lead, including viscosity, specific heat, thermal conductivity, and the thickness of the boundary layer between the surface of the steel wire and the molten lead. Figure 61 shows that the cooling rate decreases as the bath temperature increases from 475 to 550 °C (885 to 1020 °F), which is partly due to the decreasing viscosity as the temperature is increased (Ref 161). However, as the bath temperature is increased further to 690 °C (1275 °F), the cooling rate then decreases, which is partly due to the decreasing temperature difference between the steel wire and the molten

lead bath. Furthermore, it is important to note that there is no film boiling occurring in any of the three cooling processes shown.

Because of the toxicity and disposal problems with lead, there is an interest in identifying alternative quenchants. One potential alternative investigated by Narazaki was using molten sodium to quench lower-hardenability steels that require fast cooling to achieve the required depth of hardening. The physical properties of molten sodium are summarized in Table 21 (Ref 165). In this work, the temperature range of the molten sodium metal bath was 150 to 300 °C (300 to 570 °F). A cooling curve comparison of water, petroleum oil, aqueous polymer solution, molten salt, and molten sodium (at 115, 200, and 300 °C, or 240, 390, and 570 °F) is shown in Fig. 62 (Ref 165). The fastest cooling rates in the high-temperature region of the cooling curve were achievable with molten sodium relative to the other quenchants evaluated. Calculations using these data showed that the molten sodium exhibited very high heat-transfer coefficients (30,000 W/m² · K) in the high-temperature region of the cooling curves. Furthermore, cooling rates in the lower-temperature region decreased as the molten sodium bath temperature increased.

Because its nontoxicity and physical properties are similar to molten lead, bismuth was studied as an alternative to molten lead as a quenchant. The thermophysical properties of molten bismuth are shown in Table 22. Ru and Wang studied the use of molten bismuth to quench AISI 1025 carbon steel (Ref 166). The steel test specimens were austenitized at 900 °C (1650 °F) and then quenched in molten lead or molten bismuth at 400, 430, and 460 °C (750, 800, and 860 °F). Essentially, equivalent as-quenched microstructures and hardness values were obtained whether quenching into bismuth or lead. Furthermore, no apparent corrosion or bismuth reaction with the steel was observed after quenching in the molten bismuth bath. Based on this work, it was concluded that molten bismuth could be a viable alternative where molten lead baths are currently used.

Table 19 Relative cooling rates in different quenching media

Quenching medium	Cooling rate from 717 to 550 °C (1323 to 1022 °F) relative to that for water at 18 °C (65 °F)(a)	Quenching medium	Cooling rate from 717 to 550 °C (1323 to 1022 °F) relative to that for water at 18 °C (65 °F)(a)
Aqueous solution, 10% LiCl	2.07	Oil 20204	0.20
Aqueous solution, 10% NaOH	2.06	Oil, Lupex light	0.18
Aqueous solution, 10% NaCl	1.96	Water at 50 °C (122 °F)	0.17
Aqueous solution, 10% Na ₂ CO ₃	1.38	Oil 25441	0.16
Aqueous solution, 10% H ₂ SO ₄	1.22	Oil 14530	0.14
Water at 0 °C (32 °F)	1.06	Emulsion of 10% oil in water	0.11
Water at 18 °C (65 °F)	1.00	Copper plates	0.10
Aqueous solution, 10% H ₃ PO ₄	0.99	Soap water	0.077
Mercury	0.78	Iron plates	0.061
Sn ₃₀ Cd ₇₀ at 180 °C (356 °F)	0.77	Carbon tetrachloride	0.055
Water at 25 °C (77 °F)	0.72	Hydrogen	0.050
Rapeseed oil	0.30	Water at 75 °C (166 °F)	0.047
Trial oil No. 6	0.27	Water at 100 °C (212 °F)	0.044
Oil P20	0.23	Liquid air	0.039
Oil 12455	0.22	Air	0.028
Glycerin	0.20	Vacuum	0.011

(a) Determined by quenching a 4 mm (0.16 in.) nichrome ball, which, when quenched from 860 °C (1580 °F) into water at 18 °C (65 °F), cooled at a rate of 1810 °C (3260 °F) per second over the range of 717 to 550 °C (1323 to 1022 °F). This cooling rate is rated 1.00 in the table, and the cooling rates in other media are compared with it. Source: Ref 160

Table 20 Summary of thermophysical properties of molten lead

Property	Value
Melting point	327.2 °C (621 °F)
Heat to raise the temperature from 15.6 °C (60 °F) to melting point	41.9 kJ/kg (18 Btu/lb)
Working temperature range	343.3–926.7 °C (650–1700 °F)
Latent heat of fusion	26.3 kJ/kg (11.3 Btu/lb)
Mean specific heat in liquid state(a)	0.1424 kJ/kg · K (0.034 Btu/lb · °F)
Thermal conductivity(b), W/m · K	
347.1 °C	16.2
404.9 °C	17.0
456.3 °C	17.6
Electrical resistivity (Ref 163), μΩ · cm	
600.4 K	94.6
1295 K	129.6
1373 K	133
1534 K	142.7
Boiling point	1726.7 °C (3140 °F)
Density (solid)	11.35 g/cm ³ (0.41 lb/in. ³)
Density (liquid)(c)	10.24 g/cm ³ (0.37 lb/in. ³)

Dynamic viscosity: Reference 164 provides a regression equation to calculate specific heat capacity for molten lead from the melting point to 1470 K (1197 °C): $\rho_{pb} [Pa \cdot s] = 4.55 \times 10^{-4} \cdot \exp(1069/T)$ in Kelvin (K)

Reference 162 provides a regression equation to calculate specific heat capacity for molten lead from the melting point to 1300 K (1027 °C): $C_{p,pb} (J/kg \cdot K) = 175.1 - 4.961 \times 10^{-2} \cdot T + 1.985 \times 10^{-5} \cdot T^2 - 2.099 \times 10^{-9} \cdot T^3 - 1.524 \times 10^6 \cdot T^2$ in Kelvin (K). (b) Reference 162 provides an empirical equation to calculate the thermal conductivity for molten lead that is applicable from the melting point to 1300 K (1027 °C): $\lambda_{pb} (W/m \cdot K) = 9.2 + 0.011 \cdot T$ in Kelvin (K). (c) Reference 162 provides an empirical equation to calculate the density for molten lead: $\rho_{pb} (kg/m^3) = 11367 - 1.1944 \cdot T$ in Kelvin (K). Source: Ref 161

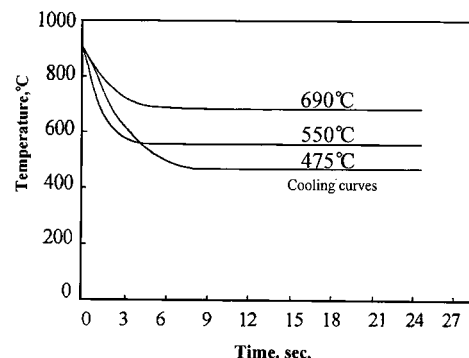


Fig. 61 Cooling curves obtained using a 5 mm (0.2 in.) diameter by 10 mm (0.4 in.) AISI 321 stainless steel wire probe with a center thermocouple in molten lead at three bath temperatures. Source: Ref 161

Table 21 Physical properties of molten sodium

Physical property	Molten sodium at 500 K
Range of liquid	98–881 °C (371–1154 K)
Thermal conductivity: Reference 164 provides an empirical equation to calculate the thermal conductivity for molten sodium that is applicable from the melting point to the boiling point: $\lambda_{Na} \text{ (W/m} \cdot \text{K)} = 104 - 0.047 \cdot T \text{ in Kelvin (K)}$	
Density: Reference 164 provides an empirical equation to calculate the density for molten sodium (equation is recommended for liquid sodium from the melting point to the boiling point): $\rho_{Na} \text{ (kg/m}^3\text{)} = 1014 - 0.235 \cdot T \text{ in Kelvin (K)}$	
Specific heat capacity: Reference 164 provides a regression equation to calculate specific heat capacity for molten sodium: $C_{pNa} \text{ (J/kg} \cdot \text{K)} = -3.001 \times 10^6 \cdot T^{-2} + 1658 - 0.8479 \cdot T + 4.454 \times 10^{-4} \cdot T^2 \text{ in Kelvin (K)}$	
Dynamic viscosity: Reference 164 provides a regression equation to calculate specific heat capacity for molten sodium from 371 to 1155 K: $\ln \eta_{Na} \text{ (Pa} \cdot \text{s)} = 556.835/T - 0.3958 \cdot \ln T - 6.4406 \text{ in Kelvin (K)}$	

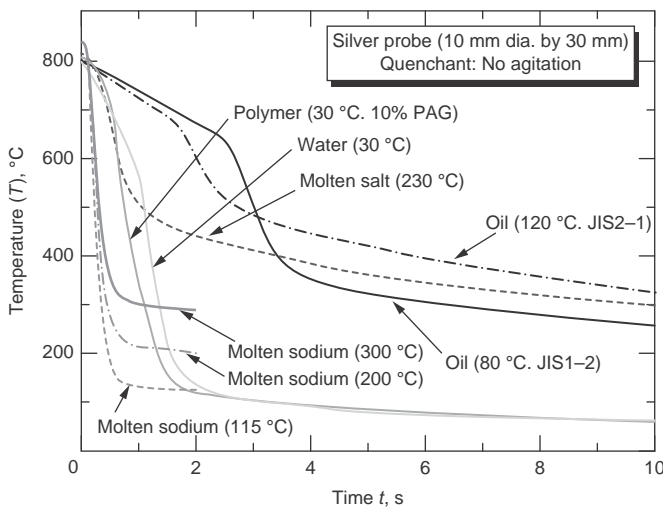


Fig. 62 Cooling curves obtained during quenching in water, petroleum oil, aqueous polymer solution, molten salt, and molten sodium (at 115, 200, and 300 °C, or 240, 390, and 570 °F). The cooling curves were obtained using a 10 mm (0.4 in.) diameter by 30 mm (1.2 in.) cylindrical silver probe with a center thermocouple.

Table 22 Physical properties of molten bismuth

Physical property	Molten bismuth
Range of liquid	271.44–1748 °C (544.59–2021 K)
Thermal conductivity: Reference 162 provides an empirical equation to calculate the thermal conductivity for molten bismuth that is applicable from the melting point to 1000 K (727 °C): $\lambda_{Bi} \text{ (W/m} \cdot \text{K)} = 12 + 1 \times 10^{-2} \cdot T \text{ in Kelvin (K)}$	
Density: Reference 162 provides an empirical equation to calculate the density for molten bismuth: $\rho_{Bi} \text{ (kg/m}^3\text{)} = 10726 - 1.2208 \cdot T \text{ in Kelvin (K)}$	
Specific heat: Reference 162 provides a regression equation to calculate specific heat capacity for molten bismuth from the melting point to 1300 K (1027 °C): $C_{pBi} \text{ (J/kg} \cdot \text{K)} = 118.2 + 5.934 \times 10^{-3} \cdot T + 71.83 \times 10^5 \cdot T^{-2} \text{ in Kelvin (K)}$	
Dynamic viscosity: Reference 164 provides a regression equation to calculate specific heat capacity for molten bismuth from the melting point to 1300 K (1027 °C): $\eta_{Bi} \text{ (Pa} \cdot \text{s)} = 4.456 \times 10^{-4} \cdot \exp(780/T) \text{ in Kelvin (K)}$	

Source: Ref 164

Table 23 Typical use temperatures for martempering oils

Viscosity at 40 °C (105 °F), SUS	Use temperatures					
	Minimum flash point		Open air		Protective atmosphere	
	°C	°F	°C	°F	°C	°F
250–500	220	430	95–150	200–300	95–175	200–350
700–1500	250	480	120–175	250–350	120–205	250–400
2000–2800	290	550	150–205	300–400	150–230	300–450

Molten Salt and Hot Oil Quenchants

Two quenching processes that require relatively high quenchant temperatures are martempering and austempering. Martempering requires that the steel part be rapidly cooled to a temperature slightly above the M_s transformation temperature, stabilized, and then cooled to room temperature. This process is conducted to minimize the potential for cracking. Typical viscosities and use temperatures for martempering oils are summarized in Table 23 (Ref 154).

Austempering is conducted by cooling the steel part to a temperature slightly above the M_s temperature and holding for a sufficient time for austenite to transform to bainite. While austempering may be performed in specially formulated petroleum oils for use at these relatively high temperatures, molten salts are usually used. Martempering and austempering processes may eliminate the need for conventional oil quenching and tempering. A schematic comparison of martempering and austempering is shown in Fig. 63.

Molten salts are usually the medium of choice for high-temperature quenching. Advantages of salt quenching include (Ref 167, 168):

- Cooling at a controlled rate will provide a completely annealed structure in highly alloyed steels, such as those shown in Table 28 (isothermal annealing).

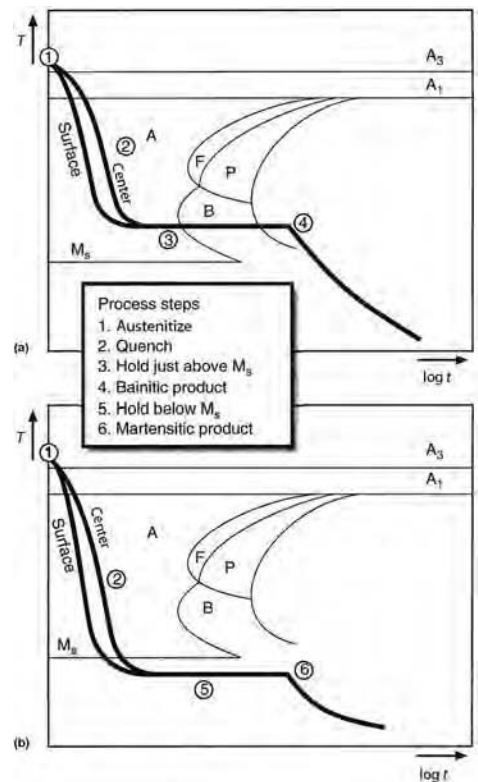


Fig. 63 Comparison of (a) martempering and (b) austempering processes

- Cooling past the pearlite nose of the transformation curve to a suitable temperature for equalization prior to martensitic transformation will reduce the risk of undesirable distortion and cracking (martempering).
- Scaling, distortion, and cracking of high-speed tool steels is minimized by cooling at a controlled rate to a suitable temperature (interrupted quenching). Surface protection is facilitated by eliminating contact with air during heating.
- The risk of cracking during martensite formation, for example, spring wire, is reduced.
- Cooling at a controlled rate allows isothermal transformation to bainite (austempering).
- The temperature within the bath is uniform and may be precisely controlled within $\pm 2\text{ }^\circ\text{C}$ ($4\text{ }^\circ\text{F}$).

Most quenching salts are either binary or ternary mixtures of potassium nitrate (KNO_3), sodium nitrite (NaNO_2), and sodium nitrate (NaNO_3). The minimum quenching temperature depends on the melting point of the salt mixture. The ratio of the salt mixture may affect the viscosity of the molten mixture, which will then affect cooling rates. Quenching temperatures of these molten salt mixtures may range from 140 to 600 $^\circ\text{C}$ (285 to 1110 $^\circ\text{F}$). Molten salt baths are susceptible to explosive degradation at temperatures above 600 $^\circ\text{C}$ (1110 $^\circ\text{F}$) (Ref 154). A comparison of the physical properties of the ternary salt bath mixture and a typical conventional petroleum oil is provided in Table 24 (Ref 169). While the specific heat is greater for petroleum oil, the thermal conductivity of the salt is approximately five times greater on a weight basis and ten times greater on a volume basis. Furthermore, molten salt does not exhibit undesirable film-boiling behavior during quenching.

The effect of increasing water content on decreasing melting point of a ternary mixture of $\text{KNO}_3/\text{NaNO}_2/\text{NaNO}_3$ is shown in Fig. 64 (Ref 171). Figure 64 also shows that the boiling point decreases rapidly as the amount of water added is increased. As long as the salt bath temperature is maintained below the boiling point of the resulting hydrated mixture, it was reported that the water content can be maintained for long periods of time. However, when hot steel is immersed into the hydrated salt mixture, the boiling point may be temporarily exceeded, and some water will be boiled off and will need to be replaced to maintain the composition. Therefore, it is better practice to quench into the salt mixture closer to the freezing point than the boiling point to reduce water losses during quenching (Ref 171). Dubal has reported that the addition of 1% water decreases the melting point of a dry salt bath by 11 $^\circ\text{C}$ (20 $^\circ\text{F}$), and the addition of 2% water decreases the melting point by 19 $^\circ\text{C}$ (35 $^\circ\text{F}$) (Ref 170).

Although ternary salt mixtures are used in the range of 150 to 600 $^\circ\text{C}$ (300 to 1110 $^\circ\text{F}$) for quenching, the addition of up to 10% water may allow the bath to be used for quenching at temperatures as low as 80 $^\circ\text{C}$ (175 $^\circ\text{F}$)

Table 24 Comparison of physical properties of a ternary salt bath mixture and a typical petroleum oil (hot oil) quenchant

Property	Ternary salt mixture	Petroleum oil
Composition	$\text{KNO}_3/\text{NaNO}_2/\text{NaNO}_3$	Hydrocarbon mixture
Operating range	150–400 $^\circ\text{C}$ (300–750 $^\circ\text{F}$)	130–220 $^\circ\text{C}$ (265–430 $^\circ\text{F}$)
Density at 200 $^\circ\text{C}$ (390 $^\circ\text{F}$), g/cm ³	1.92	0.82
Dynamic viscosity, cP		
At 200 $^\circ\text{C}$ (390 $^\circ\text{F}$)	7.5	2.9
At 315 $^\circ\text{C}$ (600 $^\circ\text{F}$)	2.9	...
Specific heat, Btu/lb · $^\circ\text{F}$	0.37	0.5
Thermal conductivity, Btu/lb · ft ²	0.32	0.07
Thermally stable to, $^\circ\text{C}$ ($^\circ\text{F}$)	540 (1000)	230 (450)
Heat-transfer coefficient, kW/m ² · K	4.5–16.5	NA
Dragout rate, g/m ²	50–100	NA

NA, not applicable. Source: Ref 169, 170

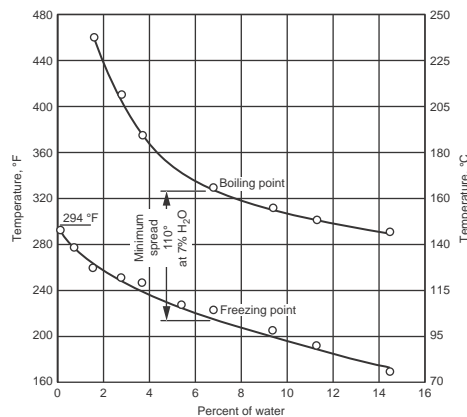


Fig. 64 Effect of water content on the freezing point and boiling point of a ternary mixture of potassium nitrate, sodium nitrite, and sodium nitrate

(Ref 168). However, more typically, water concentrations of 0.5 to 2% would be used in the more typical operating temperature range of 150 to 290 $^\circ\text{C}$ (300 to 550 $^\circ\text{F}$).

Instead of fresh water addition, salt solutions from a washing bath have been used. Also, some heat treaters use low-pressure steam instead of water (Ref 170). The saturation concentrations of water in the salt bath as a function of bath temperature are shown in Table 25 (Ref 160). Safe practice requires that water is always added to a well-agitated bath and never to an unagitated bath (Ref 170).

The quench severity of molten salt is approximately the same as that of petroleum oil, as illustrated by the Grossmann *H*-value comparison shown in Table 26 (Ref 170). Both are slower than water and brine solutions and aqueous polymer quenchants; depending on polymer structure, concentration, and agitation, quench severities may range from those of molten salt and petroleum oil to that exhibited by brine solutions.

The cooling curve behavior of a $\text{KNO}_3/\text{NaNO}_2/\text{NaNO}_3$ salt bath will increase with increasing concentrations of water, as shown in Fig. 65 (Ref 168). Interestingly, not only does the cooling rate in the high-temperature region of the cooling curve tend to increase with increasing water content, but no vapor phase

Table 25 Water saturation concentrations in $\text{KNO}_3/\text{NaNO}_2/\text{NaNO}_3$ as a function of salt bath temperature

Salt bath temperature		Saturation concentration of water, %
$^\circ\text{C}$	$^\circ\text{F}$	
370	700	0.25
315	600	0.5
260	500	1.0
205	400	2.0

Table 26 Grossmann *H*-value comparisons of common quenchant media

Quenchant	Grossmann <i>H</i> -value, in. ⁻¹
Still air	<0.1
Oil	0.2–0.4
Molten salt	0.2–0.5
Aqueous polymers	0.2–1.0
Unagitated water at room temperature	1.0
Brine	5.0

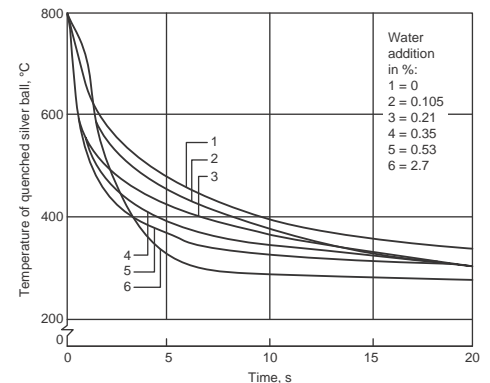


Fig. 65 Effect of increasing water content on a martempering salt bath at 200 $^\circ\text{C}$ (390 $^\circ\text{F}$). Source: Ref 168

behavior was observed until the water concentration was the maximum of that evaluated, 2.7%.

The effect of agitation on the cooling rate of a low-melting-point salt bath at 175 $^\circ\text{C}$ (350 $^\circ\text{F}$) is shown in Fig. 66 (Ref 170). The cooling rate reported is the average rate between 650 and 260 $^\circ\text{C}$ (1200 and 500 $^\circ\text{F}$). The data show that

increasing agitation substantially increases the cooling rate. As discussed previously, increasing water concentration from 0.5 to 5% results in increased cooling rates, as shown in Fig. 67 (Ref 170). A combination of water addition and agitation reportedly will increase cooling rates (quench severity) threefold.

Liščić has also demonstrated the effect of agitation rate and water addition on a hot salt bath (Degussa AS-140) at 200 °C (390 °F) on the cross-sectional Rockwell distribution after quenching 50 mm (2 in.) diameter by 200 mm (8 in.) round bars of AISI 4140 steel (Ref 172). Figure 68 shows that the greatest increase in hardness was obtained between agitated and unagitated salt. However, a further increase in hardness and depth of hardening was obtained with the addition of 2% water. Using the hardness value at ¼R for comparison, it was observed that with good agitation and the addition of 2% water, there was an additional increase of 19 HRC relative to the results obtained with no agitation and no water addition.

The depth of hardening at 47 HRC is four times greater with 2% water added than that obtained without water addition (Ref 172).

Selection of a martempering or austempering process also depends on the steel to be quenched. Table 27 shows the Rockwell hardness that can be expected for plain carbon, alloy steel, and cast iron for each process. Salt bath temperatures in the range of 195 to 350 °C (385 to 660 °F) exhibit only a minimal effect on Grossmann *H*-values (Ref 154).

Generally, alloy steels are more commonly martempered than carbon steels. However, some carbon steels with section sizes thinner than 5 mm (0.2 in.) that are typically water quenched may be martempered at 205 °C (400 °F) if the martempering oil is vigorously agitated. However, martempering does not eliminate the need for tempering (Ref 173). Steel grades that are most commonly martempered include AISI 1090, 4130, 4140, 4150, 4340, 300M, 4640, 5140, 6150, 8630, 8640, 8740, 8745, SAE 1141, and SAE 5100. Carburizing steel grades that are martempered after carburizing include AISI 3312, 4620, 5120, 8620, and 9310. Gray cast iron parts are also routinely martempered (Ref 174). Although hot oil is usually used for martempering (175 °C, or 350 °F), molten salt with the addition of water may also be used. Wahl reports that for martempering of carburized carbon steels in a salt bath, the operation is typically conducted at 180 to 200 °C (355 to 390 °F), and 0.5 to 1.0% water is added to increase the cooling rate; heat transfer occurs principally by convection (Ref 175).

Austempering has many advantages, such as when parts require high hardness and high ductility and to reduce distortion or dimensional variation or cracking. However, austempering is not universally applicable to all steels. Limitations include section size and carbon content of the specified steel. Tables 28 to 30 provide recommendations on the limitations of steel composition and alloy type on the cross-sectional size and thickness that may be austempered

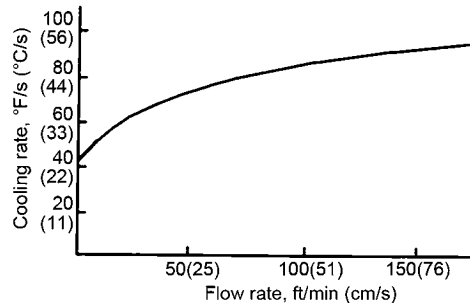


Fig. 66 Effect of agitation on the cooling rate of a low-melting-point salt at 175 °C (350 °F). Source: Ref 170

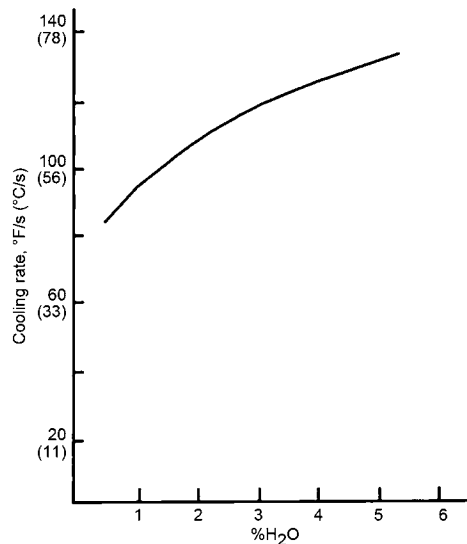


Fig. 67 Effect of increasing water concentration on the cooling rate of a low-melting-point salt at 175 °C (350 °F). Source: Ref 170

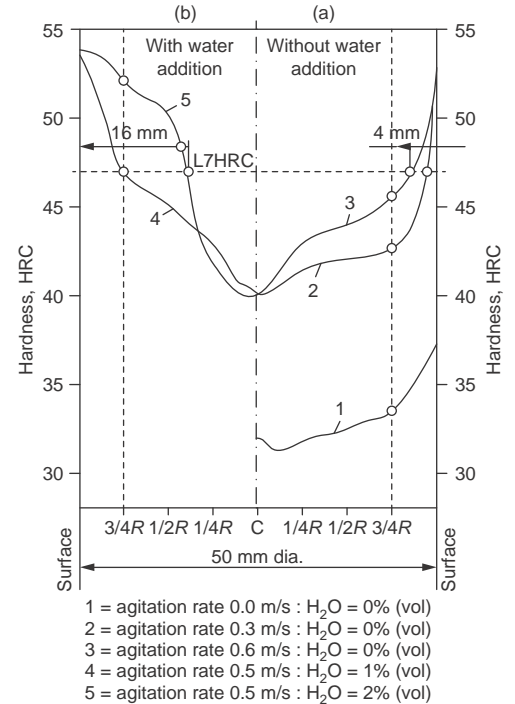


Fig. 68 Influence of agitation rate and water addition on a hot salt bath (Degussa AS-140) at 200 °C (390 °F) on the cross-sectional Rockwell distribution after quenching 50 mm (2 in.) diameter by 200 mm (8 in.) round bars of AISI 4140 steel

Table 27 Martempering versus austempering for various steels

Steel class	Cross-sectional size		Hardness HRC	
	mm	in.	Martempering	Austempering
Carbon steel	<13	<0.5	35–65	35–55
Alloy steel	<100	<4.0	35–65	35–55
Cast iron	<13	<0.5	63	...

Table 28 Effect of chemistry on maximum section size to achieve an essentially bainitic microstructure after austempering

Steel type	Maximum section		Martensite start (<i>M_s</i>) temperature		Analysis			Maximum HRC
	mm	in.	°C	°F	C	Cr/Mo	Mn	
1050	3.17	0.125	345	655	0.48/0.55	...	0.60/0.90	48/50
1065	4.75	0.187	275	525	0.50/0.70	...	0.60/0.90	50/54
1066 (1062)	7.13	0.281	260	500	0.60/0.71	...	0.85/1.15	51/54
1080	5.08	0.200	210(a)	410(a)	0.75/0.88	...	0.60/0.90	55/57
1084	5.53	0.218	200	395	0.80/0.93	...	0.60/0.90	55/57
1086	3.96	0.156	215	420	0.80/0.93	...	0.35/0.50	55/57
1090	4.75	0.187	210(a)	410(a)	0.85/0.98	...	0.60/0.90	57/60
1090(b)	20.8	0.820	205(a)	400(a)	0.85/0.98	...	0.60/0.90	Ave. = 44.5
1095	3.76	0.148	210	410	0.90/1.05	...	0.35/0.50	57/60
1350	15.9	0.625	234	453	0.48/0.53	...	1.60/1.90	53/56
5160	26.3	1.035	256	492	0.56/0.64	Cr	0.75/1.00	47
4063	15.9	0.625	245	473	0.58/0.67	0.60/1.00 Mo	0.70/0.90	53/56
50100	7.92	0.312	205	400	0.98/1.10	0.20/0.30 Cr	0.25/0.45	57/60
						0.4/0.6		

(a) Estimated *M_s* temperatures. (b) Modified austempering practice (not cited). Source: Ref 177

(Ref 176). These maximum-diameter recommendations correspond to center cooling rates that just miss the nose of the TTT curve for the steel alloy when using a salt bath held at approximately 315 °C (600 °F).

Generally, as the transformation temperature increases, the immersion time during austempering decreases. As the carbon concentration of a steel increases, the transformation time at the same transformation temperature increases. Also, heat transfer is most critical during the first second of immersion of the austenitized steel, which is the time when the greatest rate of heat removal

occurs. Heat-transfer rates can be increased by fluid flow from long free-fall or by agitation. Increasing agitation is the most effective. As discussed previously, water addition is used when the steel has marginal hardenability or larger section sizes are being quenched.

When minimum distortion is a critical concern, parts should be austenitized at the lowest possible temperature and quenched at the highest possible temperature. In cases where parts are long and thin, they may need to be suspended vertically for more uniform fluid flow around the parts, which will minimize distortion.

Table 29 Section size limitations for austempering from Ford manufacturing standards

SAE steel	Maximum cross section	
	mm	in.
1045	3.81	0.150
1062	6.35	0.250
1095	5.08	0.200
1340	7.61	0.300
4063	15.2	0.600
4150	20.3	0.800
4340	25.4	1.000
5140	25.4	1.000
8620	6.35	0.250
8630	7.61	0.300
52100	12.7	0.500

Data taken from Ford Manufacturing Standard P HT 207 (1974). Source: Ref 176

Table 30 Size limitations for various compositions

Carbon, %	Manganese, %	Approx. max. diameter	
		mm	in.
1.00	0.40	3.8	0.15
1.00	0.75	4.8	0.19
0.85	0.40	3.93	0.155
0.85	0.75	5.6	0.22
0.65	0.75	4.8	0.19
0.65	1.10	7.1	0.28
0.65	1.80	16	0.63

Source: Ref 176

Table 31 Cooling time and Grossmann *H*-value characterization of various vegetable and animal oils

Oil	Cooling time, s (700–300 °C, or 1290–570 °F)	Grossmann <i>H</i> -value, cm ⁻¹
Soybean oil	1.42	0.200
Whale oil	1.35	0.198
Sperm oil	1.45	0.200
Rapeseed oil	1.63	0.199
Castor oil	1.80	0.199
Hardened fish oil	3.30	0.125
Petroleum oil	3.87	0.142

Note: Cooling data obtained using the old JIS K 2242 silver probe with a surface thermocouple (Ref 101); quenching from 800 °C (1470 °F) into the oil at 80 °C (175 °F). Source: Ref 180

Oil Quenchants

There are primarily two types of oils that are used to quench steel: vegetable and animal fats and oils, and petroleum-derived oils. Of these, petroleum oils have been used only since approximately 1900, while vegetable and animal oils have been used for perhaps thousands of years (Ref 93). The historical use of vegetable oils was recently reviewed and is not discussed further here. While the current use of animal oils is rather limited, there is substantial renewed interest in the use of vegetable oils as steel quenchants, such as the work by de Souza, who showed that vegetable oils, as a class of fluids, typically exhibit little, if any, film-boiling behavior. This is due to the relatively high boiling points of vegetable oils (Ref 178).

Of these early studies, one of the most extensive relating to the use of vegetable and animal oils was reported by Tagaya and Tamura (Ref 179, 180). Tamura determined the Grossmann *H*-values on a number of vegetable and animal oils and compared their performance with a conventional petroleum oil quenchant. The results of this study are shown in Table 31 (Ref 180). With the exception of hardened fish oil, the different animal and vegetable oils evaluated yielded comparable *H*-values, which were

slightly higher than those obtained for the conventional petroleum oil and hardened fish oil. Fats, which are triglycerides extracted from various fish and animals, exhibit a quenching performance that is superior to petroleum oils. Fatty oils produce faster cooling rates at high temperatures than petroleum oils without accompanying film boiling, which is an important property if pearlite transformation is to be minimized during quenching and if distortion minimization is to be achieved. (Note: While the use of whale oil and sperm oils predominated as quenchants until the early 20th century, or the 1900s, it is no longer used today in 2013.)

Like water (Fig. 1), petroleum oil quenchants often exhibit all three primary cooling mechanisms—film boiling, nucleate boiling, and convective cooling—simultaneously on the steel surface during the quenching process, as shown in Fig. 69. Also, as with water quenching, the presence and stability of film boiling is a key contributor to nonuniform quenching, which may lead to distortion control and cracking problems.

The presence and duration of these cooling phases depends on a number of factors, such as quenchant temperature and agitation. However, perhaps the greatest single impact is the compositional variation of the oil used to formulate the quenchant. This is illustrated by Fig. 70, which shows the wide variation of cooling rate properties of many commonly available commercially formulated quenchants. Given the inherent variability of the quench severities of petroleum oil quenchants, the accompanying question when viewing Table 32 is “which oil”? This degree of variability would be expected to result in dramatic differences in as-quenched hardness produced by a steel alloy. This cooling complexity is compounded by the fact that the cooling properties change with time in use, and often various oils may be indiscriminately mixed in the shop, so that often the actual composition of a quench oil in use is not known.

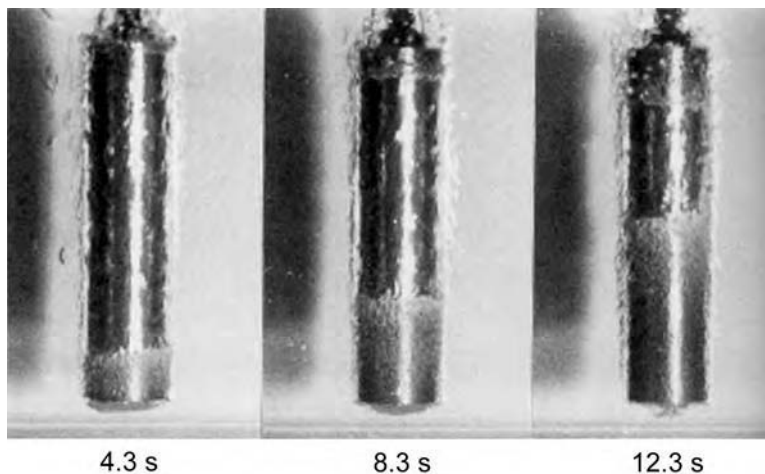


Fig. 69 Quench of a 25 mm (1.0 in.) diameter by 100 mm (4.0 in.) cylinder of CrNi steel into petroleum oil at 60 °C (140 °F) with an agitation rate of 0.3 m/s (1.0 ft/s). Courtesy of H.M. Tensi, Technical University of Munich

In this section, the various reasons for quench oil variability are addressed. This discussion is followed by further complications due to aging and contamination, and a brief summary of recommended quench bath maintenance is provided.

Petroleum oil-based quenching oils are complex mixtures based on a variety of compositions, with components differing in physical properties such as volatility and viscosity, all of which can affect overall cooling performance. Volatility of a petroleum oil is inversely proportional to its flash point, the lowest temperature at which the vapors over an oil sample (either in an open or a closed system) will ignite if exposed to a flame. The more volatile a component, the lower its flash point. Figure 71 illustrates the relative volatility of several petroleum oil components (Ref 181). Quenching oils that contain substantial quantities of typically more volatile naphthenic derivatives usually exhibit inferior characteristics, such as greater deposit formation and lower flash points than paraffinic oils. Lower flash points are particularly deleterious in heat treating applications where the oils are subjected to various sources of high temperature, particularly with respect to high interfacial temperatures between the steel and oil.

Although paraffinic basestocks are the most preferred basestock, there are others that may be used for quenchant formulation. These include (Ref 182):

- *Double hydro-treated mineral oils:* These oils are treated to remove carbon-carbon double bonds of aromatic and paraffinic structures, which results in substantial improvement in oxidative stability, somewhat higher flash points, and better cooling curve behavior for the same viscosity.
- *Refined paraffinic mineral oils:* These are the most commonly used baseoils in quenchant formulation. As a class, they exhibit relatively high flash points, excellent thermal

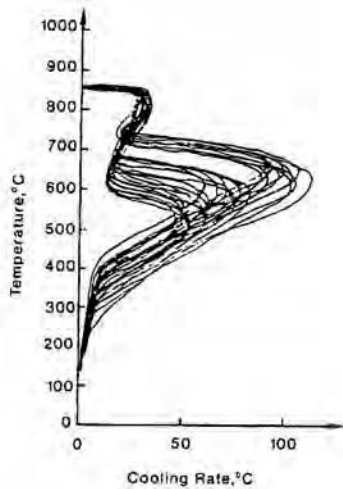


Fig. 70 Cooling rate variability that may be exhibited by various petroleum oil quenchants. Courtesy of S.O. Segerberg

Table 32 Typical Specification 31 recommendations for austenitizing, annealing, and normalizing temperatures with allowed quenching media for plain carbon and alloy steels

Steel designation	Austenitizing temperature		Normalizing temperature		Annealing temperature		Quenchant
	°C	°F	°C	°F	°C	°F	
1025	871	1600	899	1650	885	1625	Water, polymer
1035	843	1550	899	1650	871	1600	Oil, water, polymer
1045	829	1525	899	1650	857	1575	Oil, water, polymer
1095	802	1475	843	1550	816	1500	Oil, polymer
1137	843	1550	899	1650	788	1450	Oil, water, polymer
3140	816	1500	899	1650	816	1500	Oil, polymer
4037	843	1550	899	1650	843	1550	Oil, water, polymer
4130	857	1575	899	1650	843	1550	Oil, water, polymer
4135	857	1575	899	1650	843	1550	Oil, polymer
4140	843	1550	899	1650	843	1550	Oil, polymer
4150	829	1525	871	1600	829	1525	Oil, polymer
4330V	871	1600	899	1650	857	1575	Oil, polymer
4335V	871	1600	899	1650	843	1550	Oil, polymer
4340	816	1500	899	1650	843	1550	Oil, polymer
4340 Mod.	871	1600	927	1700	843	1550	Oil, polymer
4640	829	1525	899	1650	843	1550	Oil, polymer
6150	871	1600	899	1650	843	1550	Oil, polymer
8630	857	1575	899	1650	843	1550	Oil, water, polymer
8735	843	1550	899	1650	843	1550	Oil, polymer
8740	843	1550	899	1650	843	1550	Oil, polymer
Hy-Tuf	871	1600	941	1725	760	1400	Oil, polymer
300M	871	1600	927	1700	843	1550	Oil, polymer
H-11	1010	1850	871	1600	Air, oil, polymer
98BV40	843	1550	871	1600	843	1550	Oil, polymer
D6AC	885	1625	941	1725	843	1550	Oil, polymer
52100	843	1550	899	1650	Oil, polymer
9Ni-4Co-0.20C	829	1525	899	1650	Oil, water, polymer
9Ni-4Co-0.30C	843	1550	927	1700	Oil, polymer
M-50	1107	2025	Salt
AF1410	829	1525	899	1650	899	1650	Oil, polymer
Aeromet 100	885	1625	899	1650	Air, oil, polymer

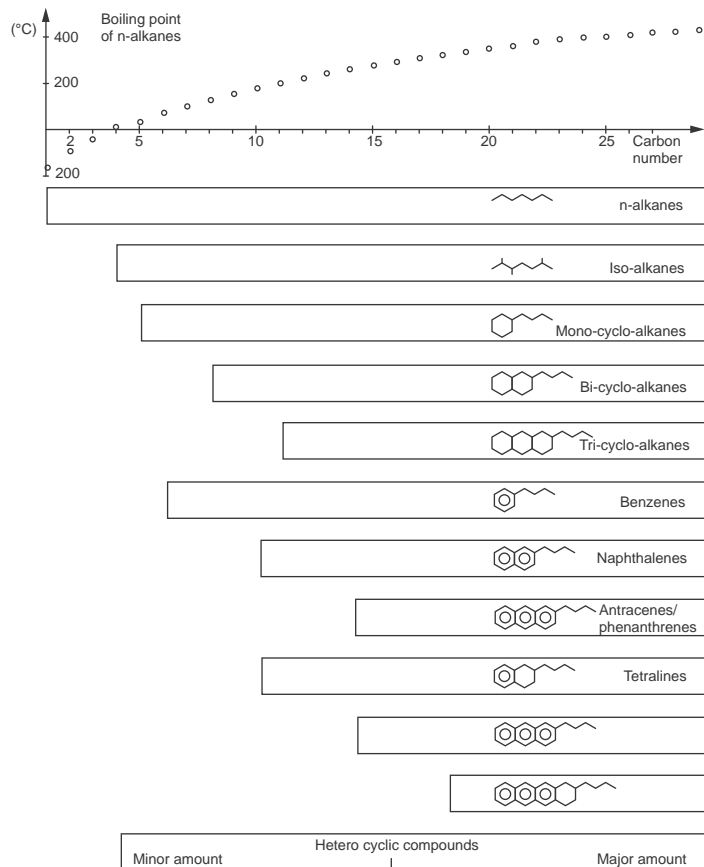


Fig. 71 Relative hydrocarbon volatility in a typical crude oil fraction

and oxidative stability, and good cooling curve behavior.

- *Refined naphthenic mineral oils:* Relative to paraffinic basestocks, they exhibit lower flash points, poorer thermal-oxidative stability, and are more difficult to separate during water-washing processes.
- *Re-refined paraffinic baseoils:* These oils are recovered basestocks that are passed through a cracker and distilled and are available in very narrow boiling point ranges. They have a limited viscosity of 100 SUS and are eco-friendly.

Protsidim et al. showed that small compositional changes in the quench oil basestock resulted in significant changes in quenching performance. Table 33 provides four examples of different potential quench oil compositions and physical properties, and Fig. 72 illustrates that these compositional variations exhibit a significant impact on the corresponding cooling rate behavior (Ref 183).

Another method of quantifying the difference in quench oils is to determine the relative ability to wet the steel surface. Tkachuk et al. measured the effect on quenching behavior exhibited by viscosity and wettability by contact-angle measurements of four quench oil compositions,

summarized in Table 34. Viscosity is determined by the molecular composition of the oil and would be expected to exhibit its greatest influence on heat transfer during convection. Surface activity (wettability) of the oil would be expected to affect the origin, growth, and detachment of the vapor bubbles from the steel surface that are formed during nucleate boiling. The assessment of wettability from contact-angle measurements is shown schematically in Fig. 73.

Cooling rate behavior of Tkachuk's petroleum oil fractions was determined by using a silver ball probe. Figure 74 provides a correlation of cooling rate with viscosity and wettability exhibited by the test oils. These data show that cooling rate increases with decreasing oil viscosity and increasing contact angle (wettability of the oil on the steel surface) (Ref 184). Taken together, these data show that as the viscosity is increased and wettability is decreased, there is a corresponding decrease in cooling capacity and duration of nucleate boiling. Tkachuk's explanation was that by increasing the viscosity, the departure time for bubbles next to the hot surface would be decreased, thus inhibiting the ability of the bubbles to remove heat. Decreasing wettability would cause the bubbles to grow in size prior to departure, thus

increasing the vapor fraction at the hot metal interface and decreasing heat-transfer efficiency.

Figure 75 shows the cooling rate curves for the four test oils shown in Table 34. Although these oils possess approximately the same boiling point, they exhibit substantially different viscosity and wettability. In addition, the cooling rate curves in Fig. 75 show that the Leidenfrost temperatures, the transition temperatures from film boiling to nucleate boiling, are also similar. However, the cooling rates exhibited by the group III aromatic hydrocarbon fraction (Table 34) was less than that exhibited by the paraffinic-naphthenic fraction (Ref 184). This study shows that the highest-quality quenching oils would preferably be formulated from paraffinic or paraffinic-naphthenic basestocks, with an objective of identifying lower viscosity and better wettability.

Yokota et al. studied the effect of petroleum oil basestock boiling point and volatility by evaluating the quenching behavior of 21 quench oils with the same viscosity (17 mm²/s, or 0.26 in.²/s, at 40 °C, or 105 °F) (Ref 185). These oils contained the same additives, and only the basestock composition was varied. Cooling curve analysis was performed according to JIS 2242:1980 (Ref 101). The cooling curve criteria were the Leidenfrost temperature and the cooling time from 800 to 400 °C (1470 to 750 °F). In general, oil quenchants with higher Leidenfrost temperatures and lower cooling times provided the best as-quenched hardness of a 0.45% C steel. The as-quenched hardness results are summarized in Fig. 76. Because all these oils possessed the same viscosity, it was determined that the variation in hardnesses observed was

Table 33 Impact of quench oil composition on physical properties

Property	Oil			
	MZM-16	I-20A	I-20AR1	I-20AR2
Hydrocarbon composition, %				
Paraffin-naphthene	73.7	71.48	67.04	62.65
Aromatic groups				
I	11.30	11.96	11.60	16.00
II	6.70	7.80	3.16	10.58
III	3.80	4.00	3.16	10.58
IV	3.60	2.00	3.84	1.40
Resins	0.50	2.10	4.00	4.10
Losses	0.40	0.66	2.96	1.48
Kinematic viscosity				
At 50 °C (120 °F), m ² /s (ft ² /s)	17.5 (188)	18.3 (197)	24.8 (267)	25.6 (276)
Flash point, °C (°F)				
Open cup	182 (360)	180 (356)	160 (320)	167 (333)
Closed cup	188 (370)	186 (367)	180 (356)	188 (370)
Oxidation test, wt% decrease	1.54	1.8	2.2	3.0
Change in closed-cup flash point, °C (°F)	None	None	+2.2 (+4.0)	+3.0 (+5.4)

Table 34 Effect of quench oil composition on viscosity and contact angle

Property	Composition			
	Paraffin/naphthene	Aromatic hydrocarbons		
		I	II	III
Kinematic viscosity				
At 50 °C (120 °F), m ² /s (ft ² /s)	32.7 (352)	51.3 (552)	66.8 (719)	172.1 (1853)
Fraction composition, °C (°F)				
Start of boiling	337 (639)	340 (644)	335 (635)	334 (633)
10% boiled off	437 (783)	415 (779)	416 (781)	420 (788)
50% boiled off	458 (856)	456 (853)	454 (849)	462 (864)
90% boiled off	498 (928)	500 (932)	503 (937)	504 (939)
Mean boiling point, °C (°F)	456 (853)	457 (855)	456 (853)	460 (860)
Composition of hydrocarbons, %				
Paraffin	35.6
Naphthene	62.6	25.2	27.1	37.3
Naphthene-aromatic	1.8	74.6	72.7	62.5
Aromatic resin	...	0.2	0.2	0.2
Contact angle of wetting, cos δ	0.908	0.898	0.896	0.889

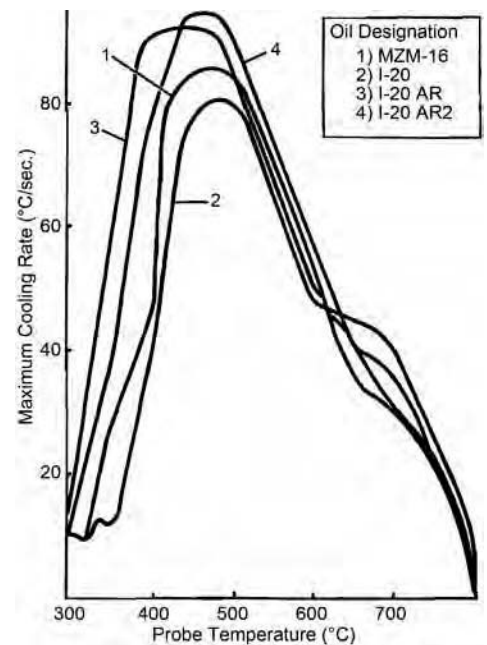


Fig. 72 Cooling rate of a spherical copper probe quenched into different petroleum oil compositions. See Table 33 for oil compositions.

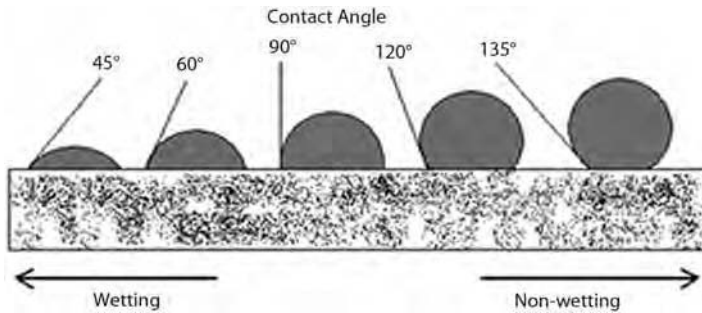


Fig. 73 Effect of fluid wettability of a fluid on a solid surface. The contact angle serves as a wettability index. Decreasing contact angles indicate increasing wettability.

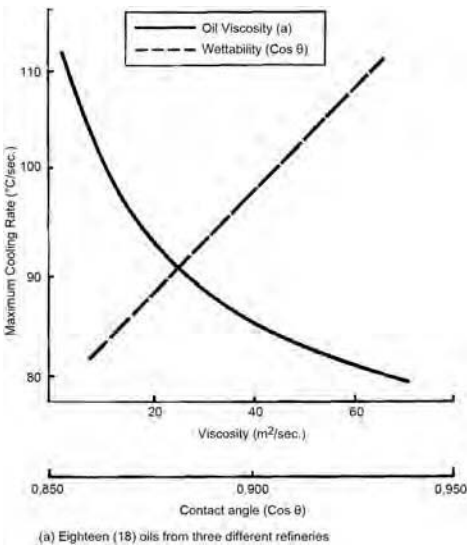


Fig. 74 Correlation of cooling rates obtained using a spherical silver probe with oil viscosity and contact angle. See Table 34 for oil compositions

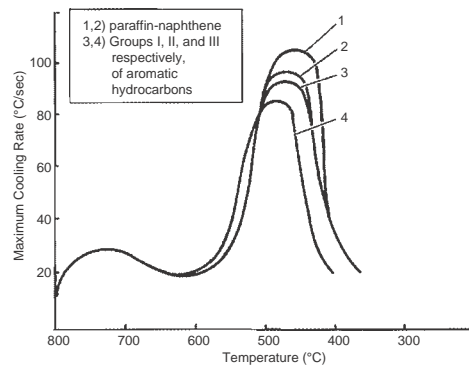


Fig. 75 Cooling rate of a silver spherical probe quenched in different hydrocarbons separated from a single oil. See Table 34 for oil compositions.

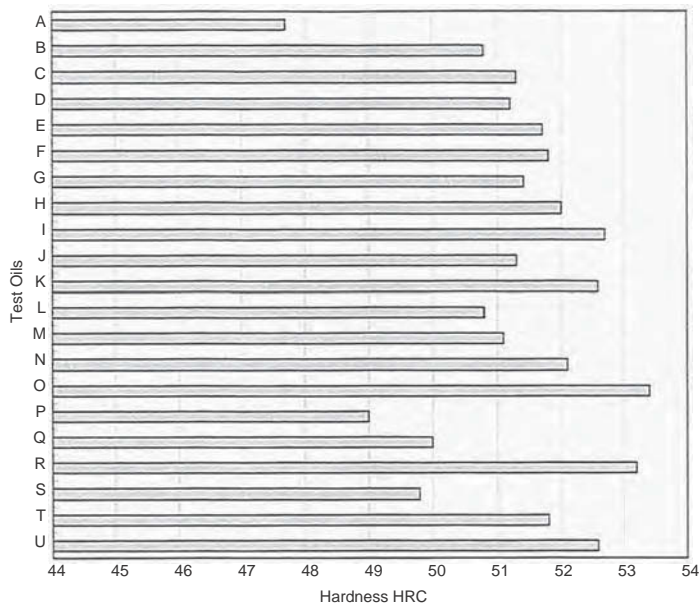


Fig. 76 Summary of as-quenched hardness variation of a 0.45% C steel with a series of petroleum oils with the same viscosity but different boiling temperature ranges. Source: Ref 185

due to the boiling point ranges of the oil base-stocks, which are composition dependent. The cooling rate with the temperature range of 350 to 300 °C (660 to 570 °F) was found to be the most critical cooling curve parameter.

The effect of the fractional composition, in 50 °C (90 °F) increments, on cooling behavior of a quenching oil was studied in detail by Tkachuk et al. (Ref 186). The conclusions from this study were:

- The composition of the petroleum oil fractions exhibits a strong effect on cooling capacity.
- A low-boiling-point oil fraction (300 to 400 °C, or 570 to 750 °F) exhibits insufficient cooling capacity in the high-temperature region due to increased vapor formation during the initial stages of cooling.
- A high-boiling-point oil (400 to 500 °C, or 750 to 930 °F) exhibits a high cooling capacity in the high-temperature region but low cooling capacity below 500 °C (930 °F) due to a reduced duration of nucleate boiling.
- A blend of the low-boiling-point fraction and the high-boiling-point fraction results in better cooling properties through the entire cooling range.

In summary, it was recommended that petroleum oil fractions should be blended to obtain the desired overall cooling properties. This procedure was reportedly how Yokota made the blends for the basestock study discussed previously (Ref 185).

Quench Oil Classification. Quench oils are selected on the basis of their ability to mediate heat transfer during the quench and are marketed based on relative quench speeds and temperature range of use. Classification designations include conventional (slow or cold), accelerated (fast), and martempering (hot) oils. Although there are other classifications, such as superfast (Ref 187) and water emulsifiable, these three general classifications are the most commonly encountered.

Martempering or hot quenching oils are used at temperatures between 95 and 230 °C (200 and 450 °F). They are usually formulated from solvent-refined mineral oils with a high paraffinic fraction to optimize thermal and oxidative stability. Stability is also enhanced by the addition of antioxidants. Typical temperature ranges for commercially available martempering oils are shown in Table 23. Because martempering oils are used at relatively high temperatures, a protective, nonoxidizing atmosphere such as an exothermic gas or nitrogen is often used, which reduces susceptibility to oxidation and permits use temperatures much closer to the flash point than when used under open-air conditions (Ref 188). Nonaccelerated and accelerated martempering oils are available.

Conventional quenching oils (also designated as cold, normal, or slow) are typically petroleum oils, which may contain antioxidants to reduce the rate of oxidative and thermal degradation. Usually, they are formulated with highly refined paraffinic oils (Ref 189). Most of these

oils have viscosities in the range of 200 to 110 SUS at 40 °C (100 °F). Conventional quenching oils do not contain additives to increase the cooling rate, but they typically do contain additives such as corrosion inhibitors and antioxidants. These oils are used for quenching highly alloyed steels such as AISI 4340 and tool steels (Ref 182, 189). Medium-speed quench oils are also available and are used for quenching medium- to high-hardenability steels.

Accelerated (fast) quenching oils are usually formulated from a petroleum oil and contain one or more rate-accelerating additives. These oils are formulated to exhibit higher cooling rates during high-temperature cooling while maintaining the slower cooling rates during lower-temperature cooling (Ref 189). Viscosities may vary from 50 to 100 SUS at 40 °C (100 °F). Accelerated quench oils are used to quench low-hardenability steels, carburized and carbonitrided components, and medium-hardenability steels with large cross-sectional sizes (Ref 182).

Wang et al. have developed superfaster quenching oils for quenching steels such as 40Cr, 40MnB, 20CrMnTi, and GCr15 to achieve higher hardness and greater depth of hardening (Ref 187). Typically, the basestocks to formulate superfaster oils are highly purified, low boiling, and narrowly fractionalized. In addition, they contain additives such as high-ash petroleum phosphonate, oil-soluble polymers, surfactants, detergents, and antioxidants. Prior to the development of these specialized accelerated oils, diesel oils, transformer oils, and machine oils were used.

A general class of emulsifiable quench oils is specially formulated to enhance removal during water washing of components, which facilitates elimination of vapor degreasing. However, because of their emulsifiable properties, they are susceptible to water contamination, which may lead to increased distortion or soft spots on the component (Ref 189).

Effect of Surface Pressure. Although it is most common to use high-pressure gas quenching with vacuum furnace operations, there are some cases where greater quench severity is necessary. In such cases, such as for thick sections or massive parts, a specially formulated petroleum oil may be used as the quenchant to provide the desired hardness and distortion control (Ref 190).

Asada and Ogino studied the effect of cooling behavior of petroleum oils and found that as the surface pressure is reduced, the duration of the film-boiling stage increases, the Leidenfrost temperature is decreased, and the convective cooling start temperature is decreased (Ref 191). Cooling curves illustrating this effect are shown in Fig. 77. Thus, by varying surface pressure, it is possible to generate a wide range of cooling behaviors from a single oil composition.

Oxidative Stability. The effect of petroleum oil oxidation throughout an accelerated aging test is monitored by measuring acid number, viscosity change, and coke formation periodically throughout the test. Initially, it was found that there was a substantial increase in these

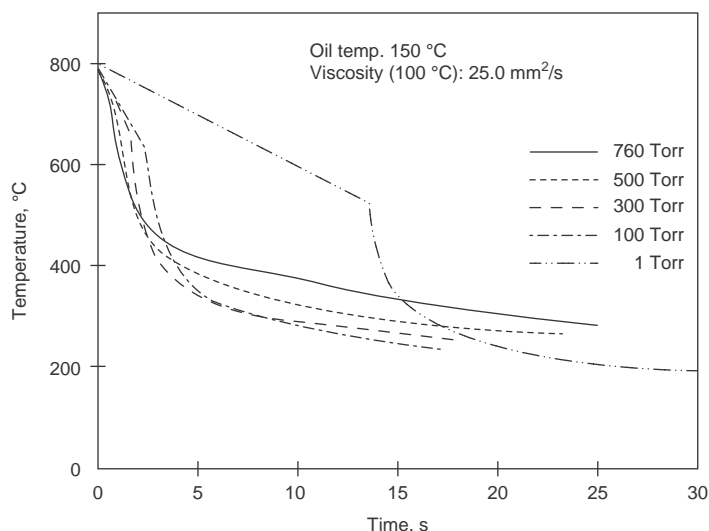


Fig. 77 Cooling curves of a martempering oil under reduced pressure, which were obtained using the JIS K2242:1980 silver probe

variables, and cooling capacity increased due to the initial formation of oxygen-containing surface-active compounds that facilitate the interfacial wetting process relative to unoxidized oil. After a short period of time, the acid number, viscosity, and coking potential stabilized. At some critical period of time, these properties increased exponentially, with a corresponding decrease in cooling capacity. Also, during this period, large amounts of sediment were formed due to polymerization of the hydrocarbon residues (Ref 192). These results are consistent with the four steps involved in oil oxidation reported by Cherkanskii and Sheindlin (Ref 193):

1. The first step involves the thermal decomposition of unsaturated and unstable paraffinic and naphthenic hydrocarbons, as indicated by soot deposition (the end product of hydrocarbon decomposition) and a slight improvement in surface brightness. The improvement in as-quenched brightness was reported to be due to the removal of oxygen and moisture dissolved in the oil. This is the chain initiation step.
2. The second step involves further hydrocarbon decomposition and the formation of peroxides, which is promoted by the presence of moisture in the protective atmosphere or by oxygen from contact with air. This is the so-called chain propagation step.
3. The final step is the chain termination step, which involves various reactions with peroxides and reactive hydrocarbon intermediates. This leads to an exponential fluid viscosity increase; alcohols, ketones, and aldehydes; in addition to carboxylic acid formation that increases the acid number (Ref 194); and particularly undesirable sediment, sludge, and varnish formation. Research has shown that oxidation by-products with molecular weights greater than 50 to 1000 are insoluble in the oil (Ref 195, 196).

Reaction Family	Prototypical Reaction
Initiation Reactions	
Primary initiation	$RH + O_2 \rightarrow R\cdot + HOO\cdot$
Bond fission	$ROOH \rightarrow RO\cdot + HO\cdot$
Hydroperoxide decomposition	$RH + R'OOH \rightarrow R\cdot + R'O\cdot + H_2O$
Propagation Reactions	
Oxygen addition	$R\cdot + O_2 \rightarrow ROO\cdot$
Alkoxy β -Scission	$RO\cdot \rightarrow R'C(O)H + R''\cdot$
β -Scission	$\cdot ROOH \rightarrow RO + \cdot OH$
Hydrogen transfer	$ROO\cdot + R'H \rightarrow ROOH + R'\cdot$
Termination Reactions	
Disproportionation	A. $2 ROO\cdot \rightarrow RO + ROH + O_2$
	B. $2 ROO\cdot \rightarrow 2 RO + O_2$
Recombination	$2 R\cdot \rightarrow RR$
Other Reactions	
Baeyer-Villiger reaction	$RCOH + R'COOOH \rightarrow 2 R'COOH$

Fig. 78 Schematic summary of general free-radical degradation mechanisms of thermal-oxidative degradation of petroleum oil quenchants. Source: Ref 197

A general summary of the mechanism of petroleum oil oxidation is provided in Fig. 78 (Ref 197). These mechanisms illustrate how carboxylic acids form by initial oxidation, and it is important to understand that these by-products are more surface active than the unoxidized oil, which contributes to faster initial cooling rates. Chain termination, for example, by recombination, explains the exponential viscosity increase observed near the end of the useful life of the quench oil. The reader is referred to Ref 194 and 197, 198, 199, 200 to 201 for additional in-depth information on thermal-oxidative degradation and its impact on physical properties of petroleum oils.

Petroleum oils are formulated with antioxidants to provide the necessary improvement in oxidative stability. Examples of antioxidants that have

been reported for this purpose include phenolic antioxidants such as ionol (Ref 183, 202), cresol (Ref 203), butylated hydroxyl toluene (Ref 204), amine-containing antioxidants such as phenyl- α -naththylamine, and amine/phenolic blends.

The impact of oxidation of a hot oil at 200 °C (390 °F) on cooling time-temperature curves superimposed on a TTT diagram for a bearing steel is shown in Fig. 79 (Ref 188). In this example, comparison of the cooling curves shows increasing cooling rates in the high-temperature cooling region with shorter film-boiling duration as the hot oil oxidizes during use, which means that pearlite is increasingly less likely to form as the oil ages. However, at the same time, the potential for bainite formation for this steel increases.

There are at least four potential reasons for petroleum oil oxidation with respect to time that will result in limiting the lifetime of the bath:

- At use temperatures below 57 °C (135 °F), the oxidation rates of inhibited petroleum oils are relatively slow. However, at temperatures above approximately 63 °C (145 °F), increased oil oxidation rates will result. It is a common assumption that oil

oxidation rates increase with every 10 °C (18 °F) increase in bath temperature, according to the Arrhenius rate rule (Ref 205).

- The antioxidant may be dragged out on the parts upon removal from the quench. This problem may be addressed by readdition of the antioxidant to the tank at appropriate intervals (Ref 206). However, this should only be done in conjunction with the quench oil supplier.
- The antioxidant may be consumed by chain-transfer reactions as part of the oil-stabilizing process. In this case, the best recourse is to replace the oil.
- Contamination by transition metal ions (Ref 207) or water will catalyze the oil oxidation process, as shown in Table 35 for an oxidatively inhibited petroleum oil formulation similar to a quenchant (Ref 208). However, when both water and the transition metal were present, the oil degradation rate was ten times greater with iron and thirty times greater with copper.

Determination of the optimum use temperature for a hot oil bath is a compromise between

the ability to achieve the desired hardness, distortion control, and elimination of cracking with the reduction of lifetime of the oil with increasing bath temperature. This is illustrated in Fig. 80, which indicates that the required hardness is not obtained at bath temperatures greater than 175 °C (350 °F), but acceptable distortion and residual stress is obtained at 150 °C (300 °F), as shown by the increment designated “AB” (Ref 209). Temperature control of the bath is critical to the success of the

Table 35 Effect of water and catalysts on oil oxidation

Catalyst	Water	Running time, h	Final acid number Mg KOH/g(a)
None	No	3500	0.17
None	Yes	3500	0.9
Iron	No	3500	0.65
Iron	Yes	400	8.1
Copper	No	3000	0.89
Copper	Yes	100	11.2

Note: Tests were run at 95 °C (200 °F) on a 150 SUS turbine-grade oil according to ASTM D943 test procedure. (a) Acid number is defined as the number of milligrams of potassium hydroxide needed to neutralize free fatty acids present in 1 g of the oil.

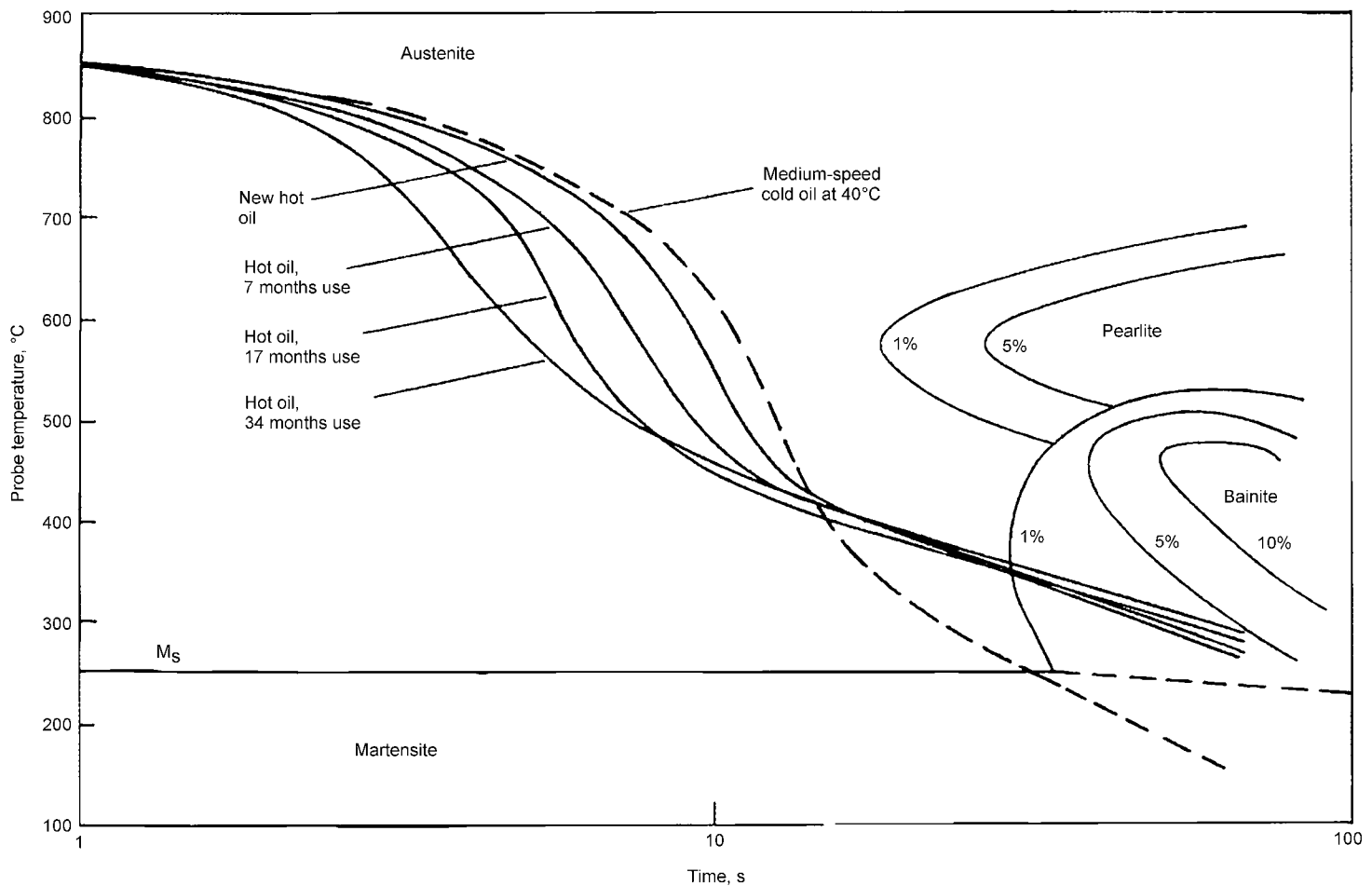


Fig. 79 Cooling time-temperature curves of a hot oil quenchant at 200 °C (390 °F) after increasing use superimposed on a time-temperature transformation curve for a bearing steel

quenching operation, and to achieve optimal results, commercial practice typically requires that the bath temperature be controlled to within $\pm 2.8\text{ }^\circ\text{C}$ ($5\text{ }^\circ\text{F}$). This is accomplished by mechanical agitation and an effective cooling system.

Cooling Rate Acceleration. In the previous discussion, it was shown that the viscosity of a petroleum oil is dependent on composition

and that cooling rates increase with decreasing viscosity. Also, the composition of a petroleum oil typically varies with the refinery, age of the refinery, different refinery practices, and variation of the feedstock. However, the preferred basestock for quenchant formulation is a solvent-refined petroleum oil, and for formulation of an accelerated oil quenchant, a basestock with a viscosity in the range of 17 to 24 cSt

at $40\text{ }^\circ\text{C}$ ($100\text{ }^\circ\text{F}$) is generally used. With a solvent-refined petroleum oil, this viscosity range provides the best compromise between low viscosity and acceptable flash point. One of the problems with lower-viscosity (meaning lower molecular weight and more volatile) base-stocks is that the film-boiling region of cooling increases as the viscosity (molecular weight) of the basestock decreases, as shown in Fig. 81 (Ref 210).

It is important to understand that although heat transfer, and therefore cooling rate, increases with decreasing viscosity, flash points decrease as well. The flash point of the oil should be at least $50\text{ }^\circ\text{C}$ ($90\text{ }^\circ\text{F}$) above the operating temperature of the quenching system. Thus, a compromise is necessary to provide acceptable margins for fire safety and, at the same time, yield the fastest cooling rates possible (Ref 204).

One type of additive that has been used to formulate accelerated quench oils is bitumen. *Bitumen* is a geological term for naturally occurring deposits of the solid or semisolid form of petroleum, specified by their viscosity at a standard temperature (typically $60\text{ }^\circ\text{C}$, or $140\text{ }^\circ\text{F}$). Some bitumens are derived from petroleum processing and contain very high-molecular-weight polar components: asphaltenes. Asphaltenes are highly variable complex structures composed of aliphatic and aromatic moieties, including heteroatoms (N,S,O). One proposed structure is shown in Fig. 82. Liquid asphalts (bitumens) are prepared by the addition of a relatively nonvolatile petroleum oil or by the addition of vegetable oils. The presence of bitumen in a quench oil has been proposed to provide cooling rate acceleration by adsorption to the hot steel surface, thus providing nucleation sites to facilitate bubble formation and

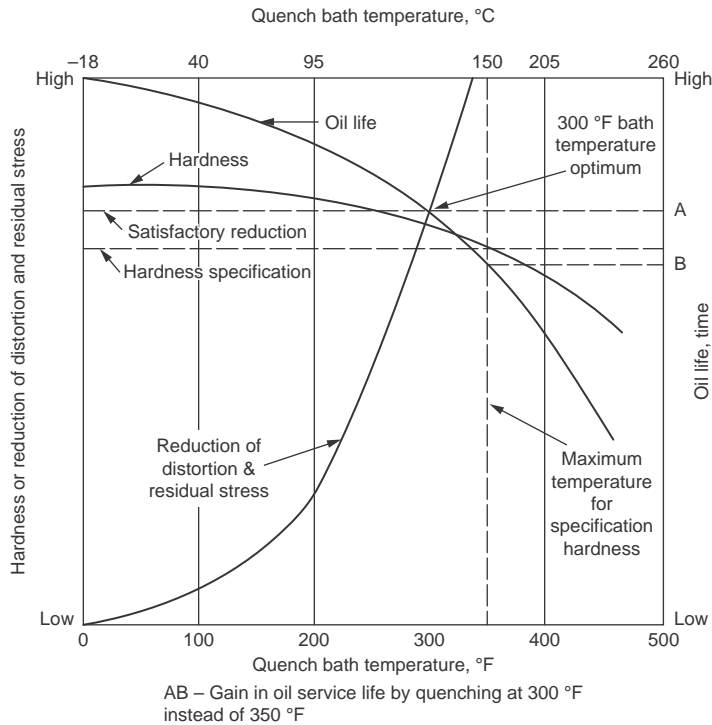


Fig. 80 Determination of optimum hot oil quenching temperature. Source: Ref 209

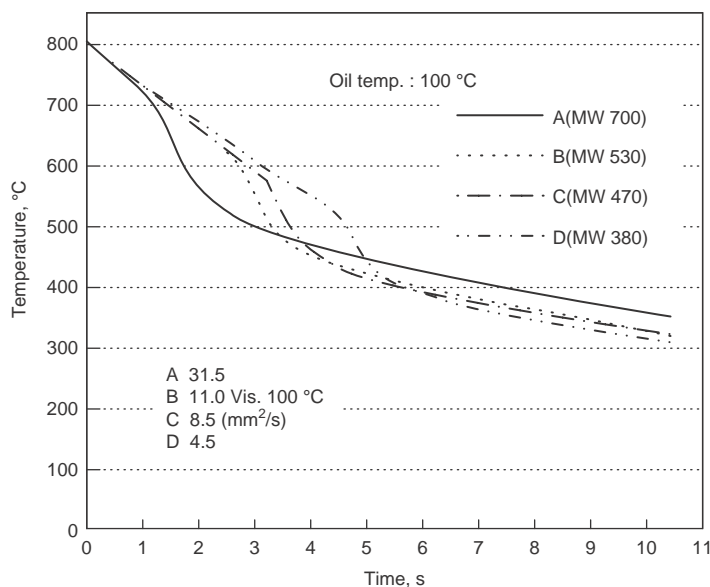


Fig. 81 Effect of molecular weight (MW) and viscosity of petroleum oil basestock on cooling curve behavior. Source: Ref 210

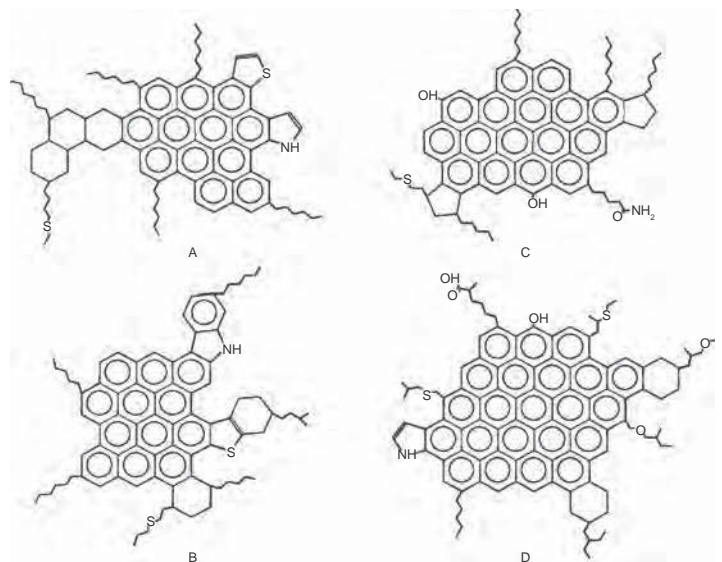


Fig. 82 Hypothetical molecular structures of asphaltenes. Asphaltene structure may vary greatly depending on the source and location. Source: Ref 211

nucleate-boiling heat transfer. Unfortunately, the original bituminous additives were not thermally stable and also were known to provide a "dirty" quench (Ref 204).

Tkachuk et al. showed that in addition to the composition of the basestock used to formulate a quench oil, faster cooling rates could be obtained by the addition of a number of additives, including calcium sulfonates (PMS-A), sodium sulfonates (NS-480) of petroleum, calcium naphthenate, and alkenyl succinimide (Ref 184, 212). Of these series of additives, the most effective was the highest molecular weight, alkenyl succinimide. Less effective were the calcium and sodium sulfonates, and the relatively low-molecular-weight calcium naphthenate actually increased the film-boiling region during cooling. As a result of this work, it was demonstrated that both viscosity and wettability were important for optimizing a quench oil formulation to maximize heat transfer, and the following conclusions were drawn:

- The cooling capacity of quench oils may be substantially increased by the optimal selection and concentration of various additives.
- High-molecular-weight, oil-soluble, surface-active compounds are effective additives to provide cooling rate acceleration in petroleum-based quench oils.
- There is a correlation between cooling rate and contact angle (wettability) of petroleum oil-based quenchants containing additives, as shown in Fig. 83 (Ref 184).

Allen et al. used a 120 by 120 by 20 mm (5 by 5 by 0.8 in.) thick austenitic stainless steel probe with a thermocouple located at the geometric center to study the effect of the addition of sodium sulfonate and another unidentified ashless additive as a cooling rate accelerator to a base oil (Ref 213). They examined the effect of these two additives at 1.5 and 3% on four parameters:

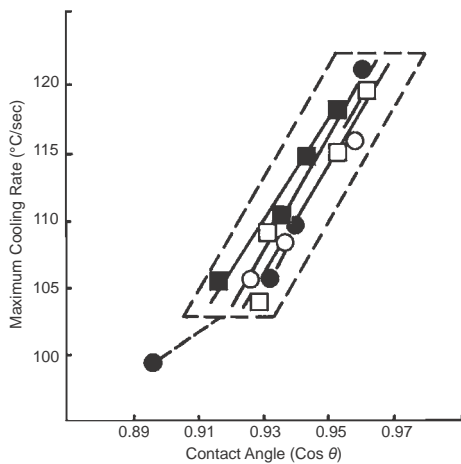


Fig. 83 Correlation between wettability and cooling rate for petroleum-based quench oils containing additives. Source: Ref 180

- Duration of the vapor blanket stage
- Temperature at which the vapor blanket breaks
- Maximum surface heat-transfer coefficient (nucleate boiling)
- Temperature at which the maximum heat-transfer coefficient occurs

The plate probe was heated to 850 °C (1560 °F) and then quenched into a bath of the experimental oil at 20 ± 1 °C (70 ± 2 °F). The results of this study, summarized in Table 36, showed that the addition of sodium sulfonate to the base oil exhibited higher surface heat-transfer coefficients than did the ashless cooling rate accelerator. However, ashless additive increased the temperature where the maximum cooling rate occurred, and the sodium sulfonate decreased it. It was observed that both additives increased the amount of oil vapor evolved during nucleate boiling. Although the ashless additive increased the oil viscosity, sodium sulfonate exhibited no significant effect. Both additives decreased the length of the vapor blanket phase, which means that these oils will permit quenching of thicker section sizes (Ref 213).

Although petroleum sulfonates have been the most common rate-accelerating additive, they do possess two important problems: relatively poor thermal stability and the presence of up to 5% water. Currently, additive companies have developed specialized sulfonates with improved thermal stability and acceptable levels of residual water content (Ref 204).

Matijević et al. performed a more recent study, with objectives analogous to those of Tkachuk, to evaluate different basestocks of similar viscosity, including those designated as base oil paraffinic, base oil naphthenic, and base oil paraffinic with two additives: calcium alkenyl phenate sulfide (Hitec 579) and calcium, sodium sulfonate (Lz 5941S). Their results also showed that cooling characteristics

depend on both the composition and type of base oil and the proper selection and concentration of the rate-accelerating additive (Ref 214).

Another more recently used class of rate-accelerating additives is low-molecular-weight hydrocarbon polymers such as polyisobutylenes (Ref 204). Typically, the degree of rate acceleration and decrease in duration of the vapor blanket stage increases with both the concentration and molecular weight of the additive. This was confirmed by Asada and Fukuhara (Ref 210).

Bright Quenching Oils. There is often a variation in the appearance of the surface steel after oil quenching, particularly after thermochemical treatment, which varies with oxidation and water contamination of the petroleum quench oils. Staining of normally bright surfaces of parts may be caused by the presence of 0.2%, or less, of sludge deposits in the oil (Ref 215). Landis and Murphy studied the generation of color bodies, which lead to staining of component surfaces (Ref 216). The results of this work showed that these color bodies were due to the presence of hydrocarbon oxidation products, aromatics, and sulfur-containing heterocyclic compounds. Although all of these potential components are significant contributors to the presence of color bodies, one of the strongest effects was due to the presence of aromatic sulfur compounds.

Mechanistically, these color bodies are formed by an acid-catalyzed oligomerization of aromatic sulfur compounds and via acid-catalyzed condensation reactions involving hydrocarbon oxidation products that are high in aromatic carbon (Ref 216). Therefore, by the mechanism proposed by Landis and Murphy, sulfur compounds have two functions: they oxidatively generate strong acids that catalyze polymerization and condensation reactions, and aromatic sulfur compounds form oligomeric products due to the presence of strong acids to produce intensely chromophoric molecular structures. One example of a color body that has been isolated is shown in Fig. 84.

Table 36 Effect of the addition of sodium sulfonate and an ashless additive to a base petroleum oil as cooling rate accelerators

Parameter	Oil composition (base oil + cooling rate accelerator)				
	None	Ashless accelerator		Sodium sulfonate	
	...	1.5%	3%	1.5%	3%
Viscosity at 40 °C (100 °F), cSt	32	33	34	36	36
Surface tension, Nm ⁻¹	0.0388	0.0334	0.0326	0.0355	0.0319
No agitation					
Duration of vapor blanket stage, s	36.5	17	16.5	21.5	16.5
Average temperature at end of vapor blanket stage, °C (°F)	600 (1110)	700 (1290)	700 (1290)	650 (1200)	650 (1200)
Mean cooling rate during nucleate boiling and transition stage, °C/s (°F/s)	10.4 (18.7)	10.7 (19.3)	14.7 (26.5)	14.2 (25.6)	20.5 (36.9)
Maximum surface heat-transfer coefficient, Wm ⁻² · K ⁻¹	921	1286	1988	1799	2592
Temperature at which maximum heat-transfer coefficient occurred, °C (°F)	476 (889)	500 (932)	526 (979)	425 (797)	400 (752)
With mild agitation					
Duration of vapor blanket stage, s	36	18.6	17.1	22.6	13.7
Maximum surface heat-transfer coefficient, Wm ⁻² · K ⁻¹	1125	1494	2058	1876	2310
Temperature at which maximum heat-transfer coefficient occurred, °C (°F)	450 (842)	500 (932)	524 (975)	425 (797)	400 (752)

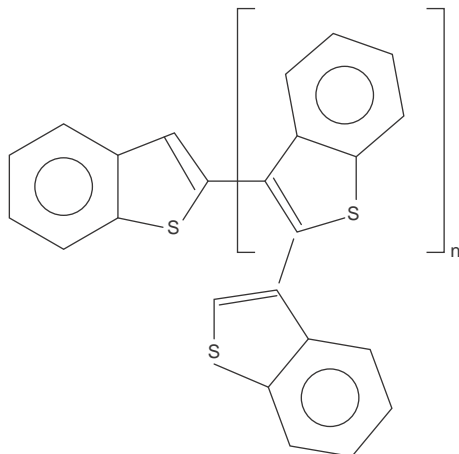


Fig. 84 Example of a color body that is formed in a petroleum oil during oxidation. Chemically, this structure is a low-molecular-weight polymeric (oligomeric) benzothioephene. Source: Ref 216

Various additives that are specific to maintaining a bright finish on as-quenched components are used for the formulation of bright quenching oils. Rudakova et al. reported that the addition of C_{20} and higher synthetic aliphatic carboxylic acids were effective for maintaining a bright as-quenched surface (Ref 217). Petroleum oil quenchants containing synthetic fatty acid still-bottom residues have also been reported to exhibit improved bright quenching properties with improved cooling rates for use in quenching bearing components (Ref 202).

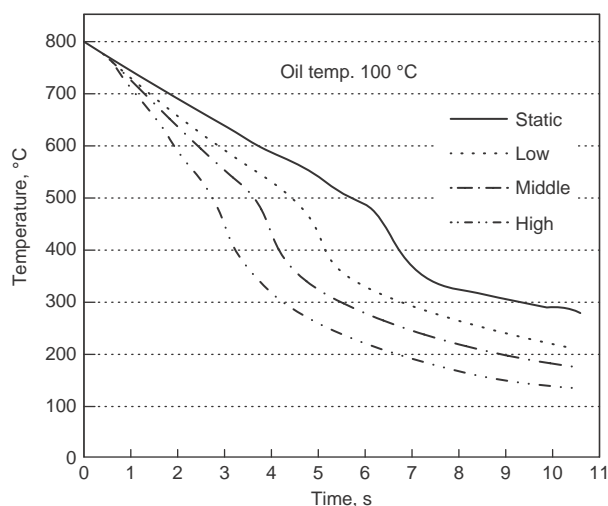
Lu studied the effect of service life on bright quenching oils (Ref 206). It was found that over time, the additive that promoted surface brightness was depleted due to drag-out on the surface of the steel upon removal from the bath. However, periodic readditization of the oil in the tank was an effective means of providing continued brightness protection of the steel surface.

Effect of Bath Temperature and Agitation.

In this article, the importance of uniform flow throughout the quench tank has been emphasized in order to obtain uniform hardening with minimum distortion problems. One of the reasons for this is that uniform flow minimizes stable pockets of film boiling around the cooling metal surface, because the presence of nonuniform film boiling is a principal cause of increased thermal stresses within an as-quenched component (Ref 218). This problem has been shown repeatedly, such as in the work reported by Asada and illustrated in Fig. 85 (Ref 210). This figure shows a strong decrease in the stability of the film-boiling region as agitation is increased.

In another study, Taraba showed the effect of agitation on the cooling behavior of a commercial accelerated oil. In this work, the degree of agitation provided is the amount of torque applied to agitate the quenchant. Although the

Fig. 85 Illustration of the effect of agitation on the cooling behavior of a petroleum oil. The cooling curves were obtained according to JIS K2242:1980 silver probe with a surface thermocouple. The oil temperature was 100°C (212°F).



agitator was capable of torque values ranging from 0 to $4.8 \text{ J} \cdot \text{s}^{-1} \cdot \text{kg}^{-1}$, the torque used in the example shown in Fig. 86 was intermediate at $2.59 \text{ J} \cdot \text{s}^{-1} \cdot \text{kg}^{-1}$. The cooling rate was measured using the ISO 9950 Inconel 600 probe shown in Fig. 24 (Ref 219). These data show that in this system, even a moderate degree of agitation was nearly sufficient to eliminate the vapor blanket formation relative to that observed with no agitation. This example does not show that agitation is necessary but that it should be as uniform as possible around the cooling component(s) throughout the quenching process.

The quench severity of a petroleum oil may be affected by both bath temperature and agitation. To evaluate the impact of agitation on bath temperature and agitation as co-variables, a three-level statistically designed cooling curve analysis experiment was conducted. The experimental variables were quenchant bath temperatures of 43 , 65 , and 88°C (110 , 150 , 190°F); linear, turbulent flow rates of 0 , 15 , and 30 m/min (0 , 50 , and 100 ft/min); and cylindrical stainless steel probe diameters of 12.5 , 25 , 37.5 , and 50 mm (0.5 , 1.0 , 1.5 , and 2.0 in.) with type K thermocouples inserted to the geometric centers. The probe length in each case was four times the diameter. Two petroleum quench oils were evaluated: a conventional (slow oil) and an accelerated (fast) oil. A total of ten experiments for each oil was performed and, after statistical analysis, a series of contour plots were prepared that illustrated the effect of these variables on the maximum cooling rate, cooling rate at 345°C (650°F), Grossmann H -value, and predicted hardness for AISI 1045 and 4140 steels.

The contour plots for the conventional petroleum oil quenchant are shown in Fig. 87, and contour plots for the accelerated petroleum oil are shown in Fig. 88. From these data, several conclusions were drawn:

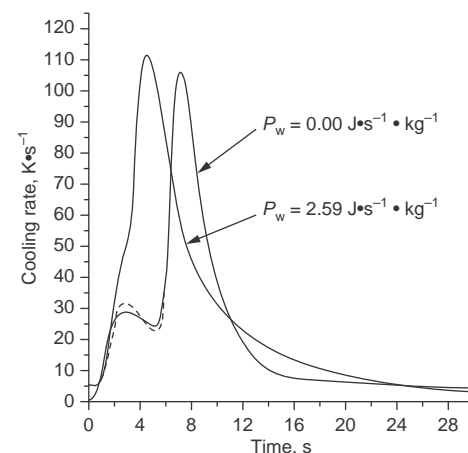


Fig. 86 Cooling rate comparison for an unagitated, accelerated petroleum oil quenchant at 50°C (120°F) with the same oil subjected to an intermediate level of agitation at a $2.59 \text{ J} \cdot \text{s}^{-1} \cdot \text{kg}^{-1}$ torque level

- The maximum cooling rate (CR_{max}) and cooling rate at 650°F (CR_{650}) were essentially independent of bath temperature but were dependent on agitation rate. The effect of agitation rate on CR_{max} and CR_{650} was greater for the conventional, unaccelerated petroleum oil.
- The Grossmann H -values for the conventional oil were independent of bath temperature but dependent on agitation rate. However, the H -values obtained for the accelerated oil were dependent on both bath temperature and agitation rate. The H -values were calculated from cooling rate data according to Ref 55.
- The Rockwell (HRC) values for a low-hardenable carbon steel (AISI 1045) and a medium-hardenability alloy steel (AISI

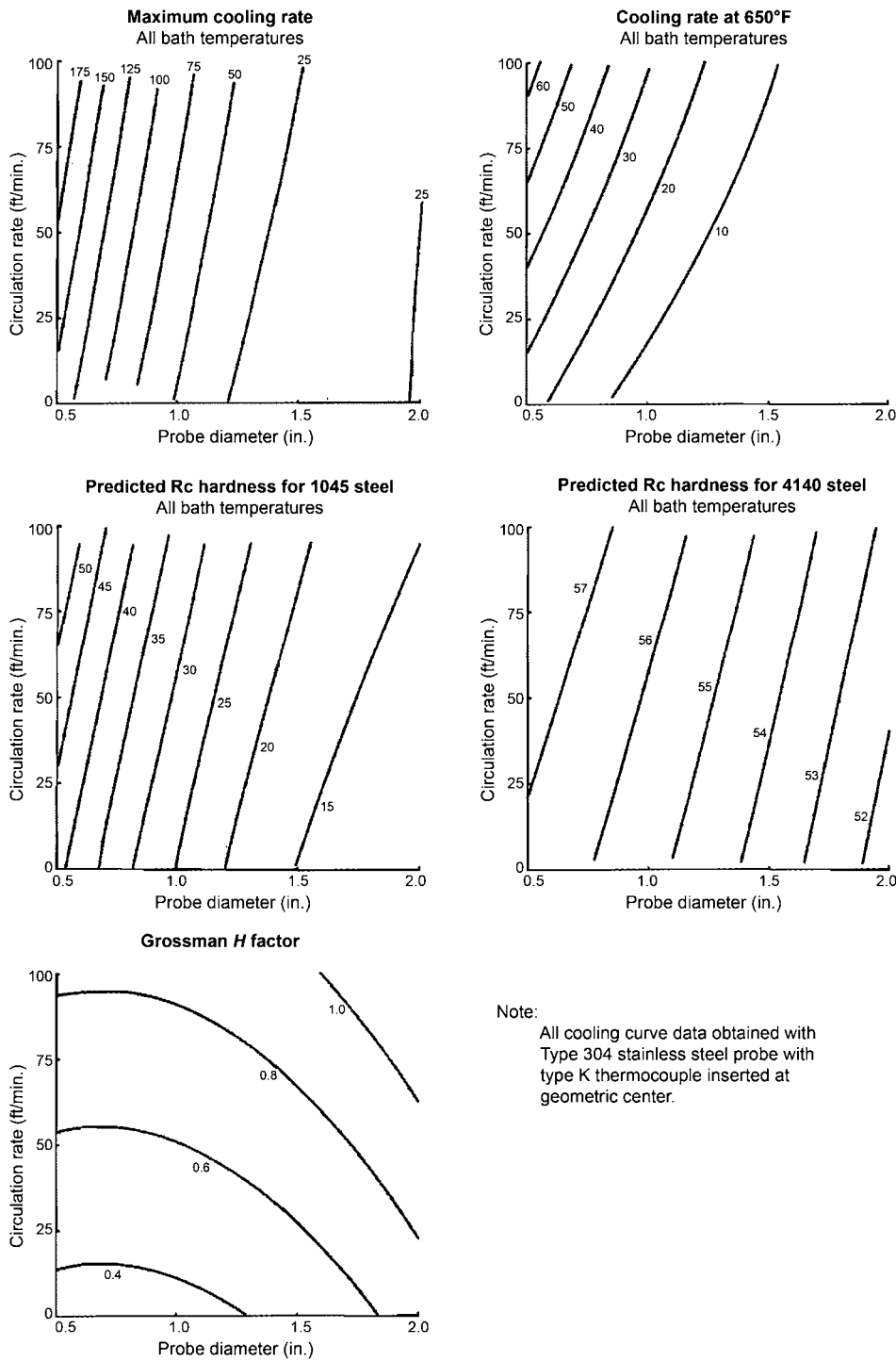


Fig. 87 Contour plots of cooling curve results obtained from statistical analysis of a conventional (slow) petroleum oil quenchant. Source: Ref 78

4140) were calculated according to the procedure described by Bates and Totten (Ref 220). The hardness values obtained for both steel grades were essentially independent of bath temperature for both the conventional and accelerated quench oils. However, the hardness values for both steel grades were dependent on the agitation rate. Not

surprisingly, this dependence was greater for the low-hardenability (1045) carbon steel.

These data show that quench severity provided by a petroleum oil can be significantly affected by the addition of additives and the degree of agitation around the component. Although, in this study, quench severity was

relatively independent of bath temperature, larger increases in bath temperature, such as 21 to 120 °C (70 to 250 °F), have been reported to result in significant changes in quench severity, particularly by producing slightly faster cooling in the film-boiling and nucleate-boiling regions due to the lower oil viscosity at higher temperature (Ref 190). However, with the exception of marquenching oils, typically the optimum quench oil use-temperature range is 50 to 65 °C (120 to 150 °F). In this much more limited temperature range, the expected increase in quench severity due to the decrease in oil viscosity by the increased bath temperature is approximately compensated by the decrease in quench severity expected by the decrease temperature difference between the cooling metal surface and oil temperature (ΔT). Herring reports that most equipment manufacturers design the size of their quench tanks to limit the instantaneous increase in bath temperature to 11 to 22 °C (20 to 40 °F) (Ref 190).

MacKenzie et al. performed a statistical analysis on the effect of a number of variables, including quench bath temperature and a number of contaminants (Ref 221). The results of this analysis showed that increasing the bath temperature had a statistically significant, although relatively small, effect by increasing the maximum cooling rate and increasing the temperature where the maximum cooling rate occurred.

Liscic also studied the effect of bath temperature and agitation on hardening by using a factorial statistical analysis experiment. Figure 89 shows the centerline-hardening curves of a cylindrical 50 mm (2 in.) diameter AISI 4135 test bar after quenching under various conditions (Ref 222). These curves represent the mean values of hardnesses of three measurements. Unagitated quench oil at 70 °C (160 °F) gave a lower hardness than when the same oil was agitated (1.67 m/s, or 5.5 ft/s) at 20 °C (70 °F), as shown by comparing the hardness values at $\frac{1}{2}R$ (curves 5 and 1). The greater the flow rate, the higher the hardness, as observed by comparing curves 1, 2, 3, and 4. Analysis of the data showed that while bath temperature did have an effect, the greatest influence was the agitation of the oil.

Although the effect of quench oil on distortion was not studied in this work, Hampshire has shown that distortion decreased with increasing bath temperature, as shown in Fig. 90 (Ref 188). The primary cause of the distortion was reported to be internal stresses created by non-uniform martensite formation, which were caused by thermal gradients formed by nonuniform flow around the component during the quench.

Table 37 illustrates the effect of agitation on the heat-transfer coefficient of an accelerated (fast) petroleum oil quenchant. These data show that the heat-transfer coefficient approximately triples as the agitation rate is increased from a still quench to 0.76 m/s (2.5 ft/s) (Ref 223). Interestingly, the accelerated quench oil at

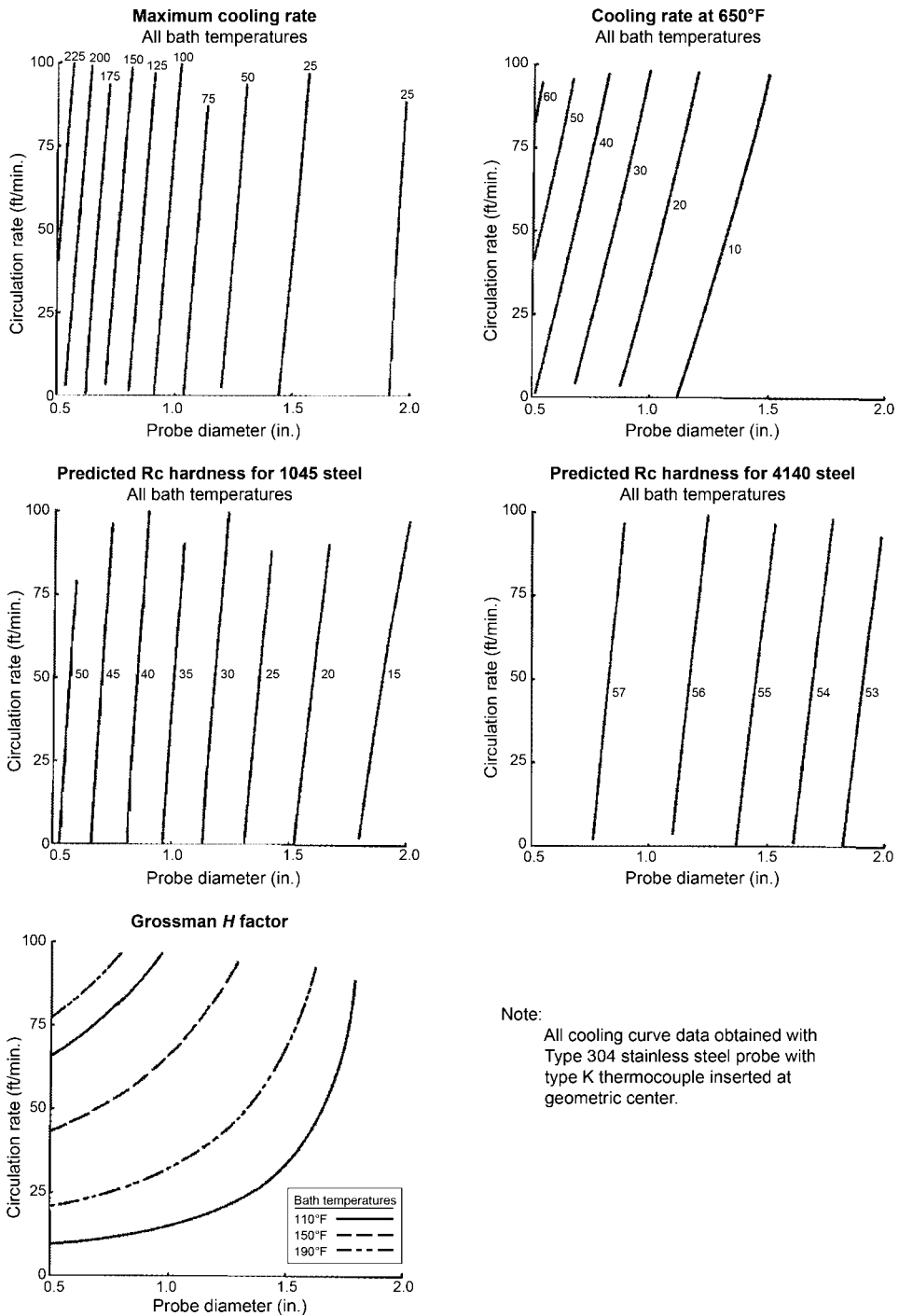


Fig. 88 Contour plots of cooling curve results obtained from statistical analysis of an accelerated (fast) petroleum oil quenchant. Source: Ref 78

60 °C (140 °F) and the martempering oil at 150 °C (300 °F) exhibited an equivalent heat-transfer coefficient at the same agitation rate of 0.51 m/s (1.7 ft/s). These data also indicate how flow variations within a tank, even if agitated, can impact the magnitude of heat transfer at localized positions around a large component or a load of smaller components. This shows

the criticality of the use of appropriate baffling and agitator placement within the quench tank.

Quench Oil Bath Maintenance

It is essential that periodic analysis of quench oils be conducted to ensure optimal

performance. A quench oil testing strategy is discussed that includes various recommended and optional procedures. These recommendations, which are based on ASTM D6710 (Ref 224), will provide the heat treater with more uniform hardening, reduced distortion and cracking, and significant improvements in operational safety.

Routine analyses of a used quenching oil should be performed approximately every three months, and more often if problems are encountered. ASTM D6710 provides a summary of recommended tests to be run. However, it is acknowledged that every test cited in ASTM D6710 will not be run at every test interval. As a minimum, it is recommended that the following tests be run at least every three months following the appropriate ASTM International testing method described previously, or its national standard equivalent:

- Crackle test (water, qualitative)
- Water content (quantitative, only if the crackle test is positive)
- Viscosity at 40 °C (100 °F) by ASTM International test method D445
- Sludge test by an appropriate ASTM International test method
- Although ASTM D3520, which uses plain nickel balls and a 25 °C (80 °F) bath temperature for conventional and fast quenching oils and 120 °C (250 °F) bath temperature for martempering oils, has been recommended in the past, this is not the preferred practice currently. Instead, it is recommended that cooling curve analysis be performed according to ASTM D6200 for the reasons described previously.

Physical Property Characterization

There are numerous specific physical property characterization procedures that may be used. The objective here is to provide representative examples of testing procedures that may be used and to provide some insight into the meaning of the results obtained. Physical property characterization is vitally important in identifying the changes that occur in quench oil during use. However, the methods for physical property characterization do not directly indicate the variations in quench severity caused by these fluid chemistry changes. Therefore, various laboratory tests to quantify quench severity have been developed (see the section “Cooling Curve Characterization” in this article) and are used in conjunction with physical and chemical property characterization.

Sampling. Fluid flow is never uniform in agitated quench tanks. Therefore, significant variations of particulate contaminants, including sludge from oil oxidation and metal scale, may be present. Therefore, it is recommended that the following sampling procedures be followed:

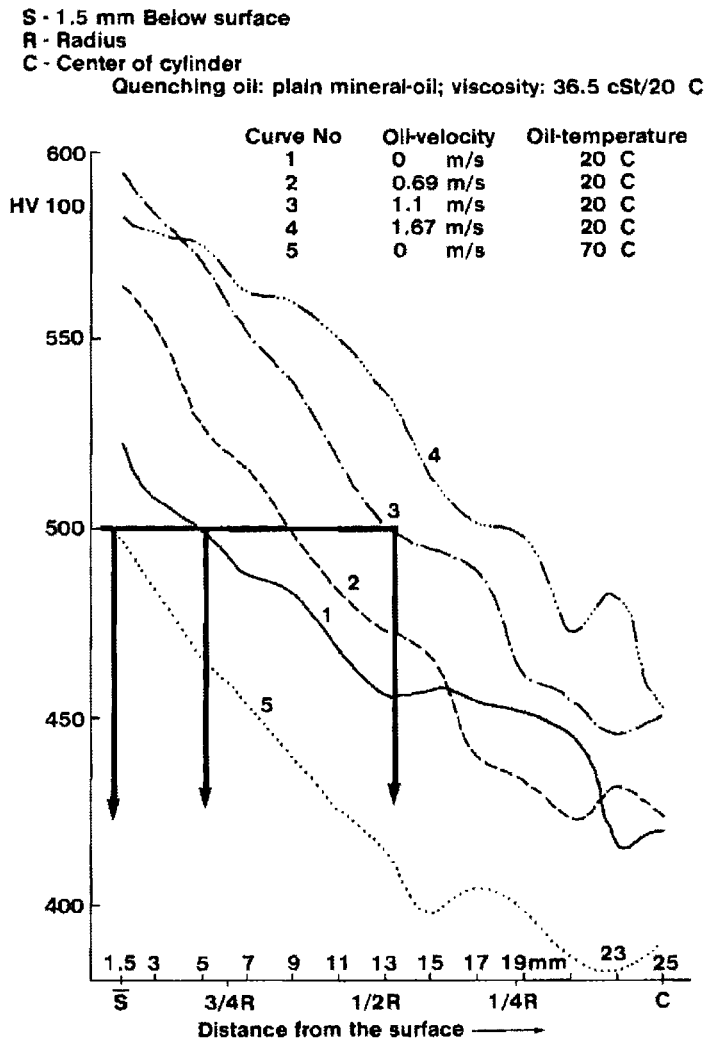


Fig. 89 Effect of agitation rate and bath temperature on through hardening of AISI 4135 steel. Source: Ref 222

- To assure as uniform a sample as possible, the quenchant should be agitated at least 1 h before immediate removal of the sample.
- For each system, the sample should be taken from the same position where maximum flow turbulence occurs, and this position shall be recorded.
- If a sample is taken from a sampling valve, the valve and associated piping should be flushed before the sample is taken.
- If the quench tank or bulk storage tank (or drum) has no agitation, then samples should be taken from the top and the bottom of the tank.
- It is important to determine and report the frequency and amounts of new quenchant additions (make-up), because large additions of new quenchant will impact the test results.
- Samples should be collected in new, clean containers. Food or beverage bottles should not be used because of the danger of contamination and leakage.

Bacon Bomb Fluid-Sampler Thief (Bacon Bomb). It is desirable to remove quenchant

samples from specific locations in the tank, especially at the bottom where periodic testing for the presence of water and sludge is necessary. One common method to obtain such samples is to use a Bacon method to obtain such samples is to use a Bacon bomb, which consists of a metal cylinder tapered at both ends and fitted internally with a plunger valve that opens automatically when the sampler strikes the bottom of the tank (Ref 225, 226). The plunger closes again when the bomb is withdrawn, forming a tight seal. The Bacon bomb may be equipped with extension rods for lowering the vessel into the tank, or it may be attached to a fine steel chain (trigger line) to lower it to the bottom and trigger the bottom valve to fill the vessel. If samples at intermediate depths are desired, the length of the trigger line may be adjusted to open the cylinder at any desired depth. After the vessel is filled, it is withdrawn from the tank, the fill stem at the bottom is opened, and the sample is put into bottles or a beaker for testing. A drawing of a Bacon bomb sampler is shown in Fig. 91.

Viscosity. As discussed previously, the quenching performance of a quench oil is

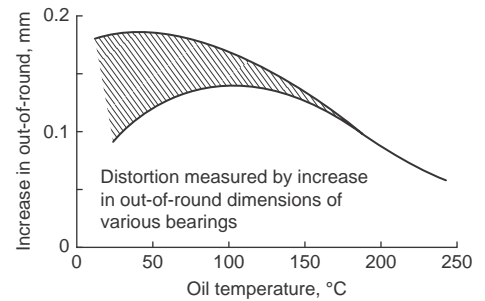


Fig. 90 Distortion as a function of oil temperature. Source: Ref 188

Table 37 Effect of agitation on heat transfer for an accelerated petroleum oil quenchant

Quench oil	Agitation rate		Heat-transfer coefficient, W/m ² · K
	m/s	ft/s	
Conventional oil at 65 °C (150 °F)	0.51	1.7	3000
Fast oil at 60 °C (140 °F)	Still	Still	2000
Fast oil at 60 °C (140 °F)	0.25	0.82	4500
Fast oil at 60 °C (140 °F)	0.51	1.7	5000
Fast oil at 60 °C (140 °F)	0.76	2.5	6500
Marquenching oil at 150 °C (300 °F)	0.51	1.7	5000

Source: Ref 223

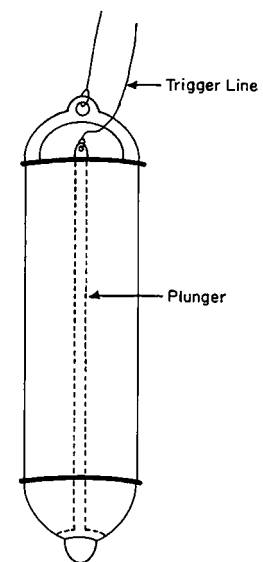


Fig. 91 Drawing of a Bacon bomb sampling vessel. Source: Ref 225

dependent on the viscosity of the oil, which varies with the bath temperature and oil deterioration during use. Kinematic viscosities are most commonly measured at 40 °C (100 °F). The most common method of viscosity determination is ASTM D445 (Ref 227).

Martempering oils are typically used at higher temperatures, and, although the viscosity may change little over a short duration of time, they may become almost solid upon cooling. Thus, the viscosity-temperature relationship (viscosity index) may be critically important with respect to pumpability and flow velocity as well as quench severity. The viscosity index is determined based on kinematic viscosity measurements at 40 and 100 °C (100 and 212 °F) for martempering oils according to ASTM D2270 (Ref 228). (Note: If viscosity in SUS is preferred, kinematic viscosity, or cSt, may be converted to SUS according to ASTM D2161, Ref 229.)

For process monitoring and the potential necessity of troubleshooting, a historical record of viscosity variation in each tank is necessary, such as the chart shown in Fig. 92 (Ref 230).

Water Content. Sources of water contamination of a quench oil may include a leaking heat exchanger, water-cooled bearings, fans, hydraulic fluids, humid environments, or from oil contamination or degradation (Ref 221). Water concentrations as low as 0.1% or less may cause soft spots, uneven hardness, or may cause the quench bath to foam greatly, increasing the potential for oil fires. Foaming potential due to water contamination is illustrated in Fig. 93. If a sufficient amount of water accumulates in the hot quench oil, an explosion caused by steam generation may result. In addition, the presence of water may darken or stain otherwise clean parts (Ref 231). Boyer and Cary have reported that more than half of all problems reported for oil quenching systems are related to water contamination of the oil (Ref 232).

If water-contaminated oil is heated, a crackling or frying sound may be heard. This is the basis of a qualitative field test with an approximate detection limit of 500 ppm (0.05% water), known as the crackle test, for the presence of water in a quench oil (Ref 233). In this test, a small quantity of the oil is heated to a temperature above the boiling point of water (>100 °C, or 212 °F). If water is present in the oil, bubbling will be observed or a crackling sound will be heard. However, water will only crackle if it is present in quantities greater than the saturation point, at which time it may be too late for the safety of the quenching system (Ref 233). In addition to being only qualitative, the crackle test is subject to false positives due to the presence of volatile solvents and gases, and the method does not measure chemically dissolved water. Nevertheless, this test does have limited utility as a rapid preliminary screening test for free and emulsified water.

The following is the test procedure for performing the crackle test (Fig. 94) (Ref 233):

1. Heat a hot plate to 160 °C (320 °F).
2. Thoroughly mix (violently agitate) the sample to assure a homogeneous suspension of the water in the oil.
3. Using a clean eye dropper, place one drop of oil on the heated hot plate and observe for:

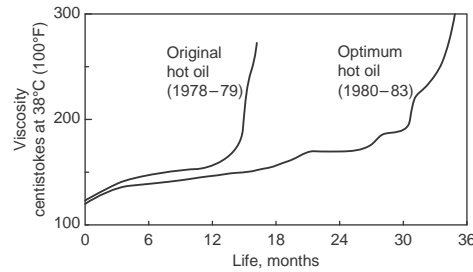


Fig. 92 Viscosity of two martempering oils as a function of time in use. Variations such as these may be observed from oil-to-oil and tank-to-tank. Source: Ref 188

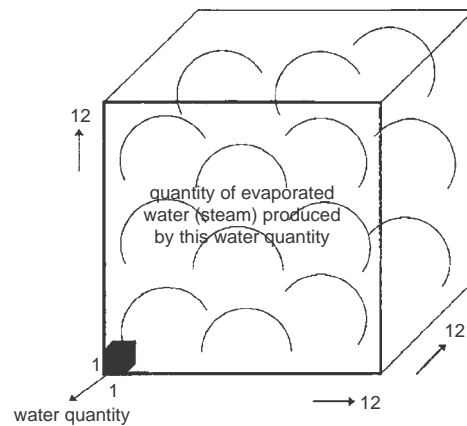


Fig. 93 Volumetric expansion of 1 mL of liquid water into 1700 mL of water vapor. This figure illustrates how small quantities of water contaminants may produce potentially very hazardous foaming in an oil quench system. Courtesy of H. Beitz, Petrofer Chemie, Hildesheim, Germany

- a. If there is no crackling sound or vapor bubble formation, then no free or emulsified water is present.
- b. If very small bubbles (0.5 mm, or 0.02 in.) are produced but disappear quickly, approximately 0.05 to 0.10% water is present.
- c. If the bubble size is approximately 2 mm (0.08 in.) and the bubbles concentrate at the center of the oil spot and then disappear, 0.1 to 0.2% water is present.
- d. If the water concentration is greater than 0.2%, then the bubbles may start out at approximately 2 to 3 mm (0.08 to 0.12 in.) initially and then grow to 4 mm (0.16 in.), with the process repeating once or twice. Higher water levels may result in violent bubbling, and a crackling sound may be heard.

An even simpler, but less quantitative, alternative method for conducting the crackle test is to heat a test tube that is one-third full of the quench oil to be tested. If an audible crackling sound occurs before the oil smokes, there is water present in the oil (Ref 215).

The most common laboratory test for water contamination below 1000 mg/kg (0.1%) in a

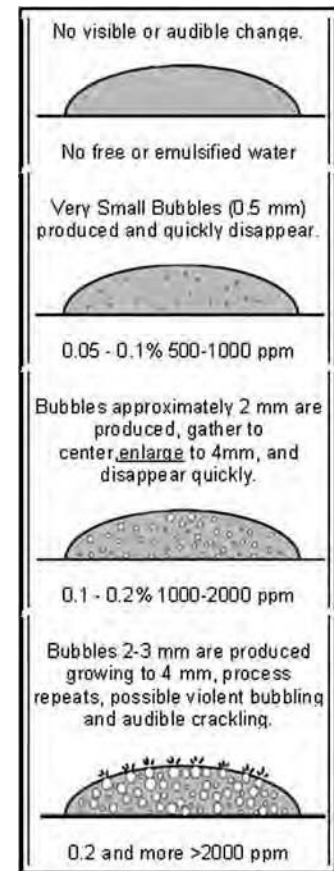


Fig. 94 Illustration of the effect of water content on visual appearance of bubble formation in the crackle test. Courtesy of Noria Corporation

quench oil is the Karl Fisher analysis (ASTM D6304) (Ref 234). This test uses the reaction of water with a Karl Fisher chemical reagent as its basis and a coulometric endpoint as the measurement. Higher water contents may be quantified by a distillation test method (ASTM D95) (Ref 235).

Flash Point. The flash point is the temperature where the oil, in equilibrium with its vapor, produces a gas that is ignitable but does not continue to burn when exposed to a spark or flame source. There are two types of flash point values that may be determined: closed cup or open cup. In the closed-cup measurement, the liquid and vapor are heated in a closed system. Traces of low-boiling contaminants may concentrate in the vapor phase, resulting in a relatively low value. When conducting the open-cup flash point, the relatively low-boiling by-products are lost during heating and have less impact on the final value. The most common open-cup flash point procedure is the Cleveland open-cup procedure described in ASTM D92 (Ref 236). The minimum open-cup flash point of an oil in an open system with no protective atmosphere should be at least 90 °C (160 °F) above the oil temperature being used. In closed systems where a protective atmosphere is used,

the minimum open-cup flash point should be at least 35 °C (65 °F) greater than the actual use temperature (Ref 224).

Acid Number. As a quench oil degrades, it forms carboxylic acids and ester by-products. These by-products may significantly affect the viscosity and viscosity-temperature properties of the quench oil and therefore its quench severity. Carboxylic acids may also act as wetting agents and increase the quench rate by increasing the wettability of the quench oil on the metal surface.

The amount of these by-products may be determined by chemical analysis. The most common method is the acid number. Because fresh oil may be alkaline or acidic, depending on the additives present, the absolute value of the acid number itself is not indicative of the quality. However, changes from the initial acid number of the fresh oil may be indicative of the degree of oxidation that has occurred, and increasing acid numbers over time indicate increased levels of by-product formation and therefore degradation.

The acid number test (ASTM D664, Ref 237, or D974, Ref 238) is conducted by first dissolving the quench oil in a solvent mixture of toluene and isopropanol to which has been added a small amount of water standard solution of potassium hydroxide (KOH). This is known as the acid number (AN) and is reported as milligrams of KOH per gram of sample (mg/g). The quench oil supplier will recommend a maximum value for a used quench oil. In the absence of such a value, ASTM D6710 recommends that the AN not exceed 2.00 mg KOH/g for a used quench oil (Ref 224).

Oil oxidation may also be monitored and quantified, even in the presence of additives, by infrared (IR) spectroscopy. Figure 95 illustrates the use of IR spectral analysis to monitor changes that occur after oil degradation. Mang and Jünemann monitored the IR stretching vibrations of C=O at 1710 cm^{-1} for carboxylic acids contained in an oxidized petroleum oil (Ref 239). Infrared analysis has been used to identify and quantify other carbonyl-containing compounds, including (Ref 224):

- Metal carboxylate salts: 1600 and 1400 cm^{-1}
- Carboxylic acids: 1710 cm^{-1}
- Metal sulfates: 1100 and 1600 cm^{-1}
- Esters: 1270 and 1735 cm^{-1}

Saponification. Quench oil degradation may produce both carboxylic acid and ester by-products. The acid number quantifies the amount of acidic by-products, and the saponification number is a quantitative measure of esters arising from oxidation and also fatty esters that may be used as additives in the quench oil. The saponification number is determined according to ASTM D94 (Ref 240). It involves heating a sample of the oil with a known amount of a basic reagent and measuring the amount of reagent consumed. Because some quench oils are formulated with components that also have saponification numbers, it

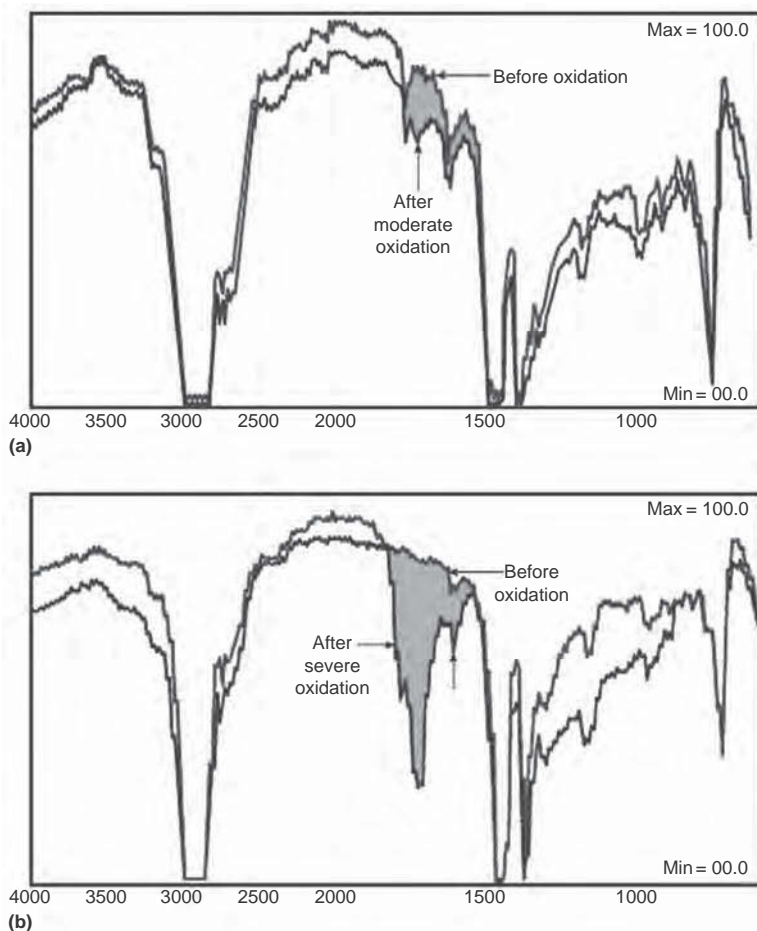


Fig. 95 Illustration of the use of infrared spectroscopy to quantitatively assess oxidative degradation of a quench oil. (a) New vs. moderately degraded quench oil. (b) New vs. severely degraded quench oil

is important not to measure an absolute value but to monitor changes over time. An increase in both the acid number and saponification number indicates an increased propensity for sludge formation. If the results of other tests are satisfactory, then saponification numbers below 3 mg KOH/g of oil may be acceptable (Ref 224).

Sludge Formation. One of the greatest problems encountered with quench oils is sludge formation. Although the various analyses given previously may indicate that a quench oil may be used, the presence of sludge may still be sufficient to cause nonuniform heat transfer, increased thermal gradients, and increased cracking and distortion. Sludge may also plug filters and foul heat-exchanger surfaces. The loss of heat-exchanger efficiency may cause overheating, excessive foaming, and possible fires.

Sludge formation is caused by oxidation of the quench oil. The oxidation reactions lead to polymerized and cross-linked molecules that are insoluble in the oil. The relative amount of sludge present in a quench oil may be quantified by the precipitation number (ASTM D91, Ref 241), which is determined by the addition

of naphtha to the oil and determining the precipitate volume after centrifuging. An alternative test that may be used is ASTM D2273 (Ref 242). Besides oil oxidation, other contributors to sludge formation include dirt, carbon residue formation, and soot from the heat treating furnace, especially if high carbon potentials are used or if the atmosphere is not in control (Ref 221, 224). It is important to maintain particle sizes in the quench oil to <1 μm to optimize quenching performance (Ref 243).

The relative propensity of sludge formation of new and used oil may be compared, providing an estimate of remaining lifetime. Experimental procedures that may be used include the Conradson carbon number (ASTM D189, Ref 244), the hot-panel coker test (Ref 245), and the rotary bomb oxidation test (ASTM D943, Ref 246). Typical hot-panel coker test values for quench oils reported by Cochran and Rizvi are 1 to 2 mg deposits for oxidatively stable formulations and 20 to 25 mg deposits for relatively unstable quench oils (Ref 246).

Induction-Coupled Plasma Analysis. When organometallic additives such as metal salts

are used as quench rate accelerators, their potential loss by processes such as degradation and drag-out can be quantified by performing a direct analysis for the metal. One of the most common procedures is induction-coupled plasma spectroscopy.

Cooling Curve Characterization

As noted, tests to determine the physical and chemical properties of a petroleum oil-based quenchant are vitally important in identifying the changes that occur in a quench oil during use. However, because these methods do not directly indicate the variations in quench severity caused by these fluid chemistry changes, various laboratory tests to quantify quench severity have been developed and are used in conjunction with physical and chemical property characterization. These tests include the hot wire test, GM Quenchometer (nickel ball) test, cooling curve analysis, and others. Of these tests, cooling curve analyses are used routinely worldwide as the preferred method for quenchant selection and for monitoring variations in used-quenchant performance. For petroleum oil-based quenchants, ASTM D6200 is recommended (Ref 96) by ASTM D6710. In this section, a number of examples are provided to illustrate the utility of cooling curve analysis for characterization of used quench oils.

Hampshire provided an example of cooling rate variation with increasing time in use. As Fig. 96 shows, maximum cooling rates and the temperature at the maximum cooling rate increase with increasing aging times. Furthermore, film boiling decreased to the point where it could not be seen at the conclusion of the test after 34 months in use (Ref 188, 247). These data suggest that although the oil viscosity was beginning to increase at the conclusion of the test, sufficient quantities of relatively volatile by-products would lead to the increased cooling rates and loss of film-boiling behavior shown. In addition, the polar carboxylic acids that are formed acted as wetting agents to enhance surface wetting of the oil, which also increases cooling rates and serves to reduce the film-boiling behavior.

Hewitt performed a similar study on the effect of increased use times on cooling properties (Fig. 97). In this case, the cooling rate progressively decreased over time. This would appear to be consistent with the drag-out of the cooling rate accelerator during use. Although it is likely that the oil oxidized, which would be expected to produce faster cooling rates, the relative impact of the loss of the cooling rate accelerator during use.

Although it is likely that the oil oxidized, which would be expected to produce faster cooling rates, the relative impact of the loss of the cooling rate accelerator is much greater in this case. The effect of water concentration on a conventional petroleum oil quenchant is shown in Fig. 98 (Ref 249). Increasing concentrations of water produced increasing maximum cooling rates, with a corresponding slight shift in the temperature where the maximum cooling rate appears, most notably at concentrations greater

than 0.01%. However, the opposite effect was obtained for an accelerated quench oil—a cooling rate decrease with increasing water concentrations—as shown in Fig. 99 (Ref 248).

MacKenzie et al. evaluated the effect of various contaminants on cooling curve performance and concluded that (Ref 221):

- The presence of hydraulic fluid, soot, salts, or water as contaminants increases the maximum cooling rate of conventional quench oils.

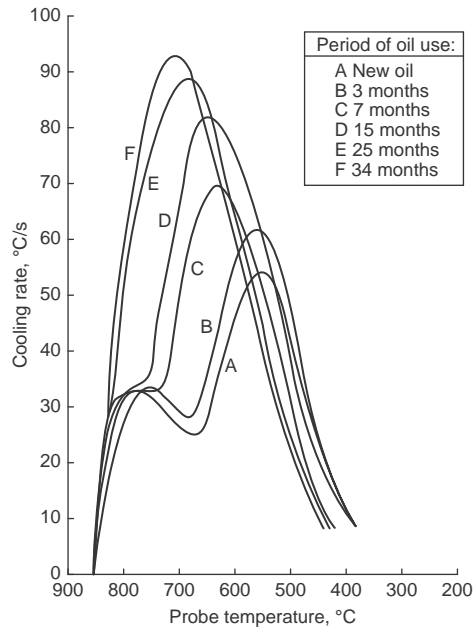


Fig. 96 Cooling rate variation of a martempering oil with increasing time in use. Source: Ref 188

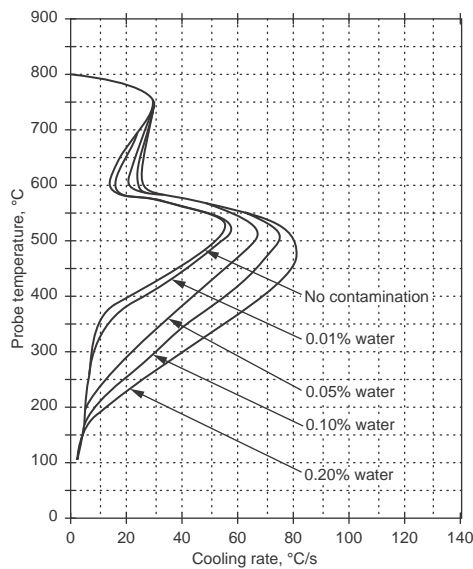


Fig. 98 Effect of increasing water contamination on a conventional quench oil. Source: Ref 249

- Oxidation decreases the maximum cooling rate and the temperature of maximum cooling, which was attributed to increasing viscosity of the quench oil.
- The presence of salt (from salt bath furnaces) and hydraulic fluid increases the maximum cooling rate by different mechanisms. Salt deposition on the cooling metal surface increases the total number of nucleation sites and therefore decreases the average size of the bubbles released during nucleate boiling, thereby increasing heat transfer. The presence of a lower-molecular-weight petroleum-based hydraulic fluid decreases the viscosity of the quench oil and reduces the boiling point of the oil. (An alternative mechanism, although not considered by the authors, is that the antiwear additives in a hydraulic fluid are surface active and therefore act as cooling rate accelerators.)
- The presence of water increases the cooling rate, which may lead to increased distortion. In addition, the presence of water creates nonuniform heat transfer on the cooling metal surface, which is also a major contributor to increased distortion and cracking (Ref 250).

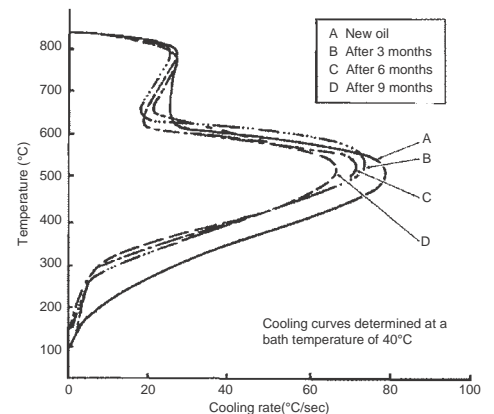


Fig. 97 Variation of cooling rate of an accelerated quench oil with increasing time in use. Source: Ref 248

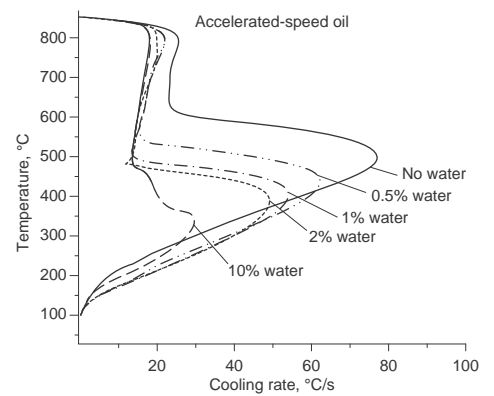


Fig. 99 Effect of increasing water contamination on an accelerated quench oil. Source: Ref 248

Oil Quench System Monitoring

After the oil quenchant is chosen and the quenching system has been established, one needs to establish the H -value of the system, as shown in the previous section on the Rushman approach. Then, the system must be monitored to detect any system changes.

Monitoring for System Changes in Quench Severity. It has been shown that the use of test pins for monitoring furnace quench systems is an effective control tool. The following test pins have been used successfully to monitor 65 °C (150 °F) fast oil quenching systems having H -values of 0.35 to 0.50.

Test Pins. The minimum quantity of test pins required should handle the testing requirements for all furnaces to be monitored for a period of one year. All test pins should be the same size and made from a single heat of steel. Previous experience has shown that for carburizing using integral quench continuous and batch furnaces, 8620H test pins have been used successfully. The pins were made from cold-drawn bar stock with a diameter (depending on availability) in the range of 15.8 to 19.1 mm (0.625 to 0.750 in.). The length was six times the diameter. A shallow groove was added to the end of each pin for attaching the pin by wire to the load. Test pins were hung in all furnace loads in a location where the processing was typical of the parts processed. By using cold-drawn stock, the pins needed only to be cut to length and grooved on a screw machine, thus minimizing the cost per pin.

The aforementioned size range was chosen so that the center core hardness would fall on the steep slope of the Jominy hardenability curve.

Testing Frequency. The testing frequency for each quench system should be as often as necessary to assure that the quenching system is in control. The minimum frequency should be once a week after an initial sampling of at least five test pins per furnace system to establish a mean center core hardness value. For a well-controlled quenching system, the range in center core hardnesses should be within 3 HRC points. The test pins were evaluated as quenched only. No tempering was permitted.

Testing Method. Each test pin was sectioned through the center of the pin, and the center core hardness was checked by Rockwell hardness; the result was recorded for each furnace. Also, the same test pin can be useful in monitoring surface hardness and/or effective case depth if used for carburizing or carbonitriding processes.

Quench Oil Toxicity. One of the most significant problems with petroleum quench oils is their toxicity, particularly their carcinogenic behavior, which is due, at least partly, to the presence of polycyclic aromatic hydrocarbons (PAHs). For example, although not all PAH structures are carcinogenic, others are strongly carcinogenic. Figure 100 illustrates a number of known PAHs with carcinogenic properties that have been found in petroleum oil-base stocks (Ref 251). Denis et al. reported that used

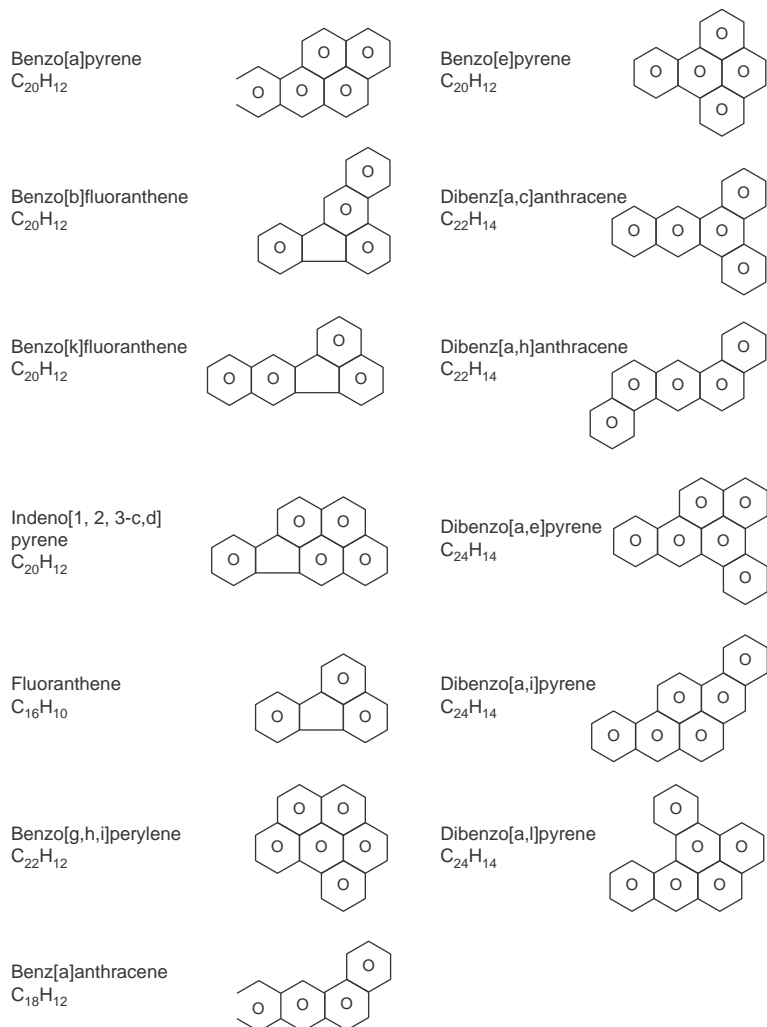


Fig. 100 Molecular structures of toxic polycyclic aromatic hydrocarbons. Source: Ref 251

quench oils contain considerable concentrations of one PAH, benzo[a]pyrene, relative to the oil in the unused condition. Table 38 summarizes these results, which show that PAH content increases substantially for used quench oils relative to fresh, unused oil. This was reportedly due to repeated heating of the quench oil when quenching hot steel, leading to the formation of PAH structures in the oil.

Simpson and Ellwood reported results of experiments conducted to monitor buildup of PAHs in quench oils over time. Quench oils from four different baths at three different heat treating companies were monitored for 6 to 18 months. In this work, the expected increase in PAH content over time was not observed, although the presence of PAHs was observed (Ref 252).

Safe Use of Petroleum Quench Oils (Ref 253)

Perhaps the greatest risk of using petroleum oil-based fluids, which are inherently flammable,

Table 38 Polycyclic aromatic hydrocarbon (PAH) content of several new and used quench oils

PAH	Concentration of PAH in quench oil, ppm	
	New	Used
Benzo[a]pyrene	0.06	34.8
	0.01	13.2
	0.25	1.2
Overall PAH content	0.36	126
	0.06	43.6
	1.55	5.4

Source: Ref 251

in contact with large masses of hot steel (at approximately 850 °C, or 1560 °F) is the obvious fire risk potential to equipment, building, and people. There have been reported cases of explosions, with resulting equipment damage and personal injury. Therefore, heat treatment operations involving an oil quench should involve careful in-depth preplanning, proper system design, and personnel training

with respect to equipment and process procedures and safety. It must be considered that even after implementation of all of these steps, there will be the possibility of failure of one or more of these vitally important links. This is a particularly important area to understand in heat treatment practice, and this section provides an overview of safety problems as they relate to petroleum oil quench tanks.

Herring has summarized some of the most common sources of explosions or fire in production quench systems. Figure 101 is a photo of a hot steel casting just prior to quenching (Ref 254). The sources of explosions or fire include (Ref 254):

- *Water contamination:* As little as 0.1% water may be unsafe.
- *Oil drag-out:* When furnace loads are allowed to drain over the oil prior to removal, there is the potential hazard of incomplete drainage. If there is sufficient residual oil due to drag-out, it may ignite as it passes through the door flame curtain. Also, if the load temperature is greater than the self-ignition temperature of the oil, the residual oil may ignite upon removal of the load from the furnace.
- *Load hangup:* If the load of hot steel seizes in a partially submerged position during transfer, a very dangerous fire may result. This may also occur in an integral quench furnace when a quench elevator door jams. Some aids to the prevention of such fires are careful design of hoists or conveyors used to lower the work load into the quench; periodic inspection of chains, sprockets, and other components that may fail; and the availability of an alternate power supply for use in the event that a power failure occurs during a quenching cycle.
- *Inner door open during the quench:* This situation may occur when the inner door sealing the furnace vestibule from the quench tank is left open to decrease transfer time.
- *High-surface-area loads:* Loads of small components with high total surface areas, such as fasteners, tend to drag out large quantities of quench oil. The volume and temperature of the oil fumes released may be sufficient to lead to a fire.
- *Oil overflow:* The ignition of oil overflowing from a tank can produce a most damaging type of fire. When an oil quench tank is located adjacent to a furnace or any other source of ignition, special precautions are required, such as providing inside overflow drains, to prevent overflowing, and outside drains, to prevent the spread of burning oil, and providing a system for detecting the presence of water in the oil (several detectors are commercially available). If the oil temperature approaches 120 °C (250 °F) with water present, foaming can result in overflow that exceeds the drain capacity.



Fig. 101 Photo of austenitized steel casting just prior to immersion into the quench oil. Source: Ref 254

- *Exceeding the flash point:* Another hazard arises when oil is heated by the workload to a temperature above its flash point. A temperature less than 10 °C (50 °F) below the flash point is considered dangerous. To minimize the temperature rise, several methods may be employed, including the use of cooling coils in the tanks, external heat exchangers, more agitation, a larger tank, or oil with a higher flash point.

Woolhead reported that there are three basic types of quench tanks commonly used in oil quenching operations (Ref 253):

- A completely open tank physically separated from the heat treating furnace
- An open tank that is connected to the furnace by means of a discharge chute
- A completely enclosed tank, within a sealed-type quench furnace (integral quench), in which the oil is normally blanketed by a gas

The first two types present the greatest fire potential because of the greatest surface area exposure to air. If a fire occurs in the chute zone of the second type of system, it may be particularly difficult to control with a specially designed CO₂ fire-suppression system. Furthermore, the second type of system is often connected to a controlled atmosphere system such as carburizing. If the oil level decreases sufficiently, there may be air ingress into the furnace, and an explosion may result. The last type creates a greater explosion hazard because the quench tank is fully enclosed and separated from the hot furnace vestibule only by an inner door.

Some of Woolhead's quench tank design recommendations for increased fire safety include (Ref 253):

- All quench tanks should be equipped with alarms to prevent overheating. Indicators should include high and low oil levels, high quenchant temperature, and inadequate cooling and agitation. One exception is those tanks with very low volume (<1000 L, or 265 gal) or surface area (1 m², or 11 ft²). Monitoring for water contamination should be performed on all quench systems, regardless of size.
- For automated quenching systems, interlocks should be provided to prevent further quenching when the oil bath temperature is 25 to 28 °C (45 to 50 °F) below the experimentally measured closed-cup flash point on the oil being used.
- Inadequate cooling should be determined by monitoring the return oil flow from the cooling system. Cooling may be provided by externally located forced-air radiators, water-cooled shell-and-tube heat exchangers, or submerged water pipes or water jacketing in the tank. If water-cooled heat exchangers are used, the quench oil pressure must be greater than the water pressure to minimize the risk of water ingress into the quench oil in the event of a leak.
- Built-in safeguards should prevent partial immersion of the hot steel into the quench oil. Partial immersion may be due to failure of the manipulators, including hoists or elevators. Overhead hoists with gravity descent are preferred for open-tank batch systems.

Figure 102 is a schematic illustration of an open quench tank for batch quench processes that incorporates Woolhead's safety recommendations (Ref 253).

Extinguishing Oil Fires. A planned program for extinguishing quenching oil fires should include:

- A quick method of extinguishing the fire without contaminating the oil, such as by smothering it with a tank cover or by the use of a carbon dioxide system
- An auxiliary method giving longer-lasting protection, such as foam, dry chemical, or draining the tank
- Periodic training of personnel in fire prevention and fire extinguishing

Facilities to drain oil from the tank to a safe location constitute one method of preventing serious fires.

Tank covers or lids can be used effectively to smother a fire in a small tank. These covers can be actuated by heat or, from a safe distance, manually.

There are two general types of carbon dioxide systems: high-pressure systems, in which the gas is stored at room temperature, and low-pressure systems, in which the gas is stored refrigerated to $-20\text{ }^{\circ}\text{C}$ ($0\text{ }^{\circ}\text{F}$).

The primary effectiveness of carbon dioxide lies in its ability to reduce the supply of oxygen at the surface of the oil to the point at which it cannot support combustion. In some systems, carbon dioxide has a cooling effect as it sublimates from a solid “snow” to a gas.

The advantages of carbon dioxide are that it does not contaminate the quenching oil or require cleanup. Disadvantages are the short duration of the protection afforded and the storage costs for a large installation.

Fire-fighting foam is a mass of fine, heat-resisting bubbles. It smothers an oil fire by floating over the oil surface and setting up into a stiff, long-lasting blanket. There are two general types of foam: chemical and mechanical (or air); both are equally effective.

An advantage of foam is its long-lasting protection. When a quench load has only partially submerged, or when the fire has heated surrounding metal, the protection must last until these sources of reignition are eliminated. Some disadvantages of foam are the cleanup problem after use and that it can cause oil over $120\text{ }^{\circ}\text{C}$ ($250\text{ }^{\circ}\text{F}$) to boil or foam unless the extinguisher is discharged several feet above the tank surface.

The dry chemical extinguisher uses mainly sodium bicarbonate discharged through heads with high-pressure nitrogen. The advantages and disadvantages of the extinguishing action are similar to those of the foam type. Dry powders have been known to contaminate quenching oil.

Polymer Quenchants

The traditional solution to cracking problems has been to reduce the quench severity of water by quenching in an oil. The trade-off, however, may be inadequate through hardening, depending on the steel composition being quenched.

Polymer quenchants provide quench rates intermediate between those achievable with oil and water. Perhaps the major driving force for the use of polymer quenchants, at least initially, has been the reduction or elimination of the fire risk potential and environmental disposal problems associated with the use of petroleum oil.

Aqueous polymer solutions have been used in the heat treating industry for more than 50 years. However, acceptance and substantial use is relatively recent. Polymer quenchants are based on water-soluble polymers, and the most common examples in use in the United States today (2013) include cellulosic derivatives, poly(vinyl alcohol), poly(sodium acrylate), poly(acrylamide), poly(vinyl pyrrolidone), poly(ethyl oxazoline), and poly(alkylene oxide) (Ref 255). See Table 39 for a selected summary of patents for major polymer types.

Although similar in some respects, individual members of the polymer quenchant family differ markedly from each other in other respects. These differences can significantly affect quenching performance. Therefore, it is

important to have a basic understanding of what differentiates these different polymers in order to better understand how to select the most suitable quenchant for the heat treating application being considered.

In this section, a very brief primer on polymers is provided. This discussion is followed by a summary of the composition of the most common water-soluble polymers, with their physical properties, that affect quenchant formulation and heat transfer at the hot metal interface during the quench. The critical parameters that must be considered to ensure successful quench process design are summarized. Finally, a summary of quenchant analysis methods to ensure continued quenching performance is provided. For more information on quenchants used for heat treatment of ferrous alloys, see also Ref 16).

Polymer Primer

A polymer is a large molecule built up by the repetition of smaller chemical units

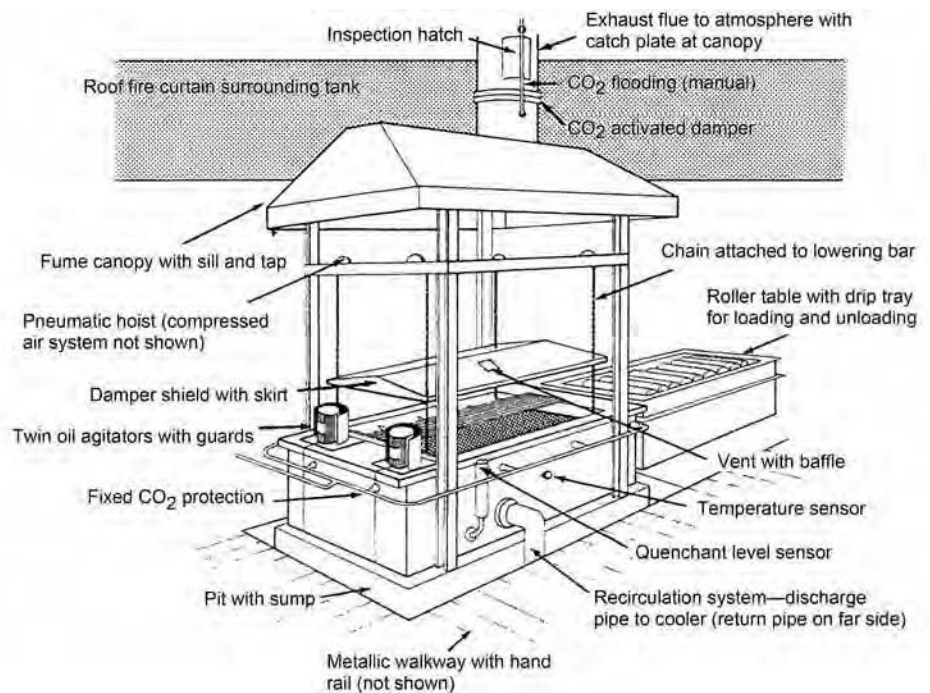


Fig. 102 Schematic of an open quench tank incorporating some of Woolhead's suggested safeguards. Source: Ref 253

Table 39 Summary of selected polymers used for quenchant formulation

Polymer	Inventor(s)	Patent No.	Date
Poly(vinyl alcohol)	E.R. Cornell	U.S. patent 2,600,920	June 10, 1952
Cellulosic derivatives	M. Gordon	U.S. patent 2,770,564	November 13, 1956
Poly(alkylene glycol)	R.R. Blackwood and W.D. Cheesman	U.S. patent 3,220,893	November 30, 1965
Poly(acrylamide)	...	British patent 1,163,345	June 1, 1967
Poly(vinyl pyrrolidone)	A.G. Meszaros	U.S. patent 3,902,929	September 2, 1975
Poly(sodium acrylate)	K.-H. Kopietz	U.S. patent 4,087,290	May 2, 1978
Poly(ethyl oxazoline)	J.F. Warchol	U.S. patent 4,486,246	December 4, 1984

called monomers. For example, poly(sodium acrylate) is prepared by the polymerization of the monomer sodium acrylate. Similarly, poly(vinyl pyrrolidone) is prepared by the polymerization of the monomer vinyl pyrrolidone. Figure 103 illustrates the synthesis of various water-soluble polymers used in quenchant formulation from their corresponding monomers (Ref 255). Some polymers are ionic, such as sodium polyacrylate, but most used for quenchants are nonionic.

The size of the polymers, or molecular weight, in Fig. 103 is dependent on the magnitude of “*n*.” The molecular weight of the polymer is equal to the molecular weight of the monomer times “*n*.” Polymers that are used as quenchants typically have average values of “*n*” from approximately 100 to more than 10,000. The term *average value of n* is used because water-soluble polymers used for quenchant formulation are not a single polymer chain with one molecular weight, but instead the polymer chain has an average distribution of *n*-values. It is important to note that polymer stability decreases with molecular size. Therefore, most, but not all, polymers used for quenchant formulation exhibit molecular weight in the range of 10,000 to 50,000. Furthermore, in practice, the smaller the polymer, the faster the quenching speeds at the same concentration, bath temperature, and agitation (Ref 256, 257).

Many heat treaters have mistakenly developed the belief that all polymers are the same and will therefore produce the same quenching results. For example, compare poly(sodium acrylate) (PSA) and poly(alkylene glycol) (PAG). The PSA polymers tend to be considerably higher in molecular weight and, because of their ionic nature, do not exhibit cloud points. (A cloud point is the solution temperature where a polymer undergoes a phase separation from water. Cloud points, when measured under atmospheric conditions, are limited to approximately the boiling point of water.) The PAG polymers, which are synthesized with two co-monomers, do exhibit cloud points that are dependent on the ratio of the co-monomers.

Therefore, the separation and purification of these two polymers, PSA and PAG, present two very different problems. Also, as with most polymer solutions of very different polymer compositions, aqueous solutions of these two polymers are not mutually compatible and cannot be mixed.

Another problem that has arisen over the years is the totally incorrect use of the term *glycol* when referring to a PAG quenchant. This terminology error has, in a number of cases, led to the formulation of a polymer quenchant that was formulated from ethylene glycol, a component in antifreeze, with absolutely disastrous results not only with respect to quenching performance but also with respect to personnel safety. Therefore, it is advisable to use the correct term for a PAG polymer-based aqueous

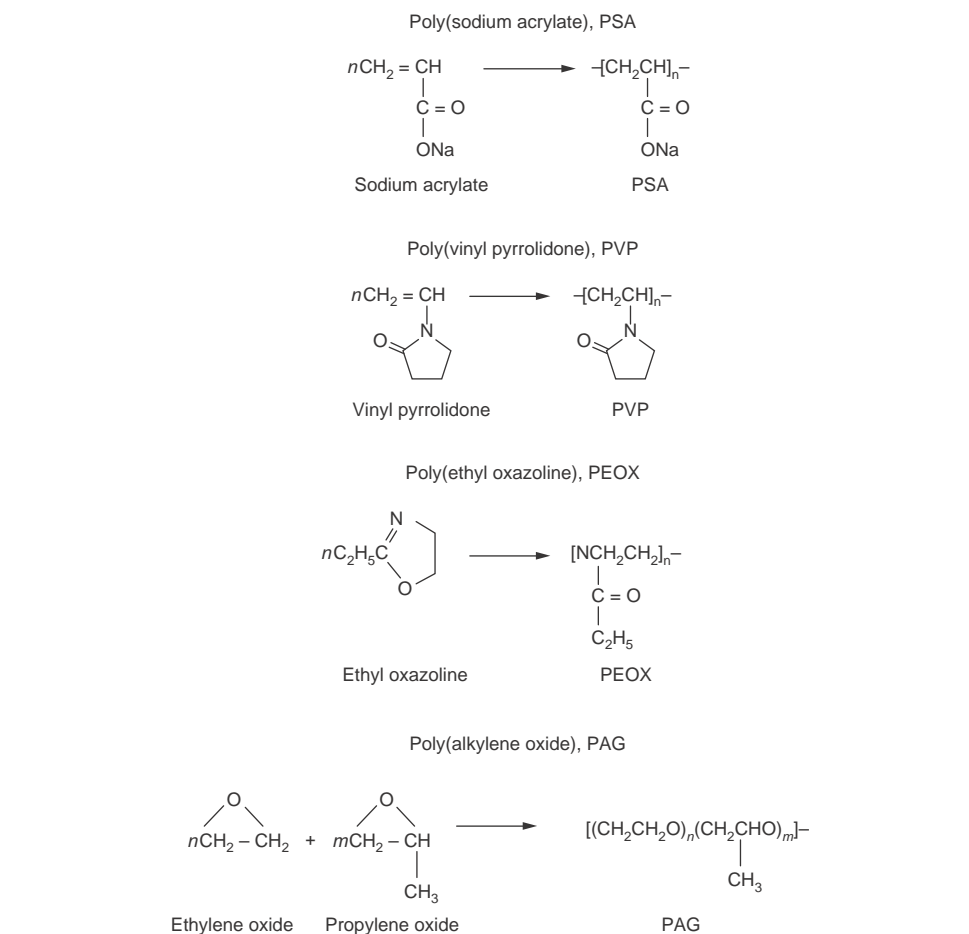


Fig. 103 Synthesis of selected water-soluble polymers, currently used for polymer quenchant formulation, from their corresponding monomers. Source: Ref 255

quenchant to cease using the misleading term *glycol* (Ref 255).

Thermal Separation/Inverse Solubility. Thermal separation of an aqueous polymer solution is based on the limited solubility of the quenchant polymer at elevated solution temperatures. Thermal separation is accomplished in practice by heating the aqueous polymer solution to a temperature greater than the critical temperature, its cloud point, at which time the polymer will separate from solution. This is a thermally reversible process so that when the solution components cool below the cloud point and agitation is applied, a homogeneous solution is formed once again. Of those aqueous polymer quenchants currently in commercial use, PAG-based polymer quenchants are the most common to undergo the thermal separation process.

Figure 104 is a schematic illustration of the thermal separation process of a homogeneous poly(alkylene glycol) aqueous solution (Ref 258). The solution is heated to a temperature in excess of its cloud point. Although the cloud point of a PAG polymer quenchant solution may range from 65 to 85 °C (149 to 185 °F), in practice, thermal separations are often performed at 90 °C (194 °F). Upon separation,

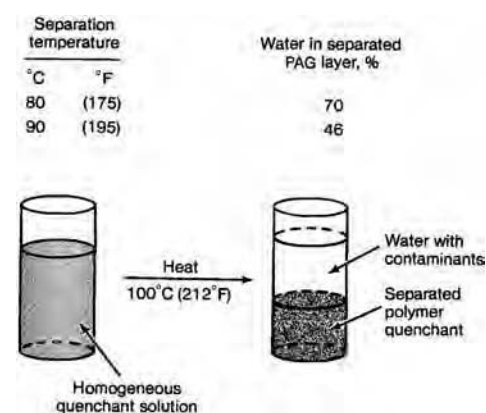
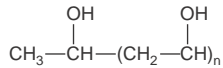


Fig. 104 Typical thermal separation procedure using inverse solubility of the polyalkylene glycol (PAG) polymer quenchant in water. Source: Ref 258

two layers are formed. The lower layer is usually the polymer-rich layer, unless the density of the salt-rich aqueous layer is greater, in which case, the layers will be inverted. Thus, a salt contaminant can be easily fractionated from the polymer (Ref 258).

Polyvinyl Alcohol

The use of aqueous solutions of polyvinyl alcohol (PVA) as quenching media was first described in U.S. patent 2,600,290, which was issued in 1952. Polyvinyl alcohol was discovered in Germany and was introduced commercially into the United States in 1939. The chemical formula for PVA is:

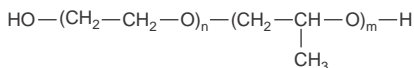


Although PVA can be regarded as a polymer of vinyl alcohol, in reality all PVA resins are made by the hydrolysis of polyvinyl acetate. The extent of hydrolysis, which can govern commercial applications, may vary from partial (87 to 89%) through fully hydrolyzed (95%) to superhydrolyzed (99.7%). Furthermore, the water solubility and quenching characteristics of PVA resins (all of which are solids) will vary with the molecular weight of the polymer.

Cooling Characteristics. Polyvinyl alcohol was introduced in the mid-1950s as an additive to water to modify its cooling rate. As the curves in Fig. 105 indicate, only slight variations in solution concentration are needed to produce changes in cooling characteristics of PVA solutions. At concentrations of less than 0.01%, the cooling characteristics at room temperature are only modestly different from those of water alone. With such small concentration variations, close control of PVA solutions is necessary. Control is complicated by the fact that quenched parts can become coated with an insoluble layer of resin, thus reducing the bath concentration. Maintaining an effective concentration requires specific control measures.

Polyalkylene Glycol

Polyalkylene glycols, or polyalkylene glycol ethers, were first introduced as a family of commercial products in the early 1940s. As shown in the subsequent diagram, these materials are formulated by the random polymerization of ethylene and propylene oxides (although higher alkylene oxides and/or aryl oxides may also be used). Although block polymerizations of these same oxides are possible, these derivatives are less attractive as quenchants.



By varying the molecular weights and the ratio of oxides, polymers having broad applicability may be produced. Certain of the higher-molecular-weight products were shown to have utility as metal quenchants when used in aqueous solution (U.S. patent 3,230,893).

Proper selection of the polymer composition, and its molecular weight, provides a PAG product that is completely soluble in water at room temperature (Ref 259). However, the selected PAG molecules exhibit the unique behavior of inverse solubility in water, that is, water insolubility at elevated temperatures. This phenomenon provides the unique mechanism for cooling hot metal by surrounding the metal piece with a polymer-rich coating that serves to govern the rate of heat extraction into the surrounding aqueous solution. As the metal part approaches in temperature the temperature of the quenchant itself (stage C in Fig. 2), the PAG polymer coating dissolves to again provide a uniform concentration in the quenchant bath.

In the section describing the cooling characteristics of water, one of the disadvantages cited for plain water is that the vapor blanket stage (stage A in Fig. 2) may be prolonged. This prolongation encourages vapor entrapment that may result in uneven hardness and unfavorable distribution of stress, which in turn may cause cracking and/or distortion. By using polyglycol quenchants, uniform wetting of the metal surface results, thereby avoiding the unevenness and accompanying soft spotting. In fact, selection of the proper PAG quenchant can provide accelerated wetting so that the cooling rates achieved are faster than water and approach those achieved by brines. Thus, brine quenching is possible without the hazards and corrosiveness attendant with the use of salts or caustic solutions.

U.S. patent 3,475,232 teaches that the addition of water-soluble alcohols, glycols, or glycol ethers with two to seven carbon atoms also can improve the wetting characteristics of PAG quenchants. Control of a multicomponent system then becomes more complex.

Whereas rusting can be a drawback when quenching with water alone, particularly where recirculation of treated water is not employed, solutions of polyglycol quenchants may be inhibited to provide corrosion protection of the quench-system components. Corrosion inhibition of quenched parts will be of short duration, so that specific protection should be provided following the tempering operation.

Cooling Characteristics. In the application of PAG quenchants for heat treating, three principal parameters are recognized to control the rate of cooling:

- Quenchant concentration
- Quenchant temperature
- Quenchant agitation

The influence of polymer concentration on cooling rates is illustrated by the cooling curves shown in Fig. 106. No specific concentrations are listed because the shape of the cooling curve, as well as the change in rate with concentration, will vary with the selection of the PAG quenchant. The slower rates of cooling achieved at the higher concentrations reflect

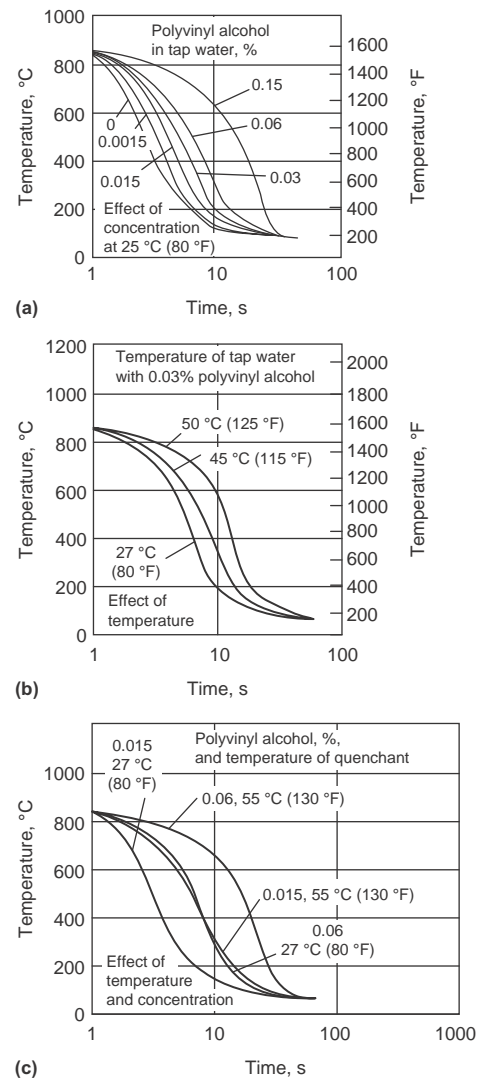


Fig. 105 Cooling curves for polyvinyl alcohol solutions

the thickness of the polymer layer that surrounds the heated part during quenching. The polyglycol quenchants also are less sensitive to minor changes in polymer concentration, which is a recognized deficiency of polyvinyl alcohol and the other film-forming polymer quenchants.

Just as water exhibits a marked decrease in cooling capability as its temperature is elevated (Fig. 107), this same loss is translated to the aqueous solutions of PAG quenchants. The curves shown in Fig. 108 are illustrative of the general trends that would occur with changes in bath temperature; more detailed data would require specific identification of the particular PAG quenchant employed.

The use of no agitation with a polyglycol quenchant would be unusual. In general, low to moderate agitation is essential to ensure that adequate replenishment of polymer occurs at the hot metal surface and to provide uniform heat transfer from the hot part to the surrounding

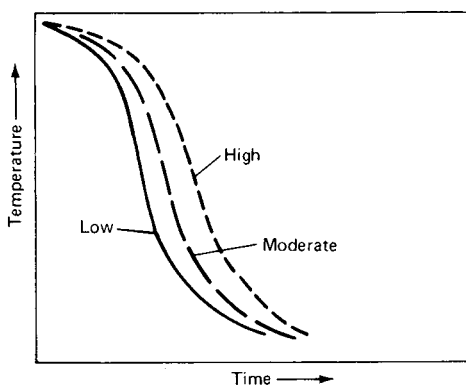


Fig. 106 Effect of concentration on cooling rate

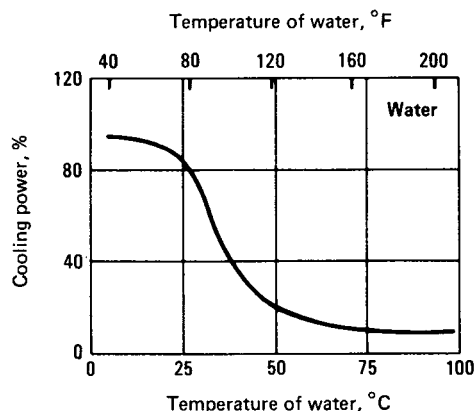


Fig. 107 Relation of surface-cooling power of water with moderate agitation and water temperature

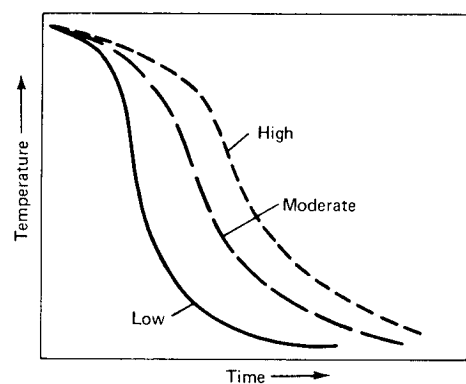


Fig. 108 Effect of temperature on cooling rate

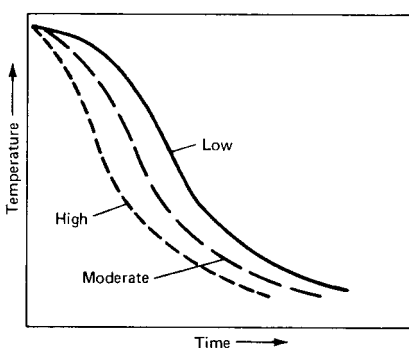


Fig. 109 Effect of agitation on cooling rate

reservoir of cooler quenchant. Vigorous agitation may be essential for achieving a rapid rate of cooling (for example, with a low-hardenability steel) to avoid undesired transformation. Figure 109 clearly illustrates that as agitation is increased, the cooling curves shift to more rapid rates.

Control Measures. The refractive index of oxyalkylene glycol polymer solutions (in the range employed for quenching) is essentially linear with concentration. Thus, the refractive index of a PAG quenchant solution serves as a measure of product concentration. Industrial-model optical refractometers that employ an arbitrary scale may be calibrated. Whereas such instruments prove invaluable for day-to-day monitoring of the quenchant concentration, the refractometer also will register other water-soluble components that are introduced to the used quenchant. When the indicated refractometer reading begins to provide erroneous numbers, some other analytical test is required to define the effective quenchant concentration. With polyglycol quenchants, kinematic viscosity measurements (which are correlated with concentration) have proven to be most useful.

As required, additional analytical tests for pH, inhibitor level, and conductance may be useful adjuncts to a successful monitoring

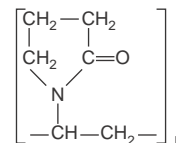
program. If the level of contaminants in the polyglycol quenchant becomes excessive (where these contaminants may be, in part, the same undesirable constituents that are detrimental to water alone, or oil), quenchant recovery can be affected thermally (Ref 260, 261). By heating the quenchant solution (in whole or in part) above the separation temperature, a more dense polymer-rich layer is obtained. Much of the water-soluble contamination can be withdrawn with the supernatant water layer. Solid contaminants such as scale or carbon would require settling, filtration, and/or centrifugation.

Because PAG quenchants are highly bio-resistant, the addition of a bactericide to the as-supplied quenchant is not required. Further, biochemical activity in use is traceable not to the polyglycol polymer itself but to the introduction of nutrient contaminants. Microbiological treatment such as is employed with other aqueous metal working fluids generally will keep under control this foreign biological activity.

Polyvinyl Pyrrolidone

Polyvinyl pyrrolidone (PVP) is derived from the polymerization of *n*-vinyl-2-pyrrolidone. It

is a water-soluble polymer characterized by its unusual complexing and colloidal properties and by its physiological inertness. Polyvinyl pyrrolidone has been available in the United States as a white, free-flowing powder manufactured in four molecular weight grades. Its structure is shown in the following diagram:



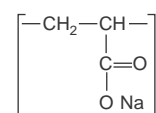
Solutions of PVP in water were first introduced as quenchant in 1975, coinciding with the issuance of U.S. patent 3,902,929. The patent defines the molecular weight range for the pyrrolidone polymer, the quantity of polymer recommended for a solution concentrate (generally about 10% polymer solids), and the preferred use of a rust inhibitor and a bactericidal preservative.

Quenchant Variables. As with other polymer-type quenchant, concentration, bath temperature, and agitation all play a role in establishing the cooling characteristics (Ref 262, 263). By comparison, the quenching rates tend to be faster during the stable film and nucleate and boiling stages but are slower during the convection stage. Because PVP does not have inverse solubility in water, only very small amounts of polymer film are retained on quenched parts at quenching temperatures from 30 °C (85 °F) to near boiling. Thus, a broader working range of temperatures for quenching can be employed.

Optical refractometer readings will provide initial control of concentration, but backup with viscosity measurements is strongly recommended. The means for removal of impurities by ultrafiltration was recently patented (U.S. patent 4,251,292). This can be done without interrupting the quenching process.

Polyacrylates

The most recent addition to commercially available polymer quenchants in the United States is a product comprising an aqueous solution of sodium polyacrylate. Introduction was made at an ASM International Heat Treating Conference/Workshop in May 1977. The following reaction illustrates that the polymer may be achieved from the direct polymerization of sodium acrylate or the alkaline hydrolysis of some polyacrylate ester:



By using the salt of an alkali metal, in this instance sodium, the polymer is provided solubility in water.

Polyacrylate quenchants represent a class of quenchants completely different from the PVA, PAG, or PVP types. The latter polymers fall into the type characterized as nonionic, that is, not ionizable or neutral. Quenchants are considered anionic, which is negatively charged. The charged character of the polymer imparts another dimension to the quenchant: strong polarity. The strong polarity provides water solubility but is also suspected of causing the polymer to operate by a different mechanism of heat extraction.

Unlike other polymer quenchants, polyacrylate solutions do not split on heating and do not form plastic films on the surface of the hot work. Their slower rate of cooling is based on the molecular weight of the polyacrylate and the subsequent viscosity of its solutions. By varying the molecular weights of the polymer, a whole family of quenchants can be designed to cover a full range of applications, from the fast quenching of water to the slow cooling of oils.

The quenching effect of the polyacrylate quenchants is a function of the three basic parameters: polymer concentration, bath temperature, and bath agitation. The effect of polymer concentration and temperature for one of the commercially

available polyacrylate quenchants is shown in Fig. 110.

The cooling curves of the polyacrylate solutions can be almost straight, which is the result of the extended vapor phase and reduced heat extraction during the boiling phase. This unique property of the polyacrylate quenchants allows their applications for hardening of crack-prone parts made of high-hardenability steels. Applications of this kind usually are unobtainable with any other polymer quenchants or require much higher concentrations of the polymer. Comparison of cooling curves of a polyacrylate quenchant with those of water, conventional quenching oil, and a few typical polymer quenchants is shown in Fig. 111.

As can be seen in Fig. 111, the cooling rates of the polyacrylate solutions are distinctly slower than those of any other polymer quenchants. This illustrates their advantages as quenchants, in particular for applications requiring a slow quenching effect.

With increasing polymer concentration and bath temperature, the cooling rate of the solutions can be slowed to the extent that many ferrous metals do not transform to martensite at all

but form bainite or pearlite. This nonmartensitic quenching can be used for new and unique heat treating procedures that are beneficial in many respects, for example, cost, energy, safety, and environmental control. Some applications of the polyacrylate solutions for nonmartensitic quenching are as follows:

- Deep carburized parts, such as bearing races, balls, and rollers, are usually double hardened in oil to obtain grain refinement. The first quenching can be done in a polyacrylate solution.
- Direct quenching of plain carbon steel with a high carbon content can be done in polyacrylate solutions to obtain similar mechanical properties as obtained by quenching and tempering or austempering, such as automotive sway bars or railroad rails made of SAE 1070 to 1090.
- Rod or wire patenting can be done in polyacrylate solutions instead of the commonly used lead or salt bath process at 510 to 565 °C (950 to 1050 °F).
- Direct quenching of hot-formed parts can be done in polyacrylate solutions to obtain good machinability without the usual necessary

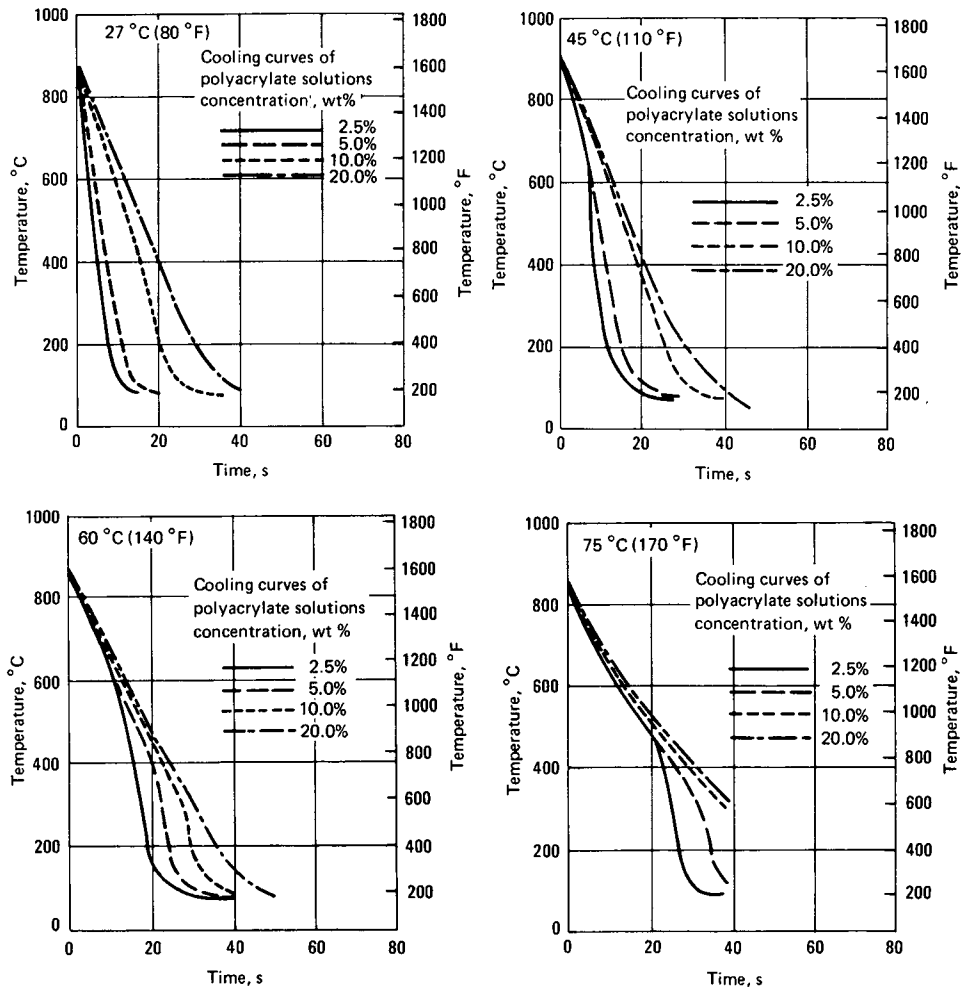


Fig. 110 Cooling rate of a polyacrylate quenchant as a function of concentration and temperature

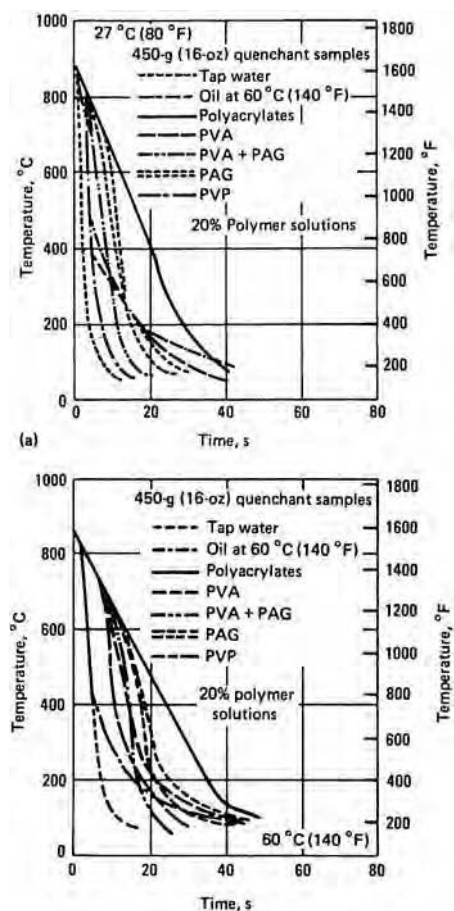


Fig. 111 Cooling rates of different polymer quenchants at 20% concentration at 25 and 60 °C (80 and 140 °F). PVA, polyvinyl alcohol; PAG, polyalkylene glycol; PVP, polyvinyl pyrrolidone

tempering process subsequent to hardening, in particular for steels of low hardenability, such as low-alloy carburizing steels.

- Cooling of hot-formed parts can be done in polyacrylate solutions to prevent excessive scaling and decarburization during slow cooling in air, whereby practically the same microstructure is obtained as during air cooling.
- Large concast steel slabs are water quenched to shorten cooling duration, thus permitting inspection shortly after casting. This is possible only for slabs of plain carbon steel with up to 0.2% C. Alloy steels and steels with higher carbon content must be air cooled, which requires several days. They would crack when water quenched. Now, the addition of polyacrylates to the slab quench water allows faster cooling of high-carbon and alloy steel slabs.

The polyacrylate quenchants also can be used for quenching aluminum alloys after solution treatment to minimize distortion and warpage.

As with any other polymer quenchants, the polyacrylate solutions require the use of agitation, the degree of which depends on the specifics of application. As a general rule, a high degree of agitation is recommended for hardening operations, whereas minimal agitation is usually sufficient for nonmartensitic quenching.

The concentration control of the polyacrylate quenchants is based on their kinematic viscosities. To take into account the influence of contamination, they also should be periodically checked with other laboratory methods, including cooling curve analysis. This service usually is provided by a quenchant supplier.

Fixtures

Fixtures are used to provide support or restraint. Support fixtures are widely used to minimize distortion during quenching. They may vary in design from a simple tray or rack to complex compartmented baskets and special holders. Distortion of parts such as shafts is minimized if they are hung or supported vertically during heating and quenching.

Circular parts, such as large rings, may be supported on flat surfaces during heating and quenching. However, this practice may cause nonuniform hardness, because it restricts the flow of quenchant. A preferred practice is to support such members on fixtures that have radial ribs, machined or ground flat, to permit free flow of the quenching medium to all areas.

Distortion of thin-walled circular members is sometimes corrected by inserting pins inside the ring to force the small diameter outward prior to tempering. The pins are a part of a turn-buckle assembly that permits adjustment. To ensure acceptable roundness after tempering and removal of the pin assembly, an overcorrection of approximately 50% is usually required. However, corrective methods such as this are practical only for small-scale production.

Restraint fixturing is costly and is used primarily for highly specialized applications. Notable examples of parts that require restraint during heating and quenching are rocket and missile casings or other large components with thin-walled sections. For such components, two or more external restraining bands may be used. An articulated internal fixture also may be required. It is built up of numerous cast or stamped pieces pinned together to provide many points of support and a free flow of quenchant to the inner surface of the workpiece. Articulated fixtures can accommodate workpieces of various diameters and lengths. The whole assembly is hung in the furnace and then lowered into the oil quench tank.

Cold Die Quenching. Thin disks, long slender rods, and other delicate parts that distort excessively when they are quenched in conventional liquid media often can be quenched between cold dies with virtually no distortion.

Example. Large, thin thrust washers, which were blanked from cold-rolled steel and contained machined oil grooves, developed considerable distortion as a result of blanking and machining stresses. A dimensional variation of 1.3 mm (0.050 in.) was common, and even larger variations sometimes occurred. Nevertheless, these washers had to be flat to within 0.13 mm (0.005 in.) after hardening.

To ensure the required flatness, the washers were squeezed between a pair of water-cooled die blocks immediately after they left the hardening furnace. The die blocks provided the necessary quenching action while maintaining flatness. When water-cooled beryllium copper die blocks were used in this application, the rate of cooling approached that obtained in water quenching.

Cold die quenching is limited to parts with a large surface area and a relatively small mass, such as washers, rods of small diameter, and thin blades.

REFERENCES

1. H.M. Tensi, A. Stich, and G.E. Totten, Fundamentals of Quenching, *Met. Heat Treat.*, March/April 1995, p 20–28
2. G.J. Leidenfrost, De Aqua Communis Nonnullus Tractus, translation of 1756 paper by C. Waves, *Int. J. Mass Transf.*, Vol 9, 1966, p 1153–1166
3. R.B. Duffy and D.T.C. Porthouse, The Physics of Rewetting in Water Reactor Engineering Core Cooling, *Nucl. Eng. and Des.*, Vol 31, 1973, p 234–245
4. A. Yamanouchi, Effect of Core Spray Cooling in Transient State after Loss of Cooling Accident, *J. Nucl. Sci. Technol.*, No. 5, 1968, p 547–558
5. T. Künzel, “Einfluss der Wiederbenetzung auf die Allotrope Modifikation Sänderung tauchgekühlter Metallkörper,” Ph.D. thesis, Faculty for Mechanical Engineering

of the Technical University of Munich, Munich, Germany, 1986

6. D. Hein, “Modellvorstellung zur Wiederbenetzung durch Fluten,” Ph.D. thesis, Technical University of Hannover, Hannover, Germany, 1980
7. H. Thimbleby, The Leidenfrost Phenomenon, *Phys. Educ.*, Vol 24, 1989, p 300–303
8. N.I. Kobasko, Chap. 2, Transient Nucleate Boiling and Self-Regulated Thermal Processes, *Intensive Quenching Systems: Engineering and Design*, N.I. Kobasko, M.A. Aronov, J. Powell, and G.E. Totten, Ed., ASTM International, 2010, p 24–44
9. H.M. Tensi and A. Stich, Characterization of Polymer Quenchants, *Heat Treat.*, May 1993, p 25–29
10. G.E. Totten and H.M. Tensi, Using Conductance to Characterize Quenchants, *Heat Treat. Prog.*, July/Aug 2002, p 39–42
11. G.E. Totten, C.E. Bates, and N.A. Clinton, Chap. 8, Other Quenching Processes, *Handbook of Quenchants and Quenching Technology*, ASM International, 1993, p 291–338
12. B. Liščić, H.M. Tensi, L.C.F. Canale, and G.E. Totten, *Quenching Theory and Technology*, 2nd ed., CRC Press, London, New York, 2010
13. N.I. Kobasko and F.A. Krivoshey, On the Mechanism of Temperature and Heat Flux Oscillations in Cooling Metallic Specimen in Aqueous Solutions of Polymers, *Rep. Acad. Ukraine*, No. 11, 1994, p 90–94
14. N.I. Kobasko, *Steel Quenching in Liquid Media under Pressure*, Naukova Dumka, Kyiv, 1980
15. H.J. Vergana-Hernandez and B. Hernandez-Morales, A Novel Probe Design to Study Wetting Kinematics during Forced Convective Quenching, *Exp. Therm. Fluid Sci.*, Vol 33 (No. 5), 2009, p 797–807
16. D.S. MacKenzie, Quenchants Used for Heat Treatment of Ferrous Alloys, *Heat Treating of Irons and Steels*, Vol 4B, *ASM Handbook*, ASM International, to be published
17. B. Taraba, S. Duehring, J. Španielka, and Š. Hadju, Effect of Agitation Work on Heat Transfer during Cooling in Oil ISO-RAPID 277 HM, *Strojniški vestnik—J. Mech. Eng.*, Vol 58 (No. 2), 2012
18. H.R. Bergman, Importance of Agitation for Optimum Quenching, *Met. Eng. Q.*, May 1971, p 17–19
19. R.T. von Bergen, The Effects of Quenching Media Selection and Control on the Distortion of Engineered Steel Parts, *Conf. Proc. Quenching and Distortion Control*, G.E. Totten, Ed., ASM International, 1992, p 275–282
20. L.V. Petrash, Cooling Power of Quenching Oils, *Met. Sci. Heat Treat.*, No. 7, July 1959, p 57–60

21. M. Narazaki, G.E. Totten, and G.M. Webster, Hardening by Reheating and Quenching, *Handbook of Residual Stress and Deformation of Steel*, G.E. Totten, M.A.H. Howes, and T. Inoue, Ed., ASM International, 2002, p 248–295
22. S. Ma, “Characterization of the Performance of Mineral Oil Based Quenchants Using the CHTE Quench Probe System,” M.S. thesis, Worcester Polytechnic Institute, Department of Materials Science and Engineering, Worcester, MA, 2002
23. M. Narazaki, S. Fuchizawa, M. Kogawara, and M. Inaba, Effects of Surface Oxidation on Cooling Characteristics during Quenching of Heated Metals in Subcooled Water, *Tetsu-to-Hagane*, Vol 79 (No. 5), May 1993, p 583–589
24. E.S. Davenport, Isothermal Transformation in Steels, *Trans. ASM*, Vol 27, 1939, p 837–886
25. E.S. Davenport and E.C. Bain, Transformation of Austenite at Constant Subcritical Temperatures, *Trans. AIME*, Vol 90, 1930, p 117–154
26. D.H. Herring, What Happens to Steel during Heat Treatment, Part Two: Cooling Transformations, *Ind. Heat.*, June 2007, p 12–14
27. T.G. Diggs, S.J. Rosenberg, and G.W. Geil, “Heat Treatment and Properties of Steel,” National Bureau of Standards Monograph 88, Library of Congress Catalog Card 66-61523, Nov 1, 1966
28. M. Eshraghi-Kakhki, M.A. Golozar, and A. Kurmanpur, Application of Polymer Quenchant in Heat Treatment of Crack-Sensitive Steel Mechanical Parts: Modeling and Experiments, *Mater. Des.*, Vol 32 (No. 5), May 2011, p 2870–2877
29. G.E. Totten, C.E. Bates, and N.A. Clinton, Chap. 2, Measuring Hardenability and Quench Severity, *Quenchants and Quenching Technology*, ASM International, 1993, p 35–68
30. J.L. Dossett, Make Sure Your Specified Heat Treatment Is Achievable, *Heat Treat. Prog.*, March/April 2007, p 23–30
31. S.P. Radzevich, Chap. 6, Gear Materials, *Dudley’s Handbook of Practical Gear Design and Manufacture*, 2nd ed., CRC Press, Boca Raton, FL, 2012, p 371–419
32. M.A. Grossmann, Chap. 3, The Nature of the Quenching Process, *Elements of Hardenability*, American Society for Metals, 1952, p 61–91
33. C.R. Jackson and A.L. Christenson, The Effect of Quenching Temperature on the Results of the End-Quench Hardenability Test, *Trans. Am. Inst. Min. Met. Eng.*, Vol 158, 1944, p 125–137
34. “Equivalent Sections of Certain Shapes to Round Bars,” Aerospace Standard AS 1260, SAE International, 1972
35. J.L. Lamont, How to Estimate Hardening Depth in Bars, *Iron Age*, Vol 152, Oct 14, 1943, p 64–70
36. N.I. Kobasko, Chap. 6, Regular Thermal Process and Kondratjev Form Factors, *Intensive Quenching Systems: Engineering and Design*, N.I. Kobasko, M.A. Aronov, J. Powell, and G.E. Totten, Ed., ASTM International, 2010, p 91–106
37. D.V. Doane, Applicability of Hardenability Concepts in Heat Treatment of Steel, *J. Heat Treat.*, Vol 1 (No. 1), 1979, p 5–30
38. M.A. Grossmann, Hardenability Calculated from Chemical Composition, *AIME Trans.*, Vol 150, 1942, p 227–259
39. J.H. Holloman and L.D. Jaffe, Chap. 6, Hardenability, *Ferrous Metallurgical Design: Design Principles for Fully Hardened Steel*, John Wiley & Sons, New York, NY, 1947, p 196–214
40. W. Crafts and J.L. Lamont, Chap. 5, Hardness and Hardenability, *Hardenability and Steel Selection*, Pittman Publishing, New York, NY, 1949, p 84–110
41. B. Liščić, Chap. 5, Hardenability, *Steel Heat Treatment Handbook*, 2nd ed., *Steel Heat Treatment: Metallurgy and Technologies*, G.E. Totten, Ed., CRC Press Taylor & Francis Group, Boca Raton, FL, 2007, p 213–276
42. H.K.D.H. Bhadeshia and R. Honeycombe, Chap. 8, *Steels: Microstructure and Properties*, 3rd ed., Elsevier Inc., New York, NY, 2006, p 167–182
43. M.A. Grossmann and E.C. Bain, Quantitative Hardenability, *Principles of Heat Treatment*, 5th ed., American Society for Metals, 1964, p 92–112
44. M.A. Grossmann, Chap. 3, The Nature of the Quenching Process, *Elements of Hardenability*, American Society for Metals, 1952, p 61–91
45. G. Krauss, Chap. 6, Hardness and Hardenability, *Steels: Heat Treatment and Processing Principles*, ASM International, 1990, p 145–178
46. T. Lund, “Carburizing Steels: Hardenability Prediction and Hardenability Control in Steel Making,” Technical Report RD 33 US 03.84, available from SKF Steel Technology, P.O. Box 133, S-182 12 Daneryd, Sweden, 1984
47. “Hardenability Bands for Carbon and Alloy H-Steels,” J1268, SAE International, May 2010
48. “Restricted Hardenability Bands for Selected Alloy Steels,” J1868, SAE International, Feb 2010
49. M.A. Grossmann, M. Asimov, and S.F. Urban, Hardenability, Its Relation to Quenching and Some Quantitative Data, *Hardenability of Alloy Steels*, American Society for Metals, 1939, p 124–190
50. M.A. Aronov, N.I. Kobasko, J.A. Powell, and J.B. Hernandez-Morales, Correlation between Grossmann *H*-Factor and Generalized Biot Number Bi_V , *Fifth WSEAS Int. Conf. on Heat and Mass Transfer (HMT '08)*, Jan 25–27, 2008 (Acapulco, Mexico), p 122–126
51. M.A. Grossmann and S. Asimow, Hardenability and Quenching, *Iron Age*, April 25, 1940, p 25–29
52. M.A. Grossmann and S. Asimow, Hardenability and Quenching, *Iron Age*, May 2, 1940, p 39–45
53. W. Crafts and J.L. Lamont, Chap. 4, Quenching, *Hardenability and Steel Selection*, Pittman Publishing, New York, NY, 1949, p 53–83
54. R.W. Monroe and C.E. Bates, Evaluating Quenchants and Facilities for Hardening Steel, *J. Heat Treat.*, Vol 3 (No. 2), Dec 1983, p 83–89
55. M.E. Dakins, C.E. Bates, and G.E. Totten, Estimating Quench Severity with Cooling Curves, *Heat Treat.*, April 1992, p 24–26
56. K. Narayan Prabhu and A. Prasad, Metal/Quenchant Interfacial Heat Flux Transients during Quenching in Conventional Quench Media and Vegetable Oils, *J. Mater. Eng. Perform.*, Vol 12, 2003, p 48–55
57. W.E. Jominy and A.L. Boegehold, A Hardenability Test for Carburizing Steel, *Trans. ASM*, Vol 26, 1938, p 575–606
58. “Standard Test Methods for Determining Hardenability of Steel,” A255-10, *ASTM International*
59. “Methods of Determining Hardenability of Steels,” J406-2009, SAE International
60. “Method of Hardenability Test for Steel (End-Quenching Method),” JIS G 0561-2006, Japanese Standards Association
61. “Hardenability Test by End Quenching,” DIN 50191 (1987-09), VDE Verlag, Germany
62. “Steel—Hardenability Test by End Quenching (Jominy Test),” ISO 642:1999, International Organization for Standardization, Switzerland
63. A.L. Boegehold, Hardenability Control for Alloy Steel Parts, *Met. Prog.*, Vol 53, May 1948, p 697–709
64. W. Crafts and J.L. Lamont, Chap. 6, Hardenability Test Methods, *Hardenability and Steel Selection*, Pittman Publishing, New York, NY, 1949, p 111–127
65. E.W. Weinman, R.F. Thomson, and A.L. Boegehold, A Correlation of End-Quenched Test Bars and Rounds in Terms of Hardness and Cooling Characteristics, *Trans. ASM*, Vol 44, 1952, p 803–844
66. G.F. Vander Voort, Hardenability, *Atlas of Time-Temperature Diagrams for Irons and Steels*, ASM International, 1991, p 73–77
67. T.F. Russell and J.G. Williamson, Section IV B, “Surface Temperature Measurements during the Cooling of a Jominy Test Piece,” Special Report 36, Iron and Steel Institute, 1946, p 34–46
68. C.R. Brooks, Chap. 3, Hardenability, *Principles of the Heat Treatment of Plain Carbon and Low-Alloy Steels*, ASM International, 1996, p 43–86
69. C.A. Siebert, D.V. Doane, and D.H. Breen, Utilization of Hardenability Concepts and

- Information, *The Hardenability of Steels—Concepts, Metallurgical Influences and Industrial Applications*, American Society for Metals, 1977, p 139–202
70. M. Asimow, W.F. Craig, and M.A. Grossmann, Correlation between Jominy Test and Round Bars, *SAE Trans.*, Vol 41 (No. 1), 1941, p 283–292
 71. W.F. Rushman, How to Determine Quench Severity of Oil and Salt Baths, *Met. Prog.*, Vol 84 (No. 6), Dec 1963, p 91–92
 72. D.A. Guisbert, Control of Quenching Systems in the Heat Treatment of Gear Products, *17th Heat Treating Society Conference Proceedings, Including the First International Induction Heat Treating Symposium*, D. Milam, D. Poteet, G. Pfaffmann, W. Albert, A. Muhlbauer, and V. Rudnev, Ed., ASM International, 1997, p 369–372
 73. E.A. Bender and H.J. Gilliland, New Way to Measure Quenching Speed, *Steel*, Dec 30, 1957, p 58–60
 74. E.A. Bender and H.J. Gilliland, Magnetic Test Accurately Compares Heat Extraction Properties of Quenching Media, *Tool. Prod.*, Sept 1958, p 55–58
 75. “Standard Test Method for Quenching Time of Heat-Treating Fluids (Magnetic Quenchometer Method),” D 3520, ASTM International, withdrawn 2008
 76. H.J. Gilliland, Measuring Quenching Rates with the Electronic Quenchometer, *Met. Prog.*, Oct 1960, p 111–113
 77. T.W. Mohr, A Better Way to Evaluate Quenchants, *Met. Prog.*, May 1974, p 85–88
 78. G.E. Totten, C.E. Bates, and N.A. Clinton, Chap. 4, Quenching Oils, *Handbook of Quenchants and Quenching Technology*, ASM International, 1993, p 129–160
 79. C.E. Bates and G.E. Totten, Quantifying Quench-Oil Cooling Characteristics, *Adv. Mater. Process.*, March 1991, p 25–28
 80. D.A. Guisbert and D.L. Moore, Correlation of Magnetic Quenchometer to Cooling Curve Analysis Techniques, *Heat Treating: Proceedings of the 16th Conference*, J.L. Dossett and R.E. Luetje, Ed., ASM International, 1996, p 451–458
 81. C.E. Bates, Research Report SORI-EAS-86-149, Southern Research Institute, Birmingham, AL, 1986
 82. “Quenchability of Oils—Hot Wire Method,” Aerospace Material Specification ARP 4206, Sept 28, 1990
 83. R.W. Foreman, Paper presented at ASM Short Course on Quenching Media, American Society for Metals, Nov 1985
 84. D.A. Guisbert and L.M. Jarvis, Influence of Test Conditions on the Cooling Curve Response of Polymer Quenchants (Tensi Agitation Device), *Heat Treating 2003: Proceedings of the 22nd Heat Treating Society Conference and the Second International Surface Engineering Congress (ASM International)*, N.B. Dahotre, R.J. Gaster, R.A. Hill, and O.O. Popoola, Ed., Sept 15–17, 2003 (Indianapolis, IN), ASM International, p 218–227
 85. D.A. Guisbert and D.L. Moore, Investigation of Agitation Chamber Design for Off-Line Cooling Curve Analysis, *17th Heat Treating Society Conference Proceedings, Including the First International Induction Heat Treating Symposium*, D. Milam, D. Poteet, G. Pfaffmann, W. Albert, A. Muhlbauer, and V. Rudnev, Ed., ASM International, 1997, p 399–401
 86. D.A. Guisbert, Precision and Accuracy of the Continuous Cooling Curve Test Method, *Heat Treating: Proceedings of the 16th Conference*, J.L. Dossett and R.E. Luetje, Ed., ASM International, 1996, p 435–437
 87. D.A. Guisbert and D.L. Moore, Influence of Test Conditions on the Cooling Curve Response of Polymer Quenchants, *19th Heat Treating Society Conference Proceedings*, S. Midea and G. Pfaffmann, Ed., ASM International, 1999, p 264–267
 88. J.D. Bernardin and I. Mudawar, Validation of the Quench Factor Technique in Predicting Hardness in Heat Treatable Aluminum Alloys, *Int. J. Heat Mass Transf.*, Vol 38 (No. 5), 1995, p 869–873
 89. G.E. Totten, C.E. Bates, and N.A. Clinton, Chap. 3, Cooling Curve Analysis, *Handbook of Quenchants and Quenching Technology*, ASM International, 1993, p 69–128
 90. G.M. Webster and G.E. Totten, Cooling Curve Analysis—Data Acquisition, *Heat Treating: Proceedings of the 16th Conference*, J.L. Dossett and R.E. Luetje, Ed., ASM International, 1996, p 427–434
 91. M.H. Le Chatelier, Les Aciers Rapides a Outils, *Rev. Metall.*, No. 9, 1904, p 334–347
 92. S. Haedicke, Le Chateliers Härteversuche, *Stahl Eisen*, Vol 24 (No. 21), 1904, p 1239–1244
 93. R.L.S. Otero, L.C.F. Canale, and G.E. Totten, Use of Vegetable Oils and Animal Oils as Quenchants: A Historical Review 1850–2010, *J. ASTM Int.*, Vol 9 (No. 1), 2011, JAI103534
 94. H.M. Tensi, A. Stich, and G.E. Totten, Chap. 9, Quenching and Quenching Technology, *Steel Heat Treatment Handbook*, 2nd ed., *Steel Heat Treatment: Metallurgy and Technologies*, G.E. Totten, Ed., CRC Press Taylor & Francis Group, Boca Raton, FL, 2007, p 607–650
 95. “Industrial Quenching Oils—Determination of Cooling Characteristics—Nickel-Alloy Probe Test Method,” ISO 9950-1995, International Organization for Standardization, Switzerland
 96. “Standard Test Method for Determination of Cooling Characteristics of Quench Oils by Cooling Curve Analysis,” D6200-01, ASTM International, 2012
 97. “Standard Test Method for Determination of Cooling Characteristics of Aqueous Polymer Quenchants by Cooling Curve Analysis with Agitation (Tensi Method), D6482-06, ASTM International, 2011
 98. “Standard Test Method for Determination of Cooling Characteristics of Quenchants by Cooling Curve Analysis with Agitation (Drayton Unit),” D6549-06, ASTM International, 2011
 99. “Industrial Quenching Oil—Determination of Cooling Characteristics—Nickel-Alloy Probe Test Method,” Chinese National Standard GB/T 7951—2004, China Association for Standardization, Beijing, China, <http://www.chinacsrmap.org/>
 100. J. Clark and R. Tye, Thermophysical Properties Reference Data for Some Key Engineering Alloys, *High Temp.—High Press.*, Vol 35/36, 2003/2004, p 1–14
 101. “Heat Treating Oils,” JIS K 2242, Japanese Standards Association, 1980
 102. “Heat Treating Fluids,” JIS K 2242, Japanese Standards Association, 2012
 103. “Standard Test Method for Determination of Cooling Characteristics of Aqueous Polymer Quenchants for Aluminum Alloys by Cooling Curve Analysis,” D7646-10, ASTM International
 104. “Cooling Performance Measuring Method for Heat Treatment Oils,” Chinese National Standard SH/T0220-92, China Association for Standardization, Beijing, China, <http://www.chinacsrmap.org/>
 105. AFNOR NFT 60178, Association Technique de Traitement Thermique, Paris, France
 106. S.I. Abu-Eishah, Correlations for the Thermoconductivity of Metals as a Function of Temperature, *Int. J. Thermophys.*, Vol 22 (No. 6), Nov 2001, p 1855–1868
 107. S.I. Abu-Eishah, Y. Haddad, A. Solieman, and A. Bajbouj, A New Correlation for the Specific Heat of Metals, Metal Oxides and Metal Fluorides as a Function of Temperature, *Lat. Am. Appl. Res.*, Vol 34, 2004, p 257–265
 108. W.J. Parker, R.J. Jenkins, C.P. Butler, and G.L. Abbott, Flash Method of Determining Thermal Diffusivity, Heat Capacity and Thermal Conductivity, *J. Appl. Phys.*, Vol 32, 1961, p 1679–1684
 109. M. Narazaki, M. Kogawara, A. Shirayori, S. Fuchizawa, and G.E. Totten, Experimental and Numerical Analysis of Cooling Curves during Quenching of Small Probes, *Heat Treating—Proc. of the 20th Conference*, Vol 2, K. Funatani and G.E. Totten, Ed., Oct 9–12 2000, ASM International, p 666–673
 110. M. Narazaki, S. Asada, and K. Fukahara, Recent Research on Cooling Power of Liquid Quenchants in Japan, *Conf. Proc. Second International Conference on Quenching and Control of Distortion*, G.E. Totten, K. Funatani, M.A.H. Howes, and

- S. Sjoström, Ed., ASM International, 1996, p 37–46
111. M. Narazaki, M. Kogawara, A. Shirayori, and S. Fuchizawa, Laboratory Test of Cooling Power of Polymer Quenchants, *Conf. Proc. Second International Conference on Quenching and Control of Distortion*, G.E. Totten, K. Funatani, M.A.H. Howes, and S. Sjoström, Ed., ASM International, 1996, p 101–109
 112. K.-J. Zhang, Factors Determining the Cooling Rate of Workpiece Surface during Quenching, *20th Congress for Heat Treatment and Surface Engineering*, G. Zhi and H. Chong, Ed., Oct 23–25, 2012 (Beijing, China), Chinese Heat Treatment Society, p 433–443
 113. K.-J. Zhang, Characteristic Parameters of Surface Cooling Process and Boiling Curves for Quenching Process, *20th Congress for Heat Treatment and Surface Engineering*, G. Zhi and H. Chong, Ed., Oct 23–25, 2012 (Beijing, China), Chinese Heat Treatment Society, p 405–416
 114. T. Lübben, F. Frerichs, and H.-W. Zoch, Rewetting Behavior during Immersion Quenching, *Strojarstvo (J. Theory Appl. Mech. Eng.)*, Vol 53, 2011, p 45–52
 115. T. Lübben and F. Frerichs, Quenching of Bearing Races—Influence of Rewetting Behavior on Distortion, *Conf. Proc. Sixth International Conference on Quenching and Control of Distortion*, D.S. MacKenzie, Ed., Sept 9–13, 2012 (Chicago, IL), ASM International, 2012, p 349–360
 116. B. Hernández-Morales and A. López-Valdéz, Experimental Determination of the Temperature Evolution within the Quenchant during Immersion Quenching in Still Water, *Int. J. Microstruct. Mater. Prop.*, Vol 6 (No. 6), 2011, p 444–454
 117. B. Hernández-Morales, H.J. Vergara-Hernández, G. Solorio-Díaz, and G.E. Totten, Experimental and Computational Study of Heat Transfer during Quenching of Metallic Probes, *Evaporation, Condensation and Heat Transfer*, A. Ahsan, Ed., In-Tech Europe, Rijeka, Croatia, 2011, p 49–72, <http://www.intechopen.com/books/evaporation-condensation-and-heat-transfer/experimental-and-computational-study-of-heat-transfer-during-quenching-of-metallic-probes>
 118. F. Frerichs and T. Lübben, The Influence of Surface Temperature on Rewetting Behavior of Hollow and Solid Cylinders, *J. ASTM Int.*, Vol 6 (No. 1), 2009, Paper ID JAI101852
 119. H.M. Tensi and A. Stich, Characterization of Polymer Quenchants, *Heat Treat.*, May 1993, p 25–29
 120. H. Tensi, P. Stitzelberger-Jacob, and T. Künzel, Monitoring and Controlling the Kinematics of Wetting to Prevent Hardening Defects, *Maschinenmarkt*, Vol 94 (No. 15), 1988, p 70–72, 74, 76
 121. M. Narazaki, M. Kogawara, A. Shirayori, and S. Fuchizawa, Influence of Wetting Behavior on Cooling Characteristics during Quenching of Hot Metal, *Proc. of the Third International Conference on Quenching and Control of Distortion* (Prague, Czech Republic), ASM International, 1999, p 405–415
 122. N.I. Kobasko, A.A. Batista, Jr., L.C.F. Canale, G.E. Totten, and V.V. Dobryvecher, Investigation of the Cooling Capacity of Coconut, Palm and Commercial Petroleum Oil by Solving the Heat Conductivity Inverse Problem, *Mater. Perform. Charact.*, accepted for publication, in production
 123. T. Lübben, J. Rath, F. Krause, F. Hoffmann, U. Fritsching, and H.-W. Zoch, Determination of Heat Transfer Coefficient during High-Speed Water Quenching, *Conf. Proc. of 15th International Metallurgy and Materials Congress (IMMC 2010)*, Nov 11–13, 2010 (Istanbul, Turkey), UCTEA Chamber of Metallurgical Engineers, p 1616–1625
 124. G.E. Totten, H.M. Tensi, and A. Stich, Temperature Measurement Accuracy in Cooling Curve Analysis, *Heat Treat. Prog.*, Vol 2 (No. 4), 2002, p 45–49
 125. N.I. Kobasko, Effect of Accuracy of Temperature Measurements on Determination of Heat Transfer Coefficient during Quenching in Liquid Media, *J. ASTM Int.*, Vol 9 (No. 2), 2012, Paper ID 104173
 126. L.C.F. Canale, X. Luo, X. Yao, and G.E. Totten, Quenchant Characterization by Cooling Curve Analysis, *J. ASTM Int.*, Vol 6 (No. 2), 2009, JAI101981
 127. G.E. Totten, M.E. Dakins, and R.W. Heins, Cooling Curve Analysis—A Historical Perspective, *J. Heat Treat.*, Vol 6 (No. 2), 1988, p 87–95
 128. H.M. Tensi and E. Steffen, Measuring of the Quenching Effect of Liquid Hardening Agents on the Basis of Synthetics, *Steel Res.*, Vol 56, 1985, p 489–496
 129. P. Damay and M. Deck, “Castrol Index—Method of Classifying Quenching Oils,” paper presented at the Int. Heat Treating Association Meeting, Sept 1990 (Lamans, France)
 130. M. Necati Özisik and H.R.B. Orlande, *Inverse Heat Transfer: Fundamentals and Applications*, Taylor and Francis, New York, NY, 2000, p 330
 131. A.N. Tikhonov and V.Y. Arsenin, *Solutions of Ill-Posed Problems*, Wiley Publishing House, New York, 1977
 132. S.E. Guseynov, “Methods of the Solution of Some Linear and Nonlinear Mathematical Physics Inverse Problem,” Doctoral thesis, University of Latvia, Riga, Latvia, 2003
 133. S.E. Guseynov, N.I. Kobasko, S.A. Andreyev, J.S. Rimshans, J. Kaupuzs, P. Morev, and N. Zaiceva, Stable Measurement of Temperature Errors during Testing of Quenchants by Methods of the Theory of Ill-Posed Problems, *Proceedings from the Sixth International Quenching and Control of Distortion Conference, Including the Fourth International Distortion Engineering Conference*, Sept 9–13, 2012 (Chicago, IL), 2012, p 646–666
 134. L.A. Kozdoba and P.G. Krukovskiy, *Methods of Solving Inverse Heat Conduction Problems*, Kyiv, Naukova Dumka, 1982
 135. P.G. Krukovskiy, *Inverse Heat and Mass Transfer Problems (General Engineering Approach)*, Kyiv, Engineering Thermal-Science Institute, 1998
 136. J.V. Beck, B. Blackwell, and C.R. St. Clair, Jr., *Inverse Heat Conduction: Ill-Posed Problems*, Wiley-Interscience, New York, 1985
 137. N.I. Kobasko, M.A. Aronov, J. Powell, and G.E. Totten, Ed., *Intensive Quenching Systems: Engineering and Design*, ASTM International, 2010
 138. G.M. Kondratjev, *Regular Thermal Mode*, GITL, Moscow, 1952
 139. N.I. Kobasko, A.A. Moskalenko, G.E. Totten, and G.M. Webster, Experimental Determination of the First and Second Critical Heat Flux Densities and Quench Process Characterization, *J. Mater. Eng. Perform.*, Vol 6 (No. 1), 1997, p 93–101
 140. N.I. Kobasko, M.A. Aronov, B.L. Ferguson, and Z. Li, Local Film Boiling and Its Impact on Distortion of Spur Gears during Batch Quenching, *Mater. Perform. Charact.*, Vol 1 (No. 1), 2012, p 1–15
 141. N.I. Kobasko, A.A. Moskalenko, V.V. Dobryvecher, and L.M. Protsenko, Intensive Quenching of Steel Parts and Tools in Water Salt Solutions of Optimal Concentration, *J. ASTM Int.*, Vol 9 (No. 2), 2012, Paper ID JAI104072
 142. H.J. French, *The Quenching of Steels*, American Society for Heat Treating, Cleveland, OH, 1930
 143. V.I. Tolubinsky, *Heat Transfer at Boiling*, Naukova Dumka, 1980
 144. S.S. Kutateladze, *Heat Transfer at Condensation and Boiling*, Mashgiz, Moscow, 1952
 145. S. Segerberg and J. Bodin, Experimental Difficulties in Achieving Reliable Cooling Curve Data, *Heat Treating: Proceedings of the 16th Conference*, J.L. Dossett and R.E. Luetje, Ed., ASM International, 1996, p 421–426
 146. M. Narazaki, G.E. Totten, and G.M. Webster, Hardening by Reheating and Quenching, *Handbook of Residual Stress and Deformation of Steel*, G.E. Totten, T. Inoue, and M.A.H. Howes, Ed., ASM International, 2002, p 248–295
 147. K. Murata and S. Nishio, Mechanism of Film-Boiling Onset in Transient Cooling Process with Highly Subcooled Water and Unstable Boiling-Cooling Phenomena,

- Tetsu-to-Hagane*, Vol 79 (No. 1), 1993, p 55–61
148. O.A. Bannykh, G.T. Bozhko, M.N. Tropkina, and P.I. Mannikhin, Oxidation of Steel during Quenching in Aqueous Solutions of Electrolytes, *Met. Sci. Heat Treat.*, Vol 26 (No. 12), Dec 1984, p 867–869
 149. G.E. Totten and K.S. Lally, Proper Agitation Dictates Quench Success—Part 1, *Heat Treat.*, Sept 1992, p 12–17
 150. G.E. Totten and K.S. Lally, Proper Agitation Dictates Quench Success—Part 2, *Heat Treat.*, Oct 1992, p 28–31
 151. The Mead velocimeter, in particular the HP-302 open-stream velocity probe, is used most often for the measurement of flow rates in water streams for pollution control. This instrument is available from Mead Instruments Corporation, P.O. Box 367, Sussex, NJ, 07461.
 152. G.E. Totten, M.E. Dakins, and L.M. Jarvis, How *H*-Factors Can Be Used to Characterize Polymers, *Heat Treat.*, Dec 1989, p 28–29
 153. “Houghton on Quenching,” Houghton International, Inc., Valley Forge, PA, 2012
 154. G.E. Totten, C.E. Bates, and N.A. Clinton, Chap. 8, Other Quenching Processes, *Handbook of Quenchants and Quenching Technology*, ASM International, 1993, p 291–338
 155. L.V. Petrash, Some Physical Phenomena during Quenching, *Met. Sci. Heat Treat.*, Vol 15 (No. 6), June 1973, p 523–526
 156. Q. Cui, S. Chandra, and S. McCahan, The Effect of Dissolving Salts in Water Sprays Used for Quenching a Hot Surface, Part 2: Spray Cooling, *J. Heat Transf.*, Vol 125, April 2003, p 333–338
 157. T. Arai and M. Furuya, Effect of Hydrated Salt Additives on Film Boiling Behavior at Vapor Film Collapse, *J. Eng. Gas Turbines Power*, Vol 131, Jan 2009, Paper ID 012902-1
 158. M.P. Mukhina, N.I. Kobasko, and L.V. Gordeeva, Hardening of Structural Steels in Cooling Media Based on Chlorides, *Met. Sci. Heat Treat.*, Vol 31 (No. 9), Sept 1989, p 677–682
 159. R.F. Kern, Distortion and Cracking II: Distortion from Quenching, *Heat Treat.*, March 1985, p 41–45
 160. R.W. Foreman, Salt Quench Rivals Oil, Synthetics in Neutral Hardening Applications, *Heat Treat.*, Oct 1980, p 26–29
 161. X. Luo, K. Chen, and G.E. Totten, Fast Primary Cooling: Alternative to Lead Baths for High-Carbon Steel Wire Patenting, *Mater. Perform. Charact.*, Vol 1 (No. 1), 2012, Paper ID MPC20120006
 162. C. Fazio, Chairperson, OECD/NEA Nuclear Science Committee Working Party on Scientific Issues of the Fuel Cycle Working Group on Lead-Bismuth Eutectic, Chap. 2, Thermophysical and Electrical Properties, *Handbook on Lead-Bismuth Eutectic Alloy and Lead Properties, Materials Compatibility, Thermal Hydraulics and Technologies*, 2007 ed., p 25–100
 163. J.A. Cahill, G.M. Krieg, and A.V. Grosse, Electrical Conductivity of Tin, Lead, and Bismuth Near Their Boiling Points with Estimates to Their Critical Temperatures, *J. Chem. Eng. Data*, Vol 13 (No. 4), 1968, p 504–507
 164. V. Sobolev, “Database of Thermophysical Properties of Liquid Metal Coolants for GEN-IV—Sodium, Lead, Lead-Bismuth Eutectic (and Bismuth),” Scientific Report SCK-CEN-BLG-1069, SCK-CEN, Belgium, Nov 2010
 165. M. Narazaki and S. Ninomiya, Molten Sodium Quenching of Steel Parts, *IFHTSE 2002 Congress* (Columbus, OH), ASM International, 2003, p 464–470
 166. J. Ru and Z. Wang, A Feasibility Study on the Use of Bismuth Bath to Replace Lead as the Quenching Media for Steel Heat Treating, *J. ASTM Int.*, Vol 5 (No. 9), 2008, Paper ID JAI101871
 167. G.T. Dubal, M.T. Ives, A.G. Meszaros, and J. Recker, Modern Applications for Salt Bath Heat Treating of Automotive Components, *The First International Automotive Heat Treating Conference*, R. Colas, K. Funatani, and C.A. Stickels, Ed., ASM International, 1998, p 90–95
 168. C. Skidmore, Salt Bath Quenching—A Review, *Heat Treat. Met.*, No. 2, 1986, p 34–38
 169. R.W. Foreman, Salt Bath Quenching, *Conf. Proc. Quenching and Distortion Control*, G.E. Totten, Ed., ASM International, 1992, p 87–94
 170. G.P. Dubal, Salt Bath Quenching, *Adv. Mater. Process.*, Vol 156 (No. 6), Nov 1999, p H23–H28
 171. E.N. Case and A.M. White, “Water in Molten Salt—Increases Quenching Power, Lowers Operating Temperatures,” white paper by American Cyanamide, Industrial Chemicals Division, New York, NY
 172. B. Liščić, State of the Art in Quenching, *Quenching and Carburizing—Third International Seminar of IFHT* (Melbourne, Australia), Institute of Materials, London, U.K., 1993, p 1–32
 173. J.L. Dossett and H.L. Boyer, Chap. 7, Heat Treating of Alloy Steels, *Practical Heat Treating*, 2nd ed., ASM International, 2006, p 125–139
 174. H.M.R. Habarakada, “Martempering and Austempering of Steel,” Sept 13, 2007, <http://austemperingandmatempering.blogspot.com/2007/11/martempering-and-austempering-of-steel.html>
 175. G. Wahl, Development and Application of Salt Baths in the Heat Treatment of Case Hardening Steels, *Proceedings of ASM Heat Treating Conference: Carburizing, Processing and Performance*, G. Krauss, Ed., July 12–14, 1989 (Lakewood, CO), ASM International, p 41–56
 176. R.L. Suffredini, Factors Influencing Austempering, *Heat Treat.*, Jan.1980, p 14–19
 177. *Heat Treating, Cleaning and Finishing*, Vol 2, *Metals Handbook*, 8th ed., American Society for Metals, 1964
 178. E.C. de Souza, M.R. Fernandes, S.C.M. Augustinho, L.C.F. Canale, and G.E. Totten, Comparison of Structure and Quenching Performance of Vegetable Oils, *J. ASTM Int.*, Vol 6 (No. 9), 2009, Paper JAI 102188
 179. M. Tagaya and I. Tamura, No. 123—Studies on the Quenching Media, Third Report: The Cooling Ability of Oils, *Technol. Rep. Osaka Univ.*, Vol 4, 1954, p 305–309
 180. M. Tagaya and I. Tamura, On the Deterioration of Quenching Oils, *Technol. Rep. Osaka Univ.*, Vol 7, 1957, p 403–424
 181. G.E. Totten, C.E. Bates, and N.A. Clinton, Chap. 8, Other Quenching Processes, *Handbook of Quenchants and Quenching Technology*, ASM International, 1993, p 291–338
 182. D.S. MacKenzie, The Chemistry of Oil Quenchants, *Heat Treat. Prog.*, Oct 2009, p 28–32
 183. P.S. Protsidim, N.Y. Rudakova, and B.K. Sheremeta, Regenerated Oils as Base of Quenching Media, *Met. Sci. Heat Treat.*, Vol 30 (No. 2), Feb 1988, p 86–88
 184. T.I. Tkachuk, N.Y. Rudakova, B.K. Sheremeta, and M.A. Altschuler, The Influence of Component Composition of Quenching Oils on the Cooling Intensity in the Bubble Boiling Period, *Met. Sci. Heat Treat.*, Vol 28 (No. 10), Oct 1986, p 755–758
 185. Y. Yokota, H. Hoshino, S. Satoh, and R. Kanai, Effect of Boiling Range of Mineral Base Stocks on Quenching of 0.45%C Carbon Steel, *Heat Treating—Proceedings of the 20th Conference*, Vol 2, K. Funatani and G.E. Totten, Ed., Oct 9–12, 2000, ASM International, p 827–832
 186. T.I. Tkachuk, N.Y. Rudakova, and M.R. Orazova, Effect of Fractional Composition of Quenching Oils in Their Cooling Capacity, *Met. Sci. Heat Treat.*, Vol 25 (No. 1), Jan 1983, p 21–22
 187. D.-H. Wang, L.-F. Su, and X.-X. Gao, Production of CS Superfast Quenching Oils, *Heat Treat. Met. (China)*, No. 10, 1991, p 44–50
 188. J.M. Hampshire, User Experience of Hot Oil Quenching, *Heat Treat. Met.*, No.1, 1984, p 15–20
 189. T.W. Dicken, Modern Quenching Oils: An Overview, *Heat Treat. Met.*, No. 1, 1986, p 6–8
 190. D.H. Herring and S.D. Balme, Oil Quenching Technologies for Gears, *Gear Solutions*, July 2007, p 22–30, 50

191. S. Asada and M. Ogino, Reduced Pressure Quenching Oil and Distortion, *Conf. Proc. Second International Conference on Quenching and Control of Distortion*, G.E. Totten, K. Funatani, M.A.H. Howes, and S. Sjoström, Ed., ASM International, 1996, p 585–593
192. T.I. Tkachuk, N.Y. Rudakova, B.K. Sheremeta, and M.R. Orazova, Effect of Oxidation on the Functional Properties of Quenching Oils, *Met. Sci. Heat Treat.*, Vol 27 (No. 9), Sept 1985, p 644–646
193. V.V. Chekanskii and B.E. Sheindlin, Bright-Quenching Properties of Mineral Oils, *Met. Sci. Heat Treat.*, Vol 10 (No. 3), March 1968, p 177–181
194. C. Chen, J. Yao, and S. Chen, Investigation on Oxidation of Quenching Oil, *20th Congress for Heat Treatment and Surface Engineering*, G. Zhi and H. Chong, Ed., Oct 23–25, 2012 (Beijing, China), Chinese Heat Treatment Society, p 417–422
195. A. Sasaki, T. Tobisu, S. Ushiyama, T. Sakai, and M. Kawasaki, Evaluation of Molecular Weight and Solubility in Oil of the Oxidation Products of Two Different Types of Oil, *Lubr. Eng.*, Vol 47 (No. 10), 1991, p 809–813
196. A. Sasaki, T. Tobisu, S. Uchiyama, and M. Kawasaki, GPC Analysis of Oil Insoluble Oxidation Products of Mineral Oil, *Lubr. Eng.*, Vol 47, 1991, p 525–527
197. J. Pfaendtner and J.J. Broadbelt, Mechanistic Modeling of Lubrication Degradation, Part I: Structure-Reactivity Relationships for Free Radical Oxidation, *Ind. Eng. Chem. Res.*, Vol 47, 2008, p 2886–2896
198. V.J. Gatto, W.E. Moehle, T.W. Cobb, and E.R. Schneller, Oxidation Fundamentals and Its Application to Turbine Oil Testing, *J. ASTM Int.*, Vol. 3 (No. 4), 2006, Paper ID JAI13498
199. J. Igarashi, Oxidative Degradation of Engine Oils, *Jpn. J. Tribol.*, Vol 35 (No. 10), 1990, p 1095–1104
200. D. Wooton, The Lubricant's Nemesis—Oxidation, *Pract. Oil Anal.*, Vol 10 (No. 3), March 2007, p 26, <http://www.machinerylubrication.com/Read/999/lubricants-oxidation>
201. D. Wooton, The Lubricant's Nemesis—Oxidation, Part II: Testing Methods, *Pract. Oil Anal.*, Vol 10 (No. 5), May 2007, p 34, <http://www.machinerylubrication.com/Read/1028/oxidation-lubricant>
202. B.K. Sheremeta, G.I. Cherednichenko, N.Y. Rudakova, Z.N. Stanitskaya, and Z.N. Drimalik, Investigation and Selection of Additives to Regulate the Basic Properties of Quenching Oils, *Met. Sci. Heat Treat.*, Vol 14 (No. 11), Nov 1978, p 832–834
203. Z.N. Ostrovskaya, N.Y. Rudakova, B.K. Sheremeta, and Z.N. Drimalik, Oils for Quenching, *Met. Sci. Heat Treat.*, Vol 17 (No. 1), Jan 1975, p 66–67
204. D. Paddle, Development Accelerated Mineral Oil Quenchants, *Ind. Heat.*, Jan 1998, p 40–42
205. W.H. Naylor, Selecting and Handling Quenching Fluids, *Met. Prog.*, Dec 1967, p 70–73
206. J. Lu, Differences in the Cooling Characteristics of Rapid Quenching Oil and Bright Rapid Quenching Oil during the Working Process, *Heat Treat. Met. (China)*, Vol 12, Dec 1990, p 48–50
207. N.M. Emanuel, Z.K. Maizus, and I.P. Skibida, The Catalytic Activity of Transition Metal Compounds in the Liquid Phase Oxidation of Hydrocarbons, *Angew. Chem. Int. Ed.*, Vol 8 (No. 2), 1969, p 97–107
208. J.A. Farris, “Extending Hydraulic Fluid Life by Water and Silt Removal,” Field Service Report 52, Industrial Hydraulics Division, Pall Corporation, Glenn Cove, NY
209. The Hardening and Tempering of Steel: Conventional and Hot Oil Quenching, *Lubrication*, Vol 37 (No. 9), 1951, p 97–112
210. S. Asada and K. Fukuhara, The Influence of Additives on Cooling Process of Mineral Quench Oil, *Heat Treating—Proceedings of the 20th Conference*, Vol 2, K. Funatani and G.E. Totten, Ed., Oct 9–12, 2000, ASM International, p 833–838
211. E. Chrisman, V. Lima, and P. Menechini, Chap. 1, Asphaltenes—Problems and Solutions in E&P of Brazilian Crude Oils, *Crude Oil Emulsions—Composition, Stability and Characterization*, M. El-Sayed Abdul-Raouf, Ed., Intech, 2012, p 3–26, http://cdn.intechopen.com/pdfs/29875/InTech-Asphaltenes_problems_and_solutions_in_e_p_of_brazilian_crude_oils.pdf
212. T.I. Tkachuk, N.Y. Rudakova, B.K. Sheremeta, and R.D. Novoded, Possible Means of Reducing the Film Period of Boiling in Hardening in Petroleum Oils, *Met. Sci. Heat Treat.*, Vol 28 (No. 10), Oct 1986, p 752–755
213. F.S. Allen, A.F. Fletcher, and A. Mills, The Characteristics of Certain Experimental Quenching Oils, *Steel Res.*, Vol 60, 1989, p 522–530
214. V. Matijević, J. Župan, and L. Pedišić, Effect of Composition on Oil Quenching Performance, *Int. Heat Treat. Surf. Eng.*, Vol 6 (No.1), 2012, p 15–18
215. J.A. Hasson, Preventative Maintenance for Quenching Oils, *Ind. Heat.*, Sept 1980, p 21–23
216. M.E. Landis and W.R. Murphy, Analysis of Lubricant Components Associated with Oxidative Color Degradation, *Lubr. Eng.*, Vol 47 (No. 7), 1991, p 595–598
217. N.Y. Rudakova, B.K. Sheremeta, and T.I. Tkachuk, The Development and Use of Special Quenching Oils, *Met. Sci. Heat Treat.*, Vol 28 (No. 10), Oct 1986, p 750–752
218. K.J. Mason and I. Capewell, The Effect of Agitation on the Quenching Characteristics of Oil and Polymer Quenchants, *Heat Treat. Met.*, No. 4, 1986, p 99–103
219. B. Taraba, S. Duehring, J. Španielka, and Š. Hajdu, Effect of Agitation Work on Heat Transfer during Cooling in Oil ISORAPID 277HM, *Strojniški Vestn. (J. Mech. Eng.)*, Vol 58 (No. 2), 2012, p 102–106
220. C.E. Bates and G.E. Totten, Quench Severity Effects on the As-Quenched Hardness of Selected Alloy Steels, *Heat Treat. Met.*, No. 2, 1992, p 45–48
221. D.S. MacKenzie, G. Graham, and J. Janowski, Effect of Contamination on the Cooling Rate of Quenching Oils, *Conf. Proc. Sixth International Conference on Quenching and Control of Distortion*, D.S. MacKenzie, Ed., Sept 9–13, 2012 (Chicago, IL), ASM International, 2012, p 746–754
222. B. Liščić, The Temperature Gradient on the Surface as a Characteristic of the Actual Quenching Intensity during Hardening (Der Temperaturgradient auf der Oberfläche als Kenngröße für die Reale Abschreckenintensität beim Härten), *Härt.-Tech. Mitt.*, Vol 33 (No. 4), 1978, p 179–191
223. B.L. Ferguson and D.S. MacKenzie, Effect of Oil Condition on Pinion Gear Distortion, *Conf. Proc. Sixth International Conference on Quenching and Control of Distortion*, D.S. MacKenzie, Ed., Sept 9–13, 2012 (Chicago, IL), ASM International, 2012, p 319–328
224. “Standard Guide for Evaluation of Hydrocarbon-Based Quench Oil,” D6710-02 (2012), ASTM International
225. M. Johnson, “Selection and Use of Equipment for the Sampling of Liquids,” Report EML-574, Environmental Measurements Laboratory, U.S. Department of Energy, New York, NY, Nov 1995, www.osti.gov/bridge/servlets/purl/184043-QMdlPIJ/.../184043.pdf
226. “Tank Sampling,” United States Environmental Protection Agency SOP 2010, Nov 16, 1994, <http://www.dem.ri.gov/pubs/sops/wmsr2010.pdf>
227. “Standard Test Method for Kinematic Viscosity of Transparent and Opaque Liquids (and Calculation of Dynamic Viscosity),” D445-12, ASTM International
228. “Standard Practice for Calculating Viscosity Index from Kinematic Viscosity at 40 and 100 °C,” D2270-10e1, ASTM International
229. “Standard Practice for Conversion of Kinematic Viscosity to Saybolt Universal Viscosity or to Saybolt Furol Viscosity,” D 2161-10, ASTM International
230. D.A. Wachter, G.E. Totten, and G.M. Webster, Quenching Fundamentals: Maintaining Quench Oils, *Adv. Mater. Proc.*, No. 2, 1997, p 48AA–48CC

231. G. Furman, Quenching, Part II, *Lubrication*, Vol 57 (No. 3), 1971, p 25–36
232. H.E. Boyer and P.R. Cary, Ed., *Quenching and Control of Distortion*, ASM International, 1988, p 44–45
233. Monitor Water-in-Oil with a Visual Crackle Test, *Prac. Oil Anal.*, March 2002, <http://www.machinerylubrication.com/Magazine/Issue/Practicing%20Oil%20Analysis/3/2002>
234. “Standard Test Method for Determination of Water in Petroleum Products, Lubricating Oils, and Additives by Coulometric Karl Fischer Titration,” D6304-07, ASTM International
235. “Standard Test Method for Water in Petroleum Products and Bituminous Materials by Distillation,” D95-05(2010), ASTM International
236. “Standard Test Method for Flash and Fire Points by Cleveland Open Cup Tester,” D92-12b, ASTM International
237. “Standard Test Method for Acid Number of Petroleum Products by Potentiometric Titration,” D 664-11a, ASTM International
238. “Standard Test Method for Acid and Base Number by Color-Indicator Titration,” D974-12, ASTM International
239. T. Mang and H. Jünemann, Evaluation of the Performance Characteristics of Mineral Oil-Based Hydraulic Fluids, *Erdöl Kohle, Erdgas, Petrochem. Brennstoff-Chem.*, Vol 25 (No. 8), 1972, p 459–464
240. “Standard Test Methods for Saponification Number of Petroleum Products,” D94-07(2012), ASTM International
241. “Standard Test Method for Precipitation Number of Lubricating Oils,” D91-02 (2012), ASTM International
242. “Standard Test Method for Trace Sediment in Lubricating Oils,” D2273-08 (2012), ASTM International
243. V. Srimongkokul, Is There a Need for Really Clean Oil in Quenching Operations? *Heat Treat.*, Dec 1990, p 27–28
244. “Standard Test Method for Conradson Carbon Residue of Petroleum Products,” D189-06(2010)e1, ASTM International
245. G.J. Cochrac and S.Q.A. Rizvi, Chap. 30, *Oxidation of Lubricants and Fuels, Fuels and Lubricants Handbook: Technology, Properties, Performance and Testing*, G.E. Totten, S. Westbrook, and R. Shah, Ed., ASTM International, 2003, p 787–824
246. “Standard Test Method for Oxidation Characteristics of Inhibited Mineral Oils,” D943-04a(2010)e1, ASTM International
247. G.E. Totten, C.E. Bates, and N.A. Clinton, Chap. 6, *Quench Bath Maintenance, Handbook of Quenchants and Quenching Technology*, ASM International, 1993, p 181–238
248. W. Hewitt, Monitoring Quench Media in the Production Heat Treatment Shop, *Heat Treat. Met.*, No. 1, 1986, p 9–14
249. R.T. von Bergen, The Effects of Quenchant Media Selection and Control on the Distortion of Engineered Steel Parts, *Conf. Proc. Quenching and Distortion Control*, G.E. Totten, Ed., ASM International, 1992, p 275–282
250. K. Funatani, “Smart Distortion Control by Quench Oil Character,” *Conf. Proc. Sixth International Conference on Quenching and Control of Distortion*, D.S. MacKenzie, Ed., Sept 9–13, 2012 (Chicago, IL), ASM International, 2012, p 373–382
251. J. Denis, J. Briant, and J.C. Hipeaux, Chap. 1, *Analysis of Oil Constituents, Lubricating Properties, Analysis and Testing*, Editions Technip, Paris, France, 2000, p 1–106
252. A.T. Simpson and P.A. Ellwood, Polycyclic Aromatic Hydrocarbons in Quench Oils, *Ann. Occup. Hyg.*, Vol 40 (No. 5), 1996, p 531–537
253. F.E. Woolhead, Controlling the Quench Oil Fire Hazzard, *Heat Treat. Met.*, No. 2, 1984, p 29–32
254. D.H. Herring, Identifying Sources of Oil Quench Fires, *Ind. Heat.*, Nov 2004, <http://www.heat-treat-doctor.com/documents/Quench%20Oil%20Fires.pdf>
255. G.E. Totten, Polymer Quenchants: The Basics, *Adv. Mater. Proc.*, Vol 137 (No. 3), 1990, p 51–53
256. G.E. Totten and G.M. Webster, Quenching Fundamentals: Maintaining Polymer Quenchants, *Adv. Mater. Process.*, June 1996, p 64AA–64DD
257. “Standard Guide for Evaluation of Aqueous Polymer Quenchants,” D6666-04 (2009), ASTM International
258. L.M. Jarvis, R.R. Blackwood, and G.E. Totten, Thermal Separation of Polymer Quenchants for More Efficient Heat Treatments, *Ind. Heat.*, Nov 1989, p 23–24
259. “UCON Quenchants User’s Manual,” Form 118-01567-605AMS, The Dow Chemical Company
260. E.R. Mueller, Polyglycol Quenchant Cleanliness: Are There Benefits? *Heat Treat.*, Oct 1983, p 24–27
261. E. Troell and H. Kristofferson, Influence of Cooling Characteristics on Aging and Contamination of Polymer Quenchants, *Conf. Proc. New Challenges in Heat Treating and Surface Engineering—Conference in Honor of Božidar Liščić*, June 9–12, 2009 (Cavtat Croatia), Croatian Society for Heat Treatment and Surface Engineering, Zagreb, Croatia, p 53–60
262. C.H. Chen, Investigation of Influence Factors on Cooling Rate of PVP Quenchant, *Proc. of Fourth International Conference on Quenching and the Control of Distortion*, Nov 23–24, 2003 (Beijing, China), Chinese Heat Treatment Society, Beijing, China, p 253–256
263. C.H. Chen and J.E. Zhou, The Orthogonal-Regression Analysis on Cooling Rate of PVP Quenchant, *J. Mater. Eng. Perform.*, Vol 11, 2002, p 527–529

Characterization of Heat Transfer during Quenching

B. Hernández-Morales, Universidad Nacional Autónoma de México, México

THE RECORD of 1548 megatonnes (Mt) during 2012 (Ref 1) for global crude steel production reflects the continuing success of steel in obtaining a variety of mechanical properties that can be achieved after processing, at a competitive cost. Although solidification processes play an important role, the final properties of a given part are tailored during processing in the solid state through the control of the microstructure. In particular, the mechanical properties sought in a part fabricated with steel can be obtained by heat treating processes, which are based on controlled heating and cooling cycles.

Quenching is a heat treating process in which the part is heated to the austenitizing temperature (to transform the microstructure into austenite), held at that temperature for a period of time (to achieve the desired previous austenite grain size and, if necessary, dissolve carbides), and rapidly cooled to room temperature (to promote the austenite-to-martensite transformation) (Ref 2). The as-quenched martensite is hard but too brittle to be used in the field; thus, quenching is usually followed by a tempering process that consists of heating the part in the ferrite + iron carbide region of the phase diagram, holding it for a given period of time, and cooling it to room temperature. The resulting so-called tempered martensite (although it is not martensite but rather fine carbide particles in ferrite) has a relatively high hardness and toughness (Ref 3).

Because quenched and tempered parts are at or near the end of the production chain, controlling these heat treating operations becomes critical. However, during quenching there are many phenomena that interact with each other and occur at different scales, which makes this a very complex process. Figure 1 summarizes the interlinked phenomena. There are three basic fields of interest:

- The thermal field (which changes with time due to heat extraction at the part/quench medium interface)

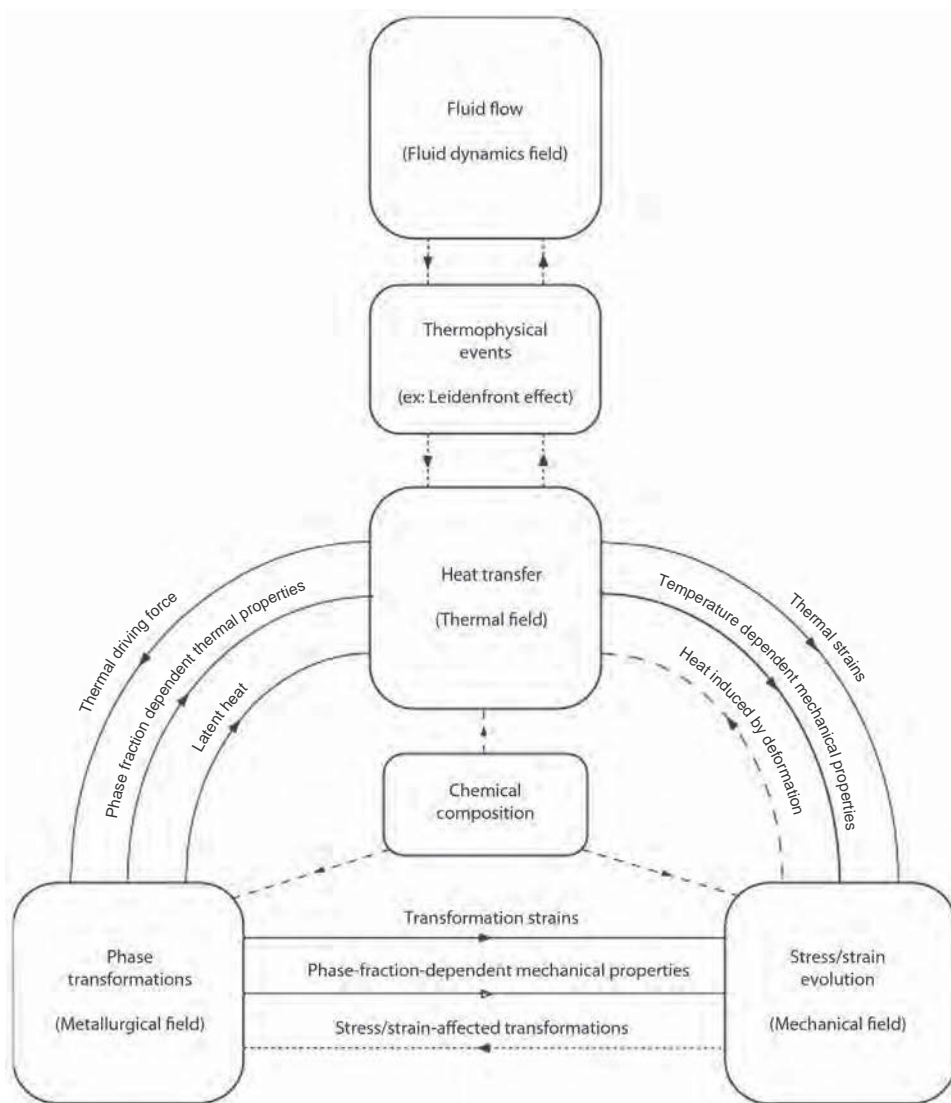


Fig. 1 Physical phenomena occurring during quenching and their couplings. Source: Ref 4. Reprinted, with permission, from *Materials Performance and Characterization*, copyright ASTM International, 100 Barr Harbor Drive, West Conshohocken, PA 19428

- The metallurgical field (which changes with time as the various phase transformations occur)
- The mechanical field (which changes with time as displacements within the part occur)

Because the quench medium is either liquid or gaseous, the fluid dynamics field within the quenchant becomes important in defining the heat extracted as the process progresses. In the figure, the causes that create the interactions among the different fields are also shown. For example, the evolution of the metallurgical field (the volume fraction evolution of each one of the microconstituents) is associated with two important effects that modify the thermal field: the rate of latent heat release and the values of the thermophysical properties (which depend on both the temperature and the phase distribution).

The initial state of each one of the basic fields must be known as precisely as possible. In this regard, it is common practice to assume a uniform thermal field at the beginning of the quench; the initial metallurgical field may include a previously formed carburized layer, prior-austenite grain size, and partially or fully dissolved carbide-forming elements. Initially, the mechanical field is the residual-stress field after austenitizing.

The mechanical properties achieved and the distortion produced by a given quenching operation are the result of the paths that each one of the fields described previously follows during the process.

The goal of steel quenching is to transform the austenite into martensite while producing as little distortion as possible. There are three distinct methodologies that may be used to design, control, and optimize an industrial process such as quenching: empirical, laboratory-scale testing, and process engineering. The level of complexity associated with the analysis as well as the required technical expertise increases from empirical procedures to laboratory-scale testing to process engineering; at the same time, the amount of knowledge generated also increases. For a given problem, any one of the three approaches (or any combination) may be convenient.

The empirical methodology is mainly used to define operational windows through experiments in which the values of a number of process variables are changed in an orderly fashion and the results obtained in the final product are compared against specific targets. A case in which an empirical methodology was used to optimize in-plant heat treating variables (austenitizing temperature and holding time) to comply with as-quenched flatness specifications for gears was presented by Lim (Ref 5). To reduce the number of experiments required, he used a factorial design to design the experimental matrix.

The empirical methodology provides very little insight into the phenomena that occur during the process, because it usually considers only

the initial and final states; on the other hand, it is not possible to measure the various system responses in situ, but rather, one must resort to laboratory-scale measurements that usually focus on only one aspect of the process. These exercises are useful mainly for comparison purposes, and therefore, it is important that they are standardized. Although they have been designed to reduce and simplify the phenomena involved, it is still possible to obtain useful data for process design and control. For example, the hardenability of a given steel is characterized based on the Jominy end-quench test, in which a bar fabricated with the steel of interest is water quenched on one of its ends, and the resulting hardness profile along the bar length (which is directly related to the evolution of the cooling rate distribution) is measured (Ref 6).

Process engineering is based on mathematical and physical modeling of the phenomena occurring in a process, complemented by in-plant and pilot-plant measurements as well as laboratory measurements (to evaluate transport and/or thermodynamic properties) (Ref 7). A comprehensive review of mathematical models of quenching processes is published by Gür and Şimşir (Ref 4). Physical modeling of quenching processes is focused on studies of fluid flow in the quench bath (Ref 8, 9).

Heat-Transfer Basics

All bodies at a temperature above zero Kelvin contain a definite amount of thermal energy (the sum of internal and kinetic energy) that is directly related to the body temperature; because the latter is easier to measure, the thermal energy state of a system is usually characterized by its temperature.

The most common method used to record temperature variations in many materials processes is based on thermocouples. They may be placed either within the part (by drilling

holes to insert them) or directly attaching them to the part surface. In the first case, the thermocouples are secured to the part using various high-temperature cements; in some investigations, precautions have been taken to improve thermal contact between the thermocouple sheath and the part. In the case of thermocouples attached to the surface part, there are two kinds of arrangements: intrinsic (the material forms part of the thermoelectric circuit) and extrinsic (the two thermocouple wires are first welded and the resulting junction is spot welded to the surface). Tseng and Saraf (Ref 10) showed that the fin effects associated with a surface-mounted thermocouple affect the measured temperatures and, consequently, they developed a mathematical model to correct it; the model can be embedded in a more general finite-element model of heat transfer within the part. The Liščić-NANMAC probe (Fig. 2) is based on drilling holes perpendicular to the probe surface to place the tip of a self-renewing thermocouple at the probe surface (Ref 11).

Along with the temperature, the cooling rate is a very important variable in heat treating. It cannot be measured directly; instead, it is calculated from the measured cooling curve (temperature versus time data), usually assuming a linear variation of the cooling curve during a short time interval. With this assumption, a two-point formula for approximating the derivative (Ref 12) is applied:

$$\text{Cooling rate} \equiv \frac{\partial T}{\partial t} \approx \frac{\Delta T}{\Delta t} \quad (\text{Eq 1})$$

where T is temperature, t is time, and ΔT is the temperature change over a small time interval (Δt).

Given that the quantity of interest is the thermal response, it is important to select an adequate frequency of data acquisition. Totten et al. (Ref 13) showed the effect of increasing this frequency (from 1 to 5 Hz) on the cooling

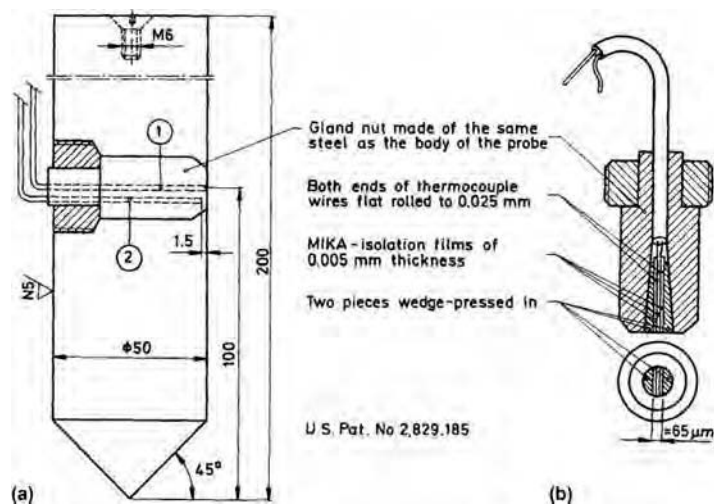


Fig. 2 (a) Schematic representation of the Liščić-NANMAC probe. (b) Detail of the NANMAC thermocouple. Source: Ref 11

rate versus time curve for a cylindrical probe (13 by 100 mm, or 0.5 by 4.0 in.) fabricated with Inconel 600 instrumented with a single thermocouple located at the geometrical center. They found that the highest value was needed to obtain a sufficiently smooth curve. A numerical derivative (such as the one used to compute the cooling rate) tends to produce rough curves, particularly when a two-point formula is applied.

The temperature distribution within a body may be modified due to heat-transfer processes. Heat transfer occurs whenever a temperature difference (driving force) is present either within a body or between separate bodies. The rate of heat transfer is quantified by the heat flow, which in turn is related to the heat flux and the heat-transfer area:

$$Q = qA_{\perp} \quad (\text{Eq 2})$$

where Q is the heat flow, q is the heat flux, and A_{\perp} is the area perpendicular to the heat flow.

Another way of modifying the thermal balance within a system is by converting its thermal energy to another form of energy, or vice versa. For example, when electric current flows through a material that offers electrical resistance, part of the electrical energy is transformed into thermal energy, which is dissipated as heat; this is the well-known Joule effect. On the other hand, when an endothermic reaction occurs, thermal energy must be supplied to contribute to the chemical energy required for the reaction.

Thus, the heat that flows into a system, the heat that flows out of a system, and the amount of thermal energy transformed into/from another form of energy combine to produce a net change of thermal energy within the system:

$$A = \sum_i Q_{E,i} - \sum_j Q_{S,j} + Q_G \quad (\text{Eq 3})$$

where A is the rate of accumulation of thermal energy within the system, $Q_{E,i}$ is the heat flow into the system through area i , $Q_{S,j}$ is the heat flow out of the system through area j , and Q_G is the rate of thermal energy transformation. Note that all dimensions in the terms in Eq 3 are [thermal energy/time], that is, denote thermal energy flow, although it is usually referred to (erroneously) as heat flow.

The rate of the thermal energy transformation term in Eq 3 (Q_G) is also known as a heat source (when another form of energy is transformed into thermal energy) or a heat sink (when thermal energy is transformed into another form of energy). This term explains the difference between sensible and latent heat: the former implies a temperature change ($A \neq 0$ in Eq 3) due to a net heat transfer to a body without heat sources/sinks, while the latter may occur isothermally ($A = 0$ in Eq 3) if the net heat transferred to/from the body is balanced by a heat source/sink associated with a phase change or nonisothermally ($A \neq 0$ in Eq 3) if such balance is not achieved.

Mechanisms of Heat Transfer. There are two basic mechanisms by which heat may be transferred: conduction and radiation (Ref 14). Conduction occurs by heat exchange between two parts of a system due to molecular motion; therefore, it is characterized by short-distance interactions and requires the presence of a medium; that is, it cannot occur in vacuum. Fourier developed a phenomenological law that relates the heat flux by conduction with the thermal gradient in the direction normal to heat flow (Ref 15). He found that the heat flux is proportional to the thermal gradient and that the proportionality constant is dependent on the material through which heat is flowing. Fourier's law is written (for example, for heat flowing in the x -direction) as:

$$q_{k,x} = -k \frac{\partial T}{\partial x} \quad (\text{Eq 4})$$

where $q_{k,x}$ is the heat flux by conduction in the x -direction, k is the material thermal conductivity, T is the temperature, and x is the x -coordinate.

Temperature is a scalar quantity (it has only magnitude), while the heat flux is a vector quantity (it has both magnitude and direction) and has from one up to three nonzero components. The minus sign in Eq 4 is required because heat always flows from a hot to a cold region, that is, against the thermal gradient.

Heat exchange by radiation occurs between two surfaces at different temperatures; the space between the surfaces may be transparent to radiation—in which case it is not taken in consideration in the calculations—or not. The nature of thermal radiation is electromagnetic, which makes it akin to light. The total amount of energy emitted by a surface may be quantified through the Stefan-Boltzmann equation (Ref 14):

$$q_{\text{rad}} = \sigma T^4 \quad (\text{Eq 5})$$

where q_{rad} is the heat flux due to radiation, σ is a constant ($5.669 \times 10^{-8} \text{ Wm}^{-2} \cdot \text{K}^{-4}$), and T is the surface temperature (expressed in Kelvin).

The Stefan-Boltzmann equation was derived for the so-called black-body surface, which is a hypothetical surface that absorbs all incoming radiation. In general, a real surface emits less radiant energy than predicted by Eq 5; therefore, the radiant thermal energy emitted by a real surface, $q_{\text{rad,real}}$, is given by (Ref 14):

$$q_{\text{rad,real}} = \epsilon \sigma T^4 \quad (\text{Eq 6})$$

with ϵ being the surface emissivity, which, for steel, varies from 0.1 to 0.3 (for a polished surface) to 0.8 (for an oxidized surface).

In many textbooks, a third mechanism, convection, is described. It occurs due to the interaction between a surface and a fluid in motion; when the fluid is moved by an external source, one refers to forced convection, while free

convection is associated with fluid flow due to density differences. In either case, heat exchange between a surface and a fluid actually occurs by conduction and radiation, and therefore, some authors prefer not to classify convection as a heat-transfer mechanism proper but rather refer to this mode of heat transfer as heat transfer with convection (Ref 14). Due to the complexity of solving both the velocity and the thermal field (which are coupled in the case of free convection and uncoupled for forced convection), it is customary to apply the so-called Newton's law of cooling to quantify the heat exchange between a surface and a fluid in contact with it (Ref 16):

$$q_{\text{int}} = -\bar{h}\Delta T = -\bar{h}(T_f - T_{\text{surf}}) \quad (\text{Eq 7})$$

where q_{int} is the heat flux transferred across the interface, \bar{h} is the heat-transfer coefficient, T_{surf} is the surface temperature, and T_f is the bulk fluid temperature. The latter is the fluid temperature outside of the thermal boundary layer (the region where significant thermal gradients do occur), and it is commonly assumed to be constant. In many texts and papers related to heat transfer during quenching, the heat-transfer coefficient is represented by α .

Boiling Heat Transfer. Boiling occurs when a vaporizable liquid is heated to a temperature above its saturation temperature (at a given pressure), resulting in a phase transition from liquid to vapor (Ref 17); although boiling is commonly associated with the formation of bubbles, at sufficiently high surface temperatures it is possible to form a film of vapor.

The different modes of boiling are classified according to the hydrodynamics of the bath and the fluid operational temperature with respect to its saturation point (Ref 17). If the liquid is quiescent, the boiling mode is termed pool boiling, whereas in forced convective boiling the liquid is set in motion by external forces. It should be noted that bubble dynamics induce mixing near the surface of the testpiece in both modes. When the operational temperature of the liquid is kept below its saturation point, subcooled boiling occurs; on the other hand, in the case of saturated boiling, the liquid is kept at a temperature slightly above its saturation point. Regarding the thermal conditions during an experimental study or a plant operation, they may be steady state (using either electric power control or surface temperature control) or transient.

Pool Boiling. The bulk of investigations on boiling has been concentrated on saturated pool boiling. In a pioneer study, Nukiyama (Ref 18) devised a power-controlled experiment to characterize the boiling behavior of saturated water at atmospheric pressure. He heated a 0.14 mm (0.006 in.) diameter nichrome wire in quiescent water at 100 °C (212 °F) and plotted the logarithm of the surface heat flux (q_s) as a function of the logarithm of the corresponding wall superheat (ΔT_{sat}), that is, the difference between the surface temperature and the liquid

saturation temperature; this graph is known as a boiling curve. He observed that the surface heat flux increases as the wall superheat increases until a maximum is reached, the boiling curve has a local minimum, and at very high wall superheat values a burn-out effect occurs. From his observations, the nucleate and film boiling regions in a boiling curve were defined. The nucleate boiling region is associated with nucleation, growth, and departure of bubbles, and its upper bound—in the boiling curve—is defined by the maximum surface heat flux, also known as the critical heat flux; on the other hand, a film of vapor covers the surface in the film boiling region. The critical heat flux is of prime importance in nuclear reactor design (Ref 19–22).

Nukiyama's experiments were conducted under steady-state conditions and controlled the electric power supplied to the wire, that is, controlled the surface heat flux. Under these experimental conditions, it is not possible to observe the region between nucleate and film boiling. The complete boiling curve under pool boiling conditions is shown, schematically, in Fig. 3. The small amount of superheat (region I) required to initiate the formation of bubbles is due to kinetic factors that limit bubble nucleation. The region in which bubbles are present consists of two different subregions; in region II, small bubbles are formed at only a few sites along the surface, while in region III (nucleate boiling), the bubbles are larger and cover the entire surface. Due to their small size, the bubbles in region II condense as they enter in contact with the liquid; in contrast, the larger bubbles in region III detach from the surface, leaving an empty area that is quickly covered by fresh liquid. As mentioned previously, the upper bound of the nucleate boiling regime is the critical heat flux. At higher temperatures, the surface is in contact with increasing amounts of vapor that hinder heat transfer, thus, the negative slope of the boiling curve in region IV, also known as transition boiling. Stable film boiling (region V) is characterized by a vapor blanket in contact with the entire surface; the vapor blanket acts as a barrier to heat transfer, which occurs by a combination of conduction and radiation through the vapor blanket. If the heat flux to the surface is further increased, the wall superheat increases to a point where radiation becomes the dominant heat-transfer mechanism, and the surface heat flux increases again.

Forced Convective Boiling. While fluid flow in pool boiling is primarily driven by bubble motion, bulk motion as well as buoyancy effects are responsible for fluid flow in forced convective boiling (Ref 24). For a given subcooling, heat extraction is increased when the fluid velocity increases, as shown schematically in Fig. 4 (Ref 25). Near the critical heat flux, the forced convective boiling curves for various fluid velocities and subcoolings merge into a single curve, known as the fully developed boiling curve. In some systems, this curve lies on

an extension of the corresponding nucleate boiling curve for pool boiling.

The need for higher cooling rates than those provided by pool boiling has prompted the development of more efficient cooling schemes based on forced convective boiling. In the metallurgical industry, spray cooling is used in press quenching of aluminum alloys because it enhances the heat-transfer rate in all regions of the boiling curve (Ref 26). Water-jet cooling is applied in run-out tables to produce high heat-extraction rates that result in ferrite grain

size refinement, producing steels with higher strengths (Ref 27). During continuous casting of steel, heat exchange between the copper mold and cooling water takes place by forced convection, which enhances heat transfer to the cooling fluid, avoiding excessive mold heating, which may lead to defects in the casting (Ref 28). Intensive quenching processes are based on a highly agitated quench medium that suppresses film boiling altogether (Ref 29). A very efficient forced convective process is jet impingement (Ref 30).

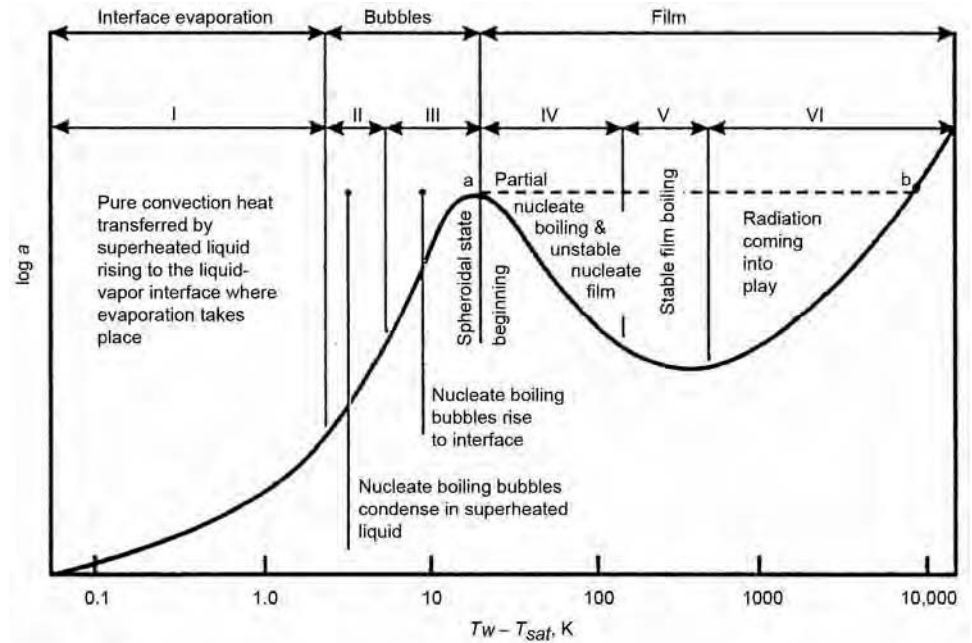


Fig. 3 Schematic of characteristic boiling curve for pool boiling in a saturated liquid. Source: Ref 23

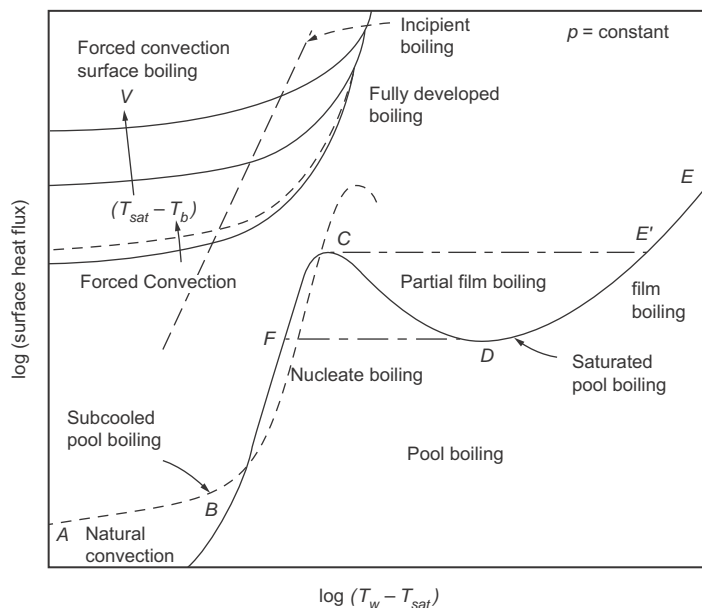


Fig. 4 Schematic comparison of forced convective boiling versus pool boiling. Source: Ref 25

Heat Generated by Microstructural Evolution

The microstructural field evolution during quenching produces the final microstructural distribution, but it also modifies the heat balance within the probe. During quenching, all solid-solid phase transformations in steels are exothermic reactions; that is, they release heat as they occur. The volumetric rate of heat released by a phase transformation from austenite to microconstituent k ($q_{G,k}$) is proportional to the rate of phase transformation:

$$q_{G,k} = \rho \Delta H \frac{\partial f_k}{\partial t} \quad (\text{Eq 8})$$

where ρ is the density, ΔH is the enthalpy of transformation per unit mass, and f_k is the fraction transformed of microconstituent k .

The volumetric rate of heat released is related to the rate of thermal energy transformation (Q_G in Eq 3) through:

$$Q_G = q_G V \quad (\text{Eq 9})$$

where V is the volume.

Under heat treating conditions, the local rate of thermal energy transformation usually overcomes the local net heat flow (refer to Eq 3), resulting in a change of slope of the temperature/time curve during the phase transformation period. Upon heating, the transformation to austenite is endothermic, which causes a slight decrease in the heating rate because of the heat absorbed by the transformation. In contrast, during cooling, the transformation is exothermic, that is, it releases heat, resulting in a temperature increase known as recalescence. For example, Fig. 5 plots the cooling curve measured with a 1.6 mm ($1/16$ in.) diameter type K thermocouple at the centerline of a 12.7 mm (0.5 in.) diameter by 50.4 mm (2.0 in.) long cylindrical probe made of AISI 4140 steel quenched in a fluidized bed consisting of alumina and air at room temperature. The numerical value of the fluidization number (the ratio of actual gas velocity to minimum fluidization velocity) is commonly used to characterize the level of fluidization of a given fluidized-bed reactor. The results in Fig. 5 refer to a fluidization number of 1.4, which indicates that the actual gas velocity through the bed is 1.4 times the value required to achieve minimum fluidization, that is, the condition under which individual particles lose contact with each other and the bed behaves as a fluid. In the early stages of the quench, the temperature decreases monotonically; at approximately 320 °C (610 °F), a change of slope is evident. The latter is due to the heat released by the austenite-to-martensite transformation, which overcomes the capacity of the quench medium to extract heat. As mentioned previously, this change in a cooling curve is referred to as recalescence. Toward the end of the transformation, the rate of heat released is compensated by the rate of heat

extraction, and the local temperature diminishes monotonically until the fluidized-bed operating temperature is reached.

The rate of formation of the new phase is defined by the type of kinetics of the solid-solid phase transformation. The objective of a quench is to transform the austenite into martensite. The austenite-to-martensite transformation is one of two types of diffusionless transformations (those in which the atoms need to move only short distances) (Ref 32). The phase transformation involves a definite orientation relationship; that is, the atoms need to move in a coordinated manner. Because there are no thermally activated events, the amount of martensite fraction transformed depends on the local instantaneous temperature alone. Koistinen and Marburger measured the volume percent of retained austenite after quenching pure iron-carbon alloys ($0.37 < \%C < 1.1$) using x-ray diffraction (Ref 33). From the experimental data, they developed an empirical equation to predict the volume fraction of retained austenite after the quench. The Koistinen-Marburger equation, in terms of volume fraction of martensite (f_M), is:

$$f_M = 1 - \exp[-\beta(M_s - T)] \quad (\text{Eq 10})$$

where T is the local current temperature, M_s is the martensite start temperature, and $\beta = 0.011 \text{ } ^\circ\text{C}^{-1}$.

The diffusional transformations (austenite transforming to ferrite, pearlite or bainite) occur at high temperatures and may be described mathematically—considering an isothermal event—using the Johnson-Mehl-Avrami-Kolomgorov equation (Ref 34, 35):

$$f_k = 1 - \exp[-bt^n] \quad (\text{Eq 11})$$

where f_k is the volume fraction ($k \equiv$ ferrite, pearlite, or bainite), and b and n are parameters to be determined experimentally.

From Eq 8, 10, and 11, it is evident that the rate of thermal energy produced by austenite decomposition during quenching depends on the rate of phase transformation, which in turn is a strong function of the current temperature. Thus, the thermal and microstructural fields are strongly coupled (Fig. 1).

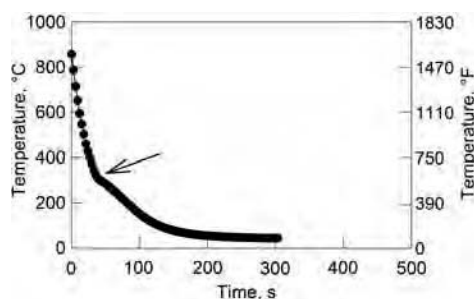


Fig. 5 Cooling curve measured at the centerline of an AISI 4140 cylindrical probe quenched in a fluidized bed (alumina plus air at room temperature) and with a fluidization number of 1.4. Source Ref 31

The relationship between the kinetics of a phase transformation and the variables temperature and time is given by a time-temperature-transformation (TTT) diagram, such as that shown schematically in Fig. 6. The characteristic “nose” is a consequence of the competing nucleation and growth events of the high-temperature transformations. The temperatures at which the austenite-to-martensite transformation starts and finishes are known as the martensite start and finish temperatures (M_s and M_f , respectively). This type of diagram is obtained through experiments conducted under isothermal conditions and is also known as isothermal transformation diagrams.

Quenching is a nonisothermal process. Therefore, continuous cooling transformation (CCT) diagrams are preferred instead of TTT diagrams to predict (roughly) the final microstructure by superimposing a measured cooling curve on the diagram. A CCT diagram is built from data obtained during experiments in which cooling is provided by a gas. However, the usual cooling conditions during a quench are very different from those obtained during gas cooling, and therefore, care must be taken if a CCT diagram is to be used for quantitative predictions.

Liquid Quenching Heat Transfer

To optimize a quenching process, it is necessary to fully understand the dynamics of the interplay between the hot part and the quenchant. Although it is possible to quench some steels in air and other gases, such as nitrogen, hydrogen, and helium, the bulk of the quenching operations are carried out using liquid quenchants (Ref 2). Therefore, heat extraction at the part surface usually occurs in the presence of boiling phenomena, with the exception of quenching in molten salts or metals, which is seldom used. Given that the size and geometry of parts quenched in a plant make it difficult

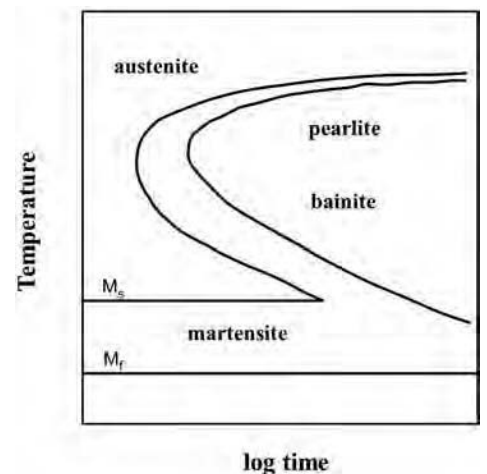


Fig. 6 Schematic representation of a time-temperature-transformation diagram

to instrument them with thermocouples, it is customary to compare the heat-extraction characteristics of quenchants by means of studying the thermal response of small-sized probes quenched in laboratory-scale equipment, a methodology known as cooling curve analysis. In some studies, the results have been extrapolated to predict the metallurgical response of actual parts.

An example of a cooling curve measured in a laboratory is shown in Fig. 7. The AISI 304 stainless steel conical-end cylindrical probe (Fig. 7a) was heated in air using an electrical resistance furnace and quenched in water at 60 °C (140 °F) flowing at 0.2 m/s (0.7 ft/s) parallel to the probe length; the cooling curve in Fig. 7(b) corresponds to the position of thermocouple T/C 3 (42.67 mm, or 1.68 in., from the top of the probe). Initially, the thermal response is constant, which indicates that the probe is still inside the furnace; at approximately 29.1 s (as determined from a video taken synchronously with the cooling curve), the probe has reached its final position within the quench bath.

Immediately after the start of the quench, a vapor film is formed surrounding the probe; the vapor film acts as a thermal resistance, reducing heat extraction. As the surface temperature decreases, the vapor film becomes unstable, giving way to the formation of discrete bubbles; bubble nucleation and growth is a very efficient form of heat extraction, and therefore, the cooling curve registers a sudden change in its rate of change. At even lower temperatures, boiling cannot be sustained, and the surface is cooled by pure convection (in this case, forced convection). Because the probe material is an austenitic stainless steel, there is no phase transformation during cooling, and the cooling curve does not show any recalescence. Pilling and Lynch (Ref 37) were the first to note this behavior while measuring the cooling curve measured at the center of 6.4 mm (0.25 in.) diameter by 50 mm (2 in.) long cylindrical carbon steel probes quenched from 850 °C (1560 °F) in vaporizable liquids; they named the three zones of the cooling curve thus described as A-, B-, and C-stage, respectively, which is a nomenclature still in use today (2013). Tagaya and Tamura videorecorded evidence of the events at the probe surface during quenching of a 10 mm (0.4 in.) diameter by 300 mm (12 in.) long cylindrical silver probe while simultaneously recording the cooling curve (Ref 38). They also identified a fourth stage (which occurs at the start of the quench): shock-film boiling.

Each one of the different stages shown in Fig. 7 results in different magnitudes of heat extracted by the quenchant, as schematically shown in Fig. 8, where the heat-transfer coefficient associated with each stage is also shown (Ref 39, 40). In the figure, immersion cooling refers to a process in which a part is cooled by immersing it in a fluid, while film cooling occurs when a film of liquid descends along the part surface to cool it.

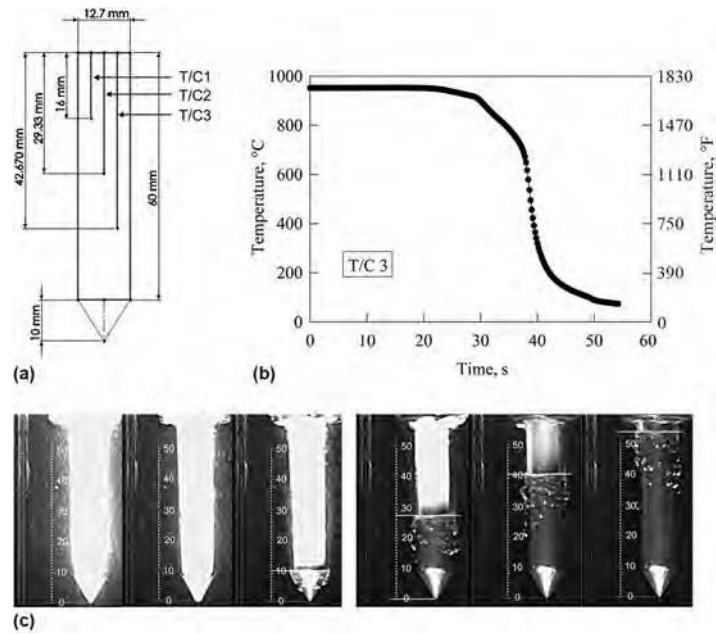


Fig. 7 (a) Schematic diagram of the conical-end probe. (b) Thermal response measured by the thermocouple labeled as T/C 3 during an experiment with water at 60 °C (140 °F) flowing at 0.2 m/s (0.7 ft/s). (c) Images taken from the video recording (the scale on the photographs is given in millimeters). Source: Ref 36

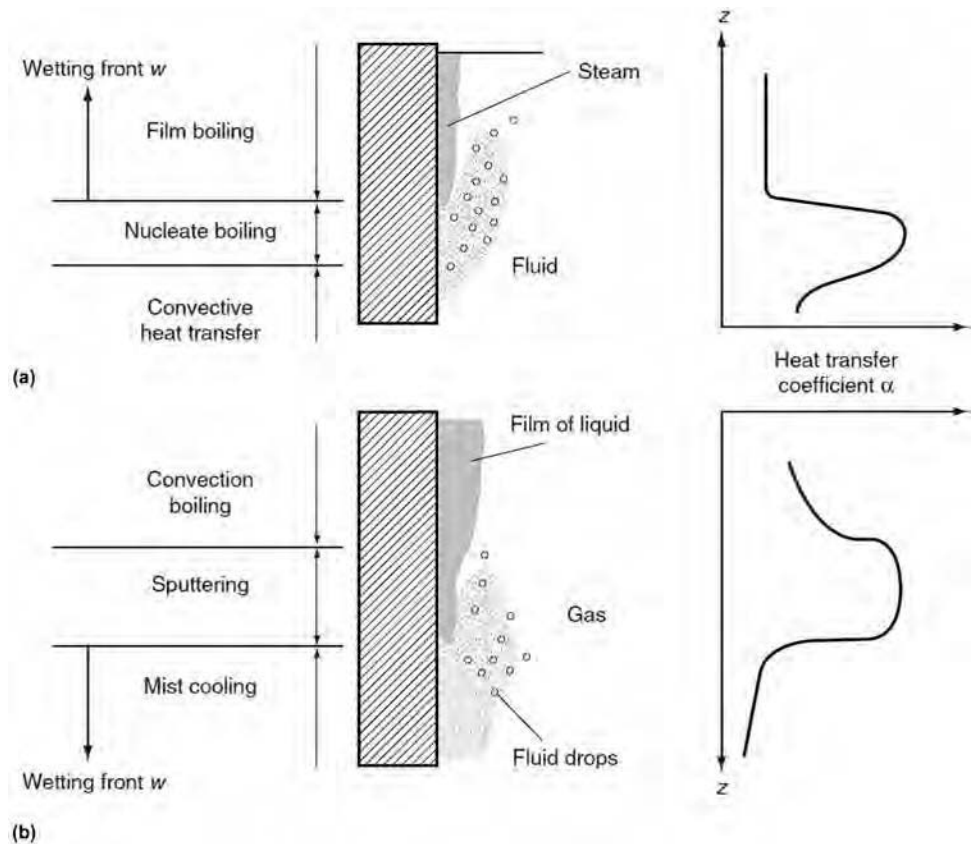


Fig. 8 Wetting behavior and change of heat-transfer coefficient (α) along the surface of a metallic probe. (a) Immersion cooling. (b) Film cooling. Source: Ref 39, 40. Reprinted, with permission, from *Fuels and Lubricants Handbook: Technology, Properties, Performance and Testing*, copyright ASTM International, 100 Barr Harbor Drive, West Conshohocken, PA 19428

Rewetting is a complex phenomenon that plays a key role in defining the heat-extraction characteristics of a liquid quenchant. The rewetting process marks the end of the vapor blanket stage and the beginning of the nucleate boiling stage; the loci of positions where this transition takes place is known as the wetting front. A related quantity is the Leidenfrost temperature (Ref 41); in the context of metal quenching, this quantity is the temperature at which film boiling ends and transition boiling starts. Another form of characterizing rewetting is by the rewetting time, which is the time at which the transition from vapor film to nucleate boiling occurs.

Quenching in oils, water, and some polymer quenchants exhibits a slow advance of the wetting front. As can be deduced from Fig. 7, not only does the wetting front position vary with time, but there is not a single value of the Leidenfrost temperature; instead, it is a function of position along the probe length. This behavior is known as non-Newtonian cooling, to distinguish it from a case in which the total area of contact between the part and the quenchant is considered to experience a single mode of heat extraction at a given time (Newtonian cooling). Although the latter assumption simplifies further calculations, it has been pointed out that it usually results in errors, as is the case with the Grossman number or H factor (Ref 42), which, nonetheless, has been used to predict the final hardness distribution.

Once the position of the wetting front has been determined as a function of time, the wetting front velocity may be estimated by fitting that curve. For example, knowing the wetting front position determined from images extracted from videorecordings during quenching of conical-end cylindrical probes quenched in water flowing (parallel to the probe length) at 0.2 m/s (0.7 ft/s), Hernández-Morales et al. (Ref 36) fitted a regression line, as shown in Fig. 9(a). A measure of the goodness of a linear regression is the coefficient of determination (R^2); if its value is close to 1, then there is a strong linear relationship between the dependent and independent variables. In the context of Fig. 9(a) the value of $R^2 = 0.994$ indicates that the relationship between the wetting front location and time may be assumed as linear, and therefore, the wetting front velocity is constant in this example. Using the same methodology, the wetting front velocity was computed as a function of bath temperature (Fig. 9b). The relationship between wetting front velocity and bath temperature was nonlinear, with the wetting front velocity decreasing as the bath temperature increased, because this condition favors a more stable vapor film and therefore higher local rewetting times. Due to the same reason, the local Leidenfrost temperature diminished (an indication of a more stable vapor film) as the water temperature increased.

Besides the cinematographic technique, there are alternative methods to characterize wetting front kinematics. Künzel et al. (Ref 43) noted that the electrical conductance between the part

surface and a counterelectrode is directly related to the breaking up of the vapor blanket. They instrumented a 15 mm (0.6 in.) diameter, 45 mm (1.8 in.) long cylindrical CrNi probe with a thermocouple at the probe center and measured the change of conductance between the sample and a circular back-plate electrode that is placed concentric with the sample. During the early stages of an experiment in boiling water, they measured a very low electrical conductance, because the vapor blanket is not only a good thermal insulator but also a good electrical insulator. As the rewetting process starts and the wetting front spreads, the surface area free from the water blanket increases and so does the measured electrical conductance; thus, the synchronous measurement of temperature and electrical conductance allows the determination of the time and temperature at which rewetting starts, as well as the portion of the probe surface that is wetted at a given time. With this information, it is possible to compute the wetting front velocity; in this particular experiment, rewetting started at the bottom, and the wetting front advanced upward at a constant velocity.

It is interesting to note that in their experiments, using a probe with a smooth surface (Fig. 10), the time at which rewetting starts (t_s , as determined from the electric conductance measurements) is shorter than the time at which a change in slope may be detected in the cooling curve measured at the core (t_u). This is a direct consequence of the thermal resistance between the probe surface and its center, which delays and dampens the measured thermal response with respect to the events taking place at the probe surface. When the surface was modified to reduce its smoothness (by machining a thread on it), the vapor blanket broke up much earlier during the experiment, but the wetted surface area was only that of the peaks of the thread; consequently, the measured electrical conductivity increased slowly until no vapor was trapped within the threads. They also studied the effect of bath agitation and subcooling and found that the wetting duration decreases when either one of those variables increase. Furthermore, they also measured the resulting hardness in Ck45 steel quenched from 880 °C (1615 °F) in water at 50 °C (120 °F); they observed a hardness distribution along

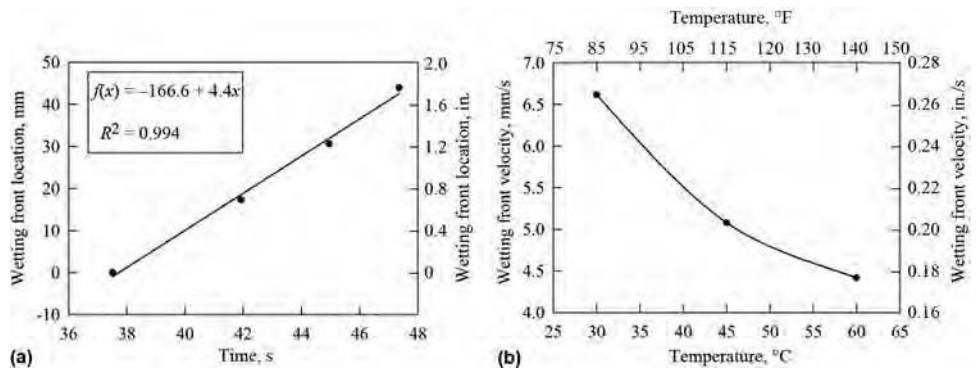


Fig. 9 Wetting front kinematics during quenching of a conical-end AISI 304 stainless steel probe in water flowing (parallel to the probe) at 0.2 m/s (0.7 ft/s). (a) Wetting front location as a function of time during quenching in water at 60 °C (140 °F). Data (symbols); linear regression (line). (b) Wetting front velocity as a function of water temperature. Source: Ref 36

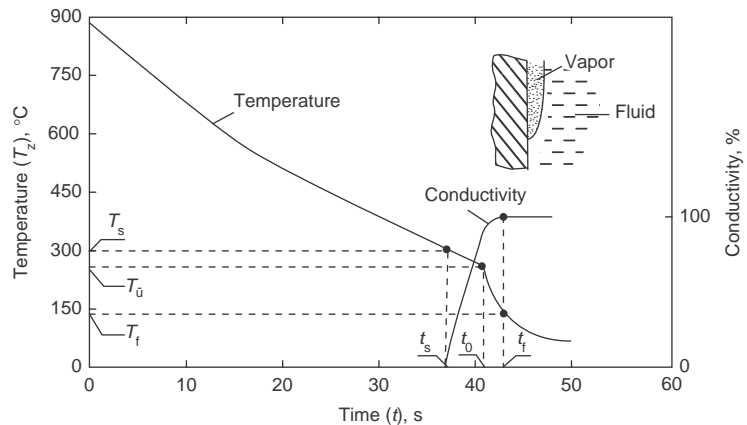


Fig. 10 Measured cooling curve (at the probe center) and electrical conductivity during quenching of a NiCr cylindrical probe with a smooth surface in still boiling water. See text. Final temperature and time, T_f and t_f . Source: Ref 43

the probe sample that was consistent with the wetting front kinematics.

Another method for determining wetting front kinematics is based on the noise associated with the formation and departure of bubbles from a heated surface. Kobasko et al. (Ref 44) quenched a 200 mm (8 in.) spherical silver probe in a bath containing 15 kg (33 lb) of quenchant. The probe was instrumented with a type K thermocouple located at the probe center and cast in place. The cooling curve was recorded with a data-acquisition frequency of 30 Hz. Within the bath, a microphone was located to monitor the noise produced during the quench; the total signal width was divided into 100 Hz bands over 200 channels. The cooling-rate history curve is shown, along with two spectrographs (frequency spectrum curves extracted from the acoustical signal), in Fig. 11. The spectrograph in the broadband (Fig. 11b) resembles the cooling-rate history curve, which is a good indication of the usefulness of the acoustical method. Moreover, even though silver probes have been known for their high sensitivity (because the high thermal conductivity of the silver greatly diminishes the lagging and damping effects), it was not possible to detect the shock-boiling stage that precedes film boiling using the cooling curve data. In contrast, the acoustical method provided evidence of shock boiling: the peak with high amplitude that occurs at less than 1 s in the spectrograph shown in Fig. 11(c).

In their study, Künzel et al. (Ref 43) also found that probe geometry has a significant effect on heat extraction during quenching. Recently, Hernández-Morales et al. have shown, using computational fluid dynamics, that this effect is directly related to the hydrodynamic conditions in the vicinity of the probe (Ref 45–48). In particular, the computed streamlines shown in Fig. 12 demonstrate that the flow field is much more uniform when using a conical-end probe as opposed to the more commonly used flat-end probe; moreover, the interaction between the fluid and the base of the flat-end probe produces boundary layer separation and a region of recirculation. As a result of the hydrodynamic conditions, the pressure distribution around the probe is also markedly different for both geometries, which directly affects the evolution of the vapor film and consequently the measured cooling curves and particularly the wetting behavior.

Frerichs and Lübben (Ref 49) studied rewetting in hollow and nonhollow cylinders by means of videorecordings (30 frames/second) and cooling curve measurements (with 0.5 mm, or 0.02 in., sheathed thermocouples located approximately 1 mm, or 0.04 in., below the probe surface). The probes were made from 303 stainless steel and were 50 mm (2 in.) in diameter with lengths varying from 100 up to 200 mm (4 to 8 in.); the probes could have hollow and nonhollow sections. The probes were heated to 850 °C (1560 °F) in a nitrogen atmosphere and quenched in 130 L (34 gal) of still high-speed oil (Isorapid 277) at 80 °C (175 °F);

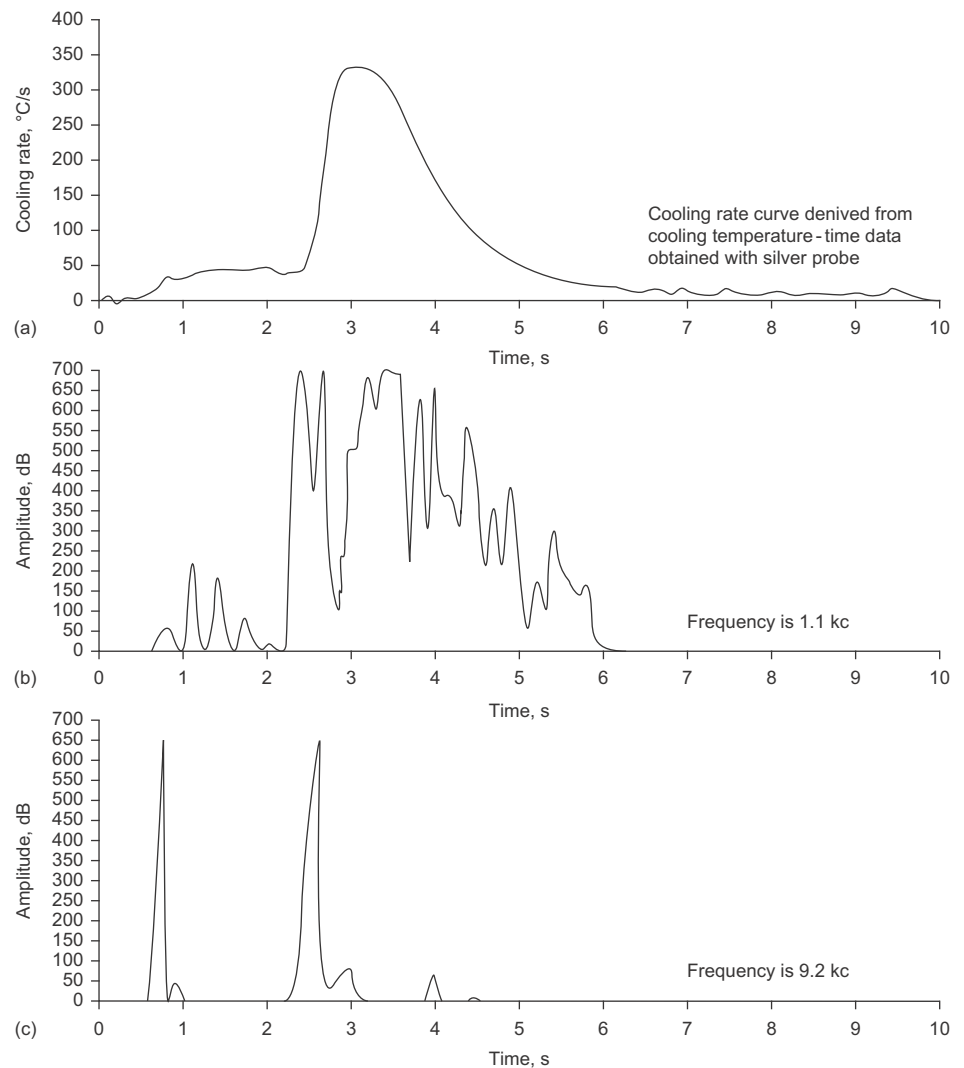


Fig. 11 Quenching of a silver sphere. (a) Cooling-rate history. (b) Broadband acoustical data. (c) Narrowband acoustical data. Source: Ref 44

care was taken to ensure that the quenchant would not fill the hollow section of the probes.

The wetting front kinematics are shown in Fig. 13 for a composite probe in which the bottom part was solid and the upper part hollow; no screws were used to attach both sections. After immersing the probe in the quenchant, the wetting front advances from bottom to top (in the solid region of the probe); at 8 s the rewetting of the hollow part occurs instantaneously, and at approximately 10.8 s the two fronts converge at the longitudinal position where the solid and hollow parts met. From this result, it is clear that the amount of solid mass (and therefore, thermal energy available) plays an important role in rewetting. The larger amount of thermal energy provided by the solid part produced a low wetting front velocity, which allowed the hollow part to cool to a temperature at which the vapor film could not be sustained before the advancing wetting front could reach the hollow part. Considering all

their experiments, the authors concluded that the formation of the wetting front needs nucleation points such as edges or surface singularities. For the solid sections, the authors could fit the position of the wetting front as a function of time by a second-order polynomial, which indicates that the wetting front velocity in the solid section is not constant.

The nonuniform heat extraction resulting from a non-Newtonian cooling, that is, nonuniform rewetting, has an impact on the thermal response and therefore the final mechanical properties and distortion. Lübben and Frerichs (Ref 50) documented rewetting during quenching of SAE 304 steel rings (133 mm, or 5.2 in., inside diameter; 145 mm, or 5.7 in., outside diameter; 26 mm, or 1.0 in., in height); the dimensions favor distortion if heat extraction is nonuniform. The rings were heated in air to 860 °C (1580 °F) and manually transferred to an agitated quench bath. The quenchant was high-speed quenching oil (Thermisol QH

10MC) kept at 60 °C (140 °F) and agitated by a propeller that generated an oil velocity of approximately 0.2 m/s (0.7 ft/s); some experiments were conducted in still oil. The quench tank had a window that allowed recording the events at the ring surfaces using a charge-coupled device videocamera; the quenching

oil used is transparent, which facilitated the videorecording. They tested both horizontal and vertical orientations and two different modes for supporting the ring in the former case. Figure 14 compares the rewetting behavior for the horizontal and vertical arrangements. Clearly, the orientation plays a significant role:

horizontal rings showed a wetting front that was homogeneous in the angular direction but asymmetric in the axial direction (starting at the bottom with the second wetting front starting at the top near the end of the rewetting process). On the other hand, vertically immersed rings showed a symmetrical wetting behavior

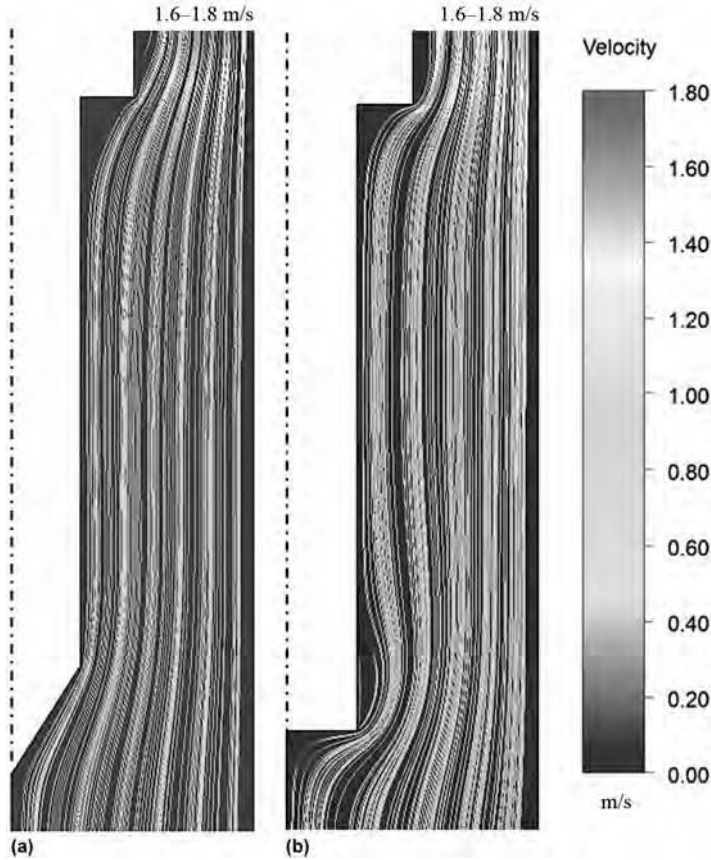


Fig. 12 Computed streamlines (m/s) in the vicinity of probes in contact with water at 60 °C (140 °F) flowing at 0.6 m/s (2.0 ft/s). (a) Flat-end probe. (b) Conical-end probe. Source: Ref 48

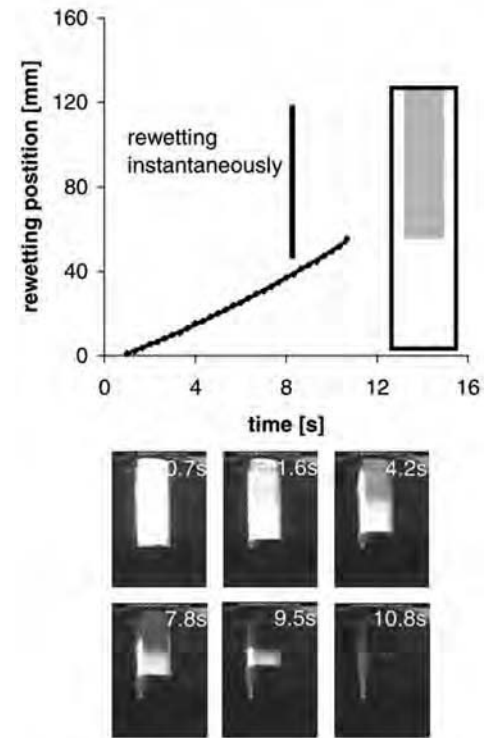


Fig. 13 Wetting front kinematics in a composite probe with solid material at the bottom, hollow in the upper part, and no screw threads. Quenched in high-speed oil at 80 °C (175 °F) without agitation. Source: Ref 49

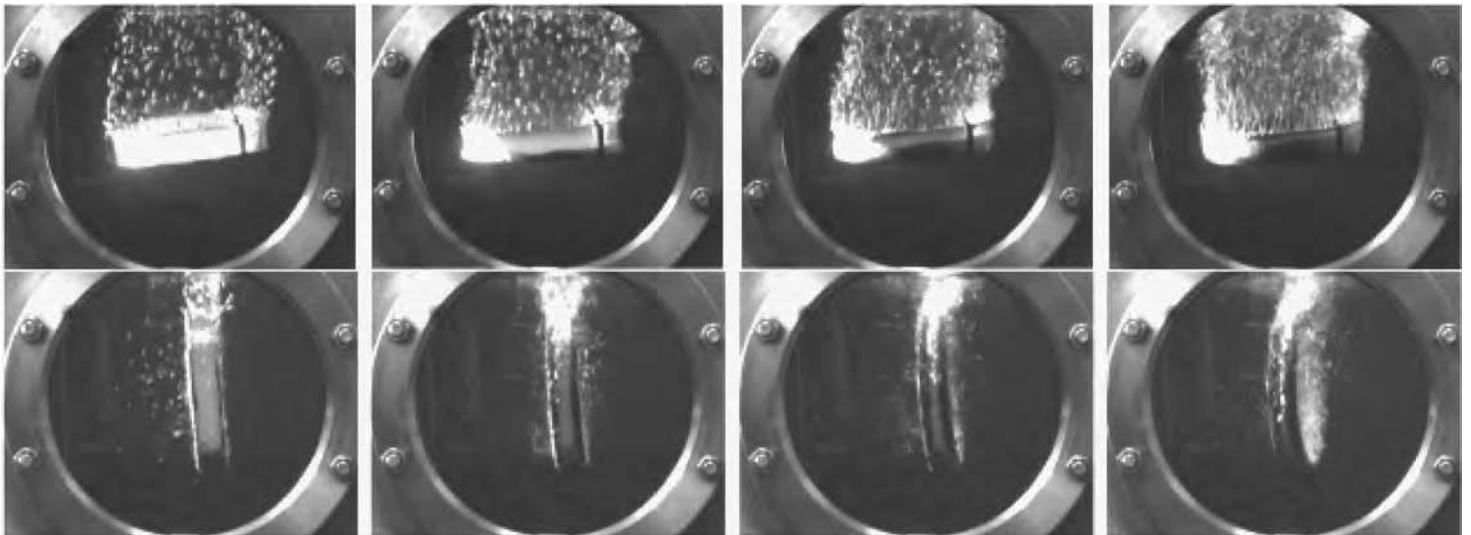


Fig. 14 Rewetting behavior at different times for horizontal (top row) and vertical (bottom row) ring orientations. Source: Ref 50

in the axial direction, with two wetting fronts starting at both sides and moving at the same velocity toward the center and asymmetrical in the angular direction. From images extracted from the videos, the position of the wetting front as a function of time was determined (Fig. 15). Because the vertically oriented rings showed two symmetrical fronts moving toward the center, the rewetting time in the axial direction was shorter (3.5 s) than in the case of the horizontally immersed rings (nearly 5 s).

Variations on the horizontal arrangement, such as different modes of holding the ring (by hanging it or supporting it), bath agitation, and support of initial temperature (either heating it together with the ring or not), did not produce significant differences in the rewetting behavior.

Intensive quenching is a process based on suppressing film boiling completely. Kobasko (Ref 51) showed that the requirement for film boiling is that the initial heat flux is higher than the first critical heat flux ($q_{in} > q_{cr1}$). The latter is the local maximum heat flux that occurs within approximately 0.1 s after immersing the hot part in the bath (Ref 44). When $q_{cr1} > q_{in}$, nucleate boiling occurs immediately after shock boiling; because nucleate boiling is a very efficient mode of heat transfer, the surface temperature drops very quickly, reaching the saturation temperature and staying at that value for a relatively long period of time in a process that Kobasko has identified as self-regulated thermal process (Ref 51). If film boiling is present, then a local minimum heat flux, the second critical heat flux (q_{cr2}), is observed (Ref 44).

Thermal Field. The temperature field evolution within the part being quenched directly affects the microstructural and dimensional changes. The heat transfer within the part is governed by conduction; therefore, the thermal field may be computed by solving a heat balance equation (Eq 3), with the heat flux defined using Fourier's law (Eq 4). When Eq 2 is applied to an infinitesimally small control volume and Fourier's law is substituted for the heat flux, the general form of the heat-conduction equation is obtained:

$$-\nabla \cdot (-k\nabla T) + q_G = \rho C_p \frac{\partial T}{\partial t} \quad (\text{Eq 12})$$

where q_G is the volumetric rate of heat generated, ρ is the part density, C_p is the part heat capacity at constant pressure, t is time, and ∇ is the nabla operator. Note that now the dimensions in each term are thermal energy/(volume \times time).

The heat conducted through the part is transferred to the quench bath at the part/bath interface. The relative importance of conductive and interface transfer, which act in series, may be assessed using the Biot number (Bi), that is, a dimensionless number defined as the ratio of thermal resistance due to conduction within the solid to thermal resistance due to interface transfer (with the latter computed using Newton's law of cooling) (Ref 52):

$$Bi = \frac{\text{Thermal resistance (conduction)}}{\text{Thermal resistance (interface)}} = \frac{\bar{h}L_C}{k} \quad (\text{Eq 13})$$

where L_C is a characteristic length associated with heat conduction. For a condition of heat flow in the radial direction of a long cylinder (often encountered in laboratory-scale testing of quenchant), the characteristic length is taken as the cylinder radius. Some authors calculate the characteristic length from the part volume and total surface area perpendicular to heat flow:

$$L_C = \frac{V}{A_{\perp}} \quad (\text{Eq 14})$$

If the Biot number is less than 0.1, the thermal resistance is dominated by the interface component, and therefore, the thermal gradients within the part may be considered as negligible, which considerably simplifies the heat-transfer problem. This special case may apply during quenching of small probes with very high thermal conductivity used for laboratory-scale cooling curve analysis, but, in general, thermal gradients within the part do occur.

To solve Eq 12 for a given application, boundary and initial conditions must be defined; this formulation is known as a mixed-boundary and initial value problem.

The initial condition is the known temperature distribution at the beginning of the process:

$$T = f_i(x_i) \text{ in region } \Omega \quad (\text{Eq 15})$$

It is common practice to assume a uniform initial temperature distribution:

$$T = \text{constant in region } \Omega \quad (\text{Eq 16})$$

There are three types of boundary conditions (Ref 53):

1. Prescribed temperature along the boundary surface (first kind, or Dirichlet):

$$T = f_i(x_i, t) \text{ on the boundary surface } S_i \quad (\text{Eq 17a})$$

2. Prescribed normal derivative of temperature or heat flux along the boundary surface (second kind, or Neumann):

$$\frac{\partial T}{\partial \hat{n}} = f_i(x_i, t) \text{ or } q = f_i(x_i, t) \text{ on the boundary surface } S_i \quad (\text{Eq 17b})$$

3. Prescribed energy exchange with the surroundings (third kind):

$$k_i \frac{\partial T}{\partial \hat{n}} + \bar{h}_i T = f_i(x_i, t) \text{ on the boundary surface } S_i \quad (\text{Eq 17c})$$

In the preceding equations, \hat{n} is the outward-drawn normal to the boundary surface i . If the right side of any of Eq 17 is equal to zero, the boundary condition is said to be homogeneous, which simplifies the analytical solution of the governing equation. From a practical point of view, homogeneous boundary conditions only occur at symmetry planes, in which case a Neumann-type boundary condition is always homogeneous.

Active Heat-Transfer Boundary Condition

For a given alloy and targeted properties, the heat-extraction history at the part surface is the key element of a quench operation, because it is directly related to the temperature field response within the part being quenched. Thus, it is very important to correctly define the active heat-transfer boundary condition, that is, the heat-transfer boundary condition at the part surface.

Given that it is very difficult to measure a transient surface temperature, a Dirichlet-type boundary condition (Eq 17a) is usually not applicable for modeling quenching operations. Instead, it is common practice to insert thermocouples into an actual part or a laboratory-scale probe to measure the local thermal response at the thermocouple hot junction; from these data it is possible to estimate the heat-transfer boundary condition either as a surface heat flux (Eq 17b) or a heat-transfer coefficient (Eq 17c).

In many investigations, the heat-transfer coefficient is computed using the Newton law of cooling, as given by Eq 7. It has been common practice to use the liquid subcooling to compute the heat-transfer coefficient:

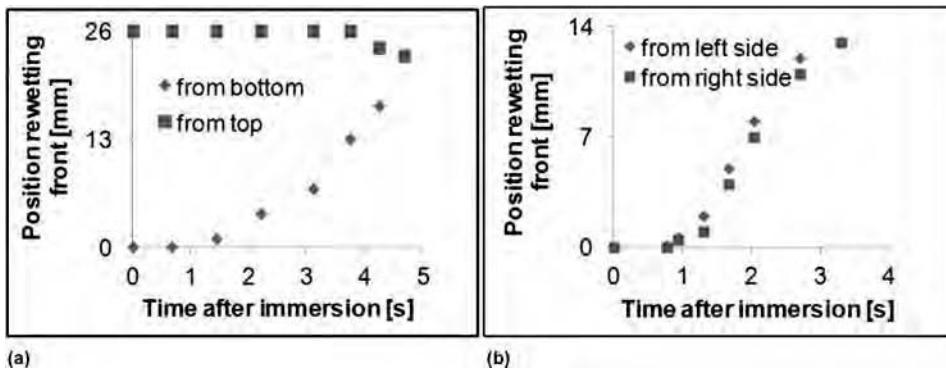


Fig. 15 Wetting front kinematics, along the axial direction, for (a) horizontally and (b) vertically oriented rings. Source: Ref 50

$$\bar{h} = -\frac{q_s}{(T_f - T_{\text{surf}})} \quad (\text{Eq 18})$$

where T_{surf} is the surface temperature, and T_f is the bulk quenchant temperature.

However, Kobasko (Ref 54) has argued that it should be calculated using the difference between the surface temperature and the saturation temperature of the quenchant (T_{sat}):

$$\bar{h} = -\frac{q_s}{(T_{\text{sat}} - T_{\text{surf}})} \quad (\text{Eq 19})$$

To distinguish between them, Kobasko refers to the values defined by Eq 18 and 19 as the effective and real heat-transfer coefficient, respectively.

In the opinion of the author, the use of the heat-transfer coefficient should be discarded in favor of the surface heat flux. The latter is a physical quantity that directly measures heat extraction at the part surface, and, as may be realized from either Eq 18 or 19, the heat-transfer coefficient does require knowledge of the surface heat flux. Also, the computer codes for modeling quenching processes are easy to modify so that they use the surface heat flux as a boundary condition instead of the heat-transfer coefficient.

The Inverse Heat-Conduction Problem.

The mathematical problem of using a measured local thermal response to estimate an active heat-transfer boundary condition is known as the inverse heat-conduction problem (IHCP), as opposed to the direct heat-conduction problem (DHCP), which consists of calculating the thermal field evolution for a given set of initial and boundary conditions. There are several scenarios in which the IHCP needs to be solved for a quench. Ideally, one is interested in estimating the active heat-transfer boundary condition during an actual quench in a heat treating plant. However, the complex geometry and big size of real parts lead to a spatial distribution of time-varying values of the heat-transfer boundary condition over the part surface, which would possibly require the solution of a three-dimensional IHCP (i.e., one that considers heat flow in three directions). In addition, the occurrence of a phase change, such as the austenite-to-martensite transformation, complicates even further the solution of the IHCP.

Instead of instrumenting an actual part, many researchers have concentrated their efforts in studying heat extraction in laboratory-scale equipment using relatively small parts or probes of simple geometry, which has led to two-dimensional heat flow or even one-dimensional heat flow IHCPs. In many cases, the materials used do not transform upon quenching; furthermore, given certain conditions, thermal gradients within the probe may be considered as negligible.

Bodies with Negligible Thermal Gradients. As mentioned previously, when the Biot number is small ($Bi < 0.1$), the thermal resistance by interface transfer, that is, on the coolant side, is much higher than the thermal resistance by conduction within the solid. In

that case, thermal gradients within the probe may be assumed negligible, and therefore, the temperature within the solid is a function of time alone. Thus, based on Eq 3, a macroscopic thermal energy balance may be set up, considering that the rate of change of thermal energy within the probe is equal to the rate of thermal energy transferred to the bath, if there are not sources/sinks of thermal energy. This approach is referred to as a lumped heat-capacity or lumped parameter analysis (Ref 52).

In terms of surface heat flux, the macroscopic heat balance is written as:

$$\rho C_p V \frac{dT(t)}{dt} = q(t) A_{\perp} \quad (\text{Eq 20})$$

where $q(t)$ is a time-varying surface heat flux, and A_{\perp} is the normal surface area. In this equation, it is assumed that the surface heat flux has a unique value, at a given time, over the whole part surface; alternatively, one could work on a slice of the probe as the computational domain.

Using the so-called Newton's law of cooling (Eq 7), this equation may be rewritten as:

$$\rho C_p V \frac{dT(t)}{dt} = -\bar{h}(t) [T_f - T(t)] A_{\perp} \quad (\text{Eq 21})$$

where $\bar{h}(t)$ is a time-varying heat-transfer coefficient. Note that with the assumption of negligible thermal gradients within the solid, the surface temperature that would normally appear within the square bracket in the right side of Eq 21 is substituted by $T(t)$.

Either Eq 20 or 21 requires the definition of an initial condition, such as:

$$T(t) = T_0, t = 0 \quad (\text{Eq 22})$$

where T_0 is the initial temperature.

The governing equation (Eq 20 or 21 plus its initial condition) may be solved in a piecewise fashion along the time coordinate to estimate the time-varying heat-transfer boundary condition using any of the standard numerical methods for solving ordinary differential equations, such as Euler, Runge-Kutta, and so on (Ref 55). If the thermophysical properties are temperature dependent, they may be assumed as constant during a given time step to avoid the need for an iterative solution.

A case in which the assumption of negligible internal thermal gradients is valid arises in the characterization of the heat extraction of a quenchant using the Japanese industrial standard (JIS) K2242 silver probe (Ref 56). The probe is a cylinder, 10 mm (0.4 in.) in diameter and 30 mm (1.2 in.) long, fabricated with silver and instrumented with a thermocouple at mid-height, near the probe surface (Fig. 16).

Narazaki et al. (Ref 57) used their LUMP-PROB computer code (which is based on the lumped parameter analysis) to estimate the heat-transfer coefficient during quenching of the JIS silver probe in 15% polymeric solution at 30 °C (85 °F) without agitation, in water at 30 °C (85 °F) without agitation, and in

oil (JIS 1-2) at 80 °C (175 °F) without agitation. They solved Eq 21 by numerically computing the derivative on the right side of the equation instead of integrating the ordinary differential equation. Their methodology includes a smoothing technique (a polynomial curve-fitting method combined with a least-squares technique) to reduce undesirable noise in the measured thermal response that would be intensified in the numerically computed derivative. Hasan et al. (Ref 58) used a similar approach, smoothing the data by using a rolling average of 11 points.

Narazaki et al. (Ref 57) tested two scenarios in their calculations: constant and temperature-dependent thermophysical properties. The estimated heat-transfer coefficient as a function of surface temperature (which, in the present case of negligible thermal gradient, is identical to the centerline temperature) for the three quenchant studied is shown in Fig. 17(a). The maximum values of the heat-transfer coefficient follow the order: water (30 °C, or 85 °F, still) > oil (80 °C, or 175 °F, still) > 15% polyacrylamide (30 °C, or 85 °F, still). Although the heat-transfer coefficient curves do not show noticeable differences when using constant or temperature-dependent thermophysical properties, a much better agreement between measured and computed (based on the estimated heat-transfer coefficients) cooling curves was obtained when temperature-dependent properties were used in the calculations (Fig. 17b).

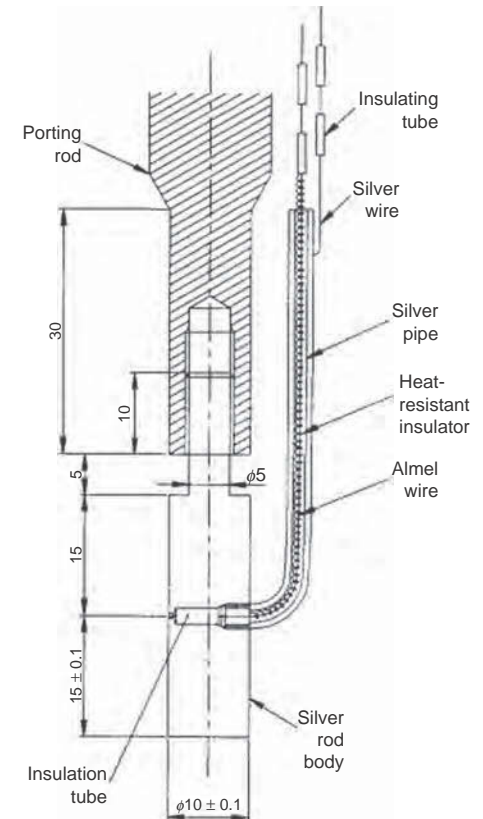
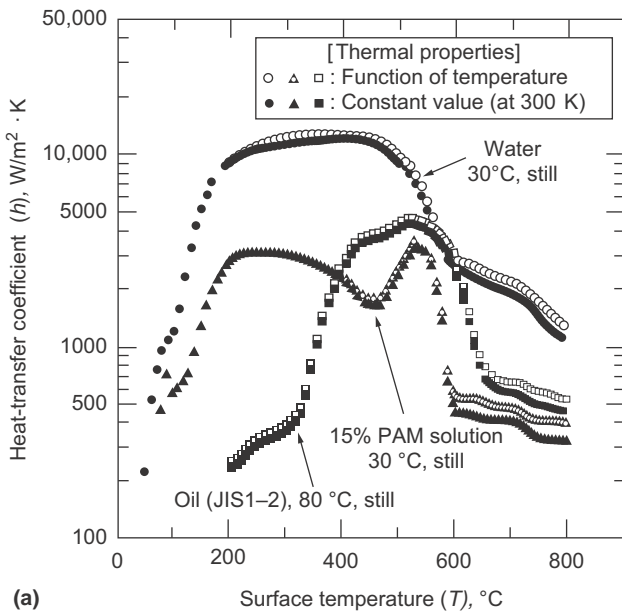
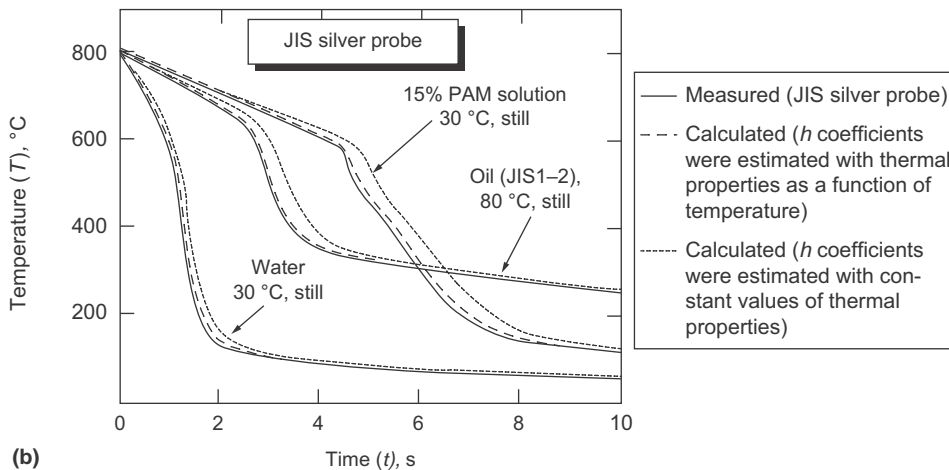


Fig. 16 The Japanese Industrial Standard silver probe. Source: Ref 57



(a)



(b)

Fig. 17 (a) Estimated heat-transfer coefficient as a function of surface temperature for 15% polymeric (polyacrylamide, or PAM) solution at 30 °C (85 °F) without agitation, for water at 30 °C (85 °F) without agitation, and for oil (JIS 1-2) at 80 °C (175 °F) without agitation. (b) Corresponding measured (solid line) and calculated cooling curves estimated with two different assumptions of h coefficients: thermal properties varying as a function of temperature (dashed line) and thermal properties held constant (dotted line). Source: Ref 57

In a separate paper (Ref 59), Narazaki et al. reported a comparison between calculated and measured cooling curves in S45C steel cylindrical probes (20 mm, or 0.8 in., diameter by 60 mm, or 2.4 in., long) quenched in still water at 30 °C (85 °F) and still 10% polyalkylene glycol aqueous solution by modifying initial estimates of the heat-transfer coefficient deduced from cooling curves measured with the JIS silver and the ISO 9950 Inconel alloy probes, which validated their methodology to estimate heat-transfer coefficients from measured cooling curves.

Bodies with Thermal Gradients. The combination of size and relatively low values of thermal conductivity of real parts (and even some small laboratory-scale probes) results in Biot number values considerably larger than 0.1, and

therefore, the thermal gradients within the solid cannot be neglected. In this case, the temperature is a function of time and at least one spatial coordinate, and therefore, a microscopic (as opposed to a macroscopic) thermal balance must be adopted. The majority of the probes used to characterize heat extraction during quenching are cylinders designed with a length-to-diameter ratio greater than four, which guarantees that there are no end effects, and, in principle, heat transfer may be assumed to be one dimensional. If a wetting front with a finite velocity does occur, then significant axial temperature gradients are generated within the part, and two-dimensional heat flow would have to be considered. However, to keep the development of the equations that follow as simple as possible, the presence of a slow-moving wetting front will not be included in the analysis.

Following the one-dimensional heat-flow assumption, the governing equation within the probe is given by:

$$\rho C_p \frac{\partial T(r,t)}{\partial t} = \frac{1}{\alpha} \frac{\partial}{\partial r} \left[r k \frac{\partial T(r,t)}{\partial r} \right] \quad (\text{Eq 23})$$

where $\alpha = k/(\rho C_p)$ is the thermal diffusivity. At the centerline, the temperature profile is symmetrical, which implies that the spatial derivative of the temperature is equal to zero:

$$\frac{\partial T}{\partial r} = 0 \quad t > 0, r = 0 \quad (\text{Eq 24})$$

At the solid/quenchant interface, the heat extracted by the fluid is characterized by a surface heat flux or a heat-transfer coefficient:

$$-k \frac{\partial T}{\partial r} = q_s(t) \quad t > 0, r = R \quad (\text{Eq 25})$$

or

$$-k \frac{\partial T}{\partial r} = -\bar{h}(t)[T_i - T_s(t)] \quad t > 0, r = R \quad (\text{Eq 26})$$

The initial condition, considering a uniform initial temperature distribution, is:

$$T(r,t) = T_0 \quad t = 0, 0 \leq r \leq R \quad (\text{Eq 27})$$

The mathematical formulation of the IHCP includes the same governing equation and centerline boundary condition, but the surface heat flux or the heat-transfer coefficient is unknown, which makes Eq 25 or 26, respectively, indeterminate. Instead, the thermal response (cooling curve) at a given position within the solid is known from measurements:

$$T(r_1,t) = Y_1(t) \quad t > 0, r = r_1 \quad (\text{Eq 28})$$

where $Y_1(t)$ is the measured thermal response.

Mathematically, the IHCP is an ill-posed problem; that is, its solution does not satisfy the conditions of existence, uniqueness, and stability (Ref 60). Moreover, the solution to the IHCP is very sensitive to measurement errors. Because of these characteristics, most of the IHCPs of technological importance require special techniques to stabilize the solution and obtain physically plausible results (Ref 60–63). It should be pointed out that all of these techniques use the solution of the associated DHCP as part of the IHCP algorithm. Because the active heat-transfer boundary condition is usually highly nonlinear, the DHCP cannot be solved analytically, and one must resort to numerical solutions such as finite differences or finite elements. The numerical solution to the IHCP may estimate the heat-transfer boundary condition sequentially, that is, estimating a single value at each time step; on the other hand, whole-domain procedures estimate all values of the heat-transfer boundary condition simultaneously. It must be stressed that the solution of an IHCP provides an estimated value; it is not possible to calculate the exact figure.

There are three basic methods to solve an IHCP: function specification, regularization, and iterative

regularization (Ref 64). The function specification method assumes a functional form (with few unknown constants) of the active heat-transfer boundary condition; the experimental data are then used to estimate the constants by means of the least-squares method (Ref 61). The least-squares function (for one-dimensional heat flow) is the sum of the square of the difference between measured and estimated temperatures for all thermocouples during a number of time steps (including the current time step and a few future time steps):

$$S = \sum_{j=1}^J \sum_{i=1}^r (Y_{ji} - T_{ji})^2 \quad (\text{Eq 29})$$

where Y is a measured temperature, T is the corresponding calculated temperature, J is the number of thermocouples, r is the number of future time steps, and the subindexes j and i represent the thermocouple and local future time step, respectively. For a single thermocouple ($J = 1$), Eq 29 reduces to:

$$S = \sum_{i=1}^r (Y_i - T_i)^2 \quad (\text{Eq 30})$$

By using experimental data spanning few time steps (the current one and up to r values), the solution to the IHCP is stabilized, which is particularly critical considering that heat transfer during quenching produces high cooling rates, which in turn implies very small time steps (high frequency of data acquisition) for which even small measurement errors result in very unstable solutions.

The least-squares procedure is based on minimizing the least-square function (S) with respect to the heat-transfer boundary condition, which may be accomplished by deriving S and equating the result to zero:

$$\frac{\partial S}{\partial \hat{q}^M} = 0 \quad (\text{Eq 31})$$

or

$$\frac{\partial S}{\partial \hat{h}^M} = 0 \quad (\text{Eq 32})$$

depending on whether the active heat-transfer boundary condition is expressed in terms of the estimated surface heat flux (\hat{q}) or the estimated heat-transfer coefficient (\hat{h}), respectively. In Eq 31 and 32, the superindex indicates that the quantity is being evaluated at time t^M .

One of the most commonly used sequential function specification algorithms in quenching is due to Beck et al. (Ref 65). In this algorithm, the thermophysical properties are assumed to be constant (and evaluated at the previous time step) at a particular location within the solid while estimating the heat-transfer boundary condition during a given time step, which is a very reasonable assumption for small computational time steps. Using this assumption, the IHCP becomes linear during a particular computational time step, which results in a very

efficient algorithm, because there is no need to iterate while estimating \hat{q}^M or \hat{h} . Also, a constant surface heat flux functional between t^{M-1} and t^M is adopted to estimate \hat{q}^M . The core of the algorithm is the following explicit equation that is used for estimating the value of the surface heat flux at time t^M when using a single thermocouple assembly:

$$\hat{q}^M = \hat{q}^{M-1} + \frac{1}{\Delta_M} \sum_{i=1}^r (Y_{M+i-1} - T_{M+i-1}) X_{M+i-1} \quad (\text{Eq 33})$$

where

$$\Delta_M = \sum_{i=1}^r (X_{M+i-1})^2 \quad (\text{Eq 34})$$

The quantity X_{M+i-1} is the sensitivity coefficient:

$$X_{M+i-1} = \frac{\partial T_{M+i-1}}{\partial \hat{q}^M} \quad (\text{Eq 35})$$

Once \hat{q}^M has been calculated, it becomes the base point for the following time step, and the temporary values of $\hat{q}^{M+1} \dots \hat{q}^{M+r-1}$ are eliminated. The procedure is repeated until the total process time is reached. To improve accuracy, it is possible to use computational time steps that are smaller than the experimental ones.

It may be shown that the definition of the sensitivity coefficient leads to a governing equation (with associated initial and boundary conditions) that has a very similar structure to that of the DHCP. Thus, the DHCP and sensitivity problems associated with the sequential function specification algorithm may be integrated in time using the same numerical technique, such as finite differences of finite elements.

On the other hand, regularization techniques are based on adding a term, called a regularizer, to the least-squares function; this term includes a parameter (α) that is selected based on what is known about the measurement errors (Ref 64). For example, in the zeroth-order Tikhonov regularization technique, the least-squares function for estimating the surface heat flux in a one-thermocouple assembly is given by:

$$S = \sum_{i=1}^I (Y_i - T_i)^2 + \sum_{i=1}^I \alpha (q_i)^2 \quad (\text{Eq 36})$$

where q_i is the estimated surface heat flux at time t_i , and I is the total number of time steps; that is, the method uses the whole time domain. Instead of using a least-squares method, the adjoint-conjugate gradient method is commonly applied to minimize S .

The iterative regularization method is also a whole-domain technique that employs the conjugate gradient method (Ref 64). The function to minimize has the form:

$$S = \sum_{i=1}^I (Y_i - T_i)^2 \quad (\text{Eq 37})$$

Beck et al. (Ref 64) used experimental data to compare the three methods described earlier. The experimental setup consisted of a 0.86 mm (0.034 in.) thick mica heater (containing a very thin planar electric heater at its center) in contact with a composite specimen that was insulated at its opposite end. The three methodologies for solving the IHCP were compared using the experimental thermal response measured at the mica/specimen interface as input and the following root mean square (rms) expression to estimate the error generated by the approximations used in the algorithm:

$$\hat{\sigma}_{\text{rms}} = \left[\frac{1}{I-1} \sum_{i=1}^I (q_i - \hat{q}_i)^2 \right]^{1/2} \quad (\text{Eq 38})$$

It should be pointed out that, in general, the actual value of the surface heat flux is not known; however, in this particular experimental setup, the current fed to the mica heater could be controlled, and therefore, the heat flux into the specimen (q_i) was known with a high degree of accuracy, which, evidently, is not the usual case. Although the results were very similar for all three methods, the authors remarked that the sequential forward selection algorithm is conceptually simpler and easier to extend to other problems of interest.

There are other techniques that have been put forward to solve the IHCP. Sánchez-Sarmiento et al. (Ref 66, 67) estimated the heat-transfer coefficient history using an optimization technique that assumes either a linear or a polynomial variation of the heat-transfer coefficient with time. Kobasko et al. have applied a technique based on the Kondratjev and the generalized Biot numbers together with the measured core cooling rate at a given temperature to estimate the effective heat-transfer coefficient during quenching in vegetable oils (Ref 68). Murio developed a methodology known as mollification (Ref 69). Felde and Totten (Ref 70) compared the performance of the conjugate gradient method, the Levenberg-Marquardt method, the Simplex method, and the Nondominated Sorting Genetic Algorithm (NSGA II), using fictitious thermal responses from two cases of theoretical heat-transfer coefficients: time-dependent and time- and local-coordinate-dependent. In the first case, all methods gave comparable results, with the conjugated gradient method showing the fastest convergence; for the second example, the best estimation was obtained using the NSGA II method.

For simplicity, the aforementioned equations have been written for a system where the heat flow may be assumed to be one dimensional. If the part geometry is complex or if slow rewetting occurs, it is likely that the active heat-transfer boundary condition would have different values at different sections of the part at a given time. This condition would lead to heat flow in more than one direction, which results in a two- or even a three-dimensional IHCP. Although the same principles explained

earlier can be extended to these groups of problems, the solution is much more involved. Some examples of multidimensional IHCP solutions can be found in Ref 70 to 75.

Regarding the design of a thermocouple arrangement within a probe or part, two points may be made. Through the concept of the sensitivity coefficient, it is possible to show that the best place to locate a thermocouple is as close to the active boundary condition as possible (Ref 76), which is consistent with the reasoning of having a lower thermal resistance between the thermocouple and the part surface, which diminishes the effects of lagging and damping of the signal that severely affect the performance of any IHCP algorithm. The presence of a probe within a field to be measured will always cause a disturbance in that field. Li and Wells (Ref 77) found that the direction of the thermocouple with respect to the active surface has a significant effect on the estimated surface heat flux; a thermocouple inserted at an angle of 90° with respect to the active surface leads to large errors in the estimated surface heat flux, which is not the case when the thermocouple is inserted parallel to the active surface. They also concluded that the presence of the hole should be considered in the inverse heat-conduction model when the Biot number is large. In a follow-up paper, Caron et al. (Ref 78) showed that the problem described previously may be corrected by defining an equivalent thermocouple hole depth when using thermocouples inserted at 90° with respect to the active surface; this equivalent depth corresponds to a fictitious depth at which the same thermal response would be measured if the thermal field were undisturbed. Figure 18 shows the surface heat flux as a function of surface temperature estimated from experimental data during rapid cooling of a disk made of AISI 316 stainless steel (Ref 78). As can be observed in the figure, the use of the equivalent depth concept (“ED” in the figure legend) corrects the estimated surface heat flux when a thermocouple inserted at 90° is used to record the thermal response.

Bodies with Internal Heat Generation. Most of the studies carried out to characterize the heat-extraction characteristics of a given quenchant through cooling curve analysis rely on using materials that do not undergo phase transformations during the quench. Although this consideration simplifies the solution of the IHCP, it has been argued (Ref 58, 79) that this approach does not aid in revealing the effect of phase transformations on the active heat-transfer boundary condition.

Prasanna Kumar conducted a series of experiments with instrumented probes made of a medium-carbon steel (AISI 1050) quenched in an aqueous solution of polyalkylene glycol (Ref 79). The probes were 25 mm (1.0 in.) diameter by 100 mm (4.0 in.) long and had a thermocouple placed at midheight, 4 mm (0.16 in.) from the probe surface. The surface heat flux and the surface temperature were estimated

by solving an IHCP that includes a source term associated with phase transformations during quenching. Considering an insulated section around the middle 10 mm (0.4 in.) of the probe, the governing equation for heat transfer within the solid is then given by:

$$\frac{1}{r} \frac{\partial}{\partial r} \left[kr \frac{\partial T(r, z, t)}{\partial r} \right] + \frac{\partial}{\partial z} \left[k \frac{\partial T(r, z, t)}{\partial z} \right] + q_G = \rho C_p \frac{\partial T(r, z, t)}{\partial t} \quad (\text{Eq 39})$$

with its corresponding initial and boundary conditions. Because the mathematical formulation couples heat transfer with the kinetics of phase

transformation, the estimated surface heat-flux values are specific to the steel grade-quenchant combination studied. The method used to solve the IHCP is based on the sequential function specification technique developed by Beck et al. (Ref 65), extended to include the phase transformation.

The measured cooling curves during the quench are shown in Fig. 19, along with the estimated cooling curves at the core and surface of the probe at midheight. As expected, the measured values fall in between the other two curves. A notable feature of the surface cooling curve is the recalescence observed at approximately 600 °C (1110 °F).

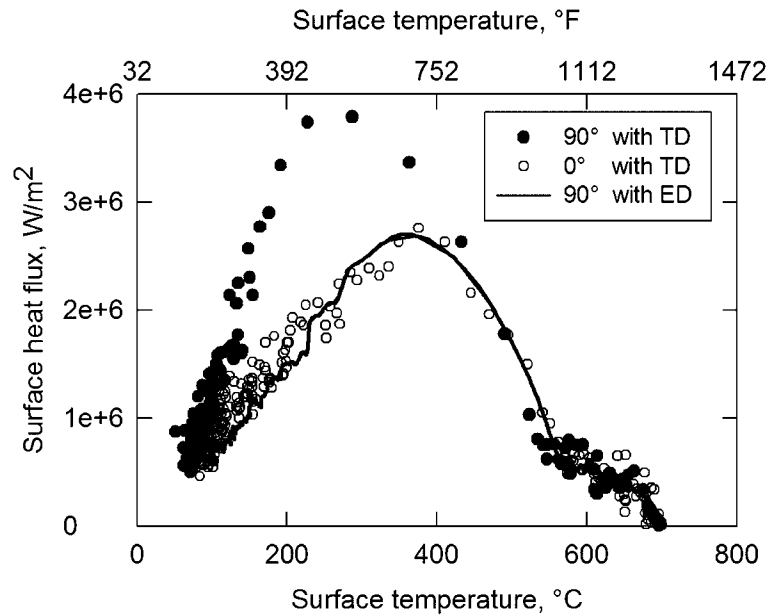


Fig. 18 Estimated surface heat flux as a function of estimated surface temperature using actual (TD) and equivalent (ED) thermocouple depths in solving the inverse heat-conduction problem for a thermocouple inserted parallel (0°) or perpendicular (90°) to the active heat-transfer surface. Source: Ref 78

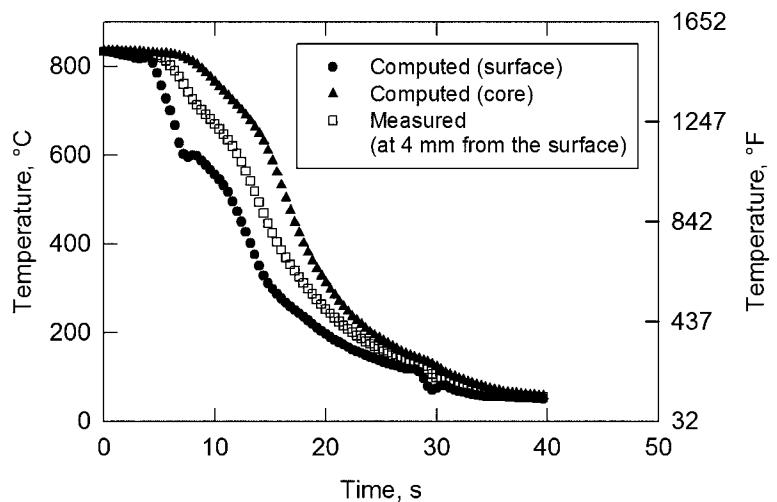


Fig. 19 Measured and computed (at the core and surface of the probe) cooling curves. Source: Ref 79. Reprinted, with permission, from *Materials Performance and Characterization*, copyright ASTM International, 100 Barr Harbor Drive, West Conshohocken, PA 19428

The estimated surface cooling curve and the computed surface ferrite and bainite volume fractions as a function of time are shown in Fig. 20. Clearly, the recalescence observed in the estimated surface cooling curve is due to the austenite-to-ferrite and, particularly, the austenite-to-bainite transformations.

The main objective of the investigation was to estimate the surface heat flux and explain its behavior. The estimated surface heat flux as a function of estimated surface temperature

and estimated surface cooling curve during quenching of an AISI 1050 steel probe are shown in Fig. 21. Most notable in the figure is the occurrence of two peaks in the surface heat-flux curve. The first peak has a value of 1.6 MW/m^2 and occurs at approximately $650 \text{ }^\circ\text{C}$ ($1200 \text{ }^\circ\text{F}$); referring to the volume fraction evolution at the probe surface (Fig. 20), it is evident that this a local maximum, caused by the start of the austenite-to-ferrite and then the austenite-to-bainite transformations that

arrest the estimated surface heat flux, causing a local decrease in the curve. Once the transformations stop (at approximately $550 \text{ }^\circ\text{C}$, or $1020 \text{ }^\circ\text{F}$), the heat-flux curve increases again until a second maximum (1.8 MW/m^2) is observed at $350 \text{ }^\circ\text{C}$ ($660 \text{ }^\circ\text{F}$); because no phase transformation occurs at the surface at this temperature, this second maximum is related to the heat-extraction characteristics of the quenchant itself. A much smaller (0.6 MW/m^2) local maximum may be observed at $100 \text{ }^\circ\text{C}$ ($212 \text{ }^\circ\text{F}$), which approximately corresponds to the boiling point of water. From these results (and those obtained at the core, which are omitted here for brevity), it becomes evident that the heat extraction during a quench is the result of an intricate interplay of heat transfer and kinetics of phase transformation.

Hasan et al. (Ref 58) quenched probes made of six different steels in water. The probes were 2 mm (0.08 in.) in diameter and 10 mm (0.4 in.) long, with a 1 mm (0.04 in.) diameter thermocouple located at the probe geometrical center; the probe dimensions were chosen to ensure that no thermal gradients would be present during the quench ($Bi < 0.1$). Due to the latter condition, the lumped parameter analysis was applied to estimate heat-transfer coefficients. Their findings were similar to those reported by Prasanna Kumar (Ref 79) in that the effect of hardenability on phase-transformation kinetics and therefore latent heat release modifies the shape of the cooling rate and heat-transfer coefficient.

Given that many IHCP algorithms involve solving the associated DHCP, including the heat-generation term in the calculations, may result in an excessive computing time. To reduce this problem, Ali et al. (Ref 80) used the full nonlinear form of the heat-conduction equation to eliminate iterations and reduce the computing time in an IHCP solver for an infinitely long cylinder that calculates the volumetric rate of heat generated by the phase transformation explicitly at the end of each time step. The algorithm was tested with simulated cooling curves in a 38.1 mm (1.5 in.) diameter cylinder made of AISI 1080 carbon steel quenched in water at $22.5 \text{ }^\circ\text{C}$ ($72.5 \text{ }^\circ\text{F}$) (Ref 81).

On the other hand, Hernández-Morales et al. (Ref 31) have pointed out that heat transfer is a phenomenon that depends on the driving force, and therefore, for a given quenchant, the heat-transfer boundary condition must be defined solely in terms of the part surface temperature. They quenched AISI 4140 cylindrical probes (12.7 mm , or 0.5 in. , diameter by 50.8 mm , or 2.0 in. , long) from temperatures below and above the austenitizing temperature to obtain a composite heat-flux history curve. By carefully selecting the segments of the cooling curves used in the IHCP, they could solve it without including the phase transformation.

Verification. Regardless of the dimensionality of the heat flow and the technique employed to solve the IHCP, it is good practice to verify

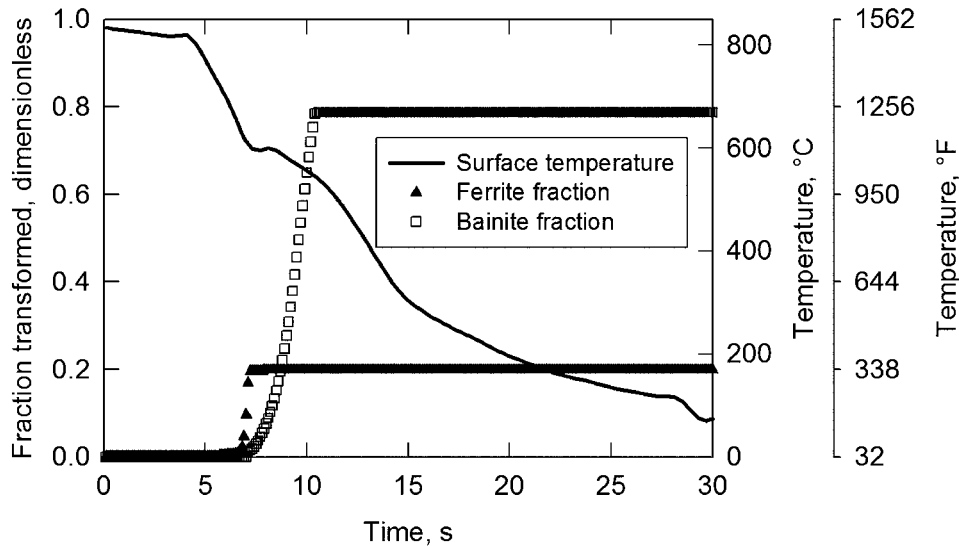


Fig. 20 Computed surface temperature (right vertical axis) and volume fraction (left vertical axis) as a function of time during quenching of an AISI 1050 steel probe. Source: Ref 79. Reprinted, with permission, from *Materials Performance and Characterization*, copyright ASTM International, 100 Barr Harbor Drive, West Conshohocken, PA 19428

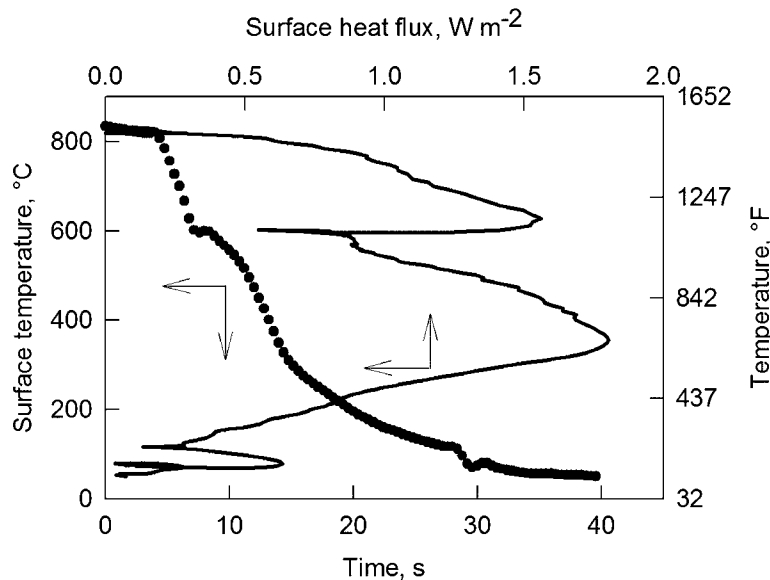


Fig. 21 Estimated surface heat flux as a function of estimated surface temperature and estimated surface cooling curve during quenching of an AISI 1050 steel probe. Source: Ref 79. Reprinted, with permission, from *Materials Performance and Characterization*, copyright ASTM International, 100 Barr Harbor Drive, West Conshohocken, PA 19428

the quality of the estimations. To accomplish this, it is advisable to generate virtual thermal responses by solving a DHCP with similar characteristics to the actual problem of interest and to compare the estimated active heat-transfer boundary condition with the values input to the DHCP solver. A function that has been used in many occasions is that of a surface heat flux that increases sharply up to a maximum and then decreases again in a rapid fashion, forming a shape that resembles a triangle (see, for example, Ref 82). Another possibility is to use an analytical solution of a DHCP to generate the virtual thermal response (Ref 65).

REFERENCES

1. "World Crude Steel Output Increases by 1.2% in 2012," Worldsteel Association, <http://www.worldsteel.org/media-centre/press-releases/2012/12-2012-crude-steel.html> (accessed Jan 31, 2013)
2. G.E. Totten, Ed., Steel, Chap. 9, in *Heat Treatment Handbook*, 2nd ed., CRC Press, Boca Raton, FL, 2006
3. C.R. Brooks, Tempering, Chap. 5, in *Principles of Heat Treatment of Plain Carbon and Low Alloy Steels*, ASM International, 1996
4. C.H. Gür and C. Şimşir, Simulation of Quenching: A Review, *Mater. Perform. Charact.*, Vol 1 (No. 1), Sept 2012
5. T.E. Lim, Optimizing Heat Treatment with Factorial Design, *J. Met.*, 1989, p 52–53
6. "Standard Test Methods for Determining Hardenability of Steel," A255, ASTM International, West Conshohocken, PA, 2010, www.astm.org (accessed Oct 2012)
7. J. Szekely, J.W. Evans, and J.K. Brimacombe, *The Mathematical and Physical Modeling of Primary Metals Processing Operations*, John Wiley & Sons, New York, 1988
8. L.C.F. Canale and G.E. Totten, Quenching Technology: A Selected Overview of the Current State-of-the-Art, *Mater. Res.*, Vol 8 (No. 4), 2005, p 461–467 (online)
9. J.B. Hernández-Morales, H.J. Vergara-Hernández, J.A. Barrera-Godínez, B. Beltrán Fragoso, and C. Álamo-Valdéz, The Influence of Flowrate and Deflector Arrangement on Distortion in Agitated Quench Tanks, *Proc. of the 23rd ASM Heat Treating Society Conference*, D. Herring and R. Hill, Ed., Sept 25–28, 2005 (Pittsburgh, PA), ASM International, 2006, p 314–319
10. T.C. Tszeng and V. Saraf, A Study of Fin Effects in the Measurement of Temperature Using Surface-Mounted Thermocouple, *Trans. ASME*, Vol 125, 2003, p 926–935
11. B. Liščić and T. Filetin, Computer-Aided Evaluation of Quenching Intensity and Prediction of Hardness Distribution, *J. Heat Treat.*, Vol 5 (No. 2), 1988, p 115–124
12. B. Carnahan, H.A. Luther, and J.O. Wilkes, *Applied Numerical Methods*, John Wiley & Sons, New York, 1969, p 128–130
13. G.E. Totten, C.E. Bates, and N.A. Clinton, *Handbook of Quenchants and Quenching Technology*, ASM International, 1993, p 83–86
14. G.H. Geiger and D.R. Poirier, *Transport Phenomena in Materials Processing*, The Minerals, Metals and Materials Society, Warrendale, PA, 1994, p 185, 372
15. J.B. Fourier, *Theorie Analytique de la Chaleur*, Paris, 1822; English translation by A. Freeman, Dover Publications, Inc., New York, 1955
16. J.P. Holman, *Heat Transfer*, 10th ed., McGraw Hill, Boston, 2010, p 10
17. V.K. Dhir, Boiling Heat Transfer, *Ann. Rev. Fluid Mech.*, Vol 30, 1998, p 365–401
18. S. Nukiyama, The Maximum and Minimum Values of the Heat Q Transmitted from Metal to Boiling Water under Atmospheric Pressure, *Int. J. Heat Mass Transf.*, Vol 9 (No. 12), 1966, p 1419–1433
19. R.B. Duffey and D.T.C. Porthouse, The Physics of Rewetting in Water Reactor Emergency Core Cooling, *Nucl. Eng. Des.*, Vol 25, 1973, p 379–394
20. M. Belhadj, T. Aldemir, and R.N. Christensen, Determining Wall Superheat under Fully Developed Nucleate Boiling in Plate-Type Research Reactor Cores with Low-Velocity Upward Flows, *Nucl. Technol.*, Vol 95, 1991, p 95–102
21. G. Yadigaroglu, The Reflooding Phase of the LOCA in PWRs, Part I: Core Heat Transfer and Fluid Flow, *Nucl. Safety*, Vol 19 (No. 1), 1978, p 20–36
22. E. Elias and G. Yadigaroglu, The Reflooding Phase of the LOCA in PWRs, Part II: Rewetting and Liquid Entrainment, *Nucl. Safety*, Vol 19 (No. 2), 1978, p 160–175
23. W.M. Rohsenow and H.Y. Choi, Chap. 9, in *Heat, Mass and Momentum Transfer*, Prentice-Hall, Englewood Cliffs, NJ, 1961
24. D.P. Incropera and F.P. De Witt, Chap. 10, in *Fundamentals of Heat and Mass Transfer*, 3rd ed., Wesley & Sons, New York, 1990
25. W.M. Rohsenow, General Boiling, *Handbook of Multiphase Systems*, G. Hestroni, Ed., Hemisphere Publishing Corp., Washington, D.C., 1982, p 6.25–6.26
26. I. Mudawar and W.S. Valentine, Determination of the Local Quench Curve for Spray-Cooled Metallic Surfaces, *J. Heat Treat.*, Vol 7 (No. 2), 1989, p 107–121
27. T. Tanaka, Overview of Accelerated Cooling of Steel Plates, *Accelerated Cooling of Rod Steel*, G.E. Ruddle and A.F. Crawley, Ed., The Metallurgical Society of the Canadian Institute of Mining, Metallurgy and Petroleum, 1987, p 187–208
28. I.V. Samarasekera and J.K. Brimacombe, Thermal and Mechanical Behavior of Continuous-Casting Billet Moulds, *Iron-making Steelmaking*, Vol 9 (No. 1), 1982, p 1–15
29. G.E. Totten, N.I. Kobasko, M.A. Aronov, and J. Powell, Overview of Intensive-Quenching Processes, *Ind. Heat.*, Vol 69 (No. 4), 2002, p 31–33
30. K. Jambunathan, E. Lai, M.A. Moss, and B.L. Button, A Review of Heat Transfer Data for Single Circular Jet, *Int. J. Heat Fluid Flow*, Vol 13 (No. 2), 1992, p 106–115
31. B. Hernández-Morales, F. López-Sosa, and L. Cabrera-Herrera, A New Methodology for Estimating Heat Transfer Boundary Conditions during Quenching of Steel Probes, *Quenching Control and Distortion*, D.S. MacKenzie, Ed., Proc. of the Sixth International Quenching and Control of Distortion Conference, Sept 9–13, 2012 (Chicago, IL), ASM International, 2012, p 81–92
32. D.A. Porter, K.E. Easterling, and M.Y. Sherif, Chap. 6, in *Phase Transformations in Metals and Alloys*, 3rd ed., CRC Press, Boca Raton, FL, 2009
33. D.P. Koistinen and R.E. Marburger, A General Equation Prescribing the Extent of the Austenite Transformation in Pure Iron-Carbon Alloys and Plain Carbon Steels, *Acta Metall.*, Vol 7, 1959, p 59–60
34. M. Avrami, Kinetics of Phase Change, Part I: General Theory, *J. Chem. Phys.*, Vol 7, 1939, p 1103–1112
35. M. Avrami, Kinetics of Phase Change, Part II: Transformation-Time Relations for Random Distribution of Nuclei, *J. Chem. Phys.*, Vol 8, 1940, p 212–224
36. B. Hernández-Morales, J.R. González-López, G. Solorio-Díaz, and H.J. Vergara-Hernández, Effect of Water Temperature on Wetting Front Kinematics during Forced Convective Quenching, *Mater. Sci. Forum*, Vol 706–709, 2012, p 1415–1420
37. N.B. Pilling and T.D. Lynch, Cooling Properties of Technical Quenching Liquids, *Trans. AIME*, Vol 62, 1920, p 665–688
38. M. Tagaya, M. Tamura, and I. Tamura, Studies on the Quenching Media (First Report)—An Analysis of Cooling Process during Quenching, *Mem. Inst. Sci. Ind. Res.*, Osaka Univ., Vol 9, 1952, p 85–102
39. B. Liscic, H.M. Tensi, G.E. Totten, and G.M. Webster, Non-Lubricating Process Fluids: Steel Quenching Technology, *Fuels and Lubricants Handbook: Technology, Properties, Performance and Testing*, G.E. Totten, S.R. Westbrook, and R.J. Shah, Ed., ASTM International, West Conshohocken, PA, 2003, p 587–634
40. P. Stitzelberger-Jakob, "Hartevorherbestimmung mit Hilfe des Benetzungsablaufes beim Tauchkühlen von Stählen," Dissertation, Faculty for Mechanical Engineering of the Technical University Munich, 1991

41. G.J. Leidenfrost, "De Aqua Communis Nonnullis Tractus," original from 1756, in C. Waves, *Int. J. Mass Transf.*, Vol 9, 1966, p 1153–1166 (translated)
42. G.E. Totten, Ed., *Heat Treatment Handbook*, 2nd ed., CRC Press, Boca Raton, FL, 2006, p 566
43. T. Künzel, H.M. Tensi, and G. Welzel, Rewetting Rate—The Decisive Characteristic of a Quenchant, *Proc. of the Fifth International Congress on Heat Treatment of Materials*, Vol 3 (Budapest, Hungary), 1986, p 1806–1813
44. N.I. Kobasko, A.A. Moskalenko, L.N. Deyneko, and V.V. Dobryvechir, Electrical and Noise Control Systems for Analyzing Film and Transient Nucleate Boiling Processes, *Recent Advances in Heat Transfer, Thermal Energy and Environment*, Aug 20–22, 2009 (Moscow, Russia), WSEAS, 2009, p 101–105
45. H.J. Vergara-Hernández and B. Hernández-Morales, A Novel Probe Design to Study Wetting Front Kinematics during Forced Convective Quenching, *Exp. Therm. Fluid Sci.*, Vol 33, 2009, p 797–807
46. B. Hernández-Morales, H.J. Vergara-Hernández, and G. Solorio-Díaz, Fluid Dynamics during Forced Convective Quenching of Flat-End Cylindrical Probes, *Recent Advances in Fluid Mechanics, Heat and Mass Transfer and Biology*, A. Zemiak and N. Mastorakis, Ed., Proc. of the Eighth WSEAS International Conference on Fluid Mechanics, Eighth WSEAS International Conference on Heat and Mass Transfer, Eighth WSEAS International Conference on Mathematical Biology and Ecology, Jan 29–31, 2011 (Puerto Morelos, Mexico), WSEAS Press, 2011, p 135–141
47. B. Hernández-Morales, H.J. Vergara-Hernández, G. Solorio-Díaz, and G.E. Totten, Experimental and Computational Study of Heat Transfer during Quenching of Metallic Probes, *Evaporation, Condensation and Heat Transfer*, A. Ahsan, Ed., InTech—Open Access Publisher, Rijeka, Croatia, 2011, p 49–72, <http://www.intechopen.com/articles/show/title/experimental-and-computational-study-of-heat-transfer-during-quenching-of-metallic-probes>
48. B. Hernández-Morales, R. Cruces-Reséndez, H.J. Vergara-Hernández, and G. Solorio-Díaz, Hydrodynamic Behavior of Liquid Quenchants in the Vicinity Quench Probes, *Quenching Control and Distortion*, D.S. MacKenzie, Ed., Proc. of the Sixth International Quenching and Control of Distortion Conference, Sept 9–13, 2012 (Chicago, IL), ASM International, 2012, p 361–372
49. F. Frerichs and T. Lübben, The Influence of Surface Temperature on Rewetting Behavior during Immersion Quenching of Hollow and Solid Cylinders, *J. ASTM Int.*, Vol 6 (No. 1), 2009
50. T. Lübben and F. Frerichs, Quenching of Bearing Races—Influence of Rewetting Behavior on Distortion, *Quenching Control and Distortion*, D.S. MacKenzie, Ed., Proc. of the Sixth International Quenching and Control of Distortion Conference, Sept 9–13, 2012 (Chicago, IL), ASM International, 2012, p 349–360
51. N.I. Kobasko, Duration of the Transient Nucleate Boiling Process and Its Use for the Development of New Technologies, *J. ASTM Int.*, Vol 8 (No. 7), 2011
52. J.P. Holman, *Heat Transfer*, 10th ed., McGraw Hill, Boston, 2010, p 141–143
53. M.N. Özisik, *Heat Conduction*, John Wiley and Sons, New York, 1980, p 13
54. N.I. Kobasko, Real and Effective Heat Transfer Coefficients (HTCs) Used for Computer Simulation of Transient Nucleate Boiling Processes during Quenching, *Mater. Perform. Charact.*, Vol 1 (No. 1), 2012
55. B. Carnahan, H.A. Luther, and J.O. Wilkes, Chap. 6, in *Applied Numerical Methods*, John Wiley & Sons, New York, 1969
56. "Heat Treating Oils," JIS K2242-1991, Japanese Standards Association, Tokyo, Japan
57. M. Narazaki, M. Kogawara, A. Shirayori, and S. Fuchizawa, Accuracy of Evaluation Methods for Heat Transfer Coefficients in Quenching, *Heat Treating Including the Liu Dai Memorial Symposium*, R.A. Wallis and H.W. Walton, Ed., Proc. of the 18th Heat Treating Conference, Oct 12–15, 1998 (Chicago, IL), ASM International, 1999, p 509–517
58. H.S. Hasan, M.J. Peet, J.M. Jalil, and H.K.D.H. Bhadeshia, Heat Transfer Coefficients during Quenching of Steels, *Heat Mass Transf.*, Vol 47, 2011, p 315–321
59. M. Narazaki, K. Osawa, A. Shirayori, and S. Fuchizawa, Influence of Validity of Heat Transfer Coefficients on Simulation of Quenching Process of Steel, *Heat Treating Including Steel Heat Treating in the New Millennium*, S.J. Midea and G.D. Pfaffmann, Ed., Proc. of the 19th Heat Treating Conference, Nov 1–4, 1999 (Cincinnati, OH), ASM International, 2000, p 600–607
60. A.N. Tikhonov and V.Y. Arsenin, *Solution of Ill-Posed Problems*, Winston & Sons, Washington, 1977
61. J.V. Beck, B. Blackwell, and C.R. St. Clair, Jr., *Inverse Heat Conduction: Ill-Posed Problems*, Wiley-Interscience, New York, 1985
62. K.A. Woodbury, Ed., *Inverse Engineering Handbook*, CRC Press, Boca Raton, FL, 2003
63. M.N. Özisik and H.R.B. Orlande, *Inverse Heat Transfer: Fundamentals and Applications*, Taylor & Francis, New York, 2000
64. J.V. Beck, B. Blackwell, and A. Haji-Sheikh, Comparison of Some Inverse Heat Conduction Methods Using Experimental Data, *Int. J. Heat Mass Transf.*, Vol 39 (No. 17), 1996, p 3649–3657
65. J.V. Beck, B. Litkouhi, and C.R. St. Clair, Jr., Efficient Solution of the Nonlinear Inverse Heat Conduction Problem, *Numer. Heat Transf.*, Vol 5, 1982, p 275–286
66. G. Sánchez Sarmiento, A. Gastón, and G. Totten, Computational Modelling of Heat Treating Processes by Use of HT-MOD and Abaqus, *Latin Am. Appl. Res.*, Vol 41, 2011, p 217–224
67. G. Sánchez-Sarmiento, A. Gastón, and J. Vega, Inverse Heat Conduction Coupled with Phase Transformation Problems in Heat Treating Process, *Computational Mechanics—New Trends and Applications*, CD-Book, Part VI, Section 1, Paper 16 (Barcelona, Spain), 1998
68. N.I. Kobasko, E.C. de Souza, L.C.F. Canale, and G.E. Totten, Vegetable Oil Quenchants: Calculation and Comparison of the Cooling Properties of a Series of Vegetable Oils, *J. Mech. Eng.*, Vol 56 (No. 2), 2010, p 131–142
69. D.A. Murio, *The Mollification Method and the Numerical Solution of Ill-Posed Problems*, Wiley-Interscience, New York, 1993
70. I. Felde and G.E. Totten, Estimation of Heat Transfer Coefficient Obtained during Immersion Quenching, *Quenching Control and Distortion*, D.S. MacKenzie, Ed., Proc. of the Sixth International Quenching and Control of Distortion Conference, Sept 9–13, 2012 (Chicago, IL), ASM International, 2012, p 447–456
71. K.J. Dowding, Multi-Dimensional Analysis of Quenching: Comparison of Inverse Techniques, *Proc. of the 18th Heat Treating Conference*, R.A. Wallis and H.W. Walton, Ed., Oct 12–15, 1998 (Chicago, IL), ASM International, 1999, p 525–534
72. D.M. Trujillo and R.A. Wallis, Determination of Heat Transfer from Components during Quenching, *Ind. Heat.*, Vol 56 (No. 7), 1989, p 22–24
73. R.I. Ramakrishnan, Quench Analysis of Aerospace Components Using FEM, *Proc. of the First International Conference on Quenching and Control of Distortion*, G.E. Totten, Ed., Sept 22–25, 1992 (Lincolnshire, IL), ASM International, 1992, p 155–164
74. A. Sugianto, M. Narazaki, M. Kogawara, and A. Shirayori, A Comparative Study on Determination Method of Heat Transfer Coefficient Using Inverse Heat Transfer and Iterative Modification, *J. Mater. Process. Technol.*, Vol 209, 2009, p 4627–4632
75. Y. Heng, A. Mhamdi, E. Wagner, P. Stephan, and W. Marquardt, Estimation of Local Nucleate Boiling Heat Flux Using a Three-Dimensional Transient Heat Conduction Model, *Inv. Prob. Sci. Eng.*, Vol 18, 2010, p 279–294
76. B. Hernández-Morales, J.K. Brimacombe, and E.B. Hawbolt, Application of Inverse Techniques to Determine Heat-Transfer

- Coefficients in Heat-Treating Operations, *J. Mater. Eng. Perform.*, Vol 1 (No. 6), 1992, p 763–772
77. D. Li and M.A. Wells, A Compensation Method for the Disturbance in the Temperature Field Caused by Subsurface Thermocouples, *Metall. Mater. Trans. B*, Vol 36, 2005, p 343–354
 78. E. Caron, M.A. Wells, and D. Li, A Compensation Method for the Disturbance in the Temperature Field Caused by Subsurface Thermocouples, *Metall. Mater. Trans. B*, Vol 37, 2006, p 475–483
 79. T.S. Prasanna Kumar, Coupled Analysis of Surface Heat Flux, Microstructure Evolution and Hardness during Immersion Quenching of a Medium Carbon Steel in Plant Conditions, *Mater. Perform. Character.*, Vol 1 (No. 1), 2012
 80. S.K. Ali, M.S. Hamed, and M.F. Lightstone, An Efficient Numerical Algorithm for the Prediction of Thermal and Microstructure Fields during Quenching of Steel Rods, *J. ASTM Int.*, Vol 5 (No. 10), 2008
 81. S.K. Ali, M.S. Hamed, and M.F. Lightstone, A Modified Online Input Algorithm for Inverse Modeling of Steel Quenching, *Numer. Heat Transf. B*, Vol 57, 2010, p 1–29
 82. A. Majorek, B. Scholtes, H. Müller, and E. Macherauch, The Influence of Heat Transfer on the Development of Stresses, Residual Stresses and Distortions in Martensitically Hardened SAE 1045 and SAE 4140, *Proc. of the First Conference on Quenching and Distortion Control*, G.E. Totten, Ed., Sept 22–25, 1992 (Chicago, IL), ASM International, 1992, p 171–179

Large Probes for Characterization of Industrial Quenching Processes

Božidar Liščić and Saša Singer, University of Zagreb

Laboratory Tests to Evaluate the Cooling Intensity of Liquid Quenchants

This section includes discussion on probes for laboratory tests and resultant curves, the scope of laboratory tests, and the calculation of the heat-transfer coefficient based on laboratory tests.

Probes for Laboratory Tests and Resultant Curves

Cooling curve tests have been the most useful means for measuring and recording the cooling intensity of liquid quenchants (oils, water, polymer solutions, and other water-based solutions) for many years, but with no standardized procedure. Small probes of different dimensions, made of different materials, have been used; therefore, a comparison among different measurements was not possible. Much later, in 1982, the Wolfson Heat Treatment Center Engineering Group in Birmingham, United Kingdom, issued "Laboratory Test for Assessing the Cooling Curve Characteristics of Industrial Quenching Media," which later served as the basis for the first international standard, ISO 9950-1995, entitled "Industrial Quenching Oils—Determination of Cooling Characteristics—Nickel Alloy Probe Test Method." According to this standard, the probe shall have a 12.5 mm (0.49 in.) diameter and a 60 mm (2.4 in.) length and shall be manufactured from an austenitic nickel-chromium superalloy that does not undergo phase transformations (no latent heat involved) and is oxidation resistant. The thermocouple type K (NiCr/NiAl), having a 1.5 mm (0.06 in.) outside diameter, is placed with its tip at the geometrical center of the probe. The assembly of the probe is shown in Fig. 1.

The surface of the probe must be passivated by heating in a furnace without a protective atmosphere. For initial calibration, and regular reconditioning, a reference fluid is used. This fluid shall be an unblended high-viscosity paraffinic mineral oil without any additive treatment, with prescribed physical characteristics. The quantity of quenching fluid to be tested is

2L (0.53 gal). The starting probe temperature is 850°C (1560 °F), and the temperature of the tested oil may be chosen according to concrete requirements, but for comparison it usually is 40°C (100 °F).

The results of tests are presented by the cooling curve, that is, the temperature as a function of time, and the cooling rate as a function of surface temperature, as shown in Fig. 2.

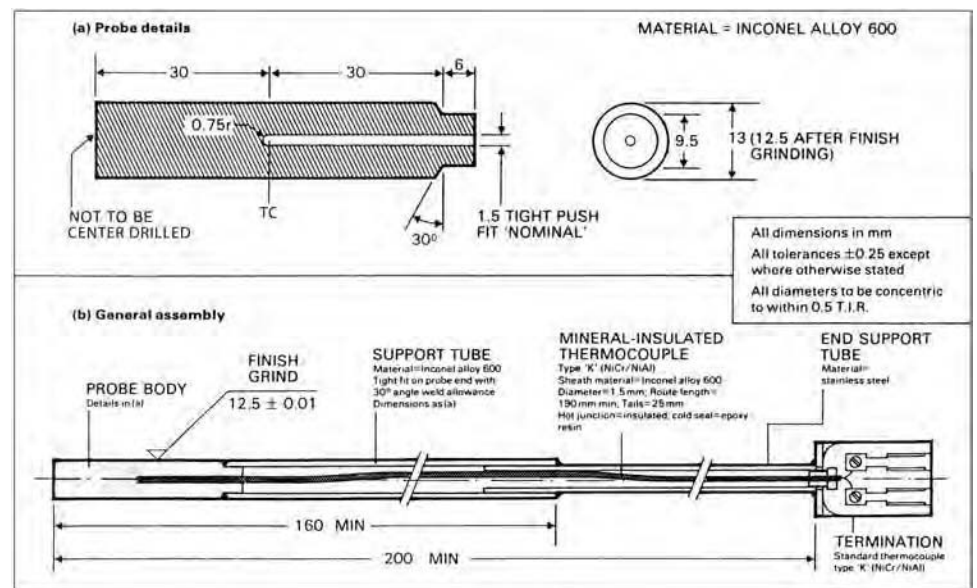


Fig. 1 Assembly of the ISO 9950 probe. TC, thermocouple; T.I.R., total indicator reading

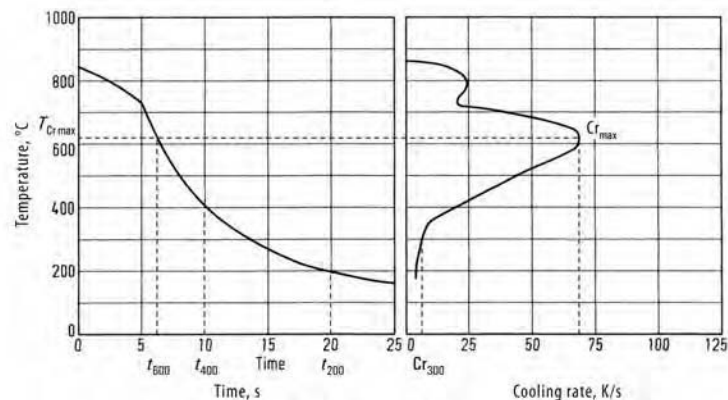


Fig. 2 Typical temperature/time and temperature/cooling rate plots when quenching the ISO 9950 probe in oil

From the temperature-versus-time plot, the following characteristic data are derived: time required for cooling the probe from the initial temperature to 600, 400, and 200 °C (1110, 750, and 390 °F). From the plot of cooling rate versus surface temperature, the characteristic data are the maximum cooling rate, the temperature at which the maximum cooling rate occurs, and the cooling rate at 300 °C (570 °F). Figure 3 shows real cooling curves and cooling rate curves of a medium-viscous mineral oil for the temperatures 50, 75, and 100 °C (120, 170, and 210 °F), measured according to ISO 9950, that is, without agitation. For digital measuring of temperatures, the frequency should be $>20 \text{ s}^{-1}$.

In the United States, ASTM International has issued the following testing standards:

- ASTM D6200 (reapproved 2007), “Standard Test Method for Determination of Cooling Characteristic of Quench Oils by Cooling Curve Analysis.” This standard is based on ISO 9950, uses the same 12.5 mm (0.49 in.) diameter by 60 mm (2.4 in.) probe made of an austenitic nickel-chromium superalloy, and the same amount of the still oil sample of 2 L (0.53 gal). The starting temperature is 850 °C (1560 °F), and the temperature of the oil is 40 °C (100 °F). The resulting curves are the same as with ISO 9950.
- ASTM D6482-6, “Standard Test Method for Determination of Cooling Characteristic of Aqueous Polymer Quenchants by Cooling Curve Analysis with Agitation (Tensi Method).” Aqueous polymer solutions are subject to much greater influences by

variation of physical and chemical parameters than oils, and polymeric quenching media exhibit very great differences in their wetting behavior. Cooling intensity of aqueous polymer quenchants depends on the concentration and molecular weight of the specific polymer, the quenchant temperature, and the agitation rate. Therefore, forced bath convection always is used when testing polymer solutions. According to this standard, the agitation device (driven by a small impeller) developed by H.M. Tensi is used. The probe and its assembly is the same as with ISO 9950. The starting temperature is 850 °C (1560 °F), and the polymer solution is heated to the desired temperature for production testing, or to 40 °C (100 °F) for comparison. Interpretation of results is essentially the same as with ISO 9950.

- ASTM D6549-06, “Standard Test Method for Determination of Cooling Characteristic of Quenchants by Cooling Curve Analysis with Agitation (Drayton Unit).” This standard is the same as ASTM D6482, with another agitation device. Instead of Tensi’s agitation device with rotating impeller, the Drayton agitation unit uses a pump.

In addition to the international standard ISO 9950, there are national standards in some countries, for example, France, Japan, and China, as shown in Table 1. They use silver probes of different dimensions.

Because the thermal conductivity of silver is 16 times higher than for an austenitic nickel-chromium superalloy or for stainless steel, the cooling curves measured by probes made of an austenitic nickel-chromium superalloy or stainless steel are not comparable with those measured by silver probes.

Figure 4 shows the Japanese new silver probe according to JIS K 2242-method B and some examples of cooling curves measured by this probe. Due to the small size and the very high heat conductivity of silver, when quenched in oil, this probe cools down to 200 °C (390 °F) in approximately 20 to 30 s, and when quenched in water, brine, or a polymer solution of low concentration, cools in less than 2 s. Such a probe is well suited for evaluation of the critical heat-flux densities.

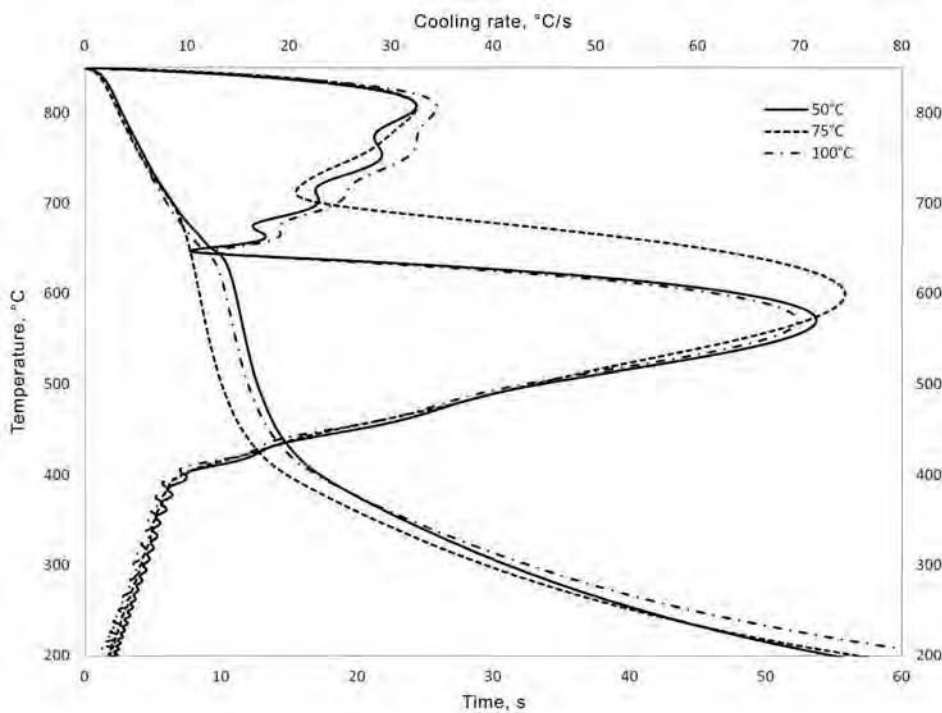


Fig. 3 Resultant cooling curves and cooling rate curves of a medium-viscous mineral oil for the temperatures 50, 75, and 100 °C (120, 170, and 210 °F), without agitation. Courtesy of the Quenching Research Center, Faculty of Mechanical Engineering and Naval Architecture, Zagreb

Table 1 Comparison of cooling curve standards: International, France, Japan, and China

Variable	ISO 9950:1995(E) (international)	AFNOR NFT-60778 (France)	JIS K 2242 (Japan)	ZB E 45003-88 (China)
Probe alloy	Alloy 600	Silver, 99.999% pure	Silver, 99.999% pure	Silver, 99.999% pure
Probe dimensions, mm (in.)	12.5 × 60 (0.49 × 2.4)	16 × 48 (0.63 × 1.9)	10 × 30 (0.4 × 1.2)	10 × 30 (0.4 × 1.2)
Standard reference oil	Mineral-oil reference quenching fluid	Mineral-oil reference quenching fluid	Diocetyl phthalate	Diocetyl phthalate
Vessel dimensions	115 ± 5 mm (4.5 ± 0.2 in.) diameter	138 mm high × 99 mm diameter (5.4 in. high × 3.9 in. diameter)	300 mL (10 oz) beaker	300 mL (10 oz) beaker
Oil volume, mL (oz)	2000 (70)	800 (30)	250 (9)	250 (9)
Oil temperature, °C (°F)	40 ± 2 (100 ± 4)	50 ± 2 (120 ± 4)	80, 120, 160 (180, 250, 320)	80 ± 2 (180 ± 4)
Probe temperature, °C (°F)	850 ± 5 (1560 ± 9)	800 ± 5 (1470 ± 9)	810 ± 5 (1490 ± 9)	810 ± 5 (1490 ± 9)

Source: Ref 1

Scope of Laboratory Tests

Laboratory tests for evaluation of the cooling intensity of liquid quenchant are used for:

- Comparison of cooling intensity among different kinds of oils, different polymer solutions, or other water-based solutions under different conditions (quenchant temperature and agitation rate), with the purpose of selecting the optimal quenchant and its condition in the concrete case
- Checking the effect of a currently used quenching fluid, or developing a new type of quenchant, when adding some additives
- Monitoring the condition of a liquid quenching bath at regular intervals, to prevent its deterioration
- Computer-aided calculation of the heat-transfer coefficient (HTC) for small cylindrical pieces

Calculation of the Heat-Transfer Coefficient Based on Laboratory Tests

Inverse Heat-Conduction Method. For small laboratory probes, one of the possibilities for HTC calculation is to solve the inverse heat-conduction problem. The temperature distribution $T(x, t)$, at a point x inside the probe, for times $t \geq 0$, is determined by the heat-conduction equation:

$$c\rho \frac{\partial T}{\partial t} = \text{div}(\lambda \text{ grad } T) \tag{Eq 1}$$

where c , ρ , and λ are physical properties of the probe, which are temperature dependent. The initial condition $T(x, 0)$ is known and the boundary condition is given by:

$$q = \lambda \frac{\partial T}{\partial n} = -\alpha(T - T_x) \tag{Eq 2}$$

where q is the surface heat-flux density, α is the surface HTC, and T_x is the external temperature of the quenchant. The inverse problem is to determine α in this boundary condition, which then is given by:

$$\alpha = -\frac{q}{T - T_x} \tag{Eq 3}$$

A small probe has only one thermocouple located at the core of the probe, and the quenchant temperature is also measured, because it is needed in Eq 3. These measured temperature curves in time are the only input data. For efficiency reasons, the probe is treated as an infinite cylinder with radially symmetric temperature distribution. This leads to a one-dimensional (1-D) heat-conduction model in Eq 1, while q and α in Eq 2 and 3 depend only on time.

Quite generally, the HTC can be calculated by iterative regularization algorithms. A general form of the function $q(t)$ or $\alpha(t)$ is prescribed, with a certain number of “free”

parameters. These parameters are computed iteratively, by repeatedly solving the heat-conduction equation (Eq 1) with the boundary condition (Eq 2), until a good fit to a selected set of measured temperature data is obtained. This procedure is applied globally in time, over the whole quenching period, as in Ref 2. Because a small probe cools relatively quickly, the whole HTC calculation is quite efficient.

Lumped Heat-Capacity Method. The fundamental concept of this method, according to Ref 3, is the following: If the probe temperature during quenching is uniform, the heat loss from the probe, Q , is equal to the decrease in the internal energy of the probe:

$$Q = hA(T_p - T_L) = C\rho V \frac{dT_p}{dt} \tag{Eq 4}$$

where Q is heat flow (W), h is the HTC at the probe surface ($\text{W/m}^2 \cdot \text{K}^{-1}$), A is the surface area of the probe (m^2), T_p is the temperature of the probe (K), T_L is the temperature of the quenching liquid (K), C is the specific heat of the probe material ($\text{J/kg}^1 \cdot \text{K}^1$), ρ is the density of the probe material (kg/m^3), V is the volume of

the probe (m^3), t is time (s), and dT_p/dt is the cooling rate of the probe (K/s^1).

If the quenchant temperature around the probe, T_L , is uniform, the next relation is derived from Eq 4:

$$q = h(T_p - T_L) = \left(C\rho \frac{V}{A} \right) \frac{dT_p}{dt} \tag{Eq 5}$$

where q is the heat-flux density (W/m^2).

From Eq 5, the HTC can be calculated directly from the cooling rate dT_p/dt :

$$h = C\rho \frac{V}{A} \left[\frac{\frac{dT_p}{dt}}{T_p - T_L} \right] \tag{Eq 6}$$

The preciseness of the values q and h depends on the accuracy of the cooling rate calculated from measured cooling curve data. The lumped heat-capacity method can be used only if the assumption of uniform probe temperature during the cooling process can be justified.

Temperature distribution in a probe depends on thermal conductivity of the probe material and the heat transfer from the surface of the

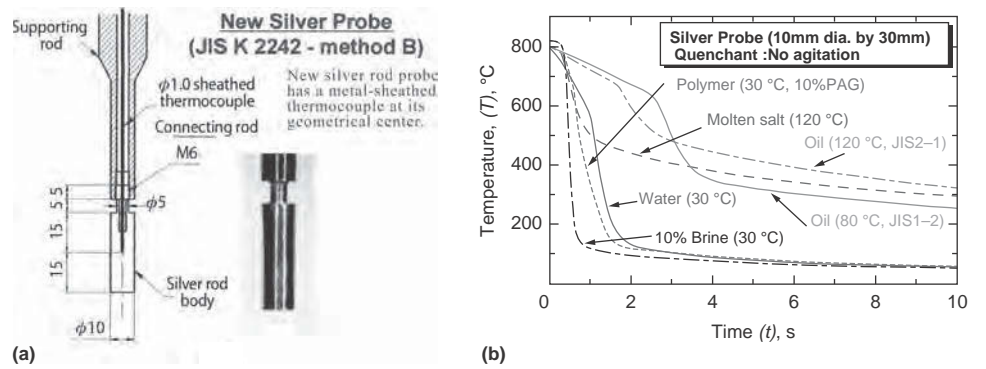


Fig. 4 (a) Japanese new silver probe according to JIS K 2242-method B. (b) Examples of cooling curves measured by this probe. PAG, poly(alkylene glycol). Courtesy of M. Narazaki

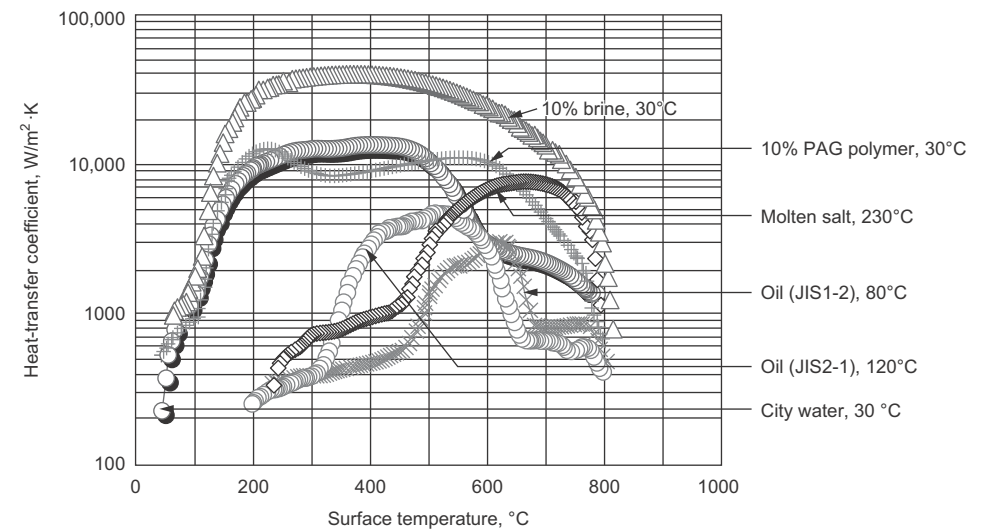


Fig. 5 Examples of heat-transfer coefficients calculated from cooling curves shown in Fig. 4(b). Courtesy of M. Narazaki

probe to the quenchant. The smaller the probe size and the higher the thermal conductivity of the probe material, the more realistic the assumption of uniform temperature of the probe. According to Kobasko, it is assumed that a temperature field in the cross section of the silver probe is uniform if the Biot number $B_i = h R/\lambda < 0.2$, where R is the radius of the probe and λ is the thermal conductivity. Figure 5 shows HTC calculated from the cooling curves shown in Fig. 4(b) using the lumped heat-capacity method.

Differences between Laboratory Tests and Characterization of Industrial Quenching Processes

When comparing cooling of a small probe in a laboratory test with cooling of real workpieces in a batch having larger mass and dimension, the following differences can be found:

- A very big difference in the cooling time. A small laboratory probe of 12.5 mm (0.49 in.) diameter, when quenched in still oil, cools down to 200 °C (390 °F) in approximately 30 to 50 s, while a cylindrical workpiece of only 50 mm (2.0 in.) diameter cools in equal conditions within 300 to 350 s.
- The HTC during nucleate boiling depends, according to Ref 4, on the probe diameter, as shown in Fig. 6. The smaller the probe diameter, the greater the HTC values. Below 50 mm (2.0 in.), this dependence is exponential.
- The initial heat flux (q_{in}) at equal cooling conditions depends on the ratio between volume and surface area (V/A). Small laboratory test probes have small volume and relatively large surface area. They cool from the beginning much faster than real workpieces having large volume and relatively small surface area. Consequently, the initial heat flux of the small probes usually is greater than the first critical heat-flux density

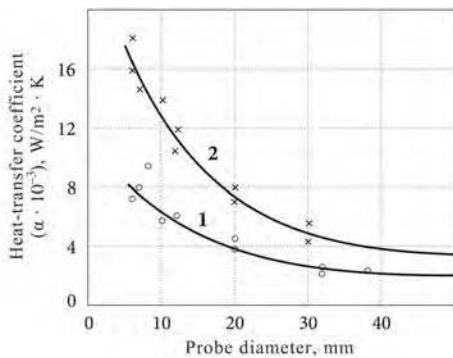


Fig. 6 Influence of probe diameter on the heat-transfer coefficient at nucleate boiling phase. 1, quenching in water of 25 to 40 °C (80 to 100 °F); 2, quenching in 12% water solution of NaOH at 20 to 30 °C (70 to 90 °F). Source: Ref 4

(q_{cr1}), and vapor film will develop. This is not always the case with real workpieces of large volume and relatively small surface area, because their q_{in} may be less than q_{cr1} .

- Technological conditions in the workshop practice (bath temperature, agitation rate and direction, loading arrangement in a batch) differ substantially from those in a laboratory test.

These are the reasons why the results obtained with small probes in laboratory tests cannot be directly transferred to real workpieces.

Requirements for a Workshop-Designed Test

Large probes for characterization of industrial quenching processes, which are used in workshop environments, must satisfy the following requirements:

- The probe itself should be of the same basic shape as the workpiece to be quenched, that is, for cylindrical workpieces, a cylindrical probe; for platelike workpieces, a platelike probe; and for ringlike workpieces, a ringlike probe. This is important because the heat flux always is perpendicular to the main surface of the body. When using a 1-D heat-transfer calculation, the supposed direction of the heat flux is as follows: for cylindrical workpieces, radial; for platelike workpieces, perpendicular to the main surface of the plate; and for ringlike workpieces, radial in two opposite directions—toward the outer and toward the inner diameter. Thermocouples should always be placed inside the cross section parallel with the main heat flux.
- The probe should be applicable to all liquid quenchants (oils, water, brine, polymer solutions, salt baths, and fluid beds) under all possible conditions and to all quenching techniques. The main purpose of the large probes for characterization of industrial quenching processes is to compare different quenchants under different conditions. There is no standard yet for the large probe itself nor for the test procedure. To select the optimal quenchant and quenching conditions in

a concrete case, one should know which one to use, for example, a still mineral oil at 60 °C (140 °F), a poly(alkylene glycol) polymer solution of 20% concentration at 40 °C (100 °F) temperature and 0.5 m/s (1.6 ft/s) agitation rate, or a salt bath at 200 °C (390 °F). The answer can be obtained only after measuring and recording the cooling curves using a large probe and calculating the HTC as a function of time and surface temperature, respectively.

The recorded results of every test are stored in the database. Once the database is filled with an adequate number of test results, a virtual comparison among different quenchants and quenching conditions, based on calculated HTCs, is possible, without repeating the test. Other possibilities a database can render are described in the section “Database of Cooling Intensities of Liquid Quenchants” in this article.

Critical Heat-Flux Densities of Liquid Quenchants

This section includes discussion on the initial heat-flux density and the importance of the first critical heat-flux density.

Initial Heat-Flux Density

For every quenching process there is an initial heat-flux density, q_{in} , which depends on the ratio between the volume (heat capacity) and the surface of the workpiece. The heat-flux density depends on the temperature gradient at the surface. Bodies with a relatively small volume and a large surface area have a greater temperature gradient and a greater initial heat-flux density than bodies with a relatively great volume and small surface area, as shown in Fig. 7. The former cools much faster than the latter.

When quenching in a vaporizable liquid, four modes of heat transfer occur at the interface of the hot workpiece and the quenchant. These are (in order of their occurrence) shock boiling (Ref 5), full film boiling, nucleate boiling, and

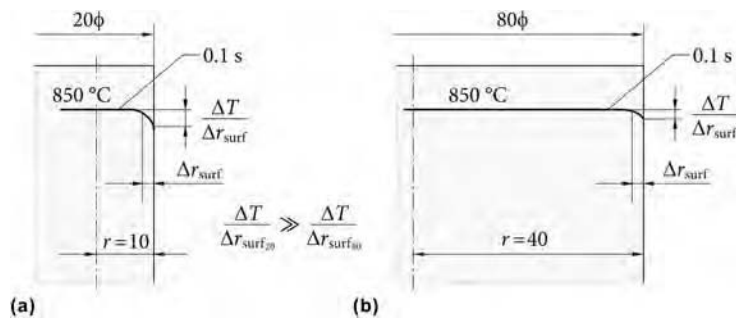


Fig. 7 Temperature gradient at the surface in the very beginning of cooling for cylinders that are (a) 20 mm (0.8 in.) in diameter by 80 mm (3.2 in.) and (b) 80 mm (3.2 in.) in diameter by 320 mm (12.6 in.)

convection. Shock boiling rarely is considered when reviewing the stages of the quenching process, because it occurs over a very short period of time, during approximately a tenth of a second. It is difficult to measure and record. Usually, a noise-sensing system is used to detect the shock-boiling mode.

Importance of the First Critical Heat-Flux Density

At every vaporizable quenchant there are two critical heat-flux densities: the first critical heat-flux density, q_{cr1} , and the second critical heat-flux density, q_{cr2} . Both are inherent properties of any vaporizable liquid. They do not change with the mass, shape, or material of the workpiece. The first critical heat-flux density is the maximum heat-flux density that causes film boiling (Ref 6). Typically, it occurs within approximately 0.1 s after immersion of the hot metal. The second critical heat-flux density is the minimum amount of thermal energy necessary to support film boiling. This is the point at which the surface of the hot workpiece has cooled sufficiently to allow the collapse of the vapor blanket, that is, the end of film boiling and the beginning of nucleate boiling, as shown in Fig. 8.

There is a relation between q_{cr1} and q_{cr2} that is valid for all vaporizable liquids:

$$\frac{q_{cr2}}{q_{cr1}} = 0.2 \quad (\text{Eq 7})$$

Because it is difficult to measure q_{cr1} directly, the proposed method is to measure q_{cr2} using a silver probe and then calculate q_{cr1} using Eq 7.

According to Ref 7, upon immersion of a workpiece into the quenchant, the initial heat-flux density, q_{in} , can be:

$$q_{in} \gg q_{cr1}; q_{in} \approx q_{cr1}; q_{in} \ll q_{cr1} \quad (\text{Eq 8})$$

When $q_{in} \gg q_{cr1}$, full film boiling (vapor blanket) will develop. When $q_{in} \approx q_{cr1}$, transition boiling is observed. When $q_{in} \ll q_{cr1}$, the film boiling stage is absent and nucleate boiling starts immediately after shock boiling. Each of these cases has different values of HTC.

The nonuniformity of the film boiling stage causes much of the distortion of the workpiece during quenching.

The first critical heat-flux density, q_{cr1} , has a great effect on the cooling rate of workpieces and their distortion. It depends on the saturation temperature of the liquid and the difference between the saturation temperature and the actual temperature of the quenchant. The bigger the difference that one can maintain between the workpiece surface and the quenchant temperature, the higher the effective cooling rate at the surface of the workpiece.

When water is applied as the quenchant, the q_{cr1} value depends on the water flow rate and the water temperature (Ref 8). It can be increased by increasing the agitation rate. The higher q_{cr1} is, the more resistant the liquid is to boiling when heat is applied. Therefore, the main purpose is to find the highest q_{cr1} in the concrete case. Once the highest q_{cr1} has been found, the temperature point of operation for that liquid is found where it is most resistant to film boiling. This can be done by repeating the test at different quench bath temperatures and available agitation rates. In addition, a small amount (e.g., 0.1%) of some chemical additives can increase the q_{cr1} value by two to three times. The kind of additive, its concentration, the water velocity, and the optimal bath temperature are held by companies as their "process know-how." Finding the highest critical heat-flux density, q_{cr1} , for a given quenchant and maintaining the quench bath at the optimal temperature will optimize the quench system for all workpieces quenched in that system, with minimum distortion. To provide uniform cooling (with no film boiling), that is, to eliminate distortion variation, the critical heat-flux density, q_{cr1} , should be greater than the initial heat-flux density, q_{in} .

Temperature Gradient Method for Evaluation of Cooling Intensity in Workshop Conditions

This section includes discussion on the theoretical principle behind and the purpose of the temperature gradient method.

Theoretical Principle

The temperature gradient method is based on the known physical rule that the heat flux at the surface of a body is directly proportional to the temperature gradient at the surface multiplied by the thermal conductivity of the material of the body being cooled:

$$q = \lambda \frac{\partial T}{\partial x} \quad (\text{Eq 9})$$

where q is the heat-flux density (W/m^2), λ is the thermal conductivity of the body material ($\text{W/m} \cdot \text{K}$), and $\partial T/\partial x$ is the temperature gradient at the body surface perpendicular to it (K/m).

Purpose of the Temperature Gradient Method

The temperature gradient method for cooling intensity of liquid quenchant was published by Liščić (Ref 9) in 1978. It is designed for the measurement and recording of the cooling intensity when real engineering components are quenched in workshop conditions.

This approach should be contrasted with Grossmann's H -factor concept, which expresses the severity of a quenchant by a single number. The temperature gradient method is based on the heat-flux density and expresses the cooling intensity by continuous change of relevant thermodynamic functions during the entire quenching process.

The method is applicable to all liquid quenchant (oils, water, brine, aqueous polymer solutions, salt baths, and fluidized beds), to different quenching conditions (bath temperatures, agitation rates, fluid pressures, and loading arrangements), as well as for all quenching techniques (direct immersion quenching, interrupted quenching, martempering, and austempering).

The main goals of this method are:

- To enable real comparison of the cooling intensity among different quenchant, quenching conditions, and quenching techniques
- To provide an unambiguous relation between the evaluated cooling intensity (I) and the resulting depth of hardening. In this regard, the following four criteria are used: the maximum of heat-flux density, q_{max} (MW/m^2); the time from immersion to the occurrence of q_{max} , $t_{q_{max}}$ (s); the integral under the heat-flux density curve (proportional to the quantity of heat extracted):

$$\int_{t_0}^{t_s} q dt \quad (\text{MJ/m}^2)$$

and time until the core temperature drops to 300°C , $t_{T_{300}}$ (s). The cooling intensity (I) is higher and the depth of hardening is greater if q_{max} and $\int_{t_0}^{t_s} q dt$ are bigger and the time intervals $t_{q_{max}}$ and $t_{T_{300}}$ are shorter.

- To provide the information about thermal stresses. In this regard, a diagram showing temperature differences between the center of the cross section and positions of other thermocouples is used.

To perform tests using the temperature gradient method in industrial practice, the Liščić/Petrofer probe is used.

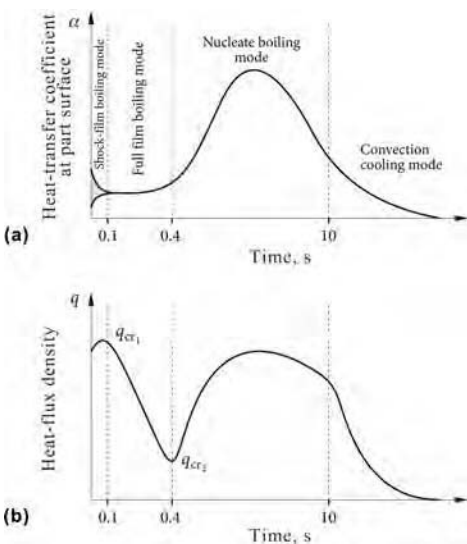


Fig. 8 (a) Four modes of cooling at quenching. (b) Critical heat-flux densities. Courtesy of N.I. Kobasko

The Liščić/Petrofer Probe

This section includes discussion on the design of the probe, the heat-extraction dynamic, and the influence of wetting kinematics.

Design of the Probe

The Liščić/Petrofer probe is a large probe designed to measure and record the cooling intensity of all kinds of liquid quenchant in a workshop environment, that is, to characterize quenching processes in industrial practice. Because of its own shape, it is applicable for axially symmetrical workpieces of any shape, primarily for diameters between 25 and 100 mm (1.0 and 4.0 in.).

The probe is a cylinder of 50 mm (2 in.) in diameter and 200 mm (8.0 in.) in length. Figure 9 is a sketch of the probe with the handle, and Fig. 10 is a photo of the probe itself.

The ratio between length and diameter, $L/D = 4:1$, assures that the heat dissipation through both ends is negligible, so that in the cross section at half-length, where the thermocouples are positioned, only radial heat flow exists. This is a prerequisite for 1-D heat-transfer calculation. The probe is made of an austenitic nickel-chromium superalloy that does not undergo structural transformations and is oxidation resistant. The probe is instrumented with three thermocouples (TCs). One sheathed TC of 1 mm (0.04 in.) outer diameter is placed at 1 mm (0.04 in.) below the surface, the second one at 4.5 mm (0.18 in.) below the surface, and the third one in the center of the cross section at the half-length of the probe. All TCs are placed along the same radius.

For the test, the probe is heated to 850 °C (1560 °F) until the central TC reaches this value, then it is transferred quickly to the quenching bath and immersed vertically. It is of utmost importance that the transfer from the furnace to the quenching bath is always performed within the same short period of time and that the probe is immersed with the same speed strictly vertically, so that equal cooling conditions can be guaranteed around its perimeter. The probe is connected to a temperature data-acquisition system that contains three analog-to-digital converters and amplifiers and a personal computer. The acquisition software enables the recording of all three TC signal outputs with a frequency of 0.02 s (50 measurements per second) during the whole quenching process and the simultaneous drawing of three cooling curves in real-time, as shown in Fig. 11.

Heat-Extraction Dynamic

The Liščić/Petrofer probe is used within the program “Temperature Gradient System (TGS) for Hardness Prediction in Quenched Axially Symmetrical Workpieces of any Shape.”

For calculation of the HTC, the measured temperatures at 1 mm (0.04 in.) below surface are used as input for the 1-D inverse heat-conduction method. The procedure of HTC calculation is described later.

After calculation of the HTC, the TGS program enables a comprehensive analysis of the

quenching process by the following thermodynamic functions:

- The calculated surface temperature (T_s) and measured temperatures at 1 and 4.5 mm (0.04 and 0.18 in.) below the surface and at the center (Fig. 12)
- Temperature differences versus time between the center and the surface, between the center and 1 mm (0.04 in.) below the surface, and between the center and 4.5 mm (0.18 in.) below the surface (Fig. 13). These graphs are used when thermal stresses are to be calculated.
- The cooling rate curves as a function of surface temperature for 1 and 4.5 mm (0.04 and 0.18 in.) below the surface and for the center of the probe

The temperature gradient method also can be used for probes of the same design having different diameters. Figure 14 shows the results obtained for such probes of 20 mm (0.8 in.).

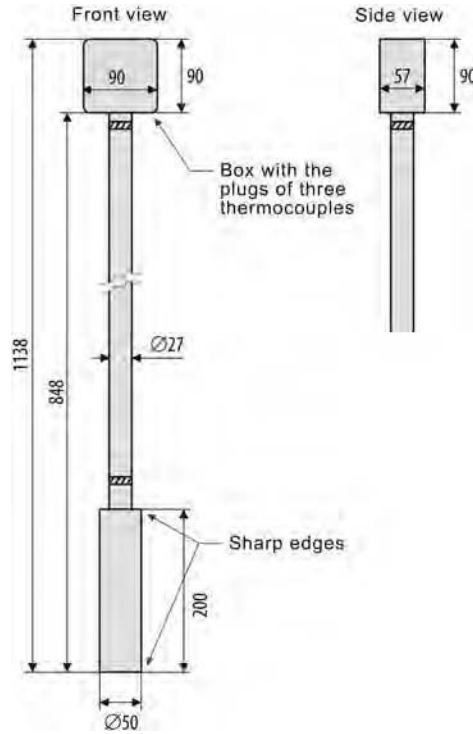


Fig. 9 Sketch of the Liščić/Petrofer probe with handle. Courtesy of Petrofer GmbH



Fig. 10 Photo of the Liščić/Petrofer probe. Courtesy of Petrofer GmbH

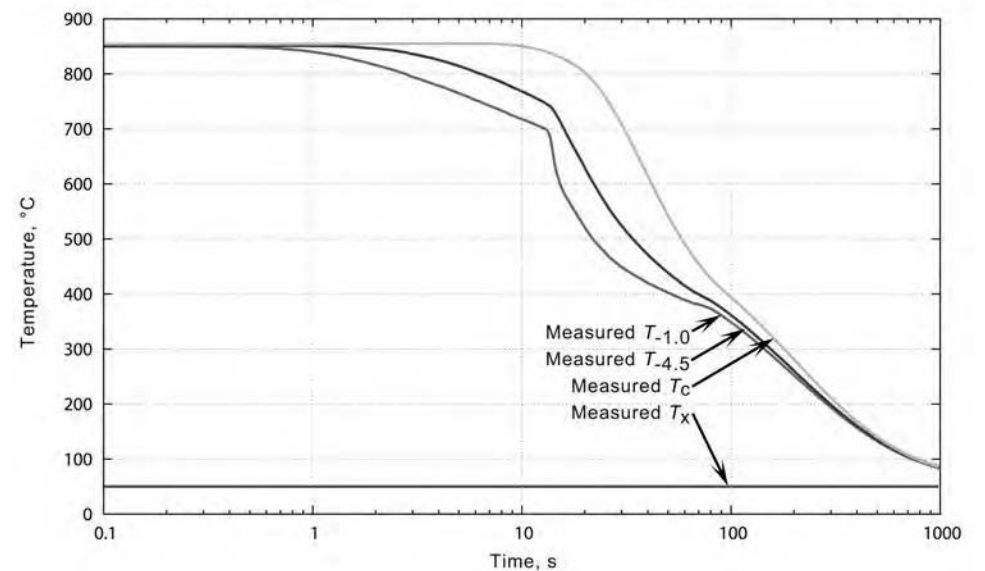


Fig. 11 Cooling curves measured by the Liščić/Petrofer probe quenched in a medium-viscosity accelerated quenching oil at 50 °C (120 °F). Courtesy of Petrofer GmbH

diameter by 80 mm (3.2 in.) and 80 mm (3.2 in.) diameter by 320 mm (12.6 in.) quenched in a low-viscous accelerated oil at 50 °C (120 °F) with medium agitation.

Irrespective of the probe diameter and mass of the probe, the temperature gradient method exhibits two very important features:

- It clearly displays the heat-extraction dynamic during the whole quenching process.
- It shows the initial heat-flux density (q_{in}) at the beginning of cooling.

To explain the heat-extraction dynamic during quenching, the features of Fig. 14(a) and (b) are first discussed. In Fig. 14, the probe of 80 mm (3.2 in.) diameter by 320 mm (12.6 in.) has a mass of 13.6 kg (30.0 lb), a surface area/volume ratio of only 56 m^{-1} , and a heat capacity of $6045 \text{ J/kg}^1 \cdot \text{K}^1$, representing a case of great volume (and heat capacity) and relatively small surface area. The probe of 20 mm

(0.8 in.) diameter by 80 mm (3.2 in.) has a mass of only 0.2 kg (0.44 lb), a surface area/volume ratio of 225 m^{-1} , and a heat capacity of only $94 \text{ J/kg}^{-1} \cdot \text{K}^{-1}$, representing a case of small volume (and heat capacity) and relatively big surface area. The heat capacity of the bigger probe is 64 times larger than the heat capacity of the smaller probe.

One would expect that the cooling time to 200 °C (390 °F) of the bigger probe would be several tens of times longer than that of the smaller probe, but it is only 7.7 times longer, as can be seen in Fig. 14(a) and (b) (395 s for the bigger probe versus 51 s for the smaller probe). The reason can be explained by comparing the temperature gradients during quenching of both probes. The smaller probe cools from the beginning faster than the bigger one, but later the maximal temperature gradient within the bigger probe ($434 \text{ }^\circ\text{C}$, or $813 \text{ }^\circ\text{F}$) is much larger than that within the smaller probe ($132 \text{ }^\circ\text{C}$, or $269 \text{ }^\circ\text{F}$), which causes larger heat

fluxes within the bigger probe. This is why the cooling time of the bigger probe is only 7.7 times longer, although its heat capacity is 64 times larger.

The initial heat-flux density (q_{in}) can be compared in the beginning of cooling. For example, 2 s after immersion of the smaller probe (Fig. 14a), the temperature gradient between the center and 1 mm (0.04 in.) below the surface was already $26.1 \text{ }^\circ\text{C}$ ($79.0 \text{ }^\circ\text{F}$). For the bigger probe at the same time, the temperature gradient between the center and 1 mm (0.04 in.) below the surface was only $12.4 \text{ }^\circ\text{C}$ ($54.3 \text{ }^\circ\text{F}$), as shown in Fig. 14(b), making a big difference in the initial heat-flux density.

This analysis shows how the Liščić/Petrofer probe based on the temperature gradient method can precisely describe the dynamic of heat extraction during the whole quenching process, as well as determine the real initial heat-flux density, depending on the volume (mass) of the workpiece.

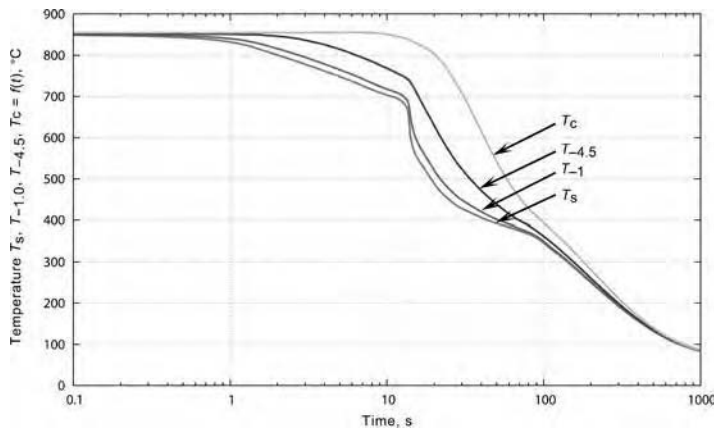


Fig. 12 Calculated surface temperature (T_s) and measured temperatures at 1 and 4.5 mm (0.04 and 0.18 in.) below the surface and in the center of the probe. Courtesy of Petrofer GmbH

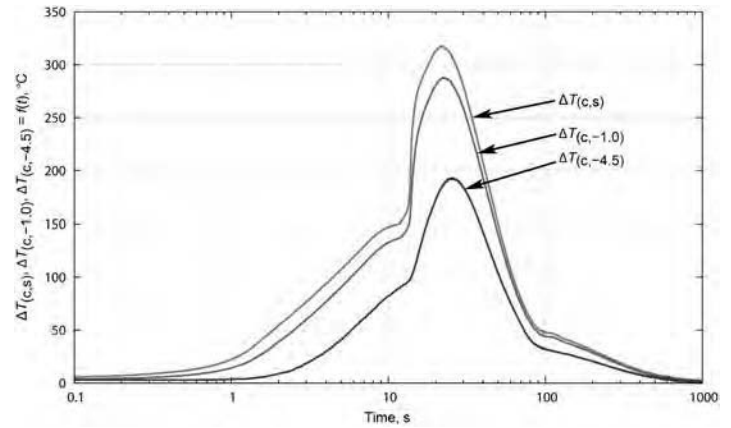


Fig. 13 Calculated temperature differences versus time between the center and the surface, between the center and 1 mm (0.04 in.) below the surface, and between the center and 4.5 mm (0.18 in.) below the surface. Courtesy of Petrofer GmbH

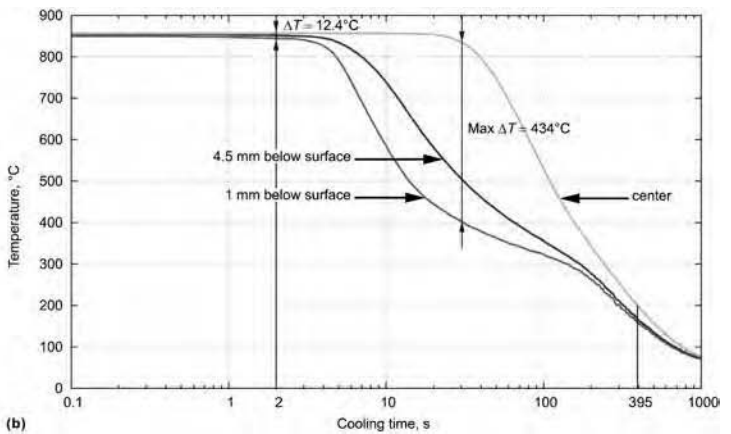
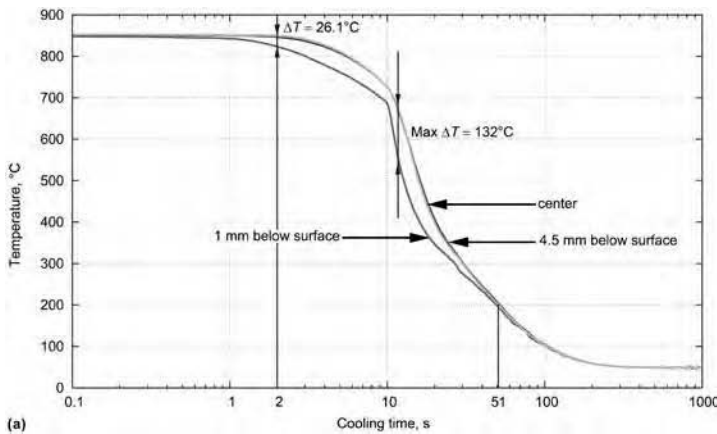


Fig. 14 Cooling curves measured by probes of the same design as the Liščić/Petrofer probe that were quenched in a low-viscous accelerated oil of 50 °C (120 °F) with medium agitation. (a) 20 mm (0.8 in.) diameter by 80 mm (3.2 in.). (b) 80 mm (3.2 in.) diameter by 320 mm (12.6 in.). Courtesy of Petrofer GmbH

Influence of Wetting Kinematics

In the cross section at half-length of the probe, only radial heat flux should exist (due to negligible heat dissipation on both ends of the probe), but the influence of wetting kinematics should not be neglected. This is a phenomenon accompanying every quenching process in evaporable liquids that causes some axial heat flow, depending on the time of rewetting (Ref 10). As shown in Fig. 15, rewetting starts in those places on the workpiece surface where film boiling (vapor blanket) collapses and nucleate boiling starts.

At each of these places at that moment, a sudden increase of the HTC occurs. Rewetting usually starts at the lower end and moves gradually as a wetting front toward the upper end of the cylinder, as shown on the left side of Fig. 16. The spreading speed of the wetting front is determined by physical properties of the body and the fluid, as well as many other factors.

During rewetting, the temperature inside the cylinder changes not only radially but also along the cylinder (z), as shown on the right side of Fig. 16 (Ref 11).

This case relates to immersion cooling of an AISI 4140 steel cylinder of 40 mm (1.6 in.) diameter by 120 mm (4.7 in.) in water at 80 °C (180 °F). Such conditions are not used in practice but have been chosen to clearly show the advancement of the wetting front. The rewetting process can have different forms and durations, from slowly moving wetting front in, for example, a quenching oil of high temperature, to abrupt explosion in some polymer solutions. Therefore, it can have lesser or greater influence on the local HTC. When using the Liščić/Petrofer probe, the calculated HTC at the half-length cross section (which depends on the cooling curve measured at 1 mm, or 0.04 in., below the surface) includes the time the wetting front reaches this point as well as the local change of HTC at that moment. When comparing results of tests for different quenchants and quenching conditions, the influence of wetting kinematics is always included. Because this influence depends on the probe itself, for a precise comparison, a probe of the same characteristics should be used.

Prediction of Hardness Distribution after Quenching Axially Symmetrical Workpieces of Any Shape

A two-dimensional (2-D) computer program has been developed by Smoljan (Ref 12, 13) for the prediction of hardness distribution in quenched axially symmetrical workpieces of any shape, based on the finite-volume method. It also contains a subroutine for drawing a 2-D contour of every axially symmetrical workpiece as well as automatic generation of the finite-element mesh for half of it.

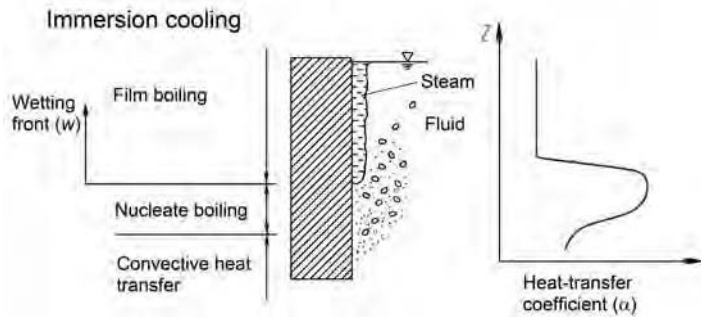


Fig. 15 Change in local heat-transfer coefficient on immersion cooling due to wetting kinematics. Source: Ref 10

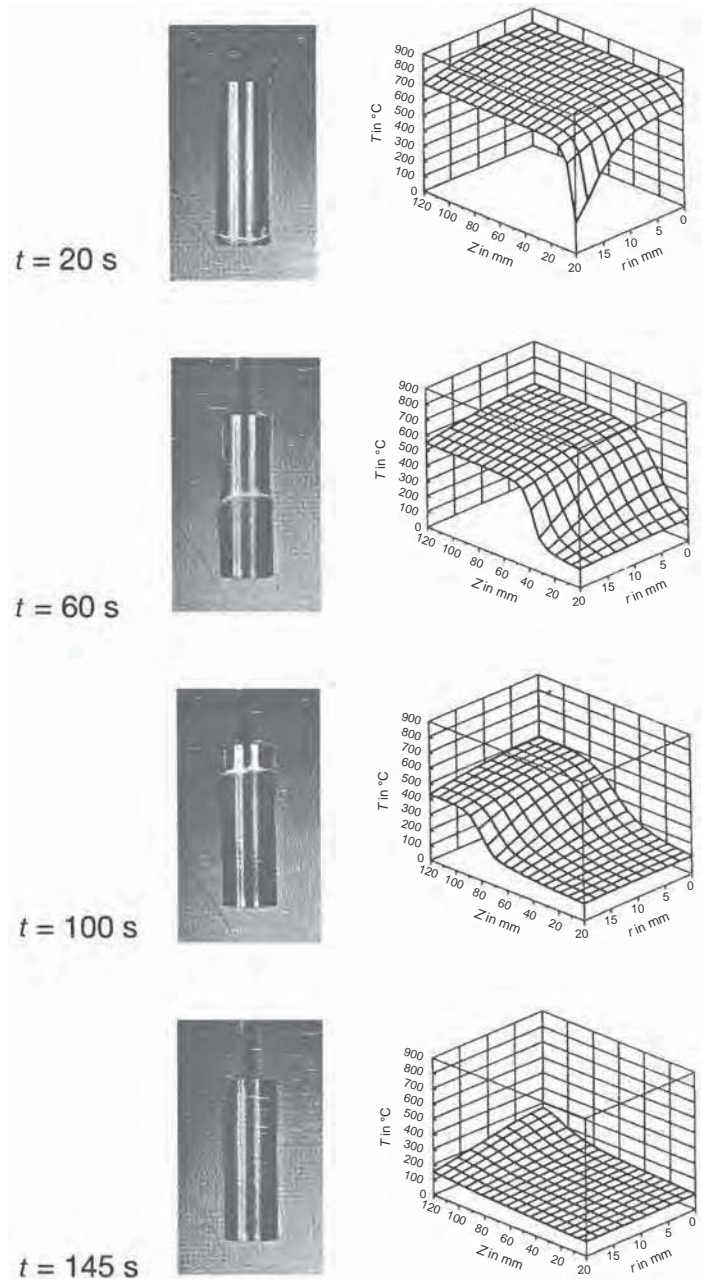


Fig. 16 Observed wetting-front advancement (left) and temperature distribution (right) calculated by using the local heat-transfer coefficient when immersion cooling an AISI 4140 steel cylinder of 40 mm (1.6 in.) diameter by 120 mm (4.7 in.) in 80 °C (180 °F) water. Source: Ref 11

By using the HTC calculated for a concrete test by the Liščić/Petrofer probe, cooling curves at every particular point of the axial workpiece section are calculated, and cooling times from 800 to 500 °C (1470 to 930 °F) ($t_{8/5}$) are determined and stored. According to Rose (Ref 14), the time $t_{8/5}$ is a relevant characteristic for phase transformation in most structural steels and, accordingly, is a decisive feature for resulting hardness after quenching.

Because there is a fixed relation between the cooling time $t_{8/5}$ and the distance from the quenched end of the Jominy specimen, for each time $t_{8/5}$, the corresponding Jominy distance can be read, as shown in Fig. 17.

The next step is to read the hardness at the relevant Jominy distance from the Jominy hardenability curve for the concrete steel in question. The whole procedure of conversion of the cooling time $t_{8/5}$ to the hardness at a particular point of the workpiece section is shown schematically in Fig. 18.

The preciseness of the hardness prediction depends first on the Jominy curve, which further depends on the chemical composition of the particular batch for every steel grade. Therefore, the most precise hardness prediction can be expected when the Jominy curve for the particular batch of the relevant steel grade is available.

Figure 19 shows the result of hardness prediction across half of the axial section of a complex axially symmetrical workpiece made of steel grade AISI 5140 quenched in oil with medium agitation.

Figure 19(a) shows the workpiece without the central hole, and Fig. 19(b) shows the same workpiece having a central hole of 20 mm (0.8 in.) diameter. The prediction of quenched hardness using colors to denote the quenched hardness (HRC) index exactly shows hardness differences between slim and thick sections, especially sharp corners, as well as areas of insufficient hardness. Note that this area is

much smaller at the workpiece with the central hole, because cooling from inside the hole has been accounted for.

By specifying the coordinates in the longitudinal (z) and radial (r) directions, one can read the particular value of hardness at every point of the axial section.

Database of Cooling Intensities of Liquid Quenchants

The TGS computer program contains two types of data files:

- Data files of a large number of structural steel grades with their respective Jominy hardenability curves
- Data files of HTCs calculated from cooling curves recorded experimentally by the Liščić/Petrofer probe. For example, Fig. 21 and 22 (in the article characterization of heat transfer during Quenching, in this volume) show the calculated HTC for this probe quenched in a medium-viscosity accelerated quenching oil at 50 °C, as a function of time and as a function of surface temperature, respectively.

Both types of data files are openly structured, so that every user can add new grades of steel and/or new HTCs calculated for other specific quenching conditions.

When using the TGS program for prediction of quenched hardness, the following steps are necessary:

1. Half of the contour of the workpiece must be drawn on the computer screen.
2. The steel grade must be selected, which automatically determines its hardenability by the relevant Jominy curve.
3. The HTC must be selected for the concrete quenching test performed by the Liščić/Petrofer probe.

Once the database is filled with an adequate number of test measurements and calculated HTCs for different quenchants and quenching conditions, the TGS enables:

- Comparison of real cooling intensities by the previously mentioned thermodynamic functions and calculated HTCs for all stored quenchants and specified quenching conditions
- Prediction of the hardness distribution for every axially symmetrical workpiece

One purpose when predicting the hardness distribution is a virtual selection of the best combination of cooling intensity and steel grade for the concrete workpiece. This is done by using different steel grades and/or different quenching conditions stored in the database, without doing one's own experiments. The Jominy curve stored in this case corresponds to an average chemical composition, starting from an austenitization temperature shown in literature.

The other purpose is to perform one's own experiments with the probe and calculate the HTC from cooling curves recorded in concrete quenching facilities and conditions. In this case, the Jominy curve should correspond to the particular batch of the relevant steel grade, obtained by the Jominy test with the same austenitization temperature as is used for hardening the concrete workpiece. In this case, a more precise hardness prediction can be expected.

Numerical Solution of the Inverse Heat-Conduction Problem

This section includes discussion of the simplified 1-D temperature-distribution model, the calculation of the HTC, and the finite-

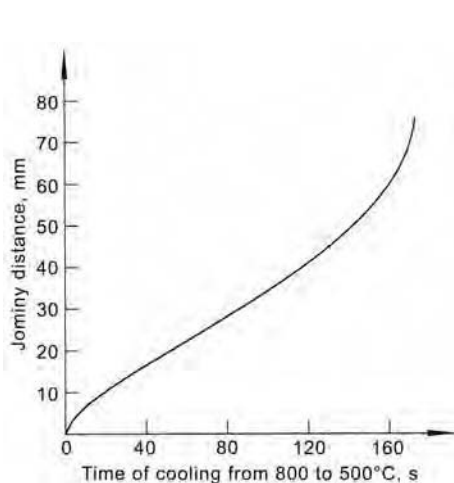


Fig. 17 Relation between time of cooling from 800 to 500 °C (1470 to 930 °F) ($t_{8/5}$) and the Jominy distance. Source: Ref 14

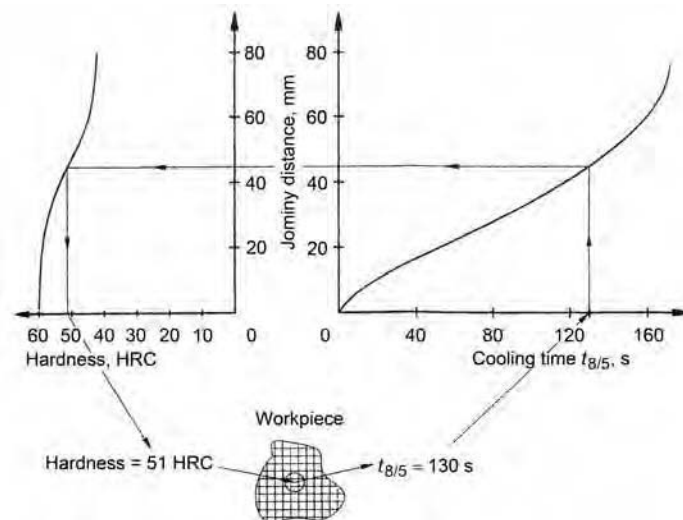


Fig. 18 Example of conversion of the cooling time $t_{8/5}$ to hardness. Source: Ref 12, 13

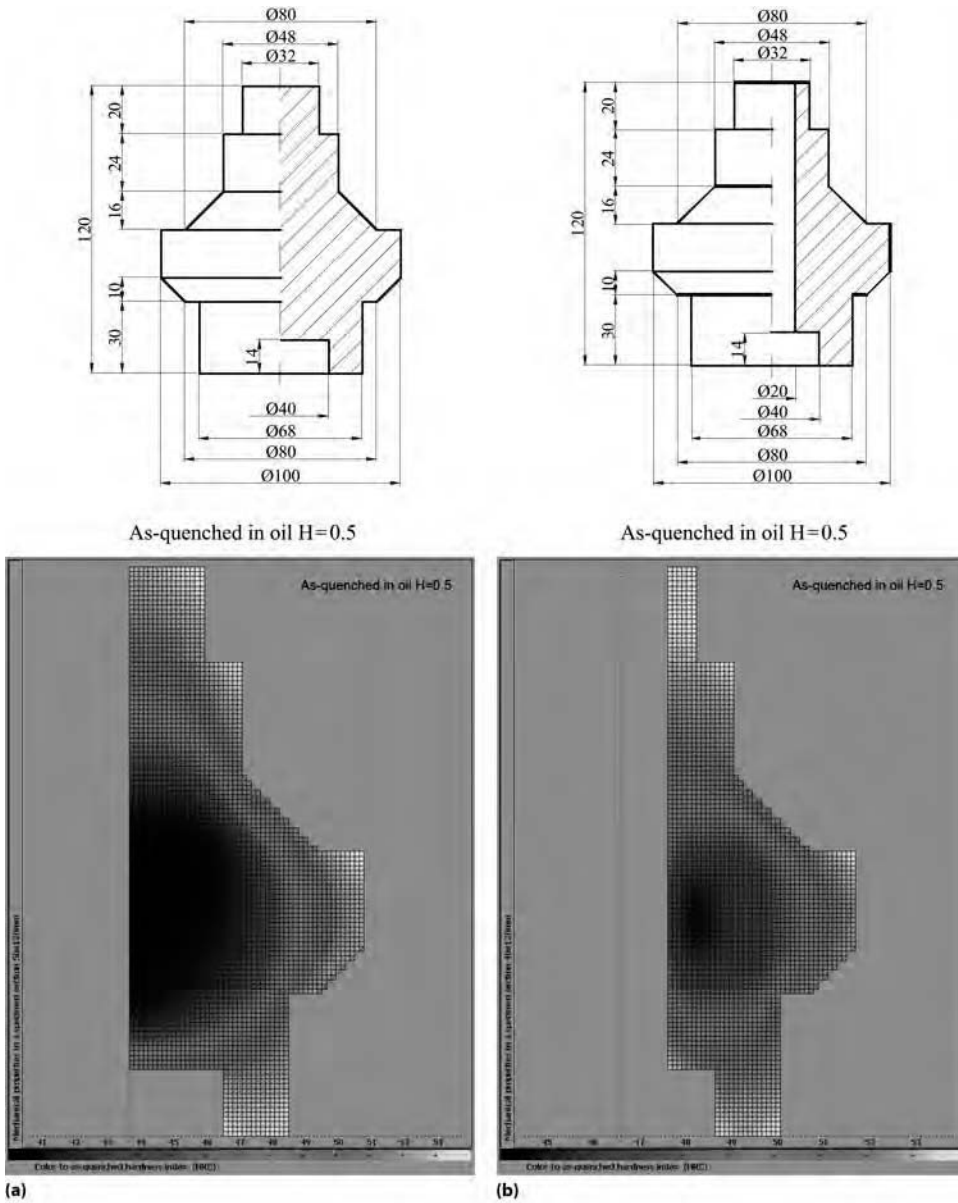


Fig. 19 Result of hardness prediction across half of the axial section of a complex axially symmetric workpiece made of steel grade AISI 5140 quenched in oil. (a) Without a central hole. (b) With a central hole of 20 mm (0.8 in.) diameter. Source: Ref 12, 13

volume method for the heat-conduction equation (HCE).

Simplified 1-D Temperature-Distribution Model

The standard probe is treated as a long, radially symmetrical cylinder of a given radius $R = 25$ mm (1.0 in.). Asymmetries and changes in the material introduced by the thermocouples are simply ignored. It is assumed that heat loss during the quenching process occurs only through the curved side of the cylinder, and the flat top and bottom sides are ignored, as if the cylinder is of infinite

length. The ignored surface area is only $1/8$ of the active surface area, which provides sufficient accuracy in practice. Finally, in a simplified 1-D model, it is assumed that the temperature (T) inside the cylinder for all times (t) depends only on the radial distance $r \in [0, R]$ from the center of the cylinder and can be written as $T = T(r, t)$.

This assumption poses severe restrictions in practical applications, and great care must be taken when using the probe to ensure that this is valid as much as possible. For example, the probe should be immersed vertically into the quenchant, and eventual quenchant agitation must be vertical as well.

With all of these assumptions, the temperature inside the cylinder is determined by the 1-D heat-conduction equation (Eq 1), written in polar coordinates without the angular component:

$$c\rho \frac{\partial T}{\partial t} = \frac{1}{r} \cdot \frac{\partial}{\partial r} \left(r\lambda \frac{\partial T}{\partial r} \right) \tag{Eq 10}$$

All physical/thermal properties c , ρ , and λ of the material must be considered as temperature dependent, because of the temperature range involved in quenching. Thus, the heat-conduction problem (Eq 10) becomes a nonlinear (or, more precisely, a quasi-linear) problem.

Because an austenitic nickel-chromium superalloy does not have phase transitions with latent heat involved, these properties are almost linear functions of T (Ref 15). They are given as tables of values for only a small number of temperatures. For the numerical solution of the heat-conduction problem, these tables first have to be converted into functions by computing a suitable approximation for each property over the whole temperature range. A simple piecewise linear interpolation in the table is sufficient for most purposes. To obtain a smoother function, cubic or quadratic splines can be used (Ref 16, 17, where the algorithms for computing such approximations are also given).

For the Liščić/Petrofer probe, all thermal properties at a given temperature are computed by Akima's piecewise cubic interpolation (Ref 16, 18) in the original tables from Ref 15. This method produces a smoother function than the ordinary piecewise linear interpolation—the first derivative is continuous—and also avoids wiggles in it.

The probe initially is heated to a certain temperature, and the initial condition $T(r, 0) = T_0(r)$ at the start of the quenching process is known. Usually, it is assumed that the probe is uniformly heated, so T_0 is constant, approximately 850°C (1560°F).

Due to symmetry, the boundary condition at the center of the cylinder ($r = 0$) must be:

$$\frac{\partial T}{\partial r} = 0 \tag{Eq 11}$$

By the infinity assumption, the probe has only one cooling surface, and radial symmetry implies that the surface HTC (α) depends only on time (t). The boundary condition (Eq 2) for $r = R$ can then be written as:

$$q_s = -\lambda \frac{\partial T}{\partial r} = \alpha(T_s - T_x) \tag{Eq 12}$$

where $T_s(t) = T(R, t)$ is the surface temperature of the cylinder, and $T_x(t)$ is the measured external temperature of the quenchant. Here, the surface heat-flux density, $q_s(t)$, is considered to be

positive when the probe cools, which is customary in industrial applications.

To determine α as a function of time in Eq 12, a temperature curve $T_n(t)$ is measured by a thermocouple located at a point $r = r_n$ near the surface of the cylinder. In the Liščić/Petrofer probe, T_n is measured at the depth $d = 1$ mm (0.04 in.), so its position is $r_n = 24$ mm (1.0 in.). Note that the whole computation is performed in consistent units, and all space coordinates are given in meters, that is, $R = 0.025$ m and $r_n = 0.024$ m.

The actual HTC calculation, to be described subsequently, is based on a simplified model that requires only two measured temperature curves in time, $T_n(t)$ and $T_x(t)$. No other input is needed, which makes it simple but fast in practice. In this model, all particular quenching conditions are reflected in only these two measured temperatures.

The probe is equipped with two additional thermocouples. One measures the core temperature, T_c , at $r = 0$, and the other one is located at the depth of 4.5 mm (0.18 in.) and measures the so-called intermediate temperature, T_i . These measured temperatures are sometimes used to calculate an approximation of the initial temperature distribution, $T_0(r)$. Apart from that, they are used only to verify the results.

Calculation of the Heat-Transfer Coefficient

The input temperatures T_n and T_x are measured at discrete times by a data-acquisition device, until some final time, t_{final} . The recorded values are rounded to a small number of decimal digits (no more than two) and also may be affected by measurement errors. Because the HTC (α) is obtained by numerical differentiation of temperature near the surface, any jumps in measured temperatures will be greatly amplified in the computed α . Therefore, before any use, both measured temperatures must be smoothed in time over the whole time range.

The primary goal of smoothing is to get rid of random measurement errors and convert discrete tables into functions of time, for all values $t \in [0, t_{\text{final}}]$. Depending on the application, there may be additional constraints in smoothing, such as the monotonicity of the smoothed temperature functions. The smoothing procedure is described later in more detail, but for now, it is assumed that the original discrete values already have been replaced by smoothed functions of time, also denoted by $T_n(t)$ and $T_x(t)$, respectively.

In principle, the HTC then can be calculated by the following global numerical procedure for solution of the inverse heat-conduction problem:

1. Take the smoothed temperature $T_n(t)$ as the fixed or Dirichlet's boundary condition for the heat-conduction equation

(Eq 10) on $[0, r_n]$. Solve this problem, for example, by using the implicit finite-difference method (Ref 19, 20). In each time step, simple iterations can be used to adjust all thermal properties to new temperatures.

2. Extend the computed solution from $[0, r_n]$ to the whole interval $[0, R]$ to find the surface temperature $T_s(t)$. This extension can be accomplished by the quasi-reversibility method of Lattès and Lions (Ref 21) or by simple extrapolation of the computed solution, if the depth $d = R - r_n$ is small with respect to the whole radius of the probe. Numerical testing shows that simple extrapolation is quite sufficient for depths up to 10% of the radius.
3. Calculate α from Eq 12 by using the smoothed external temperature $T_x(t)$ and numerical differentiation of the computed solution at the surface of the probe.

However, with standard liquid quenchants, the temperature gradient at the surface and the HTC in Eq 12 usually are very high. To keep the errors introduced by numerical differentiation within reasonable limits, the whole problem must be solved with a very fine space grid. As a result, the aforementioned procedure becomes quite slow.

To overcome this problem, the HTC is computed by an alternate procedure, which avoids explicit numerical differentiation of calculated temperatures. The heat-conduction equation (Eq 10) is written in a space-integrated form, as a heat-conservation law for the cylinder, in terms of the surface heat-flux density, q_s (Ref 22):

$$\int_0^R \left(c\rho \frac{\partial T}{\partial t} \right) (r, t) \cdot r dr = R \cdot \left(\lambda \frac{\partial T}{\partial r} \right) (R, t) = -R \cdot q_s(t) \quad (\text{Eq 13})$$

This is valid for all times, t , and already includes the symmetry boundary condition (Eq 11). The surface boundary condition (Eq 12) is represented here as the right side in Eq 13, with unknown q_s as a function of time. In accordance with this formulation, the numerical solution of the inverse problem now is based on the finite-volume method (Ref 20) and contains the following main steps:

1. Solve the heat-conservation law (Eq 13) on the whole interval $[0, R]$ to calculate the surface heat-flux density, $q_s(t)$, and the surface temperature, $T_s(t)$.
2. Compute the HTC, α , as a function of t directly from Eq 12, as:

$$\alpha = \frac{q_s}{T_s - T_x} \quad (\text{Eq 14})$$

where $T_x(t)$ is the smoothed external temperature.

The computation in step 1 is performed in a series of discrete time levels, t_i , until the final

time is reached, and it progresses by one time level in a global time-step loop:

- At each time level, t_i , the surface heat-flux density, $q_s(t_i)$, is calculated iteratively until the resulting temperature at the position r_n is exactly equal to the smoothed near-surface temperature, $T_n(t_i)$. The numerical solution of this equation, $T(r_n, t_i) = T_n(t_i)$, is done by the Brent-Dekker method (Ref 23), because it requires no derivatives and also is reasonably fast.
- Throughout these iterations, for each trial value of the surface heat-flux density, the heat-conservation law on $[0, R]$ is solved by the nonlinear implicit finite-volume method, with simple iterative adjustment of thermal properties to new temperatures. A brief outline of the algorithm is given in the next section.

In the TGS software, the calculated HTCs are used to predict the hardness distribution in a given workpiece under various quenching conditions. Because the simulated workpiece can be of any shape and dimensions, much better results are obtained if α is treated as a function of the surface temperature, T_s . This change of the independent variable, from t to T , is possible only if the calculated $T_s(t)$ is a monotone decreasing function of time. Otherwise, it may lead to different values of α at two different times, which correspond to the same value of the surface temperature at these times.

On the other hand, in practice, the surface temperature of the probe may increase at times, because of chaotic local behavior of the quenchant near the surface. This phenomenon is demonstrated by the polymer quenching example in the last section. In that example, the measured near-surface temperature, T_n , also increases over some time intervals, despite the damping effect. As expected, the calculated T_s increases even more. So, to convert α into a function of T_s , one must first compute a monotone decreasing approximation of $T_s(t)$ over the whole time interval $[0, t_{\text{final}}]$.

Note that such increases in temperature (either T_n or T_x) usually occur over relatively small periods of time. Because the probe cools globally in time, a monotone decreasing approximation of the temperature can be interpreted as local averaging (in time) of the cooling conditions at the surface of the probe. In the previous algorithm, T_s is computed from T_n . To avoid very large increases in T_s , this averaging is performed in stages:

1. At the very beginning, the measured near-surface temperature, T_n , is smoothed by a monotone decreasing function. The aim of this is to initially damp any chaotic surface effects, including the most violent jumps in q_s and α .
2. If the computed surface temperature, $T_s(t)$, does not decrease in time over the whole

time interval, a monotone decreasing approximation is computed by the same algorithm as in the initial monotone smoothing of T_n .

3. Finally, the monotone decreasing $T_s(t)$ function is substituted in Eq 14 to calculate $\alpha(t)$ and $\alpha(T_s)$.

A more conservative approach would involve replacing the last step with the monotone surface temperature $T_s(t)$ as the boundary condition for the second HTC calculation, and then use this more damped α in subsequent calculations.

Finite-Volume Method for the HCE

Time and Space Discretizations. In the numerical solution of the heat-conduction problem, both time and space coordinates are discretized by finite grids. The whole time interval $[0, t_{\text{final}}]$ is divided into a discrete sequence of increasing time levels:

$$0 = t_0 < t_1 < \dots < t_{n_r-1} < t_{n_r} = t_{\text{final}} \tag{Eq 15}$$

with time steps:

$$\tau_i = t_i - t_{i-1}, \quad i = 1, \dots, n_r \tag{Eq 16}$$

These time steps must be chosen in accordance with the thermal behavior of the probe in a particular quenchant, to avoid extreme temperature gradients in a single time step, which may result in a loss of accuracy.

With the Liščić/Petrofer probe, the finest temperature measurements are taken with a time step $\Delta t = 0.02$ s throughout the whole quenching period, with $t_{\text{final}} \approx 1000$ s. Such a fine time step provides very accurate data during the first intensive part of the quenching process but is quite unnecessary later on, when the temperature drops. Hence, three different time steps are used in Eq 16, to speed up the calculation:

1. $\tau_i = 0.02$ s, for the first 100 s
2. $\tau_i = 0.1$ s, from 100 up to 200 s
3. $\tau_i = 1$ s, from 200 s until the final time

In total, this gives approximately 6800 time levels instead of 50,000.

In the 1-D model of the probe, only the radial space coordinate must be discretized. For a prescribed number of subintervals, n_r , a uniform grid with the space step:

$$h = \frac{R}{n_r} \tag{Eq 17}$$

is generated in the interval $[0, R]$. The grid points r_j (illustrated in Fig. 20) are given by:

$$r_j = jh, \quad j = 0, \dots, n_r \tag{Eq 18}$$

Here, n_r must be sufficiently large, that is, the space step h in Eq 17 must be sufficiently small, for

accurate solution of the problem. The standard value is $n_r = 200$, or $h = 0.125$ mm (0.005 in.), for the Liščić/ Petrofer probe.

Quite generally, in a chosen formulation of the problem, all time and space derivatives are approximated by finite (or, more precisely, divided) differences with respect to the chosen grid points, and the resulting system of equations for unknown values at grid points then is solved numerically. The algorithm advances by one time level per step in a global time-step loop. So, in step i , approximate values for temperatures at time level t_i are computed at all grid points r_j . These approximate values will be denoted by T_j^i , to be distinguished from the unknown true values $T(r_j, t_i)$.

The only difference between the finite-difference method (FDM) and the finite-volume method (FVM) lies in the initial formulation of the heat-conduction problem, which then is discretized. In the FDM, the original formulation is the partial differential equation (Eq 10), with the appropriate boundary conditions (Eq 11, 12). In the FVM, the problem is written in its integral form, similar to Eq 13, and the finite-difference approximation is used for the heat flux (or the heat-flux density in 1-D models).

Control Volumes for the FVM. Grid points r_j given by Eq 17 and 18, are used to radially divide the probe into $n_r + 1$ annular finite-control volumes, as shown in Fig. 20.

In the simplified 1-D model of the probe, these volumes collapse into ordinary intervals V_j , shown at the bottom of Fig. 20.

The internal volumes V_j , for $j = 1, \dots, n_r - 1$, are cell-centered at grid points r_j :

$$V_j = \left[r_j - \frac{h}{2}, r_j + \frac{h}{2} \right], \quad j = 1, \dots, n_r - 1 \tag{Eq 19}$$

and their length is equal to the space step h . The remaining two boundary volumes:

$$V_0 = \left[0, \frac{h}{2} \right], \quad V_{n_r} = \left[R - \frac{h}{2}, R \right] \tag{Eq 20}$$

are neither vertex-centered nor cell-centered, and their length is halved. This somewhat unusual choice of control volumes is particularly well suited for the problem, because it is easy to discretize the equations with high accuracy.

The problem now is written as the heat-conservation law for each control volume V_j , to obtain the so-called semidiscretized system of equations. Space integration of the heat-conduction equation (Eq 10) over the control volume V_j , with the inner radius r_- and the outer radius r_+ , gives:

$$\int_{r_-}^{r_+} \left(c_p \frac{\partial T}{\partial t} \right) (r, t) \cdot r dr = r_+ \cdot \left(\lambda \frac{\partial T}{\partial r} \right) (r_+, t) - r_- \cdot \left(\lambda \frac{\partial T}{\partial r} \right) (r_-, t) \tag{Eq 21}$$

The right side represents the heat flow through the boundaries at r_- and r_+ , in terms of heat-flux densities at both surfaces. Here, it is easy to incorporate both boundary conditions (Eq 11,12), which already are given in terms of the heat-flux density, so there is no need for explicit numerical differentiation of temperatures.

Implicit Finite-Volume Method. The semi-discretized system of equations (Eq 21) is still valid for all times t and must be further discretized in time and space.

To ensure numerical stability of the whole algorithm, this discretization is done by the so-called implicit approach (Ref 19, 20). The

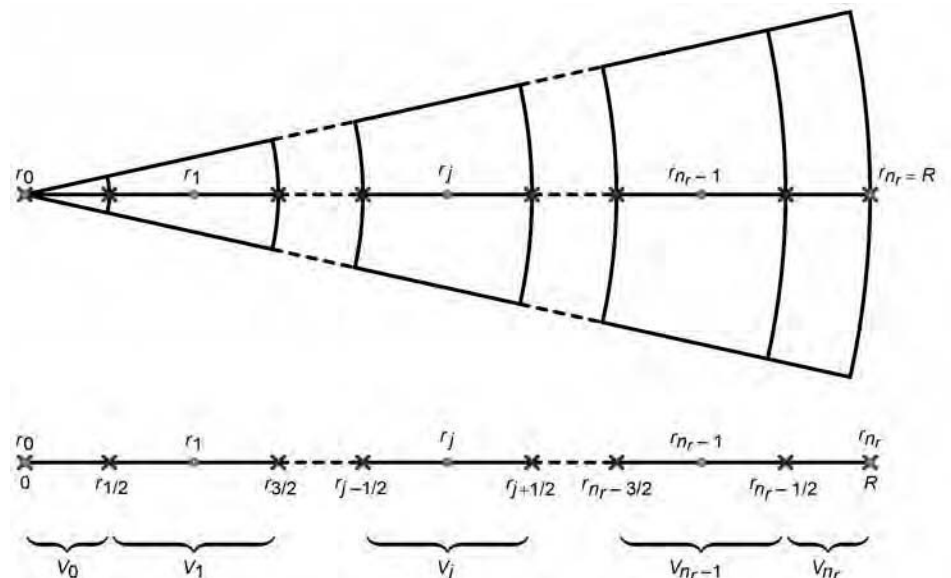


Fig. 20 Finite-control volumes for the one-dimensional heat-conduction problem

final space discretization is always performed at the new time level t_i , where the approximate solution is yet to be calculated, and all time derivatives are approximated by the backward difference, in terms of the previous time level, t_{i-1} , where the approximate solution already is known. At the first step when $i = 1$, the previous time level, $t_0 = 0$, corresponds to the known initial condition, T_0 , for the heat-conduction problem.

In the implicit FVM, Eq 21 is further discretized at the current time level t_i . Because of the choice of control volumes, the right side is easily discretized by central differences in terms of the temperatures T_j^i at grid points r_j . The integral on the left side is approximated by the midpoint quadrature formula (Ref 24). If necessary, this approximation is combined with the linear interpolation in terms of the grid-point values. The accuracy of all of these approximations is of the second order in h . Although the backward difference approximation of time derivatives is only first-order accurate in τ_i , this lower accuracy is more than accounted for in the overall numerical stability of the method.

At each time level t_i , the surface heat-flux density is calculated iteratively, until it reproduces the smoothed near-surface temperature at that time. Approximate values for $q_s(t_i)$ are generated by the surrounding Brent-Dekker algorithm for iterative solution of this equation. In each iteration, this approximate value is used in Eq 21 as the boundary condition for the outer boundary volume.

Implicit Iterative Computation of Temperatures. The discretization procedure gives a system of $n_r + 1$ equations, for $n_r + 1$ unknown temperatures T_j^i at all grid points r_j , for $j = 0, \dots, n_r$. In fact, this system has many more unknown values—it also contains thermal properties that depend on the unknown temperatures at the same time level.

However, because all thermal properties vary quite slowly with the temperature, the whole system is solved by a simple iterative adjustment of thermal properties to new calculated temperatures:

- The initial approximations for thermal properties at time level t_i are computed from the already calculated temperatures at the previous time level t_{i-1} . If time steps τ_i are not too large, this gives a very good approximation for all thermal properties.
- The thermal properties then are considered as known, as if they are constant at the corresponding spatial points. The system now becomes a tridiagonal linear system for unknown temperatures at time t_i , which is solved very quickly and accurately.
- The newly computed temperatures are used to compute better approximations for thermal properties, and the system is solved again.

These simple iterations are terminated when all computed temperatures at grid points are

stabilized almost to the full machine relative precision.

Smoothing of Measured Temperatures

Before any further processing, the measured temperatures must be smoothed in time, to remove the so-called noise in the data, which is caused by random measurement errors. This ordinary smoothing, without additional constraints, is sufficient if the computed HTC is used only as a function of time, to calculate the temperature distribution in the probe itself. On the other hand, if the HTC is used for other geometries, then it is taken as a function of the surface temperature. Here, the smoothing procedure involves an additional task; it must produce a function that is monotone decreasing in time, to eventually ensure the monotonicity of the surface temperature.

Ordinary Smoothing without Constraints

For temperatures measured in quenching, the noise introduced by random measurement errors contains only high-frequency oscillations, which are usually small in amplitude. So, the main goal of smoothing is to filter this type of noise, but the overall shape of the data should remain unchanged. Such a smoothing of data can be done either locally or globally in time by several standard algorithms.

In local smoothing, the smoothed value at a given point in time is calculated as a weighted average of a small number of nearby measurements. Very often, it is computed from a low-degree polynomial least-squares approximation (Ref 25). When applied through the whole data set, this provides a quick and simple way to obtain a locally smoothed table of values. This is quite appropriate for local smoothing of calculated $q_s(t)$ or $\alpha(t)$ values, to remove artificial oscillations introduced by the numerical solution of the inverse problem.

However, local smoothing is not adequate for smoothing of measured temperatures. To provide a freedom of choice for time levels in the HCE solution algorithm, an output of smoothing must be a smoothing function, f , that can be evaluated at any time point in the range. This function f also must be sufficiently smooth, at least continuously differentiable (the so-called C^1 smoothness), to avoid sudden jumps or discontinuities in the calculated α .

The smoothing function f is obtained by finding a suitable approximation of the measured data, that is, by solving an appropriate optimization problem. Usually, the function $f(t)$ is assumed to have a prescribed form, with a certain number of “free” parameters. For statistical reasons that justify the noise removal from the

original data, these unknown parameters are computed by solving the corresponding least-squares (LSQ) approximation problem.

In the authors’ experience, when there are no additional shape constraints on the smoothing function, the best way for global smoothing of measured temperatures is to take f as a low-degree polynomial spline. Algorithms for global smoothing by polynomial splines are given in Ref 16 and 17. The accompanying software is publically available and free to use.

Monotone Smoothing

In the TGS software, the smoothing function f must be monotone decreasing in time. Accordingly, a global numerical procedure for finding f is to compute an LSQ approximation of the measured data, except that f is restricted to be monotone. For example, monotone smoothing can be done by using cubic splines (Ref 17). This leads to a constrained optimization problem, which is more difficult to solve than the corresponding unconstrained problem. In addition, cubic splines are too smooth for temperatures measured in liquid quenchants.

For these reasons, instead of polynomial splines, continuously differentiable (C^1) exponential splines (Ref 26) are used for monotone smoothing. Such splines are more difficult to calculate, but in the end, an unconstrained LSQ optimization problem is obtained, which is then easier to solve. Moreover, for smoothing of temperatures, this form of the smoothing function offers some extra advantages.

Exponential C^1 Splines. Informally speaking, an exponential C^1 spline f is a function that is piecewisely composed of ordinary exponential functions, and these pieces are joined in such a way to give the global C^1 smoothness of the function. More precisely, the construction of f begins by specifying the so-called spline mesh. It is given as an ascending sequence of $m + 1$ knots:

$$\xi_0 < \dots < \xi_m \quad (\text{Eq 22})$$

and divides the whole interval $[\xi_0, \xi_m]$ into m subintervals $[\xi_{j-1}, \xi_j]$, for $j = 1, \dots, m$. The restriction of f on each subinterval $[\xi_{j-1}, \xi_j]$ is equal to some exponential function p_j , that is:

$$f(t) = p_j(t), \quad t \in [\xi_{j-1}, \xi_j], \quad j = 1, \dots, m \quad (\text{Eq 23})$$

where the exponential “piece” p_j is defined by:

$$p_j(t) = \begin{cases} a_j + b_j e^{d_j t} & \text{for } d_j \neq 0 \\ a_j + b_j t & \text{for } d_j = 0 \end{cases} \quad (\text{Eq 24})$$

Finally, to make f continuously differentiable on $[\xi_0, \xi_m]$, the pieces p_j must satisfy the following continuity conditions at all interior knots ξ_1, \dots, ξ_{m-1} of the spline mesh:

$$f(\xi_j) = p_j(\xi_j) = p_{j+1}(\xi_j) \\ f'(\xi_j) = p'_j(\xi_j) = p'_{j+1}(\xi_j) \quad j = 1, \dots, m-1 \quad (\text{Eq 25})$$

The interior knots also are known as the break-points of f , because the second derivative f'' has jumps at these points.

Note that each piece p_j is determined by three parameters: a_j , b_j , and d_j . This initially gives $3m$ degrees of freedom, but $2m - 2$ continuity conditions (Eq 25) imply that only $m + 2$ degrees of freedom are left for f . In fact, the exponential C^1 spline f is uniquely determined by the following $m + 2$ parameters:

- Two “global” endpoint values, $f_0 = f(\xi_0)$ and $f_m = f(\xi_m)$, which can be viewed as the boundary conditions for f
- The m values of local shape parameters d_1, \dots, d_m —one value for each subinterval of the spline mesh. They control the second derivative of f , that is, determine the local convexity or concavity of each piece.

Such a function always is monotone on the interval $[\xi_0, \xi_m]$. The trend of f is determined solely by the boundary conditions, and $f_0 > f_m$ makes f monotonically decreasing. Therefore, no additional monotonicity constraints are required for monotone smoothing.

For a given set of parameter values, the continuity equations (Eq 25) become a linear system for the remaining local parameters of all pieces. This system is quite easy to solve, either numerically or even analytically, to obtain the local form (Eq 24) of each piece. Then, p_j can be evaluated at each point t in its subinterval.

Monotone Smoothing of Measured Temperatures. Suppose that the measured data set consists of $n_d + 1$ points (t_k, T_k) , for $k = 0, \dots, n_d$, where t_k now denote the times at which the temperatures are measured (and not the time levels, as before), and $T_k = T_n(t_k)$ are the measured near-surface temperatures. In addition, it is assumed that the whole set is sorted increasingly in time:

$$0 = t_0 < t_1 < \dots < t_{n_d-1} < t_{n_d} \quad (\text{Eq 26})$$

and that the first measurement is taken at the time $t_0 = 0$.

For simplicity, the spline mesh is taken as a suitable subset of all measured times, that is, the spline knots coincide with some of the data sites t_k . Regardless of the number of knots in the mesh (which may vary), the boundary knots always are placed as:

$$\xi_0 = t_0 = 0, \quad \xi_m = t_{n_d} \quad (\text{Eq 27})$$

so that f always covers the whole time range.

The calculation is organized in several stages, as an iterative refinement of the spline mesh, to obtain better and better approximations. In each stage, the spline mesh is fixed, and the corresponding exponential C^1 spline f is computed to fit the data. At a

particular stage, some of the $m + 2$ parameters $f_0, f_m, d_1, \dots, d_m$ may have fixed values (mainly, to speed up the process), and the remaining free parameters are computed by solving the LSQ problem:

$$\sum_{k=0}^{n_d} (T_k - f(t_k))^2 \rightarrow \min \quad (\text{Eq 28})$$

to obtain the best possible fit and to remove the noise in the data as well.

This is a nonlinear unconstrained optimization problem, which can be solved by various iterative methods. However, the derivatives of f with respect to the free parameters are quite hard to compute here. To avoid that, Eq 28 actually is solved by the Nelder-Mead simplex search algorithm (Ref 27), because it uses only function values of f .

Monotone smoothing with exponential C^1 splines also can be used to provide additional information about the quenching process. If the temperatures are measured until the probe is properly cooled, and the tail-end temperatures are approximated by an exponential function, the time limit $t \rightarrow \infty$ of such an approximation provides a very good approximation of the final stationary temperature T_∞ of the whole system. This is very useful in practice, when the quenchant temperature T_x is given only as a constant value, which is usually the initial temperature of the bath.

Simulation Examples

There is a wide variety of liquid quenchants that can be used for quenching in industrial applications. The optimal choice is a difficult problem, because different quenchants may cause very different effects, especially near the surface of the workpiece. This point is illustrated by two examples, where the Liščić/Petrofer probe is used in two different quenchants: a mineral oil and a polymer solution. (Data used by permission from PetroFer Chemie H.R. Fischer GmbH + Co. KG, Hildesheim, Germany.)

From now on, to indicate the depths of thermocouples, the near-surface temperature T_n and the intermediate temperature T_i are denoted by $T_{-1,0}$ and $T_{-4,5}$, respectively. All three temperatures are measured until $t_{\text{final}} = 981$ s, with nonuniform time steps. At the beginning, the time step is $\Delta t = 0.1$ s, while at the end, it is much larger, $\Delta t = 1$ s. Each data set has 1461 points.

The external temperature T_x is not measured in time. Instead, it is given as the initial temperature of the quenching bath, and both examples have $T_x = 50$ °C (120 °F). This turns out to be rather inaccurate, and the final steady-state temperature T_∞ estimated from an exponential approximation of the last 25 °C (77 °F) in the near-surface temperature $T_{-1,0}$ is used.

Oil Quenching

In the first example, the probe is quenched in a medium-viscosity accelerated quenching oil, and the initial temperature of the probe is $T_0 = 854$ °C (1569 °F).

The original unsmoothed measured temperatures $T_c, T_{-4,5}, T_{-1,0}$, and T_x are given earlier in Fig. 11 (in that order, from the top of the figure).

Note that there is a very sharp change (or drop) in the near-surface temperature at approximately $t = 14$ s, when nucleate boiling begins. This change is slightly less visible in the intermediate temperature, because of the damping effect.

Apart from that, all temperatures appear to be very smooth, even without smoothing, because the noise is very small in magnitude. There are no other abrupt changes in quenching conditions, and the calculated surface temperature T_s also decreases in time. Therefore, an additional monotone approximation to make α a function of T_s is not required here.

The calculated heat-transfer coefficient, α , is shown in Fig. 21 as a function of time, and in Fig. 22 as a function of the calculated surface temperature, T_s .

Because the quenching is done in oil, there are no chaotic effects on the surface of the probe, and both HTC curves are fairly regular in shape. In fact, all three phases of the heat extraction are nicely visible.

The differences between measured and calculated temperatures at reference points are given in Fig. 23.

These differences or errors in the numerical simulation refer to the original measured temperatures, so they include the initial smoothing of measured near-surface temperatures, numerical solution of the heat-conduction problem (Eq 13), and the final local smoothing of calculated surface heat-flux density, $q_s(t)$.

It should be noted that all errors in $T_{-1,0}$ are entirely due to the initial monotone smoothing, because the HTC calculation exactly reproduces the smoothed near-surface temperature. Most of these errors come from random noise in the data, and only a small “regular” part reflects the monotone approximation errors.

The errors in core and intermediate temperatures are somewhat larger. This is nothing unusual, because the temperature gradients are very high here. In addition, the strict radial symmetry of temperatures in the probe is almost impossible to achieve in practice, and these errors may be caused by a slightly slanted immersion of the probe into the quenchant or by small variations in the fluid flow around the probe.

Polymer Quenching

It is well known that polymer quenching is likely to cause chaotic violent changes in

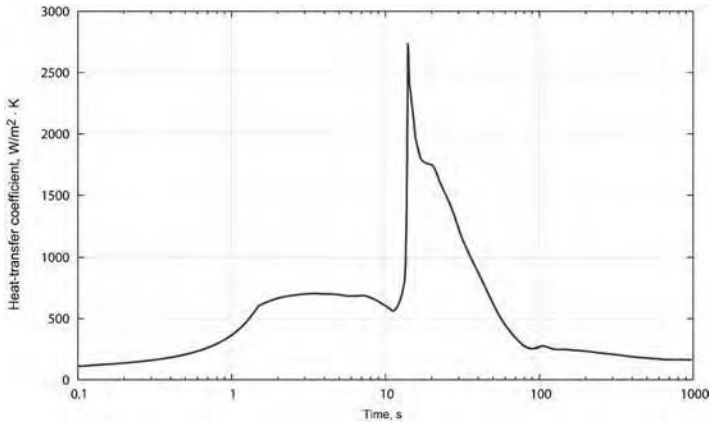


Fig. 21 Oil quenching: calculated heat-transfer coefficient, α , as a function of time. Courtesy of Petrofer GmbH

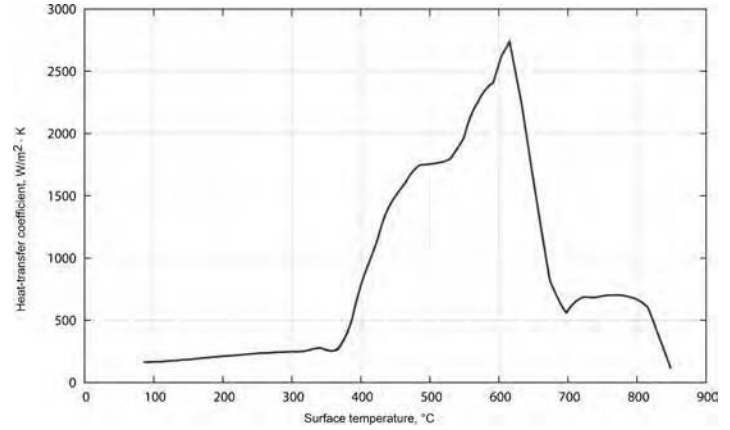


Fig. 22 Oil quenching: calculated heat-transfer coefficient, α , as a function of surface temperature. Courtesy of Petrofer GmbH

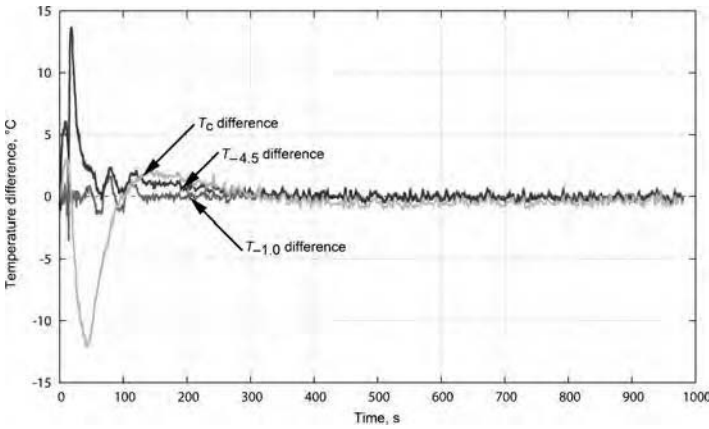


Fig. 23 Oil quenching: differences between measured and calculated core, intermediate, and near-surface temperatures. Courtesy of Petrofer GmbH

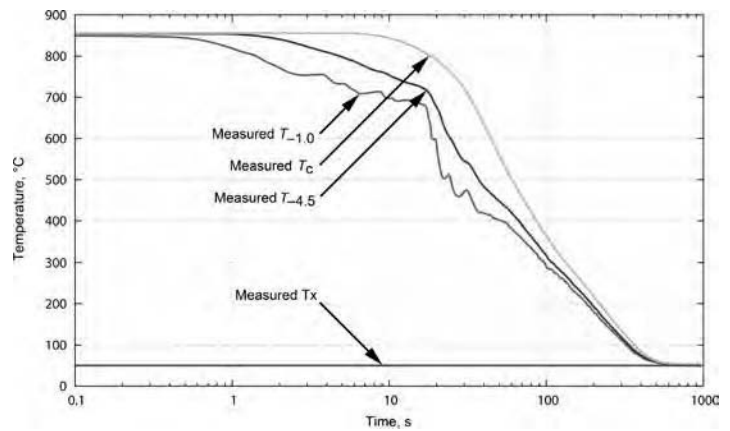


Fig. 24 Polymer quenching: measured core, intermediate, near-surface, and external temperatures. Courtesy of Petrofer GmbH

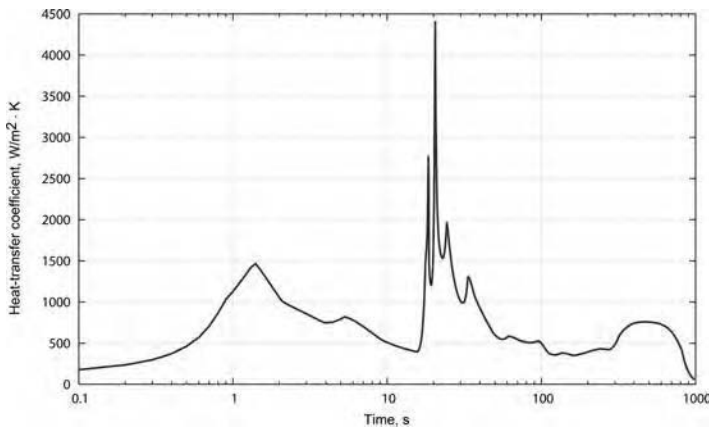


Fig. 25 Polymer quenching: calculated heat-transfer coefficient, α , as a function of time. Courtesy of Petrofer GmbH

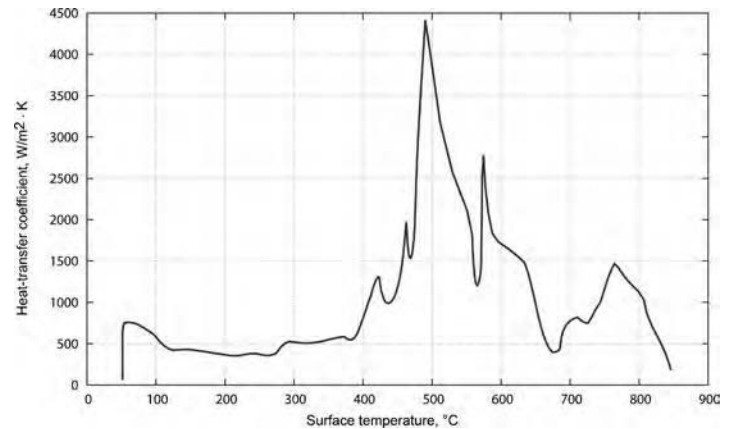


Fig. 26 Polymer quenching: calculated heat-transfer coefficient, α , as a function of surface temperature. Courtesy of Petrofer GmbH

local quenching conditions near a particular point at the surface, so that the symmetry assumption is almost certainly not valid in this case. However, in most cases, these irregularities are very local, both in time and space, and

the 1-D radial symmetry model may still be sufficiently accurate on the average to calculate the temperature distribution in the probe.

To demonstrate this, in the second example, the probe is quenched in a 10% polymer solution, and

the initial temperature of the probe is $T_0 = 855\text{ }^\circ\text{C}$. $T_0 = 855\text{ }^\circ\text{C}$ (1570 °F).

The original unsmoothed measured temperatures T_c , $T_{-4.5}$, $T_{-1.0}$, and T_x are given in Fig. 24 (in that order, from the top of the figure).

The measured near-surface temperature is very rough for the first 35 s. Moreover, it increases significantly for some periods of time, reflecting the violent conditions at the surface. In fact, these conditions are so irregular that the monotone smoothing of $T_{-1,0}$ does not help, and the calculated surface temperature, T_s , is not strictly decreasing in time. As a consequence, an additional monotone approximation of T_s is necessary to express α as a function of T_s .

The calculated heat-transfer coefficient, α , is shown in Fig. 25 as a function of time, and in Fig. 26 as a function of the monotone surface temperature, T_s .

In contrast to the previous example, both HTC curves are very irregular. Thus, despite all monotone smoothing efforts, they still reflect the quenching conditions at the surface.

The differences between measured and calculated temperatures at reference points are given in Fig. 27.

High errors in $T_{-1,0}$ for the first 35 s are now caused by the monotone approximation of $T_{-1,0}$ and reflect the nonmonotonicity in the original data.

Finally, regardless of all chaotic phenomena at the surface, the errors in core and intermediate temperatures are not much higher than in oil quenching.

REFERENCES

- G.E. Totten, G.M. Webster, H.M. Tensi, and B. Liscic, Standards for Cooling Curve Analysis of Quenchants, *Heat Treat. Met.*, No. 4, 1997, p 92–94
- I. Felde, T. Reti, G. Sarmiento, M. Guerrero, and J. Grum, Comparison Study of Numerical Methods Applied for Estimation of Heat Transfer Coefficient during Quenching, *Proc. Conf. New Challenges in Heat Treatment and Surface Engineering*, June 9–12, 2009 (Dubrovnik-Cavtat, Croatia), p 303–308
- M. Narazaki, M. Kogawara, A. Shirayori, and S. Fuchizawa, Analysis of Quenching Processes Using Lumped-Heat-Capacity Method, *Proc. Sixth Int. Seminar of IFHTSE* (Kyongju, Korea), 1997, p 428–435
- N.I. Kobasko, Thermal Processes in Quenching of Steel, *Metalloved. Term. Obrab. Met.*, Vol 3, 1968, p 2–6 (in Russian)
- N.I. Kobasko, A.A. Moskalenko, G.E. Totten, and G.M. Webster, Experimental Determination of the First and Second Critical Heat Flux Densities and Quench Process Characterization, *JMEPEG*, Vol 6, 1997, p 93–101
- N.I. Kobasko, M.A. Aronov, J.A. Powell, and G.E. Totten, *Intensive Quenching Systems: Engineering and Design*, ASTM International, 2010, p 47
- N.I. Kobasko, Why Database for Cooling Capacity of Various Quenchants Should Be Developed? *Proc. Eighth IASME/WSEAS Int. Conf. on Heat Transfer, Thermal Engineering and Environment*, Aug 20–22, 2010 (Taipei, Taiwan), p 304–309
- N.I. Kobasko, M.A. Aronov, J.A. Powell, B.L. Ferguson, and V.V. Dobryvechir, Critical Heat Flux Densities and Their Impact on Distortion of Steel Parts during Quenching, *Proc. Eighth IASME/WSEAS Int. Conf. on Heat Transfer, Thermal Engineering and Environment*, Aug 20–22, 2010 (Taipei, Taiwan), p 338–344
- B. Liščić, The Temperature Gradient at the Surface as an Indicator of the Real Quenching Intensity during Hardening, *HTM*, Vol 33 (No. 4), 1978, p 179–191 (in German)
- H.M. Tensi, Wetting Kinematics, Chapt. 5, *Theory and Technology of Quenching*, B. Liščić, H.M. Tensi, and W. Luty, Ed., Springer Verlag, 1992, p 91
- A. Majorek, H. Müller, and E. Macherauch, Computersimulation des Tauchkühlens von Stahl—Zylindern in Verdampfenden Flüssigkeiten, *HTM*, Vol 51 (No. 1), 1996, p 11–18
- B. Smoljan, Numerical Simulation of As-Quenched Hardness in a Steel Specimen of Complex Form, *Commun. Numer. Meth. Eng.*, Vol 14, 1998, p 277–285
- B. Smoljan, Numerical Simulation of Steel Quenching, *J. Mater. Eng. Perform.*, Vol 11 (No. 1), 2002, p 75–80
- A. Rose et al., *Atlas zur Wärmebehandlung der Stähle I*, Verlag Stahleisen, Düsseldorf, 1958
- “Inconel Alloy 600,” Publication SMC-027, Special Metals Corporation, 2008
- C. de Boor, *A Practical Guide to Splines* (rev. ed.), Springer, New York, 2001
- P. Dierckx, *Curve and Surface Fitting with Splines*, Clarendon Press, Oxford, 1993
- H. Akima, A New Method of Interpolation and Smooth Curve Fitting Based on Local Procedures, *J. Assoc. Comput. Mach.*, Vol 17 (No. 4), 1970, p 589–602
- A.R. Mitchell and D.F. Griffiths, *The Finite Difference Method in Partial Differential Equations*, John Wiley & Sons Ltd., Chichester, 1980
- R.M.M. Mattheij, S.W. Rienstra, and J.H.M. ten Thijsse Boonkamp, *Partial Differential Equations: Modeling, Analysis, Computation*, SIAM, Philadelphia, PA, 2005
- R. Lattès and J.-L. Lions, *Méthode de Quasi-Reversibilité et Applications*, Dunod, Paris, 1967
- A. Jeffrey, *Applied Partial Differential Equations, An Introduction*, Academic Press, an imprint of Elsevier Science, San Diego, 2003
- R.P. Brent, *Algorithms for Minimization without Derivatives*, Prentice-Hall, Englewood Cliffs, NJ, 1973
- W. Gautschi, *Numerical Analysis*, 2nd ed., Birkhäuser, New York, 2012
- F.J. Scheid, *Schaum's Outline of Theory and Problems of Numerical Analysis*, 2nd ed., McGraw-Hill, New York, 1989
- J.O. Ramsey, Estimating Smooth Monotone Functions, *J. R. Statist. Soc. B*, Vol 60, 1998, p 365–375
- S. Singer and S. Singer, Efficient Implementation of the Nelder-Mead Search Algorithm, *Appl. Num. Anal. Comp. Math.*, Vol 1 (No. 3), 2004, p 524–534

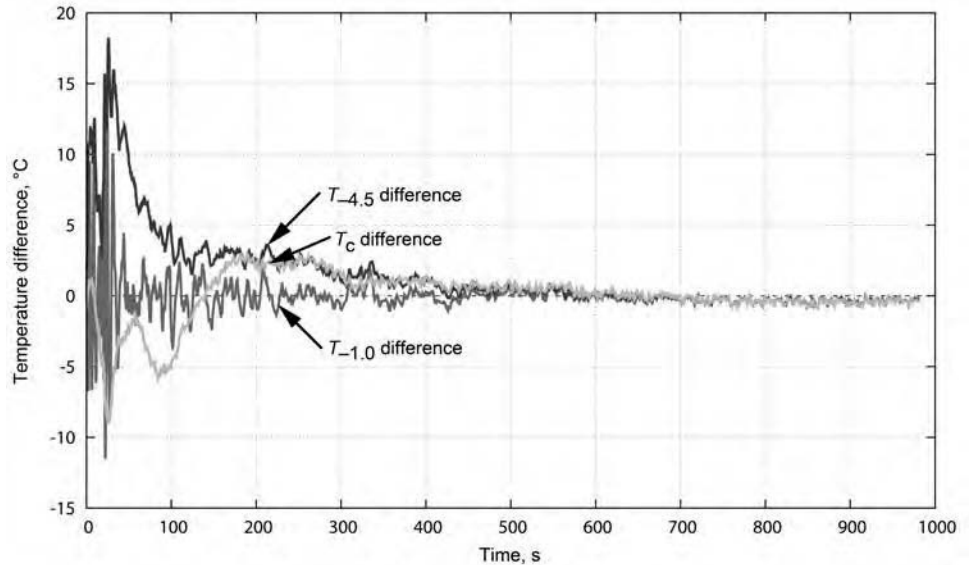


Fig. 27 Polymer quenching: differences between measured and calculated core, intermediate, and near-surface temperatures. Courtesy of Petrofer GmbH

Quench Process Sensors*

G.E. Totten, Portland State University

FLUID FLOW is critical for the control of quench severity during the quenching process. Residual stresses and often the distortion control of quenched steel parts are dependent on fluid agitation during the quenching process. Steel hardening results. Nonuniform fluid flow throughout the quench zone in production quench tanks is one of the greatest contributors to nonuniform hardness, increased thermal stresses, cracking, and distortion. Therefore, the measurement of flow characteristics during the quenching process is important.

However, although this is known, monitoring of fluid flow is rarely encountered in production quench tanks, even though it is also known that fluid flow varies greatly as a function of position in the tank. One of the reasons that fluid flow measurement is seldom performed is that, until recently, properly designed flow-measurement devices with sufficient sensitivity and ruggedness for use in the heat treating shop have not been commercially available. This article provides an overview of various measurement principles for different types of flow devices. A number of developed instruments for use in production quench tanks are described. Various methods of flow measurement in commercial quench tanks may be acceptable for adequate control to ensure a high-quality production process.

Fluid Flow in Quenching

Quenching severity is agitation dependent. Therefore, magnitude and turbulence of fluid flow around a part in the quench zone is critically important relative to the uniformity of heat transfer throughout the quenching process (Ref 1–5). One of the greatest contributors to nonuniform hardness, increased thermal stresses, cracking, and distortion is nonuniform fluid flow throughout the quench zone in production quench tanks (Ref 6). The impact of nonuniform flow on distortion and cracking has been discussed previously (Ref 7–10). These, and other, references have clearly shown the

necessity of optimizing the uniformity of fluid flow in the quench zone to provide optimum control of distortion and to minimize cracking.

Some of the classic methods of measuring fluid flow on both a laboratory and commercial scale include turbine velocimeters (Ref 11), streak photography (Ref 12, 13), pitot-static tube (Ref 14), electromagnetic current meter (Ref 15), hot-film anemometer (Ref 11), and laser Doppler velocimetry (Ref 8–11). Although none of these methods are generally unsuitable for continuously monitoring fluid flow in quench tanks during heat treatment processing, they have provided invaluable insight into the fluid mechanics of the quenching process. For example, streak photography was conducted on a model of a quench tank for an integral quench furnace.

Computational fluid dynamics (CFD) modeling is increasingly used to examine the uniformity of fluid flow in a quench tank. Totten and Lally reported one of the first examples of the application of this methodology to illustrate the nonuniformity of quench tank fluid flow (Ref 11). This work was followed by studies reported by Garwood et al. (Ref 15, 16). Bogh used CFD analysis to examine the impact on quench nonuniformity of the placement of submerged spray eductors at various locations around a rack of aluminum panels (Ref 17). More recently, Halva and Volný (Ref 18) have used CFD analysis to examine the homogeneity of fluid flow as a function of agitator placement. An example of the use of CFD modeling to design a quench system with improved flow uniformity has recently been reported by IIT Flygt (Ref 19). A study was sponsored by the Society of Automotive Engineers-Aerospace Metals and Engineering Committee to evaluate the concentration limitations to meet *Military Handbook 5* design minimums for type I quenchants for aluminum heat treating standard development. Unfortunately, the results were too scattered to achieve the desired goal. Computational fluid dynamics analysis was performed, which illustrated the variance in physical property data was likely due to flow velocity

variation in the quench tank (Ref 20). The most recently reported example of CFD modeling was conducted on a classic laboratory apparatus used for cooling-curve analysis. The results of this work showed that even this system was susceptible to significant flow variation in the quench zone (Ref 21).

These CFD studies have clearly shown that in most cases it is not possible to achieve perfectly uniform fluid flow in the quench zone. In addition, experimental work reported by Titus showed substantial variation of fluid flow in the quench zone of a batch integral quench furnace (Ref 22, 23). Therefore, from these and other studies, it is clearly important that fluid flow velocity be measured during quench processing in the workshop. Various approaches reported to measure quench severity and fluid flow are reviewed here.

Fluid Flow Measurement

This is a summary of the most important devices used for flow measurement, which are frequently reported in literature under the heading “volume meters” (Ref 24). The flow rate is the ratio of the quantity of the flowing medium, differentiated with respect to the time in which this quantity flows through a conduit cross section. The flow rate is expressed either in units of volume or units of mass. The flow velocity of the fluid can therefore be determined from the quotient of the measured volume flow rate and the cross section of the conduit.

Volumetric Measurement. In volumetric measurement methods, the flow velocity of the fluid is indicated as a function of the fluid-caused rotation of the measuring vanes of the sensor, or it can be indicated indirectly by continuous measurement of small volumes or by integration of flow-rate values. These two groups can be distinguished as measurement methods with fixed measurement chamber walls and measurement methods without fixed measurement chamber walls.

* Adapted from G.E. Totten, H.M. Tensi, and G.M. Webster, Fluid Flow Sensors for Industrial Quench Baths: A Literature Review, 21st ASM Heat Treating Society Conference Proceedings, Nov 5–8, 2001 (Indianapolis, IN), ASM International, 2001

The vane sensor is an example of a frequently used measurement method without fixed measurement chamber walls. The single-jet meter is characterized by a straight, smooth flow channel. The fluid flow acts on the rotor, causing it to rotate as shown in Fig. 1. The vane wheel sensor has the advantage that the lower limit of the measurement range is more favorable than that of other volumetric measurement methods. It is necessary to avoid excessive pressure losses, however. Although this type of meter may be encountered in the laboratory, it is seldom used as a flow-measuring device in commercial quench tanks.

A method that is used, at least on some occasions, in production quench tanks is the propeller-driven flow meter. The propellers may be placed on the fixture or fixed in the tank. Alternatively, a hand-held unit such as the Meade velocimeter, described in Ref 11, may also be used. There are various problems with these meters. They are susceptible to cavitation, and the propeller blades may wear by abrasion. In addition, they measure flow in only one direction and are not sensitive to twist. Thus, they may be inadequate indicators of the quality of agitation that the parts are being subjected to during the quenching cycle. Furthermore, when portable hand-held units are used, it is essential that they be placed in exactly the same location and position each time they are used if comparative data are to be obtained. Thus, while known and available, such measurement devices have not gained widespread acceptance for use in production environments.

Effective Pressure. Methods belonging to this group are derived from energy equations. The kinetic energy present as a result of the flow state and thus also the flow velocity are included in the physical formulas. The basis of these measurement methods is Bernoulli's equation, which states that, in a frictionless, steady-state flow, the sum of the kinetic energy, the potential energy, and the static pressure energy of a streamline is constant. If changes in the local height can be ignored, a unique relationship is obtained between the fluid pressure and the fluid velocity.

In pipe flows, the fluid is forced to travel faster or slower by internal fittings in the pipe. Pressure energy and velocity energy are therefore converted into each other. The flow velocity can be calculated from the difference in the pressures. Nozzles, diaphragms, and venturi tubes are used to constrict the cross section of the pipe.

Flow Velocity Measurement by Correlation Methods. The basis of velocity measurement by the correlation method is the assumption of random disturbances in the material being measured. These arise in flowing media as local, random variations in pressure, temperature, conductivity, electrostatic charging of the fluid, velocity, or light-transmission capacity as a result of turbulence or as a result of special types of flow, in the case of multiphase mixtures. Two measurement sensors,

arranged one after the other in the flow section, record the randomly fluctuating signals, from which a correlation computer determines the transit time. From the transit time and the geometry of the measurement section, it is possible to calculate the flow velocity of the fluid.

In the ideal case, the two measurement sensors set up in a row in the flow direction generate two signals of the same form but shifted with respect to each other by the transit time (t_1). The measurement method is based on the idea of artificially delaying the signal of the first measurement sensor by time t_2 . The job of the correlation computer is to adjust the model transit time t_2 in such a way that $t_2 = t_1$. Therefore, the signal delayed by the measurement section is the same as the artificially delayed signal. Expressed in general terms, the correlation computer must minimize the mean square deviation of the two signals.

Velocity Measurement—Means of Lasers (Transit Time Measurement). This method measures the time it takes for a dust particle to pass between two laser beams. A laser beam passes through two convex lenses and is divided by a prism into two parallel beams of equal intensity. These two beams then pass through the pipe at right angles to the flow direction. They are separated from each other by a distance d . The laser beams are focused in the center of the pipe by two lenses. Diaphragms interrupt the direct course of the beams, as illustrated in Fig. 2. When a dust particle travels through the two focal points in the center of the pipe in succession, the light is scattered by this particle. The scattered light is

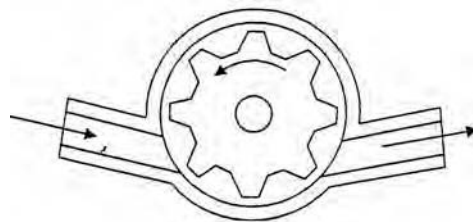


Fig. 1 Vane sensor, single-jet meter

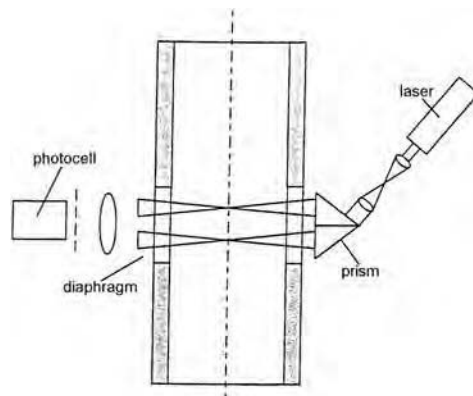


Fig. 2 Arrangement for determining the flow velocity by measuring the transit time

collected by a system of lenses, received by photocells, and converted into electrical signals. From the difference in time between the two successive pulses, the particle velocity and thus the flow velocity of the fluid in the flow field is determined.

When a source at rest emits a wave with a frequency of f_0 , an observer at rest observes the same frequency f_0 . However, if the observer is moving relative to the source, he perceives more oscillations per unit time as he moves toward the source and fewer as he moves away. This is called the Doppler effect, and it can be used to measure flow velocity, as illustrated in Fig. 3.

When a light beam passes through a flowing medium, some of the light is scattered out of the beam by the small particles in the fluid. The Doppler effect occurs twice during this scattering process. In one case, the particle is a moving observer, which sees the laser as a light source at rest; in the second case, the particle re-emits this light as a source in motion. The photocurrent consists of a constant component and a variable component with the frequency Δf . The photocurrent undergoes a frequency shift, Δf , which is proportional to the fluid flow velocity.

Heat-based flow measurement is obtained from a temperature difference that is measured in a flow field. One heat-based flow-measurement method is the heated wire method (Fig. 4), where an electrically heated metal wire, the resistance of which is a function of temperature, is introduced into a flow stream and cooled by it. The loss of heat in this case depends on the velocity of the gas passing

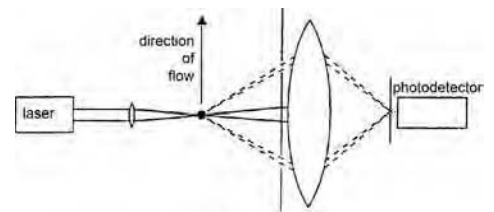


Fig. 3 Use of the Doppler effect to determine the flow velocity of flowing media

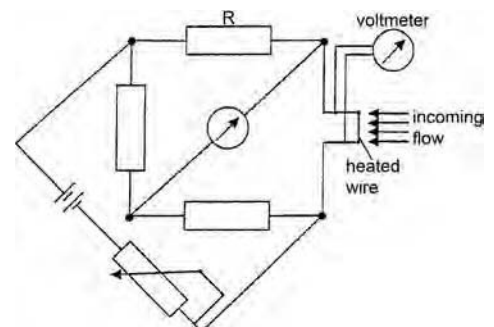


Fig. 4 Schematic illustration of the heated wire method

by, on its physical data (thermal conductivity, specific heat capacity, and density), and on the difference between the temperature of the fluid and the temperature of the wire. The use of a thermistor-based sensor has been reported; however, it was not used to continuously monitor quench severity in a commercial tank (Ref 25).

An illustration of the use of the hot wire method to examine flow uniformity in a commercial quench tank was reported by Koccevar et al. (Ref 26, 27). In this work, the cooling power of a quenchant was measured by examining the cooling profile of a heated (to 850 °C, or 1560 °F) 0.2 mm (0.008 in.) diameter by 20 mm (0.8 in.) long platinum wire. Electrical current was used to heat the wire at a constant rate of 20 °C/s (36 °F/s). Cooling power is then related to the electrical energy required to keep the temperature rise of the wire constant. (Platinum wire was used because it possesses a relatively proportional relationship between temperature and resistance.) Figure 5 illustrates the relationship between cooling power and agitation for a quench oil at different temperatures (Ref 26).

The agitation variation possible in a batch integral quench furnace was illustrated by attaching a platinum wire to different empty baskets in the quench zone. The data in Fig. 6 show that the cooling power varies significantly between the top and bottom basket, with the greatest cooling variation occurring at the position of the bottom basket (Ref 26).

Keil et al. discussed two disadvantages of the Koccevar hot wire method that inhibit its repeated and general use under production conditions (Ref 28). The first disadvantage is that the platinum wire sensor exhibits a limited life-time due to repeated heating and cooling cycles. The second disadvantage is that there is only one wire sensor; therefore, both ambient and heated wire temperatures are not measured concurrently. Because ambient temperatures are not measured, the device cannot be used for instantaneous monitoring (see the subsequent discussion). Keil et al. described the

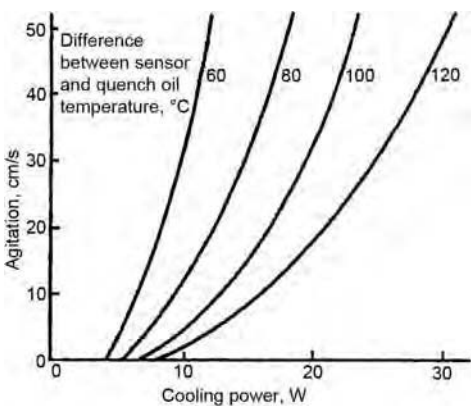


Fig. 5 Relationship between cooling power and agitation for a quench oil at 60, 80, 100, and 120 °C (140, 175, 210, and 250 °F)

construction of an alternative apparatus that can be used for continuous monitoring of quenchant agitation in a commercial quench tank. This apparatus, illustrated in Fig. 7 (Ref 29), uses two heat-conductive sheaths containing sensors that are thermally insulated from each other. A microprocessor is connected to these sensors, and a known current is applied to one sensor to calculate cooling effectiveness. A schematic illustration of the sensor is provided in Fig. 8 (Ref 29). The convection heat-transfer coefficient (*h*) is calculated from:

$$h = \frac{1/A}{\left(\frac{T_{HTR} - T_{AMB} - 1.4932}{q}\right)}$$

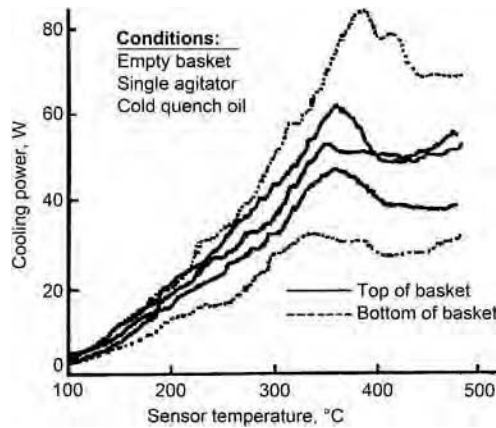


Fig. 6 Cooling power variation between different positions on the top and bottom of baskets in a batch integral quench furnace

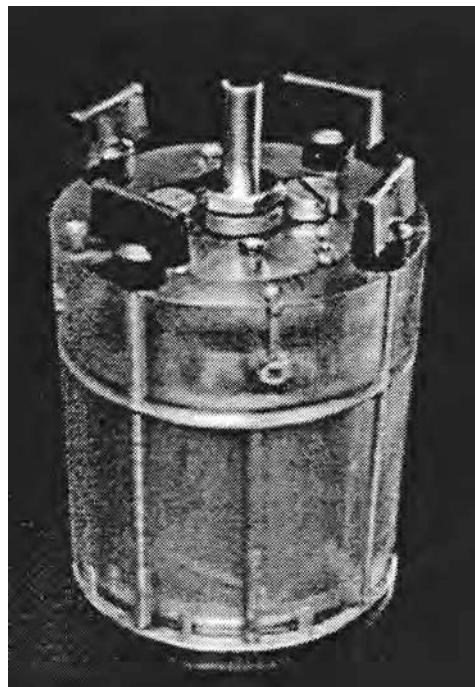


Fig. 7 Illustration of the Caterpillar quench-evaluation sensor. Source: Ref 29

where *A* is the surface area of the first conductive sheath; *T_{HTR}* is the temperature of the first sensor; *T_{AMB}* is the ambient temperature of the quenchant in the tank; and *q* is the electrical power consumed, which is calculated from *q* = *K/V₁*, where *K* is the constant current output from the voltage regulator, and *V₁* is the measured voltage drop across the resistor. The value of 1.4932 is a conductive factor to account for heat losses between the surface of the first sensor and the surface of the first heat-conductive sheath. Figure 9 illustrates the sensor assembly (Ref 30).

Velocity Measurement Using Thermal Probes. Another heat-based method is the velocity measurement using thermal probes. Thermal probes consisting of semiconductor resistors are especially suitable for the measurement of low velocities, because of their high temperature coefficients and the associated high output signals. The measurement sensor is heated electrically. A state of equilibrium is

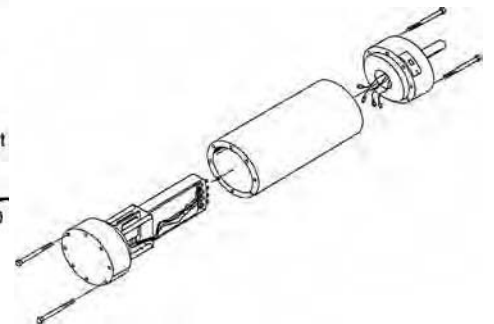


Fig. 8 Schematic illustration of the temperature sensor used for the apparatus in Fig. 7

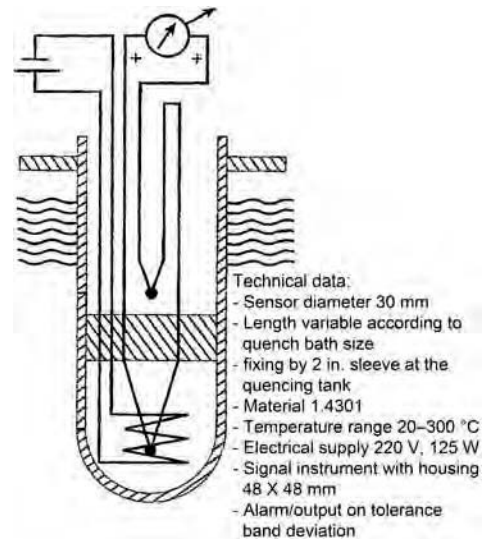


Fig. 9 Illustration of the Ipsen International Fluid-Quench Sensor instrument. An interesting illustration of flow variation during a quench occurs when an agitator fails. Such an example is provided in the Ipsen literature (Fig. 10). The failure of the agitator causes the sensor temperature difference to rise above the allowed setpoint, activating an alarm.

reached in correspondence with the cooling conditions. The temperature of the measurement sensor present in the state of equilibrium determines the resistance. Appropriate circuitry derives a signal from this resistance, and suitable measurement technology then evaluates the signal.

This group of thermal methods involves heating the medium to be measured (Ref 31). The heat balance can then be used to calculate the mass throughput and thus the flow velocity of the medium from the amount of heating power supplied to increase the temperature of the fluid and the specific heat capacity of the fluid. This is the principle used for the flow-measurement device recently developed and reported by Tensi et al. (Ref 32–34). The probe, similar to the one illustrated in Fig. 10, measures heat flux from the part to the surrounding quenchant with an unknown flow velocity and an unknown turbulence or twist. The probe geometry, as described by Tensi et al., is designed to minimize dependence on flow direction and still be highly sensitive to agitation (Ref 35). The body of the probe has a freely defined temperature (T_{probe}) that fulfills the conditions:

$$T_{Leidenfrost} > T_{probe} > T_{bath} \quad (Eq 1)$$

and

$$T_{probe} = Constant \quad (Eq 2)$$

by variation of conducted energy (E_{con}), so the probe temperature is constant. The Leidenfrost temperature ($T_{Leidenfrost}$) refers to the temperature for vapor-blanket cooling, characterized by the Leidenfrost phenomenon, namely, the formation of a uniform vapor blanket around the testpiece. The vapor blanket develops and is maintained while the supply of heat from

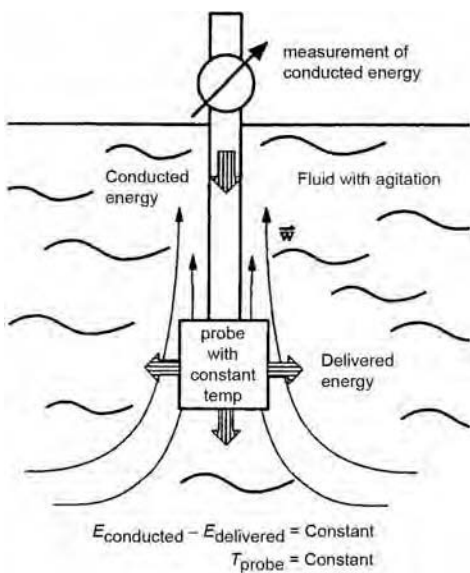


Fig. 10 Schematic of the probe used to define the agitation power of a quenching bath with forced convection, and the energy balance. Source: Ref 32

the interior of the part to the surface exceeds the amount of heat needed to evaporate the quenchant and maintain the vapor phase.

The probe permits measurements of delivered energy according to the equation:

$$E_{con} - E_{del} = Constant \quad (Eq 3)$$

Because the delivered energy (E_{del}) depends on chemical qualities of the bath as well as the bath temperature (T_{bath}) and agitation (composed from flow rate, v , and twist), a value is provided for the quality of agitation or cooling power using dimensionless flow. With this information, two other parameters may be determined:

$$E_{con} = C \times \text{Quality of agitation} \quad (Eq 4)$$

where C contains the thermal properties of the probe, including T_{probe} , the chemical properties of the bath, T_{bath} , and E_{del} . The change of the probe temperature, until achieving a stationary condition according to Eq 4, is schematically given in Fig. 11. The temperature of the probe (T_{probe}) decreases upon submersion of the probe in the quenching bath to a defined position and then increases by automatic variation of E_{con} until reaching the initial temperature of the probe (T_{probe}). Once the parameters of the probe are defined, correlation between E_{con} , T_{bath} , and quality of agitation may be determined. Measurement accuracy increases with increasing T_{probe} .

McCurdy and Coughlin have reported the use of a solid-state sensing probe (with no details regarding the construction), a measurement chamber, a microprocessor-based controller, and a plumbing system to continuously monitor the heat-transfer coefficient in the quench tank (Ref 36). The microprocessor is used to directly convert thermal energy to electrical energy. In this system, the quenchant is pumped past the sensor at a constant velocity, and an electrical current is passed through the sensor. The heat-transfer coefficient (h) is calculated from:

$$h = \frac{kP}{\Delta T}$$

where P is the dissipated power, k is a constant, and ΔT is the temperature difference between the probe surface and the surrounding quenchant. Although it was acknowledged that the data obtained were agitation-dependent, this device was used only to monitor the variation of the heat-transfer coefficient at a constant flow velocity in the probe measurement chamber. However, presumably this device could be redesigned to obtain agitation rate-dependent data.

Ipsen International has commercialized an instrument called the Fluid-Quench Sensor (Fig. 9) that reportedly can be used for continuously monitoring oil and aqueous polymer quenchants to determine fluid flow variation at different quenchant temperatures and fluid compositions (Ref 25). This instrument, like that reported by Keil et al. (Ref 28–30), measures the temperature difference between the quenchant and a higher temperature produced by a separate heat source. The temperature difference is caused by the heat flux between the applied heat and the convective heat transfer to the quenchant. It should be noted that the flow conditions at the sensor are dependent on its position relative to the agitators, the sensor must not be influenced by heat transfer from the load during the quench, and it must be possible to install the sensor without draining the quench tank.

An interesting illustration of flow variation during a quench occurs when an agitator fails. Such an example is provided in the Ipsen literature (Fig. 12). The failure of the agitator causes the sensor temperature difference to rise above the allowed setpoint, activating an alarm.

ACKNOWLEDGMENT

This article, adapted from Ref 37, includes an excerpted text and figures from H.M. Tensi, A. Haas, K. Lainer, G.E. Totten, and G.M. Webster, Sensor Tip Optimization for a Thermal Anemometer for Determining Convection Intensity in Quench Baths, *21st ASM Heat Treating Society Conference Proceedings*, Nov 5–8, 2001 (Indianapolis, IN), ASM International, 2001.

REFERENCES

1. G.E. Totten, G.M. Webster, and N. Gopinath, Quenching Fundamentals: Effect of Agitation, *Adv. Mater. Process.*, Vol 2, 1996, p 73–76
2. J. Olivier, B. Clément, J.J. Debrie, and F. Moreaux, Stirring of Quenchant: Concept and Metallurgical Results, *Trait. Therm.*, Vol 206, 1986, p 29–42 (in French)
3. Function of Proper Agitation in Quenching to Assure Uniform Physical Properties, *Ind. Heat.*, Jan 1979, p 14–17

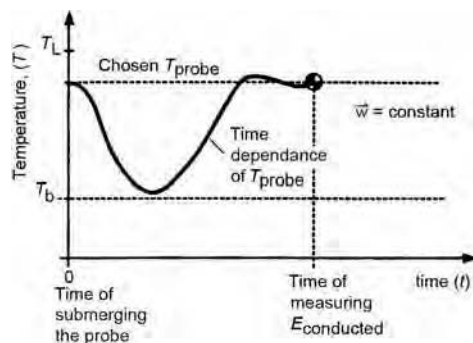


Fig. 11 Changing the temperature of the probe (T_{probe}) versus time after submerging the probe in a quenchant with defined composition, bath temperature (T_b), and an unknown local agitation force. T_L , Leidenfrost temperature; w , fluid velocity. Source: Ref 32

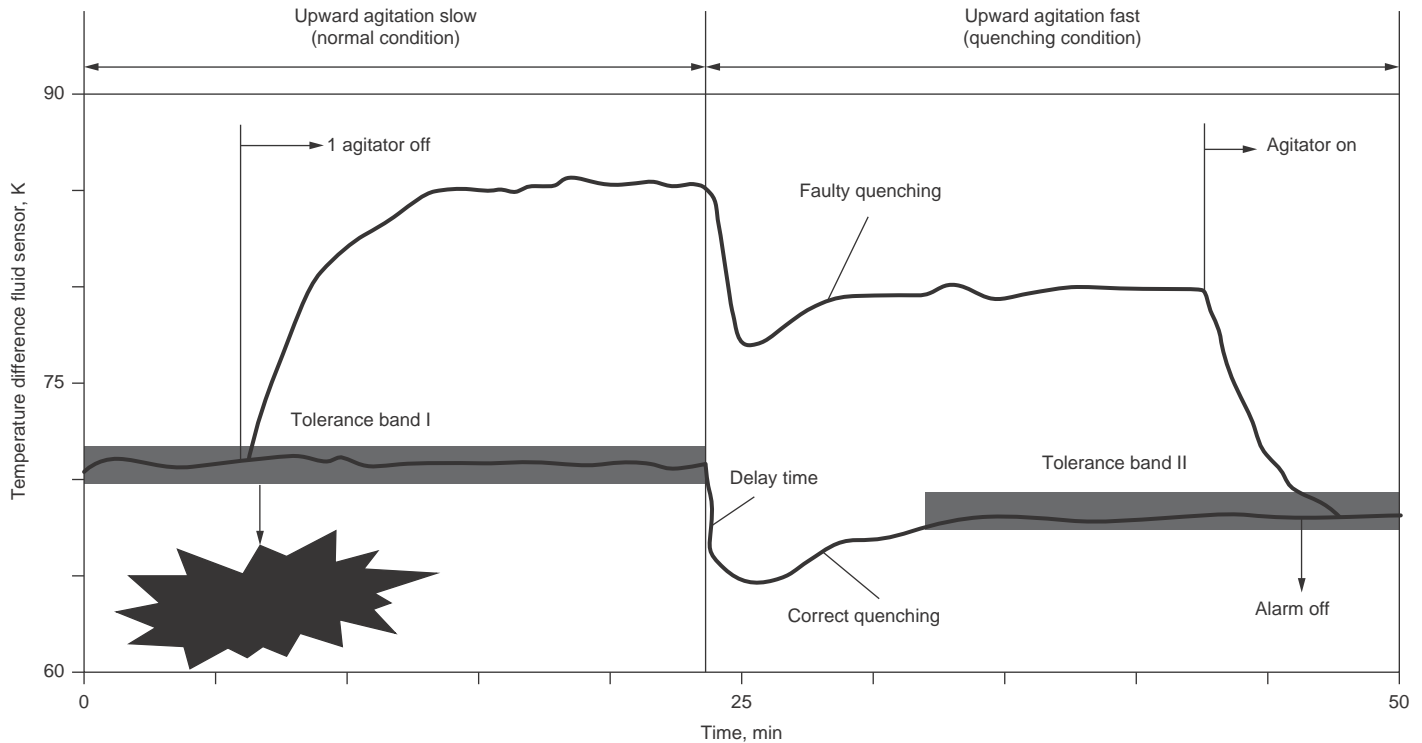


Fig. 12 Illustration of temperature differences for a correct and a faulty quench caused by an agitator failure

4. H. R. Bergmann, Importance of Agitation for Optimum Quenching, *Met. Eng. Q.*, Vol 11 (No. 2), 1971, p 17–19
5. Tensiles and Yields Are Closer with Fast Circulation of Quench Oil, *Met. Treat.*, Dec–Jan 1964–1965, p 18–19
6. “Improved Quenching of Steel by Propeller Agitation,” U.S. Steel, 1954
7. R.T. Von Bergen, in *Quenching and Control of Distortion*, G.E. Totten, Ed., ASM International, 1992, p 275–292
8. R. Kern, *Heat Treat.*, April 1985, p 38–42
9. R. Kern, *Heat Treat.*, Feb 1971, p 1–4
10. R. Kern, *Heat Treat.*, March 1985, p 41–45
11. G.E. Totten, C.E. Bates, and N.A. Clinton, *Handbook of Quenchants and Quenching Technology*, ASM International, 1993, p 339–411
12. J.Y. Oldshue, *Fluid Mixing Technology*, McGraw-Hill, New York, NY, 1983, p 162–168
13. S. Segerberg, *Heat Treat.*, May 1988, p 26–28
14. C.E. Bates, G.E. Totten, and R.L. Brennan, *Heat Treating*, Vol 4, *ASM Handbook*, ASM International, 1991, p 67–120
15. D.R. Garwood, J.D. Lucas, R.A. Wallis, and J. Ward, Modeling of Flow Distribution in Oil Quench Tank, *J. Mater. Eng. Perform.*, Vol 1 (No. 6), 1992, p 781
16. R.A. Wallis, D.R. Garwood, and J. Ward, The Use of Modeling Techniques to Improve the Quenching of Components, *Heat Treating: Equipment and Processes—1994 Conference Proceedings*, G.E. Totten and R.A. Wallis, Ed., ASM International, 1994, p 105–116
17. N. Bogh, Quench Tank Agitation Design Using Flow Modeling, *Heat Treating: Equipment and Processes—1994 Conference Proceedings*, G.E. Totten and R.A. Wallis, Ed., ASM International, 1994, p 51–54
18. J. Halva and J. Volný, Modeling the Flow in a Quench Bath, *Hutn. Listy*, No. 10, 1993, p 30–34
19. L’Agitation Submersible au Cœur des Bacs de Trempe, *Trait. Therm.*, Vol 278, 1994, p 73–75
20. D.S. MacKenzie, G.E. Totten, and N. Gopinath, CFD Modelling of Quench Tank Agitation, *Proc. of the Tenth Congress of the IFHT*, T. Bell and E.J. Mittemeijer, Ed., IOM Communications Ltd., London, England, 1999, p 655–669
21. A.J. Baker, P.D. Manhardt, and J.A. Orzechowski, On a FEM Platform for Simulation/Heat Treating Operations, *Proc. of the Second Int. Conf. on Quenching and the Control of Distortion*, G.E. Totten, M.A.H. Howes, S.J. Sjöström, and K. Funatani, Ed., ASM International, 1996, p 283–290
22. W. Titus, Understanding and Optimizing Flow Uniformity in Propeller and Impeller Agitated Quench Tanks, *Proc. of the First International Automotive Heat Treating Conference*, R. Colas, K. Funatani, and C.A. Stickels, Ed., ASM International, 1998, p 251–263
23. W. Titus, Understanding and Optimizing Flow Uniformity in Propeller and Impeller Agitated Quench Tanks, *Proc. Heat Treating Including Steel Heat Treating in the New Millennium—An Int. Symposium in Honor of Prof. George Krauss*, ASM International, 1999, p 461–466
24. K.W. Bonfig, *Technische Durchflußmessung mit besonderer Berücksichtigung neuartiger Durchflußmeßverfahren (Technical Flow Measurement with Special Consideration of New Flow Measurement Methods)*, Vulkan Verlag, Essen
25. Ipsen Fluid-Quench Sensor product brochure, Ipsen International GmbH, Germany, www.ipsen.de/en/home.html
26. M.P. Kocevar, M. Kasai, E. Nakamura, and K. Ichitani, Real Time Measurement of Cooling Power in the Furnace Tank, *Proc. of the First International Automotive Heat Treating Conference*, R. Colas, K. Funatani, and C.A. Stickels, Ed., ASM International, 1998, p 231–236
27. T. Katafuchi, Method of Evaluating Cooling Performance of Heat Treatment and Apparatus Therefore, U.S. Patent 4,563,097, Jan 7, 1986
28. G.D. Keil, W.A. Supak, and S.A. Tipton, Quench System Cooling Effectiveness

- Meter and Method of Operating the Same, U.S. Patent 5,601,363, Feb 11, 1997
29. G.D. Keil, S. Tipton, and W. Supak, Characterization of Cooling Uniformity in an Integral Batch Oil Quench, *Conf. Proc. Third International Conference on Quenching and Control of Distortion*, G.E. Totten, B. Liscic, and H.M. Tensi, Ed., ASM International, 1999, p 240–242
 30. G.D. Keil, W.A. Supak, and S.A. Tipton, Quench Cooling Effectiveness Apparatus for Continuous Monitoring, U.S. Patent 5,722,772, March 3, 1998
 31. W. Beitz and K.-H. Kuttner, *Dubbel: Taschenbuch für den Maschinenbau (Dubber's Manual of Mechanical Engineering)*, Springer-Verlag, Berlin, Heidelberg, and New York
 32. H.M. Tensi, A. Haas, K. Lainer, G.E. Totten, and G.M. Webster, Sensor Tip Optimization for a Thermal Anemometer for Determining Convection Intensity in Quench Baths, *21st ASM Heat Treating Society Conference Proceedings*, Nov 5–8 2001 (Indianapolis, IN), ASM International, 2001
 33. G.E. Totten, G.M. Webster, M. Meindl, H. Tensi, and K. Lainer, Development of a Device for Measuring the Heat-Based Flow Profiles of Fluids, *Proc. Heat Treating Including Steel Heat Treating in the New Millennium—An Int. Symposium in Honor of Prof. George Krauss*, ASM International, 1999, p 343–354
 34. H.M. Tensi, G.E. Totten, and G.M. Webster, A Proposal to Monitor Agitation of Production Quench Tanks, *Heat Treating—Including the 1997 International Induction Heat Treating Symposium*, D. Milam, D. Poteet, G. Pfaffmann, W. Albert, A. Muhlbauer, and V. Rudnev, Ed., ASM International, 1997, p 423–431
 35. H.M. Tensi, G.E. Totten, G.M. Webster, M. Meindl, and K. Lainer, Development and Technology Overview of a Fluid Flow Sensor (Sonde) for Commercial Quench Tanks, *Proc. of the Eighth Seminar of the International Federation for Heat Treatment and Surface Engineering/Croatian Society for Heat Treatment and Surface Engineering*, 2001, p 35–43
 36. D.W. McCurdy and T.H. Coughlin, Automatic Control of Polymer Quench Concentration, *Proc. of Int. Heat Treating Conference: Equipment and Processes*, G.E. Totten and R.A. Wallis, Ed., ASM International, 1994, p 347–351
 37. G.E. Totten, H.M. Tensi, and G.M. Webster, Fluid Flow Sensors for Industrial Quench Baths: A Literature Review, *21st ASM Heat Treating Society Conference Proceedings*, Nov 5–8, 2001 (Indianapolis, IN), ASM International, 2001

Intensive Quenching of Steel Parts

Michael A. Aronov, Nikolai I. Kobasko, and Joseph A. Powell, IQ Technologies, Inc.
George E. Totten, Portland State University

INTENSIVE QUENCHING is an alternative method of hardening steel parts. It provides extremely high cooling rates within the martensite-phase formation temperature range. This is in contrast to conventional quenching conducted in oil, polymer, or water that limits the cooling rate within the martensite formation range. This rule is based on the belief that slower cooling will avoid high-tensile residual stress, distortion, and a possibility of part cracking. Extensive research conducted by Dr. Kobasko in the early 1960s in the Ukraine demonstrated that avoiding a high cooling rate when material is in the martensite phase is not always necessary or optimal for obtaining the best material properties. His studies showed that a very high cooling rate within the martensite range would actually prevent quench cracking, if done correctly.

The process of intensive quenching (IQ) is a method of interrupted quenching conducted in highly agitated water. It differs from conventional oil, polymer, and water quenching by providing a much greater heat-extraction rate from the parts being quenched. The phenomenon was discovered first by laboratory experiments (Ref 1). Figure 1 shows experimental

data obtained for a cylindrical specimen made of low-alloy steel with a diameter of 6 mm (0.24 in.). The bell-shaped curve clearly illustrates a general effect of the cooling rate within the martensitic phase on crack formation: the probability of quench cracking is low for both the relatively slow conventional quenching and also for very rapid and uniform cooling (associated with the IQ process). Later, the IQ phenomenon was supported by the results of computer simulations and a large number of field experiments on a variety of actual steel parts.

Currently, two types of IQ methods are used in heat treating practice: IQ-2 and IQ-3. The IQ-2 process is a three-step procedure (referred to as an IQ-2 technique) based on fast cooling under quenchant nucleate boiling heat-transfer conditions on the part surface, slow cooling in air, and convection cooling in the quench tank. The IQ-2 process is usually applied to batch quenching. The IQ-3 process is a one-step intensive cooling method (referred to as an IQ-3 technique), where cooling at the part surface is so fast that both film boiling and nucleate boiling are completely avoided, and the basic heat-transfer mode on the part surface is simply convection. Direct convection

cooling is the key element of the IQ-3 process, and it is usually employed for single-part quenching operations.

This article provides a review of these methods and some applications. Basic principles, metallurgy, and practical applications of IQ methods for steel parts also are presented in numerous technical papers, conference proceedings, and books. A detailed description of the IQ technology, related equipment, and IQ applications is presented in the book *Intensive Quenching Systems: Engineering and Design* (Ref 3).

Mechanical Properties and Cooling Rate of Quenching

Figure 2 shows a general correlation between steel mechanical properties and the cooling rate of the part for both the conventional quenching process and the IQ process. Material mechanical properties improve with cooling rate increase during quenching, because the greater the rate of cooling, the deeper the hardened layer, and the more complete the phase transformation that takes place in steel parts.

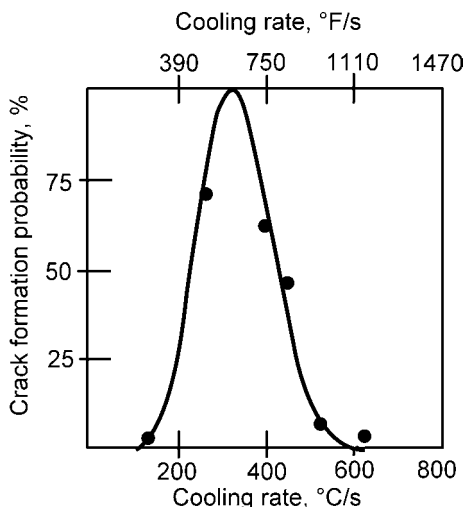


Fig. 1 Correlation between part cooling rate and probability of crack formation. Source: Ref 2

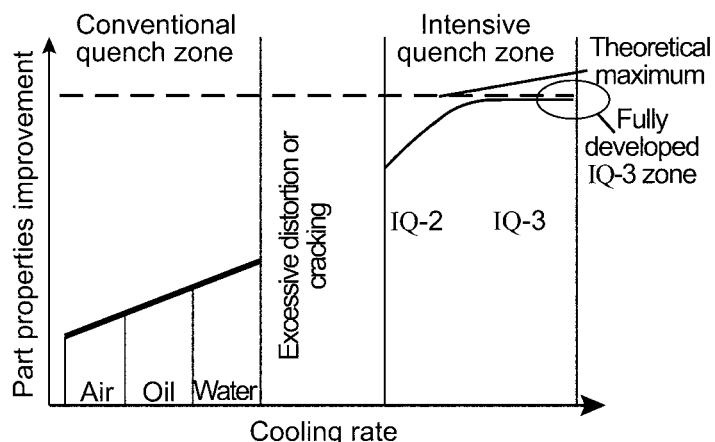


Fig. 2 General correlation between steel mechanical properties and cooling rate during quenching. IQ, intensive quenching. Source: Ref 4

The curve breaks between the conventional quenching zone and the IQ zone. This break illustrates that, in conventional quenching, the part will likely crack above a certain cooling rate. At that point, it is useless to quench faster and attempt to obtain any further improvements in the part mechanical properties on a distorted or broken part.

Figure 2 also shows that, in the IQ zone, part mechanical properties are not only greater compared to the conventional quench zone, but they continuously increase up to a certain ultimate level for the given steel type. When in the IQ zone, a faster quench rate on the part surface does not improve the part properties. This is because at the initiation of the IQ, the part surface temperature almost instantaneously becomes the same as the quenchant temperature. Said another way, after a certain intensity of quench (at a very high heat-extraction rate), the part cannot "give up" its heat any faster than the rate of heat conduction through the part. This is why one cannot quench too fast during the intensive portion of the quench. When the part surface layer has reached the temperature of the quenchant, conduction within the part sets a natural limit on the rate of cooling in the subsurface layers and the core

of the part. Because conduction is also a very rapid and a very uniform form of heat removal, intensive quenching is able to reach the ultimate goal of any quench.

Intensive Quenching and Other Quench Methods

As noted, the IQ process is an interrupted quench method conducted in highly agitated water. It differs from conventional oil, polymer, and water quenching by providing a much greater heat-extraction rate from the parts being quenched. Heat fluxes from the part surface during intensive quenching (and, as a result, the part cooling rates) are several times greater than that for conventional quenching (Ref 5, Chapters 3, 5, and 10). Extremely high heat-extraction rates result in a much greater temperature gradient throughout the part cross section. As shown subsequently, the temperature gradient is a major factor affecting the formation of very high current surface compressive stresses that prevent parts from cracking during intensive quenching. The residual surface stresses remain compressive after the IQ process is

completed. This is in contrast to conventional quenching, where residual surface stresses are usually tensile or neutral.

As an example, Fig. 3 to 5 illustrate the difference in thermal, structural, and stress conditions during the IQ process and conventional quenching in oil for a cylindrical rod of 25 mm (1 in.) diameter and made of plain carbon AISI 1045 steel. These data were generated by Deformation Control Technologies, Inc. of Cleveland, Ohio (Ref 6) using the DANTE computer program (Ref 7). As seen from Fig. 3, during IQ, the part core is still at the austenitizing temperature at a time when the martensite transformation begins on the part surface. A substantially deep part surface layer transforms into martensite by the time the phase transformation starts in the core. This is in contrast to conventional quenching in oil (Fig. 4), where the temperature lag from the part core to the surface is less than 50 °C (90 °F). This means that the phase transformation in oil takes place almost simultaneously through the entire part cross-sectional area.

Figure 5 shows a distribution of the calculated residual hoop stresses in the rod after IQ and after quenching in oil. As seen from the figure, the residual surface compressive hoop

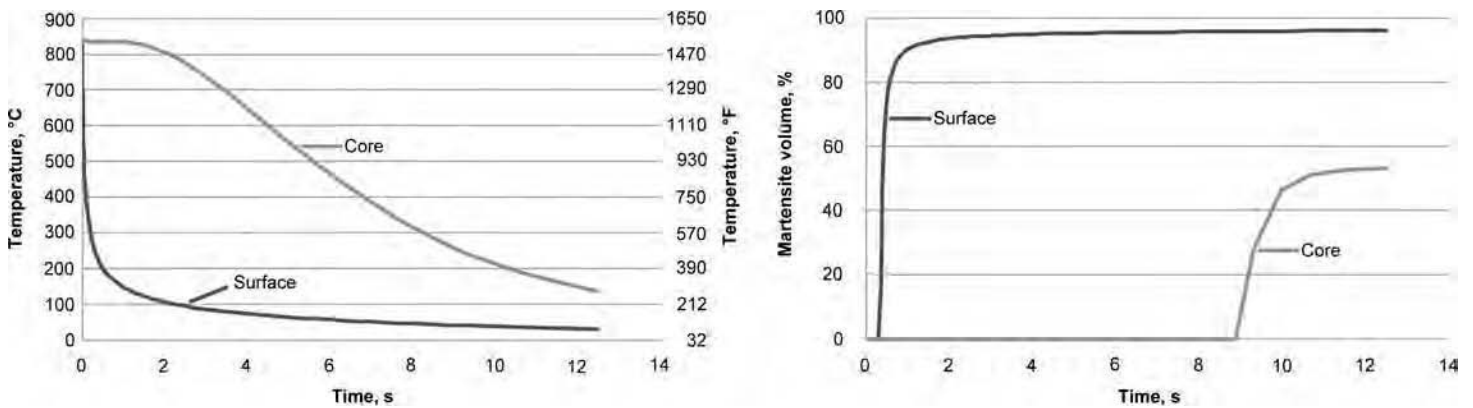


Fig. 3 Temperature and structural conditions during intensive quenching of 25 mm (1 in.) diameter rod made of 1045 steel

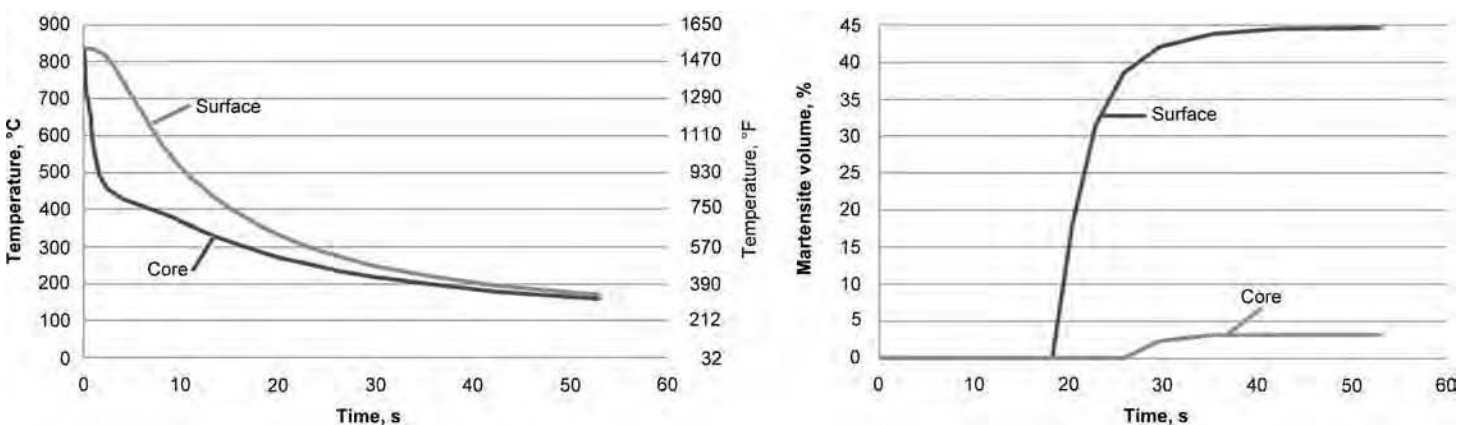


Fig. 4 Temperature and structural conditions during quenching in oil of 25 mm (1 in.) diameter rod made of 1045 steel

stresses after the IQ process are much greater compared to that after conventional quenching in oil. A value of the residual hoop surface compressive stresses after the IQ process is -1000 MPa (-144.7 ksi), while this value after oil quenching is only -294 MPa (-42.5 ksi). Two factors contribute to a higher value of the residual hoop surface compressive stresses after the IQ process:

- Formation of a much deeper martensitic surface layer at the very onset of the quench, prior to the start of the phase transformation in the part core; the deeper the martensitic shell or case, the more expansion of the material takes place in the part surface layer, and the higher the hoop surface compressive stresses around the still hot and plastic austenitic core.
- After the martensite transformation starts on the rod surface, there is substantial thermal shrinkage in the part core, resulting in pulling the part martensitic layer toward the core and inducing greater hoop compressive stresses.

The subsequent formation of martensite in the part core during intensive quenching ultimately results in the core swelling and diminishing the surface hoop compressive stresses. However, as seen from Fig. 5, after IQ, the residual surface hoop stresses are still compressive and much greater than that after oil quenching. This is in spite of the fact that the part core is martensitic (and therefore stronger) after IQ, while the core has a mixed structure after oil quenching. A phenomenon of developing high residual surface compressive stresses after IQ for through-hardened parts illustrated previously by

computer simulations is supported by numerous experimental data.

Along with uniformly fast cooling of the part shell, the key element of the IQ process is the interruption of the IQ at the proper time. The calculated time for interruption of IQ depends on part shape, part dimensions, type of steel, and ultimately the desired physical properties in accordance with the part specifications. For example, for parts made of through-hardened medium- and high-alloy steels, the quench is usually interrupted at the moment of time when surface compressive stresses are at their maximum value and the part hardened layer is at an optimum depth. A method for calculating an optimum interruption time during IQ is presented as follows.

After interruption of the intensive water quench, cooling then continues in air. The thermal energy coming from the still very hot part core tempers the martensitic surface layer, making it tougher and preventing possible cracking. On the other hand, for parts made of low- or medium-plain carbon steels having a low hardenability, or for parts made of carburized grades of steel, the interruption criterion is often calculated to provide the hardened shell or case as deep as possible.

A very commonly posed question regarding the IQ process is how it differs from induction case hardening (or shell hardening) methods. Like the IQ process, induction case hardening provides the part with residual compressive surface stresses and with a wear-resistant martensitic surface. However, unlike the IQ processes, induction case hardening strengthens only the part surface layer. The part core does not experience any phase transformations. If core

conditioning is required, the part must be through heated, quenched, and tempered prior to conducting induction case hardening. This is in contrast to the IQ methods that provide high compressive surface stresses and, at the same time, strengthen the core. Secondly, induction case hardening creates hardness and residual-stress profiles (from compressive at the surface to tensile below the surface) that are much steeper than those after IQ, because only a relatively thin part surface layer is austenitized by induction heating. Finally, the IQ process is interrupted when residual surface compressive stresses are at their maximum value, providing the part with an optimum hardened depth. The smoother hardness profile, the high residual compressive stresses, the properly toughened core, and the optimum depth of hardness after IQ processes result in better part performance characteristics—and in a single process.

In summary, the IQ process involves interrupted quenching in highly agitated water for through hardening. Both the intensity of cooling (the heat-extraction rate) and the cooling time are strictly defined depending on the part shape, dimensions, and type of steel and are determined by computer simulations. Due to greater cooling rates compared to conventional quenching, the IQ process provides a better material microstructure, deeper hardened layer, and high residual surface compressive stresses, resulting in stronger parts with better fatigue life and less energy consumed in processing. Due to the environmental benefits of IQ being a water-only quenchant, the IQ process facilitates part-by-part heat treatment operations within the manufacturing cell.

Heat Transfer during Quenching

As noted, two methods of IQ are used in practice. One is a three-step process (IQ-2) based on quenchant nucleate boiling during fast cooling, followed by slow cooling in air, and then convection cooling in the quench tank. The other method (IQ-3) is a one-step intensive cooling method based on direct convection cooling of the part surface. To better understand the fundamentals of IQ methods, it is helpful to briefly review the modes of heat transfer during quenching of steel parts in liquid quench media.

Heat Transfer during Conventional Quenching. When quenching parts in oil, polymer, or water, four consecutive modes of heat transfer take place: shock nucleate boiling, film boiling, nucleate boiling, and convection (Ref 3, Chapter 3). Figure 6 qualitatively presents the heat flux change from the part surface during quenching. The shock nucleate boiling process starts at the very beginning of part immersion into the quench bath. The heat flux from the hot part surface during this time period is very high, resulting in an almost instant initiation of the boiling process. Due to high heat flux during the shock boiling process, the rate of bubble formation is so great that, in a very

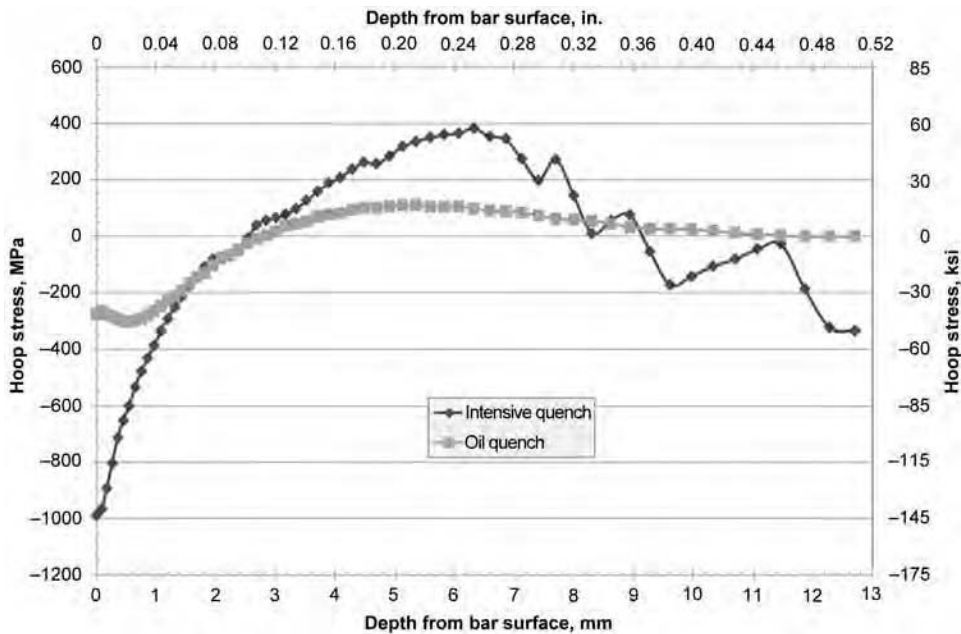


Fig. 5 Distribution of residual hoop stresses in 25 mm (1 in.) diameter rod made of 1045 steel after intensive quenching and after quenching in oil

short time period (usually approximately 0.1 s after the beginning of the quench), bubbles merge with each other to form a vapor blanket or film on the part surface. The heat flux from the part surface required for initiation of the film boiling mode of heat transfer is called the first critical heat flux density, q_{cr1} (Fig. 6). Note that the formation of the vapor blanket is a very unstable process and therefore uncontrollable. Prior to forming a vapor blanket throughout the entire part surface, areas of the film boiling move sporadically along the part surface, causing very nonuniform cooling. In addition, because the vapor blanket has low thermal conductivity, it creates a barrier for heat transfer from the hot part surface to the quenchant, resulting in sharp reduction of the heat flux from the part surface (Fig. 6) and a slowdown of the part cooling rate. The nonuniform and delayed cooling, in turn, may cause excessive part distortion and a spotty surface hardness, often called a slack quench.

Due to a gradual reduction of the part cooling rate, the temperature gradient throughout the part cross section decreases, resulting in the reduction of heat flux from the part surface. At some point, the heat flux on the surface of the part reaches a level at which it cannot support the film boiling process any longer. The vapor blanket starts to collapse, and the film boiling mode of heat transfer switches to the nucleate boiling mode. The heat flux at the part surface when the nucleate boiling process starts is called the second critical heat flux density, q_{cr2} (Fig. 6). Due to the absence of the vapor blanket (a thermal barrier) on the part surface during the nucleate boiling mode of heat transfer, the heat flux from the part surface starts to rise from q_{cr2} to its maximum value. Note that the nucleate boiling process is both a very stable and a very intensive mode of heat transfer. The average heat-transfer coefficient from the part surface during nucleate boiling is much greater than that during the nonuniform film boiling process. In the final stage of conventional quenching, as the heat flux from the part surface further reduces, the nucleate boiling process is replaced by convection heat transfer from the part surface to the liquid quenchant.

Heat Transfer during Batch Intensive Quenching (IQ-2 Process). Similar to conventional quenching, a shock boiling process initiates from the very beginning of the IQ-2 quench. However, in contrast to conventional quenching, the shock nucleate boiling process never transforms into the film boiling process. Thus, only two modes of heat transfer take place during the IQ-2 process: nucleate boiling followed by convection cooling. The film boiling process is fully eliminated in IQ water tanks due to the following measures: providing a vigorous (intensive) agitation of the quench bath, maintaining the water at close to ambient temperature, and using a small amount of water additives (usually mineral salts) that affect electrostatic conditions of the thin quenchant layer bearing against the part surface, resulting in an increase of

quenchant surface tension. All these factors increase the value of the first critical heat flux density, q_{cr1} , in the quench water. In other words, a greater heat flux from the part surface is required to bring the IQ-2 quench water to the saturated temperature needed to initiate the film boiling process at the part surface.

Another method for eliminating the film boiling process is to provide a redundant pressure above the surface of the quench bath. A detailed description of this approach is presented in Ref 3 (Chapter 8) and Ref 5. Raising the pressure in the quench chamber above the ambient pressure results in the rise of the water saturated temperature. This, in turn, causes an increase of the first critical heat flux density, q_{cr1} , which makes initiation of the film boiling process more difficult. For example, raising the pressure above the quench bath from ambient 0.1 to 0.2 MPa (1 to 2 bar) results in an increase of the water boiling temperature from 100 to 120 °C (212 to 248 °F) and an increase of q_{cr1} from 5.8 MW/m² to approximately 7.5 MW/m².

Due to the very high heat-transfer coefficient during nucleate boiling in water, the part surface temperature approaches the water boiling temperature very quickly. The part surface temperature stabilizes just above the quenchant boiling temperature for a certain time period (Fig. 7). Note that this period of cooling (characterized by a stabilized surface temperature) is absent when quenching parts in oil, due to a much smaller nucleate boiling heat-transfer coefficient in oil compared to that in IQ water tanks.

When the heat flux from the part surface drops further, the nucleate boiling process in water is replaced by the final mode of heat transfer: convection cooling (the same final cooling mode as in oil or polymer/water quenching).

Heat Transfer during Single-Part Intensive Quenching (IQ-3 Process). When implementing the IQ-3 process in high-velocity IQ systems, the water is flowing so fast along the part surface that the water does not have a chance to reach the boiling temperature. A so-called direct convection cooling takes place during the IQ-3 process. In this case, the

part surface temperature cools to the water temperature almost instantly (Fig. 7). The IQ-3 process provides the ultimate intensive cooling rate for steel parts during quenching that yields the highest as-quenched hardness and deepest quenched layer (versus conventional oil or polymer/water quenching). The IQ-3 process thus provides the maximum achievable improvement in material mechanical properties for a given alloy of steel in a given geometry.

Batch Intensive Quenching (IQ-2)

The three-step IQ method (referred to as IQ-2) is usually applied to batch quenching. As noted, the IQ-2 technique is a three-step procedure:

1. Fast cooling under quenchant nucleate boiling heat-transfer conditions on the part surface
2. Slow cooling in air
3. Convection cooling in the quench tank

During the first stage of cooling, martensite forms rapidly in the part surface layer, creating surface compressive stresses. The fast cooling is interrupted at an optimum time, when the surface compressive stresses reach their maximum value. At this point, the steel part is removed from the water quenchant. Usually, it happens at the end of the nucleate boiling stage of cooling (Fig. 7). In some cases (when the part is relatively thick), the optimum cooling time is longer than the duration of nucleate boiling, and the quench is interrupted when there is already convection heat transfer on the part surface. A method and example of calculating the optimum cooling time during the IQ-2 process is subsequently discussed in detail.

After interruption of the intensive stage of cooling, part cooling continues in air. During this second stage of IQ-2, the part surface layer, or shell, is self-tempered by the heat coming from the hot core. The part surface temperature increases while the part core decreases, resulting in equalization of the part temperature throughout its cross-sectional area. Also, in this second

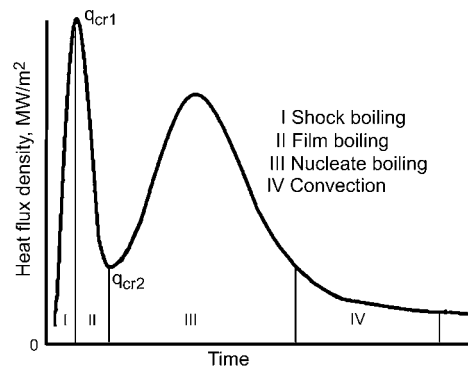


Fig. 6 Schematic of heat-transfer modes during quenching in liquid media. q_{cr1} , first critical heat flux density; q_{cr2} , second critical heat flux density. Source: Ref 3

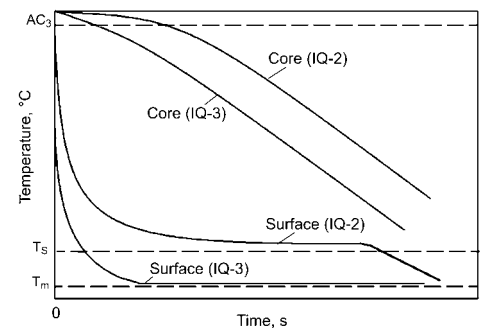


Fig. 7 Typical cooling curves at surface and core during intensive quenching processes (IQ-2 and IQ-3). AC_3 , austenitizing temperature; T_s , quenchant saturation temperature (100 °C, or 212 °F); T_m , water or water/salt solution temperature (usually 20 °C, or 68 °F)

stage, the part compressive surface stresses (developed as current compressive stresses in the first stage of cooling) are fixed. As a result of the self-tempering process, the martensitic surface layer strengthens (as toughened tempered martensite), eliminating possible part cracking during final stages of IQ-2 cooling.

In the third phase of the IQ-2 quench, the part is returned to the intensive quench tank for further convection cooling to complete the required phase transformations in the part surface layer. This third cooling step is needed to provide the maximum achievable improvement in material mechanical properties; because the first stage of cooling takes place mainly during the nucleate boiling mode of heat transfer, and even after cooling in air, the temperature of the part surface layer is still above the quenchant boiling temperature, which is above the martensite finish temperature for a majority of steels.

An analytical mathematical model of the nucleate boiling process was developed to determine the duration of this stage of IQ (Ref 3, Chapter 2). The model consists of a one-dimensional linear differential heat-conduction equation with a nonlinear boundary condition for a nucleate boiling process (Ref 5). An analytical solution of the aforementioned mathematical model for an infinite plate, infinite cylinder, and sphere is presented in Ref 5. The solution was obtained for so-called irregular and regular thermal conditions that take place during quenching of steel parts (Ref 3, 5). It was assumed that, at the moment of transition from the nucleate boiling process to convection, the heat flux densities for both modes of heat transfer are equal. In other words, the heat flux density from the part surface at the end of nucleate boiling is equal to the convective heat flux density at the beginning of convection heat transfer. The following equations for calculating the duration of the nucleate boiling process were obtained (Ref 3, Chapter 2):

$$\tau = \left[\Omega + f \ln \frac{\vartheta_I}{\vartheta_{II}} \right] \frac{K}{a} \quad (\text{Eq 1})$$

where $\Omega = 0.48$, a parameter that determines the duration of the irregular portion of the thermal process (Ω is a relatively small value compared to τ) (Ref 3, Chapter 2); $f = 3.21$; K is a parameter (known as the Kondratjev form factor) that depends on the part shape and dimensions (Table 1), in m^2 ; and a is the steel thermal diffusivity, in m^2/s .

Values ϑ_I and ϑ_{II} are calculated from Eq 2 and 3 using an iterative technique:

$$\vartheta_I = \frac{1}{\beta} \left[\frac{2\lambda(\vartheta_0 - \vartheta_I)}{R} \right]^{0.3} \quad (\text{Eq 2})$$

$$\vartheta_{II} = \frac{1}{\beta} [\alpha_{conv}(\vartheta_{II} + \vartheta_{uh})]^{0.3} \quad (\text{Eq 3})$$

where $\vartheta_0 = T_0 - T_s$; $\vartheta_{uh} = T_s - T_m$; T_s is the part temperature, in $^{\circ}C$; T_m is the quenchant

temperature, in $^{\circ}C$; λ is the steel heat conductivity, in $W/m \cdot ^{\circ}C$; R is the characteristic part dimension, in meters; α_{conv} is the convective heat-transfer coefficient in the quench tank, in $W/m^2 \cdot ^{\circ}C$; and β is a parameter depending on the properties of the quenchant and vapors.

As an example, Table 1 presents the values for the Kondratjev form factor, K , for parts of simple shapes, while Table 2 includes data for steel thermal conductivity and thermal diffusivity, respectively. A convective heat-transfer coefficient, α_{conv} , in the quench tank can be calculated approximately using known experimental correlations between a nondimensional Nusselt number, Nu , and Reynolds number, Re , for a turbulent external flow (Ref 8), or it can be determined experimentally for a specific quench tank using special probes.

The results of calculations of the nucleate boiling process duration for different steel parts were confirmed by numerous experimental data (Ref 3, Chapter 2). The following example shows a procedure for calculating the duration of the nucleate boiling process for a cylindrical part that is 80 by 320 mm (3.15 by 12.6 in.)

diameter made of medium-alloy steel. The part is quenched from the initial temperature of $860^{\circ}C$ ($1580^{\circ}F$) in an IQ tank with a water flow velocity of 1.5 m/s (5.0 ft/s). First, a Kondratjev form factor, K , is calculated using the following equation from Table 1 for a finite cylinder:

$$K = \frac{1}{\frac{5.784}{R^2} + \frac{9.87}{Z^2}} = \frac{1}{\frac{5.784}{0.04^2} + \frac{9.87}{0.32^2}} = 269.4 \times 10^{-6} m^2$$

Secondly, the values of ϑ_I and ϑ_{II} are calculated. When determining parameter ϑ_I from Eq 2, the following average values for steel thermal diffusivity and thermal conductivity within the temperature range of 100 to $860^{\circ}C$ (212 to $1580^{\circ}F$) are used: $a = 5.36 \times 10^{-6} m^2/s$ and $\lambda = 22 W/m \cdot K$ (Table 2). Note that the thermal property values for supercooled austenite are applicable to a majority of steels.

Parameter β for water at $20^{\circ}C$ ($70^{\circ}F$) is equal to 3.45; $\vartheta_0 = T_0 - T_s = 860^{\circ}C - 100^{\circ}C = 760^{\circ}C$ ($1580^{\circ}F - 210^{\circ}F = 1370^{\circ}F$).

Table 1 Values for Kondratjev form factor, K , for parts of simple shapes (results of analytical calculations)

No.	Part shape	Coefficient K, m^2	$\frac{K}{\varphi}, m^{-1}$	$K \frac{\varphi}{\pi}, m$
1	Infinite plate of thickness L	$\frac{L^2}{\pi^2}$	$\frac{2}{L}$	$\frac{2L}{\pi^2}$
2	Infinite cylinder of radius R	$\frac{R^2}{5.784}$	$\frac{2}{R}$	$0.346R$
3	Square infinite prism with equal sides of L	$\frac{L^2}{2\pi^2}$	$\frac{4}{L}$	$\frac{2L}{\pi^2}$
4	Finite cylinder of radius R and height Z	$\frac{1}{\frac{5.784}{R^2} + \frac{9.87}{Z^2}}$	$\left(\frac{2}{R} + \frac{2}{Z} \right)$	$\frac{2RZ(R+Z)}{5.784Z^2 + \pi^2 R^2}$
5	Finite cylinder, $R = Z$	$\frac{R^2}{15 \cdot 65}$	$\frac{4}{R}$	$0.256R$
6	Finite cylinder $2R = Z$	$\frac{R^2}{8.252}$	$\frac{3}{R}$	$0.364R$
7	Cube with side of L	$\frac{L^2}{3\pi^2}$	$\frac{6}{L}$	$0.203L$
8	Finite square plate with sides of L_1, L_2, L_3	$\frac{1}{\pi^2 \left(\frac{1}{L_1^2} + \frac{1}{L_2^2} + \frac{1}{L_3^2} \right)}$	$\frac{2(L_1 L_2 + L_1 L_3 + L_2 L_3)}{L_1 L_2 L_3}$	$\frac{2(L_1 L_2 + L_1 L_3 + L_2 L_3) L_1 L_2 L_3}{\pi^2 (L_1^2 L_2^2 + L_1^2 L_3^2 + L_2^2 L_3^2)}$
9	Sphere	$\frac{R^2}{\pi^2}$	$\frac{3}{R}$	$0.304R$

Table 2 Thermal conductivity, λ , and thermal diffusivity, a , of supercooled austenite versus temperature

Temperature		$\lambda, \frac{W}{mK}$	$\bar{\lambda}, \frac{W}{mK}$	$a, 10^{-6} \frac{m^2}{s}$	$\bar{a}, 10^{-6} \frac{m^2}{s}$
$^{\circ}C$	$^{\circ}F$				
100	212	17.5	17.5	4.55	4.55
200	390	18	17.75	4.63	4.59
300	570	19.6	18.55	4.70	4.625
400	750	21	19.25	4.95	4.75
500	930	23	20.25	5.34	4.95
600	1110	24.8	21.15	5.65	5.10
700	1290	26.3	21.90	5.83	5.19
800	1470	27.8	22.65	6.19	5.37
900	1650	29.3	23.4	6.55	5.55

Note: $\bar{\lambda}$ and \bar{a} at $500^{\circ}C$ ($930^{\circ}F$) (analogously at other temperatures) mean average values for the range of 100 to $500^{\circ}C$ (212 to $930^{\circ}F$)

Thus, the equation for determining ϑ_I is the following:

$$\begin{aligned}\vartheta_I &= \frac{1}{\beta} \left[\frac{2\lambda(\vartheta_0 - \vartheta_I)}{R} \right]^{0.3} \\ &= \frac{1}{3.45} \left[\frac{2 \times 22(760 - \vartheta_I)}{0.04} \right]^{0.3}\end{aligned}$$

From solving this equation, the value of ϑ_I is equal to 17.2 °C (63.0 °F). When determining parameter ϑ_{II} from Eq 3, the following values for the convective heat-transfer coefficient and parameter ϑ_{uh} are used: $\alpha_{conv} = 5000 \text{ W/m}^2 \text{ } ^\circ\text{C}$; $\vartheta_{uh} = T_s - T_m = 100 \text{ } ^\circ\text{C} - 20 \text{ } ^\circ\text{C} = 80 \text{ } ^\circ\text{C}$ (210 °F - 70 °F = 140 °F). Thus, the equation for determining ϑ_{II} is the following:

$$\begin{aligned}\vartheta_{II} &= \frac{1}{\beta} [\alpha_{conv}(\vartheta_{II} + \vartheta_{uh})]^{0.3} \\ &= \frac{1}{3.45} [5000 \times (\vartheta_{II} + 80)]^{0.3}\end{aligned}$$

From solving this equation, the value of ϑ_{II} is equal to 14.6 °C (58.3 °F). From Eq 1, the duration of the transient nucleate boiling process for the part considered is:

$$\begin{aligned}\tau &= \left[\Omega + f \ln \frac{\vartheta_I}{\vartheta_{II}} \right] \frac{K}{a} \\ &= \left[0.48 + 3.21 \ln \frac{17.2 \text{ } ^\circ\text{C}}{14.6 \text{ } ^\circ\text{C}} \right] \frac{269.4 \times 10^{-6} \text{ m}^2}{5.36 \times 10^{-6} \text{ m}^2/\text{s}} \approx 51 \text{ s}\end{aligned}$$

Single-Part IQ Process (IQ-3)

The one-step IQ method (referred to as IQ-3) is usually employed for single-part quenching operations. In contrast to the multistep cooling rates of the IQ-2 process, the IQ-3 technique involves intense one-step cooling such that heat transfer on the part surface is simply convection (direct convection cooling). As noted, when the IQ-3 process is applied, part surface cooling is so fast that both film boiling and nucleate boiling are completely avoided, and the basic heat-transfer mode on the part surface is simply convection.

The part surface temperature cools almost instantaneously to the water temperature, usually close to ambient temperature or approximately 20 °C (68 °F) during the IQ-3 process (Fig. 7). Because the water temperature is below the martensite finish temperature (M_f) for a majority of steels, the IQ-3 process creates the conditions for developing the maximum possible temperature gradient throughout the part being quenched and for developing a 100% martensitic structure in the part surface layer. As a consequence, with the IQ-3 process, the maximum achievable residual surface compressive stresses and the highest physical properties for the part are attained (for a given hardenability of steel alloy and for a given part geometry). This is also why IQ-3 can often allow the use of a less expensive, lower-alloy

steel and provide equal or better part performance (e.g., AISI 1045 substituted for AISI 4140 alloy, or AISI 1020 substituted for case-carburized AISI 8620 alloy).

In the IQ-3 method, intensive cooling is continuous and uniform over the entire part surface until compressive stresses on the part surface reach their maximum value. Note that the optimal hardened depth depends on the part geometry and type of steel, but the optimal hardened depth corresponds to the maximum surface compressive stresses. These maximized compressive surface stresses will be diminished if the core of the part is cooled further, for example, to the quenchant temperature. Therefore, the second key element of the IQ-3 process is to interrupt intensive cooling at the proper time—when compressive surface stresses are at their maximum value and to the optimum depth.

When designing an IQ-3 process, two issues should be resolved: what convective heat-transfer coefficient (HTC) on the part surface should be provided to eliminate the possibility of any type of boiling, for uniform direct convection cooling, and when the IQ process should be interrupted to provide maximum residual surface compressive stresses. The required HTC is determined by using Eq 1 to 3, assuming that the duration of the nucleate boiling process, τ , is equal to zero (hence the parameter Ω in Eq 1 is also equal to zero). With this assumption, the required convective HTC can be calculated from the following equation:

$$\alpha_{conv} \geq \frac{2\lambda(\vartheta_0 - \vartheta_I)}{R(\vartheta_I + \vartheta_{uh})} \quad (\text{Eq 4})$$

The optimum duration of the IQ-3 process for maximum residual surface compressive stresses can be determined from the following equation (Ref 3, Chapter 10):

$$\tau = \left[\frac{kBi_V}{2.095 + 3.867Bi_V} + \ln \left(\frac{T_0 - T_m}{T - T_m} \right) \right] \frac{K}{aKn} \quad (\text{Eq 5})$$

where k is a parameter equal to 1 for an infinite plate, 2 for an infinite cylinder, and 3 for a sphere; T_0 is the initial part temperature prior to quenching, in °C; T_m is the water temperature, in °C; T is the part core temperature at a time when surface compressive stresses are at their maximum value (this temperature depends on the part shape and usually is in the range of 350 to 450 °C, or 660 to 840 °F, as shown by numerous calculations) (Ref 3, Chapter 7); K is the Kondratjev form factor (Table 1); Kn is the nondimensional parameter (known as the Kondratjev number); and Bi_V is the generalized Biot number.

A generalized Biot number, Bi_V , is calculated by the following formula:

$$Bi_V = \frac{\alpha_{conv}}{\lambda} K \frac{S}{V} \quad (\text{Eq 6})$$

where S is the surface area of the part, in m^2 ; and V is the volume of the part, in m^3 . A generalized Biot number, Bi_V , is a nondimensional parameter that is similar to a conventional Biot number used for analyzing conduction heat transfer (Ref 8). The difference is that a conventional Biot number is applied to bodies of simple shapes (an infinite plate, infinite cylinder, and sphere), while a generalized Biot number is used for parts of a complex geometry. The expression $K \frac{S}{V}$ in Eq 6 represents a characteristic dimension for parts of complex shapes. Note that a characteristic part dimension used for calculating a conventional Biot number is a radius for an infinite cylinder or sphere, or a half-thickness for an infinite plate.

The Kondratjev number, Kn , is calculated using the following equation:

$$Kn = \frac{Bi_V}{(Bi_V^2 + 1.437Bi_V + 1)^{0.5}} \quad (\text{Eq 7})$$

A nondimensional parameter, the Kondratjev number, Kn , characterizes the intensity of cooling and varies in the range of 0 to 1 (for IQ processes, $Kn > 0.8$) (Ref 3, Chapter 10). The following example shows a procedure for calculating the minimum convective HTC required for implementing the IQ-3 process and an optimum cooling time for the same part as considered earlier: a cylinder of 80 by 320 mm (3.15 by 12.6 in.) diameter made of medium-alloy steel. First, a minimum HTC that provides a direct convection condition required by the IQ-3 process is calculated using Eq 4:

$$\begin{aligned}\alpha_{conv} &\geq \frac{2\lambda(\vartheta_0 - \vartheta_I)}{R(\vartheta_I + \vartheta_{uh})} = \frac{2 \times 22(760 - 17.2)}{0.04(17.2 + 80)} \\ &= 8406 \frac{\text{W}}{\text{m}^2\text{K}}\end{aligned}$$

Then, a generalized Biot number, Bi_V , and a Kondratjev number, Kn , are calculated using Eq 6 and 7:

$$\begin{aligned}Bi_V &= \frac{8406 \text{ W/m}^2\text{K}}{22 \text{ W/mK}} \times 269.4 \times 10^{-6} \text{ m}^2 \\ &\quad \times \frac{2 \times 3.14 \times 0.04 \times 0.32 \text{ m}^2 + 2 \times 3.14 \times 0.04^2 \text{ m}^2}{3.14 \times 0.04^2 \times 0.32 \text{ m}^3} \\ &= 5.79 \\ Kn &= \frac{5.79}{(5.79^2 + 1.437 \times 5.79 + 1)^{0.5}} = 0.885\end{aligned}$$

Finally, the optimum cooling time is calculated by using Eq 5, taking into account that, for cylindrical parts, maximum residual surface compressive stresses are observed when the part core temperature is 450 °C (840 °F) (Ref 3):

$$\begin{aligned}\tau &= \left[\frac{2 \times 5.79}{2.095 + 3.867 \times 5.79} + \ln \frac{860 - 20}{450 - 20} \right] \\ &\quad \frac{269.4 \times 10^{-6} \text{ m}^2}{5.36 \times 10^{-6} \text{ m}^2/\text{s} \times 0.885} \approx 65 \text{ s}\end{aligned}$$

Improvement of Steel Microstructure, Mechanical Properties, and Stress Conditions

The significantly higher quench-cooling rates used in the IQ processes versus conventional quenching methods results in a different microstructure in the parts after intensive quenching than after oil quenching. Depending on the hardenability of the material, steels subjected to IQ are harder, to a deeper level, and have a finer structure than conventionally quenched parts of the same alloy. Over the years, numerous studies of mechanical properties of intensively quenched test samples and actual parts have been conducted (Ref 2, 4, 9–20). Some of the data from the referenced studies are presented subsequently. The IQ data were compared to the same test specimens and parts quenched in oil. In all instances, the oil-quenched parts and the IQ parts were made from the same steel heat and were tempered to the same surface hardness. The IQ parts have shown superior mechanical properties. The data clearly demonstrate that the IQ process significantly improves steel mechanical properties and parts performance characteristics versus traditional oil quenching.

Through-Hardening Steels. Table 3 presents data on mechanical properties for some plain carbon and through-hardened alloy steels. Large and small cylindrical test samples with diameters ranging from 6 to 50 mm (0.25 to 2.0 in.) were used. All test samples were heated to their standard austenitizing temperature, depending on the type of steel. The samples were tempered after quenching at temperatures ranging from 370 to 500 °C (700 to 925 °F). The following steel properties were measured: tensile strength, yield strength, elongation, reduction in area, and impact strength. A detailed description of the test procedures applied is presented in Ref 9 and 16.

As an example, Fig. 8 illustrates the significant difference in microstructure for 19 mm (0.75 in.) test bars made of AISI 1045 steel after IQ and after oil quenching. The significantly finer microstructure obtained after IQ, in turn, yields better mechanical properties (Table 3) than the comparable oil-quenched steels. Note that the higher hardness of the IQ steel does not come at the expense of the ductility; in fact, the ductility is usually somewhat higher for the IQ material. This means that the majority of the IQ samples were stronger and, at the same time, more ductile when compared to the oil-quenched samples.

Generally, the IQ steels have a higher hardness to a greater depth versus the oil-quenched steels, independent of the section size of the specimen. The rapid cooling from the IQ provides a higher strength level and also better impact resistance, even at the higher strength levels achieved with IQ.

Improvement of Strength and Ductility. Intensive quenching can result in a simultaneous improvement of both material strength and ductility, an effect sometimes referred to as superstrengthening. It was first reported in Ref 21. The mechanism of the additional strengthening can be explained by the following. A residual supercooled austenite in the part surface layer plastically distorts when being subjected to high compression from the firm martensite plates that appear in the austenite. This results in the formation of an extremely high density of dislocations in the austenite that improve the material mechanical properties after quenching. The higher the cooling rate

within the martensite formation range, the greater the compression from the martensite plates and the greater the density of the dislocations. During very rapid cooling, there is not enough time for the dislocations to accumulate in the grain boundaries and to form nuclei of future microcracks. The dislocations are “frozen” in the material. Thus, the rapidly forming martensite plates act like microscopic “blacksmiths;” under conditions of high current stress during intensive cooling, the expanding plates of martensite arise explosively, deforming the austenite and creating extremely high dislocation densities. The superstrengthening effect is similar to work hardening that takes place in

Table 3 Mechanical properties improvement for plain carbon and alloy through-hardened steels

Steel	Bar diameter		Quench(a)	Core hardness, HRC	Material strength					
					Ultimate strength		Yield strength		Impact strength at 22 °C (72 °F)	
	mm	in.			MPa	ksi	MPa	ksi	J	ft · lbf
1038	30	1.2	IQ	26	842	123	622	90	84	62
			Oil	23	807	117	532	77	38	28
1045	19	0.75	IQ	37	1191	173	1125	163	54	40
			Oil	32	980	142	766	111	53	39
1045	50	2.0	IQ	28	891	129	704	102	34	25
			Oil	27	880	128	626	91	31	23
1060	19	0.75	IQ	44	1465	212	1377	200	26	19
			Oil	40	1227	178	966	140	27	20
5160	19	0.75	IQ	48	1728	251	1584	230	22	16
			Oil	47	1592	231	1472	213	22	16
5160	38	1.5	IQ	48	1886	273	1499	217	9	7
			Oil	48	1623	235	1292	187	9	7
4140	19	0.75	IQ	48	1506	218	1181	171	40	30
			Oil	45	1350	196	1125	163	22	16
4140	50	2.0	IQ	44	1447	210	1072	155	20	15
			Oil	42	1329	193	1004	146	19	14
4130	22	0.87	IQ	35	1084	157	984	143	95	70
			Oil	30	925	134	809	117	125	92
40X (5140)(b)	50	2.0	IQ	28	860	125	695	101	168	124
			Oil	20	780	113	575	83	113	83
35XM (4130)(b)	50	2.0	IQ	30	970	141	820	119	150	111
			Oil	30	960	139	775	112	54	40
25X1M (4118)(b)	50	2.0	IQ	30	920	133	820	119	170	125
			Oil	20	755	109	630	91	70	52

(a) IQ, intensive quench. (b) Russian steels with AISI equivalent in parentheses

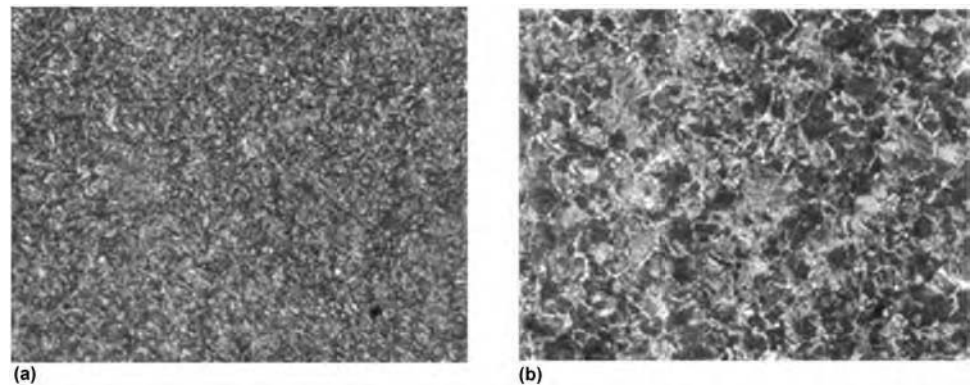


Fig. 8 Microstructure for 19 mm (0.75 in.) diameter rod made of 1045 steel after (a) intensive quenching and (b) oil quenching. Original magnification: 250 \times . Source: Ref 16

low-temperature thermomechanical treatment of steel. A detailed description of the material superstrengthening effect can be found in Ref 3, Chapter 9.

Carburized Steels. The following parameters were evaluated for samples made of carburized grades of steel (Ref 16): effective case depth (ECD), microhardness distribution from surface to core, material microstructure, and residual surface compressive stresses. Test samples of 30 mm (1.18 in.) diameter were made of plain carbon AISI 1018 steel and the following alloy steels: AISI 4320, 5120, and 8620. All samples were carburized with the same cycle: 927 °C (1700 °F) for 5 h at 0.9% C potential. After the carburization cycle was completed, the samples were furnace cooled under a protective atmosphere. All alloy steel samples were then reheated to 843 °C (1550 °F) and quenched in oil, while AISI 1018 steel samples were reheated to 860 °C (1580 °F) and quenched in the IQ water tank or in the single-part, high-velocity IQ system. All samples were tempered at 204 °C (400 °F) for 2 h.

Figure 9 presents the hardness distribution for the processed test samples over the entire diameter and for the 2.5 mm (0.1 in.) surface layer. As seen from the graph, after identical 5 h carburizing cycles, the ECD at 50 HRC for the IQ samples was the same or deeper compared to the alloy steel samples quenched in oil. This is because IQ needs less carbon in the case gradient to reach 50 HRC.

Residual-Stress Conditions. The IQ processes provides high residual surface compressive stresses for parts made of through-

hardened steels. This is in contrast to conventional quench methods that provide neutral or tensile residual stresses for these materials. As mentioned earlier, high residual surface compressive stresses after the IQ process are due to a high-temperature gradient throughout the part cross section at a time when martensite starts forming in the part surface layer (Fig. 3) and establishes high current compressive stresses. As an example, Fig. 10 and 11 present experimental data on residual surface compressive stress profiles for cold work punches made of shock-resisting S5 steel (Ref 11) and for a bearing roller made of AISI 52100 steel (Ref 16). In both cases, residual stresses were measured by the x-ray diffraction method. As seen from Fig. 10, residual surface stresses for the punch after quenching in oil are tensile of approximately 200 MPa (29 ksi), while these same stresses are compressive after IQ. The residual surface compressive stresses for the punch are in the range of -500 to -950 MPa (-72 to -138 ksi). The surface stresses are still compressive at a depth of more than 0.5 mm (0.020 in.) from the punch surface. Note that the presence of residual surface compressive stresses changes the failure mode for the IQ punches to wear from the oil-quenched punches chipping, and it improves punch service life by at least 100%. This means the user obtains at least twice as many holes punched from IQ punches versus oil-quenched punches made of the same material.

The residual surface compressive stresses for the bearing roller (Fig. 11) reach the maximum value of -230 MPa (-33.3 ksi) when quenching in the IQ water tank and -900 MPa

(-130 ksi) when quenching in the single-part processing IQ system. These residual stresses extend under the surface to a depth of 2.5 to 2.9 mm (0.10 to 0.11 in.). Note that the single-part quenching IQ process provides higher residual surface stresses compared to the test sample quenched intensively in the IQ water tank. This is because the single-part IQ method provides greater cooling rates compared to quenching in an IQ water tank.

Figure 12 shows a distribution of the residual surface compressive stresses for test samples made of carburized AISI 1018 and 8620 steels. Test samples made of 1018 steel were quenched in the IQ water tank and in the single-part processing IQ system. The results show the significantly improved residual surface stress conditions for both IQ test samples compared to the oil-quenched specimen. Figure 13 presents a residual surface stress profile for the automotive pinions made of carburized AISI 8620 steel after IQ in the IQ water tank and conventional quenching in oil. The residual stresses are compressive for both quench methods. However, as seen from the figure, the residual surface compressive stresses are approximately two times greater when applying the IQ process.

Table 4 presents values for the surface residual compressive stresses for various actual parts and test samples. As seen from the figures and Table 4, the values of surface residual stresses of up to -900 MPa (-130 psi) can be achieved when quenching parts intensively in water or water/salt solutions.

Summarizing the previous information, the following conclusions can be made:

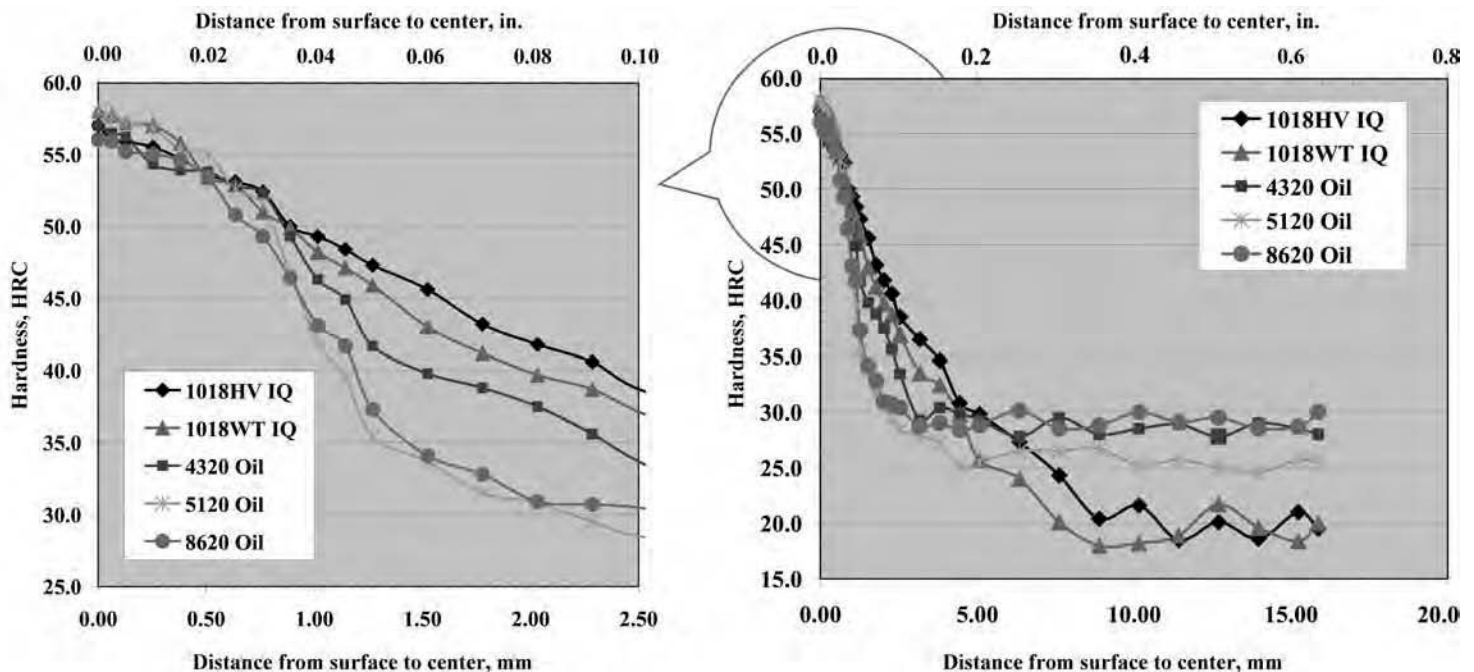


Fig. 9 Hardness distribution for test samples made of AISI 1018, 4320, 5120, and 8620 steels. IQ, intensive quenching. Source: Ref 16

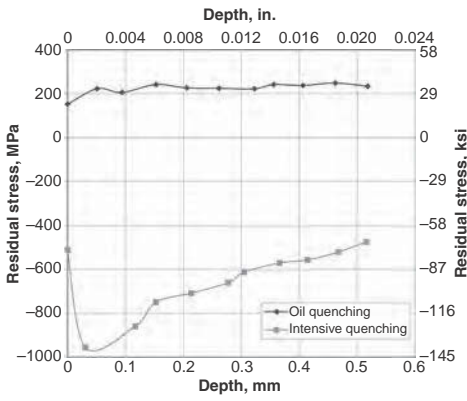


Fig. 10 Residual surface stresses for S5 steel punch. Source: Ref 11

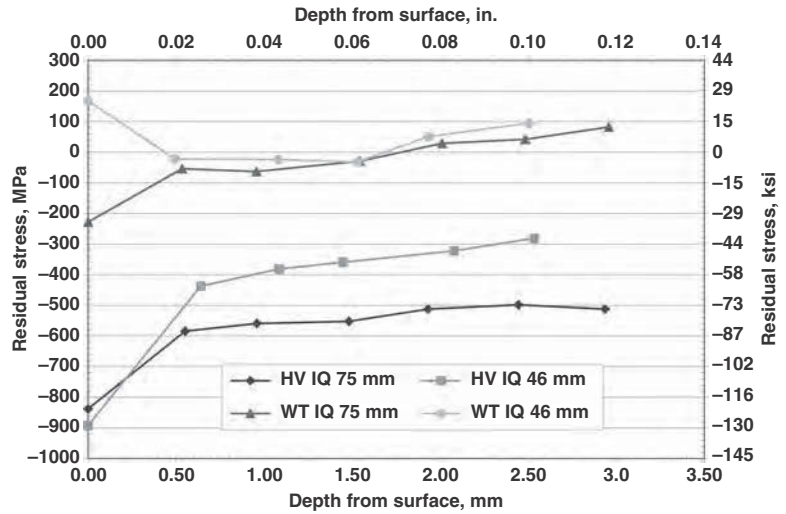


Fig. 11 Residual surface stresses for 52100 steel bearing roller. Source: Ref 16

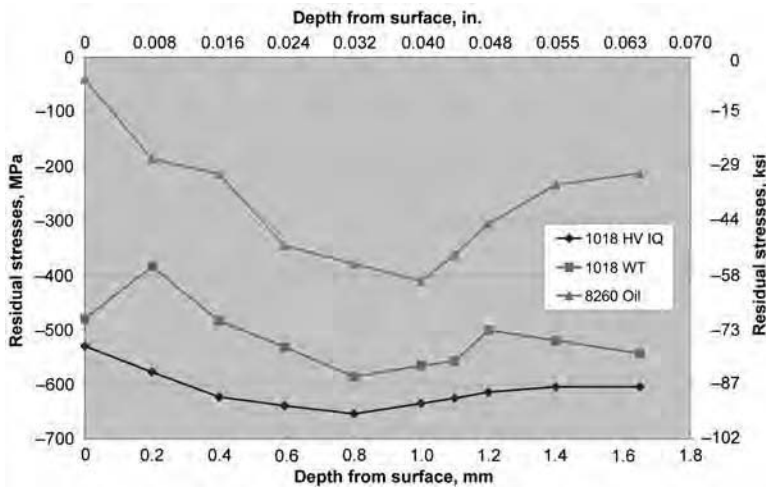


Fig. 12 Residual surface stresses for 32 mm (1.3 in.) diameter bars made of 1018 and 8620 steel. IQ, intensive quenching. Source: Ref 16

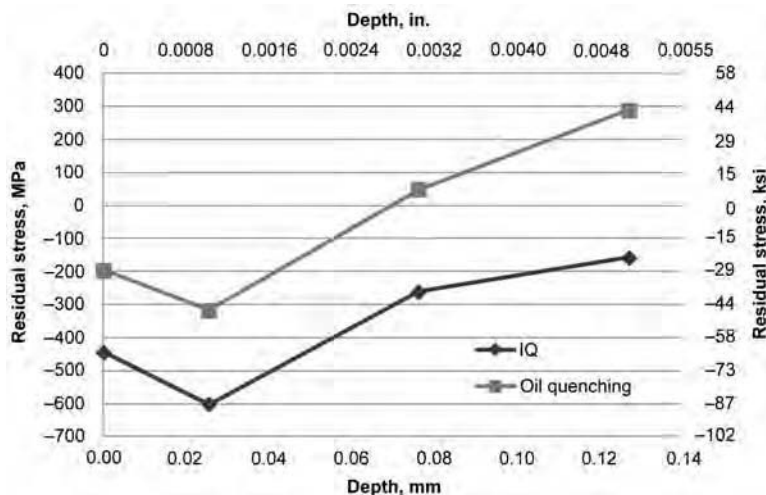


Fig. 13 Residual surface stresses for automotive pinion made of 1018 and 8620 steels. IQ, intensive quenching

Table 4 Residual surface compressive stresses after intensive quenching and tempering

Part	Residual surface compressive stresses	
	MPa	psi
52100 steel bearing ring, 22 cm (8.5 in.) diameter	-136	-20
52100 steel bearing roller, 7.5 cm (3 in.) diameter	-840	-122
52100 steel bearing roller, 4.5 cm (1.8 in.) diameter	-900	-130
4140 steel kingpin, 4.5 cm (1.8 in.) diameter	-563	-82
S5 steel punch, 4.0 cm (1.5 in.) diameter	-750	-109
5160 steel torsion bar sample, 3.5 cm (1.4 in.) diameter	-311	-45
1045 steel cylindrical part, 3.5 cm (1.5 in.) diameter	-430	-62
1547 cylindrical part, 7.29 cm (2.87 in.) diameter	-626	-91
1547 cylindrical part, 5.0 cm (2 in.) diameter	-515	-75
Pyrowear-53 carburized gear:		
Oil quench	-350	-51
Intensive quench	-800	-116

- For a given type of steel of the same section size, the IQ steel specimens generally develop higher strength and, at the same time, higher ductility than the steel samples quenched in oil. A superstrengthening of material takes place during IQ.
- The impact properties obtained from IQ steels are generally superior to the impact properties from oil-quenched steels.
- The IQ process provides high residual surface stresses for parts made of through-hardened steels, even when the part core is fully hardened.
- For carburized grades of steel, the IQ process provides a higher ECD with greater and deeper residual surface compressive stresses.
- The IQ specimens made of plain carbon carburized steel showed deeper ECDs, with higher residual surface compressive stresses, than those specimens made of alloy carburized grades that were quenched in oil.

IQ Process and Part Distortion

The two major phenomena causing part distortion during conventional quenching are thermally induced deformation and martensite phase-transformation size change (swelling). These same reasons for part distortion are also present in the IQ process. However, an absolute value of predictable part distortion after IQ is usually less compared to conventional quenching in oil. The major reasons for this include:

- More uniform cooling during IQ, due to the absence of the film boiling process and to a more uniform heat-extraction rate from the part surface in the quench bath, reduces non-predictable distortion.
- Phase transformation in the parts takes place under different thermal conditions during the IQ process.

As known, more uniform cooling during quenching results in less part distortion. However, in many cases, even with a uniform heat-extraction rate throughout the entire part surface area, the part will distort due to its shape: thin sections of the part cool faster compared to thicker sections. This causes nonuniform thermal contraction followed by nonuniform formation of the martensitic shell. The IQ process usually reduces part distortion in such cases compared to conventional quenching in oil. As an example, consider distortion for a 25 by 250 mm (1 by 10 in.) diameter keyway shaft with a 6.35 by 6.35 mm (0.25 by 0.25 in.) keyway made of AISI 1045 steel. Reference 22 presents the results of computer simulations of the distortion for the keyway shaft, as well as actual experimental shaft distortion measurements after quenching in oil and after IQ in the IQ water tank or in the single-part high-velocity IQ system. To simplify the evaluation of the shaft distortion, only one parameter characterizing the part deformation was used: the shaft bow/flatness (Fig. 14).

The results of calculations show the following dynamics of keyway shaft distortion during IQ. At the very beginning of the quench (prior to the start of martensite transformation on the part surface), the shaft is bowing toward the keyway due to the development of current tensile surface stresses at the keyway corners, which experience greater thermal contraction compared to the rest of the shaft. Note that at the initiation of the quench, the hot shaft core is still at the austenitizing temperature and very low in strength. Therefore, the material in the shaft core is plastic and does not resist bowing

of the shaft caused by thermal shrinking at the surface in the keyway corners.

The direction of the shaft bowing changes after the material at the keyway corners reaches the martensite start temperature. The formation of martensite causes the steel to expand, resulting in the development of current surface compressive stresses. These surface compressive stresses start to bend the shaft in the opposite direction (against the keyway). The reverse bending continues until the surface compressive stresses reach their maximum value. At this point, the thermally induced bow practically disappears. Continued phase transformation in the shaft causes swelling in the part core that partially cancels the compressive surface stresses. As a result, the shaft bows a little bit back toward the keyway. A calculated value of the final shaft out-of-straightness after IQ is 98 μm (Ref 22).

During conventional quenching in oil, the keyway shaft also bows first toward the keyway due to thermal shrinkage of the material prior to the start of martensite transformation. Similar to IQ, after martensite begins to form on the part surface, the current surface compressive stresses created by material expansion start to reverse the bowing of the shaft. However, because these compressive stresses are much smaller compared to those formed during the IQ process, they cannot fully compensate for the thermally induced bow. After phase transformation is completed throughout the shaft cross section, the part core swells, fully cancelling compressive stresses on the part surface, causing a reversal of the bowing toward the keyway and increasing the final shaft distortion. So, at the end of oil quenching, in contrast to IQ, the keyway shaft is bent toward the keyway (Fig. 14). A calculated value of the final shaft out-of-straightness after quenching in oil is 871 μm (Ref 22).

A good agreement between the results of calculations and the experimental data (Ref 22) supports that the dynamics of keyway shaft distortion predicted by the computer simulation and the dynamics described previously in the actual parts are correct. Table 5 presents experimental data (Ref 4) on keyway shaft final distortion after the IQ processes and after conventional oil quenching. As seen from Table 5, both IQ methods provide much less keyway shaft final distortion compared to conventional quenching in oil. The data from Table 5 also show that the single-part quenching IQ-3 process produces less part distortion compared to the batch IQ-2 method. For symmetrical parts, the distortion can be as low as 50 μm . For example, distortion for drive shafts made of

alloy carburized steel and having a diameter of approximately 40 mm (1.6 in.) with a length of 385 mm (15.2 in.) was only 50 to 70 μm after quenching one-by-one in the IQ system.

It is important to note that at the end of quenching, IQ parts usually have greater dimensions compared to identical oil-quenched parts. For example, computer simulations (Ref 23) conducted for a spur gear having 40 teeth, a module of 2.54, and a face width of 6.35 mm (0.25 in.) show that the IQ gears grew approximately 0.05 mm (0.002 in.) more in the radial direction compared to oil-quenched gears (0.18 versus 0.13 mm, or 0.007 versus 0.005 in., respectively). The major reason for this is differences in stress states and their distributions during the IQ process and conventional oil quenching. In accordance with computer simulations and actual x-ray measurements, the magnitude of residual surface hoop stresses after IQ were approximately twice the value of hoop compression from oil quenching. While the parts after IQ may swell more, this distortion in part dimensional growth is predictable and repeatable, and it can be managed by adjusting the pre-heat green size of the part. The IQ process provides repeatable distortion because more uniform cooling fully eliminates the nonpredictable and nonuniform film boiling process. Unlike random, nonuniform distortion, predictable distortion is really only expected size change, and it is usually manageable for the part maker. Therefore, an adjustment of the part green sizes can address the predictable dimensional changes resulting from the IQ process.

Design of Production IQ Systems

Currently there are two general types of IQ equipment. The first one is designed for implementing the IQ-2 quenching processes (either for batch operations or for continuous operations). These batch IQ systems are similar to those used with conventional oil quenching or batch polymer water quenching methods. The second type of IQ system is designed for implementing single-part, high-velocity IQ-3 processes. The following three key elements of the IQ processes will dictate the design of the applicable IQ equipment:

- Intensive quenching uses highly agitated plain water or low-concentration water/mineral salt solutions as a quenchant.
- With any form of IQ, it is necessary to provide a proper high heat-extraction rate uniformly over the entire part surface area, to

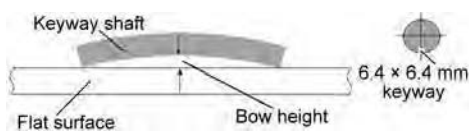


Fig. 14 Distortion of keyway shaft during intensive quenching and quenching in oil

Table 5 Keyway shaft distortion

Single-part oil quenching		Batch oil quenching		Single-part intensive quenching	
mm	in.	mm	in.	mm	in.
0.20–0.36	0.008 – 0.014	0.25–0.51	0.010–0.020	0.08–0.12	0.003–0.005

develop a uniform, strong martensitic shell and residual surface compressive stresses.

- It is necessary to interrupt IQ after a certain dwell time, the time when the current residual surface compressive stresses are at their maximum value and their optimum depth in the part.

In batch-type IQ systems, multiple parts are uniformly heated through to the austenitizing temperature, typically in a furnace in alloy baskets. For IQ, the baskets are transferred from the furnace hot zone to the IQ water quench tank. Any type of batch furnace (atmosphere, fluidized bed, or salt bath) can be used when implementing the IQ-2 process. The IQ tank can be separated from the furnace, or it can be a part of an integral quench furnace. Both of these designs are considered as follows.

Figure 15 shows an example of a production system with a stand-alone IQ water tank. The IQ system consists of an atmosphere furnace (on the left) having a work zone of 91 by 91 by 122 cm (36 by 36 by 48 in.) and an IQ water tank (on the right) of 22.7 m³ (6000 gal). A standard transfer cart is used to move the load from the furnace to the quench tank. Transfer-time considerations are no different than good conventional quenching practices; the parts should be uniformly austenitic when they enter the quench. The mild steel IQ tank is equipped with four propellers that are rotated by four 10 hp motors. Note that a similar oil quench tank would be equipped with only two propellers rotated by 5 hp motors. The IQ tank uses plain water with a low concentration of sodium nitrite salts as the quenchant. The quenchant flow velocity in the tank is approximately 1.5 to 1.6 m/s (5 to 5.2 ft/s)

as it passes over the parts. An air-cooling system maintains the quench water within the required temperature range. The maximum load mass per heat is approximately 900 kg (2000 lb).

Figure 16 presents a picture of a 91 by 91 by 183 cm (36 by 36 by 72 in.) production integral quench furnace equipped with a 39.7 m³ (10,500 gal) IQ water tank built by AFC-Holcroft Company of Wixom, Michigan, USA, and installed at the Euclid Heat Treating Co. of Cleveland, Ohio, USA. The IQ tank is equipped with four propellers that are rotated by four motors providing a total recirculation of approximately 5.67 m³/s (90,000 gal/min). The approximate velocity of the quenchant in the tank is 2 m/s (7 ft/s) past the parts. Internal directional vanes and baffles provide a uniform quenchant flow velocity through the workload. The quenching chamber is equipped with a unique lifting mechanism that provides accelerated vertical motion into and out of the quench tank. Minimizing this motion time is very important for accurately implementing the intensive cooling dwell time for IQ recipes.

The following major issues should be addressed when designing batch-type IQ systems:

- Provide a uniform water flow velocity distribution throughout the cross section of the quench tank working zone by installing a proper set of baffles at the bottom of the tank and straightening vanes in the propeller draft tubes. A variation of the water flow velocity through the quench tank work zone should be within approximately 10%.
- Provide a water flow velocity of at least 1.5 m/s (5 ft/s).

- To maintain the water temperature in the IQ tank not exceeding 25 °C (77 °F), the IQ water tank should be equipped with an air-cooling system or a chiller, or with a combined system including an air-cooling unit and a chiller.
- The propeller assembly should minimize air entrainment into the quench tank. (The presence of air bubbles in the water reduces the heat-extraction rate from the part being quenched and may affect the uniformity of cooling.)
- The propeller size and location (a depth under the water and a distance from the tank walls) and the parameters of the draft tubes should be selected to minimize the total system head resistance.

Continuous-Type IQ Systems. Figure 17 presents a sketch of an industrial continuous heat treating line using the IQ-2 quenching process (Ref 3, Chapter 10). The heat treating line includes the following major components: continuous furnace, quench tank equipped with a chute, pump, quenchant cooling system, variable-speed conveyer, washing unit, conveyer that moves the parts through the washing unit, and continuous tempering furnace equipped with its own conveyer.

In the first step of quenching, the parts are intensively cooled, first while falling through the chute and then while lying on the quench tank conveyor. The quench tank conveyor is of variable speed and moves the parts through the IQ tank to the second conveyor that is installed above the tank. During the subsequent cooling in air (while the parts are moving to the washing unit), the temperature of the parts equalizes through their cross



Fig. 15 Batch-type intensive quenching (IQ) system with stand-alone IQ water tank. Courtesy, Akron Steel Heat Treating Co.



Fig. 16 Integral quench atmosphere furnace equipped with intensive quenching water tank. Source: Reprinted from Ref 3 with permission of ASTM International

section, and a self-tempering process takes place, resulting in tempering a martensitic shell on the part. Then, the parts are intensively cooled again in the unheated washing chamber until they reach ambient temperature. Thus, the unheated washing chamber provides both the part cleaning (there is no oil to remove or skim from the washwater) and the final step of the IQ-2 process. After washing, the parts are transferred to the tempering furnace. The speeds of the quench tank conveyer and washing unit conveyer are varied and controlled in accordance with the part-specific IQ cooling recipes.

Single-Part-Processing IQ Systems. When performing the IQ-3 process, the parts are usually quenched one by one with very high-velocity water flow or jet impingement. Figure 18 presents the layout of a typical IQ system for single-part processing.

In practice, any through-heating source may be used—induction, atmosphere, and so on. The IQ-3 quench sequence is as follows. With the pump operating and the three-way valve in the bypass position, an austenitized part is placed in the lower section of the quench chamber. The air cylinders move the lower section up to the stationary upper section while locking and sealing the quench chamber in place. The three-way valve switches from the bypass to the quench position, and high-velocity water starts flowing through the quench chamber and over the austenitized part. When IQ is completed, the three-way valve switches back to the bypass position, and the water stops flowing through the quench chamber and again recirculates through the bypass line. The air cylinders open the quench chamber by moving the lower section down. The part is removed from the quench chamber lower section.

The major issue to be addressed when designing single-part quenching IQ-3 systems is to provide a high-velocity water flow uniformly around the entire part surface area. This is an especially difficult task when processing parts of complex geometry, which may cause the presence of stagnation zones at some areas of the part. The stagnation zones, in turn, may cause local film boiling, resulting in excessive part distortion. Computational fluid dynamic modeling is often required for designing an optimum quench chamber configuration in the case of complex-shaped parts processing (Ref 24).

Figure 19 presents a picture of a production high-velocity IQ system designed for processing helicopter gears. The IQ system is capable of also quenching shafts, rings, rollers, and other parts with maximum dimensions of 200 by 500 mm (8 by 20 in.) diameter. The IQ system is equipped with a water chiller for maintaining proper water temperature and an atmosphere box furnace for austenitizing the parts. The system is installed at the Euclid Heat Treating Co. of Cleveland, Ohio, USA. A similar production IQ system was developed for processing gun barrel steels and long shafts of

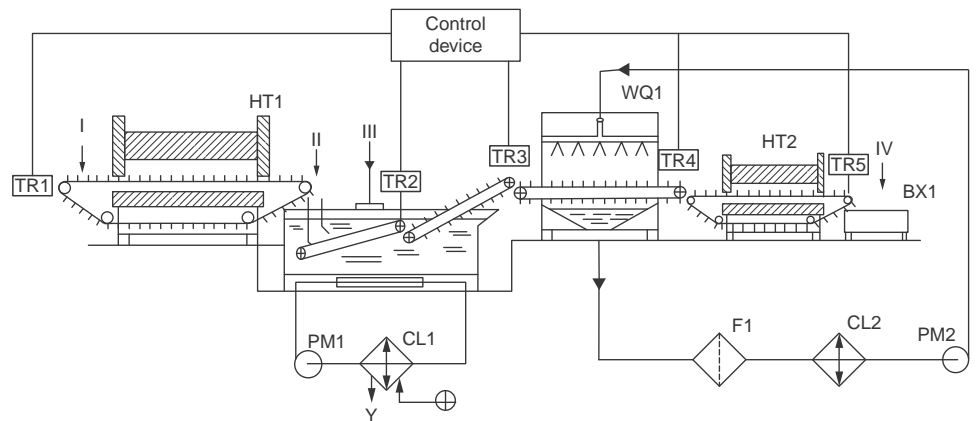


Fig. 17 Schematic of continuous-type intensive quenching system. I, loading point for steel parts onto the conveyor for heating in furnace HT1; II, chute with intensive cooling devices; III, quenching tank with two conveyers; IV, unloading point of steel parts from furnace HT2; TR1 to TR5, speed-control units for conveyor belts 1 to 5 operated by the control device; HT1 and HT2, furnaces 1 and 2; WQ1, washing and quenching device; PM1 and PM2, pumps 1 and 2; CL1 and CL2, chillers 1 and 2; F1, filter; BX1, container for heat treated parts. Source: Reprinted from Ref 3 with permission of ASTM International

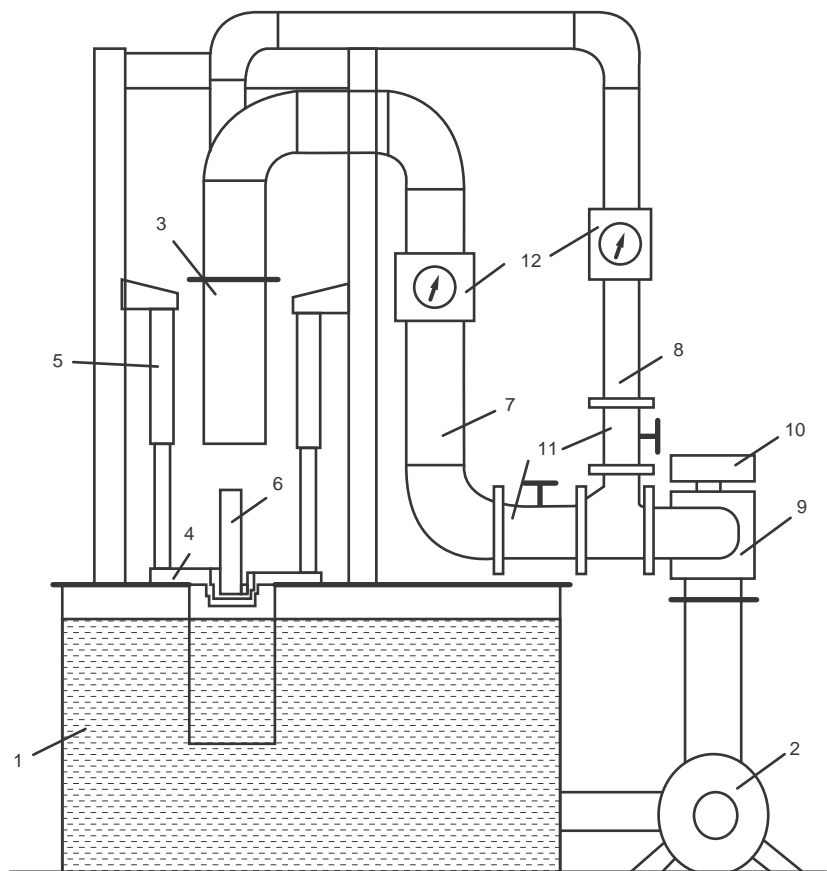


Fig. 18 Layout of typical single-part intensive quenching system. 1, water tank; 2, water pump; 3, stationary upper section of vertical quench chamber; 4, movable loading lower section of quench chamber; 5, air cylinders that move lower section up and down; 6, part to be quenched; 7 and 8, two of three water lines providing water flow through the quench chamber, and one bypass water line (not shown) used in idle conditions immediately before and after intensive quench dwell time of the part; 9, three-way valve providing water flow from the pump, either through the quench chamber or through the bypass line; 10, three-way valve actuator; 11, valves controlling water flow to quench chamber; 12, flow meters on water lines. Source: Reprinted from Ref 3 with permission of ASTM International

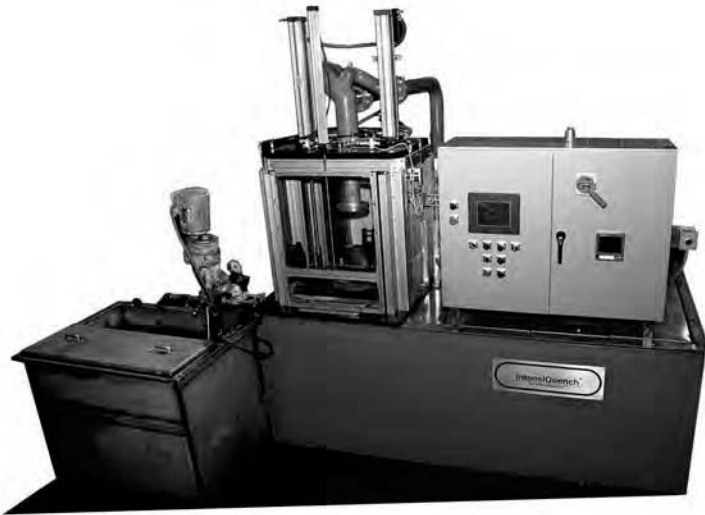


Fig. 19 Single-part production intensive quenching system for processing helicopter gears up to 200 by 480 mm (8 by 19 in.) diameter. Source: Ref 25

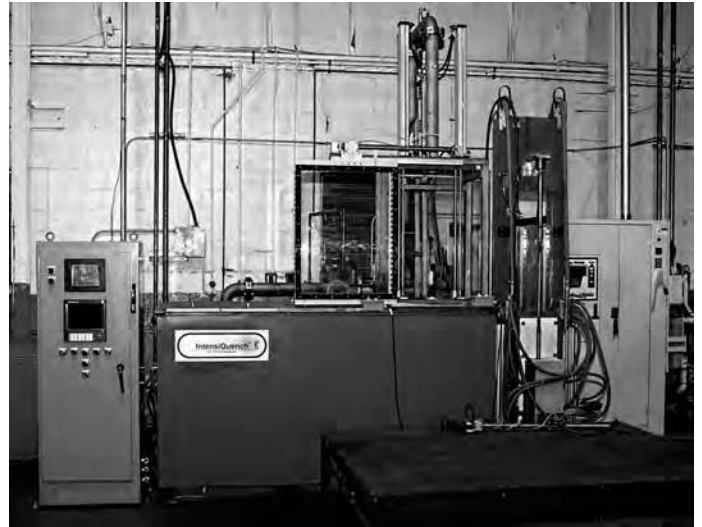








Fig. 20 Single-part production intensive quenching system for processing long shafts up to 50 mm (2 in.) diameter and 915 mm (36 in.) long. Source: Ref 25

Table 6 Practical applications of single-part intensive quenching process

Part	Improvement
 Automotive coil spring	Intensively quenched automotive coil springs made of 9259 and 9254 have longer fatigue life by 13 to 27% compared to the same springs quenched conventionally in oil, while intensively quenched lighter automotive coil springs have the same fatigue life as standard springs quenched in oil.
 Pulverizer coil spring	Intensively quenched pulverizer coil springs demonstrated 40% service life improvement in the field compared to the same springs quenched conventionally in oil.
 Output shaft	Heavy truck output shaft made of plain carbon 1040 steel and intensively quenched outperformed standard output shaft made of alloy 5140 steel and quenched in oil. Note that the use of plain carbon steel also provides material cost savings.
 Helicopter test gear	Intensively quenched helicopter test gears made of carburized Pyrowear-53 steel withstand 14% greater load for the same fatigue life as standard gears quenched in oil.
 Automotive side pinion	Automotive side pinion made of optimal-hardenability steel and quenched intensively demonstrated better fatigue performance compared to standard side pinion made of carburized 8620 steel and quenched in oil.
 Aluminum extrusion dies	Service life of intensively quenched aluminum extrusion dies made of hot work H-13 steel improves by at least 40%.

- Control of dwell time—the duration of each stage of the IQ process

In IQ-2 systems that are equipped with high-volume propellers, measurement of the revolutions per minute and amperage draw for each propeller ensures uniform and repeatable quenchant flow through the workload. In IQ-3 systems, control valves and flow meters, along with properly designed part-holding fixtures, are used to adjust and control the water flow uniformity and velocity around the part surfaces being quenched.

One of the most important control elements for IQ processes is the duration or timing of quench and quench-interruption steps. The accuracy of controlling this parameter depends on the repeatability of the conveyer speed or lifting mechanism speed when applying IQ-2 processes. Also, for batch processing with IQ-2, proper part spacing is necessary to prevent film boiling between parts in the load. For IQ-3 systems, proper application of the IQ recipe depends on the time required by a three-way valve to switch from a bypass position to a high-velocity flow position and back, as well as on the time required to close and open the quench chamber. Because the duration of quench and quench-interruption steps is typically measured in seconds, all facets of the quench should be automated.

Practical Applications of IQ Processes

Over the years, the IQ processes were proved for a number of different steel products (automotive parts, forgings, castings, railroad equipment components, tool products, fasteners, etc.). Tables 6 and 7 show some examples of steel parts and the actual benefits obtained by applying batch-type or single-part IQ methods (Ref 4, 11, 12, 13–15, 17–20).







up to 50 by 910 mm (2.0 by 36 in.) diameter (Fig. 20). This system is equipped with an induction heating unit for austenitizing the parts prior to IQ.

Control and Automation Requirements. To run IQ processes successfully and to provide

process repeatability, the following parameters should be controlled:

- Water or water/salt solution flow velocity and temperature
- Water/salt solution concentration

Table 7 Practical applications of batch-type intensive quenching process

Part	Improvement	
	Automotive ball studs	Ball studs made of plain carbon 1040 and 1045 steels and intensively quenched have the same fatigue life as standard ball studs made of alloy 4140 steel and quenched in oil.
	Automotive universal joint crosses	Universal joint crosses made of plain carbon 1018 steel and intensively quenched have the same or better performance characteristics as standard crosses made of alloy 5120 steel and quenched in oil. Note that the carburization cycle for the intensively quenched crosses was reduced by 15% compared to the standard cycle, resulting in process cost reduction as well.
	Cold work punches	Service life of intensively quenched cold work punches made of S5 steel improves by at least 2 times.
	Castings	Castings made of 8630 steel demonstrated the same or better mechanical properties as the same forged and oil-quenched parts.
	Steel mill rolls	Steel mill rolls made of ductile iron and intensively quenched have greater service life compared to the same rolls quenched in oil.
	Forged rings	Forged rings made of 1045 steel and intensively quenched have less distortion compared to the same rings quenched in oil.

One of the major limitations for applying IQ processes is part dimension and shape. Part thickness should be adequate for developing a required temperature gradient throughout the part, necessary for formation of the high current and residual surface compressive stresses. A minimum permissible part thickness depends on the part shape as well as on the type of steel; steels of less hardenability and carburized grades of steel allow for less part thickness. Based on the results of numerous IQ process studies, the IQ method, in general, is not recommended for parts with thickness of less than 10 mm (0.4 in.). The IQ process is not applicable to parts with great thickness variation, because it is practically impossible to assign a cooling time suitable for all part sections. (The thin sections of the part could be cooled completely prior to quench interruption, resulting in excessive part distortion or even cracking.)

In summary, IQ processes have been shown to increase part hardness and strength, while at the same time providing the same or better material toughness versus traditional quenching methods on typical products made of various steel types. Manufacturers of steel parts can improve their product quality and reduce their costs by using the IQ processes. Some of the

proven advantages of intensive water quenching include:

- Higher surface hardness and core toughness with a greater hardened layer depth for parts made of carburized and noncarburized grades of steel
- Reduction of the carburization cycle for the same ECD (compared to oil quenching), resulting in the significant reduction of heat treatment processing costs and an increase of heat treating equipment production rate
- Improved part microstructure (finer grain and superstrengthened martensite)
- Greater and deeper residual surface compressive stresses
- Improved material strength and toughness (superstrengthening of steel)
- Substitution of lower-alloy steels for a reduction in part costs, yet no penalty to part strength or part performance
- Possibility of making high-power density parts—lighter parts with the same or better performance characteristics and fatigue life as oil-quenched parts due to the strengthening of the material and high residual surface compressive stresses provided by the IQ process
- Less part distortion and no part cracking

- Full elimination of quench oil and associated costs (cost of quench oil, part washing, etc.), resulting in a significant reduction of the heat treatment process cost and an improved environment
- Possibility of moving heat treatment operations into the manufacturing cell for rapid, part-by-part heat treating, because the intensive water-quenching method is an environmentally friendly process

REFERENCES

1. N.I. Kobasko and N.I. Prokhorenko, Quenching Cooling Rate Effect on Crack Formation of 45 Steel, *Metalloved. Term. Obrab. Met.*, No. 2, 1964, p 53–54 (in Russian)
2. M.A. Aronov, N.I. Kobasko, J.A. Powell, et al., “Practical Application of Intensive Quenching Technology for Steel Parts and Real Time Quench Tank Mapping,” Proceedings of 19th ASM Heat Treating Society Conference (Cincinnati, OH), 1999
3. N.I. Kobasko, M.A. Aronov, J.A. Powell, and G.E. Totten, *Intensive Quenching Systems: Engineering and Design*, ASTM International, 2010
4. M.A. Aronov, N.I. Kobasko, and J.A. Powell, “Application of Intensive Quenching Methods for Steel Parts,” Proceedings of the 21st ASM Heat Treating Conference (Indianapolis, IN), 2001
5. N.I. Kobasko, *Steel Quenching in Liquid Media under Pressure*, Naukova Dumka, Kiev, 1980 (in Russian)
6. L.L. Ferguson, private communication, Aug 2012
7. “Predictive Model and Methodology for Heat Treatment Distortion,” NCMS Report 0383RE97, National Center for Manufacturing Sciences, Ann Arbor, MI, Sept 30, 1997
8. W.M. Rohsenow, J.P. Harnett, and Y.C. Cho, *Handbook of Heat Transfer*, 3rd ed., McGraw-Hill Handbooks, 1998
9. M.P. Muhina, N.I. Kobasko, and L.V. Gordejewa, Hardening of Structural Steels in Chloride Quench Media, *Metalloved. Term. Obrab. Met.*, Sept 1989, p 32–36 (in Russian)
10. M.A. Aronov, N.I. Kobasko, J.F. Wallace, and D. Schwam, “Experimental Validation of the Intensive Quenching Technology for Steel Parts,” Proceedings of the 18th ASM Heat Treating Conference (Chicago, IL), 1998
11. M.A. Aronov, N.I. Kobasko, J.A. Powell, J.F. Wallace, and D. Schwam, “Experimental Study of Intensive Quenching of Punches,” Proceedings of 19th ASM Heat Treating Society Conference (Cincinnati, OH), 1999
12. M.A. Aronov, N.I. Kobasko, and J.A. Powell, “Practical Application of Intensive Quenching Process for Steel

- Parts,” Proceedings of the 20th ASM Heat Treating Conference (St. Louis, MO), 2000
13. M.A. Aronov, N.I. Kobasko, and J.A. Powell, “Basic Principles and Metallurgy of Intensive Quenching Methods,” Proceedings of the 13th IFHTSE Congress (Columbus, OH), 2002
 14. M.A. Aronov, N.I. Kobasko, and J.A. Powell, “Intensive Quenching Technology for Tool Steels,” Proceedings of the 13th IFHTSE Congress (Columbus, OH), 2002
 15. M.A. Aronov, N.I. Kobasko, J.A. Powell, P. Ghorpade, and D. Gopal, “Application of Intensive Quenching Processes for Carburized Parts,” Proceedings of 22nd ASM Heat Treating Conference (Indianapolis, IN), 2003
 16. M.A. Aronov, N.I. Kobasko, J.A. Powell, J.F. Wallace, and Y. Zhu, “Effect of Intensive Quenching on Mechanical Properties of Carbon and Alloy Steels,” Proceedings of the 23rd ASM Heat Treating Conference (Pittsburgh, PA), 2005
 17. A.M. Freborg, Z. Li, B.L. Ferguson, and D. Schwam, “Bending Fatigue Strength Improvement of Carburized Aerospace Gears,” Proceedings of the 23rd ASM Heat Treating Conference (Pittsburgh, PA), 2005
 18. C.R. Hubbard, F. Tang, M.A. Aronov, N.I. Kobasko, et al., “Effect of Intensive Quenching on Residual Stress,” Proceedings of 23rd ASM Heat Treating Conference (Pittsburgh, PA), 2005
 19. M.A. Aronov, N.I. Kobasko, J.A. Powell, and P. Ghorpade, “Demonstrations of Intensive Quenching Methods for Steel Parts,” Proceedings of 24th ASM Heat Treating Conference (Detroit, MI), 2007
 20. B.L. Ferguson, A.M. Freborg, and Z. Li, “Improving Gear Performance by Intensive Quenching,” Proceedings of 24th ASM Heat Treating Conference (Detroit, MI), 2007
 21. N.I. Kobasko, “Effect of Structural and Thermal Stresses on Crack Formation during Steel Quenching,” Proceedings of All-Union Conference on Increase of Productivity and Profitability of Heating Furnaces (Dnepropetrovsk, Ukraine), 1967
 22. B.L. Ferguson and A.M. Freborg, “Use of Computer Simulation in Optimizing Intensive Quenching Process,” Proceedings of the 2002 IFHTSE Congress (Columbus, OH), 2002
 23. B.L. Ferguson, A.M. Freborg, and Z. Li, “Residual Stress and Heat Treatment—Process Design for Bending Fatigue Strength Improvement of Carburized Aerospace Gears,” European Conference on Heat Treatment (Berlin), 2007
 24. A. Banka, J. Franklin, B.L. Ferguson, Z. Li, and M. Aronov, “Applying CFD to Characterize Gear Response during Intensive Quenching Process,” Proceedings of 24th ASM Heat Treating Conference (Detroit, MI), 2007
 25. M.A. Aronov, N. I. Kobasko, J.A. Powell, and P. Sampson, Intensive Quenching Process Commercialization, *Ind. Heat. J.*, Oct 2012

Inverse Hardening*

B. Liščić, University of Zagreb
George E. Totten, Portland State University

INVERSE HARDENING is a term first coined in 1978 by Shimizu and Tamura (Ref 1) after studying the hardness distribution in round bars, whereby the hardness profile produced by delayed quenching is higher in the center of the bar than it is at the surface. In 1977, Loria showed that in some instances delayed quenching can increase the depth of hardening (Ref 2). Subsequently, in that same year, Shimizu and Tamura explained that the phenomenon is caused by a discontinuous change in cooling rate during quenching, such that the effect depends on the duration of the incubation time preceding the abrupt change in cooling rate (Ref 1, 3). Since then, experimental work by Liščić and Totten (Ref 4) and numerical calculations by Chen and Zhou (Ref 5) showed that the average cooling rate during delayed quenching can be higher below the surface of the workpiece than at the surface itself.

The results of these investigations made it clear that the heat-extraction dynamics during quenching, and not just the cooling time, are responsible for the hardness distribution in the quenched part. Unlike the conventional distribution, the hardness profile produced by delayed quenching is higher in the center of the bar than it is at the surface. In conventional quenching, with no discontinuous change in cooling rate, the cooling rate decreases constantly from the surface of the workpiece toward the center. In delayed quenching, the cooling rate is lower at the surface, because of relatively slow or mild cooling at the beginning of the quench, and becomes greater below the surface and toward the center, because of the subsequent abrupt, discontinuous change in heat transfer at the workpiece surface.

Heat-Extraction Dynamics

To produce inverse hardening, a steel of adequate hardenability, a workpiece of sufficiently large cross section, an appropriate cooling

medium, and the right quenching conditions are needed. If these conditions are met, this controllable delayed quenching has great potential for increasing the depth of hardening, compared with conventional quenching practice. Chen and Zhou also state that delayed quenching can reduce residual stresses and distortion (Ref 5). Liščić, Grubisic, and Totten have shown that the technique can be used to enhance resistance to both bending fatigue and impact (Ref 6).

Among the liquid quenchants, only solutions of poly(alkylene glycol) (PAG) copolymer can be tailored or preprogrammed for controllable delayed quenching. The concentration of the polymer is raised to a higher-than-normal level, because control of heat transfer is best achieved with a PAG solution of sufficiently high concentration. This provides a thicker film on the workpiece surface, thus extending the vapor-blanket stage of cooling, resulting in delayed quenching. Other important variables that must be properly controlled are bath temperature and agitation rate. Heat-transfer dynamics can also be controlled in gas-quenching applications (especially in vacuum furnaces using pressurized, high-velocity gases). Compared with liquid quenching, more time is available during cooling to adjust gas pressure and velocity, the primary cooling variables.

Since its discovery in the 1970s, the phenomenon of delayed quenching is only more recently considered for use in real-world applications for two reasons:

- Until recently, there has been no adequate way to test for and record the quenching intensity information that is required to describe the heat-extraction dynamics of real quenching processes. Neither the magnetic quenchemeter method nor cooling curve analysis of small-diameter (12.5 mm in diameter by 60 mm long) nickel alloy or silver specimens can be used for this purpose.

- Only recently has it been revealed that higher-concentration PAG solutions can be used for preprogrammed controllable delayed quenching (Ref 7).

Computer simulation software is needed to first determine whether a workpiece of specific cross section, made of a steel of specific hardenability, is suitable for quenching using controlled heat-extraction dynamics, and, if found suitable, to then optimize the relevant quenching parameters. Also required is a method for measuring and recording the heat-extraction dynamics of different quenchants—in production environments—to obtain relevant values of the heat-transfer coefficient.

Quench Analysis. The need for a way to measure quenching intensity has been met by the newly developed Temperature Gradient Quenching Analysis System (TGQAS). It can measure, record, and evaluate all quenching processes in common use, describing their heat-extraction dynamics by corresponding thermodynamic functions. The system uses the Liščić/Nanmac probe (Ref 8), which measures and records cooling at various positions in an actual part. The probe measures 50 mm in diameter by 200 mm long and is made of AISI type 304 stainless steel. It is instrumented with three thermocouples at its midlength cross section, which measure temperature at the surface, 1.5 mm below the surface, and in the center.

Typical TGQAS test data are shown in Fig. 1 for two quenchants: mineral oil at 20 °C bath temperature without agitation, and a 25% solution of PAG copolymer (UCON Quenchant E, Union Carbide Corporation) at 40 °C and 0.8 m/s agitation rate. Cooling curves are shown in Fig. 1, top, while calculated heat-flux density (Q , in W/m^2) versus time curves between different thermocouple positions are plotted in Fig. 1, bottom.

The most important characteristic of the heat-flux density data with regard to heat-extraction dynamics is the time from probe

* Adapted from B. Liščić and G. Totten, Benefits of Delayed Quenching, *Advanced Materials and Processes*, Sept 1997, p 180–184; and B. Liščić and G. Totten, Controllable Delayed Quenching, *Heat Treating: Equipment and Processes—1994 Conference Proceedings*, ASM International, p 253–262

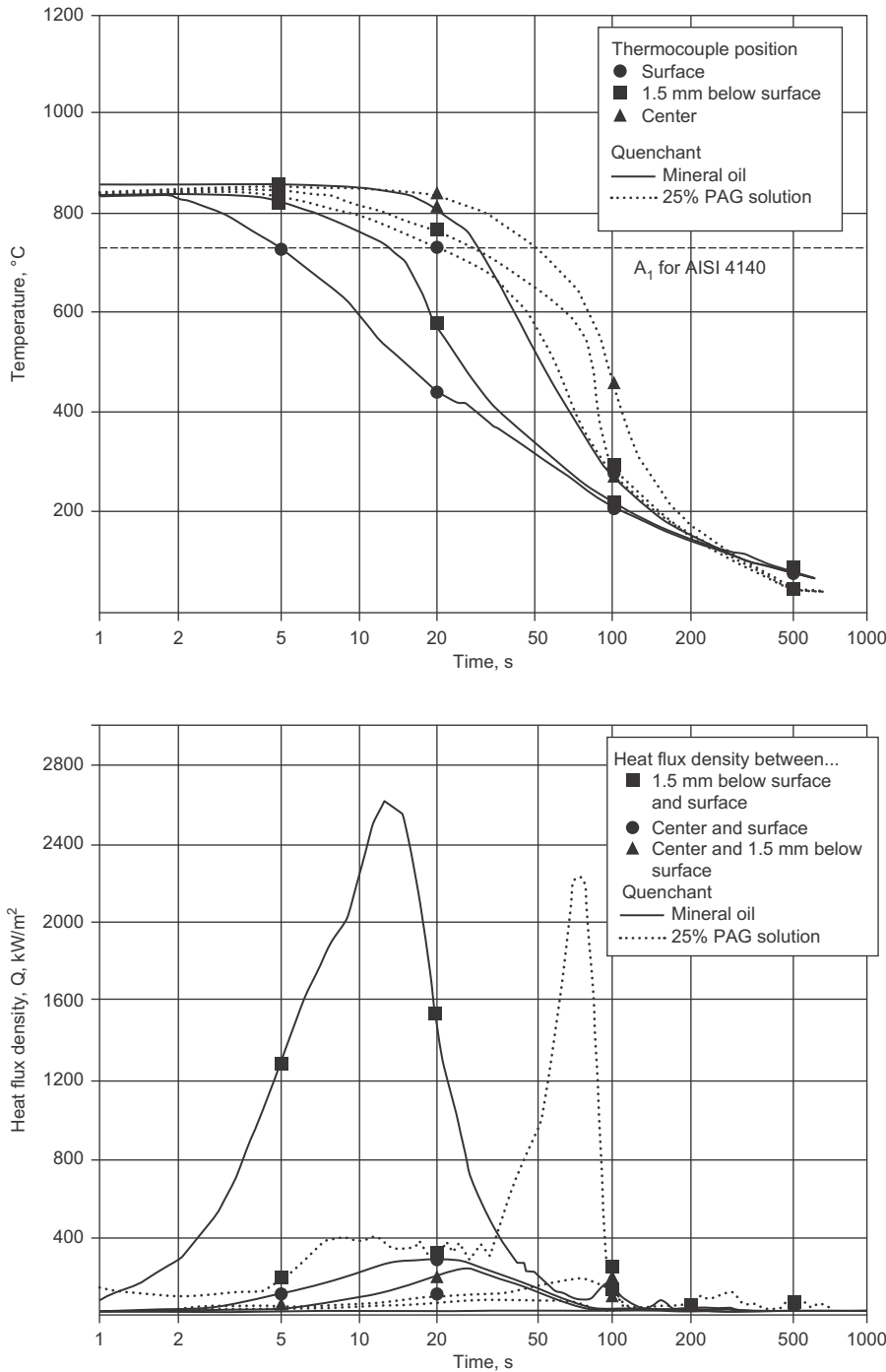


Fig. 1 Results of quenching tests using the Temperature Gradient Quenching Analysis System method and the Liščić/Nanmac probe. Quenchants are mineral oil at 20 °C without agitation and 25% poly(alkylene glycol) (PAG) copolymer solution at 40 °C and 0.8 m/s agitation rate. Top: cooling curves. Bottom: heat-flux density, Q , versus time. The polymer solution provides delayed quenching (compare the times to maximum Q).

immersion to the time where maximum heat-flux density (t_{Qmax}) occurs. The value of t_{Qmax} for the mineral oil is 14 s, whereas that for the PAG solution is 72 s. The PAG test provides an example of delayed quenching.

Because heat-flux density is the real measure of heat extraction, it is interesting to compare

the “between 1.5 mm below surface and surface” curves for both quenchants (Fig. 1, bottom). For oil quenching, only 12.5 s were needed to increase Q from 200 kW/m² to its maximum of 2600 kW/m², while 35 s were required for Q to drop back to 200 kW/m². For polymer quenching, 67 s—5.4 times more

time—were necessary to raise Q from 200 kW/m² to its maximum of 2250 kW/m², but only 23 s—1.5 times less time—were required for Q to return to 200 kW/m².

These data clearly show the distinct difference in heat-extraction dynamics between the two quenching processes. The oil quench is characterized by rapid cooling from the beginning, while the polymer quench is characterized by a long period of relatively slow cooling followed by a sudden rise in heat extraction, which occurs after the polymer film bursts. This reflects a pronounced discontinuous change in cooling rate, which has a specific influence on the transformation behavior of the steel being quenched.

Cooling rate versus surface temperature curves for the three thermocouples of the probe are shown in Fig. 2 for the mineral oil (top) and 25% PAG solution (bottom). Note that the maximum cooling rate for the polymer quenchant occurs at 1.5 mm below the surface of the probe. Now, refer back to the PAG solution cooling curve for the thermocouple at 1.5 mm below the surface (Fig. 1, top). Note the distinct change in the slope of this curve at 570 °C, which reflects the discontinuous change in cooling rate.

Temperature Fields Displayed. Using the heat-transfer coefficient versus time values calculated from the measured temperatures at the midlength cross section of the Liščić/Nanmac probe, a two-dimensional heat-transfer computer program was developed for calculating temperature fields during quenching. This program can be used to produce graphical representations of the heat-extraction dynamics during quenching. Examples for a stainless steel specimen (50 mm in diameter by 200 mm long) at 16, 42, 88, and 120 s after immersion are shown in Fig. 3 for the mineral oil (top) and 25% PAG solution (bottom). The graphics dramatize the pronounced difference in heat-extraction dynamics between the two quenchants.

It should be emphasized that for transformation kinetics, it is the cooling rates below A_1 that are critical and not those from the austenitizing temperature to A_1 . For AISI 4140 steel, for example, the A_1 temperature is 730 °C. An analysis of the average radial temperature gradients between center and surface in half-length cross sections from Fig. 3 gives the values shown in Table 1. The following information can be extracted from these values and the calculated temperature fields (Fig. 3):

- *Conventional quenching with continuous cooling rates (mineral oil test):* Cooling of the center of the specimen within the critical temperature range (700 to 400 °C) between 42 and 88 s occurs with a decreasing temperature gradient, that is, decreasing heat-extraction flux from the center to the surface. Once the surface temperature has fallen to a low value (approximately 200 °C, after 88 s), heat transfer has essentially

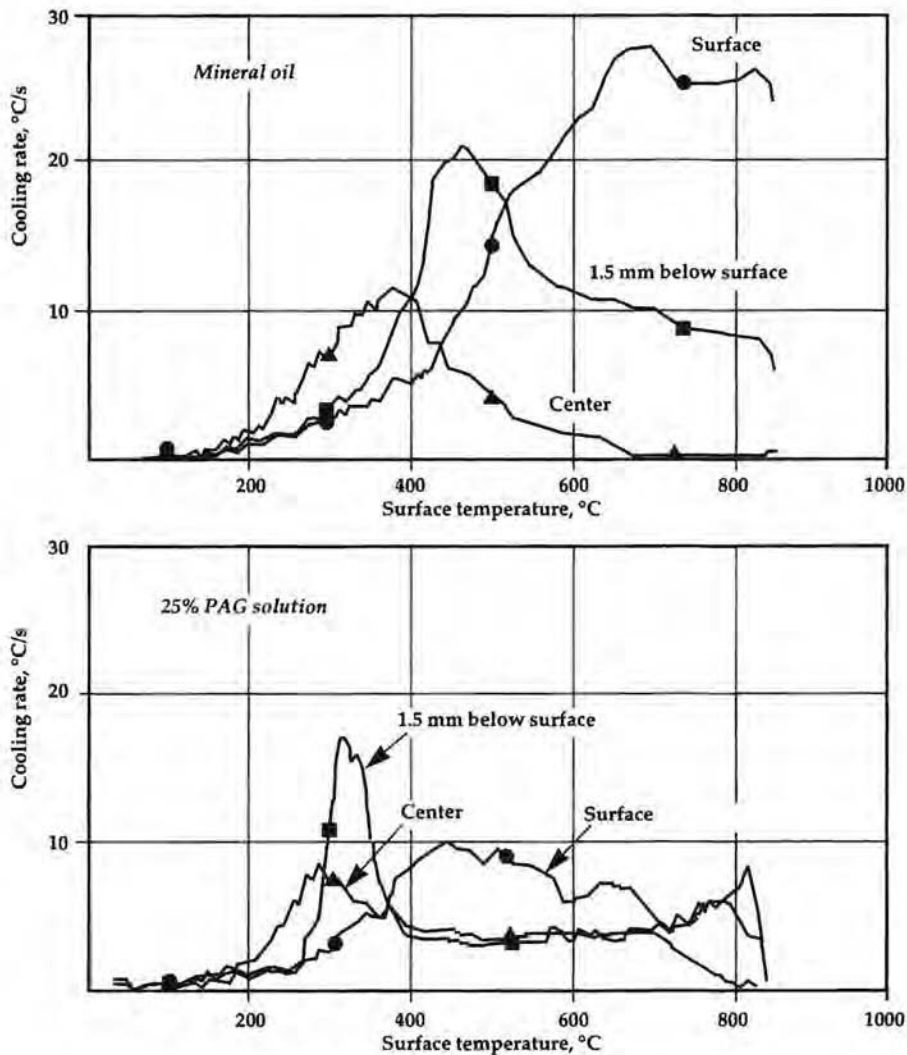


Fig. 2 Cooling rate versus surface temperature curves for quenching the Liščić/Nanmac probe in mineral oil at 20 °C without agitation (top) and 25% poly(alkylene glycol) (PAG) solution at 40 °C and 0.8 m/s agitation rate (bottom)

ceased because of the small temperature difference between the workpiece surface and the surrounding quenchant. These heat-extraction dynamics result in a normal hardness distribution: the hardness in the center is substantially lower than it is at the surface.

- *Delayed quenching with discontinuous change in cooling rate (25% PAG solution test):* Cooling of the center of the specimen within the critical temperature range (750 to 600 °C) between 42 and 88 s occurs with an increasing temperature gradient, that is, increasing heat-extraction flux from the center to the surface. The result is an increase in hardness at the center to a value above that at the surface, or inverse hardening.

Metallurgical Aspects

Two different processes are initiated at the moment the austenitized workpiece is immersed in the quenchant: heat extraction (a thermodynamic process) and microstructural transformation (a metallurgical process). Microstructural transformation actually begins at different times for each point along the radius of the cross section, when the temperature at each point drops to the A_1 temperature. The time depends on the cross-sectional size and the cooling intensity of the quenchant. The resulting hardness at a particular point depends on the constituents of the transformed microstructure, which, in turn, depend heavily on the steel hardenability, that is, on the incubation time at each isotherm. Because incubation times are counted only at

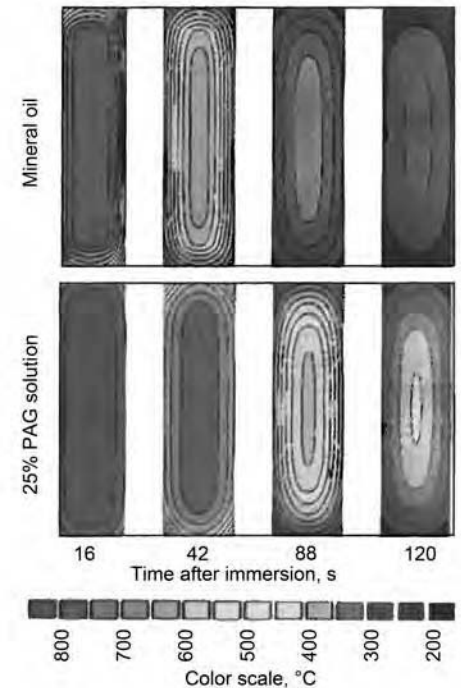


Fig. 3 Heat-extraction dynamics represented by computer simulations of temperature fields during quenching of stainless steel specimens. The two-dimensional simulations are based on heat-transfer coefficients obtained using the Liščić/Nanmac probe (calculation program by B. Smoljan; graphical interpretation program by J. Galinec). PAG, poly(alkylene glycol).

Table 1 Average temperature gradient between specimen center and surface

Immersion time, s	Average temperature gradient(a), °C/mm	
	Mineral oil	25% PAG solution(b)
16	10	2
42	12	4
88	6	10
120	4	6

(a) Half-length cross section, specimens of 25 mm radius, austenitized at 850 °C. (b) PAG, poly(alkylene glycol)

temperatures below A_1 for each point on the cross section, the cooling rate in the critical temperature range (A_1 to M_s) is of paramount importance.

Shimizu and Tamura found that the pearlitic transformation during quenching with a discontinuous change of cooling rate is different from that predicted by the conventional continuous cooling transformation (CCT) diagram, and that this transformation is related to the length of the incubation period preceding the change in cooling rate. In delayed quenching, some of the incubation period is used up at the surface of the workpiece, while none is expended at the center.

Delayed quenching is shown schematically in Fig. 4(a). The total incubation period at any

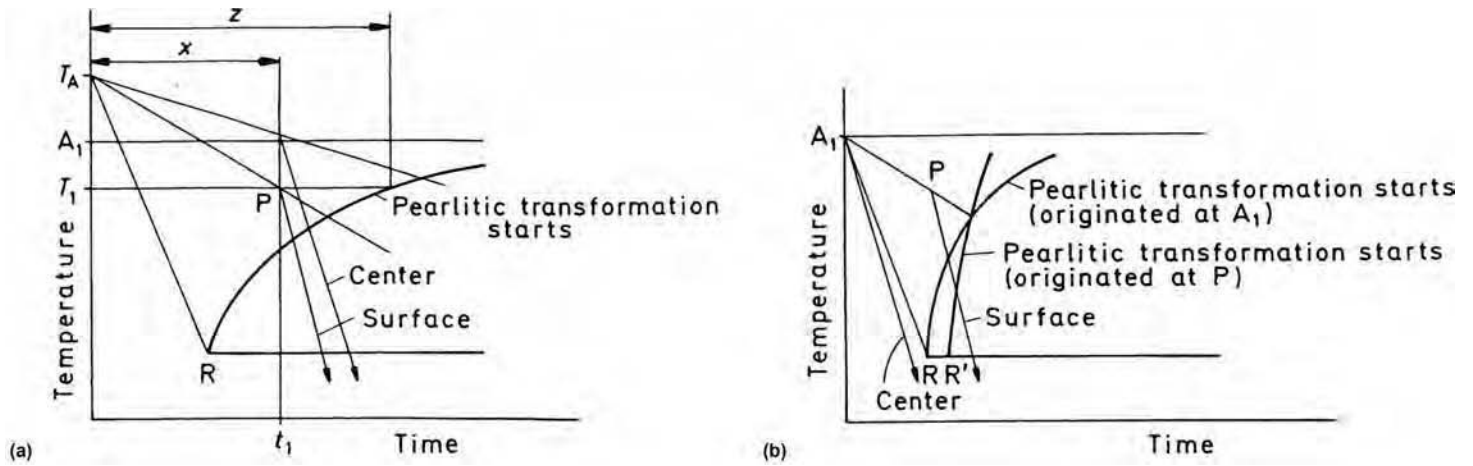


Fig. 4 Schematic of how delayed quenching causes inverse hardening. Source: Ref 3

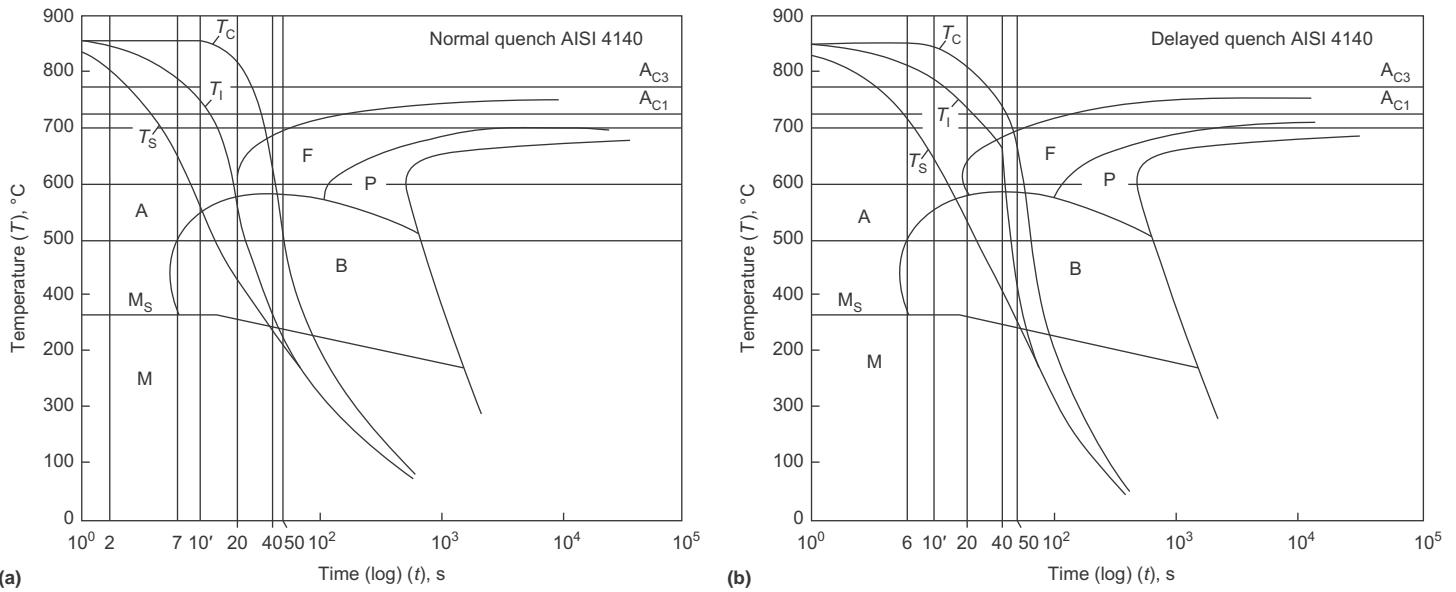


Fig. 5 Measured cooling curves superimposed on the continuous cooling transformation diagram of AISI 4140. (a) Normal quench. (b) Delayed quench. T_s , surface temperature; T_1 , temperature 1.5 mm below surface; T_c , temperature in the center

given isotherm is z , the time until the transformation starts, while x is the incubation period before the discontinuous change of cooling rate.

A discontinuous change of cooling rate has occurred at point P —time t_1 and temperature T_1 . Up to this moment, the surface of the workpiece had consumed a portion (x) of the total incubation time (z), but the center had not, because at t_1 , its temperature was still above A_1 .

Further cooling below point P proceeds at a substantially higher rate, modifying the transformation start curve, as shown in Fig. 4(b). Because none of the incubation time has been consumed at the center, the cooling curve for the center begins at the A_1 temperature—at zero time. The cooling curve for the center now does not intersect the pearlite phase field.

A center hardness higher than that of the surface is the result.

Average Cooling Rates A_1 to 500 °C within Subsurface Region. The dynamics of heat extraction during quenching and the resulting hardness at different points of the cross section lead to the conclusion that the actual cooling rates between A_1 and 500 °C at different distances from the surface play the most important role. In case of delayed quenching including a discontinuous change of cooling rate, the heat-extraction dynamics at different points are different from normal quenching.

To explain this, consider normal quenching and delayed quenching of 4140 steel, as illustrated in Fig. 5 and 6. Measured cooling curves are illustrated in Fig. 5, superimposed on the

4140 CCT diagram, for the following two quench conditions:

- Normal quench when the probe was quenched in 20 °C mineral oil without agitation
- Delayed quench when the probe was quenched in a 40 °C bath of polymer solution with 15% concentration and an agitation of 0.8 m/s

In Fig. 5, the measured cooling curves T_s for the very surface, T_1 for the point 1.5 mm below the surface, and T_c for the center of the 50 mm diameter probe have been superimposed on the CCT diagram of AISI 4140 steel. Relevant temperature fields have been plotted in Fig. 6(a) and (b) for different times during quenching onto the longitudinal cross section of the probe, based on values measured in three points

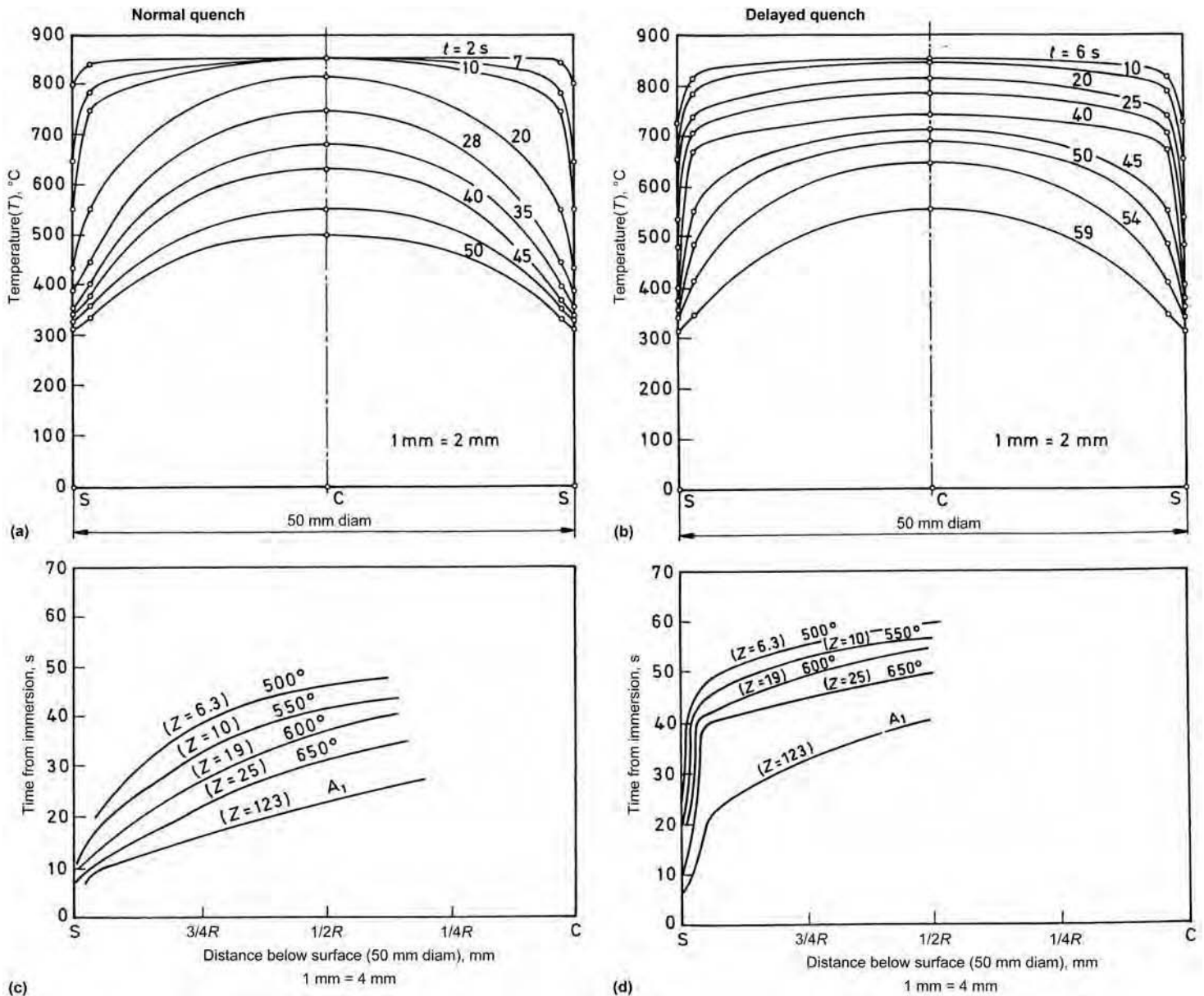


Fig. 6 Temperature distribution curves inside a 50 mm diameter cylinder derived from (a) normal quench and (b) delayed quench. Time-temperature relations in different points below the surface of a 50 mm diameter cylinder, derived from top figures: (c) normal quench and (d) delayed quench. Z , incubation period (in seconds)

mentioned for normal and delayed quenching, respectively. By intersecting the curves in this diagram with vertical lines for different distances from the surface, one can derive the respective diagrams shown in Fig. 6(c) and (d).

Figures 6(c) and (d) correlate times after immersion with curves of equal temperature (isotherms) for different distances below the surface. From the diagram in Fig. 6(c), one can read off, for example, that points at $\frac{3}{4}$ radius cool down to A_1 in 16 s and need 23 s more to cool to 500 °C, reaching it in 39 s after immersion. The incubation time for every isotherm (Z) is also given.

Comparing the diagrams in Fig. 6, one can notice the difference in temperature fields as well as the difference in times after immersion to cool down to equal isotherms for different distances below the surface. Taking the isotherms for $A_1 = 727$ °C and for 500 °C from diagrams in Fig. 6(c) and (d), it is possible to calculate the average cooling rate for this temperature range ($A_1 - 500$ °C = 227 °C) at different points from the surface up to $\frac{1}{2}$ radius. Figure 7 shows the result of such calculations. It shows a most interesting comparison of the heat-extraction dynamics between normal and delayed quenching.

In the mentioned case of normal quenching in oil, the average cooling rate in the critical temperature range A_1 to 500 °C, being high at the surface, *decreases* up to $\frac{3}{4}R$ for approximately 50%, while in the specified case of delayed quenching, this average cooling rate, being low at the surface, *increases* gradually up to $\frac{1}{2}R$. These experimentally obtained results contribute to the understanding of inverse hardness distribution as a consequence of delayed quenching.

Obviously, a controlled delay in quenching can substantially increase the depth of hardening. In this respect, a controllable delayed quenching technique has the potential to substitute for lower

hardenability of the steel in achieving a greater depth of hardening. In any case, the effect of delayed quenching on hardness distribution is closely connected with the hardenability of the steel and the cross-sectional size of the workpiece.

Quenchants Enabling Controllable Delayed Quenching

For quenching of single workpieces, the spray quenching technique lends itself to controllable delayed quenching because the start of spraying can be preprogrammed. For immersion quenching of a batch of workpieces, PAG solutions of high concentration

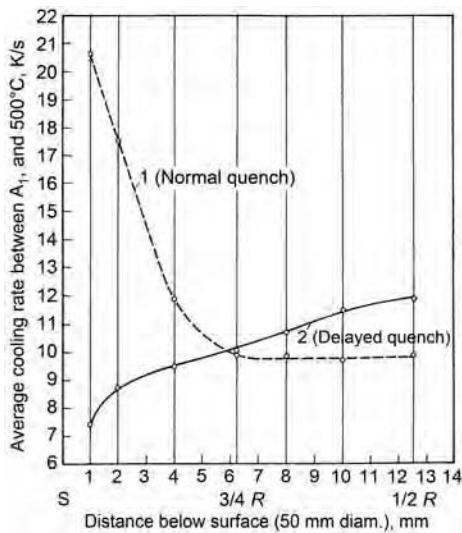


Fig. 7 Average cooling rates between A₁ and 500 °C versus distance below the surface of a 50 mm diameter cylinder. Quenching conditions: 1) oil, 20 °C, without agitation; 2) UCON-E, 15% concentration, 40 °C bath temperature, 0.8 m/s agitation rate. Source: Ref 4

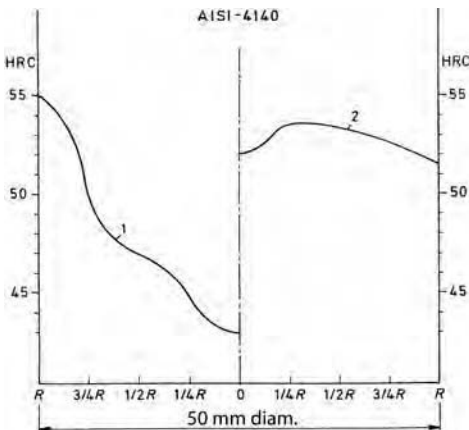


Fig. 8 Normal hardness distribution (1) after quenching in oil at 20 °C without agitation. Inverse hardness distribution (2) after quenching in UCON-E of 25% concentration, 40 °C bath temperature, and 0.8 m/s agitation rate. Source: Ref 6

are the only quenching media that, by changing the polymer concentration in the solution, enable a predetermined and controllable delay in quenching, uniformly for all parts in the batch.

The quenchant used was an aqueous solution of UCON-E, formulated with a proprietary PAG copolymer of ethylene oxide and propylene oxide (Ref 9). This polymer is a block copolymer that was developed to include the well-known process advantages of the more commonly available random PAG copolymers (Ref 10) and also to exhibit more uniform surface coverage throughout the quenching process.

When hot metal is immersed into an aqueous solution containing any polymer, a vapor blanket is formed due to the immediate volatilization of water at the hot metal interface (Ref 11). This vapor blanket is encapsulated by a polymer film. For PAG quenchants, this film is fluid and mobile. Heat transfer from the hot metal is slow during this stage because it must occur through a gas and must have the energy to rupture the film. Upon continued cooling, the encapsulated vapor ruptures the fluid film and the water escapes, with heat transfer occurring by nucleate boiling.

Higher polymer concentrations in an aqueous solution produce thicker films. As the film thickness increases, the film becomes more insulating, leading to slower heat transfer in the first period of quenching. The heat-transfer properties of this polymer film are also affected by the film strength at the hot metal interface (film strength increases with polymer molecular weight) and the viscosity of the hydrated polymer at the interface throughout the quenching process. Heat transfer is inversely proportional to the viscosity of the quenchant at the hot metal interface.

When the energy of the heat in the vapor blanket stage is sufficient to rupture the hydrated film, the heat transfer at the surface suddenly accelerates. This is the

point when a discontinuous change of cooling rate occurs. With higher polymer concentration and thicker film, the time to rupture this film is longer, providing a controllable parameter (in addition to the bath temperature and agitation rate) for delayed quenching.

Properties

Inverse hardening results in higher core hardness than the surface, when a predetermined change of heat transfer on the workpiece surface results in heat extraction primarily from the core. The increase in depth of hardening depends on steel hardenability and section size. This offers the ability to influence the hardness distribution and properties by control of heat transfer.

Hardness Distribution. The left curve in Fig. 8 is the normal hardness distribution in the cross section of a 50 mm diameter bar of AISI 4140 after quenching in unagitated mineral oil at a bath temperature of 20 °C. The curve at right is the inverse hardness distribution measured after quenching a bar of the same steel in 25% PAG solution at 40 °C bath temperature and 0.8 m/s agitation rate. Note how delayed quenching significantly increased the depth of hardening.

Low-alloy steels such as 4140 are used in the hardened and tempered condition. Normal and inverse hardness distribution curves for 50 mm diameter bars of 4140 tempered for 2 h at 480 °C are shown in Fig. 9. Tempering did not affect the shape of the normal hardness distribution curve; however, the curve for the inverse-hardened steel is now essentially uniform (flat) over the entire cross section. This is an example of the rule of thumb that during tempering, higher hardness values decrease more than lower hardness values. The ~6 HRC greater hardness in the center

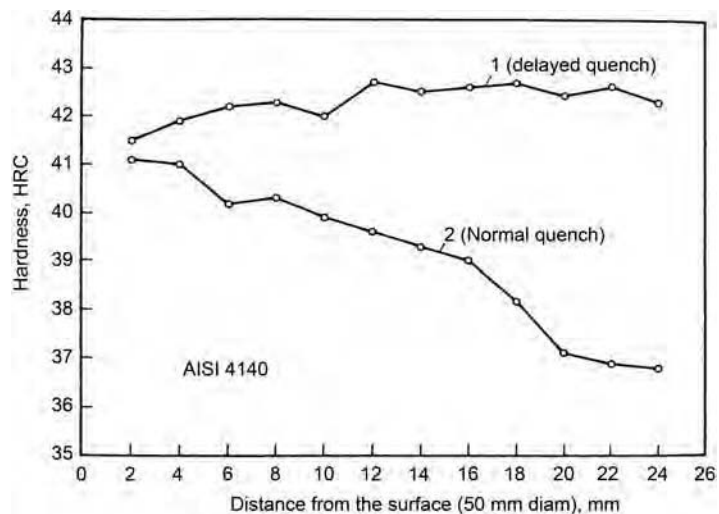


Fig. 9 Hardness distribution after tempering at 480 °C for 2 h. Source: Ref 6

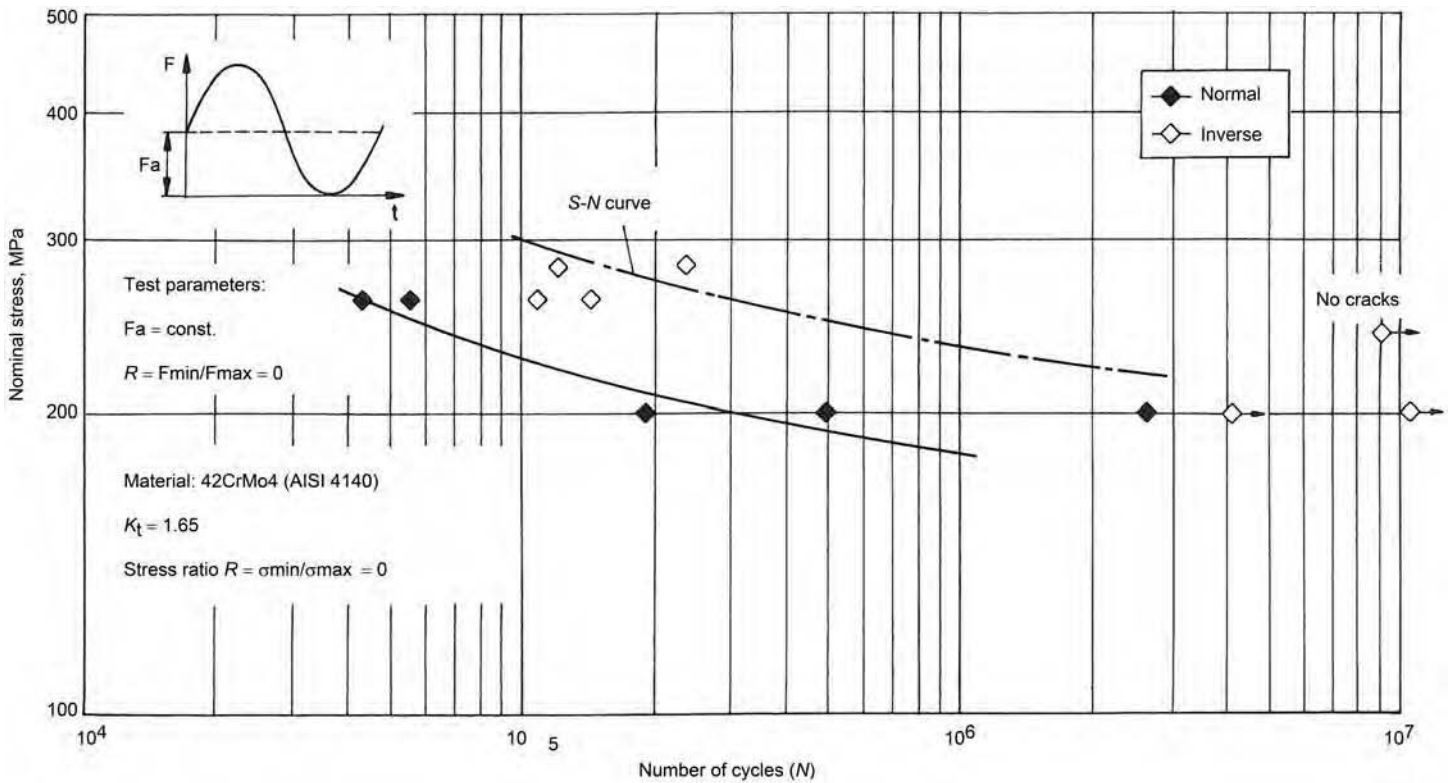


Fig. 10 Bending fatigue $S-N$ curves for AISI 4140 specimens having normal and inverse hardness distributions after quenching. All specimens were tempered for 2 h at 500 °C. Source: Ref 6

of the inverse-hardened and tempered steel provides a “guarantee” that the microstructure consists of essentially all tempered martensite. In the conventionally heat treated steel, softer constituents also are present. In terms of mechanical properties, it is well known that tempered, fine-grained martensite yields the highest toughness, particularly for high strength levels.

Effects on Fatigue Resistance. AISI 4140 specimens 50 mm in diameter by 300 mm long were tested in bending fatigue (Ref 12). All specimens were from the same heat of steel and were austenitized in a protective atmosphere at 860 °C.

Specimens heat treated to have a normal hardness distribution were quenched in used mineral oil at 20 °C, without agitation. Specimens heat treated to have an inverse hardness distribution were quenched in 25% PAG solution at 40 °C bath temperature and 0.8 m/s agitation rate. After quenching, specimens were tempered in a vacuum furnace for 2 h at 500 °C.

Information about the crack growth rate is provided by the crack growth fraction of total test length (in percent): $(N_f - N_c)/N_f$, where N_f is the number of cycles at the end of the test, and N_c is the number of cycles to initiation of the first crack. (The value of N_c is the number of cycles at which the stiffness of the specimen began to decrease.)

Fatigue tests were run at different pulsating sinusoidal loads, with a frequency of 16 Hz and a stress ratio, R , of 0. Test results (Fig. 10) are plotted as $S-N$ curves, that is, plots of nominal stress amplitude versus fatigue life (number of cycles) to initial cracking. Even though the number of tests was low, it can still be concluded that the fatigue life of specimens having an inverse hardness distribution is longer than that of specimens having a conventional hardness distribution. At 270 MPa, for example, the stress at which most of the tests were performed, fatigue life was increased by a factor of approximately 7. It was also observed that the crack growth portion of the test was more uniform for specimens having an inverse hardness distribution and amounted to 13 to 20% of total fatigue life, depending on the stress.

Summary

Controllable delayed quenching technology is based on the discontinuous change of the cooling rate that is connected with every delayed quenching. As theoretically explained, the discontinuous change of the cooling rate during quenching has a high potential to increase the depth of hardening, compared to normal quenching practice. The average cooling rate within the critical temperature range A_1 to 500 °C decreases from

the surface toward the core for normal quenching, while it increases in the case of delayed quenching. The effect of delayed quenching on hardness distribution always depends on the hardenability of the steel and the cross-sectional size of the workpiece. Delayed quenching can substitute for lower hardenability of the steel in respect to the depth of hardening. For immersion quenching of a batch of workpieces, aqueous polymer solutions (PAG) of high concentration are the only quenchants suitable for controllable delayed quenching. In addition to bath temperature and agitation rate, the main parameter to be controlled is the polymer concentration, on which the thickness of the polymer film and thus the delay in quenching depends.

REFERENCES

1. N. Shimizu and I. Tamura, An Examination of the Relation between Quench-Hardening Behavior of Steel and Cooling Curve in Oil, *Trans. ISIJ*, Vol 18, 1978, p 445-450
2. E.A. Loria, Transformation Behavior on Air Cooling Steel in A_3 - A_1 Temperature Range, *Met. Technol.*, Oct 1977, p 490-492
3. N. Shimizu and I. Tamura, Effect of Discontinuous Change in Cooling Rate during

- Continuous Cooling on Pearlite Transformation Behavior of Steel, *Trans. ISIJ*, Vol 17, 1977, p 469–476
4. B. Liščić and G.E. Totten, Controllable Delayed Quenching, *Heat Treating: Equipment and Processes—1994 Conference Proceedings*, G.E. Totten and R.A. Wallis, Ed., ASM International, 1994, p 253–262
 5. M. Chen and H. Zhou, Numerical Heat Transfer Analysis on the Effect of Enhancing the Thickness of the Hardened Layer by Delayed Quenching, *Jinshu Rechuli Xuebao (Trans. Met. Heat Treat.)*, Vol 14 (No. 4), Dec 1993, p 1–6 (in Chinese)
 6. B. Liščić, V. Grubisic, and G.E. Totten, Inverse Hardness Distribution and Its Influence on Mechanical Properties, *Proc. Second International Conference on Quenching and the Control of Distortion*, ASM International, 1996, p 47–54
 7. B. Liščić, “Investigation of the Correlation between Polymer-Solution (PAG) Concentration and Inverse Hardening Distribution Curves,” Internal Report 11/92, Laboratory for Heat Treatment, Faculty of Mechanical Engineering and Naval Architecture, University of Zagreb, Zagreb, Croatia, March 1992
 8. B. Liščić, S. Svaic, and T. Filetin, Workshop Designed System for Quenching Intensity Evaluation and Calculation of Heat Transfer Data, *Proc. First International Conference on Quenching and the Control of Distortion*, ASM International, 1992, p 17–26
 9. R.H. Harding and P.L. Matlock, U.S. Patent 33,445, reissued 1990
 10. R.R. Blackwood and W.D. Cheesman, U.S. Patent 3,220,893, 1965
 11. W. Luty, Types of Cooling Media and Their Properties, *Theory and Technology of Quenching*, B. Liščić, M. Tensi, and W. Luty, Ed., Springer Verlag, Berlin, 1992, p 248–340
 12. Test Report 7710, Fraunhofer Institut für Betriebsfestigkeit, Darmstadt, Germany, Nov 24, 1994

Gas Quenching

Volker Heuer, ALD Vacuum Technologies GmbH

Introduction

The gas quenching process is usually performed at elevated pressures and is therefore mostly referred to as high-pressure gas quenching (HPGQ). During HPGQ, previously austenitized/thermochemically treated parts are quenched in an inert gas flow in a pressure range between 1 and 20 bar with gas velocities between 0.5 and 20 m/s. When using a nozzle field, velocities can be much higher, up to 80 to 160 m/s. In a few cases, up to 25 bar pressure is applied. The HPGQ process is combined in most cases with a vacuum heat treatment, such as low-pressure carburizing (LPC), and in a few applications, HPGQ has been applied after conventional gas carburizing. The HPGQ process is usually followed by a tempering process.

In most cases, the goal of the gas quenching process is to improve hardness. Upon completion of austenitization, the parts are subjected to HPGQ to change the microstructure from austenite into martensite, thus obtaining the desired increase in hardness.

High-pressure gas quenching is an environmentally friendly and low-distortion quench process compared to liquid quenching, such as oil, polymer, or water. Dry gas quenching has the following advantages compared to liquid quenching:

- Clean part surfaces after heat treatment; no washing of parts necessary
- Environmentally friendly process (no disposal of oil, salt bath residues, or detergent residues)
- Full flexibility to control quench intensity
- Potential to reduce heat treatment distortion (unwanted changes in form and size of the part geometry during heat treatment)
- Possibility to integrate heat treatment into the production line

Process variables that influence microstructure, hardness, and distortion are summarized in Fig. 1.

The disadvantage of HPGQ is the somewhat limited quench intensity compared to liquid quench media such as oil, water, or polymer quench. Even with the recent improvements

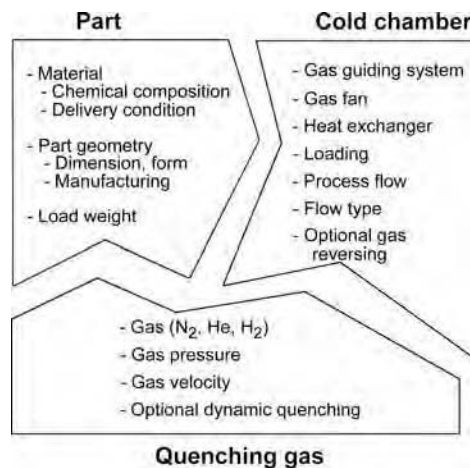


Fig. 1 High-pressure gas quenching variables that influence microstructure, hardness, and distortion

of HPGQ, very large components cannot be quenched in gas successfully unless they are made of a steel grade with excellent hardenability (see the section "Prediction of Core Hardness" in this article for more details). Nevertheless, HPGQ becomes more and more popular and displaces liquid quenching in many applications.

For the heat treatment of tool steels and high-speed steels, HPGQ is the preferred choice and has almost completely replaced liquid quench media, which were formerly used. By enhancing gas pressure and gas velocity as well as through the development of separate HPGQ quench chambers, or so-called cold chambers, the process also has become established for the hardening of low-alloyed case-hardening steels and quenched and tempered steels. To date, primary applications of HPGQ in cold chambers are gear components (wheels, shafts, synchronizers), bearing rings, and components for fuel-injection systems (nozzles, pump heads, etc.). Over the last few years, the technology of LPC in combination with HPGQ has become a preferred choice for the treatment of gear components for manual and automatic transmissions for passenger cars.

Physical Principles

At the beginning of an HPGQ process, the quench chamber is flooded with the quench gas. Depending on the type of gas and the installed equipment, it takes between 4 and 20 s to reach the desired pressure level. Then, the gas stream is circulating through the load and extracting energy from the components, while the absorbed heat of the gas is released to an integrated heat exchanger.

The amount of energy that is extracted can be described by the heat flux density, \dot{q} . According to Eq 1, the heat flux density is proportional to the heat-transfer coefficient, α . This heat-transfer coefficient is the dominating physical parameter in quenching, and the distribution of local α values on the part surface is crucial for part quality after quenching:

$$\dot{q} = \alpha \cdot (T_{\text{Surface of the part}} - T_{\text{Gas}}) \quad (\text{Eq 1})$$

Figure 2 shows the range of heat-transfer coefficients for different quenching media. These ranges are average values. The cooling rate obtained with HPGQ is similar to the cooling rate obtained with a mild oil quench. The cooling rates obtained with strong oil quenching, including agitation of the oil bath, cannot be reached with HPGQ.

Equation 2 describes the theoretical correlation between the heat-transfer coefficient, α , and the process parameters:

$$\alpha = C \cdot w^{0.7} \rho^{0.7} d^{-0.3} \eta^{-0.39} c_p^{0.31} \lambda^{0.69} \quad (\text{Eq 2})$$

where C is a constant, w is the gas velocity, ρ is the gas density, d is the part-specific diameter, η is the dynamic gas viscosity, c_p is the specific heat capacity of the gas, and λ is the thermal conductivity of the gas.

The constant C includes all other influences, such as the special aerodynamic conditions in the quench chamber, the degree of flow turbulence, and so on. Once the type of quench chamber and type of quench gas have been chosen, the gas pressure and gas velocity remain

the two crucial process parameters to adjust for the desired quench intensity.

During the course of the HPGQ process, the heat-transfer coefficient is almost constant over time (Ref 1).

When comparing the mechanisms of heat transfer between gas quenching and liquid quenching (oil, water, polymer), a fundamental difference is observed. Three different mechanisms occur during liquid quenching: film boiling, bubble boiling, and convection. As a result of these three mechanisms, the distribution of the local heat-transfer coefficients on the surface of the component is very inhomogeneous (Fig. 3). These inhomogeneous cooling conditions cause tremendous thermal and transformation stresses in the component and subsequently may lead to distortion. During HPGQ, only convection takes place, which results in much more homogeneous cooling conditions. Due to the missing phase transition in the

gaseous quench medium, HPGQ leads to reduced distortion compared to liquid quenching in many applications.

Another advantage of gas quenching is the flexibility to precisely dial in the quench intensity by varying the process parameters of gas pressure and gas velocity. The quench intensity can be adjusted specifically to the target values of the components regarding hardness and microstructure. With liquid quenching, there is less flexibility, because only the agitation and the temperature of the quenchant can be varied. This results in a much smaller process window for liquid quenching compared to HPGQ.

When using liquid quenchants over a long period of time, the heat-transfer coefficient can deteriorate due to contamination of the quench medium (Ref 3). When applying HPGQ, this is not the case; the cooling rates stay reproducible over time.

Equipment for Gas Quenching

There are two main types of equipment for gas quenching. In the so-called single-chamber furnaces, all process steps such as heating, austenitizing, an optional thermochemical treatment, and HPGQ are performed in the same chamber. As an alternative, cold chambers are dedicated for quenching only. Cold chambers are part of multichamber systems, where the heating, austenitizing, and an optional thermochemical treatment are performed in specific treatment chambers.

For both types, an integrated high-performance fan is used to circulate the gas via suitable gas-guiding systems through the hot load. The installed motor power for the gas fan is derived from the targeted gas velocity, the targeted gas pressure, and the selected type of gas. The typical installed motor power of a fan ranges from 80 to 250 kW and sometimes up to 400 kW. The heat from the load is absorbed by the gas and released to the integrated gas/water heat exchanger.

Figure 4 schematically shows the gas flow in a single-chamber furnace. Heating and quenching are performed in the same chamber, so the design of the chamber is a compromise between both functions. The gas is accelerated with one fan and guided through the load and the heat exchanger. By changing positions of the flaps and guiding plates, the direction of the gas flow can be alternated. Different single-chamber furnace designs are available, such as cubic or round chambers, quenching with gas nozzles, and chambers with one-, two- or four-directional cooling.

Figure 5 illustrates the design of a cold chamber for gas quenching. Before the HPGQ process is started, the hot load is transported into the cold chamber. After closing a pressure-tight door, the chamber is flooded with the quench gas. Two fans are used to accelerate the gas through the load and the two water-cooled heat exchangers, which are located

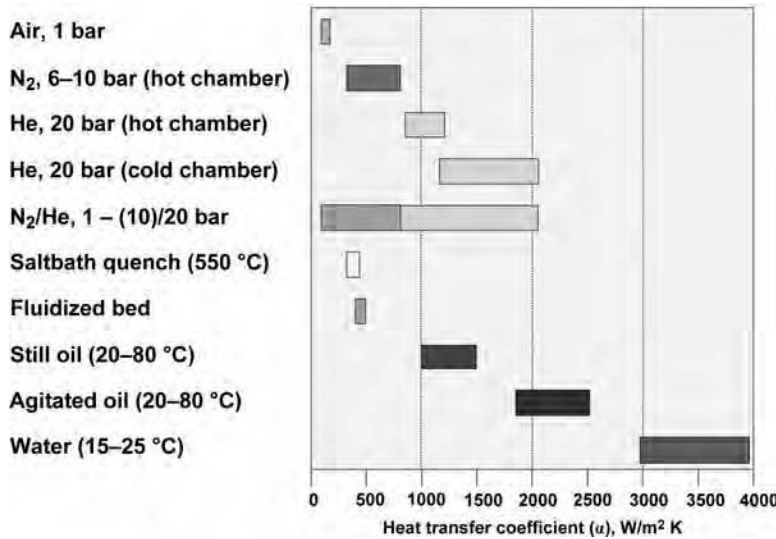


Fig. 2 Average heat-transfer coefficients for different quench media

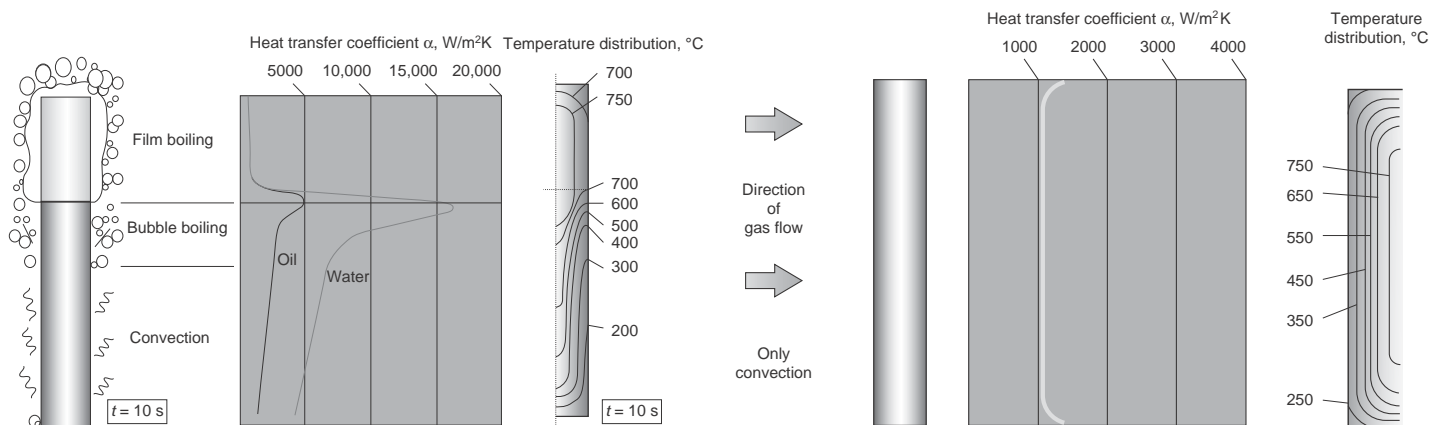


Fig. 3 Heat-transfer coefficient and temperature distribution in liquid and gas quenching. Source: Ref 2

above and below the load. Besides cooling the quench gas, the heat exchangers are used to homogenize the gas velocity.

Cold chambers provide stronger quench intensities compared to single-chamber furnaces. When designing a cold chamber, the design of the gas flow is not compromised by the other process steps, such as heating or thermochemical treatment. Due to the required space for the heating elements, in a single-chamber furnace there is a significant gap between the load and the inner furnace wall. Therefore, a significant amount of gas is not guided through the load but bypasses the load. A further advantage of the cold chamber is that only the load itself needs to be quenched and not the hot inner furnace walls, as in single-chamber furnaces.

Table 1 shows the advantages and disadvantages and the typical applications for single-chamber furnaces and for cold chambers. For both types of equipment, it is important to provide good uniformity of the gas-flow velocity in order to reach homogeneous results in terms of hardness and distortion of the components.

The uniformity of the cooling rate is usually determined by placing thermocouples into the quenched components at different positions in the load. It is recommended to measure cooling curves in the extreme positions of the load, such as the corners, the top-middle, the middle-middle, and the bottom-middle of the load. When measuring cooling curves in a cold chamber, it is mandatory to use a mobile electronic data-logging device,

which travels with the load through the entire process. The disadvantage of such a device is that it has an impact on the measured cooling curves, because it changes the quench performance due to its relatively large size.

Gas Types

Mainly three types of gas are used for HPGQ: nitrogen, helium, and argon. Hydrogen has not been established in industrial practice due to safety concerns. Hydrogen is the only ignitable quench gas and therefore requires extensive safety precautions in the technical design of such plants and for later operation. The quench gases clearly differ in their quenching capacity because of their various thermophysical properties (Table 2).

Nitrogen is used for many industrial applications. Helium is used in some applications, when higher quench rates are required. Because helium is much lighter compared to nitrogen, higher gas velocities can be provided by installing a bigger fan wheel without the need to increase the fan power. However, the high cost of helium makes it absolutely necessary to recycle the helium after each quench cycle. Argon is often used for quenching of aerospace components.

In addition to the use of pure gases, it is also possible to blend mixtures of gases. Theoretical calculations verify that the heat-transfer coefficients of gas mixtures such as helium-carbon dioxide in a mixing ratio of 60/40% range above the values of pure helium gas. Nevertheless, to date, the use of gas mixtures for quenching has not become established in practice due to the high technical effort required to supply and maintain the gas mixtures. Additionally, the use of carbon dioxide as the quench gas would lead to

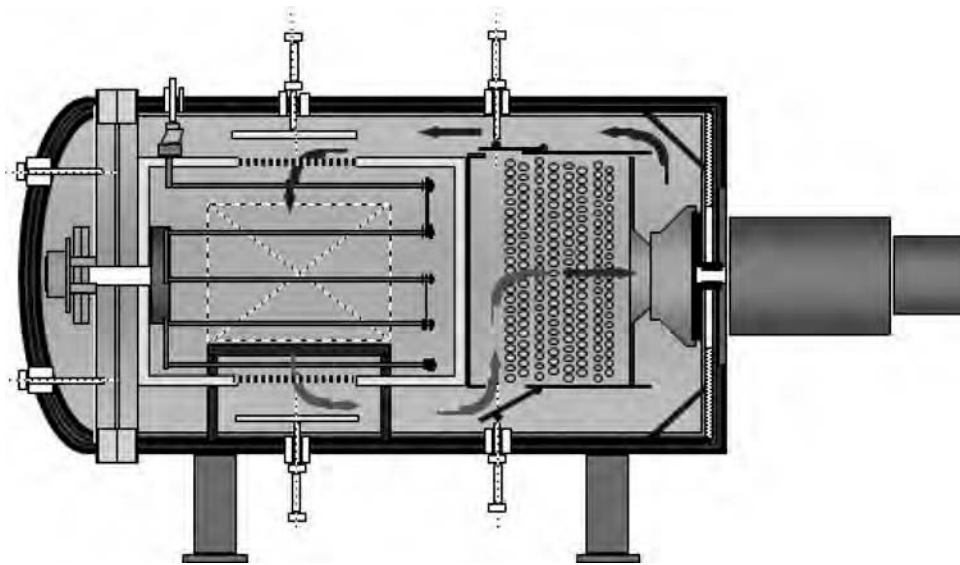


Fig. 4 Gas quenching in a single-chamber furnace (austenitizing/thermochemical treatment and quenching in one single chamber)

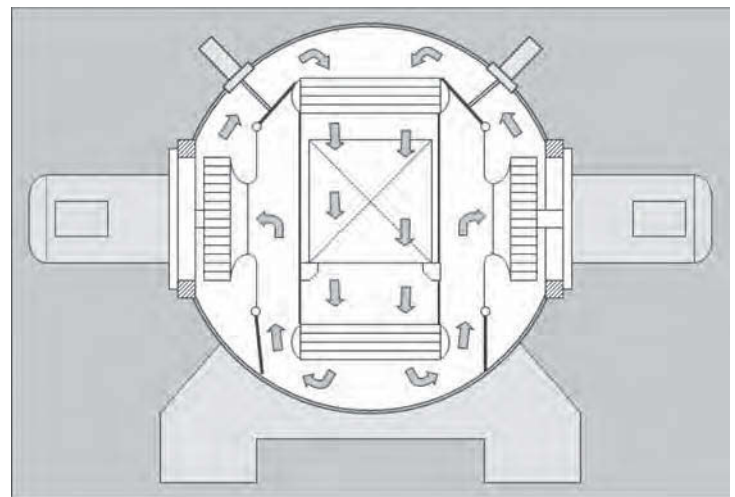
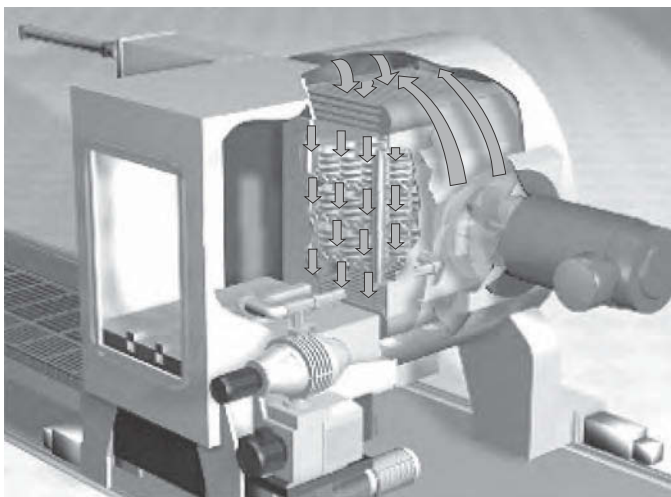


Fig. 5 Gas quenching in a cold chamber (quenching in separate chamber)

oxidation on the surface and discoloration of the parts.

Besides the use of the technical gases from Table 2, it is also possible to use dry air as a quench gas (Ref 4). The use of air inevitably leads to oxidation of part surfaces during the quench process. However, the formation of oxide layers of approximately 5 μm on typical low-alloyed case-hardening steels can be completely removed by shot peening in the subsequent production step (Ref 4). No problems have been reported regarding

surface hardness and wear properties of the parts. Quenching with air represents a genuine alternative, if the oxide layer can be removed by shot peening or hard finishing after the quench.

Cooling Curves

The quench rate depends strongly on the shape and size of the components, the design of the quench chamber, as well as the

configuration and weight of the load. However, if the type of quench chamber and quench gas have been chosen and if the load configuration has been defined, then the gas pressure and gas velocity remain the two crucial process parameters to adjust for the desired quench intensity. To determine the gas velocity of a certain quench chamber design, the local distribution of speed is measured by a hot-wire anemometer. This measurement is performed in an empty quench chamber at the level of charge support. The gas velocity of the chamber is then defined as the average value in this measurement plane. According to Eq 2, gas velocity as well as gas density influence the equation for the heat-transfer coefficient, α, with an exponent of 0.7. The gas density is directly proportional to the gas pressure. Consequently, gas pressure and gas velocity have the same impact on the heat-transfer coefficient.

As described in the section “Equipment for Gas Quenching” in this article, when analyzing cooling curves, there must be a distinction between single-chamber furnaces and cold chambers. Figures 6 and 7 show cooling characteristics of a single-chamber furnace. Cooling curves as a function of gas pressure for 25 mm diameter cylinders, which were quenched with nitrogen and a gas velocity of 7 m/s, are given in Fig. 6. In Fig. 7, cooling curves are shown for 100 mm diameter cylinders when quenched in 6 bar N₂ with a gas velocity of 7 m/s. Cooling curves for the core and the surface of the specimen are displayed. In this case, so-called gas reversing was applied for better cooling uniformity (see the section “Gas-Flow Reversing” in this article).

As of today (2013), single-chamber furnaces with higher quench intensities have been developed for special applications (Ref 5).

In single-chamber furnaces, smaller components made of medium-alloyed steel grades are usually cooled directly to ambient temperature. Big and complex-shaped components

Table 1 Comparison of single-chamber furnaces and cold chambers for high-pressure gas quenching

	Single-chamber furnace	Cold chamber
Production volume	Small-production lots	High-production throughput
Main fields of application	Tools, dies, aerospace components, gear components, bearing rings (limited size), fuel-injection components	Gear components, machine components, bearing rings, fuel-injection components
Typical steel grades for treatment	M2, M3, M42, T1, H10, H11, H13, D2, D3, A2, 440C, 4xx stainless, 3xx stainless, case-hardening steels (for small parts)	4120, 4320, 5120, 5130, 52100, 8625, 9310, 100Cr6, 20MnCr5, 27MnCr5, 18CrNiMo7-6, 8620 (for small parts), 16MnCr5 (for small parts)
Medium-high quench rates	Not possible (only with special furnaces)	Possible
Very slow quench rates	Possible (by using integrated heating system)	Not possible
Temperature measurements inside components during quenching	Possible	Not possible (only possible by using a mobile electronic data-logging device)
Gas-flow uniformity	Often limited	Optimized

Table 2 Thermophysical properties of technical gases at standard conditions of 25 °C and 1 bar

Property	Argon	Nitrogen	Helium	Hydrogen
Chemical symbol	Ar	N ₂	He	H ₂
Density at 15 °C and 1 bar, kg/m ³	1.6687	1.170	0.167	0.0841
Ratio of density compared to air	1.3797	0.967	0.138	0.0695
Molecular mass, kg/kmol	39.9	28.0	4.0	2.01
Specific heat capacity (c _p), kJ/kg · K	0.5024	1.041	5.1931	14.3
Heat conductivity (λ), W/m · K	177 × 10 ⁻⁴	259 × 10 ⁻⁴	1500 × 10 ⁻⁴	1869 × 10 ⁻⁴
Dynamic viscosity (η), N · s/m ²	22.6 × 10 ⁻⁶	17.74 × 10 ⁻⁶	19.68 × 10 ⁻⁶	8.92 × 10 ⁻⁶

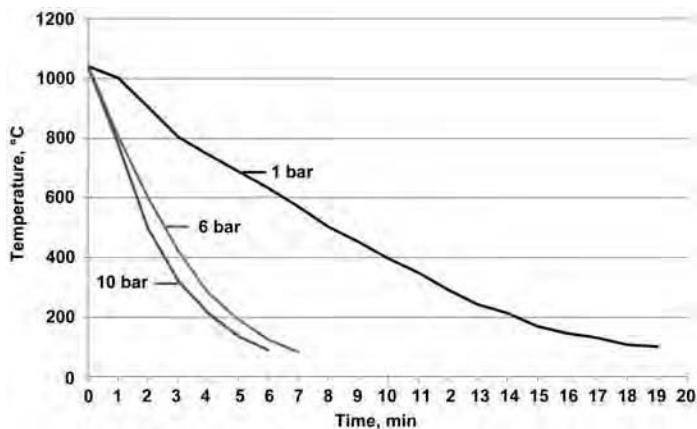


Fig. 6 Cooling curves as a function of gas pressure in 25 mm diameter cylinders quenched in single-chamber furnace (Monotherm 60/60/90; bolt charge with 540 kg gross weight; quench gas: nitrogen; gas velocity: ~7 m/s)

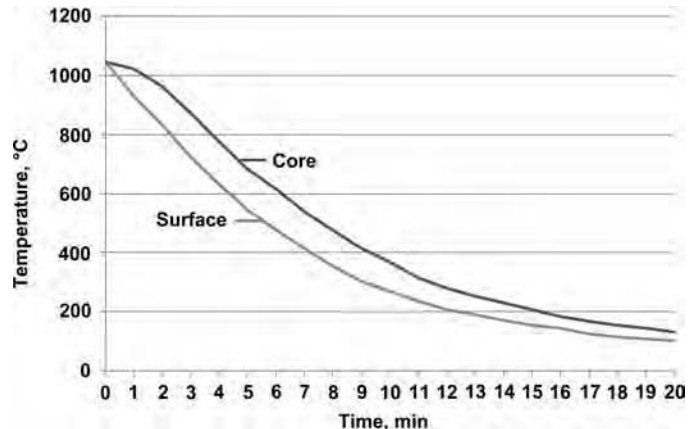


Fig. 7 Cooling curves in surface and core of 100 mm diameter cylinders quenched in single-chamber furnace (Monotherm 60/60/90; bolt charge; middle-middle position of the load; quench gas: 6 bar N₂; gas velocity: ~7 m/s; gas reversing applied)

made of high-alloyed steels are often hardened in several steps. This process is known as mar-quenching and is applied to avoid cracks during quenching and to reduce distortion of the components (Fig. 8).

As noted in the section “Equipment for Gas Quenching” in this article, the development of cold chambers led the way to providing higher quench intensities. In parallel, the maximum quench pressure has continuously increased over the years. Currently, cold chambers with a maximum pressure of 20 bar represent the standard for HPGQ of low-alloyed steels in mass production.

Besides quench pressure, the gas velocity has also increased over the years to achieve higher quench intensities. Today (2013), an average gas velocity in the range of 12 m/s and a quench pressure of 20 bar is applied when using nitrogen. When using helium, due to its low gas density, the gas velocity can be significantly enhanced without the need to increase motor power. Today, average gas velocities of up to 20 m/s can be achieved with a helium quench.

The quench intensities obtained with HPGQ in cold chambers have been determined

in various studies (Ref 1, 7). For example, cooling curves in the core of a cylindrical specimen with different diameters were experimentally determined in a cold chamber HPGQ (Ref 1). Figure 9 shows the cooling curves for a 10 mm diameter cylindrical specimen for various quench parameters, and Fig. 10 shows the cooling curves for a 50 mm diameter specimen.

The quench parameter $\lambda_{800-500}$ is often used for the characterization of the cooling rate. This value is determined by taking a reading from the cooling curve, that is, how long it takes to cool from 800 to 500 °C. Then, this value in seconds is multiplied by the factor $1/100$ to obtain the quench parameter $\lambda_{800-500}$. The $\lambda_{800-500}$ parameter is shown for three different quench conditions in a cold chamber in Fig. 11.

When trying to predict the cooling curve of complex-shaped components, it is mandatory to know the magnitude of the heat-transfer coefficient for different quench conditions. Table 3 shows heat-transfer coefficients that were determined experimentally with the help of the so-called Q-probe (Ref 8) in a cold

chamber. The cooling curves in the surface and in the core of the Q-probe were measured to obtain these data (Ref 1). Table 3 additionally shows the calculated α -values, derived from Eq 2. The measured values correspond well with the calculated values. However, it is important to realize that the constant $C = 0.10535$ is only valid for the tested type of quench chamber. Different values for constant C will apply if Eq 2 is used for other types of quench chambers.

As stated previously, the α -values can be determined experimentally by measuring the cooling curves during HPGQ. This is a well-established procedure to determine the average α -values on the surface of a component. However, if not the average value but the local distribution of α -values on different surface areas of the part and the local distribution within the charge are required, then this procedure proves to be difficult. There is another experimental method that can be used to determine the local α -values within the charge. This method is based on the analogy between energy and mass transfer (Ref 9). However, substantial experimental work is required in this method. Another possibility is to calculate the α -values with the help of computational fluid dynamics simulations. However, when doing so, it is mandatory to validate the calculation results with the help of experiments.

Prediction of Core Hardness

The quench intensity and the resulting core hardness values after HPGQ do not depend solely on the quench parameters of gas pressure and gas velocity. The resulting core hardness values depend strongly on the hardenability of the component material, on the design of the quench chamber, as well as on the configuration and weight of the load. Therefore, all predictions of core hardness results are very specific for each type of equipment and each load configuration.

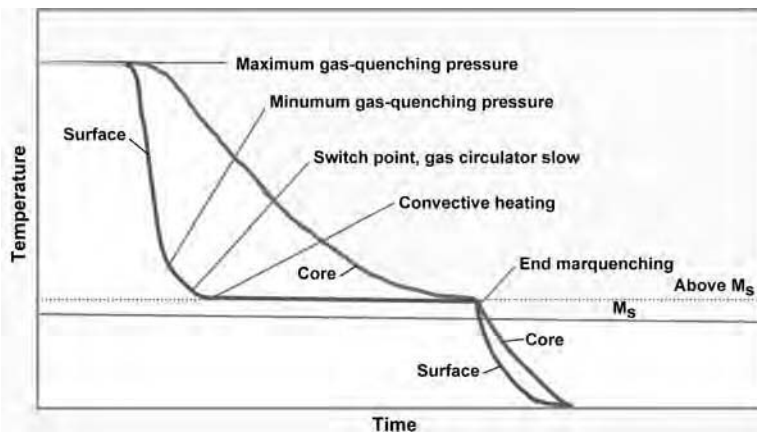


Fig. 8 Use of marquenching technology in vacuum hardening to minimize distortion. Source: Ref 6

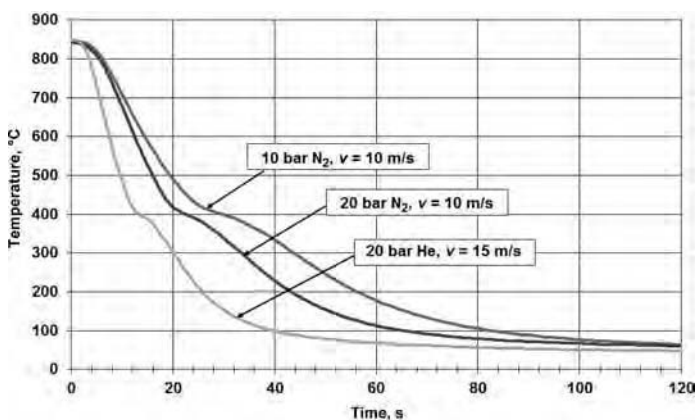


Fig. 9 Cooling curves for 10 mm diameter cylinders quenched in cold chamber (ModulTherm) with different quench parameters

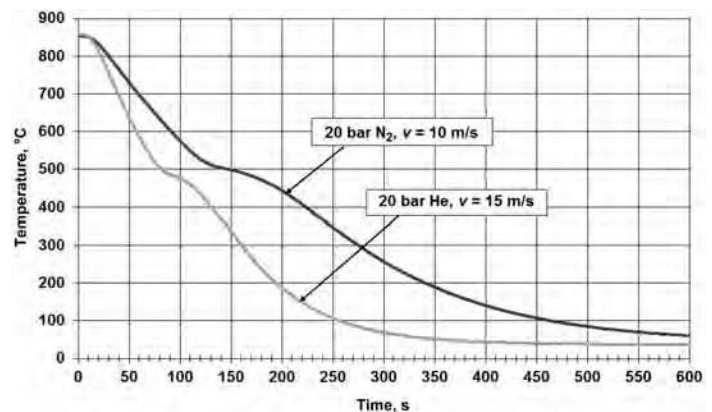


Fig. 10 Cooling curves for 50 mm diameter cylinders quenched in cold chamber (ModulTherm) with different quench parameters

Table 3 Calculated and measured heat-transfer coefficients (α) in cold chamber (ModulTherm)

Gas type	Gas pressure, bar	Gas velocity, m/s	α calculated(a), $W/m^2 \cdot K$	α experimental, $W/m^2 \cdot K$
Nitrogen	1.5	3	43	58
Nitrogen	1.5	4.8	60	75
Nitrogen	1.5	8.8	91	98
Nitrogen	10	10.1	380	380
Nitrogen	19	10.1	596	590
Helium	19	14.7	1038	990

(a) Calculated using Eq 2 with $C = 0.10535$; values for the lateral surface of a cylinder with 28 mm diameter (Q-probe), quenched in longitudinal direction. Source: Ref 1

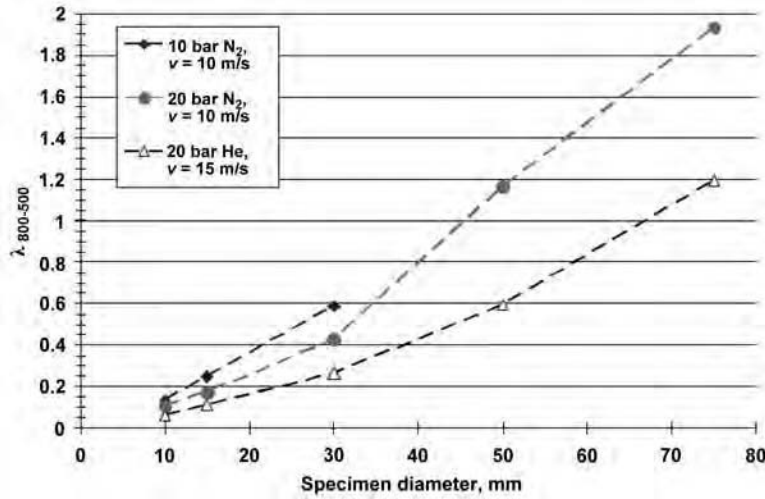


Fig. 11 Quenching parameter $\lambda_{800-500}$ as a function of the diameter of a cylindrical specimen and the quenching parameters in cold chamber (ModulTherm). Source: Ref 1

The following examples from the heat treatment of transmission components show how core hardness values can be predicted in industrial practice. When designing an HPGQ process for gear wheels or gear shafts, it must be predicted what values of tooth-root core hardness can be achieved when using different steel grades as material for the components. Once a certain steel grade has been chosen, it must be defined what quench parameters should be applied to guarantee the targeted values of tooth-root core hardness in serial production. These questions can be answered by a prediction method that is based on the Jominy hardenability curve of the steel.

The Jominy hardenability curve is a standardized test, as described in DIN EN ISO 642 (Ref 10), using a cylindrical specimen with 25 mm diameter and 100 mm height as the test probe. After austenitizing, the probe is hung vertically and quenched with a water jet of well-defined intensity. The water jet is directed toward the lower face of the cylindrical specimen. This means that with increasing distance from this face, the quench rate inside the probe is continually reduced.

After completion of the quench, the hardness profile is measured in an axis-parallel line with 0.4 mm distance to the surface. The resulting curve is the so-called Jominy curve. This curve describes the relationship between the

distance from the lower face of the probe in millimeters (the so-called Jominy value) and the achieved hardness in HRC. In addition to the experimental method as described previously, the curve can be calculated from the chemical composition of the steel grade as well (Ref 11).

The Jominy value is described in millimeters and therefore has the unit of distance, but ultimately each Jominy value is describing the local cooling rate inside the Jominy probe, because the Jominy test is a standardized quenching test. When quenching a load, every component inside the load has a certain cooling curve that can be described by a corresponding Jominy value.

When applying the prediction method, the Jominy values for different positions inside the load are determined first. As stated earlier, the cooling curves depend on the size and shape of the component to be quenched, the process parameters, the type of quench cell, and the configuration and weight of the load. That is why the determined Jominy values are only valid for a specific quench scenario with a specific combination of component geometry, quench chamber, process parameters, and load configuration.

The fundamental steps of the prediction method are depicted in Fig. 12. The goal is to predict for a given type of quench chamber

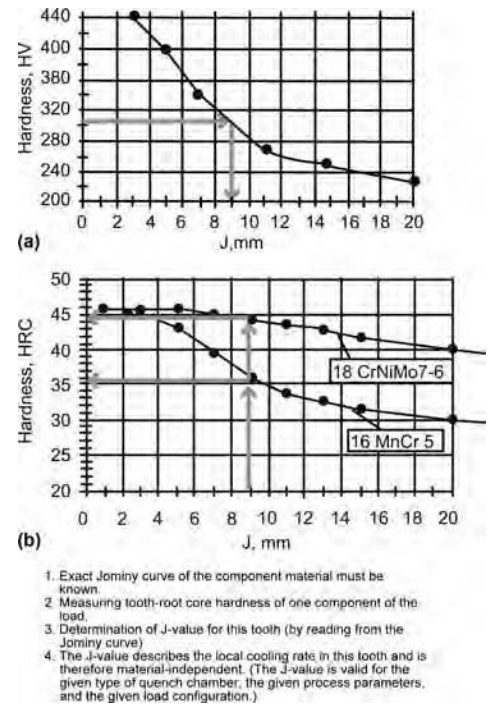


Fig. 12 (a) Prediction of tooth-root core hardness values by determination of local Jominy values inside the load. (b) Illustration of the procedure to predict tooth-root core hardness when choosing a different steel grade with a given type of quench chamber, part geometry, load configuration and weight, and given process parameters (gas pressure, gas velocity, etc.)

and given process parameters for a certain component geometry and load configuration which tooth-root core hardness is achieved when using different steel grades. To allow for such a prediction, the exact Jominy hardenability curve of the component material must be known. After completing the heat treatment cycle, the tooth-root core hardness values are determined at characteristic locations in the load (e.g., tooth-root core hardness in a component from the middle of the bottom layer of the load). With this hardness value, the corresponding Jominy value is read from the Jominy curve of the used steel. This Jominy value characterizes the local cooling rate in the tooth root of the component for the given quench scenario. A low Jominy value is equivalent to a high cooling rate, and a high Jominy value is equivalent to a low cooling rate in the tooth root.

After determination of the local Jominy value of the component, it can be predicted what tooth-root core hardness values can be achieved when choosing different steel grades. If the Jominy curves of the steel grades are known, it can be read from the Jominy curve which hardness will be achieved.

Figure 13 shows the Jominy values that were determined in the tooth root of gear wheels. The values from the bottom layer are displayed for a 20 bar He quench and a 10 bar N_2 quench.

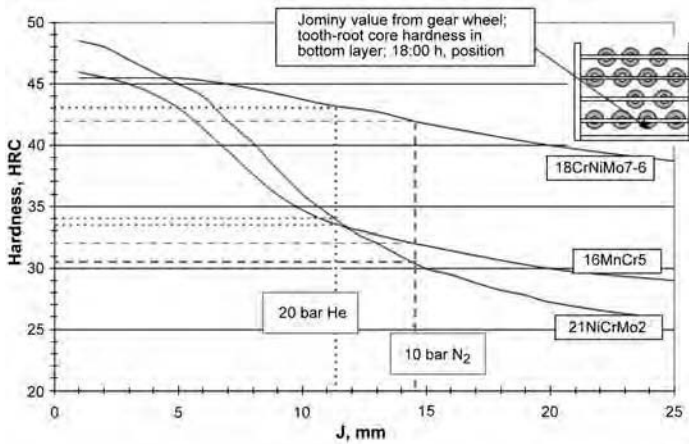


Fig. 13 Prediction of tooth-root core hardness values in the bottom layer of a load with gear wheels (hanging gears; outside diameter = 97 mm; height = 35 mm; quenched in cold chamber; ModulTherm)

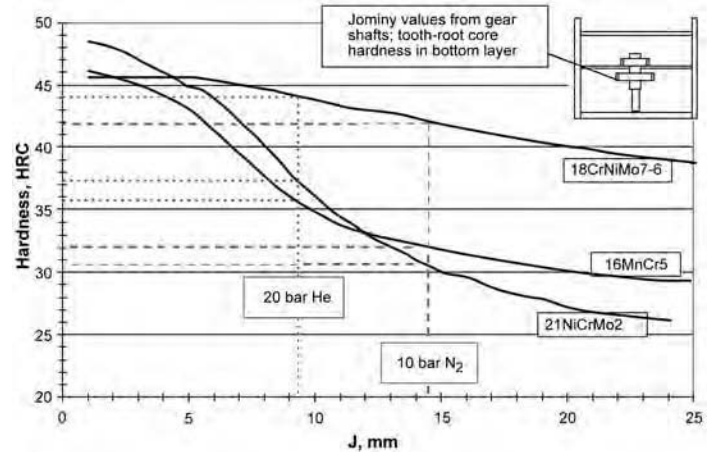


Fig. 14 Prediction of tooth-root core hardness values in the bottom layer of a load with gear shafts (outside diameter = 97 mm; height = 340 mm; quenched in cold chamber; ModulTherm)

Additionally, the Jominy curves of 16MnCr5, 21NiCrMo2, and 18CrNiMo7-6 are added to the diagram. The hardenability curves of typical HH steel qualities are displayed. Now the tooth-root core hardness values can be predicted when using these steel grades.

Figure 14 shows the Jominy values that were determined in the tooth root of gear shafts for a 20 bar He and a 10 bar N₂ quench. Again, the hardenability curves of typical HH steel qualities are displayed.

Figure 15 shows a comparison of Jominy curves of different case-hardening steels that are often processed with HPGQ in cold chambers. Generally speaking, all steel grades have a certain tolerance range of the alloying elements. Therefore, each material has a hardenability scatter band with an upper- and lower-limit curve that is defined in the material specification. The hardenability curves from Fig. 15 represent curves that are 1/3 of the scatter band below the maximum Jominy curve. When choosing the steel grade for a new application, the hardenability scatter bands must be taken into consideration.

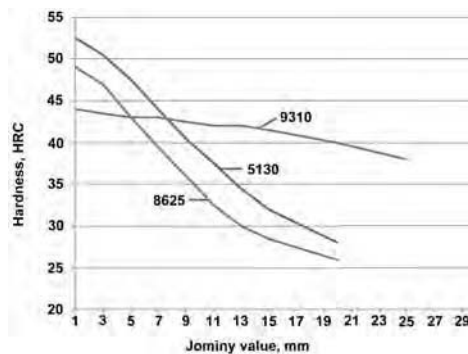


Fig. 15 Typical Jominy curves of case-hardening steels, which are often processed with high-pressure gas quenching in cold chambers. Curves indicate 1/3 of the scatter band below the maximum Jominy curve.

direction, there is less difference in the cooling curves of parts placed in different layers. This reduces the spread of distortion inside the load.

A schematic view of a quench chamber with reversing gas flow is shown in Fig. 16. To allow for alternating flow direction, the chamber is equipped with flaps that are operated pneumatically. Depending on the setting of the valves, either top-to-bottom or bottom-to-top flow direction is put into effect. The alternating flow direction is time-controlled.

As shown in Fig. 17, the cooling curves in the top and bottom layer converge when applying reversing gas flow. As a result, the spread of core hardness values within the load is significantly reduced. In the application from Fig. 17, the maximum difference in tooth-root core hardness was reduced from 90 to 40 HV.

Reversing gas flow is not only used to reduce the spread of core hardness but also to reduce the spread of distortion within the load. The following is an example for such an application. The reversing gas-flow process

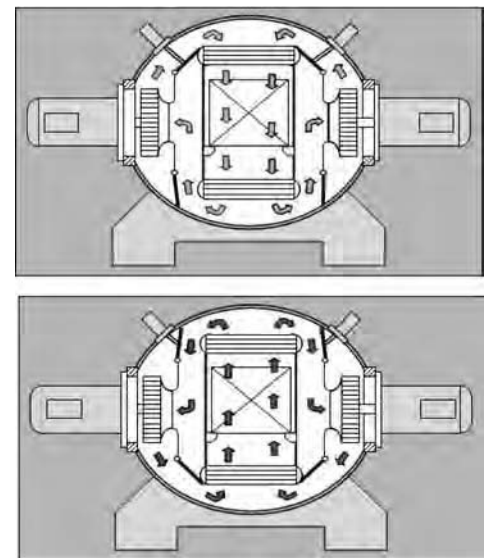


Fig. 16 Schematic illustration of a quenching chamber with reversing gas-flow technology

was applied on the final-drive pinion planetary gears of a six-speed automatic transmission (Ref 12). The gears are made of 5120 material, have an outer diameter of 31 mm, a height of 32 mm, and have 24 external teeth. One load consists of 1056 pieces treated in 9 layers (Fig.18).

Figure 19 shows the improvement that was achieved when introducing the reversing gas-flow process. When applying unidirectional gas flow, the gas flows only from top to bottom through the load. With reversing gas flow, the flow of gas alternates back and forth from top to bottom and bottom to top, as illustrated in Fig. 16. As shown in Fig. 19, with unidirectional flow, the parts in the middle and top layer of the load exhibit excessive distortion. With reversing gas flow, the helix angle variations were

Gas-Flow Reversing

High-pressure gas quenching is typically performed with a flow direction from top to bottom through the load. However, this unidirectional quench can lead to variation of the hardening results. This variation is caused by warming of the quench gas and by aerodynamic flow conditions, which differ from layer to layer due to wake effects between the layers. Modern gas-quenching chambers offer the possibility to reverse the direction of the gas flow during quenching. Reversing gas flow means that the flow of gas is alternated back and forth from top to bottom and bottom to top. By alternating the gas-flow

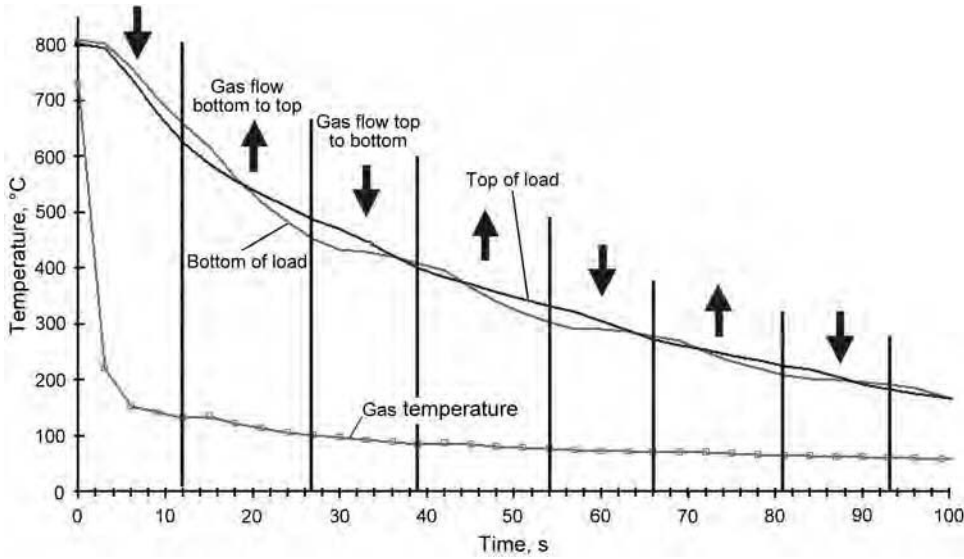


Fig. 17 Cooling curves in the tooth-root core of truck gears when applying high-pressure gas quenching with gas reversing. Cooling curves are from the top and bottom levels of the load; additionally, the direction of gas flow is indicated.

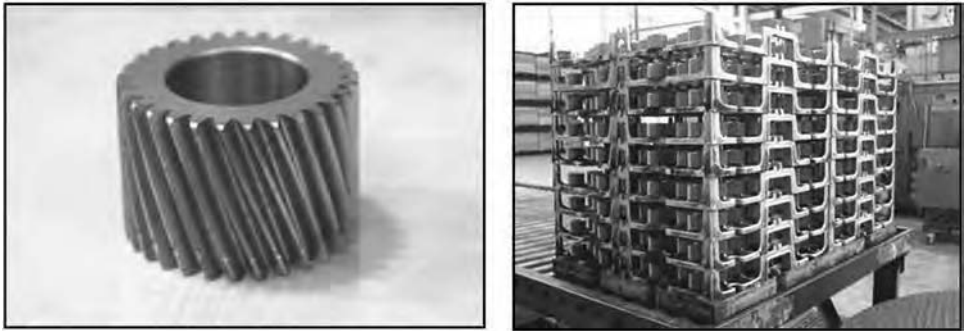


Fig. 18 Final-drive pinion planetary gear (diameter = 31 mm, 24 teeth) and production load (9 layers with 1056 pieces total)

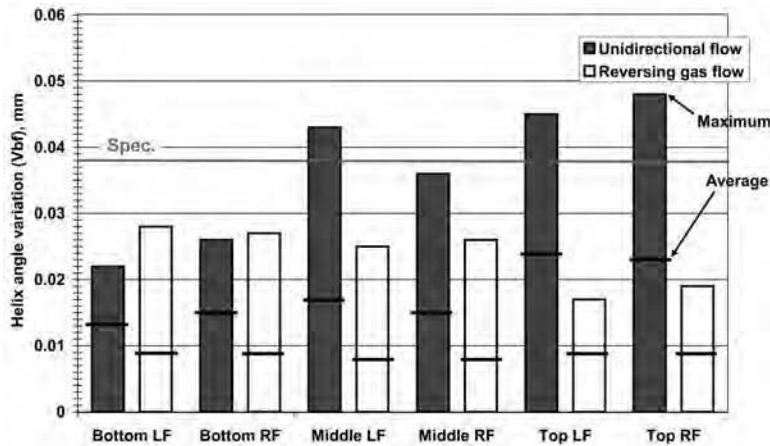


Fig. 19 Reduction of distortion by application of reversing gas flow; comparison between unidirectional and reversing gas flow (helix angle variation of final-drive pinion gears after heat treatment in bottom, middle, and top layer; LF = left flank; RF = right flank; specified maximum after heat treatment: 38 μ m)

significantly reduced. For example, for the right flank of the gears from the top layer, the maximum helix angle variation was reduced by 61%.

With the optimized reversing gas-flow process, it is not necessary to machine the teeth of these final-drive pinion gears after heat treatment. Only the bores and faces of the gear are machined after heat treatment. This example shows the significant potential to reduce distortion with reversing gas flow.

Dynamic Gas Quenching

In addition to the possibility for adjusting quench intensity precisely to the desired level and the possibility for alternating gas-flow direction, HPGQ offers the possibility for changing quench intensity during quenching. When applying this process in cold chambers, it is referred to as dynamic quenching or interrupted quenching. The goal of dynamic quenching is to reduce distortion. The variation of quench intensity is typically time-controlled. By lowering the cooling speed, the thermal and transformation stresses can be reduced, thus leading to less distortion.

It is recommended to reduce quench intensity before the martensite start temperature (M_s) is reached in any location of the part, by reducing the gas velocity. As a result, the thermal gradient and therefore the thermal stresses in the part are reduced. Furthermore, the reduction in temperature difference leads to a more simultaneous transformation into martensite in the surface and the core, which results in a reduction in transformation stresses. By reducing the thermal and transformation stresses, less plastic deformation is generated and therefore less distortion.

Figure 20 schematically shows the cooling curves during dynamic quenching. The diagram shows temperatures on the surface and in the core of different-sized parts when gas velocity is reduced to zero for a certain time. For a large specimen, the surface temperature can rise after the gas velocity is stopped, because the hot core reheats the surface. To prevent such reheating, the gas velocity should not be reduced to zero but to a level that prevents reheating.

A homogeneous temperature field inside the component and a lower cooling speed during martensite formation result in fewer thermal and transformation stresses. Based on the reduction of these stresses, the magnitude and spread of distortion is reduced.

The process of dynamic quenching is explained with two examples in the following.

Idler Gears

Figure 21 shows the helix angle variation ($f_{h\beta}$) of idler gears after application of different quench methods. The idler gears have an outside diameter of 179 mm, a height of 19 mm, 67 teeth, and are made of 16MnCr5 material.

After HPGQ without dynamics, the variation of $f_{h\beta}$ is slightly reduced compared to oil quenching. After HPGQ with dynamic quenching, the variation of $f_{h\beta}$ is significantly reduced (Ref 13).

In addition to the absolute values of $f_{h\beta}$ after heat treatment, the changes of $f_{h\beta}$ during heat treatment were determined as well. Here, changes during heat treatment mean the differences between the values before and after heat treatment. Compared to oil quenching, the average change of $f_{h\beta}$ was reduced by 37% for the left flanks of the teeth and by 17% for the right flanks of the teeth when applying HPGQ with dynamic quenching.

Internal Ring Gears

Quenching of thin-walled parts leads to distortion in terms of out-of-roundness. Figure 22 shows the runout values of a ring gear with internal toothing before and after heat

treatment. The ring gears have a diameter of 140 mm, a height of 28 mm, 98 teeth, and are made of ASTM 5130M material. The average roundness before heat treatment is 30 μm . After heat treatment on an alloy fixture and with standard HPGQ, the runout values were far beyond the required specification of 150 μm . By using a carbon-fiber-reinforced carbon (CFC) fixture, the values were reduced significantly. When using a CFC fixture in conjunction with dynamic quenching, the specification of 150 μm maximum was successfully met (Ref 14). Because the process proved to be very stable, the gear manufacturer was able to completely eliminate all hard-finishing operations.

In another application on internal ring gears made of 5130M material, the average change of runout during heat treatment was reduced to 7 μm , and the maximum change of runout was reduced to 41 μm by application of dynamic quenching (Ref 15).

In summary, heat treatment distortion can be reduced significantly by application of HPGQ and dynamic quenching. In particular, the spread of distortion can be significantly reduced. This leads to substantial cost-savings because the hard-finishing operations can be drastically reduced or even completely eliminated.

Fixtures for Gas Quenching

When designing the load configuration, it is mandatory for economic reasons to put as many parts into the load as possible while still guaranteeing the specified quality after treatment. Typical distance between parts in the load is 10 to 20 mm. The minimum distance between components should not be below 5 mm.

When designing the fixture, special attention should be given to ensure the following:

- Sufficient permeability for the gas stream to flow through the load
- Thermal mass of the fixture should be as low as possible
- Horizontal support of the components, to minimize distortion
- Robust design for easy handling of the fixtures

Ideally, a three-point contact between components and fixtures should be established. Gear wheels can be loaded either lying horizontally or hanging vertically in the fixture. Shafts must hang vertically to reduce distortion.

Two different groups of fixture materials can be used for HPGQ: high-nickel-content alloys and CFC materials. High-nickel-content alloys such as DIN 1.4818 are used in oil quenching as well. The CFC materials are made from a carbon matrix with embedded fibers, where 50

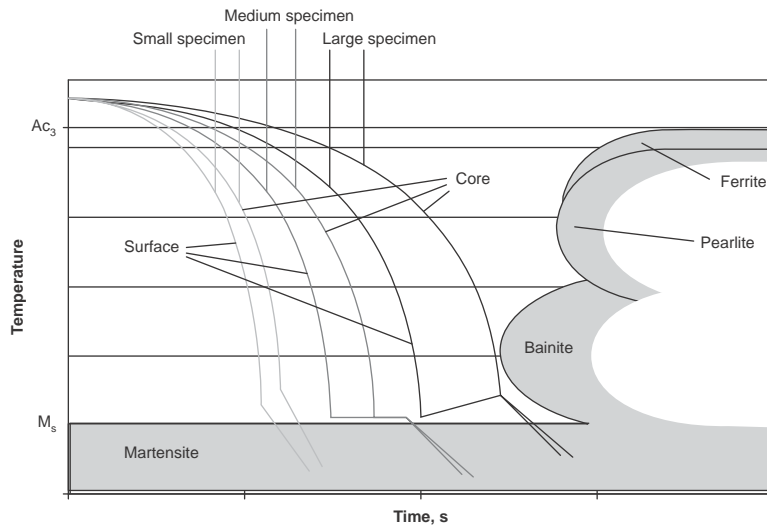


Fig. 20 Schematic illustration of dynamic quenching for different-sized specimens

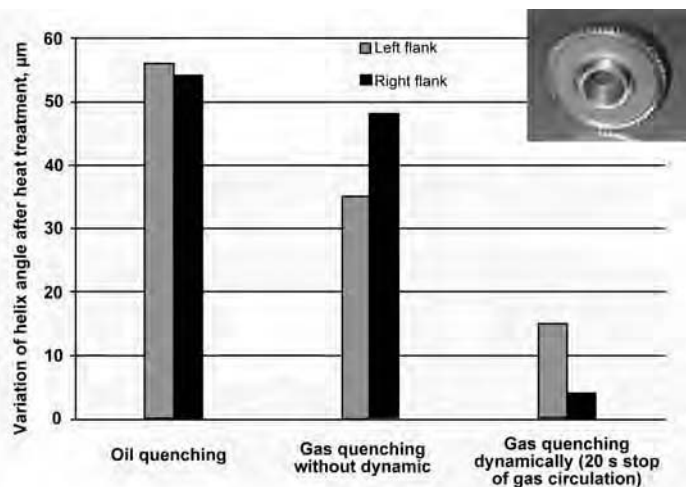


Fig. 21 Helix angle variation ($f_{h\beta\text{max}} - f_{h\beta\text{min}}$) of idler gears with 179 mm diameter made of 16MnCr5 after heat treatment with different quenching methods

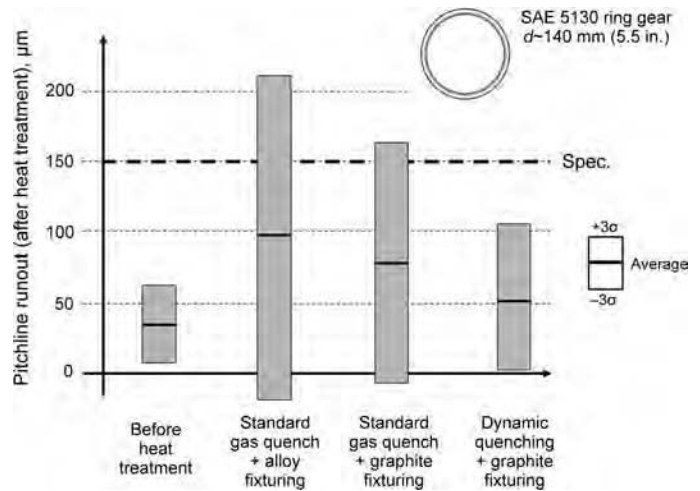


Fig. 22 Pitchline runout of internal ring gears before and after heat treatment. Material = ASTM 5130M; diameter = 140 mm; height = 28 mm; 98 teeth

to 60% of the volume consists of fibers. The CFC is a heat-resisting material that can be used at temperatures up to 2000 °C if a protective atmosphere or vacuum is applied. The strength of CFCs even increases with increasing temperature. Compared to room temperature, the hot bending strength at 1000 °C is increased by ~15%.

Fixtures made of CFC incorporate a light design and do not tend to creep during use at high temperatures. Unlike fixtures made of alloy, no bending or cracking of the fixture takes place even after many years of use. When treating components on CFC fixtures, it is guaranteed that all components are supported horizontally in the fixture. In many applications, this leads to a reduction of component distortion. The density of CFC is only 1400 to 1650 kg/m³ compared to ~7900 kg/m³ for steel. This is why CFC fixtures are much lighter than alloy fixtures and can be heated faster. However, this advantage is partly reduced by the higher specific heat capacity of CFC (~1 to 2 kJ/kg · K) compared to steel (~0.5 kJ/kg · K). A typical CFC fixture is shown in Fig. 23.

The maximum use temperature under oxygen-containing atmosphere should not exceed 350 °C. Therefore, CFC cannot be used in atmospheric gas carburizing due to the oxygen content in the process gas. The use of CFC is limited to vacuum processes such as low-pressure carburizing (LPC). These vacuum processes are often combined with HPGQ.

The CFC fixtures are usually much more expensive than alloy fixtures, but they have a much longer operating life. An operating life of 11 years or more has been proven in industrial application. When investing in CFC fixtures, the operating life is typically estimated to be 5 years, whereas the operating life of

alloy fixtures is typically estimated to be 1.5 to 2 years.

Control of Distortion with HPGQ

As with all heat treating processes, low distortion can only be achieved if the manufacturing process chain before heat treatment, including melting, casting, cutting, soft machining, and so on, is optimized and stable. It is important to create low levels of residual stress in the components before heat treatment. When blanks with excellent material homogeneity and low residual-stress level are provided, the HPGQ process can achieve low levels of distortion.

Due to the missing phase transition in the gaseous medium, HPGQ in many applications leads to reduced distortion compared to liquid quenching. For a lot of applications, it is not the absolute height of distortion that causes manufacturing problems but the spread of distortion. When the spread of distortion is low, it can be precompensated in soft machining. So, for many applications the challenge is to optimize the HPGQ in such a way that it provides a heat treatment process with very little spread of distortion within a load and over time from load to load. It was proven for many applications that HPGQ leads to a significant reduction in the spread of distortion (Ref 14, 16). Figure 24 depicts a comparison between the concentricity of bevel pinions after LPC and HPGQ and after gas carburizing and oil quenching. The bevel pinions were made of ASTM 8625 material and have a height of 280 mm and a head diameter of 85 mm. Further distortion improvements can be achieved with the application of gas-flow reversing and dynamic gas quenching.

REFERENCES

1. K. Loeser, V. Heuer, and G. Schmitt, Auswahl Geeigneter Abschreckparameter für die Gasabschreckung von Bauteilen aus Verschiedenen Einsatzstählen, *Härt.-Tech. Mitt.*, Vol 60 (No. 4), 2005, p 248–254
2. A. Stich and H.M. Tensi, *Härt.-Tech. Mitt.*, Vol 50, 1995
3. D.S. MacKenzie, G. Graham, and J. Janowski, “Effect of Contamination on the Heat Transfer of Quench Oils,” Sixth International Quenching and Control of Distortion Conference, Sept 9–13, 2012 (Chicago, IL)
4. D. Zimmermann, Anwendung von Hochdruckluft-Abschrecktechnik an einer Durchstoßanlage zur Einsatzhärtung von PKW Getriebeteilen, *Gaswärme Int.*, Vol 54 (No. 7), 2005
5. M. Korecki et al., Single-Chamber HPGQ Vacuum Furnace with Quenching Efficiency Comparable to Oil, *Ind. Heat.*, Sept 2009, p 73–77
6. *Handbuch der Kunststoffformstähle*, 1st ed., Edelstahlwerke Buderus AG, Auflage, 2002
7. M. Lohrmann, “Experimentelle und Theoretische Untersuchungen zur Vorausbestimmung des Wärmebehandlungsergebnisses beim Hochdruckgasabschrecken,” Dissertation, Universität Bremen, 1996
8. T. Lübber, “Zahlenmäßige Beschreibung des Wärmeübergangs flüssiger Abschreckmedien am Beispiel zweier Hartöle als Wesentliche Randbedingung für die Numerische Simulation von Wärmebehandlungsprozessen,” Dissertation, Universität Bremen, 1994
9. V. Heuer and K. Loeser, Experimentelles Verfahren zur Ermittlung von Wärmeüber-



Fig. 23 Heat treating fixture made of carbon-fiber-reinforced carbon. Courtesy of Graphite Materials GmbH, Zirndorf

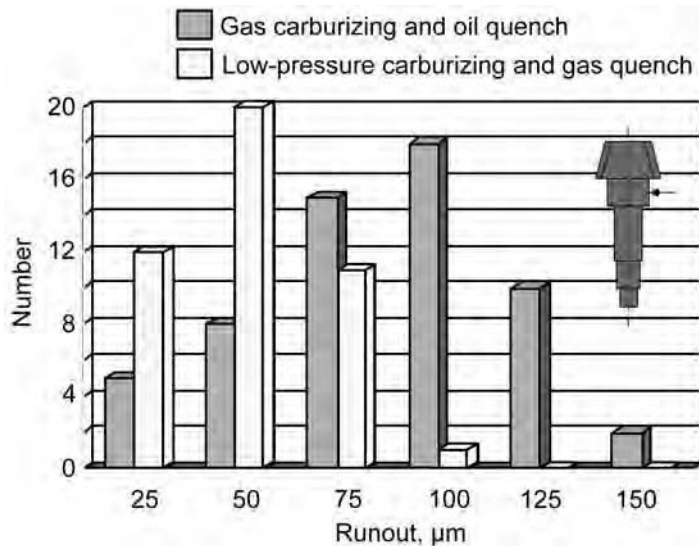


Fig. 24 Runout of pinions; comparison between low-pressure carburizing and high-pressure gas quench and gas carburizing and oil quench

- gangskoeffizienten bei der Hochdruck-Gasabschreckung, *Härt.-Tech. Mitt.*, Vol 59 (No. 6), 2004, p 432–438
10. “Stirnabschreckversuch,” DIN EN ISO 64, Jan 2000
 11. VDEh calculation sheets for Jominy hardenability curve
 12. V. Heuer, D.R. Faron, D. Bolton, M. Lifshits, and K. Loeser, Distortion Control of Transmission Components by Optimized High Pressure Gas Quenching, *J. Mater. Eng. Perform.*, to be published
 13. V. Heuer and K. Loeser, Entwicklung des Dynamischen Abschreckens in Hochdruck-Gasabschreckenanlagen, *Mater.wiss. Werkst. tech.*, Vol 34, 2003, p 56–63
 14. K. Loeser, V. Heuer, and D. Faron, Distortion Control by Innovative Heat Treating Technologies in the Automotive Industry, *Härt.-Tech. Mitt.*, Vol 61 (No. 6), 2006, p 326–329
 15. V. Heuer, D.R. Faron, D. Bolton, and K. Loeser, “Low Distortion Heat Treatment of Transmission Components,” AGMA Technical Paper 2010, ISBN 978-1-55589-979-0
 16. H. Altena, F.Schrank, and W. Jasienski, Reduzierung der Formänderung von Getriebeteilen in Gasaufkohlungs-Durchstoßanlagen durch Hochdruck-Gasabschreckung, *Härt.-Tech. Mitt.*, Vol 60 (No. 1), 2005, p 43–50

Salt Quenching

J.R. Keough, Applied Process Inc.

THE USE OF MOLTEN SALTS in the quenching of ferrous materials is covered in this article. Salts are also used for descaling, processing of nonferrous materials, nitriding, and removing various coatings and ceramic shell material. Molten salts are usually the medium of choice for high-temperature quenching. Examples are:

- Isothermal annealing of high-alloy steels
- Minimizing scaling, distortion, and cracking of high-speed tool steels
- Reducing the risk of cracking during martensite formation (e.g., spring wire)
- Formation of high-temperature transformation products

Molten salt is the quenching medium most commonly used in austempering and mar-quenching of ferrous materials because:

- It transfers heat rapidly.
- It virtually eliminates the problem of a vapor phase barrier during the initial stage of quenching.
- Its viscosity is uniform over a wide range of temperatures.
- Its viscosity is low at austempering temperatures (similar to that of water at room temperature), thus minimizing dragout losses.
- It remains stable at operating temperatures and is completely soluble in water, thus facilitating subsequent cleaning operations.
- Salts can be easily recovered from wash waters by evaporative methods and recycled.

The most common salts used for quenching are nitrite/nitrate salts: various mixtures of sodium nitrite (NaNO_2), potassium nitrate (KNO_3), and sodium nitrate (NaNO_3). A ternary diagram for those salts is shown in Fig. 1. The phase diagram illustrates the dependence of melting point on ratio of the salt mixture. The ratio of salt mixture may also affect viscosity of the medium, which can influence cooling rate (Ref 1).

The three salts shown in Fig. 1 are those most commonly used for salt quenching. Sodium nitrite is typically more expensive than the potassium salts, but it has a lower melting

temperature and, as such, drains from the quenched parts more effectively, reducing salt dragout. Systems used at low quenching temperatures primarily use a 50/50 mixture of sodium nitrite and potassium nitrate. With these nitrite-nitrate salt mixtures, water additions can be accomplished to increase quench severity. Systems operating at higher temperatures can use a 50/50 mixture of the two nitrate salts. A totally nitrate salt system *must never use water additions* because of a resultant acid reaction that can embrittle carbon steel parts and quench tank components and mechanisms. Additionally, all of these salts can be reclaimed from the washing water, which is discussed later.

Ranges of the low-temperature salts are roughly (Ref 2):

- 150 to 500 °C (300 to 930 °F) for binary mixture of equal parts of potassium nitrate and sodium nitrite
- 260 to 620 °C (500 to 1150 °F) for binary mixtures of potassium nitrate and sodium nitrate

The lowest-temperature salt mixtures can be used at operational temperatures as low as 175 °C (350 °F) with low dragout. However, melting points as low as 80 °C (175 °F) can be achieved with water additions up to 10% H_2O (Ref 3). Salt baths are subject to potential

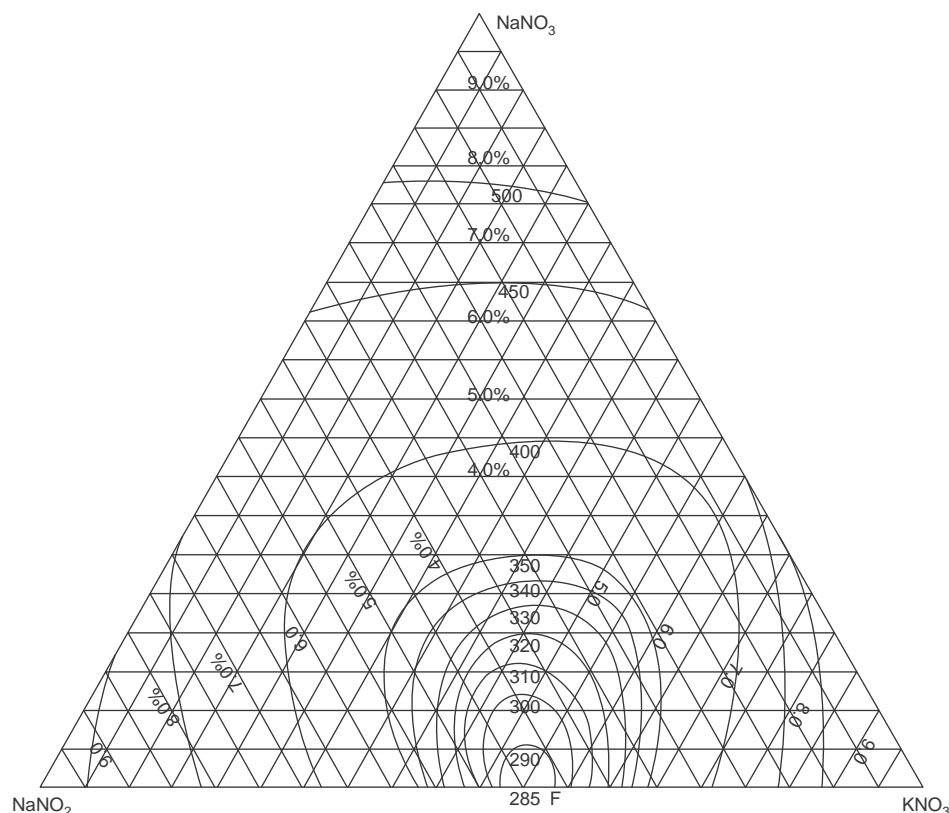


Fig. 1 Freezing point isotherm for a ternary nitrite-nitrate salt mixture. Source: Park Chemical (now Heatbath Corporation)

explosive degradation at temperatures above 600 °C (1110 °F) (Ref 4, 5).

Melting in of new salt requires that the quench salts are added at the proper ratio to a heated water bath; the volume of the salt added is roughly equal to the water. Note: if the salt is not added at the target ratio it may not melt. The heating is continued. When the solids are dissolved, additional granular salt is added with a decreasing percentage of water. This is repeated at a pace suitable for the heating capacity of the system until the new bath temperature exceeds the melt point of the target nitrite-nitrate salt mixture. Then agitation should be initiated and dry, granular salt is added (at ratio) until sufficient volume of the desired molten quench chemistry is obtained.

Equipment for Salt Quenching

The mass of the quench must be properly designed for the furnace load being quenched. A sufficient volume of cool salt must be circulated to carry the heat of the quenched parts away from the parts. A sufficient mass of quench salt must be provided as a heat sink to keep the temperature rise of the quenching bath to a low, acceptable level. A 20:1 mass ratio of quench salt to load will produce a maximum temperature spike of 8 °C (15 °F). Lesser salt-to-load ratios will result in greater temperature variations during quenching and the chance for excessive local salt decomposition.

Continuous Operation. In a continuous operation the system must be sized so that the conveyerized handling system can effectively catch and carry the parts through, and out of, the quench tank. The size and speed of the conveyor will depend on the capacity of the furnace feeding it and the required time in the salt.

If the quench is attached to an atmosphere furnace, special precautions must be taken so that carbon soot can never build up in contact with the nitrate salt, an explosion hazard that is discussed later.

The quench tank for a continuous system should be sized to maintain a constant temperature at maximum throughput with the cooling capabilities of the system being used. Some systems simply use oversized tanks and depend on convection cooling. Other systems, depending on the system manufacturer or design, have either forced-air cooling jackets, surface mounting water plate coolers, or immersion coolers to maintain the desired temperature during maximum loading.

Agitation in continuous systems usually consists of a pump system that produces an upward flow of quenchant in the area where the parts pass into the salt. The ideal flow rate for maximum cooling is the maximum laminar flow rate for the temperature and quench configuration used. This flow rate, however, may not be practical for very small or light parts that could float and become scattered or miss the conveyor.

The time in the quench is a function of the time required to cool the parts and, in the case of an isothermal heat treatment, to fully transform the part to the desired microstructure. For instance, medium-carbon steel clips may transform fully from austenite to bainite in as little as 5 min or as long as 20 min depending on the quench temperature used. A practical solution is to set the conveyor speed at 30 min. to cover the range and assure that processed parts are fully transformed. In turn, the quench conveyor is sized so that at the 30 min speed and maximum throughput the conveyor is not overloaded.

Batch Operation. Batch quenching operations must provide systems to extract heat quickly after the quench. Continuous quench systems continually add a smaller mass of quenched parts. Batch quenches, however, must deal with a large amount of heat being removed when a maximum mass load is quenched. This is accomplished with oversized quench tanks, specialized cooling systems, and agitation with flow directed by fixed or variable baffle systems. Batch quenching systems use either undirected propellers or directional pumps and baffled systems that direct the quench upward through the load.

For the maximum heat extraction rate, the speed of the quenchant should be at the maximum laminar flow rate for the salt temperature and quench configuration employed. The flow rate will be a function of the size of the quenching system and the design capacity of the agitators employed. That will define the maximum laminar (nonturbulent) flow rate achievable. An effectively agitated quench should turn the volume of the quench tank at least 100 times per hour, although many quenches allow turn rates of up to 400 quench volumes per hour.

Batch quench operations can be more flexible than continuous systems. This is needed for quenching things such as 52100 steels or cast irons that may require isothermal transformation times of several hours. In fact, some high-carbon bearing alloy steels are isothermally quenched for up to 24 h to achieve maximum properties. Austempered ductile iron (ADI) quench processes can range from 30 min to over 4 h to transform the microstructure from austenite to the acicular ferrite and carbon-stabilized austenite structure known as *austferrite*.

Step quenching is typically only used on batch-type systems being used for austempering or marquenching (martempering). It is accomplished by initially quenching the parts into a bath that is just above the martensite start (M_s) temperature for the shortest time necessary to stabilize the temperature of the parts. The parts are then transferred into the finish bath. For marquenching, the secondary bath is typically at a temperature below the M_s to produce martensite. For austempering, the primary bath is at a temperature above the M_s to drop the temperature of the part rapidly. The secondary bath is at a higher temperature

that produces the austempered (bainitic) microstructure of the desired hardness in a shorter time. Step quenching is generally used to increase the quench severity in the initial quench. Some people have even experimented with first quenching in the high-temperature salt and then transferring to a lower-temperature salt to produce a higher bainitic hardness in a shorter time.

Time and Temperature Considerations

The quenching temperature range will determine the salt selection and will also affect the time required in the bath. For marquenching (martempering), the temperature is generally near or below the M_s . For austempering, the bath temperature is held above the M_s and the resultant hardness of the transformed part is a function of the quenching temperature. Higher quench temperatures produce lower hardness structures. Lower quench temperatures produce higher hardness structures. As noted, the lowest-temperature salt mixtures can be used at operational temperatures as low as 175 °C (350 °F). Salt bath temperatures in the range of 195 to 350 °C (385 to 660 °F) have only a minimal effect on the Grossmann factor (Table 1).

Typically nitrite-nitrate quench tanks are made of plain carbon steel, but care must be taken at higher quench temperatures because plain carbon steel weakens dramatically above approximately 400 °C (750 °F). Furthermore, if the local temperature of the nitrate salt exceeds approximately 540 °C (1000 °F) it decomposes rapidly, giving off free oxygen and spot rusting the parts. This effect can be observed as brown "water spots" on parts run in continuous furnaces and brown contact marks where parts contact each other or the fixtures in batch quenches.

Transformation Time. The design of the quenching system will be affected by the range of transformation times being considered. Quenching times can range from a few minutes for marquenching or austempering of plain carbon steels, to many hours for the low-temperature austempering of high-carbon alloy steels or

Table 1 Effect of salt temperature on quench severity

A KNO_3 - $NaNO_2$ salt with a melting temperature of 135 °C (275 °F) was used with no agitation.

Salt temperature, °C (°F)	Grossman <i>H</i> factor, in. ⁻¹	
	Center	Surface
195 (385)	0.46	0.63
200 (390)	0.45	0.65
230 (450)	0.40	0.65
270 (515)	0.45	0.64
295 (560)	0.41	0.57
350 (660)	0.43	0.58

Source: Ref 1, 6

austempering of cast irons. Batch-type systems may employ multiple quenches. Continuous or semicontinuous systems must provide for a dwell time long enough for the maximum transformation time. In these systems the conveyor speed or push time must be adjustable and this may or may not affect the loading rate or push time of the austenitizing furnace.

Critical Characteristics for the Operation of Salt Quenching Systems

Composition of Quenchant (Chemical Analysis, Melt Point). As previously discussed, the salt selected is largely a function of the temperature range at which it will be used. If a salt with a higher melting point is used at a lower processing temperature, the salt will thicken or freeze on the surface of the parts as they rise from the quench and be dragged into the wash. Salt mixtures with lower melting temperatures drain more readily from the parts and have a lower viscosity over the commercial range of salt temperatures but are generally higher priced.

Contaminants. As with any quenching system, the quenchant must be properly maintained. Routine tank cleaning is required to remove rust and debris from the tank sides and bottom. If salt is reclaimed from the washing water, settling tanks, magnetic techniques, or centrifugal techniques can be used to separate undesirable particles from the water. The salt is totally dissolved in the water and will not settle out for concentrations below 10%.

After extended reclamation and reuse of the salt, carbonates can form in the bath. These form hard particles that condense on cooler surfaces. Carbonates can be mitigated by controlling the pH of the wash water with a measured acid treatment prior to reclaiming. The salt supplier should be able to define the process necessary for controlling carbonates.

Anti-caking agents can be found in some commercially premixed salts. Although these additives can minimize the agglomeration of the salt, they can also cause unwanted foaming and outgassing during initial melting. Unless the salt is added with a mechanism that requires the salt to flow freely, the use of these additives is not recommended.

Quenches in salt-to-salt systems can be difficult to reclaim. The high-temperature salts form a thin skin on the parts being removed from the austenitizing salt and transferred to the quench. Although this skin protects the parts from the ambient atmosphere, it also forms sludge in the quench salt that must be skimmed from the bath. Failure to properly remove the high-temperature salt sludge can increase the viscosity and degrade the quench severity of the quench bath.

Temperature control in the salt quench bath is critical. (Depending on the process, a control

range well within ± 20 °F, or ± 11 °C, is demanded.) Most salt quench processes require a narrow temperature range to produce the desired results. If the temperature is too low, the salt can thicken and freeze. If the salt temperature is too high, the salt can chemically crack, giving off free oxygen that can damage the parts and change the chemical ratio of the salt.

The quenching system requires a heating system sufficient to raise the temperature to the maximum process quench temperature in the absence of work. It requires a cooling system sufficient to maintain a uniform temperature while processing the maximum volume of work.

The temperature of the salt in the presence of a quenched load will vary from the bottom to the top of the load. Thermocouple placement in the quench should be such that it best approximates the average temperature of the salt in a maximum mass load. A secondary monitoring thermocouple should be provided to assure that the salt temperature has not exceeded the system minimum or maximum salt temperature. The thermocouple protection tubes can be made from mild steel. If the quench tank is heated using gas burners, mild steel can be used for the heating tubes. While the flame temperature is over 1090 °C (2000 °F), the tubes are fully immersed in the salt and temperatures do not rise much over 540 °C (1000 °F).

Agitation and Water Additions. Agitation in molten salt tanks is essential for both the quality and the safety of the system. Agitation increases the quench efficiency, increases temperature uniformity, facilitates the addition of water, and eliminates the possibility of a boiling liquid expanding vapor explosion (referred to as BLEVE). As previously noted, turning the volume of the quench tank at least

100 times per hour is an effective level of agitation. Many quenches allow turn rates of up to 400 quench volumes per hour.

Still (unagitated) salt is a rather poor heat conductor. Although it is not subject to the vapor barrier that forms in water or oil, an unagitated salt bath would be of little value as a cooling medium in heat treatment. Figure 2 shows the maximum relative quench severity of molten salt using approximate Grossman numbers for several quenchant and conditions. As can be seen, dry salt with agitation exceeds the quench severity of still mineral oil. When a small amount of water (2%) is added to an open, agitated salt bath, the quench severity approaches that of agitated additive oil. In specially designed pressurized batch quench systems, up to 12% water can be added, greatly increasing the quench severity.

When maximum quench severity is desired, the speed of the quenchant flow should be the maximum laminar (nonturbulent) flow achievable with the system. This will be affected by the agitator design, the temperature of the salt, the depth of the bath, and other factors. An effective measure is to use a variable-speed agitation system and experiment with speeds until turbulence is achieved, then reduce the final speed from that setting. The blade design on any propeller also affects the maximum achievable flow. The blades should be properly sized to smoothly push salt at the appropriate flow rate. An undersized or improperly design propeller will shear the salt at a speed well below the flow rate necessary to provide adequate flow.

The quenching severity of a nitrite-nitrate salt can be increased significantly by careful addition of water. Agitation of the salt is necessary to disperse the water uniformly. Water is continuously evaporating from the bath surface, and the rate of evaporation increases during

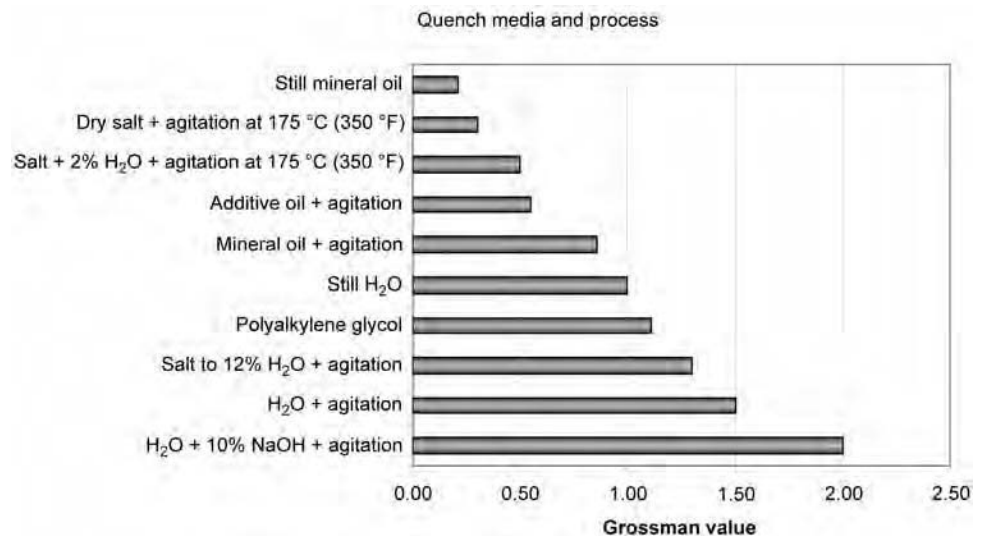


Fig. 2 Relative maximum quench severity of various quench systems compared on the Grossman scale. Source: Research performed by Applied Process Inc. and AFC Holcroft

quenching of hot work. Thus, it is necessary to add water to maintain the water concentration and a uniform quenching severity.

Water can be added with complete safety as follows:

- Water may be misted at a regulated rate into a vigorously agitated area of the molten bath.
- In installations where the salt is pump circulated, returning salt is cascaded into the quench zone. A controlled fine stream of water may be injected into the cascade of returning salt.
- The austempering bath may be kept saturated with moisture by introducing steam directly into a bath. The steam line should be trapped and equipped with a discharge to avoid emptying condensate directly into the bath.
- Steam additions of water to ADI baths is done with operating temperatures above 260 °C (500 °F).

Addition of water to increase the quenching severity of salt usually is made by directing a continuous stream of water into the molten salt bath at the agitator vortex. A protective shroud surrounds the water spray to prevent spattering. The turbulence of the salt carries the water into the bath without spattering or hazard to the operator. Water should never be added to a salt bath by hand, by bailing, or by bulk.

In baths exposed to atmospheric pressure, water can be added to the approximate percentages shown in Table 2. The percentage of water in salt can be measured by sampling a

Table 2 Amount of water that can be added to a molten salt bath with proper agitation and exposed to atmospheric pressure

Temperature, °C (°F)	Water concentration in salt, %
205 (400)	½ to 2
260 (500)	½ to 1
315 (600)	¼ to ½
370 (700)	¼

small quantity of the salt and weighing it accurately before and after dehydrating it by heating to 370 to 425 °C (700 to 800 °F). Water addition also suppresses the melt point of nitrite-nitrate salt baths. Figure 3 shows this effect.

A critical note about water addition: water addition can be done successfully with nitrite-nitrate salt mixtures to effectively increase the quench severity as mentioned previously. However, *water should never be added to an all-nitrate salt bath* because an acid reaction can occur that can embrittle the parts, as well as the mild steel structures, tanks, and conveyors. One-hundred-percent nitrate salt mixtures can be used safely and cost effectively without water addition, but the quench severity of such baths will be limited.

The Rushman method (Ref 7) is an effective way to determine the quench severity. Another quench severity test is described in Ref 8. Several suppliers also sell batch measuring devices used to quantify quench severity. They are called quench probes that measure cooling rate. The devices use either electric potential, a timed probe cooling rate, or a relative power required to heat a probe in the bath. The data or feedback from such devices can be used to adjust the agitation and/or water addition to create a specific quench severity. Performance varies, and use of probes to quantify quench severity is not universally recommended. Several brands are available from suppliers such as Thermet (India), Degussa (Germany), Houghton (United States), IVF (Sweden), and Ke Hui (China).

Loading and Handling Systems. The quench transfer and loading systems must be adequate for the purpose. They must be sized for the maximum throughput of the heat treat system.

In continuous belt-type systems, the parts must fall from the belt (without hitting baffles or chutes) directly into the quench, down through the salt, and onto a conveyor. The conveyor must be designed to catch and contain parts of all the sizes processed. It must allow free flow of quenchant around the landing area for the parts without pushing small parts off of the conveyor. It must be sized to handle the

maximum furnace throughput for the longest quench time covered in the design. Most conveyors of this type are mild steel with side plates and flights that hold the parts while the conveyor slopes upward and carries the parts to a wash conveyor.

In semicontinuous systems (such as pusher-type systems) the transfer to the quench elevator or hoist must be done smoothly to prevent mechanical damage to the parts in the soft austenitic condition. The elevator or hoist that lowers the parts into the quench must be suitable for the maximum load. The pushes under salt need to be timed to allow for cumulative push time to meet the maximum quench time allowed for the design. (The pushes may be shortened for processes requiring a shorter quench.) Semicontinuous systems can employ a secondary tank, using the first tank as the quenching tank and the second tank as the transformation tank.

In batch-type systems the transfer to the quench hoist or elevator must be done smoothly to prevent damage to the soft, hot parts. The elevator or hoist must be adequate to smoothly raise and lower a maximum gross load. The area in the quench where the parts are initially cooled must be designed to direct the quenchant up through the load smoothly, so the under-salt structure is often designed to baffle and strengthen the structure. Batch-type systems may also use a secondary (transformation) tank if long quenches are required and the throughput of the furnace exceeds that of a single-tank quench.

Preventive Maintenance. As with any heat treating system, a salt quenching system requires a rigorous routine preventive maintenance plan to assure reliable performance. The plan should be well defined, executed as defined, and the checks and follow-up actions documented.

Each salt quenching system will have a different design, maker, and function, so the items to be checked will be unique to the specific equipment type. Some of the most critical items include:

- Thermocoupling and electronic measuring and recording devices
- Agitators (bearings, blades, speed)
- Chutes and channels
- Doors and door mechanisms
- Elevator and elevator mechanisms
- Tank wall and floor
- Water addition system
- Deposits of parts, scale, or carbonate precipitates
- Timers

Well-maintained salt quenching tanks can provide reliable performance for decades, however, in environments where a wide range of quenching temperatures are used, the thermal fatigue on the steel structure can ultimately cause cracks in the steel that will need to be weld repaired.

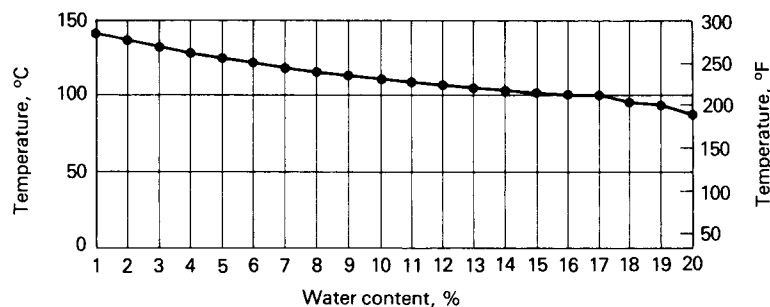


Fig. 3 Effect of water content on the freezing point of nitrite-nitrate salt bath

Environmental and Safety Considerations in Salt Quenching

Handling and Storage of Molten Salts.

Molten quenching salts should never be used or stored without agitation, especially in the presence of added water. In an extreme case with still salt, a skin or semisolid layer can develop on the surface of the bath. If there is a local hot spot under that layer and the layer is breached, even in a small way, the resultant drop in pressure can result in the instantaneous vaporization of the salt below and a resultant, explosive expansion. Agitation prevents the formation of the surface membrane and the possibility of a boiling liquid expanding vapor explosion.

Molten nitrate salt should not be used in the presence of carbon-base materials such as oils. Nitrate salts exposed to oils can create an explosive oxidation reaction. Facilities using salt should be free of oils and greases. Cloth, paper, wood, and other carbon-bearing materials should be stored in areas where they are not contaminated with salt that would result in making them more flammable. In short, salt quenching areas should be kept clean and free of organic materials.

Any containers, piping, pump or other devices used to handle or move salt must be clean, dry, and free of paint or oil. Baking of such containers and implements at a temperature above 400 °C (750 °F) is necessary before handling molten quench salt. New pipe is often coated with an organic finish. If that finish is not fully burned off and it comes into contact with molten nitrate salt, an explosive oxidation reaction will result. After pipes, containers, tools, and such have been burned off and used, they can be stored in a clean dry location and safely used subsequently for molten salt handling exclusively without re-baking.

Parts Washing, Salt Disposal, and Reclamation. After quenching, the parts have a thin film of quench salt on their surfaces. This film must be removed by water washing. Failure to properly wash the parts will cause them to corrode, the salt mixing with some machining fluids can produce a hazardous chemistry, and paint or plating adhesion will be problematic. This, necessarily, results in a quantity of water with an increasing salt content that must be dealt with safely and within legal regulations.

Although nitrites are used as meat curatives and nitrates are used as fertilizers, they are all considered to be low-level hazardous materials and are subject to national and local rules for handling and disposal. In many localities treated salt-quench wash water, with a certain maximum salt percentage, containing no chlorides or cyanates and within a codified pH range, can be discharged into the sewer. The processor must check the regulations in the local community.

Salt costs in heat treating systems with no reclamation can run from 5 to 15% of heat treat

sales. Salt costs in a facility with a fully capitalized reclamation system can be reduced to less than 2% of heat treat sales (including equipment depreciation, energy costs, pH balancing, and handling).

Salt-to-salt processors must deal with the separation of high-temperature (hardening) salt contamination in the quench salt, making salt reclamation a more expensive process. The hardening salt has a higher melting temperature and contains hazardous materials that can only be disposed of in licensed hazardous waste dumps. Figure 4 shows the solubility of hardening salt in a nitrite-nitrate salt versus the temperature of the quench.

Hardening salt can be separated by lowering the salt bath temperature to near the melt point and skimming the solid hardening salt layer from the surface. Skimming devices exist for this purpose. Atmosphere-to-salt producers can directly and economically reclaim the salt from the wash water. Salt-to-salt processors must undertake the aforementioned separation process prior to reclamation.

Salt reclamation is accomplished by acid treating of the wash water to a suitable (near neutral) pH, filtering/separating out of solids, and distillation of the salt from the wash water. Distillation can be accomplished using stand-alone, externally heated reclamation devices or with devices integrated into the quench using external power or waste heat from the heat treating process. Such systems can be purchased from heat treat equipment suppliers or custom designed for a specific facility.

Over time, reclaimed salt will increase in nitrate percentage due to the thermochemical

dynamics of the quenching process. Regular melt-point and chemical analyses will provide the user direction in salt addition to maintain the quench bath chemistry within a controlled range. Typically, salt additions to reclaimed baths are higher-percentage nitrite salts.

REFERENCES

1. R.W. Foreman, ASM National Heat Treating Conference, Sept 1988, as noted in *Handbook of Quenchants and Quenching Technology*, ASM International, 1993, p 310
2. A.K. Sinha, *Hardening and Hardenability, Ferrous Physical Metallurgy*, 1989, Butterworths, Boston, MA, p 441-522
3. C. Skidmore, Salt Bath Quenching—A Review, *Heat Treatment of Metals*, Vol 2, 1986, p 34-38
4. M.A.H. Howes, "The Cooling of Steel Shapes in Molten Salt and Hot Oil," Ph.D. thesis, London University, 1959
5. R.W. Foreman, *Heat Treat.*, Oct 1980, p 26-29
6. M.J. Sinnott and J.C. Shyne, *Trans. ASM*, Vol. 44, 1952, p 758-774
7. W.F. Rushman, How to Determine the Quench Severity of Oil and Salt Baths, *Met. Prog. Mag.*, Vol 84 (No. 6), Dec 1963, p 91-92
8. "Project A4001, Austempered Ductile Iron Data Base," 1989, ASME Gear Research Institute, Naperville, IL (now Pennsylvania State University, State College, PA)

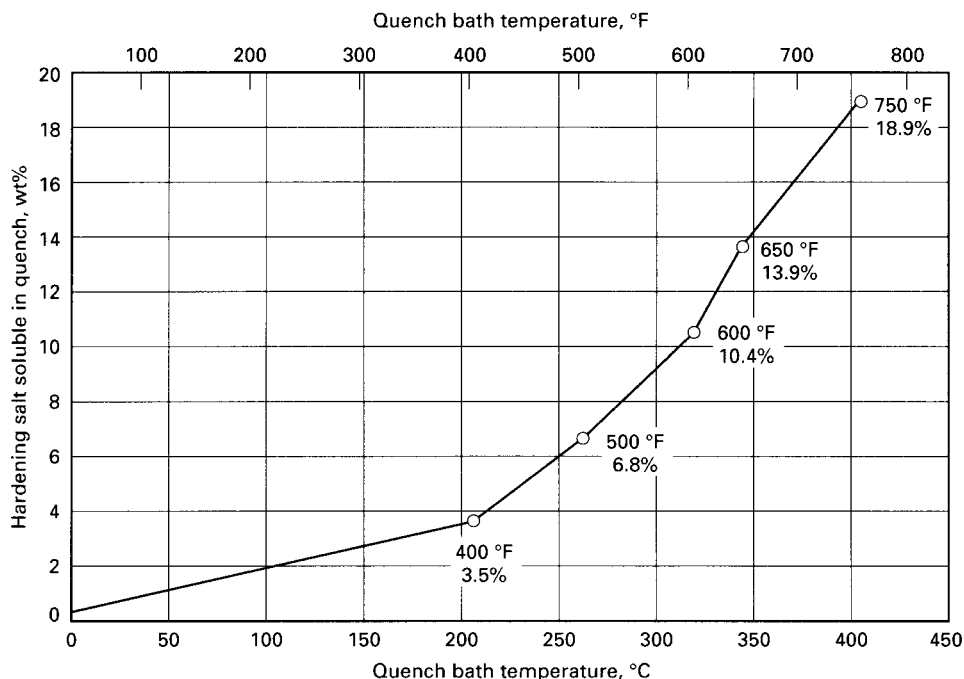


Fig. 4 Solubility of hardening salt in quench salt vs. quench temperature

SELECTED REFERENCES

- E.H. Burgdorf, Use and Disposal of Quenching Media—Recent Developments with Respect to Environmental Regulations, *Quenching and Carburizing*, 3rd Int. IFHT Seminar (Melbourne, Australia), Sept 1991, p 66–77
- D.R. Chenoweth, “Mixed-Convective, Conjugate Heat Transfer During Molten Salt Quenching of Small Parts,” US Sandia Report SAND97-8234. UC-406, Feb 1997
- P.J. Cote, R. Farrara, T. Hickey, and S.K. Pan, “Isothermal Bainite Processing of ASTM A723 Components,” US ARDEC Report ARCCB-TR-93035
- G.P. Dubal, The Basics Of Molten Salt Quenchants, *Heat Treat. Prog.*, Aug 2003, p 81
- R.W. Foreman, Salt Bath Quenching, *Proc. of the First International Conference on Quenching & Control of Distortion*, 22–25 Sept 1992 (Chicago, IL), p 8
- R.W. Foreman, Salt Quench Rivals Oil, Synthetics in Neutral Hardening Applications, *Heat Treat. Mag.*, Oct 1980
- J.R. Keough, “Austempering—A Small, Niche Heat Treatment with Large Powertrain Implications,” American Gear Manufacturers Association meeting 2004
- J.R. Keough and V. Popovski, “Large Austempered Parts—Monster Opportunities,” American Foundry Society Congress 2012
- W.R. Keough, Equipment, Process and Properties of Modern Day Austempering, *Proc. Int. Heat Treating Conference: Equipment and Processes*, April 1994
- J. Lefevre and K.L. Hayrynen, Austempered Materials for Powertrain Applications, *Proc. 26th ASM International Heat Treating Society*, 2011
- Molten Salts, *Handbook of Quenchants and Quenching Technology*, ASM International, 1992, p 309–316
- J. Rassizadehghani, Sh. Raygan, and M. Askari, Comparison of the Quenching Capacities of Hot Salt and Oil Baths, translated from *Metallovederiie I Termicheskaya Obrabotka Metallov*, (No. 5), May 2006, p 8–11
- J. Shi, S. Zou, J.J.M. Too, and R.W. Smith, On the Quenchability of Austempered Ductile Iron, *Cast Met.*, Vol 5 (No. 2), 1992
- D.E. Smith, Optimization-Based Inverse Heat Transfer Analysis for Salt Quenching of Automotive Components, *Int. J. Vehicle Des.*, Vol 25 (No.1/2), Special Issue, 2001
- L. Shu-Zhong, Problems Related to Salt Bath Quenching, *Jinshu Rechuli (Heat Treatment of Metals)*, (No. 5), Qishuyan Institute of Locomotive and Railway-Car Technology, 1991, p 59–61

Fluidized-Bed Quenching

Weimin Gao, Lingxue Kong, and Peter Hodgson, Institute for Frontier Materials, Deakin University

FLUIDIZATION occurs when fine-grained materials such as quartz sand are filled into a tank with a gas-penetrable bottom, and a gas, such as air, is blown up through the bottom at such a rate that the buoyed weight of the particles is completely supported by the drag force imposed by the gas. The particles are then able to move relative to one another. During fluidization, the bed of particles gains the appearance and many properties of a true liquid. The fluidized bed provides a means for exchanging heat between a metal part, the solid particles, and the fluidizing gas and is viable for quenching.

The potential of using the properties of the fluidized particle bed for quenching metals was first outlined in the 1950s. Since then, the use of fluidized beds has been investigated for a wide range of quenching applications, from cast iron and tool steels to aluminum alloys, and their use in industrial production is still growing (Ref 1–3).

Design of Quenching Fluidized Beds

The basic design of a quenching fluidized bed is shown schematically in Fig. 1

The bed consists of a container or retort with lateral walls and a gas-penetrable bottom (the so-called gas distributor), in which fine-grained materials, typically aluminum oxide particles, are fluidized by a passing gas introduced into the bed through the distributor. Parts to be heat treated are immersed in the fluidized bed, individually or loaded all together in a basket. Cooling of the bed to extract the heat removed from the load being quenched to maintain bed temperature is performed by external water jackets or internal tubing. This section briefly considers some of the important aspects of equipment design.

Gas Distributor. The gas distributor (also called a grid) induces a uniform and stable fluidization across the entire bed cross section. To ensure an even distribution of fluidizing gas, it is necessary to use distributors with dense gas-entry points, for instance, a sufficient number of holes in a perforated metal plate distributor, to have an adequate pressure drop through it. Otherwise, the bed will tend to fluctuate in

density with channelling and slugging. This is more important for shallow beds, such as wire patenting beds, because once channels have formed, these may persist, so that gas mainly passes up through the void regions of the bed, while nonfluidization prevails in other regions. On the other hand, because an excessive pressure drop can contribute appreciably to the power cost, it is much more practical to keep this to a minimum, consistent with approaching an even gas distribution.

The other most important design variables for a gas distributor include that it should support the weight of the bed when the gas is shut off, not become blocked by particles and atmospheric dust, not cause weepage of solids into the plenum beneath the distributor, and not cause the injected gas to directly impinge on the fixed surfaces, such as container walls or cooling tubes. More design tips and details are provided in major texts and information sources on fluidization (Ref 4).

It is practical to adopt a layer of coarse refractory particles to act as the distributor. The layer is located under the fine particle layer, and the size of its constituted particles is sufficiently large so as to remain unfluidized when the bed is operating.

Plenum. The plenum, or windbox, is the chamber immediately below the distributor. A good design of the plenum and of the connecting gas supply ducting should provide an even distribution of gas without relying solely on the pressure drop through the gas distributor. However, for the case where the ratio of the pressure drop through the distributor to the bed pressure drop is high enough, the plenum design will probably not be that important.

Container. The container is designed to fill a certain height of granules to form the fluidized bed. Refractory containers are generally used for the fluidized beds without an external cooling jacket, while retorts fabricated from a high-melting-point metal alloy are preferable for the fluidized beds with a surrounded cooling jacket to remove heat from the fluidized beds.

As with convection quenching tanks such as oil and water, the fluidized bed must be designed for a maximum temperature rise of no more than 20 to 40 °C (40 to 70 °F) during the quenching

cycle. The basic calculations used to size the container are identical in principle to that of sizing other quench systems, and thus, the heat load is calculated and related to the physical characteristics of the bed. For a continuous process, a bed with as shallow a depth as possible is preferable, because this gives the lowest pressure drop and power consumption. Beds too-deep will lead to an increase in the pressure drop through both the particle bed and gas distributor plate.

Bed Cooling and Temperature Control.

The quantity of heat that transfers to the bed from the hot parts must be carried off. For a continuous quenching fluidized bed, the rate of heat removal must be the same as the heat-release rate to maintain a constant quenching temperature. This can occur via the fluidizing gas that is blown in at a low temperature, takes the heat from the particles, and then leaves the bed at a higher temperature. By regulating the entrance temperature and the flow rate of the fluidizing gas, the temperature of the fluidized bed may be kept at a constant value. However, the primary cooling by the fluidizing gas is limited, because the velocity of the fluidizing gas through the bed cannot be forced up to more than the terminal velocity of the particles and is, generally, determined by approaching the cooling rate required by the heat treatment process for the parts. Such a fluidized bed is also limited in its production capacity per

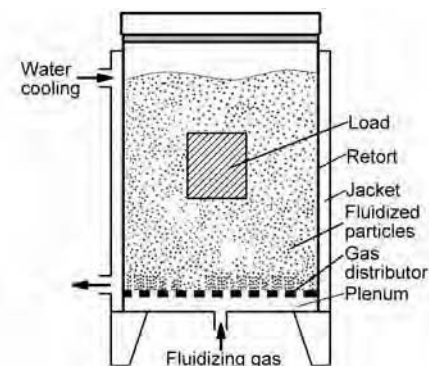


Fig. 1 Schematic representation of quenching fluidized bed

square meter of bed surface, so that a large fluidized bed must be designed to maintain the quenching temperature.

When the heat released from the hot treated parts largely exceeds the heat-removal capability of the quenching fluidized bed through only the fluidizing gas, it is necessary to use additional cooling systems and bed-temperature control means. These include a cooling container (Fig. 1), cooling pipes immersed in the bed, regular water spray, and air cooling of the bed surface (Fig. 2).

Cooling Retort. The retort is similar to that used in the external resistance-heated fluidized bed in terms of heat transfer. It is surrounded by a cooling jacket of a fluid, typically water, instead of a series of electrical elements. The amount of heat that can be removed by the cooling jacket is limited by the ratio of the area of retort surface to the bed volume. For wide, shallow beds, the cooling retort will probably be inefficient. The water jacket is preferably designed to have a higher heat-transfer rate from the retort to the cooling fluid than that from the fluidized bed to the retort. Various types of jackets can be used, such as conventional jackets with or without spiral baffles, dimple jackets, partial-pipe jackets (often called limpet jackets), and so on.

Immersed Cooling Pipes. The bed heat can be removed by cooling tubes immersed in the fluidized bed. This method provides a wide range of cooling rates, depending on the total length of the tubes, the configuration of the tubes in the bed, the cooling-fluid property, and the cooling-fluid flow rate. This cooling system with a controllable cooling-fluid flow rate provides a means to adjust and to maintain a constant temperature inside the quench bed for constant operation.

The cooling pipes can be in various shapes and configurations in fluidized beds. The heat-transfer surfaces or other fixed surfaces immersed into the beds should be either vertical or horizontal, not inclined, because oblique surfaces may cause the gas and particles to flow toward the higher end of the tubes.

When the cooling pipes are arranged along the inside wall of the container, the pipe surfaces should be separated sufficiently to avoid channelling upward in the gap, causing defluidization of the region and local gas bypass. For the cooling pipes horizontally crossing the fluidized bed, the density of the pipes per square meter bed surface should be controlled so as not to cause the bed to collapse and not to disturb the fluidization.

The heat-removal rate of the immersed cooling tube system is determined by the heat-transfer characteristics of the fluidized bed and forced convection flow through the tubes. When a fluidized bed at a temperature of T_{bed} is cooled by immersed thin tubes with a diameter of D , and the coolant inside the tubes has a temperature of T_{cf} , the rate of the heat that can be removed by per meter length of tubes can be approximated by:

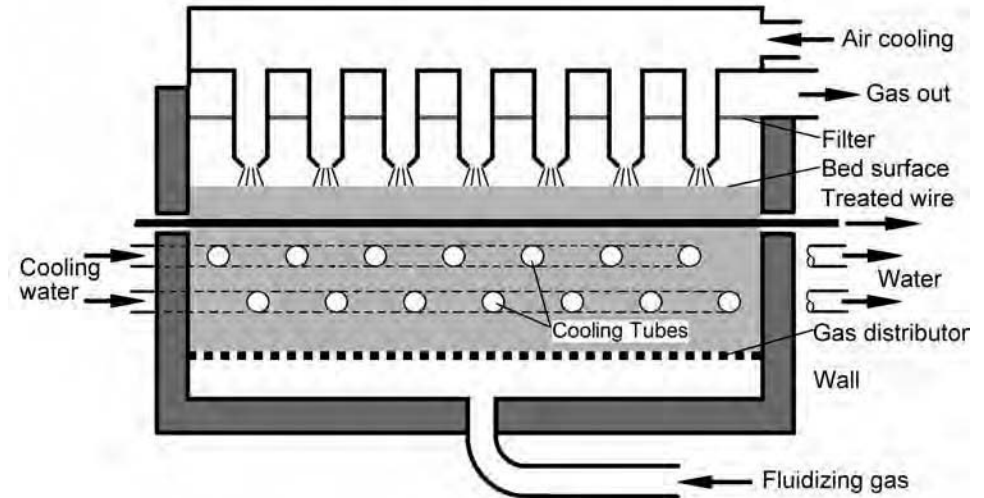


Fig. 2 Schematic representation of continuous-cooling fluidized bed with immersed cooling tubes and surface air spray cooling

$$q = \pi D \frac{h_{bed} h_{cf}}{h_{bed} + h_{cf}} (T_{bed} - T_{cf}) \quad (\text{Eq 1})$$

The convective heat-transfer coefficient between the cooling tubes and the fluidized bed, h_{bed} , is usually of the order of 300 to $500 \text{ W/m}^2 \cdot \text{K}$ (50 to $90 \text{ Btu/h} \cdot \text{ft}^2 \cdot ^\circ\text{F}$), while on the coolant side the heat-transfer coefficient for laminar flow in the cooling tubes of a length L , h_{cf} , can be determined by:

$$Nu_D = 3.66 + \frac{0.065 Re_D Pr \frac{D}{L}}{1 + 0.04 (Re_D Pr \frac{D}{L})^{2/3}} \quad (\text{Eq 2})$$

or by:

$$Nu_D = 0.023 Re_D^{0.8} Pr^{0.4} \quad (\text{Eq 3})$$

for turbulent flow, where the Nusselt number $Nu_D = Dh_{cf}/k$; the Reynolds number $Re_D = \rho v D / \mu$; the Prandtl number $Pr = C_p \mu / k$; and ρ , C_p , k , μ , and v are the density, specific heat, thermal conductivity, dynamic viscosity, and velocity of the cooling fluid, respectively. The transition from laminar to turbulent flow of the cooling fluid occurs at a Reynolds number of approximately 2300.

Water is typically used as the coolant. However, particle agglomeration may occur on the pipes, because the residual moistness in the fluidizing gas condenses against the cold cooling pipes. This leads to a particle-cake formation around the pipes, which reduces the heat transfer to the tubes and also causes the fluidized bed to rapidly block up or collapse. Therefore, it is preferable to regulate the water flow rate to control the cooling rate in order to keep the cooling-zone bed temperature above the saturation temperature of the fluidizing gas. An alternative is to use ambient air as the cooling fluid, although air has a smaller cooling capacity than

water, or use a dry fluidizing gas to avoid the condensation.

Bed Surface Spray Cooling. Spray cooling occurs when ambient air is blown into the surface-particle layer above a fluidized bed. The air contacts with the particles erupted from the bed and the particles that constitute the upper surface of the bed, removing part of the energy of the particles due to the particle-gas convective heat-transfer effects. The cooled particles return into the bed, and hot particles are drawn up to the bed surface by the fluidizing gas and cooled there, so that a continuous heat removal is implemented by the bed-surface air spray. This cooling system generally consists of a ventilator, a regulator, and ducts to transport air to the air ejectors.

The advantages of this method are no disturbance in the bed, simple equipment, and very low cost for coolant. The main disadvantage is its small heat-removal capacity for deep beds, due to the low portion of surface particles being cooled relative to all bed particles when air is used above the bed. When the air is mixed up with atomized water, the cooling capacity is enhanced, due to the latent heat of evaporation in addition to substantial single-phase convection. However, care should be taken to avoid particle agglomeration in the upper surface of the bed.

Quenching Power

Heat-Transfer Characteristics

Cooling Rates. The cooling rate in a fluidized bed is higher compared to air cooling and approximately 10% lower than molten salt quenching. However, the fluidized bed can operate at lower temperatures without solidifying.

A comparison of the cooling curves of a fluidized bed to other common types of quenchants is given in Fig. 3. It is obvious that the fluidized-bed quench is slower than water and oil. The cooling

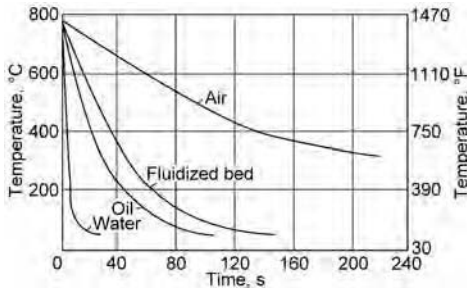


Fig. 3 Comparison of cooling curves for 16 mm (0.6 in.) diameter steel bars cooled in various quenching media from approximately 780 °C (1440 °F) to room temperature. Source Ref 3

rate in (°C/s) obtained in the fluidized bed is approximately 65% of that of the oil bath in this case. However, in high-temperature quenching, fluidized beds may provide a higher cooling rate than oil or water because there is no boiling in the fluidized beds.

Heat-Transfer Coefficients. The heat-transfer coefficient is a useful and comparable quantitative measure for assessing the quenching power of a medium. With the help of computational modeling, cooling rate and temperature change at any position in a specific part, such as at the surface and in the center, in a quenching medium can be reasonably predicted by the heat-transfer coefficient to obtain a general opinion on the possible application of the quenchant medium for the part, without the need of practical data or performing physical measurement for the quenching of the part to be treated.

The value of the heat-transfer coefficient of a fluidized bed depends on many technological factors and can vary between wide limits.

Values of some fluidized beds are given in Fig. 4 and compared with other quench media.

Fundamental Factors Affecting Quenching Power

The quenching power of fluidized beds mainly depends on particle size, particle material, fluidizing gas composition, fluidizing gas flow rate, bed temperature, and the arrangement of quenched parts with respect to one another and to the bed.

Fluidized Particles. Desirable properties of particles intended for quenching fluidized beds include appropriate particle size, density and shape, good attrition resistance, appropriate hardness, no surface stickiness, inert to high temperatures of 1500 °C (2730 °F) and above, good resistance to thermal shock, no chemical reactivity with the fluidizing gases, and no toxicity. They should also be readily available and inexpensive. The size, density, and shape determine the fluidization quality and cooling rate. The particle classification of Geldart depending on the particle diameter and the relative density difference between the fluid phase and the solid particles (Ref 5) can be used to choose the particles in regard to the fluidization quality. Rounded particles provide a good fluidization and cause less surface wear than particles with sharp corners and edges.

Particle size has the greatest influence on heat transfer in fluidized beds (Table 1). Figure 5 also illustrates changes in the cooling rate with different particle sizes. The optimum particle size is in the range of 100 to 150 μm (4 to 6 mils). Small grains show a tendency to agglomerate, an irregular fluidization, and excessive dust from the bed. The heat transfer is also considerably affected by the bed density, which, in turn, depends on the density of the particle material themselves and on the degree of their loosening. The most commonly used materials are aluminum oxide (Al₂O₃) and silicon carbide

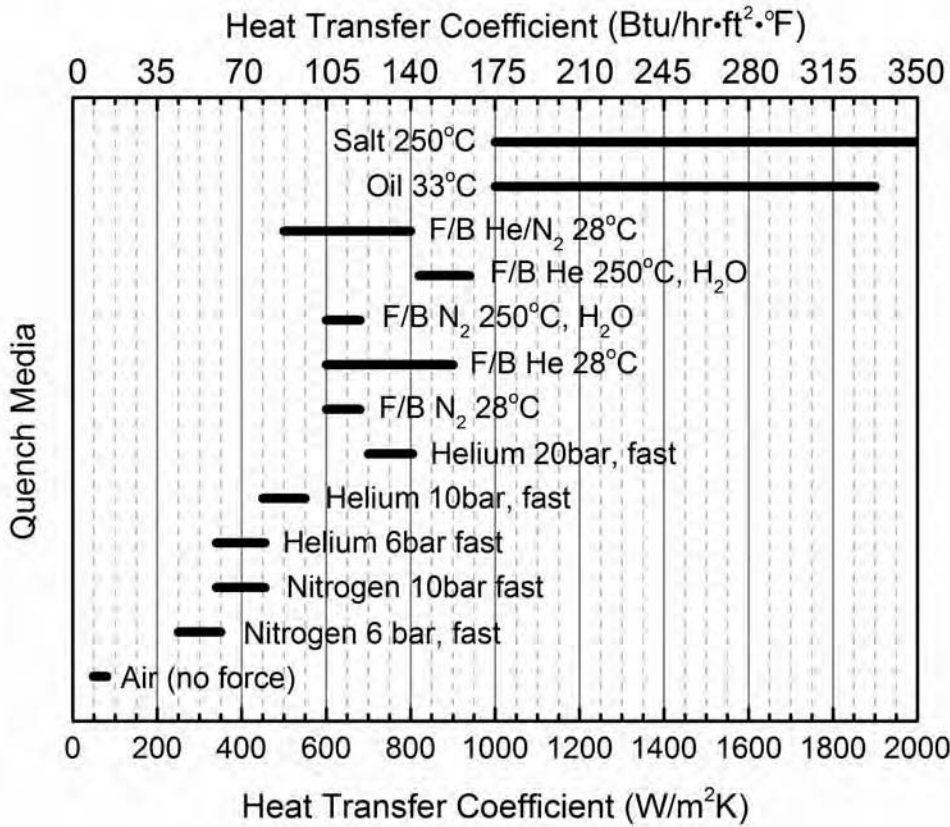


Fig. 4 Guide to the range of heat-transfer coefficients for various quench media against fluidized-bed quenching. Source: Ref 2

Table 1 Effect of grain diameter and density of fluidized bed (quartz sand) on the heat-transfer coefficient, W/m² · K (Btu/h · ft² · °F)

Density		Diameter, μm (mils)			
kg/m ³	lb/ft ³	50 (2.0)	100 (4.0)	200 (8.0)	400 (16.0)
1300	80	700 (125)	570 (100)	400 (70)	240 (40)
650	40	540 (95)	390 (70)	260 (45)	160 (30)
325	20	410 (70)	280 (50)	200 (35)	100 (20)

Source: Ref 6

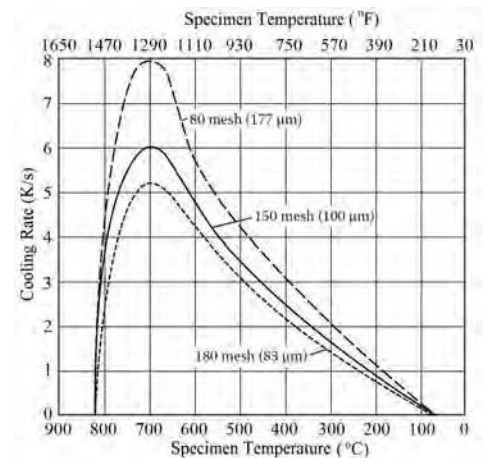


Fig. 5 Effect of alumina grain size on cooling rates for 50 mm (2 in.) diameter and 100 mm (4 in.) length steel samples quenched in an ambient-temperature fluidized bed. Source: Ref 1

(SiC) particles operated at a bed density of approximately 1761 kg/cm^3 (110 lb/ft^3). The thermal conductivity of the particles has little or no effect on the heat transfer.

Fluidizing Gas. The effect of the type of fluidizing gas on the quenching power is mainly attributed to its thermal conductivity. Higher conductivity provides a higher cooling rate, as shown in Fig. 6. Hydrogen and helium, which have thermal conductivities of 0.168 and $0.139 \text{ W/m} \cdot \text{K}$ (0.0975 and $0.0805 \text{ Btu/h} \cdot \text{ft} \cdot ^\circ\text{F}$), respectively, at room temperature, are high-thermal-conductivity gases, while nitrogen and air, which have a thermal conductivity of approximately $0.024 \text{ W/m} \cdot \text{K}$ ($0.014 \text{ Btu/h} \cdot \text{ft} \cdot ^\circ\text{F}$), are low-thermal-conductivity gases by comparison. The thermal conductivity of argon is $0.0177 \text{ W/m} \cdot \text{K}$ ($0.010 \text{ Btu/h} \cdot \text{ft} \cdot ^\circ\text{F}$) and that of steam is $0.045 \text{ W/m} \cdot \text{K}$ ($0.026 \text{ Btu/h} \cdot \text{ft} \cdot ^\circ\text{F}$). Also, mixtures of low and high thermal-conductivity gases are used. The heat-transfer coefficients that these gases can provide are given in Fig. 4. Other considerations when choosing fluidizing gas include the cost and reaction (oxidation) with the treated parts.

Air and nitrogen are generally used as the supporting gas when lower heat-transfer coefficients are acceptable. Because of the safety issues of hydrogen, helium is the preferred fluidizing gas to obtain a high cooling rate. The

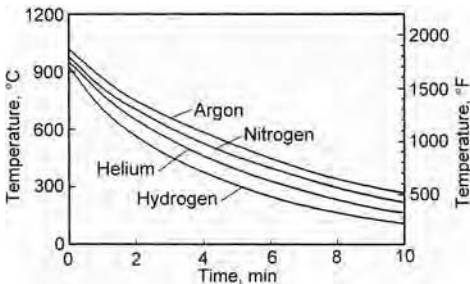


Fig. 6 Effect of gas composition on cooling rates for a 50 mm (2 in.) diameter cylinder. Source: Ref 3

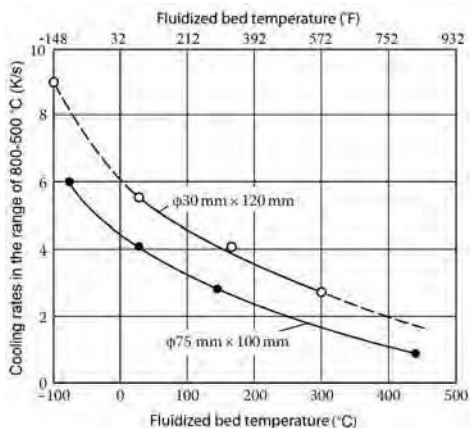


Fig. 7 Effect of fluidized-bed temperature on the center cooling rate between 800 and 500 °C (1470 and 930 °F) of steel specimens 30 × 120 mm (1.2 × 4.7 in.) and 75 × 100 mm (3 × 4 in.) in diameter. Source: Ref 1, 7, 8

high cost of helium, between 20 and 30 times the cost per cubic meter of nitrogen, is the major problem in changing over to it. The use of steam or water vaporization as an additive to the bed necessitates that the bed be operated well above the vaporizing temperature of water. A cheap and simple way to create a nonoxidizing bed atmosphere is to use cooled exhaust gas from a combustion furnace.

Fluidization Velocity. As the flow rate of the fluidizing gas from the minimum fluidization velocity increases, the heat-transfer coefficient initially increases, reaches a maximum, and then decreases. The increased velocity is required for cooling as opposed to heating. The optimum heat transfer for cooling can be achieved when the fluidizing velocity is 3 to 4.5 times the minimum fluidizing velocity

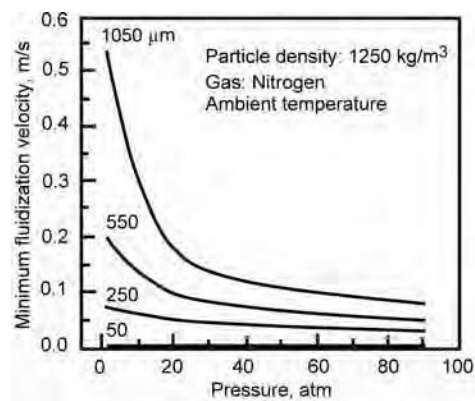


Fig. 8 Effect of pressure on minimum fluidization velocity. Source: Ref 9

required for fluidization. Typical velocities, for example, range between 0.05 and 0.08 m/s (0.16 to 0.26 ft/s) for $100 \mu\text{m}$ (0.004 in.) corundum particles. The variation of fluidization velocity can be likened to the effect of agitation in oil and water quench tanks.

Bed temperature influences the quenching capacity of a fluidized bed because of the heat-transfer coefficient at the cooled parts and the difference between the temperatures of the part and the cooling medium. The increase in heat-transfer coefficient with temperature is mainly because of the increase in thermal conductivity of the fluidizing gas around the part. A high temperature difference results in a high heat flux. Fig. 7 shows the variation of the cooling rate at specimen temperatures of 700 and $550 \text{ }^\circ\text{C}$ (1290 and $1020 \text{ }^\circ\text{F}$) as a function of the bed temperature.

Bed Pressure. Because system pressure affects thermodynamic and transport properties of the fluidizing gas, a pressurized operation yields a lower minimum fluidization velocity and enhances the heat transfer. The convective heat transfer is higher under high-pressure operations than it is under ambient pressure, due to a higher gas density and an increase in the thermal conductivities of the gas phase and the dense gas-solid phase. The effect of system pressure on fluidization and heat transfer strongly depends on particle size. For particles greater than approximately $100 \mu\text{m}$ (4 mils), pressure effects are obvious (Fig. 8, 9). Materials of this size are essentially the particles used in quenching fluidized-bed and other powders of Geldart group B and D. For particles smaller than $100 \mu\text{m}$ (Geldart group A powders), change in

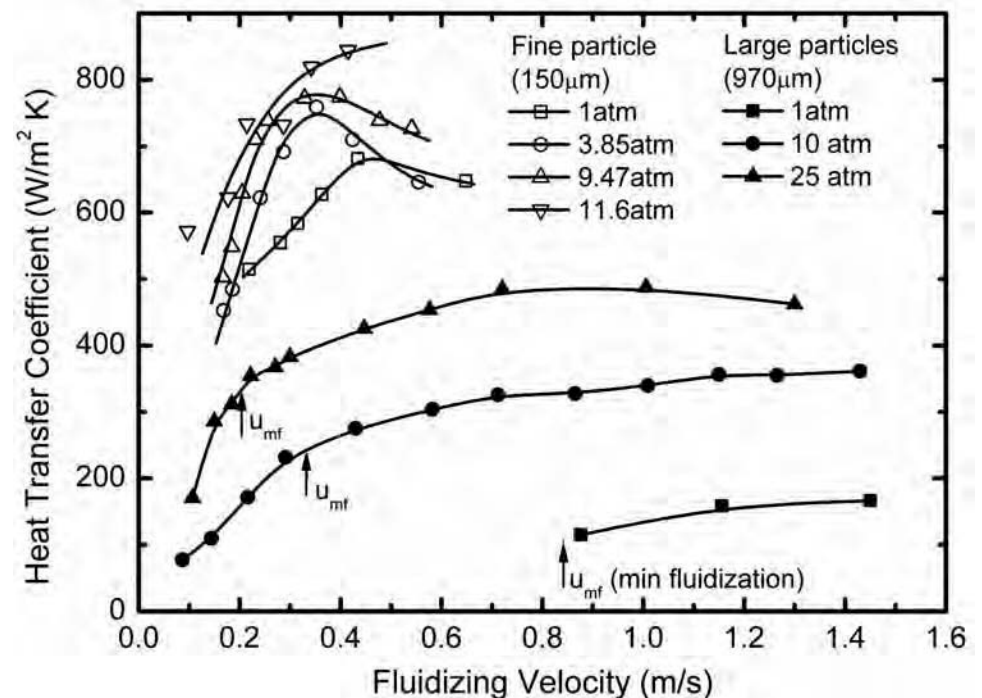


Fig. 9 Effect of system pressure on heat-transfer coefficient. Source: Ref 10 for large-particle data; Ref 11 for fine-particle data

pressure has no effect on minimum fluidization velocity (Fig. 8). High-pressure sealed quenching in a fluidized bed is capable of producing quench rates comparable to oil quenching.

Geometry of Parts and Their Configuration in a Bed. The effect of cooling rate on the shape of treated parts in fluidized beds is similar to that in other quenching media. The section size and the surface-area-to-volume ratio are essential as a single part is treated in a fluidized bed, whereas with loads comprised of several parts, the arrangement of the parts plays an important role, as shown in Fig. 10. In addition, a peculiar occurrence in quenching fluidized beds is the “shield” effect caused by deposition of the bed material on the upper surface of the treated parts and in cavities and holes (Fig. 10, 11), which adversely affects the uniformity of cooling and thus the uniformity of hardness developed. The particle shield acts like a thermal screen, hindering heat transfer. Fig. 12 shows the dependence of heat transfer on the orientation of the treated surface to the stream lines of gas and particles in a fluidized bed. To even out heat transfer between the sides and top face of a section, the workload should be continuously moved, rotated, or horizontally vibrated during cooling.

Application of Fluidized-Bed Quenching

Fluidized-bed quenching provides a number of advantages relative to quenching in molten metal and molten salt baths and oil quenching:

- There are no toxic vapors and gases, compared to salt baths, and no fire and smoke associated with quenching oil.
- The parts contain no salt residues and require no posttreatment as needed with salt baths.

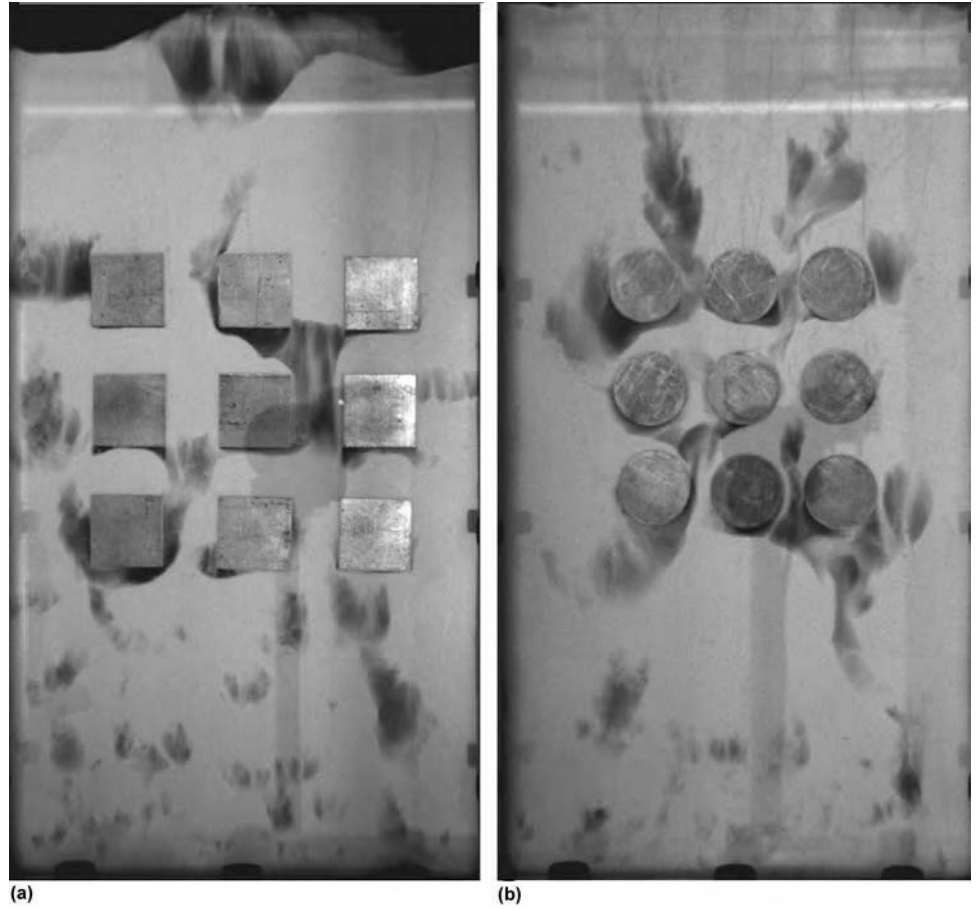


Fig. 10 Images of dense phase (light regions) and bubbles (dark regions) in Al_2O_3 fluidized beds with (a) 30 × 30 mm (1.2 × 1.2 in.) square-section parts and (b) 30 mm (1.2 in.) diameter cylinders at a fluidizing air velocity of 0.055 m/s (0.18 ft/s) (minimum fluidizing velocity = 0.021 m/s, or 0.069 ft/s)

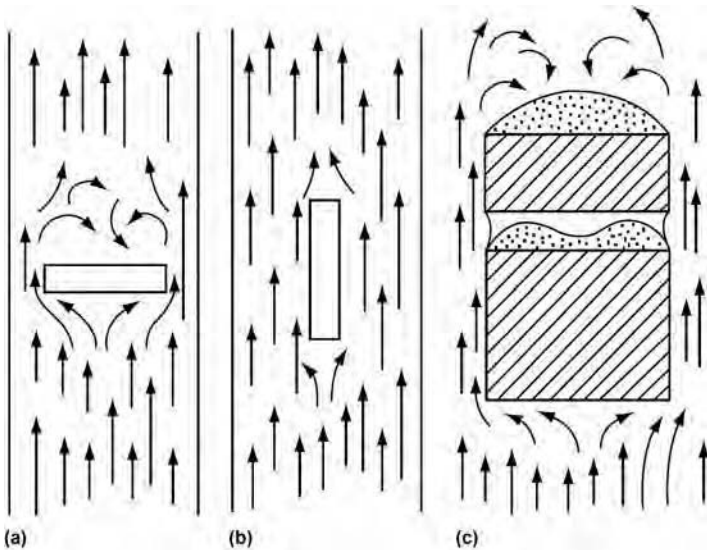


Fig. 11 Effect of part arrangement and shade phenomenon on cooling conditions. (a) Abnormal arrangement. (b) Correct arrangement. (c) Shade phenomenon. Source: Ref 12

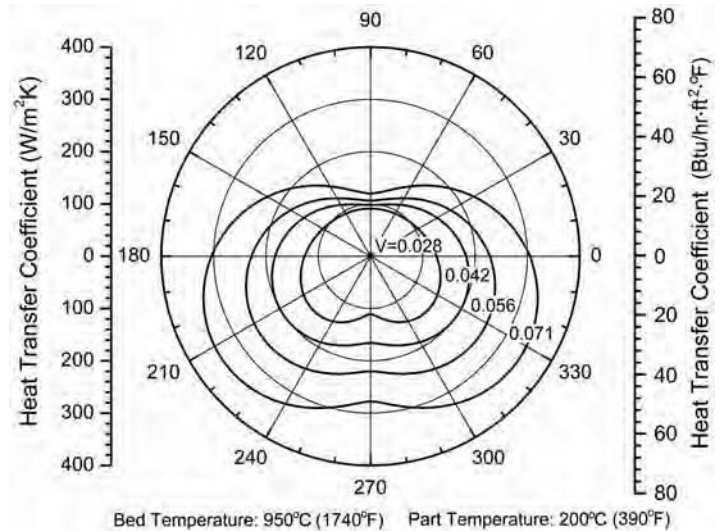


Fig. 12 Dependence of heat-transfer coefficient on the surface orientation of an 80 mm (3.2 in.) diameter by 30 mm (1.2 in.) long cylinder. Source: Ref 13

- The melting operation that is necessary with salt baths is not needed, so the fluidized bed is continuously ready for use, and energy consumption is reduced.
- Unlike vaporizable liquid quench media such as oil and water, where boiling limits the quenching rate and adversely affects uniform quenching and causes distortion, fluidized-bed quenching does not vary through the quenching process.

The major barrier to the use of fluidized beds in quenching is that they exhibit a lower quenching power than salt baths. This may rule out fluidized-bed quenching for some applications due to part geometry or alloy quench sensitivity. Cost is another significant disadvantage when expensive fluidizing gases such as helium are used and not recycled.

In addition to the aforementioned advantages, there are two important features that fluidized-bed quenching possesses. The heat-transfer coefficient can be adjusted over a wide range, because of the rapid change of gases and the flow rate of the gas within the bed. The fluidized bed can operate at any low temperature, and different-temperature quenching processes can work together. Therefore, in cases where hardness values in fluidized-bed quenching are slightly lower than those of the other quenchants, higher hardness can be obtained by slightly decreasing the fluidized-bed temperature. These, to some extent, compensate its major drawback of low cooling rate compared to salt baths.

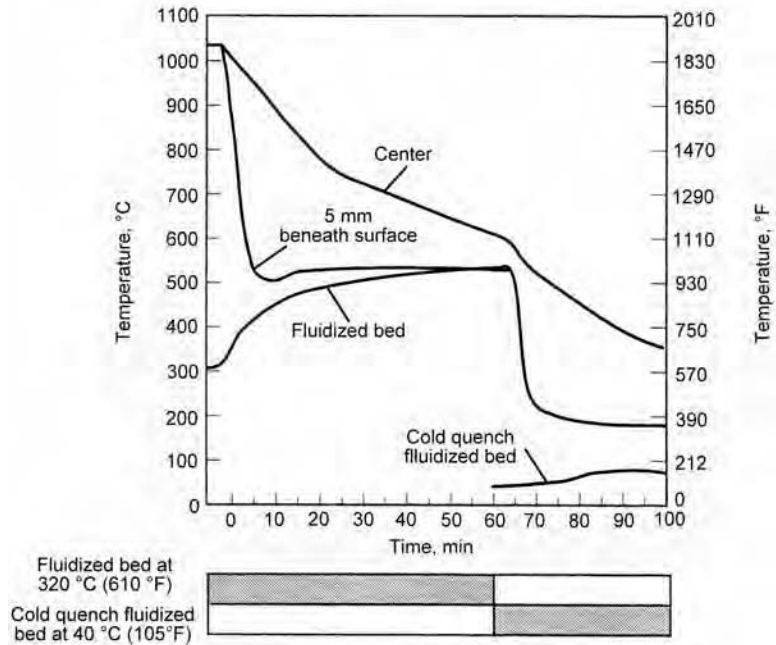
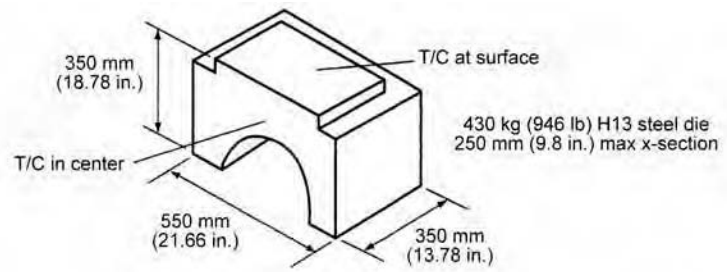


Fig. 13 Cooling curves for fluidized-bed quenching of a 430 kg (946 lb) H13 hot-work steel die casting tool. T/C, thermocouple. Source Ref 3

Fluidized-Bed Quenching Processes

Fluidized-bed quenching can be used for many grades of tool and alloy steels, and its potential for use in other applications continues to increase. It is possible for hydrogen or helium fluidized-bed cooling to replace oil quenching in a large number of applications. In heating operations and in marquenching and martempering, helium and hydrogen fluidized beds are good substitutes for salt baths in some situations. If correctly controlled, fluidized-bed quenching can replace high-pressure quenching in a vacuum furnace. Fluidized-bed quenching is also used to accelerate cooling after tempering or to heat treat aluminum alloys.

Fluidized beds can be operated in batch model for general quenching applications and in continuous model for various types of wire, tube, and strip quenching.

Conventional Batch Quenching. Fluidized-bed quenching is performed in a conventional manner, where one carrying gas is used and the treated parts stay in the fluidized bed through the cooling cycle. Low-temperature quenching of air-hardening tool steels, for example, is a typical application. The process requires that the quench rate must be severe enough to effect full metallurgical transformation of thick sections while not causing severe distortion or cracking. The quenching powers

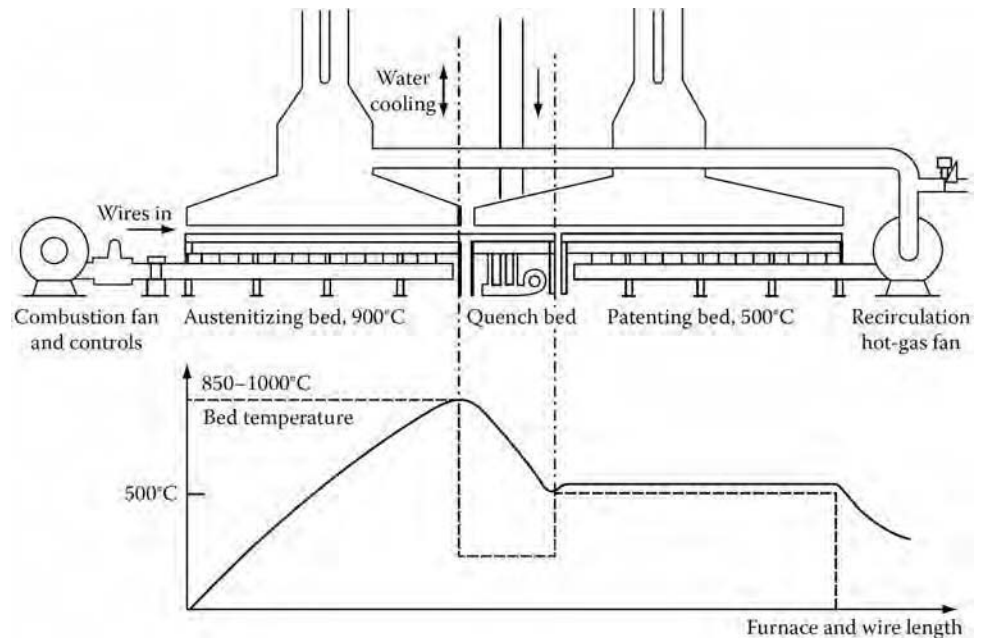


Fig. 14 Three-zone fluidized-bed arrangement and quench-temperature ranges. Source Ref 12

of various fluidized beds with respect to the carrying gas can be found in Fig. 4. With the use of hydrogen and helium, a fluidized bed affords a cooling rate similar to that of an unagitated salt bath. Using helium gas at 28 °C (82 °F), for example, the heat-transfer coefficient is in the range of 820 to 870 W/m² · K (144 to 153 Btu/h · ft² · °F), with a maximum cooling rate of 22 °C/s (40 °F/s). This cooling rate is fast enough to form satisfactory metallurgical properties in steels such as SAE 8620 (Ref 2). A fluidized bed that uses a water additive was designed to replace salt baths for austempering low-alloy steels (Ref 3).

Two-Step Batch Quenching. The conventional fluidized bed has insufficient heat-transfer characteristics to be used in the quenching of medium- and low-alloy steels because the critical stage of their cooling cycle is the first 10 s, where a high cooling rate is necessary to avoid precipitation of proeutectoid carbides at the grain boundaries. This limitation is overcome by a two-step process. In the first step, helium is used in the critical portion of the cycle (the nose of the isothermal transformation curve). In the second phase, nitrogen replaces helium for the rest of the cycle. The following are some application cases.

Case One. The two-step fluidized-bed quenching process was applied in austempering 4340 medium-carbon steel tools to replace salt processing; that is, the parts were austenitized at 920 °C (1690 °F), quenched in salt at 315 °C (600 °F), and then held for 30 min at that temperature. In fluidized-bed quenching, helium was used for the first 30 to 60 s and then the carrying gas was switched from helium to nitrogen for the remainder of the cycle. For the two-step process, the quench temperature was reduced from 330 to 295 °C (625 to 565 °F). The hardness of these parts was lower than that of those treated with the salt process. The desired result was obtained by slight reductions in the fluidized-bed temperature.

Case Two. In marquenching hot die steel H13, a fluidized bed at approximately 320 °C (610 °F) was used for 5 to 7 min in the initial critical period. When the bed temperature increased to between 500 and 520 °C (930 and 970 °F) due to the heat extracted from the hot dies, the dies were removed and finally quenched in a cold-quench fluidized bed operating at 40 °C (105 °F). The results of a typical cooling process are given in Fig. 13. The marquenching of H13 tool steels was also implemented by initially quenching the parts in a cold- or ambient-quench fluidized bed for 7 min, then transferring them to a second bed at 350 °C (660 °F), and finally cooling in a fluidized bed at ambient temperature.

Continuous Quenching. Continuous fluidized-bed quenching exhibits high flexibility and improved process control, especially when operating together with fluidized-bed heating. The most typical example uses fluidized beds for the heating and cooling operations to perform wire patenting, as shown in Fig. 14. In between two tanks for austenitizing and austempering at a temperature of approximately 500 °C (930 °F), a short, water-cooled tank for fluidized-bed quenching at approximately 100 °C (210 °F) is installed. The wire to be patented is placed in this tank for a short time so that its temperature only decreases to approximately 500 °C (930 °F). Sealed quenching with an inert gas (nitrogen)-purged hood traveling between heating furnaces and quenching fluidized beds is also a practical case.

REFERENCES

1. P. Sommer, Quenching in Fluidised Beds, *Heat Treat. Met.*, Vol 13 (No. 2), 1986, p 39–44
2. R. Reynoldson and L.M. Huynh, Quenching in Fluidised Beds for the Heat Treatment

- Industry, *Int. J. Mater. Prod. Technol.*, Vol 24 (No. 1–4), 2005, p 397–410
3. R.W. Reynoldson, *Heat Treatment in Fluidized Bed Furnaces*, ASM International, 1993
4. W.-C. Yang, *Handbook of Fluidization and Fluid-Particle Systems*, CRC Press, 2003
5. D. Geldart, Types of Gas Fluidization, *Powder Technol.*, Vol 7, 1973, p 285–292
6. H.S. Mickley and C.A. Trilling, Heat Transfer Characteristics of Fluidized Beds, *Ind. Eng. Chem.*, Vol 41 (No. 6), 1949, p 1135–1147
7. W. Luty, Study of the Thermokinetic Properties and the Range of Applicability of a Fluidized Bed as a Quenching Medium, *Heat Treat. Met.*, Vol 36 (No. 4), 1981, p 194–198
8. W. Luty, Effect of Temperature Gradient on the Quenching Power in Fluidized Beds, *J. Heat Treat.*, Vol 3 (No. 2), 1983, p 108–113
9. P. Rowe, The Effect of Pressure on Minimum Fluidisation Velocity, *Chem. Eng. Sci.*, Vol 39 (No. 1), 1984, p 173–174
10. H.J. Bock and J.-M. Schweitzer, Heat Transfer to Horizontal Tube Banks in a Pressure Gas/Solid Fluidized Bed, *German Chem. Eng.*, Vol 9 (No. 1), 1986, p 16–23
11. J.S.M. Botterill and M. Desai, Limiting Factors in Gas-Fluidized Bed Heat Transfer, *Powder Technol.*, Vol 6 (No. 4), 1972, p 231–238
12. L. Wackaw, Cooling Media and Their Properties, *Quenching Theory and Technology*, 2nd ed., CRC Press, 2010
13. W.M. Gao, P.D. Hodgson, and L.X. Kong, Experimental Investigation and Numerical Simulation of Heat Transfer in Quenching Fluidised Beds, *Int. J. Mater. Prod. Technol.*, Vol 24 (No. 1–4), 2005, p 325–344

Spray Quenching

Introduction

Adapted from "Spray Quenching" in *Handbook of Quenchants and Quenching Technology* (Ref 1)

The term *spray quenching* refers to a wide variety of quenching processes that involve heat removal facilitated by the impingement of a quenchant medium on a hot metal surface. Some of these processes have obvious differences, while others are similar and differ only in degree. Examples include the addition of droplets of water (or other volatile liquids) to a gas quenching stream in fog quenching (Ref 1); quenching with water or water/air streams (Ref 2); sprays of volatile liquid quenchants other than water (Ref 3); and high-pressure jets of an oil (Ref 4), water (Ref 5, 6–7), or aqueous polymer solution (Ref 8) under the liquid level in a bath.

One advantage of spray quenching, relative to other quench methods, is that a large and adjustable range of cooling rates is achievable by simple changes in flow rates and pressures. The high rates of heat extraction possible with sprays are critical for attaining a good depth of hardness. Segerberg (Ref 5) has examined

this and illustrated the results with the cooling curves shown in Fig. 1. Immersion quenching was performed using an oil and a polymer solution. The water flux for the spray quench was chosen to give a cooling curve with a vapor film of the same duration as that for the oil immersion quench. The quantitative impact of the higher rate of cooling found with the spray system was determined using 35 by 100 mm (1.4 by 4.0 in.) cylindrical samples of SAE 52100 ball bearing steel. These cylinders were heated to 850 °C (1560 °F) and quenched in a fast oil at 50 °C (120 °F), or a 15% aqueous solution of a polyalkylene glycol (PAG) polymer at 25 °C (77 °F), or by the water spray quenching system. Hardness distributions along the diameter of the cylinder are shown in Fig. 2. The higher cooling rates achieved by the immersion quench in the PAG solution and by the water spray quench account for the greater depth of hardness shown in Fig. 2.

Spray quenching is used to optimize heat transfer for hardening while simultaneously developing the desired distribution and level of stress (Ref 9). With spray quenching, the heat-transfer coefficient from the part to the quenching medium is directly related to the flow rate, turbulence, and impingement pressures of the quenchant at the hot surface. It is possible to adjust these parameters during the quench to yield a cooling profile achievable in no other way (Ref 2, 5, 10,11–12). Computerized adjustment of these variables during the quench also have been extensively explored (Ref 2, 5, 10, 13,14,15,16,17–18). This ability to control and vary the heat-transfer coefficient

during the quench may produce properties that would otherwise require more expensive, higher-alloy materials (Ref 9, 19–22).

The next section of this article, "Water Quenching Heat Transfer," reviews heat-transfer characteristics of immersion quenching and spray quenching with water. Liquid quenching provides high cooling rates required for the steel hardening process. Water is the most commonly used liquid in quenching because it is readily available, easy to pump, nontoxic, and inflammable. Quenching can be carried out by directly submerging the part in a quench bath, bottom reflooding, falling film, sprays, and impinging jets. Impinging jets are used to remove extensive amounts of heat locally, while sprays are used to achieve less but more uniformly distributed cooling rates.

Concepts of Spray Quenching. When quenching a hot metal part in a water bath, the cooling mechanisms vary according to regions, as illustrated in Fig. 3 (Ref 13, 23,

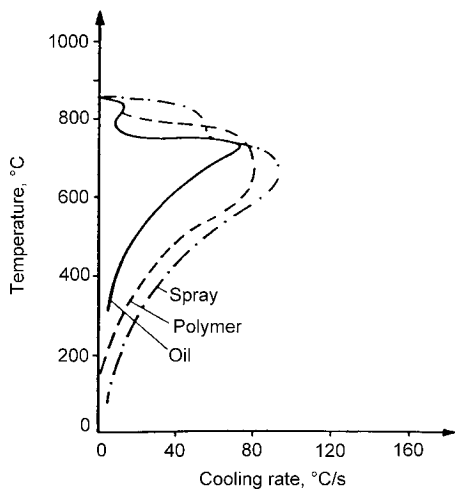


Fig. 1 Cooling rates for spray, polymer, and oil immersion quenching

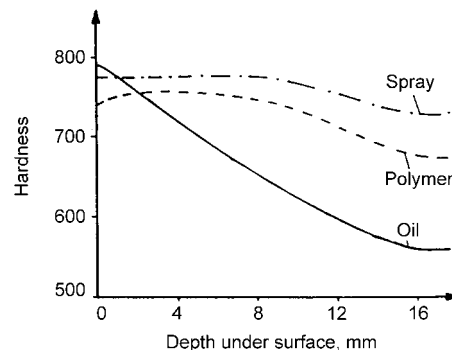


Fig. 2 Hardness distributions for spray, polymer, and oil immersion quenching

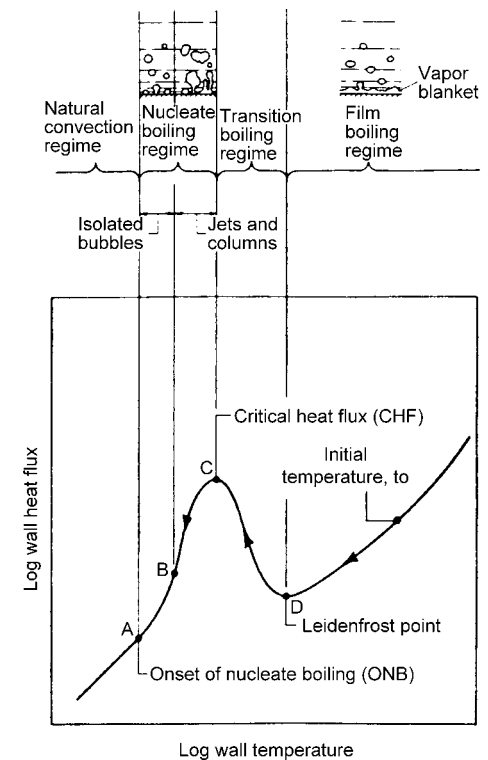


Fig. 3 Heat transfer versus surface temperature

24), showing the heat transfer from the part as a function of its surface temperature. Figure 3 also relates the surface temperature and heat-transfer coefficient to the mechanism of heat removal. Upon immersion, the part will first be surrounded by a vapor blanket, which will collapse as the part cools. The heat transfer through this vapor blanket is poor, and the part will cool slowly in this region.

The second region of the cooling curve is called the nucleate boiling region and corresponds to rapid heat transfer caused by direct contact of the part with the water. In this region, the part is still very hot and the water will boil vigorously. The high heat of water vaporization accounts for the very rapid heat transfer. In the third, or convective, cooling region, the surface of the part has cooled to a temperature below the boiling point of water. Only convective heat transfer occurs in this region.

The rate of heat removal from a quenched part can be increased by agitation, which reduces the stability of the vapor blanket that surrounds the part during the early stage of the quench. The effect of agitation on the cooling mechanism of a silver probe quenched by immersion in a 60 °C (140 °F) water bath is shown in Fig. 4 (Ref 6). A stream of water with a velocity of V_i was injected below the surface of the bath and directed at the probe. The greater the flow rate (agitation), the higher the temperature at which the vapor blanket mechanism was displaced by the much more effective nucleate boiling mechanism.

Cooling by the impact of a stream of droplets or liquid in spray quenching is also represented by Fig. 3. Fluid flow is used to accelerate the quench by rupturing the vapor blanket. The high agitation rates inherent in a spray quench also accelerate cooling in the nucleate boiling and convective cooling portions of the quench. Based on the mathematics needed to describe the spray systems, one author has stated that “spray cooling is also a sort of turbulent flow cooling” in all three regions of the cooling curve (Ref 25). In fact, it is useful to use the same terms to describe the heat-transfer mechanisms in both spray and immersion quenching.

Consider a series of water droplets moving toward the surface of a hot metal plate. The first droplet will contact the plate, and the surface temperature of the droplet at the point of contact will instantly rise. If the plate is sufficiently hot that the liquid in the contact zone is raised above its limiting superheat temperature (260 °C, or 500 °F, for water), then a portion of the liquid will evaporate in approximately 0.001 s (Ref 11). This evaporation will occur before the original spherical shape of the droplet has been significantly deformed. Because the contact region represents a small fraction of the mass of the drop, no significant heat removal from the plate will have occurred. The vapor film that forms will push the

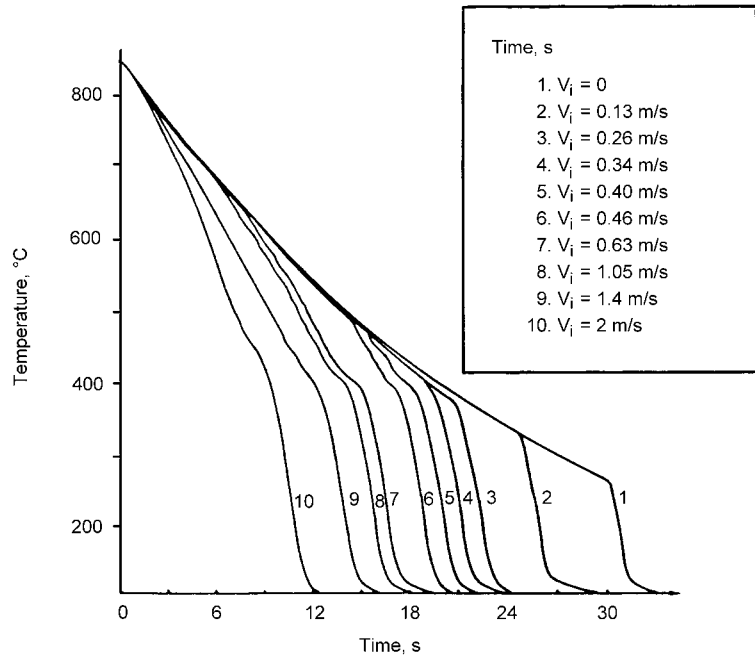


Fig. 4 Effect of agitation on the cooling curve

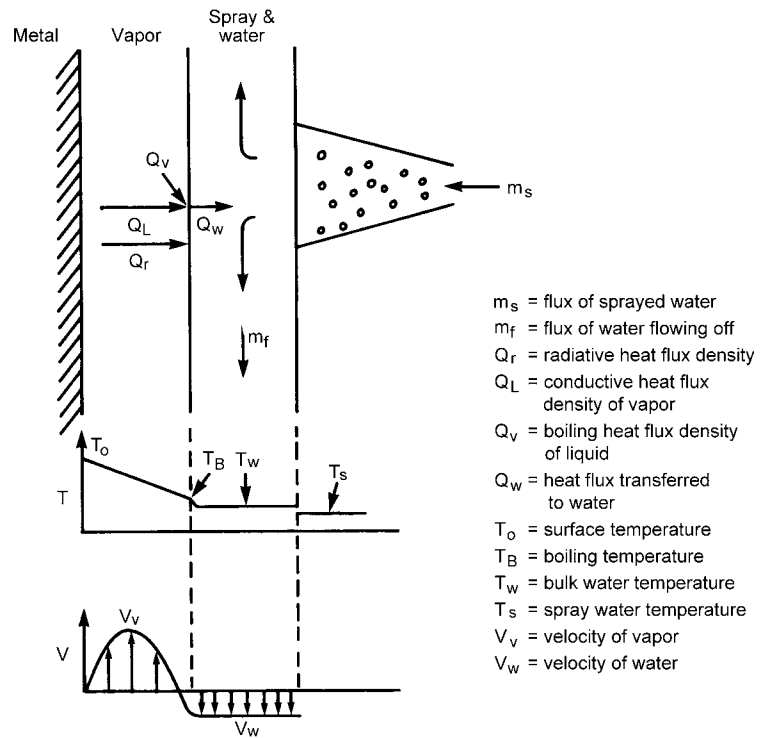


Fig. 5 Heat transfer in the vapor blanket portion of a spray quench

remaining portion of the droplet away from the plate. This vapor blanket provides a partial insulating barrier and inhibits the impact of additional droplets. Only those droplets with sufficient kinetic energy (momentum) will be able to penetrate the vapor film and strike the

plate. The result will be a film of liquid separated from the plate by a layer of vapor. This is called the film boiling or nonwetting phase.

The heat-transfer process for this state can be pictured as shown in Fig. 5 (Ref 2, 26). The heat-transfer rate through the vapor film is

relatively slow; therefore, there is a relatively slow decrease in the temperature of the plate. As the temperature falls, the thickness of the vapor film will decrease (Ref 5). At a characteristic temperature, which is dependent on the quench conditions, the droplets with higher-than-average kinetic energy will penetrate the vapor film, contact the plate, and begin to spread out on the surface. The temperature at which this occurs is called the Leidenfrost point. At this temperature, regions of the plate will be observed to be "wetted" by the quenchant.

The increased contact of the droplets with the metal surface will result in a corresponding increase in the heat transfer from the plate, causing the plate temperature to decrease more rapidly. A larger number of droplets will penetrate the film, and heat transfer will increase until the entire plate is wet with boiling liquid. At this point, the heat-transfer process is characterized by nucleate boiling. Further reduction of the plate temperature leads to an end of boiling, and the heat-transfer mechanism becomes dependent on convective cooling. In practice, the Leidenfrost temperature is found to be a function of the surface physical properties (Ref 6, 11, 27, 28) as well as its temperature (Ref 29, 30).

Water Quenching Heat Transfer

M.S. Hamed and A.B. Ahmed, McMaster University, Hamilton, Ontario, Canada

Immersion Quenching

Oils and water are the most widely used liquids in steel quenching processes. Water, although most commonly used, causes cracks and distortion for quenched parts. Uniformity

in the heat-transfer coefficient in the film and nucleate boiling regimes is required to abate such problems (Ref 31). The heat-transfer coefficient in water immersion quenching depends on the surface temperature of the part, the thermophysical properties of the part, and the initial water bulk temperature (Ref 32). Bamberger developed the following correlation of the heat-transfer coefficient in immersion quenching:

$$h_{\text{imm}} = \sqrt{K\rho C \exp\left(0.32 \frac{\theta_c - \theta_s}{\theta_b - \theta_c}\right) + h_v + h_{\text{rad}}} \quad (\text{Eq 1})$$

where:

$$h_{\text{rad}} = \sigma \varepsilon \frac{\theta_c^4 - \theta_a^4}{\theta_c - \theta_a}$$

and h_v is the stable film evaporation heat-transfer coefficient.

Investigating the heat transfer during quenching operations experimentally has many difficulties associated with it: measuring the temperature of the quenched part surface, determining the cooling rate, and quantifying the heat-transfer coefficient, especially with the two-phase nature of the flow. Recently, enormous attention has been given to modeling the heat-transfer coefficient in water immersion quenching, taking into consideration the boiling phase change. Srinivasan et al. (Ref 33, 34) developed a numerical code for immersion quenching processes. They used the most widely and commonly used relations to estimate the heat-transfer coefficient: Nusselt's method for film condensation to model film boiling, Zuber's relation for the critical heat flux, and Rohsenow's correlation for nucleate boiling. Their results matched the experimental data, except for some deviations in the case of complex shape quenching in the transition boiling regime.

The Effect of Quenching Agitation. When the part is first immersed in the water, the adjacent water layer evaporates rapidly, forming a vapor layer with low heat-transfer coefficient. Film boiling dominates until the surface

temperature falls to the Leidenfrost point or the vapor layer breaks at higher temperature. Agitation helps in breaking the vapor layer. The collapse starts from the corners of the part toward the center, augmenting the heat-transfer coefficient and increasing the cooling rate. Quenchant stirring, quenchant circulation, and submerged jet/spray mixing are the most commonly used techniques in quench tank agitation (Ref 35). Hernandez-Morales et al. (Ref 36) compared the heat-transfer rate in quenching of a steel disk in stagnant water and in agitated water. The stability of the vapor layer was severely affected by the water stirring, with an increase of 65% in the film boiling heat-transfer coefficient compared to stagnant water. Sedighi et al. (Ref 37) carried out an experimental investigation to quantify the agitation effect for flowing oil in the quench tank. They found that the time required to cool a cylinder from 860 to 100 °C (1580 to 212 °F) was reduced to half when the oil speed was quadrupled across the cylinder in the transverse configuration.

Spray Quenching

Spray quenching is superior to immersion quenching in that the cooling rate range can be adjusted by changing the flow rate and liquid pressure. Different spray and jet types can be used, as shown in Fig. 6. Spray quenching follows the boiling cure. The water droplet accelerates the quenching process by rupturing the vapor layer. The vapor layer is formed when water droplets from the spray touch the hot surface, and the liquid in contact with the plate evaporates, leaving the droplet in its spherical shape with a miniature contact with the surface. McGinnis and Holman (Ref 39) quantified the maximum heat flux from a single droplet on a heated surface. The maximum heat flux existed because of two opposing effects of the increasing temperature gradient and the weaker contact between the surface and the droplet with time. The vapor layer dramatically decreases heat removal from the surface. Because the

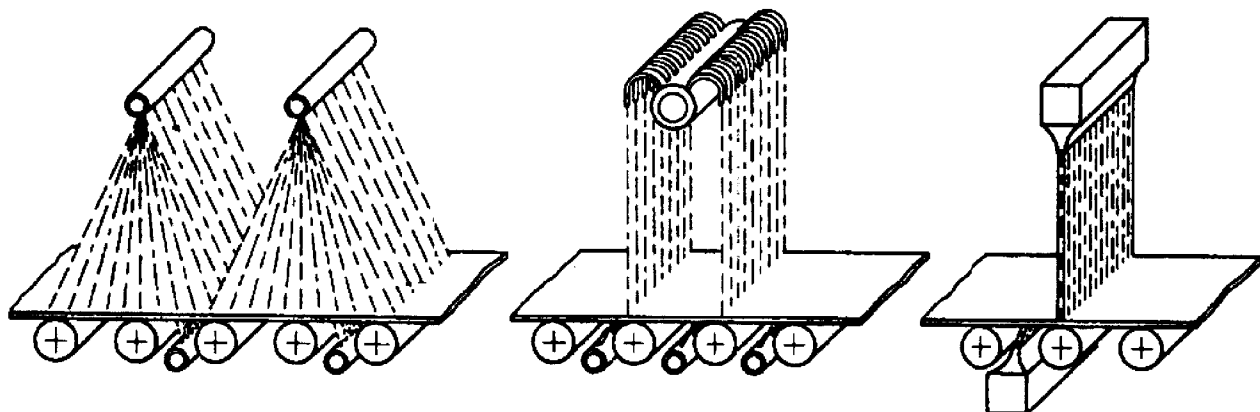


Fig. 6 The three main water-cooling configurations on runout tables. From left to right: spray, laminar, and water curtain. Source: Ref 38

droplets from the spray have high momentum, they break the vapor layer and wet the surface (Ref 35).

Sozbir et al. (Ref 40) compared low-mass-flux spray jets with air jets and found that the heat-transfer coefficient increases with the increase of the water-mass flux, between 0 and 7.67 kg/m²/s, for the mist-jet, as shown in Fig. 7. They pointed out that the increase in the heat flux was due to the fact that the droplet hits the same place on the surface. They indicated that the droplet velocity has a minor effect on the heat-transfer coefficient augmentation. High water velocity results in distortion of the droplet when it hits the surface.

Sengupta et al. (Ref 41) found that vapor film boiling in steel continuous casting is the dominant heat-transfer mode, and it is preferred because its heat-removal rate is mass-flux dependent. They established an empirical correlation for water heat-transfer coefficient with the following spray nozzle characteristics: type, nozzle separation, distance of the nozzle from the surface, and water-mass flux. Ciofalo et al. (Ref 42) carried out a transient study of the effect of different nozzles on swirl spray cooling. Their results are limited to the configurations they used. The reported heat flux is higher than the other reported heat fluxes for the same water-mass flux. Most of the empirical models developed for cooling steel plates cannot be applied for other conditions than the ones they have been developed for. Bamberger and Prinz (Ref 32) carried out experiments on spray cooling using water pressure between 0.12 and 0.5 MPa (0.017 and 0.07 ksi) and related the spray heat-transfer coefficient to the immersion heat-transfer coefficient given in Eq 1, as follows:

$$h_{spr} = 0.69 \log \frac{\dot{V}_w}{6 \times 10^{-4}} (h_{imm} - h_{rad}) + h_{rad} \quad (\text{Eq 2})$$

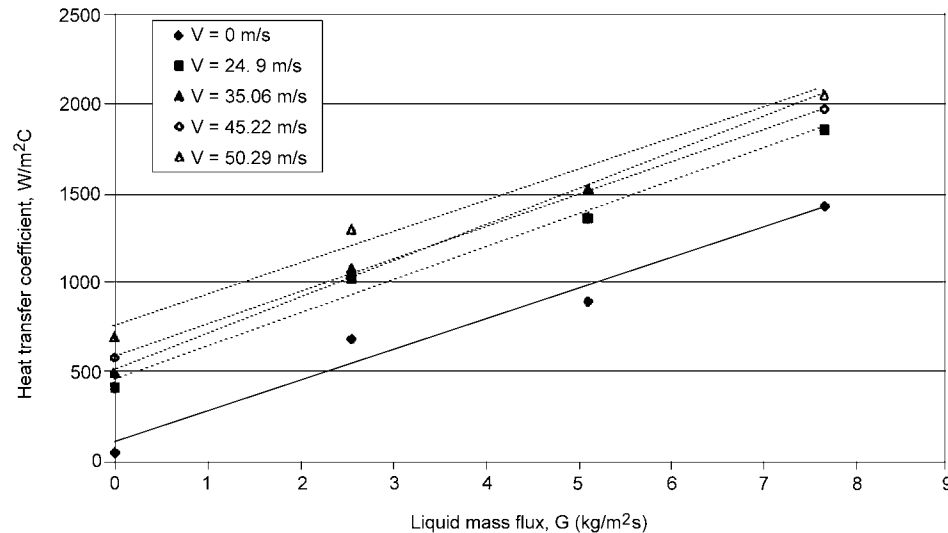


Fig. 7 Water-mass-flux effect on heat-transfer coefficient. Source: Ref 40

Mudawar and Valentine (Ref 13) carried out steady-state experiments up to 400 °C (750 °F) and were able to correlate the heat-transfer coefficient locally to the hydrodynamic properties of the spray (droplet velocity, 10.6 to 26.5 m/s, or 34.8 to 86.9 ft/s; droplet diameter, 0.434 to 2.005 mm, or 0.017 to 0.079 in.; and volumetric flux, 0.6 to 9.96 × 10⁻³ m³/s). The Nusselt number correlation in the single-phase region (Eq 3) is based on the Reynold's and Prandtl numbers. The Reynold's number is based on the characteristic velocity of the volumetric flux and the mean droplet diameter as the characteristic length. The heat-transfer rate in the nucleate boiling regime (Eq 4) is independent of the hydrodynamic properties and depends only on the surface and film temperatures:

$$Nu_{0.5} = 2.569 Re_{0.5}^{0.78} Pr_f^{0.56} \quad (\text{Eq 3})$$

$$q'' = 1.87 \times 10^{-5} (T_w - T_f)^{5.55} \quad (\text{Eq 4})$$

Jet Quenching

Because the water jet is not uniformly spread over the quenched part and it is more concentrated over a narrow region, there is hydrodynamic variations in the flow, which results in a nonuniform cooling pattern. However, impinging jets produce significantly high cooling rates. Several studies have been carried out investigating cooling rates in quenching processes using impinging jets.

Transient Studies. Ishigai et al. (Ref 43) obtained the boiling curves for a free impinging jet with jet velocity between 0.65 and 3.5 m/s (2.1 and 11.5 ft/s) and liquid subcooling of 5 to 55 °C (40 to 130 °F). They reported that the heat flux and the minimum surface

temperature are significantly affected by the degree of subcooling. At 2 m/s (6.6 ft/s) jet velocity, as the degree of subcooling increased from 5 to 15 °C (40 to 60 °F), the minimum surface temperature increased by more than 100 °C (180 °F). At higher degrees of subcooling, the heat flux tended to be constant with a decrease in the surface temperature. This phenomenon has been recently referred to as the shoulder heat flux (Ref 44), due to the intermittent surface rewetting.

Hall et al. (Ref 45) quenched a copper disk at 650 °C (1200 °F) with a water-jet velocity ranging from 2 to 4 m/s (6.6 to 13.1 ft/s). They noticed a sharp drop in the critical heat flux in the stagnation zone compared to the radial flow zone. They attributed that to the deceleration of the flow in the radial direction and the decrease in the shear force on the bubbles in the boundary layer, which led to a significant increase in the boundary layer thickness. The minimum heat flux was found to decrease with the radial position also, and the minimum temperature depended on the liquid film hydrodynamics. Mozumder et al. (Ref 46) reported similar trends. They also noted that the maximum heat flux position moves circumferentially outward following the wetting front. Karwa et al. (Ref 47) studied the wetting front propagation and hydrodynamic effects on a flat surface. Akmal et al. (Ref 48) studied the wetting front on cylindrical surfaces.

Islam et al. (Ref 49) captured different flow patterns while quenching a surface at 500 to 600 °C (930 to 1110 °F) with a 2 mm (0.08 in.) upward water jet of 5 to 80 °C (40 to 175 °F) of subcooling impinging on the surface with a velocity range from 3 to 15 m/s (9.8 to 49.2 ft/s). The six distinctive flow patterns depended on the surface thermal characteristics: material type, surface finish and aging, and surface temperature. They also studied the variations in the cooling rate due to the different boiling regimes.

Steady-State Investigations of Jet Cooling.

Wolf et al. (Ref 50) carried out steady-state experiments using a 10 mm (0.4 in.) wide water jet kept at 50 °C (120 °F) of subcooling impinging on a horizontal flat surface. The surface heat flux was controlled by the means of direct heating using a direct-current power supply. The heat-transfer coefficient was quantified for the single-phase convection, partial, and fully nucleate boiling regimes. The effect of the jet velocity, between 2 and 5 m/s (6.6 and 16.4 ft/s) was clear in the single-phase and partial boiling regimes, where the flow hydrodynamics were dominant over bubble dynamics. The jet velocity had no significant effect in the fully developed boiling regime. The heat flux was not a function of the jet velocity and the only function of the surface superheat:

$$q'' = 63.7 (T_w - T_{sat})^{2.95} \quad (\text{Eq 5})$$

Robidou et al. (Ref 44, 51) were able to investigate the entire boiling curve at the jet

stagnation point and up to a location 55 times the jet width, which was 10 mm (0.4 in.). The maximum degree of subcooling was 20 °C (70 °F), and the maximum jet velocity was 1 m/s (3.3 ft/s). The jet impinged on a flat horizontal surface indirectly heated with ten heaters in an attempt to achieve constant surface temperature. They studied the effect of subcooling, jet velocity, immersion, and jet-to-heater spacing on the different boiling regimes. In the forced convection regime, the boiling curve was shifted up with the increase of subcooling and jet velocity. However, in the nucleate boiling regime, no parameter was found to have an effect on the heat flux and the boiling curve. The critical heat flux was found to increase with the increase in jet velocity and subcooling and to decrease with the distance from the stagnation point.

Modeling of jet cooling includes global and mechanistic forms.

Global Modeling. Most of the work cited in the previous two sections involved the development of an empirical correlation of the heat flux to the jet parameters and surface superheat. Although these kinds of relations are easy and fast to apply, they are limited to the conditions for which they have been developed. Omar et al. (Ref 52) developed an empirical/analytical model to predict the stagnation heat flux from

a free planar jet impinging on a horizontal flat surface. With the assumption of enough liquid superheat around the bubbles in the bubbly layer, bubbles departed the surface and then collapsed in the layer above, at the saturation temperature. Additional disturbances are induced due to bubble dynamics, which result in an enhancement of the heat transfer. Such enhancement has been represented by an additional diffusion term in the momentum and energy equations. The total diffusivity term in the momentum and energy equations (Eq 6 and 7) is assumed to be the sum of the molecular and the proposed bubble-induced diffusivity:

$$u \frac{\partial u}{\partial x} + v \frac{\partial u}{\partial y} = -\frac{1}{\rho_l} \frac{dP}{dx} + \frac{\partial}{\partial y} \left((\epsilon_m + \nu) \frac{\partial u}{\partial y} \right) \quad (\text{Eq 6})$$

$$u \frac{\partial T}{\partial x} + v \frac{\partial T}{\partial y} = -\frac{\partial}{\partial y} \left((\epsilon_h + \alpha) \frac{\partial T}{\partial y} \right) \quad (\text{Eq 7})$$

By solving the equations in a nondimensional form, they derived Eq 8 to calculate the nucleate boiling heat flux at the surface:

$$q''_{nb} = \epsilon^{+0.5} \rho_l C_p (T_{sat} - T_\infty) \sqrt{\frac{\bar{C}V_j v}{w}} \frac{d\theta}{d\eta} \Big|_{\eta=0} \quad (\text{Eq 8})$$

Solving Eq 8 requires a value for the diffusivity ϵ . They successfully correlated the

diffusivity to nondimensional groups that represent the flow:

$$\epsilon^+ = \frac{Re_b^{x_1} Ja_{sup}^{x_4} Ja_{sub}^{x_5}}{We_b^{x_2} + x_3} \quad (\text{Eq 9})$$

where $x_1, x_2, x_3, x_4,$ and x_5 are constants representing the effect of different forces on the bubble diffusivity. The model has been validated. It gave predictions of the heat flux with variations in the range of +30 and -15% from the experimental data.

Mechanistic Modeling of Jet Cooling. On the contrary to global models, mechanistic models have the ability to quantify total heat flux, and each component of heat flux independently, based on the submodels or experimental observations for bubble maximum diameter, release frequency, and density of the nucleation sites. One of the oldest wall flux partitioning models was proposed by Griffith (Ref 53) when he noticed a subcooled boiling region with low void fraction and a less subcooled boiling region with high void fraction. In the first region, the scattered static bubbles acted as surface disturbances, and the heat flux components are due to the single-phase flow and boiling, while in the second region the heat is assumed to transfer to the liquid through condensation of the bubbles.

Based on an earlier work of flow boiling heat transfer by Basu et al. (Ref 54), Omar (Ref 55) recently applied the wall heat flux partitioning concept to the stagnation zone heat flux produced by an impinging jet. Omar assumed that the total heat flux is the sum of three partitions due to forced convection, evaporation, and transient conduction heat fluxes, as shown in Fig. 8:

$$q''_w = q''_{FC} + q''_{TC} + q''_{ev} \quad (\text{Eq 10})$$

Omar found a closure for his mechanistic model by developing submodels for the bubble growth diameter and bubble growth terminal scenario. He assumed that after the bubble grows, it may slide or collapse in place, based on whether the dynamic equilibrium or the thermal equilibrium condition would be reached first (Fig. 9). Applying these equilibrium conditions, Omar calculated the maximum bubble

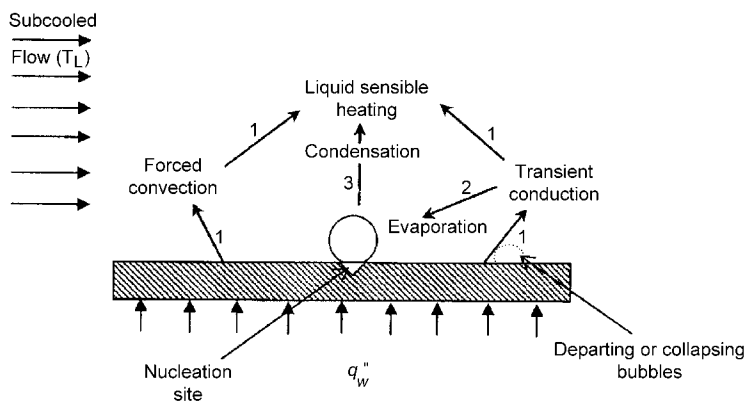


Fig. 8 Different heat flow paths. Source: Ref 55

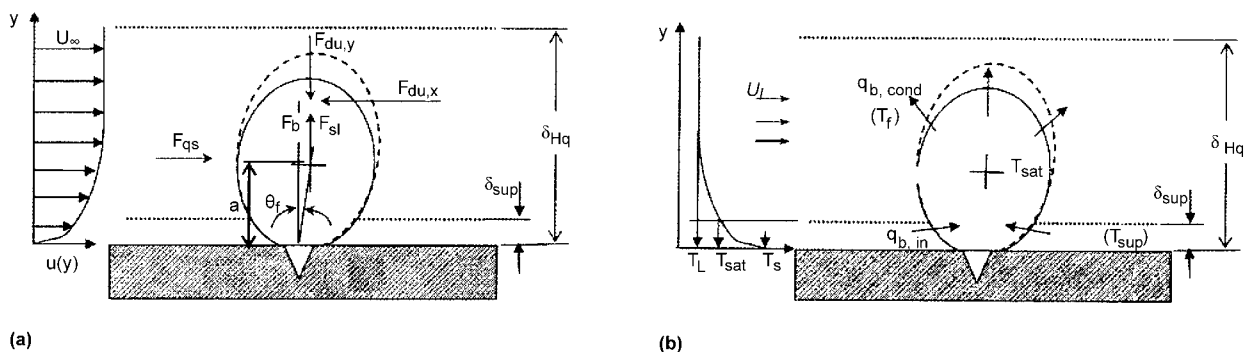


Fig. 9 Two bubble growth-termination scenarios. (a) Dynamic equilibrium. (b) Thermal equilibrium. Source: Ref 55

diameter. He used high-speed imaging and an intrusive optical probe to collect information about bubble dynamics (diameter, frequency, and number).

To find closure for his model, Omar also modeled the onset of nucleate boiling, bubble frequency, and nucleation-site density. Onset of nucleate boiling was correlated as a function of the film velocity, which is a function of the jet velocity. Using the optical probe, Omar measured the bubble frequency as a function of the dimensionless flow parameters. The model was validated using experimental data and was found to be $\pm 30\%$ accurate.

Summary

Water quenching is one of the most common ways in steel heat treatment to achieve the required hardness. Besides the enormous advantages of using water, it also serves a wide range of cooling rates in quenching. Each configuration has its difficulties in estimating the heat flux and the quenched part temperature, which requires more studies for predictiveness and expectedness of the process.

Spray quenching achieves more uniform surface cooling with no cracks and deformations, while immersion quenching is more suitable for complex large parts. Different agitation techniques are used to establish uniformity of the quenched part. Jet cooling has the capability of local cooling, which makes it, along with spray quenching, a good way to quench parts on a runout table.

REFERENCES

- G. Totten, C. Bates, and N. Clinton, *Handbook of Quenchants and Quenching Technology*, ASM International, 1993, p 239–289
- B. Liscic, *Quenching and Carburising*, Third International Seminar, Sept 1991 (Melbourne), IFHT, p 1–27
- N.V. Zimin, *Metalloved. Term. Obrab. Met.*, Nov 1967, p 62–68
- F.K. Kern, *Heat Treat.*, Sept 1986, p 19–23
- S. Segerberg, *Heat Treatment and Surface Engineering: New Technology and Practical Applications*, Sept 28–30, 1988 (Chicago, IL), ASM International, p 177–181
- F. Moreaux and G. Beck, *Heat and Mass Transfer in Metallurgical Systems*, D.B. Spalding and N.H. Afgan, Ed., Hemisphere Publishing, 1981, p 553–561
- L.N. Bokanova, V.V. Lebedev, and L.N. Markova, *Met. Sci. Heat Treat.*, Vol 31 (No. 3–4), 1989, p 159–161
- R.R. Blackwood, *Ind. Heat.*, May 1991, p 46–51
- G. Beck, *Heat and Mass Transfer in Metallurgical Systems*, D.B. Spalding and N.H. Afgan, Ed., Hemisphere Publishing, 1981, p 509–525
- G. Li, *Proc. Fourth Ann. Conf. Heat Treat.*, May 25–31, 1987 (Nanjing), Chinese Mechanical Engineering Society, p 171–175
- V.G. Labeish, *Steel USSR*, Vol 19 (No. 3), March 1989, p 134–136
- N. Hatta and H. Osakabe, *ISIJ Int.*, Vol 29 (No. 11), 1989, p 919–925
- I. Mudawar and W.S. Valentine, Determination of Local Quench Curve for Spray-Cooled Metallic Surfaces, *J. Heat Treat.*, Vol 7 (No. 2), 1989, p 107–121
- F. Moreaux and P. Archambault, *Quenching and Carburising*, Third International Seminar, Sept 1991 (Melbourne), IFHT, p 170–176
- T.A. Deiters and I. Mudawar, *J. Heat Treat.*, Vol 8 (No. 2), 1990, p 81–91
- M.A. Geller and M.S. Zheludkevich, *Metalloved. Term. Obrab. Met.*, Sept 1989, p 29–30
- F. Moreaux and P. Archambault, *Prom. Teplotekh.*, Vol 11 (No. 3), 1989, p 48–55
- P. Archambault, G. Didier, F. Moreaux, and G. Beck, *Met. Prog.*, Oct 1984, p 67–72
- T. Fukuda, T. Takayama, N. Hamasaka, K. Ohkawa, K. Tsuda, and H. Ikeda, *Netsu Shori*, Vol 29 (No. 5), 1989, p 296–301
- B.I. Medovar, A.I. Us, A.I. Krendeleva, N.B. Pivovarskii, N.A. Astaf'ev, and N.M. Shelestiuk, *Probl. Spets. Elektrometall.*, Vol 59 (No. 2), 1987, p 37–40
- N.I. Kobosko, *Metalloved. Term. Obrab. Met.*, Sept 1989, p 7–14
- H.E. Boyer and P.D. Harvey, Ed., *Surface Hardening*, American Society for Metals, 1979
- V.S. Yesaulov, A.I. Sopotkin, V.F. Polyakov, A.V. Nogovitsyn, and V.I. Semen'kov, *Izv. V.U.Z. Chernaya Metall.*, No. 8, 1990, p 82–85
- M.A. Brich, V.T. Borukhov, M.A. Geller, and M.S. Zheludkevich, *Prom. Teplotekh.*, Vol 12 (No. 6), 1990, p 58–62
- M. Mitsutsuka, *Tetsu Hagane*, Vol 54 (No. 14), 1968, p 1457–1471
- R. Jeschar, R. Maass, and C. Kohler, *Proc. AWT-Tagung Inductives Randschichtarten*, March 23–25, 1988, p 69–81
- M. Mitsutsuka, *Tetsu Hagane*, Vol 69 (No. 2), 1983, p 268–274
- M. Mitsutsuka and K. Fukuda, *Tetsu Hagane*, Vol 69 (No. 2), 1983 p 262–267
- R.G. Owen and D.J. Pulling, Multiphase Transport: Fundamentals, Reactions, Safety, Applications, *Proc. Multi-Phase Flow Heat Transfer Symp. Workshop*, 1979
- K.J. Baumeister, F.F. Simon, and R.E. Henry, paper presented at Winter Meeting of the American Society of Mechanical Engineers, 1970
- L. Canale and G. E. Totten, Quenching Technology: A Selected Overview of the Current State-of-the-Art, *Mater. Res.*, Vol 8 (No. 4), 2005, p 461–467
- M. Bamberger and B. Prinz, Determination of Heat Transfer Coefficients during Water Cooling of Metals, *Mater. Sci. Technol.*, Vol 2 (No. 4), 1986
- V. Srinivasan, K.-M. Moon, D. Greif, D.M. Wang, and M.-H. Kim, Numerical Simulation of Immersion Quench Cooling Process Using an Eulerian Multi-Fluid Approach, *Appl. Therm. Eng.*, Vol 30 (No. 5), 2010, p 499–509
- V. Srinivasan, K.-M. Moon, D. Greif, D.M. Wang, and M.-H. Kim, Numerical Simulation of Immersion Quenching Process of an Engine Cylinder Head, *Appl. Math. Model.*, Vol 34 (No. 8), 2010, p 2111–2128
- G. Totten, C. Bates, and N. Clinton, *Handbook of Quenchants and Quenching Technology*, ASM International, 1993
- B. Hernandez-Morales, J.K. Brimacombe, E.B. Hawbolt, and S.M. Gupta, Determination of Quench Heat-Transfer Coefficient Using Inverse Techniques, *Proc. First Int. Conf. on Quenching and Control of Distortion*, Vol 214, 1992, p 155–164
- M. Sedighi and C. McMahon, The Influence of Quenchant Agitation on the Heat Transfer Coefficient and Residual Stress Development in the Quenching of Steels, *Proc. Inst. Mech. Eng. B, J. Eng. Manuf.*, Vol 214, 2000, p 555–567
- G. Tacke, H. Litzke, and E. Raquet, Investigation into the Efficiency of Cooling Systems for Wide-Strip Hot Rolling Mills and Computer-Aided Control of Strip Cooling, *Accelerated Cooling of Steel: Proceedings of a Symposium Sponsored by the Ferrous Metallurgy Committee of the Metallurgical Society of AIME*, Aug 1985, p 35–54
- F. McGinnis and J. Holman, Individual Droplet Heat-Transfer Rates for Splattering on Hot Surfaces, *Int. J. Heat Mass Transf.*, Vol 12, Jan 1969, p 95–108
- N. Sozibir, Y.W. Chang, and S.C. Yao, Heat Transfer of Impacting Water Mist on High Temperature Metal Surfaces, *J. Heat Transf.*, Vol 125 (No. 1), 2003, p 70
- J. Sengupta, B. Thomas, and M. Wells, The Use of Water Cooling during the Continuous Casting of Steel and Aluminum Alloys, *Metall. Mater. Trans. A*, Vol 36, 2005, p 187–204
- M. Ciofalo, I.D. Piazza, and V. Brucato, Investigation of the Cooling of Hot Walls by Liquid Water Sprays, *Int. J. Heat Mass Transf.*, Vol 42, April 1999, p 1157–1175
- S. Ishigai, S. Nakanishi, and T. Ochi, Boiling Heat Transfer for a Plane Water Jet Impinging on a Hot Surface, *Sixth International Heat Transfer Conference* (Toronto, ON, Canada), 1987, p 445–450
- H. Robidou, H. Auracher, P. Gardin, and M. Lebouche, Controlled Cooling of a Hot Plate with a Water Jet, *Exp. Therm. Fluid Sci.*, Vol 26, 2002, p 123–129
- D. Hall, F. Incropera, and R. Viskanta, Jet Impingement Boiling from a Circular

- Free-Surface Jet during Quenching, Part 1: Single-Phase Jet, *Trans. ASME J. Heat Transf.*, Vol 123 (No. 5), 2001, p 901–910
46. A.K. Mozumder, P.L. Woodfield, M.A. Islam, and M. Monde, Maximum Heat Flux Propagation Velocity during Quenching by Water Jet Impingement, *Int. J. Heat Mass Transf.*, Vol 50, 2007, p 1559–1568
 47. N. Karwa, L. Schmidt, and P. Stephan, Hydrodynamics of Quenching with Impinging Free-Surface Jet, *Int. J. Heat Mass Transf.*, Vol 55, 2012, p 3677–3685
 48. M. Akmal, A. Omar, and M. Hamed, Experimental Investigation of Propagation of Wetting Front on Curved Surfaces Exposed to an Impinging Water Jet, *Int. J. Microstruct. Mater. Prop.*, 2008
 49. M. Islam, M. Monde, P. Woodfield, and Y. Mitsutake, Jet Impingement Quenching Phenomena for Hot Surfaces Well Above the Limiting Temperature for Solid-Liquid Contact, *Int. J. Heat Mass Transf.*, Vol 51 (No. 5–6), 2008, p 1226–1237
 50. D.D. Wolf, F.F. Incropera, and R. Viskanta, Local Jet Impingement Boiling Heat Transfer, *Int. J. Heat Mass Transf.*, Vol 39, May 1996, p 1395–1406
 51. H. Robidou, H. Auracher, P. Gardin, M. Lebouche, and L. Bogdanic, Local Heat Transfer from a Hot Plate to a Water Jet, *Int. J. Heat Mass Transf.*, Vol 39, Nov 2003, p 861–867
 52. A. Omar, M. Hamed, and M. Shoukri, Modeling of Nucleate Boiling Heat Transfer under an Impinging Free Jet, *Int. J. Heat Mass Transf.*, Nov 2009, Vol 52, p 5557–5566
 53. P. Griffith, J.A. Clark, and W.M. Rohsenow, Void Volumes in Subcooled Boiling, *U.S. National Heat Transfer Conference* (Chicago), 1985
 54. N. Basu, G.R. Warrier, and V.K. Dhir, Wall Heat Flux Partitioning during Subcooled Flow Boiling, Part 1: Model Development, *J. Heat Transf.*, Vol 127 (No. 2), 2005, p 131–140
 55. A. Omar, “Experimental Study and Modeling of Nucleate Boiling during Free Planar Liquid Jet Impingement,” Ph.D. thesis, McMaster University, 2010

Press Quenching

Arthur Reardon, The Gleason Works

PRESS QUENCHING is a specialized quenching technique that can be utilized during heat treatment to minimize the distortion of complex geometrical components. The distortion encountered in industrial heat treating operations can result from a wide variety of independent contributing factors. These include, among others, the quality and prior processing history of the material from which the component in question has been manufactured; the residual stress distribution and prior thermal history of the component; and the generation of unbalanced thermal and transformation stresses induced by the quenching operation itself. High precision components such as industrial bearing races and automotive spiral bevel gears can often distort unpredictably during unconstrained or free oil quenching as a result of these factors.

Press quenching can help to minimize the distortion of such components by using specialized tooling for generating concentrated forces that constrain the movement of the component in a carefully controlled manner. When performed correctly, this method of quenching can often achieve the relatively stringent geometrical requirements stipulated by industrial manufacturing specifications. It is routinely performed on a wide variety of complex components manufactured from both ferrous- and nonferrous-based alloys. Common steel alloys that are routinely press quenched include high-carbon through-hardening grades such as AISI 52100 and A2 tool steel, as well as low-carbon carburizing grades such as AISI 3310, 8620, and 9310.

Carburizing steels in particular can benefit from the process of press quenching, due to the nature of their processing and popularity in many of the automotive and gearing assemblies used in industrial and consumer products. Ideally, during quenching the transformation temperature should be the same throughout the entire cross section of the component so that it is capable of transforming uniformly. However, in case-carburized components, the martensite start transformation temperature is not uniform throughout the entire cross section of the part. The carbon that is diffused into the part surface during the carburizing process produces a composition gradient that results in a gradient in the transformation temperature near the surface. During quenching, this gradient can

promote or aggravate distortion issues in such components. Nonuniformities in the base material microstructure (such as in heavily segregated or improperly normalized material) can also contribute to this type of distortion. Uniformly large, thin-walled components such as large-diameter bearing races are, in general, more readily susceptible to these distortion-related issues than are relatively thick, massive, compact geometries. While press quenching cannot eliminate these effects, its use can help to minimize them.

The severity of the distortion encountered during heat treatment depends strongly on the nature of the heat treating process that is used. To minimize distortion issues during quenching, heat should be extracted from the component in as uniform a manner as possible. This can be difficult to achieve in cases where sudden changes in geometry occur, such as, for example, when thin sections are located adjacent to heavy or thick sections on the same component. A good example of this is the teeth on a gear or pinion. The teeth have a greater surface-area-to-volume ratio than the body of the gear or pinion, and they have a tendency to distort by “unwinding” during quenching. Although free or unconstrained quenching of such parts can lead to unpredictable distortion, this characteristic movement of gear teeth is so reproducible during the press-quenching operation (Ref 1) that it is often incorporated into the gear design itself to minimize post-quench grinding removals. As the workpiece is submerged into the quenching medium, the teeth tend to cool and contract more rapidly than the adjacent heavier sections. As a result of this varying quench rate, the thinner or lighter sections tend to harden more rapidly and contract, while the balance of the component is still in an expanded state. Because the heavier sections cool and contract at a relatively slower rate, they encounter resistance to their movement at the point where the thin sections adjoin them. The outcome is that the thin sections transform more quickly than the thick sections, resulting in temperature gradients and nonuniform transformation-induced stresses. This particular issue can be addressed in press quenching by selectively directing the quenchant flow toward the thicker sections and

baffling it away from the thinner sections to promote a more uniform quench. This capability is achieved primarily through the use of specialized tooling. By implementing this important technique, lower levels of transformation-induced distortion can result.

Equipment

Quenching machines initially came into widespread industrial use in the United States in the early 1930s and were used primarily in the processing of automotive ring gears for applications involving passenger cars and trucks (Fig. 1). These machines can be hydraulically or pneumatically actuated (depending on the specific design) and can use a variety of quenching media, the most common being oil. While the geometrical design and optional features may have changed dramatically in these machines over the decades since their initial introduction, their basic functionality has remained the same. A representative version of a modern quenching machine is depicted in Fig. 2. The overall design consists of several fundamental components, including the upright machine section, a control panel, a lower die table, tooling, and a base. A chiller is used for maintaining the quenchant temperature within a specified, narrow range and may be included as a part of an individual machine system or used in a central reservoir that is connected to multiple quenching machines simultaneously. The machine upright houses the upper die ram, the hydraulic manifolds, hydraulic lines, solenoids and valves, and the electrical panel control box. A control screen listing the various features that may be adjusted during the course of a quenching cycle is depicted in Fig. 3. A schematic of the base, which serves as a reservoir for the quench oil and also supports the lower die assembly, is shown in Fig. 4. The upright is recessed from the front of the machine base to allow full access to the lower die for placing the components to be quenched on the tooling or for removing them after quenching is completed when the machine is in the “out” position.

During operation, the component to be quenched is either manually or robotically



Fig. 1 One of the 64 cm (25 in.) automatic quenching machines manufactured by The Gleason Works in Rochester, NY, in the early 1930s. The operator is removing a large spiral bevel gear from the lower die assembly after the quenching operation has been completed. Courtesy of The Gleason Works, Rochester, NY



Fig. 2 Modern version of the Gleason 529 quenching machine. Courtesy of The Gleason Works, Rochester, NY

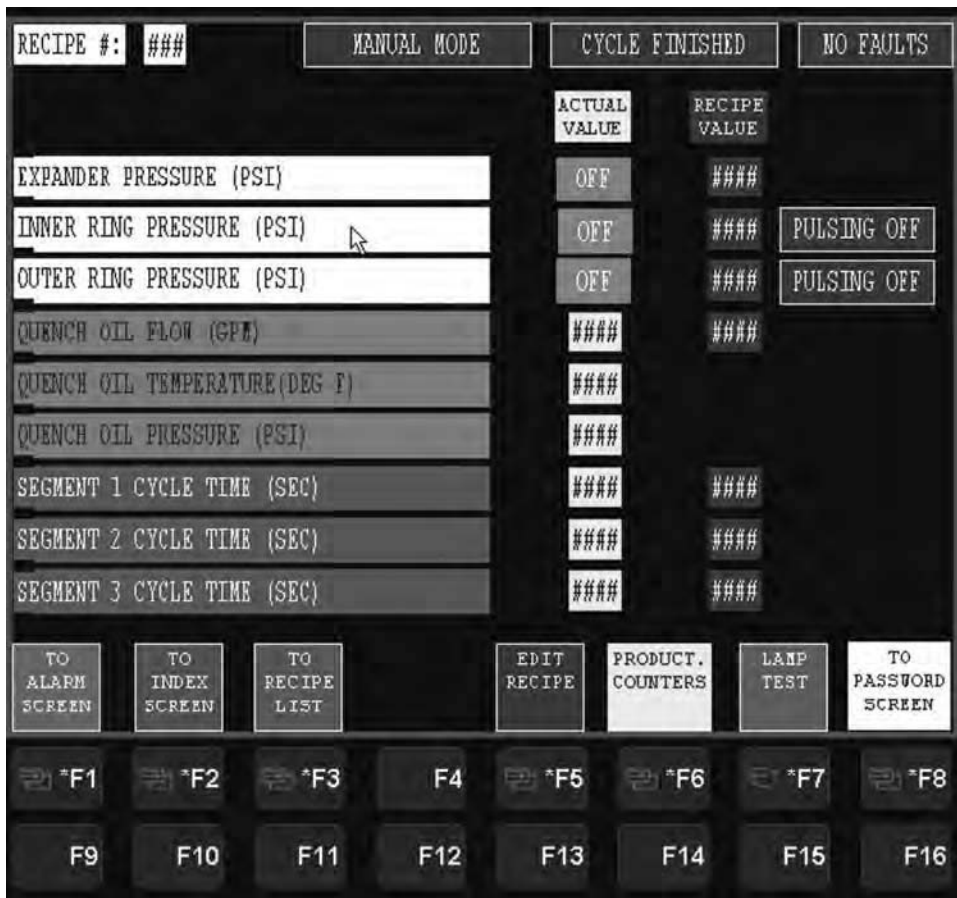


Fig. 3 Control screen showing the various parameters that may be adjusted over the course of a typical quenching cycle. Courtesy of The Gleason Works, Rochester, NY

removed from a separate furnace (usually a box, continuous rotary, or pusher-type furnace) and is placed onto the tooling of the lower die assembly. A close-up view of this die assembly is shown in Fig. 5. It should be noted that the efficiency of the transfer mechanism from the furnace to the quenching machine is often a critical parameter in press quenching. Transfer times should be kept to a minimum to minimize heat loss. If this step requires too much time, then hardness-related issues and undesirable transformation products may be generated as a result of a slack quench. After the part is successfully loaded onto the lower die assembly, the machine is actuated and the part is retracted into the machine, where it is centered below the upper hydraulic ram assembly. The outer machine guard is lowered as the assembly descends, and the center ram actuates one (or multiple) internal expanders that make contact with the inner diameter(s) of the component at the specified pressure points to maintain roundness at these locations (Fig. 6). Each of the components of the ram assembly (center expander, inner and outer dies) is controlled independently of each other through three separate proportional valves, and they are monitored via pressure transducers. A predetermined pressure level is usually maintained by the expander throughout the quench cycle, although in some machines that possess the required programming capability, this pressure may be varied over the course of the quenching cycle. The inner and outer dies are lowered to make physical contact with the upper surfaces of the component being quenched, to control alignment, dish, and part flatness during the course of the quenching cycle. The flow of quench oil, which

may be preset or preprogrammed, is then activated to quench the part.

Figure 7 illustrates an example of a quench oil circulation path that can be established within the quenching chamber. Oil is pumped into the quench chamber through apertures around the outside diameter of the lower die. As the chamber fills up surrounding the component, oil flows out of the top. If the tooling is properly designed, the direction of oil flow over the component can be adjusted to obtain the best overall results. The elongated apertures at the exit may be adjusted to restrict oil flow or

may be fully opened to maximize flow, depending on the requirements for the part in question. The lower dies are constructed from several different concentric slotted rings that may be rotated to provide full flow or to restrict oil flow to the underside of the part. These particular features can be finely adjusted to help minimize the degree of distortion attributed to uneven heat removal during quenching. Timed segments during the quenching cycle can also be used to vary both the oil flow rate and duration to establish a well-defined quenching recipe for a specific part design.

The lower die table typically rides on transverse rods and is either driven by a hydraulic or pneumatic piston. A cam allows adjustment of the individual rings in the lower die assembly. Through actuation of the cam assembly, these individual rings may be forced into a dishing or coning position to better accommodate the required part geometry (Fig. 8). A side benefit of this arrangement is the relatively fast and easy method that can be employed of cutting and installing shims under each ring as necessary to establish proper contact with the component being quenched. Proper support of the part is a critical aspect of press quenching, and tooling design plays a key role in this regard.

The oil-quenching process itself may consist of up to three general stages:

- The initial vapor blanket stage, where the first oil to come in contact the part is instantly vaporized and forms a vapor barrier

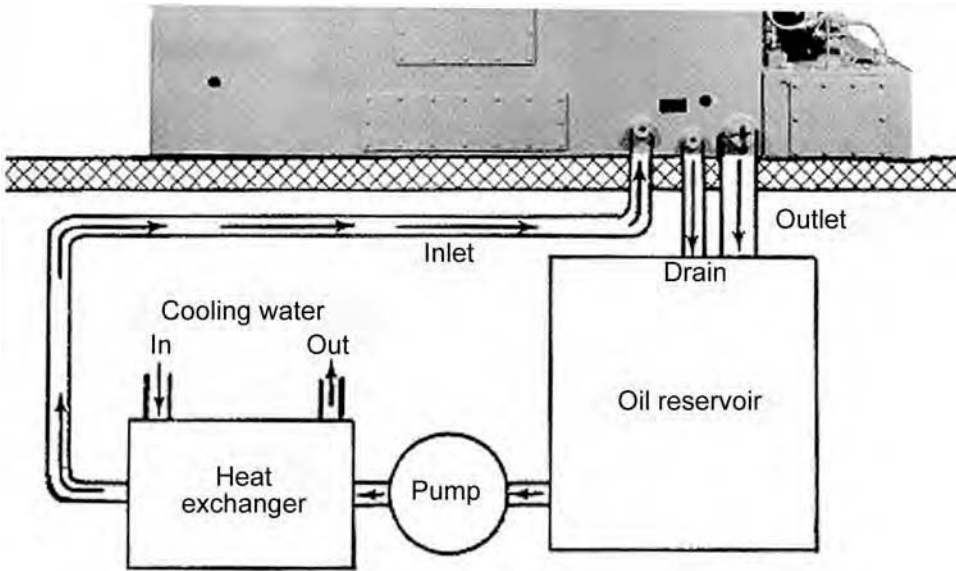


Fig. 4 Schematic representation of the oil flow from the oil reservoir to the chiller and back to the quenching machine. Courtesy of The Gleason Works, Rochester, NY



Fig. 5 Lower die assembly of a quenching machine in the "out" position. Note the spring-loaded center expander cone and the individual slotted rings. Courtesy of The Gleason Works, Rochester, NY

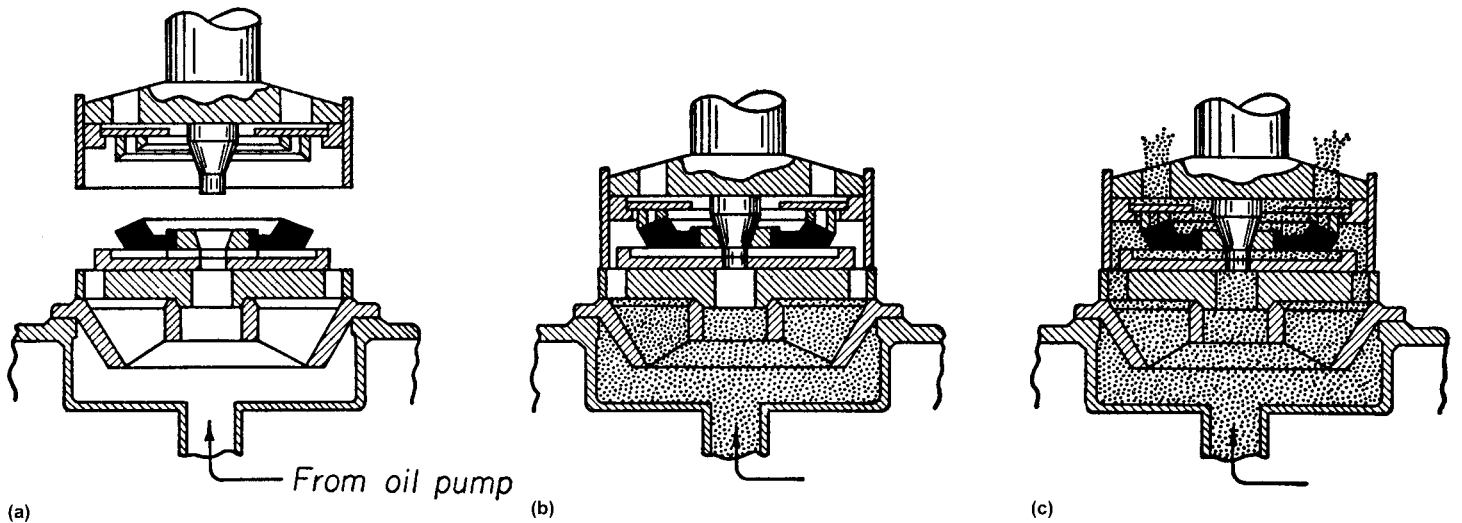


Fig. 6 (a) A hot gear placed into position on the lower die assembly is ready for press quenching. (b) Lowering the center ram and the upper inner and outer dies to make contact with the part. (c) Starting the timing cycle; the oil flow is initiated into the quenching chamber and around the part. Source: Ref 2

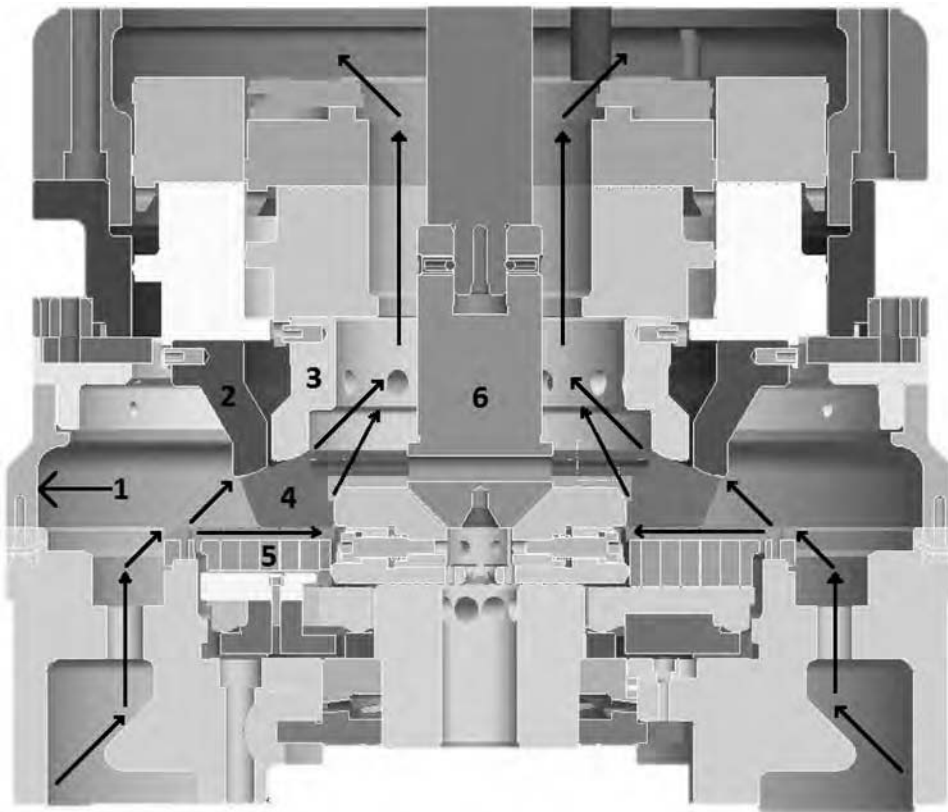


Fig. 7 Schematic diagram illustrating contact of the center expander and the inner and outer dies with the part during quenching. The various components labeled in the diagram are (1) machine guard attached to the upper die assembly; (2) outer upper die; (3) inner upper die; (4) component undergoing quench; (5) lower die assembly; and (6) center expander cone. The oil flow path in the quench chamber is depicted by the flow line arrows. Courtesy of The Gleason Works, Rochester, NY

that surrounds the part and acts as an effective thermal insulating layer

- The vapor transport stage, where oil breaks through the vapor blanket, resulting in more rapid heat transfer
- The liquid stage, where heat extraction occurs predominately by convective heat transfer

For uniform heat extraction to occur during the initial stages of quenching, the oil flow rates must be sufficient to prevent the formation of a vapor blanket. If vapor bubbles are allowed to form in areas around the surface of the component, uneven heat extraction will result that can lead to unacceptable hardness variations and distortion. After this initial quenching stage has been successfully eliminated, lower quenchant flow rates may be safely tolerated. The quenchant flow rate profile that is ultimately established for the part in question must be carefully selected so that the hardness and geometry requirements are satisfactorily met. Too slow of a quench rate will result in a slack quench, hardness variations, and undesirable transformation products. Too rapid of a quench rate could result in unacceptable part distortion and/or cracking. The establishment of the proper oil flow rate profile and selection of an

oil flow path around the part are often determined by using a trial-and-error process. Success frequently depends on the experience, knowledge, and skill of the machine operator.

The average oil temperature for most press-quenching operations typically falls somewhere within the range of approximately 25 to 75 °C (75 to 165 °F), depending on the nature of the quenching operation, the type of quench oil being used, the material in question, and post-heat-treat property requirements. Average quench oil temperatures exceeding 60 °C (140 °F) should generally be avoided as a precaution to prevent damage to the machine seals that are used to contain the quench oil. Proper and routine maintenance of the quench oil bath is important (Ref 4). It is often a neglected aspect of the press-quenching process and can lead to unexpected variations in the hardening response of the materials processed in these types of systems. As the quench oil continues to be used, the oil additives gradually break down, and fine particulates can accumulate over time, even if the oil is continuously filtered. If left undetected, this can lead to accelerated quench rates, which can compromise the integrity of the oil-quenching process. Monitoring of the quench bath for oil viscosity, flash point, water content, sludge content, and

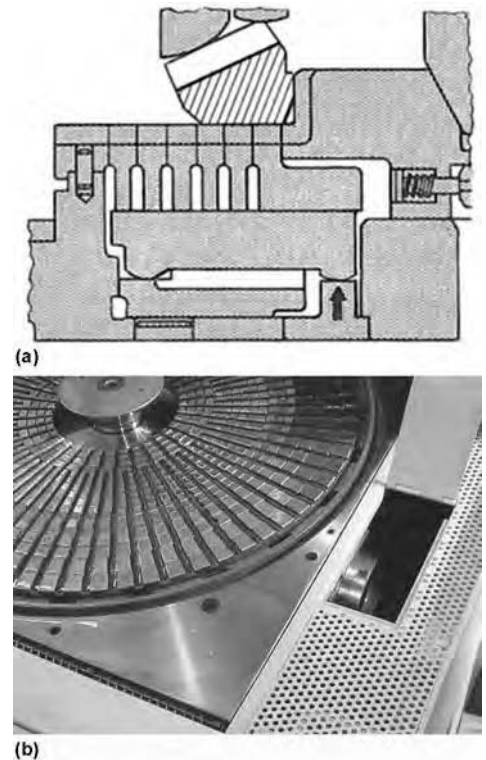


Fig. 8 (a) Schematic diagram illustrating the mechanism used to control dishing. This mechanism permits the inner ring of lower die to be raised or lowered (arrow) to compensate for dishing. Source: Ref 3. (b) Actual lower die assembly showing the dial that controls the mechanism for raising or lowering the individual slotted rings. Courtesy of The Gleason Works, Rochester, NY

precipitation number should be performed periodically based on usage. Testing of the quench oil should be performed on a quarterly basis at a minimum.

Factors in Distortion Control

In summary, the primary critical factors affecting component distortion during the press-quenching operation are:

- Quality and prior processing history of the material from which the component in question has been manufactured
- Residual-stress distribution and prior thermal history of the component
- Generation of unbalanced thermal and transformation stresses induced by the quenching operation
- Material grade and austenitizing temperature profile used
- Transfer time between the austenitizing furnace and the quenching machine
- Type, quantity, condition, and temperature of quenchant used
- Direction and selective metering of quenchant flow over the component

- Duration of quench at various flow rates
- Proper quench die tooling design, setup, and maintenance
- Locations of contact points on the component for applying pressure
- Amount of pressure applied for maintaining component geometry
- Pulsing

The last item in this list is a unique feature of press quenching. The inner and outer dies are typically pulsed during quenching to maintain the geometry of the part in order to minimize distortion. The pulse feature periodically eases the applied pressure exerted by the inner and outer dies and allows the component to contract normally as it cools, while still maintaining the desired part geometry. Without this feature, the stresses that would be induced from frictional contact between the die assembly and the part would not allow the component to contract normally as it cools. Pulsing effectively reduces this frictional contact and avoids distortion issues due to eccentricity and out-of-flatness. When properly applied, the pulsing technique keeps the dies in contact with the part throughout the quenching cycle but allows the pressure to be released and then reapplied approximately every 2 seconds. Although the inner and outer dies are typically cycled in this manner, the expander pressure is not normally pulsed. Most press-quenching machines used in industry today (2013) utilize this design feature; however, it is not a recent development. For decades, the pulsing technique has been an integral feature of semiautomatic press-quenching machines designed for high production rates. An illustration of one of these semiautomatic machine designs is shown in Fig. 9.

Each component that is press quenched requires a specific die tooling design configuration and machine setup. Expanding segmental dies are often employed to maintain bore size and roundness in bearing races and gears. If a component possesses a bore diameter that is physically too small to accommodate these segmental dies, a solid plug could be used instead to control the diameter and taper of the bore. The plug would simply be pressed out after quenching. It is imperative that when there are different locating surfaces on the lower die assembly that the dimensions between these surfaces be held to a close tolerance from piece to piece. Failure to adhere to this rule will result in inconsistent results and unwanted distortion. In addition to expanding dies, contracting dies are also available to maintain the geometrical tolerances for the outside diameter,

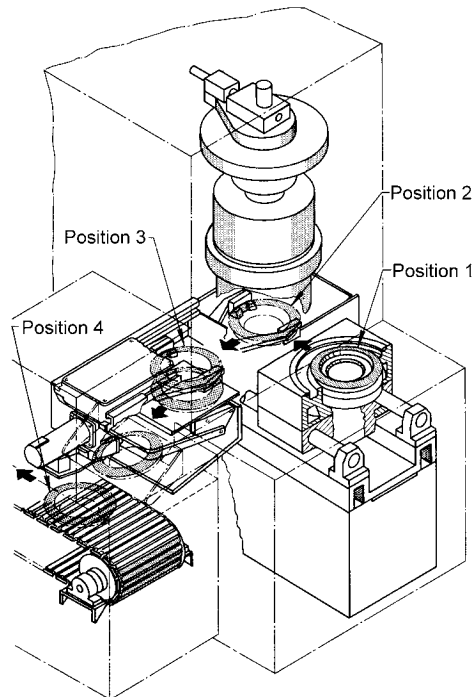


Fig. 9 Schematic diagram of four-position semiautomated press-quenching machine using the pulsing principle. Source: Ref 3, 5

where this is a critical factor. A good example of this is gears that incorporate thin web sections in conjunction with relatively heavy sections for gear teeth, bosses, and bearing diameters. Gears used in aerospace applications often incorporate several of these features, which may cause them to contract unevenly during quenching. This problem can be effectively remedied by the application of compressive loads on the outside surface of the component.

The tolerances that can be achieved through press quenching are impressive. For example, if the bore on a 230 mm (9 in.) diameter gear is held to 0.025 mm (0.001 in.) out of round in the soft condition, it can often achieve 0.064 mm (0.0025 in.) out of round after press quenching. The same gear, when placed on a surface plate, should not permit a gap that a 0.05 mm (0.002 in.) feeler gage can access anywhere between the plate and back surface of the gear. For gears up to 460 mm (18 in.) in diameter, this gap should be less than 0.075 mm (0.003 in.). These stringent tolerances are routinely achievable through press quenching, provided that the factors listed earlier are

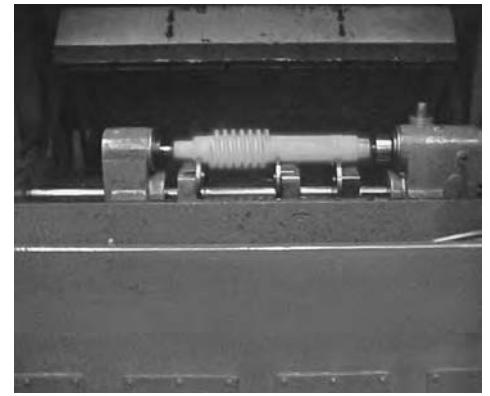


Fig. 10 Image of worm gear loaded into a roller-die quenching machine. After the machine guard is lowered, the flow of quench oil is initiated to uniformly quench the part as it rotates between centers. Courtesy of The Gleason Works, Rochester, NY

properly addressed (i.e., good-quality forgings are used, correct normalizing is performed prior to machining, good machining practices are followed with sharp cutting tools, etc.). An extension of press quenching is the roller-quenching method used for controlling distortion in long cylindrical parts, shafts, or crankshafts up to 1020 mm (40 in.) long and 200 mm (8 in.) in diameter. This technique involves using rollers to exert carefully controlled loads on a hot component while it is rotating between centers as the quenching chamber is filled with flowing oil. Figure 10 provides a representative image of one of these highly specialized quenching machines.

REFERENCES

1. L.E. Jones, Fundamentals of Gear Press Quenching, *Ind. Heat.*, April 1995, p 54
2. *Metals Handbook*, American Society for Metals, 1948, p 624
3. *Quenching and Martempering*, American Society for Metals, 1964
4. B.L. Ferguson and D.S. MacKenzie, Effect of Oil Condition on Pinion Gear Distortion, Quenching Control and Distortion, *Proc. Sixth International Quenching and Control of Distortion Conference*, Sept 9–13, 2012 (Chicago, IL), p 319–328
5. P. Cary, *Quenching and Control of Distortion*, ASM International, 1988

Wire Patenting

Xinmin Luo, Jiangsu University
George E. Totten, Portland State University

Wire Patenting Processes

Wire is one of the most important standard products of iron and steel, with multiple purposes in many industries, such as mechanical and power engineering, mine and harbor haulage, marine applications such as fishing, bridge construction, and civil engineering. Drawing is the main manufacturing process of wire, and in many cases, multiple annealing steps are needed due to the work-hardening effect when it is made. Furthermore, the final mechanical properties of wire rely on a unique heat treatment process: patenting.

Lead Baths. Lead bath patenting has been carried out in virtually every wire mill that produces high-carbon steel wire since its discovery one century ago. This is due to the many advantages offered by the medium of molten lead, which exhibits good heat-transfer characteristics, giving an adequate structure and a combination of strength and ductility that promote superior drawing. Nevertheless, molten lead baths also suffer from two main disadvantages: high cost due to expensive purity lead, drag-out losses, and equipment and maintenance costs; and toxicity resulting from lead fumes and lead dust, which are very difficult to dispose of and recycle. Problems of pollution by lead are well known and are subject to strict scrutiny and control by health and safety regulatory agencies. With an increasing environmental consciousness, it is certain that such health and safety regulations will become more stringent globally. The question should be posed by both metallurgists and environmentalists as to whether the use of molten lead will be capable of meeting future requirements in terms of environmentally conscious products. In view of the disadvantages and limitations outlined, the possibility of replacing molten lead with nontoxic media or techniques is increasingly important.

Aqueous Carboxymethyl Cellulose Solution as a Lead Bath Alternative. There have been various wire-patenting processes that have been developed as acceptable alternatives to the use of molten lead baths, including air (Ref 1), mist (Ref 2), molten salt (Ref 1), water (Ref 3,

4), fluidized-bed processes (Ref 5), and aqueous polymer solutions such as aqueous solutions of sodium polyacrylates (Ref 4). One aqueous polymer solution that has been extensively studied for use in wire patenting and which has considerable commercialization potential as an alternative to molten lead baths is an aqueous solution of carboxymethyl cellulose (CMC) (Ref 6, 7). Aqueous CMC solutions have been shown to be biodegradable and nontoxic (Ref 8–10) and to result in potentially favorable wire-patenting properties.

Spray quenching is a cooling method with good flexibility in heat treatment. A unique and important aspect is the ability to change the cooling rate during the quenching process by altering the compressed air pressure or quenchant flux according to the cooling requirement of the workpiece through a certain temperature range (Ref 11). Some aqueous polymer solutions can be used as a moderator in spray quenching to further expand the advantages of spray quenching and therefore to increase its applications (Ref 12).

Cooling Behavior Experiment Materials and Procedures

Commercial gages of wires were used for comparison. One type was 3.9 to 6.5 mm (0.15 to 0.25 in.) diameter 0.70 % C steel wires, and the other was AISI 321 austenitic stainless steel wire (with the same diameter) that will not undergo phase transformation on heating and/or cooling.

To investigate the cooling characteristics and the transformation behavior of the steel to be tested, a steel wire probe was designed (Ref 13) with a built-in thermocouple located at the geometric center, as shown in Fig. 1. When the wire probe was quenched from the austenitic temperature into a molten lead bath or an aqueous polymer solution, cooling time-temperature curves were recorded, and the cooling time-temperature data subsequently were processed using a computer to obtain cooling-rate curves (Ref 14, 15). The system is shown in Fig. 2. A schematic illustration of the fog-

cooling experimental facility is illustrated in Fig. 3; it consisted mainly of a spraying atomization system with opposite-set nozzles and compressed air and quenchant supplies. Microstructural characterizations were performed using a Nikon Epiphot 300 optical microscope and a JEOL JSM-7001F field-emission scanning electronic microscope (SEM).

Two types of aqueous polymer solutions were used for comparison. One was polyvinyl alcohol (PVA), which usually is used as a spray-cooling medium for surface induction heat treatment. In this experiment, the use concentration was 0.05 to 0.4%. The other aqueous polymer was CMC, whose molecular formula is $(C_6H_7O_2(OH)_2OCH_2COONa)_n$, and the use concentration was less than 0.05% due to its viscosity-concentration behavior.

Cooling Curves and Cooling-Rate Curves Results and Analysis

Measurement in CMC Solutions. Figure 4 shows the cooling curve and cooling-rate curve of 5 mm (0.2 in.) steel wire during patenting in

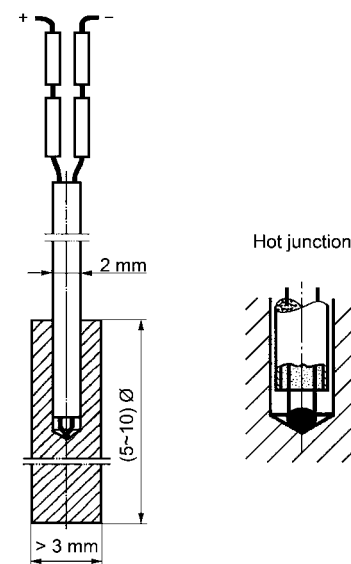


Fig. 1 Schematic illustration of steel wire probe

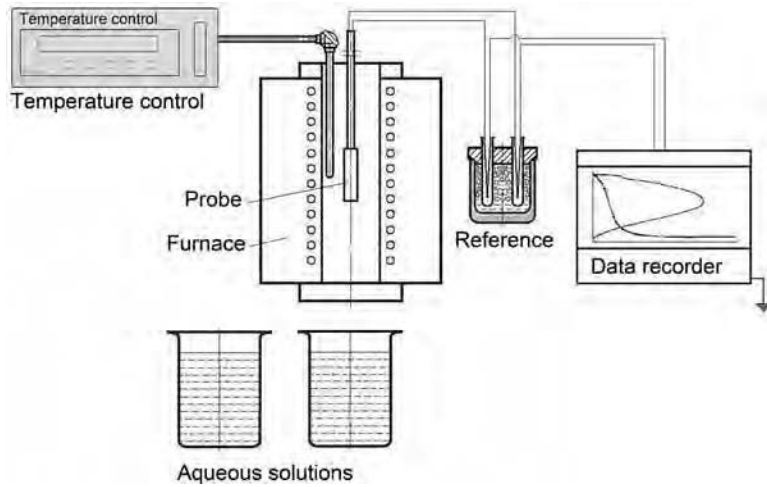


Fig. 2 System for measuring cooling curves

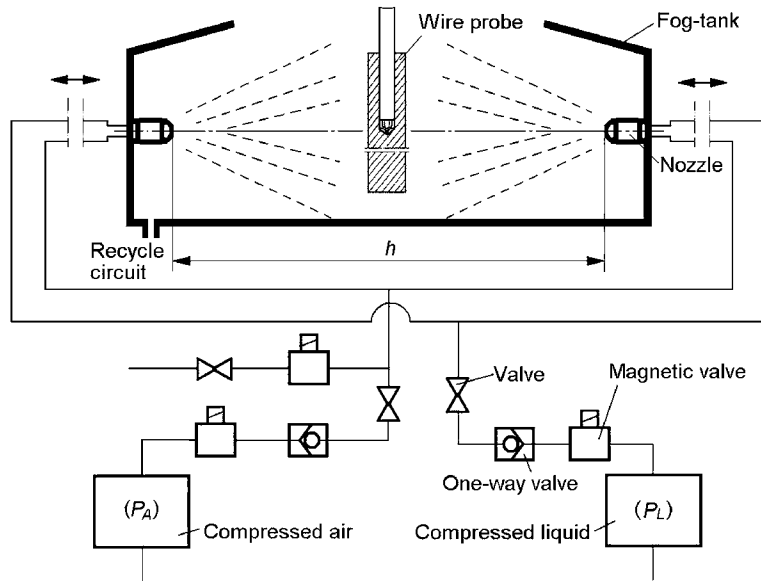


Fig. 3 Schematic diagram of experimental system for fog cooling

0.10 and 0.25% CMC aqueous polymer solutions. Hardness tests indicated that the steel wire was through hardened when immersion quenched in 0.1% CMC polymer solution, indicating that an undesirable martensite transformation occurred. However, the desired fine pearlite microstructure was obtained when quenched in the 0.25% CMC polymer solution. It is interesting that the cooling curve measured in the higher-concentration aqueous CMC polymer solution exhibited the same exothermic “hump” phenomenon during cooling as observed during lead bath patenting, although the cooling rate was approximately 40 °C/s (72 °F/s). This “zero cooling rate” shown on the cooling-rate curve of Fig. 4(b) was indicative of a pearlite-type transformation because the vapor blanket (film boiling) stage would be sufficiently long for austenite to transform into pearlite with increasing polymer

concentration. Unfortunately, the initial cooling rate still was slower, which may result in the coarser pearlite or even separation of primary ferrite from the subcooled austenite during cooling. When the wires cooled into the nucleate boiling stage, although the cooling rate is greater in the lower-temperature range, the pearlite transformation was completed.

It is well known that the cooling curves change dramatically with increasing concentrations of a polymer quenchant. Typically, the vapor blanket cooling stage is extended and cooling rates decrease as the polymer quenchant concentration increases. When the steel has cooled to the characteristic point that indicates—for vaporizable quenchants such as aqueous CMC polymer solutions—the cooling process moved from film boiling to nucleate boiling, this becomes an insurmountable obstacle for further acceleration of cooling during the

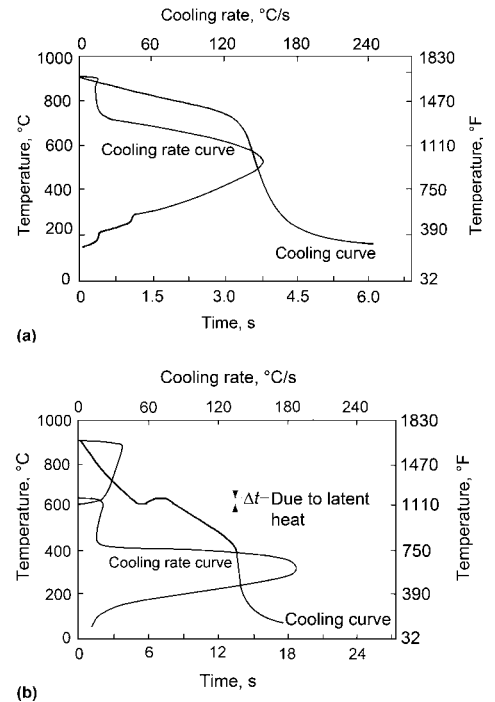
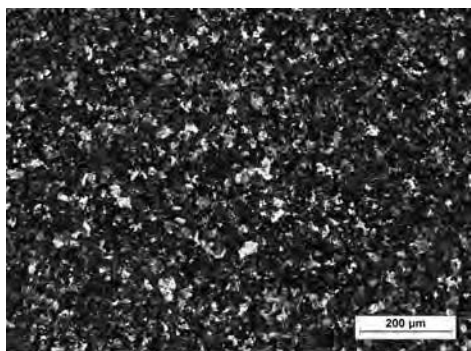


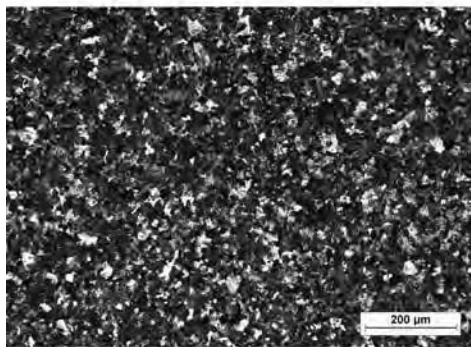
Fig. 4 Cooling curve and cooling-rate curve of 5 mm (0.2 in.) steel wire during patenting in (a) 0.10% carboxymethyl cellulose (CMC) and (b) 0.25% CMC. Note the different time scales, because cooling was substantially slower in the higher-concentration CMC solution shown in Fig. 4(b).

initial stage for patenting using one concentration of an aqueous polymer solution. Because the pearlite transformation was completed during the vapor blanket cooling stage, no additional phase-transforming latent heat would be emitted when the steel wire is passed through the lower-temperature transformation range. In fact, only when the cooling power of the cooling medium cannot be balanced with the latent heat of the steel wire it is possible for the proeutectoid ferrite to separate, which depends on the size of the steel wires and the CMC polymer quenchant concentration.

Microstructure Comparison. Optical micrographs of the microstructures of patented high-carbon steel wires are shown in Fig. 5. The microstructures exhibit fine pearlite morphology. Because of limited resolution, it was not possible to clearly distinguish differences in microstructures for these two test specimens using optical microscopy. Figure 6 shows the micrographs obtained using a field-emission SEM. At high magnification approaching the nanometer scale, it is clear the lamellar structure obtained by patenting in a lead bath is finer than that obtained when patenting in the CMC aqueous polymer solution. Although the lamellar cementite in the latter is slightly thicker but crushed due to higher transformation stress, it is not likely to negatively affect bulk deformation of the wire upon drawing (Ref 16).



(a)



(b)

Fig. 5 Optical micrographs of 0.70% C steel wire patented at 550 °C (1020 °F) in (a) lead bath and (b) 0.25% carboxymethyl cellulose aqueous solution

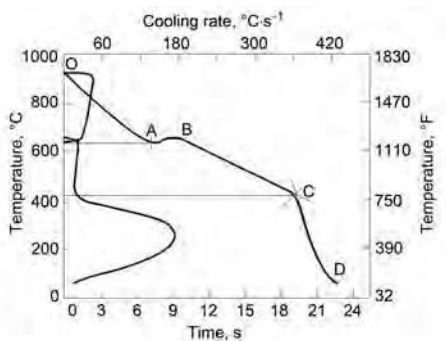
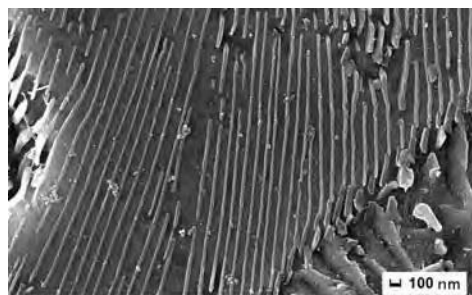


Fig. 7 Typical cooling curve and cooling-rate curve measured by a 5 mm (0.2 in.) steel wire probe in fog cooling

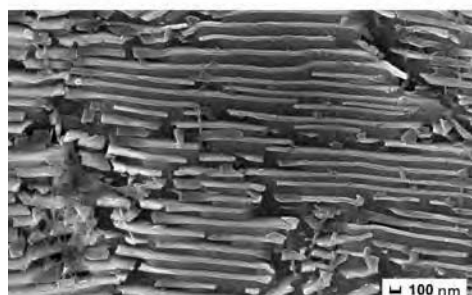
Typical Cooling Curve in Fog Cooling

Figure 7 shows the typical cooling curve and cooling-rate curve measured by a 5 mm (0.2 in.) steel wire probe in fog cooling. There are two main characteristics of this figure: the apparent pearlite transformation manifestation, and the typical three stages that occurred in immersion quenching in a vaporized quenchant. Pearlite transformation starts at point A and finishes at

point B, which indicates the temperature and the moment involved. Point C marks the transition point from the dynamic vaporizing blanket stage to the dynamic boiling stage. From the cooling-rate curve, the maximum cooling rate (v_{max}) and the average cooling rate between 900 and 600 °C (1650 and 1110 °F) ($v_{900-600}$) can be obtained and used as investigated indicators for comparison.



(a)



(b)

Fig. 6 Optical micrographs of lamellar pearlite structure of 5 mm (0.2 in.) steel wire patented at 550 °C (1020 °F) in (a) lead bath and (b) 0.25% carboxymethyl cellulose aqueous solution

Influence Order of Spray Parameter when Polymer Additive Introduced

When steel wire is being spray quenched, the cooling process becomes complicated because of the interaction of transformation heat and a number of spray parameters, and more complicated after introducing a polymer additive. To determine the influence of the spray parameters, the liquid pressure (P_L), compressed air pressure (P_A), and solution concentration were selected as the main parameters to be orthogonally tested. In the test, CMC was selected as a polymer additive (the only linear factor that influences the cooling ability), and the distance between nozzles was set at 1000 mm (40 in.). The levels in the orthogonal test were selected within the ranges favorable both for comparison and for application; the investigation targets consisted of the maximum cooling rate (v_{max}), the average cooling rate through the high-temperature range ($v_{900-600}$), and the time for pearlite transformation to begin (τ_s). All of the parameters and the results of the orthogonal test are shown in Tables 1 to 3. Because the cooling capacity in the dynamic vapor blanket stage is of most importance for patenting, v_{max} , $v_{900-600}$, and τ_s are taken as the investigated indicators, which are collected from the measured cooling curves (Ref 12).

Table 1 Levels of orthogonal test

Levels	Pressure of liquid medium (P_L)		Pressure of compressed air (P_A)		Concentration of aqueous solutions, %
	MPa	ksi	MPa	ksi	
I	0.30	0.04	0.20	0.03	0.5
II	0.20	0.03	0.15	0.02	0.1
III	0.10	0.015	0.10	0.015	0.05

Table 2 Orthogonal test array and results

Factors	Pressure of liquid medium (P_L), MPa	Pressure of compressed air (P_A), MPa	Concentration of aqueous solutions, %	Investigated indicators				
				Maximum cooling rate at dynamic vapor blanket stage of cooling curve (v_{max})		Average cooling rate between 900–600 °C (1650–1110 °F) ($v_{900-600}$)		Time for pearlite transformation to start (τ_s), s
				°C/s	°F/s	°C/s	°F/s	
1	I	I	I	60.5	108.9	38	68	6.1
2	I	II	II	93.5	168.3	59	106	4.05
3	I	III	III	87.9	158.2	57	103	4.2
4	II	I	II	88.1	158.6	44	79	5.35
5	II	II	III	86.8	156.2	58	104	4.4
6	II	III	I	44.9	80.8	30	54	8.0
7	III	I	III	50.1	90.2	35	63	6.2
8	III	II	I	40.0	72	27	49	7.6
9	III	III	II	74.0	133.2	53	95	5.9

The value “R” stands for the magnitude of the impact factor of the spray parameters at the suggested test levels. The orthogonal test results are summarized in Fig. 8, where it can be seen that the investigation targets were regularly dominated by the three main spray parameters. The order of the influence was polymer concentration (conc.), liquid pressure (P_L), and compressed air pressure (P_A), which shows a regular sequence.

Cooling Curves and Cooling-Rate Curves with Polymer Additive on Spraying. The cooling curves and cooling-rate curves under the same spraying parameters measured by a steel wire probe with a diameter of 5 mm (0.2 in.) with tap water, 0.05% PVA, and 0.05% CMC are shown in Fig. 9, left and right, respectively. These results show that spray quenching with a polymer additive could significantly improve the cooling rate above 600 °C (1110 °F), which is called the dynamic vapor blanket stage (Ref 17), but could not maintain the same regularity in the low-temperature range. Also, from these cooling curves, it can be seen from the characteristic points for the three cooling stages that spray cooling using a polymer quenchant is a more complicated heat-transfer process than observed during immersion quenching, which may be caused by either the bulk effect of the probe or the dynamic spraying process. When a steel probe is quenched in the spray fog, many very small droplets continuously collide against the hot surface and quickly vaporize to form a dynamic vapor blanket. The vapor blanket

gradually diminishes and then finally disappears as the temperature of the probe decreases, so that the entire cooling process was moderately transitioned between the three stages, which is totally different from the heat-extraction process of the deposited liquid organic polymer film on the surface of a workpiece during immersion quenching (Ref 18).

These data indicate that the polymer additive not only would form a thick polymer film on a hot workpiece surface upon spray quenching at the high-temperature range but also would change the physical properties of the spray medium, such as surface tension (σ), vapor pressure, and boiling point, to improve spray conditions. Spray media containing polymer additives form a uniform single-phase solution before atomizing, but when atomized pneumatically, a dual-phase flow of droplets and air affect the surface-cooling process during spraying and should not be neglected (Ref 17). The relationship between the work required to form many new droplet surfaces (W), the surface tension of the solution (σ), and the newly formed surface area of the droplets (ΔS) may be expressed as:

$$\sigma = W/\Delta S(N \cdot m^{-1})$$

In a spray system, the surface area of new droplets that are formed (ΔS) can be used to indicate spraying status. When the work provided for atomizing (W) is determined, the surface tension of the liquid solution (σ) will

directly influence the atomizing process. Most polymer additives behave as high-molecular-weight surfactants. When the concentration of the spray medium is very low, the binding force between the molecules in solution is primarily of the van der Waals type, which is much less than that of pure water, which is favorable for atomizing the polymer solution. The smaller the droplet, the easier vaporization occurs on the surface of a workpiece. All of these factors contributed to the accelerated cooling of the wire probe during the dynamic vapor blanket stage.

Concentration-Fog Flux Effect

This work has shown that there exists an optimum combination between polymer concentration and spray parameters to obtain the maximum cooling rate, which can be called the concentration-fog flux effect (Ref 11). Figure 10, left and right, respectively, shows the cooling curves and cooling-rate curves obtained during spray quenching with different concentrations of CMC solution using fixed spray parameters. The cooling rate achieved the maximum value in the high-temperature range when the concentration was 0.25%. Under the same conditions, there existed another maximum cooling rate at a lower temperature range. However, this occurred at a concentration of 0.05%. Conversely, when the quenching solution concentration was fixed and there was only one

Table 3 Analysis of orthogonal test results

Items(a)	Pressure of liquid medium (P_L)			Pressure of compressed air (P_A)			Concentration of aqueous solutions		
	v_{max}	$v_{900-600}$	τ_s	v_{max}	$v_{900-600}$	τ_s	v_{max}	$v_{900-600}$	τ_s
K_I	241.9	154	14.35	198.7	117	17.65	145.4	95	21.7
K_{II}	219.8	132	17.75	220.3	144	16.05	255.6	156	15.3
K_{III}	164.1	115	19.7	206.8	140	18.1	224.8	150	14.8
k_I	80.6	51.3	4.78	66.2	39	5.9	48.5	31.7	7.2
k_{II}	73.3	44.0	5.92	73.4	48	5.35	85.3	52	5.1
k_{III}	54.7	38.3	6.57	68.9	46.7	6.0	74.9	50	4.9
R	25.9	13	1.79	7.2	9	0.7	36.8	20.3	2.7

(a) $K_i = \Sigma$ (sum total at one level); $k_i = \Sigma/3$ (average value of K_i); $R = k_{imax} - k_{imin}$

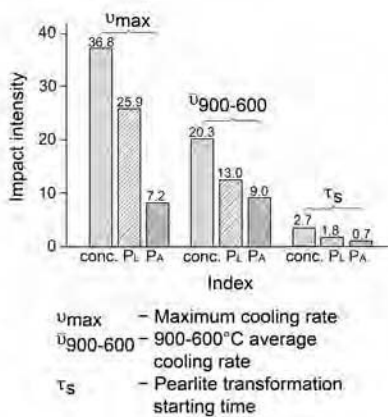


Fig. 8 Comparison of orthogonal test results

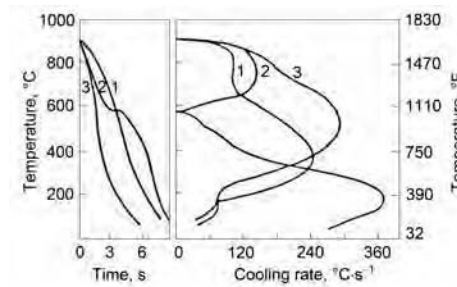


Fig. 9 Complete cooling curves (left) and cooling-rate curves (right) of fog cooling with different polymers. 1 = tap water; 2 = 0.05% polyvinyl alcohol; 3 = 0.05% carboxymethyl cellulose

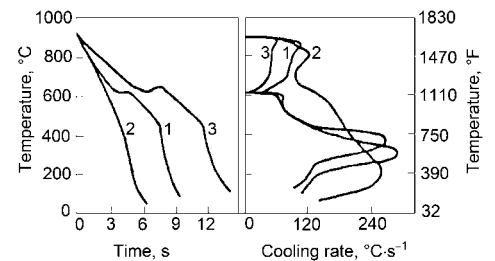


Fig. 10 Effect of polymer concentration on cooling characteristics. 1 = 0.05% carboxymethyl cellulose (CMC); 2 = 0.25% CMC; 3 = 0.5% CMC

variable spray parameter, there existed another important parameter in addition to cooling capacity and spray parameter.

Figure 11, left and right, respectively, shows the cooling curves and cooling-rate curves obtained merely by changing one spray parameter. These phenomena verify that when the surface temperature, cooling area, and thermal capacity of a wire probe are given, the total liquid amount vaporized on the cooling area of the probe is closely related to the fog flux ($\text{mL} \cdot \text{cm}^{-2} \cdot \text{s}^{-1}$). Any small change of the concentration, liquid pressure, air pressure, or distance between nozzles will cause a large variation in the flux, which therefore will result in variations of the amount of liquid vaporized on the surface of the probe. To obtain a maximum cooling rate, these three main factors—total liquid amount vaporized on the cooling surface, solution concentration, and spray parameters—should be optimized.

As the temperature of the probe surface decreases, the solutions sprayed onto the probe surface could not vaporize immediately but instead formed a layer of organic polymer film. Although this film exists dynamically, the relationship among the three main factors follows a different cooling mechanism. At the lower temperature range, the conditions to obtain a maximum cooling rate differ from those at a higher temperature range, which is not related to the patenting treatment.

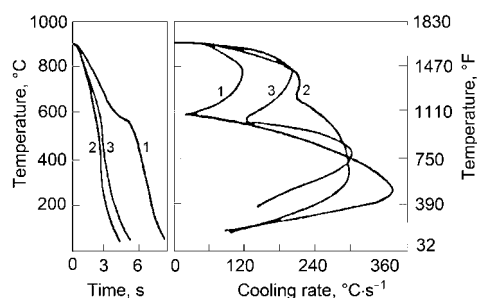


Fig. 11 Effect of atomization parameter on fog-cooling characteristics. $P_L = 0.35$ MPa; 1, $P_A = 0.1\%$ MPa; 2, $P_A = 0.2\%$ MPa; 3, $P_A = 0.25\%$ MPa

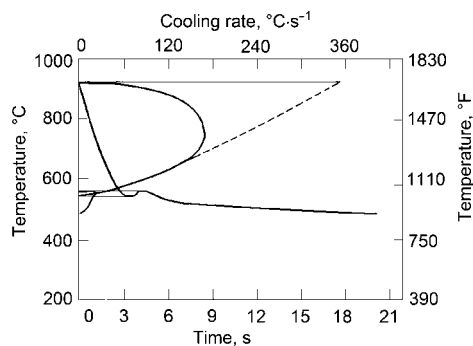


Fig. 12 Controlled fog-cooling curve and characteristic curves in 0.05% carboxymethyl cellulose aqueous solution for 5 mm (0.2 in.) wire

Controlled Fog-Cooling Patenting with CMC Additive

The cooling process exhibited during lead bath patenting was simulated by using the flexibility and controllability of spray quenching with a low concentration of the polymer additive. Figure 12 shows the cooling curve and cooling-rate curve of 5 mm (0.2 in.) high-carbon steel wire during controlled fog-cooling patenting with 0.05% CMC polymer. It can be seen that the cooling status of spray cooling with a polymer additive was similar to the cooling process in a lead bath. When pearlite transformation starts, the “hump” on the cooling-rate curve resulted from the latent heat of phase

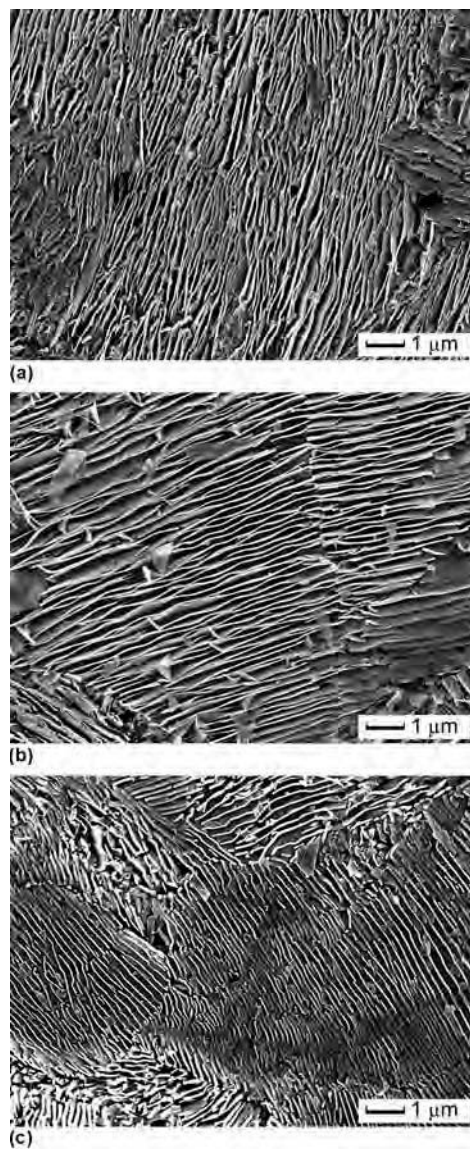


Fig. 13 Microstructure of steel wire fog-cooling patented in a 0.05% carboxymethyl cellulose aqueous solution. Scanning electron microscopy. (a) 3.9 mm (0.15 in.) diameter. (b) 5.0 mm (0.20 in.) diameter. (c) 6.5 mm (0.25 in.) diameter. $P_L = 0.35$ MPa (0.05 ksi); $P_A = 0.2$ MPa (0.03 ksi); $h = 700$ mm (28 in.)

transformation, which was much lower than that obtained with a tap water spray, indicating that the transformation would proceed under a smaller temperature range and the size of the fine pearlite colony would become finer. The typical fog-cooling patented microstructure of steel wire of different diameters obtained with a polymer additive is shown in Fig. 13. The mechanical properties of steel wires are listed in Table 4.

Conclusion

According to cooling curves and cooling-rate curves measured by wire probes and microstructure examination, the 0.70% C steel wires can complete pearlite-type transformation in a lead bath, aqueous polymer solution, and controlled fog-cooling method.

The patenting of carbon steel in higher-concentration aqueous CMC solutions is similar to a continuous cooling transformation. The pearlite-type transformation is completed in a higher temperature range before the wire comes to the bath temperature. It is important to accelerate the primary cooling rate during the high-temperature range (above the nose of the time-temperature transformation diagram) and maintain the transformation throughout a constant temperature range to obtain the correct microstructure when seeking aqueous polymer quenchant alternatives for lead baths.

A small amount of polymer additive in spraying could modify the physical properties of the spray medium and improve atomizing status, which would effectively accelerate the cooling rate of the dynamic vapor blanket stage above 600 °C (1110 °F). The concentration-fog flux effect further improves the flexibility of spraying and makes it easier to control the cooling process. The controlled fog-cooling trial of high-carbon steel wires verifies that the cooling process is steady and can simulate patenting in a lead bath for steel wire.

REFERENCES

1. T. Berntsson, E. Sapcanin, M. Jarl, and S. Segerberg, Alternatives to Lead Bath for Patenting of High Carbon Steel Wire, *Wire J. Int.*, Vol 37 (No. 5), 2004, p 82–86
2. High Tensile Steel Wire Rods Applying Mist Cooling Process, *JFE Tech. Rep.*, No. 15, May 2010, p 41–43
3. W. Weidenhaupt, Patenting in a Water Bath, *Wire*, No. 2, 2010, p 26
4. K.J. Mason and T. Griffin, The Use of Polymer Quenchants for the Patenting of High Carbon Steel Wire and Rod, *Heat Treat. Met.*, No. 3, 1982, p 77–83
5. H. Geipel, E. Forster, and W. Heinemann, Fluidized Bed, U.S. Patent 3,492,740, Feb 3, 1970

Table 4 Mechanical properties of steel wires with controlled fog-cooling patenting

Wire diameter		Tensile strength (Rm)		Elongation (A), %	Hardness, HRC
mm	in.	MPa	ksi		
3.9	0.15	1181	171	6.3	36
5.0	0.20	1047	152	7.6	31
6.5	0.25	1011	147	7.4	30

6. X. Luo and F. Li, Metallurgical Behaviors of High-Carbon Steel Wires in Lead Bath and CMC Aqueous Solutions by Cooling Curve Analysis, *Int. J. Mater. Prod. Technol.*, Vol 24 (No. 1–4), 2005, p 142–154
7. X. Luo and J. Li, Effects of Cooling Rate Fluctuation on Cooling and Transformation Behavior of Steel upon Direct Quenching, *J. ASTM Int.*, Vol 6 (No. 2), 2009, p 935–952
8. M.G. Wirick, Aerobic Biodegradation of Carboxymethylcellulose, *J. Water Pollut. Control Fed.*, Vol 46 (No. 3), 1974, p 512–521
9. C.G. VanGinkel and S. Gayton, The Biodegradability and Nontoxicity of Carboxymethyl Cellulose (DS 0.7) and Intermediates, *Environ. Toxicol. Chem.*, Vol 15 (No. 3), 1996, p 270–274
10. A.S. Turaev, Dependence of the Biodegradability of Carboxymethylcellulose on Its Supermolecular Structure and Molecular Parameters, *Chem. Nat. Compd.*, Vol 31 (No. 2), 1993, p 254–259
11. X. Luo, Feasibility of Fog-Cooling Patenting for High-Carbon Steel Wire, *Iron Steel*, Vol 26 (No. 6), 1993, p 11, 52–56
12. X. Luo, “Controlled Fog-Cooling for Patenting of High-Carbon Steel Wire instead of Lead-Bath,” Master’s thesis, Jiangsu Institute of Technology, Zhenjiang, China, 1989
13. X. Luo and S. Zhu, Merits of Small Probes in Research on Cooling Behaviour of Steel upon Quenching, *Proceedings of the 21st ASM Heat Treating Society Conference*, ASM International, 2001, p 225–229
14. S. Deda, Transformation of 70 (T7A) Steel Wire when Heated, *Steel Wire Prod.*, Vol 27 (No. 4), 2001, p 46–50
15. X. Luo, H. Liu, and M. Le, Study on the Cooling Behaviour for Steel Wire during Patenting with Wire Probe and the Cooling Curves Measured, *Heat Treat. Met.*, No. 12, 1989, p 9–14, 16
16. Y. Lin, G. Luo, X. Li, et al., Behavior of Fine Pearlite in the Course of Deformation, *J. Mater. Sci. Eng.*, Vol 26 (No. 3), 2008, p 346, 369–371
17. Y. He, “Feasibility of Water-Air Fog-Cooling for Steel Quenching,” Master’s thesis, Jiangsu Institute of Technology, Zhenjiang, China, 1987
18. H.M. Tensi, Chap. 7, Wetting Kinematics, *Quenching Theory and Technology*, 2nd ed., B. Liščić, H.M. Tensi, L.C.F. Canale, and G.E. Totten, Ed., CRC Press, Boca Raton, FL, 2010, p 179–203

Steel Heat Treatment Processes

Cleaning of Steel for Heat Treatment	265	Austenite Grain Growth.	314
Surface Contaminants on Heat Treated Parts	266	Control of Solute Concentrations in Austenite	315
Cleaning Methods.	267	Quenching and Partitioning Steel Heat Treatment	317
Cleanliness Measurement.	271	Chemical Composition and Annealing Process.	318
How Clean Is Clean?	272	Microstructure and Mechanical Properties	318
Case Studies	272	Mechanical Behavior and Stability of	
Pollution Control and Resource Recovery	273	Retained Austenite	320
Safety	273	Welding Properties	322
Summary	274	Tempering of Steels.	327
Stress-Relief Heat Treating of Steel	275	Introduction	327
Sources of Residual Stress	275	Principal Variables	327
Thermal Stress-Relief Methods.	275	Tempering Temperatures and Stages.	327
Stress Relief of Springs.	277	Tempering Time and Temperature	332
Normalizing of Steel	280	Effect of Composition	334
Introduction	280	Dimensional Change during Tempering.	336
Heating and Cooling	281	Tensile Properties and Hardness	338
Applications of Normalizing Based on Steel		Toughness and Embrittlement	339
Classification	282	Equipment for Tempering	344
Forgings	284	Special Tempering Procedures	345
Bar and Tubular Products	286	Induction Tempering.	347
Castings.	287	Austempered Steel.	352
Sheet and Strip.	287	Steels for Austempering	353
Annealing of Steel	289	Section Thickness Limitations	354
Metallurgical Principles.	289	Applications.	354
Annealing Cycles	290	Dimensional Control	357
Guidelines for Annealing.	291	Modified Austempering	357
Annealing Temperatures	291	Austempering Problems and Solutions	359
Spheroidizing.	291	Martempering of Steels	362
Process Annealing	294	Introduction	362
Annealed Structures for Machining.	294	Advantages	364
Industrial Annealing	295	Martempering Media.	364
Annealing of Steel Sheet and Strip	297	Safety Precautions	367
Annealing of Steel Forgings.	301	Suitability of Steels for Martempering.	368
Annealing of Bar, Rod, and Wire	302	Control of Process Variables	371
Annealing of Plate and Tubular Products.	303	Dimensional Control	373
Accelerated Cycling Annealing	303	Applications.	376
Subcritical Annealing and Normalizing	305	Selection of Austenitizing Equipment	377
Subcritical Temperatures	305	Selection of Martempering Equipment	377
Temperature-Time Relations	306	Martempering Bath Maintenance	378
Normalizing.	307	Racking and Handling.	380
Induction Thread Softening	307	Washing the Work	380
Austenitizing in Steels	309	Cold and Cryogenic Treatment of Steel	382
Introduction	309	Cold Treatment of Steel	382
Purposes and Overview of Austenitization.	309	Cryogenic Treatment of Steels	383
Thermodynamics and Kinetics of Austenite Formation	309		

Cleaning of Steel for Heat Treatment

Mohammed Maniruzzaman, Caterpillar Inc.
Xiaolan Wang and Richard D. Sisson, Jr., Worcester Polytechnic Institute

SURFACE TREATMENT is an important step for all manufacturing processes. The deposited or absorbed layers of various elements and contaminants change the surface characteristics and can adversely affect the surface treatment processes, such as coatings, paintings, adhesive bonding, welding, brazing, and soldering as well as the heat treatment process.

The cleaning of the part often seems a rather unimportant process in heat treatment operation compared to other surface treatment processes. However, cleaning before and after heat treatment is important for the quality of the part and sometimes dramatically influences the subsequent processes. For example, contaminants left on the surface may adversely affect the diffusion process in carburizing, nitriding, or nitrocarburizing processes. Haase et al.

(Ref 1–3) investigated the effects of various contaminants on the gas nitriding performance of steels. A set of experimental results is shown in Fig. 1. In spite of different gas-phase pre-treatments, all contaminated surfaces reduced the nitrogen uptake, resulting in no or less hardness increase than that of the cleaned reference surface. The contaminants may also cause some visible defects during the heat treatment process. The rework of defective parts is difficult; it consumes time and money and may not be feasible. The barrier contaminant layers may have to be removed mechanically, for example, by grinding or blasting, which may create other problems, such as a change in dimensions of the workpiece and the roughness of the surface. Afterwards, the parts must be heat treated again, consuming more time and money. After the parts are hardened, the surface may become

contaminated again, so additional cleaning may be required. It should be noted that the cleaning residue may also affect the heat treatment process. Silicate-based alkaline solution or silicone-based defoaming agent residue may cause spotty carburizing or nitriding. Hardness, porosity, thermal coefficient of expansion, conductivity, melting point, specific heat, and the effect of hydrogen embrittlement must be considered during surface cleaning. Hardened steels can become embrittled by hydrogen during cleaning. Pictures of workpieces before and after oil quenching heat treatment are shown in Fig. 2, which shows the visible discoloration of workpieces due to oil residue on the surface.

A cleaning system used in the heat treatment operation is comprised of the following steps (Ref 4):

1. Cleaning
2. Rinsing
3. Soil separation within the cleaning machine
4. Drying
5. Waste soil disposal

In the cleaning step, the soils are removed from the steel surface by one or a combination of three basic actions: mechanical, thermal, and chemical. Mechanical actions include abrasive surface blasting, spray jet cleaning, use of ultrasonic to loosen the dirt, hand cleaning with a brush, and so on. Thermal action involves heating the environment or cleaning medium. The chemical actions include a dissolving action or a surface-active action. In a dissolving action, the surface contaminants are absorbed by or dissolved in the cleaning medium, such as an organic solvent dissolving an oil. On the other hand, in a surface-active action, the soils are desorbed or loosened from the part surfaces with the aid of surface-active agents.

In the rinsing step, the cleaning fluid and soils are diluted with and/or displaced by soil-free fluid to an acceptable level. This step can be repeated as necessary. The diluted cleaning/rinsing solutions are removed from the part surface by evaporation or some other non-evaporative methods in the drying step.

Soil in the cleaning machine must be separated or removed periodically to minimize

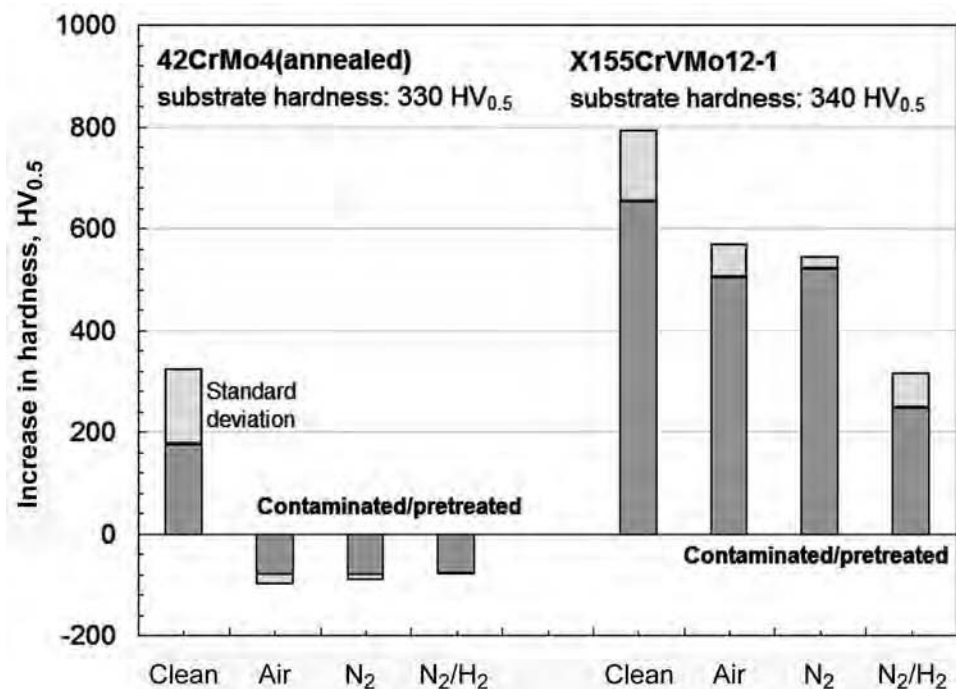


Fig. 1 Nitriding response of two steels contaminated by cutting oil and nitrided for 4 h at 520 °C (970 °F) with a nitriding potential of 10. Contaminated surfaces are pretreated at between 300 and 400 °C (570 and 750 °F) (preoxidation in air, followed by treatment in nitrogen or a mixture of nitrogen and hydrogen), and the results are compared with cleaned surface-nitrided samples. Adapted from Ref 1

recontamination of the part and the dragout of soils to the rinsing step. Disposal of waste soil is also an important step in the cleaning operation. In this step, the soils are removed from the solution so that the detergent or solvent can be reused and the soils can be recovered in a sufficiently pure form for either efficient disposal or possible reuse.

The steps for measuring the effectiveness of the cleaning system in a heat treating process are shown in a flow chart in Fig. 3. Pre- and postcleaning are used based on the cleanliness requirements for the subsequent process and the end product. The cleanliness degree can be measured by using various techniques. This article identifies the surface contaminants that may affect the heat treatment processes and the end-product quality. Various cleaning methods and the chemicals needed to clean different surface contaminants are also identified and discussed.



(a)



(b)

Fig. 2 Workpieces (a) before heat treatment and (b) after quenching

The processing procedures, equipment requirements, effects of variables, and safety precautions that are applicable to individual cleaning processes are covered in *Surface Engineering*, Volume 5 of *ASM Handbook*. Additional relevant information is also contained in the articles “Environmental Regulation of Surface Engineering,” “Vapor Degreasing Alternatives,” and “Compliant Wipe Solvent Cleaners” in the same volume of *ASM Handbook*.

Surface Contaminants on Heat Treated Parts

Before heat treating, the workpieces are treated in various ways: machining, casting, forming, joining, and other processes. The workpiece surface is influenced and changed. There are two distinct changes: mechanical

(deforming, compressing, abrasion, and so on) and chemical (phosphate layers, reaction with corrosion protection, cooling fluids, oil, and so on). Figure 4 shows a schematic of the surface of a typical workpiece before heat treatment.

The bulk material is covered by four layers: the deformed boundary layer, the reaction layer, the sorption layer, and the contamination layer. The binding energy for each layer grows weaker toward the surface. The deformed boundary layer is formed during the mechanical treatment. The reaction layer includes metal oxides, sulfides, or phosphorus compounds. Reaction layers also are formed during phosphating. They are thin but have excellent adhesion and can be very dense. On the sorption layer, compounds of the grease are bound by chemisorptions or physisorptions. The final layer is the contamination layer—the most important layer in the cleaning process. This layer contains residues of the previous processing steps, for example, oil, grease, chips, cleaner residues, or water ingredients (Ref 5).

Incoming parts from the previous operation have various contaminants on the surface. From machining, cutting fluids, chips, oil, rust preventive, water ingredients, and rust may appear on the surface. If the parts are made by casting, the contamination will contain oxides, sand, lubricant, dust, and so on. Forming and shaping will bring lubricants, oxides, and dust on the surface. Joining will bring oxides, wax, and dust on the surface.

Contaminants can be classified into five broad categories (Ref 6):

- Pigmented drawing compounds
- Unpigmented oil and grease
- Chips and cutting fluids
- Rust and scale
- Miscellaneous surface contaminants

Pigmented compounds, including graphite, molybdenum disulfide, and so on, are often used in lubricants, heat treating, and hot forming protected coatings and are left on the surface after shape forming, joining, and other processes. All pigmented compounds are difficult to remove, because of their chemical inertness to acid and alkalis and their tight adherence to the metal surface.

Common shop oils and greases, unpigmented drawing lubricants, rust-preventive oils, and quenching and lubricating oils are unpigmented oils. They can effectively be cleaned by several cleaners.

Cutting and grinding fluids used for machining can be classified into three groups:

- Plain or sulfurized mineral and fatty oils, chlorinated mineral oils, and sulfurized chlorinated mineral oils
- Conventional or heavy-duty soluble oils with sulfur or other compounds added, and soluble grinding oils with wetting agents
- Chemical cutting fluids, which are water soluble and generally act as cleaners

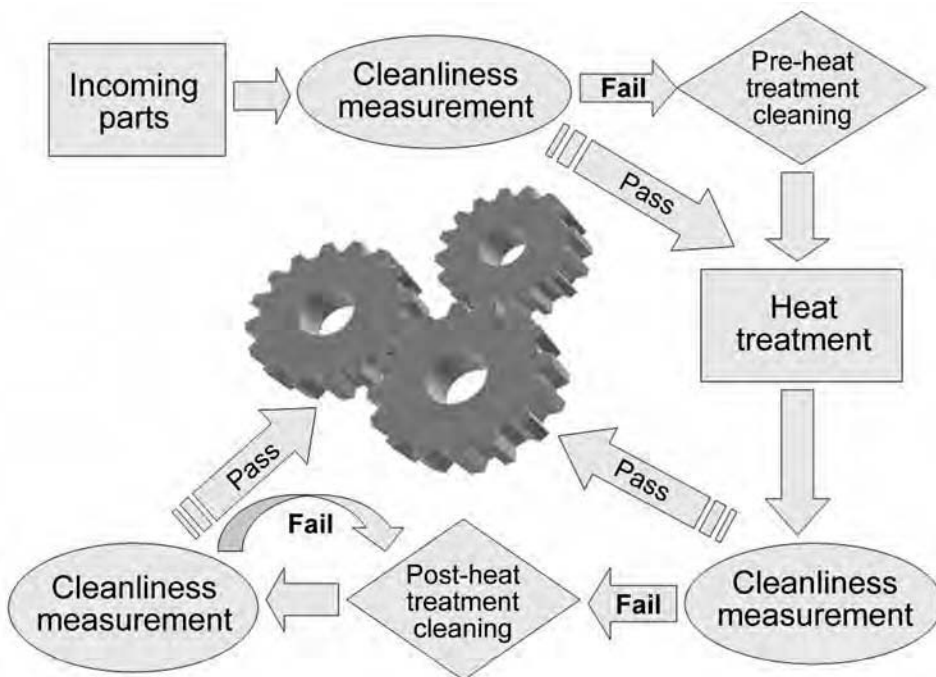


Fig. 3 Flowchart for pre- and post-heat-treatment cleaning operation

These three types of fluids are easily removed, while the chips fall away during cleaning.

Rust and scale attached on the surface are usually removed by physical methods, because of the different adhesion mechanism.

Miscellaneous surface contaminants may include polishing, buffing compounds, lapping compounds, and residue from magnetic particle inspection.

Substrate Considerations. The selection of a cleaning process must be based on the substrate being cleaned as well as the contaminants to be removed. Steels are highly resistant to alkalis and are attacked by essentially all acidic material. Corrosion-resistant steels, also referred to as stainless steels, have a high resistance to both acids and alkalis, but the degree of resistance depends on the alloying elements.

Cleaning Methods

Cleaning processes used for removing contaminants are varied, and their effectiveness depends on the requirements of the specific application. The many factors that must be considered in selecting a metal-cleaning process include (Ref 6):

- Type of soil to be removed
- Base material to be cleaned (i.e., ferrous, nonferrous, etc.)
- Importance of the condition of the surface to the end use of the part
- Degree of cleanliness required
- Existing capabilities of available facilities
- Environmental impact of the cleaning processes
- Cost
- Total surface area to be cleaned
- Fragility, size, and intricacy of the part
- Effects of previous processes
- Rust-inhibition requirements
- Materials handling factors
- Surface requirements of subsequent operations (gas carburizing, vacuum carburizing, gas nitriding, phosphate conversion coating, painting, and plating)

Only a few of these factors can be quantified. Among these factors, the type of soil to be removed, the degree of cleanliness required, and the cost are most important. A manufacturing company tends to choose as much flexibility and versatility in a facility as the cost allows. The size of the largest workpiece is used in establishing the cleaning processes, equipment sizes, and handling methods. There are various cleaning methods and media available; the selection is greatly based on the degree of cleanliness and the next procedures to be performed. If a part has a complex shape, some of the line-of-sight processes will not work very well. The presence of blind holes in a part usually indicates the need for a process that includes sprays of some type, together with a relatively higher vapor-pressure cleaner to assist the drying process. The part volume and the longest rigid dimension of the part help to determine such things as tank size for

immersion processes or pressure vessel size for supercritical fluid methods. With a simple shape, the workpiece can be cleaned effectively by immersion or immersion and spray when the parts are no more than approximately 500 mm (20 in.) across. Large parts of this type can be cleaned more effectively by spraying.

Cleaning methods can be classified into three broad categories: mechanical, chemical, and electrochemical. The mechanical cleaning methods include grinding, brushing, steam or flame jet cleaning, abrasive blasting, and

tumbling. The main chemical cleaning methods are solvent cleaning, emulsion cleaning, alkaline cleaning, acid cleaning, pickling, and descaling. The electrochemical cleaning methods are electropolishing, electrolytic alkaline cleaning, and electrolytic pickling. Figure 5 shows various cleaning methods for different contaminants. Table 1 summarizes the various cleaning methods and their effectiveness. Some of the most commonly used cleaning methods and their applicability are discussed in the following paragraphs.

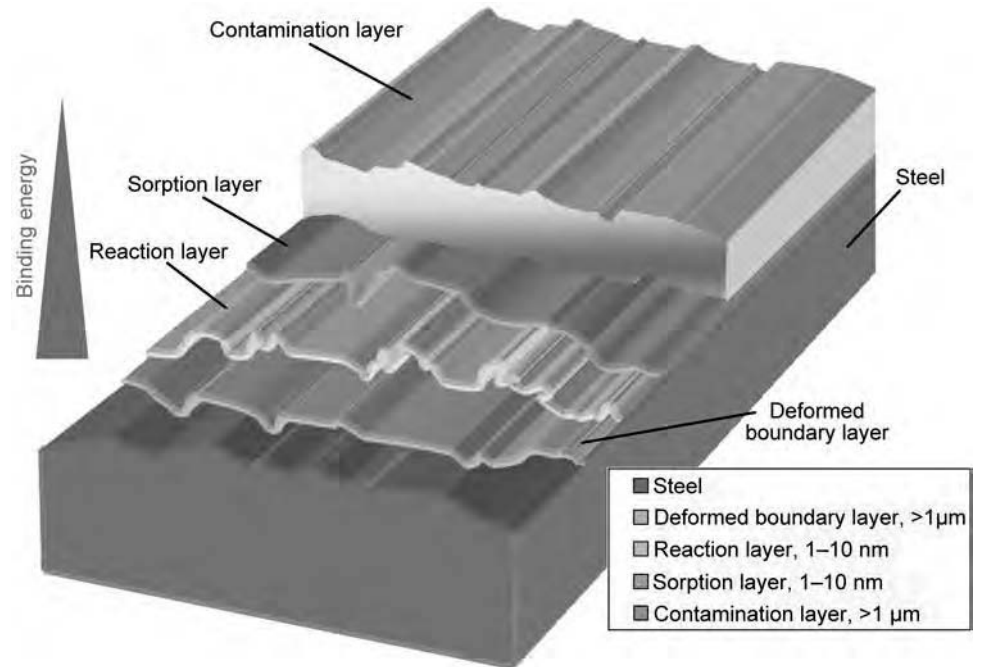


Fig. 4 Various layers on the surface of a workpiece before heat treatment

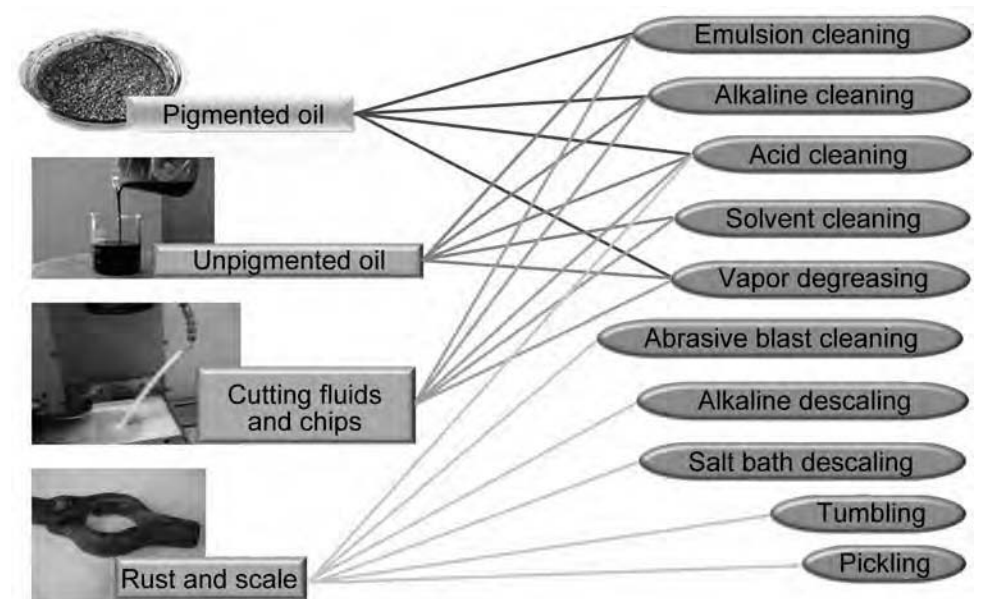


Fig. 5 Cleaning methods

Table 1 Metal-cleaning processes

Cleaning process	Cleaning media	Application	Effectiveness
Emulsion cleaning:			
<ul style="list-style-type: none"> For intermittent or occasional cleaning Particles of soils are suspended in cleaning medium, then separated from surface Prepare for phosphating and precleaning before alkaline cleaning 	<ul style="list-style-type: none"> Water- or water-solvent-based solutions Emulsions of hydrocarbon solvents such as kerosene and water with emulsifiable surfactant 	<ul style="list-style-type: none"> Pigmented drawing compounds Unpigmented oil and grease Cutting fluids and chips 	<ul style="list-style-type: none"> Faster but less thorough than alkaline cleaners Leaves a film that protects the steel against corrosion Most effective method for pigmented compounds Effective, inexpensive means of removing all three types of cutting fluids
Alkaline cleaning:			
<ul style="list-style-type: none"> Both physical and chemical actions may be used Alkaline immersion, spray cycles Removes oil and grease by saponification or emulsification Degree of cleanliness depends largely on thorough mechanical agitation 	<ul style="list-style-type: none"> Mix of ingredients such as surfactants, sequestering agents, saponifiers, emulsifiers, and chelators Also with various forms of stabilizers and extenders 	<ul style="list-style-type: none"> Some pigmented drawing compounds Unpigmented oil and grease All three types of cutting and grinding fluids Rust, light scale, and carbon smut 	<ul style="list-style-type: none"> Efficient and economical against unpigmented oil and grease. Capable of cleaning to a no-water-break surface Usually least expensive process to remove cutting fluids and polishing and buffing compounds Marginally effective against pigmented compounds. May require hand slushing and manual brushing to remove all traces of pigment
Alkaline descaling:			
<ul style="list-style-type: none"> More costly, slower than acid pickling. No metal is lost because chemical action stops when the rust or scale is removed. 			
Solvent cleaning:			
<ul style="list-style-type: none"> Applied by swabbing, static tank immersion, spray or solid stream flushing, or vapor condensation Effective as preliminary or conditioning cleaner to decrease time in final cleaner 	<ul style="list-style-type: none"> Typical organic solvents are trichloroethylene, methylene chloride, toluene, and benzene. 	<ul style="list-style-type: none"> Unpigmented common oil and grease Cutting fluids and chips of the first group (frequently) 	<ul style="list-style-type: none"> Lack of effectiveness, rapid contamination against pigmented compounds Possibility of leaving residues, often requiring additional steps More costly than alkaline or emulsion methods
Acid cleaning	<ul style="list-style-type: none"> Various organic acid solutions such as citric acid, acid deoxidizing solutions 	<ul style="list-style-type: none"> Light, blushing rust (storage rust from high humidity) 	<ul style="list-style-type: none"> Effective against light, blushing rust
Abrasive blast cleaning:			
<ul style="list-style-type: none"> Widely used with air stream or water jet 	<ul style="list-style-type: none"> Uses small, sharp particles propelled by an air stream or water jet 	<ul style="list-style-type: none"> All classes of scale and rust 	<ul style="list-style-type: none"> Preferred for removing heavy scale and paint Only allowable cleaning method for steels sensitive to hydrogen embrittlement
Tumbling	<ul style="list-style-type: none"> Can use either dry abrasives (deburring compounds) or descaling compounds 	<ul style="list-style-type: none"> Rust and scale 	<ul style="list-style-type: none"> Least expensive process against rust and scale Cannot uniformly descale complex-shaped parts with deep recesses and other irregularities
Pickling	<ul style="list-style-type: none"> Done in hot, strong solutions of sulfamic, phosphoric, sulfuric, or hydrochloric acid 	<ul style="list-style-type: none"> Scale 	<ul style="list-style-type: none"> Complete removal of scale from mill products and fabricated parts Electrolytic pickling removes scale twice as fast.
Salt bath descaling:			
<ul style="list-style-type: none"> Bath operates within temperatures of 400 to 525 °C (750 to 975 °F) 	<ul style="list-style-type: none"> Several types of salt baths are used. 	<ul style="list-style-type: none"> Scale 	<ul style="list-style-type: none"> Seldom used alone for scale removal No loss of metal No danger of hydrogen embrittlement Required water quenching may cause cracking or warping of complex parts

Abrasive blast cleaning (Ref 6–9) is the process of cleaning a hard surface by forcing small solid particles across that surface at high speeds propelled by an air stream or water jet. The contaminants are removed from the part surface by the resulting impact force. Borazon (cubic boron nitride), ceramic, corundum (alumina or aluminum oxide), dry ice, glass bead, silicon carbide (carborundum), zirconia, and alumina are usually used as the solid particles. This method is widely

used for removing all classes of scale and rust from ferrous mill products, forgings, castings, weldings, and heat treated parts. Depending on the requirement, abrasive blast cleaning can be the sole process, or it can be combined with pickling, which is applied afterward to remove the remainder. It should be noted that blasting has limited use on complex and curved surfaces and on parts with deep crevices, threads, or machined surfaces. Also, it cannot be used on parts where

the dimensions must be retained. Glass bead cleaning (blasting) is used for cleaning threaded or precision parts, high-strength steel, titanium, and stainless steel. Abrasive cleaning is also frequently used as the only allowable cleaning method for steels that are sensitive to hydrogen embrittlement.

Tumbling (Ref 6–13) is a technique for smoothing and polishing a hard substance. It is the least expensive method for removing

scale and rust, but the size and shape of parts are limited by the process. Tumbling in dry abrasives (deburring compounds) is often used for clean, small workpieces. However, complex-shaped parts with deep recesses and other irregularities cannot be descaled uniformly by tumbling and may require several hours of tumbling if that method is used. Adding descaling compounds in solution rather than deburring compounds often decreases the required time by 75%.

Solvent cleaning (Ref 6, 8, 9, 12, 13) is the dissolution of contaminants by an organic solvent. Typical solvents are trichloroethylene, methylene chloride, toluene, and benzene. The solvent can be applied by swabbing, tank immersion, spray or solid stream flushing, or vapor condensation. Vapor degreasing is accomplished by immersing the work into a cloud of solvent vapor; the vapor condenses on the cooler work surface and dissolves the contaminants. Subsequent flushing with liquid solvent completes the cleaning process. Temperature elevation accelerates the activity.

One major drawback of solvent cleaning is the possibility of leaving some residue on the surface, often necessitating additional cleaning steps. Another more significant disadvantage is the environmental impact of solvent cleaning processes. In fact, much effort is being expended on replacing solvent-based processes with more environmentally acceptable aqueous-based processes (see the article "Vapor Degreasing Alternatives" in *Surface Engineering*, Volume 5 of *ASM Handbook*).

Solvent cleaning is seldom recommended for removing pigmented compounds, except for occasional preliminary or rough cleaning before other methods. For example, parts are sometimes soaked in solvents such as kerosene or mineral spirits immediately following the drawing operation to loosen and remove some of the soil, but the principal effect of the operation is to condition parts for easier cleaning by more suitable methods, such as emulsion or alkaline cleaning.

Solvent cleaning may be used to remove common oils and greases from metal parts. Methods vary from static immersion to multistage washing. Eight methods of solvent cleaning, listed in increasing order of their effectiveness, are as follows:

- Static immersion
- Immersion with agitation of parts
- Immersion with agitation of both the solvent and the parts
- Immersion with scrubbing
- Pressure spraying in a spray booth
- Immersion scrubbing followed by spraying
- Multistage washing
- Hand application with wiper

The shape of the part influences the cycle and method selected. For example, parts that will nest or entrap fluids are cleaned by dipping in a high-flash naphtha, Stoddard solvent, or chlorinated hydrocarbon for 5 to 30 s at room

temperature. The time depends on the type and amount of soil. Parts that are easily bent or otherwise damaged are sprayed for 30 s to 2 min at room temperature. Complex parts are soaked at room temperature for 1 to 10 min.

Solvent cleaning is most widely used as a preliminary or conditioning cleaner to degrease. The shape of the parts influences the cycle and method selected. It is commonly used for cleaning between machining operations, to facilitate the inspection. Solvents can remove chips and cutting fluids by soaking (with or without agitation), hand wiping, or spraying. Cleaning with chlorinated solvents in a mechanical degreaser or brushing or spraying with petroleum solvents quickly removes most of the gross soil after buffing or polishing. A number of solvents and their properties are found in the articles on vapor degreasing and solvent cleaning in *Surface Engineering*, Volume 5 of *ASM Handbook*.

Biosolvents such as soy methyl ester, lactate ester, and other bio-derived chemicals or biosurfactants can also effectively be used as a solvent to remove oil, grease, paint, cutting fluid, and adhesives (Ref 14, 15). Soy methyl ester exhibits excellent solvent characteristics. It can replace the use of chlorinated hydrocarbon- and fluorocarbon-based solvents such as mineral spirits, lacquer thinner, xylene, methyl ethyl ketone, and other hydrocarbon degreasing solvents. Biosolvents are noncarcinogenic, nonozone depleting, nonflammable, and biodegradable.

Emulsion cleaning (Ref 6, 8, 12, 13) is the most effective way to remove pigment compounds. It relies on mechanical wetting and floating to remove contaminants from the surface. However, this method is usually added when graphite or molybdenum disulfide are on the surface. Water-solvent-based solutions, which have a concentration of 1 to 10%, used in a power spray washer, have the best results in removing pigmented compounds. The normal spray time is 30 to 60 s at 54 to 77 °C (129 to 171 °F), depending on the flashpoint of the cleaner. In continuous cleaning, two adjacent spray zones or a hot water (60 to 66 °C, or 140 to 151 °F) rinse stage located between the two cleaner spraying zones is common practice.

Cleaning with an emulsifiable solvent, a combination of solvent and emulsion cleaning, is an effective technique for removing pigmented compounds. Emulsifiable solvents may be used either full strength or diluted with a hydrocarbon solvent, 10 parts to 1 to 4 parts of emulsifiable solvent. Workpieces with heavy deposits of pigmented compound are soaked in this solution, or the solution is slushed or swabbed into heavily contaminated areas. After thorough contact has been made between the solvent and the soil, workpieces are rinsed in hot water, preferably by pressure spray. Emulsification loosens the soil and permits it to be flushed away. Additional cleaning, if required, is usually done by either a conventional emulsion or an alkaline cleaning cycle.

For removing unpigmented compounds, emulsion cleaners are widely used for

occasional or intermittent cleaning; they leave a thin layer to protect the steel piece against rust. They are mostly used in preparing the surface for phosphating, plating, and postcleaning after alkaline cleaning.

Emulsion cleaning is an effective and inexpensive means of cleaning all three types of cutting fluids by dipping or spraying. Attendant fire hazard is not great if operating temperatures are at least 8 to 11 °C (14 to 20 °F) below the flash temperature of the hydrocarbon used. Emulsion cleaning is often used with a surface-activating agent, after alkaline cleaning. It is more economical to remove the major portion of the soil by alkaline cleaning first, followed by emulsion cleaning to remove the remainder. If painting or phosphating is the next step, emulsion cleans the alkali residues and protects the painting or phosphating systems from contamination.

Alkaline cleaning (Ref 6, 8, 12, 13) is the mainstay of industrial cleaning and may employ both physical and chemical actions. These cleaners contain combinations of ingredients such as surfactants, sequestering agents, saponifiers, emulsifiers, and chelators as well as various forms of stabilizers and extenders. Except for saponifiers, these ingredients are physically active and operate by reducing surface or interfacial tension, by formation of emulsions, and by suspension or flotation of insoluble particles. Solid particles on the surface are generally assumed to be electrically attracted to the surface. During the cleaning process, these particles are surrounded by wetting agents to neutralize the electrical charge and are floated away, are held in solution suspension indefinitely, or eventually are settled out as sludge in the cleaning tank.

Alkaline cleaning can remove graphite and molybdenum disulfide pigmented hot forming and heat treating protective coatings, which are the most difficult pigmented compounds to be removed, by using hot alkaline scale-conditioning solutions. The softer pigmented compounds can usually be removed by immersion and spray cycles. The degree of cleanliness obtained depends largely on thorough mechanical agitation in tanks or barrels, or strong impingement if a spray is used. The use of ultrasonics in alkaline cleaning is also highly effective in removing tough pigmented drawing compounds.

The size of the parts is limited for alkaline immersion; the part should be no longer than approximately 508 mm (20 in.) (Ref 6). The recommended minimum spray pressure is 0.10 MPa (0.015 ksi). Larger parts can be cleaned more effectively by spraying. Energy-saving, low-temperature, solventized alkaline cleaners are available for soak cleaning. Similarly, low-temperature electrocleaners are effectively employed in industry, operating at 27 to 49 °C (81 to 120 °F).

Alkaline cleaners are efficient and economical for removing unpigmented oil and grease and can achieve a no-water-break surface. They remove oil and grease by saponification,

emulsification, or both. Silicones, paraffin, and sulfurized, chlorinated, oxidized, or carbonized oils are difficult but can be removed by alkaline cleaners. However, alkalis will contaminate paint and phosphate coating systems, so thorough rinsing is necessary. Cold water rinsing is recommended. Parts should be kept wet between stages, and delays before subsequent processing should be kept to a minimum. Alkaline cleaning is the least expensive method, and it also can be used in cleaning all three types of cutting and grinding fluids, rust-preventive oils, and soils left by polishing and buffing.

Acid Cleaning (Ref 6, 8, 12, 13). In acid cleaning, detergents, liquid glycol ether, and phosphoric acid are effective in removing pigmented compounds from engine parts, even if dried. By using a power spray, these acid solutions can clean the parts without manual scrubbing. Phosphoric acid cleaners may cause some discoloration, but they will not etch steel. Acid cleaners are usually used in a power spray. Some cleaners remove light, blushing rust and temporarily form a thin film of protection. They are high in cost but are often used in large ferrous parts, such as truck cabs. Phosphoric or chromic acid cleaners, with power spray or soak cleaning, are used in removing most cutting fluids. These methods are expensive; however, in some cases they are used because of their ability to remove light rust, such as the rust that forms on ferrous metal in storage under high humidity. A typical power spray acid cleaning cycle consists of washing the part with 15 to 19 g/L phosphoric acid at 74 to 79 °C (165 to 174 °F) for 3 to 4 min, followed by rinsing in 4 to 7.5 g/L phosphoric acid at 74 to 79 °C for 1 to 1.5 min. Various organic-acid-based solutions, such as citric acid, are also used to remove rust from stainless steels, including the 400-series and the precipitation-hardening steels.

Vapor degreasing (Ref 6, 10) is not environmentally friendly due to the use of perchloroethylene 1,1,1-trichloroethane and trichloroethylene. Therefore, it cannot be used in many states today (2013). This cleaning method has limited value for removing pigmented compounds because it may leave a residue of dry pigment that can be even more difficult to remove. However, modifications of this method, such as slushing, spraying, or ultrasonic cleaning, can be used for 100% removal of the easier-to-clean pigments, such as whitening, zinc oxide, or mica, but not for difficult-to-clean pigments, such as graphite or molybdenum disulfide. Perchloroethylene is preferred for removing water-containing soils. This method is often used for occasional or intermittent cleaning.

Vapor degreasing is an effective and widely used method for removing a wide variety of oils and greases. It has proved especially effective for cleaning soluble soil from cracks, such as rolled or welded joints. Vapor degreasing is particularly well adapted for cleaning oil-impregnated parts, such as bearings, and for

removing solvent-soluble soils from the interiors of storage tanks.

Vapor degreasing will remove the first group of cutting fluids easily and completely, but the fluids from the second and third groups cannot be completely removed. The vapor phase will not remove chips or other solid particles, but by combining with an air blowoff, chips can be removed. The operating and maintenance cost of a vapor degreaser could be as high as four times that of emulsion cleaning with the same utility (Ref 12).

Supercritical fluid (SCF) cleaning especially SCF CO₂, is a good substitute for chlorofluorocarbon-based cleaning methods (Ref 16). The SCF makes an ideal solvent because of its liquidlike density and gaslike transport properties of diffusivity and viscosity, zero surface tension, and the pressure-dependent solvent power over the range of interest. It is effective in removing numerous oils, fluids, adhesives, and chemical compounds with an 85 to 99% removal rate (Ref 17). Although SCF-based cleaning has been used in the food, fragrance, and petroleum industries for years, it is slowly gaining acceptance as an economical replacement for bulk cleaning in other manufacturing industries. Its low cost, low critical temperature (31.7 °C, or 89.1 °F) and pressure (7.3 MPa, or 72 atm), tunability by adjusting pressure and temperature to remove particular contaminants, nontoxicity, and ease of recycleability make it an excellent choice for cleaning applications.

Ultrasonic cleaning can effectively be used to remove a variety of surface contaminants by using high-frequency sound waves in the range of 20 to 200 kHz (above the upper limit of human hearing, or approximately 18 kHz) from parts immersed in aqueous media, which can be water, water with surfactants, alkaline, acid, or even organic solvents. The contaminants can be grease, cutting oil, sludge, machine chips, buffing and polishing compounds, mold-releasing agents, corrosion deposits, and other particulates. The passage of ultrasonic waves through the liquid medium creates tiny gas bubbles, which provide a vigorous scrubbing action on the parts being cleaned.

Two frequency ranges are used for cleaning metal surfaces: 20 to 40 kHz for heavy-duty cleaning of items such as engine blocks and heavy metal parts and for removal of heavy, greasy soils; and 40 to 70 kHz for general cleaning of machine parts to remove small particles (Ref 18, 19). The cleaning systems are comprised of ultrasonic transducers mounted on a radiating diaphragm, an electrical generator, and a tank filled with cleaning fluids. Ultrasonic cleaning provides excellent penetration and cleaning of intricately shaped parts, such as small crevices and tight spaces between surfaces. Its effectiveness can exceed the performance of vapor degreasing. A disadvantage of ultrasonic cleaning processes is the high capital cost of the power supplies and transducers.

The use of this process is largely restricted to applications in which other methods have proved

inadequate. Despite the high cost of ultrasonic cleaning, it has proved economical for applications that would otherwise require hand operations. Part size is a limitation, although no definite limits have been established. The commercial use of ultrasonic cleaning has been limited principally to small parts. The process is used as a final cleaner only, after most of the soil is removed by another method. Ultrasonic cleaning, in some cases, has resulted in fatigue failure of parts. Proper racking and isolation from the tank wall will often solve this problem.

An extremely high degree of cleanliness without damage is required on some expensive delicate parts (e.g., fuel injection equipment). Ultrasonic cleaning with alkaline solution, followed by spray with alkaline and immersion/spray rinsing, is ideal for this application. Ultrasonic cleaning is rapidly replacing the old pressure-solvent spray/agitated immersion technologies, which were only partially effective. Parts that normally took an hour or more to clean using solvent cleaning processes are now effectively cleaned in just a few minutes of ultrasonic cleaning. Other inherent advantages of this approach are that it is nondestructive to the parts, it uses more environmentally friendly cleaning solutions, and it is much safer with respect to the explosion dangers that are characteristic of many solvent cleaning technologies. As always, the primary drawback to ultrasonic cleaning is the comparatively high upfront capital cost.

Pickling (Ref 6–13) is used for the complete removal of surface oxide, scale, and dirt from mill products and fabricated parts by using hot, strong solutions of sulfamic, phosphoric, sulfuric, or hydrochloric acid (Ref 11). Pickling is generally used as the second step after abrasive blast cleaning or salt bath descaling, which removed the major portion. Acid concentrations of approximately 3% and a temperature of approximately 60 °C (140 °F) or lower are the most commonly used parameters in pickling.

Salt bath descaling (Ref 6) is an effective way to remove scale on carbon alloy, stainless, and tool steels. Several types of salt baths either reduce or oxidize the scale. Because it operates at a temperature range of 400 to 525 °C (750 to 975 °F), the parts are heat treated again by using this method.

Usually, salt bath descaling and quenching are followed by acid pickling as a final step in removing the last of the scale. The supplementary pickling is done with more dilute acids at lower temperatures and for shorter times than are used in conventional pickling. A solution of 3% sulfuric acid at a maximum temperature of approximately 60 °C (140 °F) is commonly used for pickling after salt bath descaling. Other acids are used at comparable concentrations. Metal loss and the danger of acid embrittlement are negligible in this type of pickling. Very high operating temperatures and high facility costs discourage widespread use of this process.

Alkaline descaling (Ref 6, 9) or alkaline derusting is used to remove rust, light scale, and carbon smut from carbon alloy, and stainless

steels and from heat-resisting alloys. The process is more costly and slower in its action than acid pickling of ferrous alloys, but no metal is lost using the alkaline method, because chemical action stops when the rust or scale is removed. Alkaline descaling also allows complete freedom from hydrogen embrittlement.

A number of proprietary compounds are available. They are composed mainly of sodium hydroxide (60% or more) but also contain chelating agents. Immersion baths are usually operated from room temperature to 71 °C (160 °F) but can be used at 93 to 99 °C (199 to 210 °F) with concentrations of approximately 0.9 kg (32 oz) of compound to 4 L of water. Required immersion time depends on the thickness of the rust or scale.

The rate of oxide removal can be greatly increased by the use of current in the bath, either continuous direct or periodically reversed. In one instance, an electrolyzed bath descaled steel parts in 1 min, as compared to 15 min for a nonelectrolytic bath doing the same job. However, parts must be racked for electrolytic descaling, which increases the cost because of the additional equipment, increased power requirement, and decreased bath capacity.

The addition of approximately 0.5 kg (18 oz) of sodium cyanide per 4 L of water increases the effectiveness of electrolyzed baths. However, when cyanide is used, the bath temperature should be kept below 54 °C (129 °F) to prevent excessive decomposition of the cyanide. One manufacturer descales heat treated aircraft parts in an alkaline descaling bath, using direct current and cyanide additions. Another manufacturer descales similar work in an alkaline bath operated at 82 to 93 °C (180 to 199 °F) with a lower concentration of descaling compound, 60 to 90 g/L, and no cyanide. The latter bath is operated at a current density of 2 to 20 A/dm² and with periodic current reversal (55 s anodic, followed by 5 s cathodic). Alkaline permanganate baths are also used for descaling. Proprietary products available are used at approximately 120 g/L, 82 to 93 °C (180 to 199 °F), 30 min or longer, depending on scale thickness and condition.

Despite the high cost of alkaline descaling baths, they can be economical. Because alkaline descaling baths are compounded for detergency as well as derusting, chemical cleaning and derusting are accomplished simultaneously. Paint, resin, varnish, oil, grease, and carbon smut are removed along with rust and scale. Thus, in a single operation, work is prepared for phosphating, painting, or electroplating. If parts are to be plated, the cost of electrolytic descaling may be comparable to that of the nonelectrolytic process, because in either case workpieces must be racked before final cleaning and plating. An electrolytic descaling bath may serve as the final cleaner.

Alkaline descalers are used for applications on critical parts such as turbine blades for jet engines, where risk of hydrogen embrittlement, loss of metal, or etched surfaces cannot be tolerated. Alkaline descaling may also be chosen

for parts made of high-carbon steel or cast iron, because acid pickling will leave smut deposits on these metals. Because of the time required, alkaline descaling is seldom used for removing heavy scale from forgings.

Electrolytic alkaline cleaning is a modification of alkaline cleaning in which an electrical current is imposed on the part to produce vigorous gassing on the surface to promote the release of soils. Electrocleaning can be either anodic or cathodic. Anodic cleaning is also called reverse cleaning, and cathodic cleaning is called direct cleaning. The release of oxygen gas under anodic cleaning or hydrogen gas under cathodic cleaning in the form of tiny bubbles from the work surface greatly facilitates lifting and removing of surface soils.

Electrolytic alkaline cleaning provides a high level of agitation close to the work surface, because of the gas generated, and is an effective method for removing polishing and buffing residues. Electrocleaners can be easily contaminated by polishing and buffing compounds as well as steel particles that may be attracted to the work. Precleaning is necessary. Parts on which mineral oil has been used as a polishing compound should always be precleaned before being electrocleaned. Use of both heavy-duty alkaline soak cleaners and electrocleaners is often necessary to provide a water-break-free surface. The presence of large amounts of animal or vegetable oils or fatty acids and abrasives in the polishing and buffing compounds will react with free caustic and form soaps in the electrocleaner, shortening its life.

Electrolytic Pickling. Although more expensive than conventional pickling, electrolytic pickling can remove scale twice as fast and may prove economical where time is limited. In an automatic plating installation, electrolytic pickling removes light scale and oxidizes during the time allowed in the pickling cycle and eliminates a preliminary pickling operation. For this purpose, a solution of 30% hydrochloric acid is used at 55 °C (130 °F) and 3 to 6 V for 2 to 3 min. Cathodic current is used.

Sulfuric acid formulas also are used electrolytically. A cycle for removing light scale from spot-welded parts is a solution of 10% sulfuric acid at 82 °C (180 °F) and 3 to 6 V for 5 to 20 s.

The main disadvantage of electrolytic pickling is its high cost. In addition to the requirement for more elaborate equipment, all workpieces must be racked.

Cleanliness Measurement

Before cleaning the parts, the amount of contaminants on the surface must be quantified. After cleaning, the degree of cleanliness also must be measured. Measuring cleanliness helps to ensure product quality.

Qualitative Tests

There are several simple methods (Ref 20–24) that can be used on the shop floor.

These techniques are totally qualitative and can be used to detect contaminants that are more than 0.1 g/in.²:

- Magnified visual inspection
- Black light
- Water-break test
- White/clean towel test
- Transparent tape test

Magnified Visual Inspection. This method requires a magnifying glass that can be used to examine a part directly and observe any gross contamination that may not be visible with the naked eye. It is a method used in non-critical cleaning applications where only gross contamination needs to be detected. It has the advantage of requiring minimum equipment. An area separate from production, such as a small laboratory, is used, and inspectors must be well trained.

Black Light. This test requires a dark room and black light source for direct visual inspection of parts. This method is a pass/fail test that will work on any material with a contaminant that fluoresces under black light, provided the part itself does not fluoresce. The operator simply places the part under the black light and inspects the part. This method has most of the same applications of magnified visual inspection. The contaminants fluoresce, so they are even easier to notice. This method is practical only for testing smaller parts.

Water-Break Test. This simple method takes advantage of the fact that many contaminants of interest are hydrophobic. This is a pass/fail test that is typically used for metal surfaces, and water is flowed over the part. If the water sheets off the surface evenly, the part is clean. If the water channels or beads on certain areas, the part is considered to be contaminated with a hydrophobic substance (oil/grease). This test can be done in production areas or as a batch test and is also usable on very large parts, such as airplane wings. To be effective, the water used in the test must be free of surfactants or other contaminants that would cause the water to flow evenly in the presence of contamination, and the part must be of a geometry that allows water to flow across the surface of interest.

White/Clean Towel Test. The part surface is wiped with a white cloth or paper. The presence of soil on the cloth or paper indicates the degree of cleanliness. This is the simplest way to test for cleanliness, but using this method will wipe off some film, left by the former cleaning processes, that protects the steel from rust.

Transparent Tape Test. A strip of transparent tape is affixed to the surface in question with firm pressure. The tape is removed and placed on a clean, white sheet of paper. The clean surface should appear as white as the original sheet of paper. For this method, the degree of contamination can be defined according to the amount of contaminant on the tape.

Quantitative Tests

As the degree of cleanliness is classified, a quantitative cleanliness measurement is also necessary on the heat treatment shop floor. The method should be nondestructive, portable, easily evaluated, and cost-effective. Gravimetric measurement and dirt catching are used in gross verification measurements. Some modern and advanced techniques can also be used on the heat treatment shop floor.

Gravimetric Measurement (Ref 20–22). This method requires a highly sensitive scale that can weigh parts to an accuracy of ± 1 mg or better. This method is used on small parts of any material to detect gross contamination, but it does not require any other equipment besides the scale. Parts must be weighed prior to being contaminated and then again after contamination. After cleaning, the part is oven dried and weighed again. The difference between the initial weight and the postcleaning weight is attributed to any residual contamination left on the part. If there is no difference in these two weights, the part is considered clean. A small laboratory is needed to conduct these tests, and large parts cannot be tested in this way.

Dirt Catching (Wash and Filter) (Ref 20). This method uses the same equipment as the direct gravimetric method and has the same issues. However, instead of weighing the part directly, a fine filter patch is weighed before the contaminants are flushed off the part and collected, and again after. A solvent is used to flush the contaminants off and through the filter patch, and the filter patch is weighed.

Advanced Techniques. There are several spectroscopy-based techniques (Ref 24–30) that can be used to identify surface contaminants on heat treated parts. Fourier transform infrared (FTIR) and Raman spectroscopy could provide spectra of the contaminants, but they need a standard reference library of known contaminants to match and identify. Low-level surface contamination on the metal surface can also be detected and measured by grazing-angle reflectance FTIR spectroscopy. Laser-induced breakdown spectroscopy is an atomic emission spectroscopy technique that is minimally destructive and uses successive nanosecond laser pulses to ablate a small amount of material from the surface. It can be used for elemental analysis of the contaminants. The instruments using these techniques are currently available in compact and portable format so that they can be used on the heat treatment shop floor. The most promising and emerging technique is direct solid probe mass spectrometry equipped with desorption atmospheric pressure chemical ionization (DAPCI) (Ref 31). DAPCI employs corona discharge directed at the surface of interest, using a carrier gas to desorb and ionize surface contaminants, such as hydrocarbon-based oil, and using mass spectrometry to record the spectra of the contaminants under ambient conditions. This device is yet to be commercialized as a portable device.

How Clean Is Clean?

“Free of oil and grease” and “remove all chips, oil, dirt, etc.” are often used as specifications. How clean is clean for heat treatment? For different processes, the cleanliness requirement is different. The required cleanliness level for a desired performance can be determined by using some means of quantifying the surface cleanliness measurement to correlate product performance with contaminant level, in that way, establishing the degree of contamination that can be tolerated. The degree of cleanliness in heat treated parts can be quantified by assigning level numbers on the scale of 1 to 5, with 1 being the best and 5 being the worst. For example, annealing and normalizing requires the most undemanding level (level 5), but gas quenching in a low-pressure carburization system has some strict requirements (level 2) on surface contamination. Once the level of cleanliness is defined, the quantifying measurement is needed to exam the level of cleanliness achieved during production to assure that the surface meets the established cleanliness requirements.

Case Studies

The level of cleanliness requirement for heat treated parts mainly depends on the subsequent operations. Several case studies discussing the cleaning methods and their effects on part surfaces are presented here.

Case Study 1 (Ref 32). In steel wire manufacturing, wires must be phosphated before reshaping. The phosphate layer allows better sliding and provides temporary corrosion protection. The phosphate layer and the support compounds must be completely removed before the heat treatment. If not, cracks will form in the glasslike iron phosphate layers.

Grün (Ref 32) experimentally investigated the cleaning of phosphate layers. Demulsifying cleaning with rinsing was necessary before dephosphating to reduce saponification to a minimum. During precleaning, the quenching oils can also be removed. To remove the phosphate layer, highly alkaline ($\text{pH} > 12$) products containing complexing agents and surfactants are used. The complexing agents are biodecomposable, and the metal complexes (zinc, iron) can be removed easily in the usual wastewater treatment.

Case Study 2 (Ref 33). Cooling lubricants and preservation agents on the workpiece surface can have a detrimental effect on the heat treatment result. The contaminants impede the diffusion process. Difficulties in heat treatment are mainly caused by graphite, molybdenum disulfide, and compounds of chlorine, sulfur, silicon, phosphorus, and boron in cooling lubricants. They form diffusion-inhibiting layers during heating. Residues can also impair the surface appearance and are often the cause of surface spotting.

Cronan (Ref 33) suggested several cleaning methods suitable to wash away contaminants. Acid cleaning, which has a pH value < 2 , can

remove oil from the surface. Hydroxide cleaning can remove oil as well. The most popular hydroxide agents are either tensile-based washing agents or builder based (hydroxides and mineral salts). The combination of appropriate cleaners and cleaning equipment can achieve good results.

Case Study 3. Clark (Ref 34) experimented with acid cleaning of 304L stainless steel. The sample was prepared in a sequence of polish, air anneal, acid clean, and passivate. Two different cleaning solutions were used: 2 vol% HF + 10 vol% HNO₃ in water, and 14 vol% Turco Nitradd (Henkel Corp.) + 25 vol% HNO₃ in water. Intergranular surface ditching, observed on many of the examined stainless steel surfaces, was shown to result from air annealing and acid cleaning of stainless steel during normal manufacturing. The ditched air-annealed and acid-cleaned stainless steel samples were more resistant to subsequent acid attack than vacuum-annealed or polished samples without ditches.

Case Study 4 (Ref 6). The gear illustrated as part 1 in Fig. 6 is made of 8620 steel, carburized and hardened to approximately 56 to 58 HRC. Although the part is processed in a controlled atmosphere, a descaling operation is required. Abrasive blasting with fine steel grit or chilled iron shot (SAE G40 or S170) proved the most economical method for cleaning large tonnages of such parts used in the manufacture of trucks, tractors, and similar vehicles. Acid pickling was precluded because of hydrogen embrittlement, and descaling in molten salt was unsuitable because of the softening effect of the high-temperature bath.

Conventional abrasive blasting may deleteriously affect the dimensions of precision gears or pinions. In these special applications, alkaline descaling or wet blasting with a fine abrasive, such as glass beads, under carefully controlled conditions is indicated.

Case Study 5 (Ref 6). Normally, abrasive blasting would be the preferred method for removing rust and scale from a rough ferrous metal casting such as part 2 in Fig. 6. Chilled iron shot or steel abrasives are usually the most economical abrasives for this purpose.

Pickling is seldom used for descaling castings, such as cast iron, because smut is deposited and must be removed by another cleaning operation. Severe pitting is also likely to result.

Salt baths have been successfully used for descaling ferrous castings, but there is danger of cracking and excessive distortion for configurations such as part 2.

Case Study 6 (Ref 6). Barrel or vibratory tumbling is probably the most economical method for removing scale or rust from steel parts such as part 3 in Fig. 6, if they are no larger than approximately 50 to 75 mm (2 to 3 in.). For similar but larger parts, abrasive blasting is usually a better choice.

However, if such parts are close to finished dimensions and these dimensions are critical, a nonabrasive method of cleaning should be chosen. If parts are made of low-carbon steel and are not heat treated, pickling in inhibited hydrochloric or sulfuric acid is satisfactory

and less expensive, and hydrogen embrittlement is not a factor. However, if such parts are made of high-carbon (or carburized) steel and are heat treated, acid pickling would be hazardous and alkaline descaling would be preferred.

Pollution Control and Resource Recovery

The cleaning of metal surfaces may generate volumes of waste. The increasing cost of waste disposal has a great impact on process cost and should be considered in selecting cleaning processes. Treatment of waste within the plant should be considered to reduce cost, reduce

liability, permit reuse of the raw material, and improve process control. A good example of closed-loop recycling is the distillation purification of vapor degreasing solvents. The federal Environmental Protection Agency (EPA) has established compliance guidelines, but state and local regulations are often more stringent. For more information, see the article "Environmental Regulation of Surface Engineering" in *Surface Engineering*, Volume 5 of *ASM Handbook*.

Safety

In the use of any metal-cleaning process, there are possible safety, health, and fire

hazards that must be considered. The degree of hazard is dependent upon such factors as the specific materials and chemicals involved, the duration of employee exposure, and the specific operating procedures.

Information is presented in Table 2 on the types of hazards that may be associated with each cleaning process and the general control measures to be used for each hazard.

The Occupational Safety and Health Administration (OSHA) has established in its General Industry Standards (29 CFR 1910) regulations pertaining to a variety of safety and health hazards. Those sections of the standards that may apply to each cleaning process are referenced in Table 2. Because of the unusual fire hazard associated with

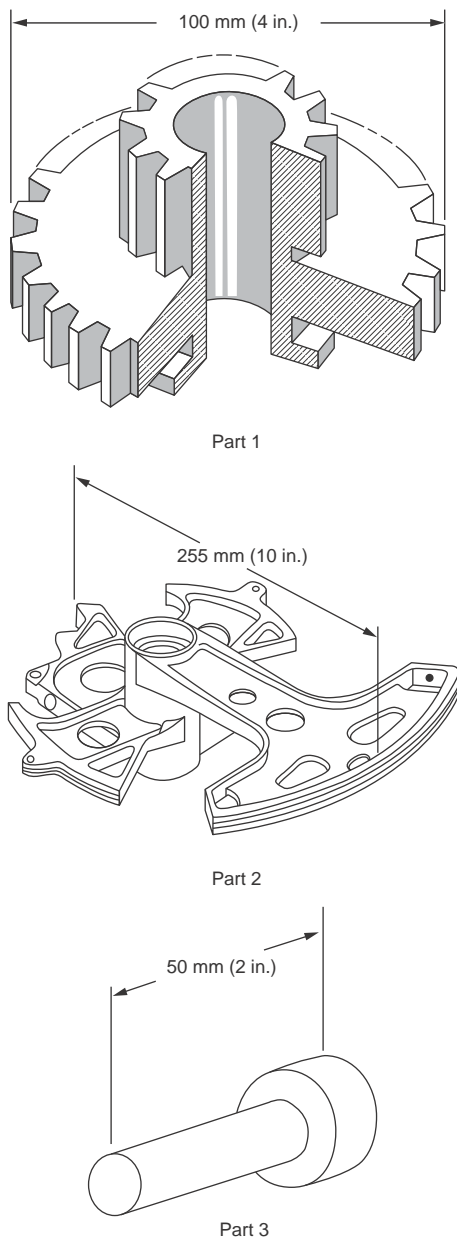


Table 2 Safety and health hazards of cleaning processes

Cleaning process	Hazard/air contaminant	Control measures	OSHA/NFPA references
Abrasive blasting	Silica dust/total dust exposures	Local exhaust ventilation Respiratory protection Goggles or face shield	(29 CFR) 1910.94(a) 1910.95
	Noise exposures	Noise exposures Hearing protective devices	1910.133 1910.134
	Skin abrasion	Leather protection garments	1910.1000 Table Z-3
Acid cleaning	Acid gas or mist exposure	Local exhaust ventilation Respiratory protection Goggles or face shield	1910.94(L) 1910.133 1910.134
	Skin contact	Impervious gloves and garments	1910.1000 Table Z-1
Alkaline cleaning	Alkaline mist exposure	Local exhaust ventilation Respiratory protection Goggles or face shield	1910.94(d) 1910.133 1910.134
	Skin contact	Impervious gloves and garments	1910.1000 Table Z-1
Emulsion cleaning	Petroleum or chlorinated hydrocarbons	Local exhaust ventilation Respiratory protection	1910.94(d) 1910.132
	Alkaline mist exposures	Local exhaust ventilation	1910.133 1910.134 1910.1000
Pickling	Skin contact	Respiratory protection Goggles or face shield Impervious gloves and garments
	Acid gas or mist exposures	Local exhaust ventilation Respiratory protection Goggles or face shield	1910.94(d) 1910.133 1910.134
	Skin contact	Impervious gloves and garments	1910.1000 Table A
Salt bath descaling	Burns	Heat-resistant gloves and garments Face shield	1910.132 1910.133
	Toxic gases	Local exhaust ventilation Respiratory protection	1910.134 1910.1000
	Fire/explosion	Proper facility design, construction, maintenance Proper controls for tank Proper work procedures	NFPA 86C, Chapter 11 ...
Solvent cleaning	Petroleum or chlorinated hydrocarbon exposure	Local exhaust ventilation	1910.94(d) 1910.132 1910.133
		Respiratory protection	1910.134 1910.1000
Tumbling	Skin contact	Impervious gloves and garments	Tables Z-1, Z-2
	Noise exposure	Noise enclosure for equipment Hearing protective devices	1910.95
Vapor degreasing	Chlorinated hydrocarbon exposure	Condenser cooling system and appropriate thermostats Minimize dragout Local exhaust ventilation	1910.94(d) ...
	Solvent decomposition products	Eliminate hot surfaces above 400 °C (750 °F) in the vicinity Eliminate sources of ultraviolet radiation in the vicinity Proper monitoring of solvent for acid buildups to prevent exothermic decomposition	1910.94(d)

Fig. 6 Sample part configurations cleaned by various processes. Source: Ref 6

OSHA/NFPA, Occupational Safety and Health Administration/National Fire Prevention Association. Source: Ref 6

salt bath descaling, an applicable chapter of the National Fire Prevention Association standards has also been referenced.

Summary

For proper assessment of the cleaning operation, four parameters must be analyzed: the substrate, the degree of cleanliness required, the nature of the soil, and the incoming water quality. (The condition of the incoming water is often overlooked in metal cleaning.) Aqueous cleaners are generally better than solvent cleaners at removing soils or particulate matter. The rinsing and drying steps are of particular concern, especially with complex geometries or parts that are susceptible to corrosion, because water can remain on the part and cause flash rust. Compared to solvents, aqueous systems generally have higher capital costs and require elaborate rinsing and drying procedures as well as tighter process controls for optimum cleaning. Spent solvents are classified as a hazardous waste. Handling and disposal of these solvents are more involved and expensive than other cleaning alternatives. There are a few emerging technologies for precision cleaning that are technologically and economically efficient and could also be used for surface cleaning of heat treated parts, such as argon/nitrogen cryogenic aerosol and ice-air jet (Ref 35, 36).

REFERENCES

- B. Haase, M. Stiles, T. Haasner, and A. Walter, Formation of Reaction Layers in Steel Machining: Impact on Surface Treatment Process, *Surf. Eng.*, Vol 5 (No. 3), 1999, p 242–248
- B. Haase, M. Stiles, and J. Dong, Improvement of Gas Nitriding Process by Prior Surface Quality Control, *Surf. Eng.*, Vol 14 (No. 1), 1998, p 31–36
- B. Haase, J. Dong, O. Irretier, and K. Bauckhage, Influence of Steel Surface Composition on Gas Nitriding Mechanism, *Surf. Eng.*, Vol 13 (No. 3), 1997, p 251–256
- J.B. Durkee II, *Management of Industrial Cleaning Technology and Processes*, 1st ed., Elsevier, 2006
- R. Grün, Cleaning as a Part of the Heat Treatment, *SurTec Tech. Lett.*, Vol 13a, 1999
- D.B. Chalk, Classification and Selection of Cleaning Processes, *Surface Engineering*, Vol 5, *ASM Handbook*, ASM International, 1994, p 3–17
- K.J. Patel, Quantitative Evaluation of Abrasive Contamination in Ductile Material during Abrasive Water Jet Machining and Minimizing with a Nozzle Head Oscillation Technique, *Int. J. Mach. Tools Manuf.*, Vol 44, 2004, p 1125–1132
- B. Kanegsberg, *Handbook for Critical Cleaning*, CRC Press, Washington, D.C., 2001, p 152
- “Standard Practice for Cleaning, Descaling, and Passivation of Stainless Steel Parts, Equipment, and Systems,” A 380-06, ASTM International, 2006
- K.E. Pearce, “Use of Emulsion Cleaning to Replace Perchloroethylene and Freon Vapor Degreasing,” P 04971, Division of Pollution Prevention and Environmental Assistance
- A. Bornmyr and B. Holmberg, *Handbook for the Pickling and Cleaning of Stainless Steel*, AvestaPolarit Welding, 1995, <http://www.stainlesspickling.co.uk/docs/cleaninghandbook.pdf>
- N. Rajagopalan and T. Lindsey, Recycling Aqueous Cleaning Solutions, *Prod. Finish. Mag.*, 1999
- E. O’Neill and A. Miremadi, Simplifying Aqueous Cleaning, *Prod. Finish. Mag.*, 2000
- “Ethyl Lactate Solvents: Low-Cost and Environmentally Friendly,” Argonne National Laboratory, 1998 Discovery Award Winner, DoE, Energy Efficiency and Renewable Energy, Office of Industrial Technologies
- T.M. Carole, J. Pellegrino, and M.D. Paster, Opportunities in the Industrial Bio-based Products Industry, *Appl. Biochem. Biotechnol.*, Vol 113–116, Humana Press, 2004, p 871–885
- G. Manivannan and S.P. Sawan, The Supercritical State, *Supercritical Fluid Cleaning—Fundamentals, Technology, and Applications*, William Andrew Publishing, 1998
- W.D. Spall and K.E. Laintz, A Survey on the Use of Supercritical Carbon Dioxide as a Cleaning Solvent, *Supercritical Fluid Cleaning—Fundamentals, Technology, and Applications*, William Andrew Publishing, 1998
- S.B. Awad and R. Nagarajan, Ultrasonic Cleaning, *Developments in Surface Contamination and Cleaning*, Elsevier Inc., 2010, p 225–280
- J.B. Durkee II, The Fundamentals of No-Chemistry Process Cleaning, *Surface Contamination and Cleaning*, Vol 1, K.L. Mittal, Ed., VSP, 2003, p 129–136
- “Cleanliness Measurement Review,” Pacific Northwest Pollution Prevention Resource Center, 1999, <http://www.pprc.org/pubs/techreviews/measure/meintro.html>
- J. Durkee, Using Simple Science to Assay Surface Cleanliness, *MetalFinish.*, Feb 2008, p 49–51, <http://www.metalfinishing.com>
- Choices for Cleanliness Verification, *Parts Clean. Web Mag.*, Witter Publishing Corporation, March 2001, p S2–S9, <http://infohouse.p2ric.org/ref/13/12911.htm>
- R.A. Wilkie and C.E. Montague, Counting on Cleanliness Measurement Technology, *Precis. Clean.*, Sept 1994
- R. Kohli, Methods for Monitoring and Measuring Cleanliness of Surfaces, *Developments in Surface Contamination and Cleaning*, Vol 4, *Detection, Characterization, and Analysis of Contaminants*, Elsevier, 2011, p 107–168
- J. Gross, *Ambient Mass Spectrometry, Mass Spectrometry*, 2nd ed., Springer-Verlag, Berlin, 2011
- R. Ghosh and Z. Zurecki, Merchant R&D, Air Products, private communications
- “Portable XRF,” Portable Analytical Solutions Ltd., Australia, <http://portablexrf.com/HowXRFWorks.html>
- D.A. Cole and L. Zhang, Surface Analysis Methods for Contaminant Identification, *Developments in Surface Contamination and Cleaning*, William Andrew Inc., 2008, p 585–652
- M.M. Szczesniak, “Surface Inspection for Contamination,” The Industrial Protective Coatings Conference and Exhibit, Nov 1999 (Houston, TX)
- J. Owsik, J. Janucki, K. Jach, R. Swierczynski, V.S. Ivanov, A.F. Kotyuk, and M.V. Ulanovski, LIBS System for Elemental Analysis of Soil Samples, *Proc. SPIE 5710, Nonlinear Frequency Generation and Conversion: Materials, Devices, and Applications IV*, 2005, p 138–323
- Z. Takáts, J.M. Wiseman, and R.G. Cooks, Ambient Mass Spectrometry Using Desorption Electrospray Ionization (DESI): Instrumentation, Mechanisms and Applications in Forensics, Chemistry, and Biology, *J. Mass Spectrom.*, Vol 40, 2005, p 1261–1275
- R. Grün, Dephosphating of Parts before Heat Treatment, *SurTec Tech. Lett.*, Vol 10, 2002
- T. Cronan, “Parts Cleaning and Its Integration into Heat Treating,” International Heat Treating Conference, 1994
- E.A. Clark, “Type 304L Stainless Steel Surface Microstructure: Performance in Hydride Storage and Acid Cleaning,” Westinghouse Savannah River Co., Aiken, SC, 1994
- W.T. McDermott and J.W. Butterbaugh, Cleaning Using Argon/Nitrogen Cryogenic Aerosols, *Developments in Surface Contamination and Cleaning*, William Andrew Inc., 2008, p 951–986
- D.V. Shishkin, E.S. Geskin, and B. Goldenberg, Practical Applications of Icejet Technology in Surface Processing, *Surface Contamination and Cleaning*, Vol 1, K.L. Mittal, Ed., VSP, 2003, p 193–212

SELECTED REFERENCES

- R.E. Luetje, Surface Cleaning, *Surface Engineering*, Vol 5, *ASM Handbook*, ASM International, 1994
- R.D. Sisson, Y. Rong, M. Maniruzzaman, X. Wang, and W. Liu, “Characterization, Evaluation and Removal of Surface Contamination from Pre and Post Heat Treated Parts,” CHTE Project Report, Center for Heat Treating Excellence (CHTE), Worcester Polytechnic Institute, Worcester, MA, 2007 and 2008
- X. Wang, M. Maniruzzaman, Y. Rong, and R.D. Sisson, The Role of Cleaning in Heat Treatment Process, *Proceedings of the 24th ASM Heat Treating Society Conference* (Detroit, MI), 2007, p 425–431

Stress-Relief Heat Treating of Steel*

STRESS-RELIEF HEAT TREATING is used to relieve stresses that remain locked in a structure as a consequence of a manufacturing sequence. This definition separates stress-relief heat treating from postweld heat treating in that the goal of postweld heat treating is to provide, in addition to the relief of residual stresses, some preferred metallurgical structure or properties (Ref 1, 2). For example, most ferritic weldments are given postweld heat treatment to improve the fracture toughness of the heat-affected zones. Moreover, austenitic and non-ferrous alloys are frequently postweld heat treated to improve resistance to environmental damage.

Stress-relief heat treating is the uniform heating of a structure, or portion thereof, to a suitable temperature below the transformation range (Ac_1 for ferritic steels), holding at this temperature for a predetermined period of time, followed by uniform cooling (Ref 2, 3). Care must be taken to ensure uniform cooling, particularly when a component is composed of variable section sizes. If the rate of cooling is not constant and uniform, new residual stresses can result that are equal to or greater than those that the heat treating process was intended to relieve.

Stress-relief heat treating can reduce distortion and high stresses from welding that can affect service performance. The presence of residual stresses can lead to stress-corrosion cracking (SCC) near welds and in regions of a component that has been cold strained during processing. Furthermore, cold strain per se can produce a reduction in creep strength at elevated temperatures.

Residual stresses in ferritic steels can cause significant reduction in resistance to brittle fracture. In a material that is not prone to brittle fracture, such as an austenitic stainless steel, residual stresses can be sufficient to provide the stress necessary to promote SCC even in environments that appear to be benign (Ref 4).

Sources of Residual Stress

There are many sources of residual stress; they can occur during processing of the

material from ingot to final product form (Ref 4, 5). Residual stresses can be generated during rolling, casting, or forging; during forming operations such as shearing, bending, drawing, and machining; and during fabrication, in particular, welding. Residual stresses are present whenever a component is stressed beyond its elastic limit and plastic flow occurs. Table 1 lists a summary of compressive and tensile residual stresses at the surface of parts fabricated by common manufacturing processes.

Bending a bar during fabrication at a temperature where recovery cannot occur (cold forming, for example) will result in one surface location containing residual tensile stresses, whereas a location 180° away will contain residual compressive stresses (Ref 6).

Quenching of thick sections results in high residual compressive stresses on the surface of the material. These high compressive stresses are balanced by residual tensile stresses in the internal areas of the section (Ref 7).

Grinding is another source of residual stresses; these can be compressive or tensile in nature, depending on the grinding operation. Although these stresses tend to be shallow in depth, they can cause warping of thin parts (Ref 8).

Welding. The cause of residual stresses that has received the most attention in the open literature is welding. The residual stresses associated with the steep thermal gradient of welding can occur on a macroscale over relatively long distances (reaction stresses) or can be highly localized (microscale) (Fig. 1). Welding usually results in localized residual stresses that approach levels equal to or greater than the yield strength of the material at room temperature.

Thermal Stress-Relief Methods

The basic premise of a stress-relief method is to produce rearrangement of atoms from their momentary equilibrium position (higher residual-stress state) to more stable positions associated with lower potential energy or stress state. Methods can be classified into three broad categories: thermal, chemical, and mechanical (Ref 9)—including the more recent mechanical method of

Table 1 Summary of compressive and tensile residual stresses at the surface of parts created by common manufacturing processes

Compression at the surface
Surface working: shot peening, surface rolling, lapping, etc.
Rod or wire drawing with shallow penetration(a)
Rolling with shallow penetration(a)
Swaging with shallow penetration(a)
Tube sinking of the inner surface
Coining around holes
Plastic bending of the stretched side
Grinding under gentle conditions
Hammer peening
Quenching without phase transformation
Direct-hardening steel (not through-hardened)
Case-hardening steel
Induction and flame hardening
Prestressing
Ion exchange
Tension at the surface
Rod or wire drawing with deep penetration
Rolling with deep penetration
Swaging with deep penetration
Tube sinking of the outer surface
Plastic bending of the shortened side
Grinding: normal practice and abusive conditions
Direct-hardening steel (through-hardened)(b)
Decarburization of steel surface
Weldment (last portion to reach room temperature)
Machining: turning, milling
Built-up surface of shaft
Electrical discharge machining
Flame cutting

(a) Shallow penetration refers to less than ~1% reduction in area or thickness; deep penetration refers to greater than ~1%. (b) Depends on the efficiency of quenching medium

vibratory stress relief (especially in the subresonant region). Chemical and mechanical methods are not discussed here.

Thermal stress-relief methods include, among others, annealing, aging, and reheat treatment (e.g., postweld heat treatment). In general, a stress-relief operation involves heating the part to a certain temperature, holding at the elevated temperature for a specified length of time, followed by cooling to room temperature. Primary reduction in residual stresses takes place during the holding period due to creep and relaxation. Thus, if computer simulation of a thermal stress-relief method is

* Revised from D.A. Canonico, Stress-Relief Heat Treating of Steel, *Heat Treating*, Vol 4, ASM Handbook, ASM International, 1991, p 33-34

considered, it generally entails a thermal-elastic-plastic-creep analysis of the part.

A number of factors influence the relief of residual stresses, including level of stress, permissible (or practicable) time for their relief, temperature, and metallurgical stability. Thermal stress relief is still conducted much as it has been done for most of the 20th century. However, advanced equipment designs have been developed for more rapid convective heating and stress relief (Ref 10). Rapid heating is defined as “any heating method that accelerates conventional furnace heating” (Ref 11). Heat-transfer rates of up to 30 times those achieved in conventional convection furnaces are possible (Ref 12). In the past, rapid heating technology has been applied primarily to the forging industry, where steel is heated to 1000 to 1250 °C (1830 to 2280 °F). It has been much less commonly encountered in the heat treating

industry, although rapid heating is enjoying increased use for stress relieving, particularly for spring wire.

Typically, stress-relieving times for specific alloys are obtained from standards such as those listed in Table 2 for wire. The stress-relieving times shown in Table 2 were developed for conventional convection-heated batch ovens. With rapid stress-relieving technology, the total stress-relieving time for 16 mm (0.63 in.) diameter chromium-silicon wire can be reduced to 10 min or less (Ref 15).

Time-Temperature Factors. Little or no stress relief occurs at temperatures below 260 °C (500 °F), and approximately 90% of the stress is relieved at 540 °C (1000 °F). The maximum temperature for stress relief is limited to 30 °C (54 °F) below the tempering temperature.

The relief of residual stresses also is a time-temperature phenomenon, such that similar relief of residual stresses can be achieved by

holding a component for longer periods at a lower temperature. Examples of time-temperature effects are shown in Fig. 2 and 3 for stress relief of specific steels.

Time-temperature effects on stress relief can be modeled parametrically by the Larson-Miller equation:

$$\text{Thermal effect} = T(\log t + 20) \times 10^{-3} \quad (\text{Eq 1})$$

where T is temperature (Rankine), and t is the time in hours. For example, holding a piece at 595 °C (1100 °F) for 6 h provides the same relief of residual stress as heating at 650 °C (1200 °F) for 1 h. The thermal effect on residual stress is described as a percentage of yield strength, as plotted in the example in Fig. 4 of data for a specific grade of steel.

The stress-relief response of steel can also be represented by curves such as those in Fig. 5. The example in Fig. 5 is from the HY-100 steel data in Fig. 3. As an example of the use of these curves, it is seen from Fig. 5 that a 1 h anneal at 450 °C (840 °F) results in approximately 50% stress relief (point X in Fig. 5a). If the same level of stress relief is desired by using 400 °C (750 °F), the time

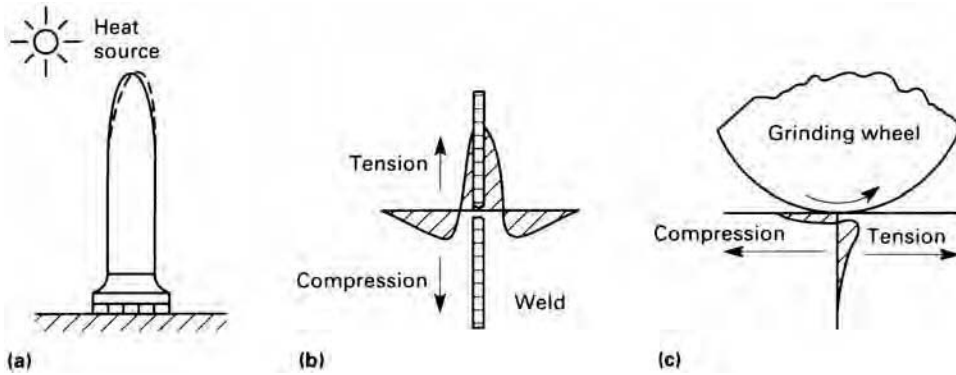


Fig. 1 Examples of the causes of residual stresses. (a) Thermal distortion in a structure due to heating by solar radiation. (b) Residual stresses due to welding. (c) Residual stresses due to grinding. Source: Ref 4

Table 2 Oven stress-relief temperatures and times for wire

Material	Specification	Temperature		Time, min
		°C	°F	
Beryllium-copper	ASTM B134 or ASTM B197	315	600	120
Blue temper	N/A	230	450	30
Brass wire	ASTM B134	190	375	30
Chrome-silicon	ASTM A401 or SAE J157	370	700	60
Chrome-silicon (Lifens)	SAE J157	385	725	60
Chrome-vanadium	ASTM A231	370	700	60
Galvanized MB class I or II	ASTM A674	230	450	30
Hastelloy C	...	330	500	30
HDMB class I or II	ASTM A227	230	450	30
High tensile hard drawn	ASTM A679	230	450	30
Inconel 600	...	650	1200	90
Inconel X700 spring temper	AMS 5699	650	1200	240
Inconel X750/1 temper	AMS 5699	650	1200	240
Monel 400	...	425	800	60
Music wire (tin coated)	ASTM A288	150	300	30
Music wire (cadmium-zinc coated)	ASTM A288	205	400	30
Music wire	AMS 5112	280	540	60
OTMB	ASTM A229	230	450	30
Phosphorus bronze (grade A)	ASTM B159	190	375	30
301 stainless steel	...	345	650	30
302 stainless steel	AMS 5688	345	650	30
304 stainless steel	ASTM A313	345	650	30
316 stainless steel	ASTM A313	345	650	60

N/A, not applicable. Source: Ref 13, 14

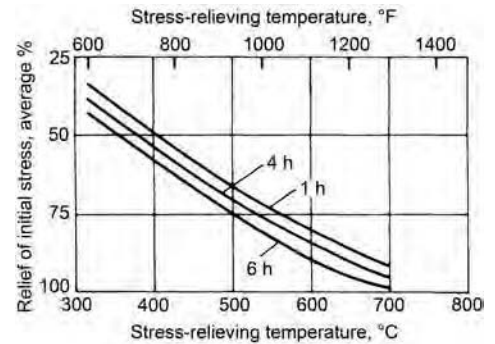


Fig. 2 Relationship between time and temperature in the relief of residual stresses in steel. Source: Ref 3

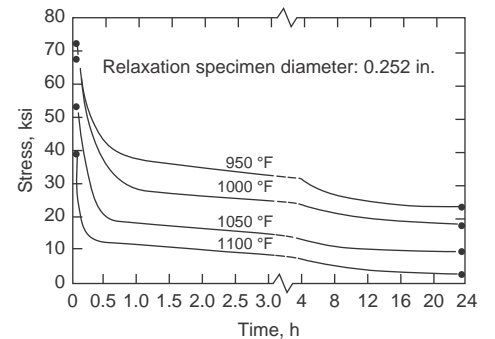


Fig. 3 Residual stress as a function of stress-relief annealing temperature and time for HY-100 steel. Source: Ref 16

required is obtained by drawing a vertical line from the 1 h/450 °C (840 °F) point until the 400 °C (750 °F) sloping curve is intersected, at which a time of 20 h is obtained at point X in Fig. 5(b) (Ref 17).

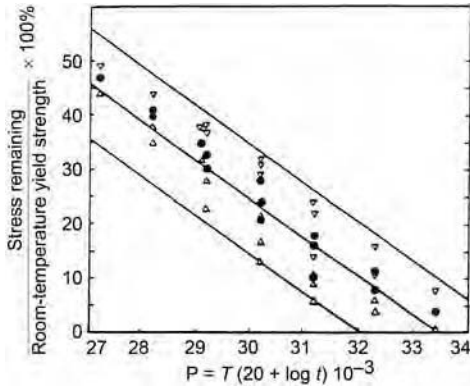


Fig. 4 Stress-relief data of a steel plotted versus the Larson-Miller equation (Eq 1). Source: Ref 16

Alloy Considerations. Relief of residual stresses represents typical stress-relaxation behavior, in which the material undergoes microscopic (sometimes even macroscopic) creep at the stress-relief temperature. Creep-resistant materials, such as the chromium-bearing low-alloy steels and the chromium-rich high-alloy steels, normally require higher stress-relief heat treating temperatures than conventional low-alloy steels. Typical stress-relief temperatures for low-alloy ferritic steels are between 595 and 675 °C (1100 and 1250 °F). For high-alloy steels, these temperatures may range from 900 to 1065 °C (1650 to 1950 °F).

For high-alloy steels, such as the austenitic stainless steels, stress relieving is sometimes done at temperatures as low as 400 °C (750 °F). However, at these temperatures, only modest decreases in residual stress are achieved. Residual stresses can be significantly reduced by stress-relief heat treating those austenitic materials in the temperature range from 480 to 925 °C (900 to 1700 °F). At the higher end of this range, nearly 85% of the residual

stresses may be relieved. Stress-relief heat treating in this range, however, may result in sensitizing susceptible material. This metallurgical effect can lead to SCC in service (Ref 18). Frequently, solution-annealing temperatures of approximately 1065 °C (1950 °F) are used to achieve a reduction of residual stresses to acceptably low values.

Some copper alloys may fail by SCC due to the presence of residual stresses. These stresses are usually relieved by mechanical or thermal stress-relief treatments. Stress-relief heat treating tends to be favored because it is more controllable, less costly, and also provides a degree of dimensional stability. Stress-relief heat treating of copper alloys is usually carried out at relatively low temperatures, in the range from 200 to 400 °C (390 to 750 °F) (Ref 5).

Resistance of a material to the reduction of its residual stresses by thermal treatment can be estimated with a knowledge of the influence of temperature on its yield strength. Figure 6 provides a summary of the yield-strength-to-temperature relationship for three generic classes of steels. The room-temperature yield strength of these materials provides an excellent estimate of the level of localized residual stress that can be present in a structure. To relieve the residual stress requires that the component be heated to a temperature where its yield strength approaches a value that corresponds to an acceptable level of residual stress. Holding at this temperature can further reduce the residual stress through the reduction of strain due to creep. Uniform cooling after residual-stress heat treating is mandatory if these levels of residual stress are to be maintained.

Stress Relief of Springs

Residual stresses are certain to be generated during spring manufacture, and stress relief is one of the most common heat treating processes used in spring manufacturing. For a given spring material with a certain strength and surface quality, residual stress is a key variable that influences fatigue resistance.

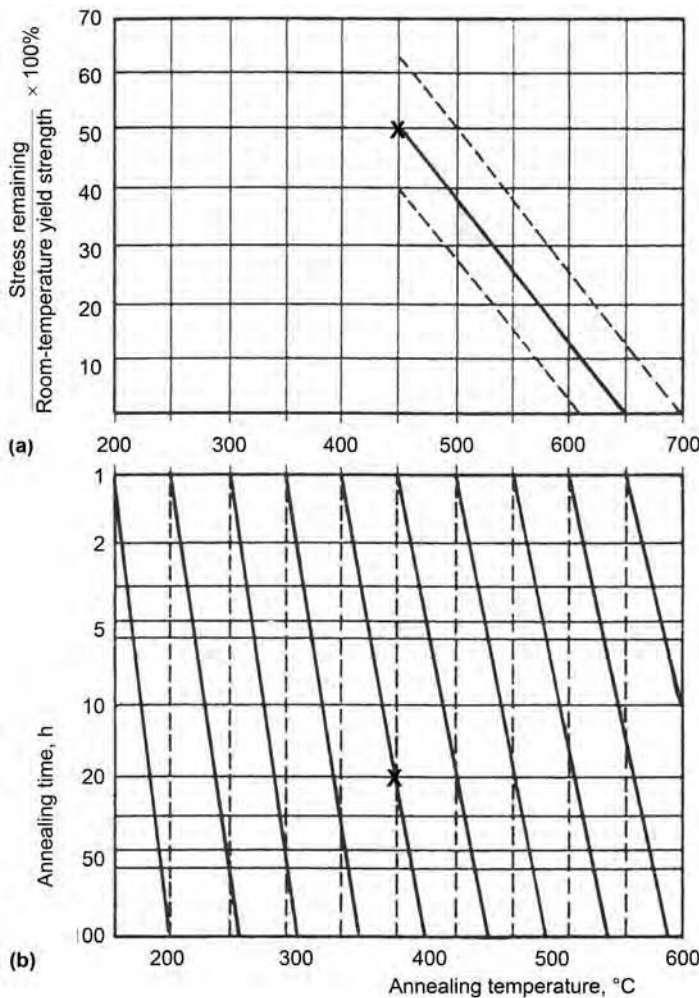


Fig. 5 Residual stress as a function of annealing time and temperature for the HY-100 steel data in Fig. 3. (a) Anneal at 450 °C (840 °F) results in approximately 50% stress relief (point X). (b) Same level of stress relief with 400 °C (750 °F) treatment requires 20 h (point X).

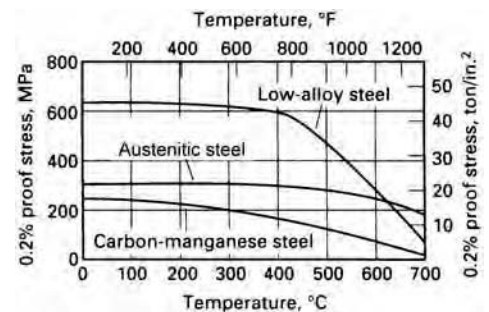


Fig. 6 Variation of yield strength with temperature for three generic classes of steel. Source: Ref 19

Compression springs, torsion springs, flat springs, and retaining rings can be stress relieved and cold set. The treatment used depends on the design and application requirements of the individual spring. Compression springs, cold wound from pretempered or hard-drawn high-carbon spring wire, should always be stress relieved to remove residual stresses produced in coiling. Extension springs are usually given a stress-relieving treatment to relieve stresses induced in forming hooks or other end configurations, but such treatment should allow retention of stresses induced for initial tension.

The treatment of wire retaining rings depends on whether the loading tends to increase or decrease the relaxed diameter of the spring. Most rings contain residual stresses in tension on the inside surface. For best performance, rings that are reduced in size in the application should not be stress relieved, while expanded rings should be. This consideration applies equally to torsion springs. It is common practice to give these springs a low-temperature heat treatment to provide dimensional stability.

Stress relieving affects the tensile strength and elastic limit, particularly for springs made from music wire and hard-drawn spring wire. The properties of both types of wire are increased by heating in the range of 230 to 260 °C (450 to 500 °F). Oil-tempered spring wire, except for the chromium-silicon grade, shows little change in either tensile strength or elastic limit after stress relieving below 315 °C (600 °F). Both properties then drop because of temper softening. Wire of chromium-silicon steel temper softens only above approximately 425 °C (800 °F).

The properties of spring steels are usually not improved by stress relieving for more than 30 min at temperature, except for age-hardenable alloys such as 631 (17-7 PH) stainless steel, which requires approximately 1 h to reach maximum strength. Typical stress-relief temperatures for steel spring wire are given in Table 3. When springs are to be used at elevated temperatures, the stress-relieving temperatures should be near the upper limit of the

range to minimize relaxation in service. Otherwise, lower temperatures are better (Ref 20).

Examples of stress-relief data are in Fig. 7 to 9 for three common spring materials (Ref 21). The data in Fig. 7 plot the effect of temperature on yield strength for a 1 h stress-relief. This is the type of analysis used to

determine recommendations for stress-relief temperatures. The data in Fig. 8 are used to refine the time required for complete stress relief. Figure 9 combines the effect of temperature for three different treatment times to quick assess optimal stress-relief temperature to achieve desired mechanical properties.

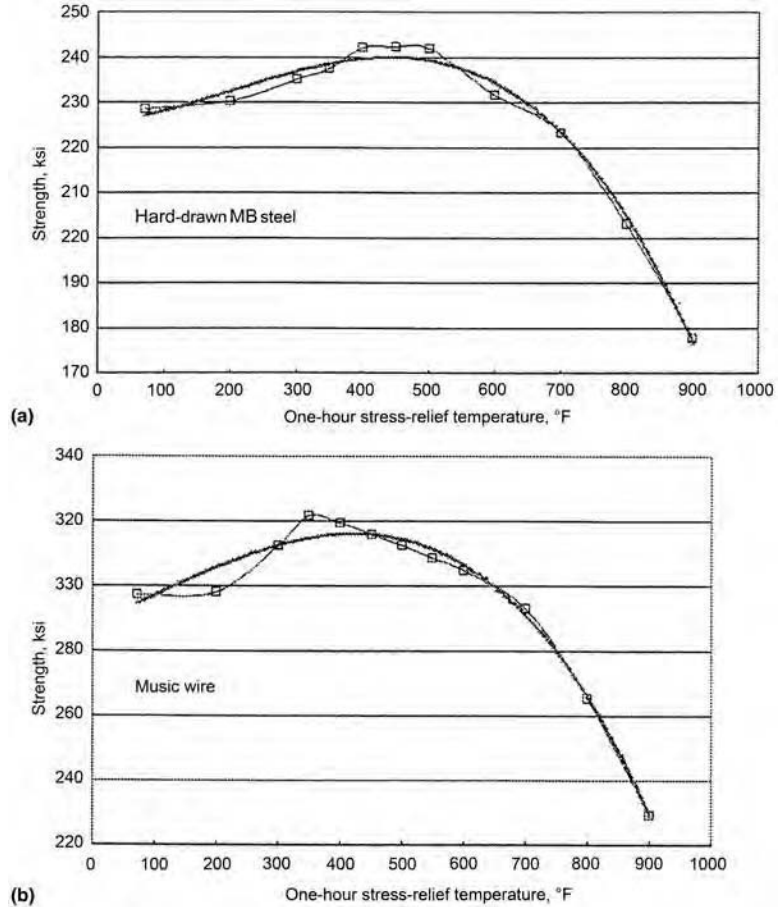


Fig. 7 Effect of temperature on 1 h stress relief of 2 mm (0.080 in.) diameter spring wire. (a) Hard-drawn carbon wire. (b) Music wire. Source: Ref 21

Table 3 Typical stress-relieving temperatures for steel spring wire

Applicable only for stress relieving after coiling and not valid for stress relieving after shot peening

Steel	Temperature(a)	
	°C	°F
Music wire	230–260	450–500
Hard-drawn spring wire	230–290	450–550
Oil-tempered spring wire	230–400	450–750(b)
Valve spring wire	315–400	600–750
Cr-V spring wire	315–400	600–750
Cr-Si spring wire	425–455	800–850
Type 302 stainless	425–480	800–900
Type 631 stainless	480 ± 6(c)	900 ± 10(c)

(a) Based on 30 min at temperature. (b) Temperature is not critical and can be varied over the range to accommodate problems of distortion, growth, and variation in wire size. (c) Based on 1 h at temperature

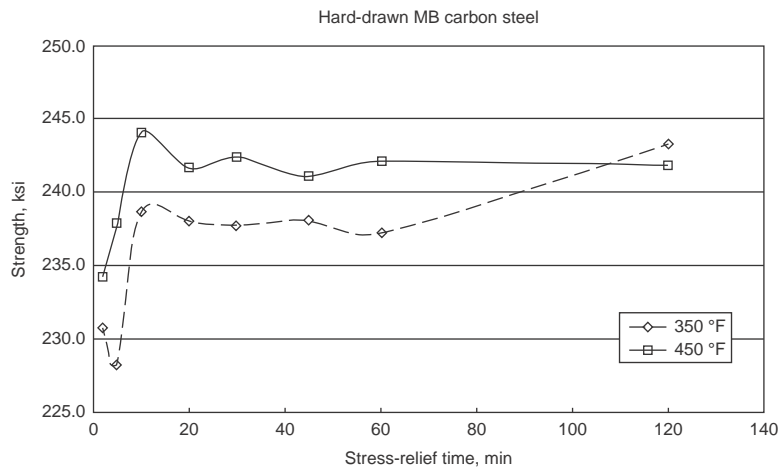


Fig. 8 Effect of stress-relief time at two temperatures for 2 mm (0.080 in.) diameter hard-drawn carbon wire. At these temperatures, the bulk of stress relief occurs after 20–30 min. Source: Ref 21

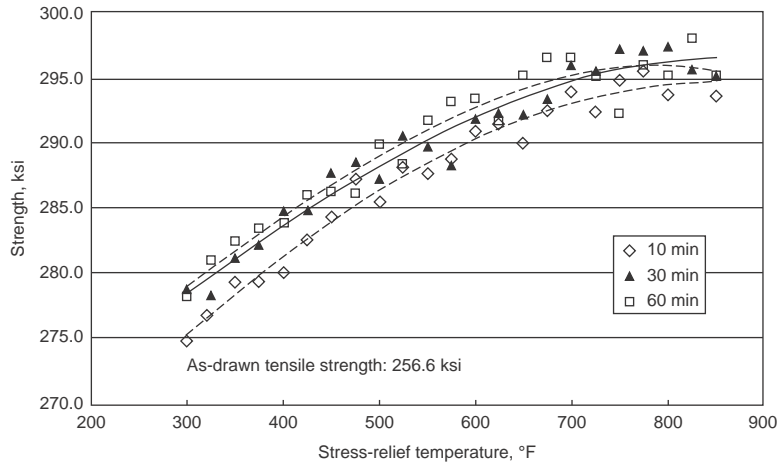


Fig. 9 Effect of stress temperature and time on 1.9 mm (0.075 in.) T-302 stainless steel wire. Source: Ref 21

REFERENCES

1. N. Bailey, The Metallurgical Effects of Residual Stresses, *Residual Stresses*, The Welding Institute, 1981, p 28–33
2. C.E. Jackson et al., *Metallurgy and Weldability of Steels*, Welding Research Council, 1978
3. Fundamentals of Welding, *Welding Handbook*, Vol 1, 7th ed., American Welding Society, 1976
4. H. Thielsch, *Defects and Failures in Pressure Vessels and Piping*, Reinhold, 1965, p 311
5. *Properties and Selection: Nonferrous Alloys and Pure Metals*, Vol 2, *Metals Handbook*, 9th ed., American Society for Metals, 1979, p 255–256
6. G.E. Dieter, *Mechanical Metallurgy*, 2nd ed., McGraw-Hill, 1976
7. J.O. Almen and P.H. Black, *Residual Stresses and Fatigue in Metals*, McGraw-Hill, 1963
8. *Machining*, Vol 3, *Metals Handbook*, 8th ed., American Society for Metals, 1967, p 260
9. R.G. Treuting, J.J. Lynch, H.B. Wishart, and D.G. Richards, *Residual Stress Measurements*, American Society for Metals, 1952, p 134
10. M. Grenier, High Speed High Precision Stress Relieving, *Springs*, Vol 41 (No. 5), Oct 2002, p 68–71
11. N. Fricker, K.F. Pomfret, and J.D. Waddington, Comm. 1072, Inst. of Gas Engineering, 44th Annual Meeting, Nov 1978
12. G.E. Totten and M.A.H. Howes, Ed., *Steel Heat Treatment Handbook*, Marcel Dekker, Inc., 1997, p 294–481
13. D. Herring, Stress Relief, *Wire Form. Technol. Int.*, Summer 2010
14. M. Grenier and R. Gingras, Rapid Tempering and Stress Relief via High-Speed Convection Heating, *Ind. Heat.*, May 2003
15. M. Grenier, R. Gingras, and G.E. Totten, Rapid Stress Relief and Tempering, *Heat Treat. Prog.*, Vol 7 (No. 4), 2007, p 36
16. A.H. Rosenstein, *J. Mater.*, Vol 6, 1971, p 265
17. C. Brooks, *Heat Treatment of Plain Carbon and Low Alloy Steels*, ASM International, 1996
18. *Properties and Selection: Stainless Steels, Tool Materials, and Special-Purpose Metals*, Vol 3, *Metals Handbook*, 9th ed., American Society for Metals, 1980, p 47–48
19. C.G. Saunders, Thermal Stress Relief and Associated Metallurgical Phenomena, *Weld. Inst. Res. Bull.*, Vol 9 (No. 7), Part 3, 1968
20. L. Godfrey, Steel Springs, *Properties and Selection: Irons, Steels, and High-Performance Alloys*, Vol 1, *ASM Handbook*, ASM International, 1990, p 302–326
21. T. Bartel, Heat Treatment, *Springs*, Oct 2007, p 13–17

Normalizing of Steel*

Introduction

Normalizing of steel is a heat treating process that is often considered from both a thermal processing and a microstructural standpoint. In terms of thermal processing, normalizing is defined as heating of a ferrous alloy to a suitable temperature above the transformation range and then cooling it in air to a temperature substantially below the transformation range. Good normalizing practice requires that:

- The piece being treated be uniformly heated to a temperature high enough to cause complete transformation of ferrite to austenite
- It remain at this temperature long enough to achieve uniform temperature throughout its mass
- It be permitted to cool in still air or in a controlled manner (such as a tunnel with cooling fans) to produce desired microstructure.

Normalizing also is described in terms of microstructure. Normalizing is used to convert

a heterogeneous structure, such as develops from a high-austenitizing-temperature treatment (e.g., during hot forging), to a finer and more uniform structure. The microstructures in Fig. 1 illustrate the effect. The annealed microstructure consists of coarse primary ferrite grains that have formed on the boundaries of large austenite grains. When the steel with this microstructure is re-austenitized in a lower temperature range, smaller austenite grains form, and a finer structure results upon air cooling (Fig. 1b).

In addition to the refinement of the prior austenite grains, there is a reduction in the size of the primary ferrite grains. This is due to the effect of the temperature of formation on the nucleation rate of these crystals. The nucleation rate of primary ferrite crystals formed isothermally is shown schematically in Fig. 2(a). In the higher temperature range, the lower the transformation temperature, the higher the nucleation rate. Figure 2(b) shows that this produces finer ferrite grains on air cooling. In

addition, the faster cooling allows less primary ferrite to form, so that more pearlite is present (Fig. 3). Also, because the pearlite forms in a lower temperature range, it will be finer and hence harder.

With appropriate processing that produces a larger percent of finer pearlite, a normalized steel would be appreciably harder than the same steel in the annealed condition. However, the purpose of normalizing varies considerably. Normalization may increase or decrease the strength and hardness of a given steel in a given product form, depending on the thermal and mechanical history of the product. The functions of normalizing may overlap with (or be confused with) those of annealing, hardening, and stress relieving. Improved machinability, grain-structure refinement, homogenization, and modification of residual stresses are among the reasons normalizing is done. Homogenization of castings by normalizing may be done to break up or refine the dendritic structure and facilitate a more even response to subsequent

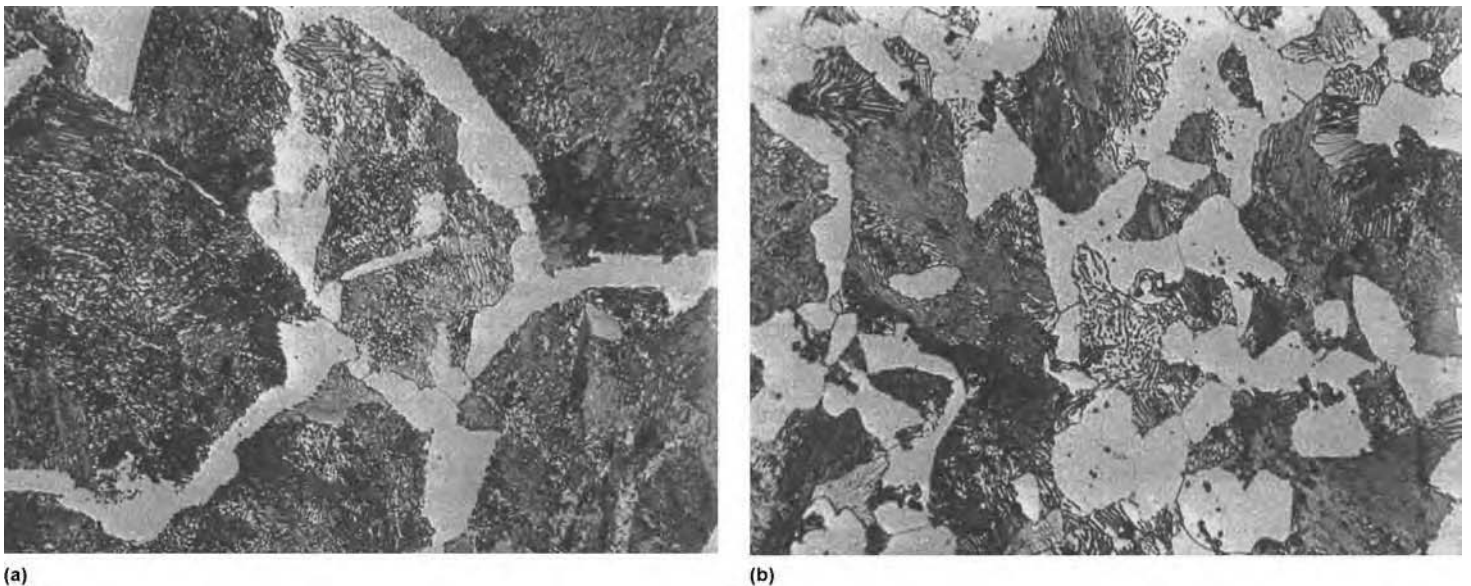


Fig. 1 Microstructures showing the refinement of primary ferrite grains by normalizing of a 0.5% C steel. (a) Air cooled from hot working range (e.g., 1200 °C, or 2190 °F). (b) Normalized after treatment in (a). Source: Ref 1

* Revised from T. Ruglic, Normalizing of Steel, *Heat Treating*, Vol 4, *ASM Handbook*, ASM International, 1991, p 35–41

hardening. Similarly, for wrought products, normalization can help reduce banded grain structure due to hot rolling, as well as large grain size or mixed large and small grain size due to forging practice.

Heating and Cooling

For normalizing, austenitizing is carried out in a temperature range slightly higher than that normally used for hardening for water quenching, to

ensure a homogeneous austenite. Typically, the work is heated to a temperature approximately 55 °C (100 °F) above the upper critical line of the iron-iron carbide phase diagram, as shown in Fig. 4; that is, above A_{c3} for hypoeutectoid steels and above A_{cm} for hypereutectoid steels. To be properly classed as a normalizing treatment, the heating portion of the process must produce a homogeneous austenitic phase prior to cooling. Figure 5 compares the time-temperature cycle of normalizing to that of full annealing. Typical normalizing temperatures for many standard steels are given in Table 1.

Uniform cooling requires free circulation of air around each piece so that there is no area in which the cooling has been restricted or accelerated. Restriction of the cooling rate will alter the operation from a normalizing to an annealing treatment.

The cooling curves in Fig. 6 demonstrate the effect of mass and section size on cooling in still air for carbon steel bars ranging from 100 to 270 mm (4 to 10½ in.) in diameter. A summary of cooling curves at the bar center is in Fig. 7. Cooling curves on a logarithmic scale are plotted in Fig. 8.

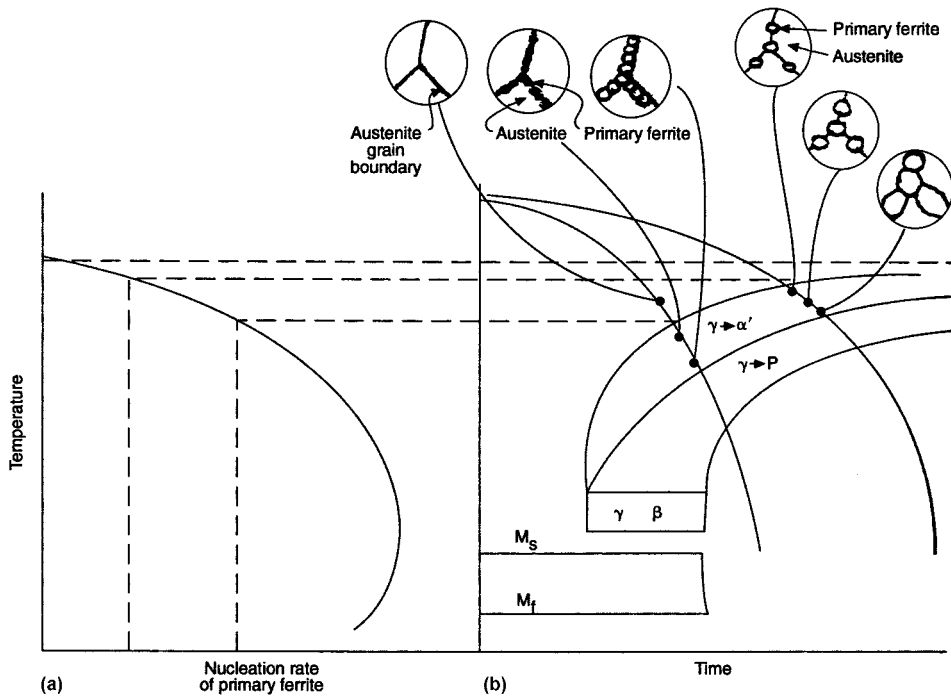


Fig. 2 Effect of normalizing process on primary ferrite formation. (a) Effect of temperature on the nucleation rate of primary ferrite at the grain boundaries of austenite. (b) Effect of cooling rate from austenite on the grain size of the primary ferrite crystals. Source: Ref 1

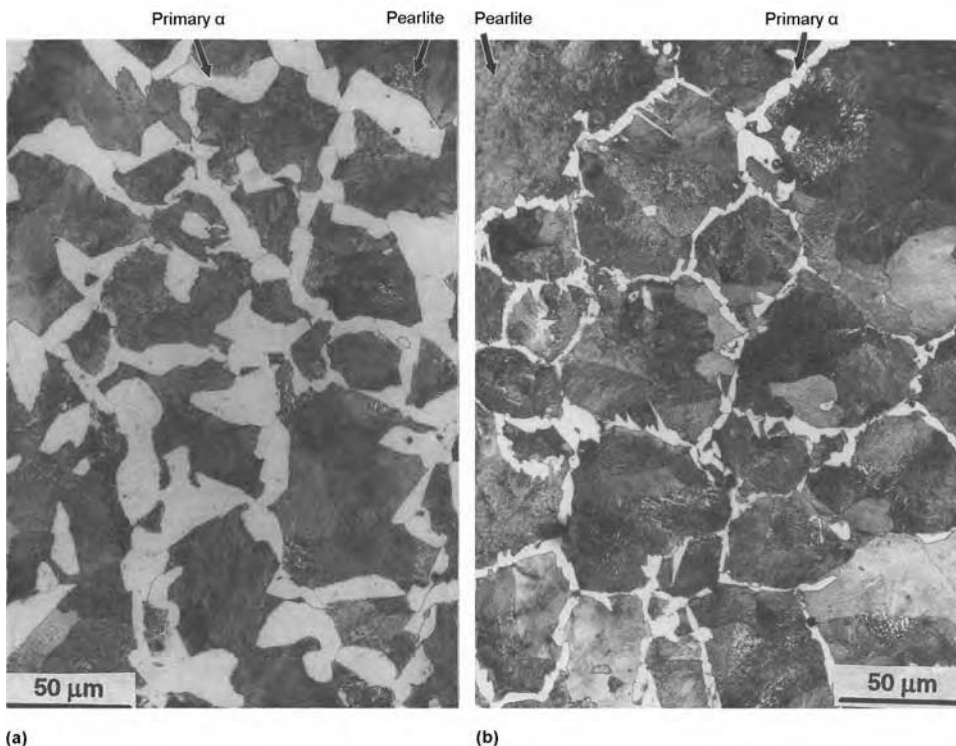


Fig. 3 Extent and finer structure of pearlite in a 0.5% C plain carbon steel from (a) furnace cooling (annealing) and (b) air cooling (normalizing). Source: Ref 1

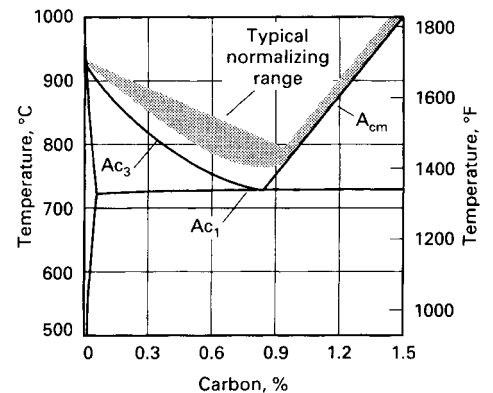


Fig. 4 Partial iron-iron carbide phase diagram showing typical normalizing range for plain carbon steels

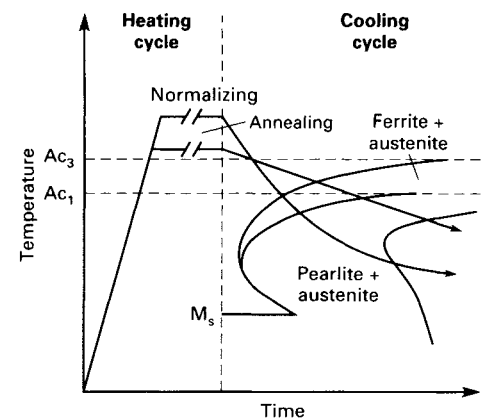


Fig. 5 Comparison of time-temperature cycles for normalizing and full annealing. The slower cooling of annealing results in higher temperature transformation to ferrite and pearlite and coarser microstructures than does normalizing. Source: Ref 2

Table 1 Typical normalizing temperatures for standard carbon and alloy steels

Grade	Temperature(a)		Grade	Temperature(a)	
	°C	°F		°C	°F
Plain carbon steels					
1015	915	1675	4815	925	1700
1020	915	1675	4817	925	1700
1022	915	1675	4820	925	1700
1025	900	1650	5046	870	1600
1030	900	1650	5120	925	1700
1035	885	1625	5130	900	1650
1040	860	1575	5132	900	1650
1045	860	1575	5135	870	1600
1050	860	1575	5140	870	1600
1060	830	1525	5145	870	1600
1080	830	1525	5150	870	1600
1090	830	1525	5155	870	1600
1095	845	1550	5160	870	1600
1117	900	1650	6118	925	1700
1137	885	1625	6120	925	1700
1141	860	1575	6150	900	1650
1144	860	1575	8617	925	1700
			8620	925	1700
			8622	925	1700
Standard alloy steels					
1330	900	1650	8625	900	1650
1335	870	1600	8627	900	1650
1340	870	1600	8630	900	1650
3135	870	1600	8637	870	1600
3140	870	1600	8640	870	1600
3310	925	1700	8642	870	1600
4027	900	1650	8645	870	1600
4028	900	1650	8650	870	1600
4032	900	1650	8655	870	1600
4037	870	1600	8660	870	1600
4042	870	1600	8720	925	1700
4047	870	1600	8740	925	1700
4063	870	1600	8742	870	1600
4118	925	1700	8822	925	1700
4130	900	1650	9255	900	1650
4135	870	1600	9260	900	1650
4137	870	1600	9262	900	1650
4140	870	1600	9310	925	1700
4142	870	1600	9840	870	1600
4145	870	1600	9850	870	1600
4147	870	1600	50B40	870	1600
4150	870	1600	50B44	870	1600
4320	925	1700	50B46	870	1600
4337	870	1600	50B50	870	1600
4340	870	1600	60B60	870	1600
4520	925	1700	81B45	870	1600
4620	925	1700	86B45	870	1600
4621	925	1700	94B15	925	1700
4718	925	1700	94B17	925	1700
4720	925	1700	94B30	900	1650
			94B40	900	1650

(a) Based on production experience, normalizing temperature may vary from as much as 27 °C (50 °F) below to as much as 55 °C (100 °F) above indicated temperature. The steel should be cooled in still air from indicated temperature.

Applications of Normalizing Based on Steel Classification

A broad range of ferrous products can be normalized. Normalizing may harden, soften, or stress relieve, depending on the condition of the product before normalizing. All of the standard low-, medium-, and high-carbon wrought steels can be normalized, as well as many castings. Many steel weldments are normalized to refine the structure within the weld-affected area. Austenitic steels, stainless steels, and maraging steels either cannot be normalized or are not usually normalized. Tool steels are generally annealed by the steel supplier.

The details of normalizing treatments applied to three typical production parts are given in

Table 2, which also lists the reasons for normalizing and gives some of the mechanical properties obtained in the normalized and tempered condition. Comparisons of typical hot-rolled or annealed mechanical properties versus typical normalized properties are presented in Table 3.

Figure 9 shows that high-carbon steels with large amounts of pearlite have high transition temperatures and therefore will fail in a brittle manner even well above room temperature. On the other hand, low-carbon steels have sub-zero transition temperatures and are quite tough at room temperature (Ref 2).

Depending on the mechanical properties required, normalizing may be substituted for conventional hardening when the size or shape of the part is such that liquid quenching may result in cracking, distortion, or excessive

dimensional changes. Thus, parts that are of complex shape or that incorporate sharp changes in section may be normalized and tempered, provided that the properties obtained are acceptable.

The rate of heating generally is not critical for normalizing; on an atomic scale, it is immaterial. In parts having great variations in section size, however, thermal stress can cause distortion.

Time at temperature is critical only in that it must be sufficient to cause homogenization. Sufficient time must be allowed for solution of thermodynamically stable carbides or for diffusion of constituent atoms. Generally, time sufficient for complete austenitization is all that is required. One hour at temperature, after the furnace recovers, per inch of part thickness, is considered to be standard. Parts often can be austenitized adequately in much less time (with a saving of energy). In cases where normalizing is done to homogenize segregated structures, longer times may be required.

The rate of cooling significantly influences both the amount of pearlite and the size and spacing of the pearlite lamellae. At higher cooling rates, more pearlite forms, and the lamellae are finer and more closely spaced. Both the increased amount of pearlite and the greater fineness of the pearlite result in higher strength and higher hardness. Conversely, lower cooling rates result in softer parts.

The effect of mass on hardness (via its effect on cooling rate) is illustrated by the data in Table 4. In any part having both thick and thin sections, the potential exists for variations in cooling rate and thus for variations in strength and hardness as well. This can also increase the probability of distortion or even cracking. Cooling rate sometimes is enhanced with fans to increase strength and hardness of parts or to decrease the time required, following the furnace operation, for sufficient cooling of parts to permit convenient handling.

After parts have cooled uniformly through their cross section to black heat below Ar_1 (the parts are no longer red, as when they were removed from the furnace), they may be water or oil quenched to decrease the total cooling time. In heavy sections, cooling of the center material to black heat may require considerable time. Thermal shock, residual thermally induced stress, and resultant distortions are factors to be considered. The microstructure remains essentially unaffected by the increased cooling rate, provided that the entire mass is below the lower critical temperature, Ar_1 , although changes involving precipitates may occur.

Carbon Steels. Table 1 lists typical normalizing temperatures for some standard grades of carbon steel. These temperatures can be interpolated to obtain values for carbon contents not listed.

Steels containing 0.20% C or less usually receive no treatment subsequent to normalizing. However, medium- or high-carbon steels are often tempered after normalizing to obtain specific properties, such as a lower hardness for

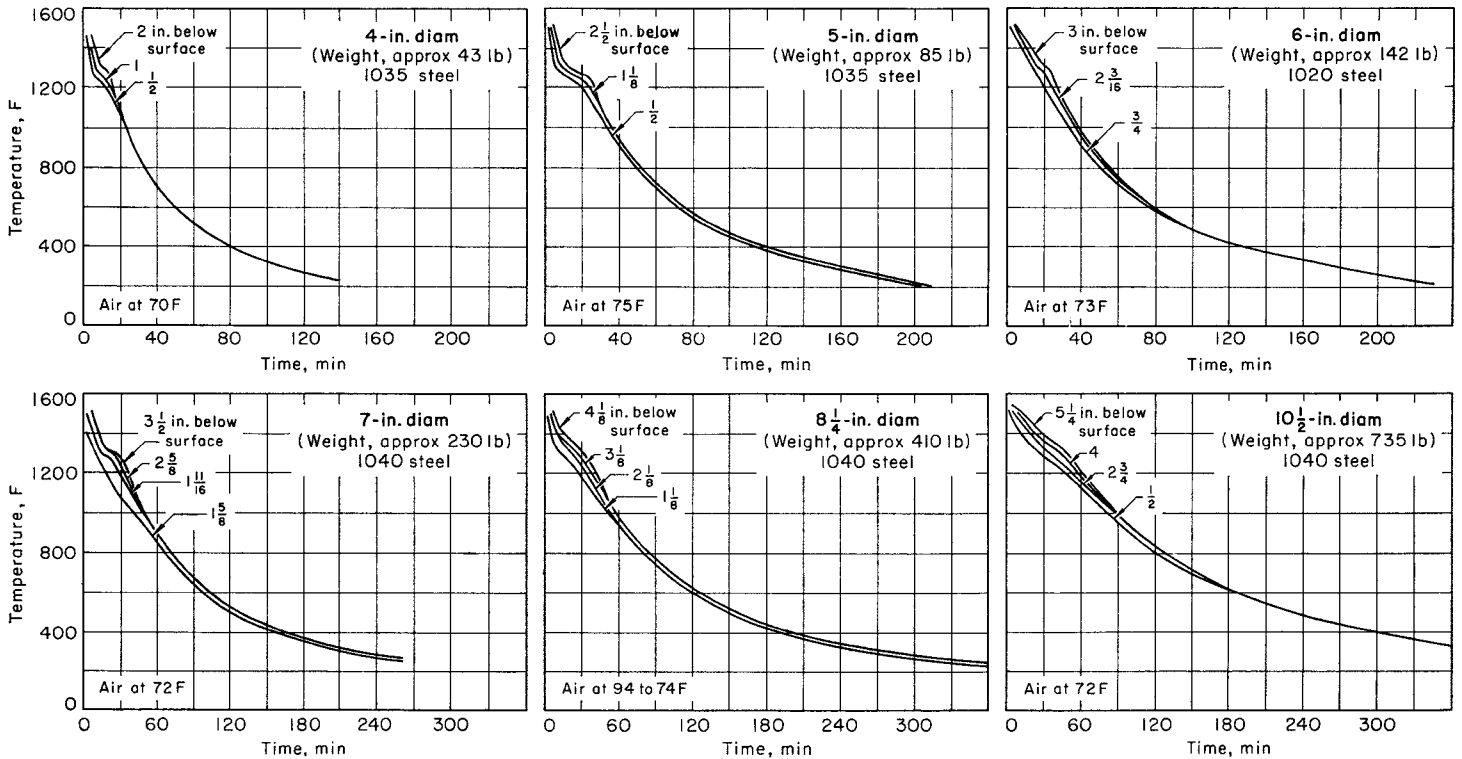


Fig. 6 Effect of mass and section on cooling curves in still air. Note the difference in the horizontal scales of the two rows.

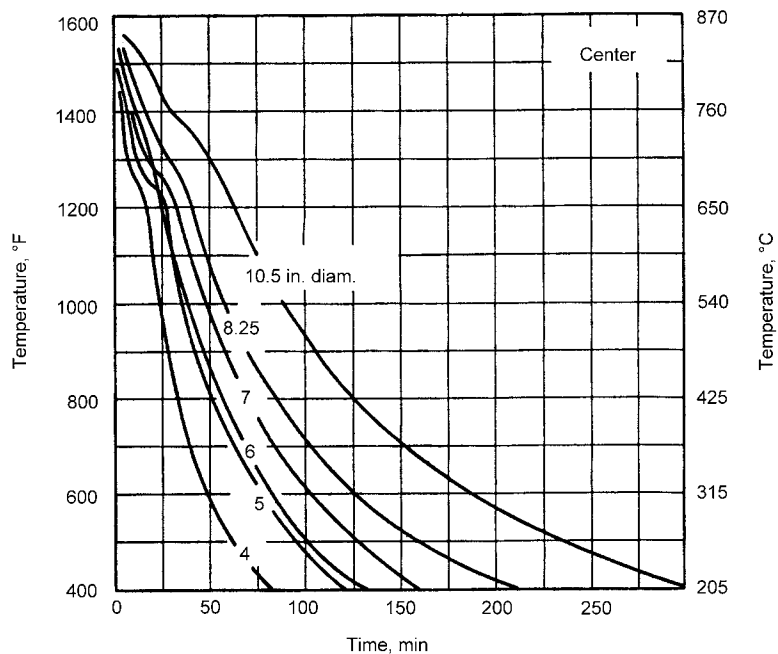


Fig. 7 Summary of center-cooling curves from Fig. 6

straightening, cold working, or machining. Whether tempering is desirable depends on specific property requirements and not on carbon content and section-size requirements. Table 3 presents typical mechanical properties of

selected carbon and alloy steels in the hot-rolled, normalized, and annealed conditions. Because of pearlite lamellae and spacing, a low- or medium-carbon steel of thin section may be harder after normalizing than a high-

carbon steel of large section size subjected to the same treatment.

Alloy Steels. For alloy steel forgings, rolled products, and castings, normalizing is commonly used as a conditioning treatment before final heat treatment. Normalizing also refines the structures of forgings, rolled products, and castings that have cooled nonuniformly from high temperatures. Table 1 lists typical normalizing temperatures for some standard alloy steels. Alloy carburizing steels such as 3310 and 4320 usually are normalized at temperatures higher than the carburizing temperature to minimize distortion in carburizing and to improve machining characteristics. Carburizing steels of the 3300 series sometimes are double normalized, with the expectation of minimizing distortion; these steels are tempered at approximately 650 °C (1200 °F) for intervals of up to 15 h to reduce hardness to below 223 HB for machinability. Carburizing steels of the 4300 and 4600 series usually can be normalized to a hardness not exceeding 207 HB and therefore need not be tempered for machinability.

Hypereutectoid alloy steels such as 52100 are normalized for partial or complete elimination of carbide networks, thus producing a structure that is more susceptible to 100% spheroidization in the subsequent spheroidize annealing treatment. The spheroidized structure provides improved machinability and a more uniform response to hardening.

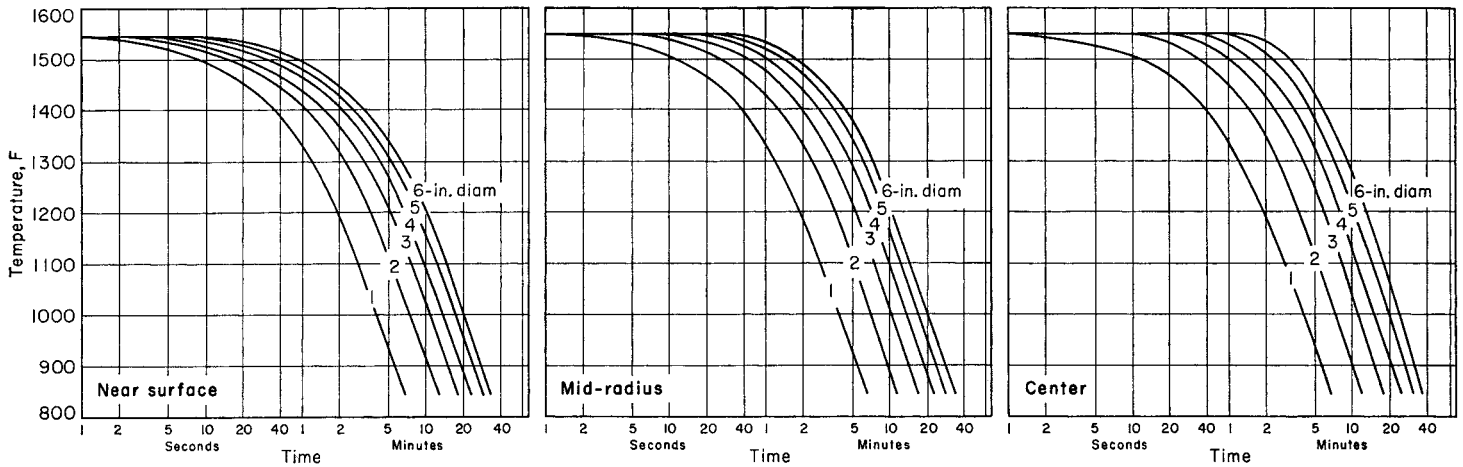


Fig. 8 Logarithmic time scale of cooling curves for steel bar of various diameters

Table 2 Typical applications of normalizing and tempering of steel components

Part	Steel	Heat treatment	Properties after treatment	Reason for normalizing
Cast 50 mm (2 in.) valve body, 19 to 25 mm (3/4 to 1 in.) in section thickness	Ni-Cr-Mo	Full annealed at 955 °C (1750 °F), normalized at 870 °C (1600 °F), tempered at 665 °C (1225 °F)	Tensile strength, 620 MPa (90 ksi); 0.2% yield strength, 415 MPa (60 ksi); elongation in 50 mm, or 2 in., 20%; reduction in area, 40%	To meet mechanical-property requirements
Forged flange	4137	Normalized at 870 °C (1600 °F), tempered at 570 °C (1060 °F)	Hardness, 200 to 225 HB	To refine grain size and obtain required hardness
Valve-bonnet forging	4140	Normalized at 870 °C (1600 °F) and tempered	Hardness, 220 to 240 HB	To obtain uniform structure, improved machinability, and required hardness

Some alloy grades require more care in heating to prevent cracking from thermal shock. They also require longer soaking times because of lower austenitizing and solution rates. For many alloy steels, rates of cooling in air to room temperature must be carefully controlled. Certain alloy steels are forced-air cooled from the normalizing temperature in order to develop specific mechanical properties.

Forgings

When forgings are normalized before carburizing or before hardening and tempering, the upper range of normalizing temperatures is used. However, when normalizing is the final heat treatment, use is made of the lower range of temperatures.

Furnaces. Any appropriately sized furnace may be used for normalizing. Furnace type and size will depend upon the specific need. In a continuous furnace, forgings to be normalized are usually placed in shallow pans, and a pusher mechanism at the loading end of the furnace transports the pans through the furnace. Furnace burners located on both sides of the furnace fire below the hearth, and

combustion products rise along the walls of the work-zone muffle and exhaust into the roof of the furnace. No atmosphere control is used. Combustion products enter the work zone through ports lining both sides of the entire hearth. A typical furnace is 9 m (30 ft) long and has 18 gas burners (or 9 oil burners) on each side. For purposes of temperature control, such a furnace is divided into three 3 m (10 ft) zones, each having a vertical thermocouple extending into it through the roof of the furnace.

Processing. Small forgings are usually normalized as received from the forge shop. A typical furnace has five pans in each of the three furnace zones. Heating is adjusted so that the work reaches normalizing temperature in the last zone. After passing through the last zone, the pans are discharged onto a cooling conveyor. The work, while still in the pans, is cooled in still air to below 480 °C (900 °F); it is then discharged into tote boxes, where it cools to room temperature. Total furnace time is approximately 3½ h, but during this period the work is held at the normalizing temperature for only 1 h.

Normalizing of large open-die forgings usually is performed in batch-type furnaces

pyrometrically controlled to narrow temperature ranges. Forgings are held at the normalizing temperature long enough to allow complete austenitizing and carbide solution to occur (usually one hour per inch of section thickness) and then are cooled in still air.

Axle-Shaft Forging. In forging an axle shaft made of fine-grained 1049 steel, only one end of the forging bar was heated to upset the wheel-flange section. When the part was examined in cross section from the flanged end to the cold end, the metallurgical conditions discussed subsequently were revealed.

The hot-worked flanged area of the axle exhibited a fine-grained structure as a result of the hot working at the forging temperature (approximately 1095 °C, or 2000 °F). However, a section adjacent to the flange, which also had been heated to the forging temperature but which had not been hot worked, exhibited a coarse-grained structure. Nearer the cool end of the shaft, a zone that reached a temperature of approximately 705 °C (1300 °F) exhibited a spheroidized structure. The cold end of the shaft retained its initial fine grain size throughout the forging operation.

In subsequent operations, this shaft was to be mechanically straightened, machined, and induction hardened. Because of the mixed grain structure, these operations posed several problems. The coarse-grained area adjacent to the flange was extremely weak in the transverse direction, and there was a possibility that fracture would occur if this section were subjected to a severe straightening operation. The spheroidized area would not respond adequately to induction hardening because the solution rate of this type of carbide formation was too sluggish for the relatively rapid rate of induction heating. Furthermore, the mixed metallurgical structure would present difficulties in machining. Consequently, normalizing was required in order to produce a uniformly fine-grained structure throughout the axle shaft

Table 3 Properties of selected carbon and alloy steels in the hot-rolled, normalized, and annealed conditions

AISI grade(a)	Condition or treatment	Tensile strength		Yield strength		Elongation(b), %	Reduction in area, %	Hardness, HB	Izod impact strength	
		MPa	ksi	MPa	ksi				J	ft · lbf
1015	As-rolled	420	61	315	46	39.0	61	126	111	82
	Normalized at 925 °C (1700 °F)	425	62	325	47	37.0	70	121	115	85
1020	As-rolled	385	56	285	41	37.0	70	111	115	85
	Normalized at 870 °C (1600 °F)	450	65	330	48	36.0	59	143	87	64
1022	As-rolled	440	64	345	50	35.8	68	131	118	87
	Normalized at 870 °C (1600 °F)	395	57	295	43	36.5	66	111	123	91
1030	As-rolled	505	73	360	52	35.0	67	149	81	60
	Normalized at 925 °C (1700 °F)	485	70	360	52	34.0	68	143	117	87
1040	As-rolled	450	65	315	46	35.0	64	137	121	89
	Normalized at 870 °C (1600 °F)	550	80	345	50	32.0	57	179	75	55
1050	As-rolled	525	76	345	50	32.0	61	149	94	69
	Normalized at 925 °C (1700 °F)	460	67	345	50	31.2	58	126	69	51
1060	As-rolled	620	90	415	60	25.0	50	201	49	36
	Normalized at 900 °C (1650 °F)	595	86	370	54	28.0	55	170	65	48
1080	As-rolled	520	75	350	51	30.2	57	149	45	33
	Normalized at 870 °C (1600 °F)	725	105	415	60	20.0	40	229	31	23
1095	As-rolled	750	109	430	62	20.0	39	217	27	20
	Normalized at 900 °C (1650 °F)	635	92	365	53	23.7	40	187	18	13
1100	As-rolled	815	118	485	70	17.0	34	241	18	13
	Normalized at 900 °C (1650 °F)	775	113	420	61	18.0	37	229	14	10
1117	As-rolled	625	91	370	54	22.5	38	179	11	8
	Normalized at 900 °C (1650 °F)	965	140	585	85	12.0	17	293	7	5
1118	As-rolled	1015	147	525	76	11.0	21	293	7	5
	Normalized at 900 °C (1650 °F)	615	89	380	55	24.7	45	174	7	5
1137	As-rolled	965	140	570	83	9.0	18	293	4	3
	Normalized at 900 °C (1650 °F)	1015	147	505	73	9.5	14	293	5	4
1141	As-rolled	655	95	380	55	13.0	21	192	3	2
	Normalized at 900 °C (1650 °F)	490	71	305	44	33.0	63	143	81	60
1144	As-rolled	470	68	305	44	33.5	54	137	85	63
	Normalized at 860 °C (1575 °F)	430	62	285	41	32.8	58	121	94	69
1188	As-rolled	525	76	315	46	32.0	70	149	109	80
	Normalized at 925 °C (1700 °F)	475	69	315	46	33.5	66	143	103	76
1137	As-rolled	450	65	285	41	34.5	67	131	107	79
	Normalized at 870 °C (1600 °F)	625	91	380	55	28.0	61	192	83	61
1141	As-rolled	670	97	400	58	22.5	49	197	64	47
	Normalized at 900 °C (1650 °F)	585	85	345	50	26.8	54	174	50	37
1144	As-rolled	675	98	360	52	22.0	38	192	11	8
	Normalized at 900 °C (1650 °F)	710	103	405	59	22.7	56	201	53	39
1340	As-rolled	600	87	355	51	25.5	49	163	34	25
	Normalized at 815 °C (1500 °F)	705	102	420	61	21.0	41	212	53	39
3140	As-rolled	670	97	400	58	21.0	40	197	43	32
	Normalized at 900 °C (1650 °F)	585	85	345	50	24.8	41	167	65	48
4130	As-rolled	835	121	560	81	22.0	63	248	92	68
	Normalized at 870 °C (1600 °F)	705	102	435	63	25.5	57	207	71	52
4140	As-rolled	890	129	600	87	19.7	57	262	54	40
	Normalized at 870 °C (1600 °F)	690	100	420	61	24.5	51	197	46	34
4150	As-rolled	670	97	435	63	25.5	60	197	87	64
	Normalized at 865 °C (1585 °F)	560	81	360	52	28.2	56	156	62	46
4320	As-rolled	1020	148	655	95	17.7	47	302	23	17
	Normalized at 870 °C (1600 °F)	655	95	420	61	25.7	57	197	54	40
4340	As-rolled	1160	168	740	107	11.7	31	321	12	9
	Normalized at 870 °C (1600 °F)	730	106	380	55	20.2	40	197	24	18
4620	As-rolled	795	115	460	67	20.8	51	235	73	54
	Normalized at 895 °C (1640 °F)	580	84	430	62	29.0	58	163	110	81
4820	As-rolled	1280	186	860	125	12.2	36	363	16	12
	Normalized at 870 °C (1600 °F)	745	108	475	69	22.0	50	217	52	38
5140	As-rolled	570	83	365	53	29.0	67	174	135	98
	Normalized at 900 °C (1650 °F)	510	74	370	54	31.3	60	149	94	69
5150	As-rolled	760	110	485	70	24.0	59	229	110	81
	Normalized at 860 °C (1580 °F)	685	99	460	67	22.3	59	197	94	69
5160	As-rolled	795	115	475	69	22.7	59	229	38	28
	Normalized at 830 °C (1525 °F)	570	83	295	43	28.6	57	167	41	30
6150	As-rolled	870	126	530	77	20.7	59	255	31	23
	Normalized at 870 °C (1600 °F)	675	98	360	52	22.0	44	197	26	19
8620	As-rolled	960	139	530	77	17.5	45	269	11	8
	Normalized at 860 °C (1575 °F)	725	105	275	40	17.2	31	197	10	7
8630	As-rolled	940	136	615	89	21.8	61	269	35	26
	Normalized at 870 °C (1600 °F)	665	97	415	60	23.0	48	197	27	20
8650	As-rolled	635	92	360	52	26.3	60	183	100	74
	Normalized at 910 °C (1675 °F)	540	78	385	56	31.3	62	149	115	83
8740	As-rolled	650	94	430	62	23.5	54	187	95	70
	Normalized at 870 °C (1600 °F)	565	82	370	54	29.0	59	156	95	70
9255	As-rolled	1025	149	690	100	14.0	45	302	14	10
	Normalized at 870 °C (1600 °F)	715	104	385	56	22.5	46	212	30	22
9310	As-rolled	930	135	605	88	16.0	48	269	18	13
	Normalized at 870 °C (1600 °F)	695	101	415	60	22.2	46	201	41	30
9310	As-rolled	930	135	580	84	19.7	43	269	14	10
	Normalized at 900 °C (1650 °F)	775	112	490	71	21.7	41	229	10	7
9310	As-rolled	910	132	570	83	18.8	58	269	119	88
	Normalized at 890 °C (1630 °F)	820	119	440	64	17.3	42	241	79	58
9310	As-rolled									
	Normalized at 845 °C (1550 °F)									

(a) All grades are fine grained except for those in the 1100 series, which are coarse grained. (b) In 50 mm (2 in.)

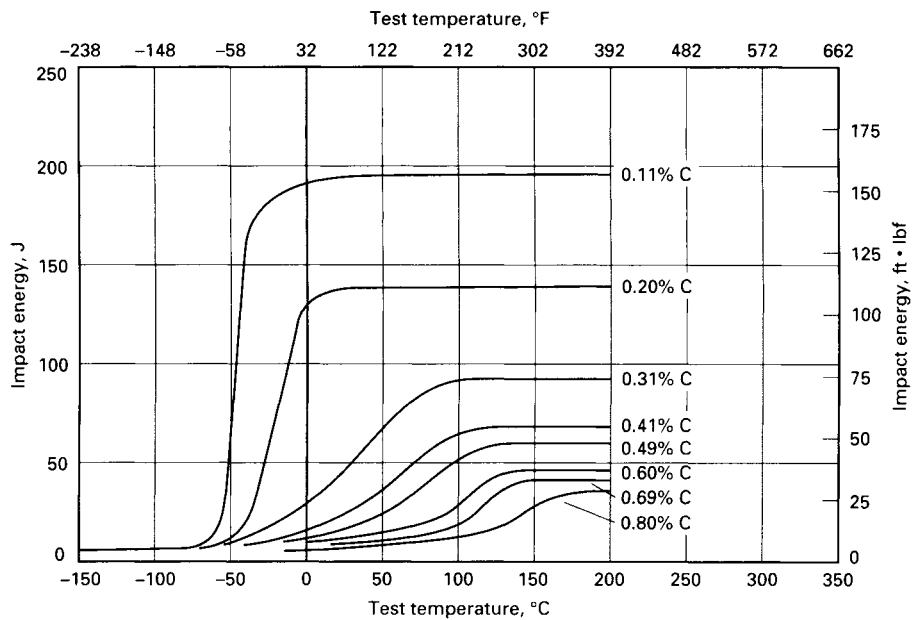


Fig. 9 Change in impact transition curves with increasing pearlite content in normalized carbon steels. Source: Ref 2

prior to straightening, machining, and induction hardening.

Low-Carbon Steel Forgings. In contrast to the medium-carbon axle shaft discussed in the preceding paragraphs, forgings made of carbon steels containing 0.25% C or less are seldom normalized. Only severe quenching from above the austenitizing temperature will have any significant effect on their structure or hardness.

Structural Stability. Normalizing and tempering is also a preferred treatment for promoting the structural stability of low-alloy heat-resistant alloys, such as AMS 6304 (0.45% C, 1% Cr, 0.5% Mo, and 0.3% V), at temperatures up to 540 °C (1000 °F). Wheels and spacer rings used in the cold ends of aircraft gas-turbine engine compressors are typical of parts subjected to such treatment to promote structural stability.

Multiple normalizing treatments are employed to obtain complete solution of all lower-temperature constituents in austenite by the use of high initial normalizing temperatures (for example, 925 °C, or 1700 °F) and to refine final pearlite grain size by the use of a second normalizing treatment at a temperature closer to the A_{c3} temperature (for example, 815 °C, or 1500 °F) without destroying the beneficial effects of the initial normalizing treatment. Double normalizing is usually applied to carbon and low-alloy steels of large dimension where extremely high forging temperatures have been used (Ref 5). Locomotive-axle forgings made of carbon steel to Association of American Railroads Specification M-126, Class F (ASTM A236, Class F), containing 0.45 to 0.59% C and 0.60 to 0.90% Mn, are double normalized to obtain a uniformly fine grain structure along with other exacting mechanical-property requirements. Forgings made of a low-carbon

steel (0.18% C) with 1% Mn intended for low-temperature service are double normalized to meet subzero impact requirements.

Bar and Tubular Products

Frequently, the finishing stages of hot-mill operations employed in making steel bar and tube produce properties that closely approximate those obtained by normalizing. When this occurs, normalizing is unnecessary and may even be inadvisable. Nevertheless, the reasons for normalizing bar and tube products are generally the same as those applicable to other forms of steel.

The machinability of steel bars and tubular products depends on a combination of hardness properties and microstructure. For a low-carbon alloy steel, a coarse pearlitic structure obtained by normalizing or annealing maximizes machinability. In the case of medium-carbon alloy steel, a lamellar pearlitic structure obtained by annealing is desirable in order to optimize machinability. For a high-carbon alloy steel, a spheroidized structure lowers the hardness and increases the machinability of the alloy. Prior processing, part configuration, and processing following machining should be taken into consideration when determining the need for annealing or normalization.

In general, annealing improves machinability more than normalization does. Normalizing is used to correct the effects of spheroidization, but the steel bar or tube still needs to be annealed. Multiple anneals and tempering are normally used on only small-diameter parts such as wire gage products. Type 4340 is one of the few steels that is typically delivered to

Table 4 Effect of mass on hardness of normalized carbon and alloy steels

Grade	Normalizing temperature		Hardness, HB, for bar with diameter, mm (in.), of:			
	°C	°F	13 (½)	25 (1)	50 (2)	100 (4)
Carbon steels, carburizing grades						
1015	925	1700	126	121	116	116
1020	925	1700	131	131	126	121
1022	925	1700	143	143	137	131
1117	900	1650	143	137	137	126
1118	925	1700	156	143	137	131
Carbon steels, direct-hardening grades						
1030	925	1700	156	149	137	137
1040	900	1650	183	170	167	167
1050	900	1650	223	217	212	201
1060	900	1650	229	229	223	223
1080	900	1650	293	293	285	269
1095	900	1650	302	293	269	255
1137	900	1650	201	197	197	192
1141	900	1650	207	201	201	201
1144	900	1650	201	197	192	192
Alloy steels, carburizing grades						
3310	890	1630	269	262	262	248
4118	910	1670	170	156	143	137
4320	895	1640	248	235	212	201
4419	955	1750	149	143	143	143
4620	900	1650	192	174	167	163
4820	860	1580	235	229	223	212
8620	915	1675	197	183	179	163
9310	890	1630	285	269	262	255
Alloy steels, direct-hardening grades						
1340	870	1600	269	248	235	235
3140	870	1600	302	262	248	241
4027	905	1660	179	179	163	156
4063	870	1600	285	285	285	277
4130	870	1600	217	197	167	163
4140	870	1600	302	302	285	241
4150	870	1600	375	321	311	293
4340	870	1600	388	363	341	321
5140	870	1600	235	229	223	217
5150	870	1600	262	255	248	241
5160	855	1575	285	269	262	255
6150	870	1600	285	269	262	255
8630	870	1600	201	187	187	187
8650	870	1600	363	302	293	285
8740	870	1600	269	269	262	255
9255	900	1650	277	269	269	269

Note: All data are based on single heats. Source: Ref 3, 4

the customer with a normalized heat treatment, due to machining specifications standard in the aircraft industry.

Tubes are easier to normalize than bars of equivalent diameter, because the lighter section thickness of tubes permits more rapid heating and cooling. These advantages help minimize decarburization and promote more nearly uniform microstructures in tube products.

Furnace Requirements. Continuous furnaces of the roller-hearth type are widely used for normalizing tube and bar products, especially in long lengths. Batch-type furnaces or other types of continuous furnaces are satisfactory if they provide some means for rapid discharge and separation of the load to permit free circulation of air around each tube as it cools. Continuous furnaces should have at least two zones: one for heating and one for soaking. Cooling facilities should be ample so that

uniform cooling can proceed until complete transformation has occurred. If tubes are packed or bundled during cooling from a high temperature, the purpose of normalizing is defeated, and a semiannealed or a tempered product results.

Generally, protective atmospheres are not used in roller-hearth continuous furnaces for normalizing bar or tube products. The scale that forms during normalizing is removed by acid pickling or abrasive blast cleaning.

Castings

In industrial practice, steel castings may be normalized in car-bottom, box, pit, or continuous furnaces. The same heat treating principles apply to each type of furnace. The effect of normalizing on hardness and toughness is compared with annealing and quench-temper treatments in Fig. 10 and 11, respectively.

Furnace Loading. Furnaces are loaded with castings in such a manner that each casting will receive an adequate and uniform heat supply. This may be accomplished by stacking castings in regular order or by interspersing large and small castings so that load concentration in any one area is not excessive. At normalizing temperatures, the tensile strength of steel is greatly reduced, and heavy unequal sections may become distorted unless bracing and support are provided. Accordingly, small and large castings may be arranged so that they support each other.

Loading Temperature. When castings are charged, the temperature of the furnace should be such that the thermal shock will not cause metal failure. For the higher-alloy grades of steel castings, such as C5, C12, and WC9, a safe furnace temperature for charging is 315 to 425 °C (600 to 800 °F). For lower-alloy

grades, furnace temperatures may be as high as 650 °C (1200 °F). For cast carbon steels and low-alloy steels with low carbon contents (low hardenability), castings may be charged into a furnace operating at the normalizing temperature.

Heating. After the furnace has been charged, the temperature is increased at a rate of approximately 225 °C/h (400 °F/h) until the normalizing temperature is reached. Depending on steel composition and casting configuration, a reduction in the rate of heating to approximately 28 to 55 °C/h (50 to 100 °F/h) may be necessary to avoid cracking. Extremely large castings should be heated more slowly to prevent development of extreme temperature gradients.

Soaking. After the normalizing temperature has been reached, castings are soaked at this temperature for a period that will ensure complete austenitization and carbide solution. The duration of the soaking period may be predetermined by microscopic examination of specimens held for various times at the normalizing temperature.

Cooling. After the soaking period, the castings are unloaded and allowed to cool in still air. Use of fans, air blasts, or other means of accelerating the cooling process should be avoided.

Sheet and Strip

Hot-rolled steel sheet and strip (approximately 0.10% C) are normalized primarily to refine grain size, to minimize directional properties, and to develop desirable mechanical properties. Uniformly fine equiaxed ferrite grains are normally obtained in hot-rolled sheet and strip by finishing the final hot-rolling operation above the upper transformation temperature. However, if part of the hot-rolling

operation is performed on steel that has transformed partially to ferrite, the deformed ferrite grains usually will recrystallize and form abnormally coarse-grained patches during the self-anneal induced by coiling or piling at temperatures of 650 to 730 °C (1200 to 1350 °F). Also, relatively thin hot-rolled material, if it is inadvertently finished well below the upper transformation temperature and coiled or piled while it is too cold to self-anneal, may possess directional properties. These conditions are unsuitable for some types of severe press-drawing applications and may be corrected by normalizing.

Normalizing also may be used to develop high strength in alloy steel sheet and strip if the products are sufficiently high in carbon and alloy contents to enable them to transform to fine pearlite or martensite when cooled in air from the normalizing temperature. In general, the hardened material is tempered to attain an optimum combination of strength and ductility. Typical mechanical properties of normalized 4130, modified 4335, and modified 4340 steel sheet are given in Table 5.

Processing. The normalizing operation consists of passing the sheet or strip through an open, continuous furnace where the material is heated to a temperature approximately 55 to 85 °C (100 to 150 °F) above its upper transformation temperature, 845 to 900 °C (1550 to 1650 °F), thus obtaining complete solution of the original structure with the formation of austenite and then air cooling the material to room temperature.

Furnace Equipment. Normalizing furnaces are designed to heat and cool sheets singly or two in a pile. They are built in the form of long, low chambers and usually comprise three sections: a preheating zone (12 to 20% of the total length); a heating, or soaking, zone (approximately 40% of the total length); and a cooling zone, which occupies the remaining 40 to 50% of the length.

Heating Arrangements. Normalizing furnaces usually are heated with gas or oil and do not employ protective atmospheres. Therefore, sheets are scaled during heat treatment. Burners are arranged along each side of the heating zone; they usually are above the conveyor but occasionally are both above and below it. The furnace roof, which is higher in the preheating and soaking zones than in the cooling zone, is usually built in sections. In most furnaces, both the preheating zone and the cooling zone are heated by the hot gases from the heating zone. However, both of these zones may be equipped with burners for more accurate temperature control. Air is excluded by regulating the draft to maintain a slight pressure within all zones.

Conveyor-Type Furnaces. In modern furnaces of the conveyor type (the only type suitable for treating short lengths), sheets are carried through each of the three zones on rotating disks made of heat-resistant alloys. These disks have polished surfaces, which prevent

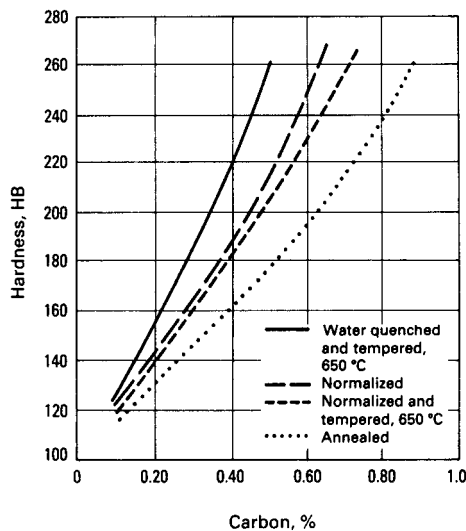


Fig. 10 Brinell hardness of cast carbon steels as a function of carbon content and heat treatment. Source: Ref 6

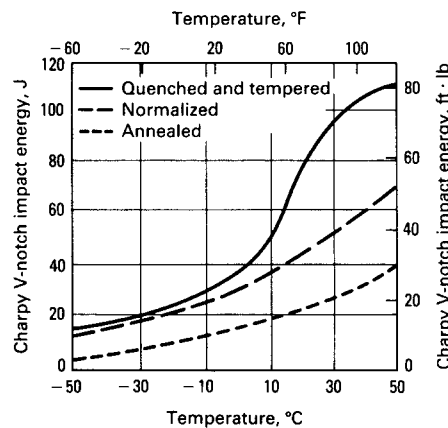


Fig. 11 Effect of various heat treatments on the Charpy V-notch impact energy of a 0.30% C steel. Source: Ref 6

Table 5 Typical mechanical properties of normalized alloy steel sheet

Grade	Thickness		Tensile strength		Yield strength(a)		Elongation(b), %	Hardness, HRC
	mm	in.	MPa	ksi	MPa	ksi		
4130	4.9	0.193	835	121	585	85	14	25
4335(c)	4.6	0.180	1725	250	1240	180	8	48
4340(c)	2.0	0.080	1860	270	1345	195	7	50

(a) At 0.2% offset. (b) In 50 mm (2 in.). (c) Modified: 0.40% Mo, 0.20% V

them from scratching the sheets, and are staggered to ensure uniform heating. The disks are mounted on water-cooled shafts, which are driven by variable-speed motors through chains and sprockets or shafts and gears. These furnaces may be up to 2.5 m (100 in.) wide and from 27 to 61 m (90 to 200 ft) long. Fuel consumption is 2.3 to 5.2×10^6 kJ/tonne (2.0 to 4.5×10^6 Btu/ton) of steel treated, and production rates vary from 2.7 to 10.9 tonnes (3 to 12 tons) per hour.

Normalizing in a three-zone conveyor-type furnace equipped with pyrometric controls is a relatively simple operation. If scratching of sheets is to be avoided, the sheets are brought to the charging table and hand laid, one or more at a time, on a rider or conveyor sheet. Heavy sheets are normalized singly, but lighter sheets may be stacked two in a pile. To control heating and retard scaling, single sheets may be laid on a rider sheet and covered with a cover sheet. Sheets are carried by disk-rollers into the preheating zone, where they absorb heat rapidly because of the large temperature differential between the sheets and the interior of the furnace and because of the large surface-to-

volume ratio. As the sheets become heated and the temperature differential is reduced, the rate of heat absorption slackens. After traveling $4\frac{1}{2}$ to 6 m (15 to 20 ft), the sheets enter the soaking zone at a temperature several degrees below the normalizing temperature. Heating is completed in the soaking zone, which is maintained at a constant temperature, and sheets are held at the required temperature for a time sufficient to convert the microstructure to austenite before they are passed into the cooling zone. The sheets emerge from the cooling zone at a temperature that can be varied between 150 and 540 °C (300 and 1000 °F) and are conveyed for a short distance on the runout table, where, after being cooled rapidly in air, they are carefully removed from the rider sheet. The trip through such a furnace is carried out at a uniform speed of 0.03 to 0.10 m/s (5 to 20 ft/min) and requires 5 to 20 min to complete.

Catenary Furnaces. The catenary, or free-loop, type of furnace is designed for continuous normalizing of cold-reduced steel unwound from coils; it does not have rolls or any other type of conveyor for supporting the material passing through the heating zone. The heating

zones of catenary furnaces range in length from 6 to 15 m (20 to 50 ft). The preheating and cooling zones usually are shorter than those in conveyor-type furnaces and, for some kinds of work, may be omitted entirely. At their exit ends, catenary furnaces may incorporate pickling or other descaling equipment for removing surface oxides formed on the steel during normalizing.

ACKNOWLEDGMENTS

Portions of this article were adapted from content by the late Professor Brooks published in C.R. Brooks, *Principles of the Heat Treatment of Plain Carbon and Low-Alloy Steels*, ASM International, 1996

REFERENCES

1. C.R. Brooks, *Principles of the Heat Treatment of Plain Carbon and Low-Alloy Steels*, ASM International, 1996
2. G. Krauss, *Steels: Heat Treatment and Processing Principles*, ASM International, 1990
3. *Modern Steels and Their Properties*, 6th ed., Bethlehem Steel Corporation, 1966
4. *Modern Steels and Their Properties*, Handbook 3310, Bethlehem Steel Corporation, Sept 1978
5. A.K. Sinha, *Ferrous Physical Metallurgy*, Butterworths, 1989
6. D. Poweleit, *Steel Castings Properties, Casting*, Vol 15, *ASM Handbook*, ASM International, 2008, p 949–974

Annealing of Steel*

Revised by Satyam S. Sahay, John Deere Asia Technology Innovation Center, Pune, India

ANNEALING is a generic term denoting a treatment that consists of heating to and holding at a suitable temperature followed by cooling at an appropriate rate, primarily for the softening of metallic materials. Generally, annealing is done by heating in furnaces, although at times, annealing by induction heating is also done when rapid heating is an effective method (such as annealing of wire after drawing).

Metallurgical Principles

Generally, in plain carbon steels, annealing produces a ferrite-pearlite microstructure (Fig. 1). Steels may be annealed to facilitate cold working or machining, to improve mechanical or electrical properties, or to promote dimensional stability.

The iron-carbon binary phase diagram (Fig. 2) can be used to better understand annealing processes (Ref 1). Although no annealing process ever achieves true equilibrium conditions, it can closely parallel these

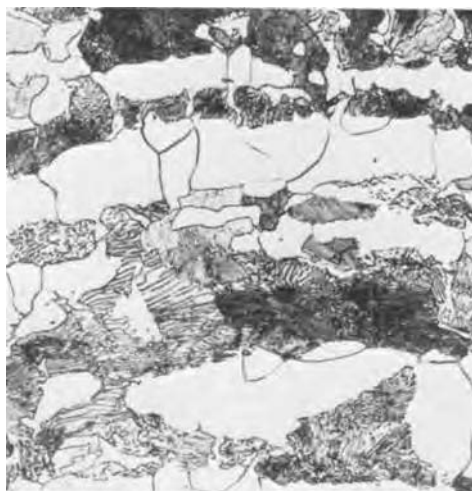


Fig. 1 Fully annealed 1040 steel showing a ferrite-pearlite microstructure. Etched in 4% picral plus 2% nital. Original magnification: 500×

conditions. In defining the various types of annealing, the transformation temperatures or critical temperatures are usually used.

Critical Temperatures. The critical temperatures define the onset and completion of the transformation to or from austenite. The equilibrium critical temperatures depicted on the binary iron-carbon phase diagram (Fig. 2) are A_1 and A_3 for hypoeutectoid steel and A_1 and A_{cm} for the hypereutectoid steel (Ref 1).

It must be noted that due to the nonequilibrium effect, the critical cooling temperatures Ar_1 , Ar_3 , and Ar_{cm} (denoted with a suffix “r” for the French word *refroidissement* meaning cooling) are lower, whereas the critical heating temperatures Ac_1 , Ac_3 , and Ac_{cm} (denoted with a suffix “c” for the French word *chauffage*) are higher than the corresponding equilibrium temperatures. Various alloying elements markedly affect these critical temperatures. For example,

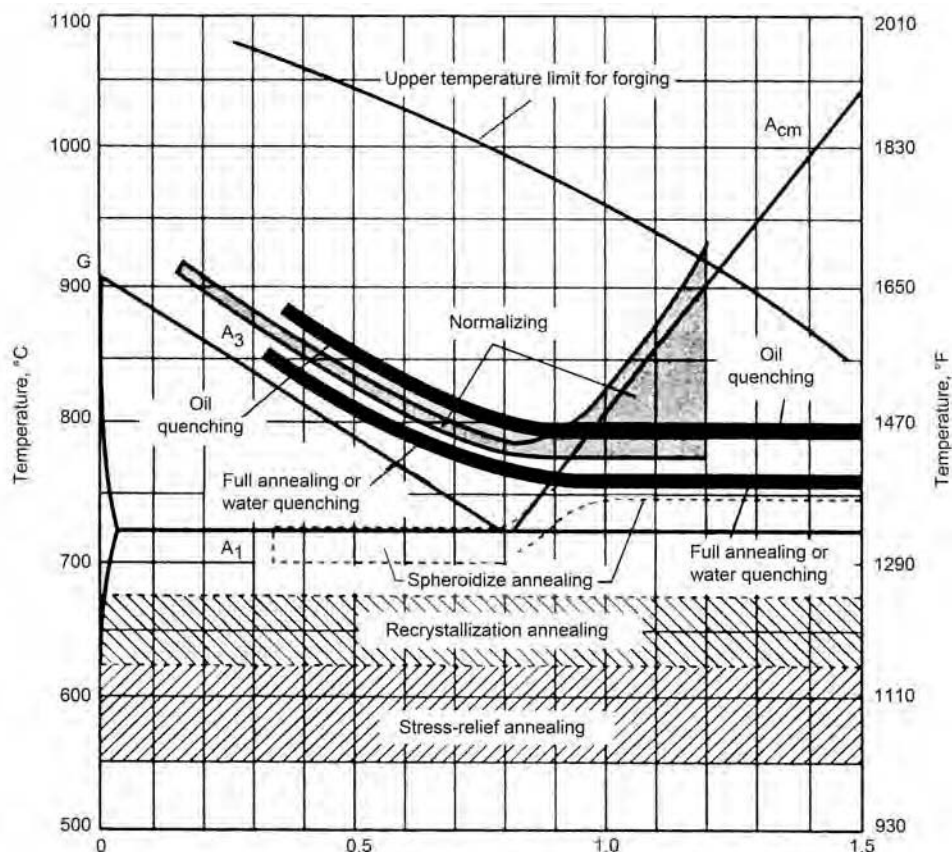


Fig. 2 Iron-carbon binary phase diagram with superimposed full annealing, process annealing, and spheroidizing treatments. Source: Ref 1

* Updated from Annealing of Steel and Continuous Annealing of Steel, *Heat Treating*, Vol 4, ASM Handbook, ASM International, 1991, p 42–66

chromium raises the eutectoid temperature, A_1 , and manganese lowers it. The upper and lower critical temperatures can be calculated using the actual chemical composition of the steel (Ref 2).

Annealing Cycles

In practice, annealing cycles are classified based on the specific purpose and the temperature to which the steel is heated and the method of cooling used. The maximum temperature may be below the lower critical temperature, A_1 (subcritical annealing); above A_1 but below the upper critical temperature, A_3 in hypoeutectoid steels, or A_{cm} in hypereutectoid steels (intercritical annealing); or above A_3 (full annealing), which has been illustrated in Fig. 2.

Because some austenite is present at temperatures above A_1 , cooling practice through transformation is a crucial factor in achieving desired microstructure and properties. Accordingly, steels heated above A_1 are subjected either to slow continuous cooling or to isothermal treatment at some temperature below A_1 at which transformation to the desired microstructure can occur in a reasonable amount of time. Under certain conditions, two or more such cycles may be combined or used in succession to achieve the desired results. The success of any annealing operation depends on the proper choice and control of the thermal cycle, based on the metallurgical principles discussed in the following sections.

Subcritical Annealing

Subcritical annealing does not involve formation of austenite. The prior condition of the steel is modified by such thermally activated processes as recovery, recrystallization, grain growth, and agglomeration of carbides. The prior history of the steel is therefore an important factor.

In as-rolled or forged hypoeutectoid steels containing ferrite and pearlite, subcritical annealing can adjust the hardnesses of both constituents, but excessively long times at temperature may be required for substantial softening. The subcritical treatment is most effective when applied to hardened or cold-worked steels, which recrystallize readily to form new ferrite grains. The rate of softening increases rapidly as the annealing temperature approaches A_1 . Cooling practice from the subcritical annealing temperature has very little effect on the established microstructure and resultant properties. A more detailed discussion of the metallurgical processes involved in subcritical annealing is provided in Ref 3.

Intercritical Annealing

Austenite begins to form when the temperature of the steel exceeds A_1 . The solubility of

carbon increases abruptly (nearly 1%) near the A_1 temperature. In hypoeutectoid steels, the equilibrium structure in the intercritical range between A_1 and A_3 consists of ferrite and austenite, and above A_3 the structure becomes completely austenitic. However, the equilibrium mixture of ferrite and austenite is not achieved instantaneously. For example, the rate of solution for a typical eutectoid steel is shown in Fig. 3. Undissolved carbides may persist, especially if the austenitizing time is short or the temperature is near A_1 , causing the austenite to be inhomogeneous. In hypereutectoid steels, carbide and austenite coexist in the intercritical range between A_1 and A_{cm} ; and the homogeneity of the austenite depends on time and temperature. The degree of homogeneity in the structure at the austenitizing temperature is an important consideration in the development of annealed structures and properties. The more homogeneous structures developed at higher austenitizing temperatures tend to promote lamellar carbide structures on cooling, whereas lower austenitizing temperatures in the intercritical range result in less homogeneous austenite, which promotes formation of spheroidal carbides.

Austenite formed when steel is heated above the A_1 temperature transforms back to ferrite and carbide when the steel is slowly cooled below A_1 . The rate of austenite decomposition and the tendency of the carbide structure to be either lamellar or spheroidal depend largely on the temperature of transformation. If the austenite transforms just below A_1 , it will decompose slowly. The product then may contain relatively coarse spheroidal carbides or coarse lamellar

pearlite, depending on the composition of the steel and the austenitizing temperature. This product tends to be very soft. However, the low rate of transformation at temperatures just below A_1 necessitates long holding times in isothermal treatments, or very slow cooling rates in continuous cooling, if maximum softness is desired. Isothermal treatments are more efficient than slow continuous cooling in terms of achieving desired structures and softness in the minimum amount of time. Sometimes, however, the available equipment or the mass of the steel part being annealed may make slow continuous cooling the only feasible alternative.

As the transformation temperature decreases, austenite generally decomposes more rapidly, and the transformation product is harder, more lamellar, and less coarse than the product formed just below A_1 . At still lower transformation temperatures, the product becomes a much harder mixture of ferrite and carbide, and the time necessary for complete isothermal transformation may again increase.

Temperature-time plots showing the progress of austenite transformation under isothermal (IT) or continuous transformation (CT) conditions for many steels have been widely published (Ref 4, 5) and illustrate the principles just discussed. These IT or CT diagrams may be helpful in design of annealing treatments for specific grades of steel, but their usefulness is limited because most published diagrams represent transformation from a fully austenitized, relatively homogeneous condition, which is not always desirable or obtainable in annealing.

In the continuous annealing process, the intercritical annealing is leveraged to develop

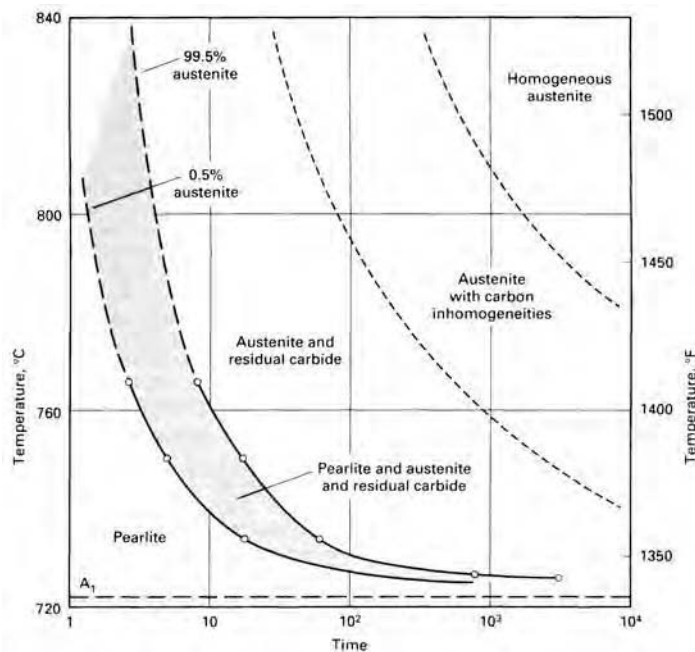


Fig. 3 Austenitizing rate-temperature curves for commercial plain carbon eutectoid steel. Prior treatment was normalizing from 875 °C (1610 °F); initial structure, fine pearlite. First curve at left shows beginning of disappearance of pearlite; second curve, final disappearance of pearlite; third curve, final disappearance of carbide; fourth curve, final disappearance of carbon concentration gradients.

dual-phase and tri-phase microstructures, with final microstructure consisting of islands of martensite in a ferritic matrix. Depending on the alloy content of the austenite pools and the cooling conditions, the austenite may not fully transform, and the microstructure will consist of martensite/retained austenite regions in a ferritic matrix.

Cooling after Transformation. After the austenite has been completely transformed, little else of metallurgical consequence can occur during cooling to room temperature. Extremely slow cooling may cause some agglomeration of carbides and, consequently, some slight further softening of the steel, but in this regard such slow cooling is less effective than high-temperature transformation. Therefore, there is no metallurgical reason for slow cooling after transformation has been completed, and the steel may be cooled from the transformation temperature as rapidly as feasible to minimize the total time required for the operation.

If transformation by slow continuous cooling has been used, the temperature at which controlled cooling may be stopped depends on the transformation characteristics of the steel. However, the mass of the steel or the need to avoid oxidation are practical considerations that may require retarded cooling to be continued below the temperature at which the austenite transformation ceases.

Effect of Prior Structure. The finer and more evenly distributed the carbides in the prior structure, the faster the rate at which austenite formed above A_1 will approach complete homogeneity. Therefore, the prior structure can affect the response to annealing. When spheroidal carbides are desired in the annealed structure, preheating at temperatures just below A_1 sometimes is used to agglomerate the prior carbides in order to increase their resistance to solution in the austenite on subsequent heating. The presence of undissolved carbides or concentration gradients in the austenite promotes formation of a spheroidal, rather than lamellar, structure when the austenite is transformed. Preheating to enhance spheroidization is applicable mainly to hypoeutectoid steels but also is useful for some hypereutectoid low-alloy steels.

Supercritical or Full Annealing

A common annealing practice is to heat hypoeutectoid steels above the upper critical temperature (A_3) to attain full austenitization. The process is called full annealing. In hypoeutectoid steels (under 0.77% C), supercritical annealing (that is, above the A_3 temperature) takes place in the austenite region (the steel is fully austenitic at the annealing temperature). However, in hypereutectoid steels (above 0.77% C), the annealing takes place above the A_1 temperature, which is the dual-phase austenite-cementite region. Figure 2 shows the annealing temperature range for full annealing

superimposed in the iron-carbon binary phase diagram. In general, an annealing temperature 50 °C (90 °F) above the A_3 for hypoeutectoid steels and A_1 for hypereutectoid steels is adequate.

Austenitizing Time and Dead-Soft Steel. Hypereutectoid steels can be made extremely soft by holding for long periods of time at the austenitizing temperature. Although the time at the austenitizing temperature may have only a small effect on actual hardnesses (such as a change from 241 to 229 HB), its effect on machinability or cold-forming properties may be appreciable.

Long-term austenitizing is effective in hypereutectoid steels because it produces agglomeration of residual carbides in the austenite. Coarser carbides promote a softer final product. In lower-carbon steels, carbides are unstable at temperatures above A_1 and tend to dissolve in the austenite, although the dissolution may be slow.

Steels that have approximately eutectoid carbon contents generally form a lamellar transformation product if austenitized for very long periods of time. Long-term holding at a temperature just above the A_1 temperature may be as effective in dissolving carbides and dissipating carbon-concentration gradients as is short-term holding at a higher temperature.

Guidelines for Annealing

The metallurgical principles discussed previously have been incorporated by Payson (Ref 6) into the following seven rules, which may be used as guidelines for development of successful and efficient annealing schedules:

- *Rule 1:* Fully homogeneous austenitized steel transforms to completely lamellar pearlitic structure after annealing, whereas heterogeneous austenitized steel transforms to nearly spheroidal annealed carbides.
- *Rule 2:* The softest condition in the steel is usually developed by austenitizing at a temperature less than 55 °C (100 °F) above A_1 and transforming at a temperature (usually) less than 55 °C (100 °F) below A_1 .
- *Rule 3:* Because very long times may be required for complete transformation at temperatures less than 55 °C (100 °F) below A_1 , allow most of the transformation to take place at the higher temperature, where a soft product is formed, and finish the transformation at a lower temperature, where the time required for completion of transformation is short.
- *Rule 4:* After the steel has been austenitized, cool to the transformation temperature as rapidly as feasible to minimize the total duration of the annealing operation.
- *Rule 5:* After the steel has been completely transformed, at a temperature that produces the desired microstructure and hardness, cool to room temperature as rapidly as

feasible to decrease further the total time of annealing.

- *Rule 6:* To ensure a minimum of lamellar pearlite in the structures of annealed 0.70 to 0.90% C tool steels and other low-alloy medium-carbon steels, preheat for several hours at a temperature approximately 28 °C (50 °F) below the lower critical temperature (A_1) before austenitizing and transforming as usual.
- *Rule 7:* To obtain minimum hardness in annealed hypereutectoid alloy tool steels, heat at the austenitizing temperature for a long time (approximately 10 to 15 h), then transform as usual.

These rules are applied most effectively when the critical temperatures and transformation characteristics of the steel have been established and when transformation by isothermal treatment is feasible.

Annealing Temperatures

From a practical sense, most annealing practices have been established from experience. For many annealing applications, it is sufficient simply to specify that the steel be cooled in the furnace from a designated annealing (austenitizing) temperature. Temperatures and associated Brinell hardnesses for simple annealing of carbon steels are given in Table 1, and similar data for alloy steels are presented in Table 2.

Heating cycles that employ austenitizing temperatures in the upper ends of the ranges given in Table 2 should result in pearlitic structures. Predominantly spheroidized structures should be obtained when lower temperatures are used.

When an alloy steel is annealed to obtain a specific microstructure, greater precision is required in specifying temperatures and cooling conditions for annealing. Table 3 presents, for a variety of standard alloy steels, typical schedules for such annealing operations.

In isothermal annealing to produce a pearlitic structure, particularly in forgings, an austenitizing temperature as much as 70 °C (125 °F) higher than that indicated in Table 3 may be selected in order to decrease the austenitizing time.

For most steels, as indicated in Table 3, annealing may be accomplished by heating to the austenitizing temperature and then either cooling in the furnace at a controlled rate or cooling rapidly to, and holding at, a lower temperature for isothermal transformation. Both procedures result in virtually the same hardness; however, considerably less time is required for isothermal transformation.

Spheroidizing

The majority of all spheroidizing activity is performed for improving the cold formability

Table 1 Recommended temperatures and cooling cycles for full annealing of small carbon steel forgings

Data are for forgings up to 75 mm (3 in.) in section thickness. Time at temperature usually is a minimum of 1 h for sections up to 25 mm (1 in.) thick; ½ h is added for each additional 25 mm (1 in.) of thickness.

Steel	Annealing temperature		Cooling cycle(a)				Hardness range, HB
			°C		°F		
	°C	°F	From	To	From	To	
1018	855–900	1575–1650	855	705	1575	1300	111–149
1020	855–900	1575–1650	855	700	1575	1290	111–149
1022	855–900	1575–1650	855	700	1575	1290	111–149
1025	855–900	1575–1650	855	700	1575	1290	111–187
1030	845–885	1550–1625	845	650	1550	1200	126–197
1035	845–885	1550–1625	845	650	1550	1200	137–207
1040	790–870	1450–1600	790	650	1450	1200	137–207
1045	790–870	1450–1600	790	650	1450	1200	156–217
1050	790–870	1450–1600	790	650	1450	1200	156–217
1060	790–845	1450–1550	790	650	1450	1200	156–217
1070	790–845	1450–1550	790	650	1450	1200	167–229
1080	790–845	1450–1550	790	650	1450	1200	167–229
1090	790–830	1450–1525	790	650	1450	1200	167–229
1095	790–830	1450–1525	790	655	1450	1215	167–229

(a) Furnace cooling at 28 °C/h (50 °F/h)

of steels. It is also performed to improve the machinability of hypereutectoid steels, as well as tool steels. A spheroidized microstructure is desirable for cold forming because it lowers the flow stress of the material. The flow stress is determined by the proportion and distribution of ferrite and carbides. The strength of the ferrite depends on its grain size, any ferrite strengthening by alloying additions (such as silicon or manganese), and the rate of cooling. Whether the carbides are present as lamellae in pearlite or spheroids radically affects the formability of steel.

Steels may be spheroidized, that is, heated and cooled to produce a structure of globular carbides in a ferritic matrix. Figure 4 shows 1040 steel in the fully spheroidized condition. Spheroidization can take place by the following methods:

- Prolonged holding at a temperature just below Ae_1
- Heating and cooling alternately between temperatures that are just above Ac_1 and just below Ar_1
- Heating to a temperature just above Ac_1 , and then either cooling very slowly in the furnace or holding at a temperature just below Ar_1
- Cooling at a suitable rate from the minimum temperature at which all carbide is dissolved to prevent reformation of a carbide network, and then reheating in accordance with the first or second methods in this list (applicable to hypereutectoid steel containing a carbide network)

It should be noted that it is difficult to establish consistent designations for critical temperatures. In discussions about heating with prolonged holding, the critical temperatures of interest should be the equilibrium temperatures Ae_1 and Ae_3 . Terminology becomes more

arbitrary in discussions of heating and cooling at unspecified rates and for unspecified holding times.

Figure 2 shows the range of temperatures used for spheroidization of hypoeutectoid and hypereutectoid steels. The rates of spheroidizing provided by these methods depend somewhat on prior microstructure, being greatest for quenched structures in which the carbide phase is fine and dispersed. Prior cold work also increases the rate of the spheroidizing reaction in a subcritical spheroidizing treatment.

An example of the effect of prior microstructure on spheroidization is given in Fig. 5 for the same 1040 steel shown in Fig. 1 (further examples are found in Ref 7). The micrograph in Fig. 5(a) shows the extent of spheroidization of the 1040 steel with a prior martensitic microstructure after holding 21 h at 700 °C (1290 °F). Figure 5(b) shows the extent of spheroidization after the same time/temperature heating cycle with a prior ferrite-pearlite microstructure. Spheroidization has occurred in the 1040 steel with the prior martensitic microstructure. On the other hand, it has only just begun in the same steel with the prior ferrite-pearlite microstructure. Figure 6 shows that after 200 h at 700 °C (1290 °F), the spheroidization process is almost completed in the prior ferrite-pearlite steel; however, traces of the pearlitic areas can still be seen.

For full spheroidizing, austenitizing temperatures either slightly above the Ac_1 temperature or approximately midway between Ac_1 and Ac_3 are used. If a temperature slightly above Ac_1 is to be used, good loading characteristics and accurate temperature controls are required for proper results; otherwise, it is conceivable that Ac_1 may not be reached and that austenitization may not occur.

Low-carbon steels are seldom spheroidized for machining, because in the spheroidized

Table 2 Recommended annealing temperatures for alloy steels (furnace cooling)

AISI/SAE steel	Annealing temperature		Hardness (max), HB
	°C	°F	
1330	845–900	1550–1650	179
1335	845–900	1550–1650	187
1340	845–900	1550–1650	192
1345	845–900	1550–1650	...
3140	815–870	1500–1600	187
4037	815–855	1500–1575	183
4042	815–855	1500–1575	192
4047	790–845	1450–1550	201
4063	790–845	1450–1550	223
4130	790–845	1450–1550	174
4135	790–845	1450–1550	...
4137	790–845	1450–1550	192
4140	790–845	1450–1550	197
4145	790–845	1450–1550	207
4147	790–845	1450–1550	...
4150	790–845	1450–1550	212
4161	790–84	1450–155	...
4337	790–84	1450–155	...
4340	790–84	1450–155	223
50B40	815–870	1500–1600	187
50B44	815–870	1500–1600	197
5046	815–870	1500–1600	192
50B46	815–870	1500–1600	192
50B50	815–870	1500–1600	201
50B60	815–870	1500–1600	217
5130	790–845	1450–1550	170
5132	790–845	1450–1550	170
5135	815–870	1500–1600	174
5140	815–870	1500–1600	187
5145	815–870	1500–1600	197
5147	815–870	1500–1600	197
5150	815–870	1500–1600	201
5155	815–870	1500–1600	217
5160	815–870	1500–1600	223
51B60	815–870	1500–1600	223
50100	730–790	1350–1450	197
51100	730–790	1350–1450	197
52100	730–790	1350–1450	207
6150	845–900	1550–1650	201
81B45	845–900	1550–1650	192
8627	815–870	1500–1600	174
8630	790–845	1450–1550	179
8637	815–870	1500–1600	192
8640	815–870	1500–1600	197
8642	815–870	1500–1600	201
8645	815–870	1500–1600	207
86B45	815–870	1500–1600	207
8650	815–870	1500–1600	212
8655	815–870	1500–1600	223
8660	815–870	1500–1600	229
8740	815–870	1500–1600	202
8742	815–870	1500–1600	...
9260	815–870	1500–1600	229
94B30	790–845	1450–1550	174
94B40	790–845	1450–1550	192
9840	790–845	1450–1550	207

condition they are excessively soft and “gummy,” cutting with long, tough chips. When low-carbon steels are spheroidized, it is generally to permit severe deformation. For example, when 1020 steel tubing is being produced by cold drawing in two or three passes, a spheroidized structure will be obtained if the material is annealed for ½ to 1 h at 690 °C (1275 °F) after each pass. The final product will have a hardness of approximately 163 HB. Tubing in this condition will be able to withstand severe deformation during subsequent cold forming.

Table 3 Recommended temperatures and time cycles for annealing of alloy steels

Steel	Conventional cooling(a)												Hardness (approx.), HB		
	Austenitizing temperature		Temperature						Cooling rate			Isothermal method(b)			
			°C		°F		Time, h	Cool to		Hold, h					
	From	To	From	To	°C/h	°F/h		°C	°F						
To obtain a predominantly pearlitic structure(c)															
1340	830	1525	735	610	1350	1130	10	20	11	620	1150	4.5	183		
2340	800	1475	655	555	1210	1030	8.5	15	12	595	1100	6	201		
2345	800	1475	655	550	1210	1020	8.5	15	12.7	595	1100	6	201		
3120(d)	885	1625	650	1200	4	179		
3140	830	1525	735	650	1350	1200	10	20	7.5	660	1225	6	187		
3150	830	1525	705	645	1300	1190	10	20	5.5	660	1225	6	201		
3310(e)	870	1600	595	1100	14	187		
4042	830	1525	745	640	1370	1180	10	20	9.5	660	1225	4.5	197		
4047	830	1525	735	630	1350	1170	10	20	9	660	1225	5	207		
4062	830	1525	695	630	1280	1170	8.5	15	7.3	660	1225	6	223		
4130	855	1575	765	665	1410	1230	20	35	5	675	1250	4	174		
4140	845	1550	755	665	1390	1230	15	25	6.4	675	1250	5	197		
4150	830	1525	745	670	1370	1240	8.5	15	8.6	675	1250	6	212		
4320(d)	885	1625	660	1225	6	197		
4340	830	1525	705	565	1300	1050	8.5	15	16.5	650	1200	8	223		
4620(d)	885	1625	650	1200	6	187		
4640	830	1525	715	600	1320	1110	7.6	14	15	620	1150	8	197		
4820(d)	605	1125	4	192		
5045	830	1525	755	665	1390	1230	10	20	8	660	1225	4.5	192		
5120(d)	885	1625	690	1275	4	179		
5132	845	1550	755	670	1390	1240	10	20	7.5	675	1250	6	183		
5140	830	1525	740	670	1360	1240	10	20	6	675	1250	6	187		
5150	830	1525	705	650	1300	1200	10	20	5	675	1250	6	201		
52100(f)		
6150	830	1525	760	675	1400	1250	8.5	15	10	675	1250	6	201		
8620(d)	885	1625	660	1225	4	187		
8630	845	1550	735	640	1350	1180	10	20	8.5	660	1225	6	192		
8640	830	1525	725	640	1340	1180	10	20	8	660	1225	6	197		
8650	830	1525	710	650	1310	1200	8.5	15	7.2	650	1200	8	212		
8660	830	1525	700	655	1290	1210	8.5	15	8	650	1200	8	229		
8720(d)	885	1625	660	1225	4	187		
8740	830	1525	725	645	1340	1190	10	20	7.5	660	1225	7	201		
8750	830	1525	720	630	1330	1170	8.5	15	10.7	660	1225	7	217		
9260	860	1575	760	705	1400	1300	8.5	15	6.7	660	1225	6	229		
9310(e)	870	1600	595	1100	14	187		
9840	830	1525	695	640	1280	1180	8.5	15	6.6	650	1200	6	207		
9850	830	1525	700	645	1290	1190	8.5	15	6.7	650	1200	8	223		
To obtain a predominantly ferritic and spheroidized carbide structure															
1320(d)	805	1480	650	1200	8	170		
1340	750	1380	735	610	1350	1130	5	10	22	640	1180	8	174		
2340	715	1320	655	555	1210	1030	5	10	18	605	1125	10	192		
2345	715	1320	655	550	1210	1020	5	10	19	605	1125	10	192		
3120(d)	790	1450	650	1200	8	163		
3140	745	1370	735	650	1350	1200	5	10	15	660	1225	10	174		
3150	750	1380	705	645	1300	1190	5	10	11	660	1225	10	187		
9840	745	1370	695	640	1280	1180	5	10	11	650	1200	10	192		
9850	745	1370	700	645	1290	1190	5	10	11	650	1200	12	207		

(a) The steel is cooled in the furnace at the indicated rate through the temperature range shown. (b) The steel is cooled rapidly to the temperature indicated and is held at that temperature for the time specified. (c) In isothermal annealing to obtain pearlitic structure, steels may be austenitized at temperatures up to 70 °C (125 °F) higher than temperatures listed. (d) Seldom annealed. Structures of better machinability are developed by normalizing or by transforming isothermally after rolling or forging. (e) Annealing is impractical by the conventional process of continuous slow cooling. The lower transformation temperature is markedly depressed, and excessively long cooling cycles are required to obtain transformation to pearlite. (f) Predominantly pearlitic structures are seldom desired in this steel.

As with many other types of heat treatment, hardness after spheroidizing depends on carbon and alloy content. Increasing the carbon or alloy content, or both, results in an increase in the as-spheroidized hardness, which generally ranges from 163 to 212 HB (Table 3). Deformation after transformation significantly accelerates the spheroidization kinetics as well as results in higher degree of spheroidization (Ref 8).

It must be noted that fine carbides dispersed in the austenite phase can initiate eutectoid transformation either by pearlite reaction or divorced eutectoid transformation (DET). While both these methods have been known

for a significantly long time, the majority of industrial spheroidization processes have been designed by leveraging the pearlite reaction. It recently has been highlighted that the DET path is more efficient in terms of transformation time (Ref 9). It has been demonstrated for the hyper-eutectoid steel that DET can be promoted over the pearlite reaction by maintaining a lower austenitization temperature and slower cooling rates (less than 830 °C, or 1525 °F, and a cooling rate slower than 500 °C/h, or 900 °F/h, for 52100 steel) (Ref 9). In the DET reaction, the pre-existing carbide particles grow directly by diffusion of carbon from the austenite matrix, resulting in a transformation product comprising

spheroidized carbides in a ferrite matrix. Compared to 10 to 16 h of spheroidization time required in the conventional continuous-cool or isothermal spheroidal anneal methods leveraging pearlite transformation, the DET spheroidization can be done in less than 1 h (Ref 9), resulting in significant savings in energy as well as furnace productivity. It was also shown that chromium addition reduces the carbide size, whereas manganese addition promotes pearlitic transformation. In a more recent study (Ref 10), it has been shown that chromium addition can be leveraged for widening the DET reaction regime, in terms of austenitization temperature and time.

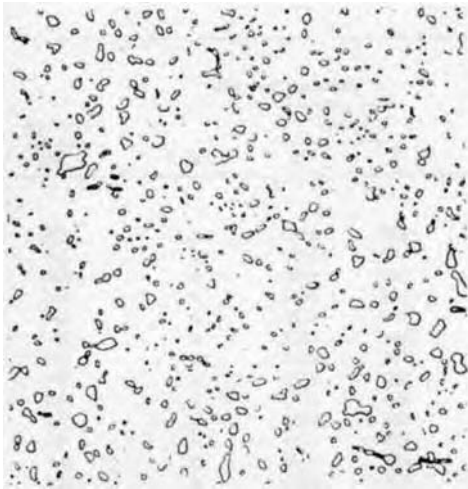
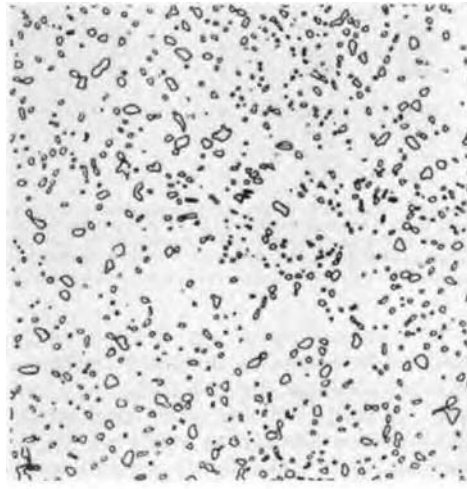
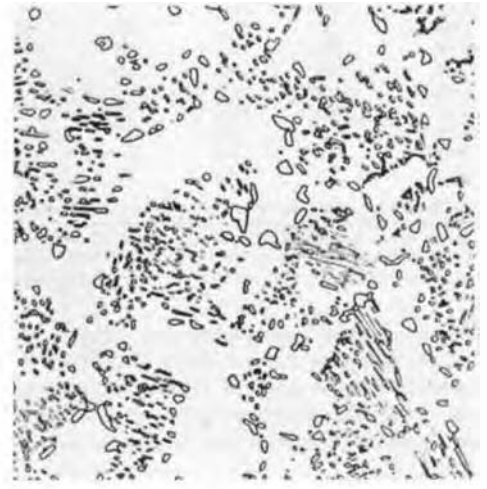


Fig. 4 Spheroidized microstructure of 1040 steel after 21 h at 700 °C (1290 °F). 4% picral etch. Original magnification: 1000×



(a)



(b)

Fig. 5 Effect of prior microstructure on spheroidizing a 1040 steel at 700 °C (1290 °F) for 21 h. (a) Starting from a martensitic microstructure (as-quenched). (b) Starting from a ferrite-pearlite microstructure (fully annealed). Etched in 4% picral plus 2% nital. Original magnification: 1000×

Process Annealing

As the hardness of steel increases during cold working, ductility decreases and additional cold reduction becomes so difficult that the material must be annealed to restore its ductility. Such annealing between processing steps is referred to as in-process or simply process annealing. It may consist of any appropriate treatment. In most instances, however, a subcritical treatment is adequate and least costly, and the term *process annealing* without further qualification usually refers to an in-process subcritical anneal.

Figure 7 shows the range of temperatures typically used for process annealing. It is often necessary to specify process annealing for parts that are cold formed by stamping, heading, or extrusion. Hot-worked high-carbon and alloy steels also are process annealed to prevent them from cracking and to soften them for shearing, turning, or straightening.

Process annealing usually consists of heating to a temperature below A_{e1} , soaking for an appropriate time, and then cooling, usually in air. In most instances, heating to a temperature between 10 and 20 °C (20 and 40 °F) below A_{e1} produces the best combination of microstructure hardness and mechanical properties. Temperature controls are necessary only to prevent heating the material above A_{e1} and thus defeating the purpose of annealing.

When process annealing is performed merely to soften a material for such operations as cold sawing and cold shearing, temperatures well below A_{e1} normally are used, and close controls are unnecessary.

In the wire industry, process annealing is used as an intermediate treatment between the drawing of wire to a size slightly larger than the desired finished size and the drawing of a light reduction to the finished size. Wire thus made is known as annealed-in-process wire.

Process annealing is used also in the production of wire sufficiently soft for severe upsetting and to permit drawing the smaller sizes of low-carbon and medium-carbon steel wire that cannot be drawn to the desired small size directly from the hot-rolled rod. Process annealing is more satisfactory than spheroidize annealing for a material that, because of its composition or size (or both), cannot be drawn to finished size because it either lacks ductility or does not meet physical requirements. Also, material that is cold sheared during processing is process annealed to raise the ductility of the sheared surface to a level suitable for further processing.

Annealed Structures for Machining

Different combinations of microstructure and hardness, considered together, are significant in terms of machinability. For instance, Fig. 8 shows that a partially spheroidized 5160 steel shaft was machined (by turning) with much less tool wear and better surface finish than the same steel in the annealed condition with a pearlitic microstructure and a higher hardness. Based on many observations, optimum microstructures for machining steels of various carbon contents are usually as follows:

Carbon, %	Optimum microstructure
0.06–0.20	As-rolled (most economical)
0.20–0.30	Under 75 mm (3 in.) diameter, normalized; 75 mm diameter and over, as-rolled
0.30–0.40	Annealed, to produce coarse pearlite, minimum ferrite
0.40–0.60	Coarse lamellar pearlite to coarse spheroidized carbides
0.60–1.00	100% spheroidized carbides, coarse to fine

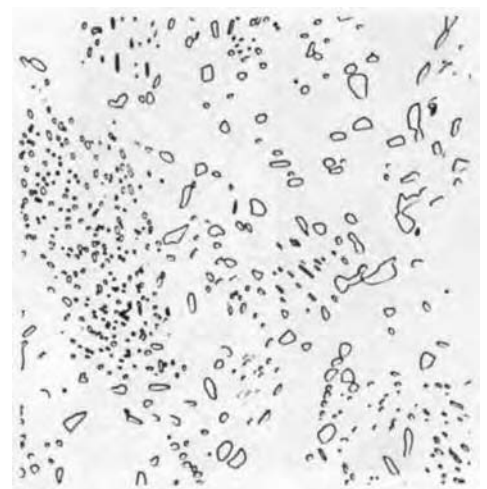


Fig. 6 The extent of spheroidization at 700 °C (1290 °F) for 200 h for the 1040 steel starting from a ferrite-pearlite microstructure etched in 4% picral. Original magnification: 1000×

The type of machining operation is also a factor. For example, certain gears were made from 5160 steel tubing by the dual operation of machining in automatic screw machines and broaching of cross slots. The screw-machine operations were easiest with thoroughly spheroidized material, but a pearlitic structure was more suitable for broaching. A semispheroidized structure proved to be a satisfactory compromise.

Semispheroidized structures can be achieved by austenitizing at lower temperatures, and sometimes at higher cooling rates, than those used for achieving pearlitic structures. The semispheroidized structure of the 5160 steel tubing mentioned previously was obtained by heating to 790 °C (1450 °F) and cooling at 28 °C/h (50 °F/h) to 650 °C (1200 °F). For this

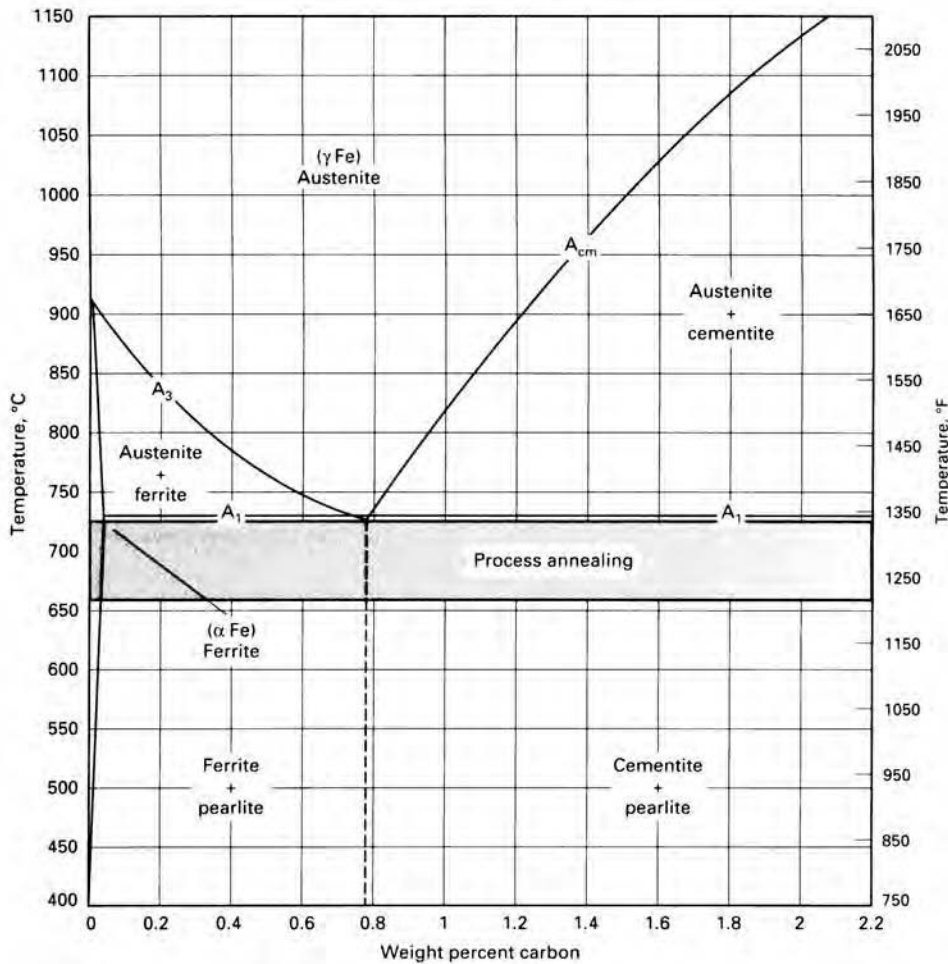


Fig. 7 Iron-carbon binary phase diagram showing the temperature region for process annealing

At lower carbon levels, structures consisting of coarse pearlite in a ferrite matrix often are found to be the most machinable. In some alloy steels, this type of structure can best be achieved by heating to temperatures well above A_{C3} to establish a coarse austenite grain size, then holding below A_{r1} to allow coarse lamellar pearlite to form. This process sometimes is referred to as cycle annealing or lamellar annealing. For example, forged 4620 steel gears were heated rapidly in a five-zone furnace to 980 °C (1800 °F), cooled to 625 to 640 °C (1160 to 1180 °F) in a water-cooled zone, and held at that temperature for 120 to 150 min. The resulting structure—coarse lamellar pearlite in a ferrite matrix—had a hardness of 140 to 146 HB (Ref 11).

Industrial Annealing

Types of Furnaces. Furnaces for annealing are of two basic types: batch furnaces and continuous furnaces (Ref 12). Within either of these two types, furnaces can be further classified according to configuration, type of fuel used, method of heat application, and means by which the load is moved through, or supported in, the furnace. Other factors that must be considered in furnace selection are cost, type of annealing cycle, required atmosphere, and physical nature of parts to be annealed. In many cases, however, the annealing cycle used is dictated by the available equipment.

Batch-type furnaces are necessary for large parts such as heavy forgings and often are preferred for small lots of a given part or grade of steel and for the more complex alloy grades requiring long cycles. Specific types of batch furnaces include car-bottom, box, bell, and pit furnaces. Annealing in bell furnaces can produce the greatest degree of spheroidization (up to 100%). However, the spheroidizing cycles in bell furnaces are long and last from 24 to 48 h depending on the grade of material being annealed and the size of the load.

Continuous furnaces such as roller-hearth, rotary-hearth, and pusher types are ideal for isothermal annealing of large quantities of parts of the same grade of steel. These furnaces can be designed with various individual zones, allowing the work to be consecutively brought to temperature, held at temperature, and cooled at the desired rate. Continuous furnaces are not able to give complete spheroidization and should not be used for products that require severe cold forming.

Furnace Atmospheres. Electric furnaces used with air atmospheres, and gas furnaces used with atmospheres consisting of the products of combustion, cannot be regulated for complete elimination of oxidation of the steel being treated. Only atmospheres independent of the fuel are generally considered satisfactory for clean or bright annealing. Excessive oxidation during annealing usually is prevented by the use of controlled atmospheres in

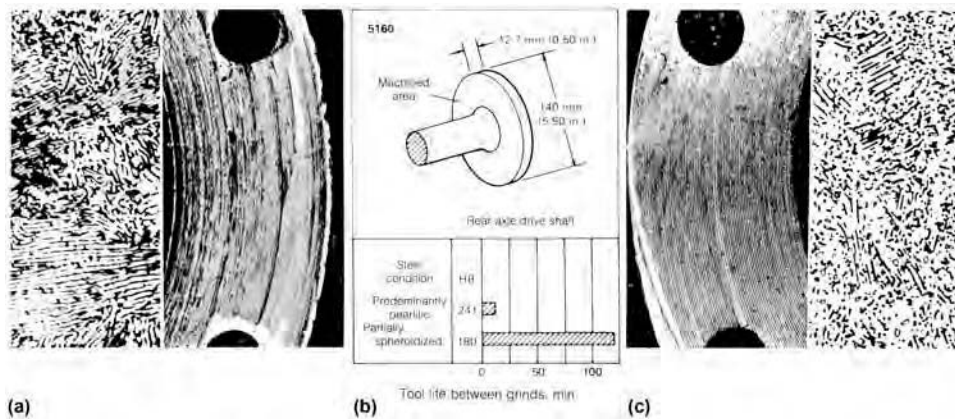


Fig. 8 Effect of partial spheroidization on surface finish and tool life in subsequent machining of 5160 steel. (a) Annealed (pearlitic) microstructure (hardness: 241 HB) and surface finish of flange after machining of eight pieces. (b) Tool life between grinds, min. (c) Partially spheroidized microstructure (hardness: 180 HB) and surface finish of flange after machining of 123 pieces

steel, austenitizing at a temperature of approximately 775 °C (1425 °F) results in more spheroidization and less pearlite.

Medium-carbon steels are much more difficult to fully spheroidize than are high-carbon

steels, such as 1095 and 52100. In the absence of excess carbides to nucleate and promote the spheroidizing reaction, it is more difficult to achieve complete freedom from pearlite in practical heat treating cycles.

conjunction with a suitable furnace that is designed to exclude air and combustion gases from the heating chamber. The gases and gas mixtures used for controlled atmospheres depend on the metal being treated, the treatment temperature, and the surface requirements of the parts being annealed. The need to eliminate decarburization as well as oxidation is often a significant factor in the selection of annealing atmospheres.

The gas most widely used as a protective atmosphere for annealing is exothermic gas. This gas is inexpensive, the raw materials for making it are readily available, and the results obtained with it are generally excellent. Hydrocarbon gases such as natural gas, propane, butane, and coke-oven gas are commonly burned in an exothermic-gas producer, creating a self-supporting, heat-producing combustion reaction. A commonly used exothermic gas mixture contains 15% H₂, 10% CO, 5% CO₂, 1% CH₄, and 69% N₂. This gas is used for bright annealing of cold-rolled low-carbon steel strip. It will decarburize medium-carbon and high-carbon steels, however, because of the carbon dioxide and water vapor it contains.

Allowable decarburization on spheroidize annealed blanks or coiled rod can be quite restrictive. As long as the furnace has excellent sealing characteristics, low-dewpoint exothermic gas can protect the steel from decarburization. Many commercial heat treaters compensate for the sealing problems of furnaces by using a blend of exothermic and endothermic gases. Depending on the carbon content of the stock that is being processed, the blend can be varied. A great deal of caution must be exercised when such blends are used, because endothermic gas forms an explosive mixture with air as the temperature drops below 760 °C (1400 °F).

Other atmospheres commonly used in annealing include endothermic-base, dissociated

ammonia, and vacuum atmospheres. Nitrogen-base atmospheres became popular among heat treaters in the 1980s due in part to rising costs of utilities such as natural gas and water. The nitrogen is blended with small percentages of additives such as methane, propane, propylene, and carbon monoxide.

Uniformity of Temperature. One potential contribution to the failure of an annealing operation is a lack of knowledge of the temperature distribution within the load of steel in the furnace. Furnaces large enough to anneal 18 Mg (20 tons) of steel at a time are not uncommon. In some large forging shops, workpieces can weigh in excess of 270 Mg (300 tons). The larger the furnace, the more difficult it is to establish and maintain uniform temperature conditions throughout the load, and the more difficult it is to change the temperature of the steel during either heating or cooling.

Furnace thermocouples indicate the temperature of the space above, below, or beside the load, but this temperature may differ by 28 °C (50 °F) or much more from the temperature of the steel itself, especially when the steel is in a pipe or box, or when bar or strip is packed in a dense charge in a quiescent atmosphere. When these conditions exist, the distribution of temperature throughout the load during heating and cooling should be established by placing thermocouples among the bars, forgings, coils, and so on. A good practice is to spot weld a thermocouple to the workpiece or to use embedded thermocouples (thermocouples placed in holes drilled into the workpiece). Regulation of the furnace during the annealing operation should be based on the temperatures indicated by these thermocouples, which are in actual contact with the steel, rather than on the temperatures indicated by the furnace thermocouples.

Uniformity across Load. The uniformity across the charge is strongly influenced by the

manner it is loaded in a furnace. For example, during the continuous annealing of rod bundles in a multizone roller-hearth furnace, the packing density of rods, as well as the bundle diameter, has significant impact on the uniformity across the bundle as well as the furnace productivity (Ref 13, 14). Figure 9 shows that, compared to the core rod, the surface rod in the bundle has a higher temperature during the heating phase, which switches to a lower temperature during the cooling phase. Furthermore, the higher packing density of the bundle enhances thermal conductivity across the bundle, resulting in a higher temperature in the core rods compared to a bundle with lower packing density (Fig. 9a). It is interesting to note that when rods are packed as bundles, due to a higher number of contact points and increased contact resistance, the temperature of the core rods decreases with a reduction in rod diameter for a fixed bundle diameter and packing fraction. This is counterintuitive because during annealing of a single rod in a continuous furnace, the core temperature decreases with an increase in rod diameter. The core temperature significantly impacts the hardness of the annealed core rod (Fig. 9d). In practice, the industrial operation is optimized by managing the hearth speed, packing fraction rod, and bundle diameters to maximize furnace productivity (Ref 14). The charge configuration effect can also be observed during coil annealing of steel sheet, as illustrated in Fig. 10(a) (Ref 15, 16). In this case, for a fixed coil diameter, reduction in sheet thickness results in increased number of contact points with lower core temperature, necessitating a higher cycle time during the batch annealing process.

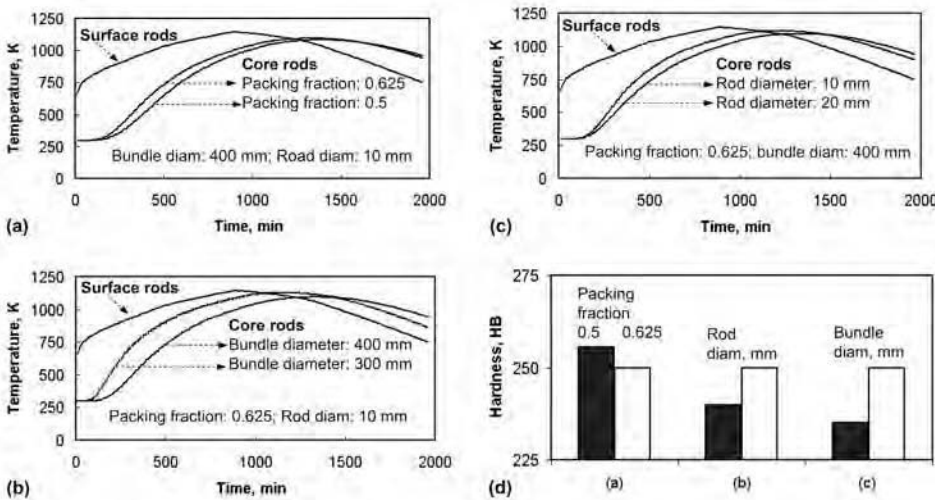


Fig. 9 Surface and core temperature profiles to examine the effect of (a) packing density, (b) bundle diameter, and (c) rod diameter. (d) Effect of temperature profile on hardness of core rods. Source: Ref 13

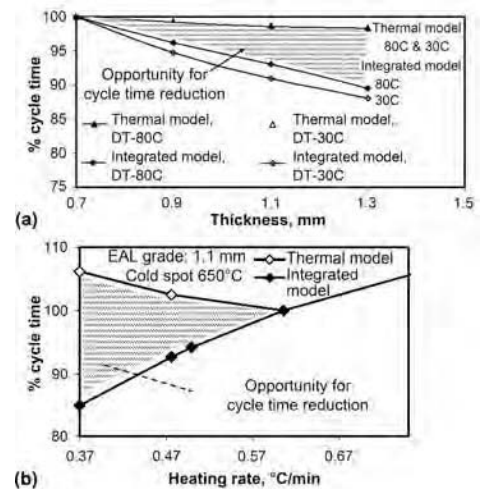


Fig. 10 During batch annealing of steel sheet coil, (a) the cycle time increases with decrease in sheet thickness for a given coil diameter due to increased contact resistance, and (b) reduction in heating rate enhances the annealing kinetics due to AlN precipitation-recrystallization-grain growth interactions. Source: Ref 16

The common practice of controlling an annealing operation through the core temperature can be deceptive due to the nonlinear phase-transformation effects. For example, during batch annealing of aluminum-killed cold-rolled steel sheet, due to the complex interplay between precipitation, recrystallization, and grain growth, heating rates have significant impact on the annealing kinetics. As a result, it is possible to reduce the heating rate yet enhance the annealing kinetics as well as the furnace productivity (Fig. 10b) (Ref 16). This is counterintuitive, because generally the heating cycle is considered to be furnace limited and there is a tendency to maximize it during industrial annealing operations.

These numerous possibilities of load configuration as well as complex interactions of governing phase-transformation kinetics in an industrial scenario can be effectively captured through mathematical modeling of the annealing operation, resulting in significant improvement in quality and furnace productivity (Ref 16–18).

Annealing of Steel Sheet and Strip

In terms of total tonnage of material processed, annealing of sheet and strip during production of steel-mill products represents the major use of annealing. Because such annealing is done to prepare the material for further processing (such as additional cold rolling or fabrication into parts), and because the temperatures employed are usually below the A_1 temperature, the more specific terms *subcritical annealing* and *process annealing* are appropriate, although common practice is to use the term *annealing* without qualification.

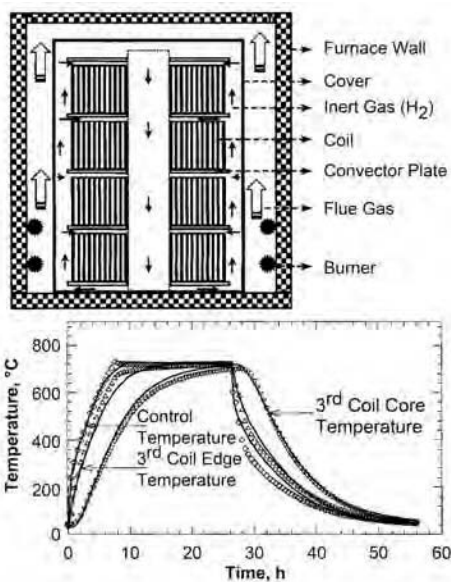


Fig. 11 (a) Schematic diagram of a batch annealing furnace. (b) Thermal profile during batch annealing of cold-rolled sheet. Source: Ref 15

Annealing of sheet steel products is performed on a commercial scale by either batch annealing or continuous annealing. In a batch annealing furnace, multiple (four to five) cylindrical cold-rolled steel coils of outer diameter in the range of 1.5 to 2.5 m (4.9 to 8.2 ft), inner diameter of 0.5 to 0.7 m (1.6 to 2.3 ft), and widths of 1.0 to 1.4 m (3.3 to 4.6 ft), weighing approximately 14 to 27 Mg (15 to 30 tons) each, are stacked on a base unit with a recirculation fan and cooling system (Ref 15). The steel coils, separated by convector plates for gas recirculation, are placed under a cylindrical steel cover and annealed in a reducing atmosphere (Fig. 11a). During the last couple of decades, two- to threefold reduction in batch annealing time has been achieved by switching from pure N_2 or $N_2 + H_2$ to pure H_2 atmosphere due to seven times higher thermal conductivity and fourteen times lower density of hydrogen gas (Fig. 11b). The slow heating and cooling rates during the batch annealing operation ensure that all carbon dissolved during annealing precipitates upon cooling. This results in excellent ductility, although some nonuniformity develops because the sheet at the outer surface and inner core of a coil experience different thermal histories.

In contrast, continuous annealing of sheet involves the rapid passage of uncoiled sheet through a two-stage furnace for times on the order of a few minutes (Fig. 12a). The first stage

rapidly heats the steel to annealing temperature between 675 and 850 °C (1250 and 1550 °F) above the A_1 temperature and soaks for approximately 1 min to achieve recrystallization and limited grain growth. This is followed by the second stage of taper cooling for partial precipitation of solute carbon from the ferrite phase and/or higher primary cooling rates for higher carbon supersaturation in the ferrite (Fig. 12b). This increases the driving force and promotes carbon precipitation during the subsequent overaging stage and prevents strain aging of the annealed sheet. The metallurgical advantages of continuous annealing over conventional batch annealing include improved product uniformity, surface cleanliness and shape, and the versatility to produce a wide range of steel grades.

Sheet Steels for Automotive Applications

Steels for automotive applications require high formability and deep-drawing characteristics, which necessitates higher normal anisotropy (\bar{r}) and high ductility. The quantity \bar{r} represents the mean of the drawability values taken from measurements in the longitudinal (L), transverse (T), and two 45° (A + B) orientations; therefore, $\bar{r} = 0.25(L + T + 45^\circ A + 45^\circ B)$. In addition, low strength and low-strain-aging index are desired.

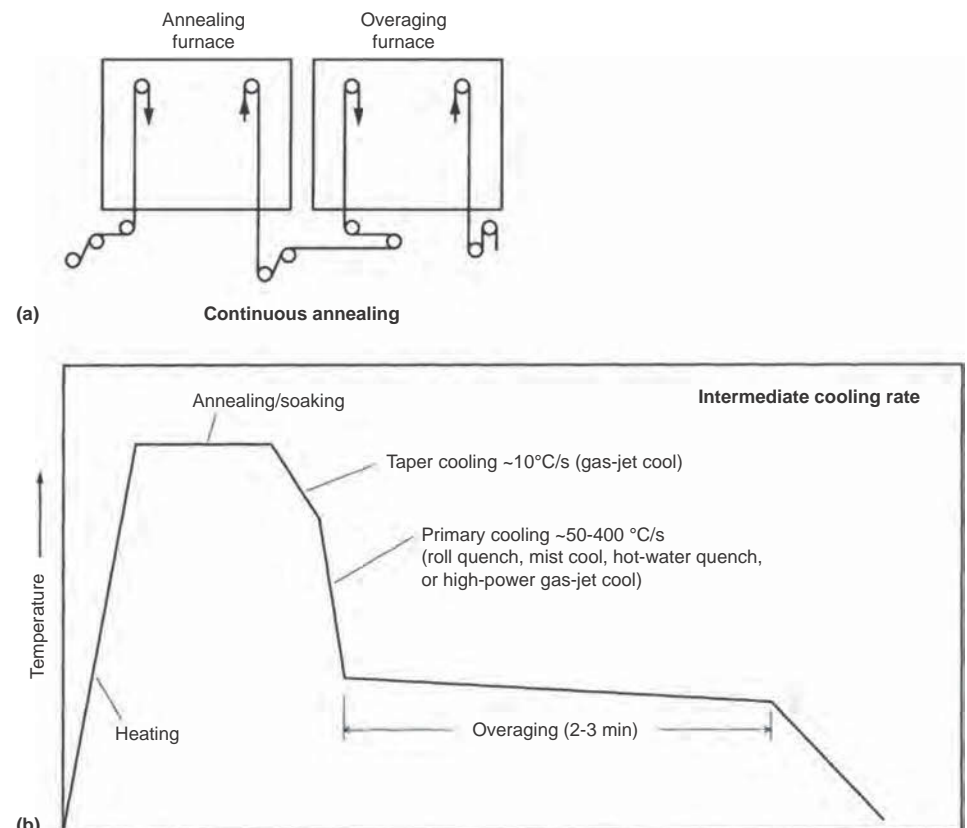


Fig. 12 (a) Schematic diagram of a continuous annealing furnace. (b) Typical continuous annealing thermal profile

The usual method of manufacturing cold-rolled sheet and strip is to produce a hot-rolled coil, pickle it to remove scale (oxide), and cold roll it to the desired final gage. Cold rolling may reduce the thickness of the hot-rolled material in excess of 90%, which increases the hardness and strength of the steel but severely decreases its ductility. If any large amount of subsequent cold working is to be done, the ductility of the steel must be restored.

Annealing of the cold-rolled steel normally is designed to produce a recrystallized ferrite microstructure from the highly elongated, stressed grains resulting from cold work. Figure 13 shows the effect of annealing on the microstructure of a low-carbon cold-rolled sheet steel. The cold-rolled microstructure is shown in Fig. 13(a) in contrast to the partially and fully recrystallized microstructures in Fig. 13(b and c). During heating of the steel, and in the first segment of the holding portion of the cycle, the first metallurgical process to occur is recovery. During this process, internal strains are relieved (although little change in the microstructure is evident), ductility is moderately increased, and strength is slightly decreased.

As annealing continues, the process of recrystallization occurs, and new, more equiaxed ferrite grains are formed from the elongated grains. During recrystallization, strength decreases rapidly, with a corresponding increase in ductility. Further time at temperature causes some of the newly formed grains to grow at the expense of other grains; this is termed grain growth and results in modest decreases in strength and small (but often significant) increases in ductility.

Most plain carbon steels are given an annealing treatment that promotes full recrystallization, but care must be taken to avoid excessive grain growth, which can lead to surface defects (such as "orange peel") in formed parts.

The rates at which the previously mentioned metallurgical processes proceed are functions of both the chemical composition and the prior history of the steel being annealed. For

example, small amounts of elements such as aluminum, titanium, niobium, vanadium, and molybdenum can decrease the rate at which the steel will recrystallize, making the annealing response sluggish and therefore necessitating either higher temperatures or longer annealing times to produce the same properties. Although the presence of these alloying elements is generally the result of deliberate additions intended to modify the properties of the sheet (as in the case of aluminum, titanium, niobium, and vanadium), some elements may be present as residual elements (molybdenum, for example) in quantities great enough to modify the response to annealing. Conversely, larger amounts of cold work (greater cold reductions) will accelerate the annealing response. Therefore, it is not possible to specify a single annealing cycle that will produce a particular set of mechanical properties in all steels; the chemical composition and the amount of cold work also must be taken into account.

Commercial-Quality, Drawing-Quality, and Deep-Drawing-Quality Steels. Commercial-quality plain carbon steel is the most widely produced steel, which is suitable for moderate forming. Drawing-quality (DQ) steel is produced to tighter mechanical-property restrictions for use in more severely formed parts. Drawing-quality special-killed steel is produced to be suitable for the most severe forming applications. Structural-quality steel is produced to specified mechanical properties other than those for the previously mentioned three grades.

The coiling temperature after hot rolling as well as the heating rate during annealing have a significant impact on \bar{r} , which is different for batch and continuous annealing operations (Ref 19, 20). The desired coiling and annealing temperatures are <600 and 720 °C (1100 and 1330 °F) for batch annealing and >700 and 850 °C (1290 and 1560 °F) for continuous annealing. The higher coiling temperature ensures complete AlN precipitation, which coarsens during high temperature during

continuous annealing and promotes strong {111} texture, resulting in high \bar{r} values. In contrast, the lower coiling temperature for the subsequent batch annealing process promotes AlN precipitation, which interacts and retards the recrystallization kinetics during its slow heating process, resulting in desirable pancake grain structure with strong {111} texture and higher deep-drawing characteristics. Furthermore, reduction in carbon and manganese content significantly enhances the \bar{r} values.

The deleterious effect of AlN particles in inhibiting grain growth during continuous annealing can be circumvented by the addition of boron (Ref 21). The addition of boron, up to the boron:nitrogen stoichiometric level, results in a lowering of strength without the necessity of resorting to high hot-mill coiling temperatures. However, a product with boron added has a low \bar{r} -value (Ref 22).

Interstitial-Free (IF) Steels. In IF steels, the elimination of interstitials (carbon and nitrogen) is accomplished by adding sufficient amounts of carbide/nitride-forming elements (generally titanium and/or niobium) to tie up carbon and nitrogen completely, the levels of which can be reduced to less than 50 ppm by modern steelmaking/casting practices, including vacuum degassing.

The choice of the microalloying additions (titanium, niobium, or titanium plus niobium) and the hot-mill coiling practice influence the recrystallization temperature (that is, the minimum temperature required on the annealing line to ensure 100% recrystallization) and product properties. A higher coiling temperature lowers the recrystallization temperature and, in conjunction with heavy cold reduction (~80%), results in superior forming properties. A high annealing temperature is preferred for increased grain growth and high \bar{r} -values. The cooling rate after annealing is not critical, and no overaging treatment is required. Because of this, the IF steels are ideally suited for the production of highly formable, continuously annealed, cold-rolled, hot-dip-coated steels.

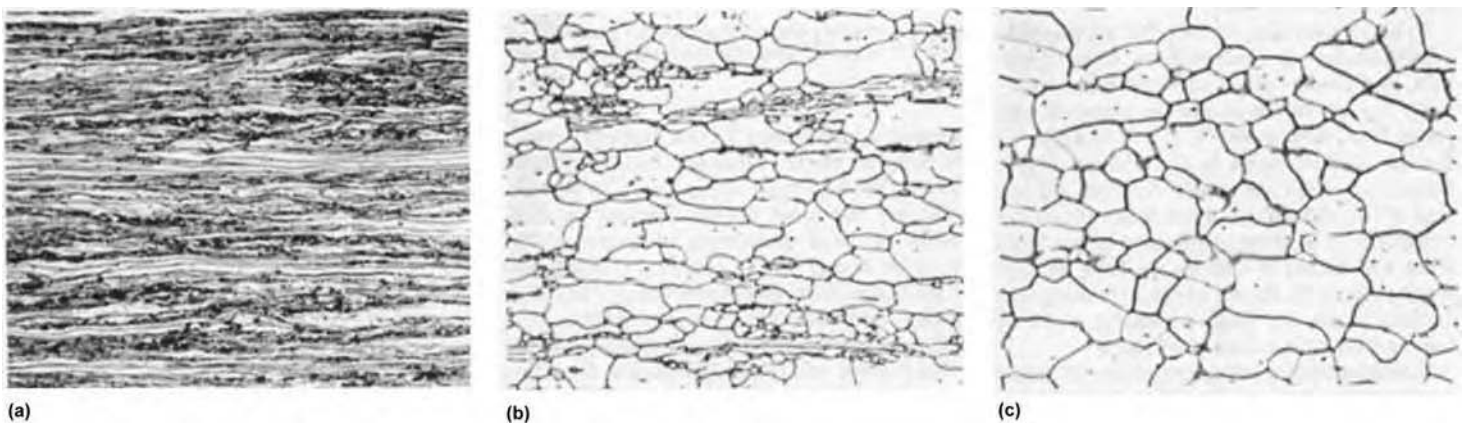


Fig. 13 A low-carbon sheet steel in the (a) as-cold-rolled unannealed condition, (b) partially recrystallized annealed condition, and (c) fully recrystallized annealed condition. Marshall's etch. Original magnification: 1000×

Depending on the processing conditions, the mechanical properties of IF steels fall in the following ranges:

- Yield strength: 130 to 170 MPa (19 to 25 ksi)
- Total elongation: 40 to 47%
- \bar{r} -value: 1.6 to 2.2
- n -value: 0.25 to 0.28

Higher yield strengths, up to 300 MPa (43 ksi), are achieved by solid-solution strengthening with phosphorus, manganese, or silicon (Ref 23).

Bake-hardening steels are characterized by their ability to exhibit an increase in yield strength due to carbon strain aging during paint-baking operations at moderate temperatures (125 to 180 °C, or 260 to 355 °F). Bake hardening has little effect on tensile strength.

Plain Carbon Steels. In the continuous annealing of plain carbon steels, the final solute carbon is restricted to less than approximately 10 ppm by the fine-tuning of the primary cooling rate and the overaging temperature/time to ensure adequate freedom from ambient strain aging. This level of solute carbon, however, is sufficient to realize a bake-hardening (175 °C, or 350 °F, for 20 min) yield strength increment of up to 50 MPa (7 ksi) (Ref 24).

In *dual-phase steels*, the martensite phase (≤ 20 to 30 vol%) suppresses ambient strain aging (Ref 25). Accordingly, a higher solute carbon concentration and a consequent larger bake-hardening yield strength increment (≤ 90 MPa, or 13 ksi) are feasible.

In *IF steels*, a bake-hardening strength increment can be generated if several conditions are satisfied (Ref 26):

- Niobium or niobium + titanium chemistry with a niobium-to-carbon atomic ratio less than or equal to 1
- High annealing temperatures (~ 850 °C, or 1560 °F) in the continuous-annealing line to permit partial dissolution of the NbC precipitates
- Rapid cooling of ≤ 20 °C/s (35 °F/s) after annealing
- No overaging, to prevent the reprecipitation of carbon

In addition, if processed on a hot-dip galvanizing line, rapid cooling between the coating pot temperature and approximately 200 °C (400 °F) is necessary to circumvent precipitation of the solute carbon as Fe₃C. A bake-hardening yield strength increment of 20 to 40 MPa (3 to 6 ksi) has been reported (Ref 23).

Solution-Strengthened and Microalloyed High-Strength Low-Alloy Steels (Ref 27–31). In solution-strengthened steels, alloying additions of manganese, phosphorus, and/or silicon are made to increase strength by substitutional solid-solution strengthening: approximately 3 MPa (0.4 ksi) per 0.1% Mn, 7 MPa (1 ksi) per 0.01% P, and 8.5 MPa (1.2 ksi) per

0.1% Si. These elements are equally effective whether the steel is batch or continuously annealed. With continuous annealing, lower alloying additions are needed to achieve a desired strength level, however, because of the finer ferrite grain size. The finer grain size is a result of, first, the very fast heating rate (compared to batch annealing), which leads to more nucleation, and, in turn, a fine grain size, and second, the short soak time (< 1 min), which prevents the growth of the fine recrystallized ferrite grains. The continuous-annealing thermal profile used to produce solid-solution-strengthened steels consists primarily of a recrystallization annealing followed by overaging, as in the case of DQ and/or deep-drawing-quality steels.

In microalloyed high-strength low-alloy (HSLA) steels, which contain microadditions of niobium, titanium, or vanadium (niobium is generally preferred), higher strength levels are achieved by precipitation strengthening and grain refinement. In a continuous-annealing process, the microalloy carbonitride particles can provide effective precipitation strengthening because the short annealing time prevents the occurrence of any appreciable particle

coarsening. In contrast, the coarsening of the precipitate particles that occurs during batch annealing results in a considerable decrease in the precipitation strengthening, although the particles do retard grain growth to some extent. As a consequence, for the same composition, a higher yield strength is achievable with continuous annealing (Fig. 14).

The HSLA steels are sensitive to the hot-mill coiling temperature, and a low-temperature coiling practice is preferred to maximize precipitation strengthening. The thermal profile on a continuous-annealing line for microalloyed HSLA steels is similar to that for the solution-strengthened steels. However, the HSLA steels require higher annealing temperatures to ensure complete recrystallization, because the carbonitride particles of niobium, titanium, and vanadium retard recrystallization.

Yield strength levels ranging from approximately 280 to 550 MPa (40 to 80 ksi) are possible and practical with solution-strengthened and microalloyed HSLA steels. Yield ratio, that is, the ratio of yield strength to tensile strength, is approximately 0.8. Like the plain carbon steels, these steels exhibit bake-hardening characteristics.

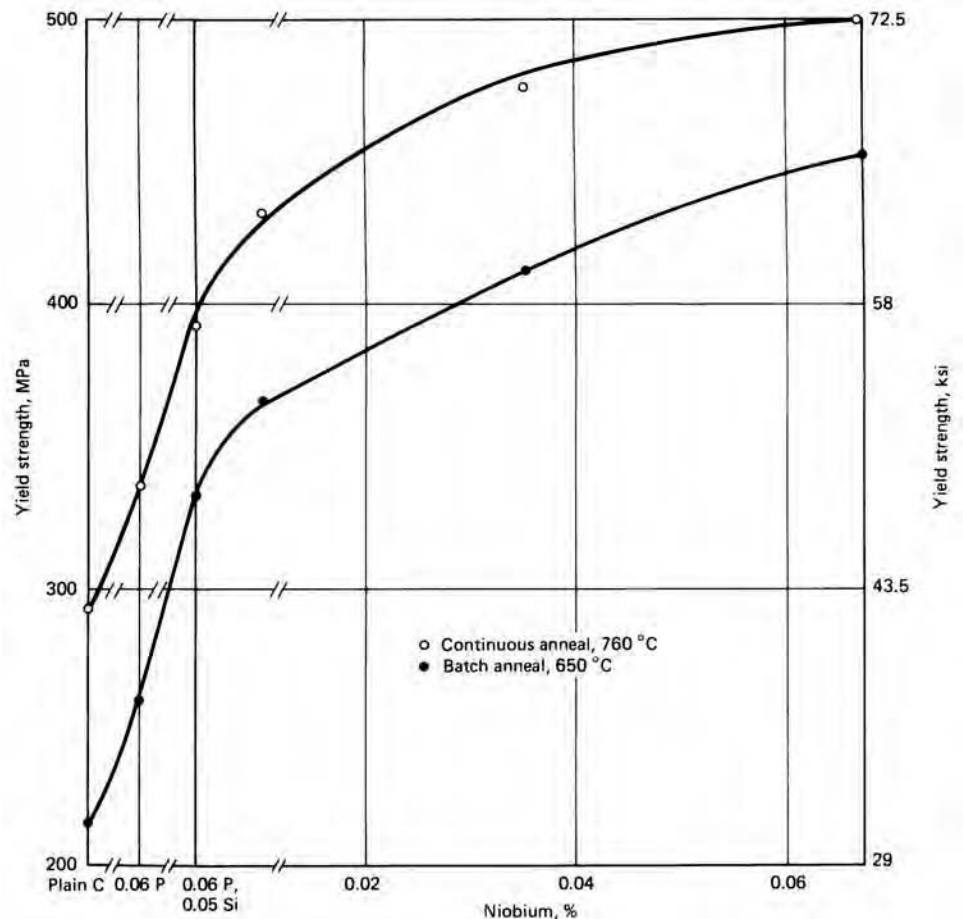


Fig. 14 Comparison of strength levels achievable by means of continuous and batch annealing of solution-strengthened and high-strength low-alloy steels. Source: Ref 27

Dual-phase steels are unique in that they deform by a continuous yielding behavior, because the martensite is a continuous source of dislocations during plastic deformation. Most other low-carbon steels that display a yield point upon deformation need to be skin passed or temper rolled to provide a source of dislocations for continuous yielding behavior. Steels displaying a yield point are undesirable for many forming operations because of the



Fig. 15 Stretcher-strain marks (Lüders bands) on the surface of a range component after forming. Original magnification: 0.25x

formation of Lüders bands (Fig. 15) that blemish the surface.

Annealing of dual-phase steels involves soaking in the intercritical or two-phase (ferrite-plus-austenite) region, followed by the transformation of some of the austenite into martensite. The martensite is responsible for the higher strength levels, especially tensile strength, of these steels (Ref 31, 32). To promote the austenite-to-martensite transformation, a critical level of hardenability is needed, depending on the cooling rate. Lower hardenability, from a reduced amount of manganese (and/or molybdenum, chromium) in the steel, can be tolerated with a higher cooling rate (Fig. 16). These steels are generally annealed for a short period (usually less than 5 min) in the intercritical range, followed by rapid cooling. The resulting microstructure is 10 to 20% martensite by volume in a matrix of ferrite. The continuous-annealing process is ideal for producing dual-phase sheet grades.

There are several types of dual-phase steels, determined by the thermal profile of the continuous-annealing line following the intercritical anneal. Low-hardenability steels can be produced most economically by directly water quenching from the intercritical annealing temperature, followed by overaging to temper the martensite. High-hardenability dual-phase steels (with high manganese and molybdenum content) are produced by lowering the quenching temperature by gas-jet cooling and lowering the overaging temperature. Furthermore, fully martensitic steels can also be

produced by annealing and water quenching. The martensitic transformation is often aided by boron addition.

Tin mill products are distinguished from their cold-rolled sheet mill counterparts chiefly by the fact that they are produced in lighter gages (0.13 to 0.38 mm, or 0.005 to 0.015 in.) and by the fact that some of them are coated with tin or chromium and chromium oxide for corrosion resistance. The sequence used for processing single-reduced tin mill products is similar to that for cold-rolled sheet, that is, pickling, cold reducing, annealing, and temper rolling of hot-rolled coils. Double-reduced products are cold rolled an additional 30 to 40% following annealing (this step replaces temper rolling). Whereas much of the tonnage produced in tin mills is batch annealed, a considerable amount is continuous annealed. (Facilities for continuous annealing currently are more prevalent in tin mills than in sheet mills.)

Because tin mill products traditionally have been produced at facilities separate from sheet mills and because applications for these products are different from those for cold-rolled sheet, tin mill products have been assigned separate designations for indicating the mechanical properties developed during annealing. A list of these temper designations is given in Table 4.

The conventional tinplate continuous-annealing lines involve soaking at 650 to 700 °C (1200 to 1300 °F), followed by slow gas-jet cooling (~10 °C/s, or 20 °F/s) to the ambient temperature. The T4 (Rockwell hardness, HR 30T = 61 ± 3) and T5 (HR 30T = 65 ± 3) tempers are being produced on these lines using plain carbon aluminum-killed chemistries.

The production of T2 (HR 30T = 53 ± 3) and T3 (HR 30T = 57 ± 3) tempers by continuous annealing have necessitated several chemistry restrictions and process modifications. The optimum carbon level is 0.02 to 0.07%, with total nitrogen restricted to less than 0.003%. Hotmill coiling is restricted to below 630 °C (1165 °F) to prevent deterioration of corrosion resistance due to the presence of coarse carbides (Ref 34). Rapid cooling (40 to 70 °C/s, or 70 to 125 °F/s) from 700 °C (1300 °F), followed by

Table 4 Temper designations for steel tin mill products

Designation	Hardness aim, HR 30T
Batch (box)-annealed products	
T1	52 max
T2	50–56
T3	54–60
Continuously annealed products	
T4 CA	58–64
T5 CA (TU)	62–68
T6 CA	67–73
Double-reduced products	
DR-8	73
DR-9	76
DR-9M	77
DR-10	80

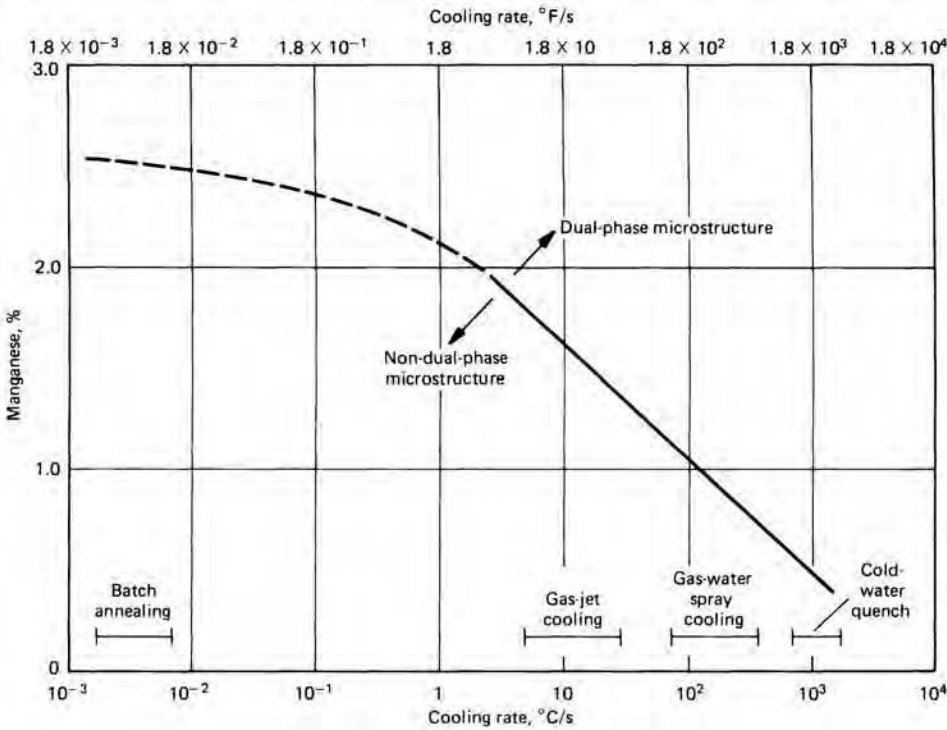


Fig. 16 Effect of cooling rate from the intercritical temperature on the manganese required to form dual-phase microstructures. Source: Ref 33

overaging at 400 to 450 °C (750 to 840 °F) for 60 s, is necessary to reduce the carbon concentration solute and, consequently, the hardness. The rapid cooling is achieved by means of high-speed gas-jet cooling systems (Ref 35).

Improved hardness distribution, improved corrosion resistance as a result of enhanced surface cleanliness, and the prevention of surface defects caused by the surface enrichment of carbon and manganese are the key advantages of continuous annealing over batch-annealed tinplate sheets.

Open-coil annealing, which is done in batch furnaces, involves loose rewinding of a cold-reduced coil to provide open spaces between successive laps. This allows the controlled atmosphere gases to be drawn between the laps, providing faster and more uniform heating and cooling than are obtained with tightly wound coils. In addition, by control of the hydrogen content and dewpoint of the atmosphere, decarburizing conditions can be established. The carbon content of the steel can thereby be reduced to low levels for such materials as enameling steel and electrical steel.

Loose rewinding of coils for open-coil annealing is done on a turntable having a vertical mandrel. As the coil is wound, a twisted wire spacer is inserted between the laps. This spacer remains in the coil during annealing and is removed after the coil has been removed from the furnace. The coil is then tightly rewound and is ready for temper rolling.

Annealing of Steel Forgings

Annealing of forgings is most often performed to facilitate some subsequent operation, usually machining or cold forming. The type of annealing required is determined by the kind and amount of machining or cold forming to be done as well as the type of material involved. For some processes it is essential that the microstructure be spheroidal, whereas for others spheroidal structures may not be necessary or even desirable.

Annealing of Forgings for Machinability. In many cases, a structure suitable for machining can be developed in low-carbon steel forgings by transferring the forgings directly from the forging operation to a furnace heated to a proper transformation temperature, holding them at this temperature for a time sufficiently long to permit all the austenite to transform, then cooling in air. In this process, the effective austenitizing temperature is the finishing temperature of forging, not the initial forging temperature. This process is capable of producing reasonably uniform structures in forgings of uniform sections. However, in forgings shaped such that some portions are cooler than others, this difference in finishing temperature will cause the structures to be dissimilar. This process generally will not produce a spheroidal structure except in high-alloy steels containing large amounts of carbide-forming elements. If

a lamellar structure is suitable for subsequent operations, however, this process can minimize the energy usage and lower costs by reducing processing and handling time.

In many instances where the product or subsequent process requires a more consistent hardness, forgings can be subcritical annealed by heating to a temperature between 10 and 20 °C (20 and 40 °F) below A_{e1} , holding sufficiently long (determined by degree of softening required), and then cooling in air (or equivalent). Care should be taken to maintain the temperature below A_{e1} to prevent formation of austenite, which would require a much lower cooling rate.

In forgings produced from higher-carbon steels with or without significant amounts of alloying elements, a spheroidal structure generally is preferable for high-speed machining operations. Direct transfer of high-carbon steel forgings to a furnace for transformation sometimes can be used as the preliminary step of an annealing cycle and as a means of preventing the possibility of cracking in deep-hardening steel parts, but seldom will produce satisfactory properties alone. Most annealing of high-carbon steel forgings is done either in a batch furnace or in a continuous tray pusher furnace. Typical schedules for spheroidizing 52100 steel in a batch furnace are as follows:

- Austenitize by holding at least 2 h at 790 °C (1450 °F), furnace cool at 17 °C/h (30 °F/h) to 595 °C (1100 °F), then air cool
- Austenitize by holding at least 2 h at 790 °C (1450 °F), cool as rapidly as practical to 750 °C (1380 °F), cool at 6 °C/h (10 °F/h) to 675 °C (1250 °F), then air cool
- Austenitize by holding at least 2 h at 790 °C (1450 °F), cool as rapidly as practical to 690 °C (1275 °F), transform isothermally by holding at this temperature for 16 h, then air cool

In all instances, the load should be distributed to promote uniform heating and cooling. Use of circulating fans in the furnace chamber will greatly aid in producing a product that is uniform in both hardness and microstructure.

A typical continuous furnace for annealing steel forgings may consist of five or six zones. An example of a specific spheroidize annealing treatment in such a furnace is given in the next section.

Annealing of Forgings for Cold Forming and Re-Forming. If a steel forging or blank requires further cold forming, it may be necessary to soften it to enhance its plastic-flow characteristics. In general, this type of annealing is done only to the extent that the forming operation requires, that is, to satisfy dimensional, mechanical, and tool-life requirements, as well as to prevent cracking and splitting. Much intermediate annealing is done successfully, but cold forming processes are best performed on parts with totally spheroidized microstructures, especially for parts made of high-carbon steels.

In one plant, both 5160 and 52100 steels have been successfully spheroidized with a common cycle in a six-zone tray pusher furnace. In this cycle, the temperatures in the six zones are 750, 750, 705, 695, 695, and 680 °C (1380, 1380, 1300, 1280, 1280, and 1260 °F). Time in each zone is 150 min. This process yields 5160 steel forgings with hardnesses of 170 to 190 RB and 52100 steel parts with hardnesses of 175 to 195 RB, both suitable for cold or warm restrike operations.

In another cold-forming plant, 15B35 steel is processed in either a continuous roller-hearth furnace or a bell furnace, depending on the severity of the cold-forming operation. The continuous furnace is a two-zone furnace with zone temperatures at 750 °C (1380 °F) and 695 °C (1280 °F). Annealing time in each zone is between 90 and 120 min. The parts then enter a water-cooled cooling bed and exit the furnace at approximately 260 °C (500 °F). Only a partially spheroidized structure is obtainable in this furnace. If a nearly full-spheroidized structure is required, bell furnaces are used (Fig. 17). A typical cycle for a 4500 kg (10,000 lb) load involves soaking at 760 °C (1400 °F) for 8 h followed by a slow cool to 675 °C (1250 °F) and a rapid cool afterward.

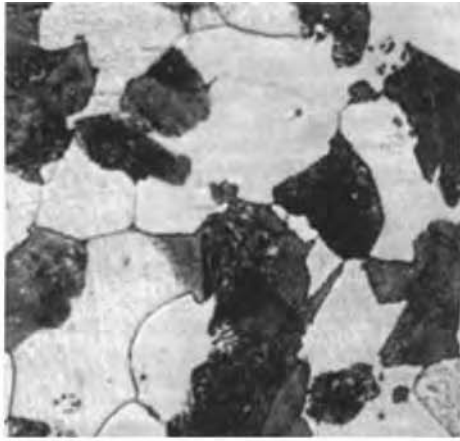
A commercial heat treater uses a further variation of the processing cycle in its bell furnaces. The cycle for a 14,000 kg (31,000 lb) load involves soaking at 765 °C (1410 °F) for 24 h, furnace cooling to 675 °C (1250 °F), and holding at that temperature for 16 h, followed by a rapid cooling.

Low-carbon steels generally can be cold formed successfully after being heated to temperatures near A_1 and then being cooled through 675 °C (1250 °F) at a controlled rate. In one plant, 5120 steel annealed 1 to 2 h at 745 °C (1375 °F) and slow cooled has been cold formed successfully. Large quantities of 1008, 1513, 1524, 8620, and 8720 steels are being cold formed after annealing cycles consisting of 1 to 6 h at 720 °C (1325 °F), followed by slow cooling. The severity of the forming operation, as well as the grade of steel and history of the part, determines the extent of annealing required. Batch furnaces, continuous tray pusher furnaces, and continuous belt furnaces are being used successfully to perform these types of annealing operations on low-carbon steels.

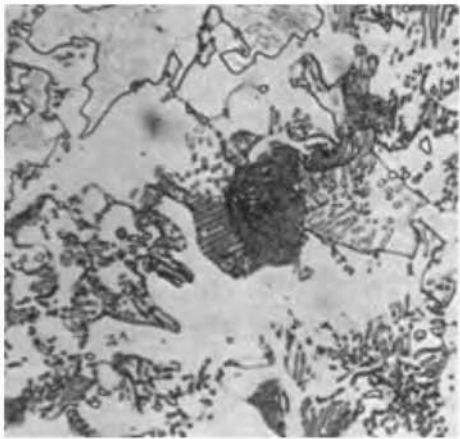
Any part that contains significant stresses resulting from cold forming or restrike operations should be reviewed for some type of stress-relief process. Stress relieving usually is done by means of time-temperature cycles that result in slight reductions in hardness. These cycles often consist of 1 h at 425 to 675 °C (800 to 1250 °F).

Annealing to Obtain Pearlitic Microstructures. Forgings—especially plain and alloy high-carbon steel forgings—are isothermally annealed to produce a pearlitic microstructure that is preferred for a subsequent process. In steels that are to be induction hardened, for

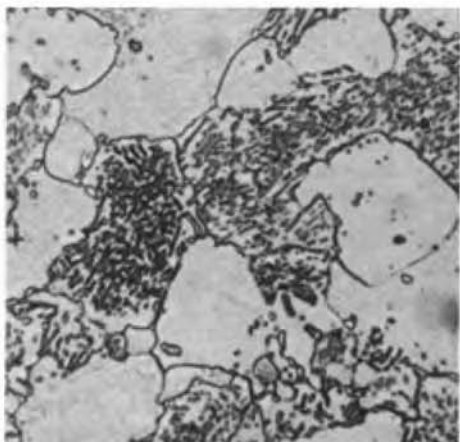
example, the carbide distribution of a fine pearlitic structure offers excellent preparation for optimum control in selective hardening while producing a reasonably machinable core



(a)



(b)



(c)

Fig. 17 Microstructures of 15B35 steel. (a) In the as-received hot-rolled condition, microstructure is blocky pearlite. Hardness is 87 to 88 HRB. (b) In the partially spheroidized condition following annealing in a continuous furnace. Hardness is 81 to 82 HRB. (c) In the nearly fully spheroidized condition following annealing in a bell furnace. Hardness is 77 to 78 HRB.

structure. Isothermal annealing to obtain line pearlite can be performed in batch or continuous furnaces; however, temperature control and uniformity are more critical than in conventional slow cooling cycles because a particular microstructure and a particular hardness level usually are desired. In one plant, a continuous belt-type furnace is used for isothermal annealing of 1070 steel forgings. The forgings are uniformly heated for 30 min at 845 °C (1550 °F), cooled to 675 °C (1250 °F), and held for 20 min, then rapidly cooled. The microstructure produced is essentially fine lamellar pearlite with a hardness of 219 to 228 HB. The hardness and the structure can be modified by adjusting the transformation temperature.

Annealing of Bar, Rod, and Wire

Significant tonnages of bar, rod, and wire are subjected to thermal treatments that decrease hardness and prepare the material for subsequent cold working and/or machining. For low-carbon steels (up to 0.20% C), short-time subcritical annealing often is sufficient for preparing the material for further cold working. Steels with higher carbon and alloy contents require spheroidizing to impart maximum ductility.

Most carbon and alloy steel coiled products can be successfully spheroidized. In batch annealing, it is helpful to use higher-than-normal temperatures (for example, 650 °C, or 1200 °F) during initial heating for purging because the higher initial temperature promotes a lower temperature gradient in the charge during subsequent heating into the temperature range between A_1 and A_3 . Use of a higher purge temperature also promotes agglomeration of the carbides in the steel, which makes them more resistant to dissolution in the austenite when the charge temperature is finally elevated. These undissolved carbides will be conducive to the formation of a spheroidal rather than a lamellar structure when transformation is complete.

Knowledge of the temperature distribution in the furnace and in the load can be a major factor in achieving a good, consistent response to spheroidization. Temperature distribution and control are much more critical in batch and vacuum furnaces, which may handle loads of up to 27 Mg (30 tons), than in continuous furnaces, in which loads of only 900 to 1800 kg (2000 to 4000 lb) may be transferred from zone to zone. Test thermocouples should be placed strategically at the top, middle, and bottom (inside and outside) of the charge during development of cycles. In spheroidizing, to minimize formation of pearlite on cooling, it is important to ensure that no part of the charge be allowed to approach A_3 . Conversely, if temperatures only slightly above A_1 are used and temperature controls are inaccurate because of poor placement of thermocouples, it is probable that the A_1 temperature will not be attained and that no austenitization will occur.

Table 5 gives typical mechanical properties that can be obtained in hypoeutectoid plain carbon steels by spheroidizing. Recommended temperatures and times for lamellar and spheroidize annealing of hypoeutectoid alloy steels are presented in Table 3.

Prior cold working increases the degree of spheroidization and provides even greater ductility. For example, 4037 steel in the as-rolled condition normally can be spheroidized to a tensile strength of approximately 515 MPa (75 ksi). If, however, the material is drawn 20% and then spheroidized (referred to as spheroidize annealed in-process), the resulting tensile strength will be approximately 470 MPa (68 ksi).

Although prior cold work can enhance response to annealing, caution must be observed in spheroidizing cold-worked plain carbon steels with 0.20% C or less. Unless a reduction of at least 20% is applied, severe grain coarsening may be observed after spheroidizing. Such grain coarsening is the result of a unique critical combination of strain and annealing temperature for the particular steel and may severely impair subsequent performance.

In the wire industry, a wide variety of in-process annealing operations have been evolved for rendering coiled material suitable for further processing that may require formability, drawability, machinability, or a combination of these characteristics. One large wire mill reports current use of 42 separate and distinct annealing cycles, the majority of which represent compromises between practical considerations and optimum properties. For example, annealing temperatures below those that may yield optimum softness sometimes must be used in order to preclude scaling of wire coils, which often can occur even in controlled-atmosphere furnaces. Even slight scaling may cause the coil wraps to stick together, which can impede coil payoff in subsequent operations.

Some of the terms used to describe various in-process annealing treatments are in common usage throughout the wire industry, whereas others have been developed within specific plants or mills. No attempt is made here to list or define all the names that refer to specific treatments.

Table 5 Typical mechanical properties of spheroidized plain carbon steels

Steel	Tensile strength			
	Hot rolled		Spheroidized	
	MPa	ksi	MPa	ksi
1010	365	53	295	43
1018	450	65	365	53
1022	470	68	385	56
1030	585	85	415	60
1038	600	87	485	70
1045	675	98	515	75
1060	860	125	550	80
1065	910	132	600	87
1524	510	74	450	65
1541	710	103	540	78

Patenting is a special form of annealing that is unique to the rod and wire industry. In this process, which usually is applied to medium- and higher-carbon grades of steel, rod or wire products are uncoiled, and the strands are delivered to an austenitizing station. The strands are then cooled rapidly from above A_3 in a molten medium—usually lead at approximately 540°C (1000°F)—for a period of time sufficient to allow complete transformation to a fine pearlitic structure. Both salt baths and fluidized beds have also been used for this purpose. This treatment increases substantially the amount of subsequent wire drawing reduction that the product can withstand and permits production of high-strength wire. Successive drawing and patenting steps may be employed if necessary, to obtain the desired size and strength level.

Austenitizing for patenting can be accomplished in oil, gas, or electric furnaces; in high-temperature lead or salt baths; or by induction or direct resistance heating. As an alternative to quenching in molten lead, continuous air cooling often is employed. Such air patenting is less expensive than lead patenting but results in coarser pearlite and often more proeutectoid ferrite, a microstructure that is less desirable from the standpoint of drawing high-strength wire.

Annealing of Plate and Tubular Products

Plate products are occasionally annealed to facilitate forming or machining operations. Annealing of plate usually is done at subcritical temperatures, and long annealing times generally are avoided. Maintaining adequate flatness can be a significant problem in annealing of large plates.

Tubular products known as mechanical tubing are used in a variety of applications that can involve machining or forming. For these products, which are made from various grades of steel, annealing is a common treatment. In most annealing cycles, subcritical temperatures and short annealing times are used to reduce hardness to the desired level. High-carbon grades, such as 52100, generally are spheroidized to facilitate machining. Tubular products manufactured in pipe mills are rarely annealed. These products normally are used in the as-rolled, the normalized, or the quenched and tempered condition.

Accelerated Cycling Annealing

Historically, the annealing cycles comprised three segments: heating, soaking, and cooling. Depending on the charge dimensions and target transformation, there could be additional soaking segments. This philosophy of minimizing the number of segments during heat treating has not changed despite significant advances in the modern programmable controllers and online-control systems. These modern control

systems enable deployment of a large number of controlled segments during the heat treating operation.

The possibility of significant acceleration in the transformation kinetics by replacing the conventional isothermal soaking segment with controlled cyclic segments has been demonstrated (Ref 36). The accelerated phase transformation during cyclic thermal processing has been observed in a variety of solid-state phase transformations, including recrystallization (Ref 37), grain growth (Ref 36), austempering (Ref 38, 39), and spheroidizing of steel (Ref 40). As compared to the conventional isothermal processing (Fig. 18a), in the cyclic processing, the phase transformation is carried out in a narrow temperature range, where the temperature is cycled in a controlled manner between the high and low temperatures (Fig. 18b). The acceleration of transformation kinetics during cyclic thermal processing has been envisioned as a novel way to reduce the energy consumption and enhance the productivity of these industrial operations.

During cyclic grain growth of aluminum-killed steel, annealing was carried out between two temperatures with an amplitude range of 75 to 120°C (165 to 250°F), where the temperature was varied with a frequency of 5 to $20^\circ\text{C}/\text{min}$ (10 to $35^\circ\text{F}/\text{min}$) (Ref 36). It was observed that cyclic annealing results in higher grain growth compared to the maximum temperature limit, with a possibility of 15%

reduction in the annealing time and 20% reduction in energy cost (Ref 41). It was also noted that during cyclic annealing, both cyclic frequency as well as amplitude have significant impact on the transformation kinetics. In addition, both the amplitude and frequency demonstrate a presence of optimum value with highest rate of transformation kinetics (Ref 36). Similar observations were made for the cyclic recrystallization of cold-rolled steel (Ref 37). In the aforementioned work, these results were also modeled and explained on the basis of an additional nonisothermal component in the rate equation.

Bainitic transformation kinetics were also precisely studied by Gleeble experiments, where accelerated kinetics, with as high as 80% reduction in time, were observed during cyclic austempering as compared to conventional isothermal austempering (Ref 38, 39). In another work, cyclic spheroidization treatment around A_{c3} was found to accelerate the spheroidization kinetics in a medium-carbon steel (Ref 40).

The accelerated kinetics were attributed to the nonisothermal effects arising from heating rate and temperature-reversal effects imposed during cyclic processing. It was hypothesized that in addition to thermal excitation, during cyclic annealing, extra nonisothermal excitation is available for grain growth, the magnitude of which increases with an increase in the heating rate (Ref 36). Furthermore, this acceleration during cyclic processing has been modeled on

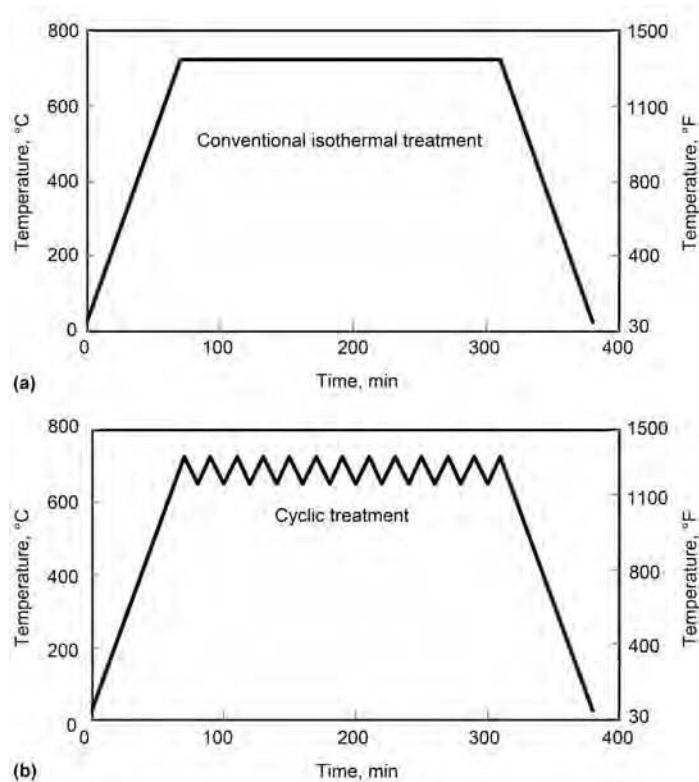


Fig. 18 (a) Conventional annealing with isothermal soaking segment. (b) Cyclic treatment with soaking segment having temperature fluctuations with controlled frequency and amplitude. The temperatures and time given here are illustrative.

the basis of thermally activated escape of an overdamped Brownian particle from the metastable state of a system driven by a time-periodic force (Ref 37), which resulted in an additional nonisothermal component in the rate constant of the Johnson-Mehl-Avrami-Kolmogorov-type kinetic models. The extra nonisothermal excitation mentioned in the hypothesis was the nonisothermal term in the rate equation.

The accelerated transformation kinetics during cyclic annealing can be effectively used by replacing the constant-temperature soaking segment with controlled cyclic perturbations, below the required isothermal temperature. The accelerated transformation kinetics during cyclic treatments will reduce the total cycle time with a resultant enhancement in productivity, whereas reduction in energy consumption will be effected due to the reduction in cycle time as well as the reduction in the mean furnace temperature during cyclic treatment. During cyclic annealing under laboratory conditions, the benefits have been quantified as 10 to 15% productivity enhancement and 15 to 20% energy reduction. It must be noted that cyclic processing is amenable to components and shapes with lower thicknesses. For example, it can be easily implemented during continuous annealing of sheets and tubes. However, due to the dampening of thermal amplitude for thick components, for example, billets, bars, or batch annealing of coils, thermal cycling may not be very effective. The importance of nonlinearity in transformation kinetics is emphasized in this work.

REFERENCES

- G. Krauss, Normalizing, Annealing and Spheroidizing Treatments, *Steels: Processing, Structure, and Performance*, ASM International, 2005, p 251–262
- K.W. Andrews, Empirical Formulae for the Calculation of Some Transformation Temperatures, *J. Iron Steel Inst.*, Vol 203, 1965, p 721
- B.R. Banerjee, Annealing Heat Treatments, *Met. Prog.*, Nov 1980, p 59
- Atlas of Isothermal Transformation and Cooling Transformation Diagrams*, American Society for Metals, 1977
- M. Atkins, *Atlas of Continuous Cooling Transformation Diagrams for Engineering Steels*, American Society for Metals, in cooperation with British Steel Corporation, 1980
- P. Payson, The Annealing of Steel, series, *Iron Age*, June and July 1943; Technical booklet, Crucible Steel Company of America
- L.E. Samuels, *Optical Microscopy of Carbon Steels*, American Society for Metals, 1980
- J. Arruabarrena, P. Uranga, B. López, and J.M. Rodríguez-Ibabe, Carbide Spheroidization Kinetics in a Low Alloy Medium Carbon Steel: Relevance of Deformation after Transformation, *Mater. Sci. Technol. (MS&T)*, 2011, p 698–705
- J.D. Verhoeven, The Role of the Divorced Eutectoid Transformation in the Spheroidization of 52100 Steel, *Metall. Mater. Trans. A*, Vol 31, 2000, p 2431–2438
- N.V. Luzginova, L. Zhao, and J. Sietsma, The Cementite Spheroidization Process in High-Carbon Steels, with Different Chromium Contents, *Metall. Mater. Trans. A*, Vol 39, 2008, p 513–521
- W. Snyder, Annealing and Carburizing Close Tolerance Driving Gears, *Met. Prog.*, Oct 1965, p 121
- H.E. McGannon, Ed., *The Making, Shaping and Treating of Steel*, 10th ed., Association of Iron and Steel Engineers, 1985
- S.S. Sahay and K. Krishnan, Model-Based Optimisation of a Continuous Annealing Operation for Bundle of Packed Rods, *Ironmaking Steelmaking*, Vol 34, 2007, p 89–94
- S.S. Sahay and P.C. Kapur, Model-Based Scheduling of a Continuous Annealing Furnace, *Ironmaking Steelmaking*, Vol 34 (No. 3), 2007, p 262–268
- S.S. Sahay, A.M. Kumar, and A. Chatterjee, Development of Integrated Model for Batch Annealing of Cold Rolled Steels, *Ironmaking Steelmaking*, Vol 31 (No. 2), 2004, p 144–152
- S.S. Sahay, K. Krishnan, M. Kulthe, A. Chodha, B. Bhattacharya, and A.K. Das, Model-Based Optimisation of a Highly Automated Industrial Batch Annealing Operation, *Ironmaking Steelmaking*, Vol 33 (No. 4), 2006, p 306–314
- S.S. Sahay, R. Mehta, S. Raghavan, R. Roshan, and S.J. Dey, BAF Tinplate Process Analytics, Modeling, and Optimization of an Industrial Batch Annealing Operation, *Mater. Manuf. Process.*, Vol 24, 2009, p 1459–1466
- S.S. Sahay, Modeling of Industrial Heat Treatment Operations, *Handbook of Thermal Process Modelling of Steels*, C. Hakan Gur and J. Pan, Ed., CRC Press, 2009, p 313–339
- W.B. Hutchinson, Development and Control of Annealing Texture in Low Carbon Steels, *Int. Met. Rev.*, Vol 29, 1984, p 25–42
- E. Kozeschnik, V. Pletenev, N. Zolotor-evsky, and B. Buchmayr, Aluminum Nitride Precipitation and Texture Development in Batch-Annealed Bake-Hardening Steel, *Metall. Mater. Trans. A*, Vol 30, 1999, p 1663–1673
- N. Takahashi et al., in *Metallurgy of Continuous-Annealed Sheet Steel*, B.L. Bramfitt and P.L. Mangonon, Ed., TMS-AIME, 1982, p 133–153
- R. Pradhan and J.J. Battisti, in *Hot- and Cold-Rolled Sheet Steels*, R. Pradhan and G. Ludkovsky, Ed., TMS-AIME, 1988, p 41–56
- Y. Tokunaga and H. Kato, in *Metallurgy of Vacuum-Degassed Steel Products*, R. Pradhan, Ed., The Minerals, Metals and Materials Society, 1990, p 91–108
- K. Yamazaki et al., in *Microalloyed HSLA Steels*, ASM International, 1988, p 327–336
- K. Nakaoka et al., in *Formable HSLA and Dual-Phase Steels*, A.T. Davenport, Ed., TMS-AIME, 1977, p 126–141
- M. Kurosawa et al., *Kawasaki Steel Tech. Rep.*, No. 18, 1988, p 61–65
- R. Pradhan, *J. Heat Treat.*, Vol 2 (No. 1), 1981, p 73–82
- R. Pradhan, in *Metallurgy of Continuous-Annealed Sheet Steel*, B.L. Bramfitt and P.L. Mangonon, Ed., TMS-AIME, 1982, p 203–227
- R. Pradhan et al., *Iron Steelmaker*, Feb 1987, p 25–30
- R. Pradhan, in *HSLA Steels: Technology and Applications*, American Society for Metals, 1984, p 193–201
- R. Pradhan, in *Technology of Continuously Annealed Cold-Rolled Sheet Steel*, R. Pradhan, Ed., TMS-AIME, 1985, p 297–317
- I. Gupta and P.-H. Chang, in *Technology of Continuously Annealed Cold-Rolled Sheet Steel*, R. Pradhan, Ed., TMS-AIME, 1985, p 263–276
- P.R. Mould, in *Metallurgy of Continuous-Annealed Sheet Steel*, B.L. Bramfitt and P.L. Mangonon, Ed., TMS-AIME, 1982, p 3–33
- T. Obara et al., in *Technology of Continuously Annealed Cold-Rolled Sheet Steel*, R. Pradhan, Ed., TMS-AIME, 1985, p 363–383
- Recent Development in CAPL Technology: CAPL for Tinplate, *Nippon Steel Tech. Rep.*, Oct 1988
- S.S. Sahay, C.P. Malhotra, and A.M. Kolkhede, Accelerated Grain Growth Behavior during Cyclic Annealing, *Acta Mater.*, Vol 51, 2003, p 339–346
- V. Sista, P. Nash, and S.S. Sahay, Accelerated Bainitic Transformation during Cyclic Austempering, *J. Mater. Sci.*, Vol 42, 2007, p 9112–9115
- V. Sista, P. Nash, and S.S. Sahay, Accelerated Bainitic Transformation during Cyclic Austempering, *Heat Treat. Prog.*, July 2008, p 45–48
- K. Krishnan, S.S. Sahay, S. Singh, and D. Pal, Modeling the Accelerated Cyclic Annealing Kinetics, *J. Appl. Phys.*, Vol 100, 2006, p 093505
- A. Saha, D.K. Mondal, and J. Maity, An Alternate Approach to Accelerated Spheroidization in Steel by Cyclic Annealing, *J. Mater. Eng. Perform.*, Vol 20, 2011, p 114–119
- S.S. Sahay, Energy Reduction via Cyclic Heat Treatments, *Heat Treat. Prog.*, Jan 2003, p 44–45

Subcritical Annealing and Normalizing

Roger N. Wright, Rensselaer Polytechnic Institute

THE TERM *anneal* encompasses many operations in steel processing (see the article “Annealing of Steel” in this Volume). While these operations vary considerably, they usually have the purpose of transforming the steel into a predictable state, and often a state that affords improved secondary processing latitude. This article provides additional details on the metallurgy and process specifics of subcritical annealing, which involves heating below the lower critical temperature (A_1), such that austenite does not form during subcritical annealing. Practical implications for induction annealing are included.

In principle, the starting microstructure can be ferrite, pearlite, bainite, martensite, tempered martensite, and combinations thereof. Often, the starting microstructure has been cold worked, with the main purpose of the anneal being to remove cold work by way of recovery and recrystallization. Somewhat parallel or overlapping stages of subcritical annealing response may be described as follows:

- Transformation of the initial microstructure to a combination of ferrite and carbide. Microstructural interpretation typically is important in regard to understanding of the transformation response. Normalizing anneals accomplish much the same purpose (discussed in this article and the article “Normalizing of Steels” in this Volume).
- Transformation of a cold-worked structure to a stress-relieved, recovered, and recrystallized structure of ferrite and carbide
- Transformation of a structure of ferrite and carbide to a structure involving globular carbides, of increased coarseness

In response “a” from subcritical annealing, if the starting microstructure is martensitic, then anneals of appropriate temperature and time will carry carbide development through the range of tempered structures, ending up (if desired) with an overtempered distribution of globular carbides in ferrite. If the starting structure is that of ferrite and pearlite, the annealing may cause a degeneration of the pearlite, en route to a structure of globular carbides in ferrite.

Most practical subcritical annealing involves responses “b” and “c”. Annealing en route to

response “b” is often called process annealing, and its purpose is to remove the effects of cold work so as to allow continued cold working with reduced risk of fracture, or simply to provide a softer, more tough and ductile structure to properly suit an application. When exceptionally low strength is desired, the anneal may be continued for a long time (for example, ten or more hours) at a temperature just below the critical temperature, to achieve a structure of ferrite and very coarse, globular carbides. Such an anneal is called a spheroidizing anneal, in view of the spheroidal morphology of the carbides. Spheroidizing anneals may cause coarsening of the ferrite structure; however, such a response is modest compared with the grain-growth dynamics possible with austenitic structures and hot working.

Subcritical Temperatures

Nominal Subcritical Annealing Temperatures for Plain Carbon and Low-Alloy Steels.

In the most elementary practices, anneals are described in terms of a temperature, presumably maintained for the order of a very few minutes for in-line, continuous processing, or an hour in the case of batch processing, or ten hours or more in the case of a spheroidization anneal. Time is important, as discussed subsequently, but it remains that anneals are unfortunately often specified only in terms of a temperature.

The iron-iron carbide phase diagram, shown in Fig. 1, provides a useful template for presenting carbon steel annealing and heat treating temperatures (Ref 1). The critical temperature, or A_1 , is 727 °C (1341 °F). Handbook recommendations for through-going process annealing of carbon steels are 11 to 22 °C (20 to 40 °F) below A_1 , or from 705 to 716 °C (1301 to 1321 °F) (Ref 1). These temperatures are rather close to the critical temperature, and operations with limited temperature control may require the targeting of somewhat lower ranges. For that matter, many casual process annealing practices involve a few hours in the 500 to 650 °C (930 to 1200 °F) range.

It must be noted that aspects of subcritical annealing response occur at temperatures

considerably below the A_1 temperature of 727 °C (1341 °F). In the case of cold-worked structures, the nominal recrystallization temperature of ferrite is 500 °C (930 °F), although lower temperatures have been cited, particularly as a threshold for stress relief and recovery. Thus, for the case of, say, a 700 °C (1290 °F), one-hour anneal, stress relief, recovery, and recrystallization occur very early in the process, and carbide transformations are the principal response over time at the threshold temperature. Air cooling is the general practice, although variations in cooling rate are of little consequence.

It should be noted that the use of temperatures and times rather in excess of the recrystallization range is often necessary to achieve through-heating of a large workpiece configuration (coil, plate, etc.) or to meet certain soaking requirements. On the other hand, use of minimally necessary temperatures and times may be desirable for rapid in-line processing or to minimize scaling.

Process annealing temperatures for low-alloy steels should reflect the effect of the alloying additions on the critical temperature. Empirical formulas have been generated to project, roughly, the effect of alloying additions (and residual elements) on the eutectoid, or critical, temperature. A representative relationship for common alloying and residual elements is as follows:

$$A_1 = 727^\circ\text{C} + [(25 \times \text{wt}\% \text{Si}) + (17 \times \text{wt}\% \text{Cr}) + (81 \times \text{wt}\% \text{Mo}) - 6.8 \times \text{wt}\% \text{Mn} - (12 \times \text{wt}\% \text{Ni})]^\circ\text{C}$$

It will be seen that the projected effects on the A_1 of the commonly present manganese and silicon will largely cancel each other in carbon and low-alloy steels. On the other hand, the projected effect on A_1 of the presence of chromium and molybdenum in a 41xx-series steel can be significant, as can the effect of nickel, chromium, and molybdenum in a 43xx steel. For example, a midrange composition for a plain carbon 1022 steel leads to the projection of essentially no change in A_1 , whereas a midrange composition for a chromium-molybdenum 4140 steel leads to a projected increase in A_1 of 33 °C (59 °F). Finally, a midrange composition for a Ni-Cr-Mo 4340

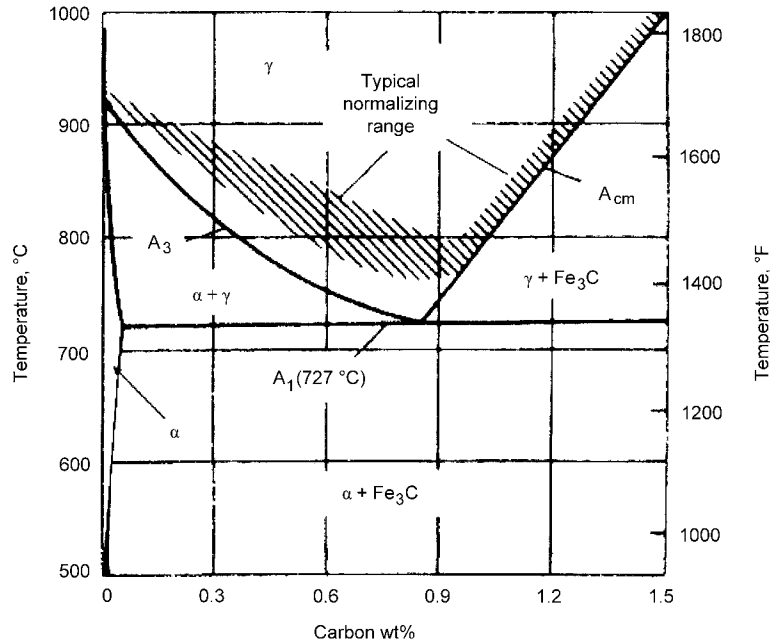


Fig. 1 Iron-iron carbide phase diagram indicating the eutectoid temperature of 727 °C (1341 °F) and the temperature range for normalizing treatments. Ferrite is designated as α , austenite is designated as γ , and iron carbide is designated as Fe_3C . Source: Ref 1

steel leads to a projected increase in A_1 of only 15 °C (27 °F), in view of the effect of nickel in lowering the A_1 .

This having been said, published values for A_1 temperatures for carbon and low-alloy steels vary significantly, and handbook recommendations for process annealing temperatures do not always reflect the subtleties of low-alloy additions. Nevertheless, refined practice and process analysis should take these alloying effects into consideration. Moreover, process anneals should not be taken in the upper temperature ranges without a careful evaluation of the actual A_1 for the steel being processed.

Nominal Subcritical Annealing Temperatures for High-Alloy Steels. Stainless steels and many tool steels generally involve alloying additions that grossly alter the austenite phase field of Fig. 1. Figure 2 displays the effect of large chromium additions on the iron-carbon system (Ref 2). Considering a chromium level of 12 wt %, pertinent to a martensitic 410 stainless steel, the diagram indicates that no austenite should form until approximately 810 °C (1490 °F). In this context, handbook recommendations for the process annealing of 410 stainless steel are usually in the 730 to 800 °C (1345 to 1470 °F) range. In passing, one should note that at higher chromium levels, the steel forms no austenite at all upon heating. Stainless steels that do not form austenite at any temperature are called ferritic, and ones that do not form ferrite in the practical processing range are called austenitic. Such steels have an annealing range that is not restricted by critical temperature considerations.

In the case of high-alloy tool steels, the restricted austenite field is somewhat similar

to that of the martensitic stainless steels, with molybdenum, vanadium, and tungsten playing roles similar to and along with that of chromium. For example, both D2 tool steel (1.55 wt% C, 11.5 wt% Cr, 0.9 wt% Mo, 0.8 wt% V) and M48 tool steel (1.50 wt% C, 3.75 wt% Cr, 5.25 wt% Mo, 3.10 wt% V, 9.75 wt% W, 8.5 wt% Co) have recommended annealing cycles that peak at 870 °C (1600 °F) for 2 h.

Temperature-Time Relations

As stated previously, handbook instructions and specifications do not always specify a time to go with a subcritical annealing temperature, and if they do, the time may reflect heat-transfer considerations for coils and large workpieces. Nonetheless, most of the practical responses of subcritical annealing are diffusion and creep related and therefore thermally activated, with a rate that is temperature sensitive. Although it is naïve to assume that a given time-temperature parameter applies to all of the subcritical annealing responses, some rough time-temperature trade-offs can be projected with the use of the Larson-Miller parameter, P , where:

$$P = T(\log t + C)$$

where T is absolute temperature (most data are in °R), t is time in hours, and C is a constant (from 15 to 25, and often set at 20 for nominal calculations). Thus, if a desired degree of stress relief is achieved in 6 h at 1100 °F (1560 °R, 593 °C, 866 K), then the Rankine-based Larson-Miller

parameter for this stress-relief response is 32.4×10^3 , based on a C -value of 20. If it is desired to achieve the same degree of stress relief in only an hour, then:

$$T = \frac{P}{[\log(t) + C]} = \frac{32.4 \times 10^3}{20} = 1620 \text{ } ^\circ\text{R}$$

where $1620 \text{ } ^\circ\text{R} = 1160 \text{ } ^\circ\text{F} = 627 \text{ } ^\circ\text{C}$.

This analysis can be extended, for purposes of approximation, to any subcritical annealing response. Suppose a high subcritical anneal has been undertaken for an hour at 710 °C (1770 °R), and it is desired to back off to 680 °C (1716 °R). The Rankine-based Larson-Miller parameter associated with this anneal is 35,400, based on a C -value of 20. Therefore, the time for the lower-temperature anneal is 4.26 h, based on:

$$\log t = (P/T) - C$$

Similarly, suppose a spheroidizing subcritical anneal has been undertaken for 24 h at 710 °C (1770 °R), and it is necessary to back off to 680 °C (1716 °R). The Rankine-based Larson-Miller parameter associated with this spheroidizing anneal is 37,840, based on a C -value of 20. Therefore, the time for the lower-temperature anneal is 113 h, based on:

$$\log t = (P/T) - C$$

As noted previously, the nominal recrystallization temperature for ferrite is only approximately 500 °C (1392 °R), and it is possible that a useful recrystallization anneal can be achieved in an hour at 500 °C. The Rankine-based Larson-Miller parameter associated with this recrystallization anneal is 27,840, based on a C -value of 20. Now, if it is desired to accomplish this anneal in 1 min (0.0167 h) for in-line, continuous processing, it is worth estimating the temperature required. The estimated temperature for a time of 1 min is 1528 °R (575 °C), based on:

$$T = P/(\log t + C)$$

Thus, there would seem to be ample latitude for the design of such an in-line recrystallization anneal.

Practical Implications for Induction Annealing. In principle, subcritical annealing cycles can be readily achieved in the workpiece by way of induction heating. This is especially the case for longer-time anneals, through-the-thickness, at temperatures that are not too close to the critical temperature. The more challenging situation is that of near-surface short-time anneals just below the critical temperature. The risk in this case is that of exceeding the critical temperature and forming austenite. Such austenite can form very quickly, and if the short-time, near-surface anneal involves relatively rapid cooling, then the austenite will become untempered

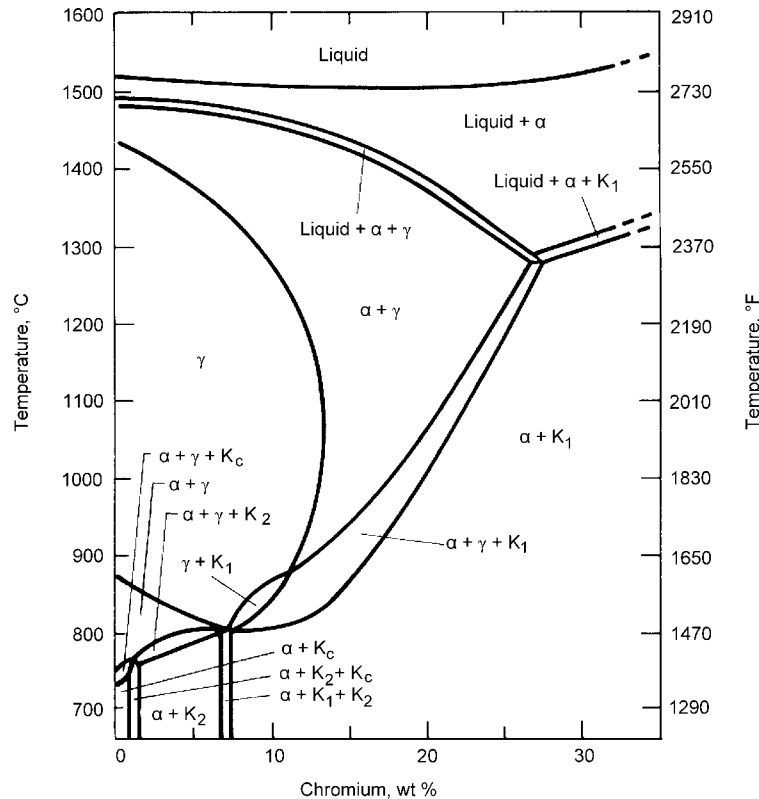


Fig. 2 Iron-chromium pseudo-binary phase diagram for a carbon content of 0.10 wt%. Source: Ref 2

martensite. The presence of even small amounts of untempered martensite can lead to embrittlement. Of course, the risk and seriousness of this phenomenon will depend on the carbon level and alloy content of the steel.

Normalizing

In the simplest concept, normalizing involves heating to achieve complete austenitization of the steel, followed by cooling in still air. (Advanced practices may involve managed cooling rates, and normalizing typically involves cooling to 400 °C, or 750 °F, in approximately 1 min.) The heating should be at a slow enough rate to minimize temperature gradients and thermal stresses. Time-at-temperature is usually not specified for a normalizing process, owing to the rapid transformation to austenite. Nonetheless, it is quite important for enough time to be allowed for the achievement of a uniform temperature throughout the workpiece. The hatched area in Fig. 1 represents the range of austenitization temperatures commonly used for normalizing. Exemplary recommended normalizing temperatures are as follows (Ref 1):

Steel grade	Normalizing temperature	
	°C	°F
1022	915	1680
1040	860	1580
4140	870	1600
4340	870	1600

Normalizing treatments transform carbon and alloy steels, of diverse process histories, into a uniform, predictable ferrite/carbide microstructure, given that carbides largely dissolve in the austenite and precipitate in fine pearlite upon cooling. Even if carbide dissolution is incomplete, the postnormalization carbide structure is nonetheless substantially refined (carbide dissolution can be facilitated by normalizing at higher temperatures). The refined carbide structure may be desirable because it is easier to dissolve in subsequent heat treatment. Normalization generally achieves the often useful goals of stress relief, recrystallization, grain-size refinement, homogenization, and improved machinability.

Stainless steels are not generally normalized. This is the case even with martensitic stainless steels, because the high degree of hardenability makes it difficult to avoid

martensite formation with air cooling. Similarly, normalization is generally not undertaken with most tool steels.

Practical Implications for Induction Normalizing. As in the case of subcritical annealing, normalization cycles can be achieved, in principle, by induction heating. This is especially the case for longer-time, through-the-thickness normalization. The major challenge would seem to be matching the rates of heating and cooling involved with conventional normalizing. As noted previously, heating rates must be slow enough to minimize temperature gradients and thermal stresses. More important, the cooling rate should involve, or be consistent with, still-air cooling. Again, the most challenging situation would seem to be that of near-surface normalizing, where inappropriately rapid cooling may result in untempered martensite formation in higher-carbon and alloy steels. The presence of even small amounts of untempered martensite can lead to embrittlement.

Induction Thread Softening

A practical application of induction normalizing and subcritical annealing is thread softening. The threaded area on carburized components, such as hypoid pinion gears, is commonly induction softened to prevent delayed fractures from occurring after the nut is torqued down during assembly. The induction softening may be done by normalizing, subcritical annealing, or a combination of the two. The method will depend on the hardenability of the steel used. If the hardenability is relatively low, the induction normalizing process may be used.

A typical process would include induction heating the threaded area above the critical temperature, followed by slow cooling by immersing the thread in a bed of vermiculite. On occasion, the process may need to be followed by an induction subcritical annealing process if the steel hardenability is sufficiently high and the carburized case rehardens after slow cooling. It is common to soften the carburized case at the root of the threads to a maximum of 45 HRC. The softening may also be done by using the subcritical annealing process. When using this method, it is normally desirable to maximize the time at temperature to achieve the necessary degree of softening. As a result, very low power settings are used in order to extend the heating time. Another way to achieve this involves pulsing the power after the desired temperature is reached. Additionally, a second subcritical anneal may be used.

The induction frequency and power requirement will depend on the size of the thread and the method being used. When the induction normalizing process is used, it is typical to

through heat the entire thread cross section to ensure a slower cooling rate. A frequency of 10 kHz or less would be common for this. One disadvantage to this process is that a larger portion of the part will be affected by the heating. The induction subcritical annealing process uses a lower temperature, so the heat input into the part will be lower. With this process, the entire thread cross section can be heated, or only the outer case region can be heated. With

the latter method, it is common to use a higher frequency, including radio frequency.

ACKNOWLEDGMENT

The author thanks Gregg Fett, Dana Corporation, for the addition of coverage on thread softening.

REFERENCES

1. H.E. Boyer and T.L. Gall, Ed., *Metals Handbook Desk Edition*, American Society for Metals, 1985, p 28-11
2. W.T. Lankford, Jr., N.L. Samways, R.F. Craven, and H.E. McGannon, Ed., *The Making, Shaping and Treating of Steel*, Association of Iron and Steel Engineers, Pittsburgh, PA, 1985, p 1338

Austenitizing in Steels

John G. Speer, Advanced Steel Processing and Products Research Center, Colorado School of Mines
Robert J. Gaster, Deere & Company, Moline Technology Innovation Center

Introduction

Austenite is the intermediate starting microstructure in many steels, which transforms during later processing or heat treatment to the microstructure desired in the particular steel alloy of interest. *Austenitization* refers to heating into the austenite phase field, during which the austenite structure is formed. Austenite is the high-temperature, face-centered cubic form of iron, stable at intermediate temperatures on the iron-carbon binary phase diagram. The austenitizing heat treatment almost always involves heating, but austenite formation also occurs during direct processing from very high temperature. For example, some newer processes involve casting and solidification directly linked with processing in the solid state, where austenite forms following solidification and transforms to the final microstructure before the steel is first cooled to room temperature. Such processes are not the focus of this article, but many of the principles related to austenitizing heat treatments are also applicable to austenite behavior during direct casting processes.

The iron-carbon equilibrium phase diagram, shown in Fig. 1, is a good starting point from which to consider austenite formation in steels. While the Fe-Fe₃C (cementite) diagram (shown using solid lines in Fig. 1) represents conditions that are metastable with respect to the true equilibrium in the iron-carbon system (where graphite is thermodynamically stable), cementite is the carbon-rich phase that is present in most commercial steels. Heating a ferrous alloy into the austenite phase field is associated with a thermodynamic driving force for austenite to replace the starting microstructure, which typically may contain ferrite, pearlite, iron carbide or cementite (Fe₃C), bainite and/or martensite, and perhaps some austenite that may have been present in the starting microstructure. Such austenite is referred to as retained austenite, resulting from incomplete transformation/decomposition during cooling from a previous processing step or sequence of steps.

Purposes and Overview of Austenitization

Steels are heated into the austenitic regime for a variety of purposes. In heat treating, austenite is formed to modify the microstructure, replacing an earlier-formed structure with a new microstructure tailored for the end use or next step in processing, via subsequent transformation at a lower temperature. For steels that are hot worked by means of rolling or forging, austenitization occurs as part of the reheating process to reduce the strength of the steel so that hot working can be accomplished with reasonable force or power inputs. Chemical homogenization can also be attained by increasing atomic mobility at high temperatures within the austenitic regime, although the kinetics of substitutional alloy redistribution are sluggish in the solid state, so homogenization may be limited in practice. However, interstitial homogenization of carbon in steels occurs more quickly, enabling the success of structure modifications in heat treatment of steels.

Partial austenitization is also employed intentionally during heat treating of some steels. For example, intercritical annealing (heating between the lower and upper critical temperatures for a particular steel, that is, between the A₁ and A₃ temperatures indicated in Fig. 1) of hypoeutectoid steels in the ferrite-plus-austenite two-phase field is used to generate intercritical ferrite in high-strength sheet products along with harder products of austenite decomposition, such as martensite in dual-phase microstructures. In hypereutectoid steels, for example, grade 52100, heating is often into the austenite-and-cementite two-phase field, whereby the presence of cementite moderates the austenite carbon concentration prior to quenching and enhances wear resistance in ball-bearing applications.

Austenitizing may involve plain carbon or low-alloy steels, where the transformations that occur upon heating primarily involve ferrite transformation and dissolution of cementite, or higher alloy steels where full or partial dissolution of alloy carbides or nitrides may be

important. The starting microstructure also influences the austenitizing response, because the scale of the microstructure influences the distances over which solute diffusion may be required, and additional processes such as tempering or recrystallization can occur during heating of steels that are martensitic or cold worked before austenitizing. Alloy content of the steel can also influence austenitizing response, because carbide-forming elements will delay the diffusion of solute carbon in rapid heating conditions such as induction hardening. Reactions with the external environment may be an additional consideration, because oxidation and scale formation occur during heating, and carburizing or nitriding reactions and so on may also occur in the austenitic regime.

While heat-transfer considerations are not the focus of this article, it should be recognized that the microstructure evolution mechanisms that occur during austenitizing are diffusional, so temperature and time have a profound influence on the austenitizing response. Heating time-frames may range from fractions of a second (in surface-hardening applications such as induction hardening) to many hours for soaking of heavy sections. Temperature gradients influence microstructure development and hot working behavior and are sometimes inherent and intentional in processing, but in most cases are minimized through careful control of heating and soaking. Commercial software is available to calculate heat-transfer characteristics and thermal behaviors during heating.

Thermodynamics and Kinetics of Austenite Formation

Selection of Austenitizing Temperature.

The presence of austenite at equilibrium can be predicted by using the phase diagram, such as in Fig. 1 for iron-carbon binary alloys, or by using thermodynamic databases for multi-component steels. In practice, austenite formation may occur under conditions that may deviate considerably from equilibrium. Figure 2

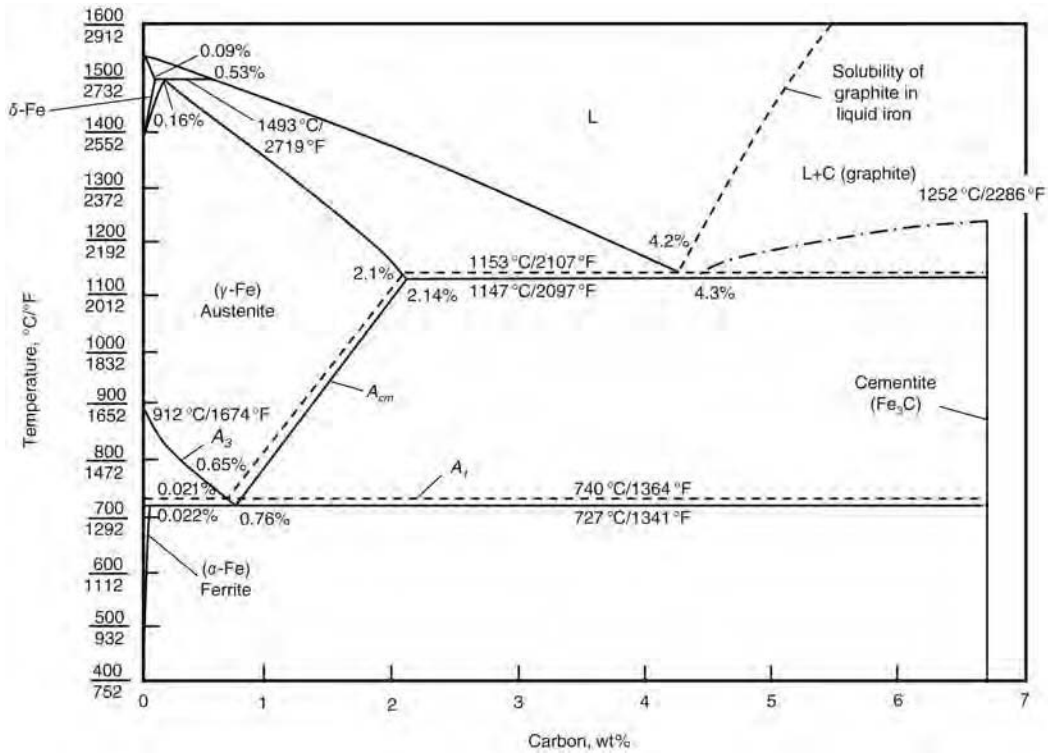


Fig. 1 Iron-carbon binary phase diagram, where solid lines indicate the metastable Fe-Fe₃C diagram and dashed lines are from the iron-graphite equilibrium diagram. Reprinted from Ref 1, adapted from Ref 2

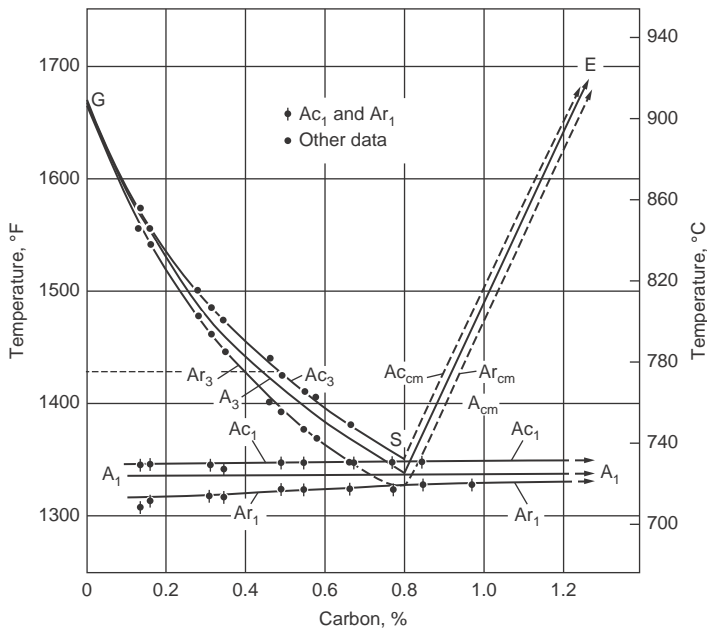


Fig. 2 Transformation temperatures from the phase diagram, along with critical temperatures for transformation during heating (c) or cooling (r) at 0.125 °C/min (0.225 °F/min). Reprinted from Ref 3

includes a portion of the iron-carbon phase diagram in the near-eutectoid region, with additional boundaries that illustrate the onset of transformation during heating or cooling. Some commonly employed heat treating nomenclature is associated with this figure, wherein the

boundaries (as may be measured based on a thermal arrest) that define critical temperatures for transformation are designated as A₁ (critical temperature for eutectoid transformation), A₃ (critical temperature for primary ferrite transformation), and A_{cm} (critical temperature for

primary cementite transformation). Additional subscripts of “c” or “r” are used to define the critical temperatures under heating or cooling conditions, respectively. The counterintuitive use of “c” as a subscript to describe heating rather than cooling stems from the French origin of these designations, wherein *chauffage* refers to heating and *refroidissement* to cooling. It should be noted that the information in Fig. 2 applies to iron-carbon binary alloys heated or cooled at 0.125 °C/min (0.225 °F/min), because the critical temperatures depend on both alloy composition and processing.

It is important to understand the critical temperatures to design appropriate heat treatment practices. For example, full austenitization is often the first step in heat treating, so the A₃ temperature for that particular steel must be exceeded to obtain the desired starting condition. In modern multicomponent steels, binary phase diagrams may not provide accurate information on critical temperatures and phase stability, however, due to the presence of other alloying elements. Commercial software packages are now available to obtain such information using computational thermodynamic databases. Experimental measurements using dilatometry are also employed to assess kinetic effects. Handbook summaries of critical temperatures can also be helpful, and Tables 1 and 2 show examples with recommended austenitizing and forging temperatures for a variety of carbon and low-alloy steels, respectively. Empirical equations are also available to

Table 1 Recommended austenitizing temperatures for several steels

Temperature			Temperature			Temperature		
Steel	° C	° F	Steel	° C	° F	Steel	° C	° F
Carbon steels			1146	800–845	1475–1550	50B60	800–845	1475–1550
1025	855–900	1575–1650	1151	800–845	1475–1550	5130	830–855	1525–1575
1030	845–870	1550–1600	1536	815–845	1500–1550	5132	830–855	1525–1575
1035	830–855	1525–1575	1541	815–845	1500–1550	5135	815–845	1500–1550
1037	830–855	1525–1575	1548	815–845	1500–1550	5140	815–845	1500–1550
1038(a)	830–855	1525–1575	1552	815–845	1500–1550	5145	815–845	1500–1550
1039(a)	830–855	1525–1575	1566	855–885	1575–1625	5147	800–845	1475–1550
1040(a)	830–855	1525–1575	Alloy steels			5150	800–845	1475–1550
1042	800–845	1475–1550	1330	830–855	1525–1575	5155	800–845	1475–1550
1043(a)	800–845	1475–1550	1335	815–845	1500–1550	5160	800–845	1475–1550
1045(a)	800–845	1475–1550	1340	815–845	1500–1550	51B60	800–845	1475–1550
1046(a)	800–845	1475–1550	1345	815–845	1500–1550	50100	775–800(c)	1425–1475(c)
1050(a)	800–845	1475–1550	3140	815–845	1500–1550	51100	775–800(c)	1425–1475(c)
1055	800–845	1475–1550	4037	830–855	1525–1575	52100	775–800(c)	1425–1475(c)
1060	800–845	1475–1550	4042	830–855	1525–1575	6150	845–885	1550–1625
1065	800–845	1475–1550	4047	815–855	1500–1575	81B45	815–855	1500–1575
1070	800–845	1475–1550	4063	800–845	1475–1550	8630	830–870	1525–1600
1074	800–845	1475–1550	4130	815–870	1500–1600	8637	830–855	1525–1575
1078	790–815	1450–1500	4135	845–870	1550–1600	8640	830–855	1525–1575
1080	790–815	1450–1500	4137	845–870	1550–1600	8642	815–855	1500–1575
1084	790–815	1450–1500	4140	845–870	1550–1600	8645	815–855	1500–1575
1085	790–815	1450–1500	4142	845–870	1550–1600	86B45	815–855	1500–1575
1086	790–815	1450–1500	4145	815–845	1500–1550	8650	815–855	1500–1575
1090	790–815	1450–1500	4147	815–845	1500–1550	8655	800–845	1475–1550
1095	790–815(a)	1450–1500(b)	4150	815–845	1500–1550	8660	800–845	1475–1550
Free-cutting carbon steels			4161	815–845	1500–1550	8740	830–855	1525–1575
1137	830–855	1525–1575	4337	815–845	1500–1550	8742	830–855	1525–1575
1138	815–845	1500–1550	4340	815–845	1500–1550	9254	815–900	1500–1650
1140	815–845	1500–1550	50B40	815–845	1500–1550	9255	815–900	1500–1650
1141	800–845	1475–1550	50B44	815–845	1500–1550	9260	815–900	1500–1650
1144	800–845	1475–1550	5046	815–845	1500–1550	94B30	845–885	1550–1625
1145	800–845	1475–1550	50B46	815–845	1500–1550	94B40	845–885	1550–1625
			50B50	800–845	1475–1550	9840	830–855	1525–1575

(a) Commonly used on parts where induction hardening is employed. All steels from SAE 1030 up may have induction hardening applications. (b) This temperature range may be employed for 1095 steel that is to be quenched in water, brine, or oil. For oil quenching, 1095 steel may alternatively be austenitized in the range 815 to 870 °C (1500 to 1600 °F). (c) This range is recommended for steel that is to be water quenched. For oil quenching, steel should be austenitized in the range 815 to 870 °C (1500 to 1600 °F). Reprinted from Ref 4

estimate critical temperatures based on alloy composition, and these can provide useful guidance for some low-alloy steels. For example, expressions of Andrews for A_{c3} and A_{c1} are reproduced as follows in Eq 1 and 2, respectively (Ref 6). (Some additional effects of manganese, chromium, copper, phosphorus, aluminum, arsenic, and titanium on A_{c3} are also mentioned in the original reference.)

$$A_{c3}(^{\circ}\text{C}) = 910 - 203\sqrt{C} - 15.2\text{Ni} + 44.7\text{Si} + 104\text{V} + 31.5\text{Mo} + 13.1\text{W} \quad (\text{Eq 1})$$

$$A_{c1}(^{\circ}\text{C}) = 723 - 10.7\text{Mn} - 16.9\text{Ni} + 29.1\text{Si} + 16.9\text{Cr} + 290\text{As} + 6.38\text{W} \quad (\text{Eq 2})$$

Both the tables and equations reflect the tendency for critical temperatures to increase with additions of austenite-stabilizing elements (such as carbon, nickel, manganese, etc.), which expand the temperature range of austenite stability, and for the critical temperature to decrease with additions of ferrite-stabilizing elements (such as silicon, chromium, and molybdenum), which expand the temperature range of ferrite stability.

The recommended temperature ranges in Table 1 reflect the need to fully austenitize while avoiding excessive austenite grain

growth. The forging temperatures in Table 2 are higher for a given alloy, reflecting the desire to reduce the forming loads while also avoiding overheating, where incipient melting at grain boundaries or other embrittling mechanisms may be encountered. (The phase diagram in Fig. 1 shows that the liquidus temperature for austenite decreases with increasing carbon for most steels, consistent with the trends in Table 2.) Reheating temperatures before hot working may also reflect the need to control dissolution of precipitates in microalloyed high-strength low-alloy steels; this application is discussed in a later section. In a carburizing heat treatment, the temperature also controls the carbon mobility and maximum solubility in austenite. Finally, partial austenitizing heat treatments may apply to either hypoeutectoid or hypereutectoid steels, such as dual-phase sheet or ball-bearing steels, as mentioned previously. In these instances, the intercritical temperature (i.e., between the A_1 and A_3 or between the A_1 and A_{cm}) simultaneously controls both the austenite composition and the fraction of austenite and ferrite or carbide.

Mechanisms and Kinetics of Austenite Formation. The initial microstructure influences the locations within the microstructure and the mechanisms by which austenite may form. Austenite nucleation is most likely to occur at interfaces, although the thermody-

Table 2 Typical forging temperatures for various carbon and alloy steels

Steel	Major alloying elements	Typical forging temperature	
		° C	° F
Carbon steels			
1010	...	1315	2400
1015	...	1315	2400
1020	...	1290	2350
1030	...	1290	2350
1040	...	1260	2300
1050	...	1260	2300
1060	...	1180	2160
1070	...	1150	2100
1080	...	1205	2200
1095	...	1175	2150
Alloy steels			
4130	Chromium, molybdenum	1205	2200
4140	Chromium, molybdenum	1230	2250
4320	Nickel, chromium, molybdenum	1230	2250
4340	Nickel, chromium, molybdenum	1290	2350
4615	Nickel, molybdenum	1205	2200
5160	Chromium	1205	2200
6150	Chromium, vanadium	1215	2220
8620	Nickel, chromium, molybdenum	1230	2250
9310	Nickel, chromium, molybdenum	1230	2250

Reprinted from Ref 5

amic characteristics that apply to different interfaces are not necessarily identical. For example, nucleation would be possible at interfaces between pearlite colonies as soon as the

temperature exceeds the eutectoid or Ac_1 , while there would not be a driving force for austenite nucleation at ferrite-ferrite interfaces (absent cementite) until much higher temperatures. In microstructures containing retained austenite, it may not be necessary for nucleation of austenite to occur, because the transformation could conceivably involve growth only of the existing austenite. Apart from the differences in nucleation behavior, the initial microstructure also influences the kinetics of austenite growth (Ref 7).

Austenite formation involves a change in crystal structure and composition. The crystal structure change is accomplished by short-range atom rearrangements at the interface, so that the body-centered cubic ferrite (or orthorhombic cementite) is transformed into face-centered cubic austenite. The kinetics of these structural rearrangements do not usually control the overall reaction kinetics, because long-range carbon and/or substitutional solute diffusion are needed to achieve the equilibrium austenite composition. The scale of (or dimensions associated with) the initial microstructure and carbon or solute distribution control the distance over which long-range diffusion occurs during austenitization and thus profoundly influence the kinetics (Ref 7). Coarse ferrite in combination with coarse alloy-enriched carbides represent the most sluggish austenitization kinetics, because the formation of homogeneous austenite requires dissolution of coarse carbides, involving redistribution of substitutional solutes, and carbon transport into the large volume previously consisting of carbon-depleted ferrite. On the other hand, martensitic or fully pearlitic starting microstructures contain the same overall solute content as the resulting austenite, so the transformation kinetics are less inhibited by the need for long-range solute transport. Fine eutectoid pearlite is a relatively simple case to consider, whereby austenite is stable just above the eutectoid temperature, and carbon redistribution is needed

only on the scale of the pearlite interlamellar spacing.

The kinetics of isothermal austenite transformation from pearlite are shown schematically in Fig. 3. Here the eutectoid (pearlite) composition is indicated by the phase diagram on the left. The transformation kinetics are shown on the time-temperature-transformation (TTT) diagrams on the right. Above the eutectoid temperature, austenite formation occurs from pearlite, while below the eutectoid temperature, austenite decomposition occurs (forming pearlite in an appropriate temperature regime). The transformation start and completion lines are asymptotic to the dashed horizontal line at the eutectoid temperature, below which austenite is not stable and above which ferrite and cementite are not stable. At a given temperature, austenite formation from eutectoid pearlite has been shown to follow the well-known Johnson-Mehl-Avrami-Kolmogorov model (Ref 8, 9) that applies to many diffusional processes. Austenite formation in Fig. 3 occurs at shorter times with increasing temperature (i.e., the reaction rate increases monotonically with temperature) and exhibits a characteristic curve shape that is distinctly different than the usual C-curve kinetics that apply to austenite decomposition in the TTT diagram applicable below the eutectoid temperature. This distinctive characteristic arises from a fundamental difference between transformations that occur following heating and cooling. In transformations that occur following cooling, the free-energy change for the transformation (i.e., thermodynamic driving force) increases at lower temperatures, while atomic mobility is greater at higher temperatures, and the balance between these two factors leads to the well-known C-curve shape. In heating transformations, the free-energy change increases with increasing temperature, and the diffusion kinetics also increase with increasing temperature, so the reaction is always faster at higher temperatures.

The austenite growth rate is shown in Fig. 4, plotting austenite radius as a function of time, for different steels and temperatures. The slopes of the lines represent the interface velocity and increase at higher temperatures. Linear behavior indicates a constant interface velocity, which is possible in this special case where the eutectoid reaction is reversed ($\alpha + Fe_3C \rightarrow \gamma$), and the product inherits the entire carbon and alloy concentration of the parent pearlite. In the more general case where the parent microstructure is inhomogeneous and austenite grows with a different chemical composition (carbon-enriched austenite in hypoeutectoid steels, for example), growth under diffusion control becomes slower as the reaction proceeds and the solute concentration gradients are reduced, resulting in nonlinear behavior. Austenite transformation of pearlite can also occur, wherein the transformations of ferrite and carbide are uncoupled such that incompletely dissolved carbides can be present in the austenite. An example is shown in Fig. 5, where an austenite crystal is growing into pearlite in the central region of the micrograph. The austenite is light gray, having transformed to martensite at room temperature. Some undissolved carbides are clearly visible in the transformed volume, sometimes referred to as ghost pearlite (Ref 12). This behavior is more likely in rapid heating/short time situations such as in induction hardening. Eventually the carbides dissolve completely, given sufficient time and temperature in the single-phase austenite field, because the austenite composition becomes further carbon enriched.

Figure 6 shows the austenite carbon concentration in a hypereutectoid alloy versus log (time) for different austenitizing temperatures. The arrows indicate the point at which ferrite is completely transformed to austenite at each temperature, and the figure shows that the austenite carbon content continues to increase after this point, as carbide dissolution continues. Austenite

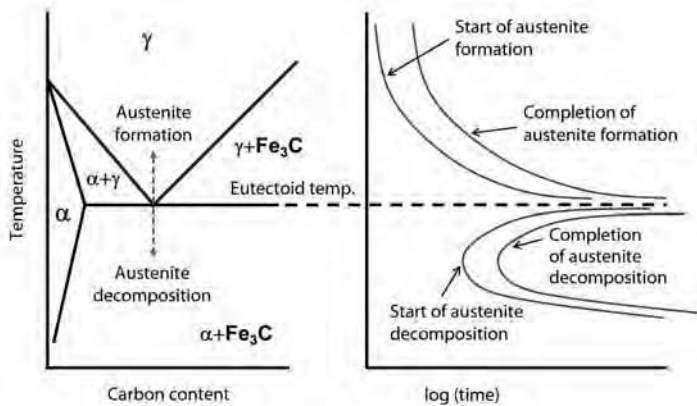


Fig. 3 Schematic iron-carbon phase diagram (left). Austenitization time-temperature diagram illustrating kinetics of isothermal austenite formation upon heating (upper right) and time-temperature-transformation diagram representing isothermal austenite decomposition upon cooling (lower right) for a eutectoid steel. Adapted from Ref 8

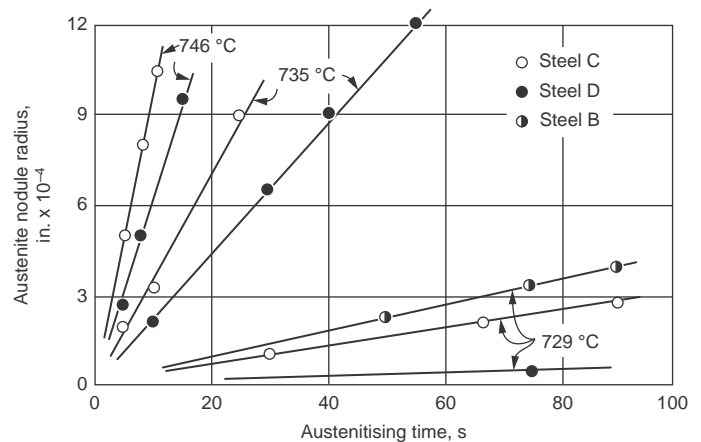


Fig. 4 Austenite grain (nodule) radius versus austenitizing time at different temperatures. Reprinted from Ref 1; original source Ref 10

formation and carbide dissolution are both faster at elevated temperature, and the equilibrium carbon concentration of the austenite increases with temperature up to the A_{cm} temperature. The decoupling of austenite growth from carbide dissolution is an important consideration, and aspects related to this behavior are sometimes reflected in TTT or time-temperature-austenitization (TTA) diagrams for specific steels.

The TTA diagram shown in Fig. 7 is for heating of a Ck 45 steel (similar to AISI 1045). This figure was adapted (Ref 12, 14–16) from the *Atlas zur Wärmebehandlung der Stähle*, which should serve as a useful reference on this topic. The light-gray Ac_2 line represents the Curie temperature below which the material is ferromagnetic. Superimposed on the temperature-time axes are also curves that reflect variations in heating rate over three orders of magnitude from 0.3 to 300 °C/s (0.54 to 540 °F/s). For this medium-carbon steel austenitized from a ferrite + partially spheroidized pearlite starting microstructure, Ac_1 represents the onset, while Ac_3 represents the completion of austenite formation. Austenite is likely to first consume the prior pearlite in this steel, because transformation of the low-carbon prior ferrite to austenite requires higher temperatures. Thus, carbide dissolution may be complete at the Ac_3 , particularly at lower heating rates.

During and persisting for some time after carbide dissolution, an inhomogeneous carbon distribution may remain in the austenite until sufficient carbon transport has occurred across the dimensions of the starting microstructure. The inhomogeneous austenite composition may be reflected through a variation in the martensite start temperature during subsequent quenching of the austenite, wherein the presence of carbon-depleted regions leads to martensite formation at higher temperatures than in homogeneous austenite. The influences of time and temperature on austenite transformation kinetics are clearly illustrated in the figure, with austenite formation and homogenization completing at much lower temperatures under

slower heating conditions. The presence and importance of inhomogeneous austenite is more relevant at high heating rates and short holding times during austenitization, such as may apply during induction hardening. While results as shown in Fig. 7 can be helpful, it should be reiterated that the positions and slopes of the curves are also dependent on prior processing and microstructure.

Austenite nucleation is likely to occur heterogeneously at pearlite colony interfaces or ferrite/carbide interfaces, although ferrite grain boundaries may also represent appropriate nucleation sites under some conditions (e.g., in pure iron or at high temperature). Austenite growth has been studied in low-carbon intercritically annealed sheet steels, where processing involves hot rolling and coil cooling (usually resulting in a ferrite + pearlite microstructure), followed by annealing in the ferrite + austenite two-phase field, and then quenching to transform the austenite to martensite and generate the dual-phase final microstructure (Ref 17). Manganese is commonly added to steels to provide hardenability.

Austenite nucleates first at the ferrite-pearlite interface and grows rapidly into pearlite, until pearlite dissolution is complete. After dissolution of pearlite, further growth of austenite into ferrite occurs, usually controlled by carbon diffusion in austenite. Because manganese partitions to austenite in preference to ferrite, final equilibration during intercritical annealing in

the two-phase field involves an additional mechanism that does not usually apply during full austenitization of low-alloy steels at elevated temperature. Manganese partitioning is quite slow, so the final redistribution of manganese and adjustment of the phase fractions occurs over very long timeframes, which are not applicable to industrial processing.

Figure 8 shows a scanning electron micrograph of the partly transformed microstructure in a 0.06C-1.5Mn steel intercritically annealed for 1 h at 740 °C (1360 °F) and slow cooled to room temperature. The inhomogeneous distribution of austenite is clear, with a predominance of ferrite retained from the starting microstructure, and austenite distributed along the ferrite grain boundaries and triple points, having formed from pearlite. The ferrite is dark gray, while the austenite (transformed to martensite in this room-temperature micrograph) is lighter in contrast. The inset illustration shows the distribution of phases after air cooling in one of the austenite islands that formed during annealing. Here, martensite is present in the outer rim, while the austenite decomposed during slow cooling into ferrite and pearlite. This phase distribution is reflective of the hardenability effects of manganese enrichment in the outer rim of the austenite. This example provides an illustration of the spatial distribution of austenite as it begins to form in a ferrite + pearlite starting microstructure and important aspects of substitutional redistribution that can occur.

Figure 9 provides a TTA diagram for 100 Cr 6 steel (similar to AISI 52100) in a spheroidized condition. This is a hypereutectoid steel with a substantial chromium addition in which

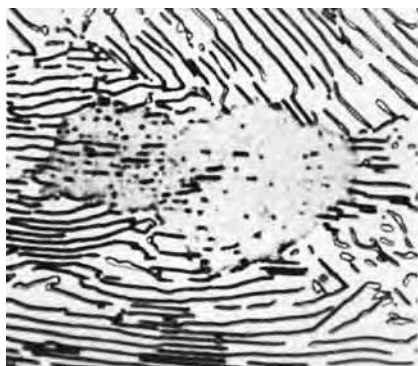


Fig. 5 Austenite formation in a eutectoid steel (0.81C, 0.07Si, 0.65Mn) held 26 s at 730 °C (1350 °F) and water quenched. Original magnification: 2000 \times . Reprinted from Ref 11

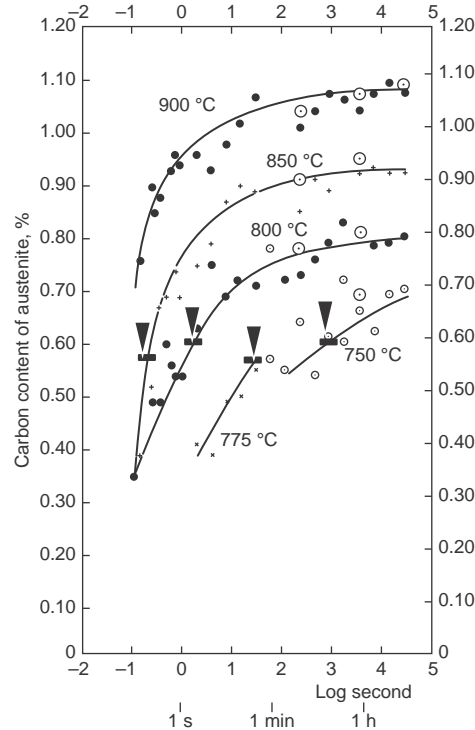


Fig. 6 Carbon content in austenite as a function of austenitizing time and temperature for a 1.27C (by weight) steel. Arrows indicate the disappearance of ferrite. Reprinted from Ref 13

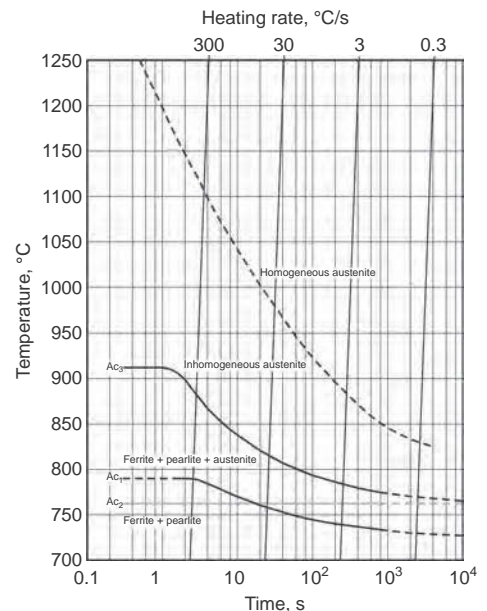


Fig. 7 Time-temperature-austenitization diagram for Ck 45 steel. Adapted from Ref 14 and 15 and reprinted from Ref 16

chromium is incorporated into the cementite, so additional considerations also apply in this steel, because carbides are stable with austenite over a range of temperatures in the intercritical regime during heating, and carbide dissolution and austenite homogenization involve slower diffusion of substitutional (chromium) atoms, as well as carbon. Here, Ac_{1b} indicates the beginning of austenite formation, where there is a driving force to transform the ferrite and dissolve some of the carbides while coarsening others. The end of ferrite transformation during heating is represented by Ac_{1e} , where the microstructure consists of austenite plus carbide. Carbide dissolution continues during further heating over a considerable range of temperatures up to the Ac_c , followed by redistribution of solute carbon and chromium during austenite homogenization.

The previous discussion considered some nonequilibrium effects related to the behavior of carbides during austenitizing. Nonequilibrium effects related to the behavior of ferrite during austenitizing also occur at rapid heating rates and short holding times, such as in induction hardening. Austenite formation in pure iron is partitionless, occurring without any carbon or solute transport, and only requires short-range atom movements to reconstruct a different lattice structure at the interface. The transformation temperature (Ac_3) is shown in Fig. 10 and varies only a small amount over a wide range of heating rates, much less in comparison to the alloys shown earlier in Fig. 7 and 9. Here, the ferrite is stable to much higher temperatures than the eutectoid temperature, so growth is very fast once the temperature is high enough that a driving force is available for transformation to austenite. (If the transformation was not fast, the temperature of transformation would be much higher at very fast heating rates.)

While commercial steels do not usually resemble pure iron, it should be recognized that large ferrite grains in the initial microstructure could exhibit behaviors similar to pure iron if they persist to high temperature without having transformed to austenite. The thermodynamics of partitionless decomposition of austenite during cooling are reasonably well understood, because such conditions apply to massive

ferrite transformation as well as martensite transformation that represents the classic situation of transformation without a composition change. The concepts are not much discussed in the context of austenite formation during heating but may have applicability at high heating rates where transformation is suppressed at low temperatures, where partitionless transformation is impossible (Ref 7, 19).

The T_o concept is used to understand driving forces for partitionless transformation and is illustrated in Fig. 11. The free energies of ferrite and austenite are shown in the upper portion as a function of carbon concentration for a temperature T_1 on the phase diagram (below); the common tangent to the free-energy curves defines the equilibrium ferrite and austenite compositions on the phase diagram. The intersection between the ferrite and austenite free-energy curves is designated T_o and lies between the equilibrium ferrite and austenite compositions, within the $\alpha + \gamma$ phase field. While the T_o does not represent equilibrium, it represents the locus of compositions and temperatures above which austenite has a lower free energy than ferrite of the same chemical composition and below which ferrite has a lower free energy than austenite. While under equilibrium transformation conditions, the temperature must exceed the A_3 curve to obtain full austenitization; under partitionless conditions there is actually a driving force for austenite to replace ferrite of the same composition once the T_o temperature is reached.

For low carbon levels applicable to ferrite, the T_o temperature is very high, so partitionless austenite formation could occur very quickly. Equally important, rapid partitionless transformation during cooling may also occur if short austenitizing times do not permit homogenization of austenite. The significance of this discussion lies in its potential application to austenite formation at rapid heating rates and short holding times in microstructures containing coarse ferrite (along with coarse pearlite, for example), such as may apply during induction hardening. Here, rapid forward and rapid reverse transformation from ferrite to austenite and then to ferrite again

may occur under partitionless conditions, wherein the final microstructure containing low-carbon ferrite has the appearance of incomplete austenitization with untransformed ferrite but in fact resulted from full austenitization without homogenization of carbon in the austenite.

Austenite Grain Growth

The desired grain size of the austenite that forms during austenitization is dependent on the application. Coarse austenite grains increase hardenability, although in practice, alloying is used to control hardenability, because finer austenite is usually preferred to refine the final microstructure, enhancing strength and toughness. Due to grain growth or grain coarsening, the austenite grain size is expected to increase with time or temperature, as shown for pure

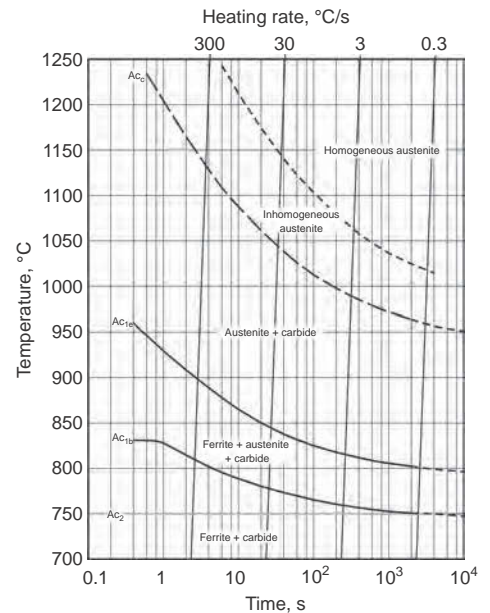


Fig. 9 Time-temperature-austenitization diagram for 100 Cr 6 steel with a ferrite + spheroidized carbide initial microstructure. Adapted from Ref 14 and 15 and reprinted from Ref 16

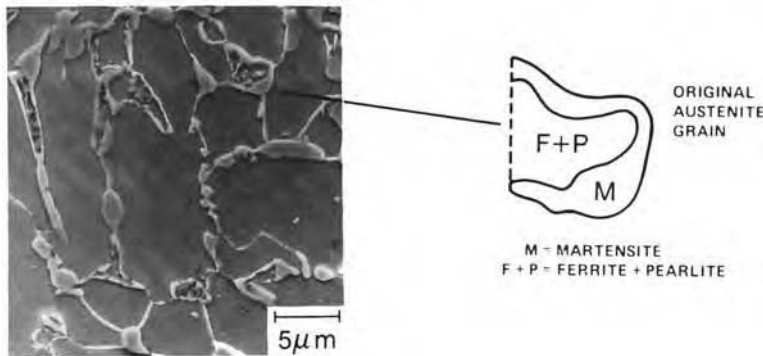


Fig. 8 Microstructure of 0.06C-1.5Mn steel intercritically annealed 1 h at 740 °C (1360 °F) and then slow cooled. Reprinted from Ref 17

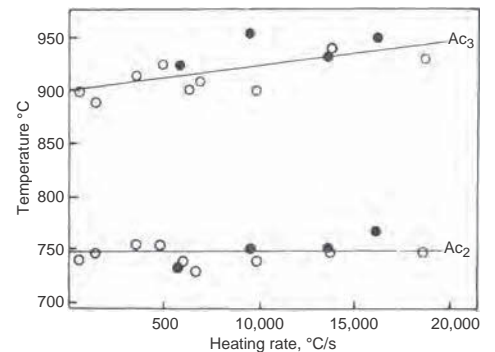


Fig. 10 Effect of heating rate on the temperature at which ferrite transforms to austenite (Ac_3) in pure iron. The Curie temperature is also shown (Ac_2). Reprinted from Ref 18

iron in Fig. 12. In alloys, the austenite grain-coarsening behavior may be different, because alloying elements in solution or in the form of precipitates may retard grain growth by means of solute drag or precipitate pinning effects, respectively, on austenite grain-boundary motion. The pinning precipitates in many steels are aluminum nitrides, AlN, and provide effective grain refinement at low temperatures in the austenite phase field during heat treatments such as normalizing, carburizing, and so on. Aluminum is added to many steels to remove oxygen from the liquid prior to casting and combines with solute nitrogen to form aluminum nitrides during cooling or reheating. The aluminum fine-grained practice is therefore available to suppress grain growth in many steels during subsequent re-austenitizing.

Figure 13 shows the ASTM International grain size number for austenite as a function of heating (austenitizing) temperature for steels that would be produced with and without an aluminum deoxidizing treatment during steel-making, the so-called fine-grained or coarse-grained practice, respectively. Note that smaller ASTM International grain size numbers represent coarser grains. In the aluminum-free coarse-grained steel, austenite grain size increases continuously with temperature. In the aluminum-added fine-grained steel, the austenite grains are pinned by AlN, and the grain size remains small up until the grain-coarsening temperature. (Other precipitates, such as vanadium nitride or niobium carbide, can also be effective at suppressing grain coarsening during re-austenitizing. See Ref 22 and 24.) A sudden increase in grain-growth kinetics occurs at the

grain-coarsening temperature, accompanied by abnormal coarsening where some grains grow much larger than the others, leading to grain sizes that may be coarser than would be observed in steels without any grain-refining additive. At still higher austenitizing temperatures, the pinning particles coarsen and lose effectiveness, so normal grain growth resumes, and austenite grain sizes are similar to the steels without grain-refining additions (Ref 22).

Because the austenite grain size has an important influence on the final microstructure and properties for a given application, it is often desirable to measure the prior-austenite grain size. The term *prior austenite* is used because the austenite grains that existed at high temperature are no longer present, having transformed to a different microstructure at room temperature. Evidence for the location of the prior-austenite grain boundaries can be readily obtained in some microstructures using careful metallographic techniques (and specialized etchants), particularly in fully martensitic microstructures (because the martensite plates/packets grow within a single austenite grain and do not cross the austenite boundaries) or in partially transformed microstructures where a specific transformation product “decorates” the prior-austenite boundaries, having nucleated only on those boundaries during transformation. In other instances, such as in low-carbon ferritic microstructures, it can be very difficult to bring out the prior-austenite microstructure. Special processing can aid in rendering the prior-austenite microstructure, to help characterize the austenitizing response of a particular steel. For example, controlled cooling may be applied to generate a transformation product located predominantly at the prior boundaries, and carburizing may be used to generate a network of cementite at the austenite grain boundaries, which remains in the microstructure after transformation during cooling (Ref 25).

Control of Solute Concentrations in Austenite

While precipitates are helpful for austenite grain-size control in many heat treatments, there are other applications where certain precipitates must be dissolved in austenite for the solutes to have their desired effect. Examples include boron-containing martensitic steels, and microalloyed high-strength low-alloy (HSLA) steels. In the boron-added steels, solute boron segregates to austenite grain boundaries and provides substantially enhanced hardenability for typical austenitizing treatments, at optimum boron levels of 10 or 20 (weight) ppm. Boron is a strong nitride former, so titanium is often added (in excess of the nitrogen concentration) to prevent BN precipitation, because boron is only effective when present in solution. An iron borocarbide phase can also form, however, so austenitizing times and temperatures must also take into consideration the precipitation kinetics of $Fe_{23}(C,B)_6$ in these steels (Ref 26).

Microalloyed HSLA steels are most often subjected to thermomechanical processing as part of hot working in the austenitic regime, modifying the final microstructure and properties. Here, small additions of niobium, for example, are added to suppress austenite recrystallization at low temperatures in the austenitic hot working regime during finish rolling, forging, and so on. The deformed (“pancaked”) unrecrystallized austenite is associated with increased austenite grain-boundary surface area, which enhances nucleation during transformation, leading to a finer microstructure and increased strength and toughness. The key mechanisms involve microalloy carbide precipitation on the austenite grain boundaries and deformation substructure (sub-boundaries) during thermomechanical processing; the precipitates pin the boundaries and suppress

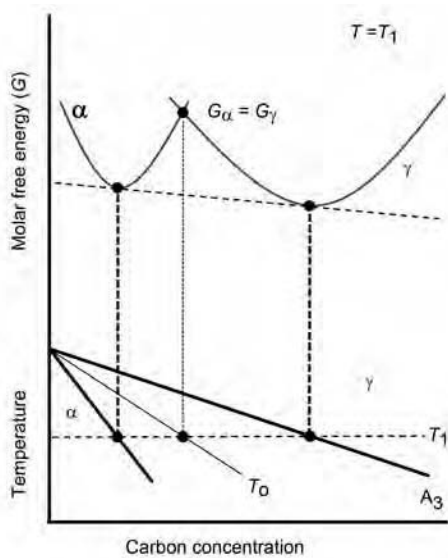


Fig. 11 Schematic illustration of the thermodynamic origin of the T_0 curve (above), where the free energies of austenite and ferrite are equal, overlaid on a portion of the iron-carbon phase diagram (below). The equilibrium ferrite and austenite (A_3) compositions are given by the common tangent to the respective free-energy curves. Adapted from Ref 20

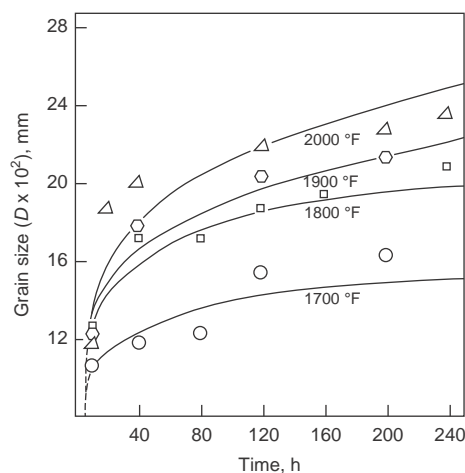


Fig. 12 Austenite grain size of pure iron as a function of austenitizing time and temperature, showing expected grain-growth behavior. Reprinted from Ref 8; original source Ref 21

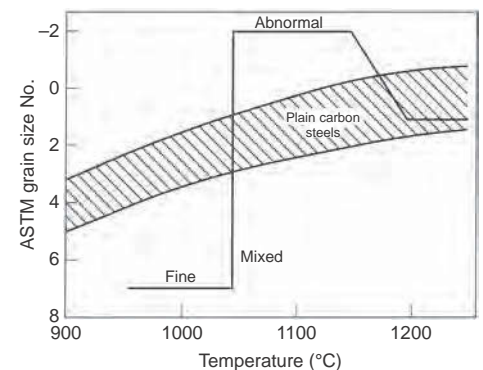


Fig. 13 Schematic illustration showing effect of austenitizing temperature on austenite grain size of plain carbon coarse-grained (shaded area) and fine-grained steels (solid line). The ASTM International grain size number “N” is defined by the relation $2^{N-1} = n$, where n is the number of grains/in.² at 100 \times magnification. Reprinted from Ref 22; see also Ref 23

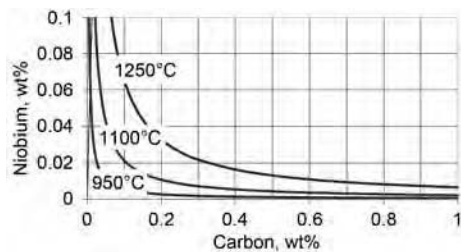


Fig. 14 Niobium carbide solubility isotherms for austenite at 950, 1100, and 1250 °C (1740, 2010, and 2280 °F)

recrystallization. For this mechanism to operate, the microalloy carbide solubility must be controlled carefully, because the carbides must be dissolved in the austenite during reheating prior to hot working and then must precipitate at lower temperatures within the hot-working regime. If the precipitates remain undissolved during reheating, they do not contribute beneficially to the thermomechanical processing response. (This mechanism should not be confused with the fine-grained practice discussed earlier, where precipitates that remain undissolved during austenitizing as part of heat treating, not hot working, help suppress austenite grain growth.)

The solubility of microalloying elements is reasonably well understood, and a variety of solubility product relationships are available in the literature for relevant carbides and nitrides (Ref 22). As an example, Fig. 14 shows solubility isotherms for niobium carbide in austenite, showing the strong dependence of NbC solubility on temperature, as well as concentrations of both carbon and niobium. The isotherms represent the loci of niobium and carbon solute concentrations in equilibrium with austenite, satisfying the solubility product expression in Eq 3, where the solute concentrations are in weight percent and the temperature is in Kelvin:

$$\log_{10}[\text{Nb}][\text{C}] = 2.26 - 6770/T \quad (\text{Eq 3})$$

For particular concentrations of carbon and niobium added to the steel, the solubility isotherms show whether or not all of the NbC is dissolved during reheating at the temperature of interest. If the niobium and carbon concentrations are below the solubility isotherm for a given temperature, then NbC can be fully dissolved in the austenite at that temperature. If the concentrations are above the solubility isotherm, then NbC precipitates should be present at equilibrium; the amount of NbC and the remaining niobium and carbon in austenite can be determined by applying appropriate mass-balance considerations (Ref 27). While these solubility considerations are critical in alloy and process designs

for thermomechanical processing, they are also applicable in designing precipitation schemes to enhance suppression of austenite grain coarsening during heat treatment and have proved effective, for example, in enabling the use of increased carburizing temperatures to accelerate carbon transport without undesired coarsening of the microstructure (Ref 24).

ACKNOWLEDGMENTS

The sponsors of the Advanced Steel Processing and Products Research Center at Colorado School of Mines are gratefully acknowledged.

REFERENCES

1. F.C. Campbell, Ed., *Elements of Metallurgy and Engineering Alloys*, ASM International, 2008, p 153
2. T.B. Massalski, H. Okamoto, P.R. Subramanian, and L. Kacprzak, *Binary Alloy Phase Diagrams*, 2nd ed., ASM International, 1990, p 843
3. R.F. Mehl and C. Wells, Constitution of High-Purity Iron-Carbon Alloys, *Met. Technol.*, Vol 4 (No. 4), TP 798, June 1937, p 1–41
4. *Heat Treating*, Vol 4, *ASM Handbook*, ASM International, 1991, p 961
5. C.J. Van Tyne, Forging of Carbon and Alloy Steels, *Metalworking: Bulk Forming*, Vol 14A, *ASM Handbook*, ASM International, 2005, p 241–260; Cites original source: J.T. Winship, Fundamentals of Forging, *Am. Mach.*, July 1978, p 99–122
6. K.W. Andrews, Empirical Formulae for the Calculation of Some Transformation Temperatures, *JISI*, Vol 203, 1965, p 721–727
7. J.J. Coryell, D.K. Matlock, and J.G. Speer, The Effect of Induction Hardening on the Mechanical Properties of Steel with Controlled Prior Microstructures, *Heat Treating for the 21st Century: Vision 2020 and New Materials Development*, Materials Science and Technology (MS&T) 2005, p 3–14
8. C.R. Brooks, *Principles of the Austenitization of Steels*, Elsevier Applied Science, 1992
9. B.C. De Cooman and J.G. Speer, *Fundamentals of Steel Product Physical Metallurgy*, AIST, 2011, p 85–89
10. G.A. Roberts and R.F. Mehl, *Trans. ASM*, Vol 31, 1943, p 615
11. L.E. Samuels, *Optical Microscopy of Carbon Steels*, American Society for Metals, 1980, p 266
12. G. Krauss, *Steels: Processing, Structure and Performance*, ASM International, 2005
13. G. Molinder, A Quantitative Study of the Formation of Austenite and the Solution of Cementite at Different Austenitizing Temperatures for a 1.27% Carbon Steel, *Acta Metall.*, Vol 4, 1956, p 565–571
14. J. Orlich, A. Rose, and P. Wiest, Zeit-Temperatur-Austenitisierung-Schaubilder, *Atlas zur Wärmebehandlung der Stähle*, Band 3 (Vol 3), Verlag Stahleisen, 1973
15. J. Orlich and H.-J. Pietrzeniuk, Zeit-Temperatur-Austenitisierung-Schaubilder 2, Teil (Part 2), *Atlas zur Wärmebehandlung der Stähle*, Band 4 (Vol 4), Verlag Stahleisen, 1976
16. K. Clarke, “The Effect of Heating Rate and Microstructural Scale on Austenite Formation, Austenite Homogenization, and As-Quenched Microstructure in Three Induction Hardenable Steels,” Ph.D. thesis, Colorado School of Mines, 2008
17. G.R. Speich, V. Demarest, and R.L. Miller, Formation of Austenite during Inter-critical Annealing of Dual-Phase Steels, *Metall. Trans. A*, Vol 12, Aug 1981, p 1419–1428
18. W.L. Haworth and J.G. Parr, The Effect of Rapid Heating on the Alpha-Gamma Transformation in Iron, *Trans. ASM*, Vol 58, 1965, p 476–488
19. E.D. Schmidt, E.B. Damm, and S. Sridhar, A Study of Diffusion and Interface-Controlled Migration of the Austenite/Ferrite Front during Austenitization of a Case-Hardenable Alloy Steel, *Metall. Mater. Trans. A*, Vol 38, April 2007, p 698–715
20. H.K.D.H. Bhadeshia, *Bainite in Steels*, 2nd ed., IOM Communications, 2001, p 9
21. H.B. Probst and M.J. Sinnott, *Trans. AIME*, Vol 203, 1955, p 215
22. T. Gladman, *The Physical Metallurgy of Microalloyed Steels*, The Institute of Materials, 1997
23. E.C. Bain, *Functions of the Alloying Elements in Steel*, American Society for Metals, 1939, p 137
24. K.A. Alogab, D.K. Matlock, J.G. Speer, and H.J. Kleebe, The Influence of Niobium Microalloying on Austenite Grain Coarsening Behavior of Ti-Modified SAE 8620 Steel, *ISIJ Int.*, Vol 47, 2007, p 307–316
25. H.W. McQuaid, The McQuaid-Ehn Test, *Metals Handbook*, American Society for Metals, 1948, p 407–408
26. K.A. Taylor and S.S. Hansen, The Boron Hardenability Effect in Thermomechanically Processed, Direct-Quenched 0.2 Pct. C Steels, *Metall. Trans. A*, Vol 21, June 1990, p 1697–1708
27. J.G. Speer, J.R. Michael, and S.S. Hansen, Carbonitride Precipitation in Niobium/Vanadium Microalloyed Steels, *Metall. Trans. A*, Vol 18, 1987, p 211–222

Quenching and Partitioning Steel Heat Treatment

Li Wang, Automotive Steel Research Institute and Baoshan Iron & Steel Company, Ltd.
John G. Speer, Colorado School of Mines

QUENCHING AND PARTITIONING (Q&P) steel is a term used to describe a series of C-Si-Mn, C-Si-Mn-Al, or other steels subjected to the recently developed quenching and partitioning heat treatment process. The purpose of Q&P steel in the context of automotive structures is to obtain a new type of ultrahigh-strength steel with good ductility to improve fuel economy while promoting passenger safety. With a final microstructure of ferrite (in the case of partial austenitization), martensite, and retained austenite, Q&P steel exhibits an excellent combination of strength and ductility, which permits its use in a new generation of advanced high-strength steels (AHSS) for automobiles. While autobody application represents the first implementation of Q&P on an industrial scale, the heat treatment concept is also applicable to a range of other potential applications.

In 2003, Speer et al. (Ref 1) first proposed an approach designated as the quenching and partitioning process to exploit novel martensitic steels containing retained austenite (Q&P steel), based on the fact that carbon can diffuse from supersaturated martensite into neighboring untransformed austenite and stabilize it to room temperature. The Q&P steel is first treated by an initial partial or full austenitization and then followed by an interrupted quench to a temperature between the martensite start (M_s) and martensite finish (M_f) temperatures, resulting in untransformed retained austenite, and an anneal or so-called partitioning treatment either at or above the initial quench temperature. With enhanced silicon alloying suppressing cementite precipitation, it is anticipated that retained austenite will be enriched with carbon expected to escape from the supersaturated martensite phase in which it has very low solid solubility. The treatment should then produce a fine acicular aggregate of carbon-depleted and potentially carbide-free martensite laths interwoven with retained austenite stabilized by carbon enrichment. As a result, with a composition of 0.2% C, 1 to 1.5% Al, and 1 to 1.5% Mn, Q&P steel (Ref 2) shows an ultrahigh strength of 1000 to

1400 MPa (145 to 200 ksi) with adequate ductility of 10 to 20%; property advancements continue to be made through research on this emerging technology. Early investigations (Ref 1) also proposed a corresponding thermodynamic model for Q&P steel and its heat treatment, which is now referred to as constrained carbon equilibrium (Ref 3).

Since first proposed in 2003, Q&P steel has gained interest for its potential to enhance properties of strength and ductility with compositions similar to transformation-induced plasticity (TRIP) steel and has been proposed as a third-generation automotive steel (Fig. 1) (Ref 4). Many researchers (Ref 5–17) have investigated the relationship between properties and microstructures of Q&P steels subjected to various heat treatments and showed that the ultrahigh strength of Q&P steel results from martensite laths, while its good ductility is attributed to TRIP-assisted behavior of retained austenite during deformation. De Moor et al. (Ref 14) examined the stability of retained austenite and showed that the TRIP effect occurs in Q&P steels, thereby effectively contributing to the significant strain hardening. Santofimia et al. (Ref 15, 16) and Takahama et al. (Ref 17)

analyzed microstructural evolution during annealing by using a model considering the influence of martensite-austenite interface migration on the kinetics of carbon partitioning and indicated that different interface mobilities lead to profound differences in the evolution of microstructures during the partitioning process. In addition, processing opportunities for Q&P steels were discussed by Matlock et al. (Ref 18) and Thomas et al. (Ref 19, 20) based on the considerations in the application of the Q&P concept to automotive AHSS production. Additional work has been subsequently published by multiple research groups. In 2009, the world's first industrially processed Q&P cold rolled sheet steel was produced by Baosteel, having a tensile strength over 980 MPa (142 ksi) and ductility over 15%. In 2012, Q&P steel with a tensile strength of 980 MPa was successfully commercialized (Ref 21–23), and a 1180 MPa (170 ksi) tensile strength Q&P sheet grade is under development. This article provides an overview of important background and product characteristics, with a focus on the automotive sheet steel application that has now reached commercialization. The Q&P heat treating concept has broader potential and

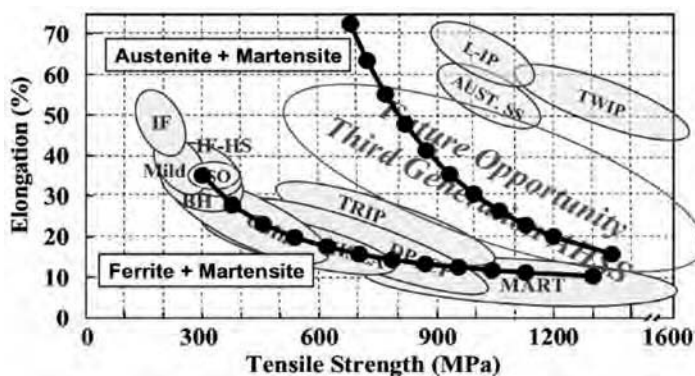


Fig. 1 Predicted potential for austenite/martensite mixtures to achieve property targets beyond those of ferrite/martensite mixtures for third-generation advanced high-strength sheet steels. Source: Ref 4

may be extended to other products and applications in the future.

Chemical Composition and Annealing Process

The chemical compositions of typical Q&P steels are listed in Table 1. The Q&P steels are hypoeutectoid iron-carbon alloys that typically contain 0.15 to 0.30% C by weight, similar to TRIP steels. The Q&P steels also contain alloying elements such as silicon that prevent the precipitation of the cementite phase (Fe₃C), which is present in typical steels at room temperature. This maintains the high carbon concentration in the austenite phase, which becomes stable at room temperature. Carbon content in current Q&P steels is limited to 0.15 to 0.30 wt% due to weldability concerns. As shown in Table 1, the manganese content in Q&P steels is relatively high, to enhance hardenability and austenite stability. Silicon is used to stabilize the austenite phase during continuous annealing and at room temperature, because silicon significantly increases the carbon activity in both ferrite and austenite and decreases carbon solubility in ferrite. As a result, silicon inhibits the formation of cementite during the partitioning stage. Because Q&P steels have already exhibited an excellent balance between ultrahigh strength and high ductility, other alloying elements have not been necessary, although opportunity is likely available to use microalloying and other concepts for additional enhancements.

Thermal Profile and Phase Transformation

The continuous annealing process and consequent phase-transformation behaviors of Q&P steels are schematically shown in Fig. 2. To produce Q&P steel with ultrahigh strength and excellent ductility, a unique annealing process is conducted to obtain the appropriate phase distribution. First, the steel is heated to a temperature above Ac₃ (annealing temperature), where the material is composed of austenite. The material is then slowly cooled to a temperature below Ar₃ (slow cooling temperature, or SC), which is approximately 740 °C (1360 °F) for the 980 MPa (142 ksi) steel grade, to allow the formation of a certain amount of proeutectoid ferrite. The ferrite phase plays a significant role in the improvement of ductility of the 980 MPa

material. The fraction of ferrite and martensite phases can be adjusted by precisely controlling SC. After slow cooling, the steel is then quenched to a temperature between M_s and M_f (quenching temperature) with a cooling rate higher than 50 °C/s (90 °F/s), wherein austenite transforms (partially) to martensite. The fractions of austenite and martensite can be controlled by this interrupted quenching process. After quenching, the steel is usually reheated to a higher temperature (partitioning temperature) and held for a couple of minutes. In a typical steel alloy, the supersaturated carbon in martensite would lead to cementite precipitation. However, the high content of silicon prevents the formation of cementite. Consequently, the excess carbon in the martensite phase partitions into the remaining austenite, because austenite with a face-centered cubic structure exhibits much higher carbon solubility than martensite with a body-centered cubic structure. Finally, the stable carbon-enriched austenite is retained when the steel is cooled to room temperature. After this unique heat treatment, the final microstructure composed of ferrite, martensite, and retained austenite is achieved. The key annealing considerations to produce Q&P steels are that fast

cooling is needed, and, at the same time, the quench arrest temperature must be easily controlled below the M_s temperature.

Microstructure and Mechanical Properties

The microstructure of commercial Q&P steels is composed primarily of martensite (50 to 80%) formed during quenching, and ferrite (20 to 40%) formed from the austenite phase during slow cooling, as well as dispersed retained austenite (5 to 10%) stabilized by carbon enrichment during partitioning. Reduced fractions of ferrite can be used in higher-strength products. Example micrographs taken with a scanning electron microscope and a light optical microscope can be seen in Fig. 3. Small nodules of retained austenite are found, and films of austenite are also present in the lath martensite. The fine Q&P microstructure is usually not well resolved by light optical microscopy. Some additional aspects related to microstructure are also included in the following sections.

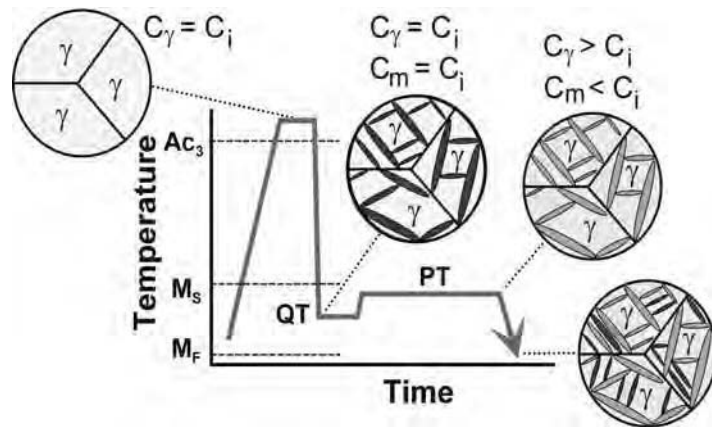


Fig. 2 Schematic illustration of the thermal profile and phase-transformation behavior of quenching and partitioning steels. QT, quenching temperature; PT, partitioning temperature

Table 1 Chemical compositions of current-generation quenching and partitioning steels

Chemical composition, wt%					
C	Mn	Si	Al	P	S
0.15–0.30	1.5–3.0	1.0–2.0	0.02–0.06	<0.015	<0.01

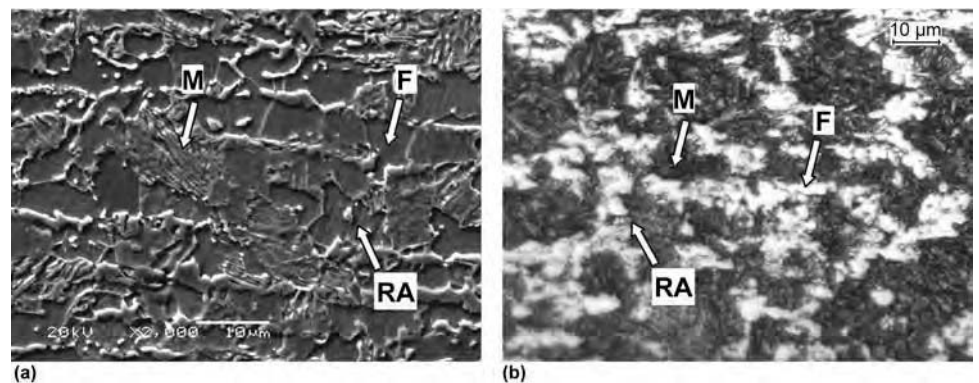


Fig. 3 Microstructure of quenching and partitioning steel obtained using (a) scanning electron microscopy and (b) light optical microscopy. M, martensite; F, ferrite; RA, retained austenite

Mechanical Properties

Carbon-enriched metastable retained austenite is considered beneficial because transformation-induced plasticity during deformation, that is, the TRIP phenomenon, can contribute to work hardening, formability, and fracture toughness. During deformation, the dispersed retained austenite progressively transforms to harder martensite, which creates a high work-hardening rate, even at higher strain levels. A typical strain-stress curve is shown in Fig. 4. It can be seen that with a tensile strength of 980 MPa (142 ksi), the total elongation of Q&P steel is approximately 20%. Mechanical properties of industrially produced Q&P steels are listed in Table 2 for

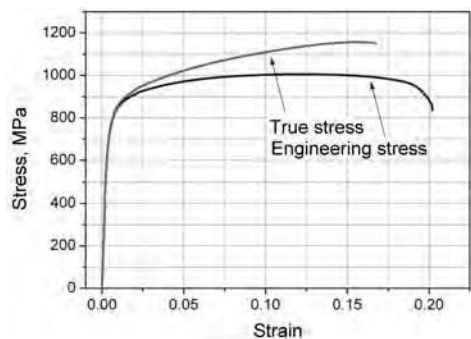


Fig. 4 Strain-stress curve of industrially produced 980 MPa (142 ksi)-grade quenching and partitioning steel

minimum tensile strength levels of 980 and 1180 MPa (142 and 170 ksi).

Applications

The Q&P steels with ultrahigh strength and excellent ductility, or formability, are well suited to help reduce weight of car bodies, with the added advantage of enhanced occupant safety. The work-hardening rates of Q&P steels are substantially higher than for conventional high-strength steels (HSS), providing significant stretch-forming capability. Compared to most other HSS with the same tensile strength, Q&P steels exhibit much higher formability; hence, they are particularly well suited for automotive structural and safety parts such as cross members, longitudinal beams, B-pillar reinforcements, sills, and bumper reinforcements, which cannot be cold formed using conventional HSS with similar strength levels. Some typical automotive parts produced from Q&P steels are shown in Fig. 5. This family of steels is at an early stage of industrial implementation and may find its way into other high-strength components for both automotive and other applications.

Forming

The Q&P steels offer high ductility for their tensile strength. For example, cold rolled Q&P 980 has a total elongation of approximately 20%, and cold rolled Q&P 1180 has a total

elongation of approximately 12%. Figure 6 shows typical forming-limit curves for cold rolled Q&P 980, dual-phase (DP) 780, and DP 980 steels. The formability of Q&P 980 is superior to that of DP 980 steel and reaches to the level of DP 780.

Dynamic Tensile Properties

Besides quasi-static tensile testing results, dynamic tensile testing of sheet steels is also important for more precise evaluation of vehicle crashworthiness in the automotive industry. Positive strain-rate sensitivity, that is, strength increases with strain rate, offers a potential for improved energy absorption during a crash event. The results of dynamic tensile testing of Q&P 980 are shown in Fig. 7. The results confirm that Q&P steel exhibits positive strain-rate sensitivity.

Application Properties of Q&P Steels

Hole-Expansion Ratio of Q&P Steels. One of the concerns for AHSS in stamping operations is the failure of sheared edges in stretching modes. The hole-expansion ratio (HER) is usually used to characterize the sheared-edge stretchability. The HER of Q&P 1180 and Q&P 980 compared to DP 980 is shown in Fig. 8. For either punched or machined edges, Q&P 1180 shows higher HER than Q&P 980 and DP 980, while Q&P 980 shows similar HER as DP 980. One possible explanation of the high HER of Q&P 1180 is its high yield strength/tensile strength ratio and uniform microstructure. It should be noted that the HER can be significantly lower for punched holes compared with machined holes. This probably is due to the reduced local elongation of the multiphase steels, which can have interfacial failure between the ductile ferrite matrix and the harder phases.

Table 2 Typical mechanical property ranges for current-generation quenching and partitioning (Q&P) steels

Steel	Yield strength		Tensile strength		Elongation, %
	MPa	ksi	MPa	ksi	
Q&P 980	650–800	95–115	980–1050	140–150	17–22
Q&P 1180	950–1150	140–170	1180–1300	170–190	8–14

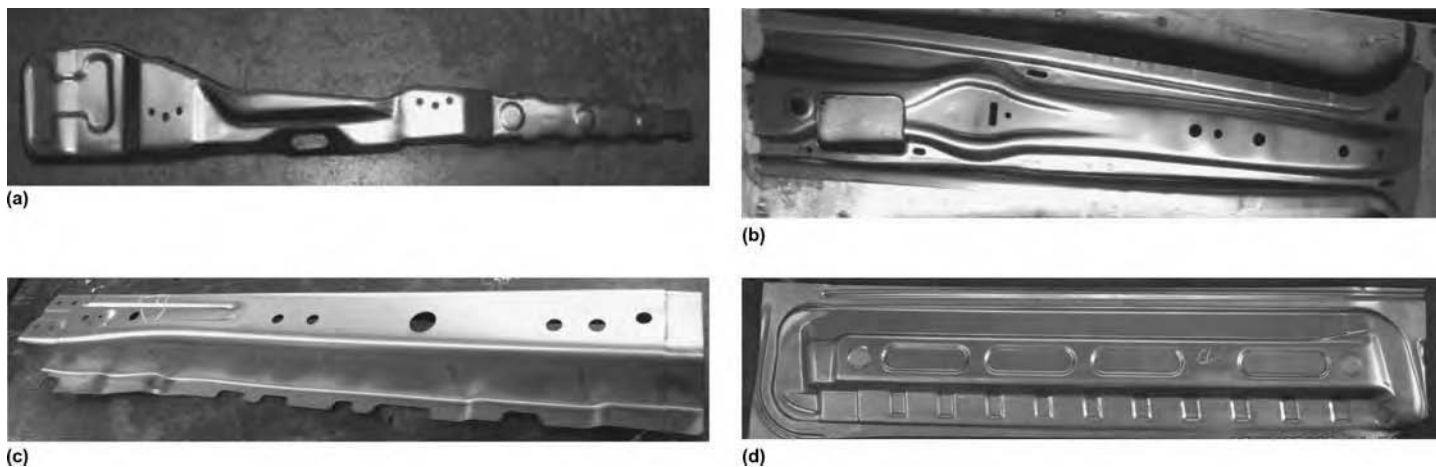


Fig. 5 (a) B-pillar reinforcement left/right. Material: 980 quenching and partitioning (Q&P) steel; gage: 2.0 mm (0.08 in.). (b) B-pillar inner. Material: 980 Q&P; gage: 1.2 mm (0.05 in.). (c) side member front floor left. Material: 980 Q&P; gage: 1.8 mm (0.07 in.). (d) Door panel inner left/right. Material: 980 Q&P; gage: 1.0 mm (0.04 in.)

Shear Fracture Behavior of Q&P Steels. Shear fracture can happen during stretching over the die radii for some part geometries at strains below the conventional forming limit of the material; thus, computer simulations often fail to predict this type of fracture using the conventional forming limit as the failure criterion. Shear fracture is another manufacturing issue to address for AHSS. The shear fracture performance of Q&P steel was evaluated by the bending-under-tension test, and a critical R/t value was determined according to the criterion developed by Hudgins (Ref 24). The critical R/t data for Q&P 980, DP 980, TRIP 780, and data for the commercial steels tested by Hudgins (Ref 24) are presented together in Fig. 9 as a function of the tensile strength. The results illustrate that the commercial steels generally show increasing critical R/t values with increasing strength in the range of tensile strength from 400 to 1100 MPa (60 to 160 ksi). Interestingly, the Q&P 980 exhibited

lower critical R/t values than those steels having 780 and 980 MPa (110 and 142 ksi) strength levels and critical R/t values close to those of other steels having 600 MPa (87 ksi) strength levels. Thus, the shear fracture performance of Q&P 980 should be better than that of some DP 980, DP 780, and TRIP 780 steels.

Springback Behavior of Q&P Steels. Many reports indicate that springback problems are much greater for AHSS than for traditional HSS. The springback angle of 1.2 mm (0.05 in.) Q&P 980 was thus compared to 1.2 mm DP 980 using the bending-under-tension test. A strong linear relationship between springback angle and normalized back force (back force/tensile strength) was found, as shown in Fig. 10. With increasing back force, the springback angle decreases. Almost no difference was observed between Q&P 980 and DP 980 when a 5 mm (0.2 in.) radius die was used. The Q&P 980 exhibited smaller springback angles than DP

980 when a 12.7 mm (0.5 in.) radius die was used, suggesting that Q&P 980 may have better springback performance than DP 980 in some situations.

Mechanical Behavior and Stability of Retained Austenite

An essential principle in the Q&P process is to maintain suitable stability of retained austenite through optimizing chemical composition (alloy elements such as carbon, manganese, silicon, etc.) (Ref 25), grain refinement (Ref 26), and phase morphology (Ref 25).

Mechanical Properties

Engineering stress-strain curves obtained on longitudinal specimens at six different temperatures are illustrated in Fig. 11. The specimens showed continuous yielding behavior, which can be interpreted as the result of the high density of dislocations introduced by martensite. The M_s^σ temperature for strain-induced transformation can characterize retained austenite stability. When the tensile temperature is in the range of M_s to M_s^σ , plastic deformation of the austenite involves stress-induced transformation at pre-existing nucleation sites, with a load drop evident during yielding. When the temperature is between M_s^σ and M_d , the stability of the retained austenite is expected to increase, perhaps leading to a transition from stress-induced transformation to strain-induced transformation. The symbol M_d refers to the minimum temperature where no martensite transformation occurs during deformation. The deformation-induced martensitic transformation

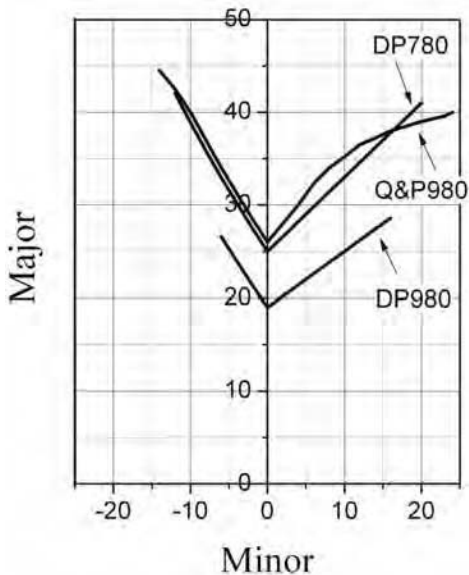


Fig. 6 Forming-limit curves for quenching and partitioning (Q&P) 980, dual-phase (DP) 780, and DP 980. Thickness: 1.2 mm (0.05 in.)

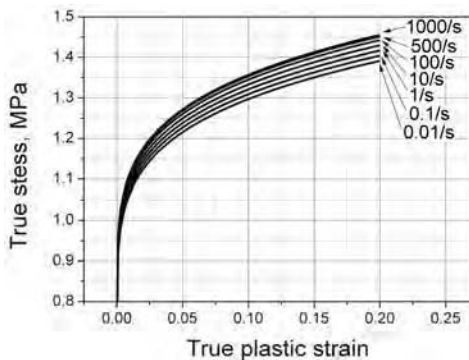


Fig. 7 Dynamic tensile testing results for Q&P 980

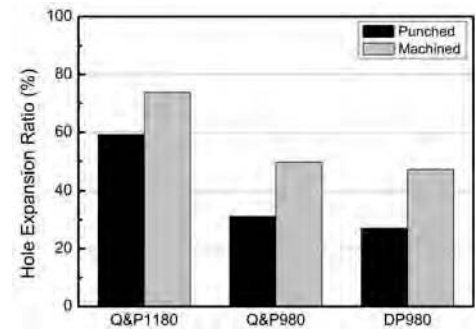


Fig. 8 Hole-expansion ratio of quenching and partitioning (Q&P) steels compared to DP 980 for punched or machined holes

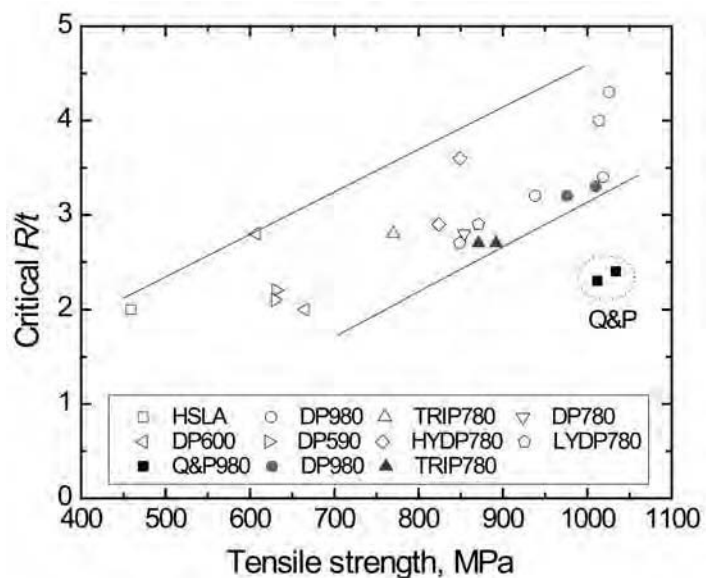


Fig. 9 Comparison of the critical R/t values for Q&P 980 and other high-strength steels. Unfilled points are from the work of Hudgins. Source: Ref 21

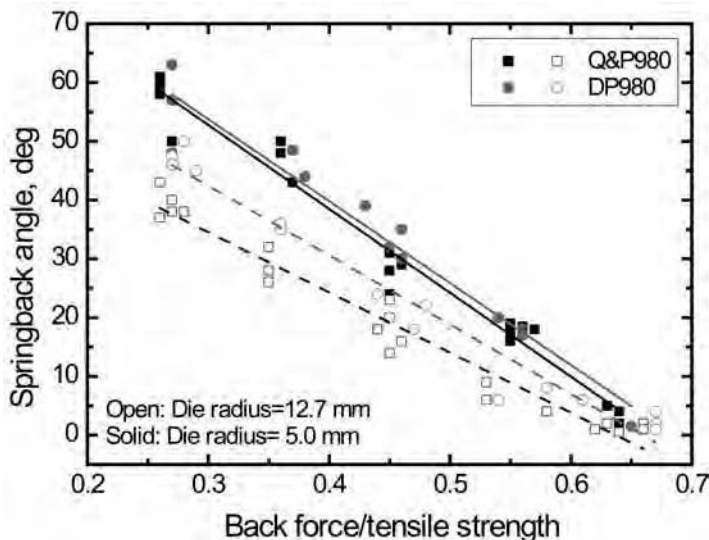


Fig. 10 Comparison of springback angle between Q&P 980 and DP 980 using the bending-under-tension test

of austenite is desired at higher strains to enhance the tensile ductility. The M_s^σ temperature of most low-alloy TRIP steels is typically in the range of -10 to $+10$ °C (14 to 50 °F) (Ref 17). However, according to interpretation of the yielding behaviors in Fig. 11, the M_s^σ temperature of the examined Q&P steel is confirmed to be below -40 °C (-40 °F). The retained austenite in the Q&P steel is thus believed to be relatively more stable compared to that in TRIP steel, which is considered beneficial to formability.

Figure 12 demonstrates the effect of testing temperature on yield strength (YS), ultimate tensile strength (UTS), and total elongation (TEL) of a Q&P 980 steel. It is observed that the YS remains relatively stable over the test temperature range in comparison to the UTS; the decrease in UTS is up to approximately 104 MPa (15 ksi) with an increase in test temperature from -40 to 60 °C (-40 to 140 °F), while the YS is rather stable. This strengthening effect at low temperature can be attributed to two factors: the result of reduction of thermally activated flow and the transformation of retained austenite, which is further elucidated subsequently. The TEL also varies significantly with testing temperature. The maximum value of TEL appears to be in the range of 0 to 20 °C (32 to 68 °F) for this steel, while TEL decreases slightly with increasing temperature above 20 °C. The austenite chemical composition and grain-size distribution influence its stability, and retained austenite with finer particle size and greater carbon concentrations is more stable and resists transformation during deformation. Further increasing the stability of retained austenite by increasing the testing temperature by 20 °C (36 °F) apparently begins to deteriorate the ductility of this steel.

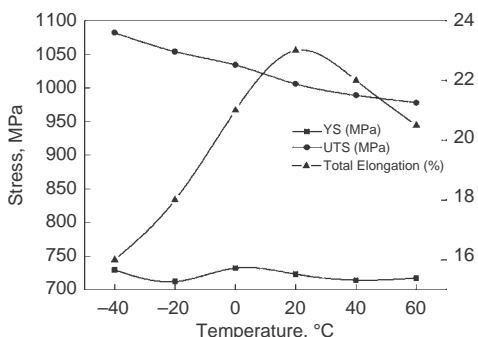


Fig. 12 Effect of test temperature on mechanical properties of Q&P 980 steel. YS, yield strength; UTS, ultimate tensile strength

Retained Austenite Transformation

Retained austenite stability is characterized at different uniaxial tensile testing temperatures by observing deformation and transformation behavior of austenite using x-ray diffraction, scanning electron microscopy, and electron backscatter diffraction (Ref 27). Evolution of the volume fraction of retained austenite (V_γ) is shown in Fig. 13, determined from x-ray diffraction of the studied Q&P sheet steel at different testing temperatures and strains. Generally, the transformation behavior of V_γ is roughly divided into two stages: a rapid decrease at low strains (stage I) and more sluggish decrease at high strains (stage II). However, in some cases, usually when tested at higher temperature, the first stage is less pronounced, and the retained austenite fraction decreases at an almost constant rate from the beginning of deformation. It should be noted here that the transformation rate ($dV_\gamma/d\varepsilon$) at lower testing temperature is faster than that at higher

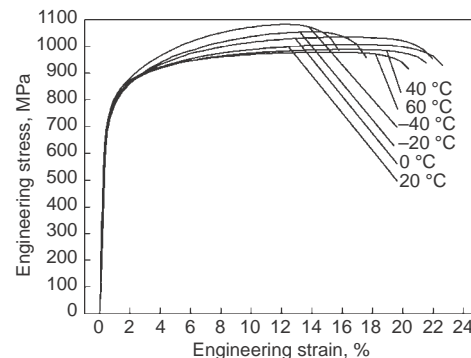


Fig. 11 Tensile engineering stress-strain curves at different temperatures

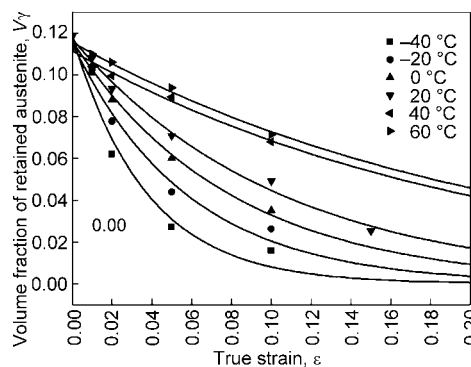


Fig. 13 Effect of strain and testing temperature on volume fraction of austenite

temperature, implying reduced mechanical stability of austenite at lower temperatures due to the smaller driving force needed for deformation-induced martensitic transformation (DIMIT). This DIMIT behavior at small strains is typical of stress-induced martensite transformation. For example, when tested at -40 °C (-40 °F), almost all the retained austenite is transformed into martensite, and only approximately 3% remains after 5% strain. At 60 °C (140 °F), however, most of the retained austenite remained untransformed even when deformed to a tensile strain of 10%. The transformation rates and the amount of retained austenite transformed at greater strains are less sensitive to testing temperature.

Microstructure Evolution with Strain

Figure 14 shows a scanning electron micrograph of a Q&P steel after polishing and etching, showing apparently three characteristics: a rough surface structure corresponds to martensite, ferrite is relatively smooth with only slight surface structure, and the retained austenite areas appear smooth with a featureless surface structure, helping to distinguish it from ferrite and martensite. This steel was intercritically

annealed before quenching, so a considerable ferrite fraction is present along with the Q&P constituent that consists of a mixture of martensite laths and retained austenite. Ideally, formable Q&P steels should not contain a substantial amount of iron carbide. The Q&P steel studied here was partitioned at 400 °C (752 °F) for a few minutes, and, in this instance, the martensite regions also contained carbides. The presence of carbides is of importance because it implies that the cementite may not have fully dissolved, and the available carbon content does not fully contribute to the stabilization of the carbon-enriched austenite in the industrial processing conditions employed.

Microstructure evolution during tensile testing at different strain levels has been examined using electron backscatter diffraction (EBSD). The microstructure of specimens undergoing different strains, that is, 0, 1, 5, and 10%, at 0 °C (32 °F) was analyzed, and Fig. 15 shows the results of a combined image-quality map and gray-scale-coded phase map. Retained austenite is distributed both as thin films and as larger blocky regimes. It is clear that the retained austenite fraction decreases with increased strain, and the remaining austenite particles are mostly the finer ones. These results support the conclusion that finer retained austenite is more stable with deformation. According to Santofimia et al. (Ref 28), the darker-gray areas refer to regions that are likely martensite, based on poor image quality due to high dislocation density, while the lighter-gray areas perhaps represent ferrite. Another method (Ref 29) has also been shown to distinguish these phases by the character of the orientation relationships between them.

The volume fraction of retained austenite measured by EBSD, where all data with confidence index lower than 0.05 were excluded from the analysis as dubious, is a little lower than the one measured by x-ray diffraction, as shown in Table 3. This behavior is consistent with other literature (Ref 30). The discrepancies between results obtained using different

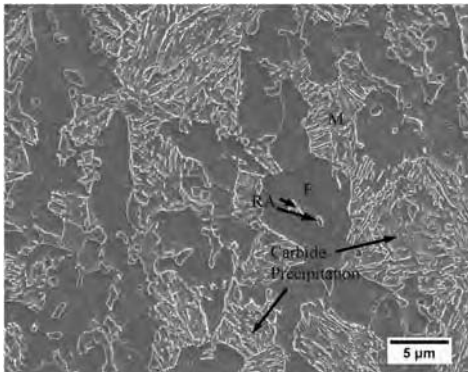


Fig. 14 Scanning electron micrograph of a quenching and partitioning steel containing intercritical ferrite (F), retained austenite (RA), and martensite (M), which is also associated with retained austenite and some carbides

methods may result from differences in sample preparation and penetration depths between the two techniques. During sample preparation, it is inevitable that some austenite transformed into martensite. The scale of the film austenite may also be below the resolution limits and cannot be identified.

Welding Properties

The Q&P 980 steel can be successfully welded with the correct set of parameters. Resistance spot welding, laser welding, and metal active gas welding have produced good results.

Resistance Spot Welding

When resistance spot welded, Q&P 980 requires less current than conventional steels because it has higher electrical resistivity. On the other hand, due to its ultrahigh base material strength, Q&P 980 needs higher electrode forces than conventional steels that have equivalent thickness.

Weld Lobe. Resistance spot welding has been accomplished using the weld schedule shown in Table 4, with a pulsed current profile as shown in Fig. 16. Three types of weld times were chosen to determine their welding current range. The actual weld times were pulse 1 = pulse 2 = 100 ms, pulse 1 = pulse 2 = 120 ms, and pulse 1 = pulse 2 = 140 ms. The weld lobe for 1.6 mm (0.06 in.) Q&P 980 is shown in Fig. 17. In this weld lobe, the minimum weld current is defined as the welding current needed to obtain a full button fracture mode when peel tested, and the maximum weld current is defined as the welding current when expulsion occurs. So, in the enclosed (shaded) zone of Fig. 17, the fracture modes of all spot welds were full button pullout when peel tested. The button size of these welds (in the shaded zone) ranged from 6.0 to 7.7 mm (0.24 to 0.30 in.).

As shown in Fig. 17, the weld current range is 8.0 to 9.8 kA (weld time: 200 ms), 8.0 to 9.4 kA (weld time: 240 ms), 7.6 to 9.4 kA (weld time: 280 ms). The weld lobe is wide enough for most applications.

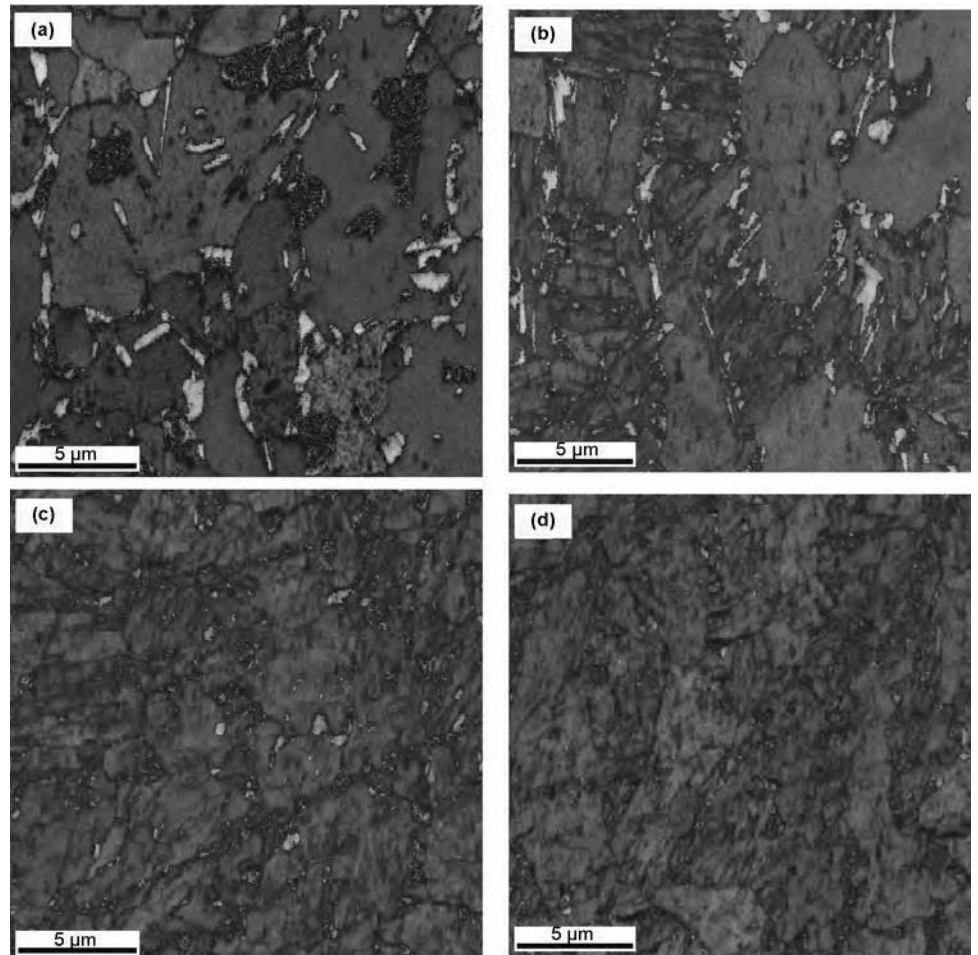


Fig. 15 Electron backscatter diffraction maps of quenching and partitioning steel tension tested at 0 °C (32 °F). White corresponds to face-centered cubic lattice (retained austenite). Gray scale indicates the image quality, where darker-gray scale indicates lower image quality (higher dislocation density). (a) 0, (b) 1, (c) 5, and (d) 10% strain

Table 3 Retained austenite volume fraction measured by x-ray diffraction (XRD) and electron backscatter diffraction (EBSD)

Method	Strain, %				
	Initial	1	2	5	10
XRD	0.116	0.105	0.088	0.060	0.035
EBSD(a)	0.112	0.104	0.080	0.053	0.03

(a) EBSD data with confidence index values greater than 0.05

Spot Weld Strength. The tensile shear strength and cross-tension strength of points “A,” “B,” and “C” (Fig. 17) are listed in Table 5. Points “A,” “B,” and “C” were located at the lower bound of the weld lobe, because it is known that, before expulsion happens, with weld current increasing, the spot weld strength increases with welding current. Overall, 1.6 mm (0.06 in.) Q&P 980 shows good spot weld strength performance.

Spot Weld Microstructure and Microhardness. A weld cross-sectional micrograph and microhardness profile for 1.6 mm (0.06 in.) Q&P 980 is shown in Fig. 18. No weld defects, such as cracks, shrinkage void, pore, no fusion, deep indentation, and so on, are noted. The weld nugget grew very well. The nugget microhardness is approximately 500 HV; its maximum hardness is 512 HV, while its minimum is 474 HV. The base material microhardness is approximately 300 HV. There is no obvious softened region in the heat-affected zone (HAZ).

Laser Welding

Laser welding has been successful using the welding parameters shown in Table 6.

Weld Joint Performance. The 1.6 mm (0.06 in.) Q&P 980 has good laser weldability. For the welding parameters in Table 6, the laser weld joint strength of 1.6 mm (0.06 in.) Q&P 980 was 1081 MPa (157 ksi), and the tensile failure was located in the base material far away from the weld seam and HAZ. Figure 19 shows the microstructure of a 1.6 mm Q&P 980 laser-welded joint. The weld seam zone is martensite, while the HAZ is martensite and ferrite. There were no weld defects found. Figure 20 is the microhardness profile of the 1.6 mm Q&P 980 laser-welded joint. Microhardnesses in both the welded seam and HAZ are higher than in the base material, and there is no obvious softened region in the HAZ.

The laser weld seam for Q&P 980 has good stretchability. Figure 21 shows Erichsen cups after testing the base material and weld seam of 1.6 mm (0.06 in.) Q&P 980. The Erichsen test performance describes the stretchability. Using this test, the Erichsen value for the laser weld seam was 7.34 mm (0.29 in.), approximately 70% of the value for the base material (10.3 mm, or 0.4 in.), and the fracture direction in the Erichsen test was perpendicular to the laser-welded seam.

Table 4 Resistance spot welding parameters

Thickness of base material		Welder	Weld electrode	Weld force		Cooling		Weld pulse
mm	in.			kN	lbf	L/min	gal/min	
1.6	0.06	Medium-frequency direct current	ISO 5821-16 × 20 (type B; diameter 6 mm, or 0.24 in.)	5.8	1305	2	0.5	3

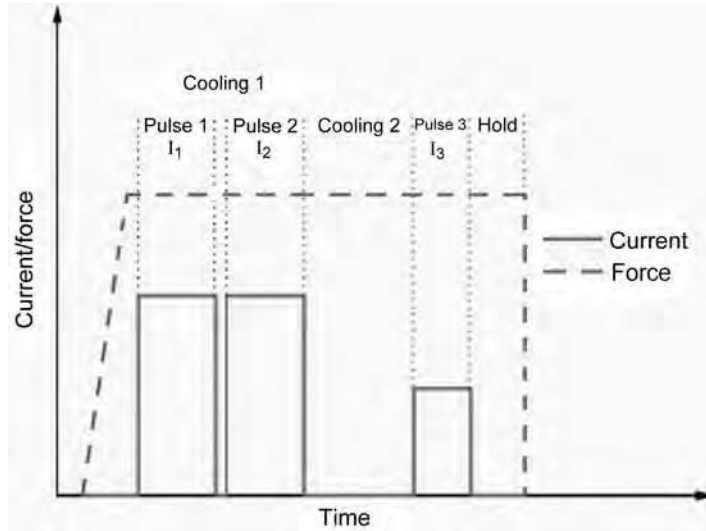


Fig. 16 Resistance spot welding pulsed current profile. Pulse 1 = pulse 2, I₁ = I₂; cooling 1 = 20 ms, cooling 2 = 200 ms; pulse 3 = 100 ms, I₃ = 4.3 kA; hold time = 100 ms

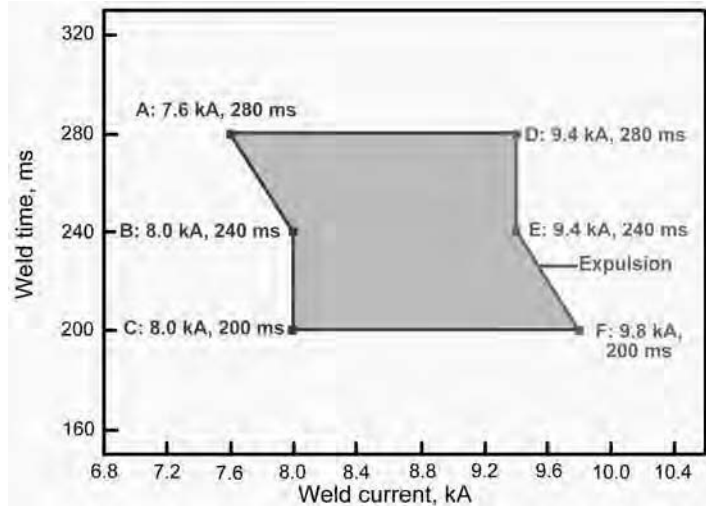


Fig. 17 Weld lobe for 1.6 mm (0.06 in.) Q&P 980

Table 5 Spot weld strength for 1.6 mm (0.06 in.) Q&P 980

Point	Button size		Tensile shear strength		Cross-tension strength	
	mm	in.	kN	lbf	kN	lbf
A	6.5	0.256	26.7	6002	12.3	2765
B	6.2	0.244	26.0	5845	11.9	2675
C	6.0	0.236	23.9	5373	11.4	2563

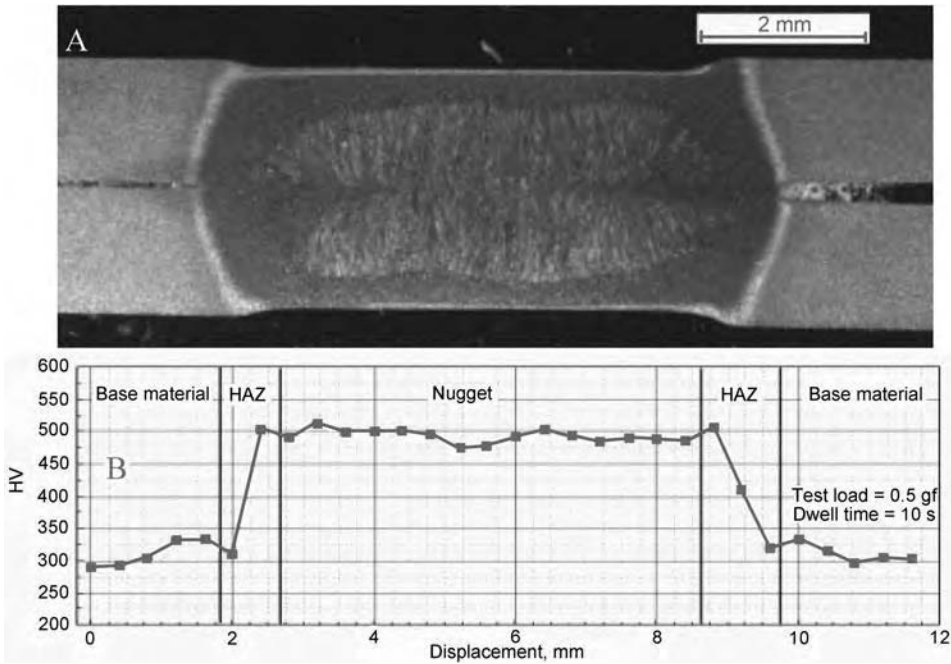


Fig. 18 Spot weld cross-sectional micrograph and microhardness profile for 1.6 mm (0.06 in.) Q&P 980. HAZ, heat-affected zone

Table 6 Laser welding process parameters

Thickness		Power, kW	Weld speed		Defocus		Weld angle, degrees	Cover gas	Quantity of gas	
mm	in.		m/min	ft/min	mm	in.			L/min	gal/min
1.6	0.06	3	5	16	0	0	0	He	15	4.0

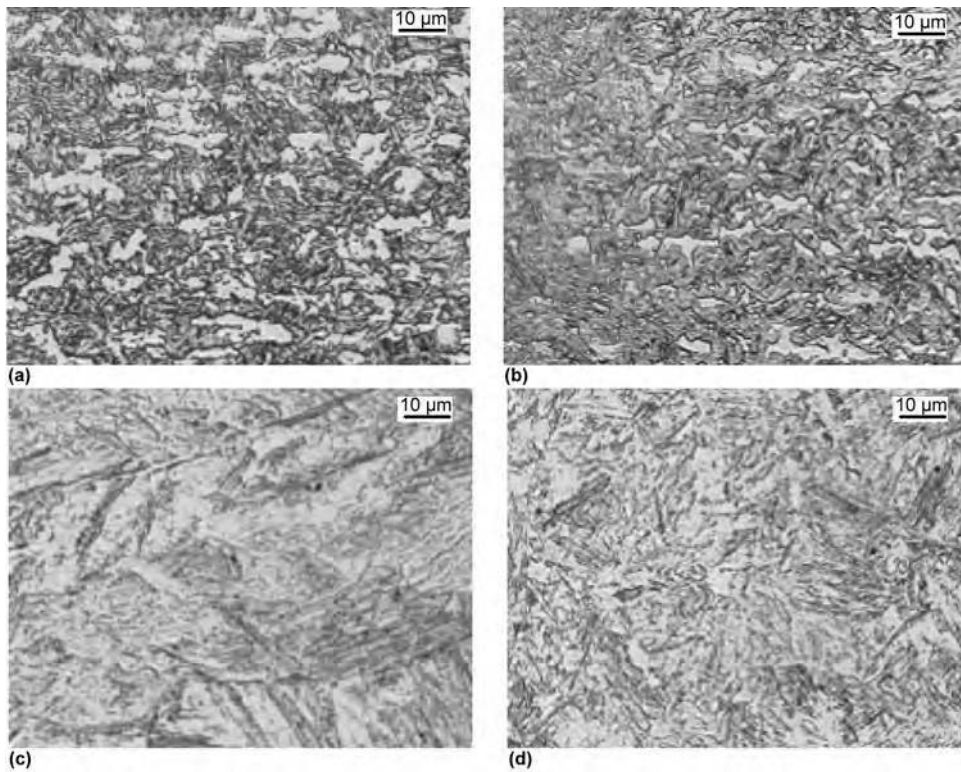


Fig. 19 Microstructures of 1.6 mm (0.06 in.) Q&P 980 laser-welded joint. (a) Base material. (b) Fine-grained heat-affected zone (HAZ). (c) Weld seam. (d) Coarse-grained HAZ

Metal Active Gas Welding

Metal active gas (MAG) welding was successful using the welding parameters shown in Table 7.

Weld Joint Performance. Despite the greater alloy content used for Q&P 980, there were no welding defects than observed with mild steel MAG welds. For the parameters listed in Table 7, the MAG weld strength of 1.6 mm (0.06 in.) Q&P 980 is 991 MPa (144 ksi). Figure 22 shows the microhardness profile of the 1.6 mm Q&P 980 MAG weld joint. The microhardness of both the welded seam and HAZ is less than 500 HV, and there is no obvious softened region in HAZ.

ACKNOWLEDGMENTS

The authors would like to thank Yong Zhong, Weijun Feng, and Xinyan Jin for providing previously unpublished data and for their assistance in the preparation of this article.

REFERENCES

1. J.G. Speer, D.K. Matlock, B.C. De Cooman, and J.G. Schroth, Carbon Partitioning into Austenite after Martensite Transformation, *Acta Mater.*, Vol 51, 2003, p 2611–2622
2. J.G. Speer, D.V. Edmonds, F.C. Rizzo, and D.K. Matlock, Partitioning of Carbon from Supersaturated Plates of Ferrite, with Application to Steel Processing and Fundamentals of the Bainite Transformation, *Curr. Opin. Solid State Mater. Sci.*, Vol 8, 2004, p 219–237
3. J.G. Speer, D.K. Matlock, B.C. DeCooman, and J.G. Schroth, Comments on “On the Definitions of Paraequilibrium and Orthoequilibrium” by M. Hillert and J. Agren, *Scr. Mater.*, Vol 50, 2004, p 697–699; *Scr. Mater.*, Vol 52, 2005, p 83–85
4. D.K. Matlock and J.G. Speer, Design Considerations for the Next Generation of Advanced High Strength Sheet Steels, *Proceedings of the Third International Conference on Structural Steels*, H.C. Lee, Ed. (Seoul, Korea), The Korean Institute of Metals and Materials, 2006, p 774–781
5. J.G. Speer, F.C. Rizzo Assunção, D.K. Matlock, and D.V. Edmonds, The Quenching and Partitioning Process: Background and Recent Progress, *Mater. Res.*, Vol 8, 2005, p 417–423
6. D.V. Edmonds, K. He, M.K. Miller, F.C. Rizzo, A. Clarke, D.K. Matlock, et al., Microstructural Features of Quenching and Partitioning: A New Martensitic Steel Heat Treatment, *Fifth International*

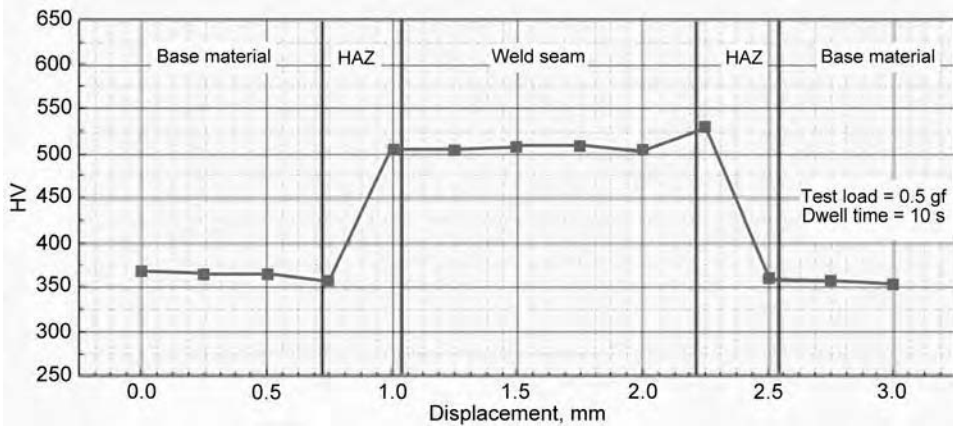


Fig. 20 Microhardness profile across 1.6 mm (0.06 in.) Q&P 980 laser-welded joint. HAZ, heat-affected zone

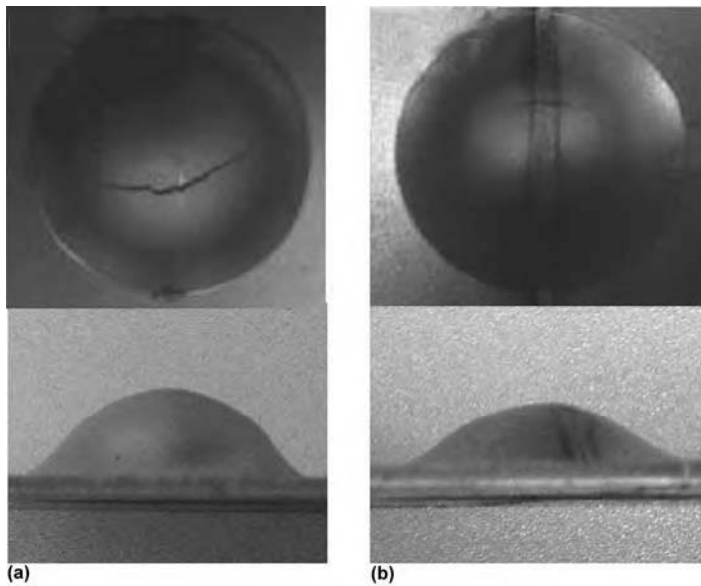


Fig. 21 Photographs of Erichsen test specimens for (a) base material and (b) laser-welded seam

Table 7 Metal active gas welding process parameters

Thickness of base material		Welding speed		Energy input		Cover gas	Filler material	Quantity of gas		Blowpipe distance	
mm	in.	cm/min	in./min	kJ/cm	Btu/in.			L/min	gal/min	mm	in.
1.6	0.06	35	14	3.6	8.7	80% Ar + 20% CO ₂	ER110S	14	3.7	12	0.5

Conference on Processing and Manufacturing of Advanced Materials, T. Chandra, K. Tsuzaki, M. Miltzer, and C. Ravindran, Ed. (Vancouver, Canada), 2006, p 4819–4825

7. D.V. Edmonds, K. He, F.C. Rizzo, B.C. De Cooman, D.K. Matlock, and J.G. Speer, Quenching and Partitioning Martensite—A Novel Steel Heat Treatment, *Mater. Sci. Eng. A*, Vol 438–440, 2006, p 25–34

8. K. He, D.V. Edmonds, J.G. Speer, D.K. Matlock, and F.C. Rizzo, Microstructural Characterisation of Steel Heat-Treated by the Novel Quenching and Partitioning Process, *EMC 2008 14th European Microscopy Congress*, Sept 1–5, 2008 (Aachen, Germany), Springer Berlin Heidelberg, 2008, p 429–430

9. S.S. Nayak, R. Anumolu, R.D.K. Misra, K.H. Kim, and D.L. Lee, Microstructure-Hardness Relationship in Quenched

and Partitioned Medium-Carbon and High-Carbon Steels Containing Silicon, *Mater. Sci. Eng. A*, Vol 498, 2008, p 442–456

10. M.J. Santofimia, L. Zhao, R. Petrov, and J. Sietsma, Characterization of the Microstructure Obtained by the Quenching and Partitioning Process in a Low-Carbon Steel, *Mater. Charact.*, Vol 59, 2008, p 1758–1764

11. C.Y. Wang, J. Shi, W.Q. Cao, and H. Dong, Characterization of Microstructure Obtained by Quenching and Partitioning Process in Low Alloy Martensitic Steel, *Mater. Sci. Eng. A*, Vol 527, 2010, p 3442–3449

12. J.G. Speer, E. De Moor, K.O. Findley, D.K. Matlock, B.C. De Cooman, and D.V. Edmonds, Analysis of Microstructure Evolution in Quenching and Partitioning Automotive Sheet Steel, *Metall. Mater. Trans. A*, Vol 42, 2011, p 3591–3601

13. G. Thomas, J. Speer, D. Matlock, and J. Michael, Application of Electron Backscatter Diffraction Techniques to Quenched and Partitioned Steels, *Microsc. Microanal.*, 2011, p 1–6

14. E. De Moor, S. Lacroix, A.J. Clarke, J. Penning, and J.G. Speer, Effect of Retained Austenite Stabilized via Quench and Partitioning on the Strain Hardening of Martensitic Steels, *Metall. Mater. Trans. A*, Vol 39, 2008, p 2586–2589

15. M.J. Santofimia, L. Zhao, and J. Sietsma, Model for the Interaction between Interface Migration and Carbon Diffusion during Annealing of Martensite-Austenite Microstructures in Steels, *Scr. Mater.*, Vol 59, 2008, p 159–162

16. M.J. Santofimia, J.G. Speer, A.J. Clarke, L. Zhao, and J. Sietsma, Influence of Interface Mobility on the Evolution of Austenite-Martensite Grain Assemblies during Annealing, *Acta Mater.*, Vol 57, 2009, p 4548–4557

17. Y. Takahama, M.J. Santofimia, M.G. Meozzi, L. Zhao, and J. Sietsma, Phase Field Simulation of the Carbon Redistribution during the Quenching and Partitioning Process in a Low-Carbon Steel, *Acta Mater.*, Vol 60, 2012, p 2916–2926

18. D.K. Matlock and J.G. Speer, Processing Opportunities for New Advanced High-Strength Sheet Steels, *Mater. Manuf. Process.*, Vol 25, 2010, p 7–13

19. G.A. Thomas, J.G. Speer, and D.K. Matlock, Considerations in the Application of the Quenching and Partitioning Concept to Hot Rolled AHSS Production, *Iron Steel Technol.*, Vol 5, 2008, p 209–217

20. G.A. Thomas, J.G. Speer, and D.K. Matlock, Quenched and Partitioned Microstructures Produced via Gleeble Simulations of Hot-Strip Mill Cooling Practices, *Metall. Mater. Trans. A*, 2011, p 1–8

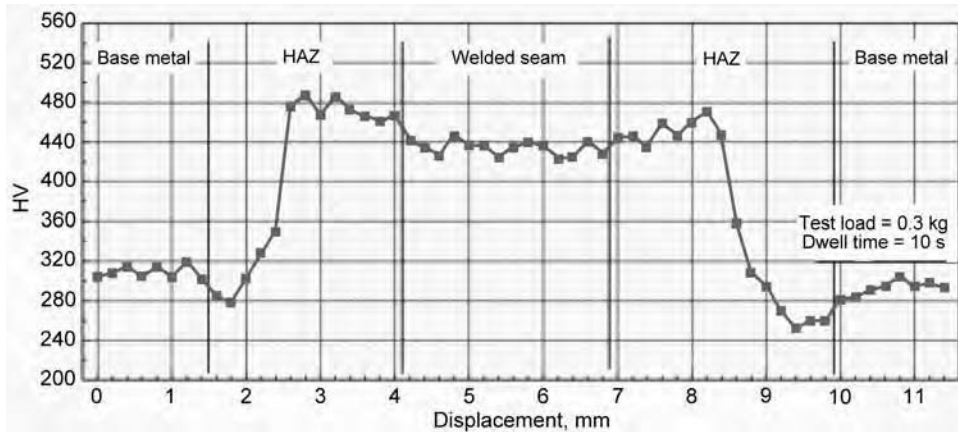


Fig. 22 Microhardness profile across 1.6 mm (0.06 in.) Q&P 980 metal-active-gas-welded joint. HAZ, heat-affected zone

21. L. Wang, W. Li, and W. Feng, "Industry Trials of C-Si-Mn Steel Treated by Q&P Concept in Baosteel," presented at SAE International Congress, 2010
22. L. Wang, X. Jin, and H. Qian, "Recent Development of Galvanizing Sheet

Steels in Baosteel," Proceedings of Galvatech 2011: Eighth International Conference on Zinc and Zinc Alloy Coated Sheet Steel (Genova, Italy), 2011

23. L. Wang and W. Feng, Development and Application of Q&P Sheet Steels, *Advanced*

Steels: The Recent Scenario in Steel Science and Technology, W. Yuqing, D. Han, and G. Yong, Ed., 2011, p 255

24. A.W. Hudgins, "Shear Fracture in Bending of Advanced High Strength Steels," Ph.D. thesis, MT-SRC-010-008, Colorado School of Mines, 2010
25. D.K. Matlock and J.G. Speer, in *Third Generation of AHSS: Microstructure Design Concepts*, A. Haldar, S. Suwas, and D. Bhattacharjee, Ed., Springer London, 2009, p 185
26. J.G. Speer, A.M. Streicher, D.K. Matlock, F. Rizzo, and G. Krauss, *Austenite Formation and Decomposition*, E.B. Damm and M.J. Merwin, Ed., TMS, Warrendale, PA, 2003, p 505
27. A.J. Clarke, Ph.D. thesis, Colorado School of Mines, Golden, CO, 2006
28. M.J. Santofimia, L. Zhao, and J. Sietsma, *Metall. Mater. Trans. A*, Vol 40, 2009, p 46-57
29. S. Zaeferrer, J. Ohlert, and W. Bleck, *Acta Mater.*, Vol 52, 2004, p 2765
30. T. Bhattacharyya, S.B. Singh, S. Das, A. Haldar, and D. Bhattacharjee, *Mater. Sci. Eng. A*, Vol 528, 2011, p 2394

Tempering of Steels*

Revised by Renata Neves Penha and Lauralice C.F. Canale, Universidade de São Paulo, Jan Vatauvuk, Universidade Presbiteriana Mackenzie, and Steven Lampman, ASM International

Introduction

Tempering of steel is a process in which previously hardened or normalized steel is heated to a temperature below the lower critical temperature (A_{c1}) and cooled at a suitable rate, primarily to increase ductility and toughness but also to increase the grain size of the matrix. Tempering usually follows quench hardening and is historically associated with the heat treatment of martensite in steels; however, tempering is also used to relieve the stresses and reduce the hardness developed during welding and to relieve stresses induced by forming and machining.

The focus of this article is on tempering after hardening to obtain specific values of mechanical properties and also to relieve quenching stresses and to ensure dimensional stability. In steel quenched to a microstructure consisting essentially of martensite, the iron lattice is the highly strained body-centered tetragonal structure (martensite) with interstitial carbon atoms, thus producing a very hard (and brittle) condition. Upon heating, the carbon atoms diffuse more easily and react in a series of distinct steps that eventually form Fe_3C or alloy carbides in a ferrite matrix of gradually decreasing stress level.

The properties of the tempered steel are primarily determined by the size, shape, composition, and distribution of the carbides that form, with a relatively minor contribution from solid-solution hardening of the ferrite. These changes in microstructure usually decrease hardness, tensile strength, and yield strength but increase ductility and toughness. Under certain conditions, hardness may remain unaffected by tempering or may even be increased as a result of it. For example, tempering a hardened steel at very low tempering temperatures may cause no change in hardness but may achieve a desired increase in yield strength.

Also, those alloy steels that contain one or more of the carbide-forming elements (chromium, molybdenum, vanadium, and tungsten) are capable of secondary hardening; that is, they may become somewhat harder as a result of tempering.

Principal Variables

Variables associated with tempering that affect the microstructure and the mechanical properties of a tempered steel include:

- Tempering temperature
- Time at temperature
- Cooling rate from the tempering temperature
- Composition of the steel, including carbon content, alloy content, and residual elements

The tempering process is very dependent on the relation of time-temperature. An inappropriate selection of these process parameters affects temper embrittlement, nonoptimal stress relief, mechanical properties, and transformation of retained austenite. Temperature and time also are interdependent variables in the tempering process. Within limits, lowering temperature and increasing time can usually produce the same result as raising temperature and decreasing time. However, minor temperature changes have a far greater effect than minor time changes in typical tempering operations.

Like many heat treatment processes, the temperature of tempering is much more important than the time of tempering. The distribution and size of carbides depends on tempering conditions. At lower tempering temperatures, for example, the microstructure is still martensitic, with the acicular needle structure beginning to round at the tips as carbides begin to form. In contrast, a ferritic matrix with a fine dispersion of carbides is the end result of high-temperature tempering. The resultant microstructure is often referred to as tempered martensite, although

tempered steel microstructures often do not contain martensite.

The effects of tempering temperatures on hardness values for several quenched steels are presented in Table 1. As expected, higher tempering temperatures result in lower hardness for both carbon steels (Fig. 1) and alloy steels (Fig. 2, 3). Unlike martensite (where only carbon influences the hardness of martensite), the hardness of quenched and tempered (QT) alloy steel is higher than that of a QT carbon steel at the same carbon level. Tempering of alloy steels also can produce alloy carbides that are harder than iron carbide (Fe_3C) in carbon steels. Toughness also is improved at higher tempering temperature, although there is a well-recognized dip in toughness at intermediate tempering temperatures for both carbon and alloy steels (Fig. 4).

Cooling Rate. Another factor that can affect the properties of tempered steel is the cooling rate from the tempering temperature. Although tensile properties are not affected by cooling rate, toughness (as measured by notched-bar impact testing) can be decreased if the steel is cooled slowly through temperatures in the range of approximately 450 to 600 °C (840 to 1110 °F), especially in steels that contain carbide-forming elements. Elongation and reduction in area may be affected also. This phenomenon is called temper embrittlement and is discussed in the section “Temper Embrittlement” in this article.

Tempering Temperatures and Stages

As recognized for many years (Ref 1), temperature is the key factor in tempering, because microstructural modifications are accelerated by increasing temperature. For carbon or low-alloy steels, the following five practical temperature ranges suggested by Grossmann and Bain

* Revised from M. Wisti and M. Hingwe, Tempering of Steel, *Heat Treating*, Vol 4, ASM Handbook, ASM International, 1991, p 121–136, with adapted text from sources listed in the Acknowledgments.

Table 1 Typical hardnesses of various carbon and alloy steels after tempering

Grade	Carbon content, %	Hardness, HRC, after tempering for 2 h at									Heat treatment
		205 °C (400 °F)	260 °C (500 °F)	315 °C (600 °F)	370 °C (700 °F)	425 °C (800 °F)	480 °C (900 °F)	540 °C (1000 °F)	595 °C (1100 °F)	650 °C (1200 °F)	
Carbon steels, water hardening											
1030	0.30	50	45	43	39	31	28	25	22	95(a)	Normalized at 900 °C (1650 °F), water quenched from 830–845 °C (1525–1550 °F); average dewpoint, 16 °C (60 °F)
1040	0.40	51	48	46	42	37	30	27	22	94(a)	
1050	0.50	52	50	46	44	40	37	31	29	22	
1060	0.60	56	55	50	42	38	37	35	33	26	
1080	0.80	57	55	50	43	41	40	39	38	32	Normalized at 885 °C (1625 °F), water quenched from 800–815 °C (1475–1550 °F); average dewpoint, 7 °C (45 °F)
1095	0.95	58	57	52	47	43	42	41	40	33	
1137	0.40	44	42	40	37	33	30	27	21	91(a)	Normalized at 900 °C (1650 °F), water quenched from 830–855 °C (1525–1575 °F); average dewpoint, 13 °C (55 °F)
1141	0.40	49	46	43	41	38	34	28	23	94(a)	
1144	0.40	55	50	47	45	39	32	29	25	97(a)	
1330	0.30	47	44	42	38	35	32	26	22	16	
2330	0.30	47	44	42	38	35	32	26	22	16	Normalized at 900 °C (1650 °F), water quenched from 800–815 °C (1475–1500 °F); average dewpoint, 16 °C (60 °F)
3130	0.30	47	44	42	38	35	32	26	22	16	
4130	0.30	47	45	43	42	38	34	32	26	22	Normalized at 885 °C (1625 °F), water quenched from 800–855 °C (1475–1575 °F); average dewpoint, 16 °C (60 °F)
5130	0.30	47	45	43	42	38	34	32	26	22	
8630	0.30	47	45	43	42	38	34	32	26	22	
1340	0.40	57	53	50	46	44	41	38	35	31	
3140	0.40	55	52	49	47	41	37	33	30	26	Normalized at 870 °C (1600 °F), oil quenched from 830–845 °C (1525–1550 °F); average dewpoint, 16 °C (60 °F)
4140	0.40	57	53	50	47	45	41	36	33	29	
4340	0.40	55	52	50	48	45	42	39	34	31	Normalized at 870 °C (1600 °F), oil quenched from 830–845 °C (1525–1575 °F); average dewpoint, 13 °C (55 °F)
4640	0.40	52	51	50	47	42	40	37	31	27	
8740	0.40	57	53	50	47	44	41	38	35	22	
4150	0.50	56	55	53	51	47	46	43	39	35	
5150	0.50	57	55	52	49	45	39	34	31	28	Normalized at 870 °C (1600 °F), oil quenched from 830–870 °C (1525–1600 °F); average dewpoint, 13 °C (55 °F)
6150	0.50	58	57	53	50	46	42	40	36	31	
8650	0.50	55	54	52	49	45	41	37	32	28	Normalized at 870 °C (1600 °F), oil quenched from 815–845 °C (1500–1550 °F); average dewpoint, 13 °C (55 °F)
8750	0.50	56	55	52	51	46	44	39	34	32	
9850	0.50	54	53	51	48	45	41	36	33	30	

Data were obtained on 25 mm (1 in.) bars adequately quenched to develop full hardness. (a) Hardness, HRB

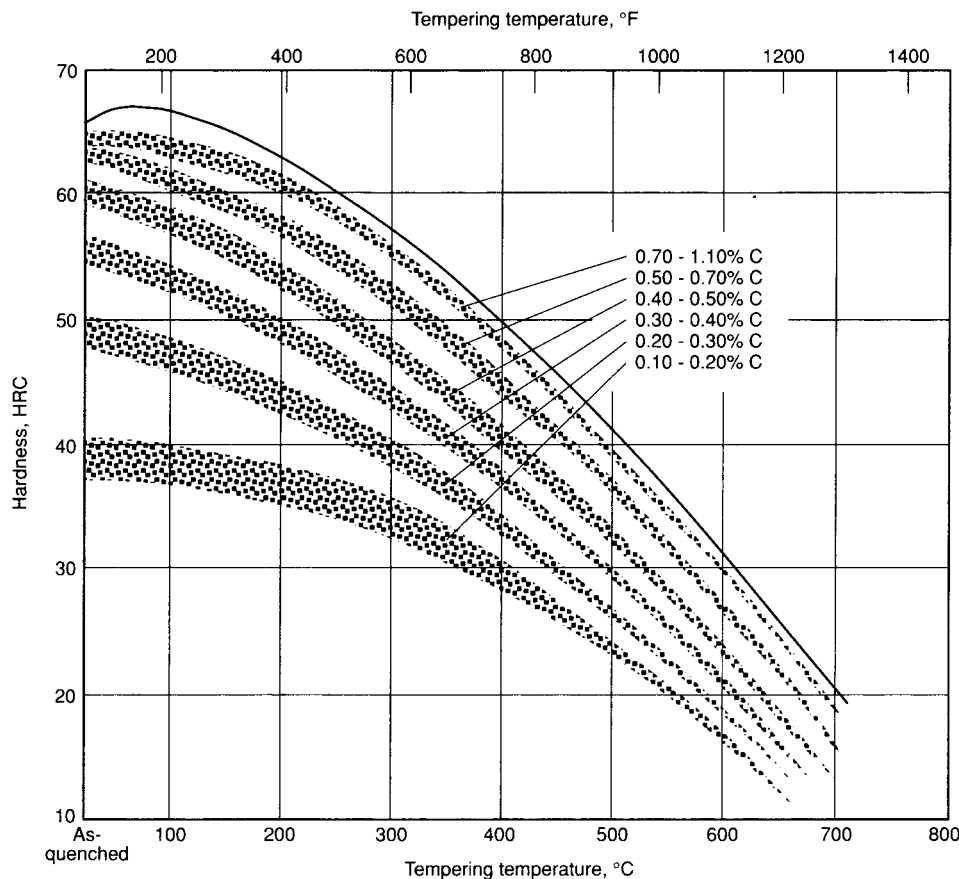


Fig. 1 Hardness of quenched and tempered plain carbon steels at various tempering temperatures. Source: Ref 1

(Ref 1) are still convenient in discussing the tempering process:

- Refrigeration, which converts more or less, and usually much, of the retained austenite to martensite
- Heating in the range of 95 to 205 °C (200 to 400 °F), in which (depending on the temperature) the martensite progressively loses its tetragonality to become cubic, and one finds the first precipitation of a transition carbide (not cementite)
- Heating in the range of 230 to 370 °C (450 to 700 °F), within which range the retained austenite is decomposed, being transformed, largely isothermally, to lower bainite (unless the retained austenite has previously been transformed to martensite by refrigeration)
- Tempering in the range of 370 to 540 °C (700 to 1000 °F), causing formation of the cementite (Fe₃C) form of carbide
- Tempering in the range of 540 to 705 °C (1000 to 1300 °F). In plain carbon steels in this range of temperature, there is merely further agglomeration of the cementite, but in alloy steels containing carbide-forming elements, tempering into this temperature range causes the first formation of very finely dispersed alloy-rich carbides, believed to take place by re-solution of cementite and contemporaneous precipitation of carbon as special alloy-bearing carbide. This reaction often results in a marked retardation of the softening process—sometimes an actual

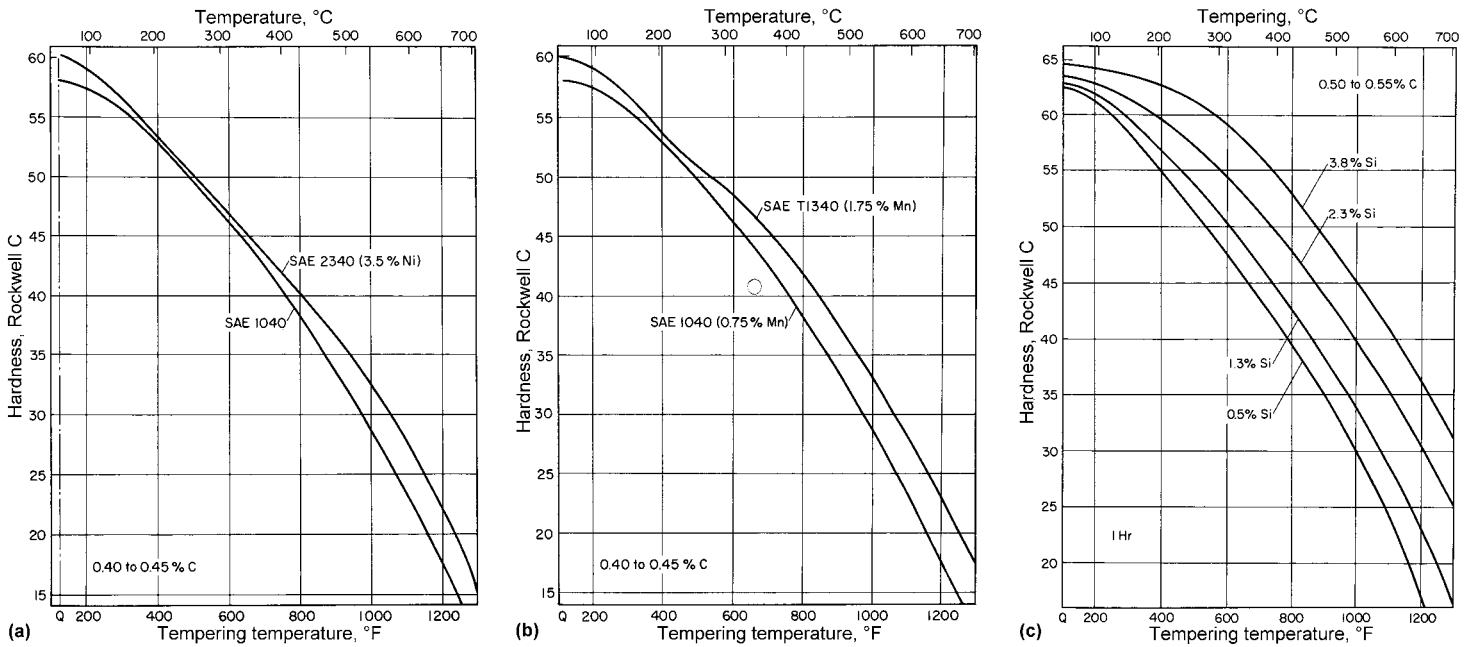


Fig. 2 Examples of alloying effects on resistance to softening during tempering as compared to carbon steel. Effect of (a) nickel, (b) manganese, and (c) silicon. Source: Ref 2

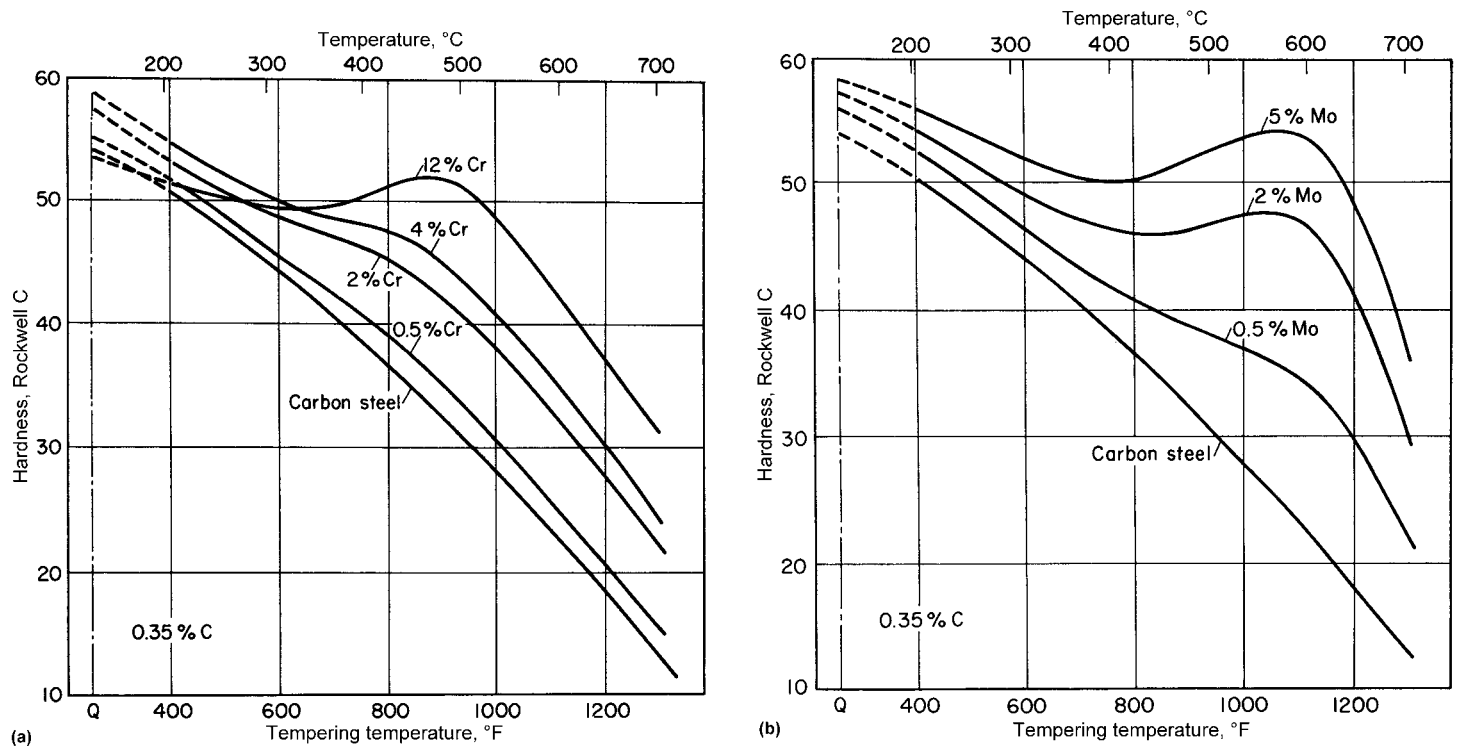


Fig. 3 Examples of secondary hardening during tempering with strong carbide-forming elements. (a) Chromium (b) Molybdenum. Source: Ref 2

increase in hardness—and is often designated secondary hardening.

Refrigeration, as discussed in another article, is only noted here as a method to reduce retained austenite. The other four temperature ranges are described in the following sections.

Tempering temperatures also are often described in terms of so-called stages, which are relatively distinct temperature ranges of microstructural change. The stages of tempering are somewhat arbitrary, as there can be considerable overlap, because reactions continually occur when a part is heated to higher and higher

temperatures. Nonetheless, the stages have been identified from various studies (Ref 3–6):

- *Stage I:* The formation of transition carbides and lowering of the carbon content of the martensite to 0.25% (typically from approximately 100 to 250 °C, or 200 to 480 °F)

- **Stage II:** The transformation of retained austenite to ferrite and cementite (200 to 300 °C, or 390 to 570 °F)
- **Stage III:** The replacement of transition carbides and low-temperature martensite by cementite and ferrite (250 to 350 °C, or 480 to 660 °F)
- **Stage IV:** Precipitation of finely dispersed alloy carbides in high-alloy steels or secondary hardening (Fig. 3).

It also has been found that stage I of tempering is often preceded by the redistribution of carbon atoms, called autotempering or quench tempering, during quenching and/or holding at room temperature (Ref 7). Other structural changes take place because of carbon atom rearrangement preceding the classical stage I of tempering (Ref 8, 9).

A summary of the microstructural changes during tempering is given in Fig. 5 and Table 2. Many other references describe this in more detail. More recent reviews are contained in Ref 2 and 11 to 13.

Tempering at 95 to 200 °C (200 to 400 °F). The tempering range of 95 to 200 °C (200 to 400 °F) is used when it is important to preserve as much hardness of strength as possible with a modest improvement in toughness. In terms of microstructure, two changes are known to take place (Ref 1): Tetragonal martensite becomes cubic, and carbon is precipitated in the form of cementite (Fe₃C) or transitional carbides (Ref 1).

This temperature range includes stage I tempering, which can begin (to a limited degree) even at room temperature and extend to 250 °C (480 °F). At the beginning of stage I tempering of low-carbon steels, the carbon atoms redistribute themselves to lower-energy sites such as dislocations. Martensite may undergo a partial loss of its tetragonal structure due to the lowering of its carbon content to 0.25 wt%. Because carbon atoms can reduce their energies more by segregating to dislocation sites than by forming transition carbides, no transition carbides form in steels with less than approximately 0.2 wt% C. In steels

containing more than 0.2 wt% C, the initial carbon segregation occurs by precipitation clustering. The very fine particles of transition carbide nucleate and grow within the martensite.

Carbon content of the martensitic matrix is reduced by the formation of transition carbides, which include epsilon (ε)-carbide (with a hexagonal crystal structure and an approximate composition of Fe_{2.4}C) and/or eta (η)-carbide (Fe₂C with an orthorhombic crystal structure). Both epsilon-carbide and eta-carbide have substantially higher carbon contents than the cementite Fe₃C that forms later when tempering is conducted at higher temperatures. When the transition carbides form, the martensite retains some degree of its tetragonal structure, because it still contains more carbon in solid solution than ferrite does. Therefore, when the total carbon content is high enough, the first stage of tempering involves the segregation of carbon to various defects in the microstructure and the conversion of martensite to low-carbon martensite and a transition carbide. During

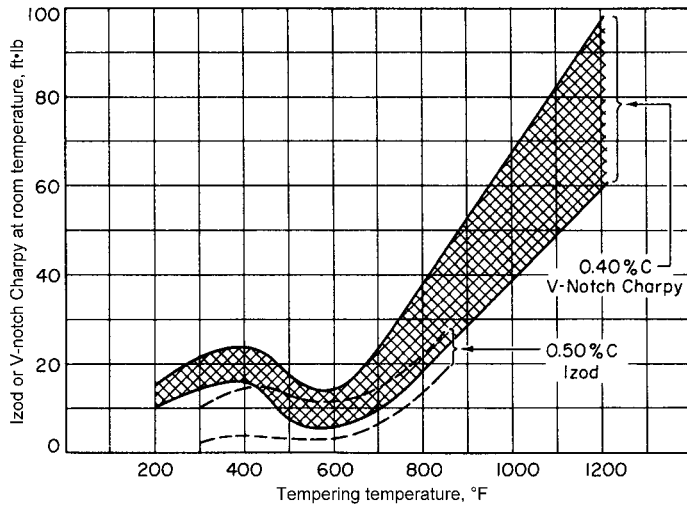


Fig. 4 Range of notch toughness at room temperature for a variety of low-alloy steels (with 0.40 and 0.50% C) after various tempering temperatures. Source: Ref 1

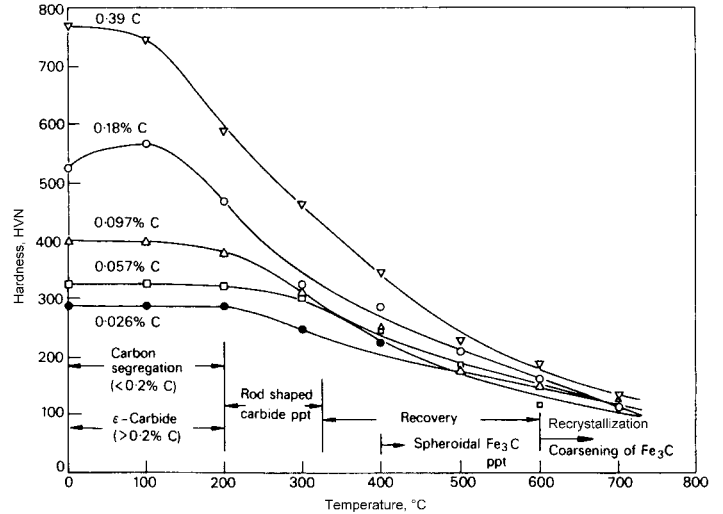


Fig. 5 Tempering stages and effect of tempering temperature on hardness of plain carbon steels. Adapted from Ref 10

Table 2 Sequence of events in tempering of steels

Temperature range		Reaction and symbol (if designated)	Comments
°C	°F		
-400 to 100	-690 to 212	Clustering of two to four carbon atoms on octahedral sites of martensite segregation of carbon atoms to dislocation boundaries	Clustering is associated with diffuse spikes around fundamental electron diffraction spots of martensite.
20 to 100	70 to 212	Modulated clusters of carbon atoms on (102) martensite planes (A2)	Identified by satellite spots around electron martensite
60 to 80	140 to 175	Long-period ordered phase with ordered carbon atoms arranged (A3)	Identified by superstructure spots in electron diffraction patterns
100 to 200	212 to 390	Precipitation of transition carbide as aligned 2 nm diameter particles (T1)	Recent work identifies carbides as eta (orthorhombic, Fe ₂ C); earlier studies identified the carbides as epsilon (hexagonal, Fe _{2.4} C).
200 to 350	390 to 660	Transformation of retained austenite to ferrite and cementite (T2)	Associated with tempered martensite embrittlement in low- and medium-carbon steels
250 to 700	480 to 1290	Formation of ferrite and cementite; eventual development of well-spheroidized carbides in a matrix of equiaxed ferrite grains (T3)	This stage now appears to be initiated by chi-carbide formation in high-carbon Fe-C alloys.
500 to 700	930 to 1290	Formation of alloy carbides in Cr-, Mo-, V-, and W-containing steels. The mix and composition of the carbides may change significantly with time (T4).	The alloy carbides produce secondary hardening and pronounced retardation of softening during tempering or long-time service exposure at approximately 500 °C (930 °F).
350 to 550	660 to 1020	Segregation and cosegregation of impurity and substitutional alloying elements	Responsible for temper embrittlement

Source: Ref 9

stage I tempering, there are also changes in the physical properties, such as electrical resistivity, which can be used to monitor the progress of the changes. However, there is not much reduction in the hardness; in fact, it can increase slightly for steels of medium-to-high carbon contents.

Tempering at 230 to 370 °C (450 to 700 °F). The approximate tempering range of 230 to 370 °C (450 to 700 °F) is scarcely ever employed in the tempering of quench-hardened steel. It lies between the tempering range (below 205 °C, or 400 °F) where high hardness is the main consideration and the tempering range (above 370 °C, or 700 °F) where toughness is the principal objective. The range between these two is avoided, probably because of the peculiar loss in toughness, as mentioned subsequently, and because of the lack of either great strength or great toughness in the resulting properties.

The tempering range of 230 to 370 °C (450 to 700 °F) is characterized chiefly by two long-known behaviors: the microstructural change in which the retained austenite (unless previously transformed by refrigeration) is now more or less isothermally transformed to lower bainite, and a loss in room-temperature notch toughness as the tempering temperature is raised. The two behaviors are wholly unconnected.

Reduction in Retained Austenite. The quantity of retained austenite can be large in alloy steels, especially those in which the martensite finish temperature is below room temperature. Tempering in the temperature range of 200 to 300 °C (400 to 570 °F) induces the decomposition of retained austenite into cementite and ferrite, or lower bainite—resulting in an increase of volume. When the retained austenite is present as a film (typically, at grain boundaries), the cementite precipitates as a continuous array of particles that have the appearance of a film (Ref 2, 13).

In steels with carbon contents below 0.5%, the retained austenite content is less than 2% by volume, if present. In Fig. 6, for example, the transformation of retained austenite in 4130 and 4340 steels (with approximately 2 and 4 vol% of retained austenite, respectively) begins above 200 °C (400 °F) and is complete by 315 °C (600 °F). As the amount of retained austenite decreases, the percentage of cementite increases.

Reduction in Toughness. Like the reduction in retained austenite, the loss in toughness after tempering in the range 230 to 370 °C (450 to 700 °F) (Fig. 4) has been known for many decades. The usual improvement in toughness occurs up to tempering temperatures of 200 °C (400 °F), but with a drop in toughness in the range of approximately 260 to 315 °C (500 to 600 °F). This effect is referred to as tempered martensite embrittlement, which is different from temper embrittlement (see the section “Toughness and Embrittlement” in this article). Given the drop in toughness, tempering at 230 to 370 °C

(450 to 700 °F) is seldom used in industry. Both plain carbon and alloy steels respond to tempering in this manner.

Tempering at 370 to 540 °C (700 to 1000 °F) (Ref 1). Once the tempering temperature of 370 °C (700 °F) has been exceeded, one enters the broad tempering range of 370 to 675 °C (700 to 1250 °F), in which a whole host of industrial products are tempered. These embrace the products in which toughness is of prime importance. When tempered in the lower part of this range, namely, 370 to 540 °C (700 to 1000 °F), the pieces attain excellent toughness while retaining a fair measure of strength. Tempering in the higher portion of the range, namely, 540 to 675 °C (1000 to 1250 °F), is applied to parts that require maximum toughness, even if much strength must be sacrificed.

The tempering range of 370 to 540 °C (700 to 1000 °F) is employed almost entirely for the plain carbon and alloy constructional steels (thus excluding tool steels, bearing steels, and case-hardened steels). This tempering range is characterized by causing an increase in toughness, while at the same time causing a considerable decrease in hardness (with its accompanying decrease in strength). These changes in mechanical properties are a result of the microstructural change: the precipitation and coalescence (initial spheroidization) of the stable carbide.

Of course, the decrease in hardness covers a broad range of hardnesses; because steels of successively higher carbon contents exhibit successively higher hardnesses as quenched, their hardnesses after tempering also cover a band of values, as illustrated in Fig. 1. Figure 1 may be used as a rough guide of the hardnesses to be expected, but it should be emphasized that it is a rough guide only; it is intended to represent only the plain carbon steels.

Typical hardnesses of 4140 or 4150 steels and 1141, 1144, or 1045 steels are listed in Tables 3 and 4 for tempering temperatures up to 650 °C (1200 °F).

Tempering at 540 to 700 °C (1000 to 1300 °F) (Ref 1). Great toughness is obtained by tempering in the high range of 540 to 675 °C (1000 to 1250 °F). In achieving this toughness, much of the strength that was achieved by quenching is lost. In spite of the loss of strength, the quenching and tempering process is still desirable, because tempered martensite is vastly tougher than a pearlitic structure of the same hardness.

The toughness that may be expected after tempering at a series of temperatures is illustrated in a general way in Fig. 4. Figure 4 shows the range of notch-impact values that may be expected in quenched and tempered 0.40 and 0.50% C steels, of a variety of alloy contents, tested at room temperature as V-notch Charpy tests or as Izod tests. When the Charpy tests are keyhole instead of V-notch, lower foot-pound values than those shown are to be expected.

The curves of Fig. 4 cover a variety of alloy compositions. There is little evidence that any particular alloy or combination of alloys will regularly furnish superior toughness at the same hardness. Rather, it is to be expected that, when testing a considerable number of heats of a single (nominal) composition, there will be found such noticeable variations in toughness as to overlap similar variations in most other alloy compositions, at the same carbon content.

Although toughness improves with tempering above 370 °C (700 °F) for carbon and low-alloy steels (Fig. 4), extended heating times or slow cooling in the temperature range of 450 to 600 °C (840 to 1110 °F) can reduce

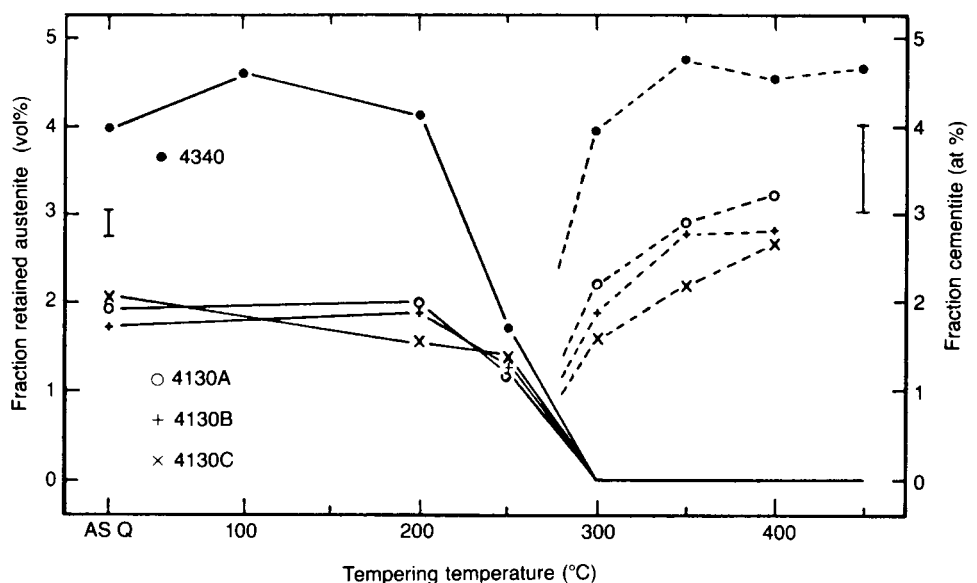


Fig. 6 Transformation of retained austenite in 4130 and 4340 steel

Table 3 Typical hardness of tempered 4140 and 4150 steels

Temper		Furnace hardened and tempered for 1 h, HRC				Induction hardened and tempered for 2 h, HRC			
°C	°F	63	60	58	55	63	60	58	55
As-quenched									
150	300	62.0	59.0	57.0	55.0	61.5	58.5	57.0	54.0
165	325	60.5	58.2	56.0	54.0	58.5	56.2	55.0	52.5
175	350	59.5	57.4	55.0	53.0	57.5	55.4	54.0	51.0
190	375	58.5	56.6	54.0	52.0	56.5	54.6	53.0	50.0
200	400	57.5	55.8	53.5	51.5	55.5	53.8	52.0	49.5
220	425	57.0	55.0	53.0	51.0	55.0	53.0	51.5	49.0
230	450	56.5	54.0	52.5	50.5	54.5	52.0	51.0	48.5
245	475	56.0	54.5	52.0	50.0	54.0	52.5	50.5	48.0
260	500	55.0	53.8	51.5	49.5	53.0	51.8	50.0	47.5
275	525	54.5	53.0	51.0	49.0	52.5	51.0	49.5	47.0
290	550	54.0	52.2	51.0	49.0	52.0	50.2	49.5	47.0
300	575	53.5	52.0	50.5	48.5	51.5	50.0	49.0	46.5
315	600	53.0	51.5	50.0	48.0	51.0	49.5	48.5	46.0
330	625	52.5	51.0	49.5	47.5	50.5	49.0	48.0	45.5
345	650	52.0	50.5	49.0	47.0	50.0	48.5	47.5	45.0
355	675	51.5	50.0	48.5	46.5	49.5	48.0	47.0	44.5
370	700	51.0	49.0	48.0	46.0	49.0	47.0	46.5	44.0
385	725	50.5	48.5	47.5	45.5	48.5	46.5	46.0	43.5
400	750	50.0	48.0	47.0	45.0	48.0	46.0	45.5	43.0
415	775	49.5	47.5	46.5	44.5	47.5	45.5	45.0	42.5
425	800	48.0	46.0	45.5	43.5	46.0	44.0	44.0	41.5
440	825	47.5	45.2	44.5	42.5	45.5	43.2	43.0	40.5
455	850	46.5	44.5	43.5	41.5	44.5	42.5	42.0	39.5
470	875	45.5	43.7	41.7	39.7	43.5	41.7	40.2	37.7
480	900	44.5	43.0	41.0	39.0	42.5	41.0	39.5	37.0
495	925	43.5	42.0	39.2	37.2	41.5	40.0	37.7	35.2
510	950	42.5	41.0	38.5	36.5	40.5	39.0	37.0	34.5
525	975	41.8	40.0	37.5	35.7	39.8	38.0	36.0	33.7
540	1000	41.0	39.0	36.5	35.0	39.0	37.0	35.0	33.0
565	1050	38.5	37.5	35.0	33.5
595	1100	37.0	36.0	33.5	32.0
620	1150	35.0	34.0	31.5	30.0
650	1200	32.5	31.5	29.0	27.5

Source: Ref 14

Table 4 Typical hardness of tempered 1141, 1144, and 1045 steels

Temper		Furnace hardened and tempered for 1 h, HRC				Induction hardened and tempered for 2 h, HRC			
°C	°F	58	55	52	48	60	58	55	52
As-quenched									
150	300	57.0	54.0	51.0	48.0	58.5	56.5	53.0	50.5
165	325	56.0	53.5	50.5	47.5	57.0	54.0	52.0	49.0
175	350	55.0	53.0	50.0	47.5	56.0	53.0	51.5	48.5
190	375	52.5	52.5	49.5	47.0	53.5	50.5	51.0	48.0
200	400	53.5	52.0	49.0	46.5	54.5	51.5	50.5	47.5
220	425	53.5	51.5	48.5	46	54.5	51.5	50.0	47.0
230	450	53.0	51.0	48.0	45.5	54.0	51.0	49.5	46.5
245	475	52.5	50.5	47.5	45	53.5	50.5	49.0	46.0
260	500	51.5	49.5	47.0	44.5	52.5	49.5	48.0	45.5
275	525	50.5	48.5	46.0	44.0	51.5	48.5	47.0	44.5
290	550	50.0	48.0	45.5	43.0	51.0	48.0	46.5	44.0
300	575	49.0	47.0	45.0	42.0	50.0	47.0	45.5	43.5
315	600	48.5	46.5	44.5	41.5	49.5	46.5	45.0	43.0
330	625	48.0	46.0	44.0	41.0	49.0	46.0	44.5	42.5
345	650	47.5	45.5	43.5	40.5	48.5	45.5	44.0	42.0
355	675	47.0	45.0	43.0	40.0	48.0	45.0	43.5	41.5
370	700	46.0	44.0	42.0	39.0	47.0	44.0	42.5	40.5
385	725	44.5	42.5	40.5	37.5	45.5	42.5	41.0	39.0
400	750	43.0	41.0	39.0	36.0	44.0	41.0	39.5	37.5
415	775	41.5	39.5	37.5	34.0	42.5	39.5	38.0	36.0
425	800	39.9	37.5	35.5	32.5	40.9	37.9	36.0	34.0
440	825	38.5	36.7	34.7	31.7	39.5	36.5	35.2	33.2
455	850	38.0	36.0	34.0	31.0	39.0	36.0	34.5	32.5
470	875	37.0	35.0	33.0	30.0	38.0	35.0	33.5	31.5
480	900	36.5	34.0	32.0	29.0	37.5	34.5	32.5	30.5
495	925	35.5	33.5	32.5	28.5	36.5	33.5	32.0	31.0
510	950	34.5	33.0	31.0	28.0	35.5	32.5	31.5	29.5
525	975	33.5	32.0	30.5	27.5	34.5	31.5	30.5	29.0
540	1000	32.5	31.0	30.0	27.0	33.5	30.5	29.5	28.5
565	1050	31.0	29.5	28.5	26.0
595	1100	29.5	28.0	27.0	24.5
620	1150	26.5	26.0	25.0	22.5
650	1200	24.5	23.5	22.5	20.0

Source: Ref 14

toughness (Fig. 7). The effect of cooling rates is more pronounced at the higher end of the temperature range in Fig. 7. This phenomenon is referred to as temper embrittlement (see the section “Toughness and Embrittlement” in this article).

Tempering Time and Temperature

Both time and temperature influence the diffusion of carbon and alloying elements and thus the extent of carbide formation and tempering. For consistency and less dependency on variations in time, components generally are tempered for 1 to 2 h in gas-fired or electric furnaces. A rule-of-thumb suggested by Thelning (Ref 16) is one hour per 25 mm (1 in.) of section thickness after the furnace load has reached a preset temperature. AMS 2759 also specifies recommended tempering conditions for various carbon and low-alloy steels. If tempering is done by induction heating, then the tempering cycle is quite sensitive to both the temperature and the time at temperature.

Generally, the desired hardness is known, and the required temperature is determined from curves such as those in Fig. 1 to 3 for specific tempering time. However, it is useful to consider equivalent tempering over a wide range of time-temperature combinations. Often, tempering can be achieved by short-time tempering at a higher temperature.

Plotting hardness versus tempering time at various tempering temperature (such as in Fig. 8 to 10) is one way of summarizing tempering data. Unless secondary hardening occurs, the changes

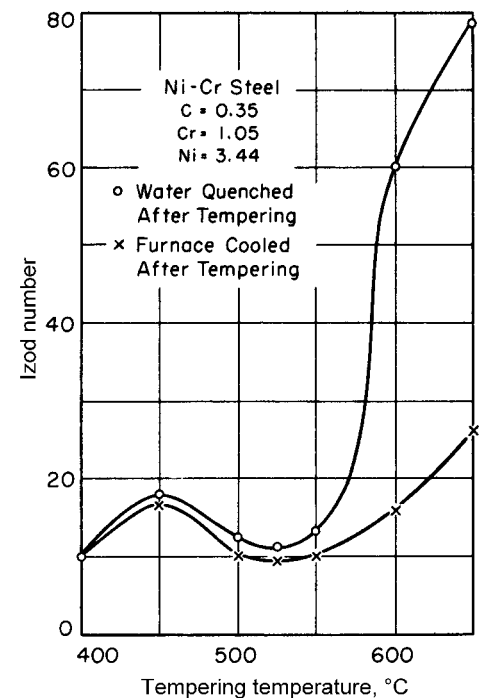


Fig. 7 Effect of cooling rate on temper embrittlement. Adapted from Ref 15

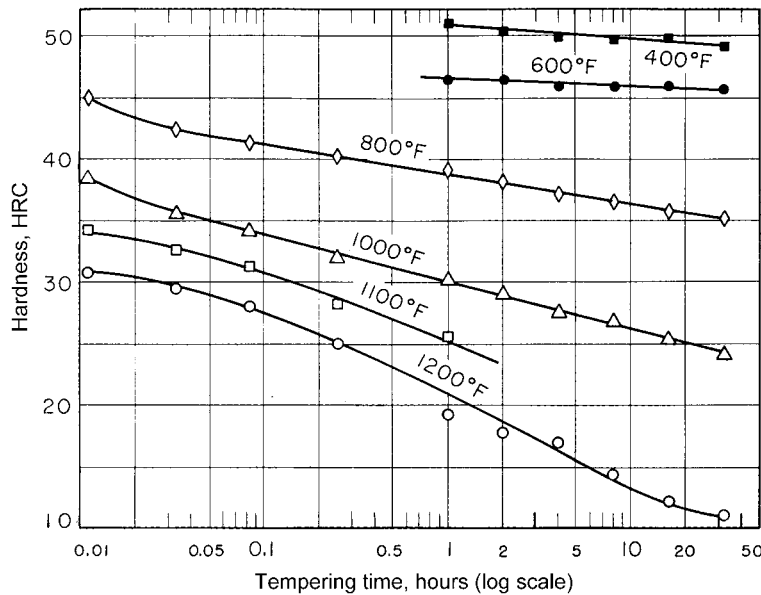


Fig. 8 Summary plot of tempering data for 1335 steel. Source: Ref 17

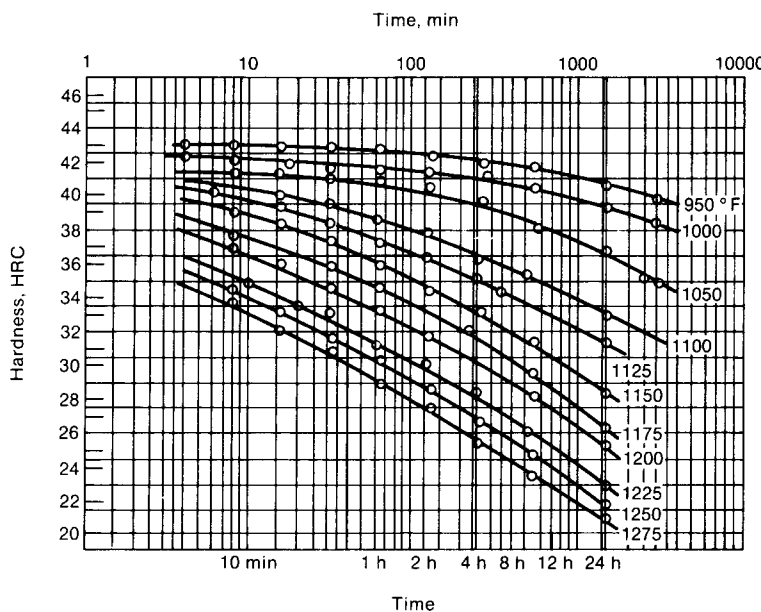


Fig. 10 Tempering behavior of a 4340 steel (0.355 C, 0.66 Mn, 0.042 P, 0.017 S, 0.28 Si) at various temperatures as a function of time. Adapted from Ref 18

in hardness are approximately linear over a large portion of the time range when the time is presented on a logarithmic scale. However, this method is time-consuming. Therefore, parametric methods have been developed to describe the time-temperature effects of tempering.

Most time-temperature parametric models of tempering relate the hardness to a function of absolute temperature (T) times the sum of a parametric constant (C) and the common logarithm of tempering time (t) as follows:

$$\text{Hardness} = \text{Function of } T \times [C + \log_{10}(t)]$$

where T is typically in degrees Kelvin, time (t) is in seconds, and C is a constant that depends

on the carbon content of the steel. This relation, similar to the Larson-Miller parametric analysis of creep data, was first proposed by Holloman and Jaffe (Ref 19) as an empirical tempering parameter to approximate hardnesses of quenched and tempered low- and medium-alloy steels under different time-temperature conditions. From their analysis of various steels, they suggested a parametric constant, C , in the range of 10 to 15, depending on the steel. Two examples are in Fig. 11.

Except when significant amounts of retained austenite are present, reasonably good correlations are obtained with the Hollomon-Jaffe method. The charts in Fig. 12 and

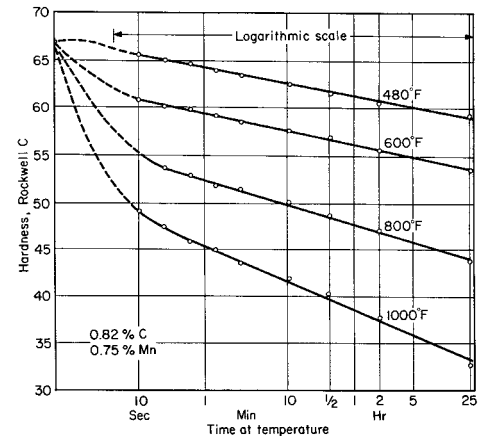


Fig. 9 Effect of tempering time on softening of 0.82C-0.75Mn steel. Source Ref 2

13 were also developed from the datasets of Hollomon and Jaffe, which included carbon and low-alloy steels. Data from high-alloy steel (stainless steels and tool steels) were *not* part of developing these two charts. Figures 12 and 13, as described subsequently, provide a basis for estimating time-temperature effects in the tempering of mechanical/forging steels and high-carbon steels, respectively.

Estimating an Equivalent Time-Temperature Condition for Tempering to a Similar Hardness. Depending on the carbon content of the steel, either Fig. 12 or 13 is used. The chart in Fig. 10 applies for steels with carbon levels of 0.15 to 0.40%. For example, if a 0.30% C steel is tempered at 505 °C (940 °F) for 10 h to achieve a certain hardness, what temperature would give the same hardness from tempering in 1 h? Tempering for 10 h at 505 °C (940 °F) falls on point A in Fig. 12. Point A lies on the hardness differential line of 62 that crosses the 1 h line (point B). In this example, the equivalent tempering temperature is thus 545 °C (1010 °F) for 1 h. The same process applies in Fig. 13 for the high-carbon steels (0.90 to 1.2% C).

Estimating Difference in Hardness from Two Tempering Treatments. The Hollomon-Jaffe charts (Fig. 12, 13) are used in a slightly different way to estimate hardness variations. For steel without large amounts of carbide-forming elements, the difference in the hardness produced by two tempering treatments is approximately equal to the differential between the Rockwell C numbers given on the chart for the two treatments. This is not true, however, for hardnesses less than C-20 Rockwell or within 3 Rockwell C numbers of the hardness before tempering.

Example: Alloy Steel with 0.30% C (Fig. 12). A 0.30%C-3%Ni steel tempered 10 h at 505 °C (940 °F) has a hardness of C-29, as determined experimentally. What would be the approximate

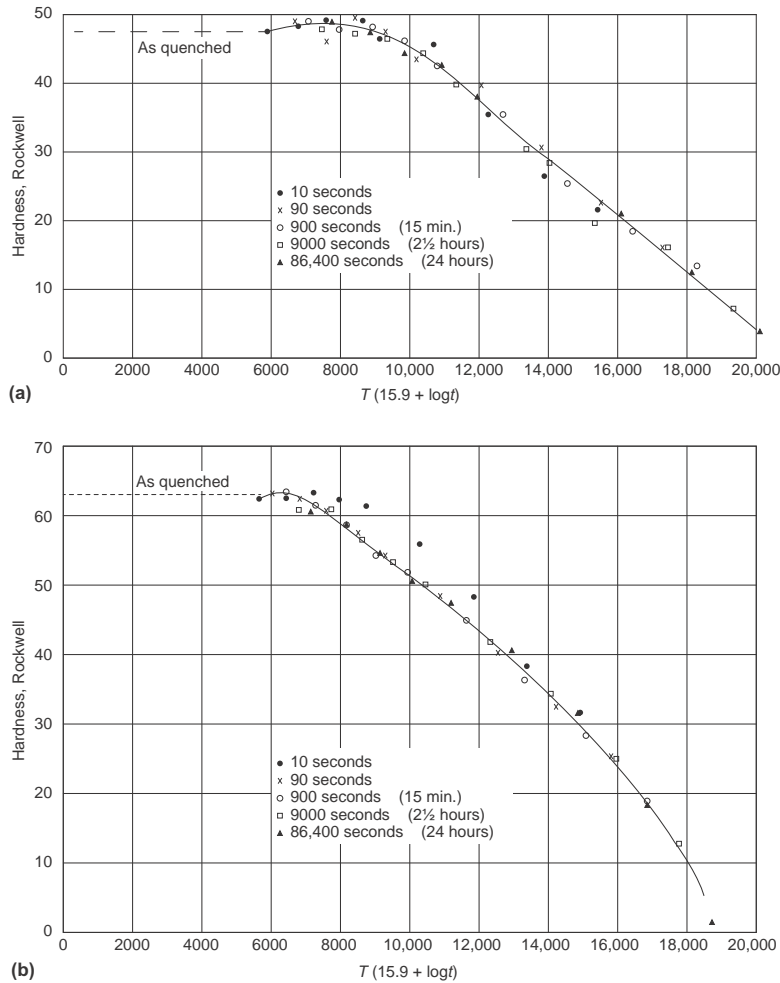


Fig. 11 Hollomon-Jaffe parametric plot of tempering behavior for (a) 0.31% C steel with a parametric of 15.9 and (b) 0.356% C steel with a parametric of 14.3. Temperature (T) in K and time (t) in seconds. Source: Ref 20

hardness if the steel were tempered 2 h at 425 °C (800 °F)?

Tempering for 10 h at 505 °C (940 °F) (point A) falls on line 62; tempering for 2 h at 425 °C (800 °F) (point C) falls on line 54. The differential is $62 - 54 = 8$. The hardness after 2 h at 425 °C (800 °F) would then be $8 + 29 = \text{Rockwell C-37}$.

Example: High-Carbon Steel (Fig. 13). A 1095 steel tempered 1 h at 595 °C (1100 °F) has a hardness of C-34, as determined experimentally. What would be the approximate hardness if the steel were tempered 4 h at 480 °C (900 °F)?

Tempering for 1 h at 595 °C (1100 °F) (point C) falls on line 65.5; tempering for 4 h at 480 °C (900 °F) (point D) falls on line 59.5. The differential is $65.5 - 59.5 = 6$. The hardness after 4 h at 480 °C (900 °F) would then be $34 + 6 = \text{Rockwell C-40}$.

Other Parametric Models. In practical use, the parametric constant (C) can vary with steel and hardness levels. Like any empirical relation, caution is needed in the use of parametric models. The method assumes full (100% martensite) as-quenched hardness without retained austenite.

Caution is also needed in extending use significantly beyond the steel compositions in a given analysis. Some examples of the Larson-Miller parametric constant are listed in Table 5.

In the analysis of various carbon and low-alloy steels by Grange and Baughman (Ref 17), the parametric constant (C) varied so much for a given steel (by a factor of 4 or more alloy steels) that the average value was of little value. However, in a trial-and-error method to minimize the scatter in the plotted data, Grange and Baughman were able to recommend a single value of $C = 18$ that was a satisfactory constant for various carbon steels (from 1026 to 1080) and low-alloy steels (4027, 4037, 4047, 4068, 1335, 2340, 3140, 4140, 4340, 4640, 5140, and 6145). Tempering data were satisfactorily modeled by the following parametric equation:

$$P = [^{\circ}\text{F} + 460][18 + \log(t, \text{ in hours})] \times 10^{-3}$$

Examples are shown in Fig. 14 and 15 for carbon steels and low-alloy steels, respectively. The variation of parameter, P , and hardness was

also plotted as a function of carbon content (Fig. 16a) for carbon steels. In relating the various values of the parameter in terms of time and temperature, Fig. 16(b) provides a way of determining the parameter for a tempering cycle.

Many methods have been used in modeling the time-temperature response of martensitic steels during tempering. A recent review is in Ref 23. In particular, a promising method is the use of artificial neural networks (ANNs), which are a nonlinear regression-type methodology for establishing the correlation between input and output variables in a physical system. The advent of neural networks is a tool for complex empirical modeling and the discovery of fundamental relationships and quantitative structure within arrays of data. An introduction on the ANN methods can be found in the article "Neural-Network Modeling" in *Fundamentals of Modeling for Metals Processing*, Volume 22A of *ASM Handbook* (Ref 24). The use of the ANN method in the modeling of tempering is reviewed in Ref 23.

Effect of Composition

The effect of carbon content on the hardness of QT carbon steel properties of tempered steels is shown in Fig. 17(a). This figure serves as the basis for determining the effects of other alloying elements on the hardness of QT low-alloy steels. All alloying increases the resistance to softening during tempering (e.g., Fig. 2 and 3 as previously noted). The main purpose of adding alloying elements to steel is to increase the hardenability, that is, to increase the depth of martensite formation upon quenching. Alloying elements retard the rate of softening, especially at the higher tempering temperatures. Thus, to reach a given hardness in a given period of time, alloy steels require higher tempering temperatures than do carbon steels.

Alloying elements can be characterized as carbide forming or non-carbide forming. Elements such as nickel, silicon, aluminum, and manganese, which have little or no tendency to occur in the carbide phase, remain essentially in solution in the ferrite and have only a minor effect on tempered hardness. Hardening due to the presence of these elements occurs mainly through solid-solution hardening of the ferrite or matrix grain size control. The carbide-forming elements (chromium, molybdenum, tungsten, vanadium, tantalum, niobium, and titanium) retard the softening process by the formation of alloy carbides. The effect of the carbide-forming elements is minimal at low tempering temperatures where Fe_3C forms; however, at higher temperatures, alloy carbides are formed, and hardness decreases slowly with tempering temperature.

The increases in resistance to softening due to alloying elements are shown in Fig. 18 and 19 at different tempering temperatures. Strong carbide-forming elements such as chromium, molybdenum, and vanadium are most effective

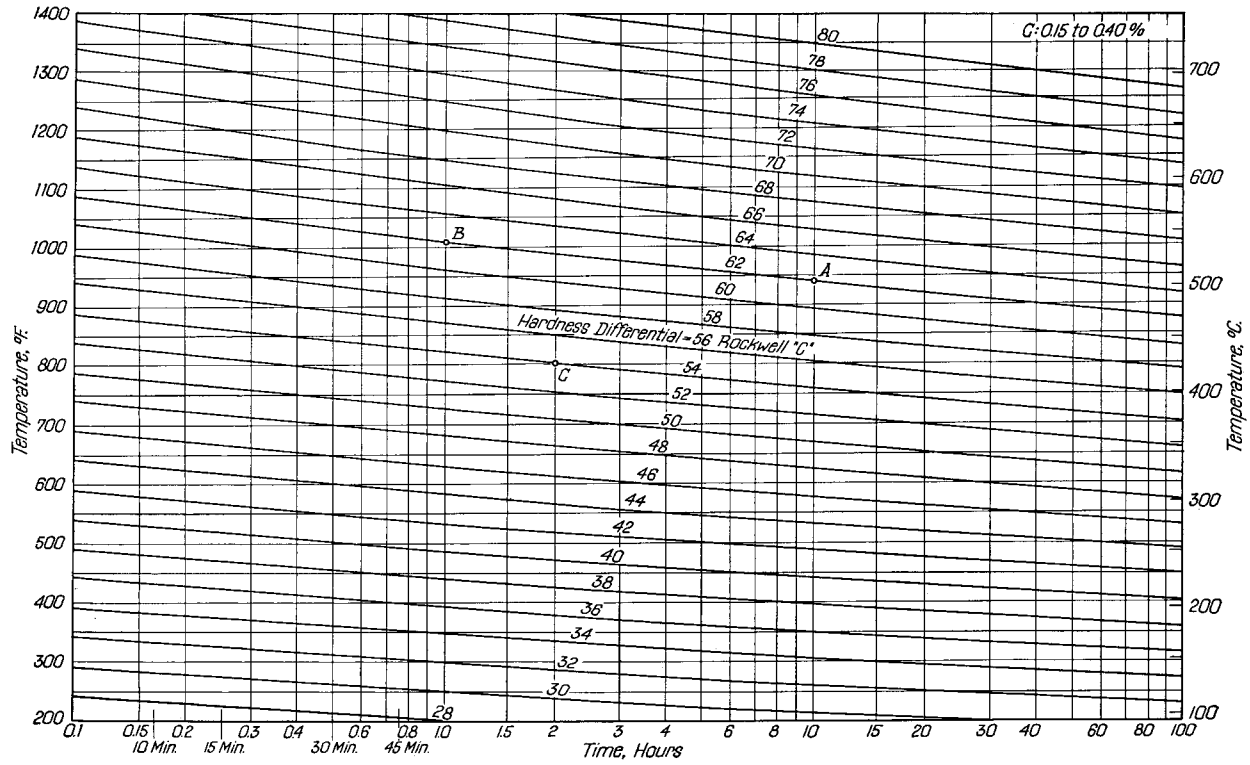


Fig. 12 Time-temperature relation in tempering mechanical and forging carbon and low-alloy steels (with carbon levels from 0.155 to 0.40%). Source: Ref 21

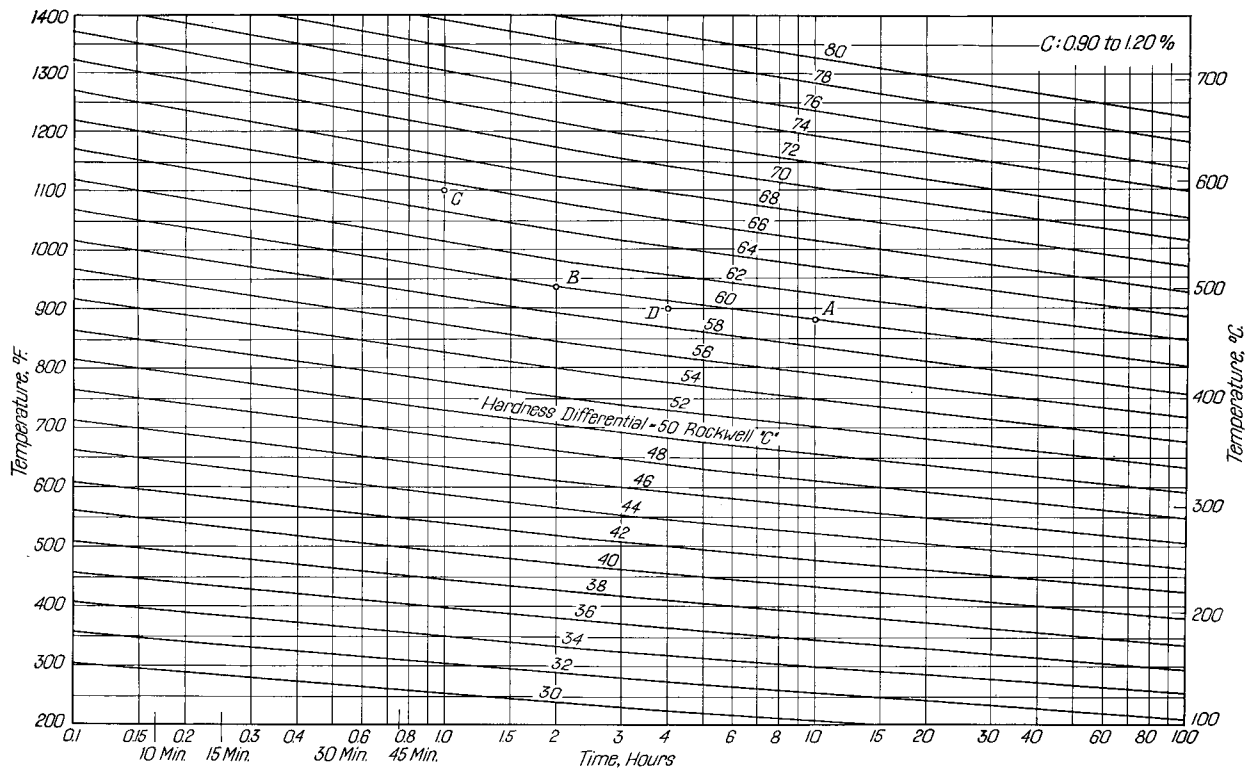


Fig. 13 Time-temperature relation in tempering high-carbon steels (with carbon levels from 0.90 to 1.20%). Source: Ref 21

in increasing hardness at higher temperatures above 205 °C (400 °F). Silicon is found to be most effective in increasing hardness at 315 °C (600 °F). The increase in hardness caused by phosphorus, nickel, and silicon can be attributed to solid-solution strengthening. Manganese is more effective in increasing hardness at higher tempering temperatures. The carbide-forming elements retard coalescence of cementite during tempering and form numerous small carbide particles. Under certain conditions, such as with highly alloyed steels, hardness may actually increase. This effect, mentioned previously, is known as secondary hardening.

Table 5 Parametric constant, C, for time-temperature tempering analysis of different materials

Material	C-value (for time in hours and temperature in R)
Low-carbon and low-alloy steels	18
Carbon-molybdenum steel	19
2¼ Cr and 1 Mo steel	23
Cr-Mo-Ti-B steel	22
18-8 stainless steel	18
18-8-Mo stainless steel	17
25-20 stainless steel	15

Source: Ref 22

The effect of molybdenum content on the tempering behavior of a 0.35% C steel is shown in Fig. 3(b). As the alloy content increases, the magnitude of the secondary-hardening effect increases. Synergistic effects of various combinations of alloying elements can occur: Chromium tends to produce secondary hardening at a lower temperature than does molybdenum, and the combination of chromium and molybdenum produces a rather flat tempering curve, with the peak hardness occurring at a somewhat lower temperature than when only molybdenum is present. The H11 and H13 steels are widely used hot working die steel that contains nominally 0.35% C, 5% Cr, 1.5% Mo, and 0.4% V. Figure 20 shows the room-temperature hardness of H11 as a function of tempering temperature. A very flat tempering curve results because of the specific combination of the three carbide-forming elements. A similar result is in Fig. 21 for H13 tool steel for various tempering times (with a parametric fit).

Other Alloying Effects. In addition to ease of hardening and secondary hardening, alloying elements produce a number of other effects. The higher tempering temperatures used for alloy steels presumably permit greater relaxation of residual stresses and improve properties. Furthermore, the hardenability of alloy steels requires use of a less drastic quench so that quench cracking is minimized. However, higher-hardability steels are prone to quench

cracking if the quenching rate is too severe. The higher hardenability of alloy steels may also permit the use of lower carbon content to achieve a given strength level but with improved ductility and toughness.

Residual elements, that is, elements not intentionally added to a steel, can cause embrittlement. The elements that are known to cause embrittlement are tin, phosphorus, antimony, and arsenic. A discussion of the specific effects of these elements can be found in the section "Temper Embrittlement" in this article.

Dimensional Change during Tempering

The body-centered tetragonal lattice of martensite has a lower density than the body-centered cubic structures of ferrite. Therefore, a decrease in volume typically occurs during tempering as the lower-density martensite decomposes into a mixture of ferrite and cementite. However, a 100% martensitic structure does not always occur after quenching, and thus, volume may not continuously decrease with increasing tempering temperature due to the transformation of retained austenite into lower-density phases.

As noted, retained austenite in plain carbon steels and low-alloy steels transforms to bainite or ferrite during stage II tempering (see the section

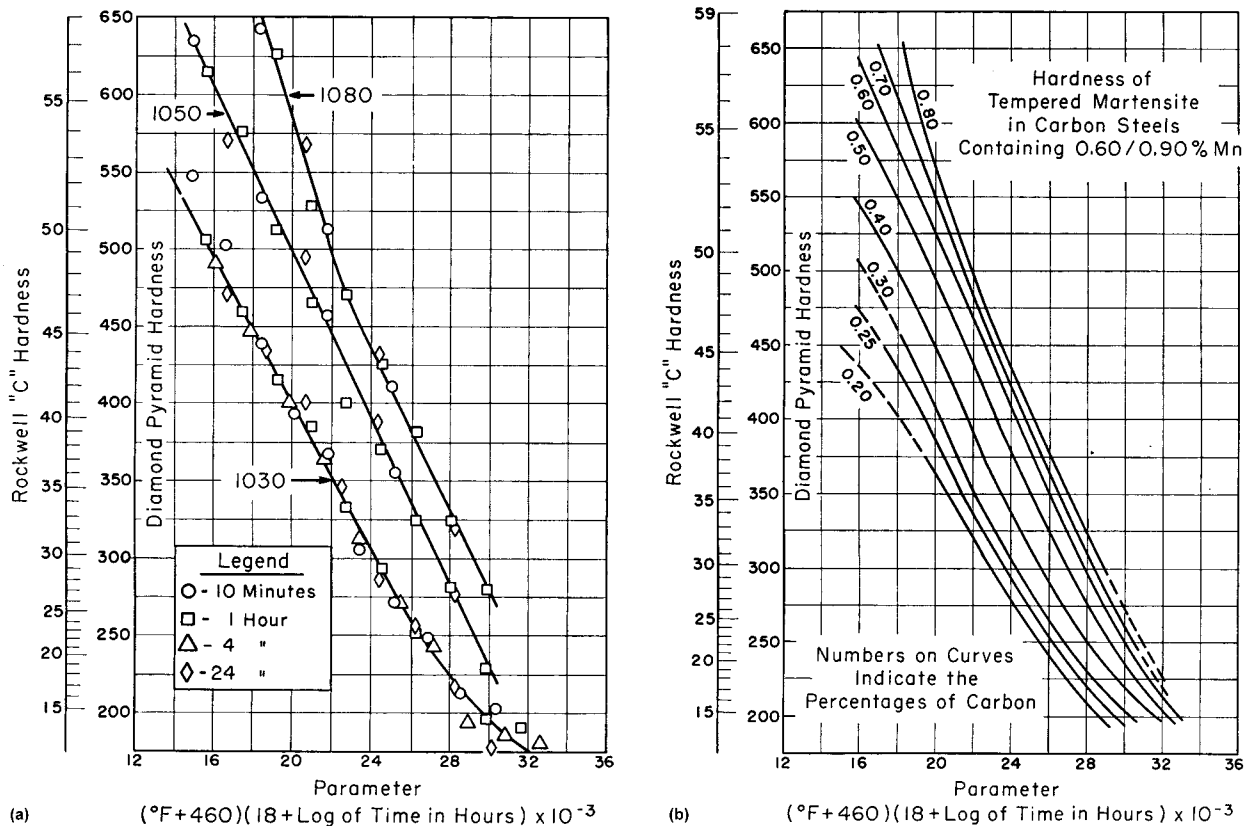


Fig. 14 Tempering curves for plain carbon steels. Source: Ref 17

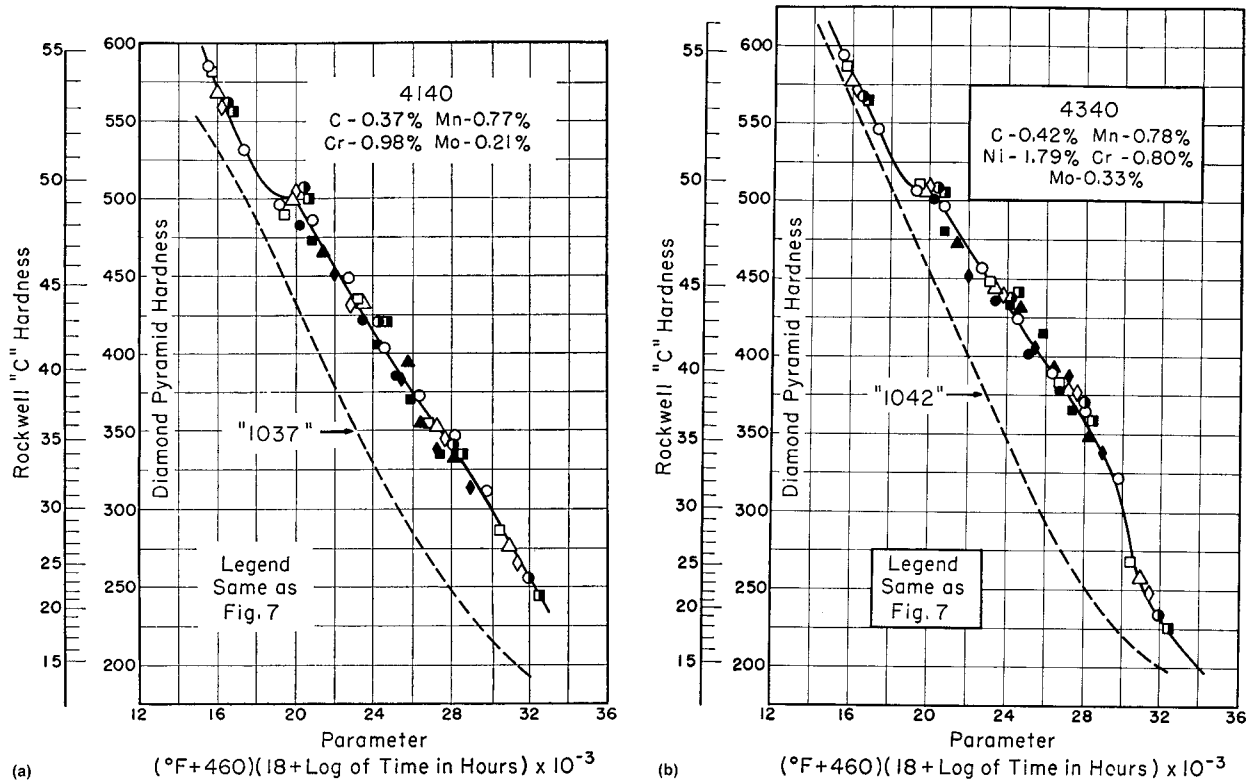


Fig. 15 Tempering curves for (a) 4140 and (b) 4340 steels. Source: Ref 17

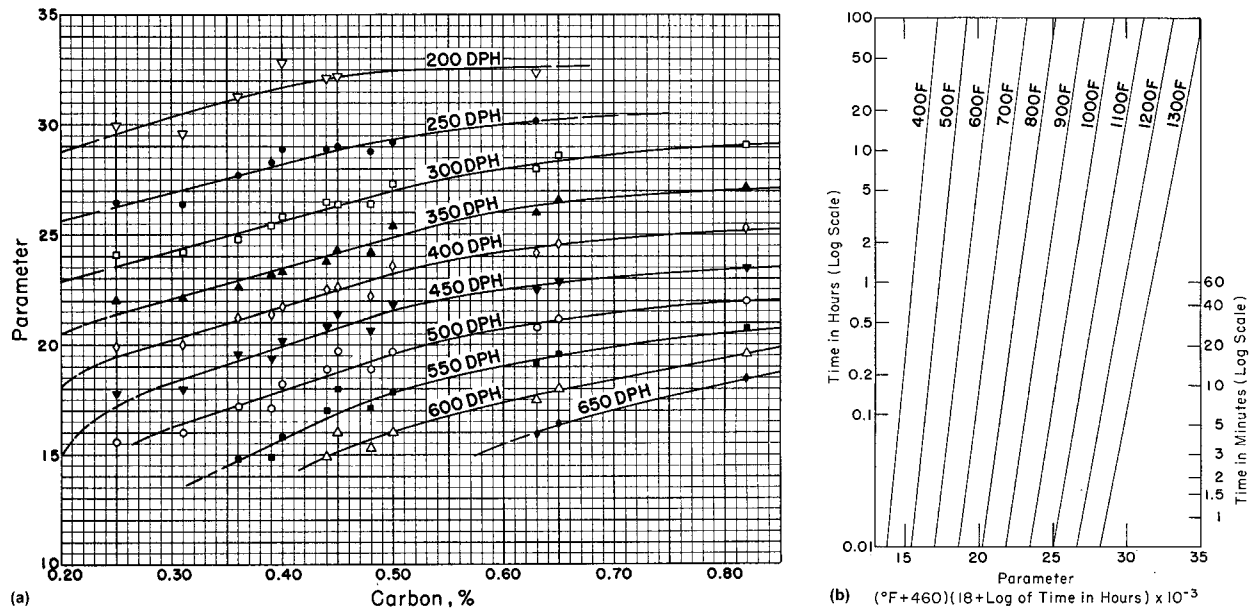


Fig. 16 Charts of tempering parameter (P) where $P = [^{\circ}F + 460] [18 + \log (t, \text{in hours})] \times 10^{-3}$. (a) Variation of P with hardness and carbon levels. (b) Chart showing relation of P with tempering time and temperature. Source: Ref 17

“Tempering at 230 to 370 °C (450 to 700 °F)” in this article). This results in an increase in volume, because austenite has a higher density than ferrite and bainite. When certain alloy steels are tempered, some retained austenite may transform to

martensite during cooling from the tempering temperature. When alloy carbides precipitate during tempering, the martensite start temperature of the retained austenite is raised, and some of the austenite may transform to martensite.

The change in dimensions of O1 tool steel plate during tempering is shown in Fig. 22. The plates were hardened from two different hardening temperatures and two different soak times. The dimensional changes, after cooling to

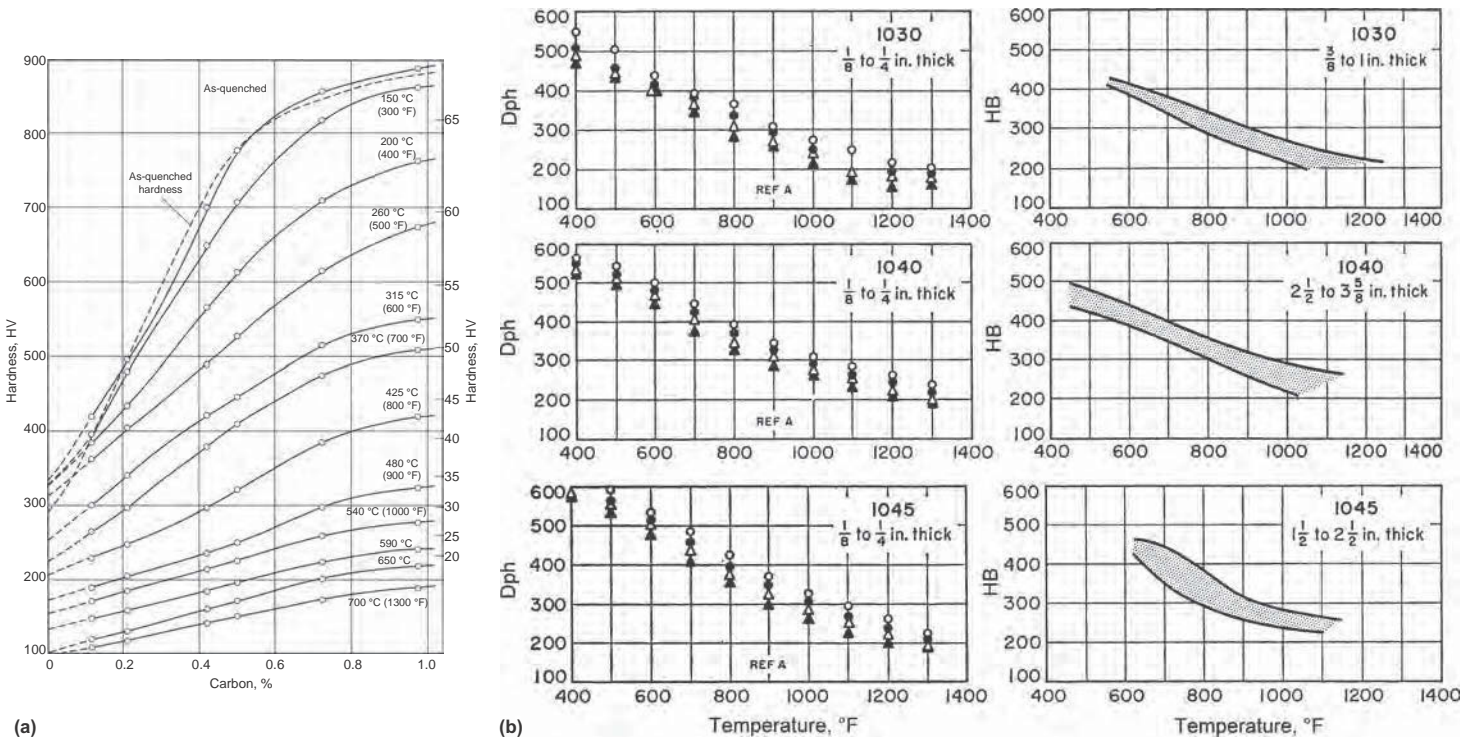


Fig. 17 Hardness of quenched carbon steels. (a) Relationship between hardness of tempered martensite with carbon content at various tempering temperatures. (b) Tempered hardness of selected carbon steels. Source: Ref 25

ambient temperature, are shown for tempering temperatures up to 400 °C (750 °F). The variation of 40 °C (70 °F) and 10 min has a negligible effect on dimensional changes. Tempering up to 200 °C (390 °F) is accompanied by a slight contraction in all directions of the plate. At a higher tempering temperature, there is an increase in the dimensions, with a maximum increase at 300 °C (570 °F), after which dimensions again decrease. The increased volume at 300 °C (570 °F) is attributed to the transformation of retained austenite to bainite. At 400 °C (750 °F), the dimensions revert to values closer to the original values, prior to quenching and tempering.

Tensile Properties and Hardness

The measurement of hardness is commonly used to evaluate the tensile properties of tempered carbon and alloy steels for low tempering. Hardness and tensile properties of two QT steels are shown in Fig. 23 and 24, with the general response being similar for the carbon and alloy steels. Empirical relationships also have been developed to correlate hardness with the tensile strength of QT carbon and low-alloy tempered steels. For example, Janitzky and Baeyertz (Ref 28) evaluated tensile properties of several QT steels (Fig. 25) and showed a roughly linear relationship between Brinell hardness and tensile strength, which can be expressed in metric units for the tensile strength (TS) as:

$$TS(\text{MPa}) = 3.6\text{HB} - 42.3$$

For example, a steel with a hardness of 363 HB would have an estimated tensile strength of 1265 MPa, which converts to 183 ksi (and is close to data plotted in Fig. 25). The tensile strength of QT steels also correlates very strongly with other tensile properties (Fig. 26, 27). This range of tensile properties provides a structural designer with many options in the use of quenched and tempered carbon and low-alloy steels.

Hardnesses of quenched and tempered steels also can be estimated by a method established by Grange et al. (Ref 25). The general equation for hardness is:

$$HV = HV_C + \Delta HV_{Mn} + \Delta HV_P + \Delta HV_{Si} + \Delta HV_{Ni} + \Delta HV_{Cr} + \Delta HV_{Mo} + \Delta HV_V$$

where HV is the estimated hardness value (Vickers).

To use this relationship, one must determine the hardness value of carbon (HV_C) from Fig. 17(a). For example, if one assumes that a tempering temperature of 540 °C (1000 °F) is used and the carbon content of the steel is 0.2% C, the HV_C value after tempering will be 180 HV. Second, the effect of each alloying element must be determined from a figure such as Fig. 18 or 19.

To illustrate the use of the Grange et al. method, the same type 4340 steel shown in Fig. 24 is used. The composition of the steel is 0.41% C, 0.67% Mn, 0.023% P, 0.018% S,

0.26% Si, 1.77% Ni, 0.78% Cr, and 0.26% Mo. Assuming a 540 °C (1000 °F) tempering temperature, the estimated hardness value for carbon is 210 HV. From Fig. 17(a), the hardness values for each of the other alloying elements are:

Element	Content, %	Hardness, HV
C	0.41	210
Mn	0.67	38
P	0.023	7
Si	0.26	15
Ni	1.77	12
Cr	0.78	43
Mo	0.26	55
Total hardness	...	380

According to Fig. 24, the hardness value after tempering at 540 °C (1000 °F) was 363 HB (see Brinell hardness values along x-axis). From hardness conversion tables (e.g., ASTM E 48 conversion table), a Brinell hardness of 363 HB equates to a Vickers hardness of 383 HV. The calculated value of 380 HV (in the preceding table) is very close to the actual measured value of 383 HV. Thus, this method can be used to estimate a specific hardness value after a quenching and tempering heat treatment for a low-alloy steel.

Variations in Hardness after Tempering. An example of the range of variation in hardness obtained after tempering is shown in Fig. 28. Variations in hardness after tempering are most frequently the result of differences in prior microstructure. Effect of prior microstructure

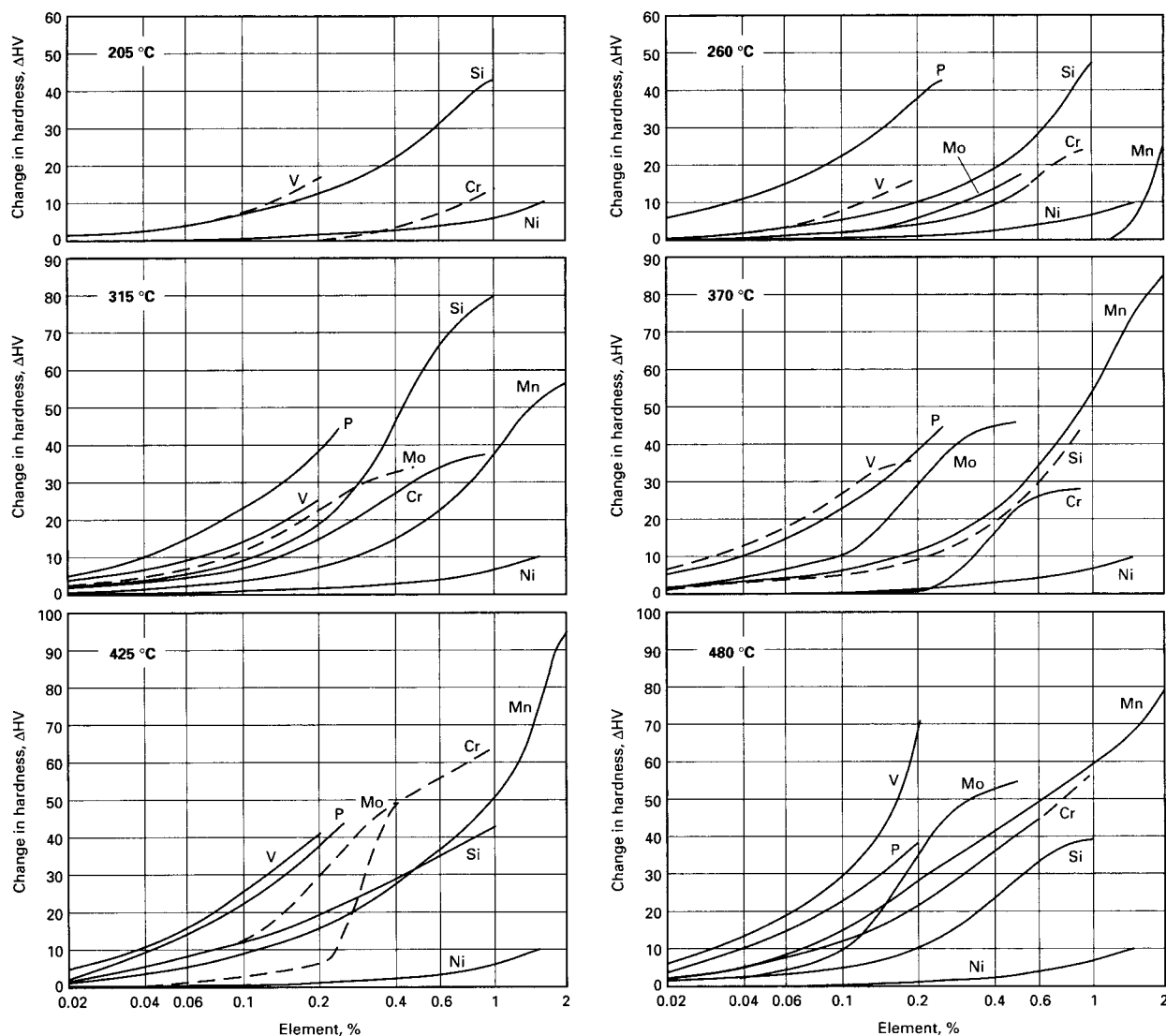


Fig. 18 Effect of seven elements (chromium, manganese, molybdenum, nickel, phosphorus, silicon, and vanadium) on the hardness of tempered martensite after tempering for 1 h at temperatures from 205 to 480 °C (400 to 900 °F). Note that manganese, molybdenum, and phosphorus have no effect on hardness at 205 °C (400 °F). Source: Ref 25

on tempered hardness is more pronounced at shorter and/or lower temperature cycles, as one may expect (Fig. 29).

When prior microstructure is the same, the control of temperature is the most important factor in the control of the tempering process. In general, the control of tempering temperature to within ± 13 °C (25 °F) is adequate and is within the practical limits of most furnace and molten-bath equipment. Temperature variations are seldom permitted to exceed ± 6 °C (10 °F) unless mechanical property requirements are correspondingly broad.

Toughness and Embrittlement

Quenched and tempered steels are susceptible to different types of embrittlement. Some are due to structural modifications during

tempering, such as tempered martensite embrittlement and temper embrittlement. However, some are due to the interaction of the environment with the quenched and tempered microstructures, such as hydrogen embrittlement and liquid metal embrittlement (see the article "Embrittlement of Steels" in *Properties and Selection: Irons, Steels, and High-Performance Alloys*, Volume 1 of *ASM Handbook*, Ref 29).

The focus of this section is on embrittlement associated with the tempering process. A map by Krauss (Ref 30) of fracture behavior of hardened steels is given in Fig. 30. It includes regions of tempered martensite and temper embrittlement, which are described in more detail in Ref 31.

Temper embrittlement (TE) occurs when carbon or low-alloy steels are tempered for extended times between 450 and 600 °C (840 and 1110 °F). The effect is more pronounced

with slower cooling rates at higher tempering temperatures (Fig. 7). It also can occur from slow cooling after exposure above this temperature range. In most instances, a short exposure time within, or rapid cooling through, this temperature range will minimize TE. However, when heat treating thick sections, this procedure may not be possible, and TE may occur.

Temper embrittlement can be reversed by retempering above the embrittlement temperature (>600 °C, or 1110 °F), followed by rapid cooling through this range to restore toughness. Steels that have been embrittled because of TE can be de-embrittled by heating to approximately 575 °C (1065 °F), holding a few minutes, and subsequently rapidly cooling or quenching. The time for de-embrittlement depends on the alloying elements present and the temperature of reheating (Ref 32). De-embrittlement is

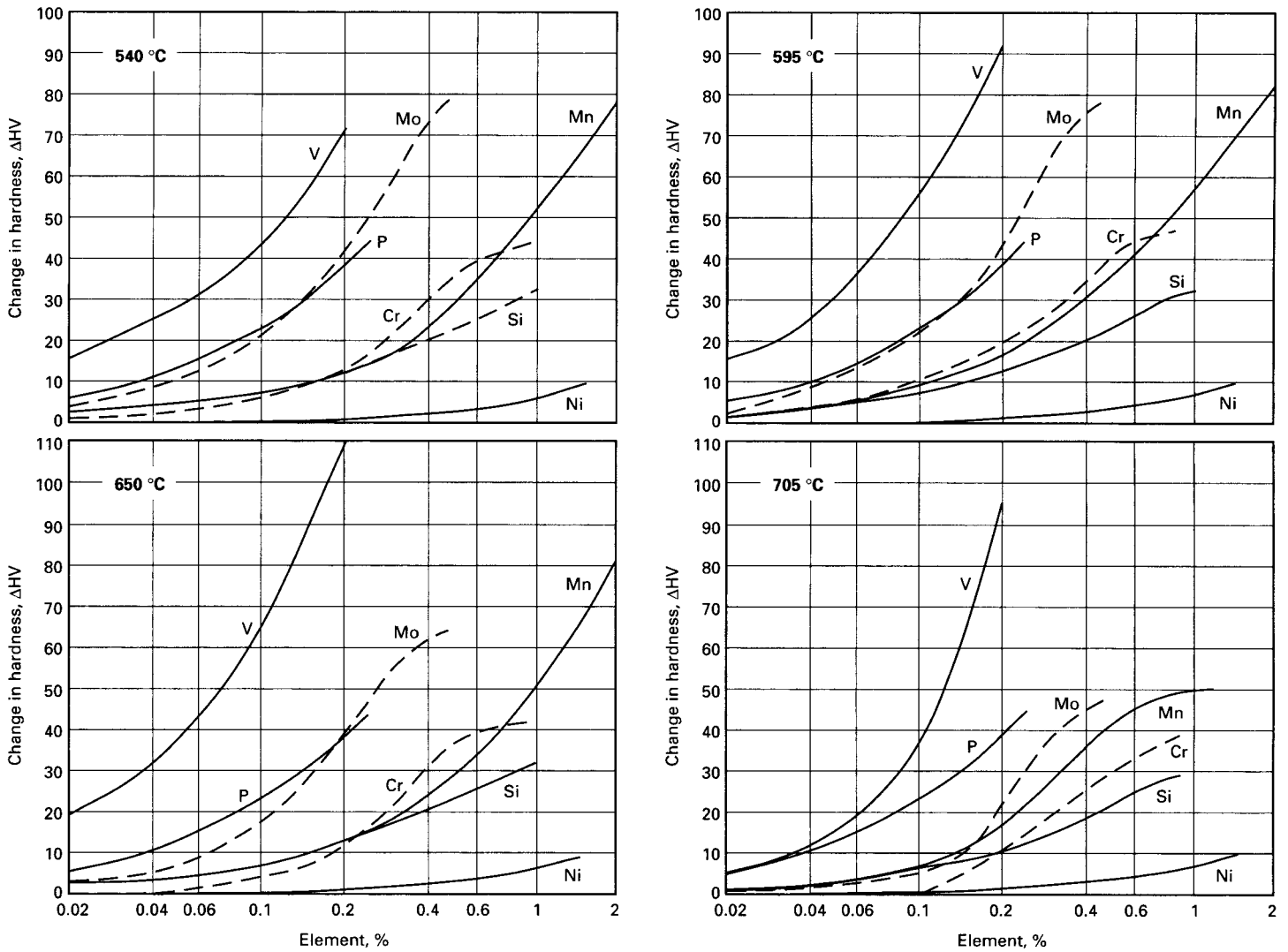


Fig. 19 Effect of seven elements (chromium, manganese, molybdenum, nickel, phosphorus, silicon, and vanadium) on the hardness of tempered martensite after tempering for 1 h at temperatures from 540 to 705 °C (1000 to 1300 °F). Source: Ref 25

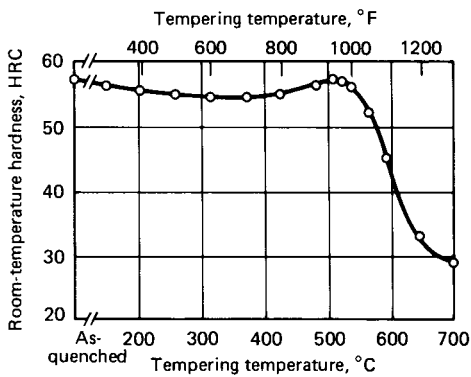


Fig. 20 Variation of room-temperature hardness with tempering temperature for H11 steel. All specimens air cooled from 1010 °C (1850 °F) and double tempered 2 h plus 2 h at temperature

accompanied by a redistribution of impurities at the grain boundaries (Ref 33).

The cause of TE is believed to be the precipitation of compounds containing trace elements, such as tin, arsenic, antimony, and phosphorus, along with chromium and/or manganese (see also the Selected References). Relatively small amounts (0.01% or less) of impurities, such as phosphorus, antimony, and arsenic, have been related to TE (Ref 1, 11, 34, 35). It takes place due to impurity segregation at the grain boundary and decohesion of the grain boundary. This leads to intergranular fracture morphology. The intergranular nature of the fracture suggests that the embrittlement occurs at the prior-austenite grain boundaries.

It has also been known that carbon steels with less than 0.5% Mn are immune to TE. Substantial additions of manganese cause susceptibility to this problem. Other alloying elements, such as chromium and nickel, also promote TE. When taken separately, they

produce a weaker effect than in the case of combined alloying. The highest embrittlement effect is observed in chromium-nickel and chromium-manganese steels. Alloy steels of very high purity are not susceptible to TE.

The beneficial influence of molybdenum on phosphorus-induced TE has been known for many years (Ref 36). Small additions of molybdenum (0.2 to 0.3%) significantly retard TE. Greater amounts of molybdenum yield no additional improvement. Although molybdenum is an effective element to reduce the susceptibility for TE, the precipitation of molybdenum-metal carbides must be addressed. To avoid precipitation, vanadium is added to steel. Vanadium is a strong carbide former, compared to molybdenum and chromium. Vanadium initially forms MC-type carbide, changing the molybdenum-to-carbon and chromium-to-carbon ratios. The increase in molybdenum-to-carbon rate is favorable for Mo₂C-type carbides; chromium-to-carbon ratio is favorable for Cr₇C₃ carbides. These changes

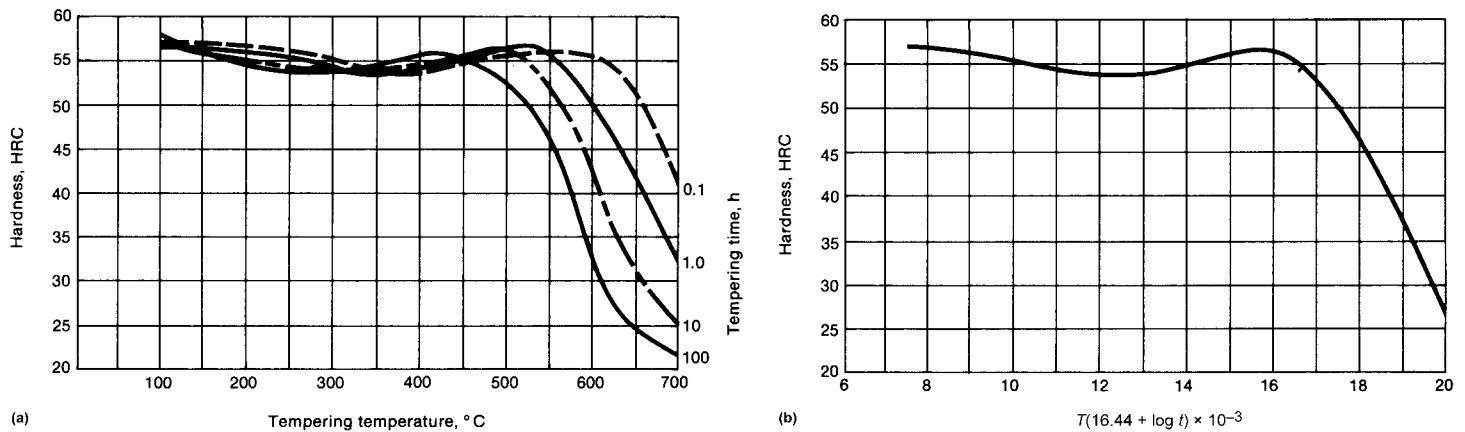


Fig. 21 Tempering curves for H13 tool steel. (a) Plotted at various tempering times. (b) Parametric plot with $P = T [16.44 + \log (t)]$, where T is absolute temperature in degrees Kelvin (K), and t is time in seconds. Source: Ref 26

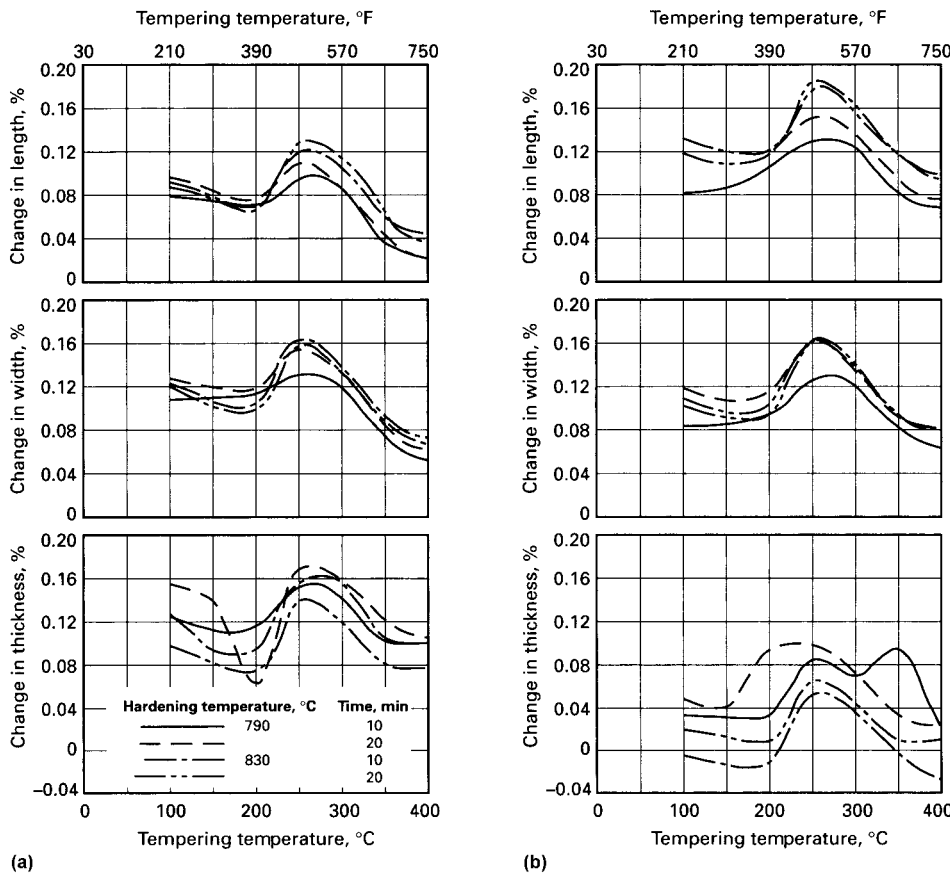


Fig. 22 Dimensional changes that occur in O1 tool steel (Bofors RT 1733) when heat treated at two hardening temperatures and two soak times using two tempering methods: (a) oil quenching and (b) martempering. Specimen dimensions were 100 × 50 × 18 mm (4 × 2 × 0.7 in.). Steel was rolled in the longitudinal direction. Source: Ref 27

slow down the precipitation of molybdenum as carbides. When the molybdenum is not in solid solution with ferrite, then the phosphorus is free to segregate and cause embrittlement.

The effect of molybdenum on suppressing TE decreases as the purity of the steel increases (Ref 37). The total content of impurities (sulfur

plus phosphorus plus nonferrous elements plus gases), expressed in atomic parts per million, ranges in values roughly as follows:

- 1500 ppm in steels of conventional purity (corresponding to the usual amounts found in air-arc-melted steel)

- 1000 ppm in very clean steel (corresponding to vacuum-melted steel)
- Approximately 500 ppm in the extraclean steels (corresponding to vacuum-melted steel using a very pure charge)

When relatively impure steel is used (with over 1500 ppm impurities and over 0.01% P), the unique role of molybdenum in minimizing TE is very important. Molybdenum does not appear to be a necessary alloying element in the production of high-purity steels (under 500 ppm impurities and under 0.001% P), which are not susceptible to TE.

Blue Brittleness. The heating of plain carbon steels or some alloy steels to the temperature range of 230 to 370 °C (450 to 700 °F) may result in increased tensile and yield strength, as well as decreased ductility and impact strength. This embrittling phenomenon is referred to as blue brittleness, because such temperatures produce a bluish temper color on the surface of the specimen (Ref 38–40).

Blue brittleness is an accelerated form of strain-age embrittlement caused by carbide and/or nitride precipitation hardening within the critical-temperature range. It can be eliminated if elements that tie up nitrogen are added to the steel, for example, aluminum or titanium. Deformation while the steel is heated in the blue-heat range results in even higher hardness and tensile strength after cooling to room temperature. If the strain rate is increased, the blue-brittle temperature range increases.

Tempered Martensite Embrittlement (TME) (adapted from Ref 41). Tempered martensite embrittlement occurs when high-strength alloy steels are tempered in the range of 200 to 370 °C (400 to 700 °F). Tempered martensite embrittlement is also referred to as 350 °C (or 500 °F) embrittlement, although the greatest alteration reportedly occurs at approximately 315 °C (600 °F). Avoiding the embrittling temperature range is necessary to prevent TME, although the range is somewhat variable.

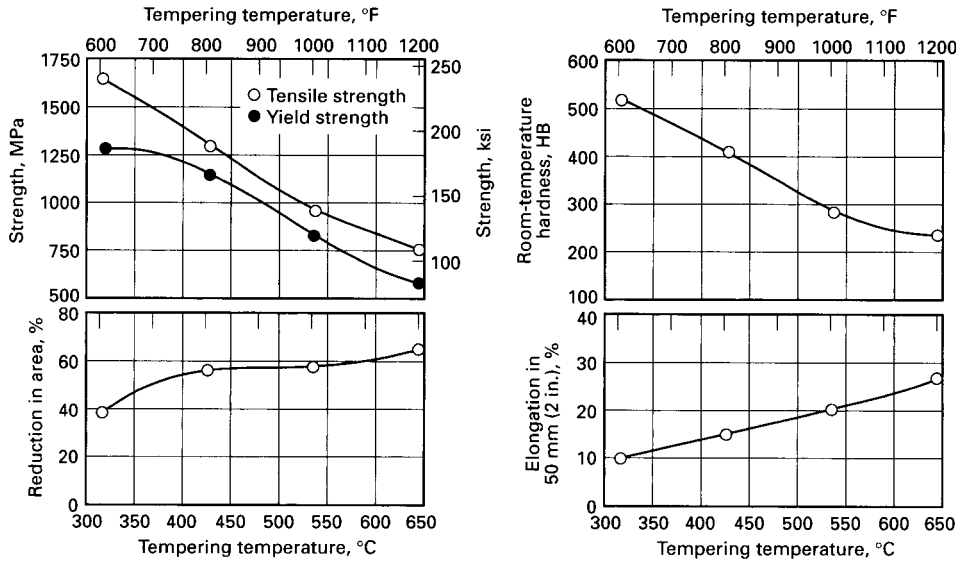


Fig. 23 Effect of tempering temperature on room-temperature mechanical properties of 1050 steel. Properties summarized are for one heat of 1050 steel that was forged to 38 mm (1.50 in.) in diameter, then water quenched and tempered at various temperatures. Composition of heat: 0.52% C, 0.93% Mn

Tempered martensite embrittlement is distinguished from TE in several ways besides the temperature range of embrittlement. First, TE is reversible as noted, while TME is not. Once TME appears, there is no heat treatment to reverse the effect, other than to re-austenitize and quench the steel, followed by tempering in an appropriate temperature range where TME does not occur. Embrittled steels can be annealed to restore maximum impact energy when necessary.

The TME mechanism also is a much more rapid process than TE. Tempered martensite embrittlement develops during the first hour of the normal tempering period and is independent of section size and/or cooling rate after tempering. In contrast, TE needs many hours to develop, and it is an important concern, mainly for heavy sections that are tempered at higher temperatures (out of embrittlement range) and cooled very slowly over a period of many hours through the critical range of embrittlement. Thus, TE is sometimes referred to as two-step temper embrittlement, while TME is sometimes referred to as one-step temper embrittlement.

Tempered martensite embrittlement occurs in the tempering range in which ϵ -carbide changes to cementite. It takes place mainly in steels with a microstructure of tempered martensite, but steels with microstructures of tempered lower bainite are also susceptible to TME. Other structures, such as upper bainite and pearlite/ferrite, are not embrittled by tempering in this region. The impact toughness after tempering at this temperature is lower than that obtained at tempering temperatures below the TME range.

Figure 31 shows the impact absorbed as a function of tempering temperature for chromium-

molybdenum steels with various phosphorus and carbon contents. The figure exhibits the effect of phosphorus and carbon on the impact toughness of low-alloy steels. There is a loss in impact toughness for steels tempered in the temperature range of 250 to 300 °C (480 to 570 °F). Steels with lower phosphorus content have superior impact properties than steels with a higher phosphorus level. Also, impact toughness decreases with increasing carbon content (Ref 42).

The mechanism causing TME is not as well defined as that which causes TE. While many studies have shown that fractures are partly or substantially intergranular, particularly with tempering at approximately 350 °C (660 °F), other studies have observed only transgranular fractures. This difference may influence the respective interpretations of the TME mechanism. The main explanations for TME are based on the effects of impurities and cementite precipitation on the prior-austenite grain boundaries.

Early studies concluded that TME was due to precipitation of thin platelets of cementite at the grain boundaries. However, TME has also been found to occur in very-low-carbon steels, and residual impurity elements have also been shown to be essential factors in TME. Use of steels with low impurity contents, particularly phosphorus, can prevent the impurity segregation contribution to total embrittlement. Steels containing either impurities or potent carbide forms are susceptible to TME.

Both intergranular (Ref 43–45) and transgranular fracture modes may be observed in TME (Ref 43, 46). Intergranular TME fracture is quite common and has been related to austenite grain-boundary phosphorus segregation during austenitization. However, the presence

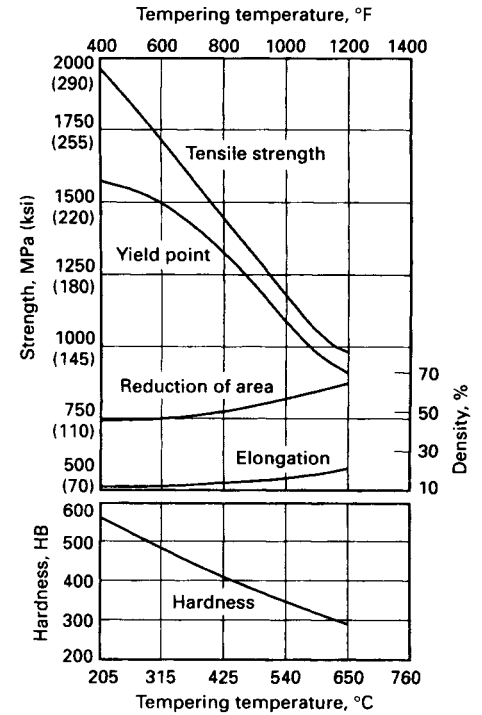


Fig. 24 Effect of tempering temperature on the mechanical properties of oil-quenched 4340 steel bar. As-quenched hardness, 601 HB. Single heat with ladle composition of: 0.41% C, 0.67% Mn, 0.023% P, 0.018% S, 0.26% Si, 1.77% Ni, 0.78% Cr, 0.26% Mo

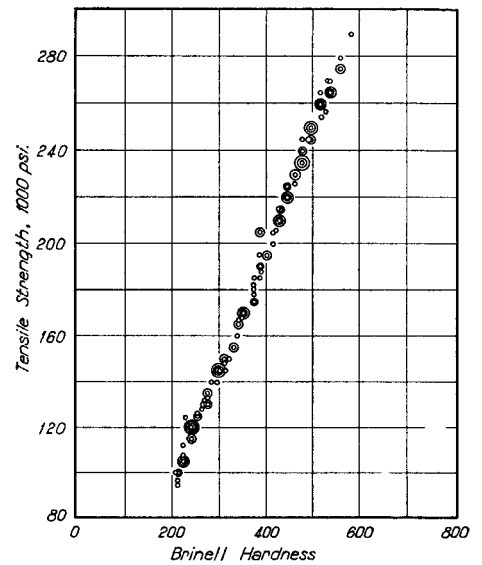


Fig. 25 Brinell hardness versus tensile strength for several quenched and tempered steels (SAE 1330, 2330, 4130, 5130, 6130). Round bars, 25 mm (1 in.) diameter, normalized, water quenched, and tempered at various temperatures from 200 to 700 °C (400 to 1300 °F). Source: Ref 28

of phosphorus at the prior-austenite grain boundary is not sufficient for the development of TME. An interaction between phosphorus and cementite is necessary for the intergranular

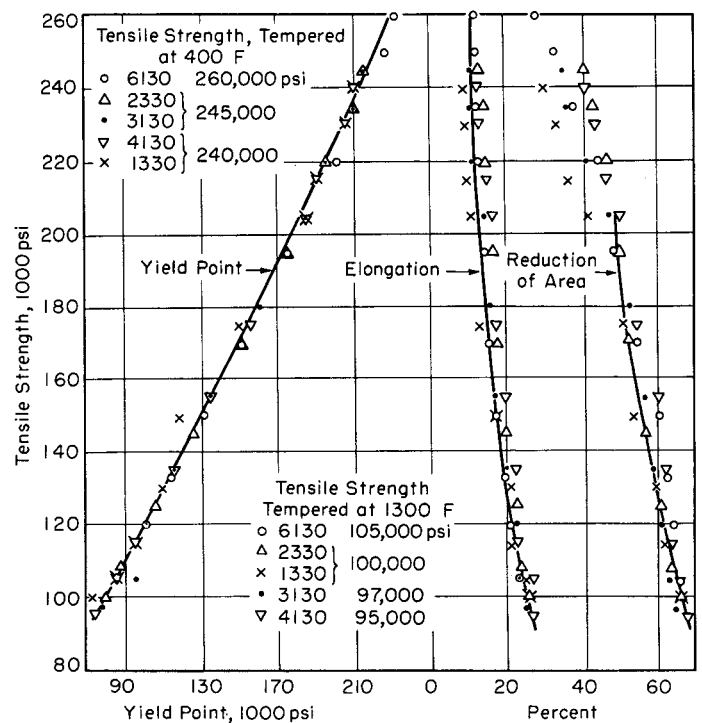
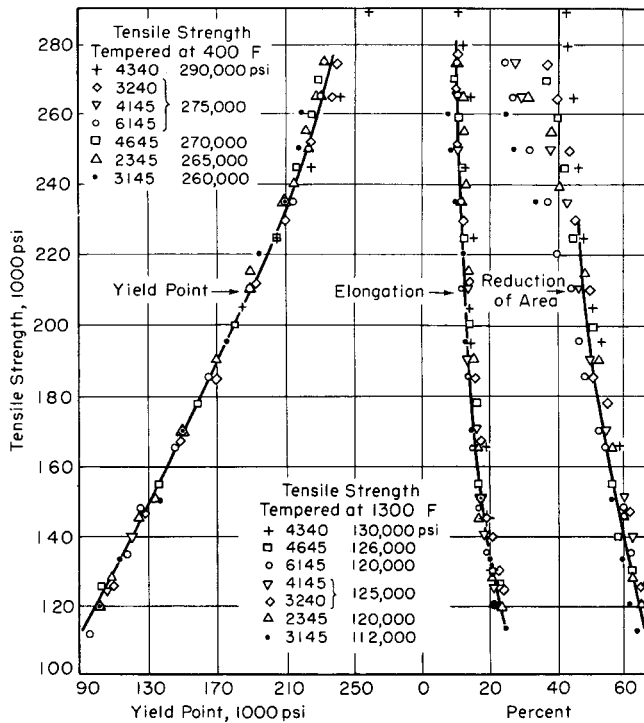


Fig. 26 Tensile properties of several oil-hardening steels (6145, 4645, 4145, 3240, 3145, 2345, 4340) tempered from 200 to 700 °C (400 to 1300 °F). Round bar, 25 mm (1 in.) diameter. Source Ref 1

Fig. 27 Tensile properties of several water-hardening steels (3130, 6130, 2330, 4130, 1330) tempered from 200 to 700 °C (400 to 1300 °F). Round bar, 25 mm (1 in.) diameter. Source Ref 1

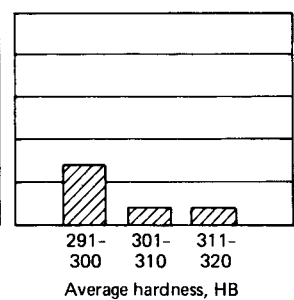
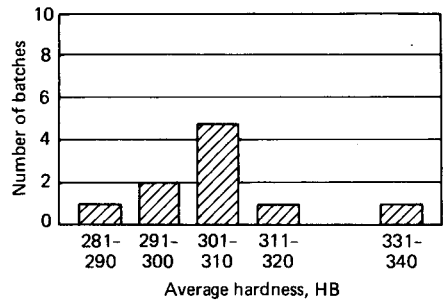
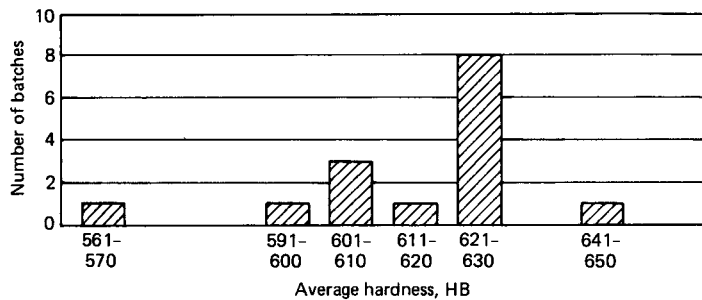


Fig. 28 Variations in room-temperature hardness after production tempering of forged 1046 steel. (a) As-quenched. (b) Tempered at 510 °C (950 °F) for 1 h. (c) Tempered at 525 °C (975 °F) for 1 h. Hardening operation was as follows: 1046 steel heated to 830 °C (1525 °F) and quenched in caustic. Forgings were heated in a continuous belt-type furnace and individually dump quenched in agitated caustic. Forgings weighed 9 to 11 kg (20 to 24 lb) each; maximum section, 38 mm (1½ in.).

mode of TME. Segregation of impurities such as phosphorus at austenite grain boundaries during austenitizing and the formation of cementite at prior-austenitic grain boundaries during tempering are responsible for the intergranular fracture mode of TME (Ref 43–45, 47).

Transgranular fractures in TME may be related to the interlath carbide thickness; thinner carbides cause interlath fracture and thicker carbides promote translath cleavage. In medium-carbon steels, transgranular TME fracture mode occurs from the formation of cementite between

parallel martensitic lathes during tempering (Ref 43, 46). During tempering, thin plates of cementite form from the transformation of retained austenite between laths of martensite in quenched medium-carbon steels. Another type of transgranular TME fracture is observed in AISI 4340-type steels (Ref 13). It is interlath cleavage induced by cracking of the cementite formed from the decomposition of retained austenite. In some low-carbon steels, embrittlement is associated with a carbide morphology that provides numerous sites for microcrack initiation and growth by microvoid coalescence.

Fracture then occurs with little gross plastic deformation.

Silicon additions to carbon steels raise the temperature range in which TME occurs (Ref 48–50), because silicon delays the conversion of the ε-carbide to cementite within the martensite laths and delays the coarsening of cementite at boundaries with higher tempering temperatures (Ref 43, 44).

Investigations using AISI 4140 steels show that austenitization temperature has an influence on the TME phenomenon. High austenitization temperature favors brittle failure modes,

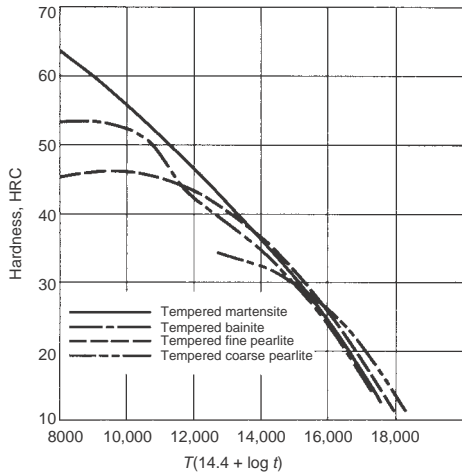


Fig. 29 Hardness as a function of the Hollomon-Jaffe parameter (T in K; t in seconds) for a 0.94% C steel with various starting microstructures. Source: Ref 19

even in specimens showing virtual absence of phosphorus segregation. High austenitization temperature also increases carbide dissolution in austenite, due to more intensive carbide precipitation and growth during tempering (Ref 44).

Equipment for Tempering

The selection of equipment for tempering is based principally on the temperature requirements and the quantity and similarity of the work to be treated. Equipment selection also depends on whether tempering is for bulk processing (accomplished by soaking entire parts in the furnace for enough time) or by selective heating of certain portions of the part (see the section “Selective Tempering” in this article).

Temperature requirements are dictated by prior heat treatment and by the properties to be developed by tempering. Bulk processing may be done in convection furnaces or in molten salt, hot oil, or molten metal baths. The selection of furnace type depends primarily on number and size of parts and on desired temperature. Table 6 gives temperature ranges, most probable reasons for use, and fundamental problems of these four types of equipment.

Convection Furnaces. The most commonly employed tempering method uses the recirculating or forced-air convection furnace, and the equipment most commonly used in conjunction with convection furnaces includes continuous belt conveyor, roller rail, or dog beam pusher systems. Batch equipment, such as box or pit types, is also used.

Forced recirculating air is the most common and efficient method of tempering because it lends itself to a wide selection of furnace designs to accommodate a variety of products and capacities. Moreover, the metallurgical

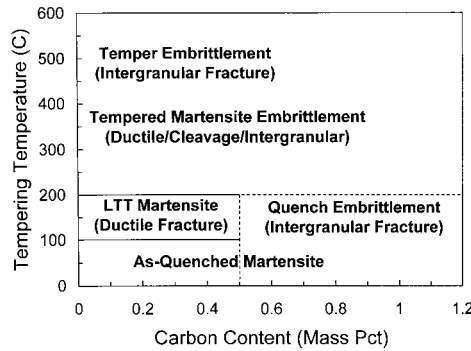


Fig. 30 Fracture response under tensile loading as a function of tempering temperature and carbon content of hardened carbon and low-alloy steels. LTT, low-temperature-tempered. Source: Ref 31

results are very good in terms of price per unit weight of yield.

Generally, convection furnaces are designed for tempering temperatures of 150 to 750 °C (300 to 1380 °F). For temperatures up to 550 °C (1020 °F), recirculated hot air is supplied to the product from a chamber separate from the work-holding area to avoid uneven heating by radiation. For temperatures of 550 to 750 °C (1020 to 1380 °F), either forced convection or radiant heating is used, depending on the metallurgical requirements of the product. To obtain closer control of metallurgical properties, recirculated forced hot air is employed; however, for greater efficiency, radiant heating is used because the transfer of radiant heat is greater as the temperature approaches 750 °C (1380 °F).

The most important phase of convection furnace design is determining the proper amount of forced air. The objective of the blower is to furnish enough hot air to the complete work area so that it is efficiently used to heat the product in the shortest time thermophysically allowed. The type of product and the material being processed dictate the required forced-air supply, which is measured at the operating temperature. Consultation with fan manufacturers can help achieve maximum efficiency of heat transfer.

Heat for the furnace can be supplied by electricity, gas, or oil. In most furnace designs, a dual heat source capability can be built in, such as gas and electricity. This allows for more than one choice of utility when there is a shortage or a cost advantage of one over the other.

Temperature control is accomplished by positioning a thermocouple at the hot-air side of the recirculating system close to the product. When this technique is used, there is minimal danger of overheating, and loads of various sizes can be handled. This method also allows the duration of processing (holding time) to be varied by moving the thermocouple location, but only within the limits of the furnace size (and/or conveyor speed, for continuous-type furnaces). Temperatures generally are held

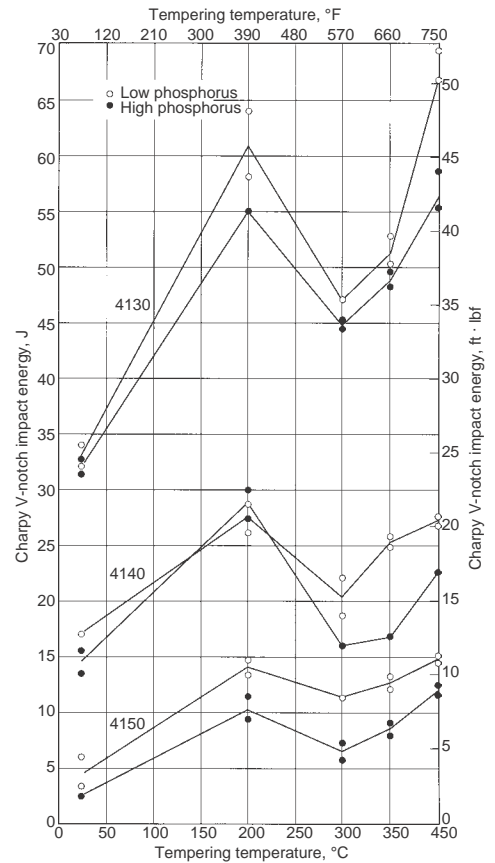


Fig. 31 Room-temperature Charpy V-notch impact energy versus tempering temperature for 4130, 4140, and 4150 steels austenitized at 900 °C (1650 °F) and tempered 1 h at temperatures shown. Source: Ref 42

within ± 5 °C (± 9 °F). If modern temperature controllers are used, baffle plates are positioned properly and furnace curtains are installed.

The efficient use of a continuous furnace cannot be attained when production quantities are small or when parts vary in size, shape, and mechanical requirements. A batch furnace is better suited for work of this type. When a continuous furnace is used for such applications, production time is lost when the furnace temperature is raised or lowered. Sometimes, when the process variables must be changed, a dummy load must be placed in the furnace to accelerate a desired reduction of temperature, or production must be stopped until the temperature is stabilized.

Salt bath furnaces may be used for tempering at 160 °C (320 °F) and above. Good heat transfer and natural convection in the bath promote the uniformity of workpiece temperature.

All moisture must be removed from parts before they are immersed in the molten salt, because hot salt reacts violently with moisture. If dirty or oily parts are immersed in the bath, the salt will become contaminated and will require more frequent rectification. Rectification with chemical or gaseous compounds controls the soluble oxides within proper limits.

Table 6 Temperature ranges and general conditions of use for four types of tempering equipment

Type or equipment	Temperature range		Service conditions
	°C	°F	
Convection furnace	50–750	120–1380	For large volumes of nearly common parts; variable loads make control of temperature more difficult
Salt bath	160–750	320–1380	Rapid, uniform heating; low to medium volume; should not be used for parts whose configurations make them hard to clean
Oil bath	≤250	≤480	Good if long exposure is desired; special ventilation and fire control are required
Molten metal bath	>390	>735	Very rapid heating; special fixturing is required (high density)

A carbon rod rectification procedure is used to remove the insoluble metallics.

All parts tempered in salt must be cleaned soon after being removed from the bath, because the salt that clings to them is hygroscopic and may cause severe corrosion. Parts with small or blind holes from which salt is difficult to clean should not be tempered in salt.

Salt bath compositions and operating temperature ranges presented in Table 7 pertain to baths in common use for tempering and are classified according to Military Specification MIL-S-10699A (Ordnance):

- Class 1 and class 2 salts are reasonably stable and seldom require rectification. If chlorides are added by carryover from a higher-temperature bath, they will cause an increase in the viscosity of the bath. Chlorides can be removed by filtering through fine screens or by cooling and settling out the insoluble chlorides as a sludge. Occasionally, carbonates become excessive. These can be removed by reaction with dilute nitric acid-base rectifiers. Upper temperature limits must not be exceeded or salt will become highly oxidizing, even toward alloy steels.
- Class 3 salts seldom require rectification. However, their high melting points (approximately 560 °C, or 1040 °F) severely restrict their useful temperature range. Also, they are decarburizing to steels at temperatures above approximately 705 °C (1300 °F).
- Class 4 salts, which are all-chloride neutral salts, are quite stable. They seldom require rectification but are restricted to temperatures above 595 °C (1100 °F).
- Class 4A salts are close relatives of class 4 salts but contain calcium chloride, which lowers the minimum working temperature to 550 °C (1025 °F). The upper limit for these salts is more restricted than that for class 4 salts.

Oil bath equipment for tempering may be similar in design to that used for salt baths, or a steel tank over hot plate burners will serve satisfactorily. Submerged electric heating elements may also be employed. Stirring is essential for temperature uniformity and satisfactory oil life. Simple, oven-type temperature controls may be employed, but localized overheating must be avoided to prevent fire and the rapid

decomposition of the oil. A standard thermometer of the proper range may be used to check the temperature of the oil.

Low-temperature tempering in a hot-oil bath is a simple and inexpensive method that is especially useful for holding work at temperature for long periods of time. The practical temperature limit is approximately 120 °C (250 °F) without special ventilation or fire protection equipment and approximately 250 °C (480 °F) with such precautions, which may include extremely efficient ventilators or inert-gas blanketing systems. When a tempering temperature above 205 °C (400 °F) is required, a salt bath is usually preferable to an oil bath.

Oils for tempering must resist oxidation and have a flash point well above the operating temperature. The most commonly used oils are high-flash-point paraffinic oils with antioxidant additives. Oils used for martempering are also satisfactory for tempering.

Molten metal baths for tempering have largely been replaced by salt baths. When employed, commercially pure lead, which melts at approximately 327 °C (620 °F), has proved to be the most generally suitable of all metals and alloys. For special applications, however, lead-base alloys having lower melting points are used. Lead oxidizes readily. Although lead itself will not adhere to clean steel, the adherence of lead oxide to steel surfaces is a problem, especially at higher temperatures. Within the range of temperatures usually employed, a film of molten salt will protect the surface of the lead bath, and the work will be easily cleaned. Above 480 °C (900 °F), granulated carbonaceous material, such as charcoal, may be used as a protective cover.

Because of its high thermal conductivity relative to the gaseous atmosphere, lead is useful for rapid local heating and selective tempering. A typical application is the tempering of a ball joint. The part is carburized and quenched to a minimum case hardness of 59 HRC and a core hardness of 30 to 40 HRC. The thread and taper are then tempered in lead to produce a maximum case hardness of 40 HRC.

Because of the high specific gravity of lead, parts tempered in molten lead will float unless held down by fixtures. All parts and fixtures must be dry when immersed in the bath to prevent the formation of steam in, and resultant violent expulsion of, the molten lead. Precautions

Table 7 Compositions and operating temperatures for salt baths used in tempering

Class	Composition of bath	Operating temperature		Fuming temperature	
		°C	°F	°C	°F
1	37–50% NaNO ₂ 0–10% NaNO ₃ 50–60% Na ₂ CO ₃	165–595	325–1100	635	1175
2	45–57% NaNO ₃ 45–57% KNO ₃	290–595	550–1100	650	1200
3	45–55% Na ₂ CO ₃ 45–55% KCl	620–925	1150–1700	935	1720
4	15–25% NaCl 20–32% KCl 50–60% BaCl ₂	595–900	1100–1650	940	1725
4A	10–15% NaCl 25–30% KCl 40–45% BaCl ₂ 15–20% CaCl ₂	550–760	1025–1400	790	1450

Source: Military Specification MIL-S-10699A (Ordnance)

also must be taken to protect personnel from industrial lead poisoning; hoods and ventilating equipment are required.

Temperature Control. For either gas or electric heat, properly adjusted potentiometers of the on-off type will control the tempering temperature within ±6 °C (±10 °F) at the thermocouple location. With proportioning controls, these instruments can maintain temperatures within ±1 °C (±2 °F) at the thermocouple location.

Special Tempering Procedures

Special processes are occasionally employed to achieve specific properties, such as those derived from steam treating or the use of protective atmospheres. The tempering mechanism in certain steels also may be enhanced by cyclic heating and cooling. A particularly important procedure employs cycles between subzero temperatures and the tempering temperature to increase the transformation of retained austenite. The term used for this procedure, *multiple tempering*, is also applied to procedures that use intermediate thermal cycles to soften parts for straightening prior to the actual tempering operation designed to achieve the desired degree of toughness and plasticity.

Selective Tempering

Selective or localized tempering is applied to parts in which adjacent areas must have significantly different hardnesses. It is used to soften specific areas of fully hardened parts or to temper areas that were selectively hardened previously. The purpose of this treatment is to improve the machinability, the toughness, or the resistance to quench cracking in the selected

zone. Induction and flame tempering are the most commonly used selective techniques because of their controllable local heating capabilities. The immersion of selected areas in molten salt or molten metal can be accomplished, but with somewhat less control. Chisels, punches, the upset ends of cold-formed rivets, and the threaded portions of carburized parts are typical examples. Localized tempering is also employed in preheating and postheating of weld areas when a lowering of the hardness in the heat-affected zone is desired.

Selective tempering entails heating a restricted area to the required tempering temperature without heating the remainder of the part to this temperature. Induction heating coils, special flame heads, and immersion in lead or salt baths are employed to achieve this selective heating. Selective tempering is also done by the use of defocused lasers or electron beam equipment. Induction heating and flame techniques are generally used in high-volume production applications and are easiest to control. Deeper penetration is achieved with low-frequency (3 to 10 kHz) induction heating and salt immersion than is obtained with the other techniques.

To obtain rapid heating for selective tempering by immersion in salt or lead baths, it is usually necessary that the bath temperature be considerably higher than the desired tempering temperature. Consequently, the immersion time becomes the controlling factor in obtaining the desired results. Lead, because of its higher rate of heat transfer, is more effective than salt. Other factors, such as ease of fixturing, part configuration, heater frequency, and cost, also influence the choice of equipment for selective tempering. In induction tempering, the same heating system can be used for both hardening and tempering.

Both of the following examples illustrate how selective tempering can be used to produce specific hardnesses in certain areas of a workpiece.

Example 1: Use of Bulk Processing and Selective Tempering to Produce a Tack Hammer with a 50 to 55 HRC Striking Head. An upholsterer's tack hammer, forged from 1086 steel, is hardened on all surfaces to 53 to 60 HRC and then is tempered in salt at 190 °C (375 °F). This treatment provides the desired combination of hardness, toughness, and magnetic properties for the horseshoe-magnet end of the hammer. However, the striking head must be selectively tempered in salt at 260 °C (500 °F) to produce the working hardness of 50 to 55 HRC.

Example 2: Use of Bulk Processing and Selective Tempering to Produce a Pipe Wrench with 47 to 52 HRC Chain Teeth and a 40 to 48 HRC Handle. A chain pipe wrench handle forging, made of 4053 steel, is fully hardened and tempered for 1 h at 355 °C (675 °F) to produce an overall hardness of 47 to 52 HRC. This is an ideal hardness for the wrench teeth but does not provide sufficient

toughness for the I-beam section of the handle. Thus, this section is selectively tempered by induction heating for 1 min at 480 °C (900 °F) to produce a hardness of 40 to 48 HRC.

Multiple Tempering

Multiple tempering is principally used to:

- Relieve the quenching and straightening stresses in irregularly shaped carbon and alloy steel parts and thereby lessen distortion
- Eliminate retained austenite and improve dimensional stability in such parts as bearing components and gear blocks
- Improve yield and impact strengths without decreasing hardness

The following examples illustrate these principal applications of the multiple-tempering process.

Example 3: Use of Multiple Tempering to Relieve Straightening-Induced Stresses in a 1046 Steel Diesel Engine Crankshaft. A six-throw, seven-bearing, counterweighted diesel engine crankshaft weighing 80 kg (175 lb) was distorted in rough machining to such a degree that cold straightening was required. The straightening operation induced additional stresses, which caused severe distortion in final machining. The problem was solved by first tempering the 1046 steel shaft at 455 °C (850 °F) to a hardness of approximately 321 HB, which allowed hot straightening. The shaft was then retempered at 480 to 540 °C (900 to 1000 °F), depending on the composition of the particular heat, to produce a hardness of 269 to 302 HB and to relieve residual stresses.

Example 4: Use of Multiple Tempering to Minimize Retained Austenite and to Improve Dimensional Stability in a W1 Tool Steel Gage Block. In the manufacture of a gage block of W1 tool steel (final hardness, 65 to 66 HRC), the block is quench hardened after rough machining. It is then subjected to three consecutive cycles, each consisting of cold treatment at -100 °C (-145 °F) for 1 h followed by tempering at 70 °C (160 °F) for 1 h. This minimizes the retained austenite and enhances dimensional stability before the block is finish ground.

Use of Fixtures

Many high-strength steel components having a tensile strength greater than 1720 MPa (250 ksi) are finish machined before final heat treatment. To minimize distortion and satisfy stringent dimensional requirements, some of these components, such as cylinders, pressure vessels, and thin parts, are held in fixtures during both hardening and tempering or during tempering only. External rings, internal mandrels, jacks, screws, weights, wedges, dies,

and other mechanical devices are used to aid in dimensional correction.

Example 5: Use of Tempering Fixture to Minimize Out-of-Round Condition in a 4135 Steel Welded Pressure Vessel. A welded pressure vessel made of 4135 steel, 380 mm (15 in.) outside diameter, 1.8 m (6 ft) long, and 3.18 mm (0.125 in.) thick, was found to be 1.3 to 3.8 mm (0.050 to 0.150 in.) out of round over its entire length when measured in the as-quenched condition. A tempering fixture consisting of a series of steel rings 125 mm (5 in.) wide reduced maximum out-of-roundness to 1.3 mm (0.050 in.) after tempering at 455 °C (850 °F) for 2½ h.

Cracking in Processing

Because of their carbon or alloy contents, some steels are likely to crack if they are permitted to cool to room temperature during or immediately following the quenching operation. This likelihood is caused by the generation of high tensile residual stresses during quenching, due to thermal gradients, abrupt changes in section thickness, decarburization, or other hardenability gradients. Another potential source is cracking due to quenchant contamination and the subsequent change in quenching severity. Accordingly, for carbon steels containing more than 0.4% C and alloy steels containing more than 0.35% C, it is recommended that the parts be transferred to tempering furnaces before they cool to below 100 to 150 °C (212 to 300 °F). Alternately, many heat treating operations use quenching oil for the tempering operation (martempering) or to avoid cooling below 125 °C (255 °F). Steels that are known to be sensitive to this type of cracking include 1060, 1090, 1340, 4063, 4150, 4340, 52100, 6150, 8650, and 9850.

Other carbon and alloy steels are generally less sensitive to this type of delayed quench cracking but may crack as a result of part configuration or surface defects. These steels include 1040, 1050, 1141, 1144, 4047, 4132, 4140, 4640, 8632, 8740, and 9840. Some steels, such as 1020, 1038, 1132, 4130, 5130, and 8630, are not sensitive.

Before being tempered, parts should be quenched to room temperature to ensure the transformation of most of the austenite to martensite and to achieve maximum as-quenched hardness. Austenite retained in low-alloy steels will, upon heating for tempering, transform to an intermediate structure, reducing overall hardness. However, in medium- to high-alloy steels containing austenite-stabilizing elements (nickel, for example), retained austenite may transform to martensite upon cooling from tempering, and thus, such steels may require additional tempering (double tempering) for the relief of transformation stresses.

Snap Draw. Steels that are susceptible to cracking at room temperature after hardening are given a low-temperature tempering treatment

(a snap draw) immediately after hardening and prior to final tempering in fixtures.

Special Microstructures

Carburized Components (portions adapted from Ref 51). Although many carburized parts are placed in service without tempering, case-hardened carburized parts are tempered to improve toughness and bending strength. Table 8 is a summary of tempering effects on mechanical properties of various carburized steels. Tempering in the range of 150 to 200 °C (300 to 400 °F) does provide benefit in terms of toughness and bending strength. Tempering carburized parts between 150 and 200 °C (300 and 400 °F) is typical when wear resistance is to be retained. However, higher tempering temperatures may apply for applications requiring impact toughness or high load durability. For example, drag racers have been known to temper gears at temperatures as high as 425 °C (800 °F) to survive the very high load conditions (Ref 51).

When selecting tempering time and temperature of carburized parts, the combination of toughness, strength, and hardness must be considered along with effects on residual stress and retained austenite. Tempering reduces the compressive stresses within the case and the tensile stresses at the core (Ref 52). Core properties cannot always be controlled by tempering when trying to achieve maximum case properties, and a favorable compressive residual-stress pattern may be retained only at the expense of overall toughness.

The influence of tempering on residual stress is shown in Fig. 32. The transformation of retained austenite and the resultant change in the relative volume of case and core are primarily responsible for the change in residual stress as a function of temperature. The effect of retained austenite on the performance varies.

The reduction of retained austenite is apparently desirable for resistance to grinding abuse and to provide dimensional stability, but some retained austenite appears to be beneficial for contact-fatigue durability.

Nonmartensitic Structures. The tempering of microstructures other than martensite and retained austenite also represents special applications of tempering. The main difference in the tempering behavior of martensite and bainite is that there is little carbon solution in the solid solution of bainite. The bainitic structure is less sensitive to tempering because carbon is mostly present as coarse carbides that contribute little to strength (Ref 11).

Reactions of structures containing substantial amounts of lower bainite are relatively similar to that of martensite in terms of the phenomena associated with carbide growth and coalescence. Upper bainite and fine pearlite formed by controlled or relatively slow cooling simply respond by carbide growth and eventual ferrite recrystallization. The softening associated with tempering in such instances is shown in Fig. 33. Impact properties of normalized and tempered or hardened and tempered structures at nearly equal hardnesses are shown in Fig. 34.

The properties of retained austenite after the martensitic and bainitic transformations are also different. The retained austenite of bainitic structures is highly stable; decomposition depends on high tempering temperatures. Steel with a structure of upper bainite contains a notable quantity of austenite, even after tempering at high temperatures (Ref 53).

Bainitic steels containing strong carbide-forming elements, such as chromium, vanadium, molybdenum, and niobium, also exhibit the secondary hardening peak. This reaction is slow if compared to martensitic structure, because the cementite in bainite is coarse (Ref 11).

Induction Tempering

Extensive production experience has demonstrated the commercial success of induction tempering for many applications. Metallurgically, the success of induction tempering has been related fundamentally to the possibility of compensating for short tempering times with higher tempering temperatures. Economically, induction tempering has proved particularly adaptable to automation in production lines.

Application. At present, two principal areas of application exist for induction tempering:

- Selective tempering, such as induction tempering of threads
- Progressive tempering of bar stock previously hardened by scanning

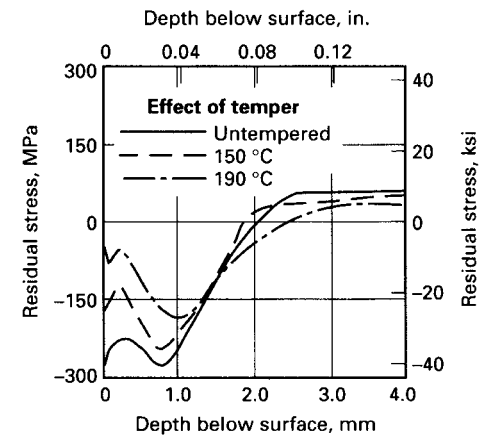


Fig. 32 Effect of tempering on residual stress in carburized steel. Bars of 8617 steel, 19 mm (0.75 in.) in diameter, were carburized, direct oil quenched, and tempered for 1 h at the indicated temperature.

Table 8 Data on as-quenched and tempered unnotched Charpy bars following gas carburizing

Sample No.(a)	AISI grade	Tempering temperature		Hardness, HRC		Case depth				Charpy impact energy		Slow bend test results					
		°C	°F	Surface	Core	Effective		Visual		J	ft-lb	Yield		Ultimate		Deflection	
						mm	in.	mm	in.			kN	lb	kN	lb	mm	in.
1	8615	As-quenched		66	36	0.89	0.035	1.02	0.040	16-20	12-15	19.6	4400	30.2	6780	0.86	0.034
2	8615	150	300	63-64	37	0.97	0.038	1.02	0.040	24-26	18-19	27.6	6200	33.2	7460	1.02	0.040
3	8615	205	400	59-61	35-36	0.91	0.036	1.02	0.040	26-30	19-22	27.6	6210	35.1	7900	1.07	0.042
4	8615	260	500	58-59	35-36	0.91	0.036	1.02	0.040	19-31	14-23	34.3	7700	39.2	8820	1.42	0.056
5	8615	315	600	55-56	36	0.84	0.033	1.02	0.040	43-56	32-41	32.0	7200	42.9	9640	1.45	0.057
6	8615	370	700	51-53	34	0.58	0.023	1.02	0.040	53-144	39-106	28.0	6300	42.2	9480	2.39	0.094
7	8615	425	800	48-49	32	0.36	0.013	1.02	0.040	175-231	129-170
8	8615	480	900	45-46	29-30	1.02	0.040	264-302	195-223	23.6	5300	35.1	7900	5.08	0.200
9	8620	As-quenched		64-66	45	1.17	0.046	1.14	0.045	24-30	18-22	22.2	5000	34.6	7780	1.09	0.043
10	8620	150	300	62-65	45-46	0.91	0.036	1.14	0.045	34-39	25-29	32.9	7400	37.4	8400	1.09	0.043
11	8620	205	400	59-60	45-46	1.09	0.043	1.14	0.045	33-60	24-44	29.8	6700	38.7	8700	1.12	0.044
12	4320	As-quenched		64	46	1.40	0.055	1.52	0.060	26-28	19-21	26.7	6000	34.3	7700	1.17	0.046
13	4320	150	300	61-63	46	1.65	0.065	1.52	0.060	38-41	28-30	27.1	6100	36.9	8290	1.14	0.045
14	4320	205	400	58-59	46-47	1.40	0.055	1.52	0.060	43-47	32-35	30.2	6800	38.4	8640	1.17	0.046
15	8617	150	300	60-61	38	0.99	0.039	0.91	0.036	22-45	16-33	28.9	6500	36.1	8100	1.12	0.044
16	4815	150	300	58	42-43	1.22	0.048	0.91	0.036	63-79	39-58
17	4820	150	300	58	40-41	0.89	0.035	0.86	0.034	58-68	43-50	28.0	6300	37.0	8320	1.40	0.055

Bars 1-14 carburized in one group; bars 15-17 carburized in one group. Unnotched Charpy bar to simulate cross section of a small differential gear tooth, carburized and direct quenched in 50 °C (120 °F) oil and tempered for 2 h. Source: Ref 51

Many machine parts vary from one section to another with respect to load and wear requirements. Often, this variation in requirements is met by a compromise of properties obtained by uniform tempering to a single hardness level. However, it is apparent that superior performance may be expected if the mechanical properties could be adjusted to meet the particular requirements in each section by selective tempering. Within certain limitations, induction tempering is an economical means of accomplishing this. These limitations are that the parts must be of such a shape and size that they can be coupled by the inductor to heat uniformly to the desired temperature in critical sections. Although this is impossible or impracticable for some parts, many can be tempered selectively by induction to obtain different degrees of hardness in the same part, with a consequent improvement in quality.

One key advantage of induction tempering is the possibility of integration with machine lines to avoid excessive handling of work, thereby minimizing labor cost. This is illustrated in the preparation of bar stock of specified mechanical properties before machining into cylinder-head studs and miscellaneous machine parts. Frequently, the tempering operation is keyed to the hardening operation, or the same equipment may be used for both induction hardening and tempering either by merely changing the work coil or by reducing the power density and the heating time.

Selection of Frequency and Power Densities. Because tempering is performed below the lower transformation temperature of 725 °C (1335 °F), lower-frequency induction tempering installations are generally used; such installations are necessary for tempering large sections to minimize any temperature gradient from the surface to the interior. Frequency selection is basically related to the required depth of heating. It should be noted that line frequencies (60 Hz) may be used for tempering parts 25 to 50 mm (1 to 2 in.) in diameter or larger. Using low frequencies and low current densities is particularly important for the induction tempering of carburized threads. Shorter cycles and higher frequencies will allow for rehardening of the thread tips and thus lead to thread failures. Because the usual objective of induction tempering is to produce uniform hardness throughout the cross section, rather than to heat the surface, the power density within the inductor is generally low, from 0.08 to 0.8 W/mm² (0.05 to 0.5 kW/in.²). Power densities may be selected on the basis of experience, tests, or data such as those presented in Table 9. Furthermore, the heating time is comparatively long to help provide uniform heating throughout the part. To meet production requirements, the length of the inductor can be increased, or more than one bar can be processed at a time.

In general, the control of induction tempering is achieved by selection of the power density and the rate of feed through the coil (scanning)

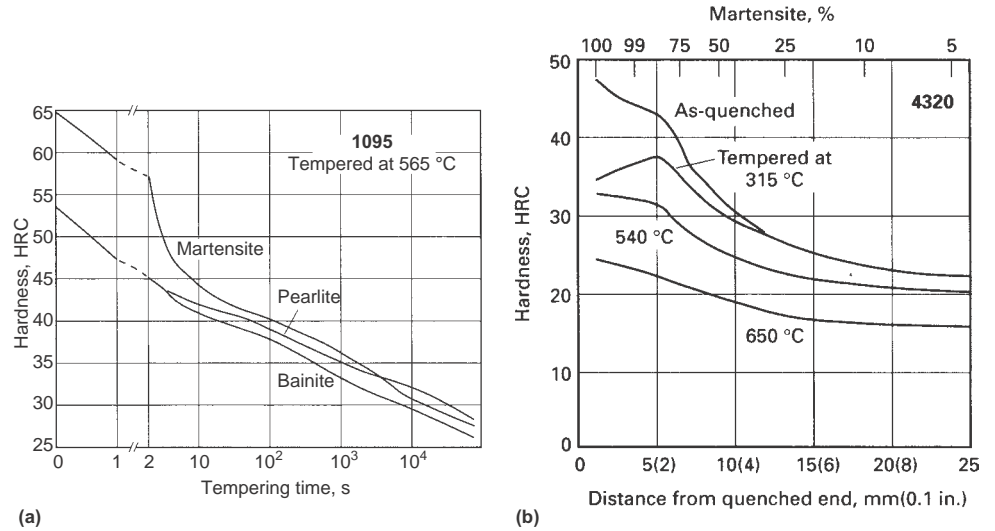


Fig. 33 Effect of prior microstructure on room-temperature hardness after tempering. (a) 1095 steel tempered at 565 °C (1050 °F) for various periods of time. (b) Room-temperature hardness before and after tempering, as well as amount of martensite present before tempering in 4320 steel end-quenched hardenability specimens tempered 2 h

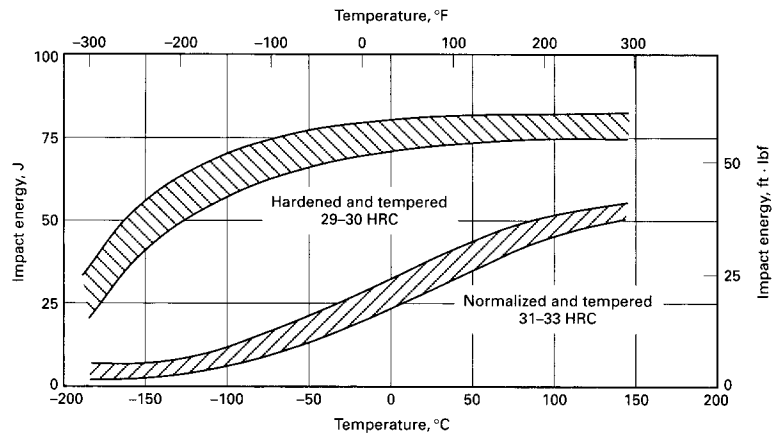


Fig. 34 Effect of microstructure on notch toughness. Variation in Charpy keyhole-notch impact energy with temperature for 4340 steel hardened and tempered to 29 to 30 HRC or normalized and tempered to 31 to 33 HRC

Table 9 Approximate power density required for tempering

Frequency(a), Hz	Input(b)			
	W/mm ²		kW/in. ²	
	150–425 °C (300–800 °F)	425–705 °C (800–1300 °F)	150–425 °C (300–800 °F)	425–705 °C (800–1300 °F)
60	0.10	0.24	0.06	0.15
180	0.08	0.22	0.05	0.14
1,000	0.06	0.19	0.04	0.12
3,000	0.05	0.16	0.03	0.10
10,000	0.03	0.13	0.02	0.08

(a) Table is based on use of proper frequency and normal overall operating efficiency of equipment. (b) In general, these power densities are for section sizes of 13 to 50 mm (½ to 2 in.). Higher inputs can be used for smaller section sizes, and lower inputs may be required for larger section sizes.

on the basis of hardness tests of the tempered product. Automatic control may be obtained at tempering temperatures above 425 °C (800 °F) by use of a special radiation pyrometer and high-speed controller. This arrangement may

be used to vary the speed of the scanning operation continuously or to control the power.

Equivalent Heating for Induction Tempering (adapted from Ref 54). Fundamentally, the temperatures for induction tempering must

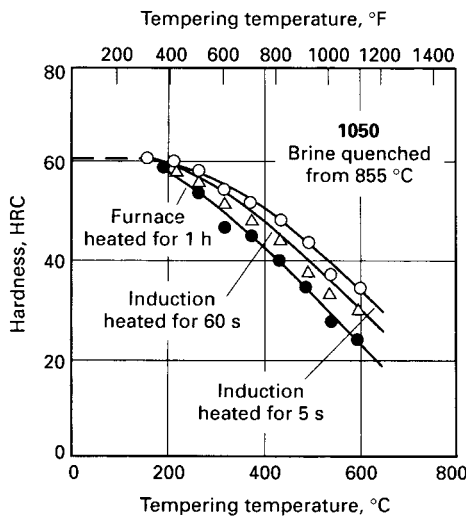


Fig. 35 Variations of room-temperature hardness with tempering temperature for furnace and induction heating

be higher than the usual furnace tempering temperatures to compensate for the short heating times on induction. Figure 35 shows the increase in tempering temperature required to produce a given hardness as the tempering time is decreased from 1 h (furnace tempering) to 60 s and 5 s (induction tempering) in 1050 steel quenched in brine from 855 °C (1575 °F). Pieces with small cross section may be air cooled immediately upon reaching the tempering temperature, while slower heating rates or short periods of time at temperature (5 to 60 s) before cooling are desirable for larger sections to allow penetration of heat. In scanning, of course, the power density, the rate of travel, and the length of the inductor will determine the time of tempering.

The Hollomon-Jaffe equation, although quite useful in conjunction with conventional tempering curves, should be applied with care for induction tempering of martensite. Firstly, it must be remembered that there is a limit above which the tempering temperature should not be raised. This, of course, is the A_1 temperature (or A_{c1} for rapid heating processes), at which carbides start to go back into solution. Secondly, it must be realized that the relation applies only to short-time tempering at a fixed temperature, that is, isothermal tempering treatments. In other words, it assumes that the temperature of the workpiece is increased instantaneously to the tempering temperature. When the heating time is of the same order of magnitude as the actual soak time, it must be taken into account.

A means by which a particular time-temperature history is accounted for in rapid heating (for instance, by induction) may be derived by a simple extension of the Hollomon-Jaffe concept. This is done by calculating the equivalent time, t^* , for a constant temperature heating cycle that corresponds to the continuous cycle. One way of doing this is illustrated in Fig. 36.

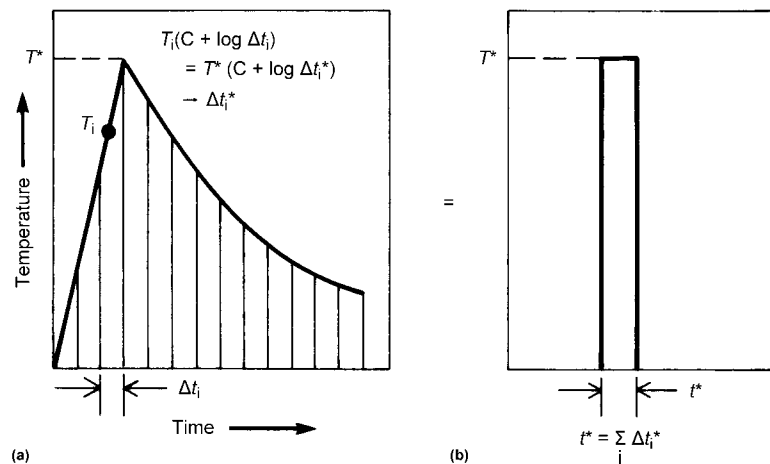


Fig. 36 Method of equivalent cooling with induction heating and isothermal heating. (a) Continuous heating cycle with induction heating to determine effective tempering time (Δt_i^*) for small intervals of the cycle. (b) Equivalent isothermal cycle with the effective tempering time, $t^* = \sum \Delta t_i^*$. Source: Ref 54

Here, the induction tempering cycle (shown schematically in Fig. 36a) consists of a heating portion and a subsequent cooling portion, the latter occurring at a somewhat lower rate. The total continuous cycle is broken into a number of very small time increments, each of duration Δt_i and characterized by some average temperature, T_i . It is assumed that the temperature for the equivalent isothermal treatment is the peak temperature of the continuous cycle, or T^* . This specification of the temperature for the isothermal cycle is arbitrary, however.

Having specified the temperature of the equivalent isothermal cycle as T^* , an effective tempering time, t^* , for this cycle can be estimated. This is accomplished by solving for the increment in t^* , or Δt_i^* , for each Δt_i in the continuous treatment by using the equation $T_i(C + \log \Delta t_i) = T^*(C + \log \Delta t_i^*)$. Summing the Δt_i^* for each portion of the continuous cycle yields the total effective tempering time, t^* , at temperature T^* and hence the effective tempering parameter $T^*(C + \log t^*)$, as shown in Fig. 36(b).

In the application of this method, care should be exercised in selecting Δt_i . These time increments should be chosen small enough so that the temperature does not change too much during the increment, thus enabling a reasonable average for the temperature T_i to be obtained and used in the aforementioned expression. For continuous heating from room temperature to typical induction tempering temperatures, a Δt_i on the order of 0.005 to 0.01 times t_{total} , where t_{total} is the total heating time, provides sufficient calculation accuracy.

Another consideration in estimating the effective tempering time is the fact that tempered steels are usually air cooled to avoid distortion. As implied previously, the cooling rates are typically much lower than the heating rates, giving rise to substantially greater times at high temperature during the cooling cycle. Therefore, the tempering that occurs during cooling must also be included in the effective

tempering parameter. To do this, the cooling rate must be measured or estimated from a heat-transfer analysis. The increments in the effective tempering time, Δt_i^* , are then estimated from this cooling curve and the aforementioned relation, and they are added to those for the heating portion of the cycle prior to calculation of the effective tempering parameter from $T^*(C + \log t^*)$.

ACKNOWLEDGMENTS

Portions of this manuscript were adapted from various references that include:

- E.C. Bain and H.W. Paxton, *Alloying Elements in Steel*, American Society for Metals, 1966
- R.A. Grange and R.W. Baughman, Hardness of Tempered Martensite in Carbon and Low-Alloy Steels, *Trans. ASM*, Vol 48, 1956, p 165–197
- R.A. Grange, C.R. Hribal, and L.F. Porter, Hardness of Tempered Martensite in Carbon and Low Alloy Steels, *Metall. Trans. A*, Vol 8, 1977, p 1780–1781
- M.A. Grossmann and E.C. Bain, Chap. 5, Tempering after Quenching, *Principles of Heat Treatment*, 5th ed., American Society for Metals, 1964, p 129–176
- S.L. Semiatin and D.E. Stutz, *Induction Heat Treatment of Steel*, American Society for Metals, 1986

REFERENCES

1. M.A. Grossmann and E.C. Bain, Chap. 5, Tempering after Quenching, *Principles of Heat Treatment*, 5th ed., American Society for Metals, 1964, p 129–176
2. E.C. Bain and H.W. Paxton, *Alloying Elements in Steel*, American Society for Metals, 1966

3. C.S. Roberts, B.L. Auerbach, and M. Cohen, The Mechanism and Kinetics of the First Stage of Tempering, *Trans. ASM*, Vol 45, 1953, p 576–604
4. B.S. Lement, B.L. Auerbach, and M. Cohen, Microstructural Changes on Tempering Iron Carbon Alloys, *Trans. ASM*, Vol 46, 1954, p 851–881
5. F.E. Werner, B.L. Auerbach, and M. Cohen, The Tempering of Iron Carbon Martensitic Crystals, *Trans. ASM*, Vol 49, 1957, p 823–841
6. G.R. Speich, Tempered Ferrous Martensitic Structures, *Metallography, Structures and Phase Diagrams*, Vol 8, *Metals Handbook*, 8th ed., American Society for Metals, 1973, p 202–204
7. G.R. Speich and W.C. Leslie, Tempering of Steel, *Metall. Trans.*, Vol 3, 1972, p 1043–1054
8. S. Nagakura, Y. Hirotsu, M. Kusunoki, T. Suzuki, and Y. Nakamura, Crystallographic Study of the Tempering of Martensitic Carbon Steel by Electron Microscopy and Diffraction, *Metall. Trans. A*, Vol 14, 1983, p 1025–1031
9. G. Krauss, Tempering and Structural Change in Ferrous Martensitic Structures, *Phase Instrumentations in Ferrous Alloys*, A.R. Marder and J.I. Goldstein, Ed., TMS-AIME, 1984, p 101–123
10. G.R. Speich, *Trans. Metall. Society AIME*, Vol 245, 1969, p 2553, in C.R. Brooks, *Principles of the Heat Treatment of Plain and Low-Alloys Steels*, ASM International, 1996
11. R.W.K. Honeycombe and H.K.D.H. Bhadeshia, *Steels Microstructure and Properties*, Edward Arnold, London, 1995
12. A.V. Sverdlin and A.R. Ness, Chap. 2, The Effects of Alloying Elements on Heat Treatment of Steel, *Steel Heat Treatment Handbook*, Marcel Dekker Inc., New York, 1997
13. G. Krauss, *Principles of Heat Treatment of Steel*, ASM International, Materials Park, OH, 1990
14. J. Dossett, private communication
15. K. Nagasawa, Temper Brittleness of Steels, *Honda Anniversary Volume*, Sendai, Oct 1936, p 1078, in M.A. Grossmann and E.C. Bain, *Principles of Heat Treatment*, 5th ed., American Society for Metals, 1964
16. K.-E. Thelning, *Steel and Its Heat Treatment*, 2nd ed., Butterworth, 1984, p 207–318
17. R.A. Grange and R.W. Baughman, Hardness of Tempered Martensite in Carbon and Low-Alloy Steels, *Trans. ASM*, Vol 48, 1956, p 165–197
18. D.K. Bullens, *Steel and Its Heat Treatment*, Wiley, 1948, in S.L. Semiatin and D.E. Stutz, *Induction Heat Treatment of Steel*, American Society for Metals, 1986
19. H. Holloman and L.D. Jaffe, Time-Temperature Relations in Tempering Steels, *Trans. AIME*, Vol 162, 1945, p 223–249
20. H. Holloman and L.D. Jaffe, Time-Temperature Relations in Tempering Steels, *Trans. AIME*, Vol 162, 1945, p 223–249 in C.R. Brooks, *Principles of Heat Treatment of Plain and Low-Alloys Steels*, ASM International, 1996
21. H. Hollomon and L.D. Jaffe, Datasheet, *Met. Prog.*, 1954
22. F.R. Larson and J. Miller, A Time-Temperature Relationship for Rupture and Creep Stresses, *Trans. ASME*, Vol 74, 1952, p 765–775
23. L.C.F. Canale, X. Yao, J. Gu, and G.E. Totten, A Historical Overview of Steel Tempering Parameters, *Int. J. Microstruc. Mater. Prop.*, Vol 3 (No. 4–5), 2008, p 474–525
24. H.K.D.H. Bhadeshia and H.J. Stone, Neural-Network Modeling, *Fundamentals of Modeling for Metals Processing*, Vol 22A, *ASM Handbook*, ASM International, 2009, p 435–439
25. R.A. Grange, C.R. Hribal, and C.F. Porter, Hardness of Tempered Martensite in Carbon and Low-Alloy Steels, *Metall. Trans. A*, Vol 8, 1977, p 1775, 1780–1781
26. S.L. Semiatin and D.E. Stutz, *Induction Heat Treatment of Steel*, American Society for Metals, 1986, from K.E. Thelning, Steel and Its Heat Treatment, *Bofors Handbook*, Butterworth, 1974
27. K.E. Thelning, Steel and Its Heat Treatment, *Bofors Handbook*, Butterworth, 1974
28. E.J. Janitzky and M. Baeyerz, Marked Similarity in Tensile Properties of Several Heat Treated SAE Steels, *Metals Handbook*, American Society for Metals, 1939, p 515
29. G.F. Vander Voort, Embrittlement of Steels, *Properties and Selection: Irons, Steels, and High-Performance Alloys*, Vol 1, *ASM Handbook*, ASM International, 1990, p 689–736
30. G. Krauss, Deformation and Fracture in Martensitic Carbon Steels Tempered at Low Temperatures, *Metall. Mater. Trans. B*, Vol 32, 2001, p 205–221
31. G. Krauss and C.J. McMahon, Jr., Low-Toughness and Embrittlement Phenomena in Steels, *Martensite*, G.B. Olsen and W.S. Owen, Ed., ASM International, 1991, p 295–321
32. B.J. Schulz, Ph.D. thesis, University of Pennsylvania, 1972
33. T. Inoue, K. Yamamoto, and S. Sekiguchi, *Trans. Iron Steel Inst. Jpn.*, Vol 14, 1972, p 372
34. I. Olefjord, Temper Embrittlement, Review 231, *Int. Metall. Rev.*, Vol 23, 1978, p 149–175
35. G. Krauss, Tempered Martensite Embrittlement in AISI 4340 Steel, *Metall. Trans. A*, Vol 10, 1979, p 1643–1649
36. M. Szczepanski, *The Brittleness of Steels*, John Wiley & Son, New York, 1963
37. D.J. Wulpi, Failures of Shafts, *Failure Analysis and Prevention*, Vol 11, *ASM Handbook*, American Society for Metals, 1986, p 459–482
38. E.O. Hall, The Deformation of Low-Carbon Steel in the Blue-Brittle Range, *J. Iron Steel Inst.*, Vol 170, April 1952, p 331–336
39. R.L. Kenyon and R.S. Burns, Testing Sheets for Blue Brittleness and Stability against Changes due to Aging, *Proc. ASTM*, Vol 34, 1934, p 48–58
40. G. Mima and F. Inoko, A Study of the Blue-Brittle Behavior of a Mild Steel in Torsional Deformation, *Trans. Jpn. Inst. Met.*, Vol 10, May 1969, p 227–231
41. B.A. Miller, Overload Failures, *Failure Analysis and Prevention*, Vol 11, *ASM Handbook*, ASM International, 2002, p 671–699
42. F. Zia Ebrahimi and G. Krauss, Mechanisms of Tempered Martensitic Embrittlement in Medium Carbon Steels, *Acta Metall.*, Vol 32 (No.10), 1984, p 1767–1777
43. J.P. Materkowski and G. Krauss, Tempered Martensite Embrittlement in SAE 4340 Steel, *Metall. Trans. A*, Vol 10, 1979, p 1643–1651
44. S.K. Banerji, C.T. McMahon, Jr., and H.C. Feng, Intergranular Fracture in 4340-Type Steels: Effects of Impurities and Hydrogen, *Metall. Trans. A*, Vol 9, 1978, p 237–247
45. C.L. Briant and S.K. Banerji, Tempered Martensite Embrittlement in Phosphorus Doped Steels, *Metall. Trans. A*, Vol 10, 1979, p 1729–1736
46. G. Thomas, Retained Austenite and Tempered Martensite Embrittlement, *Metall. Trans. A*, Vol 9, 1978, p 439–450
47. H. Ohtani and C.J. McMahon, Jr., Modes of Fracture in Temper Embrittlement Steels, *Acta Metall.*, Vol 23, 1975, p 377–386
48. W.J. Nam and H.C. Choi, Effect of Si on Mechanical Properties of Low Alloy Steels, *Mater. Sci. Technol.*, Vol 15, 1999, p 527–530
49. W.J. Nam and H.C. Choi, Effect of Silicon, Nickel, Vanadium on Impact Toughness in Spring Steels, *Mater. Sci. Technol.*, Vol 13, 1997, p 568–574
50. F.A. Darwish, L.C. Pereira, C. Gattis, and M.L. Graça, On the Tempered Martensite Embrittlement in AISI 4140 Low Alloy Steel, *Mater. Sci. Eng. A*, Vol 131, 1991, p L5–L9
51. G. Fett, Tempering of Carburized Parts, *Met. Prog.*, Sept 1982, p 53–55
52. J. Vatauvuk, M.Z. di Monte, and A.A. Couto, The Effect of Core and Carburized Surface Microstructural Stability on Residual Stress Evolution during Tempering, *J. ASTM Int.*, Vol 6 (No. 9), 2009
53. A.S. Shneiderman, Tempering of the Bainitic Structure, *Met. Sci. Heat Treat.*, Vol 20 (No. 12), 1978, p 971–974
54. S.L. Semiatin and D.E. Stutz, Chap. 6, Induction Tempering of Steel, *Induction*

Heat Treatment of Steel, American Society for Metals, 1986

SELECTED REFERENCES ON TEMPER EMBRITTELEMENT

- J.R. Low, Jr., D.F. Stein, A.M. Turkalo, and R.P. LaForce, Alloy and Impurity Effects on Temper Embrittlement of Steel, *Trans. TMS-AIME*, Vol 242, 1968, p 14–24
- C.J. McMahon, Jr., Temper Brittleness—An Interpretative Review, *Temper Embrittlement in Steel*, STP 407, American Society for Testing and Materials, 1968, p 127–167
- D.L. Newhouse and H.G. Holtz, Temper Embrittlement of Rotor Steels, *Temper Embrittlement in Steel*, STP 407, American Society for Testing and Materials, 1968, p 106–126
- I. Olefjord, Temper Embrittlement, *Int. Met. Rev.*, Vol 4, 1978, p 149–163
- T. Takeyama and H. Takahashi, Strength and Dislocation Structures of α -Irons Deformed in the Blue-Brittleness Temperature Range, *Trans. Iron Steel Inst. Jpn.*, Vol 13, 1973, p 293–302
- B.C. Woodfine, Some Aspects of Temper Brittleness, *J. Iron Steel Inst.*, Vol 173, 1953, p 240–255
- J. Yu and C.J. McMahon, Jr., The Effects of Composition and Carbide Precipitation on Temper Embrittlement of 2.25 Cr-Mo Steel: Part I, Effects of P and Sn, *Metall. Trans. A*, Vol 11, 1980, p 277–289
- J. Yu and C.J. McMahon, Jr., The Effects of Composition and Carbide Precipitation on Temper Embrittlement of 2.25 Cr-Mo Steel: Part II, Effects of Mn and Si, *Metall. Trans. A*, Vol 11, 1980, p 291–300

Austempered Steel*

Edited by John R. Keough, Applied Process Inc.

AUSTEMPERING is the isothermal transformation of a ferrous alloy at a temperature below that of pearlite formation and above that of martensite formation, as Austempering of steel offers several potential advantages:

- Increased ductility, toughness, and strength at a given hardness (Table 1)
- Reduced expansion during transformation, which minimizes distortion and lessens subsequent machining time, stock removal, sorting, inspection, and scrap
- Elimination of quench cracking
- The shortest overall time cycle to through harden within the hardness range of 35 to 60 HRC, with resulting savings in energy and capital investment
- A bainitic microstructure that is resistant to hydrogen embrittlement, even at high hardness

Steel is austempered by being:

- Heated to a temperature within the austenitizing range, usually 790 to 927 °C (1450 to 1700 °F)
- Cooled rapidly enough to avoid the formation of pearlite or ferrite to a temperature that is above the M_s , depending on the material, in the range of 204 to 400 °C (400 to 750 °F). This is generally accomplished in a bath of molten nitrite-nitrate salt but can, in some circumstances, be done with liquid spray, high-pressure gas, hot oil, or molten lead. Salt quenching is covered in more detail in the article "Salt Quenching" in this Volume.
- Allowed to transform isothermally (over several minutes or hours) to bainite at the temperature that produces the desired hardness. This is generally accomplished in a bath of molten nitrite-nitrate salt but can, in some circumstances, be done with hot oil, forced convection, or molten lead.
- Cooled to room temperature

The process is described in detail by the inventors E.S. Davenport and E.C. Bain in U.S. Patent 1,924,099. The fundamental difference between austempering and conventional

quenching and tempering is shown schematically in Fig. 1. For true austempering, the metal must be cooled from the austenitizing temperature to the temperature of the austempering bath fast enough so that no transformation of austenite occurs during cooling, and then held at bath temperature long enough to ensure complete transformation of austenite to bainite. Modifications of these procedures, constituting departures from true austempering, are discussed in the section "Modified Austempering" in this article.

Grossman and Bain found that austempered eutectoid steel parts had significantly greater impact strength than quenched and tempered parts at the same hardness (Fig. 2). Notice that

the difference in impact strength between bainite and tempered martensite increases with hardness until a hardness of approximately 52 HRC. The rapid flattening of the bainite curve above 52 HRC is related to the austempering time for the experimental samples being insufficient for complete bainitic transformation. In the higher-hardness samples (transformed at decreasing quench temperatures), the presence of increasing amounts of martensite in the microstructure from transformation in the region between the M_s and M_f further flattens the bainite curve. The curves merge where the structures both become, essentially, 100% martensite. This figure graphically shows the increased ductility of bainite compared to tempered martensite at

Table 1 Mechanical properties of 1095 steel heat treated by three methods

Specimen No.	Heat treatment	Hardness, HRC	Impact strength		Elongation in 25 mm (1 in.), %
			J	ft · lbf	
1	Water quenched and tempered	53.0	16	12	...
2	Water quenched and tempered	52.5	19	14	...
3	Martempered and tempered	53.0	38	28	...
4	Martempered and tempered	52.8	33	24	...
5	Austempered	52.0	61	45	11
6	Austempered	52.5	54	40	8

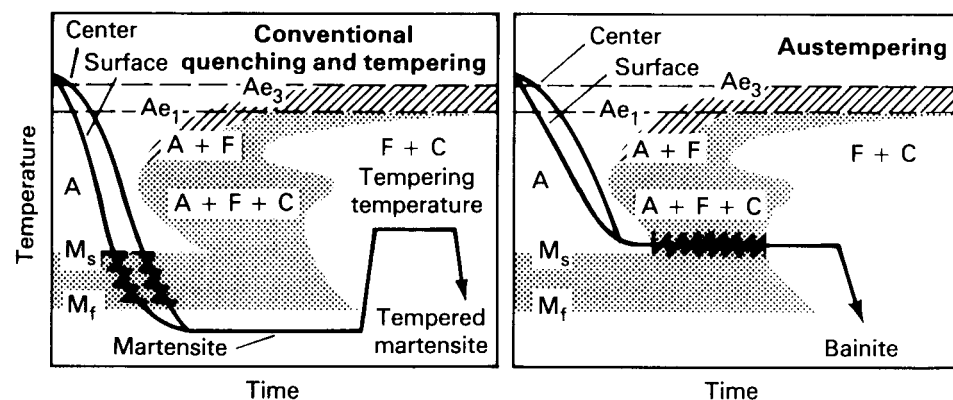


Fig. 1 Comparison of time-temperature-transformation cycles for conventional quenching and tempering and for austempering

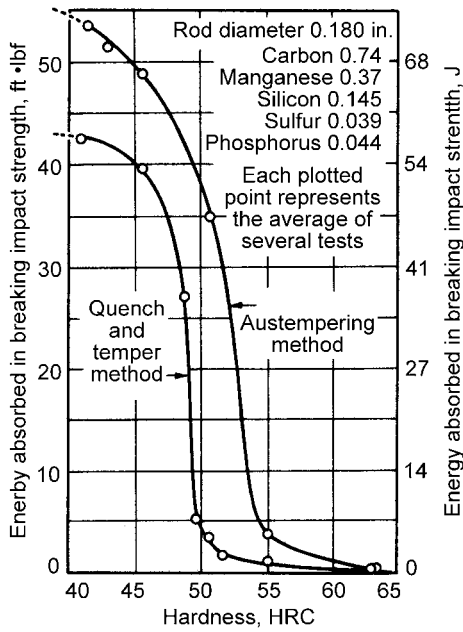


Fig. 2 Impact energy vs. hardness for the quenched and tempered (martensitic) and austempered (bainitic) methods for a eutectoid steel. Source: Ref 1

hardnesses exceeding 40 HRC. Below 40 HRC, the mechanical properties of tempered martensite are usually superior. In industrial practice, one may choose austempering below 40 HRC for low distortion and no quench cracking, but the major advantages of bainite are found at higher hardnesses.

Steels for Austempering

The selection of steel for an austempered component must be based on the configuration of the part, the processing characteristics of the heat treating equipment employed, and the hardenability and transformation characteristics of the steel alloy as indicated by time-temperature-transformation (TTT) diagrams and isothermal transformation (IT) diagrams. Some important considerations are:

- The location of the pearlite nose of the TTT or IT curve indicating the hardenability of the steel
- The maximum thermal section size of the component
- The speed of the quench being used

- The time required for complete transformation of austenite to bainite at the austempering temperature
- The M_s temperature of the steel

As indicated in Fig. 3(a), 1080 carbon steel possesses transformation characteristics that give it limited suitability for austempering. Cooling from the austenitizing temperature to the austempering bath must be accomplished in approximately 1 s to avoid the pearlite nose of the TTT curve and thus prevent transformation to pearlite during cooling. Depending on the temperature, isothermal transformation in the bath is completed within a period ranging from a few minutes to approximately 1 h. Because of the rapid cooling rate required, austempering of 1080 can be successfully applied only to thin sections of approximately 5 mm (0.2 in.) maximum.

Low-alloy 5140 steel is well suited to austempering, as indicated by the TTT curve shown in Fig. 3(b). Approximately 2 s are allowed in which to bypass the nose of the curve, and transformation to bainite is completed within 1 to 10 min at 315 to 400 °C (600 to 750 °F). Parts made of 5140 steel or of other steels with similar transformation

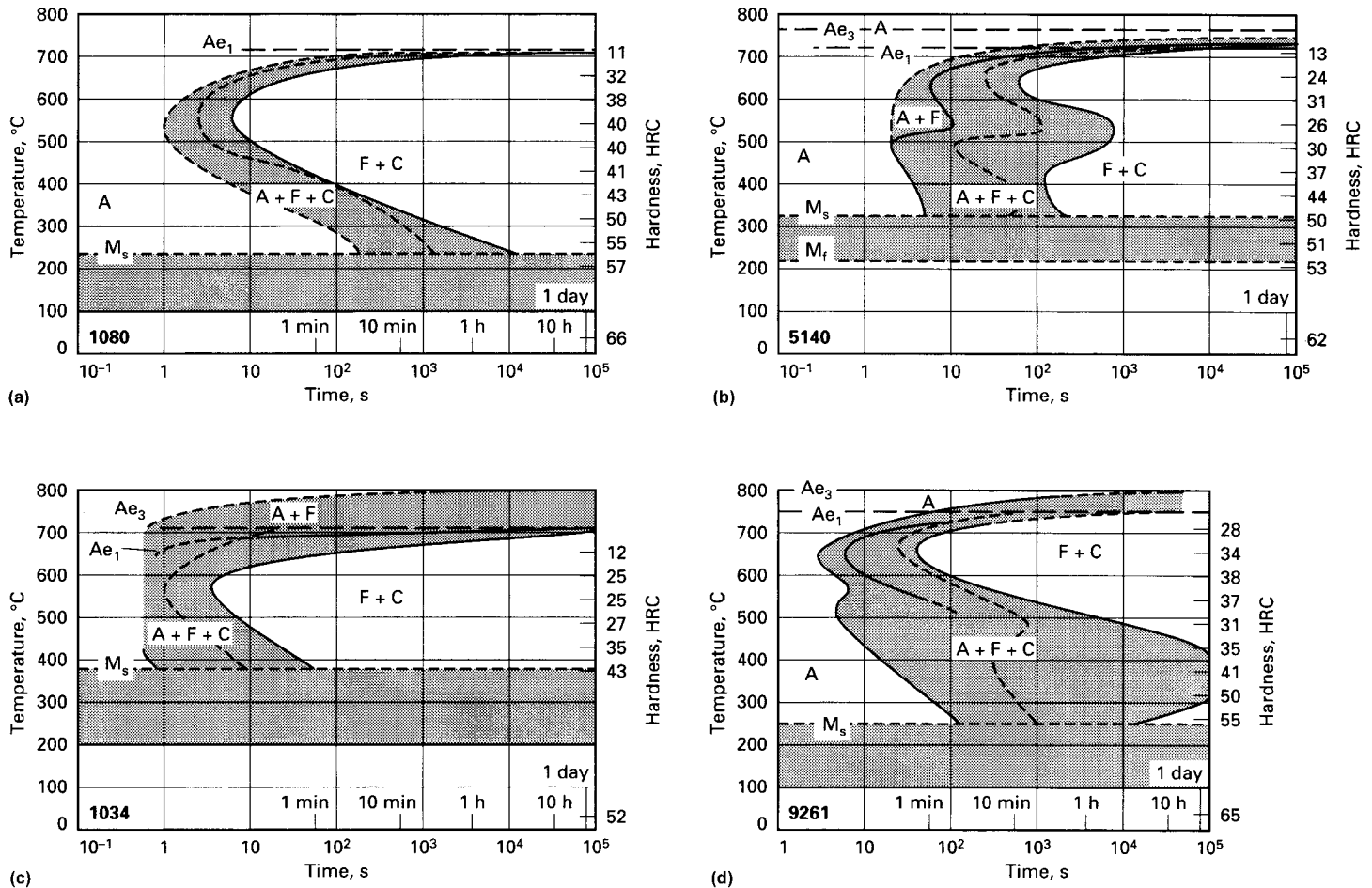


Fig. 3 Transformation characteristics of (a) 1080, (b) 5140, (c) 1034, and (d) 9261 steels

characteristics are adaptable to austempering in larger section sizes than are feasible for 1080 steel because of the greater time allowed for bypassing the pearlite nose of the curve.

Steels such as 1034 (Fig. 3c) cannot be successfully austempered. Their hardenability is insufficient, and their elevated M_s temperature would require isothermal transformation above 400 °C (750 °F), yielding a 30 to 35 HRC hardness and a mixed structure of upper bainite and pearlite, with properties inferior to tempered martensite at the same hardness.

Steels such as 9261 (Fig. 3d) with high hardenability and relatively high carbon contents are suitable for thicker sections and, with a lower M_s temperature, higher bainitic hardnesses. One process drawback is the time required for complete bainitic transformation. To produce a 55 HRC bainitic structure, a transformation time of over 4 h is required.

In addition to the steels previously indicated (1080, 5140, and 9261), steels adaptable to austempering include:

- Plain carbon steels containing 0.50 to 1.00% C and a minimum of 0.60% Mn
- High-carbon steels containing more than 0.90% C and, possibly, a little less than 0.60% Mn
- Certain carbon steels (such as 1041) with a carbon content of less than 0.50% but with manganese content in the range from 1.00 to 1.65%
- Certain low-alloy steels (such as the 5100-series steels) containing more than 0.30% C; the 1300- to 4000-series steels with carbon contents in excess of 0.40%; and other steels, such as 4140, 6145, and 9440
- Certain carbon steels (such as 10B38) with carbon content of less than 0.50%, manganese exceeding 0.60%, and microalloyed with boron for increased hardenability
- Chromium-nickel-molybdenum steels such as 4340 and 4350. The hardenability of these steels is so great that they can be through austempered in sections exceeding 50 mm (2 in.), albeit with long isothermal transformation times.

If one is familiar with the quenching speed of the processing equipment being used, commercially available programs (i.e., SteCal) for modeling the steel hardenability and isothermal-transformation characteristics are available. A modeled isothermal-transformation diagram is not only useful for determining the hardenability of material, it can also accurately predict the required austempering time for a given set of steel inputs.

The chemical composition of the steel is also the major determinant of the M_s temperature. Carbon is the most significant variable affecting the M_s . The direct effects of other alloying elements on the M_s point are much less pronounced than the effect of carbon. However, carbide-forming elements (such as molybdenum and vanadium) can tie up the carbon as

alloy carbides and prevent complete solution of carbon. The approximate M_s temperature, in degrees Centigrade, of a completely austenitized steel can be calculated by means of the following formula:

$$M_{s,C} = 538 - (361 \times \%C) - (39 \times \%Mn) - (19 \times \%Ni) - (39 \times \%Cr)$$

Expressed in degrees Fahrenheit, the formula is:

$$M_{s,F} = 1000 - (650 \times \%C) - (70 \times \%Mn) - (35 \times \%Ni) - (70 \times \%Cr)$$

These chemical relationships create another metallurgical anomaly related to parts that are to be austempered. A minor variation in surface carbon in a quench and temper process will result in a slightly higher or lower hardness as-quenched martensitic structure. A slightly decarburized surface on a part being austempered will have a higher M_s temperature and can, depending on the amount of decarburization and the selected austempering temperature, result in a thin layer of (untempered) martensite on a bainitic core. This bimodal structure results in tensile residual stresses on the surface, degrading the strength of the part and making it susceptible to environmental embrittlement. Therefore, in processing austempered parts, the process should err on the side of a slightly carburizing ambient, because bainitic hardness will be a function of the austempering temperature and is basically unrelated to the carbon content (beyond its being sufficient to lower the M_s to below the austempering temperature).

Austenitizing temperature has a significant effect on the time at which transformation begins. As the austenitizing temperature is increased above normal (for a specific steel), the pearlitic nose of the TTT curve can shift to the right because of grain coarsening, or (in hypereutectoid steels) increased carbon in solution, or the dissolution of alloy carbides and their diffusion into the austenite. In Fig. 3, for example, approximately 0.75 s is allowed for quenching 1080 steel in order to avoid the nose of the curve. However, this is based on an austenitizing temperature of 790 °C (1450 °F); higher austenitizing temperatures move the TTT curve to the right, allowing more time before transformation begins.

Practical use is sometimes made of this phenomenon in order to process compositions or section sizes that would otherwise not be suitable for austempering. However, the coarser grain sizes or dissolution of alloy carbides resulting from higher austenitizing temperatures may be detrimental to some properties (i.e., formability or resistance to contact brinelling). Therefore, it is recommended that standard austenitizing temperatures be given preference for austempering. If experience with specific compositions and parts proves that advantages can be gained from the use of a

higher temperature and that no harm will be incurred from grain coarsening, higher austenitizing temperatures may be employed.

As the austenitizing temperature of a high-carbon steel increases, the M_s temperature decreases marginally because of more complete solution of carbon. This effect on the M_s temperature, however, is small compared to the effects of the chemical composition.

Section Thickness Limitations

The maximum section thickness is important in determining whether or not a part can be successfully austempered. The maximum section that can be through hardened will, of course, also depend on the speed of quench provided by the selected processing equipment, and some general observations follow. For 1080 steel, a section thickness of approximately 5 mm (0.2 in.) is the maximum that can be austempered to a fully bainitic structure using a fully agitated salt quench. Carbon steels with lower carbon content will be restricted to a proportionately lesser thickness. Lower-carbon steels containing boron, however, can be successfully austempered in heavier sections. In some alloy steels, section thicknesses up to approximately 25 mm (1 in.) can be austempered to fully bainitic structures. In highly alloyed Ni-Cr-Mo steels, such as 4300 steels, sections in excess of 50 mm (2 in.) can be successfully through austempered in high-speed sealed salt quenches. Nevertheless, sections of carbon steel significantly thicker than 5 mm (0.2 in.) are regularly austempered in production when some pearlite is permissible in the microstructure. This is demonstrated in Table 2, which lists section sizes of austempered parts made of various steels.

The effects of section thickness on the hardness of austempered 1090 and 5160 steels are shown in Fig. 4. Hardness remains reasonably consistent to the center of a 17 mm (0.680 in.) diameter of 1090, but it becomes erratic when the diameter is increased to 21 mm (0.820 in.). A similar difference is evident for 5160 steel when the diameter is increased from 24.6 to 26 mm (0.967 to 1.035 in.).

The lower surface hardnesses indicated for 1090 and 5160 were the result of grain refinement at the surface. (Very fine grains on the surface resulting from cold finishing of the steel significantly reduce the local hardenability.) The high core hardness of the 24.6 mm (0.967 in.) diameter of 5160 is attributed to chemical segregation in the center portion of the bar and the absence of appreciable grain refinement.

Applications

Austempering usually is substituted for conventional quenching and tempering for the following reasons:

Table 2 Hardness of various steels and section sizes of austempered parts

Steel	Section size		Salt temperature		M_s temperature(a)		Hardness, HRC
	mm	in.	°C	°F	°C	°F	
1050	3(b)	0.125(b)	345	655	320	610	41–47
1065	5(c)	0.187(c)	(d)	(d)	275	525	53–56
1066	7(c)	0.281(c)	(d)	(d)	260	500	53–56
1084	6(c)	0.218(c)	(d)	(d)	200	395	55–58
1086	13(c)	0.516(c)	(d)	(d)	215	420	55–58
1090	5(c)	0.187(c)	(d)	(d)	57–60
1090(e)	20(c)	0.820(c)	315(f)	600(f)	44.5 (avg)
1095	4(c)	0.148(c)	(d)	(d)	210(g)	410(g)	57–60
1350	16(c)	0.625(c)	(d)	(d)	235	450	53–56
4063	16(c)	0.625(c)	(d)	(d)	245	475	53–56
4150	13(c)	0.500(c)	(d)	(d)	285	545	52 max
4365	25(c)	1.000(c)	(d)	(d)	210	410	54 max
5140	3(b)	0.125(b)	345	655	330	630	43–48
5160(e)	26(c)	1.035(c)	315(f)	600(f)	255	490	46.7 (avg)
8750	3(b)	0.125(b)	315	600	285	545	47–48
50100	8(c)	0.312(c)	(d)	(d)	57–60

(a) Calculated. (b) Sheet thickness. (c) Diameter of section. (d) Salt temperature adjusted to give maximum hardness and 100% bainite. (e) Modified austempering; microstructure contained pearlite as well as bainite. (f) Salt with water additions. (g) Experimental value

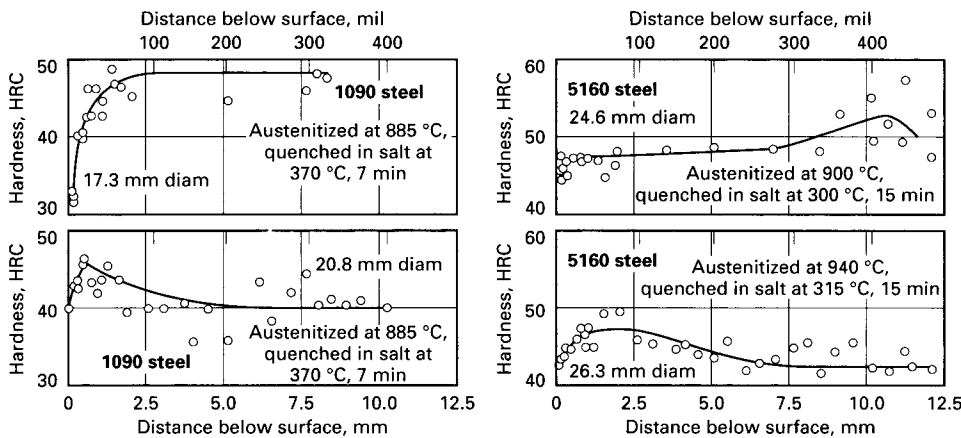


Fig. 4 Effect of section thickness on the hardness of austempered carbon and alloy steels. The 5160 steel was quenched in agitated salt containing some water. The HRC values were converted from microhardness readings taken with a 100 g load. Low values of surface hardness result from decarburization. High hardness at center of 24.6 mm (0.967 in.) 5160 is due to segregation.

- To obtain improved mechanical properties (particularly higher ductility or notch toughness at a given high hardness). Figure 5 compares the fracture morphologies of austempered versus quenched and tempered 10B53 steel.
- To decrease the likelihood of cracking and distortion
- To improve wear resistance for a given hardness
- To improve resistance to subsequent embrittlement

Historically, austempered parts have not required baking after plating. This can be attributed to the relative resistance of the bainitic microstructure to hydrogen embrittlement. This phenomenon is shown graphically in Fig. 6, where 4340 steel samples with martensitic and bainitic structures were loaded with, and without, a hydrogen ambient. The martensitic samples demonstrated a sharp drop in ductility resulting from the hydrogen, while

the effect on the bainitic structure was minimal. For this reason, bainitic fasteners well in excess of 40 HRC can be used without the fear of embrittlement.

This embrittlement advantage is also observed in the fatigue behavior of bainitic versus martensitic samples. Figure 7 demonstrates that martensitic structures have a distinct maximum hardness, above which there is a significant decrease in allowable fatigue loading. For this reason, quenched and tempered fasteners (with hardness above 39 HRC) are rarely used in applications where fatigue would be the dominant stress loading. Fully bainitic components, however, can be safely used in fatigue loading up to the maximum bainitic hardness. Makers of turf- and crop-cutting blades (knives, mower blades, flail blades) use austempered steel for its good impact strength at a hardness in excess of 40 HRC.

Austempering results in reduced distortion compared to martensitic hardening. Distortion (nonuniform shape change) occurs due to the relief of stresses induced into the part during

forming, the mechanical creep of parts at austenitizing temperatures, nonuniform transformation of the various part sections during quenching, and solid-state growth during transformation. While austempered parts are subject to the unwinding of residual stresses during heatup and the low strength and stiffness of steel during austenitizing, they are not subject to nonuniform transformation, and the transformation expansion during the bainitic reaction is much less than that of the martensitic reaction.

Transformation to martensite is, essentially, an instantaneous, temperature-related function. Therefore, when one drops a fully austenitic part into a liquid maintained at a temperature below the M_s , the moment the temperature of a specific section of the part drops below the M_s it transforms from face-centered cubic (fcc) austenite to body-centered tetragonal (bct) martensite (virtually instantaneously). The newly transformed section of the part will be hard, relatively brittle, untempered martensite. If an adjacent section of the part (say, a thicker section or a section with no end condition) drops to below the M_s some seconds later, it too must transform from soft, ductile fcc austenite to bct martensite, but the earlier transformed section(s) of the part have assumed their new dimension(s), forcing the later transforming section(s) of the part to grow where they can. This results in unpredictable distortion and even cracking. Transformation from fcc austenite to bainite (largely body-centered cubic acicular ferrite and nanocarbitides) takes place uniformly throughout the part over many minutes (or even hours), depending on the austempering temperature and the chemical composition of the steel being processed. This results in parts with no variable residual stresses, uniform growth, and no cracking.

The chemistry of the steel and the austempering temperature affect the bainitic transformation time. Table 3 shows the effect of austempering time and temperature on the hardness. When the hardness levels out, it implies that the bainitic reaction is complete.

Figure 8 shows the relationship between transformation expansion and carbon content for steel. As carbon content increases, the transformation expansion of martensite increases. The transformation expansion of bainite actually decreases with increasing carbon content. This quantifies the industrial differences regularly observed in quenched and tempered and austempered medium-carbon steel parts.

In some applications, austempering is less expensive than conventional quenching and tempering. This is most likely when small parts are treated in an automated setup wherein conventional quenching and tempering comprise a three-step operation, that is, austenitizing, quenching, and tempering. Austempering requires only two processing steps: austenitizing and isothermal transformation in an austempering bath. Subsequent reheating for tempering is not required.

With the exception of some modified austempering material/process combinations outlined

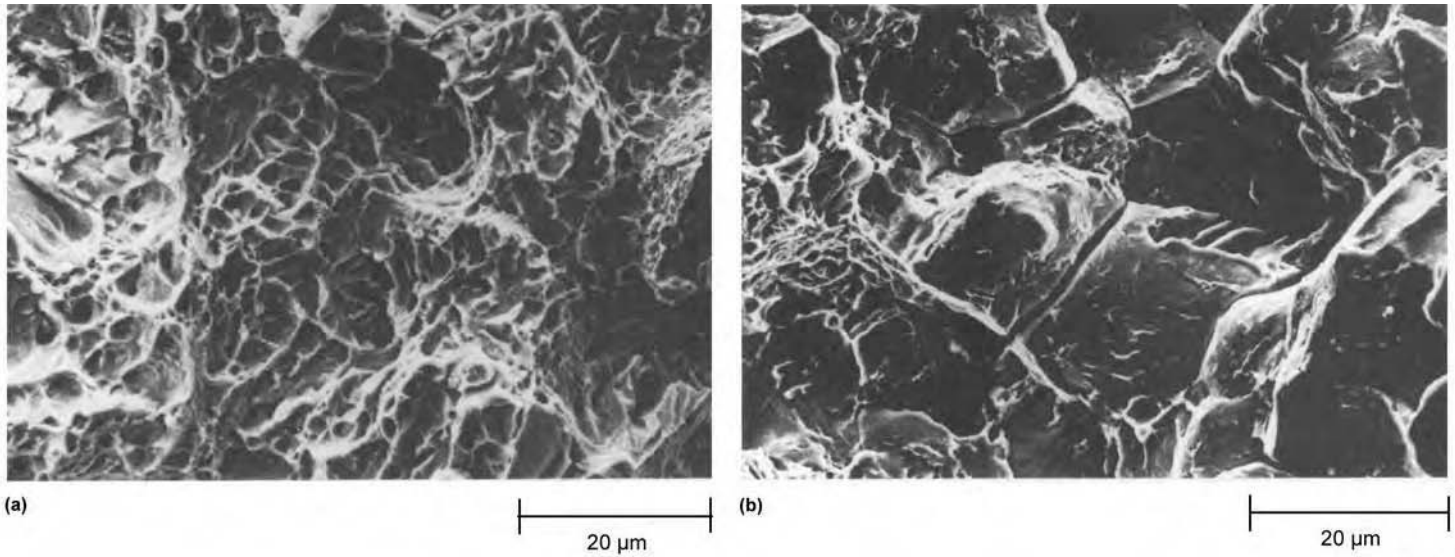


Fig. 5 Effect of heat treatment on the fracture appearance of 10B53 steel. (a) Ductile fracture surface of specimen austempered to 53 HRC. (b) Brittle fracture of specimen quenched and tempered to 53 HRC. Courtesy of Vermont America Corporation

in the “Modified Austempering” section of this article, the range of austempering applications generally encompasses parts fabricated from bars of small diameter or from sheet or strip of small cross section. Austempering is particularly applicable to thin-section carbon steel parts requiring exceptional toughness at a hardness between 40 and 50 HRC.

In austempered carbon steel parts, reduction in area is usually much higher than in conventionally quenched and tempered parts, as indicated in the following tabulation for 5 mm (0.180 in.) diameter bars of 0.85% C plain carbon steel:

Austempered mechanical properties	
Tensile strength, MPa (ksi)	1780 (258)
Yield strength, MPa (ksi)	1450 (210)
Reduction in area, %	45
Hardness, HRC	50
Quenched and tempered mechanical properties	
Tensile strength, MPa (ksi)	1795 (260)
Yield strength, MPa (ksi)	1550 (225)
Reduction in area, %	28
Hardness, HRC	50

The mechanical properties of sway bars made of 1090 steel and hardened by these two processes are listed in Table 4 (see also Table 1).

Provided that environmental embrittlement is not a design factor, it is more important that austempered parts possess desired mechanical properties than that they have a 100% bainitic structure. In Table 2, it is evident from the hardness values that several of the austempered steels have mixed structures. Higher-than-normal hardness indicates that some martensite has formed, and below-normal hardness indicates the presence of some pearlite (and/or upper bainite). The formation of pearlite is more common and results from a quenching speed too slow (or insufficient hardenability

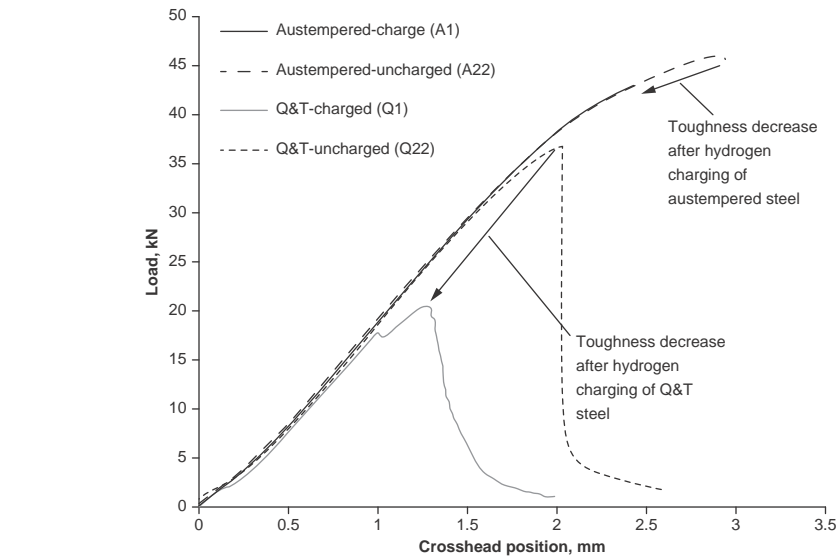


Fig. 6 Effect of hydrogen loading on martensitic and bainitic microstructures in 4340 steel samples. Q&T, quenched and tempered. Source: Ref 2

of the steel) for complete avoidance of the pearlite “nose” on the isothermal transformation curve.

In industrial austempering practice, a sizable percentage of applications are successful with less than 100% bainite. In fact, 85% bainite has been found to be satisfactory for some applications. Austempering is often modified to some degree in commercial application, and whether or not the metallurgical properties obtained conform to those obtained in true austempering is at least partially ignored if the treated parts meet service requirements. However, variations in hardenability from heat to heat may give rise to erratic results from variations in the amount of pearlite when borderline conditions are

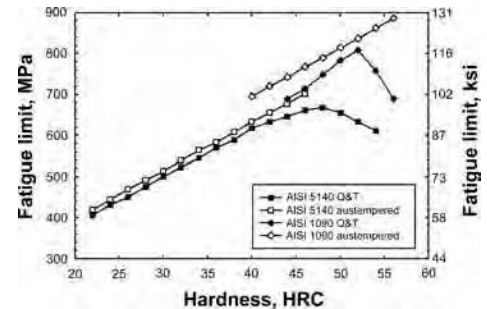


Fig. 7 There is a pronounced maxima in the fatigue limit for martensitic structures, while the fatigue limit of bainitic steel continues to increase to maximum bainitic hardness. Source: Ref 3

involved in modified austempering. When maximum property repeatability (minimum variation) is desired, the process should be designed to through harden the part to bainite.

Table 5 presents processing data for a number of specific parts made of various plain carbon, alloy, and carburizing steels; these data are representative of austempering practice in at least a dozen different manufacturing facilities.

Dimensional Control

Due to the uniform, time-dependent bainitic transformation described earlier, parts can usually be produced with less dimensional change by austempering than by conventional quenching and tempering. Austempering may be the best way to hold close tolerances without extensive straightening or machining after heat treatment. The data in Table 6 demonstrate the degree of improvement in dimensional stability attainable by austempering as compared to water or oil quenching and tempering.

The isothermal transformation process produces less dimensional variation than conventional quenching and tempering. Figure 9 shows the variation in pitch length for austempered and quenched and tempered 1050 roller chain links. Figure 10 shows the variation in height and bow for a 3 mm (0.125 in.) lever after austempering and quenching and tempering. This dimensional consistency is a hallmark of the austempering process.

Surface austempering can be successfully accomplished using induction heating of the surface and the introduction of a reducing or protective atmosphere during austenitization. The process yields a bainitic case with a pearlitic/ferritic core.

Carburizing and austempering is a high-performance steel heat treatment that combines a high-carbon bainitic case with either a bainitic or tempered martensite core to produce a component with an exceptional combination of strength and toughness. The process is done under various names, the most common trade name being Carbo-Austempering (Applied Process Inc.).

There are many property advantages to the carburizing and austempering process. They include:

- Greatly increased fatigue strength in high-load, low-cycle applications
- Higher tensile strength
- Increased elongation
- Greatly improved impact properties
- Increased wear resistance
- Less distortion
- No cracking

Table 7 compares properties of 8615 that has been carburized and austempered versus the same material carburized, quenched, and tempered. The carburizing and austempering process yields a high-carbon bainitic case and a low-carbon tempered martensitic core.

Table 3 Effect of austempering time on hardness of three steels

Steel	Austempering temperature		Rockwell hardness(a) after austempering times of:							
	°C	°F	30 min	60 min	90 min	120 min	240 min	300 min	360 min	
1095(b)	230(c)	450(c)	91	90	90	90	90	90	90	
	265(d)	510(d)	90	89	89	89	89	89	89	
8735(e)	260(f)	500(f)	51	51	49	49	48	48	47	
	315(f)	600(f)	49	45	46	46	46	46	46	
	370(f)	700(f)	40	39	38	38	38	38	37	
8750(g)	260(f)	500(f)	58	56	53	51	52	52	51	
	315(f)	600(f)	58	52	48	47	47	47	47	
	370(f)	700(f)	54	42	39	39	39	38	39	

(a) Rockwell 15-N hardness values for the 1095 steel; Rockwell C hardness values for the 8735 and 8750 steels. (b) Steel contained 0.90% C; specimen thickness, 0.25 mm (0.010 in.). Each hardness value is an average of 12 specimens; range of test values did not exceed one point on Rockwell 15-N scale. (c) Time for 100% transformation was 170 min. (d) Time for 100% transformation was 85 min. (e) Steel contained 0.37% C; specimen size, 16 × 32 × 2 mm (0.622 × 1.250 × 0.087 in.). (f) Time for complete transformation was 5 to 10 min. (g) Steel contained 0.49% C; specimen size, 25 × 25 × 3 mm (1 × 1 × 1/8 in.)

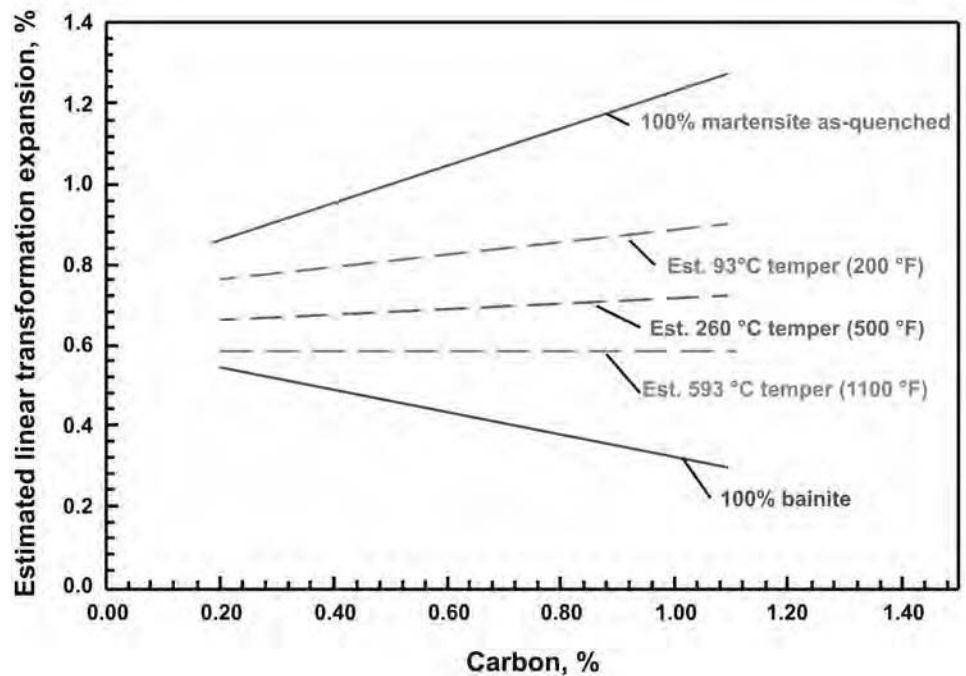


Fig. 8 Transformation-expansion comparison of martensite and bainite at various carbon contents. This applies to the commercial austempering range of 260 to 399 °C (500 to 750 °F). Source: Ref 4

Table 8 compares the properties of 4150 steel that has been carburized and austempered versus the same material carburized, quenched, and tempered. Carburizing and austempering 4150 produces a high-carbon bainitic case and a medium-carbon bainitic core. Carburizing, quenching, and tempering of 4150 produces a high-carbon martensitic case on a medium-carbon martensitic core.

Figure 11 shows the superiority of the high-load, low-cycle fatigue properties of carburized and austempered 8822 steel versus the same material carburized, quenched, and tempered.

Figure 12 shows the improved single-tooth bending properties of carburized and austempered

8620 versus conventional carburized, quenched, and tempered gear teeth.

Modified Austempering

As mentioned previously, modifications of austempering practice that give rise to mixed structures of pearlite and bainite are quite common in industrial practice. The amounts of pearlite and bainite may vary widely in different modifications of processing.

Patenting, a treatment used in the wire industry, is a significant and useful form of modified austempering in which austenitized wire or rod

is continuously quenched into a bath maintained at 510 to 540 °C (950 to 1000 °F) and held in the bath for periods ranging from 10 s (for small wire) to 90 s (for rod). Patenting provides a combination of moderately high strength and high ductility. As indicated in Fig. 13 by the line designated "modified practice," the process varies from true austempering in that the quenching rate, instead of being rapid enough to avoid the nose of the TTT curve, is sufficiently slow to intersect the nose, which results in the formation of fine pearlite.

Similar practice is usefully employed in applications involving plain carbon steels when a hardness between approximately 30 to 42 HRC is desirable or acceptable. The hardness of plain carbon steel quenched at a rate that intersects the nose of the TTT curve will vary with carbon content (Fig. 14).

Modified practices can be applied to parts having sections thicker than are normally considered practicable for austempering. These practices, however, also are subject to certain metallurgical limitations, such as the following that apply to the modified austempering of 1080 steel:

- The part to be quenched must be of sufficient mass or weight that cooling to the quench bath temperature cannot be

accomplished in the time (approximately $\frac{3}{4}$ s) allowed for avoiding the nose of the TTT curve; otherwise, the part will undergo true austempering and may be harder than desired. The temperature of the quenching medium should not be raised above 370 °C (700 °F) in an effort to retard the cooling rate, or temper brittleness may result. For small parts, isothermal annealing at 565 °C (1050 °F) is preferred to austempering for obtaining hardness in the range of 30 to 42 HRC.

- The part to be quenched is subject to a maximum, as well as a minimum, weight limit. If more than approximately 20 s is required for the center of the part to transform, or if there is a rise in bath temperature, some upper bainite may form, resulting in a variable hardness and mixed structure.
- The lower temperature limit of the quench bath depends on the weight of the part. For pieces weighing 1 to 2 kg (2 to 4 lb), the lower limit of the bath temperature is approximately 330 °C (625 °F).

From the aforementioned, it is evident that modified practices are limited by several critical factors and that some trial and error is necessary in developing an optimum cycle for parts of specific composition and section thickness.

Another form of modified austempering also entails the use of a special technique but produces results that are similar to those obtained in true austempering. This modification is used for parts that, because of their size and the type of steel from which they are made, are difficult to quench rapidly enough to avoid the nose of the TTT curve before transformation begins. In such applications, the cooling rate can be increased by first quenching the part into a bath that is slightly above the M_s temperature. For 1080 steel, this is approximately

Table 4 Comparison of typical mechanical properties of austempered and of oil-quenched and tempered sway bars of 1090 steel

Property(a)	Austempered at 400 °C (750 °F)(b)	Quenched and tempered(c)
Tensile strength, MPa (ksi)	1415 (205)	1380 (200)
Yield strength, MPa (ksi)	1020 (148)	895 (130)
Elongation, %	11.5	6.0
Reduction of area, %	30	10.2
Hardness, HB	415	388
Fatigue cycles(d)	105,000(e)	58,600(f)

(a) Average values. (b) Six tests. (c) Two tests. (d) Fatigue specimens 21 mm (0.812 in.) in diameter. (e) Seven tests; range, 69,050 to 137,000. (f) Eight tests; range, 43,120 to 95,220

Table 5 Typical production applications of austempering

Parts listed in order of increasing section thickness

Part	Steel	Maximum section thickness		Parts per unit weight		Salt temperature		Immersion time, min	Hardness, HRC
		mm	in.	kg ⁻¹	lb ⁻¹	°C	°F		
Plain carbon steel parts									
Clevis	1050	0.75	0.030	770/kg	350/lb	360	680	15	42
Follower arm	1050	0.75	0.030	412/kg	187/lb	355	675	15	42
Spring	1080	0.79	0.031	220/kg	100/lb	330	625	15	48
Plate	1060	0.81	0.032	88/kg	40/lb	330	630	6	45–50
Cam lever	1065	1.0	0.040	62/kg	28/lb	370	700	15	42
Plate	1050	1.0	0.040	0.5 kg	$\frac{1}{4}$ lb	360	675	15	42
Type bar	1065	1.0	0.040	141/kg	64/lb	370	700	15	42
Tabulator stop	1065	1.22	0.048	440/kg	200/lb	360	680	15	45
Lever	1050	1.25	0.050	345	650	15	45–50
Chain link	1050	1.5	0.060	573/kg	260/lb	345	650	15	45
Shoe-last link	1065	1.5	0.060	86/kg	39/lb	290	550	30	52
Shoe-toe cap	1070	1.5	0.060	18/kg	8/lb	315	600	60	50
Lawn mower blade	1065	3.18	0.125	1.5 kg	$\frac{3}{8}$ lb	315	600	15	50
Lever	1075	3.18	0.125	24/kg	11/lb	385	725	5	30–35
Fastener	1060	6.35	0.250	110/kg	50/lb	310	590	25	50
Stabilizer bar	1090	19	0.750	22 kg	10 lb	370	700	6–9	40–45
Boron steel bolt	10B20	6.35	0.250	100/kg	45/lb	420	790	5	38–43
Alloy steel parts									
Socket wrench	6150	0.3 kg	$\frac{1}{8}$ lb	365	690	15	45
Chain link	Cr-Ni-V(a)	1.60	0.063	110/kg	50/lb	290	550	25	53
Pin	3140	1.60	0.063	5500/kg	2500/lb	325	620	45	48
Cylinder liner	4140	2.54	0.100	15 kg	7 lb	260	500	14	40
Anvil	8640	3.18	0.125	1.65 kg	$\frac{3}{8}$ lb	370	700	30	37
Shovel blade	4068	3.18	0.125	370	700	15	45
Pin	3140	6.35	0.250	100/kg	45/lb	370	700	45	40
Shaft	4140(b)	9.53	0.375	0.5 kg	$\frac{1}{4}$ lb	385	725	15	35–40
Gear	6150	12.7	0.500	4.4 kg	2 lb	305	580	30	45
Carburized steel parts									
Lever	1010	3.96	0.156	33 kg	15 lb	385	725	5	30–35(c)
Shaft	1117	6.35	0.250	66/kg	30/lb	385	725	5	30–35(c)
Block	8620	11.13	0.438	132/kg	60/lb	290–315	550–600	30	50(c)

(a) Contains 0.65 to 0.75% C. (b) Leaded grade. (c) Case hardness

260 °C (500 °F), as shown in Fig. 13. The part is held at this temperature for only the brief time necessary to obtain temperature equalization throughout the section and is then transferred to the austempering bath at a higher temperature and allowed to transform isothermally in the normal manner (see example 4 in the following section).

Austempering Problems and Solutions

Problems encountered in austempering, together with their solutions, are discussed in the following examples.

Example 1: Reduced Distortion in U-Bolts by Austempering. In one application, a U-shaped part was formed from 1095 steel strip, 0.25 mm (0.010 in.) thick. The open end of the U varied within 0.25 mm (0.010 in.) after forming. When these parts were oil quenched from 800 °C (1475 °F) and tempered at 260 °C (500 °F), the open end of the U varied over a range of 1.3 mm (0.050 in.). However, when the parts were austempered for 90 min at 265 °C (510 °F), the dimensional spread was decreased to approximately 0.8 mm (0.030 in.).

Example 2: Reduction in Straightening Operations with Austempering. Table 6 compares the dimensional changes that occurred in stabilizer bars as a result of oil quenching and tempering with those that resulted from austempering. Approximately 20% of these bars

require straightening when oil quenched. This percentage is sharply reduced when austempering is used. With a new die setup, approximately 1 to 5% will require straightening for the first 3000 pieces while the dies are being trimmed for precise fit. After the correct fit and setup are established, straightening will drop to less than ½%. This will carry through until the die wear becomes appreciable (approximately 40,000 pieces), at which point the amount of straightening required begins to increase. Note that when straightening bainitic structures there is a great deal more springback than with martensitic structures. One will find that parts being straightened will require reverse loading well beyond practices used for quenched and tempered parts in order to return to the zero axis.

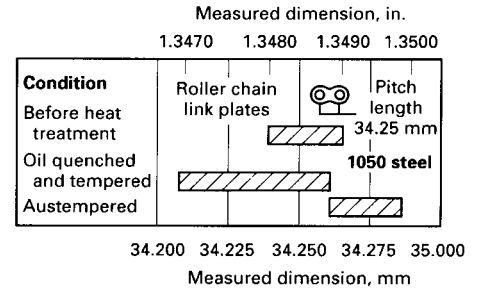


Fig. 9 Variation in pitch length of 2 mm (0.080 in.) thick link plates after austempering and after oil quenching and tempering. All link plates were austenitized at 855 °C (1575 °F) for 11 min; austempered link plates were held in salt at 340 °C (640 °F) for approximately 1 h.

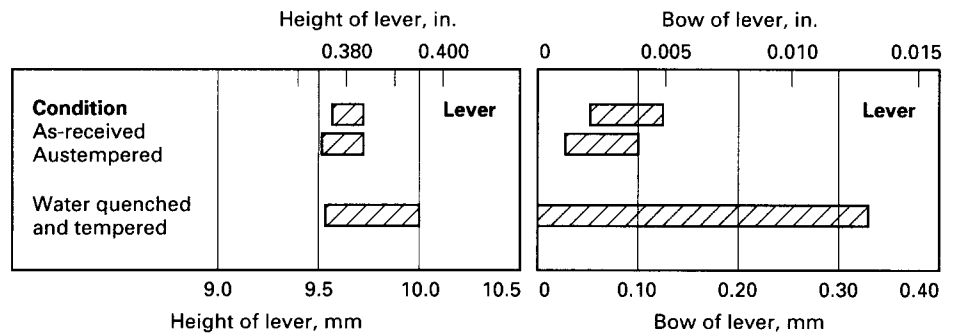
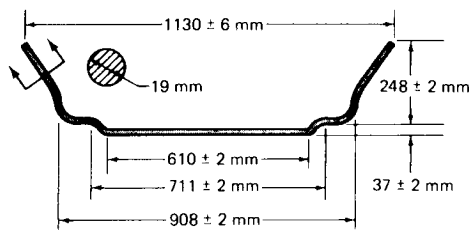


Fig. 10 Variation in dimensions of 3 mm (0.125 in.) thick levers after austempering and after water quenching and tempering. Horizontal bars represent groups of ten samples.

Table 6 Effects of oil quenching and tempering and of austempering on dimensions of stabilizer bars



Specified dimensions		Process	Measured dimension(a)					
mm	in.		High		Low		Average	
			mm	in.	mm	in.	mm	in.
1130 ± 6	44½ ± ¼	OQ & T	1133	44¾	1127	44¾	1130	44½
		Austemper	1130	44½	1126	44⅝	1127	44¾
908 ± 2	35¾ ± ⅛	OQ & T	911(b)	35⅞(b)	905(b)	35⅞(b)	910	35⅓
		Austemper	910	35⅓	910	35⅓	910	35⅓
711 ± 2	28 ± ⅛	OQ & T	714(b)	28⅞(b)	711	28	713	28⅓
		Austemper	713	28⅓	711	28	711	28
610 ± 2	24 ± ⅛	OQ & T	614(b)	24⅓(b)	611	24⅓	613(b)	24⅓(b)
		Austemper	611	24⅓	610	24	611	24⅓
248 ± 2	9¾ ± ⅛	OQ & T	249	9⅓	246	9⅓	248	9¾
		Austemper	248	9¾	246	9⅓	246	9⅓
37 ± 2	1⅓ ± ⅛	OQ & T	38	1½	36.5	1⅓	38	1½
		Austemper	38	1½	38	1½	38	1½
2(c)	⅓(0.0625)(c)	OQ & T	1.3	0.050	0.13	0.005	0.8	0.032
		Austemper	1.5	0.060	0.25	0.010	0.9	0.036

Note: OQ & T, oil quenching and tempering. (a) Data represent measurements made on 12 samples of bars processed by each method. (b) Out of specification. (c) Arm-to-arm parallel

Table 7 Properties of Carbo-Austempered and carburized quenched and tempered (Q&T) 8615 steel

	Carbo-Austempered	Carburized Q&T
Tensile strength, MPa (ksi)	1162 (169)	742 (108)
Unnotched impact energy, J (ft · lbf)	407+ (300+)	31 (23)
Elongation, %	15.9	0.9
Case hardness, HRC	55	58

Note: Effective case depth, 0.64 mm (0.025 in.); 12.8 mm (0.505 in.) diameter tensile bars. Source: Ref 5

Table 8 Properties of Carbo-Austempered and carburized quenched and tempered (Q&T) 4150 steel

	Carbo-Austempered	Carburized Q&T
Tensile strength, MPa (ksi)	2033 (295)	1033 (150)
Unnotched impact energy, J (ft · lbf)	407+ (300+)	16 (12)
Elongation, %	10.7	0.7
Case hardness, HRC	56	56

Note: Effective case depth, 0.64 mm (0.025 in.); 12.8 mm (0.505 in.) diameter tensile bars. Source: Ref 5

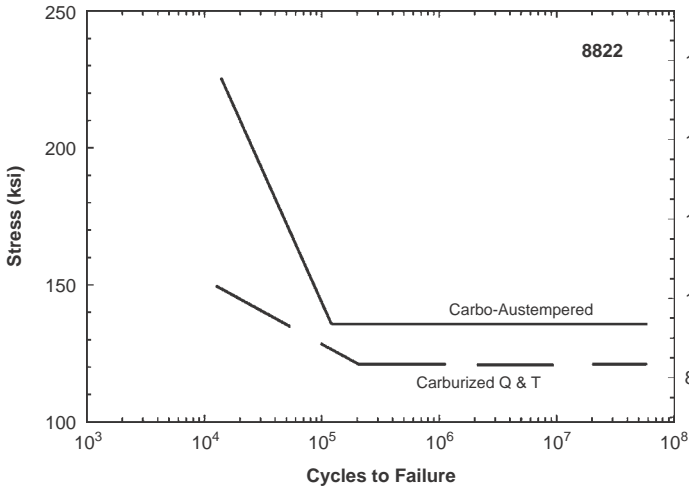


Fig. 11 Rotating-bending fatigue properties of Carbo-Austempered vs. conventionally carburized and hardened 8822 steel. Q&T, quenched and tempered. Source: Ref 5

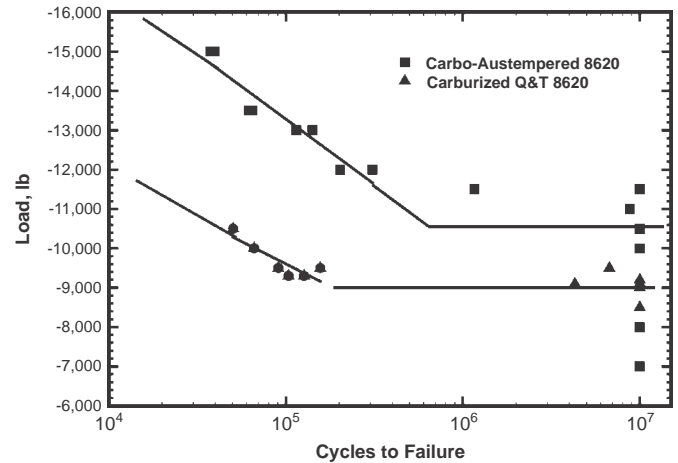


Fig. 12 Load vs. cycles to failure for Carbo-Austempered and carburized, quenched, and tempered 8620 steel gears. The estimated endurance limits are 10,500 and 9,000 lb, respectively. (Specimens at 10^7 cycles were runouts or did not fail.) Source: Ref 5

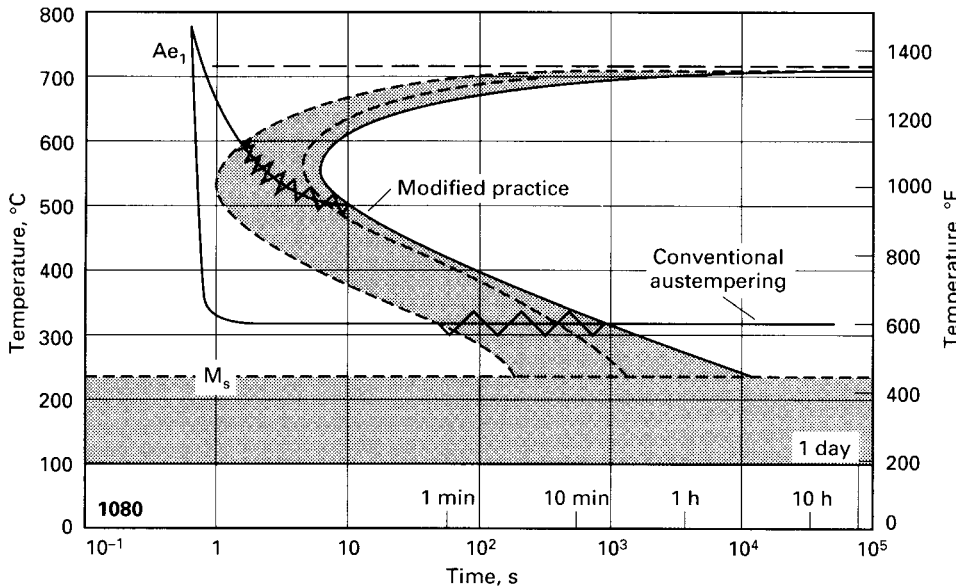


Fig. 13 Time-temperature-transformation diagram for 1080 steel showing difference between conventional and modified austempering. When applied to wire, the modification shown is known as patenting.

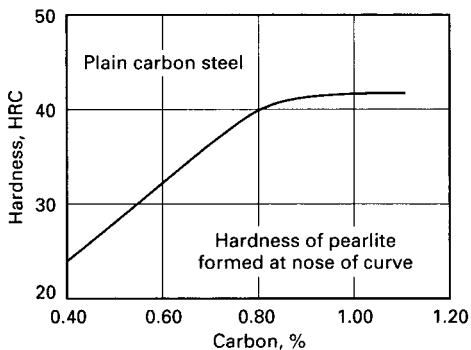


Fig. 14 Effect of carbon content in plain carbon steel on the hardness of fine pearlite formed when the quenching curve intersects the nose of the time-temperature diagram for isothermal transformation



Fig. 15 A 9.5 mm ($\frac{3}{8}$ in.) diameter 8640 steel unthreaded bolt austempered to 44 HRC and bent 90° without cracking exhibits the superiority of a bainitic microstructure at higher (>40 HRC) hardnesses. Courtesy of Applied Process Inc.

Example 3: Normalizing before Austenitizing and Austempering to Achieve Carbide Solution and Adequate Ductility. Threaded fasteners made of 1060 steel, designed to be embedded in concrete by explosive discharge, exhibited insufficient ductility after austempering. These parts were hardened by being heated to 845 °C (1550 °F) and quenched in a salt bath at 290 °C (550 °F) for 30 min. The lack of ductility is attributed to insufficient carbide solution. Parts with acceptable ductility after austempering are obtained by normalizing before final austenitizing and austempering.

Example 4: Austempering Procedure for a Steel with Borderline Hardenability. Lawn mower blades, approximately 3 mm ($\frac{1}{8}$ in.) thick and made of 0.50 to 0.60% C steel, exhibited low hardness after austempering. Low hardenability due to lower-than-normal manganese content proved to be the cause. The manganese content desired for this application should be near the high side of the allowable range (0.60 to 0.90%), but the steel for these blades contained less than 0.50% Mn. The problem was solved by first quenching the blades in a lower-temperature bath (just above M_s) for $\frac{1}{2}$ min and then transferring them to the normal austempering bath at 315 °C (600 °F) and holding for $\frac{1}{2}$ h. This technique has been successfully applied to many carbon steels that were borderline for austempering because of low hardenability in relation to the section being quenched.

Example 5: Prehardening Treatment to Dissolve the Abnormally Large Carbides Produced during Spheroidization. Chain saw components made of low-alloy Cr-Ni-V steel containing 0.65 to 0.75% C exhibited excessive brittleness in a torque test. The parts had been austenitized in a shaker hearth furnace at 830 °C (1525 °F) and quenched in an agitated salt bath at 290 °C (550 °F). Examination

disclosed excessive martensite and undissolved carbides in the microstructure. Overspheroidization prior to hardening was determined to be the cause of brittleness. This resulted in the formation of abnormally large carbides that were not dissolved during the 11 min furnace cycle, thus lowering the carbon content of the matrix and raising the M_s temperature. This caused partial transformation to martensite instead of 100% lower bainite. The problem was solved by prehardening and tempering prior to the regular heat treating cycle.

Example 6: Carburizing and Austempering Heavy-Duty Parking Pawls. Heavy-duty trucks with automatic transmissions must pass a test wherein a fully loaded vehicle is rolled down a 7% grade at 2 mph and is shifted into park. The parking pawl must engage, stop the vehicle, and sustain no damage. Traditional carburized and hardened pawls fracture the engaging tooth. Parts carburized and austempered to 55 to 60 HRC are able to sustain the impact repeatedly without failure and have been adopted by industry using investment cast, forged, and fine-blanked steel pawls that are subsequently carburized and austempered.

Example 7: Class 14 Bainitic Fasteners.

As systems become smaller, designers seek to use the smallest-diameter fasteners available. However, using quenched and tempered bolts over 39 HRC exposes the manufacturer to the chance of environmental failure, so class 8 bolts (800 MPa, or 116 ksi, tensile strength) are the general standard. Bainite is not susceptible to environmental embrittlement to maximum

bainitic hardness. Class 14.8 bainitic fasteners at 45 HRC (1400 MPa, or 203 ksi, tensile strength) can allow designers to safely use smaller-diameter fasteners. A special note: These high-hardness bainitic fasteners exhibit significant ductility. Figure 15 shows a 9.5 mm ($\frac{3}{8}$ in.) diameter unthreaded 8640 bolt austempered to 44 HRC and bent 90° without cracking.

REFERENCES

1. M.A. Grossman and E.C. Bain, Chapt. 6, Austempering and Ausforming, *Principles of Heat Treatment*, American Society for Metals, 1935/1964
2. J.M. Tartaglia, K.A. Lazzari, G.P. Hui, and K.L. Hayrynen, A Comparison of Mechanical Properties and Hydrogen Resistance of Austempered vs. Quenched and Tempered 4340 Steel, *Metall. Trans. A*, Vol 39, March 2008, p 559–576
3. W.R. Keough, Equipment, Process and Properties of Modern Day Austempering, *Proceedings of the International Heat Treating Conference: Equipment and Processes*, ASM International, April 1994
4. H. Palmero and R. Flinn, “Dilation due to Austenite Transformation as a Function of Temperature and Composition,” University of Michigan, 1973
5. K.L. Hayrynen, K.R. Brandenburg, and J.R. Keough, “Carbo-Austempering, A New Wrinkle?” Paper 2001-01-1478, Society of Automotive Engineers, 2002

SELECTED REFERENCES

- H.K.D.H. Bhadeshia, *Solid to Solid Phase Transformations in Inorganic Materials*, Vol 1, TMS, Warrendale, PA, 2005, p 469–484
- K.R. Brandenburg, K.L. Hayrynen, and J.R. Keough, Austempered Gears and Shafts—Tough Solutions, *Gear Technol.*, March/April 2001, p 42–50
- P.J. Cote, R. Farrara, T. Hickey, and S.K. Pan, “Isothermal Bainite Processing of ASTM A723 Components,” U.S. ARDEC Report ARCCB-TR-93035
- J.R. Keough, “Austempering—A Small, Niche Heat Treatment with Large Powertrain Implications,” American Gear Manufacturers Association Meeting, 2004
- J.R. Keough and V. Popovski, “Large Austempered Parts—Monster Opportunities,” American Foundry Society Congress, 2012
- W.R. Keough, Carbo-Austempering, *Proceedings of the Second International Conference on Carburizing and Nitriding with Atmospheres*, Dec 1995, p 135–142
- J. Lefevre and K.L. Hayrynen, Austempered Materials for Powertrain Applications, *Proceedings of the 26th ASM International Heat Treating Society*, 2011
- S.-Z. Li, Problems Related to Salt Bath Quenching, *Jinshu Rechuli (Heat Treat. Met.)*, No. 5, Qishuyan Institute of Locomotive and Railway-Car Technology, 1991, p 59–61
- *Mechanical Hydrogen Embrittlement Methods for Evaluation and Control of Fasteners*, ASTM International, West Conshohocken, PA, 2001, p 1–25

Martempering of Steels*

Revised by
Lauralice de C.F. Canale, University of São Paulo (Brazil)
Jan Vatauvuk, Presbyterian University Mackenzie (Brazil)
George E. Totten, Portland State University

Introduction

Martempering is a quench hardening process also known as interrupted quenching. According to Ref 1, this process was discovered by D. Lewis in 1929. The martempering process is used to avoid quenching cracks and distortion. However, because of the limited understanding of the use of transformation diagrams, martempering was not used at that time.

Ten years later, the process was better understood, and in 1943, Shepherd introduced it industrially and named it martempering (Ref 2). In this work, Shepherd showed that the heat stress due to the mass varies with the type of quench, resulting in a relative difference in temperature between the surface and the center of the workpiece. To avoid cracking, Shepherd suggested that the quenching medium should be selected to produce a minimum difference in temperature between the surface (outside) and the center (inside) at the M_s temperature. Following this thought process, he wrote "...if the cooling rate obtained in the salt bath (held at temperature just above the M_s point) would be such as to exceed the critical cooling rate, the piece could be quenched entirely in this bath, equalized in temperature, removed and allowed to cool in air. ..."

To address the different M_s temperatures that vary with different steels, he suggested a modification of the temperature of the salt bath used for the particular martempering process.

Shepherd developed some experiments to determine the time required to equalize the temperature for rounds of 1, 2, and 3 in. (25, 50, and 75 mm). He used a salt bath at 200, 260, and 315 °C (400, 500, and 600 °F). His results are summarized in Fig. 1.

Based on those results, Shepherd performed several quenching cycles with different steels. He found for NE 8442 (0.40% C, 1.43% Mn, 0.22% Si, 0.23% Ni, 0.29% Cr, and 0.32% Mo) that the relief of stress may increase the mechanical properties, as shown in Table 1.

It was mentioned that the more impressive result was related to crack development. Approximately 50% of the pieces quenched in oil cracked longitudinally. The same hardness with no tendency

toward cracks was developed from the same quenching temperature, 843 °C (1550 °F), by quenching in salt at 200 °C (400 °F), removal after 5 min, and then cooling in air.

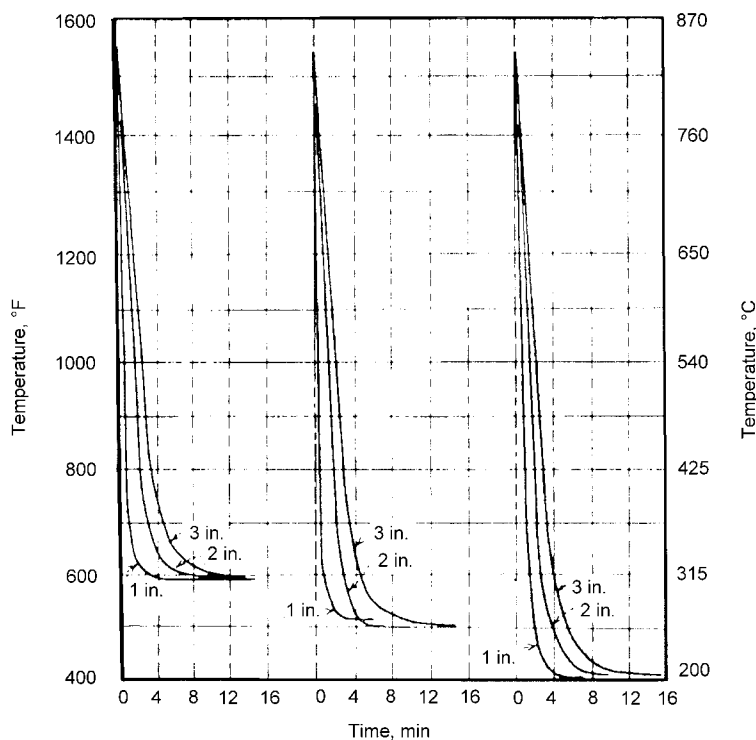


Fig. 1 Time required to equalize rounds from 843 °C (1550 °F) to the bath temperature. Adapted from Ref 2

Table 1 Mechanical properties of a 19 mm (¾ in.) round of NE8442 steel

Treatment	Yield point		Tensile strength		Elongation in 50 mm (2 in.), %	Reduction, %	Brinell hardness
	MPa	ksi	MPa	ksi			
Quench in soluble oil at 27 °C (80 °F)	1010	146	1080	156.6	19	57.3	321
Quench in salt at 200 °C (400 °F), hold 5 min, and air cool	1035	150	1124	163	18	56.4	321

* Revised from H. Webster and W.J. Laird, Martempering of Steel, Heat Treating, Vol 4, ASM Handbook, ASM International, 1991, p 137-151

Harvey (Ref 3) subsequently published "Development, Principles and Applications of Interrupted Quench Hardness," ascribing the earliest attempts at interrupted quench hardening to the year 1879, when Richard Akerman used a lead bath followed by air cooling of an austenitized steel. However, he recognized D. Lewis and O.C. Trautman as pioneers as well. Interestingly, Shepherd's work was not cited.

Harvey originally designated martempering as step quenching, and it was applied to the hardening of hacksaw blades, resulting in straighter and tougher blades relative to blades that were conventionally hardened. A U.S. patent assigned to R.F. Harvey was obtained in 1940. Figure 2 (Ref 3) illustrates three heat treatments: conventional hardening, austempering, and step quenching.

The interrupted quench hardening treatments attempt to equalize the temperature within the workpiece (quenched into a molten salt bath) before subsequent hardening proceeds during slow cooling in air. Austempering results in a bainitic transformation that, in the case of hacksaw blades, provided hardnesses of approximately 50 to 55 HRC, which were lower than those obtained with step quenching. However, Harvey observed that relative to conventional hardening, martempering offered important advantages, including less distortion, less internal stress, less cracking, greater toughness, greater fatigue life, savings in man hours through elimination of unnecessary operations such as straightening or grinding, less rejects, and higher hardness and wear life; for case-hardened work, less distortion was obtained. Conventional hardening necessitated removal of the hardest part of the case due to grinding operations (Ref 3). These conclusions were made based on the hacksaw blades work, but other applications were subsequently studied as well.

Martempering is not related to austempering, because martempering is not an isothermal process. The term *martempering* is somewhat misleading and is better described as *marquenching*, because martempering implies a tempering operation, which actually does not occur. However, the term *martempering* is used more commonly than *marquenching*. Typically, the microstructure obtained after martempering is a brittle, untempered martensite. Therefore, martempered parts should be subsequently tempered in the same manner as those conventionally quenched in oil, water, or other quenching media (Ref 4).

The time-temperature relationship of martempering and tempering are compared with those of conventional quenching and tempering in Fig. 3(a) and (b). Martempering of steel (and of cast iron) consists of:

- Quenching from the austenitizing temperature into hot oil, molten salt, molten metal, fluidized particle bed, or in a vacuum furnace at a temperature usually above the martensite start (M_s) temperature
- Holding in the quenching medium until the temperature throughout the steel is uniform

- Subsequently cooling (usually in air) at a moderate rate to minimize the formation of large temperature gradients between the surface and the center of the section

Formation of martensite occurs fairly uniformly throughout the workpiece during cooling to room temperature, thereby avoiding formation of excessive amounts of residual

stress. Straightening or forming is also easily accomplished upon removal from the martempering bath while the part is still hot. The piece will hold its shape upon subsequent cooling by fixturing or during air cooling after removal from the forming die. Martempering can be accomplished in a variety of baths, including hot oil, molten salt, molten metal, or in a fluidized bed. In addition, martempering in a

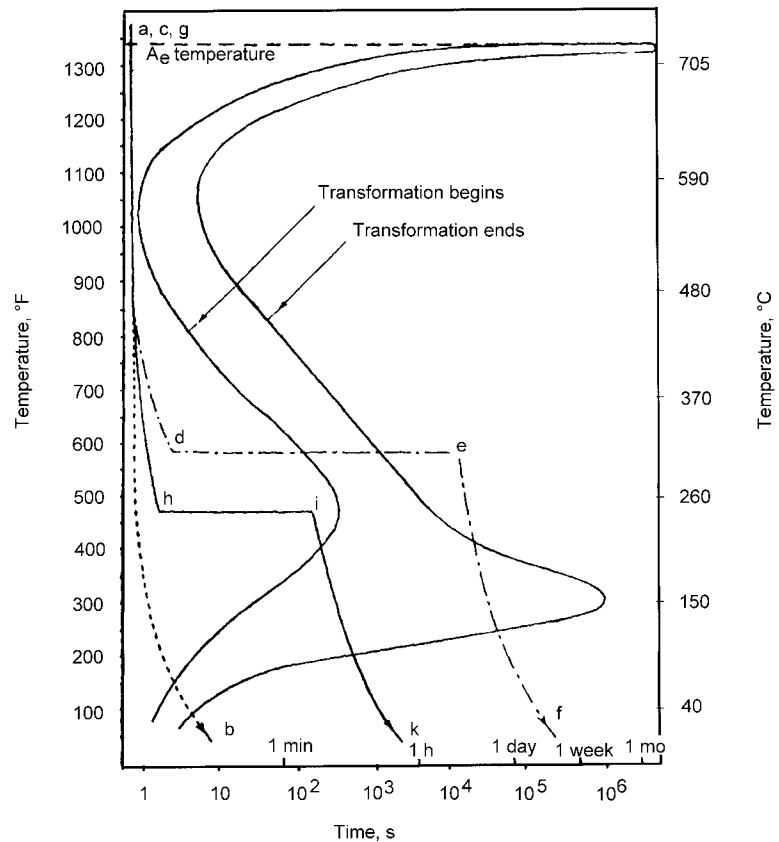


Fig. 2 Time-temperature transformation diagram showing difference between conventional hardening, austempering, and martempering (step quenching). Adapted from Ref 3

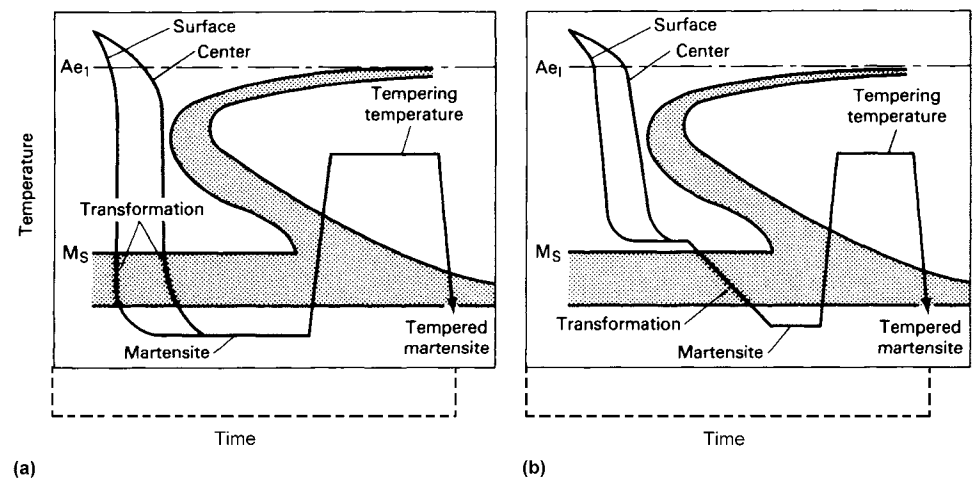


Fig. 3 Time-temperature transformation diagrams with superimposed cooling curves showing quenching and tempering. (a) Conventional. (b) Martempering. Source: Ref 5

vacuum furnace is increasingly common. Martempered parts are tempered in the same manner as conventionally quenched parts. The elapsed time before tempering is not as critical, because the stress is greatly reduced.

Modified martempering differs from standard martempering only in that the temperature of the quenching bath is below the M_s point (Fig. 4). The lower temperature increases the severity of quenching. This is important for steels of lower hardenability that require faster cooling in order to achieve a sufficient depth of hardening or when the M_s is high and bainite formation is detrimental to the finished part. Therefore, modified martempering is applicable for a greater range of steel compositions than is the standard process.

Advantages

The advantage of martempering lies in the reduced thermal gradient between surface and center as the part is quenched to the isothermal temperature and then is air cooled to room temperature. Residual stresses developed during martempering are lower than those developed during conventional quenching because the greatest thermal variations occur while the steel is in the relatively plastic austenitic condition and because final transformation and thermal changes occur throughout the part at approximately the same time. Martempering also reduces or eliminates susceptibility to cracking.

Another advantage of martempering in molten salt is the control of surface carburizing or decarburizing. When the austenitizing bath is neutral salt and is controlled by the addition of methane gas or proprietary rectifiers to maintain its neutrality, parts are protected with a residual coating of neutral salt until immersion into the marquenching bath.

Although martempering is used primarily to minimize distortion, eliminate cracking, and minimize residual stresses, it also greatly reduces the problems of pollution and fire

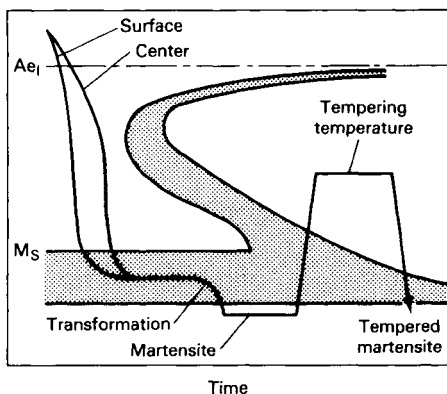


Fig. 4 Time-temperature transformation diagrams with superimposed cooling curves showing modified martempering and tempering. Source: Ref 5

hazard as long as nitrate-nitrite salts are used rather than martempering oils. This is especially true where nitrate-nitrite salts are recovered from wash waters with systems that provide essentially no discharge of salts into drains. Any steel part or grade of steel responding to oil quenching can be martempered to provide similar physical properties. The quenching severity of molten salt is greatly enhanced by agitation and water additions to the nitrate-salt bath. Both techniques are particularly beneficial in heat treating of carbon steels that have limited hardenability. Table 2 compares the properties (impact test) of different steels that were martempered and tempered with those obtained by conventional quenching and tempering.

Data regarding improved impact energy due to martempering are normally related to high-carbon steels (Ref 10). Table 2 compares the impact toughness of carbon and cold work tool steels AISI 4140, AISI 1095, and AISI O1, quenched/tempered and martempered. These results show that impact toughness increases due to martempering for high-carbon steels (AISI 1095 and AISI O1). The martempering process effect on impact toughness is negligible for the lower-hardness AISI 4140 carbon steel tempering condition. Increasing the tempering temperature reduces hardness and enhances plastic deformation in the impact test samples. In general, the mechanical energy to induce plastic deformation is much higher than the work to induce elastic deformation. The residual-stress effect is more sensitive when the resilience contribution is higher (lower plastic deformation during impact loading). Lowering the hardness for the 4140 steel (20 to 37 HRC) enhances the plastic deformation contribution to the absorbed mechanical energy, making negligible the as-quenched residual-stress difference between the quenching/tempering and martempering processes. In the same way, higher tempering temperatures prompt greater residual-stress reduction.

In many instances, martempering eliminates the need for quenching fixtures that would be required for minimizing distortion during conventional quenching and thus reduces the cost of tooling and handling. However, changing from conventional quenching to martempering may require that dimensional variations of individual parts be studied before preheat treatment dimensions are established (Ref 5).

Another virtue is that, in some cases, it is possible to perform a straightening operation

before the part has hardened. This is done when the part is just above the M_s temperature (Fig. 3b) in order to equalize the temperature (between center and surface), but it has not yet transformed to martensite. At this time, a quick straightening operation can be used to minimize the total distortion, after which the part is placed back into the quenching medium and allowed to transform (Ref 4).

Martempering Media

Although hot oil is used for modified martempering at 175 °C (350 °F) and lower, molten nitrate-nitrite salts (with water addition and agitation) are effective at temperatures as low as 175 °C (350 °F). Because of their higher heat-transfer coefficients, approximately 4.5 to 16.5 kW/m² · K (800 to 2900 Btu/h · ft² · °F) (Ref 11), molten salts offer some metallurgical and operational advantages. In salt quenching, the heat transfer mainly takes place by convection. Boiling does not occur with molten salts. Heat transfer occurs by convection. Oil-cooling characteristics are quite different from those of a molten salt martempering bath (Ref 12).

Both molten salt and hot oil are widely used for martempering. Several factors must be considered when choosing between salt and hot oil. Operating temperature is the most common deciding factor. Oils are widely used for martempering at up to 205 °C (400 °F) and sometimes at temperatures as high as 230 °C (450 °F). Molten salt is used for martempering in the range of 160 to 400 °C (320 to 750 °F).

Composition and Cooling Power of Salt. A salt commonly used for martempering is composed of 50 to 60% potassium nitrate, 37 to 50% sodium nitrite, and 0 to 10% sodium nitrate. It melts at approximately 140 °C (280 °F) and may be used within a working range of 165 to 540 °C (325 to 1000 °F). Higher-melting-point (less costly) salts can be used for higher operating temperatures. These salts are comprised of 40 to 50% potassium nitrate, 0 to 30% sodium nitrite, and 20 to 60% sodium nitrate.

The cooling power of agitated salt at 205 °C (400 °F) is approximately the same as that of agitated oil in conventional oil quenching. Addition of water to salt increases its cooling power, as indicated by the cooling curves for 1045 steel in Fig. 5 and by the hardness values in Fig. 6. The range of hardnesses measured is from the end of the bar (surface = the highest

Table 2 Literature impact data

Steel	Hardness	Quenched and tempered (impact energy)	Martempered (impact energy)	Reference
AISI 4140	20–25	111 J	126 J	Ref 6
AISI 4140	36–37	57 J	59 J	Ref 6
AISI 4140	46–47	9.6 J	18.5 J	Ref 6
AISI 1095	52.5	19 J	33 J	Ref 7
AISI O1	51.0	74 kJ/m ² (a)	114.5 kJ/m ² (a)	Ref 8, 9

(a) Reduced-size impact samples

hardness) to 1.5 mm (0.06 in.) below the surface (the lower hardness of the range shown). The cooling power of salt is compared with the cooling power of water and of three types of oil in Fig. 6.

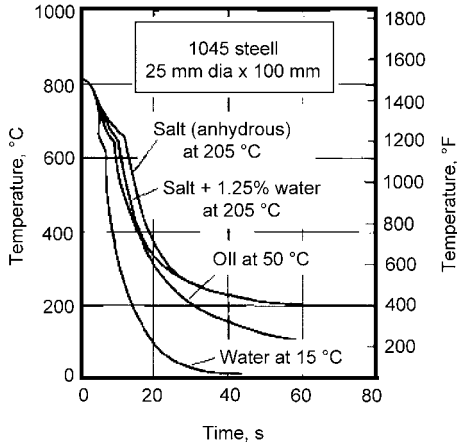


Fig. 5 Cooling curves for 1045 steel cylinders quenched in salt, water, and oil. Thermocouples located in the geometric center. Source: Ref 5

Advantages of salt in comparison with oil for martempering are as follows:

- The viscosity of salt changes only slightly over a wide temperature range.
- Salt retains chemical stability, so that replenishment is usually required only to replace dragout loss. This is not always the case, however. In an installation for high-volume martempering of cylinder liners, for instance, breakdown of the salt did occur, forming a carbonate. This occurred on quenching from an endothermic atmosphere into an open-top salt quench bath at 245 °C (475 °F). The same operation conducted with a nitrogen atmosphere in the heating furnace does not produce such breakdown.
- Salt has a wide operating temperature range.
- Salt is easily washed from the work with plain water.
- Less time is required for workpieces to attain temperature equalization in salt.
- No unusual disposal problems attend the rinsing operation.
- Salt is relatively easy to handle in powder form and easy to clean up if spilled; however, it is necessary to keep salts separated.

Disadvantages of salt in comparison with oil include the following:

- The minimum operating temperature of salt is 160 °C (320 °F).
- Quenching from cyanide-based carburizing salts is hazardous because of possible explosion.
- Explosion and splatter of high-temperature salt can occur if wet or oily parts are immersed.
- Potentially explosive reactions also occur with sooty atmospheres in atmosphere furnaces connected to martempering salt quenches.
- Quench salt can be contaminated by high-temperature neutral salt used for heating. Sludging operations are required to maintain quenching severity.
- The difference in viscosity between martempering oil and salt martempering baths causes differences in dragout at martempering temperature. Greater losses can be expected with salt martempering baths than with oil (Ref 12).

Fluidized Beds. Although fluidized beds are somewhat limited, they have the advantage of equal heat transfer throughout the entire

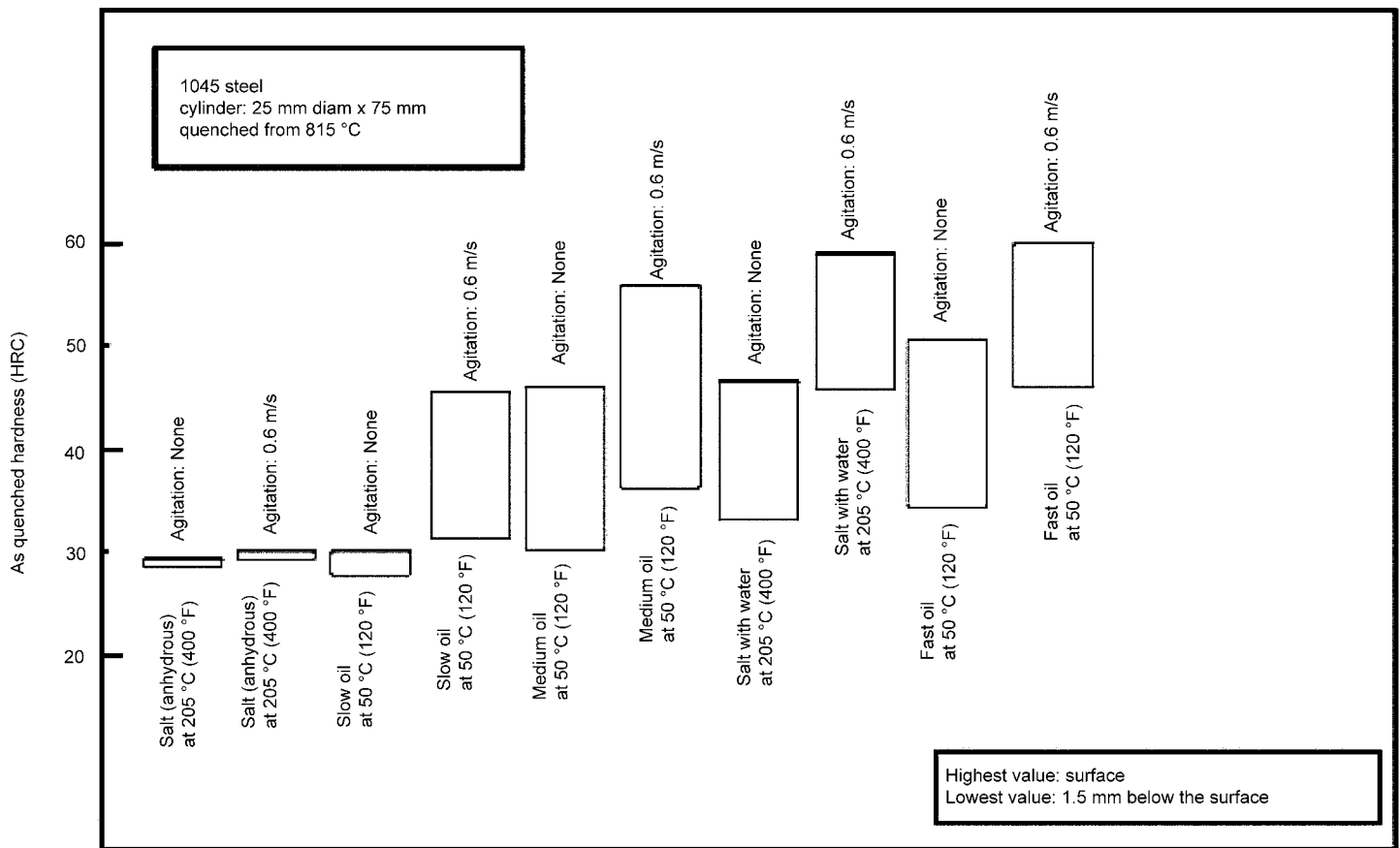


Fig. 6 Effects of quenchant and agitation on hardness of 1045 steel. Adapted from Ref 5

temperature range of quenching. This leads to a quench rate that is reproducible, does not degrade with time, and can be adjusted within wide limits. In addition, fluidized beds do not have the environmental drawbacks of oils or salt quenchant.

Oils for Martempering. Martempering or hot quenching oils are used at temperatures between 95 and 230 °C (205 and 450 °F). Non-accelerated and accelerated martempering oils are available (Ref 13). Physical properties of two oils commonly used for martempering are listed in Table 3. Such oils are compounded especially for martempering and, in comparison with conventional quenching oils, offer higher rates of cooling during the initial stage of quenching.

Most martempering oils are formulated using highly refined paraffinic base stocks, giving a good stability while operating at higher temperatures. Additives to provide oxidation resistance are incorporated in the formulation. Desired quenching speed is also obtained with the use of additives.

Leaner-alloyed parts usually require a lower viscosity martempering oil with speed improvers added. Higher-alloyed parts require higher viscosity and also speed improvers, which

permits higher oil temperatures to control distortion. Many times, the higher-viscosity oils with additives will give quenching speeds approaching that of medium-to-fast quenching oils, while thinner oils promote elimination of the vapor phase, as shown in Fig. 7 (Ref 14).

The higher operation temperature, the contact with hot parts, and the forced heating of colder oil during heatup all contribute to the martempering oil degradation. When heating up the martempering oil from ambient temperatures, low-velocity burners or resistant heaters with a maximum rating of 0.016 W/mm² should be used to keep degradation of oil to a minimum (Ref 14). Quenching oil requires special handling when used in the temperature range from 95 to 230 °C (200 to 450 °F). To prolong its life, the oil must be maintained under a protective atmosphere (reducing or neutral). Deterioration is accelerated when oil is exposed to air at elevated temperatures. For example, for every 10 °C above 60 °C (every 18 °F above 140 °F), the rate of oxidation is approximately doubled. This causes formation of acid and sludge, which may affect both the hardness and color of workpieces. Figure 8 shows the life of a hot oil developed to resist oxidation compared with the original formulation (Ref 15).

Table 3 Physical properties of two oils used for martempering of steel

Property	Value, for oil with operating temperature of	
	95 to 150 °C (200 to 300 °F)(a)	150 to 230 °C (300 to 450 °F)
Flash point (min), °C (°F)	210 (410)	275 (525)
Fire point (min), °C (°F)	245 (470)	310 (595)
Viscosity, SUS, at:		
38 °C (100 °F)	235–575	...
100 °C (210 °F)	50.5–51	118–122
150 °C (300 °F)	36.5–37.5	51–52
175 °C (350 °F)	...	42–43
205 °C (400 °F)	...	38–39
230 °C (450 °F)	...	35–36
Viscosity index (min)	95	95
Acid number	0.00	0.00
Fatty-oil content	None	None
Carbon residue	0.05	0.45
Color	Optional	Optional

(a) Temperature range for modified martempering

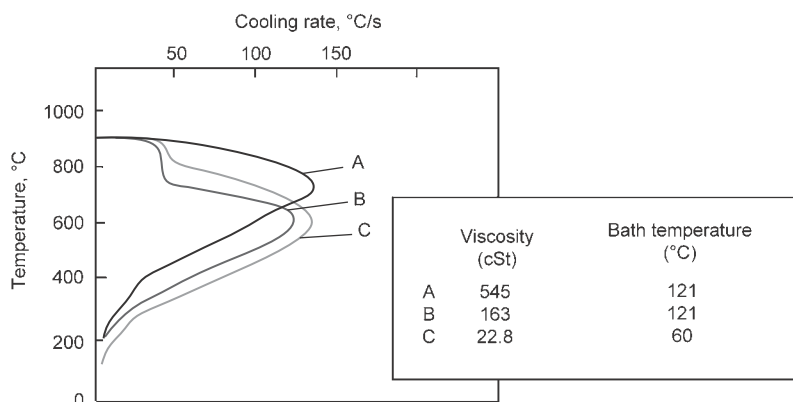


Fig. 7 Cooling-rate curves of oils from different viscosities. Adapted from Ref 14

Example 1: Martempering of Carburized Transmission Components in Oil. A manufacturer of transmission components and axles martempers carburized parts at a rate of 115 kg/h (250 lb/h) in a 7550 L (2000 gal) oil tank that is completely covered by a vestibule hood and that is located directly beneath the discharge door of the continuous carburizing furnace. The vestibule contains a protective atmosphere consisting of carburizing gases that emanate from the furnace. The vestibule is equipped with an elevator that lowers the tray of parts into the martempering oil.

The ambient temperature in the vestibule immediately above the oil is 89 to 92 °C (193 to 197 °F) when the furnace discharge door is closed. The temperature of the oil is controlled at 150 °C (300 °F). However, during high-production quenching, the temperature of the martempering oil will rise to as high as 165 °C (325 °F). The atmosphere in the vestibule protects the carburized parts and the martempering oil from oxidation. To avoid possible oil fires, the furnace discharge door is closed before the workload is lowered into the martempering oil.

The martempering oil in this tank has not been replaced in several years of continuous operation (24 h per day, 7 days per week); makeup oil is added to the tank at a rate of approximately 755 L (200 gal) per month.

Bypass or continuous types of filter units with suitable filtering media (clay, cellulose cartridge, or waste cloth) or centrifugal filtering help prolong oil life and maintain clean work. Filtering units are effective and relatively inexpensive. Oils should be circulated at a rate no lower than 0.9 m/s (180 ft/min) to break up excessive vapor that is formed during quenching.

Continuous operation of oils above 205 °C (400 °F) can cause excessive breakdown of the oils unless the correct oil is used for each specific application. Once every one to six months, the oil should be subjected to complete physical and chemical testing to determine its condition. Such testing usually includes determinations of flash point, viscosity, degree of oxidation, quenching effect, contamination, and cooling power.

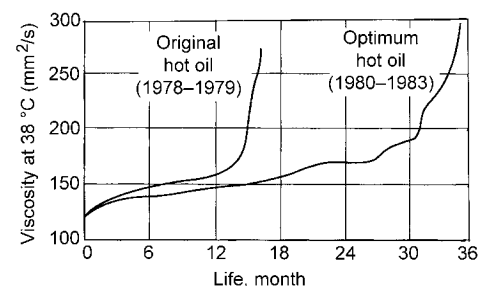


Fig. 8 Life of an optimal hot oil installed in 1980 compared with the originally-used product, assessed on the basis of viscosity increase in a laboratory test. Adapted from Ref 15

Advantages of oil in comparison with salt are as follows:

- Oil can be used at lower temperatures.
- Oil is easier to handle at room temperature.
- Less dragout loss occurs with oil.
- Oil is compatible with all austenitizing salts.

Disadvantages of oil include the following:

- Oil is limited to a maximum operating temperature of 230 °C (450 °F).
- Oil deteriorates with use, therefore requiring closer control.
- When martempered in oil, workpieces require more time to attain temperature equalization.
- Oil, whether hot or cold, is a fire hazard.
- Soap or an emulsifier is necessary to wash off the oil. Washers must be drained and refilled periodically. Oily wastes create disposal problems.

Safety Precautions

In operating a martempering installation (salt or oil), the precautions appropriate for operating any other hot liquid bath are applicable. The following operator-safety precautions are recommended:

- Operators of equipment should be thoroughly familiar with equipment manufacturer's instructions and with company safety recommendations before attempting to operate or service the equipment.
- Operators should wear gloves, face shields, and protective clothing, as required. Safety equipment contaminated with oil or nitrate-nitrite salts should be discarded.
- Adequate first-aid materials should be available where salts are used, and personnel should be trained and available in treating alkali burns.

Nitrate-Nitrite Salts. Several precautions should be taken in operating nitrate-nitrite salt baths:

- All racks, fixtures, and cleaning tools must be thoroughly cleaned of salts (hot water preferred) and thoroughly dried before being reused; otherwise, the presence of salt could contaminate the austenitizing furnace, and residual water could cause spattering of molten salt.
- All salt bath furnaces should be labeled so that the proper salt is used. Cyanide-containing salts should not be combined with nitrate-nitrite salts because such mixtures result in explosive reactions. Good housekeeping is essential to prevent accidents. Martempering salts must be stored in closed, well-marked containers. These salts are hygroscopic and will absorb water if exposed. Yellow, orange, or red coloring is

commonly used for identification of nitrate-nitrite salts. Cyanide-containing materials may be identified by white, blue, or gray. Color coding is not universally practiced but is strongly recommended. Everyone handling these materials should be familiarized with the explosion hazard of intermixing. For a discussion of attendant hazards and recommended practices, see the sections of this article entitled "Salt Contamination" and "Selection of Austenitizing Equipment."

- When water is added to a nitrate-nitrite salt to increase its quenching severity, the water should be trickled or atomized onto the surface of the bath and should never be introduced below the surface or under pressure. Otherwise, spattering or eruption can occur. Equipment manufacturers should be consulted as to recommended procedures and hardware.

- The salt bath should be equipped with a high-temperature limit controller to prevent the bath from exceeding 595 °C (1100 °F). At higher temperatures, nitrate salts decompose and may cause fire or explosion. Although nitrate-nitrite salts do not burn, they are oxidizing and will support combustion. Therefore, oxidizable materials should not be stored near the bath, and combustible materials should not be introduced into the bath unless designed for the purpose. In the event of a fire, a carbon dioxide extinguisher should be used. Sand is also effective in smothering floor fires. *To avoid explosive spread of the molten medium, water should never be used to extinguish a fire in or around a molten salt (or molten metal) bath.*
- Soot and carbonaceous materials should not be allowed to accumulate on the surface of the molten bath.
- Signs are provided by local fire departments for placing on the outside of buildings that house salt baths. These signs tell the fire department what materials are present and what means can be used to extinguish the fire.

Hot oil also requires safety precautions. Among the hazards that accompany its use are fire; overflow caused by the increase in the volume of the oil during heating; explosion, when no atmosphere cover is used over the quench tank; and contamination by water, which can result in fire.

Equipment normally used for protection against these hazards includes:

- Alarm system on temperature-control instrument. (Recommended maximum operating temperature is 55 °C, or 100 °F, below the flash point of the quenching oil.) Often, an additional system is added for maximum temperature alarm.
- An oil-level indicator
- If the oil is heated by gas-fired tubes, which are not recommended for heating martempering oils, a safety-control system to prevent firing when the air cooling system is off

- Electric heating elements should have a maximum heat flux density of 0.016 W · mm⁻² (10 W · in.⁻²).
- Expansion system to accommodate the change in volume that occurs when the oil is heated from room temperature to the operating temperature. A suitable system is a small tank equipped with an overflow return line from the main quench tank. The main tank is equipped with a small pump to return the oil from the expansion tank. The capacity of the pump is usually approximately 20 L/min (5 gal/min).
- A safety control to prevent oil from being heated unless it is agitated
- A carbon dioxide or foam system installed over the quench tank for fire protection
- A water-detection system, with automatic alarm, that monitors the oil for water content

Caution should be used in installing ventilating systems and any other system that could cause addition of water to the hot oil. When an atmosphere is used over the quenching medium, the general safety precautions outlined in the article "Gas Carburizing" in this Volume should be followed.

Although the most-used media for martempering are oil and salt, nowadays more and more martempering processes are being performed in vacuum furnaces, mainly for high-performance components (Ref 16). Some advantages are observed, offering a good potential to reduce distortion for high-strength steel and improving dimensional stability of the heat treated component.

In tool steels and high-speed steels that have a propensity to crack, distort, and change dimensions, martempering is especially useful, and a vacuum furnace is usually chosen for this operation. However, it was shown that another advantage is the compressive stress developed. Some current results were obtained by monitoring a big block test of hot-worked steel (AISI H13). The dimensions of the block were 310 by 305 by 300 mm (12.2 by 12.0 by 11.8 in.). Steel composition is provided in Table 4. Thermocouples were positioned according to Fig. 9(a) and (b). Tests were made according to American Automotive Industry/North American Die Casting Association specification.

The thermal cycles used are illustrated in Fig. 10. The difference between the cycles was in the cooling process. In one of the cycles, gas quenching at 900 kPa (9 bar) was used, and the cooling process stopped when the center achieved 60 °C (140 °F). The other used an isothermal cycle (martempering), beginning when

Table 4 Hot-worked steel chemical composition

C	Chemical composition, %				
	Si	Mo	Mn	Cr	V
0.39	1.00	1.25	0.35	5.10	0.90

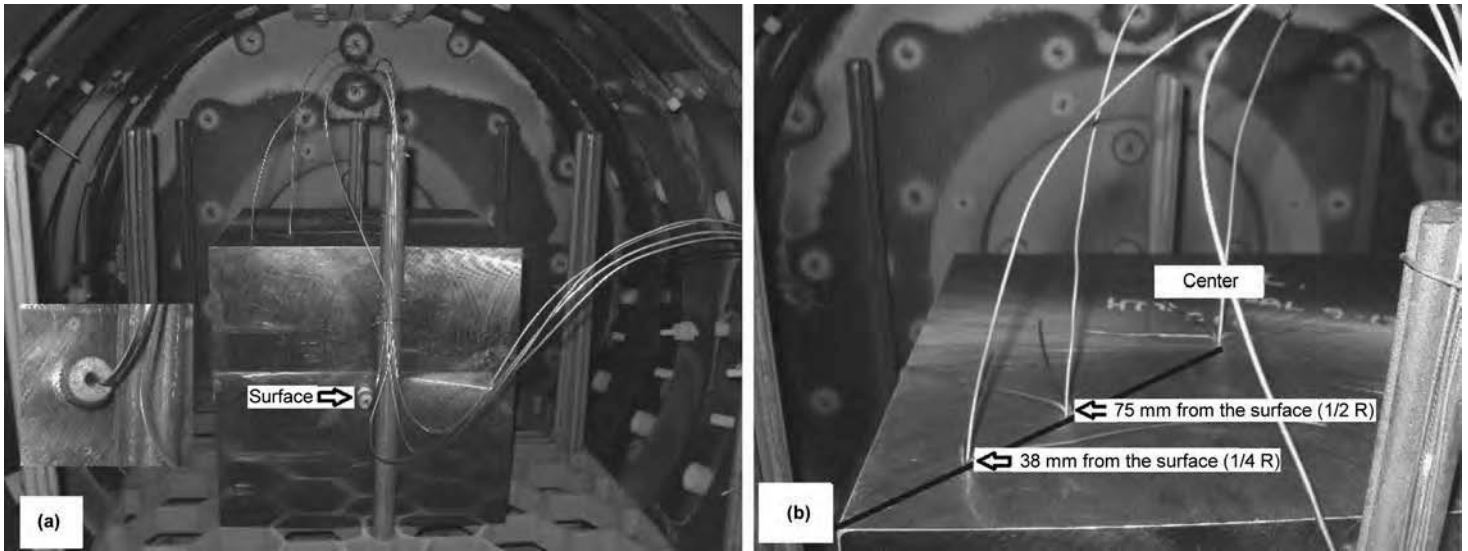


Fig. 9 Position of thermocouples for (a) quenching test and (b) martempering test. Courtesy of Isoflama Ind. Com., Indaiatuba, Brazil

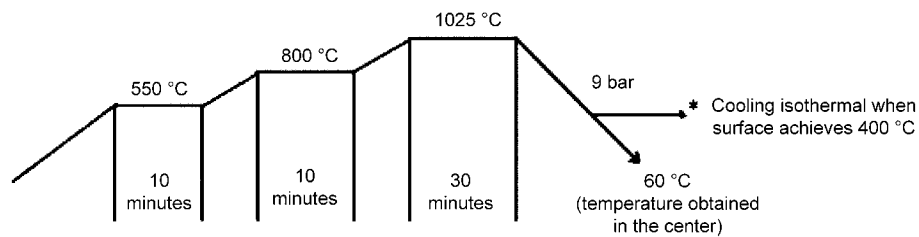


Fig. 10 Thermal cycles used in the experiment. Courtesy of Isoflama Ind. Com., Indaiatuba, Brazil

the surface temperature, during the quenching, achieved 400 °C (770 °F). Cooling curves obtained from the surface and the center for both conditions are shown in Fig. 11(a) and (b).

Temperature distribution is more homogeneous in the martempering cycle, contributing to less distortion and decreasing the potential for cracking. In this experiment, calculation of the residual stress was performed (Ref 17). Figure 12 shows results for the calculated residual stresses “X” distance from the center for both situations.

The martempering cycle produces higher surface compressive stresses compared with conventional gas quenching. Those results bring another advantage to using martempering as a heat treatment for tool steels. Fatigue properties are directly related to the value and nature of the surface residual stress. Higher compressive stresses usually promote longer fatigue life (Ref 17).

Similar tests (Ref 18) showed only the advantages of using a vacuum furnace to perform heat treatment of hot work steel once it is possible to also run martempering with success.

The martempering process is also applied in carburizing components using gas quenching systems. A modified martempering performed

in a vacuum furnace, called the StopGQ (ECM Technologies) quenching process, was presented (Ref 19). It demonstrated that besides less distortion, elimination of cracking, and better impact properties, improved fatigue resistance was also obtained. Tests were made with transmission gears. Studied situations included low-pressure vacuum gas carburizing (LPC), high-pressure gas quenching (HPGQ), and StopGQ. Gears were made from SAE 5130 steel. Chemical steel composition is provided in Table 5. After LPC, gears were submitted to three different heat treatment cycles, as shown in Fig. 13.

Because cycle 2 involves an isothermal step in the temperature range of 180 to 200 °C (355 to 390 °F) in the gas quenching process, an autotempering is obtained. A summary of the rotating-bending fatigue is shown in Fig. 14. These three conditions were analyzed: LPC + HPGQ (cycle 1), LPC + HPGQ + StopGQ (cycle 2), and LPC + HPGQ + tempering (cycle 3). The condition obtained from cycle 2, which is the modified martempering, gave an almost 30% better performance than that from cycle 3 and an approximately 10% better performance than that from cycle 1. In such tests, the hardness values (surface and center)

were similar for the three cycles unless a condition from cycle 3 presented a surface hardness that was a little lower than the others (Ref 19).

Suitability of Steels for Martempering

Alloy steels generally are more adaptable than carbon steels to martempering. In general, any steel that is normally quenched in oil can be martempered. Some carbon steels that are normally water quenched can be martempered at 205 °C (400 °F) in sections thinner than 5 mm ($3/16$ in.), using vigorous agitation of the martempering medium. In addition, thousands of gray cast iron parts are martempered on a routine basis.

The grades of steel that are commonly martempered to full hardness include 1090, 4130, 4140, 4150, 4340, 300M (4340M), 4640, 5140, 6150, 8630, 8640, 8740, 8745, SAE 1141, and SAE 52100. It is extremely difficult to use a martempering oil for quenching of low-hardenability steels such as 1045 (or lower-carbon steels in the 1000 series). Higher-carbon steels such as 1090 can be successfully martempered in oil due to lower M_s temperature and the additional time before upper-transformation products transform (Ref 14). Carburizing grades such as 3312, 4620, 5120, 8620, and 9310 also are commonly martempered after carburizing. Occasionally, higher-alloy steels such as type 410 stainless are martempered, but this is not a common practice.

Success in martempering is based on knowledge of the transformation characteristics (time-temperature transformation, or TTT, curves) of the steel being considered. The temperature range in which martensite forms is especially

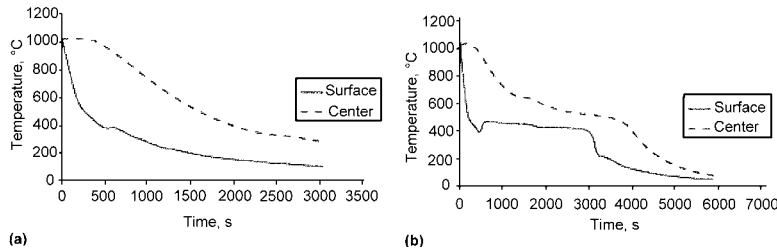


Fig. 11 Cooling curves obtained in the AISI H13 block. (a) Conventional gas quenching. (b) Martempering. Courtesy of Isoflama Ind. Com., Indaiatuba, Brazil

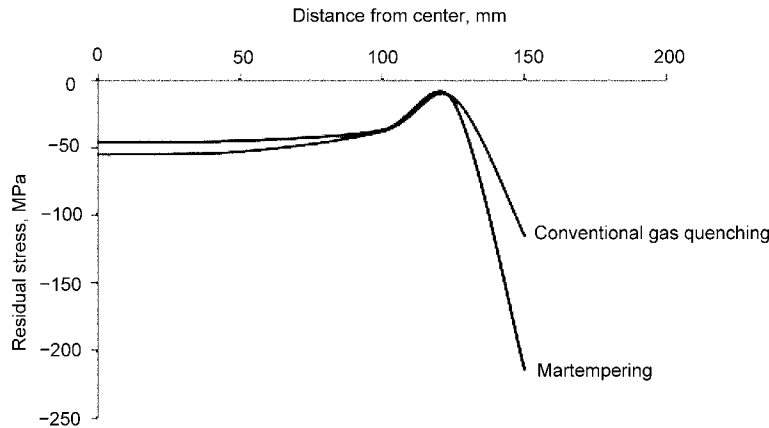


Fig. 12 Residual-stress results from conventional gas quenching and martempering in an AISI H13 block. Source: Ref 17

important. Figure 15 shows the martensite temperature ranges for 14 carbon and low-alloy steels. Two trends may be observed in these data: As carbon content increases, the martensite range widens and the martensite transformation temperature is lowered; and the martensite range of a triple-alloy (nickel-chromium-molybdenum) steel is usually lower than that of either a single-alloy or a double-alloy steel of similar carbon content.

Any steel that is to be martempered successfully must contain sufficient carbon or alloying additions to move the nose of the TTT curve to the right, thus permitting sufficient time for quenching of workpieces past the nose of the TTT curve.

The TTT diagrams for a hypoeutectoid steel (1034), which is discussed later, and a hypereutectoid steel (1090) are shown in Fig. 16. The diagram for 1090 steel is the simplest form of transformation diagram because no proeutectoid constituents (free ferrite or free carbide) are involved in the transformation at temperatures above that corresponding to the nose of the curve. The speed of transformation at the nose is related to the hardenability of the steel; when the nose of the TTT curve is far to the left on the diagram, the steel has lower hardenability; when the nose is to the right, the steel has higher hardenability. To achieve full hardening during quenching, the cooling curve of the steel must pass to the left of the curve farthest to the left on the diagram. In production, some loss in

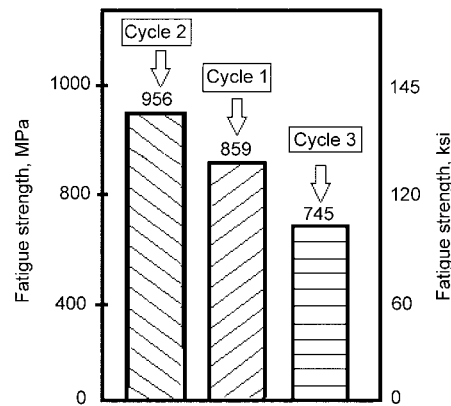


Fig. 14 Results from rotating-bending fatigue. With the increase in fatigue resistance, the torque of the existing transmission gears could also be increased. Adapted from Ref 19

as-quenched hardness is usually accepted in order to achieve minimum distortion.

A TTT diagram for a hypoeutectoid low-alloy steel (5140) suitable for martempering is shown in Fig. 17. The chromium in this steel causes the characteristic shape of the TTT curve near 540 °C (1000 °F).

The TTT diagram for an extremely high-hardenability steel (4340) is also shown in Fig. 18. The combined effect of nickel,

Table 5 SAE 5130 steel chemical composition

Chemical composition, %					
C	Si	Mn	Cr	P	S
0.28–0.33	0.15–0.35	0.7–0.9	0.8–1.1	0.035 max	0.04 max

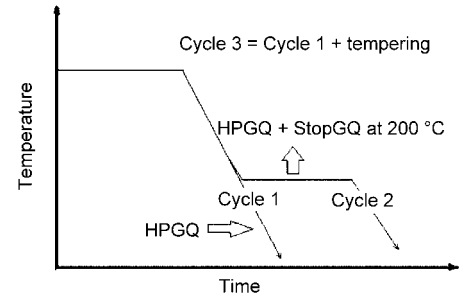


Fig. 13 Heat treating cycles 1, 2, and 3 applied in the carburized (low-pressure vacuum gas carburizing) gear load. HPGQ, high-pressure gas quenching. Adapted from Ref 19

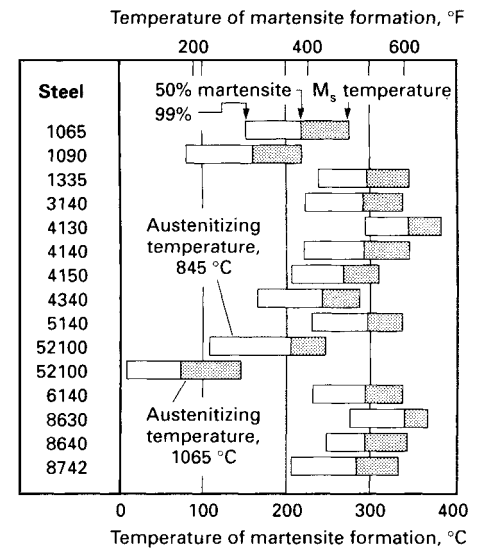


Fig. 15 Temperature ranges of martensite formation in 14 carbon and low-alloy steels

chromium, and molybdenum on hardenability is illustrated in this diagram. These elements cause a double nose on the TTT curve. The nose that occurs at approximately 480 °C (900 °F) is more significant in martempering than the one occurring near 650 °C (1200 °F). Steels having such high hardenability are easily martempered to fully martensitic structures.

Low-carbon and medium-carbon steels 1008 through 1040 are too low in hardenability to be successfully martempered, except when carburized. The TTT curve for the 1034 steel in Fig. 16 is characteristic of a steel that is unsuitable for martempering; except in sections only a few thousandths of an inch thick, it

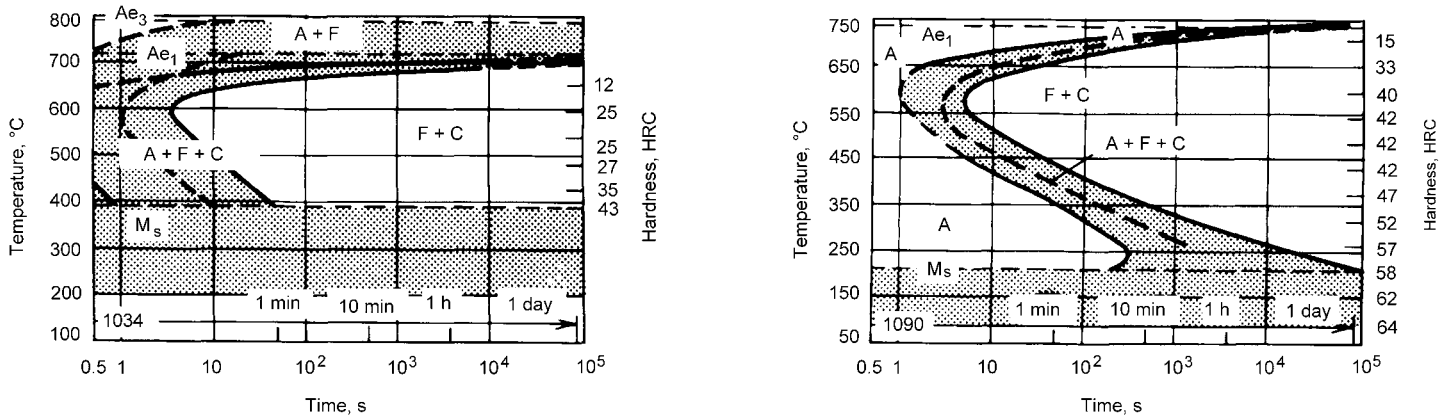


Fig. 16 Time-temperature transformation diagrams for 1034 and 1090 steels. The 1090 steel was austenitized at 885 °C (1625 °F) and had a grain size of 4 to 5.

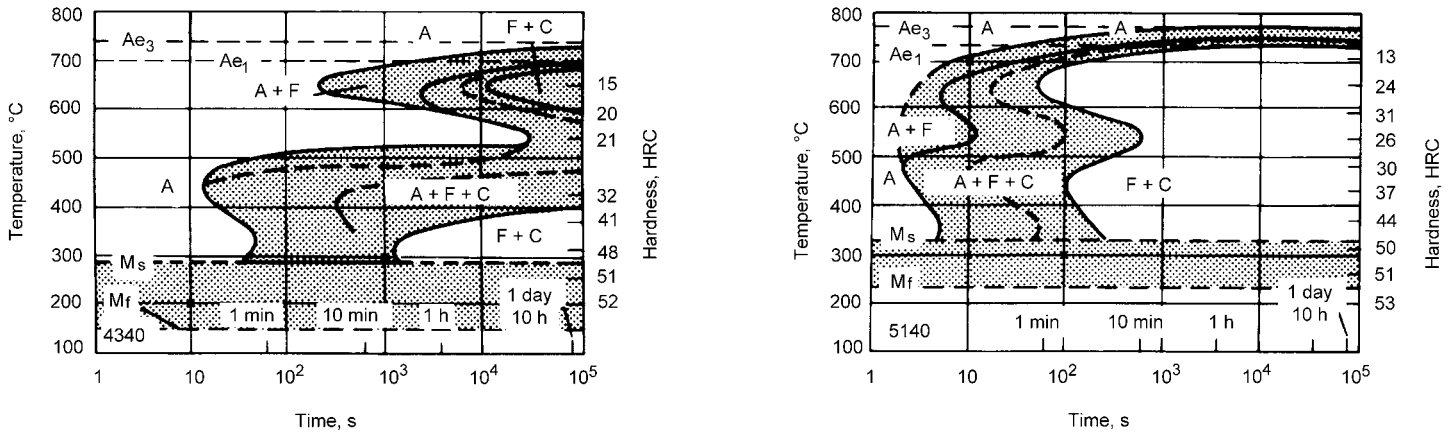


Fig. 17 Time-temperature transformation diagrams for 4340 and 5140 steels. The austenitizing temperature for both steels was 845 °C (1550 °F); grain size was 7 to 8 for 4340 and 6 to 7 for 5140.

would be impossible to quench the steel in hot salt or oil without encountering upper-transformation products.

Borderline Grades. Some carbon steels higher in manganese content, such as 1041 and 1141, can be successfully martempered in thin sections. Low-alloy steels that have limited applications for successful martempering are listed (the lower-carbon grades are carburized before martempering): 1330 to 1345, 4012 to 4042, 4118 to 4137, 4422 and 4427, 4520, 5015 and 5046, 6118 and 6120, 8115.

Most of these alloy steels are suitable for martempering in section thicknesses of up to 16 to 19 mm (5/8 or 3/4 in.). Martempering at temperatures below 205 °C (400 °F) will improve hardening response, although greater distortion may result than in martempering at higher temperatures.

Effect of Mass. The limitation of section thickness or mass must be considered in martempering. With a given severity of quench, there is a limit to bar size beyond which the center of the bar will not cool fast enough to transform entirely to martensite. This is shown in Fig. 18, which compares the maximum diameter of bar that can be hardened by

martempering, oil quenching, and water quenching for 1045 steel and five alloy steels of various hardenabilities.

For some applications, a fully martensitic structure is unnecessary, and a center hardness 10 HRC units lower than the maximum obtainable value for a given carbon content may be acceptable. By this criterion, maximum bar diameter is 25 to 300% greater than the maximum diameter that can be made fully martensitic (see lower graph in Fig. 18). Nonmartensitic transformation products (pearlite, ferrite, and bainite) were observed at the positions on end-quenched bars corresponding to this reduced hardness value, as follows:

Steel	Transformation
1045	15% pearlite
8630	10% ferrite and bainite
1340	20% ferrite and bainite
52100	50% pearlite and bainite
4150	20% bainite
4340	5% bainite

The influence of mixed structures such as these on the mechanical properties of the steel would have to be determined for each application.

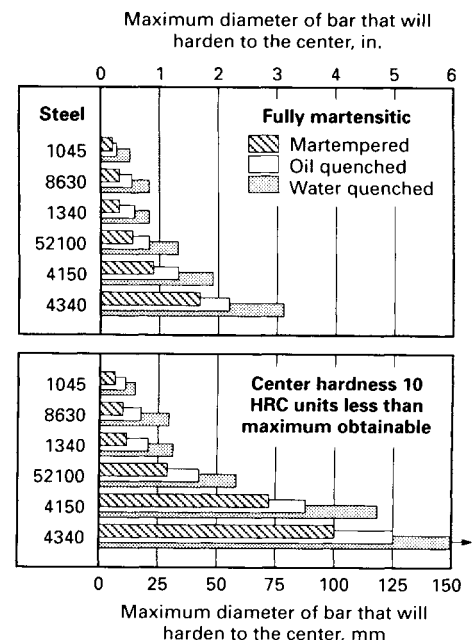


Fig. 18 Approximate maximum diameters of bars that are hardenable by martempering, oil quenching, and water quenching

Steels selected for martempering must be judged on hardenability and section size. To form the same amount of martensite for a given section size, the carbon content, alloy content, or both must be somewhat higher for martempering than for conventional (uninterrupted) quenching.

Control of Process Variables

The success of martempering depends on close control of variables throughout the process. It is important that the prior structure of the material being austenitized be uniform. Also, use of a protective atmosphere (or salt) in austenitizing is required, because oxide or scale will act as a barrier to uniform quenching in hot oil or salt.

The process variables that must be controlled in martempering include austenitizing temperature, temperature of martempering bath, time in martempering bath, salt contamination, water additions to salt, agitation, and rate of cooling from the martempering bath.

Austenitizing temperature is important because it controls austenitic grain size, degree of homogenization, and carbide solution, and because it affects the M_s temperature, which is important in establishing martempering procedures. As indicated in Fig. 19 for 52100 steel, an increase in austenitizing temperature lowers M_s temperature and increases grain size.

Temperature control during austenitizing is the same for martempering as for conventional quenching: A tolerance of 8 °C (15 °F) is common. The austenitizing temperatures most commonly used for several different steels are indicated in Table 6.

In most instances, austenitizing temperatures for martempering are the same as those for conventional oil quenching. Occasionally, however, medium-carbon steels are austenitized at higher temperatures prior to martempering to increase as-quenched hardness.

For carburized parts, low austenitizing temperatures usually yield better size control during martempering. To obtain minimum dimensional changes, the lowest austenitizing temperature that will yield satisfactory core properties should be used. The ratio of case depth to core, as well as the prior processing history of the steel (such as forging, rolling, or drawing), can also be controlling factors, particularly for critical section shapes and sizes. Austenitizing temperatures that have been used for several carburizing steels are indicated in Table 6.

Salt Contamination. When parts are carburized or austenitized in a salt bath, they can be directly quenched in an oil bath operating at the martempering temperature. However, if the parts are carburized or austenitized in salt containing cyanide, they must *not* be directly martempered in salt because the two types of salts

are not compatible and explosions can occur if they are mixed. Instead, one of two procedures should be used: Either air cool from the carburizing bath, wash, reheat to the austenitizing temperature for case and/or core in a chloride bath, and then martemper; or quench from the cyanide-containing bath into a neutral chloride rinse bath maintained at the austenitizing temperature and then martemper.

If the latter method is used, it is essential to control the amount of cyanide buildup in the neutral rinse. When tests indicate more than 5% cyanide in the chloride rinse, part of the salt should be discarded and the remainder diluted with new salt.

All fixtures must be thoroughly cleaned after martempering to prevent transfer of quenching salt to either cyanide baths or neutral chloride baths. Mixing of cyanide with nitrate-nitrite salts will cause explosion. A chloride bath that is contaminated with nitrate-nitrite salts will produce pitting and decarburization of parts immersed in it.

Temperature of the martempering bath varies considerably, depending on composition of workpieces, austenitizing temperature, and desired results. In establishing procedures for new applications, many plants begin at 95 °C (200 °F) for oil quenching, or at approximately 175 °C (350 °F) for salt quenching, and progressively increase the temperature until the best combination of hardness and distortion is obtained. Martempering temperatures (for oil and salt) that represent the experience of several plants are listed in Table 6.

Time in the martempering bath depends on section thickness and on the type, temperature, and degree of agitation of the quenching medium. The effects of section thickness and

of temperature and agitation of the quench bath on immersion time are indicated in Fig. 20.

Because the object of martempering is to develop a martensitic structure with low thermal and transformation stresses, there is no need to hold the steel in the martempering bath for extended periods. Excessive holding lowers final hardness because it permits transformation to products other than martensite. In addition, stabilization may occur in medium-alloy steels that are held for extended periods at the martempering temperature.

The martempering time for temperature equalization in oil is approximately four to five

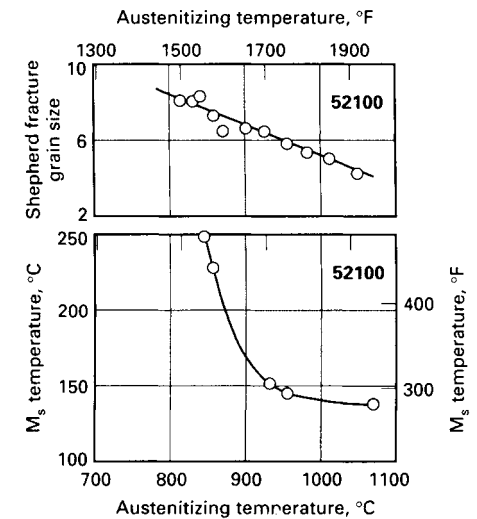


Fig. 19 Effects of austenitizing temperature on grain size and martensite start (M_s) temperature of 52100 steel

Table 6 Typical austenitizing and martempering temperatures for various steels

Grade	Austenitizing temperature		Martempering temperature			
	°C	°F	Oil(a)		Salt(b)	
			°C	°F	°C	°F
Through-hardening steels						
1024	870	1600	135	275
1070	845	1550	175	350
1146	815	1500	175	350
1330	845	1550	175	350
4063	845	1550	175	350
4130	845	1550	205–260	400–500
4140	845	1550	150	300
4140	830	1525	230–275	450–525
4340, 4350	815	1500	230–275	450–525
52100	855	1575	190	375
52100	845	1550	175–245	350–475
8740	830	1525	230–275	450–525
Carburizing steels						
3312	815	1500	175–190	350–375
4320	830	1525	175–190	350–375
4615	955	1750	190	375
4720	845	1550	175–190	350–375
8617, 8620	925	1700	150	300
8620	855	1575	175–190	350–375
9310	815	1500	175–190	350–375

(a) Time in oil varies from 4 to 20 min, depending on section thickness. (b) Martempering temperature depends on shape and mass of parts being quenched; higher temperatures in range (and sometimes above range) are used for thinner sections and more intricate parts.

times that required in anhydrous salt at the same temperature. For example, for a 25 mm (1 in.) diameter bar martempered in salt at 205 °C (400 °F) with moderate agitation, the customary immersion time is approximately 1½ to 2 min, whereas approximately 8 to 10 min are required for the bath to attain temperature equalization in oil at 205 to 220 °C (400 to 425 °F). The immersion time required in salt can be reduced by as much as 50% by addition of 0.5 to 2% water.

Water Additions to Salt. The quenching severity of a nitrate-nitrite salt can be increased significantly by careful addition of water. Agitation of the salt is necessary to disperse the water uniformly, and periodic additions are needed to maintain required water content. The water can be added with complete safety as follows:

- Water can be misted at a regulated rate into a vigorously agitated area of the molten bath.
- In installations where the salt is pump-circulated, returning salt is cascaded into the quench zone. A controlled fine stream of water can be injected into the cascade of returning salt.
- The austempering bath can be kept saturated with moisture by introducing steam directly into the bath. The steam line should be trapped and equipped with a discharge to avoid emptying condensate directly into the bath.

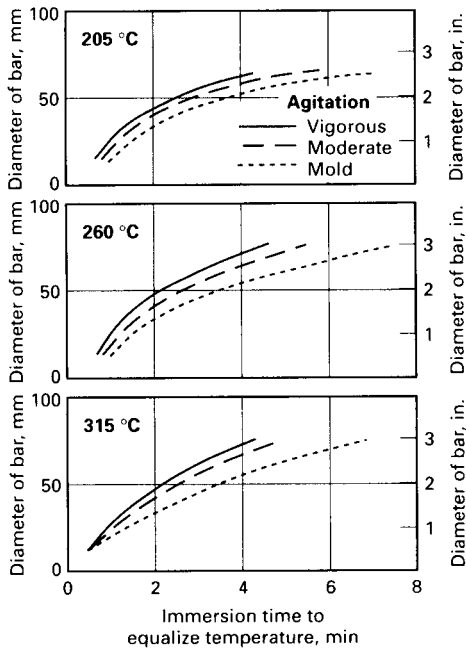


Fig. 20 Martempering time versus section size and agitation of quench bath for 1045 steel bars. Effects of bar diameter and agitation of quench bath on time required for centers of 1045 steel bars to reach martempering temperature when quenched from a neutral chloride bath at 845 °C (1550 °F) into anhydrous nitrate-nitrite martempering salt at 205, 260, and 315 °C (400, 500, and 600 °F). Length of each bar was three times the diameter.

- Steam addition of water to the bath is done on baths with operating temperatures above 260 °C (500 °F).

The addition of water to increase the severity of salt is usually made by directing a stream of water onto the molten salt at the agitator vortex. A protective shroud surrounds the water spray to prevent spattering (see the section “Safety Precautions” in this article). The turbulence of the salt carries the water into the bath without spattering or hazard to the operator. Water should never be added to a salt bath from a pail or dipper.

Water is continuously evaporating from the bath surface, and the rate of evaporation increases during quenching of hot work. Therefore, it is necessary to add water periodically to maintain the water concentration and a uniform quenching severity. The amount of water to be added varies with the operating temperature of the salt, as indicated by the following recommended concentrations:

Temperature		Water concentration, %
°C	°F	
205	400	½–2
260	500	½–1
315	600	¼–½
370	700	¼

At present, there is no known means of automatically controlling the concentration of water in molten nitrate-nitrite salt. Water is usually controlled at the discretion of the operator, who will add water as needed. On the basis of experience, however, it is possible to anticipate the need for water; here, the addition of water may be simplified by use of timers that can be adjusted to time the frequency and duration of water additions.

The presence of water is visually detectable by the operator because steam is released when the hot work is immersed into the nitrate-nitrite salt. The steam causes a visible mounding of the salt above the quench area, and there is a characteristic sizzling caused by the vapor phase.

Besides visual appearance, periodic hardness checks of the work will indicate the activity of the bath. A more exact determination can be made by removing a small quantity of the salt and weighing it accurately before and after dehydrating it by heating to 370 to 425 °C (700 to 800 °F). Another method is to determine the freezing point of a small sample and to then refer to a published curve that relates freezing point to water content for that specific salt.

The use of periodic histograms is another method for determining the quenching effect of the marquench bath. Complete statistical process control is the best method to ensure consistency of the marquench process.

Agitation of the martempering salt or oil considerably increases the hardness obtainable for a given section thickness, in comparison to

that possible in still quenching. This is demonstrated in Fig. 21, which presents data for 52100 steel that relate section thickness, hardness, and agitation.

In some instances, the rapid cooling produced by the most vigorous agitation increases distortion. Thus, mild agitation is often used in combination with water addition to obtain minimum distortion without sacrificing hardness.

Cooling from the martempering bath ordinarily is done in still air to avoid large differences in temperature between the surface and the interior of the steel. Forced-air cooling by means of fans is occasionally used on sections over 19 mm (¾ in.) thick, but caution is required if the part varies in section thickness or has more surface exposed on one section, such as on threads or serrations, because objectionable amounts of distortion can occur on rapid cooling through the martensite range. Generally, cooling of workpieces in cool oil or water after removal from the martempering bath is considered undesirable, because cooling can reestablish thermal gradients and unequal stress patterns that can increase distortion. In high-carbon steels, during conventional quenching the component is removed from the quenchant at a temperature of approximately 60 °C (140 °F) and immediately goes to tempering. This is done to decrease the potential for cracking and distortion (Ref 8).

Cooling time varies with the mass and density of the charge, the maximum section thickness of the workpiece, and the ambient air temperature. Usually, production loads of 365 to 815 kg (800 to 1800 lb) from either continuous or batch-type furnaces will require 2½ to 5 h to reach room temperature. Figure 22 shows the effect of section thickness. As indicated, the 25 mm (1 in.) diameter sections were completely cooled in approximately half the time required for complete cooling of the 75 mm (3 in.) diameter sections.

After being cooled to room temperature, martempered parts usually can be held at room

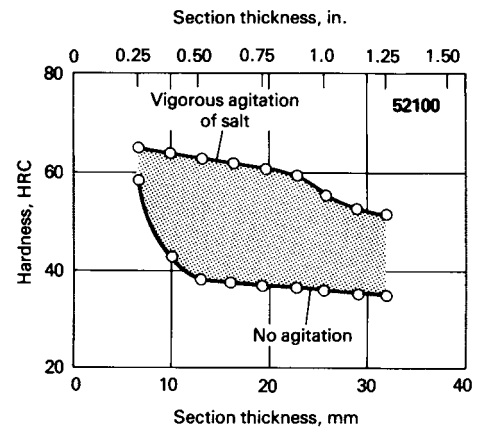


Fig. 21 Influence of agitation on surface hardness of 52100 steel in various section thicknesses martempered in hot salt

temperature for several hours, and sometimes days, without risk of cracking, because residual stresses are low compared to those in conventionally quenched parts. Holding of parts at room temperature also permits more nearly complete transformation of steels in which transformation is sluggish.

Dimensional Control

In many instances, distortion is significantly lower in martempered parts than in parts hardened by uninterrupted (conventional) quenching. However, prior processing often has a significant effect on distortion, regardless of the heat treating method used. Therefore, for some applications, martempering may fail to solve distortion problems because excessive dimensional changes occurred during heating prior to martempering.

Occasionally, it is necessary to consider the effects of fabricating stresses that occur during forging, stamping, rolling, and machining. When the workpiece is heated, these stresses can cause a significant amount of distortion. A process anneal at 650 to 705 °C (1200 to 1300 °F) after rough machining or forming usually will relieve such stresses. Any resulting change in the size or shape of the part can then be corrected by finish machining prior to austenitizing and martempering. During heating, distortion also can occur as the result of temperature differences in a part having both light and heavy sections. This condition is often corrected by preheating at 650 to 705 °C (1200 to 1300 °F) prior to austenitizing.

Relatively large parts that require extreme flatness often must be press quenched. For example, a gear 180 mm (7 in.) in diameter, 13 mm (½ in.) thick at the rim, and with a 6.4 mm (¼ in.) web could not be martempered with an acceptable degree of flatness. A large ring gear with internal teeth and a thin wall is another part for which martempering has been replaced by press quenching to obtain dimensions within acceptable limits.

The following examples describe specific situations in which distortion problems have been encountered. In some instances, the effects (on identical parts) of martempering

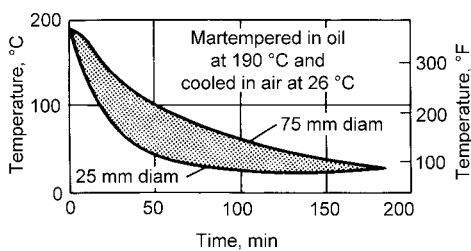


Fig. 22 Effect of section thickness on time required for air cooling of steel after martempering at 190 °C (375 °F). Temperature measurements were made at the surface. Times can be reduced by approximately 30% by forced fan cooling.

and of oil quenching are presented for comparison.

Example 2: Comparison of Distortion in Navy C Specimens after Conventional Quenching and Martempering. Figure 23 shows data for nine Navy C specimens made of a high-carbon alloy steel containing 0.95% C, 0.30% Si, 1.20% Mn, 0.50% W, 0.50% Cr, and 0.20% V that were austenitized for 40 min at 845 °C (1550 °F); three of the specimens were subjected to conventional quenching in oil at 60 °C (140 °F), three were martempered for 2 min in salt at 205 °C (400 °F), and three were martempered for 2 min in salt at 245 °C (475 °F). Each quenching medium was agitated vigorously. All specimens were tempered to 63 to 64 HRC before being measured for dimensional changes.

The data accompanying Fig. 23 indicate that the martempered specimens—especially those quenched in salt at 245 °C (475 °F)—exhibited less distortion in every dimension. These test results indicate that lower stresses result from martempering than from conventional oil quenching.

Example 3: Martempering of Bearing Races for Distortion Control. Bearing races, 215 mm (8½ in.) in outside diameter by 190 mm (7½ in.) in inside diameter by 130 mm (5½ in.), made of 52100 steel, were austenitized in chloride salt at 850 °C (1560 °F) for 25 min, martempered in salt at 230 °C (450 °F) for 2½ min, and air cooled to room temperature. The resulting hardness was 63 to 64 HRC. This treatment produced an average growth of 0.08 mm (0.003 in.) and an average distortion (out-of-roundness) of 0.25 mm (0.010 in.). Prior to heat treatment, the machined races had an average out-of-roundness of 0.18 mm (0.007 in.). Thus, the average increase in out-of-roundness was only 0.08 mm (0.003 in.).

In this application, martempering reduced grinding time from 50 to 7 min per race by permitting a reduction in the grinding stock required for conventionally oil-quenched parts.

Example 4: Warpage of Oil-Quenched Rods. Rods 6.4 mm (¼ in.) in diameter by 255 mm (10 in.) long, with a 3.2 mm (⅛ in.) hole near one end, were made from oil-

hardening drill rod. The requirements were a hardness of 60 to 62 HRC and maximum warpage of 0.25 mm (0.010 in.) (indicator reading between centers).

The rods were heated by being suspended in a salt bath at 805 °C (1480 °F), and then were quenched in oil at 55 °C (135 °F). This treatment produced the required hardness, but warpage was excessive (up to 0.76 mm, or 0.030 in.). The problem was solved by replacing oil quenching with martempering in unagitated salt at 175 °C (350 °F).

Example 5: Martempering of Carburized Gears to Reduce Distortion. Figure 24 shows a thin-wall ring gear of 8625 steel, with a flange on one end, that had to be carburized to a depth of 1.3 mm (0.050 in.) and hardened. After carburizing followed by martempering in oil at 190 °C (375 °F), out-of-roundness ranged from 0.43 to 0.66 mm (0.017 to 0.026 in.), which was not acceptable. The problem was solved by martempering and then placing the ring gears over a plug machined to the final inside diameter of the gear for cooling to room temperature. This produced acceptable parts having a maximum runout of 0.09 mm (0.0035 in.). The runout for eight gears tested before heat treating and after plug cooling is indicated in Fig. 24.

Figure 25 indicates the dimensional changes that occurred when different types and sizes of gears made of 8625H steel were carburized at 925 °C (1700 °F) to a depth of 1.0 to 1.5 mm (0.040 to 0.060 in.) and then martempered in oil at either 165 or 190 °C (325 or 375 °F).

Figure 26 shows the dimensional changes that were encountered in carburizing and martempering seven different sizes of automatic-transmission gears made of 8620H steel. The gears were martempered in oil at 150 °C (300 °F). Shrinkage of the largest gear is associated with lower core hardness in the considerably heavier section of the gear.

Figure 27 indicates the effects of various combinations of carburizing and quenching methods on the dimensions of 25-tooth reverse-idler gears for power-grader transmissions. All gears were carburized to a depth of 0.76 to 1.0 mm (0.030 to 0.040 in.). The smallest dimensional changes occurred in gears that were liquid carburized and then

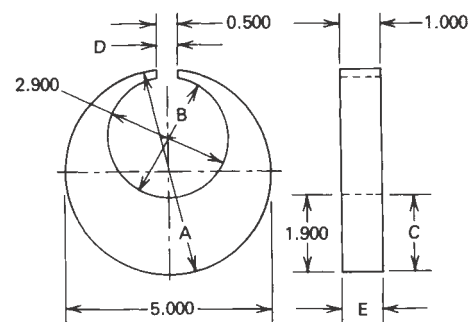


Fig. 23 Dimensional changes in Navy C specimens austenitized at 845 °C (1550 °F) and quenched in three vigorously agitated media (Example 2). Figure dimensions given in inches

Type of quench	Dimensional change, mm (mil)				
	A	B	C	D	E
Conventional (oil at 60 °C, or 140 °F)	0.21 (8.3)	0.24 (9.5)	0.20 (8.0)	0.61 (24)	0.075 (3)
Martempering in salt at					
205 °C (400 °F)	0.137 (5.2)	0.15 (6)	0.13 (5)	0 (0)	0.025 (1)
245 °C (475 °F)	0.117 (4.5)	0.075 (3)	0.0025 (0.1)	-0.05 (-2)	0.025 (1)

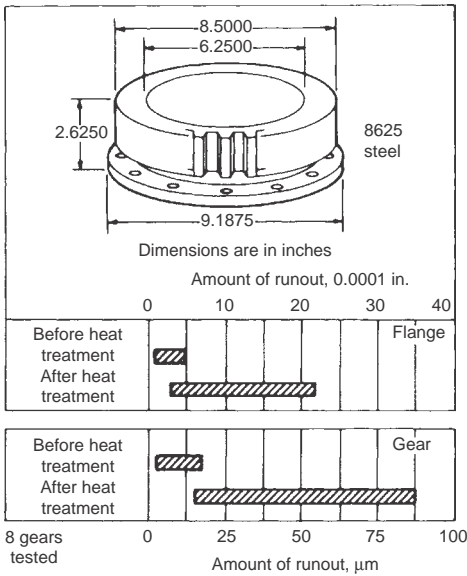


Fig. 24 Control range for 8625 steel ring gears (Example 5). Eight ring gears made of 8625 steel were carburized to a depth of 1.3 mm (0.050 in.), martempered in oil at 190 °C (375 °F), and placed on a plug for cooling to room temperature. Measurements are total indicator readings.

martempered in salt at 205 °C (400 °F); the greatest changes occurred in those that were gas carburized and quenched in agitated oil at 45 °C (110 °F).

The effect of stress relieving on out-of-roundness is also indicated in Fig. 27. The data for bore, teeth, and runout are for gears that were stress relieved before heat treating.

Example 6: Distortion in Martempering of 8625 Steel Shafts. Figures 28 and 29 are histograms of distortion data, in terms of total indicator readings, for various shafts made of 8625 steel. The shafts depicted in Fig. 28 were machined from bar stock, whereas those in Fig. 29 were forged. All shafts were carburized at 925 °C (1700 °F) and martempered in oil at 165 °C (325 °F). Also, all shafts were in the vertical position during heat treating—some suspended, and some supported on one end—as indicated in Fig. 28 and 29.

Stabilizing after Martempering. Parts such as shafts, chain-saw guides, washers, and springs require straightening or reforming after

heat treatment. This is sometimes not feasible after normal quenching and tempering. However, after such parts are removed from a martempering bath, straightening is readily accomplished, either by hand pressure or in a die press, while the parts are still essentially austenitic.

When parts are clamped between plates held at approximately 150 °C (300 °F), the parts cool to the temperature of the plate. At this temperature, depending on the M_f temperature of the steel, the transformation to martensite may be only partial, but it is usually near enough to completion for the part to set permanently before it is removed from the clamped position. At this temperature, the film of salt (melting point, approximately 145 °C, or 290 °F) adhering to the part will not freeze, and therefore, removal of the part from the clamps or die can be accomplished without difficulty. The transformation of martensite is completed during subsequent air cooling to room temperature, and the part is within dimensional tolerance.

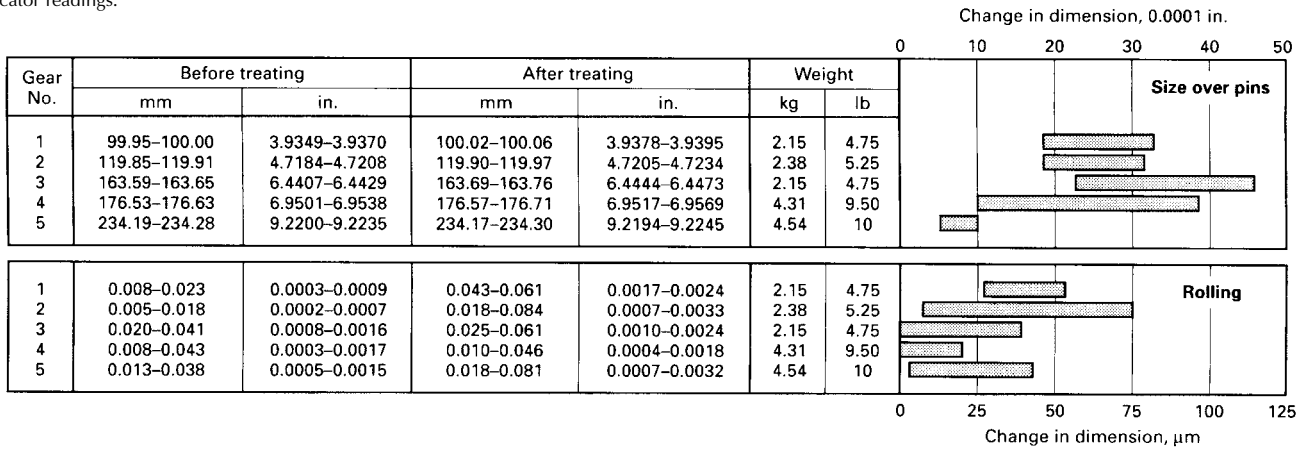


Fig. 25 Dimensional changes in carburized and martempered gears of 8625H steel (Example 5). All gears were carburized at 925 °C (1700 °F) to a depth of 1.0 to 1.5 mm (0.040 to 0.060 in.) and martempered directly from the carburizing temperature in oil at 165 °C (325 °F). Gears 1, 2, and 5 were measured over 7.32 mm (0.288 in.) diameter pins; gear 3 over 3.66 mm (0.144 in.) diameter pins; and gear 4 over 8.78 mm (0.3456 in.) diameter pins.

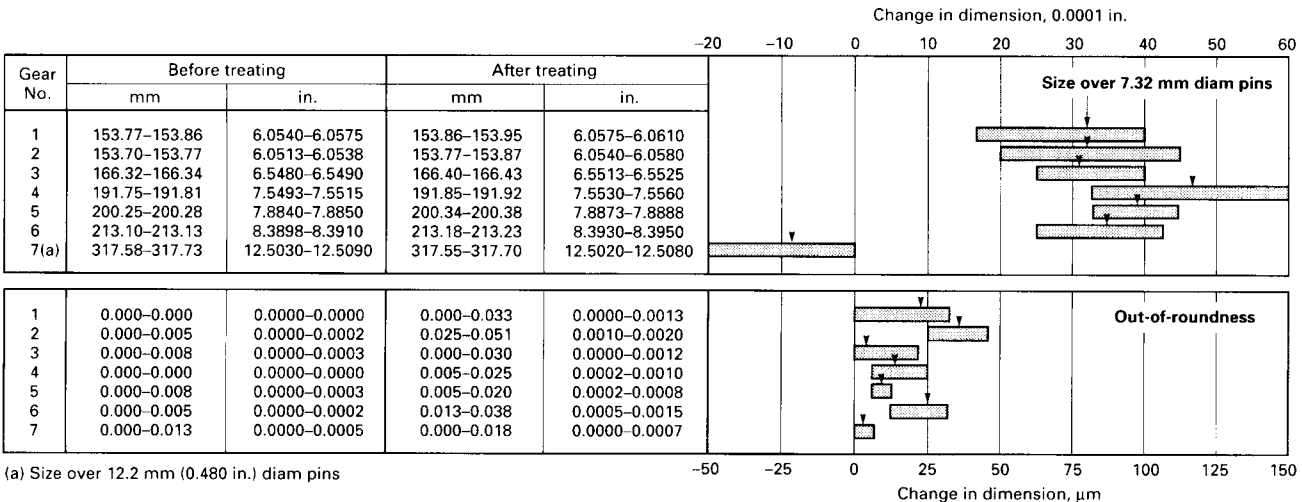


Fig. 26 Dimensional changes in carburized and martempered automatic-transmission gears made of 8620H steel. All gears were carburized at 925 °C (1700 °F) and then martempered directly from the carburizing temperature in oil at 150 °C (300 °F).

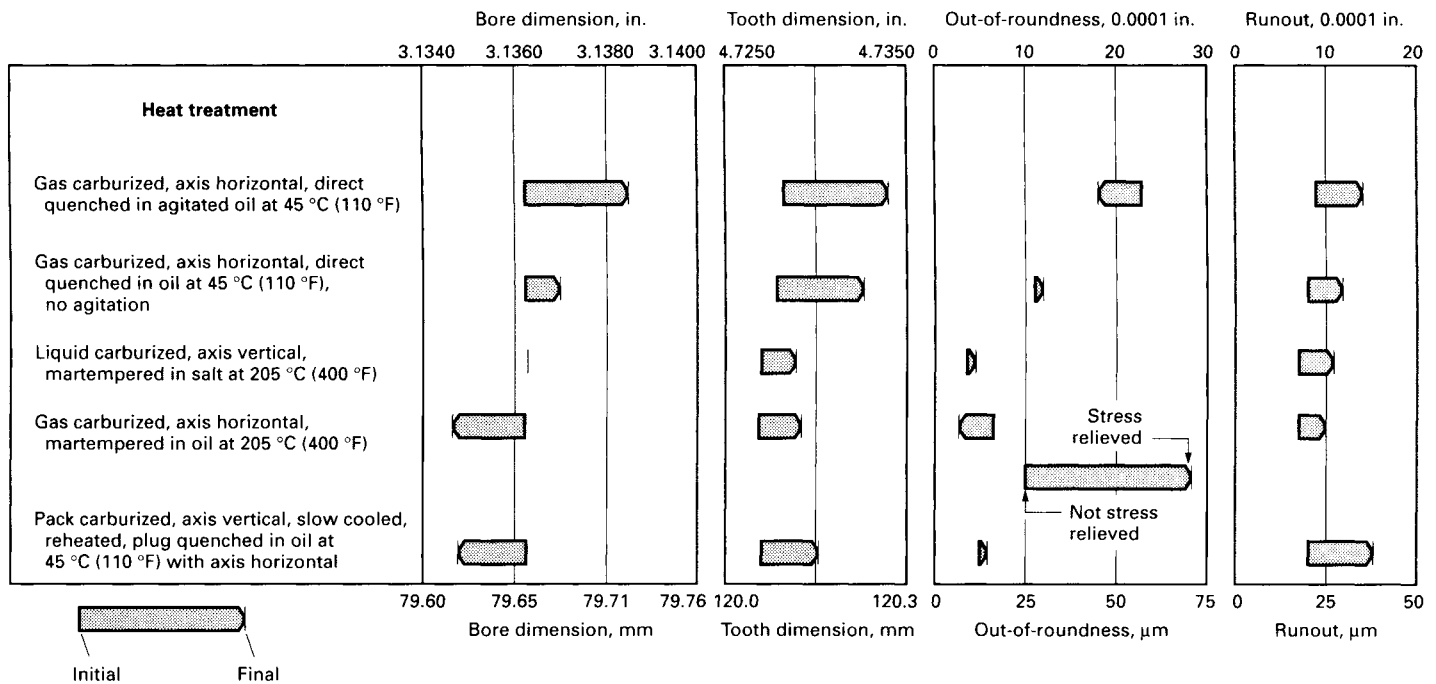


Fig. 27 Effects of various carburizing and quenching methods on dimensions of 4620H steel reverse-idler gears for power-grader transmissions. Gears were carburized to a depth of 0.8 to 1.0 mm (0.030 to 0.040 in.) and quenched to a hardness of 58 to 63 HRC.

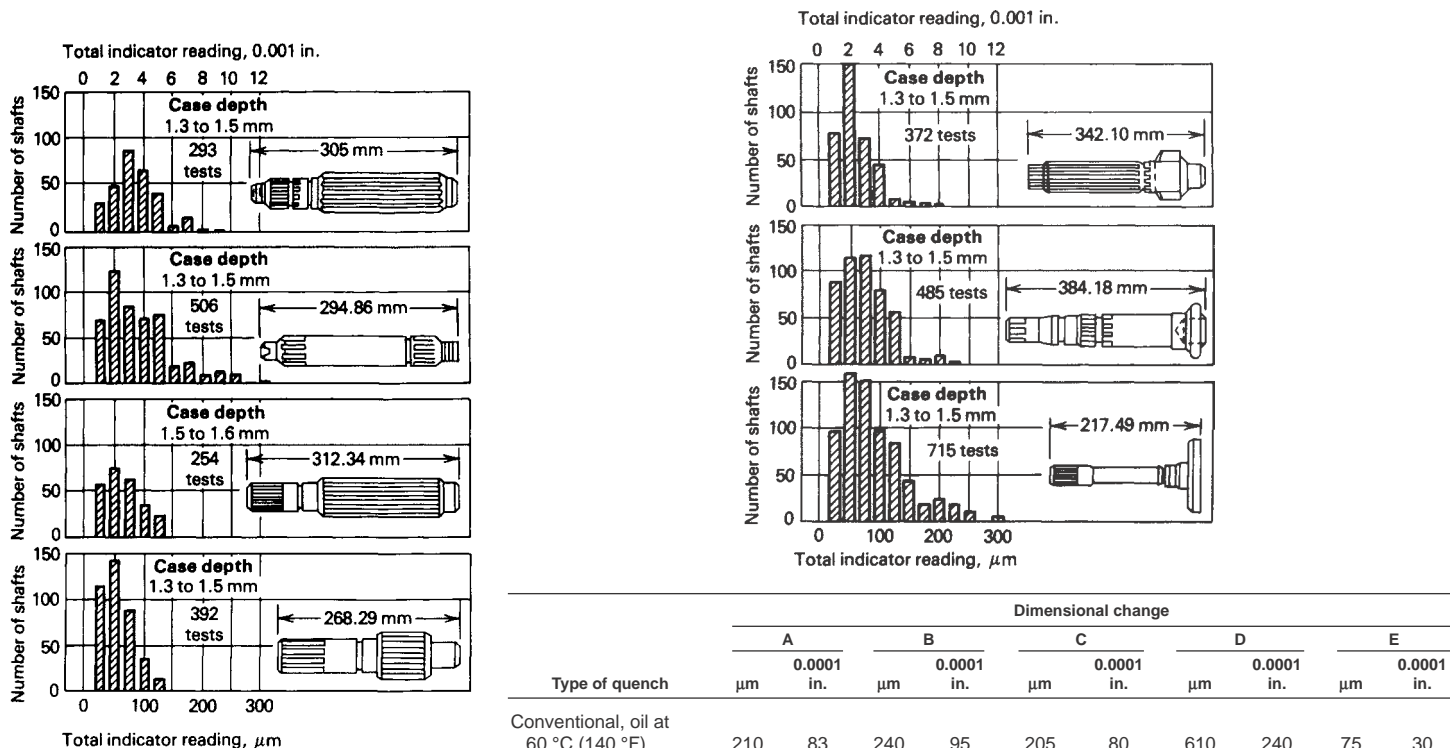


Fig. 28 Distortion in martempering (Example 6). Histograms of distortion data on shafts of 8625 steel (machined from bar stock) after carburizing at 925 °C (1700 °F) and martempering in oil at 165 °C (325 °F). Shafts were heat treated in the vertical position: the top two shafts were suspended vertically from the threaded end; the lower two shafts were supported on one end.

Fig. 29 Distortion in martempering (Example 6). Histograms of distortion data on forged shafts of 8625 steel after carburizing at 925 °C (1700 °F) and martempering in oil at 165 °C (325 °F). Shafts were supported vertically on one end during heat treatment.

Forming after Martempering. Difficult-to-form materials, such as hot work die steels (H11) and some martensitic stainless steels used for missiles, rockets, and high-speed

aircraft, can be accurately formed and hardened by austenitizing, martempering, and hot forming to shape immediately after they are extracted from the quench bath, if the

martempering temperature is above the martensite transformation temperature for the specific alloy being treated. During hot forming by rolling, forging, drawing, or extruding, the

metal consists of metastable austenite, which transforms to martensite on subsequent cooling to room temperature.

Parts of both simple and complex shape have been formed in this manner; after being air cooled to room temperature in or out of the forming die, the parts will accurately maintain their as-formed dimensions and yet be in the fully heat treated condition, requiring only a subsequent tempering operation.

This method of heat treating and forming has been successfully applied to sheet and plate that require nearly perfect flatness. It also has been used for forming type 420 stainless steel sheet into cups that require close dimensional tolerances and hardness values of 55 to 58 HRC.

Working of metastable H11 that results in deformation of 58 to 94% at 480 °C (900 °F) produces a 19 to 32% increase in tensile strength.

Applications

Typical applications of martempering in salt and oil are indicated in Tables 7 and 8, which list and describe commonly treated steel parts and give details of martempering procedures and hardness requirements. From these tables, it is evident that martempering is used for parts of diverse shapes, weights, section sizes, and steel compositions.

Although approximately a third of the applications in Table 7 and most of the applications in Table 8 are carburized parts, it is believed that in current industrial practice the tonnage of martempered through-hardening steels markedly exceeds that of martempered carburized steels. However, martempering is especially appropriate for carburized parts (particularly for splined shafts, cams, and gears) because these parts generally are more difficult to grind and more costly to fabricate, and are made to closer dimensions, than are parts made of through-hardening steels.

Special adaptations of martempering are sometimes employed to achieve desired characteristics and to solve specific problems. Such

Table 7 Typical applications of martempering steel parts in salt

Part	Grade	Maximum section thickness		Weight		Martempering conditions			
		mm	in.	kg	lb	Temperature of salt		Time in salt, min	Required hardness, HRC
						°C	°F		
Compliant tube	4130	0.8	0.03	0.11	0.25	160(a)	320(a)	5	50(b)
Thrust washer	8740	5.1	0.20	0.05	0.1	230	450	1	52 min(b)
Chain link	1045	5.6	0.22	0.11	0.25	205(c)	400(c)	1	45–50(b)
Cotton-picker spindle(d)	Type 410	6.4	0.25	0.05	0.12	315	600(c)	1½	44–48(b)
Accessory drive shaft	9310(e)	6.4	0.25	0.45	1.0	190	375	2½	90 (15N scale)
Clutch-adjustment nut	8740	7.6	0.30	0.14	0.3	230	450	2	52 min(b)
Seal ring	52100	7.6	0.30	0.18	0.4	190	375	10	65(b)
Spur pinion	3312(e)	7.6	0.30	0.23	0.5	175	350	1½	90 (15N scale)
Internal gear	4350	8.9	0.35	0.36	0.8	245	475	2	54 min(b)
Dual gear(f)	4815(e)	9.4	0.37	2.13	4.7	260	500	2	62–63(b)
Drive coupling	4340	10.2	0.40	0.27	0.6	230	450	2½	52 min(b)
Spline shaft	8720(e)	10.2	0.40	0.50	1.1	190	375	2½	90 (15N scale)
Arbor sleeve	1117L(e)	10.2	0.40	0.59	1.3	205	400	3	...
Screw-machine spindle	8620(e)	10.2	0.40	6.35	14.0	205	400	3	...
Driving barrel	4350	12.7	0.50	0.45	1.0	245	475	3	48–52(g)
Bearing race(h)	52100	12.7	0.50	13.2	29.2	220	425	2½	63–64(b)
Hog knife	9260	15.2	0.60	8.16	18.0	175(i)	350(i)	15	62(b)
Landing-gear spring	6150	19.1	0.75	14.7	32.5	260	500	2¾	56–57(b)
Internal gear	1117L(e)	25.4	1.00	1.36	3.0	205	400	3	...
Spur pinion gear(j)	4047	25.4	1.00	16.4	36.2	230(c)	450(c)	3	50–52(k)
Screw-machine sprocket	8620(e)	38.1	1.50	9.07	20.0	205	400	3	...

Note: OD, outside diameter; ID, inside diameter. (a) Salt contained 1½% water. (b) As-quenched. (c) Salt contained water. (d) 6.4 mm (¼ in.) diameter by 203 mm (8 in.) long. (e) Carburized. (f) 124 mm (4¾ in.) OD by 32 mm (1¼ in.) ID by 102 mm (4 in.). (g) Final. (h) 224 mm (8¾ in.) ID by 251 mm (9¾ in.) OD. (i) Salt contained 1% water. (j) 19 mm (¾ in.) OD by 92 mm (5¾ in.) ID by 140 mm (5½ in.). (k) As-quenched hardness of teeth

Table 8 Typical applications of martempering steel parts in oil

Part	Grade	Maximum section thickness		Outside diameter		Weight		Carburizing temperature, °C	Depth of case		Quenching temperature, °C	Temperature of martempering oil(a), °C	Surface hardness, HRC
		mm	in.	mm	in.	kg	lb		µm	0.001 in.			
Sleeve	52100	3.2	0.125	0.1	¼	790	165	58–59
Spacer plate	1065	3.2	0.125	0.1	¼	790	165	56–57
Bushing	1117	4.8	0.1875	51.0	2.009	0.2	½	910	1015–1220	40–48	910	190	58–62
	1117	6.4	0.25	76.3	3.0034	0.6	1¼	910	1015–1220	40–48	910	190	55–60
Shifter rail	1018	9.5	0.375	1.0	2½	845(b)	255–455	10–18	845	165	55–60
	1018	9.5	0.375	1.4	3½	845(b)	355–610	14–24	845	165	55–60
Spur gear	8620	12.7	0.5	320.6	12.620	12.7	28	925	1145–1525	45–60	845	150	55–60
Helical gear	4620H	19.1	0.75	331.5	13.050	16.9	37.2	925	760–1015	30–40	845	150	58–63
Herringbone gear	4820	19.1	0.75	283.2	11.150	16.3	36	925	1145–1525	45–60	845	150	55–61
Shifter rail	1141	25.4	1.0	25.4	1.0	0.9	1¾	885(b)	455–660	18–26	885	165	45–50
Spiral bevel gear	4620	25.4	1.0	210.6	8.29	5.1	11.25	925	1015–1270	40–50	845	150	55 min
Helical pinion	8617H	25.4	1.0	35.8	1.409	0.4	0.9	925	510–710	20–28	845	150	58–63
Spur gear	8625	31.8	1.250	83.8	3.300	4.3	9¾	925	1525–1725	60–68	925	190	58–62
	4817H	34.0	1.340	186.7	7.350	8.6	19	925	1400–1780	55–70	845	150	58–63
Splined shaft	8625	38.1	1.500	165.1	6.500	2.5	5½	925	1525–1725	60–68	925	190	58–62
	8625	39.7	1.564	39.7	1.564	2.7	5¾	925	1400–1980	70–78	925	190	58–62
Spur gear	8625	44.4	1.750	108.0	4.250	3.5	7¾	925	1525–1725	60–68	925	165	58–62
Splined shaft	8625	44.4	1.750	44.4	1.750	2.0	4½	925	1525–1725	60–68	925	190	58–62
	8620	50.8	2.000	50.8	2.000	5.1	11¼	925	1525–1725	60–68	925	165	58–62
Spur gear	8625	65.0	2.559	65.0	2.559	6.8	15	925	1525–1725	60–68	925	165	58–62
	8625	84.7	3.3343	245.5	9.667	11.9	26¼	925	1525–1725	60–68	925	190	58–62

(a) Minimum time in oil, 5 min. (b) Carbonitriding temperature

modified techniques, however, usually require that all conditions be closely controlled, lest still greater problems result. One special technique that has been employed is described in the following example.

Example 7: Adaptation of Martempering Involving a Brief Quench in Brine. A problem was encountered in obtaining a sufficient depth of hardness in forged balls made of 52100 steel, which ranged in diameter from 25 to 65 mm (1 to 2½ in.). Investigation ruled out both conventional oil quenching and martempering because of low hardness penetration and the existence of quenching pearlite (an intermediate transformation product) in the microstructure.

This problem was solved by preceding martempering with a brief, timed quench in agitated brine at 23 °C (74 °F). Heat treatment of the balls then consisted of:

- Austenitizing in salt at 855 °C (1575 °F) for times ranging from 15 min for 25 mm (1 in.) diameter balls to 50 min for 64 mm (2½ in.) diameter balls
- Quenching in agitated brine at 23 °C (74 °F) for times ranging from 15 s for 25 mm diameter balls to 40 s for 64 mm diameter balls and removing parts while hot (above 100 °C, or 212 °F) to accelerate evaporation of moisture
- Martempering in salt at 165 °C (325 °F) for 8 min (all diameters)
- Air cooling
- Tempering at 140 °C (285 °F) for 3 h (all diameters). By use of this treatment, the parts were successfully hardened to the desired depth. Surface hardness values were as follows:

Diameter of ball		Surface hardness, HRC
mm	in.	
27	1 ¹ / ₁₆	64.0–64.5
29	1 ¹ / ₈	64.5–65.5
32	1 ¹ / ₄	63.5–64.5
33	1 ⁵ / ₁₆	64.0–64.5
35	1 ³ / ₈	63.0–64.0
38	1 ¹ / ₂	63.0–63.5
41	1 ⁵ / ₈	63.5–64.5
43	1 ¹¹ / ₁₆	63.0–64.0
44	1 ³ / ₄	63.5–64.5
48	1 ⁷ / ₈	63.5–64.0
49	1 ¹⁵ / ₁₆	63.5–64.0
54	2 ¹ / ₈	61.5–63.5

Selection of Austenitizing Equipment

Austenitizing of steel prior to martempering may be done in virtually any furnace. This phase of the operation has been successfully accomplished in furnaces ranging from small, simple box furnaces to large, fully automated, high-production installations. Both atmosphere-controlled furnaces and molten salt baths are widely used. Fluid beds are also being used to austenitize loads prior to martempering.

The choice of austenitizing equipment depends mainly on availability, shape and size of workpieces, production requirements, and permissible distortion.

Work that is austenitized in a gaseous atmosphere can be oxidized while being transferred to an oil or salt martempering furnace. However, no special considerations are necessary when salt media are used for austenitizing before martempering in salt, because chloride salts are compatible with, and are easily separated from, the martempering bath. The composition and characteristics of a typical chloride salt medium are as follows: composition, 45 to 55% NaCl and 45 to 55% KCl; melting range, 650 to 675 °C (1200 to 1250 °F); and working range, 705 to 900 °C (1300 to 1650 °F).

If it is necessary to austenitize in a bath that contains cyanide, such as a liquid carburizing bath, the work should be transferred to a neutral salt (chloride-type) rinse at the austenitizing temperature prior to martempering in salt. Direct quenching from a noncyanide-type liquid carburizing bath is permissible (see the article “Liquid Carburizing and Cyaniding of Steels” in this Volume).

Salt bath furnaces for austenitizing (and neutral rinsing, if used) are most commonly of the submerged- or immersed-electrode type, although externally heated pots are also satisfactory.

Selection of Martempering Equipment

The furnace used for martempering is essentially a heat exchanger. Its basic functions are to absorb heat from the work being quenched and then to dissipate this heat to the surroundings to maintain a constant temperature.

In its simplest form, the martempering furnace consists of a steel pot that contains the oil or nitrate-nitrite salt and that is heated internally or externally. Such a simple furnace can be successfully used for martempering in limited production quantities. For continuous production, more complex equipment is needed to maintain optimum quenching conditions.

Fuel-fired (usually gas-fired) immersion tubes, electrodes, or immersion heaters, located across the back wall and sides of the furnace, are also used for internal heating. Occasionally, furnaces are externally heated by fuel or electricity, but such furnaces are limited to relatively small installations because they are difficult to control.

With internal heating, furnace size is unlimited and is based on production requirements. Sizes may range from 0.06 m³ (2 ft³) to lengths of more than 18 m (60 ft) and depths of more than 14 m (45 ft).

The operating temperature range for martempering usually is 165 to 595 °C (325 to 1100 °F). Temperature is measured by one or more

thermocouples (depending on the size of the furnace), which are connected to controlling pyrometers that automatically control temperature within by actuating the heating or cooling systems as required.

In continuous production, heat input from the work usually exceeds heat losses by radiation. Therefore, arrangements for cooling as well as for heating the martempering medium are required. To supplement heat losses by radiation from the surface of the bath, the exterior surface of the pot may be designed with cooling fins so that additional heat can be removed by forcing air through the cooling chamber between the pot and the casing walls. To increase heat dissipation, atomized water may be added to the stream of air. The mixture is then passed through a heat exchanger placed in the bath.

Agitation of the molten salt greatly improves the rate at which heat is extracted from the work. The furnace can be provided with a propeller-type pump that delivers the molten salt to the quench header into which the hot work is placed for quenching. By directing the flow of salt upward or downward through this quench header, effective control of the quenching severity of the salt is maintained, particularly if the speed of the pump can be varied. The salt also may be agitated by propeller mixers, centrifugal pumps, or air bubblers located to produce effective agitation in the quench area. The use of air bubblers is not recommended because they are not efficient and may cause carbonate buildup in the bath.

The furnace may have a second chamber in which the contaminating chlorides of barium, sodium, and potassium that may be carried over from the austenitizing salt bath are separated by gravity from the nitrate-nitrite martempering salt. Contaminated salt is continuously circulated through the separating chamber, and, with a drop in salt temperature, more chlorides are precipitated from solution and settle to the bottom of the separating chamber. Because clarification is continuous, a uniform quenching condition is provided at all times. When work is austenitized in an atmosphere-controlled furnace, this chamber is not required.

The equipment required for martempering in hot oil is essentially the same as that for martempering in salt. Although the operating temperature range of oil baths is lower (95 to 230 °C, or 200 to 450 °F), the problem of maintaining a constant bath temperature is the same for salt.

Examples of Equipment Requirements

Examples of equipment requirements for several specific operations are given in Tables 9 to 15. Each example is described further as follows.

Examples in Table 9. The equipment required for martempering miscellaneous carburized parts (70 g to 1.0 kg, or 0.15 to 2.2 lb, per piece) made from 4024 and 4028 steels,

at a rate of 455 kg/h (1000 lb/h), is listed in Table 9. Oil at 190 °C (375 °F) was the martempering medium used in this installation.

The parts were carburized at 915 to 925 °C (1680 to 1700 °F) to a depth of 0.5 to 0.75 mm (0.020 to 0.030 in.) in a radiant-tube, gas-fired, three-row continuous pusher furnace with automatic quenching facilities. Parts were quenched from the final zone at 895 to 905 °C (1640 to 1660 °F). The carburizing atmosphere consisted of endothermic gas provided by a gas generator and 4.8 m³/h (170 ft³/h) of natural gas.

Example in Table 10. In the operation for which equipment requirements are detailed in Table 10, oil at 150 °C (300 °F) was used as the martempering medium. In this operation, a 455 kg (1000 lb) load of 1.5 kg (3.3 lb) parts made of 8617 steel was quenched from an automatic batch-type furnace.

These parts were carburized to a depth of 1.0 mm (0.040 in.) in a radiant-tube, gas-fired batch furnace with automatic quenching facilities. The parts were carburized at 925 °C (1700 °F) and cooled in the furnace to a quenching temperature of 845 °C (1550 °F). The carburizing atmosphere consisted of endothermic gas and natural gas.

Example in Table 11. Table 11 lists details of equipment required for salt martempering 1.1 kg (2.5 lb) transmission shafts made of 5040 steel at a rate of 170 kg/h (375 lb/h). The complete treatment was as follows:

- Austenitize for 35 min in neutral chloride salt at 845 °C (1550 °F)
- Martemper for 5 min at 260 °C (500 °F)
- Air cool (30 min) to 65 to 95 °C (150 to 200 °F)
- Temper for 45 min at 425 °C (800 °F)
- Air cool (5 min) to 95 to 120 °C (200 to 250 °F)
- Wash, rinse, and dry

Hardness after tempering and cooling to room temperature was 40 to 42 HRC (required hardness was 38 to 42 HRC).

Example in Table 12. Table 12 lists equipment requirements for salt martempering 0.9 kg (2 lb) gears made of 6150 steel at a rate of 128 pieces per hour. The gears were austenitized in a 60 kV · A submerged-electrode salt pot capable of heating 180 kg/h (400 lb/h) to 870 °C (1600 °F). The austenitizing pot measured 455 by 380 by 760 mm (18 by 15 by 30 in.) and contained 180 kg (400 lb) of alkali-chloride salt at an operating temperature of 845 °C (1550 °F). Table 12 gives martempering requirements.

Example in Table 13. Details of a salt martempering furnace used in a commercial heat treating plant for quenching up to 180 kg/h (400 lb/h) are given in Table 13. This salt bath is capable of being operated at up to 400 °C (750 °F) and therefore can also be used for austempering.

Example in Table 14. Table 14 shows details of a salt martempering bath capable of cooling 210 kg/h (465 lb/h) from 845 to 260 °C (1550 to 500 °F). This specific installation is used

exclusively for heat treating piston rings made of 52100 steel.

Example in Table 15. The equipment used in one installation for martempering aircraft landing-gear parts made of 4330 steel is detailed in Table 15. Following martempering, these parts are tempered at 425 °C (800 °F), which results in a hardness of 37 to 42 HRC.

Martempering Bath Maintenance

Lack of an established maintenance schedule may result in loss of process control, damage to the equipment, or both.

Table 9 Equipment requirements for oil martempering carburized parts made of 4024 and 4028 steels

Production requirements	
Production rate, kg/h (lb/h)	455 (1000)
Weight of each piece, kg (lb)	70 g–1.0 (0.15–2.2)
Number of pieces per hour	Variable
Equipment requirements	
Capacity of quench tank, L (gal)	18,925 (5000)
Type of oil	Mineral oil (viscosity at 99 °C, or 210 °F; 110 SUS)
Temperature of oil, °C (°F)	190 (375)
Agitation	High and low, as required

Table 10 Equipment requirements for oil martempering carburized parts made of 8617 steel

Production requirements	
Weight of load, kg (lb)	455 (1000) net
Weight of each piece, kg (lb)	1.5 (3.3)
Number of pieces treated per hour	75
Equipment requirements	
Capacity of quench tank, L (gal)	7570 (2000)
Type of oil	Mineral oil with additives (viscosity at 38 °C, or 100 °F, 250 SUS)
Temperature of oil, °C (°F)	150 (300)
Agitation	Direct flow(a)
(a) Agitation provided by two 3.7 kW (5 hp) motors driving 455 mm (18 in.) propellers at 370 rpm, causing the oil to flow at a rate of 915 mm/s (36 in./s)	

Table 11 Equipment requirements for salt martempering automotive transmission shafts of 5040 steel

Production requirements	
Weight of each piece, kg (lb)	1.1 (2.5)
Pieces per fixture	14
Production per hour:	
Number of loaded fixtures	10.7
Number of pieces	150
Weight of pieces, kg (lb)	170 (375)
Equipment requirements	
Martempering furnace	Steel salt pot with resistance immersion heaters (70 kW)
Size of chamber(a)	1.22 m by 510 mm by 560 mm (48 by 20 by 22 in.)
Size of chloride-separating chamber, mm (in.)	380 by 815 by 940 (15 by 32 by 37)
Capacity of salt pot, kg (lb)	3630 (8000)
Type of salt	Nitrate-nitrite
Operating temperature, °C (°F)	260 ± 3 (500 ± 5)
Agitation, kW (hp); mm (in.)	One 2.2 (3), 150 (6) propeller pump
Cooling system(b), kW (hp); m ³ /min (ft ³ /min)	One 0.25 (1/3) blower (25.5, or 900)
(a) Total depth of salt was 940 mm (37 in.). (b) Cooling capacity of system was 215 kg/h (475 lb/h) (gross) from 845 to 230 °C (1550 to 450 °F) without exceeding 230 °C.	

Salt System Maintenance

Because martempering baths vary widely in design, shape, size, and method of operation, it is not feasible to set forth a standard maintenance schedule. Manufacturers recommendations for specific equipment should be followed; however, typical schedules for maintaining a salt bath are as follows:

Each 8 h shift:

- Check instruments and thermocouples against a standard.

Table 12 Equipment requirements for salt martempering gears made of 6150 steel

Production requirements	
Weight of each piece, kg (lb)	0.9 (2)
Pieces per furnace load	32
Production per hour(a):	
Number of pieces	128
Net work load, kg (lb)	116 (256)
Gross furnace load(b), kg (lb)	152 (336)
Equipment requirements	
Martempering furnace	Immersion-heated salt pot(c)
Size of salt pot, mm (in.)	610 by 380 by 840 (24 by 15 by 33)
Capacity of salt pot, kg (lb)	270 (600)
Type of salt	Nitrate-nitrite (2% water added)
Quenching capacity of salt pot, kg/h (lb/h)	180 (400)
Operating temperature, °C (°F)	205 (400)
Agitation	Air-operated stirrer

(a) Cycle time, 15 min. (b) Work plus fixtures: each fixture had an empty weight of 9.1 kg (20 lb) and contained eight gears. (c) Salt pot rated at 21 kV - A (3 phase, 60 cycle, 220 to 440 V) for heating to temperature range of 175 to 400 °C (350 to 750 °F); 0.37 kW (0.5 hp) blower (3 phase, 60 cycle, 220 V) used for cooling by driving room-temperature air between wall of pot and exterior shell of furnace

Table 13 Equipment requirements for salt martempering a variety of steel parts

Martempering furnace	Steel salt pot
Method of heating, mm (in.)	100 (4) immersion tube fired by natural gas(a)
Rated heat input, kW (Btu/h)	38.4 (131,000)
Operating temperature range(b), °C (°F)	205–400 (400–750)
Capacity of salt pot, kg (lb)	1725 (3800)
Type of salt	Nitrate-nitrite
Size of chloride-separating chamber(c)	205 mm by 1.07 m (8 by 42 in.)
Agitation method, kW (hp)	0.19 (¼) propeller mixer
Cooling method(d)	Air through immersion tube

(a) Gas rated at 39.12 MJ/m³ (1050 Btu/ft³). (b) Temperature automatically controlled to ±3 °C (±5 °F). (c) Depth of salt, 760 mm (30 in.). (d) Cooling capacity, 180 kg/h (400 lb/h) (gross) from 845 to 260 °C (1550 to 500 °F) without exceeding 260 °C

Table 14 Equipment requirements for salt martempering piston rings made of 52100 steel

Production requirements	
Production rate(a):	
Gross, kg/h (lb/h)	210 (465)
Net, kg/h (lb/h)	68 (150)
Equipment requirements	
Martempering furnace	Immersion-heated steel salt pot(b)
Size of work chamber(c), mm (in.)	915 by 455 (36 by 18)
Size of chloride-separating chamber(d), mm (in.)	380 by 785 (15 by 31)
Capacity of salt pot, kg (lb)	1950 (4300)
Type of salt	Nitrate-nitrite
Operating temperature of salt pot(e), °C (°F)	260 (500)
Agitation, kW (hp); mm (in.)	One 2.2 (3), 150 (6) propeller pump
Cooling system, kW (hp); m ³ /min (ft ³ /min)	One 0.25 (⅓) blower (25.5, or 900)
Cooling capacity, kg/h (lb/h); °C (°F)	210 (465) (gross) from 845 to 260 (1550 to 500)

(a) Heavy mandrels were used as fixtures to retain shape of piston rings, which accounts for wide difference between gross and net weights. (b) Resistance immersion heaters (60 kW). (c) Depth of salt, 760 mm (30 in.). (d) Depth of salt, 1.04 m (41 in.). (e) Automatically controlled to ±3 °C (±5 °F)

Table 15 Equipment requirements for salt martempering aircraft landing-gear parts of 4330 steel

Production requirements	
Production per hour, kg (lb)	One load of 270 (600)
Equipment requirements	
Martempering furnace	Immersion-heated steel salt pot(a)
Size of work chamber(b), m (in.)	1.5 by 1.9 (60 by 75)
Capacity of salt pot, kg (lb)	21,850 (48,200)
Type of salt	Nitrate-nitrite
Operating temperature of salt pot(c), °C (°F)	205 (400)
Agitation, kW (hp); mm (in.)	Two 2.2 (3), 180 (7) propeller agitators
Cooling system	Natural draft
Cooling capacity, kg/h (lb/h); °C (°F)	455 (1000) (gross) from 845–205 (1550–400)(d)

Note: Parts were treated as follows: austenitize for 45 to 60 min at 845 °C (1550 °F), martemper for 5 to 7 min at 205 °C (400 °F), air cool to room temperature, and then temper at 425 °C (800 °F) to produce a hardness of 37 to 42 HRC. (a) Resistance immersion heaters (120 kW). (b) Depth of salt, 4.72 m (186 in.). (c) Temperature automatically controlled to ±3 °C (±5 °F). (d) Maximum temperature rise to 215 °C (415 °F)

- Check neutrality of austenitizing bath (if salt containing cyanide is used for austenitizing, the cyanide content should be less than 2%).
- Remove sludge from martempering bath; mechanical separators (filter baskets or pans) eliminate the need for this operation.
- Check salt level.
- Check agitation of bath and adjust as needed.

Weekly:

- Lubricate all moving parts.
- Remove sludge or contamination from the surface of the immersion heaters (radiant tubes or electrodes) and from the walls, bottom, and top of the furnace.

Monthly:

- Check operation of all moving parts, such as blowers and pumps; adjust belt tension and alignment of shafts.
- Check electrical contacts of all contactors and relays, and repair as required; examine all electrical devices for proper operation.
- Remove fallen parts or debris from the quench header or quench area to avoid fouling.
- Check heating and cooling facilities.

Semiannually or annually:

- Remove the salt from the furnace and check the condition of the pot, pumps, and heating system.
- Clean and repair all electrical parts, such as contactors, relays, motors, and motor starters. (It is especially important to remove condensed salt from all terminals and transformers.)
- Clean and repair all moving parts and lubricate as required.

Oil System Maintenance

Following is a typical procedure for maintaining a high-temperature (175 to 205 °C, or 350 to 400 °F) oil-quench system:

Daily:

- Observe oil-temperature indicators every hour; verify the indicated temperature with a potentiometer each day.
- Check oil level in sight gage to ensure proper level and function of the automatic makeup unit.
- Check closed system frequently for proper pressure of the atmosphere blanket over the quenching oil; pressure of this blanket should be equal to furnace-atmosphere pressure.
- Check oil agitation by either observing through sight doors and noting if the pump shaft is operating at the proper speed, or, preferably, by monitoring the load on the pump motor.

- Check condition of oil on parts emerging from quench. Undue discoloration or varnishing may indicate deterioration of oil.
- Visually check the performance of gas-fired immersion-heating tubes.

Weekly:

- Check condition of oil visually and by viscosity testing; record findings on graph to note trends.
- Check speed of pump shaft with tachometer to ensure consistent oil flow.
- Check performance of temperature-control devices through on-off range to ensure positive control.
- Check thermocouple.
- Check for proper operation and elevations of quenching mechanism or elevator.
- Check and clean pilot lights.
- Check and clean electrodes in ignition system of gas burners.
- Check safety control on gas lines for heating tubes.
- Check makeup oil supply.
- Check motor-operated venting systems for proper operation, and remove carbon buildup to prevent jamming.

Semiannually:

- Drain oil from, and clean, quench tank.
- Operate and inspect functioning of mechanical elements such as elevator, oil pumps, and adjustable oil deflectors.
- Check gas-fired heating tubes.
- Inspect V-belts for pump drive and agitators; replace if necessary.
- Check condition of temperature-measuring system.
- Determine condition of oil by physical and chemical testing of various properties.

Racking and Handling

The techniques for handling parts to be martempered may be similar to those for conventional oil quenching. However, racking and fixturing can be simplified for some martempering applications because distortion is less.

Example 8: Elimination of Heavy Fixturing with Martempering. Extensive fixturing was required during conventional oil quenching of shaftlike parts made of 52100 steel. These parts were approximately 180 mm (7 in.) long and had a major diameter of 25 mm (1 in.). The fixtures weighed approximately the same as the workload.

A change from conventional quenching to martempering for 5 min in salt at 245 °C (475 °F) eliminated the need for the heavy, expensive fixtures and made it possible to hold distortion within the required limits. For martempering, the parts were placed vertically in simple

fabricated baskets. This practice also resulted in a greater “payload.”

The manner in which workpieces enter the bath generally is less critical in martempering than in conventional oil quenching. For example, large flat parts do not dish as much when martempered. However, the shape of each part must be considered individually, and some trial and error often is necessary before an optimum handling technique can be developed.

Nesting of small parts can be a problem, and development of a handling method that will result in uniform quenching often requires experimentation. A technique that proved successful for one application is described subsequently.

Example 9: Techniques to Improve Uniform Quenching during Martempering. Flat blades that were not well suited to fixturing or wiring had a tendency to nest, which caused nonuniform quenching during martempering. This problem was overcome by use of a pump that directed a heavy flow of molten salt upward through a perforated metal basket, which kept the parts separated. This technique requires that the flow of salt be regulated to the floating characteristics of the workpieces.

For fixturing of parts, one of the following considerations may apply:

- Long, slender parts should be suspended.
- Symmetrical parts, such as bearing races and cylinders, can be stacked and supported on a rack or grid.
- Flat parts, such as circular saw blades, mower blades, and clutch plates, are best supported on horizontal slotted rods that provide the necessary separation.
- Coils of wire are supported either vertically on a spider-type grid or horizontally on support rods.
- Small parts can be loaded into a perforated ladle or basket and then dumped into the quench to obtain intimate quenching of all parts.
- Fixture design should be simple, free of welds (if possible), and easy to maintain. For example, fixtures supporting vertical stacks of bearing races should be removable for periodic grinding to maintain flatness.

Proper spacing of workpieces to permit good flow of the quenchant around each part is an important consideration in martempering. Also, the combined weight of workpieces and fixtures must be limited to the extent that the heat they contain is insufficient to cause a sharp increase in the temperature of the quenchant. In this regard, the size of a salt bath furnace is determined not only by the physical size of the work but also by design requirements such as salt-separating systems, a means for agitation of the salt, and sufficient area for dissipation of heat through sidewalls.

Washing the Work

Regardless of the martempering medium used, the workload should not be washed until transformation is complete (all portions of workpieces should be near room temperature).

Martempering salts are completely water soluble, and any hot-water soaking tank or spray washer will remove all salt from accessible areas. Cold water can be used, but its washing action is much slower.

The speed of washing will depend on how much hot water unsaturated with salt flows over the salt-coated surface. Therefore, agitation will increase the washing action, and a device such as an open-impeller sump pump can be used in a soaking tank to direct a stream of hot water into recessed areas. Steam jets may be used as supplementary equipment to remove salt from sections of intricately shaped parts with difficult-to-reach recesses for which conventional washing equipment is inadequate.

Quenching oils often present washing problems. Martempering oil adheres more tenaciously to workpieces than does conventional quenching oil because of its higher viscosity, as high as 1200 Saybolt universal seconds (SUS) at 38 °C (100 °F), compared with 100 SUS at 38 °C for conventional oil.

Basically, the washing equipment is the same for both types of quenching oils, but a heavy-duty cleaner must be used to remove martempering oil. Several proprietary heavy-duty silicate-alkaline cleaners are available for cleaning parts martempered in hot oil. Vapor degreasing and steam cleaning without detergent may be used in special applications.

REFERENCES

1. M.A. Grossmann and E.C. Bain, *Principles of Heat Treatment*, 5th ed., American Society for Metals, 1964
2. B.F. Shepherd, *Martempering, The Iron Age*, Vol 4, Feb 1943, p 45–48
3. R.F. Harvey, Development, Principles and Applications of Interrupted Quench Hardening, *J. Franklin Inst.*, Vol 255, Feb 1953, p 93–99
4. H.E. Boyer, *Techniques of Quenching, Quenching Theory and Technology*, 2nd ed., B. Liscic, H.M. Tensi, L.C. Canale, and G.E. Totten, Ed., CRC Press and IFHTSE cooperation, Boca Raton, FL, 2010, p 485–507
5. *Heat Treating*, Vol 4, *ASM Handbook*, ASM International, 1991
6. B.F. Shepherd, Mechanical and Metallurgical Advantages of Martempering Steel, *Prod. Eng.*, Vol 16, 1945, p 438–441
7. J.R. Keough, W.J. Laird, and A.D. Godding, Austempering of Steel, *Heat Treating*, Vol 4, *ASM Handbook*, ASM International, 1991, p 152

8. J. Vatauvuk and F.D. Santos, Comportamento Quanto à Tenacidade ao Impacto do aço AISI O1 com Microestruturas Bainítica e Martensítica Processado por Diferentes Ciclos de Tratamento Térmico, *Temas em Tratamentos Térmicos (TTT)* (Atibaia, São Paulo, Brazil), 2008
9. F.D. Santos, H. Goldenstein, and J. Vatauvuk, The Modified Martempering and Its Effect on the Impact Toughness of a Cold Work Tool Steel, *SAE Technical Papers Series*, 2011
10. P.V. Krishna, R.R. Srikant, M. Iqbal, and N. Sriram, Effect of Austempering and Martempering on the Properties of AISI 52100 Steel, *ISRN Tribol.*, 2013
11. G.P. Dubal, The Basics of Molten Salt Quenchants, *Heat Treat. Prog.*, Aug 2003, p 81–86
12. G. Wahl, Influence of Salt Quench on Distortion, *Proceedings of the Second International Conference on Quenching and the Control of Distortion*, G.E. Totten, M.A. Howes, S.J. Sjostrom, and K. Funatani, Ed. (Cleveland, OH), ASM International, 1996, p 417–422
13. G.E. Totten, C.E. Bates, and N.A. Clinton, *Handbook of Quenchants and Quenching Technology*, G.E. Totten, C.E. Bates, and N.A. Clinton, Ed., ASM International, 1993
14. R.J. Brennan, How to Use Martempering Oils for Control of Part Distortion, *Ind. Heat.*, Jan 1993, p 29–31
15. J.M. Hampshire, User Experience of Hot Oil Quenching, *Heat Treat. Met.*, 1984, p 15–20
16. J. Prichard and S. Rush, “Vacuum Hardening High-Strength Steels: Oil vs. Gas Quenching,” Vac Aero International Inc., Jan 23, 2013, www.vacaero.com/Education-Training/Magazine-Articles/vacuum-hardening-high-strength-steels-oil-vs-gas-quenching.html
17. R.N. Penha, J.C. Vendramim, and L.C. Canale, Tensões Residuais Térmicas Obtidas Após a Martêmpera e a Têmpera a Vácuo do aço Ferramenta AISI H13, *Temas sobre Tratamentos Térmicos* (Atibaia, São Paulo, Brazil), 2012
18. B. Zieger, Vacuum Heat Treatment of Hot-Work Steel, *Proceedings of the Sixth International Tooling Conference* (Karlstad, Sweden), 2002, p 643–655
19. J.J. Since and O. Irretier, Vacuum Heat Treatment and High Pressure Gas Quenching—Aspects in Distortion Control, *Heat Process.*, Vol 8, 2010, p 1–10

Cold and Cryogenic Treatment of Steel

Revised by F. Diekman, Controlled Thermal Processing

COLD TREATING OF STEEL is widely accepted within the metallurgical profession as a supplemental treatment that can be used to enhance the transformation of austenite to martensite and to improve stress relief of castings and machined parts. Common practice identifies $-84\text{ }^{\circ}\text{C}$ ($-120\text{ }^{\circ}\text{F}$) as the optimal temperature for cold treatment. There is evidence, however, that cryogenic treatment of steel (also referred to as deep cryogenic treatment, or DCT), in which material is brought to a temperature on the order of $-184\text{ }^{\circ}\text{C}$ ($-300\text{ }^{\circ}\text{F}$), improves certain properties beyond the improvement attained at cold treatment temperatures. This discussion explains the practices employed in the cold treatment of steel and presents some of the results of using cryogenic treatment to enhance steel properties.

Cold Treatment of Steel

Cold treatment of steel consists of exposing the ferrous material to subzero temperatures to either impart or enhance specific conditions or properties of the material. Increased strength, greater dimensional or microstructural stability, improved wear resistance, and relief of residual stress are among the benefits of the cold treatment of steel. Generally, one hour of cold treatment for each 2.54 cm (1 in.) of cross section is adequate to achieve the desired results.

All hardened steels are improved by a proper subzero treatment to the extent that there will be less tendency to develop grinding cracks and therefore they will grind much more easily after the elimination of the retained austenite and the untempered martensite.

Hardening and Retained Austenite

Whenever hardening is to be done during heat treating, complete transformation from austenite to martensite generally is desired prior to tempering. From a practical standpoint, however, conditions vary widely, and 100% transformation rarely, if ever, occurs. Cold treating may be useful in many instances for improving the percentage of transformation and thus for enhancing properties.

During hardening, martensite develops as a continuous process from start (M_s) to finish (M_f) through the martensite formation range. Except in a few highly alloyed steels, martensite starts to form at well above room temperature. In many instances, transformation essentially is complete at room temperature. Retained austenite tends to be present in varying amounts, however, and when considered excessive for a particular application, must be transformed to martensite and then tempered.

Cold Treating versus Tempering. Immediate cold treating without delays at room temperature or at other temperatures during quenching offers the best opportunity for maximum transformation to martensite. In some instances, however, there is a risk that this will cause cracking of parts. Therefore, it is important to ensure that the grade of steel and the product design will tolerate immediate cold treating rather than immediate tempering. Some steels must be transferred to a tempering furnace when still warm to the touch to minimize the likelihood of cracking. Design features such as sharp corners and abrupt changes in section create stress concentrations and promote cracking.

In most instances, cold treating is not done before tempering. In several types of industrial applications, tempering is followed by deep freezing and retempering without delay. For example, such parts as gages, machineways, arbors, mandrils, cylinders, pistons, and ball and roller bearings are treated in this manner for dimensional stability. Multiple freeze-draw cycles are used for critical applications.

Cold treating also is used to improve wear resistance in such materials as tool steels, high-carbon martensitic stainless steels, and carburized alloy steels for applications in which the presence of retained austenite may result in excessive wear. Transformation in service may cause cracking and/or dimensional changes that can promote failure. In some instances, more than 50% retained austenite has been observed. In such cases, no delay in tempering after cold treatment is permitted, or cracking can develop readily.

Process Limitations. In some applications in which explicit amounts of retained austenite are considered beneficial, cold treating might be detrimental. Moreover, multiple tempering,

rather than alternate freeze-temper cycling, generally is more practical for transforming retained austenite in high-speed and high-carbon/high-chromium steels.

Hardness Testing. Lower-than-expected Rockwell C hardness (HRC) readings may indicate excessive retained austenite. Significant increases in these readings as a result of cold treatment indicate conversion of austenite to martensite. Superficial hardness readings, such as HR15N, can show even more significant changes.

Precipitation-Hardening Steels. Specifications for precipitation-hardening steels may include a mandatory deep freeze after solution treatment and prior to aging.

Shrink Fits. Cooling the inner member of a complex part to below ambient temperature can be a useful way of providing an interference fit. Care must be taken, however, to avoid the brittle cracking that may develop when the inner member is made of heat treated steel with high amounts of retained austenite, which converts to martensite on subzero cooling.

Stress Relief

Residual stresses often contribute to part failure and frequently are the result of temperature changes that produce thermal expansion and phase changes, and consequently, volume changes.

Under normal conditions, temperature gradients produce nonuniform dimensional and volume changes. In castings, for example, compressive stresses develop in lower-volume areas, which cool first, and tensile stresses develop in areas of greater volume, which cool last. Shear stresses develop between the two areas. Even in large castings and machined parts of relatively uniform thickness, the surface cools first and the core last. In such cases, stresses develop as a result of the phase (volume) change between those layers that transform first and the center portion, which transforms last.

When both volume and phase changes occur in pieces of uneven cross section, normal contractions due to cooling are opposed by transformation expansion. The resulting residual stresses will remain until a means of relief is

applied. This type of stress develops most frequently in steels during quenching. The surface becomes martensitic before the interior does. Although the inner austenite can be strained to match this surface change, subsequent interior expansions place the surface martensite under tension when the inner austenite transforms. Cracks in high-carbon steels arise from such stresses.

The use of cold treating has proved beneficial in stress relief of castings and machined parts of even or nonuniform cross section. Features of the treatment include:

- Transformation of all layers is accomplished when the material reaches $-84\text{ }^{\circ}\text{C}$ ($-120\text{ }^{\circ}\text{F}$).
- The increase in volume of the outer martensite is counteracted somewhat by the initial contraction due to chilling.
- Rewarm time is controlled more easily than cooling time, allowing equipment flexibility.
- The expansion of the inner core due to transformation is balanced somewhat by the expansion of the outer shell.
- The chilled parts are handled more easily.
- The surface is unaffected by low temperature.
- Parts that contain various alloying elements and that are of different sizes and weights can be chilled simultaneously.

Advantages of Cold Treating

Unlike heat treating, which requires that temperature be controlled precisely to avoid reversal, successful transformation through cold treating depends only on the attainment of the minimum low temperature and is not affected by lower temperatures. As long as the material is chilled to $-84\text{ }^{\circ}\text{C}$ ($-120\text{ }^{\circ}\text{F}$), transformation will occur; additional chilling will not cause reversal.

Time at Temperature. After thorough chilling, additional exposure has no adverse effect. In heat treating, holding time and temperature are critical. In cold treatment, materials of different compositions and of different configurations may be chilled at the same time, even though each may have a different high-temperature transformation point. Moreover, the warm-up rate of a chilled material is not critical as long as uniformity is maintained and large temperature gradient variations are avoided.

The cooling rate of a heated piece, however, has a definite influence on the end product. Formation of martensite during solution heat treating assumes immediate quenching to ensure that austenitic decomposition will not result in the formation of bainite and cementite. In large pieces comprising both thick and thin sections, not all areas will cool at the same rate. As a result, surface areas and thin sections may be highly martensitic, and the slower-cooling core may contain as much as 30 to 50% retained austenite. In addition to incomplete transformation, subsequent natural aging induces stress

and also results in additional growth after machining. Aside from transformation, no other metallurgical change takes place as a result of chilling. The surface of the material needs no additional treatment. The use of heat frequently causes scale and other surface deformations that must be removed.

Equipment for Cold Treating

A simple home-type deep freezer can be used for transformation of austenite to martensite. Temperature will be approximately $-18\text{ }^{\circ}\text{C}$ ($0\text{ }^{\circ}\text{F}$). In some instances, hardness tests can be used to determine if this type of cold treating will be helpful. Dry ice placed on top of the work in a closed, insulated container also is commonly used for cold treating. The dry ice surface temperature is $-78\text{ }^{\circ}\text{C}$ ($-109\text{ }^{\circ}\text{F}$), but the chamber temperature normally is approximately $-60\text{ }^{\circ}\text{C}$ ($-75\text{ }^{\circ}\text{F}$).

Mechanical refrigeration units with circulating air at approximately $-87\text{ }^{\circ}\text{C}$ ($-125\text{ }^{\circ}\text{F}$) are commercially available. A typical unit has these dimensions and operational features:

- Chamber volume, up to 2.7 m^3 (95 ft^3)
- Temperature range, 5 to $-95\text{ }^{\circ}\text{C}$ (40 to $-140\text{ }^{\circ}\text{F}$)
- Load capacity, 11.3 to 163 kg/h (25 to 360 lb/h)
- Thermal capacity, up to 8870 kJ/h (8400 Btu/h)

Although liquid nitrogen at $-195\text{ }^{\circ}\text{C}$ ($-320\text{ }^{\circ}\text{F}$) may be employed, it is used less frequently than any of the previous methods because of its cost.

Cryogenic Treatment of Steels

Cryogenic treatment, also referred to as cryogenic processing, deep cryogenic processing, deep cryogenic treatment (DCT), cryogenic tempering, and deep cryogenic tempering, is a distinct process that uses extreme cold to modify the performance of materials. (The use of the word *tempering* is a misnomer, because this is not a tempering process.)

The process is differentiated from cold treatment by the use of lower temperatures, the presence of distinct time/temperature profiles, and its application to materials other than steel (Ref 1). Cryogenic treatment has been in existence only since the late 1930s, making it a relatively new and emerging process. The late development of the process is mainly due to the fact that cryogenic temperatures have been available in useful commercial quantities only since the early 1900s.

Cryogenic treatment can provide wear-resistance increases several times those created by cold treatment with hardened steels (Ref 2). The process is not confined to hardened steels, but also shows results with most metals,

cemented carbides, and some plastics (Ref 3–5). Use of the process on metals other than steel produces similar effects as with steel. Results of the process include relief of residual stresses (Ref 6); reduced retained austenite (in hardened steel); the precipitation of fine carbides in ferrous metals (Ref 7, 8); and increased wear resistance, fatigue life, hardness, dimensional stability, thermal and electrical conductivity, and corrosion resistance (Ref 9).

What are cryogenic temperatures? The scientific community generally defines cryogenic temperatures as temperatures below $-150\text{ }^{\circ}\text{C}$ ($-238\text{ }^{\circ}\text{F}$, or 123 K) (Ref 10). This, admittedly, is an artificial upper limit. Temperatures used presently in cryogenic treatment are generally $-185\text{ }^{\circ}\text{C}$ ($-300\text{ }^{\circ}\text{F}$, or 89 K). These are temperatures easily reached with liquid nitrogen. Some work is being done with liquid helium at temperatures down to $-268\text{ }^{\circ}\text{C}$ ($-450\text{ }^{\circ}\text{F}$, or approximately 6 K).

Cryogenic treatment was made easier to achieve and more successful by the development of microprocessor-based temperature controls in the 1960s and 1970s and by the pioneering research by Randall Barron of Louisiana Tech University. Research into the process has been accelerating. The Cryogenic Society of America maintains a database of peer reviewed research papers (Ref 11).

Cryogenic Treatment Cycles

One distinct difference from cold treatment is that cryogenic processing requires a slow drop in temperature in order to reap all benefits of the process. The ramp down in temperature usually is on the order of 0.25 to $0.5\text{ }^{\circ}\text{C/min}$ (32.5 to $32.9\text{ }^{\circ}\text{F/min}$). The object of this slow ramp down is to avoid high-temperature gradients in the material that can create harmful stresses, and to allow time for the crystal lattice structure to accommodate the changes that are occurring.

Typical cryogenic treatment consists of a slow cool-down from ambient temperature to approximately $-193\text{ }^{\circ}\text{C}$ ($-315\text{ }^{\circ}\text{F}$), where it is held for an appropriate time. Hold periods range from 4 to 48 h depending on the material. At the end of the hold period, the material is brought back to ambient temperature at a rate of approximately $2.5\text{ }^{\circ}\text{C/min}$ ($36.5\text{ }^{\circ}\text{F/min}$). The temperature-time plot for this cryogenic treatment cycle is shown in Fig. 1. By conducting the cool-down cycle in gaseous nitrogen, temperature can be controlled accurately, and thermal shock to the material is avoided. Single-cycle tempering usually is performed after cryogenic treatment to improve impact resistance, although double or triple tempering cycles sometimes are used.

It is worthy of note that most time-temperature profiles have been empirically developed. Some research is being done to optimize the profiles for individual steels. For instance, some research indicates the holding time for AISI

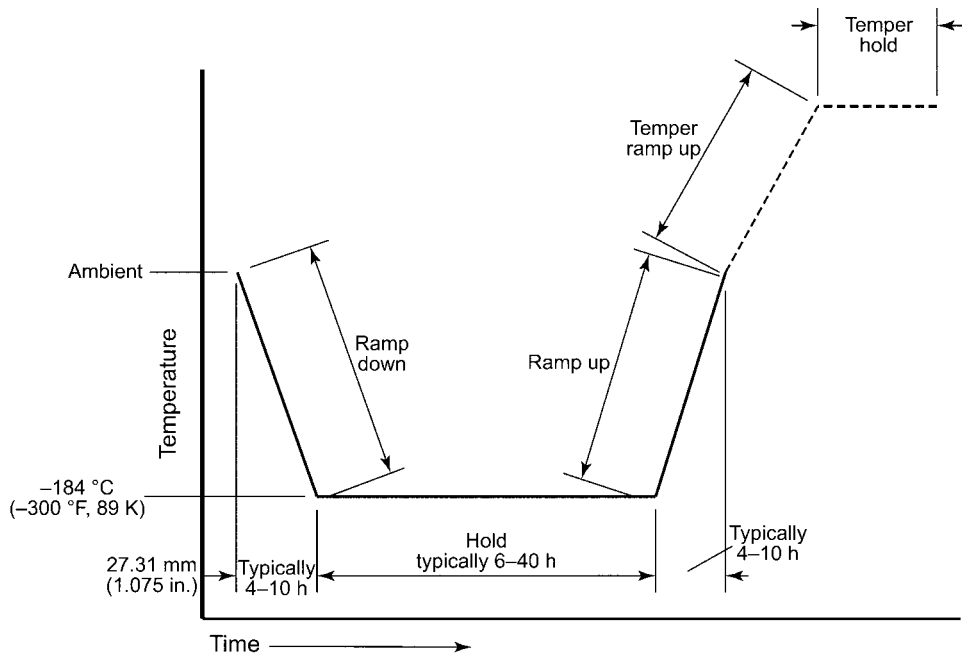


Fig. 1 Plot of temperature vs. time for the cryogenic treatment cycle. Tempering may or may not be necessary, depending on the material treated. Some materials require multiple tempering cycles. Some companies are now treating materials down to $-268\text{ }^{\circ}\text{C}$ ($-450\text{ }^{\circ}\text{F}$, or 6 K)

T42 steel should not be longer than 8 h (Ref 12). In contrast, research indicates that the hold time should be 36 h for AISI D2 (Ref 13). This indicates there is much research to be done to optimize the process for all materials. Research into the optimal ramp down times, hold times, and ramp up times would maximize the effect of the process and minimize the time needed to accomplish its results.

There are several theories behind the effects of cryogenic treatment. One theory involves the more nearly complete transformation of retained austenite into martensite. This theory has been verified by x-ray diffraction measurements. Another theory is based on the strengthening of the material brought about by precipitation of submicroscopic carbides as a result of the cryogenic treatment (Ref 7, 8). Allied with this is the reduction in internal stresses in the martensite that happens when the submicroscopic carbide precipitation occurs. A reduction in microcracking tendencies resulting from reduced internal stresses also is suggested as a reason for improved properties. Studies also show reduction in residual stresses. Another theory postulates that the extreme cold reduces the free energy of the crystal structure and creates a more orderly structure. Another area to consider is the basic effect of cold on the crystal structure of metals. Point defects in the crystal structure are temperature dependent. Lowering the temperature of the crystal structure will cause the number of point defects in the crystal structure to change according to:

$$N_d = N \exp(-E_d/kT)$$

where N_d is the number of defects present, N is the total number of atomic sites, E_d is the activation energy needed to form the defect, k is the Boltzmann constant, and T is the absolute temperature. Reducing the temperature at a suitably slow rate drives the point defects out of the structure to the grain boundaries. In other words, the solubility of vacancies and other point defects in the matrix drops. This could account for some of the effects seen in DCT.

In the past, the absence of a clear-cut understanding of the mechanism by which cryogenic treatment improves performance had hampered its widespread acceptance by metallurgists. Some confusion has arisen from the fact that there are a number of different effects on metals, many of which cannot be seen in simple microstructural examination of the material with a light microscope. The lack of easily detected microstructural changes led many to discount the process. Another reason was the generally accepted belief that nothing happens to solid objects as the temperature drops. Extreme cold has been available on earth only for about 100 years. Understanding of materials science developed with the observation that heat changes properties. Much of the early research was centered around determining whether or not cryogenic treatment actually provided the advantages claimed. Because the early research and actual industry usage have proven the validity of the process, research

now is turning to determine why the results are seen and how to maximize those results.

Uses of Deep Cryogenic Treatment

Deep cryogenic treatment is used in many ways to reduce wear. It is in common use to control distortion of metal objects, modify the vibrational characteristics of metals, increase fatigue life, reduce abrasive wear, and reduce electrical resistance. It is safe to say the applications for this process are extremely broad.

The process is in commercial use for high-speed steel (HSS) and carbide cutting tools, knives, blanking tools, forming tools, and more. Research as far back as 1973 indicates that deep cryogenic processing results in over three times life increase in end mills, 82 times life improvement in punches, over two times the life in thread dies, six times the life in copper resistance electrodes, six times the life in progressive dies, and over four to five times the life in broaches (Ref 2). Research estimates a 50% reduction in tooling costs with H13 and M2 steels that have been deep cryogenically treated (Ref 14).

Other studies have shown that DCT increases abrasion resistance of cast iron. Cast iron brake rotors consistently show a three to five times life increase when tested to SAE2707 brake dynamometers (Ref 15). This has been validated against real-world experience in passenger cars, racing cars, trucks, and mining vehicles.

Deep cryogenic treatment also has been proven to create a phase change in cemented carbide (Ref 5). A study by the National Aeronautics and Space Administration (NASA) proved the release of residual stresses in welded aluminum (Ref 6), and other studies prove increases in fatigue life in steel springs (Ref 16) and in load capacity of gears (Ref 17).

Deep cryogenic treatment is used in the automotive racing industry to increase life in virtually every engine component. Drive line components such as transmission and differential gears, suspension springs, torsion bars, axles, suspension members, and, of course, brakes are treated.

Deep cryogenic treatment also is in commercial use by musical instrument makers. Yamaha Wind Instruments has done extensive testing of DCT and offers the process on its wind instruments (Ref 18). There is much activity in the high-performance stereo industry in treating vacuum tubes, wire, power cords, vacuum tubes, transformers, connectors, and more.

Equipment for Cryogenic Treatment

All cryogenic treatment equipment is comprised of a thermally insulated container and some means of extracting the latent heat of the payload to reach the desired low temperature. In most cases the insulation is a solid material that contains small closed cells of trapped still air. The thermal conductivity of such insulation essentially is that of still, non-convecting air, assuming that the solid material

that encloses the air pockets is of thin cross section and low conductivity. Examples are polyurethane foam, aerogel, and expanded glass foam. Fifteen centimeters (6 in.) of any of these will conduct approximately (15 Btu/h.ft²) across a temperature differential of 204 °C (400 °F), which exists between the interior of a refrigerator at -195 °C (-320 °F) and ambient temperature of 26 °C (80 °F).

These solid insulating materials are relatively inexpensive and, in the case of foamed-in-place polyurethane, can readily fill irregularly shaped cavities. They all suffer from one important drawback: temperature cycling establishes a temperature gradient across the insulating slab that results in differential contraction in the material. Repeated temperature cycles ultimately result in fatigue cracking of the insulation. Energy expenditure to sustain the temperature difference goes up, and temperature uniformity within the refrigerator may deteriorate.

The use of vacuum insulation in cryoprocessor design avoids these problems. A vacuum insulated container consists of two concentric shells, usually cylindrical, separated by a small distance relative to their diameters, which are joined around the perimeter of one end of the shells. The space between the shells contains reflective insulation and is evacuated to a pressure of approximately 533 Pa (10⁻⁶ torr). This essentially eliminates heat flow by conduction and convection because most of the conducting or convecting gas has been removed. Heat gain via infrared radiation is minimized by multiple reflective layers placed in the vacuum space. Heat flow across a vacuum-insulated space, given a temperature difference across the walls of 204 °C (400 °F), is (0.008 Btu/h.ft²), a factor of 1900 better than solid insulation of 15 cm (6 in.) thickness (Ref 19). The principle mode of heat transmission into the interior of a vacuum-insulated container is metallic conduction through the perimeter that joins the inner and outer shells.

In addition to providing a barrier to heat flow relative to solid insulation, the vacuum-insulated vessel is immune to thermal cycling fatigue. Additionally, the vacuum-insulated vessel can sustain elevated operating temperatures far in excess of that permissible with the use of polyurethane. This permits the post-refrigeration tempering of components in one device, eliminating the need for a separate tempering oven.

Heat extraction from the payload is effected by the phase change of a low-boiling-point fluid. If mechanical refrigeration is used, a high-pressure fluid is allowed to expand and become a gas within an evaporator coil inside the insulated space. The evaporator coil is a heat exchanger that absorbs heat from the payload via convection, natural or forced, within the chamber. This ensures the relatively slow cooling of the payload and avoids thermal shock resulting from too rapid cooling. Rapid cooling can cause shrinkage of the outside of

the cooled component while the relatively warm interior does not shrink. Tensile stress induced this way can lead to cracking or the initiation of residual stress, especially at sharp edges. Reaching cryogenic temperatures by mechanical refrigeration for industrial size payloads requires multistage refrigeration. These are very expensive machines to build and maintain.

Fortunately, liquid nitrogen is abundant, readily available, and relatively inexpensive. It has a boiling point of -196 °C (-321 °F) and a heat of vaporization of approximately 150 Btu/liter. It is produced in huge industrial gas production facilities and delivered to the facility where the expansion and phase change occurs, free of the capital and maintenance expense demanded by in-house mechanical refrigerators.

Two other approaches have been tried but have difficulties: a hybrid of mechanical refrigeration and LN₂ (liquid nitrogen) cooling, and a controlled immersion of components into LN₂.

The hybrid approach uses mechanical refrigeration to do an initial cooling of the payload to some sub-atmospheric temperature that is well above the desired cryogenic range. At that point a spray of LN₂ droplets is showered onto the payload to bring the temperature down to the desired point. Unless the mechanical refrigeration has sufficient Btu removal rate, the payload will be substantially warmer than indicated by the thermocouple that monitors chamber temperature. This causes the LN₂ spray to come on prematurely, with the resultant rapid cooling of parts and the increased possibility of cracking.

The controlled immersion of components into LN₂ has been tried in two versions: the payload is lowered slowly into a pool of LN₂, or a chamber is slowly flooded with LN₂ so the liquid level rises to and eventually covers the payload.

Both versions suffer from a serious weakness arising from the effects of fundamental physics. First, the temperature gradient above a pool of LN₂ is very steep. Second, the rate of heat transport between warm solid and a cold gas at -195 °C (-320 °F) is much slower than the rate between the same warm solid and a liquid at -195 °C. Therefore, in either of the above versions, a slow decrease in the distance separating the part and the liquid does not ensure a slow rate of cooling of the part. The risk of thermal shock is increased by the steep temperature gradient above the liquid and the sudden increase in the heat transfer rate when liquid contact is made.

Cryogenic treatment is a process that holds great promise to modify and improve products in many markets, including reducing wear and extending the service life of many components. Continuing research efforts are being undertaken to understand the underlying science of DCT so process improvements can be made and the technology advanced.

ACKNOWLEDGMENT

Article revised and updated from E.A. Carlson, Cold Treating and Cryogenic Treatment of Steel, *Heat Treating*, Vol 4, *ASM Handbook*, ASM International, 1991, p 203-206.

REFERENCES

1. R.F. Barron, *A Study of the Effects of Cryogenic Treatment on Tool Steel Properties*,
2. R.F. Barron, Yes, Cryogenic Treatments Can Save You Money!, *Fall Corrugated Containers Conference* (Denver, CO), Technical Association of the Pulp and Paper Industry, 1973, p 35-40
3. S. Kalia, *Cryogenic Processing: A Study of Materials at Low Temperatures*, *J. Low Temp. Phys.*, Vol 158 (No. 5-6), March 2010, p 934-945
4. H.A. Stewart, A Study of the Effects of Cryogenic Treatment of Tool Steel Properties, *Forest Prod. J.*, Feb 2004, p 53-56
5. A. Yong, "Cryogenic Treatment of Cutting Tools," doctoral thesis, National University of Singapore, 2006
6. P. Chen, T. Malone, R. Bond, and P. Torres, "Effects of Cryogenic Treatment on the Residual Stress and Mechanical Properties of an Aerospace Aluminum Alloy," NASA, Huntsville, AL, 2002
7. D.N. Collins, *Cryogenic Treatment of Tool Steels*, *Adv. Mater. Process.*, 1998
8. F. Meng, K. Tagashira, R. Azuma, and H. Sohma, "Role of Eta-Carbide Precipitations in the Wear Resistance Improvements of Fe-12Cr-MO-V-1.4C Steel," *ISIJ International*, 1994
9. S. Sendooran and P. Raja, *Metallurgical Investigation on Cryogenic Treated HSS Tool*
10. R. Radebaugh, About Cryogenics, *The MacMillan Encyclopedia Of Chemistry*, New York, 2002, <http://cryogenics.nist.gov/AboutCryogenics/about%20cryogenics.htm> (accessed July 17, 2013)
11. *Cryogenic Treatment Database*, Cryogenic Society of America, Inc., Oak Park, IL, www.cryogenictreatmentdatabase.org (accessed July 17, 2013)
12. C.L. Gogte, D.R. Peshwe, and R.K. Paretkar, Influence of Cobalt on the Cryogenically Treated W-Mo-V High Speed Steel, *Cryogenic Treatment Database*, Nov 2010, www.cryogenictreatmentdatabase.org/article/influence_of_cobalt_on_the_cryogenically_treated_w-mo-v_high_speed_steel/ (accessed July 17, 2013)
13. D. Das, A.K. Dutta, and K.K. Ray, Influence of Varied Cryotreatment on the Wear Behavior of AISI D2 Steel, *Wear*, Vol 266 (No. 1-2), Jan 2009, p 297-309
14. A. Molinari et al., Effect of Deep Cryogenic Treatment on the Mechanical Properties of Tool Steels, *J. Mater. Process.*

- Tech.*, Vol 118 (No. 1–3), Dec 2001, p 350–355
15. SAE2707 Method B, Society of Automotive Engineers, July 2004
 16. D.L. Smith, “The Effect of Cryogenic Treatment on the Fatigue Life of Chrome Silicon Steel Compression Springs,” Ph.D. thesis, Marquette University, 2001
 17. A. Swiglo, “Deep Cryogenic Treatment to Increase Service Life, The Instrumented Factory for Gears, Chicago,” INFAC Industry Briefing, 2000
 18. Cryogenic Treated YTR-8335RGS Trumpets, *Yamaha Bell and Barrel*, Aug 2010, <http://yamahawinds.wordpress.com/tag/cryogenic-treatment/> (accessed July 18, 2013)
 19. J. Levine, Cryogenic Equipment, *Heat Treat. Prog.*, 2001, p 42–44

SELECTED REFERENCES

- R.F. Barron, Effect of Cryogenic Treatment on Lathe Tool Wear, in *Proceedings of the 8th International Congress of Refrigeration*, Vol 1, 1971
- R.F. Barron, Cryogenic Treatment Produces Cost Savings for Slitter Knives, *TAPPI J.*, Vol 57 (No. 5), May 1974
- R.F. Barron, Cryogenics CRYOTECH, *Heat Treat. Mag.*, June 1974
- R.F. Barron, Cryogenic Treatment of Metals to Improve Wear Resistance, *Cryogenics*, Vol 22 (No.5), Aug 1982
- R.F. Barron, “How Cryogenic Treatment Controls Wear,” presented at 21st Inter-Plant Tool and Gage Conference (Shreveport, LA), Western Electric Company, 1982
- R.F. Barron and C.R. Mulhern, Cryogenic Treatment of AISI-T8 and C1045 Steels, in *Advances in Cryogenic Engineering Materials*, Vol 26, Plenum Press, 1980
- R.F. Barron and R.H. Thompson, Effect of Cryogenic Treatment on Corrosion Resistance, *Advances in Cryogenic Engineering*, Vol 36, Plenum Press, 1990, p 1375–1379
- V.E. Gilmore, Frozen Tools, *Pop.Sci.*, June 1987
- M. Kosmowski, The Promise of Cryogenics, *Carbide Tool J.*, Nov/Dec 1981
- T.P. Sweeney, Jr., Deep Cryogenics: The Great Cold Debate, *Heat Treat.*, Feb 1986

Case Hardening of Steels

Introduction to Surface Hardening of Steels.	389	Copper Plating	399
Diffusion Methods of Surface Hardening.	389	Stop-off Paints	400
Carburizing and Carbonitriding	390		
Nitriding and Nitrocarburizing	393	Methods of Measuring Case Depth in Steels.	405
Applied Energy Methods.	395	Introduction	405
Other Methods	396	Measurement Specifications	405
Process Selection	397	Chemical Method	406
		Mechanical Methods.	407
Stop-Off Technologies for Heat Treatment.	399	Visual Methods	411
Mechanical Masking	399	Nondestructive Methods	413

Introduction to Surface Hardening of Steels*

Revised by Michael J. Schneider, The Timken Company, and Madhu S. Chatterjee, Bodycote

SURFACE HARDENING, a process that includes a wide variety of techniques (Table 1), is used to improve the wear resistance of parts without affecting the more soft, tough interior of the part. This combination of hard surface and resistance to breakage upon impact is useful in parts such as a cam or ring gear, bearings or shafts, turbine applications, and automotive components that must have a very hard surface to resist wear, along with a tough interior to resist the impact that occurs during operation. Most surface treatments result in compressive residual stresses at the surface that reduce the probability of crack initiation and help arrest crack propagation at the case-core interface. Further, the surface hardening of steel

can have an advantage over through hardening because less expensive low-carbon and medium-carbon steels can be surface hardened with minimal problems of distortion and cracking associated with the through hardening of thick sections.

There are two distinctly different approaches to the various methods for surface hardening (Table 1):

- Methods that involve an intentional buildup or addition of a new layer
- Methods that involve surface and subsurface modification without any intentional buildup or increase in part dimensions

The first group of surface-hardening methods includes the use of thin films, coatings, or weld overlays (hardfacings). Films, coatings, and overlays generally become less cost-effective as production quantities increase, especially when the entire surface of workpieces must be hardened. The fatigue performance of films, coatings, and overlays may also be a limiting factor, depending on the bond strength between the substrate and the added layer. Fusion-welded overlays have strong bonds, but the primary surface-hardened steels used in wear applications with fatigue loads include heavy case-hardened steels and flame- or induction-hardened steels. Nonetheless, coatings and overlays can be effective in some applications. With tool steels, for example, TiN and Al₂O₃ coatings are effective not only because of their hardness but also because their chemical inertness reduces crater wear and the welding of chips to the tool. Some overlays can impart corrosion-resistant properties. Overlays can be effective when the selective hardening of large areas is required.

This introductory article on surface hardening focuses exclusively on the second group of methods, which is further divided into diffusion methods and selective-hardening methods (Table 1). Diffusion methods modify the

chemical composition of the surface with hardening species such as carbon, nitrogen, or boron. Diffusion methods may allow effective hardening of the entire surface of a part and are generally used when a large number of parts are to be surface hardened. In contrast, selective surface-hardening methods allow localized hardening. Selective hardening generally involves transformation hardening (from heating and quenching), but some selective-hardening methods (selective nitriding, ion implantation, and ion beam mixing) are based solely on compositional modification. Factors affecting the choice of these surface-hardening methods are discussed in the section “Process Selection” in this article.

Diffusion Methods of Surface Hardening

As previously mentioned, surface hardening by diffusion involves the chemical modification of a surface. The basic process used is thermochemical because some heat is needed to enhance the diffusion of hardening elements into the surface and subsurface regions of a part. The depth of diffusion exhibits a time-temperature dependence such that:

$$\text{Case depth} = K\sqrt{\text{Time}} \quad (\text{Eq 1})$$

where the diffusivity constant, K , depends on temperature, the chemical composition of the steel, and the concentration gradient of a given hardening element. In terms of temperature, the diffusivity constant increases exponentially as a function of absolute temperature. Concentration gradients depend on the surface kinetics and reactions of a particular process.

Methods of hardening by diffusion include several variations of hardening elements (such as carbon, nitrogen, or boron) and of the

Table 1 Engineering methods for surface hardening of steels

Layer additions

• Hardfacing:

- Fusion hardfacing (welded overlay)
- Thermal spray (nonfusion-bonded overlay)

• Coatings:

- Electrochemical plating
- Chemical vapor deposition (electroless plating)
- Thin films (physical vapor deposition, sputtering, ion plating)
- Ion mixing

Substrate treatment

• Diffusion methods:

- Carburizing
- Nitriding
- Carbonitriding
- Nitrocarburizing
- Boriding
- Titanium-carbon diffusion
- Toyota diffusion process

• Selective-hardening methods:

- Flame hardening
- Induction hardening
- Laser hardening
- Electron beam hardening
- Ion implantation
- Selective carburizing and nitriding
- Use of arc lamps

* Revised from S. Lampman, Introduction to Surface Hardening of Steels, *Heat Treating*, Vol 4, *ASM Handbook*, ASM International, 1991, p 259–267

process method used to handle and transport the hardening elements to the surface of the part. Process methods for exposure involve the handling of hardening species in forms such as gas, liquid, or ions. These process variations naturally produce differences in typical case depth and hardness (Table 2). Factors influencing the suitability of a particular diffusion method include the type of steel (Fig. 1), the desired case hardness (Fig. 2), case depth (Fig. 3), the desired case profile, and cost.

It is also important to distinguish between total case depth and effective case depth. The effective case depth is typically about two-thirds to three-fourths the total case depth. (In some cases, the depth to the hardness value of 50 HRC or five points lower than the surface hardness is also specified.) The required

effective depth and the measurement technique must be specified so that the heat treater can process the parts for the correct time at the proper temperature.

Carburizing and Carbonitriding

Carburizing is the addition of carbon to the surface of low-carbon steels at temperatures (generally between 850 and 980 °C, or 1560 and 1800 °F) at which austenite, with its high solubility for carbon, is the stable crystal structure. With grades of steel engineered to resist grain coarsening at high temperatures and properly designed furnaces such as vacuum furnaces, carburizing above 980 °C (1800 °F) is practical to dramatically reduce carburizing time.

Hardening is accomplished when the high-carbon surface layer is quenched to form martensitic case with good wear and fatigue resistance superimposed on a tough, low-carbon steel core. Of the various diffusion methods (Table 2), gas carburization is the most widely used, followed by gas nitriding and carbonitriding.

Case hardness of carburized steels is primarily a function of carbon content. When the carbon content of the steel exceeds approximately 0.65%, additional carbon has no effect on hardness but does enhance hardenability. Carbon in excess of 0.65% may not be dissolved, which would require high temperatures to ensure carbon-austenite solid solution. Higher levels of carbon in the case will impact microstructural properties that can enhance performance characteristics such as wear, sliding contact fatigue,

Table 2 Typical characteristics of diffusion treatments

Process	Nature of case	Process temperature		Typical case depth	Case hardness, HRC	Typical base metals	Process characteristics
		°C	°F				
Carburizing							
Pack	Diffused carbon	815–1090	1500–2000	125 µm–1.5 mm (5–60 mils)	50–63(a)	Low-carbon steels, low-carbon alloy steel	Low equipment costs; difficult to control case depth accurately
Gas	Diffused carbon	815–980	1500–1800	75 µm–1.5 mm (3–60 mils)	50–63(a)	Low-carbon steels, low-carbon alloy steels	Good control of case depth; suitable for continuous operation; good gas controls required; can be dangerous
Liquid	Diffused carbon and possibly nitrogen	815–980	1500–1800	50 µm–1.5 mm (2–60 mils)	50–65(a)	Low-carbon steels, low-carbon alloy steels	Faster than pack and gas processes; can pose salt disposal problem; salt baths require frequent maintenance
Vacuum/LPC	Diffused carbon	815–1090	1500–2000	75 µm–1.5 mm (3–60 mils)	50–63(a)	Low-carbon steels, low-carbon alloy steels	Excellent process control; bright parts; faster than gas carburizing; high equipment costs
Nitriding							
Gas/LPN	Diffused nitrogen, nitrogen compounds	480–590	900–1100	125 µm–0.75 mm (5–30 mils)	50–70	Alloy steels, nitriding steels, stainless steels	Hardest cases from nitriding steels; quenching not required; low distortion; process is slow; is usually a batch process
Salt	Diffused nitrogen, nitrogen compounds	510–565	950–1050	2.5 µm–0.75 mm (0.1–30 mils)	50–70	Most ferrous metals including cast irons	Usually used for thin hard cases < 25 µm (1 mil); no continuous white layer; most are proprietary processes
Ion	Diffused nitrogen, nitrogen compounds	340–565	650–1050	75 µm–0.75 mm (3–30 mils)	50–70	Alloy steels, nitriding steels, stainless steels	Faster than gas nitriding; no white layer; high equipment costs; close case control
Carbonitriding							
Gas	Diffused carbon and nitrogen	760–870	1400–1600	75 µm–0.75 mm (3–30 mils)	50–65(a)	Low-carbon steels, low-carbon alloy steels, stainless steels	Lower temperature than carburizing (less distortion); slightly harder case than carburizing; gas control critical
Liquid (cyaniding)	Diffused carbon and nitrogen	760–870	1400–1600	2.5–125 µm (0.1–5 mils)	50–65(a)	Low-carbon steels	Good for thin cases on noncritical parts; batch process; salt disposal problems
Ferritic nitrocarburizing	Diffused carbon and nitrogen	565–675	1050–1250	2.5–25 µm (0.1–1 mil)	40–60(a)	Low-carbon steels	Low-distortion process for thin case on low-carbon steel; most processes are proprietary
Other							
Aluminizing (pack)	Diffused aluminum	870–980	1600–1800	25 µm–1 mm (1–40 mils)	< 20	Low-carbon steels	Diffused coating used for oxidation resistance at elevated temperatures
Siliconizing by chemical vapor deposition	Diffused silicon	925–1040	1700–1900	25 µm–1 mm (1–40 mils)	30–50	Low-carbon steels	For corrosion and wear resistance, atmosphere control is critical
Chromizing by chemical vapor deposition	Diffused chromium	980–1090	1800–2000	25–50 µm (1–2 mils)	Low-carbon steel, < 30; high-carbon steel, 50–60 > 70(a)	High- and low-carbon steels	Chromized low-carbon steels yield a low-cost stainless steel; high-carbon steels develop a hard corrosion-resistant case
Titanium carbide	Diffused carbon and titanium, TiC compound	900–1010	1650–1850	2.5–12.5 µm (0.1–0.5 mil)		Alloy steels, tool steels	Produces a thin carbide (TiC) case for resistance to wear; high temperature may cause distortion
Boriding	Diffused boron, boron compound	400–1150	750–2100	12.5–50 µm (0.5–2 mils)	40–> 70	Alloy steels, tool steels, cobalt and nickel alloys	Produces a hard compound layer; mostly applied over hardened tool steels; high process temperature can cause distortion

(a) Requires quench from austenitizing temperature. Source: Ref 1

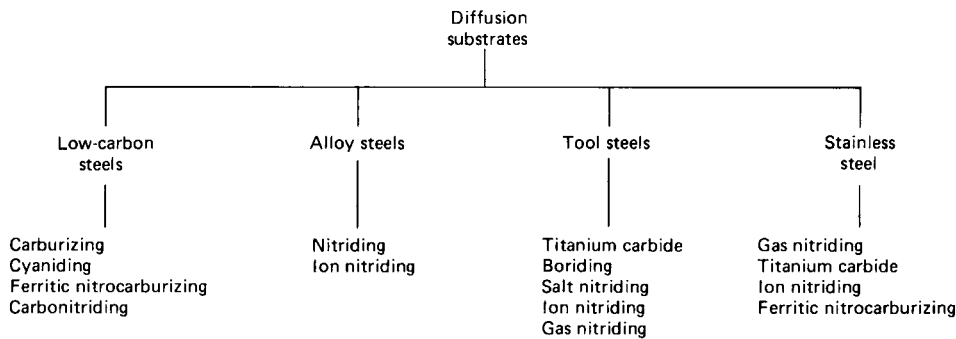


Fig. 1 Types of steels used for various diffusion processes

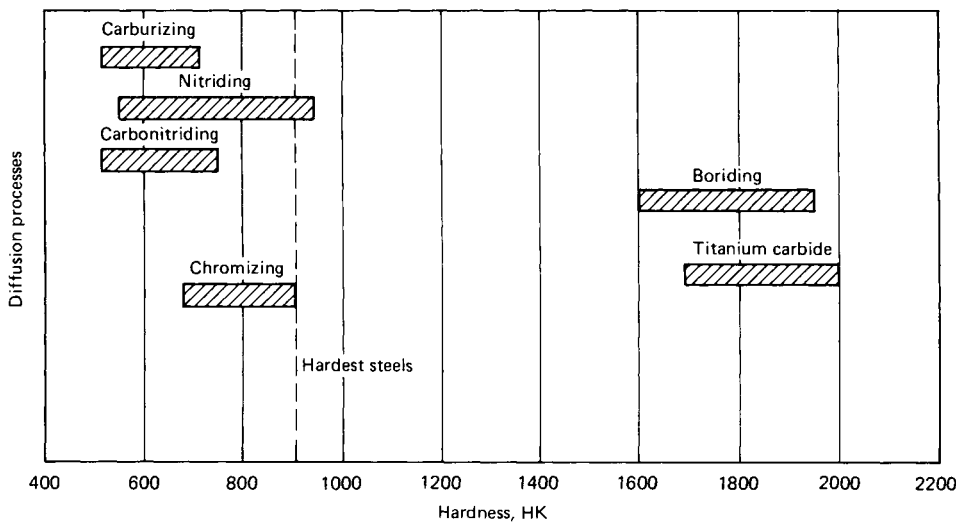


Fig. 2 Spectrum of hardness obtainable with selected diffusion processes of steel

and rolling contact fatigue. Too high a carbon level can result in excessive carbide formation and carbide networking or massive carbides that may be detrimental to performance. Therefore, it is important to understand the carbon profile needed and define it when necessary.

Case depth of carburized steel is a function of carburizing time, the steel chemistry, and available carbon (carbon potential) at the surface. When prolonged carburizing times are used for deep case depths, a high carbon potential produces a high surface-carbon content, which may thus result in excessive retained austenite or free carbides. These two microstructural elements can have adverse effects on the distribution of residual stress in the case-hardened part. Consequently, a high carbon potential may be suitable for short carburizing times but not for prolonged carburizing. Selection of carbon potential also depends on the carburizing response of a particular steel.

Carburizing Steels

Carburizing steels for case hardening usually have base-carbon contents of approximately 0.2%, with the carbon content of the carburized

layer generally being controlled at between 0.7 and 1% C (Ref 2). However, surface carbon is often limited to 0.9% (Ref 3) because too high a carbon content can result in retained austenite and brittle martensite (due to the formation of proeutectoid carbides on the grain boundaries).

Most steels that are carburized are killed steels (deoxidized by the addition of aluminum), which maintain fine grain sizes to temperatures of approximately 1040 °C (1900 °F). Steels made to coarse grain practices can be carburized if a double quench is introduced to provide grain refinement. Double quenching usually consists of a direct quench followed by a re-quench from a lower temperature.

Many alloy steels for case hardening are now specified on the basis of core hardenability. Although the same considerations generally apply to the selection of uncarburized grades, there are some distinct characteristics in carburizing applications.

First, in a case-hardened steel, the hardenability of both case and core must be considered. Because of the difference in carbon content, case and core have quite different hardenabilities, and this difference is much greater for some grades of steels than for

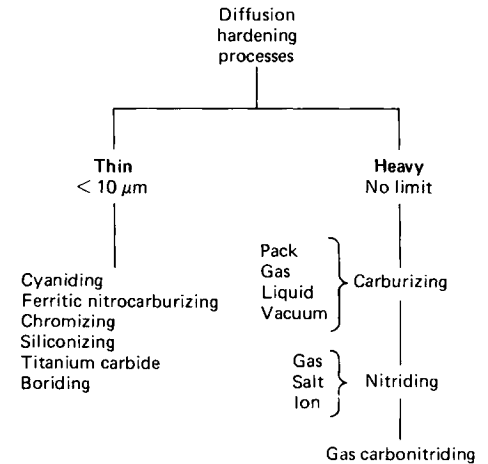


Fig. 3 Categorization of diffusion processes by typical case depth

others. Moreover, the two regions have different in-service functions to perform. Until the introduction of lean alloy steels such as the 51xx, or 86xx series, with and without boron, there was little need to be concerned about case hardenability because the alloy content combined with the high carbon content always provided adequate hardenability. This is still somewhat true when the steels are direct quenched from carburizing, so that the carbon and alloying elements are in solution in the case austenite. In parts that are reheated for hardening and in heavy-sectioned parts, however, both case and core hardenability requirements should be carefully evaluated.

The hardenability of the steels as purchased is the core hardenability. Because these low-carbon steels, as a class, are shallow hardening and because of the wide variation in the section sizes of case-hardened parts, the hardenability of the steel must be related to some critical section of the part, for example, the pitch line or the root of a gear tooth or the largest inscribed circle of a cross section such as a bearing. This is best accomplished by making a part of a steel of known hardenability, heat treating it, and then, by means of equivalence of hardness, relating the hardenability in the critical section or sections to the proper positions on the end-quench hardenability specimens, for both carburized and noncarburized part. Finally, the relationship between the thermal gradient and the carbon (hardenability) gradient during quenching of a carburized part can make a difference in the case depth measured by hardness. That is, an increase in base hardenability can produce a higher proportion of martensite for a given carbon level, yielding an increased measured case depth. Therefore, a shallower carbon profile and shorter carburizing time could be used to attain the desired result in a chosen steel.

Core Hardness. A common mistake is to specify too narrow a range of core hardness.

When the final quench is from a temperature high enough to allow the development of full core hardness, the hardness variation at any location will be that of the hardenability band of the steel at the corresponding position on the end-quenched hardenability specimen. One way to alter this state of affairs is to use higher-alloy steels. In the commonly used alloy steels having a maximum of 2% total alloy content, the range for the core hardness of sections such as gear teeth is 12 to 15 HRC points. Higher-alloy steels exhibit a narrower range; for example, in 4815 the range is 10 HRC points, while in 3310 it is 8 HRC points. Narrow-range steels are justified only for severe service or special applications.

In standard steels purchased to chemical composition requirements rather than to hardenability, the range can be 20 or more HRC points; for example, 8620 may vary from 20 to 45 HRC at the $\frac{1}{16}$ in. position. The 25-point range emphasizes the advantage of purchasing (cost) to hardenability specifications to avoid the intolerable variation possible within the ranges for standard-chemistry steels. Another way to control core hardness within narrow limits without resorting to the use of high-alloy steels is to use a final quench from a lower temperature, so that full hardness in the case will be developed without the disadvantage of excessive core hardness.

Gears, Bearings, and Low-Distortion Applications. Gears and bearings are almost always oil quenched or high-pressure gas quenched, because distortion must be held to the lowest possible level. Therefore, alloy steels are usually preferred. The lower-alloy steels such as 4023, 5120, 4118, 8620, and 4620, with a carbon range between 0.15 and 0.25%, are widely used to achieve satisfactory results. In most applications, 8620 or 5120 are preferred. The final choice, based on service experience or dynamometer testing, should be the least expensive steel that will do the job. Another steel, 1524, could be considered; although not classified commercially as an alloy steel, it has sufficient manganese to make it oil harden up to an end-quench correlation point of $\frac{3}{16}$.

For heavy-duty applications or heavy cross sections requiring core strength, higher-alloy grades such as 4320, 4817, and 9310 are justifiable if based on actual performance tests. Rather than the bench tests, actual life testing of gears in the same mountings used in service to prove both the design and the steel selection is particularly important.

The carbonitriding process extends the use of carbon steels such as 1016, 1018, 1019, and 1022 into the field of light-duty gearing by permitting the use of oil quenching in teeth of eight diametral pitch and finer. Steels selected for such applications should be specified silicon-killed or aluminum-killed fine grained to ensure uniform case hardness and dimensional control. The core properties of gears made from these types of steel resemble that of low-carbon steel, oil quenched. In the thin sections of fine-pitch

teeth, this may be up to 25 HRC. The carbonitriding process is usually limited, for economic reasons, to maximum case depths of approximately 0.6 mm (0.025 in.). In some bearing applications, 52100 materials are also carbonitrided to enhance galling properties.

Non-Gear/Bearing Applications. In other applications, when distortion is not a major factor, the carbon steels described previously, water quenched, can be used up to a 50 mm (2 in.) diameter. In larger sizes, low-alloy steels, water quenched, such as 5120, 4023, and 6120, can be used, but possible distortion and quench cracking must be avoided.

Carburizing Methods

While the basic principle of carburizing has remained unchanged since it was first introduced, the methodology has gone through continuous evolution. In its earliest application, parts were simply placed in a suitable container and covered with a thick layer of carbon powder (pack carburizing). Although effective in introducing carbon, this method was exceedingly slow, and as the production demand grew, a new method using a gaseous atmosphere was developed. In gas carburizing, the parts are surrounded by a carbon-bearing atmosphere that can be continuously replenished so that a high carbon potential can be maintained. While the rate of carburizing is substantially increased in the gaseous atmosphere, the method requires the use of a multicomponent atmosphere whose composition must be very closely controlled to avoid deleterious side effects, for example, surface and grain-boundary oxides. In addition, a separate piece of equipment is required to generate the atmosphere and control its composition or liquids, such as methanol, which must be vaporized. Despite this increased complexity, gas carburizing has become the most effective and widely used method for carburizing steel parts in high volume.

In efforts required to simplify the atmosphere, carburizing in an oxygen-free environment at very low pressure (vacuum carburizing) has been explored and developed into a viable and important alternative. Although the furnace enclosure in some respects becomes more complex, the atmosphere is greatly simplified. A single-component atmosphere consisting solely of a simple gaseous hydrocarbon, for example, methane or acetylene, may be used. Furthermore, because the parts are heated in an oxygen-free environment, the carburizing temperature may be increased substantially without the risk of surface or grain-boundary oxidation. The higher temperature permitted increases not only the solid solubility of carbon in the austenite but also its rate of diffusion, so that the time required to achieve the case depth desired is reduced. When carburizing at temperatures over 980 °C (1800 °F), properly engineered steel chemistries are recommended to mitigate the potential for grain coarsening.

Although vacuum carburizing overcomes some of the complexities of gas carburizing, it introduces a serious new problem that must be addressed. Because vacuum carburizing is conducted at very low pressures, and the rate of flow of the carburizing gas into the furnace is very low, the carbon potential of the gas in deep recesses and blind holes is quickly depleted. Unless this gas is replenished, a distinct nonuniformity in case depth over the surface of the part is likely to occur. If, in an effort to overcome this problem, the gas pressure is increased significantly, another problem arises, that of free-carbon formation, or sooting. Thus, to obtain cases of reasonably uniform depth over a part of complex shape, the gas pressure must be increased periodically to replenish the depleted atmosphere in recesses and then reduced again to the operating pressure. Clearly, a delicate balance exists in vacuum carburizing: The process conditions must be adjusted to obtain the best compromise between case uniformity, risk of sooting, and carburizing rate. Surface area and alloy content of the component are two important considerations of vacuum carburizing.

A method that overcomes the major limitations of gas carburizing yet retains the desirable features of a simple atmosphere and a higher permissible operating temperature is plasma or ion carburizing.

To summarize, carburizing methods include:

- Gas carburizing
- Vacuum carburizing or low-pressure carburizing
- Plasma carburizing
- Salt bath carburizing
- Pack carburizing

These methods introduce carbon by the use of gas (atmospheric gas, plasma, and vacuum carburizing), liquids (salt bath carburizing), or solid compounds (pack carburizing). All of these methods have limitations and advantages, but gas carburizing is used most often for high-volume production because it can be accurately controlled and requires minimal special handling.

Vacuum carburizing and plasma carburizing have found applications because the absence of oxygen in the furnace atmosphere thus eliminates grain-boundary oxidation. Salt bath and pack carburizing are still done occasionally but have relatively little commercial importance today (2013).

Process characteristics of the aforementioned carburizing methods fall into two general groups:

- Conventional methods, which introduce carbon by gas atmospheres, salt baths, or charcoal packs
- Plasma methods, which impinge positive carbon ions on the surface of a steel part (the cathode)

The main difference between the conventional and glow-discharge (or plasma) methods is the

reduced carburizing times in plasma-assisted methods. The quickly attained surface saturation also results in faster diffusion kinetics. Furthermore, plasma carburizing can produce very uniform case depths, even in parts with irregular surfaces (Ref 4, 5). This uniformity is caused by the glow-discharge plasma, which closely envelops the specimen surface, provided that recesses or holes are not too small (Ref 5).

With the conventional methods, carburization always takes place by means of a gaseous phase of carbon monoxide; however, each method also involves different reaction and surface kinetics, producing different case-hardening results. In general, with conventional methods, carbon monoxide dissociates at the steel surface:



The liberated carbon is readily dissolved by the austenite phase and diffuses into the body of the steel. For some process methods (gas and pack carburizing), the carbon dioxide produced may react with the carbon atmosphere or pack charcoal to produce new carbon monoxide by the reverse reaction of Eq 2. Because the reaction can proceed in both directions, an equilibrium relationship exists between the constituents (Fig. 4). If the temperature is increased at constant pressure, more carbon monoxide is produced (Fig. 4). In turn, the equilibrium percentages of carbon monoxide and carbon dioxide influence the carbon concentrations in steel (Fig. 5).

Quantitative algorithms for estimating case depth from carburization often focus on making the proportional relation of Eq 1 explicit (Case depth = $K\sqrt{\text{Time}}$) for gas carburization only (Ref 2, 3). However, even in gas carburization, the kinetics of carbon diffusion gives an incomplete picture of carburizing. A

comprehensive model of gas carburization must include algorithms that describe:

- Carbon diffusion
- Kinetics of the surface reaction
- Effects of steel chemistry
- Kinetics of the reaction between endogas and enriching gas
- Purging (for batch processes)
- Atmosphere control system

Reference 8 discusses possible modeling of each of these factors for gas carburization. The effects of process variables are also covered in the article "Gas Carburizing" in this Volume.

Selective Carburizing. Sometimes it is necessary to prevent carburization on certain areas of a part. For example, carburization prevention may be necessary on areas to be machined further after heat treating, or to prevent a thin area from being carburized all the way through its section, thereby becoming brittle (Ref 3). Preventing carburization in selective areas can be done with mechanical masking, stop-off compounds, or copper plating (see the article "Stop-off Technologies for Heat Treatment" for more details). Close attention to cleanliness and handling is needed to achieve the desired stop-off, and application instructions should be closely followed to achieve effective and good results. In copper plate thicknesses of approximately 0.03 mm (0.001 in.) are required.

After case hardening, selective areas of the workpieces also can be "softened" by induction tempering. External threads of gears or shafts are typical applications. This method is not suitable for steels of high hardenability. Another method of selective hardening is to remove case prior to quenching. The areas of the part that were machined after the carburize cycle will only show the core hardness because

the case layer had been removed prior to quench.

Carbonitriding

Carbonitriding is a surface-hardening heat treatment that introduces carbon and nitrogen into the austenite of steel. This treatment is similar to carburizing in that the austenite composition is changed and high surface hardness is produced by quenching to form martensite. However, because nitrogen enhances hardenability, carbonitriding makes possible the use of low-carbon steel to achieve surface hardness equivalent to that of high-alloy carburized steel without the need for drastic quenching, resulting in less distortion and minimizing potential for cracks. In some cases, hardening may be dependent on nitride formation.

Although the process of carbonitriding can be performed with gas atmospheres or salt baths, the term *carbonitriding* often refers solely to treatment in a gas atmosphere (see the article "Carbonitriding of Steels" in this Volume). Basically, carbonitriding in a salt bath is the same as cyanide bath hardening. In both processes, nitrogen enhances hardenability and case hardness but inhibits the diffusion of carbon. In many instances, carbonitriding of coarse-grained steels is more appropriate than carburizing, because of the lower temperatures and shorter cycle times.

Like carbon, nitrogen is an austenite stabilizer. Therefore, considerable austenite may be retained after quenching a carburized part. If the retained austenite content is so high that it reduces hardness and wear resistance, it may be controlled by reducing the ammonia content of the carbonitriding gas either throughout the cycle or during the latter portion of the cycle. Another result of excessive nitrogen content in the carbonitrided case is porosity (see the article "Carbonitriding of Steels" in this Volume).

Nitriding and Nitrocarburizing

Nitriding is a surface-hardening heat treatment that introduces nitrogen into the surface of steel at a temperature range (500 to 550 °C, or 930 to 1020 °F), while it is in the ferritic condition. Because nitriding does not involve heating into the austenite phase with quenching to form martensite, nitride components exhibit minimum distortion and excellent dimensional control. Nitriding has the additional advantage of improving corrosion resistance in salt spray tests.

The mechanism of nitriding is generally known, but the specific reactions that occur in different steels and with different nitriding media are not always known. Nitrogen has partial solubility in iron. It can form a solid solution with ferrite at nitrogen contents up to approximately 6%. At approximately 6% N, a compound called gamma prime (γ'), with a

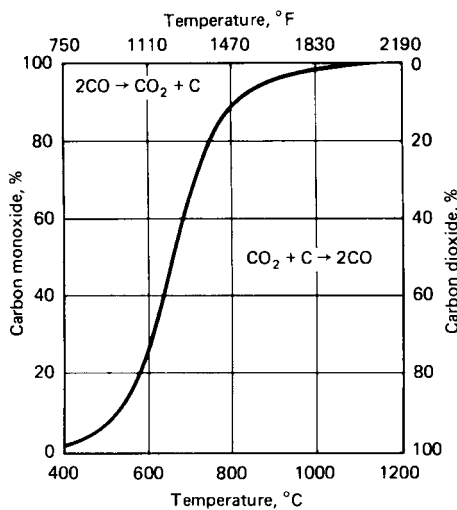


Fig. 4 Equilibrium diagram for reaction $2\text{CO} \rightleftharpoons \text{CO}_2 + \text{C}$ at pressure of one atmosphere. Source: Ref 6

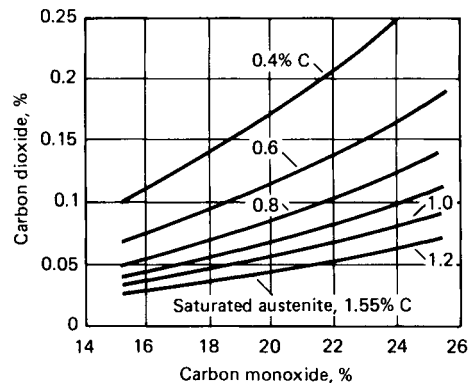


Fig. 5 Equilibrium percentages of carbon monoxide and carbon dioxide required to maintain various carbon concentrations at 975 °C (1790 °F) in plain carbon and certain low-alloy steels. $K = 89.67$. Source: Ref 7

composition of Fe_4N , is formed. At nitrogen contents greater than 8%, the equilibrium reaction product is ϵ compound, Fe_3N . Nitrided cases are stratified. The outermost surface can be all γ' , and, if this is the case, it is referred to as the white layer (it etches white in metallographic preparation). Such a surface layer is undesirable; it is very hard but is so brittle that it may spall in use. Usually it is removed; special nitriding processes are used to reduce this layer or make it less brittle. The ϵ zone of the case is hardened by the formation of the Fe_3N compound, and below this layer there is some solid-solution strengthening from the nitrogen in solid solution (Fig. 6). The Fe_3N (ϵ) formed on the outer layer is harder than Fe_4N , which is more ductile. Controlling the formation of each of these compound layers is vital to application and degree of distortion.

The depth of case and its properties are greatly dependent on the concentration and type of nitride-forming elements in the steel. In general, the higher the alloy content, the higher the case hardness. However, higher-alloying elements retard the N_2 diffusion rate, which slows the case depth development. Thus, nitriding requires longer cycle times to achieve a given case depth than that required for carburizing. Figure 7 shows some typical cycle times for nitriding versus case depth relationship for commonly used materials, such as Nitralloy 135M, Nitralloy N, AISI 4140, AISI 4330M, and AISI 4340.

Nitrided steels (Ref 9) are generally medium-carbon (quenched and tempered) steels that contain strong nitride-forming elements such as aluminum, chromium, vanadium, and molybdenum. The most significant hardening is

achieved with a class of alloy steels (nitralloy type) that contain approximately 1% Al (Fig. 6). When these steels are nitrided, the aluminum forms AlN particles, which strain the ferrite lattice and create strengthening dislocations. Titanium and chromium are also used to enhance case hardness (Fig. 8a), although case depth decreases as alloy content increases (Fig. 8b). The microstructure plays an important role in nitriding, because nitrogen can readily diffuse through ferrite, and a low carbide content favors both diffusion and case hardness. Usually, alloy steels in the heat treated (quenched and tempered) conditions are used for nitriding (Ref 6).

Nitriding steels used in the United States fall in one of two groups: aluminum-containing Nitralloys and AISI low- or high-alloy steels. There is, however, a wide gap between the characteristics of these two groups of steels, which, in Europe, is filled by CrMo and CrMoV

steels with 2.5 to 3.5% Cr. Chromium provides good hardenability and higher hardness in nitrided case than AISI low-alloy steels. Molybdenum resists softening on tempering so that high strengths can be retained even after tempering at well over the nitriding temperature. It also minimizes susceptibility to embrittlement during nitriding and increases hardenability and hot hardness. Vanadium permits easier control of heat treatment and gives higher hot hardness.

For surface hardness and toughness, the nitrided CrMo and CrMoV steels occupy a position in between Nitralloy 135M and AISI low-alloy steels. Because of lower case hardness, these materials are less brittle. Furthermore, they are less sensitive to grinding cracks and have higher hardenability. Also, they can be heat treated to higher core hardness prior to nitriding. For example, 3.5Cr-AlMo, a British

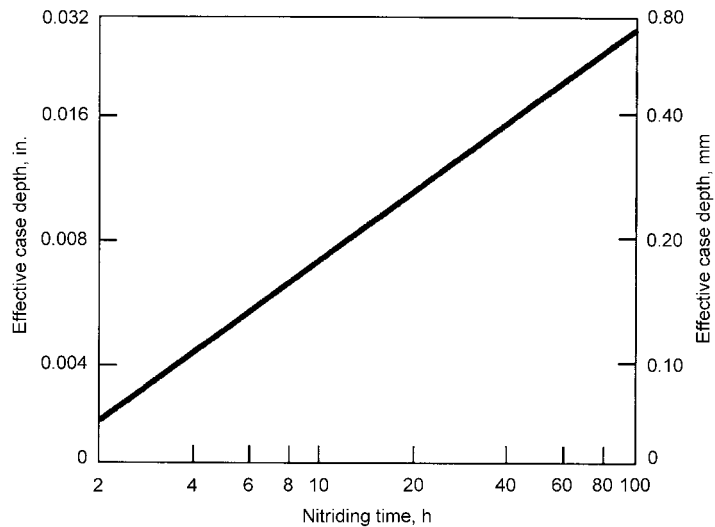


Fig. 7 Nominal time for different nitrided case depths. Source: Ref 9

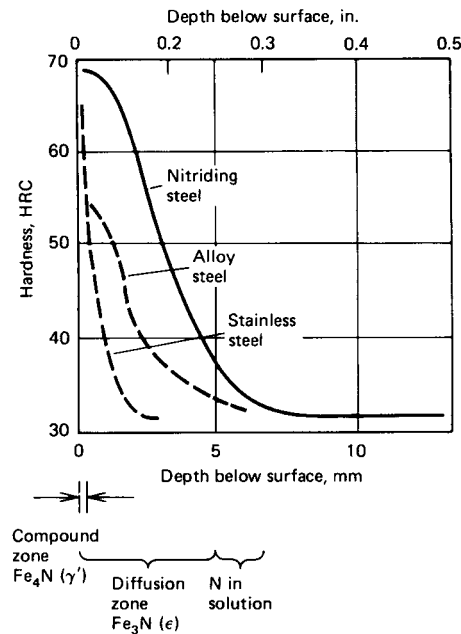


Fig. 6 Nitride case profiles for various steels. Source: Ref 1

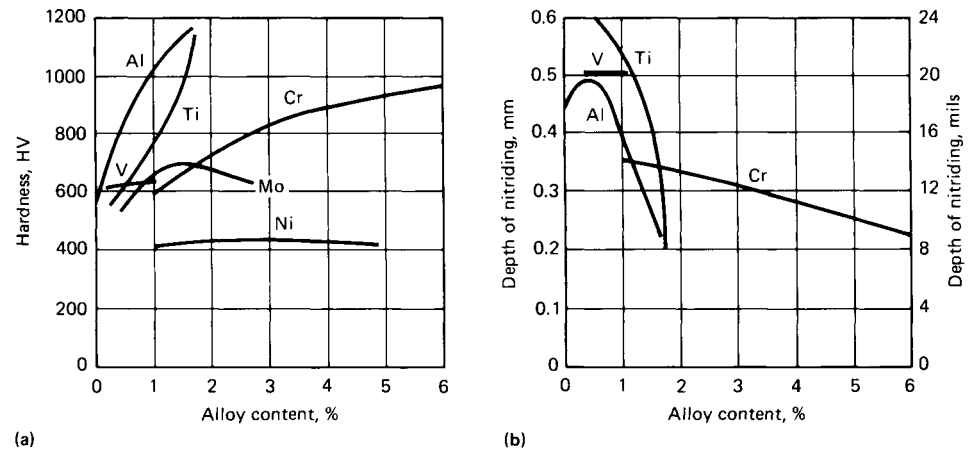


Fig. 8 Influence of alloying elements on (a) hardness after nitriding (base alloy, 0.35% C, 0.30% Si, 0.70% Mn) and (b) depth of nitriding measured at 400 HV (nitriding for 8 h at 520 °C, or 970 °F). Source: Ref 6

Steel (EN 40C), can be heat treated to 375 to 444 Brinell hardness in sections up to 63.5 mm (2.5 in.), whereas Nitralloy 135M can be heat treated to only 248 to 302 Brinell hardness in that size. In addition, the steels with 2.5 to 3.5% Cr come with low nonmetallic inclusions (higher cleanliness), even in the air-melted condition, whereas the aluminum-containing steels, such as Nitralloy 135M, require vacuum melting or degassing to achieve similar cleanliness. In general, the cleaner the material, the lower the distortion during any hardening process. Nitrided gears made from air-melted CrMo steels produce negligible distortion.

Process methods for nitriding include gas (box furnace or fluidized bed), liquid (salt bath), and plasma (ion) nitriding. In a survey of 800 commercial shops in the United States and Canada, 30% offered nitriding services, of which (Ref 10):

- 21% offered gas nitriding
- 7% offered salt bath nitriding
- 6% offered fluidized-bed nitriding
- 5% offered plasma nitriding

The advantages and disadvantages of these techniques are similar to those of carburizing. However, process times for gas nitriding can be quite long, that is, from 10 to 130 h depending on the application, and the case depths are relatively shallow, usually less than 0.5 mm (0.020 in.). Plasma nitriding allows faster nitriding times, and the quickly attained surface saturation of the plasma process results in faster diffusion. Plasma nitriding may clean the surface by sputtering.

Nitrocarburizing is a surface-hardening process that uses both carbon and nitrogen, but with more nitrogen than carbon, when compared to carbonitriding (see the article “Carbonitriding of Steels” in this Volume). Carbonitriding produces a martensitic case with nitrogen levels less than carbon levels. In contrast, nitrocarburizing involves higher levels of nitrogen with a compound layer. There are two types of nitrocarburizing: ferritic and austenitic (Ref 11). Ferritic nitrocarburizing occurs at lower temperatures in the ferritic temperature range and involves diffusion of nitrogen into the case. Austenitic nitrocarburizing is a more recently developed process with process temperatures in the range of 675 to 775 °C (1245 to 1425 °F). It also uses much higher ammonia additions and thus higher nitrogen levels in the case. This allows the formation of a surface compound zone, which is not typical of the carbonitriding process. Austenitic nitrocarburizing differs from ferritic nitrocarburizing in the ability for deeper case depths with a better load-carrying capability but may result in greater part distortion because of the higher processing temperatures and the required quenching process. Although ferritic and austenitic nitrocarburizing have higher processing temperatures than does nitriding (Table 2), they

have the advantage of being suitable for plain carbon steels.

Applied Energy Methods

Surface hardening of steel can be achieved by localized heating and quenching, without any chemical modification of the surface. The more common methods currently used to harden the surface of steels include flame and induction hardening. However, each of these methods has shortcomings that can prevent its use in some applications. For example, the disadvantages of flame hardening include the possibility of part distortion, while induction hardening requires close coupling between the part and the coil (especially when using high frequencies), which must be precisely maintained.

Flame hardening consists of austenitizing the surface of a steel by heating with an oxy-acetylene or oxyhydrogen torch and immediately quenching with water or water-based polymer. The result is a hard surface layer of martensite over a softer interior core with a ferrite-pearlite structure. There is no change in composition, and therefore, the flame-hardened steel must have adequate carbon content for the desired surface hardness. The rate of heating and the conduction of heat into the interior appear to be more important in establishing case depth than the use of a steel of high hardenability.

Flame-heating equipment may be a single torch with a specially designed head or an elaborate apparatus that automatically indexes, heats, and quenches parts. Large parts such as gears and machine toolways, with sizes or shapes that would make furnace heat treatment impractical, are easily flame hardened. With improvements in gas-mixing equipment, infrared temperature measurement and control, and burner design, flame hardening has been accepted as a reliable heat treating process that is adaptable to general or localized surface hardening for small and medium-to-high production requirements.

Induction heating is an extremely versatile heating method that can perform uniform surface hardening, localized surface hardening, through hardening, and tempering of hardened pieces. Heating is accomplished by placing a steel ferrous part in the magnetic field generated by high-frequency alternating current passing through an inductor, usually a water-cooled copper coil. The depth of heating produced by induction is related to the frequency of the alternating current, power input, time, part coupling and quench delay.

The higher the frequency, the thinner or more shallow the heating. Therefore, deeper case depths and even through hardening are produced by using lower frequencies. The electrical considerations involve the phenomena of hysteresis and eddy currents. Because

secondary and radiant heat are eliminated, the process is suited for in-line production. Some of the benefits of induction hardening are faster process, energy efficiency, less distortion, and small footprints. Care must be exercised when holes, slots, or other special geometric features must be induction hardened, which can concentrate eddy currents and result in overheating and cracking without special coil and part designs. For details, see the articles “Induction Surface Hardening of Steels” and “Induction Heat Treating Systems” in this Volume.

Laser surface heat treatment is widely used to harden localized areas of steel and cast iron machine components. This process is sometimes referred to as laser transformation hardening to differentiate it from laser surface melting phenomena (Fig. 9). There is no chemistry change produced by laser transformation hardening, and the process, like induction and flame hardening, provides an effective technique to harden ferrous materials selectively. Other methods of laser surface treatments include surface melting and surface alloying. Laser surface melting results in a refinement of the structure due to the rapid quenching from the melt. In surface alloying, elements are added to the melt pool to change the composition of the surface. The novel structures produced by laser surface melting and alloying can exhibit improved electrochemical behavior.

Laser transformation hardening produces thin surface zones that are heated and cooled very rapidly, resulting in very fine martensitic microstructures, even in steels with relatively low hardenability. High hardness and good wear resistance with less distortion result from this process. The laser method differs from induction and flame heating in that the laser can be located at some distance from the workpieces. Also, the laser light is reflected by mirrors to the focusing lens, which controls the width of the heated spot or track.

Molian (Ref 12) has tabulated the characteristics of 50 applications of laser transformation hardening. The materials hardened include plain carbon steels (1040, 1050, 1070), alloy steels (4340, 52100), tool steels, and cast irons (gray, malleable, ductile). Because the absorption of laser radiation in cold metals is low, laser surface hardening often requires energy-absorbing coatings on surfaces. Reference 12 lists some energy-absorbing coatings.

Typical case depths for steels are 250 to 750 μm (0.01 to 0.03 in.) and for cast irons are approximately 1000 μm (0.04 in.). The flexibility of laser delivery systems and the low distortion and high surface hardness obtained have made lasers very effective in the selective hardening of wear- and fatigue-prone areas on irregularly shaped machine components, such as camshafts and crankshafts.

Electron beam (EB) hardening, like laser treatment, is used to harden the surfaces of steels. The EB heat treating process uses a concentrated beam of high-velocity electrons as an

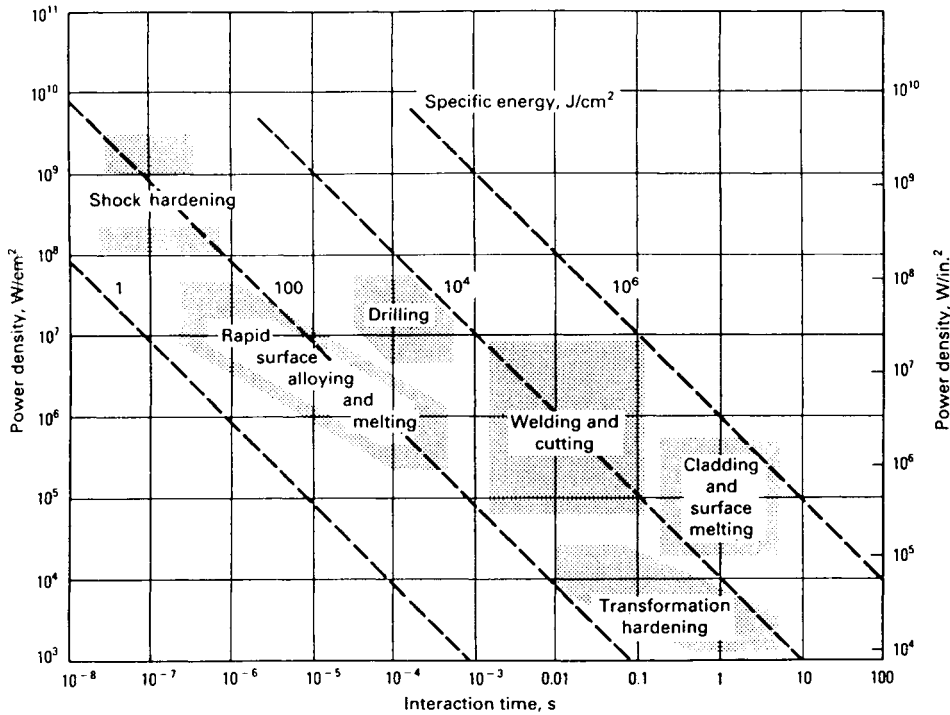


Fig. 9 Interaction times and power densities necessary for various laser surface modification processes

energy source to heat selected surface areas of ferrous parts. Electrons are accelerated and are formed into a directed beam by an EB gun. After exiting the gun, the beam passes through a focus coil, which precisely controls beam density levels (spot size) at the workpiece surface and then passes through a deflection coil. To produce an electron beam, a high vacuum of 10^{-5} torr (1.3×10^{-3} Pa) is needed in the region where the electrons are emitted and accelerated. This vacuum environment protects the emitter from oxidizing and avoids scattering of the electrons while they are still traveling at a relatively low velocity.

Like laser beam hardening, the EB process eliminates the need for quenchants but requires a sufficient workpiece mass to permit self-quenching. A mass of up to eight times that of the volume to be EB hardened is required around and beneath the heated surfaces. Electron beam hardening does not require energy-absorbing coatings, as does laser beam hardening. Processing considerations and property changes associated with EB hardening are covered in Ref 13 and 14 and in the article "Electron Beam Surface Hardening of Steels" in this Volume.

Other Methods

Diffusion coatings are deposited either by heating the components to be treated in contact with the powder coating material in an inert atmosphere (solid-state diffusion) or by heating

them in an atmosphere of a volatile compound of the coating material (out-of-contact gas-phase deposition, or chemical vapor deposition). As the coating bond is developed by diffusion, the bond strength is enhanced.

Solid-state diffusion methods include pack cementation, which is the most widely employed diffusion coating method and includes coatings based on aluminum (aluminizing), chromium (chromizing), and silicon (siliconizing). Substrate materials include nickel- and cobalt-base superalloys, steels (including carbon, alloy, and stainless steels), and refractory metals and alloys. Diffusion coatings for wear resistance are also based on boriding (boronizing) and the thermoreactive deposition/diffusion process. Of these, boron and titanium treatments offer high levels of hardness (Fig. 2), while aluminum, chromium, and silicon treatments are primarily used for corrosion resistance.

Boriding involves the diffusion of boron into metal surfaces for the enhancement of hardness and wear resistance. Boriding is most often applied to tool steels that may be hardened by heat treatment. Boriding techniques include metallizing, chemical vapor deposition, and pack cementation. For additional information, see the article "Boriding (Boronizing) of Metals" in this Volume.

Titanium Carbide. With process temperatures in the range of 900 to 1010 °C (1650 to 1850 °F), titanium and carbon will diffuse to form a diffused case of titanium carbide during chemical vapor deposition. This treatment is most commonly applied to tool steels and

hardenable stainless steels. Because the treatment is performed above the austenitizing temperatures of these steels, the core must be hardened by quenching.

Ion implantation is a surface-modification process in which ions with very high energy are driven into a substrate. Ions of almost any atom species can be implanted, but nitrogen is widely used to improve corrosion resistance and the tribological properties of steels and other alloys. Although the nitrogen content of alloy surfaces is increased by both nitrogen ion implantation and plasma nitriding, major differences exist between the two processes and the surface modifications they create. The major difference is that ion implantation can be performed at room temperature.

Ion implantation machines accelerate ions, generated by specially designed sources, at very high energies (from 10 to 500 keV). In contrast, the energy of ions and atoms in plasma nitriding is much lower (<1 keV). Ion implantation is carried out with the substrate at approximately room temperature, thereby minimizing the diffusion-controlled formation of precipitates and coarsening of the subsurface microstructure. Because the temperature of application is low and the process is carried out in accelerators with very good vacuums ($\geq 10^{-5}$ torr, or 1.3×10^{-3} Pa), clean surfaces are ensured and undesirable surface chemical reactions such as oxidation are lessened. Ion implantation is a line-of-sight process (similar to laser); that is, only relatively small areas directly exposed to the ion beam are implanted. For the coverage of areas larger than the beam, either the specimen must be translated or the ion beam must be rastered over the specimen surface.

Because of the virtual absence of diffusion-controlled case formation during ion implantation, case depths are shallow (generally <0.25 μm , or 0.010 mil). Very high strengths or hardnesses of the nitrogen-implanted surface layers compensate for the shallow case depths of ion implantation. Ion implantation is a complex, nonequilibrium process that creates significant lattice damage in the form of vacancies and interstitial point defects. Concentrations of implanted species much higher than equilibrium solubility limits may be introduced. In fact, the incorporation of high densities of atoms of significantly different size than those of the substrate lattice may produce amorphous structures or metastable phases (Ref 15).

The properties of ion-implanted surfaces and shallow case depths make ion implantation suitable for very special applications. Because the surface of the part itself is modified, the adhesion problems sometimes encountered with coated layers of high hardness do not arise. Also, because ion implantation is usually accomplished with very little heating, dimensional stability is excellent. Examples of applications of ion implantation include the surface hardening of razor blades (Ref 4) and knives (Ref 15), a

variety of tool steel applications (Ref 16), and the implantation of 52100 and 440C bearings with titanium and/or nitrogen to improve rolling-contact fatigue resistance (Ref 17–19). In the latter applications, titanium was found to reduce the coefficient of friction, and nitrogen was found to raise hardness by intermetallic compound formation. Additional information on ion implantation is given in Ref 20 and in *Corrosion*, Volume 13 of *ASM Handbook*, formerly *Metals Handbook*, 9th edition.

Surface hardening with arc lamps is used in applications that involve surface remelting or surface hardening by solid-phase recrystallization. Examples include the surface remelting of cast iron and the large-area remelting of titanium in the presence of nitrogen or methane to produce titanium carbides in the surface layer. In the surface remelting of cast irons, lasers are also used. Another area in which arc lamps are finding application is in the selective hardening of the edges on agricultural sweeps and tilling equipment blades.

Surface treating using white light from a high-power arc lamp offers several advantages over traditional methods and the beam techniques. For example, arc lamp treatment can achieve higher surface radiation intensities than can flame heating, making the procedure faster and less likely to cause distortion. Compared with induction hardening, arc lamp treatment allows much larger distances between the part and heat source, providing more flexibility in treating irregularly shaped surfaces. Unlike the EB treatment, this method does not require the use of a vacuum chamber, and an arc lamp can deliver greater power to the part surface than can a laser beam.

However, with the arc lamp method, significant power loss is encountered if arc radiation is concentrated onto surface areas smaller than the arc itself. Therefore, the illuminated spot on the sample surface should always be larger than the arc. This necessitates extremely high arc power to achieve the surface intensities needed for thermal treatment. Such high power is achieved in a very small space with specially designed arc lamps.

Process Selection

The benefits of the most common methods of surface hardening are compared in Table 3. Flame and induction hardening are generally limited to certain families of steels, such as medium-carbon steels, medium-carbon alloy steels, some cast irons, and the lower-alloy tool steels. There is no size limit to parts that can be flame hardened, because only the portion of the part to be hardened need be heated. Flame hardening is generally used for very heavy cases (in the range of approximately 1.2 to 6 mm, or 0.6 to 0.25 in.); thin case depths are difficult to control because of the nature of the heating process. Diffusion methods are compared in Table 2.

Table 3 Relative benefits of five common surface-hardening processes

Process	Benefits
Carburizing	Hard, highly wear-resistant surface (medium case depths); excellent capacity for contact load; good bending fatigue strength; good resistance to seizure; excellent freedom from quench cracking; low-to-medium-cost steels required; high capital investment required
Carbonitriding	Hard, highly wear-resistant surface (shallow case depths); fair capacity for contact load; good bending fatigue strength; good resistance to seizure; good dimensional control possible; excellent freedom from quench cracking; low-cost steels usually satisfactory; medium capital investment required; improved salt corrosion resistance
Nitriding	Hard, highly wear-resistant surface (shallow case depths); fair capacity for contact load; good bending fatigue strength; excellent resistance to seizure; excellent dimensional control possible; good freedom from quench cracking (during pretreatment); medium-to-high-cost steels required; medium capital investment required; improved salt corrosion resistance
Induction hardening	Hard, highly wear-resistant surface (deep case depths); good capacity for contact load; good bending fatigue strength; fair resistance to seizure; fair dimensional control possible; fair freedom from quench cracking; low-cost steels usually satisfactory; medium capital investment required
Flame hardening	Hard, highly wear-resistant surface (deep case depths); good capacity for contact load; good bending fatigue strength; fair resistance to seizure; fair dimensional control possible; fair freedom from quench cracking; low-cost steels usually satisfactory; low capital investment required

Transformation hardening introduces surface compressive residual stresses, which are beneficial for fatigue strength. In selective hardening, however, some residual tensile stress will exist in the region where the hardened zone meets the unhardened zone. Consequently, selective hardening by methods such as flame or induction heating should be applied away from geometric stress concentrations. Both nitriding and carburizing provide good resistance to surface fatigue and are widely used for gears and cams. In terms of bending fatigue resistance, the ideal case depth appears to be reached where the failure initiation point is transferred from the core to the surface (Ref 21). However, specification of required case depth is a complex subject, which is briefly discussed in Ref 21 for carburized steels.

REFERENCES

1. K.G. Budinski, *Surface Engineering for Wear Resistance*, Prentice-Hall, 1988
2. G. Krauss, *Steels: Heat Treatment and Processing Principles*, ASM International, 1990, p 286
3. C. Wick and R.F. Vielleux, Ed., *Materials, Finishing and Coating*, Vol 3, *Tool and Manufacturing Engineers Handbook*, Society of Manufacturing Engineers, 1985
4. B. Edenhofer, M.H. Jacobs, and J.N. George, Industrial Processes, Applications and Benefits of Plasma Heat Treatment, *Plasma Heat Treatment, Science and Technology*, PYC Édition, 1987, p 399–415
5. W.L. Grube and J.G. Gay, High-Rate Carburizing in a Glow-Discharge Methane Plasma, *Metall. Trans. A*, Vol 91, 1987, p 1421–1429
6. K.-E. Thelning, *Steel and Its Heat Treatment*, 2nd ed., Butterworths, 1984, p 450
7. ASM Committee on Gas Carburizing, Application of Equilibrium Data, *Carburizing and*

Carbonitriding, American Society for Metals, 1977, p 14–15

8. C.A. Stickels and C.M. Mack, Overview of Carburizing Processes and Modeling, *Carburizing Processing and Performance*, G. Krauss, Ed., ASM International, 1989, p 1–9
9. A.K. Rakhit, Nitriding Gears, Chap. 6, *Heat Treatment of Gears: A Practical Guide for Engineers*, ASM International, p 133–158
10. W.L. Kovacs, Commercial and Economic Trends in Ion Nitriding/Carburizing, *Ion Nitriding and Ion Carburizing*, ASM International, 1990, p 5–12
11. D. Herring, Comparing Carbonitriding and Nitrocarburizing, *Heat Treat. Prog.*, April/May 2002
12. P.A. Molian, Engineering Applications and Analysis of Hardening Data for Laser Heat Treated Ferrous Alloys, *Surf. Eng.*, Vol 2, 1986, p 19–28
13. R. Zenker and M. Mueller, Electron Beam Hardening, Part 1: Principles, Process Technology and Properties, *Heat Treat. Met.*, Vol 15 (No. 4), 1988, p 79–88
14. R. Zenker, W. John, D. Rathjen, and G. Fritsche, Electron Beam Hardening, Part 2: Influence on Microstructure and Properties, *Heat Treat. Met.*, Vol 16 (No. 2), 1989, p 43–51
15. G. Dearnaley, Ion Implantation and Ion Assisted Coatings for Wear Resistance in Metals, *Surf. Eng.*, Vol 2, 1986, p 213–221
16. J.K. Hirvonen, The Industrial Applications of Ion Beam Processes, *Surface Alloying by Ion, Electron and Laser Beams*, L.E. Rehn, S.T. Picraux, and H. Wiedersich, Ed., ASM International, 1987, p 373–388
17. D.L. Williamson, F.M. Kustas, and D.F. Fobare, Mossbauer Study of Ti-Implanted 52100 Steel, *J. Appl. Phys.*, Vol 60, 1986, p 1493–1500
18. F.M. Kustas, M.S. Misra, and D.L. Williamson, Microstructural Characterization

- of Nitrogen Implanted 400C Steel, *Nuclear Instruments and Methods in Physics Research B31*, North-Holland, 1988, p 393–401
19. F.M. Kustas, M.S. Misra, and P. Sioshansi, Effects of Ion Implantation on the Rolling Contact Fatigue of 440C Stainless Steel, *Ion Implantation and Ion Beam Processing of Materials*, G.K. Hubler, O.W. Holland, and C.R. Clayton, Ed., MRS Symposia Proceedings, Materials Research Society, Vol 27, 1984, p 675–690
20. A.H. Deutchman et al., *Ind. Heat.*, Vol 42 (No. 1), Jan 1990, p 32–35
21. G. Parrish, *The Influence of Microstructure on the Properties of Case-Carburized Components*, American Society for Metals, 1980, p 159–160, 164–165

Stop-Off Technologies for Heat Treatment

Eckhard H. Burgdorf, Manfred Behnke, and Rainer Braun, Nüssle GmbH & Co. KG
Kevin M. Duffy, The Duffy Company

CASE HARDENING may be restricted to selected portions of a surface, so that soft areas remain to allow for secondary operations such as machining, drilling, broaching, cold forming, straightening, and welding. In addition, some parts may have thin sections that would become brittle if carburizing or nitriding were allowed to occur through its section. Thus, a wide variety of stop-off technologies are used to selectively prevent the diffusion of carbon and or nitrogen during atmosphere carburizing, carbonitriding, vacuum carburizing, and various forms of nitriding. In addition to selective stop-off, technologies are also available for scale prevention in open-fired furnaces.

The stop-off methods described in this article include mechanical masking, stop-off paints/compounds, and copper plating. Two other methods of selective surface hardening are:

- Selective tempering by induction heating
- Case removal prior to quenching

Selective induction tempering involves heating and softening selective areas of the workpieces after quenching. External threads of gears or shafts are typical applications. This method is not suitable for steels of high hardenability.

Case removal prior to quenching involves keeping some machine stock on the areas that are required to remain soft. The parts are then subjected to a carburization cycle. After carburizing and slow cooling, the carburized layer is still relatively soft, allowing the removal of the machine stock. The parts are then reheated and quenched. The areas of the part that were machined after the carburizing cycle will only show the core hardness, because the case layer had been removed prior to quenching.

Mechanical Masking

In the case of internal threads, blind holes, and other areas that are too small to adequately

access, carbon and nitrogen diffusion can be minimized by inserting barriers in the form of bolts, clay, and plugs in an attempt to seal these areas from atmosphere penetration. Closely fitted conical bolts can be inserted into blind holes. Additional protection may be achieved by applying stop-off paint under the head of the bolt and/or coating the bolt threads. Another practice is to plug the holes with clay. Clay can also be used to fill the gap between the bolt and the wall of the part. Most of these options require some mechanical cleaning to remove the clay or paint after heat treatment. Plugs offer another possibility, but some means of venting the trapped air during heat-up must be employed to relieve the pressure and ensure the plug is not forced out of the hole.

In the case of external threads, a common practice is to cover the threaded area with a closely fitted heat-resistant alloy cap. This method can minimize carbon or nitrogen penetration, but by no means is it 100% effective. The caps tend to distort over time, especially if they are oil quenched, and require frequent replacement.

For plasma nitriding, shielding is used to effectively prevent nitrogen penetration. However, shielding often is not possible due to part geometry.

Copper Plating*

Copper plating has been proven to be very effective in preventing the absorption of carbon and or nitrogen during heat treatment. Copper plating can be an effective choice when 100% blockage of the case-hardening gases is needed for selective case hardening. However, it is expensive, time-consuming, and by no means environmentally friendly. Initially, the entire part is electroplated with copper. Copper is then removed by machining areas that are to be case hardened by leaving only the areas requiring stop-off plated. After heat treatment, the copper

is typically removed by stripping in cyanide or acid-based solutions.

Copper plating is used in many heat treating operations, and the choice of a plating facility familiar with these uses is important. Whether the plating is to be used for 100% assurance of zero decarburization, preparation for braze operation, or selective case hardening, the quality requirement is the same. The precleaning operations must be compatible with the alloys in question, and the uniformity of the bath chemistry must be maintained through systematic checks. The checks take the form of adhesion, porosity, and thickness. The specifications that cover these attributes can be found in MIL-C-14550, which has been superseded by AMS 2418 and ASTM B734. These specifications describe a range of thicknesses used, and most of the original equipment manufacturer aerospace specifications mandate a minimum of 0.02 to 0.05 mm (0.0008 to 0.002 in.) coverage in the required areas. The AMS 2418 standard can be used to define plating requirements and testing techniques to ensure the copper plating will be effective. If there is concern about proper adhesion, a burnishing test is described in ASTM B571.

There are many different approaches to create the selective plating, and all should be examined to determine the most cost-effective method. Among those commonly employed are rubber corks or boots to prevent the plating solution from being in contact with the area to be case hardened. Another method is to plate all over and then machine the copper free from the area requiring case development. It should be noted that if the plating is to be machined off, the plating facility must control the plating buildup to allow the machine tooling to accurately locate the surface to be removed. If the current density is not properly maintained, there will be nonuniform plating buildup, causing downstream quality issues. The use of high-density waxes and lacquers can also prevent the plating from attaching to areas desired to

* Contributed by Peter Hushek, Phoenix Heat Treating

be free of the copper plate. In this area, a careful visual examination of the unplated surfaces, typically at 10× or better, is highly advisable. A single pinhole will allow a microscopic spot of copper plate that would prevent uniform case hardening. These irregularities may show up in an etch inspection later, causing considerable production delays due to the Material Review Board or, worse yet, scrapping the lot if the prevalence is too frequent. One way of assuring that no microscopic copper is adherent is to perform a low-pressure abrasive grit blast. The pressure is low to prevent damage to the soft copper, and this slight roughening of the surface promotes a more uniform diffusion of the intended element of carbon, nitrogen, or both.

There are many baths used for copper plating, and each has its inherent benefits. The noncyanide baths have the benefit of reduced restrictions for wastewater treatment as well as air scrubbing. These baths can experience the downside risk of reduced throwing power when attempting to attain uniform coverage down a blind hole. Regardless of the bath type, there is an inherent risk that must be considered when choosing a plating service provider. The fact that copper plating is often used as an undercoating to increase the ability to plate other metals means that the heat treating orders, sometimes of infrequent and lower volumes, are often pushed aside in production scheduling. While this is not the case with all metal finish providers, it should become a discussion topic when consistent scheduling and turn times are critical to production processing.

There is also another consideration that must be considered in choosing a service provider. Some steel alloys, based on chemistry and applicability to the bath type, will require a nickel strike prior to the copper plate, to develop the required adhesion. The adhesion is critical because even an imperceptible air pocket, unseen at room temperature, will develop blisters when processed at a high temperature. These blisters often burst and expose the intended protected area to the process gases. If these areas are not planned for, subsequent postprocess machining quality delays and potential scrapping of parts can occur.

Like any process involved in metal component manufacturing, copper plating requires systematic control, regular and independent inspection of bath chemistries, rectifiers for developing current density in the parts, and standard operating procedures. It is an effective tool that can be employed when manufacturing highly reliable gears, splined shafts, and bearing surfaces. Because considerable variables come into play when deciding on the use of copper plating for each individual part, its dimension at the time of processing, the required precision of the masked areas, as well as the production volume must be factored into the proper use for a cost-effective application of this method.

Stop-off Paints

Stop-off paints refer to applied coatings for selective protection of steel parts during carburizing and nitriding. Although the term *paint* is commonly used, the term is misleading, because these stop-off products are actually coatings and should be treated as such. These coated surfaces must have a uniform coating thickness, in accordance with the manufacturer's specification, to ensure consistent results. Coating thickness usually ranges from 0.2 to 1.0 mm (0.008 to 0.04 in.). This is easily measured with a thin-film gauge. Thin-film gauges are inexpensive and easily obtained from industrial paint suppliers and industrial product distributors.

Stop-off paints are applied by brushing, immersion, spraying, or dispensing; they provide a gastight layer on the surface of the workpiece. Stop-off paints are easily adaptable to low-volume applications as well as mass production, as found in the automotive industry.

Stop-off paints have evolved from just a few products a couple of decades ago to a wide array of specifically formulated paints for each of the following processes: carburizing, deep case carburizing, carbonitriding, vacuum carburizing, nitriding, nitrocarburizing, and plasma nitriding. In addition, stop-off paints are also available for annealing processes to prevent scaling and decarburization in open-air furnaces (Table 1).

Cleaning and Curing

Part Cleanliness. Before proceeding with the proper selection of stop-off paint, it is imperative to address the cleanliness of the part surface prior to stop-off application. Ensuring the surface of the part is free from oil, grease, dust, and oxides/scale will eliminate the majority of possible failures. Allowing sufficient drying time of the paint, in accordance with the manufacturer's specification, is another requirement that cannot be overlooked.

Cleaning in Industrial Washers. The majority of industrial washers in commercial heat treating facilities and captive heat treating departments utilize single-stage washers. The washer medium is typically a hot water or an alkaline solution heated to 60 to 80 °C (140 to 180 °F). In some instances, only hot water

with a rust-inhibitor additive is used. These washers are either the spray type or a spray/dunk combination. A single-stage washer rinses the part after the wash cycle with the same emulsion used in the wash operation. This type of washer removes the majority of surface contaminants but leaves a residue of oil that can provide short-term rust prevention. The bottom line is that parts cleaned in a single-stage washer are not oil-free. Applying a stop-off coating onto a part that has a film of oil on the surface will result in spotty hardness. As the part is heated, the oil will vaporize and lift areas of the paint off the part surface. Upon inspection, hardness checks of the failed areas will show full hardness, which is evidence that paint protection was lost during the heat-up portion of the cycle.

A hot alkaline wash, as described earlier, should be sufficient if a clean water rinse is used to ensure all contaminants are rinsed off. A common practice with industrial washers with a clean water wash capability is to add a rust inhibitor to prevent oxidation of the part surface after the cleaning operation. A water rinse with a rust inhibitor, of any percentage, will result in spotty hardness under areas that have been coated with the stop-off paint.

To ensure parts are free of oil after cleaning in a single-stage washer, it is an accepted practice to thermally remove these contaminants by heating the parts above 400 °C (750 °F) to vaporize any residual surface oils left after the wash operation. These parts are then cooled to room temperature prior to paint application.

Shot/Sand Blasting. A common practice to prepare part surfaces for the application of a stop-off coating is to blast the part with steel shot, alumina oxide, garnet, or glass beads. Parts that have been blasted should be washed after the blast operation for two reasons. The majority of blast equipment utilize a media-reclamation system. The blast media is reclaimed and reused. This reclaimed media is often contaminated with oil and dirt from previous operations that is redeposited onto the part surface. Ideally, only virgin blast media should be used in these applications. Even virgin media is problematic. After blasting, the part surface is contaminated with residuals from the blast operation in the form of dust. This surface contamination inhibits adherence of the stop-off coating, resulting in nonuniform

Table 1 Summary of stop-off paints

Process	Base chemistry	Liquid carrier	Removal of residues	Special features
Carburizing/ carbonitriding	Boron oxide	Solvent	Hot water	Water washable
	Boric acid	Aqueous emulsion		Water base, water washable
Deep carburizing	Silicates + metals	Aqueous	Shotblasting, steel brush	Solvent-free
Pack carburizing	Silicates + metals	Aqueous	Shotblasting, steel brush	Solvent-free
Nitriding/ nitrocarburizing	Tin	Solvent	Shotpeening, steel brush	...
		Aqueous emulsion		
Plasma nitriding	Copper	Solvent	Wiping	Electrically conductive
	Ceramics			Nonconductive
Annealing	Silicon, silicates	Solvent	Wiping	...

protection. A note of caution: There are blast media on the market that consist of reclaimed abrasive from grinding wheels and other previous operations. These media have been processed and cleaned but can be contaminated from glues and binders, which can be left on the part surface. One must verify that the media being used is virgin material.

Hand Cleaning. When parts to be coated are too large to wash, the areas to be coated must be cleaned by hand. Various cleaning agents are available, and special care should be taken to ensure these cleaning agents are 100% effective. Because it is difficult to verify that the area cleaned by hand is free of oil, a thermal cleaning cycle following hand cleaning would offer further assurance that the area to be coated is free of contaminants. This cycle would consist of heating the part above 400 °C (750 °F).

Paint Curing/Drying. Insufficient drying time is another leading cause of stop-off paint failures. All stop-off paints use either a solvent or aqueous thinning agent. These thinning agents must be fully evaporated prior to introduction into the furnace. Insufficient drying will cause the thinning agent to outgas, lifting areas of the paint off the part surface during heatup. It is most important that the first coat be thoroughly dried before application of a second coat. Applying a coat onto a coat that has not been thoroughly cured will result in hard spots. The second coat will seal the first and prevent the thinning agent from dissipating. When heated, the thinning agent will then outgas, popping areas of the first coat off the part surface during the heat-up cycle.

Uses of Stop-off Paints

Carburizing and Carbonitriding. The most commonly used stop-off paints for carburizing

and carbonitriding are solvent or water-based coatings with boron as the main ingredient. The biggest advantage of boron-based paints is that the residues, after heat treatment, are water soluble in a hot water or alkaline wash. These paints are the best choice for applications where mechanical cleaning is not an option. The protection of threads is a typical application. These paints are widely used in the automotive industry in mass production of small- and medium-sized car components. They provide local protection during carburizing and carbonitriding, and the removal of residues during the wash operation eliminates an additional cleaning operation.

Figure 1 shows an added benefit of boron paint: the hardness response in the protected area with such a product is even lower than the core hardness, because the quenching speed is lowered due to the insulating characteristic of the paint.

The original stop-off paint, developed over 60 years ago, consisted of boron oxide and a solvent-based coating. These solvent-based paints are still used today (2013) and still offer the best protection in this class of coatings. Water-based products have been developed and offer a more environmentally friendly alternative when the use of a solvent-based paint is not acceptable. However, the use of boron in an aqueous base has limitations that can be detrimental to the interior of the furnace chamber. Both solvent- and water-based boron stop-off paints break down during the heat treating cycle. It is a time-temperature relationship. These paints offer protection up to 2 mm (0.08 in.) case depths. Beyond these depths, the paints are no longer effective. The combination of water and boron forms boric acid. The outgassing of the boric acid based coating during the atmosphere cycle can react with the silicon in the refractory, causing a eutectic and lowering the melting point of the silicon. This can result in

a glazing of the furnace chamber. The degree of glazing is dependent on the amount of paint used and number of cycles with painted parts the furnace chamber has been subjected to. The glazing will vary within the chamber due to variation of silicon in the various refractory components within the chamber. This glazing effect has also been observed on substrates used in oxygen probes. The glaze can coat the electrical contact area between the outer electrode and the inner substrate, increasing the probe resistance and offsetting readings. To correct this situation, the probe must be replaced and sent back to the manufacturer to be cleaned. The interface area between the electrode and substrate must be mechanically cleaned and tested. For these reasons, a solvent-based boron stop-off should be the first choice, because it is not subject to this phenomenon.

Boron-based paints differ from all other alternatives. When heated, these paints go into a semi-liquid state at temperature. If the coating is too thick, the mass of the paint could cause the paint to run into uncoated areas and create stop-off in addition to the intended areas. For this reason, a paint thickness of 0.2 to 1.0 mm (0.008 to 0.04 in.) should be maintained. Only one coat is required, as long as this coating is uniform. Thicker is not better. Two coats are recommended only for certain applications, such as threads. A second coat is recommended to ensure the tips of threads are adequately protected.

Deep Case Carburizing. A number of stop-off paints have been developed as an alternative to boron-based paints for case depth requirements exceeding 2 mm (0.08 in.). These silicate-based paints can provide safe protection for case depths up to 10 mm (0.40 in.), for example, large gear parts for the wind energy industry (Fig. 2) and other energy transmissions. Apart from the aqueous silicate liquid carrier, the main ingredients are metals/metal oxides. Paints containing copper are not particularly suited for carbonitriding because of the possible chemical reaction between the metal and the ammonia of the processing atmosphere. Silicate-based stop-off paints are normally applied in two or three layers, depending on the case depth in question. After heat treatment, the

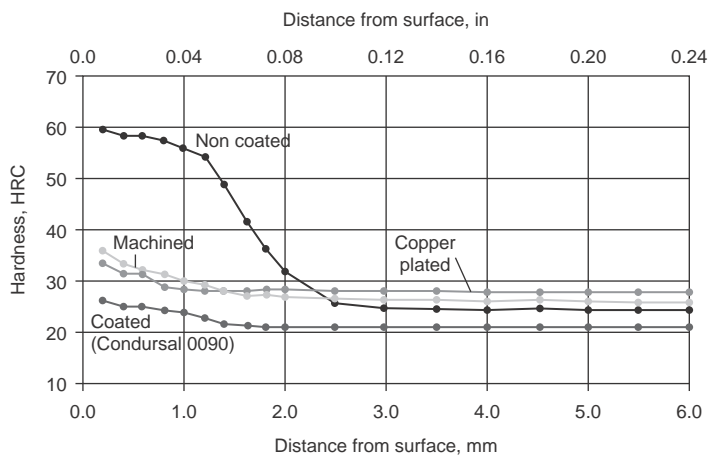


Fig. 1 Performance of different stop-off techniques for gas carburizing. Local protection of 27 mm (1.06 in.) diameter specimen of 8620H steel against carbon pickup provided by stop-off paint (Condursal 0090) compared to copper plating



Fig. 2 Gear parts for a wind turbine coated with stop-off paint (Condursal 0118) prior to case hardening

glasslike residue of the paint is not water soluble nor can it be removed using solvents. The residue is removed by shotblasting. An advantage of these paints, unlike the boron-base products, is they will not run even if the coating thickness is excessive. Also, they are not subject to the possibility of glazing the furnace interior, unlike the water-based boron paints.

Vacuum Carburizing. Stop-off paints used for vacuum carburizing are similar to those used in atmosphere carburizing. Boron paints are used for applications requiring the paint to be washed off after heat treatment.

The only boron paint that should be used in a vacuum carburizing furnace is one that has been specifically formulated for this process. Conventional boron paints can be a particular concern, especially in high-pressure vacuum quench furnaces. The extreme turbulence of the nitrogen or argon quench can blow some of the residues off the part surface and contaminate the interior of the furnace chamber. The real concern is the possibility that these residues make their way into the vacuum pump. If mechanical removal (shotblasting) of the stop-off paint is acceptable, a silicate-based copper oxide paint should be the first choice. This type of paint is extremely effective and negates the possibility of contaminating the furnace chamber during the turbulence of the quench cycle.

Nitriding and Nitrocarburizing. Stop-off for nitriding and nitrocarburizing in gas is mainly based on a fine tin powder dispersed in a lacquer consisting of a solvent + synthetic binder or water + synthetic emulsion. The stop-off effect is based on a layer of molten tin dispersed on the steel surface. It acts as a gas tight barrier, preventing the diffusion of nitrogen. It should be noted that preheating the coated parts in air must be limited to 380 °C (720 °F) maximum. Exceeding this temperature limitation will prove detrimental to the uniformity of the tin plating as required for safe protection. Residues of these paints are of a powdery appearance after the nitriding process and can be easily removed by wiping or brushing. It must be noted that a microscopic layer of tin is left on the part surface after the powdery residues are removed. Often, this does not present a problem to the functionality of the part. In the event this does present a problem, the tin layer can be removed by blasting or machining.

Occasionally, the tin layer left behind on the steel surface of the coated area is misinterpreted by metallography as a nitride layer. If there are respective doubts, a microhardness measurement helps clarify whether it is soft tin or a hard nitrided area.

It is possible that some of the powdery residuals after nitriding may come off at the end of the cycle, due to gas turbulence in the retort or during the unloading stage of the cycle. These residuals will settle on the bottom of the retort. It is recommended that the inside of the retort be vacuumed out after each cycle to ensure that residues of this powder do not re-deposit on noncoated areas of parts in the next

load. Failure to follow this procedure could result in soft spots in uncoated areas of these parts.

Typical parts for nitriding processes are crankshafts, camshafts, cam followers, valve parts, extrusion screws, die-casting tools, forging dies, extrusion dies, injectors, and plastic mold tools (Fig. 3).

Plasma Nitriding. For plasma nitriding, the most commonly used stop-off technology is shielding. If the geometry of the part does not lend itself to shielding, stop-off paints based on either copper (electrically conductive) or ceramic ingredients (nonconductive) are available. The residues of these paints are powdery and can be removed easily by wiping or brushing.

Scale Prevention. Stop-off paints are available to prevent scale and oxidation in open-fired furnaces. These paints are used for annealing, stress relieving, normalizing, and hardening. They are used in applications where a protective atmosphere is not available or is cost-prohibitive. In these applications, the entire part surface is coated. Boron paints are available that will prevent scale in applications up to a maximum temperature of 850 °C (1560 °F). After heat treatment, the residues of these paints are water soluble and easily removed in a hot water wash. These paints are not recommended in applications over 850 °C (1560 °F), because the paint is no longer water soluble, and even mechanical removal is extremely difficult.

Lacquers and ceramic-based coatings are available for applications up to 1200 °C (2190 °F). These coatings form a glasslike barrier to prevent scale from forming. On cooling, the coating will begin to spall off, due to differential expansion of the coating and the steel part. While much of the coating will break off, mechanical removal of areas of the part will typically be required.

General Considerations

Masking of steel parts during heat treatment can be successfully and economically applied using stop-off paints for practically the whole range of diffusion-based gas carburizing and nitriding processes, including the latest vacuum technologies. New products and modes of application provide a versatile and reliable technology, offering major benefits regarding cost reduction, health and safety protection of the workers, and protection of the environment compared to formerly used techniques such as copper plating.

Stop-off paints are used on expensive parts that are nearly ready for use. A lot of value has been added to each part before it is sent for heat treatment. Failure to properly clean the part surface and adhere to the manufacturer's application instructions will result in costly scrap. Also, it must be considered that the stop-off paints are not standardized but manufactured according to the proprietary formula of their



Fig. 3 Tool parts coated with stop-off paint (Condursal N633) prior to nitriding

manufacturer. Thus, it is mandatory to strictly follow the advice given in their technical documents.

A general rule of thumb states that no more than 30% of the total area of the parts within a furnace load should be coated with stop-off paint. Exceeding this amount could delay the furnace cycle due to a temporary imbalance in the furnace atmosphere. As the parts are heated, water vapor or gases generated by thermally cracked binders in the paint are released to the atmosphere. An excessive amount will cause an imbalance of the furnace atmosphere, stopping the process. In time, the furnace atmosphere will recover, but the cycle would have been interrupted, resulting in a shallower case than had been intended.

Stop-off paints typically have a minimum shelf life of one to several years. These paints should be stored at room temperature, and distribution use should always be first in, first out. Water-based paints must not be allowed to freeze. In the event freezing has occurred, the paint must be allowed to thaw to room temperature and then mixed thoroughly before application. As discussed earlier, the parts must be thoroughly cleaned and dried prior to application of the stop-off paint. Parts must be free of contaminants such as oil, grease, dust, and oxides/scale. Ideally, both parts and paint should be at room temperature (approximately 25 °C, or 77 °F) when the paint is applied. After the paint is thoroughly stirred, the coating should be applied as uniformly as possible, in such a way that the steel surface is covered completely and the steel does not shine through the painted surface. Excessive coating thickness must be avoided; it does not enhance the protective performance of the paint. However, it could cause some of the paint to run into unwanted areas, and it will definitely extend drying time. Required drying time is dependent on various factors, such as paint composition, viscosity, coating thickness, ambient and part temperature, as well as atmospheric humidity. Drying time can range from approximately 3 to 16 hours, depending on atmospheric conditions, coating thickness, and number of coats

applied. Solvent-based paints will dry relatively fast, due to the accelerated evaporation of the solvent compared to an aqueous-based paint. Drying time on all these paints can be shortened by preheating the parts at a maximum temperature of 180 °C (360 °F) in air. Exceeding this maximum temperature could cause the paint to run into noncoated areas and also compromise the effectiveness of the paint.

If parts previously coated with stop-off paints are preheated to temperatures exceeding 180 °C (360 °F), the protective performance may be affected, depending on the paint formula, the furnace atmosphere, and the preheating temperature. Thus, it is important to consider the respective advice provided by the manufacturer.

Many of these paints are hygroscopic and will absorb moisture if exposed to high humidity for extended periods of time. It is recommended that painted parts be heat treated within 24 hours of the last coat. In areas of high humidity, it is recommended that painted parts be stored in an oven at 80 °C (180 °F) maximum until they are ready to be placed into the furnace.

The painted areas of the part must be arranged or fixtured to ensure these areas do not come into contact with noncoated areas of other parts in the furnace load. If contact occurs during the furnace cycle, the protective layer may be damaged, or unwanted insulation from the gas process of neighboring parts may occur.

Care must be taken to ensure that the stop-off paint does not drip or is misapplied to unwanted surfaces. Manual cleaning of these areas is typically not sufficient. Even though the contaminated surface looks clean, case penetration in these areas may not be uniform. It is recommended that all the paint be removed mechanically by blasting, the part washed, and the paint reapplied.

After heat treatment, it is recommended that the residue of the paint does not remain on the parts for an extended period of time. The residue of some stop-off paints can react with humidity and cause a corrosive attack on the part surface.

Most stop-off paints are only effective for one atmosphere cycle. This is definitely the case with hardening cycles in which the parts are quenched. The parts must be cleaned and recoated if subsequent heat treatment is required. There is one exception to this rule. A couple of stop-off paints are available that will prevent carbon penetration during a carburizing cycle followed by atmosphere slow cooling. The parts can be cooled further in air to room temperature. These same parts can be reheated in atmosphere and oil quenched for the hardening cycle. These silicate-based paints will offer stop-off protection during both cycles, eliminating the need to recoat.

In the same furnace load, do not combine parts painted with two different stop-off paints. This situation could compromise the effectiveness of one or both of the paints. This is definitely the case if a solvent-based boron paint

and a water- or silicate-based paint are in the same load. Water- and silicate-based paints give off water vapor during the heat-up cycle, which can attack the solvent-based paint and cause it to run into uncoated areas.

Edge Effect. A common complaint is hardness found under the edges of the painted surface. This is not a failure of the paint but is caused by penetration of carbon or nitrogen through the uncoated area adjacent to the paint edge. The case diffuses into the part surface and wraps under the edge of the paint. If this is unacceptable, it can be alleviated by extending the edges of the painted surface to compensate for this condition.

Application Methods

Small numbers of parts to be selectively protected are normally coated manually by simply painting with a flat, soft brush. At the same time, stop-off paints can be tailored to the customer's needs, which allows a variety of modern semi- or fully automatic application technologies.

Prior to application of any of these technologies, proper mixing of the paint is of utmost importance. The majority of stop-off paints on the market today (2013) are non-Newtonian fluids, meaning the viscosity of the paints are always changing based on time, temperature, and other factors that can disrupt the fluid. These paints are thixotropic. Upon opening a container of paint, the contents look thick (viscous) and almost gellike. However, as the paint is sheared by the mixer, the paint becomes more fluid as the viscosity decreases, due to the shear stress caused by the mixing. Typically, these products cannot be shaken or agitated but must be mechanically mixed, either by hand or by mechanical mixer. Most stop-off paints can be used directly from the can when first opened. Thinning of the paint with either solvents or water is only required to replenish that which has been lost to evaporation. It is important that the paint be thoroughly mixed before considering the addition of thinner. Overthinning the paint can be detrimental to the effectiveness of stop-off protection.

Brushing. As mentioned previously, brushing is suited for single or small series of components, such as large gears, shafts, tools, and so on. The stop-off paint should be applied in an even, thin layer of uniform thickness by using a flat, clean brush with soft bristles. When applying the paint to the part, do not put any pressure on the brush, but allow the paint to flow off the brush in a uniform manner. Stop immediately if the paint rolls off the painted surface and back to the brush. There is oil or some other contaminant on the surface that must be removed. When storing the brush between coats, the same solvent as in the paint must be used to ensure there is no adverse chemical reaction or paint contamination.

Dipping/immersion is the simplest and most economical way to coat high volumes of lightweight parts. If the area to be coated is at the end of the part, semiautomatic or continuous systems are used to perform this task (Fig. 4). In one system (Fig. 4a), parts are loaded into a rack. The loaded rack is placed in a stationary position above a container of stop-off paint. The container is elevated to the part as required and then withdrawn. Excess paint drips into the container. The rack is removed and replaced with another rack.

In another system (Fig. 4b), parts are placed into a carrier. The carrier is indexed over a stationary container of stop-off paint. A shallow container is submerged in the paint and elevated to the parts as required. The shallow container is withdrawn into the stationary container to refill. Excess paint drips into the container. The carrier indexes from the stationary container, followed by another carrier to be processed.

Dispensing. Automatic dispensing of stop-off paint uses equipment similar to that used to apply adhesives. The process and equipment is similar to normal paint-spraying technologies, but the paint is not sprayed; it continuously flows from the nozzle like toothpaste. Many installations use this technology that requires only moderate adjustment in respect to the paint characteristics and the workpiece area to be coated. Depending on the number of parts and how sophisticated the requirements are, either simple low-cost devices (Fig. 5) or high-end computer-operated systems, including

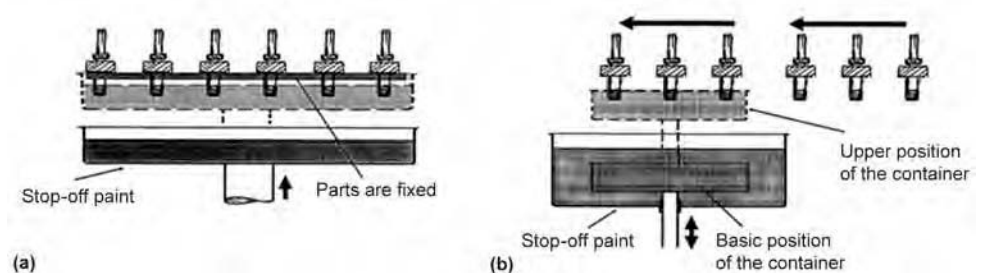


Fig. 4 Schematic view of dipping installations

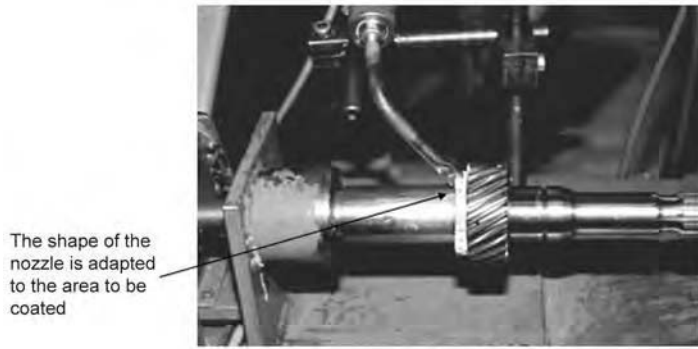


Fig. 5 Low-cost feeding installation

automatic handling systems, drying zones, and so on (Fig. 6) can be implemented. Robotics and automated handling systems provide reproducible high-production application. These systems are found in the automotive industry and are used by the manufacturers of high-production gears, such as those used in transmissions.

Spraying. Like dispensing, spraying also lends itself to high-production coating. It is especially suited for applications requiring large areas to be coated. That said, spraying has been substituted more and more by

dispensing, which offers major benefits such as reduced consumption (no overspray) and minimized mist exposure for the workers. In addition, spraying usually requires some form of masking to keep the overspray from contaminating unwanted areas.

Stamping. On large numbers of parts with intricately shaped areas to be coated, the paint can be applied by stamping. For this, a counter-piece with the mirror shape of the area to be coated is wetted with the paint and then pressed onto the workpiece. Such a process

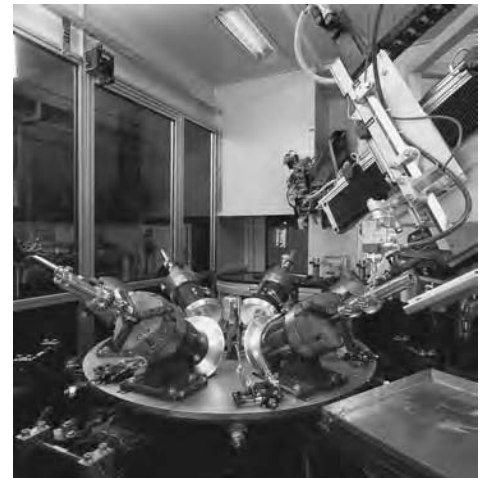


Fig. 6 High-end computer-operated feeding installation

can be semi- or fully automatically set in practice at reasonable costs.

ACKNOWLEDGMENT

The authors thank Peter Hushek, Phoenix Heat Treating, for the text on copper plating stop-off.

Methods of Measuring Case Depth in Steels

Revised by William J. Bernard III, Surface Combustion, Inc.

Introduction

Case hardening of steel is a process whose goal is to selectively harden the surface of a specimen. The hardened surface is defined as the case, while the interior is known as the core. Case depth is broadly defined as the normal distance from the surface of the steel to the start of the core.

The purpose of this article is to describe various methods of measuring case depth. Other articles describe methods to model and predict case depth in different steels for different surface-hardening processes. There are two primary methods of case hardening: diffusion methods such as carburizing, carbonitriding, nitriding, and nitrocarburizing; and thermal methods such as induction and flame hardening. In the case of diffusion methods, the chemical composition of the surface layer is modified by introducing a hardening chemical species. For thermal methods, the surface of the material is heated and quenched rapidly to form hard metastable phases (e.g., martensite), while the core retains its original microstructure.

Measurement Specifications

Measurement of case depth is highly sensitive to the type of case hardening, original steel composition, quenching condition, and even the testing method. For example, typical hardness surveys taken on cross sections at the pitch line, root fillet, and root land of a tooth in a carburized and hardened gear made of 8620H steel are shown in Fig. 1. These data illustrate the importance of well-defined specifications by showing that there are variations in effective case depth even among three areas of the same gear tooth.

Specifications such as those listed in the Selected References generally specify the following two terms.

Effective case depth is the perpendicular distance from the surface of a specimen to the

deepest point at which a specific hardness value or specific chemical composition is reached. Different standards define the hardness limit or composition value differently. For example, carburizing standards will often call for “effective case depth to 50 HRC,” “case-hardened depth to 550 HV,” or “case depth to 0.40 wt% C.” For nitriding, specifications may call for “practical nitrided case depth to core hardness + 50 HV.” For induction or flame hardening, a standard may call for “case-hardened depth to 80% of minimum surface hardness” or may allow for the effective case-depth hardness limit to vary with the carbon content of the steel, as in Table 1. Some specifications may even define case depth based on microstructure (e.g., “case depth to 50% martensite”). The effective case depth is typically found to be approximately two-thirds to three-fourths the total case depth.

Total case depth is defined as the perpendicular distance from the surface of a specimen to the point at which differences in chemical or physical properties of the case and core are no longer measurable. Total case depth sometimes is considered to be the distance from the surface to the deepest point at which the carbon content is 0.04% higher than the carbon content of the core.

It should be noted that international standards and commercial specifications may define case-depth measurement differently. When applicable, use and refer to these documents for their specific procedures. The following discussion of test procedures and technologies should only be used as a guideline of suggested practices in the absence of a governing standard’s requirements.

Case depth determined by different methods may vary significantly. For example, in one study, carburized and hardened samples of 8620 steel were prepared and submitted to five independent laboratories. Because of the amount of personal estimation involved with different case-depth measurement procedures, the results as shown in Fig. 2 and 3 vary somewhat more widely than usually encountered with other physical measurements. The results also show that when the design of a part requires a certain case depth, the method of measurement should be defined clearly. Additionally, when qualifying a process, multiple case-depth measurement methods should be employed.

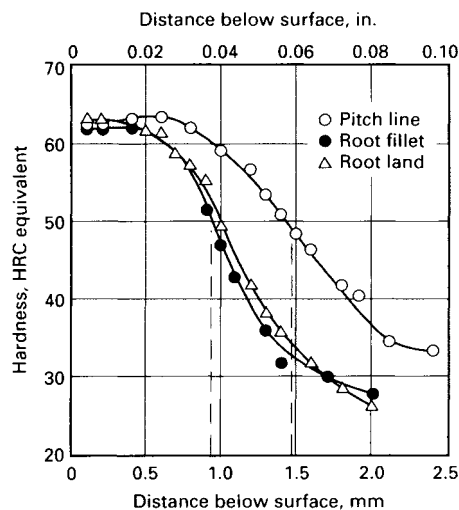


Fig. 1 Variation in hardness with distance below surface for a carburized and hardened 8620H steel gear. Effective case depths to 50 HRC: 0.94 mm (0.037 in.) at root fillet, 1.02 mm (0.040 in.) at root land, 1.45 mm (0.057 in.) at pitch line

Table 1 Recommended hardness limits as a function of carbon content for effective case depth of induction- or flame-hardened steel

Carbon content, %	Hardness Limit, HRC
0.28–0.32	35
0.33–0.42	40
0.43–0.52	45
0.53 and over	50

Source: Ref 1

Chemical Method

Chemical methods may be used to determine the total case depth developed from diffusion-based processes. If effective case depth is defined using a chemical composition limit (e.g., 0.40 wt% C), these methods can also be used. Two common methods are combustion analysis and spectrographic analysis.

Combustion Analysis. Different methods are used to determine the amount of carbon and nitrogen in steels. For carbon, typically a sample is burned in pure oxygen to convert all carbon to carbon dioxide. The carbon dioxide is then measured by infrared gas absorption and related to the weight of the original sample. Alternatively, the amount of carbon dioxide can be measured using thermal conductivity test methods. Carbon dioxide is inserted into a gas stream of helium or hydrogen. The thermal conductivity of the gas stream is measured in a test cell and compared to a standard, whereby the amount of carbon dioxide can be determined.

For nitrogen, the inert gas fusion method is used. By heating the sample in helium at high temperature ($\geq 1900^\circ\text{C}$, or 3450°F), molecular nitrogen (N_2) is released and measured by the thermal conductivity method described previously.

These test methods are highly accurate and precise; minimum detection limits of carbon and nitrogen are typically 0.002%.

Spectrographic Analysis. Carbon and nitrogen content may be determined accurately by optical emission spectroscopy. In this method, atoms are excited and ablated from the sample surface by an energy source. Typical energy sources are electric sparks or glow-discharge lamps. The excited atoms emit characteristic wavelengths of light as they lose energy. Resolving these wavelengths and their intensity from the overall emitted spectrum allows the type and amount of each element present to be found.

Whereas chemical determination by the combustion method provides an average carbon or nitrogen content for the amount of material removed by machining, the spectrograph determines the local elemental content of the specimen to a depth of 0.03 mm (0.001 in.). A comparison of carbon values obtained from five specimens by spectrographic and combustion methods is presented in Table 2.

Example Test Procedures. To ensure maximum uniformity of the case-hardening process among various types of furnaces, large heat treatment facilities often use test specimens instead of actual parts for chemical analysis. These specimens are often standardized with respect to alloy and configuration to establish schedules for various case depths and to ensure maximum uniformity among various furnaces. Case depths of actual parts then can be correlated to the test specimens.

It is good practice for test specimens to be the same grade material as the production parts and to be processed in the same load. In some

cases, a simulation procedure is used in a manner representative of the procedure to be used for actual parts. However, simulation is not recommended because the furnace load containing the test specimens should approximate actual production conditions in terms of load density, configuration, and surface area to be case hardened. These three variables affect atmosphere flow, temperature uniformity, and carbon (or nitrogen) demand. Differences in these conditions between production loads and the load that contains the specimens can lead to errors in the correlation of case depths. In addition, even if all process variables are the same, case depth determined on flat or round test specimens will often be different than case

depth determined on workpieces because of differing geometry.

A typical procedure for obtaining carburized specimens for combustion analysis is presented as follows. The accuracy of the results is highly dependent on good machining practices and well-maintained analytical equipment:

1. Prepare a cylindrical test bar of suitable material in the configuration shown in Fig. 4. Identify the bar in some manner, such as by stamping a number on the end.
2. Carburize and then quench or cool the bar as required. If the bar is slowly cooled, steps 3 through 7 can be omitted. For measurement accuracy, take care to avoid

Sample 1—8620 with core hardness Rockwell C 30, surface 0.90% C

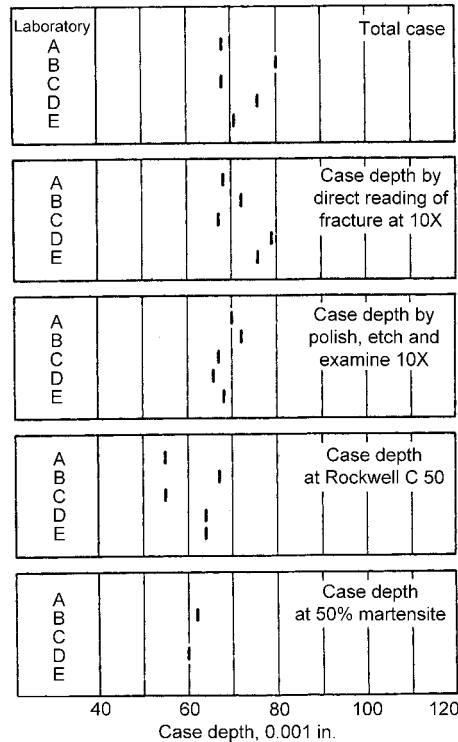


Fig. 2 Comparison of case-depth measurements on a sample of 8620 steel with core hardness of 30 HRC and 0.90% surface carbon in five different laboratories

Sample 2—8620 with core hardness Rockwell C 40, surface 0.90% C

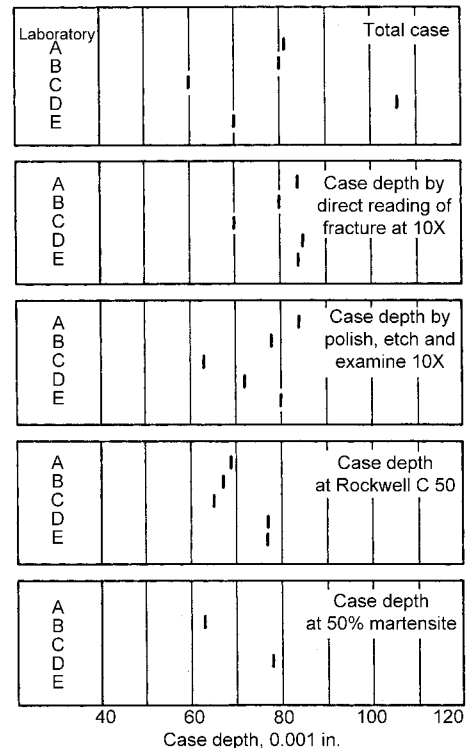


Fig. 3 Comparison of case-depth measurements on a sample of 8620 steel with core hardness of 40 HRC and 0.90% surface carbon in five different laboratories

Table 2 Carbon contents of shim stock and of surfaces of workpieces concurrently processed, as determined by spectrographic and combustion analysis

Both shim stock and workpieces were heat treated in a continuous-belt furnace with an endothermic-base atmosphere (class 301; dewpoint, -9 to -1°C , or 15 to 30°F).

Specimen No.	Carbon present, %		
	Shim stock		Workpiece surface (spectrographic analysis)
	Spectrographic analysis	Combustion analysis	
1	0.36	0.36	0.38
2	0.24	0.27	0.25
3	0.22	0.24	0.225
4	0.35	0.35	0.34
5	0.30	0.30	0.305

- excessive decarburization or distortion of the specimen during cooling.
- Wash bar with soap and water. Rinse with methanol, and dry.
 - Cut a section from the 25 mm (1 in.) diameter end for examination of microstructure.
 - Record the as-quenched surface hardness of the large-diameter end.
 - Temper the bar for the time and at the temperature specified for the part with which the test bar was carburized. Record the as-tempered hardness of the large-diameter end.
 - For ease of machining, first temper the test specimen for 1½ h at 650 °C (1200 °F). Then grit blast lightly, clean centers, and straighten bar to 0.04 mm (0.0015 in.) total indicator reading taken in three places.
 - Wash bar with soap and water. Rinse with methanol, and dry. Bars should not be handled with bare hands after cleaning and prior to machining.
 - For case depths less than 5.10 mm (0.200 in.), machine approximately 3.8 mm (0.15 in.) from the 25 mm (1 in.) diameter end to a depth of 5.0 mm (0.20 in.), to ensure that the case on the end does not contaminate the specimens for carbon analysis. An alternative is to just perform a plunge cut in the center section of the turn bar, to preclude any machining at the ends of the bar.
 - Machine the bar dry (no cutting fluid should be used). Before each machining operation, record the diameter of the bar as measured with a micrometer. Maximum allowable taper of the machined area is 0.03 mm (0.001 in.) on the radius. Machine a maximum of 0.05 mm (0.002 in.) from the radius to clean the surface. Save the chips for analysis. Next, machine the radius in increments ranging from 0.05 to 0.25 mm (0.002 to 0.010 in.), depending on the desired accuracy and expected case depth. Machine the radius in increments to a depth of 0.25 mm (0.010 in.) below the maximum expected case depth. Take three more increments of 0.25 mm (0.010 in.) from the radius or make three cuts at the expected case-depth break. Save chips from each increment for separate analysis. Take precautions to ensure that chips from each cut are not blued, burned, or

- contaminated by dirt, paper, oil, or chips from preceding cuts.
- Analyze chips or turnings using a combustion analyzer.
- Calculate and plot the carbon-gradient curve. Determine total and/or effective case depth from the curve. A sample data sheet and a carbon-gradient curve used to find effective case depth to 0.40 wt% C of a specimen are presented in Table 3A and Fig. 5, respectively.

Determination of carbon or nitrogen using the spectrographic method normally uses flat test specimens that can be taper ground, step ground, or reground incrementally after each measurement. A very small amount of material is ground from the surface (to remove oxides). Successive cuts are made and analyses are performed after each cut. Special care must be taken for accurate measurement of the depth corresponding to each elemental determination. Total and/or effective case depth is found from a plotted chemical gradient curve as in step 12 of the aforementioned combustion analysis procedure.

If glow-discharge optical emission spectroscopy is used, novel techniques allow control

of sputtering depth. Therefore, layer after layer of the sample surface can be removed and analyzed without regrinding the sample after a measurement.

Mechanical Methods

The preferred and most widely used method of measuring effective case depth is the microhardness test. This method is also preferred for measuring total depth of thin cases (≤ 0.25 mm, or 0.01 in.), such as is found in nitriding.

The microhardness test consists of making light load indentations on a prepared sample at specified linear intervals from a point near the edge of the surface through the case to a point well within the core area, as shown in Fig. 6 and 7. For case-depth measurements, the selection of a Knoop indenter is recommended so that the highest density of indentations may be obtained.

The Knoop indenter shown in Fig. 8 uses a sphero-conical diamond that produces an elongated indentation. This is especially important when measuring thin cases.

Table 3A Sample data sheet for computing case-depth values for a carbon-gradient plot

See Table 3B for definitions of dimensional factors. Data are for 8620H steel, carburized at 925 °C (1700 °F) in a 19-tray continuous pusher furnace with infrared control of carbon dioxide content in zones 2, 3, and 4. See text for explanation of procedure, and see Fig. 5 for plot of carbon gradient.

Cut No.	Dimensional factor (see Table 3b), mm									Carbon, %
	D_L	D_R	A_L	A_R	C_L	C_R	X	M	P	
0	25.35	25.36
1	25.20	25.23	0.15	0.13	0.15	0.13	0.07	0.03	0.03	0.987
2	24.98	24.99	0.22	0.24	0.37	0.37	0.18	0.06	0.13	0.953
3	24.76	24.76	0.22	0.23	0.59	0.60	0.30	0.06	0.24	0.918
4	24.49	24.47	0.27	0.29	0.86	0.89	0.44	0.07	0.37	0.871
5	24.22	24.22	0.27	0.25	1.13	1.14	0.57	0.06	0.50	0.818
6	23.94	23.91	0.28	0.31	1.41	1.45	0.71	0.07	0.64	0.787
7	23.69	23.65	0.25	0.26	1.66	1.71	0.84	0.06	0.77	0.717
8	23.41	23.38	0.28	0.27	1.94	1.98	0.98	0.07	0.91	0.675
9	23.10	23.10	0.31	0.28	2.25	2.26	1.13	0.07	1.05	0.627
10	22.80	22.78	0.30	0.32	2.55	2.58	1.28	0.08	1.21	0.583
11	22.49	22.48	0.31	0.30	2.86	2.88	1.43	0.08	1.36	0.540
12	22.19	22.17	0.30	0.31	3.16	3.19	1.59	0.08	1.51	0.483
13	21.87	21.87	0.32	0.30	3.48	3.49	1.74	0.08	1.67	0.444
14	21.59	21.56	0.28	0.31	3.76	3.80	1.89	0.07	1.81	0.401
15	21.25	21.27	0.34	0.29	4.10	4.09	2.05	0.08	1.97	0.365
16	20.80	20.75	0.45	0.52	4.55	4.61	2.29	0.12	2.17	0.328
17	20.27	20.24	0.53	0.51	5.08	5.12	2.55	0.13	2.42	0.283
18	19.72	19.68	0.55	0.56	5.63	5.68	2.83	0.14	2.69	0.245

Table 3B Definitions of dimensional factors in Table 3A

Dimensional factor in Table 3(a)	Definition
D_R, D_L	Diameters of left and right ends of turned bar, respectively. $D_{L,0}, D_{R,0}$ are diameters before turning; $D_{L,n}, D_{R,n}$ are diameters measured after each cut.
A_L, A_R	Material removed from diameter as measured from preceding cut; $A_{L,n} = D_{R,n-1} - D_{L,n}$, $A_{R,n} = D_{R,n-1} - D_{R,n}$, $n > 0$
C_L, C_R	Total diametrical depth of material removed, measured from case-hardened bar surface; $C_{L,n} = D_{L,n} - D_{L,0}$, $C_{R,n} = D_{R,n} - D_{R,0}$, $n > 0$
X	Average total radial depth of material removed from case-hardened bar surface; $X_n = (C_{L,n} + C_{R,n})/4$, $n > 0$
M	Average radial midpoint of current depth of cut as measured from preceding depth; $M_n = (X_n - X_{n-1})/2$, $n > 0$
P	Plotted depth from surface of bar corresponding to chemical analysis of turnings from this depth; $P_n = X_{n-1} + M_n$, $n > 0$

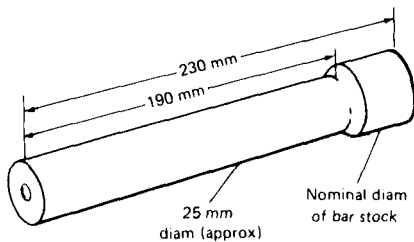


Fig. 4 Nominal configuration of standard test bar used for chemical method of carbon gradient and case-depth measurement. The 25 mm (1 in.) diameter end is finished with 80-grit sandpaper.

The use of the square pyramid Vickers indenter shown in Fig. 9 limits the ability to make closely spaced indentations and indentations close to the surface. To avoid error, there should always be a two-indentation-width space from the edge of the case to the first indentation and the same distance between subsequent indentations. The load selection is based on the need to have a sufficient number of indentations to obtain good reliable data and large enough indentations to be read accurately. Microhardness traverses are made using loads ranging from 100 to 1000 g.

Typically, specimens are prepared by cutting them perpendicular to the surface at a specified location (such as the center-length of a bar). The cut sample is then typically compression molded in a low-shrinkage thermosetting resin containing a hard filler to retain the edge of the case. The surface is then ground and polished to a point that allows accurate measurement of the microhardness indenter load impressions. It is recommended to at least polish to a 6 μm (240 μin.) finish using a napless cloth charged with diamond abrasive compound or suspension with a suitable extender. Final

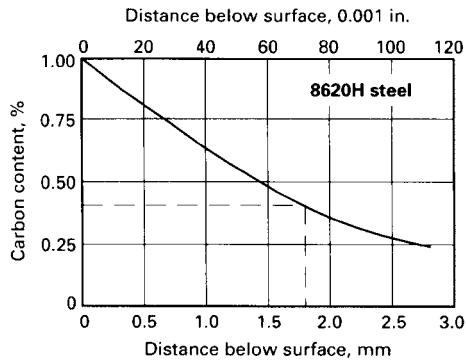


Fig. 5 Carbon gradient for carburized test bar of 8620H steel. A test bar similar to the one shown in Fig. 4 was carburized at 925 °C (1700 °F) in a 19-tray continuous pusher furnace with infrared control of carbon dioxide content in zones 2, 3, and 4. Effective case depth to 0.40% C is 1.82 mm (0.0715 in.) (indicated by broken lines). See text for explanation of procedure for calculating plot points and Table 3 for sample data sheet for this figure.

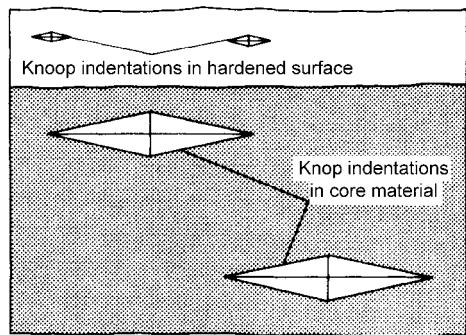


Fig. 6 Comparison of Knoop indentation using the same load in both the hardened case and soft core of a workpiece

polishing with 0.05 μm (2 μin.) alumina on a napped cloth should be limited to approximately 30 s duration to prevent edge rounding.

The accuracy of a microhardness traverse across the case and core depends on the correct preparation of the sample to be tested. In general, the same care should be taken with the

sample as if it were to be examined for microstructure. During all cutting and grinding operations, care must be taken to avoid overheating and thus tempering the sample. Each step must be performed thoroughly with ample lubrication to prevent microstructural deformation. Also, care must be taken to avoid blunting the

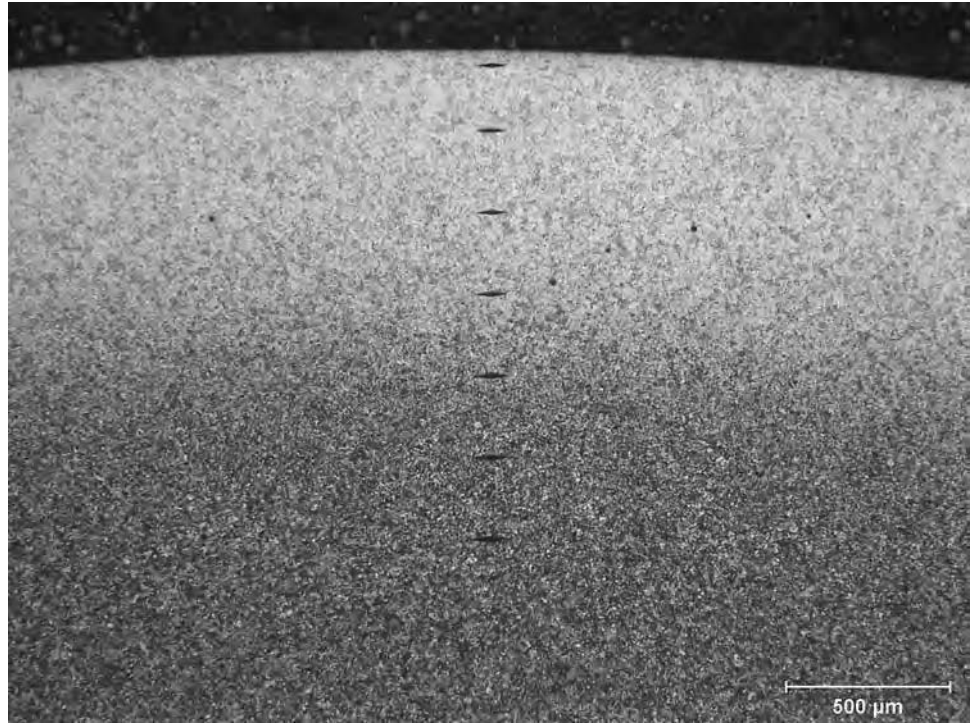


Fig. 7 Knoop survey in carburized alloy steel. 2% nital etch. Original magnification: 40×. Courtesy of Materials Evaluation and Engineering, Inc.

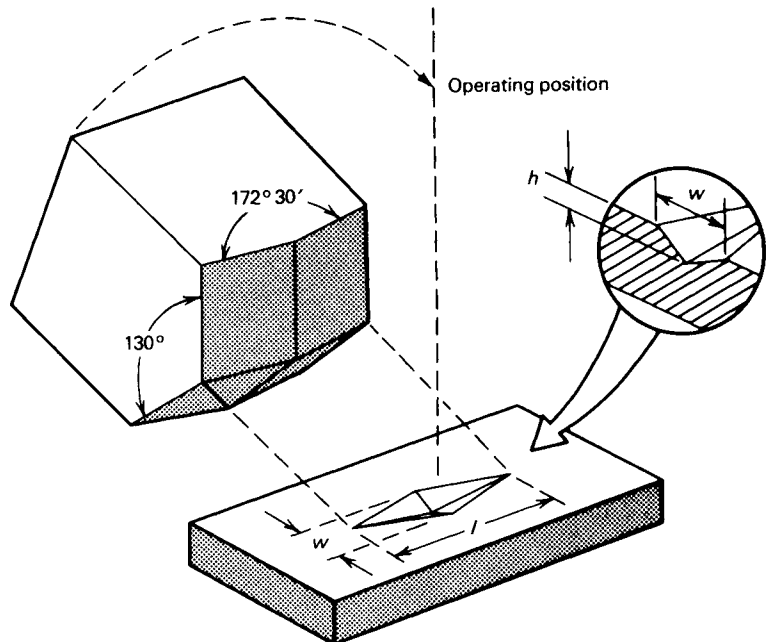


Fig. 8 Pyramidal or spheroconical Knoop indenter and resulting indentation in the workpiece

edges of the cross section to allow accurate measurement of hardness near the surface. That said, in practice, reliable microhardness readings closer than 0.01 mm (0.004 in.) to the edge of a polished specimen are difficult to obtain due to edge rounding.

It may be necessary to etch the as-polished sample to determine the demarcation between the case and the core (see visual methods that follow) or to see if temper burning has occurred. However, application of the etchant must be light. A heavy etch may affect the hardness readings and also make the visual measurement of the indentations more difficult.

Next, the specimen is typically loaded onto a microscope equipped with a Vickers (diamond pyramid) or Knoop microhardness indenter and a micrometer stage. Microhardness indenter loads are typically 0.2 to 1.0 kg. An initial impression is made adjacent to the original surface at a depth where adequate support is provided by the surrounding material to allow an accurate hardness reading. Subsequent impressions are made toward the center of the cross section (Fig. 10). Generally, the indentation process is repeated every 0.05 mm (0.002 in.) for a distance of approximately

0.5 mm (0.020 in.), unless finer readings or greater distances are required. However, successive indentations should be spaced far enough apart to preclude distortion of hardness values. Indentations can also be staggered laterally to achieve finer readings, as in Fig. 11. One final indent is usually made near the center of the sample to determine the core hardness.

Finally, the hardness data are plotted, and the effective case depth is determined from the curve. Often, this entire procedure is automated with specially designed microscopes and software.

Other specimen-preparation methods are also used. In the chord or taper-grind procedure (Fig. 12), the surface is cut or ground at an angle greater than 90°. The method effectively magnifies the distance from the surface to the core, thus allowing more indentations over an equivalent normal distance. With this method, thin cases or sharp transitions in the hardness curve within a case can be measured.

Step-grind procedures are also used (Fig. 13). Superficial hardness or microhardness readings can be taken on polished specimens similar to the chemical test bars described in the previous section. An alternate method is to section or

grind a sample to a minimum and maximum depth. Hardness readings are made and checked to see if the effective case depth falls between the two chosen limit depths. For example, if the hardness is greater than 50 HRC on the shallow step and less than 50 HRC on the deep step, the effective case depth to 50 HRC lies somewhere between the two steps.

The accuracy of microhardness testers should be checked regularly using the calibration sample provided. Care must also be taken to prevent errors due to the manual conversion of ocular indentation measurements to actual hardness numbers. Some more advanced testers display actual hardness numbers, making it unnecessary to convert ocular readings.

Because the more advanced microhardness testers are equipped to convert Knoop or Vickers measurements directly into Rockwell values, the chance for error is reduced. However, it must be remembered that any conversion of hardness values from one hardness measurement system to another introduces some error. See Table 4 and Fig. 14 for Vickers, Brinell, Knoop, and Rockwell hardness conversions.

Even when care is taken to ensure precise and accurate measurement of case depth, repeatability and reproducibility of microhardness testing can be significant. The data given in Fig. 15 correlate effective case depth to 50 HRC as measured using a microhardness traverse on the same gears by two different laboratories. Results of another gage repeatability and reproducibility study are shown in Fig. 16. In this study, a total of nine trained operators from three independent laboratories (equipped with three different microhardness testers) each performed three microhardness traverses on the same set of two samples daily for five consecutive days. The two samples had nominal effective case depths to 50 HRC of 1.3 and 3.2 mm (0.05 and 0.125 in). Approximately the same microhardness measurement

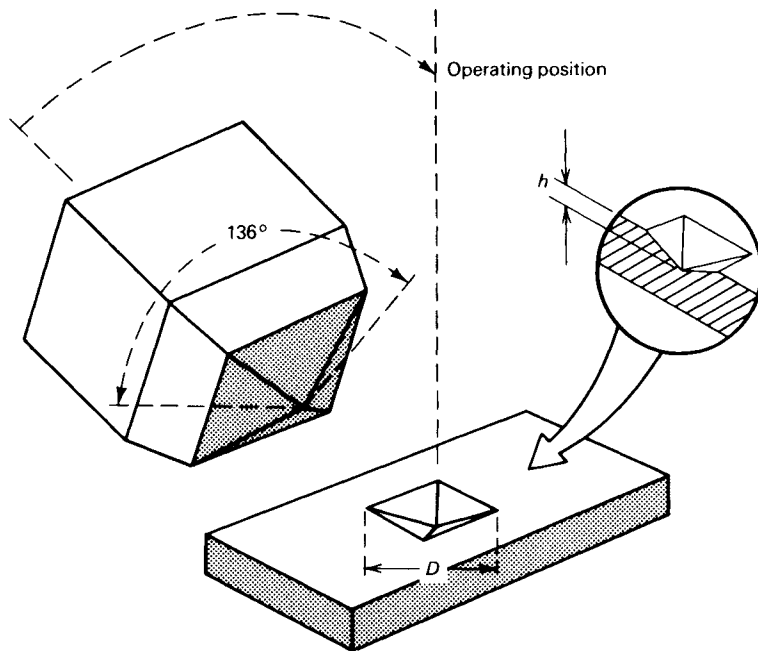


Fig. 9 Diamond pyramid indenter used for the Vickers test and resulting indentation in the workpiece. *D* is the mean diagonal of the indentation in millimeters.

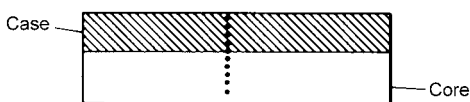


Fig. 10 Cross-sectioned specimen for hardness-traverse method of measuring depth of medium and heavy cases. Dots show locations of hardness-indenter impressions. Source: Ref 1

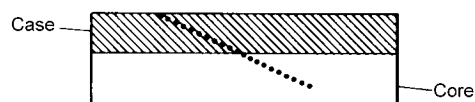


Fig. 11 Cross-sectioned specimen for hardness-traverse method of measuring depth of light and medium cases. Dots show locations of hardness-indenter impressions. Source: Ref 1

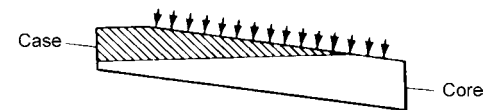


Fig. 12 Chord or taper-ground specimen for hardness-traverse method of measuring depth of light and medium cases. Arrows show locations of hardness-indenter impressions. Source: Ref 1

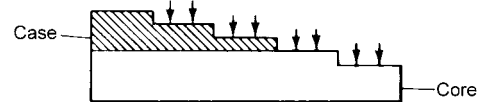


Fig. 13 Step-ground specimen for hardness-traverse method of measuring depth of medium and heavy cases. Arrows show locations of hardness-indenter impressions. Source: Ref 1

410 / Case Hardening of Steels

Table 4 Approximate equivalent hardness numbers for steel

For carbon and alloy steels in the annealed, normalized, and quenched-and-tempered conditions; less accurate for cold-worked condition and for austenitic steels. The values in **boldface type** correspond to the values in the joint SAE-ASM-ASTM hardness conversions as printed in ASTM E140, Table 1. The values in parentheses are beyond normal range and are given for information only. See Fig. 14 for plots of approximate equivalent hardness numbers for steel.

HV	HK, 500 g load and greater	HRC, 150 kg load, Brale indenter	Superficial Brale indenter			HB, 3000 kg load, 10 mm ball	
			HR15N scale, 15 kg load	HR30N scale, 30 kg load	HR45N scale, 45 kg load	Standard ball	Tungsten carbide ball
940	920	68.0	93.2	84.4	75.4
920	908	67.5	93.0	84.0	74.8
900	895	67.0	92.9	83.6	74.2
880	882	66.4	92.7	83.1	73.6	...	(767)
860	867	65.9	92.5	82.7	73.1	...	(757)
840	852	65.3	92.3	82.2	72.2	...	(745)
820	837	64.7	92.1	81.7	71.8	...	(733)
800	822	64.0	91.8	81.1	71.0	...	(722)
780	806	63.3	91.5	80.4	70.2	...	(710)
760	788	62.5	91.2	79.7	69.4	...	(698)
740	772	61.8	91.0	79.1	68.6	...	(684)
720	754	61.0	90.7	78.4	67.7	...	(670)
700	735	60.1	90.3	77.6	66.7	...	(656)
690	725	59.7	90.1	77.2	66.2	...	(647)
680	716	59.2	89.8	76.8	65.7	...	(638)
670	706	58.8	89.7	76.4	65.3	...	(630)
660	697	58.3	89.5	75.9	64.7	...	620
650	687	57.8	89.2	75.5	64.1	...	611
640	677	57.3	89.0	75.1	63.5	...	601
630	667	56.8	88.8	74.6	63.0	...	591
620	657	56.3	88.5	74.2	62.4	...	582
610	646	55.7	88.2	73.6	61.7	...	573
600	636	55.2	88.0	73.2	61.2	...	564
590	625	54.7	87.8	72.7	60.5	...	554
580	615	54.1	87.5	72.1	59.9	...	545
570	604	53.6	87.2	71.7	59.3	...	535
560	594	53.0	86.9	71.2	58.6	...	525
550	583	52.3	86.6	70.5	57.8	(505)	517
540	572	51.7	86.3	70.0	57.0	(496)	507
530	561	51.1	86.0	69.5	56.2	(488)	497
520	550	50.5	85.7	69.0	55.6	(480)	488
510	539	49.8	85.4	68.3	54.7	(473)	479
500	528	49.1	85.0	67.7	53.9	(465)	471
490	517	48.4	84.7	67.1	53.1	(456)	460
480	505	47.7	84.3	66.4	52.2	(448)	452
470	494	46.9	83.9	65.7	51.3	441	442
460	482	46.1	83.6	64.9	50.4	433	433
450	471	45.3	83.2	64.3	49.4	425	425
440	459	44.5	82.8	63.5	48.4	415	415
430	447	43.6	82.3	62.7	47.4	405	405
420	435	42.7	81.8	61.9	46.4	397	397
410	423	41.8	81.4	61.1	45.3	388	388
400	412	40.8	80.8	60.2	44.1	379	379
390	400	39.8	80.3	59.3	42.9	369	369
380	389	38.8	79.8	58.4	41.7	360	360
370	378	37.7	79.2	57.4	40.4	350	350
360	367	36.6	78.6	56.4	39.1	341	341
350	356	35.5	78.0	55.4	37.8	331	331
340	346	34.4	77.4	54.4	36.5	322	322
330	337	33.3	76.8	53.6	35.2	313	313
320	328	32.2	76.2	52.3	33.9	303	303
310	318	31.0	75.6	51.3	32.5	294	294
300	309	29.8	74.9	50.2	31.1	284	284
295	305	29.2	74.6	49.7	30.4	280	280
290	300	28.5	74.2	49.0	29.5	275	275
285	296	27.8	73.8	48.4	28.7	270	270
280	291	27.1	73.4	47.8	27.9	265	265
275	286	26.4	73.0	47.2	27.1	261	261
270	282	25.6	72.6	46.4	26.2	256	256
265	277	24.8	72.1	45.7	25.2	252	252
260	272	24.0	71.6	45.0	24.3	247	247
255	267	23.1	71.1	44.2	23.2	243	243
250	262	22.2	70.6	43.4	22.2	238	238
245	258	21.3	70.1	42.5	21.1	233	233
240	253	20.3	69.6	41.7	19.9	228	228
230	243	(18.0)	219	219
220	234	(15.7)	209	209
210	226	(13.4)	200	200
200	216	(11.0)	190	190
190	206	(8.5)	181	181
180	196	(6.0)	171	171
170	185	(3.0)	162	162
160	175	(0.0)	152	152
150	164	143	143

(continued)

Table 4 (continued)

HV	HK, 500 g load and greater	HRC, 150 kg load, Brale indenter	Superficial Brale indenter			HB, 3000 kg load, 10 mm ball	
			HR15N scale, 15 kg load	HR30N scale, 30 kg load	HR45N scale, 45 kg load	Standard ball	Tungsten carbide ball
140	154	133	133
130	143	124	124
120	133	114	114
110	123	105	105
100	112	95	95
95	107	90	90
90	102	86	86
85	97	81	81

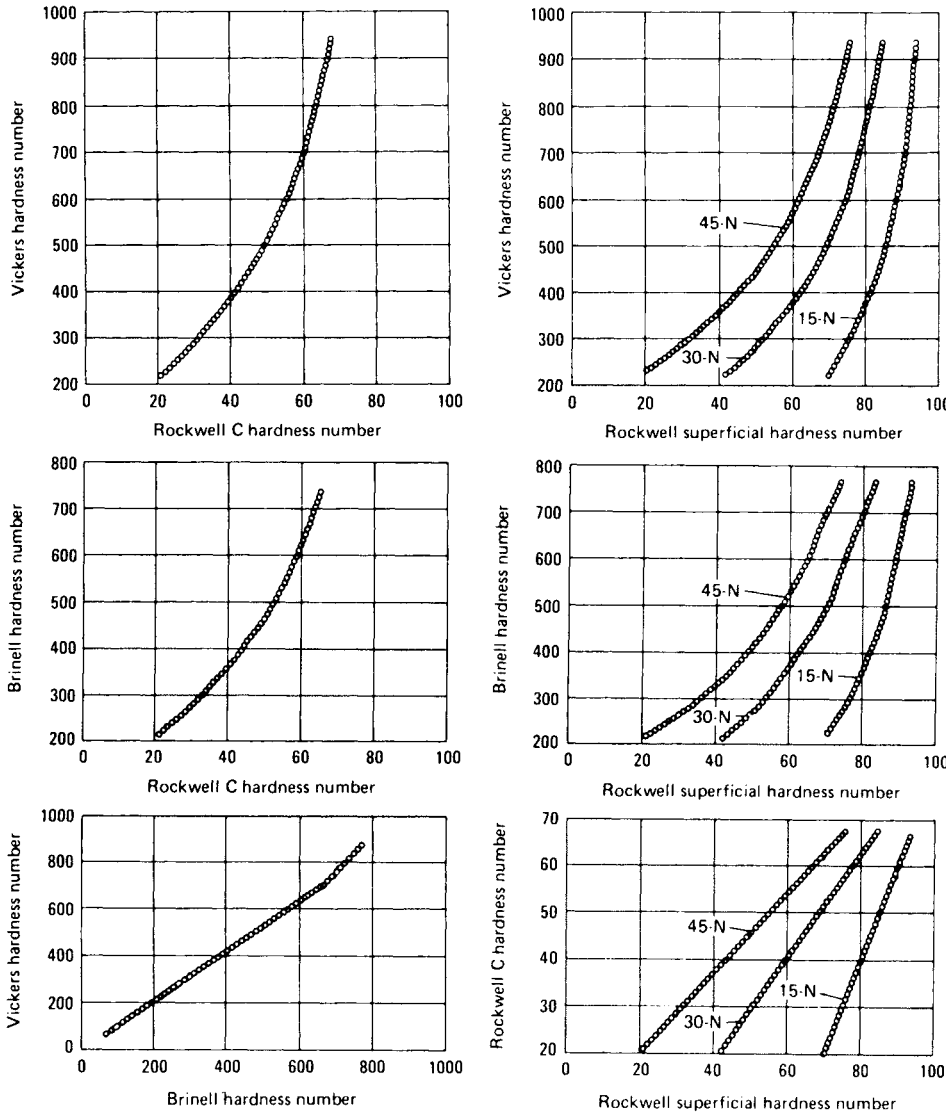


Fig. 14 Approximate equivalent hardness numbers for steel. See Table 4 for tabulated data.

variation (4 HRC) was observed regardless of the measurement depth and was consistent between the laboratories.

The data in both studies also showed that the measurement error of effective case depth increases with increasing case depth. In the latter study, expected case-depth variation was

found to be 0.2 mm (0.008 in.) for the shallower case sample and 0.8 mm (0.03 in.) for the deeper case sample. Linear interpolation between microhardness measurements is used to determine effective case depth. If the predicted variation of any two measurements is constant, the predicted error band of a linearly

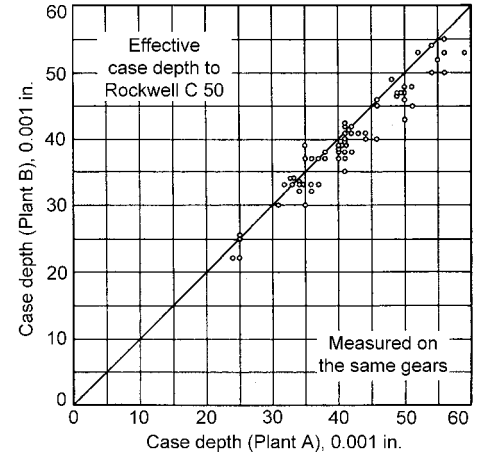


Fig. 15 Comparison of effective case depth to 50 HRC measurements made on the same gears in two different laboratories

interpolated value between two measurements increases as the slope of the line between the two points decreases. Therefore, because microhardness measurement variation is approximately constant, as the slope of the microhardness profile decreases with increasing case depth, measurement error of effective case depth increases with increasing case depth. If an effective case-depth tolerance is to be specified for a part, the tolerance should be greater than the inherent measurement error of the microhardness test method (Fig. 17).

Visual Methods

Visual methods have been classified into two general categories: macroscopic and microscopic. In macroscopic procedures, specimens normally are ground no finer than through No. 000 metallographic emery paper (600-grit silicon carbide paper), and magnifications usually do not exceed 20 diameters. The Brinell microscope, a handheld optical instrument with retical markings at intervals of 0.1 mm (approximately 0.004 in.) and 20 diameters magnification, is a convenient tool for macroscopic measurement. In microscopic procedures, complete metallographic polishing

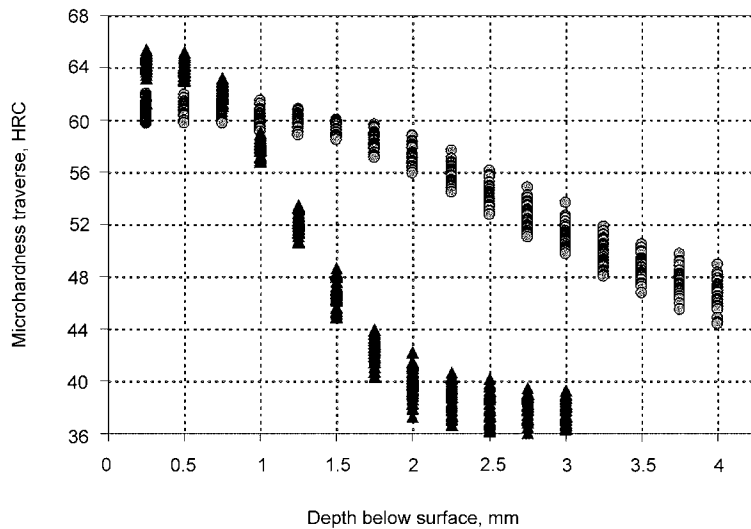


Fig. 16 Results of interlaboratory microhardness traverse gage repeatability and reproducibility study on samples with 1.3 and 3.2 mm (0.05 and 0.125 in.) effective case depth. Courtesy of Caterpillar Inc.

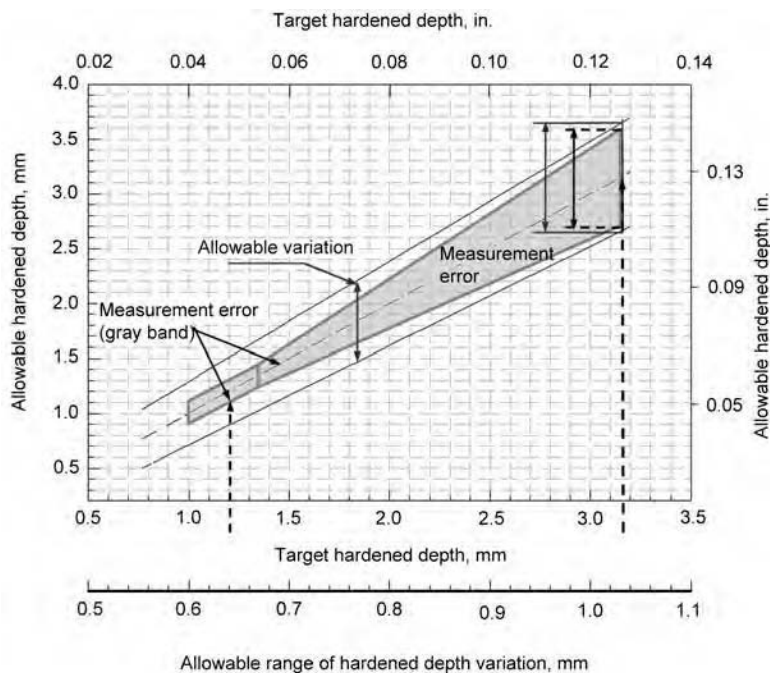


Fig. 17 Plot of expected measurement error as a function of effective case depth to 50 HRC derived from interlaboratory microhardness traverse gage repeatability and reproducibility study on samples with 1.3 and 3.2 mm (0.05 and 0.125 in.) effective case depth. A typical allowable range of variation in the measured effective case depth for the process is also plotted. Courtesy of Caterpillar Inc.

and etching generally are required, and case depths normally are read at a magnification of 100 diameters.

Macroscopic visual procedures are characterized best as quick and simple routine tests for measuring total case depth in a production environment. Typically, test specimens are compared to standard specimens whose visual

properties have been correlated to total or effective case depths found through other methods.

The most basic procedure is to fracture the test specimen and visually inspect the fracture surface. Figure 18 is an example of a gear tooth. Often, a clearly demarcated boundary is apparent that approximates total case depth, especially if the steel has shallow hardening

characteristics. If added contrast is desired, the fractured specimen can be etched in 20% nitric acid with water. In practice, test specimens that are more than 9.5 mm (0.375 in.) in diameter are not used because they are difficult to fracture.

Even more contrast can be developed if the fractured surface is roughly ground or polished. (A cut surface could also be used.) As an added benefit, relatively weaker acids can be used to heighten the contrast of these specimens (e.g., 10 or 5% nital). An alternative etching procedure for the polished specimens is to etch in 25% nital for 30 s, wash in concentrated picral, rinse in alcohol, and blow dry.

At best, these methods are good for measuring approximate total case depth. However, after correlation with another case-depth measurement method, effective case depth can be successfully estimated by measuring from the specimen surface to a selected point of the darkened zone.

The M_s method is another method of case-depth measurement which uses the fact that the martensite-start temperature (M_s point) varies with carbon content. Quenching and holding the steel for a short time at the M_s point corresponding to a given carbon content tempers the martensite formed at all lower carbon levels. Subsequent water quenching transforms austenite at all higher carbon levels to untempered martensite. Once polished and etched, the boundary between tempered (dark) and untempered (light) martensite is clearly defined; this line is normally read at 20 diameter magnification (Brinell microscope) to a precision of ± 0.05 mm (0.002 in.).

The case depth is not sensitive to small temperature changes in the quenching bath. The final selection of quenching temperature is usually done statistically to produce an equal plus-and-minus distribution of error about known carbon curves.

The main factors that affect the accuracy of this method are pearlite formation during quenching to the M_s point and time at M_s temperature. The specimen size should be sufficiently small to ensure that the severity of quench transforms all austenite of lower carbon levels to martensite without any formation of pearlite. (Specimen size may be critical for low-hardenability steels.) The time at M_s temperature should be short enough to preclude the formation of bainite, which interferes with the sharpness of the line of demarcation upon etching and can obliterate it completely. For additional information on the M_s technique, see Ref 2.

Microscopic Visual Procedures. Generally, the preparation of specimens for microscopic visual procedures is similar to the methods used for photomicrography or mechanical case-depth measurement. The specimen is then etched in 2 to 5% nital and rinsed with alcohol or water. Measurements are made with a microscope

using software or using a filar micrometer accessory that replaces one of the ocular viewing lenses.

Total case depth is found by finding the contrast boundary between the case and core or the point where no further change in microstructure occurs (Fig. 19). For many case-hardened parts, there will be a sharp transition in microstructure (and visual contrast because of the etchant

used) between case and core. However, sometimes the boundary between the case and core is not apparent, and experienced judgment must be used (e.g., carburized or carbonitrided alloy steels quenched at high temperatures). For carburized alloy steels, the M_s method described earlier has been found effective. This method can also be used for carbonitrided, cyanided, nitride, and flame- or induction-hardened cases.

Effective case depth may be determined if a microstructure corresponding to the hardness limit is empirically well defined. In the case of carburized cases, often the structure that is nearly equivalent to 50 HRC consists of approximately 85% tempered martensite and 15% intermediate quench or mixed upper-transformation products.

For carburized cases, SAE J423 (Ref 1) defines an annealing method whereby total case depth can be determined precisely using microstructural methods. Instead of annealing specimens in charcoal, as suggested in the standard, a protective atmosphere can be used. Also note that production carburizing schedules often have cooling rates similar to those described in the SAE J423 annealing method. Therefore, specimens processed under those conditions would not have to be reheated before testing, and the results of the test can be accurately correlated to a standard specimen.

Nondestructive Methods

Nondestructive case-depth measurement is an active field of research. As with all nondestructive methods, the goal is to quickly inspect 100% of parts during the production process and avoid having to destroy parts that could have otherwise been sold in the marketplace.

Nondestructive methods of measuring case depth make use of the changing electrical and magnetic properties of the material through the depth of a case-hardened workpiece. These property changes result from localized differences of material microstructure, hardness, and/or chemistry within the case.

Eddy-current tests are the most frequently used nondestructive tests in the automotive industry (Ref 3). Primary among their valuable characteristics is the speed with which tests can be performed; this makes them suitable for the automatic testing of high-production quantities. Production nondestructive evaluations of case depths are performed on parts such as piston pins; axle, transmission, and water pump shafts; and differential and transmission gears. Measured case depths range from 0.2 to 9 mm (0.008 to 0.35 in.), with agreement with destructive techniques of 0.2 mm (0.008 in.) or less. This requires equipment specifically designed for the parts being tested.

A typical system for the production precision measurement of case depths generally requires the use of master parts of known case depth to standardize the unit. With a system developed to test cold-extruded axle shafts, measurements are made on a master shaft and stored in computer memory for later comparison with measurements from unknown production parts. Computers are commonly used to control the part scanner and eddy-current instrument, acquire and analyze the data, and store the results. A typical test consists of placing the part within the test machine and then sequentially applying frequencies ranging from 5 to



Fig. 18 Induction-hardened gear tooth polished with silicon carbide abrasive paper and etched with 10% nital. Courtesy of Materials Evaluation and Engineering, Inc.

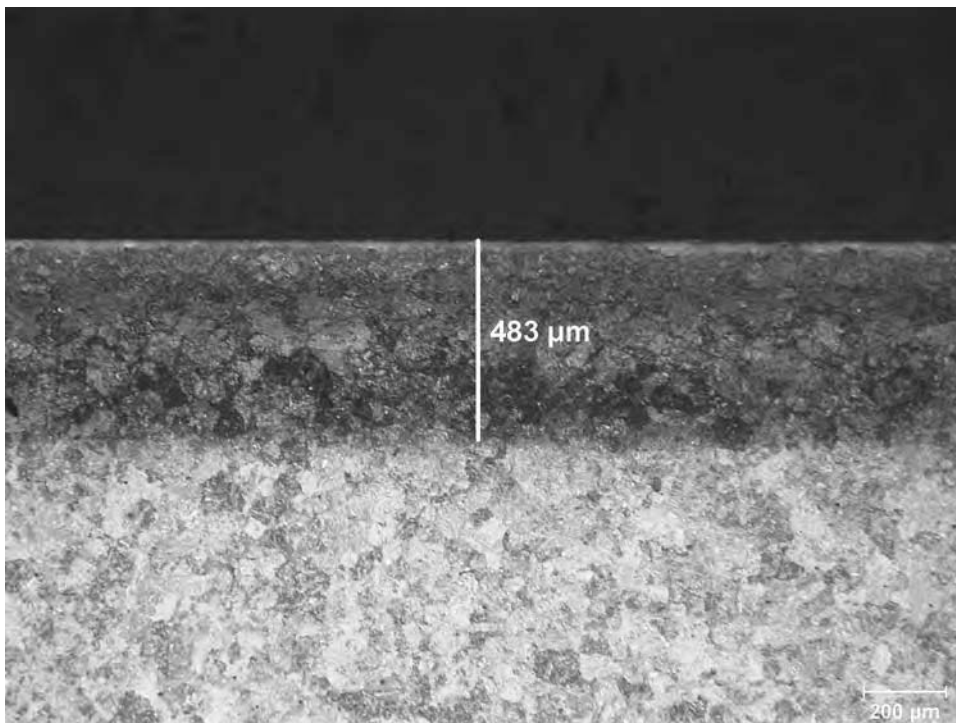


Fig. 19 Nitrided case etched with 2% nital. Original magnification: 50 \times . Courtesy of Materials Evaluation and Engineering, Inc.

10 kHz to the eddy-current coil located at the area of interest. The computer uses the responses at certain frequencies to estimate the case depth. Then, on the basis of the estimate, it selects algorithms to make a final calculation of case depth, based on multiple linear regressions of eddy-current responses at several frequencies against case depth. The particular frequencies used depend on the location on the part. Generally, they consist of a combination of one or more low frequencies (0.1 to 1.0 kHz) with one or more higher frequencies (5 to 10 kHz). The highest frequencies (5 to 10 kHz) are used for surface hardness measurements. Figure 20 illustrates the correlation that can be achieved between destructive and nondestructive case-depth measurement methods.

The accuracy of eddy-current inspection is limited by the testing conditions encountered by the instrument. Variations in workpiece temperature, surface roughness, residual stress, material chemistry, and core microstructure can affect the impedance of the material and the resultant determination of case depth. Sample cleanliness, surface roughness, and residual stresses can also affect measurement. When

measuring carburized cases, varying surface carbon concentrations may introduce additional uncertainties. It is important to recognize these variables when designing and operating nondestructive measurement systems and selecting appropriate master parts.

New variations of the eddy-current technique are in various stages of development. One technique uses handheld eddy-current sensors known as meandering winding magnetometers (Ref 4). These instruments also incorporate magnetic induction sensors.

Another new way of measuring case depth makes use of the magnetic Barkhausen noise phenomenon (Ref 5). When a variable magnetic field is applied to steel, it is not magnetized continuously. Rather, it is magnetized in discrete jumps due to the field overcoming barriers in its path (such as carbides, nitrides, dislocations, and grain boundaries). Electromagnetic and acoustic signals are generated during these jumps in magnetization. After amplifying, filtering, and analyzing these signals, they can be correlated to results of other case-depth measurement techniques to determine the range of frequencies most appropriate for case-depth determination.

Other methods apply an electric current to a test sample and then either measure the resistivity (Ref 6) or potential drop (Ref 7) or even the initial magnetic permeability between the leads. These signals, when analyzed and correlated, allow measurement of case depth and can even be used as a real-time sensor.

Ultrasonic techniques have also been used for case-depth measurement (Ref 8). These techniques measure the group velocity within the part under different frequencies and compare it to previous group velocity measurements that have been correlated with carbon content, residual stress, hardness, and grain size. Because depth of wave propagation is inversely proportional to ultrasonic frequency, various frequencies are applied to the part in order to characterize the entire case.

ACKNOWLEDGMENTS

The author thanks Larry Hanke of Materials Evaluation and Engineering, Inc. for the examples of micrographs, and Olga Rowan of Caterpillar Inc. for the examples from the interlaboratory repeatability and reproducibility study.

REFERENCES

1. "Methods of Measuring Case Depth," J423, SAE International, Warrendale, PA, Feb 1998
2. E.S. Rowland and S.R. Lyle, The Application of M_s Points to Case Depth Measurement, *Trans. ASM*, Vol 37, 1946, p 26-47
3. Automotive Applications of Eddy Current Testing, *Electromagnetic Testing*, Vol 4, 2nd ed., *Nondestructive Testing Handbook*, American Society of Nondestructive Testing, Inc., 1986, p 424-426
4. N. Goldfine and D. Clark, Introduction to the Meandering Winding Magnetometer (MWM) and the Grid Measurement Approach, *SPIE Proc.*, Vol 2944, 1996, p 186-192
5. M. Dubois and M. Fiset, Evaluation of Case Depth on Steels by Barkhausen Noise Measurement, *Mater. Sci. Technol.*, Vol 11 (No. 3), 1995, p 264-267
6. L.G. Chedid, M.M. Makhlof, and R.D. Sisson, Jr., Real-Time Carbon Sensor for Measuring Concentration Profiles in Carburized Steel, U.S. Patent 7,068,054 B2
7. J.R. Bowler et al., Alternating Current Potential-Drop Measurement of the Depth of Case Hardening in Steel Rods, *Meas. Sci. Technol.*, Vol 19 (No. 7), 1998
8. R.D. Mitra, "Case Depth Evaluation of Carburized Specimens Using Ultrasonic Methods," M.S. thesis, MIT, 1993

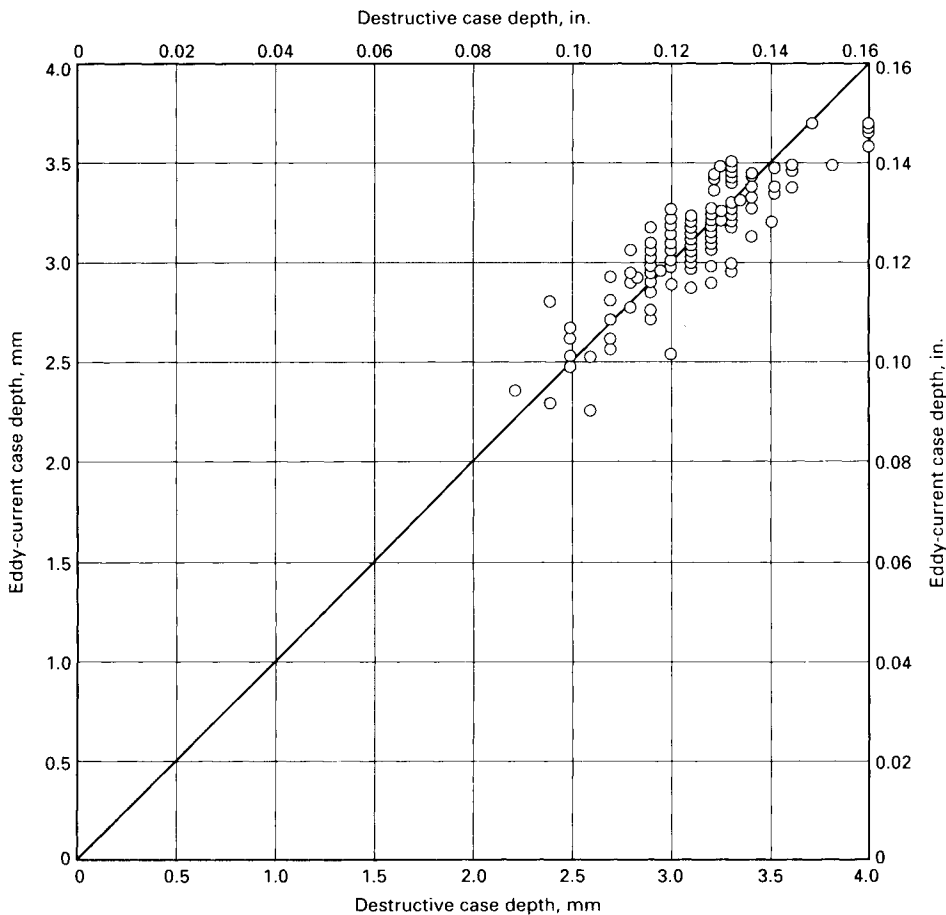


Fig. 20 Plot of axle-shaft correlation data for destructive and nondestructive case-depth measurements. Source: Ref 3

SELECTED REFERENCES

- ASM Committee on Gas Carburizing, Measurement of Case Depth, Chap. 4, *Carburizing and Carbonitriding*, American Society for Metals, 1977
- “Carburizing and Heat Treatment of Carburizing Grade Steel Parts,” AMS2759/7B, SAE International, Warrendale, PA
- “Chord Method of Evaluating Surface Microstructural Characteristics,” ARP1820B, SAE International, Warrendale, PA
- “Gas Nitriding and Heat Treatment of Low-Alloy Steel Parts,” AMS2759/6B, SAE International, Warrendale, PA
- “Hardness Depth of Heat-Treated Parts; Determination of the Effective Depth of Hardening after Nitriding,” DIN 50190-3:1979-03, Deutsches Institut für Normung, Berlin
- “Iron and Steel: Determination of the Conventional Depth of Hardening after Surface Heating,” EN 10328:2005, European Committee for Standardization, Brussels
- “Method of Measuring Nitrided Case Depth for Iron and Steel,” JIS G 0562:1993, Japanese Standards Association, Tokyo
- “Methods of Measuring Case Depth,” J423, SAE International, Warrendale, PA, Feb 1998
- “Methods of Measuring Case Depth Hardened by Carburizing Treatment for Steel,” JIS G 0557:2006, Japanese Standards Association, Tokyo
- “Standard Test Methods for Determination of Carbon, Sulfur, Nitrogen, and Oxygen in Iron, Nickel, and Cobalt Alloys by Various Combustion and Fusion Techniques,” E 1019-11, ASTM International, West Conshohocken, PA
- “Steel—Determination of Case Depth after Flame Hardening or Induction Hardening,” JIS G 0559:2008, Japanese Standards Association, Tokyo
- “Steel—Determination of Effective Depth of Hardening after Flame or Induction Hardening,” ISO 3754:1976, International Organization for Standardization, Geneva, Switzerland
- “Steels—Determination and Verification of the Depth of Carburized and Hardened Cases,” ISO 2639:2002, International Organization for Standardization, Geneva, Switzerland

Applied-Energy Case Hardening of Steels

Flame Hardening of Steels	419	Surface-Hardening Parameters	456
Methods of Flame Hardening	419	Application Tips and Troubleshooting	459
Fuel Gases	421	Electron Beam Surface Hardening	462
Burners and Related Equipment	423	Electron Beam Generation and Interaction with Material	462
Operating Procedures and Control	426	Processing Techniques	464
Preheating	427	Electron Beam Hardening Technologies	466
Depth and Pattern of Hardness	427	Electron Beam Facilities and Manufacturing Systems	
Maintenance of Equipment	428	with Integrated EB Facilities	469
Preventive Maintenance	431	Applications	471
Safety Precautions	431	Laser Surface Hardening	476
Quenching Methods and Equipment	431	Conventional Surface-Hardening Techniques	476
Quenching Media	432	Laser Surface Hardening	478
Flame-Hardening Problems and Their Causes	432	Absorptivity	479
Tempering of Flame-Hardened Parts	433	Laser Scanning Technology	480
Surface Conditions	433	Laser Annealing	481
Dimensional Control	433	Laser Cladding	481
Selection of Process	433	Laser Shock Peening	483
Selection of Material	435	Laser Heat Treatment	483
Flame Annealing	436	Thermokinetic Phase Transformations	485
Induction Surface Hardening of Steels	438	Challenges in Obtaining the Specified Hardness	487
Principles of Induction Heating	438	Influence of Cooling Rate	488
High-Temperature Electrical, Magnetic, and		Effect of Processing Parameters on Temperature,	
Thermal Properties	440	Microstructure, and Case Depth Hardness	488
Eddy-Current Distribution	443	Laser Surface Hardening of Nonferrous Alloys	491
Induction Hardening and Tempering	446		
General Equipment and Process Factors	451		

Flame Hardening of Steels*

Revised by B. Rivolta, Politecnico di Milano (Polytechnic Institute Milan)

FLAME HARDENING is a heat treating process in which a thin surface shell of a steel part is heated rapidly to a temperature above the critical temperatures of the steel. After the microstructure of the shell has become austenitic (austenitized), the part is quickly quenched, transforming austenite to martensite while leaving the core of the part in its original state. In contrast, slow cooling causes transformation, as the temperature passes through the corresponding ranges, to pearlite, bainite, and martensite, with the final structure being a combination of the three. The result is a relatively soft and ductile steel. To achieve hardness, therefore, the steel must be cooled rapidly so that it bypasses the first two transformation phases and transforms directly from austenite to martensite. Flame hardening employs direct impingement of a high-temperature flame or high-velocity combustion product gases. The part then is cooled at a rate that will produce the desired levels of hardness. The high-temperature flame is obtained by combustion of a mixture of fuel gas with oxygen or air; flame heads are used for burning the mixture.

To achieve hardness, the steel must have adequate hardenability and must be rapidly cooled. The cooling rate of the shell must be higher than the so-called martensitic critical cooling velocity, that is, the minimum quench rate to produce a completely martensitic structure (or a mixture of martensite and retained austenite).

Other intermediate critical velocities can be useful. For example, $V_1(50)$ is the critical cooling velocity that results in 50% martensite and 50% bainite (or other higher-temperature transformation products).

It is known that the martensitic critical cooling rate is strongly influenced by the alloying elements. Maynier and colleagues have developed regression equations that can be used to predict the critical cooling velocity by composition. The martensitic critical cooling velocity in °C/h, with composition in wt%, and Pa (the austenitizing parameter, a separate equation involving temperature and time) is given by the equation:

$$\text{Log } V_1 = 9.81 - (4.62\%C + 1.05\%Mn + 0.54\%Ni + 0.50\%Cr + 0.66\%Mo + 0.00183 Pa)$$

$$\text{Log } V_1(50) = 8.50 - (4.13\%C + 0.86\%Mn + 0.57\%Ni + 0.41\%Cr + 0.94\%Mo + 0.0012 Pa)$$

The influence of each element on the martensitic critical cooling rate is indicated by the magnitude of each coefficient.

The final hardness of the shell is strongly dependent on the total amount of martensite together with the alloying elements in the steel.

Maynier et al. developed equations for predicting hardness before and after tempering, with the knowledge of cooling rates and composition. The hardness of as-quenched martensite is expressed by the equation:

$$HV_{\text{martensite}} = 127 + 949C + 27Si + 11Mn + 8Ni + 16Cr + 21 \log V$$

where V is the cooling rate in °C/h.

Carbon content is the most important factor determining the level of hardness that can be obtained in steels by flame heating. The carbon amount controls hardness level and also the tendency of the part to crack and the magnitude of residual surface stresses.

Although flame hardening is used mainly to develop high levels of hardness for wear resistance, the process also improves bending and torsional strength and fatigue life.

Flame hardening can be considered similar to induction hardening both in terms of the materials processed and their applications. Flame hardening plants tend to be generally cheaper than induction hardening ones, but the operation costs often are higher. The process cannot be readily and easily automated, because induction hardening can be and is more suitable for hardening different types of uneven components. The skill of the operator is considered very important in carrying out this process successfully.

Flame hardening is applied to a wide variety of workpieces and ferrous materials for different reasons. The main advantages of flame hardening are as follows:

- It may be applied to large components where conventional furnace heating and quenching

are impracticable and/or uneconomical; typical examples include large gears, machine-ways, dies, and rolls.

- It is possible to harden a selective surface of the part, thus avoiding the heating of the whole part.
- It is more rapid than carburizing and nitriding, and larger depth of hardness can be obtained.
- A wide selection of steels may be used.

The main disadvantages of flame hardening are as follows:

- It can be somewhat difficult to measure the exact temperature on the component during the process, and, in many cases, the estimation of the surface temperature is left to the skill of the operator.
- The standardization of the process may be difficult, and it may require a specific trial run to optimize the surface temperature of the part.
- The control of the case depth may be difficult if compared with the induction-hardening process.
- Fuel gases are explosive.

For a detailed discussion of materials suitable for flame hardening and for a comparison of flame hardening with other methods used to attain similar results, see the sections "Selection of Process" and "Selection of Material" near the end of this article.

Methods of Flame Hardening

The versatility of flame-hardening equipment and the wide range of heating conditions obtainable with gas burners often permit flame hardening to be done by a variety of methods, of which the principal ones are:

- Spot or stationary
- Progressive
- Spinning
- Combination progressive-spinning

The selection of the appropriate method depends on the shape, size, and composition

* Original article by T. Ruglic, Flame Hardening of Steels, *Heat Treating*, Vol 4, ASM Handbook, ASM International, 1991, p 268–285.

of the workpiece; the area to be hardened; the depth of case required; and the number of pieces to be hardened. In many instances, more than one method will provide the desired result; the choice then will depend on comparative costs.

The spot (stationary) method, shown in Fig. 1(a), consists of locally heating selected areas with a suitable flame head and subsequently quenching. Both the component and the flame are held stationary. The heating head may be of either single-orifice or multiple-orifice design, depending on the extent of the area to be hardened. The heat input must be balanced to obtain a uniform temperature over the entire selected area. After being heated, the parts usually are quenched by immersion in water or oil, depending on the chemical composition of the steel; however, in some mechanized operations, a spray quench may be used.

Basically, the spot method requires no elaborate equipment, except perhaps fixtures and timing devices to ensure the uniform processing of each piece. However, the operation may be automated by indexing the heated parts into either a spray quench or a suitable quench bath.

The progressive method, shown in Fig. 1(b), is used to harden large areas that are beyond the scope of the spot method. The size and shape of the workpiece, as well as the volume of oxygen and fuel gas required to heat the specified area, are factors in the selection of this method. In progressive hardening, the flame head usually is of the multiple-orifice type, and quenching facilities may be either integrated with the flame head or separate from it. The flame head progressively heats a narrow band that is subsequently quenched as the head and quench traverse the workpiece.

The equipment needed for flame hardening by the progressive method consists of one or more flame heads and a quenching means mounted on a movable carriage that runs on a track at a regulated speed (flame-cutting machines are adaptable to this type of flame hardening). Workpieces mounted on a turntable

or in a lathe can be hardened readily by the progressive method; either the flame head or the workpiece may move. There is no practical limit on the length of parts that can be hardened by this method, because it is easy to lengthen the track over which the flame head travels. Single passes as wide as 1.5 m (60 in.) can be made; wider areas must be hardened in more than one pass.

When more than one pass is required to cover a flat surface, or when cylindrical surfaces are hardened progressively, such surfaces will exhibit soft bands because of overlapping or underlapping of the heated zones. These soft bands can be minimized, however, by closely controlling the extent of the overlapping. Whenever overlapping occurs, the possibility of severe thermal upset and cracking should be anticipated. Tests should be conducted to determine whether overlapping will cause cracking or other harmful effects. Simple curved surfaces may be hardened progressively by means of contoured flame heads, and some irregular surfaces may be traversed by the use of tracer template methods.

The rate of travel of the flame head over the surface is governed mainly by the heating capacity of the head, the depth of case required, the composition and shape of the work, and the type of quench used. Speeds ranging from 0.8 to 5 mm/s (2 to 12 in./min) are typical with oxyacetylene heating heads. Ordinarily, water at ambient temperatures is used as a quenchant, although air sometimes is used when a less-severe quench is indicated; under special conditions (particularly for quenching alloy steels), warm or hot water or a polymer-based synthetic quenchant may be employed.

The spinning method, shown in (Fig. 2), is applied to round or semiround parts such as wheels, cams, or gears. In its simplest form, the method uses a mechanism for rotating or spinning the workpiece, in either a horizontal or a vertical plane, while the surface is being heated by the flame head. One or more water-cooled heating heads equal in width to the

surface to be heated are employed. The speed of rotation is relatively unimportant, provided uniform heating is obtained. After the surface has been heated to the desired temperature, the flame is extinguished or withdrawn, and the work is quenched by immersion or spray or a combination of both.

The spinning method is particularly adaptable to extensive mechanization and automation. This makes it possible, for example, for all the cams on a camshaft to be hardened at the same time.

Today (2013), fully automatic flame-heating equipment is available that can treat round components up to 1.5 m (60 in.) in diameter and up to 2 Mg (2.2 tons) in weight. Much of it has been designed to treat gear wheels of all types.

Commercial machines have been built that can provide automatic control of timing, temperature, and quenching, as well as accurate control of gas flow, so that close metallurgical specifications can be met consistently. Frequently, when production is sufficient, the spinning method can be set up so that parts are either loaded manually or unloaded automatically, or they are loaded and unloaded automatically.

This method has been extended to components of irregular cross section and mass distribution. Typical are large drive wheels for tracked vehicles, cams and camshafts for marine diesel engines, and crane traveling wheels. Speed, deep hardness penetration, localized hardness zone, and uniformity of hardness pattern are the main advantages.

In one technique, a rotating flame head is used for internal spin hardening of odd-shaped parts that would present handling problems if the parts themselves were rotated. Each part is positioned by a simple handling device, and the flame head rotates inside the part.

In contrast to the progressive method, in which acetylene usually is used (because of its high flame temperature and rapid heating rates), satisfactory results can be obtained in spin hardening with natural gas, propane, or manufactured

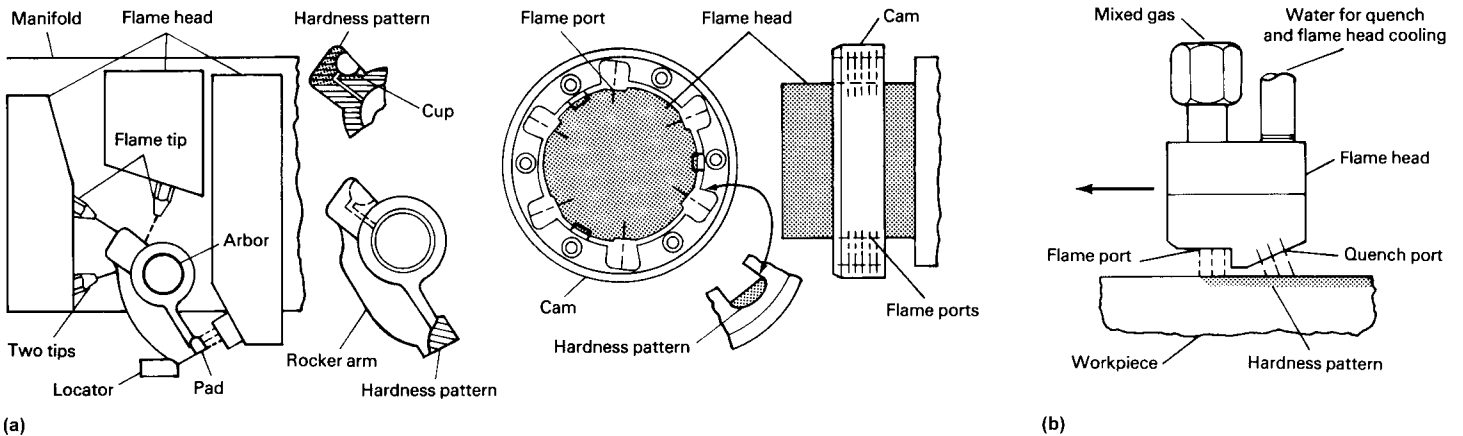


Fig. 1 Spot (stationary) and progressive methods of flame hardening. (a) Spot (stationary) method of flame hardening a rocker arm and the internal lobes of a cam; quench not shown. (b) Progressive hardening method

gas. The choice of gas depends on the shape, size, and composition of the workpiece and on the depth of case required, as well as on the relative cost and availability of each gas.

A wide choice of quenchants also is possible in the spin-hardening method. Because the flame is extinguished or withdrawn before the part is quenched, any appropriate quenchant may be used for immersion quenching. In spray quenching, the quenchant usually is water, a water-based liquid such as soluble oil, or a simulated oil in the form of a polymer-based quenchant; air also has been used.

The combination progressive-spinning method (Fig. 3), as the name implies, combines the progressive and spinning methods for hardening long parts such as shafts and rolls. The workpiece is rotated as in the spinning method, but, in addition, the heating heads traverse the roll or shaft from one end to the other. Only a narrow circumferential band is heated progressively as the flame head moves from one end of the work to the other. The quench follows immediately behind the heating head, either as an integral part of the head or as a separate quench ring.

This method provides a means of hardening large surface areas with relatively low gas flows. Progressive-spinning units designed to handle a broad range of diameters and lengths are available commercially.

Fuel Gases

Several different fuel gases are used in flame hardening. In selecting a fuel gas for a given

application, the required rate of heating and the cost of the gas must be considered, along with the initial cost of equipment and maintenance costs.

Flame hardening does not alter the composition of the base metal if done properly. Carburizing, neutral, and oxidizing flames can be used. Oxidizing flames have high oxygen ratios and can be detrimental because they produce extremely hot temperatures that can cause decarburization and overheating. A carburizing flame can prevent some decarburization but can also introduce unwanted carbon into the surface. For best results, neutral or slightly carburizing flames should be used (Ref 1).

A comparison of the heating rates of fuel gases can be made when certain fundamental properties of usable mixtures with oxygen are known. A parameter that correlates well with actual heating speed is combustion intensity, or specific flame output. This is the product of the normal velocity of burning multiplied by the net heating value of the mixture of oxygen and fuel gas. Knowledge of these two properties will aid in the selection of the most suitable fuel gas for a specific hardening speed and depth of case. The fuels of greatest commercial interest are ranked by combustion intensity (at metallurgically suitable ratios of mixture with oxygen) in the following order: acetylene, methylacetylene propadiene (MAPP), propane, and methane. Values of normal burning velocity and the heating values of metallurgically suitable mixtures are listed in Table 1.

The time required for heat penetration is another good criterion for judging the heating qualities of a fuel, provided that all other

variables remain constant. Figure 4 shows comparative heating times for stabilized MAPP, acetylene, and propane, using an efficient coupling distance for each fuel. These curves show that a greater depth of hardness can be obtained with MAPP in a shorter length of time (Ref 2).

The ratio of oxygen to fuel is very important in obtaining maximum heating efficiency from the fuel. However, oxygen-to-fuel ratios should not be confused with oxygen and fuel consumption rates, which vary with flame velocity, port size, and heating time. Stoichiometrically, acetylene requires 2½ mols of oxygen per mol of gas for complete combustion, MAPP requires 4 mols, and propane requires 5 mols. With acetylene, however, a range of only 1 to 1.5 volumes of oxygen is provided directly, with the remainder being drawn from the surrounding atmosphere. Neither MAPP nor propane has sufficient heat for flame hardening unless more oxygen is supplied, normally at a rate of four parts of oxygen per part of fuel. MAPP burns over a rather wide range of oxygen-to-fuel ratios, however, and thus permits a wider range of heat output while still providing high heat generation when necessary. The use of MAPP increases oxygen consumption, and fuel is more expensive than oxygen.

Bulk systems of supply for oxygen and fuel gases greatly reduce their cost, but of greater importance is the elimination of cylinder handling and of the residual losses usually attendant upon the use of gases in cylinders. Bulk systems also provide a more nearly

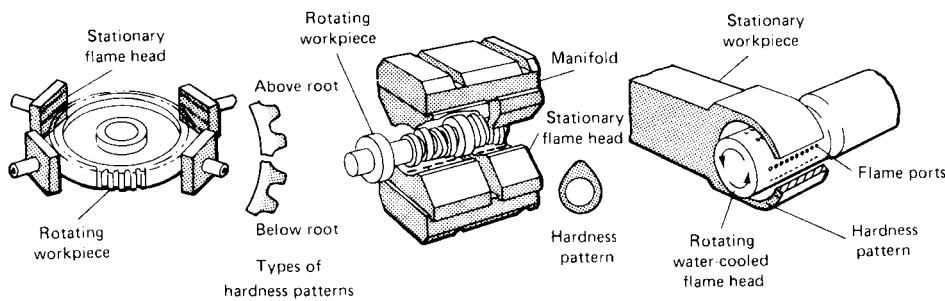


Fig. 2 Spinning methods of flame hardening. In methods shown at left and at center, the part rotates. In method at right, the flame head rotates. Quench not shown

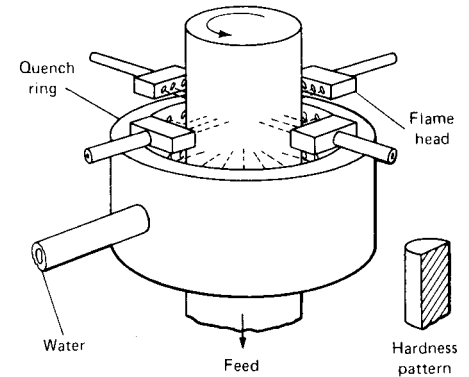


Fig. 3 Combination progressive-spinning flame hardening

Table 1 Fuel gases used for flame hardening

Gas	Heating value		Flame temperature				Usual ratio of oxygen to fuel gas	Heating value of oxy-fuel gas mixture		Normal velocity of burning		Combustion intensity(a)		Usual ratio of air to fuel gas
	MJ/m ³	Btu/ft ³	With oxygen °C	With oxygen °F	With air °C	With air °F		MJ/m ³	Btu/ft ³	mm/s	in./s	mm/s × MJ/m ³	in./s × Btu/ft ³	
Acetylene	53.4	1433	3105	5620	2325	4215	1.0	26.7	716	535	21	14,284	15,036	12
City gas	11.2-33.5	300-900	2540	4600	1985	3605	(b)	(b)	(b)	(b)	(b)	(b)	(b)	(b)
Natural gas (methane)	37.3	1000	2705	4900	1875	3405	1.75	13.6	364	280	11	3808	4004	9.0
Propane	93.9	2520	2635	4775	1925	3495	4.0	18.8	504	305	12	5734	6048	25.0
MAPP(c)	90	2406	2927	5301	1760	3200	3.5	20.0	535	381	15	7620	8025	22

(a) Product of normal velocity of burning multiplied by heating value of oxy-fuel gas mixture. (b) Varies with heating value and composition. (c) MAPP, methylacetylene propadiene

constant supply of gas at uniform pressure. A disadvantage of acetylene is that it cannot be stored in bulk, thereby requiring manifolds of cylinders.

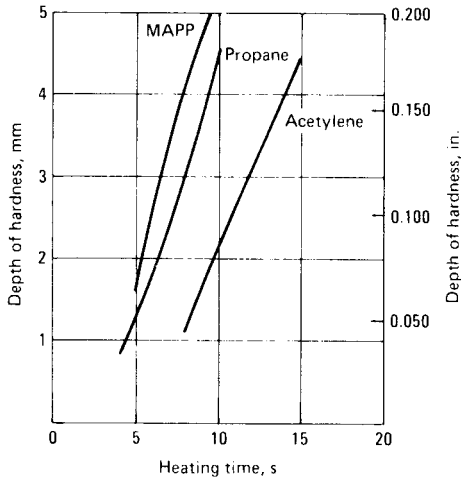


Fig. 4 Comparison of heating times for methylacetylene propadiene (MAPP), acetylene, and propane. Flame velocity, 170 m/s (550 ft/s); port size, No. 69 drill (0.74 mm, or 0.0292 in.); coupling distance, 9.5 mm (3/8 in.); material, 1036 steel. Oxygen-to-fuel ratios: MAPP, 5.0; acetylene, 1.33; propane, 4.5

Depth of Heating. Shallow hardness patterns (less than 3.2 mm, or 0.125 in., deep) can be attained only with oxy-gas fuels. The high-temperature flames obtained with oxy-gas fuels provide the fast heat transfer necessary for effective localization of the heat pattern. Deeper hardness patterns permit the use of either oxy-gas fuels or air-gas fuels. Oxy-gas fuels will localize the heat, but care is required in their application to avoid overheating the surface during the development of the deeper-seated heat. Air-gas fuels, with their slower rates of heat transfer (lower flame temperatures), minimize or eliminate surface overheating but generally extend the heat pattern beyond the desired hardness pattern. For this reason, air-gas flame hardening generally is limited to steels of shallow hardenability. In this manner, the hardness pattern is controlled by the quench rather than by the heating. The deeper-seated heat produced by air-gas flames may preclude the use of air-gas mixtures, because excessive distortion may occur. In consideration of these factors, the use of air-gas heating will depend primarily on the shape of the part insofar as the configuration favors heat localization and a lower rate of heat transfer.

Gas Consumption, Time, and Speeds. Gas consumption in flame hardening varies with the thickness of the case to be obtained; increasing

or decreasing the depth of hardening increases or decreases the amount of gas used. Massive parts increase gas consumption because of their greater internal cooling effect. To take advantage of the maximum flame temperature from the oxy-fuel gas flame, the distance from the end of the inner cone of the flame to the work should be 1.6 mm (1/16 in.).

The speed of travel of the flame head over the work in the progressive method, as well as the time of heating in the spot and spinning methods, will vary with the thickness of the case desired and the capacity of the flame head. The proximity of the quench spray to the last row of flames will affect the speed somewhat in the progressive method. Progressive and progressive-spinning speeds usually vary between 0.8 and 5 mm/s (2 and 12 in./min) for most applications, although very thin parts may require speeds of 42 mm/s (100 in./min) or more to avoid overheating or burning. Because of the intense heat involved, the necessity for accurate control of the rate of travel in the progressive and progressive-spinning methods cannot be overemphasized.

Time-temperature-depth relationships for various fuel gases used in the spot (stationary), spinning, and progressive methods of flame hardening are shown in Fig. 5. The family of curves for the spot method (Fig. 5a) was

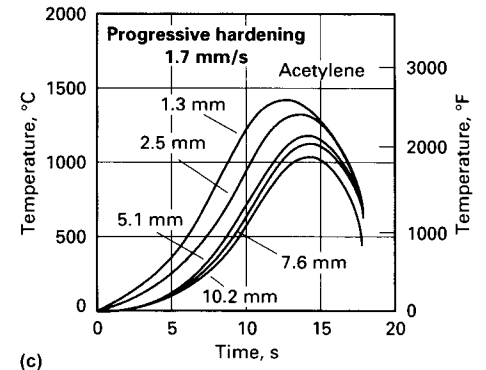
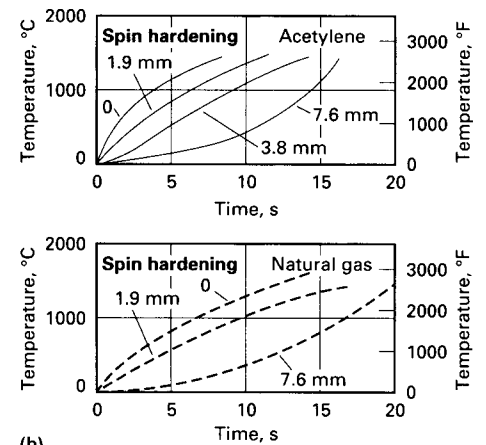
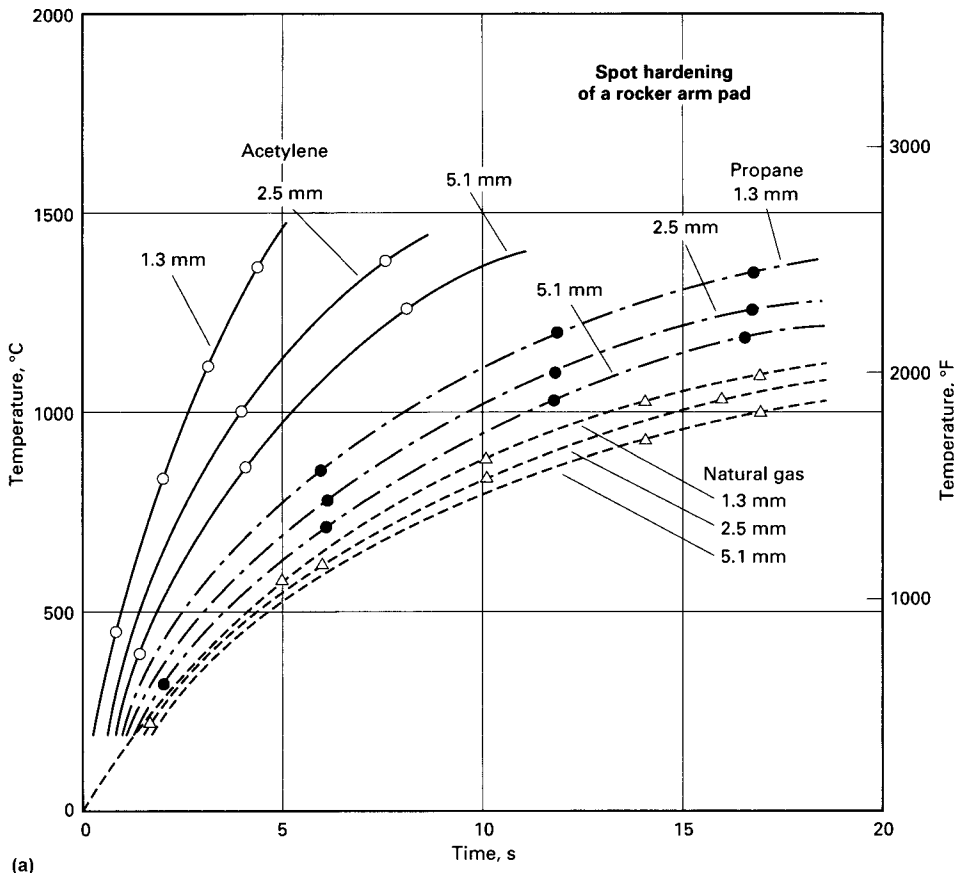


Fig. 5 Calculated time-temperature-depth relationships for spot (stationary), spinning, and progressive flame hardening. Depth of hardness given in millimeters

obtained analytically by considering the flow of heat in three dimensions away from a heated spot on the surface of a rocker arm pad. The calculations were based on heat sources of different strengths, which were varied on the basis of the combustion intensity of the gases considered (acetylene, propane, and natural gas). It is understood that the strength of the heat source also will be affected by such factors as size of tip, distance from tip to work, total gas flow, and ratio of oxygen to fuel gas; hence, these curves are intended to indicate trends in time-temperature-depth relationships rather than to provide operational values for particular applications.

The curves for the time-temperature-depth relationships of fuel gases used in the spinning method, shown in Fig. 5(b), were obtained analytically by considering the flow of heat into a cylindrical body from a heat source supplying heat uniformly over the outer cylindrical surface. It was assumed that the temperature at the axis would not be raised appreciably during surface heating and that, in spin hardening, the cylinder would be rotated rapidly enough to give the effect of substantially uniform surface heating. No temperature decrease at high values of time is indicated, because in this type of process the body is quenched immediately when the surface temperature reaches a predetermined value.

The curves for the progressive method (Fig. 5c) also were obtained analytically by considering heat flow into a body from a line source moving along a flat side of the body. The heat source strength and body configuration were chosen to be representative of progressive flame hardening. In this instance, the time variable can be correlated with travel speed if the width of the flame zone is known. For example, a flame zone 25 mm (1 in.) wide will pass over a point on the work surface in 15 s when the travel speed of the tip is 1.7 mm/s (4 in./min). This width of flame zone indicates the probability of a multirow tip, and if the heat source is as strong as assumed for computing the curves, will undoubtedly damage the work surface. Consequently, a higher travel speed would be used, for example, 2.5 mm/s (6 in./min), which would heat a point on the work for 10 s and result in hardening to a depth of approximately 2.5 mm (0.100 in.). The rapid decrease in temperature at large values of time is due to the mass quenching effect, which, in practice, would be augmented by the use of water spraying or other quenching means.

Burners and Related Equipment

Burners are basic components of equipment for all methods of flame hardening. Burners vary in design, depending on whether they are fired by an oxy-fuel or an air-fuel gas mixture. Flame temperatures obtained by oxy-fuel gas combustion are 2540 °C (4600 °F) and higher. Heat transfer is by direct impingement of the flame on the surface of the workpiece. This is the reason oxy-gas burners are more commonly

referred to as flame heads. Flame temperatures obtained by air-fuel gas combustion are considerably lower (Table 1), and heat transfer is by impingement of high-velocity combustion product gases (no direct flame) or by radiation from an incandescent refractory surface.

There is no universal flame head, and no flame head is designed specifically for one particular gas. A well-designed flame head can be used with MAPP, acetylene, or propane, for example. Better flame head design usually results in improved operation and lower gas consumption. Both acetylene and MAPP gas are somewhat reactive with copper-base alloys having more than 67% Cu. This concern is a problem only with piping systems, not torches or tips.

In general, a large number of small ports will produce a more efficient heat pattern than a few larger ports. Port spacing of 2.3 to 3.2 mm (0.090 to 0.125 in.) on centers is, in most cases, advisable. Counterboring permits higher flame velocities and is frequently advantageous or necessary when propane or MAPP is used. Because acetylene has a higher flame propagation rate,

counterboring usually is unnecessary and frequently is undesirable. Counterboring reduces coupling distance and permits a stabilized flame at higher flame velocities. For effective operation, the ratio of counterbore area to throat area should be on the order of 2 to 1. Ratios as high as 4 to 1 may be used in some cases, however (Ref 2).

Examples of modern flame heads are shown in Fig. 6.

Oxy-Fuel Gas Flame Heads. Oxy-fuel gas combustion develops flame temperatures above those at which useful metals and refractory materials can survive. Accordingly, the flame head is designed to provide a flame pattern that avoids any direct heating of its parts.

Generally, the flame head consists of a tube or a shell with one or more orifices drilled into it. The number and arrangement of orifices depend on the required area of heat coverage. Flame heads for use with oxy-fuel gas are shown in Fig. 7.

The drilled-face flame head has a limited range of application and usually is designed to meet the requirements of one specific part to

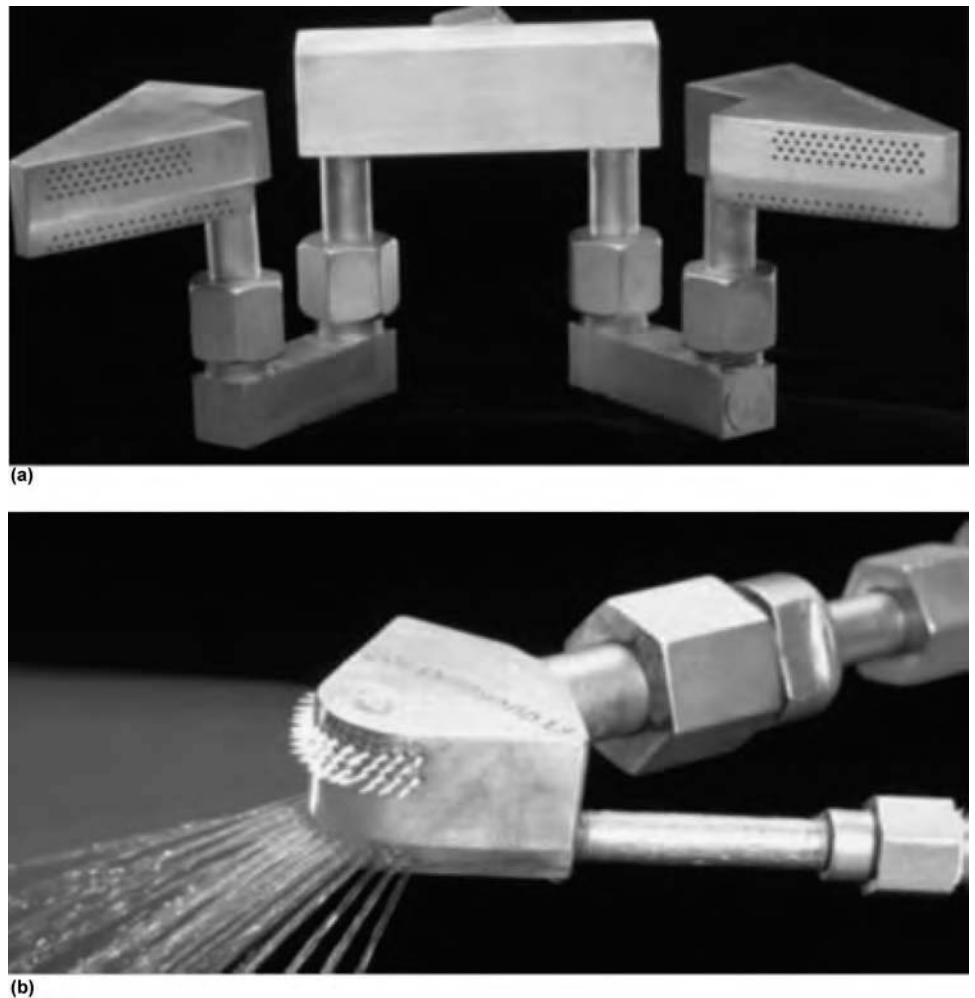


Fig. 6 Representative flame head designs. (a) Gear tooth-hardening flame head. (b) Sheave-hardening flame head. Source: Ref 3

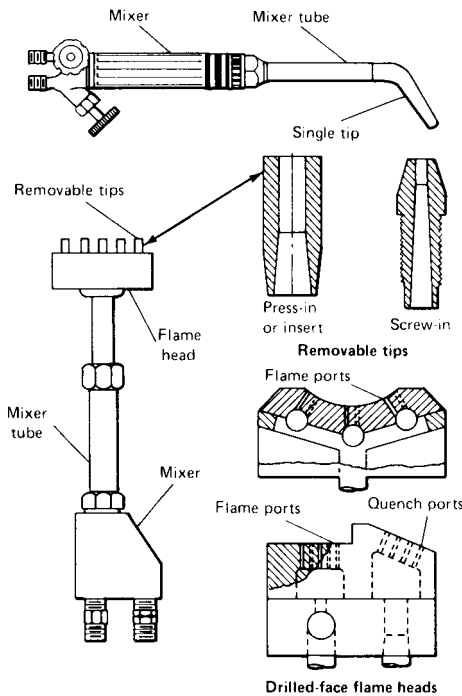


Fig. 7 Flame heads for use with oxy-fuel gas

be flame hardened in appreciable quantity. For other applications, the flame head may be fitted with removable tips of the screw-in or insert type.

The screw-in type of removable tip shown in Fig. 7 is used widely enough that it is available in off-the-shelf commercial flame heads or is supplied as a standard item by manufacturers of flame-hardening equipment; it also is simple enough that it can be made to specification by plants applying the flame-hardening treatment.

The insert, or press-in, type of tip shown in Fig. 7 is smaller than the screw-in type and permits closer spacing of orifices, approaching that of a drilled flame head. Flame heads with removable and replaceable tips can be used over a wider range of applications by removing one or more tips and replacing them with plugs.

Flame cone characteristics are affected by different drill sizes and counterbore drill sizes, as well as whether a drilled flame port is even counterbored. This also affects the heating characteristics, as shown in Table 2.

A typical flame port is a No. 69 drill (0.74 mm, or 0.0292 in.) with a No. 56 drill (1.18 mm, or 0.0465 in.) counterbore. This produces a cone length of approximately 8 mm (0.3125 in.) when the oxy-fuel gas is delivered

at a flow rate of 0.07 L/s (8.75 ft³/h) with a neutral ratio.

Integral parts of the flame system are the mixer block and the mixer tube, which mix the component fuel gases and convey them through the orifices (Fig. 7). The capacities of mixer block and mixer tube must match the number and size of the orifices; if the mixer is too small, the flame will flash back, and if the mixer is too large, the flame head will not function efficiently.

To ensure identical velocity of mixed gases at all flame orifices, it is common practice to design a flame head with baffle orifices through which the gases must pass before they are burned at the flame orifices. Two rules apply to the design of baffle orifices: first, their total area must be 1.25 to 1.50 times the area of the flame orifices; and second, the number of baffle orifices within a single baffle should be one-fourth the total number of flame orifices.

Multiple-orifice flame heads are water cooled because otherwise the high temperatures developed at and around the flame head would cause early deterioration. On flame heads used for progressive hardening, the quench water cools the head. On multiple-orifice flame heads used in the spinning and progressive-spinning methods, the cooling water is circulated through chambers integrated into the head. Single-orifice flame heads (welding torches, for example) generally are not water cooled.

Typical flame-hardening installations that use oxy-fuel gas mixtures are shown in Fig. 8. The equipment in Fig. 8(a) was designed to handle the high production of similar parts. The equipment in Fig. 8(b) was designed to harden a variety of parts by changing the flame heads and work spindle.

New equipment configurations are being designed to handle specific problems. With conventional flame-hardening equipment, for example, it is difficult to obtain a zone of uniform temperature across the surface of the tooth gap in gears. The problem of obtaining uniform depth of hardness, not only from tooth to tooth but also across the entire face width, has been solved by the development of a two-chamber burner with individual control of energy input to each chamber. The system ensures uniform heating, particularly in the tooth root, and incorporates the separate control of nozzles for tooth-root and tooth-flank hardening (Ref 4).

With this system, complex components also can be processed by spin hardening. For example, both the straight and bevel gears of a double-pinion shaft can be hardened simultaneously if the quenching-bath immersion depth is adequate. By distributing heating power between spur wheel and bevel wheel, the austenitizing temperature can be reached under the tooth roots of both gears at the same time. This requires the selection of different heat-up times for the two gears and different rates of oxygen flow to the two sets of burners (Ref 4).

Table 2 Total gas flow from one flame port at various velocities

Flame port drill size number	Flame port drill size diameter		Total gas flow, L/s (ft ³ /h)				Recommended coupling distance	
	mm	in.	At 120 m/s (400 ft/s)	At 140 m/s (450 ft/s)	At 150 m/s (500 ft/s)	At 170 m/s (550 ft/s)	mm	in.
69	0.74	0.029	0.055 (7)	0.063 (8)	0.069 (8.75)	0.076 (9.6)	9.5	0.375
64	0.91	0.036	0.079 (10)	0.089 (11.25)	0.098 (12.5)	0.108 (13.75)	11.1	0.4375
60	1.01	0.040	0.094 (12)	0.106 (13.5)	0.118 (15)	0.130 (16.5)	12.7	0.5
56	1.18	0.0465	0.134 (17)	0.150 (19)	0.167 (21.25)	0.184 (23.4)	14.3	0.5625

Source: Ref 3

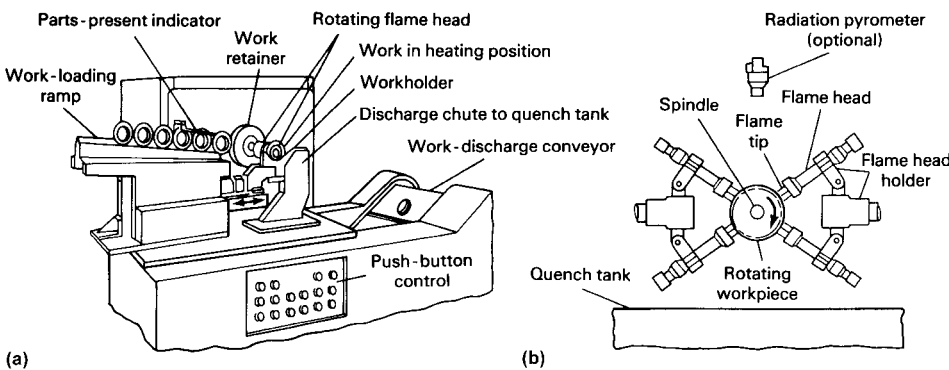


Fig. 8 Typical flame-hardening installations using oxy-fuel gas mixtures. (a) Installation for high production of similar parts: hardening the 54 mm (2 1/8 in.) bores of hubs to a depth of approximately 3.2 mm (1/8 in.). Machine has a standard, retractable spindle adapted with a rotary flame head. Spindle is driven by a variable-speed motor. Temperature of agitated quench is maintained by a water-cooled heat exchanger. (b) Installation for selective oxy-fuel gas heating of small-production lots of gears, sprockets, and flanges within size limits of the equipment. A radiation pyrometer is used here to control the heating cycle, but many operations use an electric timer instead. By changing work heads and spindles, equipment can be adapted to various parts.

Air-Fuel Gas Burners. Air-fuel gas combustion develops lower flame temperatures that are compatible with available refractory materials. Thus, burners are designed with the aim of completely using the heat generated. The burners, incorporating heat-resistant refractory liners, are of two types, generally designated as the radiant type and the high-velocity convection type (Fig. 9).

The radiant-type burner (Fig. 9a) essentially is a refractory cup in a protective metal casing. Air-gas premixing is supplied through the pipe at the back and passed through an accurately molded ceramic tip that is screwed into the pipe and located at the bottom of the cup. With numerous narrow slots molded into its periphery, the tip essentially functions as the distributing head of a multiport burner. The many small flames wash the inner surface of the cup, making it highly incandescent for rapid heat transfer by radiation. Because combustion is completed within the cup, the burner may be positioned close to the work with no flame impingement.

The standard radiant burner used in flame hardening is approximately 75 mm (3 in.) in cup diameter. It is particularly effective for spin

hardening the teeth of large gears. A single row of burners may be arranged in a ring surrounding a gear, as shown in Fig. 10(a), or multiple rows of burners may be arranged to cover completely the surface to be hardened.

The high-velocity convection burner is basically a miniature refractory-lined furnace in which heat is released at rates as high as $415 \text{ MJ/m}^3 \cdot \text{s}$ ($4 \times 10^7 \text{ Btu/ft}^3 \cdot \text{h}$). The air-gas premixture, supplied through a pipe connection, flows through the orifices of the ceramic port plate. The burner design is such that the burning gases heat the chamber lining to a temperature approaching the theoretical flame temperature. This permits preheating of the reacting gases and accelerates combustion. In this manner, gases at approximately $1650 \text{ }^\circ\text{C}$ ($3000 \text{ }^\circ\text{F}$) are discharged through a restricted slot opening to impinge on the workpiece at velocities up to 760 m/s (2500 ft/s). High-velocity convection burners are well adapted to the localized heating of parts in spin-hardening operations. Figure 10(b) shows their application for hardening the teeth of a thin gear.

Related Equipment. Burners for both the oxy-fuel gas and the air-fuel gas methods of flame hardening are implemented by pressure

regulators, valves, flowmeters, and protection devices. For the air-fuel gas method, a separate mixer and compressor are used because the mixing function is not incorporated within the burners (Fig. 11).

Materials of Construction for Burners. The metallic components of burners may be of a variety of materials, depending on the type of burner and the service to which it is subjected. The flame heads for oxy-fuel gas flame heating in nearly all instances are made of copper or a dense grade of lead-free brass (Ref 2). These metals are relatively inexpensive, have excellent thermal conductivity, and are readily machined. Because flame velocity is relatively low, there is little likelihood that the metal flame head will overheat and deteriorate as a result of the backwash of hot gases. Normally, the flow of gases within the head provides sufficient cooling to maintain a safe temperature. If additional cooling is required, the head may be water cooled. Under no circumstances should the flame head be permitted to overheat to the extent that the burner metal, brazed burner joints, or drilled flame ports are damaged.

The service life of oxy-fuel gas flame heads depends largely on the conditions of a particular application, such as containment of the heat resulting from the configuration of the piece being heated, and the degree of backwash of flame or hot gases impinging on the burner. Therefore, it is difficult to predict the exact service life that can be expected for a new application. Brass heads used for the progressive hardening of machineways have recorded an average life of 1000 to 2000 h in continuous service.

The melting points and ranges of heat resistance of available materials are not greatly different (compared with the large differences between flame temperatures and metal melting points). Life expectancy, therefore, is a relatively unimportant basis for the selection of a particular metal. Availability, cost, and ease of fabrication are likely to be more important factors in materials selection. A metal frequently used for flame heads is Muntz metal (60-40 lead-free brass); when cooling is a problem, however, copper is preferable.

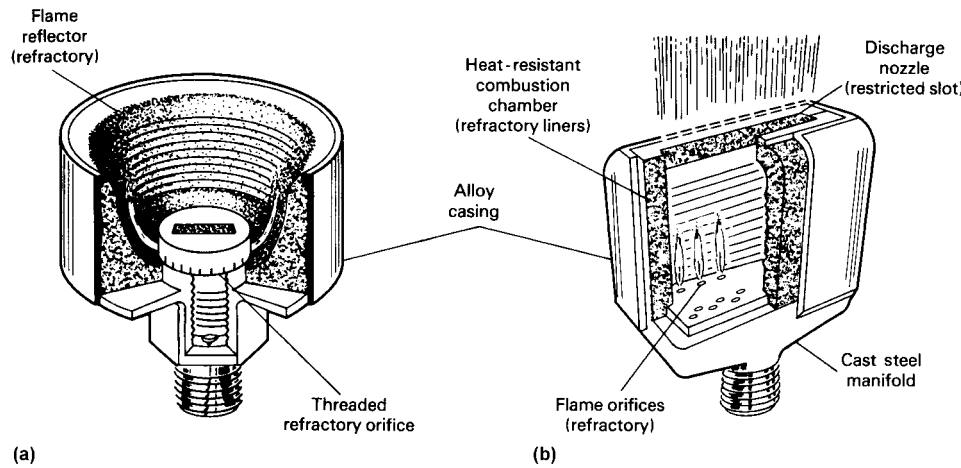


Fig. 9 Typical burners for use with air-fuel gas. (a) Radiant type. (b) High-velocity convection type (not water cooled)

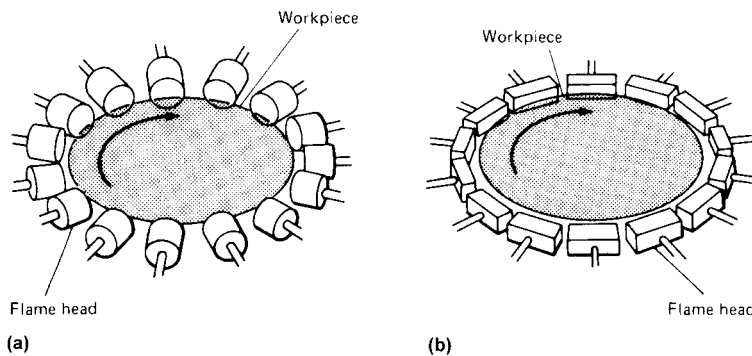


Fig. 10 Setups for flame hardening gears, idler wheels, and sprockets. (a) Radiant burners. (b) High-velocity convection burners. Wide-face parts can be heated with double or staggered rings of burners.

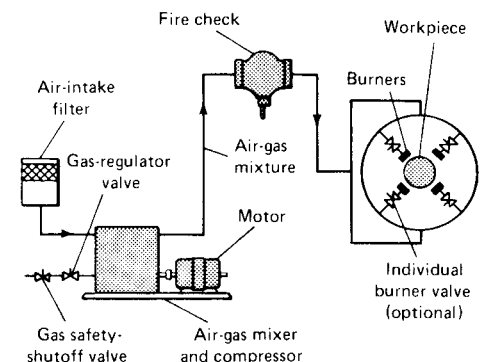


Fig. 11 Mixer-burner system for use with air-fuel gas

Screw-in tips usually are made of copper, but when higher heat resistance is required, because of secondary flame, a nickel alloy with small amounts of aluminum and titanium can be used. Insert or press-in tips usually are made of copper, but when high wear resistance of the tip bore is desired, tips made of sintered carbide are employed.

Cast iron, stainless steel, and heat-resisting alloys are used for the casings that surround the refractory cups of radiation-type air-fuel gas burners. Heat-resisting alloys may provide reasonable life at temperatures up to 1150 °C (2100 °F). Casings of high-velocity convection burners generally are constructed of stainless steel but may be of an austenitic nickel-chromium-base superalloy for more severe service. For the spin hardening of gears, either type of burner may have a useful life of 10 to 15 40-h weeks of continuous operation. In many applications, longer life for casings has resulted when the operator has exercised care in setting up and operating burners. Also, water cooling the burner casing can markedly extend its life and may be used if the added cost is justifiable and if space for the cooling arrangement is available in the heating setup.

The refractory parts of all types of air-gas burners are formed in steel dies and prefired in kilns and are capable of withstanding the most extreme temperatures generated in the burners. These parts generally fail from thermal or mechanical shock; hence, service life is unpredictable.

Operating Procedures and Control

The success of many flame-hardening applications depends largely on the skill of the operator. This is true especially when the volume of work is so small or varied that the cost of automatic-control equipment is not justified.

The principal operating variables are:

- Distance from inner cone of oxy-fuel gas flames or from air-fuel gas burner to work surface
- Flame velocities and oxygen-to-fuel ratios
- Rate of travel of flame head or work
- Type, volume, and angle of quench

These variables must be closely controlled to ensure the duplication of desired surface hardness and depth of hardness. It is highly desirable to develop a specific procedure for each item to be flame hardened. The procedure is

developed by preliminary tests on the production piece itself, if warranted, or on mock-up sections of approximately the same cross section as the production piece. After the desired contour and depth of hardened zone have been developed, the procedure is applied to production pieces and, when established, is made a part of the heat treating specification. The critical importance of developing strict procedures is demonstrated in the following case study conducted by a flame-hardening firm (Ref 5).

Example 1: Test on Flame-Hardening Procedure of 1045 Steel Bar. Each of five experienced flame hardeners was asked to flame harden a 1045 steel bar 25 by 50 by 450 mm (1 by 2 by 18 in.) using only experience and visual examination to guide the process. Only the traditionally and normally controlled variables were preset: coupling distance, 11 mm ($7/16$ in.); water pressure, 620 kPa (90 psi); quench, water; and angle of quench, 30°. Flowmeter readings were taken, speeds of travel recorded, and flame velocities determined. After treatment, each bar was ground to determine the hardness level and depth of hardness. Results are given in Table 3. Surface hardness and depth of hardness showed little consistency: Surface hardness ranged from 50 to 61 HRC and at 3.18 mm ($1/8$ in.) from 30 to 52 HRC.

The speed of travel of the flame head, or the duration of heating, should be held constant for uniform results. In the progressive method, the flames gradually heat the workpiece in front of the flame head, and sometimes this effect must be compensated for by gradually increasing the speed of travel or by precooling. At the beginning of a pass when the progressive or progressive-spinning method is being used, the flame head or heads should be manipulated or otherwise adjusted to ensure that the beginning of the area to be hardened attains the proper temperature and depth of heating as progression begins.

Gas Pressures. Oxy-fuel gas and air-fuel gas pressures should be controlled closely for uniform input of heat. Flat oxy-fuel flame heads are somewhat less efficient when used on circular or curved surfaces because each cone of flame is at a different distance from the work. Overheating causes cracking.

Oxygen-to-fuel ratio is a key factor in determining flame temperature. For example, propane produces flame temperatures of 2700 °C (4900 °F) at a 5-to-1 ratio, 2540 °C (4600 °F) at a 4-to-1 ratio, and 2370 °C (4300 °F) at a 3-to-1 ratio.

Flame velocity is one of the most important variables because when balanced with other variables, it is the main determinant of case depth. In example 1 for flame hardening 1045 steel (Ref 5), the basic flame velocity required for establishing a case depth of 3.2 to 4.8 mm ($1/8$ to $3/16$ in.) is 152 m/s (500 ft/s).

In flame hardening cast irons, where high surface temperatures are undesirable, the use of lower flame velocities is a distinct advantage. In this regard, both MAPP and propane are easy to control and are effective over a wide range of velocities. The ability to control the flame over a wide velocity range not only provides flexibility but also makes the operation much safer and results in better heat-pattern control.

Coupling distance is another key parameter in flame hardening. The relations between coupling distance and depth of hardening for three fuel gases are shown in Fig. 12. In general, the coupling distance for MAPP is equal to or very slightly greater than that for acetylene. The effect of counterboring is a shortening of the coupling distance. By the same token, coupling distance increases as flame velocity increases. Efficient coupling distances for MAPP generally range from 6.4 to 9.5 mm ($1/4$ to $3/8$ in.), depending on gas velocity and port size. A counterbored port of No. 69 drill size (0.74 mm, or 0.0292 in.) will operate efficiently at a coupling distance of 4.8 mm ($3/16$ in.).

Hardening temperatures can be judged by competent operators, but to the inexperienced ones, the heated metal will appear colder than it actually is because of the light from the burning gases; the consequent tendency is to overheat unless the operator is equipped with didymium-tinted glasses. Radiation or optical pyrometers often are used to judge more accurately the temperatures being developed. Radiation-pyrometer systems of fast response are used extensively to control work temperatures and heating times. Metallurgical examination is the best method for establishing operating conditions. Overheated spots may appear under individual flames, but with properly designed flame heads and good scanning technique, this

Table 3 Results of operator skill test

Operator	Flame velocity		Oxygen-to-fuel ratio	Travel speed		Surface hardness, HRC	Hardness at 3.18 mm (0.125 in.), HRC
	m/s	ft/s		mm/s	in./min		
1	95	313	3.6:1	3.4	8.0	61	30
2	99	324	3.1:1	2.5	6.0	50	41
3	137	451	3.1:1	1.7	4.0	57	50
4	124	407	4.2:1	1.9	4.5	55	38
5	156	511	3.3:1	2.5	6.0	60	52

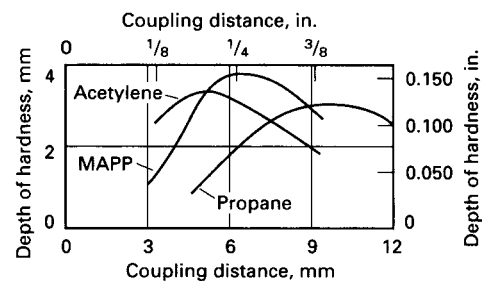


Fig. 12 Effect of coupling distance for methylacetylene propadiene (MAPP), acetylene, and propane. Flame velocity, 170 m/s (550 ft/s); port size, No. 69 drill (0.74 mm, or 0.0292 in.); material, 1052 steel. Oxygen-to-fuel ratios: MAPP, 4.5; acetylene, 1.33; propane, 4.5. Heating times: MAPP, 6 s; acetylene and propane, 8 s

effect is minimized and not readily detectable by microscopic examination.

Examples of Flame-Hardening Procedures. The interrelationship of variables can be illustrated best by specific examples of procedures used for the production hardening of actual parts. The following six examples involve the hardening of gears, cams, shafts, and flat surfaces.

A *small gear hub* made of 1052 steel was flame hardened by the spinning method at a spindle speed of 140 rpm (Table 4). The aim was to harden to 52 HRC minimum to a depth of 0.9 mm (0.035 in.) maximum above the root of the gear teeth.

A *large bevel ring gear* of 8742 steel was flame hardened by the progressive method (Table 5). The hardness aim was 53 to 55 HRC.

A *free-wheel cam* made of 1062 steel was flame hardened by the spot method (Table 6). The aim was 60 HRC minimum at the surface and 59 HRC at a depth of 1.3 mm (0.050 in.), for a width of 8.8 mm (0.345 in.) on the roller surface of the cam.

A *52100 steel shaft* was flame hardened by the progressive method to 61 to 63 HRC (Table 7).

The *roller path of a large cast alloy steel ring gear* was hardened according to the procedure outlined in Table 8. The hardness aim was 515 to 600 by portable Brinell, as specified in the last item in Table 8 (see Fig. 13).

Drop-forged wear blocks of 1040 steel were flame hardened on a conveyor to 53 to 58 HRC (Table 9).

Cam Lobe Heating. A manufacturer of cast iron automobile cams developed a production process for hardening individual cam lobes using direct flame impingement. Each cam is spin heated using a specially designed flame

head, heating the individual lobes to the desired temperature, after which the cam is dropped into a quench medium. Cam spin heating is similar to spin heating a worm shaft for hardening (Fig. 14).

In this case, hardening using flame heating gave better results than those using induction heating, due to the cracking problems associated with induction heating. The key for solving many cam-heating problems was designing a flame head that could heat an irregularly shaped cam and balancing the heat so as to heat all lobes in the same way.

Preheating

In flame hardening parts of large cross section, difficulty in obtaining the desired surface hardness and hardness penetration often can be overcome by preheating. When available power or heat input is limited, the hardened depth can be increased by preheating. The hardness data in Fig. 13 shows the effectiveness of preheating in developing hardness penetration in the ring gear discussed in Table 8.

The flame hardening of prehardened and tempered steels, especially some of the alloy steels, requires careful control of heating to avoid cracking. Preheating the part may be advisable to minimize cracking in such steels. Hardenable cast iron also is susceptible to cracking. In one application, cast iron crane wheels had to be preheated to 480 °C (900 °F) to prevent the rupture of the spokes caused by nonuniform expansion during the spin heating of the tread area.

In another application, the difficulty of heat treating the internal teeth of a planetary-gear

housing was overcome by spin hardening. The component had an irregular mass distribution, which led to large distortions when heat treating was done by ordinary flame-hardening or induction-hardening equipment. The case hardening of teeth also failed. The problem was solved by using a specially designed gear wheel spin-hardening machine with close control over heating time and power and by preheating the part with the largest mass and cross section to an accurately predetermined temperature (Ref 4).

Depth and Pattern of Hardness

In some instances, the flame-hardening procedure results in a greater depth of hardness than desired. Figure 5(a), for example, shows that spot hardening a rocker arm pad after heating 4 s at 870 °C (1600 °F) with oxyacetylene flame produces a depth of hardness of 5.1 mm (0.200 in.). If excessive, this depth may be reduced by heating the steel to the same temperature but in a shorter time. Thus, with a reduction in heating time to 3.2 s at 870 °C, the depth of hardening will be 2.5 mm (0.100 in.) (Fig. 5a). Because of the shorter heating period, the cost of hardening each pad also will be reduced.

The problem of excessive depth resulting from a spin-hardening operation may be resolved similarly, as shown in Fig. 5(b). In this operation, heating with an oxyacetylene flame for 13.5 s at 870 °C (1600 °F) produces a hardness depth of 7.6 mm (0.300 in.). Heating at the same temperature for a period of 8 s results in a hardened depth of approximately 3.8 mm (0.150 in.).

In a progressive-hardening operation with a rate of travel of 1.7 mm/s (4 in./min), a hardness depth of 5.1 mm (0.200 in.) will be produced when the heating time is 12 s at 870 °C

Table 4 Procedure for spin flame hardening a small converter gear hub (shown in Fig. 16a)

Preliminary operation
Turn on water, air, oxygen, power, and propane. Line pressures: water, 220 kPa (32 psi); air, 550 kPa (80 psi); oxygen, 825 kPa (120 psi); propane, 205 kPa (30 psi). Ignite pilots.
Loading and positioning
Mount hub on spindle. Hub is held in position by magnets. Flame head previously centered in hub within 0.4 mm (1/64 in.). Distance from flame head to inside diameter of gear teeth, approximately 7.9 mm (5/16 in.)
Cycle start
Spindle with hub advances over flame head and starts to rotate. Spindle speed, 140 rpm
Heating cycle
Propane and oxygen solenoid valves open (oxygen flow delayed slightly). Mixture of propane and oxygen ignited at flame head by pilots. Check propane and oxygen gages for proper pressure. Adjust flame by regulating propane. Heating cycle controlled by timer. Time predetermined to obtain specified hardening depth.
Propane and oxygen solenoid valves close (propane flow delayed slightly). Spindle stops rotating and retracts. Hub stripped from spindle by ejector plate. Machine ready for recycling
Propane regulated pressure, 125 kPa (18 psi); oxygen regulated pressure, 550 kPa (80 psi); oxygen upstream pressure, 400 kPa (58 psi); oxygen downstream pressure, 140 kPa (20 psi). Flame velocity (approximate), 135 m/s (450 ft/s). Gas consumptions (approximate): propane, 0.02 m ³ (0.6 ft ³) per piece; oxygen, 0.05 m ³ (1.9 ft ³) per piece. Total heating time, 9.5 s
Flame port design: 12 ports per segment; 10 segments; port size, No. 69 (0.74 mm, or 0.0292 in.), with No. 56 (1.2 mm, or 0.0465 in.) counterbore
Quench cycle
Hub drops into quench oil, is removed from tank by conveyor. Oil temperature, 54 ± 5.6 °C (130 ± 10 °F); time in oil (approximate), 30 s
Hardness and pattern aim
Hardness, 52 HRC minimum to a depth of 0.9 mm (0.035 in.) maximum above root of gear teeth

Table 5 Progressive flame hardening of ring gear teeth

Workpiece
Bevel ring gear made of 8742 steel with 90 teeth. Diametral pitch, 1.5; face width, 200 mm (8 in.); outside diameter, 1.53 m (60.412 in.)
Mounting
Gear mounted on holding fixture to within 0.25 mm (0.010 in.) total indicator runout
Flame heads
Two 10-hole, double-row, air-cooled flame heads, one on each side of tooth. Flame heads set 3.2 mm (1/8 in.) from tooth
Operating conditions
Gas pressures: Acetylene, 69 kPa (10 psi); oxygen, 97 kPa (14 psi)
Speed: 1.9 mm/s (4.5 in./min). Complete cycle (hardening pass, overtravel at each end, index time, preheat return stroke on next tooth), 2.75 min
Indexing: Index every other tooth. Index four times before immersing in coolant.
Coolant: Mixture of soluble oil and water, at 13 °C (55 °F)
Hardness aim: 53 to 55 HRC

Table 6 Spot flame hardening of a 1062 steel free-wheel cam**Preliminary operation**

Turn on water, air, oxygen, power, and propane. Line pressures: water, 205 kPa (30 psi); air, 550 kPa (80 psi); oxygen, 825 kPa (120 psi); propane, 205 kPa (30 psi). Ignite pilots.

Loading and positioning

Mount cam on flame head. Cam positioned on locating plate and two wear pads, and against three locating pins that are integral parts of flame head. Distance from flame head to cam surface, approximately 7.9 mm ($\frac{5}{16}$ in.)

Cycle start and heating cycle

Propane and oxygen solenoid valves open (oxygen flow delayed slightly). Mixture of propane and oxygen ignited at flame heads by pilots. Check propane and oxygen pressures. Adjust flame by regulating propane. Heating cycle controlled by timer. Time predetermined to obtain specified hardening depth. Propane and oxygen solenoid valves close (propane flow delayed slightly). Ejector plate (air operated) advances and strips cam from flame head.

Propane regulated pressure, 125 kPa (18 psi); oxygen regulated pressure, 585 kPa (85 psi); oxygen upstream pressure, 425 kPa (62 psi); oxygen downstream pressure, 110 kPa (16 psi). Flame velocity (approximate), 135 m/s (450 ft/s). Gas consumption (approximate): propane, 0.01 m³ (0.4 ft³) per piece; oxygen, 0.04 m³ (1.3 ft³) per piece. Total heating time, 11 s

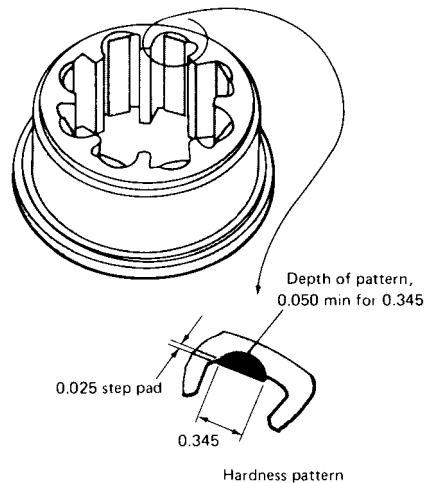
Flame port design: nine ports per row; eight rows; port size, No. 69 (0.74 mm, or 0.0292 in.), with No. 56 (1.2 mm, or 0.0465 in.) counterbore

Quench cycle

Cam drops into quench oil, is removed from tank by conveyor. Oil temperature, 54 ± 5.6 °C (130 ± 10 °F). Time in oil (approximate), 30 s

Hardness and pattern aim

Hardness, 60 HRC minimum at surface and 59 HRC minimum at a depth of 1.3 mm (0.050 in.) below surface, for width of 8.8 mm (0.345 in.) on cam roller surface. Dimensions in figure given in inches



(1600 °F), as shown in Fig. 5(c). The flame head contains two rows of flame holes that produce a heating zone 20 mm (0.8 in.) wide. If the rate of travel is increased 20% to 2 mm/s (4.8 in./min), the heating time is reduced proportionately to 10 s. This results in a hardened depth of approximately 2.5 mm (0.100 in.).

Variation in depth of hardness may occur in steels of the same nominal composition but from different heats. This is demonstrated in Fig. 15, which shows the variation in depth of hardness obtained in flame hardening hubs made of 1062 steel from three different heats. The inside diameters of these hubs were flame hardened for 12 s to produce a minimum hardness of 59 HRC at a depth of 1.9 mm (0.075 in.).

Surface Hardness Pattern. The hardness pattern of any portion of a flame-hardened surface can be determined by lightly blasting the area with fine sand. The hardened portion of the surface will be less affected than the

unheated area by the cutting action of the sand. This procedure also may be employed to indicate soft spots when the entire surface has been subjected to flame hardening. (Soft spots may result from nonuniform heating or the interference of scale on the surface.) Another procedure for determining the surface hardness pattern is to etch the area with a 10% nitric acid solution. The hardened area will appear darker than the unhardened area.

These procedures also are applicable to cross sections of hardened areas for an indication of heat penetration, and they are useful as preliminary checks on the performance of the flame-hardening setup.

Variations in the hardness of the surface are exemplified by the data shown in Fig. 16. These hardness readings taken on the surface of races made of 4063 steel cover a one-month period. The races were heated for 9 s to produce a minimum hardness of 59 HRC at 1.3 mm (0.050 in.) below the surface.

Table 7 Progressive flame hardening of a 52100 steel shaft**Setup**

Shaft held vertically between centers to within 0.1 mm (0.005 in.) total indicator runout

Flame heads

Three water-cooled flame heads, each with eight holes 1.3 mm (0.052 in.) in diameter. One torch for each flame head. Flame heads set 6.4 mm ($\frac{1}{4}$ in.) from shaft

Operating conditions

Gas pressures: Acetylene, 55 kPa (8 psi); oxygen, 76 kPa (11 psi)

Speeds: Flame head travel, 1.3 mm/s (3 in./min); speed of shaft revolution, 20 rpm

Quench: Water nozzles directly below flame heads

Hardness aim: 61 to 63 HRC

Summary. Hardness of the case in flame hardening is a function of the carbon content of the steel and will range up to 65 HRC. Medium-carbon steels with 0.40 to 0.50% C are ideal for flame hardening, but steels with carbon contents as high as 1.50% also can be flame hardened with special care. Normally, hardening depth ranges from 1.3 to 6.4 mm (0.05 to 0.25 in.). Heavier sections, such as large rolls and wheels, can have case depths of up to 13 mm (0.5 in.). Manganese-bearing alloys aid in the depth of hardening by decreasing the critical cooling rate, which contributes to deep hardening. Therefore, manganese and free-machining grades of steel are considered excellent for flame hardening.

When hardening depths are required beyond the capabilities of ordinary carbon steels (0.60 to 0.90% Mn), elevated manganese ranges such as 0.80 to 1.10%, 1.00 to 1.30%, or 1.10 to 1.40% can be used efficiently. Wear resistance in many cases is not the only critical design criterion. Under high compressive loading, the hardened layer must be deep enough not only to provide the required wear life of the part but also to contribute to the support of heavy contact loads. The case must be fully martensitic, and the material supporting the hardened layer must be of sufficient strength. However, increased hardenability may lead to cracking problems, at least with water quenching.

Maintenance of Equipment

Oxy-Fuel Gas Type of Flame Heads (Non-ferrous). Experience with nonferrous flame heads of three types of construction (drilled face, screw-in tips, and press-in tips) has shown carbon deposit, lack of proper cooling, erosion, and corrosion to be the main causes of maintenance problems common to all.

Carbon Deposit. The intermittent igniting and extinguishing of the flame causes a small deposit of carbonaceous material to build up on the sidewalls of the port, from the

Table 8 Flame hardening of roller path on side of large ring gear**Mounting on positioner**

Gear should be centered on positioner in a vertical position, to approximately 1.7 mm (0.065 in.) total indicator runout on tooth outside diameter (see schematic).

Preheating

Flame head gap: Set 75 mm (3 in.) maximum flame head at 190 mm (7½ in.) gap from flame-hardened surface and approximately 610 mm (24 in.) ahead of hardening tip.

Gas pressures: Acetylene, 89 kPa (13 psi); oxygen, 185 kPa (27 psi)

Flowmeter: 2.1 divisions for acetylene; 2.65 divisions for oxygen

Tube readings (neutral flame): Flutter, approximately ¼ division, plus or minus

Speed setting: No. 9 notch on positioner; equivalent to 2.7 mm/s (6.42 in./min) on 5.79 m (228 in.) circumference of 1.84 m (72½ in.) flame-hardened pitch circle (~35½ min/rev)

Heat cutoff: Kill preheat when spread of flame toward oncoming hardened surface produces blue-purple temper color at flame-hardening starting point. (Air-block flame head may be set up for the same purpose.)

Flame hardening

Heating-head gap. (Must be kept parallel with flame-hardened surface): Set and hold 125 mm (5 in.) flame head at 13 mm (½ in.) gap from flame-hardened surface and at an angle of approximately 35 to 40° to radius; adjust during flame hardening to follow in line with roller-path warp.

Gas pressures: Acetylene, 89 kPa (13 psi); oxygen, 185 kPa (27 psi)

Flowmeter: 2.7 divisions for acetylene; 3.2 divisions for oxygen

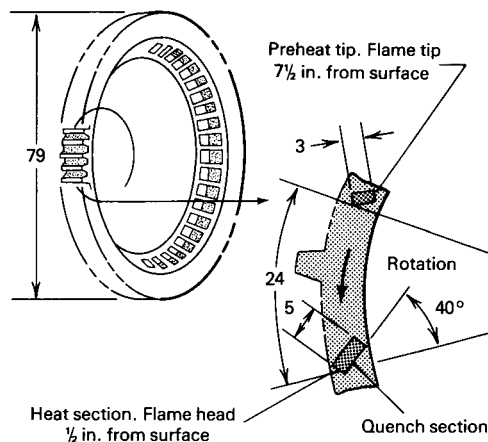
Tube readings (neutral flame): Normal flutter, approximately ¼ division; watch frequently for signs of gas failure.

Water pressure (flame-hardening quench): Set pressure-reducing valve for 205 kPa (30 psi).

Speed setting: Same as for preheating. (Note: Double-check setting just before flame hardening.)

Heat cutoff: (No overlap permissible; aim at 13 mm, or ½ in., maximum soft gap; use extreme caution.) As flame head approaches finish junction, gradually back off tip 1.6 mm (1/16 in.) during final 13 mm (½ in.) of gear travel and kill flame abruptly when nearest row of flames just reaches 6.4 mm (¼ in.) clearance from starting point of flame hardening; immediately speed up table to fastest-speed notch.

Hardness aim (except at flame-hardening junction): 515 to 600 on portable Brinell at points 50 mm (2 in.) from inside diameter of flame-hardened roller path (50 HRC at a depth of approximately 5.1 mm, or 0.2 in.); total depth of contour, 7.9 mm (5/16 in.). Schematic shows ring gear (in vertical position) and position of flame heads for hardening roller path (located on side face of ring) by procedure summarized in table. Gas cost was approximately 25% of total processing cost. Hardening extended to a depth of 4.8 mm (3/16 in.). Hardness at surface, 530 HB. For hardness gradients, see Fig. 13.



retrogression of the burning fuel below the orifice of the port as the flame is extinguished. Although small for each cycle, the deposit builds up gradually until it causes a restriction in the port and thus a variation in the velocity of the gas and therefore in the heating performance. Several thousand cycles may be completed before it is necessary to clean the head.

A slight amount of cleaning can be done without removing the head from the mixer tube. This is done by pushing through the ports a wire of the proper size or a drill one size smaller than the ports. However, care must be exercised to prevent bell mouthing or increasing the size of the port. Cleaning by this method deposits loose carbonaceous material in the fuel

chamber, and this material, propelled by the velocity of the oxygen and fuel-gas mixture, may become lodged in other ports.

Flame heads operating on volume production should be removed from the machine and thoroughly cleaned after 40 to 120 h of operation. The interval depends on the installation, the oxygen and fuel gas mixture, and the heating cycle time.

Drilled-port and insert-port heads, when removed, can be cleaned by inserting in the ports a wire of the proper size or a drill one size smaller than the ports and then immersing the heads in a suitable solvent or cleaner that will loosen the carbonaceous deposits. Again, care must be exercised to prevent bell mouthing or enlarging of the port. Also the cleaner or

solvent must not attack the head itself. After cleaning and rinsing in clean water, all traces of dirt and moisture should be blown from the ports, fuel chamber, and water lines. Screw-in tips and heads may be cleaned in the same manner.

Erosion and Corrosion. All types of heads are subjected to the by-products of combustion, which may attack the face of the burner or the tips, causing erosion and corrosion. A flash plate of chromium on the burner face has proved to be helpful in reducing erosion and corrosion. In time, the face of a drilled-port burner may erode to a point at which it is necessary to reface the head by machining and reworking the counterbore. If there is enough space between ports on drilled-port heads, the port can be repaired by drilling oversize and pressing in an insert. These inserts can be removed and replaced when necessary.

Because the oxy-fuel gas type of flame head is water cooled, it may be necessary, in localities where extremely hard water is supplied, to soften the water to keep scale from forming in the cooling passages; commercial water softeners of the zeolite or polyphosphate type may be used. Recirculating systems with heat exchangers sometimes are required.

Air-Gas Type of Burners. Failures of air-gas burner liners occur by spalling, erosion, and cracking of the refractory cup or tunnel and outlet. These liners should be inspected periodically, at intervals determined by experience with the individual installation; when conditions are severe, inspection may be required as often as once every shift.

The causes of deterioration of burner liners are thermal shock from repeated rapid heating or cooling (or both) and mechanical shock from work striking the burners. The burner casings deteriorate mainly from prolonged exposure to escaping hot gases that heat the casings locally, causing more or less progressive oxidation, cracking, growth, and, infrequently, burning. If installation space permits the use of water or air cooling, these usually can be expected to increase the life of burners. Shielding, designed to conduct hot gases away from the burners and other parts of the machine, also is valuable in reducing maintenance costs.

Mechanical Components. Because both oxy-fuel and air-fuel gas systems employ pressure gages, pressure regulators, valves, flowmeters, and safety devices, the maintenance problems associated with these accessories are common to both methods of flame hardening. Symptoms and probable causes of trouble with several mechanical components used in flame hardening are listed in Table 10.

Air-gas systems also have maintenance problems related to their compressors and blowers. Devices for protection against backfire and explosion should be serviced according to manufacturer instructions.

Electrical Components. Electrical contacts should be cleaned periodically; when the heating cycle is controlled by a timer, periodic

Table 9 Flame hardening of 1040 steel wear blocks

Preliminary operation

Clean blocks until free of scale and rust, preferably by sand or shot blasting.

Loading

Load blocks on one end of conveyor belt.

Flame head

Head contains 2 rows of No. 54 drill size (1.4 mm, or 0.055 in.) flame holes; total of 49 holes, of which 24 are plugged; 150 mm (6 in.) between centers of end holes. Head also contains single row of water-quench holes. Head set at 16 mm (5/8 in.) total gap; cone point clearance of flame, 4.8 mm (3/16 in.)

Gas pressures

Acetylene, 83 kPa (12 psi); oxygen, 150 kPa (22 psi)

Speed

Conveyor speed, 2.47 mm/s (5.83 in./min); total flame-hardening time, 1.5 min per pad

Hardness and pattern aim

Hardness, 53 to 58 HRC; total depth of hardening to core, 4 mm (5/32 in.)

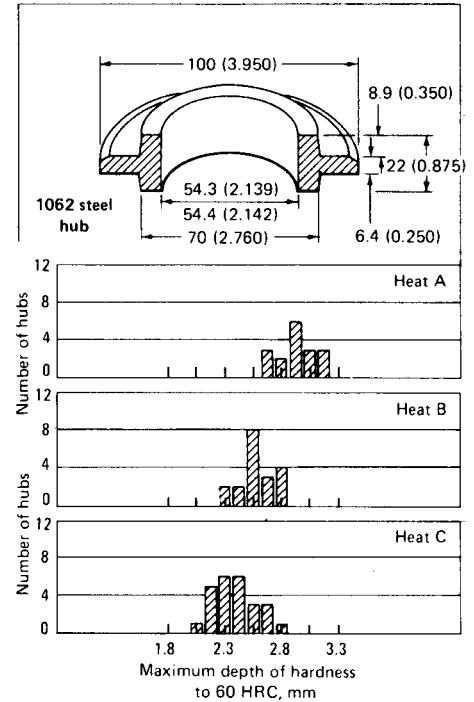
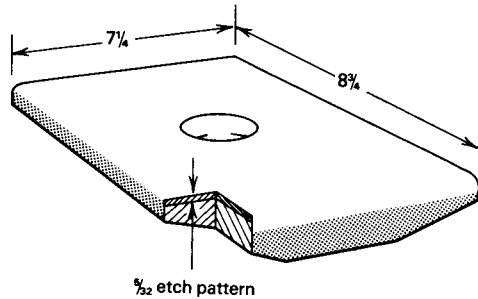


Fig. 15 Heat-to-heat variations in depth of hardness among three heats of 1062 steel hubs flame hardened on the inside diameter to a minimum of 59 HRC at 1.9 mm (0.075 in.) below the surface. Hubs were heated 12 s and quenched in oil. Hardness was measured on cross sections of heated area. Dimensions given in millimeters and, in parentheses, inches

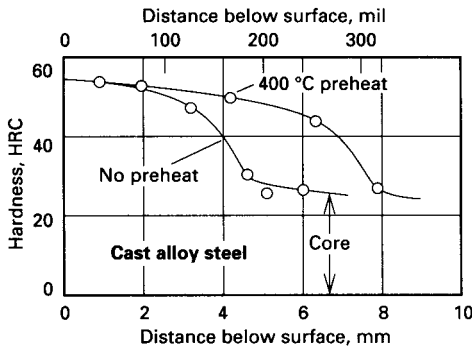


Fig. 13 Effect of preheating on hardness gradient in a ring gear. See Table 8 for preheating procedure.



Fig. 14 Worm-shaft spin heating (similar process to cam spin heating). Source: Ref 3

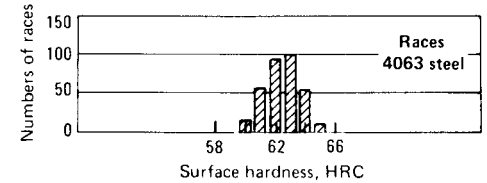


Fig. 16 Distribution of surface hardness. Results obtained during 1 month of testing flame-hardened races (4063 steel) that were heated for a total of 9 s to produce a minimum hardness of 59 HRC at a depth of 1.3 mm (0.050 in.)

checks of the timer are advisable. Generally, if the heating cycle is inaccurate, it will be evident in the inspection of the parts. If the heating cycle is controlled by a thermopile, several items must be checked. Excessive flow of cooling water through the housing will cause condensation on the lens; a deposit of any type on the lens will cause erratic results. In high-production work, the lens should be cleaned at least twice each shift, and the temperature recorder should be balanced once each shift.

Spindle and Movable Holding Fixtures. It is important that positioning of the parts and the flame head be consistent. Therefore, holding

Table 10 Maintenance problems in flame-hardening equipment

Component	Symptom of trouble	Probable cause
Pressure gage	Erratic behavior	Mechanical damage to mechanism
Gas supply pressure regulator	Failure to hold pressure setting at outlet	Broken or hardened diaphragm Too taut diaphragm Sticking stem or valve parts Damaged or dirty valve seat or plugged orifices or vents
Solenoid valve	Failure to close or open	Broken or damaged spring
Fuel valve	Flame lingers after shutoff	Defective valve mechanism or wiring
Oxygen valve	Flame popping after shutoff	Dirty seat or stem; damaged seat Damaged seat

fixtures and spindles should be periodically cleaned, checked, and lubricated. Any worn part should be replaced before it becomes improperly located.

Piping. Types of piping and fittings recommended by underwriters should be used in installing the gas lines from the gas source to the site of use. In long gas lines, means should be provided for purging accumulated condensate from the line before the gas reaches the mixing chamber or torch.

Preventive Maintenance

A typical schedule of preventive maintenance for flame-hardening equipment is as follows.

Daily tasks include:

- Check all solenoids for leaks; clean, repair, or replace, as necessary
- Replace damaged screw-in flame tips; clean dirty or clogged tips or ports
- Remove foreign material from surfaces of flame heads and movable machine parts
- Check for stable pilots
- Check for leakage of fuel gas, water, oxygen, and air
- Check level, circulation, and temperature of quench oil
- Clean lens of radiation pyrometer and balance the recorder
- Check oil level and flow of oil to spindle

Weekly tasks include:

- Check liquid level in backflash arrestor
- Check relief valve on backflash arrestor
- Lubricate all movable parts as required
- Check all fuel-gas, oxygen, and air connections for leaks (using soap solution)

Bimonthly tasks include:

- Remove and clean flame heads (frequency will vary with installation and use)

Semiannual or annual tasks include:

- Remove, clean, and repair oxygen and fuel-gas regulators
- Remove, clean, and repair all solenoids
- Check electrical contacts and wiring
- Clean heat exchanger and quench tank
- Check orifice in mixing blowpipe
- Repack motor bearings

Safety Precautions

All fuel gases are explosive when mixed with either air or oxygen within their flammable limits. However, they are widely used throughout industry and are safe when properly handled, stored, and transported in compliance with established laws of safe practice. Stabilized MAPP combines the safety and handling ease

of propane with the high heat energy of acetylene.

The following organizations have published information on cylinder storage, cylinder manifolding, acetylene generators, housing and piping systems, equipment, and operating procedures:

American Gas Association
400 North Capitol Street NW, No. 450
Washington, D.C. 20001

American Insurance Association
(formerly National Board of Fire Underwriters)
2101 L Street NW, Suite 400
Washington, D.C. 20037

Compressed Gas Association
14501 George Carter Way, Suite 103
Chantilly, VA 20151

XL Group
(formerly Industrial Risk Insurers)
100 Washington Boulevard, 6th Floor
Stamford, CT 06902

National Fire Protection Association
1 Batterymarch Park
Quincy, MA 02169

Most state and local governments follow the recommendations of these organizations in adopting regulations pertaining to gases. A study of local regulations should be made to determine whether there is any variance from standard procedures.

Operators should be taught to keep equipment clean, free of grease and oil, and in good condition, and to avoid leaks of oxygen or fuel gas by regularly testing them with soapy water free of oil and grease. They should open oxygen or fuel-gas valves slowly and be sure that the lines are purged before igniting. An air hose should be available for dispersing fuel gas that has been bled from the lines. Any spaces in and around the machine in which gases may accumulate also should be purged with the air hose. No flame or other source of ignition should be allowed in proximity to the area where fuel gas or oxygen is released into the air, and good ventilation is of primary importance.

Operators should recognize backfires or backflashes immediately and shut off the gases; the cause and extent of damage must be determined, and corrections made, before the torch is reignited. To prevent major explosions, a backflash arrestor must be installed in the fuel line.

Hand friction lighters should not be used to ignite the gases, except for very small flame heads of low gas capacity. A flame from an acetylene torch or a burner using some other gas should be used. The pilot flame should be very close to the heating head to prevent the accumulation of gas and oxygen before ignition. For automatic flame-hardening machines, the pilot light can be permanently mounted (in which case a flame detector and alarm system should be installed to give warning when the pilot light is extinguished accidentally), or electric spark ignition can be used. When

operations are stopped for any length of time, the valves in the main supply lines should be closed. These valves must not leak because even a small leak can cause a dangerous accumulation of gas.

Oil or grease may ignite violently in the presence of oxygen under pressure and must be kept away from cylinders, regulators, hoses, and other apparatus. The storage of fuel-gas cylinders must be in accordance with standards established by the Occupational Safety and Health Administration and the National Fire Protection Agency. The allowable amounts of indoor gas storage are limited, and cylinder manifold design must meet the appropriate requirements.

The cylinders in a manifold should be secured with clamps or chain to prevent them from tipping or falling. A fall or any severe bump can detonate acetylene, with disastrous consequences. Propane is not likely to detonate, but any gas under pressure is dangerous if the valve is damaged or knocked off the cylinder. In some instances, noise can be a problem in a gas-air system. Equipment should be designed to keep the noise level within generally accepted limits to avoid injury to nearby personnel.

Quenching Methods and Equipment

The proper application of a suitable quench in flame hardening is as important as proper heating. The quench must remove heat at a rate that will produce the desired structure and assist in controlling the depth of the hardened case.

The method of quenching and type of quenchant vary with the method of flame hardening. In spot hardening, immersion quenching generally is used, but spray quenching may be used.

Quenching after Progressive Heating.

Parts heated by the progressive method usually are quenched by a spray integrated into the flame head, although for steels of high hardenability, or when it is desirable to vary or adjust the distance between the heated zone and the quench, a separate spray-quench head sometimes is used. The spray quench should issue from the head at an angle away from the flame head to prevent interference with heating and must provide full coverage over the heated band. The integrated type commonly sprays the quenching medium on the work 19 to 32 mm ($\frac{3}{4}$ to $1\frac{1}{4}$ in.) behind the last row of flames. When the surface to be hardened by the progressive method is vertical or overhead, additional cooling may be required after the usual spray quench.

Quenching after Spin Heating. Parts heated by the spinning method can be quenched by several different procedures. In one, the heated part is removed from the heating area and quenched by immersion in a separate quench tank. Another method integrates quenching by making the quench tank a part of the flame-hardening machine. Parts may be heated on the machine spindle or arbor and then

quenched by being dropped into a quench tank located immediately below the arbor. Parts that are either too heavy or too fragile to be dropped may be lowered into the quench by means of arms or may be lowered into the quench while still on the arbor. Parts may be removed manually from the quench or automatically by means of a conveyor belt. A spray-quenching ring is sometimes submerged in the quench bath to increase the cooling rate.

Parts heated by the spinning method also may be quenched with quench blocks on the same plane as the flame heads. When the heating cycle is completed and the flames are extinguished, the quench is turned on. The quench blocks should cover the heated band and provide enough quenching liquid to obtain suitable and uniform hardness. There should be enough quench points around the periphery of the block to envelop the area completely with quenchant. Water or a polymer quench solution is typical for this type of quench because of the hazard of contaminating the heating heads with oil. When oil quenching is used, the oil should not contact the heating head. This may be avoided by indexing the heated part to a separate quenching station or by retracting the heating heads into a shielded area.

When air-fuel gas mixtures are employed in spin-hardening operations, the heat pattern developed, in many instances, extends beyond the limits desired. Immersion quenching in such instances could extend the hardening into areas requiring subsequent machining or contribute to an excessive amount of distortion. Localized quenching, such as that provided by quench rings, is a solution to this problem. For example, this quenching method was used in hardening the teeth of large sprockets weighing approximately 205 kg (450 lb). The entire tooth surface, including the root, was hardened to a depth of 4.8 mm ($3/16$ in.). The 10 min heating cycle completely heated the teeth and backup rim. When quenching was done by rotation of the sprocket in a ring of water spray nozzles, hardening was confined to the desired surfaces and the backup rim remained soft. A similar practice is used for hardening large gears. Parts heated by the combination progressive-spinning method usually are quenched by a spray integrated in the flame heads or by separate quench blocks located below the flame heads.

Quenching Media

With spray quenching, either integrated in the flame head or by separate quench blocks, water or a dilute polymer solution is used as the quenching medium. Quenching oils should not be allowed to come into contact with oxygen or to contaminate equipment using it. As with conventional hardening, the alloy content of the steel determines the type of quench that should be used. The quenchant may be water, a brine solution, a glycol-based polymer quench, or air.

By reducing the pressure of the quenchant, the rate of cooling by spray quenching can be reduced from the maximum for which the integrated or separate quench blocks are designed. Increasing the distance between the last row of flames and the point at which the quenchant impinges will allow the mass of metal below the area to be hardened to extract heat and thus will decrease the severity of quenching.

Quenching distance is another factor the operator must consider because the quenchant must strike the heated area while it still is at the critical temperature to avoid the formation of pearlite or other undesirable transformation products in the microstructure. If the spray head is angled too close to the flame, spotty hardness and blowouts can occur. If the angle of spray is too far away, the case may not be fully hardened.

Forced Air. In progressive hardening operations, forced air frequently is used as the quenchant for steels normally considered to be oil-quenching steels. Water is not used immediately after heating because the fast cooling action would result in surface checks. Because most of these steels have relatively low A_{r3} transformation temperatures, the forced air quickly reduces the surface temperature to a point at which water can be applied without causing surface checks. The resulting hardness usually is close to that obtained with a direct oil quench. For example, 52100 steel quenched with forced air and then with water attains a surface hardness of 60 to 61 HRC.

Forced-air quenching also is used in applications in which intermediate hardnesses are required. One example is the hardening of railroad rail ends to reduce "end-batter" by the impact of car wheels. The rails are indexed under the burners in four preheat stations and one high-heat station (high-temperature, high-velocity burner), which heats the rail to the hardening temperature of 870 °C (1600 °F) in 95 s. In a sixth station, air at 690 kPa (100 psi) is directed against the heated surface. This treatment results in a hardened structure of fine pearlite that provides wear resistance and sufficient ductility to withstand the impact of moving wheels. Water is unsuitable in this application because the high-carbon rail steel is susceptible to cracking. Rail lengths for curves, crossovers, and switches are similarly hardened; however, for these, hardening is done progressively, using oxy-gas burners and air quenching.

Immersion quenches vary in type in relation to the metal used, the hardness and depth desired, and the mass, design, and dimensional tolerances of the part. The quenching medium can be a caustic or brine solution, water, a soluble-oil emulsion, or any of a large variety of oils or simulated oils such as polymer quenches.

Self-Quenching. During any type of flame hardening other than through hardening, the mass of cold metal underneath the heated layer aids quenching by withdrawing heat. Thus, cooling rates are very high compared with rates for conventional quenching. During the progressive hardening of the teeth of gears made

from medium-carbon steels such as 4140, 4150, 4340, and 4640, for example, the combination of rapid heating and the temperature gradient between the surface and the interior of the gear results in a subsequent self-quench that is equivalent to quenching in oil.

For uniform quenching, a coolant can be used at some distance from the tooth being heated. In one application involving hardening the teeth of 4150 steel gears in the size range of 4 to 12 pitch, one tooth at a time was heated and cooled by conduction. The coolant was directed at the body of the gear. With this procedure, the hardness of the teeth was 50 to 55 HRC after the gears had been tempered at 200 °C (400 °F).

Flame-Hardening Problems and Their Causes

Problems that may occur in flame hardening and their causes include the following.

Overheating can be caused by:

- Controlling pyrometer set too high
- Millivolt compensator of controlling pyrometer set incorrectly
- Heating cycle too long
- Flame heads too close to work
- Oversized flame ports
- Excess oxygen in flame
- Excessive fuel-gas pressure
- Improper pattern of flame tip

Hardness below the minimum required can be caused by:

- Controlling pyrometer set too low
- Millivolt compensator of controlling pyrometer set incorrectly
- Heating cycle too short (underheating)
- Severity of quench too low
- Delay before quenching too long
- Part not thoroughly quenched
- Material hardenability too low for quench
- Surface decarburized

Spotty or uneven hardening can be caused by:

- Nonuniform heating
- Time interval between heating and quenching too short
- Quenching medium not sufficiently agitated
- Water in quenching oil
- Scale on work
- Improper quenching medium
- Surface decarburized

Distortion can be caused by:

- Shape of part or relationship of portion to be hardened to remainder of section not well adapted to flame hardening
- Metallurgically unsuitable prior structure
- Heating cycle too long
- Nonuniform heating

- Nonuniform quenching
- Excessive rate of quenching
- Material hardenability excessive

Shallow depth of hardening can be caused by:

- Material of low hardenability
- Excessive rate of gas flow; check for oxidizing flame
- Flame-port velocity too high
- Controlling pyrometer set too low
- Millivolt compensator of controlling pyrometer set incorrectly
- Short heating cycle or excessive scanning speed
- Severity of quench too low
- Delay before quenching too long

Excessive depth of hardening can be caused by:

- Low flow rate of gas; check for reducing flame
- Excess fuel gas in flame
- Controlling pyrometer temperature set too high
- Millivolt compensator of controlling pyrometer set incorrectly
- Flame port velocity too low

Excessive scaling can be caused by:

- Heating cycle too long
- Rates of gas flow too low
- Flame velocity too low
- Delay before quenching too long
- Improper arrangement of flame heads around periphery; overheating or banding

Tempering of Flame-Hardened Parts

It usually is desirable to temper parts that have been flame hardened; the need for tempering martensite is the same regardless of the heat treating method used to produce it. Flame-hardened steel will respond to a tempering treatment in the same manner as it would if hardened to the same degree by any other method. Standard procedures, equipment, and temperatures can be used. However, for work that is flame hardened because it is too large to be heated in a furnace, flame tempering may be the only feasible method of tempering available.

Flame Tempering. Large articles usually are hardened by the progressive method and can be tempered immediately by reheating the hardened surface with a flame head placed a short distance behind the quench. The reheating or tempering flame head must be designed correctly with regard to number and size of orifices or tips (flame ports) to produce the desired work temperature and temperature gradient in the flame-hardened zone at the flame-hardening speed.

Exact final adjustments can be made by varying the flow of gases through the flame head and by adjusting the distance between flame head and work surface. Tempering flame heads

must have smaller heat outputs than hardening flame heads because the too-rapid heating of the hardened zone can cause cracking and because, for tempering, the temperatures required are lower and temperature control usually is more critical.

Self-Tempering. On large parts flame hardened to depths of approximately 6.4 mm (1/4 in.) or more, the residual heat present after quenching may be sufficient to accomplish satisfactory relief of hardening stresses, and subsequent tempering in a separate operation may be unnecessary. Air-fuel gas heating, because of its lower rates of heat transfer, promotes the development of the deep-seated heat required for self-tempering.

When residual heat cannot be used and it is desirable to eliminate the separate tempering operation, the use of a lower-carbon steel is suggested if hardness requirements permit. The preheating of heavy parts increases the residual heat available for tempering. For this purpose, preheating may be accomplished by either heating the part in a furnace, if feasible, or by spinning the part in the burner ring with the burners firing at reduced or idling input. The choice depends on the availability of equipment and the economics involved. The exact preheat temperature will vary, depending on the size and configuration of the part and the degree of stress relief or temper desired. In each application, the exact schedule may be established on a trial basis as a preliminary step.

Surface Conditions

For wrought and cast steel parts, the surface conditions likely to be detrimental to successful

flame hardening are, in general, those that interfere with heating or quenching, cause localized overheating, initiate cracking, or result in the presence of a soft surface skin after proper heating and quenching.

Table 11 summarizes the more common defects or conditions, their origins, and the detrimental effects to be expected when they are present on flame-hardened areas. The extent of these defects determines the amount of difficulty they may cause.

Dimensional Control

Because of its ability to heat specific areas of a part selectively, flame hardening in many applications affords greater control of dimensional stability than is obtainable by furnace heating and quenching. The magnitude of the dimensional changes that occur in flame hardening is influenced by such factors as size and shape of the part, area heated, depth of heating, hardenability, and quenching medium. Figure 17, for example, shows the various dimensional changes that occurred from the flame hardening of converter gear hubs.

Selection of Process

Flame hardening basically is adaptable to surface hardening and to the through hardening of selected areas. Manufacturing specifications often call for the heat treatment of an entire part, but in many cases this is not necessary. Crane wheels, mill rolls, and gears are examples of items for which flame hardening can

Table 11 Surface conditions detrimental to flame hardening of steel parts

Defect or condition	Probable origin of condition	Detrimental effects to be expected on flame-hardened areas
Laps, seams, folds, fins (wrought parts)	Rolling mill or forging operations	Localized overheating (or, at worst, surface melting), with consequent grain growth, brittleness, and greater hazard of cracking
Scale (adherent)(a)	Rolling or forging; prior heat treatment; flame cutting	Insulating action against heating, with resulting underheated areas and soft spots Localized retardation of quench, causing soft spots
Rust, dirt(a)	Storage and handling of material or parts	Similar to scale condition as noted above left Severe rusting may result in surface pitting that will remain after hardening.
Decarburization	Present in as-received steel bar stock; heating for forging or prior heat treatment of parts or stock	In severely decarburized work, no hardening response will be found when parts are tested by file or other superficial means.(b)
Pinholes, shrinkage (castings)	Casting defects	Localized overheating (or, at worst, surface melting), with consequent grain growth, brittleness, and greater hazard of cracking
Coarse-grain gate areas (castings)	Casting gates located in areas to be flame hardened (avoid, if possible)	Increased cracking hazard during quenching, compared with nongated areas; shrinkage defects also likely in these areas
Improper welds	Parts welded with an alloy dissimilar to base metal	Weld zone reaction dissimilar to base-metal reaction. Weld may separate, requiring rewelding or scrapping of the part.(c)

(a) In addition to having detrimental effects on flame-hardened surfaces, scale, rust, or dirt in the path of the flame may become dislodged and cause fouling of oxy-fuel gas burners or react chemically with ceramic air-fuel gas burner parts (causing rapid deterioration). When such materials enter a closed quenching system, they may clog strainers, plug quench orifices, and cause excessive wear of pumps. (b) Partial decarburization lowers surface hardness as a direct function of actual carbon content of stock lost at surface, provided that steel was adequately heated and quenched. (c) To avoid these and other problems, it is mandatory that the flame hardener be given accurate and complete information on any changes in composition and past processing of the part. For example, previously hardened parts should never be flame hardened unless they have been annealed; otherwise, cracking is inevitable. Source: Ref 1

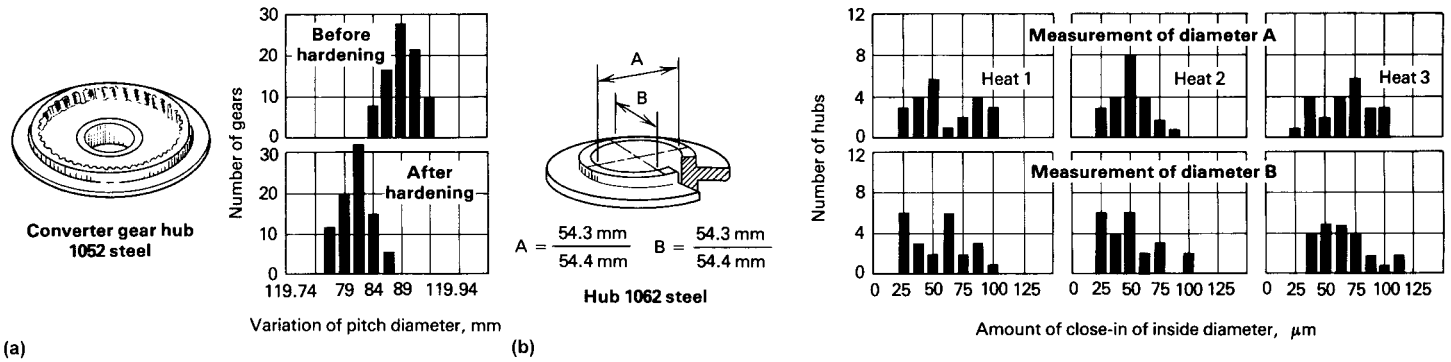


Fig. 17 Distribution of dimensional change as a result of flame hardening. (a) Change in pitch diameter of converter gear hubs made of 1052 steel. Gear teeth on inside diameter were heated for a total of 9.5 s, before being quenched in oil to provide a depth of hardness of 0.9 mm (0.035 in.) above the root. (b) Close-in of inside diameters of converter hubs made of 1062 steel. Inside diameter was heated for a total of 12 s and then oil quenched to harden to 59 HRC min at a depth of 1.9 mm (0.075 in.) below the surface. Inside diameter was finish ground after hardening.

be used to harden only the working surfaces. Dies often require hardening only along parting lines or in forming areas.

Other hardening processes that may be applicable for accomplishing the same purposes include:

- Induction hardening for surface or through hardening
- Carburizing, nitriding, and other furnace processes in which surface composition is altered to permit hardening of the case
- Application of hard facing materials to surfaces
- Through hardening of selected sections by partial immersion in molten lead or salt baths

Table 12 lists the different processes in use and describes the benefits realized from each.

Induction hardening and flame hardening are the most effective methods for selectively hardening portions of a part (gear teeth, for example) without affecting other areas. A 4150 steel shaft, 760 mm (30 in.) long, with a 25 mm (1 in.) long gear at one end, can be core hardened to 26 to 32 HRC all over (a good machining hardness), and the gear can be hardened to 55 to 60 HRC by flame or induction hardening. If carburizing or nitriding were used instead, the main shaft would have to be masked with copper, which would have to be stripped away after hardening.

The differences between these three basic types of surface-hardening processes can be small enough for certain applications that their feasibilities overlap. For example, a ring gear used in almost identical applications has been made for four customers using four different surface-heating procedures: induction hardening a 4150 steel gear, with or without separate core hardening, depending on the specific application; flame hardening the teeth of a 1045 steel gear; carburizing an 8620 or 9310 steel gear, and then finish grinding; and core hardening a 4150 steel gear to 32 to 34 HRC and then nitriding.

Careful analysis, however, no doubt would show that one of the four variations would be

Table 12 Relative benefits of five hardening processes

Carburizing	Hard, highly wear-resistant surface (medium case depths); excellent capacity for contact load; good bending fatigue strength; good resistance to seizure; excellent freedom from quench cracking; low-to-medium-cost steels required; high capital investment required
Carbonitriding	Hard, highly wear-resistant surface (shallow case depths); fair capacity for contact load; good bending fatigue strength; good resistance to seizure; good freedom from quench cracking; low-cost steels usually satisfactory; medium capital investment required
Nitriding	Hard, highly wear-resistant surface (shallow case depths); fair capacity for contact load; good bending fatigue strength; excellent resistance to seizure; excellent dimensional control possible; good freedom from quench cracking (during pretreatment); medium-to-high-cost steels required; medium capital investment required
Induction hardening	Hard, highly wear-resistant surface (deep case depths); good capacity for contact load; good bending fatigue strength; fair resistance to seizure; fair dimensional control possible; fair freedom from quench cracking; low-cost steels usually satisfactory; medium capital investment required
Flame hardening	Hard, highly wear-resistant surface (deep case depths); good capacity for contact load; good bending fatigue strength; fair resistance to seizure; fair dimensional control possible; fair freedom from quench cracking; low-cost steels usually satisfactory; low capital investment required

Source: Ref 6

most economical. Examples of false economy are common. A company may save 25¢/kg on steel but have to pay twice that amount for hot or cold straightening to correct the distortion caused by the lower heat treatability of the lower-cost steel.

In selecting a flame-hardening process, consideration must be given to the method of applying the flame to the work and to the choice of gas mixture. Oxy-gas equipment differs significantly from air-gas equipment in the design of the systems that control, deliver, and burn the gas mixtures.

The heating characteristics of the combustion mixture largely determine the degree to which the hardening and heat-affected zones can be localized in the workpiece. Shallow hardness patterns (less than 3.2 mm, or 1/8 in., deep) can be obtained with oxy-gas mixtures because the higher-temperature flames produced will provide a sufficiently rapid heat transfer to localize the heat pattern effectively. Deeper hardness patterns may permit the use of either oxy-gas or air-gas mixtures. With oxy-gas mixtures, the heat is localized, but care is required in controlling the heat-release rate to avoid overheating the surface during the development of the deeper-seated heat.

Air-gas mixtures, because of the lower rate of heat transfer obtained with them, reduce the tendency toward surface overheating but generally extend the heat-affected zone well beyond the desired hardness pattern. For this reason, air-gas flame hardening generally is limited to those applications in which the portion to be hardened may be through heated or in which materials of shallow hardenability are used. In the latter instance, the depth of the hardness pattern primarily is controlled by quenching rather than by heating intensity. Because of potential excessive distortion, the deeper-seated heat developed in a part by air-gas flames may preclude the use of this heating medium.

In view of these considerations, the success of air-gas flame hardening largely depends on the configuration of the part insofar as that configuration favors heat localization with its lower rates of heat transfer. In selective through hardening of gear and sprocket teeth, flanges, ribs, edges, and similar projections, air-gas flame heating may be applied. On the other hand, the surface hardening of gear teeth, rolls, journals, shaft areas, machineways, wear areas of forming dies, inside and outside diameters of hubs, and massive sections usually is done with oxy-fuel flame equipment. Small parts

frequently require the very small, easily controllable flame characteristics obtainable with oxy-fuel-burning equipment.

When more than one mode of flame application or combustion-gas mixture can be used for a flame-hardening operation, the selection of process and equipment becomes primarily an economic consideration. The equipment then may be chosen on the basis of the expected cost involved in meeting immediate and anticipated production requirements.

Whether or not a flame-hardening process is selected in preference to other hardening processes for a specific application is commonly determined on the basis of the suitability of the process for producing the required results, control of distortion, and cost. A specific example of the selection of flame hardening as a method of hardening is described as follows.

Example 2: Flame Hardening versus Induction Hardening of Sprocket Teeth.

Because of service failures and to avoid a design change, a sprocket manufacturer changed from induction hardening to flame hardening of sprocket teeth (Fig. 18). When induction hardened, the sprockets were failing in the web area. Failure was attributed to high stress concentration resulting from the induction through hardening of the teeth and rim. Continued use of induction hardening would have required major redesign of the part and remaking of a costly forging die.

For flame hardening, the sprocket was indexed on a small positioner, and standard flame-hardening tips were moved across the face of the tooth by means of a small flame-cutting dolly. Warm-water quenching was used to eliminate the slight surface checks that had developed with cold-water quenching. Figure 18 shows the hardness pattern developed by the standard flame tips. Failures were eliminated, sprockets hardened by this method had excellent wear qualities, and the cost of hardening was not increased.

Selection of Material

The use of flame hardening is limited to hardenable steels (wrought or cast) and cast irons. Typical hardnesses obtained for various grades of these materials by flame heating and quenching in air, oil, or water are given in Table 13.

Maximum hardness is not the sole criterion used in selecting flame hardening as a heat treatment. Proper steel selection is essential to minimize distortion, for example. Plain carbon steels should be used, if possible, instead of steels whose deep-hardening characteristics are more likely to incur higher internal stresses.

Some flame hardeners feel it is important to stress relieve all alloy steels and other steels with more than 0.40% C at 175 to 245 °C (350 to 475 °F), depending on customer specifications. This low-temperature tempering decreases hardness but also removes internal stress and restores toughness and ductility.

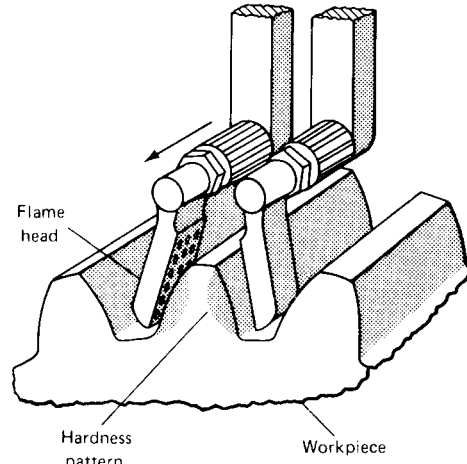


Fig. 18 Hardness pattern developed in sprocket tooth when standard flame tips were used for heating. When space permits the use of this method, hardening one tooth at a time results in low distortion.

Selective heating has the disadvantage of developing residual tensile stresses in the surface. As one area of a piece of metal is heated while the remainder stays cold, the hot metal expands; if restraint is sufficient, the heated metal will upset itself. Upon cooling, this upset metal becomes short. As it cools to room temperature, it often stabilizes in a state of tension, which can be high enough to crack the part.

When a part is to be induction or flame hardened, the materials engineer should work closely with the designer to keep the level of hardness, and the necessary carbon, as low as possible, while still meeting engineering requirements. Carbon content is the most important factor determining the level of hardness that can be attained in steels by induction or flame heating. It controls hardness level, the tendency of the part to crack, the magnitude of the part to crack, and the magnitude of residual surface stresses.

The practical level of minimum surface hardnesses attainable with water quenching for various carbon contents is shown in Fig. 19. The curve is applicable for induction hardening as well as for flame hardening. It also applies to alloy steels, except those containing stable carbide formers such as chromium and vanadium.

For best results, steels to be induction or flame hardened should be as-rolled, normalized (particularly from a high temperature), air-blast quenched, or quenched and tempered. These preferred heat treatments result in microstructures conducive to rapid and complete austenitization and full hardening. In selecting steels for either induction or flame hardening, it is important that the necessary steps be taken to ensure that the areas to be hardened are free of decarburization. Depending on stock size, steel grade, producing mill, and several other factors, the depth of decarburization for as-rolled bar may run from near 0 to 3.2 mm (0.125 in.). It should not be assumed that

Table 13 Response of steels and cast irons to flame hardening

Material	Typical hardness, HRC, as affected by quenchant		
	Air(a)	Oil(b)	Water(b)
Plain carbon steels			
1025-1035	33-50
1040-1050	...	52-58	55-60
1055-1075	50-60	58-62	60-63
1080-1095	55-62	58-62	62-65
1125-1137	45-55
1138-1144	45-55	52-57(c)	55-62
1146-1151	50-55	55-60	58-64
Carburized grades of plain carbon steels(d)			
1010-1020	50-60	58-62	62-65
1108-1120	50-60	60-63	62-65
Alloy steels			
1340-1345	45-55	52-57(c)	55-62
3140-3145	50-60	55-60	60-64
3350	55-60	58-62	63-65
4063	55-60	61-63	63-65
4130-4135	...	50-55	55-60
4140-4145	52-56	52-56	55-60
4147-4150	58-62	58-62	62-65
4337-4340	53-57	53-57	60-63
4347	56-60	56-60	62-65
4640	52-56	52-56	60-63
52100	55-60	55-60	62-64
6150	...	52-60	55-60
8630-8640	48-53	52-57	58-62
8642-8660	55-63	55-63	62-64
Carburized grades of alloy steels(d)			
3310	55-60	58-62	63-65
4615-4620	58-62	62-65	64-66
8615-8620	...	58-62	62-65
Martensitic stainless steels			
410, 416	41-44	41-44	...
414, 431	42-47	42-47	...
420	49-56	49-56	...
440 (typical)	55-59	55-59	...
Cast irons (ASTM classes)			
Class 30	...	43-48	43-48
Class 40	...	48-52	48-52
Class 45010	...	35-43	35-45
50007, 53004, 60003	...	52-56	55-60
Class 80002	52-56	56-59	56-61
Class 60-45-15	35-45
Class 80-60-03	...	52-56	55-60

(a) To obtain the hardness results indicated, those areas not directly heated must be kept relatively cool during the heating process. (b) Thin sections are susceptible to cracking when quenched with oil or water. (c) Hardness is slightly lower for material heated by spinning or combination progressive-spinning methods than it is for material heated by progressive or stationary methods. (d) Hardness values of carburized cases containing 0.90 to 1.10% C

turned and polished bar is free of decarburization unless it is specifically ordered with this requirement. Carbon-restored and cold-finished bar is available from mills in various carbon and alloy grades.

When maximum resistance to fatigue is desired, the hardened surface should contain residual compressive stresses; a recommended level is 172 MPa (25 ksi). Because surfaces hardened to depths of less than 1.9 mm (0.075 in.) are commonly residually stressed in tension, it is suggested that depth of hardening be at least 2.7 mm (0.105 in.) to ensure that residual stresses are compressive. This depth

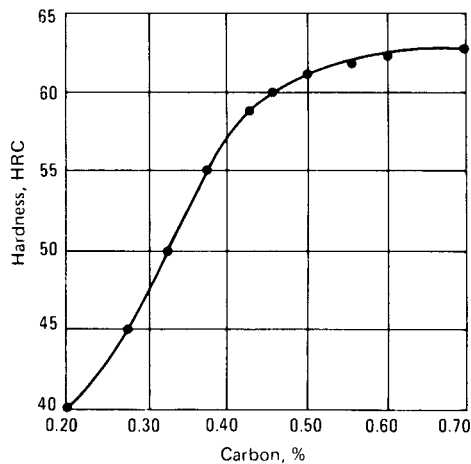


Fig. 19 Relationship of carbon content to minimum surface hardness attainable by flame or induction heating and water quenching. Practical minimum carbon contents can be determined from this curve.

is appropriate particularly for manufacturers not equipped with residual-stress-measuring equipment. Further, microstructure should be at least 90% martensite, with no ferrite visible at a magnification of 500 \times .

Carbon Steels. Plain carbon steels in the range of 0.37 to 0.55% C are the most widely used for flame-hardening applications. They can be through hardened in sections up to 13 mm ($\frac{1}{2}$ in.). This response permits the use of carbon steel for selectively flame-hardened small gears, shafts, and other parts of small cross section in which uniform properties are needed throughout the section. These same steels can be used for larger parts in which hardness is necessary only to shallow depths from 0.8 to 6.4 mm ($\frac{1}{32}$ to $\frac{1}{4}$ in.).

Carbon steels 1035 to 1053 are suitable for flame hardening; 1042 and 1045 are the most widely available and are recommended for all flame-hardening applications except when they would be incapable of meeting requirements, for example:

- Failure of a 1045 steel part to harden with a given quench would necessitate the use of a steel of higher hardenability; for example, one with higher carbon or manganese or both, or possibly an alloy steel.
- If increased depth of hardening is required, 1042 or 1045 may be inadequate where heavy sections are progressively hardened; therefore, the substitution of 1541, 1552, or an alloy steel would be necessary.
- In applications in which wear resistance is of prime importance, it may be advisable to use a steel with 0.60% C or more to produce maximum surface hardness. Steels this high in carbon content often are quenched in oil or simulated oil to avoid the possibility of cracking due to water quenching. Thus, greater hardenability may be needed with the higher carbon content.

- When a severe quench in brine or caustic is required for hardening 1042 or 1045 steel and such quenching causes cracking, a steel of higher hardenability—either carbon or alloy, which can be hardened by a less severe quench—should be selected.

Alloy Steels. The use of alloy steels for flame-hardening applications is justified only when:

- High core strength is required (through heat treatment before flame hardening) and carbon steels are inadequate to achieve this strength in the section sizes involved.
- The mass and shape of a part, restrictions on distortion, or the hazard of cracking preclude the use of carbon steel quenched in water.
- Certain alloy grades may be more readily obtainable than carbon grades (particularly the higher-manganese carbon grades) appropriate for the application. Steels such as 4135H, 4140H, 6150H, 8640H, 8642H, and 4340H are typical of the more readily obtainable alloy steels.

Carbon and alloy steel castings are widely used for flame-hardening applications. The selection of a specific composition or grade is made on much the same basis as for wrought carbon and alloy steels.

Cast Iron. Gray cast irons, ductile irons, and pearlitic malleable irons having combined carbon contents of 0.35 to 0.80% can be flame hardened and will respond the same as steel.

Cast irons having less than 0.35% combined carbon will not respond readily to flame hardening because of the inability of austenite to dissolve graphite during the extremely rapid heating that occurs during flame hardening. Flame hardening these irons produces a typical hardness of approximately 40 HRC. Malleable iron, in which all the carbon is in graphitic form, is not amenable to flame hardening for this reason.

Cast irons having combined carbon contents greater than 0.80% are difficult to flame harden because of their inherent brittleness and susceptibility to cracking when heated and quenched rapidly. The low melting point of cast iron and the presence of graphite in the microstructure make cast iron susceptible to “burning” or even localized melting during flame hardening; therefore, extreme care must be taken to reduce the rate of heating when cast iron is hardened using equipment designed specifically for flame hardening steel. For example, the distance between the inner cone and the workpiece can be increased, or the flame velocity can be decreased. The use of a flame head with smaller orifices also will decrease the heating rate.

Perhaps the most significant factor in the response of cast irons to flame hardening is prior microstructure. Irons without free ferrite in their microstructure respond almost instantly to flame or induction heating and require very little holding time at the austenitizing temperature in order to be fully hardened. With a

moderate amount of free ferrite, the response may be satisfactory, but an entirely ferritic matrix, typical of grades with high ductility, requires several minutes at 870 °C (1600 °F) to be fully hardened by subsequent cooling. A matrix microstructure of fine pearlite, readily obtained by normalizing, has a rapid response to surface hardening and provides excellent core support for the hardened case.

Other Materials. Flame hardening can be applied to other hardenable ferrous materials, for example, alloy cast irons, martensitic stainless steels, and tool steels. However, the nature of flame hardening—especially the relatively high-temperature gradients and higher-than-normal surface temperatures—may cause the retention of excessive amounts of austenite in many of the highly alloyed materials, with possible low hardness and transformation to untempered martensite in service, which is accompanied by brittleness.

Lee et al. (Ref 7, 8) investigated the properties of hardness, hardening depth, and residual stresses of 12Cr steel after a flame-hardening modification. The process increases the hardness of the steel up to 420 to 550 HV (250 HV base value), depending on the surface temperature. The investigation allowed the optimization of the process parameters according to the acceptance criteria of Siemens AG-KWU and GE Power Generation Engineering.

Carburized parts made of plain carbon or alloy steels can be flame hardened to provide a hard case of high carbon content. The depth of carburized case may vary from a few hundredths of a millimeter to 1.6 mm ($\frac{1}{16}$ in.) or more. The flame-hardening procedure is adjusted to heat the carburized case to its full depth for hardening. Because the core of low-carbon steel thus treated does not harden substantially, the method provides a means of accurately controlling the depth of hardened case.

Recently, flame hardening was used to create alloy deposits with different chemical compositions on low-carbon steel (Ref 9). Chromium-nickel alloy deposits were obtained from a plating bath with trivalent chromium and divalent nickel ions. An amorphous structure was detected in which the hardness can be significantly increased from 550 to 1460 HV after flame heating for 3 s. From the analysis of the microstructure, the hardening can be ascribed to the precipitation of nanosized carbon-related particles, which have a high hardness value and cause lattice strain fields at their precipitation sites.

Flame Annealing

The chemical reaction between oxygen and steel during flame cutting evolves intense heat, raising the temperature of the cut edge to the melting point on the surface and above the transformation temperature to a shallow depth. If the carbon or alloy content of the steel is high

enough, hardening results when the heated zone is cooled rapidly.

Carbon steels containing 0.30% C or less do not harden sufficiently to prevent the use of flame-cut pieces in structures or in subsequent fabrication where bending is involved. When cut by flame, steels containing alloying elements and steels containing more than 0.30% C may harden sufficiently to prevent the use of flame-cut pieces for some purposes.

When hardening is likely to occur along a cut edge, oxyacetylene flames applied by suitable equipment can be used either to prevent hardening or to soften an already hardened cut surface. The term *flame annealing* is applied to this process and to the selective flame softening of areas of hardened steel parts. Tool steels and certain highly alloyed steels will crack during flame cutting, or very soon after, unless they are heated to temperatures ranging from 200 to 425 °C (400 to 800 °F) before being cut.

REFERENCES

1. N.J. Fulco, Flame Hardening, *Heat Treat.*, Aug 1974, p 14–17
2. G.M. Corbett, Fuel Gases for Flame Hardening, *Weld. Res. Suppl.*, Oct 1965, p 476–479
3. M.M. Serrine, Direct Flame Impingement, *Heat Treat. Prog.*, Jan 2006, p 42–45
4. Surface Hardening Gets Better, *Iron Age Metalworking International*, Dec 1969, p 34–35
5. G.D. Orr and G.M. Kampitch, Programmable Flame Hardening Through Flow Control, *Heat Treat.*, Sept 1975, p 37–40
6. R.F. Kern, Selecting Steels for Heat-Treated Parts, Part II—Case Hardenable Grades, *Met. Prog.*, Dec 1968, p 71–81
7. M.K. Lee, G.H. Kim, K.H. Kim, and W.W. Kim, Control of Surface Hardnesses, Hardening Depths, and Residual Stresses of Low Carbon 12Cr Steel by Flame

Hardening, *Surf. Coat Technol.*, Vol 184, 2004, p 239–246

8. M.K. Lee, G.H. Kim, K.H. Kim, and W.W. Kim, Effects of the Surface Temperature and Cooling Rate on the Residual Stresses in a Flame Hardening of 12Cr Steel, *J. Mater. Process. Technol.*, Vol 176, 2006, p 140–145
9. C.A. Huang, C.K. Lin, W. Chiou, and F. Hsu, Microstructure Study of the Hardening Mechanism of Cr-Ni Alloy Deposits after Flame Heating for a Few Seconds, *Surf. Coat. Technol.*, Vol 206, 2011, p 325–329

SELECTED REFERENCE

- B. Rivolta, Flame Hardening, *Encyclopedia of Tribology*, Q.J. Wang and Y.-W. Chung, Ed., Springer and Verlag

Induction Surface Hardening of Steels*

Valery Rudnev, Inductoheat Incorporated
Jon Dossett, Consultant

INDUCTION HEATING occurs when an alternating magnetic field induces eddy currents in electrically conductive materials. Because all metals are fair electrical conductors, induction heating is applicable to several types of metal processing operations, such as melting, welding, brazing, heat treating, stress inducement, and zone refining.

Induction heat treatment is done with various metals and alloys—mainly steels and cast irons, although other materials, including light metals, aerospace materials, superalloys, and some composites, are also inductively heat treated or preheated prior to hot and warm forming operations. Induction heat treatment is attractive from the viewpoint of its speed, selective heating capabilities, low distortion, energy savings, and high production rates, among other reasons.

The advantages of using induction for heat treating are derived from its capability to generate heat within the workpiece and include the following:

- **Heat intensity:** In heat treatment, the higher heating rates play a central role in designing rapid, high-production heat treating processes. Induction heat treating of steels and cast irons may take as little as 5% or less of the time required for a furnace treatment. For example, only a few seconds are typically required to induction harden small- and medium-sized gears or journals of camshafts and crankshafts.
- **Selective heating:** Controlling the heat patterns by selecting appropriate process parameters and induction equipment allows surface and selective hardening that yield an attractive blend of properties (e.g., high strength and hardness of the component surface layers and toughness of its core that may not be affected by the heat). Such capabilities are not feasible with furnace heating processes, which are slower and heat the entire workpiece.
- **Energy savings:** In addition to eliminating idle periods, induction heat treating techniques put energy only when and where needed, improving energy efficiency and equipment

readiness. With induction heaters, there are no conditioning or idle periods such as with the use of furnace equipment.

- **Space saving:** The induction equipment has a substantially smaller footprint. Equipment can be easily incorporated in in-line processing and manufacturing cells than furnace treatment equipment.
- **Individual part traceability:** This is a very attractive feature that plays an important role in ensuring the required quality of heat treated components.
- **Low equipment maintenance cost; lean and green process with reduced labor**

Induction heating is used in a variety of steel heat treatment processes, such as steel hardening and tempering, annealing, normalizing, and stress relieving. The most popular application of induction heat treatment is the surface hardening of steels and cast irons. Although not as common as surface hardening and tempering, through hardening and tempering by induction heating have been found to be practical for a number of applications, such as piping, structural members, saw blades, and garden tools.

Induction surface hardening and tempering of steels can be used for a wide range of parts. Examples include machine tools, hand tools, crankshafts, camshafts, axle shafts, transmission shafts, splined shafts, universal joints, gears, valve seats, wheel spindles, bearings, steering knuckles, and track links. This article introduces the fundamentals of induction heating and describes the general process factors for the induction surface hardening of steels. See *ASM Handbook, Volume 4C, Induction Heating and Heat Treatment* (2014) for more information on induction equipment and other heat treating applications of induction heating.

Principles of Induction Heating

Induction heating occurs when an electrically conductive material is exposed to a varying magnetic field. The basic components of an induction

heating system are an induction coil (an inductor), an alternating-current power supply, and the workpiece itself. The coil, which may take different shapes depending on the required heating pattern, is connected to a power supply.

The basic process is illustrated in Fig. 1 with an alternating current that flows in a solenoid coil. The current generates an alternating magnetic field around the coil, and the magnitude of the magnetic field depends on the strength of the current and the number of turns in the coil.

When a material is placed inside the coil, the varying magnetic field induces an electric potential according to Faraday's law of electromagnetic induction:

$$e = -N \frac{d\Phi}{dt} \quad (\text{Eq 1})$$

which relates an induced voltage (e) to the time rate of change of the magnetic field (Φ) and the number of turns (N) in the coil. In effect, the coil acts in much the same manner as a primary winding of a transformer, with the workpiece acting as a single-turn (or short-circuited) secondary winding. Hence, the term *transformer action* is sometimes used to describe the process of electromagnetic induction. In fact, an early observation of induction heating by Michael Faraday in the mid-1800s was the undesirable heating of transformer and motor windings and laminated cores.

Heating occurs when an electrically conductive material is placed in (or near) the coil. The induced voltage creates electrical eddy currents, which have the same frequency as the current in the primary coil—but the direction of eddy currents is opposite that of the current in the coil (Fig. 1b). It is also important to note that eddy currents are generated in any electrically conductive objects that are near the coil. At any moment, the direction of the induced current in the workpiece is approximately opposite to that in the inductor coil, and, in general, its flow pattern will describe a kind of shadow image of the coil conductors. The induced currents also generate their

* Adapted from content sources listed in the Acknowledgments of this article

own magnetic fields, which are in opposition to the field generated by the coil and thereby prevent the field from penetrating to the center of the object.

The primary mechanism of heat generation occurs from the flow of eddy currents in the workpiece. A second mechanism of heat generation occurs in ferromagnetic materials when energy is dissipated during the reversal of magnetic domains. This effect in ferromagnetic materials is usually ignored in induction heating calculations, because the effect is small for the typical strength levels of magnetic fields for induction hardening. Therefore, the rate of heating in units of power (watts) is largely a function of I^2R , or Joule heating.

The heating efficiency and intensity as well as temperature distribution depend on several factors. The heating rate is affected by several variables, such as:

- Magnetic field strength (expressed in units of ampere-turns of the work coil)
- Frequency of the magnetic field
- Proximity of the workpiece to the coil conductors and its geometry
- Electrical and magnetic properties of the material, such as resistivity (ρ) and magnetic permeability (μ)

Heating rates are typically controlled by the coil voltage/current, because the field strength is roughly proportional to coil voltage/current. A key factor also is the degree of coupling between the workpiece and the magnetic field of the coil. Coupling is determined by the number of imaginary magnetic flux lines that enter the workpiece. This flux density is proportional to the coil current, and the amount of energy transferred is proportional to the square of the number of imaginary flux lines intercepted by the workpiece. The frequency of coil currents also influences the pattern of induced currents, because flux lines tend to stay closer to the coil conductors as frequency is increased.

Induction heating also is nonuniform, because the distribution of eddy currents (and heating) is concentrated near the surface. According to the commonly accepted theory of electromagnetic induction, eddy currents and power density (heat source) primarily flow near the surface layer (or "skin"). This "skin effect" must be clearly understood in practically all application of induction heating. Heat transfer and electromagnetics also are nonlinear and tightly interrelated, because the physical properties of heated materials depend strongly on temperature, magnetic field intensity, alloy chemical composition, prior microstructure, and other factors.

Except for the simplest of workpiece geometries, mathematical analysis of induction heating processes can be quite complex, because of nonuniform three-dimensional (3-D) heat generation through the workpiece, 3-D heat transfer, and the fact that the electrical, thermal, and metallurgical properties of most materials

exhibit a strong dependence on temperature. For this reason, quantitative solutions exist, for the most part, only for the heating of round bars or tubes and infinitely wide rectangular slabs and sheets. Nevertheless, such knowledge, if properly applied, may provide useful insights into the effects of coil design and equipment characteristics on heating patterns in irregularly shaped parts. This information, coupled with knowledge generated through years of experimentation in both laboratory and production environments, serves as the basis for the practical design of induction heating processes.

Induction Coils. Inductor coils for induction heat treating applications are of three types: single-shot inductors, progressive (or scanning) inductors, and special inductors. The shape of induction coils can be quite varied, depending on the size and shape of the workpiece surface that

is to be hardened and the required pattern of heating. Figure 2 shows three basic types of coils for heating for external surfaces (Fig. 2a), internal surfaces (Fig. 2b), and front surfaces (Fig. 2c) of the workpiece. The shape of the coil also influences heating patterns (see the section "Design of Induction Heating Coils" in this article).

Single-shot coils are setups in which the entire surface of the workpiece is heat treated at one time with a coil that remains stationary with respect to the part. Typically, single-shot coils are used for parts with complex geometries and parts that require irregular heating patterns. Single-shot induction heating is often combined with rotation of the workpiece to ensure more uniform heating. The coil-to-workpiece gap is very important, because the energy penetration and heating efficiency depend on it.

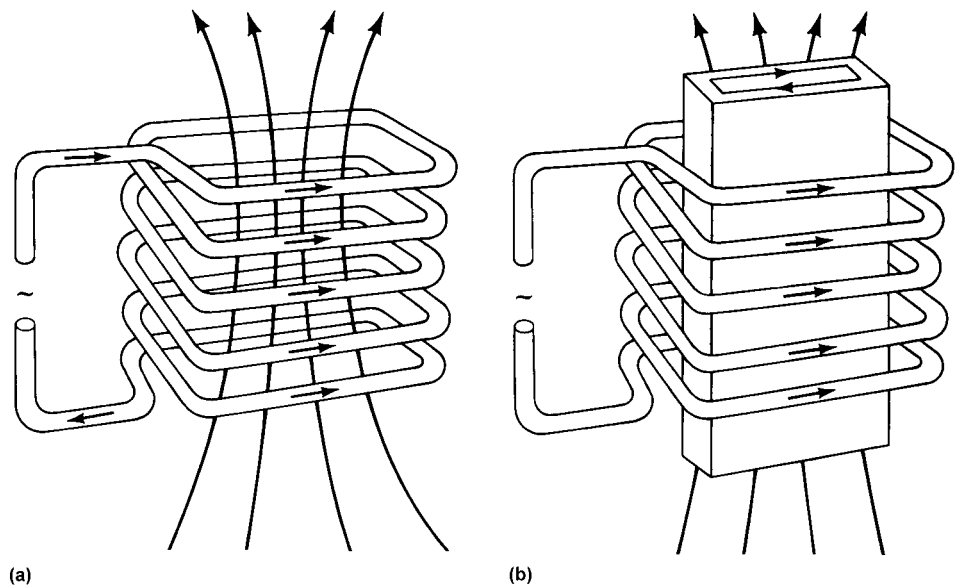


Fig. 1 Pattern of electrical currents and the magnetic field in (a) a solenoid coil and (b) conductive materials with induced eddy current (flowing in the opposite direction to the current in the coil). Source: Ref 19

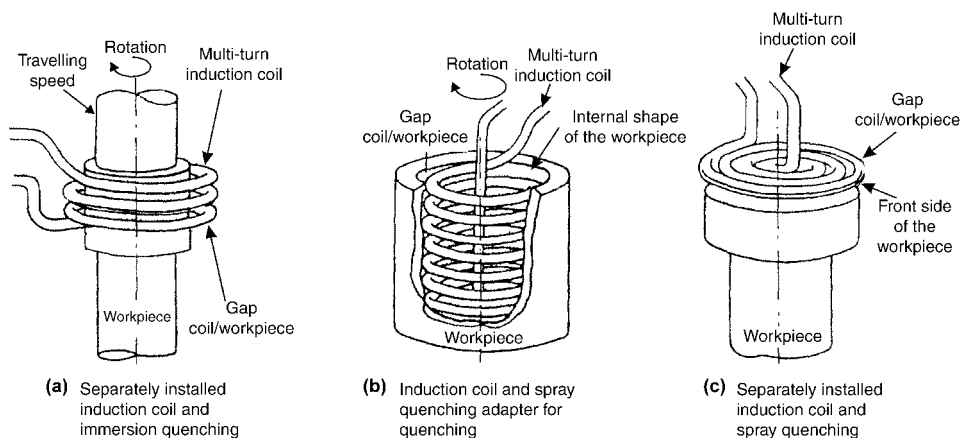


Fig. 2 Three general configurations of induction coils. Source: Ref 1, 2

If part rotation is not feasible, heating uniformity can be improved by coil copper profiling increased by using flattened tubing, by putting an offset in the coil, and so on. Flattened tubing should be placed so that its larger dimension is adjacent to the workpiece. The offsetting of coil turns (Fig. 3) provides an even horizontal heating pattern. Offsetting is most easily accomplished by annealing the coil after winding and pressing it between two boards in a vise. Profiling of induction coils can be achieved by spacing turns differently (in multi-turn inductors) or by copper machining and having variable workpiece-to-copper proximity (in single-shot inductors).

Progressive (Scanning) Coils. When parts are induction scanned, the parts are moved progressively through the coil. Thus, only a small portion of the workpiece is heat treated at any given time. Parts with a high degree of rotational or axial symmetry are often induction heated using scanning techniques.

Scan hardening inductors are particularly attractive for large and/or elongated workpieces for which a single-shot method would substantially increase coil and power supply costs. Scan inductors also provide superior flexibility compared to single-shot inductors. They allow various lengths of parts to run, can result in an easily automated process that quickly adapts to new heat treatment tasks, and can be easily integrated into a work cell.

Scan inductors may be one or more turns. The required number of turns is determined by process features or by the ability to load-match (load-tune) the coils to the power supply. This impedance (load)-matching process is particularly important if maximum power is required from the power supply.

Scan inductors with narrow heating faces are useful not only for a sharp pattern cutoff but also for obtaining short transition zones. Scan coils with wider heat faces allow faster scan rates. This is due to the simple fact that the inductor is longer. The part will be in the inductor for a longer period of time; therefore, the scan rate can be higher. The main disadvantage of the wide heating face is that it will produce a gradual pattern runout and may not meet hardness pattern specifications there. Single-turn inductors with narrow heating faces are used where a sharp pattern runout is required. An example of this would be the case where a pattern must end near a snap-ring groove.

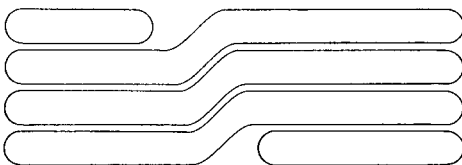


Fig. 3 Induction coil with an offset used to provide heating uniformity

High-Temperature Electrical, Magnetic, and Thermal Properties

The performance of induction heaters first and foremost depends on the electromagnetic properties of the heated metal. Electromagnetic properties of materials encompass a variety of characteristics, including magnetic permeability, electrical resistivity (electrical conductivity), saturation flux density, coercive force, and many others. While recognizing the importance of all electromagnetic properties, two of them—electrical resistivity (electrical conductivity) and magnetic permeability—are key properties that influence the depth of heating by induction (see Eq 3 and 4 in the section “Eddy Current Distribution” in this article). Thus, the electrical resistivity and relative magnetic permeability of the workpiece have a pronounced effect on the performance of an induction heating system, the coil efficiency,

and the selection of main design and process parameters (Ref 3).

Electrical Resistivity. The ability of material to easily conduct electric current is specified by electrical conductivity, σ . The reciprocal of the conductivity σ is electrical resistivity, ρ . The units for ρ and σ are Ohm-m and mho/m, respectively. For some electrically conductive materials, electrical resistivity decreases with temperature. For majority steels and cast irons, electrical resistivity increases with temperature, being a nonlinear function. Grain size has a noticeable effect on electrical resistivity, as well as plastic deformation, prior heat treatment, and some other factors. At the same time, the effect of temperature and chemical composition are two of the most pronounced factors.

The resistivities of metals vary with temperature. Figure 4 shows this behavior for two ferrous alloys: electrolytic iron, an alloy with a negligible amount of carbon, and a 1% C steel. Both alloys have a similar dependence of

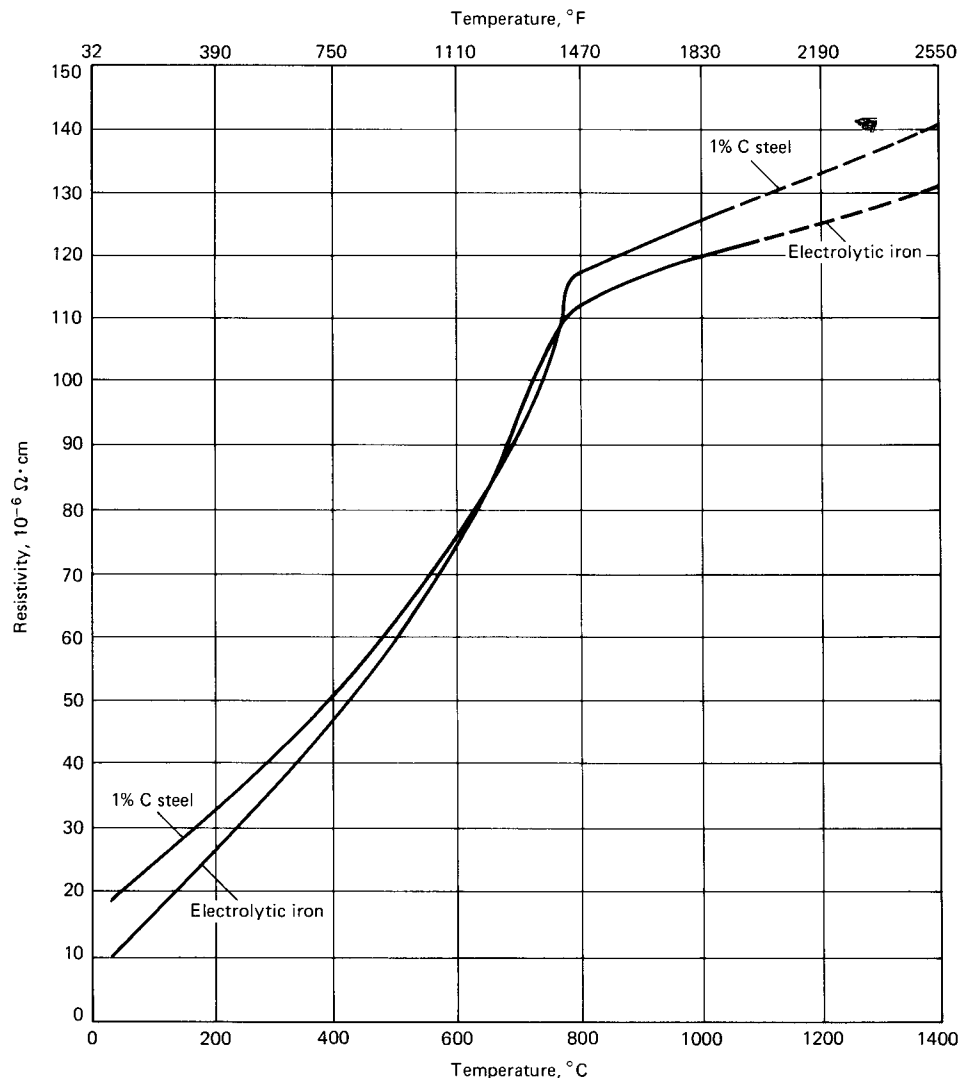


Fig. 4 Electrical resistivity versus temperature for electrolytic iron and a 1% C steel. Source: Ref 4

resistivity on temperature. This can be attributed to the fact that both consist largely of ferrite at low temperatures and austenite at high temperatures. In fact, a change in slope of the curves occurs at temperatures between 700 and 800 °C (1290 and 1470 °F)—a region in which ferrite-austenite phase transformation occurs.

Magnetic Properties of Steel. Relative magnetic permeability, μ_r , indicates the ability of a material (i.e., metal) to conduct magnetic flux better than vacuum or air. Relative magnetic permeability is a nondimensional parameter, and it has a pronounced effect on coil calculation, electromagnetic field distribution, and selection of process parameters. The constant $\mu_0 = 4\pi \times 10^{-7}$ H/m [or Wb/(A × m)] is called the permeability of free space (the vacuum). The product of relative magnetic permeability and permeability of free space is called magnetic permeability, μ , and corresponds to the ratio of the magnetic flux density (B) to the magnetic field intensity (H).

All materials, based on their magnetization ability, can be divided into paramagnetic, diamagnetic, and ferromagnetic. The relative magnetic permeability of paramagnetic materials is slightly greater than 1 ($\mu_r > 1$). The value of μ_r for diamagnetic materials is slightly less than 1 ($\mu_r < 1$). Due to insignificant differences of μ_r for both paramagnetic and diamagnetic materials, those materials are simply called nonmagnetic materials in induction heating practice. The relative magnetic permeability, μ_r , of nonmagnetic materials is assumed to be equivalent to that of air and is assigned a value of 1. Typical nonmagnetic metals are aluminum, copper, titanium, austenitic stainless steels, tungsten, and so on. In contrast to paramagnetic and diamagnetic materials, ferromagnetic materials, including iron, cobalt, nickel, and some rare earth metals, exhibit an appreciable value of relative magnetic permeability ($\mu_r \gg 1$) and are simply called magnetic materials.

Carbon steels exhibit magnetic properties and belong to the group of magnetic alloys. As the temperature increases, the relative magnetic permeability of steels decreases until the Curie temperature is reached. When steels are heated above the Curie temperature, they become nonmagnetic. Figure 5 shows the Curie temperature for plain carbon steels, as represented by the line ABCD.

Below the Curie temperature, relative permeability varies with the intensity of the magnetic field and hence the current in carbon steels. For steels with less than 0.45% C, this temperature is 768 °C (1414 °F). In higher-carbon steels, the Curie temperature follows the A_3 line on the iron-carbon phase diagram to the eutectoid composition; thereafter, it coincides with the A_1 line. Alloying elements in steels change the Curie point by small amounts. Molybdenum and silicon increase it, and manganese and nickel decrease it.

In physical terms, the decrease in magnetic permeability with temperature in carbon steel

signifies the loss of ferromagnetic properties. Below the Curie point, heating occurs as a result of both eddy-current losses and hysteresis losses. The latter are no longer present once the ferromagnetic property of steels is eliminated. Such a consideration is very important with regard to the austenitizing of steels in the hardening operation, since this is done above the Curie temperature. Figure 6 illustrates this effect (assuming that eddy-current cancellation is absent). Here it will be noticed that, below the Curie point, the amount of energy needed to heat a given mass of steel by induction is proportional to the temperature increase.

It is important to recognize that several factors are responsible for the need to increase the required power when heating a workpiece above the Curie point compared to the below-Curie temperature:

- Absence of hysteresis losses
- Reduction of the equivalent electrical resistance of the heated workpiece. As a ferromagnetic material loses its magnetic properties, the thickness of the layer where the

eddy current flows (current penetration depth) inevitably increases, which in turn decreases its electrical resistance.

- Nonlinearity of the specific heat
- Significant increase of surface heat losses (due to thermal radiation and convection) that must be compensated

Once the Curie temperature is reached, the required amount of energy per degree of temperature is substantially larger. When the final required temperatures are only slightly above the Curie temperature, very minor adjustments in the induction equipment are usually necessary (an exception includes wire and strip through-heating applications). On the other hand, when the temperatures must be relatively high, there will be a significant change in coil impedance, which may require special consideration for load-matching.

The ferromagnetic property of a material is also a complex function of grain structure, chemical composition, frequency, temperature, and magnetic field intensity. It is important to recognize that the same kind of carbon steel at the same temperature and frequency can have

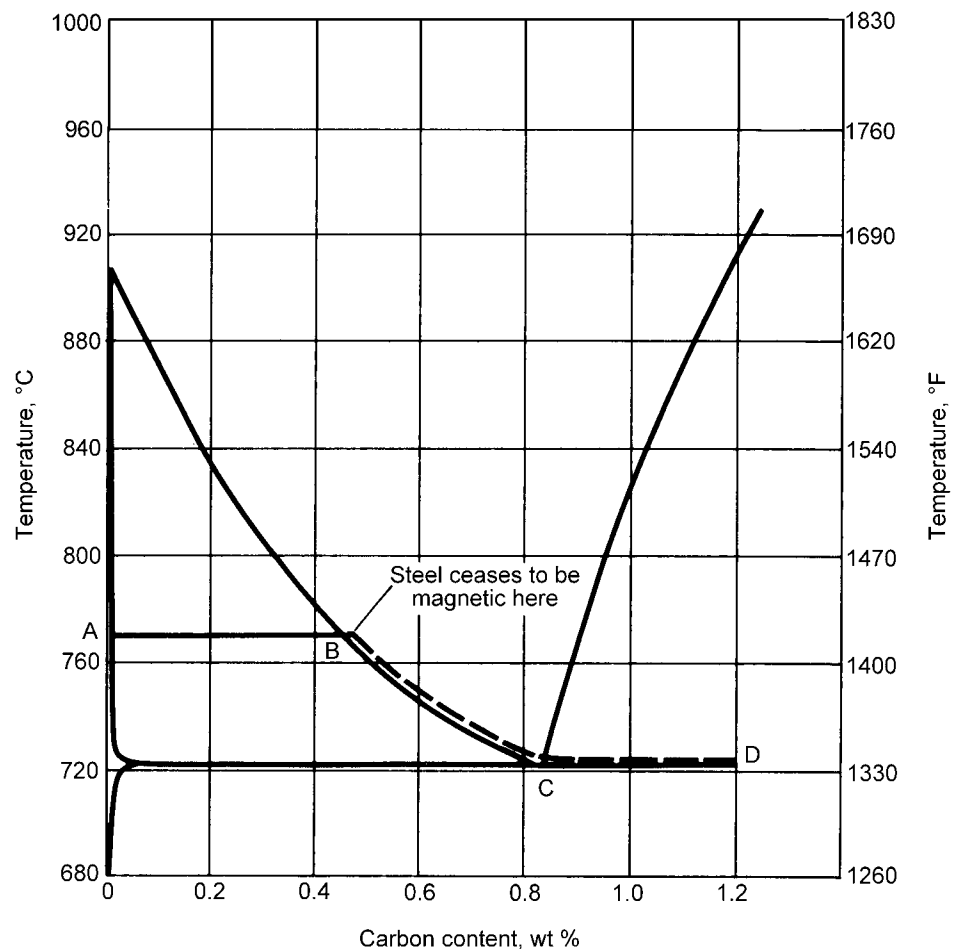


Fig. 5 Curie temperature for carbon steels. Source: Ref 4

a different value of μ_r due to differences in power applied to the induction coil, which affects the intensity of the magnetic field (H). For example, the μ_r of magnetic steels commonly used in induction heating can vary from small values, where $\mu_r = 3$ or 4, to very high values exceeding 300, depending on the magnetic field intensity (H) and temperature (T). The temperature at which a ferromagnetic body becomes nonmagnetic is called the Curie temperature (Curie point). Figure 7 illustrates the complex relationship among μ_r , temperature, and magnetic field intensity for medium-carbon steel. In the majority of induction heating applications, magnetic permeability decreases with increasing temperature. However, in a relatively weak magnetic field, μ_r may first increase with temperature and begin to drastically decline only near the Curie point. Discussion of this phenomenon is provided in Ref 3.

Chemical composition is another factor that has a marked effect on the Curie point. The Curie point of plain low-carbon steel corresponds to the A_2 critical temperature on the iron/iron-carbide phase transformation diagram. Therefore, even among plain carbon steels, the Curie temperature may be noticeably different due to the carbon content. For example, the Curie temperature of plain carbon steel AISI 1008 is clearly different from steel AISI 1060 (768 versus 732 °C, or 1414 versus 1350 °F). Depending on the heat intensity (°C/s, or °F/s), there can be some shifting of the Curie temperature due to thermal hysteresis.

Magnetic Hysteresis losses occur only in magnetic materials. As magnetic parts, such as those made from carbon steels, are heated by induction from room temperature, the alternating magnetic flux field causes the magnetic domains of the material to oscillate, because the magnetic domains change their polar orientation every cycle. Figure 8 shows an illustration of hysteresis and the effect on the magnetic flux field strength. This oscillation is called magnetic hysteresis, and a minor amount of heat is produced due to the friction produced when the domains oscillate.

For the great majority of induction heat treating applications (such as through-hardening and normalizing), a heating effect due to hysteresis losses does not typically exceed 7 to 8% compared to the heat effect due to Joule heat generated by eddy current, because the majority of the heat cycle of the component surface temperature is well above the Curie point. This makes valid an assumption of neglecting the magnetic hysteresis losses. However, in some low-temperature applications, where heated metal retains its magnetic properties during the entire heating cycle (e.g., induction tempering, low-temperature stress relieving, heating prior to galvanizing and coating of ferrous strips and wires, etc.), hysteresis heat generation can be appreciable compared to Joule heat generated by eddy-current losses, and

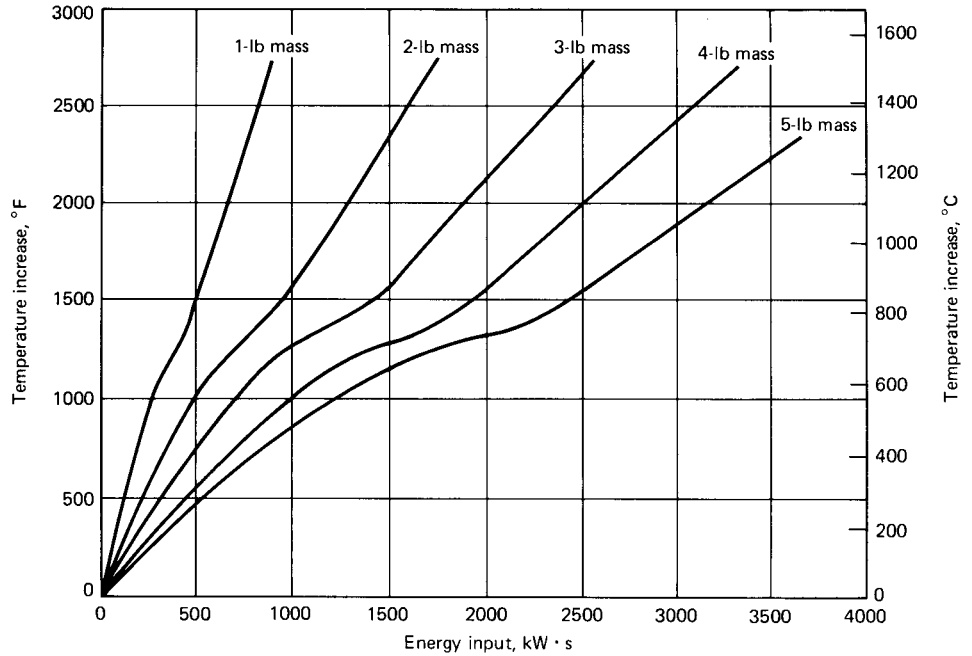


Fig. 6 Temperature increase as a function of energy input for induction-heated carbon steel. Note the decrease in heating rate as the Curie temperature (770 °C, or 1420 °F) is approached and exceeded. Source: Ref 4, 21

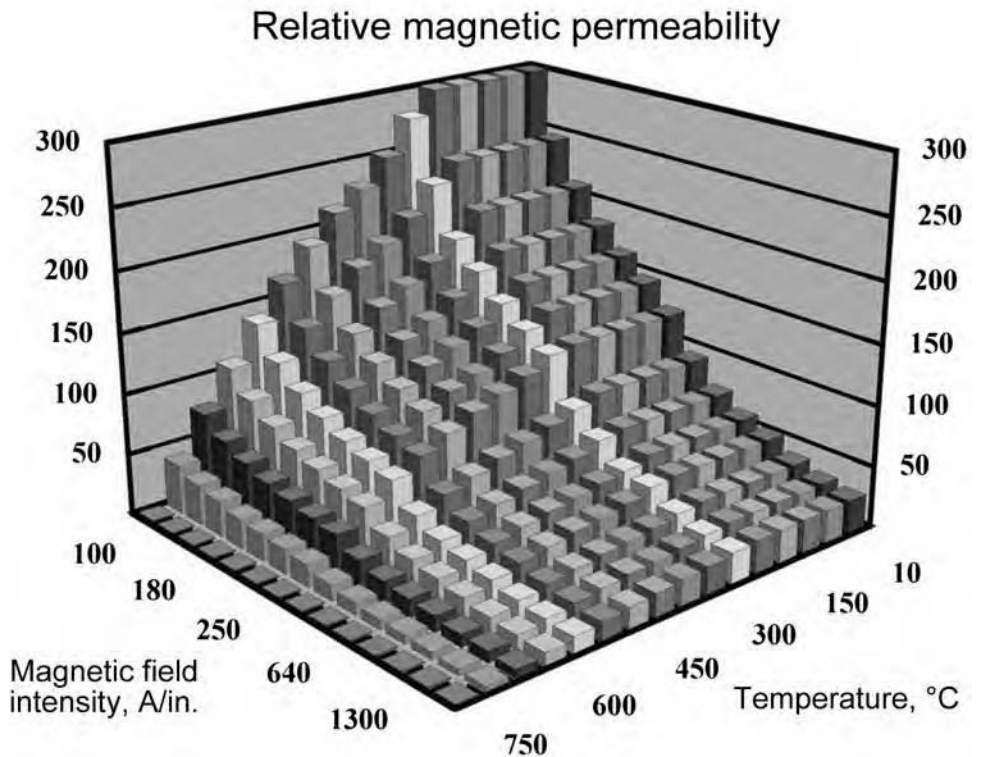


Fig. 7 Magnetic permeability as a function of temperature and magnetic field intensity. Source: Ref 6

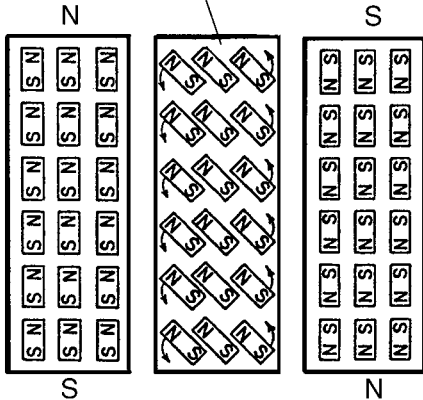
an assumption of neglecting the magnetic hysteresis may not be valid.

Thermal properties of heated materials (specific heat, thermal conductivity, heat

content, etc.) are also temperature dependent. Figure 9 shows the change in heat content (ability to absorb heat) with temperature for various materials. Steel has the ability to absorb more

Hysteresis loss

Energy is required to turn the small internal magnets around. This is like friction. The material becomes heated.



Hysteresis loss depends on the area of the hysteresis loop of the material

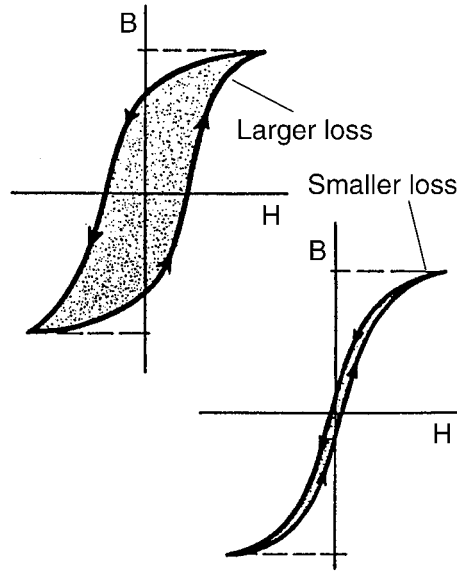


Fig. 8 Hysteresis losses from varying magnetic field. Source: Ref 5

heat as the temperature increases. This means that more energy is required to heat steel when it is hot than when it is cold.

Thermal conductivity, k , designates the rate at which heat travels across a thermally conductive workpiece. A material with higher k value conducts heat faster than a material with a low k . When thermal conductivity of the metal is high, it is easier to obtain a uniform temperature distribution within the workpiece, which is important in through-heating applications. Therefore, from the point of view of obtaining temperature uniformity, a higher thermal conductivity of metal is preferable. However, in surface- and selective-hardening applications, a high value of k is quite often a disadvantage because of its tendency to promote a heat-soaking action and equalize the temperature distribution within the workpiece. As a result of heat soaking, the temperature rise will take place not only in the required region of the workpiece that is to be hardened but in adjacent, not-to-be-hardened areas as well. The temperature increase in the adjacent areas results in the need for more power to heat the region to the desired final temperature.

Eddy-Current Distribution

As noted, eddy currents and power density (heat source) primarily concentrate near the surface layer (or "skin") of the workpiece (or any conductive materials or in close proximity to the coil). The electromagnetic skin effect is a fundamental property of induction heating, and the mathematics needed to explain the skin effect involve a differential equation that has solutions in the form of Bessel functions. These solutions demonstrate that the induced current in a large planar object (that is, a plate much thicker than the expected eddy-current penetration) decreases exponentially from the surface into the workpiece. This allows the definition of an effective depth of eddy currents known as the reference depth or penetration depth, where the current density has dropped by $1/e$ (or 37%) of its surface value.

Reference Depth from Skin Effect. The induced current density (J_x) at some distance, x , decreases exponentially from the current density at the surface (J_s), such that:

$$J_x = J_s \exp[-x/\delta] \tag{Eq 2}$$

where δ is defined as the reference depth or penetration depth. By definition, the current density at the reference depth ($x = \delta$) is thus $1/e$ (or 37%) that of the current at the surface. This is illustrated in Fig. 10, where the distance of $d = 1$ is equal to the reference depth (δ). A great majority of induced power also is concentrated within the reference depth, because power density (W) is a square of current density. Thus, the power density at the reference depth distance decreases as a function of $[1/e]^2$ from the surface (Fig. 10). From this,

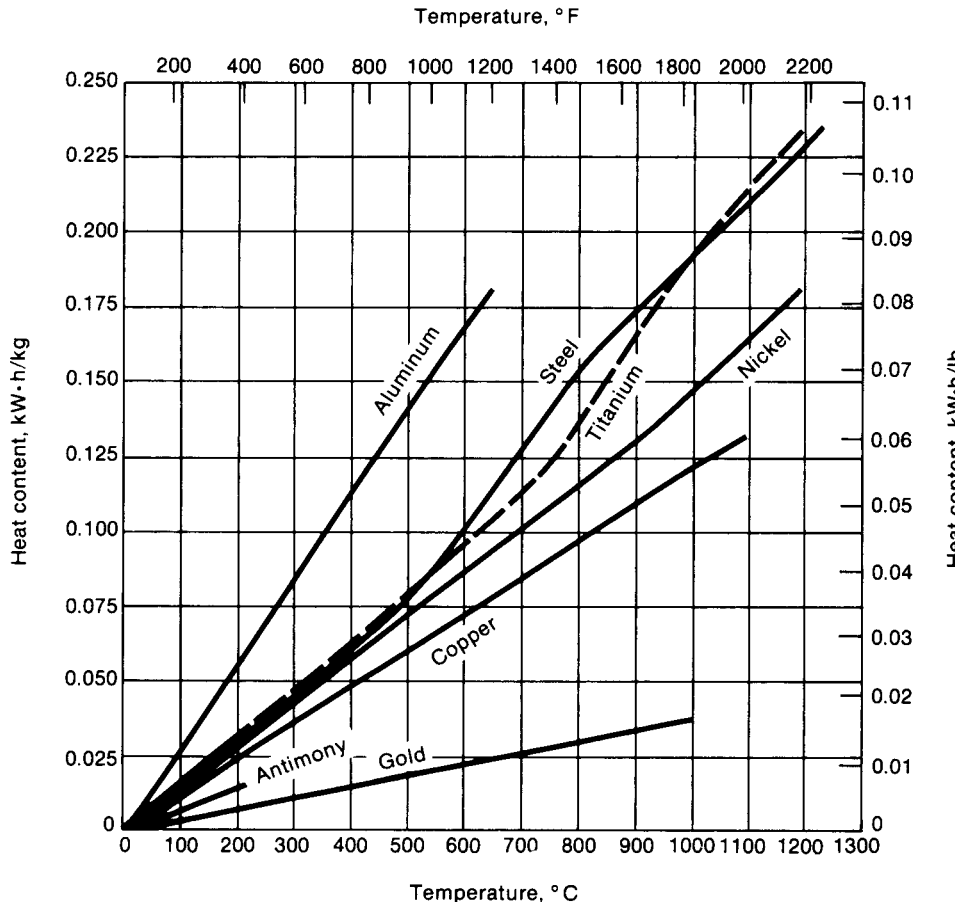


Fig. 9 Change in specific heat with temperature for various metals and steel. Source: Ref 4

one can see that approximately 63% of the current and 86% of the power induced in the workpiece will be concentrated within the reference depth near the surface.

The formula for the value of penetration depth is:

$$\delta = 503 \sqrt{\frac{\rho}{\mu_r F}} \quad (\text{Eq 3})$$

where ρ is the electrical resistivity of the metal (in units of $\Omega \text{ m}$), μ_r is its relative magnetic permeability, F is the frequency of the alternating current (in units of Hertz, or cycles per second), and δ is the penetration depth in units of meters. It is also expressed in the form:

$$\delta = 3160 \sqrt{\frac{\rho}{\mu_r F}} \quad (\text{Eq 4})$$

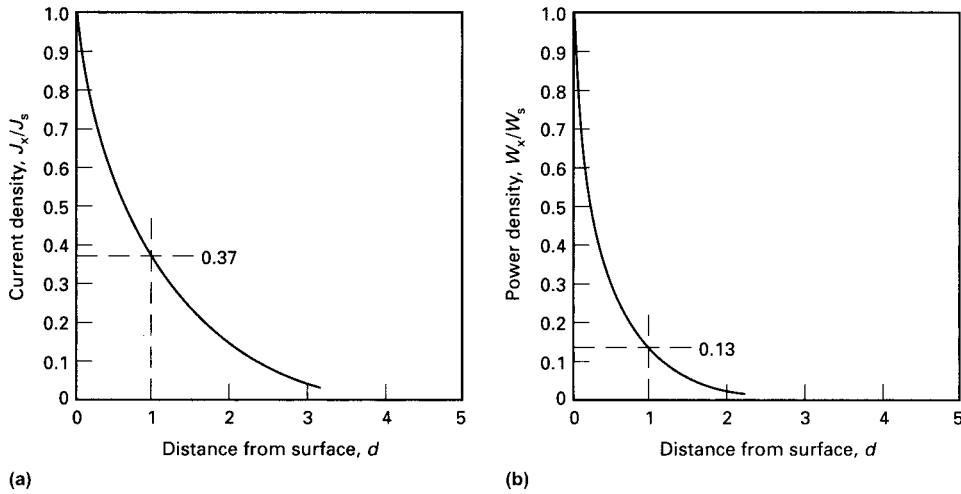


Fig. 10 Reduction of induced currents and power density as a function of distance below the surface. (a) Current density at the reference depth (δ , or here as $d = 1$) is $1/e$ (37%) that of current density at the surface. (b) Power density at the reference depth (δ) is $1/e^2$ (13%) that of power density at the surface. Source: Ref 19

where penetration depth (δ) is given in units of inches, with electrical resistivity (ρ) expressed in units of $\Omega \text{ in}$.

Many times, engineers calculate the distribution of the current density along the workpiece thickness (radius) using numerical computer simulation, Bessel functions, or numerous charts that are readily available to determine values of penetration depth (δ) versus temperature when heating different materials using various frequencies. For example, Fig. 11(a) presents plots of penetration depth at various frequencies as a function of electrical resistivity. Figure 11(a) also illustrates different frequency requirements for a given penetration depth during various steel processing methods.

However, because electrical resistivity (ρ) is a function of temperature, and relative magnetic permeability (μ_r) is a function of temperature and magnetic field intensity, the penetration depth is a nonlinear function of temperature and magnetic field intensity. Furthermore, for ferromagnetic metals, the relative permeability varies with temperature, decreasing to a value of 1 (relative to free space) at the so-called Curie temperature. Also, as the power density is increased, steels may become magnetically saturated, leading to decreased permeability and hence increased reference depth (Fig. 11b). Because of these effects, the reference depth in nonmagnetic materials may vary by a factor of 2 or 3 over a heat treatment

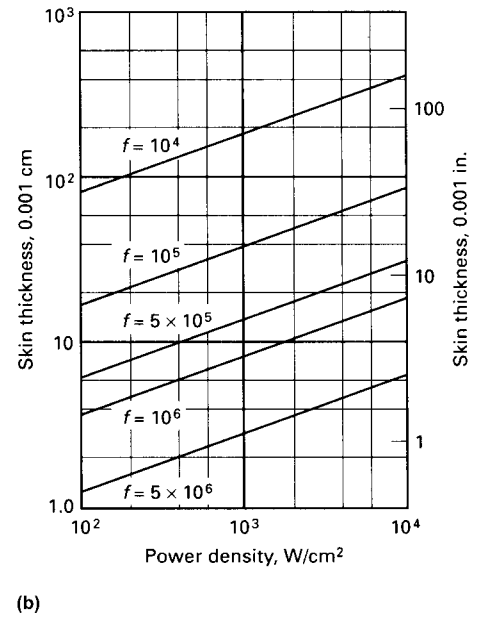
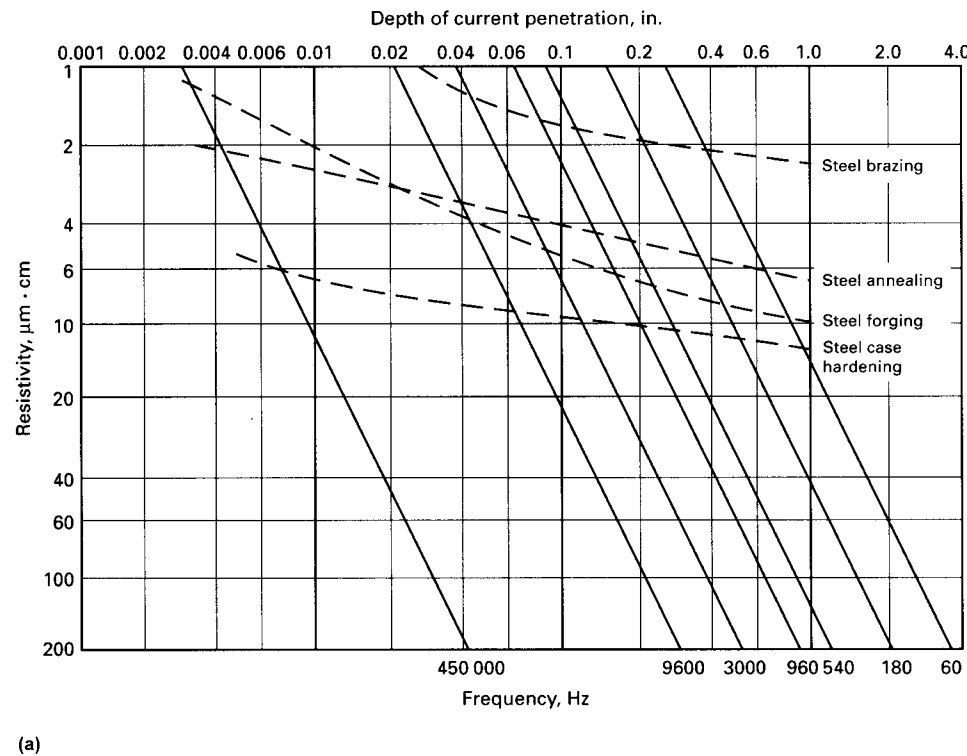


Fig. 11 Plots of penetration depth at various frequencies as a function of electrical resistivity. (a) Curves of current penetration versus frequency for induction heating with longitudinal flux. The dashed lines represent the reference depth for ferromagnetic steel below the Curie temperature for various operations. (b) Reference (skin) depth for magnetic steel as a function of power density. Source: Ref 19

temperature range, whereas for magnetic steels it can vary by a factor of 20.

It also is important to be aware that commonly accepted assumptions regarding current and power distribution due to skin effect are not valid for a great majority of induction surface-hardening applications. For example, the widely accepted assumption of exponential distribution of induced current and power is only appropriate for a solid body (workpiece) having constant values of both electrical resistivity and magnetic permeability. For the great majority of induction surface-hardening applications, the power density (heat source) distribution is not uniform, and there always are thermal gradients within the heated workpiece. These thermal gradients result in non-uniform distributions of electrical resistivity and, in particular, magnetic permeability within the heated workpiece. The presence of these nonlinearities leads to the fact that the common definition of current penetration depth being an exponential curve does not fit its principal assumption.

Current Cancellation. Current density decreases exponentially if the dimensions of the part are sufficiently large. For example, the cross-sectional size of a solid cylinder being heated must be at least four times the reference depth, otherwise current cancellation may occur. If the cross section is smaller relative to reference depth, then eddy currents in the inner regions of an object will overlap and cancel each other (assuming the use of solenoid-type inductors). This effect is illustrated in Fig. 12(a) for various ratios of object thickness (a) and reference depth (d). The dashed lines show exponential decay from either side, while the solid line gives the net current from the summation of the two dashed lines. Net heating curves (Fig. 12b) are obtained by squaring the net current density. Current cancellation directly affect a reduction of the heating efficiency.

To avoid current cancellation, frequencies for through hardening are often chosen so that the reference depth at final temperature does not exceed approximately one-fourth of the diameter for round parts and one-half the thickness for plates and slabs when using solenoid coils. When the bar diameter is less than three reference depths or the slab thickness less than two reference depths, the electrical efficiency drops sharply. By contrast, little increase in electrical efficiency is obtained when the bar diameter or slab thickness is many times more than the reference depth, but in some cases it can result in a reduction of total efficiency.

Because current cancellations reduce the efficiency of heating, the rule of thumb for good efficiency is to have the reference dimension of the part at least three times greater than the reference depth (d). The reference dimension is the diameter of round objects or the thickness of rectangular objects such as strips or slabs.

Magnetic-Wave Characterization. During induction surface hardening, the desirable frequency is often chosen in such a way that it produces a current penetration depth at the

austenitizing temperature that is 1.2 to 2 times the required case depth. If the frequency has been chosen correctly, the thickness of the non-magnetic surface layer—the layer that is heated to above Curie temperature for purposes of austenitization—is somewhat less than the current penetration depth in hot steel.

With the criterion of austenitization being an integral aspect of induction hardening, an important effect occurs that differs significantly from the commonly assumed exponential distribution. Here, the power density has its maximum value at the surface and decreases toward the core. However, at a certain distance from the surface, the power density suddenly starts to increase again, reaching a maximum value before it starts a final decline (Fig. 13,

right). This unique effect on power density distribution along the radius/thickness during induction surface heating is referred to as a magnetic-wave phenomenon (Ref 3, 6).

Originally, a hypothesis regarding a magnetic-wave phenomenon was independently introduced by Simpson (Ref 7) and Lozinskii (Ref 8). They intuitively felt that there should be situations where the power density (heat source) distribution would differ from that of the traditionally accepted exponential form. Both scientists provided a qualitative description of this phenomenon based on their intuition and understanding of the physics of the process. At the time, a quantitative evaluation of this phenomenon could not be developed due to a limitation in computer modeling capabilities

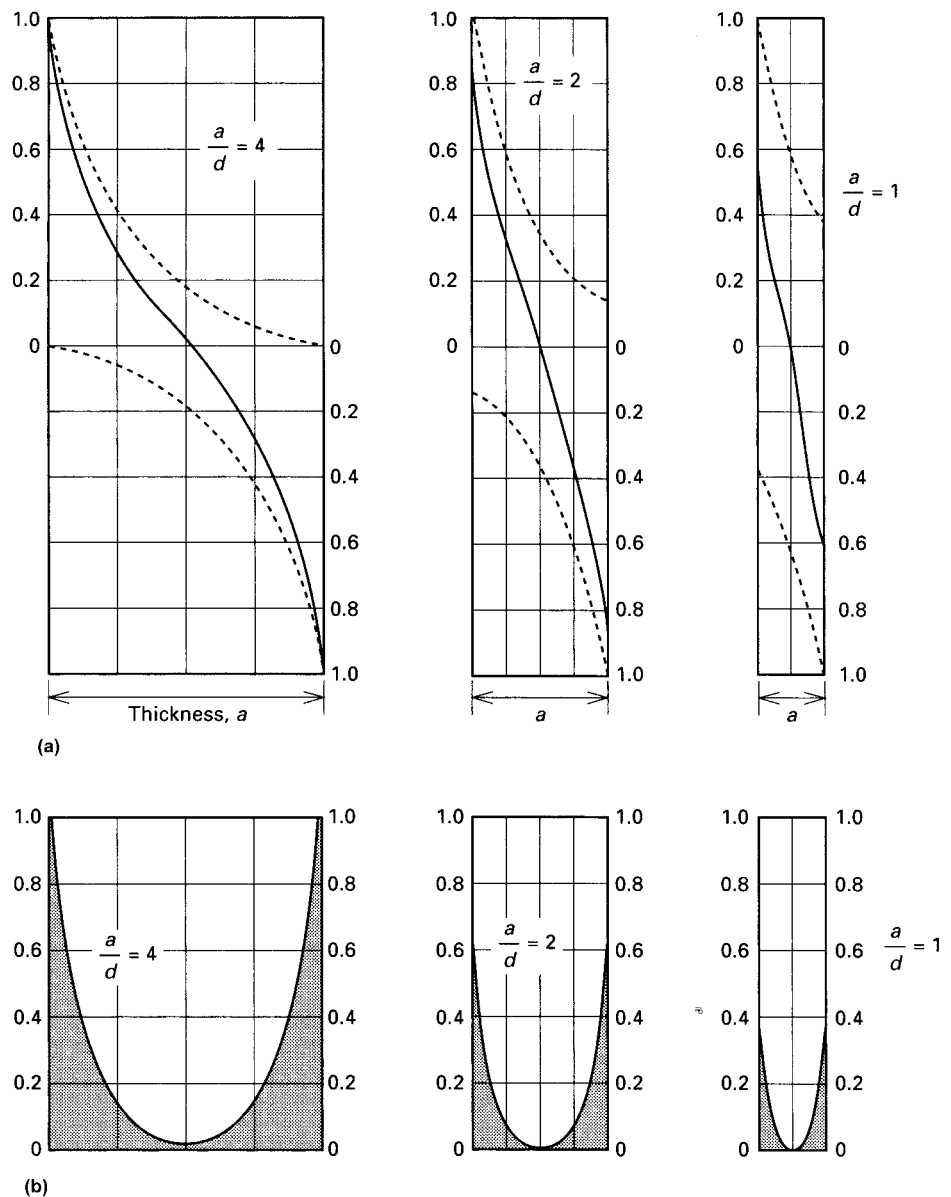


Fig. 12 Schematics showing (a) current distribution and (b) heat distribution for specimens of varying thicknesses. Source: Ref 19

and the lack of software that could simulate the tightly coupled electrothermal phenomena of induction hardening. Of course, it also was not possible to measure the power/current density distribution inside the solid workpiece during heating, without disturbing an eddy-current flow. The first publication that provided a quantitative assessment of the magnetic-wave phenomenon was Ref 6.

Modern, tightly coupled electromagnetic-thermal numerical software enables a quantitative assessment of the magnetic-wave phenomenon based on its ability to properly simulate interrelated electromagnetic and thermal phenomena. An example is given in Fig. 13, which shows the temperature profile (Fig. 13, left) and power density distribution (Fig. 13, right) along the radius of a 36 mm (1.42 in.) diameter medium-carbon steel shaft at the final stage of heating (just before quenching would be applied), using a frequency of 10 kHz. For comparison, the dotted curve represents the commonly assumed exponential curve for power density distribution, and the solid curve shows an actual magnetic-wave distribution obtained as a result of numerical computer modeling (Ref 9).

The main cause of magnetic wave relates to the phenomenon that, in induction surface hardening, carbon steel retains its magnetic properties in the subsurface region. The surface region is nonmagnetic (being heated well above the A_{c2} critical temperature for austenitization). Note that in some cases, this phenomenon can manifest itself in formation of the maximum value of heat sources being located in an internal layer of the workpiece and not at its surface.

The capability to take into consideration the phenomenon of wavelike distribution of power density has a marked effect on the choice of frequency that allows the required hardness depth to be provided.

It is important to be aware that the magnetic-wave phenomenon of power density distribution does not appear only along the radius/thickness of the workpiece. It also occurs when

studying power density distribution in the axial direction, because it occurs in through hardening of selected areas of the component.

Induction Hardening and Tempering

The hardening and tempering of steel account for the largest market in the induction heat treatment field. As with steel parts hardened by furnace heat treatment, the typical procedure for induction hardening of steel involves austenitizing and quenching to form martensite either on the surface (case hardening) or through the entire section (through hardening). The difference between heat treatment temperatures for induction heating and furnace heating is related to the inherent short heating times with induction, the treatment temperatures with induction heating are higher than the treatment temperatures with conventional furnace-based processes.

Because the induction hardening process does not change the carbon content of the steel, the selected material must have sufficient amounts of carbon and alloy content (if required) prior to induction hardening. Steels with a 0.25 to 0.65% C content are commonly used for induction hardening. H-steels (i.e., 1050H, 4340H) are preferred because they produce more consistent results due to having a specified hardenability. Martensitic stainless steels (AISI 416, 420, and 440C) as well as some iron castings also can be induction hardened (Ref 10).

Austenitizing

The primary metallurgical question that arises in induction hardening relates to austenitizing. As with austenitizing by conventional furnace techniques, time and temperature are the two

critical parameters that must be controlled. Complete austenitization occurs above the A_3 critical temperature for hypoeutectoid steel (carbon < 0.8 wt%) or the A_{cm} critical temperature for hypereutectoid steels (carbon > 0.8 wt%). The time to form a totally austenitic microstructure depends on the selected austenitizing temperature and the starting microstructure (also called an initial structure or prior structure).

In all cases, the speed with which austenite is formed is controlled by the diffusion of carbon, a process that can be accelerated a great deal by increasing the temperature. For example, the time for complete austenitization in a plain carbon steel of eutectoid composition with an initial microstructure of pearlite is decreased from approximately 400 seconds at an austenitizing temperature of 730 °C (1345 °F) to approximately 30 seconds at an austenitizing temperature of 750 °C (1380 °F), as shown in Fig. 14.

The influences of heat rate and carbon content on austenitization are plotted in Fig. 15 for various carbon steels with varying carbon levels. Time-temperature austenitization diagrams give variations of the transition temperature A_3 , with particular emphasis for some common plain carbon steels (1015, 1035, 1045, and 1070) and reference to the given

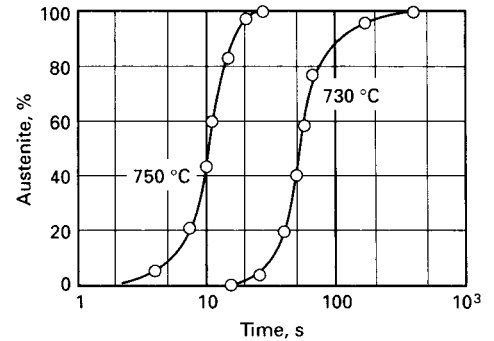


Fig. 14 Effect of austenitizing temperature on the rate of austenite formation from pearlite in a eutectoid steel

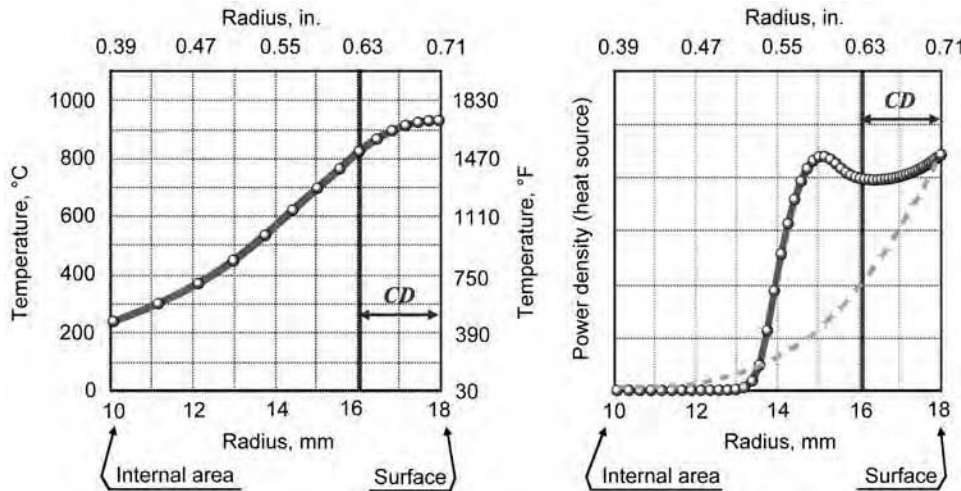


Fig. 13 Magnetic-wave effect during austenitization of a steel surface by induction heating. CD, case depth. Source: Ref 6

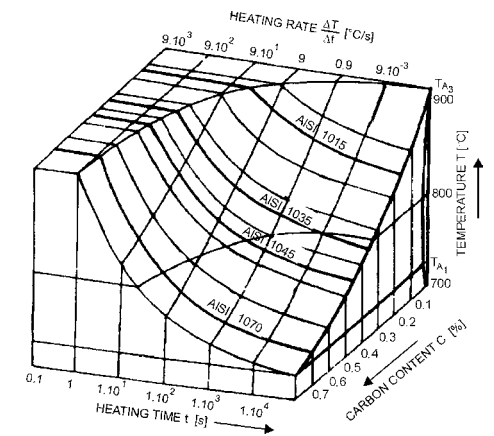


Fig. 15 Influence of heating rate and carbon content on austenitic transformation temperature. Source: Ref 11

heating rate and the corresponding heating time (Ref 11). Figure 16 plots an example of austenitizing temperatures at different cooling rates for hypoeutectic carbon steels.

These times for austenitization also can be considerably increased if the starting microstructure has carbon tied up within large, spheroidized carbide particles. This occurs because the diffusion distance for carbon, which must be transported from the carbon-rich carbide phase, is considerably larger than that of pearlite (which has thin lamellae of ferrite and carbide). Likewise, the finer bainitic and martensitic microstructures tend to be reaustenitized more readily than pearlite.

Data such as those in Fig. 14 suggest that at sufficiently high temperatures, austenite forms in a fraction of a second. This fact is relied upon in induction surface hardening (very rapid heating rates) or induction through hardening (moderate-to-rapid heating rates) in which the workpiece surface or cross section is raised to

a higher temperature than is normally used in much slower, furnace-based processes.

A tremendous amount of metallurgical research has been directed at the determination of the upper critical temperature (Ac_3) that signifies complete austenitization during continuous heating cycles, such as those used in induction heating. Because the only soaking time available for phase transformation in these cases is that time after which the equilibrium critical temperatures (Ae_3 or Ae_{cm}) are exceeded, the continuous-heating critical temperatures are always above the equilibrium ones. This difference increases with heating rate, as may be expected—an effect shown in Fig. 17 for the Ac_3 temperature for 1042 carbon steel. Here, the Ac_3 temperature is the one at which it has been estimated that the austenite reaction is complete.

These data also show that the increase in critical temperature depends on the initial microstructure. The quenched-and-tempered, or martensite, microstructure revealed the least change in Ac_3 temperature as compared to the equilibrium A_3 temperature, whereas the same steel with annealed microstructure exhibits the largest difference in Ac_3 as compared to the corresponding temperatures obtained from very slow heating rates. Such a trend is readily explained by the fact that the diffusion distance to redistribute carbon is shorter in the former instance and longer in the latter microstructure, in which carbides are much larger.

Data similar to those for 1042 steel are given in Fig. 18. For eutectoid 1080 carbon steel, the Ac_1 and Ac_3 temperatures nearly coincide during slow heat treatments. By contrast, they differ for rapid heating (Fig. 18). The lower critical temperature can be taken as one at which the reaction started, and the upper one as that at which transformation to austenite was completed. At the higher heating rates, the Ac_1 and Ac_3 are higher than at lower rates, an effect which offsets the shorter times at temperature.

The aforementioned measurements are most useful when only the surface layers of a steel part are to be austenitized and hardened. In these cases, continuous rapid heating to the Ac_3 temperature is all that is needed. In other situations, in which deeper hardening or through hardening is necessary, a certain amount of actual soaking time at temperature may be required.

Based on data such as those in Fig. 17 and 18, guidelines have been derived for the required austenitizing temperature for induction hardening of a wide range of steels (Table 1). Generally, the recommended temperatures increase with increasing A_3 temperature; they are approximately 100 °C (180 °F) above the equilibrium upper critical temperature, primarily to reduce the austenitizing time during continuous induction heating cycles. However, they are still below that at which undesirable austenite grain growth occurs in the short times characteristic of rapid induction heating processes.

Recommended austenitizing temperatures are at least another 100 °C (180 °F) higher in alloys with strong carbide-forming elements (for example, titanium, chromium, molybdenum, vanadium, niobium, or tungsten) than for carbon steels. These increases are a result of large increments in the critical temperatures of alloy steels. This is because of the kinetics of alloy carbide dissolution in austenite, which can be substantially slower than those of cementite dissolution, particularly when NbC, TiC, and VC are involved. Such increases in induction hardening temperature and time generally are not deleterious from the viewpoint of austenite grain growth, however, because of the effects of alloying.

The aforementioned recommendations for induction hardening temperatures should be used only as a guide. This is especially true for modern plain carbon steels, which are

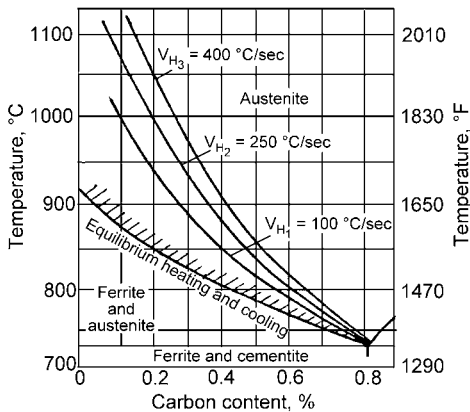


Fig. 16 Influence of induction surface heating rate on hardening temperature for hypoeutectic steels. Source: Ref 1, 8

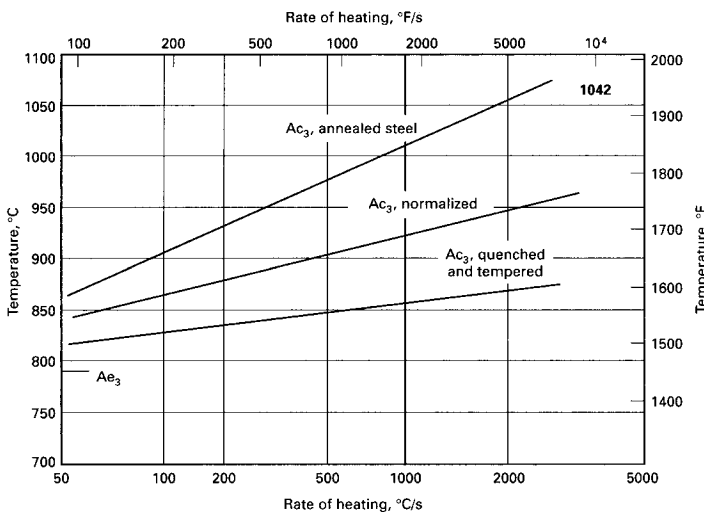


Fig. 17 Effect of prior structure and rate of heating on Ac_3 transformation temperature of 1042 steel. Source: Ref, 4, 19

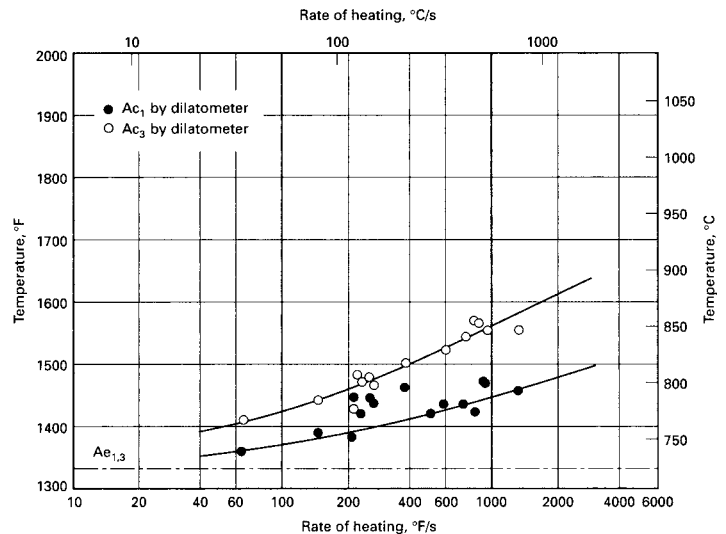


Fig. 18 Effect of heating rate on Ac_1 and Ac_3 temperatures for annealed 1080 steel. Source: Ref 4

Table 1 Approximate induction austenitizing temperatures for carbon and alloy steels

Carbon content, %	Temperature for furnace heating		Temperature for induction heating	
	°C	°F	°C	°F
0.30	845–870	1550–1600	900–925	1650–1700
0.35	830–855	1525–1575	900	1650
0.40	830–855	1525–1575	870–900	1600–1650
0.45	800–845	1475–1550	870–900	1600–1650
0.50	800–845	1475–1550	870	1600
0.60	800–845	1475–1550	845–870	1550–1600
>0.60	790–820	1450–1510	815–845	1500–1550

Note: Recommended austenitizing temperatures for a specific application will depend on heating rates and prior microstructure. Free-machining and alloy grades are readily induction hardened. Alloy steels containing carbide-forming elements (e.g., niobium, titanium, vanadium, chromium, molybdenum, and tungsten) should be austenitized at temperatures at least 55 to 100 °C (100 to 180 °F) higher than those indicated (Ref 19).

typically melted using a large percentage of scrap that may contain microalloyed high-strength low-alloy steels. Thus, the steel may still be considered to be nominally of the plain carbon type but may contain trace amounts of niobium, vanadium, and/or titanium, whose presence may greatly affect heat treating response. For this reason, it is wise to obtain a complete chemistry on each lot of steel employed in induction hardening processes or to determine proper austenitizing temperatures experimentally.

Quenching

The heating process is only one portion of the hardening operation. Quenching techniques are as varied as the heating equipment. The critical factors to be considered when determining quenching systems include the following:

- Part size and geometry
- Type of austenitizing operation (surface or through hardening) and required heat pattern
- Type of heating method (single-shot or scanning)
- Hardenability of steel, its brittleness or toughness, and quenchant required

Various quenchants have different cooling characteristics and cooling rates. Different materials and part geometry have different quenching rate requirements in order to produce a martensitic microstructure that is free of cracking and has reduced distortion. For example, free or compressed air quenching is typically used for high-hardenability steels or surface-hardened steels with small case depths in which relatively little heat needs to be removed by the thermal conduction of the cold core.

Water continues to be an excellent quenchant when used appropriately. In the early years of induction heat treating, water was widely used for quenching, with salt additives when severe quenchants were needed. In the 1950s, the introduction of fast-speed oil quenchants permitted the use of oil as a quenchant for medium-carbon steels where there were cracking tendencies because of small section size or

the presence of irregularities. Later, various water-soluble oils and plastic quenchants were introduced, followed by the introduction and use of polymer-based water quenchants that became the most popular choice today (2013). Polymer quenchants have eliminated spotty hardnesses that were caused by vapor pocket formation in immersion quenching, and they provide more flexibility and reliability at a reduced overall cost.

Concern about fires and environmental restrictions are obvious drawbacks to using oils and oil-based quenchants. These are some of the main reasons why oils are seldom used with induction.

When quenching is done improperly, several problems may arise. These may include soft spots, quench cracks, and/or excessive part distortion. Soft spots may occur when water is used as the quenchant as a result from the formation of steam pockets on the part surface, which prevent uniform and sufficiently rapid cooling for the formation of martensite in statically processed parts. This problem can also occur during the use of other aqueous-based quenchants as a result of quenchant foaming. As may be expected, the problem can be most severe in lower-hardenability steels. The problem can be alleviated by improved quench ring design or changes in the quenching device-workpiece configuration. A foam-suppressant material from the quenchant manufacturer can eliminate foaming problems.

Quench cracks from the induction hardening process are typically due to one or several of five separate factors:

- Too severe a quench (which is particularly troublesome in higher-carbon and higher-hardenability steels)
- Nonuniformity of quenching
- Changes in part contours with insufficient transitional areas
- Surface roughness (e.g., tool marks)
- Presence of irregularities (e.g., holes, keyways, grooves, etc.)

Quenching Methods. The two most common types of systems consist of spray quench rings and immersion techniques. Dunk (immersion) quenching can be used in induction heat

treating, particularly for alloy steels producing the critical cooling rates needed for complete martensitic microstructures. The workpiece is removed from the induction coil and placed into the quench tank. There are applications, such as the submerged hardening of gear teeth, in which the entire gear is submerged in the quenchant with the induction coil during an entire heating cycle. The gear tooth can be austenitized under the quenchant because the heat formed on the gear tooth produces a vapor pocket during heating of the gear that insulates and permits temperature buildup. At the end of the cycle, turning the power off allows the part to quench in place.

Spray quenching (for example, using water or water-based polymers) is the most popular method used in induction hardening applications. Spray quenching works best if the component (axle shafts, spindles, rods, and gears, for example) is rotated during the quenching, ensuring cooling uniformity. By rotating parts, the component essentially experiences a constant impingement rather than many small impingements. Uneven quenching could have a detrimental negative effect on the microstructure of the heat treated part and could result in excessive distortion and quench cracking. Fast rotation should be avoided, because quenchant may be thrown off the surface of the heat treated component, failing to provide a sufficient cooling intensity.

Quench holes in the tooling are typically placed facing the heated component at ~5 to 6 mm ($\frac{3}{16}$ to $\frac{1}{4}$ in.) intervals in a staggered pattern. The orifice size is related to the specifics of quenching requirements, including coil-to-workpiece geometry, the air gap between the quench block and the workpiece surface, quench concentration, and its pressure. In some cases, the quenchant system is built into the coil, which is called machined integral quench. In other cases, quench followers (additional quench rings or barrels) are used separately from an inductor when a high scanning rate is required. Quench followers help to ensure that a heat treated component was sufficiently quenched (Ref 3).

Spray quenches are used both in static heating and single-shot heating, where the workpiece is heated at one time, and in progressive or scan hardening. When quench rings are used for round bars, their shapes, like the coil, are generally round. The ring may be located concentric with the coil or directly underneath or alongside it, as in single-shot induction hardening setups (Fig. 19).

In induction scanning or progressive hardening, workpieces move through the quench ring and coil, with quenching occurring immediately after heating (Fig. 20). For nonsymmetric workpieces, the quenching system, like the coil, is generally the same shape as the workpiece. It is possible to design the induction coil separately from the spray (Fig. 20) or combined so that the induction coil has downward-directed spray openings for quenching in its bottom part (Fig. 20b).

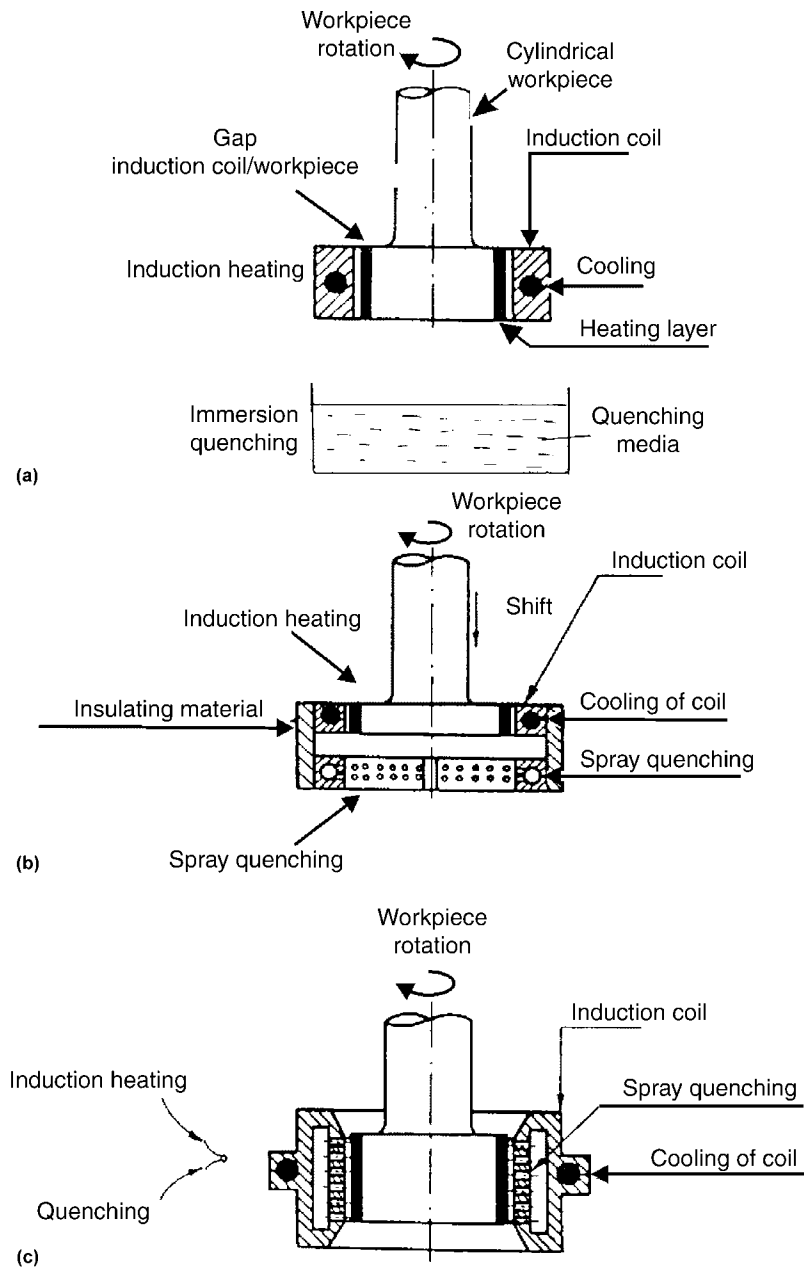


Fig. 19 Single-shot induction hardening of cylindrical workpieces. (a) Separately installed induction coil and immersion quenching. (b) Induction coil and spray quenching adapted for quenching. (c) Separately installed induction coil and spray quenching. Source: Ref 1, 2

Severity of Spray Quenching. The intensity of spray quenching (intensity of heat removal) depends on the quenchant flow rate; the angle at which the quenchant strikes the workpiece; the temperature, purity, and type of quenchant; the depth of heating; and the temperature of the heat treated component. Spray quenching typically leads to a greater quench severity than immersion quench, resulting in higher hardness and greater compressive surface residual stresses compared to conventional immersion quenching. Quenchants used include water, aqueous polymer solutions, and, to a lesser extent, oil, water mist, and forced air. Water

and aqueous polymer solutions are the most popular choices. Oil and oil-based quenchants should never be used with spray quenching.

There is a common misunderstanding regarding the ability to apply the widely published, classical cooling curves for immersion quenching to induction hardening applications. Classical cooling curves representing three stages of quenching—vapor blanket (stage A), nucleate boiling (stage B), and convective cooling (stage C)—cannot be applied directly to spray quenching. The differences are both quantitative and qualitative and include, but are not limited to, specifics of film formation and heat

transfer through the vapor blanket during the initial stage (A), as well as the kinetics of formation, growth, and removal of bubbles from the surface of the heated component during nucleate boiling (stage B) (Ref 12).

Due to the nature of spray quenching, stages A and B are greatly suppressed in time, while cooling during the heat convection stage (C) is noticeably more intense, compared with the process represented by classical cooling curves of immersion quenching.

Also, the thickness of the vapor blanket film during stage A is typically much thinner during spray quenching than when the part is submerged in a quench tank, and its magnitude depends on flow rate, impingement angle, part rotation, and other characteristics of the quenching system. This vapor film is unstable and could be frequently ruptured.

In addition, the transition between stages A and B is smoother with spray quenching than that shown by classical cooling curves for immersion quenching. During nucleate boiling (stage B), bubbles are smaller because they have less time to grow. Much larger numbers of bubbles form during spray quenching, and the intensity with which they remove heat from the surface of the component is substantially greater compared with immersion quenching.

Another factor that has a considerable effect on quench severity in selective hardening or surface hardening by induction is the thermal sink effect provided by the cold regions of the component (for example, its cold core). In the majority of induction surface-hardening applications, the core temperature does not rise significantly during the heating cycle, due primarily to a pronounced skin effect, high heat intensity, and short heating time. As a result, heat transfer from the surface of the workpiece to its core during the heating stage is not sufficient to significantly raise core temperature. A cold core complements spray quenching by further increasing the cooling intensity of austenitized regions of the part due to thermal conduction.

Note that in some induction surface-hardening applications that require shallower case depths (0.5 to 1.25 mm, or 0.02 to 0.05 in.), self-quenching can be used. Here, the effect of thermal conduction away from the surface by a sufficiently cold core provides a cooling intensity that may be high enough to miss the nose of the continuous cooling transformation curve. Such a self-quenching technique (also called mass quenching) allows a shallow case to be obtained without the use of a liquid quenchant. Regardless of its simplicity, self-quenching is seldom used in induction hardening because it is limited to very shallow case depths and the presence of a sufficiently large cold mass below the case depth, or when hardening high-hardenable or air-hardenable alloys.

When discussing spray quenching in scan hardening, it is imperative to take into consideration a comet-tail effect (Ref 13, 14). Figure 21 shows a result of computer modeling of

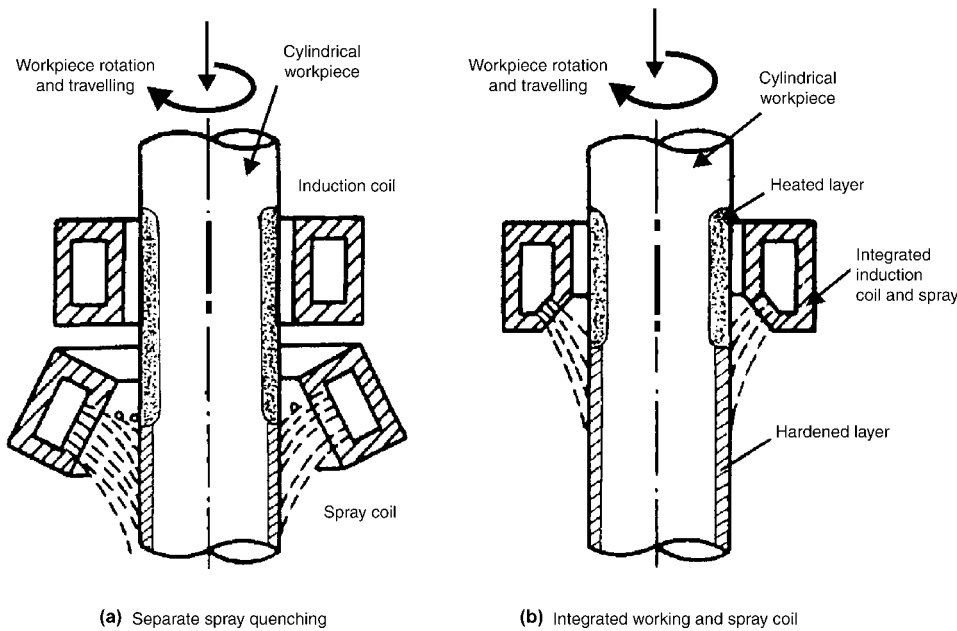


Fig. 20 Progressive (scan) hardening of cylindrical workpiece. Source: Ref 2

temperature distribution of an intermediate process stage during vertical induction scan hardening of the hollow shaft. The comet-tail effect manifests itself as heat accumulation in shaft subsurface regions below the scan inductor, being pronounced in the areas of a diameter change. Upon quenching, the temperature of the shaft surface can be cooled sufficiently below the martensite start (M_s) temperature, approaching the temperature of the quenchant. At the same time, the heat accumulated in the shaft subsurface may be sufficient for tempering back the as-quenched surface regions and could potentially result in the appearance of soft spots within the case depth. Sufficient quench-out is essential to prevent this undesirable phenomenon.

In addition to the coil/quench ring arrangements mentioned earlier, several other systems are in common use. These have been summarized by Spencer and his colleagues (Ref 15) and are depicted in Fig. 22. In brief, they consist of the following systems and operations:

- Fig. 22(a): Heat in coil; manually lift part out of coil; submerge part in tank of agitated quench medium. Used where limited production does not warrant the cost of an automated quench
- Fig. 22(b): Heat and quench in one position; quench by means of integral quench chamber in inductor (single-shot method described previously)
- Fig. 22(c): Heat in coil with part stationary; quench ring moves in place (modified single-shot scanning technique)
- Fig. 22(d): Part is hydraulically lowered into quench tank after single-shot heating.

Quench medium is agitated by submerged spray ring or propeller.

- Fig. 22(e): Vertical or horizontal scanning with integral spray quench. Single-turn inductor. Used for shallow hardening
- Fig. 22(f): Vertical or horizontal scanning with multiturn coil and separate multirow quench ring. Used for deep-case or through hardening
- Fig. 22(g): Coil scans and heats workpiece; self-quench or compressed air quench. Used in special applications with high-hardenability steels
- Fig. 22(h): Horizontal cam-fed parts are pushed through coil, then dropped onto submerged quench conveyor
- Fig. 22(i): Vertical scanning with single-turn inductor in combination with integral dual quench: one quench ring for scan hardening, the second for stationary quenching when the scanning travel stops. Used for parts having a diameter or a flange section too large to travel through the inductor, wherein it is desired to harden up to the shoulder or flange
- Fig. 22(j): Vertical scanning with single-turn inductor with integral spray quench and submerged quench in tank
- Fig. 22(k): Split inductor and integral split quench ring. Used for hardening crankshaft bearing surfaces

As-Quenched Hardness. Another important feature of induction hardening is its ability to impart as-quenched hardnesses somewhat higher than those of conventional furnace-hardened steels. This trait is illustrated in Fig. 23 for plain carbon steels of various carbon contents. Data are presented for surface

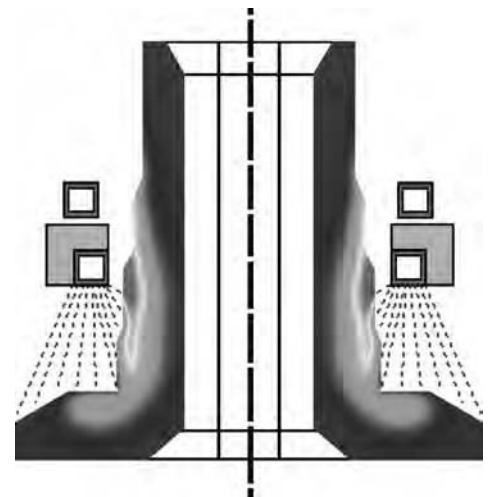


Fig. 21 Computer model of temperature distribution showing comet-tail effect manifested as heat accumulation in shaft subsurface regions below the scan inductor. Source: Ref 14

induction-hardened (curve A), furnace through-hardened (curve B), and furnace-hardened (curve C) specimens given a low-temperature heat treatment consisting of cooling to liquid nitrogen temperatures and subsequently tempering at 100 °C (210 °F).

The higher hardnesses of the induction-hardened specimens may be attributable to four sources:

- Greater quench severity
- Residual stresses
- Smaller amounts of retained austenite
- Carbon segregation

The greater quench severity is related to the cooling intensity of spray quenching that is associated with the additional cooling effect of the cold core.

As to the second effect, compressive residual stresses are developed in surface-hardened steels because of the smaller density of martensite as compared with bainite or pearlite. During cooling following austenitizing, the higher-density inner layers shrink more than the surface layers, leading to such residual stresses (and thus increments in hardness).

The third factor, smaller amounts of retained austenite in induction-hardened steels, is a result of the finer martensite generally resulting from such steel heat treatments; the martensite may also be harder because it was formed from finer-grain, less-homogeneous austenite having a larger number of imperfections.

The last factor, the increment in hardness due to carbon segregation, derives from the fact that induction austenitizing normally involves rapid heating and requires short holding times, which may lead to variation in carbon content within the austenite grains. Thus, a mixture of higher-carbon and lower-carbon martensite is formed during quenching. It is the high-carbon martensite

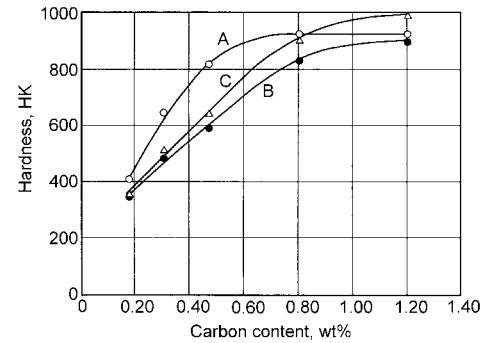


Fig. 23 Effect of carbon content on hardness in plain carbon steels. Curve A: induction hardened. Curve B: furnace hardened and water quenched. Curve C: furnace hardened, water quenched, and tempered. The quenched-and-tempered steels were treated in liquid nitrogen following water quenching prior to tempering at 100 °C (210 °F) for 2 h. Source: Ref 4

conducted at a variety of temperatures for a range of times; the hardness for each treatment is determined and then plotted, as in Fig. 24, to establish time-temperature relationships. This method, however, involves considerable time and effort.

A simpler technique uses a mathematical function known as the tempering parameter (T.P.). A number of researchers have found that the hardness of tempered martensite (as well as tempered bainite and pearlite) can be correlated to a certain function of the tempering time and tempering temperature. The formulation of the tempering parameter most widely used is that developed by Grange and Baughman:

$$T.P. = T(C + \log t)$$

where *T* is the absolute tempering temperature in degrees Rankine, *C* is a constant equal to 14.44, and *t* is tempering time in seconds.

To illustrate the application of the tempering parameter, consider the 40 HRC data discussed in Fig. 24. The tempering parameters for the two treatments are:

- T.P. furnace = (800 + 460) · (14.44 + log 3600) = 22,675
- T.P. induction = (1000 + 460) · (14.44 + log 5) = 22,105

Because the tempering parameters are almost identical, the hardness and other mechanical properties yielded by the two treatments should be nearly the same.

General Equipment and Process Factors

Although this article focuses on induction surface hardening, this section briefly describes induction heating parameters for surface hardening, through hardening, tempering, and some general heating operations in metalworking. Key process factors for induction heating are:

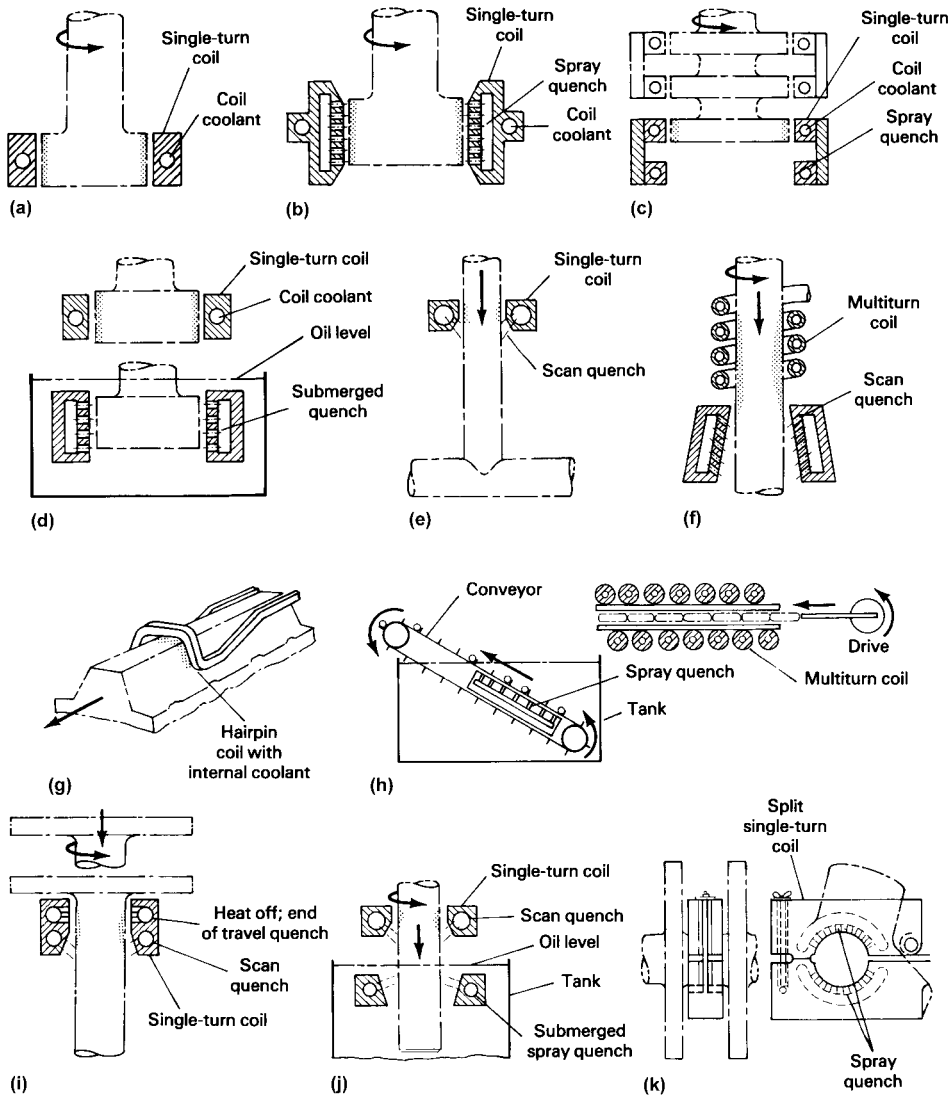


Fig. 22 Eleven basic arrangements for quenching induction-hardened parts. See text for details. Source: Ref 15

that gives rise to higher hardnesses. This effect decreases in steels whose carbon contents exceed approximately 0.6 to 0.8 wt%, above which the hardness of martensite does not change.

Induction Tempering

The major differences between induction and furnace tempering cycles lie in the times and temperatures involved. Tempering of hardened steel structures, such as martensite, involves diffusion of carbon atoms to form iron carbide (Fe₃C, or cementite). The extent of diffusion increases with both increasing temperatures and time. Thus, a short time/high-temperature treatment and a longer time/lower-temperature treatment will provide similar tempering responses. The former process would be typical

of induction treatment and the latter of furnace treatment. The data in Fig. 24 illustrate this point. The results show the tempering response for a quench-hardened 1050 steel that was tempered at a variety of temperatures between 150 and 650 °C (300 and 1200 °F). Consider, for example, the processing conditions to obtain a hardness of 40 HRC. Induction heat treatment at 540 °C (1000 °F) for 5 s gives this hardness, as does a much longer (1 h) furnace treatment at 425 °C (800 °F). Because other mechanical properties of quenched-and-tempered steels, such as yield and tensile strength, elongation, reduction in area, and fracture toughness, often correlate with hardness, these two different tempering treatments apparently yield a very similar product.

Equivalent time/temperature cycles for tempering can be determined in several ways. For example, tempering experiments can be

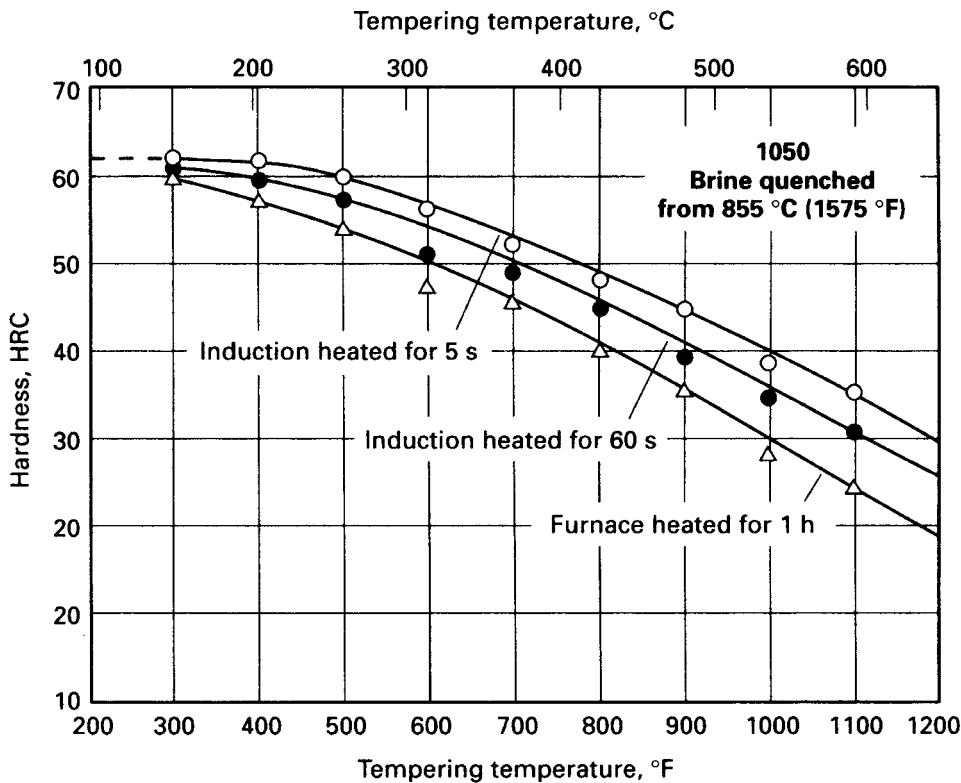


Fig. 24 Hardness as a function of tempering temperature and time for furnace- and induction-treated 1050 steel austenitized at 855 °C (1575 °F) and quenched in brine. Source: Ref 4

- Workpiece characteristics (part geometry and electrical-magnetic properties)
- Coupling distance and coil design
- Frequency selection (which affects the skin effect and thus the depth of heating)
- Power density (kilowatts per unit area exposed to the inductor)
- Heating time

The manufacturing engineer should also consider methods for part quenching, for material handling, and for the integration of heat treating cycles with other production steps.

The choice of suitable heating parameters is, to a large extent, determined by the temperature required, the depth of heating, and its pattern. Workpiece characteristics are also important. The distribution of induced current is influenced also by the magnetic and electrical characteristics of the part being heated, and because these properties change with temperature (as discussed in the preceding section), the current distribution will change as the workpiece is heated.

Optimum heating for a given workpiece and heat treatment requires detailed knowledge of the application and equipment. The first step in designing a system for induction hardening is to specify the required hardness pattern, including surface hardness, case depth, hardness pattern, and, in some cases, transition zone. The hardness pattern is directly related

to temperature distribution, which is controlled by selection of frequency, time, power, and workpiece/coil geometry. When only surface hardening is needed, induction is employed to heat the surface rapidly to temperature. For through hardening, much lower power densities and lower frequencies are typically used in order to allow heat conduction from the surface and thereby to minimize temperature gradients.

Initial guidance can come from charts or calculations for a specific set of conditions. Many induction heating equipment manufacturers have extensive computer programs based on laboratory tests, production/operating data, and mathematical modeling, which they use to recommend the proper apparatus and suggest application parameters. An estimate of what may be required for a new application can often be derived from results obtained on similar parts or by careful observation of the part itself as it is being heat treated or by applying numerical analysis (including finite-element, finite-difference, or boundary-element methods and their combinations). Final operating parameters are usually fine-tuned by experimentation.

Basic process control for most induction heating applications consists of applying power through a current-, power-, or voltage-regulated power supply for a measured period of time, and this has proved to be satisfactory for a wide variety of operations. Solid-state inverters, through their logic circuits, can provide

constant voltage, constant current, or constant power output during an entire heat cycle, and each in a particular way can help to ensure a repeatable heating effect with time under a wide variety of changing conditions. For a stationary hardening operation, either an electronic or a synchronous timer can be used to control the heating time, any needed load-matching adjustments, and application of the quench. If energy input to the product is considered an appropriate measure of control, a kilowatt-second or kilowatt-hour energy monitor can be used to terminate a heating cycle.

In terms of frequency selection, lower frequencies are more suitable as the size of the part and the case depth increase. However, power density and heating time also have an important influence on the depth to which the part is heated. This interrelationship is shown in Fig. 25 in terms of case depth for surface-hardened steel. In some instances, the determining factor in selecting the frequency is the power required to provide a power density sufficient for successful hardening, because lower-frequency induction equipment is available with higher power ratings.

Frequency Selection in Induction Heating. Frequency is the first parameter considered for induction heating. Primary considerations in the selection of frequency are depth of heating, efficiency, type of heat treatment (such as surface hardening versus through hardening or subcritical annealing), and the size and geometry of the part. It may also depend on the type of alloy, its initial microstructure, required hardness pattern, and other application factors.

As an initial starting point, Eq 3 or 4 for reference depth (δ) can be used to estimate the desired generator frequency for induction hardening of steel. For surface hardening, the desired case depth is typically taken to be equal to approximately one-half the reference depth at austenitizing temperature when selecting frequency. Compared to through-heating applications, however, frequency selection is more subtle in surface-hardening applications (see the section "Frequency Selection for Induction Surface Hardening" in this article).

By contrast, when through hardening is desired, the frequency is usually chosen such that the reference depth is a fraction of the bar diameter (or an equivalent dimension for parts that are not round). This is necessary in order to maintain adequate skin effect and to enable efficient induction heating to take place when heating using a solenoid inductor. If the reference depth is chosen to be comparable to or larger than the bar radius, then dramatic eddy-current cancellation occurs. Induced eddy current flowing on diametrically opposed surfaces of the bar will tend to go in opposite directions and thus cancel each other. To avoid this, frequencies for through hardening are often chosen so that the reference depth does not exceed approximately one-fourth of the diameter for round parts or one-half the thickness for plates and slabs when using solenoid coils.

When the bar diameter is less than four reference depths (and, in particular, less than three reference depths) or the slab thickness less than two reference depths, the electrical efficiency drops sharply. By contrast, little increase in efficiency is obtained when the bar diameter or slab thickness is many times more than the reference depth.

Power Density and Heating Time. Once the frequency has been selected, a wide range of temperature profiles can be produced by varying the power density and heating time. Selection of these two heating parameters depends on the desired heat patterns of a particular application, the production rate, and the inherent heat losses of the surface workpiece (due to thermal radiation and heat convection).

In through-heating applications, the power needed is generally based on the amount of material that is processed per unit time, the average temperature, and the heat capacity of the material at this temperature. Power specification for other operations, such as surface hardening of steel, is not as simple because of the effects of starting material condition and the desired case depth.

Surface heating is used primarily in the surface hardening of steel parts such as shafts and gears. In this type of application, high power densities and short heating times are used when thin case depths are desired. Typical power ratings for surface hardening of steel are given in Table 2. These are based on the need to heat to austenitizing temperature (Table 1) appreciably rapidly and have proven to be appropriate through the years of experience. When using these or other fixed ratings, however, the effect of heating time on case depth (Fig. 25) must be considered.

Through Heating. Power ratings for through hardening of steel are much lower than those for surface hardening, to allow time for the heat to be conducted to the center of the workpiece. After a while, the rates of increase of the surface and center temperatures become comparable due to conduction, and a fixed temperature differential persists during further heating. The allowable temperature differential permits the generator power ratings to be selected.

The basic steps in rough estimating the power rating are as follows (Ref 17, 19):

1. Select the frequency and calculate the ratio of bar diameter (or section size) to reference depth, D/δ . For most through-heating applications, this ratio will vary from approximately four to eight.
2. Using the values of the thermal conductivity (in W/in. °F) and D/δ , estimate the induction thermal factor, K_T (Fig. 26).
3. The power per unit length is calculated as the product of K_T and the allowable temperature differential (in °F) between the surface and center, $T_s - T_c$. Multiplying this by the length of the bar yields the net power required in kilowatts.

In addition to these estimates, radiation heat loss must also be considered when determining power ratings. The upper limit of radiation losses, which is defined by the emission characteristics of a blackbody, is shown in Fig. 27 as a function of temperature. Actual workpiece materials will exhibit less radiation loss than in Fig. 27 because their emissivities have lower values compared with the emissivity of blackbodies.

To avoid calculations of power requirements, tables of power densities ordinarily

used for through heating of steel (for hardening as well as other uses, such as forging) are available. One such listing is shown in Table 3. These values of power densities are based on typical electrical efficiencies and proper selection of frequency (which lead to D/δ ratios in the range of four to six). It may be noted that the larger-diameter bars, which can be heated efficiently with lower-cost, lower-frequency power supplies, typically employ smaller power densities than small-diameter

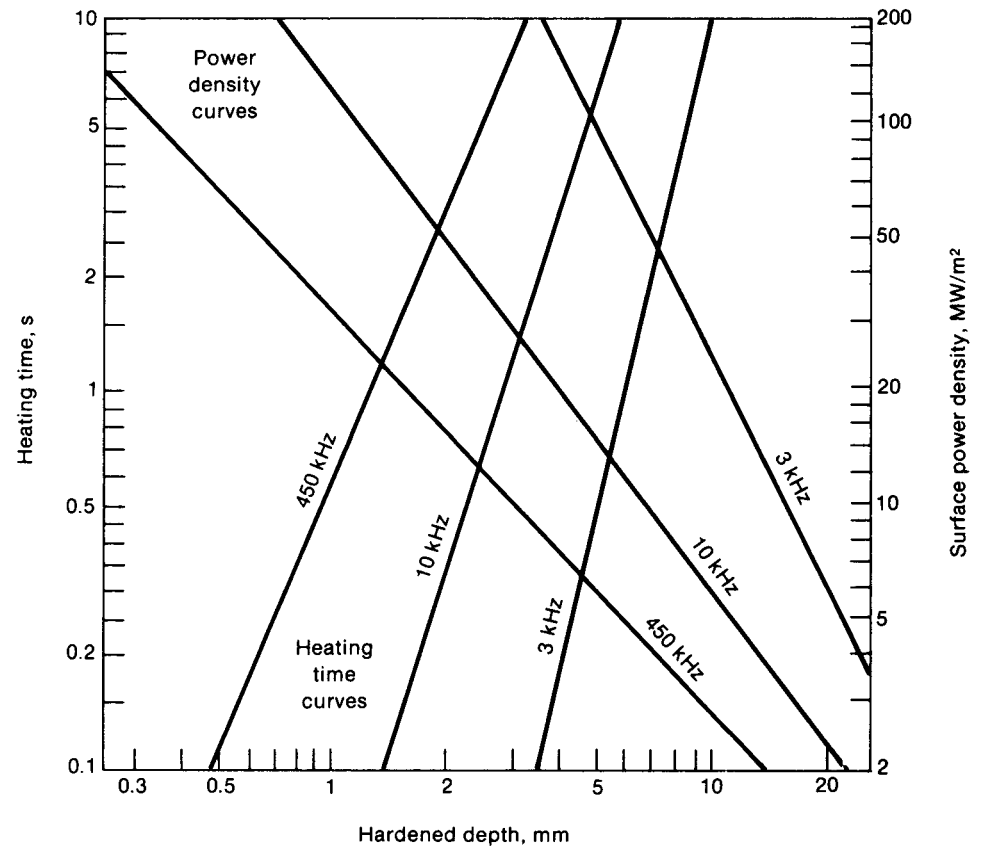


Fig. 25 Interrelationship among heating time, surface power density, and hardened depth for various induction generator frequencies. Source: Ref 8

Table 2 Typical rough estimates of power densities required for surface hardening of steel

Frequency, kHz	Depth of hardening(a)		Input(b)(c)					
			Low(d)		Optimum(e)		High(f)	
	mm	in.	kW/cm ²	kW/in. ²	kW/cm ²	kW/in. ²	kW/cm ²	kW/in. ²
500	0.381–1.143	0.015–0.045	1.08	7	1.55	10	1.86	12
	1.143–2.286	0.045–0.090	0.46	3	0.78	5	1.24	8
10	1.524–2.286	0.060–0.090	1.24	8	1.55	10	2.48	16
	2.286–3.048	0.090–0.120	0.78	5	1.55	10	2.33	15
	3.048–4.064	0.120–0.160	0.78	5	1.55	10	2.17	14
3	2.286–3.048	0.090–0.120	1.55	10	2.33	15	2.64	17
	3.048–4.064	0.120–0.160	0.78	5	2.17	14	2.48	16
	4.064–5.080	0.160–0.200	0.78	5	1.55	10	2.17	14
1	5.080–7.112	0.200–0.280	0.78	5	1.55	10	1.86	12
	7.112–8.890	0.280–0.350	0.78	5	1.55	10	1.86	12

(a) For greater depths of hardening, lower kilowatt inputs are used. (b) These values are based on use of proper frequency and normal overall operating efficiency of equipment. These values may be used for both static and progressive methods of heating; however, for some applications, higher inputs can be used for progressive hardening. (c) Kilowattage is read as maximum during heat cycle. (d) Low kilowatt input may be used when generator capacity is limited. These kilowatt values may be used to calculate largest part hardened (single-shot method) with a given generator. (e) For best metallurgical results. (f) For higher production when generator capacity is available. Source: Ref 15

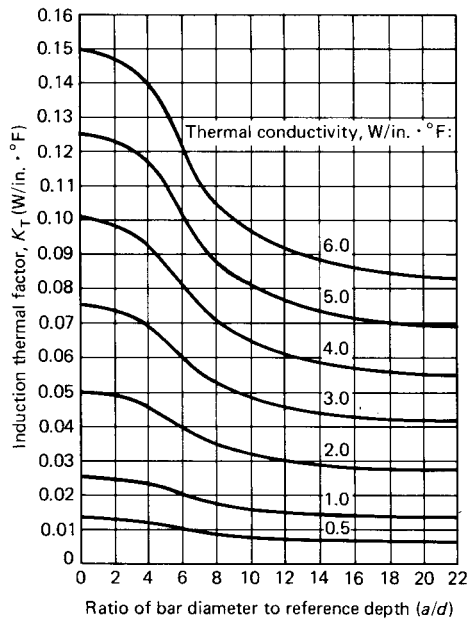


Fig. 26 Induction thermal factor for round bars as a function of the ratio of bar diameter to reference depth (a/d) and the thermal conductivity. Source: Ref 17

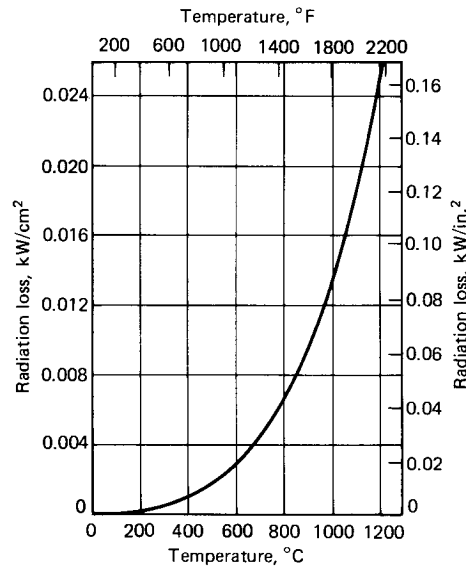


Fig. 27 Radiation heat loss as a function of surface temperature. Losses are based on blackbody radiation into surroundings at 20 °C (70 °F). Source: Ref 19

Table 3 Approximate power densities required for through heating of steel for hardening, tempering, or forming operations (Ref 19)

Frequency(a), Hz	Input(b)									
	150–425 °C (300–800 °F)		425–760 °C (800–1400 °F)		760–980 °C (1400–1800 °F)		980–1095 °C (1800–2000 °F)		1095–1205 °C (2000–2200 °F)	
	kW/cm ²	kW/in. ²	kW/cm ²	kW/in. ²	kW/cm ²	kW/in. ²	kW/cm ²	kW/in. ²	kW/cm ²	kW/in. ²
60	0.009	0.06	0.023	0.15	(c)	(c)	(c)	(c)	(c)	(c)
180	0.008	0.05	0.022	0.14	(c)	(c)	(c)	(c)	(c)	(c)
1000	0.006	0.04	0.019	0.12	0.08	0.5	0.155	1.0	0.22	1.4
3000	0.005	0.03	0.016	0.10	0.06	0.4	0.085	0.55	0.11	0.7
10,000	0.003	0.02	0.012	0.08	0.05	0.3	0.070	0.45	0.085	0.55

(a) The values in this table are based on use of proper frequency and normal overall operating efficiency of equipment. (b) In general, these power densities are for section sizes of 13 to 50 mm (½ to 2 in.). Higher inputs can be used for smaller section sizes, and lower inputs may be required for larger section sizes. (c) Not recommended for these temperatures

bars (Table 4). This is because of the greater times required for heat to be conducted to the center of the larger pieces. In addition, lower frequencies such as 60 and 180 Hz are not ordinarily recommended for through heating of steel parts with diameters less than 250 to 140 mm (9.8 to 5.5 in.), respectively, when temperatures above approximately 730 °C (1350 °F) are desired. This is due to the increased reference depth (and decreased skin effect) above the Curie temperature where the relative magnetic permeability drops to unity. An exception to this practice is the use of 60 Hz sources for induction heating of very large parts, such as steel slabs in steel mills. Tempering treatments may also use 60 Hz sources (Table 5).

When estimating power ratings for a particular application, it is important to take into consideration the expected coil efficiency and the presence of additional kilowatt losses induced

in electrically conductive bodies located in close proximity to the induction coil (e.g., rails, end plates, cabinets, magnetic concentrators, shunts, etc.) as well as transmission losses (e.g., bus bars, transformers, etc.).

Design of Induction Heating Coils. Guidelines for coil design are based largely on experience, and additional information is described in *ASM Handbook, Volume 4C, Induction Heating and Heat Treatment* (2014). Designing an induction coil is very specific to a given application, but there are several major functions that an induction coil must perform:

- Induce current in the load and accomplish the proper heating pattern with as high an electrical efficiency as possible
- Provide an impedance match to the generator so that adequate power can be transferred to the load

- Have a geometry that will accomplish the aforementioned two major functions and permit easy loading and unloading of the part being heated

The required production rate and the available power/frequency of the source may also influence coil design.

Low-frequency induction heating is generally desired for through heating of metals, particularly those with large and relatively simple cross sections. Low-frequency coils often have many turns. Generally, the lower the frequency, the larger the coil or the greater number of turns. (unless C-core or transverse inductors are used.)

Medium-to-high-frequency applications typically require specifically configured or contoured coils with the coupling adjusted for heat uniformity. In the simplest cases, coils are bent or formed to the contours of the part. Regardless of the final part contour, the most efficient coils are essentially modifications of the standard, round coil or channel-type inductors.

Coil Characterization. In static/stationary heating applications, because magnetic flux tends to concentrate toward the middle of the length of a solenoid work coil, the heating rate produced in this area is generally greater than that produced toward the ends (assuming that the lengths of the workpiece and the coil are approximately the same). Further, if the part being statically heated is long, conduction and radiation remove heat from the ends at a greater rate. To achieve uniform heating along the part length, the coil must thus be modified to provide better uniformity. The technique of adjusting the coil turns, spacing, overhang, or coupling with the workpiece to achieve a uniform heating pattern is known as coil characterization.

There are several ways to modify the flux field. The coil can be decoupled in its center, increasing the distance from the part and reducing the flux in this area. Secondly, and more commonly, having appreciable coil overhang and/or the number of turns in the center (turn density) can be reduced, producing the same effect. A similar approach—altering a solid single-turn inductor by increasing its bore diameter at the center—achieves the same result. Each of these techniques is described and illustrated in this section.

In Fig. 28(a), the coil turns have been modified to produce an even heating pattern on a tapered shaft. The closer turn spacing toward the end compensates for the decrease in coupling caused by the taper. This technique also permits through-the-coil loading or unloading to facilitate fixturing. A similar requirement in the heat treatment of a bevel gear is shown in Fig. 28(b). Here, because of the greater part taper, a spiral-helical coil is used. With a pancake coil, decoupling of the center turns provides a similar approach for uniformity.

Magnetic Flux Concentrators. The degree of coupling between the workpiece and the magnetic field of the coil is determined by the number of imaginary magnetic flux lines that

Table 4 Typical operating conditions for progressive through hardening of steel parts by induction (Ref 19)

Section size		Material	Frequency(a), Hz	Power(b), kW	Total heating time, s	Scan time		Work temperature				Production rate		Inductor input(c)	
mm	in.					s/cm	s/in.	°C	°F	°C	°F	kg/h	lb/h	kW/cm ²	kW/in. ²
Rounds															
13	½	4130	180	20	38	0.39	1	75	165	510	950	92	202	0.067	0.43
			9600	21	17	0.39	1	510	950	925	1700	92	202	0.122	0.79
19	¾	1035 mod	180	28.5	68.4	0.71	1.8	75	165	620	1150	113	250	0.062	0.40
			9600	20.6	28.8	0.71	1.8	620	1150	955	1750	113	250	0.085	0.55
25	1	1041	180	33	98.8	1.02	2.6	70	160	620	1150	141	311	0.054	0.35
			9600	19.5	44.2	1.02	2.6	620	1150	955	1750	141	311	0.057	0.37
29	1½	1041	180	36	114	1.18	3.0	75	165	620	1150	153	338	0.053	0.34
			9600	19.1	51	1.18	3.0	620	1150	955	1750	153	338	0.050	0.32
49	1½/6	14B35H	180	35	260	2.76	7.0	75	165	635	1175	195	429	0.029	0.19
			9600	32	119	2.76	7.0	635	1175	955	1750	195	429	0.048	0.31
Flats															
16	⅝	1038	3000	300	11.3	0.59	1.5	20	70	870	1600	1449	3194	0.361	2.33
19	¾	1038	3000	332	15	0.79	2.0	20	70	870	1600	1576	3474	0.319	2.06
22	⅞	1043	3000	336	28.5	1.50	3.8	20	70	870	1600	1609	3548	0.206	1.33
25	1	1036	3000	304	26.3	1.38	3.5	20	70	870	1600	1595	3517	0.225	1.45
29	1½	1036	3000	344	36.0	1.89	4.8	20	70	870	1600	1678	3701	0.208	1.34
Irregular shapes															
17.5–33	1½/6–1¾/6	1037 mod	3000	580	254	0.94	2.4	20	70	885	1625	2211	4875	0.040	0.26

(a) Note use of dual frequencies for round sections. (b) Power transmitted by the inductor at the operating frequency indicated. This power is approximately 25% less than the power input to the machine, because of losses within the machine. (c) At the operating frequency of the inductor

Table 5 Operating and production data for progressive induction tempering (Ref 19)

Section size		Material	Frequency, Hz	Power(a), kW	Total heating time, s	Scan time		Work temperature				Production rate		Inductor input(b)	
mm	in.					s/cm	s/in.	°C	°F	°C	°F	kg/h	lb/h	kW/cm ²	kW/in. ²
Rounds															
13	½	4130	9600	11	17	0.39	1	50	120	565	1050	92	202	0.064	0.41
19	¾	1035 mod	9600	12.7	30.6	0.71	1.8	50	120	510	950	113	250	0.050	0.32
25	1	1041	9600	18.7	44.2	1.02	2.6	50	120	565	1050	141	311	0.054	0.35
29	1½	1041	9600	20.6	51	1.18	3.0	50	120	565	1050	153	338	0.053	0.34
49	1½/6	14B35H	180	24	196	2.76	7.0	50	120	565	1050	195	429	0.031	0.20
Flats															
16	⅝	1038	60	88	123	0.59	1.5	40	100	290	550	1449	3194	0.014	0.089
19	¾	1038	60	100	164	0.79	2.0	40	100	315	600	1576	3474	0.013	0.081
22	⅞	1043	60	98	312	1.50	3.8	40	100	290	550	1609	3548	0.008	0.050
25	1	1043	60	85	254	1.22	3.1	40	100	290	550	1365	3009	0.011	0.068
29	1½	1043	60	90	328	1.57	4.0	40	100	290	550	1483	3269	0.009	0.060
Irregular shapes															
17.5–33	1½/6–1¾/6	1037 mod	9600	192	64.8	0.94	2.4	65	150	550	1020	2211	4875	0.043	0.28
17.5–29	1½/6–1¾/6	1037 mod	9600	154	46	0.67	1.7	65	150	425	800	2276	5019	0.040	0.26

(a) Power transmitted by the inductor at the operating frequency indicated. For converted frequencies, this power is approximately 25% less than the power input to the machine, because of losses within the machine. (b) At the operating frequency of the inductor. One mitigating effect that must be considered when establishing power requirements for austenitizing is the delay between the time at which the power is turned off and the time at which the quench is applied. Following heating, the temperature at the surface drops more rapidly than that at the center of the workpiece. Eventually, the center temperature becomes greater. Because of this, the heating and cooling cycles can often be adjusted to compensate for the nonuniform heating that characterizes induction processes. Thus, greater input power and higher heating rates can sometimes be realized than when quenching follows immediately after heating.

enter the workpiece. This magnetic flux density is proportional to the coil current, and the amount of energy transferred is proportional to the square of the number of flux lines intercepted by the workpiece. The frequency of coil currents also influences the pattern of induced currents, because flux lines tend to stay closer to the coil conductors as frequency is increased.

Flux leakage refers to the magnetic flux that does not thread through the heated material. The degree of flux leakage depends, in part, on the gap between the current-carrying surface of the coil conductors and the workpiece. This so-called air gap is of greater concern as frequency

increases, because flux lines tend to stay closer to the surface of coil conductors as frequency is increased.

Flux leakage can also be reduced by the use of flux concentrators, which are ferromagnetic materials purposely placed on or near the coil assembly. These devices provide a path of low magnetic reluctance and facilitate the concentration of flux lines in desired regions. If a ferromagnetic material is introduced into the coil field, it will provide a low-reluctance path for the flux (with minimum energy dissipation). This low-reluctance path reduces the stray flux and tends to gather flux lines, thereby concentrating the field. The use of flux concentrators

improves the load power factor and may also reduce coil current requirements.

Flux concentrators can play a very important role in enhancing the induction heating process when they are properly applied in and around the induction coil. The major uses of flux concentrators are to (Ref 3, 16):

- Improve heating at coil ends
- Improve the heating effect of internal coils
- Improve the heating effect of proximity or stray field coils
- Improve the general efficiency of an induction coil
- Provide shielding effect

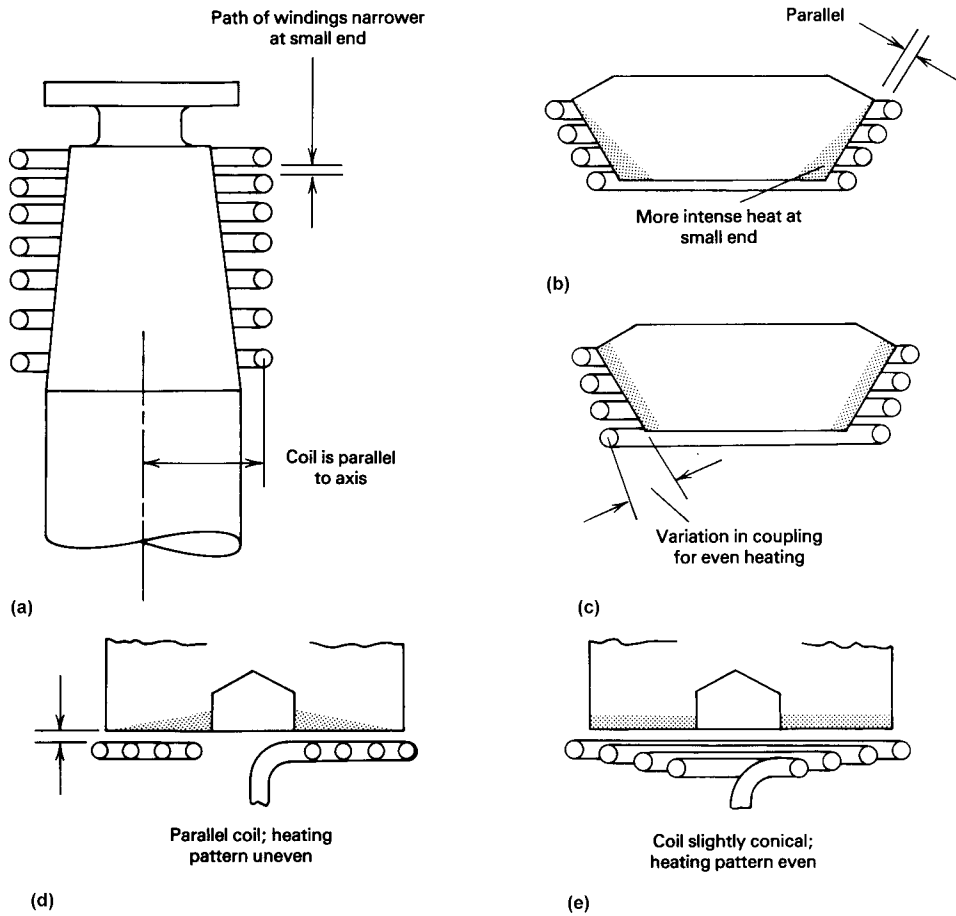


Fig. 28 Adjustment (coil characterization) of induction heating patterns for several parts by varying the coupling distance or turn spacing. Source: Ref 19

For example, flux concentrators applied at coil ends will increase heat intensity there and may help to make the heat pattern more uniform along the coil length. The performance from coils used to heat the inside or bore of a part also can be improved by placing the flux concentrator or core inside the coil. Transverse flux coils can heat more effectively when a flux concentrator is placed on the face opposite the heating face.

Modern, high-permeability, low-electrically-conductive materials are routinely used in a manner similar to that of magnetic flux cores in power transformers or motors. Different applications may call for different materials.

The material chosen for a flux concentrator depends on the applied frequency, the kind of service, and the degree of exposure to radiated heat. Commonly used materials include stacks of silicon-steel laminations used at frequencies below 15 kHz or ferrites and various iron- and ferrite-base composites for higher frequencies, including those in the radio-frequency range (Ref 3, 16).

There is a common misconception that the use of flux concentrators automatically means an increase in coil efficiency. Flux

concentrators improve the efficiency, partly by reducing the stray losses (by reducing the reluctance of the air path), but also by reducing the equivalent electromagnetic coupling distance between the coil and the workpiece. However, because the flux concentrator is an electrically conductive body and conducts high-density magnetic flux, there is some power loss generated as heat within it, due to Joule effect and hysteresis loss. This phenomenon could cause a reduction of electrical efficiency and the need for designing a special water-cooling system to remove the heat from the concentrator. The first two factors (reducing stray losses and coupling distance) counteract power loss, but the change in electrical efficiency is a result of all factors (Ref 3, 16). Therefore, in some cases, an efficiency reduction can actually take place after applying a magnetic flux concentrator. Typically, in induction-hardening applications using single-turn or two-turn inductors, the use of a magnetic flux concentrator noticeably increases coil efficiency.

Special care should be taken when applying flux concentrators to multiturn coils, because the voltage across coil turns can be significant, and a short current path may develop through

the concentrator. In this case, the reliability of the concentrator electrical insulation plays an essential role in induction coil design.

Surface-Hardening Parameters

Frequency Selection for Induction Surface Hardening. Frequency selection is appreciably more subtle for surface-hardening applications compared to through-heating applications. In surface-hardening (case-hardening) applications, a hard surface layer may be required at a particular surface (for example, inside diameter, outside diameter, butt end, fillet, etc.) of the heat treated component.

According to a classic definition of the skin effect (see earlier discussion), approximately 86% of all power induced by induction coil will be concentrated in the surface layer, called the current penetration depth. Frequency and temperature have a dominant effect on the magnitude of current penetration depth in steels and cast irons. By controlling the depth of current penetration, it is possible to austenitize selective areas of the component that require hardening without affecting the rest of the component. Depending on the required hardness case depth, the frequency selection for surface-hardening applications ranges from 60 Hz (hardening of large mill rolls) to greater than 450 kHz (hardening small pins).

It is also important to recognize that, in some cases, the frequency selection can be affected by an economical factor as well. A higher frequency rating usually reflects a higher capital cost for the equipment.

Induction heat treating practitioners typically divide frequencies into three categories: low frequency (below 10 kHz), medium frequency (from 10 to 90 kHz), and high frequency (above 90 kHz). With frequency increase, the depth of heating is decreased according to Eq 2 and 3.

Various case depths and hardness patterns can be achieved with the same inductor by changing the frequency, power density, and duration of heating. Figure 29 shows an impressive example of the diversity of achievable induction-hardening patterns when hardening gearlike components (Ref 3). The image at the left in Fig. 29 shows various hardness patterns that were obtained on the same carbon steel shaft with variations in heat time, frequency, and power density. The images at the right show a similar effect when surface hardening a spur gear. As a general rule, with encircling coils, when it is necessary to harden only the tips of the gear tooth, a higher frequency and high power density are applied; to harden the tooth roots, use a lower frequency. A high power density in combination with a relatively short heat time generally results in a shallow pattern, while a low power density and extended heat time produces a deep pattern with wide transition zones.

For illustration purposes, Fig. 30 shows sketches of three cases related to frequency

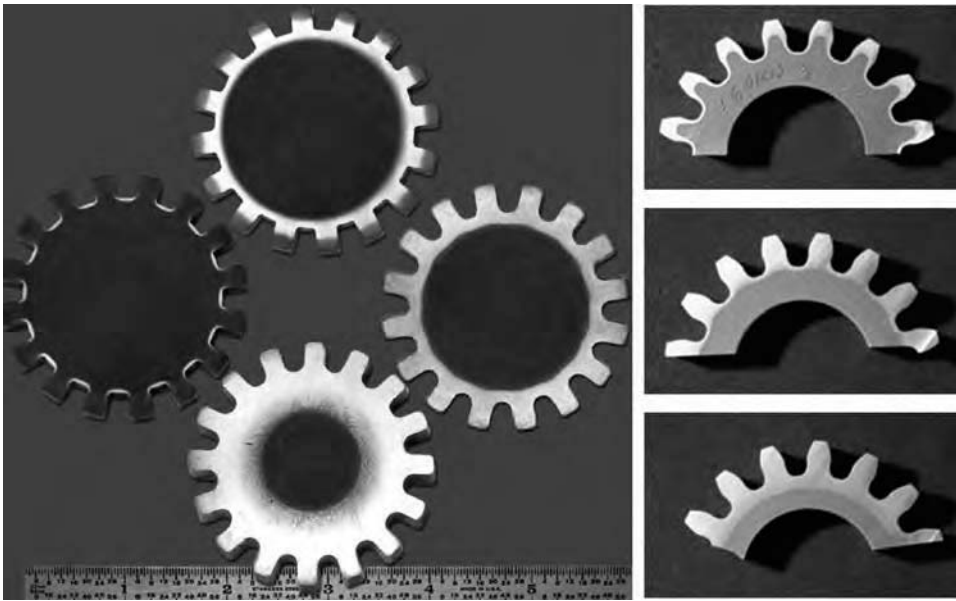


Fig. 29 Variety of induction-hardening patterns obtained by using variations in frequency, heat time, and power density. (Courtesy of Inductoheat Inc.)

selection when surface hardening of a solid shaft (Ref 3). In all three cases, it was possible to achieve the same case depth (indicated as a dotted line) while using three appreciably different frequencies designated as too high, too low, and optimal frequency. If the frequency is too high for the specified case depth, resulting in a too-small current penetration depth (Fig. 30, left), additional heating time is needed to allow the heat to be conducted to the desired depth to obtain the required hardness depth. Not only does this add unnecessary cycle time, but it may also lead to noticeable overheating of the surface, resulting in excessive grain growth, decarburization, scale formation, incipient melting, grain-boundary liquation, and other undesirable metallurgical phenomena.

Conversely, if the chosen frequency is appreciably lower than optimal frequency, it produces a depth of heating significantly greater than necessary. The result is a large heat-affected zone, additional shape distortion of the heat treated component, and unnecessary waste of energy to heat the greater-than-required mass of metal (Fig. 30, middle). In some cases, the penetration depth can be so large compared to the required hardened case depth that it will not be possible to meet a pattern specification, because the maximum permissible case depth is exceeded or the pattern repeatability may be altered.

Generally speaking, the desirable frequency results in a current penetration depth at a temperature above the Curie point within the range of 1.2 to 2.4 times the required hardness case depth. In this case, the surface of the component will not be overheated, and additional heat that is generated below the case depth will be

just sufficient to compensate for the cooling/soaking effect of the cold core.

Keeping in mind the aforementioned drawbacks of using other-than-optimal frequencies, it should be stated that in many cases it is possible to achieve the desirable hardness patterns by using an appropriate combination of power density, frequency, and heat time (as illustrated in Fig. 30). The basic rule is that when a shallow case depth is required, it may be possible to achieve the same case depth with a lower-than-recommended frequency by using a higher power density and a shorter heat time (faster scan rate). Conversely, if a deeper pattern is required, a higher-than-optimal frequency and a lower power density in combination with longer heat time should be used.

In the majority of cases, the frequencies used in surface hardening of regular-shaped components result in a pronounced skin effect, which eliminates the concern of eddy-current cancellation. However, if the workpiece has an irregular shape (e.g., C-shaped tubes, odd-shaped parts, or slotted cylinders), the eddy current may be forced to flow on the outside and inside areas of the part, with the potential of cancelling each other (Ref 3). The basic rule of thumb to avoid current cancellation in such cases is that the chosen frequency should result in a value of current penetration depth that would be no more than one-fourth the thickness of the current-conducting path (Ref 3).

Rules of Thumb. Over the years, industry has accumulated numerous “rules of thumb” for calculating process parameters for induction surface hardening. Most of those rules are extremely subjective and only related to the selection of frequency and power when

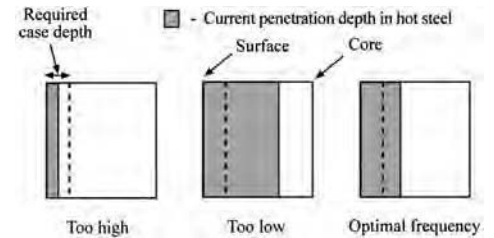


Fig. 30 Comparison of required case depth versus current penetration depths in hot steel at various frequencies. Source: Ref 3

performing single-shot hardening or scan hardening of regular-shaped cylinders (i.e., solid shafts) made from plain carbon steels. Some recommendations are shown in Table 2.

According to another rule of thumb, the required frequency for surface hardening of solid cylinders with a case depth ranging from 1.6 to 5 mm (0.05 to 0.2 in.) can be determined based on Eq 5 or 6:

$$\left(\frac{6.5}{X_{CD}}\right)^2 < \text{Frequency(kHz)} < \left(\frac{16.6}{X_{CD}}\right)^2 \quad (\text{Eq 5})$$

$$\text{Frequency(kHz)} \cong \left(\frac{9.8}{X_{CD}}\right)^2 \quad (\text{Eq 6})$$

where X_{CD} is the required case depth (in millimeters).

Example. If a 3 mm (0.12 in.) case depth is required, the calculation for the frequency range is:

$$\left(\frac{6.5}{3}\right)^2 < \text{Frequency(kHz)} < \left(\frac{16.6}{3}\right)^2$$

According to Eq 5, an appropriate frequency range will be 4.7 kHz < 30.6 kHz. In comparison, the most desirable frequency according to Eq 6 will be 10.7 kHz.

Components of smaller sizes (smaller outside diameter) shift the expression (Eq 5) toward using higher frequencies. In contrast, lower frequencies could be used when induction case hardening larger-sized parts.

Power Selection. The typical power ratings given in Table 2 are based on the need to heat to temperature very rapidly, and they have proven to be appropriate through years of experience. Two examples serve to show that these numbers should be used only for rough estimation.

First, consider induction hardening the surface of a small-diameter shaft by a 500 kHz generator. For a case depth of 0.75 mm (0.03 in.), 6.5 cm² (1 in.²) of surface requires 0.00064 kWh (2.18 Btu), or 2.30 kW-seconds, of energy to be heated to 870 °C (1600 °F). Thus, a generator that can supply 1.55 kW/cm² (10 kW/in.²) of surface, operating at 100% efficiency, can heat the surface in 0.23 s. In practice, it will take noticeably longer because of

generator and coil losses as well as the fact that some of the power is used to heat the inner layers of the workpiece, due to thermal conduction to temperatures below the transformation temperatures.

As another illustration, consider case hardening a larger-diameter shaft to a depth of 7.6 mm (0.3 in.) using a 1 kHz generator. The energy required is 10 times that for the previous example, or 3.55 kW-seconds/cm² (22.9 kW-seconds/in.²) of surface. Similarly, a power rating of the order of 15.5 kW/cm² (100 kW/in.²) would be required to surface heat the shaft to temperature in an identical time. Because cost and the likelihood for surface overheating increase with power rating, a power of only 1.55 kW/cm² (10 kW/in.²) or slightly more would also be optimal in this instance. The time to heat to temperature at this power level would still be only 2.3 s under idealized conditions, or probably around 2 to 3 times this period in practice. For other case depths and frequencies, it may be noted from Table 2 that a power rating of approximately 1.55 kW/cm² (10 kW/in.²) of surface to be treated is the typical recommendation.

However, the microstructure of steel prior to heat treatment has a pronounced effect on the results of the heat treatment, and it is imperative to keep in mind that most rules of thumb assume hardening of fine-grained, normalized, homogeneous, ferritic-pearlitic prior structures with a carbon content of approximately 0.4 to 0.5%. Even for the same grade of steel (AISI 1042), the required induction-hardening temperature range depends on the heat intensity as well as the prior microstructure of the steel:

- 880 to 1095 °C (1620 to 2000 °F) for annealed prior microstructures
- 840 to 1000 °C (1550 to 1830 °F) for normalized prior microstructures
- 820 to 930 °C (1510 to 1710 °F) for quenched-and-tempered prior microstructures

Tempered martensite ensures rapid transformation, which lowers the temperature required for austenite formation. This results in a fast, consistent response of the steel to induction hardening with minimum amounts of grain growth, shape/size distortion, and surface oxidation; a minimum required heating energy; and a well-defined—or “crisp”—hardness pattern having a narrow transition zone. This type of initial structure can even result in slightly higher hardness and a deeper hardened case depth as well as lower coil power compared with other prior structures. Normalized microstructures, consisting of homogeneous, fine pearlitic structures, also are responsive to austenitization. In contrast, steels with large stable carbides (spheroidized microstructures) have poor response to induction hardening and also result in the need for prolonged heating and significantly higher temperatures to complete austenitization.

After selecting the frequency and power density, the last parameter is the duration of heat. Typically, induction-hardened components are heated to hardening temperatures within several seconds or even during a fraction of a second (i.e., gear contour hardening using a dual-frequency source). Upon choosing an appropriate frequency and power density based on one of the aforementioned criteria, the duration of heat can also be determined after several heat trials and evaluation of obtained hardness patterns. Numerical computer modeling (e.g., finite-element analysis) can provide more accurate results than rough-estimation techniques that are based on simplified formulas, graphs, or tables.

Heating Times for Austenitization. The information given earlier (Fig. 25) is useful for estimation of frequency and power density for surface and through hardening and tempering. However, the question often arises as to the heating time that one should use. For through-heating applications, this is a relatively straightforward calculation based on the heat capacity and weight of the workpiece, the input power, the system efficiency, and the desired final temperature. In a through-hardening application, only a minimum time need be estimated in this manner. Longer times can often be used without deleterious results.

On the other hand, time is a critical factor in surface-hardening operations. If the heating time is too long, the workpiece may reach austenitizing temperature at locations deeper than necessary for the desired case thickness. As noted, prior microstructure also has a more pronounced effect on the time required for austenitization when shorter heating times are involved. This can dramatically influence the selection of heat time, power, and, in some instances, frequency.

Rapid heating also reduces the effect of thermal conduction and tends to austenitize only the area where eddy currents were induced (i.e., the outer surface layer). This results in a very short transition zone. With an increase in heat time, thermal conductivity begins to play an increasingly appreciable role, allowing the heat to soak from higher-temperature surface areas toward lower-temperature internal regions, leading to a fuzzy transition area of the hardened pattern and requiring a greater amount of energy.

Longer heating times lead to grain growth, the formation of coarse martensite, a larger transition zone, surface oxidation, and increased shape distortion. Physics dictates that if a greater amount of heat is induced in the workpiece, then a larger mass of steel will be heated, leading to greater workpiece expansion which often results in more shape distortion. Therefore, to decrease the distortion of hardened components, it is desirable to keep the heating time as short as possible. However, there are limits to shortening the heating time while also achieving the minimum required transformation temperature to create a homogeneous austenite at the depth to be hardened.

Short heating times may be undesirable when:

- A combination of unreasonably high frequency and/or surface power density leads to surface overheating and undesirable microstructures.
- A combination of high frequency and/or surface power density produces a substantial temperature gradient during heating that causes cracking of more brittle materials (i.e., high-carbon steels and gray cast irons). In such cases, it may be desirable to use longer heating times with lower power density.
- Geometrical irregularities (sharp corners, holes, keyways, grooves, edges, etc.) cause hot and cold spots. In these cases, a less intensive heat and longer heat times are also desired, including the use of dwells before quenching to allow thermal conduction to reduce the temperature of hot spots and equalize heat distribution.

Methods to Establish the Heating Time for Surface Hardening.

Three methods are available to establish the heating time for surface-hardening operations. One involves a trial-and-error procedure in which the power and heating time are varied until the needed hardness and hardened depth are obtained. The hardened depth is determined metallographically by sectioning and acid etching. If the case is too shallow, the power input and/or heating time should be increased. Conversely, if it is too deep, the power and/or the heating time should be decreased. Metallography will also show the presence of various microstructural constituents, such as martensite or the presence of upper transformation products, which can be used as an indication of proper or improper austenitization.

A second method of determining appropriate surface-hardening parameters, including heating time, is through the use of graphs such as the ones shown in Fig. 25 and 31. Figure 25 gives the relation between frequency, applied power density, heating time, and hardened depth for steels that are austenitized at temperatures between 850 and 900 °C (1560 and 1650 °F) using a single-shot induction heating method. As illustrated in the figure, it is apparent that, for a given power density and heating time, shallow case depths require higher frequencies, or, at a fixed frequency, shallow case depths need high power densities for shorter times.

Figure 31 is a similar nomograph designed for surface hardening via a scanning technique. The curves give the approximate relationship between power density and heating time in the coil for various case depths. Note that the curves apply only to a 10 kHz power supply. A similar set of curves can be used for other frequencies. Whenever possible, the greatest operating efficiencies are obtained by using operating conditions close to the steeper part of the curves.

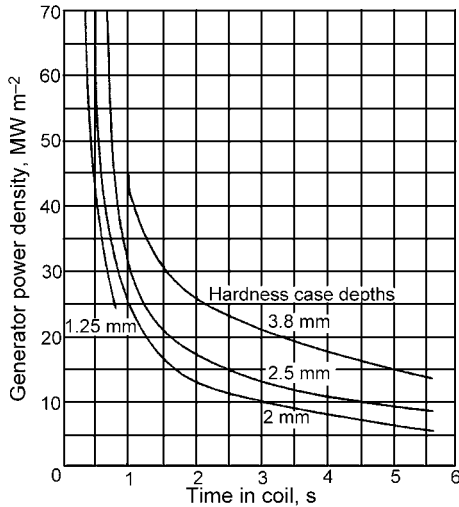


Fig. 31 Relationship between power density, time in coil, and hardened depth for shaft hardening via a scanning method. Generator frequency = 10 kHz; minimum scanning rate = 50 mm/s¹; minimum shaft diameter = 16 mm (0.6 in.). Source: Ref 18

A third method of determining optimal process parameters for surface hardening is related to the use of numerical computer modeling, which became increasingly popular in the last five years.

However, it is imperative to remember that using rules of thumb as well as the use of rough-estimation techniques can be misleading in determining an optimal combination of process parameters. Material specifics, prior structure, geometry, and functionality can influence results. Numerical computer modeling may help in obtaining better recommendations.

Application Tips and Troubleshooting

Parts with Complex Geometries. Complex-shaped parts with geometrical stress raisers (i.e., holes, sharp corners, grooves, undercuts, diameter changes, etc.) can present challenges in avoiding localized overheating and cracking and obtaining the required hardness pattern. Sharp corners and poor chamfering or rounding of holes and edges can lead to local overheating, resulting in excessive thermal stresses and excessive grain growth that may, in turn, cause cracks to form. If a part consists of a combination of thick and thin sections, the thick sections may not come up to the required temperatures during heating as quickly as the thin sections. Inductor profiling and the use of special process settings can help to overcome this problem (Ref 3).

Thickness variations of complex-geometry parts may create some difficulties in obtaining the required heat treating pattern during quenching as well, because there may be a noticeable cooldown difference between

thinner sections compared to massive areas. Special adjustments in inductor design and quench blocks should be made.

The proper choice of design parameters (applied frequency, power density, coil geometry, steel selection, etc.) allows the heat treater to obtain the required heat treating pattern even in cases when an undesirable combination of electromagnetic end effect and thermal edge effects seem unsuitable for hardening by induction.

Induction Surface Hardening of Powder Metallurgy Parts. Surface hardening of ferrous powder metallurgy (PM) parts is an important application of induction hardening, and PM parts have several peculiarities compared with hardening wrought steels and cast irons. Inconsistent results are often observed when induction hardening highly porous (low-density) PM parts. The composition and homogeneity of PM materials also affect induction hardening.

Density and/or porosity may include cracking and variations in surface hardness and case depth. Low-density PM parts are good candidates for cracking, because interconnected pores contribute to decreased part strength and rigidity compared with wrought materials. In addition, the poor thermal conductivity of porous PM parts encourages the development of hot spots, requiring intense quenching, which results in severe thermal gradients that also increase the tendency for cracking. Variations of electrical resistivity and magnetic permeability lead to variations in the amount of power induced within the PM workpiece and the depth of eddy-current penetration, resulting in heat pattern variation.

Electrical resistivity, thermal conductivity, and magnetic permeability are strongly dependent on the amount of porosity in the sintered compact. This helps explain why the induction-hardening response of PM parts is more sensitive to variations in material properties than that of castings or forgings. The effects of density reduction (porosity increase) on some properties and induction-hardening parameters are given in Table 6.

Low density (high porosity) negatively affects hardenability. Therefore, when induction hardening PM parts, good practice requires having a density of at least 7.0 g/cm³ (0.25 lb/in.³) but preferably 7.2 g/cm³ (0.26 lb/in.³) or greater. This will help ensure

consistent heat treating results, particularly when hardening internal surfaces that have undercuts, teeth, splines, sharp corners, slots, and other stress raisers.

Composition and Homogeneity. Density and porosity are not the only factors that affect the induction hardening of PM parts. Material composition is another. Copper, nickel, and molybdenum are the most commonly used steel powder alloying elements. Depending on their specific composition and alloying techniques, some parts may have a greater tendency to crack. Copper-alloyed PM steels require particular attention when developing an induction-hardening recipe.

Other factors that affect the heat treating quality of a PM part are the homogeneity of its microstructure (material segregation), surface condition, and parameters of the heat treating process, as well as specifics of prior processing operations such as sintering. In the case of sintering, factors include the process sequence, atmosphere used, pressure, temperature, degree of sintering, and graphite segregation. High-temperature sintering is preferred because it improves microstructural homogeneity and ensures good diffusion. However, decarburization of the surface prior to induction hardening should be avoided.

The alloying method used to produce the powder also can have a marked effect on heat treating results. Among alloying techniques are admixing, diffusion alloying, prealloying, hybrid alloying, and the metal injection molding method. The technique used can affect material segregation and chemical and microstructural heterogeneity, due to different areas of the part undergoing abnormal phase transformations during cooling. For example, large inclusions may form that can serve as stress raisers, increasing the potential for cracking and/or inconsistent hardness readings.

It is quite common for PM parts to absorb 2% oil by weight. Therefore, steps must be taken to ensure that quenchants remain clean and that sufficient ventilation is provided.

Other media frequently used include water-based polymer quenchants and water (containing appropriate additives). Note that oils typically require higher hardening temperatures than polymer quenchants and water.

Shape/size distortion and warping due to heat treating are usually less for PM components

Table 6 Effect of density reduction (porosity increase) on some properties and induction-hardening parameters

Property	Change	Influence on induction heat treatment process
Thermal conductivity	Decrease	Less soaking action from high-temperature to low-temperature regions. Larger temperature gradients and thermal stresses during heating. Slower cooling during quenching
Electrical resistivity	Increase	Larger current penetration depth
Magnetic permeability	Decrease	Larger penetration depth and lower coil electrical efficiency
Hardenability	Decrease	More severe quench required to provide the same case depth
Structural homogeneity	Worse	Inconsistency of hardening: variations in surface hardness, case depth, hardness scatter, and residual stress data. Tendency for cracking during hardening

Source: Ref 3

than for their wrought steel counterparts. The degree of shape deformation strongly depends on part/coil geometry and hardness pattern, and usually is determined experimentally.

Powder metallurgy steel parts often have a variable surface-to-core or outside-diameter-to-inside-diameter density. The density at the surface to be hardened typically is 7.5 g/cm³ (0.27 lb/in.³) or higher. This gradually decreases to a base density of 7.0 g/cm³ (0.25 lb/in.³) at the center of the part.

When determining process parameters for induction hardening of PM parts, energies and frequencies higher than those used for wrought alloys of similar composition often are chosen. Closer process control also is required. Preheating is sometimes necessary to avoid cracking and to obtain the required heat treating pattern of parts with appreciable stress raisers.

As with conventional furnace heat treatments, problems such as surface decarburization, surface defects (e.g., seams, laps, etc.), distortion, cracking, and dimensional changes should be considered in the design of induction-hardening processes. Any surface defects remaining from the steelmaking process can also cause cracks and/or undesirable metallurgical structures.

Surface Decarburization. Decarburization is the loss of carbon from the surface of steel after being heated to sufficiently high temperature without a protective atmosphere during manufacture. Because the carbon content of steel determines the hardness level that can be achieved in austenitized and quenched parts, surface decarburization causes a soft surface hardness that can lead to tensile stresses at the surface, which in turn reduce strength and can cause cracking.

All medium- and high-carbon steel bars have surface decarburization to some degree, because of the method of steel manufacture. This condition as well as others resulting from the steelmaking process (seams, laps, etc.) must be removed prior to heat treatment in order to achieve the desired result. The Recommended Stock Removal tables for various sizes of bar stock are published by the American Iron and Steel Institute and are available from steel manufacturers. Forging processes also contribute to surface decarburization of steel, which must be removed from forgings prior to induction hardening.

The actual induction-hardening process can add only a small amount of decarburization—on the order of approximately 0.02 mm (0.0008 in.) depth of decarburization after induction heating for 5 s at 960 °C (1760 °F). In addition, microstructural and chemical inhomogeneities (such as banding), which are carried through the melting and hot rolling operations during steel production, particularly in resulfurized grades such as 1137, 1141, and 1144, may affect the ability to obtain a uniformly heat treated product.

Distortion. Dimensional changes developed during hardening operations have two main sources: residual stresses and volume changes associated with phase transformation. For many

surface-hardening applications, the dimensional changes associated with these effects are usually minimal; in some surface-hardening jobs, such as hardening of shafts with grooves, they are not. Similarly, through-hardening applications can produce size changes that are not negligible. Those due to residual stresses (arising from thermal or phase-change effects) vary with material, part shape, and processing parameters. On the other hand, dimensional alterations resulting from phase changes can be estimated from the data in Table 7.

It is seen that volume change is greatest when a martensitic structure is produced in a part with a starting spheroidized microstructure. Less change can be expected after hardening a part with an initial bainitic or fine pearlitic structure.

In contrast to the dimensional changes associated with hardening, those in tempering generally involve volume decreases. This trend occurs when carbon is precipitated from solution in martensite, leading to a higher-density microstructure of ferrite and carbides. In steels in which austenite is retained following quenching, however, bainite or pearlite formation from the austenite may produce volume increases during tempering. For these reasons, tempering may give rise to overall dimensional decreases or increases.

Parts distortion is commonly caused by relief of residual stresses, uneven heating, nonuniform quenching, or hardening nonsymmetrical parts. In many cases, the problem can be controlled by modifications to inductors, quenching systems, or part-handling techniques during heating and quenching. When the workpiece has an axisymmetric shape, it is very important to place the induction coil so that symmetric heating and quenching is achieved, resulting in uniform thickness of the hardened layer with a martensitic microstructure.

Distortion during austenitizing usually results from relief of residual stresses introduced during forging, machining, and so on or from nonuniform heating. When the cylindrical part (i.e., shaft) is only surface austenitized and hardened, the cool metal in the core of the workpiece minimizes distortion. Small amounts of distortion in induction-surface-hardened parts with shallow cases are often eliminated by means of a subsequent mechanical sizing (e.g., grinding, straightening) operation. Furthermore, the use of induction scanning, in which only a small portion of the workpiece is

Table 7 Change in volume during transformation to differing phases of steel

Transformation	Change in volume, %
Spheroidized pearlite → austenite	-4.64 + 2.21 · (% C)
Austenite → martensite	4.64 - 0.53 · (% C)
Spheroidized pearlite → martensite	1.68 · (% C)
Austenite → lower bainite	4.64 - 1.43 · (% C)
Spheroidized pearlite → lower bainite	0.78 · (% C)
Austenite → upper bainite	4.64 - 2.21 · (% C)
Spheroidized pearlite → upper bainite	0

heated at any one time, is helpful in preventing problems of this type. Scanning is also helpful in keeping distortion levels low in through-hardening applications. In these instances, rotation of the part enhances the heating uniformity and decreases the likelihood for nonuniformities in the final shape. It is important to note that part wobbling during rotation (which may occur due to excessively worn bearings) cannot be compensated by part rotation.

Distortion resulting from quenching is a function largely of the austenitizing temperature, the uniformity of the quench, and the quench medium. Higher austenitizing temperatures, which give rise to higher transitional and residual stresses, increase the amount of nonuniform contraction during cooling. Severe quenches such as water or brine, which also tend to produce high residual stresses, can lead to severe distortion as well. The problem can be especially troublesome when alloy steels are quenched into water. However, these steels usually have sufficient hardenability such that oil or high-concentration polymer quenchants can often be employed instead.

Part distortion may also occur as a result of nonuniform starting microstructure in a part to be induction hardened. For example, decarburization that varies around the periphery can give rise to distortion because of variations in the volume changes that accompany the formation of martensite.

Cracking. In extreme cases, distortion may lead to cracking. This cracking is intimately related to part design as well as the transitional and residual stresses that are developed. Components with large discontinuities in cross section are particularly difficult to heat treat, for this reason. In addition, many times there is a limiting case depth beyond which cracking can potentially occur (Fig. 32); in these instances, tensile stresses near the surface of the induction-hardened part, which balance the compressive residual stresses generated, can be blamed for the cracking problem.

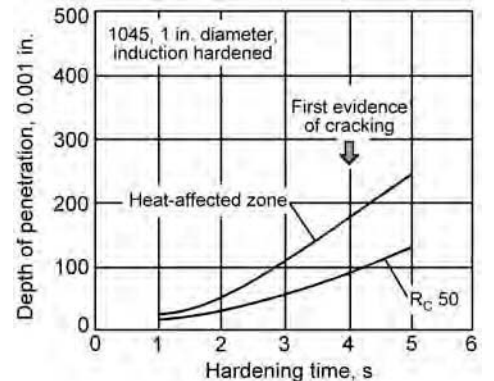


Fig. 32 Effect of heating time on hardened depth and tendency toward quench cracking of machined and ground 1045 steel bars induction heated (450 kHz, 50 kW generator) and water quenched to a surface hardness of HRC 62. Source: Ref 15

Steel composition also plays a role in the tendency toward cracking in induction-hardening applications. This tendency increases as the carbon or alloy content is increased. The effect of carbon on the tendency toward quench cracking is greatest in through-hardened parts and arises because of its influence on the depression of the M_s temperature and the hardness of the martensite. This is not to say, however, that critical levels of constituents can be specified, because other factors such as case depth (in surface-hardening applications), part design, and quench medium are also important.

As the carbon content is increased, the M_s temperature is lowered. Because the transformation occurs at lower temperatures, larger surface tensile residual stresses are produced. (Note that surface residual stresses, which are tensile in nature, are often generated during through-hardening processes. Subsequent tempering can reduce such residual stresses.) These residual stresses have a greater effect at lower temperatures, at which ductility is lower than at higher temperatures. Moreover, the ductility/toughness of higher-carbon martensite at a given temperature is lower than that of lower-carbon martensite. Therefore, the combination of high tensile residual stresses and low ductility/toughness contributes to quench cracking.

However, inasmuch as hardness increases with carbon content, quench-cracking problems can often be minimized by employing slower cooling rates (through the use of a milder quenchant), by decreasing the difference between the austenitizing and quenching temperatures, both of which tend to reduce residual stresses, or by using an interrupted quench. Sometimes, higher-hardenability steels must be used to take advantage of these alternatives. Also, in some situations, quench-cracking problems can be alleviated by switching to lower-carbon or more ductile/tough steels.

Besides low toughness and ductility, induction hardening of high-carbon steels is associated with an increased amount of retained austenite, unless cryogenic treatment is used. Transformation of retained austenite could occur during service life, leading to increased distortion and brittleness.

Even if distortion and quench cracking are not a problem, the dimensional changes that occur as a result of induction heat treatment

should be evaluated, particularly if little or no machine finishing is to follow hardening and tempering of close-tolerance parts.

ACKNOWLEDGMENTS

The contents of this article were adapted with permission of the copyright holder ASM International:

- Grum, Induction Hardening, *Failure Analysis of Heat Treated Steel Components*, ASM International, 2008
- P.A. Hassell and N.V. Ross, Induction Heat Treating of Steel, *Heat Treating*, Vol 4, *ASM Handbook*, ASM International, 1991, p 164–202
- “Induction Heat Treatment,” Lesson 14, ASM Course on Advanced Heat Treating, ASM International
- V. Rudnev, Simulation of Induction Heat Treating, *Metals Process Simulation*, Vol 22B, *ASM Handbook*, ASM International, 2010, p 501–546
- S.L. Semiatin and S. Zinn, *Induction Heat Treating of Steel*, ASM International, 1988

REFERENCES

1. J. Grum, Induction Hardening, *Materials Science and Technology Series*, Vol 1, Faculty of Mechanical Engineering, Ljubljana, 2001
2. K.E. Thelning, Chap. 6.6: Induction Hardening, *Steel and Its Heat Treating*, *Bofors Handbook*, Butterworth, London and Boston, 1975, p 432–451
3. V. Rudnev, D. Loveless, R. Cook, and M. Black, *Handbook of Induction Heating*, Marcel Dekker, New York, 2003
4. S.L. Semiatin and D.E. Stutz, *Induction Heat Treating of Steel*, American Society for Metals, 1986
5. S.L. Semiatin and S. Zinn, *Induction Heat Treating of Steel*, ASM International, 1988
6. V. Rudnev, R. Cook, D. Loveless, and M. Black, Induction Heat Treatment: Basic Principles, Computation, Coil Construction, and Design Considerations, *Steel Heat Treatment Handbook*, G. Totten and

- M. Howes, Ed., Marcel Dekker, New York, 1997, p 765–872
7. P.G. Simpson, *Induction Heating Coil and System Design*, McGraw-Hill, New York, 1960
8. M.G. Lozinskii, *Industrial Applications of Induction Heating*, Pergamon Press, London, 1969
9. V. Rudnev, Computer Modeling Helps Identify Induction Heating Misassumptions and Unknowns, *Ind. Heat.*, Oct 2011, p 59–64
10. J. Grum, Induction Hardening, *Failure Analysis of Heat Treated Components*, ASM International, 2008, p 417–502
11. W. Amende, Transformation Hardening of Steel and Cast Iron with High-Power Lasers, Chap. 3, *Industrial Applications of Lasers*, H. Koenner, Ed., John Wiley & Sons, Chichester, 1984, p 79–99
12. V. Rudnev, Metallurgical Insights for Induction Heat Treaters, Part 2: Spray Quenching Subtleties, *Heat Treat. Prog.*, Aug 2007, p 19–20
13. V. Rudnev, Spray Quenching in Induction Hardening Applications, *J. ASTM Int.*, Vol 6 (No. 2), Jan 2009
14. V. Rudnev, Professor Induction Series: Induction Heating, Q&A, *Heat Treat. Prog.*, Sept 2009, p 29–32
15. T.H. Spencer et al., *Induction Hardening and Tempering*, American Society for Metals, 1964
16. V. Rudnev, An Objective Assessment of Magnetic Flux Concentrators, *Heat Treat. Prog.*, Nov/Dec 2004, p 19–23
17. C.A. Tudbun, *Basics of Induction Heating*, Rider, N.Y., 1960
18. J. Davies and R. Simpson, *Induction Heating Handbook*, McGraw-Hill, Ltd., 1979
19. P.A. Hassell and N.V. Ross, Induction Heat Treating of Steel, *Heat Treating*, Vol 4, *ASM Handbook*, ASM International, 1991, p 164–202
20. “Induction Heat Treatment”, Lesson 14, ASM course on Advanced Heat Treating, ASM International
21. F.W. Curtis, *High-Frequency Induction Heating*, McGraw-Hill, New York, 1950

Electron Beam Surface Hardening

Rolf Zenker and Anja Buchwalder, Technical University Bergakademie Freiberg
Institute of Materials Engineering, Freiberg, Germany

ELECTRON BEAM HARDENING (EBH) is one of the most modern surface-hardening technologies, with some special characteristics in comparison to other heat treatment technologies. Electron beam hardening is similar to other surface heat treatment processes in that the material to be hardened is heated to the austenitization temperature, held at that temperature for a short period, and then quenched. Martensitic transformations occur that generally differ neither thermodynamically nor kinetically from the transformations occurring under conventional conditions. Electron beam hardening belongs, as does laser beam hardening (LBH), to the process group known as short-cycle heat treatments. When compared to all other conventional volume and surface-layer heat treatment processes, the temperature-time (T - t) cycles are characterized by significantly higher austenitizing temperatures, T_A (with T_A close to the melting temperature, T_M), as well as considerably higher heating and cooling rates (10^3 to 10^4 K/s) and short austenitization times (0.1 to 3 to 5 s). Another similarity to LBH as opposed to conventional heat treatments, which need additional cooling media, is that cooling occurs from T_A via self-quenching, that is, the heat produced in the material by the electron beam (EB) or laser beam flows rapidly into the material mass. The advantages of EBH when compared to other surface hardening, including LBH processes, arise in particular from the physical characteristics of the EB, which can be transformed with exceptional readiness into technical and technological advantages. The most advantageous characteristics of electron beams are their excellent formability and deflectability, which allow beam deflection frequencies of up to 100 kHz.

Other important facts are the high productivity and low cost of the EB process. Thermal EB processes are realized in a vacuum. In the past, processing under vacuum was described as a disadvantage. However, because of the inert effect of the vacuum, secondary negative effects (oxidation, decarburization, or hydrogen embrittlement) are avoided. In modern EB facilities, the process sequences and facility layouts are optimized such that the evacuation

period does not impair the productivity of the machine.

During the last 30 years, EB surface technologies have been implemented at the industrial scale, with various interesting and innovative applications. As a result of the high-frequency beam deflection technique (Ref 1–4) and its further development (Ref 5–10), EBH has become more and more efficient. Both the basics of the interaction of electrons with materials and their effects on structure and properties have been investigated (Ref 9, 11–20), and the progress in industrial application has been advanced (Ref 7, 9, 10, 16, 19–21). Results regarding the combination of EBH with nitriding and/or hard coating have already been published and are used in industrial applications (Ref 22–25). Electron beam surface treatments are used, in particular, for enhancing internal stress conditions, surface hardness, and wear resistance. The success of EB surface treatment depends, among other things, on the technology chosen and the material to be treated, combined with a suitable beam deflection technique that is related to the geometry of the component, especially its surface contour. The energy of the beam must be transferred into the material in order to achieve surface-layer properties and gradients that enable the material to cope with relevant stress conditions.

Today (2103), there are not only numerous innovative solutions in the field of EBH, but modern EB facilities and complete manufacturing systems are also available. Electron beam hardening is employed as a job-shop solution for individual one-off part treatment, for small- and medium-sized series production with associated component variety, and for large-series mass production.

The challenge is to find intelligent solutions for processing in connection with suitable facilities concepts.

There are other EB surface-layer technologies in which, in contrast to EBH, the material zones subjected to energy input by EB change to the liquid state up to a certain depth, such as remelting (without additives), and alloying, dispersing, or cladding (with additives), for example. These treatment variations

are especially advantageous in applications for nonhardenable ferrous materials (e.g., austenitic and ferritic steels or cast iron materials) and lightweight alloy materials based on magnesium, aluminum, and titanium, as well as copper- or nickel-base alloys. Such processing technologies, however, are not the focus of this article.

This article aims to illustrate the principles of thermal EB technologies and to characterize the technical and technological possibilities for EBH in comparison to other surface-layer hardening processes. Furthermore, this article seeks to present modern EB facilities and present the state of current industrial application via numerous examples of use.

This article deals with the topical knowledge about modern EBH technology.

Electron Beam Generation and Interaction with Material

Electron Beam Generation

Figure 1 shows a schematic configuration of an EB machine. The electron beam is produced in an electron beam generator through the emission and acceleration of free electrons (beam generation) and is centered, shaped, focused, and deflected (beam guidance). When the beam impacts the material to be processed in the working chamber, various interaction processes occur.

The generation of the EB is based on the thermal emission of electrons. In industrial processes, a tungsten cathode is preferred for use. This cathode is directly (band cathode) or indirectly (bolt cathode) heated to very high temperatures (>2500 °C, or 4530 °F). This causes numerous electrons to emerge from the cathode surface and to form a so-called “electron cloud,” into which new electrons are constantly emitted and from which others return to the surface of the cathode material (Fig. 2).

Through application of a high voltage (60 to 150 kV) in the beam-generation system between the cathode and anode (Fig. 2b), the electrons are accelerated in the direction of

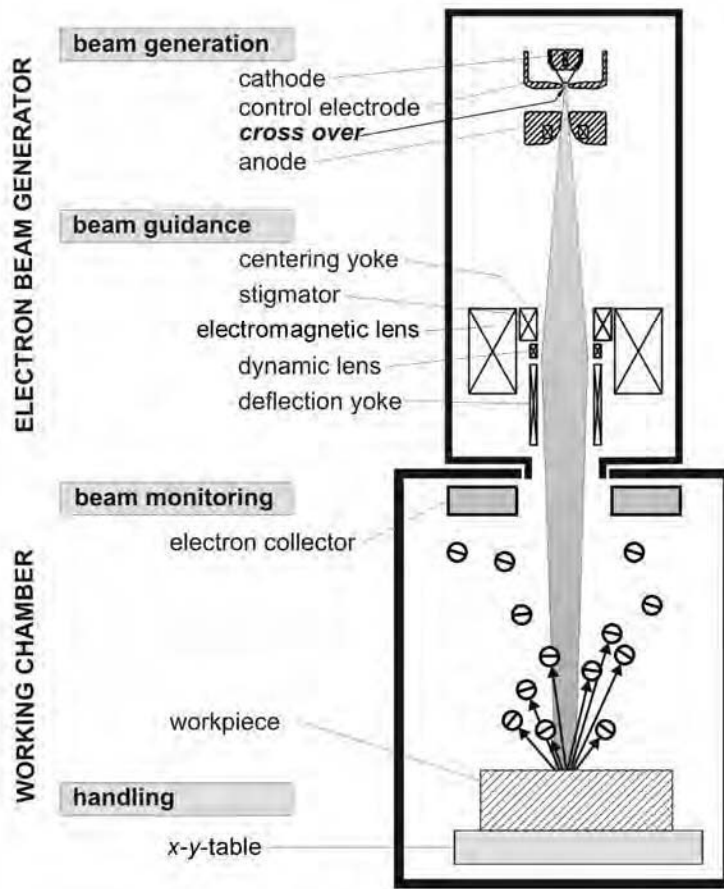


Fig. 1 Schematic of main assemblies and functional elements of an electron beam machine

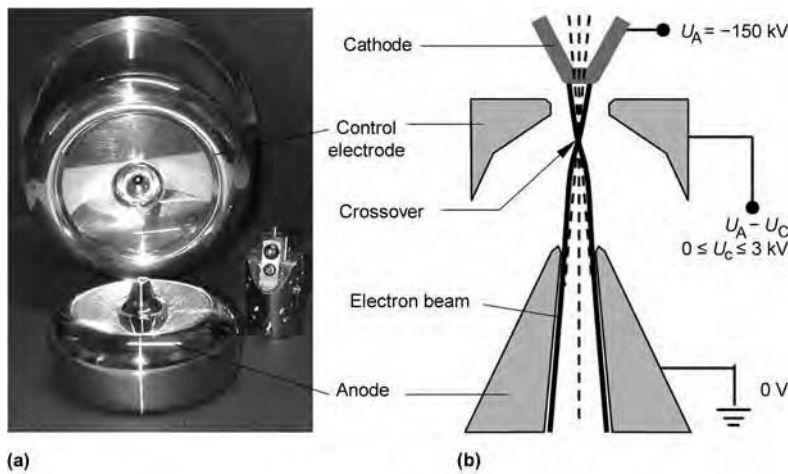


Fig. 2 Beam-generation system. (a) Components. (b) Schematic. Courtesy of pro-beam

the anode (up to $\frac{2}{3}$ the speed of light). The accelerated electrons continue their path through a hole in the anode toward the beam exit of the EB generator (Fig. 3a). A control electrode between cathode and anode regulates the amount of electrons transmitted by way of

a control voltage ($0 \leq U \leq -3$ kV with respect to the cathode potential), thus regulating the beam intensity (Fig. 2).

To produce a beam of the smallest possible diameter with concentric energy distribution (Gaussian function) and low divergence, the

raw beam is manipulated by electromagnetic devices, such as the centering yoke (Fig. 3b), stigmator (Fig. 3c), and focusing lenses (Fig. 3d), after passing the anode. As a general result of these measures, an EB is formed with a diameter between 0.1 and 1.0 mm (0.004 and 0.04 in.), mostly 0.3 to 0.4 mm (0.012 to 0.016 in.), in focus.

So that larger areas on components can be influenced in a targeted way using EB, an additional beam-deflection mechanism is required (Fig. 3e). The electromagnetic deflection coil is capable of deflecting the EB in the x - and y -directions very quickly (deflection frequency, $f \leq 100$ kHz). A dynamic lens establishes additional degrees of freedom in the z -direction (by changing the distance of the focus plane to the beam generator in synchronization with the x/y deflection pattern). With such a system, it is possible to produce different deflection figures and energy-transfer patterns (Fig. 3e; see also the section "Processing Techniques" in this article).

Electron Beam Interaction with Material

When the electrons impact the material surface, different interaction processes arise (Fig. 4). Due to so-called inelastic scattering, the kinetic energy of the electrons is transferred into various kinds of energy and causes generation of secondary particles within a thin absorption layer in the surface region of the material. In the energy range of interest for EBH, the thickness of the energy-absorption layer is given by the electron range, S (μm), which can be approximated by the equation (Ref 26, 27):

$$S = 6.67 \times 10^{-7} \left(\frac{U_A^{5/3}}{\rho} \right) \quad (\text{Eq 1})$$

where U_A is the acceleration voltage of the electron beam generator in volts, and ρ is the density of the material in g/cm^3 (Ref 26, 27). For ferrous metals, typical acceleration voltages of the beam range from 60 to 150 kV, and typical electron range values are >8 to $36 \mu\text{m}$.

Because of the intense interaction between the beam electrons and the atoms of the target material, the beam electrons lose their energy rapidly. The majority of this energy lost by the electrons is transformed into heat in the absorption volume (Fig. 4).

Due to elastic scattering, a certain portion of the beam electrons is not absorbed but reflected back into the vacuum by the target material. These backscattered electrons carry away from the workpiece but can be used for process monitoring and control (see the section "Processing Techniques" in this article). Further energy losses occur via thermal radiation, x-radiation, and the emission of thermal electrons (Fig. 4). The x-rays generated can be used for analytical purposes, although this has, to date, been carried out exclusively in laboratory settings.

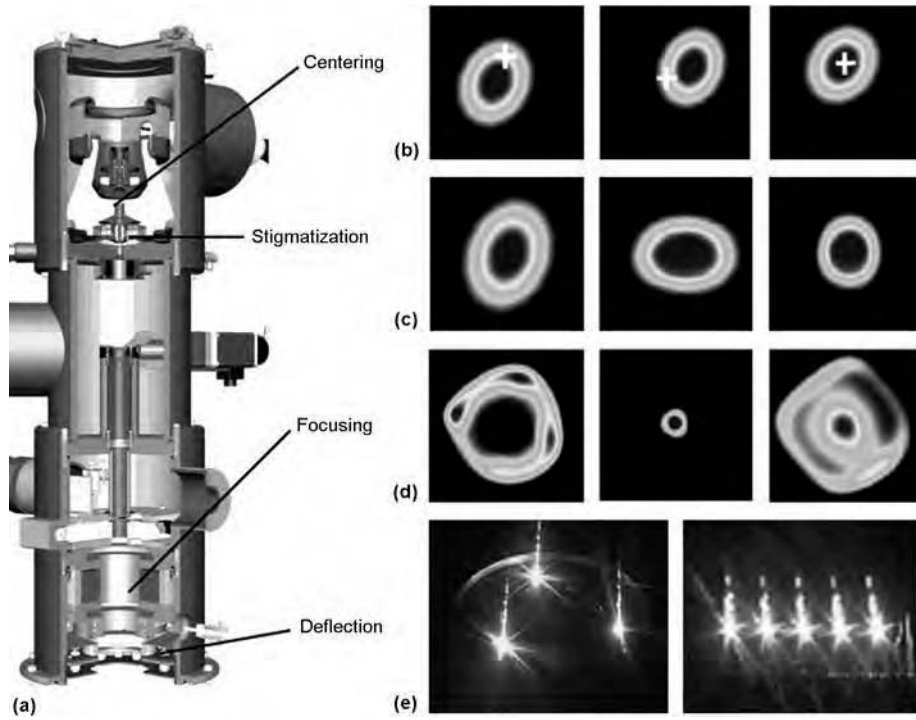


Fig. 3 (a) Functional elements of an electron beam generator. (b) Effects of beam centering. (c) Correction of astigmatisms. (d) Beam focusing. (e) Beam deflection. Courtesy of pro-beam

Heat Transfer

Approximately 75 to 80% of the power generated by the electron beam is converted to heat when the beam is applied perpendicular to the material surface.

As a result of the energy transfer, it is the material in the energy absorption volume that is heated first. This results in a temperature gradient toward the interior of the component. Because of thermal conduction in the direction of this gradient, the regions adjacent to the absorption volume are heated accordingly. The longer the duration of the energy transfer, the farther the heated zone of the material extends beyond the actual energy-absorption volume. The temperature field, $T(x, y, z, t)$, that results is described by the thermal conductivity equation:

$$\left(\frac{\partial}{\partial t} - a \frac{\partial^2}{\partial r^2}\right) T(x, y, z, t) = \begin{cases} \frac{v(x, y, z, t)}{\rho c} & \text{for } 0 \leq t \leq t_H \\ 0 & \text{for } t_H \leq t \end{cases}$$

with $a = \frac{\lambda}{\rho c}$ (Eq 2)

where \mathbf{r} is a vector in space defined by $|\mathbf{r}|^2 = (x^2 + y^2 + z^2)$, and a is the temperature diffusivity resulting from the heat conductivity (λ), the specific heat (c), and the density (ρ) of the material (Ref 26, 27). The term $v(x, y, z, t)$ describes the spatial heat source distribution in the energy-absorption volume and their temporal evolution, which extends over the energy-transfer duration (t_H). The solution to the equation of thermal conductivity (Eq 2)

for different source distributions $v(x, y, z, t)$ and various boundary conditions in the technical literature covering thermodynamics (Ref 28).

One general result of the resolved thermal conductivity equation (Eq 2) is of great importance for EBH (Ref 27). This is the sudden energy transfer that occurs within a time $t_H \rightarrow 0$. In this case, the energy-absorption layer is heated up rapidly when hit by the EB but cools down much slower due to heat conduction into the bulk material afterward. So, the energy-absorption layer acts as a heat accumulator that discharges at a constant relaxation time (τ):

$$\tau \approx \frac{S^2}{a} \quad \text{(Eq 3)}$$

This means that the energy-absorption layer maintains the energy transfer into the interior of the workpiece for a certain time even after the pulsed beam action has ceased (Ref 27). As a result, it is immaterial for the temperature field in a distance $z > S$ below the surface whether a particular energy flow density is transferred to the surface either continuously or in a pulsed fashion, provided the cycle time of pulses is shorter than the time τ given by Eq 3. Because of the interdependence of Eq 1 and 3, however, the heat-retaining capacity of the energy-absorption layer and the discharge-time constant will strongly increase with the acceleration voltage of the EB (Ref 27). Depending on the acceleration voltage and material, this results in values of τ in a range

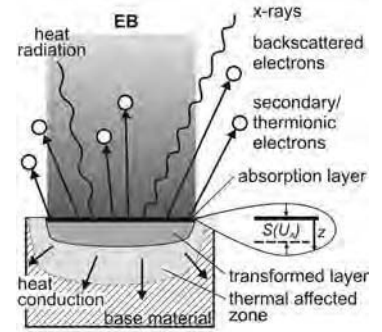


Fig. 4 Interaction of electrons with material. EB, electron beam

from a few microseconds to a few hundred microseconds.

Figure 5 shows the conditions of energy transfer for two different scenarios:

- Constant power density, P , in the energy-transfer field (Fig. 5a)
- Constant surface, T_S (isothermal), during energy transfer (Fig. 5b)

At constant power density, the surface temperature varies directly with \sqrt{t} (Fig. 5a). To achieve constant surface temperature, power density must be changed proportionally to $1/\sqrt{t}$ (Fig. 5b) (Ref 27).

Processing Techniques

Beam-Deflection Technique

The density and distribution with which electrons impact the material surface are deciding factors for the effectiveness of the EB. As opposed to EB welding, extended areas shall be thermally influenced during EB surface treatment.

The development of the two-dimensional high-speed scanning beam-deflection technique (Ref 1, 2) in 1986 was the beginning of a new era in thermal EB technologies, and for surface treatment in particular, because this was the key to the cost-efficient application of high-power beams in a geometrically precise manner. Since 2000, three-dimensional beam deflection has been available for EB processing (Ref 5–8).

Without deflection, the EB takes effect at one energy-transfer spot. Its size varies for EBH facilities from at least 0.1 to 0.4 mm (0.004 to 0.016 in.) (focused beam diameter) up to some millimeters in diameter (defocused EB). However, the EB can also be deflected so that the energy transfer takes place in every position within a programmed interaction area, depending on the technically limited deflection angle, with a maximum area of typically 200 by 200 mm² (0.3 by 0.3 in.²). Using high-frequency beam-deflection techniques, nearly arbitrary, lateral energy-dose distributions of energy or locally defined lateral dosed-energy distribution

can be defined: homogeneous concentrated (e.g., several programmed spots) or an energy-transfer field with analytically prescribed local power density variation (e.g., proportional to $1/\sqrt{x}$ as needed for surface isothermal heating of moving workpieces).

Two basic techniques can be distinguished. First, the component to be treated or the EB deflection field (or both) is moved relative to each other when the beam interacts with the material. Although the energy transfer to a given surface area happens within a short time (determined by the relative speed of motion and the dimension of the deflection field), this variant is called the continuous interacting (CI) technique because the EB power is kept constant during the process. Second, the

component to be treated and the EB deflection field are fixed, but the beam power is controlled in dependence on time. Because the energy-transfer times required are usually short (typically 0.1 to 2 s), this variant is called the flash technique (Fig. 6).

Continuous EB Interaction (CI Technique)

When using the CI technique, a rectangular energy-transfer field with a width of up to 200 mm (8 in.) and a length ranging from 3 to 20 mm (0.12 to 0.8 in.) is usually programmed. This parameter window covers the majority of applications. The component moves with a feed

rate of 5 to 20 mm/s⁻¹ through the EB deflection field. In this way, tracks are formed (Fig. 6) along which the material is thermally influenced (e.g., hardened). A simple rectangular field with constant energy distribution over the entire area means that, in the feed direction, the surface temperature of the material is lower at the beginning than at the end of the field (Fig. 5a).

In the case of surface isothermal energy transfer, a field with variable energy density in the feed direction is passed over the component; therefore, the energy density is higher at the front of the field than at the end (Fig. 5b). The resulting temperature-time profile beneath the distance from the surface is shown in Fig. 7. In material layers below the surface, the maximum temperature is reached after a finite time, and its value decreases with increasing surface distance. These processes are defined by the field energy density, by exposure time (field length, feed rate), and, above all, by the thermal conductivity of the material.

Electron Beam Flash Technique

The flash technique (Fig. 6) is the method of choice for EBH of components with face areas to be hardened, sometimes with complex shapes, because the energy-transfer field can be flexibly adjusted to the surface geometry of the component. During beam-effect EB energy transfer, the field and component are fixed to each other. The projection ratio of curved surfaces, height differences, and variable incidence angles must be considered when programming the energy-transfer field. Figure 8(a) shows a component with a flat surface and a ring-shaped energy-transfer area for which a ring-shaped energy-transfer field must be programmed. To avoid overheating (melting) of the component being treated, positions of the EB deflection field and of the component must be positioned exactly. During exposure of the EB, the energy input, that is, the beam current, I_B , is continually reduced (Fig. 8b). The surface temperature thus remains constant during the entire process, as in the case of surface isothermal energy transfer with the CI technique. The T - t cycles at different distances beneath the surface in

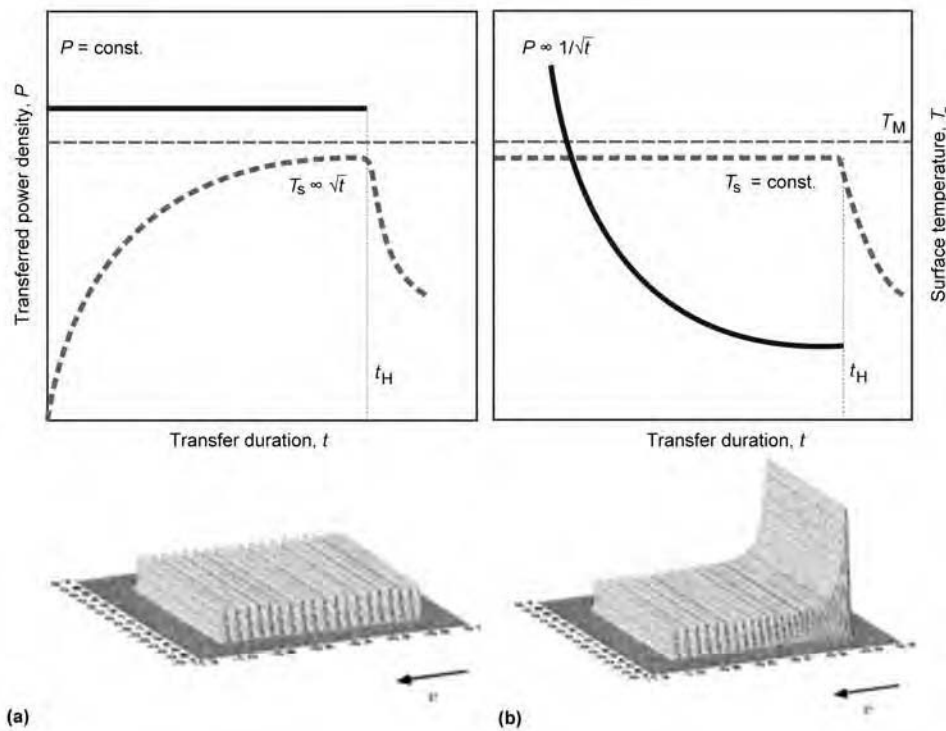


Fig. 5 Relation between transferred power density (P) and surface temperature (T_s) for two cases: (a) $P = \text{constant}$ and (b) $T_s = \text{constant}$

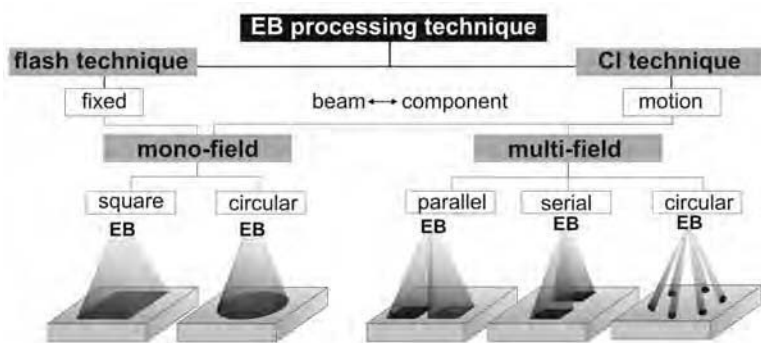


Fig. 6 Schematic of processing techniques for electron beam (EB) hardening. CI, continuous interacting

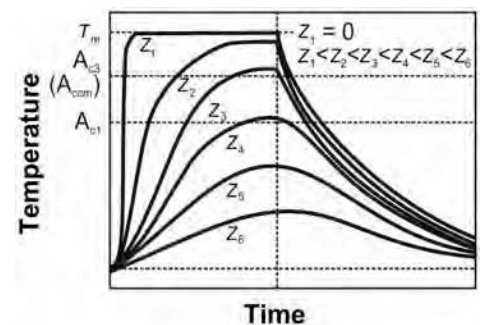


Fig. 7 Surface isothermal energy transfer in the continuous interaction technique. Temperature-time profiles as a function of distance from the surface (z)

the material volume are comparable to those of the CI technique as well (Fig. 7, 8b).

Multifield EB-Deflection Technique

Another highly efficient variant of the EB-deflection technology is the multifield technique (Fig. 6).

These process variants can be used advantageously when several areas of a component that are accessible to an EB are to be treated. Enabled by the high deflection frequencies of the EB, energy can be transferred quasi-simultaneously to different treatment zones, whereas other surface regions of the component remain unaffected. This process variant excels in efficiency due to high area throughput and reduced handling efforts.

Multifield EB deflection can be used in the CI or flash techniques. Details are discussed in the section “Applications” in this article, in connection with concrete components.

Multiprocess Technique

In multiprocess techniques, two or more different heat treatment processes are carried out in a single pass of the component through simultaneously acting energy-transfer fields. The best-known multiprocess-deflection technique is EBH plus tempering performed in one process run.

Prerequisites for this combination include that the materials to be treated should exhibit high thermal conductivity and a sufficient degree of hardenability. After a given surface region has passed the first (EBH) field, the self-quenching process must be completed before the second (tempering) field can be entered. This means that the distance between the EBH field and the tempering field must be sufficiently large. The EB multifield variation

is therefore preferred for use on nonalloy and low-alloy steels.

Another process combination, preheating plus EBH, was developed for high-alloy steels to allow for adjustments for larger transformation depths. Because of the low thermal conductivity of these materials, the energy input must be “dosed” in several stages to avoid surface overheating (melting). This combination is solely realized as a CI process; for example, two or more energy-transfer fields with different energy contents move simultaneously along a track across the component. The effect of well-dosed energy input is comparable with that of the multipulse flash technique.

The advantages of multiprocess technologies are high productivity and new possibilities for changing material structures and properties (by virtue of very short local thermal cycles).

Electron Beam Hardening Technologies

Characteristics

The principle of the processes taking place in the material during EBH is represented schematically in Fig. 9(a). The power density within the energy-transfer field must be low enough that the melting temperature (T_M) of the material is not exceeded but high enough that the material is heated to a temperature above the upper transformation temperature (T_{UT}). A suitable exposure time ensures the material is completely transformed down to the desired hardening depth. At a certain distance from the surface, only the lower transformation temperature (T_{LT}) is reached, and, in this zone, an incomplete transformation occurs. Even below that region, further thermally induced changes in the material properties can be observed (heat-affected zone).

In contrast to conventional volume-hardening technologies and as a result of the high heating rates during EBH, the transformation temperatures shift to higher values (A_{c1} , A_{c3} , A_{ccm} by approximately 100 to 200 K). To reach maximum EBH depths within the shortest possible holding times, the austenitizing temperature must be set considerably higher than in conventional hardening. Typically, a temperature value approximately 10% below the melting temperature of the phase that melts at the lowest temperature is chosen.

The EBH technique is confined to steels and cast irons with carbon contents $\geq 0.25\%$, a requirement that represents the value for conventional hardening. A selection of ferrous materials for which established industrial experience in EBH exists is given in Table 1.

For volume hardening and other thermal surface-hardening processes (such as flame hardening and induction hardening), the choice of the right quenching medium is of crucial importance for the hardening process results. For EBH, the quenching rates tied to self-quenching (10^3 to 10^4 K/s $^{-1}$) lie distinctly above the values achievable even by quenching in water.

Microstructure

Given optimal irradiation conditions and sufficiently large component volumes, the depth of EBH depends on the energy input, chemical composition, and previous heat treatment of the material (Fig. 10). In general, low thermal conductivity due to a higher carbon and alloying element content reduces the EBH depths. After EBH with the same process parameters, a normalized or soft-annealed state exhibits a hardening depth that is lower by approximately 5 to 15% than those achieved with a hardened and tempered state, mainly due to the more inhomogeneous distribution of carbon in the former.

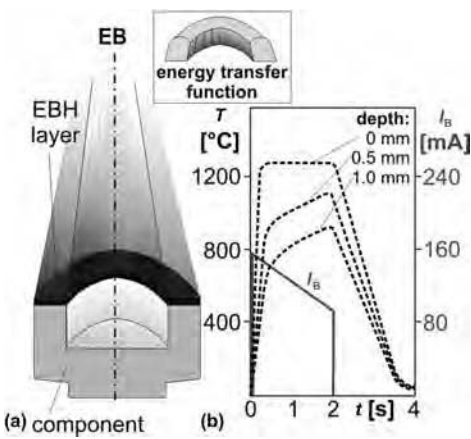


Fig. 8 (a) Surface isothermal energy transfer in the flash technique. EB, electron beam; EBH, electron beam hardening. (b) Component and energy-transfer field. Temperature-time profiles depend on distance from the surface (left axis) and time-dependent control of the beam current (right axis).

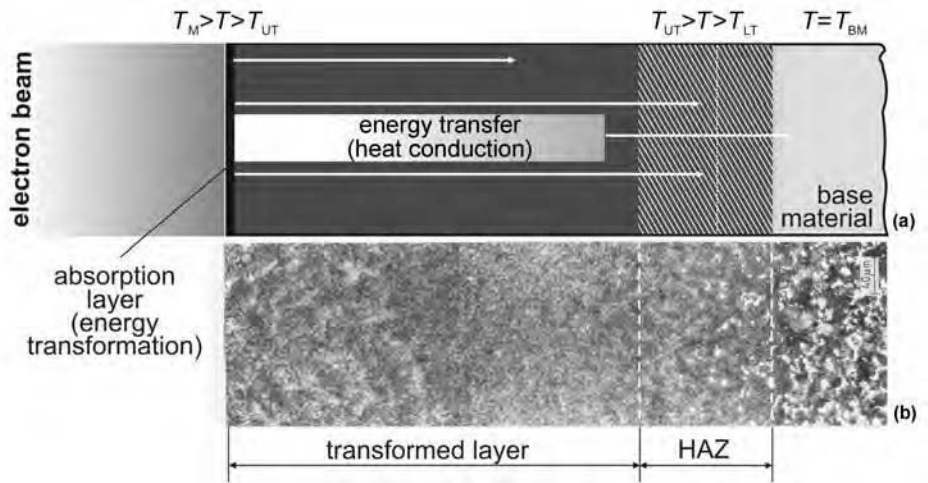


Fig. 9 Principle of electron beam hardening as a solid-phase process. (a) Schematic and (b) example microstructure of low-alloy steel. HAZ, heat-affected zone

Table 1 Selected steels suitable for electron beam hardening

Material			Composition, wt%								
AISI	UNS No.	DIN(a)	C	Si	Mn	P	S	Cr	Mo	Ni	V
Carbon and low-alloy steels											
1030	G10300	C30	0.27–0.34	≤0.4	0.50–0.80	≤0.045	≤0.045	≤0.40	≤0.10	≤0.40	...
1045	G10450	C45	0.42–0.50	0.17–0.37	0.50–0.80	≤0.040	≤0.040	≤0.050	≤0.10	≤0.30	...
...	...	30CrMoV9	0.26–0.34	≤0.4	0.40–0.70	≤0.035	≤0.035	2.3–2.7	0.15–0.25	≤0.6	0.1–0.2
...	...	37MnSi5	0.33–0.41	1.1–1.4	1.1–1.4	≤0.035	≤0.035
1039	G10390	40Mn4	0.36–0.34	0.25–0.5	0.8–1.1	≤0.035	≤0.035
1340	G13400	42MnV7	0.38–0.45	0.17–0.37	1.60–1.90	≤0.035	≤0.035	≤0.030	≤0.10	≤0.30	0.07–0.12
...	...	55Cr 1	0.52–0.60	0.17–0.37	0.5–0.8	≤0.035	...	0.2–0.5	...	≤0.30	...
4140	G41400	42CrMo4	0.38–0.45	0.17–0.37	0.50–0.80	≤0.035	≤0.035	0.90–1.20	0.15–0.25	≤0.30	≤0.06
...	...	50CrV4	0.47–0.55	0.4	0.7–1.1	≤0.035	≤0.030	0.90–1.20
Tool steels											
...	...	C70W1	0.65–0.75	0.10–0.30	0.10–0.40	≤0.030	≤0.030
W1	T72301	C100W1	0.95–1.04	0.15–0.30	0.15–0.25	≤0.020	≤0.020	≤0.020	...	≤0.20	...
E52100	G52986	100Cr6	0.95–1.05	0.17–0.37	0.20–0.45	≤0.027	≤0.027	1.30–1.65	...	≤0.30	...
...	A485	100CrMn6	0.93–1.05	0.45–0.70	1.0–1.2	≤0.025	≤0.015	1.40–1.65
Cold work tool steels											
...	...	75Cr1	0.70–0.80	0.25–0.50	0.50–0.80	≤0.030	≤0.030	0.30–0.40
O2	T31502	90MnV8	0.85–0.95	0.15–0.35	1.80–2.00	≤0.030	≤0.030	0.07–0.12
D2	T30402	X155CrMoV12-1	1.45–1.60	0.10–0.60	0.20–0.60	≤0.030	≤0.030	11–13	0.7–1.0	...	0.70–1.00
D3	T30403	X210Cr12	1.9–2.2	0.10–0.60	0.20–0.60	≤0.030	≤0.030	11–13
Hot work tool steels											
L6	T61206	55NiCrMoV6	0.50–0.60	0.10–0.40	0.65–0.95	≤0.030	≤0.020	0.60–0.80	0.25–0.35	1.5–1.8	0.07–0.12
H11	T20811	X38CrMoV5-1	0.33–0.41	0.8–1.2	0.25–0.5	≤0.030	≤0.020	4.8–5.5	1.1–1.5	...	0.30–0.50
...	...	X42Cr13	0.36–0.42	≤1.0	≤1.0	≤0.030	≤0.030	12.5–14.5
Spring steel											
1070	G10700	Ck67	0.65–0.72	0.25–0.50	0.60–0.80	≤0.035	≤0.035	≤0.035	...	≤0.30	...
9255	G92550	55Si7	0.52–0.60	1.6–2.0	0.60–0.90	≤0.025	≤0.025	≤0.4	≤0.1	≤0.4	...

(a) DIN, Deutsche Industrie-Normen

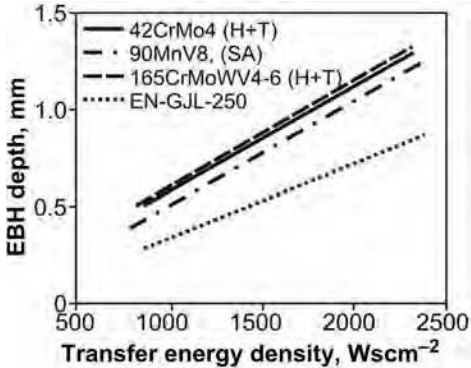


Fig. 10 Influence of transfer energy density, chemical composition, and previous heat treatment on electron beam hardening (EBH) depth for steels and cast iron. H+T, hardened + tempered; SA, soft annealed

The microstructures (phases) resulting from EBH are considerably finer than those formed after conventional volume hardening. Essentially, however, the same transformation mechanisms take place. The effect of the carbon and the alloying elements is also comparable.

The martensitic microstructure of hypoeutectoid steels has a lathlike morphology with small bundles of short, nearly parallel laths (Fig. 11a, 12a). Hypereutectoid steels are characterized by platelike martensite with different percentages of retained austenite and additional partially undissolved carbides (Fig. 11a, 12b).

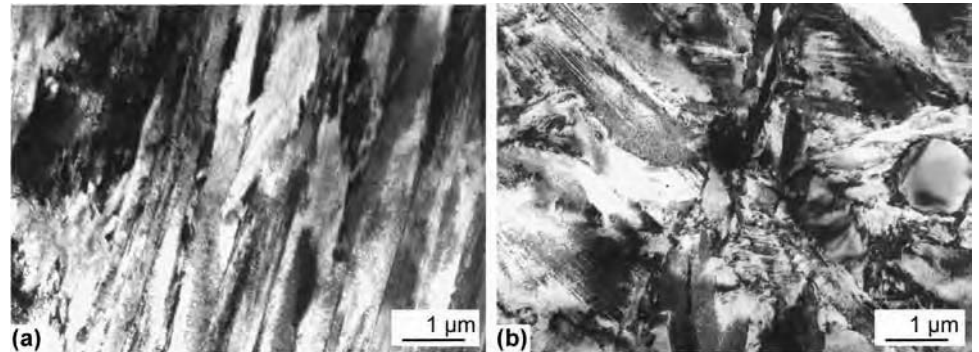


Fig. 11 Transmission electron microscopy images showing influence of carbon content on microstructure after electron beam hardening. (a) Lathlike and (b) platelike martensite

The changing of the $T-t$ cycles with distance from the surface affects the microstructure (Fig. 12). The transformation products become finer and are distributed less homogeneously, and a change of the percentage of martensite morphological variants occurs. At the transition from the EBH layer to the base material, the material is only partly austenitized, and nontransformed ferrite and/or pearlite, or undissolved carbides, appear beside newly formed martensite.

Pearlite-containing cast irons are also EB hardenable by martensitic transformation of the former pearlitic matrix (Fig. 12c). The graphite is not transformed, but the carbon can diffuse from the graphite into the ferrous matrix

at the edges of the graphite particles in spite of the short temperature cycle. For former ferritic-matrix areas, martensite forms along the border between graphite and the ferrous matrix after quenching. If a former pearlitic matrix is enriched with carbon by diffusion out of the graphite, martensite and retained austenite will be present after quenching.

Surface Properties

Surface hardness is the parameter most commonly used to characterize the success of EBH. In the vast majority of cases, this value will lie

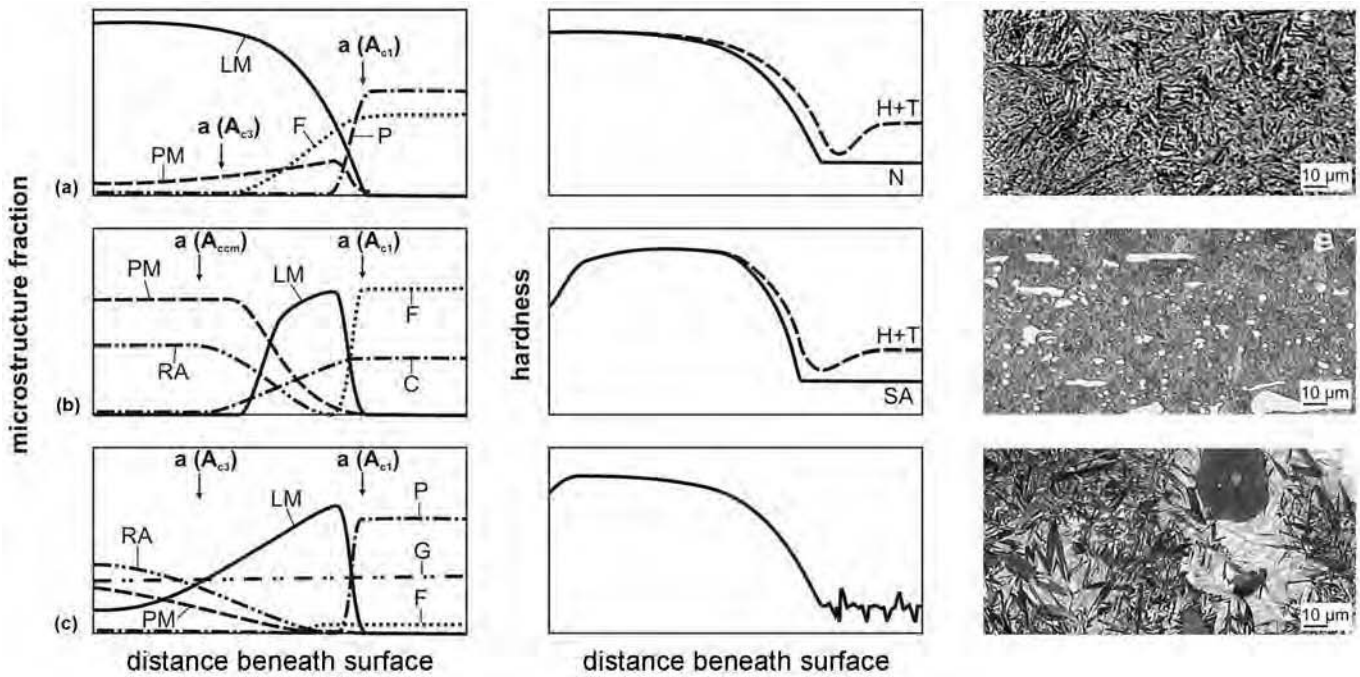


Fig. 12 Influence of chemical composition (carbon content) and previous heat treatment on transformation-depth profiles, hardness profile, and microstructure for (a) hypoeutectoid steel, (b) hypereutectoid steel, and (c) cast iron. H+T, hardened + tempered; N, normalized; SA, soft annealed; LM, lathlike martensite; PM, platelike martensite; RA, retained austenite; F, ferrite; P, pearlite; C, cementite; G, graphite

above that achieved with conventional hardening methods, due to the finer microstructure. The difference in hardness in comparison to the tempered or hardened and annealed state in Fig. 13 can be attributed to the fact that, in the vast majority of cases, tempering is unnecessary after EBH. Exceptions include, in particular, materials with a high risk of crack formation (such as, for example, 90MnCrV8 steel). Figure 13 shows that the abrasive wear density, W_R , correlates with the surface hardness.

With respect to the particular conditions of use, hardness is not, in many cases, a truly meaningful term. To more comprehensively classify the result of treatment, wear tests can be used. They provide insight into the performance characteristics of tribological systems.

Completely different wear mechanisms can be addressed by contact fatigue and compressive strength measurements. In both cases, a metallic counterpart (e.g., a tool steel roller or a carbide disc) moves against a wearing component; that is, the conditions inside bearings are simulated. As shown in Fig. 14, both parameters can be significantly improved through EBH in comparison to conventional treatments.

The considerations thus far refer exclusively to surface properties; however, this method generally does not allow conclusions to be drawn regarding the characteristics of the EBH layer in its entirety, and certainly not regarding the layer-matrix compound. As mentioned previously, different transformation processes occur due to the temperature gradients

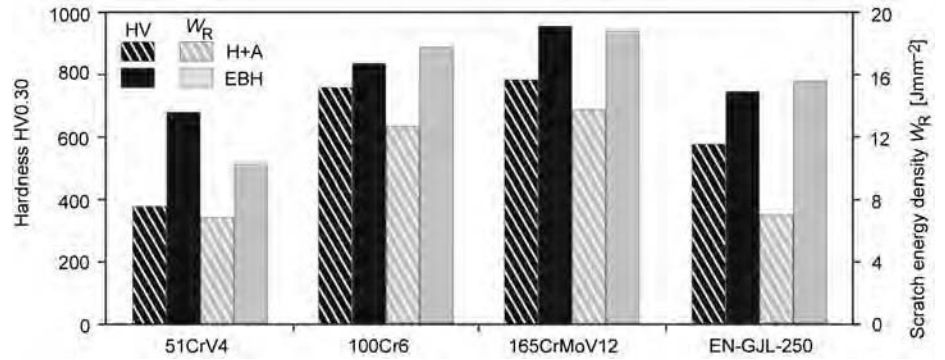


Fig. 13 Hardness and scratch energy density for different iron-base alloys. W_R , abrasive wear density; H+A, hardened + annealed; EBH, electron beam hardened

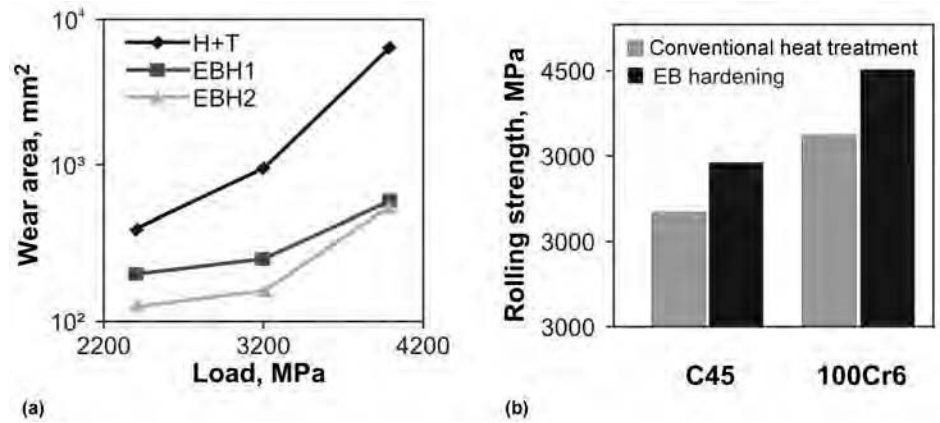


Fig. 14 Influence of (a) load conditions and (b) carbon content on fretting fatigue for different previous heat treatments. H+T, hardened + tempered; EBH, electron beam hardened

between the surface and the core, which produce different microstructures as a result. These processes vary from material to material. Different properties and property gradients result. The choice of EB parameters (temporal and spatial energy input) is, of course, of significant importance in this process.

Component Specifics

Electron beam surface-layer treatment is a technological process in which—as with many other processes, too—the characteristics of the component (size, volume, mass, geometry, surface contour, wall thickness) must be harmonized with those of the process (restricted energy-transfer area, irradiation conditions). The effect of self-quenching is limited by the component volume and the material thickness. If the energy introduced cannot be removed well enough or quickly enough, the component heats up; that is, the surface-to-core temperature gradient becomes flatter, and the critical cooling rate for the formation of martensite is not reached (Fig. 15a).

The incidence angle of the EB is determined by the component contour, and this angle determines the EBH depth via the angular dependencies of the area projection ratio and the electron backscattering. Without taking additional measures, the decrease in transformation depth amounts to approximately 50% at an EB arrival angle of $\approx 60^\circ$ against the surface normal (Fig. 15b).

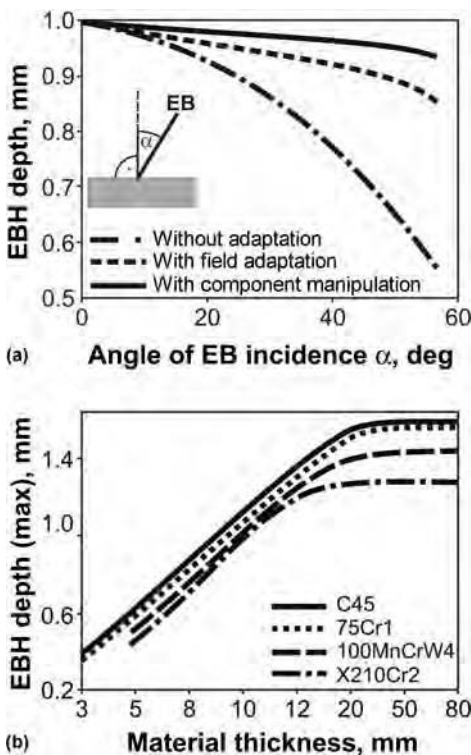


Fig. 15 Influence of (a) angle of electron beam (EB) incidence and (b) material thickness on the electron beam hardening (EBH) depth

However, restrictions regarding the applicability of EBH may result especially from the criterion that the EB must have preferably straight access to the surface to be treated. In Fig. 16, various surface contours are classified in terms of their suitability for EBH. Interior contours (e.g., drills) must have an aspect ratio (diameter to depth) of ≥ 1 to be hardened by oblique irradiation. Certain contours such as cutting edges, thin walls, or undercuts make the configuration of the energy-transfer fields challenging. The main issue in this respect is the avoidance of local melting through overheating. In such critical cases, the use of a temperature-controlled power regulator proves to be extremely helpful.

As outlined previously, EBH excels in precise control of the temperature-time regime, localization, and the total amount of energy transferred to the component. Thus, the thermal EB treatment can be limited exactly to the stressed surface regions of the component and to the EBH depth, required by the load conditions. In this way, the thermal effect can be reduced considerably. Hence, the distortion of components known from conventional heat treatment is dramatically decreased in EBH and lies within the usual production tolerance limits.

Contrary to laser surface treatment, EBH does not demand special surface preparation. The EB does not require additional absorption layers but can easily penetrate into metallic bright as well as coated metallic material, even at unfavorable incidence angles and through thin oxidation or phosphatization layers, thermochemically produced layers, and hard coatings such as TiN, TiAlN, and CrN. Because of the last-mentioned lower density of the layer materials, electron absorption will even be improved.

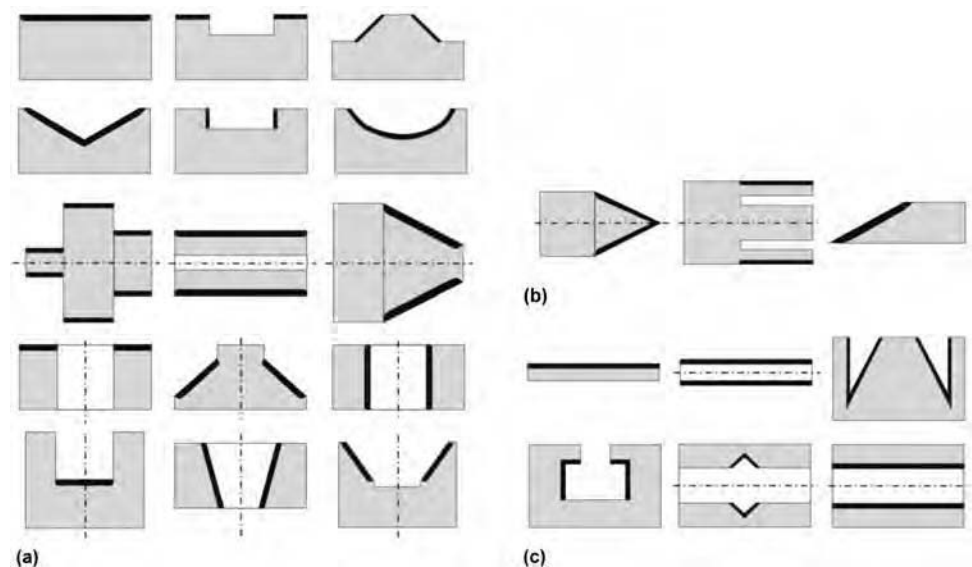


Fig. 16 Classification of contours with regard to electron beam hardening. (a) Most suitable. (b) Limited suitability. (c) Unsuitable

Surface smoothness is generally not critical. For high roughness values, it is even possible for smoothing to occur via melting of the roughness peaks. For components that will not be mechanically processed after EBH, it must be considered, however, that the roughness prior to the EB treatment is decisive for the end result and that, in EBH, surface deformation occurs (depending on the depth of hardening) on the micrometer scale up to a maximum of 15 μm .

Material allowance for subsequent machining can thus be omitted or kept small. In cases where very high requirements regarding the dimensional tolerances are in place, an oversizing of 0.1 mm (0.004 in.) is recommended, which can simultaneously compensate for the very small dimensional and shape deviations that eventually occur during the EBH process.

Components must be free from dirt, processing solutions, and preservatives. The removal of such residues can be achieved by chemical or mechanical means.

Electron Beam Facilities and Manufacturing Systems with Integrated EB Facilities

All EB facilities have the same basic technical design and consist of the following main subassemblies and devices (Fig. 17):

- Electron beam generator
- Working chamber with operating system
- High-voltage generator
- Vacuum system for EB generator and working chamber

- Cooling system for EB generator and vacuum system
- Computer numerical control (CNC) system for beam control, power circuits, components manipulation, and vacuum system
- Process observation and control (electron optical monitoring) and/or optical system

The EB facilities (Fig. 18–20) and the manufacturing system with integrated EB facility (layout depicted in Fig. 21) differ from each other with respect to:

- Degree of flexibility: single- or multipurpose facility
- Structural and technical configuration of the working chamber: transfer facilities, lock-type shuttle facilities, manufacturing systems, specialized designs
- Number of generators: single- or multigenerator facility

The beam-generation system and the working chamber are, vacuumwise, separated from each other by a flow resistor (usually established by the anode hole) and differentially pumped because of the different pressure requirements. The EB generator must be operated under high-vacuum conditions (10^{-5} to 10^{-6} mbar) to protect the hot cathodes against erosion and to prevent high-voltage breakdowns. Depending on the application, the working chamber with handling systems is evacuated to a soft vacuum (10^{-2} to 10^{-3} mbar) or a high vacuum (10^{-5} to 10^{-6} mbar). For process observation and/or control, EB facilities are equipped with optical and/or electron optical monitoring systems.

The electron optical monitoring system uses the fact that the number and main direction of secondary and backscattered electrons depend on the material and surface relief of the target (Fig. 1, 4). With collectors placed beneath or integrated into the EB generator, these characteristics can be recorded in synchronization with the EB while it is scanning the surface. This imaging method has several advantages. First, it is highly resistant to debris, that is, condensed vapors or splashes created upon EB action at the worksite; therefore, it is reliable in long-term processes. Second, it eliminates misalignment between the optically determined position and the practical EB impact location that magnetized components may cause. Third, it shows not only outer contours but also the contrast between different materials. Last, it produces reflection-free images. In connection with electronic image processing and control systems, the electron collector signals can also be used for process control.

There are two-step and single-step solutions available for this task. During the former, the component contour is determined by electron optical imaging and displayed for the operator or saved to the control system in a first step. These (real-time or prerecorded) contour data are used to adjust component manipulation and beam guidance. In the second step, the EB treatment occurs exactly in the desired surface regions.

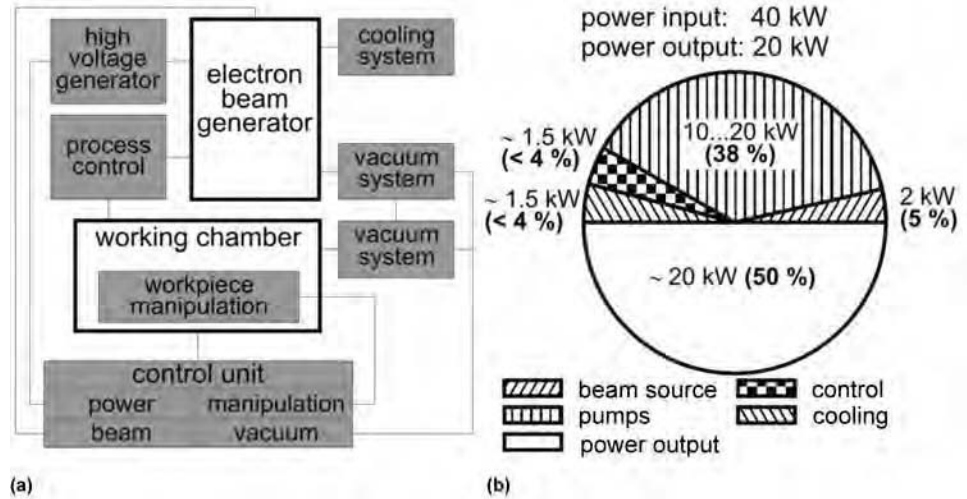


Fig. 17 (a) Basic configuration and (b) energy balance of an electron beam machine with 20 kW beam power output



Fig. 18 Universal-chamber electron beam machine for hardening, welding, engraving, and structuring. Chamber volume: 0.5 m³; beam parameters: 60 kV, 10 kW. Courtesy of FOCUS



Fig. 19 Load-lock cycle facility for hardening. Chamber volume: 0.04 m³; beam parameters: 60 kV, 6 kW. Courtesy of PTR

For the single-step process (CI technique), an EB scan field suitable for observation advances a following EBH field and registers a reference contour, for example, an edge, and transmits its position to the CNC. Magnetic declination and edge displacements, for example, through distortion resulting from prior processing and/or thermal expansion occurring during EB treatment, can be compensated for by using this method.

For each application, investment costs must be balanced against productivity when choosing the right concept of the EB facility or EB system. This concerns the design of the EB facilities on the one hand and the optimization of technological process runs on the other. Common strategies are mainly focused on:

- Elimination of nonproductive evacuation time (by minimization of chamber volume or multichamber arrangements)
- Assurance of suitable throughput of components (by adapted components handling/beam power rating/deflection technology)

These concepts are particularly important in the case of highly productive mass-production facilities. For instance, designing so-called zero-volume chambers that are fitted in size and shape to a specific component makes sense for single-purpose machines used in large-scale production.

If, however, the treatment time is long compared with the evacuation time, or if a big assortment of different components is to be handled (as in a job shop), larger single-chamber facilities are preferred, which are less costly than multichamber systems and offer a higher degree of flexibility than zero-volume chambers.

Electron Beam Facilities

Electron beam facilities are operator- and particularly environment-friendly because they neither need harmful supply media nor produce toxic waste. They also have outstanding high-energy efficiency.



Fig. 20 Load-lock shuttle facility for hardening and welding. Chamber volume: 2 m³ (71 ft³); beam parameters: 60 kV, 10 kW. Courtesy of pro-beam

Although they operate according to the same basic principle, the two load-lock shuttle facilities (Fig. 19, 20) can be differentiated according to their chamber size and their component-handling method. While the small machine can only be loaded manually, the system shown in Fig. 20 can also be loaded automatically. The principle behind this system type is that different process steps can be carried out simultaneously in an exactly timed regime. Carriages on the preparation bed are loaded with components. Another component carriage is located in the prechamber for pre-evacuation up to working pressure, while the EB components undergo hardening in the working chamber. After finishing the hardening process, the door between the working chamber and the prechamber opens, and the component carriages are exchanged. After the automatic closure of the chamber door, the EB immediately begins to harden the components. The prechamber is vented and opened, and the carriage with the processed components is removed from the prechamber and exchanged with the fully loaded carriage on the preparation bed. Then, the refilled prechamber is evacuated again. Depending on chamber size (0.5 to 2.5 m³, or 18 to 88 ft³), the unproductive time, during which the EB is switched off, lies between 5 and 20 s. This is markedly shorter than is the case for single-chamber machines.

Manufacturing Systems with Integrated EB Facility

For even higher EBH economic viability, EB facilities can be integrated in fully automatic manufacturing systems (Fig. 21). The component handling can occur manually or automatically. Then, the components pass through stations for washing (preheating), EB treatment (e.g., hardening, welding), cooling, quality control, and unloading. With systems of this complexity, and depending on the size of the components, the chamber size, and the hardening task, cycle times between approximately 10 and 30 s can be achieved.

Although EB technology has reached a high level of development, there is still huge innovation potential. Concepts for numerous EBH tasks are available, and new applications are constantly being developed (see the section "Applications" in this article).

It can be expected that new technologies and customer needs will also trigger the design of new EB systems and facilities in the future.

Applications

Characteristics

From both engineering and technological standpoints and with respect to its economic viability, experience to date has shown that

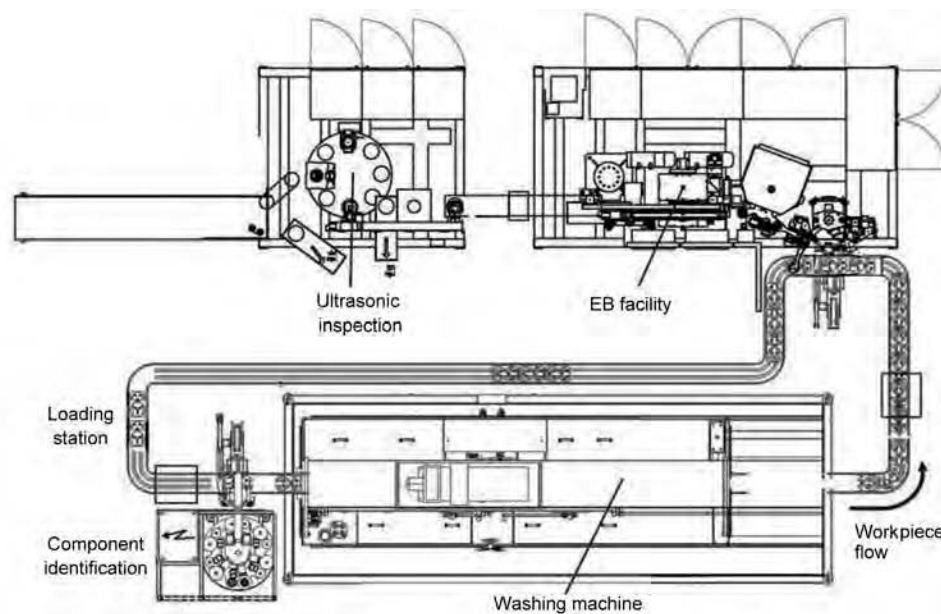


Fig. 21 U-type manufacturing system with integrated electron beam (EB) facility (layout) for welding or hardening with integrated EB facility. Chamber volume: 0.6 m³ (21 ft³); beam parameters: 60 kV, 6 kW. Courtesy of pro-beam

The EB machine shown in Fig. 18 is a small universal chamber for microprocessing and is used in job-shop production of small-sized individual components or small series. It can perform EB hardening, welding, structuring, and engraving. The chamber is manually loaded, evacuated, and vented after the process upon every exchange of components. The evacuation times amount to approximately 0.5 to 2 min.

Single-purpose EB systems with more than one vacuum chamber are used for increasing

the productivity in mass production. While loading is carried out in one working chamber, the EB operates in a second one (double-chamber machine). After loading the first chamber and finishing EB processing in the second chamber, the beam is switched to the first chamber, and so on. Other concepts with high productivity are load-lock shuttle or load-lock cycle and load-lock transfer facilities (Fig. 19) with more than two chambers (one pre-evacuation chamber in front of and another one behind the working chamber).

EBH can compete well with other heat treatment and surface treatment methods. Numerous examples of the application of EBH have been developed, and they are summarized in Table 2 according to their geometric characteristics.

For components that are geometrically simple and for surfaces that are, with respect to their irradiation conditions, relatively uncomplicated to harden, the rapid processing speed of EBH makes it especially attractive. For complex component contours, the relative ease and diversity of EB guidance and control is of great benefit.

In the case of precision parts and slim or thin-walled components, the low shape and/or dimensional deviations typically met in EBH can be decisive for its use.

Because EBH is inherently vacuum based and has a short time-treatment process, decarburization and oxidation are avoided. In this way, EB-hardened components meet the highest surface-quality requirements.

Additional measures with respect to beam guidance can expand the fields of application of EBH. Magnetic beam-bending devices, for instance, enable the hardening of surfaces that are not directly accessible to a straight beam. Even inside walls, for example, of hollow cylinders, can be treated. Further options include multifield beam-guiding techniques and multiprocess technologies (Fig. 6). The use of such technological solutions for advanced beam guidance allows for highly efficient realization of these modern surface-treatment technologies.

Connecting Rods

Connecting rods are EB hardened using a CI rotating monofield technique. Due to its asymmetry and the relatively large diameter of the surface to be hardened, a connecting rod, made of C70 steel (Fig. 22b), is to be horizontally fixed and centered with respect to the beam generator (Fig. 22a). The ring-shaped face region is locally treated by a rotating energy-transfer field (Fig. 22a) and can be precisely hardened locally without distortion (Fig. 22c). In this EBH zone, hardness values reach

800 HV0.30. Due to the very limited local EBH zone (Fig. 22c), very little energy is transferred to the component, which is minimally heated. In the two crack-zone areas of the connecting rod, the energy input is interrupted twice over a beam path length of 2 mm (0.08 in.) to avoid melting in this area. Such peculiarities are with a view to beam-control programming and are easy to implement. Connecting rods are produced very economically in large-scale production. Treatment times are 5 s per component.

Pump Cams

Contrary to the EBH of connecting rods, in the case of pump cams (Fig. 23a) the cam (and not the CI monofield) moves around its own rotational axis under a rectangular energy-transfer field. The external contours of the pump cam, made of a tempering steel (51CrMo4), are first rapidly locally heated to the austenitizing temperature and then hardened (to approximately 800 HV0.30) by self-quenching to a depth of up to 0.3 mm (0.012 in.), defined by a hardness limit of 550 HV0.30 (Fig. 23b). The incidence angle of the EB at and the distance of the surface from the beam generator changes continuously during the treatment. To adjust for a uniform EBH layer thickness over the entire hardening area, the rotational speeds and/or the beam current along the contour of the cam are continuously adjusted. Programming of the EB parameters (beam current, rotation velocity) in the area of the drill poses an additional challenge (Fig. 23a).

Using this treatment variation, a softened slope zone is unavoidable (Fig. 23d). However, this overlapping area can be located on the flank of the cam, apart from the radius, where the highest load occurs. The decrease in hardness in this narrow (approximately 0.5 mm, or 0.02 in.) zone is equivalent to a maximum 50% of the surface hardness (Fig. 23c) and is not of importance for this component. Special programming solutions, such as soft-zone optimization with respect to the load profile, can also be used, thus avoiding soft zones in the slope area.

Camshafts

Camshafts with different design concepts (solid, hollow, or assembled) and made of different materials (steel or cast iron) can be EB hardened using the CI multifield technique for energy transfer during rotation of the cam shaft. Generally, cam shafts are made of unalloyed or low-alloyed steels (e.g., C55, 51CrV4, 42CrMo4). However, EB hardening is also used for camshafts made of nodular cast iron, such as EN-GJS-600. In the case of assembled cam shafts, the cams are made of 100Cr6 steel.

The EBH process is comparable with that of the pump cam described previously. It is a peculiarity of EBH of camshafts that, if neighboring cams have similar angular orientation and if the axial gap between them is not too wide, a CI technique with two energy-transfer fields side by side can be applied. In this way, one can treat both cams simultaneously and nearly double the process productivity.

Because the surface deformation of different materials is very small (4 to <10 μm), it is not necessary to employ a grinding process after EB treatment, although a finishing process is carried out in most cases.

An advantage of the EBH process is that the thickness of the hardened layer can be varied depending on the load conditions around the cam contour (e.g., for cams, 0.4 + 0.1 mm, or 0.016 + 0.004 in.; for bearings, 0.2 + 0.1 mm, or 0.008 + 0.004 in.) (Fig. 23a). The layer thickness can be reduced in contour segments with lower loading (e.g., flanks). In the more highly loaded radius areas, the EBH-layer thickness must be higher. Consequently, the heat transfer into the camshaft can be minimized, which is important with regard to tempering effects and possible deformation of the camshaft. It should be mentioned that the EBH process effects no distortions of the shaft, so that the EBH process can be realized as the last production step. For particular precision requirements, a finishing step (removing 3 to 4 μm) must be added.

Table 2 Examples of electron-beam-hardened components

Basic geometrical shape	Selected examples
Plane surfaces	Bearing pads, face plates, rolling guide elements, machine beds, guide grooves of various components, grapple bars, jaws, guide rails, stop bars, fixing plates, gripper bars, webs, work holders
Cylindrical components: Circumference plane	Quills, shafts (Fig. 24), rollers, guides, rods, machine tapers, cam rings, wire-drawing drums, support rings, valve rings, screw sleeves, molds, cam disk, bushings, crankshafts, brake drums, pump cams (Fig. 23), thread rings, pins, stator shafts, wheel drivers, folding rollers, car pins, rotors, slotted shaft (Fig. 26)
Face plane	Pressure rings, seat rings, guide bars, front and teething rings, connecting rods (Fig. 22), pressure pins, curved segments, armature contact faces, lock bolt, track rings, guide rings, injector boxes (Fig. 25), spur gearing rings
Spatially-curved surfaces	Cam plates, driving links, kneader blocks, screw sleeves, extruder screws, lift bars, lock components, glass molds, mold components, slewing shaft
Cutting edges (tools)	Cutting heads, drilling heads, cutting blades, mill disks, wipers, stator knives, propeller knives, slicer knives, ploughshares, activated blades, mill blades

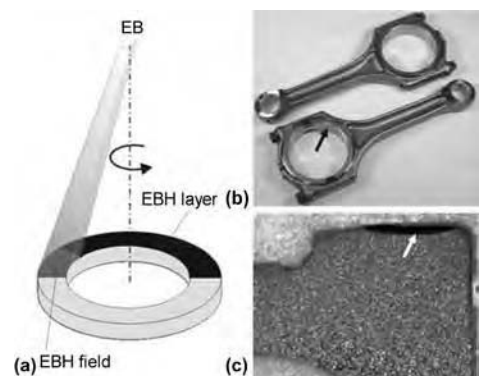


Fig. 22 (a) Electron beam hardening (EBH) with rotating energy-transfer field (continuous-interacting monofield technique) of (b) connecting rods. (c) Hardened zone

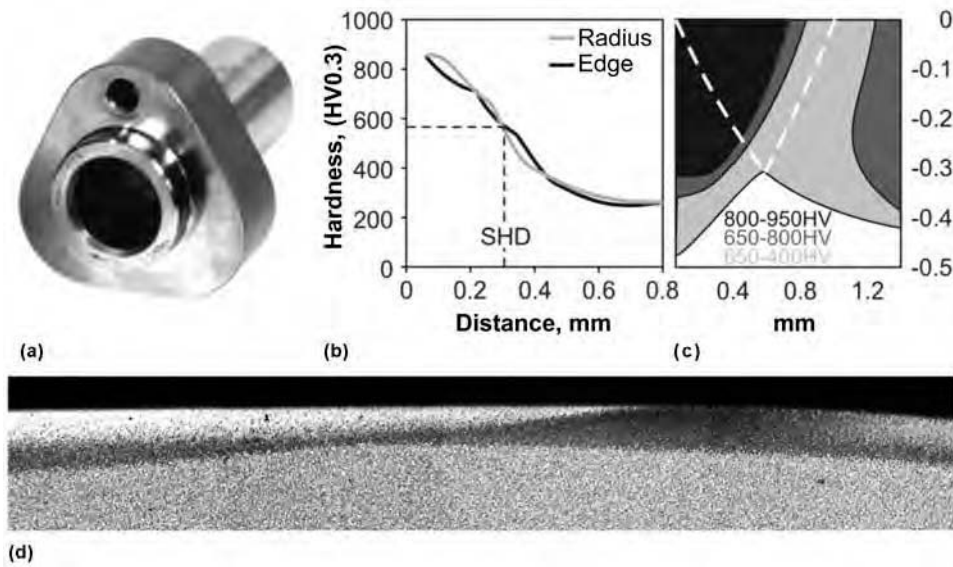


Fig. 23 (a) Electron beam hardening of pump cams with the continuous-interacting monofield technique. (b) Hardness depth profile. (c) Hardness mapping in the slope area. (d) Microstructure of slope area

Shafts

The EBH process with the CI multifield technique was used, for example, for a shaft made of 51CrV4 steel (Fig. 24a). To protect the running surfaces from wear, all three peripheral contact areas were EB hardened simultaneously in one cycle and over the entire circumference (Fig. 24a). The unavoidable small soft slope zone can be positioned at a chosen point above the circumference. In the given application, however, this is not a matter of importance.

Electron beam technology solves this hardening task much more economically than any other surface heat treatment technology. The technological cycle time of EBH takes up to 6 s per component. Because the shaft will experience only low stresses in operation, the depth of hardening can be restricted to approximately 0.3 mm (0.012 in.). This keeps the heat load to the component low and prevents distortion. Therefore, reworking is not required.

Valve Seats

Another example from the automotive industry is EBH of valve seats in cast iron (EN-GJS-600) diesel cylinder heads. The main challenge posed by this task is in minimizing the distortion of the cylinder head to avoid subsequent rework (grinding). This could be achieved using EB flash technology in combination with a ring-shaped EB flash energy-transfer field as an alternative to induction hardening. It was possible to treat a four-valve, six-cylinder head in 60 s. It is an additional advantage of EBH that no quenching media are required, thanks to the self-quenching effect. The short-cycle

energy transfer can be performed with high energy density in these contact areas, but it is realized with minimum heat transfer into the surrounding material. To confine the hardened zone to the valve seat, exact positioning of the ring-shaped energy-transfer field is necessary. This adjustment is carried out by means of electron optical monitoring and the process-control system during the first 0.25 s of the initial heating phase. In this short time interval, the temperature in the energy-transfer area is still below the transformation temperature to austenite. Austenite formation and subsequent hardening occur only in the area that is further heated by the aligned beam, that is, in the desired hardening zone.

Enabled by the described self-positioning of the EB to the valve seat, this EBH technology is flexible with regard to the various geometrical conditions or manufacturing tolerances of different cylinder heads.

Injector Boxes

The monoflash hardening method of valve seats described previously can be varied by introducing a multipulse flash technique. Here, the total energy required is transferred by a series of short pulses (Fig. 25d). This has the advantage that, despite the short exposure time related to an individual pulse (typically 0.3 s), the energy transfer occurs in a moderate manner, because programmed pauses between the pulses offer enough time for heat propagation into the material body, thus preventing undesired surface melting (Fig. 25d).

This processing variant was applied to the EBH of injector boxes (Fig. 25) made of 42CrMo4 steel. Regardless of the small volume

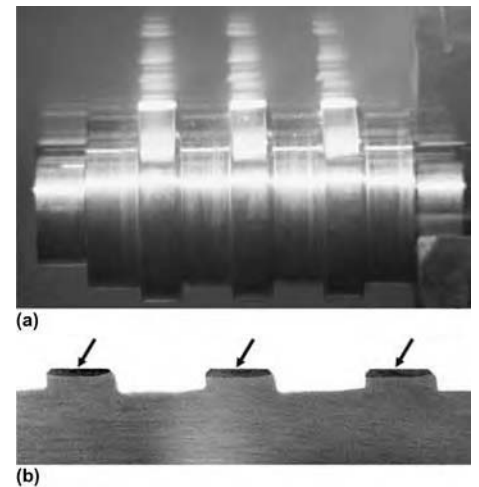


Fig. 24 (a) Electron beam hardening of a shaft with the continuous-interacting multifield technique. (b) Cross section of hardened layers

of this component (Fig. 25b), relatively thick EBH layers of 0.8 mm (0.03 in.) (Fig. 25c) could be realized using 0.3 s pulses and 0.15 s pauses (Fig. 25d). The EB interaction time was 1.35 s, and the resulting process period (including the self-quenching phase) was approximately 2 to 3 s. Aided by pyrometric control (Fig. 25a), surface melting of the contact area of the injector box could be excluded.

Slotted Shafts

The EBH of slotted shafts (Fig. 26a) was performed using the monoflash multifield technique. The component was made of 42Mn7 steel. The contact surfaces in the slots (marked in the cross section in Fig. 26b) must be protected against wear. The hardening occurs through the simultaneous action of three adjacent rectangular energy-transfer fields. The energy density distribution in each field was adjusted to compensate for the different beam incidence angles, reaching up to 60° for the outer fields (Fig. 26a). The result is a constant EBH depth of 0.5 mm (0.02 in.) along the entire slot length (Fig. 26b). Due to the localized and balanced heat input and thanks to the advantages of self-quenching, hardening-related deviations in shape and dimensions lie within range of the manufacturing tolerances; that is, there is a de facto absence of distortion. Although 12 (4 × 3) contact surfaces must be treated per component, the technological total treatment time for EBH, including positioning, requires only up to 8 s, and the production (cycle) time is approximately 14 s per component. In this way, an annual production quantity of more than 1 million components can be produced with a suitably designed and dedicated EB system.

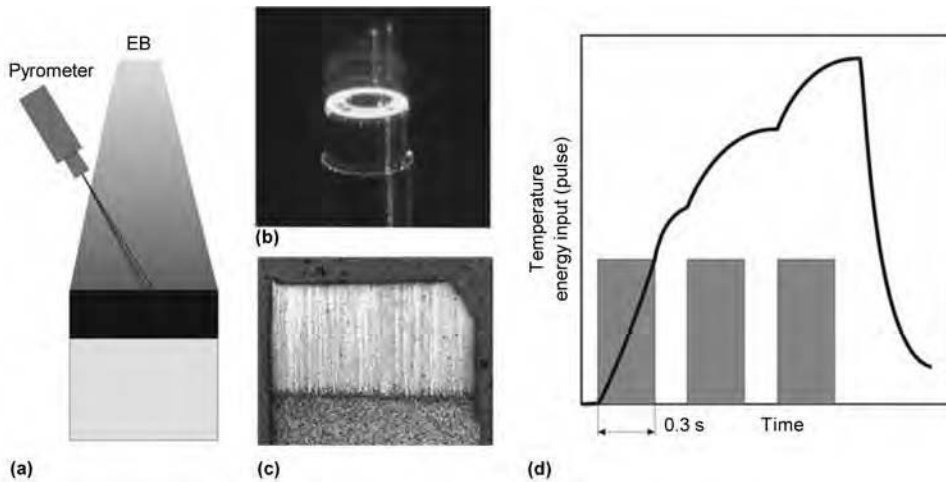


Fig. 25 (a) Electron beam (EB) hardening with the multiflash monofield technique of (b) an injector box (video still). (c) Cross section of hardened layer. (d) Temperature and energy vs. time profile

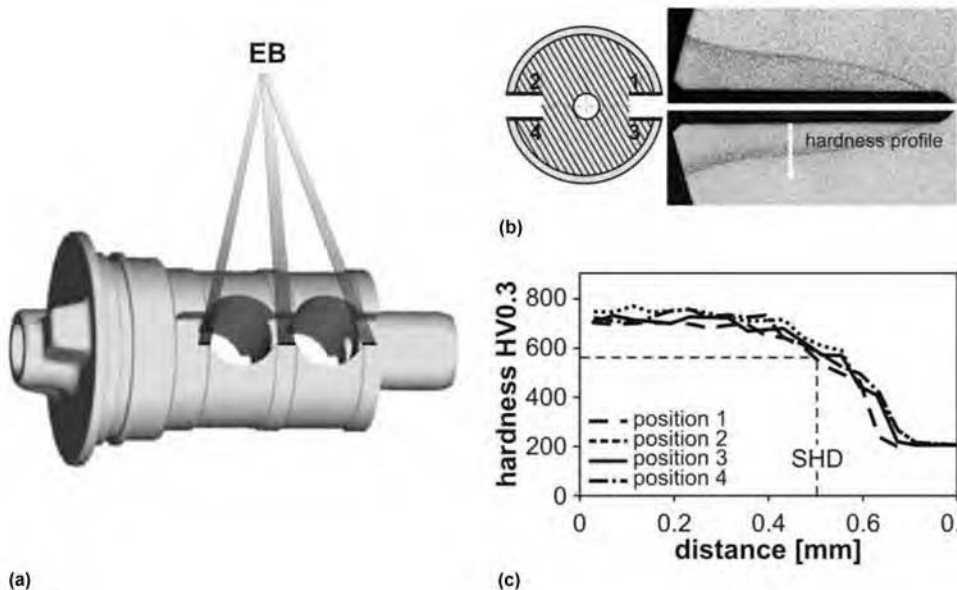


Fig. 26 (a) Electron beam (EB) hardening of a slotted shaft using the single-flash multifield technique to (b) harden positions 1 to 4 of the component, with cross section of EB-hardened layers at positions 2 and 4. (c) Hardness-depth profiles of positions 1 to 4.

ACKNOWLEDGMENT

This article is the result of research and development activities carried out over more than 25 years. The results of basic research are integrated as well as those from industrial development projects. The authors wish to thank all unnamed friends and colleagues for their innovative contributions in this long period of scientific cooperation.

Special thanks go to Prof. Dr.-Ing. habil. H.-J. Spies and Dr. G. Mattausch for the critical review of the article and the helpful references.

REFERENCES

1. S. Schiller and S. Panzer, Thermische Oberflächenmodifikation Metallischer Bauteile mit Elektronenstrahlen, *Metall*, Vol 39 (No. 3), 1985, p 227–232
2. S. Schiller and S. Panzer, Thermal Surface Modification by HF-Deflected Electron Beams, *Proc. Int. Conf. The Lasers vs. EB—State of the Art*, Part 2 (Reno, NV), 1985, p 16–32
3. S. Schiller and S. Panzer, Thermal Surface Modification by Electron Beam High-

- Speed Scanning, *Ann. Rev. Mater. Sci.*, Vol 18, 1988, p 121–140
4. S. Schiller and S. Panzer, Härten von Oberflächenbahnen mit Elektronenstrahlen, Teil 1: Verfahrenstechnische Grundlagen, *HTM*, Vol 42 (No. 5), 1987, p 293–300
5. A. Reichmann, D. Leffler, and R. Bartel, Entwicklungsstand der FEP-Strahlableitungssteuerung für Elektronenstrahlanlagen, *Proc. Sixth Int. Conf. Beam Technology*, April 26–28, 2004 (Halle, Germany), p 102–107
6. T. Löwer, U. Clauss, and D. v. Dobeneck, Innovations in Electron Beam Welding Stimulate New Applications, *Proc. Eighth EBT*, June 5–10, 2006 (Varna, Bulgaria), p 101–104
7. R. Zenker, Elektronenstrahl-Mehrschicht-Technik—Neue Möglichkeiten und Perspektiven für die Randschichtbehandlung, *Stahl Eisen*, No. 2, 2007, p 26–28
8. T. Löwer, D. v. Dobeneck, M. Hofner, C. Menhard, T. Ptaszek, and S. Thiemer, Neue Verfahren in der Thermischen Materialbehandlung mit dem Elektronenstrahl durch Quasi-Trägheitslose Strahlbewegung, *Proc. Sixth Int. Conf. Beam Technology*, April 26–28, 2004 (Halle, Germany), p 63–67
9. R. Zenker, Wärmebehandlung mit dem Elektronenstrahl, *HTM*, Vol 45 (No. 4), 1990, p 230–243
10. R. Zenker, Härten mit dem Elektronenstrahl, *Stahl*, No. 2, 1992, p 57–60
11. R. Zenker, Gefüge- und Eigenschaftsgradienten beim Elektronenstrahlhärten, *HTM*, Vol 45 (No. 5), 1990, p 307–319
12. R. Zenker, N. Frenkler, and H. Buschbeck, Les Technologies du Traitement Thermique Superficiel par Faisceau d'électrons—État de L'art, *Rev. Fr. Métall.*, No. 4, 1995, p 91–94
13. R. Zenker, Electron Beam Surface Modification, Part 1: EB Hardening, *Lasers Eng.*, No. 1, 1991, p 121–144
14. R. Franke and I. Haase, Influence of Outer Zone Handling on Rolling Wear Characteristics of Cast Iron Materials for Cam Shafts, *Tribol. Schmier.tech.*, Vol 46 (No. 5), 1999, p 33–39
15. R. Zenker, N. Frenkler, and T. Ptaszek, Neuentwicklungen auf dem Gebiet der Elektronenstrahl-Randschichtbehandlung, *HTM*, Vol 54 (No. 3), 1999, p 143–149
16. R. Zenker, *Elektronenstrahl-Randschichtbehandlung*, *Innovative Technologie für Höchste Industrielle Ansprüche*, 2nd ed., pro-beam AG & Co. KGaA, 2010
17. R. Zenker, Structure and Properties of Electron Beam Surface Treatment, *Adv. Eng. Mater.*, Vol 6 (No. 7), 2004, p 581–588
18. R. Zenker, Electron Beam Surface Treatment: Industrial Application and Prospects, *Surf. Eng.*, Vol 12 (No. 4), 1996, p 9–12
19. R. Zenker, A. Buchwalder, N. Frenkler, and S. Thiemer, Modern Electron Beam Technologies for Soldering and Surface

- Treatment, *Vak. Forsch. Praxis*, Vol 17 (No. 2), 2005, p 66–72
20. R. Zenker, Modern Thermal Electron Beam Processes—Research Results and Industrial Applications, *Metall. Ital.*, Vol 101 (No. 4), 2009, p 55–62
 21. R. Zenker, Surface Treatment Using Electron Beam—Development Results and Current State of the Application in an Industrial Scale, *J. Jpn. Soc. Heat Treat.*, Vol 49, 2009, p 137–140
 22. R. Zenker, H.J. Spies, A. Buchwalder, and G. Sacher, Combination of High Energy Beam Processing with Thermochemical and Hard Protective Coating: State of the Art, *IHTSE*, Vol 1 (No. 4), 2007, p 152–155
 23. R. Zenker, Electron Meets Nitrogen: Combination of Electron Beam Hardening and Nitriding, *IHTSE*, Vol 3 (No. 4), 2009, p 141–146
 24. H.-J. Spies, R. Zenker, and K. Bernhard, Duplex-Randschichtbehandlung von Metallischen Werkstoffen mit Elektronenstrahl-technologien, *HTM*, Vol 53 (No. 4), 1998, p 222–227
 25. R. Zenker, G. Sacher, A. Buchwalder, J. Liebich, A. Reiter, and R. Häßler, Hybrid Technology Hard Coating—Electron Beam Surface Hardening, *Surf. Coat. Technol.*, Vol 202, 2007, p 804–808
 26. S. Schiller, U. Heisig, and S. Panzer, *Electron Beam Technology*, John Wiley & Sons, 1982
 27. S. Schiller, U. Heisig, and B. Furchheim, Electron Beam Hardening, *Heat Treating*, Vol 4, *ASM Handbook*, ASM International, 1991, p 297–311
 28. R. Bird, W. Stewart, and E. Lightfoot, in *Transport Phenomena*, John Wiley & Sons, 1960, p 390

SELECTED REFERENCES

- S.-H. Choo, S. Lee, and M.G. Golkovski, Effects of Accelerated Electron Beam Irradiation on Surface Hardening and Fatigue Properties in an AISI 4140 Steel Used for Automotive Crankshaft, *Mater. Sci. Eng. A*, Vol 293, 2000, p 56–70
- Á. Csizmazia, T. Réti, M. Horváth, and I. Oláh, Partial Electron Beam Hardening of Cast Iron Camshafts, *Mater. Sci. Forum*, Vol 473–474, 2005, p 447–452
- K.P. Friedel, J. Felba, I. Pobol, and A. Wymyslowski, A Systematic Method for Optimizing the Electron Beam Hardening Process, *Vacuum*, Vol 47 (No. 11), 1996, p 1317–1324
- T.R. Gonser, Computer Sharpens EB Hardening, *Am. Mech.*, Vol 11, 1981, p 139–142
- J. Hick, Rapid Surface Heat Treatments—A Review of Laser and Electron Beam Hardening, *Heat Treat. Met.*, Vol 10 (No. 1), 1983, p 3–11
- W. Hiller and R.M. Silva, Second Electron Beam Processing Seminar (Frankfurt, Germany), Universal Technology Corporation, Dayton, OH, 1972, p 3g1–3g32
- J.-R. Hwang and C.-P. Fung, Effect of Electron Beam Surface Hardening on Fatigue Crack Growth Rate in AISI 4340 Steel, *Surf. Coat. Technol.*, Vol 80, 1996, p 271–278
- J. Rödel and H.-J. Spies, Modelling of Austenite Formation during Rapid Heating, *Surf. Eng.*, Vol 12 (No. 4), 1996, p 313–318
- R.G. Song, K. Zhang, and G.N. Chen, Electron Beam Surface Treatment, Part I: Surface Hardening of AISI D3 Tool Steel, *Vacuum*, Vol 69, 2003, p 513–516
- Q.J. Wang and Y.W. Chung, Ed., *Electron Beam Surface Technologies*, Vol 1, *Encyclopedia of Tribology*, Springer, 2013
- C.-C. Wang and J.-R. Hwang, Surface Hardening of AISI 4340 Steel by Electron Beam Treatment, *Surf. Coat. Technol.*, Vol 64, 1994, p 29–33
- R. Zenker, Electron Beam Surface Modification State of the Art (Review), *Mater. Sci. Forum*, Vol 102–104, 1992, p 459–476
- R. Zenker, W. John, D. Rathjen, G. Fritsche, and B. Kämpfe, Electron Beam Hardening, Part 2: Influence on Microstructure and Properties, *Heat Treat. Met.*, No. 2, 1989, p 43–51
- R. Zenker and M. Müller, Electron Beam Hardening, Part 1: Principles, Process Technology and Prospects, *Heat Treat. Met.*, No. 4, 1988, p 79–88
- R. Zenker, M. Müller, M. Murawski, and B. Furchheim, Electron Beam Hardening, Part 3: Technological Aspects and Industrial Application, *Heat Treat. Met.*, No. 1, 1990, p 15–21

Laser Surface Hardening

Soundarapandian Santhanakrishnan, Indian Institute of Technology Madras
Narendra B. Dahotre, University of North Texas

THE MANUFACTURING COST, energy consumption, and service life of components and tools are major concerns to any industry. In this endeavor, laser manufacturing has become a state-of-the-art technology. This technology provides a clean manufacturing environment resulting in superior-quality products. A brief timeline of laser technology development is summarized in Table 1 (Ref 1). Today (2013), laser beam emission ranges from ultraviolet to infrared wavelengths (191 to 10,600 nm). Depending on the active medium used and its physical characteristics, industrial lasers are classified by the type of active medium: solid state, gas, and liquid (Table 2, Ref 2). Lasers are used in several fields of applications, such as measurement and quality-control tools, nano-macro materials manifestation, biomedical, and so on. Among these, laser materials processing, such as heat treatment, cladding, alloying, and hard facing, is among the fastest growing fields (Fig. 1).

Each year, several billion dollars are spent in the defense, nuclear, automotive, aerospace, and ship-building industries to repair or replace high-value components (Ref 3, 4). To save money, material, manpower, and time, laser surface hardening (LSH) is used on high-value parts to repair instead of replace, thereby extending service life (Ref 5). Laser surface hardening offers many advantages over conventional techniques (physical vapor deposition, chemical vapor deposition, sputtering, sol-gel); localized/bulk surfaces with superior surface resistance properties (wear, fatigue, corrosion, fracture, erosion, heat) can be obtained. Laser surface hardening is a noncontact process that in turn provides a chemically inert and clean environment as well as flexible integration with operating systems. High volume of production with superior surface quality and reasonable manufacturing cost are the foremost advantages.

Conventional Surface-Hardening Techniques

For several decades, many conventional surface-hardening techniques have been used to enhance the surface and mechanical properties

of ferrous and nonferrous alloys. Various conventional surface-modification techniques are discussed extensively in the following sections (Fig. 2).

Physical Vapor Deposition

Physical vapor deposition (PVD) is a thin-film atomizing deposition process. In this process, material in the form of vaporized plasma-state atoms or molecules is injected in and under a pressured chamber; the plasma particles deposit on the cold substrate, forming a thin film on it. Normally, the film thickness varies from few nanometers to micrometers. However, in some circumstances, multilayer functionally graded films near half a millimeter can also be obtained. A small-to-large area (more than 10 m²) with complex-shaped substrates (glass, metals, tool bits) can be deposited using different elements, alloys, and compounds (TiN, TiC) at a deposition rate of 1 to 10 nm²/s.

Chemical Vapor Deposition

Chemical vapor deposition (CVD) is a process to continually deposit the atoms or molecules of a chemical vapor precursor species on the substrate. This process is often accomplished under a hydrogen-base atmosphere at an elevated temperature. The deposited material may react with other gaseous species in the system to yield by-products such as oxides and nitrides. Chemical vapor deposition processing is generally accompanied by volatile-reaction by-products and unused precursor species with deposition rates of 5 to 100 nm²/min. The advantages and disadvantages of PVD and CVD are illustrated in Fig. 3.

Sputter Deposition

Sputtering is the process whereby atoms or molecules of a material are ejected (or vaporized) due to the momentum transfer from an atomic-sized energetic bombarding particle impinging on the target surface (Ref 6). These vaporized particles will then condense upon and coat a substrate material. Typically, sputtering is performed using gaseous ions from

plasma that are then accelerated and directed toward the target. The system uses plasma produced and controlled by magnetron guns. For sputtering to be a useful coating process, a number of criteria must be met. First, ions of sufficient energy must be created and directed toward the surface of a target to eject atoms from the material. Second, ejected atoms must be able to move freely with little impedance toward the object to be coated. In this, low pressures are required to maintain high ion energies and to prevent too many atom-gas collisions after ejection from the target. Sputtering is a high-rate vacuum coating technique for depositing metals, alloys, and compounds onto a wide range of materials with thicknesses up to approximately 5 μm (0.2 mil). It exhibits several important advantages over other vacuum coating techniques, which has led to the development of a number of commercial applications ranging from microelectronics fabrication to simple decorative coatings (Ref 6).

Ion Plating

Ion plating uses continuous or periodic bombardment of atomic-sized energetic particles to deposit a thin film on a substrate. The energetic particles used for bombardment are usually ions of an inert or reactive gas. It can be done in either a plasma environment or a vacuum environment. By using a reactive gas in the plasma, films of compound materials can be deposited. Ion plating can provide dense coatings at relatively high gas pressures, where gas scattering can enhance surface coverage. Ion plating is used to deposit hard coatings of compound materials, adherent metal coatings, optical coatings with high densities, and conformal coatings on complex surfaces. Thin-film deposition for optical and electronic devices and corrosion and wear resistance are primary applications.

Electroplating, Electroless Plating, and Displacement Plating

Electroplating is the deposition on the cathode of metallic ions from the electrolyte of an

Table 1 Timeline of laser technology development

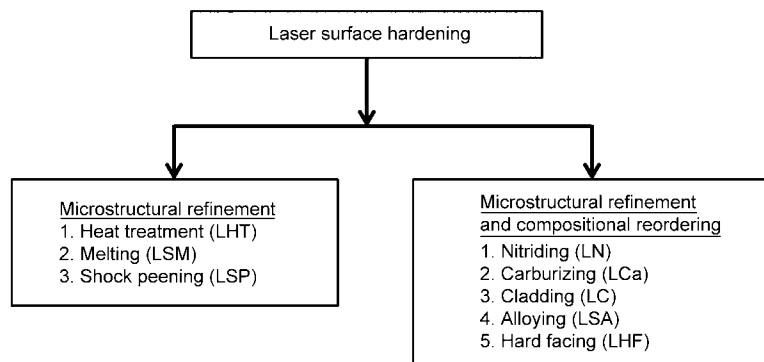
Year	Event	Year	Event
1916	Albert Einstein proposes stimulated emission	1966	Ed Gerry and Arthur Kantrowitz invent gas-dynamic CO ₂ laser, which eventually reaches hundreds of kilowatts
1928	Indirect evidence for stimulated emission reported by Rudolf Ladenburg	1967	Dye laser tuned for the first time by Bernard Soffer and B.B. McFarland at Korad
1940	Light amplification by stimulated emission proposed by Valentin Fabrikant	1967	Jack Dymont develops stripe-geometry diode laser
1951	Stimulated emission at 50 kHz observed by Edward Purcell and Robert Pound, Harvard	1968	Argon-laser treatment of diabetic retinopathy developed by Francis L'Esperance, Eugene Gordon, and Ed Labuda
1954	Charles Townes and James Gordon produce first microwave maser at 24 GHz at Columbia University	1969	Ruby laser pulses range the moon by bouncing off retroreflector placed by Apollo 11 astronauts
Summer 1957	Townes starts investigating optical maser	1970	Nikolai Basov of Lebedev Institute reports pulsed ultraviolet lasing by xenon excimers
October 1957	Townes talks with Gordon Gould about optical pumping and optical maser	1970	Zhores Alferov demonstrates first room-temperature continuous-wave diode laser
November 1957	Gould coins the word <i>laser</i> and proposes Fabry-Pérot resonator in first notebook	1970	First low-loss optical fiber made by Robert Maurer, Donald Keck, and Peter Schultz at Corning
December 1958	Townes and Arthur Schawlow publish detailed optical maser proposal in <i>Physical Review</i>	1970	Ben Snavely demonstrates continuous-wave dye laser at Kodak
1959	Advanced Research Projects Agency issues \$999,000 contract to TRG Inc. to develop laser based on Gould proposal	1971	Rudolf Kazarinov and R.A. Suris propose concept behind quantum cascade laser
May 1960	Theodore Maiman demonstrates ruby laser at Hughes Research Labs	1972	Erich Ippen and Charles Shank produce 1.5 ps pulses
Summer 1960	TRG Inc. and Bell Labs duplicate ruby laser	1974	First laser scanner demonstrated in a supermarket
July 1960	Headlines announce laser discovery, predict uses from communications to weapons	1974	Rare-gas halide excimer lasers invented; several types demonstrated
November 1960	Peter Sorokin and Mirek Stevenson, IBM, make first four-level solid-state laser, uranium in CaF ₂	1974	Two-photon Doppler-free spectroscopy developed independently by Theodor Hänsch at Stanford and David Pritchard at Massachusetts Institute of Technology
December 1960	Ali Javan, William Bennett, and Donald Herriott of Bell Labs make helium-neon laser, the first continuous-wave laser and the first gas laser	1976	Bell Labs' accelerated aging tests predict million-hour lifetimes for GaAs diode lasers
1961	First neodymium laser in calcium tungstate, Leo Johnson and Kurt Nassau, Bell Labs	1976	J. Jim Hsieh operates InGaAsP diode emitting at 1.25 μm at room temperature
1961	First neodymium-glass laser, Elias Snitzer, American Optical	1977	John M.J. Madey operates first free-electron laser oscillator
1961	Second harmonic of ruby generated by Peter Franken	1978	MCA-Philips begins test marketing helium-neon laser player of 12 in. videodisks
1961	Trion Instruments founded in Ann Arbor, MI, to make lasers	1979	Philips shows prototype compact disk player
1961	Quantatron founded by Maiman to make lasers; later becomes Korad	1980	Bell announces plans for TAT-8, first transatlantic fiber-optic cable
November 1961	Ruby laser repairs detached retina in first patient at Harkness Eye Institute in New York	1980	Supermarket scanners become common
1962	Red helium-neon laser invented by Alan White and Dane Rigden, Bell Labs	1982	Peter Moulton develops titanium-sapphire laser
1962	First semiconductor diode laser, Robert Hall, GE Research and Development Labs, followed in weeks by three other groups	1982	Audio compact disk players introduced in Japan
1962	Spectra-Physics and Perkin-Elmer introduce \$8000 infrared helium-neon laser in March; sales take off when they introduce red version in autumn	1983	Ronald Reagan launches Strategic Defense Initiative
1962	Lawrence Livermore National Laboratory forms groups to study prospects for laser fusion	1984	First commercial diode-pumped neodymium lasers emit 100 mW continuous wave
1962	Air Force Chief of Staff Gen. Curtis LeMay praises prospects for laser nuclear defense	1985	Spectra Diode Labs introduces 200 mW array of ten continuous-wave GaAlAs diode laser stripes
1963	Herbert Kroemer proposes heterostructures to improve diode lasers. Zhores Aleferov and Rudolf Kazarinov at Ioffe Institute in Russia file patent on double-heterostructure laser	1985	Sony makes continuous-wave AlGaInP diode emitting at 671 nm in red
1963	First ion laser demonstrated in mercury by Earl Bell at Spectra-Physics	1985	First room-temperature vertical cavity surface-emitting laser by Kenichi Iga
1963	Nitrogen laser invented by H.G. Heard	1986	David Payne makes erbium-fiber laser tunable across 25 nm near 1535 nm
1964	Snitzer demonstrates first fiber amplifier	1987	Payne reports 26 dB gain at 1536 nm in erbium-doped fiber amplifier
1964	William Bridges discovers pulsed argon-ion laser at Hughes; Eugene Gordon develops continuous-wave argon at Bell	1987	Pulses from dye laser compressed to 6 fs by Richard Fork at Bell
1964	First three-dimensional laser holograms displayed by Emmett Leith and Juris Upatnieks	1988	TAT-8, the first transatlantic fiber cable, is completed
1964	Kumar Patel makes CO ₂ laser at Bell Labs	1989	Spectra Diode Labs produces 76 W continuous wave from 1 cm diode array
1964	Joseph Geusic and LeGrand Van Uitert make first Nd:YAG laser at Bell	1989	Isamu Akasaki demonstrates blue light-emitting diode of GaN
1965	Kumar Patel reaches 200 W continuous wave from CO ₂ laser	1994	Nichia Chemical offers 450 nm nitride light-emitting diodes with 2% electrical conversion efficiency
1965	Coherent Radiation founded to manufacture CO ₂ lasers	1994	Federico Capasso at Bell Labs demonstrates quantum cascade laser
1965	William Silfvast and Grant Fowles make helium-cadmium laser	1995	Pulse length of titanium-sapphire reaches 8 fs
1965	J.V.V. Kasper and George C. Pimentel make first chemical laser, HCl	1996	Shuji Nakamura of Nichia reports first blue diode laser, made from InGaN
1965	Coherent anti-Stokes Raman spectroscopy demonstrated by Robert Terhune at Ford	2000	Titanium-sapphire pulses compressed to 5 fs
1966	Peter Sorokin makes first dye laser at IBM; Fritz P. Schaefer independently invents dye at Max Planck Institute	2000	Peak of technology stock bubble; the American stock exchange NASDAQ exceeds 5000 during the 2000 Optical Fiber Communication Conference and Exposition. In March 2002, TAT-8 submarine cable retired after failure because its capacity was too small to justify the cost of repairs.
1966	Charles Kao and George Hockham propose communications through low-loss, single-mode optical fibers	2004	Ozdal Boyraz and Bahrom Jalali, first silicon Raman laser at the University of California, Los Angeles
		2006	John Bowers, first silicon laser
		2007	John Bowers and Brian Koch, first mode-locked silicon evanescent laser
		2010	First 10 petawatt laser at Lawrence Livermore National Laboratory

Source: Ref 1

Table 2 Types of industrial lasers

Type of laser	Wavelength, nm	Pump source
Solid-state lasers(a)		
Nd:YAG	1064	Flashlamp, laser diode
Ruby	694	Flashlamp
Nd:glass	1062	Flashlamp, laser diode
Alexandrite	700–820	...
Titanium-sapphire	700–1100	Other laser
Er:YAG	2940	Flashlamp, laser diode
Nd:YLF	1047	Flashlamp, laser diode
Gas lasers		
HeNe	632.8	...
Argon	488, 514.5	...
Krypton	520–676	...
HeCd	441.5, 325	...
CO ₂	10600	Transverse (high-power) or longitudinal (low-power) electrical discharge
CO	2600–4000 and 4800–8300	Transverse (high-power) or longitudinal (low-power) electrical discharge
ArF	191	...
KrF	249	...
XeCl	308	...
XeF	351	...
Copper vapor	510.6, 578.2	...
Gold vapor	628	...
Semiconductor lasers		
InGaAs	980	...
AlGaInP	630–680	...
InGaAsP	1150–1650	...
AlGaAs	780–880	...
Liquid dye lasers		
Rhodamine 6G	570–640	...
Coumarin 102	460–515	...
Stilbene	403–428	...

(a) YAG, yttrium-aluminum-garnet; YLF, yttrium-lithium-fluoride. Source: Ref 2

**Fig. 1** Laser surface-hardening techniques

electrolysis cell. Chromium, nickel, zinc, tin, indium, silver, cadmium, gold, lead, and rhodium elements are commercially deposited from aqueous solutions. Some alloy compositions, such as copper-zinc, copper-tin, lead-tin, gold-cobalt, tin-nickel, nickel-iron, nickel-phosphorus, and cobalt-phosphorus, are also commercially deposited. Conductive

oxides, such as PbO and CrO₃, can also be deposited by electroplating. Typically, the anode of the electrolytic cell is of the material being deposited and is consumed in the deposition process. In some cases, the anode material is not consumed, and the material to be deposited comes only from the electrolyte solution. In electroless or autocatalytic

plating, no external voltage/current source is required. The voltage/current is supplied by the chemical reduction of an agent at the deposit surface. The reduction reaction is catalyzed by a material, which is often boron or phosphorus. Materials that are commonly deposited by electroless deposition are nickel, copper, gold, palladium, platinum, silver, cobalt, and nickel-iron alloys. Displacement plating is the deposition of ions in solution on a surface, and it results from the difference in electronegativity of the surface and the ions.

Laser Surface Hardening

The use of lasers to modify the surfaces of metals in order to increase the resistance of heat, wear, corrosion, and erosion has significant growth potential for manufacturing industries. In LSH, higher heating and cooling rates of 10^8 to 10^{10} °C/s are involved to modify the surface and mechanical properties of the metallic components. These higher heating and cooling rates could generate superior microstructures and excellent surface and mechanical properties. Laser surface hardening has demonstrated its capability to tailor properties of a surface locally as well as in bulk (Ref 7, 8).

Majumdar and Manna (Ref 9) reported that the power density of the laser and its interaction time with the material determines the heating and cooling cycle (Fig. 4). The heating and cooling frequency and duty ratio determine the final microstructure of the laser-treated surface. The final microstructure determines the mechanical and surface properties of the components. The laser materials processes are divided into three categories based on the ratio of the power density with respect to the interaction time: heating (without melting/vaporizing), melting (no vaporization), and vaporization. Surface-transformation hardening requires low-power density to avoid surface melting. High peak power density is required to perform the surface melting, cladding, alloying, and hardfacing processes. High power density within a short interaction time is required to perform the cutting, deep drilling, and other similar machining operations.

In general, laser surface modification is classified into the following five categories: laser surface heat treatment, laser surface melting (skin melting or glazing), laser direct metal deposition (cladding, alloying, and hardfacing), laser physical vapor deposition, and laser shock peening. In laser surface heat treatment, no melting takes place, whereas in laser surface melting, a thin surface layer of the workpiece is melted, and, as a result of the rapid quenching, a harder and more wear-resistant structure is obtained. In laser deposition, a second

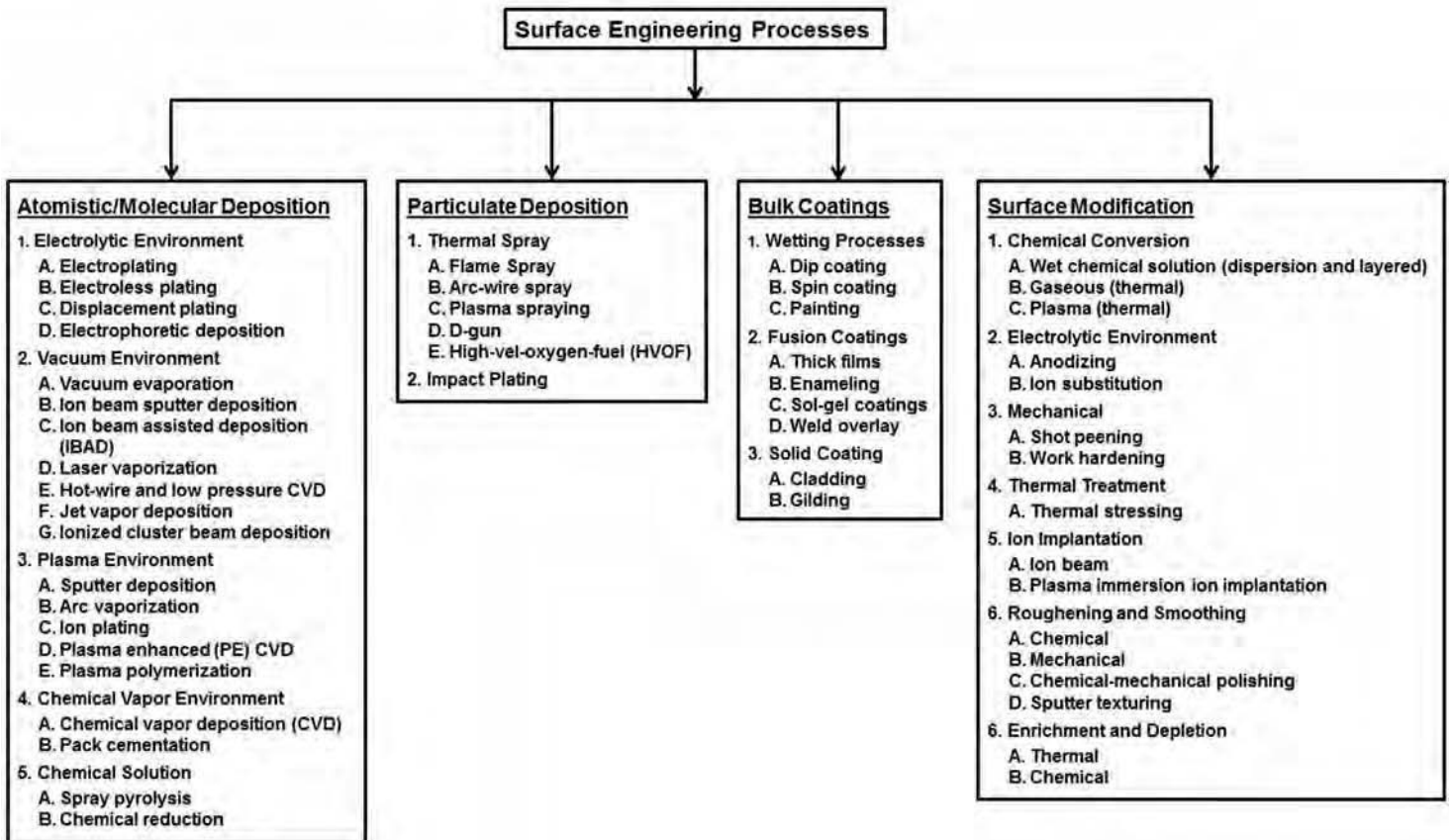


Fig. 2 Conventional surface-hardening techniques

Relationship of hard coating processes, parameters, and technology

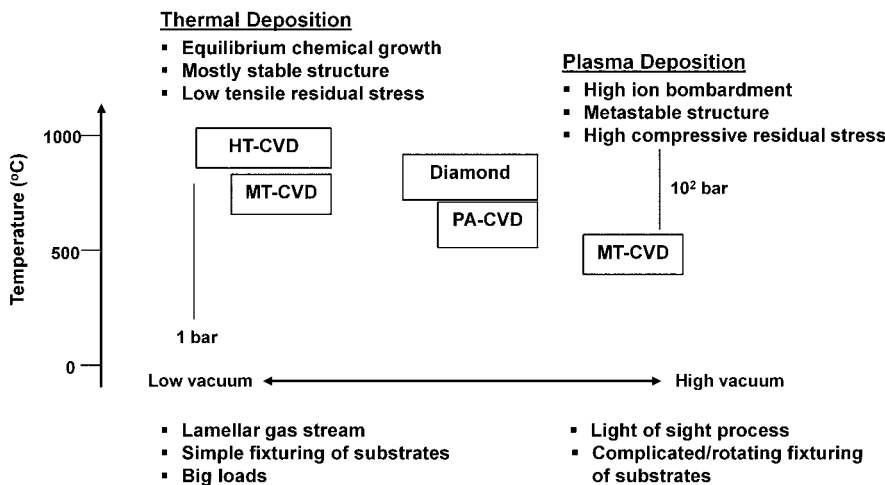


Fig. 3 Advantages and disadvantages of physical and chemical vapor deposition processes. HT-CVD, high-temperature chemical vapor deposition; MT-CVD, mid-temperature chemical vapor deposition; PA-CVD, plasma-assisted chemical vapor deposition. Source: H. G. Pregel et al., 1998

material is applied to the surface and melted by the laser beam, either to alloy with a thin surface layer of the substrate or to metallurgically bond to the substrate. However, in laser physical vapor deposition, the second material is applied in vapor form, and no melting takes place. Laser shock peening, however, generates shock waves, which induce compressive residual stresses on the surface of the material and so alter its properties.

Absorptivity

Laser radiation can be described as electromagnetic waves, which comprise electric (*E*) and magnetic (*H*) field vectors. Absorption of light results predominantly from the interaction of electromagnetic radiation with the electrons (either free or bound) of the material. When the electromagnetic radiation passes over the electron, it exerts a force and sets the electrons into motion by the electric field of the radiation (Ref 2). The force exerted by the electromagnetic

radiation on the electron can be expressed as:

$$F = eE + e\left(\frac{v}{c} \times H\right) \tag{Eq 1}$$

where v is the velocity of the electron, and c is the speed of light. If it is considered that the electric and magnetic field carry the same amount of energy, then, according to Eq 1, the contribution of magnetic field to the force is smaller than that of the electric field by a factor of the order of v/c . Hence, the most significant term in Eq 1 is eE . The absorbed radiation thus results in increasing the total energy of the charged particles, such as kinetic energy of the free electrons, excitation energy of the bound electrons, and so on. Once excited, charged particles spontaneously relax down to a lower energy level, thereby releasing energy radiatively, translating in at least partial heat. Hence, the absorption process is sometimes referred to as the secondary source of energy inside the material and is used to determine the extent of various effects on the material during laser-material interactions.

The absorption of laser radiation in the material is generally expressed in terms of the Beer-Lambert law (Ref 10):

$$I(z) = I_0 e^{-\mu z} \tag{Eq 2}$$

where I_0 is the incident intensity, $I(z)$ is the incident intensity at depth of penetration of z , and μ is the absorption coefficient. Thus, the intensity of the laser radiation becomes attenuated inside the material. The length over which the significant attenuation of laser radiation takes place is often referred to as the attenuation length (L) and is given by the reciprocal

of the absorption coefficient:

$$L = \frac{1}{\mu} \tag{Eq 3}$$

For a strongly absorbing material, the absorption coefficients are in the range of 10^5 to 10^6 cm^{-1} , such that the attenuation lengths are in the range 10^{-5} to 10^{-6} cm (Ref 11).

Laser surface hardening needs lower power density with smaller interaction time compared to welding and cutting processes. For power densities less than 10^5 W/cm^2 , a majority portion (~90%) of the incident infrared energy is reflected away from the laser-material interaction zone (Ref 12). Therefore, in practice, it is essential to apply a black coating on the substrate surface to enhance effective absorptivity. Without such a coating, only a small fraction of the laser beam energy will be conducted into the bulk substrate material, thus failing to acquire the desired surface temperature. Absorptivity is therefore one of the most important parameters directly influencing the LSH process. Although much research on absorptivity has been reported in this regard (Ref 12), it is very difficult to determine an accurate absorptivity because it depends on many parameters, such as surface roughness, irradiation angle, and surface coating. The absorptivity ($A = (L_A - L_R)/L_A$) is derived from the applied laser energy (L_A) and the reflected energy (L_R). The ability of the material surface to radiate energy is known as emissivity (e), expressed as a function $e = f(\lambda, T, t)$ of the wavelength of the laser (λ), temperature (T), and time (t) (Ref 13). The emissivity values of different metals are summarized in Table 3.

The laser energy absorbed by the material during the laser-material interaction is converted into heat by degradation of the ordered and localized primary excitation energy. The typical overall energy relaxation times are of the order of 10^{-13} s for metals (10^{-12} to 10^{-6} s for nonmetals). The conversion of light energy into heat and its subsequent propagation by conduction into the material, convection, and radiation in the surrounding atmosphere controls the temperature distribution in the material. Depending on the magnitude of the rise in temperature, heating, melting, and vaporization can occur. Furthermore, the ionization of vapor during laser irradiation may lead to generation of plasma. In addition to the thermal effects, the laser-material interactions may be associated with photochemical processes such as photoablation of the material.

The laser light intensity can be produced with different spatial transversal and longitudinal distribution patterns within the beam. These are called transverse electromagnetic modes (TEM_{mn}), characterized by integer indices m and n . TEM_{00} represents a Gaussian mode beam. Higher-order modes TEM_{mn} with m and/or n greater than zero are less focusable than Gaussian modes.

Laser Scanning Technology

In LSH, the focal beam spot geometry and its energy distribution are very important to obtain a desired heating and cooling rate, which in

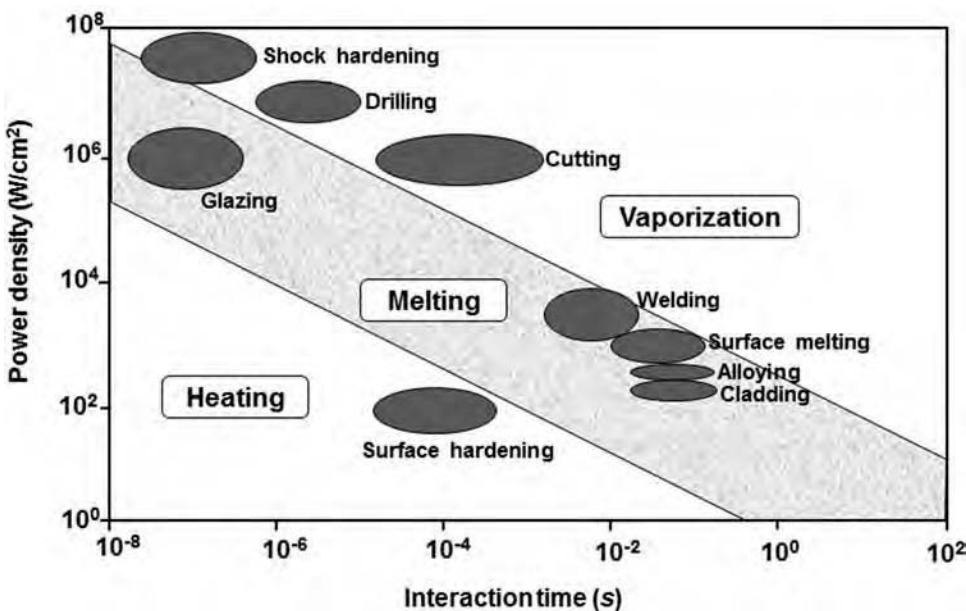


Fig. 4 Chart of laser power density and beam interaction time for various laser applications

Table 3 Emissivity values of different metals at 100 °C (212 °F)

Material	Surface condition	Emissivity
Aluminum	As-received plate	0.09
Aluminum	Oxidized	0.2
Aluminum	Polished	0.05
Aluminum	Rough	0.07
Brass	Oxidized	0.61
Brass	Polished	0.03
Chromium	Polished	0.1
Copper	Oxidized	0.7
Copper	Polished	0.03
Granite	Polished	0.85
Granite	Rough	0.88
Iron, cast	Oxidized	0.64
Iron, cast	Polished	0.21
Iron and steel	Hot rolled	0.6
Iron and steel	Oxidized	0.6
Iron and steel	Polished	0.07
Iron and steel	Galvanized	0.07
Magnesium	As-received plate	0.18
Magnesium	Polished	0.07
Nickel	Polished	0.05
Nickel	Oxidized	0.37
Silver	Polished	0.03
Stainless steel	Polished	0.18
Stainless steel	Oxidized	0.85
Titanium	Polished	0.15
Stainless steel	Oxidized	0.40
Zinc	Oxidized	0.11
Zinc	Polished	0.05

Source: Ref 14

turn generates the specified microstructure and surface properties (Ref 15). In general, a circular laser beam spot with Gaussian energy distribution is used for melting-based microstructure and chemical compositional transformed hardening processes (laser cladding, laser alloying, laser hardfacing). A rectangular or square laser beam spot with uniform energy distribution (top-hat intensity distribution profile) is used for nonmelting processes (laser annealing, laser transformation hardening, laser shock peening) where microstructure changes occur (Ref 12, 16). The quality of the TEM_{mn} laser beam is quantified as a factor K (Ref 16). For example, in the case of TEM₀₀ (Gaussian) K = 1, this K value decreases for higher TEM modes (K = 0.57 for TEM₀₁). Sheikh and Li (Ref 15) have designed various nonconventional beam geometry, such as circular (C), rectangular-short (RS), rectangular-long (RL), triangular-forward (TF), and triangular-reverse (TR), and the maximum obtained heating and cooling rates (HR/CR) were given as the sequence of HR/CR = C > TR > RL > TF > RS. Several custom-designed optical systems (peritech, SCANLAB, and so on) are commercially available to tailor the laser beam spot geometry and energy distribution (Ref 17). By using a scanning technology with optical beam expander, any specific laser beam spot geometry and energy distribution can be obtained, allowing a single laser system to be used for multiple applications (Fig. 5).

Laser Annealing

Laser annealing is a nonmelting process where an epitaxial regrowth of thin defective or amorphous layers are formed (Ref 18). The transformation of small-grain polycrystalline or amorphous layers into large-grain crystalline material is due to laser-induced recrystallization. The advantages of laser annealing are short

processing time and better process control, good surface crystallinity of laser-recrystallized materials, the process temperature is well below melting and therefore the outcome is solid-phase transformation, and its velocity is more than several meters per second. Toyserkani and Khajepour (Ref 18) mentioned that substrate preheating is advantageous to obtain the specified phase at lower laser-light intensities. Previous studies (Ref 19, 20) demonstrated laser-induced recrystallization was achieved for a large number of materials (aluminum, copper, nickel, etc.). After laser-induced recrystallization, corrosion and wear resistance improved. Katakam et al. (Ref 21) demonstrated the site-specific stress-induced selective nanocrystallization in laser-processed amorphous Fe-Si-B alloy. The mechanism was attributed to the enhanced diffusivity at the edges of the laser track due to a reduced diffusion activation barrier. A homogeneously devitrified nanocrystalline microstructure at the interface and predominantly an amorphous phase at the center of the laser track were seen. The retention of an amorphous phase in the regions experiencing a tensile stress and a compressive stress occurred at devitrification regions.

Laser Cladding

In the laser cladding (LC) process, clad material is welded to the surface of the substrate. During LC, a high-power laser is used to melt powder particles or feeding wire on the substrate.

Cook et al. (Ref 22) demonstrated that a denser-microstructure laser clad with a stable bond to the substrate was generated at high temperature. The clad structure on the components enhances/improves surface properties such as resistance to wear, corrosion, and heat. Several methods are used to achieve a thin layer of clad in the laser cladding process:

- Injecting powder particles into the substrate molten pool generated by the high-power-density laser beam
- Feeding the wire into the focal spot of the laser beam to melt it over the substrate
- Preplacing a thin layer of powder on the substrate to expose it to the high-density laser beam

The laser cladding process by powder injection has proved to produce a uniform, defect-free, and good metallurgically bonded clad on the substrate. Syed et al. (Ref 23) studied the influence of the powder-feeding direction (front side and rear side) with respect to the laser scanning direction. The angle and position of the powder-feeding nozzle greatly affect the clad geometry. A small variation in the powder feed rate could significantly generate larger variations in the geometrical features and microstructure of the clad. The front feeding direction was found to produce a smooth, uniform, and good metallurgically bonded clad. In addition, a dense, crack-free, nonporous cladding and a small heat-affected zone (HAZ) were seen.

In LC, a strong coupling between the laser beam, powder particles, and the molten pool occurs. A larger fraction of the laser power reaches the substrate, while a smaller fraction of the laser power is captured by the powder particles that will heat it up. The laser power attenuated by the powder particles and the related fluctuation of laser energy apparently changes the shape of the molten pool. The variation of molten pool shape has a significant effect on the workpiece absorption with respect to the laser beam. A number of processing parameters, such as laser power, scanning speed, powder feed rate, laser focal spot, and thermophysical properties of the materials, are involved in the laser cladding process to achieve the desired clad geometry (height and width) and surface properties. The temperature generated in the cladding process is a function of processing parameters such as laser power, scanning speed, beam angle with respect to the substrate, and the absorptivity of the clad material and the substrate to the laser beam. The clad geometry, the dilution of the clad material to the substrate, and the HAZ generated in the cladding process are the function of the thermophysical properties of the clad material and the substrate, temperature, and time. The microstructure evolution and the corresponding mechanical and surface properties produced in the cladding process depend on the rates of heating and cooling cycles, temperature gradient, and the subsequent rate of solidification.

Surface hardness obtained through LC is primarily a function of the build material and its microstructure. According to the Hall-Petch relationship, hardness is linearly proportional to the reciprocal square root of the grain size (Ref 24). It is applicable for grain sizes above approximately 0.1 mm (0.004 in.) (Ref 25), so it is appropriate for laser direct metal deposition

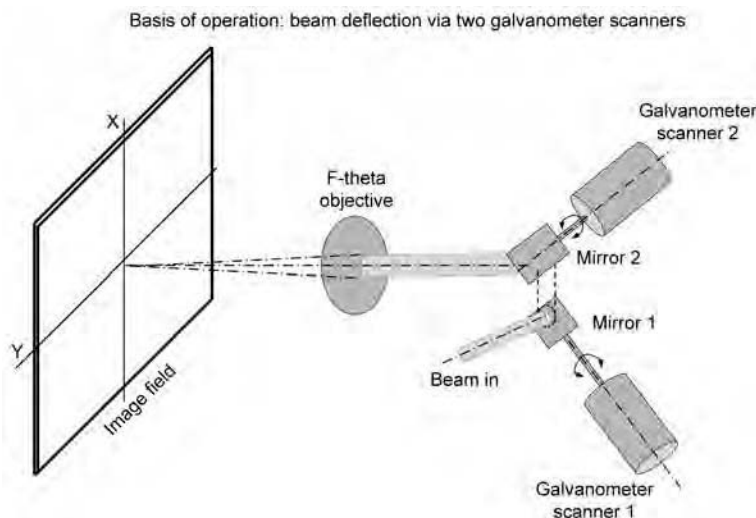


Fig. 5 Schematic of laser scanning technology

(LDMD). In turn, the microstructure is a function of the thermal gradients and cooling rates during solidification and is related to the cooling rate by the Kurz and Fischer relationships (Ref 26), which can be summarized as the microstructural scale being approximately proportional to the reciprocal cube root of the cooling rate during solidification. Consequently, hardness increases with cooling rate. Surface hardness has been found to increase with traverse speed but decrease with powder particle size and laser power when substrate and deposition material are the same. The hardness often varies with surface position; faster cooling rates near the base of a structure, where the heat flow is approximately three-dimensional, tend to give an initially harder surface, but reheating by subsequent layer deposition eventually leads to the upper portion of a wall being harder (Ref 27). Sometimes, the type of material used causes unusual hardness profiles. One example is the sudden drop in surface hardness when moving down a martensitic steel wall prepared by LDMD due to the tempering of the structure by the addition of subsequent layers (Ref 28). Studies of LDMD using dissimilar materials or elemental powder blends indicate that the hardness is primarily determined by the dilution ratio or feed proportions due to those factors determining elemental composition and influencing cooling rate.

A major application of LC is in the repair and refurbishment of high-value components such as tools, turbine blades, and military components. Conventional methods use welding to retrieve these damaged components; however, these methods are usually destructive due to the highly distributed temperature over the area of repair. This thermal destruction causes a low mechanical quality, cracks, porosity, and a very short life of the component. Laser cladding can provide a permanent structural repair and refurbishment on many alloys (e.g., aluminum alloys) that are generally considered unweldable by conventional methods. The success of laser cladding technology in this area is due to the small heat zone, rapid solidification, increased cleanliness, lower dilution, and increased controllability over the depth of the HAZ (Ref 18).

Titanium-base alloys, nickel-base superalloys, and cobalt-base alloys are some of the important alloys that are deposited on different substrates, such as unalloyed steels, alloyed steels, hardened steels, stainless steels, aluminum alloys, cast irons, and nickel- or cobalt-base alloys (Ref 18). The low-heat-input property of laser cladding makes it highly attractive for jet engine component repairs, in which metal depositions are required to be applied to superalloys. These superalloys are highly susceptible to strength loss and physical distortion when exposed to excessive temperature variations.

In recent years, researchers have been working on enhancing laser cladding to construct prototypes and production tooling, even for precision metal parts made from different commercial

alloys, such as H13 tool steel, 306 and 304 stainless steels, nickel-base superalloys (e.g., Inconel 625, 690, 708, 2024), aluminum, composite, and titanium-base material (e.g., Ti-6Al-4V). The feature of the technology provides the functionally graded material-deposition capability, which is applicable in many aerospace components in which a lightweight but hard external surface is requested.

Differences between Laser Cladding, Alloying, and Glazing

Adding powder to the melt pool may create three different products, depending on the type and amount of material added. In laser alloying, a small amount of powder is fed into the melt pool. As such, homogeneous mixing throughout the melt region may be obtained. Laser cladding resembles laser alloying except that dilution by the substrate is kept to a minimum and more addition of material to the surface is required. In laser glazing, a metallic glass coating is deposited to provide an environmentally effective surface in terms of wear and corrosion. The principal advantage of laser glazing is that it alters microstructures without changing the composition. Using laser cladding, the following advantages can be

obtained compared to other surface material processing (Ref 18, 29):

- Low heat input and thus narrow HAZ and reduced distortion, with minimal machining required
- Reduced alloy material loss
- Minimal clad dilution of base metal (less than 2%), enabling the special properties of the clad material to be maintained
- Flexibility and ease of automation
- Complete metallurgical bonding to the substrate, resulting in high-integrity coating

In general, laser cladding is an effective means of changing the microstructure and thus the mechanical properties of thin layers of a substrate where the surface area to be processed is large enough. In LC, four characteristic metallurgical regions are observed. The first region represents the clad material. The second region represents the dilution zone. The third region is a HAZ, and the final region is the substrate. Each region has a specific microstructure and metallurgical properties that depend on the materials and the deposition process parameters used. Results from previous studies of laser melting, laser cladding, alloying, and hardfacing of various ferrous alloys are summarized in Tables 4 to 7.

Table 4 Laser surface melting of ferrous alloys

Material system	Outcome	Reference
Inconel 600	Enhanced oxidation resistance through microstructural homogeneity	Ref 30
Pearlitic steel	Superior wear resistance via homogeneous microstructure and glazing layer formation	Ref 31
S31603, S30400, S32760	Higher cavitation erosion and corrosion resistance	Ref 32
AK 321	Microstructural homogeneity and high localized corrosion resistance	Ref 33
UNS S42000	Excellent hardness, cavitation erosion, and pitting corrosion resistance by higher retained austenite	Ref 34
X165CrMoV12-1	Increased hardness (retaining higher-temperature austenite phase)	Ref 35
AISI 310, AISI 304, AISI 420, AISI 430	Microstructural homogeneity (fine cellular dendritic structure) and enhanced corrosion resistance	Ref 36
AISI 316	Enhanced resistance to stress-corrosion cracking	Ref 37
AISI 304	Pitting corrosion protection due to dissolution of N ₂ and formation of nitrides	Ref 38
CK60	Improved hardness, wear, and corrosion resistance due to higher martensite phase transformation	Ref 39
P21, 440C	Higher corrosion resistance through maximum Ni ₃ Al dissolution and carbide refinement	Ref 40
41Cr4	Improved wear resistance	Ref 41
AISI 440C	Corrosion-resistance enhancement due to higher dissolution of Cr ₇ C ₃ and retained austenite	Ref 40
ASP2060	Hardness improvement and better corrosion protection	Ref 42
SKD6	Higher mechanical properties	Ref 43
AISI 304L	Improvement of pitting corrosion resistance	Ref 44
2Cr13, 1Cr18Ni9T	Increased cavitation resistance	Ref 45
ASTM A516	Higher hardness by martensite phase transformation	Ref 46
AISI 420	Higher wear resistance	Ref 47
3CR12	Enhanced pitting corrosion resistance	Ref 48
Alloy 800H	Higher corrosion resistance due to microstructural homogeneity, Cr ₂ O ₃ layer formation	Ref 49
M2, AISI 316L	Inhomogeneous absorptivity due to rapid melting and self-quenching	Ref 50
M2, ASP23, ASP30	Higher corrosion protection due to microstructural refinement and higher carbide dissolution	Ref 51
Waspaloy	Increased mechanical properties	Ref 52
DF2	Hardness improvement by martensite transformation	Ref 53
M2	Improved hardness and wear resistance	Ref 54
SAE 52100	Enhanced hardness, wear, and corrosion resistance due to microstructural refinement and higher dissolution of carbides and nitrides	Ref 55, 56
42CrMo	Hardness improvement	Ref 57
UNS S30400, S31603, S32100, S34700, S31803, S32950	Enhanced corrosion resistance attributed to homogeneous microstructure and higher dissolution of chromium carbides	Ref 58
18Ni-300	Enhanced mechanical properties (hardness, tensile strength, Young's modulus)	Ref 59
AISI 304	Improved corrosion resistance	Ref 60

Table 5 Laser cladding of ferrous alloys

Substrate (clad)	Outcome	Reference
Medium-carbon steel (Stellite 6)	Improved wear resistance	Ref 61
Mild steel (ASTM S31254)	Enhanced pitting corrosion resistance	Ref 62
Martensitic steel (Ni)	Higher wear and fatigue resistance	Ref 63
Inconel 600 (Inconel 600)	Increased hardness by using controlled process parameters	Ref 64
AISI 316L (Ni-Cr ₃ C ₂)	Higher wear resistance than Ni alloy coating	Ref 65
AISI 316L (ZK60/SiC)	Higher corrosion resistance	Ref 66
E24 (Stellite 6 + WC)	Enhanced mechanical properties through microstructural refinement	Ref 67
Plain carbon steel (AISI 316L)	Hardness improvement	Ref 68
BS 970 080M40 steel (Cr + Ni)	Increased surface hardness	Ref 69
SAE 1045 (Cu + Al)	Mechanical and electrical properties modification	Ref 70
A36 mild steel (Fe + Al)	Superior hardness	Ref 71
IF steel (Co-Cr-W-Ni-Si + SiC _p)	Improved wear resistance attributed to microstructural refinement and higher dissolution of Si ₂ W, CoWSi, Cr ₃ Si, CoSi ₂ phases	Ref 72
AISI 316L (NiTi)	Higher hardness and cavitation erosion resistance	Ref 73
	Higher hardness and cavitation erosion resistance attributed to higher dissolution of Fe, Cr, and N	Ref 74
AISI 316L (Ni, Cr ₃ C ₂ , WC)	Enhanced hardness and erosive-corrosive wear performance result from higher carbide dissolution	Ref 75
AISI 1010 (Fe-B-C, Fe-B-Si, Fe-BC-Si-Al-C)	Improved hardness, wear, and corrosion resistance	Ref 76
A36 (Co-Ti)	Superior hardness due to larger TiCo ₃ formation	Ref 77
Low-carbon steel (Fe + Si)	Higher hardness attributed to microstructural refinement and higher Si dissolution	Ref 78
Low-carbon steel (WC, Co)	Improved adhesion strength and higher hardness	Ref 79
Mild steel (Fe + SiC)	Higher protection to load, wear, and corrosion	Ref 80
AISI 304 steel (CoMoCrSi)	Superior hardness and wear resistance through microstructural refinement	Ref 81
AISI 1045 (Fe, Ni, Si, B, V)	Amorphous structural attainment results in higher hardness and wear resistance	Ref 82
AISI 316L (SiC)	Hardness and wear-resistance enhancement	Ref 83
AISI 316L (Ni, Co, Fe, Stellite)	Improved load and wear resistance	Ref 84
AISI 316L (Co)	Hardness and mechanical properties enhancement	Ref 85
AISI 304 (AISI 431)	Microstructural-refinement-induced higher hardness and wear resistance	Ref 86
Vanadis 4 (CPM 10V, Vanadis 4)	Improved hardness through heterogeneous microstructures (carbides, martensite, retained austenite)	Ref 87
ASTM A283Gr.D steel (Fe-Al-Si)	Controlled process variables aid an enhanced hardness and wear resistance	Ref 88
45 steel (NiCuMoW)	Higher mixed dissolution of borides, nitrides, and carbides results in increased hardness and wear resistance	Ref 89

Table 6 Laser surface alloying of ferrous alloys

Substrate (alloy)	Outcome	Reference
AISI 304 (Mo, Ta)	Mo- and Ta-base intermetallic formation results in increased corrosion and wear resistance	Ref 90
Mild steel (Fe, Cr, Si, N)	Refined microstructure (Fe-Cr-Si-N) formation and increased corrosion resistance	Ref 91
AISI A7 (Ti)	Improved wear and tribological properties	Ref 92
Inconel 800H (Al)	Al-rich surface has improved oxidation and wear resistance	Ref 93
Cr-Mo steel (Cr)	Rich scale Cr ₂ O ₃ formation and oxidation resistance at high temperature	Ref 94
AISI 1040 (TiB ₂)	Enrichment of boride phases and improved wear and tribological properties	Ref 95
UNS-S31603 (Co, Ni, Mn, Cr, Mo)	Ceramic/intermetallic formation and enhanced resistance to corrosion and erosion	Ref 96
AISI 1040 (NiCoCrB)	Improved corrosion and erosion resistance	Ref 34
Carbon steel (TiB ₂)	Enhanced oxidation and wear resistance attributed to higher boride dissolution	Ref 97
H13 (TiC)	Corrosion- and erosion-resistance protection	Ref 98
S31603 (CrB ₂ , Cr ₃ C ₂ , SiC, TiC, WC, Cr ₂ O ₃)	Superior wear resistance resulting from higher dissolution of carbides and borides	Ref 99
SAE 1045 (Cu)	Enhanced tribological property	Ref 100
AISI 1040 (SiC)	Increased hardness and wear resistance due to higher Fe ₂ Si, Fe ₃ Si, Fe ₇ C ₃ , and Fe ₃ C formation	Ref 101
AISI 316 (WC)	Enrichment of higher W and carbide dissolution result in superior hardness and cavitation erosion resistance	Ref 102
X40CrMoV5-1 (TiC)	Hardness and tribological properties improvement	Ref 103
	Fine-grained dendritic microstructural refinement results in increased wear resistance	Ref 104
Gray cast iron (NiCr)	Corrosion- and wear-resistance improvement attributed to refinement of composition and microstructure	Ref 105
32CrMoV12-28 (TiC, WC)	Rapid melting and solidification-induced homogeneous microstructures and higher hardness	Ref 106
AISI 1010 (Ni)	Improved hardness	Ref 107
17-4PH (C, Ni, Co, WC)	Extreme refinement of microstructures and hard-phase (Fe ₆ W ₆ C, W ₂ C) formation result in high mechanical strength and excellent corrosion and fatigue resistance	Ref 108
Mild steel (Si)	Hardness improvement and enhanced wear resistance attributed to iron silicide and nitride formation	Ref 109
X40CrMoV5-1 (TaC-VC)	Abrasion wear-resistance improvement attributed to higher carbide dissolution	Ref 110
70MnV (NiCr-Cr ₃ C ₂)	Microstructural refinement and hard phase (Cr ₇ C ₃ , Fe ₃ C, martensite) presence result in enhanced hardness and wear resistance	Ref 111
40Cr (Mo + Y ₂ O ₃)	Improved hardness and wear resistance	Ref 112
Steel (Al)	Formation of aluminides results in enhanced oxidation resistance	Ref 113
X2CrNiMo17-12-2, X6Cr13, X2CrNiMo22-8-2 (SiC)	Enriched Si, C, and Fe ₃ Cr ₇ result in higher hardness and wear resistance	Ref 114

Laser Shock Peening

In laser shock peening (LSP), high-energy-density ($\sim 10^7$ J/m²) laser plasma is used to propagate compressive residual stresses into the target material, which in turn further impedes crack initiation and propagation, thus extending the service life of metallic components. In this process, a thermoprotective coating or absorbing layer (black paint or tape) is applied on the metallic target surface. A layer of dielectric material (glass/water/quartz) is placed on top of the absorbing layer. The applied higher-energy-density laser beam instantly vaporizes the absorbing layer and produces plasma that expands rapidly, creating very high pressures (GPa) at the interface as a result of the recoil momentum of the ablated material. The high pressure results in shock waves that are transmitted throughout the material and induce compressive stresses in the material (Ref 128). This technology has been used for more than three decades in the aerospace industry to increase fatigue life and wear resistance of jet engine turbine blades. Recently, Zhang et al. (Ref 129) proposed microscale laser shock peening (mLSP) as a promising process to enhance the fatigue life of microcomponents such as microelectromechanical systems actuators, medical implants, microswitches, relays, and blades of microimpellers. The mLSP does not require high-energy laser systems; both continuous and pulsed modes with high repetition rate are applied to induce high-level compressive residual stresses (400 MPa, or 58 ksi) into the microcomponents, which in turn reduce overall production cost. A top-hat uniform energy-distribution laser beam is said to be more suitable for LSP to obtain more uniform residual-stress distribution and the resulting uniform fatigue and wear properties.

Laser Heat Treatment

Steel is the most common and versatile material used in many industrial applications (automotive, aerospace, defense, nuclear). High-value steel parts (gears, pistons, rings, wheels) working in severe abrasive and loading conditions often need to be changed due to loss of their mechanical and surface properties. In view of this, companies spend several billion dollars each year to replace these parts. Therefore, they are good candidates for case/surface hardening, often only at selective regions where the part highly interacts with severe abrasive conditions. However, the remaining bulk material core properties (more flexible and ductile and less brittle) should be retained.

In general heat treating, the process to enhance the wear, heat, and corrosion-resistant properties of high-value parts involves either diffusion or selective hardening. In conventional diffusion-based techniques (carburizing, nitriding, carbonitriding), a low-carbon steel is

heated in bulk, and externally supplied carbon and other alloying elements further diffuse into the surface layer, followed by quenching rapidly in air or water or oil to obtain a specified hardness. Selective hardening advantageously traps the diffused free carbon in the steels via both rapid heating and quenching that makes it harder than normal phase transformations. Induction, flame, and arc are normally used for achieving selective hardening. In fact, each one of them has severe drawbacks, such as poor reproducibility, auxiliary quenching, environmental issues, deeper thermal penetration, noncontrollable distortion, and long process setup time (Table 8). A high distortion and long process setup time are also some of the disadvantages of conventional heat treatment processes. Laser heat treatment (LH) uses both intense heating (10^5 W/cm²) and a rapid self-cooling cycle ($>10^3$ °C/s), which in turn produces localized superior surfaces resistant to heat, wear, fatigue, fracture, erosion, and corrosion. In this route, LH uses both material and energy effectively and also extends the service longevity of high-value parts.

Over the last three decades, CO₂ (10,600 nm) and neodymium: yttrium-aluminum-garnet (Nd: YAG) (1060 nm) laser-based heat treatments have been quite well established; however, recently, direct diode laser (808 to 940 nm) has gained more attention by the industry to perform localized hardening because it combines higher wall-plug efficiency and better absorption by metals due to operating in shorter range of wavelengths with lower capital and operating costs (Table 9).

In LH, as mentioned earlier, localized hardening is achieved through phase transformations. The metallurgical phase transformations taking place inside the material modify the surface properties (wear, fatigue, erosion, corrosion). The metallurgical phase transformations consist of a heating and cooling cycle. In heating, a narrow, thin layer of the metallic component is rapidly and locally heated to a temperature above the Ac₁ temperature for transforming the initial parental ferrite/pearlite ($\alpha + \text{FeC}$) phases to the austenite (γ) phase, where

the carbon is dissolved in the steel. If the temperature is above Ac₃ and below melting temperatures, the whole parental $\alpha + \text{FeC}$ phases are transformed completely into γ phase (Fig. 6a–c). Subsequently, the efficient conduction of heat to the surrounding bulk mass of material induces a self-quenching effect. The self-quenching at higher cooling rate would not allow any reverse transformation and the secretion of carbon, because it brings the heated surface temperature below the martensite starting (M_s) temperature. Instead of a mixed-phase structure, a very hard metastable martensite (α') structure is formed. Below the M_s temperature, the austenite is completely transformed into martensite (Fig. 6c, d). This condition does not further allow the carbon to excrete to other phases but remains in the metastable crystal structure (body-centered tetragonal). The secretion of carbon from the parental phases, $\alpha + \text{FeC} \rightarrow \gamma$ and $\gamma \rightarrow \alpha'$ is schematically shown in Fig. 7. Therefore, the heat treated metallic component case depth hardness depends on the temperature-time-dependent phase changes and the changes in carbon solubility caused by solid-state phase transformations.

The metal components to be hardened by induction, arc, or flame are heated to a temperature above the Ac₁ temperature for transforming the initial parental ferrite/pearlite ($\alpha + \text{FeC}$) phases to the austenite (γ) phase. In contrast to LH, the heated component is cooled down suddenly in an auxiliary source such as water, oil, or as-heated conditions to room temperature. Due to the larger variation of cooling rate, the outer layer cools faster than the deeper section, which cools more slowly. This quenchant-used inhomogeneous cooling rate allows time to reverse the transformation, forming a mixed phase (martensite, bainite, ferrite) at the end of the process. The mixed phases generate non-uniform case depth hardness.

The careful selection of processing parameters is a primary and major task to obtain the desired surface and mechanical properties. Either experimental investigations or numerical optimization techniques can be used to obtain the necessary processing parameters. The final

surface and mechanical properties are highly influenced by a group of processing parameters. For a single-pass heat treatment (SPHT), the laser power, scanning speed, beam focal spot size, and thermophysical properties of the material are major concerns to achieve the desired surface and mechanical properties. For multipass laser heat treatment (MPLHT), the SPHT processing parameters plus the size of overlap, length of scan, and geometry of the component play a major role in obtaining hardness uniformity of the heat treated material.

Moreover, industry's concerns are to achieve uniform hardness of the heat treated material and a small HAZ for treating a larger surface area (Fig. 8). When a larger surface area is heat treated, multiple scans by laser beam with slight overlaps are applied. Under this condition, the new heating cycle during the successive scan disturbs the normal cooling cycle of the heat treated material, which may generate a tempered microstructure. This tempering effect, in addition to hardening, will affect the homogeneity of phase transformations, microstructures, and hardness uniformity. The phase transformations, microstructure homogeneity, and uniform hardness are highly influenced by heat management defined by the length of scan and size of overlap.

Based on the austenitization starting (Ac₁) and ending (Ac₃) temperatures, three different conditions may occur during the heating cycle of the MPLHT process:

- If the material is heated more than Ac₃, the material is fully austenitized, and in the cooling cycle, it should be transformed into martensite.
- For temperatures between Ac₁ and Ac₃, a partial austenitization (bainite, ferrite, and pearlite) is achieved.
- For a temperature less than Ac₁, tempering (carbides, ferrite, and pearlite) occurs.

Table 7 Laser hardfacing of ferrous alloys

Substrate (hard phase)	Outcome	Reference
AISI 1045 (TiC, Ni-Cr-B-Si-C)	Rapid melting and solidification-induced hard phase (chromates, borides, carbides) result in higher structural stability and mechanical properties	Ref 115
AISI 316L (Colmonoy 5)	Ni-rich dendrites and eutectic borides exhibit higher mechanical properties	Ref 116
ANSI C-5, C-2 (AlMgB ₁₄)	Higher adhesion strength, hardness, and wear resistance	Ref 117
Medium-carbon steel (S42000 + Si ₃ N ₄)	Silicon nitride addition results in enhanced surface hardness	Ref 118
Low-carbon steel (Ni, Co)	Improved mechanical properties	Ref 119
AISI 1045 (TiC-VC)	Microstructural refinement (graphite, FeTi, and FeV) provides superior hardness and good wear resistance	Ref 120
AISI 316L (Si ₃ N ₄ , Ti)	Retained austenite with Ti ₅ Si ₃ results in enhanced wear and corrosion resistance	Ref 121
Q235 (Ni, CeO ₂)	Addition of Ni and CeO ₂ improves load and wear resistance	Ref 122
AISI 316L (WC, Si, Ni)	WC and Fe ₅ Si ₃ formation increases hardness and wear resistance	Ref 123
60CrMn4 (NiCrBSiCFe)	Ni ₃ (BC) formation and Ni-rich with Cr precipitates provide excellent resistance to load, wear, and corrosion	Ref 124
AISI 316L (Ni-Mo-Cr-Si)	Variation in solidification rate, cooling rate, and compositional variation results in heterogeneous microstructure (Mo-rich intermetallic) and higher hardness	Ref 125
Ductile iron (E309L)	Superior hardness and wear resistance attributed to Fe-Cr-C formation	Ref 126
43C steel (Stellite-6)	Excellent wear resistance	Ref 127

Table 8 Comparison of heat treatment techniques

Heat sources	Advantages	Disadvantages
Induction	Fast process Deep case depth obtainable Lower capital cost than laser High coverage area	Downtime for coil change Quenchant required Part distortion Electromagnetic forces may disturb surface conditions
Flame	Cheap, flexible, and mobile	Poor reproducibility Quenchant required Part distortion Environmental problems
Arc	Relatively cheap and flexible	Limited hardening Large thermal penetration Poor control to avoid melting
Laser	Minimal distortion Selective localized hardening Quenchant-free Case depth controllable Limited postmachining	High capital cost Multiple passes give local tempering

Table 9 Comparison of high-power laser systems

Factors	CO ₂	Nd:YAG	Diode
Wavelength, μm	10.6	1.06	0.808
Metal absorption, %	5–10	25–35	30–40
Average wall-plug efficiency, %	10	10	30
Approximate electrical power consumption of the lasers, kW	50	30	10
Required laser power, kW	5	8	3
Maximum power density, W/cm ²	10 ⁸	10 ⁹	10 ⁶
Electrical power cost per hour (at 0.09 \$/kWh), \$/h	4.50	2.70	0.90
Capital cost, \$/W	150–300	200–600	100–300

Nd:YAG, neodymium: yttrium-aluminum-garnet. Source: Ref 4

Thermokinetic Phase Transformations

The thermokinetic (TK) process of LSH consists of heating and cooling cycles (Fig. 9). The final surface and mechanical properties produced in LSH are based on the TK metallurgical phase transformations taking place inside the treated material. The TK phase transformation is a function of temperature, time, and the thermophysical properties of the materials.

The diffusion of carbon to steels, forming a metastable martensite, takes several stages in conventional heat treatment (CHT) in contrast to LH, which has two steps. At room temperature, the hypoeutectoid steel microstructure consists of a mixture of ferrite and pearlite. When the material is exposed to laser beam radiation, the localized region of the metallic surface is heated quickly above the austenitization (A_{C3}) temperature. In contrast, in CHTs, to reach complete austenitization (above A_{C3}), the material must cross the A_{C1} , P_s , and A_{C3} temperatures. Here, A_{C1} , P_s , and A_{C3} are the temperatures for the beginning of austenitization, the start of pearlite formation, and the completion of austenitization, respectively. During heating, if the heating temperature is enough to reach the A_{C1} temperature, the initial phase (ferrite and pearlite) starts to transform into austenite. Further heating of the material reaches the P_s temperature. At this temperature, the pearlite is instantaneously transformed into austenite. At temperatures above A_{C3} , the ferrite is completely transformed into austenite. A shorter time in this temperature range (above A_{C3}) allows homogenization of austenite.

In CHTs, the heated material is immediately quenched in oil or water and air that initiates the cooling cycle. Depending on the rates of cooling, the heat treated material goes through

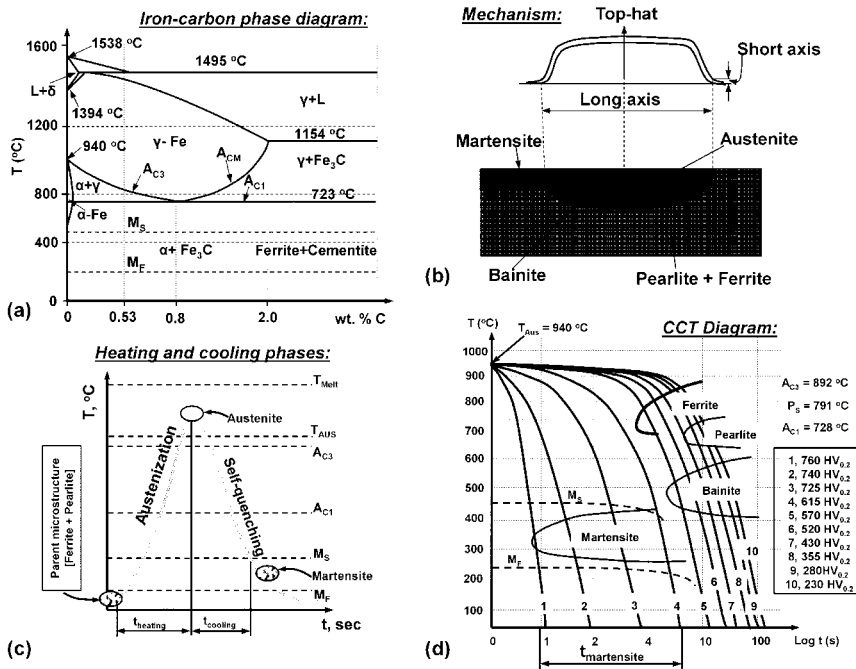


Fig. 6 (a) Iron-carbon phase diagram. (b) Laser beam-material interaction. (c) Heating and cooling phases. (d) Continuous cooling transformation (CCT) diagram. Source Ref 162

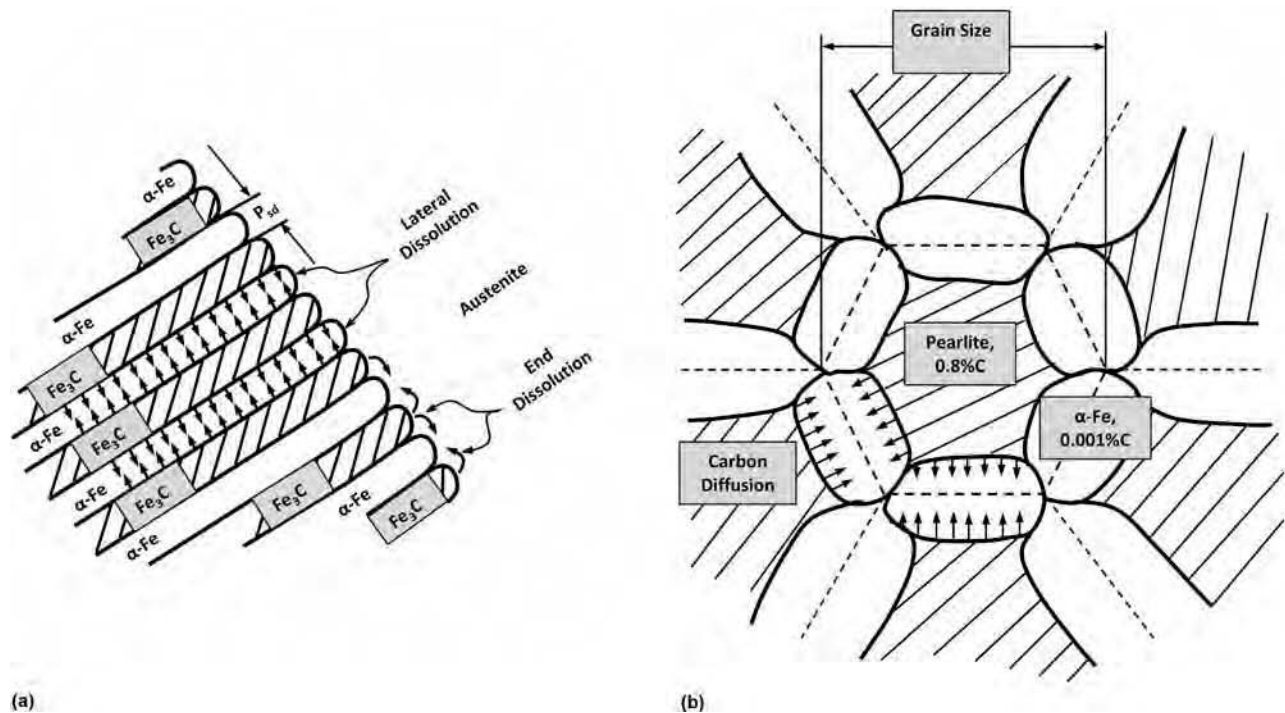


Fig. 7 (a) Austenitization and (b) homogenization of austenite during phase-transformation hardening process

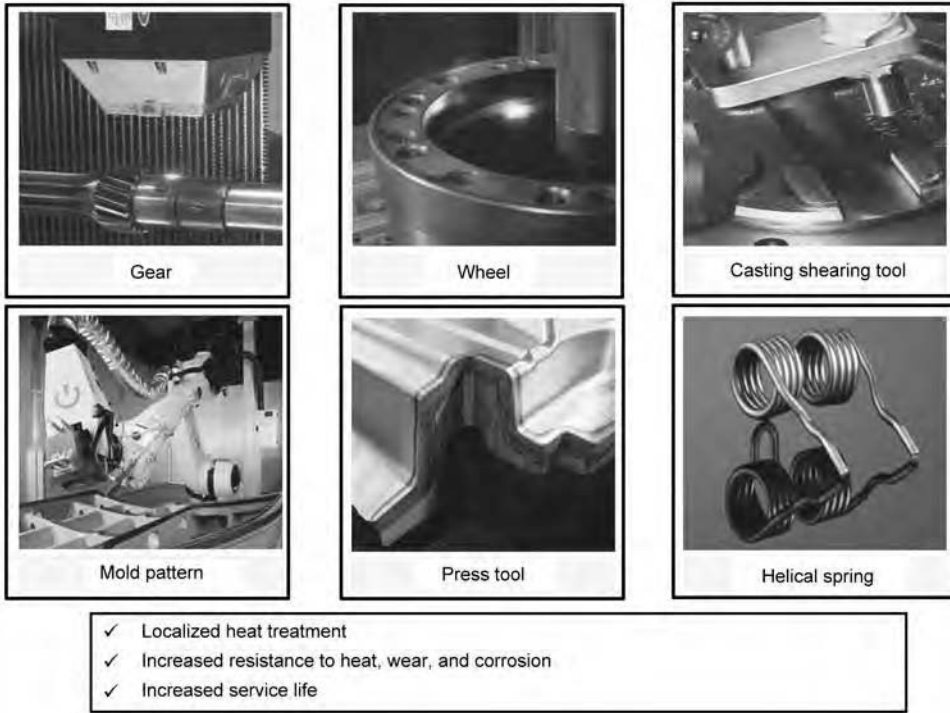


Fig. 8 Localized laser surface hardening industrial components

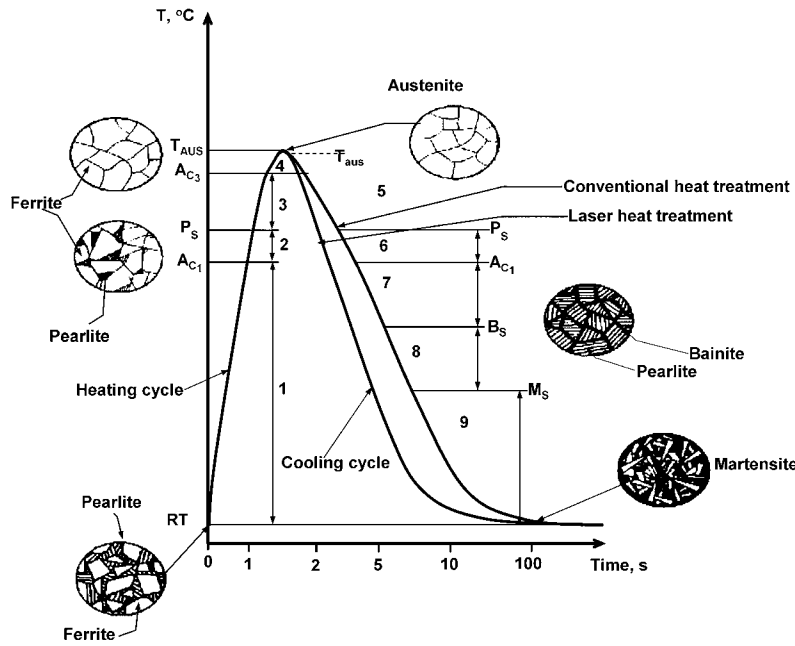


Fig. 9 Thermokinetic phase transformations during the hardening process

different phase transformations. When the temperature reaches the A_{r3} (starting temperature of transformation of austenite), the austenite starts to revert back to ferrite. The austenite-ferrite transformation continues until it reaches the P_s temperature. After the cooling cycle temperature reaches the P_s temperature, the

austenite rapidly transforms into pearlite. The austenite-pearlite transformation continues until it reaches the B_s (bainite starting) temperature. Below the B_s temperature, austenite-bainite transformation occurs. With continued cooling to the M_s (martensite starting) temperature, the austenite begins to transform into

hard, metastable martensite. With further cooling below the M_s temperature, martensite transformation proceeds and completes at the M_f (martensite finish) temperature.

In LH, when the laser beam moves to the next location, the efficient conduction by the surrounding bulk mass of the material provides a severe self-quenching effect (acts as a heat sink). This self-quenching effect instantly brings the heated surface temperature below the M_s temperature, forming a hard, metastable martensite microstructure.

The metallurgical phase transformations occur at several critical transformation temperatures (A_{c1} , P_s , A_{c3} , A_{r3} , A_{r1} , B_s , M_s , and M_f) (Eq 4 to 12). These transformation temperatures play a major role in generating a different mixture of phases with various fractions. The final surface and mechanical properties of the heat treated parts are solely dependent on the sum of fractional values of phases and their hardnesses and the thermophysical properties.

Kasatkin et al. (Ref 130) constructed the non-additive elements empirical relationships for steels to calculate the A_{c1} and A_{c3} temperatures. Kirkaldy and Venugopalan (Ref 131) developed the empirical relationships to calculate the P_s , B_s , and M_s temperatures. These transformation temperatures are used to predict the microstructure and hardness for steels. Steven and Haynes (Ref 132) presented the empirical relationships of steel compositions to predict the A_{r1} and A_{r3} temperatures. Hojerslev (Ref 133) designed the experimentally evaluated empirical relationships for calculating the M_s and M_f temperatures:

$$A_{c1} = 723 - 7.08Mn - 37.7Si - 18.1Cr + 44.2Mo + 8.95Ni + 50.1V + 21.7Al + 3.18W + 297S - 830N - 11.5CSi - 14.0MnSi - 3.10SiCr - 57.9CMo - 15.5MnMo - 5.28CNi - 6.0MnNi + 6.77SiNi - 0.80CrNi - 27.4CV + 30.8MoV - 0.84Cr^2 - 3.46Mo^2 - 0.46Ni^2 - 28V^2 \quad (Eq 4)$$

$$A_{c3} = 910 - 370C - 27.4Mn + 27.3Si - 6.35Cr - 32.7Ni + 95.2V + 190Ti + 72.0Al + 64.5Nb + 5.57W + 332S + 276P + 485N - 900B + 16.2CMn + 32.3CSi + 15.4CCr + 48.0CNi + 4.32SiCr - 17.3SiMo - 18.6SiNi + 4.80MnNi + 40.5MoV + 174C^2 + 2.46Mn^2 + 6.86Si^2 + 0.322Cr^2 + 9.90Mo^2 + 1.24Ni^2 - 60.2V^2 \quad (Eq 5)$$

$$A_{cm} = 244.4 + 992.4C - 465.1C^2 + 46.7Cr + 19.0CCr - 6.1Cr^2 + 7.6Mn + 10.0Mo - 6.8CrMo - 6.9Ni + 3.7CrNi - 2.7CrNi + 0.8Ni^2 + 16.7Si \quad (Eq 6)$$

$$P_s = A_{c1} - 10.7Mn + 29Si + 16.9Cr \quad (Eq 7)$$

$$Ar_3 = 910 - 310C - 80Mn - 20Cu - 15Cr - 55Ni - 80Mo + 0.35(h - 8) \quad (\text{Eq 8})$$

$$Ar_1 = P_s - 305.4C - 118.2Mn \quad (\text{Eq 9})$$

$$B_s = P_s - 58C - 35Mn - 15Ni - 34Cr - 41Mo \quad (\text{Eq 10})$$

$$M_s = 561 + 474C - 33Mn - 17.7Ni - 12.1Cr - 7.5Mo + 10Co - 705Si \quad (\text{Eq 11})$$

$$M_f = M_s - 215 \quad (\text{Eq 12})$$

where C, Mn, Cr, Mo, and so on are the steel composition in weight percent, and h is the thickness of the material in meters.

For larger surface area laser heat treatment, multiple scanning should be applied that includes repetitive cycles of heating and cooling, which in turn leads to higher chances of producing mixed phases of tempered martensite. Under equilibrium thermodynamic conditions, the proportion of martensite can be determined using the Koistinen and Marburger equation:

$$X_m = 1 - X_a \exp(-0.011(M_s - T)) \text{ if } M_s > T > M_f \quad (\text{Eq 13})$$

where X_m and X_a are the fractions of martensite and austenite, and M_s and M_f are martensite starting and finishing temperatures, respectively. A complete martensite transformation can be achieved when the cooling cycle temperature rapidly reaches the M_f temperature. In continuous laser scanning, the normal cooling cycle is affected by successive heating cycles, which in turn affect the actual phase transformation. Such effects include tempering of the martensite formed in the previous laser scan by the subsequent laser scans.

The fraction of tempered martensite (X_{tm}) can be calculated using the Johnson-Mehl-Avrami equation:

$$X_{tm} = 1 - \exp(-\beta^n) \quad (\text{Eq 14})$$

where β and n are the transformation nature and reaction constant. In LSH, the TK phase transformation process is far away from the actual equilibrium phase transformation. Hence, under the nonisothermal condition prevailing during LSH, the following equation can be used to calculate the phase fraction:

$$\beta = \int k(T) dt = \int k_0 \exp\left(-\frac{Q}{RT}\right)^n dt \quad (\text{Eq 15})$$

where Q is the reheating activation energy, R is the universal gas constant, and k_0 is material constant. Based on the reheating temperature,

the volume fraction of tempered martensite can be calculated. The final hardness (Ref 134, 135) can be calculated using the additivity rule of mixture of fractions of phases and hardness (Eq 16 to 22):

$$HV_{\text{final}} = X_m HV_m + X_{tm} HV_{tm} \quad (\text{Eq 16})$$

$$HV_{tm} = X_{\epsilon C} HV_{\epsilon C} + X_z HV_z + X_{Fe_3C} HV_{Fe_3C} \quad (\text{Eq 17})$$

$$X_{Fe_3C} = XX_m \frac{C_m - C_z}{C_{Fe_3C} - C_z} \text{ if } 250^\circ\text{C} < T < Ac_1 \quad (\text{Eq 18})$$

$$X_z = XX_m - X_{Fe_3C} \text{ if } 250^\circ\text{C} < T < Ac_1 \quad (\text{Eq 19})$$

$$X_{\epsilon C} = XX_m \frac{C_m - C_z}{C_e - C_z} \text{ if } 250^\circ\text{C} > T \quad (\text{Eq 20})$$

$$X_z = XX_m - X_{\epsilon C} \text{ if } 250^\circ\text{C} > T \quad (\text{Eq 21})$$

$$C_m = X_{tm} C_m + X_{\epsilon C} C_{\epsilon} + X_z C_z + X_{\gamma} C_{\gamma} \quad (\text{Eq 22})$$

A range of tempered microstructure is generated when the material is tempered between 100 °C (212 °F) and the Ac_1 temperatures. A precipitation of ϵ -carbide (Fe_2C) within the martensite is formed between the tempering temperatures of 100 to 200 °C (212 to 392 °F). In this temperature range (100 to 200 °C), the martensite is still supersaturated with carbon, whereas martensite decomposition occurs at higher temperatures (Ref 136). For a tempering temperature between 200 and 350 °C (392 and 662 °F), the martensite decomposes into ferrite and cementite. A cementite (Fe_3C) precipitation within the martensite occurs between the tempering temperature of 350 and 500 °C (662 and 932 °F). The tempering temperature between 500 and 700 °C (932 and 1292 °F) induces more precipitation of carbides within the martensite. Further, if the tempering temperature is above 700 °C (1292 °F), the retained austenite is destabilized due to the precipitation of carbides. During this destabilization process, the austenite could release internal stresses that transform the austenite partially or totally into martensite. This new structure is called tempered martensite (Ref 136). The aforementioned tempering effects could produce nonuniform case depth hardness. The tempering effect in the overlapped region is highly influenced by the carbon diffusion at various levels of activation energy and the cooling rate generated in the LH process. Moreover, the carbon atom diffusion in carbon and alloyed steels is easier than for other alloying elements due to its lower diffusion activation energy. From this perspective, the tempering is a process controlled by the diffusion of carbon atoms. In light of this, because LH is a time-temperature, material-dependent process, the surface temperature

must be controlled to obtain a specified case depth hardness. The numerical simulation using experimental boundary conditions and parameters is a well-established cost-effective approach to investigate the effects of processing parameters on the variation of temperature, phase transformations, microstructures, and case depth hardness. The numerical simulations could intuitively reduce the number of experimental trials that involve large amounts of materials, money, and time.

Challenges in Obtaining the Specified Hardness

Although laser hardening has numerous advantages, including generating superior surface (resistance to heat, wear, and corrosion) and mechanical (hardness and fatigue stresses) properties with higher processing speed, it has some challenges in producing uniform hardness in the heat treated material. The hardness (HV, kgf/mm²) uniformity of the heat treated material is controlled by the dual-cycle (rapid heating and cooling) phase transformations throughout the depth of the heat treated surface region (D , mm). The metallurgical phase transformations are activated by a group of processing parameters. The major influential processing parameters are:

- *Laser process characteristics*: wavelength, beam focal spot diameter, power distribution, mode of operation (continuous wave or pulsed), scanning speed, length of scan, and size of overlap for larger-surface-area treatment
- *Thermophysical properties of the materials*: specific heat, thermal conductivity, density, and cross-sectional thickness of the material
- *Surface conditions*: coarse or fine microstructure and surface absorptivity
- *Boundary conditions*: natural or forced convections

Any misfit between the processing parameters leads to a problem of nonuniformity in hardness of the depth of heat treated material. The problem can be due to overheating, underheating, and undercooling of the heat treated surface of the material and can result in partial melting and partial austenitization, which in turn can lead to incomplete and/or undesired phase transformation and unintended and inferior material properties at the surface. The severe effect of tempering and the resulting nonuniformity in hardness of the heat treated material in larger-surface-area heat treatment is one such undesired effect.

The laser focal spot (d , mm) determines the width of heat mark (w , mm). Multiple scanning of a laser beam with minimum overlap is desired to heat treat larger surface areas. In this case, the active heating cycle during the successive scan over the overlap region disturbs the cooling cycle in the previous scan; hence, the

disturbed cooling cycle may generate a tempered microstructure. This effect continues during successive scans, and the magnitude of this effect depends on the number of subsequent scans and the process parameters (energy density, beam diameter, scan speed). This tempered microstructure, in addition to the hardened microstructure, will affect the level and uniformity of the hardness of heat treated material.

The variation of hardness with respect to the change of scan length, L_s (shorter, medium, longer) for varying austenitization starting (Ac_1) and ending (Ac_3) temperatures may happen under three different conditions:

- Overheating ($T_{temp} > Ac_3$) that results from a shorter path with longer interaction time (due to slow scanning speed) leads to retention of a fraction of austenite (Fig. 10a). The mixture of retained austenite with transformed martensite results in a hardness reduction in the overlapped region that affects the hardness uniformity of the material.
- Optimal heating ($Ac_1 < T_{temp} < Ac_3$), a medium path, a balanced heat accumulation, and cooling maintained in the overlapped region produces a fairly uniform hardness in the heat treated material (Fig. 10b).
- Underheating ($T_{temp} < Ac_1$) that results from a longer scan path with shorter interaction time (due to rapid scanning speed) leads to generation of only a tempering effect (Fig. 10c). This tempering effect produces a non-uniform hardness in the heat treated material (Fig. 10d).

Influence of Cooling Rate

In LH, the cooling rate has a significant effect on achieving the desired microstructure and specified mechanical properties. The rates of heating and cooling are mainly determined by the laser energy density as the product of laser power density and interaction time apart from materials composition and boundary conditions. In particular, the cooling rate (Eq 23) has a more prominent effect on specified hardness:

$$C_R = \frac{\partial T}{\partial t} = -2\pi k \left(\frac{v}{P_{eff}} \right) (T - T_0)^2 \quad (Eq\ 23)$$

where C_R is the cooling rate ($^{\circ}C/s$), k is the thermal conductivity ($W/m \cdot ^{\circ}C$), v is the scanning speed (m/s), P_{eff} is the effective laser power (W), T is the instantaneous temperature ($^{\circ}C$), and T_0 is the room temperature ($^{\circ}C$).

A case study is presented to explain the effect of cooling rate on the variation of microstructure and case depth hardness. In this study, a cold air jet was used to provide additional cooling on the heat treated surface during the process. Cold air pressure from 0 to 2 bar

(increments of 0.2 bar) was used to determine the effect of cooling by cold air on the heat treated surface. A laser power of 800 W, scanning speed of 100 mm/s (4 in./s), overlap size of 0.3 mm (0.012 in.), and scan length of 25 mm (1.0 in.) were used to heat treat the coupon. After 1 bar of cold air pressure, the cooling rate increased significantly, which in turn increased the hardness (Fig. 11). Scanning electron micrographs clearly show that more volume fraction of martensite phase (approximately 36%) evolves when cooling is used (Fig. 12a) compared to without cooling (Fig. 12b). Additional cooling by cold air could effectively increase the cooling rate (18%) that is inherently dominated by the convection and conduction effects in the bulk mass of the material. This further drastically reduces the time to reach M_s from Ac_3 , which in turn

allows more austenite to transform into martensite for increased hardness ($\sim 12\%$). Thus, the final hardness of the heat treated coupon depends on two important factors: the volume fraction of each phase (ferrite, pearlite, bainite, and martensite) with the material composition (carbon, silicon, manganese, molybdenum, chromium, nickel, and vanadium) and the cooling rate (C_R).

Effect of Processing Parameters on Temperature, Microstructure, and Case Depth Hardness

Laser hardening is a nonreversible isothermal process, where the phase changes have undergone both the rapid heating and cooling cycle.

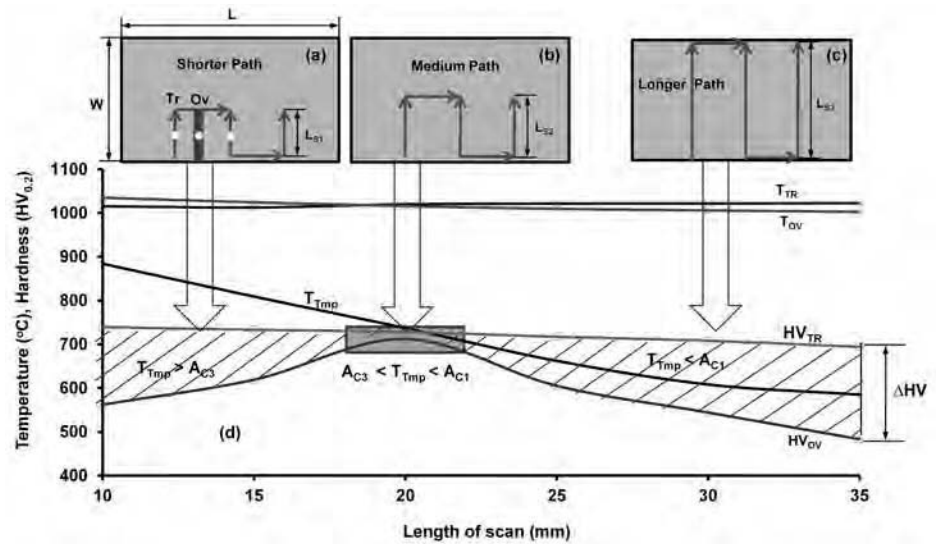


Fig. 10 Schematic presentation of influence of scan length effect. (a) Short path. (b) Medium path. (c) Long path. (d) Variation of case depth hardness for continuous laser scanning

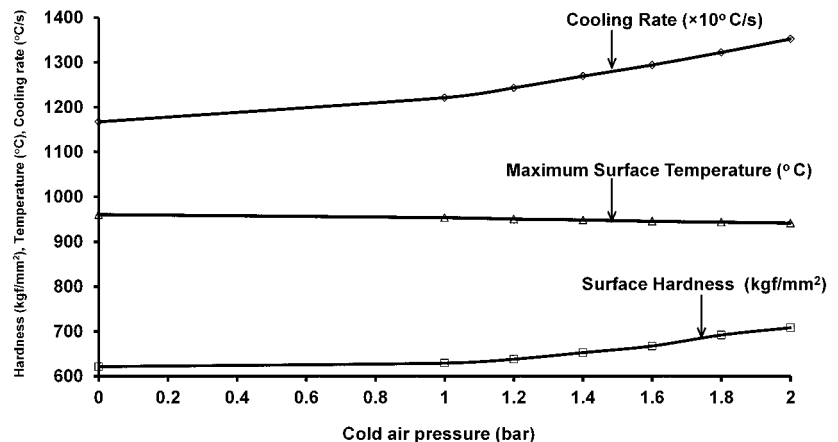


Fig. 11 Effect of additional cooling on increase of hardness for continuous laser scanning

In the case of a single pass, due to rapid self-quenching, the phase transformation is highly likely to arbitrarily skip the nose of the isothermal transformation curve, thereby avoiding the formation of bainite, ferrite, and pearlite phases, and obtain a complete martensite transformation. On the contrary, different phase transformations can occur during continuous laser scanning, depending on the variation of cooling rates and associated tempering. The mixture of phases affects the uniformity of microstructures and hardness.

For any given application, the component is required to be heat treated for uniform hardness to a desired depth from the surface. The uniformity of hardness distribution across the depth of heat treatment depends on the tempering temperature generated during successive scans of the laser beam over the previously heat treated area. The nonuniform hardness distribution across the depth of heat treatment can be the result of excessive heat generated and a minimum/uneven cooling rate or a combination of both and/or vice versa (Tables 10 to 12). The power density and transformation/interaction time (scanning speed) play major roles in determining the variation of surface temperature, tempering temperature, phase transformations, microstructure formation, and hardness (Tables 10 to 12). Power density is a function $[f(\dot{q}) = f(P, A, \beta, \eta)]$ of the laser power (P), laser beam spot area (A), laser efficiency (β), and absorption coefficient (η) of the laser beam with the material. The interaction time:

$$t_i = \frac{d}{v}$$

is defined as the ratio between laser beam diameter and scanning speed (v , mm/s).

For continuous laser scanning, in addition to power density and interaction time, one more important factor, heat management, which is defined as the ratio between the size of overlap and length of scan, is a key for determining tempering and the resultant phase transformations, microstructure, and hardness uniformity (Table 10). The overlapped region temperature and tempering temperature increase linearly with the increase in size of overlap for fixed laser power, scanning speed, and size of overlap (Table 11). A similar trend can also be expected when length of scan decreases; the tempering temperature increases linearly for a fixed laser power, scanning speed, and size of overlap (Table 12).

At smaller length of scan and bigger size of overlap, the transformation temperature reaches far above the Ac_3 temperature, and the time required for diffusion of carbon in austenite is not enough to fully transform it to martensite. Therefore, a mixed-phase structure containing retained austenite and martensite results in a decrease in hardness. At longer length of scan and smaller size of overlap, the tempering temperature remains below the Ac_1 temperature,

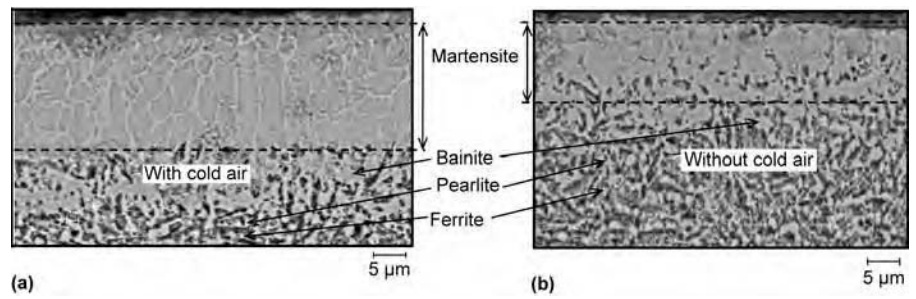


Fig. 12 Scanning electron micrographs showing (a) with and (b) without additional cooling

Table 10 Effect of processing parameters on the variation of temperature and case depth hardness

Example No.	Laser power, W	Scanning speed, mm/s	Overlap, mm	Length of scan, mm	Laser energy density, J/mm ²	Temperature(a), °C			Depth(b), μm		Hardness(c), kgf/mm ²	
						T_{tr}	T_{ov}	T_{imp}	D_{tr}	D_{ov}	HV_{tr}	HV_{ov}
1	700	50	0.1	25	0.119	917	882	552	125	90	616	590
2	700	100	0.1	25	0.059	869	837	543	110	75	580	561
3	700	150	0.1	25	0.039	824	785	491	105	60	543	497
4	700	50	0.2	25	0.237	928	908	568	135	120	632	603
5	700	100	0.2	25	0.119	912	864	549	125	110	607	576
6	700	150	0.2	25	0.079	831	808	511	115	105	551	509
7	700	50	0.3	25	0.356	984	953	618	155	145	661	638
8	700	100	0.3	25	0.178	948	914	571	140	120	649	608
9	700	150	0.3	25	0.119	910	813	504	130	110	605	536
10	800	50	0.1	25	0.136	1002	952	610	140	105	683	650
11	800	100	0.1	25	0.068	986	924	601	130	95	662	621
12	800	150	0.1	25	0.045	927	901	559	125	80	631	592
13	800	50	0.2	25	0.272	1013	998	734	160	135	696	679
14	800	100	0.2	25	0.136	1007	956	621	145	125	684	651
15	800	150	0.2	25	0.091	941	913	567	135	110	640	606
16	800	50	0.3	25	0.408	1093	1042	795	185	160	765	721
17	800	100	0.3	25	0.204	1029	1018	739	220	215	728	714
18	800	150	0.3	25	0.136	992	917	698	150	130	663	609
19	900	50	0.1	25	0.153	1020	963	628	155	115	709	656
20	900	100	0.1	25	0.076	1015	937	578	140	105	698	639
21	900	150	0.1	25	0.051	998	925	582	130	100	679	621
22	900	50	0.2	25	0.306	1033	1009	728	170	145	717	688
23	900	100	0.2	25	0.153	1016	994	713	155	135	703	663
24	900	150	0.2	25	0.102	1010	929	574	145	130	689	635
25	900	50	0.3	25	0.459	1136	1059	873	195	170	791	732
26	900	100	0.3	25	0.229	1090	1049	812	180	160	765	726
27	900	150	0.3	25	0.153	1024	999	756	160	150	712	699

(a) T_{tr} , average temperature at track; T_{ov} , average temperature at overlap; T_{imp} , tempering temperature. (b) D_{tr} , average depth of heat treatment at track; D_{ov} , average depth of heat treatment at overlap. (c) HV_{tr} , average hardness at track; HV_{ov} , average hardness at overlap

Table 11 Effect of size of overlap on the variation of surface temperature, tempering temperature, and hardness

Fixed laser power, 800 W; scanning speed, 100 mm/s; length of scan, 25 mm

Example No.	Overlap, mm	Temperature(a), °C			HV _{0.2} (b), kgf/mm ²		
		T_{tr}	T_{ov}	T_{imp}	HV_{tr}	HV_{ov}	ΔHV
1	0.1	995	936	617	704	541	163
2	0.2	1012	963	642	713	601	110
3	0.3	1025	1018	746	725	713	12
4	0.4	1022	1034	811	736	624	112
5	0.5	1026	1039	893	741	572	169
6	0.6	1031	1043	934	749	535	214

(a) T_{tr} , average temperature at track; T_{ov} , average temperature at overlap; T_{imp} , tempering temperature. (b) HV_{tr} , average hardness at track; HV_{ov} , average hardness at overlap; ΔHV , difference of average hardness between the track and overlap

and the associated time for diffusion of carbon in austenite steers the isothermal transformation path through the nose, crossing bainite, ferrite, and pearlite phase regions for formation of a

mixture of phases that contribute to a decrease in hardness. Thus, it can be clearly realized that the decrease in hardness during continuous laser scanning is due to tempering attributed

to heat management, which in turn affects the homogeneity of phase transformations, microstructure, and uniformity of hardness (Tables 10 to 12).

Hardness uniformity is a function $[f(HV) = f(T_{tmp})]$ of tempering temperature. Tempering temperature is a function $[f(T_{tmp}) = f(Ov, L_s)]$ of size of overlap and length of scan.

Therefore, hardness uniformity in continuous laser scanning is a function $[f(HV_{uniformity}) = f(Ov, L_s, P, v)]$ of size of overlap, length of scan, laser power, and scanning speed. Three important cases can be obtained by the variation of size of overlap, length of scan, laser power, and scanning speed. Scanning electron micrographs for complete martensite transformation at 0.204 J/mm^2 for MPLHT are shown in Fig. 13. A detailed review of LH of various ferrous alloys is given in Table 13.

Table 12 Effect of length of scan on the variation of surface temperature, tempering temperature, and hardness

Fixed laser power, 800 W; scanning speed, 100 mm/s; overlap, 0.3 mm

Example No.	Length of scan, mm	Temperature(a), °C			HV _{0.2} (b), kgf/mm ²		
		T _{tr}	T _{ov}	T _{tmp}	HV _{tr}	HV _{ov}	ΔHV
1	10	1018.25	1038.57	893	743	567	176
2	15	1014.79	1027.36	814	739	625	114
3	20	1016.16	1014.62	743	726	711	15
4	25	1024.52	1007.23	659	714	613	101
5	30	1019.61	1001.15	611	704	539	165
6	35	1020.85	998.35	574	687	476	211

(a) T_{tr}, average temperature at track; T_{ov}, average temperature at overlap; T_{tmp}, tempering temperature. (b) HV_{tr}, average hardness at track; HV_{ov}, average hardness at overlap; ΔHV, difference of average hardness between the track and overlap

Case 1: (T_{tmp} > A_{c3}). For a larger-sized overlap and shorter scan length, the tempering temperature is above the A_{c3} temperature. A higher temperature leads to re-austenitization, followed by formation of a mixture of retained austenite and martensite after self-quenching.

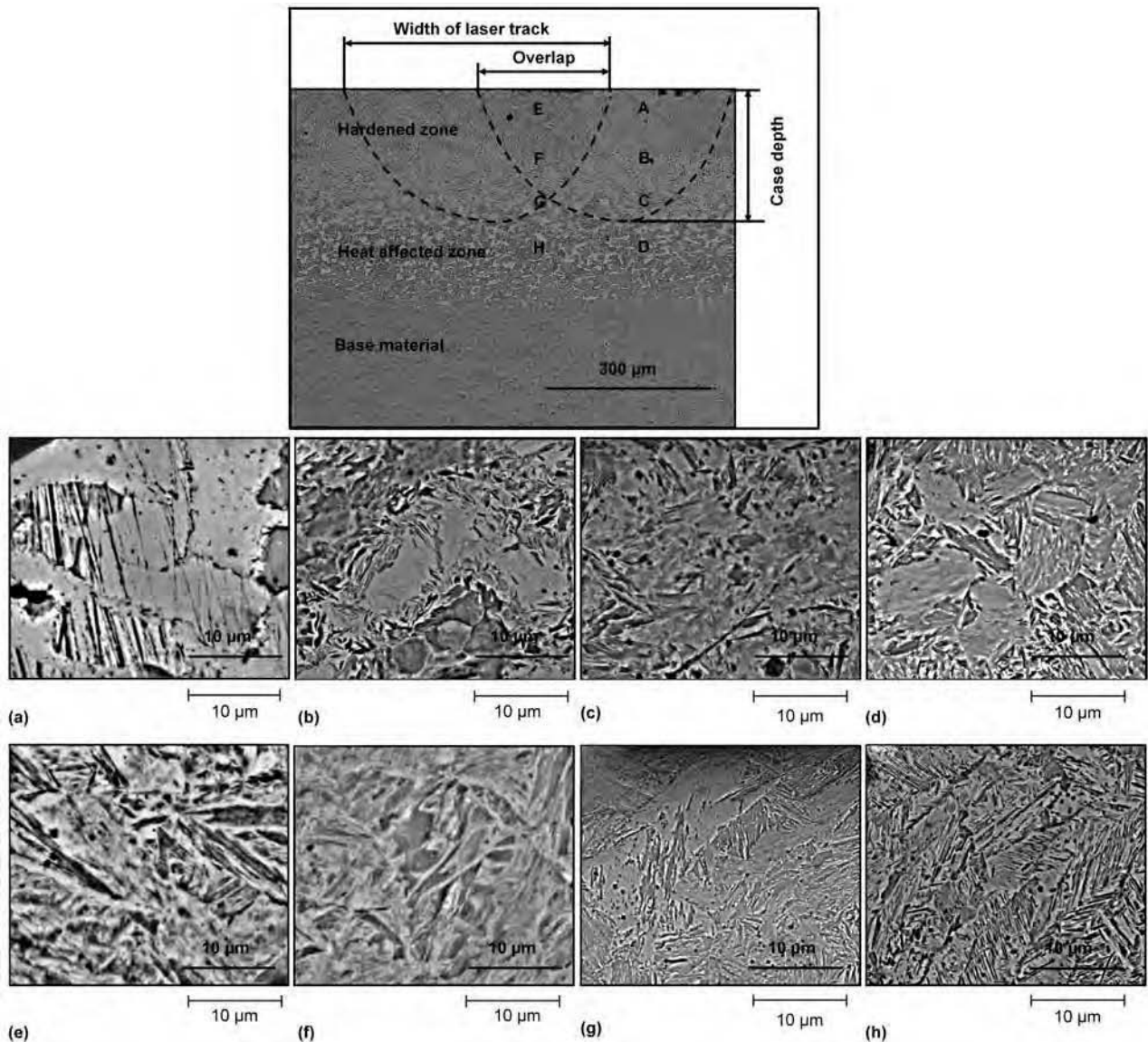


Fig. 13 Scanning electron micrographs for complete martensite transformation (0.204 J/mm^2) during continuous laser scanning

Case 2: ($Ac_1 > T_{tmp} < Ac_3$). For a medium-sized overlap and scan length, the tempering temperature falls between the Ac_1 and Ac_3 temperatures. A full austenitization occurs in the heat treated material; then, by rapid cooling, a complete martensite transformation can be obtained.

Case 3: ($T_{tmp} < Ac_1$). For a smaller-sized overlap and longer scan length, the tempering temperature falls below the Ac_1 temperature. The time allowed for diffusion of carbon in the austenite is not enough to pass through the nose of isothermal transformation for bainite, ferrite, and pearlite formation. At the end of the cooling cycle, the metastable martensite already formed in the overlapped region decomposes into the phases of bainite and ϵ -carbide as the product of solid-phase transformation. Thus, a mixture of martensite, bainite, and ϵ -carbide phases can be obtained.

Laser Surface Hardening of Nonferrous Alloys

In many industrial applications such as transportation, construction equipment, defense, nuclear, and so on, the strength-to-weight ratio is a critical factor. For these applications, low-density-based light metals, namely, aluminum, magnesium, and titanium, are used (Tables 14 to 17). Apart from light weight and high specific strength, these metals, such as aluminum, possess good electrical and thermal conductivities; magnesium has good formality, and titanium can provide corrosion protection (Ref 164). The materials substitution from ferrous alloys to nonferrous alloys (aluminum, magnesium, titanium) has led to a huge potential for their use in many industrial applications. However, these nonferrous alloys are not hard enough to use in wear- and corrosion-resistance applications during severe loading conditions (Ref 165). Hence, these alloys need surface modification to enhance their resistance to wear, heat, and corrosion. In light of this, over the last several decades, LSH has been used to tailor wear-, corrosion-, heat-, and abrasion-resistance properties. A detailed survey of the LSH of aluminum (Table 18), magnesium (Table 19), and titanium (Table 20) alloys and their outcomes is reported. These details can be used as a reference for performing LSH on the given nonferrous alloys.

REFERENCES

1. J. Hecht, Short History of Laser Development, *Opt. Eng.*, Vol 49, 2010, p 1–23
2. N.B. Dahotre and S. Harimkar, *Laser Fabrication and Machining of Materials*, Springer, New York, 2007
3. G. Overton, S.G. Anderson, D.A. Belforte, and T. Hausken, Laser Marketplace 2010: How Wide Is the Chasm? *Laser Focus World*, Jan 2010

Table 13 Laser heat treatment of ferrous alloys

Material system	Outcome	Reference
En31	Improved wear and frictional properties	Ref 137
AISI 15B21H	Hardness and fatigue properties enhancement	Ref 138
AISI W112	Wear-resistance improvement	Ref 139
En18	Improved hardness and wear resistance via martensitic phase transformation	Ref 140
En8 steel	Improved hardness through martensite phase transformation	Ref 141
AISI 420, AMS 5898	Wear properties enhancement	Ref 142
Medium-carbon steel	Structural stability gained through enhanced hardness	Ref 143
AISI 440C	Enhanced hardness and erosion resistance (martensite, retained austenite, fine carbides)	Ref 144
2Cr13	Superior hardness, wear and oxidation resistance	Ref 145
AISI 4140, AISI A2, AISI D2	High hardness and fatigue resistance through enhanced martensite phase and compressive stress	Ref 146
C45E	Hardness improvement	Ref 147
En 8	Higher hardness and wear resistance	Ref 148
AISI 1536	Improved multipass hardness uniformity	Ref 149
En8, En24T	Larger-area hardness improvement using top-hat laser beam energy distribution	Ref 8
SAE 52100	High hardness and wear resistance	Ref 150
AISI 1045	Closed-loop control guarantees higher hardness uniformity	Ref 151
Medium-carbon steel	Enhanced hardness over more dissolution of Cr_xC_y	Ref 152
S45C	Hardness improvement	Ref 153
AISI 4140	Higher hardness achievement by experimental and modeling approaches	Ref 154
	Phase transformation induces residual stress and hardness improvement	Ref 155
AISI H13	Increased hardness by martensite phase transformation	Ref 156
SM45C	Higher case hardness via controlled laser process variables	Ref 157
AISI 420	Enhanced hardness and pitting corrosion resistance through refined microstructures	Ref 158
AISI 420B	Higher surface hardness	Ref 159
C40	Superior wear resistance and hardness	Ref 160
AISI O1	Case depth hardness improvement	Ref 161
AISI S7	Multipass case depth enhances hardness uniformity	Ref 162

Table 14 Physical and mechanical properties of aluminum, magnesium, titanium, and iron

Property	Aluminum	Magnesium	Titanium	Iron
Density, kg/m ³	2700	1740	4500	7870
Melting temperature, °C	660.32	649	1667	1538
Boiling temperature, °C	2520	1090	3285	2862
Thermal conductivity at 0–100 °C, W/m ⁻¹ · K ⁻¹	238	155.5	16	80.4
Specific heat at 0–100 °C, J/kg ⁻¹ · K ⁻¹	917	1038	528	450
Coefficient of thermal expansion at 0–100 °C, 10 ⁻⁶ · K ⁻¹	23.5	26.0	8.9	11.8
Compressive strength, MPa	...	80	930	240
Fracture toughness, MPa√m ²	...	28	85	125
Modulus of elasticity, GPa	70	45	115	211
Modulus of elasticity/density	0.026	0.026	0.026	0.027
Constant rigidity, wt%	50	37	...	100

Source: Ref 163

Table 15 Mechanical properties of aluminum and its alloys

Material	Nominal composition, %	Density, g/cm ⁻³	Thermal conductivity at 100 °C, W/m ⁻¹ · K ⁻¹	Modulus of elasticity, GPa
Al	Al 99.5	2.70	218	69
	Al 99.0	2.70	209	...
Al-Cu	Cu 4.5	2.75	180	71
	Cu 8	2.83	138	...
Al-Mg	Cu 12	2.93	130	...
	Mg 3.75	2.66	134	...
	Mg 5	2.65	130	...
Al-Si	Mg 10	2.57	88	71
	Si 5	2.67	159	71
Al-Si-Cu	Si 11.5	2.65	142	...
	Si 10, Cu 1.5	2.74	100	71
Al-Si-Cu-Mg	Si 4.5, Cu 3	2.76	134	71
	Si 17, Cu 4.5, Mg 0.5	2.73	134	88
Al-Cu-Mg-Ni	Cu 4, Mg 1.5, Ni 2	2.78	126	71
	Cu 10, Fe 1.25, Mg 0.25	2.88	138	71
Al-Cu-Fe-Mg	Si 12, Cu 1, Mg 1, Ni 2	2.71	121	71
	Si 23, Cu 1, Mg 1, Ni 1	2.65	107	88
Al-Li	Li 2	2.56	...	77
	Mg 3, Li 2	2.52	...	79
Al-Li-Mg	Li 3, Mg 2	2.46	...	84
	Al-Zn-Mg	Zn 10, Cu 1, Mn 0.7, Mg 0.4	2.91	151

Table 16 Physical and mechanical properties of magnesium and its alloys

Material	Nominal composition, %	Density, g/cm ³	Thermal conductivity at 100 °C, W/m ⁻¹ · K ⁻¹	Ultimate tensile strength, MPa	Hardness, VHN
Pure Mg	Mg 99.97	1.74	167	185	30–35
Mg-Mn	Mn 1.5	1.76	142	232	35–45
Mg-Al-Zn	Al 3, Zn 1, Mn 0.3	1.78	84	232	50–60
	Al 6, Zn 1, Mn 0.3	1.81	84	293	60–70
	Al 8, Zn 1, Mn 0.3	1.81	84	293	65–75
Mg-Zn-Mn	Zn 2, Mn 1	1.78	...	232	...
	Zn 1, Zr 0.6	1.8	134	263	55–70
Mg-Zn-Zr	Zn 3, Zr 0.6	1.8	125	270	60–70
	Zn 5.5, Zr 0.6	1.83	117	270	60–80
	Y 4, RE 3.4, Zr 0.6	1.84	51
Mg-Y-RE-Zr	Y 5.1, RE 3, Zr 0.6	1.85	52
	RE 2.7, Zn 2.2, Zr 0.7	1.8	100
Mg-RE-Zn-Zr	RE 1.2, Zn 4, Zr 0.7	1.84	113
	RE 2.5, Zn 6, Zr 0.7	1.87	109
	Th 0.8, Zn 0.5, Zr 0.6	1.76	121
Mg-Th-Zn-Zr	Th 3.0, Zn 2.2, Zr 0.7	1.83	105
	Th 5.5, Zn 1.8, Zr 0.6	1.87	113
	Ag 2.5, RE 2, Zr 0.6	1.82	113
Mg-Ag-Re-Zr	Ag 1.5, RE 2.2, Zr 0.7	1.81	113
	Zn 6.5, Cu 1.3, Mn 0.8	1.87	122	340	60–80
Mg-Ag-RE-Th-Zr	Ag 2.5, RE 1, Th 1, Zr 0.7	1.83	113	270	65–80

Table 17 Physical and mechanical properties of titanium and its alloys

Material	Nominal composition, %	Density, g/cm ³	Thermal conductivity at 20–100 °C, W/m ⁻¹ · K ⁻¹	Tensile strength, MPa	Modulus of elasticity, GPa
CP titanium	Commercially pure	4.51	16
IMI 230	Cu 2.5	4.56	13	620	125
IMI 260/261	Pd 0.2	4.52	16	...	125
IMI 315	Al 2, Mn 2	4.51	8.4	720	120
IMI 317	Al 5, Sn 2.5	4.46	6.3	860	120
IMI 318	Al 6, V 4	4.42	5.8	1160	106
IMI 550	Al 4, Mo 4, Sn 2, Si 0.5	4.60	...	1200	116
IMI 551	Al 4, Mo 4, Sn 4, Si 0.5	4.62	5.7	1300	113
IMI 679	Al 2.25, Sn 11, Zr 5, Mo 1, Si 0.2	4.84	7.1	1230	108
IMI 680	Al 2.25, Sn 11, Mo 4, Si 0.2	4.86	7.5	1350	115
IMI 685	Al 6, Zr 5, Mo 0.5, Si 0.25	4.45	4.8	1020	124
IMI 829	Al 5.5, Sn 3.5, Zr 3, Nb 1, Mo 0.3, Si 0.3	4.53	7.8	965	120
IMI 834	Al 5.8, Sn 4, Zr 3.5, Nb 0.7, Mo 0.5, Si 0.35, C 0.06	4.55	...	1067	120

Paper 7913_20, SPIE Conference on Laser Resonators and Beam Control XIII, Jan 2011

18. E. Toyserkani and A. Khajepour, *Laser Cladding*, CRC Press, Florida, 2005
19. S.T. Picraux and D.M. Follstaedt, in *Laser-Solid Interactions and Transient Thermal Processing of Materials*, J. Narayan, W.L. Brown, and R.A. Lemons, Ed., North-Holland, New York, 1983, p 751
20. L. Buene et al., *Appl. Phys. Lett.*, Vol 37, 1981, p 583–590
21. S. Katakam, J.Y. Hwang, H. Vora, S. Harimkar, R. Banerjee, and N.B. Dahotre, Laser-Induced Thermal and Spatial Nanocrystallization of Amorphous Fe-Si-B Alloy, *Scr. Mater.*, Vol 66, 2012, p 538–554
22. C.M. Cook and J.M. Haake, Monitoring and Controlling the Temperature in a High Power Direct Diode Laser Surface Hardening Application, *20th ASM Heat Treating Society Conference Proceedings*, 2000, p 183–191
23. W.U.H. Syed, A.J. Pinkerton, and L. Li, A Comparative Study of Wire Feeding and Powder Feeding in Direct Diode Laser Deposition for Rapid Prototyping, *Appl. Surf. Sci.*, Vol 247, 2005, p 268–276
24. C.Y. Liu and J. Lin, Thermal Processes of a Powder Particle in Coaxial Laser Cladding, *Opt. Laser Technol.*, Vol 35, 2003, p 81–86
25. K. Takaki et al., Determination of Heat and Ion Fluxes in Plasma Immersion Ion Implantation by In Situ Measurement of Temperature Using Laser Interferometer, *Surf. Coat. Technol.*, Vol 136, 2001, p 261–264
26. W. Kurz and D.J. Fisher, *Fundamentals of Solidification*, Trans Tech Publication, 1990
27. J. Mazumder, A. Schifferer, and J. Choi, Direct Materials Deposition: Designed Macro and Microstructure, *Mater. Res. Innov.*, Vol 3, 1999, p 118–131
28. M.L. Griffith et al., Understanding the Microstructure and Properties of Components Fabricated by Laser Engineered Net Shaping LENS, *Proc. of the Solid Freeform and Additive Fabrication Conference*, 1999 (San Francisco, CA), 2000, p 9–20
29. E. Kennatey-Asibu, *Principles of Laser Materials Processing*, John Wiley & Sons, Inc., Hoboken, NJ, 2009
30. S. Ghosh, G.L. Goswami, A.R. Biswas, R. Venkatramani, and S.P. Garg, Surface Melting Using Laser for Improvement in Oxidation Resistance of Inconel 600, *Trans. Indian Inst. Met.*, Vol 50 (No. 4), 1997, p 287–290
31. R.J. DiMelfi, P.G. Sanders, B. Hunter, J.A. Eastman, K.J. Sawley, K.H. Leong, and J.M. Kramer, Mitigation of Subsurface Crack Propagation in Railroad Rails by

4. K. Kincade, Diode Lasers Test Their Mettle in Surface Treatment, *Laser Focus World*, 2006, p 95–97
5. M. Hendriks, Repair instead of Replace, *Laser Focus World*, July 2010
6. S. Swann, Magnetron Sputtering, *Phys. Technol.*, Vol 19, 1988, p 67–75
7. G.R.B.E. Romer and J. Meijer, Metal Surface Temperature Induced by Moving Laser Beams, *Opt. Quantum Electron.*, Vol 27, 1995, p 1397–1406
8. I.R. Pashby, S. Barnes, and B.G. Bryden, Surface Hardening of Steel Using a High Power Diode Laser, *J. Mater. Process. Technol.*, Vol 139, 2003, p 585–588
9. J.D. Majumdar and I. Manna, Laser Processing of Materials, *Sadhana*, Vol 28, 2003, p 495–562
10. W.M. Steen, *Laser Material Processing*, Springer, New York, 1998
11. W.W. Duley, *Laser Processing and Analysis of Materials*, Plenum Press, New York, 1983
12. H.G. Woo and H.S. Cho, Three-Dimensional Temperature Distribution in Laser Surface Hardening Processes, *Proc. Inst. Mech. Eng. B*, Vol 213, 1999, p 695–712
13. F. Meriaudeau, Real Time Multispectral High Temperature Measurement: Application to Control in the Industry, *Image Vision Comput.*, Vol 25, 2007, p 1124–1133
14. “FLIR Manual,” FLIR Systems, Inc., Jan 2012, <http://support.flir.com>, accessed June 2012
15. M.A. Sheikh and L. Li, Understanding the Effect of Non-Conventional Laser Beam Geometry on Material Processing by Finite Element Modeling, *Proc. IMechE*, Vol 224, 2009, p 1061–1072
16. L. Pawlowski, Thick Laser Coatings: A Review, *J. Therm. Spray Technol.*, Vol 8 (No. 2), June 1999, p 279–295
17. A. Laskin and V. Laskin, “Applying of Reflective Beam Shapers of Circular Symmetry to Generate Non-Circular Shapes of Homogenized Laser Beams,”

Table 18 Laser surface hardening of aluminum alloys

Material system	Outcome	Reference
Laser heat treatment		
Al-Li-Cu	Improved oxidation resistance	Ref 166
Al 7075-T651	Better corrosion resistance due to microstructural refinement	Ref 167
A356	Homogeneous microstructure results in increased hardness and tensile strength	Ref 168
AW6016	Increased tensile shear strength	Ref 169
AlSi ₆ Cu ₄ , EN-AW 6082	Improved hardness and wear resistance as a result of fine grain structures and dispersion hardening	Ref 170
AA7449-T7651	Microstructural refinement and enhanced mechanical properties	Ref 171
Laser surface melting		
Al 2024-T351	Microstructural refinement and element redistribution result in better pitting corrosion resistance	Ref 172
Al-Si alloy	Enhanced corrosion resistance attributed to Al grain refinement and Si enrichment	Ref 173
LM25	Improved wear resistance	Ref 174
Al 2014-T6	Refinement of microstructures (columnar, cellular, dendrite) results in increased mechanical and corrosion properties	Ref 175
Al-Cu	Rapid microstructural confinement causes increased hardness	Ref 176
Al 6013	Increased fatigue and corrosion resistance due to AlN and Al ₂ O ₃ formation	Ref 177
AA2050-T8	Enhanced corrosion resistance attributed to less galvanic coupling (Al-Cu-Fe-Mn, Al-Zr-Ti)	Ref 178
Al-Fe	Higher load and wear resistance result from heterogeneous microstructure (metastable and stable phases, intermetallics, oxides) formation	Ref 179
AlSi ₇ Mg _{0.3}	Improved load and wear resistance due to AlN-phase formation	Ref 180
	Laser-aided carbon diffusion and AlC formation result in enhanced wear resistance	Ref 181
Laser shock peening		
Al 2024-T62	Elastic properties (Poisson's ratio, Young's modulus) modification	Ref 182
Al 6061-T6	Enhanced wear and fatigue resistance	Ref 183
Al-Si-Mg	Fatigue strength increased	Ref 184
AA 7075-T7351	Improved fatigue resistance attributed to deeper compressive residual stress formation	Ref 185
LY2	Grain refinement and higher density dislocations cause increased hardness and elastic modulus	Ref 186
Al 7050-T7451	Increased fatigue induced by deeper compressive residual stresses	Ref 187
Al 2050-T8	Hardness and corrosion improvement due to high-order compressive stress inducement	Ref 188
Al 2050-T8	Beneficial electrochemical resistance attributed to compressive stress stimulus	Ref 189
Al 7050-T7451	Higher fatigue resistance exhibited by shock-induced compressive stresses and resultant high dislocation density within the grains	Ref 190
Al 6061-T6	Increased hardness and surface roughness	Ref 191
Al 6082-T651	Higher corrosion resistance due to Al ₂ O ₃ enrichment	Ref 192
Al 7075-T651	Enhanced fatigue resistance	Ref 193
LY2	Increased surface roughness and hardness due to shock-induced compressive residual stress formation	Ref 194
5A06	Surface strengthening through increased hardness and wear resistance	Ref 195
Laser cladding		
AA6061 (Mo-WC)	Superior hardness and wear resistance attributed to WC, Al ₃ Mo, Al ₂₂ Mo ₅ , Al ₁₇ Mo ₄ , (Al ₅ W) ₁₂ H, Mo ₂ C, Al ₄ C ₃ , and WAl ₁₂ hard-phase formation	Ref 196
AlSi10Mg (AlSi10Mg)	Enhanced fatigue resistance	Ref 197
Laser surface alloying		
A359 (A359, SiC)	Improved mechanical properties (flow stress)	Ref 198
AA6061 (SiC, Si ₃ N ₄)	Superior hardness; cavitation erosion and pitting corrosion resistance result from Al ₄ C ₃ , Al ₄ SiC ₄ , and AlN formation	Ref 199
A5083 (TiC, Cu)	Improved hardness and wear resistance result from heterogeneous structural refinement (TiC, Al ₂ Cu, Al ₄ Cu ₉)	Ref 200
Al 6061 (NiCrSiB)	Superior hardness; cavitation erosion and corrosion resistance result from hard-phase (NiAl, Ni ₃ Al, NiAl ₃ , Ni ₂ Al ₃) formation	Ref 201
Al 1100 (Al-Cu)	Microstructural homogeneity and porosity elimination result in increased elastic modulus and wear resistance	Ref 202
A5052 (Fe-Al)	Hardness and wear-resistance improvement due to FeAl ₃ and Fe ₂ Al ₃ formation	Ref 203
Al 1100 (WC + Co + NiCr)	Hardness and wear-resistance improvement attributed to mixed carbide (WC, W ₂ C, Al ₄ C ₃ , Al ₉ Co ₂ , Al ₃ Ni, Cr ₂₃ C ₆ , and Co ₆ W ₆ C) formation	Ref 204
Al 1100, AlMg1SiCu, AlSi10Mg (Fe ₂ O ₃)	Superior hardness attributed to Al ₂ O ₃ , Al ₁₃ Fe ₄ , Al ₃ FeSi ₂ formation	Ref 205

Table 19 Laser hardening of magnesium alloys

Material system	Process type(a)	Outcome	Reference
Mg- ZK60 + SiC	LSM	Microstructural refinement and enhanced corrosion resistance	Ref 206
AZ91	LSM	Improved corrosion resistance	Ref 207
Mg + SiC (Al-Si)	LC	Addition of Al and Si results in higher corrosion resistance	Ref 208
AZ91D, AM60B	LSM	Homogeneous microstructural refinement produces enhanced corrosion resistance	Ref 209
MEZ (SiC)	LHF	Hard-phase (SiC) inducement improves wear resistance	Ref 210
WE43, ZE41 (Al)	LC	Enhanced hardness and corrosion resistance attributed to Al ₃ Mg ₂ and Al ₁₂ Mg ₁₇ intermetallic formation	Ref 211
AZ31, AZ61, WE43	LSM	β-phase refinement results in better corrosion resistance	Ref 212
ZK60/SiC (Al + Zn)	LC	Increased corrosion resistance	Ref 213
Mg-Al-Zn-Mn-Ce	LSM	Enrichment of Mg ₁₇ Al ₁₂ finer dendrites provides good corrosion resistance	Ref 214
Mg-Zn (Mg-Zn)	LC	Higher hardness attributed to homogeneous microstructures	Ref 215
AZ31, AZ61	LSM	Hardness and wear-resistance enhancement result from microstructural refinement	Ref 216
AZ91D (Al + Si + Al ₂ O ₃)	LC	Superior hardness attributed to higher dispersion of Si, Al ₂ O ₃ , and Mg ₁₇ Al ₁₂	Ref 217
AZ91HP (Al-Si)	LC	Improved hardness, wear, and corrosion resistance result from multiple Mg intermetallics (Mg ₂ Si, Mg ₁₇ Al ₁₂ , Mg ₂ Al ₃) formation	Ref 218
AZ91D (CeO ₂)	LC	Corrosion resistance increased	Ref 219
ZM5 (Al + Ir)	LC	Better corrosion resistance attributed to combinatorial influence of grain refinement and dissolution of Al-rich intermetallics (AlIr, Mg ₁₇ Al ₁₂)	Ref 220

(continued)

(a) LSM, laser surface melting; LC, laser cladding; LHF, laser hardfacing; LSA, laser surface alloying

Table 19 (Continued)

Material system	Process type(a)	Outcome	Reference
Mg-Al (Ni, Cu, Al)	LSA	Enrichment of Ni solid phase results in superior corrosion and wear resistance	Ref 221
ACM720	LSM	Enhanced hardness, wear, and corrosion resistance due to grain refinement and solid-solution strengthening	Ref 222
ZE41 (Al + Si)	LC	Increased corrosion resistance attributed to Mg ₁₇ Al ₁₂ formation	Ref 223
AZ91D	LSM	Homogeneous microstructural refinement provides wear resistance	Ref 224
MRI 153M (Al + Al ₂ O ₃)	LC	Superior hardness attributed to Al ₂ O ₃ phase refinement	Ref 225
AZ91D (Al + Si)	LC	Superior hardness and wear resistance strengthened by Mg ₂ Si and Mg ₁₇ Al ₁₂ phases	Ref 226
AZ91 (Ni)	LSA	Higher Young's modulus and wear resistance attributed to MgNi ₂ phase formation	Ref 227
ZE41	LSM	Homogeneous microstructural refinement results in enhanced hardness and wear resistance	Ref 228
AZ31B	LSM	Improved mechanical properties (tensile strength)	Ref 229
AZ91D (Al + SiC)	LC	Improved hardness and wear resistance attributed to composite mixture of SiC and β-Mg ₁₇ Al ₁₂ phases	Ref 230
ZE41 (Al + Si)	LC	Rapid microstructural refinement (Al-Mg, Mg ₂ Si) results in higher load resistance	Ref 231
AZ31B (Al)	LSM/LC	Higher Mg ₁₇ Al ₁₂ intermetallic refinement results in enhanced corrosion and wear resistance	Ref 232
AZ91D	LSM	Higher tribological properties due to Mg ₁₇ Al ₁₂ formation	Ref 233

(a) LSM, laser surface melting; LC, laser cladding; LHF, laser hardfacing; LSA, laser surface alloying

Table 20 Laser surface hardening of titanium alloys

Material system	Outcome	Reference
Laser heat treatment		
Ti40, Ti-6Al-4V	Surface texture and wear properties enhancement	Ref 234
Ti-6Al-4V	Improved pitting corrosion resistance due to solute-partitioning effect reduction and Al segregation	Ref 235
CP-Ti alloy	Wetting characteristics improvement	Ref 236
ASTM grade 3 Ti	Hardness improvement by phase transformation	Ref 237
Ti-6Al-4V	Enhanced hardness	Ref 238
Laser surface melting		
Ti-6Al-4V	Wear resistance enhancement	Ref 239
CP-Ti alloy	Improved abrasive wear resistance	Ref 240
α-Ti	Microstructural refinement and martensite transformation result in improved mechanical properties	Ref 241
Laser shock peening		
Ti-15-3	Improved adhesive strength	Ref 242
CP-Ti	Improved mechanical properties (tensile, modulus of elasticity, hardness)	Ref 243
	Better hardness and tensile strength	Ref 244
TC17	Greater load resistance attributed to compressive residual stress formation	Ref 245
Ti-2.5Cu, Ti-54M, LCB	Fatigue resistance improvement	Ref 246
Laser cladding		
CP-Ti (Ni + Cr)	Higher wear resistance	Ref 247
CP-Ti (Ti + C)	Improved frictional resistance	Ref 248
BT9 (Ti ₃ Si ₃ /NiTi ₂)	Superior load and wear resistance attributed to composite intermetallic (Ti ₃ Si ₃ /NiTi ₂) formation	Ref 249
BT20 (BT20)	Microstructural homogeneity results in enhanced hardness and wear resistance	Ref 250
Laser surface alloying		
IMI 318 (SiC)	Wear resistance and hardness improvement	Ref 251
Ti-6Al-4V (SiC)	Mechanical properties enhancement by microstructural refinement	Ref 252
Ti-6Al-4V (NiAl + ZrO ₂)	Greater hardness and tribological properties due to higher hard-phase (AlZr ₃ , Ti ₃ Al, Al ₂ O ₃) formation	Ref 253
BT9 (Cr-Ni-Si)	Excellent wear resistance due to large Cr ₁₃ Ni ₅ Si ₂ enrichment	Ref 254
CP-Ti (Ni + Pd)	Corrosion-resistance improvement	Ref 255
BT9 (TiCo/Ti ₂ Co)	Dominant wear resistance	Ref 256
CP-Ti (TiN-B-Si-Ni)	Higher hardness, oxidation and frictional resistance	Ref 257, 258
Ti (TiB)	Hardness improvement due to higher boride formation	Ref 259
Ti-6Al-4V (TiB)	Increased wear resistance	Ref 260
Ti-6Al-4V (graphite)	Microstructural refinement (TiC) results in improved wear and erosion resistance	Ref 261

Laser Surface Modification, *Surf. Coat. Technol.*, Vol 106, 1998, p 30–43

32. C.T. Kwok, H.C. Man, and F.T. Cheng, Cavitation Erosion and Pitting Corrosion of Laser Surface Melted Stainless Steels, *Surf. Coat. Technol.*, Vol 99, 1998, p 295–304
33. Q.Y. Pan, W.D. Huang, R.G. Song, Y.H. Zhou, and G. Zhang, The Improvement of Localized Corrosion Resistance in Sensitized Stainless Steel by Laser Surface Remelting, *Surf. Coat. Technol.*, Vol 102, 1998, p 245–255

34. C.T. Kwok, H.C. Man, and F.T. Cheng, Cavitation Erosion and Pitting Corrosion Behaviour of Laser Surface-Melted Martensitic Stainless Steel UNS S42000, *Surf. Coat. Technol.*, Vol 126, 2000, p 238–255
35. R. Wu, C. Xie, M. Hu, and W. Cai, Laser-Melted Surface Layer of Steel X165CrMoV12-1 and Its Tempering Characteristics, *Mater. Sci. Eng. A*, Vol 278, 2000, p 1–4
36. A. Conde, R. Colac, R. Vilar, and J. de Damborenea, Corrosion Behaviour of

Steels after Laser Surface Melting, *Mater. Des.*, Vol 21, 2000, p 441–445

37. N. Parvathavarthini, S. Saroja, R.K. Dayal, and H.S. Khatak, Studies on Hydrogen Permeability of 2.25%Cr-1% Mo Ferritic Steel: Correlation with Microstructure, *J. Nucl. Mater.*, Vol 288, 2001, p 187–196
38. A. Conde, I. Garcia, and J.J. de Damborenea, Pitting Corrosion of 304 Stainless Steel after Laser Surface Melting in Argon and Nitrogen Atmospheres, *Corros. Sci.*, Vol 43, 2001, p 817–828

39. D.I. Pantelis, E. Bouyiouri, N. Kou-loumbi, P. Vassiliou, and A. Koutsomichalis, Wear and Corrosion Resistance of Laser Surface Hardened Structural Steel, *Surf. Coat. Technol.*, Vol 298, 2002, p 125–134
40. C.T. Kwok, K.I. Leong, F.T. Cheng, and H.C. Man, Microstructural and Corrosion Characteristics of Laser Surface-Melted Plastics Mold Steels, *Mater. Sci. Eng. A*, Vol 357, 2003, p 94–103
41. M. Kulka and A. Pertek, Microstructure and Properties of Borided 41Cr4 Steel after Laser Surface Modification with Re-Melting, *Appl. Surf. Sci.*, Vol 214, 2003, p 278–288
42. S. Kac and J. Kusinski, SEM Structure and Properties of ASP2060 Steel after Laser Melting, *Surf. Coat. Technol.*, Vol 180–181, 2004, p 611–615
43. Y. Suna, S. Hanakia, M. Yamashitaa, H. Uchidaa, and H. Tsujii, Fatigue Behavior and Fractography of Laser-Processed Hot Work Tool Steel, *Vacuum*, Vol 73, 2004, p 655–660
44. P.H. Chong, Z. Liu, X.Y. Wang, and P. Skeldon, Pitting Corrosion Behaviour of Large Area Laser Surface Treated 304L Stainless Steel, *Thin Solid Films*, Vol 453–454, 2004, p 388–393
45. M. Szkodo and B.G. Girén, Cavitation Erosion of Steels Processed by CO₂ Laser Beams of Various Parameters, *J. Mater. Process. Technol.*, Vol 157–158, 2004, p 446–450
46. K.A. Qureshi, N. Hussain, J.I. Akhter, N. Khan, and A. Hussain, Surface Modification of Low Alloy Steel by Laser Melting, *Mater. Lett.*, Vol 59, 2005, p 719–722
47. R. Colac and R. Vilar, On the Influence of Retained Austenite in the Abrasive Wear Behaviour of a Laser Surface Melted Tool Steel, *Wear*, Vol 258, 2005, p 225–231
48. P.H. Chong, Z. Liu, P. Skeldon, and P. Crouse, Characterisation and Corrosion Performance of Laser-Melted 3CR12 Steel, *Appl. Surf. Sci.*, Vol 247, 2005, p 362–368
49. K.T. Voisey, Z. Liu, and F.H. Stott, Inhibition of Metal Dusting of Alloy 800H by Laser Surface Melting, *Appl. Surf. Sci.*, Vol 252, 2006, p 3658–3666
50. M. Badrossamay and T.H.C. Child, Further Studies in Selective Laser Melting of Stainless and Tool Steel Powders, *Int. J. Mach. Tools Manuf.*, Vol 47, 2007, p 779–784
51. C.T. Kwok, F.T. Cheng, and H.C. Man, Microstructure and Corrosion Behaviour of Laser Surface Melted Stainless Steels, *Surf. Coat. Technol.*, Vol 202, 2007, p 336–348
52. K.A. Mumtaz, P. Erasenthiran, and N. Hopkinson, High Density Selective Laser Melting of Waspaloy, *J. Mater. Process. Technol.*, Vol 195, 2008, p 77–87
53. S. Dao, M. Hua, T.M. Shao, and H.Y. Tam, Surface Modification of DF-2 Tool Steel under the Scan of a YAG Laser in Continuously Moving Mode, *J. Mater. Process. Technol.*, Vol 209, 2009, p 4689–4697
54. B.D. Joo, J.-H. Jang, J.-H. Lee, Y.-M. Son, and Y.-H. Moon, Selective Laser Melting of Fe-Ni-Cr Layer on AISI H13 Tool Steel, *Trans. Nonferrous Met. Soc. China*, Vol 19, 2009, p 921–924
55. J.D. Majumdar, A.K. Nath, and I. Manna, Studies on Laser Surface Melting of Tool Steel, Part I: Surface Characterization and Its Electrochemical Behavior, *Surf. Coat. Technol.*, Vol 204, 2010, p 1321–1325
56. J.D. Majumdar, A.K. Nath, and I. Manna, Studies on Laser Surface Melting of Tool Steel, Part II: Mechanical Properties of the Surface, *Surf. Coat. Technol.*, Vol 204, 2010, p 1326–1329
57. C. Li, Y. Wang, and B. Han, Microstructure, Hardness and Stress in Melted Zone of 42CrMo Steel by Wide-Band Laser Surface Melting, *Opt. Lasers Eng.*, Vol 49, 2011, p 530–535
58. C.T. Kwok, K.H. Lo, W.K. Chan, F.T. Cheng, and H.C. Man, Effect of Laser Surface Melting on Intergranular Corrosion Behaviour of Aged Austenitic and Duplex Stainless Steels, *Corros. Sci.*, Vol 53, 2011, p 1581–1591
59. K. Kempen, E. Yasa, L. Thijs, J.-P. Kruth, and J. Van Humbeeck, Microstructure and Mechanical Properties of Selective Laser Melted 18Ni-300 Steel, *Phys. Proced.*, Vol 12, 2011, p 255–263
60. C.Y. Cui, X.G. Cui, Y.K. Zhang, Q. Zhao, J.Z. Lu, J.D. Hu, and Y.M. Wang, Microstructure and Corrosion Behavior of the AISI 304 Stainless Steel after Nd:YAG Pulsed Laser Surface Melting, *Surf. Coat. Technol.*, Vol 206, 2011, p 1146–1154
61. H. So, C.T. Chen, and Y.A. Chen, Wear Behaviours of Laser-Clad Stellite Alloy 6, *Wear*, Vol 192, 1996, p 78–84
62. M.A. Anjos, R. Vilar, and Y.Y. Qiu, Laser Cladding of ASTM S3 1254 Stainless Steel on a Plain Carbon Steel Substrate, *Surf. Coat. Technol.*, Vol 92, 1997, p 142–149
63. D.W. Zhang, T.C. Lei, J.G. Zhang, and J.H. Ouyang, The Effects of Heat Treatment on Microstructure and Erosion Properties of Laser Surface-Clad Ni-Base Alloy, *Surf. Coat. Technol.*, Vol 115, 1999, p 176–183
64. J. Kim and Y. Peng, Plunging Method for Nd:YAG Laser Cladding with Wire Feeding, *Opt. Lasers Eng.*, Vol 33, 2000, p 299–309
65. D.W. Zhang, T.C. Lei, and F.J. Li, Laser Cladding of Stainless Steel with Ni-Cr₃C₂ for Improved Wear Performance, *Wear*, Vol 251, 2001, p 1372–1376
66. T.M. Yue, Q.W. Hu, Z. Mei, and H.C. Man, Laser Cladding of Stainless Steel on Magnesium ZK60rSiC Composite, *Mater. Lett.*, Vol 47, 2001, p 165–170
67. M. Zhong, W. Liu, K. Yao, J. Goussain, C. Mayer, and A. Becker, Microstructural Evolution in High Power Laser Cladding of Stellite 6 + WC Layers, *Surf. Coat. Technol.*, Vol 157, 2002, p 128–137
68. A.J. Pinkerton and L. Li, The Effect of Laser Pulse Width on Multiple-Layer 316L Steel Clad Microstructure and Surface Finish, *Appl. Surf. Sci.*, Vol 208–209, 2003, p 411–416
69. S. Barnes, N. Timms, B. Bryden, and I. Pashby, High Power Diode Laser Cladding, *J. Mater. Process. Technol.*, Vol 138, 2003, p 411–416
70. D.W. Zeng, C.S. Xie, and M.Q. Wang, In Situ Synthesis and Characterization of Fe_p/Cu Composite Coating on SAE 1045 Carbon Steel by Laser Cladding, *Mater. Sci. Eng. A*, Vol 344, 2003, p 357–364
71. S.F. Corbin, E. Toyserkani, and A. Khajepour, Cladding of an Fe-Aluminide Coating on Mild Steel Using Pulsed Laser Assisted Powder Deposition, *Mater. Sci. Eng. A*, Vol 354 (No. 1–4), 2003, p 48–57
72. M. Li, Y. He, and G. Sun, Laser Cladding Co-Based Alloy/SiC_p Composite Coatings on IF Steel, *Mater. Des.*, Vol 25, 2004, p 355–358
73. F.T. Cheng, K.H. Lo, and H.C. Man, A Preliminary Study of Laser Cladding of AISI 316 Stainless Steel Using Preplaced NiTi Wire, *Mater. Sci. Eng. A*, Vol 380, 2004, p 20–29
74. K.Y. Chiu, F.T. Cheng, and H.C. Man, Laser Cladding of Austenitic Stainless Steel Using NiTi Strips for Resisting Cavitation Erosion, *Mater. Sci. Eng. A*, Vol 402, 2005, p 126–134
75. D. Zhang and X. Zhang, Laser Cladding of Stainless Steel with Ni-Cr₃C₂ and Ni-WC for Improving Erosive-Corrosive Wear Performance, *Surf. Coat. Technol.*, Vol 190, 2005, p 212–217
76. I. Manna, J.D. Majumdar, B.R. Chandra, S. Nayak, and N.B. Dahotre, Laser Surface Cladding of Fe-B-C, Fe-B-Si and Fe-BC-Si-Al-C on Plain Carbon Steel, *Surf. Coat. Technol.*, Vol 201, 2006, p 434–440
77. H. Alemohammad, S. Esmaili, and E. Toyserkani, Deposition of Co-Ti Alloy on Mild Steel Substrate Using Laser Cladding, *Mater. Sci. Eng. A*, Vol 456, 2007, p 156–161
78. D. Dong, C. Liu, B. Zhang, and J. Miao, Pulsed Nd:YAG Laser Cladding of High Silicon Content Coating on Low Silicon Steel, *J. Univ. Sci. Technol. Beijing*, Vol 14 (No. 4), 2007, p 321–326
79. C.P. Paul, H. Alemohammad, E. Toyserkani, A. Khajepour, and S. Corbin, Cladding of WC-12Co on Low Carbon Steel Using a Pulsed Nd:YAG Laser, *Mater. Sci. Eng. A*, Vol 464, 2007, p 170–176

80. J.D. Majumdar, B.R. Chandrar, A.K. Nath, and I. Manna, Studies on Compositionally Graded Silicon Carbide Dispersed Composite Surface on Mild Steel Developed by Laser Surface Cladding, *J. Mater. Process. Technol.*, Vol 203, 2008, p 505–512
81. M.J. Tobar, J.M. Amado, C. Álvarez, A. García, A. Varela, and A. Yáñez, Characteristics of Tribaloy T-800 and T-900 Coatings on Steel Substrates by Laser Cladding, *Surf. Coat. Technol.*, Vol 202, 2008, p 2297–2301
82. M. Qing-Jun, W. Xin-Hong, Q. Shi-Yao, and Z. Zeng-Da, Amorphous of Fe₃₈Ni₃₀-Si₁₆B₁₄V₂ Surface Layers by Laser Cladding, *Trans. Nonferrous Met. Soc. China*, Vol 18, 2008, p 270–273
83. J.D. Majumdar, A. Kumar, and L. Li, Direct Laser Cladding of SiC Dispersed AISI 316L Stainless Steel, *Tribol. Int.*, Vol 42, 2009, p 750–753
84. F. Wang, H. Mao, D. Zhang, and X. Zhao, The Crack Control during Laser Cladding by Adding the Stainless Steel Net in the Coating, *Appl. Surf. Sci.*, Vol 255, 2009, p 8846–8854
85. F. Lusquinos, R. Comesaña, A. Riveiro, F. Quintero, and J. Pou, Fibre Laser Micro-Cladding of Co-Based Alloys on Stainless Steel, *Surf. Coat. Technol.*, Vol 203, 2009, p 1933–1940
86. I. Hemmati, V. Ocelík, and J.T.M. De Hosson, The Effect of Cladding Speed on Phase Constitution and Properties of AISI 431 Stainless Steel Laser Deposited Coatings, *Surf. Coat. Technol.*, Vol 205, 2011, p 5235–5239
87. J. Leunda, C. Soriano, C. Sanz, and V. Garcia Navas, Laser Cladding of Vanadium-Carbide Tool Steels for Die Repair, *Phys. Proced.*, Vol 12, 2011, p 345–352
88. L. Zhao, M. Zhao, D. Li, J. Zhang, and G. Xiong, Study on Fe-Al-Si In Situ Composite Coating Fabricated by Laser Cladding, *Appl. Surf. Sci.*, Vol 258, 2012, p 3368–3372
89. H. Liu, C. Wang, X. Zhang, Y. Jiang, C. Cai, and S. Tang, Improving the Corrosion Resistance and Mechanical Property of 45 Steel Surface by Laser Cladding with Ni60CuMoW Alloy Powder, *Surf. Coat. Technol.*, June 2012
90. O.V. Akgun and O.T. Inal, Laser Surface Melting and Alloying of Type 304L Stainless Steel, *J. Mater. Sci.*, Vol 30, 1995, p 6105–6112
91. H.C. Chong, T.T. Wen, and L.T. Ju, Microstructure and Electrochemical Behaviour of Laser Treated Fe-Cr and Fe-Cr-Si-N Surface Alloyed Layers on Carbon Steel, *Mater. Sci. Eng. A*, Vol 190, 1995, p 199–205
92. T.R. Jervis, M. Nastasi, A.J. Griffin, Jr., T.G. Zocco, T.N. Taylor, and S.R. Foltyn, Tribological Effects of Excimer Laser Processing of Tool Steel, *Surf. Coat. Technol.*, Vol 89, 1997, p 158–164
93. A. Gutierrez and J. de-Damborenea, High-Temperature Oxidation Behaviour of Laser-Surface-Alloyed Incoly-800H with Al, *Oxid. Met.*, Vol 47 (No. 3–4), 1997, p 259–275
94. I. Manna, K.K. Rao, S.K. Roy, and K.G. Watkins, Surface Engineering in Materials Science, *TMS Conference Proceedings*, S. Seal, N.B. Dahotre, J.J. Moore, and B. Mishra, Ed., Warrendale, PA, 2000, p 367–376
95. A. Agarwal and N.B. Dahotre, Mechanical Properties of Laser-Deposited Composite Boride Coating Using Nanoindentation, *Metall. Mater. Trans. A*, Vol 31, 2000, p 401–408
96. C.T. Kwok, F.T. Cheng, and H.C. Man, Laser Surface Modification of UNS S31603 Stainless Steel, Part I: Microstructures and Corrosion Characteristics, *Mater. Sci. Eng. A*, Vol 290, 2000, p 55–73
97. A. Agarwal, L.R. Katipelli, and N.B. Dahotre, Elevated Temperature Oxidation of Laser Surface Engineered Composite Boride Coating on Steel, *Metall. Mater. Trans. A*, Vol 31, 2000, p 461–473
98. W. Jiang and P. Molian, Nanocrystalline TiC Powder Alloying and Glazing of H13 Steel Using a CO Laser for Improved Life of Die-Casting Dies, *Surf. Coat. Technol.*, Vol 135, 2001, p 139–149
99. F.T. Cheng, C.T. Kwok, and H.C. Man, Laser Surfacing of S31603 Stainless Steel with Engineering Ceramics for Cavitation Erosion Resistance, *Surf. Coat. Technol.*, Vol 139, 2001, p 14–24
100. D.W. Zeng, C.S. Xie, and K.C. Yung, Mesostructured Composite Coating on SAE 1045 Carbon Steel Synthesized In Situ by Laser Surface Alloying, *Mater. Lett.*, Vol 56, 2002, p 680–684
101. G. Thawari, G. Sundararajan, and S.V. Joshi, Laser Surface Alloying of Medium Carbon Steel with SiC, *Thin Solid Films*, Vol 423, 2003, p 41–53
102. K.H. Lo, F.T. Cheng, C.T. Kwok, and H.C. Man, Improvement of Cavitation Erosion Resistance of AISI 316 Stainless Steel by Laser Surface Alloying Using Fine WC Powder, *Surf. Coat. Technol.*, Vol 165, 2003, p 258–267
103. L.A. Dobrzański, M. Boneka, E. Hajduzek, A. Klimpel, and A. Lisiecki, Application of High Power Diode Laser (HPDL) for Alloying of X40CrMoV5-1 Steel Surface Layer by Tungsten Carbides, *J. Mater. Process. Technol.*, Vol 155–156, 2004, p 1956–1963
104. L.A. Dobrzański, M. Bonek, E. Hajduzek, and A. Klimpel, Alloying the X40CrMoV5-1 Steel Surface Layer with Tungsten Carbide by the Use of a High Power Diode Laser, *Appl. Surf. Sci.*, Vol 247, 2005, p 328–332
105. M. Zhong, W. Liu, and H. Zhang, Corrosion and Wear Resistance Characteristics of NiCr Coating by Laser Alloying with Powder Feeding on Grey Iron Liner, *Wear*, Vol 260, 2006, p 1349–1355
106. L.A. Dobrzański, K. Labisz, E. Jonda, and A. Klimpel, Comparison of the Surface Alloying of the 32CrMoV12-28 Tool Steel Using TiC and WC Powder, *J. Mater. Process. Technol.*, Vol 191, 2007, p 321–325
107. A. Hussain, I. Ahmad, A.H. Hamdani, A. Nussair, and S. Shahdin, Laser Surface Alloying of Ni-Plated Steel with CO₂ Laser, *Appl. Surf. Sci.*, Vol 253, 2007, p 4947–4950
108. J. Yao, L. Wang, Q. Zhang, F. Kong, C. Lou, and Z. Chen, Surface Laser Alloying of 17-4PH Stainless Steel Steam Turbine Blades, *Opt. Laser Technol.*, Vol 40, 2008, p 838–843
109. J.D. Majumdar, Development of Wear Resistant Composite Surface on Mild Steel by Laser Surface Alloying with Silicon and Reactive Melting, *Mater. Lett.*, Vol 62, 2008, p 4257–4259
110. L.A. Dobrzański, E. Jonda, and A. Klimpel, Laser Surface Treatment of the Hot Work Tool Steel Alloyed with TaC and VC Carbide Powders, *Arch. Mater. Sci. Eng.*, Vol 37, 2009, p 53–60
111. G. Sun, Y. Zhang, C. Liu, K. Luo, X. Tao, and P. Li, Microstructure and Wear Resistance Enhancement of Cast Steel Rolls by Laser Surface Alloying NiCr-Cr₃C₂, *Mater. Des.*, Vol 31, 2010, p 2737–2744
112. W.U. Anqi, L. Qibin, and Q. Shuijie, Influence of Yttrium on Laser Surface Alloying Organization of 40Cr Steel, *J. Rare Earths*, Vol 29 (No. 10), 2011, p 1004–1008
113. S.R. Pillai, P. Shankar, R.V. Subba-Rao, N.B. Sivai, and S. Kumaravel, Diffusion Annealing and Laser Surface Alloying with Aluminium to Enhance Oxidation Resistance of Carbon Steels, *Mater. Sci. Technol.*, Vol 17 (No. 10), 2001, p 1249–1252
114. Z. Brytan, L.A. Dobrzański, and K. Pakiel, Sintered Stainless Steel Surface Alloyed with Si₃N₄ Powder, *Arch. Mater. Sci. Eng.*, Vol 50 (No. 1), 2011, p 43–55
115. Q. Li, T.C. Lei, and W.Z. Chen, Microstructural Characterization of Laser-Clad TiC_p-Reinforced Ni-Cr-B-Si-C Composite Coatings on Steel, *Surf. Coat. Technol.*, Vol 114, 1999, p 278–284
116. T.A.M. Haemers, D.G. Rickerby, F. Lanza, F. Geiger, and E.J. Mittemeijer, Hardfacing of Stainless Steel with Laser Melted Colmonoy, *J. Mater. Sci.*, Vol 35, 2000, p 5691–5698
117. R. Cherukuri, M. Womack, P. Molian, A. Russell, and Y. Tian, Pulsed Laser Deposition of AlMgB₁₄ on Carbide Inserts for Metal Cutting, *Surf. Coat. Technol.*, Vol 155, 2002, p 112–120
118. C.-K. Sha and H.-L. Tsai, Hardfacing Characteristics of S42000 Stainless Steel Powder with Added Silicon Nitride Using

- a CO₂ Laser, *Mater. Charact.*, Vol 52, 2004, p 341–348
119. M. Toma, Laser Fusing of Alloy Powders for Applying Hard Facing Layers onto a Mild Steel Substrate, *Damascus Univ. J.*, Vol 21 (No. 2), 2005, p 95–111
 120. W. Xin-hong, Z. Zeng-da, and Q. Shi-yao, Microstructure of Fe-Based Alloy Hardfacing Reinforced by TiC-VC Particles, *J. Iron Steel Res. Int.*, Vol 13, 2006, p 51–55
 121. A. Viswanathan, D. Sastikumara, P. Rajarajana, H. Kumar, and A.K. Nath, Laser Irradiation of AISI 316L Stainless Steel Coated with Si₃N₄ and Ti, *Opt. Laser Technol.*, Vol 39, 2007, p 1504–1513
 122. S.H. Zhang, M.X. Li, T.Y. Cho, J.H. Yoon, C.G. Lee, and Y.Z. He, Laser Clad Ni-Base Alloy Added Nano- and Micron-Size CeO₂ Composites, *Opt. Laser Technol.*, Vol 40, 2008, p 716–722
 123. A. Viswanathan, D. Sastikumara, H. Kumar, and A.K. Nath, Formation of WC-Iron Silicide (Fe₅Si₃) Composite Clad Layer on AISI 316L Stainless Steel by High Power (CO₂) Laser, *Surf. Coat. Technol.*, Vol 203, 2009, p 1618–1623
 124. S. Abdi and S. Lebailli, Alternative to Chromium, A Hard Alloy Powder NiCrBCSi (Fe) Coatings Thermally Sprayed on 60CrMn4 Steel: Phase and Comportements, *Phys. Proced.*, Vol 2, 2009, p 1005–1014
 125. R. Awasth, S. Kumar, D. Srivastava, and G.K. Dey, Solidification and Microstructural Aspects of Laser-Deposited Ni-Mo-Cr-Si Alloy on Stainless Steel, *Indian Acad. Sci.*, Vol 75, 2010, p 1259–1266
 126. M. Shamanian, S.M.R. Mousavi Abarghouie, and S.R. Mousavi Pour, Effects of Surface Alloying on Microstructure and Wear Behavior of Ductile Iron, *Mater. Des.*, Vol 31, 2010, p 2760–2766
 127. R. Lupoi, A. Cockburn, C. Bryan, M. Sparkes, F. Luo, and W. O'Neill, Hardfacing Steel with Nanostructured Coatings of Stellite-6 by Supersonic Laser Deposition, *Light: Sci. Appl.*, Vol 1, 2012
 128. E. Kannatey-Asibu, Jr., Advantages and Disadvantages of Laser Shock Peening, *Principles of Laser Materials Processing*, Wiley, Hoboken, NJ, 2009, p 636
 129. W. Zhang et al., Microscale Laser Shock Peening of Thin Films, Part I: Experiment, Modeling and Simulation, *J. Mater. Sci. Eng.*, Vol 126, 2004, p 10–17
 130. O.G. Kasatkin and B.B. Vinokur, Calculation Models for Determining the Critical Points of Steel, *Met. Sci. Heat Treat.*, Vol 26 (No. 1–2), 1984, p 27–31
 131. J.S. Kirkaldy and D. Venugopalan, in *Phase Transformations in Ferrous Alloys*, D.A.R. Marder and J.I. Goldstein, Ed., AIME, New York, 1983, p 128–148
 132. W. Steven and A.G. Haynes, The Temperature of Formation of Martensite and Bainite in Low Alloy Steels, *J. Iron Steel Inst.*, Vol 183, 1956, p 349–359
 133. C. Hojerslev, *Tool Steels*, Riso National Laboratory, Roskilde, 2001
 134. A. Jablonka, K. Harste, and K. Schwerdtfeger, Thermomechanical Properties of Iron and Iron-Carbon Alloys: Density and Thermal Contraction, *Steel Res.*, Vol 62 (No. 1), 1991, p 24–33
 135. E. Faroozmehr and R. Kovacevic, Thermokinetic Modeling of Phase Transformation in the Laser Powder Deposition Process, *Metall. Mater. Trans. A*, Vol 40, 2009, p 1935–1943
 136. G.E. Totten, *Steel Heat Treatment Handbook: Metallurgy and Technologies*, CRC Taylor & Francis, Oregon, 2006
 137. X.M. Zhang, H.C. Man, and H.D. Li, Wear and Friction Properties of Laser Surface Hardened EN31Steel, *J. Mater. Process. Technol.*, Vol 69 (No. 1), 1997, p 162–165
 138. P.D. la-Cruz, M. Oden, and T. Ericsson, Effect of Laser Hardening on the Fatigue Strength and Fracture of a B-Mn Steel, *Int. J. Fatigue*, Vol 20 (No. 5), 1998, p 389–398
 139. R. Sagaro, J.S. Ceballos, A. Blanco, and J. Mascarell, Tribological Behaviour of Line Hardening of Steel U13A with Nd:YAG Laser, *Wear*, Vol 225–229, 1999, p 575–580
 140. J. Senthil Selvan, K. Subramanian, and A.K. Nath, Effect of Laser Surface Hardening on En18 (AISI 5135) Steel, *J. Mater. Process. Technol.*, Vol 91, 1999, p 29–36
 141. R. Komanduri and Z.B. Hou, Thermal Analysis of the Laser Surface Transformation Hardening Process, *Int. J. Heat Mass Transf.*, Vol 44, 2001, p 2845–2862
 142. M. Heitkemper, A. Fischer, C. Bohneb, and A. Pyzalla, Wear Mechanisms of Laser-Hardened Martensitic High-Nitrogen Steels under Sliding Wear, *Wear*, Vol 250, 2001, p 477–484
 143. R.A. Ganeev, Low-Power Laser Hardening of Steels, *J. Mater. Process. Technol.*, Vol 121, 2002, p 414–419
 144. K.H. Lo, F.T. Cheng, and H.C. Man, Laser Transformation Hardening of AISI 440C Martensitic Stainless Steel for Higher Cavitation Erosion Resistance, *Surf. Coat. Technol.*, Vol 173, 2003, p 96–104
 145. S. Tianmin, H. Meng, and T.H. Yuen, Impact Wear Behavior of Laser Hardened Hypoeutectoid 2Cr13 Martensite Stainless Steel, *Wear*, Vol 255, 2003, p 444–455
 146. M. Heidkamp, O. Kessler, F. Hoffmann, and P. Mayr, Laser Beam Surface Hardening of CVD TiN-Coated Steels, *Surf. Coat. Technol.*, Vol 188–189, 2004, p 294–298
 147. J. Grum and T. Kek, The Influence of Different Conditions of Laser-Beam Interaction in Laser Surface Hardening of Steels, *Thin Solid Films*, Vol 453–454, 2004, p 94–99
 148. R. Kaul, P. Ganesh, P. Tiwari, R.V. Nandedkar, and A.K. Nath, Characterization of Dry Sliding Wear Resistance of Laser Surface Hardened En8 Steel, *J. Mater. Process. Technol.*, Vol 167, 2005, p 83–90
 149. S. Skvarenina and Y.C. Shin, Predictive Modelling and Experimental Results for Laser Hardening of AISI 1536 Steel with Complex Geometric Features by a High Power Diode Laser, *Surf. Coat. Technol.*, Vol 201, 2006, p 2256–2269
 150. A. Basu, J. Chakraborty, S.M. Shariff, G. Padmanabham, S.V. Joshi, G. Sundararajan, J.D. Majumdar, and I. Manna, Laser Surface Hardening of Austempered (Bainitic) Ball Bearing Steel, *Scr. Mater.*, Vol 56, 2007, p 887–890
 151. F. Lusquinos, J.C. Conde, S. Bonss, A. Riveiro, F. Quintero, R. Comesaña, and J. Pou, Theoretical and Experimental Analysis of High Power Diode Laser (HPDL) Hardening of AISI 1045 Steel, *Appl. Surf. Sci.*, Vol 254, 2007, p 948–954
 152. H. Pansar, Relationship between Processing Parameters, Alloy Atom Diffusion Distance and Surface Hardness in Laser Hardening of Tool Steel, *J. Mater. Process. Technol.*, Vol 189, 2007, p 435–440
 153. H.J. Shin, Y.T. Yoo, D.G. Ahn, and K. Im, Laser Surface Hardening of S45C Medium Carbon Steel using ND:YAG Laser with a Continuous Wave, *J. Mater. Process. Technol.*, Vol 187–188, 2007, p 467–470
 154. R.S. Lakhkar, Y.C. Shin, and M.J.M. Crane, Predictive Modelling of Multi-Track Laser Hardening of AISI 4140 Steel, *Mater. Sci. Eng. A*, Vol 480, 2008, p 209–217
 155. N.S. Bailey, W. Tan, and Y.C. Shin, Predictive Modeling and Experimental Results for Residual Stresses in Laser Hardening of AISI 4140 Steel by a High Power Diode Laser, *Surf. Coat. Technol.*, Vol 203, 2009, p 2003–2012
 156. J.H. Lee, J.H. Jang, B.D. Joo, Y.M. Son, and Y.H. Moon, Laser Surface Hardening of AISI H13 Tool Steel, *Trans. Nonferrous Met. Soc. China*, Vol 19, 2009, p 917–920
 157. J. Kim, M. Lee, S. Lee, and W. Kang, Laser Transformation Hardening on Rod-Shaped Carbon Steel by Gaussian Beam, *Trans. Nonferrous Met. Soc. China*, Vol 19, 2009, p 941–945
 158. B. Mahmoudi, M.J. Torkamany, A.R.S.R. Aghdam, and J. Sabbaghzade, Laser Surface Hardening of AISI 420 Stainless Steel Treated by Pulsed Nd:YAG Laser, *Mater. Des.*, Vol 31, 2010, p 2553–2560
 159. G. Tani, L. Orzi, and A. Fortunato, Prediction of Hypoeutectoid Steel Softening due to Tempering Phenomena in Laser

- Surface Hardening, *CIRP Ann., Manuf. Technol.*, Vol 57, 2008, p 209–212
160. M. Pellizzari and M.G. De Flora, Influence of Laser Hardening on the Tribological Properties of Forged Steel for Hot Rolls, *Wear*, Vol 271, 2011, p 2402–2411
 161. J. Jiang, L. Xue, and S. Wang, Discrete Laser Spot Transformation Hardening of AISI O1 Tool Steel Using Pulsed Nd:YAG Laser, *Surf. Coat. Technol.*, Vol 205, 2011, p 5156–5164
 162. S. Santhanakrishnan and R. Kovacevic, Hardness Prediction in Multi-Pass Direct Diode Laser Heat Treatment by On-Line Surface Temperature Monitoring, *J. Mater. Process. Technol.*, Vol 212, 2012, p 2261–2271
 163. E.A. Brandes and G.B. Brook, *Smithells Light Metals Handbook*, Butterworth-Heinemann, Oxford, 1998
 164. T. Abbott, Why Choose Magnesium? *Fourth International Light Metals Technology Conference (LMT 2009)* (Gold Coast, Australia), Trans Tech Publications Ltd., 2009, p 3–6
 165. K. Funatani, Emerging Technology in Surface Modification of Light Metals, *Surf. Coat. Technol.*, Vol 133–134, 2000, p 264–272
 166. N.H. Prasad and R. Balasubramaniam, Influence of Laser Surface Treatment on the Oxidation Behaviour of an Al-Li-Cu Alloy, *J. Mater. Process. Technol.*, Vol 68, 1997, p 117–120
 167. T.M. Yue, C.F. Dong, L.J. Yan, and H.C. Man, The Effect of Laser Surface Treatment on Stress Corrosion Cracking Behaviour of 7075 Aluminium Alloy, *Mater. Lett.*, Vol 58, 2004, p 630–635
 168. R. Akhter, L. Ivanchev, and H.P. Burger, Effect of Pre/Post T6 Heat Treatment on the Mechanical Properties of Laser Welded SSM Cast A356 Aluminium Alloy, *Mater. Sci. Eng. A*, Vol 447, 2007, p 192–196
 169. R. Rechner, I. Jansen, and E. Beyer, Influence on the Strength and Aging Resistance of Aluminium Joints by Laser Pre-Treatment and Surface Modification, *Int. J. Adhes. Adhes.*, Vol 30, 2010, p 595–601
 170. J. Borowski and K. Bartkowiak, Investigation of the Influence of Laser Treatment Parameters on the Properties of the Surface Layer of Aluminum Alloys, *Phys. Proced.*, Vol 5, 2010, p 449–456
 171. G. Fribourg, A. Deschamps, Y. Bréchet, G. Mylonas, G. Labeas, U. Heckenberger, and M. Perez, Microstructure Modifications Induced by a Laser Surface Treatment in an AA7449 Aluminium Alloy, *Mater. Sci. Eng. A*, Vol 528, 2011, p 2736–2747
 172. R. Li, M.G.S. Ferreira, A. Almeida, R. Vilar, K.G. Watkins, M.A. McMahon, and W.M. Steen, Localized Corrosion of Laser Surface Melted 2024-T351 Aluminium Alloy, *Surf. Coat. Technol.*, Vol 81, 1996, p 290–296
 173. T.T. Wong and G.Y. Liang, Effect of Laser Melting Treatment on the Structure and Corrosion Behaviour of Aluminium and Al-Si Alloys, *J. Mater. Process. Technol.*, Vol 63, 1997, p 930–934
 174. P.A. Dearnley, J. Gummersbach, H. Weiss, A.A. Ogwu, and T.J. Davies, The Sliding Wear Resistance and Frictional Characteristics of Surface Modified Aluminium Alloys under Extreme Pressure, *Wear*, Vol 225–229, 1999, p 127–134
 175. P.H. Chong, Z. Liu, P. Skeldon, and G.E. Thompson, Large Area Laser Surface Treatment of Aluminium Alloys for Pitting Corrosion Protection, *Appl. Surf. Sci.*, Vol 208–209, 2003, p 399–404
 176. M.A. Pinto, N. Cheung, M.C. F. Ierardi, and A. Garcia, Microstructural and Hardness Investigation of an Aluminum-Copper Alloy Processed by Laser Surface Melting, *Mater. Charact.*, Vol 50, 2003, p 249–253
 177. W.L. Xu, T.M. Yue, H.C. Man, and C.P. Chan, Laser Surface Melting of Aluminium Alloy 6013 for Improving Pitting Corrosion Fatigue Resistance, *Surf. Coat. Technol.*, Vol 200, 2006, p 5077–5086
 178. F. Viejo, A.E. Coy, F.J. García-García, M.C. Merino, Z. Liu, P. Skeldon, and G.E. Thompson, Enhanced Performance of the AA2050-T8 Aluminium Alloy Following Excimer Laser Surface Melting and Anodising Processes, *Thin Solid Films*, Vol 518, 2010, p 2722–2731
 179. M.M. Pariona, V. Teleginski, K.D. Santos, S. Machado, A.J. Zara, N.K. Zurba, and R. Riva, Yb-Fiber Laser Beam Effects on the Surface Modification of Al-Fe Aerospace Alloy Obtaining Weld Fillet Structures, Low Fine Porosity and Corrosion Resistance, *Surf. Coat. Technol.*, Vol 206, 2012, p 2293–2301
 180. E. Sicard, C. Boulmer-Leborgne, C. Andreazza-Vignolle, P. Andreazza, C. Langlade, and B. Vannes, Excimer Laser Treatment for Aluminium Alloy Mechanical Property Enhancement, *Surf. Coat. Technol.*, Vol 100–101, 1998, p 440–444
 181. F. Fariaut, C. Boulmer-Leborgne, E.L. Menn, T. Sauvage, C. Andreazza-Vignolle, P. Andreazza, and C. Langlade, Excimer Laser Induced Plasma for Aluminium Alloys Surface Carburizing, *Appl. Surf. Sci.*, Vol 186, 2002, p 105–110
 182. Y.K. Zhang, X.R. Zhang, X.D. Wang, S.Y. Zhang, C.Y. Gao, J.Z. Zhou, J.C. Yang, and L. Cai, Elastic Properties Modification in Aluminum Alloy Induced by Laser-Shock Processing, *Mater. Sci. Eng. A*, Vol 297, 2001, p 138–143
 183. U.S. Santana, C.R. Gonzalez, G.G. Rosas, J.L. Ocana, C. Molpeceres, J. Porro, and M. Morales, Wear and Friction of 6061-T6 Aluminum Alloy Treated by Laser Shock Processing, *Wear*, Vol 260, 2006, p 847–854
 184. K. Masaki, Y. Ochi, T. Matsumura, and Y. Sano, Effect of Laser Peening Treatment on High Cycle Fatigue Properties of Degassing-Processed Cast Aluminum Alloy, *Mater. Sci. Eng. A*, Vol 468–470, 2007, p 171–175
 185. O. Hatamleh, J. Lyons, and R. Forman, Laser and Shot Peening Effects on Fatigue Crack Growth in Friction Stir Welded 7075-T7351 Aluminum Alloy Joints, *Int. J. Fatigue*, Vol 29, 2007, p 421–434
 186. K.Y. Luo, J.Z. Lu, L.F. Zhang, J.W. Zhong, H.B. Guan, and X.M. Qian, The Microstructural Mechanism for Mechanical Property of LY2 Aluminum Alloy after Laser Shock Processing, *Mater. Des.*, Vol 31, 2010, p 2599–2603
 187. Y.K. Gao, Improvement of Fatigue Property in 7050-T7451 Aluminum Alloy by Laser Peening and Shot Peening, *Mater. Sci. Eng. A*, Vol 528, 2011, p 3823–3828
 188. B. Rouleau, P. Peyre, J. Breuils, H. Pelletier, T. Baudin, and F. Brisset, Characterization at a Local Scale of a Laser-Shock Peened Aluminum Alloy Surface, *Appl. Surf. Sci.*, Vol 257, 2011, p 7195–7203
 189. H. Krawiec, V. Vignal, H. Amar, and P. Peyre, Local Electrochemical Impedance Spectroscopy Study of the Influence of Aging in Air and Laser Shock Processing on the Micro-Electrochemical Behaviour of AA2050-T8 Aluminium Alloy, *Electrochim. Acta*, Vol 56, 2011, p 9581–9587
 190. X.D. Ren, Y.K. Zhang, H.F. Yongzhuo, L. Ruan, D.W. Jiang, T. Zhang, and K.M. Chen, Effect of Laser Shock Processing on the Fatigue Crack Initiation and Propagation of 7050-T7451 Aluminum Alloy, *Mater. Sci. Eng. A*, Vol 528, 2011, p 2899–2903
 191. S. Sathyajith, S. Kalainathan, and S. Swaroop, Laser Peening without Coating on Aluminium Alloy Al-6061-T6 Using Low Energy Nd:YAG Laser, *Opt. Laser Technol.*, Vol 45, 2013, p 389–394
 192. U. Trdan and J. Grum, Evaluation of Corrosion Resistance of AA6082-T651 Aluminium Alloy after Laser Shock Peening by Means of Cyclic Polarisation and EIS Methods, *Corros. Sci.*, Vol 59, 2012, p 324–333
 193. J. Vázquez, C. Navarro, and J. Domínguez, Experimental Results in Fretting Fatigue with Shot and Laser Peened Al 7075-T651 Specimens, *Int. J. Fatigue*, Vol 40, 2012, p 143–153
 194. F.Z. Dai, J.Z. Lu, Y.K. Zhang, K.Y. Luo, Q.W. Wang, L. Zhang, and X.J. Hua, Effect of Initial Surface Topography on the Surface Status of LY2 Aluminum Alloy Treated by Laser Shock Processing, *Vacuum*, Vol 86, 2012, p 1482–1487

195. L. Lu, T. Huang, and M. Zhong, WC Nano-Particle Surface Injection via Laser Shock Peening onto 5A06 Aluminum Alloy, *Surf. Coat. Technol.*, Vol 206, 2012, p 4525–4530
196. P.H. Chong, H.C. Man, and T.M. Yue, Microstructure and Wear Properties of Laser Surface-Cladded MoWC MMC on AA6061 Aluminum Alloy, *Surf. Coat. Technol.*, Vol 145, 2001, p 51–59
197. E. Brandl, U. Heckenberger, V. Holzinger, and D. Buchbinder, Additive Manufactured AlSi10Mg Samples Using Selective Laser Melting (SLM): Microstructure, High Cycle Fatigue, and Fracture Behaviour, *Mater. Des.*, Vol 34, 2012, p 159–169
198. Y. Li, K.T. Ramesh, and E.S.C. Chin, The Compressive Viscoplastic Response of an A359/SiC_p Metal-Matrix Composite and of the A359 Aluminum Alloy Matrix, *Int. J. Solids Struct.*, Vol 37, 2000, p 7547–7562
199. H.C. Man, C.T. Kwok, and T.M. Yue, Cavitation Erosion and Corrosion Behaviour of Laser Surface Alloyed MMC of SiC and SiN on Al Alloy AA6061, *Surf. Coat. Technol.*, Vol 132, 2000, p 11–20
200. S. Tomida, K. Nakata, S. Saji, and T. Kubo, Formation of Metal Matrix Composite Layer on Aluminium Alloy with TiC-Cu Powder by Laser Surface Alloying Process, *Surf. Coat. Technol.*, Vol 142–144, 2001, p 585–589
201. H.C. Man, S. Zhanga, T.M. Yue, and F.T. Cheng, Laser Surface Alloying of NiCr-SiB on Al6061 Aluminium Alloy, *Surf. Coat. Technol.*, Vol 148, 2001, p 136–142
202. L. Dubourg, H. Pelletier, D. Vaissiere, F. Hlawka, and A. Cornet, Mechanical Characterisation of Laser Surface Alloyed Aluminium-Copper Systems, *Wear*, Vol 253, 2002, p 1077–1085
203. S. Tomida and K. Nakata, Fe-Al Composite Layers on Aluminum Alloy Formed by Laser Surface Alloying with Iron Powder, *Surf. Coat. Technol.*, Vol 174–175, 2003, p 559–563
204. S. Nath, S. Pityana, and J.D. Majumdar, Laser Surface Alloying of Aluminium with WC + Co + NiCr for Improved Wear Resistance, *Surf. Coat. Technol.*, Vol 206, 2012, p 3333–3341
205. S. Dadbakhsh and L. Hao, Effect of Al Alloys on Selective Laser Melting Behaviour and Microstructure of In Situ Formed Particle Reinforced Composites, *J. Alloy. Compd.*, Vol 541, 2012, p 328–334
206. T.M. Yue, A.H. Wang, and H.C. Man, Improvement in the Corrosion Resistance of Magnesium ZK60/Si Composite by Excimer Laser Surface Treatment, *Scr. Mater.*, Vol 38 (No. 2), 1997, p 191–198
207. D. Schippman, A. Weisheit, and B.L. Mordike, Short Pulse Irradiation of Magnesium Based Alloys to Improve Surface Properties, *Surf. Eng.*, Vol 15 (No. 1), 1999, p 23–26
208. A.H. Wang and T.M. Yue, YAG Laser Cladding of an Al-Si Alloy onto an Mg/SiC Composite for the Improvement of Corrosion Resistance, *Compos. Sci. Technol.*, Vol 61, 2001, p 1549–1554
209. D. Dube, M. Fiset, A. Couture, and I. Nakatsugawa, Characterization and Performance of Laser Melted AZ91D and AM60B, *Mater. Sci. Eng. A*, Vol 299 (No. 1), 2001, p 38–45
210. J.D. Majumdar, B.R. Chandra, R. Galun, B.L. Mordike, and I. Manna, Laser Composite Surfacing of a Magnesium Alloy with Silicon Carbide, *Compos. Sci. Technol.*, Vol 63, 2003, p 771–778
211. S. Ignata, P. Sallamand, D. Grevey, and M. Lambertin, Magnesium Alloys (WE43 and ZE41) Characterisation for Laser Applications, *Appl. Surf. Sci.*, Vol 233, 2004, p 382–391
212. G. Abbas, Z. Liu, and P. Skeldon, Corrosion Behaviour of Laser-Melted Magnesium Alloys, *Appl. Surf. Sci.*, Vol 247, 2005, p 347
213. Z. Mei, L.F. Guo, and T.M. Yue, The Effect of Laser Cladding on the Corrosion Resistance of Magnesium ZK60/SiC Composite, *J. Mater. Process. Technol.*, Vol 161, 2005, p 462–466
214. S.Y. Liu, J.D. Hu, Y. Yang, Z.X. Guo, and H.Y. Wang, Microstructure Analysis of Magnesium Alloy Melted by Laser Irradiation, *Appl. Surf. Sci.*, Vol 252, 2005, p 1723–1731
215. A.H. Wang, H.B. Xia, W.Y. Wang, Z.K. Bai, X.C. Zhu, and C.S. Xie, YAG Laser Cladding of Homogenous Coating onto Magnesium Alloy, *Mater. Lett.*, Vol 60, 2006, p 850–853
216. G. Abbas, L. Li, U. Ghazanfar, and Z. Liu, Effect of High Power Diode Laser Surface Melting on Wear Resistance of Magnesium Alloys, *Wear*, Vol 260, 2006, p 175–180
217. Y. Jun, G.P. Sun, H.Y. Wang, S.Q. Jia, and S.S. Jia, Laser (Nd:YAG) Cladding of AZ91D Magnesium Alloys with Al + Si + Al₂O₃, *J. Alloy. Compd.*, Vol 407, 2006, p 201–207
218. Y. Gao, C. Wang, Q. Lin, H. Liu, and M. Yao, Broad-Beam Laser Cladding of Al-Si Alloy Coating on AZ91HP Magnesium Alloy, *Surf. Coat. Technol.*, Vol 201, 2006, p 2701–2706
219. X. Yue and L. Sha, Corrosion Resistance of AZ91D Magnesium Alloy Modified by Rare Earths—Laser Surface Treatment, *J. Rare Earths*, Vol 25, 2007, p 201–203
220. C. Changjun, W. Maocai, W. Dongsheng, J. Red, and L. Yiming, Laser Cladding of Al + Ir Powders on ZM5 Magnesium Base Alloy, *Rare Met.*, Vol 26 (No. 5), 2007, p 420–425
221. T.M. Yue and T. Li, Laser Cladding of Ni/Cu/Al Functionally Graded Coating on Magnesium Substrate, *Surf. Coat. Technol.*, Vol 202, 2008, p 3043–3049
222. A.K. Mondal, S. Kumar, C. Blawert, and N.B. Dahotre, Effect of Laser Surface Treatment on Corrosion and Wear Resistance of ACM720 Mg Alloy, *Surf. Coat. Technol.*, Vol 202, 2008, p 3187–3198
223. P. Volovitch, J.E. Masse, A. Fabre, L. Barrallier, and W. Saikaly, Microstructure and Corrosion Resistance of Magnesium Alloy ZE41 with Laser Surface Cladding by Al-Si Powder, *Surf. Coat. Technol.*, Vol 202, 2008, p 4901–4914
224. Y. Jun, G.P. Sun, and S.S. Jia, Characterization and Wear Resistance of Laser Surface Melting AZ91D Alloy, *J. Alloy. Compd.*, Vol 455, 2008, p 142–147
225. M. Hazra, A.K. Mondal, S. Kumar, C. Blawert, and N.B. Dahotre, Laser Surface Cladding of MRI 153M Magnesium Alloy with (Al + Al₂O₃), *Surf. Coat. Technol.*, Vol 203, 2009, p 2292–2299
226. Y. Yang and H. Wu, Improving the Wear Resistance of AZ91D Magnesium Alloys by Laser Cladding with Al-Si Powders, *Mater. Lett.*, Vol 63, 2009, p 19–21
227. J.D. Majumdar and I. Manna, Mechanical Properties of a Laser-Surface-Alloyed Magnesium-Based Alloy (AZ91) with Nickel, *Scr. Mater.*, Vol 62, 2010, p 579–581
228. W. Khalfaoui, E. Valerio, J.E. Masse, and M. Autraic, Excimer Laser Treatment of ZE41 Magnesium Alloy for Corrosion Resistance and Microhardness Improvement, *Opt. Lasers Eng.*, Vol 48, 2010, p 926–931
229. S. Ha, S.J. Kim, S. Hong, C.D. Yim, D.I. Kim, J. Suh, K.H. Oh, and H.N. Han, Improvement of Ductility in Magnesium Alloy Sheet Using Laser Scanning Treatment, *Mater. Lett.*, Vol 64, 2010, p 425–427
230. B.J. Zheng, X.M. Chen, and J.S. Lian, Microstructure and Wear Property of Laser Cladding Al + SiC Powders on AZ91D Magnesium Alloy, *Opt. Lasers Eng.*, Vol 48, 2010, p 526–532
231. A. Fabre and J.E. Masse, Friction Behavior of Laser Cladding Magnesium Alloy against AISI 52100 Steel, *Tribol. Int.*, Vol 46, 2012, p 247–253
232. R. Paital, A. Bhattacharya, M. Moncayo, Y.H. Ho, K. Mahdak, S. Nag, R. Banerjee, and N.B. Dahotre, Improved Corrosion and Wear Resistance of Mg Alloys via Laser Surface Modification of Al on AZ31B, *Surf. Coat. Technol.*, Vol 206, 2012, p 2308–2315
233. C. Taltavull, B. Torres, A.J. Lopez, P. Rodrigo, E. Otero, and J. Rams, Selective Laser Surface Melting of a Magnesium-Aluminium Alloy, *Mater. Lett.*, Vol 85, 2012, p 98–101

234. C. Langlade, A.B. Vannes, J.M. Krafft, and J.R. Martin, Surface Modification and Tribological Behaviour of Titanium and Titanium Alloys after YAG-Laser Treatments, *Surf. Coat. Technol.*, Vol 100–101, 1998, p 383–387
235. T.M. Yue, J.K. Yu, Z. Mei, and H.C. Man, Excimer Laser Surface Treatment of Ti-6Al-4V Alloy for Corrosion Resistance Enhancement, *Mater. Lett.*, Vol 52, 2002, p 206–212
236. M.C.M. Lucas, L. Lavis, and G. Pillon, Microstructural and Tribological Study of Nd:YAG Laser Treated Titanium Plates, *Tribol. Int.*, Vol 41, 2008, p 985–991
237. D.S. Badkar, K.S. Pandey, and G. Buvashekar, Effects of Laser Phase Transformation Hardening Parameters on Heat Input and Hardened-Bead Profile Quality of Unalloyed Titanium, *Trans. Nonferrous Met. Soc. China*, Vol 20, 2010, p 1078–1091
238. Y. Lu, H.B. Tang, Y.L. Fang, D. Liu, and H.M. Wang, Microstructure Evolution of Sub-Critical Annealed Laser Deposited Ti-6Al-4V Alloy, *Mater. Des.*, Vol 37, 2012, p 56–63
239. B.S. Yilbas, J. Nickel, A. Coban, M. Sami, S.Z. Shuja, and A. Aleem, Laser Melting of Plasma Nitrided Ti-6Al-4V Alloy, *Wear*, Vol 212, 1997, p 140–149
240. M. Grenier, D. Dube, A. Adnot, and M. Fiset, Microstructure and Wear Resistance of CP Titanium Laser Alloyed with a Mixture of Reactive Gases, *Wear*, Vol 210, 1997, p 127–135
241. G.X. Luo, G.Q. Wu, Z. Huang, and Z.J. Ruan, Microstructure Transformations of Laser-Surface-Melted Near-Alpha Titanium Alloy, *Mater. Charact.*, Vol 60, 2009, p 525–529
242. P. Molitor and T. Young, Investigations into the Use of Excimer Laser Irradiation as a Titanium Alloy Surface Treatment in a Metal to Composite Adhesive Bond, *Int. J. Adhes. Adhes.*, Vol 24, 2004, p 127–134
243. I. Watanabe, M. McBride, P. Newton, and K.S. Kurtz, Laser Surface Treatment to Improve Mechanical Properties of Cast Titanium, *Dent. Mater.*, Vol 25, 2009, p 629–633
244. A.P. Quintina, I. Watanabe, E. Watanabe, and C. Bertrand, Microstructure and Mechanical Properties of Surface Treated Cast Titanium with Nd:YAG Laser, *Dent. Mater.*, Vol 28, 2012, p 945–951
245. C. Ziwen, X. Haiying, Z. Shikun, and C. Zhigang, Investigation of Surface Integrity on TC17 Titanium Alloy Treated by Square-Spot Laser Shock Peening, *Chin. J. Aeronaut.*, Vol 25, 2012, p 650–656
246. E. Maawada, Y. Sano, L. Wagner, H.G. Brokmeier, and C. Genzel, Investigation of Laser Shock Peening Effects on Residual Stress State and Fatigue Performance of Titanium Alloys, *Mater. Sci. Eng. A*, Vol 536, 2012, p 82–91
247. Y. Fu and A.W. Batchelor, Laser Nitriding of Pure Titanium with Ni, Cr for Improved Wear Performance, *Wear*, Vol 214, 1998, p 83–90
248. B. Courant, J.J. Hantzpergue, and S. Benayoun, Surface Treatment of Titanium by Laser Irradiation to Improve Resistance to Dry-Sliding Friction, *Wear*, Vol 236, 1999, p 39–46
249. H.M. Wang and Y.F. Liu, Microstructure and Wear Resistance of Laser Clad Ti₅Si₃/NiTi₂ Intermetallic Composite Coating on Titanium Alloy, *Mater. Sci. Eng. A*, Vol 338, 2002, p 126–132
250. W. Wang, M. Wang, Z. Jie, F. Sun, and D. Huang, Research on the Microstructure and Wear Resistance of Titanium Alloy Structural Members Repaired by Laser Cladding, *Opt. Lasers Eng.*, Vol 46, 2008, p 810–816
251. S. Mridha and T.N. Baker, Metal Matrix Composite Layer Formation with 3 m SiC_p Powder on IM1318 Titanium Alloy Surfaces through Laser Treatment, *J. Mater. Process. Technol.*, Vol 63, 1997, p 432–437
252. M.S. Selamat, L.M. Watson, and T.N. Baker, XRD and XPS Studies on Surface MMC Layer of SiC Reinforced Ti-6Al-4V Alloy, *J. Mater. Process. Technol.*, Vol 142, 2003, p 725–737
253. C.K. Sha, J.C. Lin, and H.L. Tsai, The Impact Characteristics of Ti-6Al-4V Plates Hardfacing by Laser Alloying NiAl + ZrO₂ Powder, *J. Mater. Process. Technol.*, Vol 140, 2003, p 197–202
254. L.N. Jian and H.M. Wang, Microstructure and Wear Behaviours of Laser-Clad Cr₁₃Ni₅Si₂-Based Metal-Silicide Coatings on a Titanium Alloy, *Surf. Coat. Technol.*, Vol 192, 2005, p 305–310
255. C.B. Pinzon, Z. Liu, K. Voisey, F.A. Bonilla, P. Skeldon, G.E. Thompson, J. Piekoszewski, and A.G. Chmielewski, Excimer Laser Surface Alloying of Titanium with Nickel and Palladium for Increased Corrosion Resistance, *Corros. Sci.*, Vol 47, 2005, p 1251–1269
256. Y. Xue and H.M. Wang, Microstructure and Wear Properties of Laser Clad TiCo/Ti₂Co Intermetallic Coatings on Titanium Alloy, *Appl. Surf. Sci.*, Vol 243, 2005, p 278–286
257. Y.S. Tian, C.Z. Chen, D.Y. Wang, and T.Q. Lei, Laser Surface Modification of Titanium Alloys—A Review, *Surf. Rev. Lett.*, Vol 12 (No. 1), 2005, p 123–130
258. Y.S. Tian, C.Z. Chen, D.Y. Wang, Q.H. Huo, and T.Q. Lei, Laser Surface Alloying of Pure Titanium with TiN-B-Si-Ni Mixed Powders, *Appl. Surf. Sci.*, Vol 250, 2005, p 223–227
259. P. Chandrasekar, V. Balusamy, K.S. Ravi Chandran, and H. Kumar, Laser Surface Hardening of Titanium-Titanium Boride (Ti-TiB) Metal Matrix Composite, *Scr. Mater.*, Vol 56, 2007, p 641–644
260. Y.S. Tian, Growth Mechanism of the Tubular TiB Crystals In Situ Formed in the Coatings Laser-Borided on Ti-6Al-4V Alloy, *Mater. Lett.*, Vol 64, 2010, p 2483–2486
261. A.F. Saleh, J.H. Abboud, and K.Y. Benyounis, Surface Carburizing of Ti-6Al-4V Alloy by Laser Melting, *Opt. Lasers Eng.*, Vol 48, 2010, p 257–267

SELECTED REFERENCES

- M.F. Asby and K.E. Easterling, The Transformation Hardening of Steel Surfaces by Laser Beams, Part I: Hypoeutectoid Steels, *Acta Metall.*, Vol 32 (No. 11), 1984, p 1935–1948
- K.Y. Benyounis, O.M. Fakron, and J.H. Abboud, Rapid Solidification of M2 High-Speed Steel by Laser Melting, *Mater. Des.*, Vol 30, 2009, p 674–678
- D. Gu, Z. Wang, Y. Shen, Q. Li, and Y. Li, In-Situ TiC Particle Reinforced Ti-Al Matrix Composites: Powder Preparation by Mechanical Alloying and Selective Laser Melting Behavior, *Appl. Surf. Sci.*, Vol 255, 2009, p 9230–9240
- N. Guermazi, K. Elleuch, H.F. Ayedi, V. Fridrici, and P. Kaps, Tribological Behaviour of Pipe Coating in Dry Sliding Contact with Steel, *Mater. Des.*, Vol 30, 2009, p 3094–3104
- Y.V. Ingelgem, I. Vandendael, D.V. Broek, A. Hubin, and J. Vereecken, Influence of Laser Surface Hardening on the Corrosion Resistance of Martensitic Stainless Steel, *Electrochim. Acta*, Vol 52, 2007, p 7796–7801
- J.C. Ion, Laser Transformation Hardening, *Surf. Eng.*, Vol 18, 2002, p 14–31
- S. Kac and J. Kusinski, SEM and TEM Microstructural Investigation of High-Speed Tool Steel after Laser Melting, *Mater. Chem. Phys.*, Vol 81, 2003, p 510–512
- M. Li, Y. Wang, B. Han, W. Zhao, and T. Han, Microstructure and Properties of High Chrome Steel Roller after Laser Surface Melting, *Appl. Surf. Sci.*, Vol 255, 2009, p 7574–7579
- Y. Li, J. Yao, and Y. Liu, Synthesis and Cladding of Al₂O₃ Ceramic Coatings on Steel Substrates by a Laser Controlled Thermite Reaction, *Surf. Coat. Technol.*, Vol 172, 2003, p 57–64
- C. Lin, Y. Wang, Z. Zhang, B. Han, and T. Han, Influence of Overlapping Ratio on Hardness and Residual Stress Distributions in Multi-Track Laser Surface Melting Roller Steel, *Opt. Lasers Eng.*, Vol 48, 2010, p 1224–1230
- J. Majumdar, Laser Heat Treatment: The State of the Art, *J. Met.*, Vol 35, 1983, p 18–26
- K.A. Mumtaz and N. Hopkinson, Selective Laser Melting of Thin Wall Parts Using Pulse Shaping, *J. Mater. Process. Technol.*, Vol 210, 2010, p 279–287

- H. Pantsar and V. Kujanpaa, Effect of Oxide Layer Growth on Diode Laser Beam Transformation Hardening of Steels, *Surf. Coat. Technol.*, Vol 200, 2006, p 2627–2633
- P.S. Peercy et al., *Laser and Electron Beam Interactions with Solids*, North Holland, New York, 1982, p 401–406
- P. Peyre, P. Aubry, R. Fabbro, R. Neveu, and A. Longuet, Analytical and Numerical Modeling of the Direct Metal Deposition Laser Process, *J. Phys. D, Appl. Phys.*, Vol 41, 2008, p 1–10
- R.K. Rao, B. Venkataraman, M.K. Asundi, and G. Sundararajan, The Effect of Laser Surface Melting on the Erosion Behaviour of a Low Alloy Steel, *Surf. Coat. Technol.*, Vol 58, 1993, p 85–92
- A. Röttger, S. Weber, and W. Theisen, Supersolidus Liquid-Phase Sintering of Ultrahigh-Boron High-Carbon Steels for Wear-Protection Applications, *Mater. Sci. Eng. A*, Vol 532, 2012, p 511–521
- M.J. Tobar, C. Álvarez, J.M. Amado, A. Ramil, E. Saavedra, and A. Yáñez, Laser Transformation Hardening of a Tool Steel: Simulation-Based Parameter Optimization and Experimental Results, *Surf. Coat. Technol.*, Vol 200, 2006, p 6362–6367
- J.W. Xie, P. Fox, W. O'Neill, and C.J. Sutcliffe, Effect of Direct Laser Re-Melting Processing Parameters and Scanning Strategies on the Densification of Tool Steels, *J. Mater. Process. Technol.*, Vol 170, 2005, p 516–523
- C. Yan, L. Hao, A. Hussein, and D. Raymond, Evaluations of Cellular Lattice Structures Manufactured Using Selective Laser Melting, *Int. J. Mach Tools Manuf.*, Vol 62, 2012, p 32–38
- E. Yasa and J.-P. Kruth, Microstructural Investigation of Selective Laser Melting 316L Stainless Steel Parts Exposed to Laser Re-Melting, *Proced. Eng.*, Vol 19, 2011, p 389–395
- B.S. Yilbas, Theoretical and Experimental Investigation Melting of Steel Samples, *Opt. Lasers Eng.*, Vol 21, 1997, p 297–307
- H.G. Prengel, W.R. Pfouts, and A.T. Santhanam, State of the Art in Hand Coatings for Carbide Cutting Tools, *Surf. Coat. Technol.*, Vol 102, 1998, p 183–190

Carburizing and Carbonitriding of Steels

Introduction to Carburizing and Carbonitriding	505	Carbon Gradients	571
Introduction	505	Hardness Gradients	571
History	505	Process Control	571
General Process Description	506	Control of Case Depth	572
How to Carburize	509	Dimensional Changes	574
Basic Carburizing Reactions	510	Quenching Media	574
Advantages and Limitations	512	Salt Removal (Washing)	575
Carburizing Steels	514	Typical Applications	576
Quality Assurance	514	Precautions in the Use of Cyanide Salts	577
Possible Complications	516	Disposal of Cyanide Wastes	578
Methods of Carburizing and Carbonitriding	518		
Evaluation of Carbon Control in Carburized Parts	522	Low-Pressure Carburizing	581
Hardness Testing	522	Process	581
Microscopic Examination	522	Physical Principles	582
Analysis of Consecutive Cuts	523	Equipment for Low-Pressure Carburizing	583
Analysis of Shim Stock	524	Carburizing Strategies	584
Analysis of Rolled Wire	526	Prediction of Carbon Profiles	585
Spectrographic Analysis	526	Applications	586
Electromagnetic Testing	527	Quality Control of the LPC Process in Mass Production	587
		High-Temperature LPC	587
Gas Carburizing	528	Plasma Carburizing	591
Thermodynamics and Kinetics	528	Principles of Plasma Carburizing	591
Carbon Sources and Atmosphere Types	532	Carburizing Reaction in Plasma Carburizing	593
Carbon-Transfer Mechanism	535	Advantages and Disadvantages	594
Carburizing Modeling and Case Depth Prediction	536	Production Equipment	595
Carburizing Equipment	538	Application Example	596
Furnace Temperature and Atmosphere Control	540		
Carburizing Cycle Development	544	Carbonitriding of Steels	599
Process Planning	547	Process Description	600
Dimensional Control	555	Case Composition	601
Case Depth Evaluation	556	Depth of Case	603
		Case-Depth Uniformity	603
Pack Carburizing	560	Hardenability of Case	604
Introduction	560	Hardness Gradients	605
Advantages and Disadvantages	560	Void Formation	605
Carburizing Medium and Compounds	561	Control of Retained Austenite	605
Process Control	562	Furnace Atmospheres	606
Furnaces for Pack Carburizing	562	Temperature Selection	609
Carburizing Containers	563	Quenching Media and Practices	610
Packing	564	Tempering	611
		Hardness Testing	612
Liquid Carburizing and Cyaniding of Steels	565	Applications	613
Cyanide-Containing Liquid Carburizing Baths	565	Carbonitriding of Powder Metallurgy Parts	614
Cyaniding (Liquid Carbonitriding)	566	Ammonia Guidelines	614
Noncyanide Liquid Carburizing	567		

Introduction to Carburizing and Carbonitriding

Allen J. Fuller, Jr., Amsted Rail Company, Inc.

Introduction

There are many occasions when it is beneficial for a component to have the strength and wear resistance of a high-carbon steel on the outside while simultaneously possessing the toughness and ductility of a low-carbon steel in its center. A heat treating solution to provide such a composite was discovered centuries ago. This process has been known by many names, including cementation and later as case hardening. *Carburization* is the modern term used to describe the variety of processes that produce this case/core composite.

Carburization is the process of intentionally increasing the carbon content of a steel surface so that a hardened case can be produced by martensitic transformation during quenching. The steel is heated above the upper critical temperature (Ac_1), and carbon is introduced into the austenite phase as a solid solution. It is necessary that the steel be austenitized, because the solubility (and also, consequently, the diffusivity) of carbon in ferrite is very low compared to that of austenite. The carbon at the surface is then allowed to diffuse into the steel, so that a sufficient carbon profile or gradient is achieved below the surface. After a sufficient carbon profile is achieved, the steel is then quenched for transformation (martensitic) hardening of the high-carbon case.

Carburization has the ability to produce mechanical properties in steel that are markedly superior to those obtained from other methods of heat treatment, such as through hardening. Carburizing is particularly competitive in situations where fatigue resistance (especially bending, torsion, and rolling contact) is important. The primary characteristic that distinguishes a carburized component from one that is through hardened is the carbon profile or gradient. Through-hardened steels have uniform carbon content throughout the cross section of the component, whereas a carburized part has a higher carbon concentration at the surface that tapers down to the base carbon content of the steel at its core. It is this gradient that

gives a carburized component its beneficial properties.

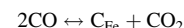
The unique properties of a carburized component are made possible by a combination of material properties (strength and hardness) that vary as a function of depth from the surface. These properties are the result of the complex interaction between the carbon content and the cooling rate. Because both the carbon content and the cooling rate vary across the section of a carburized component, different microstructures and properties are produced at different depths. The result is a component that delivers its greatest strength at the surface, where it is most effective. This has significant implications in terms of fatigue strength, because fatigue cracks typically originate at or near the surface of stressed components.

A closely related process is carbonitriding. Like carburizing, carbonitriding involves heating above the upper critical temperature (Ac_1) to austenitize the steel. In carbonitriding, however, both nascent (atomic) nitrogen and atomic carbon are added to the surface in solid solution with austenite. Nitrogen is a powerful austenite stabilizer, thus facilitating the formation of a solid solution with carbon in austenite. Nitrogen also speeds the rate of carbon diffusion. Like carburizing, case hardening is achieved by martensitic transformation during quenching. Because nitrogen is a powerful austenite stabilizer, the upper critical temperature (Ac_1) for any given steel is lower with nitrogen, thus allowing for lower transformation temperatures during carbonitriding as compared to carburizing. Nitrogen also increases the hardenability of the case so that many plain low-carbon steels respond to carbonitriding and oil quenching that would not ordinarily harden after being carburized and oil quenched.

This article introduces the basic fundamentals of carburizing, its advantages and limitations, and the methods of carburizing. Carbonitriding, as a method similar to carburizing but with important distinctions, is briefly compared to carburizing in the section “Methods of Carburizing and Carbonitriding” in this article. More details are in the article “Carbonitriding of Steels” in this Volume.

History

The origins of carburization have been lost to history, but it is believed that the first carburized tools were produced unintentionally as a result of making tools out of nonhomogeneous bloom iron. Archaeologists have found carburized implements dating over 3000 years old in western Turkey. It seems likely that early iron workers discovered that when they heated iron in hot coals for an extended period of time, the iron would become stronger than usual, even to the point of being competitive with the then state-of-the-art bronze tools being manufactured by their competitors. As iron workers sought to soften iron in forges in preparation for forming, they unknowingly heated the iron above its critical temperature (Ac_1). This resulted in two important conditions being satisfied simultaneously: 1) The iron was transformed from ferrite (α -iron) to austenite (γ -iron); 2) the combustion gases of the charcoal fuel in the forge shifted from CO_2 to CO as a result of the Boudouard reaction. The solubility of carbon in austenite is much higher than that of ferrite, and the carbon monoxide gas provided plenty of carbon for diffusion by means of the following reaction:



The elevated temperature necessary to transform the ferritic iron into austenite also increases the rate of diffusion, such that carbon diffuses into the iron at a significant rate, creating a new and extremely important material—steel. Under the proper conditions, the carbon content can increase to the point that the steel becomes hardenable. The discovery of cementation in the production of steel and tools is credited by some historians for helping to advance the Iron Age.

Carburization became an important process and found widespread use throughout the 1800s. During this period, carburization was performed by surrounding the part to be carburized with a carbonaceous material, such as

charred leather, ground animal bones, or wood charcoal. These materials were then sealed in an iron box that was heated to a temperature above the A_{c1} temperature and held for sufficient time to achieve the desired case, typically 2 to 6 h. The box would then be cooled and the part removed and hardened in a separate heat treatment. This technique became known as pack carburization.

Scientists began to understand that it was the decomposition of the carbonaceous materials into carbon monoxide, and not direct contact with the solid carbon, that made carburization possible. This realization presented the possibility of developing gaseous carburizing atmospheres that could replace solid carbon sources altogether. In the early 1900s, experiments with gaseous atmospheres for carburization were being conducted. Gas carburizing was found to show great promise, but the furnace technology at that time was not yet sufficiently advanced to permit the use of gas carburizing on a commercial scale. Because of these limitations, pack carburization would remain the leading method of production until World War II. During this period, the heat treater remained limited to establishing the process by trial and error at that time because there was little available in terms of predictive calculations.

During World War II—undoubtedly in response to the increased demand for armaments and bolstered by advancements in furnace design and manufacture—gas carburizing began to take over as the dominant method of manufacture.

In 1943, F.E. Harris published equations that revolutionized how the industry understood the process of carburization. His approach provided a powerful quantitative tool for predicting the outcome when carburizing at saturation levels in austenite. Harris demonstrated that the (total) case depth could be calculated by the following relationship:

$$D = 802.6 \frac{\sqrt{t}}{10^{(3720/T)}}$$

where D is the total case depth (millimeters), t is time at temperature (hours), and T is the absolute temperature (Kelvin).

Harris' work formed the foundation for continued advances in quantitative carburizing that has greatly improved the understanding of this commercially important process. Although the Harris equation applies to carburizing at saturation levels in austenite (which applies in the case of the pack carburizing), it also provides an important conceptual foundation in understanding the control of carburization at conditions below saturation (as in gas carburizing).

General Process Description

The primary object of carburizing is to provide a hard, wear-resistant surface with surface residual compressive stresses that improve the

useful life of components. The steel is austenitized and brought into contact with an environment of sufficient carbon potential to cause absorption of carbon at the surface and, by diffusion, to create a carbon concentration gradient between the surface and the interior of the metal. The objective is to increase the carbon content at the surface from that of the base alloy (typically 0.2%) to between 0.8 and 1.1%.

Two factors may control the rate of carburizing: the carbon-absorption reaction at the surface and the diffusion of carbon into the metal. Carburizing generally is done at temperatures in the range of 850 to 950 °C (1550 to 1750 °F). However, temperatures as low as 790 °C (1450 °F) and as high as 1100 °C (2010 °F) have been used. Although the carburizing rate can be greatly increased at temperatures above approximately 950 °C (1750 °F), the service life of most furnace equipment is degraded by operation at higher temperatures. This serves to limit the carburizing temperature at which processes can be operated economically.

Carbon Gradient. The gradient of carbon content between the surface and the center is the signature feature of a carburized component. The high-carbon layer at the surface is known as the case, and the low-carbon center is known as the core. The methods for the measurement of case depth are described later. A representative carbon concentration gradient for a carburized component appears in Fig. 1. Note how the hardness profile follows the carbon profile. The profile for a particular component will depend on the specific process parameters, including the desired surface carbon and the desired case depth.

Martensite Start Temperature. Carbon content has a powerful effect on the martensite start (M_s) temperature of steel, and this in turn

is a significant contributor to the unique properties of a carburized component. Figure 2 shows the effect of carbon content on the M_s temperature as well as the corresponding microstructure and retained austenite levels. The inverse relationship between carbon content and M_s temperature results in suppression of the M_s temperature at the surface of a carburized component.

In components made from through-hardened steels, the carbon content is uniform throughout the cross section. During quenching, the martensitic transformation begins at the surface and progresses inward as conduction reduces the temperature of successive layers. The center transforms last.

In a carburized component, the higher carbon content at the surface decreases the M_s temperature. During quenching, the surface begins cooling, but because of the lower M_s temperature, the surface does not begin to transform immediately. As heat flows out of the component by conduction, the temperature profile crosses the M_s temperature profile at a point below the surface, and martensite begins to form while the surface remains austenitic. The result is that the martensitic transformation does not begin at the surface, as one might expect, but rather at a depth below the surface. Soon thereafter, the surface drops below its M_s temperature and transforms to martensite. This “inside-out” hardening has a profound effect on the residual-stress profile of a carburized component.

Beneficial Residual-Stress Profile. The key to the success of carburized components is the suppression of M_s , as discussed in the previous section. As the layer of steel beneath the surface transforms into martensite, it expands as a result of the crystallographic change associated with the austenite-to-martensite

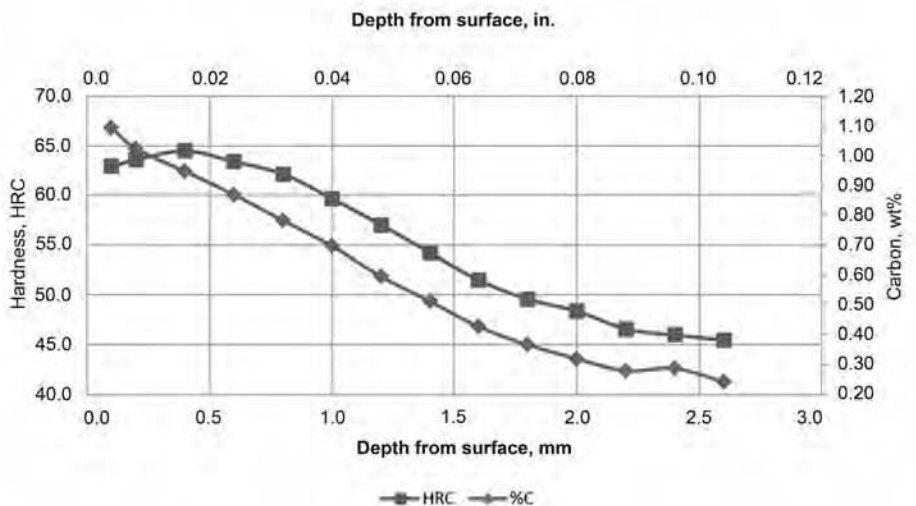


Fig. 1 Representative carbon profile on an AISI 8620 steel rod of approximately 25 mm (1 in.) diameter after carburizing at 950 °C (1750 °F) for 12 h in an enriched endothermic atmosphere. The rod was subsequently austenitized at 850 °C (1560 °F) and oil quenched, untempered. Courtesy of Amsted Rail Brenco

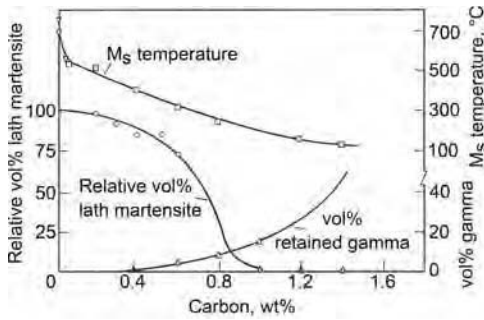


Fig. 2 Effect of carbon content in iron-carbon alloys on the martensite start (M_s) temperature, the relative proportions of lath and plate martensite, and the volume percent retained austenite. Source: Ref 1

transformation. Martensite formation results in an increase of both hardness and strength. Moments later, when the surface (with its lower M_s) transforms, it similarly tries to expand. However, because the surface is constrained by the volume underneath that has already transformed, expansion is inhibited. This causes the surface to enter a state of residual compression. Because all static components must be in balance, the surface compressive residual stress is balanced by a tensile stress at the core of the component (Fig. 3a). If a bending load is applied to the component, the applied stresses will match the profile given in Fig. 3(b). Note that the greatest magnitude of applied stress is realized at the surface of the component, while the stress drops to zero at the center. If a component with a compressive residual stress such as that in Fig. 3(a) is loaded as in Fig. 3(b), then the resulting stress profile will look like that in Fig. 3(c).

The resulting compressive residual stresses at the surface serve to arithmetically reduce the magnitude of an applied stress on the component. A component with a compressive residual stress at the surface can support a load higher than its material properties would otherwise allow. This phenomenon has the effect of increasing the practical load-carrying capacity of the component (Fig. 3c). The same principle of overcoming applied tensile stress with residual compression is used in prestressed concrete beams. Through-hardened steels do not readily produce this type of residual-stress profile. If a through-hardened component and a carburized component are compared in the same application and both have the same hardness, the carburized component will generally support a greater load before yielding. Alternatively, the use of carburization could allow a smaller, lighter component to replace a larger, heavier one made of through-hardening steel while supporting an equivalent load.

The benefit of surface compressive residual stresses applies not only to static loading but to fatigue loading. As can be seen in Fig. 4, the fatigue limit of rollers in pure rolling is much higher for the carburized steel than for the alternative processes. This is a direct result

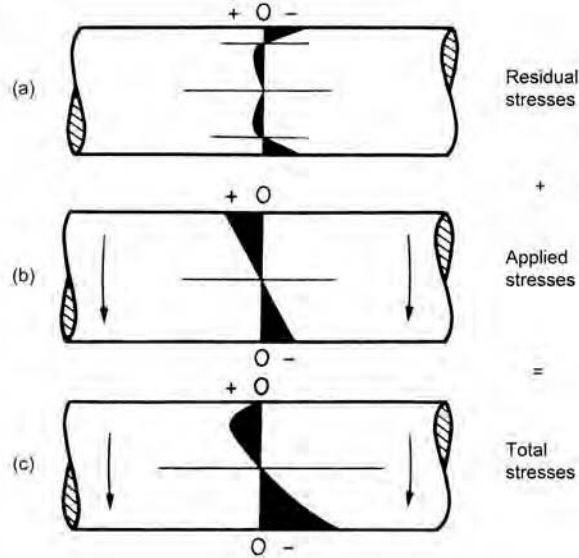


Fig. 3 Illustration showing how residual stresses associated with a carburized surface reduce the effect of surface stress due to an applied load. Source: Ref 1

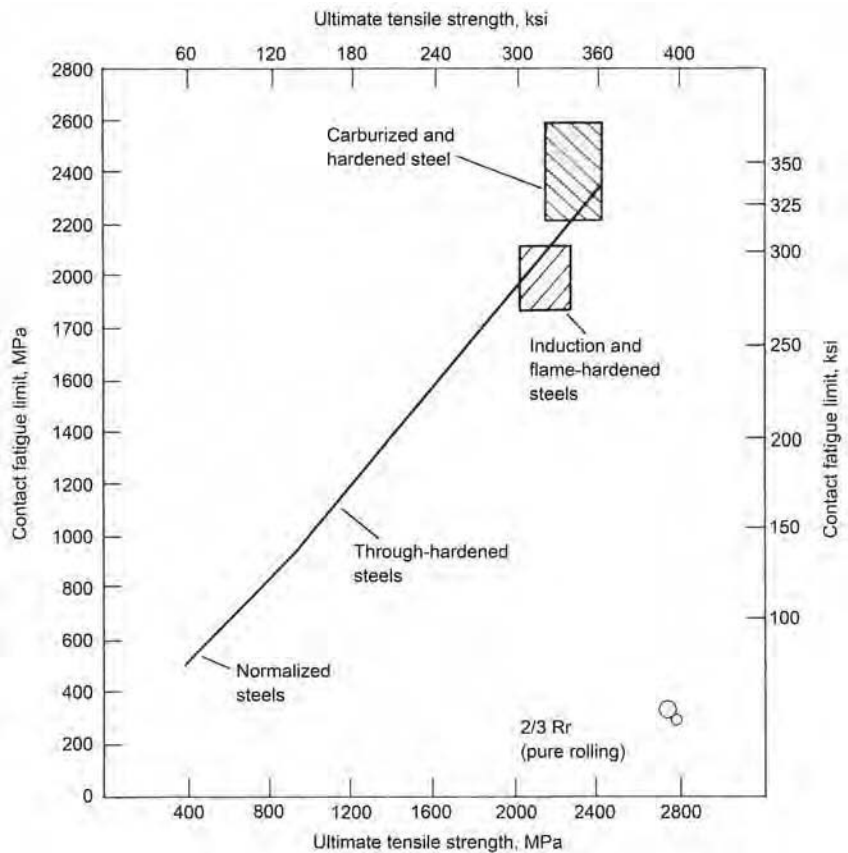


Fig. 4 Rolling contact fatigue test results. Test material run against a case-hardened surface. Deep cases used on all surface-hardened discs or rollers. Source: Ref 1

of the compressive residual-stress profile that carburizing produces.

Strength and Hardness. While the carbon profile serves to create a beneficial residual-stress profile, it also serves to produce substantial changes in the mechanical properties. Figure 5 shows the relationship between carbon content and hardness for various microstructures. From this diagram, it can be seen that the hardness of martensite increases dramatically up to approximately 0.7% C, at which point the hardness begins to plateau. In a carburized component, the surface carbon is typically greater than 0.7%, so the hardness will be highest near the surface and then decrease with depth. The gradient in hardness is due to a combination of decreasing carbon content and cooling rates from the quench. The effective cooling rate at each position is determined by its distance from the surface, with positions closer to the surface seeing a more rapid quench and deeper positions seeing a progressively slower effective quench rate. The achieved strength and hardness at each point on the profile is a function of both position and carbon content.

It is worth noting that the highest hardness in a carburized component is often just below the surface (Fig. 1). This seemingly contradictory behavior is typically due to the influence of higher carbon and thus higher retained austenite levels at the surface. Austenite is softer than martensite, so when it is present in sufficient proportions, it has the effect of reducing the overall hardness. This effect tends to be rather shallow.

The relationship between tensile strength and bending fatigue is illustrated in Fig. 6. Because of the relationship between hardness and tensile strength, it can be seen that the bending fatigue strength of a carburized component will be highest at the surface, where fatigue cracks usually initiate. Carburized components match the strength and hardness of through-hardened steels, so they would be expected to exhibit similar fatigue life. However, while both carburized and through-hardened components benefit from the relationship between hardness and tensile strength, carburized components are unique in that they derive additional fatigue strength from the presence of compressive residual stresses at the surface.

Design Considerations. When designing a carburized component, there are numerous variables that can be controlled to suit a particular application. Such variables include surface carbon content, surface hardness, case microstructure, case depth (either effective or total), core strength, and hardness. Some applications may even specify the level of surface retained austenite and residual stress.

The most important consideration is what case depth is required. The case depth has implications both for the cost of the component (due to energy consumption and processing time) and the load-carrying capacity of the

finished part. The choice of what case depth to use is often based on experience with similar applications. However, such a method is subject to error because it could either specify a deeper case than necessary, wasting resources and increasing cost, or it could fail to account for differing operating conditions and loads, which

could result in a case too shallow to adequately support the required loads. A thorough design approach must consider the loads that are anticipated in service and then match the case depth to these loads. Table 1 provides a general comparison of case depths for different application conditions.

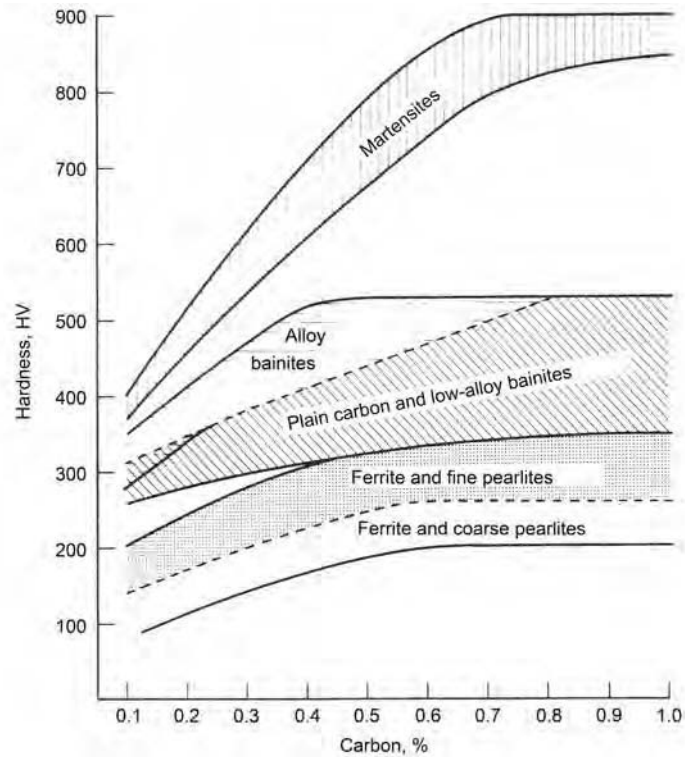


Fig. 5 Effect of carbon on the hardness of various microstructures observed in plain carbon and low-alloy steels. Source: Ref 1

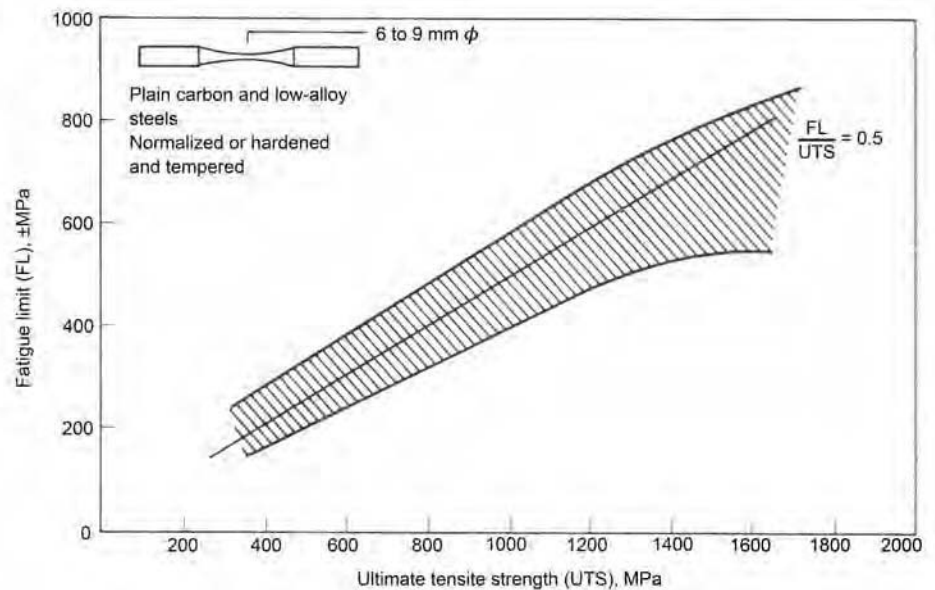


Fig. 6 Relationship between rotating-bending fatigue limit and tensile strength for through-hardened steels. Source: Ref 1

It is important to remember that the ultimate tensile strength of the carburized case changes with the hardness at each depth on the carbon profile. This gives the designer a unique opportunity to customize the strength of the component to the application.

As an example of how to design a component for a specific application, consider a component intended for a contact application such as a gear or roller bearing. For contact applications, it has been proposed that the principal failure mode occurs where the shear stresses experienced by a component exceed the shear fatigue limit at any given depth below the surface of the component (Fig. 7).

The first step is to determine the shear stress profile that the component will experience under the anticipated service loads. This can be done with mathematical models such as those proposed by Hertz and Stribeck. Computer models such as finite-element analysis

have also been used to estimate the maximum shear stresses for certain applications. Once the shear stress profile is known, it is then possible to work backward to the desired hardness profile by determining the shear fatigue strength required to counter the applied shear stress at each point along the stress profile. Then, by using the relationship between shear fatigue strength, ultimate tensile strength (shear fatigue strength $\approx 0.31 \times$ Ultimate tensile strength), and hardness, it is possible to translate the applied shear stresses into a hardness value necessary to match that stress. By employing an appropriate factor of safety, the necessary hardness profile (and therefore case depth) to adequately support the applied shear stress can be determined.

How to Carburize

It is possible to create the conditions necessary for carburization through a wide variety of methods and equipment types, but all carburizing processes have the following characteristics in common.

Low-Carbon Base Steel. Steels for carburization typically have a carbon content ranging from 0.15 to 0.30%. The most common carbon content is approximately 0.2%, although occasionally steels with a carbon content as high as 0.50% are used for special applications. Carburizing steels can be plain carbon or low-alloy steels. They provide the substrate for the carburizing process as well as the material that will provide the core properties.

Carbon-Rich Source. This will contribute the carbon for diffusion into the surface of the low-carbon base steel. A variety of carbon-containing materials may be used. The carbon can be delivered as a solid, liquid, or gas. Historically, everything from charred animal bones to natural gas and methanol has been used.

Gaseous media are the most commercially viable and constitute the bulk of the carburizing capacity in the world, although solid and liquid media are still used in special circumstances.

Heat. Carburization requires that the steel be able to accept carbon into its crystallographic structure. This is facilitated by the fact that the interstitial spaces available in the austenite unit cell are larger than those in the ferrite unit cell. These larger interstitial spaces make carbon significantly more soluble in austenite than in ferrite. To make carburization possible, the process must take place at a temperature above the Ac_1 temperature. Conveniently, carburization is a diffusion-based process, so the temperature required to transform the component to an austenitic structure also provides the necessary driving force to facilitate the diffusion of carbon from the medium into the steel in a commercially viable timeframe. The speed at which carbon diffuses into the surface is proportional to the temperature, so it is possible and often economically beneficial to operate the carburization process at the highest possible temperature in order to minimize processing time by increasing the diffusion rate. It is important to consider that the savings found in higher processing temperatures must be weighed against the increased cost of equipment maintenance.

Container. In most cases, the container will be a furnace with burners or elements to introduce heat energy, and inlets for the carbonaceous medium to enter and blanket the workpiece. The container (or vessel) must include some method of placing the workpiece and medium in intimate contact during the heating process. This container serves several functions: to prevent loss of the medium and to insulate the process to prevent excessive loss of energy. The container will also serve to isolate the surface of the workpiece from undesirable substances that can impede or reverse the carburization reaction, such as oxygen. Anything can serve the role of container if it performs these functions. Examples of common carburizing containers are provided in Table 2.

Time. Carburization is a diffusion-based process, so time is required to effect the changes in carbon concentration necessary to achieve the desired properties. The length of time required will depend on many factors, including the desired depth of the high-carbon layer (known as the case depth) and the maximum temperature available (based on limitations of the container and energy source). For economic reasons, it is usually desirable to have the

Table 1 Typical range of case depths for carburized parts in general areas of applications

Application	Case depth	
	μm	in.
High wear resistance, low-to-moderate loading. Small and delicate machine parts subject to wear	≤ 500	≤ 0.020
High wear resistance, moderate-to-heavy loading. Light industrial gearing	500–1000	0.020–0.040
High wear resistance, heavy loading, crushing loads, or high-magnitude alternating bending stresses. Heavy-duty industrial gearing	1000–1500	0.040–0.060
Bearing surfaces, mill gearing, and rollers	1500–6350	0.060–0.250

Source: Ref 2

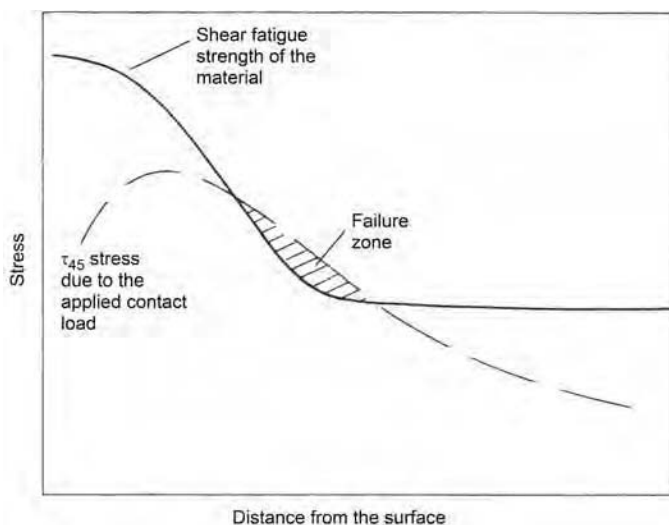


Fig. 7 Strength versus stress considerations for the crushing of a carburized case. Based on Sharma et al.'s explanation. Source: Ref 1

Table 2 Types of carburizing containers

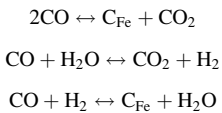
Carburizing method	Container
Pack	Metal box
Liquid (molten salt)	The liquid salt itself serves to deliver the carbon and isolate the component from oxygen.
Gas/atmosphere	Furnace shell, positive pressure
Vacuum	Furnace shell, low pressure

processing time as short as possible. This can be accomplished by increasing the process temperature, but this approach requires consideration of reduced equipment service life and increased maintenance costs, as well as possible undesirable effects on the component such as increased surface oxidation and grain growth. Usually, a compromise temperature is used that provides a reasonable balance between processing time and other factors.

Basic Carburizing Reactions

There are certain chemical reactions that are common to all carburizing methods. Carburization is a complex process where multiple reactions occur simultaneously. These reactions control the delivery (carburization) or removal (decarburization) of carbon from the surface and the oxidation or reduction of steel. The success or failure of the process depends on ensuring that the reactions are driven in the intended direction until the desired surface equilibrium and case depth are reached. Reactions and mass transfer take place in four distinct zones: the medium, the boundary layer, the surface, and within the steel. This is represented graphically in Fig. 8.

When considering generic carburizing, the following reactions are involved:



These reactions control the balance of carbon monoxide, carbon dioxide, and water vapor. The first equation is of particular utility in controlling the carburization process. The second equation, known as the water-gas reaction and in combination with the first equation, describes the relationship between carbon potential and water content at the boundary layer/iron interface.

Diffusion and the Effects of Time and Temperature. Because carburization is a diffusion-dependent process, it is worthwhile to look at the basic concepts that describe the behavior of carbon diffusion in steel. Quantitative work in diffusion became possible in 1855 when Adolf Fick introduced of a formula to describe the “flux” of gases from a region of high concentration to one of low concentration. In a single dimension, this equation, which became known as Ficks’ First Law, is written as:

$$J = -D \left(\frac{dc}{dx} \right)$$

where *J* is the diffusion flux or rate of diffusion per unit area, *D* is the diffusion coefficient of carbon in steel, and (*dc/dx*) is the concentration gradient (carbon with respect to distance). This equation assumes that the rate of transfer is proportional to the concentration gradient as measured perpendicular to the surface in question.

Basic diffusion takes place wherever there is a concentration gradient. In the case of carburization, the concentration gradient of concern is that of carbon. In carburization, the required gradient is created through the use of a low-carbon steel and a high-carbon medium. By placing the two in intimate contact at a suitable temperature, the conditions necessary to allow transfer of carbon from the medium (liquid, solid, or gas) into the workpiece are created. The speed of carbon diffusion in steel is greatly influenced both by temperature and the magnitude of the concentration gradient.

Given sufficient time, carbon will continue to transfer from the medium into the steel until equilibrium is achieved and the concentration is equal throughout the steel and the medium. Through carburization is not commonly practiced for commercial components, but this technique does have application in shim stock analysis, which is discussed later.

Increasing the rate of diffusion by maximizing the carbon gradient is exploited in the

“boost-diffuse” technique, where a higher carbon potential is used early in the process (boost phase) and reduced to a lower carbon potential in the latter half of the process (diffuse phase). Boost-diffuse has been shown to reduce the overall time required to achieve a particular case depth when compared to single-step carburization, where the carbon potential is held constant throughout the process.

To predict the effects of carburization, one must first determine the value for the diffusivity of carbon in austenite. Numerous formulas for this value have been proposed (Ref 3). The formula for a particular process and material is used from best fit with the empirical experience. There are two main approaches to calculating diffusivity of carbon in austenite. One approach is to consider only the effect of temperature; the other is to consider the combined influences of temperature and carbon content. First, a temperature-dependent diffusivity (*D_T*) is considered:

$$D_T = 0.162 \exp \left(\frac{-137,800}{RT} \right) \tag{Eq 1}$$

where *D_T* is the diffusivity of carbon in austenite (cm²/s), *R* is the ideal gas constant (8.31 J/mol · K), and *T* is the absolute temperature (Kelvin).

Values for Eq 1 are plotted in Fig. 9. It is evident from Fig. 9 that the diffusivity of carbon in austenite increases with temperature. It is this relationship that is exploited during the carburizing process and why it is beneficial to use the highest possible carburizing temperature in production.

D_T is useful for estimations, but it is understood that the diffusivity of carbon in austenite is also highly affected by the carbon concentration of the steel. This makes using a temperature- and carbon-content-dependent diffusivity, *D_(C,T)*, a more realistic approach.

Like *D_T*, there are many *D_(C,T)* formulas available to choose from. A commonly used formula for *D_(C,T)* is:

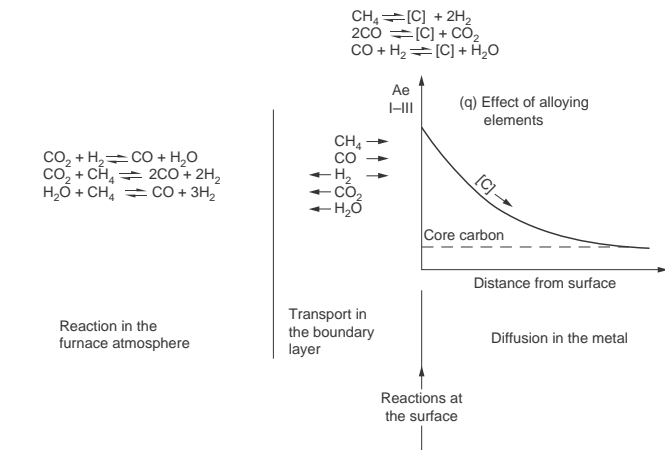


Fig. 8 Schematic representation of the various steps in the gas carburizing process. This diagram is specific for gas carburizing. Source: Ref 1

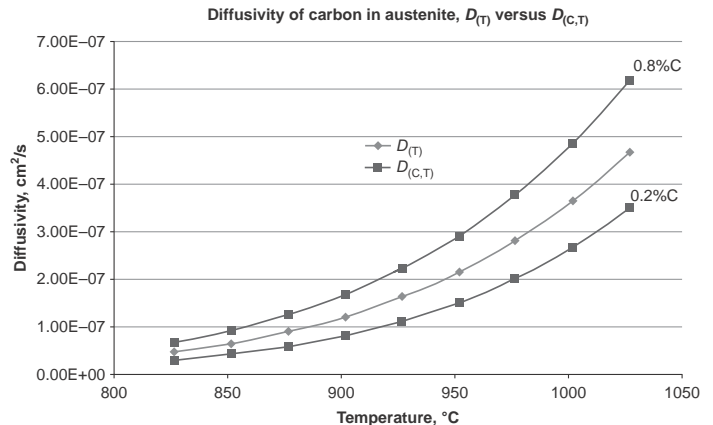


Fig. 9 Comparison of *D_T* and *D_(C,T)* at 0.2 and 0.8 wt% C. Because *D_T* is independent of carbon content, it is the same for both 0.2 and 0.8 %.

$$D_{(C,T)} = 0.47 \exp\left(-1.6 \times C - \frac{37,000 - 6,600C}{RT}\right) \quad (\text{Eq 2})$$

where $D_{(C,T)}$ is the carbon- and temperature-dependent diffusivity of carbon in austenite (cm^2/s), C is the carbon content (weight percent), R is the ideal gas constant ($1.99 \text{ cal/mol} \cdot \text{K}$), and T is the absolute temperature (Kelvin).

Because the values of Eq 2 are a function of both temperature and carbon content, a comparison between D_T and $D_{(C,T)}$ at two different carbon levels (0.2 and 0.8%) is shown graphically in Fig. 9. Note that D_T is greater than $D_{(C,T)}$ at lower carbon concentrations, but that as the carbon content increases, this relationship is reversed and the $D_{(C,T)}$ diffusivity of carbon in austenite is higher. It is this behavior that is exploited during boost-diffuse carburization.

Once a method of calculating diffusivity has been chosen, a useful formula for estimating the carbon profile resulting from the carburization process can be derived from Fick's Second Law and appears as:

$$C_{(x,t)} = C_s \left[1 - \left(1 - \frac{C_i}{C_s} \right) \text{erf} \left(\frac{x}{2\sqrt{Dt}} \right) \right]$$

where $C_{(x,t)}$ is the carbon content in weight percent at a depth x and time, t ; C_s is the carbon content in weight percent at the surface; C_i is the carbon content in weight percent of the base material; x is the depth (centimeters); t is the time (seconds); D is the diffusivity of carbon in austenite (cm^2/s); and erf is the error function of the argument.

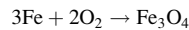
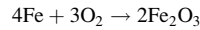
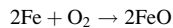
This formula can be used to predict the effects of several key process variables, including temperature, time, and surface carbon level, and is valid for what is known as single-stage carburization. Single-stage carburization takes place at a constant temperature and surface carbon content. Some production processes use a

technique known as boost-diffuse carburization. This is done to take advantage of the increased diffusivity that occurs at higher carbon levels during the early stages, with the goal of reducing overall process time.

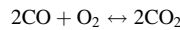
Predicted carbon profiles using $D_{(C,T)}$ at various processing times are plotted in Fig. 10. Plots such as this are easily accomplished using common spreadsheet applications. The practicality of such an estimate can be seen in Fig. 11, where 8620-grade steel was carburized in a single-stage process at a temperature of 963°C (1765°F) and a surface carbon potential of 1.30%. Neither prediction matches the experimental data exactly, but the profile calculated using $D_{(C,T)}$ is a better fit for the actual carbon profile than is the profile calculated using D_T , especially at greater values of x , which are the most important for determining case depth.

Many controls companies now offer instrumentation and computer simulation software that use proprietary diffusion equations based on variations of the concepts presented here.

Oxidation. The reactions that occur at the surface of steel during carburization are complex and numerous. In addition to the carbon monoxide and carbon dioxide reactions described previously, many carburizing processes also must contend with oxidation. Oxidation can be described by the following reactions:



The oxygen for these reactions is provided by the CO/CO₂ reaction:

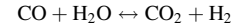


This reaction is important in describing the formation of intergranular oxidation and also in helping control carburizing processes through

the use of zirconia oxygen probes. The principle of operation for zirconia oxygen probes is described in the next section.

Atmosphere Measurement and Control.

For a carburizing process to deliver the desired results, the heat treater must be able to produce the required carbon potential in the carburizing medium. Fortunately, the numerous simultaneously occurring reactions can be exploited for this purpose. One reaction in particular has been found to be of primary importance in the control of gas carburizing atmospheres. It is known as the water-gas reaction:



This reaction can be used to show that there is a relationship between the carbon potential of an atmosphere and its water content. The relationship between water and carbon dioxide has proven to be particularly useful for this purpose. This relationship is displayed graphically for manufactured endothermic gas carburizing atmosphere produced from propane and natural gas (methane) in Fig. 12 and 13.

This relationship has been used for many years as the principal method to measure carbon potential. For many years, instruments that measured the dewpoint of carburizing atmospheres by means of adiabatic expansion were the primary means of determining the quality of carburizing atmospheres.

Dewpoint measurement was a tremendous advancement in the technology of carburizing, but it was limited by the fact that adiabatic expansion instruments cannot be used for continuous monitoring.

In the 1980s, the zirconia oxygen probe began to supplant dewpoint measurement as the primary measurement method for carburizing atmospheres. An advantage of the zirconia oxygen probe over dewpoint measurement is that zirconia probes are well suited to continuous monitoring of the carburizing atmosphere

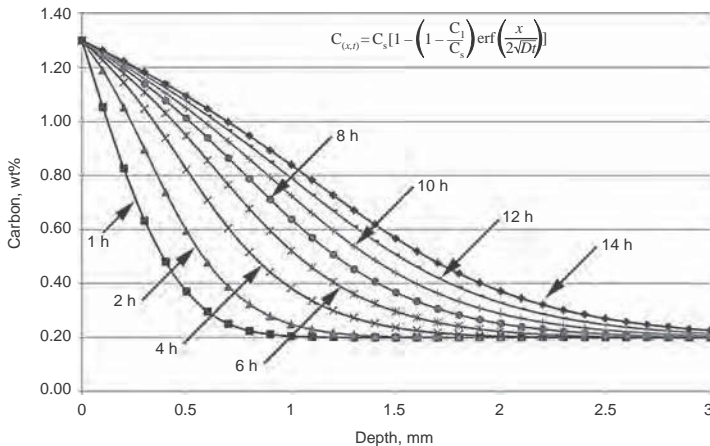


Fig. 10 Estimated single-stage carbon profiles at various carburizing times using a composition-dependent diffusivity coefficient, $D_{(C,T)}$

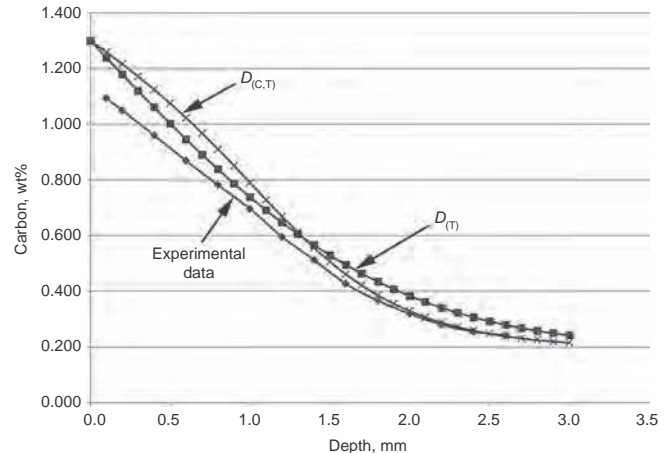
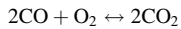


Fig. 11 Comparison of actual carbon profile with profiles predicted with experimental data using alternate methods for determining diffusivity using $D_{(T)}$ and $D_{(C,T)}$

and are continually calibrated by the oxygen in the air outside the furnace. This has opened the door for tremendous advances in instrumentation to control carburizing processes.

Oxygen probes work on the assumption that the following reaction is in equilibrium:



From this equation, it can be seen that there is a relationship between the oxygen content of the atmosphere and the CO:CO₂ ratio.

Certain materials have been found to exhibit measurable changes in electrical conductivity due almost exclusively to the transfer of oxygen ions through the material matrix. One such material, zirconia, when stabilized by small additions of other oxides such as Y₂O₃, has been found to be particularly useful in this regard. The added oxides serve to create oxygen vacancies in the zirconia matrix, which greatly facilitate the mobility of oxygen ions through the substrate. Placing platinum electrodes on either side of the zirconia substrate permits the measurement of conductivity across the material (Fig. 14).

This property is extremely useful because it is relatively simple to precisely measure the change in conductivity of the zirconia material. The following relationship describes the change of zirconia probe potential with oxygen content:

$$v(\text{millivolts}) = 0.0496T \log_{10} \frac{P_0}{P_1}$$

where T is the absolute temperature (Kelvin), P_0 is the oxygen partial pressure at the inner electrode (reference), and P_1 is the oxygen partial pressure at the outer electrode (atmosphere).

The oxygen content of the carburizing atmosphere can be easily determined by measuring the voltage of the sensor and knowing the oxygen content of a reference gas (typically room air). The oxygen content of the reference air is used to calculate the dewpoint of the atmosphere by using the relationship between

oxygen and water content. The specific formulas used to produce these values are typically proprietary to each manufacturer. To allow for small “fine-tuning” adjustments, these algorithms typically include an adjustment factor that is intended to be used by the heat treater to improve measurement accuracy by bringing the probe output into line with actual furnace conditions. A typical oxygen probe installation is represented in Fig. 15.

How can a heat treater know the actual atmosphere conditions inside the furnace? A simple technique known as the shim stock test is often used for this purpose (see the article “Evaluation of Carbon Control in Carburized Parts” in this Volume). The shim stock test involves inserting a thin foil of low-carbon steel into the furnace atmosphere through a special port in the furnace wall (Fig. 16). The shim itself is usually made of AISI grade 1010 steel at a thickness of between 0.025 and 0.075 mm (0.001 and 0.003 in). A special fixture is typically fabricated to hold the specimen. Due to its thin cross section, the shim rapidly reaches the carburizing temperature and assumes equilibrium with the carbon potential of the furnace atmosphere. The actual time required will depend on the furnace temperature, carbon potential, and shim thickness, but it is typically less than 1 h.

Historically, the carbon content of the shim was determined by precisely weighing the shim before and after carburization and calculating the carbon pickup by the weight difference. However, with today’s (2013) prevalence of combustion-type carbon analyzers, it is simpler to analyze the strip to determine the actual carbon content.

If the shim test is performed properly, the result will provide the heat treater with the carbon potential in the furnace atmosphere at the time of the test. This information can be used to select the appropriate adjustment factor to adjust the oxygen probe so that it reads the actual carbon potential of the furnace.

There are some precautions to consider when performing shim stock analysis:

- The shim should be cleaned both before and after exposure with a solvent such as alcohol to remove any residues or contamination.
- The shim test result will only be meaningful if the furnace atmosphere is stable.
- Oxidation of the test strip must be prevented because it will affect the results. It is good practice to withdraw the strip into the sample port and allow it to cool before unsealing the port and exposing the shim to air.
- The shim will only represent the particular zone or location in which it is tested. For best results, the shim port should be close to the oxygen probe. Fortunately, it is common practice for most furnace manufacturers to include a port in close proximity to the probe.
- Depending on the carbon content of the furnace, a properly prepared shim should appear either bright and clean or matte gray. Discoloration (blue or brown) indicates that the shim has oxidized. Interaction of oxygen with a hot shim will lead to decarburization of the shim and skewed carbon values.

Advantages and Limitations

When deciding if carburization is the best process for producing a component, it is helpful to consider its advantages and disadvantages when compared to competing methods.

Advantages

Lower Material Costs. Carburizing steels are characterized by low carbon content. The low carbon content offers some benefits to the steelmaker, which can be passed on to the component manufacturer. The hardenability of most carburizing steels is low enough to avoid hardening during the rolling and finishing operations at the steel mill. This means that the steel can often be introduced into the manufacturing process in the as-rolled or hot-rolled condition without the need for annealing. This can save a significant cost by avoiding the

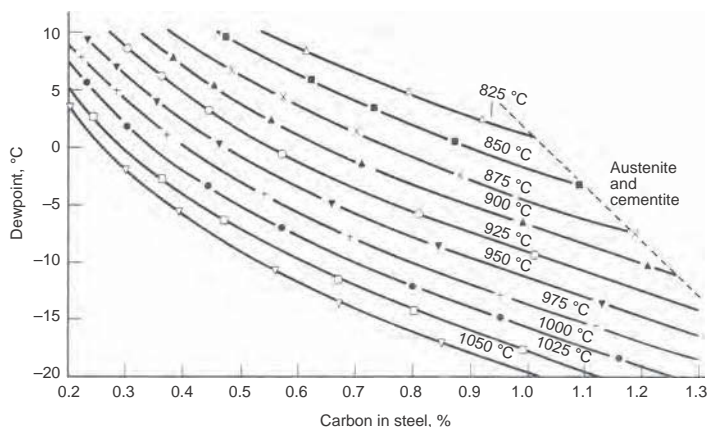


Fig. 12 Theoretical dewpoint versus carbon potential in propane endo. Source: Ref 1

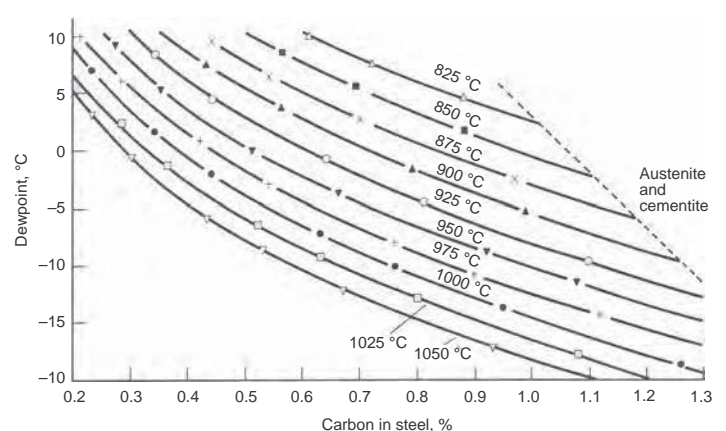


Fig. 13 Theoretical dewpoint versus carbon potential in natural gas endo. Source: Ref 1

necessity for annealing at the steel mill. By comparison, through-hardening uses medium-to-high-carbon steels. Steel grades with carbon contents greater than 0.30% can be too hard to be easily machined. These grades usually require some sort of anneal before leaving the steel mill, which adds significant cost. The use of low-carbon carburizing steels can avoid these additional costs.

Greater Ease of Machining. Compared to higher-carbon through-hardening grades, carburizing steels are typically easier to machine. This is because carbon content directly affects mechanical properties, such as strength and hardness.

As previously discussed, steels with a carbon range of 0.15 to 0.30% can often be machined directly after hot forming operations without the need for an intermediate annealing step, such as is usually required with high-carbon steels. This flexibility can be of significant financial benefit to the component manufacturer both in terms of energy consumption and cycle time.

The lower energy input required to machine low-carbon steels permits greater productivity and lower costs for consumables (such as machining inserts). Capital equipment costs can be reduced by the fact that lower machining effort permits the use of less rigid machine tools.

Greater Freedom during Forming. Carburizing steels tend to have lower yield strengths and rates of work hardening than medium- and high-carbon steels, which facilitates cold forming, and permits transfer directly to machining without subsequent annealing operations.

Tailored Mechanical Properties. The use of carburization gives the designer great flexibility. By controlling the carburizing process parameters, the engineer can choose the surface hardness, load-carrying capacity, and surface microstructure to suit various requirements.

Development of Compressive Residual Surface Stresses. The natural tendency of carburization to produce compressive residual stresses at the surface of components is a significant advantage that is often overlooked. Compressive residual stresses contribute to higher load-carrying capacity and greater resistance to damage. Compressive residual stresses can also provide greater fatigue life.

Widespread Use. Because carburization is such a commercially successful process, there are many commercial and captive heat treating facilities available that can provide heat treating services. Those wanting to bring carburizing in-house will find that the necessary equipment is widely available.

Limitations

Capital Cost. Heat treating equipment is costly, regardless of the method chosen. Procuring the equipment to carburize components will often require significant expenditures. Initial costs include furnaces and atmosphere generators. A small batch-type carburizing furnace can cost several hundred thousand dollars or more. A large continuous furnace line may cost well over a million dollars. The following additional expenses should be considered:

- With new installations, additional expenses should be anticipated for utility connections.

- Furnace racks or trays to hold the workpieces during heat treatment must also be purchased. Carburizing atmospheres will gradually degrade alloy fixtures and furnace hardware over time, so replacement will be an ongoing cost.

Energy Consumption. Carburization requires substantial time at temperature to achieve the required surface carbon content and case depth. This requires energy to heat and maintain equipment and components at the designated carburizing temperature. Competing processes do not require this step.

Distortion. The very nature of the carburization process creates the potential for changes in the geometry of the component. There are chemical, thermal, and microstructural effects that the designer must consider. To compensate for distortion, the designer may have to heat treat the component with additional stock that will allow the component to be finish-ground to the final size. This adds cost through the additional material that must be purchased and processed, as well as the cost of the final grinding operation.

Depending on the complexity and geometry of the component, some amount of fallout for dimensional nonconformance may need to be planned for. Some components may have a geometry that allows them to be hardened in what is known as a quench press. A quench press uses special tooling to hold and constrain the component while simultaneously flooding it with quenchant. The use of a quench press can greatly improve the dimensional stability of carburized components.

Time-delayed dimensional change can be caused by the transformation of retained austenite in a component. Retained austenite is metastable at temperatures below the lower critical temperature, so it is thermodynamically available to transform if sufficient energy is provided in the form of heat or shear stress.

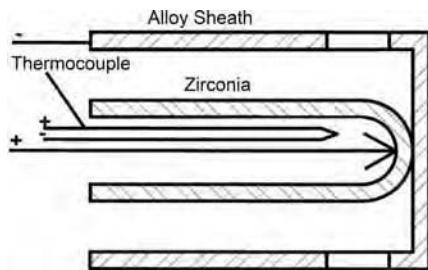


Fig. 14 Schematic of a zirconia oxygen probe. Source: Ref 4

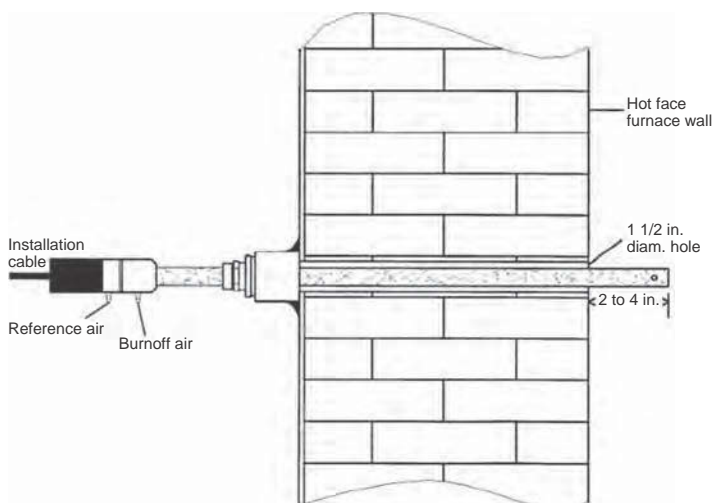


Fig. 15 Typical oxygen probe installation in a carburizing furnace. Source: Ref 4

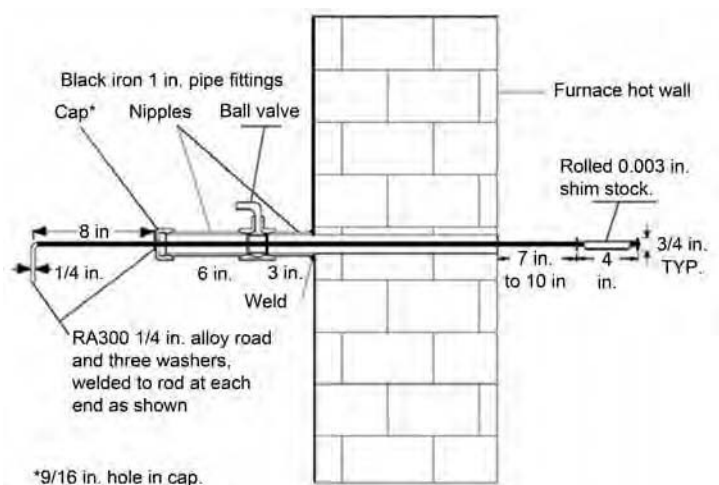


Fig. 16 Schematic of the hardware required to perform a shim stock test in an atmosphere furnace. Source: Ref 5

When transformation does occur, a portion of the austenite grains will transform into fresh martensite, causing the characteristic volume change that takes place when face-centered cubic transforms into body-centered tetragonal. This volume change can dramatically affect the residual-stress level of a component, which in turn can cause measurable changes in part geometry. This can be avoided by ensuring that the retained austenite content of the component is no higher than necessary.

Carburizing Steels

The distinguishing characteristic of carburizing steels is a low carbon content. Carburizing steels typically have a carbon content of between 0.10 and 0.30%, although steels with higher carbon contents are sometimes used in special applications. Carburizing steels can be plain carbon or alloy steels containing small amounts of alloying elements, typically manganese, chromium, nickel, and molybdenum. There are many grades available. Some popular carburizing steel grades are described in Table 3. These alloying additions are intended to either increase hardenability or enhance other properties, such as impact strength.

The steels listed in Table 3 are a sampling of grades commonly used in North America. There are various steel chemistries in use in different regions around the world, many of which are analogous to certain AISI or SAE grades. Grade selection should be based on local availability and the ability to satisfy the case and core requirements. There is usually a standard grade available to meet most applications, but in rare cases, the application may have special requirements that dictate the extra cost of using a custom grade.

Carburizing steels should be treated for grain refinement, because the elevated temperatures and extended times of commercial carburizing processes can create the potential for undesirable grain growth in the finished part.

With the rise in popularity of vacuum carburizing, there has been a greater interest in carburizing at temperatures above 980 °C (1800 °F).

When carburizing above 995 °C (1825 °F), consideration must be given to factors such as furnace construction, process used (vacuum and/or atmosphere furnace), alloy fixture life, and workpiece material. Grain growth and intergranular oxidation at the surface are undesirable effects that can occur more rapidly at high temperatures. Various combinations of alloying elements are being used by steel manufacturers to resist these deleterious effects. It is important to recognize that steel grades used to make components that will be carburized at high temperatures may need to compensate for loss of elements in vacuum high-temperature carburizing. Certain alloying elements such as niobium may be added to help prevent grain growth.

Quality Assurance

Because of the many variables that must be controlled during carburization, managing process variation is a constant challenge. Modern instrumentation and equipment makes it possible to produce repeatable results. However, proper operation and maintenance of carburizing equipment is essential to success. Due to the high temperatures employed and the chemical activity of carburizing gases, the equipment used to perform carburizing will deteriorate over time, so constant attention is necessary.

Numerous test methods have been developed to verify that the desired outcome has been obtained after carburization. Because the distinguishing characteristic of carburization is the high-carbon martensitic case, most specifications involve tests to verify the surface hardness, carbon and hardness profile, and microstructure.

The use of statistical process control (SPC) to monitor and control critical process variables has also been shown to be of great value in the successful operation of a carburizing process. An effective process control program using SPC can detect furnace maintenance and operational issues before they adversely affect product quality.

Surface hardness is the most basic and easiest test that can be performed to verify that carburization has occurred. Test methods such as the Rockwell, Vickers, and Knoop hardness

tests have been in use since the early 1900s, and they are still relevant today (2013).

The hardness range for a carburized and hardened case will vary depending on the intended application, but it will generally range from approximately 55 to 65 HRC.

Core hardness is the hardness in the center of the component, usually in a noncarburized region. Core hardness is measured by the same methods as surface hardness. Core hardness is determined by the size and heat treatment method of the part and can range anywhere from 25 to 45 HRC. Unlike surface hardness, the testing of core hardness is a destructive test, because it usually involves cutting a component to gain access to the core. Core hardness will vary in a component as a function of section thickness. Depending on the geometry of the component, it may be necessary to define exactly where the core hardness will be evaluated.

The carbon gradient is the defining characteristic of a carburized component. While the surface carbon can be estimated by its effect on surface hardness and microstructure, this does not reveal anything about the depth and slope of the carbon gradient between the surface and the core. One method that can be used to confirm that the process has produced the intended result is to measure the actual carbon content at a defined depth from the surface.

The technique required to perform this test will depend very much on part geometry. One method that has been used on axially symmetrical parts is to chuck the component in a lathe and turn the surface down to the depth of interest, then turn down a bit further and collect the turnings for analysis. If this is done with the necessary precision, it is possible to collect the turnings at various depths of cut and analyze them using a combustion analyzer.

Case Depth. The designer is expecting the carburized case to extend to a certain depth into the component in order to provide the mechanical properties and load-carrying capacity that the component requires. This necessitates the determination of the carbon gradient. There are several ways to define this depth.

Total case depth is defined as the perpendicular distance from the surface of a carburized component to the point at which differences in

Table 3 Common carburizing steels

AISI grade	Relative cost	Nominal composition, wt%					Comments
		C	Mn	Ni	Cr	Mo	
1020	Very Low	0.2	0.45	Plain carbon steel. Low core hardenability
4023	Low	0.23	0.80	0.25	Low-hardenability grade commonly used in automotive applications
4320	Moderate/high	0.2	0.55	1.82	0.50	0.25	Higher hardenability for improved core response in thicker cross sections. Somewhat longer processing times than 8620
4620	Moderate	0.2	0.55	1.85	...	0.25	Nickel/molybdenum steel. Used only where nominal hardenability and core response are required
4820	High	0.2	0.60	3.5	...	0.25	Increased nickel content for improved core toughness. Slower response results in longer processing times
5120	Low	0.2	0.80	...	0.80	...	Commonly used in automotive applications. Propensity to form carbides if carburized too close to saturation
8620	Low/moderate	0.2	0.85	0.55	0.50	0.20	Most commonly specified steel for carburizing. Excellent carburizing response, with good hardenability for most section sizes
8720	Moderate	0.2	0.85	0.55	0.5	0.25	Similar to 8620 but with additional molybdenum for increased core hardenability
9310	Very high	0.1	0.50	3.25	1.2	0.12	Increased nickel content for maximum core toughness. Slower response results in longer processing times

chemical or physical properties of the case and core can no longer be distinguished. Total case depth is sometimes practically defined to be the distance from the surface to the deepest point at which the carbon content is 0.04% higher than the carbon content of the core. Generally, the term *total case depth* is considered too vague for use in carburizing specifications because of the practical difficulty in determining the exact point where the carbon profile transitions between the case and the core.

Effective case depth or hardened depth is defined as the perpendicular distance from the surface of a hardened case to the depth at which a specified level of hardness is obtained. This method is the most practical and most widely used for determining case depth. The industry standard hardness criterion is HRC 50. Defining case depth to other hardness values is occasionally used for special applications but is not common. When other criteria are used, they should be properly defined.

Carburized case depth is defined as the perpendicular distance from the surface of a carburized case to the depth at which a specified level of carbon is obtained. It is a hybrid of the total case and effective case methods. The specified carbon level is selected to approximately correlate to a particular depth of interest, such as the near-surface or the effective case depth. For medium-to-low-alloy carburizing steels, the depth to HRC 50 will correlate to a carbon level of 0.3 to 0.4 wt% C. Often, 0.35 wt% C is used as the specified carbon level for carburized case depth.

The depth of carbon is most easily measured indirectly by measuring the effect that the carbon has on the hardenability and hardness of the steel. Because it is the easiest method to perform and quantify, effective case depth is the predominant measurement method. A microhardness tester is useful for this purpose. To measure effective case depth, a specimen is cut with its face perpendicular to the component surface. A microhardness tester equipped with a Vickers, Knoop, or similar indenter is then used to place small indentations into the specimen at defined distances from the surface, continuing until the hardness drops below the hardness of interest. By determining the intercept of the defined hardness of interest (say, 50 HRC) with the hardness gradient, the effective case depth is easily determined (Fig. 17). Instruments for checking microhardness are available from a variety of manufacturers.

Case Microstructure. To achieve the mechanical properties necessary to take advantage of the carburizing process, a carburized component must be quenched to form martensite. Martensite exists in two major forms: lath and plate. These two forms, while identical in crystallographic structure, differ in morphology and mechanical properties.

Low-Carbon (Lath) Martensite. Lath martensite is the predominant form of martensite at carbon levels below approximately 0.6%, and it disappears altogether at carbon levels

above 1.0%. As such, lath martensite is the form of martensite that is typically encountered in the core of a carburized component. Lath martensite is less strong than plate martensite, but has greater impact resistance (Fig. 18).

High-Carbon (Plate) Martensite. Plate martensite begins to form when the carbon content is greater than approximately 0.6%. As the carbon content increases above 0.6%, the proportion of plate martensite increases until, at approximately 1.0%, lath martensite disappears

completely and plate martensite becomes the dominant microstructure. Plate martensite is characteristically identified by the presence of large “needles,” often accompanied by varying amounts of retained austenite. Plate martensite is stronger than lath martensite but also less impact resistant.

Retained Austenite. Depending on the case carbon content and the specific heat treatment process used, the component may contain a significant amount of retained austenite. Retained

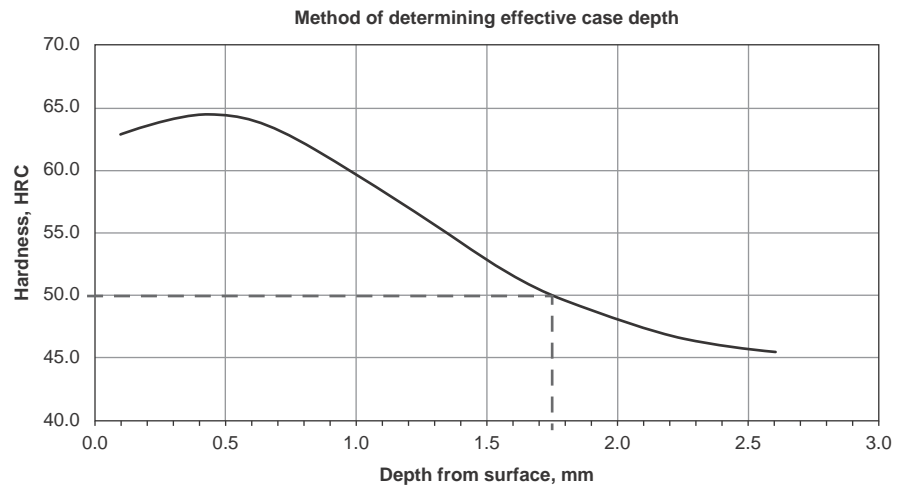


Fig. 17 Method of determining effective case depth at 50 HRC by means of microhardness profile (converted to HRC). In this example, the effective case depth is 1.75 mm (0.069 in.).

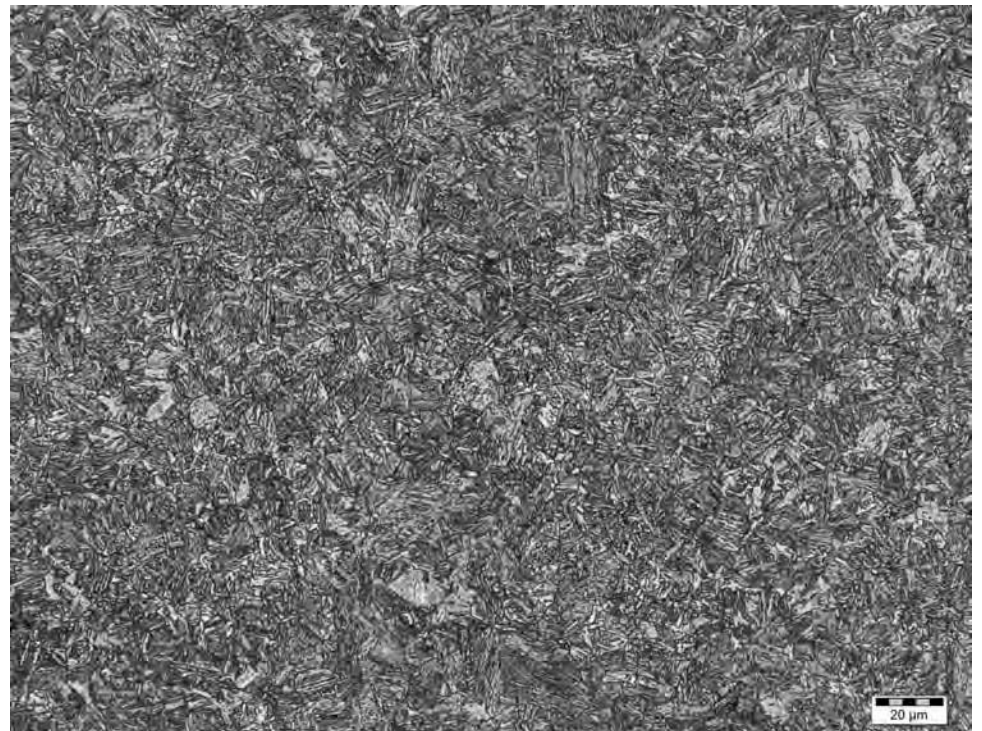


Fig. 18 Typical low-carbon (lath) martensite microstructure with some acicular ferrite. 8620-grade steel. Nital etch. Original magnification: 500×

austenite is so named because it is a high-temperature phase that is retained at room temperature after quenching and tempering. Normally, austenite is not stable below the lower critical temperature (A_{c3}) and is not normally present in ordinary alloy steels at room temperature. However, in many case-carburized applications, retained austenite is present due to suppression of the M_s temperature, non-equilibrium cooling, and the M_f being below the quench temperature. Retained austenite is metastable at temperatures below the lower critical temperature, so it is thermodynamically available to transform if sufficient provocation is offered by the environment. The driving force for the transformation of austenite to “fresh,” untempered martensite can come from the application of shear stresses in service or from post-heat-treatment exposure to elevated temperatures.

Retained austenite can either be detrimental or beneficial, depending on the application. For instance, many gears and roller bearings are intentionally designed with certain levels of retained austenite in the case, because it has been shown to prolong service life in situations where rolling or sliding contact fatigue are a primary concern.

Retained austenite is almost exclusively a case microstructural feature and presents itself as indistinct, light-colored areas in the spaces between plate martensite plates (which appear as needles). Figures 19 and 20 show microstructures with two different levels of retained austenite.

Possible Complications

Despite its many benefits, carburization is very process-sensitive. With so many variables to control, it is common to encounter certain types of conditions that may be detrimental to some degree, depending on the application.

Decarburization. The intent of the carburizing process is to create a carbon gradient into the surface of a steel component in order to achieve certain mechanical properties. However, process interruptions and equipment problems can lead to a reversal of the carbon gradient. By diffusion, carbon migrates from a region of high concentration to a region of low concentration. If, during heat treatment, the carbon potential of the atmosphere drops below that of the steel surface, the carbon flow will reverse, and decarburization of the component will occur. This is obviously undesirable because if it progresses too far, decarburization will compromise the beneficial properties that the heat treater and designer intended.

Common causes of decarburization in gas carburizing are outright furnace failures, that is, leaks, blown radiant tubes, open doors, and atmosphere generator problems. If the degree of decarburization is slight, it presents itself as a martensitic microstructure with a lower

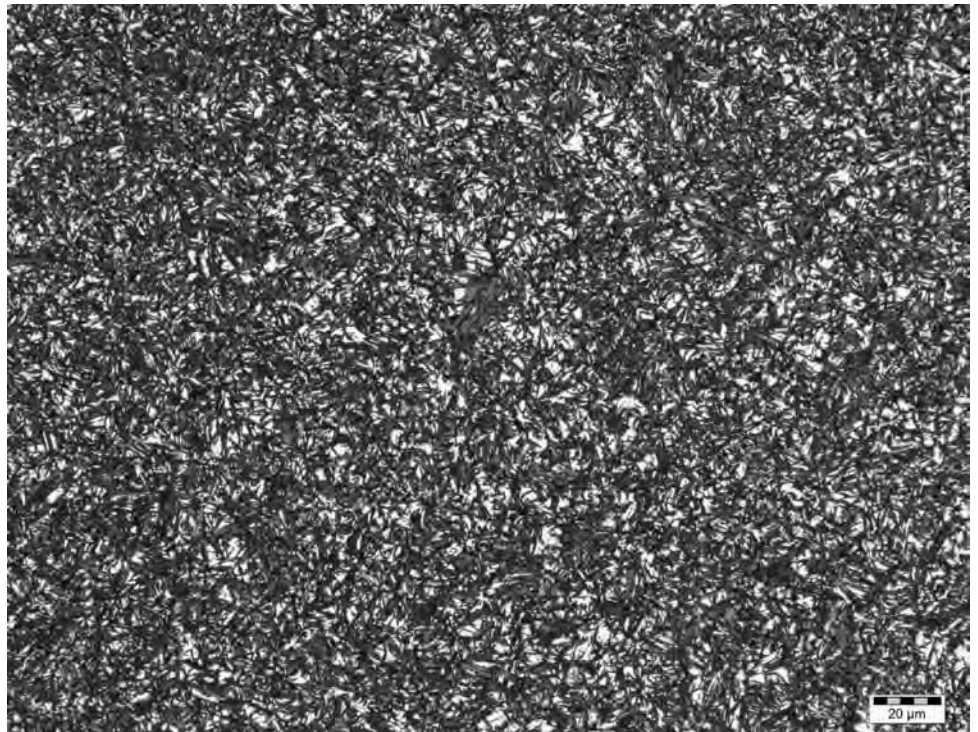


Fig. 19 Case microstructure of plate martensite and ~30% retained austenite (by x-ray diffraction). Nital etch. Original magnification: 500×

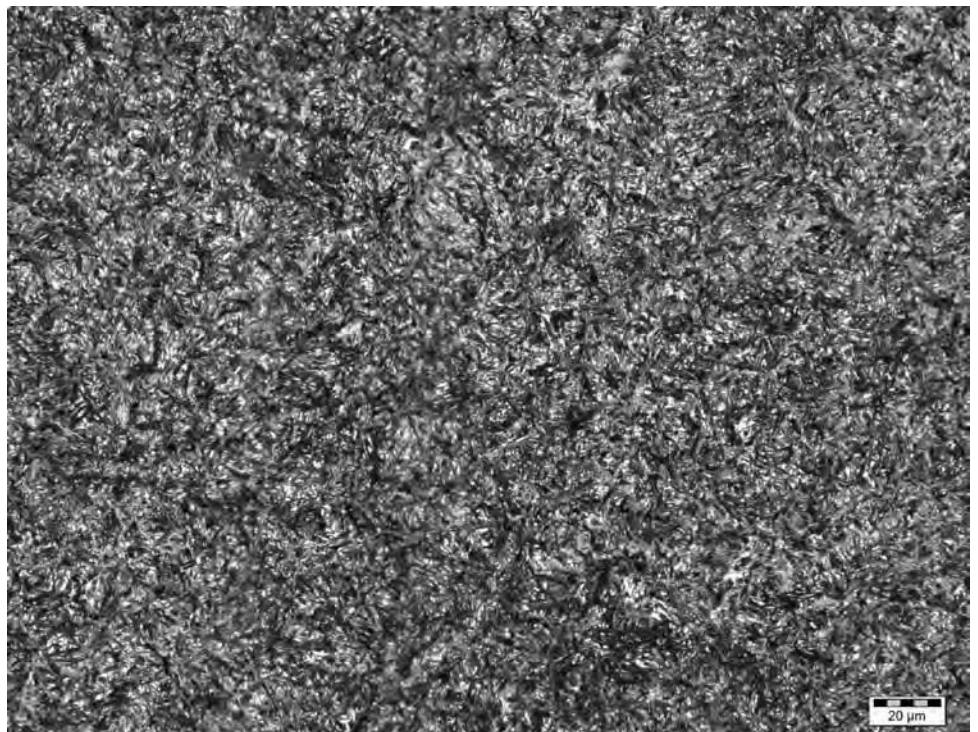


Fig. 20 Case microstructure of plate martensite and ~15% retained austenite (by x-ray diffraction). Grade 8620. Nital etch. Original magnification: 500×

retained austenite content. This may not be a problem, but slight decarburization reduces the level of compressive residual stress near the surface. If decarburization is enough for the

surface to revert back to ferrite, corrective action is required. Excessive surface decarburization can lead to low surface hardness and poor fatigue strength.

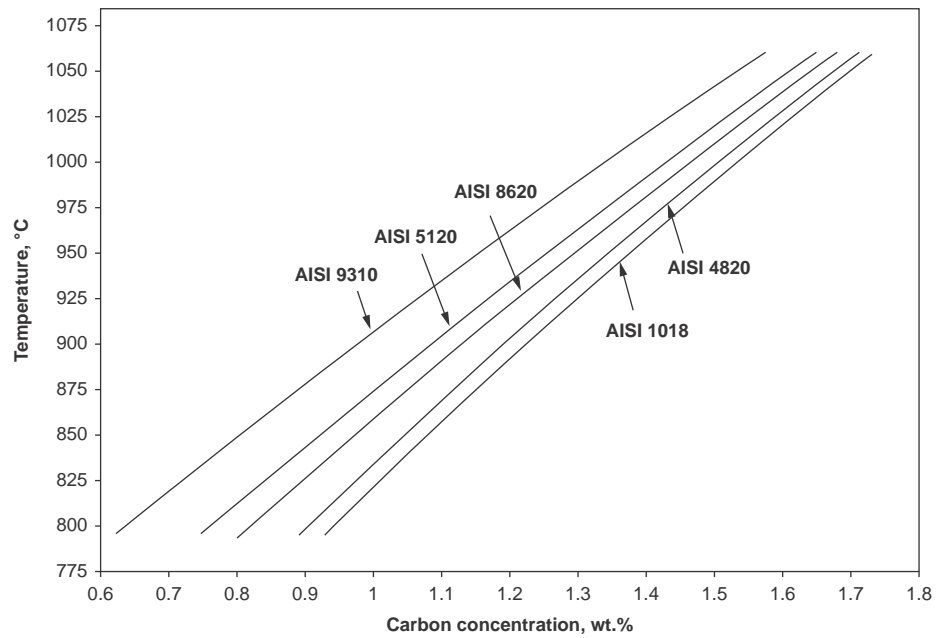
If the depth of decarburization is very shallow or less than the depth of metal removal from post-heat-treatment finishing operations, its impact may be negligible. Surface decarburization can be present even if the required case depth is achieved. This can make rework operations difficult because, in most cases, the processing required to recarburize the surface will drive the case depth even deeper, sometimes with undesirable consequences.

Carbides are relatively hard and brittle compared to carburized steel, so they are generally considered undesirable in a carburized component. Carbides are especially troublesome in rolling or sliding contact application, because they can act as fatigue crack initiation sites. Carbides tend to precipitate at grain boundaries, which can decrease the impact toughness of the material.

Regardless of the cause, carbides are typically seen near the surface of the carburized component, where the carbon content is at its highest. Carbides are typically caused by one of two conditions:

- **Excessive carbon content:** If the surface carbon of the carburizing medium is higher than the saturation carbon level of the steel (Fig. 21), it will begin to form iron carbide. There is no known benefit to carburizing at carbon levels higher than saturation. It is generally considered good practice to carburize at a carbon concentration just below the saturation carbon level, to maximize the increased diffusion rate achieved at higher carbon levels. The appropriate carbon potential can be easily controlled through the use of modern atmosphere-monitoring equipment and instrumentation. Maximum solubility limits of carbon in austenite are listed in Table 4 at typical carburizing and quench temperatures for some common carburizing steels.
- **Slow cooling from the carburizing temperature:** When carburizing, it is normal for the carbon content at the surface to exceed the eutectoid composition of the steel. While the steel remains at carburizing temperatures, the carbon remains in solution, but as the component cools, it must pass through the austenite-Fe₃C field of the phase diagram. If the cooling rate is sufficiently fast, the carbon cannot precipitate out of solution. However, if the cooling rate is too slow, carbide will begin to precipitate as an equilibrium structure at the austenitic grain boundaries. This tendency can be minimized by cooling rapidly through the austenite-Fe₃C field to limit the time that the component spends in the austenite-carbide field.

Carbides present in an etched microstructure as distinct, light-colored, round-cornered features that can be present in a variety of morphologies ranging from discrete, individual carbides to a network around the prior-austenite grain boundaries (Fig. 22), also known as a continuous carbide network.



Compositions used in calculations of saturation limits						
	1018	4118	4820	5120	8620	9310
C	0.18	0.2	0.2	0.2	0.2	0.1
Mn	0.75	0.8	0.6	0.8	0.8	0.55
Cr		0.5	—	0.8	0.5	1.2
Ni			3.5		0.55	3.25
Mo			0.25		0.2	0.1

Fig. 21 Carbon saturation limit in austenite for common AISI steel grades, calculated using Thermo-Calc. Source: Ref 6

Table 4 Carbon solubility limits in austenite at some typical temperatures for carburizing and hardening

Steel	Maximum solubility of carbon (wt%) in austenite (from Fig. 21) at:		
	925 °C (1700 °F)	845 °C (1550 °F)	800 °C (1475 °F)(a)
1018	1.3	1.07	...
4820	1.27	1.03	...
5120	1.17	0.91	...
8620	1.21	0.96	...
9310	1.06	0.79	0.64

(a) Quench from 800 °C (1475 °F) applicable for 9310

Masking is the prevention of carburization on a portion of the surface by means of a barrier. Masking can be either intentional or accidental.

Intentional masking may be employed when it is desirable to leave a specified area of the component soft for future processing (machining, drilling, etc.) or when having a hardened surface at some portion of the component is

objectionable. This can be accomplished by plating with a barrier metal such as copper or by using commercially available stopoff coatings, which are formulated to act as a barrier to the transfer of carbon (see the article "Stop-off Technologies for Heat Treatment" in this Volume).

Unintentional masking results when carbon diffusion into the steel surface is accidentally

inhibited, resulting in less surface carbon or case depth than intended. This can affect large or small regions of a component. Unintentional masking can be caused by chemical contamination of the surface or by physical obstruction of the surface by incidental contact between the component and other parts or fixtures during processing. This is often caused by residual fluids from previous operations that have dried on the surface or by surface corrosion. Unintentional masking is typically combated by selecting metalworking fluids that are compatible with carburizing or by washing parts prior to carburizing to remove residues. This condition is difficult to identify, but it can usually be detected by low surface hardness. Low case depth is only detectable by metallographic sectioning of components.

Masking directly affects the carbon composition at the surface (and therefore the microstructure), so it can be detected on finish-ground surfaces by inspecting after the application of a suitable etchant. Unintentional masking will appear as a mottled or splotchy surface.

Intergranular Oxidation. The presence of internal oxidation at the surfaces of parts that are case hardened by pack or gas carburizing has been known for 50 years or more. The high-temperature transformation products, which can form as a direct consequence of internal oxidation, have subsequently been found to have adverse influences on certain strength properties of affected parts; therefore, these products are of some concern to metallurgists and engineers.

The use of oxygen-free gas carburizing atmospheres or vacuum carburizing processes is known to eliminate the oxidation process, and nitrogen-base atmospheres are said to reduce it. However, conventional gas carburizing using the endothermic carrier gas is still the most popular method of case hardening, and its use will continue for many years. Thus, the problems related to internal oxidation will persist as long as the conventional process lives (Ref 7).

Intergranular oxidation (Fig. 23) is unavoidable in gas-carburized steels, but it is predictable. In a normally operating furnace, intergranular oxidation typically develops at a rate of 0.0025 mm (0.0001 in.) per 0.25 mm (0.010 in.) of case depth, maxing out at a depth of approximately 0.013 mm (0.0005 in.). Intergranular oxidation penetration much greater than 0.013 mm (0.0005 in.) usually indicates that there is a significant atmosphere leak in the furnace.

Methods of Carburizing and Carbonitriding

Table 5 summarizes the advantages and disadvantages of different carburizing methods. Each method is described in more detail in separate articles of this Volume. The related

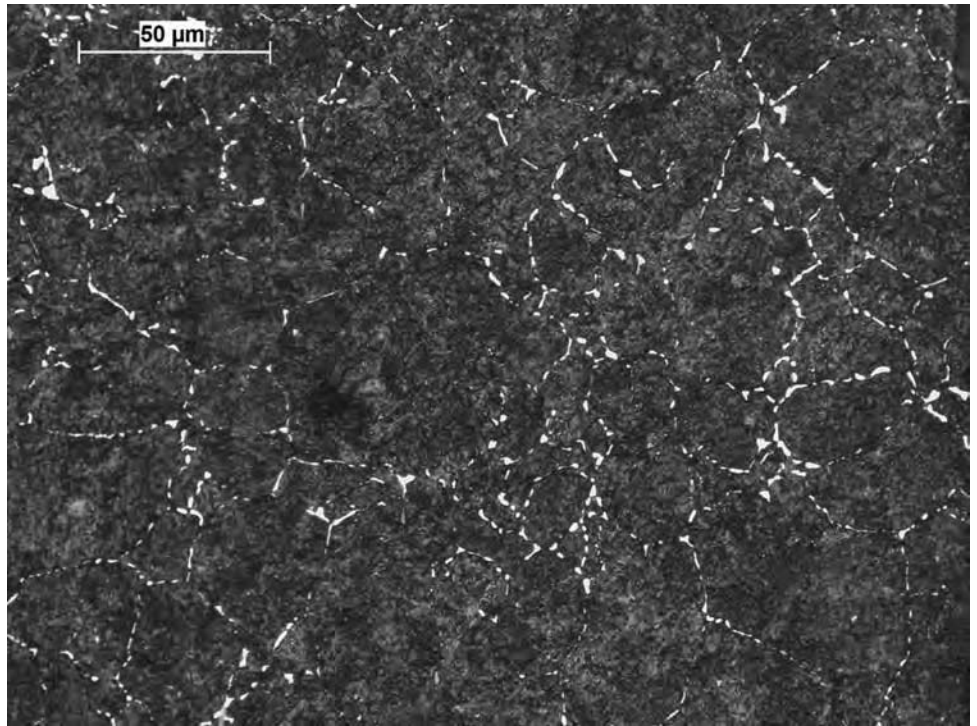


Fig. 22 Network carbides in a carburized case. Note how carbides outline the prior-austenite grain boundaries. 8620-grade steel. Nital etch. Original magnification: 500×

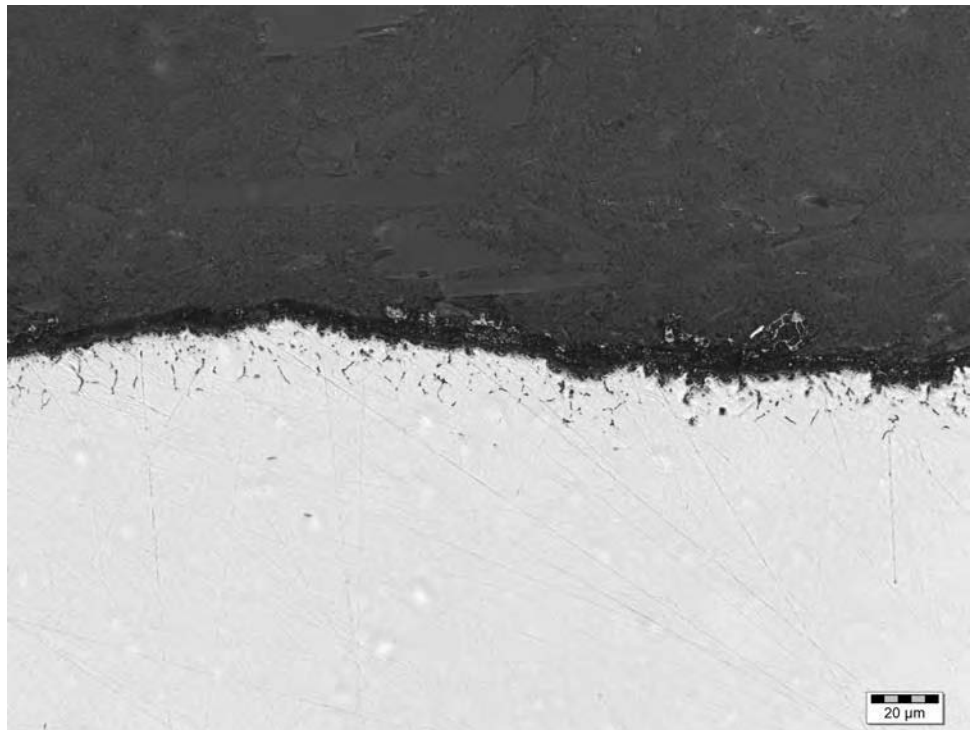


Fig. 23 Intergranular oxidation at the surface of a carburized component. Unetched. Original magnification: 500×

process of carbonitriding is also briefly compared in this section with more details in the article "Carbonitriding of Steels" in this Volume.

Pack carburizing is the original carburizing technique, and therefore, it dates back several thousand years. It has been replaced by gas and vacuum carburizing and is no longer a

Table 5 Advantages and disadvantages of carburizing methods

Advantages	Disadvantages
Pack carburizing	
Low capital requirements No atmosphere generation required	Labor-intensive Control of case depth and carbon is difficult. Direct quenching is impractical. Energy- and time-intensive due to the necessity of heating the additional mass of the container Some pack compounds (such as barium carbonate) are hazardous. Process is very dirty and requires that parts be cleaned before hardening.
Liquid carburizing	
Rapid heatup can produce case equivalent to other methods in less time. Selective carburization is possible by immersing only a portion of the component in the salt.	Molten salts present safety and environmental challenges. Salt residue can contaminate downstream processes. Not easily adapted to high-volume or continuous operation
Gas carburizing	
Easily scaled to large-volume production and continuous operation Atmosphere is easily instrumented and controlled.	Significant capital equipment costs Safety and environmental issues surrounding the use and exhaust of atmosphere gases and products of combustion Surface intergranular oxidation can be controlled but is unavoidable.
Parts can either be direct-quenched or rehardened in a separate operation.	
Low-pressure (vacuum) carburizing	
Intergranular oxidation eliminated Reduced energy consumption when compared to gas carburizing. No generators required; power used only when running a load Low environmental impact Parts are very clean after processing.	Capital equipment costs typically highest of all methods Not easily adapted to high-volume or continuous operation Difficult to exactly duplicate microstructure from conventional liquid quench processes with high-pressure gas quench due to limited cooling rates available

commercially significant process. Although essentially obsolete, pack carburizing is still practiced by educational institutions and small tool shops that lack modern carburizing facilities.

Pack carburizing involves placing a component in a metal container, surrounding it with a suitable powdered carbonaceous material, sealing the container, heating it to the carburizing temperature range, and holding it there for a suitable period of time.

During pack carburizing, the carbonaceous material in the box decomposes, filling the box with carbon monoxide. At this point, pack carburizing actually behaves much like gas carburizing. Over the years, various carbon sources have been used. Biological sources have been used from the beginning and remain in use to some extent today (2013). Examples of materials used for pack carburizing are crushed animal bones, charred leather, charcoal, or coke. Modern pack carburizing compounds are typically based on charcoal or coke with the addition of various alkaline metal carbonates that serve as activators or catalysts.

The box is a crucial piece of equipment. It serves as the container or furnace that holds the atmosphere created by the reactions of the compound. Ideally, a box should be as small and light as possible to minimize the amount of time and energy required to heat the entire assembly. The box may be fabricated out of a variety of materials ranging from plain carbon steel to stainless steel or high-temperature alloys. Materials selection will be driven by the size of the box and if it is intended to be reused.

The mass and cross section of a pack carburizing box make quenching directly from carburizing impractical, so pack-carburized

components must be hardened and quenched in a separate operation.

Liquid Carburizing or Salt Bath Carburizing. Traditional liquid carburizing, also known as salt bath carburizing, involves the carburization of a component by immersion into a molten salt bath containing cyanides. This should not be confused with a relatively new process known as liquid induction carburizing, which is discussed later in this section.

Liquid carburizing is a process that has been largely replaced by gas and vacuum carburizing. Although it is still used by some shops that have access to legacy equipment, it is commercially obsolete.

Traditional liquid carburizing involves heating of the component in a bath of liquid salts containing cyanide. The liquid salt provides an efficient medium for heat conduction into the component, and the cyanide provides the carbon for diffusion.

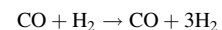
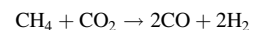
In traditional liquid carburizing, components are carburized in a salt bath by lowering them into the molten salt by means of a hoist or other lifting device. This method of charging parts provides a unique opportunity: Parts can be preferentially carburized by selecting how much of the component is immersed into the salt. Other masking or stopoff methods may be used, but compatibility of the stopoff with the salt must be determined before use.

Liquid induction carburizing is a relatively new, nontraditional carburizing method. Unlike the molten salt bath used in traditional liquid carburizing, liquid induction carburizing uses a room-temperature liquid hydrocarbon bath. The component is heated to carburizing temperatures by an induction coil while immersed in the liquid hydrocarbon. Carburization occurs as the liquid hydrocarbon dissociates on the

surface of the heated component. In addition to acting as a carbon source, the liquid hydrocarbon bath also serves as a quenchant and protects the component from oxidation. The configuration of the liquid induction carburizing process permits the component to be carburized, hardened, and tempered in the same fixture. Because part heating is not constrained by the limitations of a traditional furnace, liquid induction carburizing can make use of high carburizing temperatures (approximately 1200 to 1250 °C, or 2190 to 2280 °F), resulting in relatively short processing times. This ability also presents the intriguing possibility of expanding the scope of carburization to materials other than steel. Liquid induction carburizing has been used to develop carbide cases with significant thickness on various refractory metals, such as titanium, vanadium, chromium, zirconium, niobium, molybdenum, tantalum, and tungsten. While still experimental in nature, liquid induction carburizing has found limited use in medical and aerospace applications.

Gas carburizing is the most commercially significant carburizing technique. The distinguishing characteristic of gas carburizing is the technique of enveloping the workpiece in a gaseous atmosphere that is generated from hydrocarbons such as methane, propane, butane, or methanol.

In considering the case of natural gas (methane), the key reactions would be:



The atmosphere is typically delivered by a carrier gas into which a sufficient amount of the

hydrocarbon gas is added to produce the desired carbon potential. The most common carrier gas is known as an endothermic gas. It is produced by passing the hydrocarbon over a nickel catalyst at temperatures of 980 to 1000 °C (1800 to 1830 °F). The most common hydrocarbon used to produce endothermic gas is natural gas or methane (CH₄). The composition of a typical methane-based endothermic gas is approximately 40% H₂, 40% N₂, and 20% CO, with small amounts of water vapor, CO₂, and unreacted CH₄. Endothermic gas must be handled with caution because it is both flammable, due to its H₂ content, and an inhalation hazard, due to its carbon monoxide (CO) content.

Endothermic gas serves as a protective atmosphere at elevated temperatures. Its H₂ and CO content will protect parts from scale and oxidation. However, its carbon potential is too low to carburize on its own. To create the required carbon potential, straight hydrocarbon is added to the endothermic atmosphere in the proper proportion to produce the desired result. This is known as enrichment.

Gas carburization usually takes place by first heating the load under cover of straight endothermic gas. The load is allowed to heat through and stabilize at the carburizing temperature while the endothermic gas protects it from oxidation (although some degree of intergranular oxidation is inevitable). Once the load has equalized at the desired temperature, carbon-potential control is activated and the enriching hydrocarbon is added to achieve the desired carbon potential. The load is held at temperature for a time sufficient to achieve the required case depth, at which point the enriching gas addition is stopped and the load is either cooled to an appropriate hardening temperature and quenched (direct quench) or allowed to cool to room temperature and then hardened in a separate operation (rehardening). Rehardening is sometimes used where a finer grain size is required after heat treatment.

There are two main approaches to the carburization step. One is known as single-stage carburization and the other is known as boost-diffuse. In single-stage carburization, the carbon content is held constant throughout the carburization step.

In boost-diffuse carburizing, the time for the carburizing step is divided into two phases. In the first stage, known as the boost phase, the carbon potential of the atmosphere is set nearly to saturation and held for a time sufficient to diffuse maximum carbon into the surface. In the second, or diffuse stage, the carbon potential is lowered to that of the desired final surface carbon, and the high carbon content at the surface is allowed to diffuse into the steel to produce the desired carbon and hardness profile. Boost-diffuse carburization has been demonstrated to produce an effective case depth equivalent to that of single-stage carburization in less time. The boost-diffuse process is best suited to batch furnaces, where the entire

carburization step takes place in the same furnace chamber or zone.

Gas carburizing is used in both batch and continuous processes. A wide variety of furnaces types, configurations, and sizes are in use around the world.

Low-Pressure (Vacuum) Carburizing. Vacuum carburizing, or more properly, low-pressure carburizing, is a far second to gas carburizing in terms of worldwide carburizing capacity, but it is growing in popularity and has some distinct advantages over gas carburizing that make it the preferred process for certain applications.

In vacuum carburizing, the vacuum is actually a very low-pressure atmosphere created by a vacuum pump. Carburizing is made possible by breaking the vacuum at the appropriate time in the cycle with a partial pressure of a hydrocarbon gas such as propane, acetylene, or some other suitable hydrocarbon blend. A carrier gas such as nitrogen is sometimes used to provide a neutral partial pressure in the chamber and to dilute the hydrocarbon. Carburization occurs in the vacuum furnace as the hydrocarbon gas comes into contact with the surface of the steel. Unlike gas carburizing, methane is rarely used in vacuum carburizing because it does not dissociate well at the ordinary carburization temperatures. Propane and acetylene are better choices for vacuum carburizing.

For carburization to take place, the surface of the component must be free of oxides. For this reason, it is important that the vacuum be established in the vessel before the temperature gets high enough to form oxides on the workpiece (approximately 550 °C, or 1020 °F). Maintaining a sufficient vacuum reduces the oxygen available to produce intergranular oxidation on the component, so intergranular oxidation can essentially be eliminated.

Many vacuum furnaces are designed to permit quenching of the load by the introduction of inert gas at relatively high pressures once

carburization is complete. This makes it possible to carburize, harden, and even temper a load in the same chamber. This technique works best with lighter loads, thinner-section parts, and high-hardenability steels. There are applications where high-pressure gas quenching is unable to reproduce the exact microstructure obtained in a traditional liquid quench. If a particular microstructure is necessary that can only be produced with a faster quench rate, it may be necessary to harden the components in a separate operation or use a multichamber vacuum furnace, where it is possible to have a separate chamber dedicated to a liquid quench (Fig. 24).

Carbonitriding. As noted in the introduction of this article, carbonitriding is a modified form of carburizing rather than a form of nitriding. The modification consists of introducing ammonia into the gas carburizing atmosphere in order to add nitrogen to the carburized case. The ammonia in the atmosphere dissociates on the surface of the component, generating nascent nitrogen. The nitrogen then diffuses into the steel simultaneously with the carbon. Steels with carbon contents up to 0.2 wt% are commonly carbonitrided. Typically, carbonitriding takes place at lower temperatures and shorter times than gas carburizing, producing a shallower case—typically from 0.075 to 0.75 mm (0.003 to 0.030 in.) deep.

Carbonitriding differs from carburizing and nitriding in that carburized cases normally do not contain significant nitrogen, and nitrided cases consist primarily of nitrogen, whereas carbonitrided cases contain both. One major advantage of carbonitriding is that the nitrogen absorbed during processing lowers the critical cooling rate of the steel. Thus, the hardenability of the case is significantly greater when nitrogen is added by carbonitriding than when the same steel is carburized. Carbonitriding also increases the case hardness (Fig. 25). Full hardness with less distortion can be achieved with

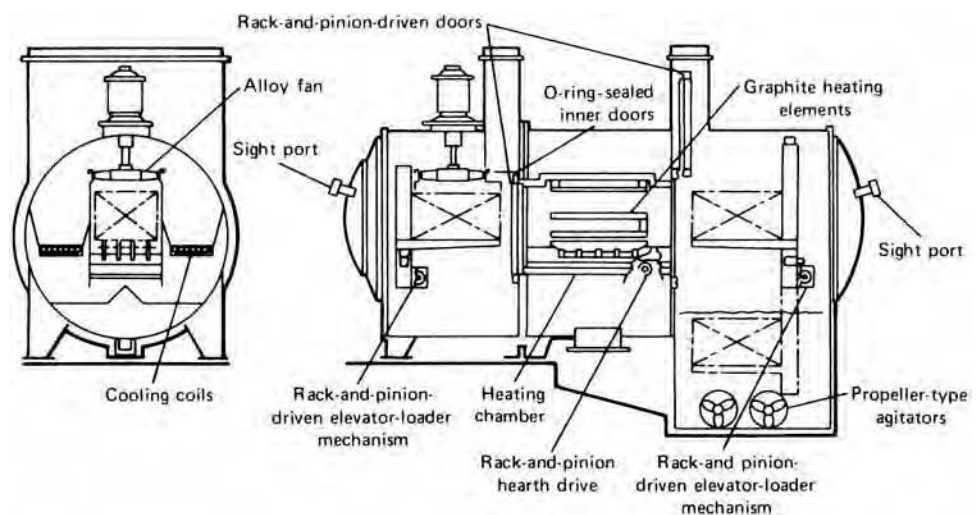


Fig. 24 Three-chamber vacuum furnace with an oil quench chamber

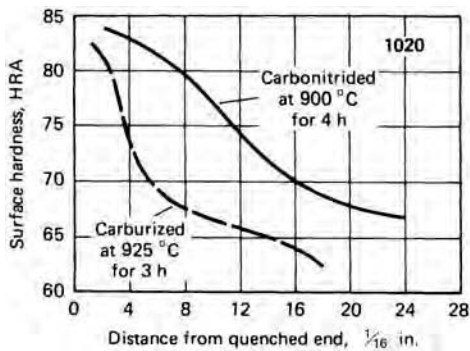


Fig. 25 End-quench hardenability curve for 1020 steel carbonitrided at 900 °C (1650 °F) compared with curve for the same steel carburized at 925 °C (1700 °F). Hardness was measured along the surface of the as-quenched hardenability specimen. Ammonia and methane contents of the inlet carbonitriding atmosphere were 5%; balance was carrier gas.

oil quenching, or, in some instances, gas quenching is possible by using a protective atmosphere as the quenching medium.

Often, carburizing and carbonitriding are used together to achieve much deeper case depths and better engineering performance than could be obtained by using only the carbonitriding process. The process generally consists of carburizing at 900 to 955 °C (1650 to 1750 °F) to give the desired total case depth (up to 2.5 mm, or 0.10 in.), followed by carbonitriding for 2 to 6 h in the temperature range of 815 to 900 °C (1500 to 1650 °F) to add the additional carbonitrided case. The parts can then be oil quenched to obtain a deeper effective case depth and thus a harder case than would have resulted from the carburizing process alone. The addition of the carbonitrided surface increases the case residual compressive stress level and thus improves contact fatigue resistance, as well as increases the case strength gradient. When the carburizing/

carbonitriding processes are used together, the effective case depth at 50 HRC to total case depth ratio may vary from approximately 9 to 19 mm (0.35 to 0.75 in.), depending on the case hardenability, core hardenability, section size, and quenchant used.

ACKNOWLEDGMENTS

The author thanks the following people for their assistance:

- Chris Dunkley, Olympus America, Inc., for use of a metallograph and photography
- Liesl Diefenderfer, Amsted Rail Brenco, for assistance with carbon and hardness profiles, metallography, and proofing
- Mike Schneider, The Timken Company, for suggesting the author write this article and for technical assistance
- Gary Keil and Olga Rowan, Caterpillar, for brainstorming and technical assistance
- Olga Rowan, Caterpillar, for calculating carbon saturation limits (Fig. 21) using Thermo-Calc
- Saveliy Gugel, Sanova LLC, for assistance regarding liquid induction carburization
- Reinhard Rieder, Amsted Rail Brenco, for technical assistance regarding vacuum carburization
- Soli Deo gloria

REFERENCES

1. G. Parrish and G.S. Harper, *Production Gas Carburizing*, Pergamon Press, 1985
2. W.F. Gale and T.C. Totemeier, Ed., Chapt. 29, Heat Treatment, *Smithells Metals Reference Book*, Butterworth-Heinemann, 2003
3. O. Karabelchtchikova, "Fundamentals of Mass Transfer in Gas Carburizing," Dissertation, Worchester Polytechnic Institute, 2007

4. "Gold Probe Instruction Manual, Rev. C," Super Systems, Inc.
5. T. Loetze, "Shim Stock Analysis," Technical paper, Super Systems Inc.
6. Thermo-Calc Software TCFE7 Steels/Fe-Alloys Database, Version 7, Stockholm, Sweden
7. G. Parrish, Chapt. 1, *Carburizing Microstructures and Properties*, ASM International, 1999

SELECTED REFERENCES

- J. Davis, Ed., *Surface Hardening of Steels: Understanding the Basics*, ASM International, 2002
- S. Gugel, Liquid Induction Carburizing/LIN-CARB/The First Induction Technology in Thermochemical Processing of Various Steels and Alloys, *21st Heat Treating Society Conference Proceedings*, ASM International, 2001
- G. Krauss, *Steels: Processing, Structure, and Performance*, ASM International, 2005
- T. Loetze, "Shim Stock Analysis (Technical Data)," Super Systems Inc.
- T. Loetze, "Zirconia Sensor Theory (Technical Data)," Super Systems Inc.
- *Metals Handbook Desk Edition*, 2nd ed., ASM International, 1998
- G. Parrish, *Carburizing: Microstructures and Properties*, ASM International, 1999
- M. Schneider, personal correspondence, Dec 2013
- V.K. Sharma, G.H. Walter, and D.H. Breen, An Analytical Approach for Establishing Case Depth Requirements in Carburised Gears, *J. Heat Treat.*, Vol 1, 1980
- W. Smith, *Structure and Properties of Engineering Alloys*, 2nd ed., McGraw-Hill, 1993
- J. Verhoeven, *Fundamentals of Physical Metallurgy*, Wiley, 1975

Evaluation of Carbon Control in Carburized Parts

Gary D. Keil and Olga K. Rowan, Caterpillar Inc.

WHEN STEEL PARTS are heated in an atmosphere that can either carburize or decarburize the surface, it is desirable to have a method of evaluating the accuracy of atmosphere control systems and the effect of the atmosphere on the surface carbon concentration and subsurface carbon profile in parts. Some of the methods discussed in this article are similar to the methods for measuring case depth produced by carburizing or carbonitriding described in the article "Methods of Measuring Case Depth in Steels" in this Volume.

Hardness Testing

The following are examples of different hardness test methods used to measure the effectiveness of surface carbon control. All possible sources of error should be considered before adopting a particular method, including evaluation of the depth of the hardness indenter penetration in relation to the desired depth of carbon evaluation:

- Surface hardness measurements taken under at least two conditions of loading (for example, Rockwell C and superficial Rockwell 15N)
- Superficial Rockwell 15N tests on steps ground below the surface to significant depths
- Microhardness measurements on a cross section through the carbon control zone
- Superficial hardness or microhardness taken on an oblique cut surface. This method is standardized in SAE J423 and SAE ARP 1820 and would be an alternative to the step-grind method.

Detection of partial or complete decarburization with a combination of Rockwell testing loads requires development of hardness-checking procedures and hardness limits established with samples having known levels of decarburization. If maximum hardness is required at the surface, as in wear applications or applications requiring high contact fatigue resistance, decarburization less than 0.08 mm (0.003 in.) deep

may not be readily revealed by surface Rockwell hardness measurements. Very shallow levels of decarburization require microhardness testing, metallographic evaluation, or a proper file hardness check.

Superficial Rockwell 15N testing on steps ground below the surface to significant depths provides an indication of carbon profile and the effectiveness of carbon-control systems. For example, if a carbon restoration operation were being performed and the original decarburization were deeper than anticipated, the low carbon in the incompletely restored zone between the carbon-restored zone and the core could be detected by the step-grind and hardness test method, whereas it may not be detectable by a surface hardness reading.

Microhardness testing on a cross section through the carbon-control zone is one method of evaluating carbon control. With this method, each hardness impression is supported by metal of like composition. Variations in carbon content that affect hardness can be detected at any depth. This method has the disadvantage of requiring a metallographically prepared cross section and special hardness-testing equipment that may not be readily available in all laboratories.

When hardness testing is used to evaluate carbon control, it should be remembered that the maximum as-quenched hardness is attained at approximately 0.80% C in plain carbon steels and at lower carbon contents in alloy steels, depending on the types and percentages of alloying elements present. If variations in carbon content above the level required to produce maximum hardness are significant, hardness measurements are not capable of evaluating carbon control. Low hardness in quenched parts or test specimens can be caused by many different process problems, such as insufficient quenching, excessive retained austenite, or low carbon content. Therefore, hardness measurements should be supplemented by metallographic evaluation or other test methods outlined subsequently to determine the proper root cause of low hardness and enable proper process corrective actions.

Microscopic Examination

Microscopic examination reveals surface carbon variations that are manifested by variation in microstructure. The effect of carbon content on microstructure varies from steel to steel. It also varies for a given steel, depending on the thermal treatment of the sample. When using either the pearlite/ferrite ratio or the carbide/pearlite ratio to estimate carbon content in non-martensitic microstructures, it should be noted that cooling rates strongly affect these ratios. Rapid cooling rates suppress formation of proeutectoid phases, resulting in higher pearlite ratios. The microscopic method of estimating carbon content is best used on steels with which experience has been gained in correlating microstructures on samples subjected to similar cooling rates with carbon gradients determined by quantitative carbon measurements.

If annealed samples are used, annealing must be carried out in the proper atmosphere, or errors may result from carburization or decarburization during the annealing cycle. The use of an inert atmosphere or a copper-plated sample is best. The microscopic method can detect smaller variations in carbon content than hardness testing, but does not yield quantitative data for very slight variations in carbon content. Because metallographic evaluation requires destructive sample preparation, appropriate testpieces are used when expensive parts are involved. Microscopic examination can be used to determine the microstructural constituents discussed as follows.

Ferrite. The presence of ferrite on the surface usually indicates partial or total decarburization. Total decarburization at the steel surface is typically accompanied by partial decarburization below the surface.

Pearlite. When the steel is annealed, a microstructure consisting of 100% pearlite indicates eutectoid carbon content. The ratio of pearlite to free ferrite for hypoeutectoid steels or the ratio of pearlite to proeutectoid carbide for hypereutectoid steels can be used to estimate carbon content.

Austenite. Carburization may cause some steels to retain excessive amounts of austenite in the near-surface region after hardening. Because both austenite and ferrite are soft, microscopic examination should be used to distinguish a sample with excessive retained austenite from one that has become decarburized.

Martensite. Variations in response to etching can indicate variations in carbon content. Familiarity with the microstructure of a particular steel and the etching response versus known carbon variation is important for the correct interpretation of etching variations.

Analysis of Consecutive Cuts

The analysis of consecutive cuts can be used to accurately evaluate the carbon concentration profile of carburized parts. This method requires very accurate machining of samples to obtain reliable information. This type of evaluation is usually performed on cylindrical test bars (often called carbon step bars) heat treated together with the work load. In the bearing industry, turnings are often obtained directly from as-carburized bearing rings, and the samples are referred to as cut rings.

The consecutive-cuts method is used most frequently on carburizing parts to quantitatively measure the carbon gradient and evaluate the case depth to a specific carbon level (i.e., the carburized case depth). This method is particularly useful in understanding the shape of a carbon gradient as it relates to carburizing process parameters, such as selection of boost-diffuse time ratios and carbon potentials at various stages of the carburizing cycle.

Carbon step bars should be made of the same grade of steel as that of the workpieces and should be accurately machined on centers to true cylindrical shape with minimum taper. Dimensions of a typical carbon step bar are shown in Fig. 1, although the diameter of the bar can be adjusted to represent critical regions of the workpieces to be evaluated. The length of the test bar need only be sufficient to allow enough turnings for a carbon analysis using the combustion method in accordance with ASTM E1019-11 and a check analysis.

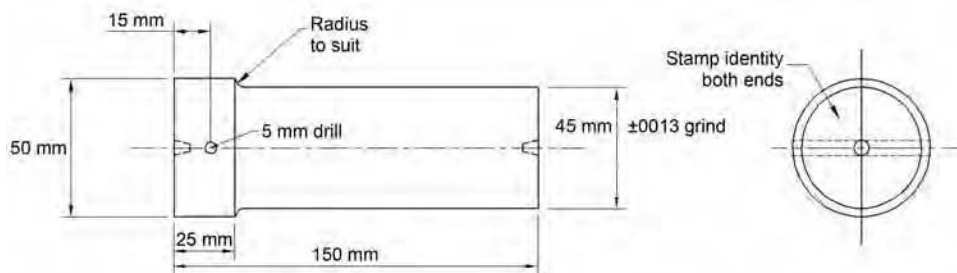


Fig. 1 Typical carbon step bar used for analysis of consecutive cuts

Before machining, the carbon step bar should be thoroughly cleaned with degreasing cleaner to remove any remnants of soot or quench oil. Bars should not be handled with bare hands after cleaning and prior to machining. Lathes used to cut sample chips must be capable of cutting less than 0.015 mm (0.0006 in.) taper over the test length. Carbon step bars are cut dry at very slow speeds to avoid burning, which would lower the carbon level and invalidate the sample. Chips should be collected on clean paper or in a clean chip tray and must be completely free of contamination by oil or grease. The lathe should be cleaned well to remove residual chips and oil from the tool holder before chucking a new sample and between cuts, to prevent mixing of chips from previous cuts. Often, ceramic inserts are used to avoid contamination of sample chips caused by tool breakdown when using carbide inserts. It is recommended that chip breakers be used to keep chips small.

Before making sample cuts, machine off the end material to remove all carburized material, and index the start of each cut from the previous cut, as shown in Fig. 2. To detect the effect of the final atmosphere exposure on the near-surface carbon gradient, three to four initial cuts of 0.025 mm (0.001 in.) thickness should be made. Thereafter, greater-depth cuts can be made through the case. Table 1 shows a typical series of recommended cuts for a 45 mm (1.8 in.) carbon step bar. Carbon step bars should be carefully measured before and after each cut, and the actual diameters recorded on the sample chip envelope. The carbon content is correlated to the average depth of the cut and is calculated as follows:

$$\text{Depth} = (0.5 \cdot D_i - 0.25 \cdot D_b - 0.25 \cdot D_a)$$

where D_i is the initial diameter of the bar, D_b is the diameter before the cut, and D_a is the diameter after the cut.

Evaluation of Surface Carbon using Data from the Consecutive-Cuts Method. Generally, carbon step bars are not used to measure surface carbon content. However, the data can be used to estimate the surface carbon concentration quite accurately after certain carburizing cycles. Specifically, carburizing cycles conducted at a single temperature setpoint and

an atmosphere carbon potential below the carbon saturation limit in austenite (i.e., steady-state carburizing), followed by rapid cooling or quenching, create carbon profiles that are linear in the region extending from the surface to approximately $\frac{1}{2}$ of the total affected depth. The surface carbon concentration on steady-state carburized bars can be estimated by extrapolating the straight-line portion of the carbon profile to the vertical axis on a plot of carbon versus depth, as shown in Fig. 3. However, on boost-diffuse cycles, the surface carbon concentration on the step bar can be either higher, lower, or equal to the atmosphere carbon potential of the diffuse stage, depending on the boost-diffuse time ratio and the duration of the diffuse stage. In addition, the carbon profile after a boost-diffuse cycle is generally not linear; therefore, linear extrapolation will not be accurate. Even though the trend of the near-surface measurements can be used to estimate the surface carbon, one must understand that this is not exact.

The method of cooling carbon step bars can alter the carbon gradient near the surface. Carbon profiles obtained on carbon step bars are most representative of the actual carburized parts when the step bars are cooled with parts under the same cooling conditions. Carbon step bars that are hardened with parts are generally too hard for accurate machining of test chips, particularly for very shallow cuts at the surface. Annealing at 600 °C (1110 °F) in an inert atmosphere can soften the bars sufficiently to machine chips, but the annealing process can often distort the test bars into an out-of-round condition, making analysis of the first shallow cuts inaccurate. To keep step bars round and minimize machining problems, it is best to cool carbon step bars in air or the furnace atmosphere of a cooling chamber. Cooling in air may cause some decarburization up to a depth of 0.15 mm (0.006 in.). For example, to evaluate the carbon gradient on parts subjected to press quenching, a test bar is loaded onto the tray and subjected to the carburize cycle with the piece parts. When the parts are removed from the press quench chambers for quenching, the carbon step bar is also withdrawn and allowed to air cool. The step bar will be soft enough to machine accurately but will exhibit some carbon loss at the surface. Although the surface carbon

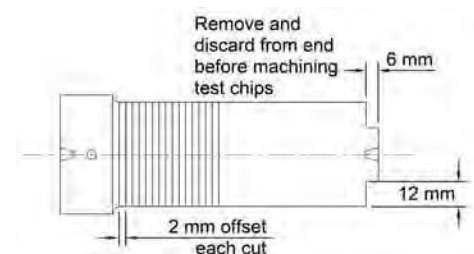
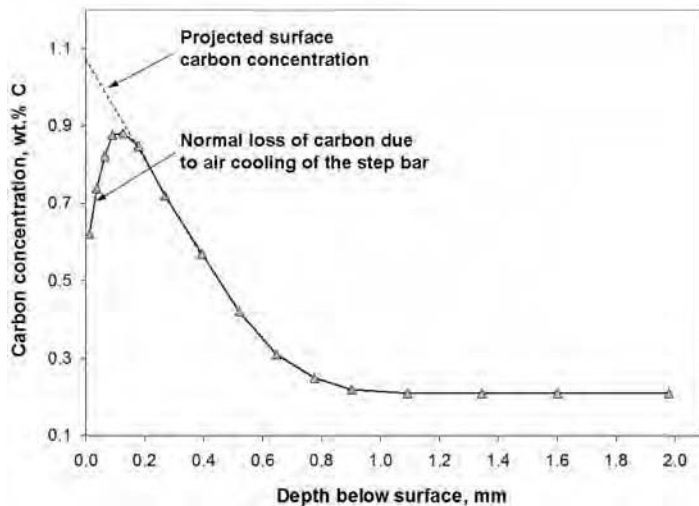


Fig. 2 Machining cuts on a carbon step bar

Table 1 Typical recommended cuts for 45 mm (1.8 in.) carbon step bar

Cut	Stock removal on radius		Stock removal on diameter		Diameter after cut		Nominal depth of cut	
	mm	in.	mm	in.	mm	in.	mm	in.
1	0.025	0.001	0.05	0.002	44.95	1.771	0.012	0.0005
2	0.025	0.001	0.05	0.002	44.90	1.769	0.037	0.0015
3	0.025	0.001	0.05	0.002	44.85	1.767	0.062	0.0024
4	0.025	0.001	0.05	0.002	44.80	1.765	0.087	0.0034
5	0.050	0.002	0.10	0.004	44.70	1.761	0.125	0.005
6	0.050	0.002	0.10	0.004	44.60	1.757	0.175	0.007
7	0.125	0.050	0.25	0.01	44.35	1.747	0.262	0.010
8	0.125	0.050	0.25	0.01	44.10	1.738	0.387	0.015
9	0.125	0.050	0.25	0.01	43.85	1.728	0.512	0.020
10	0.125	0.050	0.25	0.01	43.60	1.718	0.637	0.025
11	0.125	0.050	0.25	0.01	43.35	1.708	0.762	0.030
12	0.125	0.050	0.25	0.01	43.10	1.698	0.887	0.035
13	0.250	0.010	0.50	0.02	42.60	1.678	1.075	0.042
14	0.250	0.010	0.50	0.02	42.10	1.659	1.325	0.052
15	0.250	0.010	0.50	0.02	41.60	1.639	1.575	0.062
16	0.500	0.020	1.00	0.04	40.60	1.600	1.950	0.077
17	0.500	0.020	1.00	0.04	39.60	1.560	2.450	0.097
18	0.500	0.020	1.00	0.04	38.60	1.521	2.950	0.116
19	0.500	0.020	1.00	0.04	37.60	1.481	3.450	0.136

**Fig. 3** Method of extrapolating carbon gradient on step bar to determine the corresponding carbon profile in parts after steady-state carburizing

measurement is not representative of the piece part, the carbon gradient for depths greater than 0.15 mm (0.006 in.) accurately represents the carbon profile of the piece parts.

Carbon step bars cooled with parts under atmosphere may experience carbon loss or carbon pickup from the atmosphere during cooling. Some furnaces are designed to move the load from the carburizing chamber to a separate cooling chamber filled with nitrogen atmosphere and equipped with circulating fans. Nitrogen is normally considered to be an inert gas that does not react with the surface to remove carbon. However, when steel part surfaces are exposed to an atmosphere changing from approximately 20 to 23% CO to 0% CO, the rapid drop in CO content causes a rapid drop in the carbon potential and subsequent carbon loss at the steel surface. Because most cooling chambers have relatively high cooling rates, exposure time to low-carbon

atmosphere is short, and decarburization will be minimal depending on the mass of the part. Large parts that cool slower will experience greater carbon loss than smaller parts. However, in virtually all cases, this carbon loss is easily restored by reheat hardening in a proper atmosphere. Carbon step bars cooled with the parts will be soft enough to accurately machine test chips, and the resulting carbon profile is representative of the part carbon profile, including the loss of carbon at the surface if the mass of the test bar is approximately the same as the piece part. To accurately measure surface carbon loss from cooling chamber atmospheres on large parts, special large carbon step bars of similar size are required to ensure similar cooling rates and carbon loss.

Parts that are carburized above the saturation limit or near the saturation limit of carbon in austenite and cooled slowly (for example, large loads in pit-type carburizing furnaces)

may nucleate and grow carbides in the near-surface region. Carbon step bars run with these types of loads are soft enough to accurately machine test chips. If the step bar is made of the same alloy as the piece part, the measured carbon profile in the step bar will be representative of piece parts, including the surface region. If substantial levels of carbides are present at the surface, there will be two distinct gradients in the overall carbon profile, as shown in Fig. 4. One carbon gradient represents the normal carbon diffusion profile from the surface to the core, and the other represents the carbon gradient of the carbide region near the surface.

Analysis of Shim Stock

Measurement of atmosphere carbon potential is most accurately done with shim stock, either by weight gain or by combustion analysis for carbon content, in accordance with ASTM E1019-11.

A 0.1 to 0.15 mm (0.004 to 0.006 in.) thick piece of SAE 1010 plain carbon shim (approximately 25 by 100 mm, or 1.0 by 4.0 in.) is attached to an alloy rod that is inserted into the furnace through a port on the furnace wall. The shim stock is exposed to the carburizing atmosphere for a period of time sufficient to through carburize the shim and reach equilibrium with the carbon level in the gas atmosphere. The minimum required exposure time depends on the carburizing temperature and the thickness of the shim. Table 2 gives the minimum exposure time necessary to through carburize a 0.13 mm (0.005 in.) thick shim at various carburizing temperatures. Exposure for too little time may not permit carbon levels in the shim to equilibrate with the carbon in the gas atmosphere and will yield low readings not representative of the actual carbon potential in the furnace. As long as the furnace atmosphere composition is stabilized and controlled below the carbon saturation limit, shim exposure time in excess of the minimum required time to through carburize will not adversely affect the accuracy of the shim stock test.

If the weight-gain method is used, the shim is weighed before and after exposure to the furnace atmosphere. The gain in weight, as determined on an analytical balance scale with at least four decimal points accuracy, is used to calculate the carbon potential in the furnace atmosphere as:

$$C_p = \left(\frac{\text{Weight gain} \cdot 100}{\text{Final weight}} \right) + C_0$$

where C_p is the atmosphere carbon potential (wt%), and C_0 is the base carbon concentration in the steel part (wt%).

Figures 5(a) to (c) show the arrangement for exposing shim stock to the furnace atmosphere. The following procedures should be followed to ensure accurate shim test results:

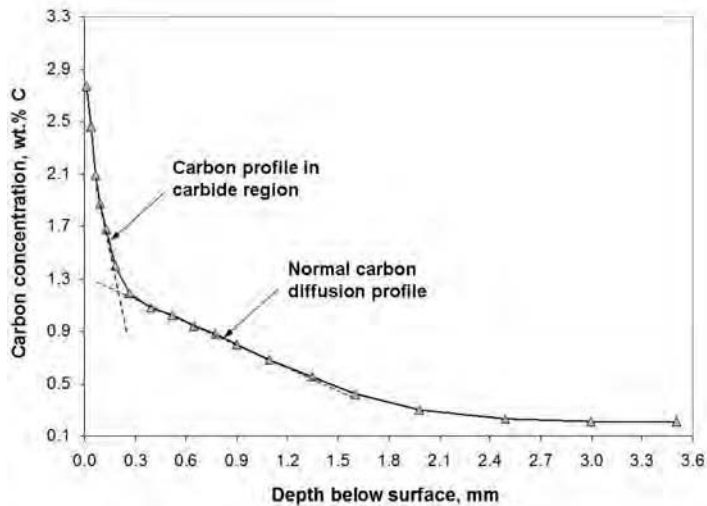


Fig. 4 Carbon concentration profile with carbide region in near-surface region

Table 2 Minimum carburizing time required to through carburize 0.13 mm (0.005 in.) thick shim stock at various carburizing temperatures

Temperature		Shim exposure time, min
°C	°F	
840	1545	45
860	1580	38
880	1620	32
900	1650	27
920	1690	22
940	1725	18
960	1760	16

cool, as shown in Fig. 5(c). Thin shims cooled quickly (less than 5 s) in either endothermic atmosphere or air will yield the same result if analyzed by the combustion method.

- The shim should be cleaned and accurately weighed or submitted for combustion analysis. Shims should not be handled barehanded prior to analysis, because this may leave fingerprints that can affect the accuracy of the carbon reading.

Special precautions include the following:

- The shim should not be rolled or wrapped tightly around the carbon potential rod. This permits only partial exposure of the shim to the atmosphere, causing a low carbon reading, and complicates removal of the shim for reweighing. Proper anchoring of the shim on the rod is accomplished by simply crimping the corners of the shim over the rod or wiring the shim to the rod at the ends of the shim, leaving the center area open to the atmosphere.
- The rod should not be withdrawn slowly or stepwise, because the composition of the shim can be altered by exposure to intermediate-temperature atmosphere in the wall section that does not have the same carbon potential as the furnace atmosphere.
- Slight oxide discoloration is typically not a problem on shims analyzed by the combustion method. If the weight-gain method of analysis is used, the oxide may cause slightly higher carbon readings to be obtained due to the weight of the oxide.
- If soot is present on the surface of the shim, it should be cleaned off prior to analyzing the shim.

The carbon analysis of a shim stock is representative of the carbon potential only if the furnace atmosphere is below the carbon saturation limit in austenite. While it is possible to calculate numerical values for atmosphere carbon potentials greater than saturation, they do not represent the actual carbon potential of the atmosphere, and the shim stock will not level off and equilibrate at the calculated supersaturated value. This phenomenon is demonstrated in Fig. 6, which shows the effect of exposure time

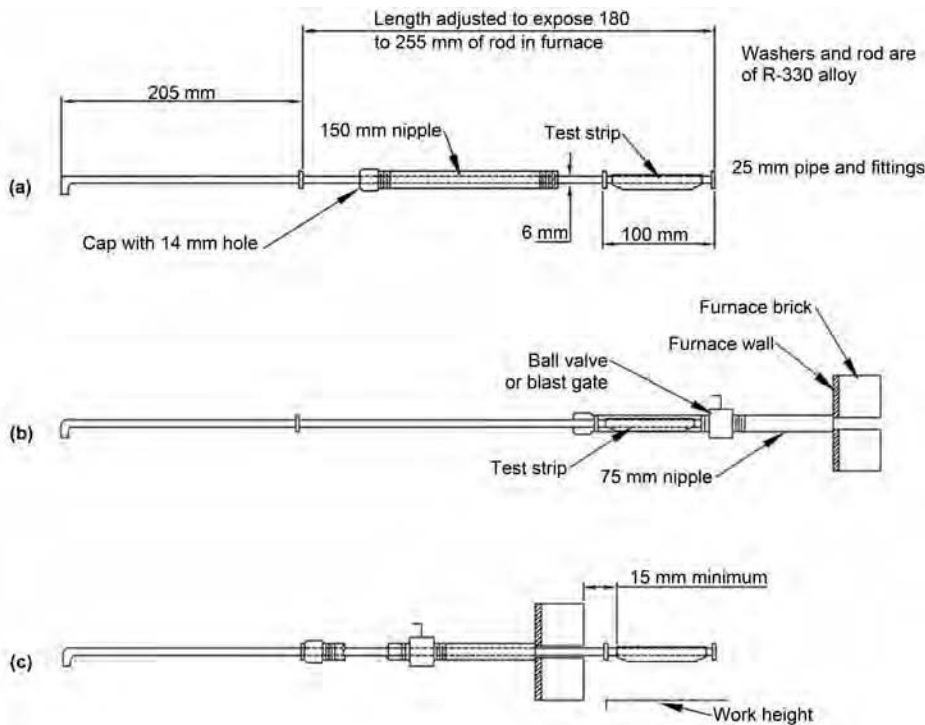


Fig. 5 Arrangement for exposing shim stock to furnace atmosphere for evaluation of carbon potential. (a) Assembly of shim stock on rod. (b) Assembly ready for insertion into furnace (same position used for cooling of shim). (c) Shim inserted into furnace atmosphere above work height

- Assemble alloy rod and shim as shown in Fig. 5(a). Shim should be cleaned well prior to insertion and must be free of oil and fingerprints.
- Ensuring first that the shim port valve is closed, insert the rod into the outer shim port section as shown in Fig. 5(b).
- Open the shim port valve and insert the shim stock into the furnace atmosphere above the

work height to a point at least 150 mm (6.0 in.) from the wall. Testing should be performed when the furnace atmosphere is under stable conditions and not subject to atmosphere composition spikes caused by door openings or other events.

- At the end of the recommended exposure time, shims should be withdrawn quickly into the outer pipe section and allowed to

on the experimentally measured carbon values of shims exposed to furnace atmospheres with calculated carbon potentials 0.15% below and 0.15% above the saturation limit (1.25% C) at 925 °C (1700 °F). When using shim stock in a controlled atmosphere with carbon potential below the carbon saturation limit in austenite, carbon concentration in the shim increases rapidly until it equilibrates with the carbon potential in the gas phase. Shim exposure in excess of the minimum time required to through carburize will not affect the carbon level attained in the shim, as shown in Fig. 6(a). If, however, shim stock is exposed to an atmosphere with carbon potential exceeding the carbon saturation limit in austenite, iron carbides will precipitate and grow within the shim. In this case, the overall carbon level in the shim will continue to increase with time (and not equilibrate with the calculated carbon potential) as the amount of carbide volume fraction increases, as shown in Fig. 6(b).

The validity of shim stock results can be determined by comparison of analysis values to the saturation carbon limit in austenite at a given carburizing temperature, as shown in Table 3. Shim stock analysis values greater than the carbon saturation only serve to inform that the atmosphere

is above saturation. The absolute carbon value in a supersaturated shim is not representative of the actual carbon potential in the furnace atmosphere and should not be used to adjust correction factors in atmosphere control systems.

Shim stock gives an accurate measure of the gas atmosphere carbon potential at the point of insertion. The carbon level attained in the shim is determined by the temperature of the shim and the exact composition of gas phase surrounding it. Therefore, carbon levels measured by shim stock are representative of the carbon potential of the atmosphere exposed to production parts only if the shim and the carburized parts are at the same temperature and exposed to the same gas composition.

It is important to realize that shim stock analysis is intended to provide a measurement of the atmosphere carbon potential, not the surface carbon level of the carburized part. Unless the part is thin enough to through carburize, the carbon level at the steel part surface does not reach thermodynamic equilibrium with the carbon in the atmosphere. For parts that are direct quenched from the carburize cycle, the surface carbon will normally be lower than the shim carbon reading. For parts that are reheat

hardened after carburizing, the part surface carbon can be either lower, higher, or equal to the shim reading, depending on whether carbides have precipitated in the part during the cooling or reheating process steps. The measurement of actual part surface carbon should be performed directly on parts by using a method of spectrographic analysis described subsequently.

Analysis of Rolled Wire

Rolled iron wire that is flattened into strip less than 0.13 mm (0.005 in.) thick may also be used for measuring carbon potential in the furnace atmosphere in much the same manner as shim stock is used, except that there are small differences in the design of the fixture on which the rolled wire is placed.

Spectrographic Analysis

The surface carbon concentration profile of a part can be accurately determined by spectrographic analysis. This method makes use of an arc spark source vacuum spectrometer, which permits the measurement of spectral lines in the ultraviolet region where air would ordinarily absorb much of the emitted radiation. Spectrographic analysis is normally performed on flat test specimens that can be taper ground, step ground, or reground incrementally after each carbon determination. Special care must be taken to ensure that the depth corresponding to each carbon determination is measured accurately. Typically, the depth of cut is smaller than the depth of burn from the spectrographic analysis. For best accuracy, the sample should have a sufficiently large flat surface area to allow multiple burns at each depth increment.

Measuring surface carbon content and the near-surface carbon gradient to a depth of 100 μm (4000 $\mu\text{in.}$) can be performed with

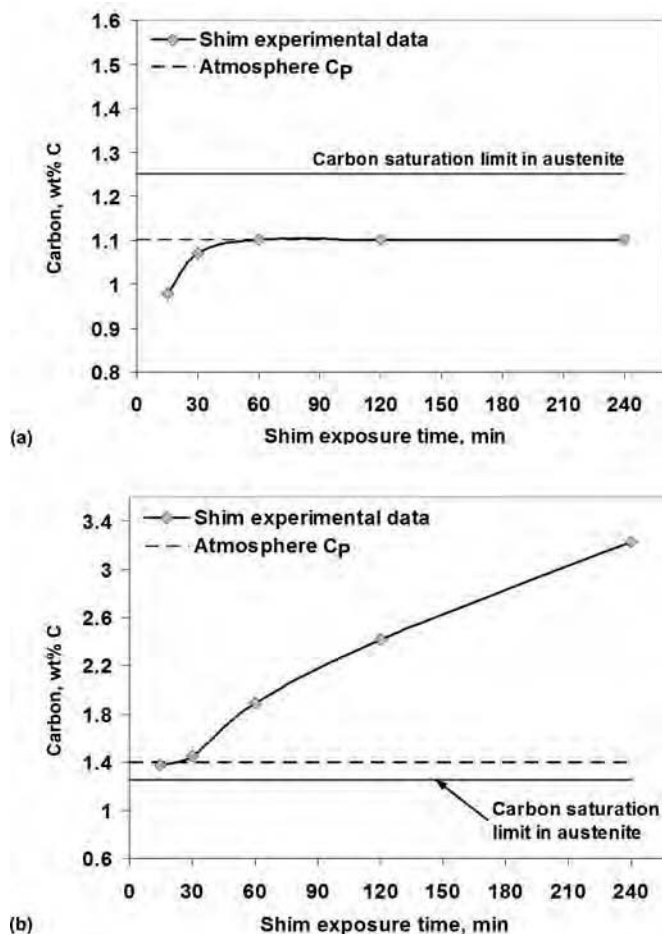


Fig. 6 Comparison of shim carbon readings analyzed by the combustion method with the atmosphere carbon potential at 925 °C (1700 °F). (a) 1.1 and (b) 1.4 wt% C atmosphere carbon potential

Table 3 Carbon saturation limit in austenite of plain carbon steel at various carburizing temperatures

Temperature		Carbon potential, wt% C
°C	°F	
810	1490	0.88
820	1510	0.91
830	1525	0.94
840	1545	0.97
850	1560	1.01
860	1580	1.04
870	1600	1.07
880	1620	1.10
890	1635	1.13
900	1650	1.17
910	1670	1.20
920	1690	1.23
930	1705	1.27
940	1725	1.30
950	1740	1.33
960	1760	1.37
970	1780	1.40
980	1800	1.44
990	1815	1.47
1000	1830	1.50

instruments that use glow-discharge optical emission spectroscopy (GDOES) coupled with continuous quantitative depth profiling. This method allows the continuous measurement of chemical constituent gradients (including nitrogen and other elements) with nanometer resolution, whereas traditional arc spectroscopy operates by averaging material on the micrometer scale. The analysis can only be performed on a flat surface; thus, flat testpieces should be included in loads of gears, bearings, or other round parts to provide an acceptable test surface.

Electromagnetic Testing

Two types of electromagnetic nondestructive tests have been used to evaluate the case depth of case-hardened parts. One compares the magnetic properties of a part with those of a test standard, and the other measures coercive force, which is then converted to case depth through use of a calibration chart.

Magnetic-Comparator Testing. The electromagnetic test is performed by placing the part to be tested in an induction coil. A reference part of known electromagnetic response is placed in a second coil. Both parts are simultaneously subjected to identical electromagnetic fields, and their responses to these fields are compared by an electronic balancing circuit. Any imbalance between responses (indicated by a meter) is a function of the following properties of the test object: chemical composition, microstructure,

case depth, surface flaws, residual stress, and work hardening.

Many electromagnetic instruments are capable of breaking down an electromagnetic response into inductive components, resistive components, third-harmonic amplitude, and phase differences. The user must correlate these variables with the property or properties to be evaluated.

Standards and Test Procedures. The electromagnetic (eddy-current) test for case depth measurement can be used only as a comparison test. Thus, the accuracy and usefulness of this test depend on the proper development of standards and test procedures. Acceptance and rejection standards are required for each part design to be evaluated. Once standards are developed and instrument settings are selected, production parts can be tested by comparison with the standards. Sufficient destructive testing must be carried out to produce the data required for the construction of a chart or graph by which meter readings can be converted to case depths with reasonable confidence. Periodic destructive testing should be carried out to reconfirm this correlation.

In a production situation involving many parts and wide differences in specified case depth, it is difficult and expensive to establish standards for all parts. To overcome this problem, a procedure has been developed in which a standard test specimen is processed with each heat. Case depth of the test specimen is determined by magnetic comparison. The standards for carburizing a testpiece are developed using the procedure described previously, and these standards are correlated with actual parts by periodic destructive testing. One example of

Table 4 Reliability of electromagnetic test for case depth determination

Error	Case depth reading error	
	mm	in.
Average error	0.1	0.004
Maximum error (3% of the time)	0.44	0.017
Minimum error (18% of the time)	0	0

a standard test specimen is 11 mm square by 75 mm long (0.4 by 3.0 in.) and made from a cold-finished bar of coarse-grained, silicon-killed SAE 1018 modified steel with residual elements held to low levels. Testing of the standard specimen may yield results that are different from those obtained with actual parts, but once a correlation is established with the standard testpiece rather than actual parts, the testpiece may be used with sufficient reliability.

Effectiveness and Limitations. Table 4 shows electromagnetic test reliability for the determination of case depth.

The magnetic-comparator test will indicate whether a production lot is acceptable or of questionable quality. Destructive tests must then be conducted on questionable lots to determine which variables are out of specification and to assist in devising corrective measures. Case depths of up to 5 mm (0.2 in.) may be measured. This method has been found to be more reliable for induction-hardened cases than for carburized cases. The chief variable that can adversely affect measurements is the case-to-core transition zone, which is much wider in carburized cases than in induction-hardened cases.

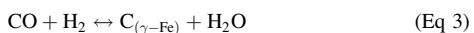
Gas Carburizing

Olga K. Rowan and Gary D. Keil, Caterpillar Inc.

CARBURIZING is a case-hardening process in which steel parts (usually low-carbon steel) are heated to an austenitizing temperature and exposed to a carbon-rich atmosphere. Carbon is absorbed at the surface and diffuses down the chemical potential gradient to create a carbon-rich surface and a decreasing carbon concentration profile with a low-carbon steel core. Subsequent hardening of the carburized parts produces a hardness profile that is dependent on the carbon gradient, steel hardenability, and quench severity of the hardening operation. The carburized and hardened case enhances wear and fatigue resistance and produces surface residual compressive stresses. Gas carburizing is the most common and commercially the most important variant of carburizing. Gaseous hydrocarbons, such as methane (CH₄), propane (C₃H₈), and butane (C₄H₁₀), or vaporized hydrocarbon liquids, are normal sources of carbon in the gas atmosphere.

Thermodynamics and Kinetics

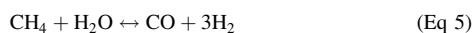
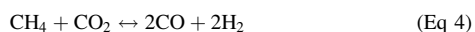
Gas Carburizing Reactions. From a thermodynamic standpoint, generation of the carburizing atmosphere is a rather complex process involving the interaction of numerous gas species and their simultaneous reactions with each other and the steel surface. Of the various chemical reactions occurring in the carburizing atmosphere, only the following three reactions are important and determine the rate of carbon transfer from the gas carburizing atmosphere to the steel surface (Ref 1):



Although the reaction in Eq 1 is commonly used to calculate the carburizing potential of an atmosphere, the reaction in Eq 3 dominates the rate of carburizing (Ref 2). The reaction in Eq 2 contributes to a lesser extent in gas-based carburizing than the reactions in Eq 1 and 3. The by-products

of the carburizing reactions, CO₂ and H₂O, act as decarburizing agents. The fact that these reactions are reversible enables the carbon potential of the atmosphere to be controlled to a specific level by maintaining a careful balance between the amount of CO-CO₂ and H₂O-H₂ present in the gas atmosphere. The implication of the thermodynamics is that the levels of CO and H₂ must be constantly replenished to sustain a carburizing atmosphere that proceeds in the forward direction. (Ref 3).

Gas carburizing atmospheres are often generated by enriching an endothermic carrier gas with methane. The carburizing potential of endothermic gas without hydrocarbon enrichment is not sufficient to produce significant carburization solely by CO decomposition at typical carburizing temperatures. Enriching with a hydrocarbon gas boosts the carbon potential of the endothermic carrier gas and provides a means of controlling the carburizing atmosphere. The primary purpose of the enriching gas is to regenerate CO and H₂ gas constituents by reducing decarburizing CO₂ and H₂O agents and thus directing carburizing gas reactions (Eq 1 and 3) to the right:



The net result of the chemical reactions in Eq 1 and 4 or the reactions in Eq 3 and 5 indicates that for every atom of carbon absorbed by the steel surface, one molecule of methane is consumed to maintain the CO concentration, and two additional molecules of hydrogen are introduced to the atmosphere. A sufficient carrier gas flow must be established in the gas carburizing furnace to mitigate H₂ dilution and to maintain the desired CO level. In continuous furnaces, carrier gas flows that typically produce atmosphere with H₂ levels ~2 to 3% higher than the nominal H₂ level of the carrier gas are deemed sufficient and enable good CO-level retention and overall control of the process. H₂ levels higher than 3% above nominal carrier gas composition indicate insufficient carrier gas flow. Hydrogen-diluted atmospheres are characterized by CO levels below nominal carrier gas levels and contain higher free-

methane levels. In batch furnaces, carburizing atmospheres after load introduction and during heatup often exhibit high H₂ and CH₄ levels for a relatively short period of time, then decay to levels similar to those described for continuous carburizers. Although the intended role of adding methane is to regenerate the carburizing CO species, it can also do one of the following: 1) exist in the atmosphere as unreacted free methane, 2) react directly at the steel surface according to the reaction in Eq 2, or 3) decompose to form soot.

Carburizing atmospheres formed by hydrocarbon enrichment do not reach true thermodynamic equilibrium—thus resulting in residual methane in the carburizing chamber (Ref 4). Residual methane is observed in all types of carburizing atmospheres, and therefore, a limited amount (up to 1.5%) is considered normal. Larger concentrations of residual methane (>1.5%) have a stronger driving force for soot formation (Ref 5, 6). Gas atmospheres with more than 2% residual methane are often regarded as “out of control” because further enriching gas additions do not increase the effectiveness of the reduction reactions in Eq 4 and 5, but rather promote soot formation and higher levels of unreacted free methane in the gas atmosphere.

Calculation of Equilibrium Gas Composition. Thermodynamic data for gas equilibrium are useful in determining the carburizing potential of a furnace atmosphere despite the non-equilibrium conditions encountered in a typical industrial process. The gas chemical reaction (Eq 3) approaches equilibrium fast enough to permit calculations of the equilibrium atmosphere composition. The same carburizing response can be expected from different furnaces with different atmosphere gas flow rates when the following factors are held constant:

- Steel chemical composition
- Carbon potential, as calculated from CO/CO₂, or CO/O₂ partial pressure measurements
- Carburizing time
- Carburizing temperature

The following approach can be used to calculate the equilibrium gas composition in the furnace after hydrocarbon gas enriching (Ref 7):

- Mixing air and natural gas in a fixed ratio at a constant temperature produces an atmosphere consisting of seven gaseous species: CO, CO₂, H₂, H₂O, C_xH_y, O₂, and N₂. Summation of partial pressures of all gas constituents at ambient atmospheric pressure is 1. Therefore, if the partial pressures of six gas components are known, the partial pressure of the seventh component can be determined.
- The ratio of C/H atoms is fixed by the stoichiometry of the hydrocarbon gas and can be used to relate the partial pressures of CO, CO₂, C_xH_y, H₂, and H₂O.
- The ratio of O/N atoms is fixed by the stoichiometry of air composition and relates the partial pressure of N₂ to CO, CO₂, H₂O, and O₂.
- The ratio of C/O atoms is fixed by the air-to-fuel gas ratio and relates the partial pressure of C_xH_y to CO, CO₂, H₂O, and O₂.
- Further, considering H₂O/H₂, CO/CO₂, and CH₄/CO₂ equilibrium gas reactions and their Gibbs free energies provides three additional equations relating the unknown partial pressures.
- Further mathematical simplifications reduce the seven equations described earlier to a system of four equations with four unknowns (partial pressure of CO, CO₂, H₂, and H₂O) that can be solved simultaneously using a nonlinear least-square optimization routine.

Kinetics of Gas Carburizing Reactions.

Kinetics of various gas-steel interactions and the mechanism of their reactions in the CO-H₂-CO₂-H₂O system have been studied by Fruehan (Ref 8, 9) and Grabke (Ref 10) using gravimetric, resistometric-relaxation methods and isotope exchange reactions. More specific to the industrial gas carburizing application, Kaspersma and Shay (Ref 11, 12) experimentally determined rate constants for the main carburizing and decarburizing chemical reactions in N₂-base carburizing atmospheres using low-carbon shim stock. Combining the effect of the individual reaction rate constants and typical partial pressures of the furnace atmosphere constituents, the overall reaction rates were calculated, as shown in Table 1 (Ref 13).

Table 1 Rate constants (*k*) for carburizing (+) and decarburizing (–) chemical reactions

Chemical reaction for rate constant	Reaction rate, mol/cm ² min
2CO $\xrightarrow{k_1}$ C _(γ-Fe) + CO ₂	+5.6 × 10 ⁻⁷
CO ₂ + C _(γ-Fe) $\xrightarrow{k_2}$ 2CO	-1.3 × 10 ⁻⁶
H ₂ + CO $\xrightarrow{k_3}$ C _(γ-Fe) + H ₂ O	+1.8 × 10 ⁻⁵
H ₂ O + C _(γ-Fe) $\xrightarrow{k_4}$ H ₂ + CO	-1.5 × 10 ⁻⁵
CH ₄ $\xrightarrow{k_5}$ C _(γ-Fe) + 2H ₂	+3 × 10 ⁻⁷
2H ₂ + C _(γ-Fe) $\xrightarrow{k_6}$ CH ₄	-2.7 × 10 ⁻⁸

Note: Temperature = 927 °C (1701 °F); calculations assumed the following furnace atmosphere using endothermic gas composition of 20 vol% CO, 40 vol% H₂, 3 vol% CH₄, 1800 ppm H₂O, and 1800 ppm CO₂. Source: Ref 13

Carburization by CO + H₂, carburizing reaction in Eq 3, was determined to proceed approximately 31 times faster than carburization by direct CO decomposition and 59 times faster than carburizing by direct CH₄ decomposition at the steel surface. Decarburization by H₂O is approximately 16 times faster than it is by CO₂. The data also showed that CH₄ is much less effective as a carburizing agent than any of the higher-molecular-weight hydrocarbons (Ref 12).

Grabke (Ref 10) and Collin et al. (Ref 1) developed expressions to describe the reaction rate coefficients for CO and CH₄ decomposition reactions (Eq 1 and 2) and CO + H₂ reaction (Eq 3), respectively:

$$k_1 = 184 \cdot \left(\frac{P_{CO_2}}{P_{CO}}\right)^{-0.3} \cdot P_{CO_2} \cdot \exp\left(\frac{-22,400}{T}\right) \quad (\text{Eq 6})$$

$$k_2 = 1.96 \cdot 10^{-2} \cdot P_{H_2}^{1.5} \cdot \exp\left(\frac{-17,600}{T}\right) \quad (\text{Eq 7})$$

$$k_3 = \frac{4.75 \cdot 10^5 \cdot \exp\left(\frac{-27,150}{T}\right) \cdot \frac{P_{H_2O}}{\sqrt{P_{H_2}}}}{1 + 5.6 \cdot 10^6 \cdot \exp\left(\frac{-12,900}{T}\right) \cdot \frac{P_{H_2O}}{\sqrt{P_{H_2}}}} \quad (\text{Eq 8})$$

where *k_i* is the reaction rate coefficient for *i*-th chemical reaction (centimeter/second), *P_i* is the partial pressure of the *i*-th gas constituent in the furnace, and *T* is the absolute temperature (Kelvin).

Calculation and Measurement of Carbon Potential. The atmosphere carbon potential at a given temperature is calculated from the equilibrium gas composition and the corresponding carbon activity. From thermodynamics of gas chemical reactions, the carbon activity in the gas atmosphere can be calculated

from any of the three carburizing reactions as follows:

$$a_{C_1}^{\text{gas}} = \frac{P_{CO}^2}{P_{CO_2}} \cdot K_1, \text{ where } K_1 = \exp\left(\frac{20,530.65}{T} - 20.98\right) \quad (\text{Eq 9})$$

$$a_{C_2}^{\text{gas}} = \frac{P_{CH_4}}{P_{H_2}^2} \cdot K_2, \text{ where } K_2 = \exp\left(\frac{10,949.68}{T} - 13.31\right) \quad (\text{Eq 10})$$

$$a_{C_3}^{\text{gas}} = \frac{P_{CO} \cdot P_{H_2}}{P_{H_2O}} \cdot K_3, \text{ where } K_3 = \exp\left(\frac{16,333.11}{T} - 17.26\right) \quad (\text{Eq 11})$$

where *a_C^{gas}* is the carbon activity in the gas phase, *P_i* is the partial pressures of *i*-th gas constituent in the gas atmosphere, and *K₁*, *K₂*, and *K₃* are the equilibrium constants calculated from the Gibbs free energy of the corresponding gas chemical reactions.

The carbon activity is related to the carbon content of austenite by the expression (Ref 14):

$$\ln a_C^{\text{gas}} = \ln y_C + \frac{9167 \cdot y_C + 5093}{T} - 1.867 \quad (\text{Eq 12})$$

with

$$y_C = \frac{4.65 \cdot w}{100 - w} \quad (\text{Eq 13})$$

where *T* is the absolute temperature (Kelvin), *y_C* is the atom ratio of carbon to iron, and *w* is the weight percent carbon in austenite. Figure 1 and Table 2 show the calculated carbon potential in the gas atmosphere as a function of carbon activity at various temperatures.

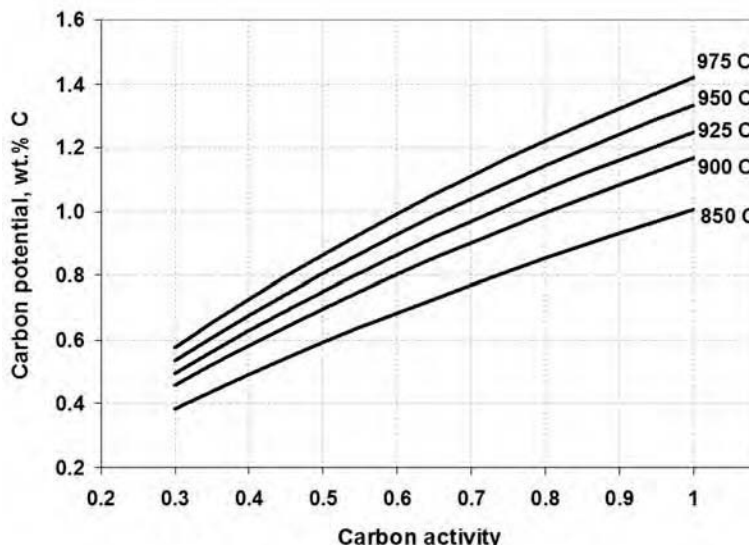


Fig. 1 Correlation of carbon potential and carbon activity at various carburizing temperatures

Table 2 Correlation of carbon potential and carbon activity at various carburizing temperatures

Carbon activity	Carbon potential, wt% C				
	850 °C (1560 °F)	900 °C (1650 °F)	925 °C (1700 °F)	950 °C (1740 °F)	975 °C (1790 °F)
0.3	0.39	0.46	0.50	0.54	0.58
0.4	0.49	0.58	0.63	0.68	0.73
0.5	0.59	0.70	0.75	0.81	0.87
0.6	0.68	0.80	0.86	0.93	0.99
0.7	0.77	0.90	0.97	1.04	1.11
0.8	0.85	1.00	1.07	1.14	1.22
0.9	0.93	1.08	1.16	1.24	1.32
1	1.01	1.17	1.25	1.33	1.42

In carburizing atmospheres controlled to carbon potentials below saturation, the carbon potential calculated from carbon activity defined by Eq 9 and 11 will typically yield the same value and will match the carbon value measured by accurate shim stock analysis of the atmosphere. However, when the actual measured partial pressures of CH₄ and H₂ of the same atmosphere are used to calculate the carbon activity defined by Eq 10, the calculated carbon potential is usually much higher (well above the carbon saturation limit) and does not match the value of atmosphere shim stock analysis. This observation is normal in industrial carburizing furnaces where thermodynamic equilibrium is not achieved and the residual methane concentration exceeds the equilibrium CH₄ level. For example, a gas carburizing furnace using a combination of natural gas and endothermic gas with 20% CO, controlled to 1.1 wt% C at 925 °C (1700 °F), should have a calculated CH₄ content of 0.22 vol% at equilibrium. Typical measured CH₄ levels are in the 1.0 vol% range. The kinetic rate of the carburizing reaction (Eq 3) is approximately 2 orders of magnitude higher than the rate of carburizing by CH₄ (Eq 2) and therefore it dominates the overall carbon flux into the steel surface. Accordingly, experimentally measured shim stock readings are typically found to agree with the carbon potential calculated from Eq 9 and 11 according to the reactions in Eq 1 and 3.

Calculation of the atmosphere carbon potential by the reaction in Eq 3 requires input of the measured CO, H₂, and H₂O vapor concentration. In practice, high-accuracy continuous measurement of water vapor in carburizing atmospheres is difficult. However, the water-gas reaction:



has a relatively high reaction rate and serves to effectively establish an equilibrium between the CO, CO₂, H₂, and H₂O, ensuring that the carbon potentials calculated according to Eq 1 and 3 are equal. High-accuracy measurement of CO and CO₂ with nondispersive infrared (NDIR) analyzers is well established; thus, calculation of the atmosphere carbon potential from the ratio of CO/CO₂ according to the

reactions in Eq 1 and 9 is an effective way of characterizing the carbon potential of the dominant reaction in Eq 3 without the need to measure water vapor directly.

Zirconia oxygen probes are significantly lower in cost than NDIR analyzers and are more commonly applied in industrial gas carburizing applications. The calculation and control of carbon potential by oxygen probe is based on the following equilibrium reaction:



The voltage output of a zirconia oxygen sensor in millivolts, with air as a reference gas, is a function of the absolute temperature (T) in Kelvin and the oxygen partial pressure (P_{O_2}) according to the expression:

$$\text{emf} = 0.04953 \cdot T \cdot \log_{10} \left(\frac{P_{\text{O}_2}}{0.2095} \right) \quad (\text{Eq 16})$$

Carbon activity can be calculated from the partial pressure of CO and O₂ at a given carburizing temperature (Kelvin):

$$a_{\text{C}}^{\text{gas}} = \frac{(P_{\text{CO}})}{\sqrt{P_{\text{O}_2}}} \cdot K, \text{ where } K = \exp \left(-\frac{13,434.52}{T} - 10.54 \right) \quad (\text{Eq 17})$$

For furnace atmospheres with stable CO levels, such as those using carrier gases produced in separate endogas generators, many control systems provide reasonable accuracy when the CO level is constant over time and is equal to the carrier gas nominal value. Atmospheres with unstable CO levels, such as those generated in-situ with hydrocarbon gas-air mixes or vaporized hydrocarbon liquid-nitrogen mixes, require measurement of actual CO levels with NDIR systems to obtain the best furnace control accuracy.

When atmospheres are subjected to sudden equilibrium upsets by large air introduction during door openings, introduction of combustion products by leaking burner tubes, or water leaks, the carbon potential is usually more accurately determined by CO₂ measurement rather than O₂ measurement. The CO₂ is held in equilibrium with the CO, H₂, and H₂O by the water-gas reaction (Eq 14), whereas the partial pressure of O₂ reaches equilibrium slower and may not accurately indicate carbon potential.

Validation of Carbon Potential via Shim Stock. Measurement of atmosphere carbon potential and validation of the calculated carbon potential from the gas atmosphere analysis is most accurately done with shim stock using combustion analysis for carbon content in accordance with ASTM E1019-11. A 0.1 to 0.15 mm (0.004 to 0.006 in.) thick piece of plain carbon shim stock (approximately 25 by 100 mm, or 1.0 by 4.0 in.) is attached to an alloy rod that is then inserted into the furnace through a port in the furnace wall. The shim

stock is exposed to the carburizing atmosphere for a period of time sufficient to reach equilibrium with the carbon level in the gas atmosphere (i.e., through carburize the shim). The minimum required exposure time depends on the carburizing temperature and thickness of the shim. Table 3 shows the minimum exposure time necessary to through carburize a 0.13 mm (0.005 in.) thick shim at various carburizing temperatures. Exposure for too little time may be insufficient to equilibrate carbon levels in the shim with carbon in the gas atmosphere and may yield low-carbon readings not representative of the actual carbon potential in the furnace. As long as the furnace atmosphere composition is stabilized and controlled below the carbon saturation limit, shim exposure time in excess of the minimum required time to through carburize will not adversely affect the accuracy of the shim stock test.

It is important to realize that shim stock analysis is intended to provide a measurement of atmosphere carbon potential, not the surface carbon level of the carburized part. Unless the part is thin enough to through carburize, carbon level at the steel part surface does not reach thermodynamic equilibrium with the carbon in the atmosphere and will always be lower than the shim carbon reading. The measurement of actual part surface carbon should be performed directly on parts by using one of the methods described in the article "Evaluation of Carbon Control in Carburized Parts" in this Volume.

Shim stock gives an accurate measure of the gas atmosphere carbon potential at the point of insertion. The carbon level attained in the shim is determined by the temperature of the shim and the exact composition of gas phase surrounding it. Therefore, carbon levels measured in shim stock are representative of the carbon potential of the atmosphere exposed to production parts only if the shim and the carburized parts are at the same temperature and exposed to the same gas composition.

Placement of the shim stock should be at least 150 mm (6.0 in.) into the working zone of the furnace to avoid the cool wall effect. Care must be taken that the holder rod does not interfere with parts that may move (e.g., in pusher-type furnaces) during the period that the shim is inserted. Shims should be cleaned well prior to insertion and must be free of oil

Table 3 Minimum carburizing time required to through carburize 0.13 mm (0.005 in.) thick shim stock at various carburizing temperatures

Temperature		Shim exposure time, min
°C	°F	
840	1545	45
860	1580	38
880	1620	32
900	1650	27
920	1690	22
940	1725	18
960	1760	16

and fingerprints. After insertion for the recommended time at a given carburizing temperature, shims should be withdrawn quickly into the cool part of the shim port (filled with furnace atmosphere) or withdrawn to rapidly air cool. Thin shims cooled quickly (less than 5 s) in either endothermic atmosphere or air will yield the same result if analyzed by the combustion method. Thin shims react quickly to changing atmosphere conditions or upsets caused by furnace cycling and/or door openings. For this reason, shim stock tests should be conducted during periods of atmosphere stability for the minimum exposure time sufficient to through carburize the shim.

Characterizing an atmosphere by calculation of the carbon potential is only valid for atmospheres with carbon potentials below saturation. While it is possible to calculate numerical values for atmosphere carbon potentials greater than saturation, they do not represent the actual carbon potential of the atmosphere, and shim stock readings will not level off and equilibrate at the calculated supersaturated value. This concept is demonstrated in Fig. 2 and Fig. 3, which show the effect of exposure time on the measured shim readings in atmospheres with calculated carbon potentials 0.15% below and 0.15% above the saturation limit (1.25% C) at 925 °C (1700 °F). When using shim stock in a controlled atmosphere with carbon potential below the carbon saturation limit in austenite, carbon concentration in the shim increases rapidly until it equilibrates with the carbon potential in the gas phase. Shim exposure in excess of the minimum time required to through carburize will not affect the carbon level attained in the shim, as shown in Fig. 2(a). If, however, shim stock is exposed to an atmosphere with carbon potential exceeding the carbon saturation limit in austenite, iron carbides will precipitate and grow within the shim, as seen in Fig. 3. In this case, the overall carbon level in

the shim will continue increasing with time (and not equilibrate with the calculated carbon potential) as the amount of carbide volume fraction increases, as shown in Fig. 2(b).

It is important that the validity of shim stock readings be confirmed by comparison to the carbon saturation limit in austenite at a given carburizing temperature, as shown in Table 4. Shim stock analysis values greater than the carbon saturation serve only to inform the heat treating engineer that the atmosphere is above saturation. The absolute carbon value in a supersaturated shim is not representative of the actual carbon potential in the furnace atmosphere and should not be used to adjust "correction" factors in atmosphere control systems.

Effect of Steel Alloy Composition. Alloy composition of the steel has an influence on the carbon activity and carbon diffusivity in austenite. Alloying elements affect the characteristic distribution of carbon atoms in the alloyed austenite matrix and the localized forces of their interactions (Ref 15, 16). Figures 4(a) to (c) schematically show the effect of various alloying elements on the distribution of interstitial carbon atoms and carbon activity in the austenite (Ref 17). In general, carbide-forming elements (molybdenum, chromium, vanadium, tungsten, etc.) induce positive atomic interaction and tend to attract interstitially diffusing carbon atoms (Fig. 4c). Such deviations from randomness impede carbon long-range diffusion in the matrix and decrease the overall rate of carbon diffusion. Austenite-stabilizing elements (nickel, copper, etc.) exhibit negative atomic interactions and tend to repel carbon atoms (Fig. 4b). As their binding energy decreases, there will be localized volumes with increased carbon diffusivity. For low-alloyed steels this influence may be negligible, while for medium- and high-alloyed steels the effect of alloying may be significant and should be taken into consideration.

Carbon activity in austenite (a_C^{steel}) is defined as:

$$(a_C^{\text{steel}}) = \gamma \cdot (\text{wt}\%C) \quad (\text{Eq 18})$$

where γ is the activity coefficient of carbon in austenite. The activity coefficient of carbon in alloyed austenite is corrected with a multiplying factor q according to Eq 19 and 20 derived by Collin et al. (Ref 1) based on work by Ellis et al. (Ref 18) and Newmann and Person (Ref 19):

$$\gamma_C = q \cdot \frac{1.07}{1 - 19.6 \cdot C_{\%}} \cdot \exp\left(\frac{4798.6}{T}\right) \quad (\text{Eq 19})$$

where

$$q = 1 + [\%Si] \cdot (0.15 + 0.033[\%Si]) - [\%Mn] \cdot (0.0365) - [\%Cr] \cdot (0.13 - 0.0055[\%Cr]) + [\%Ni] \cdot (0.03 + 0.00365[\%Ni]) - [\%Mo] \cdot (0.025 + 0.01[\%Mo]) - [\%Al] \cdot (0.03 + 0.002[\%Al]) - [\%Cu] \cdot (0.016 + 0.0014[\%Cu]) - [\%V] \cdot (0.22 - 0.01[\%V]) \quad (\text{Eq 20})$$

Although the presence of silicon and nickel in steel increases the carbon activity and the coefficient of carbon diffusion in austenite, their presence in steel impedes the carburizing process (Ref 17). This phenomenon can be explained by significant reduction in the mass transfer coefficient from the gas atmosphere to the steel surface and lower total carbon flux entering the steel surface (Ref 20). Similarly, while the presence of carbide-forming elements, such as chromium, manganese, and vanadium, in steel lowers the carbon diffusivity in austenite, it increases the rate of carbon transfer from the atmosphere to the steel surface and accelerates the overall rate of carburizing. These phenomena become more convoluted as the composition of alloy steels grows increasingly complex.

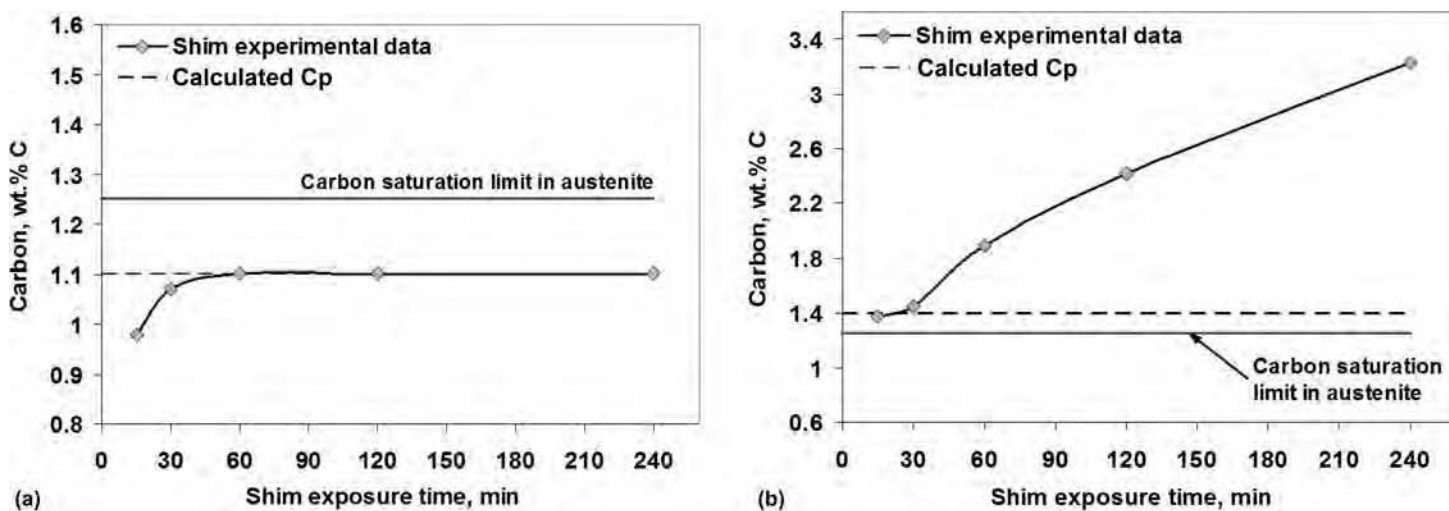


Fig. 2 Comparison of shim carbon readings, analyzed by LECO combustion method, with the atmosphere carbon potential at 925 °C (1700 °F). (a) 1.1 and (b) 1.4 wt% C atmosphere carbon potential

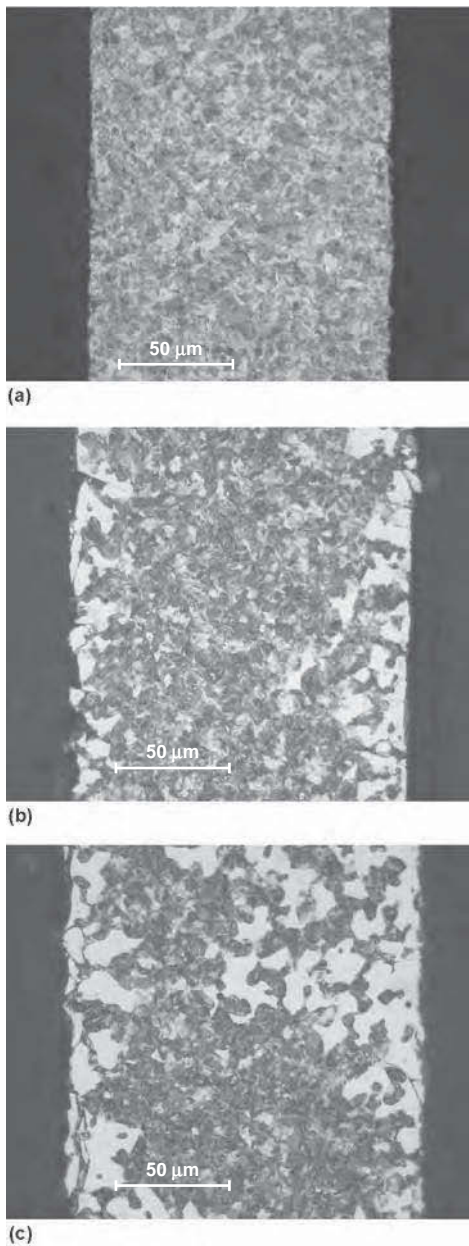


Fig. 3 Microstructure of the cross section of SAE 1020 shim stock carburized at 925 °C (1700 °F) in 1.4 wt% C (supersaturated) atmosphere carbon potential for different exposure times. (a) 30 min. (b) 2 h. (c) 4 h

Figure 5 shows experimentally measured carbon concentration profiles in different steel grades subjected to the same carburizing cycle for 1 and 2 h (Ref 20). The primary differences in the carbon profiles after 1 h are observed at the near-surface layer, which is explained by the effect of the alloy elements on the carbon activity and the instantaneous carbon flux into the steel surface. As carburizing time proceeds, the differences in the carbon profiles are more distinct all along the gradient as a result of the combined effect of the alloy composition on the carbon activity and carbon diffusivity in austenite.

Table 4 Carbon saturation limit in austenite (i.e., $a_C = 1$) at various carburizing temperatures, calculated according to Eq 12 and 13

Temperature		Carbon potential, wt% C
°C	°F	
810	1490	0.88
820	1510	0.91
830	1530	0.94
840	1545	0.97
850	1560	1.01
860	1580	1.04
870	1600	1.07
880	1620	1.10
890	1635	1.13
900	1650	1.17
910	1670	1.20
920	1690	1.23
930	1710	1.27
940	1725	1.30
950	1740	1.33
960	1760	1.37
970	1780	1.40
980	1800	1.44
990	1815	1.47
1000	1830	1.50

The presence of carbide-forming elements reduces the maximum solubility limit in austenite, moving the A_{cm} line toward a lower carbon level; therefore, surface carbides may form during carburizing of medium-to-high-alloy steels even when the shim stock carbon reading is below the carbon saturation limit in plain carbon austenite (Table 4). Therefore, carbon potential process setpoints should account for the alloy effect of the actual parts being carburized. When setting up a new process or periodic audits of the existing carburizing process performance, carburized part quality should be verified with a microstructural analysis on a sample of similar alloy composition.

The part alloy composition also influences the relationship between surface carbon content and surface hardness. Because carbon is an austenite stabilizer, when using alloys containing other austenite-stabilizing alloys the surface carbon content must be tailored to limit retained austenite levels and to optimize surface hardness. For example, with nonalloyed steel, maximum surface hardness can be achieved with surface carbon controlled to a range of 0.6 to 1.0 wt% C, whereas alloys containing 2 wt% Ni-Cr require control limits of 0.55 to 0.7 wt% C (Ref 21).

Carbon Sources and Atmosphere Types

Atmospheres can be created by several methods, and each method provides a different inherent level of controllability. The choice of atmosphere type usually is governed by cost, availability of carbon sources, and required accuracy of the carbon control.

In the early generations of gas carburizing, parts were carburized directly in hydrocarbon

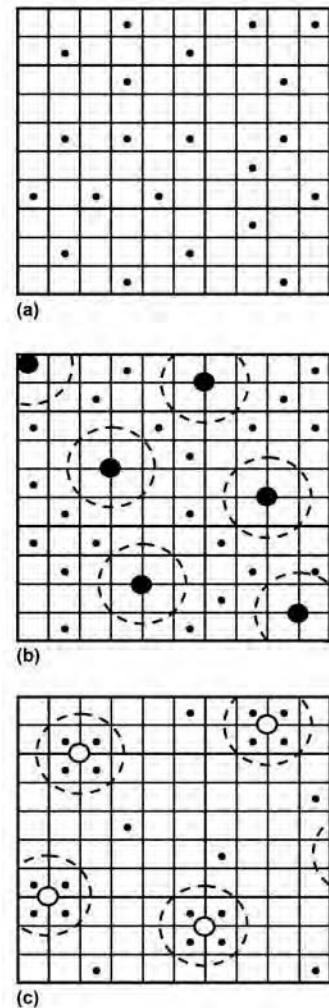


Fig. 4 Effect of alloying element on carbon activity: distribution of carbon atoms in lattice of iron. (a) Unalloyed Fe-C. (b) Fe-C-X (X increases activity of carbon). (c) Fe-C-Y (Y decreases activity of carbon). Source: Ref 17

gases such as straight natural gas, natural gas/nitrogen mixes, or uncontrolled vaporized hydrocarbon liquids. Such atmosphere carbon sources are so rich that the solubility of austenite limit is reached at the surface of the steel, and some carbides may form if proper diffusion techniques are not used. (In earlier editions of the *Metals Handbook*, the carbon gradient produced by maintaining saturated austenite at the surface of the steel is referred to as the normal carbon gradient.) This mode of gas carburizing is still practiced in certain applications involving very dense loads (such as small parts in rotary retort carburizers) at higher carburizing temperatures, and process controls are carefully monitored with piece part evaluations. The more prevalent practice in modern heat treating facilities is to use atmospheres containing greater than 15% CO and controlling residual species such as CO_2 , H_2O , or O_2 to adjust the furnace atmosphere carbon level so that:

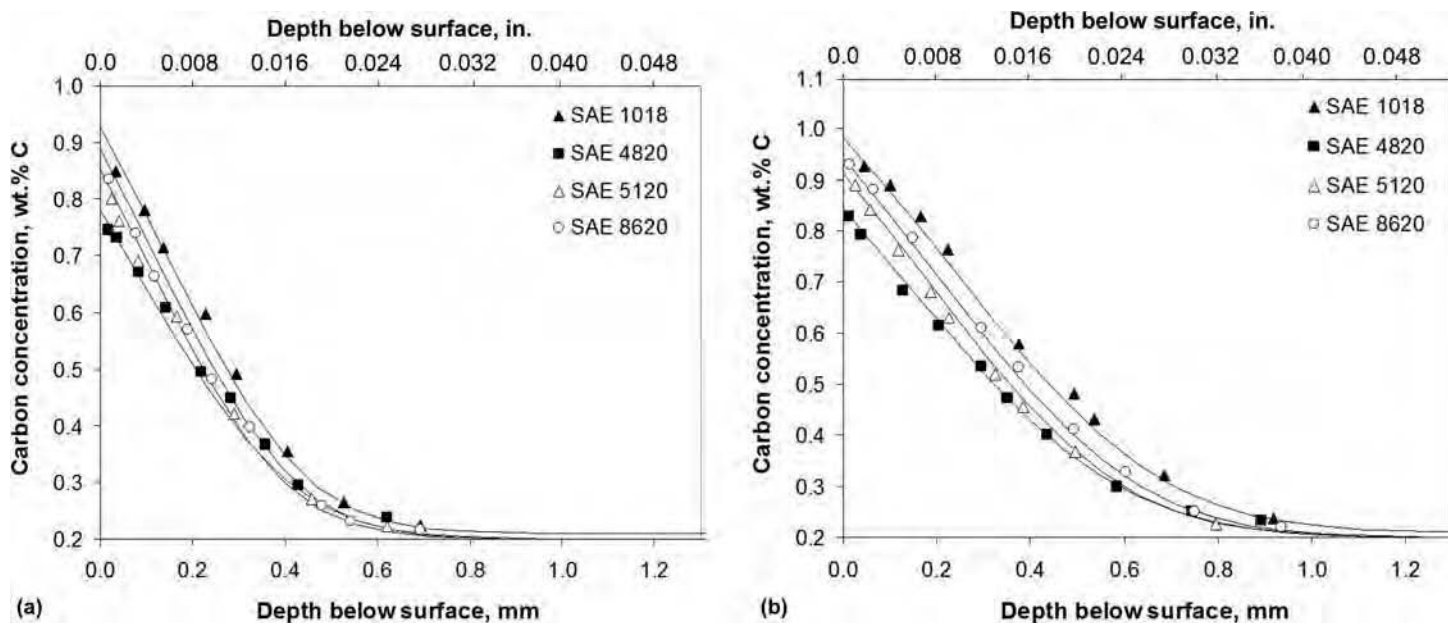


Fig. 5 Carbon concentration profiles in various steel grades after carburizing at 925 °C (1700 °F) and 1.1 wt% C for (a) 1 and (b) 2 h. Source: Ref 20

Table 5 Nominal CO concentration and air/hydrocarbon gas ratio of endothermic carburizing atmospheres generated from air and various hydrocarbon gases

Type of hydrocarbon gas	Air/hydrocarbon ratio	CO, vol%
Methane	2.47	20.3
Natural gas	2.47	20.3
Propane	7.74	23.4
Butane	9.55	23.9

- Final carbon concentration at the surface of the parts is below the solubility limit in austenite and within a specified range to meet hardness and hardened depth requirements.
- Sooting of the furnace atmosphere is minimized.

Controllability of the furnace atmosphere is established by several factors:

- Inherent stability of the CO level in the atmosphere
- Slope of the correlation curves of the controlling residual species (CO_2 , H_2O , O_2) relative to the carbon potential in the atmosphere
- Effectiveness of enriching gas in reducing CO_2 and H_2O to CO and H_2

Selection of CO Level

Most gas carburizing atmospheres are operated in the 15 to 30% CO range to provide the optimum carburizing rate with minimum soot and IGO formation. The typical CO levels for the atmospheres produced by reacting air with

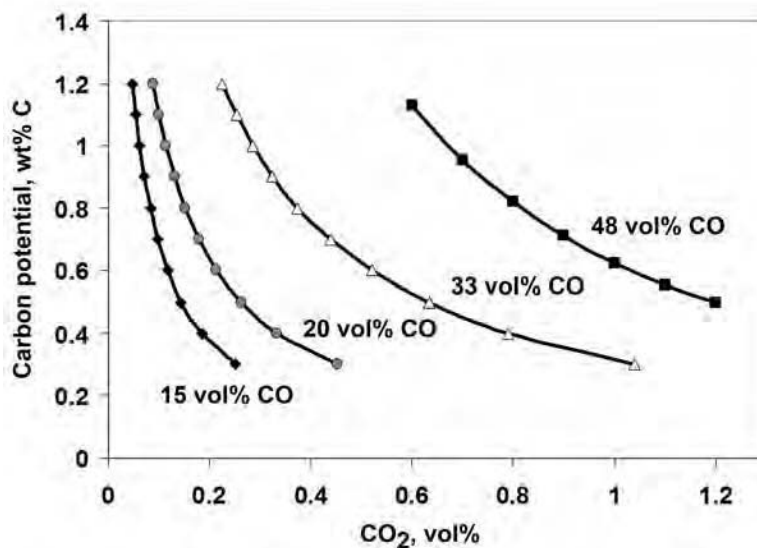


Fig. 6 Relationship between CO_2 concentration and carbon potential for gas carburizing atmospheres at 925 °C (1700 °F) with various CO concentration levels

different hydrocarbon gases, such as natural gas, pure methane, propane, and butane, are shown in Table 5.

In general, gas atmospheres with higher CO levels provide higher surface reaction rates, with a theoretical maximum occurring with a 50/50 mixture of CO/H_2 (Ref 8, 22). Higher CO levels can provide some advantage in shallow case carburizing, where the kinetics of carburizing are predominantly controlled by the surface chemical reactions. For case depths deeper than 1.0 mm (0.04 in.), this advantage is diminished because the total carbon flux is dominated by the diffusion rate of carbon.

Higher CO atmospheres also require a higher corresponding $\text{CO}_2/\text{H}_2\text{O}/\text{O}_2$ equilibrium level to achieve the same carbon potential. As shown in Fig. 6, the slope of carbon potential versus CO_2 decreases at higher CO contents. This decreases sensitivity of carbon potential to small changes in CO_2 concentration and improves atmosphere controllability. However, for any given carbon potential, higher CO atmospheres exhibit higher overall oxygen content that increase the rate of intergranular oxide (IGO) formation. Higher CO atmospheres are also more prone to soot formation, particularly when CO levels exceed 30%.

Since the carbon potential of an atmosphere is proportional to the $(\text{CO})^2/(\text{CO}_2)$ ratio, atmospheres with inherently stable CO levels are easier to control than those with dynamic levels. The stability of CO in a particular atmosphere is governed largely by the method or system used to create the carrier gas. Some carrier gases are created by the reaction of a fuel (typically a hydrocarbon gas or vaporized liquid with a carbon/oxygen ratio equal to or greater than the desired atmosphere) with air in an endothermic gas-type generator. The desired composition of the output gas is achieved by the adjustment of a single variable: the input fuel/air ratio to maintain a specific output CO_2 or dew point level. The CO levels of atmospheres created in this manner are inherently stable and are fixed by the ratio of oxygen/nitrogen in the air and the carbon/hydrogen ratio of the hydrocarbon gas used. Other carrier gases can be created by the direct injection of multiple gases or mixtures of gases and hydrocarbon liquids into the furnace chamber (Ref 23, 24). These systems have the advantage of allowing the user to create different CO levels, but the greater number of input variables drives the need for more sophisticated control systems.

The selection of atmosphere system type and CO operating level should involve consideration of the partial pressure of CO inherently produced as a result of gas chemical reactions of the intended enriching gas and air. Air commonly is carried into carburizers via door openings, part transfer, or trim air introduced for control of carbon potential. For endothermic carrier gas produced from natural gas or in-situ carrier gas generated by nitrogen-methanol adjusted to a 20% CO level, and enriched with natural gas the enriching gas reaction with introduced air produces the same 20% CO level as the carrier gas. If the same nitrogen-methanol atmosphere operated at 20% CO is enriched with propane, the propane-air reaction produces 23% CO and tends to increase the overall CO content when added. The shift in CO level is relatively small and usually within the capability and response time of control systems using CO analyzers. Alternatively, this problem can be avoided by adjusting the nitrogen/methanol ratio of the carrier gas to 23% CO when using propane as an enriching gas. Larger, more rapid upsets of CO are possible with atmospheres such as 50/50 CO-H_2 when air or products of combustion from flame screens are carried into the furnace by door openings, introducing N_2 into the atmosphere.

Endothermic Carburizing Atmospheres

Endothermic carrier gas (endogas) is a blend of carbon monoxide (CO), hydrogen (H_2), and nitrogen (N_2) with small amounts of carbon dioxide (CO_2), methane (CH_4), water vapor (H_2O), and oxygen (O_2) produced by reacting a hydrocarbon gas such as natural gas

(primarily methane), propane, or butane with air. Endogas is usually produced in a separately fired retort furnace (endogas generator) using an air-to-hydrocarbon gas feed ratio to produce an oxygen/carbon ratio slightly greater than 1.0. The gas mixture then is passed through a heated catalyst that accelerates the rate of chemical reactions. Typically, endothermic gas generators are operated at temperatures of 1050 to 1070 °C (1920 to 1960 °F) to maximize reaction efficiency. In a well-designed generator operated within the flow capability of the catalyst and heating system, the endothermic gas will reach a composition consistent with true equilibrium calculated at the highest temperature reached in the catalyst bed, which typically is approximately 50 °C (90 °F) lower than nominal generator operating temperature. Gas generators are equipped with heat exchangers to rapidly cool the gas and “freeze” the composition prior to transporting to furnaces via pipe systems.

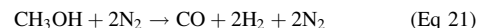
Since carbon potential is defined by the temperature of a part surface in a furnace and the composition of the gas exposed to the part surface, the term *carbon potential* should not be used to describe the composition of generated endothermic carrier gas. A single gas generator can supply gas to multiple furnaces operating at a variety of temperatures, yielding a different furnace atmosphere carbon potential in each case. When the endothermic carrier gas is reheated in the furnace, the composition of the carrier gas will shift from the generator output composition to a composition established by the furnace temperature. Table 6 shows the maximum carbon potential that can be achieved at a given furnace temperature with an endothermic carrier gas produced by the reaction of natural gas and air in a generator operated at 1050 °C (1920 °F) and controlled to a CO_2 level of 0.2%. The data presented in the table assume no significant presence of soot that would increase carbon potential, or air leakage or other sources of oxygen that would reduce the carbon potential of a reheated carrier gas in the furnace. Note that a natural gas-air endothermic gas controlled to 0.2% CO_2 at the generator will produce only a maximum of 0.53% carbon potential in a furnace operated at 925 °C (1700 °F); thus, enriching gas is required to raise the carbon potential to levels typically used in gas carburizing. Richer carrier gases require less enrichment at the furnace; however, endothermic generators controlled to produce gases with less than 0.15% CO_2 reduce generator output capability and increase soot formation within the catalyst bed.

In-Situ-Generated Nitrogen-Methanol Atmospheres. Nitrogen-methanol has become the most commonly used in-situ-generated carrier gas in recent years. When using in-situ atmospheres, separately fired endothermic gas generators are no longer required, and the atmosphere can be turned on / off with relative ease. Nitrogen-methanol systems also can be adjusted to provide various CO levels, ranging from zero (pure nitrogen) to 33% CO (straight

Table 6 Maximum carbon potential attainable in a furnace atmosphere at various temperatures using 20 vol% CO endothermic carrier gas controlled to 0.2 vol% CO_2 without further hydrocarbon enrichment at the furnace

Furnace temperature		Carbon potential, wt% C
°C	°F	
850	1560	0.75
875	1610	0.68
900	1650	0.6
925	1700	0.53
950	1740	0.46

methanol) (Ref 24). Upon entering the furnace, methanol cracks to form CO and H_2 . The nitrogen-to-methanol ratio usually is chosen to create an atmosphere with a specific CO content. For a nominal 20 vol% CO, nitrogen is blended with methanol in a 2:1 molar ratio:



Pure methanol has a carbon/oxygen ratio of 1.0 and requires a source of oxygen addition to form an atmosphere with a carbon/oxygen ratio slightly less than 1.0, which is typical of controlled carburizing atmospheres. Sooting may occur in an idling, nonloaded furnace if normal infiltration of air into the furnace and/or trace water content in the methanol (methanol is hygroscopic) is too small. Introduction of controlled amounts of air can be used to reduce sooting. Heat is required to vaporize methanol, and the cracking of methanol to CO and H_2 is endothermic. Methanol cracking efficiency decreases with decreasing temperature. Therefore, successful cracking is favored by higher furnace temperatures and lower rates of carrier gas usage. A target or sparging plate usually is incorporated at the point of methanol injection to break up the alcohol stream and to disperse it into the atmosphere for complete cracking. Damaged or missing sparging plates can result in the direct impingement of methanol on parts and formation of cold spots. The presence of lower-than-expected CO levels in furnace atmospheres is symptomatic of incomplete cracking, although variations in CO levels are more commonly caused by fluctuations in the input ratio of nitrogen to methanol.

Accurate carbon potential control requires that both the CO and CO_2 (or O_2 from oxygen probe) levels be known and that the atmosphere CO level must be controlled to a stable value. Control systems usually are programmed to use a fixed CO level input into the controller. Maintaining stable CO levels can be challenging because liquid methanol is difficult to meter and control accurately by input flow control alone, particularly at carrier gas flow rates <3000 l/h. Carbon control systems using fixed CO values generally allow manual input of a correction factor based on shim stock analysis

but often do not provide sufficient accuracy over time, because CO fluctuations typically occur at frequencies higher than shim stock checks. High-accuracy carbon potential control systems measure CO content with NDIR analyzers and control methanol flow to maintain a preset CO value.

Nitrogen of high purity (approximately 10 ppm residual CO₂ and H₂O vapor) is produced by liquifying air and then using the differences in boiling points of the various constituents to effect the separation of nitrogen. In most instances, liquid nitrogen is shipped from an air-separation plant to the heat treating plant and stored in vacuum-insulated vessels. Nitrogen of lesser purity can be produced on site by a variety of means:

- *Combustion processes:* Air is burned with natural gas, and the CO₂ and H₂O are stripped from the gas by absorption and condensation.
- *Pressure swing absorption or vacuum swing absorption:* Air is separated by using zeolite molecular sieves.
- *Membrane air separation:* Differences in molecular permeation rates through thin-walled fibrous tubes are used to separate oxygen and nitrogen.

Low-purity, less expensive nitrogen also can be used with methanol to form satisfactory furnace atmospheres. However, because the oxygen content of the nitrogen should be kept relatively constant, the nitrogen-generation process must be designed with this requirement in mind.

Nitrogen-methanol atmosphere systems require special equipment and operating procedures for safety. These requirements are detailed in the NFPA 86 Standard for Ovens and Furnaces.

Other In-Situ Atmospheres. Some furnaces use in-situ atmospheres created by the direct reaction of a hydrocarbon gas and air within the furnace (Ref 25–27). As with nitrogen-methanol, atmospheres of this type have the benefit of not requiring separate endothermic gas generators and can be relatively easy to turn-on/turn-off. However, carburizing furnaces typically operate at lower temperatures than endothermic gas generators and have limited catalytic surfaces to help drive gas reactions to completion. Furnaces must be designed to operate safely at very low positive pressures with tight-fitting doors and low-effluent flow rates to create the high residence times needed for complete gas reaction. These systems have not gained wide popularity due to inherent problems with low CO levels, high residual methane levels, and sooting.

Carbon-Transfer Mechanism

The mass transfer mechanism during gas carburizing is a complex phenomenon that involves several distinct stages (Ref 28, 29):

1. Chemical reactions take place in the gas phase.
2. The carburizing species diffuse through a boundary layer toward steel surface.
3. Absorption of the reacting species occurs on the steel surface, and chemical reactions take place at the gas-steel interface.
4. Diffusion of the absorbed carbon atoms in the steel occurs down the chemical potential gradient.

According to the thermodynamics of irreversible processes (Ref 17), the driving force for mass transfer during carburizing is the gradient in the carbon chemical potential. The chemical potential is determined by the carburizing temperature and the thermodynamic carbon activity:

$$\mu_C = \mu_C^0 + RT \ln a_C \quad (\text{Eq 22})$$

where μ_C is the chemical potential of carbon in austenite, R is the universal gas constant, T is the absolute temperature (Kelvin), and a_C is the carbon activity in austenite.

Total carbon transfer from the atmosphere to the steel is determined by the rate-limiting process and controls the rate of carburization. Figure 7 schematically shows the carbon transport mechanism and the primary control parameters: the mass transfer coefficient (β) defining the flux of carbon atoms from the atmosphere to the steel surface (J_{atm}), and the coefficient of carbon diffusion in steel (D_C), which, in conjunction with Fick's first law, defines the flux of carbon atoms in steel (J_{steel}).

In theory, the maximum carburizing rate is obtained when the rate of carbon transfer from the atmosphere to the steel surface is equal to or greater than the rate of carbon diffusion in steel. Such a diffusion-controlled process would

have no deficiency of carbon supplied to the steel surface for its further absorption and diffusion in the steel. In practice, however, the nonequilibrium carbon transfer from the atmosphere to the steel surface, including the surface reactions, is often reported to be the rate-limiting factor, especially at the beginning of the carburizing process (Ref 5, 28, 29). Later in the process, the overall carburizing rate becomes diffusion controlled (Ref 30). Therefore, when modeling gas carburizing, the process can be considered mixed-controlled and defined by the carbon flux balance at the gas-steel interface (Ref 31, 32).

The mass-transfer coefficient (β) encompasses the effect of all gas phenomena at the gas boundary between the atmosphere and steel surface, including diffusion of the reacting gases through the boundary layer and absorption of the carburizing species on the steel surface (Ref 28). As shown in Fig. 7, the mass transfer coefficient characterizes the thickness of the boundary gas layer at the gas-steel interface and determines the maximum flux of carbon atoms through the steel surface, available for further carbon diffusion in steel (Ref 33). If the value of β is increased, the resulting carburized depth would increase.

While it is commonly agreed that β is a function of the gas atmosphere composition (Ref 1, 5, 32), there is some discrepancy in the reported effect of carburizing temperature on β . Wünnig (Ref 3) and Rimmer et al. (Ref 34) reported β on the order of 10^{-5} and independent of the carburizing temperature. A number of studies (Ref 28, 35, 36) found β to be directly proportional to the carburizing temperature. Munts et al. (Ref 37) measured β ranging from 2×10^{-5} to 2×10^{-4} cm/s at 800, 900, and 1000 °C (1470, 1650, and 1830 °F) using the wire resistance method. In a more recent

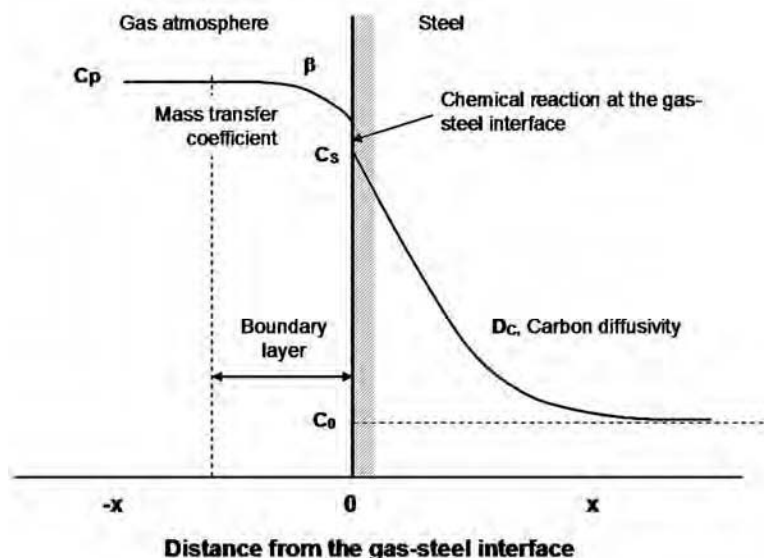


Fig. 7 Schematic representation of carbon transport in carburizing

work (Ref 38), the authors calculated β directly from the carbon concentration profiles based on direct flux integration and reported β ranging from 1.2 to 2×10^{-5} cm/s for the typical range of industrial carburizing conditions (0.9 and 1.1 wt% carbon potential and 900 to 950 °C, or 1650 to 1740 °F, temperatures). The mass transfer coefficient also has been reported to vary with the alloy composition of the steel (Ref 20, 35).

Carbon Diffusion in Austenite. Once CO molecules reach the steel surface and dissociate into absorbed carbon atoms and CO₂, the rate of further carbon transport becomes limited by the rate of carbon diffusion in steel. The combined effects of time, temperature, and carbon concentration on the diffusion of carbon in austenite can be expressed by Fick's laws of diffusion. Fick's first law states that the flux of the diffusing carbon atoms (J) perpendicular to a plane surface of unit cross-sectional area is proportional to the local carbon gradient perpendicular to the plane and can be expressed as:

$$J = -D_C \frac{\partial C}{\partial x} \quad (\text{Eq 23})$$

where D_C is the coefficient of carbon diffusion in austenite, C is the carbon concentration in steel, and x is the distance from the surface. Fick's second law establishes the mass balance within an elemental volume of steel and states that the rate of carbon accumulation is the difference between the flux of carbon atoms into the elemental volume and the flux of carbon atoms out of the elemental volume. Combining the two laws leads to a second-order parabolic partial differential equation that describes the carbon diffusion process in austenite:

$$\frac{\partial C}{\partial t} = \frac{\partial}{\partial x} \left(D_C \frac{\partial C}{\partial x} \right) \quad (\text{Eq 24})$$

where D_C is the coefficient of carbon diffusion in austenite, C is the carbon concentration in steel, t is time, and x is the distance from the surface.

The coefficient of carbon diffusion in austenite is a function of carburizing temperature, carbon concentration, and alloy composition. Carbon diffusion is thermally activated and increases exponentially with increasing carburizing temperature. Carbon diffusivity also increases with increasing carbon concentration due to distortion of the austenite lattice and increase in thermodynamic carbon activity. Several carbon diffusivity models have been published (Ref 1, 32, 39,40–41) that agree well within the range of carburizing temperatures. According to one of them, carbon diffusivity [cm^2/s] can be calculated as (Ref 39):

$$D_C = 0.47 \cdot \exp \left(-1.6 \cdot C - \frac{37,000 - 6,600 \cdot C}{RT} \right) \quad (\text{Eq 25})$$

where C is weight percent carbon, T is absolute temperature (Kelvin), and R is the gas constant (1.99 cal/mol K).

Effect of Surface Finish. Carburizing is typically applied to steel parts that are machined to final or near-final shape prior to carburizing. Depending on the part surface finish requirement, the type of machining operation, and the selection of machining process parameters, steel parts may exhibit a wide range in the surface finish that may affect the kinetics of gas carburizing.

Figure 8 shows schematically the chemical reactions that occur simultaneously during the process near the steel surface (Ref 42). Gas carburizing most rapidly proceeds by CO molecule decomposition, that has an estimated size range of 1.58 - 2.8 nm depending on the orientation of the molecule. Therefore, the interfacial surface area (i.e., surface of the part at microscopic level) defines the intensity of their interactions and the magnitude of total carbon flux across the gas-steel interface.

The effect of surface roughness on the kinetics of mass transfer in gas carburizing has been investigated in Ref 42. Rougher surface finishes provide a greater number of available sites for CO molecule decomposition, which results in a higher density of absorbed carbon atoms and overall greater carbon pickup. Figure 9 shows the total carbon flux and the mass transfer coefficient (β) as a function of the peak-to-valley roughness and the relative surface area of the parts. Parts with larger interfacial surface area (i.e., surface roughness) were found to enhance the instantaneous carbon flux through the gas-steel interface. From a kinetic standpoint, the greater rates of mass transfer establish a steeper carbon gradient at the near-surface area, promoting a greater rate of carbon diffusion in steel. As a result, parts with larger surface area attained higher carbon concentration profile, as shown in Fig. 10.

Effect of Preoxidation. Preoxidation prior to carburizing of high-alloy steel with alloy content >2 wt% Cr, commonly used in the aircraft industry, may help alleviate the problem of nonuniform carburizing (Ref 2, 43). Alloy steels with elevated levels of chromium and/or silicon form passive oxide surface layers under normal carburizing conditions. This layer inhibits absorption of carbon at the gas-steel interface and may result in a nonuniform carburized case depth. These high alloy steels benefit from preoxidation in air or other strong oxidizing environment prior to carburizing. Oxidation in air produces a porous iron-base

oxide rather than the dense, passive Cr₂O₃ or SiO₂ oxides and thus permits a more uniform ingress of carbon at the surface. As a result, a more uniform and deeper carburized depth is attained (Ref 2).

Preoxidation of low-to-medium-alloy steel grades with total alloy content below 2 wt% does not seem to provide any advantages in accelerating gas carburizing. Figure 11 shows the carbon concentration profiles of SAE 4122 samples carburized for 2 and 15 h at 930 °C (1710 °F) with prior preoxidation for 30 min at 425 °C (800 °F) and without preoxidation. No differences were observed in either case microstructure or carbon profile attained.

Carburizing Modeling and Case Depth Prediction

Process modeling and simulation are cost-effective tools to evaluate the effect of various material and process factors important for carburizing process design and optimization. In the 1940s, F.E. Harris developed an empirical technique for determining total case depth based on total carburizing time and temperature (Ref 44). Historically, this technique has been applied in industry with adequate results to single-stage carburizing (or boost-diffuse at constant process temperature) in plain carbon steels. Harris' equation assumes saturated austenite at the steel surface. In practice, however, the surface carbon concentration in steel varies with carburizing time and is typically lower than the carbon potential in the gas atmosphere. The resulting case depth will be shallower than that predicted by Harris' equation in industrial carburizing processes when the atmosphere carbon potential controlled below the carbon saturation limit in austenite. Most importantly, it should be recognized that Harris' depth prediction is used to estimate the total case depth, not the effective case depth, which rarely is used for industrial process design and specification.

Diffusion Modeling. The gas carburizing process is modeled using a parabolic, second-order, partial differential equation for carbon diffusion in steel and a set of boundary conditions accounting for the mass transfer coefficient at the steel surface and kinetics of the gas carburizing reactions:

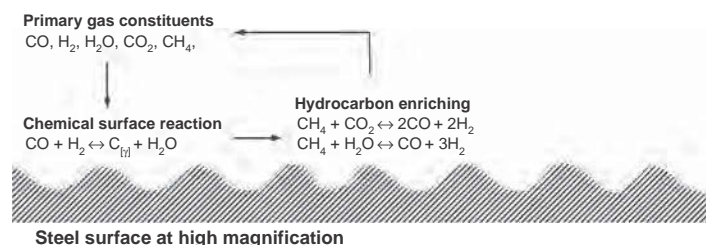


Fig. 8 Schematic of the gas atmosphere – steel interaction in gas carburizing. Source: Ref 42

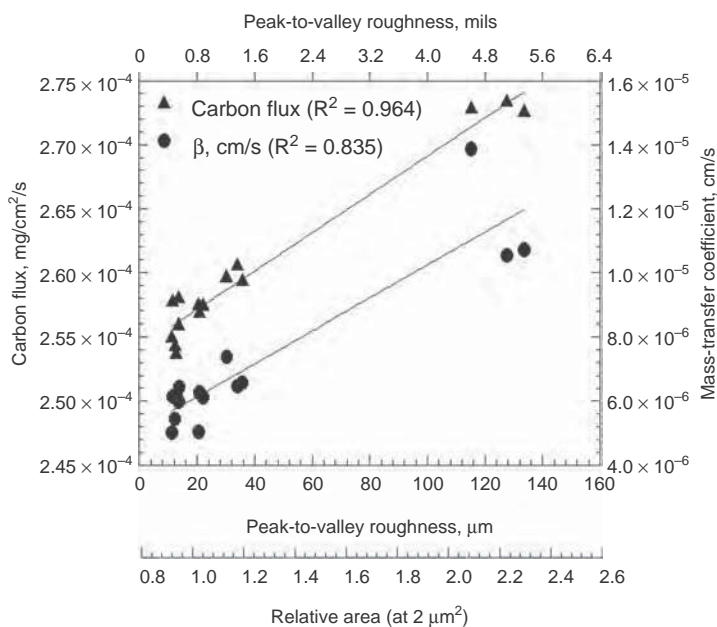


Fig. 9 Total carbon flux (triangular marks) and mass transfer coefficient (circle marks) as a function of the relative area at 2 μm² scale and peak-to-valley surface roughness. Source: Ref 42

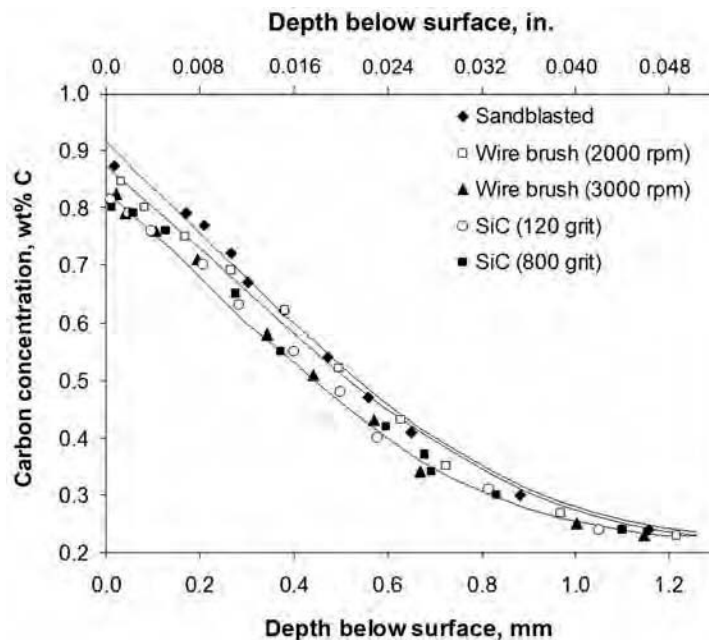


Fig. 10 Carbon concentration profiles in parts with different surface finishes carburized at 925 °C (1700 °F) and 0.95 wt% C for 3 h. Source: Ref 42

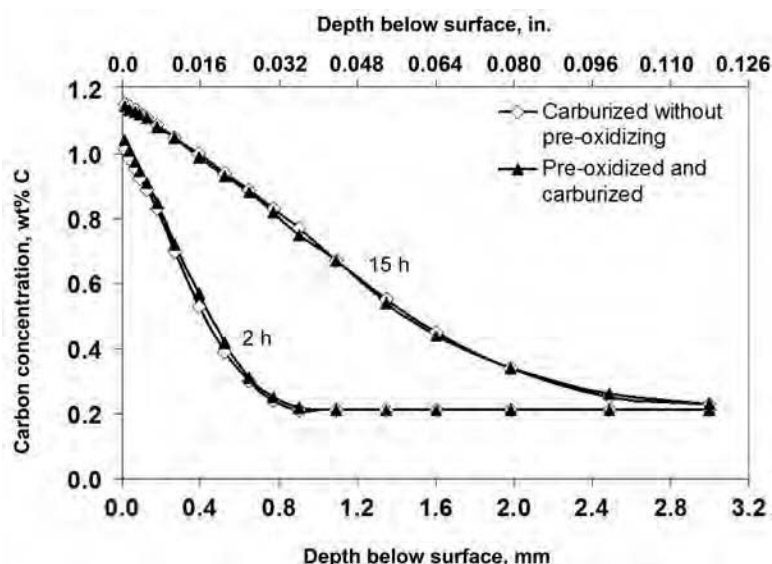


Fig. 11 Carbon concentration profiles in SAE 4122 after 2 and 15 h carburizing at 930 °C (1710 °F) and 1.2 wt% carbon potential with and without preoxidation for 30 min at 425 °C (800 °F)

$$\frac{\partial C}{\partial t} = \frac{\partial}{\partial x} \left(D_C \frac{\partial C}{\partial x} \right) + u \cdot \frac{D_C}{r + ux} \cdot \frac{\partial C}{\partial x} \quad (\text{Eq 26})$$

where $u = -1$ is used for a convex surface, $u = 0$ for a plane surface, and $u = 1$ for a concave surface; D_C is the coefficient of carbon diffusion in steel; C or $C(x,t)$ is the position- and time-dependent carbon concentration in steel; r is the radius of the curvature; x is the distance from the surface; and t is time.

In a controlled process without soot accumulation, the carbon flux produced by the surface

chemical reactions (Eq 1,2–3) is equal to the flux of carbon atoms in steel, yielding a flux balance condition at the gas-steel interface:

$$\sum_i^n \frac{k_i}{a_{\text{surf}_i}} (a_C^{\text{gas}} - a_C^{\text{surf}}) = -D_C \frac{da_C^{\text{surf}}}{dx} \quad (\text{Eq 27})$$

where k_i is the rate coefficient of the atmosphere chemical reactions (cm/s); a_C^{gas} and a_C^{surf} are the carbon activity in the gas atmosphere and at the steel surface, respectively; D_C is the

coefficient of carbon diffusion in steel (cm²/s); and x is the distance from the surface (cm). For carbon concentration profiles below 1 wt% C, the mass transfer coefficient (β) can be expressed as the ratio between the rate coefficient for the chemical reactions and the corresponding carbon activity at the steel surface (Ref 28, 45):

$$\beta = \sum_i^n \frac{k_i}{a_{\text{surf}_i}}$$

The rate of exchange at the surface is directly proportional to the difference between the surface carbon concentration and the carburizing potential of the atmosphere. Thus, the flux balance boundary condition at the surface can be expressed as:

$$\beta(C_p - C_s) = -D_C \frac{\partial C}{\partial x} \quad (\text{Eq 28})$$

where β is the mass transfer coefficient (cm/s), C_p is the carbon potential in the gas atmosphere (wt% C), C_s is the carbon concentration at the steel surface (wt% C), D_C is the coefficient of carbon diffusion (cm²/s), C (wt% C) is the carbon concentration in steel, and x is the distance from the surface (cm).

Analytical Solutions. Crank (Ref 46) provided mathematical solutions to the diffusion equation for a variety of boundary conditions and part configurations. These analytical solutions can be used to predict the carbon gradient and carburized depth for any combination of time, temperature, and surface carbon concentration. When chemical reactions at the steel

surface are taken into account, the differential equation for diffusion has no simple analytical solution (Ref 47). Analytical solutions for transient diffusion are limited to models with carbon diffusivity independent of local carbon concentration that is not representative of the industrial carburizing process. While analytical solutions to the diffusion equation with concentration-dependent carbon diffusivity are available for steady-state diffusion, numerical methods must be used for time-dependent (transient) diffusion.

Numerical Approach. The numerical approach is based on transformation of the continuum governing partial differential equation (Eq 26) with the corresponding boundary conditions into a set of finite-difference equations. The Dusinberre numerical method (Ref 46) provides solution to the diffusion equation with the boundary conditions formulated by Eq 28 for a semi-infinite part geometry initially at uniform carbon concentration. The method is accurate to a second order and provides a stable convergent solution. Solution to a one-dimensional diffusion problem is obtained by:

$$C_i^{t+\Delta t} = \frac{\Delta t}{(\Delta x)^2} \left[D_i^t \left(C_{i-1}^t - 2C_i^t \left(\frac{(\Delta x)^2}{D_i^t \Delta t} - 2 \right) + C_{i+1}^t \right) + \frac{(D_{i+1}^t - D_{i-1}^t)(C_{i+1}^t - C_{i-1}^t)}{4} \right] \quad (\text{Eq 29})$$

where C is the carbon concentration, D is the coefficient of carbon diffusion corresponding to a particular location (node i) and time, Δx is the node spacing, and Δt is the time increment. Given the mass transfer coefficient at the steel surface, carbon concentration at the boundary nodes can be calculated as:

$$C_{\text{surf}}^{t+\Delta t} = \frac{1}{M} \cdot \left[2N \cdot C_p + [M - (2N + 2)]C_{\text{surf}}^t + 2C_{x_1}^t \right] \quad (\text{Eq 30})$$

where

$$M = \frac{D_c \cdot \Delta t}{(\Delta x)^2} \text{ and } N = \frac{\beta}{D_c} \cdot \Delta x \quad (\text{Eq 31})$$

Two stability criteria must be satisfied simultaneously: $M > 2$ and $M > 2N + 2$. The maximum stable time increment is determined from the following expression, based on the selected node spacing (Δx), D and β coefficients:

$$\Delta t < \frac{(\Delta x)^2}{2\beta \cdot \Delta x + 2D} \quad (\text{Eq 32})$$

The numerical approach to modeling carbon diffusion in austenite during gas carburizing has been well validated and documented in numerous publications (Ref 1, 40, 48, 49). It should be noted, however, that these models do not account for formation of secondary phase(s) and may not yield accurate results

when modeling carburizing response in stainless steel or other alloys with high concentrations of carbide-forming elements. Modeling gas carburizing response in multicomponent systems requires input of thermodynamic and kinetic data and can be modeled numerically with the use of computer code (Ref 50, 51) or using available commercial software (Ref 52–54).

Carburizing Equipment

Gas carburizing furnaces vary widely in physical construction, but they can be divided into two major categories of furnaces: batch and continuous. In a batch-type furnace, the work load is charged and discharged as a single unit or batch. In a continuous furnace, the work enters and leaves the furnace in a continuous stream. Continuous furnaces are favored for the high-volume production of similar parts with total case depth requirements of less than 2 mm (0.08 in.).

Batch Furnaces. The most common types of batch furnaces are pit furnaces and horizontal batch furnaces. Pit furnaces are usually placed in a pit with the cover or lid located just above floor level (Fig. 12). Pit furnaces are typically used for large parts requiring long processing times. If the work is to be direct quenched, the load must be moved through air before quenching. As a result, parts will be covered by an adherent black scale that may require shot blasting or acid pickling.

Horizontal batch furnaces are frequently used for carburizing and direct quenching. Many of these furnaces are called sealed-quench, or integral quench, furnaces, where carburized parts are discharged from the furnace into a vestibule that covers an oil quench tank (Fig. 13). Parts can be kept free of oxidation prior to quenching, because the furnace atmosphere also flows through the vestibule. Sealed-quench batch furnaces are capable of processing many different types of loads with widely varying case depth requirements. Like pit furnaces, sealed-quench furnaces can be made gastight, with the result that positive furnace pressures are easily achieved.

Continuous Furnaces. Types of continuous furnaces used for carburizing include mesh belt, shaker hearth, rotary retort, rotary hearth, roller hearth, and pusher designs. Many of these furnaces can be built with sealed oil quenching so that oxide-free parts can be produced. Some of these furnaces can be sealed well enough that positive furnace pressures can be maintained, but mesh belt furnaces, on the other hand, are open to the air at either end. Because air cannot be positively excluded, carburizing in these furnaces is often difficult to control.

The carbon-rich atmospheres used in gas carburizing rapidly degrade most common Fe-Ni-Cr alloys used for internal furnace parts. Internal furnace structures made from highly

alloyed steel, such as retorts, roller rails, roller hearth rollers, and mesh belts, require periodic replacement and add to the cost and downtime of operating the furnace. The most commonly applied continuous furnace design is the pusher furnace (Fig. 14). Pusher furnaces have the advantage of being inherently gastight designs, use fewer internal alloy parts, and generally support trays of parts with ceramic refractory piers and rails. Pusher furnaces can be designed to incorporate multiple carburizing and/or diffusion chambers operating at independent temperatures and carbon potentials. Designs can also include an atmosphere and temperature-controlled cooling chamber, sealed dunk quench chamber and/or press-quench chamber. Pusher furnaces can also be designed with pre-heat chamber to enable heating of parts to the carburizing temperature in an atmosphere controlled to low carbon levels (near part base carbon content). This prevents uneven carburizing of parts (outside versus center of loads) when introduced into the first carburizing zone and reduces sooting in the first zone by preventing contact of the carburizing atmosphere with cold parts. Parts can also be preheated in air, but this practice is limited to approximately 420 °C (790 °F) maximum to avoid loose scale formation on parts. Pusher furnaces also enable the use of sidewall fans for better atmosphere circulation. With sidewall fans, the atmosphere wind flow can be well directed beneath the hearth and up through the load with greater velocity and uniformity than can be achieved with radial roof fan designs. This is particularly important when carburizing densely loaded parts that require accurate case depth control on both outside and inside surfaces, such as bearing races, bushings, and piston pins.

Furnace Internal Pressure. Furnaces should be operated at a positive pressure so that if the furnace has small leaks, air does not enter into the furnace. Pressures of 12 to 37 Pa (0.09 to 0.28 torr, or 0.05 to 0.15 in. of water column)

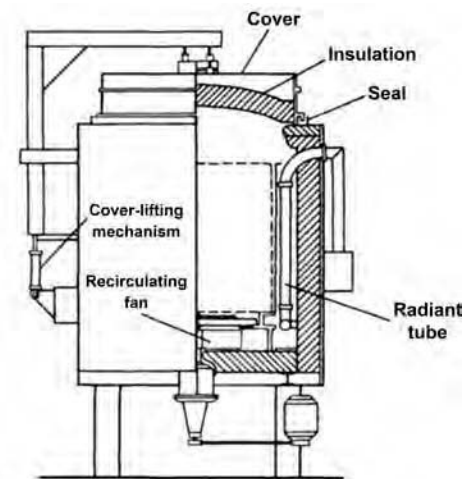


Fig. 12 Pit batch carburizing furnace. Dashed lines indicate location of workload.

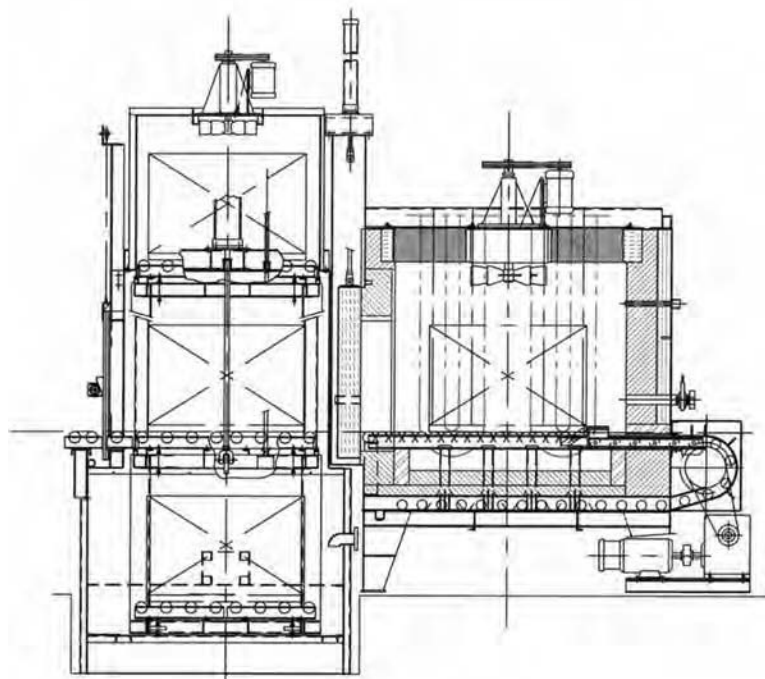


Fig. 13 Typical gas-fired integral quench furnace

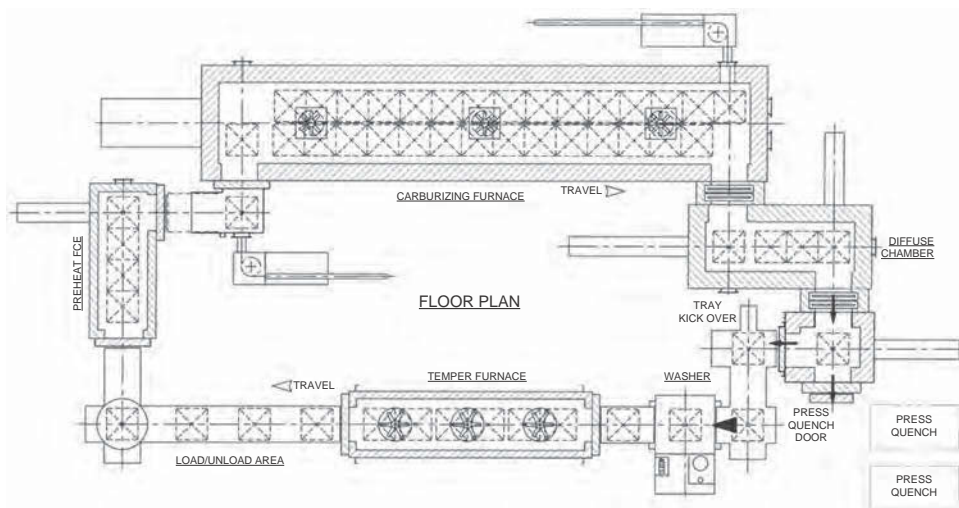


Fig. 14 Typical multichamber continuous pusher-type furnace

are usually satisfactory for carburizing furnaces. The furnace pressure can be controlled by adjusting either the orifice size in the atmosphere vent lines or the carrier gas flow rate.

The pressure differential (furnace pressure minus ambient pressure, measured at the same height) will have its smallest value at the lowest point in the furnace, because the hot gases inside a furnace are low in density. The minimum furnace pressure needed (at any height) to maintain a positive differential at all heights (P_{\min}) can be calculated from the relation:

$$P_{\min} = H(D_A - D_F) \quad (\text{Eq 33})$$

where H is the internal height of the furnace chamber, D_A is the density of ambient air outside the furnace, and D_F is the density of the atmosphere inside the furnace. In general, $D_A \gg D_F$, and a suitable minimum value for the furnace pressure in pascals is:

$$P_{\min} = H(0.117) \quad (\text{Eq 34})$$

where H is in cm, and it is assumed that the ambient air is at 1 kPa (1 atm) pressure and

20 °C (70 °F). Even though the furnace pressure is nominally positive, air can still enter the furnace through small openings if there are local fluctuations in the ambient pressure. It should be noted that a large cooling fan blowing at the furnace may raise the ambient pressure locally by as much as 25 Pa (0.19 torr, or 0.1 in. water column).

Finally, the rate at which the furnace atmosphere responds to changes in inlet gas composition depends on the mean residence time of the atmosphere gases in the furnace. The mean residence time (t_{res}) is approximately:

$$t_{\text{res}} = \frac{(V \cdot T_A)}{(F \cdot T_F)} \quad (\text{Eq 35})$$

where V is the furnace volume; F is the carrier gas flow rate measured at T_A , the absolute ambient temperature; and T_F is the absolute furnace temperature. Residence times in carburizing furnaces vary from approximately 2 to 15 min. If the inlet gas flows are changed, it takes approximately three residence times to effect 95% of atmosphere change. Therefore, batch furnaces, in which the atmosphere composition must be changed during the course of a processing cycle, are usually operated with shorter residence times than those used in continuous furnaces. It is often considered an advantage to use high flow rates of carrier gas to achieve faster recovery of the atmosphere when parts are charged. However, the same result can be achieved more economically by using an automatic control system to regulate the flow of the hydrocarbon enriching gas.

Sooting and Burnout. During normal operation of a gas carburizing furnace, soot will form over time in various regions of the furnace, particularly in areas where the atmosphere is allowed to cool or come in contact with cold parts. As the furnace becomes sooted, the carbon potential of the furnace atmosphere becomes difficult to control or uncontrollable. Enriching gas additions no longer react to reduce CO_2 and H_2O efficiently, and free methane levels will increase and result in additional soot. The higher the operating carbon potential of a furnace, the faster soot formation occurs. If the point is reached where the carbon potential cannot be effectively controlled, the only practical solution is to empty the furnace, introduce air, and burn out the soot. Some care is necessary in burning out accumulated soot to prevent local overheating in the furnace. Typically, the furnace temperature is set at approximately 815 °C (1500 °F) for burnout, and air is admitted to the furnace, either by opening doors or introducing a flow of air. The rise in temperature due to the combustion of soot should be monitored, and the air supply should be reduced if the temperature rise is more than 5 °C. A properly controlled furnace will require burnout only once every three to four weeks. Furnaces operating at higher carbon potentials or with very high surface area loads may require burnout on a more frequent basis.

Modern automatic atmosphere-control systems minimize soot formation by maintaining a constant atmosphere composition below the carbon saturation limit in austenite and by matching carbon supply in the atmosphere to carbon demand at the steel surface. However, some soot formation is inevitable, particularly in the first zone of continuous furnaces where atmosphere comes in contact with cold parts. There are also some locations, such as sight ports and gas sample lines, where soot will continue accumulating as the furnace is used. Soot also may form in unheated furnace vestibules as the furnace atmosphere gas cools upon entering the vestibule.

Carburizing atmospheres can penetrate surface regions of refractory fiber insulation, open firebrick joints, crevices between refractory brick, and alloy components that extend from the hot face of the chamber to the furnace shell. As the atmosphere is cooled in these crevice regions, solid soot will precipitate and expand, causing heaving of brick and delamination of refractory fiber. Damage of this type can be reduced with good furnace construction using tight refractory joints and minimizing the paths for atmosphere penetration into cooler regions.

Furnace Conditioning. It is necessary to dry out and condition a furnace before it is used for carburizing production when it is first put into operation after a long shutdown or after it has been overhauled and relined with new firebrick. Drying out after bricking involves heating the furnace at 100 to 150 °C (210 to 300 °F) for a period of time (often many hours or up to a few days) until there is no longer visible steaming. The furnace is then brought to operating temperature very slowly (typically 10 °C/hour maximum) to avoid damage to brick and alloy due to expansion. Drying can be accelerated by introducing dry nitrogen during the furnace conditioning. Conditioning the refractory for carburizing consists of admitting a carburizing carrier gas and allowing the atmosphere to react with the internal components of the furnace for at least several hours to as long as several days before enriching gas is added. Conditioning ensures that the internal components of the furnace equilibrate with the carburizing atmosphere, so that chemical reactions between the atmosphere and the workpieces will not be slowed by reactions between the atmosphere and the furnace lining. When a carburizing atmosphere is introduced into an empty furnace that has been idle for some time or that has just been burned out to remove soot, it is found that the amount of enriching gas needed to maintain a given carbon potential is much higher than would be expected after the furnace is conditioned. Once a furnace is conditioned, the levels of enriching gas needed to sustain a given carbon potential remain fairly constant but then begin to increase as soot forms, which signals the need for burnout.

Metal Dusting in Furnace Alloy. A major cause for gas carburizing furnace maintenance downtime occurs on alloy components that

extend from the hot face of the chamber through the refractory to the shell or other cold regions. Affected components include chain guides, pusher head and chain assemblies (portions that rest in the furnace wall), fan shafts, burner tube support rods, and alloy stools. Failure occurs as a general type of corrosion or deep pitting in areas of the alloy surface exposed to carbon-rich atmosphere in the temperature range of 430 to 650 °C (810 to 1200 °F) (Ref 55), similar to that shown for a pusher head axle pin in Fig. 15. Corrosion damage can result in metal thickness loss of 12 mm (0.5 in.) per year. Metal dusting (carbon rot) can be virtually eliminated by use of high-nickel alloys that contain several percent of cobalt, tungsten, and molybdenum, such as those listed in Table 7.

Furnace Temperature and Atmosphere Control

Control of a gas carburizing process involves accurate measurement and adjustment of temperature, time, and atmosphere carbon potential. Historically, numerous publications and experimental data relative to gas carburizing were presented from a cycle time, temperature, and gas input point of view. While this type of information is valuable, the actual carbon potential achieved in a carburizing furnace is governed by the atmosphere flow rates, air infiltration, level of furnace conditioning, and amount of soot present. It can also be impacted by catastrophic maintenance events, such as burner tube failures that allow the introduction of combustion products (i.e., a large amount of CO₂ and H₂O vapor) into the furnace atmosphere. For these reasons and the prevalence of good atmosphere-measurement systems, the furnace atmosphere-control approach presented in this article is based on measurements of the actual atmosphere parameters rather than gas input flows.

Temperature Control and Uniformity. Temperature uniformity in carburizing furnaces is important for achieving good carbon profile and hardened depth uniformity. In well-constructed carburizing furnaces, good wind circulation ensures uniform atmosphere composition throughout the furnace. Since carbon potential at the steel surface is determined by the composition of the atmosphere exposed to the part

surface and the part temperature, uniform gas composition coupled with nonuniform temperatures results in variation in the carbon potential within the part workspace. Areas of the load exposed to higher temperatures have higher diffusion rates that increase the rate of case depth formation but lower effective carbon potential. This results in lower instantaneous carbon flux into the steel surface and lower surface carbon concentration. The opposite occurs for areas of the load exposed to lower temperatures. In both cases, the combined effect of the changes in carbon diffusivity and carbon potential on the overall rate of case depth formation is nearly offsetting. As shown in Fig. 16, temperature variation has a large effect on surface carbon concentration but a relatively small effect on the carburized case depth. For an atmosphere controlled to a constant CO₂ or O₂ level, a temperature variation of ±10 °C (18 °F) at 930 °C (1706 °F) will produce a change of ±0.08 wt. % in carbon potential. Therefore, accurate control of carbon potential can be achieved only when there is good temperature uniformity and thermocouples are correctly positioned to detect part temperature. Limits of allowable temperature variation for a carburizing furnace can be calculated from product specification limits for case depth and surface carbon variation. Some users utilize AMS 2750 to define furnace classes, required temperature uniformity, and other aspects of temperature measurement, control, and related thermocouple maintenance. Most users in the United States specify carburizing furnaces capable of ±5 °C (9 °F) temperature uniformity.

The effects of temperature variation within the load caused by variations in heating rate can be reduced by heating parts in carrier gas (or near-neutral atmosphere) and not adding enriching gas until the parts have reached carburizing temperature. A well-designed pusher-type furnace with radiant tubes arranged both below the hearth and above the load is capable of ±3 °C (5.4 °F) temperature uniformity. Carburizing furnaces should be equipped with two thermocouples in each furnace zone located as close as possible to the workpieces. One thermocouple is intended for the temperature controller, while the second thermocouple is used as the over-temperature controller. If a hole or crack develops in a thermocouple-protection tube, the thermocouple will come in contact with the furnace atmosphere, become partially carburized, and yield incorrect readings. In this event, both the protection tube and thermocouples



Fig. 15 Example of metal dusting in a 25 mm (1.0 in.) diameter RA 330 alloy pusher head axle pin exposed to rich carburizing atmosphere at approximately 550 °C (1020 °F) for 1 year

Table 7 Furnace alloys resistant to metal dusting (carbon rot) corrosion

Alloy name	Alloy chemical composition, wt%						
	Cr	Ni	Si	Mn	Mo	W	Co
RA 333	28	36	1.5	...	3	3	3
Supertherm	22	48	1	1	...	5	15
Super 22H	28	48	1	1	...	5	3

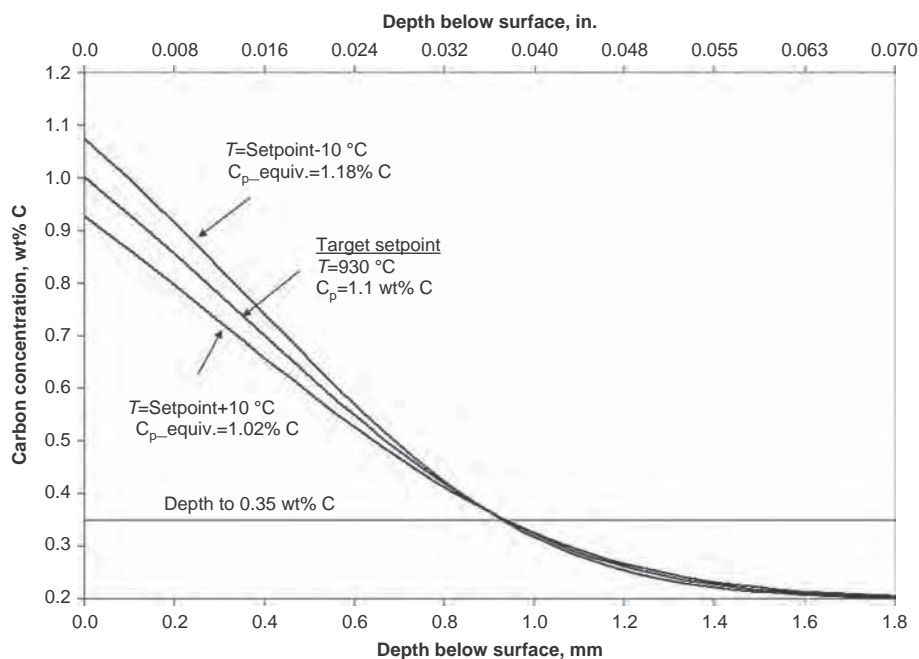


Fig. 16 Variation in the carbon concentration profile caused by ± 10 °C (18 °F) temperature error at a nominal 930 °C (1710 °F) and 1.1 wt% carbon potential setpoint

must be replaced. Thermocouple failure due to exposure to carburizing atmosphere is normally characterized by a loss of signal output that will cause the temperature-control system to call for heat, leading the chamber toward an over-temperature condition. If the over-temperature thermocouple has experienced the same damage and loss of output, it cannot properly sense the actual rise in temperature, resulting in a major over-temperature condition and potential furnace damage. For this reason, temperature-control and over-temperature thermocouples should never be placed in the same protection tube.

Atmosphere Introduction and Uniformity.

Atmosphere carrier gas and enriching gas are typically manifolded together and introduced through inlet pipes in each zone near the circulating fans. Enriching gas is usually not introduced in the first zone of a continuous carburizing furnace to minimize soot formation. Air added for controlling carbon potential should be introduced via a separate inlet to avoid burnback of atmosphere into the inlet pipe. Atmosphere inlet pipes should be located so that incoming atmosphere does not directly impinge on thermocouples or piece parts. In continuous furnaces, carrier gas is usually split between zones in equal amounts. Carrier gas flows are normally held constant (with timed high flows often implemented with door openings or events that cause negative pressure) and enriching gas (trim gas) and trim air additions that are made by the atmosphere controller for each zone as needed. Enriching gas flow should be sufficient to satisfy the need of the atmosphere controller in each zone and should not exceed 10 to 15% of the carrier

gas flow. The bulk flow and direction of the atmosphere through a furnace is mainly established by the size and position of the effluent ports. Flappers or bushings installed on the end of the effluents can be adjusted to vary the flow out of a particular effluent pipe. If infrared CH₄ analyzers are installed, the flow pattern of enriching gas throughout the furnace can easily be detected and be adjusted using the free-methane levels as a tracer.

Given a good temperature uniformity in the furnace, the single largest factor relative to achieving good carburized depth uniformity is having an atmosphere wind velocity of 1 to 2 m/s (3.3 to 6.6 ft/s) throughout the load. Furnaces must be equipped with internal fans and associated refractory construction to ensure that the atmosphere is well circulated through the workload. For dense part loads, sidewall fans and wind-turning refractory brick in the hearth bottom provide the best possible movement of atmosphere throughout the load. Individual parts within the workload should be well spaced to allow the atmosphere to penetrate the load. Care should be taken, when loading parts on screens in baskets, that only the minimum number of screens are used and the openings are not plugged with soot that could interfere with wind flow.

Quenching Uniformity. When direct quenching full loads of parts, critical parts such as gears are usually placed on fixtures to control their spacing and orientation entering the quenchant. When commissioning a new furnace and quench system, it is a good practice to measure the quenchant velocity with a propeller-type flow-measurement device attached to various locations and heights on the tray. This

information can be used to optimize design of the quenchant-delivery system for maximum uniformity. Good quality can normally be obtained when flow rates are a minimum of 0.6 m/s (2.0 ft/s) throughout the workload area. Using an excessive number of screens at the bottom of baskets or using screens plugged with soot can dramatically reduce the quenchant flow through the load, resulting in high levels of nonmartensitic transformation products at the part surface.

Control-System Features. Regardless of the variable being controlled or the instrumentation being used, a major feature of every control system should be a set of signal devices that warns operating personnel of major malfunctions. Virtually all new furnaces are controlled with programmable logic controllers (PLCs) and human-machine interfaces that provide a cost-effective means of collecting and displaying alarm condition information. For instance, a power failure normally renders the atmosphere-control system inoperative. It also shuts down the furnace heating system. If the furnace temperature drops below 760 °C (1400 °F), there is an increased danger of an explosion. A temperature-activated, battery-powered audible or visible alarm warns of a decrease in temperature in time to allow the furnace doors to be opened and the combustible mixture to be burned out or purged with an inert gas before the temperature drops below the danger point. If the furnace pressure drops below a predetermined minimum because of loss in the gas flow supply, there is a danger of explosion due to air infiltration. Such a condition should activate an alarm system to enable immediate operator response to initiate a furnace burnout or to trigger an inert gas purge system. Operators should be well trained on emergency procedures and understand how to respond to furnace problems, particularly those involving loss of atmosphere. If inert gas purging is used, the reserve supply of inert gas should be monitored and an alarm system installed that will signal if the gas supply drops below a predetermined dangerous level. Many modern inert gas storage systems include automatic communication of tank levels to the inert gas supplier. There should always be enough inert gas in reserve to purge the combustibles out of all connected furnaces. The furnace design, control system, and operating practice should comply with National Fire Protection Association 86 recommendations and other statutory requirements.

Major changes in the furnace pressure occur when furnace doors open and close, particularly with inner doors between hot chambers and cold vestibules. When an inner door opens, it normally rises into a cold space, heating and expanding the atmosphere in that area. This gas expansion causes a pressure rise in the furnace, which is typically relieved by flappers that open on effluents. When inner doors are closed, the door is lowered out of the cold region, causing the atmosphere to cool rapidly and shrink in volume. This can create a strong

negative pressure that can draw air into cold vestibules and cause a pop or explosion. To prevent this, many furnaces incorporate a high flow of carrier or inert gas during times of negative pressure to mitigate the risk of air infiltration into chambers operating below 760 °C (1400 °F). The magnitude and duration of such pressure changes is strongly governed by the speed of door opening and closing, with higher speeds causing larger fluctuations. Because many doors are operated with air cylinders that tend to increase in speed as internal seals wear, the PLC is often used to monitor door opening and closing times and provide alarms when times become too short.

Selection of Atmosphere-Control System Type. Atmosphere-control systems for gas carburizing furnaces generally use oxygen probes, NDIR analyzers, or combinations of both. High-accuracy systems may also incorporate thermal conductivity analyzers for H₂ and paramagnetic O₂ analyzers to detect sample system air leaks. If CO levels are known and stable, oxygen probe systems provide reasonable accuracy at relatively low cost. The voltage output of a zirconia oxygen sensor, with air as a reference gas, is a function of the absolute temperature (*T*) and the oxygen partial pressure (*P*_{O₂}) according to Eq 16. The oxygen partial pressure is used to calculate the carbon potential using Eq 12, 13, and 17. Oxygen probes have the advantage of not requiring a gas sample system and provide a continuous direct current millivolt output that is a convenient input for digital atmosphere controllers. Many commercial oxygen probe controllers incorporate a thermocouple input and will display and control to a setpoint that directly reads in carbon potential. Care should be taken to ensure that the oxygen probe is located so that the internal thermocouple reading matches the temperature of the zone and part temperature. Oxygen probes cannot be calibrated, and the output can vary over time due to soot accumulation and/or deterioration of the electrodes. Soot accumulation within oxygen probe sensors used in carburizing furnaces is a common problem. Many oxygen probe systems incorporate a burnout system that interrupts the control action to introduce a small flow of air to the probe tip for burnout. Then the probe re-equilibrates with the atmosphere and resumes operation. On batch furnaces, these burnouts are often performed at noncritical times of the cycle, such as transfer of the load out of the heating chamber. Oxygen probe control systems do not provide good accuracy on systems with unstable CO levels. If not coupled with an NDIR analyzer system to measure CO, the drift in the oxygen probe signal over time due to electrode deterioration can be detected only by a secondary check, such as shim stock.

Atmosphere-control systems that incorporate NDIR analyzers, particularly those that measure CO, CO₂, and CH₄, provide the best accuracy (Ref 6). Although NDIR analyzers are more costly than oxygen probe systems and require

gas sampling systems and associated maintenance, high-accuracy NDIR analyzers are available that can be calibrated to certified gas standards. The CO₂ analyzers should be selected based on their ability to accurately and repeatably detect CO₂ levels in the intended operating range. The relationship of carbon potential to CO₂ level at various carburizing temperatures is shown for natural gas-air endo (nominal 20% CO) in Table 8. As the operating temperature and carbon potential increase, the sensitivity of carbon potential to small changes in CO₂ increases.

From a practical point of view, analyzers selected for high-accuracy measurement of carbon potential should be capable of measuring CO₂ levels as low as 30 ppm with 5 ppm accuracy. Low-level resolution is diminished by higher detection ranges, but typically a CO₂ analyzer optimized for a 6000 ppm (0.6 vol%) full-scale range and capable of 2% of reading (relative) accuracy will provide good results. Absolute accuracy of readings is dependent on the accuracy of gas standards and software interference correction factors for other gas species present in the atmosphere. Hydrogen does not have an infrared absorption band but can influence the infrared absorption band of CO₂ at 4.4 μm (173 μin.) (Ref 56). This effect, known as spectral broadening or background broadening, can cause a 10% increase in the measured CO₂ reading in endothermic gas at a nominal 0.1 vol% CO₂ level. This effect can be reduced by using calibration gases containing hydrogen concentrations similar to those of the furnace carrier gas. Variations in hydrogen concentration around a calibration gas level still could produce some error, but often this is negligible. In situations where the hydrogen variations are large (such as ±20%), the effect can be totally eliminated by measuring H₂ concentration with thermal conductivity and applying cross compensation to the CO₂ measurements. Pursuit of the correct absolute value is not essential for good carbon potential control, as long as the atmosphere-control system is capable of controlling to a value determined by shim analysis to provide the desired carbon level on a consistent basis. However, the correct absolute value of CO₂ in the atmosphere is necessary when correlating shim stock

Table 8 Relationship between carbon potential and CO₂ level at various carburizing temperatures for endothermic gas generated from natural gas (nominal 20% CO)

Carbon potential, wt% C	CO ₂ , vol%		
	980 °C (1800 °F)	960 °C (1760 °F)	930 °C (1710 °F)
1.25	0.0495	0.0597	0.0796
1.2	0.0525	0.0631	0.0845
1.1	0.0592	0.0714	0.0955
1	0.0673	0.0811	0.1087
0.9	0.0775	0.0934	0.1244
0.8	0.0901	0.1082	0.1451

readings to the carbon potential in the furnace determined from the thermodynamic equilibrium calculations.

The carbon potential of an atmosphere can be determined using the CO + H₂ reaction (Eq 3) by measurement of the water vapor content. It is typically done by determining the dew point-dew point, which is defined as the temperature below which the water vapor in a volume of atmosphere at a constant barometric pressure will condense into liquid water. The relationship between dew point and the partial pressure of water in the atmosphere is given by:

$$\text{Dewpoint} = \frac{5422.18}{14.7316 - \ln P_{\text{H}_2\text{O}}} - 273.16 \quad (\text{Eq 36})$$

The speed, accuracy, cost, and limitations of dew point measurement is dependent on the type of dew point-measurement instrument used, as described in greater detail in the article "Furnace Atmosphere Control in Heat Treating" in *Heat Treating*, Volume 4 of *ASM Handbook*, 1991. The speed and accuracy of dew point measurement declines at very low water vapor levels. In industrial gas carburizing, the equilibrium water vapor contents are very low (−5 to −20 °C, or 23 to −4 °F, dew points) at higher temperatures and high carbon potentials, where the process normally demands higher levels of accuracy. Most dew point analyzers depend on some type of threshold vapor condensation to measure the water vapor. Sample gas streams of carburizing atmospheres, even though highly filtered, will precipitate small amounts of soot when chilled, forming deposits on sensor surfaces. Dew point analyzers are also sensitive to errors arising from condensed water in the sample system that contaminates the sample stream. Equipment to calibrate dew point analyzers with precisely known water content sample gas is complex and not suitable for most carburizing shop environments. Therefore, dew point measurement is not commonly used in industrial carburizing applications that require high accuracy and rapid controller response time.

Implementing Atmosphere Carbon Potential Control. Most modern gas carburizing furnaces incorporate some means of automatic atmosphere control. There are various types of systems, ranging from those that control carbon potential using measurement of a single atmosphere species to those that measure all of the major atmosphere components and control carbon potential and CO levels in the furnace, including cross-check calculations for accuracy (Ref 57). Figure 17 gives a schematic representation of a simple control system using a single residual species as the primary input to the atmosphere controller. These systems are most effective when used with stable CO atmospheres. The most commonly employed system of this type uses an oxygen probe; however, the control scheme shown in Fig. 17 can be used with a single CO₂ analyzer or dew point analyzer. The controller compares the input value to the desired

setpoint and provides output signals to enriching gas or air trim valves. Although solenoids can be used, a system incorporating position proportional actuators connected to adjustable port valves provides smooth control and the ability to adjust the maximum trim gas flow to the needs of a particular furnace zone.

It is an advantage to establish a convention regarding atmosphere-controller output, such that increasing percent output is intended to increase the richness of the atmosphere; that is, increasing the flow of enriching gas and/or decreasing the flow of control air. Both proportional valves can be connected to the same atmosphere controller 4 to 20 mA output loop and adjusted so that lower output ranges of the controller modulate air flow and upper ranges modulate enriching gas. Figure 18 shows a sample atmosphere-controller output diagram

for a gas carburizing furnace (zone) that normally needs enriching gas additions to maintain a carbon potential setpoint but occasionally requires small amounts of air for optimum control. In this case, 0% output delivers the maximum flow of air to the zone. Air flow decreases as the percent output signal from the controller increases, until there is no flow of air at 20% output. As the signal increases from 20 to 100% output, the enriching gas proportional valve opens toward maximum enriching gas flow. Depending on the needs of the zone, the zero point of no trim gas flow can be set at any percent output value, or the entire proportional output range can be used to control a single enriching gas or trim air valve. The advantage of this system is that a single 0 to 100% output scale can move the atmosphere with maximum air flow at 0% output to

maximum enriching gas flow at 100% output. When coupled to proportional actuators on adjustable port valves, the system can be adjusted to optimize trim gas flows for virtually any furnace zone requirement.

Furnaces with atmospheres that have unstable CO levels, such as those using nitrogen-methanol or the atmospheres with high levels of residual methane or hydrogen, can be controlled accurately with systems that employ multispecies measurement. These systems use NDIR analyzers or can couple NDIR analyzers, thermal conductivity analyzers (for hydrogen measurement), and O₂ probe systems together, as shown in Fig. 19.

Although these systems are more expensive, the ability to measure CO, CH₄, and H₂ concentration enables better understanding of the condition of the gas carburizing furnace. The CO measurement can be used to control the CO concentration to a constant level in nitrogen-methanol or similar systems. The actual CO level can be used to calculate the atmosphere carbon potential using either the CO-O₂ relationship or the CO-CO₂ relationship. Users can select one method for primary control and use the other one as a cross-check or system alarm. Measurement of the H₂ level allows the user to evaluate if the proper carrier gas flow is being used in a particular zone by ensuring that the increase in H₂ concentration during carburizing is limited to 2 to 3 vol% above the normal H₂ level in the carrier gas. Residual methane levels are also an indication of proper carrier gas flow during the initial setup but are more valuable in the long run as an indicator of the need for furnace burnout. Some systems incorporate a paramagnetic-type O₂ analyzer calibrated for O₂ levels in the low percent range to detect air leakage into the sample gas. Because furnace atmospheres typically have O₂ levels in the 10⁻¹⁸ partial pressure range, any oxygen detected in the sample analyzed on an external gas analyzer system in the percent range is caused by leakage into the sample stream. This is important, because a 1 vol% O₂ level in the sample means the sample has been diluted with 5 vol% air, thus causing a 5% relative error in the measured CO₂ value and calculated carbon potential.

Gas Sampling. Gas samples for the analysis of atmosphere composition should be taken from a point in the furnace chamber as close as possible to the work being treated. This will lower the likelihood of obtaining a sample of stagnant gas that may be present near the furnace wall. The sampling point should also be as far as possible from the atmosphere inlet ports and from burner tubes.

Velocity of Sample Gas Flow. Empirical data indicate that when CO₂ or H₂O vapor is to be measured, the velocity of gas flow through the sampling tube should be at least 1.2 m/s (3.9 ft/s). This velocity almost completely prevents reactions between the gas constituents by reducing the time in the intermediate-temperature range, which exists mainly in the

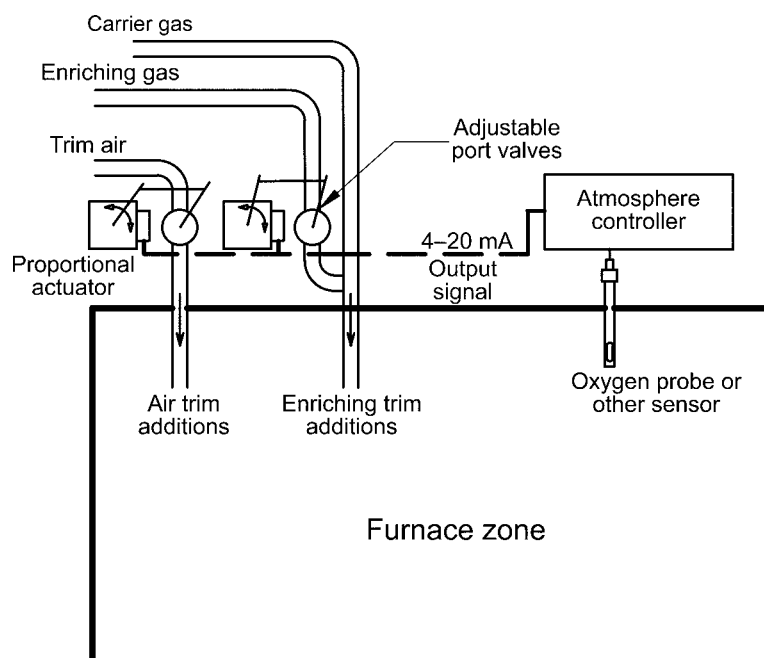


Fig. 17 Example of atmosphere-control system with single residual species sensor

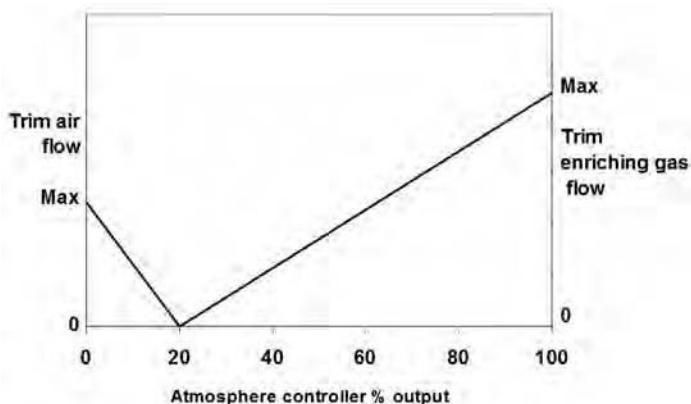


Fig. 18 Example of dual-proportional trim gas/trim air flow-control system

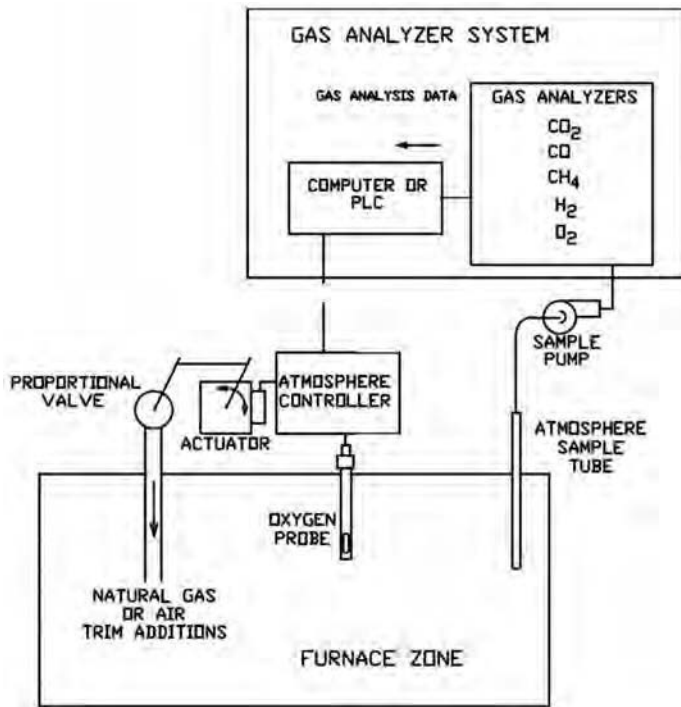


Fig. 19 Example of atmosphere-control system with multispecies control sensors. PLC, programmable logic controller

portion of the tube that passes through the furnace wall. At lower velocities, the water-gas reaction will take place at lower temperatures, resulting in higher CO_2 concentration and lower concentration of H_2O vapor. If the carbon potential of the furnace atmosphere is high, CO may decompose into CO_2 and soot. This will further increase CO_2 concentration and will affect the H_2O vapor content through the water-gas reaction. When sooting occurs in the sampling tube, the gas sample delivered to the analyzer has a higher CO_2 content than actually exists in the furnace. Based on analysis of the sample, the controller would increase the flow of enriching gas, which would put the furnace out of control and compound the sooting problem in the probe. Because the minimum gas sample velocity required for the sample tube is higher than that velocity required at the analyzer, bypass systems are used to keep the sample flow rate high and fresh at the analyzer.

The minimum flow rate can be investigated by lowering the flow of sample gas while ensuring that the atmosphere carbon potential is held constant for a period of time. The CO_2 level will remain constant until a minimum flow is reached, at which point the measured CO_2 level will increase rapidly upon decreasing further the flow rate. Gas sample systems should not be operated with a dew point of the atmosphere that is at or near room temperature, to avoid water condensation in the sample system that may damage analyzers. If gas-analyzer systems are coupled with an O_2 probe control, the sample system can be shut off if the O_2 probe is operated below a certain millivolt level, to

prevent introduction of a wet atmosphere into the sample system.

Some furnace-control systems incorporate an automatic N_2 blowout that momentarily disables gas flow to the NDIR system and pulses N_2 through the sample tube into the furnace to keep the tube clear of soot. If used, N_2 blowout valves should incorporate a block-and-bleed system to prevent leakage of N_2 into the gas sample, because N_2 would not be detectable in the NDIR system. Sample tubes should be lined with a high-purity quartz glass liner to reduce catalytic effects that the probe body alloy material may have on the sample gas, thus altering the measured composition.

Procedures and Precautions. It is important that sufficient time be allowed for purging the furnace chamber and porous refractory prior to taking a gas sample from a batch-type furnace without a charging vestibule or from a continuous furnace during startup. Otherwise, high-atmosphere dew points that may occur at the beginning of a cycle will cause condensation in the sample line that will affect subsequent measurements. For batch-type furnaces, this delay can be accomplished automatically with an electrical limit switch operated when the furnace door or cover seal is broken and a time-delay relay set up for the proper purging time. In continuous furnaces, the sample pump should be turned off, or the sample line should be blocked with a manual valve.

In pusher-type continuous furnaces, the periodic opening of the furnace doors may cause large changes in atmosphere composition. When manual instruments are used, samples should

be taken at the same time in each push cycle (preferably just before a push), in order to compare the results. Use of an automatic analyzer that continuously monitors the atmosphere will permit observation of the effects of venting, resealing doors, and changing the purge flows to the vestibules.

Carburizing Cycle Development

Carburizing Process Parameters (Temperature, Carbon Potential, and Time). Successful operation of the gas carburizing process depends on the control of three principal variables:

- Temperature
- Atmosphere composition or carbon potential
- Time

Other variables that affect the amount of carbon transferred to parts include the degree of atmosphere circulation, steel alloy composition, and surface preparation of the parts.

Temperature. Carburizing temperatures must be uniform throughout the workload to produce uniform case depth and surface carbon concentration. The maximum rate at which carbon can be added to steel is limited by the rate of carbon diffusion in austenite. Higher temperatures allow the use of higher carbon potential atmospheres and promote a faster rate of carburized case depth evolution. Carburizing most commonly is performed at 925 to 930 °C (1700 to 1710 °F). This temperature permits a reasonably rapid carburizing rate without excessive austenite grain growth or deterioration of furnace equipment, particularly alloy trays and fixtures. For case depths greater than 2 mm (0.08 in.), the carburizing temperature is often raised to a temperature range of 955 to 980 °C (1750 to 1800 °F) to shorten the carburizing time and limit the depth of IGO formation. Although higher temperatures produce shorter carburizing times, the relative sensitivity and accuracy of the carbon potential control system is reduced at higher operating temperatures.

Shallow case carburizing frequently is done at lower temperatures to take advantage of the better case depth control permitted by a slower rate of carburizing. When parts are direct hardened from the gas carburizing process, the temperature is typically lowered and equalized at the hardening temperature prior to quenching.

Carbon potential is defined as the amount of carbon in the furnace atmosphere at a given temperature that is in thermodynamic equilibrium with the weight percent carbon dissolved in unalloyed austenitic steel, such as plain carbon shim stock. The rate of carbon transfer from the gas atmosphere to the steel part is proportional to the difference between the carbon potential in the furnace atmosphere and the actual, instantaneous carbon concentration at the part surface. Higher carbon potentials provide higher carburizing rates and must be

controlled carefully when operating near the saturation limit to avoid carbide formation at the surface of the part and excessive soot formation in the furnace. In all endothermic-type atmospheres, where CO is the principal carburizing species, lower carbon potential atmospheres have higher CO₂ contents that raise the overall equilibrium partial pressure of oxygen and increase the rate of IGO formation in alloys containing chromium, manganese, and silicon.

The effect of time on case depth is interdependent with the carburizing temperature and atmosphere carbon potential. High carburizing temperatures and high-atmosphere carbon potential promote greater carbon flux from the gas phase to the part surface and greater carbon diffusion rate and therefore will require shorter times to achieve a target case depth. The effect of time and temperature on total case depth is shown in Fig. 20. The data given, originally published by Harris (Ref 44) in 1944, are computed assuming saturated austenite at the surface of the workpieces. In industrial practice, where the atmosphere carbon potential and the corresponding surface carbon content are controlled below the carbon saturation limit in austenite, the total carbon penetration depth will be less than the depth predicted by the Harris equation. Thus, the actual case depth achieved may differ significantly from the values given in Fig. 20. More complex mathematical models that allow for variations in temperature and atmosphere carbon potential with time can be constructed to allow a better prediction of case depth, as discussed in the previous sections.

In addition to the time at the carburizing temperature, several hours may be required to bring large workpieces or heavy loads of smaller parts to the operating temperature. For work quenched directly from the carburizing furnace, the cycle may be lengthened further by allowing time for the work to cool from the carburizing temperature to approximately 840 to 850 °C (1540 to 1560 °F) prior to quenching. If the workload is exposed to the carburizing atmosphere during heating, some carburizing will occur before the nominal start of carburizing. Similarly, additional diffusion and interchange of carbon with the atmosphere will occur during cooling prior to quenching. This must be accounted for in cycle design, particularly in pit and pusher carburizing furnaces.

Design of Carburizing Cycle. Carburizing cycles are normally developed to produce a given carbon profile (i.e., surface carbon and carburized depth) such that when imparted to a particular alloy, the final required hardness profile is established by the hardening process. Setpoints for temperature, time, and carbon potential can be determined by process modeling using various carbon gradient prediction programs or from experience and empirical data derived from test cycles. Inherently, carburization is a slow, forgiving process. Parts usually are at elevated temperature for several hours, and periodic fluctuations in temperature or carbon potential usually are of little consequence.

As long as average conditions are maintained, without large or prolonged excursions from setpoint conditions, it is unlikely that carburized depth will be adversely affected. Likewise, a few minutes difference from programmed time in the furnace usually will be of little consequence for carburized parts. Only carburizing and diffusion times, not total furnace time, should be counted toward the time required to develop a given depth of case. Preheating time is usually disregarded because little carburizing takes place in this part of the cycle.

Gas carburizing can be performed in a steady-state or boost-diffuse mode. Steady-state carburizing is conducted at a constant temperature with a constant carbon potential setpoint throughout the whole cycle. In steady-state carburizing, the surface carbon level increases continuously toward the gas atmosphere carbon potential but never reaches it. The forward movement of carbon atoms into the surface is characterized by the instantaneous carbon flux

defined as the product of the coefficient of mass transfer, β , through the near-surface boundary layer and the difference between the atmosphere carbon potential and the instantaneous carbon concentration at the steel surface. Figure 21 illustrates the effect of carburizing time on carbon concentration profile in steel with 0.2 wt% base carbon during steady-state carburizing at 925 °C (1700 °F) and 1 wt% carbon potential. While in some practices a saturation carbon potential is used to enable maximum carburizing rate, most often steady-state carbon potential is constrained by the maximum allowable part surface carbon content for acceptable carburizing performance.

Carburizing rates can be accelerated significantly by using boost-diffuse-type cycles. For case depths greater than 0.6 to 0.8 mm (0.02 to 0.03 in.), boost-diffuse-type cycles maximize the carburizing rate and, with the proper boost-diffuse time ratio, produce a carbon gradient with a distinct plateau near the

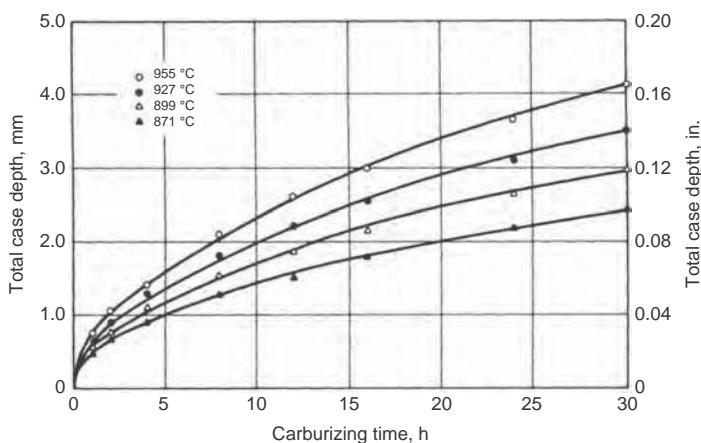


Fig. 20 Plot of total case depth versus carburizing time at four selected temperatures in a saturated carbon potential atmosphere per Harris. Source: Ref 44.

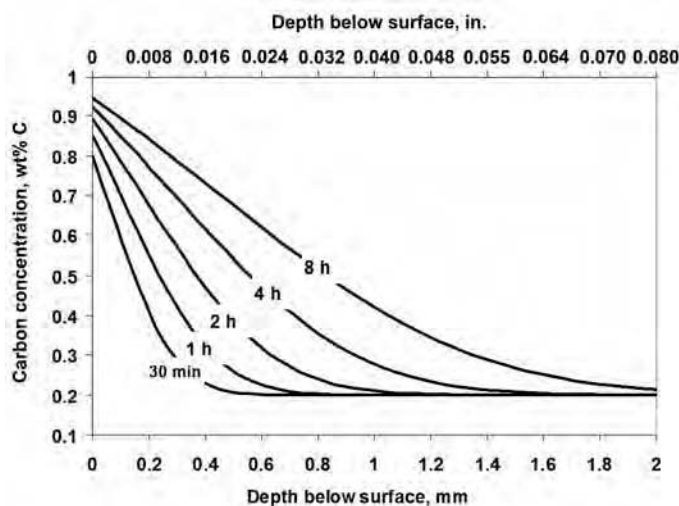


Fig. 21 Carbon concentration profile evolution during steady-state carburizing at 925 °C (1700 °F) and 1 wt% carbon potential

surface. For any given carburizing temperature, there is an optimum boost-diffuse time ratio for each carburizing depth, with the ratio of diffuse time becoming longer for deeper case depths. Carbon gradient modeling programs can be used to simulate the carbon profile that will be created by any set of time, temperature, and carbon potential conditions and allow the user to determine the optimum boost-diffuse carbon potential setpoints and time ratio. While these simulation programs provide the user with a relatively quick and easy way to evaluate the effect of operating parameters, simulation program output must be balanced with the actual operating limits of the furnace and control system.

The boost step is conducted at a relatively high temperature and a high carbon potential to enable greater carbon flux from the gas atmosphere to the steel surface and a greater rate of carbon diffusion into the steel. During the diffuse cycle, the gas atmosphere carbon potential is lowered to a level slightly greater than the desirable carbon level in the final part. Although called a diffuse cycle, the surface carbon is reduced both by diffusion of carbon into the core and loss of carbon back to the atmosphere via reversal of the surface carburizing reaction. It is important to establish the correct ratio between boost and diffuse duration to obtain a carbon concentration profile with a characteristic flat plateau near the surface and to produce desirable compressive residual stresses for better fatigue performance.

Figure 22 shows the effect of diffuse time on the carbon concentration profile. Insufficient diffuse times may result in failure to achieve a plateau surface carbon gradient or may negatively impact the magnitude of surface compressive residual stresses. Excessive diffuse times reduce the carburizing time advantage of boost-diffuse carburizing and will result in a carbon profile monotonously decreasing from the steel surface toward the core that may lower near-surface compressive residual stresses. Carbon profiles with a subsurface peak should be avoided, because they can produce a residual tensile surface stress. Mathematical models for carbon diffusion in steel, described in the previous section, can be very helpful in determining an optimal combination of temperature, carbon potential, and time required to produce a desired carbon profile with minimum cycle time and minimum operating cost.

The diffusion portion of the cycle may be conducted at the same temperature as the boost cycle segment (more common with deep case cycles) or combined with lowering of the temperature to the hardening temperature prior to quenching (more common with shallow case cycles) if parts are direct hardened. In addition to minimizing processing time, several other factors affect the choice of processing parameters. In continuous furnaces that may not always be separated into distinct boost-diffuse zones by means of internal doors, there is a limit to the magnitude of the differences in

temperature and carbon potential that can be sustained over the length of the furnace. Similarly, in batch furnaces, the rate at which the temperature can be lowered depends on the thermal inertia of the furnace, the carburizing load characteristics, and the magnitude of the heat losses. In the absence of a detailed mathematical model incorporating furnace operating characteristics, some trial-and-error experimentation may be required to find the operating setpoints that produce the desired results.

Selection of Atmosphere-Control Setpoints. Once the process temperature and carbon potential have been determined, appropriate control levels of the residual species (CO_2 , O_2 , or dew point) can be selected from Fig. 23 to 25. If using batch furnaces, most boost-diffuse ratios can be implemented easily by programming the cycle segment timers. For continuous furnaces, the boost and diffuse conditions are implemented in separate zones of the furnace, and the boost-diffuse ratio is fixed by the furnace design and the relative number of trays in the boost and diffuse zones. The boost and diffuse zones of continuous furnaces are typically operated at fixed

temperatures and atmosphere levels, and variation in case depth is achieved by changes to the overall cycle time. Depending on the allowable case depth range and overlap of different part case depths, it may be necessary to push empty trays between lots of parts when implementing a case depth change. Continuous pusher-type furnaces are most efficiently operated on large lots of similar case depth parts with minimum case depth changeover. Continuous furnaces typically produce high quality and uniformity, because the critical process conditions are relatively easy to hold constant over time. Batch furnaces provide the flexibility of running each cycle under different time, temperature, and atmosphere conditions. Case depth uniformity from batch to batch is affected by the ability of the furnace to respond to input conditions as programmed. Depending on the conditioning level and amount of soot present in a batch furnace, the actual atmosphere levels achieved may not reach setpoint or may lag substantially the temperature in a given cycle segment. If cycle segment timers are designed to begin timing when both temperature and atmosphere setpoints are achieved, the overall

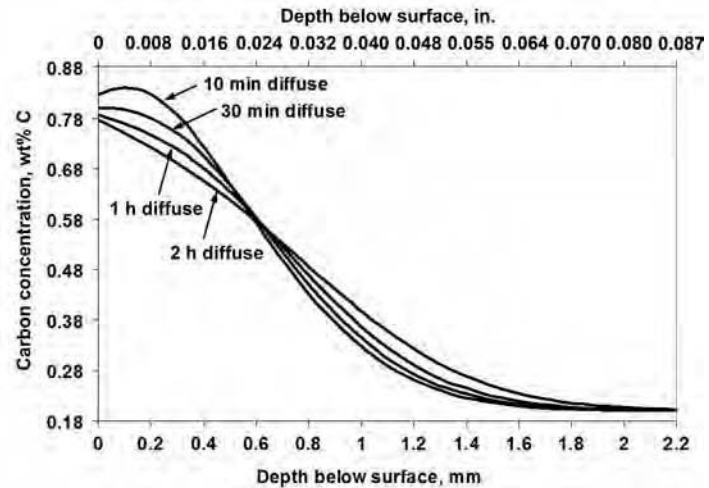


Fig. 22 Effect of diffuse time on carbon concentration profile. Boost at 925 °C (1700 °F), 1.15 wt% C, 4 h with various diffuse times at 925 °C (1700 °F), 0.8 wt% C

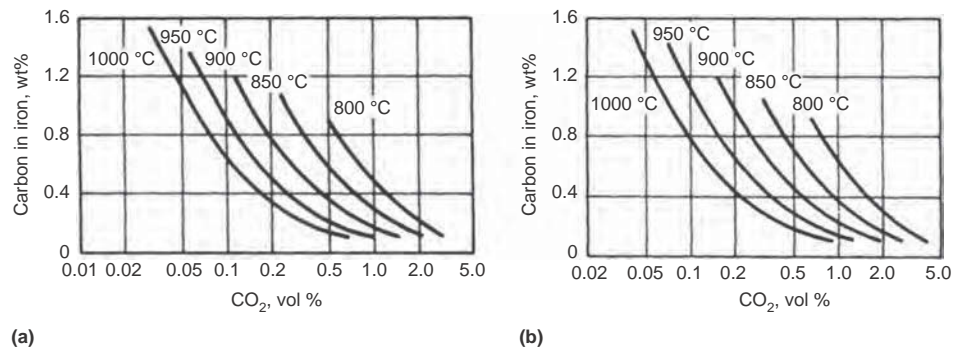


Fig. 23 Relationship between CO_2 content and carbon potential for endothermic gas generated from (a) methane and air or (b) propane and air

cycle times and case depth may vary from one batch to another one.

In most gas carburizing furnaces, whether batch or continuous type, carbon potential of a particular zone is calculated using zone temperature. If, during the cycle, the load is cooled from the carburizing temperature to a lower temperature for direct quench hardening, batch furnaces and continuous furnaces differ in terms of how the carbon potential at the part surface (governed by part temperature) responds during cooling. In batch furnaces, when the furnace temperature is lowered, the furnace and load cool at approximately the same rate; thus, the furnace thermocouple reading is a relatively good indicator of part temperature, and the carbon potential calculated using the zone temperature is a good indicator of the carbon potential at the part surface. However, cooling of loads to the hardening temperature in continuous furnaces is usually accomplished by moving the load from a zone of higher temperature into a zone at lower temperature. The furnace zone carbon potentials are calculated using the zone temperature, but the carbon potential at the surface of a part is governed by part temperature. When the higher-temperature load first enters the lower-temperature zone, the temperature of the parts is significantly higher than the zone temperature, causing the carbon potential at the surface of the parts to be lower than the zone carbon potential. The drop in carbon potential at the surface of the part causes a rapid drop in surface carbon to a level significantly below the zone carbon potential. As the load travels through the zone of lower temperature, the parts begin to cool and equilibrate with the zone temperature, and the carbon potential at the surface of the part begins to rise toward the zone carbon level. The relationship between zone carbon potential and surface carbon concentration on the part in a tunnel-type carburizer is shown in Fig. 26.

The final surface carbon in a continuous furnace where parts are cooled before quenching can be modeled by software simulation and verified in practice. Normally, the carbon potential of the latter zones is adjusted to produce the correct final surface carbon for a given overall push rate. For shallower case parts with short cycle times, the carbon level in final zones must be set higher than desired part surface carbon compared to deeper case parts with longer cycle times and more residence time in the final zones. Once the cycle time/zone carbon potential relationships are established, continuous gas carburizing furnaces will produce very consistent surface carbon and carburized case depths. To obtain consistent surface carbon when cooling loads in tunnel-type continuous furnaces, case depth cycle changes must involve a change to both the cycle push time and the latter zone carbon potential setpoints. If only the cycle time is changed, then shallower case depth parts will typically exhibit lower surface carbon than deeper case parts.

Process Planning

Designers usually specify surface hardness, core hardness, effective case depth and/or carburized depth, and sometimes microstructure requirements required for a part to withstand service load and stresses for a given application. It is the task of the process engineer to develop the carburizing treatment that will produce the desired properties. Some of the considerations involved in setting up the processes include:

- Preparation of parts for carburizing
- Available carburizing equipment
- Case microstructure (in terms of retained austenite, IGO, nonmartensitic transformation products, and decarburization)
- Residual stress
- Alloy selection
- Operating schedules
- Direct hardening versus reheat hardening
- Quenchants
- Tempering
- Selective carburizing

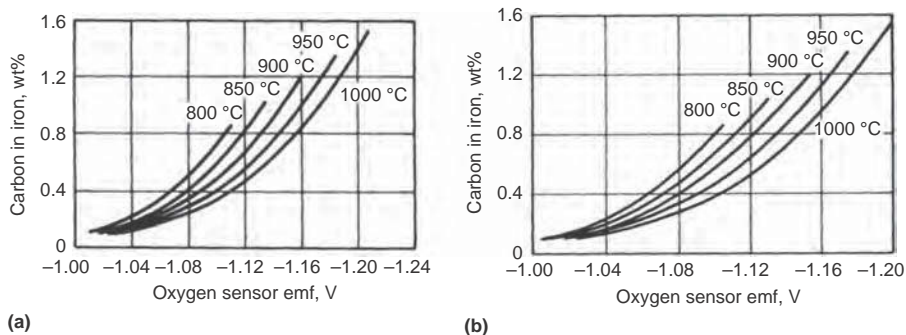


Fig. 24 Relationship between O₂ probe electromotive force (emf) measurement and carbon potential for endothermic gas generated from (a) methane and air or (b) propane and air

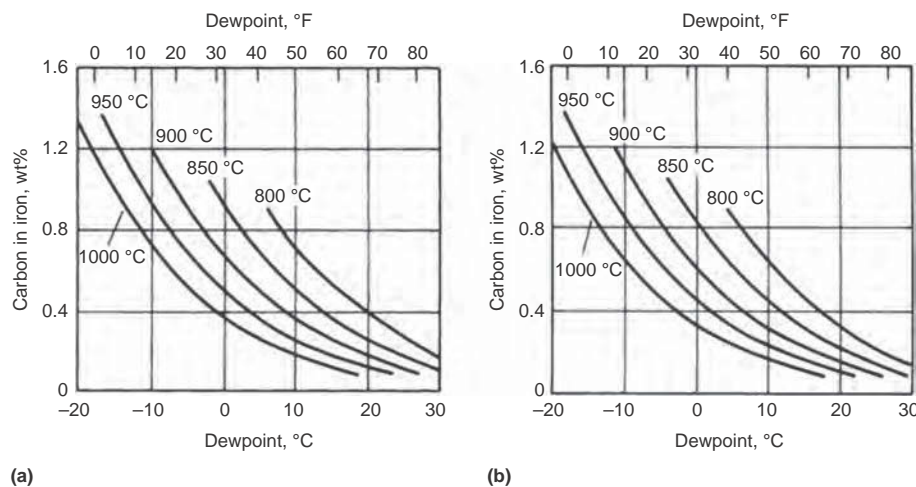


Fig. 25 Relationship between dew point and carbon potential for endothermic gas generated from (a) methane and air or (b) propane and air

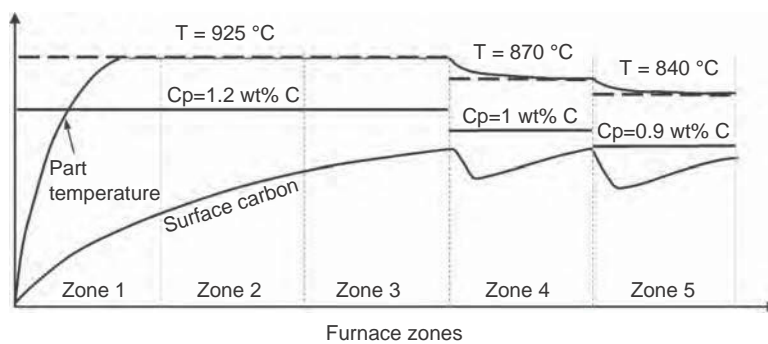


Fig. 26 Surface carbon and part temperature as load moves from a zone of higher temperature and carbon potential to a zone of lower temperature and carbon potential in a continuous tunnel type furnace

Understanding the Case Depth/Hardened Depth Relationship. Most part drawings specify a depth to a specific hardness level, often called the effective case depth or hardened depth. Achieving a desired hardness level (typically 50 HRC) at a specified depth requires that a proper carbon profile, and hence carbon content at the specified depth, be achieved. While various modeling tools can be used to accurately predict steel carburizing response to gas atmosphere composition, carburizing temperature, and time, it is imperative that the process designer understands how various carbon profiles are manifested as hardness profiles in various alloys and part section sizes subjected to a particular quench severity during hardening.

For heavier part section sizes or lower quench severities coupled with lower-alloy base materials, carbon content near 0.4 wt% may be required at the specified effective case depth to achieve 50 HRC. Smaller section sizes, higher-hardenability steel grades, and/or the use of higher quench severities can reduce the carbon content needed at the specified effective case depth closer to 0.30 to 0.32% to achieve the same 50 HRC hardness. Many companies select steel alloys that enable an effective case depth to 50 HRC to be achieved at 0.35% C (or slightly lower carbon level) with a particular quench. Carburizing cycles for various depths are then designed around carburized depths to 0.35% C. When selecting the steel grade for a particular part application, design engineers should consider the cost tradeoff of steel alloy cost for hardenability versus carburized depth and associated carburizing time and heat treatment cost.

Preparation of Parts for Carburizing. Parts, trays, and fixtures should be thoroughly cleaned before they are charged into a carburizing furnace. Often, they are washed in a hot alkaline solution. Some users preoxidize washed parts, trays, and fixtures by heating in an oxidizing atmosphere at 400 °C (750 °F) before carburizing, to remove traces of organic contaminants. During preoxidizing at temperatures below 500 °C (930 °F), a very thin oxide layer forms on parts, which is subsequently reduced by the carburizing atmosphere. Preoxidizing parts at temperatures above 500 °C (930 °F) promotes formation of a heavy oxide layer that may become flaky and loose. When parts are heated in the carburizing atmosphere, the heavy oxides are reduced to form a layer of iron on the surface of the part. This thin layer of iron or portions of the layer may survive shot cleaning after hardening and flake off in service.

Parts may have various layers of contaminants present at the steel surface prior to carburizing that could impact their response to gas carburizing. For controlled and predictable carburizing response, parts should be free of rust, scale, oil, or cutting fluid contaminations prior to carburizing. Table 9 summarizes commonly used cleaning methods for various types of steel surface contamination.

Over the past 20 years, there have been both mechanical and chemical processing changes

Table 9 Cleaning methods for various types of steel surface contamination

Type of contamination	Cleaning method
Heavy oil	Alkaline cleaning, acid cleaning, emulsion cleaning, vapor degreasing
Light oil	Alkaline cleaning, acid cleaning, emulsion cleaning, solvent cleaning, vapor degreasing
Cutting fluid	Alkaline cleaning, acid cleaning, emulsion cleaning, vapor degreasing
Rust and scale	Acid cleaning, abrasive blast cleaning, alkaline cleaning, salt bath descaling, general mechanical blast cleaning, tumbling, pickling

that have impacted the metal-cleaning industry. Most notably, these have involved the minimization of chromic acids and vapor degreasing. Today (2013), metal cleaning is generally done by using a combination of chemical and mechanical methods. This can be accomplished by changing one or more of the following components: time, temperature, pressure, and chemical concentration. When pressure, temperature, time, or chemical concentration is increased, cleaning effectiveness is improved. Often, an increase in one of these components decreases the effectiveness of one or more of the other components. In most cases, selection of the cleaning process settings is done such that it optimizes total cost or addresses other facility-specific issues that relate to such matters as health and safety, environment, energy, and so on.

Alkaline cleaners are generally known to remove oils, whereas acids are known to remove rust. However, both types of cleaners can be effective with oil removal as well as rust removal. Beyond adjusting the cleaning parameters, many of the cleaning chemical manufacturers can provide cleaning solutions with surfactants and other additives that have been demonstrated to improve oil removal with acidic products and rust with alkaline products. (Acid cleaning of high-strength steels may cause hydrogen embrittlement. To reduce the possibility of hydrogen embrittlement, the time of exposure of the steel to the acid should be minimized.)

Residues from alkaline washer solutions deposited on parts, particularly those with silicates, can cause spotty carburizing as well as give the parts a blotchy appearance. The use of silicone-based defoaming agents in washer solutions may cause spotty carburizing. In addition, alkaline residues can adversely affect the life of heat-resistant furnace alloys. Quenching salts remaining on trays and fixtures can also damage furnace hardware (for example, silicon carbide rails in pusher furnaces). Chlorine- or sulfur-containing residues on parts will release gases that can react with brickwork, the protective oxide films on heat-resistant alloy fixtures, or the workload. Parts should be cleaned in a timely manner, because residues left to sit on the metal surface may become increasingly difficult to remove.

Spray and immersion cleaning are the most commonly used metal-cleaning processes today (2013), because many companies have moved away from the traditional vapor degreasing processes. It is quite possible that new cleaning processes that incorporate both CO₂ and nitrogen may become more popular. These types of materials, which are generally used in precision cleaning processes, may find additional applications in the general metal-cleaning industry because they leave very little residue. Additionally, most of these operations are generally more environmentally friendly.

Retained Austenite. A hardened carburized case usually consists of a mixture of martensite and retained austenite for parts that are direct quenched from carburizing. For parts that are reheat hardened, the case microstructure consists of a mixture of martensite, retained austenite, and potentially (depending on the total case carbon content and the hardening temperature) finely distributed carbides. In conventional gas carburizing where carbon potential is controlled below the carbon saturation limit in austenite, microstructural constituents, such as proeutectoid carbides, bainite, and pearlite are generally avoided. The amount of retained austenite is related to the (M_s - M_f) transformation temperature range of the surface, which is governed strongly by the quench cooling rate, surface carbon content and other austenite stabilizers in solution prior to quenching. For reheat-hardened parts, the surface carbon content in solution is dependent on the hardening temperature when total surface carbon content of the as-carburized part is greater than the eutectoid composition. In virtually all cases, the martensite finish (M_f) temperature is below the quenchant temperature, and some amount of austenite will be retained after quenching. The microstructures shown in Fig. 27 demonstrate the strong effect of carbon content in solution prior to direct quenching. Retained austenite measurements via x-ray diffraction (XRD) revealed 65, 50, and 30% corresponding to 1.2, 1, and 0.75 wt% C at the steel surface, respectively. When near-surface carbon levels are equal, there is little to no effect of part temperature prior to quenching during the direct-hardening operation. Figure 28 shows case microstructures of three parts carburized to produce the same carbon profile with 0.85 to 0.9 wt% surface carbon and a carburized depth (to 0.35 wt% C) of 1 mm (0.04 in.), quenched in oil directly from 900, 925, and 950 °C (1650, 1700, and 1740 °F). The XRD measurements revealed 43 to 46% retained austenite measurements on all parts.

Nickel is used in many of the common carburizing alloys to increase toughness. However, since nickel is a strong austenite-stabilizer, it also tends to increase the amount of retained austenite. Higher-nickel-containing alloys such as SAE 9310 and SAE 3311 are often run at carbon potentials less than 0.9 wt% to limit retained austenite. Nitrogen also affects austenite stability. Care must be used to limit the amount

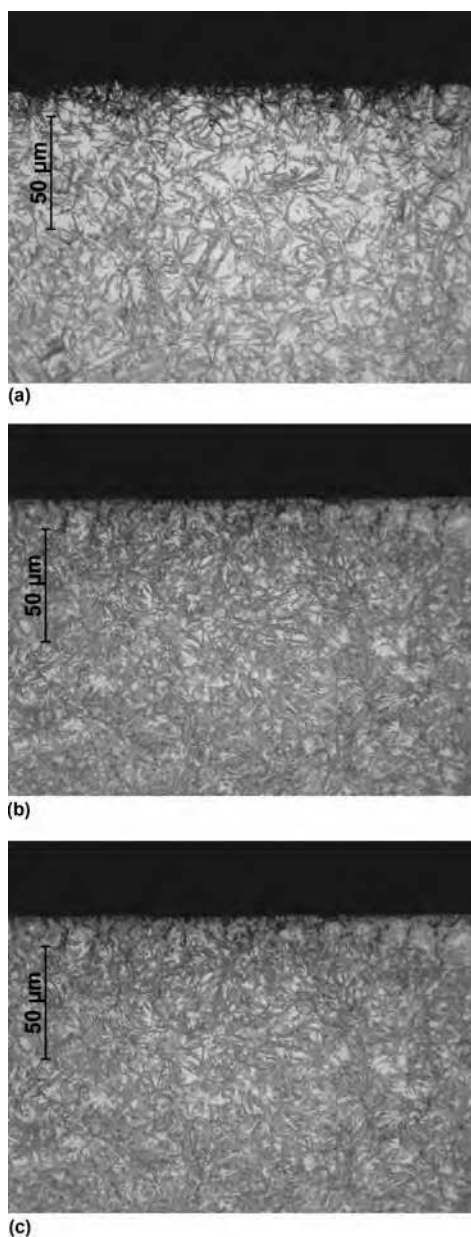


Fig. 27 Effect of carbon concentration in solution on retained austenite in SAE 4122 steel directly quenched in oil. (a) 1.2 wt% surface carbon (65% retained austenite). (b) 1 wt% surface carbon (50% retained austenite). (c) 0.75 wt% surface carbon (30% retained austenite)

of nitrogen introduced into the surface when ammonia is added to the atmosphere near the end of the gas carburizing cycle to enhance surface hardenability. Excessive nitrogen levels may cause high levels of retained austenite and low surface hardness.

The quench cooling rate also affects the level of retained austenite. Figure 29 shows case microstructures of SAE 4122 with 0.85 wt% surface carbon level quenched in oil and water from 850 °C (1560 °F). The corresponding XRD measurements revealed 35% retained austenite in the oil-quenched part and 29% retained austenite in

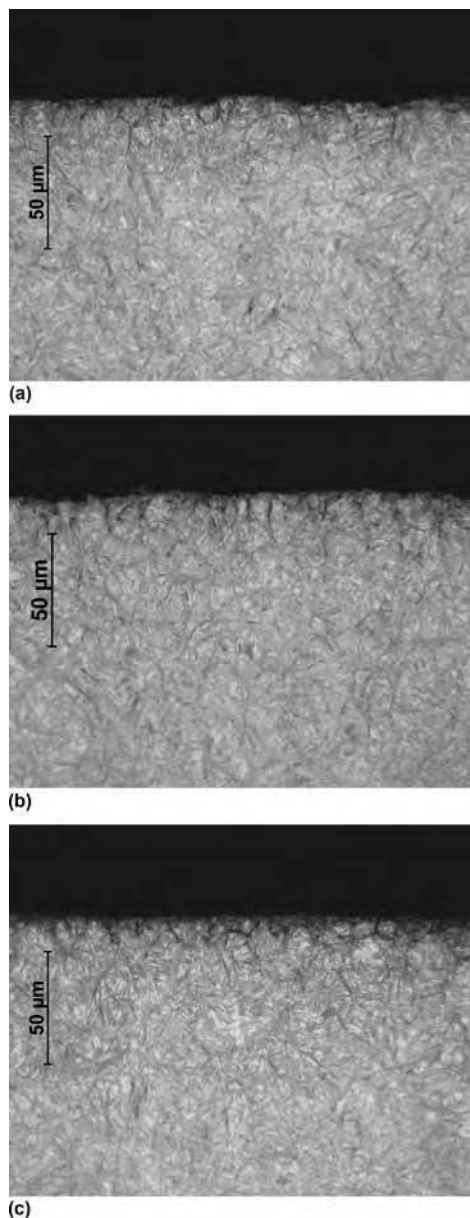


Fig. 28 Effect of part temperature prior to direct quenching on retained austenite in SAE 4122 steel. (a) 950 °C (1740 °F). (b) 925 °C (1700 °F). (c) 900 °C (1650 °F). All samples contain no. 9 wt% C and 43 to 46% retained austenite.

the water-quenched part. Slower cooling rates, although continuous, result in incremental stabilization, wherein the longer incremental time at temperatures below the M_S allow the austenite to stabilize. As a result, the slower cooling rate of the oil-quenched sample results in a higher level of retained austenite in the final structure.

Effect of Retained Austenite on Residual Stress. The amount of austenite that remains untransformed in the microstructure of carburized and hardened parts upon quenching influences the residual-stress pattern. In general, retained austenite due to high carbon content reduces compressive residual stresses. The distribution and the magnitude of the residual

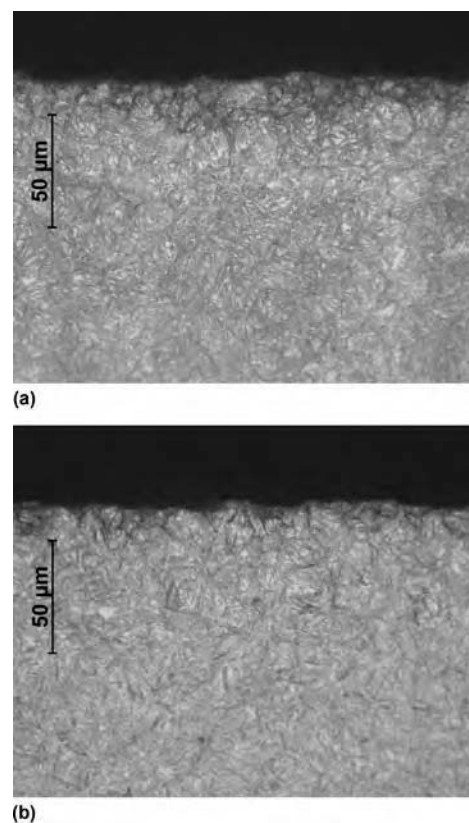


Fig. 29 Effect of cooling rate on retained austenite in SAE 4122 after carburizing and quenching in (a) water (29% retained austenite) and (b) oil (35% retained austenite)

stresses are determined by the extent and sequence of the austenite-to-martensite transformation, as shown in Fig. 30. An increase in retained austenite decreases hardness and residual stresses by reduction of the degree of transformation to martensite (and its accompanying expansion that leads to formation of compressive residual stresses). Maximum compressive residual stresses occur at some distance from the surface, where the ratio of martensite to austenite is very high. Lower values of compressive residual stress occur at the carburized surface, where the proportion of martensite to austenite is lower.

Retained Austenite and Dimensional Stability. Retained austenite is unstable and has the ability to transform to martensite during service of the component. This may occur because of a drop in temperature to levels much lower than the quench temperature but most often occurs when the retained austenite becomes deformed and transforms due to stress-induced transformation. The change in crystal structure causes volume expansion and may result in performance problems for parts that must maintain a specific fit or tolerance. Issues with dimensional stability of the part can lead to failure by wear, loss of lubrication, or galling when running clearances and fits are lost.

Often, carburized parts intended for higher temperature applications, such as high-temperature

bearings, are tempered at higher tempering temperatures to ensure dimensional stability during service. Tempering above 260 °C (500 °F) helps to reduce the amount of retained austenite, but it also results in lower case hardness. Post-case-hardening refrigeration is an effective means for reducing retained austenite. The amount of retained austenite can be reduced significantly by cooling the quenched parts to -40 to -100 °C (-40 to -148 °F). Normally, processes are designed to transfer parts to the subzero treatment process within a few hours after hardening, because the austenite stabilizes with time and will become more resistant to transformation to martensite. When close-tolerance-ground parts are involved, this treatment should precede finish grinding, because the subzero transformation results in a positive volume change. Subzero treatment of parts that are to be tempered should precede final tempering.

Effect of Retained Austenite on Performance. Retained austenite has a strong effect on

surface hardness. A decrease in case hardness usually is found when the amount of retained austenite exceeds approximately 25%. Therefore, for abrasive wear applications, where a high surface hardness is the main performance requirement, the amount of retained austenite should be minimized to maximize hardness and wear life.

High surface compressive residual stresses are favored to negate applied tensile stresses and improve resistance to fatigue crack initiation and propagation. The presence of retained austenite reduces both strength and compressive residual stresses, resulting in lower fatigue resistance. The degree of the fatigue limit reduction depends on the relative proportions of martensite and retained austenite and austenite grain size, as shown in Fig. 31 (Ref 59). Likewise, retained austenite decreases the limit where the first detectible plastic strain is observed, as shown in Fig. 32 (Ref 60).

On the other hand, austenite-containing case-hardened surfaces deform more readily than a wholly martensitic surface or a martensite/bainite surface, contributing more toward improved durability at high stress levels. Contact fatigue life can be improved when austenite content is quite high, for example, in the range of 30 to 40%, or when strengthened by increased levels of nitrogen.

Intergranular Oxidation. In gas carburizing where the primary carburizing agent is CO and the furnace is operated at normal carbon potentials in the 900 to 1000 °C (1650 to 1830 °F) range, the partial pressure of oxygen always is high enough to readily oxidize chromium, silicon, and manganese. Oxygen diffuses into the surface of the steel, forming a thin surface layer of fine IGO particles and a deeper zone of particles distributed along prior-austenite grain boundaries. Thickness of the oxidized layer depends on time, temperature, and the partial pressure of oxygen in the furnace atmosphere. Intergranular oxidation may result in the formation of nonmartensitic transformation products (Ref 61, 62) and has been reported to lower bending fatigue resistance (Ref 63, 64). Although product specifications can vary widely, IGO depths in the 10 to 20 μm (400 to 790 μin.) depth range are typically acceptable, depths in the 20 to 25 μm (790 to 985 μin.) range are considered borderline, and depths greater than 30 μm (1180 μin.) usually are deemed excessive.

For deep case parts with IGO limits, higher carburizing temperatures must be used to meet oxide depth specification limits. At higher temperatures, both the rate of IGO formation and carburized depth formation are increased. However, the increase in case depth formation occurs faster than the increase in IGO formation, with the net effect that a shallower depth of oxides always is obtained at higher carburizing temperatures for the same carburized case depth. Depth of IGO is also influenced by the atmosphere CO content and carbon potential. The driving force for IGO formation increases with increasing partial pressure of oxygen in the furnace atmosphere. For any given carbon potential, a carrier gas with higher CO content will have a higher corresponding equilibrium O₂ level than a lower-CO atmosphere. At a given temperature and CO level, lower carbon potential atmospheres have higher equilibrium O₂ levels than high carbon potential atmospheres. Therefore, parts form IGO at a slower rate in the higher carbon potential boost portion of a cycle than in the lower carbon diffuse portion. Overall, IGO depths are minimized by using higher carburizing temperatures, lower CO-content carrier gases, and the highest possible boost/diffuse time ratio (the highest carbon potential not exceeding the carbon saturation limit in austenite).

Intergranular oxides are best observed metallographically in the unetched or very lightly etched condition. Figure 33 shows the effect of gas carburizing parameters on the depth of

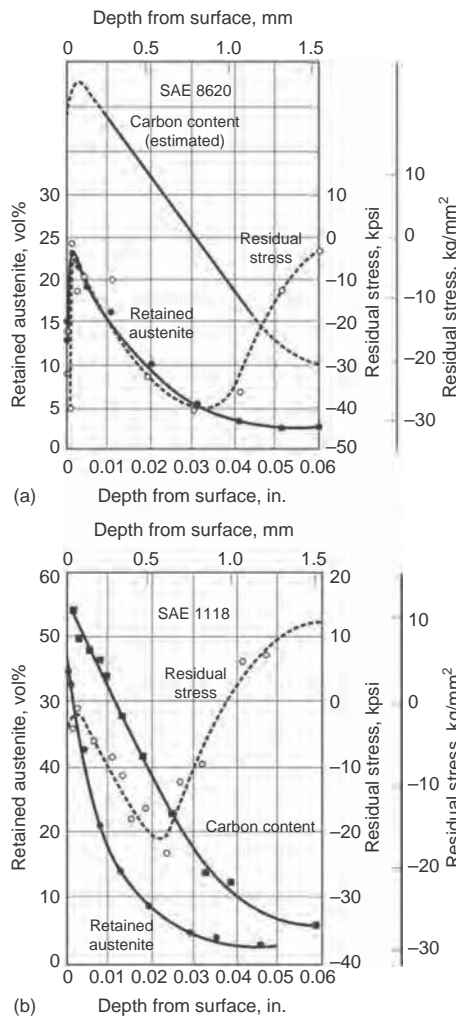


Fig. 30 Relationship between carbon gradient, retained austenite, and residual stress produced in carburized and hardened steels. (a) SAE 8620. (b) SAE 1118. Source: Ref 58

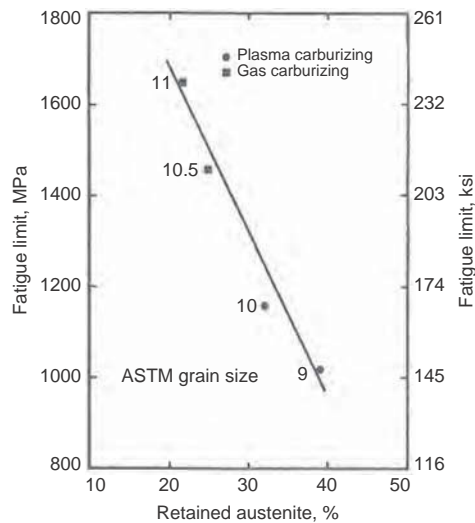


Fig. 31 Fatigue limits of plasma- and gas-carburized parts as a function of retained austenite. Source: Ref 59

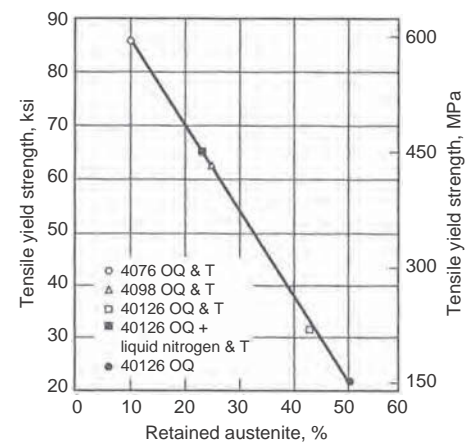


Fig. 32 Dependence of stress for first detectable plastic strain (~0.0001) on retained austenite content. OQ, oil quenched; T, tempered; AQ, air quenched. Source: Ref 60

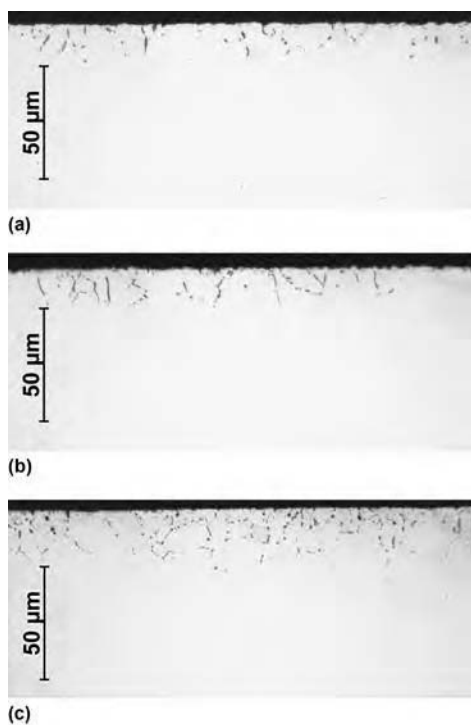


Fig. 33 Intergranular oxides in SAE 4122 after various carburizing and direct-hardening cycles to produce 2 mm (0.08 in.) hardened case depth. (a) Carburizing at 980 °C (1800 °F), boost carbon potential = 1.3 wt% C, 6.25 h; diffuse carbon potential = 0.9 wt% C, 45 min; equalize at 850 °C (1560 °F), carbon potential = 0.9 wt% C, 1 h. (b) Carburizing at 925 °C (1700 °F), boost carbon potential = 1.2 wt% C, 12 h; diffuse carbon potential = 0.9 wt% C, 45 min; equalize at 850 °C (1560 °F), carbon potential = 0.9 wt% C, 1 h. (c) Steady-state carburizing at 925 °C (1700 °F), carbon potential = 0.95 wt% C, 17 h; equalize at 850 °C (1560 °F), carbon potential = 0.9 wt% C, 1 h

IGO in SAE 4122 steel carburized to a depth of 2.0 mm (0.08 in.) with different temperatures and atmosphere carbon potential. Parts carburized at the higher temperature and higher carbon potential (Fig. 33a) reveal the shallowest depth of IGO, and parts carburized at a steady-state low temperature and lower carbon potential revealed the greatest depth of IGO (Fig. 33c). As seen in Fig. 33 and reported in Ref 64, low-temperature grain-boundary oxides have a characteristic globular appearance, while elongated and thicker grain-boundary oxides dominate at higher carburizing temperatures.

Surface Nonmartensitic Transformation Products (NMTP). Other nonmartensitic constituents are often associated with oxides that locally deplete the matrix of chromium, manganese, and silicon and thus reduce the local steel hardenability. Oxides also provide a free surface that serves to heterogeneously nucleate nonmartensitic transformation products. Depending on quench severity and hardenability of the matrix surrounding the oxide, levels of nonmartensitic formation may range from a barely visible thickening of the oxide to a full layer of pearlite in the IGO region. Surface

NMTP is also a good indicator of quench severity and failure to adequately break down the vapor blanket during the initial stages of quenching. In some shops, the NMTP layer is prevented by spiking the atmosphere with a small percentage of ammonia (approximately 1 to 3% of carrier gas flow) for a short period of time to introduce nitrogen into the surface prior to quenching. The duration and flow of ammonia additions must be well controlled, because nitrogen is a potent austenite stabilizer, and excessive flow will result in high retained austenite levels and low surface hardness. Ammonia spiking does not address the root cause of low quench severity that can also cause high levels of subsurface nonmartensitic transformation products and low core hardness. If properly applied, ammonia spiking can effectively make up for the loss of matrix hardenability associated with the IGO region.

Decarburization. Although proper carburizing temperature, time, and carbon potential produce the desired case depth and near-surface carbon content, exposure to a low-carbon atmosphere at the end of a gas carburizing cycle (even for very short times) can result in a surface layer of low-carbon martensite, bainite, pearlite, or ferrite. Some continuous-type furnaces have press quench chambers equipped with slot doors that can be opened multiple times to withdraw single parts for press quenching. As parts are transferred through air to quench presses, the surface undergoes cooling and carbon loss, both of which move the surface toward ferrite formation. Although dependent on part section size, transfer times through air should be limited to 45 s to avoid formation of free ferrite at the surface. Press quenching chambers can be contaminated by air infiltration during multiple door openings, which rapidly lowers the carbon potential of the press quench atmosphere. The rate of surface carbon loss in low-carbon endothermic gas is faster than air. Exposure to very low carbon potential endothermic atmosphere for as little as 15 s can result in a surface layer of pearlite, bainite, or free ferrite. An example of partial surface decarburization that resulted from exposure to low-carbon-potential endothermic atmosphere for 60 s is shown in Fig. 34. Thin layers of decarburization can be difficult to detect with direct surface hardness indentations but can be effectively detected by file hardness checks. This type of decarburization can be reduced or eliminated with good flame screen coverage of press quench openings, coupled with timed high flows of carrier gas and/or enriching gas.

Decarburization can also occur when parts are carburized and then cooled under nitrogen for subsequent reheat hardening. In batch integral quench furnaces equipped with top cooling chambers, endothermic gas moves with the load as it is transferred from the hot chamber into the slow-cool chamber. As nitrogen flows into the slow-cool chamber, the CO level is reduced from a nominal 20 to 23% level to 0% as

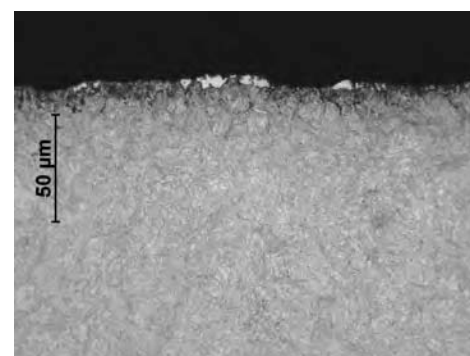


Fig. 34 Decarburization on surface of SAE 4122 gear exposed to low-carbon-potential endothermic atmosphere for approximately 1 min at end of carburizing cycle

cooling proceeds. Because the carbon potential is proportional to the $(P_{CO})^2/(P_{CO_2})$, the carbon potential drops rapidly at the beginning of the cooling cycle while the part surfaces are still hot, causing a thin layer of decarburization. Decarburization of as-carburized parts may be a problem for parts that are reheat hardened in air atmosphere (such as induction hardening). However, but the surface carbon is easily restored by hardening in a furnace with atmosphere controlled to the proper carbon potential.

Residual Stress. Carburized parts typically exhibit high surface compressive residual stresses after hardening. The elevated carbon content of the case lowers the M_s temperature of the surface below the M_f temperature of the core. Therefore, the carburized surface transforms to martensite later in time than the core material below the carburized case. The transformation timing difference between the carburized case and core after quenching promotes formation of compressive residual stresses in the case, balanced by tensile residual stresses in the core.

The presence of such residual-stress distribution provides a significant advantage for applications that involve high surface tensile stresses, such as those created by bending or torsional loading. The magnitude of the compressive residual stresses at the surface depends on the ratio of the case-to-core thicknesses and the carburized depth. Surface compressive residual stresses are high for parts with a large core-to-case ratio. When the ratio of core to case is low, the residual-stress distribution pattern will have low surface compressive residual stresses and high tensile stresses in the core. Figure 35 shows the effect of the effective case depth on the compressive residual stresses (Ref 65). Given the same part geometry and similar process parameters, the near-surface compressive residual stresses decrease with increasing carburized depth.

Alloy Selection. Frequently used carburizing steels are listed in Table 10. Carburizing steels usually are selected on the basis of case and core hardenability. Comparative hardenability

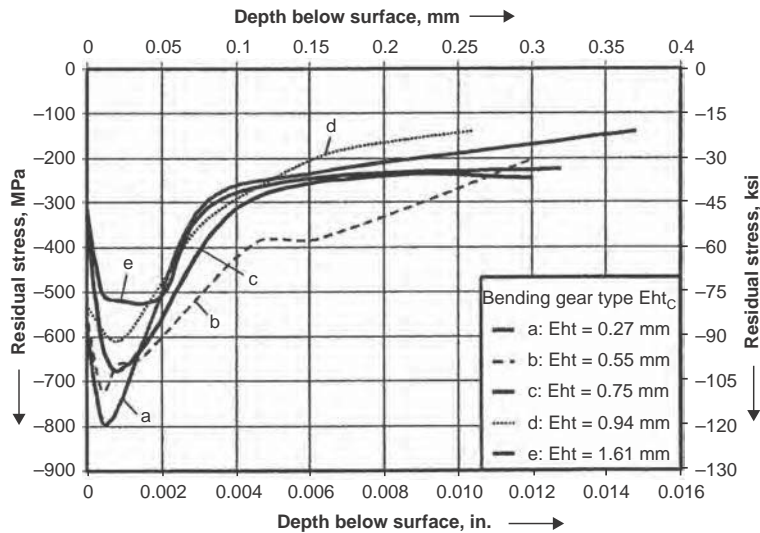


Fig. 35 Residual-stress distribution for gears with different case depth. Eht defined case depth at Vickers hardness 550 HV1. Source: Ref 65

Table 10 Chemical composition of common carburizing steel grades

Steel	Composition, %					
	C	Mn	Ni	Cr	Mo	Other
Carbon steels						
1010	0.08–0.13	0.30–0.60	(a)(b)
1018	0.15–0.20	0.60–0.90	(a)(b)
1019	0.15–0.20	0.70–1.00	(a)(b)
1020	0.18–0.23	0.30–0.60	(a)(b)
1021	0.18–0.23	0.60–0.90	(a)(b)
1022	0.18–0.23	0.70–1.00	(a)(b)
1524	0.19–0.25	1.35–1.65	(a)(b)
1527	0.22–0.29	1.20–1.50	(a)(b)
Resulturized steels						
1117	0.14–0.20	1.00–1.30	0.08–0.13 S
Alloy steels						
3310	0.08–0.13	0.45–0.60	3.25–3.75	1.40–1.75	...	(b)(c)
4023	0.20–0.25	0.70–0.90	0.20–0.30	(b)(c)
4027	0.25–0.30	0.70–0.90	0.20–0.30	(b)(c)
4118	0.18–0.23	0.70–0.90	...	0.40–0.60	0.08–0.15	(b)(c)
4320	0.17–0.22	0.45–0.65	1.65–2.00	0.40–0.60	0.20–0.30	(b)(c)
4620	0.17–0.22	0.45–0.65	1.65–2.00	...	0.20–0.30	(b)(c)
4815	0.13–0.18	0.40–0.60	3.25–3.75	...	0.20–0.30	(b)(c)
4820	0.18–0.23	0.50–0.70	3.25–3.75	...	0.20–0.30	(b)(c)
5120	0.17–0.22	0.70–0.90	...	0.70–0.90	...	(b)(c)
5130	0.28–0.33	0.70–0.90	...	0.80–1.10	...	(b)(c)
8617	0.15–0.20	0.70–0.90	0.40–0.70	0.40–0.60	0.15–0.25	(b)(c)
8620	0.18–0.23	0.70–0.90	0.40–0.70	0.40–0.60	0.15–0.25	(b)(c)
8720	0.18–0.23	0.70–0.90	0.40–0.70	0.40–0.60	0.20–0.30	(b)(c)
8822	0.20–0.25	0.75–1.00	0.40–0.70	0.40–0.60	0.30–0.40	(b)(c)
9310	0.08–0.13	0.45–0.65	3.00–3.50	1.00–1.40	0.08–0.15	(b)(c)
Special alloys						
CBS-600	0.16–0.22	0.40–0.70	...	1.25–1.65	0.90–1.10	0.90–1.25 Si
CBS-1000M	0.10–0.16	0.40–0.60	2.75–3.25	0.90–1.20	4.00–5.00	0.40–0.60 Si 0.15–0.25 V
Alloy 53	0.1	0.35	2	1	3.25	1.00 Si, 2.00 Cu, 0.10 V

(a) 0.04 P max. 0.05 S max. (b) 0.15–0.35 Si. 0.035 P max. (c) 0.04 S max

data for these alloys can be found in SAE specifications J1268 and J1868 (Ref 66, 67). In general, carburized plain carbon steels with less than 1% Mn should be water quenched to form a martensitic case. Plain carbon steels with 0.6 to 1% Mn can be oil quenched if case

hardness is enhanced with the addition of nitrogen by carbonitriding.

Alloy steels are used for most heavily loaded parts. The choice of alloy system and hardenability level depends on several factors, including microstructure and core property

requirements, part section size, and available quench severity. The choice of alloy system is affected by core toughness requirements and allowable levels of grain-boundary IGO as well as alloy cost and regional availability of alloying elements. Alloys that use low-cost hardenability elements such as manganese and chromium will form higher levels of IGO (and loss of surface hardenability) than alloys that use the higher-cost elements such as nickel and molybdenum.

Chromium-nickel-molybdenum steels such as SAE 8620 and SAE 4320, manganese-chromium-molybdenum steels such as SAE 4120, and manganese-chromium grades such as SAE 5120 provide a balance between cost, hardenability, and ease of processing that leads to their use for many parts. More expensive steels, such as SAE 9310 and 3310, are used for critical gearing and bearing applications. Some special carburizing alloys, CBS 1000M, for example, have secondary hardening characteristics that provide resistance to softening for temperatures up to approximately 550 °C (1020 °F).

Direct Hardening versus Reheat Hardening. Hardening of carburized components is achieved by cooling at a rate sufficient to produce desired metallurgical characteristics. Direct hardening at the end of the carburizing process is the most economical way of hardening carburized components. Alternatively, carburized parts may be slow cooled and then reheated to above the Ac₃ temperature and subsequently quenched. This hardening method may be preferred or required in the following situations:

- For grain size and retained austenite control
- When the material grade does not allow microstructure requirements to be met with direct quenching
- When an intermediate subcritical heat treatment or machining operations for dimensional control or selective carburizing are required
- When direct hardening is not possible due to production scheduling or equipment limitation

The type of furnace used for gas carburizing often has a bearing on whether the parts should be directly hardened or slow cooled and reheat hardened. Pusher-type continuous furnaces, for example, are well suited to direct hardening and quenching, because they can be controlled to obtain virtually any desired cycle of temperature changes and can be coupled with various types of quenches.

Since reheat hardening involves additional thermal cycling, it is typically more expensive and results in higher distortion unless die or plug quenches are incorporated. As better controls have become available for regulating furnace atmospheres and as the use of fine-grain steels has become the norm, the need for reheat hardening has diminished within some industries.

Direct hardening and reheat hardening may produce significantly different microstructures

(particularly retained austenite levels), depending on the surface carbon content and hardening temperature. When surface carbon contents are at or below eutectoid composition, the surface microstructures of direct-hardened and reheat-hardened parts are generally indistinguishable, as shown for two samples with 0.75% C in Fig. 36(a) and (b). When the surface carbon content is higher than eutectoid composition, the microstructure is governed by the amount of carbon in solution in the austenitic phase prior to hardening. For reheat-hardened parts, carbon in excess of the eutectoid composition will precipitate as fine carbides when the part is reheated to the lower critical temperature (A_1). As the parts are heated above the A_1 , the carbon in the austenite at the surface is increased by both carburizing from the atmosphere and dissolution of the fine carbides. Typically, the parts are not reheated to a sufficient temperature to completely dissolve the fine carbides. The carbon content at the surface is partitioned between the austenite and carbide phases and is often higher in total carbon content than the carbon potential of the hardening furnace atmosphere. This higher-carbon content is a result of austenite absorbing the required carbon from the furnace atmosphere during heating, rather than the dissolution of carbide to obtain the required austenite-carbide equilibrium. Thus, for parts with the same hypereutectoid surface carbon levels, direct-hardened parts will have a microstructure of martensite and retained austenite, and reheat-hardened parts will have a microstructure consisting of martensite, retained austenite, and fine carbides, as shown in Fig. 36(c) and (d). The lighter-etching surface regions of the microstructure in Fig. 36(d) are the result of slight carbon loss at the surface during slow cooling. When reheated, the slightly depleted surface region does not nucleate the fine carbides.

Quenchants. Carburized parts can be quenched in brine or caustic solutions, water, water-based polymer quenchants, oils, or molten salt. The more rapid the quench, the lower the requirements for steel hardenability, but the greater the likelihood of distortion. If a part is used in the as-heat-treated condition (i.e., no post-heat-treatment finishing operations to control dimensions), marquenching into molten salt or hot oil may be used. Rings and shafts are often press quenched by clamping in a fixture while hot and sprayed with oil to reduce distortion. The choice of alloy and quenchant and the manufacturing process design are interrelated and must be compatible.

Tempering. For good wear resistance in service, carburized and hardened components are typically quenched to produce a martensitic case with an insignificant amount of retained austenite. The high-carbon martensite has a body-centered tetragonal crystal lattice and is metastable and relatively brittle in the as-quenched condition. Untempered martensite continues changing with time to some degree even at room temperature. Tempering after

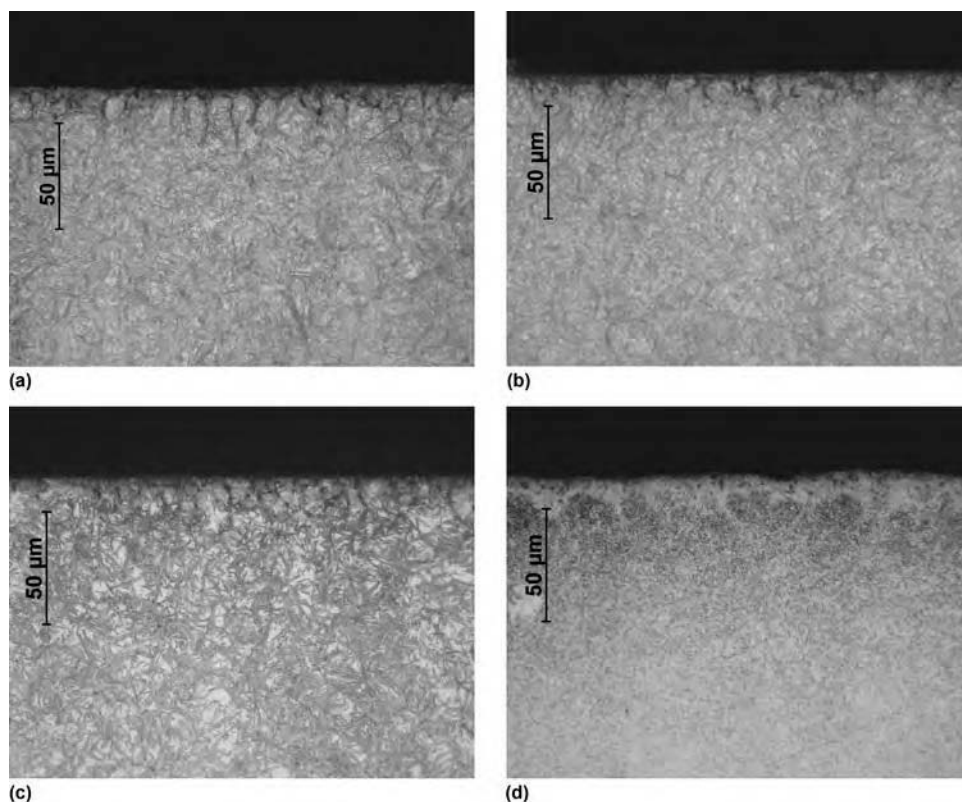


Fig. 36 Effect of direct quenching and reheat hardening in SAE 4122 after gas carburizing at various surface carbon contents. (a) Direct quenched with 0.75 wt% surface carbon. (b) Reheat hardened with 0.75 wt% surface carbon. (c) Direct quenched with 1 wt% surface carbon. (d) Reheat hardened with 1 wt% surface carbon

carburizing and hardening helps to transform unstable as-quenched martensite to tempered martensite, resulting in greater dimensional stability and a marked decrease in brittleness of the component.

As high-carbon martensite is tempered, carbides precipitate, increasing the density (volume contraction), reducing the hardness the residual stress. Thus, the response of case hardness to tempering can be complex and is affected by the fraction of retained austenite present initially. Density changes during tempering affect the relief of residual stresses produced by quench hardening. Figure 37 (Ref 68) shows the effect on stress relief of tempering for 1 h at various temperatures. Stress relief occurs at lower tempering temperatures, as the amount of carbon dissolved in austenite increases. The dependence of stress relief on tempering temperature in carburized parts is qualitatively similar to these results, although more complex behavior can be expected in steels with high levels of retained austenite.

The decrease in hardness with tempering is shown in Fig. 38. The data are given for four steel-grade samples carburized and quenched directly from 925 °C (1700 °F). The Rockwell C hardness values shown were converted from Rockwell A for surface hardness and from Vickers microindentation hardness for the sub-surface values. It should be noted that the

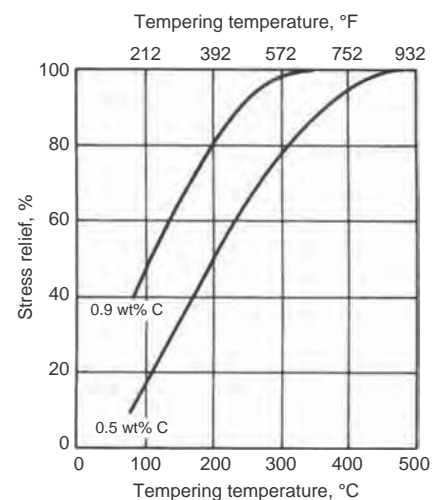


Fig. 37 Plot of stress relief versus tempering temperatures held for 1 h for two surface carbon concentration levels in austenite. Source: Ref 68

hardness changes very little for tempering temperatures up to 205 °C (400 °F). However, a substantial degree of stress relief will occur, as indicated in Fig. 37.

Selection of tempering temperature should be based on the desired mechanical properties and specifics of the service application. Generally,

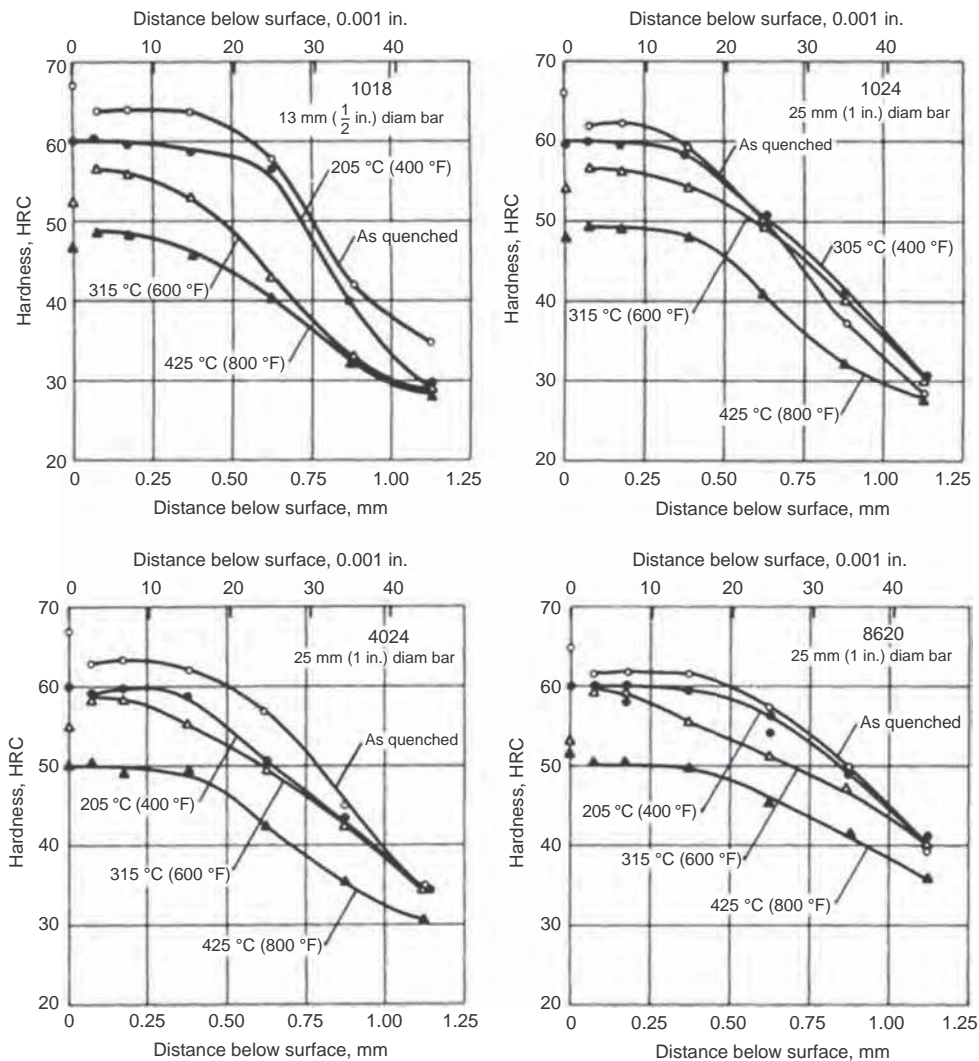


Fig. 38 Effect of tempering on hardness in carburized cases for selected steels. Samples were carburized at 925 °C (1700 °F) for 4.5 h, then oil quenched and tempered.

higher tempering temperatures result in greater ductility but lower hardness and strength, and vice versa. The selected tempering temperature should satisfy both of the following criteria:

- It should be as high as can be tolerated, considering the resulting hardness and toughness.
- It should be at least as high as the maximum service temperature to which the parts will be exposed in service.

Typically, tempering of carburized and hardened components in the range of 150 to 205 °C (300 to 400 °F) improves subsequent dimensional stability. If the best possible stability is required, as in some instrument bearings, a sub-zero treatment may be included prior to tempering to reduce retained austenite.

Carburized pinions and gears are invariably tempered for critical applications. For example, carburized parts for aircraft applications invariably are tempered. Gears that are shot peened after carburizing and hardening to improve

surface compressive stress always are tempered at 150 °C (300 °F) minimum to prevent chipping of the teeth during the peening operation. Depending on as-quenched hardness, parts may be tempered after carburizing and hardening to adjust surface hardness to a level that optimizes hardenability.

It is important to remember that tempering reduces compressive residual stresses within the case and balancing tensile stresses within the adjacent core. It also tends to shift the location of the peak compression closer to the case-core interface. Therefore, resistance to bending and torsional fatigue may be best if the parts are not tempered at all. Tempering is omitted on many thin-cased parts (0.5 mm, or 0.02 in., case depth or less) that are not finished after heat treatment.

Selective Carburizing. To function properly, some parts must be selectively carburized, that is, carburized only on certain surfaces. Some gears are carburized only on teeth, splines, and bearing surfaces. In addition to

satisfying the performance requirements of a part, selective carburizing may facilitate the machining or welding of noncarburized surfaces in the hardened condition.

Surfaces that are not to be carburized must be protected by a coating or shield that is impervious to the carburizing atmosphere. Various means are employed to protect or stop off selected surfaces from the atmosphere.

Copper plating to a minimum thickness of 13 μm (515 μin.) is widely used for this purpose because it is relatively easy to apply, is machinable and does not contaminate furnace atmospheres. Prior to carburizing a large, 915 mm (36 in.) diameter 4620 steel ring gear, for example, the gear is copper plated on the inside-diameter flange area only to permit finish machining, after hardening, of the bore and bolt holes located in the flange. Surfaces that are not to be copper plated can be coated with a chemical-resistant lacquer, which is removed prior to carburizing. After carburizing, the copper can be chemically stripped from the part or removed in subsequent machining operations.

Ceramic coatings in the form of paint can also protect selected surfaces from carburizing. Surfaces must be thoroughly cleaned before ceramic paint is applied, and the first coat must be allowed to dry before a second coat is applied. Ceramic paint coatings must adhere tightly in order to be impervious to the carburizing atmosphere. The application of ceramic paint to the bushing and button recesses of a rock bit cutter, for example, has been used in production.

Stopoffs. Blind holes can be stopped off by inserting copper plugs or by filling them with clay. If air is entrapped by the plug, a means of venting must be provided to relieve the pressure buildup during heating. Through holes may be plugged at either end to limit access by the atmosphere, thereby minimizing carburization. Internal threads can be protected by the insertion of a copper screw, and external threads by capping with a copper nut. If a steel screw or nut is used, the threads should be coated with a stopoff material to facilitate removal. The success of all stopoff methods depends largely on the care used in their applications. Seldom are mechanical stopoffs completely effective in production.

If parts are cooled slowly after carburizing, they will be soft enough to permit the removal of the case in selected areas by machining. After subsequent reheating and quenching, these areas will remain lower in carbon and relatively soft. Operations can also be planned so that the case on a hardened part can be removed selectively by grinding. This practice usually is confined to small areas and generally to cases less than 1.3 mm (0.05 in.) in depth.

A part that has been carburized may be locally softened by induction heating. The heat may just temper the part or, for steels with low hardenability, may actually normalize the area to be softened. This practice is used to soften threads on carburized shafts in the automotive industry.

Dimensional Control

Good distortion-control practices during gas carburizing and subsequent hardening operations ensure that the as-hardened part dimensions meet print requirements or that subsequent final machining operations and total manufacturing cost are minimized. Nevertheless, some growth and distortion will be encountered in all carburized parts. Distortion occurs when localized stresses in the component exceed the yield strength of the material during various stages of thermal processing.

Distortion in the carburized components is typically revealed in two forms: size change that is manifested through the net volumetric changes of the component without changes in its geometrical form, and shape distortion, revealed through nonsymmetrical dimensional changes. In general, distortion is managed by adjusting dimensions of the green-machined parts to compensate for heat treatment size change and shape distortion. Although green dimensional adjustment is generally effective, there are many factors that affect distortion. Some of these factors may not be sufficiently predictable to provide consistent expected dimensional change.

Factors Affecting Distortion

Factors affecting distortion after carburizing include:

- Part size, shape, and section size changes
- Residual stresses existing in parts prior to heat treatment
- Shape changes induced by heating too rapidly
- Multiple thermal cycles
- Lack of temperature uniformity within individual parts and throughout the load during heating and cooling
- Method of stacking or fixturing parts during carburizing and quenching
- Influence of increasing case depth on part growth
- Quench severity and uniformity
- Quenchant medium and temperature
- Material hardenability

Residual Stress. There are many potential sources of residual stress that may exist in parts prior to carburizing that, when subsequently relieved during carburizing, may result in distortion. Although it creates additional heat treatment cost, distortion-sensitive parts are often isothermally annealed prior to machining. However, additional residual stress may be induced by the machining operations, which may require subsequent stress-relief operations.

Parts Loading and Furnace Alloy Tooling. Inadequate part support during gas carburizing and poorly designed or warped furnace alloy tooling may cause sagging or creep of the parts

between supports, resulting in shape distortion prior to quenching. Plain carbon and low-alloy steels have very low yield strength at typical carburizing temperature and are capable of distorting under their own weight. Thus, special care should be taken to ensure that the carburized parts are adequately supported in the furnace during carburizing. For example, large or long and complex-shaped parts should be supported at critical positions or suspended vertically in some cases.

Heating Rate. Distortion can be caused by high heating rates that induce thermal gradients and stresses. Often, this can be minimized by using lower heating rates or programmed stepped heating with holds in the 400 to 750 °C (750 to 1380 °F) temperature range.

Hardening. Reheat hardening may be required after gas carburizing due to carburizing equipment limitations, the need for grain size refinement, or the need for intermediate machining operations. Typically, carburizing coupled with direct quenching results in less distortion. Carburizing and direct quenching minimizes distortion by bringing about phase transformations with only one thermal cycle. Every additional heating-cooling cycle produces additional volume changes and internal stresses that may result in more part distortion.

Quenching. The choice of quenching medium depends on hardenability, size, and shape of the carburized component. Quench rate should be fast enough to produce required case and core hardness and microstructure. The quench flow in many types of batch- or dunker-type quenches may be very nonuniform. Therefore, the quench velocity uniformity should be specified when purchasing new equipment and measured when equipment is commissioned. Typically, a well-designed quench will exhibit velocity uniformity throughout the work space of ± 0.15 m/s (0.5 ft/s).

Methods for Distortion Control

A variety of methods, to be described, are used to minimize distortion. All of them add to heat treating cost, but they may be cost-effective when total production costs are considered. In the high-volume production of precision components, such as automotive transmission gears, a general objective is to hold constant all of the processing variables affecting growth and distortion and to compensate for heat treatment dimensional change in the green machined (unhardened) part. For example, the lead angle of a helical gear may change after carburizing and hardening if the gear undergoes a change in length. A well-disciplined test lot process should be implemented that includes before and after heat treatment dimensional assessment using the intended heat treatment production process. It is important that test lots for distortion assessment be performed with production tooling and the intended

production loading pattern. The number of parts in a test lot should be sufficient to establish sound dimensional data results. Once parts are placed in production, they should be checked periodically to ensure that processing conditions that affect distortion have not changed.

Fixturing can be used to separate parts and allow more uniform heating to carburizing temperature, better gas atmosphere uniformity during carburizing, and better quenchant flow through the load. Fixturing adds labor cost (fixtures are often loaded and unloaded manually) as well as operating cost because the fixtures may weigh as much as, or more than, the workload. However, proper fixturing is usually effective in reducing variations in growth and distortion, thereby allowing compensation for the changes in the shape of the green part.

Marquenching, or martempering, involves quenching in molten salt or hot oil, where the quenchant temperature is above the M_s temperature (the temperature at which martensite starts to form from austenite upon cooling) of the case but below the M_s temperature of the core. Consequently, the core transforms to a mixed microstructure of martensite, bainite, and ferrite while the parts are in the quenchant. The case transforms to martensite when the parts are cooling in air after leaving the quenchant. Distortion is reduced due to lower thermal gradient between the case and core during phase transformation.

Press quenching and other means of quenching in fixtures, such as plug or cold die, are effective in reducing distortion. Press quench distortion control can be accomplished by two methodologies: plastic deformation of the part by the dies prior to initiation of the quenchant flow and/or various levels of die contact or pressure with the part after quenching flow has been initiated but before martensitic transformation begins. Often when die quenching large parts, the die pressure may be pulsed to a low level to allow part thermal shrinkage and avoid die mark damage or die-caused distortion. While quench presses may have automated loading systems, they are often loaded manually, one part at a time. Quenching in fixtures adds significantly to the cost of heat treating, but there may be no practical alternative for limiting distortion of certain parts, for example, thin-walled rings and slender shafts.

Straightening is often employed to reduce the distortion of heat treated shafts. There always is a risk of cracking the case when straightening carburized parts, so it is the usual practice to straighten after tempering. Some manufacturers find it best to straighten while parts are still hot from the tempering furnace. In one instance, shafts that cracked upon straightening after tempering could be straightened without cracking immediately after quenching. Many straighteners are equipped with acoustic emission sensors to detect cracking. Selective peening also has been used as a method for straightening parts.

Case Depth Evaluation

In a well-controlled carburizing process, parts may be exposed up to ± 0.05 wt% variation in carbon potential and ± 8 °C (14 °F) temperature variation, comprised of ± 3 °C (5 °F) accuracy of thermocouple reading and ± 5 °C (9 °F) typical temperature variation in the carburizing chamber. In addition, most steel-grade specifications allow for 0.05 wt% C total variation in the base steel composition. Figures 39(a) and (b) show the corresponding variation in the carburized depths, assuming the worst-case scenario of the process parameters and base carbon material variation.

For boost-diffuse carburizing at 925 °C (1700 °F) and carbon potential setpoints of 1.1 and 0.9 wt% C for boost and diffuse segments, respectively, a total case depth variation (at 0.35 wt% C) of 0.24 mm (0.010 in.) may be observed in the parts carburized to 1 mm (0.04 in.) target case depth (Fig. 39a). Because the slope of the carbon profile decreases for deeper depths, case depth variation due to heat treatment process and base carbon content increases with increasing depth magnitude and may reach up to 0.5 mm (0.02 in.) variation at a 2 mm (0.08 in.) depth (Fig. 39b). Note that although the difference in surface carbon concentration due to base carbon concentration is negligible variations in base carbon content have a significant effect on the total variation of the case depth, particularly at deeper case depths.

Case Depth Measurement

Carburized case depth usually is specified as the perpendicular distance from the surface of a carburized case to the depth at which a specified level of carbon is obtained. Typically, the specified carbon level is selected to approximately correlate to the effective case depth (or hardened depth) and depends on the steel hardenability, quench severity, and section size. For medium-to-low-alloy steel carburizing grades, the depth to 50 HRC will correlate to a carbon level of 0.3 to 0.4 wt% C. Often, 0.35 wt% C is used as the specified carbon level for carburized case depth. Also used is the term *total case depth*, which is defined as the depth from the surface to the point where differences in chemical or physical properties of the case and core no longer can be distinguished. Total case depth sometimes is considered to be the distance from the surface to the deepest point at which the carbon content is 0.04% higher than the carbon content of the core. Generally, the term *total case depth* is considered too vague for use in carburizing specifications because of the gradual carbon profile transition between the case and core. However, some carbonitrided parts and induction case-hardened parts will have a sharp transition in microstructure clearly separating case and core. Only in these instances is total case depth defined well enough to be useful as a specification. Methods

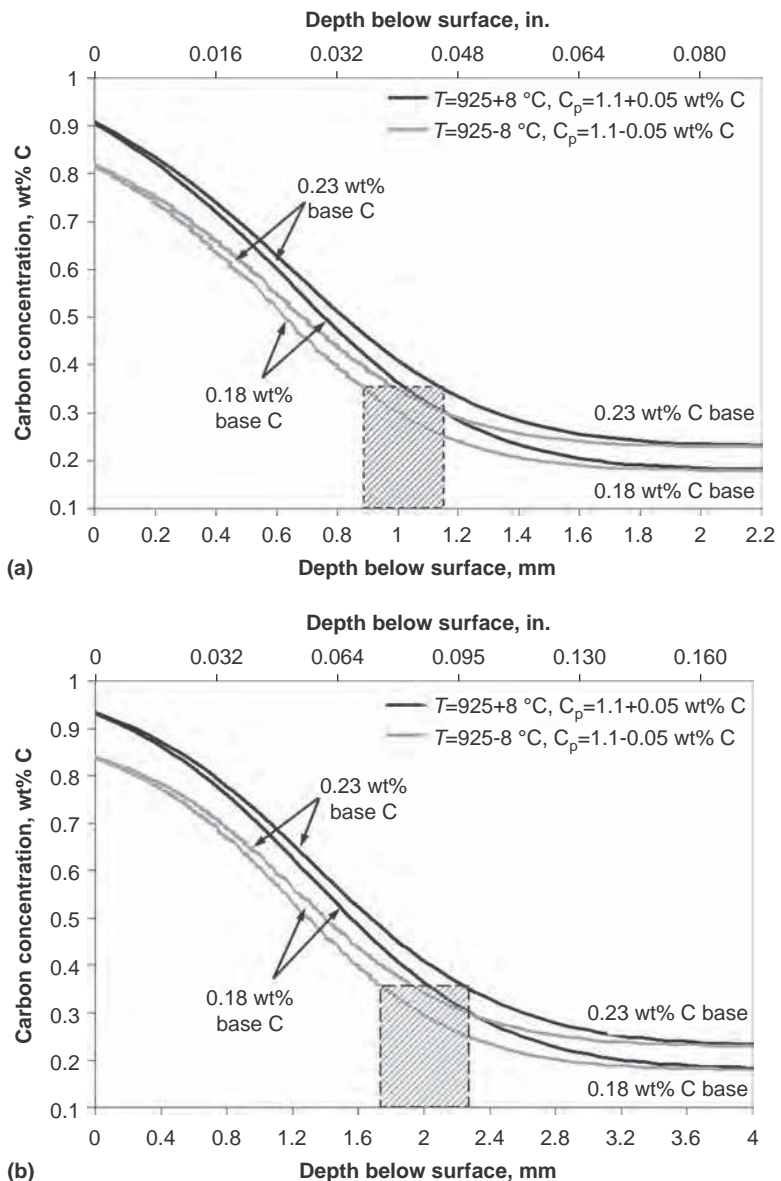


Fig. 39 Carburized case depth variation due to typical variations in temperature and furnace atmosphere carbon potential in parts with 0.2 wt% C base carbon, carburized to produce target (a) 1 mm (0.04 in.) and (b) 2 mm (0.08 in.) case depth

of measuring case depth are described in detail in SAE Recommended Practice J423.

Many parts, such as gears, consist of some surfaces that are convex, some that are relatively flat, and some that are concave. It usually is found that the carburized case depth will be lower at the concave surface (the root) and greater at the convex surface (the tooth tip). The effect of surface curvature on effective case depth is shown in Fig. 40. These data are computed for a particular case:

- Surface carbon, 1 wt%
- Core carbon, 0.2 wt%
- Diffusion time/temperature sufficient to produce a carburized case depth (to 0.4 wt% C) of 1 mm (0.04 in.) beneath the flat surface of a slab of infinite thickness

As follows from Fig. 40, the same treatment that will produce an effective case depth of 1 mm (0.04 in.) in a plane slab of 3 mm (0.12 in.) in half-thickness will produce a case depth of 1.13 mm (0.045 in.) in a rod of 3 mm (0.12 in.) radius, a case depth of 1.28 mm (0.05 in.) in a sphere of 3 mm (0.12 in.) radius, and a case depth of 0.93 mm (0.037 in.) in a circular hole of 3 mm (0.12 in.) radius. The effect of surface curvature is quite pronounced if the radius of curvature of the surface is less than approximately five times the effective case depth beneath a flat surface. The effect of curvature is small when the radius of curvature of the surface is more than 10 times the effective case depth. Surface curvature also affects cooling. The parts with marginal hardenability may exhibit a greater difference between convex and

concave surfaces when the case depth is defined in terms of depth to a specified hardness rather than depth to a specified carbon content. These facts must be kept in mind when comparing case depth at various locations on a part and when comparing case depths measured on parts and on testpieces.

Effective Case Depth (Hardened Depth). Effective case depth to a specified hardness value is best measured by means of a microindentation hardness traverse on a polished metallographic section cut normal to the surface in accordance with ASTM E384-11. Vickers (diamond pyramid hardness) and Knoop indenters may be used with loads of 1 to 1000 gram-force. Specifications can be written in terms of a microindentation hardness value or in terms of HRC hardness, where it is understood that microindentation hardness (HV, HK) is converted to HRC in accordance with ASTM E140-07. Surface hardness, which is often a part of carburizing specifications, is normally required to be taken directly on the surface, with the hardness scale indicated on the part print. For many parts, the geometry does not permit this, and surface hardness is obtained by extrapolating subsurface microindentation hardness values to the surface. Alternatively, the microindentation hardness at a depth of 0.1 mm (0.004 in.) beneath the surface can be defined as the surface hardness. It is difficult to obtain reliable microindentation hardness readings closer than 0.1 mm (0.004 in.) to the edge of a polished section because of failure of the edge to adequately support the hardness indenter or edge rounding that may occur during polishing.

The accuracy limitations of any microindentation hardness measurement equipment should be well understood before measured hardened depth is used to evaluate statistical process capability or process performance parameters. Figure 41 gives the results of a gage repeatability and reproducibility study showing typical variation in the hardened depth measurements obtained from 1.3 and 3.2 mm (0.05 and 0.13 in.) nominal case depth parts (Ref 69). The same set of two samples was measured in three independent laboratories using different microindentation hardness traverse testers and loads. In each lab, three microindentation hardness traverse profiles were measured daily by each of the three participating trained operators for five consecutive days. The observed measurement variation was consistent at each laboratory. Microindentation hardness measurement variation at each depth was observed to be approximately 4 HRC points regardless of the depth magnitude, creating a characteristic band of microindentation hardness profile uncertainty in any given carburized part. Further linear interpolation to a depth of 50 HRC yields hardened depth values with characteristic hardened depth uncertainty. As the slope of the microindentation hardness profile decreases with increasing case depth, the hardened depth measurement error increases.

Thus, if enough measurement repetitions are performed, a 0.2 mm (0.008 in.) range depth variation may be expected on a carburized part with a nominal 1.3 mm (0.05 in.) hardened depth, and a 0.8 mm (0.03 in.) range variation in a 3.2 mm (0.13 in.) nominal hardened depth.

Figure 42 shows a chart of typical allowable hardened depth variation for various target

depths. As the hardened depth measurement error increases with increasing case depth, it may completely consume the allowable hardened depth variation tolerance band. In addition, some heat treatment process variation (i.e., temperature, carbon potential, or time variation from the predetermined setpoint parameters or within any given load) is inevitable and will result in even greater likelihood of exceeding the allowable depth tolerance. Therefore, before hardened depth measurements are used for statistical process control, the measurement system accuracy must be validated as acceptable in accordance with ASTM F1503 for any given specification range. If greater than normal process control is required, it is best

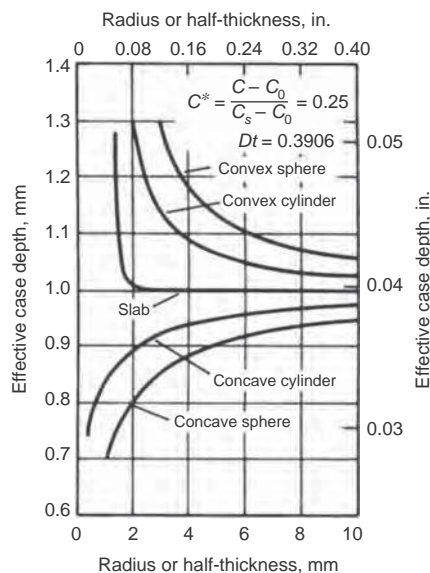


Fig. 40 Influence of surface curvature on effective case depth. C^* , normalized carbon content; C , concentration of diffusing substance; C_0 , base carbon content of the alloy; C_s , surface carbon content (often taken to be the maximum dissolved carbon content in austenite at the carburizing temperature); D , diffusion constant, having units (distance)²/time; t , time

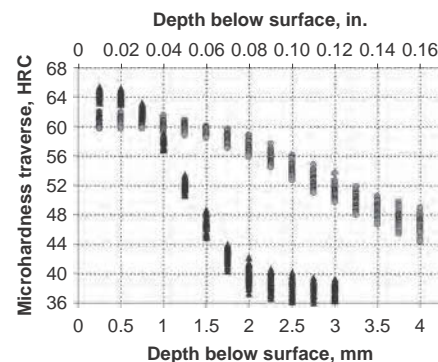


Fig. 41 Results of gage repeatability and reproducibility study showing typical variation in the hardened depth measurements obtained from 1.3 and 3.2 mm (0.05 and 0.13 in.) nominal case depth parts. The same two samples were measured by three trained operators, three measurements per day each, for five consecutive days. Source: Ref 69

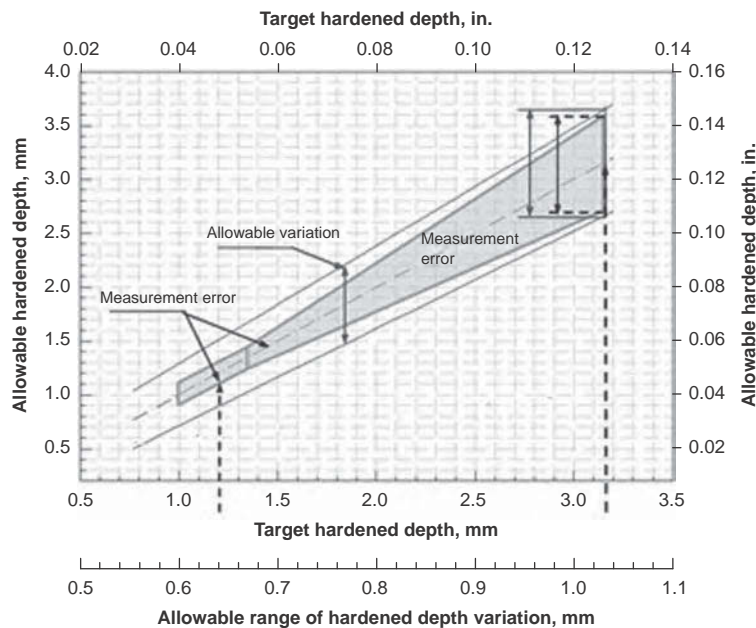


Fig. 42 Typical allowable hardened depth variation versus target hardened depth with the associated measurement errors, assuming a perfectly centered process performance with respect to the allowed hardened depth tolerance. Source: Ref 69

accomplished by continuous measurement and control of the key heat treatment process parameters, such as time, temperature, carbon potential, and quench severity.

Carburized case depth is most frequently measured on testpieces of the same alloy composition processed simultaneously with the workload. Carburized case depth can be measured by using the spectrographic method on a small flat sample or by using a carbon step bar. The analysis of carbon step bars by the consecutive cuts procedure, as described in the article "Evaluation of Carbon Control in Carburized Parts" in this Volume.

Another test for case depth makes use of the principle that the M_s temperature depends primarily on the dissolved carbon content of austenite. A carburized sample or part is austenitized, quenched in a bath at a precisely controlled temperature, held for a few minutes to allow tempering of the martensite formed, and then quenched to room temperature. A polished, etched section will reveal a line of demarcation between the martensite tempered in the salt bath (dark) and the untempered martensite formed during the final quench (white). The location of the line of demarcation corresponds to a specific carbon content. The appropriate quenching bath temperature can be found from a correlation between M_s temperature (in degrees Fahrenheit) and steel alloy composition (Ref 70):

$$M_s = 930 - 600 \cdot (\%C) - 60 \cdot (\%Mn) - 50 \cdot (\%Cr) - 30 \cdot (\%Ni) - 20 \cdot (\%Si + \%Mo + \%W) \quad (\text{Eq 37})$$

If the quenching bath temperature is chosen to be the M_s temperature for 0.4 wt% C in a given alloy, then the austenitizing temperature must be high enough to dissolve at least this much carbon in austenite, typically 830 °C (1530 °F).

Surface hardness is often measured on the plant floor on workpieces using a superficial hardness test, Rockwell 15N, for example. Because of the rather light load, the necessity for supporting pieces well, and the importance of a smooth surface, values tend to be unreliable. However, such checks of surface hardness are often necessary to detect the presence of a shallow, decarburized layer such as may occur if parts experience a delay when transferred from the carburizing furnace to the quench bath.

ACKNOWLEDGMENTS

The authors appreciate the assistance of Tim Knight, Bob Hartseil, Jeff Johnson, and other metallurgical lab staff at Caterpillar Inc. for their experimental and metallurgical lab work. The authors also would like to thank Scott Johnston and Fausta Lyons, Caterpillar Inc., and Professor David van Aken, Missouri Science & Technology University, for their assistance and valuable discussion.

REFERENCES

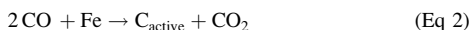
1. R. Collin, S. Gunnarson, and D. Thulin, A Mathematical Model for Predicting Carbon Concentration Profiles of Gas-Carburized Steel, *J. Iron Steel Inst.*, Vol 210 (No. 10), 1972, p 785–789
2. O. Boudouard, *Ann. Chim. Phys.*, Vol 24 (No. 5), 1901, p 85
3. M.L. Schmidt, Pre-Oxidation Prior to Gas Carburizing: Theory and Its Effect on Pyrowear 53 Alloy, *Carburizing Processing and Performance*, G. Krauss, Ed., ASM International, 1989, p 83–100
4. J. Wunning, Weiterentwicklung der Gasaufoftechnik (Advances in Gas Carburizing Technique), *Härt.-Tech. Mitt.*, Vol 23 (No. 3), 1968, p 101–109
5. U. Wyss, R. Hoffmann, and F. Neumann, Basic Requirements for Reducing the Consumption of Carburizing Gases, *J. Heat Treat.*, Vol 1 (No. 3), 1980, p 14–23
6. D.W. McCurdy and S.J. Midea, Benefits of Improved Carburizing Accuracy Using 3-Gas IR Compensation of Oxygen Probes, *International Automotive Heat Treating Conference*, 1998, p 29–31
7. O. Karabelchtchikova, "Fundamentals of Mass Transfer in Gas Carburizing," Ph.D. dissertation, Worcester Polytechnic Institute, 2007
8. R.J. Fruehan, Rate of Carburization of Iron in CO-H₂ Atmospheres, Part I: Effect of Temperature and CO and H₂ Pressures, *Mach. Des.*, Vol 4 (No. 9), Sept 1973, p 2123–2127
9. R.J. Fruehan, Rate of Carburization of Iron in CO-H₂ Atmospheres, Part 2: The Effect of H₂O and H₂S, *Mach. Des.*, Vol 4 (No. 9), Sept 1973, p 2129–2132
10. H.J. Grabke and G. Hoerz, Kinetics and Mechanisms of Gas-Metal Interactions, *Ann. Rev. Mater. Sci.*, Vol 7, 1977, p 155–178
11. J.H. Kaspersma and R.H. Shay, Mechanism for Carburization of Iron by CO-Based Mixtures in Nitrogen at 925 °C, *Metall. Trans.*, Vol 1213, 1981, p 77–83
12. J.H. Kaspersma and R.H. Shay, A Model for Carbon Transfer in Gas Phase Carburization of Steel, *J. Heat Treat.*, Vol 1 (No. 4), 1980, p 21–28
13. D.C. Miller, Accelerated Carburizing through Special Control of Furnace Atmosphere and Reactions, *Ind. Heat.*, Aug 1982, p 37–40
14. D.J. Bradley, J.M. Leitnaker, and F.H. Horne, *High Temp. Sci.*, Vol 12, 1980, p 1–10
15. S.S. Babu and H.K.D.H. Bhadeshia, Diffusion of Carbon in Substitutionally Alloyed Austenite, *J. Mater. Sci. Lett.*, Vol 14 (No. 5), 1995, p 314–316
16. K.E. Blazek and P.R. Cost, Carbon Diffusivity in Iron-Chromium Alloys, *Trans. Jpn. Inst. Met.*, Vol 17 (No. 10), 1976, p 630–636
17. A.A. Zhukov and M.A. Krishtal, Thermodynamic Activity of Alloy Components, *Met. Sci. Heat Treat.*, Vol 17 (No. 7–8), 1975, p 626–633
18. T. Ellis, I.M. Davidson, and C. Bodsworth, Some Thermodynamic Properties of Carbon in Austenite, *J. Iron Steel Inst.*, Vol 201, 1963, p 582–587
19. F. Neumann and B. Person, Beitrag zur Metallurgie der Gasaufoftechnik, *Härt.-Tech. Mitt.*, Vol 23, 1968, p 296–310
20. O.K. Rowan and R.D. Sisson, Jr., Effect of Alloy Composition on Carburizing Performance of Steel, *J. Phase Equilibria Diffus.*, Vol 30 (No. 3), June 2009, p 235–241
21. C. Dawes and D.F. Tranter, Production Gas Carburizing Control, *Heat Treat. Met.*, Vol 31 (No. 4), 2004, p 99–108
22. L. Lefevre and D. Domergue, High Efficiency Carburizing Process, *Heat Treat. Met.*, Vol 3, 2001, p 59–62
23. A. Cook, Nitrogen-Based Carbon Controlled Atmosphere—An Alternative to Endothermic Gas, *Heat Treat. Met.*, Vol 3 (No. 1), 1976, p 15–18
24. J. Slyke and L. Sproge, Assessment of Nitrogen-Based Atmospheres for Industrial Heat Treating, *J. Heat Treat.*, Vol 5 (No. 2), 1988, p 97–114
25. C.A. Stickels and C.M. Mack, Gas Carburizing of Steel with Furnace Atmospheres Formed in-Situ from Propane and Air, Part II: Analysis of the Characteristics of Gas Flow in a Batch-Type Sealed Quench Furnace, *Metall. Trans. B*, Vol 11 (No. 3), 1980, p 481–484
26. C.A. Stickels, C.M. Mack, and M. Brachaczek, Gas Carburizing of Steel with Furnace Atmospheres Formed in-Situ from Propane and Air, Part I: The Effect of Air-Propane Ratio on Furnace Atmosphere Composition and the Amount of Carburizing, *Metall. Trans. B*, Vol 11 (No. 3), 1980, p 471–479
27. C.A. Stickels, C.M. Mack, and J.A. Piepzak, Gas Carburizing of Steel with Furnace Atmospheres Formed in-Situ from Air and Hydrocarbon Gases, *Ind. Heat.*, Vol 49 (No. 6), 1982, p 12–14
28. P. Stolar and B. Prenosil, Kinetics of Transfer of Carbon from Carburizing and Carbonitriding Atmospheres, *Met. Mater.*, Vol 22 (No. 5), 1984, p 348–353
29. R. Collin, Mass Transfer Characteristics of Carburizing Atmospheres, *Met. Soc.*, 1975, p 121–124
30. H.W. Walton, Mathematical Modelling of the Carburizing Process for Microprocessor Control, *Heat Treat. Met.*, Vol 10 (No. 1), 1983, p 23–26
31. T. Turpin, J. Dulcy, and M. Gantois, Carbon Diffusion and Phase Transformations during Gas Carburizing of High-Alloyed Stainless Steels: Experimental Study and Theoretical Modeling, *Metall. Trans. A*, Vol 36 (No. 10), 2005, p 2751–2760

32. A. Ruck, D. Monceau, and H.J. Grabke, Effects of Tramp Elements Cu, P, Pb, Sb and Sn on the Kinetics of Carburization of Case Hardening Steels, *Steel Res.*, Vol 67 (No. 6), 1996, p 240–246
33. O. Karabelchthcikova and R.D. Sisson, Jr., Carbon Diffusion in Steel—A Numerical Analysis Based on Direct Flux Integration, *J. Phase Equilibria Diffus.*, Vol 26 (No. 6), Dec 2006, p 598–604
34. K. Rimmer, E. Schwarz-Bergkampf, and J. Wunning, Geschwindigkeit der Oberflächenreaktion Bei der Gasaufkohlung (Surface Reaction Rate in Gas Carburizing), *Härt.-Tech. Mitt.*, Vol 30 (No. 3), 1975, p 152–160
35. B.A. Moiseev, Y.M. Brunzel, and L.A. Shvartsman, Kinetics of Carburizing in an Endothermal Atmosphere, *Met. Sci. Heat Treat.*, Vol 21 (No. 5–6), May–June 1979, p 437–442
36. T. Sobusiak, Influence of Carburizing Parameters on Carbon Transfer Coefficient, *Trans. Mater. Heat Treat.*, Vol 25 (No. 5), 2004, p 390–394
37. V.A. Munts and A.P. Baskatov, Rate of Carburizing of Steel, *Met. Sci. Heat Treat.*, Vol 22 (No. 5–6), May–June 1980, p 358–360
38. O. Karabelchthcikova and R.D. Sisson, Jr., Calculation of Gas Carburizing Kinetics from Carbon Concentration Profiles based on Direct Flux Integration, *Defect Diffus. Forum*, Vol 266, 2007, p 171–180
39. G.G. Tibbetts, Diffusivity of Carbon in Iron and Steels at High Temperatures, *J. Appl. Phys.*, Vol 51 (No. 9), 1980, p 4813–4816
40. J.I. Goldstein and A.E. Moren, Diffusion Modeling of the Carburization Process, *Metall. Trans. A*, Vol 9 (No. 11), 1978, p 1515–1525
41. J. Agren, Revised Expression for the Diffusivity of Carbon in Binary Fe-C Austenite, *Scr. Metall.*, Vol 20 (No. 11), 1986, p 1507–1510
42. O. Karabelchthcikova, C.A. Brown, and R.D. Sisson, Jr., Effect of Surface Roughness on the Kinetics of Mass Transfer during Gas Carburizing, *Härt.-Tech. Mitt.*, Vol 63 (No. 5), 2008, p 257–264
43. C.A. Stickels, Gas Carburizing of Highly Alloyed Steels, *International Automotive Heat Treating Conference*, 1998, p 32–36
44. F.E. Harris, Case Depth—An Attempt at a Practical Definition, *Met. Prog.*, Vol 44, 1943, p 265–272
45. R. Collin, S. Gunnarson, and D. Thulin, Influence of Reaction Rate on Gas Carburizing of Steel in a CO-H₂-CO₂-H₂O-CH₄-N₂ Atmosphere, *J. Iron Steel Inst.*, Oct 1972, p 777–784
46. J. Crank, *The Mathematics of Diffusion*, Oxford University Press, Oxford, U.K., 1975, p 8–9, 42–62
47. R. Collin, M. Brachaczek, and D. Thulin, Influence of Reaction Rate on Gas Carburizing of Steel in a CH₄-H₂-N₂ Atmosphere, *J. Iron Steel Inst.*, Vol 207 (No. 8), 1969, p 1122–1128
48. J. Agren, Numerical Calculations of Diffusion in Single-Phase Alloys, *Scand. J. Metall.*, Vol 11 (No. 1), 1982, p 3–8
49. O. Karabelchthcikova and R.D. Sisson, Jr., Carburizing Process Modeling and Sensitivity Analysis Using Numerical Simulation, *Proc. MS&T 2006* (Cincinnati, OH), p 375–386
50. J. Agren, Numerical Treatment of Diffusional Reactions in Multicomponent Alloys, *J. Phys. Chem. Solids*, Vol 43 (No. 4), 1982, p 385–391
51. K. Bongartz, D.F. Lupton, and H. Schuster, Model to Predict Carburization Profiles in High Temperature Alloys, *Metall. Trans. A*, Vol 11 (No. 11), 1980, p 1883–1893
52. A. Borgenstam, A. Engstrom, L. Hoglund, and J. Agren, DICTRA, A Tool for Simulation of Diffusional Transformations in Alloys, *J. Phase Equilibria*, Vol 21 (No. 3), 2000, p 269–280
53. E. Kozeschnik, Multicomponent Diffusion Simulation Based on Finite Elements, *Metall. Trans. A*, Vol 30 (No. 10), 1999, p 2575–2582
54. A. Engstrom, L. Hoglund, and J. Agren, Computer Simulation of Carburization in Multiphase Systems, *Mater. Sci. Forum*, Vol 163–166 (No. 2), 1994, p 725–730
55. J. Kelley, “Rolled Alloys Bulletin 401,” Sept 2002, p 26
56. W.P. Houben, Background Broadening Effects in Nondispersive Infrared Gas Analysis, *Analysis Instrumentation: Proceedings of the Annual ISA Analysis Instrumentation Symposium*, Vol 19, 1981, p 51–61
57. M. Okumiya, Y. Tsunekawa, K. Kurahashi, J. Takebe, and A. Maeda, Hybrid Carbon Potential Control in Gas Carburizing Using Natural Gas as the Enriched Gas, *International Surface Engineering Congress—Proceedings of the First Congress*, 2003, p 63–67
58. D.P. Koistinen, The Distribution of Residual Stresses in Carburized Cases and Their Origin, *Trans. ASM*, Vol 50, 1958, p 227–241
59. J.L. Pacheco and G. Krauss, Microstructure and High Bending Fatigue Strength of Carburized Steel, *J. Heat Treat.*, Vol 7 (No. 2), 1989, p 77–86
60. R.H. Richman and R.W. Landgraf, Some Effects of Retained Austenite on the Fatigue Resistance of Carburized Steel, *Metall. Trans. A*, Vol 6, 1975, p 955–964
61. R. Chatterjee-Fischer, Internal Oxidation during Carburizing and Heat Treatment, *Metall. Trans. A*, Vol 9, 1978, p 1553–1560
62. W.E. Dowling, W.T. Donlon, W.B. Cople, and C.V. Darragh, Fatigue Behavior of Two Carburized Low Alloy Steels, *Carburizing and Nitriding with Atmospheres, Proceedings of the Second Conference*, Dec 1995, p 55–60
63. K.C. Evanson, G. Krauss, and D.K. Matlock, Surface Oxides and Bending Fatigue in Gas Carburized SAE 4320 Steels, *Heat Treating, Proceedings of the 20th Conference*, Oct 2000, p 9–12
64. M. Bykowski, G. Krauss, and J.G. Speer, Effect of Carburizing Temperature on Near-Surface Characteristics That Influence Rolling Contact Fatigue Performance, *Fourth VHCF-4 Conference*, TMS, 2007, p 195–201
65. T. Tobie, P. Oster, and B.R. Hohn, Systematic Investigations on the Influence of Case Depth on the Pitting and Bending Strength of Case Carburized Gears, *Gear Technol.*, Vol 22 (No. 4), 2005, p 40–48
66. *SAE Handbook*, Vol 1, Society of Automotive Engineers
67. Hardenability Curves, *Properties and Selection: Irons, Steels, and High-Performance Alloys*, Vol 1, *ASM Handbook*, ASM International, 1990
68. R.L. Brown, H.J. Rack, and M. Cohen, Stress Relaxation during the Tempering of Hardened Steel, *Mater. Sci. Eng.*, Vol 21 (No. 1), Oct 1975, p 25–34
69. O.K. Rowan, G.D. Keil, T.E. Clements, Analysis of Hardened Depth Variability Process Potential and Measurement Error in Case Carburized Components, *JMEP* (to be published 2014)
70. E.S. Rowland and S.R. Lyle, *Trans. ASM*, Vol 37, 1946, p 27–47

Pack Carburizing*

Introduction

Pack carburizing is a process in which carbon monoxide derived from a solid compound decomposes at the metal surface into nascent carbon and carbon dioxide. The basic reactions are:



The nascent carbon is absorbed into the metal, and the carbon dioxide immediately reacts with carbonaceous material present in the solid carburizing compound to produce fresh carbon monoxide.

Energizers or catalyst compounds are very often added with carbon to force the reaction in the direction favoring the formation of carbon monoxide (Ref 1). The energizing compounds include barium carbonate ($BaCO_3$), calcium carbonate ($CaCO_3$), potassium carbonate (K_2CO_3), and sodium carbonate (Na_2CO_3). The energizers facilitate the reduction of carbon dioxide with carbon to form carbon monoxide, and the amount of energizer does not change in a closed system. Carburizing continues as long as enough carbon is present to react with the excess carbon dioxide. Pack carburizing is typically conducted at approximately 920 to 940 °C (1690 to 1720 °F) for 2 to 36 h (Ref 2), but higher process temperatures are used (see the section "Process Control" in this article).

In pack carburizing, as in other carburization processes, the carbon-concentration gradient obtained is a function of carbon potential, carburizing temperature and time, and the chemical composition of the steel. Two process-control attributes peculiar to pack carburizing are:

- There may be a variation in case depth within a given furnace load due to dissimilar thermal histories within the carburizing containers.
- Distortion of parts during carburizing may be reduced because the compound can be used to support the parts.

Steel Composition. Any carburizing grade of carbon or alloy steel is suitable for pack carburizing. It is generally agreed that the diffusion rate of carbon in steel is not markedly influenced by the chemical composition of the steel. Chemical composition does have an effect on the activity of carbon and can affect the carbon level at saturation for a particular temperature.

Depth of Case. Even with good process control, it is difficult to obtain parts with total case-depth variation of less than 0.25 mm (0.010 in.) from maximum to minimum in a given furnace load, assuming a carburizing temperature of 925 °C (1700 °F). Commercial tolerances for case depths obtained in pack carburizing begin at ± 0.25 mm (0.010 in.), and, for deeper case depths, increase to ± 0.8 mm (0.03 in.). Lower carburizing temperatures provide some reduction in case-depth variation because variation in the time required for all parts of the load to reach carburizing temperature becomes a smaller percentage of total furnace time. Because of the inherent variation in case depth and the cost of packing materials, pack carburizing normally is not used on work requiring a case depth of less than 0.8 mm (0.03 in.). Typical pack-carburizing temperatures selected to produce different case depths on a variety of production parts are given in Table 1.

Distortion normally becomes more pronounced as processing temperature is increased. In some instances, carburizing temperature is selected on the basis of the maximum amount of distortion that can be tolerated. In any case, following proper container packing procedures will help minimize distortion.

Selective Carburizing. Stopoff techniques described in the article on gas carburizing in this Volume apply to selective carburization by pack carburizing. In addition, it may be possible to permit any portion of a part that is not to be carburized to protrude from the carburizing container. Alternatively, an inert or lightly oxidizing material may be packed around those areas of a part that are not to be carburized.

Advantages and Disadvantages

Pack carburizing is no longer a major commercial process. This has been mainly due to replacement by more controllable and less labor-intensive gas and liquid carburizing processes. However, any labor cost advantage that gas carburizing or liquid carburizing may have over pack carburizing can be negated should workpieces require additional steps such as cleaning and the application of protective

Table 1 Typical applications of pack carburizing

Part	Dimensions(a)				Weight		Steel	Carburizing			
	OD		OA		kg	lb		Case depth to 50 HRC		Temperature	
	mm	in.	mm	in.				mm	in.	°C	°F
Mine-loader bevel gear	102	4.0	76	3.0	1.4	3.1	2317	0.6	0.024	925	1700
Flying-shear timing gear	216	8.5	92	3.6	23.6	52.0	2317	0.9	0.036	900	1650
Crane-cable drum	603	23.7	2565	101.0	1792	3950	1020	1.2	0.048	955	1750
High-misalignment coupling gear	305	12.0	152	6.0	38.5	84.9	4617	1.2	0.048	925	1700
Continuous-miner drive pinion	127	5.0	127	5.0	5.4	11.9	2317	1.8	0.072	925	1700
Heavy-duty industrial gear	618	24.3	102	4.0	150	331	1022	1.8	0.072	940	1725
Motor-brake wheel	457	18.0	225	8.9	104	229	1020	3.0	0.120	925	1700
High-performance crane wheel	660	26.0	152	6.0	335	739	1035	3.8	0.150	940	1725
Calender bull gear	2159	85.0	610	24.0	5885	12,975	1025	4.0	0.160	955	1750
Kiln-trunnion roller	762	30.0	406	16.0	1035	2280	1030	4.0	0.160	940	1725
Leveler roll	95	3.7	794	31.3	36.7	80.9	3115	4.0	0.160	925	1700
Blooming-mill screw	381	15.0	3327	131.0	2950	6505	3115	5.0	0.200	925	1700
Heavy-duty rolling-mill gear	914	36.0	4038	159.0	11,800	26,015	2325	5.6	0.220	955	1750
Processor pinch roll	229	9.0	5385	212.0	1700	3750	8620	6.9	0.270	1050	1925

(a) OD, outside diameter; OA, overall (axial) dimension

* Revised from R.W. Foreman, Pack Carburizing of Steels, *Heat Treating*, Vol 4, ASM Handbook, ASM International, 1991, p 325-328

coatings in carburizing stopoff operations. Environmental concerns have also led to reduced use of pack carburizing. It still has application to some specialized uses, however.

Advantages. Among the principal advantages of pack carburizing are:

- It has low equipment and operating costs.
- It can make use of a wide variety of furnaces because it produces its own contained environment.
- It is ideally suited for slow cooling of work from the carburizing temperature, a procedure that may be advantageous for parts that are to be finish machined after carburizing and before hardening.
- Compared to gas carburizing, it offers a wider selection of stopoff techniques for selective carburizing.

Disadvantages. By its nature, pack carburizing is less clean and less convenient than other carburizing processes. Other disadvantages generally associated with pack carburizing include:

- It is not well suited to production of shallow case depths where strict case-depth tolerances are required.
- It cannot provide the degree of flexibility and accuracy of control over surface carbon content and carbon gradient that can be obtained in gas carburizing.
- Long heatup time is required to reach process temperatures. More processing time is required for pack carburizing than for gas or liquid carburizing because of the necessity of heating and cooling the extra thermal mass associated with the compound and the container.
- It is not well suited for direct quenching or quenching in dies; it is difficult (but possible) to harden directly from the carburizing box. Extra handling and processing are required to cool down and reheat to austenitizing temperatures.
- Decarburization can occur if components are allowed to air cool without protection.
- Grinding is necessary to remove surface porosity.
- It is labor intensive.

Carburizing Medium and Compounds

The basic component of the carburizing medium is ground wood charcoal (approximately 3 to 5 mm, or 0.12 to 0.20 in., granules) or coke, which is mixed with carbonates of barium, sodium, calcium, lithium, or potassium. The common commercial carburizing compounds are reusable and contain 10 to 20% alkali or alkaline earth metal carbonates bound to hardwood charcoal or to coke by oil, tar, or molasses. Barium carbonate is the principal energizer, usually comprising approximately

50 to 70% of the total carbonate content. The remainder of the energizer usually is made up of calcium carbonate, although sodium carbonate and potassium carbonate also may be used. It should be noted that barium carbonate, now designated by government regulations as a health hazard due to its toxicity and the disposal problems it presents, is gradually being phased out by U.S. manufacturers as a catalyst in pack-carburizing operations.

Hardwood charcoal is more reactive than coke as a source of carbon for pack carburizing. Nevertheless, coke offers certain advantages, such as minimum shrinkage, good hot strength, and good thermal conductivity. More-active carburizing compounds therefore contain both charcoal and coke, with typical compounds containing a greater percentage of coke.

Addition Rate. Because of losses associated with the use of pack-carburizing compounds, new compound usually is added to the used compound before it is returned to service. The loss in energizer normally is somewhat higher than loss of the rest of the compound. Therefore, somewhat larger percentages of new compound are used to ensure that the energizer level does not drop below approximately 5 to 8%. When direct quenching or severe mechanical handling methods are used, the addition rate may be as high as one part new compound to two parts used compound. When furnace cooling and careful handling methods are used, the addition rate may be one part new compound to three to five parts used compound.

Used compound often is screened to remove fines. The compound is then thoroughly mixed with the make-up material. Because many compounds, particularly those of the coated-charcoal type, are extremely friable, they require careful

handling to minimize losses due to formation of dust or fines.

Evaluation of Carburizing Compounds.

Evaluation of compounds can be done by subjecting a specified weight of compound to a series of standardized carburizing cycles, treating a new steel sample in each sample until the carburizing potential of the compound is depleted (indicated by shallow case depths). Four batches of unused carburizing compound (Table 2) received over a period of six months from various manufacturers were evaluated to determine whether they would be suitable for addition to the hoppers that supplied boxes used in pack carburizing gears, pins, shafts, and special washers to a case depth of 1.5 mm (0.060 in.), in continuous furnaces. Weight, screen analyses, and chemical analyses of the as-received compounds are shown in Table 2.

Carburizing tests were conducted on the four compounds as follows. A sample of 1020 steel, 50 mm (2 in.) long and 16 mm ($\frac{5}{8}$ in.) in diameter, was packed with approximately 600 g (21 oz) of unused compound in a laboratory carburizing box, subjected to a standard cycle of 9 h at 925 °C (1700 °F), and furnace cooled. The test was repeated 19 times with a new steel sample for each cycle, without adding fresh compound.

Case depth was determined microscopically after each of the 20 cycles. Variation in case depth and the cycles producing rich cases, acceptable cases, and erratic cases are shown in Fig. 1. In addition, shrinkage was determined by weight loss after each cycle and after blowing out dust after the 20th cycle. Cumulative shrinkage of two batches of pack-carburizing compounds during 20 consecutive 9 h carburizing cycles at 925 °C (1700 °F) is plotted in Fig. 2.

Table 2 Evaluation of pack-carburizing compound

Item	Batch number			
	1	2	3	4
Physical data				
Weight, lb/ft ³	28.0	32.6	38.6	41.0
Fineness, percentage through:				
0.371 in. screen	99.9	99.9	99.3	99.4
0.131 in. screen	0.1	1.0	1.0	0.4
0.100 in. screen	0.03	0.5	0.2	0.2
Chemical analysis, %				
Moisture	0.2	0.2	0.2	0.2
Sulfur	1.05	0.4	0.6	0.7
Sodium carbonate	Nil	Nil	Nil	Nil
Barium carbonate	12.2	9.2	11.5	11.1
Calcium carbonate	Nil	Nil	Nil	Nil
Charcoal	Nil	Nil	0.2	Nil
Coke	87.8	90.8	88.3	88.9
Ash	9.0	7.4	8.1	8.2
Total weight loss during 20 carburizing runs, % (See Fig. 2 for cumulative record for batches 1 and 3)				
By shrinkage	47.2	38.5	34.2	35.8
By blowing out dust	10.9	8.3	12.7	14.2
Total weight loss	58.1	46.8	46.9	50.0

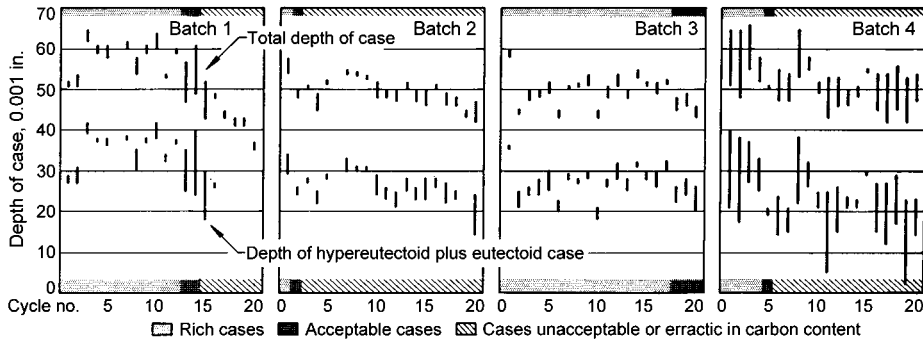


Fig. 1 Variation in case depth produced from 20 consecutive cycles of four different batches of compounds for pack carburizing (Table 2)

Process Control

In pack carburizing, as in other carburization processes, the carbon-concentration gradient obtained is a function of carbon potential, carburizing temperature and time, and the chemical composition of the steel. Pack carburizing normally is performed at temperatures ranging from 815 to 955 °C (1500 to 1750 °F). In recent years, the upper limits have been steadily raised, and carburizing temperatures as high as 1095 °C (2000 °F) have been used.

Because most pack-carburized parts are reheated and quenched from a lower temperature after being carburized and slow cooled, grain growth is not a concern when high carburizing temperatures are used. The larger concern would be the presence of surface carbides due to the higher surface carbon levels at saturation from the higher carburizing temperature.

Surface Carbon Content. Under equilibrium conditions, carbon content obtained at the surface of the work increases directly with an increase in the ratio of carbon monoxide to carbon dioxide. For given gas mixtures, the available carbon is higher at the lower temperatures (Fig. 3, 4). Although values from these two experimentally derived charts in Fig. 3 and 4 are not exactly the same, they show the basic trend of the equilibrium isotherms of CO and CO₂ mixtures with carbon concentration in iron. Thus, more carbon is made available at the work surface by the use of energizers and carburizing materials that promote formation of carbon monoxide.

In pack carburizing, the rate of evolution of carbonaceous gas is fixed and is almost always in excess of the rate required to supply the necessary carbon for a saturated surface layer. The surface carbon content is approximately that of the saturation limit for carbon in austenite (Fig. 3). At operating temperature, the desired average carbon level throughout the case is directly dependent on the carburizing temperature. When eutectoid (0.8 wt% C) cases are desired, the carburizing temperature is normally approximately 815 °C (1500 °F). As more carbon is required in the case, the temperature is

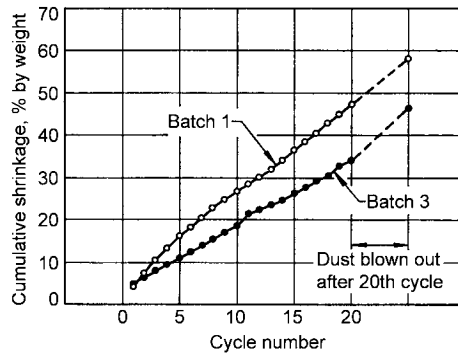


Fig. 2 Cumulative shrinkage of two batches of pack-carburizing compound during 20 consecutive 9 h carburizing cycles at 925 °C (1700 °F). Dust was blown out after the 20th cycle. Shrinkage for batches 2 and 4 (Table 2) was intermediate to the data shown for batches 1 and 3.

increased. Although the carbon potential of the compound can be varied to limit the surface carbon content, control of temperature serves the same purpose and is easier to achieve. Carbon potential (for a given gas mixture) is higher at low temperatures, but cementite (rather than saturated carbon in austenite) forms at the surface with higher CO levels and low temperatures (Fig. 3).

Carburizing Rates and Case Depth. Carbon potential refers only to available carbon at the surface and not the rate of carburization and the depth of carbon diffusion into the case. The rate at which the carburized case is formed increases rapidly with temperature. If a factor of 1.0 is representative of 815 °C (1500 °F), the factor increases to 1.5 at 870 °C (1600 °F) and to more than 2.0 at 925 °C (1700 °F). Improved containers, fine-grained steels, and other improvements now permit the use of a wide variety of temperatures.

The rate of change in case depth at a particular carburizing temperature is proportional to the square root of time. The rate of carburization is thus highest at the beginning of the cycle and gradually diminishes as the cycle is

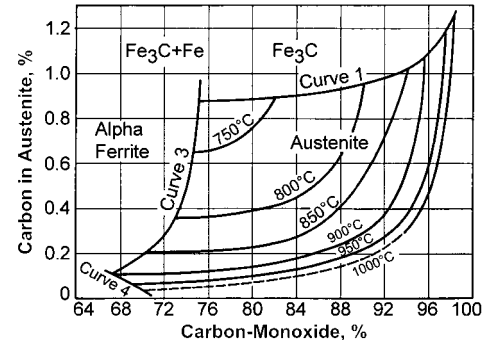


Fig. 3 Isotherms of carbon in austenite at high levels of carbon monoxide. Source: Ref 3

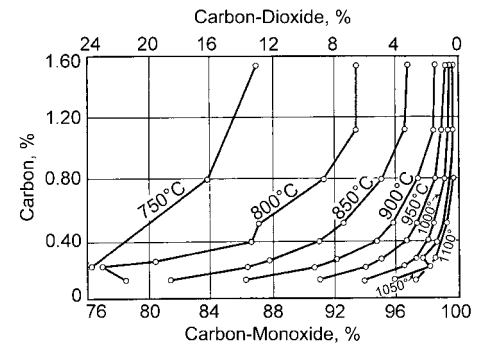


Fig. 4 Isotherms showing equilibria between various CO-CO₂ mixtures and iron with various carbon contents at a series of temperatures. Source: Ref 3

extended (Fig. 5). Higher temperatures also promote carbon diffusion and increase the case depth (Fig. 6).

Example. A rock bit section made of 4815 steel was pack carburized with a compound of charcoal (16 to 30 mesh or finer) with approximately 8 to 15% potassium carbonate energizer. Carburizing at 925 °C (1700 °F) for approximately 9 h produced a case depth of about 1.65 mm (0.065 in.) with approximately 1.0% C at the surface.

Furnaces for Pack Carburizing

The suitability of a furnace for pack carburizing depends on its ability, at reasonable cost, to provide adequate thermal capacity and temperature uniformity (furnaces must be controllable to within ±5 °C, or ±9 °F, and must be capable of uniform through heating to within ±8 to ±14 °C, or ±14 to ±25 °F) and provide adequate support for containers and workpieces at the required temperatures.

Modern heating systems and furnace construction provide ample heating capacity and temperature uniformity over a wide range of temperatures. A variation of ±8 °C (±14 °F) throughout the entire working section of a large

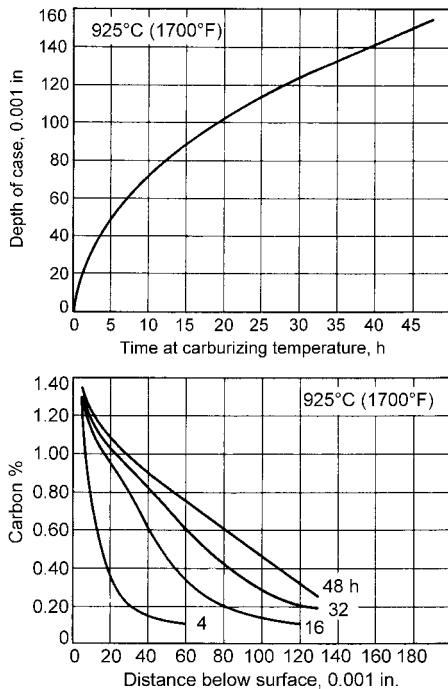


Fig. 5 Effect of duration of pack carburizing on case depth and carbon gradient in 3115 steel carburized in a compound containing hardwood charcoal, coke, and sodium carbonate

furnace can be easily maintained. Many furnaces incorporate automatic compensation for heat losses at doors or other connection points. Combustion systems that maintain constant pressure or constant flow permit close temperature control on variable loads. Zoning is also a major contributor to control. To maintain good uniformity, it is necessary to load the furnace as uniformly as possible and to allow adequate space between containers—50 to 100 mm (2 to 4 in.) or more—to permit circulation of the heating gases.

The three types of furnaces most commonly used for pack carburizing are the box, car-bottom, and pit types. Box furnaces are loaded by mechanical devices or by in-plant transportation equipment. Car-bottom furnaces provide for convenient loading of heavy units. A car-bottom furnace with a car at each end allows a second car to be loaded while the furnace is in use, which minimizes the heat loss and downtime between batches. Pit furnaces are general-purpose furnaces that may be used for carburizing and other heat treating operations that require minimum floor space.

Adequate support of containers and work-pieces does much to minimize distortion. It also helps maintain the shape and extend the life of carburizing containers. Three or more points of support should be used in car-bottom furnaces. The container should be blocked above the hearth to allow circulation around, and proper shimming of, the container. In box-type furnaces, silicon carbide and certain other hearth materials provide excellent wear

resistance to maintain the shape of the hearth. Their high thermal conductivity helps promote temperature uniformity.

Furnaces for pack carburizing have a minimum number of parts that are subject to high wear or that require frequent maintenance. Very few alloy parts inside the furnace are subjected to thermal fatigue, and a minimum of auxiliary equipment is needed. The personnel who operate these furnaces do not need extensive technical training.

Carburizing Containers

Materials. Carburizing containers are made of carbon steel, of aluminum-coated carbon steel, or of iron-nickel-chromium heat-resisting alloys. Although uncoated carbon steel boxes scale severely during carburizing and have short lives (Fig. 7), they often are the most economical for processing odd lots and unusual shapes.

Aluminum coating can significantly extend the life of a carbon steel container, making this material potentially the lowest in cost per hour per unit weight carburized.

In the long run, heat-resisting alloys are the most economical container materials for carburizing large numbers of moderate-sized parts. However, because heat-resisting alloys are considerably higher in initial cost than plain or aluminum-coated carbon steel, they must be used continuously if they are to approach the lowest possible prorated cost.

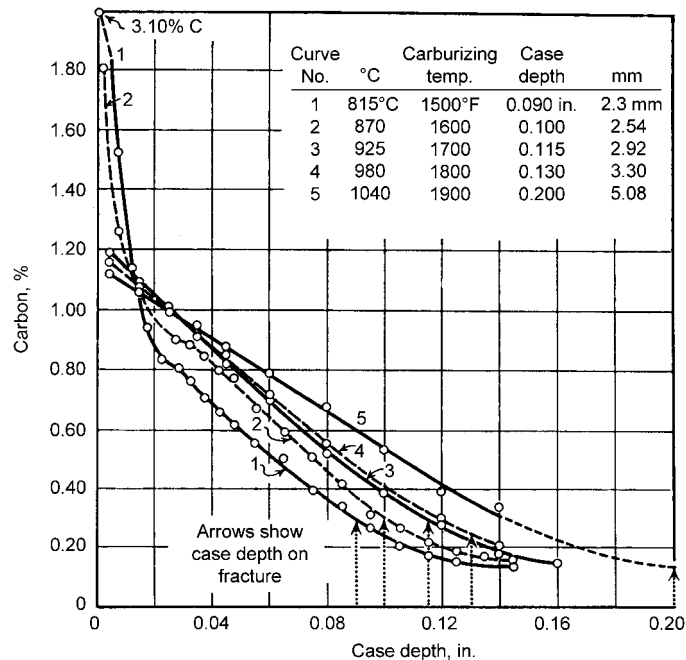


Fig. 6 Case depth-carbon content curve. Shows the effect of carburizing temperature on carbon concentration after pack carburizing at temperature given. Source: Ref 3

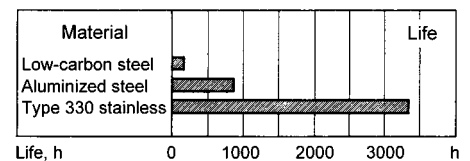


Fig. 7 Service life comparison of three materials for containers for pack carburizing

Design and Construction. For containers of all three materials, the trend has been toward lighter construction from sheet or plate, rather than the heavier cast construction. These lighter containers require ribbing, corrugating, or other bracing methods to make them rigid enough to withstand long periods at high temperature. Containers often are equipped with braced lifting eyes or hooks, special lid-receiving sections, and test-pin openings.

A carburizing container should be no larger than necessary. If possible, it should be narrow in at least one dimension to promote uniform heating of the contents. A properly designed box will provide a cooling rate high enough to minimize formation of a carbide network in the case but low enough to avoid distortion or excessive hardening.

Lid Construction. Lids for carburizing containers vary from simple sheet-metal plates to built-up lids of metal and refractory material. The lid may add rigidity to the container. It must be tight enough to prevent air from entering and burning the compound, yet not so tight

as to prevent easy expulsion of excess gas generated within the container. Lids must be capable of venting the container, and the venting means must be able to withstand the intense heat liberated by combustion of flammable gas. Lids that fit too loosely can be partly sealed with clay-based cements.

Conditioning. Before new alloy carburizing containers are placed in service, they may be conditioned by "precarburizing" without a work load. This pretreatment eliminates the possibility of the container, rather than the work load, being carburized during the first production carburizing cycle.

Packing

Components are placed in a steel box with a spacing of approximately 25 mm (1.0 in.) between the components. The box can be sealed with clay to contain the liberated gas. Intimate contact between compound and workpiece is not necessary; however, when properly packed, the compound will provide good support for the workpiece. The layer of compound surrounding the work must be heavy enough to allow for shrinkage and to maintain a high carbon potential during the entire cycle, but not so heavy as to unduly retard heating of the workpiece to carburizing temperature. If the container can be designed to conform to the shape of the workpiece, the compound will be of both uniform and minimum thickness.

Work-load density—that is, net weight (piece weight) divided by gross weight (weight of the carburizing container, compound, and workpieces)—is an important factor in the efficiency of pack carburizing, because it affects heating and cooling time. The smaller this percentage, the lower the relative efficiency of the process. Table 3 shows work-load densities for three different carburized parts.

Procedure. Packing of the workpieces in a compound is a dusty and disagreeable operation

Table 3 Work-load densities in pack carburizing

Part	Dimensions(a)				Weight per piece				Net weight, % of gross weight
	OD		OA		Net		Total(b)		
	mm	in.	mm	in.	kg	lb	kg	lb	
Roll	75	3	1220	48	37	82	72	159	51
Crane wheel	560	22	125	5	130	287	150	331	87
Gear	660	26	205	8	285	628	440	970	65

(a) OD, outside diameter; OA, overall (axial) dimension. (b) Total weight of work plus packing material plus container, divided by number of pieces in pack

(one of the reasons this process is losing favor in industry). For this reason, grouping of boxes, workpieces, and compound should be carefully planned so as to minimize handling of the compound. If possible, workpieces should come to the packer already stacked and sorted, preferably on open trays or in pans.

First, a layer of compound from 13 to 50 mm ($\frac{1}{2}$ to 2 in.) deep is placed in the empty box. The part or parts are then stacked in the container, and, if necessary, metal or ceramic supports or spacers are applied and internal container supports are inserted.

Whenever possible, workpieces should be packed with the longest dimension vertical to the base of the container. This is extremely important in processing long parts such as shafts and rolls because it minimizes the tendency of these parts to sag. Suspension of the work within the container or within the furnace is useful in minimizing distortion in relatively thin or delicate parts. For applications where small teeth or small holes are to be uniformly carburized, a 6- or 8-mesh material should be used to ensure good filling.

After the compound is sufficiently tamped, a final layer is placed on top of the parts. The thickness of the top layer varies according to the type of work, depth of case, type of container, and shrinkage rate of the compound, but it should be adequate to ensure that the work will be covered after shrinkage and other

movements have occurred. A minimum depth of 50 mm (2 in.) is recommended. In the final step, the lid is put in place.

Process-Control Specimens. To control and evaluate the carburizing process, test pins or shims normally are included in the charge. To provide valid results, section sizes and locations of test specimens must closely approximate those of the workpieces. Placing a test pin close to a workpiece often will produce a thermal history identical to that of the workpiece.

For control purposes, many containers are equipped with a test-pin section that can be removed from the load during the carburizing cycle. After the pins have been quenched and fractured, case-depth readings made on them aid in evaluating whether satisfactory carburizing results are being obtained and in determining when the prescribed case depth has been attained.

REFERENCES

1. A. Hultgren, *J. Iron Steel Inst.*, July 1951, p 245–257
2. W.F. Gale and T.C. Totemeier, Ed., Chap. 29, Heat Treatment, *Smithells Metals Reference Book*, 8th ed., Elsevier Butterworth-Heinemann, 2004
3. M.A. Grossman, A Review of Some Fundamentals of Carburizing, *Carburizing*, American Society for Metals, 1938

Liquid Carburizing and Cyaniding of Steels*

Revised by Jon Dossett, Consultant

LIQUID CARBURIZING is a process used for case hardening steel or iron parts. The parts are held at a temperature above A_{c1} in a molten salt that introduces carbon and nitrogen, or carbon alone, into the metal. Most liquid carburizing baths contain cyanide, which introduces both carbon and nitrogen into the case. Salt bath processes containing cyanide such as those described in this article were previously used for carburizing and carbonitriding and also for nitriding and ferritic nitrocarburizing. Starting in the 1970s, use of cyanide baths diminished due to operator and environmental concerns. Another type of liquid carburizing bath, however, uses a special grade of carbon, rather than cyanide, as the source of carbon. This bath produces a case that contains only carbon as the hardening agent.

Liquid carburizing may be distinguished from cyaniding (which is performed in a bath containing a higher percentage of cyanide) by the character and composition of the case produced. Cases produced by liquid carburizing are lower in nitrogen and higher in carbon than cases produced by cyaniding. Cyanide cases are seldom applied to depths greater than 0.25 mm (0.010 in.); liquid carburizing can produce cases as deep as 6.35 mm (0.250 in.). For very thin cases, liquid carburizing in low-temperature baths may be employed in place of cyaniding.

Diffusion of the carbon from the surface toward the interior produces a case that can be hardened, usually by fast quenching from the bath. Carbon diffuses from the bath into the metal and produces a case comparable with one resulting from gas carburizing in an atmosphere containing some ammonia. The main process difference is that liquid carburizing involves faster heatup (due to the superior heat-transfer characteristics of salt bath solutions). Therefore, cycle times for liquid carburizing are shorter than those for gas carburizing.

However, salt bath processes containing cyanide can cause violently poisonous reactions if allowed to come into contact with scratches or wounds (on the hands, for example) or fatal if fumes are inhaled or taken internally. Use has diminished with increased national, state, and local restrictions on disposal and effluent discharges. Of major concern has been the cyanide content from the processes and processed parts cleaning fluids. Although much was done in the area of waste treatment and waste disposal, in many instances these added costs caused the cyanide-bearing processes to no longer be economically viable. There was a switch to the gaseous versions of each of these processes, which were much more environmentally friendly. Cyanide wastes, whether dissolved in quench water or in the form of solid salt from pots, pose a serious disposal problem (see the section "Disposal of Cyanide Wastes" in this article).

Liquid carburizing and cyaniding are done in salt bath furnaces that may be heated either externally or internally. In an externally heated furnace, heat is introduced into an annular space between the salt pot and the surrounding insulation, which usually is made of firebrick. In an internally heated furnace, heat is introduced directly into the salt. Both internally and externally heated furnaces generally have insulated lids that slide to open the bath and allow workpieces and fixtures to be positioned, usually with an overhead crane or with similar mechanized lifting equipment. Additional information on equipment is available in the article "Salt Bath Heat Treatment and Equipment" in this Volume.

Cyanide-Containing Liquid Carburizing Baths

Light case and *deep case* are arbitrary terms that have been associated with liquid carburizing

in baths containing cyanide. There is necessarily some overlapping of bath compositions for the two types of case. In general, the two types are distinguished more by operating temperature or by cycle times than by bath composition. Therefore, the terms *low temperature* and *high temperature* are preferred.

Both low-temperature and high-temperature baths are supplied in different cyanide contents to satisfy individual requirements of carburizing activity (carbon potential) within the limitations of normal dragout and replenishment. In many instances, compatible companion compositions are available for starting the bath or for bath makeup, and for regeneration or maintenance of carburizing potential.

Low-temperature cyanide-type baths (light-case baths) are those usually operated in the temperature range from 845 to 900 °C (1550 to 1650 °F), although for certain specific effects this range is sometimes extended to 790 to 925 °C (1450 to 1700 °F). Low-temperature baths are best suited to formation of shallower cases. Low-temperature baths are generally of the accelerated cyanogen type containing various combinations and amounts of the constituents listed in Table 1 and differ from cyaniding baths in that the case produced by a low-temperature bath consists predominantly of carbon. Low-temperature baths are usually operated with a protective carbon cover; however, when the carbon cover on a low-temperature bath is thin, the nitrogen content of the carburized case will be relatively high. Cyaniding baths produce cases that are approximately 0.13 to 0.25 mm (0.005 to 0.010 in.) deep and that contain appreciable amounts of nitrogen.

In a low-temperature cyanide-type bath, several reactions occur simultaneously, depending on bath composition, to produce various end products and intermediates. These reaction products include the following: carbon (C), alkali carbonate (Na_2CO_3 or K_2CO_3), nitrogen

* Revised from A.D. Godding, Liquid Carburizing and Cyaniding of Steels, *Heat Treating*, Vol 4, ASM Handbook, ASM International, 1991, p 329-347

Table 1 Operating compositions of liquid carburizing baths

Constituent	Composition of bath, %	
	Light case, low temperature 845–900 °C (1550–1650 °F)	Deep case, high temperature 900–955 °C (1650–1750 °F)
Sodium cyanide	10–23	6–16
Barium chloride	...	30–55(a)
Salts of other alkaline earth metals(b)	0–10	0–10
Potassium chloride	0–25	0–20
Sodium chloride	20–40	0–20
Sodium carbonate	30 max	30 max
Accelerators other than those involving compounds of alkaline earth metals(c)	0–5	0–2
Sodium cyanate	1.0 max	0.5 max
Density of molten salt	1.76 g/cm ³ at 900 °C (0.0636 lb/in. ³ at 1650 °F)	2.00 g/cm ³ at 925 °C (0.0723 lb/in. ³ at 1700 °F)

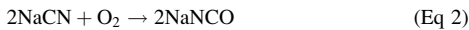
(a) Proprietary barium chloride-free deep-case baths are available. (b) Calcium and strontium chlorides have been employed. Calcium chloride is more effective, but its hygroscopic nature has limited its use. (c) Among these accelerators are manganese dioxide, boron oxide, sodium fluoride, and sodium pyrophosphate.

(N₂ or 2N), carbon monoxide (CO), carbon dioxide (CO₂), cyanamide (Na₂CN₂ or BaCN₂), and cyanate (NaNCO).

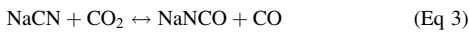
Two of the major reactions believed to occur in the operating bath are the cyanamide shift and the formation of cyanate:



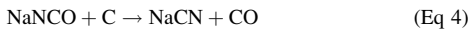
and either



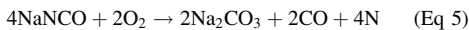
or



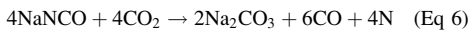
Reactions that influence cyanate content proceed as follows:



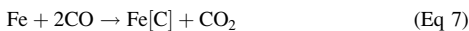
and either



or



Equations 5 and 6 deplete the activity of the bath and lead to an eventual loss of carburizing effectiveness unless suitable replenishment practice is followed. Equations 1 and 3 are at least partly reversible. Reactions that produce either carbon monoxide or carbon are beneficial in producing the desired carburized case, as for example:



and

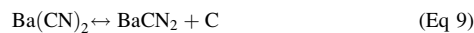


Low-temperature (light-case) baths are usually operated at higher cyanide contents than high-temperature (deep-case baths). The preferred operating cyanide contents shown in Table 2 provide a case that is essentially

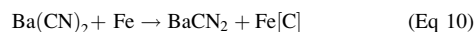
eutectoidal (>0.80% C). If a hypoeutectoid (<0.80% C) case is desired, the bath is operated at the lower end of the temperature/cyanide range. Conversely, operation at the higher end of the suggested range favors formation of a hypereutectoid surface carbon content.

High-temperature cyanide-type baths (deep-case baths) are usually operated in the temperature range from 900 to 955 °C (1650 to 1750 °F). This range may be extended somewhat, but at lower temperatures the rate of carbon penetration decreases, and at temperatures higher than approximately 955 °C (1750 °F), deterioration of the bath and equipment is markedly accelerated. However, rapid carbon penetration can be obtained by operating at temperatures between 980 and 1040 °C (1800 and 1900 °F).

High-temperature baths are used for producing cases 0.5 to 3.0 mm (0.020 to 0.120 in.) deep. In some instances, even deeper cases are produced (up to approximately 6.35 mm, or 0.250 in.), but the most important use of these baths is for the rapid development of cases 1 to 2 mm (0.040 to 0.080 in.) deep. These baths consist of cyanide and a major proportion of barium chloride (Table 1), with or without supplemental acceleration from other salts of alkaline earth metals. Although the reactions shown for low-temperature liquid carburizing salts apply in some degree, the principal reaction is the so-called cyanamide shift. This reaction is reversible:



In the presence of iron, the reaction is:



Cases produced in high-temperature liquid carburizing baths consist essentially of carbon dissolved in iron. However, sufficient nascent nitrogen is available to produce a superficial nitride-containing skin, which aids in resisting wear and which also resists softening during tempering and other heat treatments requiring higher-than-normal operating temperatures.

Table 2 Relation of operating temperature to sodium cyanide content in barium-activated liquid carburizing baths

Temperature		NaCN, %		
°C	°F	Min	Preferred	Max(a)
815	1500	14	18	23
845	1550	12	16	20
870	1600	11	14	18
900	1650	10	12	16
925	1700	8	10	14
955	1750	6	8	12

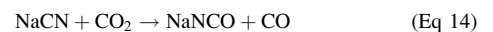
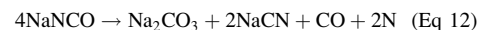
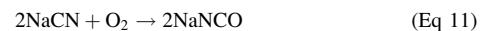
(a) The maximum limits are based on economy. If 30% NaCN is exceeded, there is danger that NaCN will break down, with production of carbon scum and attendant frothing. To correct such a condition, the bath temperature should be lowered and the NaCN content should be adjusted to the preferred value.

Combination Treatment. It is not uncommon for the carburizing cycle to be initiated in a high-temperature bath and then for the work load to be transferred to a low-temperature carburizing bath. Not only does this practice provide a maximum rate of carburizing, but quenching the work from the low-temperature bath reduces distortion and minimizes retained austenite.

Cyaniding (Liquid Carbonitriding)

Cyaniding, or salt bath carbonitriding, is a heat treating process that produces a file-hard, wear-resistant surface on ferrous parts. When steel is heated above Ac₁ in a suitable bath containing alkali cyanides and cyanates, the surface of the steel absorbs both carbon and nitrogen from the molten bath. When quenched in mineral oil, paraffin-based oil, water, or brine, the steel develops a hard surface layer, or case, that contains less carbon and more nitrogen than the case developed in activated liquid carburizing baths.

Because of greater efficiency and lower cost, sodium cyanide is used instead of the more expensive potassium cyanide. The active hardening agents of cyaniding baths—carbon monoxide and nitrogen—are not produced directly from sodium cyanide. Molten cyanide decomposes in the presence of air at the surface of the bath to produce sodium cyanate, which in turn decomposes in accordance with the following chemical reactions:



The rate at which cyanate is formed and decomposes, liberating carbon and nitrogen at

Table 3 Compositions and properties of sodium cyanide mixtures

Mixture grade designation	Composition, wt%			Melting point		Specific gravity	
	NaCN	NaCO ₃	NaCl	°C	°F	25 °C (75 °F)	860 °C (1580 °F)
96-98(a)	97	2.3	Trace	560	1040	1.50	1.10
75(b)	75	3.5	21.5	590	1095	1.60	1.25
45(b)	45.3	37.0	17.7	570	1060	1.80	1.40
30(b)	30.0	40.0	30.0	625	1155	2.09	1.54

(a) Appearance: white crystalline solid. This grade also contains 0.5% sodium cyanate (NaNCO) and 0.2% sodium hydroxide (NaOH); sodium sulfide (Na₂S) content, nil. (b) Appearance: white granular mixture

Table 4 Effect of sodium cyanide concentration on case depth in 1020 steel bars

Samples are 25.4 mm (1.0 in.) diam bars that were cyanided 30 min at 815 °C (1500 °F).

NaCN in bath, %	Depth of case	
	mm	in.
94.3	0.15	0.0060
76.0	0.18	0.0070
50.8	0.15	0.0060
43.0	0.15	0.0060
30.2	0.15	0.0060
20.8	0.14	0.0055
15.1	0.13	0.0050
10.8	0.10	0.0040
5.2	0.05	0.0020

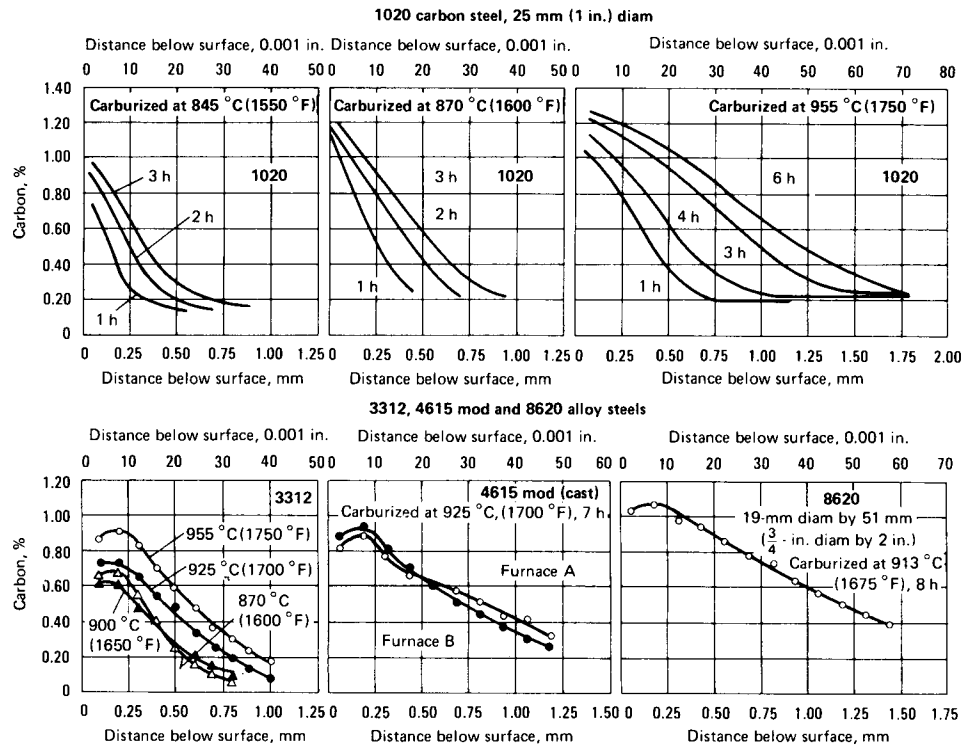


Fig. 1 Carbon gradients produced by liquid carburizing of carbon and alloy steels in low-temperature and high-temperature baths. The 1020 carbon steel bars were carburized at 845, 870, and 955 °C (1550, 1600, and 1750 °F) for the periods shown. The data on 3312 alloy steel show the effect of four different carburizing temperatures on carbon gradient (time constant at 2 h). The data on modified 4615 steel castings indicate the slight differences in gradients obtained in two furnaces employing the same carburizing conditions (7 h at 925 °C, or 1700 °F). These data and the data on 8620 steel parts showing a decrease in carbon content near the surface caused by diffusion of carbon during reheating to austenitizing temperature.

the surface of the steel, determines the carbonitrating activity of the bath. At operating temperatures, the higher the concentration of cyanate, the faster the rate of its decomposition. Because the rate of cyanate decomposition also increases with temperature, bath activity is greater at higher operating temperatures. A fresh cyaniding bath must be aged for approximately 12 h at a temperature above its melting point to provide a sufficient concentration of cyanate for efficient carbonitrating activity. For the aging cycle to be effective, any carbon scum formed on the surface must be removed. To eliminate scum, the cyanide content of the bath must be reduced to the 25 to 30% range by addition of inert salts (sodium chloride and sodium carbonate). At the

bath aging temperature—usually about 700 °C (1290 °F)—the rate of its decomposition is low.

Bath Composition. A sodium cyanide mixture such as grade 30 in Table 3, containing 30% NaCN, 40% Na₂CO₃, and 30% NaCl, is generally used for cyaniding on a production basis. This mixture is preferable to any of the other compositions given in Table 3. The inert salts sodium chloride and sodium carbonate are added to cyanide to provide fluidity and to control the melting points of all mixtures. The 30% NaCN mixture, as well as the mixtures containing 45, 75, and 97% NaCN, may be added to the operating bath to maintain a desired cyanide concentration for a specific application.

The carbon content of the case developed in cyanide baths increases with an increase

in the cyanide concentration of the bath, thus providing considerable versatility. A bath operating at 815 to 850 °C (1500 to 1560 °F) and containing 2 to 4% cyanide may be used to restore carbon to decarburized steels with a core carbon content of 0.30 to 0.40%, while a 30% cyanide bath at the same temperature will yield a 0.13 mm (0.005 in.) case containing 0.65% C at the surface in 45 min. Sodium cyanide concentration also has some effect on case depth, as shown for 1020 steel in Table 4.

Noncyanide Liquid Carburizing

Liquid carburizing can be accomplished in a bath containing a special grade of carbon instead of cyanide as the source of carbon. In this bath, carbon particles are dispersed in the molten salt by mechanical agitation, which is achieved by means of one or more simple propeller stirrers that occupy a small fraction of the total volume of the bath. Agitation is also believed to introduce greater exposure and absorption of oxygen in the air.

The chemical reaction involved is not fully understood but is thought to involve adsorption of carbon monoxide on carbon particles. The carbon monoxide is generated by reaction between the carbon and carbonates, which are major ingredients of the molten salt. The adsorbed carbon monoxide is presumed to react with steel surfaces, much as in gas or pack carburizing.

Operating temperatures for this type of bath are generally higher than those for cyanide-type baths. A range of approximately 900 to 955 °C (1650 to 1750 °F) is most commonly employed. Temperatures below approximately 870 °C (1600 °F) are not recommended and may even lead to decarburization of the steel. The case depths and carbon gradients produced are in the same range as for high-temperature cyanide-type baths (see Fig. 1 to 3 for data on carbon and low-alloy steels), but there is no nitrogen in the case. The carbon content is slightly lower than that of standard carburizing baths that contain cyanide.

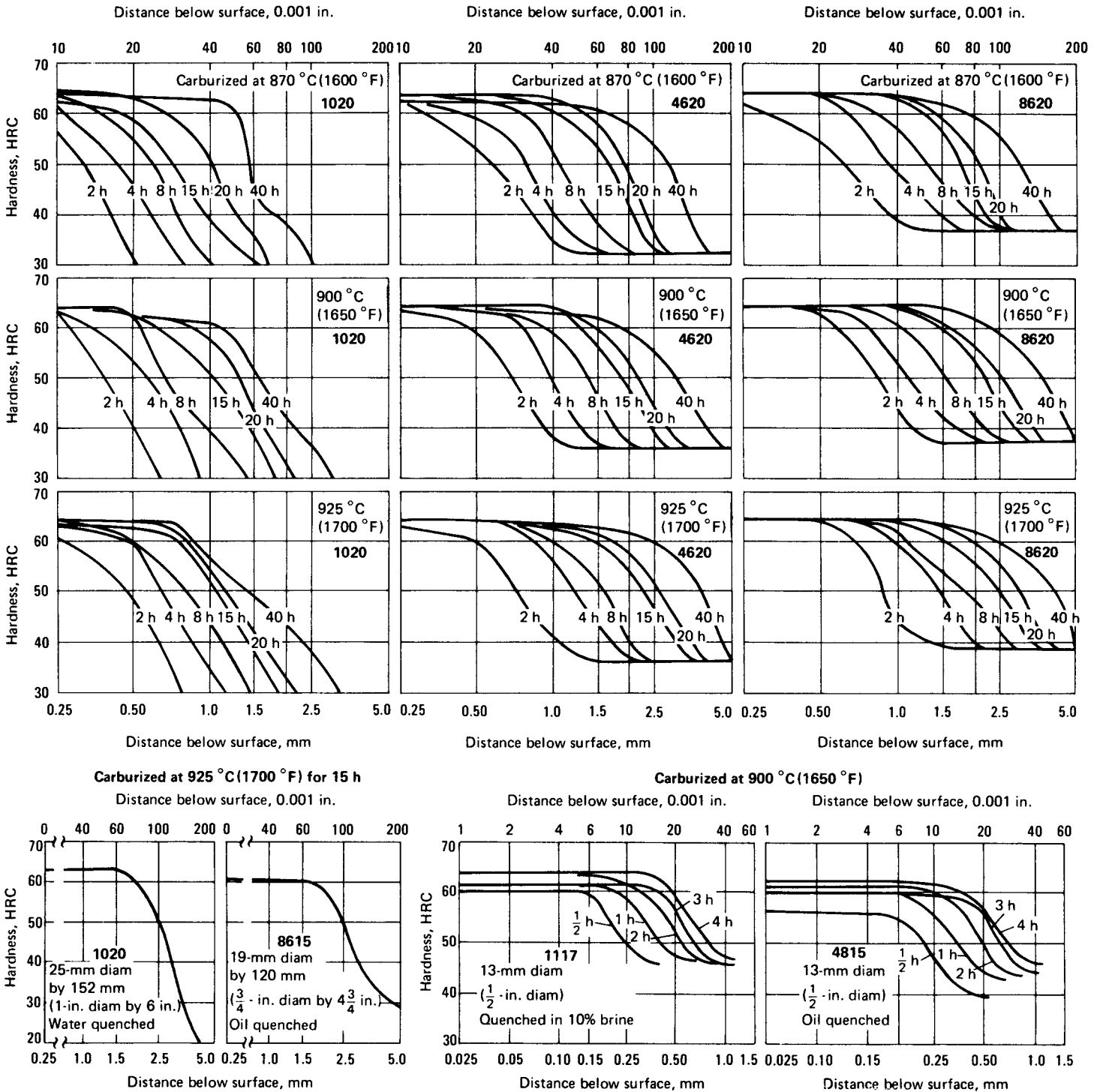


Fig. 2 Case-hardness gradients for two carbon steels and four low-alloy steels showing effects of carburizing temperature and time. Specimens measuring 19 mm diam by 51 mm (3/4 in. diam by 2 in.) were carburized, air cooled, reheated in neutral salt at 845 °C (1550 °F), and quenched in nitrate/nitrite salt at 180 °C (360 °F).

Temperatures above 955 °C (1750 °F) produce more rapid carbon penetration and do not adversely affect noncyanide baths, because no cyanide is present to break down and cause carbon scum or frothing. Equipment deterioration is the chief factor that limits operating temperature.

Parts that are slowly cooled following noncyanide carburization are more easily machined than parts slowly cooled following cyanide carburization, because of the absence of nitrogen in noncyanide-carburized cases. For the same reason, parts that are quenched following noncyanide carburization contain less retained

austenite than parts quenched following cyanide carburization.

Safety and Disposal of Noncyanide Carburizing Salts. Noncyanide carburizing salts are safe to dispose of directly in municipal or natural water if first diluted to acceptable dissolved-solids levels. There are no significant

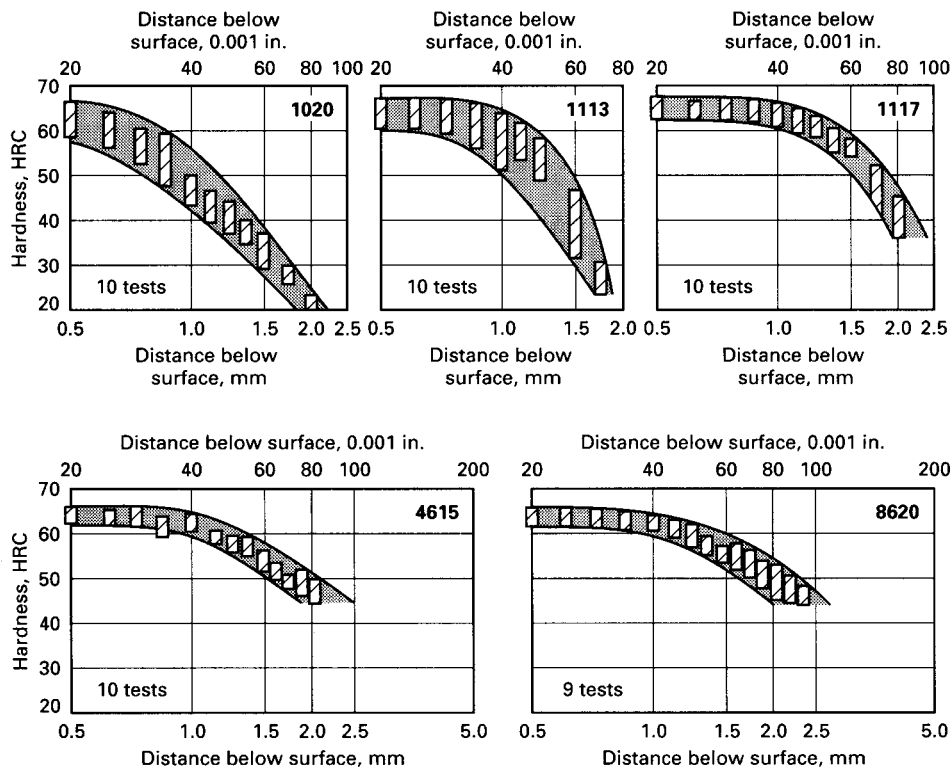


Fig. 3 Case-hardness gradients for selected steels showing scatter resulting from normal variations

chemical hazards in the proper use of these salts. They are somewhat alkaline and should be washed from the skin or eyes if contact is made. When they are used as molten salts, the usual precautions apply: avoid introduction of moisture into the bath and prevent the hot salt from contacting the body. Further information is available from Occupational Safety and Health Administration (OSHA) and Environmental Protection Agency (EPA) publications.

Noncyanide Carburizing Process (Ref 1). A noncyanide process for the liquid carburizing of steel that consists of a chloride mixture containing a small amount of specially selected carbon has recently been made commercially available. This carbon additive is a blend of selected graphite materials. The mixture should be held in a pot constructed of series 300 stainless steel, Inconel, or a ceramic material.

The chloride mixture laden with carbon is nontoxic and produces a classic carbon case that contains no nitrogen. Parts that have been carburized with this chloride-carbon material can be quenched directly into any nitrate/nitrite salt bath without the need for a neutral wash. Such a step is not recommended with cyanide carburizing salts, because of their incompatibility with strong oxidizers (for example, nitrates and nitrites).

This carbon-containing chloride mixture has the following properties:

Melting point, °C (°F)	663 (1225)
Working range, °C (°F)	954–982 (1750–1800)
Specific heat, J/kg · K (cal/g · °C)	
Solid	960 (0.23)
Liquid	1050 (0.23)
Heat of fusion, kJ/kg (Btu/lb)	414 (178)
Density at 954 °C (1750 °F), g/cm ³ (lb/in. ³)	1.44 (0.0520)

Initial Startup. A new bath is prepared by melting the chloride salt mixture and bringing it to an operating temperature of 954 °C (1750 °F). When the bath is molten and has stabilized at operating temperature, small amounts of carbon additive are introduced in the melt until a 13 to 25 mm (0.5 to 1.0 in.) thick cover remains on the surface.

Because the addition of carbon into the bath is necessary to achieve carburizing potential, the bath should be aged at heat for approximately 2 h before processing work through the bath. An adequate carbon cover should be maintained over the bath at all times while at operating temperature to ensure consistent results.

The bath level is maintained via additions of the chloride salt mixture; the carbon cover is maintained by additions of the graphite additive.

Control of Case Depth. Figure 4 shows typical effective case depths (to 50 HRC) obtainable in AISI 1117 carbon steel. Because

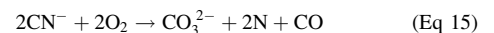
variables such as surface condition and alloy content can affect the quality and depth of a carburized surface, test coupons should be prepared and examined in order to determine optimum operating parameters.

Maximum carbon penetration can be achieved if parts are cleaned and descaled prior to the noncyanide carburizing Pure Case process. Most soils and oils can be removed with alkaline cleaner. Scale and heavy oxides may require mechanical cleaning (that is, sandblasting) or acid pickling prior to carburizing in the noncyanide mixture. It is vital that parts be completely dry before immersing the components in the molten bath.

Low-Toxicity and Regenerable Salt Bath Processes (Ref 2, 3). Extensive development work has been carried out in recent years to make salt bath processes ecologically attractive. The low-toxicity nitrocarburizing process Tufftride TF1, which incorporates a nontoxic regenerator to produce the required composition within the working bath, was successfully developed in the mid-1970s (Ref 4, 5). Therefore, it was apparent that the objective of research on carburizing and carbonitriding should be directed at developing a cyanide-free regenerator to yield the required level of CN⁻ in the process bath. By using a base salt and a regenerator that are both cyanide-free, such a technique would avoid handling, storage, and transportation problems; eliminate the need to bail out the bath; and ease disposal requirements.

Early research to establish an ecologically acceptable process revealed that in order to maintain the high quality hitherto associated with salt bath carburizing, it was necessary to retain CN⁻ as the active carburizing constituent. Existing alternatives for the development of a new and ecologically safe carburizing process rapidly showed that the quality of the salt bath could only be maintained by using cyanide in the carburizing bath.

Experimental work with alternative active constituents, such as silicon carbide and suspended graphite, showed these approaches to be impracticable. Melts containing silicon carbide became viscous, generating large amounts of sludge, while graphite suspensions were difficult to control and distribute evenly throughout the molten bath. None of the options to CN⁻ allowed the desired reproducibility with respect to close control of carburized case depth and carbon content. The fundamental carburizing reactions taking place in a salt bath at a temperature on the order of 930 °C (1705 °F) involve the decomposition of cyanide by oxygen:



followed by the subsequent diffusion of carbon into the surface of the component:



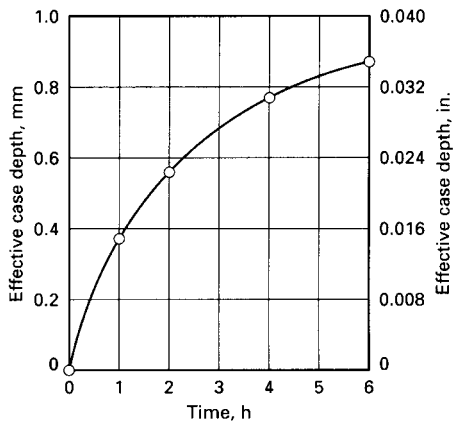


Fig. 4 Plot of carbon penetration versus holding time at 955 °C (1750 °F) for 1117 resulfurized carbon steel heat treated with Pure Case, a noncyanide carburizing process

A small amount of nitrogen also diffuses into the surface, depending on the temperature and composition of the bath. Experience has shown that salt baths completely free from cyanide do not yield reproducible results on a production scale. This not only applies to controlling the surface carbon content but also to the uniformity of carbon diffusion over the surface of the component.

Therefore, a cyanide-free regenerator had to be developed that would produce the required amount of cyanide in the bath. This aim was achieved by the use of an organic polymeric material that converts part of the carbonate present in the molten bath to CN^- . This regenerator is known as CeControl, and the process is designated as Durofer (Ref 6, 7). The Durofer process is compared to conventional salt bath carburizing in Fig. 5.

Process Control. The chemical reaction between the regenerator and the carburizing melt does not produce an increase in the molten salt volume, and, consequently, it is no longer necessary to bail out inactive salt. Therefore, the Durofer process does not produce toxic waste salt. The regenerator is manufactured in pellet form and is added to the molten bath by use of an automatic vibratory feeder. The equipment doses the molten salt with a regulated number of pellets at preset intervals, both when work is in the bath and during idling periods. Any deviation from the control range can be detected by regular analysis of the CN^- content and adjustments carried out on the autoregeneration system to compensate for any irregularity. As shown in Fig. 6, the advantage of automatic regeneration is that a very consistent CN^- level can be maintained in the bath, resulting in uniform and reproducible carburizing.

Experience has shown that the optimum surface carbon value is 0.8% for alloy steels, and 1.1% is generally accepted as the optimum surface carbon value for unalloyed steels. A choice

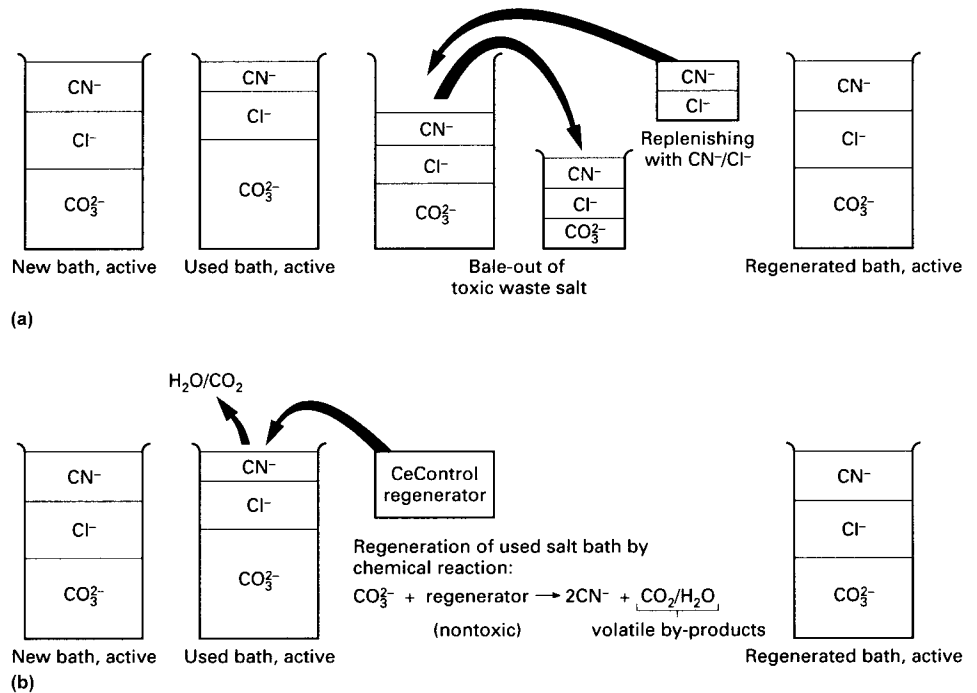


Fig. 5 Sequence of operations for two salt bath carburizing processes. (a) Conventional, requiring daily replenishment of bath with salts having high CN^- concentrations. (b) Durofer, in which CN^- level is maintained with addition of organic polymer material (CeControl regenerator) that converts carbonate in molten salt bath to CN^-

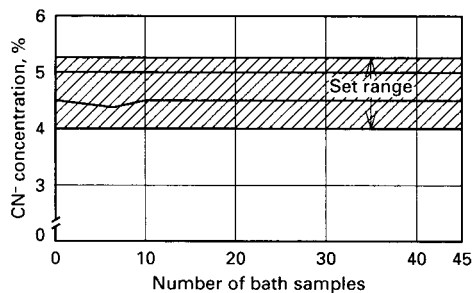


Fig. 6 The consistency of the CN^- level maintained in the Durofer process. Test data compiled over 10 working days (3 shifts/day) in a carburizing bath at 930 °C (1705 °F) using CeControl 80 regenerator

of base salt is available for use with the new regenerator to give these two carburizing conditions, designated CeControl 80B and CeControl 110B, respectively. Figure 7 shows carbon profiles obtained for samples of SAE 1015 steel after carburizing for 60 min at 930 °C (1705 °F) by the Durofer process using both of these base salts.

Process Bath Preparation. The Durofer process bath is initially prepared by melting out the base salt, which may be either CeControl 80B or CeControl 110B, depending on the application requirements. The carburizing activity is promoted by adding CeControl regenerator via the automatic feeder, increasing the CN^- content up to approximately 4.5%. Control level is reached in approximately 5 h,

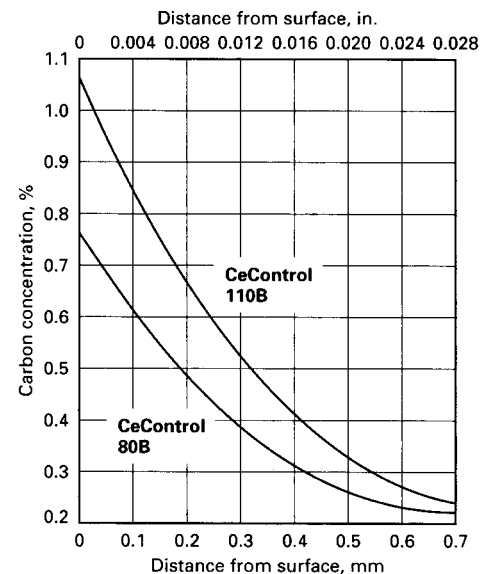


Fig. 7 Plots of carbon concentration versus carbon penetration for 1015 steels that were carburized at 930 °C (1705 °F) for 1 h with two different Durofer process base salt regenerators

when the addition rate is adjusted to that necessary to maintain control. The amount of regenerator required to maintain control is approximately 0.08 to 100 kg (0.18 to 220 lb) bath capacity per hour, for a working bath operating with a graphite economizer at

950 °C (1740 °F). Reduction of the molten salt level due to salt dragout by the workload is restored by additions of the appropriate cyanide-free base salt.

Quenching. As in traditional salt bath carburizing, components carburized in the Durofer process can be quenched into water or oil. However, the composition of the Durofer bath also permits direct quenching into molten nitrate or nitrite salt baths to minimize distortion (Ref 8). In addition to this technical advantage, the chemical nature of the salt quench decomposes the CN⁻, carried over on the components from the Durofer bath, to harmless carbonate. Thus, the need for detoxification of solid deposits in the quench medium and wash-water effluent is eliminated.

Carbon Gradients

Figure 1 shows carbon gradients produced by liquid carburizing 1020 steel bars at 845, 870, and 955 °C (1550, 1600, and 1750 °F) for various lengths of time at carburizing temperature. Carbon-gradient data for two wrought alloy steels (3312 and 8620) and one cast alloy steel (4615 mod) are also shown. After carburizing, the 8620 steel parts were austenitized at 840 °C (1540 °F) and quenched in oil at 55 °C (130 °F). The 4615 steel parts were austenitized at 790 °C (1450 °F), quenched in salt at 190 °C (375 °F) for 3 min, and cooled in air.

Carbon penetration (case depth) in liquid carburizing is determined primarily by the carburizing temperature and the duration of the carburizing cycle. A simple formula for estimating total case depths (measured to base carbon level) obtainable in liquid carburizing is:

$$d = k\sqrt{t} \quad (\text{Eq 17})$$

where d is case depth, k is a constant that represents the penetration in the first hour at temperature, and t is the time at temperature in hours. Typical values of k at three different temperatures are 0.30 mm at 815 °C (0.012 in. at 1500 °F), 0.46 mm at 870 °C (0.018 in. at 1600 °F), and 0.64 mm at 925 °C (0.025 in. at 1700 °F).

Hardness Gradients

A hardness gradient or variation in hardness at different depths below the surface is established in parts that are quenched following liquid carburization. The data in Fig. 2 show typical hardness gradients obtainable with carbon and low-alloy steels and illustrate the influence of carburizing temperature, duration of carburizing, quenching temperature, and quenching medium. Data on 1020, 4620, and 8620 steels are plotted for cycles of 2, 4, 8, 15, 20, and 40 h. These specimens were air cooled from carburizing temperatures of 870, 900, and 925 °C (1600, 1650, and 1700 °F),

reheated in neutral salt at 845 °C (1550 °F), and quenched in molten salt at 180 °C (360 °F). Although the depth of case at maximum hardness is progressively extended in the alloy steels with increases in time and temperature, increases in carburizing temperature have the effect of foreshortening the curves plotted for the 1020 steel. Differences between the responses of 1020 and 8615 steels are shown to be less pronounced after carburizing at 925 °C (1700 °F) for 15 h and quenching directly from the carburizing temperature. A final series of curves indicates the results obtained with 1117 and 4815 steels after carburizing at 900 °C (1650 °F) for periods ranging from ½ to 4 h. The 4815 steel was quenched in oil, and the 1117 steel was quenched in a 10% brine solution.

The indentation hardness data presented in Fig. 3 for five different steels indicate the effects of normal variations in practice on the hardness gradient. The shaded bands represent the scatter in results obtained from multiple tests of each steel. Although similar surface hardnesses are obtained with all five steels, depth of hardness increases with the alloy content of the steel. A comparison among the hardnesses of these five steels at a depth of 1 mm (0.040 in.) illustrates this variation. Although a minimum case hardness of 60 HRC cannot be maintained to a depth of 1 mm (0.040 in.) with 1020 (0.30 to 0.60% Mn) steel, it can sometimes be achieved with 1113 (0.70 to 1.00% Mn) steel and can almost always be achieved with 1117 (1.00 to 1.30% Mn), 4615, and 8620 steels.

Process Control

Cyaniding Time and Temperature. Bath operating temperatures for cyanide hardening vary between 760 and 870 °C (1400 and 1600 °F). Temperatures near the lower end of this range are favored for minimizing distortion during quenching from the bath temperature. Higher temperatures are selected to exceed the Ac₃ point of the steel, to achieve faster

penetration, and, depending on alloy content, to produce a fully hardened core after quenching.

When low-carbon and alloy steels are to be cyanided to produce a surface capable of resisting high contact loads, the surface usually must be backed up with a fine-grained, tough core. This requires an operating bath temperature of approximately 870 °C (1600 °F).

The high file hardness of salt-bath-cyanided steel parts is a combined effect of carbon and nitrogen absorption in the carbonitrided case (Table 5). Usually, immersion times range from 30 min to 1 h and produce case depths and surface carbon and nitrogen concentrations corresponding to those in Table 5. Lower temperatures will provide results proportionately lower than those given in Table 5.

Externally heated salt baths can be held within closer temperature limits (± 8 °C, or ± 14 °F) when a proportional control system employing electronic instrumentation is used. Control by means of valves (on-off or high-low control) requires mechanical instrumentation and is less accurate, although for a majority of applications it is entirely adequate.

Internally heated salt baths (immersed or submerged electrodes) may be regulated to ± 5 °C (± 9 °F) with either mechanical or electronic on-off controllers. In either type, the temperature-control instrument operates a relay that actuates a large circuit breaker that in turn connects or disconnects the 440 V power to the step-down transformer. Welded thermocouples may be used in installations that employ electrode heating. For safety, two thermocouples are recommended: one for temperature control and one for excess temperature cutoff.

Control of Bath Composition. Control of sodium cyanide content is the most important factor in maintaining the effectiveness of a liquid carburizing bath.

Analysis of a noncyanide liquid carburizing bath is achieved by a rapid performance test in which a 1008 steel wire 1.6 mm ($\frac{1}{16}$ in.) in diameter is immersed for 3 min in the bath, then is water quenched and mechanically bent through 90°. The bath is well activated if the wire breaks before reaching the full 90° bend.

Table 5 Effect of cyaniding temperature and time on case depth and surface carbon and nitrogen contents

Material thickness, 2.03 mm (0.080 in.); cyanide content of bath, 20 to 30%

Steel	Case depth after cyaniding for:				Analysis after 100 min at Temperature(a)	
	15 min		100 min		Carbon, %	Nitrogen, %
	mm	in.	mm	in.		
Cyanided at 760 °C (1400 °F)						
1008	0.038	0.0015	0.152	0.006	0.68	0.51
1010	0.038	0.0015	0.152	0.006	0.70	0.50
1022	0.051	0.0020	0.203	0.008	0.72	0.51
Cyanided at 845 °C (1550 °F)						
1008	0.076	0.0030	0.203	0.008	0.75	0.26
1010	0.076	0.0030	0.203	0.008	0.77	0.28
1022	0.089	0.0035	0.254	0.010	0.79	0.27

(a) Carbon and nitrogen contents were determined from analysis of the outermost 0.076 mm (0.003 in.) of cyanided cases.

A more reliable test of activity can be made by running a 1012 silicon-killed test bar for 1 h, water quenching, and measuring Rockwell C hardness. Readings above 58 HRC indicate a well-activated bath.

Graphite Cover. A graphite cover must be maintained on the surface of a cyanide bath for reduced radiation loss and reduced cyanide loss at 870 to 955 °C (1600 to 1750 °F) and during idling. Either natural flake or artificial graphite powders may be used. The former provides a more fluid cover that has less tendency to cling to the work. However, because natural graphite has a higher ash content, it introduces more impurities into the bath, which can be a problem, particularly at low operating temperatures. Furthermore, to avoid corrosion of parts, natural graphite that contains sulfur should not be used.

A noncyanide liquid carburizing bath must also have a graphite cover. A higher rate of graphite consumption, compared with a cyanide bath, is characteristic. Frequent replenishment (commonly every hour) is necessary for maintenance of proper bath activity.

Daily maintenance routines for liquid carburizing furnaces, whether fuel-fired or electrode-heated, differ in only a few details. The following items, with exceptions as noted, comprise a typical daily maintenance schedule for all types of salt bath equipment:

- Check temperature-control system, using an auxiliary pyrometer and thermocouple. An indicating potentiometer with a long extension wire can be mounted near the furnaces and will provide accurate temperature checks faster than will a laboratory-type instrument.
- Check color of exhaust smoke from the combustion chamber of fuel-fired furnaces. A bluish-white or white smoke indicates salt leakage.
- Remove sludge from bottom of pot while furnace is still at idling temperature, which normally is 705 to 730 °C (1300 to 1350 °F). The electrodes of internally heated furnaces should be scraped clean, and electric power should be shut off during the sludging and cleaning operation.
- Add fresh salt to compensate for dragout losses. If required, make room for addition of fresh salt by bailing.
- To help maintain bath composition and reduce surface heat losses, add graphite cover material to provide a thin but continuous cover.
- Check bath activity by testing for cyanide content or by quenching and examining the fracture case depth.
- If possible, rotate the pot of a fuel-fired furnace at least once a week to minimize the effects of flame impingement and thus extend pot life.
- If a salt pot is leaking and the salt is still active, remove the salt and place it in sturdy steel containers. This salt may be broken up

and reused in starting another pot (however, it is not recommended that such salt be used thereafter for replenishment).

- Prior to replacement of a pot in a resistance-heated or fuel-fired furnace, the combustion chamber should be rebuilt if contaminated with salt, to avoid rapid pot failure.
- Consult operating and maintenance instructions provided by the furnace manufacturer and salt supplier.

Shutdown and Restarting. For shutdowns of two days or longer, externally heated furnaces need not be idled; the heat may be shut off completely. During cooling and reheating, however, the pot should be covered to guard against violent expulsion of salt. The cover recommended by the manufacturer should be used.

It is generally advisable to idle electrode furnaces at 705 to 730 °C (1300 to 1350 °F), even over shutdown periods of one to two weeks. This simplifies restarting and eliminates possible damage to power transformers from condensation of moisture on the windings. For noncyanide carburizing furnaces with steel liners, idling above 845 °C (1550 °F) is recommended. During the idling period, the bath should be protected with a heavy carbon cover. The bath does not visibly fume at idling temperatures; therefore, ventilating air should be reduced. Excessive ventilating air should be avoided, because it will accelerate burnoff of the carbon cover. During the idling period, the transformer tap switch should be set at low voltage or idling tap. This will guard against possible overheating in the event that control-circuit difficulties arise while the equipment is unattended. An extra thermocouple and monitoring instrument equipped with warning alarms is recommended for use in such applications.

Control of Case Depth

The degree of uniformity of case depth obtained in normal production operations is indicated in Fig. 8 by data on 1020, 1117, and 8620 steels. Figures 8(a) to (c) are based on information obtained with process-control specimens and show depth of case as a function of distance below the surface in terms of a hardness of 50 HRC or higher. These data indicate that variations in case depth can be held within narrow limits when controlled carburizing procedures are employed. At a carburizing temperature of 900 °C (1650 °F), the 1117 steel produced a deeper case to 50 HRC than did the 1020 and 8620 steels, which were carburized at 855 °C (1575 °F). Nevertheless, the total spread in case depth for any one of these steels did not exceed 0.13 mm (0.005 in.). Data presented in Fig. 8(d) indicate the range of hardnesses obtained at depths of 0.25 and 1.25 mm (0.010 and 0.050 in.) below the surface of liquid-carburized 8620 steel. These data, based

on 24 tests, indicate a slightly larger spread in hardness at 0.25 mm (0.010 in.) than at 1.25 mm (0.050 in.) below the surface.

Whereas the information in Fig. 8 deals with carburizing cycles of 2 and 2.5 h at temperatures ranging from 855 to 915 °C (1575 to 1675 °F), the data presented in Fig. 3 pertain to a much longer carburizing time (9½ h) at 925 °C (1700 °F). The spread in case depth at 50 HRC is considerably wider than for the light-case work on which Fig. 8 is based.

Additional data on case depth as a function of time and temperature are given for ten steels in Fig. 9. These data also reflect various criteria that have been applied to evaluate case depth, for example, data relating case depth to minimum hardness, carbon content, and pearlite content.

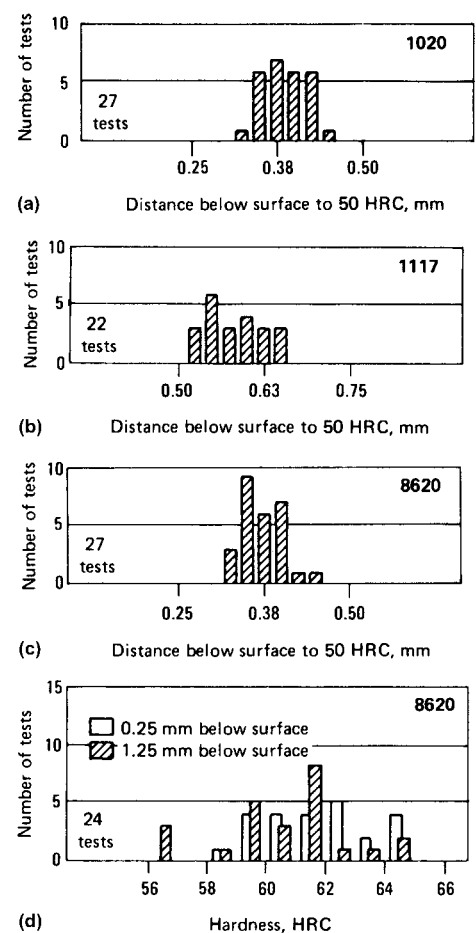


Fig. 8 Comparative case-depth and case-hardness data obtained for liquid carburizing process-control specimens made of three steels. (a) Data are for 11 mm diam by 6.4 mm (0.4375 in. diam by 0.25 in.) specimens carburized 2 h at 855 °C (1575 °F), brine quenched and tempered at 150 °C (300 °F). (b) Data are for 15.9 mm (0.625 in.) diam specimens carburized 2 h at 900 °C (1650 °F) and brine quenched. (c) Data are for 12.7 mm diam by 6.4 mm (0.50 in. diam by 0.25 in.) specimens carburized 2 h at 855 °C (1575 °F), oil quenched, and refrigerated to -85 °C (-120 °F). (d) Data are for 19 mm diam by 51 mm (¾ in. diam by 2 in.) specimens carburized 2.5 h at 915 °C (1675 °F) and water quenched.

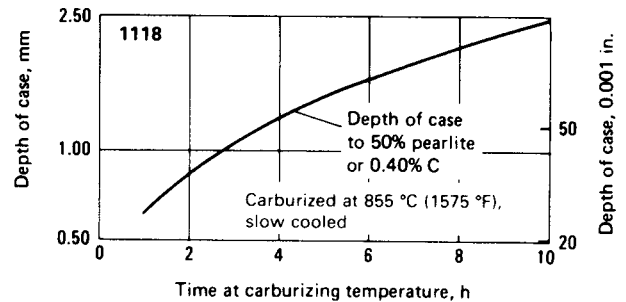
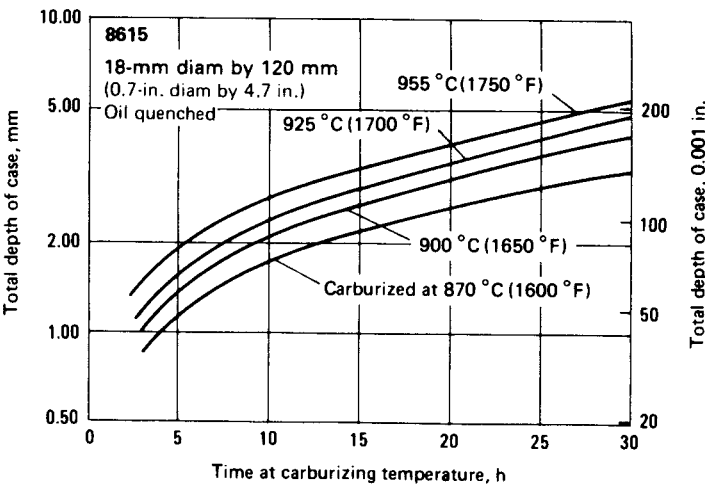
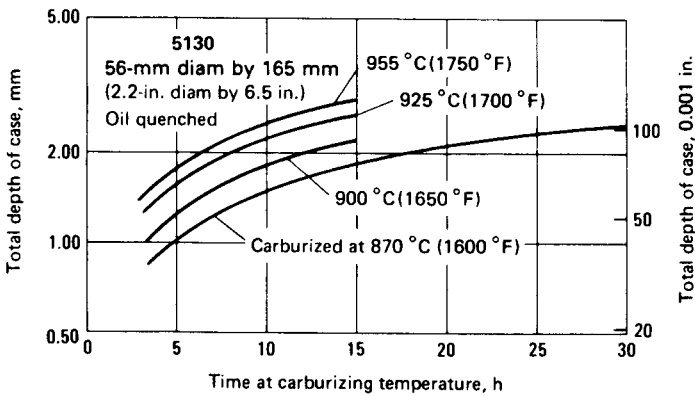
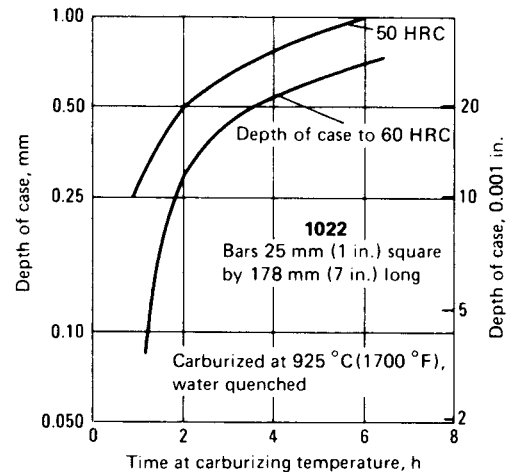
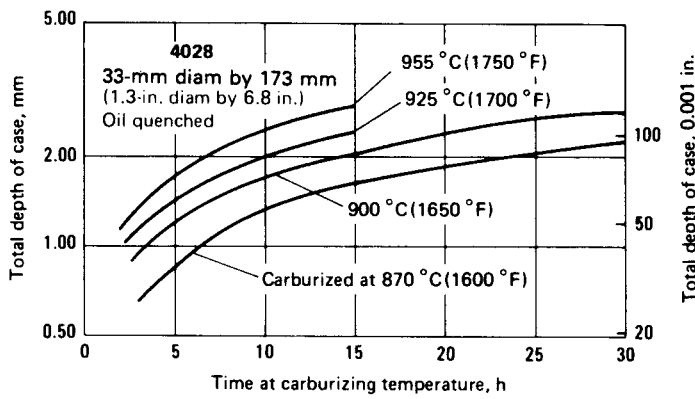
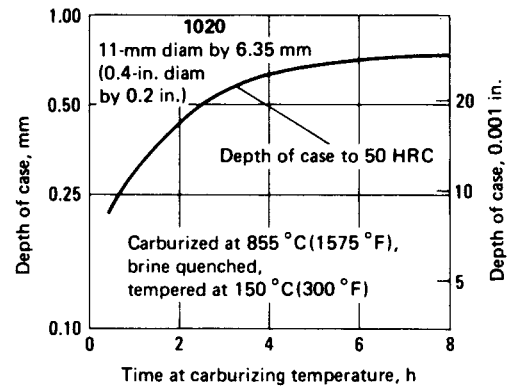
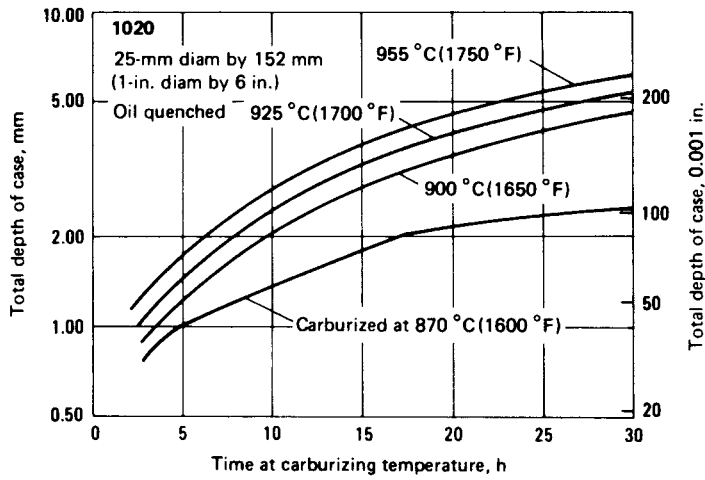


Fig. 9 Effect of time and temperature on case depth of liquid-carburized steels

Dimensional Changes

All parts undergo dimensional changes as a result of carburizing and hardening. From a production standpoint, it is important to know the nature and amount of dimensional change, or distortion, that can be anticipated, and the corrective action that may be taken to hold dimensional changes to a minimum. The following examples relate dimensional change to several shapes that vary in complexity.

Example 1: Carburized, Quenched, and Tempered 8615H Steel Gear with 60 to 62 HRC Surface Hardness. The small gear shown in Fig. 10(a) closed in along the bore from a minimum dimension of 17.22 mm (0.6780 in.) prior to heat treatment to a minimum of 17.14 mm (0.6750 in.) after heat treatment. In contrast, only slight contraction of the outer bearing surface occurred. The gears, made of 8615H steel, were carburized at 915 °C (1675 °F) to a depth of 0.51 to 0.64 mm (0.020 to 0.025 in.), reheated to 840 °C (1540 °F), quenched in oil at 55 °C (130 °F), and then tempered at 190 °C (375 °F) to a surface hardness of 60 to 62 HRC.

Example 2: Carburized, Quenched, and Stress-Relieved 8620 Steel Gear with 61 to 63 HRC Surface Hardness. The bearing race shown in Fig. 10(b) was subjected to more elaborate processing to minimize dimensional variations before and after carburizing. This 8620 steel forging was normalized and stress relieved prior to being carburized. After being rough

ground, it was liquid carburized for 14 h at 925 °C (1700 °F) to produce a minimum case depth of 2.3 mm (0.090 in.). It was air cooled, reheated to 845 °C (1550 °F), and salt bath quenched at 180 °C (360 °F). After being cooled to room temperature, it was tempered for 2 h at 175 °C (350 °F). Final case hardness was 61 to 63 HRC; core hardness was 40 to 43 HRC.

To minimize distortion, which was excessive when these bearing races were wired, a fixture was used throughout the heat treating cycle. As indicated by the dimensional data, the combination of fixturing and elaborate processing produced favorable results in terms of out-of-roundness and flatness. Dimensional discrepancy was held to 0.10 mm (0.004 in.) maximum, and in several instances, distortion was held to 0.025 mm (0.001 in.).

Example 3: Normalized, Tempered, Carburized, Quenched, and Retempered 4615 Modified Steel Crankshaft. The crankshaft shown in Fig. 10(c), a shell-mold casting made of boron-modified 4615 steel, was initially normalized for 1 h at 955 °C (1750 °F) and then tempered for 1 h at 620 °C (1150 °F). After being machined, the part was liquid carburized at 925 °C (1700 °F) (case depth, 1.14 to 1.40 mm, or 0.045 to 0.055 in.), air cooled, reheated to 790 °C (1450 °F), quenched for 5 min in salt at 190 °C (375 °F), air cooled, and tempered for 1 h at 165 °C (325 °F). The dimensional data, which apply to a length measurement at one end of the shaft only, indicate a

high degree of dimensional stability with a slight tendency in the direction of shrinkage.

Quenching Media

Most conventional quenching media, including water, brine, caustic solution, oil, and molten salts, are suitable for quenching parts that have been liquid carburized. However, the suitability of each medium must be related to specific parts and depends primarily on the hardenability of the steel, surface and core hardness requirements, and the amount of allowable distortion.

Water and brine are the quenchants most commonly used for carbon steels. A water quench is usually maintained at 20 to 30 °C (70 to 90 °F) and agitated. Water helps to dissolve the film of carburizing salt and thus creates a localized brine that suppresses the vapor phase. With continuous use, salt concentration (chlorides, carbonates, and cyanides) increases, and fresh water must be added periodically to control the concentration of contaminants and maintain a desired temperature. Sodium chloride brine (5 to 10%) and caustic (3 to 5%) solutions are used to obtain more drastic quenching. The noncyanide liquid carburizing salt provides a brine-type quench when maintained around 10% concentration by water addition. The effectiveness of brine and caustic can be severely curtailed by an excessive accumulation of contaminants. When a caustic solution is

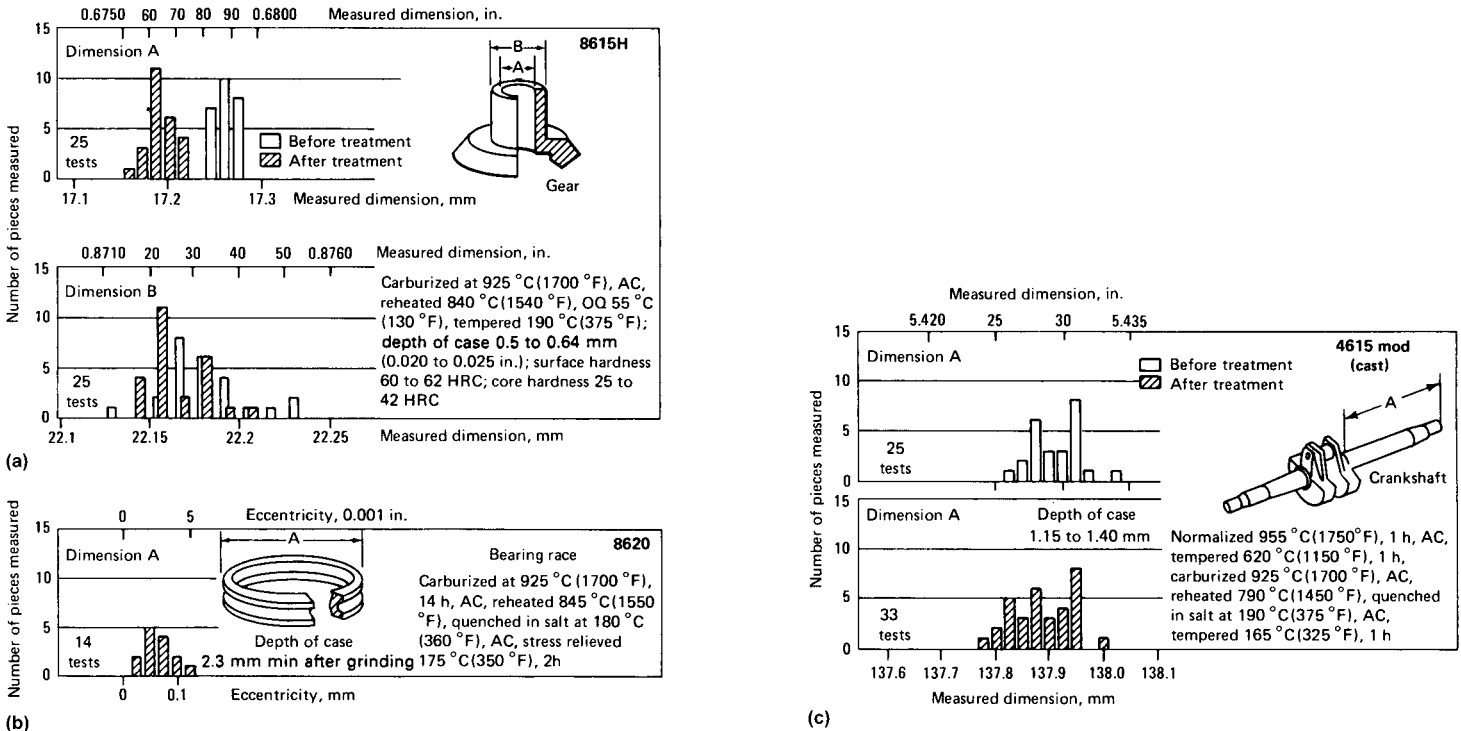


Fig. 10 Dimensional data relating selected low-alloy steel production parts before and after liquid carburizing and hardening. AC, air cooled; OQ, oil quenched

used for quenching, care must be taken to ensure that racks, baskets, and fixtures are washed free from caustic and dried before being returned to the carburizing bath. Small amounts of caustic carried back to the bath will lower its cyanide content significantly.

A water-soluble polymer is sometimes used to modify the quenching rate of a water quench. However, such additives should be avoided in a quenchant used with a liquid carburizing line, unless frequent replacement or continuous salt removal by ultrafiltration can be employed. The polymers may be precipitated by salt carried into the quench, or salt buildup in the quench may render their effect variable. Either condition is undesirable.

Oil quenching is less drastic than water quenching and produces less distortion. It is often desirable to fortify the mineral oil with nonsaponifiable additives that increase its quenching effectiveness and lengthen its useful life. To minimize distortion, special oils are available that can be used at temperatures as high as 175 °C (350 °F). Normally, liquid-carburized parts are quenched directly into agitated oil maintained within the range from 25 to 70 °C (80 to 160 °F).

Quenching oil should be kept free of moisture and should be agitated by propellers or impeller-type pumps. Compressed air should not be used for agitation. Because some salt will inevitably precipitate in the oil bath, periodic desludging is necessary. Screens should be placed in front of the lines leading to pumps to prevent entry of sludge.

Salt bath quenching in a nitrate-nitrite bath further minimizes distortion. Salt quench baths are compatible with cyanide as well as noncyanide liquid carburizing baths. *However, parts should never be transferred directly from a carburizing bath containing more than 5% cyanide to a nitrate-nitrite quench bath, because this will result in a violent reaction and may cause an explosion.* To avoid such reactions, immersion in a neutral salt bath (45 to 55% NaCl, 45 to 55% KCl) held at the desired temperature must precede quenching in a nitrate-nitrite bath. The neutral bath should be tested periodically for sodium cyanide content; it is general practice to limit cyanide content to a level of less than 5%. This level is never reached, as a rule, because of oxidation of the cyanide by oxygen in the air. The neutral stabilizing bath can be used alternatively for through hardening of carbon and alloy steels, provided that complete cyanide oxidation has not occurred.

Many liquid carburizing facilities case harden components at 925 to 955 °C (1700 to 1750 °F), and workpieces are then transferred directly to a neutral chloride salt at 845 °C (1550 °F) for stabilization and finally quenched directly into a marquenching oil at 175 to 260 °C (350 to 500 °F), depending on alloy and hardness requirements. Distortion of the workpieces is minimized when parts are air quenched after carburizing and then reheated prior to quenching.

All traces of nitrate should be removed from quenching fixtures before they are reimmersed in a carburizing bath. This can be accomplished by rinsing in hot water.

The buildup of high-temperature chlorides in a nitrate-nitrite bath impairs its quenching severity. It is desirable, therefore, to remove the chlorides as fast as they are being delivered. Various means of chloride removal are available, and the selection depends on furnace design. Where chloride is allowed to settle to the bottom of the quench area or an area provided for gravity separation, the chlorides can be collected in sludge pans; periodically, either the pans are removed or the bottoms of the pans are manually desludged. Some furnace designs employ continuous filtration of chlorides as the suspended crystals pass through filter baskets; the operator removes the baskets periodically to dump the collected chlorides and then returns the baskets to the furnace.

Maintenance of Quenching Baths. Although a limited amount of dissolved salt increases the efficiency of a water quench bath, amounts in excess of 10% retard the quenching rate. Controlled addition of fresh water to the bath, together with a continuous overflow, serves to keep salt concentration at an acceptably low level. It may be required that the overflow be chemically treated in a special reservoir prior to disposal in order to eliminate cyanide pollution (see the section "Disposal of Cyanide Wastes" in this article). For this reason, changing the water quench bath at scheduled intervals may be more convenient in small operations. For water tanks that are vigorously agitated, it is recommended that a false bottom—in the form of a perforated plate—be used to permit settling of heavier solids, which can be removed during periods of downtime.

Carryover of liquid carburizing salts into brine quench tanks actually helps maintain brine concentration. However, salt concentration should not exceed 10%. The same control of salt content applies to caustic tanks; concentration of caustic must be maintained by additions of sodium hydroxide to control the quench rate of the solution.

Some of the precautions that must be observed in the use of oil baths have already been discussed. It should be recognized that liquid carburizing salts do not dissolve in, or combine with, mineral quenching oils. Salt sludge must be removed periodically, either by mechanical means or by filtering through screens.

Proper maintenance of salt quench baths also requires sludging of contaminants. Use of separating chambers to collect these contaminants has already been discussed. Another technique involves continuous filtering out of higher-melting-point salts by pumping the contaminated quench salts through a filter maintained at a lower temperature. The contaminants are deposited on a wire-mesh basket, and the usable salts are returned to the quench tank.

Quenching Cyanided Parts. Cyanided steel parts are quenched in fast-quenching oils,

water, or aqueous salt solutions. Selection of the quenchant depends on the composition of the steel, the required as-quenched hardness, and the shape of the workpiece.

Water or aqueous salt solutions should be as free as possible of dissolved gases, which may cause soft spots. For this reason, pumps or impellers should be used to agitate the quenching water or brine. Compressed air should not be used as the primary means of agitation; mechanical agitation is preferred.

For maximum hardness, the quenchant should be as cold as is feasible and should be well agitated. Typical quenchant temperatures range from room temperature to approximately 25 °C (75 °F) for plain water and up to approximately 50 °C (120 °F) for 5 to 10% aqueous salt solutions, including solutions of sodium chloride, sodium hydroxide, or proprietary salt mixtures that provide corrosion protection. Use of higher temperatures with water-based quenchants causes insufficient hardness or soft spots.

Quenching oils are commonly used at temperatures from 50 to 85 °C (120 to 185 °F). Only petroleum-based quenching oils should be used for quenching cyanided parts.

Salt Removal (Washing)

The ease or difficulty with which salt can be removed from liquid-carburized parts depends primarily on how simply or intricately shaped the parts are and whether they were quenched in water or in oil. To some extent, removal of salt may be complicated by the presence of insoluble residues. Water-quenched parts of simple design and with no blind holes or deep recesses usually are easy to clean. They may be rinsed thoroughly in water at approximately 80 °C (180 °F) and then coated with a rust-preventive fluid or soluble oil. Parts that are rinsed free of cyanide by immersion in a chloride salt and then isothermally quenched in a nitrate-nitrite salt are easily cleaned by agitated hot-water washing and rinsing. It is also possible to reclaim the nitrate-nitrite salt from the wash water.

Oil-quenched parts are more difficult to clean because the oil must be removed before the salts can be dissolved. Some salts may be insoluble. Use of power washers with hot water or emulsion cleaners is effective. An economical cleaning procedure begins with soaking of parts in hot water to float off the oil and remove the soluble salts. The parts may then be transferred to a hot agitated dilute alkaline cleaner having high sequestering properties. (Silicated cleaners and those containing carbonates or phosphates are not recommended, because of the formation of insoluble barium compounds in the presence of barium-containing salts.) If a white, powdery overlay of barium carbonate remains on the parts, it may be removed—following removal of all cyanide—by immersion in a dilute solution of acetic or inhibited hydrochloric acid.

Complex parts with blind holes, recesses, and threads are difficult to clean, particularly if they have been oil quenched. Liquid carburizing of parts that contain blind holes for which the depth exceeds twice the diameter is not recommended unless such holes can be plugged. Agitated hot water or a steam jet is probably the best solvent for salt held in recesses, crevices, and blind holes. Normally, it will remove all soluble salts and will soften insoluble residues. When part shape and

tolerances permit, tumbling for 10 to 30 min in a mild alkali and a small quantity of sand is most effective in removing insoluble surface residues.

Washing of Cyanided Parts. Cyanide-hardened parts are easy to wash, even after oil quenching, because cyanide and sodium carbonate are good detergents and because all the components of the salt bath are water soluble. The work may be soaked in a tank of agitated boiling water, rinsed in clean hot water, and

then rustproofed (if required). Power spray washers, using hot water in a two-stage system, also give satisfactory results.

Typical Applications

The applicability of liquid carburizing is evidenced by the variety of parts listed in Tables 6 and 7, all of which were heat treated on a

Table 6 Typical applications of liquid carburizing in cyanide baths

Part	Weight		Steel	Depth of case		Temperature		Time, h	Quench	Subsequent treatment	Hardness, HRC
	kg	lb		mm	in.	°C	°F				
Carbon steel											
Adapter	0.9	2	CR	1.0	0.040	940	1720	4	AC	(a)	62-63
Arbor, tapered	0.5	1.1	1020	1.5	0.060	940	1720	6.5	AC	(a)	62-63
Bushing	0.7	1.5	CR	1.5	0.060	940	1720	6.5	AC	(a)	62-63
Die block	3.5	7.7	1020	1.3	0.050	940	1720	5	AC	(a)	62-63
	1.1	2.5	CR	1.3	0.050	940	1720	5	AC	(a)	59-61
Disk	1.4	3	1020	1.3	0.050	940	1720	5	(b)	(b)	56-57
Flange	0.03	0.06	1020	0.4-0.5	0.015-0.020	845	1550	4	Oil	(c)	55 min(d)
Gage rings, knurled	0.09	0.2	1020	1.5	0.060	940	1720	6.5	AC	(a)	62-63
Hold-down block	0.9	2	CR	1.0	0.040	940	1720	4	AC	(a)	62-63
Insert, tapered	4.75	10.5	1020	1.3	0.050	940	1720	5	AC	(a)	62-63
Lever	0.05	0.12	1020	0.13-0.25	0.005-0.010	845	1550	1	Oil	(c)	(e)
Link	0.007	0.015	1018	0.13-0.25	0.005-0.010	845	1550	1	AC
Plate	0.007	0.015	1010	0.25-0.4	0.010-0.015	845	1550	2	Oil	(c)	(e)
Plug	0.7	1.6	CR	1.5	0.060	940	1720	6.5	AC	(a)	62-63
Plug gage	0.45	1	1020	1.5	0.060	940	1720	6.5	AC	(a)	62-63
Radius-cutout roll	7.7	17	CR	1.5	0.060	940	1720	6.5	AC	(a)	62-63
Torsion-bar cap	0.05	0.1	1022	0.02-0.05	0.001-0.002	900	1650	0.12	Caustic	(f)	45-47
Resulfurized steel											
Bushing	0.04	0.09	1118	0.25-0.4	0.010-0.015	845	1550	2	Oil	(c)	(e)
Dash sleeve	3.6	8	1117	1.1	0.045	915	1675	7	AC	(g)	58-63
Disk	0.0009	0.002	1118	0.13-0.25	0.005-0.010	845	1550	1	Brine	(c)	(e)
Drive shaft	3.6	8	1117	1.1	0.045	915	1675	7	AC	(h)	58-63
Guide bushing	0.2	0.5	1117	0.75	0.030	915	1675	5	(i)	...	58-63
Nut	0.04	0.09	1113	0.13-0.25	0.005-0.010	845	1550	1	Oil	(c)	(e)
Pin	0.003	0.007	1119	0.13-0.25	0.005-0.010	845	1550	1	Oil	(c)	(e)
Plug	0.007	0.015	1113	0.075-0.13	0.003-0.005	845	1550	0.5	Oil	(c)	(e)
Rack	0.34	0.75	1113	0.13-0.25	0.005-0.010	845	1550	1	Oil	(c)	(e)
Roller	0.01	0.03	1118	0.25-0.4	0.010-0.015	845	1550	2	Oil	(c)	(e)
Screw	0.003	0.007	1113	0.075-0.13	0.003-0.005	845	1550	0.5	Oil	(c)	(e)
Shaft	0.08	0.18	1118	0.25-0.4	0.010-0.015	845	1550	2	Oil	(c)	(e)
Spring seat	0.009	0.02	1118	0.25-0.4	0.010-0.015	845	1550	2	Oil	(c)	(e)
Stop collar	0.9	2	1117	1.1	0.045	925	1700	6.5	AC	(g)	60-63
Stud	0.007	0.015	1118	0.13-0.25	0.005-0.010	845	1550	1	Oil	(c)	(e)
Valve bushing	0.02	0.05	1117	1.3	0.050	915	1675	8	AC	(g)	58-63
Valve retainer	0.45	1	1117	1.1	0.045	915	1675	7	(i)	...	58-63
Washer	0.007	0.015	1118	0.25-0.4	0.010-0.015	845	1550	2	Oil	(c)	(e)
Alloy steel											
Bearing races	0.9-36	2-80	8620	2.3	0.090	925	1700	14	AC	(g)	61-64
Bearing rollers	0.20	0.5	8620	2.3	0.090	925	1700	14	AC	(g)	61-64
Coupling	0.03	0.06	8620	0.25-0.4	0.010-0.015	845	1550	2	Oil	(c)	(e)
Crankshaft	0.9	2	8620	1.0	0.040	915	1675	6.5	AC	(h)	60-63
Gear	0.34	0.75	8620	1.0	0.040	915	1675	6	AC	(g)	60-63
	0.03	0.06	8620	0.075-0.13	0.003-0.005	845	1550	0.5	Oil	(c)	(e)
Idler shaft	0.45	1	8620	0.75	0.030	915	1675	5	(i)	...	58-63
Pintle	4.5-86	10-190	8620	1.5	0.060	925	1700	12	(i)	...	58-63
Piston	0.20	0.5	8620	1.3	0.050	915	1675	8	AC	(g)	60-63
Plunger	0.45-82	1-180	8620	1.3	0.050	915	1675	8	(i)	...	58-63
Ram	2.3-23	5-50	8620	1.1	0.045	915	1675	7	(i)	...	58-63
Retainer	0.0009	0.002	9317	0.1-0.2	0.004-0.008	845	1550	0.33	Oil	(j)	(e)
Spool	0.45-54	1-120	8620	1.3	0.050	925	1700	7	(i)	...	58-63
Thrust cup	0.20	0.5	8620	1.1	0.045	915	1675	7	(i)	...	58-63
Thrust plate	5.4	12	8620	2.3	0.090	925	1700	14	AC	(g)	60-64
Universal socket	1.8	4	8620	1.5	0.060	915	1675	10	AC	(g)	58-63
Valve	0.01	0.03	8620	0.4-0.5	0.015-0.020	845	1550	4	Oil	(j)	60 min(d)
Valve seat	0.20	0.5	8620	1.1	0.045	915	1675	7	AC	(g)	60-63
Wear plate	0.45-3.6	1-8	8620	1.3	0.050	915	1675	7	AC	(g)	60-63

CR, cold rolled; AC, air cooled. (a) Reheated at 790 °C (1450 °F), quenched in caustic, tempered at 150 °C (300 °F). (b) Transferred to neutral salt at 790 °C (1450 °F), quenched in caustic, tempered at 175 °C (350 °F). (c) Tempered at 165 °C (325 °F). (d) Or equivalent. (e) File-hard. (f) Tempered at 205 °C (400 °F). (g) Reheated at 845 °C (1550 °F), quenched in salt at 175 °C (350 °F). (h) Reheated at 775 °C (1425 °F), quenched in salt at 195 °C (380 °F). (i) Quenched directly in salt at 175 °C (350 °F). (j) Tempered at 165 °C (325 °F) and treated at -85 °C (-120 °F)

Table 7 Typical applications of liquid carburizing in noncyanide baths

Part	Weight		Steel	Case depth		Temperature		Time, h	Quench	Subsequent treatment	Hardness, HRC
	kg	lb		mm	in.	°C	°F				
Production tools	0.5–2.0	1.1–4.4	1018	0.375	0.015	925	1700	0.5–1.0	Brine	...	50–60
Bicycle forks	1.4	3.1	1017(a)	0.05–0.08	0.002–0.003	925	1700	0.085	Brine	Temper at 425 °C (795 °F)	60
Shift lever and ball	~1.5	~3.3	1040, 1017(b)	0.25	0.010	925	1700	0.67	Air cool 30 s in brine	...	File hard
Screw machine spindles	0.8	1.8	4620, 8620	0.89	0.035	(c)	(c)	6.0	Molten salt, 205 °C (400 °F)	...	60–63
Clock screws and studs	0.005	0.011	1006, 1113	0.08–0.10	0.003–0.004	955	1750	0.2	Brine	...	62–64
Flat head screws	0.015	0.033	1122	0.15	0.006	925	1700	0.33	Molten salt, 290 °C (550 °F)	...	56

(a) Partial immersion. (b) Carburizer brass braze. (c) Preheat at 840 °C (1545 °F); carburize at 920 °C (1690 °F)

production basis. For ease of reference, the parts in Table 6 have been separated according to type of steel (carbon, resulfurized, or alloy), and the parts in each group have been arranged in alphabetical order. Tables 6 and 7 also provide details, wherever they were available, regarding case depth, carburizing temperature and cycle time, method of quenching, subsequent treatment, and surface hardness.

The parts listed in Table 6 were carburized in cyanide-type baths. Noncyanide carburizing baths can be used with slight adjustments in operating conditions to do much of the carburizing described in Table 7. Noncyanide carburizing is particularly applicable to parts treated at temperatures above 900 °C (1650 °F). Some specific applications for noncyanide liquid carburizing of production parts are listed in Table 7.

In general, liquid carburizing is best suited to small and medium-sized parts. Very large parts, such as rock-bit drill rods 6 m (20 ft) long and rings 2 m (7 ft) in diameter, are too large to be conveniently processed in salt and are commonly carburized by pack methods. Because of the problems associated with salt removal, carburizing in salt baths is not recommended for parts containing small holes, threads, or recessed areas that are difficult to clean.

Stopoffs and Selective Carburizing

Selective carburizing can be accomplished in liquid carburizing baths by stopping off carbon penetration with either copper plate or copper-base paint. Because cyanide-based salts can dissolve copper, salt baths with relatively low cyanide contents are necessary. One successful formulation operates at 8 to 10% NaCN with approximately 45% BaCl₂ energizer. Noncyanide carburizing salts will not dissolve copper.

When copper plate is employed to prevent carbon penetration, the copper layer should be fine-grained, dense, and without pinholes or other porosity. Smooth surfaces require lower plating thicknesses than do rough surfaces. Copper plate thicknesses recommended for protection against liquid carburizing for various times are as follows:

Time, h	Copper plate thickness	
	mm	in.
Low-temperature salts		
<1	0.013	0.0005
1–5	0.020	0.0008
High-temperature salts		
<7	0.025	0.0010
7–15	0.040	0.0015
15–30	0.050	0.0020

Partial Immersion. Another method for selective carburizing in liquid carburizing baths entails partial immersion of the workpiece in the salt bath so that only the immersed areas are carburized. With this method, unless a clean-cut breakoff between carburized and non-carburized areas is required, the use of copper plate or copper-base paint is unnecessary.

Oxidation of the work at the bath surface can be reduced if the parts are initially immersed an inch or two deeper than required, to coat them with salt, and are then withdrawn to the required depth. A piece of plain carbon steel pipe with the bottom closed by welding can be inserted in a corner of the bath to displace salt if a precise adjustment of the bath level is necessary. Typical parts that are well suited to carburizing by the partial-immersion technique are shown in Fig. 11.

Combined Carburizing and Brazing

It is possible to braze and carburize steel parts simultaneously in either a cyanide or a noncyanide liquid carburizing bath, provided that the operating temperature of the bath is high enough to cause the brazing alloy to flow. Initially, the parts are cleaned and degreased and then the components are assembled with brazing alloy enclosed in the joints. One suitable brazing alloy, in the form of wire or thin strip, contains 55% Cu and 45% Zn, melts at 880 °C (1620 °F), and makes a sound joint at 900 to 925 °C (1650 to 1700 °F). No flux is required.

The assembly is immersed in the liquid carburizing bath for a time long enough to produce the desired case depth and at a temperature high enough to cause the brazing alloy to

flow. It is then quenched to harden the steel and complete the braze. Press-fit assemblies with carefully designed lap joints are ideal for this application.

Precautions in the Use of Cyanide Salts

Cyanides cause violently poisonous reactions if allowed to come into contact with scratches or wounds (on the hands, for example); they are fatal if taken internally. Also, fatally poisonous fumes are evolved when cyanides are brought into contact with acids. The white deposits that form on hoods and cooler furnace parts consist mainly of sublimed sodium carbonate, with small amounts of sodium, potassium, and barium salts, but may contain some cyanide as the result of splashing.

When cyanide salts are removed from the storage container, the container should be opened in the room in which the cyanide is to be used. The salts should be removed from the container with a metal scoop or gloved hands, or by being dumped out as required. When not in use, the container should be covered with its original cover or with a metal substitute cover.

The precautions that should be observed in handling cyanide-type carburizing salts are the same as for any other cyanide mixture. Work material must be clean and dry, and the bath must be enclosed and well ventilated. Even the slight amount of moisture that may be deposited on parts and fixtures as a result of atmospheric humidity will cause spatter in contact with molten salt. Accordingly, operators should be equipped with long protective gloves, protective aprons, and safety glasses or face shields. Further information is available from OSHA and EPA publications. When adequate precautions are observed, carburizing salts should not present serious hazards to health or safety.

Remelting a frozen cyanide bath in externally heated furnaces can be potentially hazardous because of the expansion of the salt and gases as the salts are heated. This hazard is not encountered with immersed-electrode furnaces because the salts melt from the top down. If remelting is done in externally heated furnaces, however, the following precaution should be

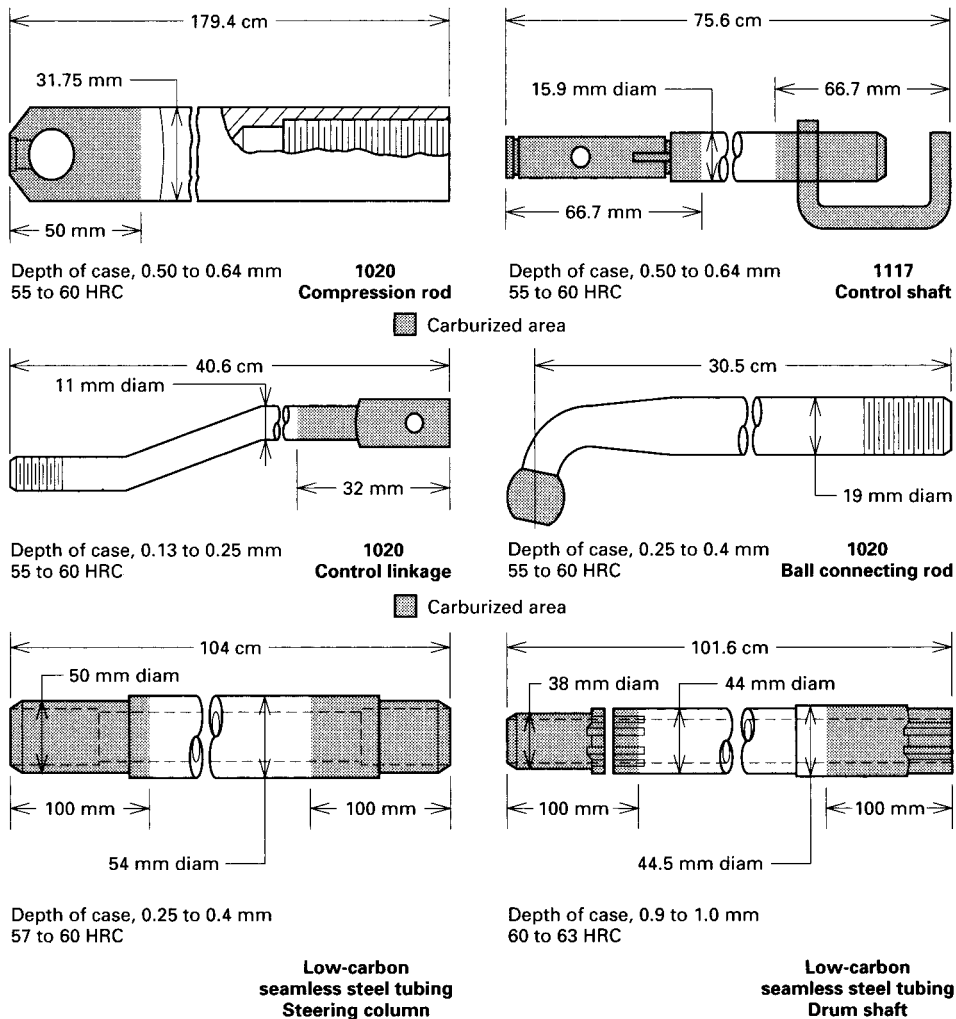


Fig. 11 Typical parts selectively carburized by partial immersion. Only the portion that is to be carburized is immersed in the bath. Area to be carburized is shaded.

observed: a steel or cast iron wedge should be inserted in the center of the bath before the bath freezes. One end of the wedge should make contact with the bottom of the pot; the other end should extend at least 10 cm (4 in.) above the surface of the bath. Before the bath is remelted, the wedge should be tapped with a hammer, loosened, and removed. The space previously occupied by the wedge will provide a vent for expanding salt and gases during remelting. No attempt should be made to remove a wedge from a bath that is not completely solidified, because molten salt may be forcibly blown out through the opening created.

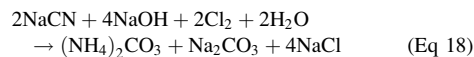
Disposal of Cyanide Wastes

Cyanide wastes, whether dissolved in quench water or in the form of solid salt from pots, pose a serious disposal problem. The cyanide contents of these wastes must be chemically altered to render the material nonpoisonous before it is discharged into sewers or streams.

Because of the toxicity of cyanide wastes, local ordinances and pollution authorities must be consulted regarding the proper disposal of wastes.

Chemical Treatment. The simplest treatment consists of oxidizing the cyanide in an alkaline solution to which is added either chlorine gas or its equivalent in the form of a hypochlorite compound, such as sodium or calcium hypochlorite (bleaching powder). The choice between gas or powder depends on the quantity of cyanide to be treated, on the availability of facilities and experienced personnel for handling the oxidizing agents, and on economics. For small quantities of cyanide solutions, it may be more practical to use a hypochlorite compound than to use chlorine gas.

Depending on the oxidizing agent employed, several reactions take place when cyanide is converted into a disposable form. One reaction with chlorine gas is as follows:



This reaction indicates that, for each kilogram (2.2 lb) of sodium cyanide, 1.42 kg (3.13 lb) of chlorine gas and 1.6 kg (3.5 lb) of sodium hydroxide are required. Because of probable side reactions, however, practical experience indicates an actual requirement of slightly more than 2 kg (4.4 lb) of chlorine for each kilogram of sodium cyanide present in the waste solution. When a hypochlorite compound is used, the amount of powder required may be estimated on the basis of available chlorine content in the compound.

Solid cyanide wastes must be dissolved in water before they can be treated. A tank of suitable capacity, equipped with a coarse screen set well above the bottom, will facilitate solution of the solid material. The tank should also have an agitator, and, for chlorine gas, a perforated pipe placed well below the solution level is required.

When cyanide wastes are to be treated with chlorine gas, the cyanide content must first be determined and the proper amount of caustic added. The gas is then introduced slowly while the temperature of the solution is kept below 50 °C (120 °F). If a sodium hypochlorite solution is used, sufficient caustic should be added to raise the pH of the cyanide solution above 8.5. The reaction between cyanide and the oxidizing agent should continue until a slight excess of chlorine is present in the solution. This can be determined by testing with starch iodide paper or with a solution of potassium iodide and starch. Both the iodide paper and starch solution will turn blue in the presence of free chlorine.

Treatment Equipment (Ref 9). The equipment shown in Fig. 12 is used to treat cyanide and barium salts. There is nothing new in cyanide treatment chemistry, and it has been used satisfactorily since the 1930s in batch and continuous treatment processes. It uses sodium or calcium hypochlorite salts. Sodium hypochlorite solutions containing from 10 to 15% available chlorine are available from local chemical suppliers. Calcium hypochlorite, sold in the granular or tablet forms, contains in excess of 70% available chlorine. This is also available from local chemical suppliers. Chlorine gas could also be used, but many wastewater treatment plants prefer to use the hypochlorite salts.

Theoretically, 1.24 kg (2.73 lb) of available chlorine is required to oxidize 0.5 kg (1 lb) of cyanide as CN to the cyanate form. Another way to state this is that 0.66 kg (1.45 lb) of available chlorine is required per 0.5 kg (1 lb) of sodium cyanide. The presence of other oxidizable substances would increase the chemical requirements. The reaction is practically instantaneous; therefore, the allowance of 10 min for completion of the reaction is sufficient. Ferrous or ferricyanides are not removed by this reaction.

The treatment should be performed above a pH of 10 to ensure that the resulting by-product is cyanate and to minimize the evolution of cyanogen chloride. No instances are known

where the reaction is required to be conducted beyond the cyanate stage. This reaction results in the evolution of carbon dioxide and nitrogen. It requires in excess of 3.2 kg (7 lb) of available chlorine per 0.5 kg (1 lb) of cyanide (as CN) and two pH adjustments—one above 10 for the first reaction and the other to 6.5.

The aforementioned treatment to the cyanate stage should produce an effluent containing less than 0.2 mg/L of CN amenable to chlorination.

The equipment shown in Fig. 12 can be used for batch treatment of rinses, water quenches, and spent salt. The latter must first be dissolved by placing it in a perforated basket that is immersed in water or a cyanide-rich rinse, while providing agitation. The concentration of sodium cyanide in the solution should not be allowed to exceed 5%, because of the evolution of heat due to the exothermic character of the reaction.

Another procedure for destroying cyanide in higher concentrations is by the use of heat and electrolysis in a plating bath, followed by treatment with sodium hypochlorite to remove the residual cyanide.

Hypochlorination is required for the removal of the cyanide residual because of the reduction in the effectiveness of electrolysis as the cyanide concentration decreases.

The treatment of cyanide solutions should be performed either under a hood or in tanks provided with ventilating ducts.

Figure 13 illustrates a continuous treatment operation with the first rinse being recirculated through cooling coils, with a side stream being treated. The second (still) rinse is also treated. The addition of sodium hypochlorite is controlled by an oxidation-reduction potential electrode assembly through a controller. Maintenance of pH is effected by a pH electrode assembly through a controller that activates metering pumps connected to sulfuric acid and caustic soda solutions. Only one of these solutions is used.

One indirect way to check for the removal of the cyanide amenable to chlorination after treatment is to check for residual chlorine by immersing a paper strip of potassium iodide starch indicator, which turns purple when chlorine is in excess of 10 mg/L.

The final result of the treatment is a treated liquid and a sludge. The latter is dewatered by filtration and carted to a suitable disposal site. The filter cake should not be hazardous, according to the tests prescribed by the EPA. Because the quantity of the sludge should be relatively small, it can be stored and periodically filtered.

The treatment effluent may not pass the test for total cyanides due to the presence of ferro- or ferricyanides, because these cannot be destroyed by chlorine compounds at ambient temperature. If the treated wastewater contains total cyanide in excess of 1.2 mg/L on any one day or a monthly average of 0.65 mg/L, an application can be made to the regulatory agency for approval of a limitation of, respectively, 0.86 and 0.32 mg/L as amenable

cyanide. Ferrocyanides that are not amenable to chlorination do not show in this test; therefore, even if the limits on the concentration of cyanide are lower, they are less restrictive than the larger figures because they do not include the ferro- or ferricyanides that are not removable by chlorine treatment at room temperature.

Electrochemical Treatment. Although chemical treatment may be entirely adequate to meet local regulations, an electrochemical process has been used to destroy free cyanide. In the electrochemical process, cyanide wastes in aqueous solution are circulated through an electrochemical reactor. Within the reactor, an applied direct-current potential oxidizes the

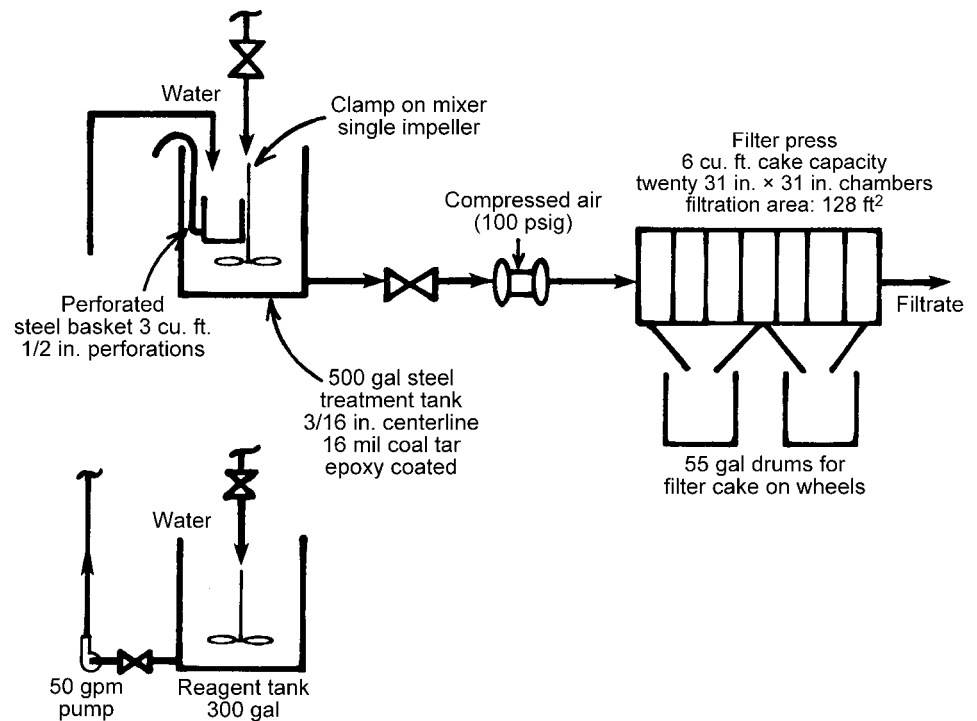


Fig. 12 Basic system for batch treatment of waste water containing cyanide or barium salts Ref 9

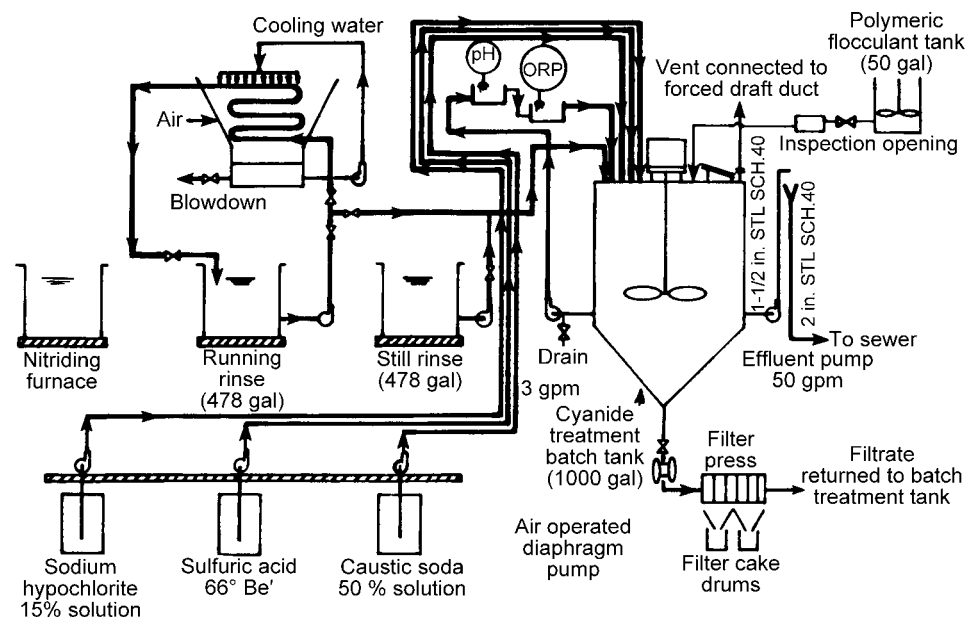
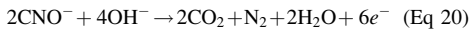
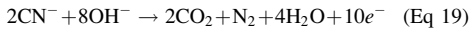


Fig. 13 Treatment of rinses from nitriding operations. ORP, oxidation-reduction potential Ref 9

free cyanide and cyanate according to the reactions:



Free cyanide and cyanate are converted to the nontoxic gases carbon dioxide and nitrogen, which are allowed to escape freely from the vented storage tank into which the reacted solution is circulated.

The electrochemical process is most effective at high cyanide-ion concentrations. With continual recirculation between storage tank and reactor, cyanide can be reduced to 1 ppm or less in approximately 100 to 150 h. By combining electrochemical and chemical treatments, effective treatment can usually be achieved at minimum cost. Electrochemical removal is used to reduce cyanide concentration to ≈ 200 to 500 ppm, and then chemical treatment is used to complete the reduction.

Electrochemical treatment offers the following advantages:

- The process uses only electricity—no chemicals are required.

- Cost per unit weight of cyanide treated is low, depending only on the cost of electricity (approximately 6.6 kW · h/kg, or 3 kW · h/lb of free CN^-).
- Capital investment is higher than alkaline chlorination.
- The process is simple to control, requiring only periodic determination of cyanide concentration.
- There are no toxic or otherwise harmful reaction products.
- Upon reaching a concentration of 1 ppm cyanide, the oxidized effluent usually may be drained and further diluted by plant effluent.
- The process can also be used to convert nitrite into nitrate.

The only significant disadvantage is that the process is time-consuming when levels of cyanide below 200 ppm must be achieved. Increasing the number of reactors decreases process times.

REFERENCES

1. "Pure Case Noncyanide Carburizing Process," Technical Data Sheet, Heatbath Corporation
2. F.W. Eysell, Regenerable Salt Baths for Carburizing, Carbonitriding, and Nitrocarburizing: A Contribution to Protecting the Environment, *FWP J.*, Oct 1989
3. L.S. Burrows, Durofer—A Low-Toxicity Salt-Bath Carburizing Process, *Heat Treat. Met.*, Vol 4, 1987
4. P. Astley, Liquid Nitriding: Development and Present Applications, *Heat Treatment '73*, Book 163, The Metals Society, 1975, p 93–97
5. P. Astley, Tufftride—A New Development Reduces Treatment Costs and Process Toxicity, *Heat Treat. Met.*, Vol 2, 1975, p 51–54
6. H. Kunst and B. Beckett, Cyanide-Free Regenerator for Salt Bath Carburizing, *Heat Treatment '84*, Book 312, The Metals Society, 1984, p 16.1–16.5
7. R. Engelmann, Paper presented at the 39th Heat Treatment Colloquium, Oct 5–7, 1983 (Wiesbaden, West Germany)
8. C. Skidmore, Salt Bath Quenching—A Review, *Heat Treat. Met.*, Vol 13, 1986, p 34–38
9. W. Zabban, Technical Note: Environmental Regulations and Treatment for Salt Baths, *J. Heat Treat.*, Vol 6 (No. 2), 1988, p 117

Low-Pressure Carburizing

Volker Heuer, ALD Vacuum Technologies GmbH

LOW-PRESSURE CARBURIZING (LPC) has been established over the past few years as one of the most popular case-hardening processes. Low-pressure carburizing is often referred to as vacuum carburizing. As with all case-hardening processes, the goal is to obtain a part with a solid, tough core and a hard, wear-resistant surface. It is applied to increase the fatigue limit of dynamically loaded components. Typical applications include gear parts, machine components, bearing components, as well as injection systems for engines. Case hardening essentially consists of three steps. First, the parts are austenitized, then carburized, and once the required carbon profile is reached, they are quenched. The microstructure in the surface layer (the case-hardening layer) of a case-hardened part is specified for functional surfaces (e.g., tooth flanks of gear wheels) as follows:

- Martensite is present, with a maximum of 20 to 30% retained austenite.
- Bone carbides or carbide networks are not permitted; finely dispersed carbides are permitted.
- Structure is free of bainite up to a depth of 70% of the case-hardening layer from the part surface.

Process

Figure 1 depicts a typical carbon profile, and Fig. 2 shows a typical hardness profile after

a case-hardening process. In this example, the surface hardness is 750 HV, the core hardness is 350 HV, and the case-hardening depth (CHD) is 0.8 mm (0.03 in.). The common definition of case-hardening depth is the distance from the surface in which the hardness is still above the hardness limit of 513 HV (50 HRC).

The LPC process takes place in a pressure range between 5 and 15 mbar (4 and 11 torr) and a temperature range between 870 and 1050 °C (1600 and 1920 °F). In most cases, the carburizing temperature is between 920 and 980 °C (1690 and 1800 °F). During the complete process, the treated components are not exposed to any traces of oxygen. The typical CHDs of components processed with LPC are specified between 0.3 and 3 mm (0.012 and 0.12 in.), depending on the size and the application of the component.

Figure 3 shows the LPC process in a schematic diagram. First, the charge enters the furnace chamber under vacuum, followed by convective heating under a nitrogen atmosphere close to 1 bar (750 torr). Convective heating offers a quicker and more homogeneous heating of the load compared to vacuum heating alone. Subsequently, another heating phase under vacuum takes place. The actual carburizing and diffusion starts after all parts have reached the specified carburizing temperature. Carburizing takes place by applying a routine of alternating pulses and diffusion steps.

Oxygen-free hydrocarbons such as acetylene C_2H_2 (ethyne) are used as a carbon source. The hydrocarbons are injected into the furnace chamber, creating a pressure of a few millibars. On the surface of the treated parts, the hydrocarbons dissociate thermally. Subsequently, the surface carbon content rises to the point of saturation within a short time, which results in a high mass flow of carbon into the material. Before carbide formation may take place, the supply of carburizing gas is stopped, and the carbon diffuses into the material. Once the surface carbon content is sufficiently reduced, the carburizing gas is injected into the furnace chamber again. These so-called pulses are repeated until the part has absorbed a sufficient amount of carbon. After completion of the carburizing pulses, a longer diffusion step takes place. This final diffusion step is used to obtain the required surface carbon content. Depending on the steel type and the desired amount of retained austenite, the target for surface carbon content is typically between 0.65 and 0.85% (Fig. 1).

In addition to acetylene, other carbon sources such as propane (C_3H_8) or cyclohexane (C_6H_{12}) can be used. However, acetylene is by far the most commonly used carbon source for LPC.

Depending on the furnace size and geometry of the treated components, the surface area of a carburized load can be between 0.5 and 21 m² (5 and 225 ft²).

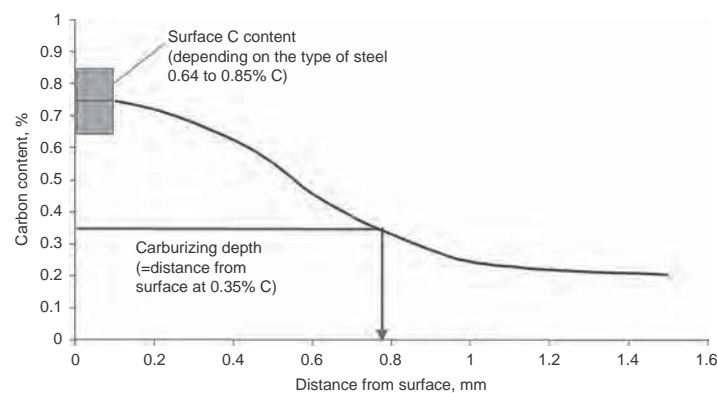


Fig. 1 Example of a carbon profile after case hardening

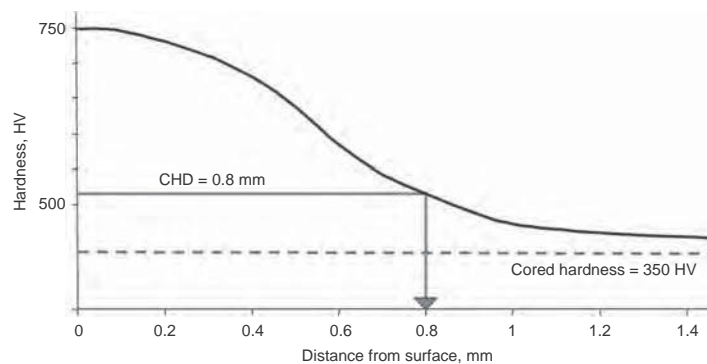


Fig. 2 Example of a hardness profile after case hardening. CHD, case-hardening depth

Once the targeted carbon profile is obtained, the parts are quenched. Quenching can be initiated either from carburizing temperature or from a lower hardening temperature. In most cases, high-pressure gas quenching (HPGQ) with either nitrogen or helium is applied after LPC. In some applications, oil quenching is applied after LPC. Details regarding the HPGQ process can be found in the article “Gas Quenching” in this Volume.

Contrary to atmospheric gas carburizing, where the case depth is achieved by control of the carbon potential, LPC is a recipe-controlled process. The process parameters of temperature, flow rate of carburizing gas, time, and pressure are defined in the heat treating recipe and controlled throughout the process to achieve the specified carbon profile.

The high mass transfer of carbon into the components during LPC leads to significantly shorter treatment times compared to conventional gas carburizing (Table 1).

When combining LPC with HPGQ, the process provides the following advantages

compared to gas carburizing combined with oil quenching:

- Excellent carburizing homogeneity, even for components with complex shapes
- Intergranular oxidation (IGO) and surface oxidation are avoided.
- Shorter cycle times
- Potential for further reduction of cycle time when applying high-temperature LPC (see the section “High-Temperature LPC” in this article)
- Possibility to integrate heat treatment into the production line
- Conditioning of the equipment is not necessary.
- Parts after heat treatment are clean; washing of parts is not necessary.
- Environmentally friendly process (small consumption of resources; no disposal of oil, salt bath residues, or detergent residues)
- Potential to reduce heat treatment distortion (unwanted changes in form and size of the part geometry during heat treatment)

The disadvantages include the higher equipment cost and the somewhat limited quench intensity of HPGQ, compared to oil quenching. Very large components cannot be quenched in gas successfully, unless they are made of a steel grade with excellent hardenability.

A detailed introduction into the technology of vacuum heat treatment including LPC is given in Ref 1.

Physical Principles

When acetylene comes in contact with the surface of the steel at temperatures above 870 °C (1600 °F), it dissociates thermally. The acetylene molecules dissociate into carbon and hydrogen:



However, the real chemical reactions that take place are much more complex and can be reduced into nine main reactions, as illustrated in Fig. 4.

Detailed literature about the pyrolysis of acetylene and the surface reactions during LPC can be found in Ref 2 to 5. The kinetics of the LPC process were analyzed in an extensive study, with the help of a special thermobalance (Ref 6, 7). The height of the carbon mass transfer into the material is a function of steel grade, process temperature, and the number, length, and timing of the carburizing pulses. When working at a pressure range between 5 and 15 mbar (4 and 11 torr), the process pressure has no influence on carbon mass transfer.

The carbon yield that is absorbed by the load is approximately 65% when using acetylene. This value was determined empirically in industrial application. The carbon yield is defined as the amount of carbon absorbed by the load in relation to the total amount of carbon injected into the furnace chamber.

Once the carbon is absorbed into the material, the same diffusion laws apply as in conventional gas; that is, the diffusion of carbon in austenite follows Fick’s law.

Low-pressure carburizing provides an oxygen-free surface after treatment. The process gases and the furnace atmosphere are free of oxygen. Therefore, IGO and surface oxidation of the components are safely prevented. Figure 5 shows a comparison of the surfaces after LPC and after atmospheric gas carburizing.

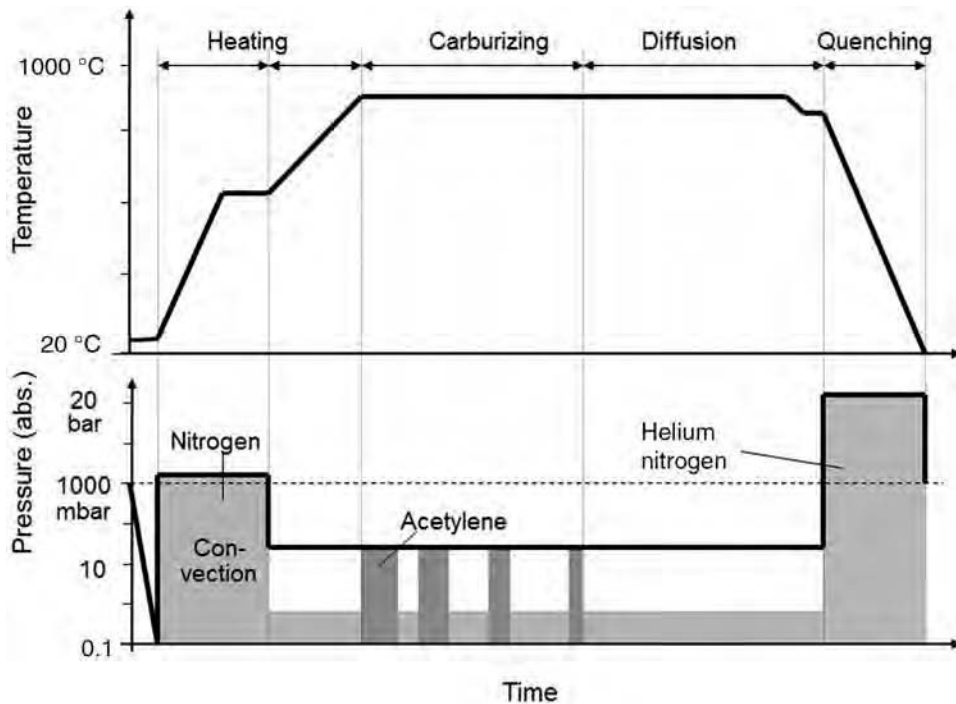


Fig. 3 Schematic diagram of the low-pressure carburizing and high-pressure gas quenching process

Table 1 Comparison of treatment times for low-pressure carburizing and atmospheric gas carburizing

Application	Material	Treatment temperature		Case-hardening depth		Treatment time(a), h	
		°C	°F	mm	in.	Low-pressure carburizing	Gas carburizing
Internal gear	28Cr4 (ASTM 5130)	900	1650	0.3	0.012	0.75	1.5
Gear	16MnCr5	930	1705	0.6	0.024	2	2.75
Shaft	16MnCr5	930	1705	0.8	0.032	2.75	4
Gear	18CrNiMo7-6	960	1760	1.6	0.063	7.5	9.5

(a) Treatment time = Carburize + Diffuse + Lower to hardening temperature

Figure 6 depicts the distribution of alloying elements close to the surface after LPC and after atmospheric gas carburizing. During LPC in some applications, the surface content of manganese is reduced by evaporation of manganese. During gas carburizing, metal oxides are formed at the surface due to IGO, which cannot be avoided in gas carburizing. The formation of metal oxides leads to a depletion of chromium, manganese, and molybdenum at a depth between 5 and 15 μm (0.2 and 0.6 mil).

In recent years, the use of acetylene has been steadily established in industrial practice, substituting for propane, which was the favorite carbon source. The carbon yield of propane is approximately 25% compared to acetylene at approximately 65%. Compared to propane, acetylene is better suited to homogeneously carburize parts with complex shapes, such as injection nozzles. Even bulk loads can be carburized successfully with acetylene.

Injection nozzles have blind holes with a length-to-diameter (L/D) ratio of up to 15. When using propane, blind holes with an L/D ratio of up to 2 can be carburized homogeneously; when using acetylene, L/D ratios up to 20 can be treated successfully (Ref 8).

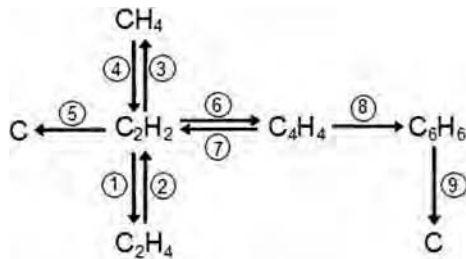


Fig. 4 Dissociation reactions during acetylene pyrolysis. Source: Ref 2

Equipment for Low-Pressure Carburizing

The LPC process can be run in two different types of equipment. In single-chamber furnaces, the LPC and the HPGQ processes are performed in the same chamber. As an alternative, treatment chambers are dedicated for LPC only. These treatment chambers are part of multichamber systems, where HPGQ is performed in specific cold chambers. The applied carburizing strategies are identical for both types of equipment.

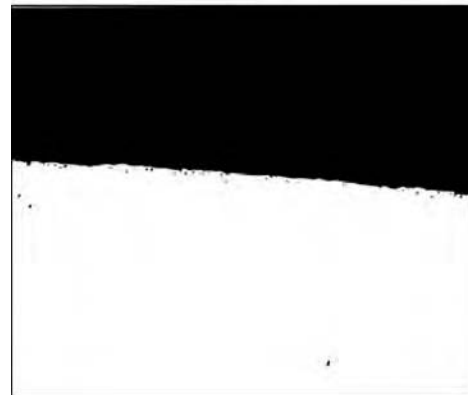
For both types, the vacuum vessel is water cooled. In single-chamber furnaces, the inner insulation typically consists of hard felt made of graphite. In treatment chambers, the inner insulation typically consists of layers of ceramic-fiber modules (e.g., $\text{Al}_2\text{O}_3 + \text{SiO}_2$) and hard felt made of graphite on the inside. Because the ceramic fiber is hygroscopic, it cannot be used in single-chamber furnaces, which are opened to atmosphere after each furnace cycle.

In multichamber systems, the treatment chambers are always at temperature and under vacuum, whereas single-chamber furnaces are cooled down and ventilated with air at the end of each furnace cycle. Therefore, multichamber systems are more energy efficient and have a longer service life.

The work zone is typically heated electrically by graphite elements. The carburizing gas enters the work zone through small tubes made of ceramics or nickel-base alloys (e.g., Inconel). The flow rate of carburizing gas is precisely controlled by mass flow controllers. Typical tube diameters range from 5 to 10 mm (0.2 to 0.4 in.). The tubes are arranged symmetrically inside the chamber to achieve a homogeneous distribution of the carburizing gas. A vacuum pump set is connected to the chamber to control the process pressure, which is usually chosen at a level between 5 and 15 mbar (4 and 11 torr).

Formation of soot or tar in the chamber occurs if the process pressure is too high. The

Low-pressure carburizing: without intergranular oxidation



Atmospheric gas carburizing: with intergranular oxidation



Fig. 5 Surface layer after carburizing to a case depth of 0.7 mm (0.03 in.). Material is SAE 5115; scale is 1000:1.

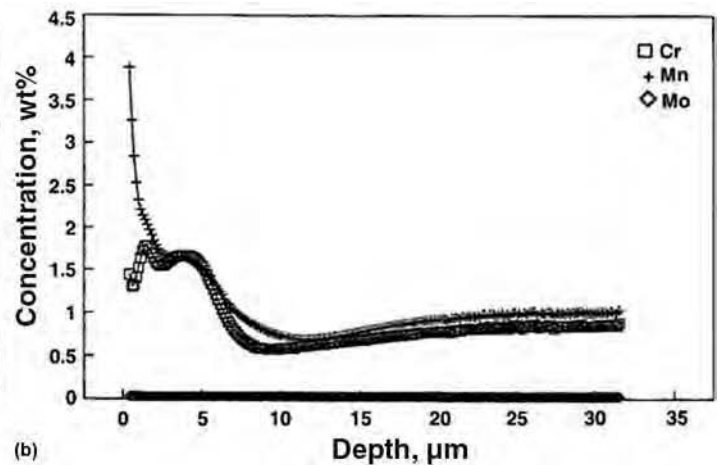
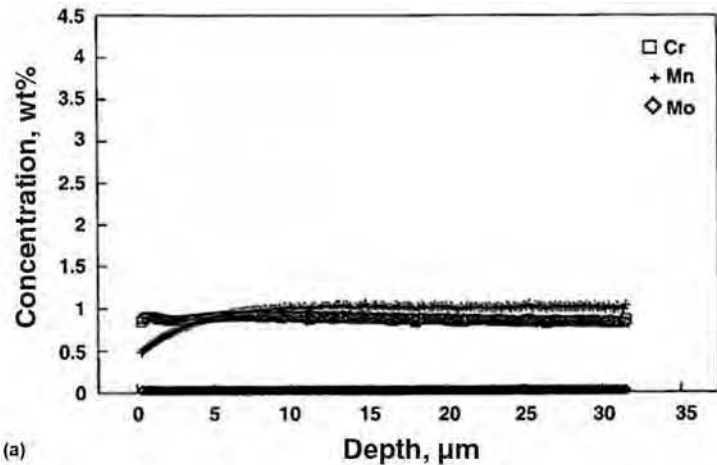


Fig. 6 Distribution of alloying elements close to the surface after (a) low-pressure carburizing and (b) atmospheric gas carburizing. Material is SAE 5115.

same applies for the flow rate of carburizing gas. If the flow rate is significantly above the rate necessary to carburize the given surface area of the load, formation of soot or tar occurs. However, when choosing the correct process parameters and when undertaking regular maintenance, soot and tar is not a threat for applying LPC in mass production.

The load sits in the chamber on a charge support made of graphite and silicon carbide. Fixtures for treatment of loads with LPC are made of either alloy with high nickel content or carbon-fiber-reinforced carbon material. More details regarding fixtures used for LPC and HPGQ are given in the article “Gas Quenching” in this Volume.

Figures 7 and 8 show examples of vacuum systems used for the LPC process. Figure 7(b) depicts a view into a single-chamber furnace with graphite heating elements, charge support, nozzles for the carburizing gas, and nozzles for the quench gas.

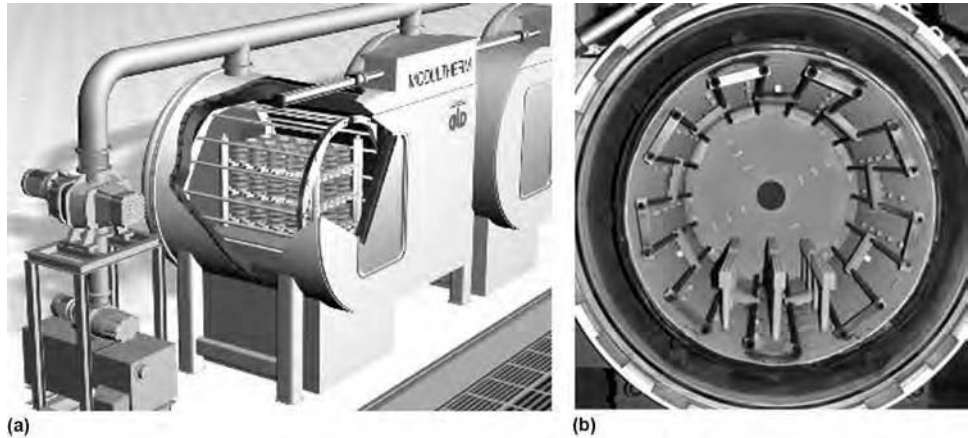


Fig. 7 Vacuum systems for the low-pressure carburizing process. (a) Treatment chamber as part of a multichamber system. (b) View into a single-chamber furnace

Carburizing Strategies

The development of the carbon profile during LPC is dictated by the number and the length of the alternating carburizing pulses and diffusion steps. To establish the shortest possible process cycle, the goal is to enrich to the saturation limit the surface of the treated components in each carburizing pulse. This saturation limit is defined as the carbon content where carbides start to be precipitated. Usually, the first pulse is longer than the following pulses, because the component is not enriched with carbon yet and is thus able to absorb more carbon.

Figure 9 schematically shows the alternating carburizing pulses and diffusion steps and the resulting effect on surface carbon content. The length of the final diffusion step depends on the targeted surface carbon content before quenching.

The saturation limit differs from steel grade to steel grade and is a function of temperature. With increasing temperature, the limit of carbide precipitation is shifted to higher carbon contents (Fig. 10).

While the development of the carbon profile is defined by the number, length, and timing of the carburizing pulses, the surface area of the load is accounted for by adjusting the flow rate of carburizing gas during the pulses.

To achieve the desired microstructure of the components after LPC, it is important to examine the development of carbon content close to the surface of the components.

Figure 11 shows an example where the sequence of carburizing pulses and diffusion steps was defined incorrectly. This example shows an LPC process for 18CrNi8 material at 940 °C (1725 °F). The diffusion steps between pulses were too short, thus leading to a carbon content above 1.18% during the course of the



Fig. 8 Multichamber system for low-pressure carburizing process in mass production. ModulTherm (ALD Vacuum Technologies) with ten treatment chambers

process. As a result, the components were oversaturated with carbon, resulting in precipitation of massive carbides. The length of the final diffusion step was chosen correctly, resulting in a surface carbon content of 0.69% C, thus avoiding the formation of excessive amounts of retained austenite.

Figure 12 depicts an example where the diffusion steps between pulses were defined correctly. Therefore, the carbon content was below 1.17% during the course of the process, and thus, the precipitation of carbides was avoided. However, the final diffusion step was

too short; therefore, the final surface carbon content before quenching was too high. This resulted in the formation of large amounts of retained austenite.

An optimized carburizing strategy is shown in Fig. 13. A proper sequence of pulses and diffusion steps and the correct length of the final diffusion step are used. As a result, the microstructure is free of any carbides and large amounts of retained austenite.

The proper sequence of pulses and diffusion steps can be easily determined by the use of simulation software for prediction of carbon

profiles; see the section “Prediction of Carbon Profiles” in this article.

Table 2 shows an example of the carburizing strategy for material 8630 processed with LPC using acetylene and targeting a case depth of 0.6 mm (0.02 in.). The length of the heating

phase (convective and vacuum heating) before the first carburizing pulse depends on the size of the treated components and the size of the load. The flow rate of acetylene during the pulses is adjusted according to the surface area of the load.

- Chemical composition of the steel grade of the components
- Saturation limit of the carbon content for the steel grade
- Carburizing temperature
- Targeted carburizing depth
- Targeted surface carbon content
- Surface area of the load

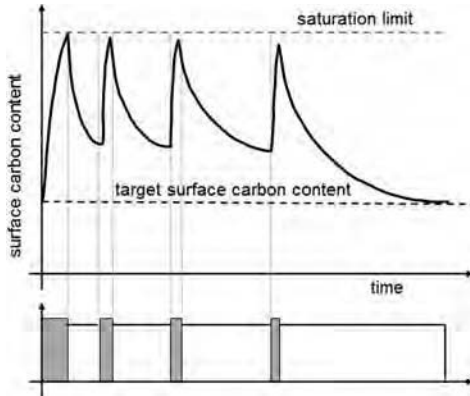


Fig. 9 Schematic of change of surface carbon content during low-pressure carburizing defined by alternating carburizing pulses and diffusion steps

Prediction of Carbon Profiles

The mass transfer of carbon and the diffusion into the material during LPC can be simulated by means of commercially available software. Such programs are based on a mathematical description of the carbon dissociation and adsorption of the carbon at the surface of the parts and equations that describe the diffusion of the carbon into the material (Ref 6). While the carbon transport to the surface in LPC differs significantly from that in atmospheric gas carburizing, the same diffusion laws apply for the carbon transport within the material. The function and the results of simulation software are exemplarily described in Ref 10. To calculate the carbon profile, the following data are entered as input parameters into the simulation program:

The program calculates the number and duration of carburizing pulses and diffusion steps as well as the required flow rate of the carburizing gas for each carburizing pulse. Furthermore, it is possible to calculate in reverse and to determine the expected carburizing depth for a given process with given temperature, carburizing pulses, and diffusion steps. In most cases, these calculations are one-dimensional, not taking possible edge effects into account.

In addition, the simulation program is a powerful tool to achieve the targeted microstructure after LPC. The program shows the formation of the carbon profile as a function of time for different distances from the surface. Therefore, it is possible to optimize carburizing strategies

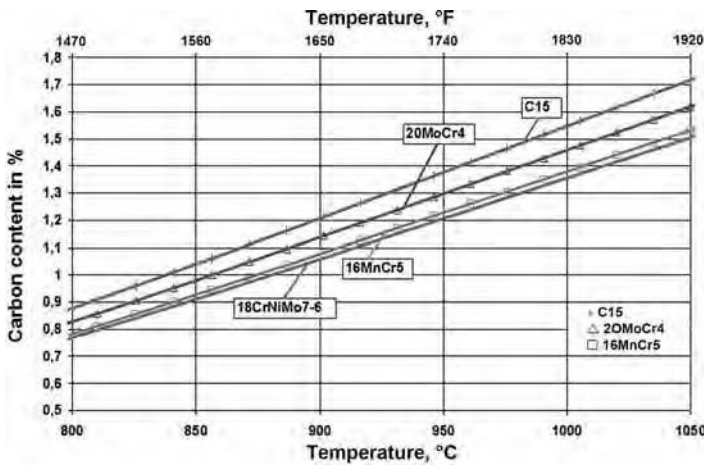


Fig. 10 Limits of carbide precipitation for different case-hardening steels (calculated according to Ref 9)

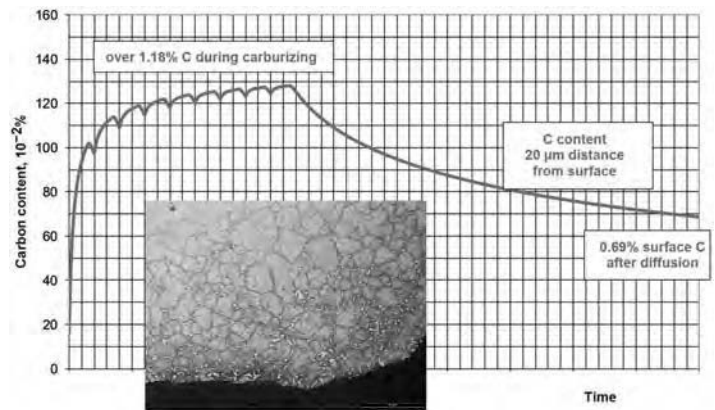


Fig. 11 Carburizing strategy resulting in unwanted carbide formation. Carburizing temperature is 940 °C (1725 °F); material is 18CrNi8.

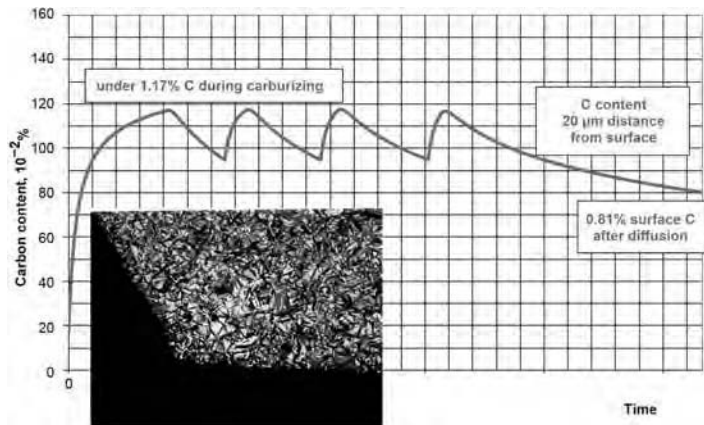


Fig. 12 Carburizing strategy resulting in unwanted formation of retained austenite. Carburizing temperature is 940 °C (1725 °F); material is 18CrNi8.

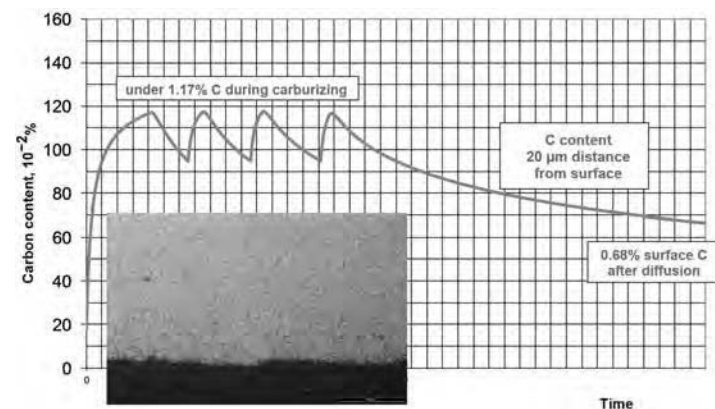


Fig. 13 Optimized carburizing strategy to achieve an optimized microstructure. Carburizing temperature is 940 °C (1725 °F); material is 18CrNi8.

in order to meet the microstructural specification, that is, the absence of large quantities of carbides or excessive amounts of retained austenite.

With the help of more complex finite-element method simulation programs, it is possible not only to simulate carbon profiles but to predict microstructures as well as the resulting core hardness after quenching (Ref 11). In special cases, heat treatment distortions are numerically simulated as well (Ref 12). However, due to the extensive effort in setting up the model and defining the boundary conditions, and due to the large required computing times, the simulation of heat treatment distortion has not yet become established as a standard tool in industrial practice.

Applications

Automotive Applications. Figures 14 and 15 show typical examples of loads with automotive gear components processed with LPC.

Another main field of application for LPC is components used for fuel-injection systems, such as nozzle bodies. Figure 16 shows the specification of a nozzle made of 18CrNi8 material after heat treatment. The special challenge during case hardening of this component is to guarantee homogeneous carburizing despite the complex shape of the nozzle (Ref 13). The component requires tight control with carburizing, evident in the blind hole, while at the same time partial overcarburizing must be prevented, for example, in the island.

The nozzles are treated with LPC using acetylene and are gas quenched with nitrogen. Areas that do not require carburizing are covered with mechanical masks. The components are austenitized twice and quenched twice to increase fatigue strength. This is followed by a deep freezing step at $-100\text{ }^{\circ}\text{C}$ ($-148\text{ }^{\circ}\text{F}$) to transform any retained austenite into martensite and then followed by tempering. Figure 17 shows the measured hardening profile after treatment at various measuring points (Ref 13).

Aerospace Applications. Figures 18 and 19 depict typical applications of LPC for aerospace components.

For aerospace products, one of the most critical requirements is the geometrical stability of the components during application. It is well known that retained austenite will transform to martensite when subjected to a certain level of stress or to a certain load (stress-induced transformation). Furthermore, retained austenite will transform to martensite when subjected to cold temperatures. This change in microstructure will result in growth of the component. Therefore, the level of retained austenite in the hardened case of the components must be controlled, which is why in many cases the components are subjected to a cryogenic

Table 2 Example of carburizing strategy for material 8630 at $960\text{ }^{\circ}\text{C}$ ($1760\text{ }^{\circ}\text{F}$) and targeting a case-hardening depth of 0.6 mm (0.02 in.)

Low-pressure carburizing process with acetylene; heating phase before carburizing must be customized according to the size of the treated components and the load size.

Sequence	Temperature		Time
	$^{\circ}\text{C}$	$^{\circ}\text{F}$	
Convective heating	960	1760	80 min
Vacuum heating	960	1760	30 min
Carburizing pulse (C_2H_2)	960	1760	90 s
Diffusion step (N_2)	960	1760	9 min
Carburizing pulse (C_2H_2)	960	1760	60 s
Diffusion step (N_2)	960	1760	11 min
Carburizing pulse (C_2H_2)	960	1760	60 s
Final diffusion (N_2)	960	1760	25 min
Quenching

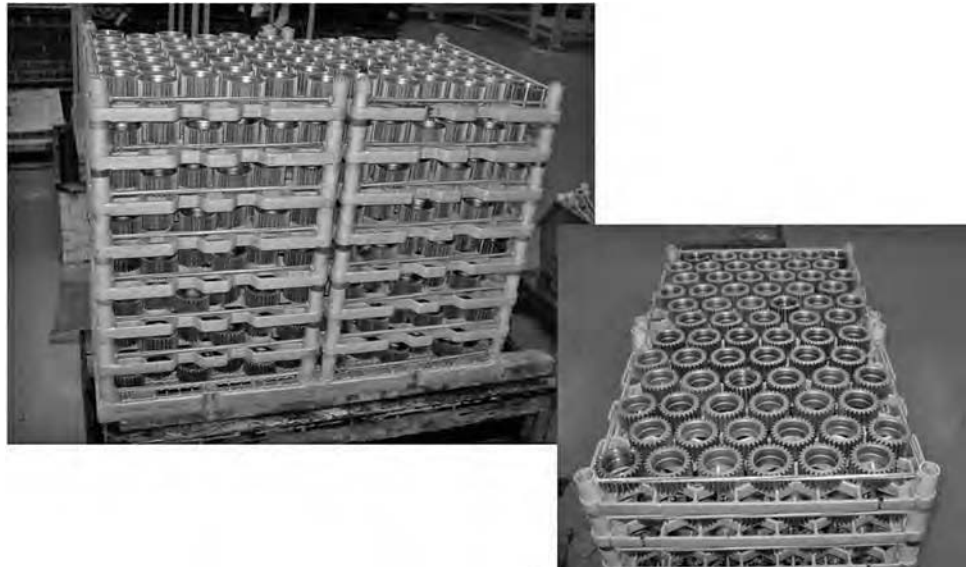


Fig. 14 Load configuration for low-pressure carburizing of sun gears. 20MnCr5HH gear wheel; 576 parts per batch; cycle time, 215 min; carburizing temperature, $945\text{ }^{\circ}\text{C}$ ($1735\text{ }^{\circ}\text{F}$); nitrogen, 8 bar (6000 torr); case-hardening depth, 0.65–0.75 mm (0.026–0.030 in.); core hardness, 35–38 HRC

treatment after quenching and before tempering. With such a cryogenic treatment at temperatures below $-73\text{ }^{\circ}\text{C}$ ($-99\text{ }^{\circ}\text{F}$) (preferred at -85 or $-100\text{ }^{\circ}\text{C}$, or -121 or $-148\text{ }^{\circ}\text{F}$), the amount of retained austenite is reduced dramatically. The specified time at temperature varies for such a cryogenic treatment, depending on the cross-sectional thickness of the components. However, a minimum of 2 h is often specified.

For example, precision bearings made of material M50NIL are first low-pressure carburized and oil quenched and then subjected to multiple cryogenic/tempering cycles. At a depth of 0.05 mm (0.002 in.) from the surface, the content of retained austenite is determined with an x-ray diffraction method to less than 2% (Ref 15).

As described in the section “Carburizing Strategies” in this article, the LPC process offers a high-flexibility carburizing strategy. This is advantageous for many aerospace applications. For example, to prevent the formation

of excessive amounts of retained austenite when treating the material SAE 9310, the carburizing temperature is limited to $930\text{ }^{\circ}\text{C}$ ($1705\text{ }^{\circ}\text{F}$) for atmospheric gas carburizing. With LPC, however, the carburizing strategy can be adjusted to target for a low level of retained austenite. Hence, LPC allows the use of higher carburizing temperatures for this material.

In a few special aerospace applications, the components are treated with multiple-step carburizing, which is used to achieve different carbon profiles on the very same component. To do so, the parts are first partly protected from carburizing (e.g., coated with copper). Then, the first LPC treatment is performed. After cooling with an optional annealing step, the copper is partly removed. Another possibility is to machine additional gear teeth or additional splines. Then, the next LPC treatment is performed. After the final LPC step, the parts are quenched. By applying this multiple-step

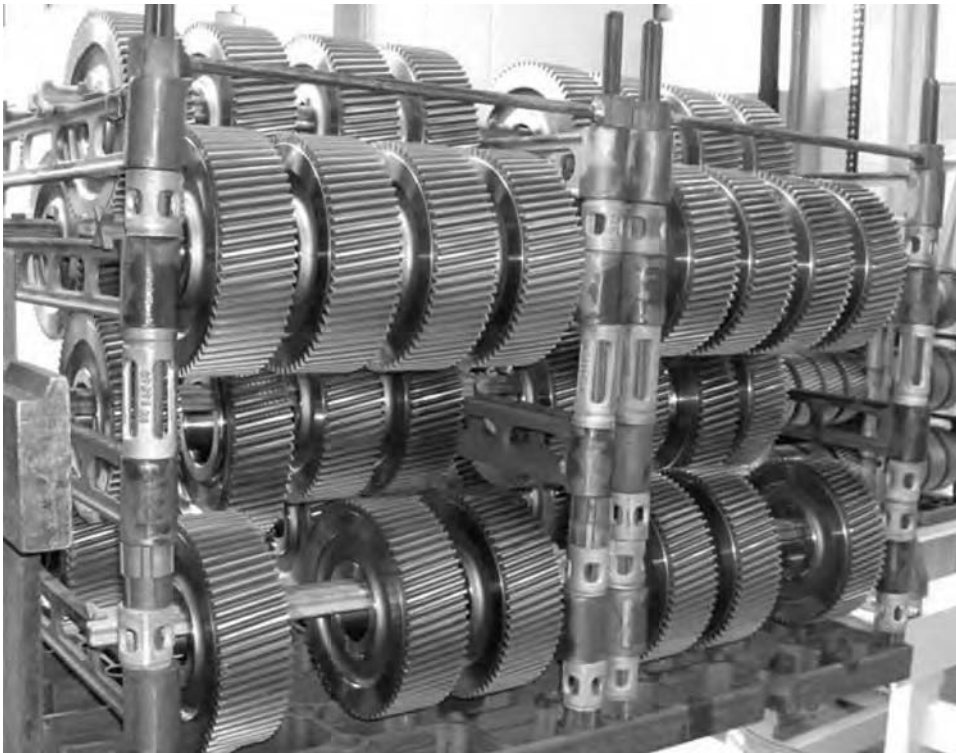


Fig. 15 Load configuration for low-pressure carburizing of ring gears. 16MnCr5 gear wheel; 44 parts per batch; cycle time, 450 min; carburizing temperature, 930 °C (1705 °F); helium, 18 bar (13,500 torr); case-hardening depth, 0.85–0.95 mm (0.034–0.037 in.); core hardness, 27–30 HRC

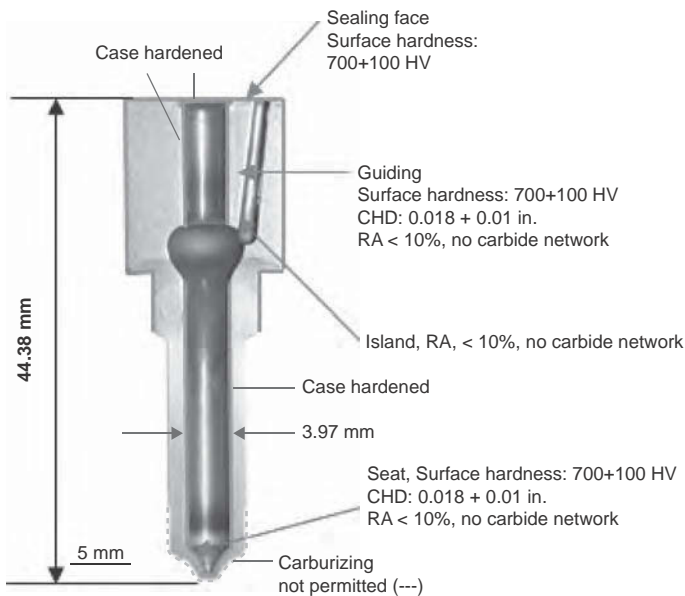


Fig. 16 Specification of a nozzle body for a diesel injection system. Source: Ref 13

carburizing, it is possible to provide uncarburized areas and areas with two different carbon profiles, and consequently two different CHDs, on the very same component.

Other Applications. Besides applications for the automotive and aerospace industry,

LPC is successfully used for other components as well. For example, hydraulic components, wear plates, industrial chains, industrial transmissions, axles, die-cutting punches, and components for the agricultural and power tools industries are often processed with LPC.

Quality Control of the LPC Process in Mass Production

To allow the LPC process to be established in mass production, reliable methods of quality control have been developed and implemented in industry over the last few years. Before the start of production of a component, the so-called production part approval process (PPAP) load is treated and analyzed intensively for quality. Components from the corners and the middle of the PPAP load are checked carefully for surface hardness, hardness profile, core hardness, and microstructure. In some cases, the carbon profile and distortion are analyzed and documented as well.

Once the PPAP load is validated and production has started, the frequency of quality checks is reduced.

Modern systems for LPC are equipped with a process-monitoring device. This device controls if the main process parameters deviate from the recipe values. If so, the load is labeled with a “red flag.” Depending on the severity of the red flag, the loads are either scrapped immediately or checked very carefully for quality and if they can be released for assembly or not.

Another method often applied in industry is the use of carbon buttons. These are discs, with standardized size and made of standardized material, that travel with the load through the process. The weight increase of the discs is an indicator if the load has indeed absorbed the targeted amount of carbon during the LPC process.

Table 3 shows the ways and means and the frequency of quality checks as typically applied in industry.

High-Temperature LPC

As shown in Table 1, the high mass transfer of carbon into the components results in significantly shorter treatment times for LPC compared to atmospheric gas carburizing. The advantage of LPC can be further enhanced by increasing the carburizing temperature. With increasing carburizing temperature, the diffusion rate rises sharply, and thus, carburizing time is significantly reduced (Fig. 20).

Furthermore, the limit for carbide precipitation shifts to higher values. According to the iron-carbon diagram, the precipitation limit is increased in unalloyed steel (i.e., C15) from 1.3% C at 930 °C (1705 °F) to 1.65% C at 1030 °C (1885 °F) (Fig. 10).

Consequently, high-temperature carburizing allows the targeting of higher surface carbon content in each carburizing pulse. The now higher concentration gradient leads to a further reduction of treatment time. (This additional reduction of carburizing time is not reflected in Fig. 20.)

Table 4 illustrates the treatment times for LPC of 18CrNiMo7-6 at different temperatures

for a case depth of 1.5 mm (0.06 in.). It shows that the total process time is reduced by 40% if the carburizing temperature is elevated from 930 to 1030 °C (1705 to 1885 °F).

The potential for improvement grows with higher case depth requirements. For material 15CrNi6 and a case depth of 3 mm (0.12 in.), for example, a total process time reduction of 55% was verified when the carburizing temperature was increased from 950 to 1050 °C (1740 to 1920 °F) (Ref 17).

However, high carburizing temperatures above 980 °C (1795 °F) may lead to grain growth. Components with coarse or mixed grains have the following disadvantages:

- Higher macroscopic heterogeneity
- Less toughness, especially in the carburized area
- Lower root-bearing capacity

Especially for dynamically loaded parts, the formation of coarse grains can reduce service life substantially. As a countermeasure, microalloyed materials were developed that do not have a tendency to develop coarse grains (Ref 18 to 20), even at high carburizing temperatures above 1050 °C (1920 °F). These microalloyed steels have, besides the defined content of nitrogen and aluminum, a defined content of the elements titanium and niobium.

The ratio between nitrogen, aluminum, niobium, and titanium should be chosen according to the targeted carburizing temperature. In many cases, the amount of niobium is defined to be 300 to 400 ppm in order to create carbonitrides in the material. Additionally, the process chain of steelmaking is defined and adjusted in such a way that an optimum distribution of aluminum nitrides and niobium carbonitrides is achieved. Several microalloyed grades have been developed and were successfully tested by component manufacturers. The use of these microalloyed materials is necessary to exploit the vast potential of process time reduction through high-temperature carburizing by means of LPC.

High-temperature LPC realizes new production philosophies, such as one-piece flow manufacturing. With the accelerated LPC process, it is possible to integrate case hardening fully into the manufacturing line (Ref 21). Instead of centralizing all heat treatment operations in one central hardening shop, all heat treating operations can be integrated into the flow of production by installing compact LPC units into each manufacturing line (Fig. 21).

In this new concept, the components are not treated in conventional big batches with multiple layers, but they are treated in small batches consisting of one layer only. The single-layer treatment provides homogeneous heating, carburizing, and precisely controlled gas quenching. All the variations from layer to layer are eliminated, which leads to reductions in distortion variation within the load (Ref 22).

In addition, this production philosophy allows strong cost-savings for logistics. Furthermore, the manufacturing line can be completely automated because the parts are taken one by one from the soft machining unit, heat treated in time with the cycle time of soft machining, and passed down one by one to the hard machining

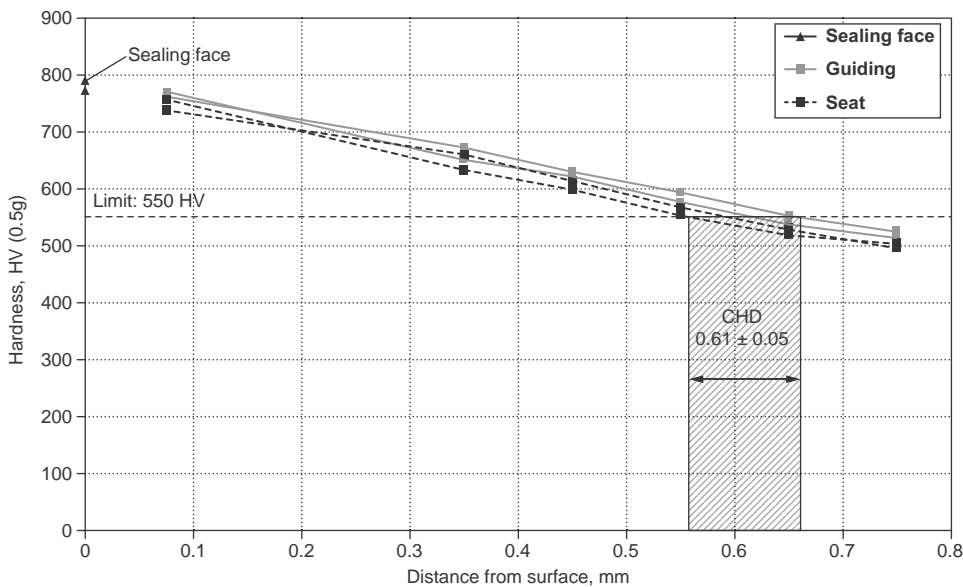


Fig. 17 Hardness profile for various measuring points on the nozzle. Source: Ref 13

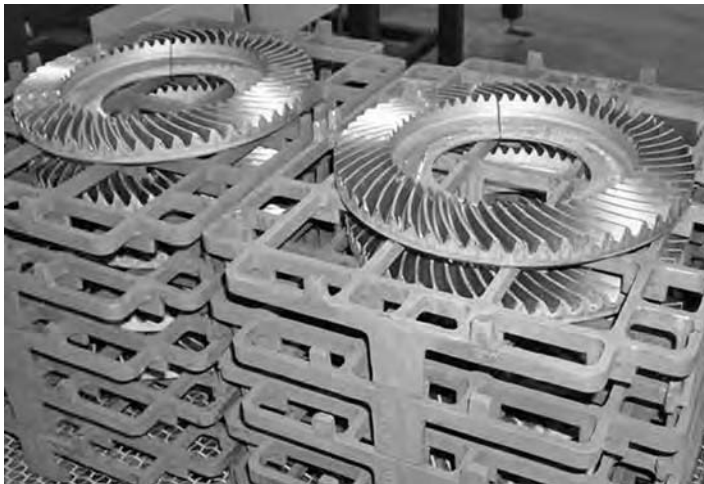


Fig. 18 Load configuration for low-pressure carburizing of transmission gears used in landing box. SAE 9310; 12 parts per batch; carburizing temperature, 960 °C (1760 °F); nitrogen, 6 bar (4500 torr); case-hardening depth, 1.4–1.65 mm (0.055–0.065 in.). Source: Ref 14

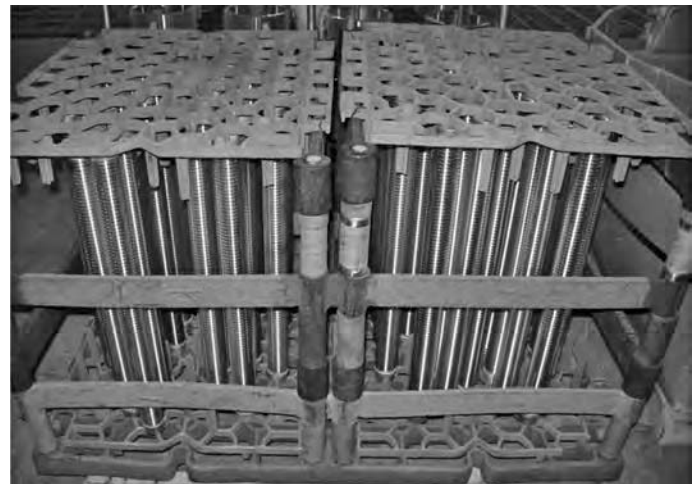


Fig. 19 Load configuration for low-pressure carburizing of ball screws. SAE 8620; carburizing temperature, 960 °C (1760 °F); nitrogen, 20 bar (15,000 torr); case-hardening depth, 1.4–1.65 mm (0.055–0.065 in.). Source: Ref 14

Table 3 Typical quality control of the low-pressure carburizing process

Quality-control step	Frequency
Surface hardness check	Three components per every load
Cutting one component from the load for conventional metallography, hardness profile, and core hardness evaluation	From every second to every tenth load of mass production
Process monitoring	Every production load
Carbon button	Optional; measures weight increase of standardized disc to evaluate carbon absorption of the disc
Nondestructive testing	Optional; eddy current
Distortion checks (measure geometry of components before and after the process)	Depending on the component and application, distortion may need to be checked; when checking distortion, usually one to three components are checked for distortion from every load up to every tenth load of mass production.

Table 4 Treatment times for low-pressure carburizing of 18CrNiMo7-6 at different temperatures (case depth = 1.5 mm, or 0.06 in.)

Process step	Time at treatment temperature, h		
	930 °C (1705 °F)	980 °C (1795 °F)	1030 °C (1885 °F)
Loading	0.25	0.25	0.25
Heating	1.5	1.75	2
Carburizing and diffusion	8.5	5	3
Lowering to hardening temperature	0.75	1	1.25
Quenching and unloading	0.5	0.5	0.5
Bottom to bottom	11.5	8.5	7
Total treatment time reduction	...	25%	40%

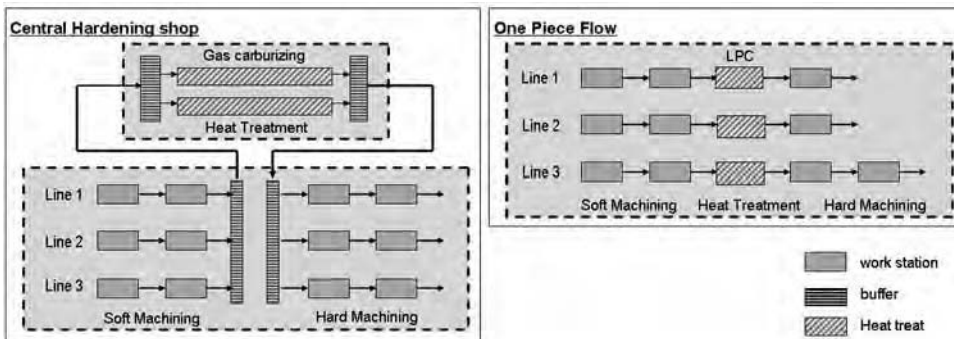


Fig. 21 Component manufacturing with central hardening shop and with one-piece flow (integrated manufacturing lines applying high-temperature low-pressure carburizing, or LPC). Source: Ref 21

unit. Only the application of high carburizing temperatures allows the needed reduction of treatment times so that the cycle time of carburizing matches the cycle time of machining.

REFERENCES

1. D.H. Herring, *Vacuum Heat Treatment*, BNP Media II, 2012
2. D. Buchholz et al., Modellierung des Pyrolyseverhaltens von Ethin unter den Bedingungen des Niederdruckaufkohlen von Stahl, *HTM*, Vol 62 (No. 1), 2007, p 5–12
3. D. Buchholz et al., Simulation der Pyrolyse- und der Oberflächenreaktionen von Ethin beim Niederdruckaufkohlen von Stahl, *HTM*, Vol 63 (No. 2), 2008, p 75–83

4. F. Graf, "Pyrolyse und Aufkohlungsverhalten von C2H2 bei der Vakuumaufkohlung von Stahl," Dissertation, Universität Karlsruhe, 2007
5. W. Gräfen and K. Seehafer, "Einsatzhärten in Theorie und Praxis," Fachtagung Härterei 2009, Münchener Werkstofftechnik-Seminar, March 19–20, 2009
6. M. Steinbacher, B. Clausen, F. Hoffmann, and H.-W. Zoch, Steigerung der Vorhersagegenauigkeit bei der Berechnung des Kohlenstoffprofils von Niederdruckaufkohlungsprozessen, *HTM*, Vol 6, 2007
7. M. Steinbacher, "Thermogravimetrische Messungen beim Niederdruckaufkohlen als Grundlage für Simulationen," Dissertation, Fachbereich Produktionstechnik, Univ. Bremen, Germany, 2012
8. W. Gräfen and B. Edenhofer, Acetylen-Unterdruckaufkohlung—Eine Neue und

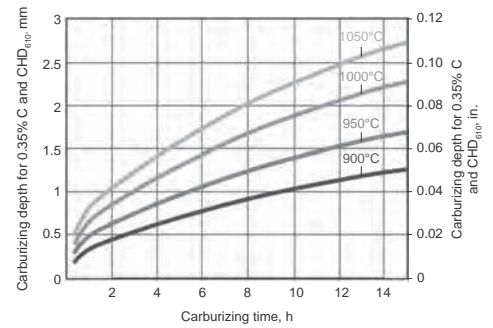


Fig. 20 Carburizing depth as a function of carburizing temperature and duration (without heating). CHD, case-hardening depth. Source: Ref 16

- überlegene Aufkohlungstechnologie, *HTM*, Vol 56 (No. 3), 2001, p 185–190
9. D. Liedtke, "Einsatzhärten," *Stahl Merkblatt* 452, Ausgabe, 2008
10. B. Reinhold, "Simulation der Aufkohlung von Einsatzstählen bei der Vakuumaufkohlung," presented at the European Congress on Total Quality in Heat Treatment, April 14–15, 2005 (Maastricht, Netherlands)
11. J. Kleff, S. Hock, and D. Wiedmann, Wärmebehandlungs-Simulation bei ZF-Anwendungsentwicklung und Vorhersage der Kernhärte an Bauteilen, *HTM*, Vol 6, 2008, p 351
12. K. Heeß, *Maß- und Formänderungen infolge Wärmebehandlung von Stählen*, Vol 3, neu bearbeitete Auflage, Expert Verlag, 2007
13. B. Reinhold, "Processing Diesel Injection Components," presented at the Vacuum Carburizing Symposium, Sept 23, 2008 (Dearborn, MI)
14. D. Herring, personal correspondence, March 2013
15. S. Carey and D.H. Herring, Low-Pressure Carburizing Process Development of M50NiL, *Heat Treat. Prog.* May/June 2007, p 43
16. *Die Prozeßregelung beim Gasaufkohlen und Einsatzhärten*, Autorenkollektiv AWT-FA 5; AK4, Expert Verlag 1997
17. A. Koch, H. Steinke, F. Brinkbäumer, and G. Schmitt, Hochtemperatur-Vakuumaufkohlung für große Aufkohlungstiefen an hoch belasteten Rundstahlketten, *Der Wärmebehandlungsmarkt*, Apr 2008, p 5–7
18. F. Hippenstiel et al., Innovative Einsatzstähle als maßgeschneiderte Werkstofflösung zur Hochtemperaturaufkohlung von Getriebekomponenten, *HTM*, Vol 57, 2002, p 290
19. F. Hippenstiel, Tailored Solutions in Microalloyed Engineering Steels for the Power Transmission Industry, *Mater. Sci. Forum*, Vol 539–543, 2007, p 4131–4136
20. M. Frotey, T. Sourmail, C. Mendibe, F. Marchal, M.A. Razzak, and M. Perez, "Grain Stability during High Temperature

Carburizing: Influence of Composition and Manufacturing Route,” Presented at HärtereiKongress, Oct 10–12, 2012 (Wiesbaden, Germany)

21. V. Heuer, K. Loeser, G. Schmitt, and K. Ritter, “Integration of Case Hardening into the Manufacturing Line: One Piece

Flow,” AGMA Technical Paper 11FTM23, 2011

22. V. Heuer, K. Loeser, T. Leist, and D. Bolton, “Enhancing Control of Distortion through One Piece Flow-Heat Treatment,” AGMA Technical Paper 12FTM23, 2012

SELECTED REFERENCES

- M. Steinbacher, B. Clausen, F. Hoffmann, et al., Thermogravimetrische Messungen zur Charakterisierung der Reaktionskinetik beim Niederdruck-Aufkohlen, *HTM*, Vol 4, 2006

Plasma Carburizing

Brigitte Clausen, Stiftung Institut für Werkstofftechnik, Bremen, Germany
Winfried Gräfen, Hanomag Härtol Gommern Lohnhärtereier GmbH, Gommern, Germany

THE PLASMA CARBURIZING PROCESS, also called ion carburizing, is basically a low-pressure carburizing process making use of a high-voltage electrical field applied between the load to be treated and the furnace wall, producing activated and ionized gas species responsible for the carbon transfer to the workpieces. The process possesses some unique features, such as the ability to carburize passivating and sintered metals, a high reproducibility, and the possibility to cover parts that cannot be carburized mechanically. The process had its peak of industrial utilization in the years between 1990 and 2000 but has lost its importance due to the rising use of low-pressure carburizing using acetylene in the late 1990s.

In the first trials by Edenhofer (Ref 1), it was noticed that an enormous amount of the carbon present in the atmosphere diffused into the surface of the sample when glow-discharge conditions occur between the sample (cathode) and the furnace (anode). Quantitative measurements showed that up to 90% of the supplied methane is converted into diffusible carbon (Ref 2). Further advantages include:

- High carbon-transfer velocities
- No soot formation
- Surfaces free of internal oxidation
- Homogeneous carburizing depth (e.g., in blind holes)
- Easy partial treatment due to mechanical cover

These results led to a high demand for plasma carburizing furnaces. Several examples of applications can be found in Ref 3, 4, 5, 6 to 7. In contrast to plasma nitriding, the importance of plasma carburizing is abating, because most advantages are easier to achieve in a low-pressure carburizing process (see the article "Low-Pressure Carburizing (LPC)" in this Volume) without the additional investment in a plasma generator and electrical isolation. Only one example for a still-working plasma process in industrial measure could be found in the investigation for this article. The example is presented at the end of the article.

Principles of Plasma Carburizing

A plasma carburizing process can be applied in a low-pressure carburizing furnace with some extra effort. The furnace must be isolated electrically from the heating and the batch, which will be connected to the plasma generator. The generator applies a voltage of approximately 600 V between the batch and the grounded furnace. It results in a current density in the range of 1 mA/cm² on the batch. The voltage must be pulsed in the range of microseconds to avoid arc discharges. Because every connection between the batch and heating chamber causes a short circuit, and carbon is a good conductor, the cleanliness of the isolation must be monitored. A plasma process requires a visual observation. Apart from calculations concerning the optimal pressure and the batch design, this visual observation offers certainty that the batch is carburized uniformly and no hollow cathode occurs. Figure 1 shows a schematic drawing of a plasma carburizing furnace.

For the plasma process, the gases methane, hydrogen, and argon should be provided. If carbonitriding processes are planned, nitrogen

should be held available. With the addition of propane and acetylene, plasma-powered low-pressure carburizing processes are possible. Because the carbon transfer in plasma carburizing processes is approximately as high as in a low-pressure carburizing process with acetylene as process gas, the process must be divided into carburizing and diffusing segments. The length of these segments is dependent on the carbon transfer. Figure 2 shows a schematic process procedure. The process starts with the evacuation of the furnace. The batch is heated up to process temperature. In the last heating segment, the sputter process is started. It is carried out with an inert gas or hydrogen, and the plasma is used to clean the surface. Thereafter, the plasma process is started with the carburizing gas. After a duration calculated from the mean carbon transfer, the furnace is evacuated again and kept at low pressure until the surface carbon content drops to approximately 0.6 mass% due to diffusion into the matrix. After diffusion, the next carburizing segment can start. The duration of the segments is calculated from empirical values. The addition of nitrogen allows the formation of reactive nitrogen-containing species in the process. Thus, nitrogen can be absorbed by the surface and change the carburizing into a carbonitriding process.

Theoretical Background on Glow-Discharge Plasma. A plasma is an electrically generated gaseous mixture consisting of positively and negatively charged particles as well as neutral species and electrons. Although gaseous in nature, it has a cohesive and stable form with a net electrical charge of zero. Plasmas occur in many places throughout the cosmos but do not exist in stable form on Earth due to the rather special conditions they require for initiation. Nevertheless, the necessary conditions can be easily achieved, and thus, stable man-made plasmas can be produced. Such plasmas have been widely employed in a variety of important industrial applications, such as welding, catalyzing chemical reactions, laser pumping, polymer stabilization, and coating processes such as physical and chemical vapor deposition.

The plasma used for case carburizing is the glow discharge (Ref 8–10). This glow-discharge

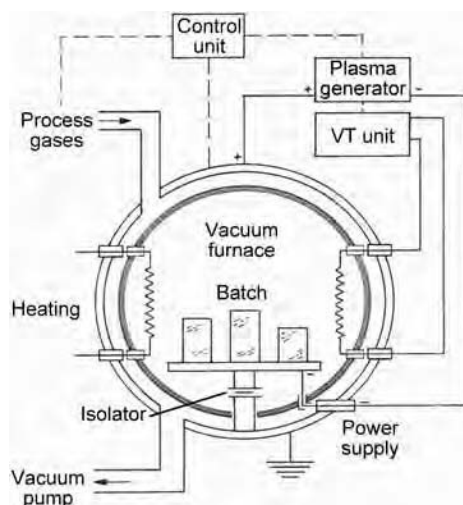


Fig. 1 Schematic drawing of a plasma carburizing furnace. Courtesy of IPSEN International

plasma contains a very high density of electrons ($1 \times 10^{12}/\text{cm}^3$) with an average energy in the range of 1 to 10 electron volts (eV)—an energy range very effective in ionizing and dissociating diatomic molecules. Further characteristics of a glow discharge are a typical degree of ionization of 10^{-4} and a current density of approximately $1 \text{ mA}/\text{cm}^2$. Thus, plasma provides a ready and prolific source of chemically active atoms, and, in plasma (ion) carburizing, this is its principal function.

A glow-discharge plasma can be established and maintained by placing two metal electrodes at opposite ends of a glass enclosure and evacuating it to a few hundred pascals (Pa) of pressure. Upon applying a direct-current voltage of a few hundred volts, a striated visible glow consisting of various regions (shown schematically in Fig. 3) is observed.

In plasma (ion) carburizing, only the cathode and negative glows in the vicinity of the negative electrode are important. It is in this region of highest field strength (the cathode fall region) that ionization of the residual gas in the tube occurs. In fact, most of the advantages achieved by ion carburizing may be attributed to the physical processes that occur in this region. Here, the electron and ion velocities are sufficiently high to dissociate molecules of the low-pressure gas and thus provide the active species required. Because this region is very near the cathode, it is also highly probable that these activated species will reach the cathode during their lifetime and thus be available for reaction with the cathode surface or absorption into it. More detailed information about the electron and ionic processes that occur in the cathode fall region can be found in the literature (Ref 8–10).

Range and Limitations of Glow-Discharge Plasma. While glow-discharge plasma can be made to occur over a rather wide range of conditions, there are, nevertheless, some constraints that must be observed to ensure stability and a constant supply of active carbon. Referring again to Fig. 3, only the positive column constitutes “true” plasma, that is, an ionized gas having no net space charge. This positive column, however, is not essential to the stability of the discharge and may be eliminated by bringing the two electrodes closer together. In fact, if the pressure and the voltage are held constant and the distance between anode and cathode (d) in Fig. 3 is decreased, the positive column simply shrinks in length until it disappears as the anode enters the Faraday dark space. The discharge parameters do not change appreciably until the anode approaches the negative glow. Even with the anode very near the negative glow, the discharge is still stable, but at a slightly higher voltage.

As d is further decreased, however, the voltage necessary to maintain stable operation will increase unless the pressure is increased to maintain approximately the same total amount

of gas between the electrodes as when d was large. As shown by the Paschen curves in Fig. 4, the voltage required to maintain a stable discharge in a gas at low pressure is a function of both the pressure, P , and the distance, d , between the electrodes—actually, the product of P and d . Thus, as d is decreased, the pressure must be increased to permit operation at the minimum voltage.

Voltage Levels in Plasma Carburizing. Although it would be advantageous to be able to operate at the minimum voltage, in ion carburizing there are other, more important conditions to be met. For example, it is essential that the plasma completely covers the cathode so that the case over the entire surface of the workpiece (the cathode) will be of uniform depth. A plot of voltage versus current in a

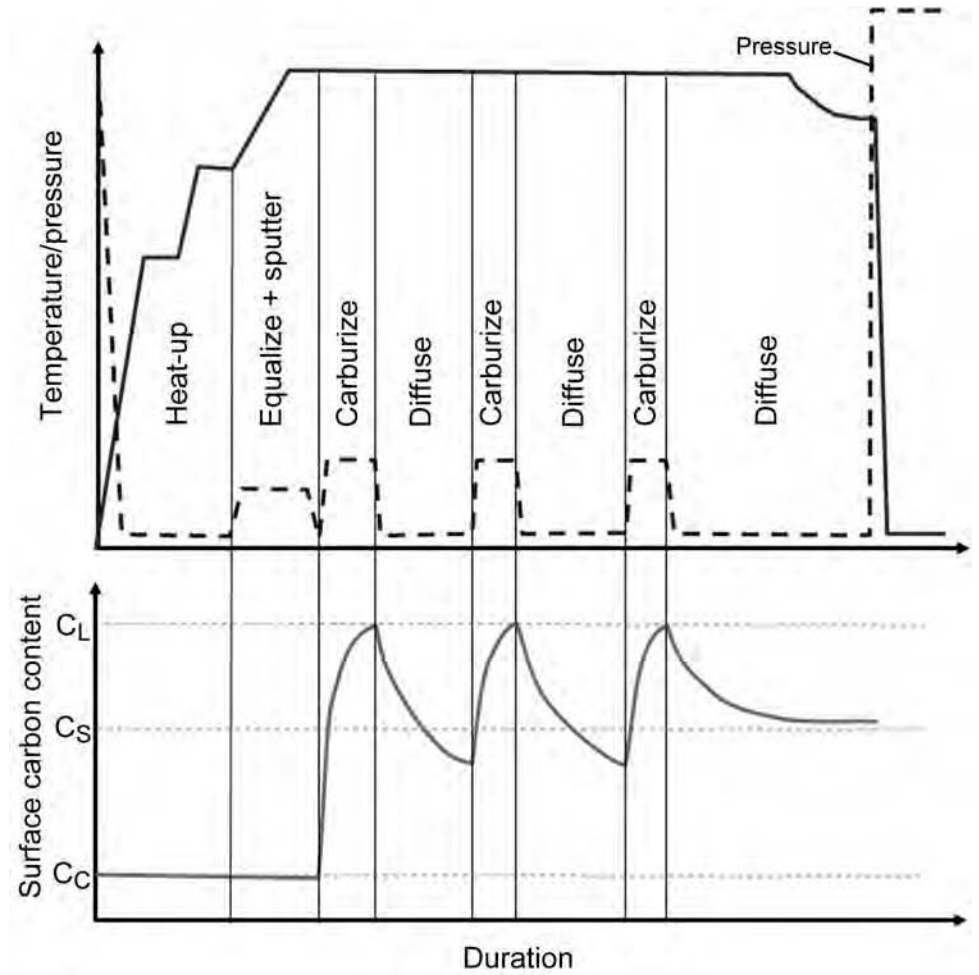


Fig. 2 Schematic process procedure

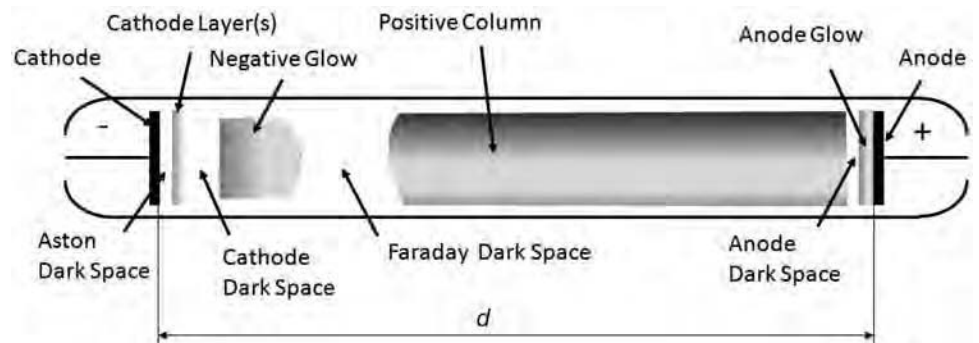


Fig. 3 Luminous and dark spaces of a glow discharge. Source: Ref 9

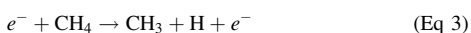
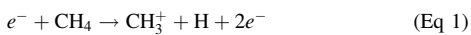
gas at low pressure is shown in Fig. 5. The minimum voltage required ensuring complete coverage of the cathode is indicated by "X," which is a voltage just above the constant voltage of the "normal" glow region. Although the voltage must be high enough to ensure that the point "X" is on the positive slope region of the current-voltage characteristic curve (for stability), it should not be any greater than that required for complete coverage, because higher voltages simply increase the tendency of the discharge to pass into the arc mode (Fig. 5). Thus, in actual practice, the voltage is interrupted continuously in pulses of a few microseconds length to minimize the tendency of the discharge to abruptly enter the arc mode and damage the part.

Coverage and Wrap-Around Effect. While the need to adjust the operating conditions to ensure that the glow sheath completely covers the workpiece may appear to be a troublesome constraint, this requirement is, in fact, an important advantage. Because a surface reaction will occur on the metal part only where the glow discharge is in contact with it, operation under conditions where complete coverage occurs ensures that the case will be of fairly uniform depth over the part—even on those areas that are not directly opposite (facing) the counterelectrode (the anode).

Deep recesses and blind holes are also carburized, provided the depth-to-diameter ratio is not too large (<12:1). To permit penetration of the glow discharge, a hole must have a diameter at least twice the thickness of the plasma sheath. The depth of the penetration of the plasma and therefore the extent of downhole carburizing will depend on the pressure and the interelectrode distance, d . This has important consequences in furnace design and furnace loading, as well as an influence on the operating parameters.

Carburizing Reaction in Plasma Carburizing

The plasma carburizing process is carried out with the process gases methane or propane. The carbon-transfer process during plasma carburizing is explained with methane. The important processes of electrons with other molecules in pure methane glow discharges are the following (Ref 11–13):



The production of the molecule CH_3 and the ions CH_3^+ and CH_4^+ are necessary for the

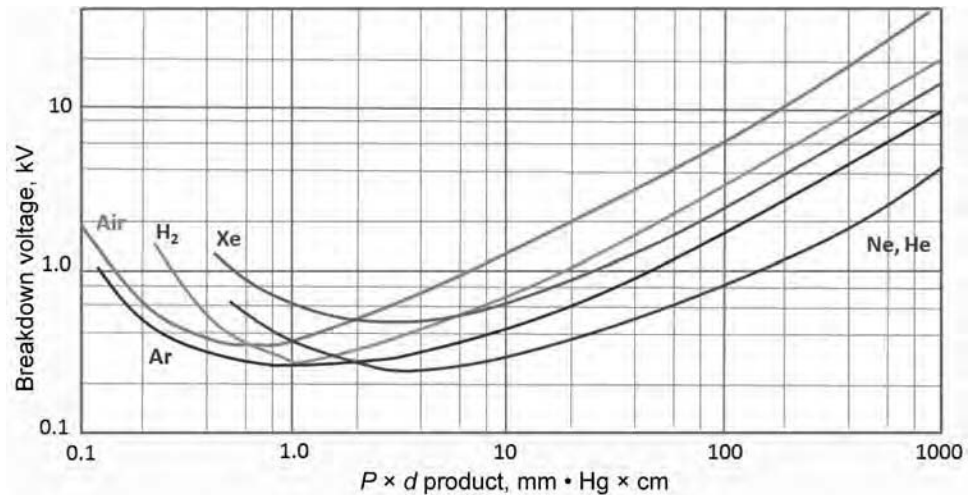


Fig. 4 Paschen curves for a direct-current glow discharge between parallel-plate electrodes for various gases, showing the breakdown voltage versus the product of the gas pressure (P) and the distance (d) between the electrodes

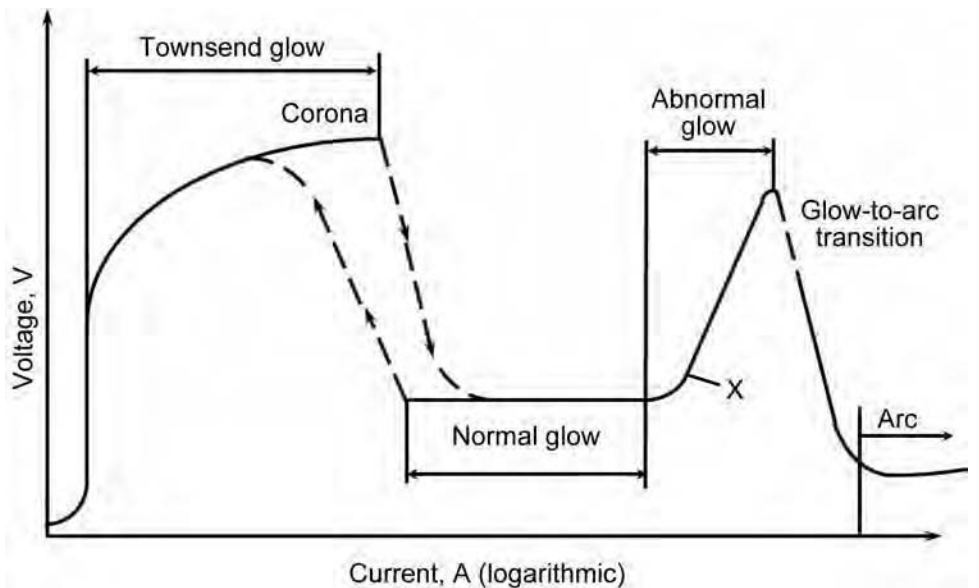


Fig. 5 Schematic current-voltage characteristic for electrical discharges in a gas at low pressure. X, minimum voltage required to ensure complete coverage of the cathode

carbon transfer from the glow discharge to the surface area of the workpiece (Ref 11). The positive-charged ions CH_3^+ and CH_4^+ are accelerated to the cathode due to the voltage of the discharge. Because the weights of CH_3^+ and CH_4^+ ions are nearly the same as the weight of CH_3 radicals, these molecules are moved to the cathode through collision reactions, too. The CH_3^+ and CH_4^+ ions and CH_3 radicals are adsorbed from the surface of the batch (cathode), crack in atomic carbon and hydrogen, and diffuse into the steel (Fig. 6) (Ref 13).

The atomic carbon is dissolved in the face-centered cubic lattice of the austenite, and the hydrogen atoms diffuse through the lattice and

leave the steel in the diffusion segments of the carburizing cycle. The carbon transfer of glow discharges depend on the current density, voltage, frequency, type of gas, gas mixture, process gas pressure, and temperature. Figure 7 shows the influence of current density on carbon transfer at a pressure of 5 mbar and a temperature of 950 °C (1740 °F) as an example of the different parameters.

Diffusion Characteristics. The laws of diffusion are not affected by the employment of plasma in the carburizing process:

$$\dot{m} = -D \frac{\partial C}{\partial x} \quad (\text{Eq 5})$$

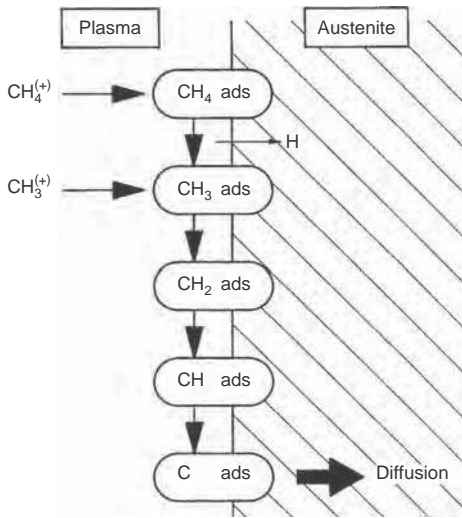


Fig. 6 Surface reactions during plasma carburizing. Source: Ref 13

The carbon flux (\dot{m}) is proportional to the carbon gradient ($\partial C/\partial x$) in the surface and the diffusion coefficient (D). The context is visualized in Fig. 8. The carbon gradient can be increased by covering the surface with diffusible carbon. The surface carbon content will increase to the temperature- and alloy- dependent solution limit (Fig. 9) and start to build carbides if the supply is not reduced. The increased gradient between surface and core content increases the carbon diffusion into the metal primarily in the first seconds of carburizing. Like vacuum carburizing, plasma carburizing is performed in an oxygen-free environment, which permits higher temperatures and thus higher diffusion rates. Both the higher diffusion rate and the carbon uptake lead to an increase of the carburizing velocity. The best effect is achieved in a combination of higher carburizing temperature and higher carbon uptake (Fig. 8).

On the other hand, it must be remembered that an increase in carburizing temperature leads to grain growth in conventional carburizing steels (Fig. 10). If the mechanical features of the treated parts are of importance, the microstructure must be refined before the hardening procedure, or specially alloyed grain-stable steels must be used (Ref 15). Another point that must be taken into account is the lifetime of furnaces and batch racks, which decreases disproportionately with increasing process temperature. Heavy components carburized at higher temperatures are in danger of losing their shape by creep due to their own weight.

Advantages and Disadvantages

Most advantages of the plasma carburizing process are based on processing at low pressures and are therefore the same as for low-pressure carburizing processes:

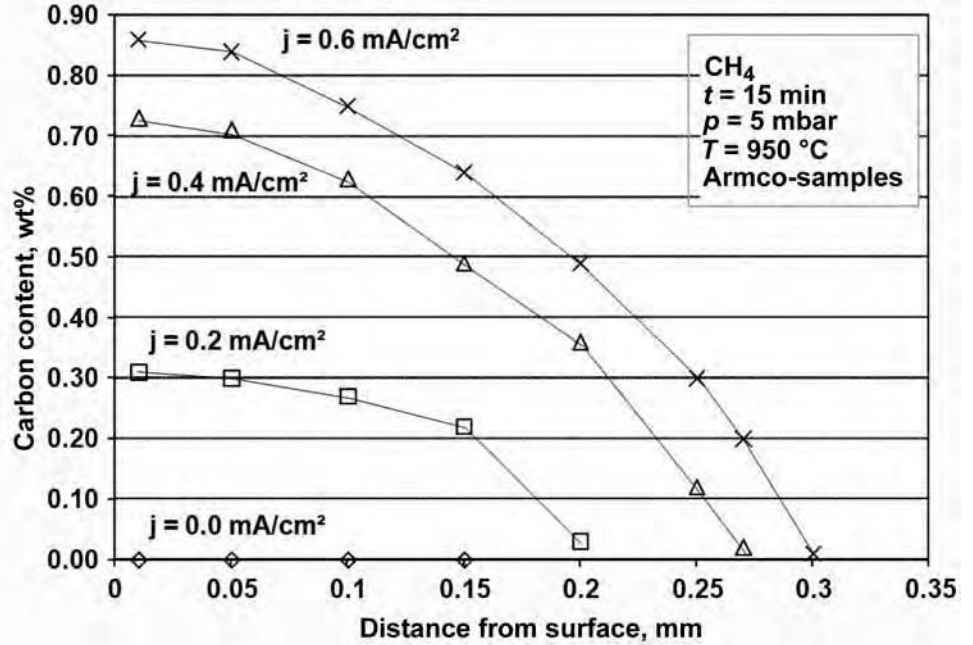


Fig. 7 Carbon transfer as a function of current density. Source: Ref 12

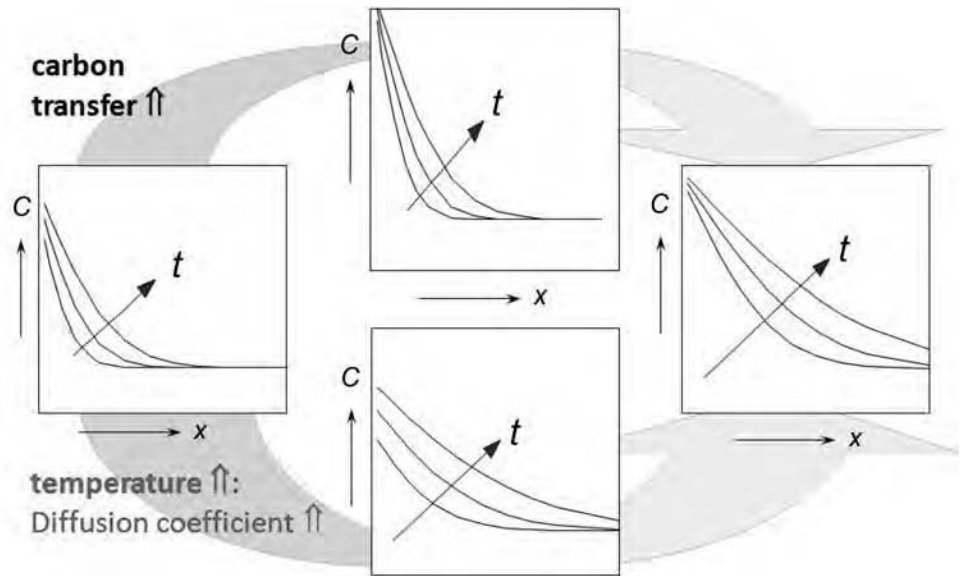


Fig. 8 Correlation between carbon uptake, temperature, and carbon supply at the surface

- High carburizing rates
- Surfaces free of internal oxidation
- Carburizing of parts with complex geometries possible
- No emission of heat and dangerous gases to the environment
- Easy integration in production lines
- No conditioning of furnaces needed
- High reproducibility
- Possible application of higher carburizing temperatures
- Shorter cycle durations
- Low input of energy and carburizing gases

Apart from these common advantages, the plasma carburizing process has some unique features that are briefly discussed as follows.

The main disadvantage of plasma carburizing is the sensitivity of the process. The use of carbon-dispensing gases combined with high voltages makes the process delicate. In comparison to gas carburizing processes, it must be claimed that despite all efforts, it is still not possible to measure a carbon-uptake corresponding value or even the temperature in the batch. The control of the process is therefore unsatisfactory.

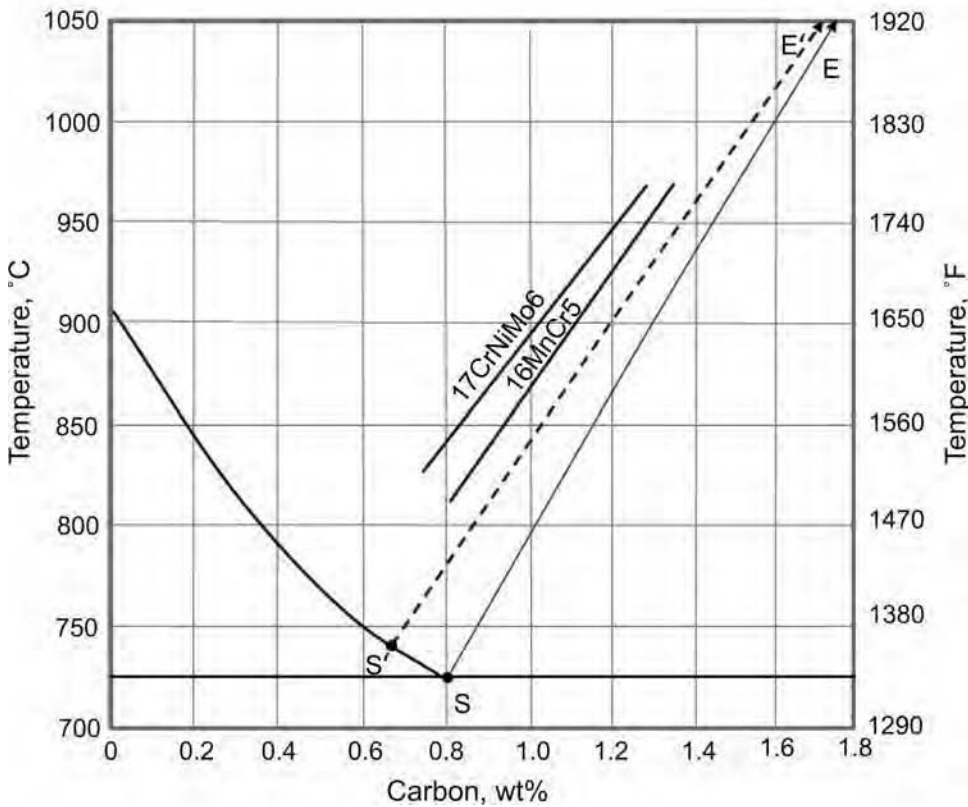


Fig. 9 Low-carbon region of the iron-carbon composition diagram complemented with calculated solubility limits for 16MnCr5 and 17CrNiMo6. Source: Ref 14

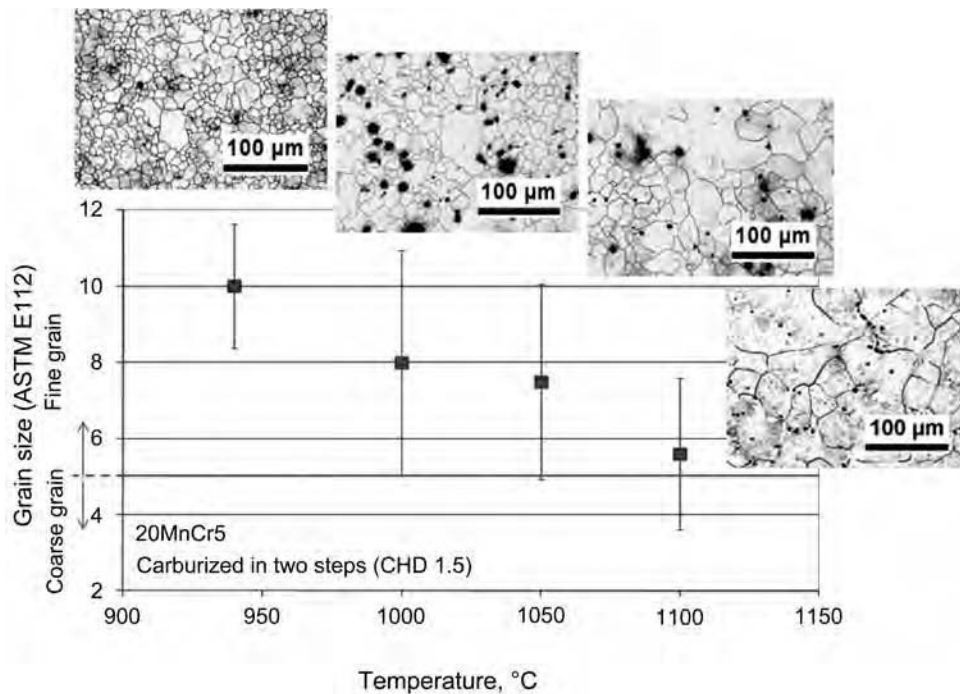


Fig. 10 Grain growth in conventional carburizing steels with increasing carburizing temperature

Mechanical Masking. In every other carburizing process, masking of, for example, core threads entails great effort. In plasma carburizing processes with methane, every thread can be masked with a simple nut (or screw), because carburizing definitely does not take place were the plasma glow is not glowing.

Carburizing Sinter Metals. Carburization of sinter metals in conventional gaseous or low-pressure processes effects an increase of the carbon content in the whole part, because the gases penetrate the porous structure. In plasma carburizing processes with methane, the carburizing treatment will be limited to the surface, because below 1130 °C (2065 °F) the nonactivated methane does not carburize the microstructure. A case-hardening treatment is therefore only possible in a plasma carburizing process.

Carburizing of Stainless Steels. Stainless steels have a passivating surface that makes it impossible to carburize them uniformly in conventional processes. In plasma carburizing processes, the surface can be activated by a sputter plasma using argon or hydrogen. The passive layer is not rebuilding at low pressures. Carburization can take place even at low temperatures to avoid the forming of chromium carbides.

Influence of Pulse Length on Carbon Input. The high carbon input of low-pressure carburizing processes is not always an advantage. As stated in the technical basics, the carburizing segments last until the carbon solution limit is reached (Fig. 2) and are followed by a diffusion segment. Throughout the process, a carbon profile forms in the surface. The amount of carbon needed to reach the solution limit decreases continuously in the process. With a constantly high carbon input, this results in an extreme shortage of the carburizing periods. The carbon input cannot be reduced by carburizing gas dilution or current reduction below a minimum value without risking a lack in homogeneity of carbon uptake in the batch. In low-pressure carburizing processes without plasma, support of this effect may result in carburizing periods below 1 min at carburizing depths above 1 mm (0.04 in.) (if the formation of carbides is to be avoided).

The plasma carburizing process offers new possibilities because the carbon input can additionally be influenced by the length of the current pulses. Contrary to plasma nitriding, the pulse-pause ratio can be chosen freely, because the batch is heated independently in the plasma carburizing process. It is possible to start with longer pulses and reduce them within the process, so that the carburizing periods always offer an optimal length and carbon supply (Ref 16).

Production Equipment

Plasma carburizing furnaces do not differ much from low-pressure carburizing furnaces. They consist of a vacuum-tight, double-wall,

water-cooled outer shell equipped with a vacuum pump system and an inner hot zone mainly consisting of graphite board insulation and graphite heating elements. The quenching process can be carried out in the very same way as after a low-pressure (vacuum) carburizing process. It is important that the load hearth support consists of electric insulators. The high-frequency pulsed power supply is connected to the batch through the load hearth support.

Loading Requirements and Limitations

Parts cannot be shovel loaded, because the plasma envelope would be mechanically masked. To carburize, the plasma envelope must surround the component part. Thus, the parts must be fixtured or positioned such that they do not contact each other. Further, the distance between parts must be adjusted in a way that a hollow cathode is excluded. The distance must exceed the double visible glow thickness to achieve this aim.

The thickness of the cathode visible glow or luminescence is a function of the pressure, gas composition, and temperature. The glow luminescence becomes thicker as the temperature increases due to the kinetic activity, and it becomes thinner with increasing pressure. A visual observation is helpful to avoid a hollow cathode and to observe the glow enveloping the batch.

Process Parameters

Experience has shown that results gained in plasma carburizing equipment cannot always be transferred to other equipment (Ref 17). Results are basically influenced by the shape of the heating chamber and the power characteristic of the plasma generator. Specific trials in a new furnace are inevitable.

Surface Condition. The plasma carburizing process is not sensitive to surface contamination. Heavily rusted samples can lead to a decrease in carbon uptake, but contamination occurring in normal industrial life does not harm the result or the homogeneity of the result (Ref 17).

Temperature influences the results by increasing the solution limit (Fig. 2) and the diffusion coefficient of carbon in steel. Further, the temperature influences the voltage-current characteristic, effecting a higher current density at higher temperatures at similar voltages (Ref 17).

Composition of Atmosphere/Gas Flow Rate. To ensure homogeneous carburization of the batch, a minimal furnace, current density, and batch-size-dependent amount of methane must be applied. A dilution of the process gas methane can be realized with nitrogen but is not necessarily needed. A sensible value can be found at approximately 100 SL (standard liters) $\text{CH}_4/(\text{h} \cdot \text{m}^2)$ (Ref 17).

Pressure. The pressure used for plasma carburizing processes ranges between 100 and

800 Pa (0.015 and 0.116 psi). If the plasma is glowing stable, the pressure has no effect on the carburization of plain surfaces. The carburization of blind and through holes can be influenced positively by higher pressure. The depth of the penetration of the plasma and therefore the extent of downhole carburizing will depend on both the pressure and the interelectrode distance, d . The width of the plasma glow should be thinner than half of the hole diameter. To ensure even carburization, a visual observation of the formation of the plasma luminescence or visible glow is necessary in covering the whole surface of the load. The visual check also verifies that no hollow-cathode effects are observed.

Voltage, Current, Pulse—Power Density. Voltage and current density are connected in the temperature, gas composition, and pressure-dependent voltage-current characteristic (Fig. 5). The current is operated between the minimal current density, providing a glow of the plasma luminescence on the whole surface of the batch, and the maximal current density below the current that results in an arc discharge. An example of the influence of current density on carbon transfer was given in Fig. 7. The carbon transfer rate (\dot{P}) increases with increasing power density, expressed as the product of voltage (U) and current (I) per unit area (A):

$$\dot{P} = \frac{U \cdot I}{A} \cdot \frac{t_{\text{Pulse}}}{t_{\text{Pulse}} + t_{\text{Pause}}} \quad (\text{Eq 6})$$

The equation shows that with stable process parameters for voltage, current, and pressure, the carbon uptake in the carburizing process can be controlled by reducing or increasing the length of the pauses between two pulses.

Application Example

Today (2013), there is only one user still applying plasma carburizing on an industrial basis. The process is described in the following example (Ref 18).

Diesel injection components are very complex-shaped and highly stressed parts. Usually, they are manufactured from special purified case-hardening or heat treatable steel grades and must be heat treated with severe requirements regarding distortion and cleanliness. This is because the parts are soft machined to a near-net shape geometry, and washing after heat treatment is undesirable. The injector body made of DIN 1.5920 steel exhibits a center bore hole and a sealing face at the lower end, and both are requested to be case hardened (Fig. 11). Four threads of different geometries are not permitted to be carburized. The outer surface is permitted but not requested to be carburized.

To fulfill these requirements, it is necessary to mask the part in a way that allows the plasma only to cover the faces to be carburized. This is

carried out by enclosing a certain number of parts completely within a graphite box and additionally masking the threads at the upper and lower end of the center bore hole of each part by metal sleeves (Fig. 12).

For the preparation of the load, eight of the graphite boxes are filled with the prewashed parts, and then the boxes are placed on two levels of a cast alloy rack. The load size is approximately 100 injector bodies and is limited to the usable volume of the furnace.

The equipment used for the plasma carburizing heat treatment process is an eight-chamber inline vacuum furnace manufactured by ALD



Fig. 11 Shape of investigated injector body. Source: Ref 18

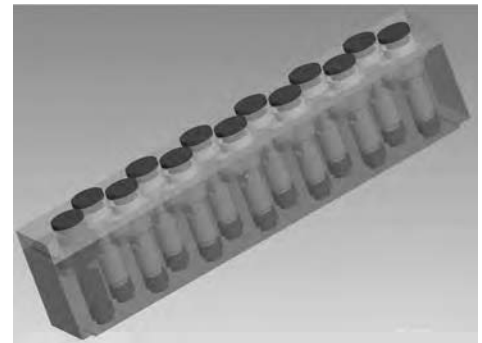


Fig. 12 Three-dimensional model of heat treatment fixture for injector bodies made of graphite. Source: Ref 18

and especially adapted to the size of the parts to be carburized (Fig. 13).

The plasma process is carried out at 900 °C (1650 °F) in a CH₄-Ar-H₂ gas mixture at a pressure of approximately 7 mbar, a voltage of approximately 600 V, and a current density of approximately 4.0 mA/cm². After the last diffusion cycle, the parts are lowered to hardening temperature. During the last cycle, the load stays in the quenching chamber to be cooled down with 10 bar nitrogen and a fan motor power of 125 kW. The heat treatment proceeds with a subzero treatment at -100 °C (-150 °F), followed by tempering at 180 °C (355 °F) for 2 h.

Figure 14 shows two microhardness profiles after the complete heat treatment. Surface hardness and case-hardening depth are within the specification and are very close together at the different locations, indicating that the plasma carburizing process is capable of producing a very uniform case even on complex-shaped parts with small through and blind holes.

This example takes advantage of the main unique features of the plasma carburizing process:

- The parts are mechanically masked on the surfaces that will not be carburized.
- The process is integrated into a production line.
- The reproducibility is used for a process with nonchanging parameters.

Due to the results achieved with low-pressure carburizing in recent years and the design-related problems of plasma carburizing furnaces, the technique is expected to become obsolete in coming years.

REFERENCES

1. B. Edenhofer, Carbonitrieren im Plasma der Glimmentladung, *Härt.-Tech. Mitt.*, Vol 28 (No. 3), 1973, p 165–172
2. W.L. Grube, Progress in Plasma Carburizing, *J. Heat Treat.*, Vol 1, 1980, p 40–49
3. Y. Yoneda and S. Takami, Ion Carburizing Process for Industrial Applications, *Proc. of Vacuum Metallurgy*, Science Press, Princeton, 1977, p 135–156
4. F. Hombeck and W. Rembges, User Experience with an Integral Quench Plasma (Ion)-Carburizing Furnace, *Proc. of Heat Treatment '84*, May 2–4, 1984 (London), The Metals Society, London, 1984, p 51.1–51.9
5. B. Edenhofer, M.H. Jacobs, and J.N. Georges, Industrial Processes, Applications and Benefits of Plasma Heat Treatment, *Proc. of International Seminar on Plasma Heat Treatment*, Sept 21–23, 1987, PYC édition, Paris, 1987, p 399–415
6. F. Schnatbaum, Plasmadiffusionsbehandlung von Sinterwerkstoffen, *HTM*, Vol 48 (No. 3), 1993, p 172–181
7. W. Gräfen, Die Plasmaaufkohlung in der industriellen Anwendung, *HTM*, Vol 53 (No. 6), 1998, p 390–394
8. A. von Engel, *Ionized Gases*, Oxford and the Clarendon Press, 1955
9. B. Chapman, *Glow Discharge Processes*, Wiley-Interscience, John Wiley and Sons, 1980
10. J. Reece Roth, *Principles*, Vol 1, *Industrial Plasma Engineering*, IOP Publishing Ltd., 1995



Fig. 13 Heat treatment plant VMKQ8 PC 40/40/40. Source: Ref 18

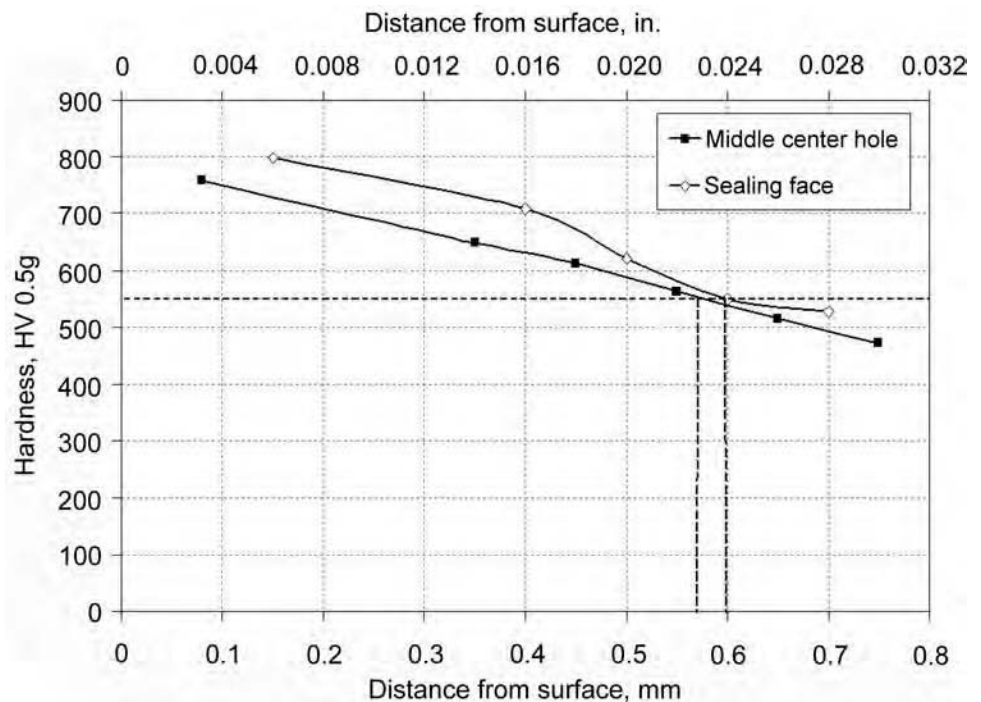


Fig. 14 Two hardness profiles on the carburized surfaces of an injector body. Source: Ref 18

11. T. Rose, "Messungen und Modellbetrachtungen zur Spezies und Energieverteilung von Ionen und Neutralteilchen an der Kathode von Glimmentladungen," Berichte des Forschungszentrum Jülich, 2662, Institut für Plasmaphysik Jül-2662, Assoziation EUROATOM KFA D 62, Dissertation Universität Düsseldorf, 1992
12. J.W. Bouwman and W. Gräfen, Anwendungen von thermischen Hochtemperaturprozessen in Vakuumanlagen, *BHM* (No. 3), 2001, p 68–76
13. B. Edenhofer, J.G. Conybear, and G.T. Legge, Opportunities and Limitations of Plasma Carburizing, *Heat Treat. Met.*, Vol 1, 1991, p 6–12
14. H.J. Grabke, D. Grassl, F. Hoffmann, D. Liedtke, F. Neumann, H. Schachinger, K.-H. Weissohn, J.A. Wüning, U. Wyss, and H.-W. Zoch, *Die Prozessregelung beim Gasaufkohlen und Einsatzhärten*, Expert Verlag, Renningen-Malsheim, 1997
15. E.P. Degarmo, J.T. Black, and R.A. Kohser, Materials and Processes in Manufacturing Update, *Materials and Processes in Manufacturing*, 9th ed., Wiley, 2003, p 116
16. K.T. Rie, F. Schnatbaum, and A. Melber, Process for Hardening of Work Pieces in a Pulse-Plasma Discharge, European Patent 0 552 460, Dec 11, 1992
17. B. Clausen, "Neue Verfahrensansätze auf dem Gebiet der Einsatzhärtung von Stählen und deren Auswirkungen auf Bauteileigenschaften," Forschungsberichte aus der Stiftung Institut für Werkstofftechnik, Bremen, Band 43, Shaker Verlag Aachen, 2009
18. B. Reinhold, Plasma Carburizing: Exotic with Potential, *Int. Heat Treat. Surf. Eng.*, Vol 3 (No. 4), 2009, p 136–140

Carbonitriding of Steels*

Jon Dossett, Consultant

CARBONITRIDING is a modified form of carburizing that involves the introduction and diffusion of atomic nitrogen (N) into the surface steel during carburization. The process is done by introducing ammonia (NH₃) during carburization, so that nitrogen atoms are available to enter and diffuse into the surface. Nitrogen in the case has several beneficial effects. Small amounts facilitate carbon diffusion and dissolution in iron (Ref 1), with some increase in hardness (Fig. 1, Ref 2). Nitrogen contents above approximately 0.20 wt% also have a marked effect on hardenability. This allows case hardening by oil quenching of plain carbon and low-alloy steels that would otherwise require water quenching. Full hardness with less distortion can be achieved with oil quenching or, in some instances, even gas quenching, employing a protective atmosphere as the quenching medium.

Carbonitriding also imparts some additional wear resistance compared to ordinary case hardening.

Like carburizing, the process temperatures for carbonitriding are above the upper critical (Ac₃), but carbonitriding typically is done at a lower temperature than carburizing—between 775 and 900 °C (1425 and 1650 °F) versus 870 and 1065 °C (1600 and 1950 °F) for carburizing—and for a shorter time. At higher carbonitriding temperatures, ammonia additions are less effective as a source of atomic nitrogen (N) for the case, because higher temperatures raise the rate of spontaneous decomposition of ammonia into molecular nitrogen (N₂), and hydrogen increases. Molecular nitrogen also does not easily diffuse, nor does it contribute to case hardenability. Thus, lower process temperatures are needed to maintain an effective source of atomic nitrogen.

Because gas carbonitriding typically is carried out at a lower temperature and for a shorter time than for gas carburizing, the case is usually shallower than that of production carburizing. Carbonitrided cases are usually between 0.075 and 0.75 mm (0.003 and 0.030 in.) deep. However, even though carbonitriding uses a lower process temperature, small amounts of nitrogen can be beneficial in the diffusion process. At lower concentrations, nitrogen raises the diffusion coefficient of carbon in austenite and increases the activity of carbon in austenite, as a result of the superficial concentration of carbon in the primary layer from the furnace atmosphere (Ref 1). Thus, for a given case depth, the carbonitriding process can be done at a temperature approximately 50 °C (90 °F) lower than the comparable carburizing temperature to achieve the same case depth.

Steels commonly carbonitrided include those in the 1000, 1100, 1200, 1300, 1500, 4000, 4100, 4600, 5100, 6100, 8600, and 8700 series, with carbon contents up to approximately 0.25%. Also, many steels in these same series with a carbon range of 0.30 to 0.50% are carbonitrided to case depths up to approximately 0.3 mm (0.01 in.) when a combination of a reasonably tough, through-hardened core and a hard, long-wearing surface is required (shafts and transmission gears are typical examples). Steels such as 4140, 5130, 5140, 8640, and 4340 for applications such as heavy-duty gearing are treated by this method at 845 °C (1550 °F). Where core properties are not important, carbonitriding permits the use of low-carbon steels, which cost less and may have better machinability or formability.

Carbonitriding has been known since the early 1900s but was little used until approximately 1935. Its use increased rapidly in the postwar years (Ref 3). Over the years, the carbonitriding process has been given many names, such as dry cyaniding, gas cyaniding, nicarbing, and others (Ref 4, 5). The nitriding process of nitrocarburizing also has been improperly used as reference to the carbonitriding process. Part of this confusion is that the term *carbonitriding* seems to imply a nitriding process. However, carbonitriding is a modified form of

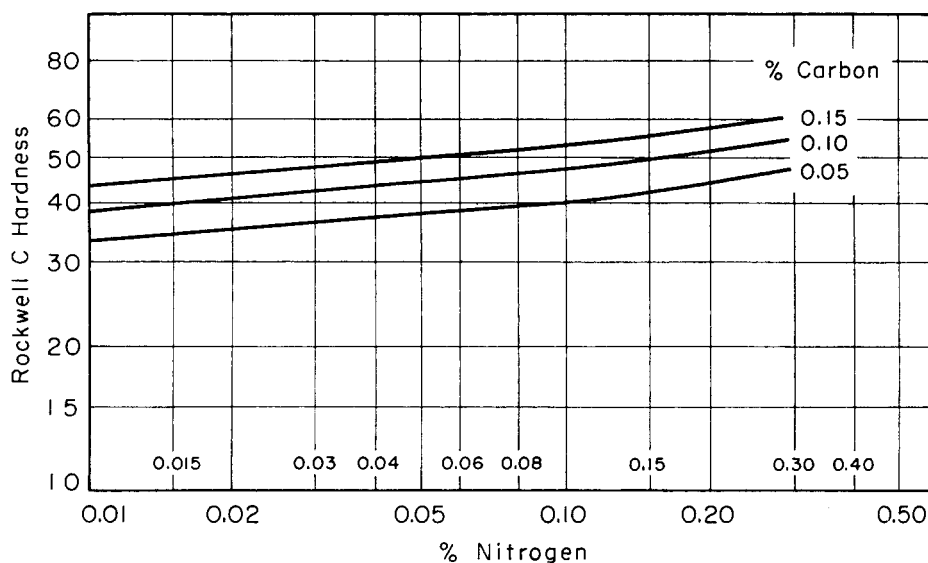


Fig. 1 Effect of nitrogen on the attainable hardness of martensite in steels with carbon levels of 0.05, 0.10, and 0.15 wt%. Quenched to produce fully martensitic structure free from residual carbides and residual nitrides. Source: Ref 2

* Revised from J. Dossett, Carbonitriding of Steels, *Heat Treating*, Vol 4, ASM Handbook, ASM International, 1991, p 376–386

carburizing, while nitrocarburizing is a nitriding process with higher levels of nitrogen in the case and a compound layer on the surface.

Carbonitriding produces a martensitic case with nitrogen levels less than carbon levels, such as the typical carbonitrided case shown in Fig. 2 with approximately 0.80% C and 0.30 % N at the surface. In contrast, nitrocarburizing involves higher levels of nitrogen with a compound layer (Fig. 3). There are two types of nitrocarburizing: ferritic and austenitic. Ferritic nitrocarburizing occurs at lower temperatures in the ferritic temperature range and involves diffusion of nitrogen into the case (Fig. 3a). Austenitic nitrocarburizing (Fig. 3b) is a more recently developed process (Ref 7, 8), with process temperatures in the range of 675 to 775 °C (1245 to 1425 °F). It also uses much higher ammonia additions and thus has higher nitrogen levels in the case. This allows the formation of a surface compound zone, which is not typical of the carbonitriding process. Austenitic nitrocarburizing differs from ferritic nitrocarburizing in its capability for deeper case depths with better load carrying but may result in greater part distortion because of the higher processing temperatures and the required quenching process.

Process Description

Carbonitriding can be carried out in a salt bath (i.e., similar to liquid cyaniding) or in a

furnace gas atmosphere cyaniding. Because of problems in disposing of cyanide-bearing wastes, gas carbonitriding is now often preferred over liquid cyaniding.

Key to controlling carbonitriding processes to obtain optimum case characteristics is to control both the case carbon and nitrogen. The rate of nitrogen pickup depends on the free ammonia content of the furnace atmosphere and not the percentage of ammonia in the inlet gas. Unfortunately, no state-of-the-art sensor for monitoring the free ammonia content of the furnace atmosphere has yet been developed.

During gas carbonitriding, the primary reactions producing carbon and nitrogen are (Ref 1):

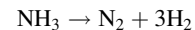
$C + CO_2 \rightleftharpoons 2CO$	Reaction 1(a)—carbon source
$CH_4 \rightleftharpoons C + 2H_2$	Reaction 1(b)—carbon source
$C + H_2O \rightleftharpoons CO + H_2$	Reaction 2
$2NH_3 \rightleftharpoons N_2 + 3H_2$	Reaction 3
$NH_3 \rightleftharpoons N + 3/2H_2$	Reaction 4
$1/2N_2 \rightleftharpoons N$	Reaction 5
$HCN \rightleftharpoons C + N + 1/2H_2$	Reaction 6
$CO + 2NH_3 \rightleftharpoons CH_4 + H_2O + N_2$	Reaction 7
$CO + NH_3 \rightleftharpoons HCN + H_2O$	Reaction 8
$CO_2 + H_2 \rightleftharpoons CO + H_2O$	Reaction 9
$CH_4 + H_2O \rightleftharpoons CO + 3H_2$	Reaction 10
$CH_4 + CO_2 \rightleftharpoons 2CO + 2H_2$	Reaction 11

Reactions 1 to 6 play a direct and active part in the production of both atomic carbon and nitrogen for diffusion. Atomic nitrogen is created in reactions 4 to 6 and is available to the steel for diffusion, together with the carbon. Decomposition of molecular nitrogen (N_2) into atomic

nitrogen (N) (reaction 5) is a key reaction for the process temperatures of carbonitriding.

Higher carbonitriding temperatures are less effective in generating atomic nitrogen (N) from ammonia additions to the atmosphere. This is because the rate of spontaneous decomposition of ammonia to molecular nitrogen (N_2) and hydrogen increases as the temperature is raised. The dependence of nitrogen potential on temperature is given in Fig. 4 (Ref 9). Figure 5 also shows that lower temperatures favor increased surface nitrogen concentrations and the effects of ammonia addition on carbon potential. At a given temperature, the fraction of the ammonia addition that spontaneously decomposes is dependent on the residence time of the atmosphere in the furnace: the higher the total flow of atmosphere gases, the lower the fraction of the ammonia addition that decomposes to nitrogen and hydrogen.

The effect addition of ammonia has on CO_2 content of the furnace is attributable to dilution of the furnace atmosphere by ammonia and its dissociation products from reaction 3:



A reduction in carbon potential would be expected with a reduction in CO_2 in the furnace atmosphere. However, even when CO_2 is maintained constant in the furnace, actual carbon potentials decrease with increasing ammonia additions (Fig. 5). The carbon potential possible with a given carbon dioxide level is higher in a carburizing atmosphere than in a carbonitriding atmosphere. Dilution with nitrogen and hydrogen affects measurements of oxygen potential in a similar manner; the carbon potential possible with a given oxygen potential is higher in a carburizing atmosphere than in a carbonitriding atmosphere. Water vapor content (dewpoint), however, is much less affected by this dilution. Thus, the amount of dilution and its resulting effect on the atmosphere composition depends on the processing temperature, the amount of ammonia introduced, and the ratio of the total atmosphere gas flow rate to the volume of the furnace.

It is possible to select process conditions to obtain almost any desired combination of carbon and nitrogen content within the case. As noted, available nitrogen content is restricted by treatment temperature, and this must be taken into account when considering higher temperatures for carbonitriding. An example is shown in Fig. 6 for 925 °C (1695 °F) treatment, from which it is possible to select process conditions that will provide any desired combination of carbon and nitrogen in the case. Figure 6 also indicates that the nitrogen content achieved for any given ammonia addition level (0 to 20%) is unaffected by the carbon potential of the furnace.

Often, carburizing and carbonitriding are used together to achieve much deeper case depths and better engineering performance for parts than could be obtained using only the carbonitriding process. This process is applicable particularly with steels with low case

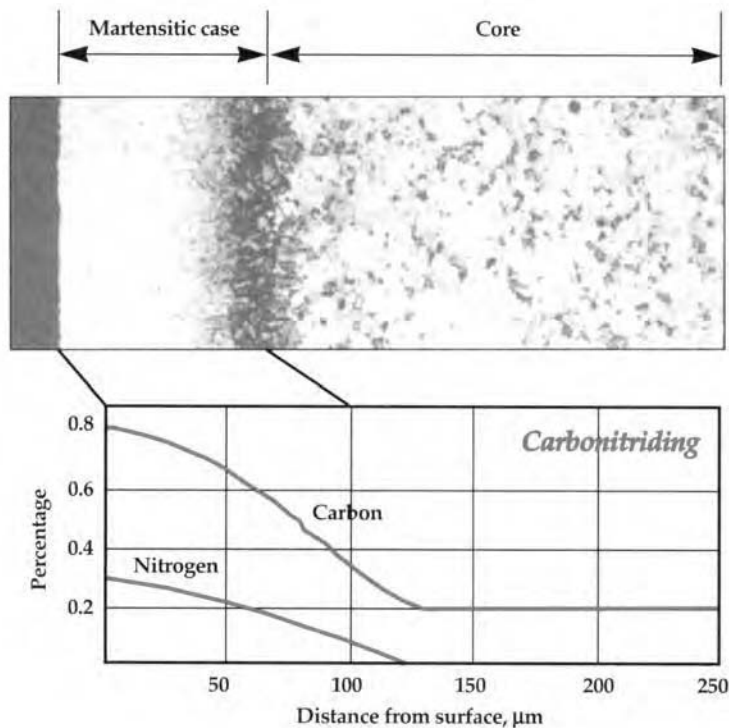


Fig. 2 Typical carbonitrided surface with carbon predominating in a martensitic case. Carbonitriding temperature was 850 °C (1560 °F). Source: Ref 5, 6

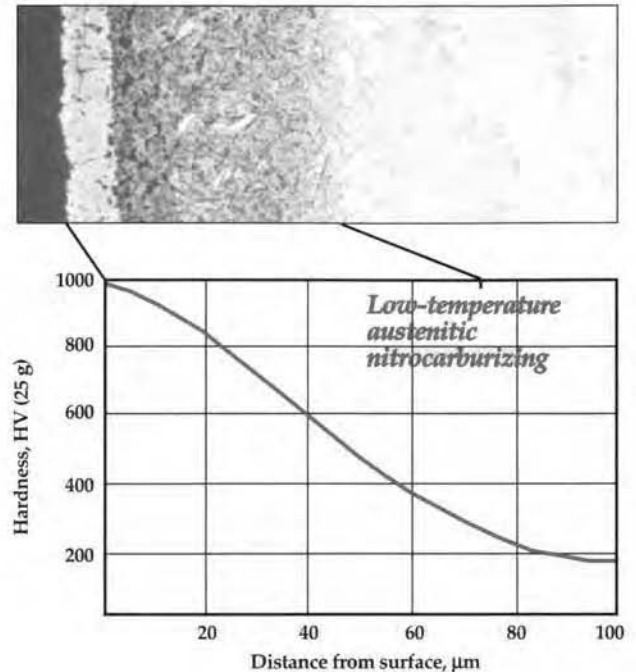
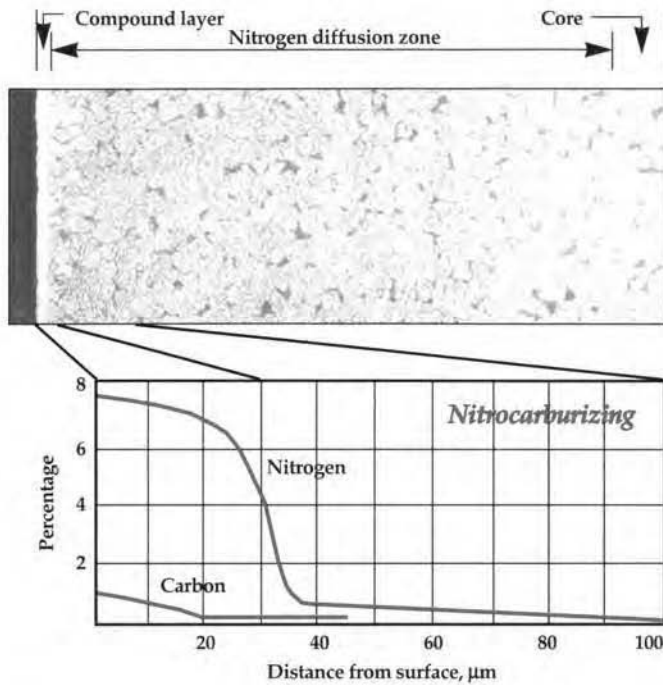


Fig. 3 Nitrocarburized steel surfaces. (a) Ferritic nitrocarburizing at 570 °C (1060 °F), where nitrogen is the predominant element in the compound layer of epsilon (ε) carbonitride. (b) Low-temperature austenitic nitrocarburizing at 700 °C (1290 °F), with a martensitic or bainitic microstructure beneath the ε-carbonitride layer. Sources: Ref 5, 6

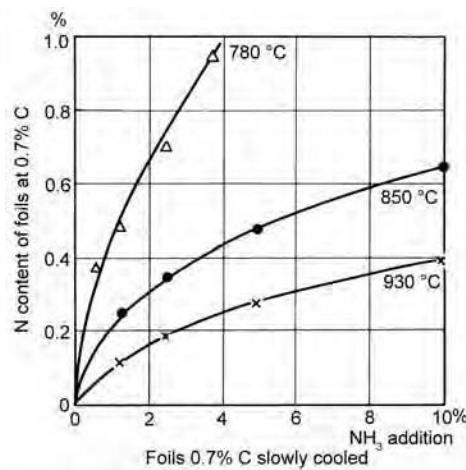


Fig. 4 Nitrogen potential as a function of temperature and ammonia additions in a furnace atmosphere. Source: Ref 9

hardness, that is, the 1000-, 1100-, and 1200-series steels. The process generally consists of carburizing at 900 to 955 °C (1650 to 1750 °F) to give the desired total case depth (up to 2.5 mm, or 0.100 in.), followed by carbonitriding for 2 to 6 h in the temperature range of 815 to 900 °C (1500 to 1650 °F) to add the desired carbonitrided case depth. The subject parts can then be oil quenched to obtain a deeper effective and thus harder case than would have resulted from the carburizing process alone. The addition of

the carbonitrided surface increases the case residual compressive stress level and thus improves contact fatigue resistance as well as increases the case strength gradient.

When the carburizing/carbonitriding processes are used together, the ratio of effective case depth (50 HRC) to total case depth may vary from approximately 0.35 to 0.75 depending on the case hardenability, core hardenability, section size, and quenchant used. A more shallow effective or total case depth can be achieved with a given carbonitriding process by using fine-grained steels containing higher amounts of aluminum (Ref 12) or titanium. The nitrogen from the process forms nitrides with the aluminum or titanium. This combined nitrogen does not improve case hardenability.

Sometimes ammonia is only added during the decreased temperature portion of a carburizing cycle for certain parts to increase the resistance to surface pitting fatigue (see also the section “Pitting Resistance of Transmission Gears” in this article). This modified process has the effect of increasing the surface hardenability, and it can partially negate the effect of surface alloy depletion and the creation of non-martensitic transformation products (NMTP) in a carburized case.

Nonmartensitic transformation products are caused by a reduction of surface hardenability in the carburizing process, and one method of improving the surface hardenability is to add ammonia to the carburizing process. However, the effectiveness of ammonia additions on

NMTP depends on the steel composition. For example, 8620 and 5120 steels respond differently to nitrogen additions, owing to the different amount of nitride formers (chromium, manganese) and to the alloying elements imparting hardenability (Ref 13). In 8620 steel, the amount of NMTP near the surface was reduced to as low as 8% (in the near-surface 20 μm) with various levels of ammonia additions during the complete cycle and at the end of the carburizing cycle. Alloy 5120 was much more sensitive to the amount of ammonia added, due to the effects of manganese sulfide (MnS) formation on hardenability. The depletion of solute manganese resulted in greatly diminished hardenability along prior-austenite grain boundaries and resulted in an increased depth of NMTP with additions of 3 or 5% ammonia (Ref 13).

Case Composition

The composition of a carbonitrided case depends on the process variables of temperature, time, and atmosphere composition. With the effect of ammonia additions on carbon potential, the carbon content of a carbonitrided case is less than that of a carburized case at the same time-temperature conditions (Fig. 7).

The type of steel may also influence the composition of a carbonitrided case. In terms of steel type, the case depth achieved during a

given carbonitriding process will be somewhat lower in steels containing higher amounts of strong nitride formers such as aluminum or titanium. Very small quantities of prussic acid (hydrocyanic acid) also occur on the steel surface when penetration of both carbon and nitrogen is accelerated (Ref 1).

Carbonitriding can be carried out at such low temperatures as to produce a compound layer, so called because Fe-C-N compounds are formed at the surface. In certain wear applications, this type of case structure is suitable. To produce this layer of compound, higher percentages of ammonia are required. It is usually unnecessary to liquid quench parts carbonitrided in this manner. However, because the diffusion rate of nitrogen and the rate of formation of the compound are so slow at temperatures below 705 °C (1300 °F), such practice is economically applicable only to shallow cases in applications in which dimensional tolerances would be difficult to maintain if the parts were treated at higher temperatures. When temperatures fall below the austenitic level, this process is called ferritic nitrocarburizing (Ref 7, 8).

Example 1: Effect of Atmosphere Dewpoint on Case Composition from Carbonitriding. Figure 8 shows carbon and nitrogen gradients and case hardness data for 1018 carbon steel and 8620 low-alloy steel that were carbonitrided for 4 h at 845 °C (1550 °F) in a batch-type radiant-tube furnace. These test data were obtained under normal production conditions, employing a standard carbonitriding cycle. All test specimens were carbonitrided along with production loads of 23 kg (50 lb) of gears and shafts.

The carbonitriding atmosphere was controlled by an infrared control unit and consisted of an endothermic gas at 14.2 m³/h (500 ft³/h), ammonia at 0.7 m³/h (24 ft³/h), propane at 0.007 to 0.021 m³/h (0.25 to 0.75 ft³/h), and 0.32 to 0.34% CO₂. The dewpoint of the atmosphere was maintained at -7 to -6 °C (19 to 21 °F) throughout the carbonitriding cycle. All specimens were quenched from the carbonitriding temperature (845 °C, or 1550 °F) into warm oil at 55 °C (130 °F); they were neither tempered nor subjected to subzero treatment.

As the dewpoint of a carbonitriding atmosphere is increased, carbon concentration decreases and nitrogen concentration remains fairly constant. This characteristic response is demonstrated by the data in Fig. 9 for a 1020 steel carbonitrided at 845 °C (1550 °F) for 4 h, which show that, with the ammonia content of the carbonitriding atmosphere set at high (5%) and low (1%) levels, an increase in the concentration of water vapor (decrease in atmosphere carbon potential) in the inlet gas lowered the profiles of carbon concentration but did not appreciably affect nitrogen concentrations. (Although the dewpoint of the atmosphere in the carbonitriding furnace, rather than the dewpoint of the inlet gas, is the controlling factor, data based on the inlet-gas dewpoint demonstrate

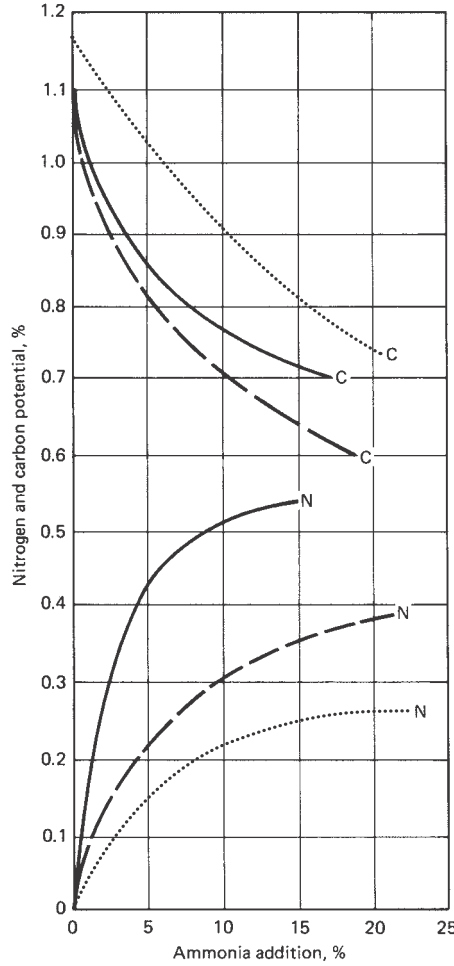


Fig. 5 Effect of ammonia additions on nitrogen and carbon potentials determined using low-carbon steel foil. For three sets of conditions: solid lines, 3 h at 850 °C (1560 °F) and 0.29% CO₂; dashed lines, 1 h at 925 °C (1695 °F) and 0.13% CO₂; dotted lines, 1 h at 950 °C (1740 °F) and 0.10% CO₂. Source: Ref 10

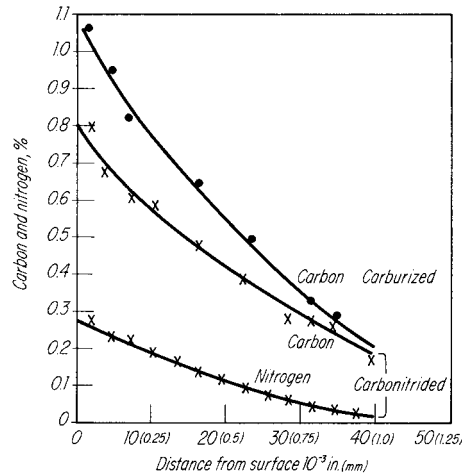


Fig. 7 Layer analysis of carburized and carbonitrided mild steel. Circle: carburized at 0.12% CO₂ for 4 h at 925 °C (1695 °F). X: carbonitrided at 0.12% CO₂ for 4 h at 925 °C (1695 °F) plus 10% NH₃. Source: Ref 11

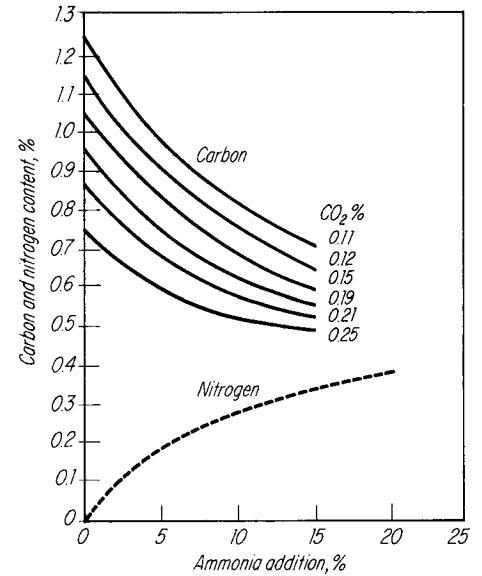


Fig. 6 Effect of ammonia level on equilibrium carbon and nitrogen content at 925 °C (1695 °F). Source: Ref 11

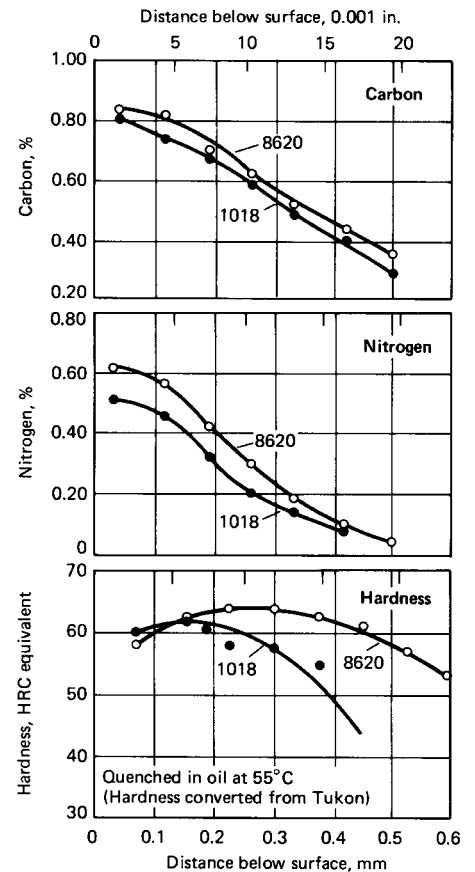


Fig. 8 Carbon, nitrogen, and hardness gradients for carburized 1018 and 8620 steels. See text for processing details.

the general effects of raising and lowering dew-point on case composition.)

Depth of Case

Preferred case depth is governed by service application and by core hardness. Case depths of 0.025 to 0.075 mm (0.001 to 0.003 in.) are commonly applied to thin parts that require wear resistance under light loads. Case depths up to 0.75 mm (0.030 in.) may be applied to parts (such as cams or small gears) for resisting high compressive loads. Case depths of 0.63 to 0.75 mm (0.025 to 0.030 in.) may be applied to

shafts and gears that are subjected to high tensile or compressive stresses caused by torsional, bending, or contact loads.

Medium-carbon steels with core hardnesses of 40 to 45 HRC normally require more shallow case depths than steels with core hardnesses of 20 HRC or below.

Measurements of the case depths of carbonitrided parts may refer to effective case depth or total case depth, as with reporting case depths for carburized parts. For very thin cases or when lower-carbon steels are processed, usually only the total case depth is specified. In general, it is easy to distinguish case and core microstructures in a carbonitrided piece, particularly

when the case is thin and is produced at a low carbonitriding temperature; more difficulty is encountered in distinguishing case and core when high temperatures, deep cases, and medium- or high-carbon steels are involved. Whether or not the core has a martensitic structure is also a contributing factor in visual case-depth evaluation.

Effect of Time and Temperature. Based on a survey of industrial practice, Fig. 10 shows case depths for different combinations of total furnace treating time and temperature. (Note that all values given for case depth are for effective case depth unless otherwise stated.)

Case-Depth Uniformity

Case-depth uniformity in carbonitriding depends on temperature uniformity within the furnace chamber, adequate circulation and replenishment of atmosphere, and distribution of the furnace charge so that it is uniformly exposed to the atmosphere.

Accurate control of treatment time is also a factor in controlling case-depth uniformity. All parts in a load should be at a uniform temperature prior to exposure to the carbonitriding atmosphere in order to achieve uniform results when the processing times are short.

Example 2: Variations in Case Depth of Carbonitrided 1010 Steel. Case-depth variations typical of carbonitriding at 775 to 800 °C (1425 to 1475 °F) are shown in Fig. 11. The data were obtained on two parts that were carbonitrided along with large production lots. One of these parts, a rack made of 1010 steel, was carbonitrided at 790 to 800 °C (1450 to 1475 °F) in a horizontal batch furnace equipped with an enclosed quench tank. Acceptable limits of case depth for these racks were 0.05 to 0.13 mm (0.002 to 0.005 in.).

The other part, a pinion shaft of 5140 steel, was carbonitrided at 775 °C (1425 °F) for 8 h and then quenched in oil at approximately 75 °C (170 °F). Attainment of acceptable case depth of 0.2 to 0.3 mm (0.008 to 0.012 in.) was 100% in 25 tests.

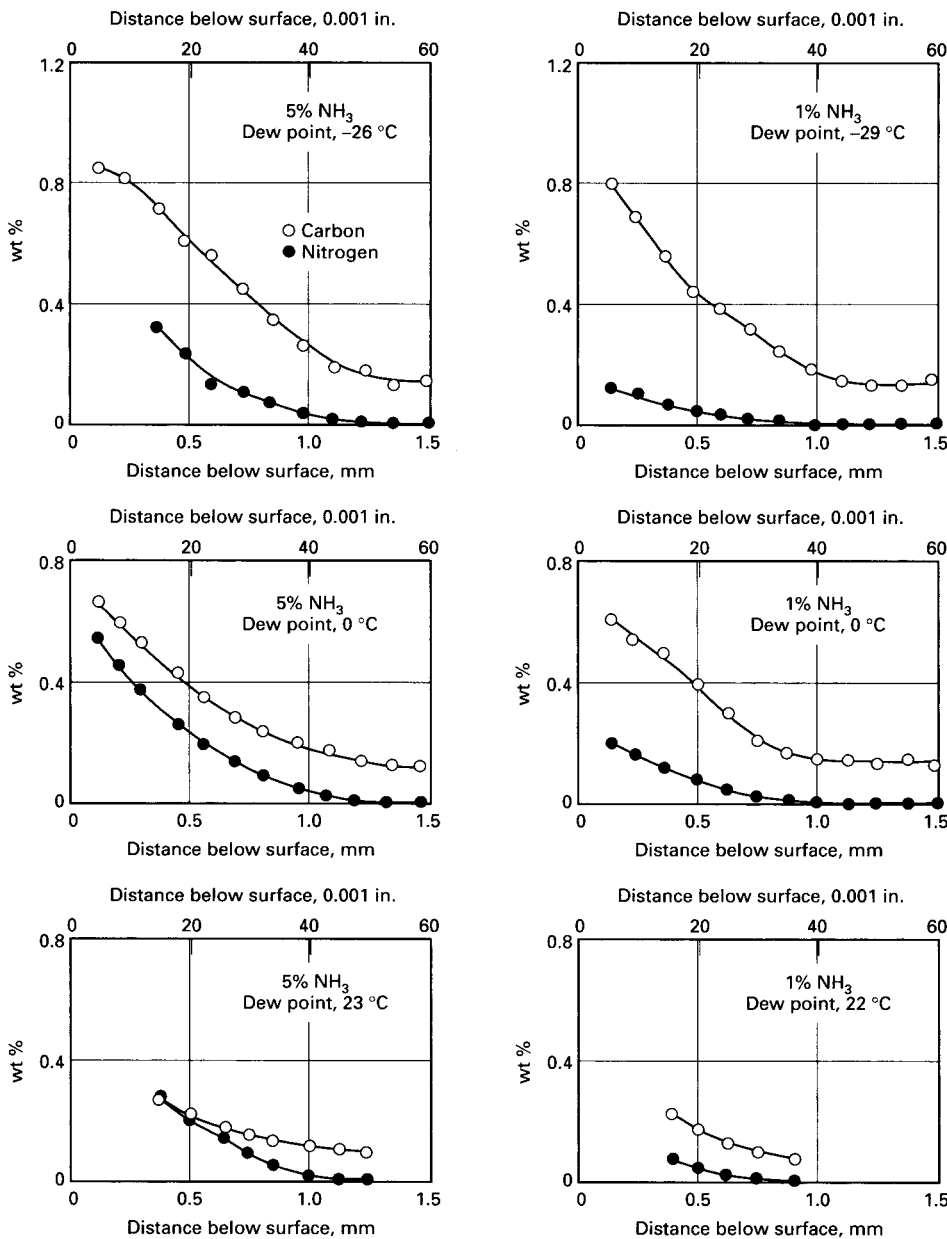


Fig. 9 Effects of ammonia concentration and inlet-gas dewpoint on carbon and nitrogen gradients in a 1020 steel carbonitrided at 845 °C (1550 °F) for 4 h and air cooled. Inlet gas also contained 5% methane; balance, carrier gas. Source: Ref 10

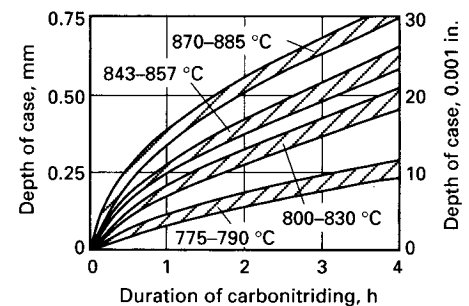


Fig. 10 Results of a survey of industrial practice regarding effects of time and temperature on effective case depth of carbonitrided cases

Although the data in this example may be considered typical, they do not fully reflect the high degree of uniformity of case depth that can be achieved. For example, one plant reports total case-depth uniformity of ± 0.025 mm (± 0.001 in.) within a load and between loads in more than 100+ cycles for case depths as low as 0.125 mm (0.005 in.) on small parts carbonitrided in 455 kg (1000 lb) gross-capacity batch furnaces. Time, temperature, and processing variables were automatically controlled. The parts were also preheated to a uniform temperature using only endothermic gas prior to actually starting the carbonitriding process.

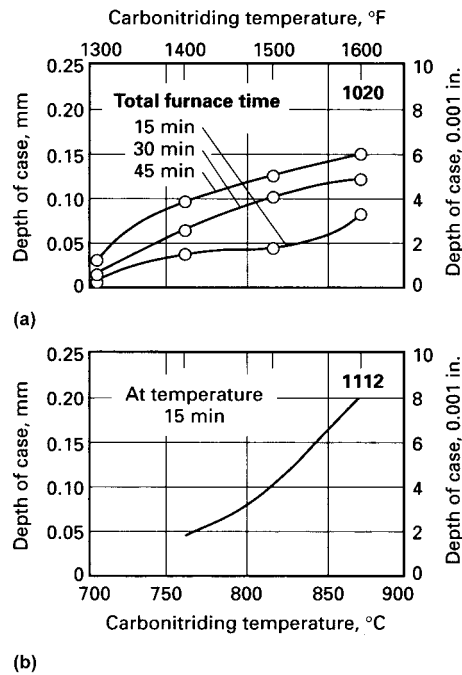


Fig. 11 Effects of temperature and of duration of carbonitriding on effective case depth. Both sets of data were obtained in the same plant. Note that the graph in (a) (for 1020 steel) is in terms of total furnace time, whereas the graph in (b) (for 1112 steel) is for 15 min at temperature.

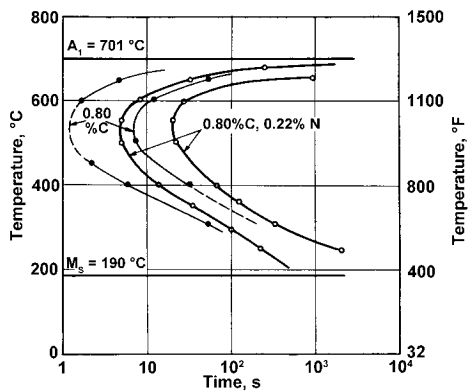


Fig. 12 Effect of nitrogen on the isothermal transformation of 0.8% C steel. Transformation curves of steel with 0.8% C included for comparison. Sources: Ref 9, 14

Hardenability of Case

One major advantage of carbonitriding is that the nitrogen absorbed during processing lowers the critical cooling rate of the steel. This can be seen in a shift in the nose of the isothermal transformation diagram (Fig. 12) from detailed studies by Přenosil (Ref 14). Nitrogen levels above 0.20% have a marked effect on transformation behavior, while nitrogen below 0.20% had hardly any effect (Fig. 13). Higher nitrogen also considerably lowers the martensite start (M_s) and austenite (A_1) transformation temperatures (Table 1).

Hardenability of a carbonitrided case is significantly greater than for the same steel that is only carburized (Fig. 14). Because higher process temperatures reduce the effectiveness of ammonia as a source of atomic nitrogen, hardenability can be affected at higher carbonitriding temperatures. Alloying elements may also interfere with the effect of nitrogen on hardenability. Conversely, nitrogen seems to interfere with the hardenability effect of boron (Ref 15).

Improved hardenability permits the use of steels on which uniform case hardness ordinarily could not be obtained if they were only carburized and quenched (for example, plain

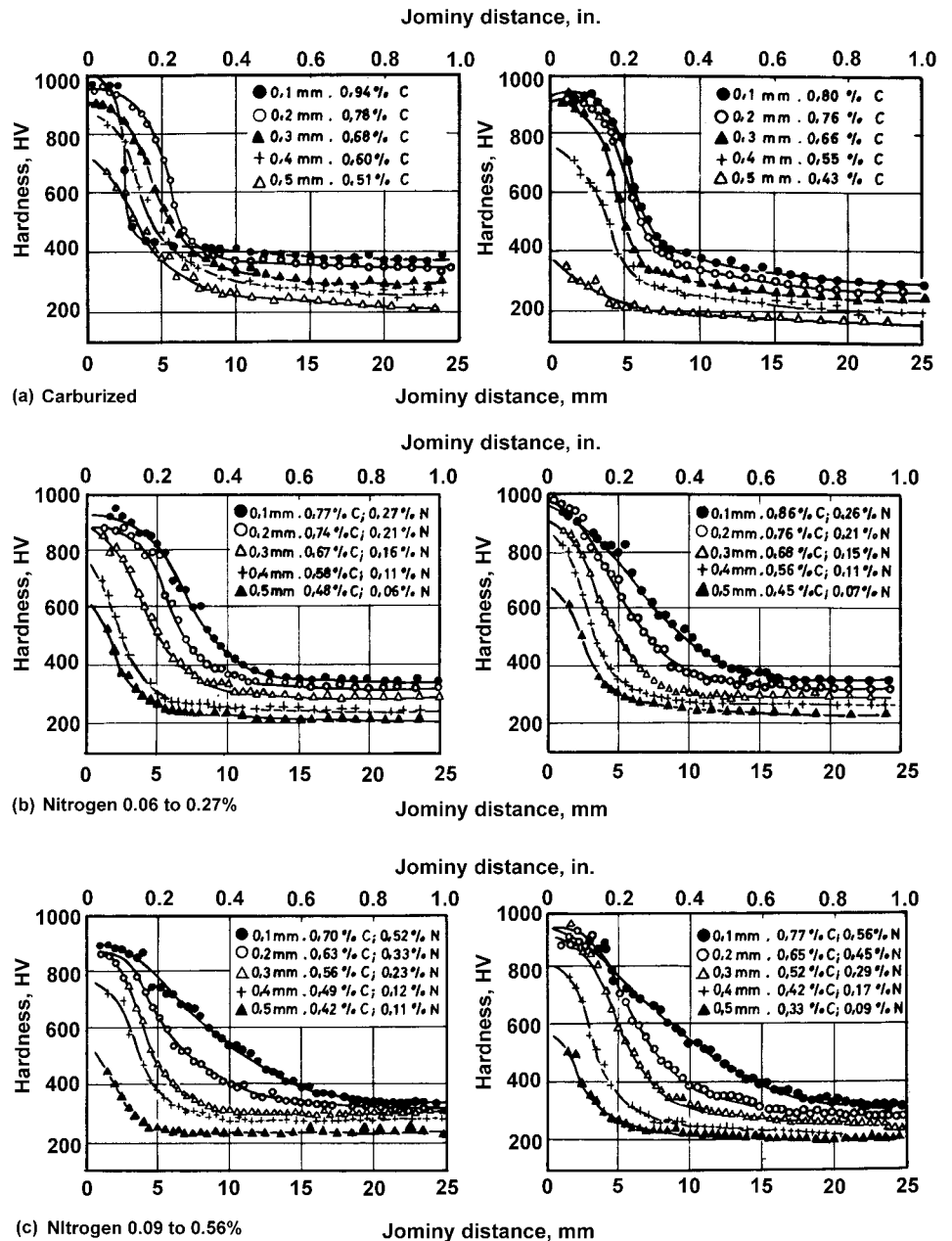
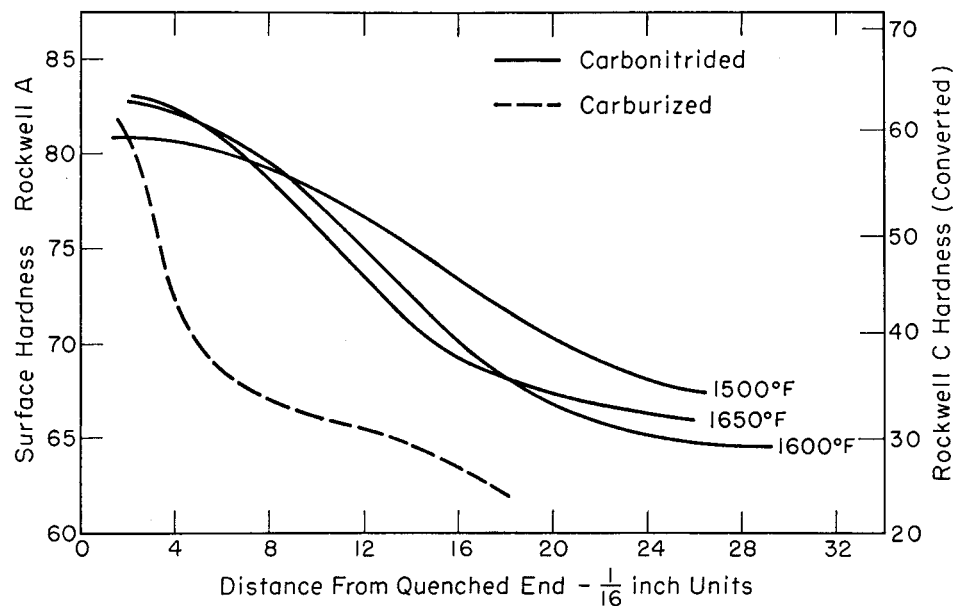


Fig. 13 Hardenability comparison of carburized and carbonitrided steel. Jominy specimens of base steel (0.08 % C, 0.19% Si, 0.40% Mn) were austenitized at 820 °C (1510 °F) for 30 min. Source: Ref 9, 14

Table 1 Effect of nitrogen on austenite (A_1) and martensite start (M_s) transformation temperatures of 0.8 wt% steel

Nitrogen, %	A_1		M_s	
	$^{\circ}\text{C}$	$^{\circ}\text{F}$	$^{\circ}\text{C}$	$^{\circ}\text{F}$
0.0	720	1330	205	400
0.39	682	1260	154	309
0.66	670	1240	108	226

Source: Ref 9

**Fig. 14** End-quench hardenability curve for 1020 steel carbonitrided at three different temperatures compared with curve for the same steel carburized at 925 °C (1700 °F). Hardness was measured along the surface of the as-quenched hardenability specimen. Ammonia and methane contents of the inlet carbonitriding atmosphere were 5% balance, carrier gas. Source: Ref 15

carbon steels that tend to have soft spots upon water quenching). Nitrogen also makes it possible to oil quench steels such as 1010, 1020, and 1113 to obtain martensitic case structures. Because of lower processing temperatures and/or the use of less severe quenches, carbonitriding may produce less part distortion and better control of dimensions than carburizing, and thus may eliminate the need for straightening or final grinding operations. Where core properties are not important, carbonitriding permits the use of low-carbon steels, which cost less and may have better machinability or formability.

Hardness Gradients

Hardness at various levels in the case depends on the microstructure. Hardness gradients associated with the microstructures of 1117 steel are presented in Fig. 15. When the carbonitriding atmosphere was relatively high in ammonia (11% NH_3), the nitrogen content of the case was high, and enough austenite was

retained after quenching to lower the hardness to 48 HRC, 500 g (1.1 lbf) load, at a depth of 0.025 mm (0.001 in.) below the surface. The amount of retained austenite was decreased, and hardness consequently was increased, either by lowering the ammonia flow rate from 0.57 to 0.14 m^3/h (20 to 5 ft^3/h), which reduced the ammonia content of the furnace atmosphere from 11 to 3%, or by introducing a 15 min diffusion period at the end of the carbonitriding operation. Either treatment increased the hardness to meet or exceed a specified minimum value of 55 HRC, 500 g (1.1 lbf) load at 0.025 mm (0.001 in.) below the surface.

Similar data relating ammonia content to hardness for 1018 steel carbonitrided at 790 °C (1455 °F) for 2½ h and at 845 °C (1550 °F) for 2½ h are shown in Fig. 16.

Void Formation

Subsurface voids or porosity in the case structure (Fig. 17) may occur in carbonitrided parts if

the processing conditions are not adjusted properly. Porosity in the case would result in such parts being unusable. Although details of the mechanism of void formation are not completely understood, this problem has been related to excessive ammonia additions. Table 2 summarizes the factors that have been shown singly or in combination to contribute to void formation. No attempt has been made to quantify the interaction of the material and process variables presented in Table 2. Rather, this information should be used as a guide for avoiding or eliminating porosity problems. It should also be noted that the reprocessing of parts previously carbonitrided can, in many instances, lead to void formation.

Surface porosity can also be caused by using an improper grade of ammonia containing moisture (water vapor).

Control of Retained Austenite

Nitrogen lowers the transformation temperature of austenite and the martensite start (M_s) temperature (Table 1). Therefore, a carbonitrided case usually contains more retained austenite than a carburized case of the same carbon content. Because available nitrogen (at a given ammonia level) is higher at the lower process temperatures, an increase in retained austenite can occur in the case at lower processing temperatures (Fig. 18, Table 3). Retained austenite also can become high when alloy steels are carbonitrided.

Retained austenite has low indentation hardness and is undesirable in many applications. It can be extremely detrimental in components of close-fitting assemblies, for example, shaft and sleeve assemblies wherein the shaft is intended to rotate or reciprocate in the sleeve. The delayed transformation of austenite to martensite at ambient temperature results in a volume increase that may cause moving parts to bind or "freeze" in service.

Because the amount of retained austenite is normally at a maximum near the steel surface, it can be removed from symmetrical contours by grinding. However, care must be exercised in grinding high retained austenite surfaces because of the increased possibility of grinding burn or checking. If grinding is not required for any reason other than to remove retained austenite, it also may be considered an expensive operation.

The most economical way to minimize retained austenite is by selection of preferred steels and control of the carbonitriding process. Minimizing retained austenite in the carbonitrided case is assisted by modification of several processing factors:

- *Furnace temperature:* An increase in furnace temperature will reduce the nitrogen content of the outer portions of the case, thus minimizing the amount of retained austenite. However, it is far better to reduce

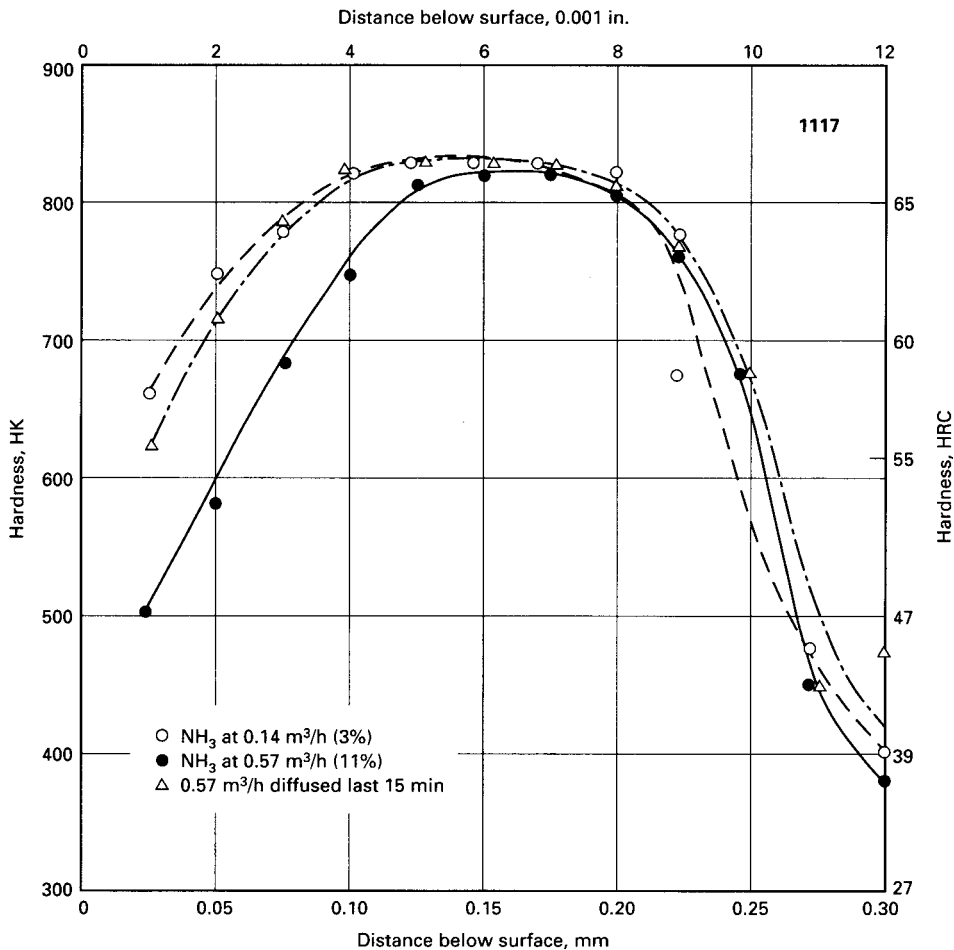


Fig. 15 Hardness gradients in 1117 steel carbonitrided at 815 °C (1500 °F) for 1½ h and quenched in oil. Required minimum hardness of 630 HK (55 HRC) at 0.025 mm (0.001 in.) below the surface was met by reducing the percentage and flow rate of ammonia or by adding a diffusion period after carbonitriding, as indicated. Atmosphere consisted of endothermic carrier gas (dewpoint, -1 °C, or 30 °F) at 4.25 m³/h (150 ft³/h), natural gas at 0.17 m³/h (6 ft³/h), and ammonia in the amounts indicated.

ammonia flow rather than depend on increased temperature to lower the nitrogen content.

- **Carbon potential:** Lowering the carbon potential will also help reduce retained austenite.
- **Ammonia content:** The ammonia content of the carbonitriding atmosphere should be restricted to the minimum required to obtain the desired hardenability. A 1 to 5% ammonia content in the inlet gas is usually a satisfactory starting point; a lower content decreases the rate of penetration but may be desirable to minimize retained austenite and to avoid case porosity.

The amount of retained austenite also can be significantly decreased by subzero-temperature treatments that allow lower-temperature martensitic transformation. This involves cooling the quenched parts to -40 to -100 °C (-40 to -150 °F). An example is shown in Fig. 19. Subzero treatment of parts that are to be tempered

should precede final tempering, or finish grinding when close-tolerance ground parts are involved. Subzero treatment may cause microcracks in the case, particularly in coarse-grained steels.

Furnace Atmospheres

Almost any furnace suitable for gas carburizing can be adapted to carbonitriding. Whether dense or shallow (openly spaced) work loads are to be processed, the furnace must be equipped with a fan to circulate the atmosphere. For work that is to be clean and bright after quenching, the furnace must be equipped with protective-atmosphere vestibules to the quench area.

The atmospheres used in carbonitriding generally comprise a mixture of carrier gas, enriching gas (methane, propane, etc.), and ammonia. Basically, the atmospheres used in carbonitriding are

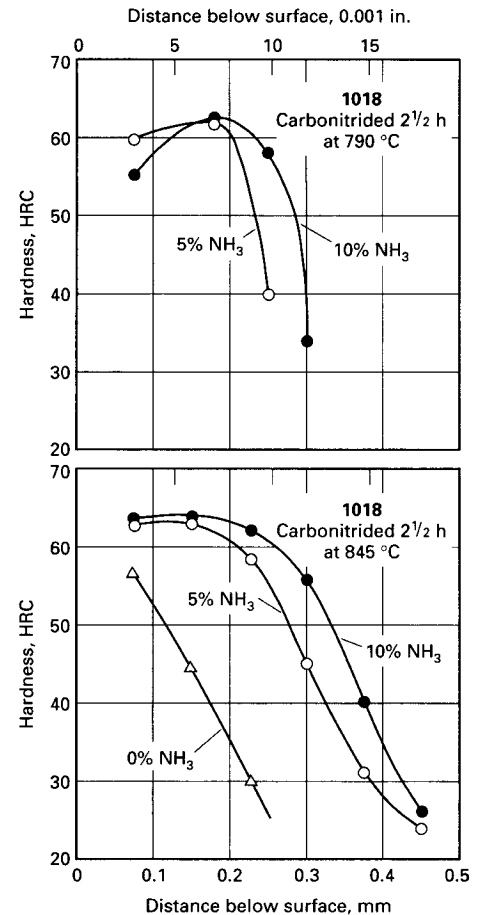


Fig. 16 Effect of ammonia content of carbonitriding gas on hardness gradient

produced by adding from generally about 2 to 5% ammonia to a standard gas-carburizing atmosphere.

Control of furnace atmosphere becomes more critical when lower austenitizing temperatures may be required (see the section "Temperature Selection" in this article). In particular, retained austenite becomes a factor at lower process temperatures. For applications where carbonitriding will not be followed by a grinding operation or subzero treatment, the recommendation is to keep carbon concentration near 0.70% and nitrogen near 0.30% (Ref 16). Thus, when carbonitriding, heat treaters should consider dropping the conventional 0.85 to 0.90% C aim used for straight carburizing by at least 10 points.

Milano did a series of tests in which surface carbon is held as close to 0.70% as possible to help substantiate whether or not maximum hardness levels and wear resistances found at various depths below the surface can be attained at the surface by dropping the surface carbon level to 0.70% and the nitrogen level to 0.30%. For example, Fig. 20 shows hardness decreasing as carbon rises; however, nitrogen varies independently of carbon.

Control of Atmospheres

The three types of gases that comprise carbonitriding atmospheres usually are measured through flowmeters and may be premixed just before they enter the furnace. Large continuous furnaces require addition of the gas mixture at several points to provide the desired composition within the chamber. Control of the atmosphere usually is obtained by producing a carrier gas that is as constant in chemical composition and dewpoint (carbon potential) as practical, with a fixed ammonia addition, and by varying the enriching gas either manually or automatically to give the desired carbon and nitrogen composition in the carbonitrided case. In varying the enriching gas, care must be taken not to introduce excessive amounts of hydrocarbon into the furnace, because this will cause sooting. Heavy deposits of soot, in addition to making the work difficult to clean, have a detrimental effect on alloy furnace parts and may impede the rate of carbonitriding.

Ammonia Content. The following are among factors to be considered in establishing ammonia content for the influent gas:

- *Atmosphere turnover:* Frequently, lower ammonia percentages must be used with high rates of furnace-gas change (that is, total gas flow divided by furnace chamber volume) to produce a specific microstructure for a specific furnace and load.
- *Recirculation rate:* Generally, increases in recirculation rate, and hence in atmosphere uniformity, permit the use of lower ammonia concentrations.
- *Furnace-cycle time:* The rate of absorption of nitrogen in austenite decreases with time; hence, short furnace cycles and low case depths require higher ammonia percentages.
- *Furnace temperature:* Higher ammonia percentages often must be used with higher furnace temperatures.
- *Load size, density, and surface area:* As size, density, and surface area of the load increase,

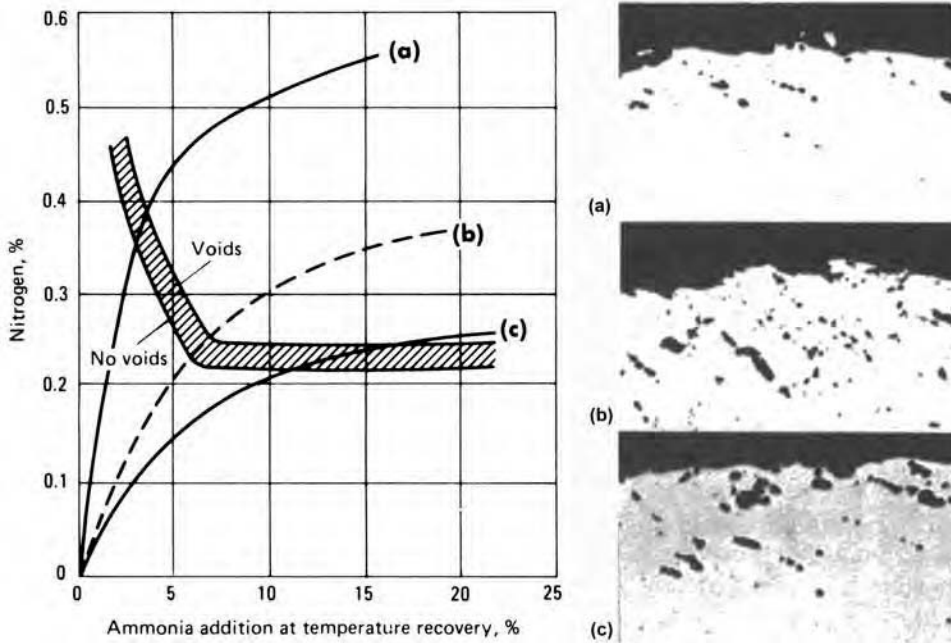


Fig. 17 Effect of ammonia additions on nitrogen content and formation of subsurface voids in foils. (a) 850 °C (1560 °F) 0.29% CO₂. (b) 925 °C (1695 °F) 0.13% CO₂. (c) 950 °C (1740 °F) 0.10% CO₂. Source: Ref 11

Table 2 Effect of material/variables on the possibility of void formation in carbonitrided cases

Material/processing variables(a)	Possibility of void formation
Temperature increase	Increased
Longer cycles	Increased
Higher case nitrogen levels	Increased
Higher case carbon levels	Increased
Aluminum-killed steel	Increased
Increased alloy content of steel	Decreased
Severe prior cold working of material	Increased
Ammonia addition during heat-up cycle	Increased

(a) All other variables held constant. Sources: Based on data in Fig. 17, Ref 8 and 15

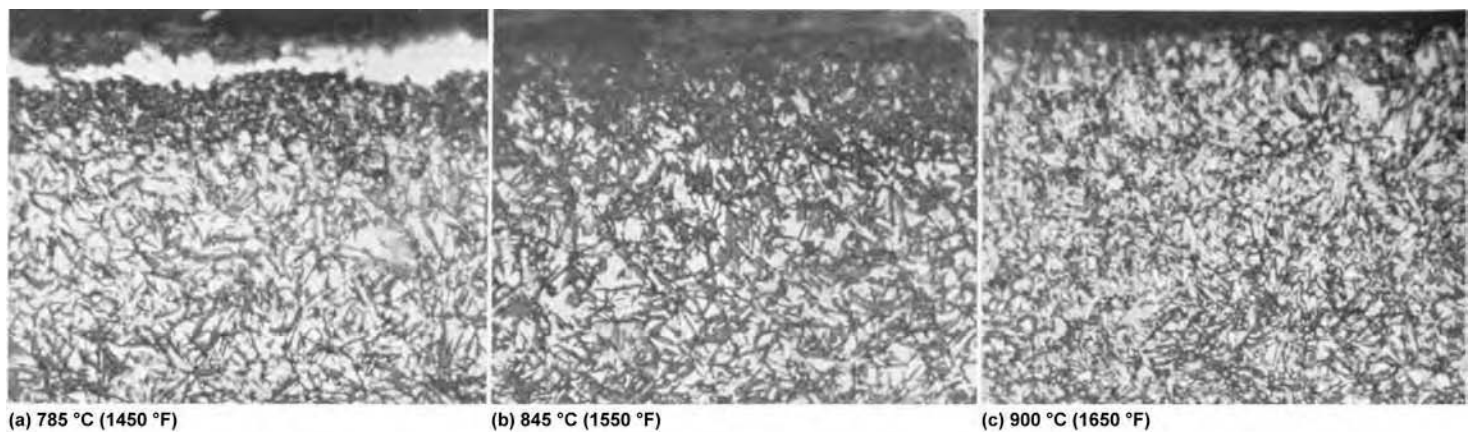
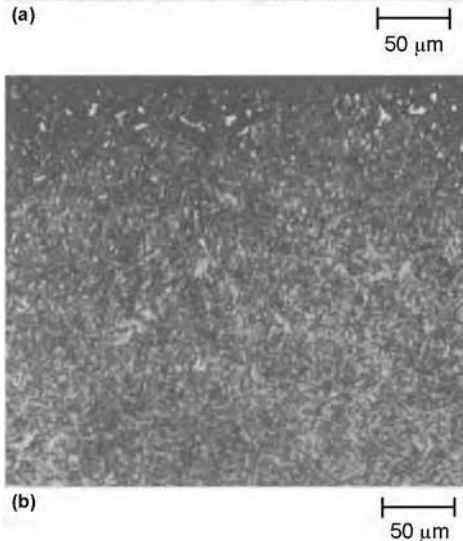
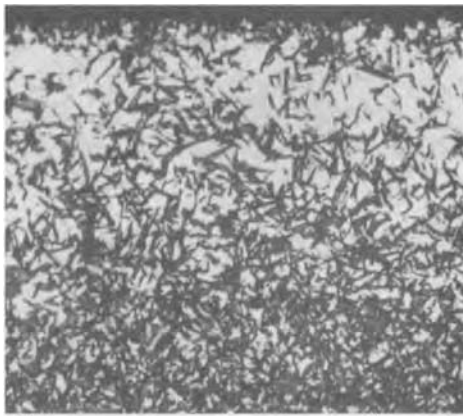


Fig. 18 Retained austenite in 1018 steel carbonitrided at three different temperatures. Bar 28.5 mm (1 1/8 in.) in diameter quenched in 55 °C (130 °F) oil. See also Table 3. Source: Ref 16

Table 3 Hardness and wear of carbonitrided 1018 steel

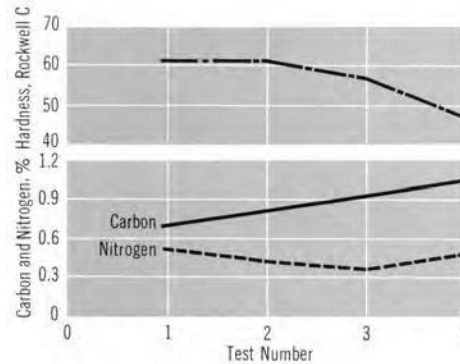
		Dewpoint			Temperature		Hardness(a), Rockwell C				
NH ₃ , %	CO ₂ , %	°C	°F	Cycle time, h	°C	°F	0.075 mm (0.003 in.)(b)		Carbon, %	Nitrogen, %	Wear, g
							Surface				
2.5	0.22	-9	16	3	900	1650	63	62	0.80	0.281	0.00027
2.5	0.31	-7	20	4	845	1550	60	58	0.88	0.397	0.00029
2.5	0.40	-5	23	5	785	1450	60	55	0.98	0.402	0.00038
5	0.22	-9	16	3	900	1650	63.5	61	0.78	0.380	0.00028
5	0.31	-7	20	4	845	1550	62.5	58	0.82	0.382	0.00035
5	0.40	-5	23	5	785	1450	61	58	0.85	0.590	0.00039

(a) Quenched with oil at 55 °C (130 °F). (b) Distance below surface. Source: Ref 16

**Fig. 19** Effect of low-temperature hold on retained austenite in carbonitrided 8617 steel bar. (a) Carbonitrided 4 h at 845 °C (1550 °F) in 8% ammonia, 8% propane, and remainder endothermic gas. Oil quenched and tempered 1.5 h at 150 °C (300 °F). Structure is tempered martensite (dark) and retained austenite. (b) Carbonitrided and tempered 8617 bar as in (a), except held 2 h at -75 °C (-100 °F) between quench and tempering. The structure is scattered carbide in a matrix of tempered martensite. Most of the retained austenite was transformed during low-temperature hold. Both 3% nital etch. Original magnification: 200×

a higher flow rate of ammonia is required to match the increase in nitrogen demand.

- *Carbon potential/hydrocarbon addition:* Lower ammonia percentages can normally be used with higher carbon potentials. However, as the load size or surface area of the

**Fig. 20** Surface hardness of carbonitrided C1018 with variation in carbon content while nitrogen remains fairly constant. Four specimens processed at 845 °C (1550 °F) in 2.5% ammonia atmosphere, quenched in 55 °C (130 °F) oil. Source: Ref 16

load increases, hydrocarbon additions of up to 25% by volume may be necessary to adequately control the carbon potential early in the cycle or for shallow case depths.

- *Type of steel:* The minimum percentage of ammonia required for hardenability depends largely on steel composition. Austenite retention increases with an increase in ammonia content. Therefore, lower ammonia contents should be used with alloy steels, particularly those containing nickel or high manganese, and with higher-manganese carbon steels such as 1117, 1118, and 1024.

Only enough ammonia should be added to sustain the carbonitriding reactions in the atmosphere; excess ammonia does not contribute to the nitrogen content of the case and can lead to void formation, as discussed earlier. Usually, 2.5 to 5% ammonia is sufficient to produce satisfactory nitrogen content in the case.

Contaminants must be avoided in order to maintain an effective atmosphere in the furnace chamber. Infiltration of air and leaks in radiant tubes cause products of combustion, which are detrimental to the atmosphere, to enter the work chamber. Even the work load itself can provide a source of contamination. When significant amounts of grease, oil, cleaning agents, moisture, or quenching salts are present on surfaces of the work load, these materials can seriously

contaminate the atmosphere. This source of contamination can be avoided by cleaning the work with a suitable agent before charging and by the use of purging cycles.

Influence of Furnace Type

Different types of furnaces require different percentages of entering component gases and different volumes of gases, depending on turnover (the number of gas changes per hour). Major variables include the reactions of the gas with the furnace brickwork and alloy; the tightness of the furnace and number of door openings (shaker-hearth and belt furnaces will have an opening between the door and hearth at all times); and the degree of circulation of gases, as related to load density and surface area of work. Data on the interrelationship of rate of gas flow, furnace volume, and number of gas changes per hour, as a function of type of furnace, are given in Table 4. From these data it is evident that:

- For brick-lined batch furnaces, fewer gas changes per hour are required as the furnace volume increases (ostensibly because relatively less gas leakage through furnace-door openings occurs as furnace volume increases).
- Shaker-hearth (or belt-type) furnaces require much higher gas flows per unit volume because of large losses of atmosphere through the fixed door opening at the charge end of the furnace.

Batch Furnace Atmospheres. For maximum uniformity of case composition and case depth, the load must be heated uniformly to the carbonitriding temperature, and an adequate supply of atmosphere maintained at constant composition must be circulated throughout the load. Processing uniformity may be significantly improved by preheating parts in an atmosphere of endothermic gas for 15 to 60 min to ensure temperature uniformity within the load before adding enriching gas and ammonia for the actual carbonitriding portion of the cycle.

As in gas carburizing, the composition of the atmosphere for carbonitriding should be carefully controlled for consistent results. After the rate of flow of ammonia and the temperature have been established, the ammonia flow should be held to limits of approximately $\pm 10\%$ of the predetermined flow gage reading. If similar parts are to be processed requiring the same ammonia addition, a stainless steel orifice plate can be installed in the ammonia supply line. This will ensure a constant and reproducible ammonia flow and prevent unintentional, and possibly detrimental, ammonia additions. Because of the generally lower carbon content of the carbonitrided case, the lower operating temperature (which permits higher dewpoints and more carbon dioxide), and the higher hardenability of the carbonitrided case, greater latitude is possible for control parameters

(oxygen potential, water vapor, carbon dioxide, and/or methane contents) than for the same steel composition using the carburizing process.

For example, when carburizing at 925 °C (1700 °F) to obtain a case carbon content of 0.90 ± 0.05% or 0.80 ± 0.05%, it is desirable to hold the dewpoint within ±0.5 °C (±1 °F), and the carbon dioxide content within ±0.005%, of the control values; when carbonitriding at 815 °C (1500 °F) to obtain a case carbon content of 0.80 ± 0.05%, it is desirable to hold the dewpoint within ±1.5 °C (±3 °F), and the carbon dioxide content within ±0.03%, of the control values. The carbon dioxide levels corresponding to a certain carbon potential will not be the same for carbonitriding and carburizing, as discussed earlier.

Dewpoint instruments that contain a lithium chloride cell are not recommended for use with carbonitriding atmospheres, because ammonia will cause deterioration of the lithium chloride. If an infrared instrument for CO₂ is used, it is recommended that stainless steel tubing be used instead of copper to avoid the corrosive action

of the ammonia. Aluminum tubing can be used successfully if care is taken to avoid any possibility of producing water condensate in the sample lines. In general, the advice of the instrument manufacturer should be obtained before using these devices with carbonitriding atmospheres.

Because of the relatively shallow carbonitrided case, turnings from test bars are not frequently employed for determining carbon content. Metallographic examination and the control of case microhardness gradient are common process-control methods. However, the most commonly used process-control setups incorporate a regulator to control ammonia flow.

Better control of furnace atmospheres can be obtained when the parts to be carbonitrided and the work baskets are free of dirt and oil. Sintered powder metallurgy parts containing oil must be "burned out" in a tempering furnace before they are carbonitrided.

Continuous Furnace Atmospheres. Setting up a program for efficient and dependable

control of a carbonitriding atmosphere in a continuous furnace is similar to that for a batch furnace. Good circulation of atmosphere and good control of temperature are of prime importance. It is advantageous to introduce ammonia only to those areas in which the temperature of the work is equal to the operating temperature for carbonitriding. If the furnace is of appreciable internal length, approximately 3 m (9.8 ft) or more, it is important to introduce the mixture of carburizing gas and ammonia at frequent intervals over the length of the furnace where the work is at temperature and in regions where the temperatures may be decreased for metallurgical reasons near the end of the cycle.

Temperature Selection

Choice of carbonitriding temperature is based on a number of considerations, including steel composition, dimensional control, fatigue and wear properties, hardness, microstructural constituents, cost, and equipment. If lower temperatures are required, control of furnace atmosphere becomes more critical (Ref 16).

As an example, test results on hardness and case composition are plotted in Fig. 21 for three process temperatures at two levels of ammonia. Specimens treated at the higher temperature (900 °C, or 1650 °F) had the most uniform and consistent martensitic case (Fig. 22) and the best wear properties (Table 3).

Although higher temperatures permit the use of higher concentrations of ammonia, ammonia content must be decreased as the alloy content of the steel increases to minimize austenite retention. To this extent, temperature,

Table 4 Influence of type of furnace on mixture and flow rate of carbonitriding gases

Type of furnace	Constituents of gas, % by volume			Total gas flow,		Furnace volume,		Gas changes/h
	Ammonia	Natural gas	Carrier gas	m ³ /h	ft ³ /h	m ³	ft ³	
Batch, brick-lined	10.4	20.8	68.8	6.8	240	0.29	10	23.5
Batch, brick-lined	4	6	90	14.5	510	1.42	50	10.2
Batch, brick-lined	8.3	8.3	83.3	10.2	360	2.55	90	4.0
Batch, brick-lined	5	20	75	11.3	400	8.50	300	1.3
Continuous, brick-lined	3.4	2.3(a)	94.3	42.0	1480	8.07	285	5.2
Continuous, brick-lined	7	7	86	28.3	1000	25.5	900	1.1
Continuous, brick-lined	5	4	91	31.1	1100	25.5	900	1.2
Shaker-hearth, metal-lined	2.5	2.5	95	6.2	220	0.06	2	110.0

(a) C₃H₈

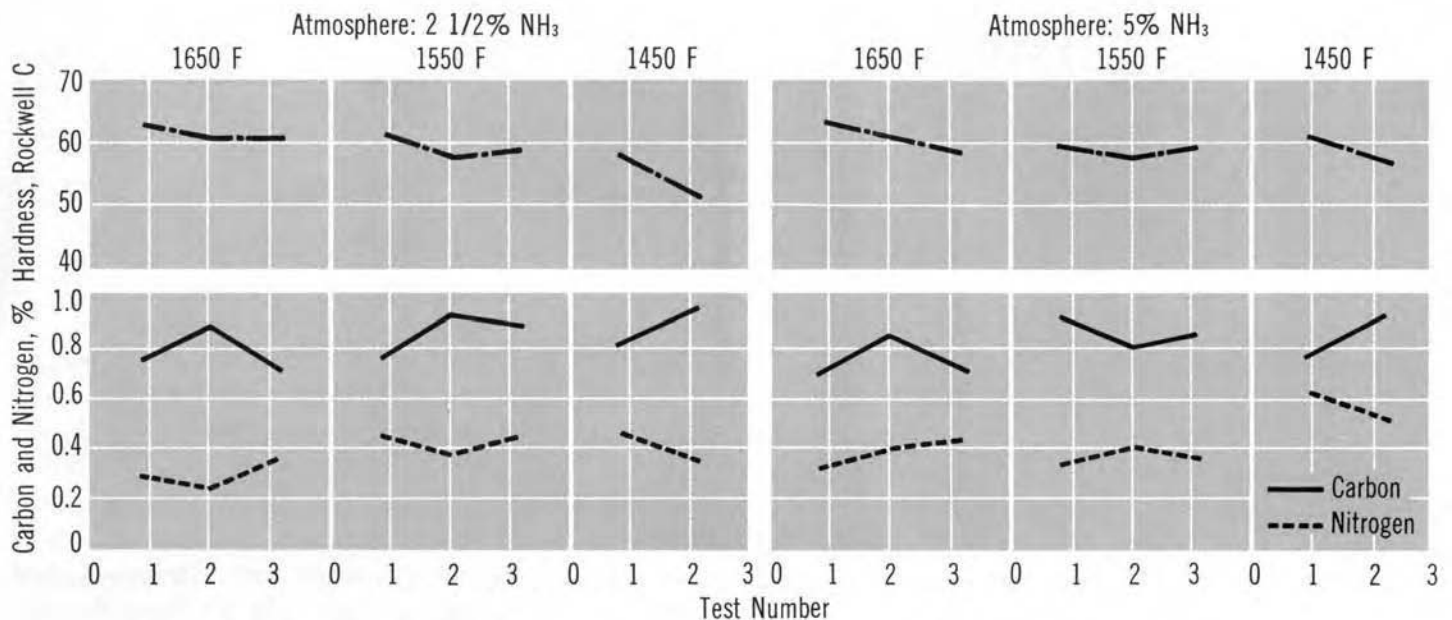


Fig. 21 Correlations of hardness (0.075 mm, or 0.003 in., below surface) with carbon and nitrogen contents of surfaces of 1018 steel after carbonitriding at indicated temperatures and ammonia levels (all quenched in 55 °C, or 130 °F, oil). In general, hardnesses drop slightly with lower temperatures, partly due to more retained austenite at lower process temperatures. See also Table 3 for processing atmospheres. Source: Ref 16

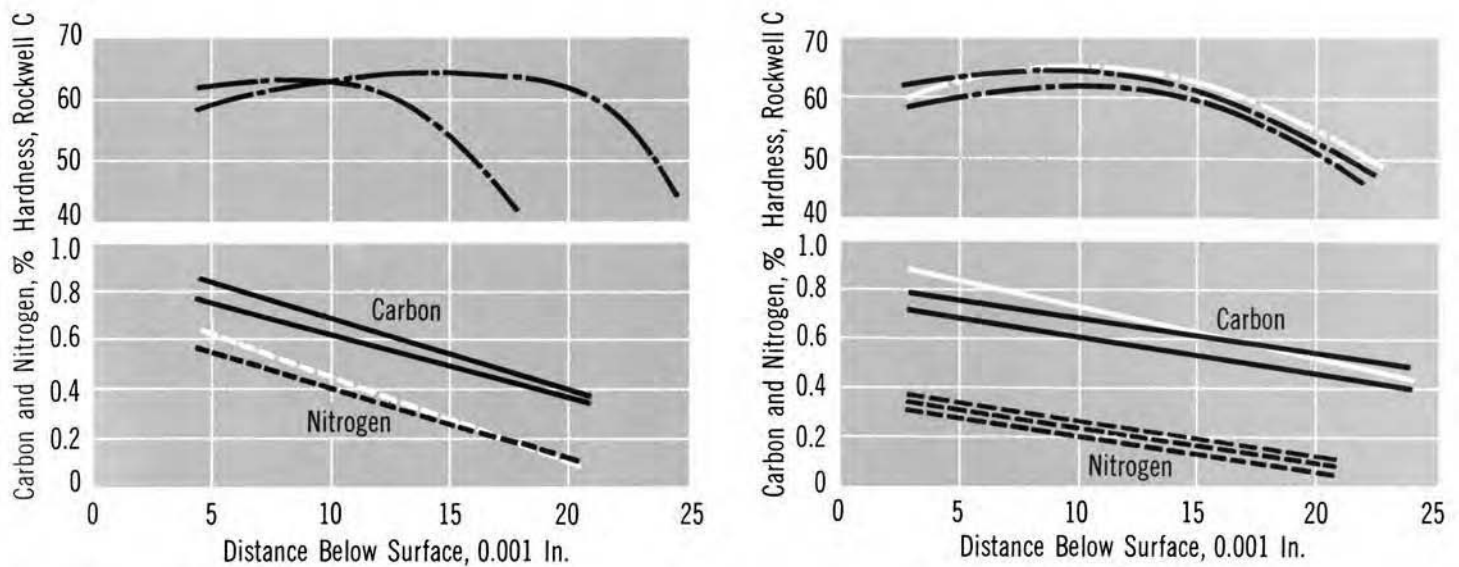


Fig. 22 Case hardness and composition of carbonitrided 1018 steel specimens, each line representing a different specimen at process temperatures of (a) 785 °C (1450 °F) and (b) 900 °C (1650 °F). The higher process temperature provides more consistent results and uniform case. 5% ammonia atmosphere, quenched in 55 °C (130 °F) oil. Source: Ref 16

atmosphere, and alloy content are closely interrelated.

Distortion and quench temperatures also must be considered in temperature selection. Dimensional control is often the most important consideration in the selection of carbonitriding temperature. The following two examples illustrate the relation between carbonitriding temperature and dimensional stability.

Example 3: Effect of Carbonitriding Temperature on Dimensional Stability of 1010 Steel Rack. A 1010 steel rack 11.75 cm long by 1 mm thick (4.63 in. long by 0.040 in. thick) could not be kept within limits of straightness tolerance (and, because of brittleness, it could not be straightened) after it was quenched from a carbonitriding temperature of 845 °C (1550 °F) into warm oil at approximately 65 to 70 °C (150 to 160 °F). The part had a case-depth requirement of 0.075 mm (0.003 in.) and a flatness requirement of 0.05 mm (0.002 in.) over its entire length. Lowering the temperature to the range of 790 to 800 °C (1450 to 1475 °F) significantly reduced distortion and increased ductility to within acceptable limits. Although temperatures below 790 °C (1450 °F) may have resulted in even less distortion and more ductility, they were not used because of the increase in time required to produce the desired case depth.

Example 4: Effect of Carbonitriding Temperature on Dimensional Stability of 1010 Steel Production Parts. Figure 23 presents data pertaining to the effect of carbonitriding temperature on the dimensional stability of three production parts. All three parts of 1010 commercial-quality steel sheet were processed in batch-type equipment at temperatures ranging from 790 to 845 °C (1450 to 1550 °F). The atmospheres consisted of endothermic

gas at 7 m³/h (250 ft³/h), enriching gas at 0.8 m³/h (30 ft³/h), and ammonia at 0.14 m³/h (5 ft³/h). Dewpoints were maintained at -1 to -4 °C (25 to 30 °F). Depending on temperature, furnace times were varied to produce specified case depths of 0.13 to 0.20 mm (0.005 to 0.008 in.).

Equal numbers of parts were hand loaded in baskets and processed in a batch furnace. The parts shown in Fig. 23(a) and (b) were loaded with their axes in the vertical position; parts such as those in Fig. 23(c) were randomly loaded. Baskets and parts were quenched in slightly agitated oil at 60 to 70 °C (140 to 160 °F).

Data in Fig. 23 represent eight heats for the part in Fig. 23(a) and three heats for each of the two other parts. All parts were within inside-diameter tolerance before carbonitriding.

For the parts carbonitrided at four temperatures, the least distortion resulted at the lowest temperature. Distortion is lower at lower temperatures because there is more ferrite in the structure at the lower temperature and consequently less volume expansion on quenching. However, for the part with the smallest inside diameter (Fig. 23c), dimensional variation was not affected by a reduction in temperature.

Temperature also has a direct bearing on core hardness. Steels treated at the higher carbonitriding temperatures and quenched from above the upper critical temperature of the core will produce higher core hardnesses. These high core hardnesses are usually desirable in applications involving high surface loads, because a strong core is needed to support the hardened case.

Special fabrication and service requirements of a particular part may restrict the choice of carbonitriding temperature. For instance, in one application, cold headed pins used in door-catch mechanisms required both riveting

quality and wear resistance. A carbonitriding temperature of 790 °C (1450 °F) satisfied both requirements by producing a soft center for riveting and a thin, file-hard case for wear resistance.

Quenching Media and Practices

Whether carbonitrided parts are quenched in water, oil, or gas depends on the allowable distortion, metallurgical requirements (such as case and core hardness), and type of furnace equipment employed.

Water Quenching. If the accompanying distortion is tolerable, parts made of low-carbon steel may be quenched in water. For example, shift-lever pins made of B1212 steel are water quenched.

Water quenching usually is restricted to those furnaces in which the work is transferred from the furnace into the air prior to quenching, thus avoiding possible contamination of the furnace atmosphere by water vapor. However, water quenching from a rotary retort furnace is feasible, provided the quench chute is equipped with gas ejectors and a water-distribution system for condensing water vapor.

It should be noted that ammonia is very soluble in water and forms a product (NH₄OH) that is extremely corrosive to copper-base materials. In continuous operations where water is exposed to an ammonia-bearing atmosphere, brass agitators, copper tube bundles in heat exchangers, and similar copper-alloy components should be avoided.

Gas Quenching. Parts that have small mass (such as thin stampings) may be quenched in a stream of cooled atmosphere gas or nitrogen. Gas or atmosphere quenching serves principally

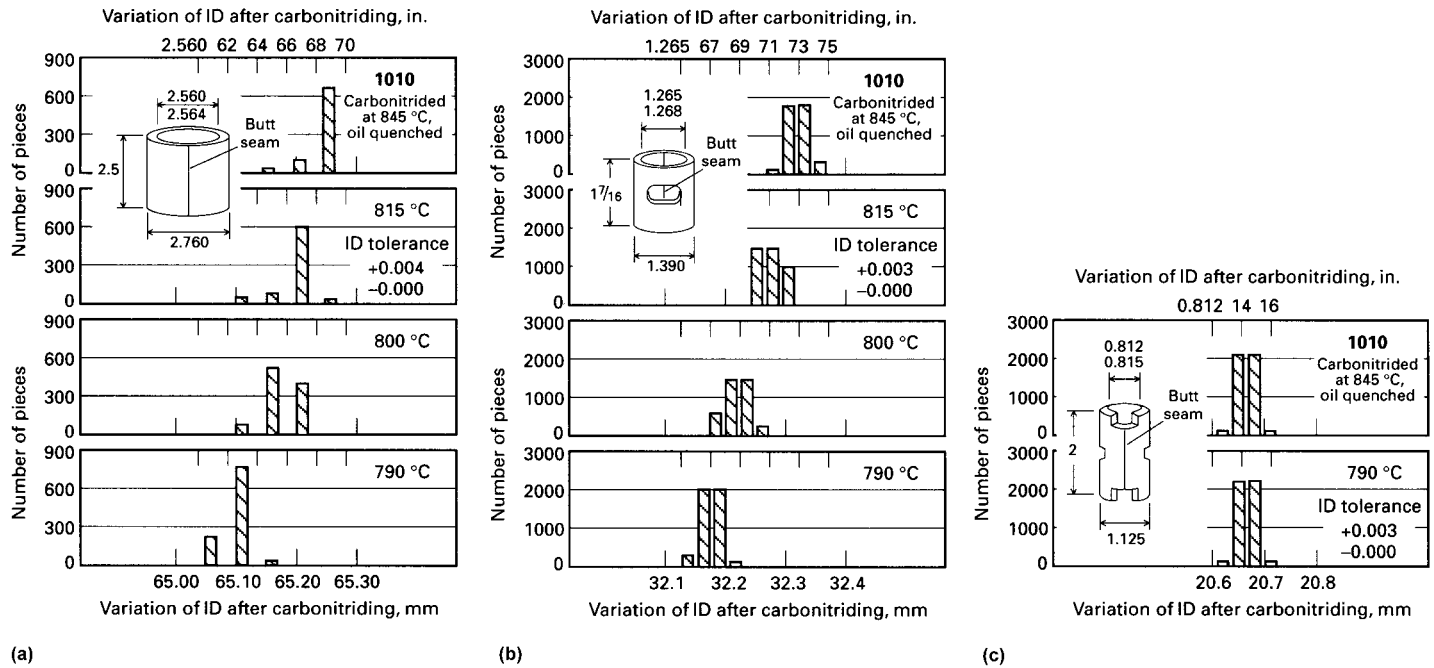


Fig. 23 Effect of carbonitriding temperature on dimensional stability of three 1010 steel production parts. Parts were carbonitrided to produce a case depth of 0.13 to 0.20 mm (0.005 to 0.008 in.) with minimum surface hardness of 89 HR15N. Gas ratios and dewpoints were essentially the same for all temperatures. Time at temperature was 15 to 45 min, depending on temperature. ID, inside diameter. Part dimensions and tolerances given in inches

to reduce distortion, thus eliminating the high costs of straightening.

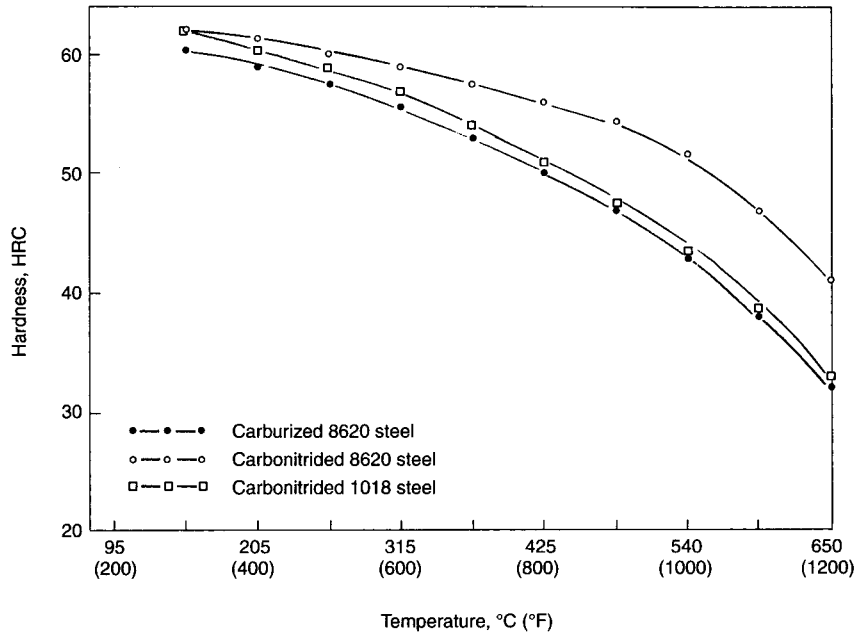
In gas quenching, parts must be loaded into furnace trays carefully so that the surfaces of the parts can be cooled rapidly enough to produce the desired hardness. Trays should be loaded and stacked so that the total mass of the load does not exceed that which can be satisfactorily quenched.

Tempering

Many shallow-case carbonitrided parts are used without tempering. The presence of nitrogen in the carbonitrided case increases its resistance to softening (Fig. 24), and the increase varies with the amount of nitrogen in the case. Resistance to tempering may be desirable where service operating temperatures are abnormally high, or where hot straightening is employed.

Tempering data obtained on carbonitrided cases of 1018 steel are given in Fig. 25. The data relate temper resistance to both carbonitriding temperature and the ammonia content of the atmosphere. Figure 26 presents a summary of the effects of carbonitriding temperature and ammonia content on temper resistance, derived from the same specimens referred to in Fig. 25.

Because tempering a carbonitrided case at 425 °C (795 °F) and above results in a marked increase in notch toughness (Table 5), parts that are to be subjected to repeated shock loading are invariably tempered to avoid impact and impact-fatigue failures. Most carbonitrided gears are tempered at 190 to 205 °C (375



8620 carburized steel			8620 carbonitrided steel			1018 carbonitrided steel		
°C	°F	HRC	°C	°F	HRC	°C	°F	HRC
150	300	60.5	150	300	62.0	150	300	62.0
205	400	59.0	205	400	61.5	205	400	60.5
260	500	57.5	260	500	60.0	260	500	59.0
315	600	55.5	315	600	59.0	315	600	57.0
370	700	53.0	370	700	57.5	370	700	54.0
425	800	50.0	425	800	56.0	425	800	51.0
480	900	47.0	480	900	54.0	480	900	47.0
540	1000	43.0	540	1000	51.5	540	1000	43.5
595	1100	38.0	595	1100	47.0	595	1100	38.5
650	1200	32.0	650	1200	41.0	650	1200	32.5

Fig. 24 Tempering curves for carburized and carbonitrided steels (all oil quenched). Source: Ref 17

to 400 °F) to reduce surface brittleness and yet maintain a minimum case hardness of 58 HRC. Alloy steel parts that are to be surface ground are tempered to minimize grinding cracks. Low-carbon steel parts are frequently tempered at 135 to 175 °C (275 to 350 °F) to stabilize austenite and minimize dimensional variations. Tapping screws made of 1020 steel are tempered at 260 to 425 °C (500 to 795 °F) to reduce breakage in tapping holes in sheet metal. In contrast, parts that are case hardened primarily for wear resistance, such as dowel pins, brackets, and washers, need not be tempered.

Hardness Testing

The selection of a method of testing the surface hardness of carbonitrided steels depends primarily on the effective case depth on the

parts to be tested. For effective case depths of 0.65 mm (0.025 in.) and above, accurate surface Rockwell C readings can be obtained. As the effective case depth decreases, lighter hardness testing loads must be used to obtain accurate surface hardness values. The Rockwell 15-N scale can be used in most instances for case depths of 0.25 to 0.40 mm (0.009 to 0.015 in.). On case depths of less than 0.25 mm, none of the Rockwell scales are reliable; testing may be done with files or a microhardness tester.

In file-hardness testing, parts with surface hardnesses that are less than full file hardness (64 to 68 HRC) can be tested with files that have been tempered to the desired hardness range. Surface hardness for such parts may be specified as Mfh 60, indicating that the part must be file hard to a mill file tempered to 60 HRC. However, a sample with high austenite content may

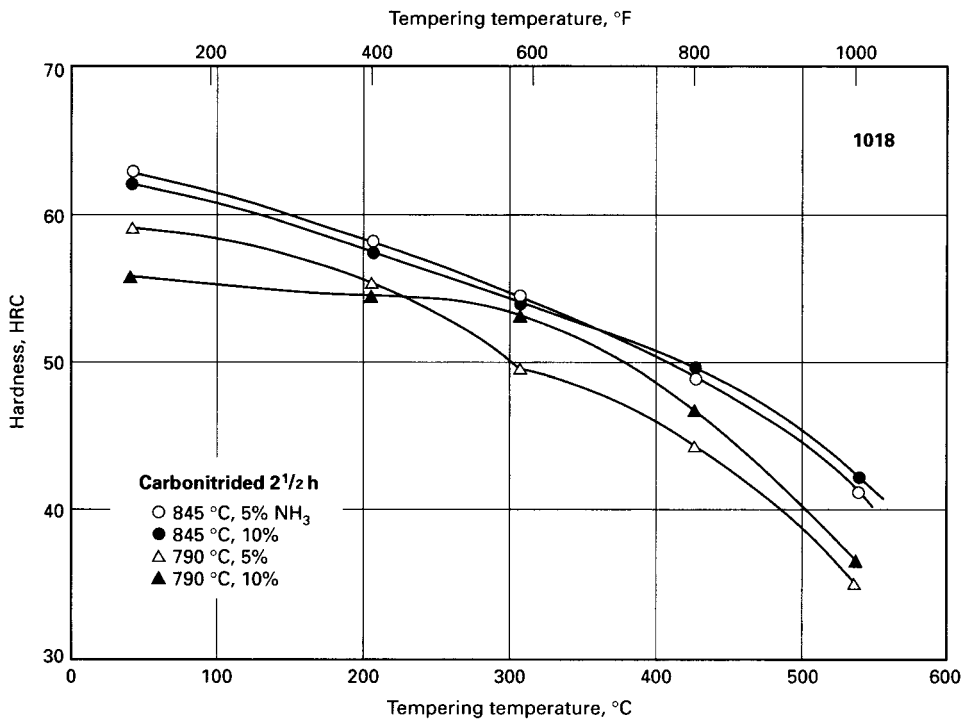


Fig. 25 Decrease of surface hardness with increasing temperature for specimens of 1018 steel carbonitrided under the conditions indicated. Rockwell C hardness converted from Rockwell 30N. See also Fig. 26.

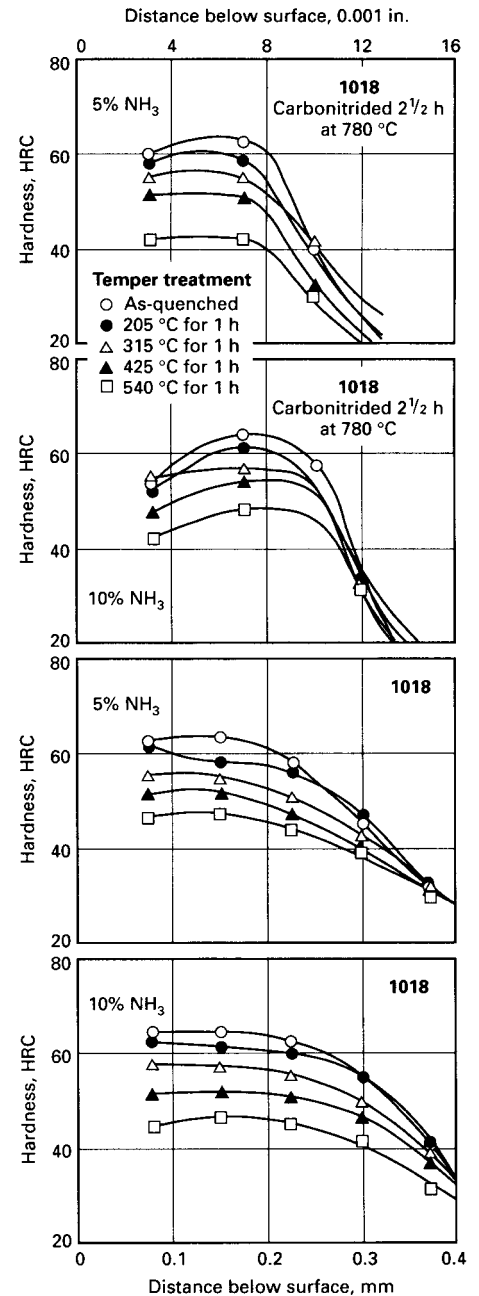


Fig. 26 Effect of tempering temperature on hardness gradients in carbonitrided cases. Rockwell C hardness converted from Vickers. Specimens were the same as in Fig. 25 and were tempered as indicated.

Table 5 Effect of tempering on Charpy V-notch impact strength of carbonitrided 1041 steel

Specimens were carbonitrided at 845 °C (1550 °F) for 3 h in an atmosphere containing 7% ammonia and were oil quenched from the carbonitriding temperature. Specimens were copper plated before machining of V-notch to permit exposure of the notch to the carbonitriding atmosphere.

Test	Tempering temperature		Impact strength		Hardness(a), HRC distance below surface, mm (in.)								
	°C	°F	J	ft · lb	Surface(b)	Core	0.075 (0.003)	0.15 (0.006)	0.25 (0.01)	0.38 (0.015)	0.64 (0.025)	1.0 (0.04)	1.4 (0.055)
1	As-quenched	As-quenched	1.4	1	60	53	63	64	64	63	61	61	58
2	370	700	2, 2	1.5, 1.5	47	46	57	57	55	54	49	50	50
3	425	800	29, 29	21.5, 21.5	42.5	43	57	57	56	55	49	47	47
4	480	900	69, 60	51, 44	38	38	54	54	52	50	42	38	38
5(c)	480	900	47, 52	35, 38
6	540	1000	78, 81	57.5, 60	35	32	49	50	50	47	36	33	32

(a) Converted from Vickers hardness. (b) Surface hardness is less than hardness at 0.075 mm (0.003 in.) below the surface because of retained austenite. (c) Tested at -18 °C (0 °F); all other tests at room temperature

indicate an indentation hardness of only 52 HRC and still resist a file hardened to 66 HRC.

Applications

Although carbonitriding is a modified carburizing process, its applications are more restricted than those of carburizing. As has been stated previously, carbonitriding is largely limited to case depths of approximately 0.75 mm (0.03 in.) or less, while no such limitation applies to carburizing. Two reasons for this are that carbonitriding is generally done at temperatures of 870 °C (1600 °F) and below, whereas, because of the time factor involved, deeper cases are produced by processing at higher temperatures; and the nitrogen addition is less readily controlled than is the carbon addition, a condition that can lead to an excess of nitrogen and, consequently, to high levels of retained austenite and case porosity when processing times are too long.

The resistance of a carbonitrided surface to softening during tempering is markedly superior to that of a carburized surface, as shown in Fig. 24. Other notable differences exist in terms of residual-stress pattern, metallurgical structure, fatigue and impact strength at specific hardness levels, and effects of alloy composition on case and core characteristics.

Steel Selection

For many applications, carbonitriding the less expensive steels will provide properties equivalent to those obtained in gas-carburized alloy steels. The following examples illustrate choices of carbonitrided carbon steels for applications ordinarily requiring alloy steels.

Example 5: Use of Carbonitrided 1010 Aluminum-Killed Steel. Camshaft eccentrics stamped from 1010 aluminum-killed steel 4 mm (0.16 in.) thick were carbonitrided to a depth of 0.25 to 0.50 mm (0.01 to 0.02 in.) and a minimum surface hardness equivalent to 58 HRC. The required metallurgical properties for this application could have been attained also with carbonitrided or gas-carburized 1011 or 1016 steel. However, the 1010 steel had the advantage of facilitating the stamping operation because of its lower carbon and manganese contents and fine grain size.

Example 6: Use of Carbonitrided 1117 Steel. Small gears for electromechanical servo units varying from 6.3 mm diameter by 12.7 mm length (¼ in. by ½ in.) to 51 mm diameter by 6.3 mm thick (2 in. by ¼ in.) were machined from 1117 steel bar stock. The parts were carbonitrided in a batch integral quench atmosphere furnace, loaded in mesh baskets. Smaller gears were run in single layers with separator screens between a maximum of three layers deep per basket. The larger-diameter gears were fixtured vertically using spiral spring separators.

The process was to carbonitride the gears at 855 °C (1575 °F) for 1½ h to produce an effective case depth of 0.20 to 0.38 mm (0.008 to 0.015 in.) with a final surface hardness of 89 HR15N, minimum. The automatic carbon-control system (oxygen probe with proportional natural gas addition) was set at 0.80% C, and 3% ammonia (by volume) was added to the automatically control-generated endothermic atmosphere.

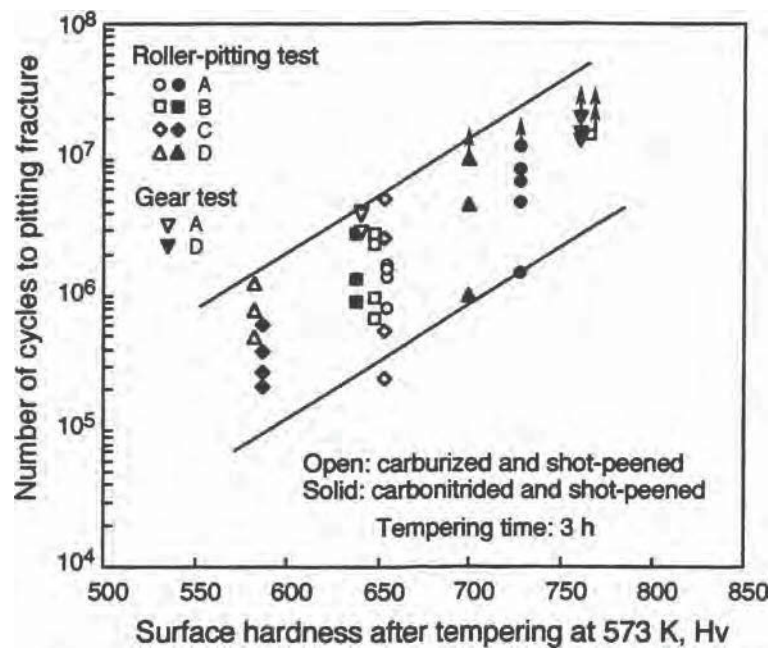
Pitting Resistance of Transmission Gears

Resistance to softening during tempering is a very important factor in reducing surface pitting fracture of transmission gears. Contact surface temperatures of transmission gears can reach almost 300 °C (570 °F) during operation under high stress. Pitting resistance is related

not only to the surface hardness but also to the retardation of softening during tempering. A positive correlation exists between the pitting lifetime of various case-hardened steels and the surface hardness of the steels after tempering at 300 °C (570 °F) (Fig. 27).

Nitrogen introduced by carbonitriding also has been shown to be more effective at improving the resistance to softening than by increasing the amount of silicon, chromium, and molybdenum in conventionally carburized steel (Ref 18). The optimal chemical composition of steel for carbonitriding to a high case amount of nitrogen for contact fatigue strength of automotive gears is proposed to be 0.7% Si, 1.5% Cr, and 0.45% Mo.

Example 7: Eliminating Pitting Fatigue in Pinion Gears. Another example involves a change from carburizing to carbonitriding to eliminate pitting fatigue for planetary pinion gears for automatic transmissions. The helical



Base composition

Steel	C	Si	Mn	P	S	Cr	Mo
A	0.22	0.67	0.30	0.009	0.024	1.50	0.44
B	0.21	0.68	0.30	0.009	0.023	2.52	Tr.
C	0.22	0.68	0.30	0.009	0.025	1.52	Tr.
D	0.19	0.06	0.78	0.006	0.016	1.09	0.45

Carbon and nitrogen contents in surface of as-heat-treated specimens

Steel	Treatment	Surface content, mass%	
		Carbon	Nitrogen
A	Carburizing	0.69	0.05
	Carbonitriding	0.85	1.14
B	Carburizing	0.77	0.05
	Carbonitriding	0.77	1.32
C	Carburizing	0.72	0.05
	Carbonitriding	0.80	1.10
D	Carburizing	0.77	0.04
	Carbonitriding	0.74	0.82

Fig. 27 Effect of surface hardness after tempering on the pitting resistance of carburized and carbonitrided steels. Pitting test specimens cut from normalized steel bar were carbonitrided at 900 °C (1650 °F) for 4 h and then at 840 °C (1545 °F) for 4 h in an atmosphere of endothermic gas (RX gas) enriched with butane gas and a 7 vol% ammonia gas mixture, diffusing carbon and nitrogen simultaneously into the steel, followed by quenching in oil at 50 °C (120 °F). Carburized specimens were also prepared with chemical analysis as indicated. Source: Ref 18

gears were hobbled and shaved and were made from 8620 steel bar stock. The specified heat treatment required a carbonitrided effective case depth of 0.46 to 0.58 mm (0.018 to 0.023 in.) at the pitch line, with a minimum hardness of RA80 after oil quenching and tempering at 175 °C (350 °F). The parts were approximately 30.5 mm diameter by 51 mm length (1.2 in. by 2 in.) with a 15.9 mm ($\frac{5}{8}$ in.) bore.

The parts were loaded vertically on fluted stem fixtures with separators between the gears and were then carbonitrided in a two-row, four-zone pusher furnace having three zones of control. The furnace was 18 trays in length. Each zone of control had individual automatic carbon addition using oxygen probes with a setpoint of 0.78% C. Each furnace zone had fan circulation with manual addition and flowmeter control of endothermic gas additions. Flow-restrictive stainless steel orifices were added to the ammonia inlet lines of each of the three control zones to ensure a 4% by volume ammonia addition. The furnace was heated to 845 °C (1550 °F) (all zones), and the push cycle was 20 min for each row (total carbonitriding time was approximately 6 h). The parts were oil quenched in agitated 100 SUS fast oil (60 °C, or 140 °F) and washed and tempered at 175 °C (350 °F). The unwind in the gears after heat treatment was built into the machining operation, and the parts did not require a gear profile grind before use. This eliminated the pitting fatigue problem.

Carbonitriding of Powder Metallurgy Parts

Carbonitriding is widely used as a process for case hardening parts made by powder metallurgy techniques from ferrous powders. Densities of the sintered compacts vary from approximately 6.5 g/cm³ (0.23 lb/in.³) up to those approaching that of wrought steel. Parts may or may not be copper infiltrated prior to carbonitriding.

Carbonitriding is effective in case hardening iron compacts made from electrolytic iron powders. Four characteristics of these compacts make case hardening by carburizing difficult: high martensite transformation temperature (M_s), very low hardenability, less surface oxidation, and inherent porosity, resulting in high rates of carbon penetration.

Carbonitriding at 790 to 815 °C (1450 to 1500 °F) solves these problems; lower rates of diffusion at these temperatures permit control of case depth and allow buildup of adequate carbon in the case. The effects of nitrogen in retarding the pearlite transformation result in sufficient hardenability to allow oil quenching.

File-hard cases (with microhardnesses equivalent to 60 HRC) and normal, predominantly martensitic structures can be consistently obtained. Shallow cases are obtainable, although the allowable range of case depth must be increased over that used for wrought steels.

Typical ranges of case depth are 0.08 to 0.20 mm (0.003 to 0.008 in.) and 0.15 to 0.30 mm (0.006 to 0.012 in.).

The high rate of carbon and nitrogen penetration that occurs as the result of porosity is demonstrated in Fig. 28 for parts made of iron powder conforming to ASTM B310, class A. Although the rate of penetration decreases with increasing density, case depths for the higher densities (7.20 to 7.30 g/cm³, or 0.260 to 0.264 lb/in.³) are much deeper than those obtained with a wrought steel (7.87 g/cm³, or 0.284 lb/in.³). Most commercial iron-powder compositions exhibit this type of response to carbonitriding; however, copper-infiltrated compacts are considerably more resistant to the penetration of carbon and nitrogen.

Tempering. Carbonitrided iron powder metallurgy parts are usually tempered, despite the fact that there is little danger of cracking untempered pieces. Tempering accomplishes the incidental result of facilitating tumbling and deburring operations. Although tempering is potentially capable of removing oil picked up and held in the pores in the part, air tempering of oil-quenched powder metallurgy parts is normally limited to temperatures not exceeding 205 °C (400 °F) because of the fire hazard at higher temperatures. Carbonitrided iron powder metallurgy parts are usually tempered at temperatures slightly higher than the temperatures used for carbonitrided wrought steel parts. Special cleaning procedures to remove oil, thus eliminating fire hazards, are incorporated in the processing steps when the tempering temperature exceeds 205 °C.

Ammonia Guidelines

The ammonia system required for carbonitriding may consist of a number of cylinders of liquid ammonia that are connected to a common manifold. In general, ammonia from only a part of the supply is employed; the remainder is held in reserve. The flow from each cylinder should be sufficiently low to prevent freezing of the valves. Only stainless steel valves and schedule 80 or stainless steel piping are recommended.

Outside bulk storage and vaporizing systems are much preferred to cylinder banks, considering the advantage of a constant, uninterrupted source on the uniformity of work quality. In general, when bulk storage is used, two-stage pressure regulation is used to ensure a constant and uniform ammonia flow. The first stage regulates the pressure for delivery to the furnace, whereas the final pressure regulation, at the furnace, controls the pressure to the process.

Ammonia used for carbonitriding must be anhydrous ammonia of 99.9+% purity. Grade designations such as premium, refrigeration, and metallurgical are used to specify suitable materials. Grades known as commercial and agricultural contain appreciable amounts of

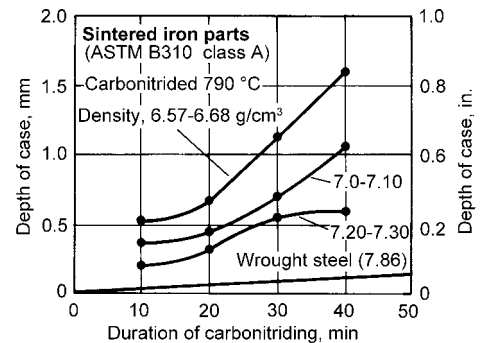


Fig. 28 Increase of case depth with decrease in density of iron powder metallurgy parts carbonitrided for various periods of time at 790 °C (1455 °F). Curve for steel is based on total furnace time and represents the average of the 775 to 790 °C (1425 to 1455 °F) band shown in Fig. 10.

carbon dioxide, water, and oils, which prohibit their use in furnace atmospheres.

Most ammonia is produced from natural gas, so costs and availability are related to natural gas supplies.

Safety

Gaseous carbonitriding media are highly toxic, flammable, and explosive. The safety precautions that must be taken to protect equipment and personnel are essentially the same as those used in gas carburizing.

Ammonia cylinders should not be located near the furnaces, in direct sunlight, or near flammable gases or other combustibles. It is recommended that the ammonia supply be placed in a room that is well ventilated at the ceiling and separated from the work area by a fire-resistant wall.

Because ammonia is lighter than air, as well as a moderate fire hazard and a toxic material, an automatic sprinkling system is recommended. Gas masks should be readily available but should not be stored in the same area as the ammonia. A sulfur stick can be used to check for ammonia leaks. Additional recommendations pertaining to safety in ammonia systems can be obtained from fire insurance companies.

Under no circumstances should combustible gas be introduced into the furnace when the furnace temperature is less than 760 °C (1400 °F). When a lower operating temperature is required, the furnace should be heated to 760 °C and purged with generator gas before the temperature is decreased. This type of operation can be very dangerous and should be done only by qualified personnel.

REFERENCES

1. W.F. Gale and T.C. Totemeier, Ed., Chap. 29, Heat Treatment, *Smithells Metals Reference Book*, 8th ed., Butterworth-Heinemann, 2004

2. A.E. Nehrenberg et al., Effects of Carbon and Nitrogen on the Attainable Hardness of Martensitic Steels, *Trans. ASM*, Vol 47, 1955, p 785–793
3. G. Rengstorff, M. Bever, and C.F. Floe, The Carbonitriding Process of Case Hardening Steel, *Met. Prog.*, Nov 1949, p 651
4. Carbonitriding, *Heat Treating, Cleaning and Finishing*, Vol 2, *Metals Handbook*, 8th ed., American Society for Metals, 1964, p 119
5. D. Herring, Comparing Carbonitriding and Nitrocarburizing, *Heat Treat. Prog.*, April/May 2002, p 17
6. C. Dawes, Nitrocarburizing and Its Influence in the Automotive Sector, *Heat Treat. Met.*, Vol 18 (No. 1), 1991.1, p 19–30
7. T. Bell, M. Kinali, and G. Munstermann, Physical Metallurgy Aspects of the Austenitic Nitrocarburizing Process, *Heat Treat. Met.*, Vol 2, 1987, p 47–51
8. F.K. Cherry, Austenitic Nitrocarburizing, *Heat Treat. Met.*, Vol 1, 1987, p 1–5
9. K.-E. Thelning, *Steel and Its Heat Treatment*, Butterworths, 1975
10. F.A. Clarkin and M.B. Bever, The Role of Water Vapor and Ammonia in Case Hardening Atmospheres, *Trans. ASM*, Vol 47, 1955, p 794–806
11. R. Davies and C.G. Smith, A Practical Study of the Carbonitriding Process, *Met. Prog.*, Vol 114 (No. 4), Sept 1978, p 40–53
12. E.R. Mantel and M.M. Shea, Hardening Response of Carbonitrided Rimmed and Aluminum-Killed SAE 1010 Steels, *J. Heat Treat.*, Vol 4 (No. 3), 1986, p 237–246
13. W.E. Dowling, W.T. Donlon, and J.P. Wise, *Proc. of 18th Heat Treating Conference*, Oct 12–15, 1998 (Chicago), ASM International, 1998, p 387–397
14. B. Přenosil, Properties of Carbonitriding Layers Forming as a Result of Carbon Diffusion in Austenite, *Härt.-Tech. Mitt.*, Vol 21 (No. 1), 1996, p 24–66 (in German)
15. G.W. Powell, M.B. Bever, and C.F. Floe, Carbonitriding of Plain Carbon and Boron Steels, *Trans. ASM*, Vol 46, 1954, p 1359–1371
16. N.P. Milano, Getting the Most from Carbonitrided Surfaces, *Met. Prog.*, July 1965, p 80
17. J.L. Dossett and H.E. Boyer, *Practical Heat Treating*, 2nd ed., ASM International, 2006, p 154
18. Y. Watanabe, N. Narita, Y. Matsushima, and K. Iwasaki, Effect of Alloying Elements and Carbonitriding on Resistance to Softening during Tempering and Contact Fatigue Strength of Chromium-Containing Steels, *Heat Treating: Proceedings of the 20th Conference*, Vol 1 and 2, K. Funatani and G.E. Totten, Ed., ASM International, 2000, p 52–61

Nitriding and Nitrocarburizing of Steels

Fundamentals of Nitriding and Nitrocarburizing	619	Common Problems	673
Introduction	619	Rules of Thumb	674
1. Advent of Nitriding	619	Safety Precautions	674
2. Nitrided/Nitrocarburized Microstructure, Thermodynamics, and Kinetics	620	Equipment	674
3. The Iron-Nitrogen Phase Diagram	621	Liquid Nitriding of Steels	680
4. Nitriding Potential and the Lehrer Diagram	622	Liquid Nitriding Applications	680
5. Controlled Nitriding	623	Liquid Nitriding Systems	680
6. Carburizing Potential and Controlled Carburizing	624	Liquid Pressure Nitriding	681
7. Controlled Nitrocarburizing	625	Aerated Bath Nitriding	681
8. Local Equilibria and Stationary States	626	Case Depth and Case Hardness	683
9. Microstructural Development of the Compound Layer	628	Operating Procedures	683
10. Kinetics of Compound-Layer Growth	633	Equipment	684
11. Microstructural Development of the Diffusion Zone	635	Maintenance Schedules	684
12. Kinetics of Diffusion-Zone Growth	639	Safety Precautions	685
Epilogue	641	Liquid Nitrocarburizing	685
Gas Nitriding and Gas Nitrocarburizing of Steels	647	Nontoxic Salt Bath Nitrocarburizing Treatments	686
Introduction	647	Wear and Antiscuffing Characteristics of the Compound Zone Produced in Salt Baths	687
Terminology for Gas Reactions	648	Appendix 1—Liquid Salt Bath Nitriding Noncyanide Baths	688
Low-Temperature Nitriding and Nitrocarburizing	649	Appendix 2—Liquid Salt Bath Nitriding	689
Nitriding	651	Plasma (Ion) Nitriding and Nitrocarburizing of Steels	690
Ferritic and Austenitic Nitrocarburizing	656	Introduction	690
Other High-Temperature Processes	657	Process History and Developments	690
Nitriding Processing	659	Glow-Discharge Process	693
Atmosphere Control	661	Plasma Nitriding Furnaces	695
Measuring the Potentials	665	Process Control	696
Temperature Control	668	Case Structures and Formation	698
Impact of Measuring Errors	669	Workpiece Factors	699
Simulation of Nitriding Processes	669	Ion Nitriding Applications	700
Inspection and Quality Control	669	Plasma Nitrocarburizing	701
Lab Equipment and Sample Preparation	670		
Selective Nitriding	673		

Fundamentals of Nitriding and Nitrocarburizing

E.J. Mittemeijer, Max Planck Institute for Intelligent Systems (formerly Max Planck Institute for Metals Research) and Institute for Materials Science, University of Stuttgart

Introduction

The nitriding process, which involves the introduction of atomic nitrogen (N) into the surface of a component, has been a most versatile and efficacious method of surface treatment of (usually) iron-base materials for many decades. The advent of nitriding as a technical process in the early 20th century was the work of Adolph Machlet (American Gas Company) in the United States (Ref 1) and Adolph Fry (Krupp Works) in Germany (Ref 2). The nitriding process has since become a technology of ever growing importance, finding an even at present still widening field of applications. In the course of time, a great number of process variants have been developed. One principal development is the process of nitrocarburizing, whereby carbon is introduced simultaneously with nitrogen.

Different methods exist for introducing atomic nitrogen, or both atomic nitrogen and atomic carbon, into the surface of steel. As described in other articles in this Volume, various nitriding/nitrocarburizing atmospheres can be indicated:

- Gas (NH₃-H₂) mixtures (see “Gas Nitriding and Gas Nitrocarburizing of Steels”)
- Salt (cyanate-cyanide) baths (see “Liquid Nitriding of Steels”)
- Plasmas (ionized gases, as, for example, based on N₂-H₂ gas mixtures) (see “Plasma (Ion) Nitriding and Nitrocarburizing of Steels”)

Powder media (based on CaCN₂, calcium-cyanamide, which delivers NH₃ upon reaction with H₂O from an added “activator”) have been successfully applied in the laboratory (Ref 3) but have not found technological application.

This article provides an overview of the current understanding of essential aspects of the thermodynamics and kinetics of the nitriding and nitrocarburizing of iron-base materials. The focus of this article is on the scientific

background of nitriding/nitrocarburizing with gaseous processes. The reason is that only the gaseous treatments allow for precise control of the thermodynamic conditions, even if only in the laboratory. Thus, the chemical potentials of nitrogen and carbon at the surface of the component to be nitrided/nitrocarburized (the nitriding/carburizing “power”) can be varied over a wide range in a controlled manner (i.e., these chemical potentials can be assigned specified values), whereas such prescribed variation of these chemical potentials is not possible in the case of the other processes mentioned. This leaves unimpeded that reproducible results by salt bath and plasma nitriding/nitrocarburizing processes can be obtained, but the thermodynamic conditions of these processes are ill-defined, thereby obstructing development of corresponding process variants that can be tuned in the above sense.

After a brief overview of the early history and the basics of the generated microstructure and properties, the interpretation of the “normal” iron-nitrogen phase diagram and the “potential” Lehrer diagram are discussed. Next, the essential elements for realizing (in practice) controlled nitriding and controlled nitrocarburizing are treated to some extent. Special attention is paid to the occurrence of local equilibria and stationary states. The concept of the “diffusion path” is highlighted in order to understand the complicated microstructures that develop in the iron-carbonitride compound layer upon nitrocarburizing. The very pronounced interaction of carbon and nitrogen atoms dissolved on the same sublattice of interstitial sites is demonstrated by recent diffusion experiments. The role of alloying elements, Me, is characterized by employing the distinction of strong, intermediate, and weak Me-N interactions, for the evolution of the microstructure of both the compound layer and the diffusion zone. The cardinal role of the so-called “excess nitrogen” for the nitriding kinetics is emphasized. Possibilities to describe the time (and temperature)

dependencies of the nitriding/nitrocarburizing processes are summarized.

1. Advent of Nitriding

On May 25, 1906, a patent application was filed by A. Machlet that proposed to avoid oxidation of steel components by replacing the air atmosphere in the retort with ammonia. This patent was granted on June 24, 1913 (Patent 1,065,697). Apparently, soon after submitting this patent application in 1906, Machlet discovered that treating such components in an ammonia atmosphere at elevated temperature led to a “skin, casing, shell or coating” that was very hard and difficult “to tarnish, corrode, rust, or to oxidize.” This invention was presented as a patent application filed on March 19, 1908. The patent was granted (also on June 24, 1913) as Patent 1,065,379. This patent (Ref 1) represents the invention of the nitriding process in the United States! In a further patent application filed on July 12, 1907, Machlet in fact introduced the (gaseous) nitrocarburizing process, with a hydrocarbon gas combined with ammonia as the treatment atmosphere and including a subsequent treatment in pure ammonia. This patent was granted on April 14, 1914 (Patent 1,092,925).

In Germany, the nitriding process of steel for surface hardening was developed by A. Fry (Ref 2). In particular Fry’s work led to the technological application of nitriding as a surface engineering process, especially by his development of steels (containing aluminum as an alloying element) dedicated to nitriding.

Starting with these early developments, a great number of process variants have been developed with significantly different effects on the structure and properties of the surface after nitriding/nitrocarburizing (see, for example, the article “Gas Nitriding and Gas Nitrocarburizing of Steels” in this Volume).

2. Nitrided/Nitrocarburized Microstructure; Thermodynamics, and Kinetics

The nitriding process typically involves the introduction of nitrogen into the surface-adjacent zone of a component, usually at a temperature between 500 and 580 °C (773 to 853 K). Depending on the nitriding “power” of the nitriding atmosphere surrounding the component, a nitrided zone emerges that, especially in the case of ferritic iron-base alloys or ferritic steels nitrided at temperatures lower than 590 °C (863 K), can be subdivided into (Fig. 1):

- A *compound layer* (of thickness, say, up to several 10 μm), largely composed of iron nitrides, as γ' -Fe₄N_{1-x} and ϵ -Fe₂N_{1-z} (see the iron-nitrogen phase diagram reproduced in Fig. 2, and see Table 1)
- A *diffusion zone* (of thickness, say, up to several 100 μm), where, in the case of pure iron or carbon steel, after nitriding, upon either slowly cooling or upon aging subsequent to quenching, the nitrogen dissolved at the nitriding temperature precipitates as iron nitrides in the diffusion zone, or, in the case of steel containing alloying elements with affinity for nitrogen, as aluminum and chromium, alloying element nitrides precipitate during nitriding

The technological importance of nitriding is derived from the pronounced increase of the resistances against fatigue, wear, and corrosion, which can be achieved by tuned applications of the nitriding process.

The pronounced property improvement is, roughly speaking, due to the high hardness, the internal stresses, and the modified chemistry in the nitrided zone. It can be crudely said that, in general, favorable wear and corrosion properties can be due to specific compound layers and that favorable fatigue and also wear properties (if the compound layer has been removed after nitriding or its formation has been avoided) can be ascribed to the diffusion zone (Fig. 1).

Nitrocarburizing processes, as compared to nitriding processes, largely influence the composition and constitution of the compound layer and thus can be relevant for wear (and corrosion) properties.

To understand what is happening during nitriding/nitrocarburizing and to be able to optimize the process in view of desired properties, it is imperative to understand the thermodynamics and kinetics of the process. Such basic understanding is less common than one may expect and, in view of the experience of approximately one century of nitriding, amazingly has only rather incompletely been obtained. Hence also to this day, research on nitriding and nitrocarburizing is timely. From a scientific point of view, the properties of interstitially dissolved elements as nitrogen and carbon in iron-base matrices are intriguing because their mobility on the sublattices of interstitial sites can

be large and their interaction can be strong, also because of their surrounding strain fields accommodating the misfit of the sizes of the atom and the interstitial site.

To understand the nitriding/nitrocarburizing process, full understanding of its thermodynamics does not suffice at all. The kinetics of the various process steps (as mass transfer from

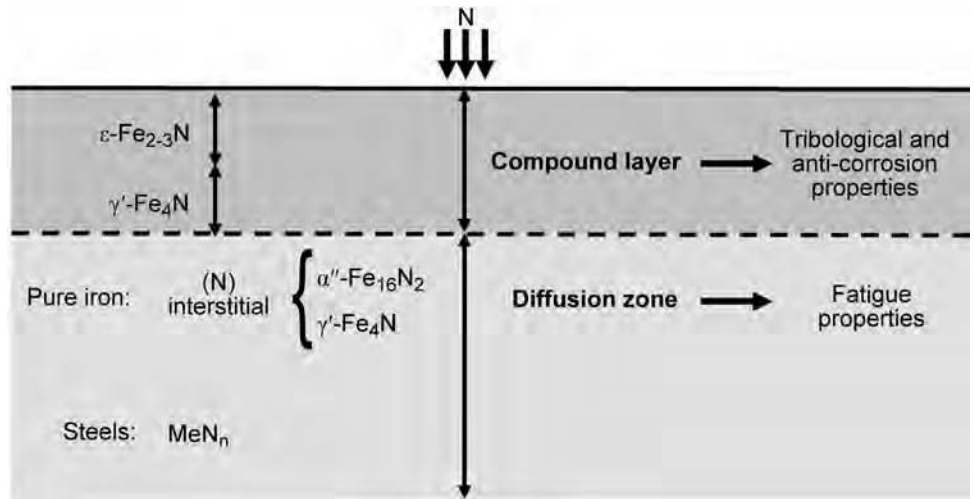


Fig. 1 Schematic cross section of nitrided region of an iron-base ferritic specimen/component showing the compound layer and the diffusion zone with their (possible) constituents

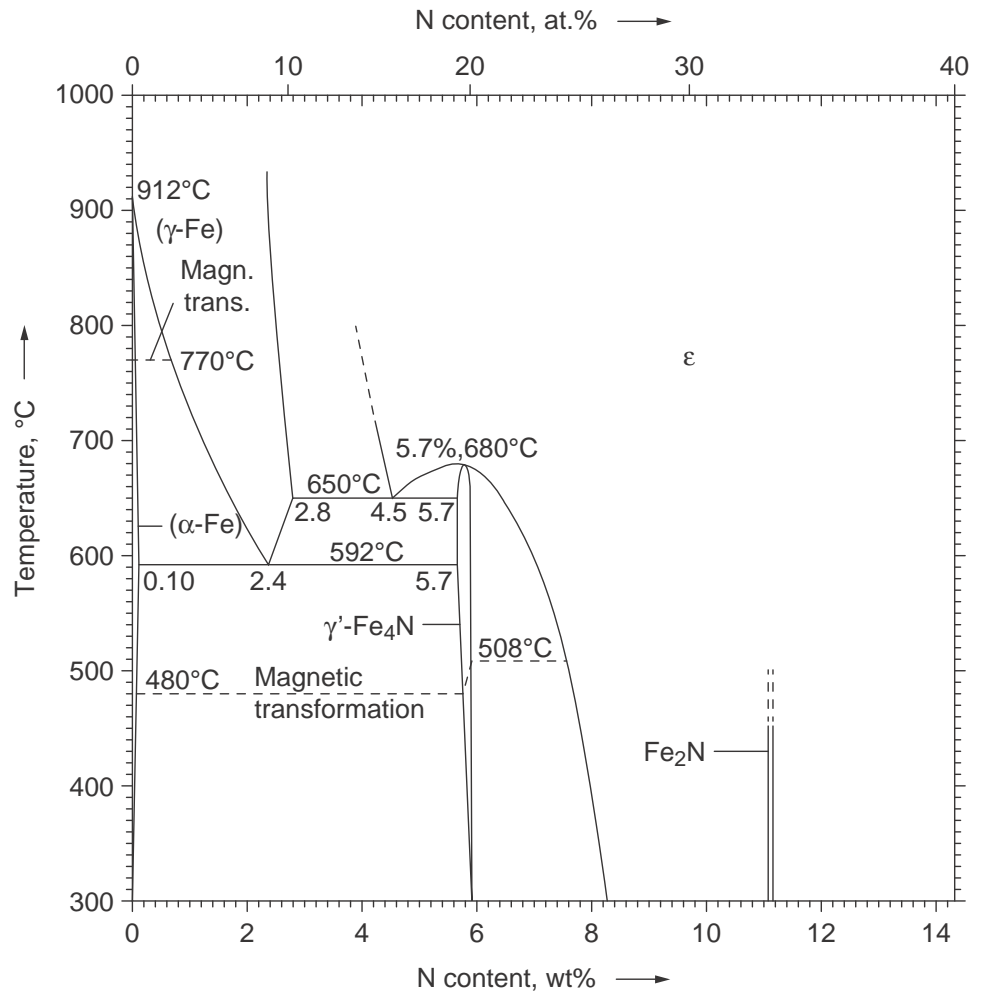


Fig. 2 Iron-nitrogen phase diagram. Redrawn from Ref 4

the nitriding/nitrocarburizing atmosphere to the substrate, diffusion, and precipitation) are of at least equal importance, albeit recognizing that the thermodynamics of the process constrain the possible kinetics.

Physical materials science has not been able until now to generally provide a description of the kinetics of a process once its thermodynamics have been established; if the Gibbs energies of the beginning and end stages are known, only seldom it is possible to provide a quantitative description of the kinetics (i.e., only rarely can the path taken by the system in the energy landscape of the system be predicted as a function of the independent, or state, variables) (Ref 14).

This serves to indicate that also in the field of nitriding/nitrocarburizing, even supposing that our understanding of thermodynamics is complete (which is not the case), the complex kinetic phenomena encountered (e.g., in the case of nitrocarburizing; see Section 9.2) have obstructed until now the presentation of a theoretical treatment comprehensively integrating the thermodynamics and kinetics of nitriding/nitrocarburizing.

The previous text should not suggest ignorance of any scientific background, and, indeed, a lot of research has been done in recent years that has provided accumulated fundamental knowledge of specific aspects of nitriding/nitrocarburizing. The following attempts to provide an overview of the current basis of our understanding, including results of recent research.

References 15 and 16 are well-known, previous review papers but are more limited and of rather different character and scope.

3. The Iron-Nitrogen Phase Diagram

Interpretation and The Development of Porosity

There is a lot of misunderstanding among heat treatment practitioners and also in the literature regarding the interpretation of the stability, metastability, and instability of nitride and carbide (and carbonitride and nitrocarbide) phases in iron-base materials. This already is manifested upon discussing the iron-nitrogen phase diagram.

Phase-stability regions for the iron-nitrogen system are usually presented in a “normal” phase diagram: temperature versus nitrogen content (Fig. 2; for temperatures below 300 °C, or 573 K, see Ref 17). “Normal” phase diagrams, as presented in the compilation of, for example, Ref 4, present stability regions for phases as a function of temperature and composition at 1 atm pressure. If this would hold for the iron-nitrogen phase diagram presented in Fig. 2, then all phases shown as, for example, the solid solutions α -Fe[N] (nitrogen ferrite) and γ -Fe[N] (nitrogen austenite) and the nitrides γ' -Fe₄N_{1-x} and ε -Fe₂N_{1-z} are unstable. Indeed, if the kinetics allow (i.e., the temperature is high enough and the needed time is of practical length), these phases decompose in Fe (solid) and N₂ (gas), which are the stable

phases at normal temperatures and pressure for the iron-nitrogen system. This is the origin of the well-known porosity in the compound (nitride) layer (Ref 18–20) that already develops during the nitriding process, because the nitride not in contact with the outer atmosphere

is simply the nitride at elevated temperature at approximately 1 atm pressure and thus is prone to decomposition in Fe and N₂ (see Fig. 3; see also Fig. 8 and 9 and their discussion in Section 9). Even nitrogen ferrite (α -Fe[N]), as produced by a nitriding treatment, is super-

Table 1 Crystal structures and composition ranges of Fe-N-C phases

Phase	Crystal structure	Nitrogen content, at.%	Carbon content, at.%	Lattice parameter references
α -Fe[N,C]	Body-centered cubic Fe N and C disordered in octahedral interstices	<0.4	<0.1	Ref 5–8
γ -Fe[N,C]	Face-centered cubic Fe N and C disordered in octahedral interstices	<10.3	<9.1	Ref 5–8
α'' -Fe ₁₆ N ₂	Body-centered tetragonal Fe sublattice N ordered in octahedral interstices	~12.5 (structural N vacancies can occur)(Ref 9)	...	Ref 10
γ' -Fe ₄ N _{1-x}	Face-centered cubic Fe sublattice N ordered in octahedral interstices	19.4–20	<0.7	Ref 11
ε -Fe ₃ (N,C) _{1+y}	Hexagonal close-packed Fe sublattice N and C more or less ordered in octahedral interstices	15–33	<8	Ref 12 (only for ε -Fe ₃ N _{1+y})
Θ -Fe ₃ C	Orthorhombic Fe sublattice C in bicapped trigonal prisms	~0	25	Ref 13

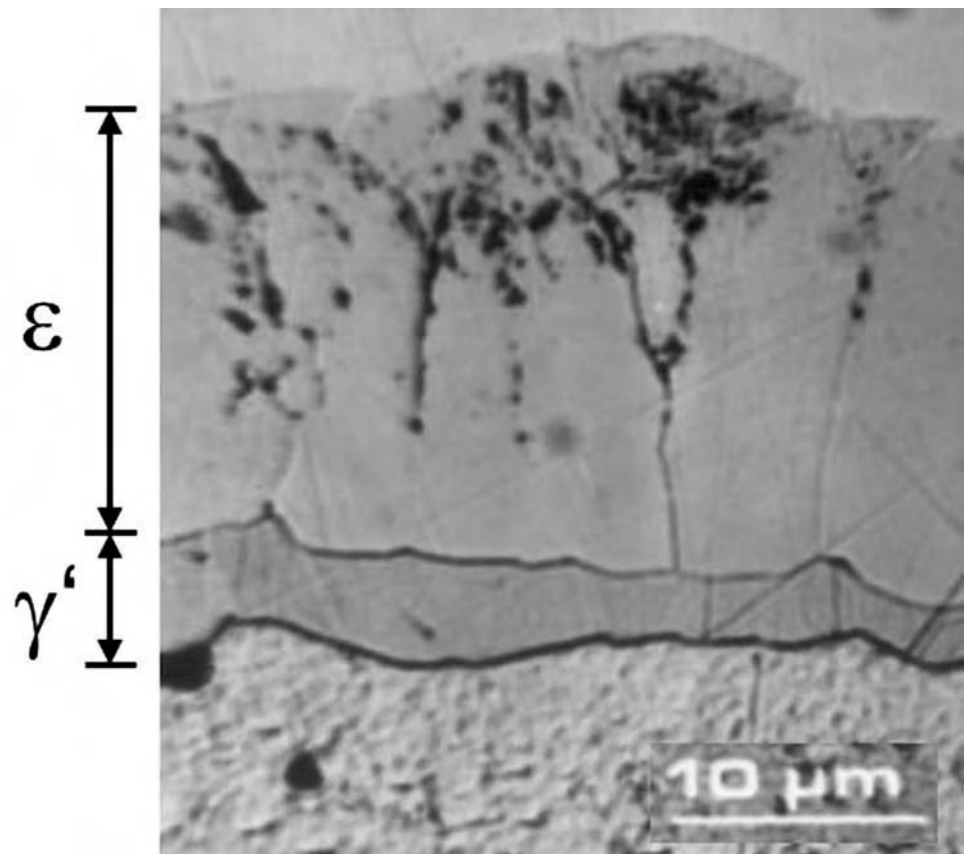


Fig. 3 Porosity in the ε sublayer, as developed during nitriding of an α -Fe substrate at 570 °C (843 K) for 7 h at $r_{N_2} = 1.93 \text{ atm}^{-1/2}$, by the association of dissolved nitrogen as N₂ gas molecules at grain boundaries in the sublayer but also within the grains of the sublayer. The porosity is most pronounced in the surface-adjacent part of the sublayer, because this is the oldest part of the sublayer and this part of the sublayer has the largest dissolved nitrogen content, implying a larger driving force for N₂ gas formation close to the surface than at larger depths. The pressure in the pores is so large that local distortion at the surface leads to local bulging out of the nitrided material. The developing pores at the grain boundaries can coalesce in advanced stages of nitriding, leading to “open” grain boundaries in contact with the outer nitriding atmosphere (see also Fig. 9b and its discussion in Section 9). Light optical micrograph of cross section; etched in 1 vol% Nital; oblique illumination, green light. Courtesy of M.A.J. Somers

saturated with dissolved nitrogen and can decompose into practically nitrogen-less iron and N_2 , that is, show pore development, after nitriding for a long time, as shown in dedicated experiments, although this is not generally recognized.

Genuine equilibrium for the phases mentioned at normal temperatures and pressures can only be realized at the surface of the specimens by contact with a nitriding medium of fixed chemical potential of nitrogen. Hence, the usual iron-nitrogen phase diagram (Fig. 2) represents the equilibria between an iron-nitrogen phase, or two or (maximally) three iron-nitrogen phases, and a medium of largely variable chemical potential of nitrogen. Such a medium is an NH_3 - H_2 gas atmosphere of constant composition that can be varied over a wide range. Evidently, then, whereas at a certain temperature a single-phase region in the iron-nitrogen phase diagram can represent equilibria with a range of nitriding atmospheres of variable value of the chemical potential of nitrogen, a two-phase region in the iron-nitrogen phase diagram at a certain temperature presents the equilibrium with a nitriding atmosphere of a single, specific value of the chemical potential of nitrogen. This knowledge is needed for understanding of the Lehrer diagram dealt with in the next section.

The discussion in the preceding paragraph also implies that the whole nitrided zone of a nitrided component, even if the component would be homogeneously (through) nitrided, and apart from (possibly) the very surface of the component is not in (far from) thermodynamic equilibrium.

Within this context, it should moreover be realized that the possibility to nitride in NH_3 - H_2 gas mixtures is a fortunate consequence of slow ammonia-dissociation kinetics: at the usual nitriding temperatures and pressures ammonia gas should thermodynamically be practically fully decomposed in nitrogen gas and hydrogen gas. However, this is a slow process, and thus, for example, by maintaining a sufficiently high flow rate in the nitriding furnace, such dissociation can be more or less avoided (see Sections 5 and 8). Only in this way can nature be prompted to impose a high chemical potential on the surface of the component to be nitrided.

The preceding two paragraphs illustrate that much of materials science involves dealing with systems in states far from equilibrium.

A discussion similar to that for the iron-nitrogen phase diagram can be given for the iron-carbon phase diagram, as published in compilations as given by Ref 4. Indeed, cementite is an unstable phase at normal temperatures and pressures and prone to decomposition in iron and carbon (graphite), which is indeed happening (kinetically possible) at elevated temperature within reasonable times. Upon inspection, there are similarities between the iron-nitrogen and iron-carbon phase diagrams. This implies that graphite and molecular nitrogen gas play similar roles for the iron-carbon and iron-nitrogen systems, respectively. This has led one German

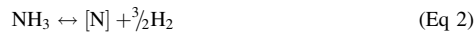
researcher (Ref 21) to propose the name “Molnit” (“molnite” in English) for this molecular nitrogen gas as the pendant for “Graphit” (“graphite”).

4. Nitriding Potential and the Lehrer Diagram

The nitriding of a solid M in an NH_3 - H_2 gas mixture can formally be imagined as the result of bringing N_2 gas into contact with M under a certain pressure. This statement is a consequence of the Gibbs energy (and thus the chemical potential) being a state variable. Therefore, the route followed to reach a certain (final) state is irrelevant for the value of the Gibbs energy of that (final) state. Thus, nitriding in an NH_3 - H_2 gas mixture can be conceived as the sum of the following (hypothetical) reactions (the subsequent treatment and also that of Section 6, “Carburizing Potential and Controlled Carburizing,” is largely derived from the one presented in Ref 20):



giving



where [N] represents nitrogen dissolved in the solid substrate M. Establishment of the equilibrium (Eq 2) implies the occurrence of local equilibrium at (only) the surface of the substrate M (see Section 8).

Equation 1(a) implies that:

$$\frac{1}{2} \mu_{N_2,g} = \mu_{N,s} \quad (\text{Eq 3})$$

where $\mu_{N_2,g}$ and $\mu_{N,s}$ represent the chemical potentials of nitrogen in the gas atmosphere and the solid substrate, respectively. Assuming ideal gases or, at least, adopting a constant fugacity coefficient,* it follows from Eq 3:

$$\frac{1}{2} \mu_{N_2,g}^0 + \frac{1}{2} RT \ln \left[\frac{p_{N_2}}{p^0} \right] = \mu_{N,s}^0 + RT \ln [a_{N,s}] \quad (\text{Eq 4})$$

where μ_i^0 is the chemical potential of component i ($i = N_{2,g}$ or N_s) in the reference state (temperature dependent at the selected pressure of the reference state; see the following), R is the gas constant, T is the absolute temperature, p_{N_2} is the partial pressure of the (hypothetical) nitrogen gas in Eq 1(a) and (b), p^0 is the pressure of N_2 in the reference state,** and $a_{N,s}$ is the activity of nitrogen in the substrate. Now $\mu_{N,s}^0$ is selected such that:

$$\frac{1}{2} \mu_{N_2,g}^0 = \mu_{N,s}^0$$

Then it is obtained:

$$a_{N,s} = \sqrt{\frac{p_{N_2}}{p^0}} \quad (\text{Eq 5a})$$

Using the equilibrium constants, K , of Eq 1(b) and 2:

$$K_{(1b)} = \frac{p_{N_2}^{1/2} \cdot p_{H_2}^{3/2}}{p_{NH_3} \cdot p^0}$$

$$K_{(2)} = \frac{a_{N,s} \cdot p_{H_2}^{3/2}}{p_{NH_3} \cdot \sqrt{p^0}}$$

it follows:

$$a_{N,s} = K_{(1b)} \cdot \sqrt{p^0} \cdot r_N = K_{(2)} \cdot \sqrt{p^0} \cdot r_N \quad (\text{Eq 5b})$$

with the so-called nitriding potential (r_N) defined by:

$$r_N \equiv \frac{p_{NH_3}}{p_{H_2}^{3/2}} \quad (\text{Eq 6})$$

where p_{NH_3} and p_{H_2} are the partial pressures of the gas components NH_3 and H_2 .

The pressure of the reference state for the gas components is selected as one pressure unit (usually 1 atm), requiring that the partial pressures of all gas components in the equations must be expressed in the same unit as the pressure of the reference state. As a consequence of this step, the numerical value of the nitrogen activity, $a_{N,s}$, can be interpreted as the square root of the pressure (in pressure units) of the hypothetical nitrogen gas occurring in Eq 1(a) and (b).

The phase-stability regions for the iron-nitrogen system can obviously be visualized in a diagram showing temperature versus chemical potential of nitrogen of the atmosphere surrounding the specimen, provided “local equilibrium” with the surface of the specimen has been realized. This “potential diagram” should not be confused with a “normal” phase diagram presenting the phase-stability regions in a diagram showing temperature versus nitrogen content of the iron-nitrogen alloy.

The described given treatment makes clear that there is a one-to-one relationship between the chemical potential of nitrogen, $\mu_{N,s}$, and the nitrogen activity, $a_{N,s}$ (Eq 3, 4), and the nitriding potential, r_N (Eq 5b). So, instead of the previously described potential diagram, corresponding diagrams are obtained upon plotting temperature versus nitrogen activity (activity diagram) or upon plotting temperature versus nitriding potential. The latter diagram for the iron-nitrogen system has, for the first time, been presented by Lehrer (Ref 22) and is called the “Lehrer diagram.” The activity diagram and the Lehrer diagram for the iron-nitrogen system are shown in Fig. 4(a) and (b), respectively.

* In this latter case, the fugacity coefficient is thought to be incorporated in the reference chemical potential $\mu_{N_2,g}^0$ (cf. Eq 4).

** The pressure of the reference state is taken equal for all gas components, and thus, $p_{N_2}^0$ is replaced by p^0 . Normally, p^0 is taken equal to 1 atm (see the following).

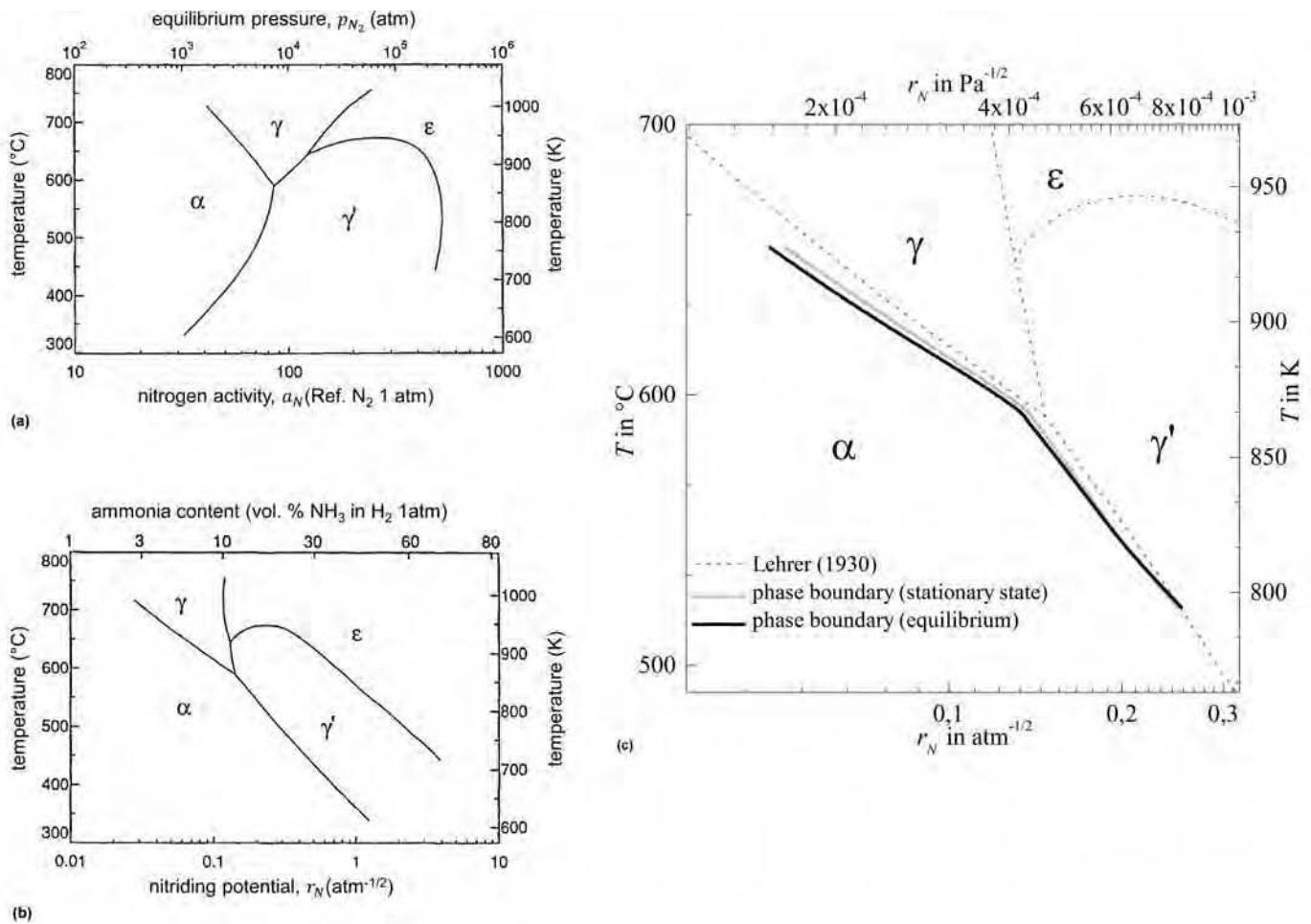


Fig. 4 (a) Temperature vs. nitrogen activity (Eq 5b). The corresponding equilibrium pressure of the hypothetical N_2 gas occurring in Eq 1(a) and (b), as calculated using Eq 5(a) with the reference pressure, p^0 , taken as 1 atm, has been indicated on the abscissa shown at the top of the figure. This (very high) equilibrium pressure actually must be read as a fugacity (see text following Eq 3) (taken from Ref 20). (b) Lehrer diagram of temperature vs. nitriding potential (cf. Eq 6). The ammonia content in an NH_3 - H_2 gas mixture at 1 atm total pressure corresponding with a given nitriding potential has been indicated on the abscissa shown at the top of the figure (taken from Ref 20). (c) Part of the Lehrer diagram showing the original α/γ' and α/γ phase boundaries as presented by Lehrer (Ref 22) and the corresponding newer data pertaining to the experimentally accessible stationary states and the (hypothetical) (local) equilibria derived as described in section 8.1 and, in particular, Ref 23. Source: Ref 23

It should be realized that a two-phase *field* as in the normal iron-nitrogen phase diagram does not occur in the potential diagram, the activity diagram, or the Lehrer diagram, because at each temperature, the chemical potentials of nitrogen (the nitrogen activities, the nitriding potentials) are the same for the two iron-nitrogen phases in equilibrium with each other and the surrounding nitriding atmosphere; that is, the two-phase stability “region” in the Lehrer diagram is given by a *line*. Similarly, the eutectoid, where three solid phases, α -Fe[N], γ -Fe[N], and γ' -Fe $_3$ N $_{1-x}$, are in equilibrium with each other and the surrounding nitriding atmosphere, is represented by a *point* in the Lehrer diagram.

It is impressive to establish how high the quality of the experimental work performed by Lehrer in 1930 was; up until now, only minor modifications of the experimental data in the Lehrer diagram have been necessary. However, as discussed in the Section 8.1, the α/γ' and α/γ phase-boundary lines in the experimental

Lehrer diagram above approximately 580 °C (853 K) may actually represent stationary states rather than (local) equilibrium. The transition of local equilibrium (at lower temperatures) to stationary state (at higher temperatures) occurs at decreasing temperature for increasing nitriding potential, and thus, in the case of iron nitrides present at the surface of the specimen, the transition from local equilibrium to stationary state can occur at a temperature distinctly lower than for nitrogen ferrite (see Section 8.1).

The most recent evaluation of the α/γ' and α/γ phase boundaries in the Lehrer diagram is shown in Fig. 4(c), together with the original Lehrer phase-boundary lines. The experimentally determined coordinates of the triple-point $\alpha/\gamma'/\gamma$ (where the eutectoid reaction $\gamma \rightarrow \alpha + \gamma'$ runs) are $T = 593$ °C (866 K) and $r_N = 0.139$ $\text{atm}^{-1/2}$. However, these data intrinsically refer to the in-reality-occurring stationary state at the surface; the coordinates of the triple-point $\alpha/\gamma'/\gamma$ in the (hypothetical above approximately

580 °C, or 853K) Lehrer diagram pertaining to (local) equilibria (at the surface of the specimen/component) are $T = 593$ °C (866 K) and $r_N = 0.135$ $\text{atm}^{-1/2}$; for full discussion, see Section 8 and Ref 23. The solubility of nitrogen in α -Fe at this point is 0.441 at.% (Fig. 2), which is the maximum equilibrium solubility of nitrogen in ferrite. This last result follows from substitution of r_N in the absorption function of ferrite describing the equilibrium solubility of ferrite as a function of r_N and T (Ref 23).

5. Controlled Nitriding

To be able to steer the outcome of the nitriding process, the chemical potential of nitrogen in the nitriding atmosphere must be controlled; that is, it should be set and maintained at a certain selected value, or it should be varied in a prescribed way. In the context of the treatment in Section 4, it then follows that control of the

nitriding potential in an $\text{NH}_3\text{-H}_2$ gas mixture is imperative. This can be achieved by nitriding in a flow of $\text{NH}_3\text{-H}_2$ gas mixture that is of a fixed composition (corresponding to the desired nitriding potential).

A stationary gas atmosphere is inappropriate, because NH_3 will tend to decompose (catalytically activated by the surface of the iron-base component and/or the furnace walls) to realize equilibrium with respect to its thermal decomposition in the gas atmosphere, which should be avoided (if controlled nitriding is the goal). This implies that a certain minimum (linear) gas flow rate is required (see Fig. 4 in Ref 24). A simple way to check this is to determine the gas composition at the entrance of the furnace and at the outlet; these should be identical. One could imagine that the gas from the outlet is reused as entrant gas at the inlet.

To apply the aforementioned approach, additional kinetic conditions must be met:

- Equilibrium (Eq 2) is established instantaneously (in any case, fast as compared to the nitriding time). This is not fully the case; at the start of nitriding, some time is needed to attain the activity/concentration of nitrogen in the solid at the surface corresponding with local equilibrium at the surface of the solid with the gas atmosphere (i.e., corresponding to the fixed nitriding potential, Eq 5b). See the discussion in Section 8.
- Other gas components potentially present in the furnace should behave as inert gases. For example, this holds for the presence of N_2 , which may have been added to the gas atmosphere; it can be taken for certainty that equilibrium (Eq 1a) is not established.
- The iron-nitrogen phases of the solid as developed in the nitrided zone (not at the very surface) are not in thermodynamic equilibrium, and therefore, these iron-nitrogen phases (underneath the surface) in principle can decompose, causing N_2 gas development and thus the formation of pores. Ideally, the kinetics of this process should be infinitely slow at the nitriding temperature. Unfortunately, that is not the case, and thus, appreciable porosity can occur during nitriding, especially close to the surface, which is the oldest part of the nitrided zone and which is the part of the nitrided zone where the largest nitrogen concentration/activity occurs and thus where the thermodynamic driving force for the decomposition is largest. Indeed, especially the surface-adjacent $\varepsilon\text{-Fe}_2\text{N}_{1-z}$ phase is known to show porosity. As a consequence, transport of nitrogen through the nitrided zone (induced by the loss of dissolved nitrogen by pore formation) is nonnegligible, and a local equilibrium cannot be established at the surface. However, the situation could have been worse: if nature would have given much faster kinetics to these decomposition processes in the solid iron-nitrogen phases, no nitriding process of iron-base components would be possible.

Epilogue. The phenomenon of severe pore formation is not restricted to only the $\varepsilon\text{-Fe}_2\text{N}_{1-z}$ phase. Nitrogen austenite ($\gamma\text{-Fe}[\text{N}]$) can accommodate much more nitrogen than nitrogen ferrite ($\alpha\text{-Fe}[\text{N}]$), up to approximately 10.3 at.% N versus approximately 0.4 at.% N (Table 1), and the driving force for its decomposition is larger compared to the case of nitrogen ferrite. Also, because of higher temperatures necessary for austenitization by nitriding (cf. Fig. 2), the kinetics of its decomposition can be relatively fast.

Thus, only a thin layer of austenite at the surface can be maintained upon continued nitriding of a pure iron foil in the austenite-phase field (Fig. 2) beyond the time necessary for complete transformation of the entire, originally pure iron foil to nitrogen austenite. The experiment discussed here (Ref 25) involved nitriding a pure iron foil with a thickness of 1 mm (0.04 in.) at 810 °C (1083 K) in a 5% $\text{NH}_3\text{-95}\%\text{H}_2$ flowing gas mixture for times up to 93 h. (The entire foil had transformed to nitrogen austenite after approximately 24 h.) Underneath the nitrogen-austenite layer at the surface, which is stabilized by nitrogen uptake at the surface from the nitriding atmosphere, the originally produced nitrogen austenite at these depths has decomposed into $\alpha\text{-Fe}$ and N_2 , leading to severe pore development. These pores develop preferentially at the grain boundaries in the nitrogen-austenitic foil, where grain boundaries run approximately perpendicular to the surface. By subsequent coalescence of the pores, channels at these grain boundaries are formed, which are in contact with the outer atmosphere.

Continued nitriding then merely implies “pumping” of nitrogen through the system without the gain of nitrogen being realized by the specimen. Nitrogen enters the specimen through the surface of the specimen, where the thin layer of nitrogen austenite is located, and leaves the specimen in the ferritic regions within the specimen at the channel walls, according to $2[\text{N}]_{\alpha\text{-Fe}} \rightarrow \text{N}_2\uparrow$ (Ref 25).

6. Carburizing Potential and Controlled Carburizing

Carburizing of steel can be realized, in a CO-CO_2 gas atmosphere for example. The definition of a carburizing potential is possible in terms of just the CO and CO_2 gas components alone, as long as no other gas components are present that can react with CO and CO_2 . However, the desired nitriding effect in a nitrocarburizing gas atmosphere involves the presence of H_2 (see Section 4), which introduces additional reactions involving CO and CO_2 that obstruct a unique definition of a carburizing potential in the case of nitrocarburizing (see the next section). To prepare for a discussion of nitrocarburizing, first a treatment for the case of carburizing in a CO-CO_2 gas mixture is given that parallels the one given for nitriding in Section 4.

Carburizing in a CO-CO_2 gas mixture can be conceived as the sum of the following (hypothetical) reactions:



giving:



where C_{Gr} denotes a hypothetical graphite, playing a role as the hypothetical N_2 gas in Eq 1(a) and (b), and $[\text{C}]$ represents carbon dissolved in the solid substrate M . Establishment of the equilibrium (Eq 8a), which is called the *Boudouard reaction*, implies the occurrence of local equilibrium at (only) the surface of the substrate M (cf. Sections 4 and 8).

Equation 7(a) implies that:

$$\mu_{\text{C}_{\text{Gr},s}} = \mu_{\text{C},s} \quad (\text{Eq 9})$$

where $\mu_{\text{C}_{\text{Gr},s}}$ and $\mu_{\text{C},s}$ represent the chemical potentials of carbon of the (hypothetical) graphite and the solid substrate, respectively. It follows from Eq 9:

$$\mu_{\text{C}_{\text{Gr},s}}^0 + RT \ln(a_{\text{C}_{\text{Gr},s}}) = \mu_{\text{C},s}^0 + RT \ln(a_{\text{C},s}) \quad (\text{Eq 10})$$

where μ_i^0 is the chemical potential of component i ($i = \text{C}_{\text{Gr},s}$ or C,s) in the reference state (temperature dependent at the selected pressure of the reference state; see the following), R is the gas constant, T is the absolute temperature, $a_{\text{C}_{\text{Gr},s}}$ is the activity of the (hypothetical) graphite in Eq 7(a) and (b), and $a_{\text{C},s}$ is the activity of carbon in the substrate. Now, $\mu_{\text{C},s}^0$ is selected such that $\mu_{\text{C}_{\text{Gr},s}}^0 = \mu_{\text{C},s}^0$. Then it is obtained:

$$a_{\text{C},s} = a_{\text{C}_{\text{Gr}}} \quad (\text{Eq 11a})$$

Using the equilibrium constants, K , of (Eq 7b) and (Eq 8a):

$$K_{(7b)} = \frac{(a_{\text{C}_{\text{Gr},s}} \cdot p_{\text{CO}_2}) \cdot p^0}{p_{\text{CO}}^2}$$

$$K_{(8a)} = \frac{(a_{\text{C},s} \cdot p_{\text{CO}_2}) \cdot p^0}{p_{\text{CO}}^2}$$

it follows:

$$a_{\text{C},s} = \frac{K_{(7b)} \cdot r_{\text{C}}}{p^0} = \frac{K_{(8a)} \cdot r_{\text{C}}}{p^0} \quad (\text{Eq 11b})$$

with a so-called carburizing potential, $r_{\text{C},a}$, defined by:

$$r_{\text{C},a} \equiv \frac{p_{\text{CO}}^2}{p_{\text{CO}_2}} \quad (\text{Eq 12a})$$

where p_{CO} and p_{CO_2} are the partial pressures of the really present gas components CO and CO_2 .

The reference state for the carbon dissolved in M is selected as graphite at 1 atm. As a

consequence of this step, the numerical value of the carbon activity, $a_{C_{Gr,s}}$, of the hypothetical graphite appearing in Eq 7(a) and (b) can have a value deviating considerably from 1.

The above presented treatment makes clear that there is a one-to-one relationship between the chemical potential of carbon, $\mu_{C,s}$, and the carbon activity, $a_{C,s}$ (Eq 9, 10), and the carburizing potential, r_C (Eq 11b). So, the carburizing potential can be used as a direct measure for the chemical potential of carbon in the solid at the surface, provided that "local equilibrium" at the surface prevails (see Section 8). Thus, as long as pure carburizing is considered, the carburizing potential, as defined by Eq 12(a) for the CO-CO₂ gas mixture as carburizing atmosphere, can be applied as a carburizing controlling parameter, similar to the nitriding potential in the case of nitriding.

For carburizing on the described basis, kinetic constraints must be satisfied that are more or less parallel with those formulated for nitriding in the previous section:

- A stationary gas atmosphere is inappropriate. As follows from the thermodynamics of equilibrium (Eq 7b) at 1 atm, graphite formation (sooting) could, in principle, occur to a significant extent at 1 atm at temperatures below approximately 700 °C (973 K). For the CO-CO₂ gas mixture, such sooting can kinetically be avoided by applying a gas flow rate high enough to avoid the formation of graphite (soot) due to the relatively slow kinetics of equilibrium (Eq 7b).
- Equilibrium (Eq 8a) should be established instantaneously (cf. Section 8). This is not the case, and such effects are nowadays taken into account in procedures for controlled carburizing.
- The iron-carbon phases of the solid as developed in the carburized zone (not at the very surface) are not in thermodynamic equilibrium, and therefore, these iron-carbon phases (underneath the surface) in principle can decompose, causing graphite development. Such graphite formation can lead to *metal dusting*, i.e. disintegration of iron carbides, produced in the carburizing process, into iron and graphite.

As an interesting point, it is noted that such sooting and metal dusting phenomena appear to be suppressed if NH₃ is added to the carburizing gas mixture, that is, nitrocarburizing (Ref 26, 27). Moreover it is shown in Ref 26 and 27 that appropriate choice of the gas composition in CO-H₂-N₂-NH₃ gas mixtures allows the growth of massive cementite layers on ferrite (α -Fe).

7. Controlled Nitrocarburizing

Carburizing can also be achieved by putting specimens/components in a CO-H₂-H₂O atmosphere according to:



which is called the *heterogeneous water gas reaction*. By a treatment similar to that given for the Boudouard reaction (Eq 8a) in a pure CO-CO₂ gas mixture, a carburizing potential can be defined as a direct measure for the chemical potential of carbon in the solid at the surface, provided that local equilibrium at the surface prevails (see Section 8). This carburizing potential for a pure CO-H₂-H₂O gas mixture is given by (following a treatment completely analogous to the one in the previous section):

$$r_{C,b} \equiv \frac{p_{CO} \cdot p_{H_2}}{p_{H_2O}} \quad (\text{Eq 12b})$$

Carburizing can also be achieved by putting specimens/components in a CH₄-H₂ atmosphere according to:

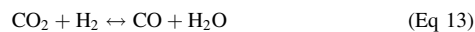


Again, like the Boudouard reaction in a pure CO-CO₂ atmosphere (Eq 8a) and the heterogeneous water gas reaction (Eq 8b), a carburizing potential can be defined as a direct measure for the chemical potential of carbon in the solid at the surface, provided that local equilibrium at the surface prevails. This carburizing potential for a pure CH₄-H₂ gas mixture is:

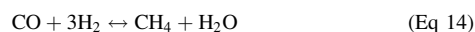
$$r_{C,c} \equiv \frac{p_{CH_4}}{p_{H_2}^2} \quad (\text{Eq 12c})$$

Obviously, the carburizing potential for realizing the same chemical potential of carbon in the gas atmosphere can have completely different values and dimensions (units) for different carburizing atmospheres (Eq 12a-c). This is trivial. The relevance of the previous discussion is to demonstrate that in the presence of a (carburizing) gas atmosphere comprising the components CO, CO₂, H₂, H₂O, and CH₄ (Eq 8a-c), it is generally impossible to characterize the chemical potential of carbon in the gas atmosphere by either $r_{C,a}$, $r_{C,b}$, or $r_{C,c}$ (Eq 12a-c). This recognition has the following unpleasant consequence for gaseous nitrocarburizing.

A gas atmosphere (initially) containing NH₃ and H₂ gas components, to establish a nitriding reaction, and CO and CO₂ gas components, to establish a carburizing reaction, is subject to side reactions between these gas components:



which is called the *homogeneous water-gas reaction*, and:



Thus, the simultaneous presence of the gas components CO, CO₂, H₂, H₂O, and CH₄ in a nitrocarburizing gas atmosphere must be considered. One may hope that of the various carburizing equilibria (Eq 8a-c), possibly only one is established fast. It has been found that equilibrium (Eq 8b), the heterogeneous

water-gas reaction, is established much faster than the equilibria (Eq 8a and c) in the case of carburizing pure iron (in the ferritic or austenitic state) (Ref 28). However, whether this statement also holds if nitrides, carbides, carbonitrides, or nitrocarbides are at the surface of the specimen (developed in the course of the treatment) is unknown. Moreover, the simultaneous occurrence of the side reactions (Eq 13, 14) will complicate any calculation/prediction and control of the nitrocarburizing reaction; application of a nitriding potential and a carburizing potential on the basis of the gas inlet composition appears senseless.

An approach is possible that avoids the ambiguity of the definition of the chemical potential of carbon according to either of the equilibria (Eq 8a-c) and that, at the same time, accounts for the occurrence of the side reactions (Eq 13 and 14), as follows. It can be shown that if the gas composition is chosen and controlled such that equilibria (Eq 13 and 14) are established (i.e., imposed), then, as a consequence, the chemical potentials of carbon in the gas phase, according to any of the three equilibria (Eq 8a-c) are equal (Ref 29, 30). Thus, any further considerations concerning which of the three equilibria is first established or not and the consequences of changes in the gas composition by reactions (Eq 13 and 14) are unnecessary.

Thus, it is possible to nitrocarburize with chosen chemical potentials, separately for nitrogen and carbon, in the gas atmosphere. This has been demonstrated in Ref 29, which can be considered as the outcome of a development departing from Ref 30 to 32. In this case, the nitriding potential can still be defined as given by Eq 6 and given a value accordingly, as equilibrium (Eq 2) is the only nitriding pathway in the gas atmosphere considered. To use the notion carburizing potential is not meaningful. Only if one of the possible carburizing reactions is the operating pathway for carburizing, one could define the carburizing potential by the corresponding formulation (one of the three Eq 12a, b, or c). That such a case occurs in reality is uncertain (see discussion following Eq 14).

The logical consequence of this discussion would be to simply characterize a nitrocarburizing atmosphere, as discussed here and having a constant composition establishing the equilibria (Eq 13 and 14), as a nitrocarburizing atmosphere of specific chemical potentials of nitrogen and carbon. At present, this approach appears to be the only feasible way toward controlled nitrocarburizing and, until today (2013), has been established only in the laboratory (Ref 29).

It should be recognized that the chemical potentials of nitrogen and carbon, as set for the gas atmosphere, are only equal to the chemical potentials of nitrogen and carbon in the specimen (at its surface) if local equilibrium at the surface of the specimen has been established. This may take a relatively long time, especially in nitrocarburizing treatments, and leads to complicated microstructural developments of the

compound layer composed (largely) of iron carbonitrides (see Section 9.2).*

Of course, more side reactions than considered previously may be considered as possible in a nitrocarburizing atmosphere. Thus, for possibly produced gas components, in particular O_2 , C_2H_2 (acetylene), C_2H_4 (ethylene), C_2H_6 (ethane), and HCN , it can be shown that their partial pressures are so low that their formation and thus their effect on the gas composition and the chosen values of the chemical potentials of carbon and nitrogen are negligible (Ref 29).

8. Local Equilibria and Stationary States

8.1 Gas-Solid Interface. The imposition of a fixed chemical potential of nitrogen, and, in the case of nitrocarburizing, also a fixed chemical potential of carbon, at the surface of the specimen/component implies that the gas composition in the furnace should not change from the desired inlet composition. Thus, in the case of nitriding, any thermal dissociation of ammonia in the furnace must be avoided (or the degree of this dissociation should be known precisely, and be controllable, at the surface of the specimen/component). If the gas-atmosphere equilibrium is at 1 atm and at a temperature above approximately 350 °C (623 K), ammonia would be practically fully dissociated. Hence, a stationary gas atmosphere is inappropriate for controlled nitriding. Because this dissociation is a relatively slow process but catalytically activated by the presence of iron (the specimen and possibly the furnace walls; see Fig. 4 in Ref 24), this thermal dissociation in the case of nitriding iron-base specimens/components can be made negligible by application of a sufficiently large (linear) gas flow rate in the furnace. However, if the nitriding potential must be very large (i.e., for an NH_3 - H_2 gas mixture implying a fraction of NH_3 approaching 100%), even a tiny amount of thermal dissociation of ammonia causes the real nitriding potential to deviate distinctly from the one calculated from the gas composition at the furnace inlet. Such a situation is not expected for the nitriding of iron-base materials but happens, for example, upon nitriding nickel to produce a Ni_3N compound layer requiring an extremely large nitriding potential (e.g., performing nitriding with a gas composed of pure ammonia at the gas inlet, which corresponds with $r_N = \infty$ at the gas inlet, Eq 6) (Ref 33).

Now, take a closer look at the establishment of equilibrium (Eq 2). At the surface of the specimen, ammonia molecules are adsorbed and dissociate by stepwise removal of hydrogen atoms (Ref 34). This leads to adsorbed individual nitrogen atoms at the surface, N_{ads} :



Next, two routes can be followed by the adsorbed nitrogen atoms. They can dissolve into the solid substrate, which is the desired effect:



or they recombine at the surface and desorb, which counteracts nitriding (Fig. 5):



Local equilibrium at the gas-solid interface (Fig. 5) can be established under the following conditions:

- Dissolution of nitrogen only occurs according to Eq (16).
- The diffusion of dissolved nitrogen from the surface to larger depths is negligible.
- The equilibrium according to Eq 16 is established, which can be taken as certain because the rate of nitrogen uptake according to Eq 16 is very fast compared to the rates of the reactions corresponding with Eq 15 and 17.
- The equilibrium according to Eq 15 is established (i.e., the forward and backward reactions according to Eq 15 are equal).

Under these conditions, the chemical potential of nitrogen in the gas atmosphere (related one-to-one to the nitriding potential; Eq 4, 5b, and 6), as determined from the NH_3 and H_2 contents in the gas atmosphere, can be equal to the chemical potential of nitrogen in the solid substrate at its surface.

It should be recognized that, in principle, as long as transport of nitrogen from the surface into the bulk of the specimen occurs, a genuine equilibrium at the surface cannot occur, albeit it can be approached very closely; in this sense, the term *local equilibrium* is somewhat misleading. In the beginning stage of nitriding a nitrogen-less specimen, the diffusion of dissolved nitrogen from the surface to larger depths can be significant, compared to the rate of nitrogen uptake according to Eq 15 and 16, due to the occurrence of a pronounced gradient for the dissolved nitrogen content in the solid at the surface (cf. Fick's first law). Then, upon gradual saturation of the substrate, a gradual increase of the dissolved nitrogen content at the surface occurs until the dissolved nitrogen content at the surface equals the equilibrium value (Fig. 6).

However, if the recombination and desorption of the adsorbed nitrogen according to Eq 17 occurs with a nonnegligible rate** compared to the rate of nitrogen uptake according to Eq 15 (assuming the equilibrium, Eq 16, is always established), then the chemical potential

of the dissolved nitrogen at the surface of the specimen is smaller than that determined from the NH_3 and H_2 contents in the gas atmosphere (cf. Eq 2), which leads to the consideration of two different cases:

- If no significant diffusion of dissolved nitrogen into the bulk of the specimen occurs, a time-independent situation (at constant temperature and constant pressure) at the surface is established as a consequence of equal rates of nitrogen uptake (Eq 15; equilibrium, Eq 16, is always established) and nitrogen desorption (Eq 17), and thus, although no equilibrium of the surface of the solid with the gas atmosphere according to only Eq 2 is established, a so-called stationary state at the gas-solid interface has been realized, characterized by a smaller content of dissolved nitrogen in the solid substrate at the surface than would occur if equilibrium at the gas-solid interface would prevail according to only Eq 2. This state of affairs is illustrated in Fig. 5 (Ref 24, 34).
- If significant diffusion of dissolved nitrogen into the bulk of the specimen does occur, as at the start of nitriding a nitrogen-less specimen, a similar situation as described in the preceding paragraph for the absence of significant recombination and desorption of adsorbed nitrogen emerges; a gradual increase of the concentration of dissolved nitrogen occurs. However, in contrast with the case described in the preceding paragraph, the eventual concentration of dissolved nitrogen in the solid at the surface does not equal the equilibrium value but is smaller than that. Using kinetic data from Ref 34 to 36 for the reactions considered here, such an evaluation of the dissolved nitrogen (surface) concentration for an α -Fe

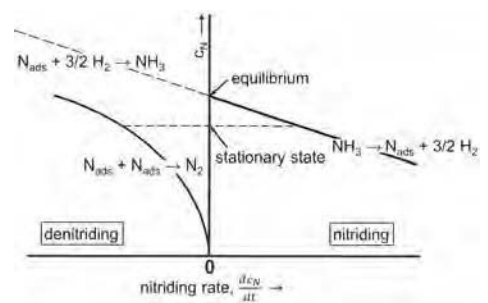


Fig. 5 Concentration of dissolved nitrogen in the solid (at the surface), c_N , vs. the nitrogen-uptake rate, dc_N/dt . If the nitrogen-uptake rate according to Eq 16 is relatively very fast and the desorption according to Eq 17 can be neglected, then equilibrium at the surface of the solid is established, if the forward and backward reactions according to Eq 15 are of equal magnitude; that is, the dynamic equilibrium as given by Eq 15 is then established at the surface of the solid. However, if the rate of nitrogen desorption according to Eq 17 cannot be neglected, such a local equilibrium is not realized. Instead, a stationary state occurs that is given by equality of the (net) nitriding rate due to (net) decomposition of NH_3 and the denitriding rate due to nitrogen desorption from the surface. Source: Ref 24 as adapted from Ref 34

* The carbon solubility of a ferritic pure-iron substrate is so low (<0.1 at.% C; Table 1) that the carbon uptake by nitrocarburizing is effectively confined to the compound layer.

** The nitriding reaction according to Eq 17 can be neglected due to its comparatively low rate (Ref 35) and the usually low partial pressure of nitrogen, p_{N_2} (usually <1 atm), in the gas atmosphere.

foil of 500 μm thickness, nitrided at 580 °C (853 K), and with $r_{\text{N}} = 0.104 \text{ atm}^{-1/2}$ is shown in Fig. 6 (the first such calculation was presented in Ref 37, neglecting the role of recombination and desorption of the adsorbed nitrogen atoms, Eq 17; this contribution was included in a later work, Ref 38, leading to, for the conditions considered, only marginal differences, in accordance with the results shown in Fig. 7). A detailed description of the calculation procedure and a summary of the available kinetic data is provided in the Appendix of Ref 23 (which is the first presentation in the English literature of these rate-constant data as provided in the original Ref 28, 34, and 35, written in German; also a drastic correction of a rate constant as provided in Ref 28 is presented there).

The tendency to recombination and desorption of N_{ads} becomes significant above approximately 580 °C (853 K) for pure iron (ferrite) as substrate. The difference between the equilibrium concentration, $c_{\text{N,eq}}$, and the lower stationary value of the concentration, $c_{\text{N,st}}$, at the surface of the nitrided component increases with increasing temperature and nitriding potential (Fig. 7). Then, the result obtained for the content of dissolved nitrogen in the solid at the surface, that is, $c_{\text{N,st}}$, does not correspond with the chemical potential of nitrogen in the gas atmosphere, as determined from the NH_3 and H_2 contents in the gas atmosphere and as expressed by the nitriding potential (Eq 4–6).

Clearly, in view of the results shown in Fig. 7, at the usual nitriding temperatures (500 to 580 °C, or 773 to 853 K), local equilibrium at the surface of at least pure iron can be supposed, provided the diffusion rate of the absorbed nitrogen to larger depths is negligible as compared to the nitrogen-uptake rate, that is, only at later stages of nitriding (Fig. 6). At higher temperatures and/or at relatively high nitriding potentials, the contribution of the recombination and desorption according to Eq 17 can no longer be neglected. For example, at a nitriding temperature of 580 °C (853 K, a nitriding temperature applied in practice), the nitriding potential should not be larger than $6.1 \text{ atm}^{-1/2}$ (pertaining to a nonexceptional 75% NH_3 -25% H_2 gas mixture), in order that the difference of $c_{\text{N,eq}}$ and $c_{\text{N,st}}$ is smaller than 1%. Under the latter conditions, nitrogen ferrite is likely not the equilibrium phase at the surface of the specimen/component, but assuming that the rate constants for Eq 15 to 17 for iron nitride at the surface of the specimen/component do not differ much from those for pure iron (no such data for the iron nitrides are available), the preceding sentence suggests that nitriding, under conditions such that, in particular, ϵ -iron nitride occurs at the surface of the specimen/component, can be associated with the occurrence of a stationary state at the surface already at temperatures distinctly lower than 580 °C (853 K; see the experimental results presented in Fig. 3 of Ref 24).

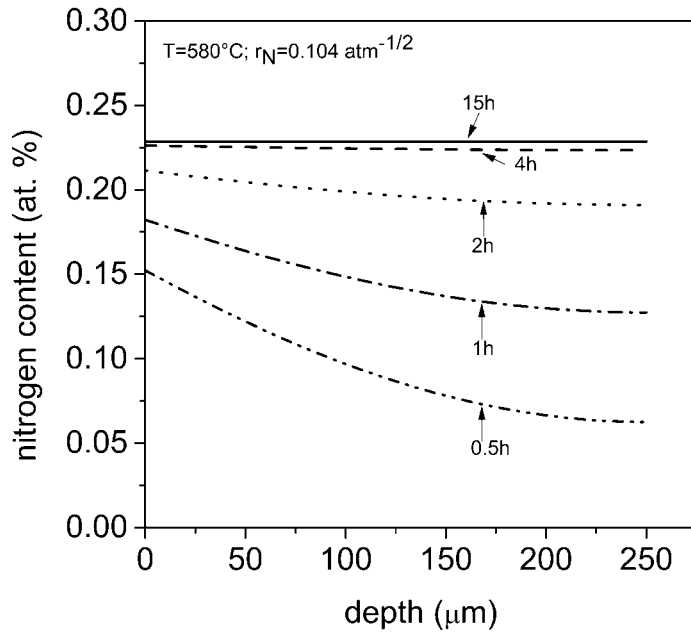


Fig. 6 The development of the nitrogen concentration-depth profile in an α -Fe foil of 500 μm thickness upon nitriding in an NH_3 - H_2 gas mixture of $r_{\text{N}} = 0.104 \text{ atm}^{-1/2}$ at 580 °C (853 K). Three competing reactions are considered here: (1) nitriding according to Eq 15 (equilibrium, Eq 16, is assumed to be realized instantaneously; see the text and the caption for Fig. 5); (2) diffusion of absorbed nitrogen into the initially unsaturated solid; and (3) recombination of adsorbed nitrogen and its subsequent desorption according to Eq 17. The rate equations and the rate constants (as given by and as derived from data in Ref 35 and 36) for these calculations have been described in detail in the Appendix of Ref 23, departing from original treatments in Ref 28 and 34 to 36. In view of the temperature and nitriding potential pertaining to the case considered here, the difference between the value of the dissolved nitrogen content at the surface according to local equilibrium, $c_{\text{N,eq}}$, and the lower stationary value of this concentration, $c_{\text{N,st}}$, as observed after homogenization of the solid has been realized is marginal (cf. Fig. 7).

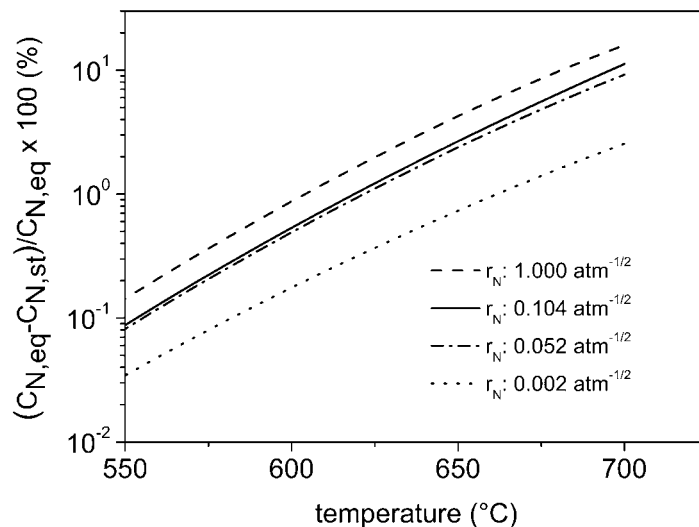


Fig. 7 The difference between the value of the dissolved nitrogen content at the surface according to local equilibrium, $c_{\text{N,eq}}$, and the lower stationary value of this concentration, $c_{\text{N,st}}$ (as illustrated in Fig. 5), as a function of temperature for various nitriding potentials. Obviously, these results hold for a homogeneous solid (here: nitrogen ferrite) having a nitrogen concentration at all depths equal to that in the solid at the surface. These calculated results thus pertain to the competition of (cf. the caption of Fig. 6) nitriding according to Eq 15 (Equilibrium, Eq 16, is assumed to be realized instantaneously; see text and the caption of Fig. 5) and recombination of adsorbed nitrogen and its subsequent desorption according to Eq 17. As shown in the Appendix of Ref 23, an analytical equation relating $c_{\text{N,eq}}$ and $c_{\text{N,st}}$ can be given.

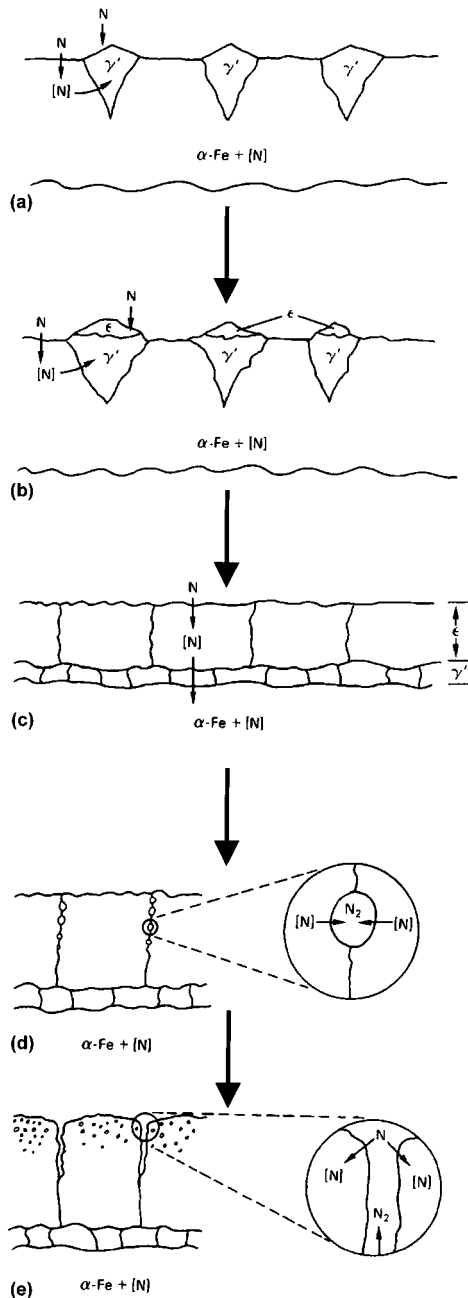


Fig. 8 Schematic illustration of the progressive microstructural stages of compound-layer formation and evolution upon nitriding α -Fe. (a) Nucleation of γ' nitride at the surface followed by its growth by nitrogen supply via the γ' nuclei formed, but in particular also by nitrogen supply via the ferrite that surrounds them, as an efficient bypass possibility using the much faster diffusion of nitrogen through ferrite than through the nitride. (b) At the same time, ϵ phase may develop on top of the γ' particles before these have produced, by lateral growth, a closed layer. (c) As a result, a double ϵ/γ' layer has formed, and further growth can only be established by nitrogen transport through both sublayers. (d) Decomposition of (especially ϵ) iron nitride underneath the surface of the compound layer occurs for extended stages of nitriding, leading to development of pores filled with N_2 gas at grain boundaries and even within the grains. (e) Coalescence of pores at grain boundaries (usually oriented more or less perpendicular to the surface) leads to channels at grain boundaries in contact with the outer nitriding atmosphere. Source: Ref 19, 39, and 41

The previously mentioned consideration has as a consequence that the phase boundaries presented in the potential Lehrer diagram (Fig. 4b) above approximately 580 °C (853 K) (and above lower temperatures at high nitriding potentials as correspond to the development of iron nitrides) are incorrect, because the experimentally determined nitriding potential for the phase boundary (at a certain temperature) corresponds to a stationary state rather than a (local) equilibrium. The true nitriding potential, characterizing the chemical potential of the hypothetical gas atmosphere in equilibrium with the solid (at the phase boundary) and given by the NH_3 and H_2 contents of that hypothetical gas atmosphere, will be smaller than the experimentally determined one (see the results shown for the α/γ phase boundary in Fig. 4c and the discussion at the end of the Section 4). The effect may be considerably larger for the γ'/ϵ phase boundary, as indicated in the previous paragraph.

8.2 Solid-Solid Interface. Upon nitriding of an iron substrate, various iron-nitrogen phases may develop in the nitrided surface-adjacent zone of the substrate. In particular in the case of pure iron, these phases can occur as a layered structure, with the order of iron-nitrogen phases corresponding with a decrease in the local chemical potential of nitrogen in the solid with increasing depth beneath the surface, in accordance with the iron-nitrogen phase diagram (Fig. 2) and the activity and potential (Lehrer) diagrams (Fig. 4) (see Section 9).

At the interfaces between two such iron-nitrogen phases (layers), a situation described as local (metastable; see the following) equilibrium (cf. the previous discussion) can occur if the compositions of both phases at the interface comply with those pertaining to the metastable equilibria presented by the phase diagram (note that realizing true thermodynamic equilibrium in the solid, underneath the surface, requires decomposition of these phases in Fe and N_2 , as discussed in Section 3 in this article). The accumulation or depletion of nitrogen at either side of the solid-solid interface implies that local equilibrium can only be maintained if the mobility of the interface is infinitely large, so that the redistribution of nitrogen, to restore the local equilibrium situation at the interface, is instantaneous. In this case and if the accumulation/depletion of nitrogen at the interface is due to diffusional transport of nitrogen in the (layer) system, the phase transformation at the interface is a diffusion-controlled one (Ref 14). Evidently, during growth of the nitrided zone, implying a net inward transport of nitrogen, also across the interface considered, and recognizing the real, finite rate of interface migration, genuine equilibrium cannot be established at the interface, but it can be closely approached.

In the case of nitrocarburizing, the occurrence of local equilibrium at a solid-solid interface implies that the nitrogen concentrations at both sides of the interface and the carbon concentrations at both sides of the interface

must correspond with the metastable (ternary) phase diagram. To indicate one of the possible complications with two diffusing components, it is conceivable that local equilibrium at a solid-solid interface could be realized for one of the components, whereas this may not be possible for the other component.

The evidence until now suggests that at the solid-solid interfaces in the nitrided/nitrocarburized zone of iron-base specimens/components, local equilibrium is closely approached.*

9. Microstructural Development of the Compound Layer

9.1 Microstructural Development of the Compound Layer during Nitriding. A schematic presentation of the development of the compound layer upon nitriding α -Fe is provided in Fig. 8 (Ref 39–41); micrographs of the two-phase compound layer are shown in Fig. 9 for cases of less (Fig. 9a, lower temperature, shorter time) and more (Fig. 9b, higher temperature, longer time) porosity. At the start of the nitriding process, nitrogen is dissolved in the ferrite matrix. At the moment that the solubility of nitrogen in ferrite (at the surface) equals and becomes larger than that compatible with the α/γ' equilibrium, γ' iron nitride must form thermodynamically. This need not occur at the start of nitriding; an apparent incubation time for nitride formation occurs (Ref 37, 38). After a certain time, the nitrogen concentration in the solid at the surface has risen to a level allowing the development of γ' iron nitride as a result of the competition of:

- Nitrogen supply to the surface from the gas via dissociation
- Removal of dissolved nitrogen from the surface by diffusion into the interior of the specimen/component
- Removal of nitrogen adsorbed at the surface by recombination and desorption from the surface (see discussion in Section 8.1)

The γ' nitride particles nucleated at the surface initially do not form a closed layer (Fig. 8a). They grow largely via supply of nitrogen from the ferrite that surrounds them, rather than by nitrogen diffusion through the particles, because the diffusion of nitrogen through ferrite is much faster than that through the nitride. Yet, after some time, lateral growth of the nitride particles at the surface leads to a closed layer. Depending on the nitriding potential applied, before a closed layer has formed, ϵ iron nitride may have

* This assumption of the occurrence of local equilibria at solid-solid interfaces in diffusion zones is often taken for granted, and the compositions in both phases at the interface have then been interpreted as defining phase boundaries in the corresponding phase diagram. However, this cannot be generally true, and therefore, phase boundaries determined in this way and taken up in published phase diagrams may be flawed.

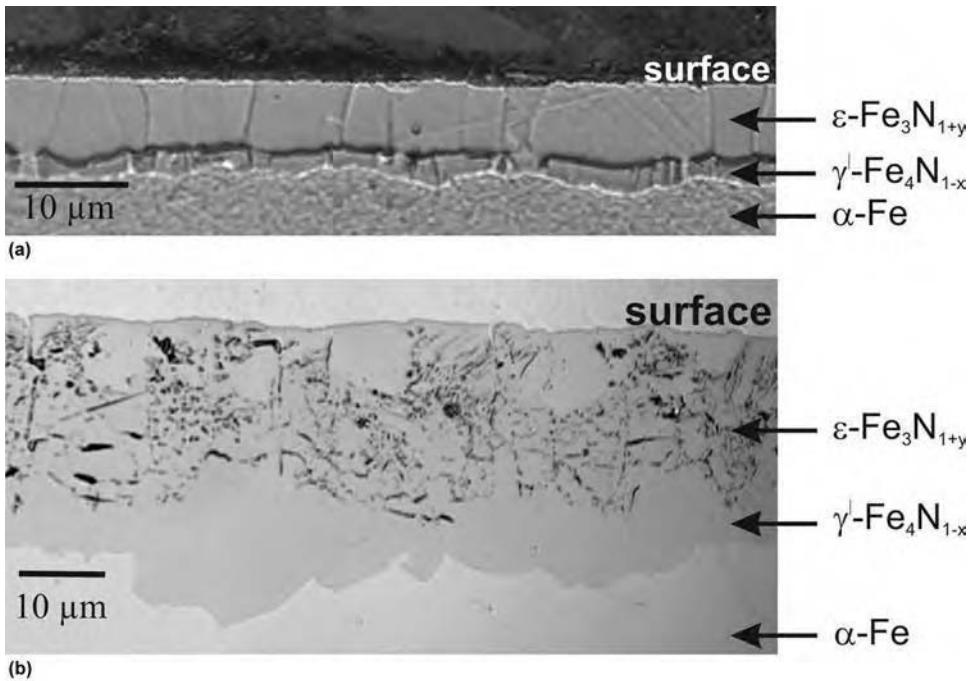


Fig. 9 Cross sections of nitrided pure α -Fe (light optical micrographs, after etching in 1.0 vol% Nital containing 0.1 vol% HCl). (a) Nitrided at 550 °C (823 K) for 5 h at $r_N = 2.37 \text{ atm}^{-1/2}$. (b) Nitrided at 560 °C (833 K) for 20 h at $r_N = 2.37 \text{ atm}^{-1/2}$. The dark spots and stripes observed in the ϵ sublayer for the specimen corresponding to (b) are due to porosity developing during nitriding in the iron nitride underneath the surface, due to its metastability. Inter- and intragranular pores can form. Source: Ref 41; cf. Fig. 3 and Section 3

nucleated on top of the γ' particles. After closure of the nitride surface layer, further growth of the ϵ/γ' compound layer requires diffusion of nitrogen through the layer from top to bottom.

As discussed in Section 3 of this article, the iron nitrides beneath the very surface are not in thermodynamic equilibrium; they tend to decompose in Fe and N_2 . This leads to porosity upon prolonged nitriding, especially in the oldest part of the compound layer, which is also the most nitrogen-rich part of the compound layer and the part adjacent to the surface (Fig. 8d and e; see also Fig. 3 and 9b). Only in the surface-adjacent region (where the ϵ phase occurs) is porosity visible with a light microscope. The γ' iron nitride, underneath the ϵ iron nitride and not in contact with the nitriding atmosphere, tends to decompose as well and develop porosity, which usually cannot be observed with a light microscope but at higher magnification with an electron microscope. This is also the case for the nitrogen ferrite, constituting the diffusion zone underneath the γ' iron nitride.

9.2 Microstructural Development of the Compound Layer during Nitrocarburizing. The microstructural evolution of the compound layer produced upon nitrocarburizing ferritic iron is much more complicated than in the case of nitriding. Of course, this relates to the occurrence of the simultaneous inward diffusion of two components, nitrogen and carbon, and the more complex metastable (see Section 3) phase equilibria of the ternary Fe-C-N system. Until now, only a few papers have appeared in the

literature presenting a more or less systematic study of the microstructural changes accompanying compound-layer growth during nitrocarburizing (Ref 31, 42–45). The following summarizes the common, but still limited, basis of understanding, based largely on results presented in Ref 31 and 45.

Local equilibria appear to be established at the interphase boundaries in the compound layer, whereas, at the same time, a local equilibrium (or a stationary state) does not prevail at the gas-solid interface, at least not in the beginning of the nitrocarburizing. As a matter of fact, such a conclusion also holds for the case of nitriding (see Section 9.1). The occurrence of local equilibria within the nitrocarburized zone implies that the chemical potentials of nitrogen and carbon (and iron) vary in a continuous manner through the nitrocarburized zone, from the surface to the nonaffected core. This can be associated with the formation of phases in a sequence and of compositions as prescribed by a so-called *diffusion path* at constant temperature in the (metastable) phase diagram (Ref 46, 47).

Thus, for the case of nitriding, pertaining to the binary metastable iron-nitrogen phase diagram, the order of phases (from top to bottom of the nitrided zone) would then be $\epsilon/\gamma'/\alpha$, as shown in Fig. 8 and 9 and discussed in Section 9.1 (provided the nitriding potential of the nitriding atmosphere is high enough to allow formation of ϵ nitride). Draw a horizontal line in Fig. 2 at the nitriding temperature and proceed from the right (corresponding to relatively

high chemical potential of nitrogen) to the left (corresponding to relatively low chemical potential of nitrogen); also see the discussion in Sections 3 and 4.

To determine on this basis the sequence and compositions of the carbonitride phases in the compound layer developing upon nitrocarburizing, a diffusion path should be drawn in an isothermal section of the Fe-C-N phase diagram for the temperature at which the nitrocarburizing is carried out. *The diffusion path is defined by the course of the (laterally, i.e., at constant depth) averaged composition in the direction perpendicular to the original interface of the diffusion couple concerned*—here, perpendicular to the surface of the specimen/component. Not only do thermodynamics govern the course of the diffusion path, but kinetics can be decisive as well.

As follows by application of Gibbs' phase rule, at constant temperature and constant pressure, in the case of the binary system iron-nitrogen, only one phase can be present over a certain depth range covering a certain variation in the (laterally averaged) composition (if local equilibrium prevails). The presence of two phases in contact represents a nonvariant situation; the two phases are in contact only at a specific depth, that is, at a specific set of values for the chemical potentials of the components iron and nitrogen, and at a specific set of values of the compositions of both phases in contact. This is compatible with Fig. 8 and 9 discussed in Section 9.1. Note that as a consequence, the phases ϵ and γ' occur as sublayers in that order, from top to bottom, in the compound layer developing upon nitriding iron.

Similarly, it follows that in the compound layer at constant temperature and constant pressure, in the case of the ternary system Fe-C-N, one or, at most, two phases can be present over a certain depth range covering a certain variation in the laterally averaged composition (if local equilibrium prevails). The presence of three phases in contact represents a nonvariant situation; the three phases are in contact only at a specific depth, that is, at a specific set of values for the chemical potentials of the components iron, carbon, and nitrogen, and at a specific set of values of the compositions of the three phases in contact. Hence, only the thermodynamics of the system can already induce a complicated microstructure of the compound layer in the case of nitrocarburizing. Note that a sequence of sublayers (with each phase represented by a sublayer, as is the case for nitriding of iron; see above discussion) is not expected in the case of nitrocarburizing of iron, already because two phases can be in contact over a certain depth range, which does represent a (local) equilibrium situation.

As an example, a schematic presentation of the microstructural development, in particular the phase constitution, of the compound layer obtained upon nitrocarburizing α -Fe at 580 °C (853 K) is provided in Fig. 10 and described subsequently (Ref 45). {The nitrocarburizing conditions for these experiments involved a

gas mixture composed of 15.44 vol% NH_3 , 57.59 vol% H_2 , 20 vol% CO , and 6.61 vol% N_2 ; the gas flow rate was $13.5 \text{ mm} \cdot \text{s}^{-1}$, as calculated for room temperature (Ref 45). If no side reactions occur in the gas atmosphere (but see next sentence), a nitriding potential for this gas mixture can be given as $r_{\text{N}} = 0.35 \text{ atm}^{-1/2}$ (Eq 6). The carburizing potential for this gas mixture would be infinite; however,

because of side reactions in the gas atmosphere, an effective carburizing potential/chemical potential of carbon operates (Ref 48.)

In the following discussion of the microstructural development, the phase constitution is presented as a sequence of sublayers containing one or two phases (see previous discussion) indicated by their symbols and separated by the symbol "/"; thus, the notation $\varepsilon/\varepsilon + \gamma'$

indicates that at the surface, an ε sublayer occurs which is followed at some depth by a dual-phase $\varepsilon + \gamma'$ sublayer (see stage 6 in Fig. 10), and that underneath the last sublayer, the substrate occurs but is not separately indicated.

At the start of nitrocarburizing, a single-phase layer of cementite (θ) forms at the surface (stage 1). The ε carbonitride phase develops subsequently at the layer/substrate interface, and a

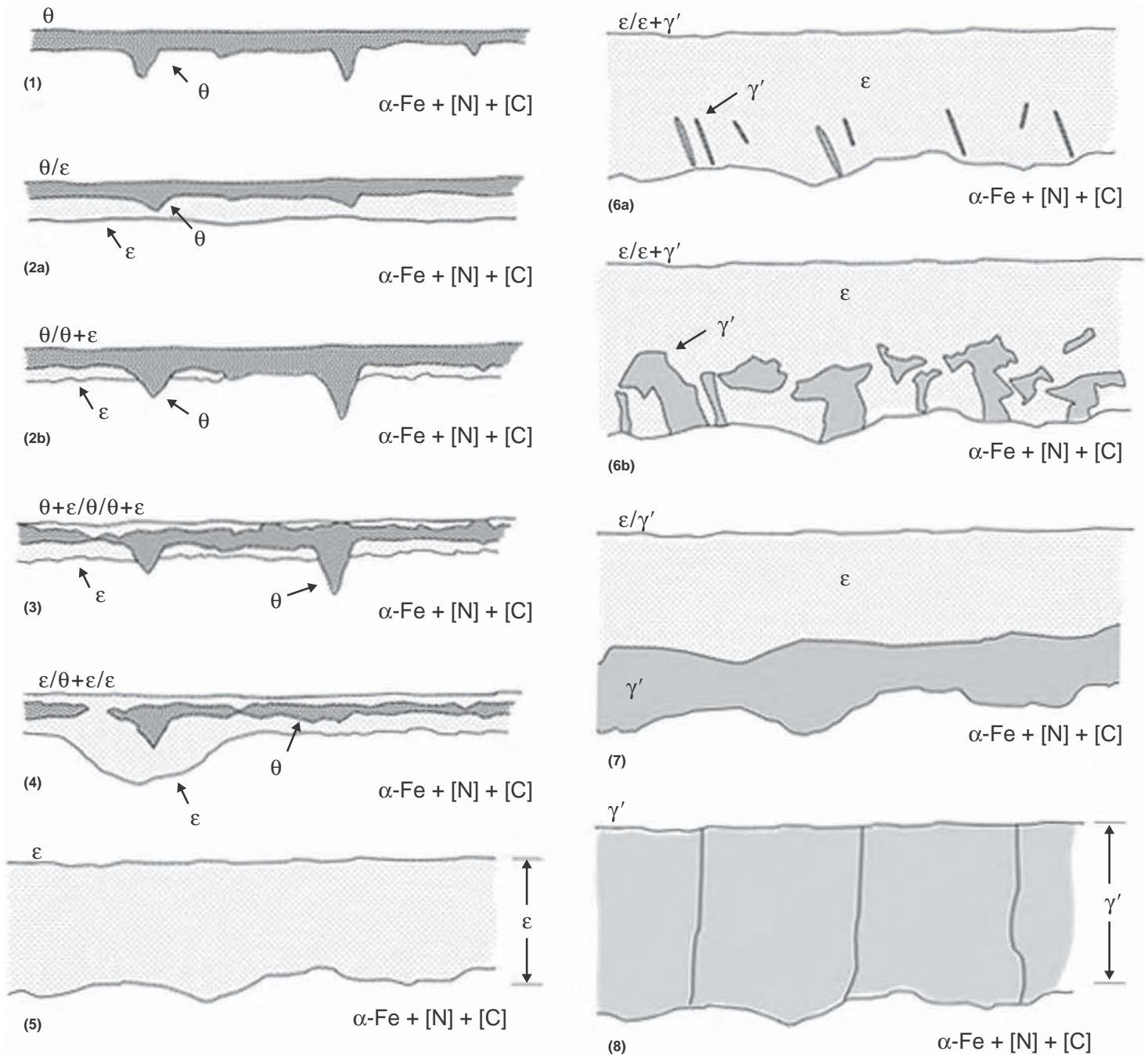


Fig. 10 Schematic illustration of the progressive microstructural stages of compound-layer formation and evolution upon nitrocarburizing α -Fe. The results pertain specifically to a treatment temperature of approximately 580°C (853 K). The process starts with the formation of a carbon-rich phase (cementite) and proceeds in the direction of nitrogen-rich phases along diffusion paths, as sketched for successive nitrocarburizing times in Fig. 11. The following successive stages have been indicated: (1) single-phase cementite (θ) layer, (2a) θ/ε double layer, (2b) $\theta/\theta + \varepsilon$ layer, (3) $\theta + \varepsilon/\theta + \varepsilon$ layer, (4) $\varepsilon/\theta + \varepsilon/\varepsilon$ layer, (5) single-phase ε layer, (6a) ε with some γ' developing in regions close to the interface with the substrate, (6b) $\varepsilon/\varepsilon + \gamma'$ layer, (7) ε/γ' double layer, and (8) single-phase γ' layer. Source: Ref 45

θ/ϵ double layer (stage 2a) or a $\theta/\theta + \epsilon$ double layer (stage 2b) results. The amount of ϵ phase in the compound layer then increases strongly by growth of ϵ into the substrate and also in the opposite direction, by conversion of θ into ϵ (stages 3 and 4; that such $\theta \rightarrow \epsilon$ conversion can occur was shown for the first time in Ref 49). This growth phase ends with a single-phase ϵ (compound) layer (stage 5). Continued nitrocarburizing induces emergence of (the carbon-poor) γ' phase close to the interface with the substrate, and thus, an $\epsilon/\epsilon + \gamma'$ double layer is formed (stages 6a and 6b), which is succeeded by an ϵ/γ' double layer (stage 7). Thereafter, the amount of γ' phase in the compound layer increases until a single-phase compound layer results (stage 8).

These results, as obtained in Ref 45, have been presented here with the recognition that 580 °C (853 K) is a nitrocarburizing temperature often applied in practice, and indeed, microstructures as presented as stages 5 and 6 in Fig. 10 have frequently been observed in practice after treatment times of, say, 2 to 4 h at the temperature concerned (580 °C, or 853 K). Stage 8 has been observed after a treatment time of 24 h, which is much longer than treatment times applied in practice.

For all types of nitrocarburizing atmospheres (including salt baths and plasmas), it cannot be claimed that precisely the same sequence of microstructures as presented in Fig. 10 occurs in the compound layer (Ref 39). However, the general conclusion from observations as well as the previous discussion is that *the microstructural evolution of the compound layer developing upon nitrocarburizing proceeds from a carbon-rich phase (cementite, θ) into the direction of carbon-poorer and nitrogen-richer phases (ϵ and γ').*

The change (with treatment time) of the composition and the phase constitution at the surface of the compound layer immediately makes clear that neither a local equilibrium nor a stationary state (see Section 8) occurs at the gas-solid interface, at least not for the largest part of the period of time in the nitrocarburizing experiments pertaining to Fig. 10, implying that this certainly holds for the nitrocarburizing treatments in (commercial) practice. The initial development of cementite (not generally recognized, because this cementite at the interface with the substrate disappears in the subsequent stage of the process) was first reported in Ref 43 for salt bath nitrocarburizing and in Ref 39 for gaseous nitrocarburizing. This occurrence of cementite can be discussed as follows.

The rate of carbon transfer from the nitrocarburizing medium, that is here from CO, is much higher than that of nitrogen transfer, that is, from NH₃ (Ref 28). Further, the solubility of carbon in the substrate (ferrite) is very small and, in any case, much smaller than that of nitrogen (Table 1). Then, recognizing that the diffusion coefficients of carbon and nitrogen in ferrite do not differ strikingly (Ref 50), it follows that the ferrite substrate at the surface is saturated with carbon much faster than with

nitrogen, leading to the initial formation of cementite (which has a negligible solubility for nitrogen) at the surface of the substrate and not of a nitrogen-rich(er) carbonitride that appears to comply with local equilibrium at the surface or with a stationary state at the surface (see the results for long(er) treatment times as indicated in Fig. 10). Upon continued treatment, the ferrite substrate at the substrate/compound-layer interface becomes gradually enriched in nitrogen (by diffusion of nitrogen through the grain boundaries of the cementite, Ref 51), and then the ϵ phase can nucleate there (Fig. 10, stage 2).

Whereas the composition and phase constitution at the surface are controlled by kinetics, it can be shown that, given this constraint, the microstructure within the compound layer, dependent on the composition and phase constitution at the surface, is controlled by thermodynamics: local equilibria prevail at the solid-solid phase interfaces within the compound layer. The way to make this likely is by drawing diffusion paths (see the beginning of this section) in the metastable ternary Fe-C-N phase diagram (Ref 52) at the treatment temperature (Fig. 11). For the various stages shown in Fig. 10, suggestions for diffusion paths, representing the change of the lateral average

composition and phase constitution as a function of depth, have been made (schematically) in Fig. 11 (Ref 45). That this is possible indicates that the depth dependence of the lateral average composition and the thermodynamics of the Fe-C-N system (fully) govern the microstructure within the compound layer.

This section is concluded with a paragraph about a special microstructural feature that can be observed in particular if larger fractions of ammonia occur in the gas atmosphere. In that case, distinct porosity can develop in the compound layer (see Section 3), in particular in the ϵ (carbo)nitride phase/(sub)layer. Such a situation has not been considered in the previous discussion and in Fig. 10. After these pores, preferentially nucleated at grain boundaries, have coalesced and induced channel formation along these grain boundaries, they can have direct contact with the outer nitrocarburizing atmosphere. Then, a preferential uptake of carbon has been observed to take place via these channel walls at some depth beneath the surface (Fig. 12a), leading eventually to cementite formation at the channel walls (Fig. 12b); even a cementite sublayer has been observed to develop subsequently (Ref 42). One can

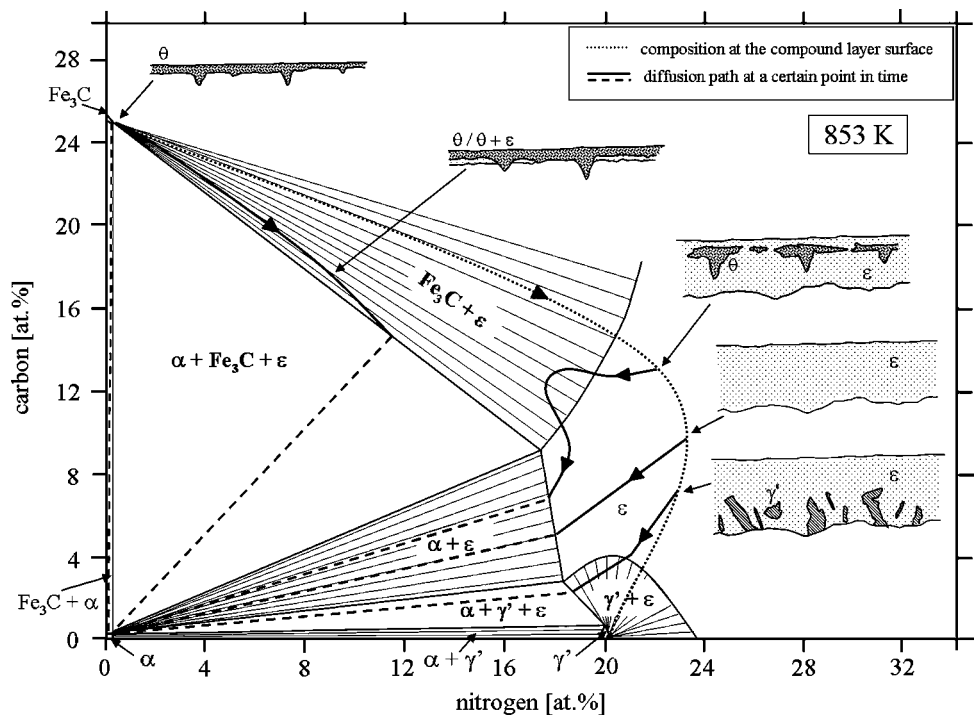


Fig. 11 Diffusion paths in the isothermal section of the Fe-C-N phase diagram at 580 °C (853 K) for various stages of compound-layer development upon nitrocarburizing α -Fe at 580 °C (853 K) and as shown in Fig. 10. On this basis, the time-dependent microstructural evolution of the compound layer can be illustrated for the case that local equilibrium at solid/solid interfaces occurs, which appears to be the case for nitrocarburizing (and nitriding; see text). A diffusion path represents, at a given time, the course of the lateral gross composition and the phase constitution, going from the top to the bottom of the compound layer; see the solid lines indicated with arrows for those parts of the diffusion paths where a continuous change of the gross composition as a function of depth occurs, and the dashed lines for depths where a jump in the gross composition takes place. The time-dependent change of the gross composition at the surface of the compound layer is represented by the dotted line indicated with an arrow. It should be noted that the isothermal section of the Fe-C-N phase diagram shown here is that given in Ref 52, on the basis of experimental data, which is incompatible with the calculated isothermal section according to the CALPHAD database (2008). Source: Ref 45

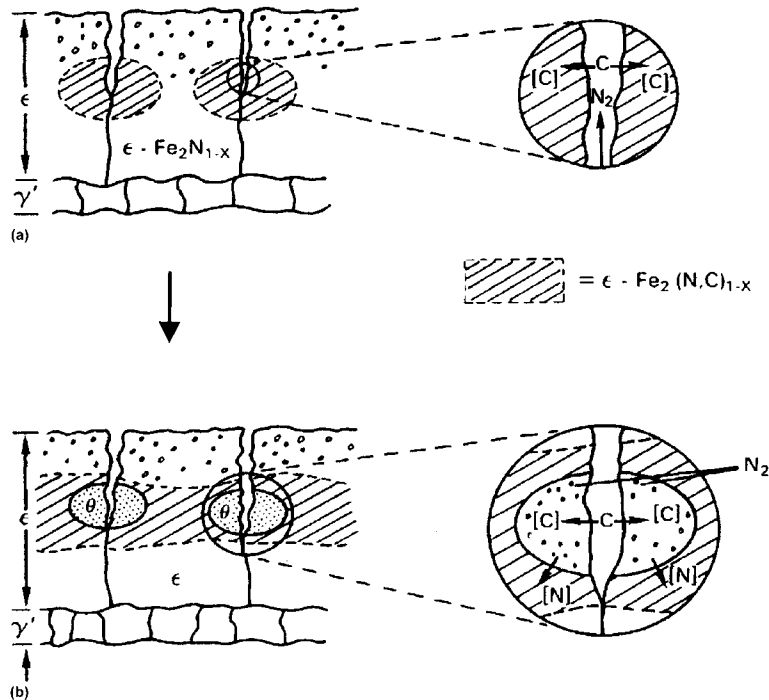


Fig. 12 Carbon uptake through "open" grain boundaries/channels in contact with the outer nitrocarburizing atmosphere. (a) Preferential carbon uptake is observed to take place via the channel walls at some distance from the outer surface (in this case, nitrocarburizing took place in a CO-containing gas atmosphere: 3 vol% CO; 53 vol% NH_3 , and 44 vol% H_2 at 570 °C, or 843 K). (b) The carbon enrichment in the ϵ phase at these depths can eventually lead to cementite formation. The associated transformation of the original ϵ phase to cementite (θ) adjacent to the channel walls leads to fine pores (filled with N_2 gas), because the cementite has a very low solubility for nitrogen. Source: Ref 39

speculate about the origin of this phenomenon. It can be suggested that the outer gas atmosphere can penetrate the channels, after these have established an opening at the outer surface, and that at the fresh channel walls the kinetics of carbon uptake may be much faster than that of nitrogen uptake, as discussed earlier for the formation of cementite at the surface of the substrate at the start of nitrocarburizing. The driving force for the decomposition of the ϵ phase, giving rise to pore/channel formation, is largest close to the outer surface, because the nitrogen content of the ϵ phase is largest there. Thus, the initial presence of a large amount of N_{ads} at the fresh channel walls may be most pronounced at the channel walls close to the outer surface, which thus could effectively block the occurrence of a gas-solid reaction (Eq 8a) at these depths at the channel walls close to the outer surface.

9.3 Microstructural Development of the Compound Layer in the Presence of Alloying Elements. Steels subjected to a nitriding treatment often possess alloying elements having distinct chemical affinity for nitrogen (see Section 10). The question emerges how the presence of these alloying elements influences the formation of the compound layer. To provide an answer, one must distinguish between a group of alloying elements that has an apparently strong-to-intermediate interaction with nitrogen (alloying elements belonging to this

group are titanium, vanadium, and chromium) and a group of alloying elements that has an apparently weak interaction with nitrogen (alloying elements belonging to this group are aluminum, molybdenum, and silicon). (For the classification of strong, intermediate, and weak Me-N interaction, which expresses a net outcome of the precipitation promoting change of chemical Gibbs energy and the precipitation obstructing misfit energy, see Section 5.4 in Ref 53; see also Section 11.2 in this article).

Strong interaction implies that upon the start of nitriding, an immediate precipitation of MeN_n nitride particles in the ferritic matrix is invoked. Then, as soon as the amount of nitrogen dissolved in the ferrite matrix at the surface of the specimen exceeds the solubility limit of nitrogen, a compact (largely) iron-nitride compound layer develops at the surface of the specimen. During growth of this iron-nitride compound layer, the MeN_n nitride particles, which already have precipitated in the matrix (the diffusion zone), are incorporated in the compound layer by overrunning them (Ref 41, 54–56).

Underneath the iron-nitride compound layer, iron-nitride developments along grain boundaries of the matrix can often be observed (Fig. 13). This phenomenon can be explained as follows:

- Segregation at grain boundaries of the alloying element Me, already in the unnitrided condition, leads to preferred precipitation

of Me-nitride at grain boundaries in the diffusion zone below the compound layer. As a consequence, Me-depleted regions adjacent to such grain boundaries occur. The prevailing supersaturation of nitrogen in these regions then, in the absence of Me, can lead to the development of iron nitride adjacent to such grain boundaries.

- The initially developed nanosized, largely coherent MeN precipitates (see Section 11.2), in the so-called continuous precipitation (CP) region, may coarsen via a discontinuous coarsening reaction (Ref 14, 57), which results in the development of a lamellar, discontinuously coarsened (DC) microstructure (Ref 58–60). The ferrite matrix surrounding the continuous, nanosized, largely coherent precipitates can contain much more excess nitrogen (see Section 11.3) than the ferrite matrix in the DC region. Thus, the occurrence of DC is accompanied by release of a huge amount of excess nitrogen that either locally enhances the nitrogen supersaturation of ferrite, leading to the precipitation of nitride along grain boundaries and also at the CP/DC interface, or associates at the grain boundaries under formation of pores filled with N_2 gas, coalescence of which leads to the development of open grain boundaries/cracks (refer to the discussion on pore formation in the iron-nitride compound layer in Sections 3 and 9.1). The penetration of the outer nitriding atmosphere through the cracks opened to the surface then leads to the development of iron nitride along the crack faces (see discussion of Fig. 12).

Weak interaction implies that, upon the start of nitriding, not an immediate but a (very) slow precipitation of MeN_n nitride particles can occur. Such a delayed precipitation reflects the pronounced misfit strain field that is associated with the development of MeN_n precipitates. In this case, a competition between the slow precipitation of MeN_n and the development of iron nitride can occur. Consider the case that nitriding takes place under conditions which allow the development of γ' iron nitride. The solubility of Me in γ' iron nitride can be small, as, for example, holds for aluminum and molybdenum. Then, precipitation/development of γ' iron nitride occurs either after a partitioning of Me in the ferrite matrix, as by a preceding precipitation of Me as MeN_n , has been realized, to make possible the development of Me-free γ' iron nitride, or the γ' iron nitride is forced to nucleate and grow with Me dissolved in it. The difficulty in the precipitation of both MeN_n and γ' iron nitride allows the absorbed nitrogen to diffuse deeply into the specimen, leading to a (unusually) high nitrogen supersaturation of the ferrite matrix. Eventually, such nitrogen supersaturation brings about the development of γ' iron nitride, with Me dissolved in it, across the depth range of high-nitrogen supersaturation. As a result, a peculiar, platelike morphology of γ' ,

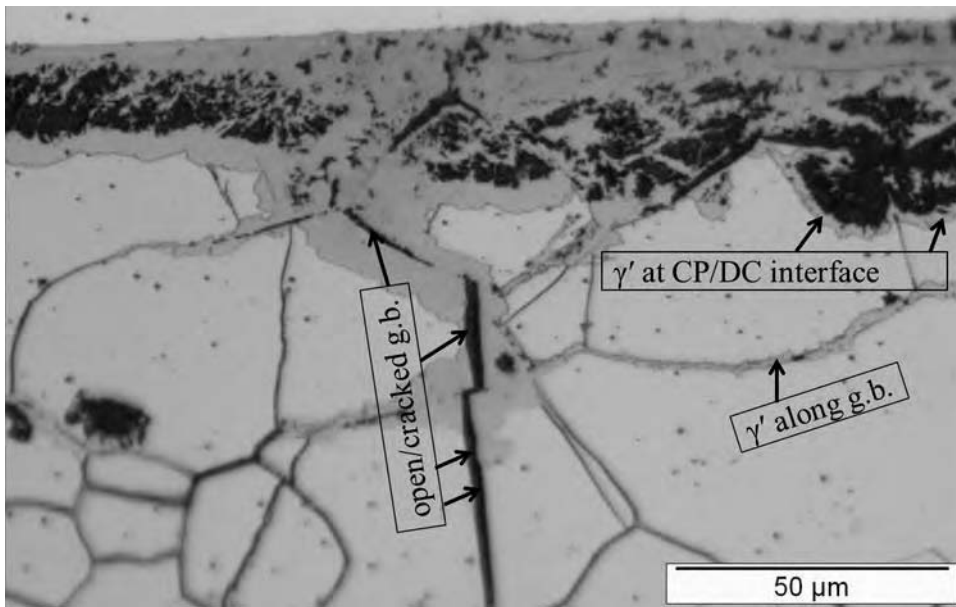


Fig. 13 Cross section of nitrided Fe-Me alloy specimen with a “strong” Me-N interaction (see text). Here, Me = V; Fe-4at.%V specimen nitrided at 580 °C (853 K) for 4 h with $r_N = 0.8 \text{ atm}^{-1/2}$ (light optical micrograph; after etching in 2 vol% Nital). γ' nitride has formed not only as a layer at the surface but also along the “open” grain boundaries (g.b.) in the matrix and along the interface between the zones of continuous precipitation (CP) (of VN) and of discontinuous coarsening (DC). Source: Ref 56

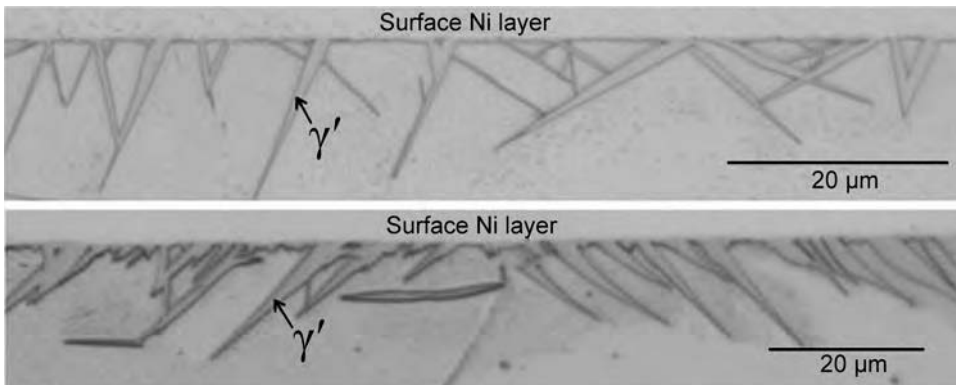


Fig. 14 Cross sections of nitrided Fe-Me alloy specimens with a “weak” Me-N interaction (see text). (a) Fe-4.7at.%Al specimen nitrided at 500 °C (773 K) for 10 min with $r_N = 1.73 \text{ atm}^{-1/2}$. (b) Fe-1at.%Mo alloy specimen nitrided at 480 °C (753 K) for 2 h with $r_N = 0.7 \text{ atm}^{-1/2}$. Note the unusual plate-type morphology of the developed γ' iron nitride (light optical micrographs, cross sections etched in 2 vol% Nital). Source: Ref 61 and 62, respectively

deeply penetrating the specimen, occurs (for an example, see Fig. 14) (Ref 56, 61, 62).

The results discussed in the preceding paragraph pertain to iron-base alloys, with Me as an element of weak interaction with nitrogen, in recrystallized condition. If these materials have been deformed (e.g., by cold rolling), at the start of nitriding immediate precipitation of MeN_n can occur (defect/dislocation-facilitated nucleation), and a compact compound layer of (largely) iron nitride develops at the surface that incorporates the already precipitated MeN_n particles (by overrunning them) (Ref 62). This is just as in the case for Me as an alloying element experiencing a strong interaction with nitrogen.

It is concluded that compound layers not only can be avoided (by proper selection of

the nitriding potential, which should not exceed a critical value), but that they can be microstructurally and morphologically modified by incorporating in the ferritic matrix, in dissolved state, alloying elements Me having a weak Me-N interaction (Me = aluminum, molybdenum, and silicon) next to elements Me having a strong Me-N interaction (Me = titanium, vanadium, and chromium).

10. Kinetics of Compound-Layer Growth

It is often taken for granted that growth of an iron-nitride layer upon nitriding or an

iron-carbonitride layer upon nitrocarburizing is kinetically controlled by the inward diffusion of the interstitial components. Of course, this does not hold for the beginning stage of layer growth as long as no local equilibrium or stationary state has been realized at the surface of the layer (see discussion in Section 8.1). This has an important consequence for the nucleation of (carbo)nitrides at the surface of the specimen/component, which is discussed first for the case of nitriding pure iron and the development of an iron-nitride layer at the surface in the following section.

The nitrogen-uptake rate is the outcome of competing processes:

- The dissociation process (Eq 2)
- The recombination and desorption process (Eq 17) at the gas-solid interface
- The diffusion process in the solid substrate (see Sections 8.1 and 9.1)

If rate-constant and diffusion-coefficient data are available, the joint result of these processes can be calculated numerically (see the Appendix of Ref 23). Hence, recognizing that local equilibrium, or a stationary state, is not established instantaneously at the surface in the case of nitriding, the nitrogen concentration-depth profiles cannot be calculated straightforwardly on the basis of (analytical or numerical) solutions of only Fick's second law.

An example of the evolution of the nitrogen concentration-depth profile with time at constant temperature for the case of nitriding pure iron is shown in Fig. 6. Indeed, the surface concentration of nitrogen gradually increases to attain a constant value only after pronounced nitriding. This behavior, for the normal nitriding conditions considered here, is dictated by the competition between the dissociation of NH_3 at the surface and the inward diffusion of nitrogen; the effect of the recombination of adsorbed nitrogen at the surface and its subsequent desorption as nitrogen gas is negligible at temperatures below 580 °C (853 K) and not very high nitriding potentials (Fig. 7).

The effect shown in Fig. 6 has as consequence that, even if the nitriding potential and temperature predict the development of, for example, γ' iron nitride, then nucleation of this nitride at the surface can only occur after distinct nitriding time has passed; γ' nucleation can occur (at the earliest) at the moment that the surface concentration of nitrogen surpasses the value compatible with the α/γ' equilibrium. Hence, an *incubation time* for iron-nitride formation occurs. This effect was first recognized and quantitatively predicted and experimentally verified in Ref 37. In the calculations of Ref 37, the contribution of the recombination and desorption process at the surface was neglected. In a later work (Ref 38), this effect was taken into account; the difference in resulting incubation time for

iron-nitride nucleation at the surface is only a few percent at most, in accordance with the previous discussion.

Only after a closed (carbo)nitride layer has formed at the surface and a stationary state or local equilibrium situation occurs at the surface of the layer may interstitial diffusion processes in the (carbo)nitride layer control the rate of layer growth.

Surprisingly little information on interstitial diffusion in (growing) iron-nitride layers on ferrite is available in the literature (Ref 63–66). This holds even more so for (growing) iron-carbonitride layers on ferrite (Ref 67). Especially in the case of iron-carbonitride compound layers, the microstructure can be so complicated, as exemplified by the presence of (if local equilibrium prevails, at most) two phases over a certain depth range in the layer (see Section 9.2), that a more or less straightforward analysis of diffusion processes is obstructed. Hence, researchers aiming at characterizing the kinetics of layer growth, on the basis of parameters as diffusion coefficients, look for geometries that are laterally invariable. This is guaranteed, in principle, for the binary iron-nitrogen system; if the two nitrides ϵ and γ' occur in the compound layer upon nitriding an α -Fe substrate, then the ϵ phase is present as a sublayer on top of a γ' sublayer, on top of the α -Fe substrate (see Fig. 8 and 9 and Section 9.1). This microstructure of planar, parallel ϵ and γ' sublayers is the one most frequently investigated (apart from the case of a single γ' layer on top of an α -Fe substrate). For the ternary Fe-N-C system, such a dual-sublayer microstructure is only possible for restricted ranges of chemical potentials of nitrogen and carbon in the nitrocarburizing atmosphere and limited ranges of temperature and time (and pressure); for example, see stage 7 in Fig. 10. The only work performed until now devoted to diffusion analysis of both nitrogen and carbon upon nitrocarburizing α -Fe followed this strategy (Ref 67).

The diffusional flux of only nitrogen in an iron-nitride layer growing on ferrite can be characterized by a single diffusion coefficient: the intrinsic diffusion coefficient of nitrogen, D_N . (Note that at the normal nitriding and nitrocarburizing temperatures, the iron in the system can be considered as immobile.) Thus, the flux of nitrogen, J_N , and the gradient of the nitrogen concentration in the nitride layer, dc_N/dx , are related by D_N according to Fick's first law:

$$J_N = -D_N \cdot \frac{dc_N}{dx} \quad (\text{Eq 18})$$

Such descriptions of diffusional mass transport become essentially more complicated if more than one diffusing component must be considered. Thus, for the case of simultaneous diffusion of nitrogen and carbon in an iron-carbonitride layer, Fick's first law must be written as:

$$J_k = J_{kk} + J_{kj} = -\left(D_{kk} \cdot \frac{dc_k}{dx}\right) - \left(D_{kj} \cdot \frac{dc_j}{dx}\right) \quad (\text{Eq 19})$$

with $k = N, j = C$, and with $k = C, j = N$. So, instead of only one intrinsic diffusion coefficient, now four intrinsic diffusion coefficients are required to describe the fluxes of nitrogen and carbon: D_{NN}, D_{NC}, D_{CC} , and D_{CN} . The coefficient D_{NC} describes the contribution to the diffusional transport of nitrogen due to the concentration gradient of carbon, and D_{CN} describes the contribution to the diffusional transport of carbon due to the concentration gradient of nitrogen. Each intrinsic diffusion coefficient is given by the self-diffusion coefficient of the diffusing component considered, D_k^* , multiplied by the so-called thermodynamic factor, θ_{kj} (Ref 46):

$$D_{kj} = D_k^* \cdot \theta_{kj} \quad (\text{Eq 20})$$

In principle, both the self-diffusion coefficients and the thermodynamic factors depend on concentration. These thermodynamic factors express the thermodynamic interaction of nitrogen and carbon, leading to the diffusional cross effects as outlined in Eq 19. It appears that in the case of simultaneous diffusion of nitrogen and carbon in iron-carbonitride, these contributions, as exposed by D_{NC} and D_{CN} , can be very distinct (see the following).

The growth of an ϵ/γ' double layer on top of a ferrite substrate during nitrocarburizing can be described by considering the (mass) balances that describe the shifts of the ϵ/γ' interface and

the γ'/α interface, by infinitesimal distances $d\xi$ and $d\zeta$, respectively, resulting from the diffusive fluxes arriving at and departing from the interfaces (Fig. 15) (Ref 63, 67):

$$\begin{aligned} \text{Growth of } \epsilon \text{ sublayer: } & \left(c_k^{\epsilon/\gamma'} - c_k^{\gamma'/\epsilon}\right) \cdot d\xi + W_{k,\epsilon} \\ & = \left(J_k^{\epsilon/\text{gas}} - J_k^{\gamma'/\epsilon}\right) \cdot dt \end{aligned} \quad (\text{Eq 21a})$$

$$\begin{aligned} \text{Growth of } \gamma' \text{ sublayer: } & \left(c_k^{\gamma'/\alpha} - c_k^{\alpha/\gamma'}\right) \cdot d(\zeta - \xi) + W_{k,\gamma'} \\ & = \left(J_k^{\gamma'/\epsilon} - J_k^{\alpha/\gamma'}\right) \cdot dt \end{aligned} \quad (\text{Eq 21b})$$

with $c_k^{I/II}$ as the concentration of component k in phase/sublayer I at the I/II interface, $J_k^{I/II}$ as the flux of component k in phase/sublayer I at the I/II interface, and $W_{k,I}$ as the amount of component k necessary to maintain the concentration-depth profile of component k in sublayer I. This set of equations (four in the case of simultaneous diffusion of nitrogen and carbon) reduces to one equation if γ' iron-nitride layer growth is considered.

On the basis of Eq 21, the diffusion coefficients are determined by making layer-growth rate measurements ($v^{\epsilon/\gamma'} = d\xi/dt$ and $v^{\gamma'/\alpha} = d(\zeta - \xi)/dt$) and concentration-depth profile measurements. Results presented in the literature pertain to experiments where, for the single γ' layer or for the ϵ/γ' bilayer, and at constant temperature, parabolic growth is

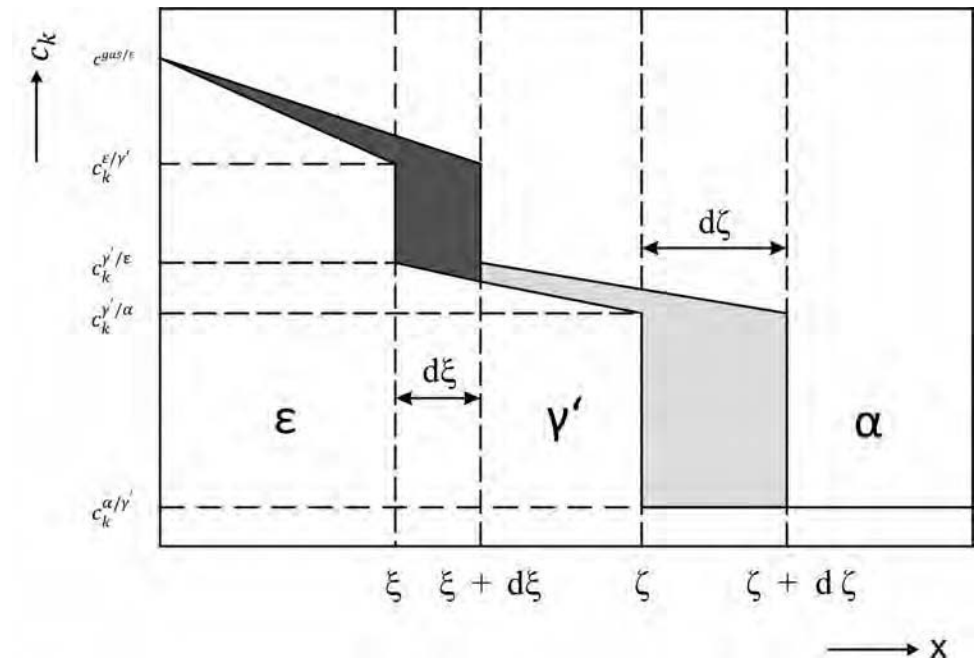


Fig. 15 Schematic concentration-depth profile of the interstitial component k in the compound layer of the I/II (here: ϵ/γ') double-layer morphology. The concentration profiles in both sublayers have been taken linearly. The dark-gray area represents the amount of component k per unit area cross section (perpendicular to the surface of the specimen) to be accumulated in sublayer II to realize a shift of the I/II interface by a distance $d\xi$ into the sublayer II. The light-gray area represents the amount of component k per unit area cross section (perpendicular to the surface of the specimen) to be accumulated in sublayer II to realize a shift of the II/ α interface by a distance $d\zeta$. Source: Ref 63, 67

assumed for the (sub)layer thickness. Such parabolic growth is expected for constant surface concentrations and constant interface concentrations and an initially fully saturated substrate or an initially unsaturated substrate of infinite thickness. Additional assumptions that have been made in such analyses are, for example, the supposition of linear concentration-depth profiles in the sublayers and constant (i.e., independent of concentration) intrinsic or self-diffusion coefficients (Ref 63, 67).

In the case of growth of only a γ' iron-nitride layer upon nitriding ferrite, adopting the self-diffusion coefficient of nitrogen as independent of concentration, the experimentally observed concave curvature of the nitrogen concentration-depth profile in the massive γ' layer near the surface could be ascribed to the concentration dependence of the thermodynamic factor (Eq 20) (Ref 68). If porosity occurs near the surface of the γ' iron-nitride layer, the penetration of the outward gas atmosphere along open grain boundaries (owing to coalesced pores developing at the grain boundaries; see Sections 3 and 9) can contribute distinctly to such concave curvature of the nitrogen concentration-depth profile (Ref 69). A summary of available data on the diffusion coefficients of nitrogen in the γ' and ε iron-nitride phases, at the typical nitriding temperatures, is provided in Ref 24. Data at considerably lower temperatures (360 to 400 °C, 633 to 673 K) are presented in Ref 66.

The only work until now devoted to the kinetic analysis of simultaneous diffusion of nitrogen and carbon in ε iron-carbonitride upon nitrocarburizing ferrite is presented in Ref 67. The window of experimental parameters (see the introductory paragraphs of this section)

was such that an ε/γ' bilayer occurred at the surface of the nitrocarburized ferrite. The γ' phase can incorporate only little carbon (Fig. 11); in the analysis, the γ' sublayer was taken as stoichiometric Fe_4N , the nitrogen and carbon concentration profiles in the ε sublayer were taken linear (validated experimentally), and the four intrinsic diffusion coefficients in the ε phase (see text following Eq 19) were taken as independent of concentration. The results obtained for D_{NN} , D_{NC} , D_{CC} , and D_{CN} upon nitrocarburizing at 550 °C (823 K) demonstrate that D_{NC} is approximately as large as D_{NN} and that D_{CN} equals approximately $\frac{1}{4}D_{\text{CC}}$. Hence the “off-diagonal” diffusion coefficients, D_{NC} and D_{CN} , are as significant as the “diagonal” ones, D_{NN} and D_{CC} . This implies the occurrence of strong thermodynamic interaction of nitrogen and carbon, which are dissolved on the same sublattice of octahedral interstitial sites as provided by the hexagonal close-packed parent lattice of iron atoms (Table 1). As an illustration, the nitrogen flux contributions J_{NN} and J_{NC} and the carbon flux contributions J_{CC} and J_{CN} (Eq 19) at the gas/ ε interface are shown in Fig. 16; J_{NC} can be as large as J_{NN} , and J_{CN} can be as large as J_{CC} .

11. Microstructural Development of the Diffusion Zone

With respect to the development of the diffusion zone, a distinction between nitriding and nitrocarburizing need not be made; carbon, as compared to nitrogen, does not dissolve to a significant extent in the ferritic matrix (Table 1). Carbon, as a species offered by a thermochemical process such as nitrocarburizing,

plays a pronounced role only in the development of the compound layer (see Section 9.2). In other words, the virtue of nitrocarburizing is restricted to its effect on the development of the compound layer of (largely) carbonitrides at the surface of the specimen/component.

11.1 Iron Nitrides in Pure Iron and Carbon Steels. In the absence of alloying elements with affinity for nitrogen, at the nitriding temperature no precipitation of nitrides can occur in the diffusion zone, and hence, the absorbed nitrogen stays in solid solution; the nitrogen atoms reside in random distribution at octahedral interstices of the body-centered cubic α -Fe parent lattice. Upon slow cooling after nitriding at relatively high temperature, the γ' iron nitride, $\text{Fe}_4\text{N}_{1-x}$, based on a face-centered cubic iron sublattice with an ordered distribution of nitrogen on octahedral interstices leading to a primitive cubic translation lattice, can precipitate. Continued cooling, if the supersaturation allows, can then lead to the precipitation of an intermediate nitride: α'' - Fe_{16}N_2 , which has a body-centered tetragonal iron sublattice with an ordered distribution of nitrogen on octahedral interstices leading to a body-centered tetragonal translation lattice (Table 1; see Fig. 17). Alternatively, if the specimen has been quenched, so that all nitrogen is still in solid solution (actually, effectively only possible with specimens that are relatively thin, such as foils), aging at room temperature and at temperatures until approximately 150 to 160 °C (423 to 433 K) leads to the development of regions with a α'' - Fe_{16}N_2 crystal structure, followed at higher temperature by the emergence of γ' - $\text{Fe}_4\text{N}_{1-x}$. (Note that local enrichment plus ordering of nitrogen atoms suffices for α'' no rearrangement of iron atoms is required, Ref 70; for a

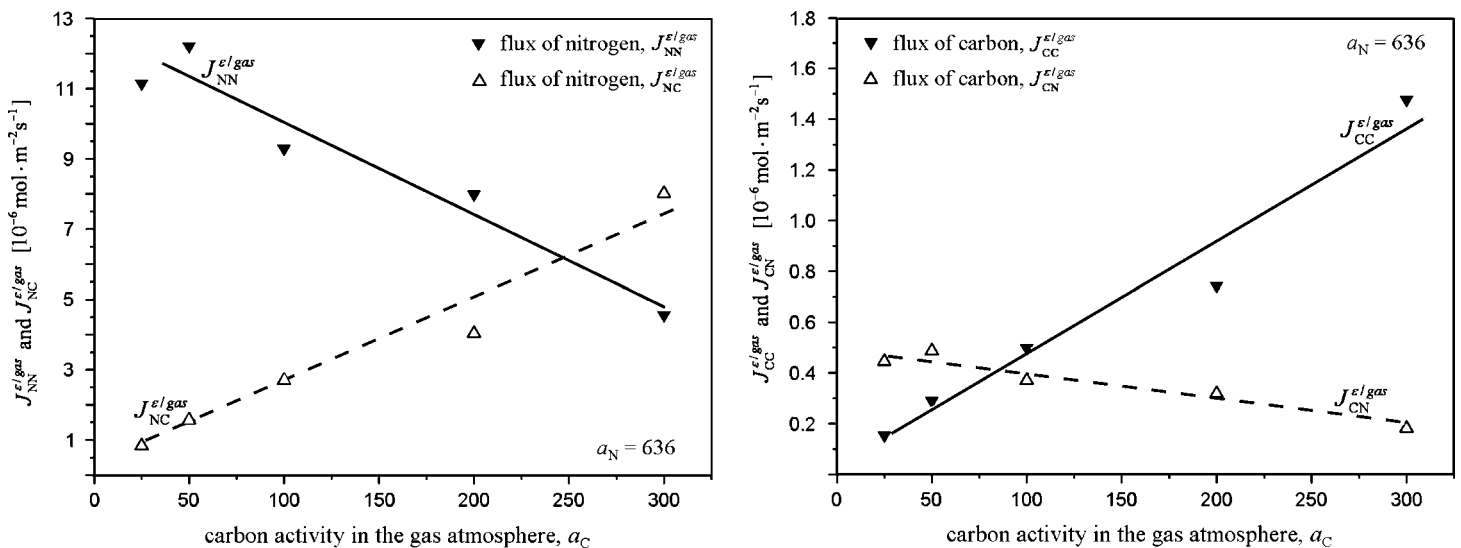


Fig. 16 Diffusive fluxes of nitrogen and carbon at the surface of the ε/γ' compound layer for a nitrocarburizing time of 4 h at 550 °C (823 K) as a function of the chemical potential of carbon in the gaseous nitrocarburizing atmosphere (here represented as the carbon activity, see Sections 6 and 7) for a fixed chemical potential of nitrogen in the gaseous nitrocarburizing atmosphere (here represented as the nitrogen activity; see Sections 4 and 7). The chemical potentials of nitrogen and carbon were controlled by the method described in Section 7. The fluxes J_{NN} and J_{NC} represent the nitrogen fluxes carried by the nitrogen concentration gradient and the carbon concentration gradient, respectively; similarly, the fluxes J_{CC} and J_{CN} represent the carbon fluxes carried by the carbon concentration gradient and the nitrogen concentration gradient, respectively (see Eq 19). Source: Ref 67

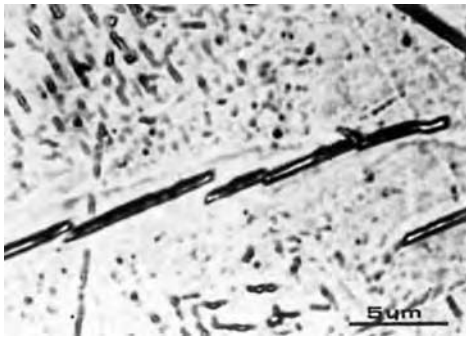


Fig. 17 Cross section of the diffusion zone of a nitrided α -Fe specimen. The specimen was powder nitrided (see the "Introduction" of this article) in a box (for 8 h at 545 °C, or 818 K; Ref 3) and thereafter very slowly cooled, leading to relatively coarse γ' and α'' iron nitrides (the small and large precipitates visible in the micrograph). (Normally, the α'' iron-nitride precipitates are only visible by applying higher magnifications, as provided by a transmission electron microscope.) Light optical micrograph; oblique illumination, oil immersion, after etching in 0.5 vol% Nital. Source: Ref 3

discussion of this process, see Ref 14, pages 421 to 422.)

11.2 Crystalline and Amorphous Alloying Element Nitrides in Iron-Base Alloys. The introduction into the matrix of alloying elements, Me, with (chemical) affinity for nitrogen is intended to induce the precipitation of tiny, possibly (semi)coherent, Me-nitride precipitates in the diffusion zone, which pronouncedly enhances the mechanical properties of the diffusion zone (as, for example, reflected by a strongly improved fatigue resistance, Ref 71; see also Ref 14, pages 576 to 580). The following binary Fe-Me systems, with respect to Me-nitride development upon nitriding, have been documented in the literature: iron-chromium (Ref 3, 58, 59, 72), iron-aluminum (Ref 73, 74), iron-vanadium (Ref 60, 75), iron-titanium (Ref 76, 77), iron-molybdenum (Ref 78, 79), and iron-silicon (Ref 80–82). This list of systems is not exhaustive, and the references given have been restricted to those reporting largely on the microstructure developing upon Me-nitride precipitation. More references can be found in the publications listed here, and specific ones are also given later in this section.

The notions "strong" and "weak" interaction of Me and N have already been touched upon in Section 9.3. They can be discussed as follows.

The Me-N interaction in ferrite, with Me and N as dissolved solutes, can be defined as the ratio of energy gained (chemical Gibbs energy) and the energy required (misfit-strain, and interfacial, Gibbs energy) upon precipitation of MeN_n nitride particles from the super-saturated ferritic Fe-Me-N matrix. For values of such an interaction parameter for a number of alloying elements that leads to a ranking of these alloying elements regarding their strength of interaction, see the examples in Table 6 in Ref 53. This interaction parameter facilitates the characterization of two extreme behaviors of Me-nitride precipitation (Fig. 18) (Ref 83):

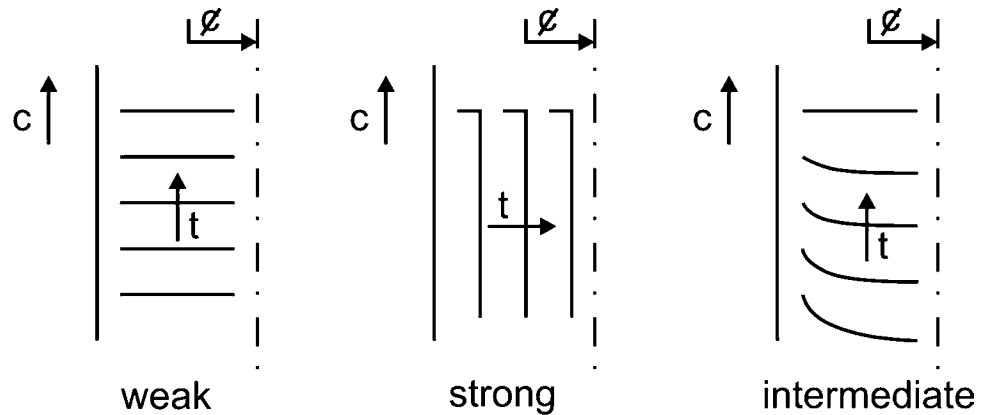


Fig. 18 Types of Me-N interaction as revealed by the emerging nitrogen concentration-depth profiles. The symbols C , t , and z denote nitrogen concentration, nitriding time, and depth below the surface, respectively. Source: Ref 83

- **Weak interaction:** The nitride-precipitation process progresses with the same rate at every depth below the surface (for a foil of finite thickness, see the following). A nitrogen gradient is virtually absent. This can be formulated as follows: nitriding a foil of finite thickness would first lead to nitrogen saturation of the ferrite matrix throughout the foil (i.e., homogeneous nitriding) before the nitride precipitation occurs (with a rate of nitrogen consumption distinctly slower than the rate of nitrogen uptake by the specimen, such that the state of homogeneous nitriding is effectively maintained).
- **Strong interaction:** A surface-adjacent region (case) develops, where all Me atoms have precipitated as nitride. A sharp case/core boundary occurs, and nitrogen in the core is virtually absent.

The type of crystal structure of Me nitride most frequently encountered is the NaCl-type crystal structure, based on a face-centered cubic translation lattice; this holds for TiN, VN, CrN (see also the discussion in Appendix A of Ref 53), and also for the cubic (rock salt) AlN (which can be favored over the equilibrium hexagonal modification, of AlN, wurtzite; Ref 84). The cubic Mo_2N crystal structure can be conceived as a NaCl-type crystal structure with 50% vacancies on the nitrogen sublattice (Ref 79). The lattice parameter of the unit cell of these NaCl-type crystal structures for MeN is closely equal to:

$$a_{\alpha\text{-Fe}}\sqrt{2}$$

where $a_{\alpha\text{-Fe}}$ indicates the lattice parameter of body-centered-cubic α -Fe. Thus a {100} habit plane and an orientation relationship of the following type can be expected:

$$(001)_{\alpha\text{-Fe}} // (001)_{\text{MN}}; [100]_{\alpha\text{-Fe}} // [110]_{\text{MN}}$$

Obviously, three variants (one for each cube plane of the matrix) of this (so-called Bain, also

called Baker-Nutting) orientation relationship can occur. These predictions are in agreement with the experimental observations. Then, a coherent interface along the $\{100\}_{\alpha\text{-Fe}}$ plane can be expected, a linear misfit on the order of a few percent. The linear misfit perpendicular to the habit plane is very much larger, of the order 40% and more. Hence, the nitrides develop as tiny platelets, say, 10 nm long and 1 nm thick, depending on the precise nitriding conditions (Ref 85). In agreement with this discussion, a high-resolution transmission electron microscopy image shows the platelet faces to be coherent, whereas (misfit) dislocations can be detected at the platelet edges (Fig. 19).

If more than one alloying element is present, such as $\text{Me}_1 = \text{Cr}$ and $\text{Me}_2 = \text{Al}$ (a combination of alloying elements met in well-known nitriding steels), one may wonder whether separate precipitation of Me_1 nitride and Me_2 nitride will occur or that a mixed nitride $(\text{Me}_1)_x(\text{Me}_2)_{1-x}\text{N}$ will precipitate. It has been recently shown that for $\text{Me}_1 = \text{Cr}$ and $\text{Me}_2 = \text{Al}$ and for $\text{Me}_1 = \text{Cr}$ and $\text{Me}_2 = \text{Ti}$, the mixed nitride, with NaCl-type crystal structure, is preferred to precipitate (Ref 86–88). This can be understood as follows (Ref 89):

- **For $\text{Cr}_x\text{Al}_{1-x}\text{N}$:** The formation of the equilibrium NaCl-type CrN precipitate is relatively fast, whereas development of the equilibrium hexagonal AlN is relatively very slow, owing to its large volume misfit with the ferritic matrix. The misfit-strain energy of the CrN precipitates can be reduced by the uptake of aluminum. Also, because the diffusion of chromium and aluminum in the ferrite matrix is very slow compared to the diffusion of nitrogen, the aluminum atoms are "dragged" into the developing cubic NaCl-type CrN precipitates. (Note that the NaCl-type crystal structure is a possible crystal structure for AlN; see previous discussion and Ref 84.) The system thus accepts the gain of a smaller-than-maximum

amount of Gibbs energy, released by nitride precipitation, as an intermediate solution; $\text{Cr}_x\text{Al}_{1-x}\text{N}$ precipitates develop.

- For $\text{Cr}_x\text{Ti}_{1-x}\text{N}$: The equilibrium precipitates CrN and TiN have the same NaCl-type crystal structure. The interaction parameter

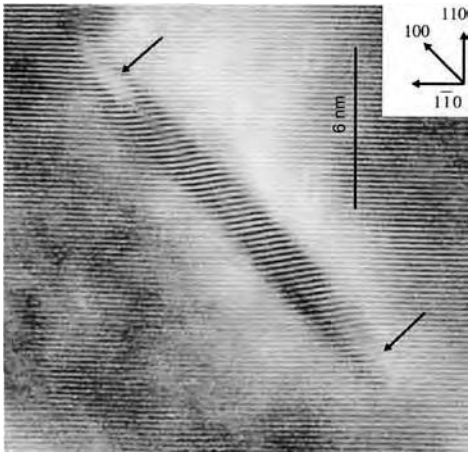


Fig. 19 Vanadium-nitride precipitate (rocksalt-type crystal structure) in an α -Fe (body-centered cubic, or bcc) matrix (high-resolution transmission electron microscopy). At the top right corner, crystallographic directions referring to the bcc lattice of the α -Fe matrix are shown. The set of (110) lattice planes in the α -Fe matrix continues as a set of (111) planes in the VN platelet, as indicated by the black-white line contrast in the micrograph, which traverses the matrix and the particle (a thin platelet) in a continuous way; the interface between the matrix and the faces of the nitride platelet is coherent. The curvature of the lattice fringes is due to elastic accommodation of the misfit between matrix and platelet. Misfit dislocations occurring at the platelet extremities have been indicated by arrows; these can be conceived as a consequence of the misfit in directions perpendicular to the platelet faces, as experienced at the platelet circumference, being (very) much larger than parallel to the platelet faces (Fe-2.2at.%V alloy nitrided for 25 h at 640 °C, or 913 K). Source: Ref 85

(see previous discussion) for titanium-nitrogen is appreciably larger than that for chromium-nitrogen. So, the driving force for TiN to precipitate is much larger than that for CrN to precipitate. The misfit-strain energy of the TiN precipitates can be reduced by the uptake of chromium. Also, because diffusion of chromium and titanium in the ferrite matrix is very slow compared to the diffusion of nitrogen, the chromium atoms are “dragged” into the developing cubic NaCl-type TiN precipitates. The system thus accepts the gain of a smaller-than-maximum amount of Gibbs energy, released by nitride precipitation, as an intermediate solution; $\text{Cr}_x\text{Ti}_{1-x}\text{N}$ precipitates develop.

Note the subtle distinction of contributing factors promoting the precipitation of a mixed nitride, $(\text{Me}_1)_x(\text{Me}_2)_{1-x}\text{N}$, for both systems in the previous consideration.

The formation of the mixed nitride releases a considerable amount of Gibbs energy. However, thermodynamically the precipitation of the separate equilibrium nitrides is favored. Indeed, it was shown that, after nitriding at 580 °C (853 K) and by annealing at 700 °C (973 K), the metastable $\text{Cr}_x\text{Al}_{1-x}\text{N}$ precipitates in the diffusion zone become depleted of aluminum, followed by subsequent precipitation of the released aluminum as hexagonal AlN in the interior and at grain boundaries of the ferritic matrix in the diffusion zone (Ref 87).

A peculiar, interesting observation has been made upon nitriding iron-base iron-silicon solid solution. A distinct chemical driving force exists for the formation of Si_3N_4 from a super-saturated Fe-Si-N solid solution. Yet, this precipitation process is very slow, leading to practically ideally weak nitriding kinetics (Fig. 18, Ref 83). The very slow rate of nitride

precipitation is undoubtedly due to the very large volume misfit of over 100% between nitride precipitate and ferrite matrix. It was a great surprise to observe that the nitride precipitates that eventually develop are not of crystalline nature but are amorphous (albeit of the composition Si_3N_4) (Ref 80); it is extremely rare for nature to favor the amorphous modification over the crystalline one for the precipitate in a solid-state precipitation process. For small-sized precipitates associated with a relatively large interface/volume ratio, a relatively low value of the energy of the interface between the amorphous precipitate and the crystalline ferrite matrix, compared to the interfacial energy in the case of the crystalline modification of the precipitate, can stabilize the amorphous modification such that it is preferred over the crystalline modification (Ref 80). The amorphous precipitates developing at 580 °C (853 K) initially occur as bands along the ferrite grain boundaries; at later stages, cuboidal amorphous nitride particles develop within the ferrite grains (Ref 81). The faces of the cuboidal amorphous precipitates (Fig. 20) are parallel to $\{100\}_{\alpha\text{-Fe}}$, suggesting that the interface between amorphous Si_3N_4 and α -Fe preferably forms along $\{100\}_{\alpha\text{-Fe}}$. At higher temperatures (650 °C, or 923 K), amorphous Si_3N_4 precipitates with a strangely eight-legged (octopod-shaped) morphology occur (Fig. 20a, b) (Ref 82); the initially cubically shaped amorphous particles, with a shape morphology dictated by favorable interface energy (see previous discussion), experience growth especially along the $\langle 111 \rangle$ directions of the crystalline ferrite matrix as a consequence of the very large volume misfit (see earlier discussion) and the elastically strongly anisotropic nature, in particular at higher temperatures, of the ferrite matrix.

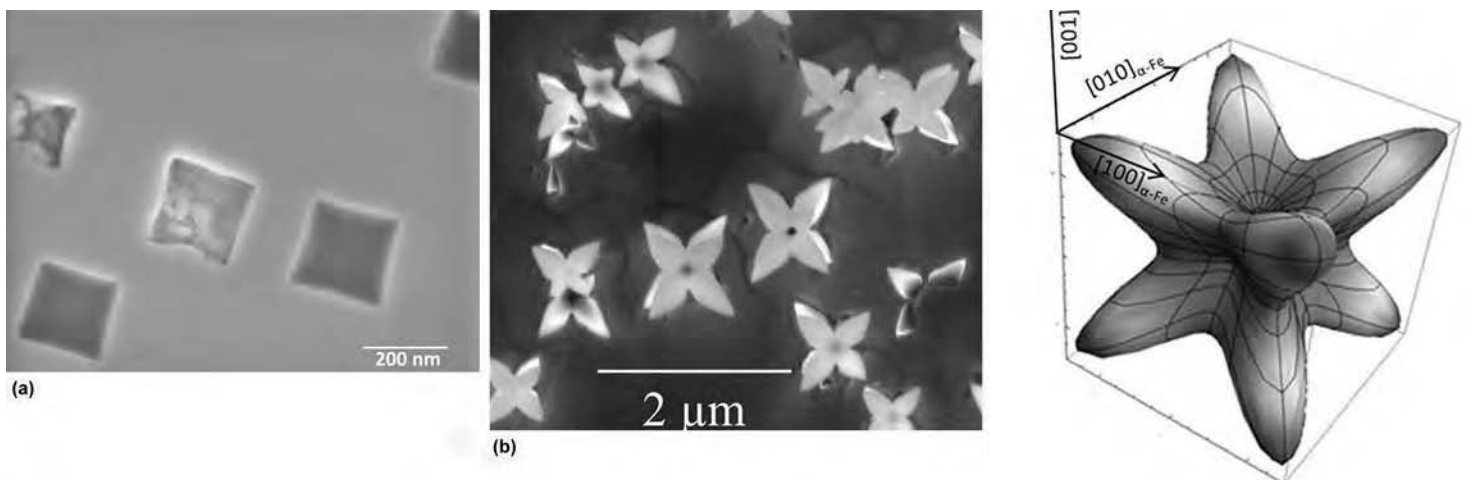


Fig. 20 Amorphous Si_3N_4 precipitates developing upon nitriding iron-silicon alloys. (a) At relatively low nitriding temperature, cubically shaped amorphous silicon nitride precipitates develop; the cubical shape, with faces parallel to $\{100\}$ planes of the α -Fe matrix, is governed by favorable interface energy (Fe-4.5at.%Si alloy specimen nitrided at 600 °C, or 873 K, for 40 h with $r_N = 0.02 \text{ atm}^{-1/2}$; scanning electron micrograph from cross section polished with colloidal silica solution OPS). (b) At higher temperature, eight-legged (octopod-shaped) amorphous silicon nitride particles occur as a consequence of preferred growth along the $\langle 111 \rangle$ directions of the α -Fe matrix due to the very large volume misfit and the anisotropic elasticity of the α -Fe matrix (Fe-4.5at.%Si alloy specimen nitrided at 650 °C, or 923K, for 48 h with $r_N = 0.02 \text{ atm}^{-1/2}$, scanning electron micrograph from jet-electropolished section). Source: Ref 81 and 82, respectively

Another peculiar microstructural consequence of weak Me-N interaction is observed upon nitriding iron-aluminum alloy under conditions where no compound (iron-nitride) layer can develop. (For the developing microstructure in case iron nitride can develop, see the description of weak interaction in Section 9.3.) Upon nitriding of a specimen of Fe-4.65at.%Al, a high density of microcracks appears along the original grain boundaries in the ferrite matrix. These microcracks arise by recombination of nitrogen originally dissolved in the matrix. This process happens because of the slow precipitation of hexagonal wurtzite-type AlN; the diffusion to the grain boundaries of the dissolved nitrogen (followed by its recombination and pore formation, which, by pore coalescence, causes open, cracked grain boundaries) competes with the slow AlN precipitation. As a consequence, AlN precipitates occur in the center of the grains, and precipitate-free zones are present along the open, cracked grain boundaries. Upon continued nitriding, inward diffusion of nitrogen brings about a full nitriding of the initially only partially nitrided grains. Then, the microcracks become closed due to the compressive stress that develops in the nitrided zone—a remarkable process of *self-healing* (Ref 90).

11.3 Types of Absorbed Nitrogen; Excess Nitrogen. The amount of nitrogen taken up in the nitrided zone, where (largely coherent) alloying element nitride precipitates have developed, can significantly exceed the amount of nitrogen predicted, assuming that all Me has precipitated as the expected MeN_n nitride and that the remaining ferrite matrix contains the equilibrium amount of dissolved nitrogen. The difference between the actual observed nitrogen content and this expected value is called “excess nitrogen.”

Detailed research has revealed that (at least) three kinds of absorbed nitrogen can be distinguished (Fig. 21) (Ref 53, 91–96):

- *Type I:* Nitrogen strongly bonded to the nitride precipitates (Fig. 21). This nitrogen cannot generally (easily) be removed by denitriding in a reducing atmosphere (such as pure H_2 gas).
- *Type II:* Nitrogen adsorbed at the (coherent) interface of the nitride plate with the matrix. For MeN of NaCl-type crystal structure, and in view of the orientation relationship and platelet morphology mentioned in Section 11.2, it can be anticipated that these adsorbed nitrogen atoms reside in octahedral interstitial sites of the surrounding ferrite matrix opposite to the Me atoms in the MeN platelet at the platelet/matrix interface (Fig. 21a). For a monolayer MeN, this would mean that the actual composition at the location of the nitride platelet can be indicated as MeN_3 . The adsorbed nitrogen atoms are less strongly bonded than the type I nitrogen atoms and thus can generally be removed by denitriding.

- *Type III:* Nitrogen dissolved in octahedral interstitial sites of (and throughout) the ferrite matrix (Fig. 21b). The misfit strain field surrounding the nitride platelet of NaCl-type crystal structure, in accordance with the discussion in the previous section, is of tetragonal nature, implying that the ferrite surrounding the nitride platelet is severely tetragonally distorted (Fig. 22). The elastic straining of the surrounding ferrite matrix is associated with a hydrostatic stress component of tensile nature that leads to a thermodynamically induced enhanced solubility of nitrogen (Ref 53).

Thus, excess nitrogen is the sum of the adsorbed nitrogen (type II nitrogen) and the surplus dissolved nitrogen (i.e., the actual amount of dissolved nitrogen minus the amount of dissolved nitrogen in the absence of misfit stress). The total amount of excess nitrogen taken up by the

specimen/component is by no means marginal; type II excess nitrogen, adsorbed at the nitride/matrix interfaces, can in practical cases be 50% of the amount of nitrogen necessary to precipitate all Me as MeN, of NaCl-type crystal structure, and the amount of excess nitrogen dissolved in the ferrite matrix can be of the order of the equilibrium amount of dissolved nitrogen. The occurrence of excess nitrogen (thus) has a great impact on the nitriding kinetics (see Section 12).

11.4 Nitriding Carbide-Containing Steels.

In physical metallurgy, the following rule of thumb holds: oxides are more stable than nitrides, which, in turn, are more stable than carbides. Therefore, upon nitriding a quenched and tempered steel containing alloying elements, with affinity for both carbon and nitrogen, the alloying element carbide particles, which result from the quenching and tempering treatment performed before nitriding, can be

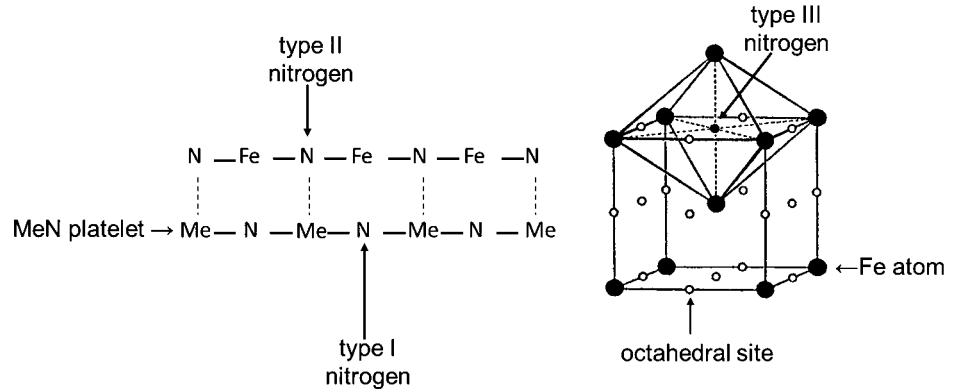


Fig. 21 Schematic presentation of the three types of absorbed nitrogen. (a) Type I nitrogen is bonded to Me in the MeN platelet (of NaCl-type crystal structure; a monolayer is shown for the case of a Bain, or Baker-Nutting, orientation relationship with the ferrite matrix; see text). Type II nitrogen is adsorbed at the interface between the ferrite matrix and the MeN platelet in the octahedral interstices in the ferrite matrix in direct contact with the Me atoms in the MeN platelet. (b) Type III nitrogen is the nitrogen dissolved in the ferrite matrix at octahedral interstitial sites. Source: Ref 75

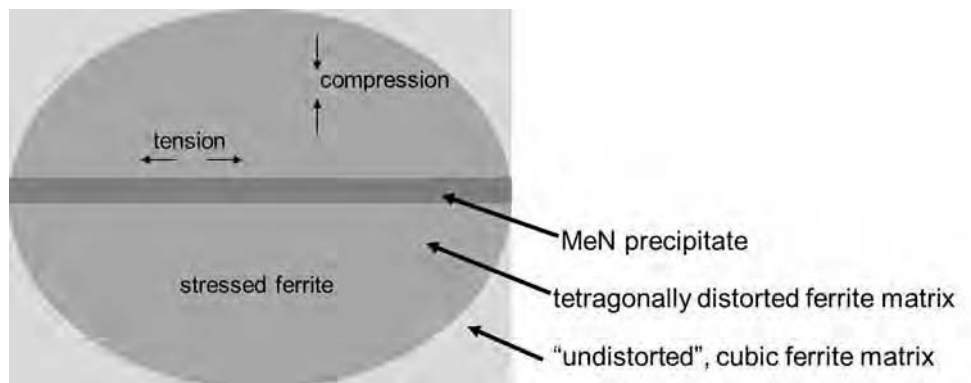


Fig. 22 Schematic view of a MeN platelet (of NaCl-type crystal structure for the case of a Bain, or Baker-Nutting, orientation relationship with the ferrite matrix; see text) with its surrounding misfit-stress field in the ferrite matrix. An expansion parallel to the platelet/matrix interface and a compression perpendicular to this interface are induced by elastic accommodation of the precipitate/matrix misfit. Thus, the ferrite matrix surrounding the platelet is tetragonally distorted. Source: Ref 75

replaced by nitride particles. This can occur by transformation of the existing carbide particles upon their reaction with nitrogen in the diffusion zone (Ref 97). This process takes place relatively slowly and therefore occurs not only at but also in the wake of the nitriding front moving into the specimen/component. The released carbon atoms can diffuse outward in the direction of the compound layer, precipitate as carbide (cementite) along grain boundaries in the diffusion zone, and diffuse inward to the unnitrided core, where a pronounced carbide development can occur. All three effects have been observed (Ref 97, 98). The micrograph in Fig. 23(a) exhibits such precipitated carbides along grain boundaries that run more or less parallel to the surface. This preferred orientation of these carbides is caused by the presence of a compressive residual stress parallel to the surface acting in the diffusion zone (see Section 11.18 in Ref 14). The nitrogen and carbon concentration-depth profiles shown in Fig. 23(b) highlight the presence of carbides (at grain boundaries) in the diffusion zone (indicated by arrows and dashed lines in the figure) and the development of a zone of carbon enrichment underneath the (nitrogen) diffusion zone.

12. Kinetics of Diffusion-Zone Growth

If no compound layer forms at the surface of the specimen/component, the nitrogen concentration-depth profile as it develops in pure ferrite (α -Fe)

and in carbon steels not containing alloying elements with affinity for nitrogen is the outcome of the following competing processes:

- The dissociation process (Eq 2)
- The recombination and desorption process at the gas-solid interface (Eq 17)
- The diffusion process in the solid substrate (see Section 8.1 and the first paragraphs of Section 10).

The nitrogen concentration-depth profiles generally cannot be calculated straightforwardly on the basis of (analytical or numerical) solutions of only Fick's second law. Numerical calculations incorporating the processes mentioned are required (Fig. 6).

In the following, it is assumed that a stationary state or local equilibrium has been closely attained at the surface (if nitriding/nitrocarburizing occurs under conditions that do not allow the formation of a compound layer) or that local equilibrium has been realized at the interface of the compound layer and the diffusion zone in the substrate. Further, it is taken for granted that any diffusion and uptake of carbon in the diffusion zone can be neglected, recognizing the very small solubility of carbon in ferrite (Table 1).

If the conditions indicated in the preceding paragraph hold, the development of the diffusion zone in pure iron and carbon steels then is rate controlled by the inward diffusion of nitrogen in ferrite alone. This becomes different for the diffusion-zone development in iron-base alloys containing alloying elements with affinity for nitrogen. In that case, the kinetics of

the precipitation process of the MeN_n nitrides can have a strong impact on the nitriding kinetics and thus on the development of the nitrogen concentration-depth profiles. These precipitation kinetics can be controlled by the nucleation (activation energy of nucleation), the growth (activation energy of growth; the growth may be interface or diffusion controlled or of mixed mode), and the impingement mechanisms (see Chapter 9 in Ref 14). Thus, the inward diffusion of nitrogen into the ferrite matrix is only one of a number of processes that together control the kinetics of nitriding. Current knowledge does not provide an encompassing model taking into account the full complexity of the nitriding process in alloyed ferritic matrices.

Only for the case of strong Me-N interaction (for the definition of strong and weak Me-N interaction, see Section 11.2) can a simple relationship between the thickness of the nitrided region and the nitriding time at constant temperature be given. To this end, and in the absence of a developing compound layer, the following assumptions are made:

- The nitrogen dissolved in the ferrite matrix exhibits Henrian behavior (Ref 20). This implies that the diffusion coefficient of nitrogen in the ferrite matrix, D_N , is independent of the dissolved nitrogen content.
- The reaction of dissolved nitrogen with dissolved Me, leading to the nitride MeN_n (or the mixed nitride $(\text{Me}_1)_x(\text{Me}_2)_{1-x}\text{N}_n$), takes place only and completely at a sharp interface between the nitrided zone and the nonnitrided core.

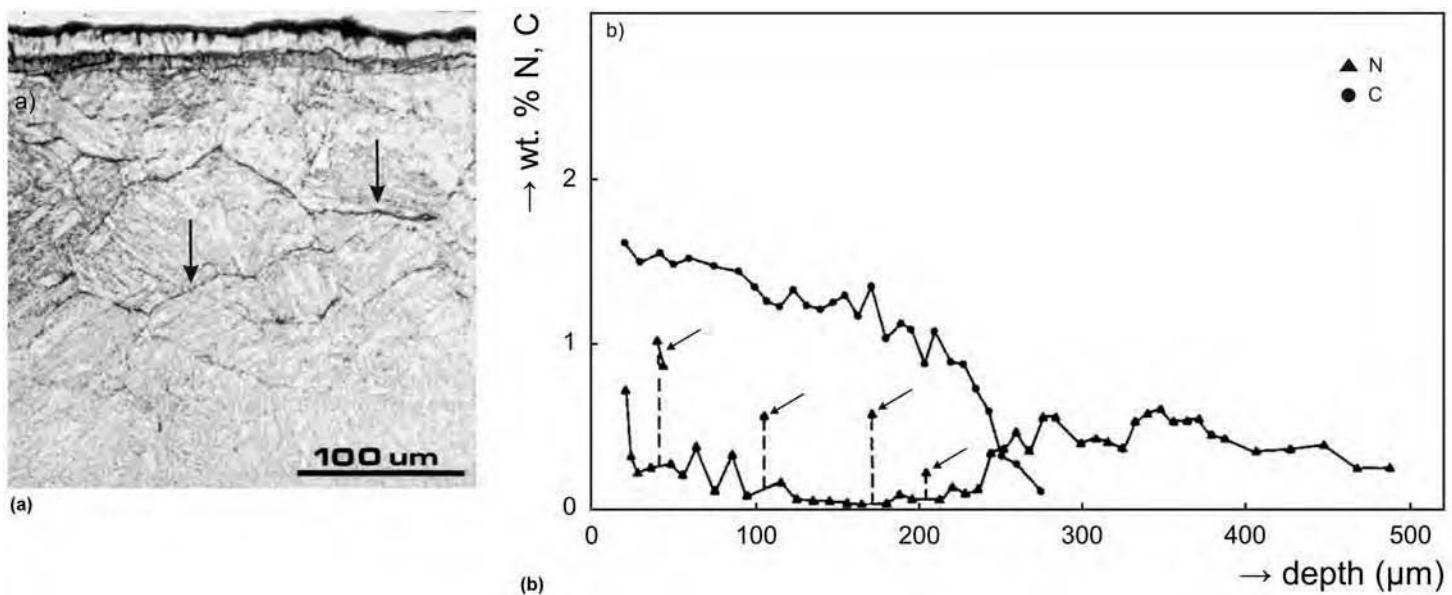


Fig. 23 (a) Cementite precipitates that developed along former austenite-grain boundaries more or less parallel to the surface upon nitriding a quenched and tempered steel (see arrows in the micrograph; light optical micrograph of cross section of quenched and tempered 24CrMo13, or En14B, steel, salt bath nitrided at 580 °C, or 853 K, for 2 h; cross section after Murakami etching that stains carbides black). (b) Nitrogen and carbon concentration-depth profiles in the diffusion zone of a quenched and tempered 24CrMo 13 (En14B) steel (salt bath nitrided at 580 °C, or 853 K, for 4 h) as determined by electron probe microanalysis. The presence of carbide (cementite) at grain boundaries is revealed by the abrupt rise of the carbon content (see the arrows and dashed lines in the figure); also, the occurrence of a carbon-rich zone underneath the nitrogen diffusion zone is exposed. Source: Ref 98; see also Fig. 16 in Ref 98

- The amount of nitrogen that is required for building up the concentration profile in the ferrite matrix of the nitrided zone is negligible in comparison to the amount of nitrogen that is consumed at the reaction interface.
- Diffusion of Me can be neglected and is not nitriding-rate determining.
- Local equilibrium prevails at the nitriding medium/specimen interface, so that the surface concentration of dissolved nitrogen is equal to the lattice solubility of nitrogen, c_N^s , as given by the chemical potential of nitrogen in the nitriding atmosphere.

With these assumptions and approximating the concentration gradient of dissolved nitrogen with $-c_N^s/z$, where z is the depth coordinate of the reaction front, the amount of nitrogen (per unit area cross section perpendicular to the diffusion direction/specimen-surface normal) that reaches the reaction front in the time period dt is equal to $(-c_N^s \cdot D_N/z) \cdot dt$. This nitrogen amount must equal the nitrogen amount required to move the reaction front a distance dz , that is, $n \cdot c_{Me} \cdot dz$, where c_{Me} is the Me concentration. Upon integration of the resulting differential equation for constant temperature, the following parabolic relationship for z and t is obtained:

$$z^2 = t \cdot \left[\frac{2c_N^s \cdot D_N}{n \cdot c_{Me}} \right] \quad (\text{Eq 22})$$

An equation of this type is well known and has been applied before in the case of internal oxidation (Ref 99).

If a compound layer develops simultaneously, the treatment dealt with here may be applicable as well on the basis of the following consideration. The compound layer is thin compared to the substrate, and the compound layer grows much slower than the depth range covered by the nitrogen concentration-depth profile in the substrate. Then, the consumption of part of the substrate by the growth of the compound layer may be neglected. Then, also, in the presence of a growing compound layer, Eq 22 can be applied if strong Me-N interaction occurs, with $z = 0$ as the position of the interface of compound layer and diffusion zone.

The validity of Eq 22 can be verified with two examples. According to Eq 5(b), the activity of nitrogen in the solid at the surface is proportional with the nitriding potential, assuming that local equilibrium at the surface prevails. In the ferrite substrate, Henry's law holds for the dissolved nitrogen (Ref 20). Hence, c_N^s is proportional with r_N . Then, according to the crude model represented by Eq 22, the depth of the nitrided front, z , must be approximately proportional with $(r_N)^{1/2}$, as observed experimentally (Fig. 24) (Ref 100). Also according to Eq 22, the squared depth of the nitrided front is proportional with t/c_{Me} . The concentration-depth profiles shown in Fig. 25 pertain to an Fe-7wt%Cr alloy specimen and an Fe-20wt%

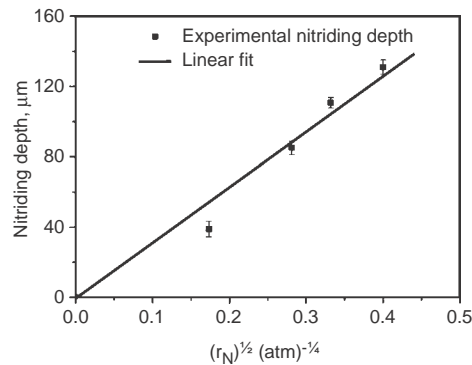


Fig. 24 Nitriding depth (extent of the diffusion zone), z , as a function of the square root of the nitriding potential, $r_N^{1/2}$, for Fe-7wt%Cr alloy specimens nitrided at 580 °C (853 K) for 4 h. Source: Ref 100

Cr alloy specimen nitrided under the same conditions for 7 and 15 h, respectively. According to the proportionality t/c_{Me} , the squared nitriding depths for these specimens should have the ratio $1/3$, which not very well agrees with the experimental result. The discrepancy is ascribed to the difference in the concentration of dissolved nitrogen at the surface, exhibiting the effect of excess dissolved nitrogen depending on the amount of alloying element nitride precipitate (see the caption of Fig. 25).

Still confining ourselves to the idealized case of strong Me-N interaction, two distinct modifications with respect to the aforementioned highly simplified model are necessary. First, it appears unrealistic to assume that all Me is precipitated instantaneously upon the arrival of nitrogen; the dissolved nitrogen concentration does not drop from its saturation level at one specific depth abruptly to zero. Instead, a depth range at the nitriding front can be discerned over which a more or less gradual change of dissolved nitrogen to practically nil occurs. Then, recognizing that a certain solubility product for Me and N in equilibrium with MeN_n holds (Ref 102), it becomes clear that not all Me is precipitated at once upon arrival of the nitriding front. Only when, after some time, the dissolved nitrogen has reached its saturation level, the maximum amount of Me has precipitated; in the meantime, the nitriding front has progressed further into the specimen/component. Second, the various kinds of nitrogen in the specimen have different effects on the nitriding kinetics (Ref 101). One must discern types I, II, and III of nitrogen as discussed in Section 11.3 (see also Fig. 21). The nitrogen taken up in the nitride platelets (obviously) and also the excess nitrogen adsorbed at the faces of the nitride platelets do not contribute to the nitrogen diffusion process; nitrogen of types I and II is *immobile nitrogen*. The nitrogen dissolved in the ferritic matrix can diffuse; nitrogen of type III is *mobile nitrogen*. (Note that the amount of dissolved nitrogen can be a multiple of the equilibrium amount of dissolved

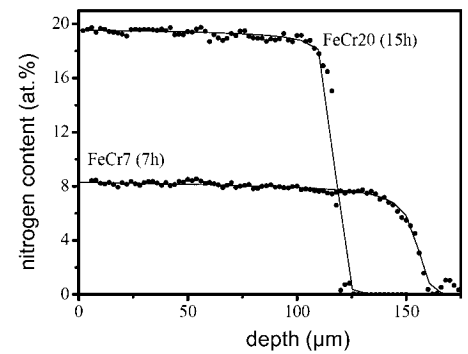


Fig. 25 Nitrogen concentration-depth profiles of nitrided Fe-7wt%Cr alloy and Fe-20wt%Cr alloy specimens nitrided for 7 and 15 h, respectively, at 580 °C (853 K) with $r_N = 0.1 \text{ atm}^{-1/2}$. The experimental data (points in the figure) were obtained by electron probe microanalysis. The full lines through the data are the results of fits of the model described in Section 12 to the experimental data, with the following results for the fitting parameters: $c_N^s = 0.35 \text{ at.}\%$, $b = 1.18$, and $K_{\text{CrN}} = 0.02 \text{ nm}^{-6}$ for the Fe-7wt%Cr specimen; and $c_N^s = 0.26 \text{ at.}\%$, $b = 1.176$, and $K_{\text{CrN}} = 0.02 \text{ nm}^{-6}$ for the Fe-20wt%Cr specimen. Source: Ref 101

nitrogen in pure ferrite; dissolved excess nitrogen occurs due to the misfit strain fields surrounding the nitride platelets.) These considerations led to the following nitriding model, which can only be evaluated numerically (Ref 101).

The inward diffusion of nitrogen in the ferritic matrix can be described with Fick's second law:

$$\frac{d c_N(z, t)}{dt} = D_N \cdot \frac{d^2 c_N(z, t)}{dz^2} \quad (\text{Eq 23})$$

where $c_N(z, t)$ is the nitrogen dissolved in the ferritic matrix at depth z , at time t , and at temperature T . The formation of nitrides MeN_n removes dissolved mobile nitrogen from the ferritic matrix. This nitrogen then becomes trapped as immobile nitrogen. The formation of MeN_n can be described as:



where Me and N denote alloying element and nitrogen dissolved in the α -Fe matrix. The equilibrium constant of this reaction, K , equals $1/K_{\text{MeN}_n}$, with the solubility product K_{MeN_n} given by:

$$K_{\text{MeN}_n} = [\text{Me}] \cdot [\text{N}]^n \quad (\text{Eq 25})$$

where $[\text{Me}]$ and $[\text{N}]$ denote the concentrations of dissolved Me and dissolved N in the α -Fe matrix. The precipitation of MeN_n will take place at a certain location if there it holds:

$$[\text{Me}] \cdot [\text{N}]^n > K_{\text{MeN}_n} \quad (\text{Eq 26})$$

In solving Fick's second law (Eq 23), it must be tested at every location (depth z) for every

time (step) if the solubility product, K_{MeN_n} , is surpassed. If this is the case, (instantaneous strong interaction) precipitation of MeN_n , at the location considered, should be allowed for until $[Me] \cdot [N]^n = K_{MeN_n}$. On this basis, a numerical finite-difference (explicit method) solution method can be developed to solve Fick's second law, subject to the prevailing boundary conditions (Ref 101). The presence of immobile excess nitrogen (nitrogen of type II) can be accounted for by changing the stoichiometry of the nitride particles: MeN_n becomes MeN_b , with $b = n + x$, where x denotes the contribution of the immobile excess nitrogen. Note that x depends on the platelet thickness (for a monolayer of MeN ($n = 1$), $x = 2$; see Section 11.3). The presence of mobile excess nitrogen, that is, the amount of dissolved nitrogen in excess of the equilibrium amount for pure α -Fe, is accounted for by adopting a model presented in Ref 53 (Ref 103).

The effects of mobile and immobile nitrogen can be assessed considering the results of simulations shown in Fig. 26(a). If only the existence of mobile excess nitrogen is assumed, as expressed by higher values for c_N^s , a significantly larger extent (depth) of the nitrided zone occurs as compared to the absence of mobile excess nitrogen (see dashed line versus full line in Fig. 26a). If only the existence of immobile excess nitrogen is assumed, as expressed by a value of b larger than n ($= 1$ for the present case of CrN precipitation), a smaller penetration depth of nitrogen occurs (see dotted line versus full line in Fig. 26a). The used values for c_N^s and b are realistic values, as follows from the experimental results presented in Ref 58, 92–96, 101, and 103. In view of the pronounced influences of the immobile and mobile excess nitrogen on the nitriding kinetics, it is imperative

to incorporate the presence of excess nitrogen in any model for the nitriding kinetics.

The role of the solubility product K_{MeN_n} is illustrated in Fig. 26(b). The transition of the nitrided zone to the unnitrided zone (i.e., the reaction front) becomes less sharp as the solubility product increases. Relatively large K_{MeN_n} values imply that (at the nitriding front) not all dissolved N reacts instantaneously with Me to MeN_n , and thus, the extent of the nitrided zone is larger for larger K_{MeN_n} , although in association with a more gradual transition from the nitrided zone to the nonnitrided core of the specimen/component. Note that the amounts of immobile and mobile excess nitrogen can depend on nitriding time at constant temperature, because they depend on the extent of MeN_n precipitation and on the stage of aging (and size) of the MeN_n precipitate particles; the solubility product, K_{MeN_n} , should not depend on nitriding time at constant temperature.

Results of fitting the previously described model to experimentally determined nitrogen concentration-depth profiles are shown in Fig. 25 for two iron-chromium alloys of different chromium content, nitrided under the same conditions for different times, and in Fig. 27 for an iron-vanadium alloy nitrided at different temperatures. The model, in a correspondingly modified form, can also be applied to the nitriding of ternary Fe-Me₁-Me₂ alloy specimens (Ref 104). In all these cases, the model provides a satisfactory fit to the experimental data. For interpretation of the values obtained for the fit parameters, as, for example, the value of b and, for example, as a function of the temperature, see Ref 53, 101, and 103.

Considering the case of weak Me-N interaction, considerable complication is added to a possible model description of the nitriding

kinetics compared to the models presented above for the case of strong Me-N interaction. In this case, precipitation of MeN_n does not occur instantaneously once the solubility product is surpassed locally. Nucleation and growth as thermally activated, time-dependent processes in a state of changing (with time and place) supersaturation and (soft) impingement as mechanisms controlling the MeN_n precipitation process must be considered (Ref 14, 81, 83, 84, 105). This is already a difficult materials science problem for supersaturated homogeneous specimens. The nitriding process mandates that a comprehensive model for the nitriding kinetics must account for the simultaneously inward diffusion of nitrogen, leading, at constant temperature, to time and location dependencies of the supersaturation, and thus, strongly locally different time-dependent kinetics of the precipitation process occur. A feasible approach may be to adopt a relatively simple model for the precipitation kinetics (Johnson-Mehl-Avrami-Kolmogorov models are popular but of limited ability to describe reality, Ref 14) and to combine such a model with a numerical solution for the inward diffusion process of nitrogen. This is an area of research where no results of practical importance have already been obtained.

Epilogue

The nitriding process and its variants offer great challenges to the materials scientist and the materials engineer. As an illustration, and instead of offering a list of conclusions, the author here refers to a few major themes of fundamental importance for scientific understanding of nature that have been highlighted in this review:

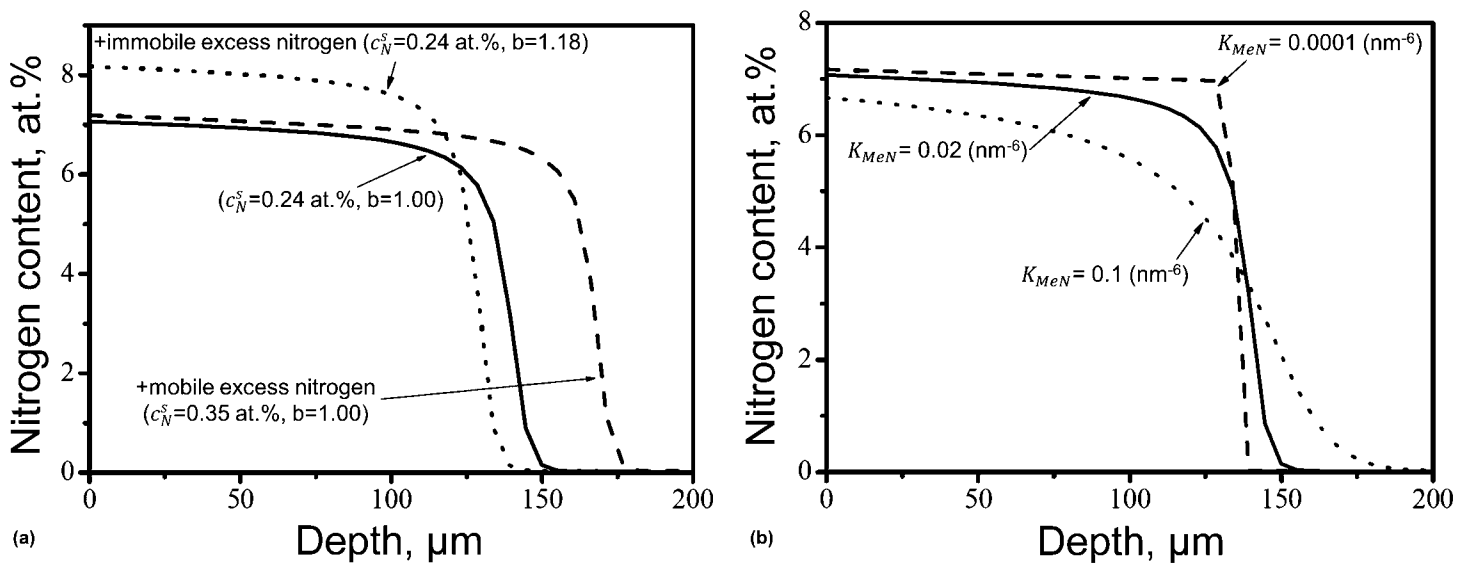


Fig. 26 (a) Effect of mobile and immobile excess nitrogen on the development of the nitrogen concentration-depth profile. (b) Effect of the solubility product, K_{CrN} , on the development of the nitrogen concentration-depth profile. The examples shown in (a) and (b) pertain to a Fe-7wt%Cr alloy sheet nitrided at 580 °C (853 K) for 7 h with $r_N = 0.1 \text{ atm}^{-1/2}$. Source: Ref 101

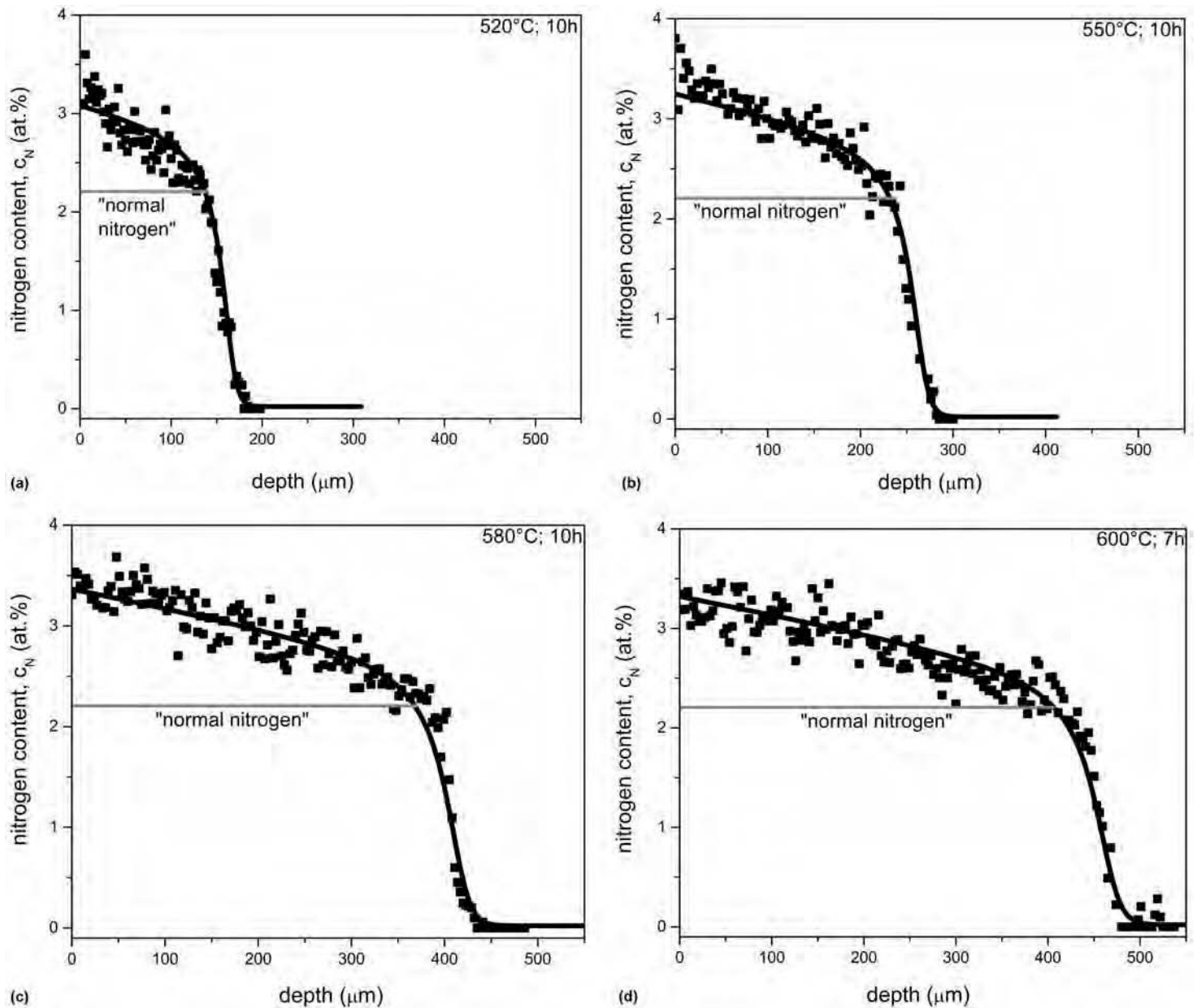


Fig. 27 Nitrogen concentration-depth profiles of nitrided Fe-2wt%V alloy specimens nitrided at $r_N = 0.103 \text{ atm}^{-1/2}$. The experimental data (points in the figure) were obtained by electron probe microanalysis. The full lines through the data are the results of fits of the model described in Section 12 to the experimental data. (a) Nitrided at 520 °C (793 K) for 10 h. (b) Nitrided at 550 °C (823 K) for 10 h. (c) Nitrided at 580 °C (853 K) for 10 h. (d) Nitrided at 600 °C (873 K) for 7 h. The horizontal lines indicated with “normal nitrogen” in the figures indicate the nitrogen content taken up if only nitrogen incorporated in the MeN (here VN) precipitates (with all vanadium precipitated) and nitrogen dissolved in the ferrite matrix according to the equilibrium state (unstressed) would occur; the real amounts of nitrogen taken up are distinctly larger, indicating the presence of considerable amounts of excess nitrogen. Source: Ref 103

- The interpretation of equilibrium has been put into perspective in the sense that for the iron-nitrogen system the definition of equilibrium has been based on the NH_3 and H_2 contents of the surrounding gas atmosphere and the sole occurrence of explicitly defined, balanced forward and backward reactions. More than 80 years after Lehrer, we have come to recognize the effect of the occurrence of so-called stationary states as a consequence of the participation of

further reactions in the exchange of nitriding medium and object. These stationary states could be considered as (dynamic) equilibria as well. However, the choice of a “reference” equilibrium (here, establishment of equilibrium, Eq 2; see Section 4), which can alternatively be described by establishment of equilibrium (Eq 15) together with (infinitely fast) establishment of Eq 16 (Section 8.1), in fact necessitates the introduction of the notion of stationary state, and thereby,

the experimentally determined Lehrer diagram does not partially represent genuine “reference” equilibria.

- Multicomponent diffusion in solids is a relatively rarely investigated phenomenon. It plays a great role in the nitrocarburizing of iron-base specimens/components. It strikes to find out that the first, rigorous study devoted to the simultaneous inward diffusion of nitrogen and carbon in a Fe-C-N phase was published only in 2013 (see

Section 10). The very pronounced strength of the nitrogen-carbon interaction in an Fe-N-C phase is expressed by the so-called thermodynamic factors. Knowing these will ultimately lead to an experiment-based description of the thermodynamics of ternary Fe-C-N phases, and thereby, much controversy in the literature about the ternary Fe-C-N phase diagram will eventually be removed.

- The role of the alloying element nitride/matrix misfit stress in seriously influencing the capacity for nitrogen uptake, that is, the emergence of excess nitrogen, has in recent years been shown to be a general phenomenon (Section 11.3). It has not been widely recognized that both the immobile and the mobile excess nitrogen greatly influence the nitriding kinetics (Section 12). Any future successful modeling of nitriding kinetics for practical applications will have to incorporate the occurrence of immobile and mobile excess nitrogen.
- The chemistry of steels developed for nitriding purposes has been largely determined in an empirical way. Research of fundamental nature is beginning to unravel the effect and interplay of (substitutionally dissolved) alloying elements on especially the kinetics of nitriding. As an example of such a result of potentially pronounced practical consequence, it has been suggested recently that combining an alloying element of so-called strong Me-N interaction (in particular, these alloying elements have been considered until now as useful for nitriding purposes) with an alloying element of weak Me-N interaction can lead to controllable, large microstructural and morphological modification of the compound layer (Section 9.3).

It is true, but only seemingly so, that some of the results and insights discussed in this article may be of no practical consequence. This would be a misleading conclusion. The materials engineer needs fundamental knowledge that allows the development of models and equipment to control and tune the nitriding/nitrocarburizing process. Reconsidering the state-of-the-art as described in a review paper published in 1997 (Ref 24), it must be concluded that our scientific understanding has made distinct progress during the ensuing fifteen or more years and as reviewed in this article. However, we are still far from tuned application of the nitriding/nitrocarburizing process, notwithstanding the many developments in practice of the last years, including new process variants that have improved controllability/reproducibility. However, to predict (i.e., to understand) the outcome of the nitriding/nitrocarburizing process in practice is not possible, other than on the basis of empiricism/experience. Unfortunately, this situation is not much different from that in 1997. As a salient example, it is mentioned that the development of a nitriding sensor, as compared to the description in Ref 24, has not

made much progress; control and knowledge of the chemical potential of nitrogen at the surface of the component during nitriding in technological practice is still no easy task. Moreover, for the case of nitrocarburizing, a method allowing simultaneous control and knowledge of both the chemical potential of nitrogen and the chemical potential of carbon, an absolute requirement for controlled and tuned nitrocarburizing, has been published only very recently and, for the time being, has been applied only in the laboratory (Section 7).

There is no doubt that, even after more than 100 years of nitriding/nitrocarburizing, future developments in materials science and engineering will be instrumental in bringing about distinctly deeper understanding of the thermodynamics and kinetics of nitriding and nitrocarburizing, in association with the emergence of accompanying engineering concepts.

ACKNOWLEDGMENTS

This article could not have been written were it not for the long-term cooperation with Prof. Marcel Somers (Technical University of Denmark, Lyngby) and Dr. Jan Slycke (formerly SKF Engineering and Research Centre, Nieuwegein, The Netherlands; now retired) and the intensive cooperation with the author's co-workers, Dr. Andreas Leineweber, Dr. Sai Ramudu (Sairam) Meka, and Dr. Ralf Schacherl. Dr. Sairam Meka and Dipl.-Ing Bastian Rheingans read and discussed with the author a (part of the) first draft of this article and suggested valuable modifications. Dr. Ralf Schacherl assisted in the preparation of all figures; Fig. 4 (c), 6, and 7 are essentially based on calculations performed by Dr. Minsu Jung. The author's former Ph.D. students contributed essentially to the understanding attained that led to this article, including Herman Rozendaal, Marcel Somers, and Mohammad Biglari, who were involved in the nitriding project in Delft; and Ralf Schacherl, Tatiana Liapina, Santosh Hosmani, Nicolas Vives Diaz, Thomas Gressmann, Marc Nikollussi, Arno Clauss, Sai Ramudu Meka, Kyung Sub Jung, Thomas Woehrl, Holger Selg, Benjamin Schwarz, Matei Fonovic, Holger Goering, Maryam Akhlaghi, and Tobias Steiner, who are former and current Ph.D. students involved in the nitriding project in Stuttgart.

REFERENCES

1. A. Machlet, Treatment of Steel, Iron, etc., U.S. Patent 1,065,379, 1913
2. A. Fry, Stickstoff in Eisen, Stahl und Sonderstahl, Ein neues Oberflaechenhaertungsverfahren, *Stahl Eisen*, Vol 43, 1923, p 1271-1279 (in German)
3. E.J. Mittemeijer, A.B.P. Vogels, and P.J. van der Schaaf, Morphology and Lattice Distortions of Nitrided Iron, Iron-Chromium Alloys and Steels, *J. Mater. Sci.*, Vol 15, 1980, p 3129-3140

4. T.B. Massalski, Ed. in Chief, *Binary Alloy Phase Diagrams*, 2nd ed., ASM International, 1996
5. H.A. Wriedt and L. Zwell, Lattice Dilatation of Alpha-Iron by Nitrogen, *Trans. AIME*, Vol 224, 1962, p 1242-1246
6. P. Ferguson and K.H. Jack, Quench-Aging and Strain-Aging of Nitrogen-Ferrite, in *Proc. Heat Treatment '81*, The Metals Society, London, p 158-163
7. L. Cheng, A. Böttger, T.H. de Keijser, and E.J. Mittemeijer, Lattice Parameters of Iron-Nitrogen Martensites and Austenities, *Scr. Metall. Mater.*, Vol 24, 1990, p 509-514
8. M. Onink, C.M. Brakman, F.D. Tichelaar, E.J. Mittemeijer, and S. van der Zwaag, The Lattice Parameters of Austenite and Ferrite in Fe-C Alloys as Functions of Carbon Concentration and Temperature, *Scr. Metall. Mater.*, Vol 29, 1993, p 1011-1016 (including thermal expansion data)
9. M.J. van Genderen, A. Böttger, and E.J. Mittemeijer, Formation of α'' Iron Nitride in FeN Martensite: Nitrogen Vacancies, Iron-Atom Displacements and Misfit-Strain Energy, *Metall. Mater. Trans. A*, Vol 28, 1997, p 63-77
10. M.J. van Genderen, A. Böttger, R.J. Cernik, and E.J. Mittemeijer, Early Stages of Decomposition in Iron-Carbon and Iron-Nitrogen Martensites: Diffraction Analysis Using Synchrotron Radiation, *Metall. Trans. A*, Vol 24, 1993, p 1965-1973
11. M.A.J. Somers, N.M. van der Pers, D. Schalkoord, and E.J. Mittemeijer, Dependence of the Lattice Parameter of γ' Iron Nitride, Fe₄N_{1-x}, on Nitrogen Content; Accuracy of Nitrogen Absorption Data, *Metall. Trans. A*, Vol 20, 1989, p 1533-1539 (including thermal expansion data)
12. T. Liapina, A. Leineweber, E.J. Mittemeijer, and W. Kockelmann, The Lattice Parameters of ϵ -Iron Nitrides: Lattice Strains Due to a Varying Degree of Nitrogen Ordering, *Acta Mater.*, Vol 52, 2004, p 173-180
13. P. Villars and L.D. Calvert, in *Pearson's Handbook of Crystallographic Data for Intermetallic Phases*, American Society for Metals, 1985, p 1520, 2162
14. E.J. Mittemeijer, *Fundamentals of Materials Science*, Springer-Verlag, Berlin Heidelberg, 2010
15. K.H. Jack, Nitriding, *Proc. Heat Treatment '73*, The Metals Society, London, p 39-50
16. T. Bell, Ferritic Nitrocarburizing, *Heat Treat. Met.*, Vol 2, 1975, p 39-49
17. S. Malinov, A.J. Böttger, E.J. Mittemeijer, M.I. Pekelharing, and M.A.J. Somers, Phase Transformations and Phase Equilibria in the Fe-N System at Temperatures below 573 K, *Metall. Mater. Trans. A*, Vol 32, 2001, p 59-73
18. B. Prenosil, Einige neue Erkenntnisse ueber das Gefuege von um 600 °C in der

- Gasatmosphäre carbonitrierten Schichten, *Härt.-Tech. Mitt.*, Vol 28, 1973, p 157–164 (in German)
19. M.A.J. Somers and E.J. Mittemeijer, Porenbildung und Kohlenstoffaufnahme beim Nitrocarburieren, *Härt.-Tech. Mitt.*, Vol 42, 1987, p 321–331 (in German)
 20. E.J. Mittemeijer and J. Slycke, Chemical Potentials and Activities of Nitrogen and Carbon Imposed by Gaseous Nitriding and Carburising Atmospheres, *Surf. Eng.*, Vol 12, 1996, p 152–162; see also (for a German version) E.J. Mittemeijer and J.T. Slycke, Die thermodynamischen Aktivitäten von Stickstoff und Kohlenstoff verursacht von Nitrier- und Carburiergasatmosphären, *Härt.-Tech. Mitt.*, Vol 50, 1995, p 114–125
 21. W. Schroeter, Zu einigen Beziehungen zwischen den Systemen Fe-C und Fe-N,-Diskussion ueber ein stabiles Zustandssystem Fe-N, *Wiss. Z. Tech. Hochsch. Karl-Marx-Stadt*, Vol 24, 1982, p 795–809 (in German)
 22. E. Lehrer, Ueber das Eisen-Wasserstoff-Ammoniak-Gleichgewicht, *Z. Elektrochem.*, Vol 36, 1930, p 383–392 (in German)
 23. J. Stein, R.E. Schacherl, M. Jung, S.R. Meka, B. Rheingans, and E.J. Mittemeijer, Solubility of Nitrogen in Ferrite; The Fe-N Phase Diagram, *Int. J. Mat. Res.*, DOI 10.3139/146.110968
 24. E.J. Mittemeijer and M.A.J. Somers, Thermodynamics, Kinetics and Process Control of Nitriding, *Surf. Eng.*, Vol 13, 1997, p 483–497
 25. E.J. Mittemeijer, P.F. Colijn, M. van Rooijen, P.J. van der Schaaf, and I. Wierszyllowski, in *Proc. Heat Treatment '81, Discussion: Surface Heat Treatments—Austenitic*, The Metals Society, London, p 220–221
 26. T. Gressmann, M. Nikolussi, A. Leineweber, and E.J. Mittemeijer, Formation of Massive Cementite Layers on Iron by Ferritic Carburising in the Additional Presence of Ammonia, *Scr. Mater.*, Vol 55, 2006, p 723–726
 27. A. Leineweber and E.J. Mittemeijer, Cementite-Layer Formation by Ferritic Nitrocarburising, *HTM J. Heat Treat. Mater.*, Vol 63, 2008, p 305–314
 28. H.J. Grabke, Kinetik und Mechanismen der Oberflächenreaktionen bei der Auf- und Entkohlung und Auf- und Entstickung von Eisen in Gasen, *Arch. Eisenhuettenwes.*, Vol 46, 1975, p 75–81 (in German)
 29. A. Leineweber, T. Gressmann, and E.J. Mittemeijer, Simultaneous Control of the Nitrogen and Carbon Activities during Nitrocarburising of Iron, *Surf. Coat. Technol.*, Vol 206, 2012, p 2780–2791
 30. A.T.W. Kempen and J.C. Wortel, The Influence of Metal Dusting on Gas Reactions, *Mater. Corros.*, Vol 55, 2004, p 249–258
 31. H. Du, M.A.J. Somers, and J. Ågren, Microstructural and Compositional Evolution of Compound Layers during Gaseous Nitrocarburizing, *Metall. Mater. Trans. A*, Vol 31, 2000, p 195–211
 32. S. Hoja, H. Kluemper-Westkamp, F. Hoffmann, and H.-W. Zoch, Mit Nitrier- und Kohlenskennzahl geregeltes Nitrocarburieren, *HTM J. Heat Treat. Mater.*, Vol 65, 2010, p 22–29 (in German)
 33. M. Fonovic, A. Leineweber, and E.J. Mittemeijer, Nitrogen Uptake by Nickel in NH₃-H₂ Atmospheres, *Surf. Eng.*, in press. DOI 10.1179/1743294413Y.0000000173
 34. H.J. Grabke, Reaktionen von Ammoniak, Stickstoff und Wasserstoff an der Oberfläche von Eisen; I. Zur Kinetik der Nitrierung von Eisen mit NH₃-H₂-Gemischen und der Denitrierung, *Ber. Bunsenges. Phys. Chem.*, Vol 72, 1968, p 533–541 (in German)
 35. H.J. Grabke, Reaktionen von Ammoniak, Stickstoff und Wasserstoff an der Oberfläche von Eisen; II. Zur Kinetik der Nitrierung von Eisen mit N₂ und der Desorption von N₂, *Ber. Bunsenges. Phys. Chem.*, Vol 72, 1968, p 541–548 (in German)
 36. H.J. Grabke, Conclusions on the Mechanism of Ammonia-Synthesis from the Kinetics of Nitrogenation and Denitrogenation of Iron, *Z. Phys. Chem. Neue Folge*, Vol 100, 1976, p 185–200
 37. H.C.F. Rozendaal, E.J. Mittemeijer, P.F. Colijn, and P.J. van der Schaaf, The Development of Nitrogen Concentration Profiles on Nitriding Iron, *Metall. Trans. A*, Vol 14, 1983, p 395–399
 38. P.B. Friehling, F.B. Poulsen, and M.A.J. Somers, Nucleation of Iron Nitrides during Gaseous Nitriding of Iron; Effect of a Preoxidation Treatment, *Z. Metallkd.*, Vol 92, 2001, p 589–595
 39. M.A.J. Somers and E.J. Mittemeijer, Verbindungsschichtbildung während des Gasnitrierens und des Gas- und Salzbadnitrocarburierens, *Härt.-Tech. Mitt.*, Vol 47, 1992, p 5–12 (in German)
 40. R. Hoffmann, E.J. Mittemeijer, and M.A. J. Somers, Verbindungsschichtbildung beim Nitrieren und Nitrocarburieren, *Härt.-Tech. Mitt.*, Vol 51, 1996, p 162–169 (in German)
 41. S.S. Hosmani, R.E. Schacherl, and E.J. Mittemeijer, Compound Layer Formation on Iron-Based Alloys upon Nitriding; Phase Constitution and Pore Formation, *HTM Z. Werkst. Wärmebeh. Fertigung*, Vol 63, 2008, p 139–146
 42. M.A.J. Somers and E.J. Mittemeijer, Formation and Growth of Compound Layer on Nitrocarburizing Iron: Kinetics and Microstructural Evolution, *Surf. Eng.*, Vol 3, 1987, p 123–137
 43. M.A.J. Somers, P.F. Colijn, W.G. Sloof, and E.J. Mittemeijer, Microstructural and Compositional Evolution of Iron-Carbonitride Compound Layers during Salt-Bath Nitrocarburizing, *Z. Metallkd.*, Vol 81, 1990, p 33–43
 44. T. Woehrl, A. Leineweber, and E.J. Mittemeijer, Influence of the Chemical Potential of Carbon on the Microstructural and Compositional Evolution of the Compound Layer Developing upon Nitrocarburizing of α -Iron, *HTM J. Heat Treat. Mater.*, Vol 65, 2010, p 243–248
 45. T. Woehrl, A. Leineweber, and E.J. Mittemeijer, Microstructural and Phase Evolution of Compound Layers Growing on α -Iron during Gaseous Nitrocarburizing, *Metall. Mater. Trans. A*, Vol 43, 2012, p 2401–2413
 46. J.S. Kirkaldy and D.J. Young, *Diffusion in the Condensed State*, The Institute of Metals, London, 1978
 47. F.J.J. van Loo, Multiphase Diffusion in Binary and Ternary Solid-State Systems, *Prog. Solid State Chem.*, Vol 20, 1990, p 47–99
 48. M. Nikolussi, A. Leineweber, and E.J. Mittemeijer, Growth of Massive Cementite Layers; Thermodynamic Parameters and Kinetics, *J. Mater. Sci.*, Vol 44, 2009, p 770–777
 49. E.J. Mittemeijer, W.T.M. Straver, P.F. Colijn, P.J. van der Schaaf, and J.A. van der Hoeven, The Conversion Cementite \rightarrow ϵ -Nitride during the Nitriding of Fe-C-Alloys, *Scr. Metall.*, Vol 14, 1980, p 1189–1192
 50. M. Weller, Point Defect Relaxations, *Mater. Sci. Forum*, Vol 366–368, 2001, p 95–140
 51. M. Nikolussi, A. Leineweber, and E.J. Mittemeijer, Nitrogen Diffusion through Cementite Layers, *Philos. Mag.*, Vol 90, 2010, p 1105–1122
 52. M. Nikolussi, A. Leineweber, E. Bischoff, and E.J. Mittemeijer, Examination of Phase Transformations in the System Fe-N-C by Means of Nitrocarburising Reactions and Secondary Annealing Experiments; The $\alpha+\epsilon$ Two-Phase Equilibrium, *Int. J. Mater. Res.*, Vol 98, 2007, p 1086–1092
 53. M.A.J. Somers, R.M. Lankreijer, and E.J. Mittemeijer, Excess Nitrogen in the Ferrite Matrix of Nitrided Binary Iron-Based Alloys, *Philos. Mag. A*, Vol 59, 1989, p 353–378
 54. S.S. Hosmani, R.E. Schacherl, and E.J. Mittemeijer, Microstructure of the “White Layer” Formed on Nitrided Fe-7wt.% Cr Alloys, *Int. J. Mater. Res.*, Vol 97, 2006, p 1545–1549
 55. S.S. Hosmani, R.E. Schacherl, and E.J. Mittemeijer, Morphology and Constitution of the Compound Layer Formed on Nitrided Fe-4wt.% V Alloy, *J. Mater. Sci.*, Vol 44, 2009, p 520–527
 56. S.R. Meka and E.J. Mittemeijer, Abnormal Nitride Morphologies upon Nitriding Iron-Based Substrates, Vol 65, 2013, *JOM*, p 769–775

57. D.B. Williams and E.P. Butler, Grain Boundary Discontinuous Precipitation Reactions, *Int. Met. Rev.*, Vol 26, 1981, p 153–183
58. P.M. Hekker, H.C.F. Rozendaal, and E.J. Mittemeijer, Excess Nitrogen and Discontinuous Precipitation in Nitrided Iron-Chromium Alloys, *J. Mater. Sci.*, Vol 20, 1985, p 718–729
59. R.E. Schacherl, P.C.J. Graat, and E.J. Mittemeijer, Gaseous Nitriding of Iron-Chromium Alloys, *Z. Metallkd.*, Vol 93, 2002, p 468–477
60. S.S. Hosmani, R.E. Schacherl, and E.J. Mittemeijer, Nitriding Behavior of Fe-4wt%V and Fe-2wt%V Alloys, *Acta Mater.*, Vol 53, 2005, p 2069–2079
61. S.R. Meka, E. Bischoff, R.E. Schacherl, and E.J. Mittemeijer, Unusual Nucleation and Growth of γ' Iron Nitride upon Nitriding Fe-4.75 at.%Al Alloy, *Philos. Mag.*, Vol 92, 2012, p 1083–1105
62. H. Selg, E. Bischoff, I. Bernstein, T. Woehrle, S.R. Meka, R.E. Schacherl, T. Waldenmaier, and E.J. Mittemeijer, Defect-Dependent Nitride Surface-Layer Development upon Nitriding of Fe-1at.% Mo Alloy, Vol 93, 2013, *Philos. Mag.*, p 2133–2160
63. M.A.J. Somers and E.J. Mittemeijer, Layer-Growth Kinetics on Gaseous Nitriding of Pure Iron; Evaluation of Diffusion Coefficients for Nitrogen in Iron Nitrides, *Metall. Mater. Trans. A*, Vol 26, 1995, p 57–74
64. H. Du and J. Ågren, Gaseous Nitriding Iron—Evaluation of Diffusion Data of N in Gamma-Phase and Epsilon-Phase, *Z. Metallkd.*, Vol 86, 1995, p 522–529
65. L. Torchane, P. Bilger, J. Dulcy, and M. Gantois, Control of Iron Nitride Layers Growth Kinetics in the Binary Fe-N System, *Metall. Mater. Trans. A*, Vol 27, 1996, p 1823–1835
66. T. Liapina, A. Leineweber, and E.J. Mittemeijer, Phase Transformations in Iron-Nitride Compound Layers upon Low-Temperature Annealing: Diffusion Kinetics of Nitrogen in ϵ - and γ' -Iron Nitrides, *Metall. Mater. Trans. A*, Vol 37, 2006, p 319–330
67. T. Woehrle, A. Leineweber, and E.J. Mittemeijer, Multicomponent Interstitial Diffusion in and Thermodynamic Characteristics of the Interstitial Solid Solution ϵ -Fe₃(N, C)_{1+x}: Nitriding and Nitrocarburizing of Pure α -Iron, Vol 44A, 2013, *Metall. Mater. Trans. A*, p 2548–2562
68. T. Woehrle, A. Leineweber, and E.J. Mittemeijer, The Shape of Nitrogen Concentration-Depth Profiles in γ' -Fe₄N_{1–2}, *Metall. Mater. Trans. A*, Vol 43, 2012, p 610–618
69. M.A.J. Somers and E.J. Mittemeijer, Development and Relaxation of Stress in Surface Layers; Composition and Residual Stress Profiles in γ' -Fe₄N_{1–x} Layers on α -Fe Substrates, *Metall. Trans. A*, Vol 21, 1990, p 189–204
70. E.J. Mittemeijer, A.B.P. Vogels, and P.J. van der Schaaf, Aging at Room Temperature of Nitrided α -Iron, *Scr. Metall.*, Vol 14, 1980, p 411–416
71. E.J. Mittemeijer, Fatigue of Case-Hardened Steels; Role of Residual Macro- and Microstresses, *J. Heat Treat.*, Vol 3, 1983, p 114–119
72. B. Mortimer, P. Grieveson, and K.H. Jack, Precipitation of Nitrides in Ferritic Iron Alloys Containing Chromium, *Scand. J. Metall.*, Vol 1, 1972, p 203–209
73. H.H. Podgurski and H.E. Knechtel, Nitrogenation of Fe-Al Alloys, Part I: Nucleation and Growth of Aluminum Nitride, *Trans. Metall. Soc. AIME*, Vol 245, 1969, p 1595–1602
74. M.H. Biglari, C.M. Brakman, and E.J. Mittemeijer, Crystal Structure and Morphology of AlN Precipitating on Nitriding of an Fe-2 at.% Al Alloy, *Philos. Mag. A*, Vol 72, 1995, p 1281–1299
75. N.E. Vives Diaz, S.S. Hosmani, R.-E. Schacherl, and E.J. Mittemeijer, Nitride Precipitation and Coarsening in Fe-2.23 at.% V Alloys: XRD and (HR)TEM Study of Coherent and Incoherent Diffraction Effects Caused by Misfitting Nitride Precipitates in a Ferrite Matrix, *Acta Mater.*, Vol 56, 2008, p 4137–4149
76. D.H. Jack, The Structure of Nitrided Iron-Titanium Alloys, *Acta Metall.*, Vol 24, 1976, p 137–146
77. D.S. Rickerby, S. Henderson, A. Hendry, and K.H. Jack, Structure and Thermochemistry of Nitrided Iron-Titanium Alloys, *Acta Metall.*, Vol 34, 1986, p 1687–1699
78. J.H. Driver and J.M. Papazian, The Electron and Field Ion Metallography of Zones in Nitrided Fe-Mo Alloys, *Acta Metall.*, Vol 21, 1973, p 1139–1149
79. H. Selg, E. Bischoff, R.E. Schacherl, T. Waldenmaier, and E.J. Mittemeijer, Molybdenum-Nitride Precipitation in Recrystallized and Cold-Rolled Fe-1at% Mo Alloy, *Metall. Mater. Trans. A*, DOI: 10.1007/s11661-013-1762-3
80. E.J. Mittemeijer, M.H. Biglari, A.J. Böttger, N.M. van der Pers, W.G. Sloof, and F.D. Tichelaar, Amorphous Precipitates in a Crystalline Matrix; Precipitation of Amorphous Si₃N₄ in α -Fe, *Scr. Mater.*, Vol 41, 1999, p 625–630
81. S.R. Meka, K.S. Jung, E. Bischoff, and E.J. Mittemeijer, Unusual Precipitation of Amorphous Silicon Nitride upon Nitriding Fe-2at.%Si Alloy, *Philos. Mag.*, Vol 92, 2012, p 1435–1455
82. S.R. Meka, E. Bischoff, B. Rheingans, and E.J. Mittemeijer, Octapod-Shaped, Nanosized, Amorphous Precipitates in a Crystalline Ferrite Matrix, Vol 93, *Philos. Mag. Lett.*, 2013, p 238–245
83. M.H. Biglari, C.M. Brakman, M.A.J. Somers, W.G. Sloof, and E.J. Mittemeijer, On the Internal Nitriding of Deformed and Recrystallized Foils of Fe-2 at.% Al, *Z. Metallkd.*, Vol 84, 1993, p 124–131
84. M.H. Biglari, C.M. Brakman, E.J. Mittemeijer, and S. van der Zwaag, The Kinetics of the Internal Nitriding of Fe-2 at.% Al Alloy, *Metall. Mater. Trans. A*, Vol 26, 1995, p 765–776
85. T.C. Bor, A.T.W. Kempen, F.D. Tichelaar, E.J. Mittemeijer, and E. van der Giessen, Diffraction-Contrast Analysis of Misfit Strains around Inclusions in a Matrix: VN Particles in α -Fe, *Philos. Mag. A*, Vol 82, 2002, p 971–1001
86. A.R. Clauss, E. Bischoff, S.S. Hosmani, R.E. Schacherl, and E.J. Mittemeijer, Crystal Structure and Morphology of Mixed Cr_{1–x}Al_xN Nitride Precipitates: Gaseous Nitriding of a Fe-1.5 wt pct Cr-1.5 wt pct Al Alloy, *Metall. Mater. Trans. A*, Vol 40, 2009, p 1923–1934
87. A.R. Clauss, E. Bischoff, R.E. Schacherl, and E.J. Mittemeijer, Phase Transformation of Mixed Cr_{1–x}Al_xN Nitride Precipitates in Ferrite, *Philos. Mag.*, Vol 89, 2009, p 565–582
88. K.S. Jung, R.E. Schacherl, E. Bischoff, and E.J. Mittemeijer, Nitriding of Ferritic Fe-Cr-Al Alloys, *Surf. Coat. Technol.*, Vol 204, 2010, p 1942–1946
89. K.S. Jung, R.E. Schacherl, E. Bischoff, and E.J. Mittemeijer, Normal and Excess Nitrogen Uptake by Iron-Based Fe-Cr-Al Alloys: The Role of the Cr/Al Atomic Ratio, *Philos. Mag.*, Vol 91, 2011, p 2382–2403
90. S. Meka, S.S. Hosmani, A.R. Clauss, and E.J. Mittemeijer, *Int. J. Mater. Res.*, Vol 99, 2008, p 808–814
91. H.H. Podgurski and F.N. Davis, Thermochemistry and Nature of Nitrogen Absorption in Nitrogenated Fe-Ti Alloys, *Acta Metall.*, Vol 29, 1981, p 1–9
92. M.H. Biglari, C.M. Brakman, E.J. Mittemeijer, and S. van der Zwaag, Analysis of the Nitrogen-Absorption Isotherms of Cold-Rolled Fe-2at%Al Specimens with Different AlN-Precipitate Dimensions, *Philos. Mag. A*, Vol 72, 1995, p 931–947
93. S.S. Hosmani, R.E. Schacherl, and E.J. Mittemeijer, Nitrogen Uptake by an Fe-V Alloy: Quantitative Analysis of Excess Nitrogen, *Acta Mater.*, Vol 54, 2006, p 2783–2792
94. S.S. Hosmani, R.E. Schacherl, L. Litynska-Dobrzynska, and E.J. Mittemeijer, The Nitrogen-Absorption Isotherm for Fe-21.5 at.% Cr Alloy: Dependence of Excess Nitrogen Uptake on Precipitation Morphology, *Philos. Mag.*, Vol 88, 2008, p 2411–2426
95. S.S. Hosmani, R.E. Schacherl, and E.J. Mittemeijer, Nitrogen Absorption by Fe-1.04 at.% Cr Alloy: Uptake of Excess Nitrogen, *J. Mater. Sci.*, Vol 43, 2008, p 2618–2624

96. K.S. Jung, S.R. Meka, R.E. Schacherl, E. Bischoff, and E.J. Mittemeijer, Nitride Formation and Excess Nitrogen Uptake after Nitriding Ferritic Fe-Ti-Cr Alloys, *Metall. Mater. Trans. A*, Vol 43, 2012, p 934–944
97. P.C. van Wiggeren, H.C.F. Rozendaal, and E.J. Mittemeijer, The Nitriding Behaviour of Iron-Chromium-Carbon Alloys, *J. Mater. Sci.*, Vol 20, 1985, p 4561–4582
98. P.F. Colijn, E.J. Mittemeijer, and H.C.F. Rozendaal, Light-Microscopical Analysis of Nitrided or Nitrocarburized Iron and Steels, *Z. Metallkd.*, Vol 74, 1983, p 620–627
99. J.L. Meijering, Internal Oxidation in Alloys, *Advances in Materials Research*, Vol 5, H. Herman, Ed., Wiley Interscience, New York, 1971, p 1–81
100. S.S. Hosmani, R.E. Schacherl, and E.J. Mittemeijer, The Kinetics of the Nitriding of Fe-7Cr Alloys; The Role of the Nitriding Potential, *Mater. Sci. Technol.*, Vol 21, 2005, p 113–124
101. R.E. Schacherl, P.C.J. Graat, and E.J. Mittemeijer, The Nitriding Kinetics of Iron-Chromium Alloys; The Role of Excess Nitrogen; Experiments and Modelling, *Metall. Mater. Trans. A*, Vol 35, 2004, p 3387–3398
102. Y. Sun and T. Bell, A Numerical Model of Plasma Nitriding of Low Alloy Steels, *Mater. Sci. Eng. A*, Vol 224, 1997, p 33–47
103. S.S. Hosmani, R.E. Schacherl, and E.J. Mittemeijer, Kinetics of Nitriding Fe-2 wt% V Alloy: Mobile and Immobile Excess Nitrogen, *Metall. Mater. Trans. A*, Vol 38, 2007, p 7–16
104. K.S. Jung, R.E. Schacherl, E. Bischoff, and E.J. Mittemeijer, The Kinetics of the Nitriding of Ternary Fe-2 at pct Cr-2 at pct Ti Alloy, *Metall. Mater. Trans. A*, Vol 43, 2012, p 763–773
105. J.S. Steenaert, M.H. Biglari, C.M. Brakman, E.J. Mittemeijer, and S. Van der Zwaag, Mechanisms for the Precipitation of AlN on Nitriding of Fe-2 at%Al, *Z. Metallkd.*, Vol 86, 1995, p 700–705

Gas Nitriding and Gas Nitrocarburizing of Steels

K.-M. Winter, Process-Electronic GmbH, a member of United Process Controls
 J. Kalucki, Nitrex Metal Inc.

Introduction

Gas nitriding is a family of thermochemical case-hardening processes whereby, respectively, nitrogen (nitriding), nitrogen and carbon (nitrocarburizing), or nitrogen and sulfur (sulfonitriding) are introduced into the surface of a solid ferrous alloy, typically but not exclusively in the ferritic state of the material, without supporting plasma. See the article “Plasma (Ion) Nitriding and Nitrocarburizing of Steels” in this Volume for details on plasma nitriding.

The nitrided layer created during treatment typically consists of a surface layer of iron nitrides and iron carbonitrides—referred to as a compound layer (also known as a white layer, due to its appearance in an etched micrograph). Underneath the white layer is a diffusion zone,

which also contains carbonitrides of alloying elements (Fig. 1) or a supersaturated metallic matrix of either expanded austenite or expanded martensite (or a mixture of the two), depending on the identity of the starting material. This structure was previously known as S-phase (see the section “Low-Temperature Nitriding and Nitrocarburizing” in this article).

The principal reasons for nitriding and nitrocarburizing are:

- To improve wear resistance:
 - High hardness (compound layer, diffusion zone, expanded austenite)
 - Improved pitting resistance (diffusion zone, expanded austenite)
 - Chemical resistivity (compound layer)
 - Low coefficient of friction (compound layer)

- To improve strength behavior:
 - Improved fatigue life (diffusion zone, expanded austenite)
- To improve resistivity against the following forms of corrosion:
 - Neutral salt solutions (compound layer)
 - Atmospheric corrosion (compound layer)
 - Chloride ions—pitting (compound layer)
 - Liquid metal (compound layer)
 - Pitting (crevice) corrosion (expanded austenite)
- To improve heat resistivity up to nitriding/nitrocarburizing temperature (diffusion zone)

Nitriding typically aims for a load-resisting case created by the diffusion of nitrogen into the alloy lattice and by forming a diffusion zone with nitride precipitates. This area of high hardness results from lattice distortion caused

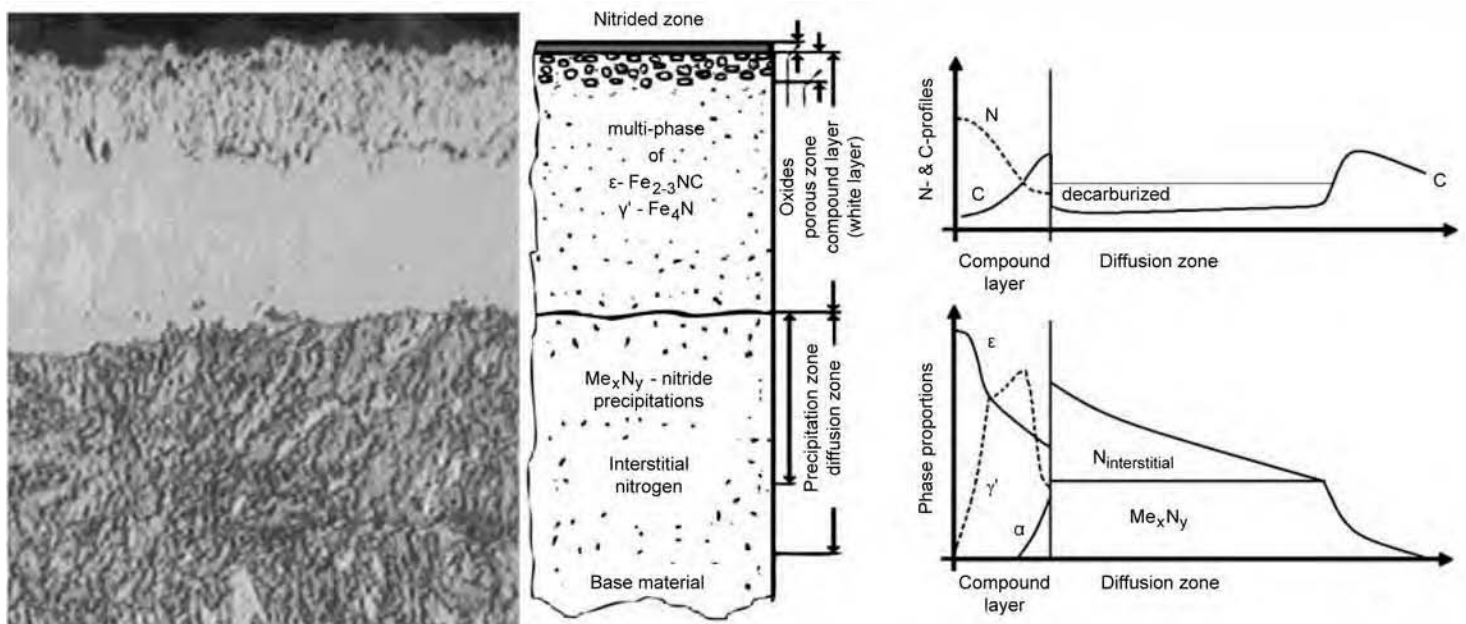


Fig. 1 Micrograph (left) of a nitrocarburized C45 (courtesy of IWT Bremen, Germany) and schematic view (middle) of a nitrided layer according to Ref 1. The graphs to the right display nitrogen and carbon profiles as well as the different phases in the compound layer in nitrided technical steel, containing carbon and nitride-forming elements according to Ref 2.

by alloy nitrides. Nitrocarburizing, on the other hand, is aimed at forming an iron-carbonitride compound layer on the very surface of a treated part in order to obtain higher corrosion and wear resistance.

Adding a dense, closed Fe_3O_4 magnetite layer of approximately 1 to 3 μm on top of the compound layer by a postoxidation treatment subsequent to nitrocarburizing noticeably increases corrosion resistance. Sulfonitriding and oxysulfonitriding create iron sulfides in the very surface of the compound layer, enhancing the dry-running properties.

Nitriding and nitrocarburizing create only little distortion compared to carburizing or conventional hardening. There is some growth, but the volumetric changes are relatively small. The nitriding temperature typically ranges between 495 and 565 °C (925 °F and 1050 °F). Ferritic nitrocarburizing typically is carried out at slightly higher temperatures, between 550 and 585 °C (1020 and 1085 °F), but still below A_{c1} in the iron-nitrogen system for ferritic steels.

Quenching is not required to produce the hard case but may be favorable in some cases. Because there is no phase transformation of the core material, nitriding and nitrocarburizing below A_{c1} in the iron-nitrogen system does not increase core strength; therefore, all hardenable steels must be hardened and tempered prior to nitriding. Nitrocarburizing is also applied to alloy or low-alloy steels in the annealed state. The tempering temperature must be high enough to guarantee structural stability at the nitriding/nitrocarburizing temperature; the

minimum tempering or aging temperature should be at least 30 °C (55 °F) above the maximum nitriding/nitrocarburizing temperature. After hardening and tempering, and before nitriding, the parts must be thoroughly cleaned (see the section "Cleaning" in this article).

In addition, there are special treatments for stainless steel nitriding that involve either low-temperature nitriding (below 450 °C, or 840 °F) to obtain a shallow case of high hardness or high-temperature nitriding (also referred to as solution nitriding) above 1000 °C (1830 °F) that creates comparably deep austenitic diffusion zones. Both processes do not form a compound layer and show no precipitation of chromium nitrides, preserving the corrosion-resistance properties.

Another high-temperature nitriding variant used to enhance the hardness of nitrided diffusion layers on low-carbon, low-alloyed steels is performed at temperatures between 700 and 800 °C (1290 and 1470 °F). High-temperature nitriding requires quenching in order to obtain the final hardness and to avoid chromium precipitation during cooling, which will impair the corrosion performance. There is also the process of austenitic nitrocarburizing at temperatures between 595 and 720 °C (1100 and 1330 °F). Besides the faster growth of the compound layer and case depth due to the faster diffusion at higher temperatures, austenitic nitrocarburizing produces an austenitic layer below the compound layer. By tempering, this layer can be transformed to a fine structure of high hardness.

When the high-temperature variants result in a phase transformation in (or part of) the core material, more distortion is created compared to the variants performed below A_{c1} in the iron-nitrogen system. Of the various processes outlined in this section, Table 1 gives an overview of processes categorized after the desired properties of the parts to be treated and the material these parts are made of.

Terminology for Gas Reactions

Nitriding and nitrocarburizing are thermochemical processes that depend on both temperature and chemical reactions. Such chemical reactions take place in the process atmosphere, where gas molecules will react with each other by breaking down and/or combining to create new molecules, but also between the atmosphere and the metal surface and within the metal structure. Terminology for these reactions is summarized here, as used in this article.

These reactions are driven by the chemical potentials of the reacting species, which can be seen as a potential energy that either will be released or must be spent in order to make these reactions happen. Because every single molecule in a gas mixture and every single atom in a solid has a specific chemical potential, the total chemical potential of a species comes to the number "x" of species "i" times their specific potential; this would be true for ideal conditions (i.e., ideal gases). To adjust

Table 1 Nitriding and nitrocarburizing processes

Process type	Temperature range	Diffusing elements	Process gases/media	Pressure range	Goal
Low-temperature nitriding/nitrocarburizing of stainless steels	Below 450 °C (840 °F)	N, (C)	NH_3 , N_2 , H_2 , dNH_3 , N_2 , CO , C_xH_y , $\text{C}_x\text{H}_y\text{N}_z\text{O}$	Atmospheric	S-phase diffusion zone of high hardness. No loss of corrosion-resistance properties. Dramatic improvement of pitting/crevice corrosion performance
Nitriding (Oxynitriding, 1) (Sulfonitriding, 2) (Oxysulfonitriding, 3) Nitriding of stainless steels	500–550 °C (930–1020 °F) Partially up to 580 °C (1075 °F)	N (S)	NH_3 , N_2 , H_2 , dNH_3 (1: air, N_2O , H_2O) (2: S, H_2S) (3: SO_2)	Typically atmospheric but also low-pressure processes between 200 mbar and 1 bar and high-pressure variants up to 12 bar	Deep wear-resistant diffusion zone with high hardness with only restricted compound layer
Ferritic nitrocarburizing (FNC)	550–580 °C (1020–1075 °F)	N, C	NH_3 , N_2 , H_2 , dNH_3 , CO , CO_2 , C_xH_y	Typically atmospheric; low-pressure and high-pressure variants possible (see nitriding)	Similar to classical nitriding with a depassivation stage prior to the nitriding stage, removing oxides of alloying elements such as Cr, Ni, and others that otherwise will effectively block the nitriding process. The process will bind all chromium in the surface to chromium nitrides, resulting in a loss of the corrosion-resistance properties. ϵ - and γ' -iron nitride compound layer of high hardness and only a small underlying diffusion zone. The compound layer also increases the base material resistance to corrosion, except for stainless steels.
Austenitic nitrocarburizing (ANC)	595–720 °C (1100–1330 °F)	N, C			Due to the higher temperature, ANC creates a thicker compound layer and a deeper diffusion zone within the same process time compared to FNC. In addition, it produces an austenitic layer below the compound layer. As in FNC, the compound layer increases the base material corrosion resistance, except for stainless steels.
High-temperature nitriding of low-carbon, low-alloyed steels	700–800 °C (1290–1490 °F)	N	NH_3 , N_2	Atmospheric	Creates a diffusion zone of high hardness after quenching
Solution nitriding of stainless steels	1050–1150 °C (1920–2100 °F)	N	N_2	0.1 to 2 bar, depending on temperature and steel grade	Creates a diffusion zone with high hardness and excellent corrosion-resistance properties. Process requires quenching in order to obtain the high hardness.

the chemical potential to real conditions where the molecules and/or atoms will interact with each other, the number x is replaced by the chemical activity (a), where a_i is a function of its concentration, x_i , and an activity coefficient, γ_i :

$$a_i = \gamma_i \times x_i$$

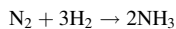
The chemical potential also depends on temperature; as with higher temperatures, the atoms and molecules will move faster, resulting in higher kinetic energy. Consequently, the activity coefficient and therefore the activity itself is a function of temperature. In that sense, the activity can be thought of as the chemically effective concentration of the species in the mixture at the actual process conditions.

In a gas mixture, concentrations are typically measured in partial pressures (p), and the sum of all partial pressures in the mixture will build the total pressure (p_0) of the mixture, in this case representing the furnace pressure. The activity of any gas i in the mixture is:

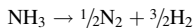
$$a_i = \gamma_i \times \left(\frac{p_i}{p_0} \right)$$

Because nature favors conditions with low potential energy, it will tend to establish equilibrium between the chemical potentials of each species and their reaction products in the mixture.

Ammonia is technically produced by combining nitrogen gas with hydrogen gas under conditions with high temperature (400 to 500 °C, or 750 to 930 °F) and high pressure (150 to 250 bar) and requiring a catalyst to make this reaction happen:



Consequently, the energy spent is stored in the ammonia molecule, making this molecule unstable and forcing a reaction where the ammonia will break down into its original components:

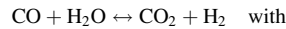


The equilibrium will be established when the driving force for both reactions will be equal at the given temperature (T) and pressure. The equilibrium coefficient (K_{eq}) can be derived by the activities and written as a function of the partial pressures of ammonia (NH_3), nitrogen gas (N_2), and hydrogen gas (H_2):

$$K_{eq} = f(T) = \frac{p_{NH_3}}{[(p_{N_2})^{1/2} \times (p_{H_2})^{3/2}]}$$

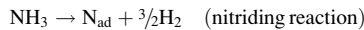
A reaction that typically takes place in nitrocarburizing atmospheres is the so-called water-gas shift reaction (or homogeneous water-gas reaction), where carbon monoxide, carbon dioxide, hydrogen, and water vapor tend to

establish equilibrium by moving oxygen from carbon to hydrogen:



$$K_w = f(T) = \frac{p_{CO_2} \times p_{H_2}}{[p_{CO} \times (p_{H_2O})]}$$

where K_w is the equilibrium coefficient for the water-gas reaction. If reactions take place on the very surface of an iron part, nitrogen or carbon may be given away into the metal lattice and therefore not react with other molecules in the gas. The reaction is written as:



where N_{ad} is the atomic nitrogen adsorbed. The equilibrium coefficient between the gas phase and nascent (atomic) nitrogen (N) in solution is:

$$K_1 = f(T) = \frac{a_N \times p_{H_2}^{3/2}}{p_{NH_3}}$$

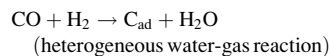
The nitrogen activity in iron thus can be expressed as:

$$a_N = \frac{K_1 \times p_{NH_3}}{[p_{H_2}]^{3/2}}$$

The partial pressure ratio of ammonia to hydrogen is called the nitriding potential (K_n):

$$K_n = \frac{p_{NH_3}}{[p_{H_2}]^{3/2}}$$

Analog to the nitriding reaction, a carburizing reaction can also be expressed where a carbon atom will react with the iron surface:



Equilibrium and carbon activity (a_C) are:

$$K_2 = f(T) = \frac{a_C \times p_{H_2O}}{p_{CO} \times p_{H_2}}$$

$$a_C = \frac{K_2 \times p_{CO} \times p_{H_2}}{p_{H_2O}}$$

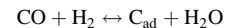
The partial pressure ratio between carbon monoxide, hydrogen, and water vapor describes the carburizing potential of this reaction:

$$K_C(\text{heterogeneous}) = \frac{p_{CO} \times p_{H_2}}{p_{H_2O}}$$

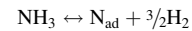
Neither nitriding potential nor carburizing potential should be mistaken for a nitrogen potential or a carbon potential, because these numbers are defined to express the mass percentage of nitrogen and carbon dissolved in the near surface of iron at equilibrium. In carburizing of iron in an austenitic state, for example, the carbon potential can be derived by transforming

the carbon activity back into the number of carbon atoms in solution and further into the resulting mass percentage. Because nitriding and nitrocarburizing processes normally take place at temperatures where the iron is still in a ferritic phase (where the solubility of nitrogen and carbon is very low, and with the process aiming for a phase change to create a compound layer), these processes use the nitriding and carburizing potentials for atmosphere control.

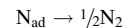
Surface reactions of the metal with the atmosphere under equilibrium conditions also may involve the removal of nitrogen and carbon atoms from the iron surface by reaction with the surrounding process atmosphere. In carburizing, for example, decarburization can occur when moisture reacts with carbon in the iron:



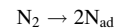
Likewise, a similar reaction can occur for the nitriding reaction, such that ammonia gas may be formed just above the part surface:



However, because the energetically more-favored reaction is the formation of nitrogen gas, the dominant denitriding reaction is:



Using activities, it is also possible to convert from ammonia-driven nitriding reactions to nitriding reactions using nitrogen gas:



This reaction is used in high-temperature nitriding, at normal nitriding conditions, and for creating a compound layer; the nitrogen activity induced by nitrogen is not high enough and would require extremely high pressures.

Low-Temperature Nitriding and Nitrocarburizing

The goal of low-temperature nitriding and nitrocarburizing is a diffusion zone of high hardness (up to 1800 HV) approximately 20 to 40 μm (0.001 to 0.002 in.) thick, while at the same time avoiding the formation of chromium nitrides and chromium carbides, in order to maintain, or even improve, the corrosion-resistance properties of stainless steels.

The process does not create a compound layer but a diffusion zone that is supersaturated by carbon and nitrogen and is known as expanded austenite (previously called S-phase). For martensitic and ferritic steels, expanded martensite can develop. This layer can be designed as a duplex layer, where the outer part contains nitrogen and the inner part contains carbon (Fig. 2), or as a uniform nitrided layer containing only nitrogen (alternatively, a carburized layer can be formed that contains only carbon). The advantage of the duplex layer is a

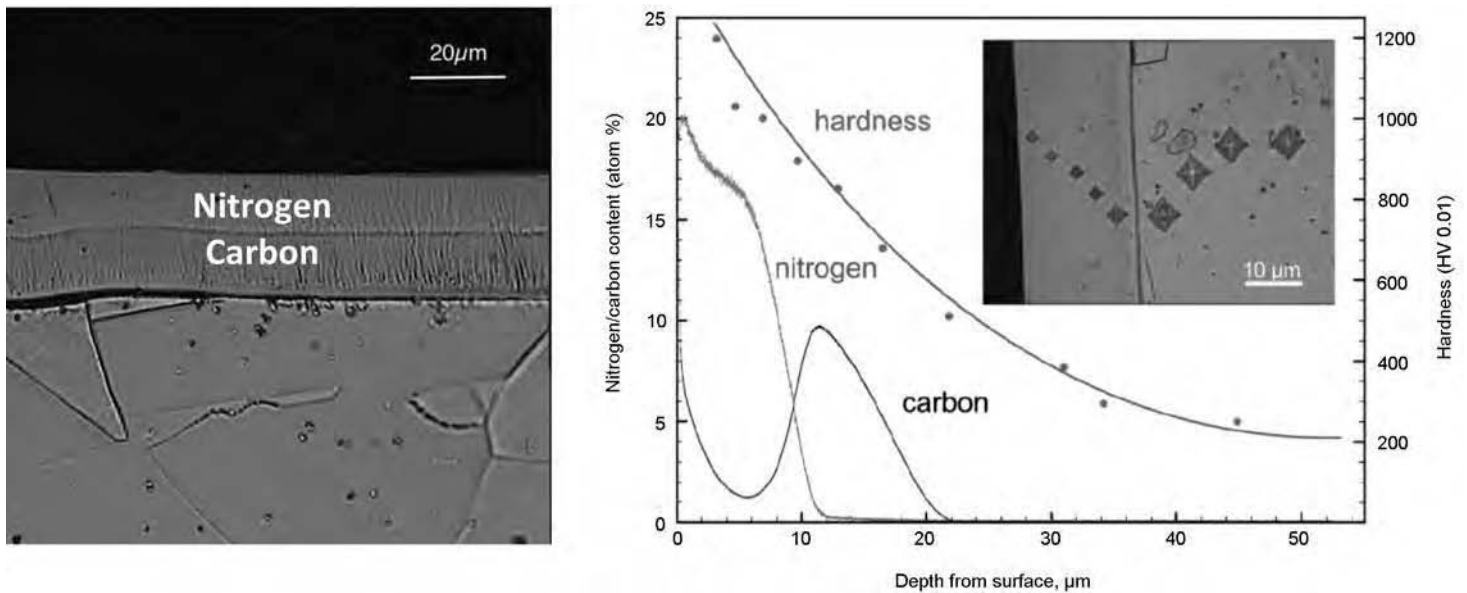


Fig. 2 The micrograph to the left shows a duplex layer of nitrogen- and carbon-expanded austenite. The distribution of nitrogen and carbon in the surface layer, as shown to the right, results in a smooth transition in compressive stresses from the hardened surface to the soft base alloy. Courtesy of Expanite A/S, Denmark

gradual case-core transition with a smooth change in hardness (Fig. 2) and residual stresses.

Application. The excellent corrosion-resistance property of stainless steels is caused by a high percentage (≥ 12 mass%) of the alloying element chromium, which forms a very stable passive layer of chromium oxides on the part surface, protecting the steel from further corrosion. Unfortunately, stainless steel is a soft material that suffers from extensive wear and therefore restricts the applicability of the material. Adding a small layer of high hardness while maintaining the corrosion resistance and improving pitting and crevice corrosion resistivity opens a wide field of applications, especially in the food and medical industries.

Applicable steels are all austenitic and martensitic stainless steels, A286, 465, duplex stainless steels, precipitation-hardenable stainless steels, Hastelloy C22 and C276, Inconel 625 and 718, but also titanium (alloys).

Thermodynamic Background. At low temperature, stainless steels are able to hold high amounts of nitrogen and/or carbon because of the strong affinity of chromium atoms for nitrogen and carbon. Because the diffusion coefficient of chromium is very low compared to the diffusion coefficient of the interstitials nitrogen and carbon, the time needed to precipitate chromium nitrides is longer than the time needed to create a surface zone consisting of a supersaturated solid solution of nitrogen/carbon of high hardness. Christiansen and Somers (Ref 3) presented a graph displaying the time needed to transform a nitrogen-expanded austenite of several steels into chromium nitrides if exposed to temperature and, in this way, losing their corrosion-resistance properties.

Figure 3 shows a reverted plot of the presented data, clearly illustrating that a short

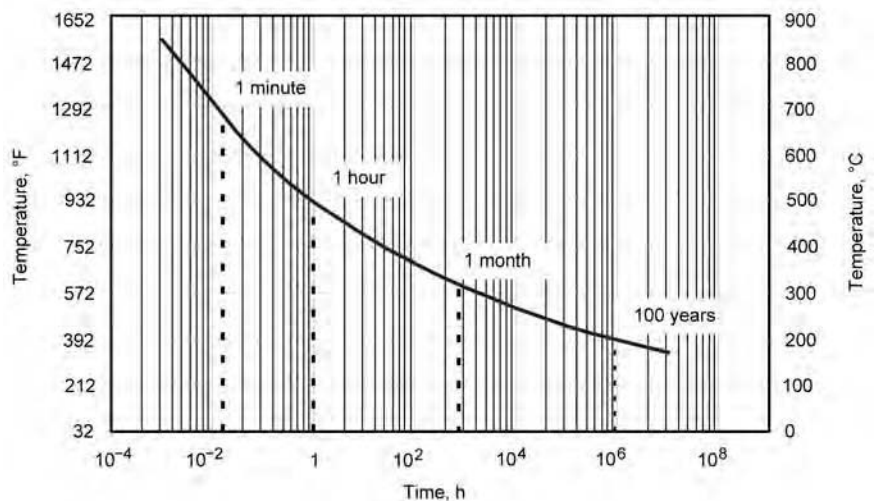


Fig. 3 Time-temperature graph for the stability of nitrogen-expanded austenite in AISI 316, based on data given by Christiansen and Somers (Ref 3). The plot displays the time needed to precipitate 50% of the originally obtained S-phase structure.

process time of 1 h requires a process temperature much lower than 500 °C (930 °F), because otherwise, half of the produced expanded austenite would precipitate to chromium nitrides during heat treatment. The temperature for the formation of chromium carbides is approximately 100 °C (180 °F) higher. Typical process temperatures for nitriding and nitrocarburizing stainless steels are below 440 °C (825 °F).

Process Description. The major problem in nitriding and nitrocarburizing of stainless steels is the self-healing surface passivation by a spontaneous formation of chromium oxides (Cr_2O_3), prohibiting the penetration of carbon and nitrogen. For this reason, all nitriding

processes designed to treat steels with high chromium content must start with a depassivation or activation stage.

The activation stage typically starts at room temperature after a nitrogen, argon, or vacuum purge, where the activation agent is put into the furnace prior to the process or injected while heating up the furnace. Activation may also be a series of stages using one or more activation agents and carried out at different temperatures.

The activation stage is followed by the nitriding/nitrocarburizing stage, where the nitrogen and carbon sources are injected. The stage time depends on temperature and the target thickness

of the expanded austenite. The nitriding stage is followed by a cooling stage, typically using an inert gas such as nitrogen or argon to purge the furnace.

There are several industrial processes available using different agents for activation and as carbon and nitrogen sources. For example, Expanite (Expanite A/S, Denmark) has patented the use of carbon-nitrogen compounds such as urea ($\text{CH}_4\text{N}_2\text{O}$) or formamide (CH_3NO) for activation (international patent WO 2011/009463 A1) and as carbon and nitrogen carriers, allowing for a parallel activation and nitriding/nitrocarburizing while heating, resulting in comparatively short overall heat treating cycles; the layer thickness and composition, such as simplex or duplex phases, are thermodynamically controlled. The patent gives an example where a sample of AISI 316 was nitrocarburized to a total case of 10 μm while being heated to 440 $^\circ\text{C}$ (825 $^\circ\text{F}$) within 45 min and subsequent cooled to room temperature within 10 min.

Nano-S (Nitrex Metal Inc., Canada) or NV-Nitriding (Air Water Inc., Japan) start with an in-furnace depassivation followed by a nitriding or nitrocarburizing stage using ammonia (NH_3) as a nitrogen source and hydrocarbons (C_xH_y) or carbon monoxide (CO) as a carbon source.

Other processes require coating of externally activated parts with a thin layer of iron (European patent 0248431 A2) or nickel (Ref 4) (U.S. patent 07431778 B2) and so on to prevent a repassivation after activation or while heat treating with oxygen-containing compounds; such a coating is permeable for carbon and nitrogen atoms.

Nitriding

Classical nitriding typically aims for a load-bearing diffusion zone of high hardness with only a limited compound layer (Fig. 4). During the process, nitrogen atoms diffuse into the material surface and, in the presence of nitride-forming elements, produce nitrides stable at nitriding temperatures. The increase in hardness after nitriding is then given by a solid solution of nitrogen in ferrite/martensite (or austenite) and the distribution of iron-base or alloying element nitrides.

Application. Of the alloying elements commonly used in commercial steels, aluminum, chromium, vanadium, tungsten, and molybdenum are beneficial in nitriding because they form nitrides that are stable at nitriding temperatures. Molybdenum, in addition to its contribution as a nitride former, also reduces the risk of embrittlement at nitriding temperatures. Other alloying elements, such as nickel, copper, silicon, and manganese, have little, if any, effect on nitriding characteristics. Aluminum-containing steels (0.85 to 1.50 mass% Al) yield the best nitriding results in terms of total alloy content, if they contain chromium as well. Even if aluminum is a strong nitride former, aluminum nitride (AlN)

does not nucleate easily in the ferrite matrix and will not give good hardness, nor does it develop a clear diffusion zone. This occurs first when chromium is also present in solid solution. Recently, it was demonstrated that mixed nitrides (Cr, Al)N develop (Ref 5). Chromium-containing steels can approximate these results if their chromium content, dissolved in the matrix and not bound to carbides, is sufficiently high enough. Unalloyed carbon steels are not well suited to nitriding because the hardness increase in the diffusion zone is limited.

The following steels can be gas nitrided for specific applications:

- Aluminum-containing low-alloy steels, preferably containing chromium
- Medium-carbon, chromium-containing low-alloy steels of the 4100, 4300, 5100, 6100, 8600, 8700, and 9800 series
- Hot work die steels containing 5 mass% Cr, such as H11, H12, and H13
- Low-carbon, chromium-containing low-alloy steels of the 3300, 8600, and 9300 series
- Air-hardening tool steels, such as A-2, A-6, D-2, D-3, and S-7
- High-speed tool steels, such as M-2 and M-4
- Nitronic stainless steels, such as 30, 40, 50, and 60
- Ferritic and martensitic stainless steels of the 400 and 500 series
- Austenitic stainless steels of the 200 and 300 series as well as certain Inconels and Incolloys
- Precipitation-hardening stainless steels, such as 13-8 PH, 15-5 PH, 17-4 PH, 17-7 PH, A-286, AM350, and AM355

Aluminum-containing steels produce a nitrided case of very high hardness and excellent wear resistance. However, the nitrided case also has low ductility, and this limitation should be carefully considered in the selection of aluminum-containing steels. In contrast, low-alloy chromium-containing steels provide a nitrided case with considerably more ductility

but with lower hardness. Nevertheless, these steels offer substantial wear resistance and good antigalling properties. Tool steels, such as H11 and D2, yield consistently high case hardness with exceptionally high core strength. Table 2 gives the average hardness increase for selected materials.

Thermodynamic Background. The modified Lehrer iron-nitrogen diagram (Fig. 5) shows the phase boundaries between ferrite (α), Fe_4N γ' -nitrides, Fe_{2-3}N ϵ -nitrides, and austenite (γ). Depending on the nitriding potential of the nitriding atmosphere:

$$K_N = \frac{P_{\text{NH}_3}}{[P_{\text{H}_2}]^{3/2}}$$

and the process temperature, nitriding either produces a surface layer of interstitially placed nitrogen atoms in the face-centered cubic iron lattice or creates a compound layer of iron nitrides once the maximum solubility for nitrogen is exceeded. At typical nitriding temperatures ranging between 495 and 565 $^\circ\text{C}$ (925 and 1050 $^\circ\text{F}$), it is not possible to create an austenitic iron phase. To create body-centered cubic γ -iron, the temperature must be raised above 595 $^\circ\text{C}$ (1100 $^\circ\text{F}$), and K_N must be set accordingly, resulting in a nitrogen content of approximately 2.35 mass%. K_N is typically measured in units of $1/\sqrt{\text{bar}}$.

When using ammonia and dissociated ammonia only, the nitriding potential can easily be transferred into different parameters (see also the section "Atmosphere Control" in this article).

Dissociation (sometimes referred to as dissociation rate), residual ammonia (R_{NH_3}), and hydrogen (H_2) in the furnace atmosphere can be measured using applicable equipment (see the section "Measuring the Potentials" in this article). Because ammonia thermally dissociates into hydrogen and nitrogen following the reaction:

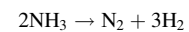


Table 2 Typical hardness increase obtained by nitriding

Material	Hardness prior to nitriding, HV	Hardness obtained by nitriding, HV
Iron	~120	~250
Low-alloyed carbon steels		
AISI 1045	~180	~350
Medium-carbon, chromium-containing low-alloy steels		
1.1% Cr (AISI 4140)	~240	~600
2.5% Cr (AISI 4340)	~240	~750
Nitriding steels (Cr and Al)	~240	~1000
Tool steels (12% Cr)	~600	>1000

Source: Ref 6

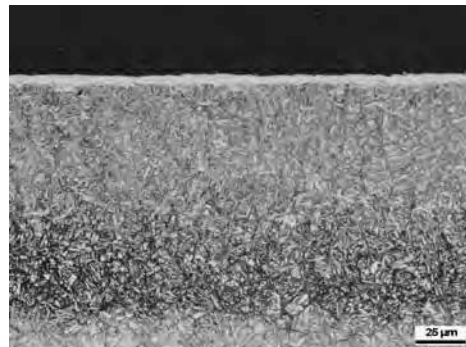


Fig. 4 Micrograph of nitrided X40CrMoV5-1. Courtesy of IWT Bremen, Germany

the nitriding potential can be determined from measurement of the exhaust of an atmospheric furnace:

$$K_N = \frac{R_{NH_3}/100\%}{\left[\frac{3}{4} \times \left(1 - \frac{R_{NH_3}}{100\%}\right)\right]^{3/2}}$$

$$K_N = \frac{\left[\frac{(100\% - 4/3 \times H_2)}{100\%}\right]}{\left[\frac{H_2}{100\%}\right]^{3/2}}$$

$$K_N = \frac{\left[\frac{(100\% - Diss.)}{100\%}\right]}{\left[\frac{3}{4} \times Diss.\right]^{3/2}}$$

where the dissociation rate (Diss.) is:

$$Diss. = 100\% - R_{NH_3}$$

$$Diss. = 4/3 \times H_2$$

The solubility for nitrogen and therefore the phase boundaries as well are influenced by the presence of carbon and other alloying elements. It can be clearly observed that when maintaining a nitriding potential above the boundaries toward iron nitrides, the nitrided layer will result not only in a diffusion zone but also create a compound layer of noticeable thickness. Table 3 explains the general influence of nitriding conditions and material on the nitriding result.

Process Description. Parts are treated in a different manner depending on the required nitriding specifications. SAE AMS 2759/6 specifies the procedure for gas nitriding of low-alloy and tool steels by the use of ammonia and dissociated ammonia. The specification limits the compound layer thickness to either a maximum of 0.0005 in. (class 1) or a maximum of 0.001 in. (25 μm) (class 2):

- Class 1 requires two nitriding stages, with the first stage at 940 to 1050 °F (505 to 565 °C) maintaining a dissociation rate of 15 to 35% and the second stage at 975 to 1050 °F (525 to 565 °C) maintaining a dissociation rate of 65 to 88%. The duration of the first stage shall be approximately 20% of the total nitriding time.
- Class 2 requires only one stage, at 940 to 1050 °F (505 to 565 °C) maintaining a dissociation rate of 15 to 35%.

The two-stage nitriding process with the second stage at an increased temperature is also known as the Floe process (U.S. patent 2,437,249).

The advantage of having two stages, with the first stage at a lower temperature, is that the lower thermal dissociation rate of ammonia during the first stage results in a higher nitriding potential compared to the second stage, where the higher temperature will automatically cause a higher thermal dissociation, hence reducing

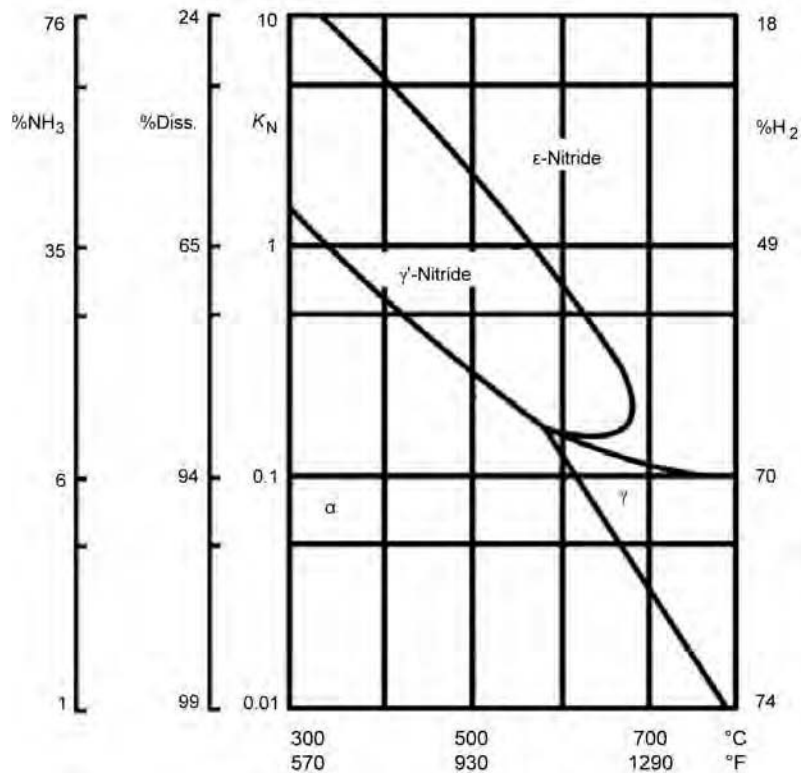


Fig. 5 Modified Lehrer iron-nitrogen diagram displaying the phase boundaries to γ'- and ε-nitrides as a function of temperature and nitriding potential (K_N), dissociation, residual ammonia, and hydrogen for an ammonia and a dissociated ammonia atmosphere. Source: Ref 7

Table 3 Influence of nitriding conditions and material on the nitriding result

	Compound layer thickness	Case (surface) hardness	Case (surface) hardness increase	Effective case depth	Case (surface) hardness depth	(Effective case depth - case hardness depth)/effective case depth
Nitriding conditions:						
Higher temperature	↑↑	= ↓	= ↓	↑	↑	= ↓
Longer soak time	↑	= ↓	= ↓	↑	↑	= ↓
Higher K _N	↑↑	=	=	=	=	=
Material composition:						
Higher Cr concentration	= ↓	↑	↑	↓ ↓	↑	↓
Higher Al concentration	↑	↑↑	↑↑	= ↓	↓	↑
Higher C concentration	= ↑	↓	↓	= ↓	↓	↑
Material structure:						
Normalized	=	= ↑	↑	=	↑	↓
Hardened, increasing tempering temperature	=	↓	↓	=	↓	↑

Source: Ref 2

the nitriding potential naturally at constant flow rates. Another advantage is the formation of fine, dispersed, small nitride precipitations at the lower temperature, with a higher hardness and fatigue strength compared to nitriding only at high temperatures.

The newer SAE AMS 2759/10A specifies the nitriding potential to be used instead of the dissociation rate. The specification limits the compound layer thickness in the same way as the older AMS 2759/6 but adds class 0, where no compound layer is permitted. For all classes and all steels, the nitriding potential maintained

during the first nitriding stage is well within the ε- range, and, depending on the allowed compound layer thickness, the nitriding potential will be lowered to the γ'-range or down to the α-γ'-boundary for the second nitriding stage. Using the nitriding potential instead of the dissociation rate allows for the use of nitrogen-diluted atmospheres.

Table 4 gives the process stages for several nitriding variants applied on low- and medium-alloy steels as well as stainless steels. After loading, the furnace is typically heated to a temperature of 300 to 350 °C (570 to 660 °F).

Table 4 Typical stages for several nitriding variants

Stages	Typical low chromium	Typical high chromium	Variant 1	Variant 2	Variant 3
Load				X	
N ₂ purge	...	X	(X)	X	...
NH ₃ purge	X
Heat to preoxidation/activation temperature	Air	N ₂ or activation agent avoids further oxidation	NH ₃	dNH ₃ or H ₂ flow removes oxides (Activate)	150 °C (300 °F) max NH ₃ flow. Oxidation by NH ₃ + air \geq NH ₃ + H ₂ O + H ₂ + N ₂
Hold for preoxidation/activation	Oxidize with air	Oxidize with water or activate	...	(Activate)	Hold at 150 °C (300 °F) max until furnace is fully purged with NH ₃
N ₂ purge	X	X	...	X	...
Heat to 1st nitriding stage	Heat with N ₂ or NH ₃ flow	Heat with N ₂ or NH ₃ flow	Heat with NH ₃ flow	Heat with N ₂ or NH ₃ flow	Heat with NH ₃ flow
Hold for 1st nitriding stage			Nitride with NH ₃ + dNH ₃ /N ₂		
Heat to 2nd nitriding stage			(NH ₃ + dNH ₃ /N ₂)		
Hold for 2nd nitriding stage			(NH ₃ + dNH ₃ /N ₂)		
Cool with process gas			(Optional, to obtain lower porosity)		
Cool with N ₂ purge until furnace is fully purged with nitrogen			X		
Unload				X	

Depending on the chromium content of the material to be treated, heating may be done in air, or the furnace may be vacuum or nitrogen purged prior to heating, to avoid further oxidation and allow for the injection of flammable gases. Variant 3 starts with a high ammonia flow while heating but requires the heating to be stopped at a maximum temperature of 150 °C (300 °F) until the furnace is fully purged with ammonia (5 times the furnace volume).

At a first temperature hold, contaminants will be evaporated, and the part surface will be activated for further nitriding. Depending on the chromium content, this may be done in a preoxidation stage (<3 to 5 mass% Cr) to remove any organic residuals from the part surface or in an activation stage to remove chromium oxides. Preoxidation of high-alloyed steels, if not activated, should preferably be carried out in a temperature range of 400 to 500 °C (750 to 930 °F).

After preoxidation and sometimes as well as prior to activation, the furnace will be nitrogen or vacuum purged (see the section "Safety Purge" in this article) and backfilled with either nitrogen or ammonia. Once filled with either nitrogen or ammonia, the furnace will be heated to the process temperature. In most cases, it may be favorable to start the ammonia flow while heating, to create a tiny layer of iron nitrides (see the section "Nucleation" in this article), thus promoting a uniform nitrogen uptake throughout the process.

Following the specifications and depending on the allowed compound layer thickness, nitriding will be carried out using either one or two nitriding stages. The principal advantage of double-stage nitriding is the ability to reach higher nitriding potentials at lower temperatures, promoting a high saturation of the surface layer and an acceleration of the propagation of the diffusion front by applying a higher temperature in the second stage. A lower potential in the second stage reduces the formation of the compound layer on the surface of the case. On the other hand, there is no technical reason for a second stage at a higher temperature, except when specified otherwise or if high potentials (a low dissociation rate) cannot be reached at

higher temperatures due to an insufficient ammonia supply or if low potentials (a high dissociation rate) cannot be reached at lower temperatures due to the absence of a dissociated ammonia or hydrogen.

Applying a higher temperature during the second stage:

- May lower the case hardness but improve the stress distribution, resulting in higher ductility
- Will increase the case depth, relative to process time
- May lower the core hardness, depending on the prior tempering temperature and the total nitriding cycle time
- May lower the apparent effective case depth because of the loss of core hardness, depending on how the effective case depth is defined

After nitriding, the furnace is cooled to a temperature of 100 to 150 °C (212 to 300 °F) or lower for unloading. This is typically done using a high-nitrogen flow to purge the flammable and/or toxic gases out of the furnace. Prior to unloading, the total nitrogen flow must be at least 5 times the volume of the furnace (see the section "Safety Purge" in this article). In some cases, it may be advantageous to cool the furnace in two stages, where, while cooling to 300 to 400 °C (570 to 750 °F), the process gas flow of the last nitriding stage is maintained, reducing the disintegration of the compound layer and the formation of porosity.

For nitriding of stainless steels, several industrial processes are available, such as Nitreg-S (Nitrex Metal Inc., Canada), LintrideSS (Bodycote, formerly known as Malcomizing, United Kingdom), or NV-Nitriding (Air Water Inc., Japan), to name a few, which differ mainly in the activation agent used.

Controlling the Case Depth. Case depth and case hardness, the two criteria most commonly referred to in the control of case properties, vary not only with the duration and other conditions of nitriding but also with steel composition, prior structure, and core hardness (Fig. 6 to 9).

With increasing amount of nitride-forming elements, the formation of alloy nitrides will increase hardness but, on the other hand, slow down the propagation of the case depth.

Carbon also has an influence on case depth and hardness. With increasing amount of carbon, surface hardness will drop, and the effective case depth may be lowered. Especially when alloyed steels are tempered at temperatures above the nitriding temperature, as suggested, carbon and chromium will form chromium carbides; thus, the bound chromium is not able to participate in developing a precipitation layer of high hardness by forming chromium nitrides.

For further information on how to modify process parameters, see "Controlling Diffusion Zone and Compound Layer" in the section "Nitriding Processing" of this article.

High- and Low-Pressure Nitriding. With increasing furnace pressure while maintaining a constant nitriding potential, the partial pressures of ammonia and hydrogen will also increase. Because this increase will not be linear due to the nonlinear ratio defining the nitriding potential, the ratio between ammonia and hydrogen decreases (Table 5). According to Jung (Ref 10), this will also increase the nitrogen-transfer speed, resulting in faster growth of the compound layer for low- and mild-alloy steels, provided the nitriding potential is set to achieve ϵ - or γ' -nitrides, but also in faster propagation of the diffusion zone (if the nitriding potential is set in a range to create only a restricted compound layer).

Consequently, when expanding the calculations given in Table 5 toward low pressures, the corresponding nitrogen-transfer speeds can be estimated, as shown in Table 6.

Calculating the expected nitrogen-transfer speeds toward lower pressures suggests that if the pressure is gradually decreased, at one point the nitrogen availability (better said, the number of ammonia molecules hitting the part surface) will be too low to support a sufficient flux through the surface. This minimum pressure or the corresponding minimum nitrogen flux is dependent on the material composition.

Tests performed by Jordan et al. (Ref 11) showed that, when nitriding samples of AISI

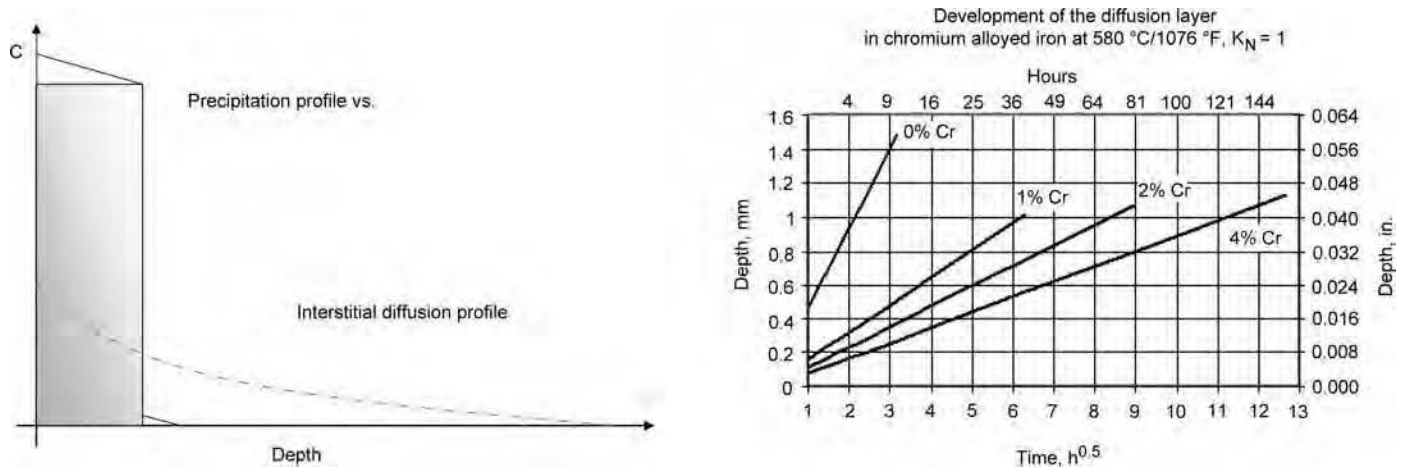


Fig. 6 With increasing amount of nitride-forming elements, more and more nitrogen, diffusing through the surface, will be bound in nitrides, slowing down the propagation of the precipitation front. This effect is often explained as the lower diffusion speed of nitrogen in alloyed steels. The calculated development of the diffusion zone follows the t -law. Source: Ref 8

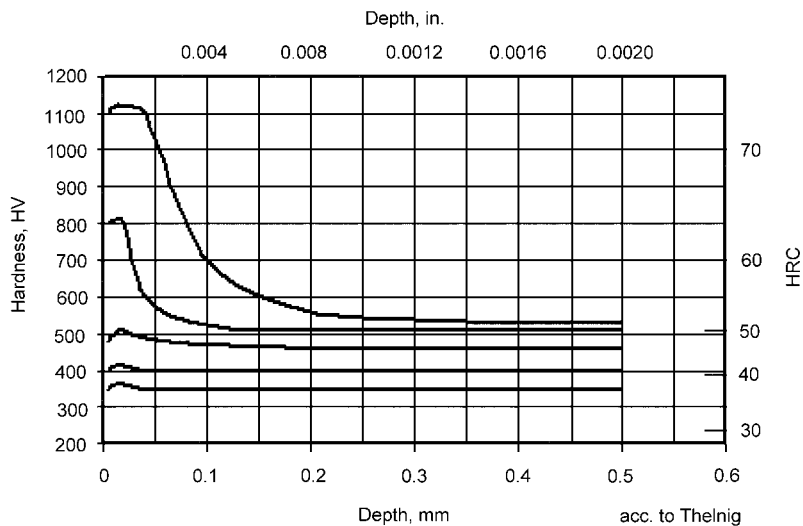


Fig. 7 Influence of pre-heat-treatment temperature on the resulting hardness of X210CrW12, nitrided for 10 h at 580 °C (1075 °F). Besides the expected loss in core hardness due to the increasing temperature while tempering, chromium will also be increasingly converted into stable chromium carbides. These carbides will not transform into chromium nitrides during nitriding. Source: Ref 9

4140 at absolute pressures of 128 and 812 torr (170 and 1093 mbar) in a temperature range of 524 to 538 °C (975 to 1000 °F), the nitriding results still gave a good correlation with the thermodynamics known from atmospheric nitriding. The nitriding potential at the α - γ' -boundary, calculated by adjusting the measured exhaust percentages of ammonia and hydrogen to match the partial pressures at furnace pressure, fits the Lehrer diagram.

While high-pressure nitriding has the advantage of a higher nitrogen flux and therefore a faster diffusion and/or compound layer formation, low-pressure nitriding offers a perfect gas

distribution throughout the load, even without a convection fan in the furnace chamber. Both processes require special equipment.

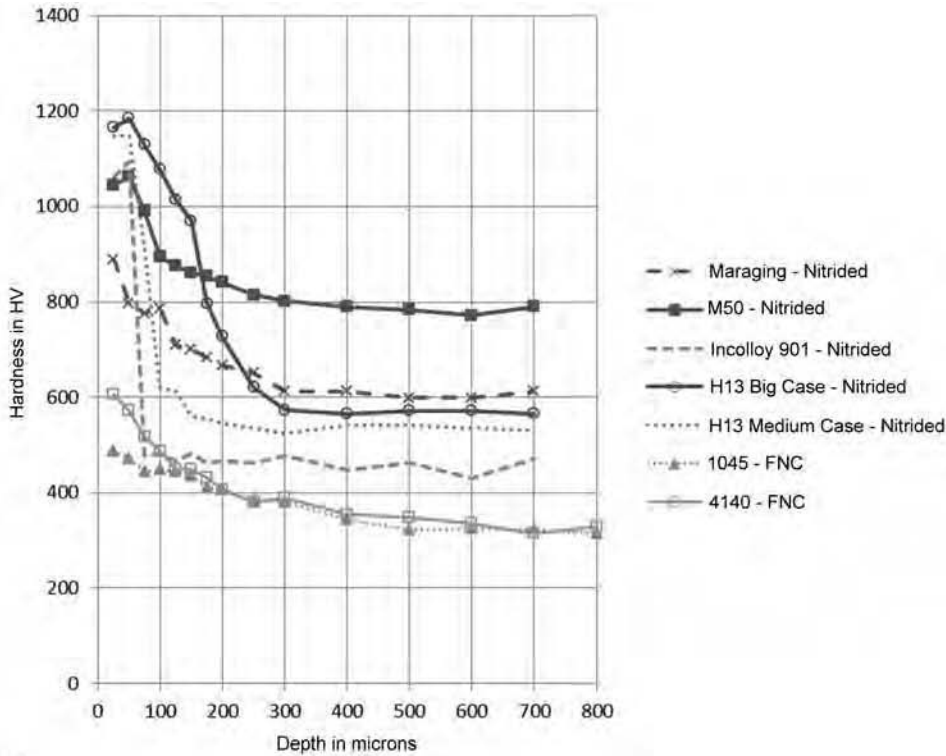
The so-called pressure nitriding (U.S. patents 2,596,981 and 2,779,697) is a process where a sealed retort is filled with ammonia up to a pre-determined pressure and then heated to process temperature. The ammonia will gradually decompose during the nitriding stage and, at the same time, increase the pressure within the retort. This does not allow for a controlled process; however, the nitriding potential will decrease over process time, hence naturally restricting the compound layer thickness and case depth.

The ALLNIT process (BMI, France) is a low-pressure gas nitriding process using a process atmosphere made from ammonia, nitrogen, and nitrous oxide (N_2O) as the ammonia dissociation and adsorption accelerator. The low process pressure provides an advantage to uniformly nitride small bores, cavities, and complex geometries by having lower gas consumption compared to traditional atmospheric nitriding. Adding carbon-bearing gases allows for low-pressure nitrocarburizing. ALLNIT may be followed by a postoxidation. This process requires vacuum equipment and may require longer cycle times.

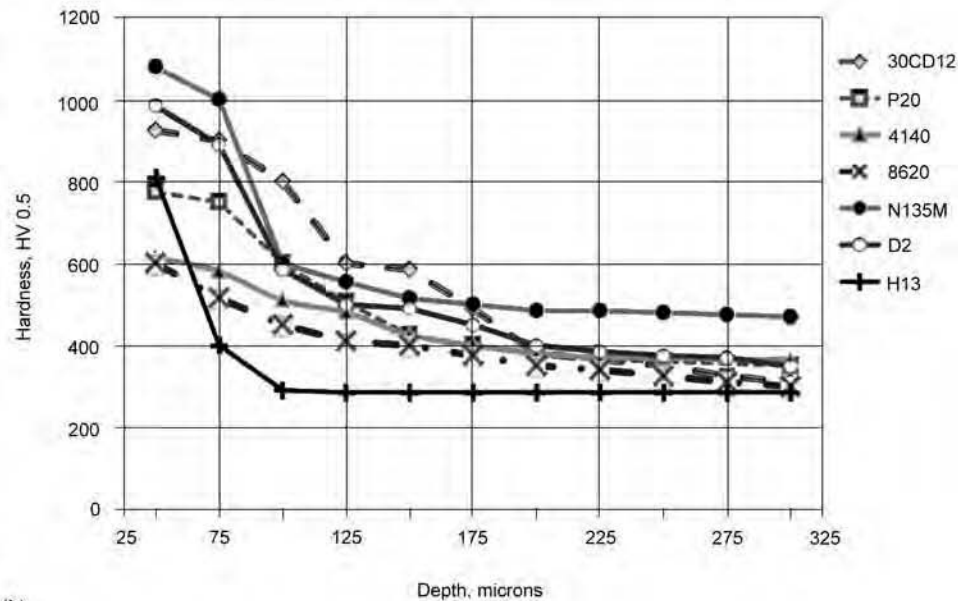
Nitrogen-Diluted Atmospheres. When diluting an ammonia/dissociated ammonia atmosphere with nitrogen, the availability of reactive nitrogen decreases. Because molecular nitrogen does not significantly participate in the nitriding reaction at normal nitriding temperatures, the effect of nitrogen dilution on the nitrogen-transfer speed can be compared to low-pressure nitriding.

To achieve a uniform nitriding result, the atmosphere must not be diluted beyond a percentage where the nitrogen flux is too low to support the diffusion into the part surface. Tests performed by Zimdars (Ref 12) showed that oxynitriding samples of 20MnCr5N at a constant nitriding potential of $K_N = 3$ at 550, 570, and 590 °C (1020, 1060, and 1094 °F) while gradually increasing the dilution first, reduced the white layer thickness, and then started to reduce the case depth. The effect increases with increasing temperature due to the faster nitrogen uptake at higher temperatures.

Nevertheless, in some cases, nitrogen may be used to control dissociation or nitriding potential; however, this control variant requires consideration of the previously discussed influence on nitrogen availability (atmosphere control).



(a)



(b)

Fig. 8 Hardness profiles. (a) Typical hardness profiles on commercially treated steels. FNC, ferritic nitrocarburizing. (b) Hardness profiles achieved on various steels after nitriding at 530 °C (985 °F) for 5 h. Profiles grow steeper with increasing amount of strong nitride formers. Courtesy of Nitrex Metal Inc., Canada

Oxynitriding is a nitriding process with the addition of an oxidizing gas, typically air or water, to enhance the nitriding reaction, especially for chromium-containing steels. According to Spies and Vogt (Ref 13), applying a high nitriding potential and an oxidizing potential:

$$K_O = p_{H_2O}/p_{H_2}$$

just above the oxidation limit of iron (Fig. 10) while nitriding high-alloy steels causes the formation of Fe₃O₄ magnetite, and once the chromium is precipitated to chromium nitrides, the

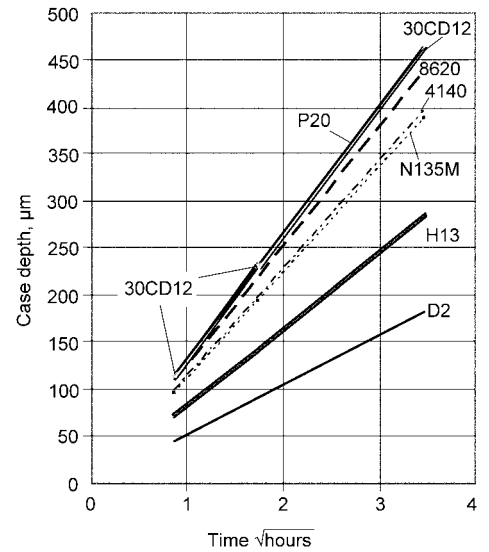


Fig. 9 Development of case depth for various steels, nitrided at 530 °C (985 °F), as a function of time

iron oxides will be transformed into iron nitrides, creating a compound layer. At low nitriding potentials, there will be a concurrent formation of iron oxides and chromium nitrides at the beginning of the process. The iron oxide layer, being permeable to nitrogen, forms a precipitation layer with no or only a restricted compound layer. In addition, oxynitriding may minimize the carbide precipitation in the diffusion zone of chromium-alloyed steels by a controlled decarburization.

Adding air, oxygen, or another highly oxidizing gas such as nitrous oxide, also known as laughing gas (N₂O), bears an explosion hazard (see the section “Safety Precautions” in this article). Therefore, the process is best carried out by using water injection. It is also possible to use carbon dioxide (CO₂) to create the oxidation potential, because CO₂ will be reduced by H₂ to CO and H₂O. Because this will also create a carburizing potential, it technically resembles a nitrocarburizing process.

Sulfonitriding and Oxysulfonitriding. The goal of sulfonitriding is a sulfurized compound layer with a low coefficient of friction, precluding the seizure of mating parts. Such a layer can be achieved by adding gaseous hydrogen sulfide (H₂S) to the nitriding atmosphere or by first forming a nitrided compound layer using a low ratio of gaseous hydrogen sulfide added to the ammonia flow and, in a second stage, sulfurizing the nitrided compound layer by a high ratio of hydrogen sulfide to an inert carrier gas (Japanese patent JP 02-270958).

Oxysulfonitriding uses sulfur dioxide (SO₂) as the sulfurizing gas, resulting in faster formation of the compound layer due to the oxygen bound in the gas.

Sulfonitriding and oxysulfonitriding can be applied on carbon steels but also on alloyed steels and cast iron.

Table 5 Partial pressures of hydrogen and ammonia and relative nitrogen-transfer speed at increasing furnace pressures at 570 °C (1060 °F), ammonia/dissociated ammonia atmosphere, and a constant nitriding potential of $K_N = 3 \text{ 1}/\sqrt{\text{bar}}$

Variable	Value			
$K_N = p\{\text{NH}_3\}/p^{1.5}\{\text{H}_2\} = 3, \text{ bar (torr)}$	1 (750)	4 (3000)	8 (6000)	12 (900)
$P\{\text{H}_2\}, \text{ bar (torr)}$	0.33 (248)	0.94 (705)	1.57 (1178)	2.11 (1583)
$P\{\text{NH}_3\}, \text{ bar (torr)}$	0.56 (420)	2.75 (2060)	5.92 (4440)	9.19 (6890)
Relative nitrogen-transfer speed	1.0	3.33	5.57	7.47

Source: Ref 10

Table 6 Partial pressures of hydrogen and ammonia and relative nitrogen-transfer speed at decreasing furnace pressures at 570 °C (1060 °F), ammonia/dissociated ammonia atmosphere, and a constant nitriding potential of $K_N = 3 \text{ 1}/\sqrt{\text{bar}}$

Variable	Value			
$K_N = p\{\text{NH}_3\}/p^{1.5}\{\text{H}_2\} = 3, \text{ bar (torr)}$	1 (750)	0.8 (600)	0.5 (375)	0.2 (150)
$P\{\text{H}_2\}, \text{ bar (torr)}$	0.33 (248)	0.28 r (210)	0.19 (143)	0.09 (68)
$P\{\text{NH}_3\}, \text{ bar (torr)}$	0.56 (420)	0.43 (323)	0.25 (188)	0.08 (60)
Relative nitrogen-transfer speed	1.0	0.77	0.43	0.13

Thermodynamic Background. The modified Fe-N-C diagram (Fig. 12) shows the phase boundaries between Fe_4N γ' -nitrides, Fe_{2-3}NC ϵ -carbonitrides, and Fe_3C cementite. The surface layer will be composed of varying amounts of nitrogen and carbon, depending on the temperature, nitriding potential, and carburizing potential. As previously described (in the section “Terminology for Gas Reactions” in this article), the nitriding potential is:

$$K_N \left[\text{in units of } \frac{I}{\sqrt{\text{bar}}} \right] = \frac{p_{\text{NH}_3}}{[p_{\text{H}_2}]^{3/2}}$$

while the carburizing potential of the atmosphere is:

$$K_{\text{CB}}[\text{bar}] = \frac{p_{\text{CO}}^2}{p_{\text{CO}_2}} \quad (\text{according to the Boudouard reaction})$$

$$K_{\text{CW}}[\text{bar}] = \frac{p_{\text{CO}} \times p_{\text{H}_2}}{p_{\text{H}_2\text{O}}} \quad (\text{heterogeneous water - gas reaction})$$

Note that Fig. 12 uses carbon activity instead of carburizing potentials, and the phase diagram is calculated for a temperature of 575 °C (1065 °F).

Process Description. There are several older commercial processes available, mainly differing in the carburizing gas added to the ammonia (Table 9). Because these processes did not include control of the according potentials, typical specifications for nitrocarburized parts will ask for a compound layer of a certain thickness, say 15 to 20 μm , mainly consisting of ϵ -carbonitrides and with a porosity of less than 30%. With the availability of potential-controlled nitrocarburizing (see the section “Atmosphere Control” in this article), these rather fuzzy requirements are more often replaced by detailed specifications.

SAE AMS 2759/12 specifies the procedure for K_N - K_C -controlled gas nitrocarburizing of carbon and high-strength, low-alloy steel, low-alloy steel, tool steel, and cast iron. The goal of the procedure is a compound layer of defined thickness and with a specified porosity. Class 1 must not exceed 15% of the total compound layer thickness, and class 2 must be at least 10% but not exceeding 40% of the total compound layer thickness.

Activation is typically not needed because nitrocarburizing is mainly performed on carbon and low-alloy steels, and the addition of oxidizing carbon-bearing gases such as CO_2 will automatically result in a mild activation that can be compared to oxynitriding.

The process is performed in a manner similar to a nitriding process but at slightly higher temperatures. Typical nitrocarburizing temperatures range between 550 and 580 °C (1020 and 1075 °F), below Ac_1 of the steel to be treated. Dissociation is overall lower when compared to a nitriding process, forcing a high nitriding potential, which, in combination with the carburizing potential, will result in fast growth of a compound layer. The influence of process parameters on the development of a compound layer can be taken from Table 3. At the end of the nitrocarburizing

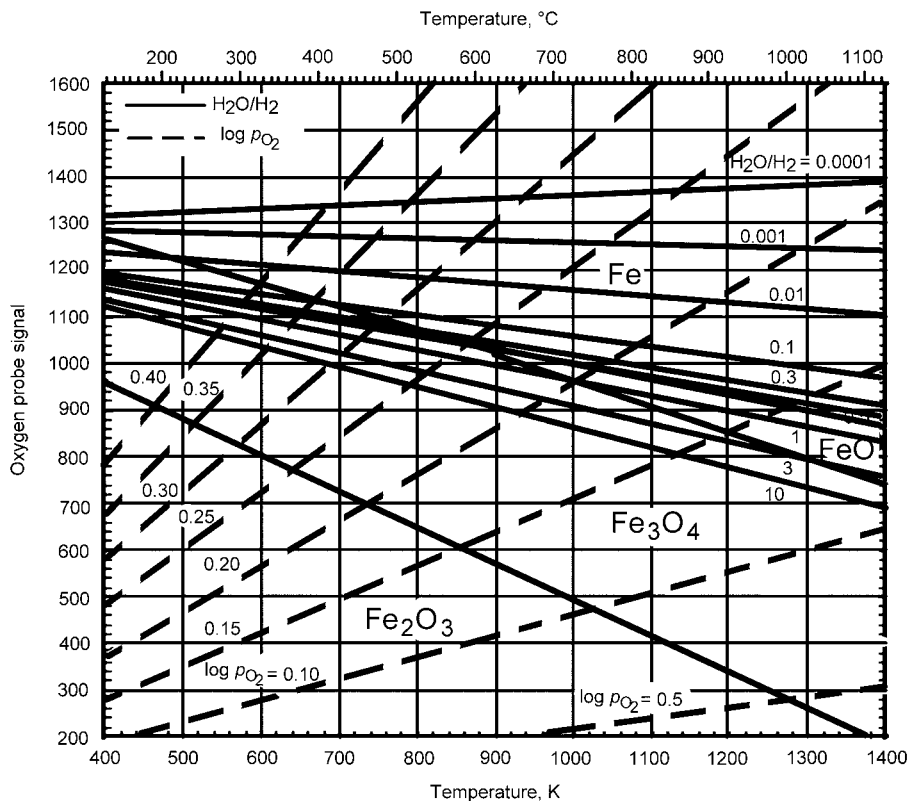


Fig. 10 Iron-oxygen diagram. Source: Ref 14

Ferritic and Austenitic Nitrocarburizing

Nitrocarburizing typically aims for a compound layer of high hardness that is preferably composed of Fe_{2-3}NC ϵ -carbonitrides and only a shallow case depth compared to nitriding that is able to support the stability of the brittle compound layer.

Application. Nitrocarburizing is typically applied to carbon steels, low-alloy steels, and also tool steels and cast iron to improve the corrosion resistance and, by lowering the

coefficient of friction, improve resistivity for adhesion and abrasion. The upper part of a compound layer typically has a porous structure, as shown in Fig. 11. In some cases, this porosity may be of advantage, but in most cases porosity should be as low as possible. Nitrocarburizing may be followed by postoxidation, resulting in even higher corrosion resistance and producing a dark-blue to black finish.

Table 7 provides an overview on how the compound layer composition and thickness should be built in order to withstand typical work conditions. Table 8 gives the expected compound layer hardness for several steels.

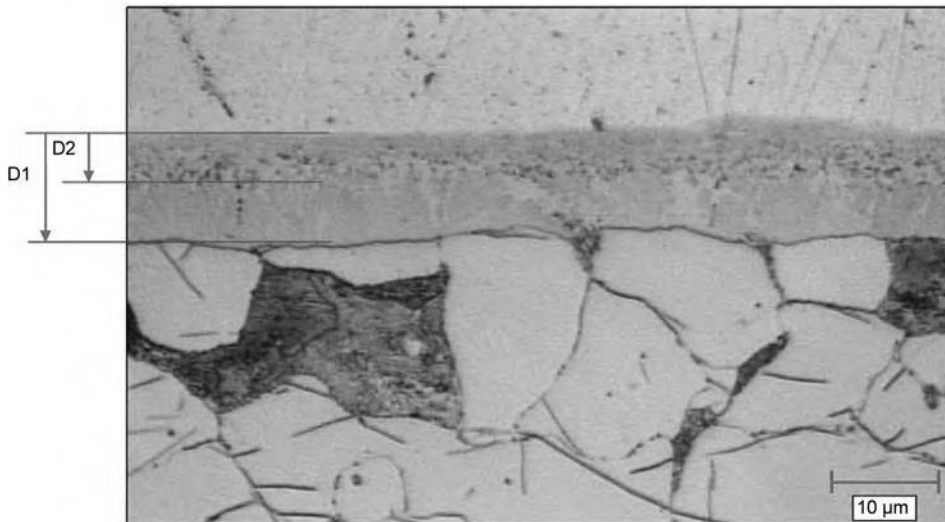


Fig. 11 Micrograph of a nitrocarburized AISI 1018 D1 as the compound layer thickness, with D2 the thickness of the porous section. The percentage of porosity (commonly referred to as porosity) is $D2/D1 \times 100\%$. Courtesy of Nitrex Metal Inc., Canada

Table 8 Compound layer hardness for different steel groups

Steel family	Example	Hardness of compound layer, HV _{0.02}
Unalloyed carbon steels	Ck15–Ck60	700–900
Alloyed carburizing steels	16MnCr5	800–1000
Alloyed hardening steels	34Cr4, 42CrMo4	800–1000
Nitriding steels	31CrMoV9, 34CrAlMo5	1200–1600
Alloyed cold work steels	X165CrMoV12	1200–1600
Hot work tool steels	X40CrMoV5-1	1200–1600
High-speed steels	S6-5-2	1300–1700
Spheroidal graphite cast iron	GGG60	500–900

Source: Ref 17

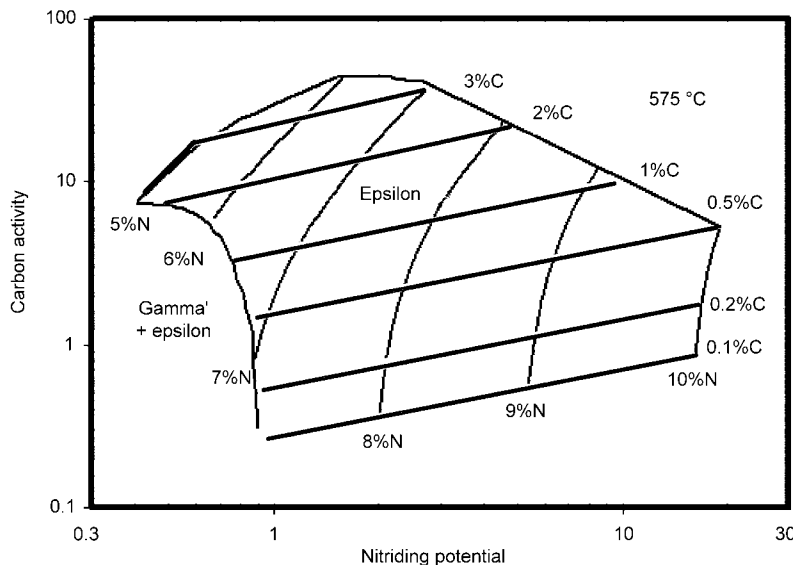


Fig. 12 Nitrocarburizing diagram displaying isoconcentration lines for nitrogen and carbon, calculated according to Kunze (Ref 18). The diagram gives the expected compound layer composition, depending on nitriding potential and carbon activity at 575 °C (1065 °F). Source: Ref 1

stage(s), the parts will often be cooled to a temperature typically below 530 °C (985 °F) for an additional postoxidation stage in order to enhance corrosion resistivity (see also “Postoxidation” in the section “Nitriding Processing” in this article).

Instead of furnace cooling, the parts may also be quenched (gas or liquid) to reduce porosity

and to avoid nitride needle formation. While slowly cooling a nitrogen-saturated lattice, the nitrogen solubility decreases, forcing nitrogen in supersaturated solution out of the solution and into the grain boundaries. This structure of intergranular nitrides takes the shape of needles when observed in a micrograph. Because these

Table 7 Possible stresses and best-suited compound layer properties

Work condition	Composition	Thickness, μm
Abrasion	$\epsilon(\gamma')$ postoxidized	>10
Adhesion	$\epsilon(\gamma')$	>10
Liquid metal attack	$\epsilon(\gamma')$ postoxidized	>10
Tribo-oxidation	ϵ or γ' , postoxidized or with high porosity to absorb lubricants	>10
Contact fatigue	$\epsilon(\gamma')$	0 to <10
Corrosion	$\epsilon(\gamma')$ postoxidized	~ >20

Source: Ref 15, 16

nitrides are much harder than the surrounding material, they act as wedges, reducing the resistance to crack propagation. Some parts, such as ball joints or synchronizer gears, are required to be free of intergranular nitrides to perform in conditions where impacts are common.

Controlling the Compound Layer. Compound layer thickness, composition, and porosity are the normal property goals (Table 7). According to Ebersbach (Ref 19), the corrosion resistance of a nitrocarburized part will dramatically increase if the compound layer is composed of ϵ -carbonitrides with a total nitrogen-plus-carbon content $[N + C]$ of at least 8.6 mass% (Fig. 13) and with a $C/[N + C]$ ratio between 0.02 and 0.2. Information on how to influence the nitrocarburizing results is given in “Controlling Diffusion Zone and Compound Layer” in the section “Nitriding Processing” in this article.

Austenitic Nitrocarburizing. Because plain carbon steels do not form a diffusion zone of high hardness, this zone is not hard enough to support the compound layer. Therefore, the general purpose of austenitic nitrocarburizing is to create a diffusion zone underneath the compound layer with a high enough hardness to support the compound layer to withstand Hertzian stresses. By raising the nitrocarburizing temperature above A_{c1} (of the nitrogen- and carbon-saturated diffusion zone), the diffusion zone is transformed from ferrite to austenite. Neither the compound layer nor the base material will be affected. The treatment temperature ranges between 595 and 720 °C (1100 and 1330 °F).

While cooling slowly, the austenitic structure of low-alloyed steels will transform into the Fe-Fe₄N eutectoid, called braunite (a pendant to pearlite in the iron-carbon system). Fast cooling or quenching will result in retained Fe-N-C austenite, which may be transformed to martensite and bainite with a hardness of 750 to 900 HV by cryogenic treatment and subsequent tempering at approximately 300 °C (570 °F).

Other High-Temperature Processes

N-Quench (Ref 21) is a process developed by Nihon Techno Ltd., Japan, for case hardening of low-alloyed, low-carbon steels. At temperatures between 700 and 800 °C (1290 and 1490 °F), the parts are exposed to an atmosphere consisting of either ammonia or an ammonia-nitrogen mixture. At these temperatures, the surface layer is transformed into

gamma phase, containing more than a wt % N. After nitriding, the parts will be quenched to obtain nitrogen martensite.

The material below the nitrided layer is not hardened. Typical surface hardness exceeds

800 HV. While distortion is still comparable to gas nitriding, the higher temperature allows for shorter cycle times and less gas consumption. A hardened layer of 20 μm can be achieved within 40 min.

Typical applications include:

- Clutch plates
- Spools
- Bearing holders
- Thrust washers
- Knitting machine parts

Table 9 Commercial nitrocarburizing processes

Procedure	Process gases	Mass% N in compound layer	Mass% C in compound layer
Nitemper (Ipsen USA)	50% NH ₃ , 50% exogas	8–10	1.7–10.5
Nitrotec (Mamesta)	NH ₃ + exogas + air	Not specified	Not specified
Nitroc (Aichelin)	NH ₃ + 50% exogas or ~10% CO ₂	~9	~1
Deganit (Degussa)	50% NH ₃ + 50% exogas (1st stage) 50% NH ₃ + 50% endogas (2nd stage)	Not specified	1–1.7
Nitroflex (AGA)	NH ₃ + CO/CO ₂	8.5–10.5	Not specified
Typical	NH ₃ + 3–10% CO ₂	<10.5	0.5–1.2

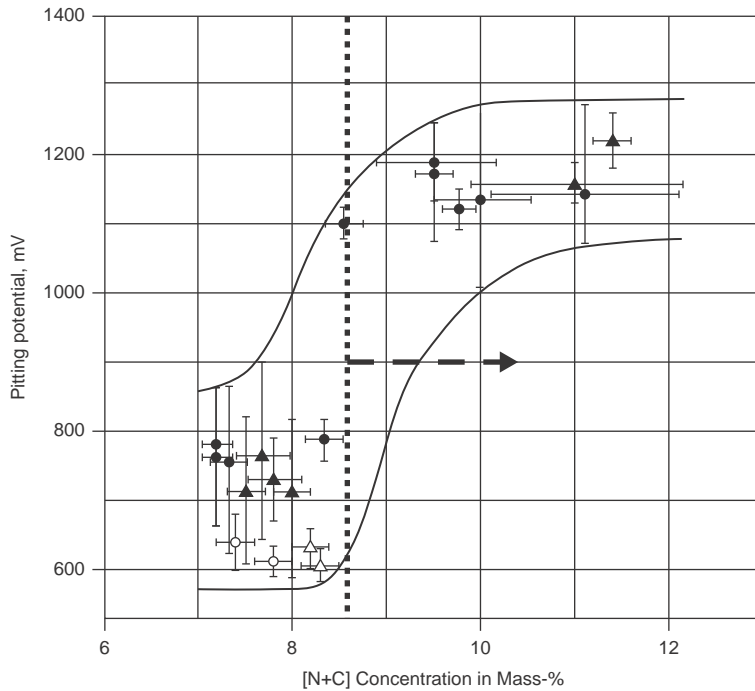


Fig. 13 The corrosion resistance of a nitrocarburized part will dramatically increase if the compound layer is composed of ε-carbonitrides and the [N + C] content in the compound layer is at least 8.6 mass%. The graph shows how the pitting potential jumps by more than 200 mV when crossing the recommended minimum composition. ○, gas nitrocarburized; ●, gas nitrocarburized plus oxidized; △, salt bath nitrocarburized; ▲, salt bath nitrocarburized plus oxidized. Source: Ref 20

Solution nitriding (Ref 22) aims for a diffusion zone of high hardness on stainless steels, without losing, or sometimes even improving, the corrosion-resistance properties of the base material (SolNit, Ipsen International).

At high temperatures between 1050 and 1150 °C (1920 and 2100 °F), nitriding can be performed using nitrogen gas. Following Sievert’s law, the solubility of nitrogen (c_N) in iron (Fig. 14) is proportional to the square root of the partial pressure of nitrogen:

$$c_N = \sqrt{p_{N_2}}$$

Maintaining corrosion resistance requires chromium not to be bound to nitrides or carbides in order to form passivating chromium oxides after the heat treatment. Depending on steel composition, temperature and nitrogen pressure must be controlled in such a way that the percentage of dissolved nitrogen does not force the formation of chromium nitrides but still provides maximum hardness. Figure 15 (Ref 23)

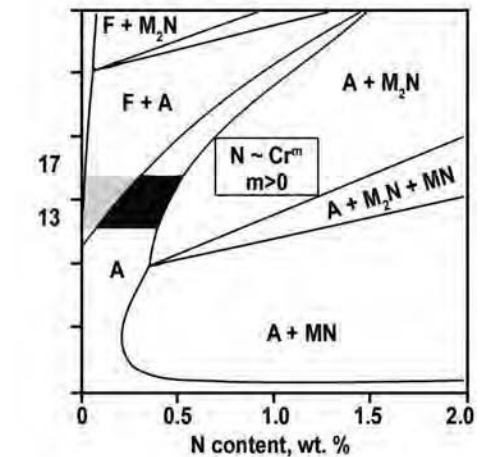
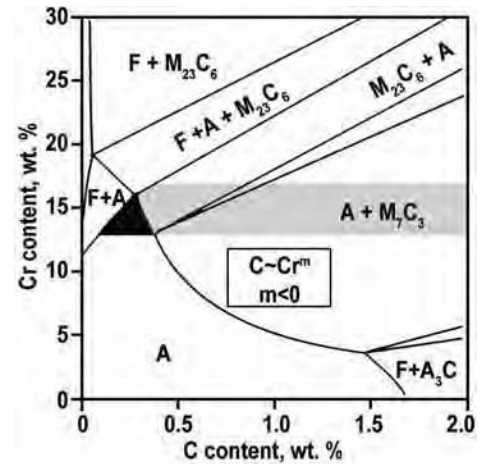


Fig. 15 Influence of chromium content on the solubility of carbon and nitrogen in austenite at 1100 °C (2010 °F). Adapted from Ref 23

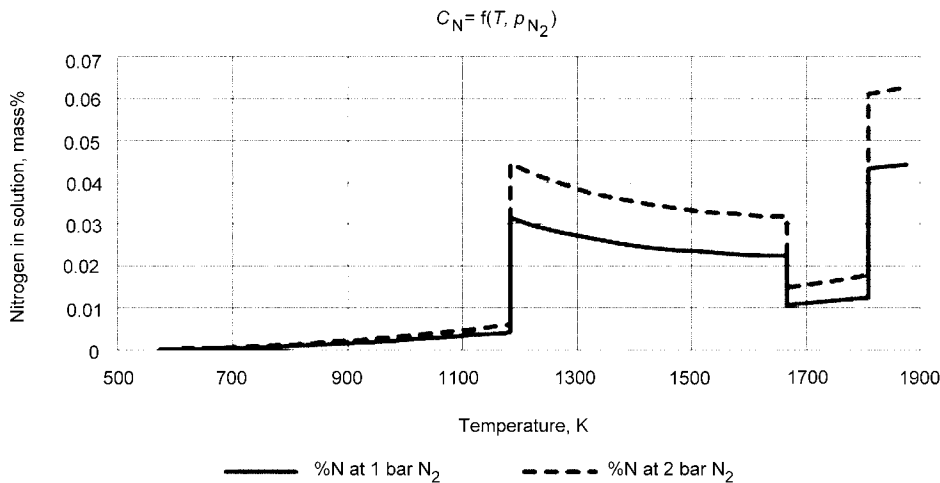


Fig. 14 Nitrogen solubility in iron as a function of temperature and nitrogen pressure

shows the solubility of nitrogen and carbon, depending on the chromium content, at 1100 °C (2010 °F). Typical furnace pressure ranges between 0.1 and 2 bar (75 to 1500 torr). The high process temperatures and process times of 15 to 240 min provide case depths of 0.2 to 2.5 mm (0.01 to 0.1 in.). The development of the case depth follows the laws of diffusion and is proportional to the square root of time:

$$x \sim \sqrt{t}$$

After diffusion treatment, the load must be quenched to prevent chromium oxide precipitation and therefore maintain corrosion resistance. Depending on the steel composition, the parts will be treated in a different manner. In austenitic stainless steels, the surface will consist of austenite with up to 0.9 mass% N in solution, with a surface hardness only slightly higher compared to the core hardness. In martensitic stainless steels, the nitrogen-saturated surface will contain a high amount of retained austenite that will be transformed into martensite by a subsequent cryogenic treatment and tempering above 450 to 480 °C (840 to 895 °F). The process requires a vacuum furnace with integrated gas or oil quench and also able to withstand high pressures up to 2 bar (1500 torr).

Typical applications are austenitic or martensitic stainless steel parts, such as:

- Tools for plastic processing machines
- Components of gearboxes
- Bearings of jet turbines
- Pumps and valves of fluid machines
- Surgical instruments
- Cutlery
- Implants
- Sanitary accessories
- Membranes

Nitriding Processing

Cleaning. Because nitrogen transfer is blocked by any contamination on the part surface, nitriding requires thorough cleaning to remove organic residuals prior to the nitriding process. Part production involves various synthetic additives from cutting fluids, anticorrosion additives, as well as remnants from abrasive wheels containing aluminum oxide. They all contribute to nonuniform nitriding, flaking layers, and other surface defects.

Table 10 Typical surface condition after machining

Thickness	Composition	Properties
Environment
Contamination layer	>1 μm	Machining residuals
Sorption layer	1–10 nm	Rich on carbon and oxygen, water
Reaction layer	1–10 nm	Metal oxides
Deformed boundary layer	>1 μm	Base material
Base material

Source: Ref 24

According to Haase (Ref 24), the typical surface condition of a machined part will show a contamination layer consisting of dirt and residuals, such as oil and grease but also shavings and chippings. Below this contamination layer is a sorption layer of water and hydrophobic agents such as hydrocarbons. Below this film, metal oxides and a more or less deformed base material can be found (Table 10).

While most parts can be successfully nitrided after vapor degreasing or cleaning in water with specific cleaning agents, some machine-finishing processes, such as buffing, finish grinding, lapping, and burnishing, may produce surfaces that retard nitriding and result in uneven case depth and distortion.

This may require abrasive cleaning with aluminum oxide grit or other abrasives, such as garnet or silicon carbide, immediately prior to nitriding. Any residual grit must be brushed off before parts are loaded into the furnace. From a practical point of view, those methods are not used unless there is a problem with passivated layers and surface deformations, typical of fine blanking. However, wet glass-bead blasting is a delicate yet effective way of cleaning certain parts.

As a general rule, vapor degreasing does not remove synthetic additives and water-soluble contaminants. Water and specific industrial cleaning agents (tensides) are used to remove mineral and nonmineral contaminants. Some of the cleaning agents are high pH, while ultrasonic cleaners often use specifically designed neutral pH cleaning agents. Parts also should be handled with clean gloves.

Safety Purge. Nitriding and nitrocarburizing processes are typically carried out at temperatures below the 750 °C (1380 °F) safety temperature known from atmospheric carburizing. Staying above this temperature would ensure that all flammable species in a furnace atmosphere would immediately burn, and an explosive gas mixture could not form.

Because nitriding and nitrocarburizing, except for solution nitriding, is performed below the self-ignition temperature of the flammable gases used, such an explosive mixture may build up. Tables 11 and 12 give the lower and upper explosion limits for various gases in air and nitrous oxide as well as the self-ignition temperatures of various gases.

Therefore, whenever the furnace atmosphere is supposed to change from oxygen/air to flammable gases or vice versa, the furnace must be purged with either an inert gas, typically nitrogen, or the furnace must be depressurized to a

point where either the amount of oxygen or the amount of flammable gases is low enough to prevent explosion hazards.

According to the safety regulations given by National Fire Prevention Association (NFPA) 86 and the safety recommendations of the German Association for Heat Treatment and Material Science (AWT) Committee 8, a safety purge with inert gas requires a gas volume of five times the furnace volume or pumped down to a pressure below 45 mbar (AWT) or 0.1 torr (NFPA) absolute.

Preoxidation. Nitriding and nitrocarburizing often start with a preoxidation stage that may be part of the nitriding process or may be done separately in a preoxidation furnace. Note: Water preoxidation does not burn any contamination with hydrocarbons.

Preoxidation can be thought of as an additional cleaning. The preoxidation temperature is approximately 300 °C (570 °F), above the vaporization temperature of hydrocarbons and cleaning agents. Therefore, the furnace is heated with air to the preoxidation temperature and held at temperature for approximately 30 to 45 min. Other contaminating films may be disintegrated by iron oxide formation.

Preoxidation may also be carried out by using water vapor with or without an additive of weak water-soluble acid. In this case, the preoxidation time is much shorter. Three minutes preoxidation with water is equivalent to approximately 30 min preoxidation with air. Therefore, it is favorable to heat the furnace to preoxidation temperature in nitrogen or air prior to injecting the water. Water preoxidation produces exclusively Fe₃O₄ magnetite, whereas air preoxidation produces magnetite and Fe₂O₃ hematite.

Table 11 Explosion limits for various gas-air mixtures

Process gas	Lower explosion limit, %	Upper explosion limit, %
H ₂ in air	3.75	75.1
H ₂ + 40% N ₂ in air	3.65	37.3
NH ₃ in air	13.3	32.9
NH ₃ + 20% N ₂ in air	14.1	20.9
H ₂ in N ₂ O (Ref 25)	3–6	84
CH ₄ in N ₂ O (Ref 25)	5	50

Source: ASTM E686-98

Table 12 Self-ignition temperatures of various process gases

Process gas	Self-ignition temperature	
	°C	°F
Hydrogen (H ₂)	~530	~985
Ammonia (NH ₃)	~650	~1200
Endogas (20% CO, 40% H ₂ , 40% N ₂)	~560	~1040
Carbon monoxide (CO ₂)	~610	~1130
Methane (CH ₄)	~640	~1185
Propane (C ₃ H ₈)	~510	~950

Source: AWT Committee 8

The formation of iron oxides will have some activating effect and will promote a faster growth of iron nitride grains on the surface at the beginning of the nitriding/nitrocarburizing stage (Ref 26).

Steels with higher chromium concentrations, especially stainless steels, cannot be nitrided after preoxidation. This type of steel requires a special activation stage to remove chromium oxides prior to the nitriding stage.

Activation/Depassivation. When nitriding or nitrocarburizing steels with high chromium content, parts must be depassivated, a process also referred to as activation.

To remove the passivating chromium oxides from the part surface, the oxygen partial pressure must be maintained to a very low level. The modified Ellingham diagram (Fig. 16) shows that at a temperature of 400 °C (750 °F), the partial pressure of oxygen must be controlled to less than 10^{-50} bar (7.5×10^{-48} torr). The corresponding signal of an internal oxygen probe would have to be above 1650 mV. Alternatively, the graph also displays the partial pressure ratios of:

$$\frac{p_{H_2}}{p_{H_2O}} \text{ at approximately } 10^8$$

$$\frac{p_{CO}}{p_{CO_2}} \text{ at approximately } 10^7$$

There have been successful attempts by using pure carbon monoxide or extremely dry hydrogen, but, in most cases, an addition of acid-forming agents is used for activation. Most of the activation agents require special cleaning or filtering of the exhaust gas.

Examples of activation methods include:

- U.S. Patent 5,340,412 describes the use of fluorine or fluoride-containing gas where the preferred agent would be a gas mixture containing 30,000 to 50,000 ppm of NF_3 . The amount of fluorine is chosen to reach good activation but prevent the furnace material from being exposed to an overly aggressive gas.
- EP1707646B1 describes activation by using a mixture of carbon monoxide and ammonia heated to at least 300 °C (570 °F) to form cyanide (HCN) and water. The HCN breaks the chromium oxides.
- DE19730372B4 describes the use of citric acid ($C_6H_8O_7$) for preoxidation/activation and post-oxidation. The citric acid is less aggressive and more suitable for the equipment.

Other possible agents used for activation are chemical compounds containing chlorine, such as polyvinyl chloride or ammonium chloride, but also sulfur and phosphorus.

The EXPANITE process (international patent WO 2011/009463 A1) uses the same agents for

activation and for nitriding/nitrocarburizing, so there is no sharp boundary between activation and nitriding.

Nucleation. To ensure a uniformly nitrided layer, the surface of the parts should be covered by a thin, closed layer of iron nitrides at the very beginning of the nitriding process. This layer will then act as a reservoir for further nitrogen diffusion. According to Somers et al. (Ref 28), nucleation starts with formation of Fe_4N γ' -nitride or of dual-phase Fe_4N γ' and $Fe_{2-3}N$ ϵ -nitride nuclei. Such nuclei will grow and eventually form a closed layer.

Fast and perfect nucleation requires a high availability of ammonia at the beginning of the nitriding/nitrocarburizing process. This can be achieved by filling the furnace with ammonia, either at already comparably low temperatures or by exchanging the atmosphere as fast as possible at higher temperatures by a high flow of ammonia. Figure 17 shows the formation of iron nitride nuclei during the first 3 min at 575 °C (1065 °F).

Depending on component geometry, it may be useful to heat the parts to nitriding temperature in an inert atmosphere and then to wait for the temperature to equalize prior to nucleation. In particular, if parts have sections with high mass and low mass, such as fins and so on, starting the ammonia flow at lower temperatures would result in overnitriding the thin sections and undernitriding the thick sections, due to their different heating times.

Postoxidation. Adding a Fe_3O_4 magnetite layer approximately 1 to 3 μm thick on top of the compound layer increases the corrosion-resistance properties and further reduces the coefficient of friction. While the corrosion resistivity of a 12 μm ϵ -compound layer already matches the 40 μm chromium plating, applying postoxidation nearly quadruples the time in a salt spray test (Ref 29). Figure 18 shows the surface layer of nitrided and postoxidized C15; the iron oxides partially close the pores of the iron nitride structure.

Postoxidation is typically carried out in a temperature range of 450 to 520 °C (840 to 970 °F). The furnace is cooled to this temperature and typically purged with nitrogen prior to injecting the oxidizing agent. The duration ranges between 30 and 45 min; the lower the temperature, the more dense is the resulting magnetite layer. Oxidizing agents are water (vapor) or nitrous oxide.

Postoxidation may be controlled using an in situ oxygen probe, where the oxygen partial pressure is maintained to match the desired iron-oxygen phase (Fig. 10).

Controlling Diffusion Zone and Compound Layer. The diffusion of interstitials such as nitrogen and carbon is described by Fick's laws:

$$J = -D \frac{dc}{dx} \text{ (Fick's first law)}$$

where the flow, J , of the interstitial is determined by the diffusion coefficient, D , and the

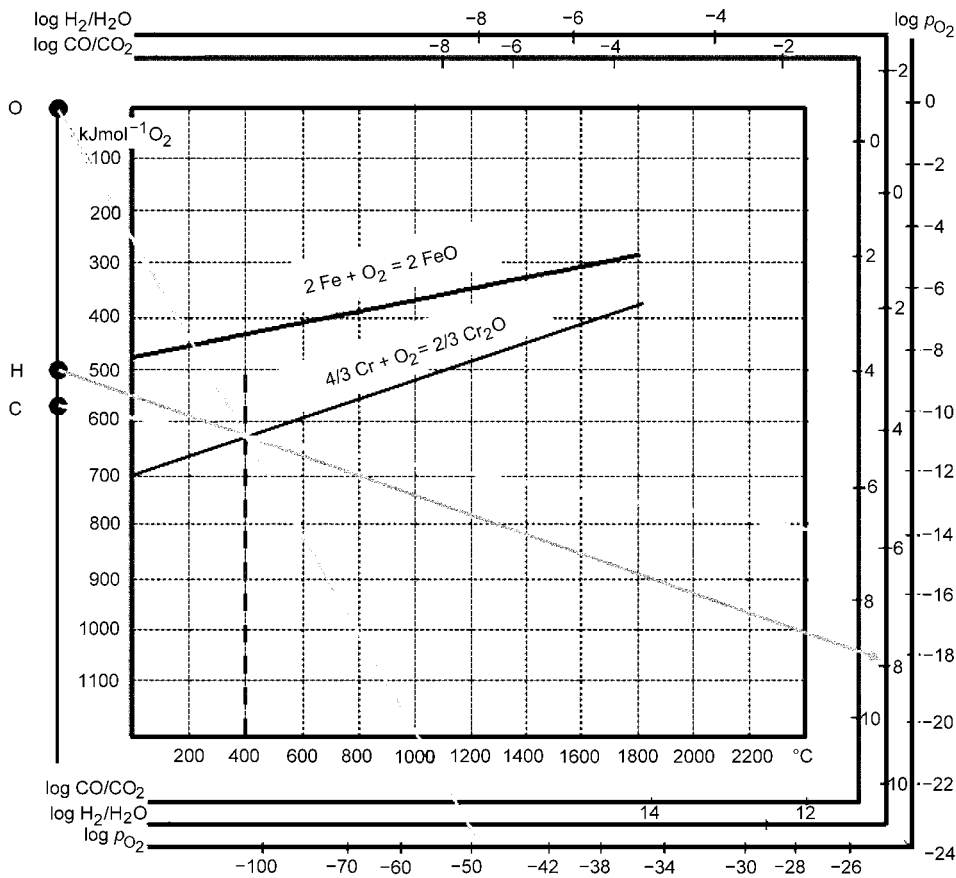


Fig. 16 Modified Ellingham diagram. Source: Ref 27

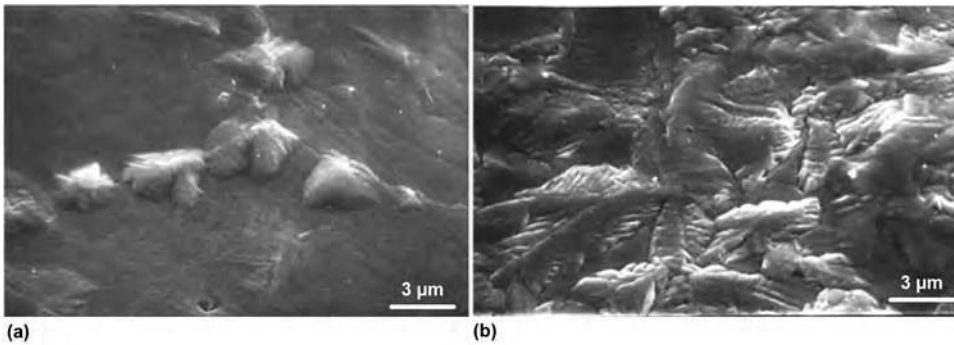


Fig. 17 Scanning electron microscope images of the nucleation of iron nitrides on a part surface after (a) 1 min and (b) 3 min at a nitriding temperature of 575 °C (1065 °F). Courtesy of IWT Bremen, Germany

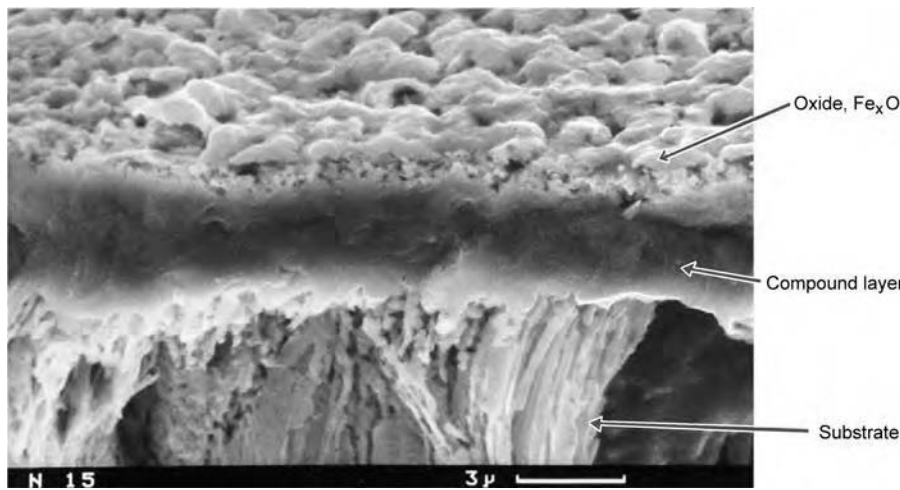


Fig. 18 Nitrided and postoxidized C15. Oxidation just began; iron oxides partially cover the porous compound layer below. Courtesy of IWT Bremen, Germany

concentration gradient, dc/dx . The differential change in concentration (dc) per time fraction (dt) can be evaluated by:

$$\frac{dc}{dt} = D \frac{d^2c}{dx^2} \text{ (Fick's second law)}$$

The concentration of the interstitial after time, t , at the position x while maintaining a concentration (c_0) on the surface can be calculated by:

$$c(x, t) = c_0 \operatorname{erfc} \left[\frac{x}{\sqrt{4Dt}} \right]$$

with $\operatorname{erfc} []$ being the complementary Gauss' error function. The length $\sqrt{4Dt}$ is called the diffusion length; the diffusion coefficient, D , and the maximum solubility, c_s , increase with temperature:

$$D = D_0 \exp[-Q/(RT)]$$

with Q being the activation energy, R the universal gas constant, and T the temperature in Kelvin. The formation of the diffusion zone thereby caused propagation of the precipitation

front, and therefore, the formation of total and effective case depth is determined by time, temperature, and the solubility of nitrogen at temperature, affected by the alloying elements. Nitride-forming elements such as aluminum, chromium, titanium, and vanadium will readily consume the diffusing nitrogen and therefore slow down the inward diffusion of nitrogen; according to Kunze (Ref 30), the resulting depth of the precipitation front can be estimated by:

$$s = \sqrt{\frac{c_s}{c_{NF} + \frac{1}{2}c_s} 2Dt}$$

with (c_s) being the solubility of nitrogen in the alpha matrix, and (c_{NF}) the total concentration of nitrogen bound in nitrides of nitride-forming elements. Non-nitride-forming elements such as nickel will lower the solubility c_s of nitrogen in the iron matrix and therefore slow down the interstitial diffusion.

If the case depth should be doubled, the duration of the nitriding stage must be four times longer, maintaining the same temperature and nitriding potential. On the other hand, when

staying with the same stage time, the temperature would have to be increased by approximately 83 °C (150 °F), and the nitriding potential must be adjusted to achieve the corresponding surface concentration, matching the Lehrer diagram.

The influence of temperature and time on the compound layer (Fig. 19) follows similar effects, but, in contrast to the aforementioned precipitation front, there is a considerable nitrogen flux into the diffusion layer, because iron is only a weak nitride-forming element. Because the flux is diffusion controlled, the relation between compound layer thickness and time can be estimated as:

$$s \sim \sqrt{t}$$

To build a compound layer, the activity of nitrogen must be high enough to force the formation of iron nitrides, respectively iron carbonitrides. Nitride-forming elements will lower the activity of nitrogen unless not yet transformed into nitrides. For this reason, formation of a white layer on top of high-alloyed steel will typically require a higher nitriding potential and a longer nitriding time. Aluminum, on the other hand, will promote compound layer formation, which may be explained by its much higher diffusion coefficient in iron, creating nitrides in a very short time compared to other nitride-forming elements, such as chromium. Table 13 gives the diffusion coefficients in iron for some elements at nitriding temperatures. Carbon increases nitrogen activity and promotes formation of iron carbonitrides at lower nitriding potentials.

Doubling the compound layer thickness requires approximately a four times longer nitriding stage at constant temperature and nitriding potential. *Increasing the temperature by 10 °C (18 °F) and adjusting the nitriding potential will promote an increase of approximately 10% on the compound layer thickness.* Table 14 gives some basic factors for adjusting case and compound layer thickness to time and temperature. Note that, depending on the material, there is a maximum thickness of compound layer that can be achieved.

Because all of the aforementioned mechanisms are highly dependent on temperature, temperature uniformity and accuracy of temperature control are mandatory. The precision of temperature control and uniformity defines the class of furnace given in NFPA 86 and AMS 2750 D.

The second prerequisite is maintaining perfect atmosphere circulation and uniformity, so that all parts experience the same atmosphere potential. Atmosphere circulation also supports uniformity of temperature.

Atmosphere Control

Dissociation Rate and Nitriding Potential.

In nitriding, dissociation rate, residual ammonia, and nitriding potential are mainly determined by

Temperature		$K_N, \sqrt{\text{bar}}$	Time, min	Compound layer thickness	
$^{\circ}\text{C}$	$^{\circ}\text{F}$			Min	Max
480	896	5.06	2400	9	14
550	1022	2.64	240	8	12
600	1112	214	30	10	12
640	1184	1.44	15	10	13

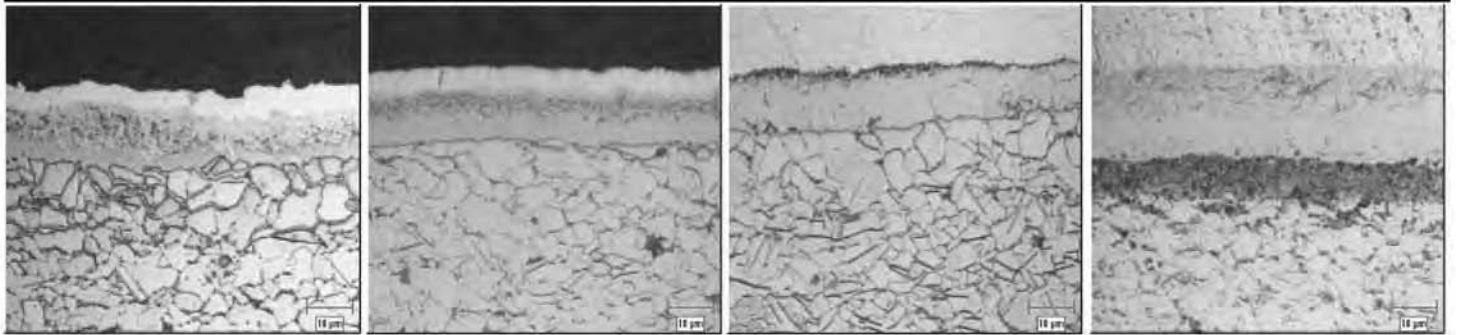


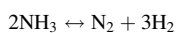
Fig. 19 Nitrocarburizing time to create a compound layer of approximately 10 μm on a microalloyed 1006 (high strength, low alloy) steel at varying temperatures. The nitriding potential has been adjusted to match the temperature and is controlled using NH_3 and dissociated NH_3 with a 10 vol% CO_2 addition to the process gas. The far-right micrograph shows the typical brownish austenitic structure below the compound layer due to the high temperature. Courtesy of Nitrex Metal Inc., Canada

Table 13 Calculated diffusion coefficients of elements in iron at nitriding temperatures

Calculation based on data provided by Eckstein (Ref 31). The ratio D_i/D_N shows the relative diffusion coefficient of a species compared to nitrogen in the according structure.

Element	Iron phase	$D, \text{cm}^2\cdot\text{s}^{-1}$		$D, \text{cm}^2\cdot\text{s}^{-1}$	
		500 $^{\circ}\text{C}$ (930 $^{\circ}\text{F}$)		595 $^{\circ}\text{C}$ (1105 $^{\circ}\text{F}$)	
H	α	3.03×10^{-4}	5084	3.72×10^{-4}	1603
	Γ	1.31×10^{-5}	76,036
C	A	4.14×10^{-8}	0.695	1.73×10^{-7}	0.75
	Γ	9.78×10^{-10}	5,696
N	A	5.95×10^{-8}	1	2.32×10^{-7}	1
	Γ	3.03×10^{-4}	...	1.72×10^{-10}	1
	$\text{Fe}_4\text{N}-\gamma'$	3.98×10^{-10}	0.0067
	$\text{Fe}_{2-3}\text{NC}-\epsilon$	9.96×10^{-11}	0.0017
Al	Γ	8.30×10^{-13}	4.8×10^{-3}
	A	1.62×10^{-18}	2.73×10^{-11}	1.30×10^{-16}	5.59×10^{-10}
Si	Γ	4.94×10^{-16}	2.88×10^{-6}
	A	5.71×10^{-17}	9.60×10^{-10}	3.88×10^{-15}	1.67×10^{-8}
Ti	Γ	1.16×10^{-16}	6.77×10^{-7}
	A	3.06×10^{-17}	5.14×10^{-10}	2.05×10^{-15}	8.82×10^{-9}
Cr	Γ	3.61×10^{-14}	...	4.23×10^{-15}	2.46×10^{-5}
	A	4.54×10^{-18}	7.63×10^{-11}	3.05×10^{-16}	1.31×10^{-9}
Co	Γ	3.69×10^{-20}	2.15×10^{-10}
	A	1.67×10^{-16}	2.81×10^{-9}	1.02×10^{-14}	4.39×10^{-8}
Mo	Γ	9.41×10^{-17}	5.48×10^{-7}
	A	2.09×10^{-23}	3.51×10^{-16}	3.29×10^{-21}	1.42×10^{-14}
W	Γ	1.83×10^{-24}	1.07×10^{-14}
	A	3.33×10^{-17}	5.60×10^{-10}	1.97×10^{-15}	8.46×10^{-9}
Fe	γ	1.04×10^{-19}	...	1.03×10^{-17}	5.98×10^{-8}

the thermal catalytic dissociation of ammonia and the ammonia inlet flow rate. The thermodynamic equilibrium of the reaction:



at normal nitriding conditions is almost fully on the side of dissociated ammonia. At atmospheric pressure and a nitriding temperature

of 525 $^{\circ}\text{C}$ (975 $^{\circ}\text{F}$), the residual ammonia percentage in equilibrium is less than 2% in volume. While the equilibrium depends on temperature only, the speed that determines how fast the ammonia will dissociate is dependent on temperature and the catalytic surface in the furnace. Tests performed in an industrial-sized pit-type furnace with a volume of approximately 2.5 m^3 (96.5 ft^3) showed that the

half-life of ammonia at 500 $^{\circ}\text{C}$ (930 $^{\circ}\text{F}$) was approximately 80 min. Raising the temperature to 575 $^{\circ}\text{C}$ (1055 $^{\circ}\text{F}$) shortened the half-life to 8 min (Fig. 20).

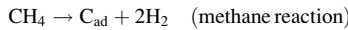
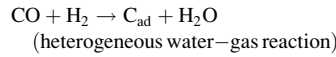
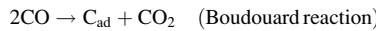
Consequently, increasing the nitriding potential (decreasing the dissociation rate) requires increasing the ammonia flow and vice versa. When lowering the nitriding potential by reducing the ammonia flow, there may be a point where the minimum flow of process gas will still be too high to support a low potential. To overcome this situation, the preferred procedure is to mix the ammonia with predissociated ammonia, maintaining a constant flow just above the minimum flow required to keep the slight overpressure needed to operate the furnace safely. The use of predissociated ammonia is recommended because the gas mixture in the furnace still follows the boundary conditions given in the Lehrer diagram.

If dissociated ammonia is not available, hydrogen may also be used to decrease the nitriding potential. Nitrogen, on the other hand, does not work in the same manner, because the effect of nitrogen dilution mainly changes the dynamics of the catalyst. As long as the amount of ammonia molecules in the furnace atmosphere is high enough to fully cover the catalytic surface, the nitriding potential will be slightly lowered. Once ammonia is rarified, and parts of the catalytic surface are no longer covered by fresh molecules, the nitriding potential begins to rise again, but not the nitriding effect. Beyond this point, control no longer works.

Small furnaces typically require a higher ammonia flow versus furnace volume ratio, and the maximum possible flow must be adjusted accordingly. Large furnaces have a rather small catalytic surface-to-volume ratio and should be equipped with a predissociated ammonia supply if used to nitride large parts that require a restricted compound layer.

Carburizing Potential. In nitrocarburizing, the carburizing potential should be controlled concurrently with the nitriding potential. In typical installations, carbon dioxide and end-gas are the most popular carbon sources used, although some applications use hydrocarbons such as methane or propane. Similar

to carburizing, the carburizing effect of the process atmosphere can be driven by a variety of reactions, depending on the process gas supply:



where C_{ad} describes the carbon adsorbed by the iron surface. Of these three reactions, the heterogeneous water-gas reaction is by far the

most efficient one. Each of these reactions also establishes its own equilibrium, depending on temperature:

$$K_1 = f(T) = \frac{a_c \times p_{\text{CO}_2}}{p_{\text{CO}}^2}$$

$$K_2 = f(T) = \frac{a_c \times p_{\text{H}_2\text{O}}}{p_{\text{CO}} \times p_{\text{H}_2}}$$

$$K_3 = f(T) = \frac{a_c \times p_{\text{H}_2}^2}{p_{\text{CH}_4}}$$

The activity of carbon (a_c) can be seen as a measure of the chemically effective concentration of carbon in the iron-carbon mixture. Rearranging the equations leads to:

$$a_c = \frac{K_1 \times p_{\text{CO}}^2}{p_{\text{CO}_2}}$$

$$a_c = \frac{K_2 \times p_{\text{CO}} \times p_{\text{H}_2}}{p_{\text{H}_2\text{O}}}$$

$$a_c = \frac{K_3 \times p_{\text{CH}_4}}{p_{\text{H}_2}^2}$$

Table 14 Factors on how nitriding time and temperature affect diffusion zone (case depth) and compound layer thickness

The factors given for a variation of the nitriding time require constant temperature and nitriding potential; the factors given for a temperature variation require constant nitriding time and the nitriding potential adjusted to match the identical position to the phase boundaries given in the Lehrer diagram (see factors on K_N). The factors represent the average factors calculated for a temperature range of 500 to 580 °C (930 to 1075 °F).

Factor on stage time	Factor on case depth and compound layer thickness	Temperature variation (ΔT), K	Factor on K_N in α -Fe	Factor on K_N in Fe_4N	Factor on K_N in $\text{Fe}_2\text{-}_3\text{N}$	Factor on case depth	Factor on compound layer thickness
0.05	0.22	-50	1.45	1.81	1.86	0.66	0.6
0.1	0.32	-40	1.34	1.60	1.63	0.72	0.66
0.2	0.45	-30	1.24	1.41	1.44	0.78	0.74
0.5	0.71	-20	1.15	1.26	1.27	0.85	0.81
0.75	0.87	-10	1.07	1.12	1.13	0.92	0.9
1	1	0	1	1	1	1	1
1.1	1.05	+10	0.93	0.90	0.89	1.09	1.11
1.2	1.1	+20	0.87	0.81	0.80	1.18	1.23
1.5	1.22	+30	0.82	0.73	0.71	1.28	1.36
2	1.41	+40	0.77	0.66	0.64	1.39	1.51
3	1.73	+50	0.72	0.60	0.58	1.51	1.67
4	2
5	2.24

The partial pressure ratios in the previous equations are called the carburizing potentials, K_C , for the following reactions:

$$K_{\text{CB}} = \frac{p_{\text{CO}}^2}{p_{\text{CO}_2}} \quad (\text{Boudouard})$$

$$K_{\text{CW}} = \frac{p_{\text{CO}} \times p_{\text{H}_2}}{p_{\text{H}_2\text{O}}} \quad (\text{water gas})$$

$$K_{\text{C-CH}_4} = \frac{p_{\text{CH}_4}}{p_{\text{H}_2}^2} \quad (\text{methane})$$

Note that none of the carburizing potentials match the carbon potentials used in carburizing processes. Unfortunately, the carburizing potentials do not match in numbers and therefore do not cause identical changes in the part surface, if controlled to the same number. To invoke the same conditions, those potentials must be adjusted by their activities. The data provided can be straightforwardly obtained from tabulated thermodynamic data (e.g., in Ref 33). For an example, the reader is referred to Ref 34. The equations were taken directly from DIN 1998 (Ref 35):

$$\log_{10}(a_c) = \log_{10}(K_{\text{CB}}) + 8817/T - 9.071$$

$$\log_{10}(a_c) = \log_{10}(K_{\text{CW}}) + 7100/T - 7.496$$

$$\log_{10}(a_c) = \log_{10}(K_{\text{C-O}_2}) + 5927/T - 4.545$$

$$\log_{10}(a_c) = \log_{10}(K_{\text{C-CH}_4}) + 4791/T - 5.789$$

Controlling the carburizing potential is discussed using the potentials according to the heterogeneous water-gas reaction and the Boudouard reaction. Figure 21 gives the K_N - K_{CB} control range for various carburizing gases, with K_N being controlled by modifying the ratio of ammonia to dissociated ammonia.

Both K_{CW} and K_{CB} are determined by CO as the driving force and by H_2O , respectively; CO_2 , on the other hand, somehow acting like brakes. It is obvious that the carbon monoxide

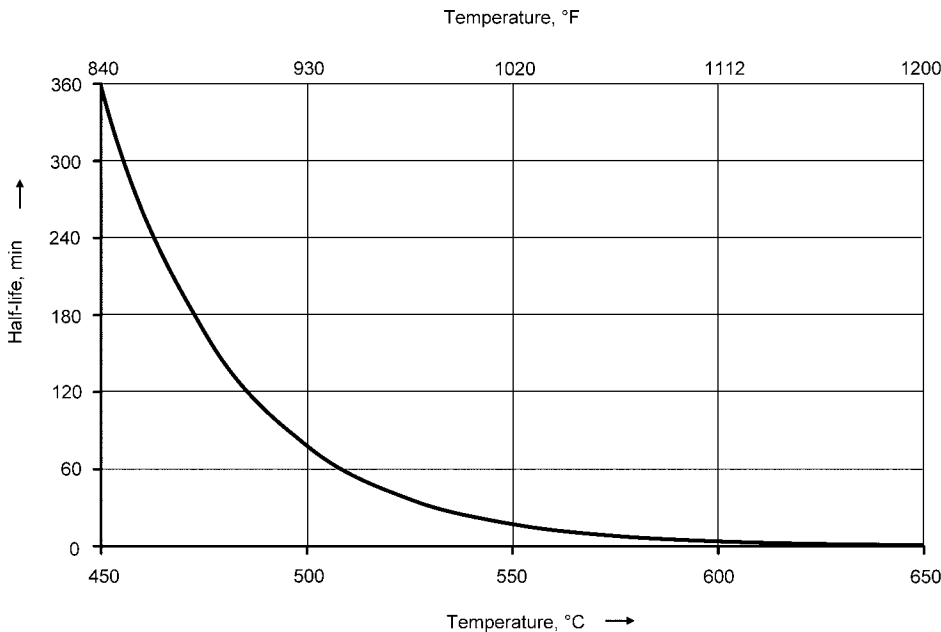


Fig. 20 Half-life of ammonia in a typical retort furnace with 2.5 m³ (96.5 ft³) volume at varying temperatures. Source: Ref 32

percentage in the process gas must be raised in order to achieve higher carbon contents in the part surface layer. Still, most typical nitrocarburizing processes use CO₂ as a carbon source.

How is it possible to gain some speed while stepping on the brakes? Due to the water-shift reaction, CO₂ is reduced to CO by forming water vapor with the hydrogen available from the ammonia dissociation. Nevertheless, this is not very effective, because the maximum carburizing potential will theoretically be reached by nearly closing the CO₂ supply, which also reduces the carbon availability and therefore the carburizing effect. Tests performed by IWT Bremen, the research institute of the German Association for Heat Treatment and Material Science (AWT), showed that for carbon steels a percentage of 10 vol% CO₂ in an ammonia/dissociated ammonia atmosphere will allow for a carbon percentage of approximately 1 to 1.2 mass% in an ε-compound layer. For certain applications, it may be favorable to reach higher percentages.

According to Naumann and Langenscheid (Ref 36), forming the preferred ε-phase is a function of temperature, nitrogen percentage, and carbon percentage. In that way, it is possible to exchange the nitrogen with carbon within certain limits. The advantage of a high-carbon compound layer is improved temperature stability, accompanied by a lower tendency to form porosity. This effect is used in the SAE AMS 2759/12 nitrocarburizing specification, with a goal of a defined percentage of porosity in the compound layer.

To increase the carbon content in the compound layer, the carburizing potential must be raised by adding carbon monoxide. A typical carbon monoxide source would be endogas, with CO contents of either 20 vol% (natural gas/air) or 23 vol% (propane/air). Because CO does not carry an additional oxygen atom to counterweigh the ratios of $[p^2\{\text{CO}\} \div p\{\text{CO}_2\}]$ and $[p\{\text{CO}\}p\{\text{H}_2\} \div p\{\text{H}_2\text{O}\}]$, the carbon potential will theoretically go infinite; in a real process, the atmosphere will start to soot. Controlling the carburizing potential therefore requires a second gas with a higher amount of oxygen. This may be air, but for obvious safety reasons, the preferred solution should be either an addition of carbon dioxide or water vapor. Using endogas bears another disadvantage; due to its high amount of hydrogen (40 vol% natural gas/air, 31 vol% propane/air), the nitriding potential is decreased with increasing endogas addition, requiring a higher ammonia flow.

The most effective and readily achieved solution for controlling the carburizing potential is the use of a mixture of CO and CO₂. The percentage of carburizing gas [CO + CO₂] on the total process gas flow is set constant, that is, to 10%, and the ratio of CO versus CO₂ is modified to adjust the carburizing potential. The nitriding potential will not be noticeably affected, allowing for a smooth K_N - K_{CB} or K_N - K_{CW} control. Of course, it would likewise be possible to use water vapor instead of carbon dioxide, but this either requires additional equipment to produce the steam or a

much more delicate control to inject only very little amounts of liquid water.

Oxidizing Potential. Some processes such as oxynitriding or oxynitrocarburizing, as well as additional process stages such as postoxidizing, ask for control of a preferred oxidizing potential, K_O :

$$K_O = \frac{p_{\text{H}_2\text{O}}}{p_{\text{H}_2}}$$

In nitriding atmospheres, this requires the addition of an oxygen-bearing gas. In the past, but still today (2013), a controlled percentage of air will be added to the process gas, thus oxidizing hydrogen produced by thermal dissociation of ammonia to water vapor. Other applications use nitrous oxide, also known as laughing gas (N₂O), to achieve the same effect. Both species, O₂ and N₂O, are highly reactive and theoretically able to create an explosive mixture (see the sections "Safety Purge" and "Safety Precautions" in this article). Therefore, newer attempts have switched from injecting air or nitrous oxide to injecting water or carbon dioxide. While water would be the preferred solution, the addition of carbon dioxide basically turns the original nitriding process into a nitrocarburizing process.

In nitrocarburizing atmospheres with carbon monoxide and/or carbon dioxide addition, there is automatically an oxidizing potential. Nitrocarburizing atmospheres that exclusively add hydrocarbons will require the addition of an oxygen-bearing gas, preferably water. Maintaining a too high oxidizing potential during a nitrocarburizing process may result in an oxidized layer that, later in the process, may be reduced and nitrided. The resulting compound layer is very fragile, of high porosity, and will immediately break out once the part is in use.

In a postoxidation stage, where typically water is the only process gas injected into the furnace, the K_O may reach an uncontrolled potential. Therefore, it is useful to also inject a small amount of ammonia or dissociated ammonia, with the hydrogen balancing the water vapor.

Preoxidation or activation is typically not yet controlled, but it may be favorable to consider such a feature for future use when setting up the control equipment. The comparably low temperatures in a preoxidation or the activation stage require the use of a heated oxygen probe.

Instead of the oxidizing potential, K_O , oxygen partial pressure ($p\{\text{O}_2\}$) or $\log_{10}[p\{\text{O}_2\}]$ may be used as the controlled process variable. The iron-oxygen diagram shown in Fig. 10 gives the relation between K_O , $\log_{10}[p\{\text{O}_2\}]$, and the millivolt signal of an in situ oxygen probe as a function of temperature.

Weight-Percentage Control. Instead of controlling K_N and K_C concurrently, it is also possible to have the potentials set automatically

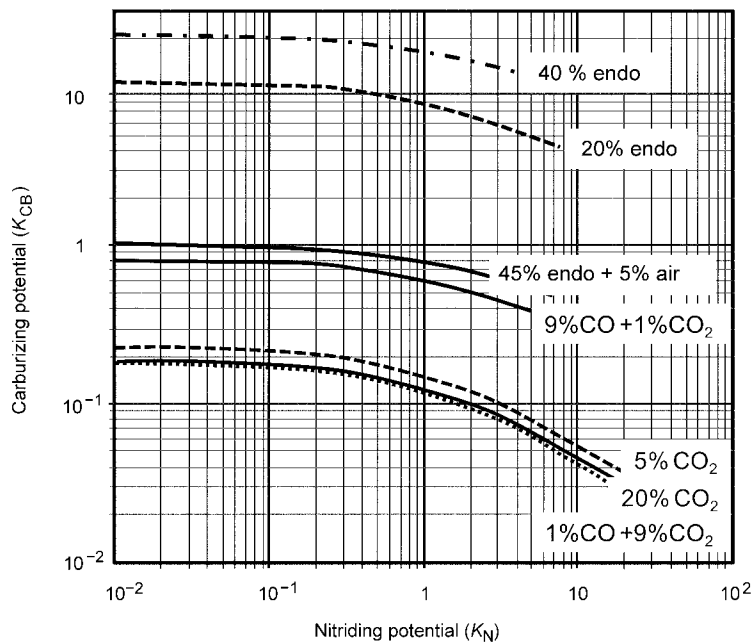


Fig. 21 K_N - K_{CB} control ranges at 580 °C (1075 °F) in ammonia/dissociated ammonia atmospheres with indicated addition of carbon gases. Adding CO₂ shows a reversed control behavior; increasing the CO₂ percentage in the process gas results in lower carburizing potentials. Endogas, carrying 20% CO, must be mixed with air (or CO₂ or H₂O) to avoid cementite formation. Using a mixture of CO and CO₂ allows for a wide control range in K_{CB} . Source: Ref 32

to aim for a given percentage of nitrogen and carbon in the compound layer (Ref 37) (Fig. 12, 22), hence defining the hot working capabilities and the percentage of porosity to be achieved by a nitrocarburizing process. The relation between temperature, nitriding potential, carburizing potential, and the expected compound layer composition on iron has been evaluated by Kunze (Ref 18), providing the necessary calculations.

The advantage of this target-oriented control variant is the ability to use the desired compound layer composition as a setpoint for the K_N - K_C controller.

Phase Control. Another target-oriented control variant allows for nearly eliminating porosity in the compound layer. The nitriding potential will be controlled to stay parallel to the phase boundaries to match the temperature-dependent dissociation pressure of the created iron nitride (Ref 39) (Fig. 22).

Considering that iron nitrides may also be formed by applying sufficient nitrogen pressure in the function of process temperature, an iron nitride tends to break down into iron and molecular nitrogen, locally creating the same pressure.

The Fe_4N γ' -nitride at 500 °C (930 °F) is kept in shape by a local pressure of more than 6000 atm; fortunately, the dissociation of ammonia at a nitriding potential of only 0.3 1/ $\sqrt{\text{bar}}$ provides the same pressure. To maintain the structural integrity of a Fe_2N ϵ -nitride, the nitriding potential at the same temperature must be raised to 2 1/ $\sqrt{\text{bar}}$, matching a nitrogen pressure of more than 300,000 atm.

Consequently, during a process, whenever the nitriding potential will no longer provide the pressure required to maintain the surface composition of the compound layer, such layer will break down to an iron nitride or iron carbonitride of lower order. The nitriding atom being released will easily react with another nitrogen atom to form molecular nitrogen by literally ripping a hole in the compound layer, causing porosity. Such an N_2 formation preferably occurs at energetically favorable locations in the microstructure, such as grain boundaries, dislocations, and so on.

Phase control maintains the appropriate pressure through all stages of the process, especially while cooling, and forms a uniform, dense compound layer (Fig. 23) with nearly no porosity at all. Applying a magnetite layer on top of the compound layer results in extraordinary corrosion resistance.

Zero-Flow Nitriding. On the contrary to the previously discussed K_N control policies, zero-flow nitriding, a process developed by Seco/Warwick Corp., Poland, uses a unary atmosphere of ammonia (Ref 40). The adjustment of the nitriding potential is performed by temporarily stopping and reactivating the ammonia flow into the furnace; hence, the process is the most efficient in the use of ammonia. The amount of ammonia needed to maintain the potential is controlled using a gas analyzer.

The control method requires tight control of the furnace pressure to avoid a situation where the pressure drops below atmospheric pressure, especially while in a cooling stage.

Catalytic nitriding is based on Russian technology and was developed by JSC Nakal Industrial furnaces (U.S. patent 7,931,854 B2). The Nakal system uses only ammonia. The gas is passed through a catalyst impregnated in an aluminum oxide and silicon carbide block and located inside the furnace, in order to ionize the ammonia to create a reactive gas (NH_3^+) and to accelerate the diffusivity of nitrogen into the base metal. According to Nakal, this acceleration of reactivated nitrogen atoms increases the growth rate of the diffusion layer without affecting the formation of a compound layer. As in all other potential-controlled nitriding processes, control of the nitrogen potential allows nitriding to achieve zero compound layer, exclusively γ' - Fe_4N compound layers, or epsilon ϵ - $Fe_{2-3}N$ compound layers.

Unlike other nitriding processes, catalytic nitriding is performed by controlling the nitrogen potential (mass% N) measured by an oxygen probe and calculated by a computer system.

Measuring the Potentials

Potentials in nitriding and nitrocarburizing are summarized in Table 15. Various methods of measurement are done, depending on the specification and requirements that must be followed.

Water Burette (Pipette). As long as automated measurement and control is not required and the process atmosphere consists of ammonia and dissociated ammonia only, the dissociation

rate can easily be verified using a water burette (Fig. 24).

The device consists of a water reservoir and a cylindrical burette with a printed scale used to measure the ammonia content of the furnace gas. A three-way valve is used to allow either water or furnace gas to flow through the device. A second valve opens or closes the exhaust of the gas cylinder. For the measurement, the water cylinder is filled with water, the three-way valve opened to the gas inlet, and the exhaust valve opened. Next, the gas cylinder is purged with furnace gas, then the exhaust valve is closed and the three-way valve opened to water. The water comes in contact with the furnace gas and reacts with the ammonia (which is hydrophilic), creating ammonia hydroxide (NH_4OH). This causes the water to enter the gas cylinder. The height of the water level represents the percentage of residual ammonia in the furnace gas. The dissociation equals 100% minus the residual ammonia.

The nitriding potential can be derived from residual ammonia from dissociation, assuming the percentage of dissociated ammonia consists of 75 vol% hydrogen and 25 vol% nitrogen:

$$K_N = \frac{\left[\frac{R_{NH_3}}{100\%} \right]}{\left[\frac{3/4 \times Diss.}{100\%} \right]^{3/2}}$$

In nonatmospheric pressure conditions, the nitriding potential must be adjusted to the furnace pressure by:

$$K_{N_{eff}} = K_N \times 1/\sqrt{\text{Pressure}}$$

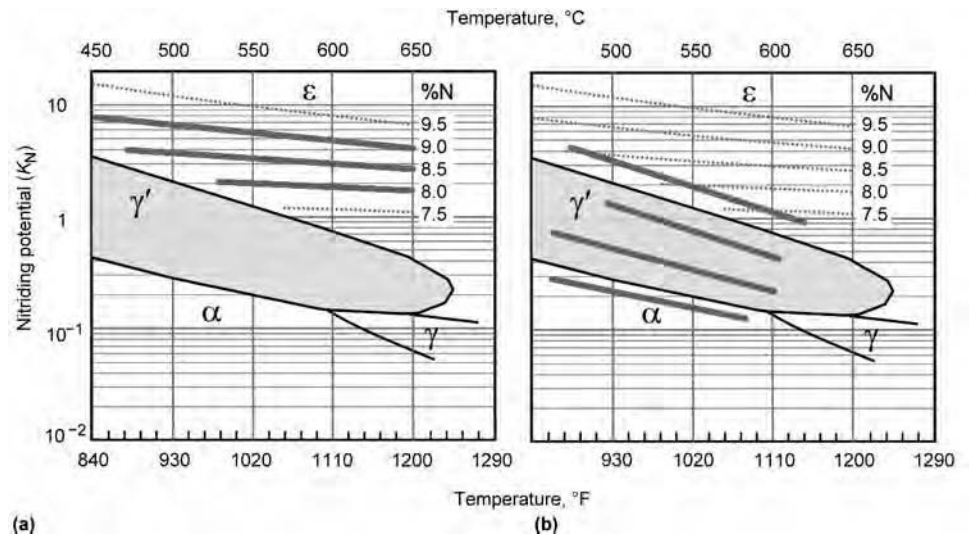


Fig. 22 Lehrer diagram. (a) Weight percentage controls nitriding potential along the isoconcentration lines. (b) Phase controls the potentials parallel to the phase boundaries. Source: Ref 7, 38

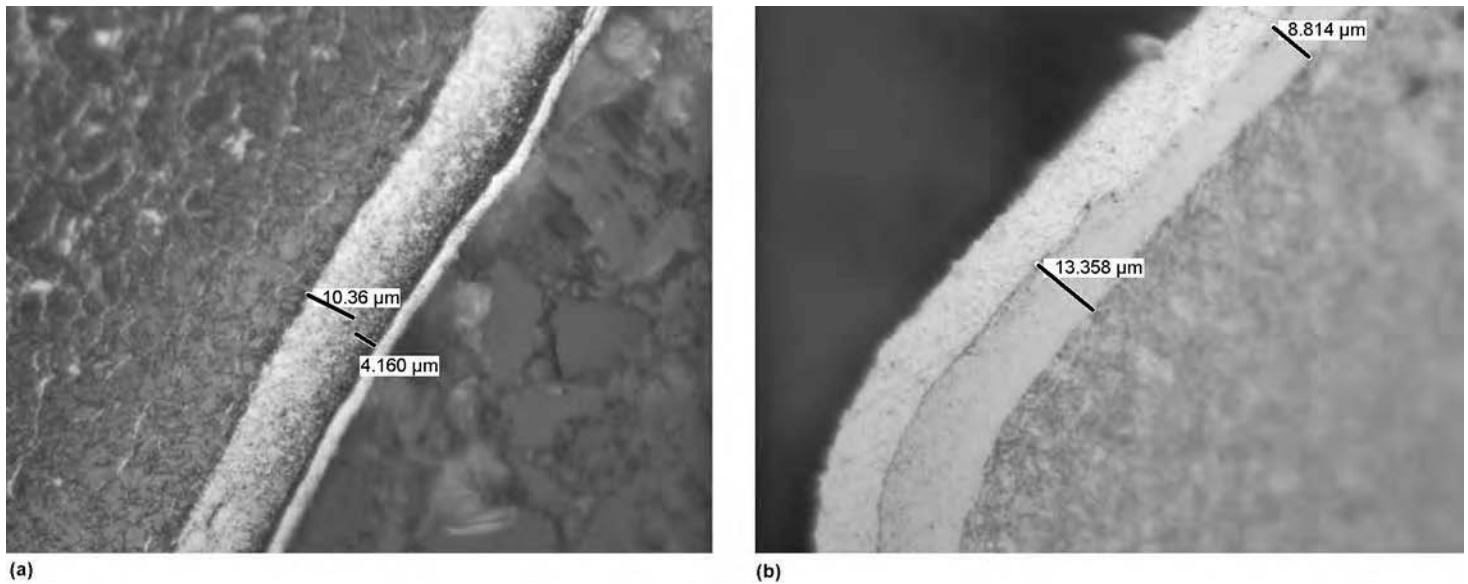


Fig. 23 Micrographs of (a) traditionally and (b) phase-controlled compound layers. Both parts have been treated in commercial heat treating loads. Courtesy of Linde Material Handling Systems, Germany

Table 15 Summary of potentials in nitriding and nitrocarburizing

Reaction potential and units	Equation
Dissociation in terms of residual ammonia (R_{NH_3}), %	Dissociation = $100\% - R_{NH_3}$
Nitriding potential, $\sqrt{\text{bar}}$	$K_N = \frac{P_{NH_3}}{[p_{H_2}]^{3/2}}$
Carburizing potential (Boudouard reaction), bar	$K_{CB} = \frac{P_{CO}^2}{P_{CO_2}}$
Carburizing potential (heterogeneous water-gas reaction), bar	$K_{CW} = \frac{P_{CO} \times P_{H_2}}{P_{H_2O}}$
Carburizing potential (methane reaction), $\sqrt{\text{bar}}$	$K_{C-CH_4} = \frac{P_{CH_4}}{P_{H_2}^2}$
Oxidation potential	$K_O = \frac{P_{H_2O}}{P_{H_2}}$

The nitriding potential is:

$$K_N = \frac{\left[\frac{(1 - H_2)}{75\%} \right]}{\left[\frac{H_2}{100\%} \right]^{3/2}}$$

The impact on the measured hydrogen percentage caused by, respectively, the presence of ammonia in a nitriding atmosphere and the presence of ammonia, water vapor, and carbon dioxide in a nitrocarburizing atmosphere is shown in Fig. 26.

Another method to measure the hydrogen content in a furnace uses the effect of palladium or similar metals that are permeable to hydrogen. For example, the HydroNit (Ipsen International, Ref 41) sensor consists of a tube of such a metal that is injected into the furnace, similar to an oxygen probe. The hydrogen diffuses into the measuring tube until there is equilibrium with the hydrogen content in the process atmosphere. The hydrogen partial pressure is measured by a normal pressure gage mounted at the open end of the measuring tube.

Pressure Increase. The Ivanit (IVA, Germany, Ref 42) control approach uses the effect of ammonia doubling its volume when dissociating into hydrogen and nitrogen. Cyclically, the furnace is closed on the inlet and on the exhaust, and the pressure increase is measured. The pressure increase is proportional to the ammonia dissociated during the measuring time. If the composition of the inlet gases is known, this can be transformed into a so-called dissociation degree and further into the nitriding potential.

Note that the dissociation degree quantifies the percentage of inlet ammonia being dissociated and does not match the dissociation

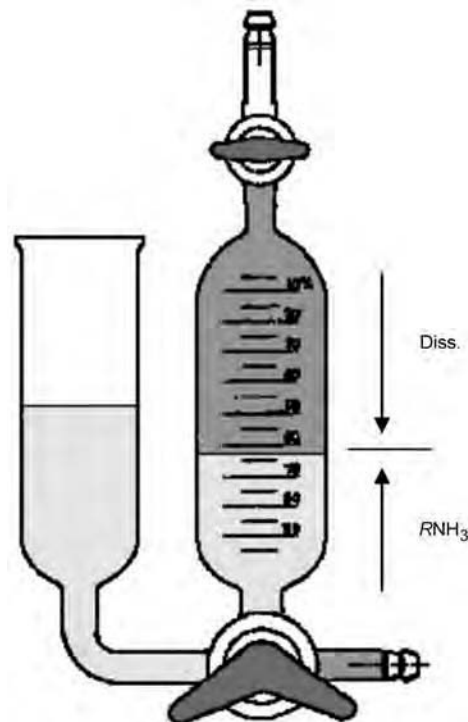


Fig. 24 Water burette

Hydrogen Analyzer. In an ammonia/dissociated ammonia atmosphere, the dissociation and nitriding potential can be derived by measuring the hydrogen percentage or hydrogen partial pressure in the furnace atmosphere. Most hydrogen analyzers measure the thermal conductivity of the sampling gas. Of all gases used in a nitriding or nitrocarburizing gas, hydrogen has by far the highest thermal conductivity (Fig. 25).

Assuming that the thermal conductivity (TC) of nitrogen is 1 and the thermal conductivity of hydrogen is 6.67, the percentage of hydrogen in a H_2-N_2 mixture becomes (simplified, in reality the curve is slightly bent by viscosity):

$$H_2 : N_2 = \frac{100\%[\text{measured } TC - 1]}{6.67 - 1}$$

Note that this is not the real hydrogen percentage in a nitriding or nitrocarburizing atmosphere, because the measurement will be shifted by the presence of ammonia, water vapor, and carbon dioxide, not having exactly the same thermal conductivity as nitrogen. The dissociation is:

$$\text{Dissociation} = H_2/0.75$$

quantifying the percentage of dissociated ammonia in the exhaust gas.

Infrared analyzers can be used to measure nonsymmetrical gas molecules. Such molecules act like a spring if stimulated by a signal matching one of their resonance frequencies. The sampling gas is fed into a measuring chamber where typically a broadband infrared signal is sent through the sampling gas. The signal is picked up at the end of the measuring path, and the loss in signal strength (amplitude) on the corresponding resonance frequency is proportional to the number of stimulated molecules.

Infrared analyzers are typically used to measure ammonia, carbon monoxide, carbon dioxide, or hydrocarbons. The problem with measuring ammonia is the cross sensitivity to water vapor. Most infrared analyzers for ammonia require drying the gas before entering the analyzer. The CO-CO₂ infrared analyzers are typically not ammonia resistant.

The measured ammonia percentage can be used to calculate dissociation and nitriding potential. Knowing the percentages of carbon monoxide and carbon dioxide enables calculation of the carburizing potential according to the Boudouard reaction.

Oxygen Probe. Zirconium dioxide is permeable to oxygen ions. If one side of the measuring cell is exposed to the furnace gas and the

other side is exposed to a reference gas with known oxygen percentage, oxygen molecules on the side with the higher percentage of oxygen will be ionized to O²⁻. The ions will diffuse to the other side until the electrical potential caused by the carrier shift is in equilibrium with the driving force of the diffusion (Ref 43). The potential can be measured as an electrical voltage, depending on temperature and the partial pressure ratio of the two oxygen percentages of the furnace gas and the reference gas. The voltage is known as the Nernst voltage, or emf:

$$emf = \frac{RT}{4F \times \ln \left[\frac{p_{O_2}}{p'_{O_2}} \right]}$$

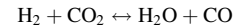
where *R* is the universal gas constant, *T* is the temperature in Kelvin, *F* is the Faraday constant, *p*{O₂} is the oxygen partial pressure in the furnace gas, and *p'*{O₂} is the oxygen partial pressure in the reference gas. Note that the signal of an oxygen probe is typically measured as a positive voltage.

Because the partial pressures of hydrogen and water vapor are in equilibrium with the partial pressure of oxygen, the millivolt signal of an oxygen probe with air reference can be used to derive the oxidizing potential:

$$\log_{10}(K_O) = \log_{10} \left[\frac{p_{H_2O}}{p_{H_2}} \right]$$

$$\log_{10}(K_O) = \frac{\left[\text{Signal(mV)} - \frac{1292.2784}{T} + 0.3264 \right]}{0.0992}$$

Assuming the partial pressures of carbon dioxide and carbon monoxide are in equilibrium with the partial pressure of hydrogen and water vapor following the water-gas reaction:



with

$$\log_{10}(K_W) = \log_{10} \left[\frac{p_{H_2O} \times p_{CO}}{p_{H_2} \times p_{CO_2}} \right] = -\frac{1717}{T} + 1.575$$

and knowing the total percentage of the inlet CO_x enables estimation of the carburizing potentials according to Boudouard and the heterogeneous water-gas reaction. Because establishing the water-gas equilibrium will not be instantaneous but depends on temperature and catalytic surface, a more accurate result can be achieved by additionally measuring carbon monoxide.

Lambda probes are a special form of oxygen probes originally designed to control the combustion in an automotive engine. As the exhaust gas of the engine is measured at a comparably low temperature, the zirconium dioxide element is heated. Lambda probes also use an air reference, and the signal is close to the signal of an in situ oxygen probe at 560 °C (1040 °F). Therefore, the signal must be converted to match the furnace temperature.

Typical Combinations. Many commercially available measuring systems combine a hydrogen analyzer with an in situ oxygen probe (Fig. 27). To measure the potentials correctly, the gas flows must be known. In combination with a potential control, where typically flow controllers or mass flow controllers are used, the actual flows are automatically read and fed into the calculation. This setup measures *K_N*, *K_C*, and *K_O*.

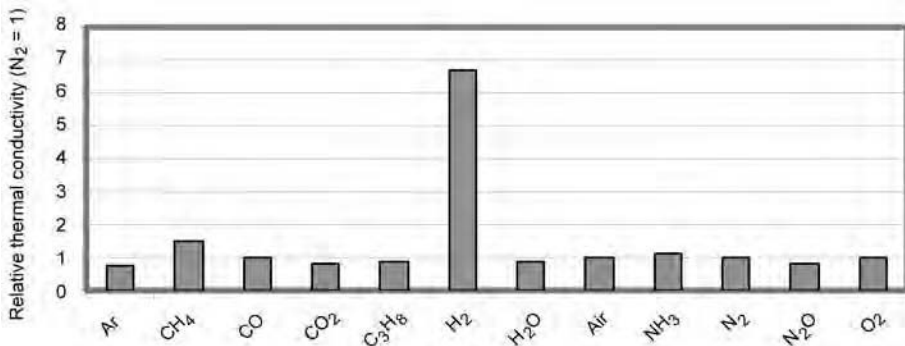


Fig. 25 Thermal conductivity of gases at 150 °C (300 °F), relative to the thermal conductivity of nitrogen

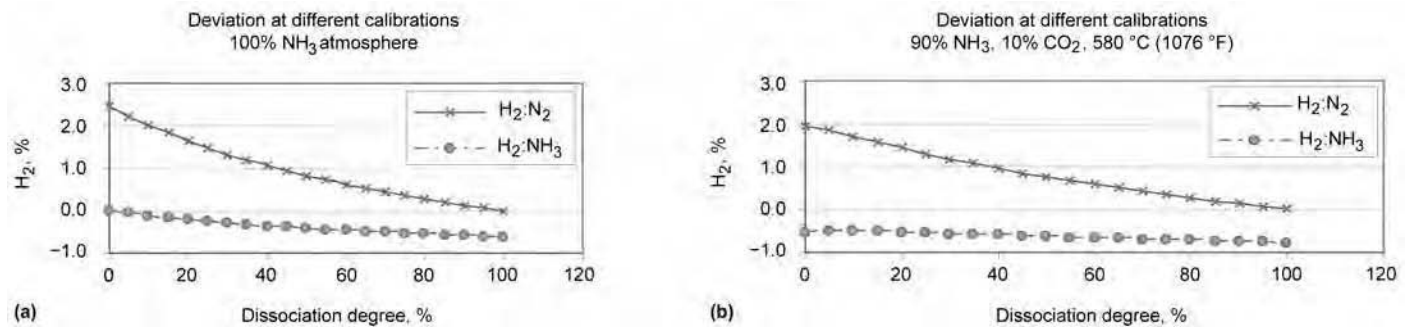


Fig. 26 Error of measured hydrogen percentages in (a) a nitriding atmosphere and (b) a typical nitrocarburizing atmosphere using a thermal conductivity analyzer. The presence of ammonia shifts the reading to higher percentages; the presence of water vapor and carbon dioxide shifts the reading to lower percentages. The top lines show the error of an H₂:N₂-calibrated analyzer; the bottom lines show the error of an H₂:NH₃-calibrated analyzer. Source: Ref 14

A combination of two oxygen probes (Ref 44), one measuring the millivolt signal of the furnace atmosphere and the second measuring the millivolt signal of the furnace atmosphere after full catalytic dissociation of the residual ammonia, provide the percentage of residual ammonia by:

$$\text{emf}_Q = \frac{p_{\text{H}_2\text{O}}}{p_{\text{H}_2}} (\text{furnace gas})$$

$$\text{emf}_E = \frac{p'_{\text{H}_2\text{O}}}{p'_{\text{H}_2}} (\text{fully dissociated})$$

where

$$p'_{\text{H}_2\text{O}} = \frac{p_{\text{H}_2\text{O}}}{\left[1 + p_{\text{NH}_3}\right]}$$

$$p'_{\text{H}_2} = \frac{p_{\text{H}_2} + \frac{3}{2} p_{\text{NH}_3}}{\left[1 + p_{\text{NH}_3}\right]}$$

The relation between the signals and the dissociation degree, α , and the nitriding potential, K_N , in the furnace is:

$$\Delta U = \text{emf}_E - \text{emf}_Q$$

$$= 0.0992 \times T \times \log_{10} \left[1 + \frac{3}{2} \left(\frac{p_{\text{NH}_3}}{p_{\text{H}_2}} \right) \right]$$

with:

$$\frac{1}{\alpha} = \left[1 + \frac{3}{2} \left(\frac{p_{\text{NH}_3}}{p_{\text{H}_2}} \right) \right]$$

so that:

$$K_N = \frac{(1 - \alpha)\sqrt{1 + \alpha}}{\frac{3}{2}\alpha^{3/2}}$$

provided the atmosphere has a certain amount of humidity. Additional gases require corrections based on mass balances.

The so-called QE sensor combines the two measurements in one sensor having an integrated catalyst and using the fully dissociated furnace gas as reference, measuring the change in millivolt signal otherwise derived from two separate sensors.

The Datanit sensor (SCR SA, Switzerland) (Ref 45) is a measuring system consisting of a pressure gage, two hydrogen analyzers, and a heated oxygen probe. First, it measures the furnace pressure, the hydrogen percentage, and the oxygen partial pressure of the furnace atmosphere; then it fully dissociates the residual ammonia using an internal catalyst and measures the hydrogen percentage after full dissociation. The increase in hydrogen can be recalculated to the residual ammonia in the furnace atmosphere, with the so-derived nitriding potential being independent from nitrogen additions to the process gas. The oxygen partial pressure can be used to derive the oxidizing potential and the carburizing potential, if the gas flows are known.

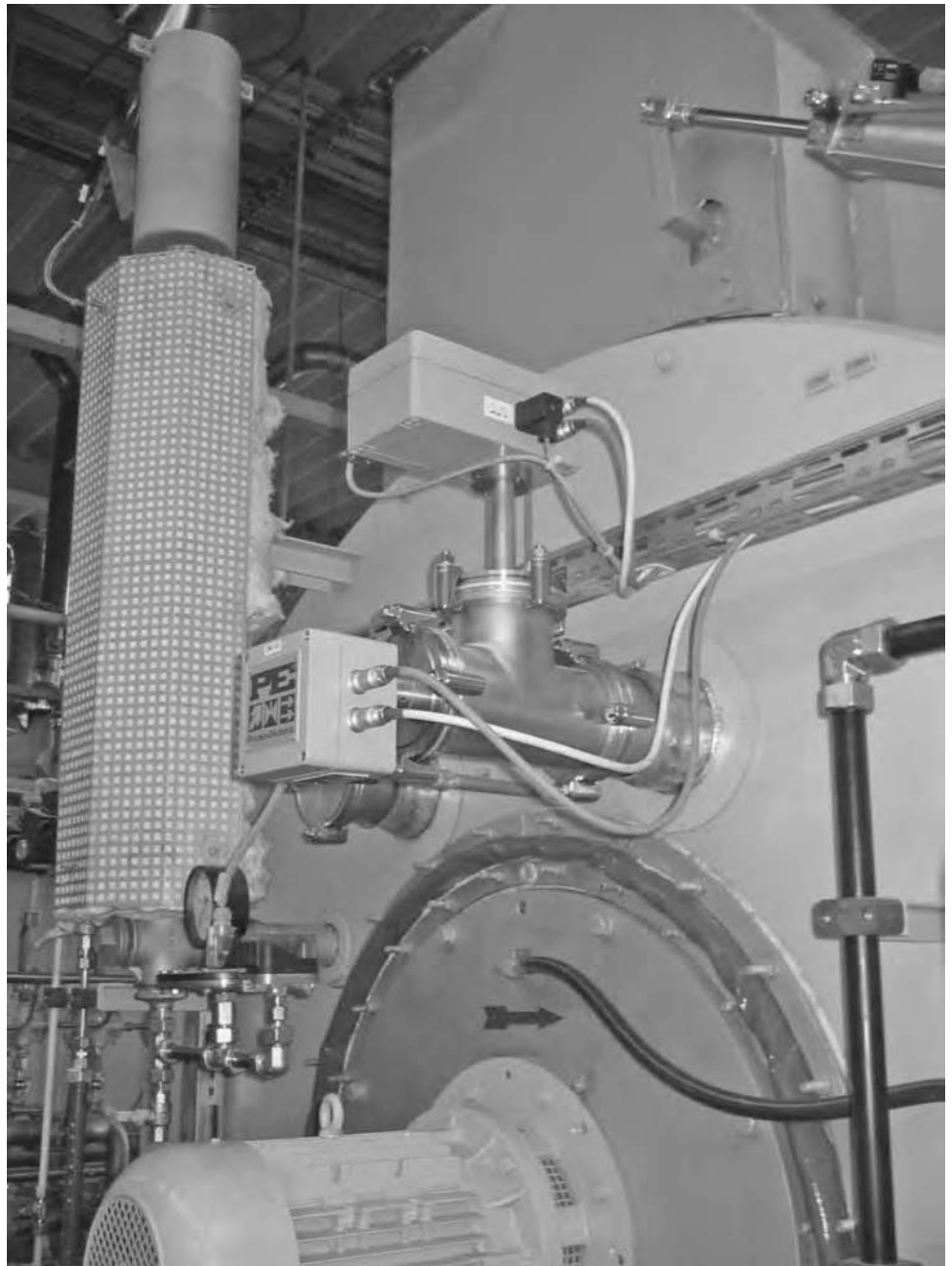


Fig. 27 H₂-O₂ measuring system for nitriding and nitrocarburizing atmospheres mounted on the back side of a horizontal retort furnace. The hydrogen analyzer is mounted on top of the flange, with the oxygen probe sticking from the back into the furnace retort. Courtesy of Process-Electronic GmbH, Germany

Temperature Control

Close control of nitriding temperature is essential to prevent uneven heating as well as distortion of parts. Nitriding furnaces are typically equipped with a cascaded temperature control. This control concept uses two control loops (controller plus thermocouple): the main loop to control the process temperature close to the load, and the zone loop to control the heat source. The heat source temperature

setpoint should be limited so that it does not exceed a maximum temperature, usually 5 to 15 °C (10 to 25 °F) above the nitriding temperature. These two control loops, in conjunction with fan circulation, normally result in control of furnace temperature to within ±3 to ±6 °C (±5 to ±10 °F). The cascaded control also reduces the likelihood of overheating if the control couple fails. Bigger furnaces may use more than one heating zone, in which case each heating zone is controlled by a separate loop.

Impact of Measuring Errors

Every measuring device has a specified accuracy and a maximum allowed for measuring error, in other words, a certain uncertainty. Often, the accuracy of a measuring device is mistaken as the resolution of the analog input used in the analyzer electronic circuit. The specified uncertainty, on the other hand, also takes into account other influences such as drift, pressure deviations, temperature deviations, and so on.

These in-built errors in measuring the atmosphere as well as the temperature require control of the potentials in such a way that the expected result will stay safely within the targeted specifications. Figure 28 displays a Lehrer diagram with fuzzy boundaries, allowing for an absolute error of $\pm 1\%$ in an H_2 measurement used for the K_N control and a temperature deviation throughout the load of $\pm 5^\circ C$ ($\pm 9^\circ F$).

Simulation of Nitriding Processes

There have been many attempts to predict nitriding and nitrocarburizing results by using mathematical models, and most of the scientific work has been done for applying thermodynamics on nitriding of pure iron (Ref 47) and binary (Ref 48) or ternary alloys (Ref 49) of iron with nitride-forming elements such as titanium, chromium, aluminum, and/or carbon.

In pure iron, were the interfaces between the distinct ϵ and γ' nitride phases in the compound layer as well as the maximum solubility of nitrogen in the diffusion layer can be derived from the iron-nitrogen phase diagram, the accompanying nitriding conditions can be identified from the Lehrer diagram (Ref 50, 51). Likewise, for nitrocarburizing of pure iron, solubility of nitrogen and carbon as well as the phase boundaries between nitrides, carbonitrides, and cementite can be derived from the ternary Fe-N-C diagram (Ref 18) as well as the growth kinetics of the compound layer (Ref 51).

In steels, with the presence of alloying elements and carbon, the growth of the diffusion zone and the compound layer are likewise affected. In particular, the pure single-phase layers of γ' and ϵ nitrides will be replaced by a multiphase mixture, and, due to the presence of carbon, the ϵ phase will predominantly occur.

Early models based purely on thermodynamics (Ref 52) and taking into account the influence of the alloying elements, including carbon, on the maximum solubility and the diffusion coefficient of nitrogen showed good correlation for low-alloyed and carbon steels but have not been able to visualize multiphase compound layers. Another major problem is the idea of using equilibrium conditions, whereas the real process depends mainly on kinetics. More recently developed models use advanced

mathematical and numerical approaches, such as neural networks (Ref 53) or phase-field calculations (Ref 54).

A more pragmatic approach is to use an empirical model, based on test results of treating real steels and using a library of parameters to describe their behavior in varying nitriding and nitrocarburizing conditions (Ref 55), with some being commercially available (Ref 56).

A type of hybrid has been developed by the Worcester Polytechnic Institute (Ref 57, 58), which presented a nitriding model based on first calculating the phase diagram for the particular steel and then matching the varying nitrogen concentration to the nitriding potentials. The diffusion coefficients for nitrogen in the multiphase compound layer and the diffusion layer have been determined by trial runs. The outcome of this model shows very good correlation for simulations of various steels.

Inspection and Quality Control

Nitrided parts typically must meet the following requirements:

- Core hardness
- Surface hardness
- Case depth, total or effective
- Compound layer thickness, typically restricted
- Microstructure

Nitrocarburized parts must meet the following requirements:

- Core hardness
- Surface hardness

- Case depth, total or effective
- Compound layer thickness, composition and percentage of porosity
- Oxide layer thickness, if postoxidized
- Microstructure
- Corrosion resistance

Quality control is typically performed by treating test coupons with each furnace load. The coupons must be of the same material and heat treated to the same core hardness as the corresponding parts, and they should be placed in locations that are representative of the nitriding conditions of the furnace.

The inspection may include:

- Visual inspection, where nitrided parts shall exhibit a uniform dull-gray appearance. Postoxidized parts shall exhibit a dark-blue-to-black finish.
- Testing core and surface hardness shall be performed in accordance with ASTM A370, E92, or E384. For conversion between scales, see ASTM E140, and for correlation with strength, see ASTM A370. Testing hardness of the compound layer shall be done using microhardness techniques only.
- For microstructure, the case shall exhibit a uniform distribution of nitrides diminishing gradually from surface to core. There shall be no evidence of continuous nitride network in the grain boundaries. Metallographic examination shall be made at a magnification not lower than $400\times$.
- The presence of a compound layer on non-austenitic steels and cast irons shall be determined by a chemical spot test. The test shall be performed by applying a drop of copper

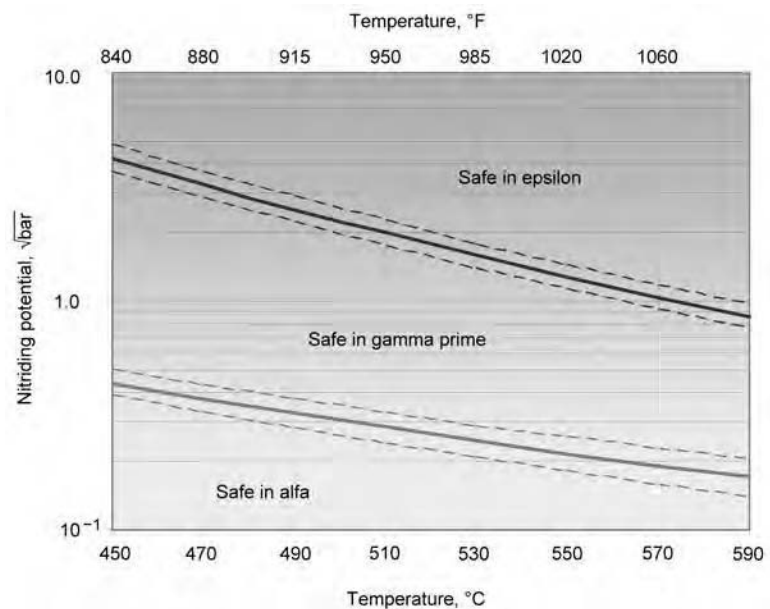


Fig. 28 Impact of measuring errors on phase boundaries in the iron-nitrogen Lehrer diagram, allowing for $\pm 5^\circ C$ ($\pm 9^\circ F$) and $\pm 1\%$ H_2 . Source: Ref 46

sulfate solution or copper ammonium chloride solution to a clean, nitrocarburized surface. If, after 15 s, the spot to which the drop was applied turns red, due to the deposition of copper, a compound layer is not present.

- The thickness of the compound layer is typically measured by metallographic methods. A prepared cross section of the nitrided surface is etched with an etchant that darkens the case but not the iron nitride layer; thus, this layer appears white and can be measured microscopically. The thickness of compound layers shall be determined in accordance with the procedure of SAE J423 or ARP1820 microscopic methods, at a magnification of 500× minimum.
- The composition of the compound layer can be evaluated by a special etching, allowing for a distinction between γ' and ϵ phases. For example, when nitrocarburized specimens are etched with 2% Nital and Murakami reagent (20 mg KOH, 20 mg $K_3Fe(CN)_6$ in 100 mL water) at 80 °C (175 °F), the compound layer shows brown areas of ϵ -carbonitrides and white areas of γ' -nitrides (Ref 59).
- The extent of porosity of a compound layer shall be measured as the percentage of the distance between the surface and the end of the dense porous zone of the total compound layer thickness, as revealed by etching with 2% Nital. Where observed, the deeper-situated spikes of porosity following the grain boundaries and jutting out in the direction of the core shall not be taken into account.
- The total case depth shall be the depth of the dark-etching subsurface zone, determined metallographically. On those alloys that do not respond by darker etching, case depth shall be the depth below the surface at which microhardness is 10% higher than that of the core, as determined by a Knoop or a Vickers hardness traverse, in accordance with ASTM E384.
- The effective case depth in gas nitriding is defined as the depth where the hardness is equal to the core hardness plus 4 HRC points (50 HV), if not specified otherwise. Hardness values are obtained in accordance with ASTM E384.

Compound layer thickness and composition may also be determined by glow-discharge optical emission spectrometry analysis, if the depth scale is externally calibrated. A Fe_4N γ' -nitride layer will show a nitrogen content of approximately 5.9 to 6.1 mass%; $Fe_{2-3}N$ ϵ -nitrides start at approximately 7.5 mass% and can reach nitrogen contents up to 11.1 mass%. In a nitriding process, carbon will tend to diffuse out from the base material. Because the compound layer has a lower diffusivity for carbon, carbon will accumulate on the interface between the compound layer and the diffusion zone, and the compound layer thickness can

be estimated by the position of the carbon peak (Fig. 29).

The $Fe_{2-3}NC$ ϵ -carbonitrides can form at much lower nitrogen contents, provided the carbon content is high enough to support the formation of the carbonitride. A good estimation may be to take the total content of carbon and nitrogen to be higher than 7.5 mass% for ϵ , and the nitrogen content dropping below approximately 5 mass% for estimating the total compound layer thickness (Fig. 30). Carbon contents above approximately 3 mass% may cause cementite formation (Fig. 31).

Suitable etchants for macroscopic and microscopic examination are shown in Table 16.

Data obtained from quality inspection should be recorded and filed with the furnace records and data obtained during the process, such as temperature, potentials, and/or dissociation and gas flows.

Lab Equipment and Sample Preparation

A minimum of equipment is needed to evaluate the thickness of compound layers, the case depth, and to produce a hardness curve. The equipment available ranges from very basic and mostly manual instruments to very complex systems. Basic equipment is less costly but often requires more technical training. It also limits the speed of evaluations, their number, and the ability to log and transmit data such as hardness curves and digital pictures. Complex equipment usually involves a computer with dedicated software and drivers connected

to a hardness tester. While the lab technician may choose the areas to be tested on the computer monitor, stepper motors actually move the samples and the turret with different magnifications, as well as the indenter. This equipment has the ability to document and log data; its ease of use saves time, especially when large numbers of samples must be processed for production part approvals or quality control of current production.

Regardless of the complexity, the following is needed:

- *Cut-off saw*: Consists of a shielded disk saw, complete with a vise to hold samples, light, and a cooling system. It is usually manual.
- *Mounting press*: Consists of a hydraulic press with integrated pressure gages and heating and cooling systems. It can be manual or automatic.
- *Polishing*: Automatic or semiautomatic polishing systems have interchangeable wheels, a water spout, and a turret that applies the correct pressure on the sample being polished. The turrets are designed to hold multiple samples. Manual polishing tables have various abrasive strips, and the lab technician manually polishes the mounted samples by rubbing on the strips, while water is running.
- *Microscope with hardness tester*: as described previously

Because of the etchants (Table 16) used and because of the thermosetting phenol formaldehyde resin often used to mount the samples, a sink with running water and a fume evacuation hood are necessary.

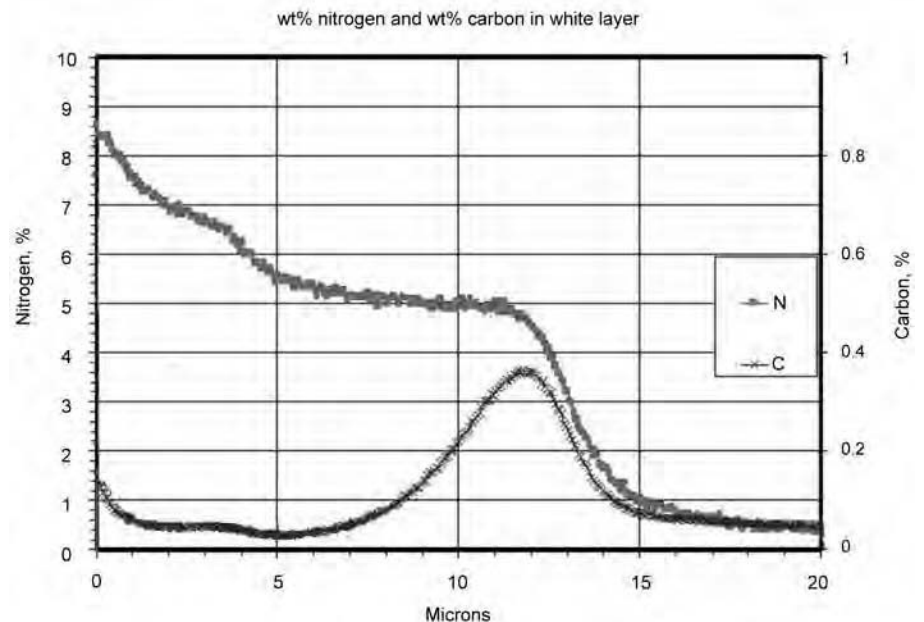


Fig. 29 Glow-discharge optical emission spectrometry analysis of a nitrided C15. The peak in carbon indicates the boundary between the compound layer and diffusion zone. The position of this peak may be used to determine the compound layer thickness. Courtesy of IWT Bremen, Germany

Hints

Choice of Sample. Unless specified or provided by the customer, a sample representative of the load should be obtained. It must be

the same steel grade, same heat treatment, and same surface finish. The sample should also be cleaned in the same way as the part it is supposed to represent, and it should be handled with clean gloves.

Sample Location. Some procedures and customers may require specific locations for parts, or a random test. If the furnace is known to be uniform in temperature and gas circulation, it is good to wire the sample with a clean wire anywhere in the load (or sampling port—some furnaces have a port designed especially for samples).

Cut-Off Saw. Plan the cuts before placing the sample in the saw. The cuts must be perpendicular to the surface; if they are not, a thicker or thinner case depth will be seen under microscopic examination. This is particularly true when evaluating a curved surface or a radius. The cut-off saw will “eat” approximately 3.2 mm (1/8 in.) of material. Beware when cutting a small, round bushing. Cutting along the diameter will leave angled surfaces and the wrong perception of case depth and compound layer thickness. This also applies to cutting a round bar at an angle to produce an ellipse (Fig. 32). Therefore, the position of the sample in the vise is crucial, as is planning, which avoids too many cuts.

The second precaution is the cutting speed. Despite cooling, the amount of heat generated by the abrasive disk may be enough to burn the surface, especially in harder materials. If sparks are visible despite cooling, reduce the pressure exerted on the disk. It will destroy the sample and the blade of the saw.

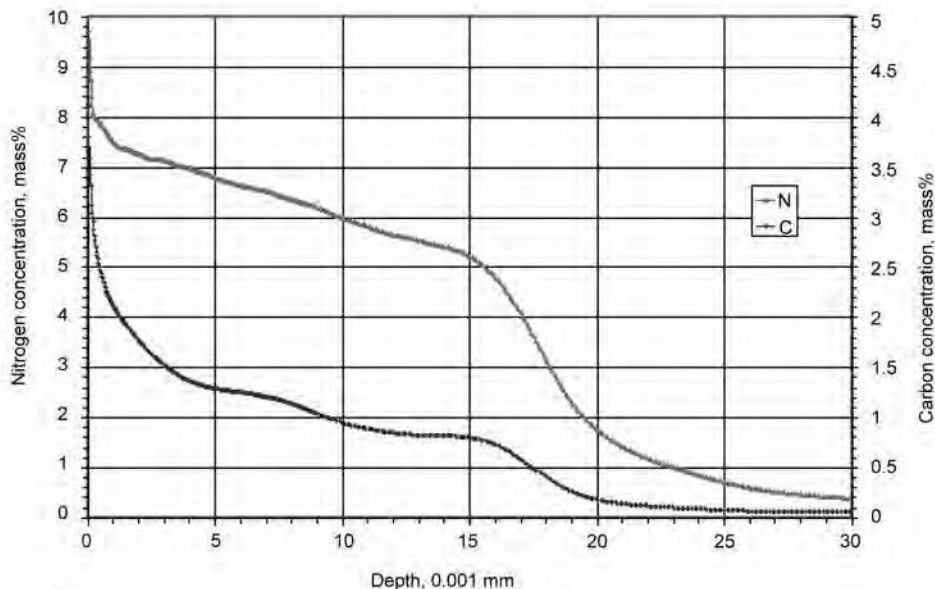


Fig. 30 Glow-discharge optical emission spectrometry analysis of a nitrocarburized AISI 1010, aiming for a high carbon concentration in the compound layer. The compound layer thickness is given at the point where the total percentage of carbon and nitrogen drops below approximately 6 mass%.

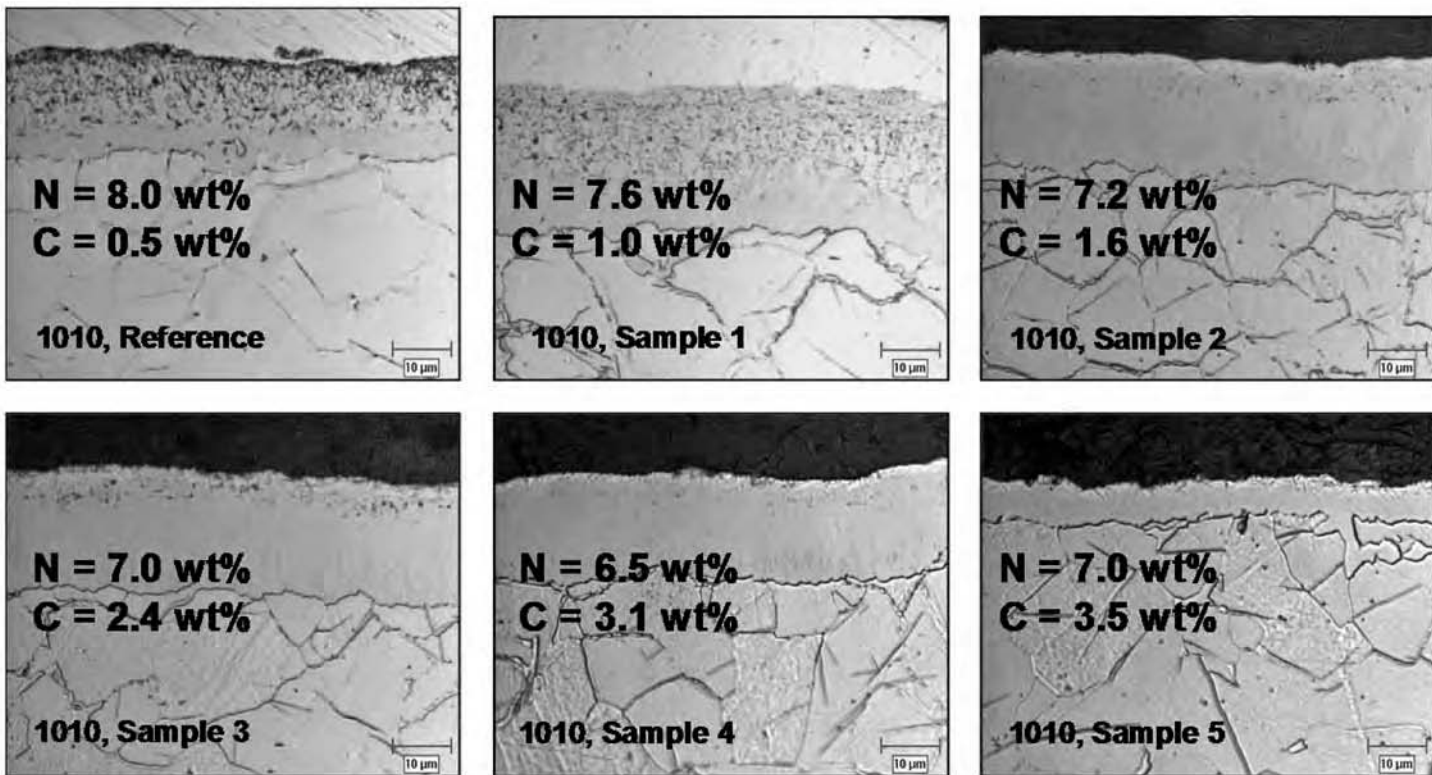


Fig. 31 Varying the compound layer composition on nitrocarburized AISI 1010, aiming for an ϵ phase with increasing carbon contents. Nitrocarburized at 580 °C (1075 °F) for 2.5 h, furnace cooled while purged with nitrogen. Increasing the carbon content decreases the amount of porosity created while cooling. A carbon content above 3 mass% slows the formation of the compound layer and may result in a layer with high amounts of cementite (sample 5). Source: Ref 37

Table 16 Selection of etchants used for lab inspection

Etchant	Composition	Concentration	Conditions	Comments
Nital	Ethanol Nitric acid	100 mL 1–10 mL	Immersion up to a few minutes	Most common etchant for iron, carbon, and alloys steels and cast iron; immerse sample from seconds to minutes
Murakami's	$K_3Fe(CN)_6$ KOH Water	10 g 10 g 100 mL	Premix KOH and water before adding $K_3Fe(CN)_6$	Chromium and alloys (use fresh and immerse); reveals carbides in iron and steels
Modified Murakami's	$K_3Fe(CN)_6$ Potassium hydroxide Water	30 g 30 g 150 mL	1 s to several minutes by immersing or swabbing	Premix KOH and water before adding $K_3Fe(CN)_6$
...	Hydrochloric acid Selenic acid Ethyl alcohol	20–30 mL 1–3 mL 100 mL	Immerse at room temperature for 1–4 min	Color etching; colors carbides and γ' phase in heat-resisting steels
...	Ammonium bifluoride Potassium metabisulfite Water	20 g 0.5 g 100 ML	Immerse at room temperature for 1–2 min	Color etching; etching of austenitic stainless steel and welds

Source: Ref 60

Surface Hardness Measurement

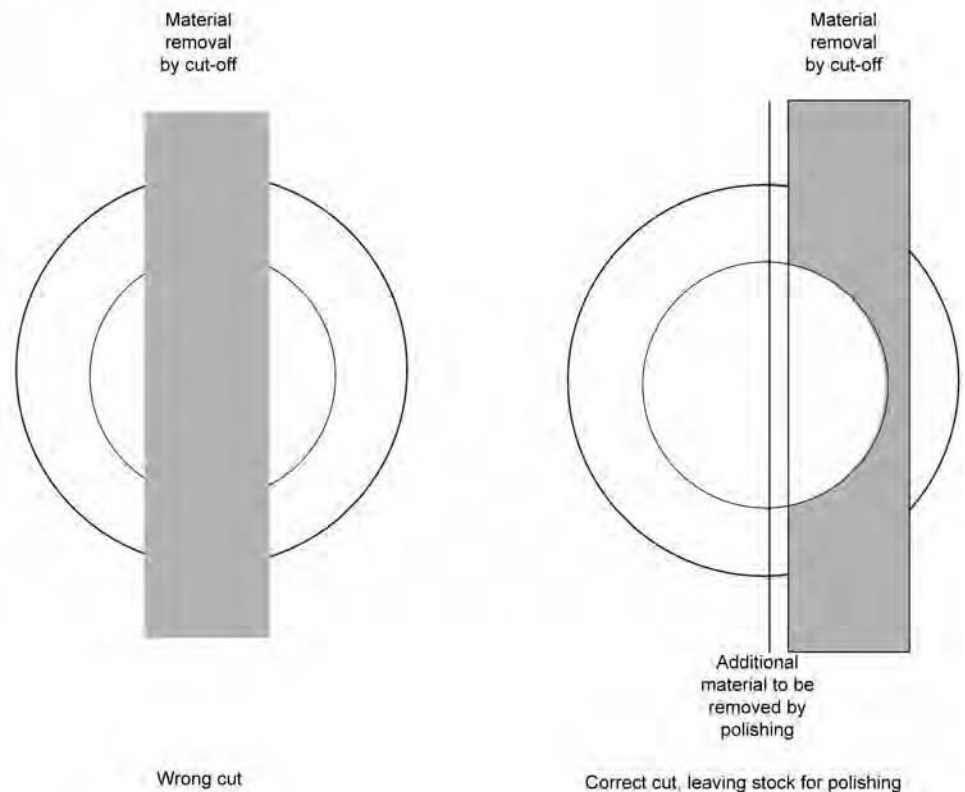
The measurement of surface hardness does not require the sample to be mounted. The nitrided surface must be parallel to the plate of the hardness tester and lightly polished with fine-grit paper (600 grit) to offer good visual contrast.

Note: A difference in the length of the diagonals of the imprint means the sample is not parallel to the testers' table or the surface is inclined.

The clear imprint is then analyzed by the hardness tester. In manual or semiautomatic models, the technician adjusts hairlines to the diagonals of the pyramid-shaped imprint. The resultant reading is compared by the computer or manually by verifying the number obtained against a reference chart where readings obtained under each load have a corresponding, precalculated Vickers hardness. Each reference chart is specific to the hardness tester model and manufacturer.

Surface hardness can be taken with different loads. Any load over 1 N (1 kgf) may produce a composite reading of nitrided case hardness and core hardness. Drawings, specifications, and other documents often specify the required load. For example, a specific hardness requirement under 150 N (15 kgf) will give a precise idea if the nitrided case thickness produces the correct gear surface hardness when combined with a specific core hardness. This is why the combination of a minimum case depth (please note: no maximum) and a minimum surface hardness using 150 N (15 kgf) provides a floating specification, where the nitriding process must adjust to a higher (or lower) core hardness.

Finally, some specifications mention Rockwell C hardness (HRC). Rockwell C is generally not used to verify surface hardness of nitrided or nitrocarburized samples. It uses a high load along with a secondary load that will crush the surface—actually through the surface—and give a somewhat composite reading. A heat treated H13 material will often attain 46 to 48 HRC.

**Fig. 32** How to cut samples for lab inspection

When nitrided, it will reach 1100 to 1200 HV—over 70 HRC when converted. However, the same layer will be evaluated at 49 to 52 HRC when subject to the actual Rockwell indenter.

This is why the specifications must be converted into HV by using a chart, and a Vickers hardness tester must be used for testing. The results may need to be reported in HRC and therefore converted again.

Metallographic Preparation

Mounting. The sample must be placed flat face (cut face) down on the piston of the mounting press. Then the piston is lowered into the cylinder, and a measured amount of mounting plastic (often phenolic plastic, usually in powder or grain form) is added with a spoon. The cylinder is closed and starts heating/compacting the powder. As the pressure and

temperature are attained, cooling water typically cools the sample.

When the sample is ready, the top of the cylinder unscrews and the piston is raised, to remove the sample. The surface of the piston must be kept clean for the next sample.

Mark the back of the mounted sample with an engraving tool to identify the sample.

Polishing. This part of the process requires the right sequence of abrasives, the right alignment of samples with abrasive wheels or strips, and the right pressure. When polishing manually, it is essential to maintain the sample surface always parallel to the polishing surface; otherwise, the sample will become rounded and will need constant focus adjustments under the hardness tester.

Depending on the desired quality of the sample, polishing can have a variable number of steps. If a fast evaluation is needed to verify that case depth and hardness comply with a requirement, a rougher sample will save time; however, more work is needed to achieve a picture-perfect sample with no traces of the abrasive wheel from the cut-off saw. The general sequence of polishing usually goes through the following:

- 180-grit paper
- 320-grit paper
- 600-grit paper
- 9 μ m polishing fluid on a special surface
- 3 μ m polishing fluid
- 0.05 μ m polishing fluid

At the end of every sequence, it is important to verify if the surface is free from earlier, rougher finish or grooves.

Note: On soft materials (carbon steel, cast iron), it is easy to peel or split the white layer and have nothing to evaluate. To prevent this, the sample should be either reinforced with a springlike metal band (sold by lab supply companies; used also to maintain upright fine samples in the mounting press) or nickel plated using a power supply and a heated solution of nickel sulfate, nickel chloride, and boric acid. This miniature nickel-plating system conserves well and only needs the addition of fresh nickel to replace the anode. Note that nickel may intrude into pores and therefore make it more difficult to detect the pores.

The sample should be reinforced before being mounted, and pressure should be kept light during polishing.

Hardness Profile

Hardness testers vary in construction and complexity. The general rule of thumb is to place the sample aligned and, if the steel section is rectangular, aligned as much as possible to the x - z axis. This will help when navigating along the edges, say from left to right, while continuously observing the surface.

Hardness can be measured with loads of 0.5 to 500 N (0.05 to 50 kgf). When a sample cross section is analyzed, a light weight is needed, usually 1 N (0.1 kgf). A specific drawing, specification, or customer request may specify a different load. Loads in excess of 10 N (1 kgf) are usually used for superficial hardness tests.

The profile is a compilation of hardness readings taken at regular space intervals, going from the surface toward the core of the sample. Indentations are spaced so as not to influence each other. Regardless of the pattern chosen to prepare a hardness profile, it is important remain perpendicular to the surface. All hardness testers have crossing hairlines to guide the indenting process and keep it perpendicular.

When compiling a hardness profile, these readings taken immediately on the edge of the sample may be discarded. Often, the indent will be incomplete, or the load will split the surface adjacent to the edge. Also, the evaluation of materials such as cast irons may require more indentations, to allow the discard of results obtained on graphite flakes, for example. Other soft inclusions will produce similar effects.

Unexpected spikes in the profile often mean that an indentation must be verified or redone. Errors are common on high-hardness readings, where a fine adjustment of the hairline—visually just touching or sitting on the end of a diagonal—makes a potentially big difference. However, a hardness profile that shows, despite corrections, a tendency for hardness to increase toward the core before dropping off (producing a hump) could be an indication of the presence of intergranular nitrides forming a network at a distance from the surface.

It takes a certain amount of training and practice to correctly evaluate samples.

Selective Nitriding

Certain manufacturing processes or drawings require masking on areas that must remain nitriding free. While mechanical masking works well in plasma nitriding, gas nitriding (and ferritic nitrocarburizing) require the use of stopoff paints or coatings. Several types of paints are available on the market; they are either tin/chromium oxide base or use a proprietary mix of finely ground ceramics.

Oil-based paints have been phased out in favor of newer water-based formulations; however, the latter require surfaces to be oil free. Oil-based paints are more forgiving on oil-contaminated surfaces. Because stopoff paints are usually very thick, they require frequent mixing before application, and each coat must thoroughly dry before the next one is applied. Coats of wet paint can bubble up, contaminating adjacent areas while reducing their effectiveness on surfaces to be masked.

Recessed areas, bores, and holes may be protected with bolts, inserts, and masking paint or paste.

Most masking coatings can be removed with wire brushes. It is recommended to refer to the material safety data sheet and the supplier's instructions on precautions to be taken. Often, dust masks and industrial dust collectors are recommended.

Some applications, mostly in the aerospace industry, require masking by copper plating. This form of masking also requires special copper plating removal after nitriding.

Common Problems

Low Case Hardness, Shallow or Uneven Case Depth. Steel characteristics that affect case hardness and depth include:

- Composition unsuitable for nitriding
- Improper microstructure
- Parts not hardened and tempered prior to nitriding
- Low core hardness
- Machining (burns, elongated grain structure)
- Smears and plastic deformation from fine-blanking, broaching, or other cutting tools
- Remnants of remelted layers from electroerosion
- Surface passivation, inadequate cleaning/surface contamination, polishing pastes, or other foreign matter

Nitriding/nitrocarburizing conditions that affect the case hardness and depth include:

- Temperature too low, slowing down the diffusion
- Temperature too high, exceeding pre-heat-treatment temperature and causing a loss in core hardness
- Nitriding potential too low and dissociation rate too high, caused by insufficient ammonia flow. Prolonged exposure of furnace parts and workbaskets to nitriding conditions may result in a bigger catalytic surface, where, at one point, the maximum ammonia flow is no longer able to support the desired potentials.
- Insufficient circulation may result in nonuniform temperature or gas distribution throughout the load.
- Insufficient time at process temperature

Discoloration of Parts. Discoloration may be caused by:

- Improper or inadequate prior surface treatment, including etching, washing, degreasing, and phosphate coating
- Oil in the retort, which may be caused by inadequate cleaning of parts (especially those with deep holes and recesses), loss of pressure at the seal or overheating the seal, and leakage at the base or other parts of the furnace

674 / Nitriding and Nitrocarburizing of Steels

- Air in the retort caused by an inadequate seal, leakage due to inadequate sealing around pipes or thermocouples, or introduction of excess air
- Moisture in the retort caused by leakage from the cooling chamber or water being sucked in from the water bottle during rapid cooling with inadequate gas flow

Excessive dimensional changes may be caused by:

- Inadequate stress relieving prior to nitriding
- Parts made from a mixed material stock with different core hardness and tempering limits below the process temperature
- Inadequate support of parts during nitriding
- Asymmetrical masking with nitriding stop-off paints or coatings
- Symmetrical accumulation of surface contaminants (e.g., dried coolant with aluminum oxide from polishing wheels)
- Inappropriate design of parts, such as wide variations in section thickness
- Unequal cases on various surfaces of parts, resulting from nonuniform conditions (created by furnace design or the manner in which parts are arranged in the load) or variations in absorptive power of surfaces (resulting from stopoff practices or from variations in surface metal removal, surface finishing technique, or degree of cleanliness)

Cracking and spalling of nitrified surfaces may be caused by dissociation in excess of 85% and also by (especially for aluminum-containing steels):

- Design (particularly sharp corners)
- Excessively thick white layer
- Decarburization of surface in prior heat treatment
- Improper heat treatment
- Contamination by cooling fluids that provide rust protection (water based)

Compound Layer Thicker Than Permitted.

A white layer deeper than permitted may be caused by:

- Nitriding temperature is too high
- Percentage of dissociation below the recommended minimum (15%) during the first stage
- First stage held too long
- Percentage of dissociation too low during the second stage
- Fast purging with raw ammonia instead of cracked ammonia or nitrogen, above 480 °C (900 °F) during slow cooling

Rules of Thumb

Rules of thumb include the following:

- Have the parts properly cleaned and depassivated.

- Increasing the temperature will increase the diffusion zone and compound layer thickness, provided the atmosphere allows for the formation of a compound layer, but may lower the core hardness and effective case depth.
- The nitriding potential must match the desired phase on the part surface. Carbon will shift the boundary toward ϵ phase to lower nitriding potentials; increasing amounts of nitride-building elements will shift the boundary to higher nitriding potentials, respectively.
- Nitride-forming elements have a high impact on the nitrogen flux needed to saturate the structure; therefore, diluting the nitriding atmosphere with too much nitrogen or treating the parts at too low a pressure will stop the proper nitriding of high-alloyed steels earlier compared to low-alloyed or carbon steels.
- Increasing the furnace pressure will increase the growth of the white layer, but this effect will be slowed down in steels that contain more of the nitride-building alloying elements.
- Stamped parts may behave similar to non-stamped parts with higher carbon content due to surface deformation.
- Heavy surface deformation prior to heat treating may cause lubricants such as cutting oil and others to burn into the surface and form a passivation layer, thus reducing the ability of nitrogen to pass the surface.

Safety Precautions

In North America, norms specific to the design, operation, and classification of ovens and furnaces as well as peripheral installations such as ammonia dissociators, piping, and so on are encompassed by NFPA 86, "Standard for Ovens and Furnaces." This publication covers all aspects of equipment, including safety, location, construction, gas use and storage, control systems, fire protection, and so on. In Europe, the main norm pertaining to heat treating equipment is EN 746, "Industrial Thermo-Processing Equipment."

The safety norms cited previously do not exclude other local standards and regulations, such as electric codes and machinery safety regulations. All norms evolve to adapt to new engineering solutions and technologies. Their most recent version must be consulted every time heat treating equipment is modified or upgraded, to ensure it is up to code according to the latest requirements. The following paragraphs give an overview of some selected potential hazards.

Nitriding and nitrocarburizing processes require the use of flammable, toxic, and suffocating gases. Transportation, storage, and piping must be in accordance with national safety standards and local standards and

regulations. All storage containers, valves, and piping should be examined periodically.

Although ammonia is classified as a nonflammable compressed or liquefied gas, ammonia gas is flammable and can produce explosive mixtures with air. Moist ammonia in contact with air is corrosive, and leaks in any portion of the system must be avoided.

Endogas, dissociated ammonia, as well as ammonia partially dissociated at nitriding temperatures contain high amounts of hydrogen, bearing a high risk of fire and explosion hazards.

Carbon monoxide, also being a part of endogas, is flammable and can produce explosive mixtures with air. Carbon monoxide is colorless, odorless, and tasteless but highly toxic.

Carbon dioxide and nitrogen cause asphyxiation; chlorine or other suffocating agents used for activation cause intense irritation of the bronchial tubes and lungs, resulting in pulmonary edema.

Because of the concentrations of such species in exhaust gases, *these gases must be vented to the outside atmosphere* and not into an enclosed area.

For all gas supply installations, adequate ventilation and precautions should be taken to avoid accumulation. Despite a ventilation system, all confined spaces are potentially dangerous. In addition to furnaces, this includes pits and other structures.

Nitriding and nitrocarburizing furnaces typically operate below the so-called safety temperature known from carburizing furnaces, above which all flammable gases would immediately burn (oxidize) when in contact with oxygen (Table 12). For this reason it must be granted that no explosive gas mixture is produced at any time (Table 11). Prior to opening the furnace to air, a safety purge must be performed to ensure that no flammable gases come in contact with oxygen. For the same reason, whenever the inlet process gas is switched between flammable gases and highly oxidizing gases such as air, oxygen, or nitrous oxide, a safety purge must be performed. In addition, it must be ensured that no air can enter the furnace when it contains a flammable process atmosphere, by maintaining and securing a given overpressure.

Equipment

All nitriding and nitrocarburizing equipment must comply with the safety standards given in the section "Safety Precautions" in this article.

Furnaces

Several furnace designs are in common use in gas nitriding installations. All of these incorporate certain essential features:

- A means of sealing the charge to exclude air and other contaminants while containing the controlled atmosphere

- An inlet line for introducing atmosphere, and an outlet line for exhausting used atmosphere
- A means of heating and appropriate temperature controls
- A means, such as a fan, for circulating atmosphere and equalizing temperature throughout the workload

The vertical retort furnace (Fig. 33) is typically placed in a pit; parts to be nitrided are loaded into a workbasket or on a rack, which is lowered into the heating chamber or a retort. Heating elements in most modern furnaces are in ambient air, while the load and the nitriding atmosphere are sealed in a retort. In retortless designs, radiant tubes or electric heating elements are calculated to limit the heat emitted and to reduce the undesirable dissociation of ammonia. Most furnace types have a lid with an incorporated gas circulation fan or retort fan. The gasket between the retort and the lid is usually made from a temperature-resistant silicone material; however, older furnaces had oil or sand seals. Some furnaces use special inflatable seals.

The incoming gases are mixed into the furnace atmosphere and circulated throughout the furnace by the retort fan. Spent atmosphere is exhausted. To improve temperature uniformity and proper gas circulation, furnaces often use a double wall or baffle.

Cooling may be achieved by starting a blower to direct cool air between the heating elements and the retort. In other designs, the retort is moved to a cooling station equipped with a blower. Cooling speed may be improved by using devices such as heat exchangers, where the atmosphere from within the load area is directed through a radiator cooled with fast-flowing water or coolant.

Pit furnaces offer a high load ratio relative to their cost and the space they occupy in a plant.

Horizontal retort furnaces (Fig. 34) are very similar to pit furnaces, except for their horizontal position. This working position allows the furnace designers to install atmosphere inlets and outlets in the back of the furnace. The lid is now a door that can be opened on a hinge or raised and lowered. The design allows for installation in a location with a low ceiling that does not allow pit excavation or servicing with a crane. The load is placed horizontally inside the furnace, similar to a chamber furnace, and allows automatic loading using a charge car. The weight of the load does not rest directly on the retort of the furnace, as it may seem, but is transferred to a support structure. Because the furnace door/lid is fixed, the retort is allowed to thermally expand toward the back of the furnace.

The horizontal furnace is more complex than the pit furnace and accommodates a smaller load relative to its size; the load shape, being rectangular, must fit into the cylindrical retort. Nevertheless, for mass manufacturing it is possible to install several horizontal furnaces serviced by

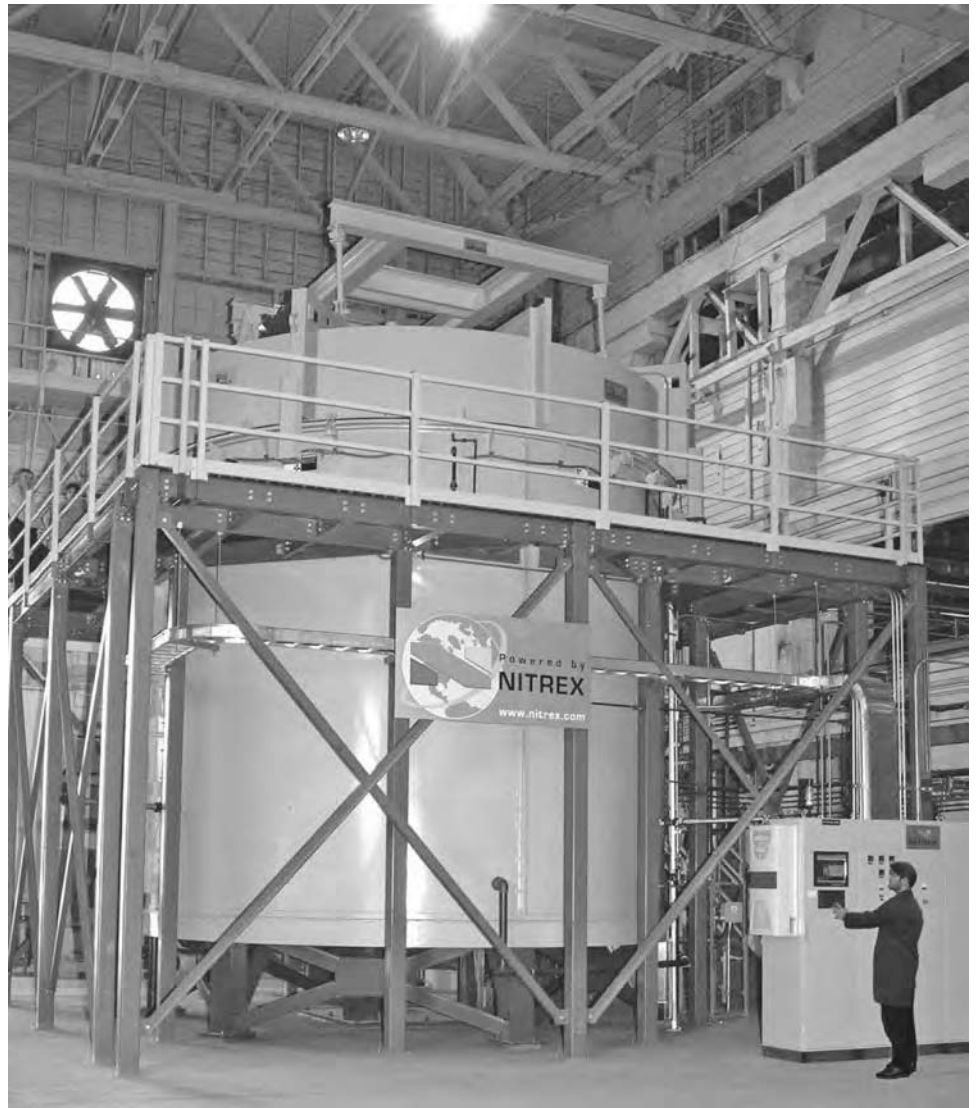


Fig. 33 Vertical retort furnace. Courtesy of Nitrex Metal Inc., Canada

an automated charge car. The addition of a horizontal preheat furnace, able to perform preoxidation, will shorten cycle times. The presence of a horizontally loaded washing machine completes the entire line. In this way, the horizontal furnace is an excellent choice for high-volume manufacturing and complete plant automation (including the so-called lights-out plants).

Cooling, gas circulation, temperature distribution, and so on are identical to the vertical retort furnace.

The bell-type movable furnace can be seen as an upside-down pit furnace. In this design, the retort is lifted and the lid is now a base; this base can support a mass that exceeds the load-bearing capacity of most retorts. This allows for easy loading, treatment, and unloading of large components. The stationary base is equipped with atmosphere inlet and outlet, control thermocouple, circulating fan, and outlets for electric power and controls. Parts to be



Fig. 34 Horizontal retort furnace. Courtesy of Nitrex Metal Inc., Canada

nitrided are loaded into workbaskets, which are placed on a work support at the furnace base or, in the case of large components, stacked directly on the base. Once loaded, the retort is lowered over the base. Seals are similar to the types used in the pit furnace. The weight of the furnace does not rest directly on any seal but on a supporting surface. Heat is provided by a heating bell, which is lowered over the retort and rests at the bottom on a flat portion of the retort. Heat passes through the retort walls and is transferred to the workload by radiation and convection as the atmosphere is circulated. Cooling is achieved by replacing the heating bell with a cooling bell, which draws air up around the retort walls and out at the top of the bell. This air movement is accomplished by a fan in the top of the cooling bell.

It is customary to provide more bases than heating and cooling bells. This permits more efficient use of the bells. A cooling bell is not essential where there is no demand for rapid cooling as a means of increasing output of the base; the quality of nitriding achieved is equivalent to that achieved using a cooling bell, but the heat radiated from the retort can be a source of discomfort to persons working in the immediate area.

Box-type movable furnaces with two stationary locations for workbaskets also have been used for nitriding. Each location is equipped with atmosphere inlet and outlet, control thermocouple, circulating fan, and separate controls. Parts to be nitrided are loaded into baskets, which are placed on a heavy metal plate at each location. A cover is placed over the charge and settles into a groove in the plate that is filled with fine chrome ore, thus effecting the seal. Lugs on the cover fit into a U-shaped holder through which pins are driven to secure the cover to the plate.

The furnace then is moved into position over the charge on rails, after which sliding doors at each end of the furnace are lowered. Heat passes through the walls of the cover and is transferred to the load by radiation and convection as the atmosphere is circulated. When the box furnace has been rolled into position over the work in the basket on the second plate, cooling is achieved for the work on the first plate by transfer of heat to the surroundings, either by natural or forced circulation of air. Usually, natural air circulation is rapid enough to permit cooling and recharging before the box furnace is again available.

Box furnaces of similar design are in use in which the furnace is stationary and the locations for the workloads are movable. The cover that closes over the load is similar to the retort used with the bell-type furnace.

Tube Retorts. In nitriding the inside diameters of tubes, the tube itself may act as the retort after it has been sealed (usually by welded-on covers) at both ends. A calculated volume of ammonia is sealed in the tube (after the tube has been purged of air), and the tube is heated in a suitable furnace. After the heating cycle, the tube is cooled in still

or recirculated air, and the covers are removed. Individual parts may be sealed in tube retorts and processed in this same manner (see the section "High- and Low-Pressure Nitriding" in this article).

Batch/integral quench furnaces can be used in the same manner as horizontal retort furnaces. These furnaces have no internal retort and are mostly used for nitrocarburizing. Gas distribution and temperature uniformity are typically not as good as in retort furnaces. The availability of an internal quench enables a suppression of nitride needle precipitation.

Pusher furnaces, similar to the ones known from carburizing, may be used for nitriding or ferritic nitrocarburizing. For safety reasons, these furnaces must be equipped with a sealed loading and unloading chamber that can be purged with nitrogen, to prevent outside air from coming in contact with the process atmosphere whenever a new load is pushed into the furnace or a treated load is pushed out of the furnace. Gas distribution and temperature uniformity are typically not as good as in retort furnaces. Pusher furnaces are exclusively used for high-volume production where parts must be treated identically, load after load.

Conveyor belt furnaces may be used for nitrocarburizing of small parts. Because this type of furnace is open to atmosphere on both sides, the furnace pressure must stay well above atmospheric pressure to prevent air from coming in contact with the process atmosphere. Typically, these furnaces have a long cooling section attached to the heated section. Gas distribution and temperature uniformity are

typically not as good as in retort furnaces. Conveyor belt furnaces are exclusively used for high-volume production where parts must be treated identically, load after load.

Continuous batch-type furnaces (Fig. 35) are mostly devoted to high-production volumes with short at-temperature processes. They are composed of self-contained chambers, separated by gastight gates, and linked together by a transport mechanism. Each chamber is separately managed with its own heating system and gas circulation fan. Chambers can be designed for component preheating, nitriding, ferritic (or austenitic) nitrocarburizing, gas or liquid quench, or solely fast cooling. The control system manages all the chambers, executes the different steps of the recipe in sequence, and communicates with the charge car that brings in new baskets. This makes the continuous furnace suitable for fully automated lights-out plants.

Fixtures

Fixtures for nitriding are similar in design to those used in gas carburizing. Under nitriding conditions, ammonia and dissociation products can react chemically with materials in retorts, fans, workbaskets, and fixtures. This reaction contributes to further dissociation of ammonia, robs the work of atomic nitrogen, and produces an excess of hydrogen. To reduce this reaction to a minimum, furnace parts and fixtures usually are made of alloys containing high percentages of nickel and chromium. Under certain conditions or after extended use, even these alloys develop

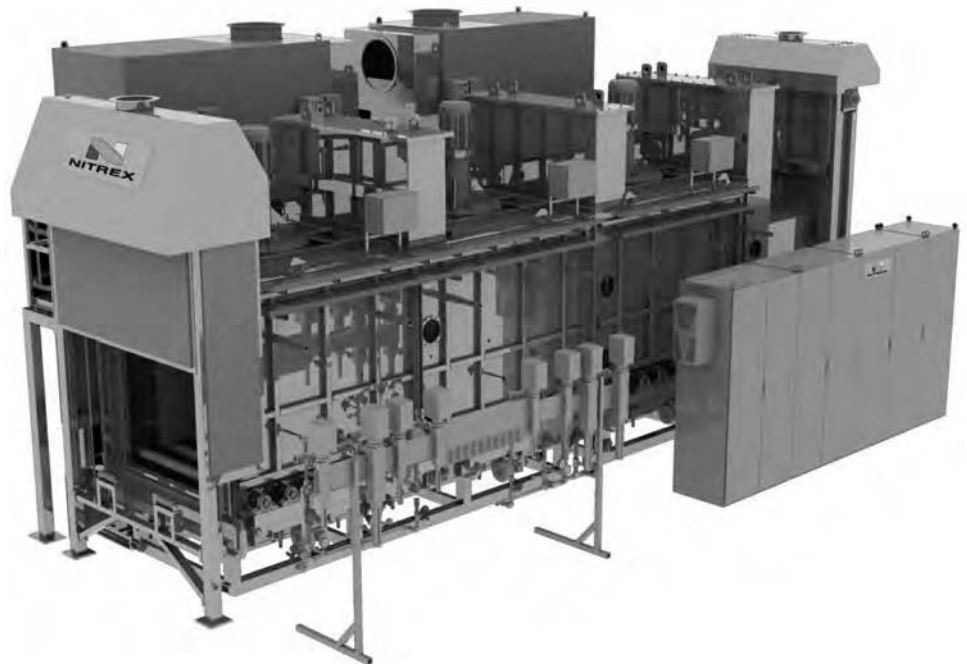


Fig. 35 Schematic view of a multichamber continuous furnace. Courtesy of Nitrex Metal Inc., Canada

a surface that interferes with normal processing; their usefulness can be restored, however, by heating them in an air atmosphere and holding them for a period of time at elevated temperature, followed by sandblasting to remove scale.

Enamel-coated carbon steel containers are satisfactory as long as the coating remains intact. Some alloys have been coated with high-temperature glass to extend their usefulness.

Low-carbon steel is unsatisfactory as a container material because it absorbs nitrogen, and the nitrided inside surface of the container becomes brittle. Besides embrittling the container, the nitrided surface also catalyzes the decomposition of the ammonia in contact with it and thereby interferes with the proper nitriding of workpieces.

Furnace Control System

The furnace control system is typically comprised of a process control unit. Basic units may rely on simple programmable logic controllers and basic gas control with preset flow meters and solenoid valves. More advanced controls feature user-friendly interfaces. Their capabilities include process building, process execution, data logging and encryption (required by some quality systems and norms), and hardware operation. Because advanced controls often incorporate the ability to automatically adjust the atmosphere to the desired control parameter (such as dissociation rate or nitriding potential), they rely on gas analyzers and more complex gas-distribution systems. Instead of opening and closing solenoid valves, those systems would communicate directly with flow meters or mass flow controllers to control, monitor, and record actual gas flows.

Ammonia Supply

Gas nitriding makes use of anhydrous liquid ammonia (refrigeration grade, 99.98% NH_3 by weight), which is available either in cylinders or in bulk (tank truck, trailer transport, and tank car). Layouts for ammonia installation and engineering data pertaining to their operation and maintenance may be obtained from suppliers of ammonia.

Usually, a storage tank is situated outside the building in which the nitriding equipment is located. At moderate outdoor temperatures, the liquid ammonia will absorb enough heat from the atmosphere to vaporize and fulfill gas requirements. On very hot days, the pressure of the gas may build up enough to actuate the pressure-relief valves. On the other hand, at low temperatures (below -7°C , or 20°F) or when very large volumes of gas are being used, an additional heat source or a vaporizer is needed.

Special Precautions. To avoid leaks, exceptionally good pipe-fitting practice must be followed. Specific pipe-joint compounds must be

used. One type of compound contains fine powdered lead, which is mixed in an insoluble, non-setting lubricant; another type is an oxychloride mixture with graphite, which, in setting, expands to form a very hard seal. When properly applied, certain high-strength, corrosion-resistant tapes also are satisfactory, as are welded joints.

Materials used for valves, piping, gages, regulators, and flow-measuring devices are similar for all installations; only iron, steel, stainless steel, and aluminum can be used because ammonia corrodes zinc, brass, and bronze. Piping should be made of extra-heavy black iron (except for vent lines, which may be made of standard-weight black iron or galvanized iron). Fittings should be made of extra-heavy malleable iron or forged steel. Valves should be made of steel and should be of the high-pressure, back-seating type.

Pressure Regulation. Ammonia gas from the supply tank or cylinder bank is under pressures up to 1380 kPa (200 psi), depending on the temperature of the gas. This pressure is reduced to approximately 14 to 105 kPa (2 to 15 psi) by means of pressure regulators.

Another reduction may be made just ahead of each furnace or dissociator to approximately 255 to 1015 mm (10 to 40 in.) water column, or an adequate pressure to supply from $1\text{ m}^3/\text{h}$ (approximately $35\text{ ft}^3/\text{h}$) or more in small furnaces to $40\text{ m}^3/\text{h}$ ($1500\text{ ft}^3/\text{h}$) on very large furnaces. Such supply lines are arranged to feed from a common line operating in manifold fashion at pressures not exceeding approximately 10 kPa (1.5 psi). Equipment to obtain this last reduction may be furnished with the dissociator or furnace.

The flow of gas into furnaces or dissociators is regulated by a suitable valve and is measured by a device such as a flow meter. This device also serves to permit a visible check that gas is moving through the lines. Flow and pressure may be monitored by contact points that close and sound an alarm at predetermined settings. On very large furnaces where high gas flows may be required, it is desirable to manifold the gas downstream of the flow meter and introduce it into the furnace at several locations, to prevent a local cool spot at a single point of entry.

Exhaust Gas. Depending on the stage of the cycle, the exhaust gas may contain air, air and ammonia, or ammonia plus hydrogen and nitrogen. Because of the variable composition of exhaust gas and the customary use of only a single exhaust line, the exhaust gas should be conducted to the outside atmosphere and released at as high an elevation as is practical. Terminating the exhaust line inside a building may be considered when all of the following conditions can be met:

- Nitrogen is used as the purge gas during heating and cooling.
- The exhaust gas is flared (burned) at the terminal during the nitriding cycle.

- The building is ventilated according to regulations applicable to the heat treating industry.

Note that environmental considerations and regulations (such as dictated by the Environmental Protection Agency, or EPA) may dictate a more sophisticated approach to handling exhaust gas.

To provide a slight backpressure within the furnace, an oil-containing bubble bottle or water bubbler may be installed in the exhaust line. As an alternative, a throttle valve installed in the exhaust line may be used to restrict the flow of exhaust gases and maintain a slight backpressure in the furnace. This pressure is indicated on a manometer (water type) and maintained at approximately 25 to 50 mm (1 to 2 in.) water column.

ACKNOWLEDGMENTS

The authors would like to thank IWT Bremen for allowing the use of some of their impressive photographs of nitrided surfaces. Gratitude is also extended to Prof. Dr. Hans-Joachim Spies of TU Freiberg and Prof. Dr. Ulrike Ebersbach of HTWK Leipzig for allowing the use of material based on their research and for providing detailed background information. Likewise, the authors would like to thank Dr. Edenhofer of Ipsen International for information on solution nitriding. Thanks are also given for material received from Expanite A/S, Denmark, about low-temperature processes and from Nitrex Metal Inc., Canada.

The authors express a very special thanks to the following reviewers for help with the article: Prof. Dr. Franz Hoffmann, IWT Bremen; Prof. Dr. Richard D. Sisson, Worcester Polytechnic Institute; and Prof. Dr. Marcel A.J. Somers, Technical University of Denmark. In particular, Professor Somers gave tremendous support and discussed many sections of the article through e-mail exchanges with the authors.

Last but not least, the authors thank Paulo Abrantes and Paul Gofas from Nitrex Canada for their input and for helping to create most of the illustrations.

REFERENCES

1. K.H. Weisssohn and K.-M. Winter, Nitrieren—Nitrocarburieren, *Gaswärme Int.*, Vol 8, 2002, p 328–336
2. H.-J. Spies and D. Bergner, Innere Nitrierung von Eisenwerkstoffen, *HTM J. Heat Treat. Mater.*, Vol 47 (No. 6), 1992, p 346–356
3. T.L. Christiansen and M.A.J. Somers, Low Temperature Gaseous Surface Hardening of Stainless Steel: The Current

- Status, *Int. J. Mater. Res.*, Vol 100, 2009, p 1361–1377
4. T. Christiansen and M.A.J. Somers, Randschichthärtung von rostfreiem Stahl durch Gasnitrierung und Gascarburierung bei niedrigen Temperaturen, *HTM J. Heat. Treat. Mater.*, Vol 60 (No. 4), 2005, p 207–214
 5. M.A.J. Somers, private conversation
 6. J.H. Kerspe et al., *Aufgaben und Verfahren in der Oberflächenbehandlung*, modified, Expert Verlag, Renningen, Germany, 2000, p 167
 7. E. Lehrer, Über das Eisen-Wasserstoff-Ammoniak-Gleichgewicht, *Z. Elektrochem.*, Vol 36, 1930, p 383–392
 8. K.-M. Winter, Gaseous Nitriding: In Theory and in Real Life, *Proc. of the ASM Conference and Exposition*, 2009, p 55–62
 9. K.-E. Thelning, *Steel and Its Heat Treatment*, 2nd ed., Butterworths, 1984
 10. M. Jung, *Entwicklung eines geregelten Drucknitrierprozesses*, Mensch & Buch Verlag, 1999
 11. D. Jordan, H. Antes, V. Osterman, and T. Jones, Low Torr-Range Vacuum Nitriding of 4140 Steel, *Heat Treat. Prog.*, March/April 2008, p 33–38
 12. H. Zimdars, “Technologische Grundlagen für die Erzeugung nitridhaltiger Schichten in stickstoffangereicherten Nitrieratmosphären,” Dissertation, Freiberg, 1987
 13. H.-J. Spies and F. Vogt, Gasoxinitrieren hochlegierter Stähle, *HTM J. Heat. Treat. Mater.*, Vol 52 (No. 6), 1997, p 342–349
 14. K.-M. Winter, Atmosphere Sensors and Controls, *Proc. of the ASM Conference and Exposition*, 2005, p 95–105
 15. H.-J. Spies, Stand und Entwicklung des kontrollierten Gasnitrierens, *Neue Hütte*, Vol 36 (No. 7), July 1991, p 255–262
 16. F. Hoffmann, Presentation at the 2012 Nitriding and Nitrocarburizing Seminar, IWT (Bremen, Germany)
 17. H. Klümper-Westkamp, Presentation given at the 2012 Nitriding Seminar, IWT (Bremen, Germany)
 18. J. Kunze, Thermodynamische Gleichgewichte im System Eisen-Stickstoff-Kohlenstoff, *HTM J. Heat. Treat. Mater.*, Vol 51 (No. 6), 1996, p 348–354
 19. U. Ebersbach, Korrosionsverhalten von nitriertem/nitrocarburisiertem und oxidiertem Stahl, *HTM J. Heat. Treat. Mater.*, Vol 62 (No. 2), 2007, p 62–70
 20. U. Ebersbach, F. Vogt, J. Naumann, and H. Zimdars, Lochfraßbeständigkeit von oxidierten Verbindungsschichten in Abhängigkeit vom (N+C)-Gehalt der ϵ -Phase, *HTM J. Heat. Treat. Mater.*, Vol 54 (No. 4), 1999, p 241–248
 21. N. Sato, M. Ojima, Y. Tomota, and K. Inaba, Surface Modification by Nitriding-Quenching for Steels, *Proc. of the 17th International Federation on Heat Treatment and Surface Engineering Congress 2008* (Kobe), p 220
 22. H. Berns and S. Siebert, Randaufsticken nichtrostender Stähle, *HTM J. Heat. Treat. Mater.*, Vol 49 (No. 2), 1994, p 123–128
 23. R. Zaugg, B. Edenhofer, W. Gräfen, J.W. Bouwman, and H. Berns, Fortschritte beim Stickstoff-Einsatzhärten von nichtrostenden Stählen nach dem SolNit-Verfahren, *HTM J. Heat. Treat. Mater.*, Vol 60 (No. 1), 2005, p 7; published in English in B. Edenhofer, M. Heninger, and J. Zhou, A Cost-Effective Case-Hardening Process for Stainless Steels, *Ind. Heat.*, June 2008
 24. B. Haase, Bauteilreinigung vor/nach der Wärmebehandlung, *HTM J. Heat. Treat. Mater.*, Vol 63 (No. 2), 2008, p 104–114
 25. U. Pfahl and J.E. Shepherd, “Nitrous Oxide Consumption and Flammability Limits of H_2-N_2O Air and $CH_4-N_2O-O_2-N_2$ Mixtures,” Explosion Dynamics Laboratory Report FM97-16, Graduate Aeronautical Laboratories, California Institute of Technology, Pasadena, CA
 26. P.B. Friehling and M.A.J. Somers, On the Effect of Pre-Oxidation on the Nitriding Kinetics, *Surf. Eng.*, Vol 16, 2000, p 103–106
 27. H.J.T. Ellingham, *J. Soc. Chem. Ind. (London)*, Vol 63, 1944, p 125
 28. M.A.J. Somers and E.J. Mittemeijer, Model Description of Iron-Carbonitride Compound-Layer Formation during Gaseous and Salt-Bath Nitrocarburizing, *Mater. Sci. Forum*, Vol 102–104, 1992, p 223–228
 29. H.J. Spies, Einfluss des Gasnitrierens auf die Eigenschaften der Randschicht von Eisenwerkstoffen, *Sonderband Nitrieren und Nitrocarburieren*, 30 Jahre Studienrichtung und Institut für Werkstofftechnik, Bergakademie Freiberg, 2004, p 190–203
 30. J. Kunze, Nitrogen and Carbon in Iron and Steel Thermodynamics, *Phys. Res.*, Vol 16, Akademie-Verlag, Berlin, 1990
 31. H.-J. Eckstein, *Wärmebehandlung von Stahl*, VEB Deutscher Verlag für Grundstoffindustrie, Leipzig, 1969, p 92–93
 32. K.-M. Winter, S. Hoja, and H. Klümper-Westkamp, Controlled Nitriding and Nitrocarburizing—State of the Art, *HTM J. Heat. Treat. Mater.*, Vol 66 (No. 2), 2011, p 68–75
 33. I. Barin and O. Knacke, *Thermochemical Properties of Inorganic Substances*, Springer-Verlag, Berlin, Heidelberg, New York, Verlag Stahleisen m.b.H., Düsseldorf, 1973
 34. E.J. Mittemeijer and T.J. Slycke, Potentials and Activities in Gaseous Nitriding and Carburizing, *Surf. Eng.*, Vol 12 (No. 2), 1996, p 154
 35. DIN 17022 Part 3, in *DIN Taschenbuch 218, Werkstofftechnologie 1, Wärmebehandlungstechnik*, Beuth Verlag, 1998, p 21–22
 36. F.K. Naumann and G. Langenscheid, Beitrag zum System Eisen-Stickstoff-Kohlenstoff, *Arch. Eisenhüttenwes.*, Vol 36 (No. 9), 1965, p 122–126
 37. K.-M. Winter, Phase Controlled Gaseous Nitriding and Nitrocarburizing, *Proc. of the ASM Conference and Exposition*, 2007
 38. H.-J. Spies, H.-J. Berg, and H. Zimdars, Fortschritte beim sensorkontrollierten Gasnitrieren und—nitrocarburieren, *HTM J. Heat. Treat. Mater.*, Vol 58 (No. 4), 2003, p 189–197
 39. K.-M. Winter, “New Measurement and Control Techniques for Predictable Results in Ferritic Nitrocarburizing,” presented at the FNA Conference and Exposition, 2010
 40. L. Maldzinski, M. Bazel, M. Korecki, A. Miliszewski, and T. Przygonski, Industrial Experiences with Controlled Nitriding Using a Zeroflow Method, *Heat Treat. Prog.*, July/Aug 2009
 41. HydroNit Sensor brochure, Ipsen International
 42. R. Hoffmann, I. Kleffmann, and H. Steinmann, Erfahrungen mit der Ivanit-Sonde, Teil 2: Überlegungen zum Ammoniakzerfall, *HTM J. Heat. Treat. Mater.*, Vol 60 (No. 4), 2005, p 216–222
 43. *Die Prozessregelung beim Gasaufkohlen und Einsatzhärten*, AWT Committee 5, Expert Verlag, 1997, p 65
 44. R. Hoffmann, E.J. Mittemeijer, and M.A.J. Somers, Die Steuerung von Nitrier- und Nitrocarburierprozessen, *HTM J. Heat. Treat. Mater.*, Vol 49 (No. 3), 1994
 45. O. Crevoiserat and C. Béguin, Contrôle des processus de nitruration et de nitrocarburisation gazeuses avec la sonde Datanit, *Berichtsband der ATTT-AWT-SVW-VWT Nitriertagung 2002* (Aachen), p 331–339
 46. K.-M. Winter, Auswirkungen von Messfehlern auf das Behandlungsergebnis beim Nitrieren und Nitrocarburieren, *Gaswärme Int.*, Vol 60 (No. 3), 2011, p 133–140
 47. W.-D. Jentzsch, F. Esser, and S. Böhmer, Mathematisches Modell für die Nitrierung von Weicheisen in Ammoniak/Wasserstoff-Gemischen, *Neue Hütte*, Vol 26 (No. 1), Jan 1981
 48. R.E. Schacherl, “Growth Kinetics and Microstructures of Gaseous Nitrided Iron Chromium Alloys,” Dissertation, 2004
 49. P.C. Van Wiggeren, H.C.F. Rozendaal, and E.J. Mittemeijer, The Nitriding Behaviour of Iron-Chromium-Carbon Alloys, *J. Mater. Sci.*, Vol 20, 1985, p 4561–4582
 50. B.-J. Kooi, M.A.J. Somers, and E.J. Mittemeijer, An Evaluation of the Fe-N Phase Diagram Considering Long-Range Order of N Atoms in γ' - Fe_4N_{1-x} and ϵ - Fe_2N_{1-z} , *Metall. Mater. Trans. A*, Vol 27, April 1996, p 1063–1071
 51. M.A.J. Somers, Thermodynamics, Kinetics and Microstructural Evolution of the Compound Layer; A Comparison of the States of Knowledge of Nitriding and Nitrocarburizing, *Heat Treat. Met.*, Vol 27 (No. 4), 2000, p 92–102

52. D. Heger and D. Berger, Berechnung der Stickstoffverteilung in gasnitrierten Eisenlegierungen, *HTM*, Vol 46 (No. 6), 1991
53. T. Malinova, S. Malinov, and N. Pantev, Simulation of Microhardness Profiles for Nitrocarburized Surface Layers by Artificial Neural Network, *Surf. Coat. Technol.*, Vol 135, 2001, p 258–267
54. Y.A. Tijani, “Modeling and Simulation of Thermochemical Heat Treatment Processes: A Phase Field Calculation of Nitriding in Steel,” Dissertation, Bremen, 2008
55. L. Maldzinski, W. Liliental, G. Tymowski, and J. Tacikowski, New Possibilities for Controlling Gas Nitriding Process by Simulation of Growth Kinetics of Nitride Layers, *Surf. Eng.*, Vol 15 (No. 5), 1999, p 377–348
56. “Compound Layer Module ECS CLT-NHD,” Stange-Elektronik GmbH
57. M. Yang, R.D. Sisson, Jr., B. Yao, and Y.H. Sohn, Simulation of the Ferritic Nitriding Process, *Int. Heat Treat. Surf. Eng.*, Vol 5 (No. 3), 2011, p 122–126
58. M. Yang, “Nitriding—Fundamentals, Modeling and Process Optimization,” Dissertation, Worcester Polytechnic Institute, 2012
59. J.B. Mane, R.C. Prasad, and B. Radhakrishnan, The Influence of Nitrocarburizing on Wear Behaviour of Forging Dies, *Proc. of the 26th Heat Treating Society Conference*, 2011, p 230
60. Pace Technologies, Tucson, AZ, www.metallographic.com

Liquid Nitriding of Steels*

Reviewed and corrected by George Pantazopoulos, ELKEME Hellenic Research Centre for Metals S.A.

LIQUID NITRIDING (nitriding in a molten salt bath) employs the same temperature range as gas nitriding, that is, 510 to 580 °C (950 to 1075 °F). The case-hardening medium is a molten, nitrogen-bearing, fused-salt bath containing either cyanides or cyanates. Unlike liquid carburizing and cyaniding, which employ baths of similar compositions, liquid nitriding is a subcritical (that is, below the critical transformation temperature) case-hardening process; thus, processing of finished parts is possible because dimensional stability can be maintained. Also, liquid nitriding adds more nitrogen and less carbon to ferrous materials than that obtained through higher-temperature diffusion treatments.

The liquid nitriding process has several proprietary modifications and is applied to a wide variety of carbon, low-alloy steels, tool steels, stainless steels, and cast irons.

Liquid Nitriding Applications

Liquid nitriding processes are used primarily to improve wear resistance of surfaces and to increase the endurance limit in fatigue. For many steels, resistance to corrosion is improved. These processes are not suitable for many applications requiring deep cases and hardened cores, but they have successfully replaced other types of heat treatment on a performance or economic basis. In general, the uses of liquid nitriding and gas nitriding are similar, and at times identical. Gas nitriding may be

preferred in applications where heavier case depths and dependable stopoffs are required. Both processes, however, provide the same advantages: improved wear resistance and anti-galling properties, increased fatigue resistance, and less distortion than other case-hardening processes employing through heating at higher temperatures. Four examples of parts for which liquid nitriding was selected over other case-hardening methods appear in Table 1.

The degree to which steel properties are affected by liquid nitriding may vary with the process used and the chemical control maintained. Thus, critical specifications should be based on prior test data or documented information.

Liquid Nitriding Systems

The term liquid nitriding has become a generic term for a number of different fused-salt processes, all of which are performed at subcritical temperature. Operating at these temperatures, the treatments are based on chemical diffusion and influence metallurgical structures primarily through absorption and reaction of nitrogen rather than through the minor amount of carbon that is assimilated. Although the different processes are represented by a number of commercial trade names, the basic subclassifications of liquid nitriding are those presented in Table 2.

A typical commercial bath for liquid nitriding is composed of a mixture of sodium and potassium salts. The sodium salts, which

comprise 60 to 70% (by weight) of the total mixture, consist of 96.5% NaCN, 2.5% Na₂CO₃, and 0.5% NaCNO. The potassium salts, 30 to 40% (by weight) of the mixture, consist of 96% KCN, 0.6% K₂CO₃, 0.75% KCNO, and 0.5% KCl. The operating temperature of this salt bath is 565 °C (1050 °F). With aging (a process described in the section "Operating Procedures" in this article), the cyanide content of the bath decreases, and the cyanate, and carbonate contents increase (the cyanate content in all nitriding baths is responsible for the nitriding action, and the ratio of cyanide to cyanate is critical). This bath is widely used for nitriding tool steels, including high-speed steels, and a variety of low-alloy steels, including the aluminum-containing nitriding steels.

Another bath for nitriding tool steels has a composition as follows:

Component	Amount, %
NaCN	30.00 max
Na ₂ CO ₃ or K ₂ CO ₃	25.00 max
Other active ingredients	4.00 max
Moisture	2.00 max
KCl	rem

A proprietary nitriding salt bath has the following composition by weight: 60 to 61% NaCN, 15.0 to 15.5% K₂CO₃, and 23 to 24% KCl.

Several special liquid nitriding processes employ proprietary additions, either gaseous or solid, that are intended to serve several

Table 1 Automotive parts for which liquid nitriding proved superior to other case-hardening processes for meeting service requirements

Component	Requirement	Material and process originally used	Resultant problem	Solution
Thrust washer	Withstand thrust load without galling and deformation	Bronze, carbonitrided 1010 steel	Bronze galled, deformed; steel warped	1010 steel nitrided 90 min in cyanide-cyanate bath at 570 °C (1060 °F) and water quenched(a)
Shaft	Resist wear on splines and bearing area	Induction harden through areas	Required costly inspection	Nitride for 90 min in cyanide-cyanate salt bath at 570 °C (1060 °F)
Seat bracket	Resist wear on surface	1020 steel, cyanide treated	Distortion; high loss in straightening(b)	1020 nitrided 90 min in cyanide-cyanate salt bath and water quenched(c)
Rocker arm shaft	Resist water on surface; maintain geometry	SAE 1045 steel, rough ground, induction hardened, straightened, finish ground, phosphate coated	Costly operations and material	SAE 1010 steel liquid-nitrided 90 min in low-cyanide fused salt at 570 to 580 °C (1060 to 1075 °F)(d)

(a) Resulted in improved product performance and extended life, with no increase in cost. (b) Also, brittleness. (c) Resulted in less distortion and brittleness, and elimination of scrap loss. (d) Eliminated finish grinding, phosphating, and straightening

purposes, such as accelerating the chemical activity of the bath, increasing the number of steels that can be processed, and improving the properties obtained as a result of nitriding.

Cyanide-free liquid nitriding salt compositions have also been introduced. However, in the active bath, a small amount of cyanide, generally up to 5.0%, is produced as part of the reaction. This is a relatively low concentration, and these compositions have gained widespread acceptance within the heat-treating industry because they do contribute substantially to the alleviation of a potential source of pollution.

Three processes, liquid pressure nitriding, aerated bath nitriding, and aerated low-cyanide nitriding, are described in the sections that follow.

Liquid Pressure Nitriding

Liquid pressure nitriding is a proprietary process in which anhydrous ammonia is introduced into a cyanide-cyanate bath. The bath is sealed and maintained under a pressure of 7 to 205 kPa (1 to 30 psi). The ammonia is piped to the bottom of the retort and is caused to flow vertically. The percentage of nascent nitrogen in the bath is controlled by maintaining the ammonia flow rate at 0.6 to 1 m³/h (20 to 40 ft³/h). This results in ammonia dissociation of 15 to 30%.

The bath contains sodium cyanide and other salts, which permits an operating temperature of 525 to 565 °C (975 to 1050 °F). Because the molten salts are diffused with anhydrous

ammonia, a new bath does not require aging and may be put into immediate operation employing the recommended cyanide-cyanate ratio, namely, 30 to 35% cyanide and 15 to 20% cyanate. Except for dragout losses, maintenance of the bath within the preferred ratio range is greatly simplified by the anhydrous ammonia addition, which serves continuously to counteract bath depletion.

The retort cover may be opened without causing complete interruption of the nitriding process. Loss of pressure within the retort results in a reduction in the nitriding rate. However, when the retort is sealed and pressure is reinstated through the resumption of ammonia gas flow, nitriding proceeds at the normal rate.

Depth of case depends on time at temperature. The average nitriding cycle is 24 h, although total cycle time may vary between 4 and 72 h. To stabilize core hardness, it is recommended that all parts be tempered at a temperature at least 28 °C (50 °F) higher than the nitriding temperature before they are immersed in the nitriding bath.

Hardness gradients and case depths resulting from pressure nitriding of 410 stainless steel, AISI type D2, and SAE 4140 are shown in Fig 1, 2, and 3.

Aerated Bath Nitriding

Aerated bath nitriding is a proprietary process (U.S. Patent 3,022,204) in which measured amounts of air are pumped through the molten

bath. The introduction of air provides agitation and stimulates chemical activity. The cyanide content of this bath, calculated as sodium cyanide, is maintained at preferably about 50 to 60% of the total bath content, and the cyanate is maintained at 32 to 38%. The potassium content of the fused bath, calculated as elemental potassium, is between 10 and 30%, preferably about 18%. The potassium may be present as the cyanate or the cyanide, or both. The remainder of the bath is sodium carbonate.

This process produces a nitrogen-diffused case 0.3 mm (0.012 in.) deep on plain carbon or low-alloy steels in a 1½ h cycle. The surface layer (0.005 to 0.01 mm, or 0.0002 to 0.0005 in. deep) of the case is composed of ϵ Fe₃N and a nitrogen-bearing Fe₃C; the nitrided case does not contain the brittle Fe₂N constituent.

Beneath the compound zone of Fe₃N, a diffusion zone exists that consists of a solid solution of nitrogen in the base iron. Depth of nitrogen diffusion in 1015 steel as a function of nitriding time at 565 °C (1050 °F) is shown in Fig 4. The outer compound layer provides wear resistance, while the diffusion zone improves fatigue strength.

It should be noted that only chromium-, titanium-, and aluminum-alloyed steel respond well to conventional bath nitriding. Plain carbon (nonalloyed) steels respond well to aerated bath nitriding but not to conventional nitriding. Thus, the aerated process should be specified for nitriding all plain carbon steels because test data show that plain carbon steel will not develop adequate hardness in a nonaerated

Table 2 Liquid nitriding processes

Process identification	Operating range composition	Chemical nature	Suggested post treatment	Operating temperature		U.S. patent number
				°C	°F	
Aerated cyanide-cyanate	Sodium cyanide (NaCN), potassium cyanide (KCN) and potassium cyanate (KCNO), sodium cyanate (NaCNO)	Strongly reducing	Water or oil quench; nitrogen cool	570	1060	3,208,885
Casing salt	Potassium cyanide (KCN) or sodium cyanide (NaCN), sodium cyanate (NaCNO) or potassium cyanate (KCNO), or mixtures	Strongly reducing	Water or oil quench	510–650	950–1200	
Pressure nitriding	Sodium cyanide (NaCN), sodium cyanate (NaCNO)	Strongly reducing	Air cool	525–565	975–1050	
Regenerated cyanate-carbonate	Type A: Potassium cyanate (KCNO), potassium carbonate (K ₂ CO ₃); Type B: Potassium cyanate (KCNO), potassium carbonate (K ₂ CO ₃), 1–10 ppm, sulfur (S)	Mildly oxidizing	Water, oil, or salt quench	580	1075	4,019,928
		Mildly oxidizing	Water, oil quench, or salt quench	540–575	1000–1070	4,006,643

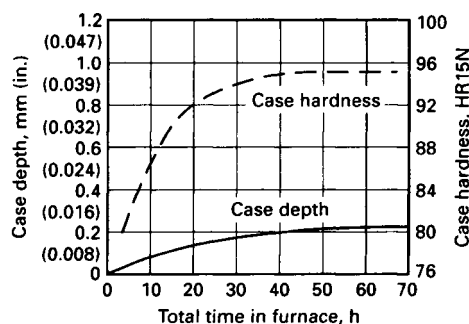


Fig. 1 Results of liquid pressure nitriding on type 410 stainless steel (composition, 0.12C-0.45Mn-0.41Ni-11.90Cr; core hardness, 24 HRC)

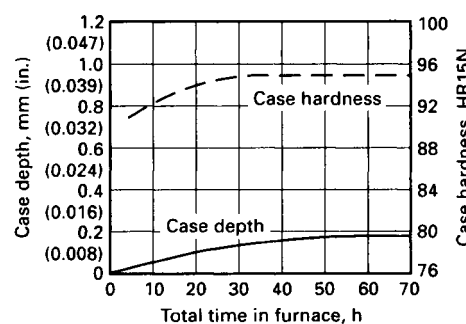


Fig. 2 Results of liquid pressure nitriding on AISI type D2 tool steel (composition, 1.55C-0.35Mn-11.50Cr-0.80Mo-0.90V; core hardness, 52 HRC)

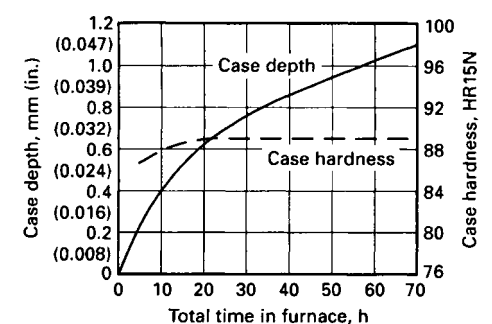


Fig. 3 Results of liquid pressure nitriding on SAE 4140 low-alloy steel (composition, 0.38C-0.89Mn-1.03Cr-0.18Mo; core hardness, 35 HRC)

nitriding bath. However, the full effect of nitriding will not be realized unless an alloy steel is selected. See the section "Hardness of Compound Layer" in Appendix 1 of this article.

Aerated Cyanide-Cyanate Nitriding. Another aerated process for liquid nitriding is a high-cyanide, high-cyanate system that is proprietary (U.S. Patent 3,208,885). The cyanide content of the fused salt is maintained in the range of 45 to 50% calculated as potassium cyanide, and the cyanate content is maintained in the range of 42 to 50% calculated as potassium cyanate. Makeup salt consists of a precise mixture of sodium and potassium cyanides that are oxidized by aeration to the mixed cyanate. The ratio of sodium ions to potassium ions is important in duplicating the integrity of the compound zone and the diffusion zone.

The process is performed in a titanium-lined container, and it produces a compound zone of ϵ iron nitride to a depth of 0.010 to 0.015 mm (0.0004 to 0.0006 in.) and a diffusion zone of 0.356 to 0.457 mm (0.014 to 0.018 in.) in plain carbon steels with a 90-min treating time, as

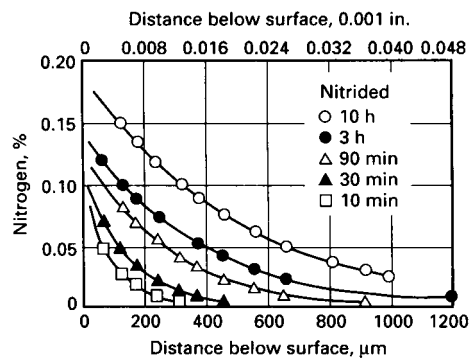


Fig. 4 Nitrogen gradients in 1015 steel as a function of time of nitriding at 565 °C (1050 °F), using the aerated bath process



Fig. 5 Nitrided case and diffusion zone produced by cyanide-cyanate liquid nitriding. The characteristic needle structure is seen only after a 300 °C (570 °F) aging treatment. Depth of compound zone about 0.01 mm

shown in Fig 5. The surface hardness of the compound zone may vary between 300 HK and 450 HK if carbon or low-alloy steels are being treated. Surface hardness of stainless steels treated by this process may reach 900 HK as shown in AMS 2755B, a portion of which is reproduced in Appendix 2 of this article.

Aerated Low-Cyanide Nitriding. Environmental concerns have led to the development of cyanide-free processes for liquid nitriding. In these proprietary processes, the base salt is supplied as a cyanide-free mixture of potassium cyanate and a combination of sodium carbonate and potassium carbonate, or sodium chloride and potassium chloride. Minor percentages of cyanide develop during use in these compositions. The problem is overcome in one process (U.S. Patent 4,019,928), by quenching in an oxidizing quench salt that destroys the cyanide and cyanate compounds (which have pollution capabilities) and produces less distortion than that resulting from water quenching. An alternate method utilized by U.S. Patent 4,006,643 is the incorporation of lithium carbonate plus minute amounts of sulfur (1 to 10 ppm) in the base salt to hold cyanide formation to below 1.0%.

These low-cyanide processes have been shown in tests to produce the same results as those developed in the previously mentioned liquid nitriding processes. The diffusion curves

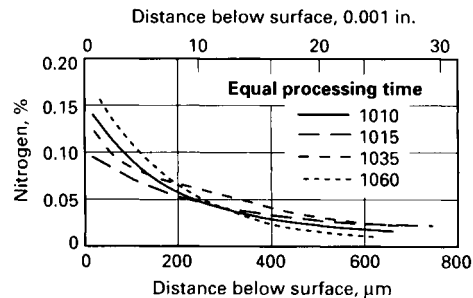


Fig. 6 Effect of carbon content in carbon steels on the nitrogen gradient obtained in aerated bath nitriding

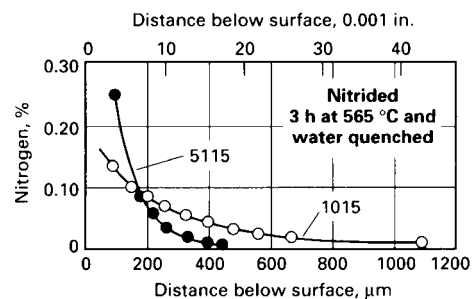


Fig. 7 Comparison of nitrogen gradients in a low-carbon steel and in a low-alloy steel containing chromium, both nitrided by the aerated bath process

and case depths are quite similar to those shown in Fig 1, 2, and 3. Because a high cyanate (65 to 75% KCNO) level in the absence of cyanide would be expected to produce iron nitride compound zones slightly lower in carbon and slightly higher in nitrogen, it is good practice to develop new tests and operational data when converting to one process from another. Excerpts from the AMS 2753 specification developed for low-cyanide liquid salt bath nitriding are shown in Appendix 1.

Case Hardness. According to AMS 2755C, case hardness varies markedly with the alloy being nitrided. Hardness and other requirements of this specification are summarized in Appendix 2.

Effects of Steel Composition. Although the properties of alloy steels are improved by the compound and diffusion layers, relatively greater improvement is achieved with plain carbon steels of low and medium carbon content. For example, the improvement in fatigue strength of unnotched test bars of 1015 steel nitrided by this process for 90 min at 565 °C (1050 °F) and water quenched (to further enhance fatigue properties) is roughly 100%. Improvement obtained with similarly treated test bars made of 1060 steel is about 45 to 50%.

The diffusion of nitrogen in carbon steels is directly affected by carbon content, as shown in Fig 6. The nitride-forming alloying elements also inhibit nitrogen diffusion. For example, the inhibiting effect of chromium on diffusion is shown in Fig 7, which compares nitrogen in a low-carbon steel (1015) and a chromium-containing low-alloy steel (5115).

Although the visible nitrogen diffusion zone shown by the Fe_4N needles in Fig 5 can be measured under the microscope to a depth of approximately 0.41 mm (0.016 in.), actual nitrogen penetration can be measured up to 1.02 mm (0.040 in.) as shown in Fig 8. This nitrogen is in solution, is under stress, and is precipitated as Fe_4N . It is responsible for the fatigue improvement resulting from liquid nitriding. The improvement is more apparent in plain carbon steels, resulting in the substitution of these steels for high-carbon and low-alloy steels in many applications (Table 3).

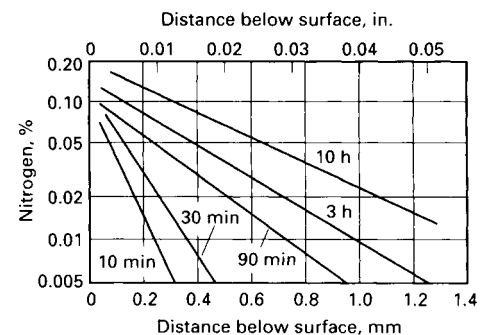


Fig. 8 Nitrogen diffusion in AISI 1015 steel

Case Depth and Case Hardness

Data indicating depth of case obtained in liquid nitriding various steels in a conventional bath at 525 °C (975 °F) for up to 70 h are shown in Fig 9. The steels include three chromium-containing low-alloy steels (4140, 4340, and 6150), two aluminum-containing nitriding steels (SAE 7140 and AMS 6475), and four tool steels (H11, H12, M50, and D2). All were nitrided in a salt bath with an effective cyanide content of 30 to 35% and a cyanate content of 15 to 20%. Case depths were measured visually on metallographically prepared samples that were etched in 3% nital. Before being nitrided, samples were tempered to the core hardnesses indicated.

Figure 10 presents data on case hardness obtained in liquid pressure nitriding the following alloy steels and tool steels: SAE 7140, AMS 6475, 4140, 4340, medium-carbon H11, low-

carbon H11, H15, and M50. The various core hardnesses, nitriding temperatures, and cycle times were as noted in the graphs in Fig 10. Case depth and hardness results are comparable to those obtained in single-stage gas nitriding.

High-Speed Steels. Compared to gas nitriding of high-speed steel cutting tools, liquid nitriding can produce a more ductile case with a lower nitrogen content.

Operating Procedures

Among the important operating procedures in liquid nitriding are the initial preparation and heating of the salt bath, aging of the molten salts (when required), and analysis and maintenance of salt bath composition. Virtually all steels must be quenched and tempered for core properties before being nitrided or stress relieved for distortion control. So prior heat treatment may be considered an essential part of the operating procedure.

Prior Heat Treatment. Alloy steels usually are given a prior heat treatment similar to that preferred for gas nitriding. Maintenance of dimensional and geometric stability during liquid nitriding is enhanced by hardening of parts prior to nitride treatment. Tempering temperatures should be no lower than the nitriding temperature and preferably slightly above.

Depending on steel composition, the effect of core hardness is similar to that encountered in gas nitriding.

Starting the Bath. Case-producing salt compositions may vary with respect to manufacturers, but they are basically sodium and potassium cyanides, or sodium and potassium cyanates. Cyanide, the active ingredient, is oxidized to cyanate by aging as described below. The commercial salt mixture (60 to 70% sodium salts, 30 to 40% potassium salts) is melted at 540 to 595 °C (1000 to 1100 °F). *During the melting period, a cover should be placed over the retort to guard against spattering or explosion of the salt, unless the equipment is*

Table 3 Improvement in fatigue properties of low-temperature liquid nitrided ferrous materials

Steel type	Property improvement, %
Low-carbon steels	80-100
Medium-carbon steels	60-80
Stainless steels	25-35
Low-carbon, chrome manganese steels	25-35
Chrome alloy, medium-carbon steels	20-30
Cast irons	20-80

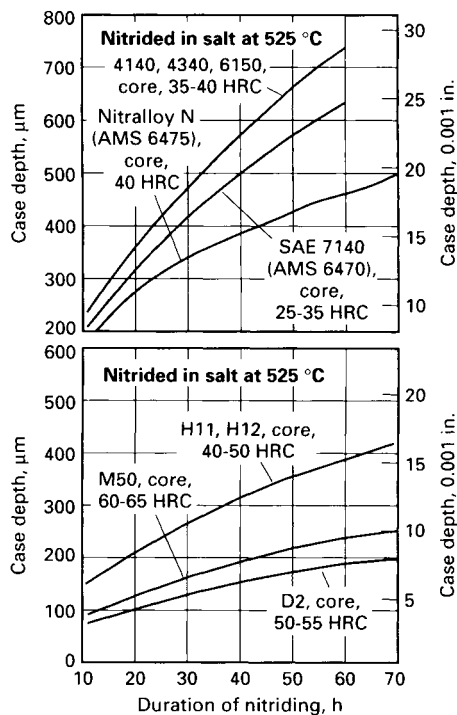


Fig. 9 Depth of case for several chromium-containing low-alloy steels, aluminum-containing steels, and tool steels after liquid nitriding in a conventional salt bath at 525 °C (975 °F) for up to 70 h

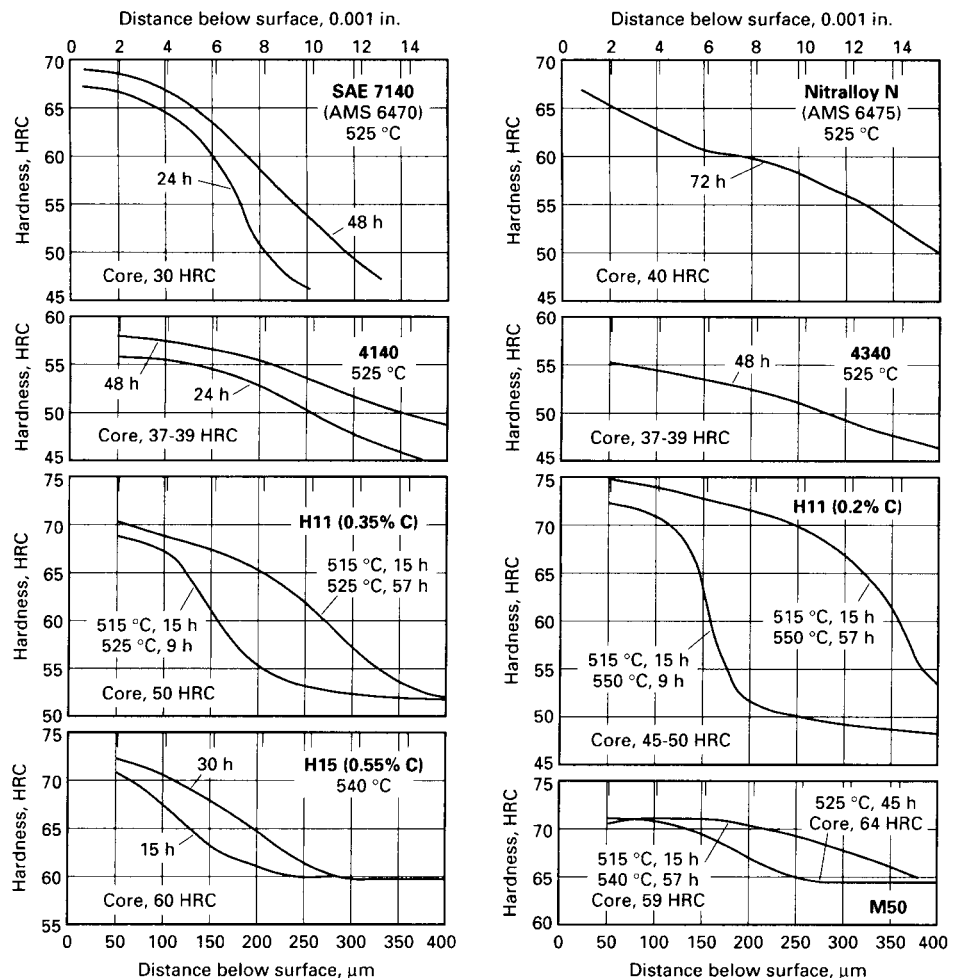


Fig. 10 Hardness gradients for several alloy and tool steels nitrided in salt by the liquid pressure process. Rockwell C hardness values are converted from Knoop hardness measurements made using a 500 g load. Temperatures are nitriding temperatures.

completely hooded and vented. It is mandatory that the salts be dry before they are placed in the retort; the presence of entrapped moisture may result in an eruption when the salt mixture is heated.

Externally versus Internally Heated Salt Baths. Salt baths may be heated externally or internally. For externally heated salt baths, startup power should be limited to 37% of total capacity until signs of melting are apparent on all sides of the salt bath. For internally heated salt baths, natural gas flame torches having a moderate flame are effective in melting a pool of molten salt for a conductive path between electrodes.

Aging the Bath. Liquid nitriding compositions that do not contain a substantial amount of cyanate in the original melt must be aged before use in production. Aging is defined as the oxidation of the cyanide to cyanate. Aging is not merely a function of temperature alone, but also depends on the surface-to-volume ratio of the molten bath. It is the surface air (oxygen) to salt contact that oxidizes cyanide to cyanate.

Molten salts in conventional baths should be aged by being held at 565 to 595 °C (1050 to 1100 °F) for at least 12 h, and no work should be placed in the bath during the aging treatment. Aging decreases the cyanide content of the bath and increases the cyanate and carbonate contents. Before nitriding is begun, a careful check of the cyanate content should be made. Nitriding should not be attempted until the cyanate content has reached at least the minimum operating level recommended for the bath.

Bath Maintenance. To protect the bath from contamination and to obtain satisfactory nitriding, all work placed in the bath should be thoroughly cleaned and free of surface oxide. An oxide-free condition is especially important when nitriding in low-cyanide salts. These compounds are not strong reducing agents and therefore are incapable of producing a good surface on any oxidized work. Either acid pickling or abrasive cleaning is recommended prior to nitriding. Finished clean parts should be preheated before being immersed in the bath to rid them of surface moisture.

A high cyanate content (up to about 25%) will provide good results, but carbonate content should not exceed 25%. Carbonate content can be readily lowered by cooling the bath to 455 °C (850 °F) and allowing the precipitated salt to settle to the bottom of the salt pot. It can then be spooned from the bottom by means of a perforated ladle.

To minimize corrosion at the air-salt interface, salts should be completely changed every three or four months (replacement of salt is usually far more economical than replacement of the pot). When the bath is not in use, it should be covered; excessive exposure to air causes a breakdown of cyanide to carbonate and adversely affects pot life.

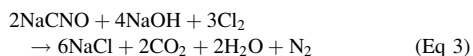
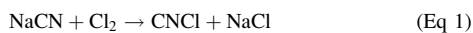
The ratio of cyanide content to cyanate content varies with the salt bath process and the

composition of the bath. The commercial NaCN-KCN bath, after aging for one week, achieves a ratio of 21 to 26% cyanide to 14 to 18% cyanate. The bath used in liquid pressure nitriding operates with a cyanide content of 30 to 35% and a cyanate content of 15 to 20%. The aerated bath is controlled to a ratio of 50 to 60% cyanide to 32 to 38% cyanate. The aerated noncyanide nitriding process is controlled to a ratio of 36 to 38% cyanate to 17 to 19% carbonate.

Oxidation products that promote unfavorable temperature gradients must be periodically removed from all baths. In normal operation, overheating of any bath (above 595 °C, or 1100 °F) should be avoided.

Safety. Some of the compositions employed in liquid nitriding processes contain sodium cyanide or potassium cyanide, or both. These compounds can be handled safely with proper equipment and neutralized by chemical means before discharge. *The compounds are highly toxic, however, and great care should be exercised to avoid taking them internally or allowing them to be absorbed through skin abrasions. Contact between the compounds and mineral acids also generates another hazard: the formation of hydrogen cyanide (HCN) gas, an extremely toxic product. Exposure to hydrogen cyanide can be fatal.*

Neutralization of Cyanide Waste. The destruction of cyanide by chlorine is believed to proceed in three steps, according to the following equations:



The first reaction (Eq 1), oxidation to cyanogen chloride, is almost instantaneous, occurring at all pH levels. The second reaction (Eq 2) is the formation of cyanate from cyanogen chloride under caustic alkaline environment. The rate of formation is primarily dependent upon the pH, and at a pH of 11 or higher, is virtually completed in minutes. At pH values lower than 10.5 the rate of hydrolysis is slowed considerably, and pHs below this value should be avoided due to the toxicity of the cyanogen chloride.

The next step (Eq 3), decomposition of the cyanate to harmless nitrogen and carbon dioxide, is pH dependent and is accelerated by a decreasing pH. At a pH of 7.5 to 8.0, about 10 to 15 min are required for the reaction to go to completion. At a pH of 9.0 to 9.5, about 30 min are required.

In practice, about 8.0 parts of chlorine and 7.3 parts of sodium hydroxide per part of cyanide are required for the overall reaction. Occasionally, chlorination to cyanate only is sufficient

because the cyanate ion is only 1/1000th as toxic as cyanide. About 3.2 parts of chlorine and 3.8 parts of sodium hydroxide per part of CN are required for the oxidation of cyanides to cyanates.

The waste will also contain small amounts of heavy metal cyanides in addition to the sodium or potassium cyanide. These will be broken down and the metal salts precipitated in reactions analogous to those for the sodium cyanide. Some metal complexes react much more slowly with the chlorine as oxidant. Silver cyanide, for instance, may require at least an hour of retention time for complete destruction.

Equipment

Salt bath furnaces used for nitriding may be heated by gas, oil, or electricity, and are essentially similar in design to salt bath furnaces used for other processes. Although batch installations are most common, semi-continuous and continuous operations are feasible. Generally, the same furnace equipment can be used for other heat-treating applications by merely changing the salt.

A variety of materials are used for the pots, electrodes, thermocouple protection tubes, and fixtures employed in salt bath nitriding, depending primarily on the salt mixture and process. For example, low-carbon steel is sometimes used for furnace liners although titanium is recommended for one of the processes (U.S. Patent 3,208,885). Inconel 600 is presently being applied to the noncyanide process described in U.S. Patent 4,019,928. Type 430 stainless steel is recommended for a low-cyanide process described in U.S. Patent 4,006,643. Cast HT alloy is a satisfactory fixture material, and type 446 stainless steel has been used for fixtures and thermocouple protection tubes. One plant reports the successful use of Inconel pots in liquid pressure nitriding; the same plant reports also that electrodeposited nickel performs satisfactorily as a stopoff in the liquid pressure bath. In general, however, nickel-bearing materials are not recommended for nitriding salt baths.

Maintenance Schedules

Certain maintenance procedures should be performed on a daily and weekly basis to ensure optimum operation of the salt bath used for nitriding.

Daily. The following procedures should be done on a daily basis:

- Check temperature-measuring instruments
- Check flowmeters, if these are required for air or anhydrous ammonia
- Check surface condition of work for desired steel-gray color and possible pitting
- Check case depth and case hardness to determine operating condition of the bath

Weekly. The following procedures should be done on a weekly basis:

- Analyze salt bath composition at least once a week; a semiweekly analysis is preferred. Make necessary additions to maintain level
- Check air-salt interface on pot for undercutting. Remove salts and recharge whenever undercutting is observed
- Check bath for nickel content. To remove traces of nickel, a steel plate-out panel should be placed in the bath overnight
- Contamination in the form of $\text{Na}_4\text{Fe}(\text{CN})_6$ (a complex ferrocyanide that forms in cyanide-type baths) should be removed from the bath by holding the bath at 650°C (1200°F) for about 2 h to settle out the compound in the form of sludge

Safety Precautions

The following safety precautions should be observed when operating salt bath furnaces for nitriding steels:

- Operating personnel must be carefully instructed in handling the poisonous cyanide-containing salts
- All chemical containers must be clearly marked to indicate contents
- Personnel should be provided with facilities for washing their hands thoroughly to prevent contamination by the cyanide salts
- Shields, gloves, aprons, and eye protection should be worn by operating personnel
- Parts and workpiece support fixtures should be preheated to drive off any moisture that may be present before they are immersed in the molten salt bath
- Proper venting of furnace and rinse tanks to the outdoors is recommended in order to provide safety against fumes and spattering and to minimize corrosion in the work area
- *Nitrate-nitrite salts must not come in contact with nitriding salts in the molten state. Contact will result in an explosion. Storage of these salts should be properly labeled and stored apart*

Liquid Nitrocarburizing

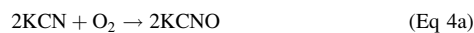
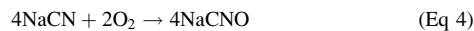
In liquid nitrocarburizing processes, both carbon and nitrogen are absorbed into the surface. High-cyanide nitrocarburizing baths have been in use since the late 1940s. Initially, the sulfur-containing variant was used to produce a wear-resistant surface of iron sulfide (see Process 2). A sulfur-free high-cyanide bath was developed in the mid-1950s, now known as aerated bath nitriding (Process 1). This process and a low-cyanide variant of it (Process 4) are commonly used.

Both Processes 1 and 2 are similar in that components are typically preheated to about

350 to 480°C (660 to 900°F), and then transferred to the nitrocarburizing salt bath at 570°C (1060°F). The major components of the baths for both processes are normally alkali metal cyanide and cyanate. Salts are predominately potassium, with sodium.

Liquid nitrocarburizing processes are used to improve wear resistance and fatigue properties of low-to-medium carbon steels, cast irons, low-alloy steels, tool steels, and stainless steels.

Process 1: High Cyanide without Sulfur. At the treatment temperature of 570°C (1060°F), the process is controlled largely by two reactions, an oxidation reaction and a catalytic reaction. The oxidation reaction involves transformation of cyanide to cyanate:



Though this reaction can proceed by natural oxidation of the cyanide bath, eventually leading to the desired cyanate content, the mechanism of natural aging does not provide the higher cyanate level made possible with aeration. To provide agitation and stimulate chemical activity, therefore, dry air is introduced into the bath.

The catalytic reaction involves breaking down cyanate in the presence of the steel components being treated, thus supplying carbon and nitrogen to the surface:

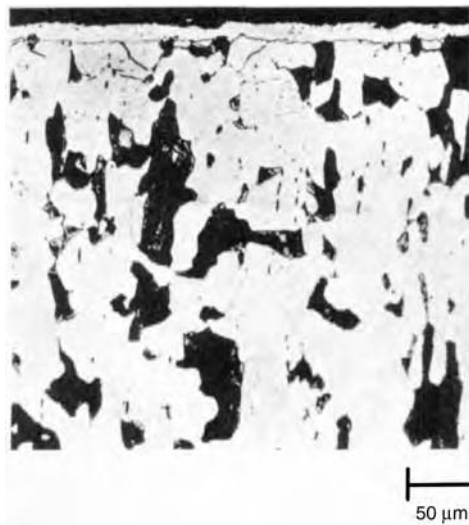
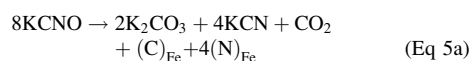
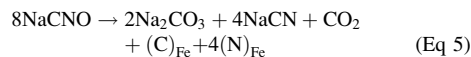
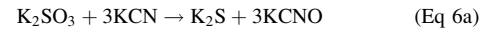
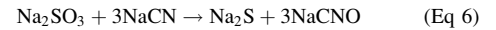


Fig. 11 Metallographic appearance of salt bath nitrocarburized mild steel after 1.5 h at 570°C (1060°F) followed by water quenching

As a result of this treatment, a wear-resistant compound zone, rich in nitrogen and carbon, is formed on component surfaces (Fig 11).

Process 2: High Cyanide with Sulfur. The same basic oxidation and catalytic reactions of Process 1 also occur in this process. In addition, further reactions take place because of sulfites in the melt. These sulfites are reduced to sulfides, in conjunction with the oxidation of the cyanide to cyanate, as follows:



Thus, the sulfur present in the bath acts as an accelerator, with the result that the cyanate is produced more readily than if the sulfur compounds were absent. Consequently, external aeration is not normally used in the process. Potassium and sodium cyanates produced by the reactions in Eq 4 and 6 catalytically decompose at the surface of ferrous materials to liberate carbon monoxide and nascent nitrogen. The carbon monoxide dissociates to liberate active carbon. The carbon, in conjunction with the nascent nitrogen, diffuses into the material being treated to form the compound zone.

The exact mechanism by which sulfur is impregnated into the material is not clear. Various sulfides react with the component being treated to form iron sulfide; this is the black deposit observed on the surface of components after treatment.

The compound layer formed on mild steel after a 90-min treatment, followed by water quenching, is shown in Fig 12. The compound layer formed by cyanide salt bath nitrocarburizing treatments, and, in particular, by the sulfur-containing high-cyanide process, contains an

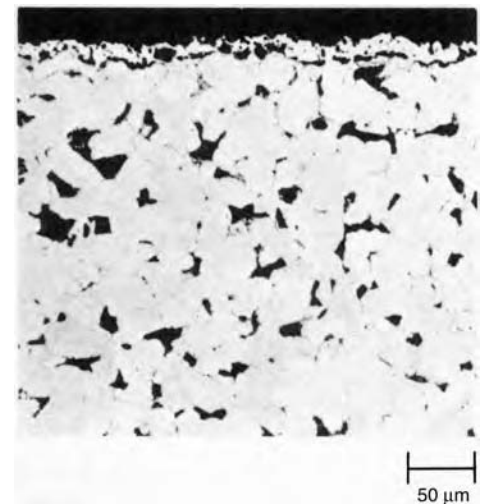


Fig. 12 Metallographic appearance of mild steel after similar treatment to Fig 11. Iron-sulfide inclusions in the outer region of the compound zone are apparent after this treatment, in which sulfur acts as an accelerator.

outer region of microporosity. These pores, which readily absorb oil, may assist the anti-scuffing properties of treated components under lubrication conditions.

Although little systematic investigation has been done to establish the optimum thickness of the compound layer for maximum improvement in wear and anti-scuffing properties, it is believed that comparable results are obtained provided the layer is 10 to 20 μm (400 to 800 $\mu\text{in.}$) thick.

Composition and Structural Analysis of the Compound Layer. X-ray diffraction investigations into the structure of the compound layer formed by the two high-cyanide salt bath nitrocarburizing processes have indicated a variety of carbon and nitrogen-base phases.

One study of cyanide nitrocarburizing treatments indicated that the best anti-scuffing properties were obtained when the compound layer consisted mainly of a hexagonal close-packed (hcp) phase of variable carbon and nitrogen concentration. Examination of the appropriate isothermal section of the iron-carbon-nitrogen ternary phase diagram (Fig 13) indicates that this phase is the ϵ carbonitride phase. Furthermore, it is believed that provided the ϵ phase was predominant within the compound layer,

small amounts of other phases, particularly Fe_4N and Fe_3C , had no serious adverse effects on anti-scuffing behavior. It has been shown that with Process 1, compound layers with less than about 2% C and less than about 6% N contained a mixture of the ϵ iron carbonitride and Fe_4N . With these processing times in excess of 3 h, the proportion of Fe_4N was found to decrease. Furthermore, when more than 2% C was in the compound layer, a compound with the structure of cementite, $\text{Fe}_3(\text{CN})$, could also be detected.

In samples treated by Process 1, a high level of oxygen within the compound layer has been reported. But whether the presence of oxygen, which is known to accelerate the formation of the compound layer by promoting the cyanide-to-cyanate oxidation reaction, is essential for improved frictional properties has not been rigorously established.

Similarly, the question arises as to whether sulfur, present in Process 2, contributes significantly to enhanced anti-scuffing properties. The predominant presence of an ϵ carbonitride phase is required for enhanced anti-scuffing properties. Electron probe microanalysis of the compound layers formed by the two processes are presented in Fig 14.

Nontoxic Salt Bath Nitrocarburizing Treatments

Environmental considerations and the increased cost of detoxification of cyanide-containing effluents have led to development of low-cyanide salt bath nitrocarburizing treatments.

Cyanates are the active nitriding constituent of both high-cyanide and low-cyanide nitrocarburizing baths. Reduction of the cyanide content permits markedly higher cyanate concentrations in the low-cyanide baths; this results in greatly increased nitriding activity. Unlike the reducing high-cyanide baths, the nominal cyanate and carbonate composition of the low-cyanide baths is oxidizing. The baths are composed of primarily potassium salts with some sodium salts. During nitriding, cyanates yield nitrogen to the steel and form carbonates. Cyanate concentration is maintained by the use of organic regenerators, which supply nitrogen to reform cyanates from carbonates.

Process 3: Low Cyanide with Sulfur. This patented process confers sulfur, nitrogen, and presumably, carbon and oxygen to surfaces of ferrous materials. The process is unique in that lithium salts are incorporated in the bath

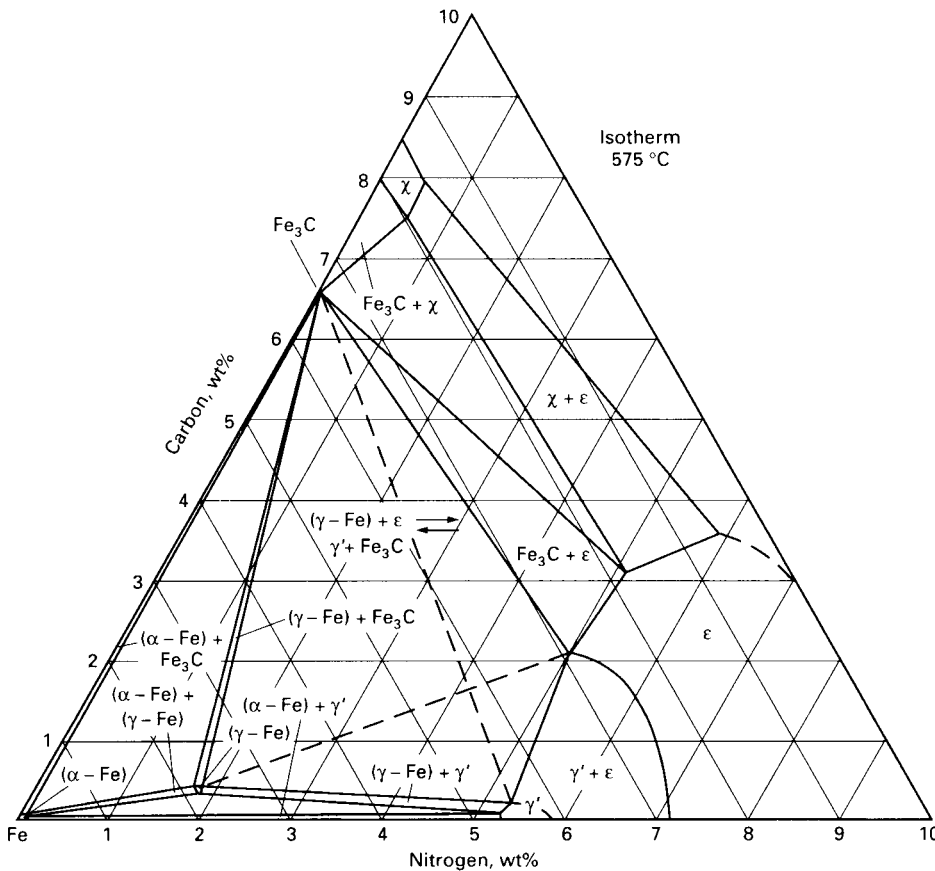


Fig. 13 Phase diagram at 575 °C (1065 °F) of the ternary iron-carbon-nitrogen system

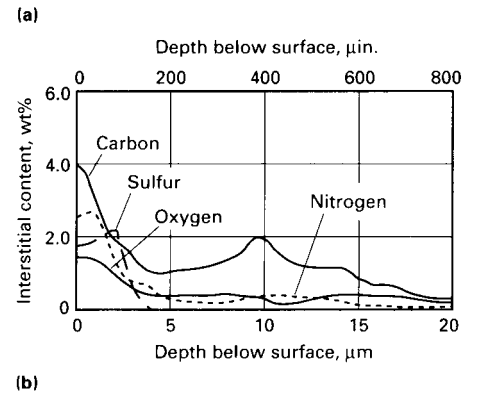
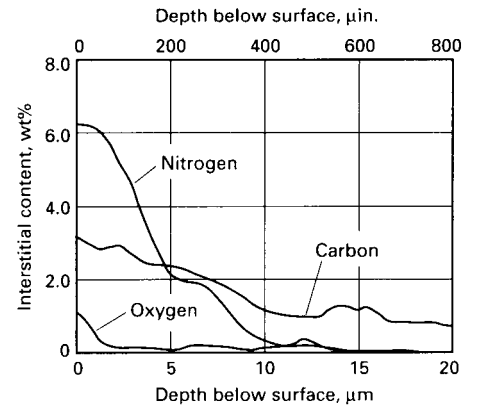


Fig. 14 Electron microprobe traces of compound layers. (a) Nitrogen, carbon, and oxygen in the compound layer formed by Process 1. (b) Nitrogen, carbon, oxygen, and sulfur in the compound layer formed by Process 2. Both treatments, 90 min

composition. Cyanide is held to very low levels: 0.1 to 0.5%. Sulfur species, present in the bath at concentrations of 2 to 10 ppm, cause sulfidation to occur simultaneously with nitriding. Sulfur levels near 10 ppm result in an apparently porous compound zone (Fig 15); the dark areas are actually iron sulfide nodules, not voids. This compound zone is similar to the high-cyanide, sulfur-containing nitrocarburizing process that has, however, columnar iron-sulfide inclusions.

Bath composition can be adjusted to lower sulfur levels (2 ppm) to form a less porous layer with a lower iron sulfide content.

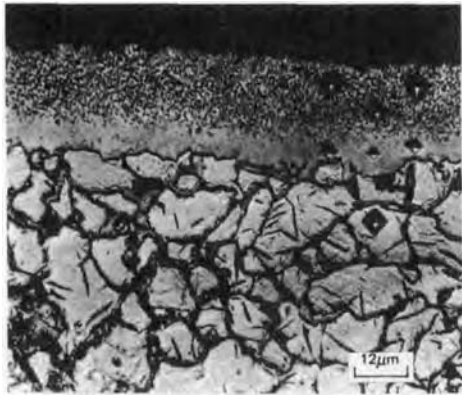


Fig. 15 Sample of plain carbon steel after low-cyanide salt bath nitrocarburizing treatment (Process 3). The high level of apparent porosity is a characteristic of high sulfur content in the compound zone; dark areas are actually iron-sulfide nodules, not voids.

A compound layer 20 to 25 μm (800 to 1000 $\mu\text{in.}$) thick forms in 90 min at 570 $^{\circ}\text{C}$ (1060 $^{\circ}\text{F}$) on AISI 1010 steel, compared with the 8 to 10 μm (320 to 800 $\mu\text{in.}$) layer formed by the high-cyanide sulfur-bearing nitrocarburizing process in the same time. Figure 16 shows the thickness of the compound layer as a function of the treatment time for the nontoxic and cyanide-based treatments.

Process 4: Low Cyanide without Sulfur. A low-cyanide alternative to the cyanide-based Process 1 has been developed. This process, like Process 3, is a cyanate bath with no lithium or sulfur compounds and very low cyanide levels (2 to 3%). Melon, an organic polymer, is used for bath regeneration.

When water quenching is employed, the low level of cyanide permits easier detoxification. Alternatively, quenching into a caustic-nitrate salt bath at 260 to 425 $^{\circ}\text{C}$ (500 to 795 $^{\circ}\text{F}$) may be used for cyanide/cyanate destruction.

Processing temperature for Process 4 is 570 to 580 $^{\circ}\text{C}$ (1060 to 1080 $^{\circ}\text{F}$); the rate of compound zone formation is comparable to that of

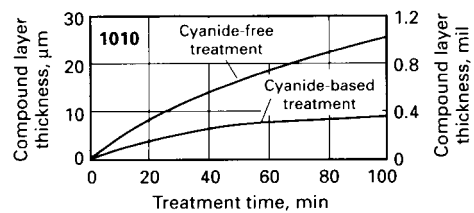


Fig. 16 Comparison of compound zone thickness produced by low-cyanide and cyanide-based treatments containing sulfur

Process 3. Metallurgical results are virtually identical with the cyanide-based Process 1.

Wear and Antiscuffing Characteristics of the Compound Zone Produced in Salt Baths

The resistance to scuffing after salt bath nitrocarburizing treatments has been frequently tested with a Falex lubricant testing machine (Fig 17, 18, 19). A 32 by 6.4 mm (1.25 by 0.25 in.) test piece is attached to the main drive shaft by means of a shear pin, and two anvils or jaws having a 90° V-notch fit into holes in the lever arms. During testing, the jaws are clamped around the test piece, which rotates at 290 rpm, and the load exerted by the jaws is gradually increased. Both test pieces and jaws can be immersed totally in a small tank containing lubricant or other fluid, or tests can be carried out dry.

Table 4 lists results of a few representative Falex tests for plain low-carbon steels both before and after cyanide salt bath nitrocarburizing treatments. The untreated low-carbon steel specimens do not show any significant scuffing resistance even when tested under oil-lubricated conditions. After treatment, however, even when tested dry, there is a considerable improvement in antiscuffing properties. Specimens tested in the dry condition after salt bath nitrocarburizing generate so much heat that they eventually become red hot and are extruded under the applied load. Untreated test pieces seize at relatively low loads before becoming red hot, whereas treated

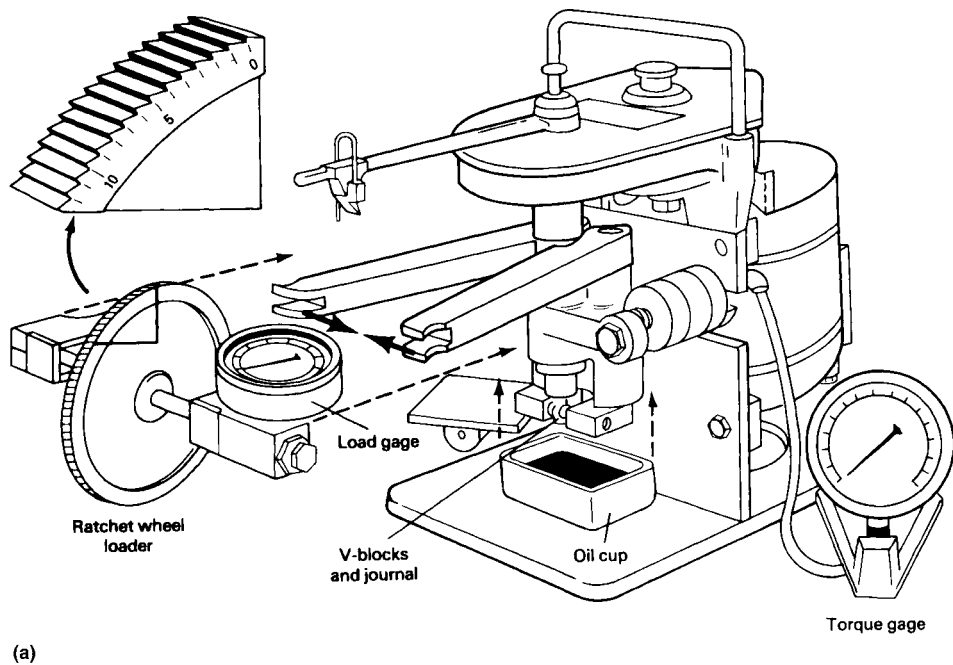


Fig. 17 Lubricant tester used to measure endurance (wear) life and load-carrying capacity of either dry solid-film lubricants or wet lubricants in sliding steel-on-steel applications. (a) Key components of instrument. (b) Exploded view showing arrangement of V-blocks and rotating journal

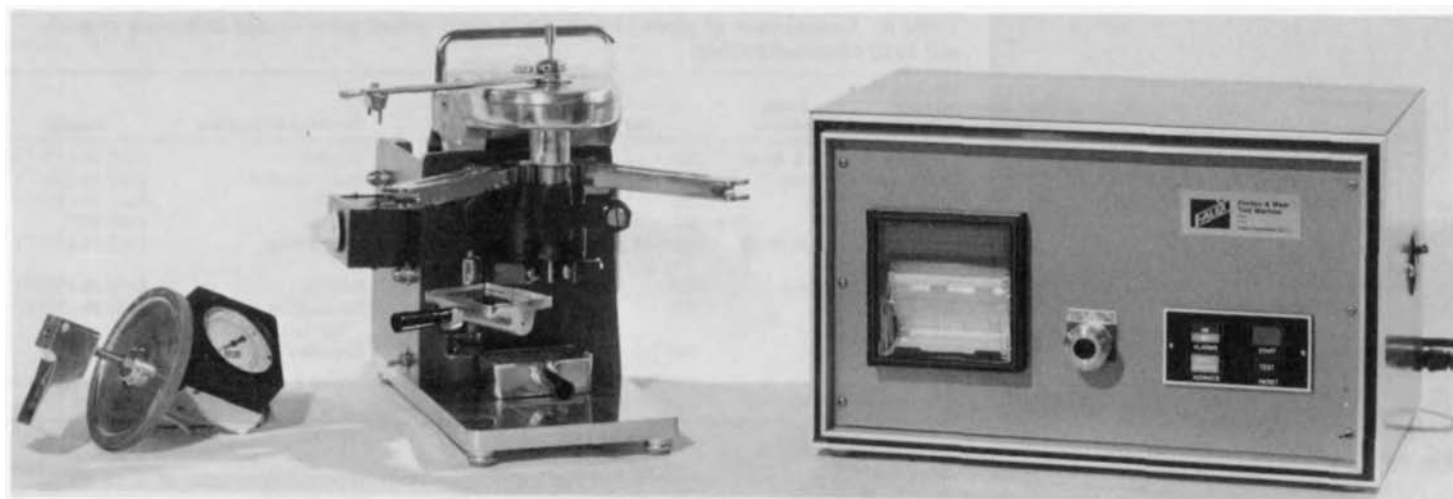


Fig. 18 Lubricant-testing machine incorporating a recorder to monitor the torque data used to determine wear life of the sample journal. The instrument provides both an instantaneous readout of the torque via a digital display and a continuous permanent record of torque values during the test on a strip chart. Workpiece failure is indicated by a torque rise of 1.1 N · m (10 lbf · in.) above the steady-state value or breakage of the shear pin, whichever failure criteria is reached first (per ASTM D 2625-83). Courtesy of Falex Corporation

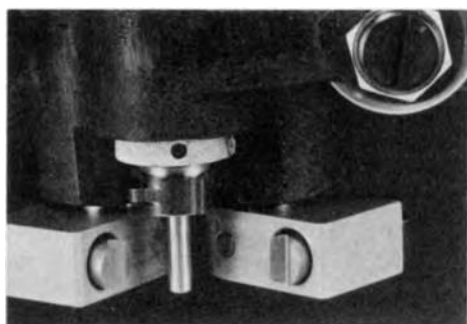


Fig. 19 Close-up view of a journal and V-block setup ready for testing in a lubricant-testing machine. Wear is indicated by a reduction or distortion in the diameter of the journal as well as deformation of the notch in the V-block. Courtesy of Falex Corporation

samples, even after extrusion, show no signs of scuffing. During testing in oil, the specimens become highly polished. Similar Falex test results are reported for low-cyanide salt bath nitrocarburizing treatments.

Appendix 1*—Liquid Salt Bath Nitriding Noncyanide Baths

Hardening. Parts requiring core hardness shall be heat treated to the required core hardness before processing. Tempering to produce the specified core hardness shall be at a temper-

* Adapted from AMS 2753A (Jan 1985)

Table 4 Comparison of plain carbon steels wear tested prior to and following cyanide salt bath nitrocarburizing

Condition of test pieces and jaws	Testing medium(a)	Applied load		Condition of test pieces	Material
		kgf	lbf		
Untreated	SAE 30 oil	320	700	Scuffed	En32 (0–15% C)
Untreated	Water	270	600	Badly scuffed	En32 (0–15% C)
Untreated	Air	320	700	Scuffed	En32 (0–15% C)
Untreated	Air	205	450	Scuffed	AISI 1045
Treated(b)	SAE 30 oil	Limit of gage, 1150	Limit of gage, 2500	No scuffing	En32 (0–15% C)
Treated(b)	Water	450	1000	Scuffed	En32 (0–15% C)
Treated(b)	Air	760	1675	No scuffing, became hot and extruded	En32 (0–15% C)
Treated(c)	Air	660	1450	Extruded	AISI 1045

(a) Falex scuffing tests at 290 rpm in EN8 (0.4% C) jaws, 90 min running time. (b) Treatment 2, cyanide nitrocarburizing salt bath, with sulfur present as an accelerator. (c) Treatment 1, cyanide nitrocarburizing salt bath

ature not lower than 590 °C (1090 °F), except when tempering is conducted in conjunction with nitriding.

Stress Relief. Parts in which residual stresses may cause cracking or excessive distortion due to thermal shock or dimensional change because of metallurgical transformations during nitriding shall be stress relieved prior to final machining. Stress relieving shall be performed at a temperature not lower than 590 °C (1090 °F).

Cleaning. Parts, at the time of nitriding, shall be clean and free of scale or oxide, entrapped sand, core material, metal particles, oil, and grease, and shall be completely dry.

Preheating. Parts shall be preheated in air at 260 to 345 °C (500 to 650 °F) to maintain bath temperature and to avoid thermal shock upon immersion in the nitriding salt.

Nitriding. Parts shall be immersed in an aerated cyanate bath as indicated in Table 5.

Quenching. Following treatment, parts shall be quenched in fused salts, water, oil, soluble oil solution, or air. Parts, except those made of air-hardening tool steels, may be cooled to 290 to 400 °C (550 to 750 °F) prior to actual quenching, when permitted by the purchaser.

Depth of compound layer shall be determined in accordance with SAE J423, microscopic method, at magnification of 500×, as indicated in Table 6.

Quality of Compound Layer. Any continuous surface porosity present shall not extend deeper than one-half the observed depth of the compound layer, determined by examining specimens metallographically at 500× magnification.

Hardness of compound layer shall be determined by microhardness measurements in accordance with ASTM E 384 on the nitrided surface or on metallographically

prepared cross sections of the nitrided case using Knoop or another appropriate hardness tester, as agreed upon by purchaser and vendor (see Table 7).

Appendix 2*—Liquid Salt Bath Nitriding

Nitriding salts shall consist of a mixture of sodium and potassium cyanide and other salts.

Salt Bath. The cyanate, cyanide, and iron contents of the bath shall be controlled within percentages by weight:

Content	Concentration, %	
	min	max
Cyanate determined as KNCO	42	50
Cyanide determined as KCN	45	50
Iron determined as $\text{Na}_4\text{Fe}(\text{CN})_6$	0.20	

Nitriding. Parts shall be immersed in an aerated cyanide-cyanate bath as indicated in Table 8.

Quenching. Following treatment, the parts shall be quenched in water, oil, soluble oil solution, or air. Parts, except those made of air-hardening tool steels, may be cooled to 290 to 400 °C (550 to 750 °F) prior to actual quenching, when permitted by the purchaser.

Depth of case shall be determined in accordance with SAE J423 (microscopic method) at 500× magnification as indicated in Table 9.

Case Quality. Any surface porosity present shall not extend deeper than one-half the observed depth of the compound layer, determined by examining specimens metallographically at 500× magnification.

Case hardness shall be determined by microhardness measurements in accordance with ASTM E384 on the nitrided surface or on metallographically prepared cross sections of the nitrided case using Vickers, Knoop, or another appropriate hardness tester, as agreed upon by purchaser and vendor (see Table 10).

Table 5 Recommended procedures for liquid salt bath nitriding in noncyanide baths

Material	Recommended time, h		Temperature	
	min	max	°C	°F
Carbon and low-alloy steels	1	2	580 ± 5	1075 ± 10
Tool and die steels (structural)	½	3	540–580	1000–1075
Tool steels (cutting)	½	1	540–580	1000–1075
Corrosion- and heat-resistant steels	1	2	580 ± 5	1075 ± 10
Ductile, malleable, and gray cast iron	1	4	580 ± 5	1075 ± 10
Powder metal products (ferrous)	½	2	580 ± 5	1075 ± 10

Table 6 Depth of compound layer after liquid salt bath nitriding in a noncyanide bath

Material	Case depth(a)	
	mm	in.
Carbon and low-alloy steels	0.0038–0.02	0.00015–0.001
Tool and die steels (structural)	0.003–0.012	0.0001–0.0005
Tool and die steels (cutting)	... 0.003	... 0.0001
Corrosion- and heat-resistant steels	0.0038–0.02	0.00015–0.001
Ductile, malleable, and gray cast iron	0.0038–0.02	0.00015–0.001
Powder metal products (ferrous)	0.0038–0.02	0.00015–0.001

(a) Ranges show minimum and maximum case depth.

Table 7 Hardness of the compound layer obtained after liquid salt bath nitriding in a noncyanide bath

Material	Hardness, min (HK at 100 gf load)
Carbon steels	300
Low-alloy steels	450
Tool and die steels	700
Corrosion- and heat-resistant steels	900
Ductile, malleable, and gray cast iron	600
Powder metal products (ferrous)	600

Table 8 Recommended procedures for liquid salt bath nitriding in cyanide-cyanate baths

Material	Recommended time, h		Temperature	
	min	max	°C	°F
Carbon and low-alloy steels	1	2	570 ± 5	1060 ± 10
Tool and die steels (structural)	½	3	540–570	1000–1060
Tool steels (cutting)	½	1	540–570	1000–1060
Corrosion- and heat-resistant steels	1	2	570 ± 5	1060 ± 10
Ductile, malleable, and gray cast iron	2	4	570 ± 5	1060 ± 10
Powder metal products (ferrous)	½	2	570 ± 5	1060 ± 10

Table 9 Depth of case measurements obtained following liquid salt bath nitriding in cyanide-cyanate baths

Material	Case depth	
	mm	in.
Plain carbon and low-alloy steels	0.004–0.03	0.00015–0.001
Tool and die steels (structural)	0.003–0.0	0.0001–0.0005
Tool and die steels (cutting)	... 0.003	... 0.0001
Corrosion- and heat-resistant steels	0.004–0.03	0.00015–0.001
Ductile, malleable, and gray cast iron	0.004–0.03	0.00015–0.001
Powder metal products (ferrous)	0.004–0.03	0.00015–0.001

(a) Ranges show minimum and maximum case depth.

Table 10 Hardness of the compound layer obtained after liquid salt bath nitriding in a cyanide-cyanate bath

Material	Hardness, min (HK at 200 gf load)
Plain carbon steels	300
Low-alloy steels	450
Tool and die steels	700
Corrosion- and heat-resistant steels	900
Ductile, malleable, and gray cast iron	600
Powder metal products (ferrous)	600

* Adapted from AMS 2755C (April 1985). Process also referred to as the "Tufftride" process

Plasma (Ion) Nitriding and Nitrocarburizing of Steels

Jan Elwart and Ralph Hunger, Bodycote

Introduction

Plasma nitriding (also known as ion nitriding, plasma ion nitriding, or glow-discharge nitriding) is a method of surface hardening using glow-discharge technology to introduce nascent (elemental) nitrogen to the surface of a metal part for subsequent diffusion into the material. The key difference between gas and ion nitriding is the mechanism of delivering nascent nitrogen into the surface of the workpiece. High-voltage electrical energy is used to form a low-pressure ionized gas (or plasma) containing nitrogen ions that are accelerated to impinge on the workpiece. This ion bombardment heats the workpiece, cleans the surface, and supplies atomic nitrogen to the surface. As a variant of steel nitriding, the nitrocarburizing of steel (Ref 1) also is done by the plasma method.

Ion nitriding, when compared to conventional (gas) nitriding, offers more precise control of the nitrogen supply at the workpiece surface. Other advantages of ion nitriding are:

- Improved control of case thickness
- Better control of nitriding potential and elimination of nitride networks
- Lower temperatures (as low as 375 °C, or 700 °F, due to plasma activation)
- Lower distortion
- No environmental hazard (freedom from using ammonia)
- The capital cost of the equipment is higher than for gas nitriding, but this can be offset by better plant utilization due to faster process cycles and more repeatable metallurgy.
- Reduced energy consumption
- Ability to automate the nitriding process in production lines and integrate into cell manufacture
- Ability to shield areas where nitriding is not desired by simple mechanical masking or protective pastes

Limitations of ion nitriding include:

- Inhomogeneous plasma distribution
- Limited temperature control
- Expensive equipment

Localized overheating and the potential for arcing also are limitations for conventional ion nitriding, where the workpieces are subjected to very high voltages to create heating from plasma conditions on the part surface. This problem is mitigated by pulsed direct-current plasma generators with auxiliary (external) heating of the furnace. The relatively recent development of active-screen plasma nitriding (Ref 2), where the plasma is generated on a screen surrounding the parts, also offers improved temperature control and more effective application of plasma nitriding of more intricate parts or varied workloads (Ref 3, 4).

Process History and Developments

The systematic investigation into the effect of nitrogen on the surface properties of steel began in the early part of the 20th century with the independent investigation of gas nitriding. Adolph Machlet (American Gas Company, Elizabeth, NJ) was granted a U.S. patent in 1913 for nitriding steels and cast iron at temperatures above 480 °C (900 °F) in ammonia. However, the monumental work of Dr. Adolph Fry (Krupp Works, Essen, Germany) was the key in developing special alloy steels (containing specifically aluminum) for case hardening. The so-called Nitralloy steels were derived from Fry's work and patent in 1921.

The plasma technique for nitriding was first investigated as a metallurgical processing tool by German physicist Dr. Wehneldt (1871–1944), who postulated that weak glow discharge could be developed into glow discharge with high current density for industrial use (Ref 5). However, he was unable to control it as a nitriding process due to the instability of the glow discharge—referred to as a lumina storm, such that the discharge dances away from the high-voltage cathode. Dr. Bernhard Berghaus (1896–1966) picked up Wehneldt's idea and successfully developed the process with a team of forty scientists, engineers, and

technicians at a research and development lab in Berlin (Ref 5).

The process developed by Berghaus was patented in Germany (Ref 6) and used as an alternative to gas nitriding in Germany during the time period of 1934 to 1943. The first practical applications were gearings and gun barrels several meters in length. Berghaus (Fig. 1) later settled in Zürich to escape Nazi persecution. Over the period 1957 to 1967, the German company Gesellschaft zur Förderung der Glimmentladungsforschung, funded by the Regional Government of Norderhein-Westfalen, undertook research into the physics, chemistry, and metallurgy of glow-discharge plasmas. The plasma technique also arrived in the United States during the 1950s, with General Electric as one of the first U.S. companies to recognize the usefulness of the process on a wide variety of materials (Ref 7).

Ionon, a private company owned by Berghaus in Köln, was responsible for the industrial exploitation of the technology generated. After the death of Berghaus, the process was acquired by the Klöckner Steel group in 1967 and was commercialized in 1970 under the name Klöckner Ionon. This technology formed the basis of the international commercialization of the technique (Ref 8). Thus, the first name in common use was ion nitriding and also the term *ionitriding*. To standardize the name within the German Deutsche Industrie-Normen, it later became plasma nitriding.

Direct-Current Plasma Nitriding (1970–1980). The first industrial-designed-sized furnaces by Klöckner Ionon were cold-walled furnaces that used water to cool the furnace walls. In comparison to other nitriding technologies, the plasma method offered significant advantages of lower operating costs (reduced consumption of energy and gases), precise depths of white layer compounds, and the nitriding of stainless steels. Plasma nitriding also provided safety and environmental benefits with no poisonous gas emissions.

However, in the initial stages of furnace building in 1970, modern electronic devices

and computer systems were not available to control the process. Therefore, the early plasma nitriding systems required operator control with a number of difficulties, including direct application of plasma on the parts to be treated, the risk of arcing, the so-called hollow-cathode effect, and nonuniform temperature. These issues required well-trained and highly skilled operators.

Direct-current (dc) plasma nitriding systems have a vacuum chamber, where the part to be treated is placed on a conducting metal plate (cathode) inside a metal chamber acting as the anode of the system (Fig. 2). The chamber is evacuated to a suitable low pressure, followed by bleeding a controlled amount of gas (typically a mixture of N_2 with some H_2) until an appropriate treatment pressure is obtained. High voltage is applied to the cathode and the metal part. Glow-discharge voltages are on the order of 1000 V or perhaps more, depending on the pressure and mixture of the gas. Hydrogen gas is typically added to promote the cleaning process.

Under the influence of this voltage, the nitrogen gas is dissociated, ionized, and accelerated toward the workpiece (the cathode). The positively charged nitrogen ion then acquires an electron from the cathode (workpiece) and emits a photon. This photon emission during the formation of nitrogen ions to their atomic state results in the visible glow discharge (Fig. 3) that is characteristic of plasma techniques. Upon impact with the workpiece, the kinetic energy of the nitrogen atoms is converted into heat, which can completely (or in combination with an auxiliary heating source) raise the load to nitriding temperature.

Because the pressure is low, very little heat is lost by convection from the part to the container. If the glow completely covers the part, the current is constant per unit area, resulting in a very uniform case (Fig. 4). However, cold-walled furnaces (with constant dc power supplies) present several limitations that include:

- Overheating, arcing, and edge effects due to the large bias voltage applied to the workpiece
- Difficulty in maintaining uniform temperature in components or workloads with different mass or complex configurations
- Difficulty in nitriding closely adjacent surfaces (due to the hollow-cathode effect), which places limits on the density of parts in a workload and the nitriding of deep, small-diameter holes
- High energy consumption to heat the part from just plasma heating

Pulsed-Current Plasma Nitriding. Attempts to address the shortcomings of dc plasma systems have involved the use of auxiliary heating and the use of pulsed biased power. During the mid-1970s, scientists at the University of



Fig. 1 Bernhard Berghaus in 1947 at his institute with a pit furnace developed for plasma nitriding of gun barrels.

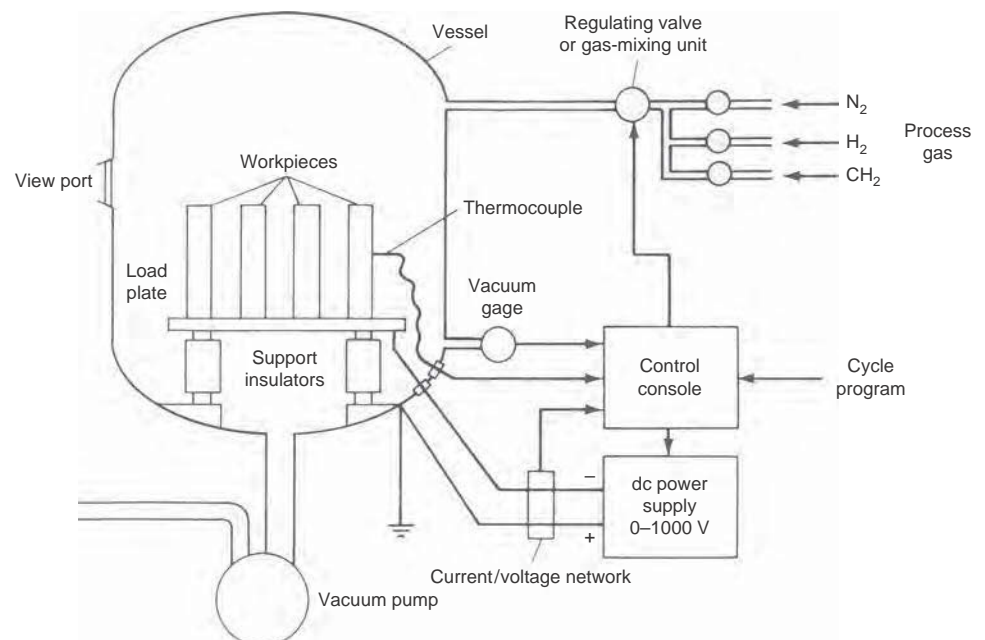


Fig. 2 Cold-walled plasma nitriding furnace and controls

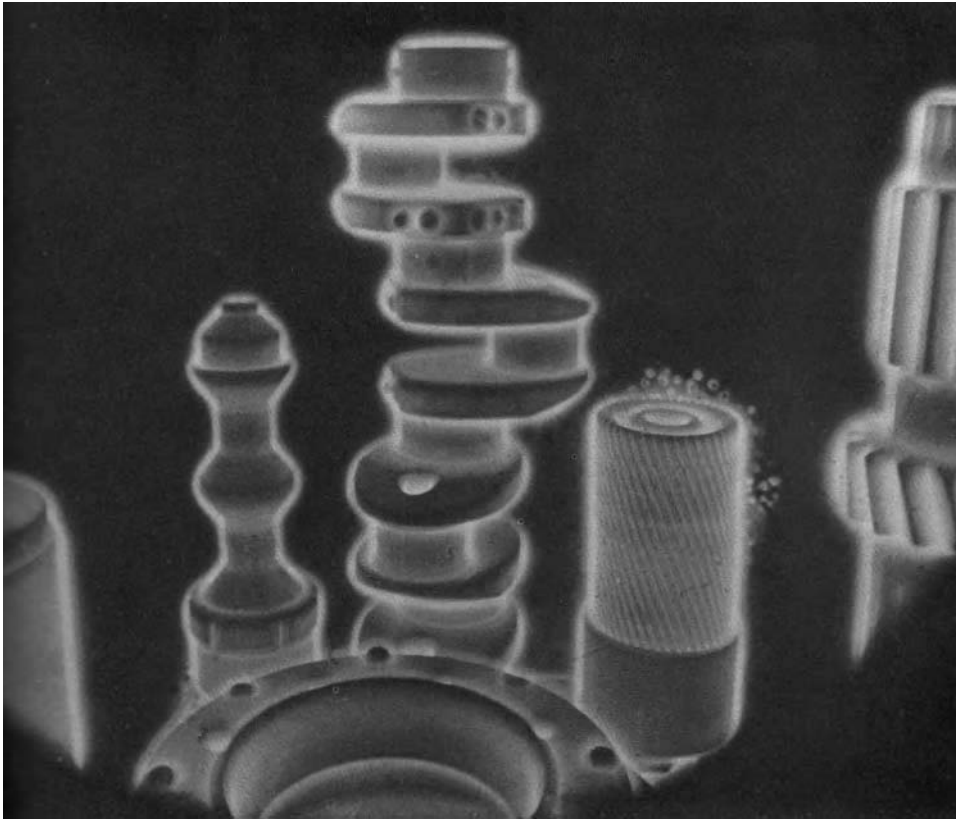


Fig. 3 Glow discharge during plasma nitriding. Source: Ref 9

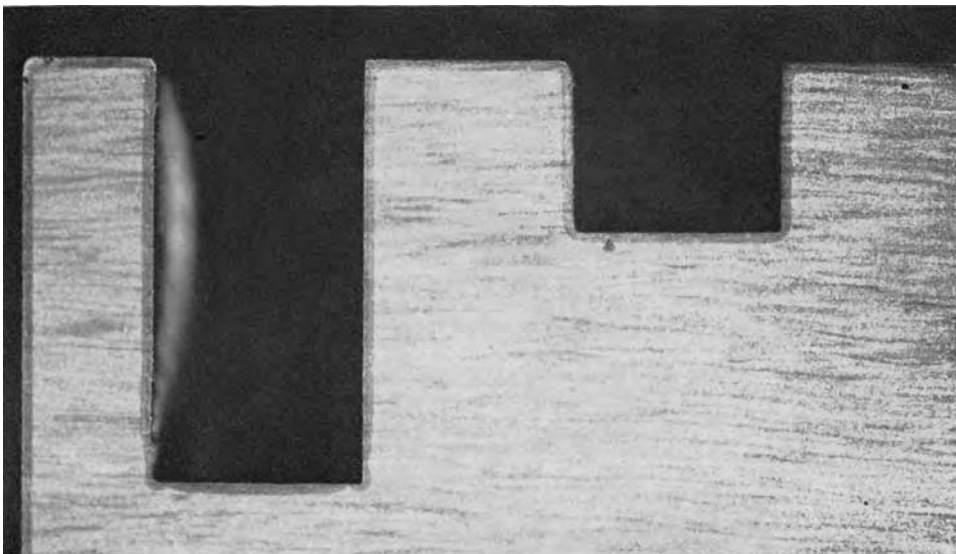


Fig. 4 Uniform case from plasma nitriding. Source: Ref 10

Aachen in Germany worked on better methods of controlling the glow discharge and other associated phenomena, such as arc discharging. The procedure developed at Aachen was that of pulsed-dc technology, which simply means interrupted power to the point of power shut-down. This technique offered many advantages

to process engineers in terms of control of the nitriding procedure.

In the early 1980s, new pulsed plasma nitriding technologies emerged on the German market and in Austria. The changes in the furnace design with auxiliary heating systems and the change from dc power supplies to pulsed-power

design improved temperature uniformity and energy savings. The new technologies also were much easier to handle for the operators.

In addition, new electronic devices and automatic gas-flow controls, together with newly developed computer systems, facilitated the design of new furnaces and process improvement, now offering some advantages compared to the old technology, especially the electrical energy consumptions. During the next 15 years, this new type of furnace and process became the industrial standard.

A pulsed-current ion nitriding system is shown in Fig. 5. The parts to be nitrided are cleaned, usually by vapor degreasing, loaded into the vacuum vessel, and secured. The subsequent process of plasma nitriding can be broken down into four steps: vessel evacuation, heating to nitriding temperature with or without plasma, nitriding at temperatures, and a subsequent cool-down step.

The pulsed-current ion nitriding system has been partly successful in improving temperature control with parts of varying mass in a load. However, applications are still limited to relatively homogeneous loads, because high voltage is still applied directly to the parts being treated (Ref 11).

Active-Screen Plasma Nitriding. Active screen invented in 1999 (Ref 2), is a technology that has been developed and commercially used in recent years. This is a technology that partly resolves the difficulties of conventional plasma nitriding in terms of temperature control, edge effects, and the hollow-cathode effect (see the section "Glow-Discharge Process" in this article). This allows more capability to nitride deep, small-diameter holes or to bulk load many small parts close together within a furnace load.

With the active screen, the plasma is no longer applied to the workload but rather to a metallic screen that surrounds the parts (Fig. 6). The parts to be nitrided are either placed on a floating potential or a light bias is applied. Under these conditions, plasma forms on the screen and not on the parts. Therefore, temperature control can be achieved by regulating the plasma power on the active screen. The plasma heats up the active screen, and radiation from the screen provides the heat that brings components to the required temperature for treatment. In this way, the whole workload heats up to the correct nitriding temperature.

The screen also supplies the active species. The plasma on the screen contains a mixture of ions, electrons, and other active nitriding species, which are then encouraged to flow through the screen and over the workload by a specially designed gas flow. The active-screen method has the ability to treat parts with a large range of geometries within one batch. As such, very complex-shaped components can be treated. Because the plasma does not form on the component surface, the arcing damage and the edge effect can be eliminated. The active species can even enter blind holes, producing

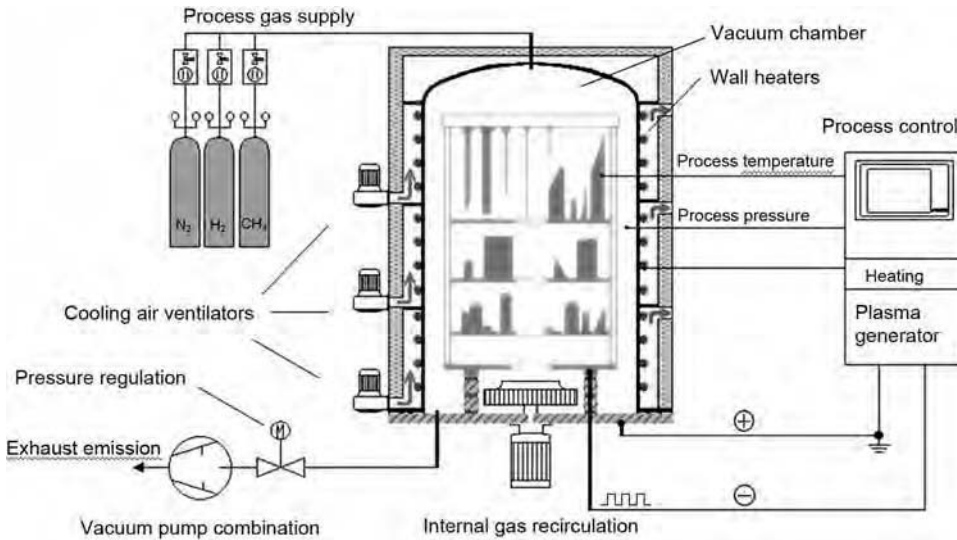


Fig. 5 Hot-walled plasma nitriding furnace. Examples of varying load configurations are illustrated in the chamber. Courtesy of Platag GmbH, Siegen, Germany

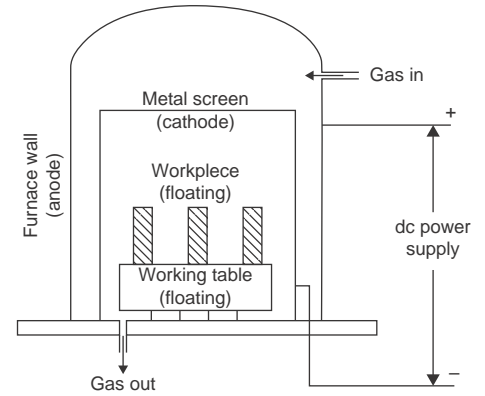


Fig. 6 Schematic of furnace configuration for active-screen plasma nitriding

uniform modified layers on all parts of different geometry and size in a heavily loaded chamber (Ref 12, 13). In addition, the active-screen plasma technique also provides the possibility of treating nonelectrical-conducting materials such as steel with an oxidized surface and polymeric materials that are unattainable with a conventional dc plasma system (Ref 4).

Glow-Discharge Process

The mechanism of nitrogen atom production and transfer from the medium to the component surface is one of the principal differences between plasma nitriding and gas or bath nitriding. Unlike conventional gas nitriding, the nitriding potential of the low-pressure atmosphere is essentially independent of the temperature of the charge. Nascent (atomic) nitrogen is ionized by the high voltage, such that electrons are stripped from nitrogen atoms. The electrons then accelerate toward the anode (furnace wall), while the anions (positively charged nitrogen ions) accelerate toward the cathode (or workpiece, in the case of conventional and pulsed-dc systems). Various mass-transfer mechanisms occur during this process, but atomic nitrogen enters the surfaces and combines with iron and alloying elements as it diffuses into the material.

Voltage-Current Conditions of Plasma Glow Discharge. Gas atoms ionize at high voltage. The breakdown voltage (V_B) of a gas depends on the gas pressure, gas composition, and the distance (d) between two parallel plates (acting as the anode and cathode). The behavior of breakdown voltage is described by Paschen curves (Fig. 7), named after the person who described this phenomenon. At a constant pressure, the breakdown voltage becomes smaller as the gap between the anode and cathode is reduced, until a minimum is reached. After the

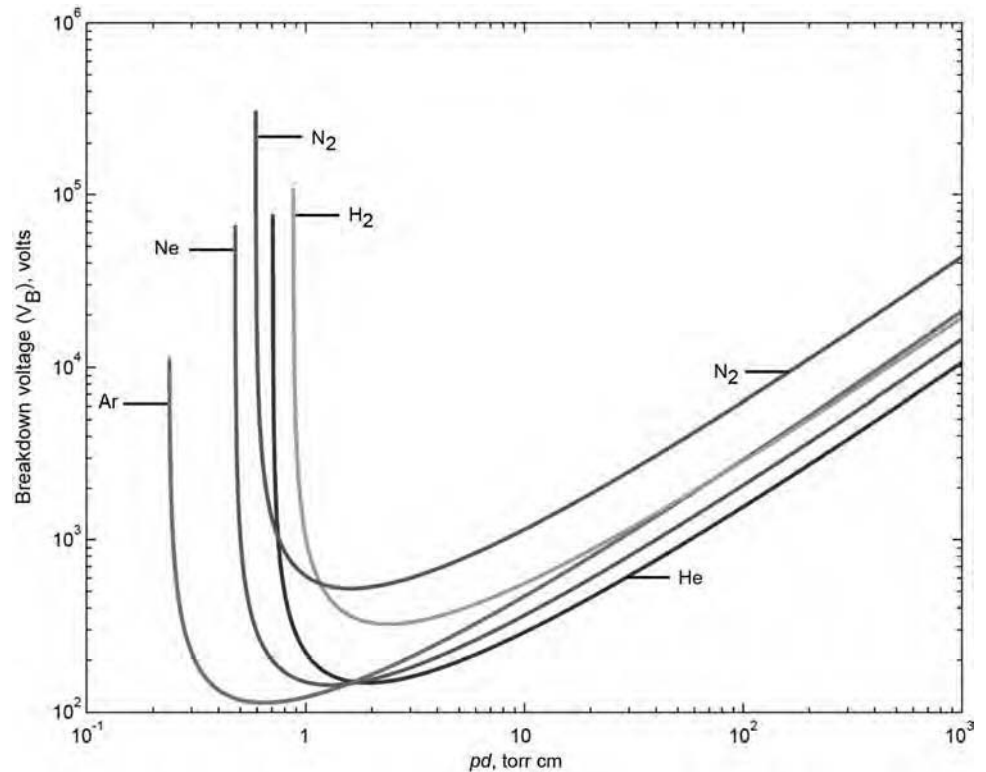


Fig. 7 Paschen curves of the breakdown voltage (V_B) for various gases as a function of gas pressure (p) and separation distance (d) between the voltage plates

minimum, further reductions in the anode-cathode gaps result in large increases in the breakdown voltage. Alternatively, if the gap (d) is held constant while the pressure (p) increases (from a vacuum), then the breakdown voltage first drops dramatically as the gas pressure increases, until the minimum is reached. After the minimum is reached, further increases in pressure result in a continuing increase of the breakdown voltage.

Ionization of a gas generates electrical currents, and the general voltage-current behavior of an ionized gas is illustrated in Fig. 8. The breakdown voltage (V_B) is in the region of corona discharge, where the initial onset of glow discharge begins, as described further in the following sections for the different regions of plasma discharge. Each region of Fig. 8 represents different conditions or mechanisms of current production from gas ionization.

Background Ionization Region. When voltage is first applied to a gas and increased, the electrons within that gas can be charged to the point where an electrical ignition of the gas will occur. This can be likened to the spark that occurs when an automobile spark plug is charged with high voltage. The air in the plug gap is electrically charged to the point where a spontaneous spark occurs. In the process chamber, the electrons accelerate toward the anode, while positive ions (anions) accelerate toward the cathode. When the process voltage is increased, then an increase of current density occurs.

Self-Maintained Region (Townsend Discharge). As voltage increases, gas ionization progresses into the next phase of Townsend discharge. This region on the curve is the area in which more electrons can be released by further gas ionization, which generates even further gas ionization. The area can be considered to be a chain reaction and is thus referred to as a self-maintained region.

Corona Discharge (Transition to Glow Discharge). Corona discharge is an unstable region indicating the beginning of glow discharge. The discharge is unstable with high partial discharge of current with drops in plasma resistance. Current density increases with a drop in voltage, and voltage stability cannot be maintained within this region of the ionization curve.

Subnormal Glow Discharge. In this region, a more consistent and stable fuzzy glow occurs over the surface of the cathode.

Normal Glow Region. This is the region where the glow seam completely covers the work. Its thickness will be determined by the chamber vacuum pressure and the process voltage.

Abnormal Glow Region (for Nitriding). In this region, the glow seam completely covers the steel work surface uniformly, following the geometric profile of the workpiece. This is the region where process pressure is adjusted to ensure penetration sufficient for current and thickness of the glow seam to nitride blind holes and cavities.

Arc Discharge Region. As the current density increases, another unstable region of voltage drop occurs, resulting in sharp increases in current and arcing. Serious overheating, localized melting, and pitting can occur. Arcing, similar to a lightning strike, can be visible through the sight glass of the process chamber.

Pressure and Gas Composition. According to the Paschen curves (Fig. 7), the breakdown voltage and thus the conditions for glow discharge depend on the gas composition and pressure. For example, if the N_2 concentration of a gas mixture (with N_2 to H_2) is increased (while also keeping the voltage-control setting fixed and the overall chamber pressure fixed), then a reduction in the voltage bias occurs. This decrease in bias voltage for a constant current can be explained by a reduction in plasma resistance as the ratio of N_2 to H_2 decreases.

Along with proper voltage, gas pressure is a key variable in maintaining a suitable glow seam. There is no ideal pressure value, but there is a range in which the pressure can be adjusted to suit the operating parameters of the particular material and geometry. Higher pressure generates a glow seam that goes within a surface recess, while a lower pressure generates a glow seam that is foggier around features of the cathode. Typical ion nitriding is generally performed at absolute pressure levels of 50 to 1000 Pa (0.007 to 0.14 psi).

Hollow-Cathode and Edge Effects. When the part is the cathode and plasma is produced directly on the surface of the part (as in conventional and pulsed-dc systems), two important effects are edge effect and the hollow-cathode effect. The edge effect is due to electric-field distortions around the corners and edges of a part, resulting in nonuniformity of the surface layer.

The hollow-cathode effect is another limitation of conventional and pulsed-dc systems.

The hollow-cathode effect occurs when parts are located close to each other, or if they have adjacent surfaces (such as deep, small-diameter holes) in close proximity. Closely adjacent surfaces can result in overlap of the discharge regions of adjacent surfaces when the cathode fall zone becomes as large as the separation between two surfaces in close proximity with each other (Fig. 9). In this situation, electrons bounce back and forth, and the oscillations raise plasma density, part temperature, and localized overheating or even melting.

Active-screen plasma nitriding does not have the problem of edge effects and the hollow-cathode effect. Because the part is not the cathode in active-screen plasma nitriding, the problems of overheating and edge effect are mitigated. Active-screen plasma nitriding also allows parts to be placed in closer proximity or to have parts with more intricate geometries (with adjacent surfaces in closer proximity).

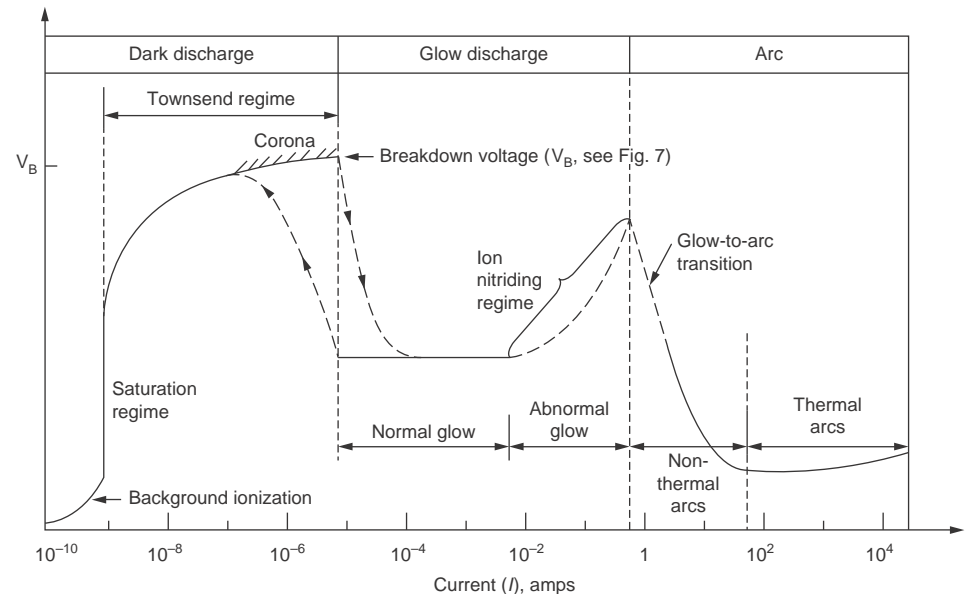


Fig. 8 Voltage versus current characteristics of different types of discharge of an ionized gas (plasma)

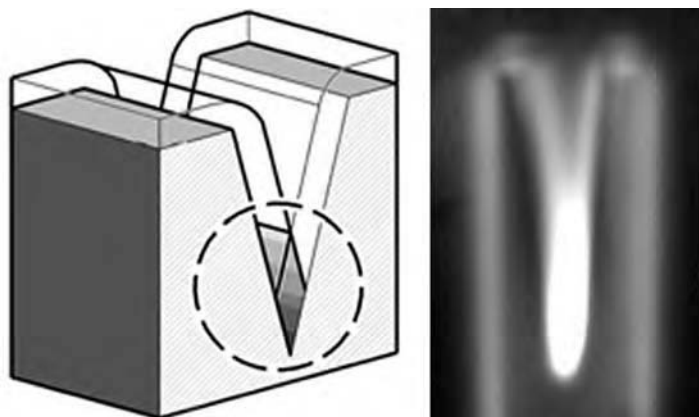


Fig. 9 Hollow-cathode effect. Circled area will produce hollow-cathode effect as seen in the photo. Source: Ref 14

Mass-Transfer Mechanisms. During the glow-discharge process, different alloy or iron atoms combine with the nitrogen as it diffuses into the material, forming a hardened surface and case. Several models have been proposed in the past to explain the mass transfer during plasma nitriding. The models include sputtering and recondensation, nitrogen implantation, low-energy $N_mH_n^+$ bombardment, nitrogen adsorption, and neutral and ion adsorption (Ref 15). According to Li and Bell (Ref 15), the sputtering and recondensation model appears to be the most likely mechanism for nitrogen mass transfer in both dc and active-screen plasma nitriding.

In the sputtering-recondensation model of dc plasma nitriding, iron atoms are sputtered (detached) from the workpiece (cathode) from the impact of accelerating ion species. The detached iron atoms then enter the cathode potential drop region and subsequently react with active nitrogen in the plasma to form iron nitride (Fig. 10). The iron nitride (FeN) particles then can be backscattered and deposited on the cathode, which further can decompose to cause the release of atomic nitrogen into the iron ferritic lattice to form a case (Ref 16). Reference 15 further proposes a similar process

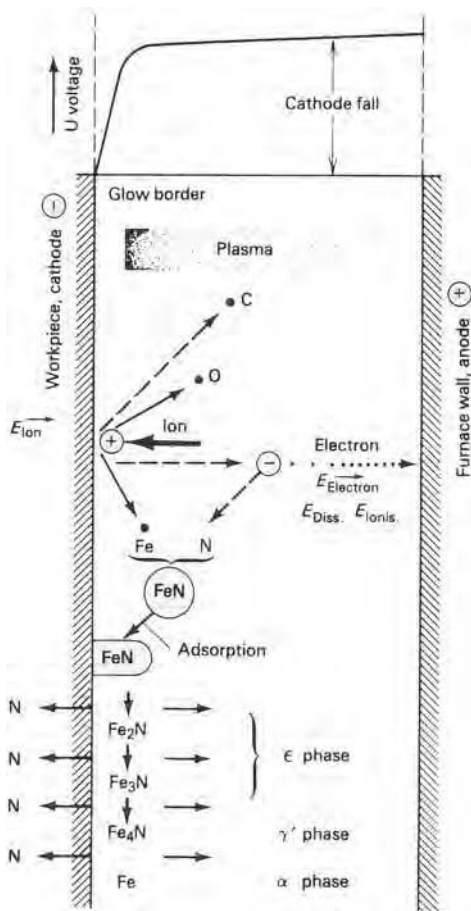


Fig. 10 Mass-transfer mechanisms during ion nitriding

for active-screen plasma nitriding, except that the sputtering occurs from the active screen, with backscattering causing the deposition and decomposition of iron nitride on the workpiece surface (Fig. 11).

Plasma Nitriding Furnaces

Plasma furnaces require an isolated hearth (or support fixturing for workpieces) to ensure electrical isolation between the anodic vacuum vessel and the high voltage applied to either the workpieces or the active screen as the cathode surface. The isolated-hearth arrangement is divided into three basic areas:

- High-voltage feed-through arrangement, which carries the voltage through the vessel wall while maintaining a good vacuum seal
- Load-support insulators, which carry the actual load weight while providing good dielectric qualities
- Charge plate or fixture, which has the workpieces placed on it or provides mechanical masking if desired

In conventional plasma nitriding, sight ports placed around the vessel provide a view of the ion nitriding process and are necessary for checking the load and ensuring that the selected parameters are accurately maintained and that no detrimental hollow-cathode disturbances (overlapping glow-discharge envelopes) have developed.

Vessel evacuation is performed by a combination of pumps such as rotary vane and root pumps so that pressure is reduced to a level below 10 Pa (0.0015 psi). This is necessary to remove most of the initial air and any contaminants. Higher vacuum levels can be achieved but are not necessary for most materials.

As noted, the method of load heating to the nitriding temperature has evolved over the years. In cold-walled furnaces, heat is generated only by the plasma energy around the part.

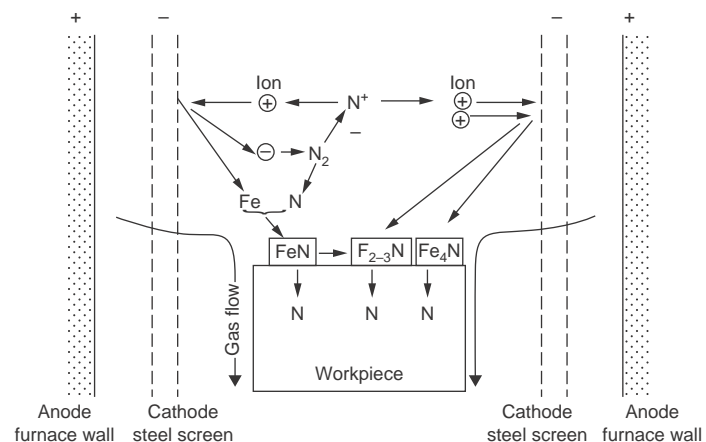


Fig. 11 Mass-transfer mechanisms during active-screen ion nitriding. Adapted from Ref 15

A combination of wall heaters and gentle plasma heating is the most common method used to heat the work load. Today (2013), external resistance heaters in hot-walled furnaces are normally used to bring the load to nitriding temperatures (375 to 650 °C, or 700 to 1200 °F) with or without the help of glow discharge. Some general process differences between cold-walled and hot-walled (pulsed-dc) furnaces are listed in Table I.

During plasma nitriding, the temperature inside the vessel may vary from 350 to 580 °C (660 to 1080 °F). After the glow-discharge process, the voltage and process gas flow are terminated, and the load is cooled. Cooling is accomplished by backfilling with nitrogen or other inert gases and recirculating the gas from the load to a cold surface wall. To improve the cycle time, a rapid cooling system can be included.

Cold-Walled Plasma Furnaces. A cold-walled furnace normally has no heating elements. In some cases, the furnace manufacturer will design a furnace with supplementary elements to assist the plasma heating. These elements would most likely be found within the furnace process chamber and usually are electrically isolated to prevent them from being nitrated.

The primary component of the cold-walled furnace is constructed in much the same way as a conventional vacuum furnace, consisting of inner and outer vessels. The inner vessel, or vacuum vessel, is usually fabricated from stainless steel, and the outer water jacket is usually manufactured from carbon steel. A water-cooling area between the two vessels conducts any heat losses from the inner vacuum vessel to the water and to a heat exchanger. The vessel sidewall usually is fitted with a sight port for observing the plasma conditions in the work area. Electrical lines through the base feed power to the cathode.

In cold-walled furnaces, heat is generated by the kinetic energy developed from ionic bombardment, and heating is controlled simply by

Table 1 General features of cold-walled and hot-walled plasma nitriding furnaces

Feature	Cold wall, constant direct current	Hot wall, pulsed direct current
Starting temperature of glow discharge	Room temperature	At a suitable elevated temperature, usually approximately 200 °C (400 °F)
Plasma current requirement for workpiece heating	Approximately 5 mA/cm ² to that of sufficient heating	Approximately 0.2 mA/cm ² with auxiliary heating
Workpiece voltages for heating	Higher current requires high voltages, which increases the risk of arcing or localized overheating. General voltages of the cold-walled constant direct-current system are approximately 600 to 800 V. Risk of arcing at 700 kV	Input voltage is not as high (400 to 500 V) away from the arc-discharge region. Hot-walled furnaces also use partial-pressure conditioning with hydrogen or nitrogen as a thermal-conductance gas.
Heating time	Usually more time for heatup than hot wall	Can be approximately 15 times faster than cold wall
Voltage control during glow discharge	Applied voltage is constant. This makes temperature control more difficult (see text for Fig. 16). A change in voltage to reduce temperature changes current density and the cathode-fall voltage distance (glow seam).	With a pulsed voltage, high voltage can be used without risk of overheating or arc discharge. Sensitivity to variations in conditions for proper glow-seam conditions is easier to control.
Heating up of the furnace wall (anode)	Scattered electrons heat the furnace wall (anode), and water cooling of the furnace wall is needed.	Wall temperatures can safely go up to temperatures of approximately 650 °C (1200 °F) without concern of a heat buildup. External blowers control wall temperatures.
Glow seam in deep blind holes	Higher pressure required for glow seam in deep holes, but increasing the operating pressure causes a corresponding increase in current density, followed by an increase in part surface temperature.	With the same pressure-temperature combination as a constant direct-current system, the hot-walled/pulsed system maintains sufficient plasma power by varying the duty cycle (pulse variation), even with a changing voltage and current density.

Adapted from Ref 17

voltage and current density regulation. Heating of loads from the glow-discharge process can present some difficulty, because moisture and other impurities on the work surface tend to cause arcing to the parts in the initial stages of the heating cycle. The methods to extinguish or prevent arcs also lengthen the heating cycle significantly.

Hot-Walled Plasma Pulsed-dc Furnaces.

Resistance heaters in hot-walled furnaces are normally used to bring the load to nitriding temperatures (375 to 650 °C, or 700 to 1200 °F), with or without the help of glow discharge. The vessel vacuum chamber is usually a hot-walled design (Fig. 12), but dual-walled and water-cooled designs are sometimes used. The vessel can be horizontally or vertically loaded in a drop-bottom, pit, or bell arrangement. Typically, no internal insulation is required because of the lower temperature (less than 650 °C, or 1200 °F) and the desire to create sufficient heat loss to support a steady dc power supply output to the workload.

Sputter cleaning is done in hot-walled furnaces before nitriding. After the chamber is evacuated to the appropriate vacuum level, the process chamber is backfilled with hydrogen gas, and the external heating elements are switched on to heat the workload, which is heated by convection. Once the process temperature has reached approximately 230 °C (450 °F), the sputter cleaning procedure begins as hydrogen ions atomically blast the workpiece surfaces, a more thorough and effective method than aqueous cleaning. Holding time at the sputter-clean temperature is determined by the initial surface cleanliness but generally is not more than 20 to 30 min. If the workpiece surfaces are badly contaminated, a gaseous mixture of up to 10% argon and 90% hydrogen should be used. To avoid surface etching, do not use more than 10% argon in the mixture.



Fig. 12 Hot-walled plasma nitriding furnace. Arrows indicate air blowers that cool the external wall of the vessel. Courtesy of Plateg GmbH

Process Control

Modern ion nitriding systems use microprocessor systems that control or monitor parameters such as work temperature, vessel wall temperature, vacuum (absolute pressure) level, plasma parameters, auxiliary heating source, and gas-mix composition. The supply of active ions is determined largely by the discharge parameters of voltage and current. This capability has a number of unique advantages; for example, materials that would lose their core strength under conventional nitriding conditions can be ion nitrided and still maintain core strength if the nitriding temperature is below the temper-

perature. This also reduces distortion considerably. Depending on the desired layer composition and case depth, process temperatures range from 530 to 570 °C (990 to 1060 °F) for times from 3 to 40 h.

The thickness of the glow seam can be altered by pressure, temperature, mixture of gas composition, dc voltage, and current. Typically, a large or thick glow envelope is created with higher temperature, lower pressure, high hydrogen concentration of the gas composition, and higher dc voltage and current. Under normal conditions, 6 mm (0.25 in.) thick glow discharge is desirable unless conditions exist with small bores or gaps; in such cases, a

thinner glow envelope is desirable to prevent local overheating. A uniform glow-discharge envelope also is necessary for proper case uniformity, especially when part geometry is complex.

Case depth depends on the nitriding current (proportional to the nitrogen ion flux), temperature, and process time. For the same processing time, case depth attained with ion nitriding is higher than gas nitriding. For example, Fig. 13 shows the results of case depth versus treatment time for AISI 4140 steel ion nitrided at 510 °C (950 °F) and gas nitrided at 525 °C (975 °F). Similar results also are achieved with Nitalloy 135M steel. As in gas nitriding, higher case depth is obtained with AISI 4140 steel than with Nitalloy 135M. However, Nitalloy 135M produces higher surface hardness. Similar to gas nitriding, time for ion nitriding varies with case depths and material. Figure 14 depicts the time required for different case depths and two gear materials.

Atmosphere and Pressure Control. After the workload is heated to the desired temperature, process gas is injected at a flow rate determined by vessel size and surface area of the load. A gas-mixing panel is used for blending gases. The process gas is normally a mixture of nitrogen, hydrogen, and, at times, small amounts of methane or argon. In the presence of this process gas, the load (or screen in active-screen nitriding) is maintained at a high negative dc potential.

The nitrogen-hydrogen ratio determines the composition of the compound layer:

- With $H_2 < N_2$ (at ratios of 1:3 or 1:4), the compound layer is ϵ ($Fe_{2-3}N$).
- With $H_2 > N_2$ (at a ratio of 3:1), the compound layer is γ' (Fe_4N).
- With $H_2 \gg N_2$ (at a ratio of 8:1), there is no compound layer.

A typical composition for a γ' compound layer would be 75% H and 25% N. For ϵ compound layer only, a typical gas mixture would be 70% N, 27% H, and 3% methane. The mixing is usually done automatically by mass-flow controllers.

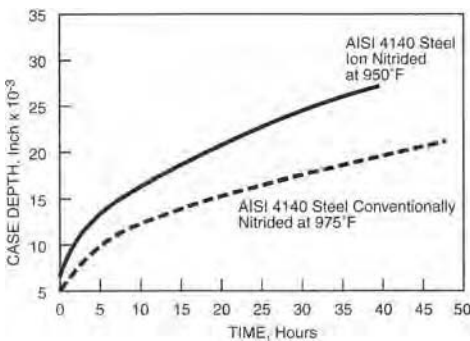


Fig. 13 Comparison of case depth vs. process time for ion and gas nitriding of 4140 steel. Source: Ref 18

Control is accomplished in two stages. First, the amount of gas inlet is controlled by mass flow controllers and provides a constant gas flow. A butterfly valve on the evacuation line between the vessel and the vacuum pump controls the amount of gas being evacuated until the desired pressure setpoint is met.

As noted, pressure is one of the principal areas of control, along with proper voltage to create plasma discharge. Once sufficient glow-discharge conditions occur, the process pressure ensures penetration of blind holes and cavities (Fig. 15). If pressure is too low, the glow is too broad to follow contours of the surface. If the pressure is too high, then the glow seam on the cathode will become intermittent, thus requiring a higher voltage to maintain adequate glow discharge. However, higher voltages increase the risk of arcing in both conventional dc and pulsed-dc systems.

Part Temperature. Perhaps even more important than control of process temperature is control of part temperature. Many factors within the furnace chamber influence temperature uniformity, and therefore, part temperature must be monitored. The part and process temperature are measured by considering the thinnest part and the thickest part within the process chamber. Part temperatures are usually held to within a tolerance band of ± 5 °C (10 °F). If a thermocouple cannot be attached to the workpiece, then it should be attached to dummy test coupons that are representative of the workpiece cross-sectional area and the material being treated. Radiation thermometers also may be used to monitor part temperature, even in the case of active-screen nitriding (Fig. 16).

Power-Supply Controls. Plasma nitriding power supplies must provide an output voltage from 0 to 1000 V. Typical current ratings range from 25 to 500 A (dc), depending on the size of the vessel and workload. The four major functions of the power supply for both constant-dc and pulsed-dc systems are:

- Create glow-discharge conditions, shown in Fig. 8
- Ensure good temperature uniformity within the workload area

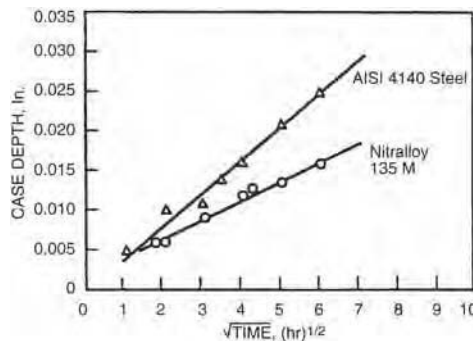


Fig. 14 Case depth vs. square root of ion nitriding time for Nitalloy 135M and 4140 steel. Source: Ref 18

- Heat the workload
- Prevent arc-discharge conditions

With a conventional dc power supply, fulfillment of the aforementioned conditions is somewhat limited, because the first three conditions are linked together. Figure 17(a) schematically shows the power characteristics of a continuous dc power supply for plasma nitriding. The gap for nitriding glow discharge is between the lines P_{min} and P_{max} , and the power of the plasma, P_{plas} , must be between these values. The area below the line P_{temp} is equal to the energy input necessary to balance the energy losses of the system and to hold the temperature in the workload at the desired value. Controlling plasma power to maintain adequate temperature thus is difficult with mixed loads of different part geometries and sizes.

Pulsed-dc plasma systems offer a better method of temperature control. In pulsed systems, the time between pulses is varied to balance the energy losses and provide sufficient power (P_{temp}) to maintain temperature. By this method, the temperature adjustment is separated from the other process parameters. Typical pulse-time values are between 5 and 100 μs , while pause time can vary between 5 and 200 μs (Ref 20). The sum of the areas under each pulse is equal to the area under the line P_{temp} (Fig. 17b). The ratio of pulse to pause is variable over a wide range to control the power input by the plasma in the workload, so that it will be possible to use an auxiliary heating system (such as external heating) for better temperature control within the process chamber.

Arc Detection and Suppression. Modern plasma generators with fast arc detection and suppression are able to handle the unstable conditions at process initiation. As noted, arcing can occur because the glow-discharge process causes the removal of surface impurities, which are always present. The impurities are removed in the form of an arc, in which there is a sudden decrease in voltage and increase in current. Because of this, both minimum and maximum current levels and voltage rate of change (dV/dt) and voltage/current relationships (slope) must be constantly monitored. When an arc is detected, the power output is momentarily switched off within microseconds to avoid any possible damage.

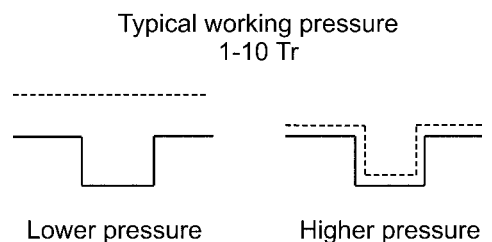


Fig. 15 Effects of gas pressure on the glow seam during plasma nitriding

Case Structures and Formation

The case structure of nitrided steel includes a diffusion zone with or without a compound zone (Fig. 18). The compound zone is the region where the γ' (Fe_4N) and ϵ (Fe_{2-3}N) intermetallics are formed. Because carbon in the material aids ϵ formation, methane is added to the process gas when an ϵ -layer is desired. The compound layer is called a white layer because it appears white on a polished, etched cross section under a metallograph. The hardness of the white layer is essentially independent of alloy content, because its constituents are only compounds of iron and nitrogen.

Case structure depends on the type and concentration of alloying elements and the time-temperature exposure of a particular nitriding treatment. Because the formation of a

compound zone and/or a diffusion zone depends on the concentration of nitrogen, the mechanism used to generate nascent nitrogen at the surface of the workpiece obviously affects the case structure.

In conventional gas nitriding, the nascent nitrogen is produced by introducing ammonia (NH_3) to a work surface that is heated to at least 480°C (900°F). Under these conditions, the ammonia, catalyzed by the metal surface, dissociates to release nascent nitrogen into the work and hydrogen gas into the atmosphere of the furnace. The nitriding potential, which determines the rate of introduction of nitrogen to the surface, is determined by the NH_3 concentration at the work surface and its rate of dissociation.

In contrast, ion nitriding allows the use of nitrogen gas (N_2) instead of ammonia, because the gas dissociates to form nascent nitrogen

under the influence of the glow discharge. Therefore, the nitriding potential can be accurately controlled by the regulation of the N_2 content in the process gas. This allows more precise determination of the composition of the entire nitrided case. Ion nitriding allows selection of a monophasic layer of either ϵ or γ' or total prevention of white-layer formation (Fig. 19).

Diffusion Zone of a Nitrided Case. The diffusion zone of a nitrided case can best be described as the original core microstructure with some solid solution and precipitation strengthening. In iron-base materials, the nitrogen exists as single atoms in solid solution at lattice sites or interstitial positions until the limit of nitrogen solubility ($\cong 0.4$ at.% N) in iron is exceeded. This area of solid-solution strengthening is only slightly harder than the core. The depth of the diffusion zone depends on the nitrogen concentration gradient, time at a given temperature, and the chemistry of the workpiece.

As the nitrogen concentration increases toward the surface, very fine, coherent precipitates are formed when the solubility limit of nitrogen is exceeded. The precipitates can exist both in the grain boundaries and within the lattice structure of the grains themselves. These precipitates, nitrides of iron or other metals, distort the lattice and pin crystal dislocations and thereby substantially increase the hardness of the material.

In most ferrous alloys, the diffusion zone formed by nitriding cannot be seen in a metallograph with standard etching methods because the coherent precipitates are generally not large enough to resolve. In Fig. 20, for example, martensite in the diffusion zone cannot be visually distinguished from that in the core. In some materials, however, the nitride precipitate is so

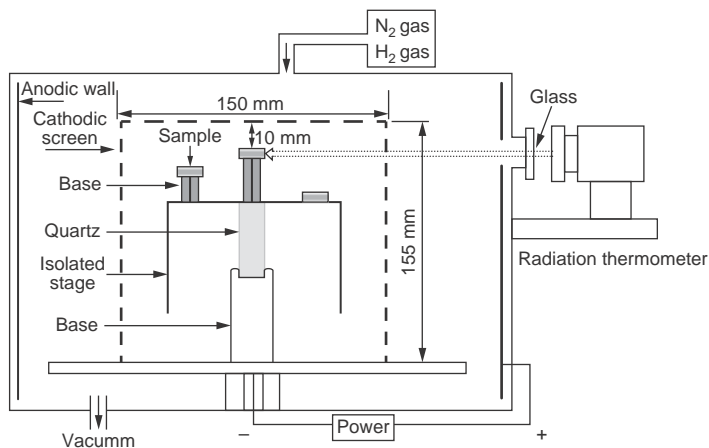


Fig. 16 Example of radiation thermometer for monitoring part temperature during active-screen plasma nitriding. Source: Ref 19

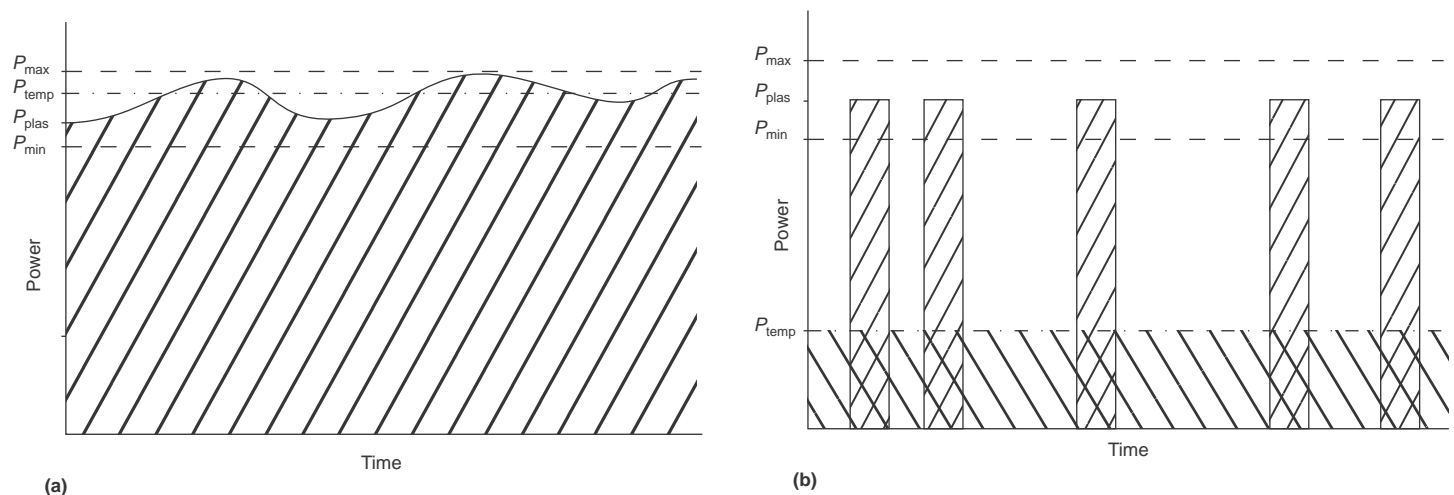


Fig. 17 Power characteristics during (a) continuous direct-current (dc) plasma nitriding and (b) pulsed-dc plasma nitriding. Abnormal glow discharge (Fig. 8) occurs between P_{\min} and P_{\max} . The power required for plasma nitriding (P_{plas}) is in this region. The time-average power required to maintain the workload at desired temperature is P_{temp} . During pulsed-dc operation (b), the pulse widths are constant and short enough to prevent arcing. The duration of pauses between pulses is varied to control temperature, such that the area under the pulses is equal time-average power (P_{temp}) to maintain the workload at desired temperature. Source: Ref 17

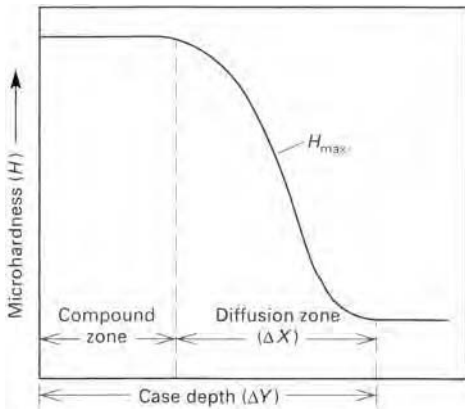


Fig. 18 Factors affecting the microhardness profile of a nitrided steel. The hardness of the compound zone is unaffected by alloy content, while the hardness of the diffusion zone is determined by nitride-forming elements (Al, Cr, Mo, Ti, V, Mn). ΔX is influenced by the type and concentration of alloying elements; ΔY increases with temperature and decreases with alloy concentration.

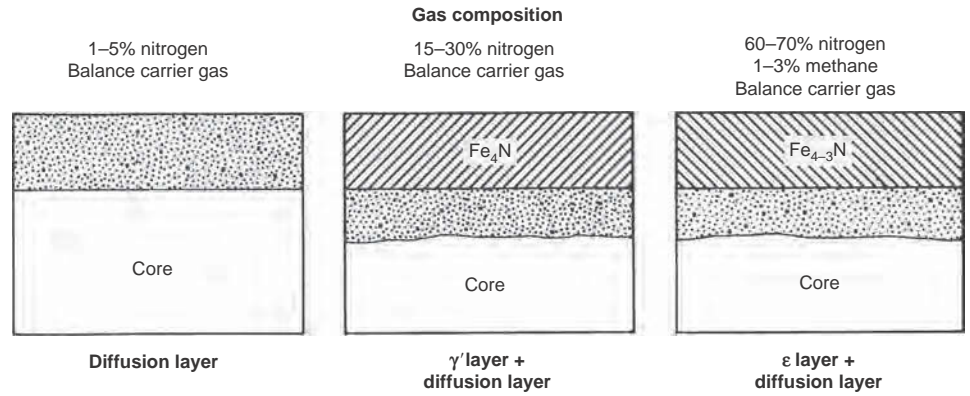


Fig. 19 Typical gas compositions and the resulting metallurgical configurations of ion-nitrided steel

extensive that it can be easily seen in an etched cross section (Fig. 21). For stainless steel and standard nitriding processes, the area of chromium precipitates can be seen in an etched microsection due to the loss of corrosion resistance compared to the stainless-base material (Fig. 22).

Workpiece Factors

In general, the response of a material to nitriding depends on the presence of strong nitride-forming elements. Plain carbon steels can be nitrided, but the diffused case is not significantly harder than the core. The strongest nitride formers are aluminum, chromium, molybdenum, vanadium, and tungsten.

The premier nitriding steels are the Nitralloy series, which combine approximately 1 wt% Al with 1.0 to 1.5 wt% Cr. Other alloys that form excellent diffused cases are the chromium-bearing alloys, such as the SAE 4100, 4300, 5100, 6100, 8600, 8700, 9300, and 9800 series. Other good nitriding materials include most tool and die steels, stainless steels, precipitation-hardening alloys, nickel-base alloys, and titanium.

Parts made by powder metallurgy (PM) can also be ion nitrided, but precleaning is more critical than with wrought alloys. A baking operation should precede ion nitriding PM parts to break down or release agents and/or to evaporate any cleaning solvents.

Effect of Prior Microstructure. As with other diffusion methods, the initial microstructure can also influence the response of a material to nitriding. In the case of alloy steels, a quenched and tempered structure is considered to produce optimum nitriding results. The tempering temperature should be 15 to 25 °C (30 to 50 °F) above the anticipated nitriding

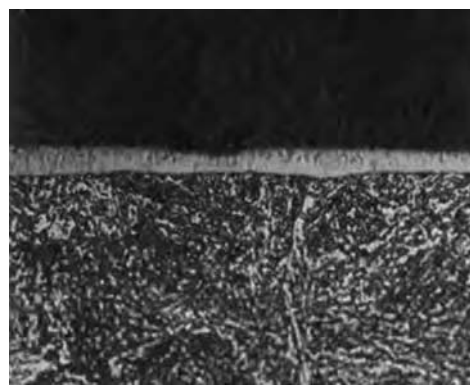


Fig. 20 Compound layer on the ion-nitrided surface of quenched and tempered 4140 steel. The compound layer is supported by a diffused case, which is not observable in this micrograph. Nital etched. Original magnification: 500×

temperature to minimize further tempering of the core during the nitriding process.

If the nitriding of a nonmartensitic matrix is desired, it is important that prior heat treatment be accompanied by fast cooling to provide a relatively low-temperature austenite transformation and retain a high percentage of the nitride-forming element in solution for subsequent precipitation.

Hardness profiles for typical ion-nitrided alloys are shown in Fig. 23. The hardness increase of an ion-nitrided layer is virtually the same as for any nitriding process with the same nitrogen concentration profile. As previously mentioned, the hardness of the diffused case depends on precipitation hardening, while that of the white layer depends on the type and thickness of the compound formed. Because the white layers are compounds of only iron and nitrogen, the hardness of these layers is essentially independent of alloy content.

White-Layer Properties. In general, case depth and white-layer composition should be selected for the predicted operating conditions of the nitrided component. The ϵ -layer is best for wear and fatigue applications that are

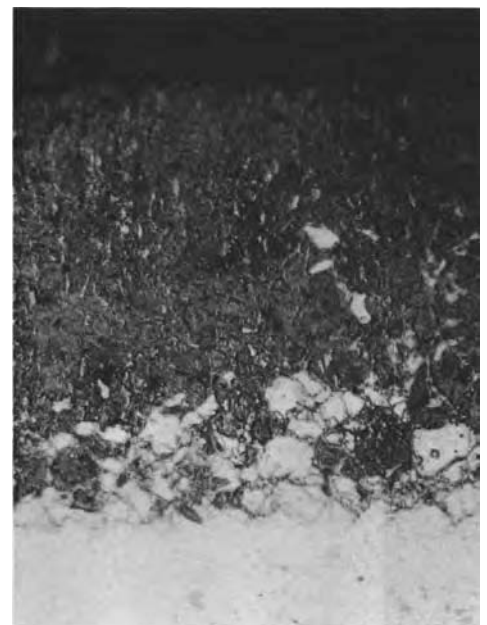


Fig. 21 Observable diffusion zone on the unetched (white) portion of an ion-nitrided 416 stainless steel. Nital etched. Original magnification: 500×

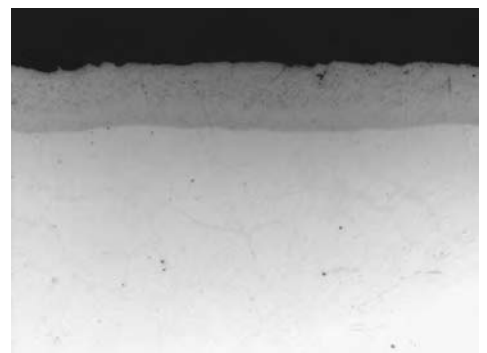


Fig. 22 Nitrided austenitic stainless steel AISI 304 (570 °C, or 1060 °F; 58 h). Nital etched. Original magnification: 500×

relatively free of shock loading or high localized stresses. The γ' -layer is somewhat softer and less wear resistant but is tougher and more forgiving in severe loading situations. The white layer also provides increased lubricity. In addition to mechanical properties, the white layer, which is relatively inert, provides increased corrosion resistance in a variety of environments.

Fatigue strength, in addition to hardness and wear resistance, is significantly improved by nitriding (Fig. 24). The formation of precipitates in the diffused case results in lattice expansion. The core material, in an attempt to maintain its original dimension, holds the nitrided case in compression. This compressive stress essentially lowers the magnitude of an applied tensile stress on the material and thus effectively increases the endurance limit of the part.

Ion Nitriding Applications

Various alloy steel and cast iron wear components, including gears, crankshafts, cylinder liners, and pistons, are excellent candidates for the plasma nitriding process. In general, case depth and white-layer composition should be selected for the anticipated operating conditions of the nitrided component.

Components used in fuel injection systems experience erosive wear from the fuel and fatigue from rapid cycling of fuel pressure. Ion nitriding greatly enhances the resistance to both of these effects.

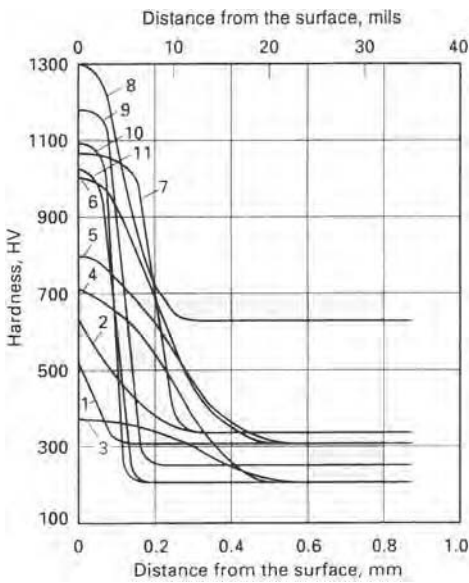


Fig. 23 Hardness profile for various ion-nitrided materials. 1, gray cast iron; 2, ductile cast iron; 3, AISI 1040; 4, carburizing steel; 5, low-alloy steel; 6, nitriding steel; 7, 5% Cr hot-worked steel; 8, cold-worked die steel; 9, ferritic stainless steel; 10, AISI 420 stainless steel; 11, 18-8 stainless steel

The increased lubricity of white layers combined with hardness and fatigue strength has generated significant growth of the ion process in the tool and die industry. Hot work dies, which usually fail by thermal fatigue and sticking, have particularly benefited from ion nitriding following quenching and tempering. Also, nitriding of cast iron stamping will replace the environmental-critical process of hard chrome plating.

Low-temperature nitriding processes are used to improve mechanical properties of stainless steel, such as resistance against cold welding or improvement of wear resistance. Applications can be found in the oil and gas industry, for example, ball valves, or in general industrial applications, such as nitrided threads for nuts and bolts, in order to prevent cold welding effects.

Because ion nitriding is essentially a line-of-sight process, it is possible to mask using simple physical shields to interrupt the flow of nitrogen-species ions. For example, the end of a shaft can be masked by simply placing a loose-fitting sheet metal can around it. Thus, areas of a part that may need to stay soft either for further machining or for welding can easily be maintained in a non-nitrided condition.

Sputtering and Ion Nitriding of Stainless Steels. Ion nitriding has a strong advantage over competing processes in the case of stainless steels, particularly austenitic or 300-series materials. The chromium oxide passive layer on the surface of these materials represents a barrier to nitriding and must be removed prior to processing. With the gas nitriding of stainless steels, several processes, such as wet blasting, pickling, and chemical reduction, have been developed to remove the oxide. With ion nitriding, however, this passive layer can be removed

by sputtering hydrogen and argon in the vessel itself just prior to introducing the process gas. However, sputtering is detrimental to surface quality needed on medical parts, for example.

When good corrosion resistance is needed, precipitation of chromium nitrides and the loss of corrosion resistance can be avoided by selecting appropriate treatment parameters, especially lower temperatures and longer treatment times.

Alternative to Carbonitriding for Dimensional Control. Ion nitriding has become a replacement for carbonitriding in some cases. The growing demand in the industry for dimensional control and reduction or elimination of machining after heat treatment is the driving force for enhancement of ion nitriding.

The distortion of carbonitrided parts occurs in three ways:

- Heating to the austenitic range relieves residual stress.
- Oil quenching introduces high thermal stresses and some localized plastic deformation.
- The expansion of the case during martensite formation can cause some part distortion.

Ion nitriding can be performed at temperatures much lower than for carbonitriding, which minimizes the amount of residual stress relieved. Because loads are gas cooled, they do not experience distortion from temperature gradients or martensite formation.

Duplex Processes. When used in combination with physical vapor deposition (PVD) coatings such as TiN, TiAlN, or CrN, nitriding has been found to sufficiently improve adhesion of PVD layers as well as significantly improve tribological properties of PVD coatings by helping the base material to provide better adhesion for the coating. Nitriding and

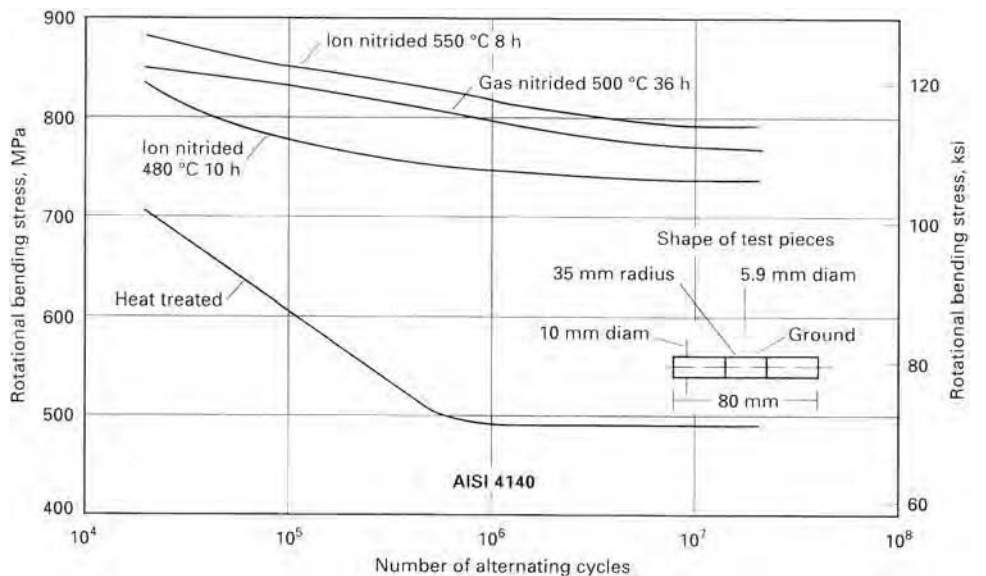


Fig. 24 Effect of nitriding on fatigue strength

coating can be done in one installation but is also often done in two steps on different installations. It is critically important to maintain good control of the plasma nitriding process to prevent the formation of a compound layer that will negatively influence the adhesion of the PVD coating.

Plasma Nitrocarburizing*

Plasma nitrocarburizing is, in essence, a variant of the plasma nitriding method. Mixtures of hydrogen, nitrogen, and a carbon-bearing gas, such as methane or carbon dioxide, are used for the nitrocarburizing process, which is carried out at 570 °C (1060 °F) to produce a compound layer of $>5 \mu\text{m}$ and a surface hardness of $\geq 350 \text{ HV}$ (Ref 21). The microprocessor-controlled unit ensures that the treatment schedules are undertaken in the correct sequence. Following nitrocarburizing, the workpieces are allowed to cool under controlled vacuum conditions.

In terms of metallurgy, the monophase ϵ -structure is strongly preferred with respect to the tribological properties of nitrocarburized steels. Unlike gas and salt bath nitrocarburizing, plasma nitrocarburizing has had problems with controlling the quality and character of the compound layer structure to achieve the monophase ϵ -carbonitride on a regular basis (Ref 22). Accordingly, with plasma nitrocarburizing the compound layer usually consists of ϵ - and γ' -phases for low-carbon-level atmospheres.

Under equilibrium conditions of gas nitrocarburizing, increasing the carbon level in the

atmosphere should produce the monophase ϵ -structure. However, under nonequilibrium thermodynamic conditions prevailing in the glow-discharge plasma, an increase in the carbon level does not automatically produce a 100% ϵ -structure, and yet cementite does appear above a certain limit of the carbon level (Ref 23). Laboratory studies using methane as the source of carbon in the plasma gas have shown that some stabilization of the ϵ -phase is possible, but above a certain limit (depending on the substrate materials), the cementite always appears and soot formation is difficult to prevent. The use of controlled additions of oxygen-bearing gases to reduce the activity of carbon has shown some promise in stabilizing the ϵ -phase, and the kinetics of compound layer growth are increased.

Experiments using 90% nitrogen/hydrogen atmospheres with controlled additions of carbon dioxide (up to 2.5%) have been carried out at 570 °C (1060 °F) for 2 h (Ref 24). It was found that:

- With pure iron, increasing the carbon dioxide stabilized the ϵ -phase, and an essentially monophase ϵ -structure was formed at 1% carbon dioxide level (Fig. 25a, b). A further increase in carbon dioxide level to 2% led to the formation of surface oxides.
- With plain carbon steel, increasing the carbon dioxide level again stabilized the ϵ -phase, but a mixture of the ϵ - and γ' -phases was invariably present (Fig. 26a, b).
- With a low-alloy chromium-bearing steel, EN40B (0.20 to 0.28% C, 0.10 to 0.35% Si, 0.45 to 0.70% Mn, 3.0 to 3.5% Cr, 0.45 to 0.65% Mo), the γ' -phase was

suppressed by even 0.5% carbon dioxide, but cementite compounds were invariably formed (Fig. 27a, b)

These controlled laboratory experiments clearly illustrate the lack of tolerance of the plasma nitrocarburizing process to minor variations in atmosphere condition. Accordingly, current industrial plasma nitrocarburizing practice, although meeting engineering mechanical property specifications, can be anticipated to show variations in microstructural characteristics.

Nonetheless, plasma nitrocarburizing has applications. One is nitrocarburizing of sintered PM components. Traditionally, PM components have been nitrocarburized using salt bath technology. This technique usually results in salt entrapment within the pores of the metallic structure. Frequently, these salts are highly toxic, and consequently there are handling problems and safe working procedures must be employed. Before PM parts enter the vacuum chamber of the plasma unit, lubricants added during PM processing must be removed. A method to remove lubricants is described in Ref 21. Using this method, it is now routinely possible to plasma nitrocarburize PM parts.

Modern systems of plasma nitriding and nitrocarburizing also are flexible. In a typical plasma nitrocarburizing unit, many different programs can be stored for different applications, and the equipment can be integrated in series in a manufacturing production line. In the equipment illustrated in Fig. 28, loads of 3000 automotive seat slider rails were nitrocarburized automatically for more than 5 years

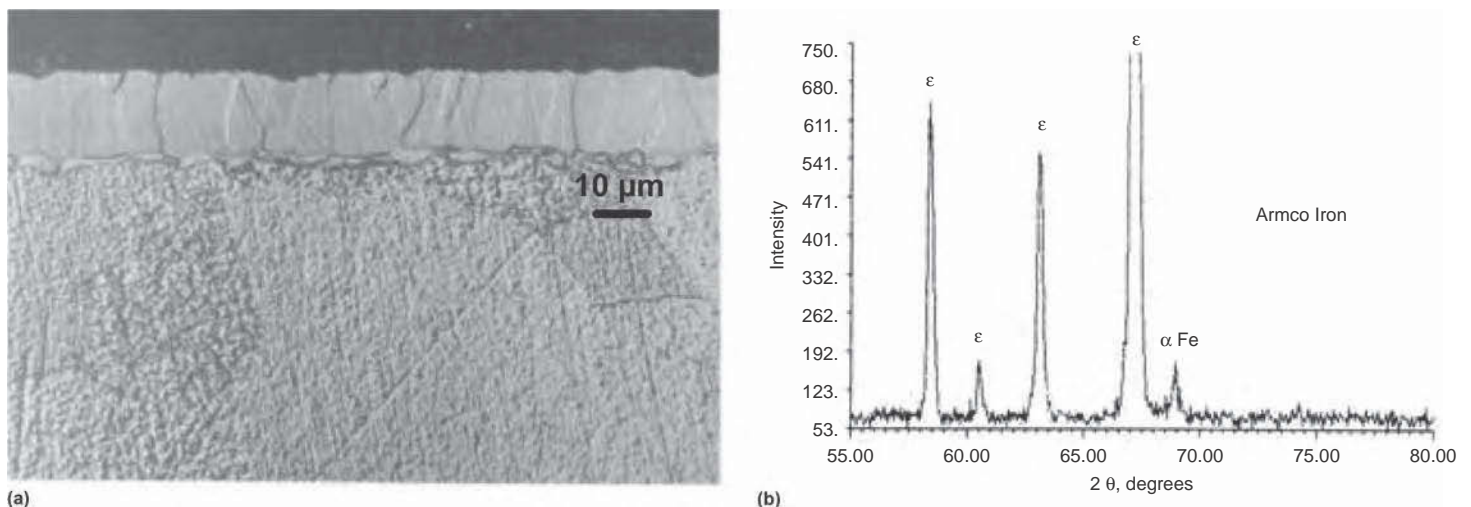


Fig. 25 (a) Microstructure of Armco iron plasma nitrocarburized at 570 °C (1060 °F) for 3 h at a gas pressure of 3.5 mbar. Gas mixture: 90 vol% N_2 , 1 vol% CO_2 , 9 vol% H_2 . Etched in a 1 mL mix of hydrochloric acid (HCl) and ethanol (1 part concentrated HCl + 10 parts ethanol) plus 99 mL 5% Nital. (b) X-ray diffraction pattern of the compound layer of the sample

* Adapted from T. Bell, Gaseous and Plasma Nitrocarburizing of Steels, *Heat Treating*, Vol 4, ASM Handbook, ASM International, 1991, p 425-436

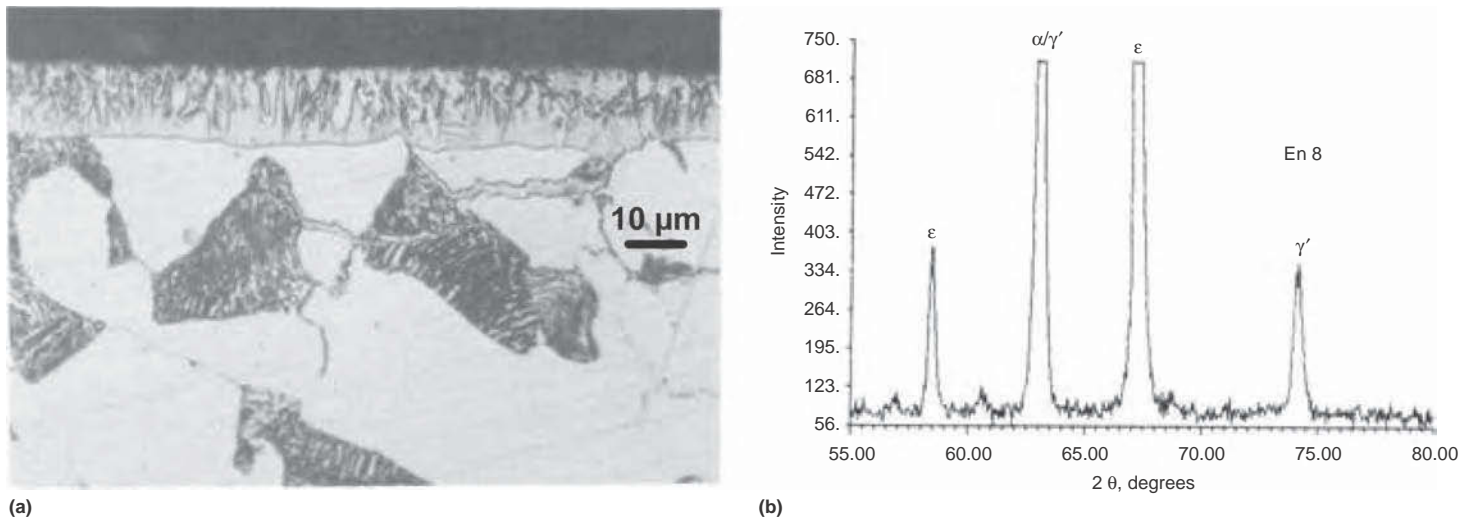


Fig. 26 (a) Microstructure of a plasma-nitrocarburized EN8 steel sample with (b) the corresponding x-ray diffraction pattern. See Fig. 25 for processing details.

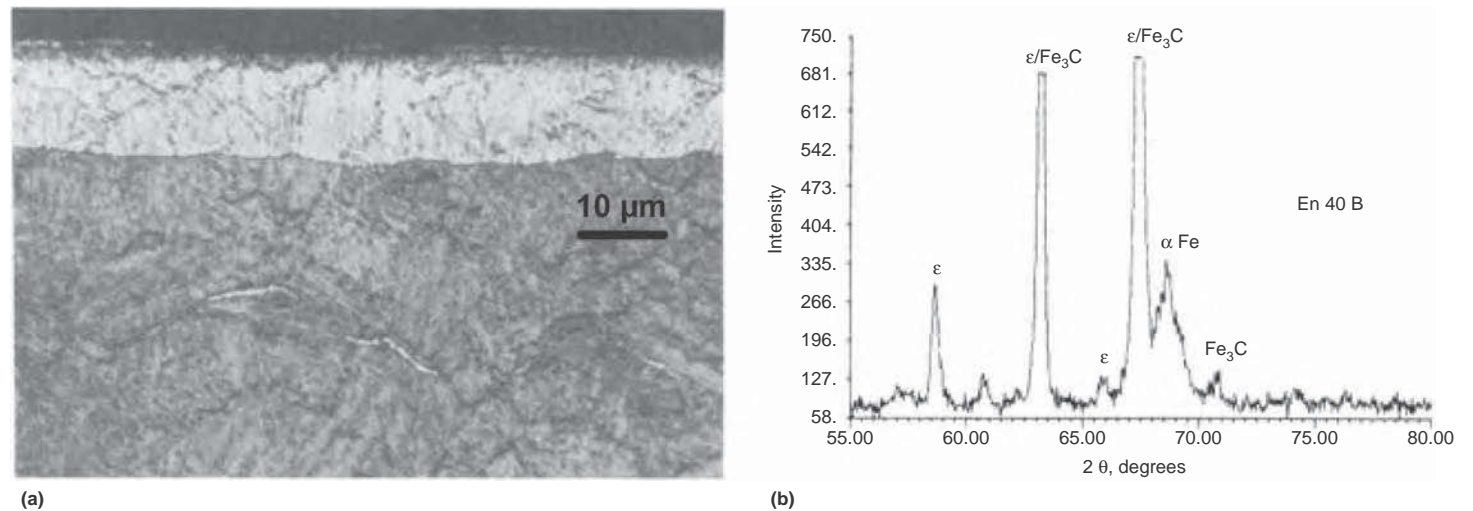


Fig. 27 (a) Microstructure of a plasma-nitrocarburized EN40B steel sample with (b) the corresponding x-ray diffraction pattern. See Fig. 25 for processing details.

without any significant technical or metallurgical problems.

ACKNOWLEDGMENTS

The authors acknowledge use of materials from the following cited publications:

- T. Bell, Gaseous and Plasma Nitrocarburizing of Steels, *Heat Treating*, Vol 4, *ASM Handbook*, ASM International, 1991, p 425–436
- D. Pye, *Practical Nitriding and Ferritic Nitrocarburizing*, ASM International
- A.K. Rakhit, *Heat Treatment of Gears: A Practical Guide for Engineers*, ASM International, 2000, p 159–169

REFERENCES

1. T. Bell, Gaseous and Plasma Nitrocarburizing of Steels, *Heat Treating*, Vol 4, *ASM Handbook*, ASM International, 1991, p 425–436
2. J. Georges, U.S. Patent 5,989,363, No. 23, 1999
3. T. Bell and C.X. Li, Active Screen Plasma Nitriding of Materials, *Int. Heat Treat. Surf. Eng.*, Vol 1 (No. 1), 2007
4. C.X. Li, Active Screen Plasma Nitriding—An Overview, *Surf. Eng.*, Vol 26 (No. 1–2), Feb 2010, p 135–141
5. F. Hombeck, Forward View of Ion Nitriding Applications, *Ion Nitriding*, T. Spalvins, Ed., ASM International, 1987, p 169–178
6. B. Berghaus, German Patents, DPR 668,639, 1932; DPR 851,560, 1939
7. C.K. Jones, D.J. Sturges, and S.W. Martin, Glow Discharge Nitriding in Production, *Met. Prog.*, Dec 1973, reprinted in *Source Book on Nitriding*, P.M. Unterweiser and A.G. Gray, Ed., American Society for Metals, 1977, p 186–187
8. F. Hombeck, The Environmentally Harmless Plasma Thermochemical Process, *Proceedings of Surface Engineering and Heat Treatment, Past, Present and Future*, Institute of Metals, London, Dec 1990
9. B. Edenhofer, Production Ionitriding, *Met. Prog.*, Vol 109, March 1976, p 38
10. K. Jones and S.W. Martin, *Met. Prog.*, Vol 85, Feb 1964, p 95
11. P. Collignon, J. Georges, and C. Kunz, “Active Screen Plasma Nitriding—An

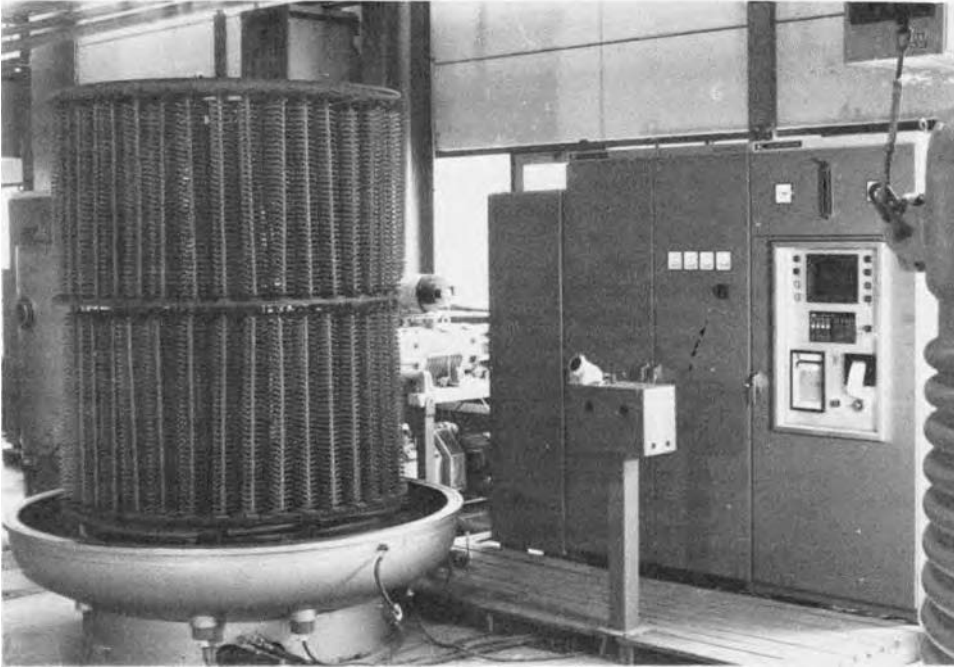


Fig. 28 Plasma nitrocarburizing installation for heat treating a load of 3000 automotive seat rails. Courtesy of Klockner Ionon GmbH

- Efficient, New Plasma Nitriding Technology,” *Industrial Heating*, BNP Media, <http://www.industrialheating.com/articles/90179-active-screen-plasma-nitriding-an-efficient-new-plasma-nitriding-technology> (accessed June 3, 2013)
12. J. Georges, TC Plasma Nitriding, *Proceedings of the 12th International Federation of Heat Treatment and Surface Engineering Congress*, Vol 3 (Melbourne, Australia), 2000, p 229–235
 13. J. Georges and D. Cleugh, Active Screen Plasma Nitriding, *Stainless Steel 2000—Thermochemical Surface Engineering of Stainless Steel*, T. Bell and K. Akamatsu, Ed., The Institute of Materials, U.K., 2001, p 377–387
 14. M. Axinte, C. Nejneru, A. Stroe, and M. Agop, Experimental Investigations on the Plasma Nitriding Process Control Using Ionic Triode, *Metal. Int.*, Vol 18 (No. 1), Jan 2013, p 26
 15. C.X. Li and T. Bell, Principles, Mechanisms and Applications of Active Screen Plasma Nitriding, *Heat Treat. Met.*, Vol 1, 2003, p 1–7
 16. B. Edenhofer, Physical and Metallurgical Aspects of Ion Nitriding, *Heat Treat. Met.*, Vol 1, 1974, p 23–28, 59–67
 17. D. Pye, *Practical Nitriding and Ferritic Nitrocarburizing*, ASM International, 2003
 18. A.K. Rakhit, *Heat Treatment of Gears: A Practical Guide for Engineers*, ASM International, 2000, p 159–169
 19. A. Nishimoto et al., Effect of Gas Pressure on Active Screen Plasma Nitriding Response, *J. ASTM Int.*, Vol 8 (No. 3), 2011
 20. R. Gruen, Pulse Plasma Treatment: The Innovation for Ion Nitriding, *Ion Nitriding Proceedings*, ASM International, 1987, p 143–147
 21. W. Rembges, Ion Nitriding Applications Grow for Automotive Components, *Heat Treat.*, March 1990
 22. K.-T. Rie and T.H. Lampe, *Proc. Heat Treatment '84*, The Metals Society, London, 1984, p 33.1–33.6
 23. J. Hadfield, “An Investigation of the Layers Produced by Plasma Nitrocarburising,” M.Sc. thesis, University of Birmingham, 1986
 24. E. Haruman, “Plasma Nitrocarburizing,” Ph.D. thesis, University of Birmingham, 1991

SELECTED REFERENCE

- J. Reece Roth, *Industrial Plasma Engineering*, Department of Electrical and Computer Engineering, University of Tennessee, Knoxville, Published by Institute of Physics Publishing, 2001

Diffusion Coatings

Pack Cementation Processes	707	Coating Mechanism and Types.	726
Aluminizing	707	Carbide Coating Nucleation and Growth	727
Siliconizing	708	Nitride Coating Nucleation and Growth	728
Chromizing	708	Factors Controlling the Growth Rate of Coatings	729
Boriding (Boronizing) of Metals	709	Coating Processes	730
Characteristic Features of Boride Layers	709	Controlling Coating Reagent Conditions	732
Boriding of Ferrous Materials	713	High-Temperature Salt Bath Carbide Coating	733
Boriding of Nonferrous Materials	716	High-Temperature Fluidized-Bed Carbide Coating	735
Thermochemical Boriding Techniques	717	Low-Temperature Salt Bath Nitride Coating	736
Applications of Thermochemical Boriding	721	Properties of Coated Parts	737
Chemical Vapor Deposition	722	Practical Applications	738
Thermoreactive Deposition/Diffusion Process for Surface		Supercarburizing	741
Hardening of Steels	725	Supercarburizing with Conventional Carburizing Steel	741
Introduction	725	Steels for Supercarburizing	744

Pack Cementation Processes

PACK CEMENTATION is the most widely employed method of diffusion coating. In general, diffusion coatings are deposited either by heating the components to be treated in contact with the powder coating material in an inert atmosphere (solid-state diffusion) or by heating them in an atmosphere of a volatile compound of the coating material (out-of-contact gas-phase deposition; or chemical vapor deposition, CVD). The pack cementation process is a modified CVD deposition batch process that involves heating a closed/vented pack to an elevated temperature (e.g., 1050 °C, or 1920 °F) for a given time (e.g., 16 h), during which a diffusional coating is produced.

The most widely used pack coating methods (Table 1) are those based on aluminum (aluminizing), chromium (chromizing), and silicon (siliconizing). Substrate materials include nickel- and cobalt-base superalloys, steels (including carbon, alloy, and stainless steels), and refractory metals and alloys. Multicomponent pack cementation coatings have been developed from chromium/aluminum and chromium/silicon processing for high-temperature corrosion resistance.

In general, simple binary alloys, for example, iron-chromium and nickel-aluminum, are not as effective for oxidation resistance as a ternary alloy using the interaction of two oxidation-resistant elements. A variety of alloys have been coated with chromium/aluminum (low-carbon and alloy steels; types 410, 304, and

316 stainless steels; and nickel-base superalloys) and chromium/silicon (low-carbon and low-alloy steels, types 304 and 409 stainless steels, Incoloy 800). Each alloy requires a specific pack chemistry to obtain optimal coating composition for superior oxidation resistance.

This article briefly reviews pack cementation processes of aluminizing, chromizing, and siliconizing. Pack cementation processes are also described in the articles “Boriding (Boronizing) of Metals” and “Thermoreactive Deposition/Diffusion Process for Surface Hardening of Steels” in this Volume. The traditional pack consists of four components: the substrate or part to be coated, the master alloy (i.e., a powder of the element or elements to be deposited on the surface of the part), a halide salt activator, and a relatively inert filler powder. The master alloy, the filler, and the halide activator are thoroughly mixed together, and the part to be coated is buried in this mixture in a retort. When the mixture is heated, the activator reacts to produce an atmosphere of source element(s) halides that diffuse into the pack and transfer the source element(s) to the substrate on which the coating is formed.

Aluminizing

An aluminizing pack cementation process is commercially practiced for a range of alloys,

including nickel- and cobalt-base superalloys, steels, and stainless steels. Simple aluminide coatings resist high-temperature oxidation by the formation of an alumina protective layer and can be used up to approximately 1150 °C (2100 °F), but the coating can degrade by spallation of the oxide during thermal cycling. For extended periods of time at temperatures in excess of 1000 °C (1830 °F), interdiffusion of the coating will cause further degradation, and therefore, practical coating life is limited to operating temperatures of 870 to 980 °C (1600 to 1800 °F).

Pack compositions, process temperatures, and process times depend on the type of base material to be aluminized. Materials fall into one of the following general classifications:

- *Class I:* carbon and low-alloy steels and copper
- *Class II:* ferritic and martensitic stainless steels and austenitic stainless steels with less than 20% Ni
- *Class III:* austenitic stainless steels with 21 to 40% Ni and iron-base superalloys
- *Class IV:* nickel- and cobalt-base superalloys

As a general rule, overall aluminum diffusion is slower as the nickel, chromium, and cobalt contents increase. Therefore, higher temperatures and longer process times are required to produce greater aluminum diffusion

Table 1 Typical characteristics of pack cementation processes

Process	Nature of case	Process temperature		Typical case depth	Case hardness, HRC	Typical base metals	Process characteristics
		°C	°F				
Aluminizing (pack)	Diffused aluminum	870–980	1600–1800	25 µm–1 mm (1–40 mils)	<20	Low-carbon steels, nickel- and cobalt-base superalloys	Diffused coating for oxidation resistance at elevated temperatures
Siliconizing by chemical vapor deposition	Diffused silicon	925–1040	1700–1900	25 µm–1 mm (1–40 mils)	30–50	Low-carbon steels	For corrosion and wear resistance, atmosphere control is critical.
Chromizing by chemical vapor deposition	Diffused chromium	980–1090	1800–2000	25–50 µm (1–2 mils)	Low-carbon steel, <30; high-carbon steel, 50–60	High- and low-carbon steels, nickel- and cobalt-base superalloys	Chromized low-carbon steels yield a low-cost stainless steel; high-carbon steels develop a hard corrosion-resistant case.
Titanium carbide	Diffused carbon and titanium, TiC compound	900–1010	1650–1850	2.5–12.5 µm (0.1–0.5 mil)	>70(a)	Alloy steels, tool steels	Produces a thin carbide (TiC) case for high resistance wear; temperature may cause distortion.
Boriding	Diffused boron, boron compounds	400–1150	750–2100	12.5–50 µm (0.5–2 mils)	40–70	Alloy steels, tool steels	Produces a hard compound layer, mostly applied over hardened tool steels; high process temperature can cause distortion.

(a) Requires quench from austenitizing temperature

thicknesses as the base material goes from class I to class IV.

As described in Ref 1, the pack cementation aluminizing coating process is performed in a pack consisting of the following mixture:

- Aluminum—in the form of a pure metal powder or alloy powder
- Filler—a ceramic powder phase, to prevent sintering of the mix during high-temperature processing. Usually aluminum oxide is used
- Activator—a volatile halide, usually an ammonium or sodium halide, to act as a chemical transfer medium for the aluminum

The precleaned steel parts to be pack aluminized are placed in a retort, or reactor vessel, with the pack mixture. Using ammonium halide (NH_4X , where X is fluorine, chlorine, bromine, or iodine) as the activator, a sequence of high-temperature reactions occurs when aluminum is deposited on the surfaces of an iron-base alloy.

The pack cementation aluminizing process is used to improve the performance of steels in high-temperature corrosive environments. The complex aluminide intermetallic coatings formed during the process exhibit superior resistance to oxidation, carburization, and sulfidation. Table 2 provides a partial listing of commercial applications for the pack aluminizing process. Typical applications include carbon steel heat-exchanger tubes used in sulfuric acid plants, low-alloy steel pipes and fittings used in petroleum refinery heaters, type 304 stainless steel vessels used in flue gas desulfurization systems, and HK or HP cast tubing for ethylene pyrolysis units.

Siliconizing

Siliconizing, the diffusion of silicon into steel, occurs similarly to aluminizing. There are pack and retort processes in which parts are subjected to gas atmospheres that react with the heated part surface to produce nascent silicon that diffuses into the substrate to be coated. In a pure silicon pack that is activated with

Table 2 Partial list of commercial applications of pack cementation aluminizing

Industry	Component	Typical materials aluminized
Hydrocarbon processing	Refinery heater tubes	2¼%Cr-1%Mo steel
	Ethylene pyrolysis furnace tubes	Incoloy 802
	Hydrodesulfurizer furnace tubes	2¼%Cr-1%Mo steel
	Delayed coker furnace tubes	9%Cr-1%Mo steel
	Catalyst reactor screens	347 stainless steel
	Catalyst reactor grating	Carbon steel
Sulfuric acid Industrial furnace components	Gas-to-gas heat exchanger tubes	Carbon steel
	Aluminum plant furnace parts	Carbon steel
	Heat treating pots	Carbon steel
	Structural members	High-nickel alloy steel
Steam power and cogeneration	Thermowells	Carbon and stainless steels
	Waterwall tubes	2¼%Cr-1%Mo steel
	Fluidized-bed combustor tubes	2¼%Cr-1%Mo steel
	Waste heat boiler tubes	Carbon steel
	Economizer and air preheater tubes	2¼%Cr-1%Mo steel
	Superheater tubes	2¼%Cr-1%Mo steel
Flue gas scrubbers Chemical processing	NO_x/SO_x removal units	304 stainless steel
	Reactor vessels and tubing	304/316 stainless steel
Cement	Cooler grates	Stainless steel, HP, HK

ammonium chloride (NH_4Cl), silicon tetrachloride (SiCl_4) and trichlorosilane (SiHCl_3) gases form, which are reduced by hydrogen gas to deposit elemental silicon on the surface of the part. Another process involves tumbling parts in a retort with SiC. When a temperature of 1010 °C (1850 °F) is reached, silicon tetrachloride gas is introduced, which reacts with the part and the SiC particles to produce a concentration gradient of silicon on the part surface as the silicon diffuses into the substrate. The process normally takes place on low-carbon steels, and these steels develop case depths up to 1 mm (0.040 in.) with a silicon content of 13 wt%. Case depths developed on these siliconized steels have hardnesses of approximately 50 HRC and therefore can be used for wear resistance. The presence of silicon on the surface allows for the formation of a stable silicon dioxide (SiO_2) phase in oxidizing environments and excellent corrosion resistance.

Chromizing

Chromium can be applied in the same manner as aluminum and silicon to produce a chromium-rich coating, and many of the same

principles of aluminizing packs apply to chromizing packs. Parts are packed in chromium powder with an inert filler such as aluminum oxide. A halide salt activator is added that changes to the vapor phase at the processing temperature and serves as a carrier gas to bring chromium to the surface of the part. Diffusion coatings can be formed on nickel-base superalloys by pack cementation using ammonium chloride as a chromium-alumina activator. These coatings usually contain 20 to 25 wt% Cr at the outer surface and involve approximately equal rates of interdiffusion of chromium and nickel. Significant depletion of aluminum and titanium from the alloy surface occurs, thus producing a coating that is a solid solution of the chromium in the remaining nickel-base superalloy. The deposited coating is usually overlaid with a thin layer of α -chromium, which must be removed chemically.

REFERENCE

1. D.M. Mattox, Diffusion Coatings, *Surface Engineering*, Vol 5, *ASM Handbook*, ASM International, 1994, p 611–620

Boriding (Boronizing) of Metals*

Craig Zimmerman, Bluewater Thermal Solutions

BORIDING, also known as boronizing, is a thermochemical diffusion-based surface-hardening process that can be applied to a wide variety of ferrous, nonferrous, and cermet materials. Boriding is typically performed on metal components as a solution for extending the life of metal parts that wear out too quickly in applications with severe wear. Boriding has often been able to increase the usable service life of high-wear metal components by factors ranging from double to ten times the wear life when compared to many conventional heat treatments and platings. The process typically involves heating metal components to temperatures of 700 to 1000 °C (1300 to 1830 °F) for 1 to 12 h, in contact with a boronaceous solid powder, paste, liquid, or gaseous medium. This allows boron to diffuse into metal surfaces and form hard, wear-resistant metal-boride compound layers. Pack cementation boriding is the most commonly used technique in industry; however, additional techniques, such as gas boriding, plasma boriding, electroless salt bath boriding, electrolytic salt bath boriding, and fluidized-bed boriding, have been developed. Work has also been performed to explore the use of multicomponent boriding.

This article presents a variety of methods and media used for boriding and their advantages, limitations, and applications. Physical and chemical vapor deposition (PVD and CVD), plasma spraying, and ion implantation are alternative nonthermochemical surface-coating processes for the deposition of boron or co-deposition of boron and metallic element(s) onto a suitable metallic or nonmetallic substrate material. This article briefly describes the CVD process, which has emerged to be dominant among the metal-boride deposition processes.

Characteristic Features of Boride Layers

During boriding, boron atoms are absorbed as interstitials into the lattice of the substrate metal. Boron atoms diffuse over time to deeper

depths below the metal surface and react with the substrate material to form metal-boride compounds (Ref 1–6). These compounds eventually form a solid continuous metal-boride compound layer below the original surface of the workpiece, extending to depths determined by the amount of boron diffusion that occurs. The resulting boride layer may consist of either a single-phase boride or a polyphase boride layer (Ref 7). The morphology (Fig. 1), growth rates, and phase composition of the boride layer is influenced by the alloying elements in the base material. The microhardness of the boride layer also depends strongly on the composition and structure of the boride layer and the composition of the base material (Table 1).

Advantages. Boride layers possess a number of characteristic features with special advantages over conventional case-hardening processes such as carburizing, carbonitriding, nitriding, and nitrocarburizing. The main advantage is that boride layers have extremely high hardness values (between 700 and 3370 HV) with high melting points of the constituent phases (Table 1). The typical surface hardness

values of borided steels compared with other treatments and other hard materials are listed in Table 2 and shown in Fig. 2. This clearly illustrates that the hardness of boride layers produced on carbon steels is much greater than that produced by any other conventional surface (hardening) treatments; it also exceeds that of the hardened tool steel, hard chrome electroplate, and is equivalent to that of tungsten carbide and many PVD coatings.

The boride layer combination of a high surface hardness with a low surface coefficient of friction also makes a significant contribution in combating the main wear mechanisms: adhesion, tribo-oxidation, abrasion, and surface fatigue (Ref 4, 5, 11). This has enabled mold makers and component design engineers to substitute easier-to-machine, lower-cost steels for the base metal while still being able to obtain wear resistance and antigalling properties superior to those of the original material treated with conventional methods (Ref 12). Figure 3 shows the effect of boriding on abrasive wear resistance of borided AISI 1045 steel (C45), titanium, and tantalum

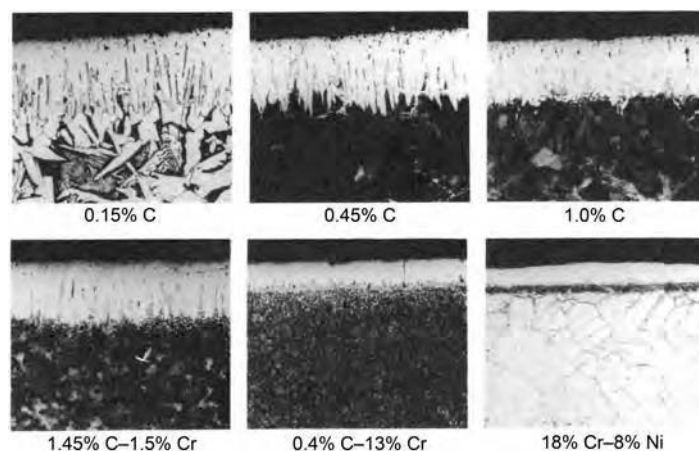


Fig. 1 Effect of steel composition on the morphology and thickness of the boride layer. Source: Ref 8

* Reviewed and revised from A.K. Sinha, Boriding (Boronizing) of Steels, *Heat Treating*, Vol 4, *ASM Handbook*, ASM International, 1991, p 437–447

Table 1 Melting point and microhardness of different boride phases formed during boriding of various substrate materials

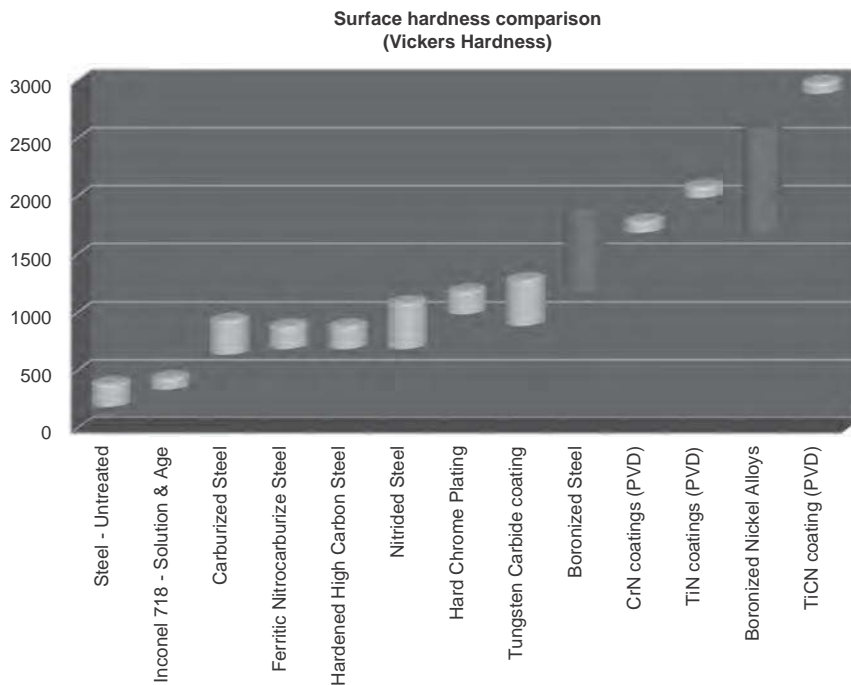
Substrate	Constituent phases in the boride layer	Microhardness of layer, HV or kg/mm ²	Melting point	
			°C	°F
Fe	FeB	1900–2100	1390	2535
	Fe ₂ B	1800–2000
Co	CoB	1850
	Co ₂ B	1500–1600
	Co ₃ B	700–800
	Co ₂ B	2200 (100 g)(a)
Co-27.5 Cr	Co ₂ B	~1550 (100 g)(a)
	Co ₃ B (?)	700–800
	Ni ₄ B ₃	1600
Ni	Ni ₂ B	1500
	Ni ₃ B	900
	...	1700 (200 g)(b)
Inco 100	Mo ₂ B	1660	2000	3630
	MoB ₂	2330	~2100	~3810
	Mo ₂ B ₅	2400–2700	2100	3810
W	W ₂ B ₅	2600	2300	4170
	TiB	2500	~1900	3450
Ti	TiB ₂	3370	2980	5395
	TiB
	TiB ₂	3000 (100 g)(a)
Nb	NbB ₂	2200	3050	5520
	NbB ₄
Ta	Ta ₂ B	...	3200–3500	5790–6330
	TaB ₂	2500	3200	5790
	HfB ₂	2900	3250	5880
Hf	ZrB ₂	2250	3040	5500
Zr	ReB	2700–2900	2100	3810
Re				

(a) 100 g load. (b) 200 g load. Source: Ref 3, 9, 10

Table 2 Typical surface hardness of borided steels compared with other treatments and hard materials

Material	Microhardness, kg/mm ² or HV
Boride mild steel	1600
Borided AISI H13 die steel	1800
Borided AISI A2 steel	1900
Quenched steel	900
Hardened and tempered H13 die steel	540–600
Hardened and tempered A2 die steel	630–700
High-speed steel BM42	900–910
Nitrided steels	650–1700
Carburized low-alloy steels	650–950
Hard chromium plating	1000–1200
Cemented carbides, WC + Co	1160–1820 (30 kg)
Al ₂ O ₃ + ZrO ₂ ceramic	1483 (30 kg)
Al ₂ O ₃ + TiC + ZrO ₂ ceramic	1738 (30 kg)
Sialon ceramic	1569 (30 kg)
TiN	2000
TiC	3500
SiC	4000
B ₄ C	5000
Diamond	>10,000

Source: Ref 3

**Fig. 2** Comparison of surface hardness results of various heat treatments and coatings. PVD, physical vapor deposition

as a function of number of revolutions (or stressing period) based on the Faville test. Figure 4 shows the influence of steel composition on abrasive wear resistance. Figure 5 shows a comparison of wear rates during a pin-on-disk wear trial

of untreated, carburized, and borided 1018 steel surfaces.

Besides having extremely high hardness and wear resistance, other additional advantages of boriding include:

- Boriding can considerably enhance the corrosion-erosion resistance of ferrous materials in nonoxidizing dilute acids (Fig. 6) and alkali media and is increasingly used to this advantage in many industrial applications (Ref 4, 5). Boride layers in ferrous materials greatly improve resistance to corrosive attack by hydrochloric, hydrofluoric, phosphoric, and sulfuric acids (Ref 4, 5, 14).
- The hardness of the boride layer can be retained at higher temperatures than cases formed by conventional heat treatments. Boride layers have been used at service temperatures up to 650 °C (1200 °F), where nitrided, nitrocarburized, carburized, and carbonitrided cases would be softened from tempering or diffuse away over short periods of time (Fig. 7).
- A wide variety of steels, including through-hardenable steels, are compatible with the processes (Ref 15).
- A wide variety of nonferrous materials, such as nickel-base superalloys, cobalt alloys, titanium alloys, and others, may be successfully borided.
- Borided surfaces have moderate oxidation resistance (up to 850 °C, or 1550 °F) and are quite resistant to attack by molten metals (Ref 16).
- Borided parts have an increased fatigue life and service performance under oxidizing and corrosive environments (Ref 16).
- Antigalling properties are greatly improved by boriding. Spherical balls and mating seats that form the seals in ball valves which slide against one another under high contact pressures can have galling failures if untreated. Boriding is an excellent treatment to prevent galling failure of these surfaces (Ref 17).

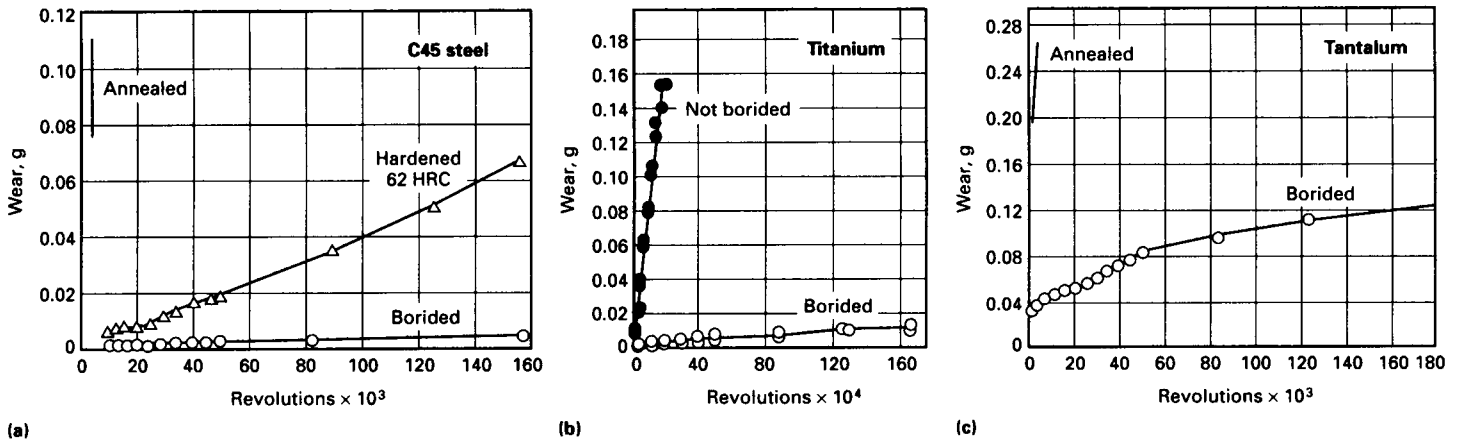


Fig. 3 Effect of boriding on wear resistance (Faville test). (a) 0.45% C (C45) steel borided at 900 °C (1650 °F) for 3 h. (b) Titanium borided at 1000 °C (1830 °F) for 24 h. (c) Tantalum borided at 1000 °C (1830 °F) for 8 h. Source: Ref 13

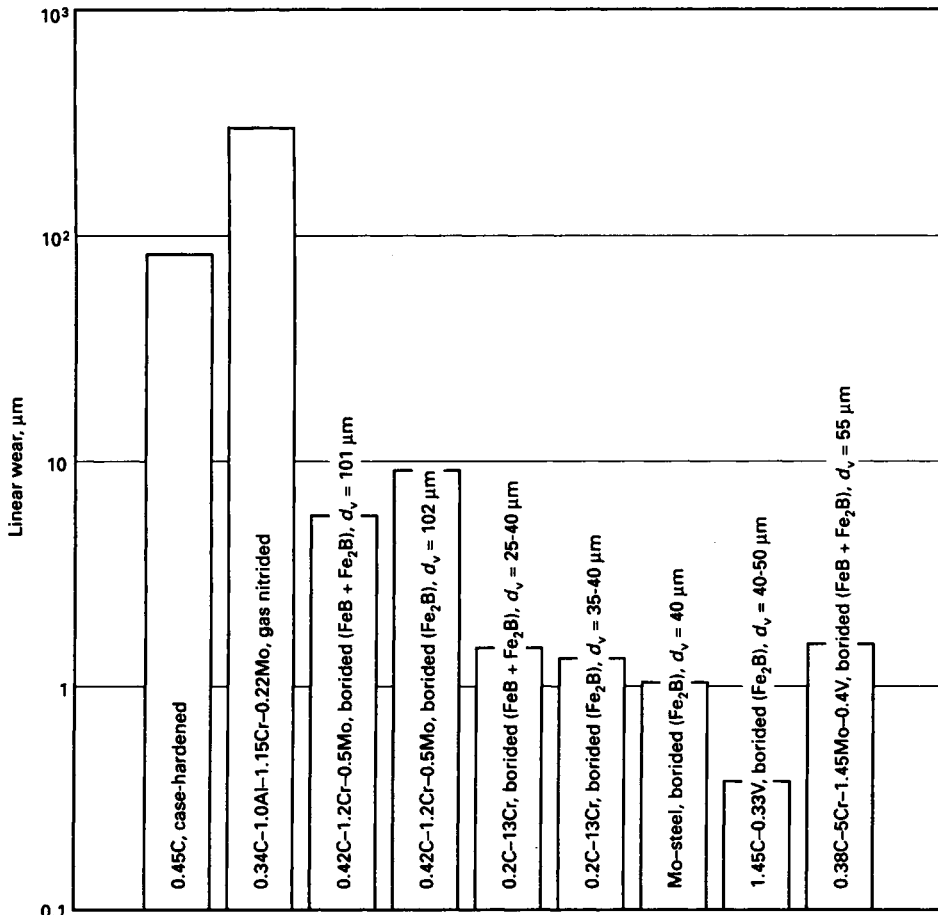


Fig. 4 Effect of steel composition (nominal values in wt%) on wear resistance under abrasive wear (d = thickness of the boride layer). Test conditions: DP-U grinding tester, SiC paper 220, testing time 6 min. Source: Ref 8, 11

Disadvantages of boriding treatments include:

- Boriding techniques require immersing parts to be treated in a boronaceous medium that becomes consumed during processing, which is typically costly and more labor-intensive than other thermochemical surface-hardening treatments, such as carburizing and nitriding. Both carburizing and nitriding case-hardening processes have a cost advantage over boriding, mainly because carbon and nitrogen sources are more readily available and can be safely used in a gaseous state. Boriding is usually only selected for applications where conventional carbon- and nitrogen-base case-hardening processes simply cannot offer enough wear and/or corrosion resistance. In some severe wear applications, components that are case hardened by conventional methods still wear out very frequently and require periodic replacement. The high cost of replacing components as they wear out, in addition to the cost of machine downtime as worn parts are being replaced, can supersede the higher heat treatment costs of boriding. For these high-wear or corrosive applications, boriding is of value because the parts can last several times longer in service and do not require frequent replacement and machine downtime.
- The growth (increase in volume) resulting from boriding is 5 to 25% of the layer thickness (for example, a 25 μm, or 1000 μin., layer would have a growth of 1.25 to 6.25 μm, or 50 to 250 μin.); its magnitude depends on the base material composition but remains consistent for a given combination of material and treatment cycle. However, it can be predicted for a given part geometry and boriding treatment. For treatment of precision parts, where little stock removal is permitted, an allowance of ~20 to 25% dimensional increase of the final boride layer thickness must be provided.

- Boriding can often be combined with other heat treatments. Neutral hardening of steels is possible after boriding to improve the core hardness and overall strength of components. Carburizing has also been performed in conjunction with boriding to take

advantage of the ultrahigh hardness of the boride layers along with the benefit of having a deeper carburized case below the boride layer (Ref 18). Solution treatment and aging after boriding has been performed on nickel-base superalloys (Ref 19).

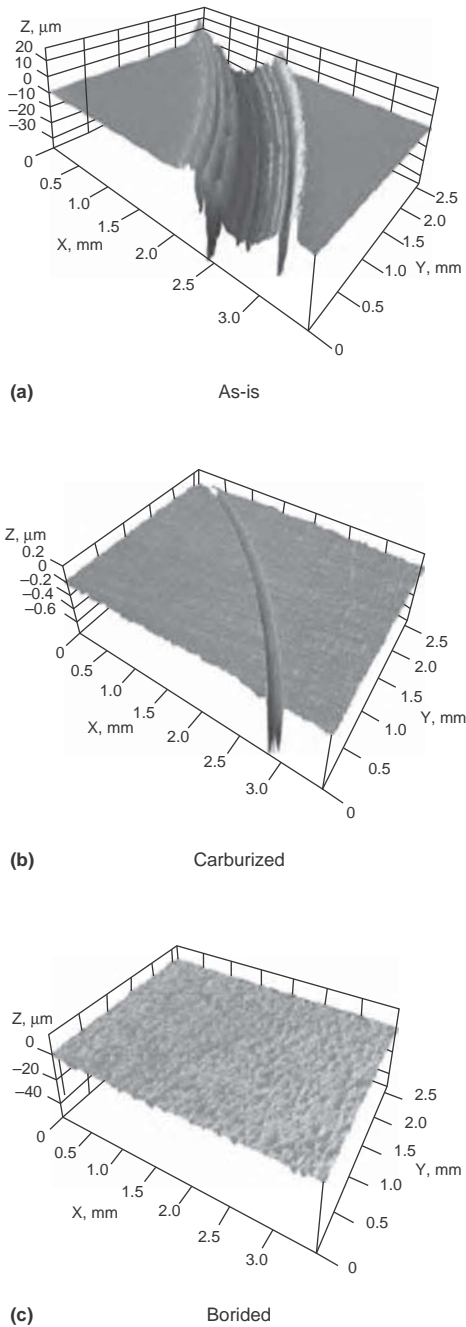


Fig. 5 Comparison of wear resistance between (a) untreated, (b) carburized, and (c) borided 1018 steel in pin-on-disk wear test. Courtesy of A. Erdemir, Argonne National Laboratory

- Dimensional control of ferrous parts during boriding can be problematic. Boriding is typically a high-temperature process, and critical dimensional tolerances can distort due to high-temperature creep, relieving of stresses, and phase transformations of the substrate material that can occur at these processing temperatures. Postmachining or grinding after boriding is very difficult to perform due to the extreme high hardness and brittle nature of the boride layer. Many

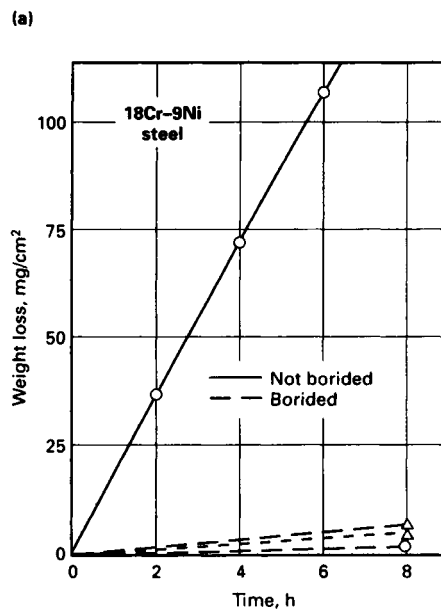
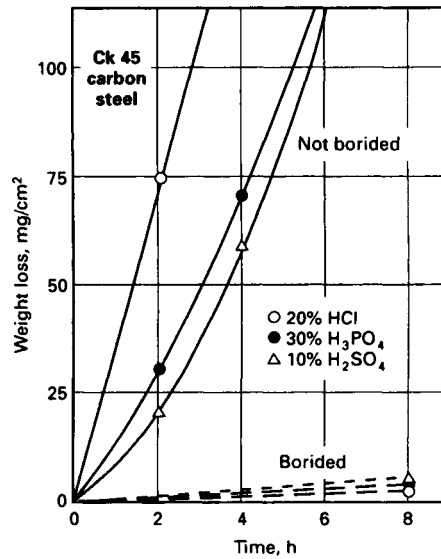


Fig. 6 Corroding effect of mineral acids on boronized and nonboronized (a) 0.45% C (Ck 45) steel and (b) 18Cr-9Ni (X10CrNiTi18 9) steel at 56 °C (130 °F). Source: Ref 4, 5, 14

- components that have tight dimensional tolerances are not suited for boriding because these tolerances may not be maintained.
- Partial removal of the boride layer for closer tolerance requirements is made possible only by a subsequent diamond lapping or very carefully controlled slow grinding using hard media because conventional grinding causes fracture of the layer (Ref 3).
- In general, the rolling-contact fatigue properties of borided alloy steel parts are very poor compared to carburized and nitrided steels at high contact loads (2000 N, or 450 lbf). This is why boriding treatments of

gears are limited to those screw designs where transverse loading of gear teeth is minimized (Ref 3).

- There is frequently a need to harden and temper or solution treat and age the components after boriding (Ref 19), which requires a vacuum, salt bath, or inert atmosphere to preserve the integrity of the boride layer. These additional heat treatment processes after boriding are an additional source of dimensional distortion and can only be performed after boriding, when the parts may be very difficult to final grind to finished dimensions.

Thermal Stability of Boride Layers at Elevated Service Temperatures. Boriding is often performed on components that operate at elevated service temperatures, due to the thermal stability of boride layers and their ability to retain high hardness at those elevated operating temperatures. Many carburized components are tempered at low tempering temperatures and will soften and lose their mechanical properties if exposed to service temperatures above their final tempering temperature, which is commonly performed between 570 and 750 °C (300 and 400 °F). Nitriding is often selected as a case-hardening process for parts exposed to high operating temperatures, where carburized parts would become tempered and soften, such as forging dies, extrusion dies, die-casting dies, and valve or pump components. However, nitriding is typically performed at temperatures between 1795 and 2010 °C (975 and 1100 °F), and those nitride layers will quickly decompose due to nitrogen diffusing away from the surface case if used at service temperatures above 540 °C (1000 °F). One advantage of boriding treatments is that the boride layers are stable at high operating temperatures and can survive without decomposition or loss of hardness at temperatures up to 650 °C (1200 °F).

A study was performed to characterize the long-term thermal stability of boride layers at 650 °C (1200 °F). Multiple samples of AISI 1018 plain carbon steel and Inconel 718 were borided together to form a boride layer with depths of 0.18 and 0.076 mm (0.007 and 0.003 in.) on the 1018 steel and Inconel 718, respectively. After the boriding treatment, each piece was held at 650 °C (1200 °F) for different exposure times. The goal of this study was to determine how long the boride layers could survive exposure to 650 °C (1200 °F) temperature and if any degradation of the layers would be observed due to diffusion of boron atoms into the substrate or exiting the surface at that temperature. After each timed exposure to 650 °C (1200 °F) temperature was complete, each test-piece was sectioned to expose the cross section of the testpiece and then mounted, ground, polished, and etched with acid solutions to reveal the boride layer and base metal microstructure. Micrographs of the boride layers for low-carbon steel and Inconel 718 are shown in

Fig. 7 after various exposure times to 650 °C (1200 °F) temperature. It can be observed that no loss of boride layer depth or change in microstructure has occurred after 30 days of exposure to 650 °C (1200 °F) temperature.

Boriding of Ferrous Materials

The boriding process consists of two types of reaction (Ref 8). The first reaction takes place between the boron-yielding substance and the component surface. The nucleation rate of the particles at the surface is a function of the boriding time and temperature. This produces a thin, compact boride layer.

The subsequent second reaction is diffusion controlled, and the total thickness of the boride layer growth at a particular temperature can be calculated by the simple formula:

$$d = k\sqrt{t} \quad (\text{Eq 1})$$

where d is the boride layer thickness in centimeters; k is a constant, depending on the temperature; and t is the time in seconds at a given temperature. The diffusivity of boron at 950 °C (1740 °F) is 1.82×10^{-8} cm²/s for the boride layer and 1.53×10^{-7} cm²/s for the diffusion zone. As a result, the boron-containing diffusion zone extends more than 7 times the depth of the boride layer thickness into the substrate (Ref 20). It has been proposed that a concentration gradient provides the driving force for diffusion-controlled boride layer growth (Ref 21).

The most desirable microstructure after boriding ferrous alloys is a single-phase boride layer consisting only of Fe₂B. In some cases, a dual-phase layer consisting of an outer darker-etching phase of FeB and an inner bright-etching phase of Fe₂B may also be formed. The formation of either a single- or dual-phase boride layer in steels depends on several factors.

Characteristics of Dual-Phase FeB and Fe₂B Layers. The formation of a single Fe₂B phase (with a sawtooth morphology due to preferred diffusion direction) is more desirable than a dual-phase layer with FeB and Fe₂B together. The boron-rich FeB phase is considered undesirable, in part, because FeB is more brittle than the Fe₂B layer. The FeB formation is also undesirable because FeB and Fe₂B are formed under tensile and compressive residual stresses, respectively, due to differences in expansion/contraction during cooling from the boriding temperature, because they have different coefficients of thermal expansion. Crack formation is often observed at or in the neighborhood of the FeB/Fe₂B interface of a dual-phase layer. These cracks may lead to flaking and spalling when a mechanical strain is applied (Ref 6) or even separation (Fig. 8) when a component is undergoing a thermal and/or mechanical shock.

In some cases where a dual-phase boride layer is present, simply handling borided surfaces after processing can create stresses sufficient to induce spalling. In other cases, spalling can occur simply from the stresses

induced by cooling the boride layers with differing coefficients of thermal expansion from the boriding temperature to ambient. Therefore, the boron-rich FeB phase should be avoided or minimized in the boride layer (Ref 6).

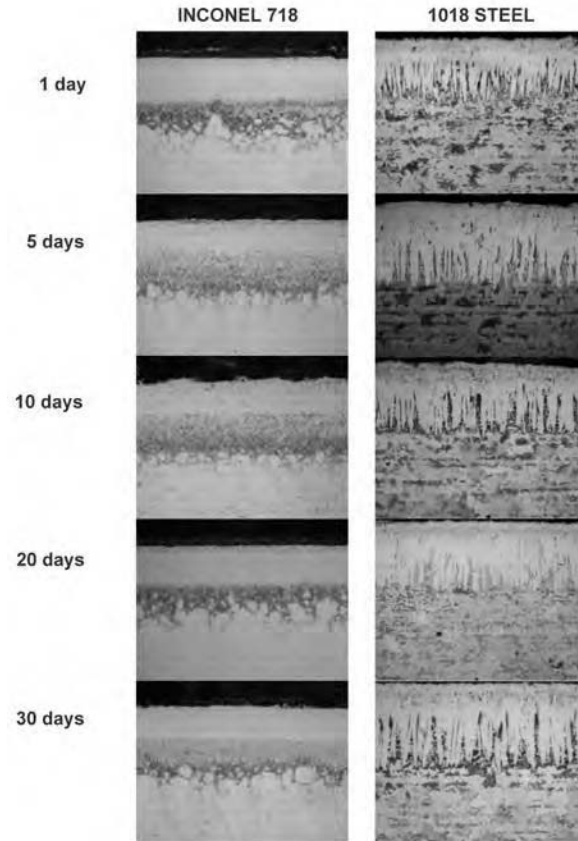


Fig. 7 Microstructure of boride layers after varying exposures to 650 °C (1200 °F) service temperatures after boriding

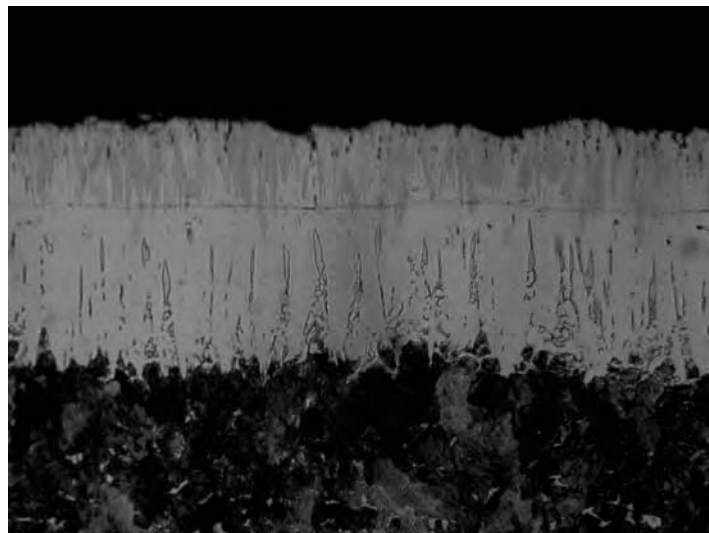


Fig. 8 Separation of dual-phase FeB (dark teeth) and Fe₂B (light teeth) boride layer on an AISI 1045 steel (borided at 927 °C, or 1700 °F, for 6 h). Original magnification: 200×

It has also been reported that tribological properties depend on the microstructure of the boride layer. The dual-phase FeB-Fe₂B layers are not inferior to those of monophase Fe₂B layers, provided that the porous surface zone directly beneath the surface is removed (Ref 22). Alternatively, a thinner layer is favored because of less development of brittle and porous surface-zone formation and flaking.

Properties of FeB layers are as follows:

- Microhardness of approximately 19 to 21 GPa (2.7 to 3.0 × 10⁶ psi)
- Modulus of elasticity of 590 GPa (85 × 10⁶ psi)
- Density of 6.75 g/cm³ (0.244 lb/in.³)
- Thermal expansion coefficient of 23 × 10⁻⁶ m/m per °C between 200 and 600 °C (400 and 1100 °F) (Ref 8, 23)
- Composition with 16.23 wt% B
- Orthorhombic crystal structure with four iron and four boron atoms per unit cell
- Lattice parameters: $a = 4.053 \text{ \AA}$, $b = 5.495 \text{ \AA}$, and $c = 2.946 \text{ \AA}$

Properties of Fe₂B Layers. The formation of single-phase Fe₂B layers with a sawtooth morphology is desirable in the boriding of ferrous materials (Ref 24). A single Fe₂B phase can be obtained from a dual FeB-Fe₂B phase by a subsequent vacuum or salt bath treatment for several hours above 800 °C (1470 °F), which may be followed by oil quenching to increase substrate properties (Ref 25, 26).

Typical properties of Fe₂B include:

- Microhardness of approximately 18 to 20 GPa (2.6 to 2.9 × 10⁶ psi)
- Modulus of elasticity of 285 to 295 GPa (41 to 43 × 10⁶ psi)
- Thermal expansion coefficient of 7.65 to 9.2 × 10⁻⁶ m/m per °C in the range of 200 to 600 °C (400 to 1100 °F) and 100 to 800 °C (200 to 1500 °F), respectively (Ref 8, 23)
- Density of 7.43 g/cm³ (0.268 lb/in.³)
- Composition with 8.83 wt% B
- Body-centered tetragonal structure with 12 atoms per unit cell
- Lattice parameters: $a = 5.078 \text{ \AA}$ and $c = 4.249 \text{ \AA}$

The solubility of boron in ferrite and austenite is very small (<0.008% at 900 °C, or 1650 °F), according to the iron-boron phase diagram (Ref 27). According to Brown et al. (Ref 28) and Nicholson (Ref 29), the phase diagram exhibits an $\alpha/\gamma/\text{Fe}_2\text{B}$ peritectoid reaction at approximately 912 °C (1674 °F), based on their findings of higher solubility of boron in ferrite than in austenite at the reaction temperature. However, later work revealed a higher solubility of boron in austenite compared to that in ferrite, thereby suggesting the reaction is eutectoid in nature (Ref 30).

Methods to Prevent/Eliminate Dual-Phase FeB/Fe₂B Layers during Pack Cementation Boriding That May Result in Spalling. When steel surfaces are borided using the most common powder pack cementation method, boron

atoms are diffused into the surface of the steel. A large concentration of boron atoms begins to build up just below the surface of the steel and will start diffusing inward. As the boriding process continues, the surface concentration of boron will continue to rise, and boron will continue to diffuse deeper into the substrate. When the boron concentration of a steel surface reaches approximately 33 at.% B, enough boron is present that Fe₂B iron boride compounds will begin to form. Over short periods of time after commencing boriding, a continuous solid surface layer of Fe₂B compound will form. The boride layer that is considered to be most desirable is a single-phase compound layer of Fe₂B. Longer boriding times will lead to deeper layers of Fe₂B iron boride compounds, because higher concentrations of boron will be present at deeper depths below the steel surface.

However, if steel surfaces continue to be borided for longer times to create deeper boride layers, the surface boron concentration will continue to rise as more boron continues to enter into the steel surface. The boron concentration at the surface will begin to approach 50 at.% B, and a different iron boride compound will start to form at the surface where the boron concentrations are highest. This second type of iron boride compound with a higher boron content is FeB. This layer will form right at the surface of the steel and will exist to a depth where the local boron concentrations remain above 50%. At depths where the boron concentration falls below 50 at.% B, an Fe₂B iron boride compound layer will be present. At deeper depths, the boron concentration will fall to below 33%, where no iron boride compounds will be present beyond that depth.

When very long cycle times or high boriding temperatures are employed to create a very deep boride layer thickness, it will result in large amounts of boron being diffused into the surface. At some point during deeper boriding processes, a transition may occur where the boride layer will change from a single-phase iron boride layer of Fe₂B into a two-phase compound layer with both FeB present at the surface and Fe₂B present at deeper depths below the surface. The single-phase Fe₂B layer is desirable, because as the parts cool down from the boriding process temperature, the Fe₂B layer will contract more rapidly than the steel substrate, and at room temperature, it will be under compressive residual stress. Two-phase boride layers are undesirable because the FeB layer will not contract as rapidly as either the Fe₂B or the substrate as the parts are cooled from the boriding process temperature, and the FeB layer will be in a state of tensile compressive stress. Because Fe₂B and FeB compounds have different thermal expansion coefficients and contract at different rates during cooling, it is common to observe cracking between the two layers, and the outer FeB layer will often spall or fracture off the surface (Fig. 8). Sometimes, this cracking will occur immediately

after the parts are cooled, and spalling will be observed as shiny, clean, silver spots where the boride layer breaks off the steel surface after boriding. Other times, it will not crack or spall right away, but as the parts are stressed or put under strains during handling or in service, the FeB layer will start to crack off the surface very easily.

One other factor that can affect the ease of dual-phase layer creation is the base alloy selection. Higher-alloy-content steels have a lower boron diffusivity rate and will generally slow down boron diffusion toward the core, resulting in more boron remaining near the surface. This means that the higher-alloy steels will typically exhibit FeB beginning to form earlier, because the boron atoms remain near the surface and will have shallower total boride layer depths at the point where FeB begins to form. Many plain carbon steels may be borided to have 0.10 to 0.15 mm (0.004 to 0.006 in.) deep layers before FeB begins to form at the surface. Sometimes, low- to medium-alloy-content steels may be borided to only 0.05 to 0.10 mm (0.002 to 0.004 in.) boride layer depths before FeB forms at the surface. Tool steels are typically boronized to only 0.025 to 0.05 mm (0.001 to 0.002 in.) boride layer depth to avoid FeB formation. Highly alloyed materials, such as stainless steels, are extremely difficult to boride because FeB forms at the surface almost immediately, due to boron remaining near the surface and diffusing much more slowly into the material. These highly alloyed materials are very prone to spalling problems after boriding. On highly alloyed materials, only very shallow boride layers are recommended, to reduce the possibility of spalling problems. Some of the best candidate materials for boriding are plain carbon or low-alloy steels, which are beneficial because these materials are typically lower-cost steels as well.

One problem with powder-pack boriding processes is that the parts are in the boriding powders during the entire process, and the rate of boron flux into the surface and the activity of boron in the powder pack cannot be adjusted or slowed down during the latter portions of the process. One remedy that can be employed is vacuum or salt bath annealing the parts after boriding, to allow for further diffusion of boron toward the core of the material without adding more boron to the surface (Ref 25, 26). Annealing the steel components after boriding can allow for additional boron diffusion toward the core to reduce the surface concentration of boron. This practice can be employed to dissolve any FeB compounds and allow them to transform back into a single-phase layer of Fe₂B. However, it can cause other problems because there is a volume difference between the two iron boride compounds, and as FeB is converted into Fe₂B, it can leave voids in the layer due to volume contraction. The other problem with this remedy is that sometimes the cracks and spalling occur immediately after cooling down from the boriding process, before

the postannealing process can be performed. Hardening of borided steels also allows for additional boron diffusion to occur during subsequent austenitizing treatments that are sometimes employed on borided components.

This problem can also be alleviated by using alternative boriding processes instead of pack cementation boriding. Electrolytic salt bath boriding, electroless salt bath boriding, gas boriding, and fluidized-bed boriding are alternative processes where the components being treated could be borided and then held at austenitizing temperatures to allow further boron diffusion from the surface to occur without the necessity of cooling the parts between the boost and diffusion steps. Pulsed boost and diffuse methods have been developed for electrolytic salt bath boriding to control and limit the boron concentration of the surfaces being treated to prevent FeB formation (Ref 26).

A final remedy that can be performed to reduce the possibility of producing dual-phase boriding layers is the use of boriding powders with lower boron activity, which will effect lower flux rates of boron into the surfaces of the steel at a given boriding temperature without reducing the diffusion rates of boron through the austenite. Because many variations of boriding powders have been developed, it is possible to design boriding powders that will boride more slowly. Lowering the concentration of boron sources in a boriding powder such as B_4C will result in slower boriding rates and reduce the potential for forming the FeB phase.

One other factor that can affect boride layer development is the geometry of the components being treated. Components with sharp edges or corners can have elevated surface concentrations of boron due to boron fluxing into the substrate from multiple angles. Elevated boron concentration at sharp corners can result in two-phase FeB/Fe₂B boride layers in these localized spots, where sharp edges and corners will become more prone to spalling (Fig. 9, 10). Care must be taken in treating parts with sharp corners or edges, such as cutting tools, to avoid deeper boride layers, because cutting edges may spall off if a two-phase layer exists. Chamfering or rounding any sharp edges or square corners prior to boriding is recommended, to assist in preventing spalling at those sharp edges. Masking one side of sharp corners to stopoff the boriding from one face or selectively paste boriding only one face can also assist in preventing the formation of deep boride layers with dual-phase layers prone to spalling.

Ultimately, the best practice to ensure that a single-phase Fe₂B layer is produced is to limit the boride layer thickness for each material to depths where it is known that a single-phase boride layer can be produced. Thin boride layers have been proven to be very effective in dramatically improving the wear and service life of many components. In many cases, it is unnecessary to attempt to produce thicker boride layers, which can actually degrade the

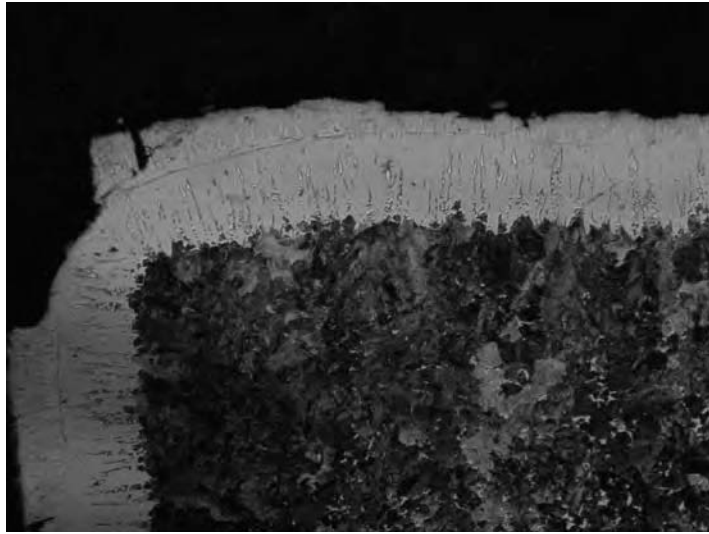


Fig. 9 Spalling of a dual-phase FeB and Fe₂B boride layer at a corner of AISI 1045 steel where outer portion of boride layer is cracking off the surface of the corner. (borided at 927 °C, or 1700 °F, for 6h) 100×

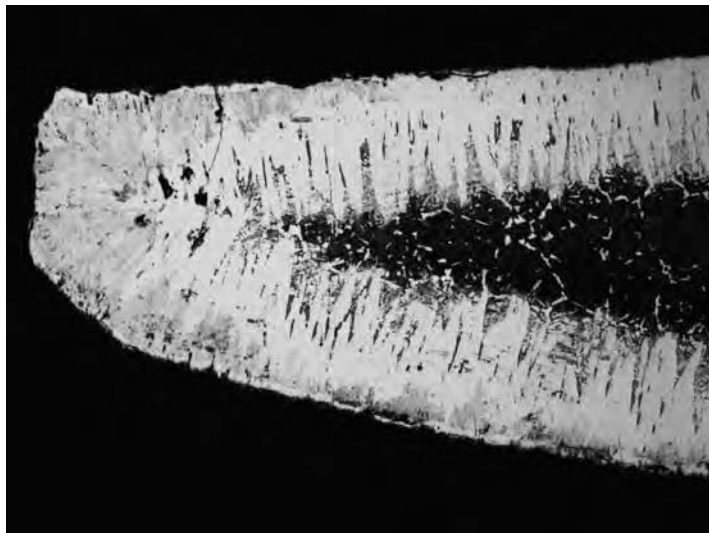


Fig. 10 Oversaturation of boride layer with FeB phase present at tip of an AISI 4130 cutter blade. Cracking of the tips is observed on part surfaces and in microstructure.

wear performance of the boride layer. Thicker boride layers may not always perform as well as a thinner boride layer, due to problems with dual-phase layer formations and spalling of the FeB.

Ferrous Materials for Boriding. With the exception of aluminum- and silicon-bearing steels, boriding can be carried out on most ferrous materials, such as plain carbon, alloy, structural, tool, stainless, and cast steels; commercially pure iron; gray and ductile cast irons; and sintered iron (Ref 31, 32). Because boriding is conducted in the austenitic range, air-hardening steels may be simultaneously borided and hardened by air cooling after boriding. Water-hardening grades are not generally

borided because of the susceptibility of the boride layer to thermal shock during subsequent hardening operations. Oil-hardening and salt-hardening processes have been successfully performed after boriding on many plain carbon and low-alloy steels without cracking the boride layers. Similarly, resulfurized and leaded steels should not be used because they have a tendency toward case spalling and case cracking. Nitrided steels should not be used because of their sensitivity to cracking (Ref 33). Stainless steels are also not recommended unless the boriding process can be controlled to produce only single-phase boride layers of Fe₂B, which can be difficult and usually allows for only very thin boride layers to be created.

Influence of Alloying Elements. The mechanical properties of the borided alloys depend strongly on the composition and structure of the boride layers. The characteristic sawtooth configuration of the boride layer is dominant with pure iron, unalloyed low-carbon steels, and low-alloy steels. As the alloying element and/or carbon content of the substrate steel is increased, the development of a jagged boride/substrate interface is suppressed, and for high-alloy steels a smooth interface is formed (Ref 34, Fig. 1). Alloying elements mainly retard the boride layer thickness (or growth) caused by restricted diffusion of boron into the steel, because alloying elements act as a diffusion barrier. Figure 11 shows the effect of alloying additions in steel on boride layer thickness (Ref 35, 36). In highly alloyed steels, alloying elements will slow the diffusivity of boron in austenite, preventing it from easily diffusing inward. The slower diffusion of boron inward creates higher concentrations of boron near the surface of these highly alloyed steels. This explains why dual-phase boride layers with boron-rich FeB compounds precipitating at the surface are observed after shorter boriding cycles with shallower total boride layer depths in higher-alloyed steels compared to low-alloy or plain carbon steels. Plain carbon and low-alloy steels are some of the best materials for boriding because they can form deeper boride layers before FeB precipitates begin to form at the surface.

Carbon does not dissolve significantly in the boride layer and does not diffuse through the boride layer. During boriding, carbon is driven (or diffused away) from the boride layer to the matrix and forms, together with boron,

borocementite, $\text{Fe}_3(\text{B,C})$ (or, more appropriately, $\text{Fe}_3(\text{B}_{0.67}\text{C}_{0.33})$ in the case of Fe-0.08% C steel), as a separate layer between Fe_2B and the matrix (Ref 37, 38).

Like carbon, silicon and aluminum are not soluble in the boride layer, and these elements are pushed from the surface by boron and are displaced ahead of the boride layer into the substrate, forming iron silicoborides— $\text{FeSi}_{0.4}\text{B}_{0.6}$ and Fe_3SiB_2 —underneath the Fe_2B layer. Steels containing high contents of these ferrite-forming elements should not be used for boriding because they reduce the wear resistance of the normal boride layer (Ref 1); they produce a substantially softer ferrite zone beneath the boride layer than that of the core (Ref 39). At higher surface pressure, this type of layer buildup results in the so-called “eggshell” effect; that is, at greater thicknesses, an extremely hard and brittle boride layer penetrates into the softer intermediate layer and is consequently destroyed (Ref 40).

A reduction in both the degree of interlocking tooth structure and the boride depth can occur with high-nickel-containing steels. Nickel has been found to concentrate below the boride layer; it enters the Fe_2B layer and, in some instances, promotes the precipitation of Ni_3B from the FeB layer (Ref 11, 41–43). It also segregates strongly to the surface from the underlying zone corresponding to the Fe_2B layer. This is quite pronounced in both Fe-14Ni and austenitic stainless steels. Consequently, gas boriding of austenitic stainless steels appears to be a more appropriate treatment for producing a low-porosity, homogeneous, single-phase Fe_2B layer because of the lower boron activity of the gaseous mixture (Ref 43).

Chromium considerably modifies the structure and properties of iron borides. As the chromium content in the base material increases, progressive improvements in the following effects are observed: formation of boron-rich reaction products, decrease in boride depth, and flattening or smoothening of the coating/substrate interface (Ref 44). A reduction of boride thickness has also been noticed in ternary Fe-12Cr-C steels with increasing carbon content (Ref 43). Manganese, tungsten, molybdenum, and vanadium also reduce the boride layer thickness and flatten out the tooth-shaped morphology in carbon steel. The distribution of titanium, cobalt, sulfur, and phosphorus in the boride layer has not been well established.

Heat Treatment after Boriding. Borided parts can be hardened in air, oil, salt bath, or polymer quenchant and subsequently tempered. Austenitizing should be carried out in an oxygen-free protective atmosphere or in a neutral salt bath (Ref 8). Any atmospheres containing ammonia should be strictly avoided, because nitrogen additions to the boride layer can render the boride layers extremely brittle as boron nitride compounds form.

Boriding of Nonferrous Materials

Nonferrous materials such as nickel-, cobalt-, and molybdenum-base alloys as well as refractory metals and their alloys and cemented carbides can be borided. Copper cannot; therefore, it provides a good masking agent for boriding. It should be noted that when boriding of nonferrous materials is performed, different metal-boride compounds will be formed instead of FeB and Fe_2B . Boriding of nickel alloys is reported to form Ni_2B , Ni_3B , and Ni_4B_3 boride compound layers. Boriding of titanium alloys will form TiB and Ti_2B boride compound layers. Boriding of cobalt will form CoB, Co_2B , and Co_3B (Table 1). Boriding of nickel, titanium, and cobalt alloys has been performed by industry for special applications.

Boriding of nickel can be performed by gas boriding, powder-pack boriding, salt bath boriding, and fluidized bed. It has been done in a gaseous $\text{BCl}_3\text{-H}_2\text{-Ar}$ mixture in the temperature range of 500 to 1000 °C (930 to 1830 °F) (Ref 9), whereas Permalloy is pack borided with 85% B_4C and 15% Na_2CO_3 or 95% B_4C and 5% $\text{Na}_2\text{B}_4\text{O}_7$ powder mixture at 1000 °C (1830 °F) for 6 h in H_2 atmosphere. Nickel boride layers are much harder than iron boride layers, with microhardness values typically ranging from 1700 to 2000 HV on many grades (Ref 9). Nickel boride layers are also more brittle and prone to spalling than iron boride layers. Boriding of nickel-base superalloys is typically performed with very thin boride layer depths (5 to 15 μm , or 0.2 to 0.6 mil), because thicker boride layers are more prone to spalling.

Boriding of titanium and its alloys has been performed using gas boriding, powder-pack cementation, salt bath boriding, and fluidized

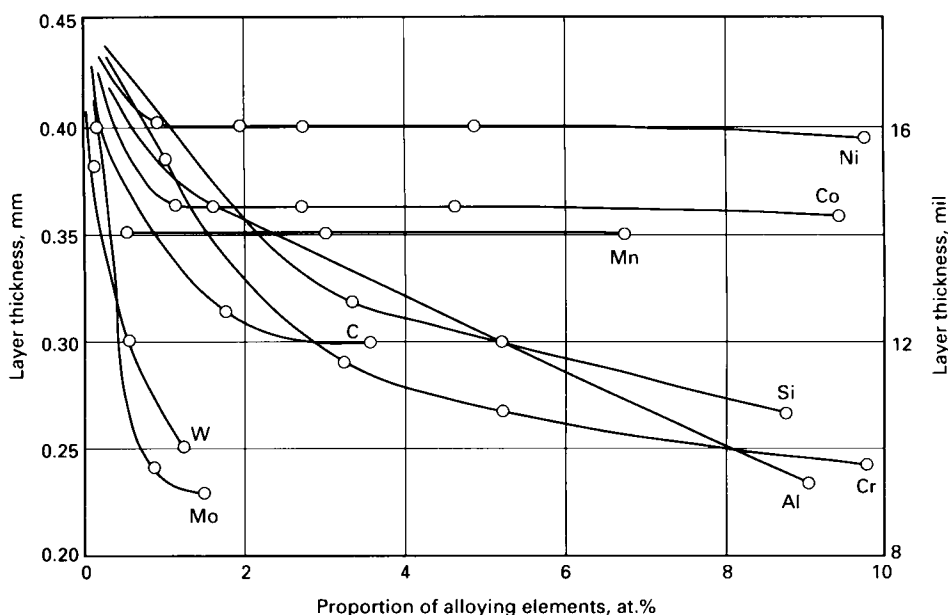


Fig. 11 Effect of alloying elements in steel on boride layer thickness. Source: Ref 35, 36

bed. Because titanium is more sensitive to reactions with oxygen, boriding must be performed in an ultrapure, oxygen-free environment to form high-quality TiB and Ti₂B boride layers. Pack boriding in oxygen-free amorphous boron in combination with high-vacuum (0.0013 Pa, or 10⁻⁵ torr) and high-purity argon atmosphere or gas boriding with H₂-BCl₃-Ar gas mixture is preferred. Boriding of titanium has also been successfully performed in a fluidized bed using argon gas as the fluidizing gas and B₄C and halogen-containing boriding powder in the bed (Ref 45). Electrolytic salt bath boriding has also been successfully performed on titanium alloys, where the bath is free from oxygen. The microhardness readings of boride layers formed on titanium and refractory metals are very high compared to those formed on cobalt and nickel (Table 1). Boride layers formed on tantalum, niobium, tungsten, molybdenum, and nickel do not exhibit tooth-shaped morphology as with titanium.

Thermochemical Boriding Techniques

Because extensive investigations have been carried out on boriding of ferrous materials, the following techniques focus mainly on the boriding of ferrous materials.

Pack Cementation Boriding

Pack cementation boriding (Ref 46–48) is the most widely used boriding process in industry because of its relative ease of handling, safety, the ability to change the composition of the powders, the need for limited equipment, and the resultant economic savings (Ref 1). The process involves packing parts in a boriding powder mixture contained in a 3 to 5 mm (0.1 to 0.2 in.) thick, heat-resistant steel box so that surfaces to be borided are covered with an approximately 10 to 20 mm (0.4 to 0.8 in.) thick layer of boriding powder. Many different boriding compounds have been used for pack boriding. They include solid boron-yielding substances, diluents, and activators.

The common boron-yielding substances are boron carbide (B₄C), ferroboration, and amorphous boron; the last two have greater boron potential, provide a thicker layer, and are more expensive than B₄C (Ref 48). Silicon carbide (SiC) and alumina (Al₂O₃) serve as diluents, and they do not take part in the reaction. However, SiC controls the amount of boron and prevents caking of the boriding agent. The compounds NaBF₄, KBF₄, (NH₄)₃BF₄, NH₄Cl, Na₂CO₃, BaF₂, and Na₂B₄O₇ are boriding activators.

Typical compositions of commercial solid boriding powder mixtures include:

- 5% B₄C, 90% SiC, 5% KBF₄
- 50% B₄C, 45% SiC, 5% KBF₄

- 85% B₄C, 15% Na₂CO₃
- 95% B₄C, 5% Na₂B₄O₇
- 84% B₄C, 16% Na₂B₄O₇
- Amorphous boron (containing 95 to 97% B)

The parts conforming to the shape of the container are packed (Fig. 12) and covered with a lid, which rests inside the container and is weighted with an iron slug or stone to ensure an even trickling of the boriding agent during the boriding treatment. It is then heated to the boriding temperature in an electrically heated box or pit furnace with open or covered heating coils or a muffle furnace for a specified time. The container should not exceed 60% of the furnace chamber volume. In principle, boriding should be accomplished in such a way that high internal stresses are relieved, which, in turn, eliminates cracks or spalling. With the packing process, the powder may be reused by blending with 20 to 50 wt% of fresh powder mixture. In this case, the powder should be discarded after five or six cycles.

Environmental Concerns with Pack Cementation Boriding. Many of the boriding powder mixtures use a halide-containing activator. One problem with pack cementation boriding is that these halide-containing activators melt and/or vaporize at the boriding temperatures. Compounds of fluorine and chlorine are released as vapors as the powder packs are heated to the boriding process temperatures. Typical by-products of heating boriding powders are BF₃, BCl₃, fluorine (F₂), and/or chlorine (Cl₂), which can be highly toxic and/or carcinogenic; however, they also play an important role in the boriding process because they react with the metal surfaces to transfer boron to the substrate. Additionally, hydrofluoric acid (HF) and hydrochloric acid (HCl) vapors can be formed when the emitted gases react with atmospheres, such as hydrogen,

endothermic gas, exothermic gas, or air, after the vapors exit the powder pack. If large quantities of boriding powder are to be used, both indoor and outdoor air-quality testing should be performed to ensure that all boriding gaseous emissions do not pose a threat to worker safety or exceed legal limits for emissions to the environment. A gas-capture system with a wet or dry scrubber system is recommended to treat and neutralize all the acid and toxic gas before emitted gases are released. Concerns for the by-product fluorine (F₂) include:

- Toxic
- Occupational Safety and Health Administration (OSHA) permissible exposure limit (PEL) of 0.1 ppm time-weighted average (TWA)
- Immediately dangerous to life and health limit of 25 ppm

Concerns for the by-product hydrofluoric acid (HF) include:

- Highly corrosive and toxic
- OSHA PEL of 3 ppm TWA
- National Institute for Occupational Safety and Health short-term exposure limit of 6 ppm

Additionally, the emitted gases from boriding processes may attack and degrade the brickwork inside a furnace, along with ductwork that the fumes may contact. The fumes from boriding processes are also known to form glassy deposits on metal components inside the furnace, such as boriding retorts, hearth rails, radiant tubes, and other components, if any air, water vapor, or oxygen is present in the furnace.

Case Depth. The thickness of the boride layer depends on the substrate material being processed, boron potential of the boriding compound (Fig. 13), boriding temperature, and time (Fig. 14). In ferrous materials, the heating rate, especially between 700 °C (1300 °F) and the boriding temperature (800 to 1000 °C, or 1470 to 1830 °F), should be high in order to minimize the formation of FeB (Ref 8).

It is usual practice to match the case depth with the intended application and base material. As a rule, thin layers (for example, 15 to 20 μm, or 0.6 to 0.8 mil) are used for protection against adhesive wear (such as chipless shaping and metal-stamping dies and tools), whereas thick layers are recommended to combat erosive wear (for example, extrusion tooling for plastics with abrasive fillers and pressing tools for the ceramic industry). The commonly produced case depths are 0.05 to 0.25 mm (0.002 to 0.010 in.) for low-alloy and low-carbon steels and 0.025 to 0.076 mm (0.001 to 0.003 in.) for high-alloy steels. However, case depths >0.089 mm (>0.0035 in.) are uneconomical and produce dual-phase boride layers in highly alloyed materials such as stainless steels and some tool steels (Ref 33).

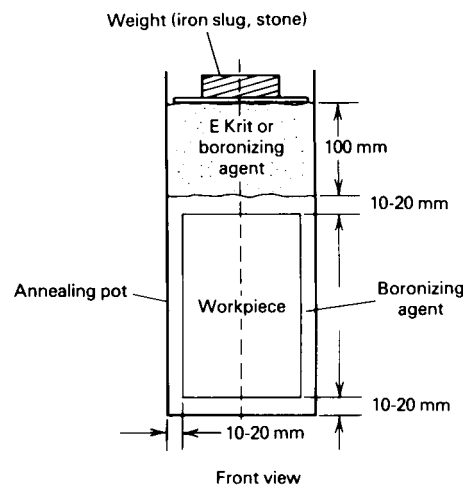


Fig. 12 Diagram of the packing of a single geometrical part in a pack boriding box. Source: Ref 1

Other Boriding Processes

Paste boriding is used commercially when pack boriding is difficult, more expensive, or only selective boriding of certain surfaces of a workpiece is desired while leaving the balance of the component untreated. In this process, a paste of 45% B₄C (grain size 200 to 240 μm, or 8 to 9 mils) and 55% cryolite (Na₃AlF₆, flux additive, Ref 6), or conventional boriding powder mixture (B₄C-SiC-KBF₄) in a good binding agent (such as nitrocellulose dissolved in butyl acetate, aqueous solution of methyl cellulose, or hydrolyzed ethyl silicate), is repeatedly applied (that is, brushed or sprayed) at intervals over the entire or selected portion of parts until, after drying, a layer approximately 1 to 2 mm (0.04 to 0.08 in.) thick is obtained. Subsequently, the ferrous materials are heated inductively, resistively, or in a conventional furnace to 800 to 1000 °C (1470 to 1830 °F) for several hours. In this process, a protective atmosphere (for example, argon, cracked NH₃, or N₂) is necessary. Endothermic gas atmospheres should not be used for paste boriding because the boriding process will be disrupted due to reactions between the endothermic gas and the boriding vapors formed by the boriding paste. A layer in excess of 50 μm (2 mils) thickness may be obtained after inductively or resistively heating to 1000 °C (1830 °F) for 20 min (Fig. 15). This process is of special interest for large components or for those requiring partial (or selective) boriding (Ref 8).

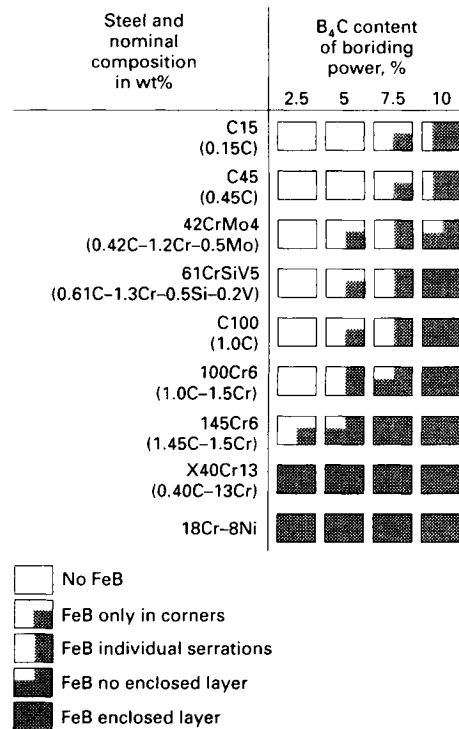


Fig. 13 Diagram showing the influence of B₄C content of the boriding powder on the proportion of FeB phase in the boride layer of various steels borided with pack powder at 900 °C (1650 °F) for 5 h. Source: Ref 11

Liquid boriding is grouped into electroless and electrolytic salt bath processes. These processes have several advantages and disadvantages. The advantages include:

- Both electroless and electrolytic salt bath boriding can be performed without the use of halide-containing chemicals, meaning that the processes will not emit harmful fumes of fluorine, HF, BF₃, chlorine, HCl, and BCl₃ common to powder-pack cementation boriding.
- Single-phase layers of Fe₂B are more readily formed because the boron potential of the electrolytic salt bath can be pulsed on and off to allow additional diffusion of boron toward the core for periods of time without additional boron being added to the surface (Ref 26).
- Direct quenching is possible from boriding salt baths, which is not possible using

powder-pack cementation boriding for parts that require higher core hardness. Powder-pack boriding requires slow cooling of the treated components, cleaning, and then reautenitizing in a protective atmosphere prior to quenching.

- Electrolytic salt bath boriding can be used to form thick boride layers in very short treatment times, although care must be taken to prevent FeB formation that can occur with high boriding rates (Ref 26).

The disadvantages include:

- Removal of excess salt and unreacted boron is essential after the treatment; this step may prove to be expensive and time-consuming and can lead to premature rusting of components after treatment due to exposure to salts.

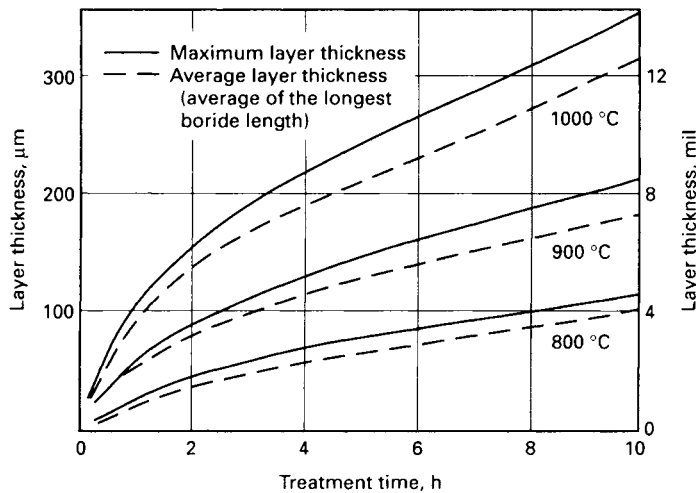


Fig. 14 Effect of pack boriding temperature and time on the boride layer thickness in a low-carbon (Ck 45) steel. Source: Ref 31, 32

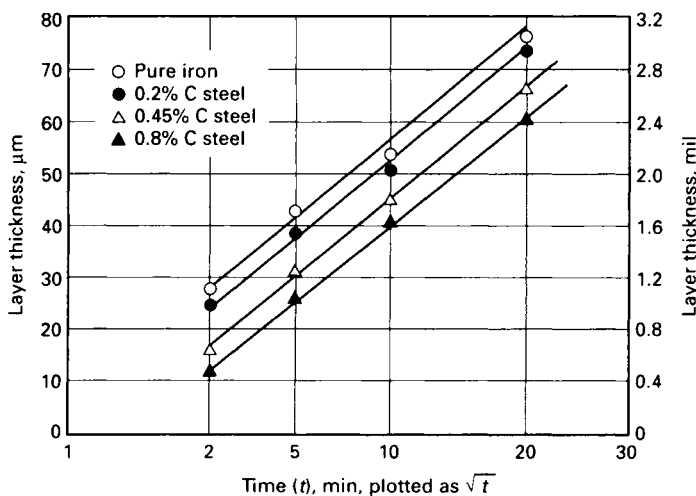


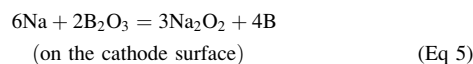
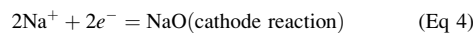
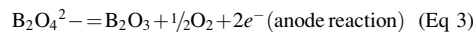
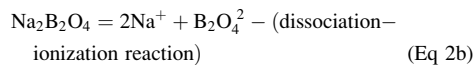
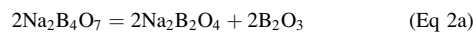
Fig. 15 Linear relationship between boride layer thickness versus square root of time (\sqrt{t}) for iron and steel boronized with B₄C-Na₂B₄O₇-Na₃AlF₆-base paste at 1000 °C (1830 °F). Source: Ref 46

- Maintaining a constant chemistry of the boriding salt baths over time is difficult, because testing is not a simple process and the salt bath may require periodic rectification at frequent intervals as the boriding agents become consumed.
- To achieve boriding reproducibility, bath viscosity is not allowed to increase. This is done by recharging with salt, which involves high maintenance costs.
- In some situations, protection from corrosive fumes may be required.
- In electrolytic salt bath boriding, fixturing design must incorporate good electrical connections, which must be maintained over time.
- In electrolytic salt bath boriding, the surface areas of the anodes and cathodes (workpieces) must be known in order to calculate required amperage settings for each load, such that a desired current density (A/in.²) is generated. As different load sizes and workpiece geometries are being treated, the surface areas of the loads must be calculated or known in order to select different current settings for each load configuration, such that each load can be processed at the optimum current density setting (Ref 26).
- Specialized salt bath furnaces that can withstand the high melting temperatures and corrosive attacks on refractory materials associated with molten borax salt must be constructed.

Electroless salt bath boriding of ferrous materials is carried out in a borax-based melt at approximately 900 to 950 °C (1650 to 1750 °F), to which about 30 wt% B₄C is added (Ref 49). The boriding action can be further improved by replacing up to 20 wt% B₄C with ferroaluminum, because it is a more effective reductant. However, superior results have been found by using a salt bath mixture containing 55% borax, 40 to 50% ferroboration, and 4 to 5% ferroaluminum (Ref 50). It has also been shown that 75:25 KBF₄-KF salt bath can be used at temperatures below 670 °C (1240 °F) for boriding nickel alloys, and at higher temperatures for ferrous alloys, to develop the desired boride layer thickness.

Electrolytic Salt Bath Boriding. In this process, the ferrous part acting as the cathode and a graphite anode are immersed in the electrolytic molten borax at 900 to 1010 °C (1650 to 1850 °F), with typical treatment times that can range from 5 min to 4 h and using a current density of approximately 0.15 A/cm² (1.0 A/in.²) (Ref 26, 51). The parts are then air cooled. In general, the parts are rotated during the treatment to obtain a uniform layer. A high current density produces a thin coating on low-alloy steels in a short time. For high-alloy steels of greater thickness, lower current densities are required for a longer time (Ref 26, 52). According to Kartal et al.

(Ref 53), the formation of boride layers in either electrochemical or thermochemical boriding (e.g., paste, liquid, pack, or spark plasma sintering) is essentially identical. The main diversity of these two boriding techniques is the manner of boron reduction; in electrochemical boriding, the formation of atomic boron on the cathode (substrate) is suggested to take place as a sequence of reactions (Eq 2–5); whereas, in thermochemical boriding, the atomic boron on the substrate is produced as a result of the chemical reactions between the boron sources (B₄C, or borax, etc.) and the reducing agents (SiC, or ferrosilicon, etc.). The following step is the adsorption and subsequent diffusion of atomic boron into the interstitial sites to grow iron borides (Fe₂B and FeB) in accordance with the amount of penetrated boron as a function of process time and temperature as well as the composition of the steel substrate (Ref 53):



Although saturation of the cathode surface with adsorbed boron atoms is the direct function of the applied current in electrochemical boriding, beyond a certain value of critical current density (CCD) at which the surface of the sample is fully occupied with boron atoms, the thickness of the boride layer becomes independent from the increase in current density. The CCD (or limiting current density) has been found to occur at 0.2 A/cm² (1.3 A/in.²) (Ref 53).

Other satisfactory electrolytic salt bath compositions include:

- KBF₄-LiF-NaF-KF mixture for parts to be treated at 600 to 900 °C (1100 to 1650 °F) (Ref 52)
- 20KF-30NaF-50LiF-0.7BF₂ mixture (by mol%) at 800 to 900 °C (1470 to 1650 °F) in 90N₂-10H₂ atmosphere
- 9:1 (KF-LiF)-KBF₄ mixture under argon atmosphere (Ref 54)
- KBF₄-NaCl mixture at 650 °C (1200 °F) (Ref 55)
- 90(30LiF + 70KF)-10KBF₄ mixture at 700 to 850 °C (1300 to 1560 °F)
- 80Na₂B₄O₇-20NaCl at 800 to 900 °C (1470 to 1650 °F) (Ref 56)

Gas boriding may be accomplished with:

- Diborane (B₂H₆)-H₂ mixture
- Boron halide-H₂/or (75:25 N₂-H₂) gas mixture
- Organic boron compounds such as (CH₃)₃B and (C₂H₅)₃B

Boriding with B₂H₆-H₂ mixture is not commercially viable due to the highly toxic and explosive nature of diborane (Ref 1, 3). When organic boron compounds are used, carbide and boride layers form simultaneously. Because BBr₃ is expensive and difficult to handle (with violent reactions with water), and because BF₃ requires high reduction temperature (due to its greater stability) and produces HF fumes, BCl₃ remains the attractive choice for gas boriding.

When parts are gas borided in a dilute (1:15) BCl₃-H₂ gas mixture at a temperature of 700 to 950 °C (1300 to 1740 °F) and a pressure up to 67 kPa (0.67 bar), a boride layer 120 to 150 μm (5 to 6 mils) thick is reported to be produced at 920 °C (1690 °F) in 2 h (Ref 57). Recent work has suggested the use of 75:25 N₂-H₂ gas mixture instead of H₂ gas for its better performance, because of the production of boride layers with minimum FeB content. The latter phase can be easily eliminated during the subsequent diffusion treatment before hardening (Ref 58). This process can be applied to titanium and its alloys as well.

Plasma Boriding. Mixtures of both B₂H₆-H₂ and BCl₃-H₂-Ar may be used successfully in plasma boriding (Ref 59, 60). However, the former gas mixture can be applied to produce a boride layer on various steels at relatively low temperatures, such as 600 °C (1100 °F), which is impossible with a pack or liquid boriding process (Ref 61). It has been claimed that plasma boriding in a mixture of BCl₃-H₂-Ar gases exhibits good features, such as better control of BCl₃ concentration, reduction of the discharge voltage, and higher microhardness of the boride films (Ref 62). Figure 16 shows a schematic layout of a plasma boriding facility.

The dual-phase layer is characterized by visible porosity, occasionally associated with a black boron deposit. This porosity, however, can be minimized by increasing the BCl₃ concentration. Boride layers up to 200 μm (8 mils) in thickness can be produced in steels after 6 h treatment at a temperature of 700 to 850 °C (1300 to 1560 °F) and a pressure of 270 to 800 Pa (2 to 6 torr) (Ref 63).

Advantages of this process include:

- Control of composition and depth of the borided layer
- Increased boron potential compared to conventional pack boriding
- Finer plasma-treated boride layers
- Reduction in temperature and duration of treatment

- Elimination of high-temperature furnaces and their accessories
- Savings in energy and gas consumption

The only disadvantage of the process is the extreme toxicity of the atmosphere employed. As a result, this process has not gained commercial acceptance. To avoid the aforementioned shortcoming, boriding from paste (containing a mixture of 60% amorphous boron and 40% liquid borax) in a glow discharge at the impregnating temperature has recently been developed, which is found to greatly increase the formation of the surface boride layer (Ref 64).

Fluidized-Bed Boriding. A recent innovation is boriding in fluidized beds (Fig. 17), which involve bed material of coarse-grained silicon carbide particles, a special boriding powder such as Ekabor WB, and an oxygen-free gas such as N_2 - H_2 mixture (Ref 65). When electricity is used as the heat source, the bed serves as a faster heat-transfer medium. This is usually equipped with quench and tempering furnaces.

This process offers the following advantages:

- High rates of heating and flow, as well as direct withdrawal of the parts, provide shorter operating cycle times (that is, rapid boriding).
- Temperature uniformity with low capital cost and flexibility is ensured.
- A fluidized furnace is very tight because of upward pressure of the gas.
- This process produces reproducibility, close tolerances, and a very uniform finish on mass-produced parts.

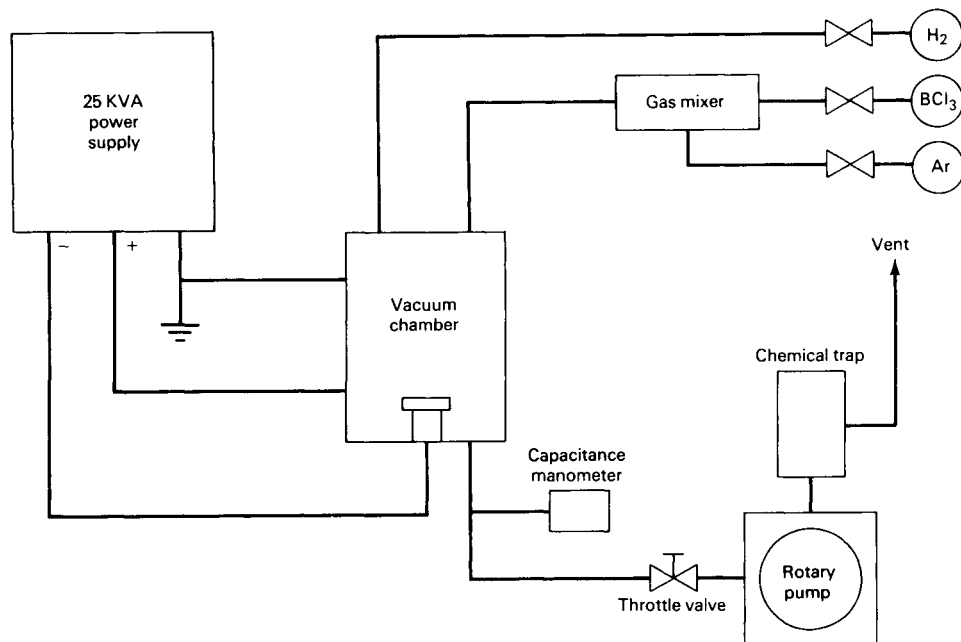


Fig. 16 Layout of plasma boronizing facility. Source: Ref 25

- This process can be adaptable to continuous production and can lend itself to automation as the parts are charged and withdrawn intermittently.
- Quenching (and subsequent tempering) of the parts is possible immediately after this treatment.
- The operating cost is low (due to reduced processing time and energy consumption) for mass production of boronized parts.
- Cleaning problems associated with powder-pack processing, such as powder sintering and bonding to component surfaces, or problems associated with salt bath boriding, such as salt residue removal, are eliminated.

An important disadvantage lies in the continuous flushing of the boriding agent within the retort by the inert gas. The exhaust gases containing enriched fluorine compounds must be cleaned absolutely, for example, in an absorber filled with dry $CaCO_3$ chips, to avoid environmental problems (Ref 40). Alternatively, a pulsed fluidizing process can considerably decrease the amount of exhaust gases (Ref 26, 40).

Multicomponent boriding is a thermochemical treatment involving consecutive or simultaneous diffusion of boron and one or more metallic elements, such as aluminum, silicon, chromium, vanadium, and titanium, into the component surface. This process is carried out at 850 to 1050 °C (1560 to 1920 °F) and involves two steps:

1. Boriding by conventional methods—notably pack, paste, and electrolytic salt bath methods (Ref 66). Here, the presence of FeB is tolerated and, in some cases, may prove

2. Diffusing metallic elements through the powder mixture or borax-based melt into the borided surface. If the pack method is used, sintering of particles can be avoided by passing argon or H_2 gas into the reaction chamber.

There are six multicomponent boriding methods (Ref 3, 66): boroaluminizing, borosiliconizing, borochromizing, borochromtitanizing, borochromvanadizing, and borovanadizing.

Boroaluminizing. When boroaluminizing involves boriding followed by aluminizing, the compact layer formed in steel parts provides good wear and corrosion resistance, especially in humid environments (Ref 8, 36, 66).

Borosiliconizing results in the formation of FeSi in the surface layer, which enhances the corrosion-fatigue strength of treated parts (Ref 68).

Borochromizing (involving chromizing after boriding) provides better oxidation resistance than boroaluminizing, the most uniform layer (probably comprising a solid-solution boride containing iron and chromium), improved wear resistance compared with traditionally borided steel, and enhanced corrosion-fatigue strength. In this case, a post-heat-treatment operation can be safely accomplished without a protective atmosphere (Ref 2, 69, 70).

Borochromtitanized structural alloy steel provides high resistance to abrasive wear and corrosion as well as extremely high surface hardness, 5000 HV (15 g load) (Ref 66). Figure 18 shows the microstructure of the case of a borochromtitanized constructional alloy steel part exhibiting titanium boride in the outer layer and iron-chromium boride beneath it.

Borovanadized and borochromvanadized layers are quite ductile, with their hardnesses exceeding 3000 HV (15 g load). This drastically

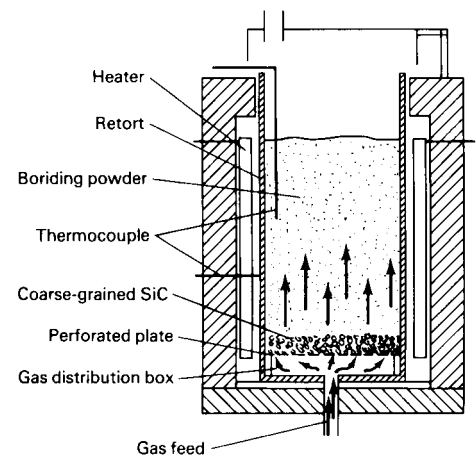


Fig. 17 Diagram of a fluidized bed for boriding. Source: Ref 4, 5

Table 3 Multicomponent boriding treatments

Multicomponent boriding technique	Media type	Media composition(a), wt%	Process steps investigated(a)	Substrate(s) treated	Temperature, °C (°F)	Reference
Boroaluminizing	Electrolytic salt bath	3–20% Al ₂ O ₃ in borax	S	Plain carbon steels	900 (1650)	67
Boroaluminizing	Pack	84% B ₄ C + 16% borax	S	Plain carbon steels	1050 (1920)	68
Borochromizing	Pack	97% ferroaluminum + 3% NH ₄ Cl	B-Al	Plain carbon steels	Borided at 900 (1650) Chromized at 1000 (1830)	2
		5% B ₄ C + 5% KBF ₄ + 90% SiC (Ekabor II)	Al-B			
Borosiliconizing	Pack	78% ferrochrome + 20% Al ₂ O ₃ + 2% NH ₄ Cl	S	0.4% C steel	900–1000 (1650–1830)	2
		5% B ₄ C + 5% KBF ₄ + 90% SiC (Ekabor II)	B-Cr			
Borovanadizing	Pack	60% ferrovanadium + 37% Al ₂ O ₃ + 3% NH ₄ Cl	Cr-B	1.0% C steel	Borided at 900 (1650) Vanadized at 1000 (1830)	2
			B-Si			
			Si-B			
			B-V			

(a) S, simultaneous boriding and metallizing; B-Si, borided and then siliconized; Al-B, aluminized and then borided
Source: Ref 3

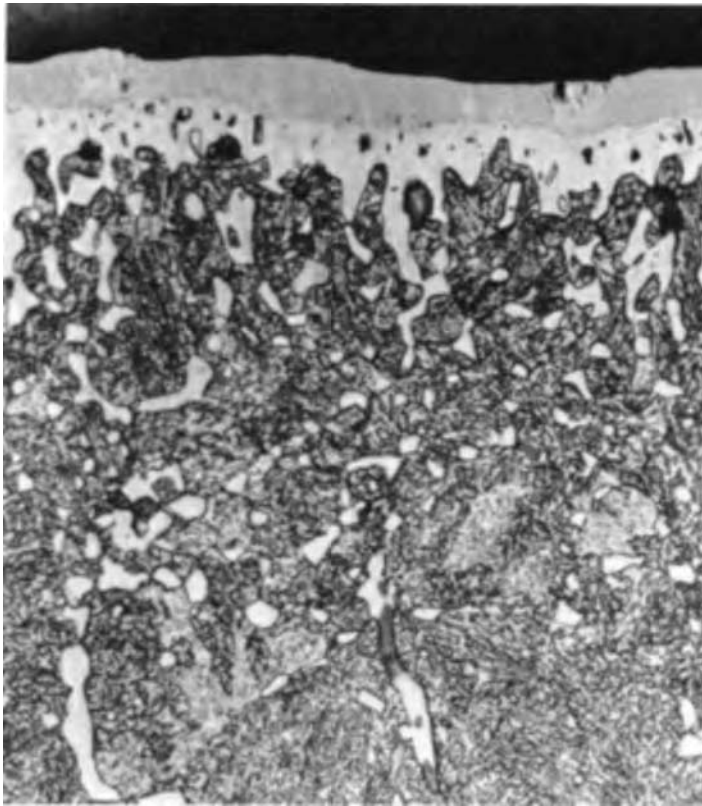


Fig. 18 Microstructure of the case of a borochromtitanized construction alloy steel. Source: Ref 8, 66

reduces the danger of spalling under impact loading conditions (Ref 66).

Applications of Thermochemical Boriding

Presently, borided parts have been used in a wide variety of industrial applications (Table 4) because of the numerous advantageous properties of boride layers. In sliding and adhesive wear situations, boriding is applied to:

- Spinning steel rings, steel rope, and steel thread guide bushings (made of DIN St 37 steel)

- Grooved gray cast iron drums (thread guides) for textile machinery
- Four-holed feed water-regulating valves (made from DIN 1.4571 or AISI 316 titanium steel)
- Burner nozzles, swirl elements, and injector tops for steel oil burners in the chemical industry (Ref 4, 5)
- Drive, worm, and helically toothed steel gears in various high-performance vehicle and stationary engines (Ref 3)
- Ball valves and seats

As abrasive wear-resistance materials, borided stainless steels are used for parts such as screw cases and bushings, perforated and

slotted hole screens, rollers, valve components, fittings, guides, shafts, and spindles. Borided Ti-6Al-4V is used for parts such as leading-edge rotor blade cladding for helicopter applications. Other applications in this category include:

- Agricultural machinery parts
- Ground-engaging tools
- Nozzles of bag-filling equipment
- Extrusion screws, cylinders, nozzles, and reverse-current blocks in plastic production machinery (extruder and injection molding machinery) (Ref 1)
- Bends and baffle plates for conveying equipment for mineral-filled plastic granules in the plastics industry
- Punching dies (for making perforations in accessory parts for cars), press and drawing matrices, and necking rings (made from S1 tool steel)
- Press dies, cutting templates, punched plate screens (made of DIN St 37 steel)
- Screw and wheel gears, bevel gears (from AISI 4317 steel)
- Steel molds (for the manufacture of ceramic bricks and crucibles in the ceramics industry), extruder barrels, plungers and rings (from 4140 steel)
- Extruder tips, nonreturn valves and cylinders (for extrusion of abrasive minerals or glass-fiber-filled plastics, from 4150 steel)
- Casting fillers for processing nonferrous metals (from AISI H11 steel)
- Transport belts for lignite coal briquettes

Borided parts also find applications in die-casting molds; bending blocks; wire draw blocks; pipe clips; pressing and shaping rollers, straightening rollers, engraving rollers, and rollers for cold mills; mandrels; press tools; bushings; guide bars; disks; casting inserts; various types of dies, including cold heading, bending, extrusion, stamping, pressing, punching, thread rolling, hot forming, injection molding, hot forging, drawing, embossing, and so on, in A2, A6, D2, D6, H10, H11, O2, and other tool steels (Ref 48).

Borided steel parts have also been used as transport pipe for molten nonferrous metals

Table 4 Proven applications for borided ferrous materials

Substrate material			Application
AISI	BSI	DIN	
...	...	St37	Bushes, bolts, conveyer tubes, base plates, runners, blades, thread guides
1020	...	C15 (Ck15)	Gear drives, pump shafts
1043	...	C45	Pins, guide rings, grinding disks, bolts
		St50-1	Casting inserts, nozzles, handles
1138	...	45S20	Shaft protection sleeves, mandrels
1042	...	Ck45	Swirl elements, nozzles (for oil burners), rollers, bolts, gate plates
		C45W3	Gate plates
W1	...	C60W3	Clamping chucks, guide bars
D3	...	X210Cr12	Bushes, press tools, plates, mandrels, punches, dies
C2	...	115CrV3	Drawing dies, ejectors, guides, insert pins
		40CrMnMo7	Gate plates, bending dies
H11	BH11	X38CrMoV51	Plungers, injection cylinders, sprue
H13	...	X40CrMoV51	Orifices, ingot molds, upper and lower dies and matrices for hot forming, disks
H10	...	X32CrMoV33	Injection molding dies, fillers, upper and lower dies and matrices for hot forming
D2	...	X155CrVMo121	Threaded rollers, shaping and pressing rollers, pressing dies and matrices
		105WCr6	Engraving rollers
D6	...	X210CrW12	Straightening rollers
S1	~BS1	60WCrV7	Press and drawing matrices, mandrels, liners, dies, necking rings
D2	...	X165CrVMo12	Drawing dies, rollers for cold mills
L6	BS224	56NiCrMoV7	Extrusion dies, bolts, casting inserts, forging dies, drop forges
		X45NiCrMo4	Embossing dies, pressure pad and dies
02	~BO2	90MnCrV8	Molds, bending dies, press tools, engraving rollers, bushes, drawing dies, guide bars, disks, piercing punches
E52100	...	100Cr6	Balls, rollers, guide bars, guides
		Ni36	Parts for nonferrous metal casting equipment
		X50CrMnNiV229	Parts for unmagnetizable tools (heat treatable)
4140	708A42 (En19C)	42CrMo4	Press tools and dies, extruder screws, rollers, extruder barrels, nonreturn valves
4150	~708A42 (CDS-15)	50CrMo4	Nozzle base plates
4317	...	17CrNiMo6	Bevel gears, screw and wheel gears, shafts, chain components
5115	...	16MnCr5	Helical gear wheels, guide bars, guiding columns
6152	...	50CrV4	Thrust plates, clamping devices, valve springs, spring contacts
302	302S25 (EN58A)	X12CrNi188	Screw cases, bushes
316	~316S16 (EN58J)	X5CrNiMo1810 G-X10CrNiMo189	Perforated or slotted hole screens, parts for the textile and rubber industries Valve plugs, parts for the textile and chemical industries
410	410S21 (En56A)	X10Cr13	Valve components, fittings
420	~420S45 (EN56D)	X40Cr13 X35CrMo17	Valve components, plunger rods, fittings, guides, parts for chemical plants Shafts, spindles, valves
Gray and ductile cast iron			Parts for textile machinery, mandrels, molds, sleeves

Source: Ref 4, 5, 31, 32

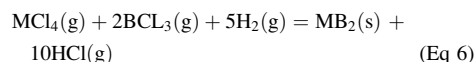
such as aluminum, zinc, and tin alloys (made from DIN St 37), corrosion-resistant transport pipe elbows for vinyl chloride monomer, grinding disks (made from DIN Ck 45), die-casting components, air foil erosion-resistant cladding, data printout components (for example, magnetic hammers, wire printers), and engine tappets (Ref 15).

Boronized Permalloy is used for magnetic head applications. Boronized cemented carbides are used as drawing dies, guiding parts, and dimensional measurement parts. Some examples of multicomponent boriding include improving the wear resistance of austenitic steels (borochromizing), of parts for plastics-processing machines (borochromtitanizing), and of dies used in the ceramics industry (borochromizing) (Ref 66).

Chemical Vapor Deposition

Metal boride coatings or deposition via chemical vapor deposition (CVD) of TiB_2 , ZrB_2 , rare earth borides, and so forth on steel, refractory

metals, and alloys have been made using the following chloride reaction:



Good deposition of some borides is obtained under the conditions listed in Table 5. Among these boride coatings, much research work has been directed toward the deposition of TiB_2 .

The CVD process for the deposition of TiB_2 or ZrB_2 coatings on various substrate materials is carried out by passing a mixture of $TiCl_4$ (or $ZrCl_4$) and BCl_3-H_2 gas mixture over a heated part placed in a vacuum chamber, where the gas decomposes into atomic boron and titanium (or zirconium) and subsequent deposition of TiB_2 (or ZrB_2) occurs at the component surface when the appropriate deposition temperature and gas pressure are maintained (Table 5). It is necessary to adjust the gas flow so that the atomic ratios are:

- B/Ti = 1 to 2 and H/Cl = 6 to 10 for TiB_2
- B/Zr = 1.0, and H/Cl = 20.0 for ZrB_2

It is further noticed that when $B/(B + Cl) = \sim 0.4$, the TiB_2 deposit becomes dense with a {1010} or {1120} preferred orientation, which is often associated with a columnar appearance (Ref 72) and microhardness values of approximately 3300 to 4500 HV (50 g load). For a good, adherent deposit of TiB_2 on steel and cemented carbides, it is desirable to precoat the substrate with corrosion-resistant layers of cobalt and TiC, respectively (Ref 72–74).

Advantages and Applications. This process has several advantages, such as the high purity of the deposit; a relatively high rate of deposition; close chemical composition control; high resistance to thermal shock, erosion, and/or corrosion at elevated temperatures; and large economic savings for the mass production of small parts. As a result, TiB_2 coatings are variously used on cemented carbide cutting inserts (Ref 74), on graphite electrodes in aluminum reduction cells, and on letdown valves in coal conversion reactors (Ref 75, 76). The $ZrBr_2$ coatings on graphite are sometimes used as a spectrally selective surface at elevated temperatures (Ref 77).

Table 5 Chemical vapor deposition conditions for some borides

Boride	Precursors	Temperature		Pressure		After (Ref 71)
		°C	°F	kPa	torr	
HfB ₂	HfCl ₄ -BCl ₃ -H ₂	1400	2550	0.4	3	Gebhardt and Cree (1965)
NbB ₂	NbBr ₅ -BBr ₃	850-1750	1560-3180	0.003-0.025	0.025-0.2	Armas et al. (1976)
Ni-B	Ni(CO) ₄ -B ₂ H ₆ -CO	150	300	87	650	Mullendore and Pope (1987)
SiB ₄	SiH ₄ -BCl ₃ -H ₂	800-1400	1470-2500	6.5-80	50-600	Dirkx and Spear (1984)
SiB _x	SiBr ₄ -BBr ₃	975-1375	1790-2500	0.007	0.05	Armas and Combesure (1977)
TaB ₂	TaBr ₅ -BBr ₃	850-1750	1560-3180	0.003-0.025	0.025-0.2	Armas et al. (1976)
	TaCl ₅ -B ₂ H ₆	500-1025	930-1875	100	760	Randich (1980)
TiB ₂	TiCl ₄ -BCl ₃ -H ₂	1200-1415	2200-2580	0.4-2	3-15	Gebhardt and Cree (1965)
	TiCl ₄ -B ₂ H ₆	600-900	1100-1650	100	760	Pierson and Mullendore (1980)
	TiCl ₄ -BCl ₃ -H ₂	750-1050	1380-1920	100	760	Caputo et al. (1985)
	TiCl ₄ -BCl ₃ -H ₂	1200	2200	6.5	50	Desmaison et al. (1987)
ZrB ₂	ZrCl ₄ -BCl ₃ -H ₂	1400	2550	0.4-0.8	3-6	Gebhardt and Cree (1965)

Source: Ref 71

REFERENCES

- A. Graf von Matuschka, *Boronizing*, Hanser, 1980
- R. Chatterjee-Fischer, *Härt.-Tech. Mitt.*, Vol 36 (No.5), 1981, p 248-254
- P. Dearnley and T. Bell, *Surf. Eng.*, Vol 1 (No. 3), 1985, p 203-217
- W.J.G. Fichtl, "Saving Energy and Money by Boronizing," Paper presented at the meeting of the Japan Heat Treating Association, Nov 25, 1988 (Tokyo)
- W.J.G. Fichtl, "Boronizing and Its Practical Applications," Paper presented at the 33rd Harterei-Kolloquium, Oct 5-7, 1977 (Wiesbaden); *Heat Treat. Met.*, 1983, p 79-80
- A. Galibois, O. Boutenko, and B. Voyzelle, *Acta Metall.*, Vol 28, 1980, p 1753-1763, 1765-1771
- R. Chatterjee-Fischer, *Powder Metall.*, Vol 20 (No. 2), 1977, p 96-99
- R. Chatterjee-Fischer, Chap. 8, in *Surface Modification Technologies*, T.S. Sudarshan, Ed., Marcel Dekker, Inc., 1989, p 567-609
- S. Motojima, K. Maeda, and K. Sugiyama, *J. Less-Common Met.*, Vol 81, 1981, p 267-272
- O. Knotek, E. Lugscheider, and K. Leuschen, *Thin Solid Films*, Vol 45, 1977, p 331-339
- K.H. Habig and R. Chatterjee-Fischer, *Tribol. Int.*, Vol 14 (No. 4), 1981, p 209-215
- D.J. Bak, *New Design News*, Feb 16, 1981, p78
- R. Chatterjee-Fischer and O. Schaaber, *Proceedings of Heat Treatment '76*, The Metals Society, 1976, p 27-30
- W.J.G. Fichtl, *Härt.-Tech. Mitt.*, Vol 29 (No. 2), 1974, p 113-119
- Mater. Eng.*, Aug 1970, p 42
- R.S. Petrova, N. Suwattananont, and V. Samardzic, *J. Mater. Eng. Perform.*, Vol 17 (No. 3), 2008, p 340-345
- B. Venkataraman and G. Sundararajan, The High Speed Sliding Wear Behaviour of Boronized Medium Carbon Steel, *Surf. Coat. Technol.*, Vol 73 (No. 3), 1995, p 177-184
- Y.A. Alimov, *Pham. Chem. J.*, Vol 9 (No. 5), May 1975, p 324-336
- H.C. Child, *Metall. Mater. Technol.*, Vol 13 (No. 6), 1981, p 303-309
- H. Kunst and O. Schaaber, *Härt.-Tech. Mitt.*, Vol 22 (No. 1), Translations HB 7122-I and HB 7122-II, 1967, p 1-25
- M.J. Lu, *Härt.-Tech. Mitt.*, Vol 38 (No. 4), 1983, p 156-159
- W. Liliental, J. Tacikowski, and J. Senatorski, *Proceedings of Heat Treatment '81*, The Metals Society, 1983, p 193-197
- H. Kunst and O. Schaaber, *Härt.-Tech. Mitt.*, Vol 22, Translation HB 7122-III, 1967, p 275-292
- D.N. Tsipas, J. Rus, and H. Noguerra, *Proceedings of Heat Treatment '88*, The Metals Society, 1988, p 203-210
- P.A. Dearnley, T. Farrell, and T. Bell, *J. Mater. Energy Sys.*, Vol 8 (No. 2), 1986, p 128-131
- G. Kartal, S. Timur, V. Sista, O.L. Eryilmaz, and A. Erdemir, *Surf. Coat. Technol.*, Vol 206 (No. 7), Dec 2011, p 2005-2011
- T.B. Massalski, *Binary Alloy Phase Diagrams*, American Society for Metals, 1986
- A. Brown et al., *Metall. Sci.*, Vol 8, 1974, p 317-324
- M.E. Nicholson, *J. Met.*, 1954, p 185-190
- T.B. Cameron and J.E. Morral, *Met. Trans. A*, Vol 17, 1986, p 1481-1483
- W. Fichtl, N. Trausner, and A.G. Matuschka, Boronizing with Ekabor, *Elektroschmelz Kempten, GmbH*
- W. Fichtl, *Oberflächentechn. Metallpraxis*, Vol 11, 1972, p 434
- "Boroalloy Process," Process Data Sheet 4, Lindberg Heat Treating Company
- A.J. Ninham and I.M. Hutchings, *Wear of Materials*, Vol 1, ASME, New York, 1989, p 121-127
- M.E. Blanter and N.P. Bosedin, *Metalloved. Term. Obra. Met.*, Vol 6, 1955, p 3-9
- G.V. Samsonov and A.P. Epik, in *Coatings on High Temperature Materials*, Part I, H.H. Hausner, Ed., Plenum Press, 1966, p 7-111
- J.J. Smit, Deift University of Technology, Laboratory of Metals, unpublished research, 1984
- C.M. Brakman, A.W.J. Gommers, and E.J. Mittemeijer, *Proceedings of Heat Treatment '88*, The Institute of Metals, 1988, p 211-217
- H.C. Fiedler and W.J. Hayes, *Met. Trans. A*, Vol 1, 1970, p 1070-1073
- W.J.G. Fichtl, *Jahr. Oberflachen Tech.*, Vol 45, Metall-Verlag, 1989, p 420-427
- G. Palombarini, M. Carbuicchio, and L. Cento, *J. Mater. Sci.*, Vol 19, 1984, p 3732
- V.I. Pokmurskii, V.G. Protsik, and A.M. Mokrava, *Sov. Mater. Sci.*, Vol 10, 1980, p 185
- P. Goeurist, R. Fillitt, F. Thevenol, J.H. Driver, and H. Bruyas, *Mater. Sci. Eng.*, Vol 55, 1982, p 9-19
- M. Carbuicchio and G. Sambogna, *Thin Solid Films*, Vol 126, 1985, p 299-305
- K.G. Anthymidis and D.N. Tsipas, *J. Mater. Sci. Lett.*, Vol 20, 2001, p 2067-2069
- V.A. Volkov and A.A. Aliev, *Steel USSR*, Vol 5 (No. 3), 1975, p 180-181
- I.N. Kiolin, V.A. Volkov, A.A. Aliev, and A.G. Kucznetsov, *Steel USSR*, Vol 7 (No. 1), p 53-54
- N. Komutsu, M. Oboyashi, and J. Endo, *J. Jpn. Inst. Met.*, Vol 38, 1974, p 481-486
- L.S. Lyakhovich, *Improving the Life of Forming Tools by Chemico-Thermal Treatment*, NIINTI, Minsk, 1971 (in Russian)
- K. Hosokawa, T. Yamashita, M. Veda, and T. Seki, *Kinzoku Hyomen Gitjutsu*, Vol 23 (No. 4), 1972, p 211-216, Translation RTS 7945
- H. Orning and O. Schaaber, *Härt.-Tech. Mitt.*, Vol 17 (No. 3), Translation BISI 3953, 1962, p 131-140
- H.C. Fiedler and R.J. Sieraksi, *Met. Prog.*, Vol 99 (No. 2), 1971, p 101-107
- G. Kartal, O.L. Eryilmaz, G. Krumdick, A. Erdemir, and S. Timur, Kinetics of Electrochemical Boriding of Low Carbon Steel, *Appl. Surf. Sci.*, Vol 257, 2011, p 6928-6934
- A. Bonomi, R. Habersaat, and G. Bienvenu, *Surf. Technol.*, Vol 6, 1978, p 313-319
- V. Danek and K. Matiasovsky, *Surf. Technol.*, Vol 5, 1977, p 65-72
- K. Matiasovsky, M.C. Paucirova, P. Felner, and M. Makyta, *Surf. Coat. Technol.*, Vol 35, 1988, p 133-149
- L.P. Skugorawa, V.I. Shylkov, and A.I. Netschaev, *Metalloved. Term. Obra. Met.*, No. 5, 1972, p 61-62
- F. Hegewaldt, L. Singheaser, and M. Turk, *Härt.-Tech. Mitt.*, Vol 39 (No. 1), 1984, p 7-15

59. E. Filep, Sz. Farkas, and G. Kolozsvary, *Surf. Eng.*, Vol 4, 1988, p 155–158
60. A.M. Staines, *Met. Mater.*, Vol 1, 1985, p 739–745
61. P. Casadesus, C. Frantz, and M. Gantois, *Met. Trans. A*, Vol 10, 1979, p 1739–1743
62. A. Raveh, A. Inspektor, U. Carmi, and R. Avni, *Thin Solid Films*, Vol 108, 1983, p 39–45
63. T. Wierzchon, J. Bogacki, and T. Karpinski, *Heat Treatment of Metals*, 1980.3, p 65
64. S.A. Isakov and S.A. Al'tshuler, *Transl. Metalloved. Term. Obra. Met.*, No. 3, March 1987, p 25–27
65. A.V. Matuschka, N. Trausner, and J. Zeise, *Härt.-Tech. Mitt.*, Vol 43 (No. 1), 1988, p 21–25
66. R. Chatterjee-Fischer, *Met. Prog.*, Vol 129 (No. 5), 1986, p 24, 25, 37
67. S.Y. Pasechnik et al., in *Protective Coatings on Metals*, Vol 4, G.V. Samsonov, Ed., Consultants Bureau, 1972, p 37–40
68. N.G. Kaidash et al., in *Protective Coatings on Metals*, Vol 4, G.V. Samsonov, Ed., Consultants Bureau, 1972, p 149–155
69. G.V. Zemskov et al., *Izv. V.U.Z. Chernaya Metall.*, Vol 10, Translation BISI 15286, 1976, p 130–133
70. R.L. Kogan et al., *Zashch. Pokrytiya Met.*, Vol 10, Translation VR/1103/77, 1976, p 100–102
71. D.G. Bhat, Chap. 2, in *Surface Modification Technologies*, T.S. Sudarshan, Ed., Marcel Dekker, 1989, p 141–208
72. T. Takahachi and R. Kamiya, *J. Cryst. Growth*, Vol 26, 1974, p 203–209
73. H.O. Pierson and A.W. Mullendore, *Thin Solid Films*, Vol 95, 1982, p 99–104
74. K. Voigt and R. Westphal, *Proceedings of the Tenth Plansee Seminar*, Vol 2, Risley Translation 4877, 1981, p 611–622
75. D.G. Bhat, *Surface Modification Technologies*, T.S. Sudarshan and D.G. Bhat, Ed., The Metallurgical Society, 1988, p 1–21
76. H.O. Pierson, in *Chemically Vapor Deposited Coatings*, H.O. Pierson, Ed., The American Ceramics Society, 1981, p 27–45
77. E. Randich, *Thin Solid Films*, Vol 83, 1981, p 393–398

Thermoreactive Deposition/Diffusion Process for Surface Hardening of Steels

Toru (Tohru) Arai, Consultant

Introduction

The thermoreactive deposition and diffusion (TRD) process is a heat-treatment-based method to form coatings, with compacted layers of carbides, nitrides, or carbonitrides, onto some carbon/nitrogen-containing materials, including steels. The coatings can have greater thickness and higher bond strengths to substrates in comparison with coatings produced by chemical vapor deposition (CVD) and especially by physical vapor deposition (PVD).

The TRD coatings are formed due to the strong affinity of carbide-forming elements (CFEs) and nitride-forming elements (NFEs) in coating reagents to the carbon/nitrogen atoms in substrates of the parts to be coated.

The growth of thicker coatings is realized by continuous supply of carbon/nitrogen by thermal diffusion from inside to the substrate surface, caused by the concentration gradient. The degree of affinity to carbon/nitrogen can be judged with free-energy changes for formation of carbides/nitrides.

Carbide-forming elements include titanium, zirconium, hafnium, vanadium, niobium, tantalum, chromium, tungsten, molybdenum, and manganese. All of these elements are also nitride-forming elements. It has been confirmed that carbide and nitride coatings of these elements can be formed on iron-, nickel-, and cobalt-base materials, if a well-considered choice of coating reagents, substrate materials, and process parameters can be employed.

Figures 1 and 2 exhibit the in-depth variation of x-ray intensities of the major elements in carbide/nitride coatings formed on steels. These coatings are almost completely composed of carbon/nitrogen and CFEs/NFEs. Major components of the substrates, such as iron, cannot be observed in the coatings. Furthermore, Fig. 3 clearly exhibits the fact that growth of the carbide coatings begins on the outside surface of the substrate. As shown in Fig. 4, very thick coatings, such as 20 μm (0.8 mil), can easily be formed by selecting substrates that have a large carbon content in the matrix phase at the

coating temperature. For example, gray cast irons and low-alloyed high-carbon steels treated at high coating temperatures have a high bonding strength to substrates that will perform well in practical applications.

The active CFEs/NFEs that can work for formation of coatings are generated from the added CFE/NFE reagents mixed into other reagents. Addition of carbon/nitrogen to the coating reagents is not recommended, because the added carbon/nitrogen in the coating reagents can deteriorate the simplicity of chemical reactions related to formation of active CFEs/NFEs in the reagents. Moreover, it can compel more efforts to retain qualities such as thickness and crystal structures and properties

such as bonding strength and so on. Coatings that are formed only by the reaction between the CFEs/NFEs existing in the coating reagents and the carbon/nitrogen in substrates of the workpieces to be coated can ensure so-called metallurgical bonding. Thus, it is well recognized that the bonding strength of coatings to substrates by TRD is greater than that of PVD and CVD, even with greater thicknesses such as 5 to 20 μm (0.2 to 0.8 mil).

Adding carbon or nitrogen into the parts to be coated is usually not recommended, because there are numerous types of industrial irons and steels that already contain sufficient amounts of carbon. Furthermore, carburizing and nitriding can easily add more carbon/nitrogen to ferrous metals, if it necessary prior to coating.

In the nature of coated layers and their application fields, the TRD process should be classified as a thin hard coating together with CVD and PVD, rather than the typical thermal diffusion processes such as carburizing, nitriding, boriding, and so on. Equipment for TRD

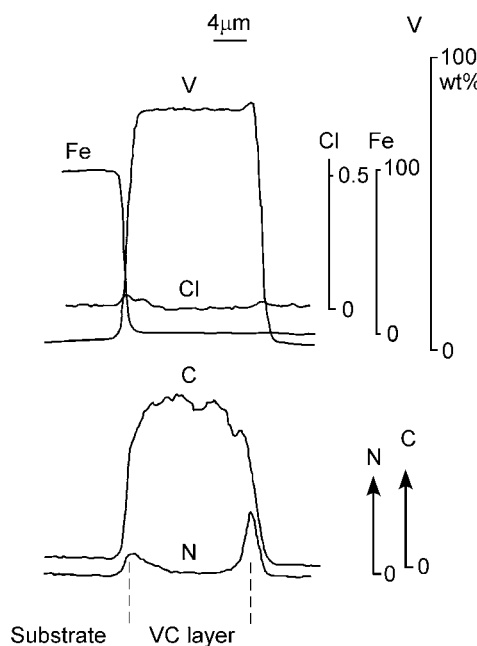


Fig. 1 In-depth variation of x-ray intensity of vanadium, carbon, iron, and other elements in vanadium carbide coatings formed on W1 by high-temperature fluidized beds with the addition of 10 wt% ferrovanadium powders. Coating temperature: 1000 °C (1830 °F); time: 2 h

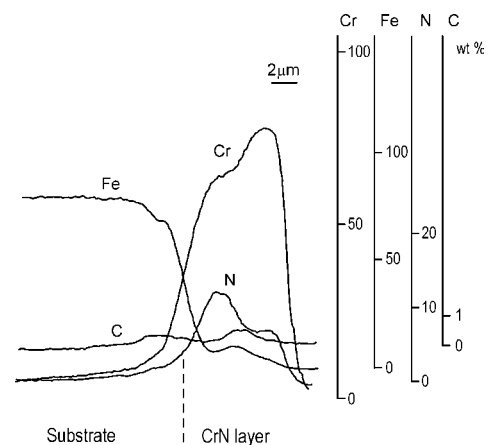


Fig. 2 In-depth variation of x-ray intensity of chromium, iron, nitrogen, and carbon in chromium nitride coatings formed on preliminarily nitrided H13 by low-temperature chloride baths with the addition of 20 wt% Cr powders. Coating temperature: 570 °C (1060 °F); time: 8 h. Preliminary nitriding in salt bath: 570 °C (1060 °F); time: 3.5 h

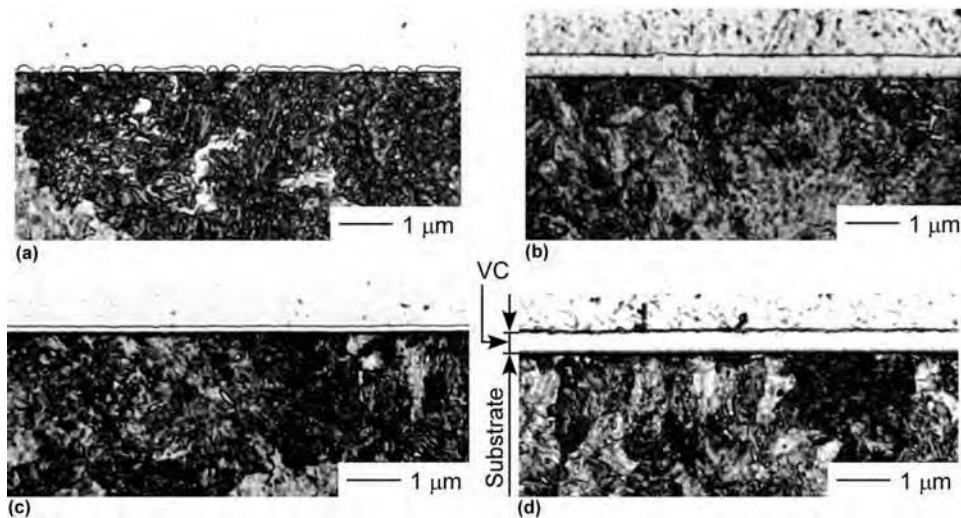


Fig. 3 Optical cross-sectional views of vanadium carbide coatings formed on W1 by high-temperature borax baths with the addition of 20 wt% V pentoxide flakes and 5 wt% boron carbide powders at various temperatures and times. (a) 900 °C (1650 °F), 3 min. (b) 900 °C, 30 min. (c) 1000 °C (1830 °F), 1 min. (d) 1000 °C, 30 min

coating is fundamentally similar to the conventional equipment used for heat treatments, although small modifications are necessary for TRD processing. Therefore, TRD coating equipment is less expensive in comparison with those for carbide/nitride coating by CVD and PVD. Excellent adhesion strength, even with much thicker coatings, and uniform coating thickness, even on narrow, recessed areas, and simultaneous core hardening and so on can be listed as advantages over CVD and PVD.

The TRD process can be performed by use of molten salt bath, fluidized-bed, and pack cementation methods using solid reagent powders. The first productive carbide coating process was developed by Toyota Central Research and Development Labs, Inc., using the borax salt bath immersion method (Ref 1, 2), and practical applications started in 1969 in Japanese industries. The process is therefore popularly called the Toyota diffusion process, the TD process, or the thermal diffusion process. However, the designation of TRD, proposed by the author, is becoming more commonly used, because it faithfully describes the growth mechanism of the coatings, which has been clarified through extensive research. The process has been expanded further by Toyota to the carbide coating and the carbide/nitride coating by use of fluidized beds (Ref 3) and chloride-based low-temperature salt baths. Fluidized-bed carbide coating and low-temperature salt bath nitride coating have been practiced since 1990 and 1996, respectively.

Some papers, published before Toyota's achievements, reported formation of carbide layers by use of salt baths and powder packing, although the quality of the coatings was insufficient for current industrial demands. Most of them (for example, Ref 4) should be in the category of TRD.

Coating Mechanism and Types

If the CFEs and NFEs in coating reagents are kept in contact with workpiece substrates at raised temperatures, they instantaneously bond chemically with carbon/nitrogen at the exposed surfaces to make carbide/nitride grains on the contact surfaces due to large affinity, that is, small free-energy changes for carbide/nitride formation.

The carbide/nitride grains thus formed grow to thick coatings on the substrate surfaces by continuous reaction between the CFEs/NFEs in the coating reagents and the carbon/nitrogen atoms at the surface of the coatings that are successively supplied from deeper levels of the substrates due to thermal diffusion. Hence, the diffusion rate of carbon/nitrogen in substrates is one of the most important factors for the growth rate of coatings. The large diffusion rate of carbon needed to create thick coatings is achieved in the temperature ranges for steel hardening but not in the range for steel tempering. However, nitrogen can diffuse more easily at low temperatures, such that sufficiently thick nitride layers can be created at temperature ranges normally employed for high-temperature tempering for steels. Thus, TRD can produce carbide coatings at austenitizing/hardening temperatures and can produce nitride coatings at the lower subcritical tempering temperatures for steels.

The TRD coating onto nitrided low-carbon steels can produce carbonitride layers at large growth rates because it uses both carbon and nitrogen. Furthermore, it can reduce the possibility of a hardness drop underneath carbide coatings that could be caused by decreased carbon contents. In this manner, the nitride coatings formed at low temperatures should be

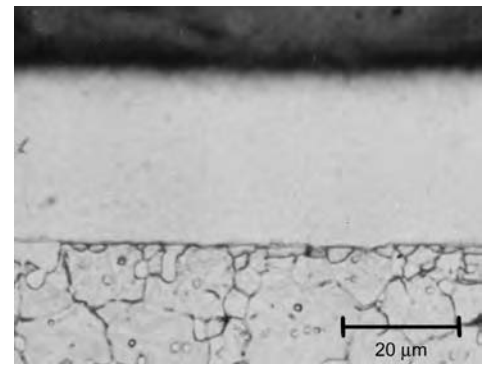


Fig. 4 Optical cross-sectional view of niobium carbide coating with remarkably large thickness formed on D3 by high-temperature borax bath. Coating temperature: 1000 °C (1830 °F); time: 24 h; 10 wt% Fe-Nb powders

strictly referred to as carbonitrides because they can include carbon in addition to nitrogen.

The TRD coating produces layers of carbides, nitrides, and carbonitrides on the substrate metals, such as iron-, nickel- and cobalt-base alloys. The TRD coatings can also be produced on solid carbides and nitrides, such as silicon carbide (SiC) and silicon nitride (Si₃N₄), as long as the CFEs/NFEs in the coating reagents have a larger affinity to carbon/nitrogen than those of the CFEs/NFEs in the substrates (Ref 5). A solid carbon, such as graphite, can have carbide coatings also.

The CFEs/NFEs capable of forming coatings (active CFE/NFE) are available in molten salt and mixtures of the CFEs/NFEs containing material powders and activators, usually halides, that are heated in airtight vessels (powder-packing process) or in fluidized beds (fluidizing-bed process).

Types of Coatings Formed. The carbide and nitride coatings reported to form on carbon/nitrogen-containing metallic materials, such as steels, cobalt alloys, and nickel alloys, can be listed as following:

High-temperature borax baths	Single and alloyed carbides of V, Nb, Ta, Cr, W, Mo Single and alloyed nitrides of V and Nb
High-temperature halide baths	Single and alloyed carbides of Ti, Zr, V, Nb, Ta, Cr, Mo, W, Mn Single and alloyed nitrides of Ti, Zr, V, Nb, Ta, Cr, Mo, W, Mn
High-temperature fluidizing beds and packing boxes	Single and alloyed carbides of Ti, Zr, V, Nb, Ta, Cr, Mo, W, Mn Single and alloyed nitrides of Ti, Zr, Nb, Cr, Mo, W
Low-temperature halide baths	Single and alloyed nitrides of V and Cr
Low-temperature fluidizing beds and packing boxes	Single nitride of Cr and V

Some of the carbide/nitride coatings can take different types of crystal lattices, depending on the ratio of the number of atoms of CFE/NFE and carbon/nitrogen in the coatings, for example, V_2C and VC , $Cr_{23}C_6$ and Cr_7C_3 , V_2N and VN , and Cr_2N and CrN . However, these differences usually do not have any remarkable effect on their performance in practical applications.

The alloyed carbide/nitride coatings (consisting of, for example, vanadium and niobium, vanadium and chromium, or niobium and chromium) can be formed in any coating process. However, it has been confirmed that the compositions of alloyed TRD carbide/nitride coatings, namely, the concentrations of each CFE/NFE, usually change during their growth, as exemplified in Fig. 5, depending on coating temperature and the mixing ratio for the CFE/NFE reagents. Also, the type of CFE/NFE has the largest effect, through the differences in degree of affinity to carbon/nitrogen and the types of crystal lattices of each carbide/nitride (Ref 6, 7).

Multiple coatings of the same and/or different types of carbides are possible, within any combination of vanadium carbide, niobium carbide, and chromium carbide, at least (Ref 8). Remarkably large mixing of the first coating CFEs/NFEs and the second coating CFEs/NFEs during the second coating process has not been observed.

Coatings can grow on CVD TiC layers and PVD TiN layers, although there is a large risk of peeling off caused by the poor adhesion strength of CVD and PVD coatings.

Copper plating can stop the formation of TRD carbide/nitride coatings, because the carbon/nitrogen atoms in the workpiece substrates cannot diffuse through the plating to the surface and react with the CFE/NFE. Therefore, copper plating is employed for localized TRD coating. On the other hand, TRD carbide coatings can grow on nickel-plated and chromium-plated steels. Carbon atoms in the workpiece substrates can easily move to the plating surfaces by thermal diffusion, changing their structures to chromium carbide or carbon-rich nickel.

In a case where the CFE has a relatively weak affinity to carbon, a large diffusion rate, and large solubility limits in substrate metals, such as chromium carbide coating onto low- and medium-carbon steels, the formed coatings consist of both a chromium carbide (outer) and a chromium-iron solid-solution layer (inside), as in the conventional chromizing process (Ref 9, 10).

Also, TRD can make layers of compounds between the CFE and the major elements in substrates, in some cases. Typical examples are $NbNi_3$, VNi_3 , $NbCo_3$, and VCo_3 on nickel- and cobalt-base alloys having relatively small carbon contents. Preliminary carburizing on these alloys can lead to formation of only compacted carbide layers. Quantitative balances of the carbon and elements in substrates should be a major determinant for the types of coatings.

Carbide Coating Nucleation and Growth

Growth on Metallic Phases in Substrates.

At carbide coating temperatures, the structures of plain carbon steels and low-alloy steels consist of mostly austenite and zero to a few percent iron-base carbides, M_3C (Fe_3C). High-carbon, high-alloy steels, on the other hand, are composed of alloy carbides, such as $M_{23}C_6$, M_7C_3 , and MC , as well as austenite. This means that carbon atoms existing in carbide grains cannot be used as easily for carbide formation as the carbon atoms in metallic phases.

The growth of carbide coatings at a very early stage, such as in a few seconds, has been observed by using the salt bath process (Ref 11, 12). Scanning electron microscopy observation of the surface of very thin steel blocks revealed that the coatings of vanadium carbide, niobium carbide, and chromium carbide started to grow in molten borax baths at $820^\circ C$ ($1510^\circ F$) in a very short time, such as 5 s. The carbide grains then grew to thick layers via three steps: primary nucleation and growth of grains smaller than $0.1 \mu m$ (0.004 mil) (hereafter called the first step); generation of very fine-grained carbide particles on the first-step layers, producing a very smooth surface (the second step); and growth to thick carbide layers that have columnar grains with strong preferred orientations or

equiaxed grains with random orientations (the third step). A similar growth behavior of vanadium carbide coatings has been reported in powder packing (Ref 13).

As for surface roughness of the third-step coatings, vanadium carbide coatings are superior to niobium carbide and chromium carbide coatings. The surfaces of niobium carbide and chromium carbide coatings formed at low coating temperatures, such as $900^\circ C$ ($1650^\circ F$), are not as smooth as vanadium carbide coatings. However, there are no big differences in smoothness between these three coatings as far as the higher coating temperatures are concerned. Differences in carbide species, types of substrates, and coating conditions have remarkable effects on the timing of transition to the next step for all three step behaviors. Figure 6 demonstrates the fracture morphology of vanadium carbide coatings formed on W1 at the coating temperature (Ref 11). The change of carbide grain size and shape during growth to thick coatings can be clearly recognized. It can also be exaggerated by the extremely higher coating temperature for a carbon steel, resulting in too-thick coatings, such as $30 \mu m$ (1.2 mil). Figure 7 illustrates the effect of bath temperature on changes in preferred orientation during growth of the vanadium carbide (Ref 11). A similar phenomenon has been observed for chromium carbide coatings (Ref 12). The higher coating temperatures tend to create equiaxed grains rather than grains with strongly preferred orientation.

It has been recognized through laboratory testing and practical use that surface finishing of hard material coatings, such as carbides and nitrides, can have a tremendous effect on tribological properties in comparison with other industrial materials. It is also noted that coatings constructed with equiaxed grains should have better mechanical strength compared to coatings with columnar grains. Selection of coating conditions should be done in consideration of such information.

Growth on Exposed Carbon and Carbide Grains on Workpiece Surfaces.

Exposed carbide grains at substrate surfaces should have some effect on the growth behavior of carbide coatings and various properties of coated parts.

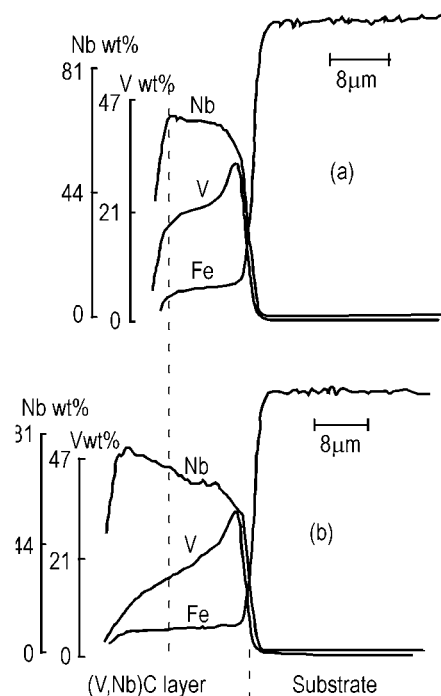


Fig. 5 In-depth variation of x-ray intensity of vanadium, niobium, and iron in vanadium-niobium-alloyed carbide coatings formed on W1 by high-temperature borax baths with the addition of 10 wt% ferrovanadium and ferri niobium powders. Coating temperature: $1000^\circ C$ ($1830^\circ F$); time: (a) 1 h and (b) 8 h

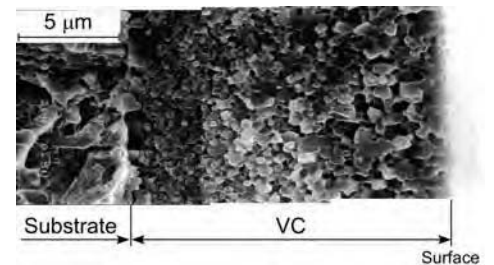


Fig. 6 Fracture morphology of vanadium carbide coatings on W1 formed by high-temperature borax baths with the addition of 20 wt% V pentoxide flakes and 5 wt% boron carbide powders. Coating temperature: $1000^\circ C$ ($1830^\circ F$); time: 4 h

It has been confirmed that only the CFEs in coating reagents, which have a greater affinity to carbon, can take out the carbon atoms in the carbide grains to contribute to TRD carbide growth, and their growth rates were almost the same as those on austenite (direct deposition). In case of weak affinity, no deposition or greatly delayed deposition of the primary carbide grains was observed, although the surface of the carbide grains can be covered by the coating carbides by lateral growth of the carbides that have already grown on the austenite (indirect deposition). This phenomenon was clarified by use of experimental cast alloys containing extremely coarsened alloy carbide grains (Ref 14).

The growth rates of coatings on carbide grains by indirect deposition are smaller than those on austenite, and therefore, the coating surfaces formed on substrates, with large grains of carbides for indirect deposition, tend to have small or large dents. This can be easily observed in the coatings on gray cast irons, as exemplified in Fig. 8(a) and (b) (Ref 15). The coatings of vanadium, niobium, and chromium are generated by indirect deposition on graphite grains in cast irons.

The small dents on the coating surface may offer a positive effect, such as micro-oil pools under some tribological conditions. On the other hand, cross-sectional observation reveals that large graphite flakes existing near the surface of gray cast irons can destroy the coatings during coating cycles and also in use.

In practical applications of industrial steels, generation of small dents by indirect growth has been recognized thus far only in chromium carbide coating onto 440C (Fig. 8c), because the carbide grains in industrial steels are usually not so coarse. Preliminary coatings of vanadium carbide and niobium carbide can solve the problem because these carbides grow on the chromium carbide grains by direct growth and ensure uniform growth of chromium carbide layers on previously coated vanadium carbide and niobium carbide layers.

There are some other industrial materials with microstructures composed of both metallic phases and grains of carbides or nitrides. These are cemented carbides and the carbide-steel cermets such as Ferro-TiC, high-carbon cobalt alloys such as Stellite, and alloyed cast irons. The TRD coatings are successfully applied to these materials, with no serious problems.

The TRD carbides/nitrides can grow on carbide/nitride ceramics, such as silicon carbide and silicon nitride, at growth rates similar to those on steels (Ref 5). However, the details of growth behavior have not yet been examined.

Nitride Coating Nucleation and Growth

The entire surface of nitrided layers formed on low-alloy steels is covered with iron-nitrogen compound layers and diffusion layers underneath

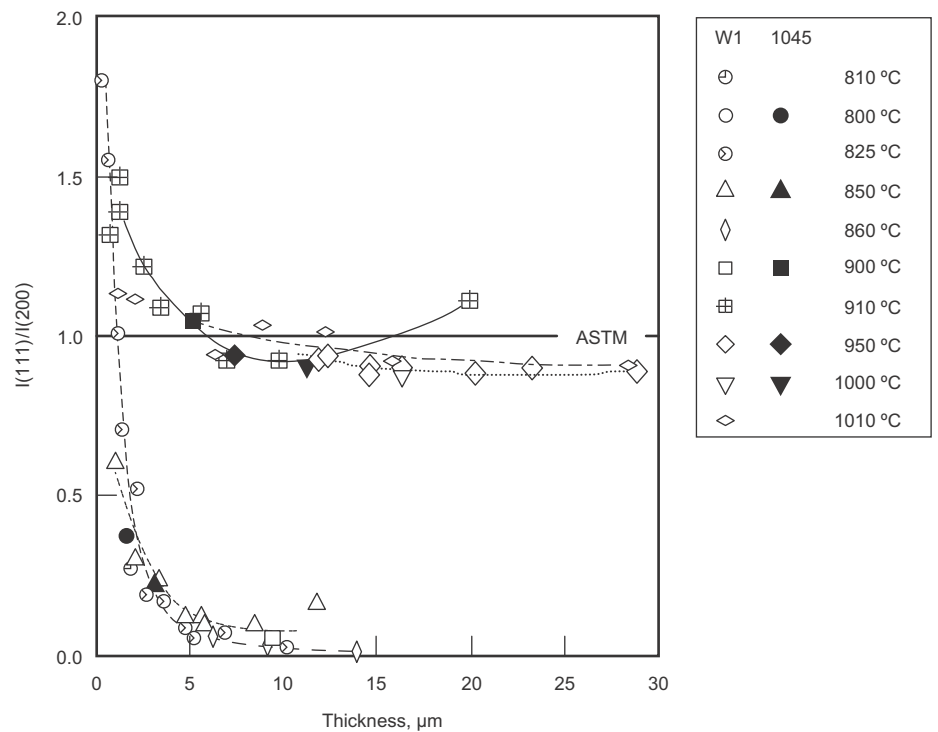


Fig. 7 Variation of x-ray intensity ratio, $I(111)/I(200)$, of vanadium carbide coatings during growth by prolonged coating at various coating temperatures

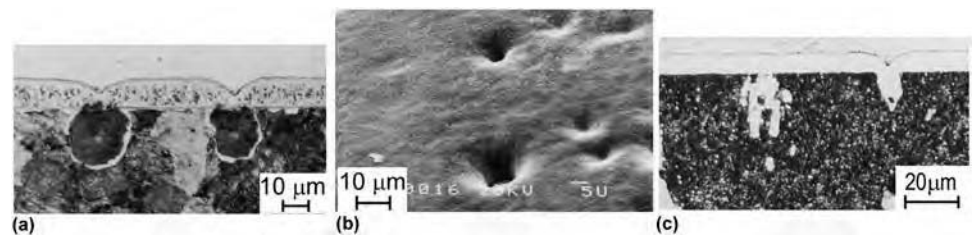


Fig. 8 Surface and cross-sectional views of carbide coatings formed by high-temperature borax baths, showing small dents on coated surfaces caused by indirect deposition on (a) graphite and carbide grains, (b) vanadium carbide on ductile cast iron, 900 °C (1650 °F), 4 h, and (c) chromium carbide on 440C, 1000 °C (1830 °F), 2 h

the compound layers. The top surface of nitrided layers formed on high-carbon, high-alloy steels should have some exposed grains of carbides that may contain some amount of nitrogen during the nitriding cycles. The TRD nitride coatings can grow on the iron-nitrogen compound layers using nitrogen atoms in the compound layers. Growth behavior of TRD coatings on carbide grains has not yet been examined. However, the presence of small carbide grains in industrial steels would not seriously hinder the ability to form nitride layers during TRD processing. The process can be successfully applied on high-speed tool steels.

The TRD coatings formed by the process consist of either double layers—Cr₂N (outer) and CrN (inner), V₂N (outer) and VN (inner)—or single layers of CrN and VN. The entire layer consists of coated nitride layers, residual iron-nitrogen compound layers, and the diffusion zone (Fig. 9a).

Observations of the detailed growth behavior, as in carbide coating, have not been reported. It seems to be very difficult to obtain a similar observation because of the very fine crystal sizes that form at low coating temperatures. Figure 9(b) shows the fracture surface of H13 coated for 3 h at 570 °C (1060 °F) in chloride salt baths. After 8 h, the coatings had grown to form a 7 μm (0.28 mil) thick layer, of which the inner 5 μm (0.2 mil) was composed of columnar grains and the outer 2 μm (0.08 mil) of globular grains (Ref 16). It has been noted that, according to transmission electron microscopy observations, the CrN compound layer was composed of evenly distributed nanometer-sized CrN grains.

As for growth behavior in low-temperature nitride coatings, detailed research has been carried out in the salt bath process (Ref 17–19) and the fluidized-bed process (Ref 20, 21). These

papers are very useful sources for further understanding of growth behavior. For example, detailed observation by Cao of phase transformation in chromium nitride formation showed that most chromium nitride coatings grew on the surface, but chromium atoms also diffuse deeper into substrates to nucleate chromium nitride (Ref 19). It has been observed that, during coating growth, chromium diffused into the surface side of nitrated compound layers. On the other hand, the deep side of compound layers can change their structures, depending on coating temperatures, nitriding temperatures, and chemical composition of the substrates used.

Factors Controlling the Growth Rate of Coatings

Amount of Active CFE/NFE. As shown in Fig. 10 to 13, coating thickness reaches its

maximum level with the addition of only a small amount of CFE/NFE reagent, meaning that a CFE/NFE reagent as small as 5 to 10 wt% yielded enough active CFE/NFE to combine with all of the carbon/nitrogen available from the substrates, regardless of the type of coating methods and carbide species. The amount of added reagents that yield coatings of the saturated thickness can be referred as the minimum required amount of CFE/NFE reagents (MRA-CFE/NFE reagents), and the amount of active CFE/NFE needed for the saturated thickness is the minimum required amount of active CFE/NFE (MRA-A CFE/NFE).

In the case of more than the MRA-A CFE/NFE being present, the sole factor in deciding growth rates of carbide/nitride layers is the amount of carbon/nitrogen atoms that can be obtained from inside the substrates over time. Furthermore, in the case of high-carbon, high-alloyed steels and high-carbon cobalt alloys such as Stellite, the amounts of available

carbon are determined not by the carbon content in the whole substrate material but by the carbon content in the metallic phase: austenite, in the case of steels, and chemical compositions, amounts, sizes, and distributions of alloyed carbide grains. If the substrates consist of cermets such as cemented carbides, the carbon contents in the cobalt phases as well as the cobalt percentages in the alloys determine the available carbon contents.

The coatings having higher CFE/NFE contents, as found with V_2C , $Cr_{23}C_6$, V_2N , Cr_2N , and so on, were observed on the coatings of VC, Cr_7C_3 , VN, and CrN in some coating conditions. It is believed that the active CFE/NFE in excess of what is required to make V_2C , $Cr_{23}C_6$, V_2N , and Cr_2N is waiting in the coating reagents for the arrival of carbon/nitrogen at the surface from inside the substrates, suggesting that the amount of carbon/nitrogen available from the inside substrates is a determining factor.

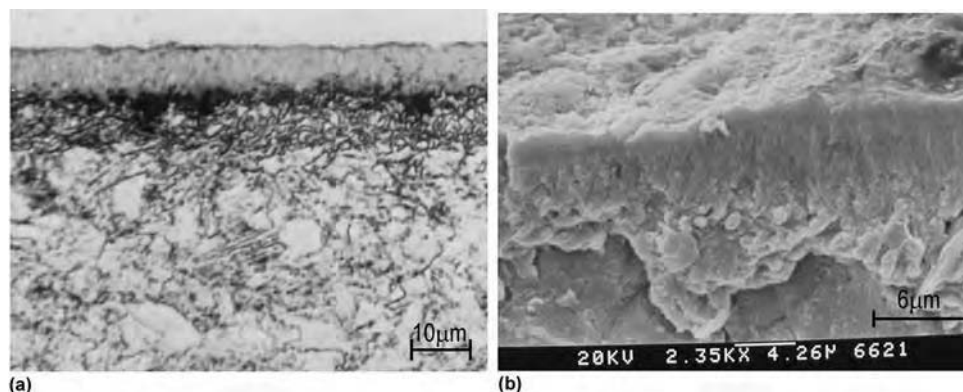


Fig. 9 Cross-sectional view of chromium nitride coatings formed on 1045 by low-temperature chloride baths with the addition of 20 wt% Cr powders. (a) Optical observation of polished cross section. Coating temperature: 570 °C (1060 °F), time: 8 h; preliminary nitriding in salt bath: 570 °C, time: 1.5 h. (b) Electron microscopy observation of fractured section of H13. Coating temperature: 580 °C (1075 °F), time: 3 h; preliminary nitriding in salt bath: 570 °C, time: 8 h

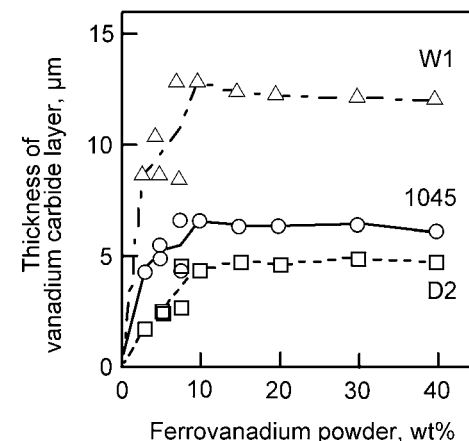


Fig. 10 Effect of amount of ferrovanadium powders in borax baths on thickness of vanadium carbide coatings formed in high-temperature borax baths. Coating temperature: 950 °C (1740 °F); time: 4 h

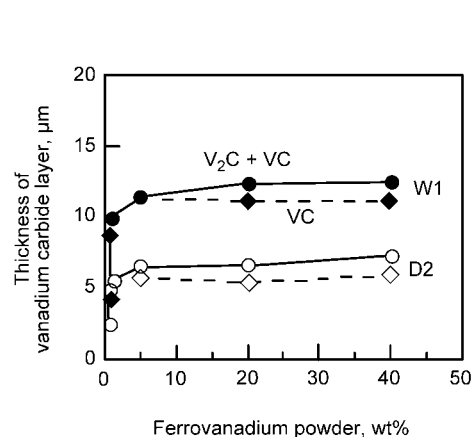


Fig. 11 Effect of amount of ferrovanadium powders in fluidized beds on thickness of vanadium carbide coatings formed in high-temperature fluidizing beds. Coating temperature: 1000 °C (1830 °F); time: 2 h

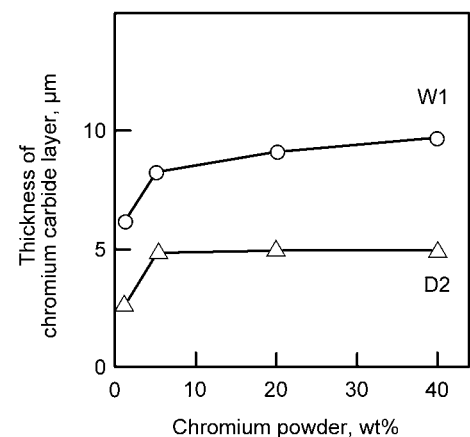


Fig. 12 Effect of amount of chromium powders in fluidized beds on thickness of chromium carbide coatings formed in high-temperature fluidizing beds. Coating temperature: 1000 °C (1830 °F); time: 2 h

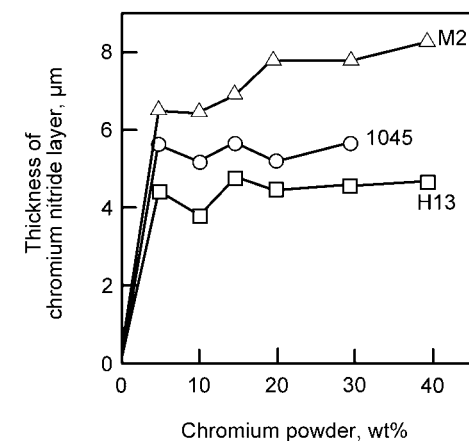


Fig. 13 Effect of amount of chromium powders in chloride baths on thickness of chromium nitride coatings formed in low-temperature chloride baths. Coating temperature: 570 °C (1060 °F); time: 8 h. Salt bath nitriding: 570 °C; time: 3.5 h

In the case of coating nitride and carbonitride onto nitrided steels, the thickness of the iron-nitrogen compound layers has a determining effect, as does their composition. The depth of nitrogen diffusion layers also should have minor effects.

Types of Carbide/Nitride Species. In the case where greater than the MRA-A CFE/NFE is present, remarkable differences have not been observed in the growth rate of coatings between any carbide/nitride species. It is a legitimate consequence, because chemical bonding at elevated temperatures usually proceeds rapidly.

Coating Temperatures and Times. As with other diffusion treatments, the parabolic law can be applied between coating times for all the coatings by TRD, as exemplified in Fig. 14 (Ref 11, 12, 15, 22).

The increased diffusion velocity of carbon/nitrogen in substrates by higher coating temperatures leads to thicker coatings, as in other diffusion treatments. However, the effect of coating temperatures is more remarkable in the case of high-carbon, high-alloyed metals, because high temperatures accelerate more dissolution of carbide grains into austenite, resulting in higher carbon content in the matrix phases (Fig.15) (Ref 22). Figure 16 shows the times needed to obtain 4 and 7 μm (0.16 and 0.28 mil) thick coatings on various industrial steels. Coating at temperatures as high as 1050 °C (1920 °F) can decrease the times greatly. However, the actual coating operation would be almost impossible with conventional external salt bath furnaces, and coating higher than 1100 °C (2010 °F) was done in salt baths prepared in a small heat-resisting alloy pot that was dipped into conventional internal-heating salt baths.

Chemical compositions of substrate materials, matrix phases, and carbide grains have an effect on the dissolution, composition, and size of carbide grains. Furthermore, formation of solid-solution layers and compound layers should have some degree of effect on the diffusion rates of carbon in matrix phases, although

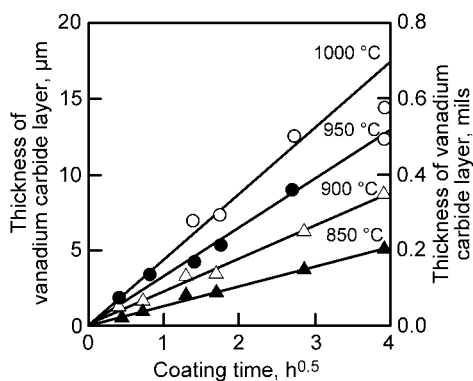


Fig. 14 Effect of coating temperatures and times on thickness of vanadium carbide coatings formed on W1 by high-temperature borax baths with the addition of 20 wt% ferrovanadium powders

it may not be so considerable as far as the industrial materials are concerned.

Thickness of Substrates. Carbon/nitrogen atoms for TRD coating are supplied only from substrates. Therefore, the maximum thickness that can be formed is limited by the thickness and the carbon/nitrogen content of the substrates. However, TRD coating can produce coatings with thicknesses similar to those by PVD even on substrates with thicknesses as thin as 0.1 mm (0.004 in.) if high-carbon steels are used as substrates. The TRD coatings have been satisfactorily applied to razor-sharp blades for cutting of rubber products, textile filament, and so on.

Coating Processes

Coating Processes in General Use. Active CFEs/NFEs can be produced either in molten-salts or by generating CFE/NFE-containing gases that are produced through the reaction between solid halides and CFE/NFE-containing solid particles in reaction chambers such as powder-packing boxes and fluidizing beds.

The following methods of performing TRD coating are recommended after considering the ease of making high-quality coatings, the marketability of reagents, production costs, properties of coatings, and demands for the coated products in markets. The following methods have been successfully employed in the past and at present and would be put into actual production in the near future:

- *High-temperature borax bath immersion, using CFE in borax:* Vanadium carbide, niobium carbide, chromium carbide, and their alloys as (V, Nb)C, (V, Nb, Cr)C, and so on, along with multilayered coatings of these carbides
- *High-temperature fluidized bed immersion, using powders of CFE/NFE-containing metals, aluminum oxide powders as the fluidizing-bed material, and particles of halide compounds or gaseous halides as activators:* Vanadium carbide

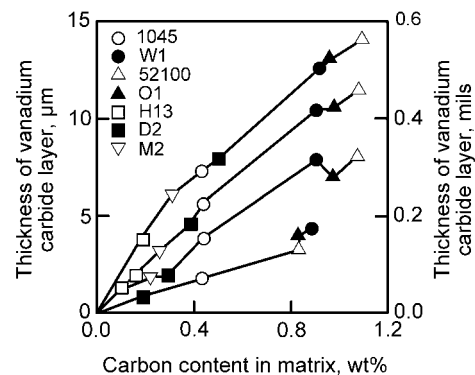


Fig. 15 Effect of carbon contents in matrix phase (austenite) at different coating temperatures on thickness of vanadium carbide coatings in high-temperature borax baths with the addition of 20 wt% ferrovanadium powders. Coating time: 4 h

- *High-temperature powder-packing methods, using powders of CFE/NFE-containing metals, aluminum oxide powders as neutral compounds, and halide compound powders as the activator:* Vanadium carbide and chromium carbide
- *Low-temperature salt bath immersion onto prenitrided steels, using powders of NFE-containing metals in chloride salt:* Chromium nitride on the prenitrided layers
- *Low-temperature fluidized-bed immersion onto prenitrided steels, using powders of NFE-containing metals, gaseous halide compounds as activators, and aluminum oxide powder as fluidizing materials:* Chromium nitride on the prenitrided layers

The borax bath high-temperature carbide coating has now found substantial acceptance in various fields worldwide. Fluidized-bed high-temperature carbide coating has also found acceptance as an alternative to the salt bath process, where problems can be experienced with cleaning off salt residues and removing masses of salt that can become difficult to remove from small, long holes in workpieces. The chloride salt bath low-temperature nitride coating is gradually penetrating into applications in the casting, hot forging, and metal stamping industries. Fluidized-bed low-temperature nitride coating is now starting to be employed in more applications in the same fields, such as extrusion dies.

Various types of steels are being used as workpiece substrates. However, cemented carbides, Stellite, and cast irons are also used for special applications.

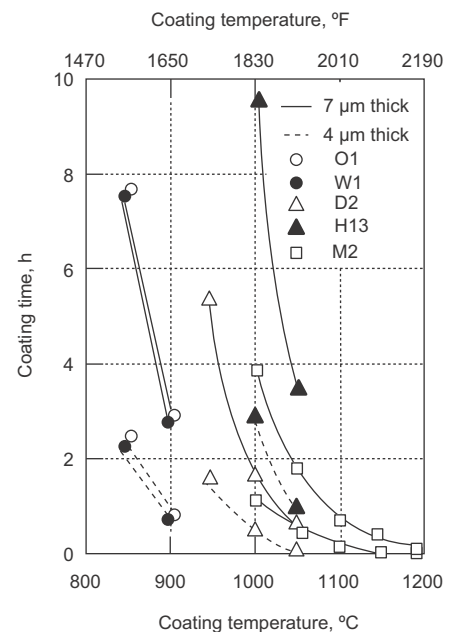


Fig. 16 Coating time required to form 4 and 7 μm (0.16 and 0.28 mil) thick carbide coatings on various substrate steels by the high-temperature carbide coating processes in common to carbide species and coating methods: salt baths or fluidized beds

Selection of Coating Processes. Tables 1 and 2 show advantages and disadvantages and characteristics of various processes. The most important advantages of the salt bath processes are the ease of achieving simultaneous hardening of steel substrates by various quenching methods. The process has large flexibility

not only for selection of the quenching method but also for substrate materials, sizes and shapes of workpieces, and treating times. Therefore, it has great versatility for small production tools, such as dies, molds, and various jigs and wear parts to be used in mass production.

In the salt bath processes, an appreciable time is needed to remove the salt reagents solidified within long, slender holes in the workpieces. The fluidized-bed processes have some advantages over the salt bath processes, for example, easy control of very precise dimensions, such as less than 10 μm (0.4 mil), due to excellent thermal uniformity. However, the processes require much more expensive coating equipment.

The greatest advantage of the low-temperature processes is the minimized distortion problems. However, the nitride coatings made by the low-temperature TRD processes are inferior to the carbide coatings in terms of coating hardness and therefore abrasive wear resistance.

Selection of Substrate Materials and Distortion Control. Carbide and nitride coatings can grow on a wide range of industrial materials as long as they contain carbon/nitrogen, even in very small amounts, such as 0.05 wt%. Therefore, there is large flexibility in the selection of substrates. However, the following two items must be kept in mind for appropriate selection for practical applications: the load-bearing capability of substrates and the ease of distortion control in application of the high-temperature TRD coating.

The TRD carbide/nitride coatings can develop microcracking by deformation of the substrates due to applied load during use; thus, the substrates must have high strength. The larger load requires a higher substrate hardness; thus, in the case of steel substrates, the following are typically selected: low-alloyed tool steels and cold working die steels (D series) for 60 HRC, high-steel tool steels for 64 HRC, superhigh-speed steels for 68 HRC, and cemented carbides for HRC higher than 68. If the wear problems are caused by friction, for example, with textile fibers as in filament guides, very small pressures are applied to the substrates and

Table 1 Advantages and disadvantages of various coating processes

Coating process	Advantage	Disadvantage
High-temperature salt bath process	<ul style="list-style-type: none"> • Less expensive equipment • Stable quality of coating • Quench hardening by various methods • Wide applicability regarding substrate materials, shape, and size 	<ul style="list-style-type: none"> • Bath maintenance required • Salt reagents must be washed off • Distortion problem • Temperature nonuniformity • High working environment • Most expensive equipment
High-temperature fluidized-bed process	<ul style="list-style-type: none"> • No need to wash off reagents • Stable quality of coating • Better throwing power • Uniform coating temperature • Tight dimensional control • Smaller shape distortion 	<ul style="list-style-type: none"> • Good equipment design required for substrate steel hardening
High-temperature powder-packing process	<ul style="list-style-type: none"> • Less expensive equipment 	<ul style="list-style-type: none"> • Unstable coating • Possibility of reagent powder sticking • Large distortion • Large temperature nonuniformity • Posthardening necessary to achieve high hardness
Low-temperature salt bath process	<ul style="list-style-type: none"> • Least expensive equipment • No distortion 	<ul style="list-style-type: none"> • Prenitriding required • Bath maintenance required • Salt reagents must be washed off (easier than high-temperature salts)
Low-temperature fluidized-bed process	<ul style="list-style-type: none"> • No need to wash off reagents • Uniform coating temperature • No distortion 	<ul style="list-style-type: none"> • Prenitriding necessary • Unstable coating quality • Expensive equipment
Low-temperature powder-packing process	<ul style="list-style-type: none"> • Less expensive equipment • No distortion 	<ul style="list-style-type: none"> • Prenitriding necessary • Large temperature deviation

Table 2 Characteristics of various coating processes

Coating process	Substrate hardening	Cooling/quenching method	Posttreatment needed	Quality issues
High-temperature salt bath process	During cooling from coating operation	Oil, salt, air, or nonoxidizing gas cooling	Wash in hot water and/or polish off the covered salt reagents	<ul style="list-style-type: none"> • High substrate hardness can be ensured. • Countermeasures required for workpiece shapes likely to result in shape distortion (thin, long, complicated geometries) • Countermeasures required for tolerances smaller than ±20 μm • Lengthy time requirement for removal of salt-filled deep blind
High-temperature fluidized-bed process	During cooling from coating operation	Gas cooling in attached cooling chamber	Remove attached reagent powder by brushing	<ul style="list-style-type: none"> • Substrate hardening cannot be done more easily than salt bath process. • Dimensional control is easier than salt bath process. • Removing reagent powder from deep holes can be easier.
High-temperature powder-packing process	No hardening or preliminary hardening	Usually impossible	Remove attached reagent powder by tumbling barrel	<ul style="list-style-type: none"> • Treatment of large numbers of small workpieces is easier. • Unstable formation of coatings • Labor required for picking up workpieces from coating powders • Possible damage by impingement of reagent powders • High-quality prenitriding required
Low-temperature salt bath process	Preliminary hardening and then nitriding	Not needed	Wash in hot water and/or polish off the covered salt reagents	
Low-temperature fluidized-bed process	Preliminary hardening and then nitriding	Not needed	Remove attached reagent powder by tumbling barrel	<ul style="list-style-type: none"> • High-quality prenitriding required • Possible damage by impingement of reagent powders
Low-temperature powder-packing process	Preliminary hardening and then nitriding	Not needed	Remove attached reagent powder by tumbling barrel	<ul style="list-style-type: none"> • Treatment of large numbers of small workpieces is easier. • High-quality prenitriding required • Unstable formation of coatings • Labor required for picking up workpieces from coating powders

coatings, and only good wear resistance of the coatings can solve the problem without requiring a hardened substrate. The use of unhardened steels, such as 1045, allows for reduction of cost through less alloy content and no requirement to harden the substrate materials.

Ease of distortion control is another important factor that should be considered in the selection of proper substrates, in combination with the load-bearing capability. Steels with high hardenability, such as air hardening tool steels, can decrease shape distortion. High-alloy tool steels and D-series, H-series, and high-speed steels are highly recommended to maximize dimension control and maintain tolerances as tight as ± 0.05 mm (0.002 in.) by employment of high-temperature tempering where minimal size change can be achieved. Dimensions of the parts made of these steels can be precisely adjusted by use of the secondary hardening behaviors, that is, decomposition of retained austenite, tempering of martensite, and so on.

For use as cutting tools, high-speed steels should be austenitized at approximately 1200 °C (2190 °F) to obtain extremely high hardness and superior resistance to high-temperature softening against thermal loading. However, in forming uses, in which resistance to high-temperature softening is not required, powder metallurgy high-speed steels are highly recommended, because they can be hardened to 65 to 68 HRC at 1025 °C (1875 °F) coating temperature, which is most popularly used in TRD coating. Furthermore, some high-speed steels that can be hardened to 64 to 66 HRC at 1025 °C (1875 °F) TRD coating temperature are gradually being introduced into practical use. Eliminating the need for reaustenitizing to perform hardening greatly decreases the possibility of distortion problems.

High-temperature TRD coatings can be applied to either hardened or unhardened steel substrates, with no differences in their thickness. However, a workpiece that has been hardened under the conditions close to those in the coating and finish-ground to the targeted dimensions makes it easier to realize tight dimensional control. It has been confirmed that employment of annealing between prehardening and coating is usually unnecessary, as long as the coating temperatures are kept below 1050 °C (1920 °F).

It should be kept in mind that good control of possible distortion problems, both for size changes and shape changes, is key to the success of high-temperature TRD coating, and the problems have been solved satisfactorily in a wide variety of applications, including various tooling and machine components. For perfect distortion control, not only expert knowledge of heat treatment but engineering skills in industrial production should be fully utilized.

Control of Coating Thickness. As shown previously in the section "Factors Controlling the Growth Rate of Coatings," coating temperature is the largest determining factor for coating thickness, as long as large amounts of the

effective CFEs/NFEs are kept in the coating reagents. Therefore, well-controlled coating temperatures are absolutely essential. However, unlike the ordinary salt bath hardening that uses internally heated baths, borax baths should use externally heated salt baths. This may cause large gaps between the temperature indications obtained with thermocouples placed outside of the pots and the actual temperatures of the baths. The salt bath temperature drops during loading of cold workpieces, and time is needed to recover and reach the targeted coating temperature. This recovery time may vary with numerous factors, such as the salt temperature before loading, the loaded workpiece sizes, preheating temperatures for the workpieces, furnace design, pot sizes, and so on. Keep in mind that, unlike the conventional chloride salts for hardening, TRD borax baths have very high viscosity, and the resulting low fluidity even at high TRD temperatures can interrupt the quick flow of heat from the pot wall area to the center of the salt bath. In the case of large-diameter pots (up to several hundred millimeters), more than 10 h would be needed to heat the baths to the targeted coating temperatures.

Good basket design, placement and orientation of the workpieces into the baskets, and several movements of the baskets in the baths—up and down and/or rotating—during each coating cycle are highly recommended to assist in reducing recovery time and ensuring good temperature uniformity throughout the bath. Temperature measuring near the baskets/workpieces by thermocouples inserted through small holes in the furnace lids should be very informative and allow for better process control, although it is not simple to engineer and operate with because of the lid design and its need to be moved.

If the times needed for recovering bath temperatures have not been added to the coating time, from loading to unloading, the actual times effectively worked for coating growth at the targeted temperatures could be much shorter than expected, and the coatings would be much thinner than expected.

Differences between the targeted thickness and the thickness actually obtained do not bring serious problems, because it has been confirmed that the thickness of TRD coatings does not have a serious effect on various properties and performances in the use of TRD-coated products. Furthermore, the length of coating time does not have a large effect on the coating thickness due to the parabolic law rule. The more critical issue is the lower substrate hardness of the coated workpieces caused by the short coating times at the targeted temperatures. The lower substrate hardness being less than expected suggests the possibility of a smaller load-bearing capability of the substrates and large dimensional movements caused by a change of structures as the amount of retained austenite, the carbon content in martensite, and so on varies.

Controlling Coating Reagent Conditions

Importance of Active CFE/NFE versus MRA-A CFE/NFE. The existence of active CFE/NFE more than MRA-A CFE/NFE can ensure formation of coatings with the same thickness, as long as the coating temperatures and times are kept unchanged. Therefore, keeping more than MRA-A CFE/NFE should be the primary concern for realizing a successful coating operation.

The birth of new active CFEs/NFE in coating reagents, with no rest, is vital to keeping more than MRA-A CFE/NFE. Active CFEs/NFEs are continuously consumed not only by coatings formation but also by changing to inactive CFEs/NFEs due to, in the case of salt bath processes, reaction with oxygen in air and, in the case of fluidized-bed processes, purging out by fluidizing gases. In concrete terms, it is absolutely necessary to maintain closed contact, with no intermission, between each of the CFE/NFE reagent powders and the salt reagents (salt bath process) or gas (fluidized-bed and packing processes).

It is better to keep in mind that, in very many cases, poor coating quality is not caused by the entire consumption of CFE/NFE reagents added thus far but rather by the decreased or lack of production of active CFEs/NFEs caused by improper maintenance. The addition of too much CFE/NFE reagents vigorously worsens the condition of coating reagents and often induces serious difficulties in daily coating. The addition of too much CFE/NFE reagents is not only useless but also harmful.

How to Ensure Consistent Production of Active CFEs/NFEs. Close contact of the entire surface of each particle of the CFE/NFE reagents with molten salts or activator gases produces active CFE/NFE. However, the CFE/NFE reagents in both the salt baths and fluidized beds are likely to migrate to the bottom areas due to their density/gravity being larger than those of either the salts or fluidizing reagents. They can become agglomerated and make a sludgelike or hard cakelike deposition, and the reduced chances of contact with the salts or activator gases can decrease the production of new active CFEs/NFEs. Frequent stirring (agitation) of the baths and proper selection of particle sizes of both fluidizing reagents and CFE/NFE reagents should be key to eliminating the problem. Selection of CFE/NFE particle size is also important in the salt bath process. Large particles can sink too quickly. Too-fine particles can stay longer on the bath surface and become oxidized by air.

Diagnosis of Coating Ability. Recognizing the amount of active CFEs/NFEs needed to stay in the system is desired. However, any tests or devices to perform quantitative measurements that are suitable for production sites have not been found. Therefore, the following method is recommended by Toyota for knowing and maintaining active CFEs/NFEs greater

than the MRA-A CFE/NFE required in the treating medium.

It has been found that coating baths have two different regions even after being freshly produced: the zone in which workpieces can be coated (effective zone) and the region in which coatings cannot be formed (ineffective zone). The ineffective zone is first formed at the surface area of treating baths and beds but gradually or rapidly grows toward the bottom area, until it finally reaches the bottom by decreasing the active CFEs/NFEs to less than MRA-A CFE/NFE. The effective zone and the ineffective zone are thought to be equivalent to the zone that had more than and less than MRA-A CFE/NFE, respectively.

Based on this finding, a very simple way to measure the height of the ineffective and effective zones, on time, was employed by Toyota. It can be called "the steel rod test." A long carbon steel rod is immersed for 10 to 30 min, followed by water quenching or air cooling, and then washing off the salt or powders to look at the rod surface color and any remaining powders. Careful monitoring of daily changes of the depth of the effective or ineffective zones before and after stirring the bath is worth doing to gain the sound judgment needed to make a determination about whether it is necessary to add reducing reagents or agitate the bath bottom area to make the sludgelike CFE/NFE reagents float upward.

The surface coated with carbides and nitrides exhibits its own colors. Therefore, the existence of coatings can be tested by visual observation alone. The copper sulfate test and corrosion tests can be helpful to define the existence of coatings as well. Portable x-ray fluorescence analyzers can also instantaneously show the thickness of the coatings.

High-Temperature Salt Bath Carbide Coating

Externally heated salt furnaces equipped with pots of heat-resisting alloys, as shown in Fig. 17(a), are usually employed. It is recommended that furnaces with pots larger than 150 to 200 mm (6 to 8 in.) diameter have an agitator (stirrer), as shown in Fig. 17(c). The agitator should be designed so that it can readily move to different positions in the pot, horizontally and vertically, to achieve two types of tasks: make a swirl of downward flow at the bath surface, and make an upward flow near the bath bottom, as shown in Fig. 17(b). The former is for the easy addition of CFE/NFE reagents into the bath. The latter is to mix up the sludgelike salt accumulated at the bottom area into the main salt. Large lids on top of furnaces minimize heat loss from the upper side of the baths.

Preparation of Coating Bath and Its Maintenance

Reagents. Anhydrous borax should be employed for the main bath reagent. In comparison

with chloride salts for steel hardening, borax has the disadvantages of higher viscosity and difficult removal during washing in water. However, it is quite difficult to find other reagents that can be rated on par with borax in the stability of coating formation. Complete or partial replacement with chloride salts was examined by some researchers, but it ended unsuccessfully because of unstable coating formation.

Powders (200 to 300 mesh) of ferroalloys or pure metals, such as ferrovanadium, ferroniobium, ferrochromium, and chromium, are added as the CFE/NFE reagents in borax in the ratio of 10 to 20 wt% at the early stage of process development. The 200 to 300 mesh was determined to be optimal with respect to ease of mixing into the baths and the time needed to reach the bath bottom.

It was confirmed that oxygen in air atmosphere has a harmful effect on bath lives, as in most other metal treatments. Furthermore, the active and inactive CFEs/NFEs in borax baths are defined as the lower degree of CFE/NFE oxides, such as V_2O_3 , Nb_2O_3 , and so on, and the higher degree of CFE/NFE oxides, such as

V_2O_5 , Nb_2O_5 , respectively (Ref 23, 24). This finding led to the use of reducing agents in the baths, added with metal powders, and finally the co-addition of both reducing reagents and CFE/NFE oxides.

The co-addition of oxides and reducing reagents brought some advantages, such as moderate viscosity, greater ease of washing off attached salt, and decreasing sludge at the bath bottom.

There are a number of different materials that can be used for the reducing reagent, but each has various advantages and disadvantages, and it was very difficult to make the best choice.

Powder of boron carbide, ferroaluminum (-200 mesh), and small lumps of aluminum are currently being used in consideration of various aspects. However, there are two possible problems to be kept in mind. The addition of too much reducing reagent may make borided layers by the reduction of boron oxide, B_2O_3 , in borax, although this means that boriding can be done by using the same equipment. As shown in Fig. 18, carbide coatings are formed within the limited ratio of the reducing reagents

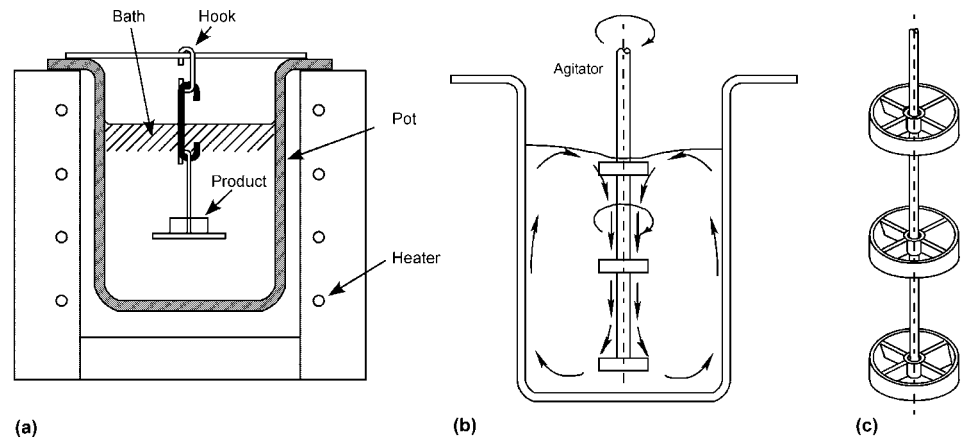


Fig. 17 Schematic representation of equipment for high-temperature borax bath process

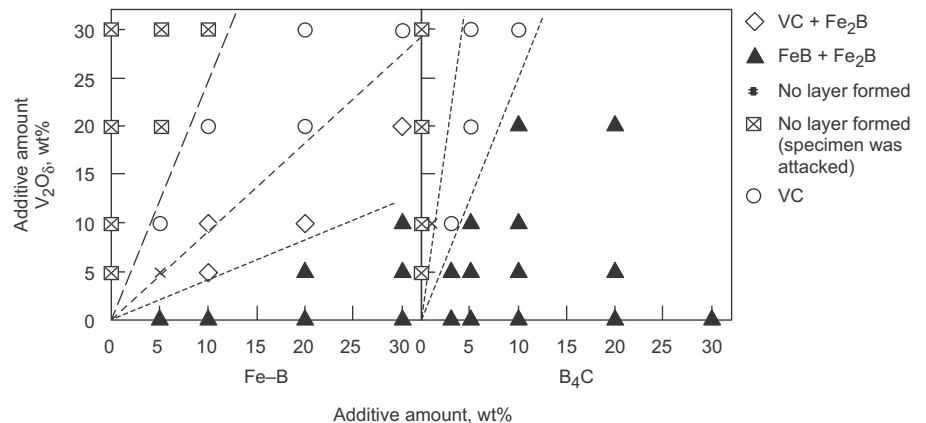


Fig. 18 Example of relationship between the amount of carbide-forming element oxides and reducing reagents added in high-temperature borax baths and the types of coatings formed on steels. Coating temperature: 950°C (1740°F); time: 1 h; W1

and CFE/NFE reagents (Ref 9, 10). Scrapped aluminum lumps are cheapest, but careful use is highly recommended. Molten aluminum, if it remained in the baths as drops of aluminum melt, even after agitation, can vigorously attack the workpieces.

Preparation of Coating Bath and Its Maintenance. Little by little, add the CFE/NFE reagents and reducing reagents to the borax bath while it is being stirred, carefully monitoring the bath level due to gas bubble generation. The salt baths, thus formed, can gain the ability for coating formation within a half-day. However, CFE/NFE reagents start to settle toward the bottom sooner or later, due to their larger density. Stirring of the baths should be continued for a few hours to keep the added reagents floating in the baths to ensure production of enough active CFEs/NFEs. Figure 19 shows recovery of the effective height by agitation (elapsed time: 0 h) and decrease by no agitation (elapsed time: 2 to 8 h).

Daily monitoring of depth changes of the effective and ineffective zones by the steel rod test is the cheapest, least labor-intensive way of maintaining good bath condition. Figure 20 illustrates an example of recording the bath conditions over approximately a month, showing daily changes of the effective depth and the measures taken against the problem. Dropping of the effective zone was observed almost every morning, but it was recovered by stirring at the bottom area, not the surface area, of the bath. The increased depth of the effective zone by only stirring means that enough CFE/NFE reagents stay in the bath to ensure that more than the MRA-A CFE/NFE exists. If there was no effective zone recovery at first, make sure that adequate stirring of the bath bottom was done. If no remarkable recovery is achieved, even with repeated agitation of the bottom area, it may mean that a shortage of CFE/NFE reagents exists in the bath. Well-considered bath maintenance can ensure stable operations. Some baths performed well for years without complete replacement of the entire bath salts.

Careful observation of the surface of the rods after washing off the attached salt yields useful information about the inside of the baths, such as height of the sludge-rich zone at the bottom, presence of hard, cakelike precipitates, and so on. If the existence of large amounts of heavy sludge in the bottom area was recognized, it is recommended that the stirring conditions be improved.

Evaluation of temperature uniformity in the baths is obtainable by measurement of the coating thickness formed on the rods. Because of the high coating temperature, it is not easy to measure the temperature distribution in the baths, even with thermocouples.

Possible Quality Issues

There is a unique quality issue that can be caused by a special characteristic of molten

borax, that is, surface damage from the strong capability to melt oxides that are inherent in the molten borax. It can be called oxidation and succeeding corrosion. During transfer to the cooling devices, molten borax can flow locally from the coated workpieces to expose the coated surfaces directly or through a very thin covering of the bath components. The molten salt still remaining on those surfaces very quickly, as in seconds, can oxidize

and dissolve the exposed areas. The problem is more frequently observed on the areas from which the molten borax salt easily flows down to expose the formed carbide coatings in air atmosphere, for example, the edge portions of top faces of the workpieces. Figure 21 exemplifies spotty damage at the upper edge portion of a ring die. This type of damage can be easily detected by observation of surface color.

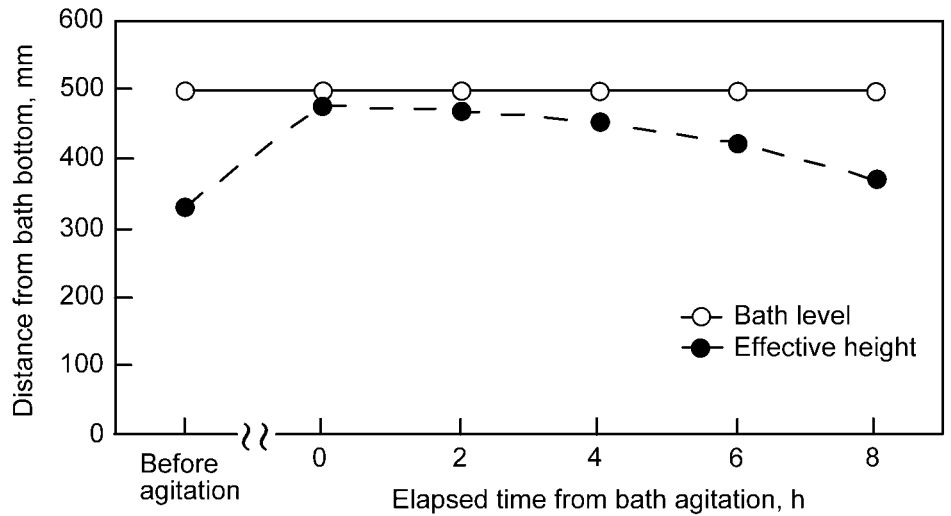
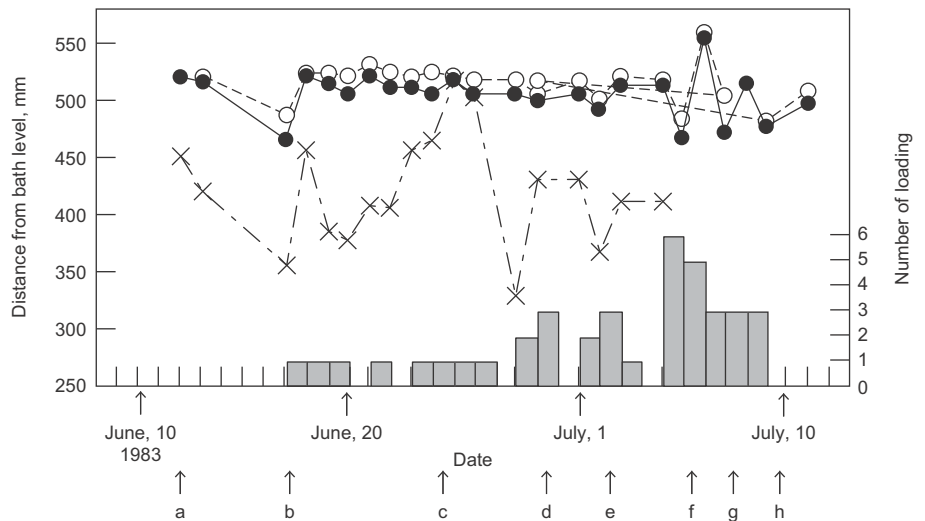


Fig. 19 Example of bath agitation effect on effective heights in a borax bath with additions of vanadium pentoxide flakes and boron carbide powders



Addition	Amount of additions (kg)							
	a	b	c	d	e	f	g	h
B ₄ C	7.5	1.1	0.3	0.3	1.2	2.4	0.6	0.6
V ₂ O ₅	30.0	2.4	1.2	1.2	4.8	4.8	2.4	2.4
Borax	112.5	9.0	4.5	4.5	8.4	16.8	9.0	9.0

Fig. 20 Example of effective height change for vanadium carbide coating in continuous run of a borax bath with additions of vanadium pentoxide flakes and boron carbide powders. Operating temperature: 1025 °C (1875 °F); pot size: 400 mm (16 in.) diameter and 650 mm (26 in.) deep

The problem can be eliminated by quenching not in a gaseous medium but in a liquid medium, such as a salt bath; putting steel blocks near the places in the problem areas to stop the downward flow of salt; and putting steel blocks above the places in the problem area, so that the salt dropping down from the steel blocks can supply more salt to the problem places.

In most cases, the damaged workpieces can be easily recovered by a recoating operation after polishing the damaged area to eliminate unevenness between the damaged and undamaged areas.

High-Temperature Fluidized-Bed Carbide Coating

Application of fluidized beds on carbide/nitride coating was started by Toyota for chromium carbide and some other carbides (Ref 3, 25) and tried successfully for titanium carbide (Ref 26).

Figure 22 shows the TRD coating equipment that was applied for small metal stamping punches in Japan. It consists mainly of a conventional fluidizing-bed reactor heated by external electric elements, a feeder for the solid activator, a cooling/quenching chamber, and an exhaust gas treating device. A gas supplier capable of precise flow rate control can be employed instead of the pellet feeder if gaseous activators such as HCl are used instead of a solid activator such as ammonium chloride (NH_4Cl).

High-purity aluminum oxide powders, 100- to 120-mesh grain size, are used as fluidizing-bed materials. As CFE/NFE reagents, powders of 100 to 120 mesh were mixed into the aluminum oxide powders by 5 to 20 wt%. Ferrovandium, ferrochromium, ferrotitanium, and chromium are typical examples. While being kept fluid, the heavier CFE/NFE powders tend to gradually settle and accumulate on the diffusion

plates, resulting in agglomeration. Furthermore, CFE/NFE powders and aluminum powders can become sintered together to make hard cakes, especially at the bottom area. Proper powder sizes should be selected.

Disc-shaped pellets of commercial ammonium chloride for fertilizers were used very satisfactorily. However, they were substituted with hydrogen chloride gas because of the availability of the fertilizer pellets, and hydrogen chloride eliminated the problem that can be caused by the presence of nitrogen, that is, deposition of vanadium nitride on ferrovandium powders and aluminum oxide powders.

Preparation of Coating Beds and Their Maintenance. In fluidized beds, the active CFEs/NFEs, probably VCl_2 , CrCl_2 , and so on, are produced through the reaction between the CFE/NFE reagents being fluidized and the gaseous halide gases mixed in the fluidizing gas.

The active CFEs/NFEs are very quickly purged from the beds, together with fluidizing gas, unlike in the powder-packing boxes. Therefore, large amounts of powders of CFE/NFE reagents and activator gases should be added to the beds, ensuring a good fluidizing condition in which each powder can move around in the beds without making lumps caused by the sticking of metal to metal and/or metal to oxide reagents. It should be kept in mind that the addition of large amounts of CFE/NFE reagents and activator, and the resulting reaction products between both, provides more opportunity for poor fluidization. The use of halides makes aluminum oxides stickier. Furthermore, covering aluminum powders and CFE/NFE reagent powders by carbides and/or nitrides, which were formed by the reactions, can stimulate the problem.

Therefore, optimizing all of the factors related to formation of active CFEs/NFEs as well as the fluidizing conditions of the beds should be key for coating process success. Elimination of lumps of reagents by screening and the addition of new powders of CFEs/NFEs is often required.

Monitoring the fluidizing condition can be done by observing fluctuations in the fluidizing-gas pressure underneath the gas diffuser plate as well as the differences in the indicated temperatures obtained from more than two thermocouples, which are placed at different positions on the outer wall of the retort. In fluidizing beds in good condition, no fluctuation in gas pressure and temperatures can be observed. Poor fluidizing causes large fluctuations in both the gas pressure and the temperatures.

The steel rod test is also very useful for this process. Changes in surface appearances, such as color, sticking of the reagent powders, and so on, provide some information regarding the bed condition.

The following is an example of a bed condition that was successfully operated in actual production:

- Fluidizing reagent: aluminum oxide, 80 to 120 mesh
- CFE/NFE reagent: ferrovandium, 100 to 200 mesh, 5 to 20 wt%
- Activator: ammonium chloride pellets or hydrogen chloride, 0.03 to 0.08 vol% as HCl
- Fluidizing gas: argon 0.1 to 0.2 L/min (0.03 to 0.05 gal/min) for 1 cm^2 (0.16 in.^2) cross section of fluidizing retort

As long as good fluidizing of the beds is kept stable, the beds can ensure good coating quality for several months or more. As shown in Fig. 23, the same coating thickness can be easily maintained.

Possible Quality Issues. Unstable fluidizing can bring serious problems, such as local overheating and variations in coating thickness. The locally increased impingement effect by hard particles, produced by inhomogeneous gas flow, yields serious erosion damage to weak workpiece positions, such as edge portions and thin thickness areas. Sticking of the powdery reagents and microscopic spalling of the coatings, and the resulting poor surface quality, are also observed in the case of poor fluidizing.



Fig. 21 Example of oxidation and succeeding corrosion observed at the upper edge of a ring coated by high-temperature borax baths. No carbide coatings on spotty bright areas surrounded with black areas

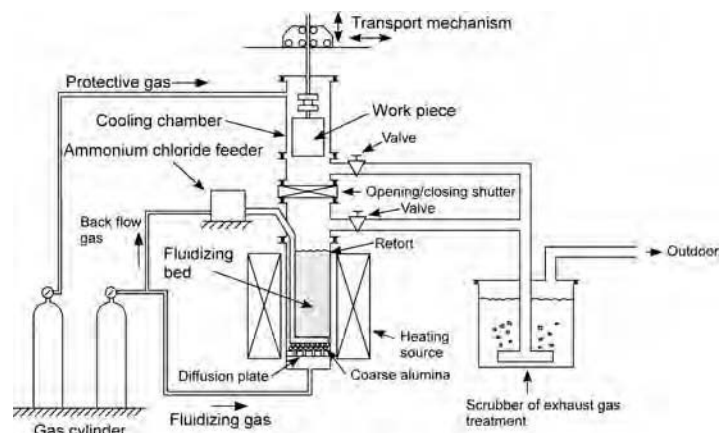


Fig. 22 Schematic representation of equipment for high-temperature fluidized-bed process

Low-Temperature Salt Bath Nitride Coating

Salt baths for quenching and high-temperature tempering of steels can be used without any large modifications. A simple agitator is attached in furnaces with as large as 400 to 500 mm (16 to 20 in.) diameter pots to mix up the sludgelike salt at the bottom area. Therefore, the equipment needed for this coating process can be less expensive, compared with any other carbide/nitride coating processes, if equipment expense for nitriding is not considered.

The process can make various nitrides, such as niobium, titanium, hafnium, zirconium, manganese, and so on, using powders of pure metals or ferroalloys as NFE reagents. However, coatings of vanadium nitride (Ref 27, 28) and chromium nitride (Ref 29) are easier than other nitrides.

Active NFEs in the low-temperature salt bath process seem to be halogenated NFEs as CrCl_3 , VCl_3 , and CrF that are produced by the reaction between halogen elements and NFEs in the baths. Consequently, a wide variety of these materials can be listed. However, mixtures of NFE powders and chloride-base salts, which have widespread use in heat treating of metals, are currently being used. Examples include 15 to 20 wt% of -200 mesh powders of metals or alloys of NFE, such as chromium, ferrochromium, ferrovandium, and so on, and the commercialized neutral salts for high-temperature tempering of steels. The co-addition of small amounts of chromium chloride, CrCl_2 , is also done.

However, during the early stages of research, it was found that the height of the effective zone lowers very quickly toward the bath bottom. It was easy to imagine that a too-low chloride salt viscosity was the problem. The chloride salts have large fluidity, unlike borax, and the added NFE powders very quickly settled toward the bath bottom, making a zone of poor NFE in the upper zone of the baths. The problem has been overcome by the addition of reagents, which can increase bath viscosity.

It was confirmed that various reagents can work for this purpose, and very fine graphite powder (-1200 mesh) has been used successfully, with additions of 0.5 to 1 wt% (Fig. 24). However, increasing viscosity can be achieved only with properly sized viscosity increasers. For example, graphite powders of 200 to 325 mesh would not work well. It has been reported that ferroboration, boron carbide, silicon oxide, and so on could work in appropriate sizes. There may be chemical reaction effects between these viscosity increasers and other reagents; however, this has not yet been discussed.

Preparation of the Coating Bath and Its Maintenance. Add viscosity increaser powders to the fused chloride bath while stirring, until the increased viscosity of the bath is clearly

recognized. Then add NFE powders, little by little, into the bath while agitating more vigorously, so that the NFE powders disperse uniformly in the bath. Continue agitating the bath for several hours with the expectation of perfect mixing. After several hours, the bath will have a good capability for coating, and the depth of the ineffective zone will be minimized.

The steel rod test is highly recommended to maintain large effective zones, as done in the high-temperature salt bath process.

Very long bath life can be ensured without complete bath renewal as long as good agitation of the bath is repeated. The bath absorbed water in the air was reused for the coating operation after drying by heating.

Possible Quality Issues. The nitrided layer necessary for TRD nitride coating should have compound layers as thick as 5 to 20 μm (0.2 to 0.8 mil), because thicker compound layers make thicker nitride coatings. Any type of compound— $\epsilon\text{-Fe}_{2.3}\text{N}$ (up to approximately 11 wt% N), $\gamma'\text{-Fe}_4\text{N}$ (approximately 6 wt% N), and $\zeta\text{-Fe}_2\text{N}$ (approximately 11 wt% N)—is acceptable. The depth of the diffusion layers is not as important because of very low nitrogen content (less than approximately 0.1% N). The largest concern is possible quality problems in the preliminary nitriding layers made by conventional nitride treaters. They usually make only thin compound layers and are more likely to produce various defects to obtain unusually

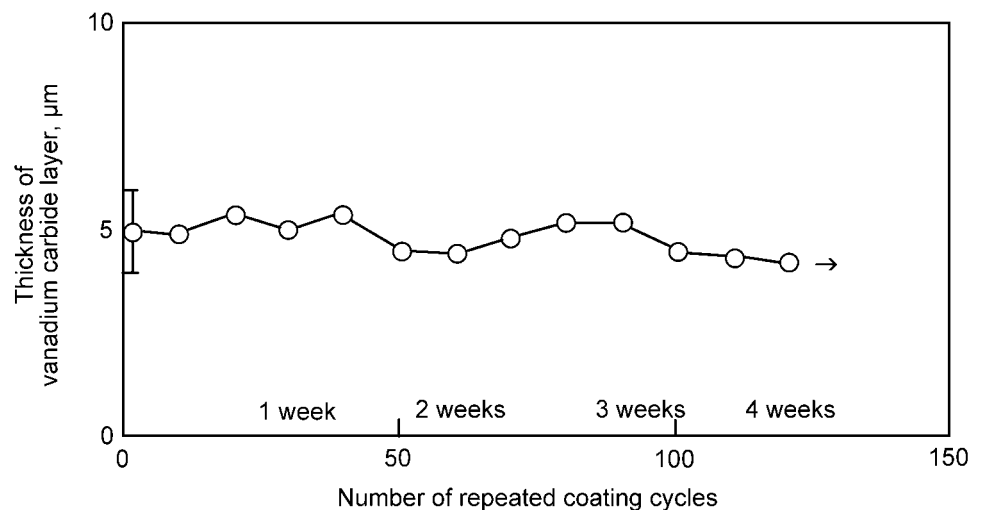


Fig. 23 Stable uniformity of thickness of vanadium carbide coatings in continuous operation of high-temperature fluidized bed with addition of 10 wt% ferrovandium. Activator: ammonia chloride pellets; D2; temperature: 1025 °C (1875 °F); time: 0.5 h

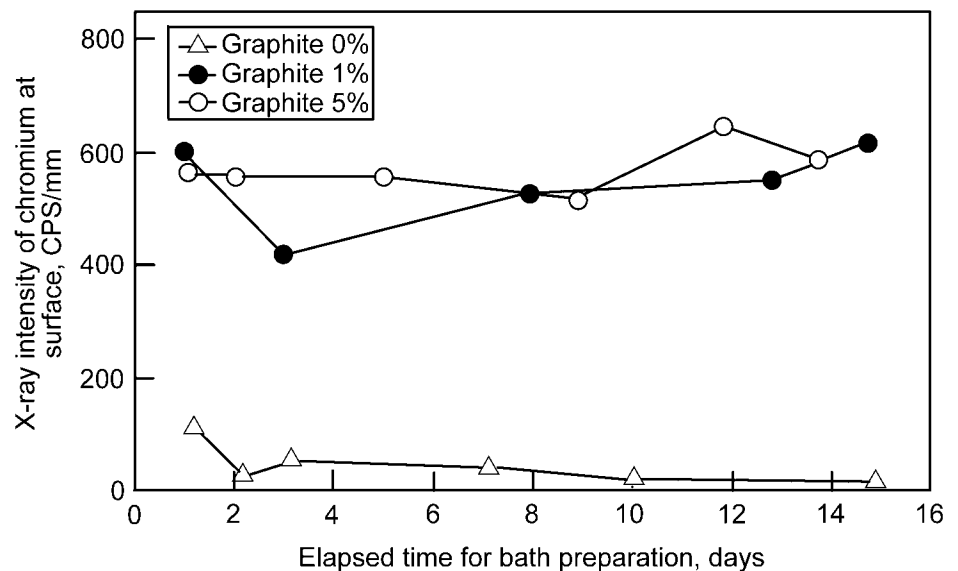


Fig. 24 Effect of addition of graphite powders on chromium coating stability in low-temperature salt bath chromium nitride coating. CPS, counts per second

thick compound layers. These are microdefects such as porosity, microcracks at the surface and interior, uneven compound layer depth, and very low toughness of nitrided parts, as well as surface roughness. The surface roughness of the TRD-coated parts, with the goal of improving tribological properties, should be smoother than normal nitriding. The TRD coating cannot repair any types of quality problems caused by nitriding.

Properties of Coated Parts

The TRD coatings are composed of layers constructed from very fine crystal grains of carbides/nitrides. As a result, TRD coatings are superior not only to the conventional diffusion surface treatments but also to PVD and CVD.

The TRD coatings improve various types of general tribological properties (Ref 10, 12, 16, 25, 27–29) as well as process tribological properties, which deal with tribology under materials processing conditions, such as sheet metal forming, bulk forging, die casting, and so on (Ref 9, 10, 12, 16, 22, 25, 28, 30–35). As for abrasive wear, TRD coatings are excellent due to their extremely high hardness. They also reduce adhesive wear, because they have less affinity to the metallic countermetals and thus less fretting wear, in which both abrasive and adhesive wear occur. Figure 25 shows an example of an evaluation of general tribological behaviors against steels.

The superiority of TRD coatings in materials processing operations has been widely evaluated through the use of various simulation tests, as shown in Fig. 26 and 27 (Ref 30, 31, 35). Excellence of process tribological properties is specific to the carbides and nitrides themselves.

However, it is also noteworthy that TRD coatings adhere very strongly to substrates, because they exploit metallurgical bonding rather than mechanical bonding, as shown in Fig. 28 and 29. References 22 and 36 to 38 provide evaluations of bonding strength under conditions that more closely simulate those for actual use of coated parts than the scratch test.

Most carbide/nitride coatings are also remarkably resistant to corrosion (Ref 22). Chromium carbide/nitride coatings have

excellent resistance to oxidation (Ref 22, 28). As for the buildup of aluminum on casting tools under actual die-casting conditions, TRD coatings of vanadium carbide, niobium carbide, and chromium nitride have received the highest evaluation ratings among many types of surface treatments (Ref 1, 9, 22, 33–35, 39–42).

Applications of TRD carbide coating to steels do not induce remarkable deterioration of their mechanical properties. A number of laboratory tests demonstrated that no serious

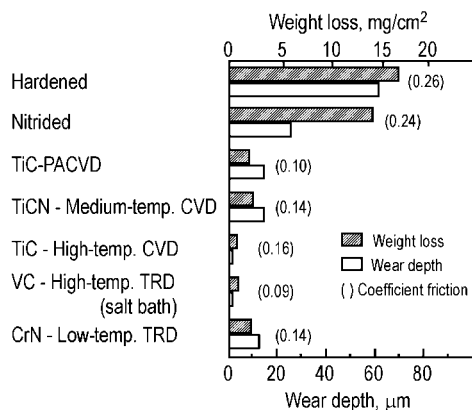


Fig. 25 Comparison of wear depth and friction coefficient of various coatings, obtained by Falex tester. Countermaterials: Cr-Mo structural steel; substrate: M2; sliding velocity: 0.1 m/s (0.33 ft/s); applied load: 400 kgf (4000 N); testing period: 4 min; lubricant: none. PACVD, plasma-assisted chemical vapor deposition; CVD, chemical vapor deposition; TRD, thermoreactive deposition/diffusion

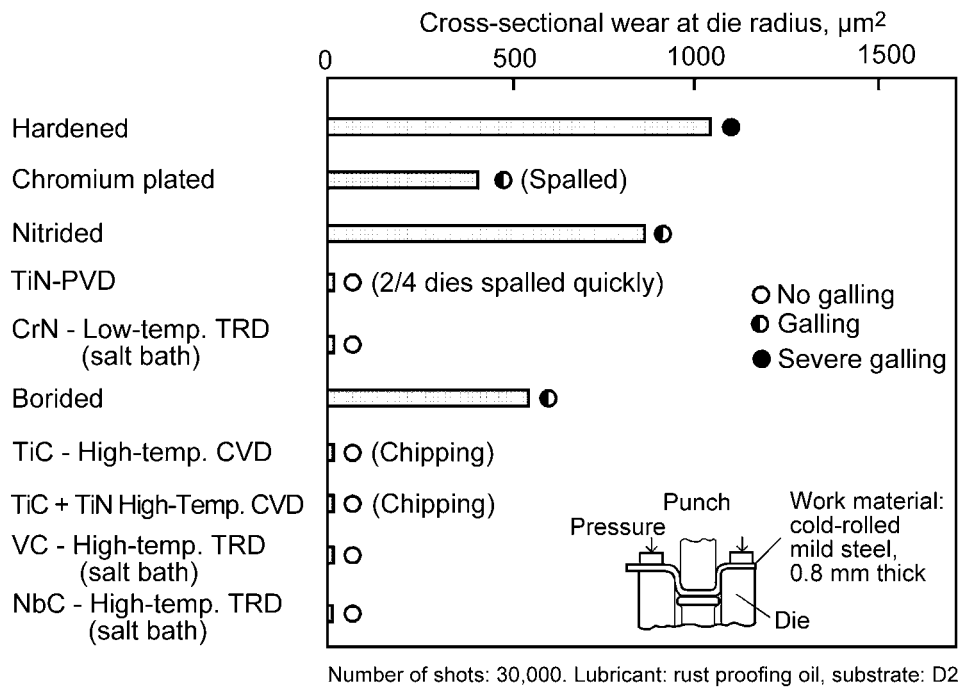


Fig. 26 Comparison of wear, scuffing, and chipping observed in sheet steel bending tests. PVD, physical vapor deposition; TRD, thermoreactive deposition/diffusion; CVD, chemical vapor deposition

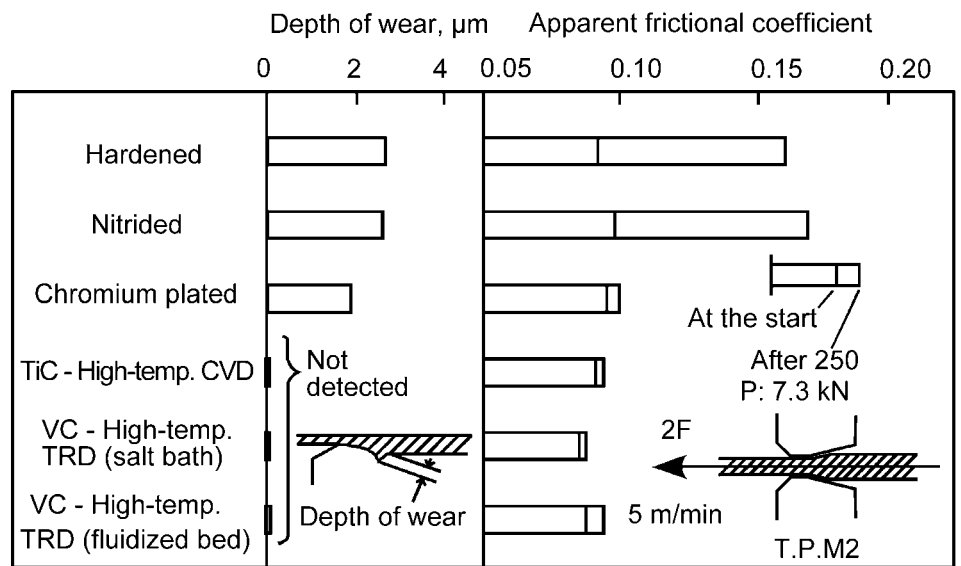


Fig. 27 Comparison of friction coefficient and wear observed in steel sheet ironing tests. CVD, chemical vapor deposition; TRD, thermoreactive deposition/diffusion

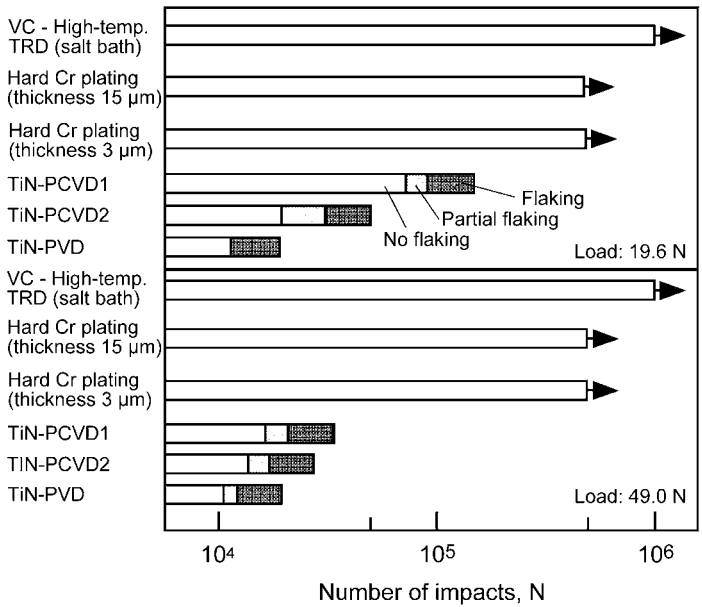


Fig. 28 Comparison of number of repeated impacts that lead to flaking of coatings in repeated hammering with a cemented carbide ball of 6.35 mm (0.25 in.) diameter. TRD, thermoreactive deposition/diffusion; PCVD, plasma chemical vapor deposition; PVD, physical vapor deposition

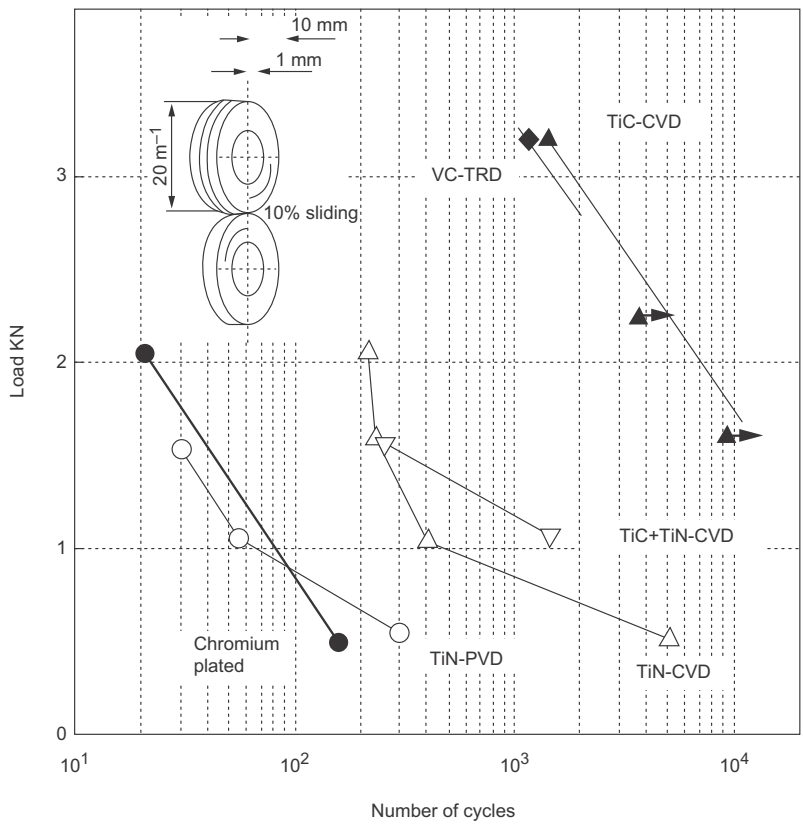


Fig. 29 Comparison of numbers of cycles at which flaking of coatings occurred in a rolling test with 10% sliding. CVD, chemical vapor deposition; TRD, thermoreactive deposition/diffusion; PVD, physical vapor deposition

deterioration occurred, even with very thick coatings of 20 μm (0.8 mil), in static and dynamic bending strength (Ref 9, 10, 43) and fatigue strength (Ref 6, 9, 10, 44). Furthermore, in some circumstances, the coatings improved fatigue strength. Large compressive residual stresses in the coating surface can delay the initiation of cracking (Ref 36). Resistance to heat checking also can be improved by carbide coatings (Ref 42).

Most people are likely to make an unwarranted assumption that cracking occurs first at the surfaces of hard and brittle coatings and then penetrates into the substrates to induce catastrophic failure of the coated parts. However, careful observation of the damage behaviors of shearing punches for high-strength steels, warm forging punches for spring steels (Ref 45), and very sharp cutting edges for hard woods (Ref 46) suggests that deformation and the resulting cracking of the substrates by applied load induced the damage onto the coatings. It is concluded that TRD carbide coatings, and perhaps nitride coatings as well, are very strong and tough.

Practical Applications

The coatings that have found practical applications in Japan and elsewhere include vanadium carbide (V₂C, VC), vanadium-niobium-alloyed carbide (V, Nb)C, vanadium-niobium-chromium-alloyed carbide (V, Nb, Cr)C, chromium carbides (Cr₇C₃, Cr₂₃C₆) by the high-temperature salt bath process, vanadium carbide by the fluidized-bed process, and chromium nitride (Cr₂N, CrN) by the low-temperature salt bath process. Chromium nitride (Cr₂N, CrN) by the low-temperature fluidized-bed process will soon be put into practical application. The coatings of chromium carbide and vanadium carbide by powder packing and their improved processes are being applied to some types of machine components. These carbides/nitrides have excellent tribological properties. Chromium carbides and chromium nitrides feature the best resistance to oxidation.

The TRD process has been used in practical applications since the early 1970s in Japan, just after the development of the molten borax bath process, which allowed simple and less expensive equipment to be used in obtaining the excellent properties of coated parts. They have now found substantial acceptance in various industrial fields worldwide.

Major applications include the following:

- Production tooling, such as molds and wear parts used in materials processing, for example, metal forging, sheet metal stamping, and metal casting (Ref 16, 28, 33, 39-41, 44, 47)
- Related wear parts for the processing of non-metallic materials, including rubber, plastics, clays, ceramics, papers, timbers, glass, and synthetic fibers

- Wear parts of various production machines used in dealing with metals and nonmetallic materials
- Parts of some consumer equipment, such as automobiles, motorcycles, and bicycles

Tool steels and cemented carbides are employed for the tooling and wear parts of production equipment used in cold forging (Ref 48). For consumer equipment parts, structure steels, including bearing steels, are usually used. There is little demand for cast irons.

Of the various surface-treatment methods in the heat treatment category, only TRD coatings form compact carbide and nitride layers. Furthermore, the greater adhesion strength caused by metallurgical bonding and the higher coating thickness has enhanced the versatility of TRD coatings. They are suitable for use in situations where abrasive wear and severe galling by high mechanical loads may otherwise cause damage, for example, in sheet metal stamping of high-strength steels. As for the problem related to stamping of high-strength steel that the world automobile industry faces, very informative reports have been published (Ref 49).

ACKNOWLEDGMENTS

The author wishes to express thanks to former colleagues at Toyota Central Research and Development Labs, Inc., who worked for development and improvement of the processes, and to many other people who contributed valuable information and suggestions regarding the practical application of the process in worldwide industries.

REFERENCES

1. T. Arai, Carbide Coating Process by Use of Molten Borax Bath in Japan, *J. Heat Treatment*, Vol 18 (No. 2), 1979, p 15–22
2. T. Arai, H. Fujita, M. Mizutani, and N. Komatsu, Formation of Carbide Layers on Steels Immersed in Fused Borax Bath, *J. Jpn. Inst. Met.*, Vol 40 (No. 9), 1976, p 925–932
3. T. Arai, J. Endo, and H. Takeda, Chromizing and Boriding by Use of a Fluidized Bed, *Proc. Fifth International Congress on Heat Treatment of Materials Conference*, Oct 20–24, 1986, p 1335–1341
4. L.E. Campbell, V.D. Barth, R.F. Hoeckelman, and B.W. Gonser, Salt Bath Chromizing, *J. Electrochem. Soc.*, Vol 96 (No. 4), 1949, p 262–273
5. T. Arai and H. Oikawa, Nitride and Carbide Formation onto Ceramics by Molten Salt Dipping Method, *Proceedings of Sintering '87*, Vol 2, Elsevier Applied Science, Nov 4–7, 1987, p 1385–1390
6. H. Fujita and T. Arai, Complex Carbide Layers Formed on the Steels in Molten Borax Baths Containing V and Cr, Nb and Cr, *J. Surf. Finish. Soc. Jpn.*, Vol 42 (No. 10), 1991, p 1019–1025
7. T. Arai, H. Fujita, and N. Komatsu, Complex Carbide V-Nb-C Layer on Steel Immersed in Fused Borax Baths, *J. Jpn. Inst. Met.*, Vol 41 (No. 5), 1977, p 438–444
8. H. Fujita and T. Arai, Two Carbide Layers Formed on the Steels Immersed Twice in Molten Borax Baths Containing V, Nb or Cr, *J. Surf. Finish. Soc. Jpn.*, Vol 42 (No. 1), 1991, p 116–121
9. T. Arai, H. Fujita, Y. Sugimoto, and Y. Ohta, Diffusion Carbide Coatings Formed in Molten Borax Systems, *J. Mater. Eng.*, Vol 9 (No. 2), 1987, p 183–189
10. T. Arai, H. Fujita, Y. Sugimoto, and Y. Ohta, “Diffusion Carbide Coating Formed in Molten Borax Systems (Reaction in Borax Bath and Properties of Carbide Coated Steels),” Paper 8512-008, *Conference on Surface Modification and Coatings* (Materials Week '85), Oct 14–16, 1985 (Toronto, Canada), ASM International
11. T. Arai and S. Moriyama, Growth Behavior of Vanadium Carbide Coatings on Steel Substrates by a Salt Bath Immersion Coating Process, *Thin Solid Films*, Vol 249, 1994, p 56–61
12. T. Arai and S. Moriyama, Growth Behavior of Chromium Carbide and Niobium Carbide Layers on Steel Substrates, Obtained by Salt Bath Immersion Coating Process, *Thin Solid Films*, Vol 259, 1995, p 174–180
13. A. Mlynareczak and K. Jastrebowski, Bildung und Wachstum von Vanadiumkarbidschichten beim Vanadieren von Werkzeugstählen, *Neue Hütte*, Vol 7, July 1990, p 259–263 (in German)
14. T. Arai, Behavior of Nucleation and Growth of Carbide Layers on Alloyed Carbide Particles in Substrates in Salt Bath Carbide Coating, *Thin Solid Films*, Vol 229 (No. 1), 1993, p 171–179
15. T. Arai, S. Moriyama, and Y. Sugimoto, Vanadium Carbide Layers Formed on Cast Irons Immersed in Molten Borax Baths, *Jpn. Foundryman Soc.*, Vol 60 (No. 2), 1988, p 104
16. Y. Sugimoto, Y. Ohta, and T. Arai, Low Temperature Salt Bath Chromium Carbonitride Coating Method, *J. Surf. Finish. Soc. Jpn.*, Vol 46 (No. 12), 1995, p 1119–1124
17. C. Wu, C. Luo, and G. Zou, Microstructure and Properties of Low Temperature Composite Chromized Layer on H13 Steel, *J. Mater. Sci. Technol.*, Vol 21 (No. 2), 2005, p 251–255
18. H. Cao, C. Wu, J. Liu, C. Luo, and G. Zou, A Novel Duplex Low-Temperature Chromizing Process at 500 °C, *J. Mater. Sci. Technol.*, Vol 23 (No. 6), 2007, p 823–827
19. H. Cao, C.P. Luo, J. Liu, and G. Zou, Phase Transformations in Low-Temperature Chromized 0.45 wt.% C Plain Carbon Steel, *Surf. Coat. Technol.*, Vol 201, 2007, p 7970–7977
20. D.M. Fabijanic, G.L. Kelly, J. Long, and P.D. Hodgson, A Nitrocarburizing and Low-Temperature Chromising Duplex Surface Treatment, *Mater. Forum*, Vol 29, 2005, p 77–82
21. P.C. King, R.W. Reynoldson, A. Brownrigg, and J.M. Long, Cr(N,C) Diffusion Coating Formation on Pre-Nitrocarburized H13 Tool Steel, *Surf. Coat. Technol.*, Vol 179, 2004, p 18–26
22. T. Arai and S. Harper, Thermoreactive Deposition/Diffusion Process for Surface Hardening of Steels, *Heat Treating*, Vol 4, *ASM Handbook*, ASM International, 1991, p 448–453
23. H.C. Child, S.A. Plumb, and J.J. McDermott, Carbide Layer Formation on Steels in Fused Borax Baths, *Proc. International Conference Organized by the Metals Society, Heat Treatment '84* (London), 1984, p 5.1–5.7
24. S.B. Fazluddin, A. Koursaris, C. Ringas, and K. Cowie, Formation of VC Coating on Steel Substrates in Molten Borax, *Surface Modification Technologies VI*, Minerals, Metals and Materials Society, 1993, p 45–59
25. K. Nakanishi, H. Takeda, H. Tachikawa, and T. Arai, Fluidized Beds Carbide Coating Process—Development and Its Application, *Congress Book of Heat & Surface '92, The Eighth International Congress on Heat Treatment of Materials*, Nov 17–20, 1992 (Kyoto Japan), p 507–510
26. S. Kinkel, G.N. Angelopoulos, and W. Dahl, Formation of TiC Coatings on Steels by a Fluidized Bed Chemical Vapor Deposition Process, *Surf. Coat. Technol.*, Vol 64, 1994, p 119–125
27. T. Arai, H. Fujita, Y. Sugimoto, and Y. Ohta, “Vanadium Carbonitride Coatings by Immersing into Low Temperature Salt Baths,” Paper 8820-0001, *Heat Treatment and Surface Engineering*, New Technology and Practical Applications, Proc. Sixth International Conference on Heat Treatment of Metals, Sept 28–30, 1988 (Chicago, IL)
28. T. Arai, H. Fujita, Y. Sugimoto, and Y. Ohta, Vanadium Carbonitride Coating by Immersing into Low Temperature Salt Bath, *Heat Treatment and Surface Engineering*, G. Krauss, Ed., ASM International, 1988, p 49–53
29. Y. Ohta, Y. Sugimoto, and T. Arai, Low Temperature Salt Bath Coating of Chromium Carbonitride, *Congress Book of Heat & Surface '92, The Eighth International Congress on Heat Treatment of Materials*, Nov 17–20, 1992 (Kyoto Japan), p 503–506
30. T. Arai and Y. Tsuchiya, Evaluation of Wear and Galling Resistance of Surface Treated Die Steels, *Proc. First International Conference, Advanced Technology of Plasticity*, Vol 1, 1984, p 225–230
31. K. Dohda, S. Kashiwaya, Y. Tsuchiya, and T. Arai, Compatibility between Tool Materials and Aluminum in Sheet Metal Ironing,

- Trans. North Am. Manuf. Res. Instit. SME*, Vol XXI, 1993, p 127–132
32. J.L. Anderson, K. Krebs, G. Kann, and N. Bay, Quantitative Evaluation of Lubricants and Tool Surfaces for Ironing of Stainless Steel, *Proc. First International Conference on Technology in Manufacturing Processes '97* (Gifu, Japan), 1997, p 358–364
 33. Y. Tsuchiya, H. Kawaura, K. Hashimoto, H. Inagaki, and T. Arai, Core Pin Failure in Aluminum Die Casting and the Effect of Surface Treatment, *Trans. 19th International Die Casting Congress and Exposition*, Nov 3–6, 1997 (Minneapolis, MN), North American Die Casting Association, p 315–323
 34. R. Shivpuri, S.I. Chang, Y.-L. Chu, and M. Kuthirakulathu, An Evaluation of H-13 Die Steel, Surface Treatments and Coatings for Wear in Die Casting Dies, T-91-OC3, *Proc. North American Die Casting Association* (Detroit, MI), 1993, p 391–397
 35. T. Arai and Y. Tsuchiya, Role of Carbide and Nitride in Antigalling Property of Die Materials and Surface Coatings, Metal Transfer and Galling in Metallic Systems, *Proc. Symposium Sponsored by the Non-Ferrous Metals Committee of Metallurgical Society and the Erosion and Wear G2 Committee of ASTM*, Oct 8–9, 1986 (Orlando, FL), p 197–216
 36. S. Hotta, K. Saruki, and T. Arai, Endurance Limit of Thin Hard Coated Steels in Bending Fatigue, *Surf. Coat. Technol.*, Vol 70, 1994, p 121–129
 37. Y. Tsuchiya, T. Arai, and S. Shima, Damage Behavior of Hard Coatings under Reciprocating Impact, *J. Jpn. Soc. Technol. Plast.*, Vol 37 (No. 429), 1996, p 1065–1070
 38. T. Arai, H. Fujita, and M. Watanabe, Evaluation of Adhesion Strength of Thin Hard Coatings, *Thin Solid Films*, Vol 154, 1987, p 387–401
 39. T. Arai and N. Komatsu, Carbide Coating Process by Use of Salt Bath and Its Application to Metal Forming Dies, *Proc. 18th International Machine Tool Design and Research Conference*, Sept 14–16, 1977, p 225–231
 40. T. Arai and T. Iwama, Carbide Surface Treatment of Die Cast Dies and Die Components, Paper G-T81-092, Proc. 11th International Die Casting Congress/Exposition, *Society of Die Casting Engineers*, June 1981
 41. P. Hairy and M. Richard, Reduction of Sticking in Pressure Die Casting by Surface Treatment, Paper T97-102, *Proc. 19th International Die Casting Congress/Exposition*, Nov 3–7, 1997 (Minneapolis, MN), p 307–314
 42. T. Tsuchiya, H. Kawaura, K. Hashimoto, H. Inagaki, and T. Arai, Paper T97-103, *Trans. 19th International Congress and Exposition*, Nov 3–6, 1997 (Minneapolis, MN), p 315–323
 43. T. Arai, Carbide Coating Process by Use of Molten Borax, Part I: Process and Application to Cold Forging Dies in Japan, *Wire*, Vol 30 (No. 3), 1981, p 102–104
 44. S. Hotta, K. Saruki, and T. Arai, Fatigue Strength at a Number of Cycles of Thin Hard Coated Steels with Quench-Hardened Substrates, *Surf. Coat. Technol.*, Vol 73, 1995, p 5–13
 45. T. Arai, Tool Materials and Surface Treatments, *J. Mater. Process. Technol.*, Vol 35, 1992, p 515–528
 46. C. Kato, J.A. Bailey, J.S. Stewart, T. Arai, and Y. Sugimoto, The Wear Characteristics of a Woodworking Knife with a Vanadium Carbide Coating only on the Back Face, Part II: The Influences of Tool Materials on the Self-Sharpening Characteristics, *Mokuzaï Gakkaiishi*, Vol 40 (No.12), 1994, p 1317–1326
 47. T. Arai, Carbide Coating Process by Use of Molten Borax, Part II: Process and Application to Cold Forging Dies in Japan, *Wire*, Vol 31 (No. 5), 1981, p 208–210
 48. T. Arai, Substrate Selection for Tools Used with Hard Thin Film Coatings, *Metalforming*, June 1998, p 31–39
 49. T. Katagiri, Y. Yamasaki, and A. Yoshitake, Effect of Tool Coatings on Galling Prevention in Forming of High Strength Steel, *Proc. Third International Conference on Tribology in Manufacturing Process* (Yokohama, Japan), 2007, p 41–46

SELECTED REFERENCES

- T. Arai, H. Fujita, Y. Sugimoto, and Y. Ohta, Vanadium Carbonitride Coating by Immersing into Low Temperature Salt Bath, *Heat Treatment and Surface Engineering*, G. Krauss, Ed., ASM International, 1988, p 49–53
- T. Arai and S. Harper, Thermoreactive Deposition/Diffusion Process for Surface Hardening of Steels, *Heat Treating*, Vol 4, *ASM Handbook*, ASM International, 1991, p 448–453
- T. Arai and N. Komatsu, Carbide Coating Process by Use of Salt Bath and Its Application to Metal Forming Dies, *Proc. 18th International Machine Tool Design and Research Conference*, Sept 14–16, 1977, p 225–231
- T. Arai and Y. Tsuchiya, Role of Carbide and Nitride in Antigalling Property of Die Materials and Surface Coatings, Metal Transfer and Galling in Metallic Systems, *Proc. Symposium Sponsored by the Non-Ferrous Metals Committee of Metallurgical Society and the Erosion and Wear G2 Committee of ASTM*, Oct 8–9, 1986 (Orlando, FL), p 197–216
- S. Hotta, K. Saruki, and T. Arai, Fatigue Strength at a Number of Cycles of Thin Hard Coated Steels with Quench-Hardened Substrates, *Surf. Coat. Technol.*, Vol 73, 1995, p 5–13
- T. Katagiri, Y. Yamasaki, and A. Yoshitake, Effect of Tool Coatings on Galling Prevention in Forming of High Strength Steel, *Proc. Third International Conference on Tribology in Manufacturing Process* (Yokohama, Japan), 2007, p 41–46
- K. Nakanishi, H. Takeda, H. Tachikawa, and T. Arai, Fluidized Beds Carbide Coating Process—Development and Its Application, *Congress Book of Heat & Surface '92, The Eighth International Congress on Heat Treatment of Materials*, Nov 17–20, 1992 (Kyoto, Japan), p 507–510
- Y. Ohta, Y. Sugimoto, and T. Arai, Low Temperature Salt Bath Coating of Chromium Carbonitride, *Congress Book of Heat & Surface '92, The Eighth International Congress on Heat Treatment of Materials*, Nov 17–20, 1992 (Kyoto, Japan), p 503–506

should be between points F and C as the steel is reheated to T again. The carbon concentration of austenite moves to point C because the C_p of furnace gas is point C. In other words, the residual undissolved carbides remain unchanged and the carbon concentration of austenite over time moves to point C. Some of the carbides dissolve; at the same time some of them grow. The carbide will precipitate and grow once the temperature is cooled to point D. If this operation is repeated, the carbide will precipitate and grow continually (Ref 10).

In 1970, steel was carburized at 920°C (1690°F) for 4 h ($C_p = 0.9\%$), then it was quenched in oil. The steel then was processed by carburizing at 920°C for 3 h ($C_p = 1.2\%$) and then quenched in oil. In other words, the steel was carburized and quenched at the C_p near eutectoid composition first, then the carbide formed by the nucleus of undissolved carbides and impurity elements after the reheated carburizing.

Further improvement was made by Japanese investigators (Ref 11, 12). The carburizing was conducted to make the surface carbon content higher than eutectoid composition because the C_p was lower than A_{cm} . After that, when the C_p was higher than A_{cm} , the carbide grew as the steel was heated to higher than A_{c1} by a speed lower than $20^\circ\text{C}/\text{min}$ ($35^\circ\text{F}/\text{min}$) and then the heat was kept at a range lower than 950°C (1740°F).

The carburizing process of the conventional carburizing steel had been researched by Chinese materials heat treatment workers. The carburized layer with large amounts of round, fine, and uniform particulate carbides was obtained in 20CrMnTi, 12Cr2Ni4A, and 18Cr2Ni4WA steel (Ref 13).

In the cycle carburizing conducted on 20CrMnTi steel (Ref 1), the carburized layer contained dispersed carbides, and the carbon content in the surface was up to 1.25%. The high-carbon-potential solid penetration enhancers and pretreatment carburizing were applied on 35CrMo steel (Ref 14), and the result was that the carburized layer with dispersed particulate carbides was obtained and the carbon content in the surface was up to 2.7%. The circulating supercarburizing process was used on 20Cr steel (Ref 15) and the supersaturated carburizing layer with high carbon content was obtained. The surface hardness of the supersaturated carburizing layer with dispersed particulate carbides was up to 912 HV (0.1g), and the wear resistance of the supercarburized steel was more than 20% compared to conventional carburizing. As a result, supercarburizing as well as workpiece strengthening can be realized on conventional carburizing steel by controlling the nucleation, growth, and precipitation of the carbides.

In the following, conventional carburizing steel 20CrMnTi is an example to introduce the supercarburizing process, mechanical properties, and microstructure (Ref 16). Table 1 shows the chemical constitution and transition point of 20CrMnTi steel. After being normalized at 880°C

Table 1 Chemical composition and transition point of 20CrMnTi steel

C	Composition, %						Transition point, $^\circ\text{C}$ ($^\circ\text{F}$)				
	Mn	Cr	Si	Ti	S	P	A_{c1}	A_{c3}	A_{r3}	A_{r1}	M_s
0.19	0.96	1.22	0.29	0.087	≤ 0.04	≤ 0.04	760 (1400)	840 (1544)	775 (1427)	665 (1229)	374 (705)

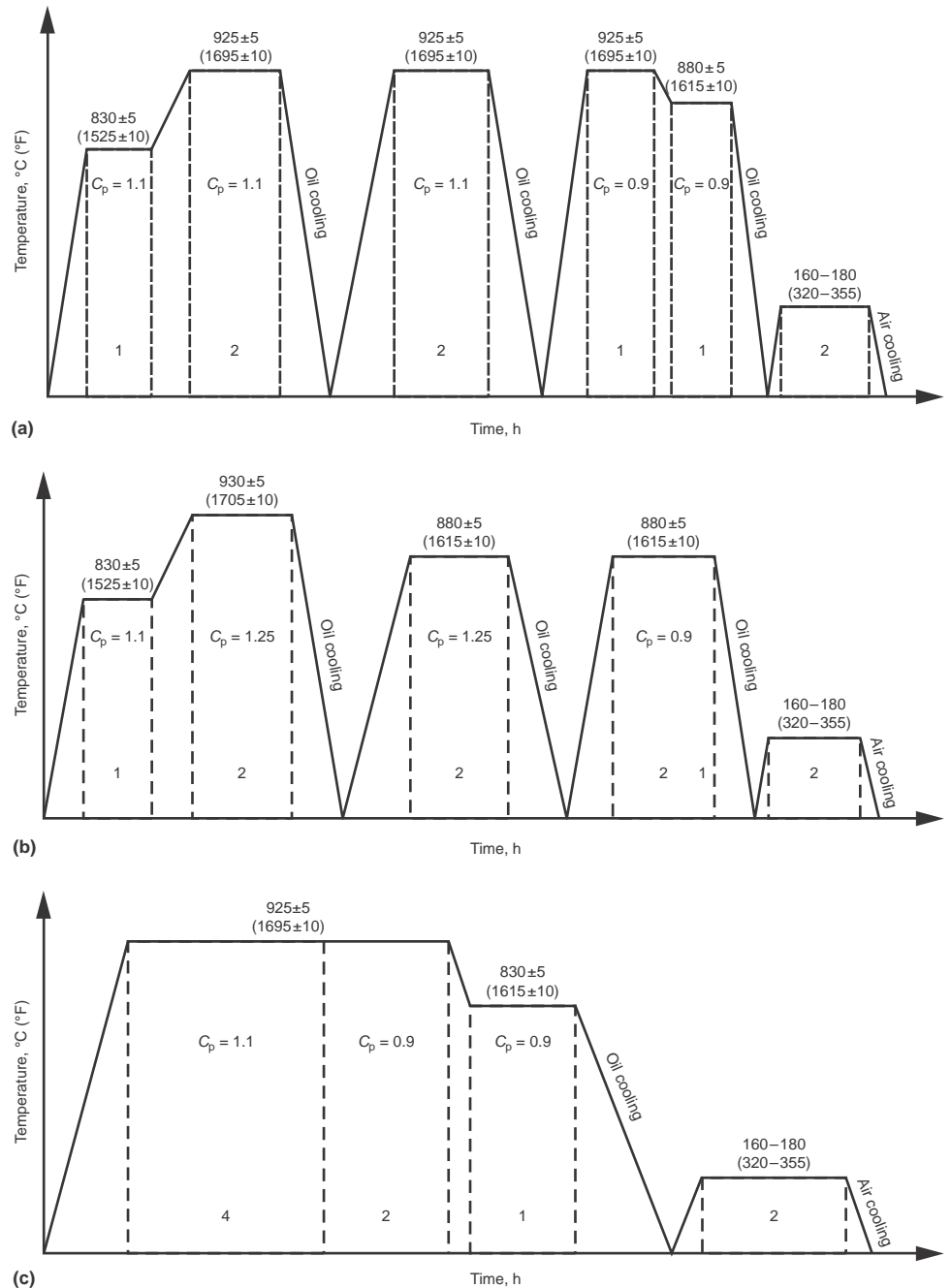


Fig. 2 Process curves of (a) supersaturated carburization, Process A, (b) supersaturated carburization, Process B, and (c) conventional carburization. C_p , carbon potential

to 890°C (1615 to 1635°F), the 20CrMnTi steel was processed into the standard sample for the ML-10-type abrasive wear testing machine, and the optical sample was $8\text{ mm} \times 10\text{ mm}$ ($0.31\text{ in.} \times 0.39\text{ in.}$) in size.

The carburizing equipment is a dual-chamber box-type gas carburizing furnace with the cooling apparatus located in the front chamber. During the thermal cycling stage, the sample is pulled out to the front chamber from the

heating chamber. After the oil is cooled to room temperature, the steel is heated in the heating chamber, completing the cycle. Kerosene was used as the carburizing agent with methanol diluent. The C_p was monitored by oxygen probe. The C_p in the furnace was controlled by adjusting the carburizer drops through an automatic control solenoid valve. The C_p in the furnace was checked by testing the carbon content in the pure iron foil. The process curves of carburizing are shown in Fig. 2.

The isothermal section drawing of Fe-Cr-C at 850 °C (1560 °F) is shown in Fig. 3. It can be seen that the steel will be in the two-phase region of $\gamma + M_3C$ at the C_p of 1.1 and the temperature of 830 ± 5 °C (1525 ± 10 °F). At this condition, the composition of the austenite is not uniform and the grain size is very fine, the solubility of carbon in austenite is very low, and the C_p is relatively high. However, the displaced atom of chromium, titanium, and so forth in the austenite can diffuse only for a

short range, which is beneficial to obtaining a large amount of fine carbides (Ref 17). In the subsequent carburizing process, it provides the favorable conditions for the formation of (Fe, Me)₃C carbide.

At the C_p of 1.1, the following two-cycle carburizing treatment is adopted: 925 ± 5 °C → room temperature → 925 ± 5 °C (1695 ± 10 °F → room temperature → 1695 ± 10 °F). During the oil cooling stage (925 ± 5 °C → room temperature), the supersaturated carbon atoms in the austenite are hard to diffuse, thus the austenite transforms into the α solid solution with saturated carbons (martensite). During the heating process (room temperature → 925 ± 5 °C), the martensite decomposes into carbide and the carbon content decreases gradually. As the steel is heated to higher than A_{r1} , the austenite begins to form and the carbon content decreases gradually. The existing carbide begins to dissolve but does not dissolve completely. The alloy carbides of chromium, titanium, and so forth are especially hard to dissolve, and the irregularly shaped carbide tends to become spherically shaped. Simultaneously, the new carbide nucleates and grows continually.

If this process is repeated, a large amount of fine carbides can be obtained in the carburizing layer (Ref 18). Although repeated thermal cycling carburizing can refine the grain size and increase the amount of carbide effectively, too much cycle carburizing time is not conducive to improving carburizing efficiency (Ref 15, 17). Considering the actual economic efficiency and technical requirements in the production process, dispersed carbides can be formed in the carburizing layer by the application of precarburing and two-cycle carburizing treatment (Process A in Fig. 2a). During the last stage of carburizing, the C_p is changed from 1.1 to 0.9. After diffusion carburizing for

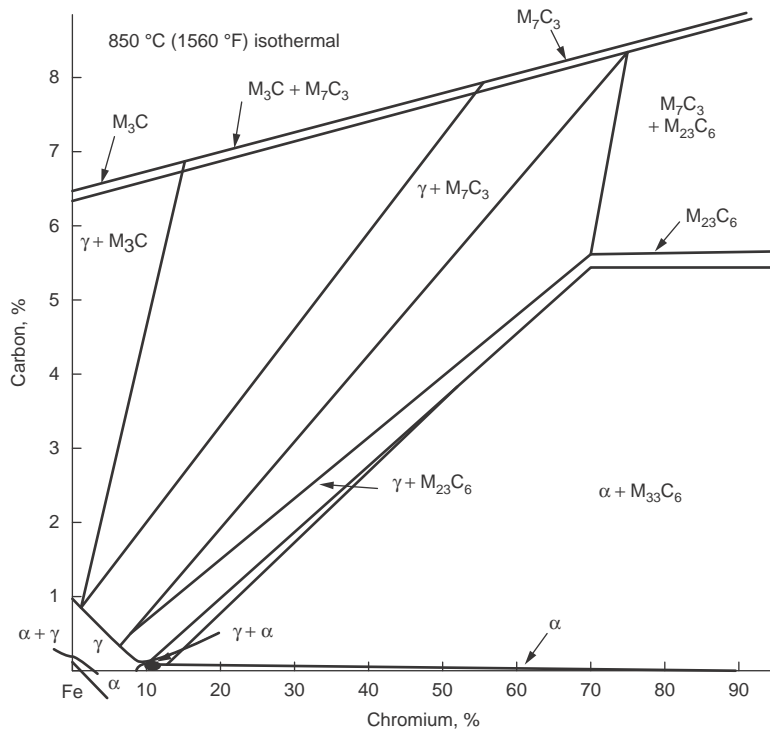


Fig. 3 Isothermal section drawing of Fe-Cr-C at 850 °C (1560 °F)

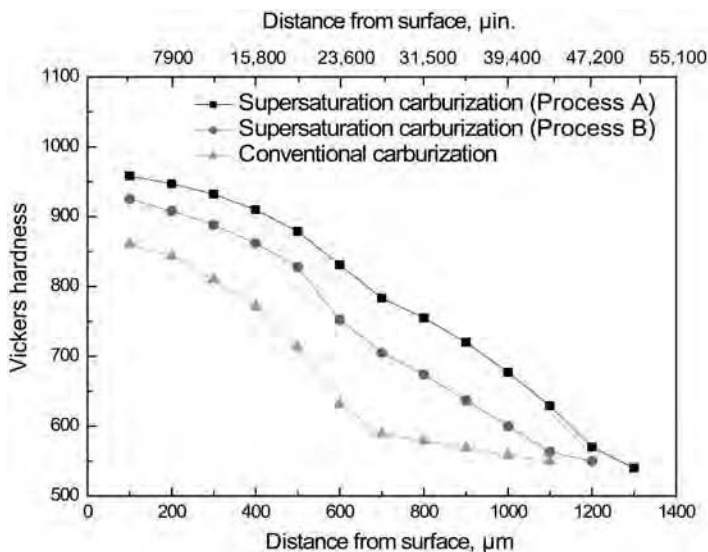


Fig. 4 Microhardness distribution of the carburized layer

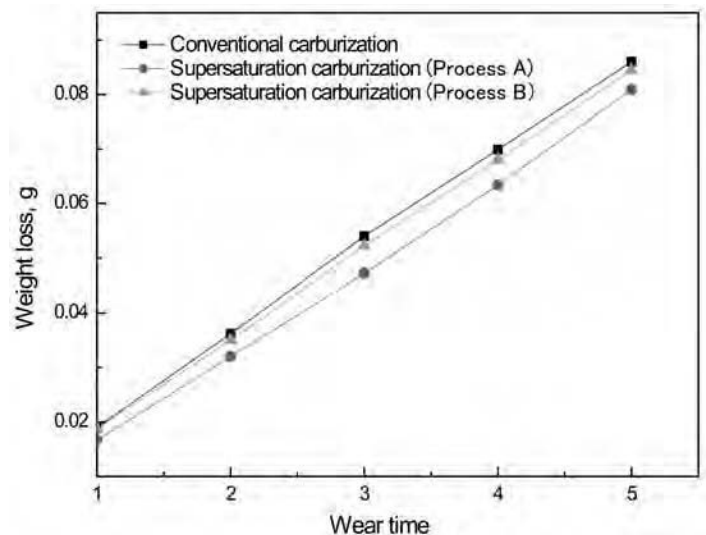


Fig. 5 Abrasion characteristic curves of the carburized samples

an hour, the distribution of the carbon concentration slows and the depth is expanded further.

Compared to the conventional carburized layer, a large amount of dispersed particulate alloy carbides is distributed in the martensite matrix, which results in the high hardness of the carburized layer. The supersaturation carburized layer from Process A (Fig. 2a) results in finer and more evenly distributed carbides in the carburized layer than for Process B. The better microstructure from Process A results in higher hardness (Fig. 4). Figure 5 illustrates the relationship between wear weight loss and wear time. The microhardness of a supersaturation carburized layer is up to 958 HV (0.1 g), which is 1.1 times that of a conventional carburized layer (Fig. 4).

The wear resistance of a supersaturation carburized layer is higher than that of a conventional carburized layer. At the same wear resistance, the wear loss weight of a supersaturation carburized layer is only 80% of a conventional carburized layer. It can be concluded that in the 20CrMnTi steel, after the treatment of pre-carburizing + two-cycle carburizing and quenching + low tempering, the microhardness and the wear resistance can be improved 10 and 20%, respectively.

Steels for Supercarburizing

In order to generate carbides, the supercarburizing process needs a higher C_p in the furnace. However, a C_p that is too high can easily form carbon black in the production process; therefore, steel suitable for supercarburizing should meet the following conditions (Ref 19):

Table 2 Composition of experimental steel

Composition, wt%								
C	Mn	Si	Mo	Cr	P	S	V	Fe
0.35	1.37	0.90	0.40	3.20	0.020	0.025	0.50	bal

- A large amount of carbides can be formed at the given C_p .
- The carbides can be formed for a short time at a given depth.
- The shape, size, and distribution of carbides can be regulated.

It is hard to achieve supercarburizing if carbon steel without alloying elements is used. However, using steel with carbide-forming elements such as chromium, molybdenum, and vanadium can realize supercarburizing easily.

A composition suitable for supercarburized steel is: 0.1~0.4% C, 0.7~0.9% Si, 2.7~3.2% Cr, 1.1~1.4% Mn, 0.4~0.6% Mo, and 0.3~0.5% V (Ref 20). The affinity of alloying elements such as chromium, molybdenum, and vanadium on the carbon is very strong; a large amount of alloy carbide precipitates once the carbon concentration exceeds the saturated concentration of austenite. During this process, the carbon is hard to diffuse from the surface to the interior of the steel, so the carbon concentration in austenite is lower than that of the equilibrium concentration (Ref 21).

The precipitation of chromium and molybdenum alloying carbides during the carburizing process can inhibit the grain growth of austenite. Compared to carbon steel, the grain size of the steel containing chromium and molybdenum alloying elements is much finer. The finer grains result in a large number of grain boundaries, which provides more channels for carbon diffusing to be internal. Thus, the existence of chromium and molybdenum alloying carbides is favorable for increasing the carbon concentration depth of the carburized layer (Ref 22). Additionally, the chromium and molybdenum alloying elements can inhibit the homogenization of the austenite component and increase the composition heterogeneity in the grains, which is favorable to the nucleation of carbides (Ref 23). If the C_p is enhanced appropriately, the dispersive carbides can be formed successfully in this alloy steel using the same technology. Supercarburizing this steel can be realized easily using simple carburizing technology.

In recent years, steel suitable for supercarburizing has been investigated by many researchers. The carburized layer with dispersive carbides was obtained in Cr12 steel in Ref 9. In investigation of 25W3Mo4Cr2V7Co5 steel (Ref 24), uniformly distributed particulate carbides were obtained using supercarburizing technology at 1050 °C (1920 °F) for 8 h. The average size of carbides obtained was approximately 4 to 6 μm (157 to 236 $\mu\text{in.}$), and the largest size was only 10 μm (394 $\mu\text{in.}$). Carburizing was conducted on three sections of W6Mo5Cr4V2Al high-speed steel in Ref 25, and the carbon content in the surface was up to 3.2%. Investigation of Cr3MoMnSi steel (Ref 26) resulted in a 1.8% C content on the surface and an HRC 66 surface hardness by quenching at 800 °C (1470 °F) followed by cold treatment at -70 °C (-95 °F) and tempering at 150 °C (300 °F). The supercarburizing also was achieved in H13 steel (Ref 27), with Cr_7C_3 carbides formed, and the size of these carbides being between 200 and 300 nm (8 to 12 $\mu\text{in.}$). In addition, alloy steel suitable for supercarburizing was investigated (Ref 28). The surface hardness of Fe-0.48%V and Fe-1.49%V steel can reach 1000 HV under the conditions of $C_p = 1.4$, carburizing 5 h at 950 °C (1740 °F), followed by water quenching. The shared characteristics of these steels are that all of them contain strong carbide-forming elements such as chromium, molybdenum, vanadium, and so forth; however, the carburizing technology used is very simple.

By using solid-state electronic theory with programming based on matrix theory, the component design experience formula for multiples of carbon in low-alloy steel was established (Ref 29). Based on the results of that research, a new supercarburizing steel, 35Cr3SiMnMoV, was investigated (Ref 20). This type of supercarburizing steel has been applied in cold drawn steel tube molding. In the following sections, the supercarburized steel composition, the carburizing characteristics, mechanical properties testing, and microstructure analysis are discussed for 35Cr3SiMnMoV steel (Ref 23).

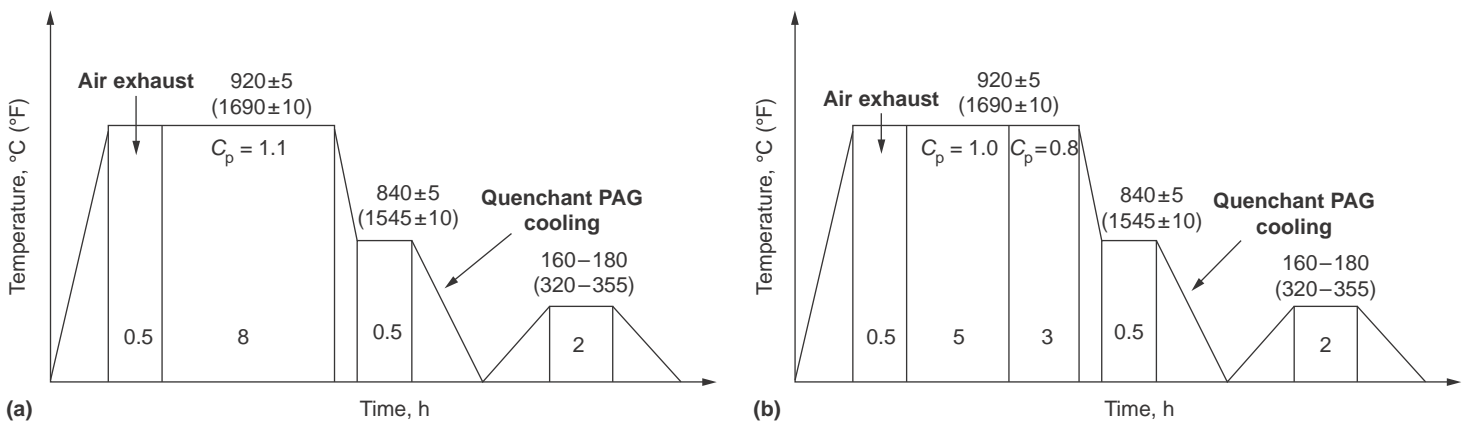


Fig. 6 (a) Supersaturated carburization process curves of 35Cr3SiMnMoV steel. (b) Conventional carburization process curves of 20CrMnMo, 20Cr2Ni4 steel. C_p , carbon potential. PAG, polyalkylene glycol

The 35Cr3SiMnMoV steel was smelted by a medium-frequency coreless furnace. The composition is shown in Table 2. After the normalizing treatment at 880 °C (1615 °F), the 35Cr3SiMnMoV steel was machined to produce an optical sample and a wear test sample.

The carbonization was done in a drip-type gas carburizing furnace with acetone as the carburizing agent and methanol as the diluent. Oxygen probe was used to control carbon potential. The quenching medium chosen was 5% polyalkylene glycol (PAG) water-soluble quenching liquid. Figure 6 shows the supersaturated carburization process curves of 35Cr3SiMnMoV steel and the conventional carburization process curves of 20CrMnMo, 20Cr2Ni4 steel.

The supersaturated carburization sample of 35Cr3SiMnMoV steel was selected. After surface cleaning by ultrasonic means, the microstructure was observed by scanning electron microscope (SEM), as shown in Fig. 7. The phase analysis of the supercarburized layer was conducted by x-ray diffraction (XRD) analyzer. The XRD pattern of the carburized layer on 35Cr3SiMnMoV steel is shown in Fig. 8.

The microstructure of the supercarburized layer is tempered martensite, carbide, and retained austenite, as shown in Fig. 7. The amount of carbide is approximately 30 to 40%, and the fine particulate carbides distributed uniformly. The shape of some of the carbide is wormlike. The existence of strong carbide-forming elements chromium, molybdenum, and vanadium in steel can seriously hinder austenitic component homogenization. The austenite at the peak area of constituent fluctuations will be in the supersaturated state once the carbon concentration exceeds the supersaturated carbon concentration. At this peak area, the austenite will be at a nonsteady state for the large lattice distortion. If the partial lattice distortion energy induced by the carbide precipitation is larger than that of the increase of free enthalpy, the carbide will precipitate dispersively. By XRD, as shown in Fig. 8, it can be seen that M_7C_3 and M_2C alloying carbide with short curing speed is formed, thus a large amount of fine particulate carbide can be obtained in the Fe_3C . The austenitic grain boundary still is the priority position for carbide precipitation. Figure 7 shows that some 3 to

6 μm (118 to 236 $\mu\text{in.}$) rod carbides were distributed at the austenitic grain boundaries. It was thought to be the result of coalescence of fine carbides. Silicon, as a non-carbide-forming element, has a tendency toward grain-boundary segregation. The silicon at grain boundaries can inhibit the carbide precipitation, thus greatly reducing the possibility of the formation of the mesh carbide. Additionally, silicon can reduce the aggregation growth rate of carbides by inhibiting the diffusion of carbon. The 35Cr3SiMnMoV steel contains both strong carbide-forming elements (chromium, molybdenum, vanadium) and non-carbide-forming elements (silicon), which is the reason for being able to obtain a supercarburized layer with dispersive carbides using simple carburizing technology.

The carburized workpiece is required to have a certain hardness and depth of a carburized layer. The hardness distribution of supercarburized layer of 35Cr3SiMnMoV steel and conventional carburized layer of 20CrMnMo and 20Cr2Ni4 steel is shown in Fig. 9.

The microhardness of a supercarburized layer of 35Cr3SiMnMoV steel is higher than that of a conventional carburized layer. At the depth of 175 μm (6900 $\mu\text{in.}$) from the surface, the microhardness of a supercarburized layer is up to 1025 HV (0.1 g), which is approximately 20% higher than a 20CrMnMo and 20Cr2Ni4 conventional carburized layer.

Figure 10 shows the wear curves of the carburized layer. It illustrates that the abrasion resistance of a supercarburized layer is higher than for a conventional carburized layer. Under the same testing conditions, the mass loss of a supercarburized layer is only approximately 60% of a conventional carburized layer. It demonstrates that the dispersive particulate carbides at the matrix of cryptocrystalline martensite not only improves the microhardness of a carburized layer but also increase its abrasion resistance.

Originally, the cold drawn steel tube mold was treated by thermal refining and cyaniding. Then they switched to Cr12MoV steel treated by quenching and tempering, but its mechanical properties and service life were not satisfactory, so the cost ultimately was higher. The 35Cr3SiMnMoV steel treated by supercarburizing, quenching, and low tempering was applied to the stainless steel tube production line by Taiyuan Iron and Steel (Group) Co. The cold drawing process of the stainless steel is shown in Fig. 11. After drawing more than 72 tonnes (72 metric tons, or 80 tons) of various materials of stainless steel pipe, the face of the mold was bright and only slight wear was found by macroscopic examination. No obvious change in size occurred and the mold could be used continually.

After the treatment of supercarburizing, quenching, and low tempering, the microhardness and abrasion on the surface of 35Cr3SiMnMoV steel is very high. Durability also is very high. Compared to Cr12MoV steel (treated by

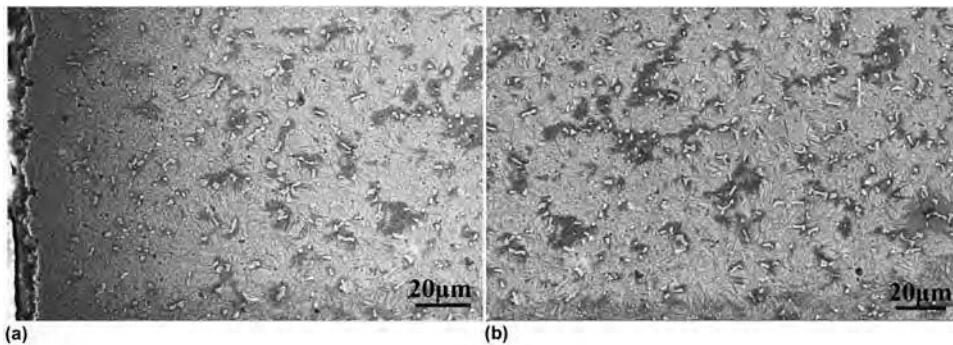


Fig. 7 Scanning electron microscope images of (a) the surface, and (b) the inside of the supercarburized layer treated by quenching and tempering

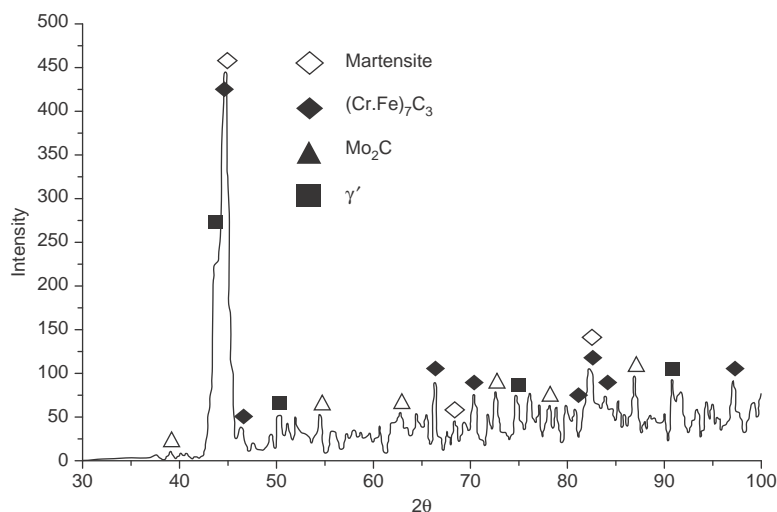


Fig. 8 X-ray diffraction pattern of the carburized layer on 35Cr3SiMnMoV steel

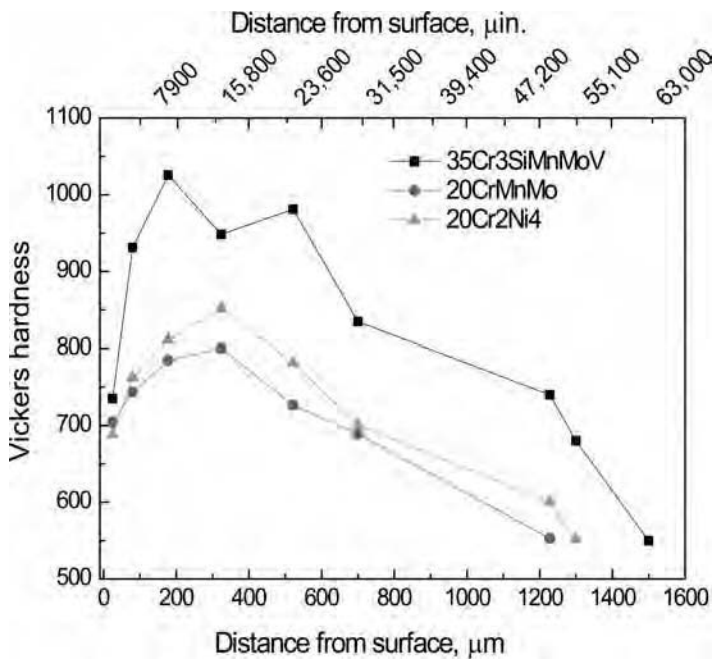


Fig. 9 Hardness distribution of supercarburized layer of 35Cr3SiMnMoV steel and conventional carburized layer of 20CrMnMo and 20Cr2Ni4 steel

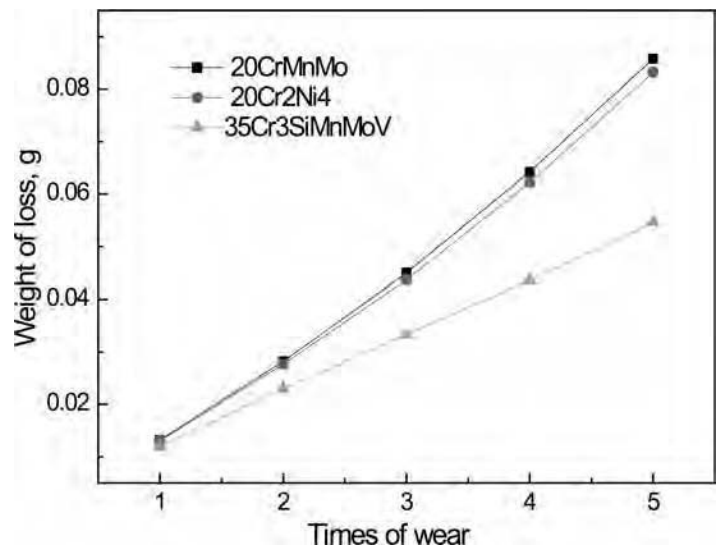


Fig. 10 Wear curves of the carburized layer



Fig. 11 Cold drawing process of stainless steel

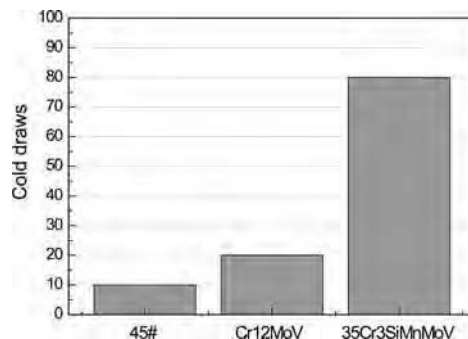


Fig. 12 Comparison of service life of three types of steel

quenching and tempering) and 45# steel (treated by thermal refining and cyaniding), the 35Cr3SiMnMoV steel (treated by supercarburizing, quenching, and low tempering) not only exhibits high mechanical properties but also has lower cost and has overcome the cyanide pollution problem. During the process of improving practical engineering applications, service life of supercarburized steel has been improved significantly, as shown in Fig. 12. As a result, the application of supercarburized steel can produce good economic and social benefits.

REFERENCES

- L.-D. Liu and F.-S. Chen, Super-carburization of Low Alloy Steel in a Vacuum Furnace, *Surf. Coat. Tech.*, Vol 183 (No. 2-3), May 2004, p 233-238
- T. Kimura and K. Namiki, Plasma Carburizing Characteristics and Fatigue Properties of Super Carburizing Steel, *Denki Seiko Jan. Vol 63 (No. 1)*, 1992, p 4-14
- T. Kimura and K. Namiki, Plasma Super Carburizing Characteristics and Fatigue Properties of Chromium Bearing Steels, *Conf. Proc. Heat and Surface '92 (Kyoto, Japan)*, 1992, p 519-522
- Z.S. Hou and H.F. Zhou, Carbide Extreme Value and Carbon Potential Threshold, *Trans. Met. Heat Treat.*, Vol 13 (No. 1), 1992, p 1-6
- T. Naito, Y. Kibayashi, and K. Nakamura, High-Carbon Cementation Technique, *J. Heat Treat.*, Vol 26 (No. 2), 1986, p 157-161
- H.S. Ming, T. Takayama, and T. Nishizawa, in Japanese, Carbide Dispersion Carburizing of a 12%Chromium Steel, *J. Japan Inst. Metals*, Vol 45, (No. 11). 1981, pp 1195-120
- M. Tsujikawa, S. Noguchi, N. Yamauchi, N. Ueda, and T. Sone, Effect of Molybdenum on Hardness of Low-Temperature Plasma Carburized Austenitic Stainless Steel, *Surf. Coat. Tech.*, Vol 201 (No. 9-11), Feb 2007, p 5102-5107
- Y. Sarikaya and M. Önal, High Temperature Carburizing of a Stainless Steel with Uranium Carbide, *J. Alloy Compd.*, Vol 542, Nov 2012, p 253-256
- H. Jiménez, M.H. Staia, and E.S. Puchi, Mathematical Modeling of a Carburizing Process of a SAE 8620H Steel, *Surf. Coat. Tech.*, Vol 120-121, Nov 1999, p 358-365
- S.M. Hao, Application of Carbide-Dispersion Carburizing and Its Mechanism, *J. Northeast Inst. Tech.*, No. 3, 1983, p 21-30
- T. Naito, Practical Cementation Quenching, Japan, Asakura Shoten, in Japanese, 1970, p 225
- Y. Abe, High Carbon Cementation, *Kinzoku Zairyo (Metallic Material) in Japanese*, (No. 6), 1977, p 32-35
- Z. Qin and Q. Zhu, Performance of Granular Carburized Layer and Its Formation Process, *Aviat. Tech.*, Nanjing Aeronautical Institute, (No. 4), 1988, p 8-10
- Y. Qi, Carbide Dispersion Carburizing in Solidity, *Working Tech.*, No. 2, 1999, p 16-18
- B.-J. Zhang, J.-Y. Shi, and S.-J. Teng, Microstructure and Wear Resistance of Supersaturation Carburized Layer on 20Cr Steel, *Heat Treat. Met.*, Vol 32 (No. 8), 2007, p 84-86
- J.-Y. Shi, J. Yu, and X. Tian, Study on Supersaturated Carburization Process for

- 20CrMnTi Steel, *Working Tech.*, Vol 39 (No. 12), 2010, p 147–149
17. K. Hua, Athermal Thermochemical Treatment, *Heat Treat. Met.*, (No. 1), 1986, p 17–22
 18. K. Zhao, X. Deng, and Z. Peng, Study on Thermocycling Carburizing of 20 and 20CrMnTi Steels, *Heat Treat. Met.*, (No. 12), 1991, p 3–8
 19. K. Tamamoto, Plasma Cementation Method, Netsushori (Heat Treatment) 2005, p 128–132
 20. J. Shi, X. Tia, B. Zhang, W. Liang, and Z. Hou, Super-carburizing Steel, China National Invention Patent 200710062035.8
 21. X. Lifang, *Technology of Metal Heat Treatment*, Harbin Institute of Technology Press, 1985, p 111
 22. T. Liu and T. Qu, The Carburization with High Concentration and Its Applications, *J. Benxi College of Metallurgy*, Vol 2 (No. 2), 2000, p 1–4
 23. J. Shi, B. Zhang, G. Xie, J. Yu, and W. Liang, Study on Supersaturation Carburization of 35Cr3SiMnMoV Steel, *Trans. Mater. Heat*, Vol 31 (No. 4), 2010, p 133–136
 24. C. Wang, Z. Shi, and Z. Qi, Carbides and Properties of Overcarburized Steel 25W3Mo4Cr2V7Co, *Special Steel*, Vol 15 (No. 3), 1994, p 13–16
 25. X. Gong, W. Ye, Y.Z. Zhou, and X. Li, Study on the Structures and Properties of High Concentration Carburized Layer, *Hot Work. Tech.*, (No. 3), p 11–13
 26. D. Xu, Study on High Carbon Concentration Carburization, *Heat Treat. Met.* (No. 2), 1994, p 27–31
 27. Z.-J. Yu, D.-I. Wang, Y. Liu, S.-M. Hao, and G. Zhao, Carbide Dispersion Carburizing of Steel H13, *J. Mater. Metall.*, Vol 1 (No. 4), 2002, p 311–316
 28. D. Wang, Y. Liu, S. Hao, and G. Zhao, Carbide Dispersion Carburization of Fe-0.48%V and Fe-1.69%V, *J. Northeastern U.*, Vol 23 (No. 9), 2002, p 854–857
 29. J. Shi and G. Xie, Application of Empirical Electron Theory of Solids and Molecules to Composition Design of Multi-Component Medium-Low-Alloy Steels, *J. Wuhan U. Tech.—Mater. Sci. Ed.*, Vol 27 (No. 1), 2012, p 9–17

INDEX

Index Terms

Links

A

ABAQUS	63			
Absorbed nitrogen	627	632	635	638
Absorptivity	479	481	487	
Accelerated cycling annealing	303–304			
Active heat-transfer boundary condition				
bodies with internal heat generation	171–172			
bodies with negligible thermal gradients	168–169			
bodies with thermal gradients	169–171			
direct heat-conduction problem (DHCP)	168			
inverse heat-conduction problem (IHCP)	168	169–170	171	
Newton's law of cooling	168			
overview	167–168			
verification	172–173			
Active-screen plasma nitriding	692–693			
ADI. <i>See</i> Austempered ductile iron (ADI)				
Advanced high-strength steels (AHSS)	317	319	320	
Aerated bath nitriding				
aerated cyanide-cyanate nitriding	682			
aerated low-cyanide nitriding	682			
case hardness	682			
overview	681			
steel composition, effects of	682			
Aerated cyanide-cyanate nitriding	682			
Aerated low-cyanide nitriding	682			
Aerospace applications				
liquid induction carburizing	519			
low-pressure carburizing (LPC)	586–587			
press quenching	256			
Agitation. <i>See also</i> Fluid flow				
bodies with negligible thermal gradients	168			
equipment				
draft tubes	117–118			

Index Terms

Links

Agitation (Cont.)

overview	115		
propellers	116–117		
pumps	115–116		
workpiece, movement of	116		
H-steels	51		
intensive quenching (IQ)	199		
low-melting salt bath	127–128		
martempering	372		
molten salts	236		
oil quenchants	137–139		
as process variable, quenching	94	114–115	
propellers	116–117		
in quenching medium	20–21		
quenching severity	192		
rewetting	164	166	
salt quenching	233	234–235	236
water quenching heat transfer	247		
AHSS. See Advanced high-strength steels (AHSS)			
Air-quenching media	122		
ALLNIT process	654		
Allotropy	3	4	
Alloy steels			
flame hardening	436		
normalizing	283–284		
selection for hardenability	49–50		
Alloying			
annealing	305	306	
austenite grain growth	314		
boriding	716		
carburized hardenability test	36		
carburizing steels	514		
continuous annealing	299		
electron beam process	462		
hardenability, affecting	45	46	51
high-alloy steels	306		
induction surface hardening	447		
induction surface hardening, PM parts	459		

Index Terms

Links

Alloying (Cont.)

isothermal transformation (IT) diagrams	18–20			
laser alloying	481	482		
laser surface hardening	476	478		
laser surface heat treatment	395			
low-alloy steels	305			
martensite hardness and hardenability	14	26		
plain carbon steels	305			
Q&P	317			
supercarburizing	744			
temper embrittlement	340			
tempering	334	336		

Alloying elements

annealing	299			
boriding, ferrous materials	716			
boron	46			
chromium	46			
hardenability, factors affecting	45–46			
manganese	46			
molybdenum	46			
nickel	46			
synergistic combinations	46			

Alloys

aluminum alloys	151	161	238	243
	482	493		
chromium alloys	641			
cobalt alloys	710	716	722	726–727
	728	729		
iron-carbon alloys	8	9	162	318
magnesium alloys	493			
nickel alloys	540	716	719	726–727
titanium alloys	494	710	716	717
zinc alloys	478	722		

Aluminizing

708

Aluminum

austenite grain growth	315			
boron factors	87			
multiplying factors	83			

Index Terms

Links

Aluminum oxide (Al₂O₃)	240			
AMAX	63			
American Gas Association	431			
American Insurance Association	431			
Ammonia				
annealing	296			
batch furnace atmospheres	608	609		
boriding	716			
carbonitriding	393	520	599	600
	601	602	614	
carbonitriding atmospheres	607			
carbonitriding temperature selection	609	610		
catalytic nitriding	665			
content, carbonitriding	606	607–608		
continuous furnaces atmospheres	609			
deep case carburizing	401			
exhaust gas	677			
fixtures, nitriding	676	677		
furnace atmospheres	606			
gas carburizing	549	551		
gas nitriding	677			
gas nitriding, ammonia supply	677			
guidelines, carbonitriding	614			
hardenability of case, carbonitriding	604			
hardness gradients, carbonitriding	605			
high- and low-pressure nitriding	653–654			
hydrogen analyzer	666			
infrared analyzers	667			
iron-nitrogen phase diagram	622			
Ivanit control approach	666–667			
liquid carburizing and cyaniding	565			
liquid pressure nitriding	681	684	690	698
low-temperature nitriding and nitrocarburizing	651			
nitriding	619	626	631	651–652
	653			
nitriding, atmosphere control	661–665			
nitriding, common problems	673	674		

Index Terms

Links

Ammonia (*Cont.*)

nitriding, measuring the potentials	665–668	
nitriding processing	660	
nitrocarburizing	395	
nitrocarburizing, ferritic and austenitic	656	
nitrogen-diluted atmospheres	654	
N-quench	657	
pressure regulation	677	
production of	649	
retained austenite, control of	605–606	
safety precautions	615	674
special precautions	677	
sulfonitriding	655	
tempering, carbonitrided parts	611	
tube retorts	676	
vertical retort furnace	675	
void formation	605	
water burette (pipette)	665	
water quenching	610	
zero-flow nitriding	665	

Annealing

accelerated cycling annealing	303–304	
alloying elements	299	
austenitizing time and dead-soft steel	291	
bar, rod, and wire	302–303	
cooling after transformation	291	
cycles	290	
defined	289	
flame annealing	436–437	
guidelines	291	
induction annealing	306–307	
intercritical annealing	290–291	
laser annealing	481	
machining, annealed structures for	294–295	
metallurgical principles	289–290	
overview	289	
plate	303	
prior structure, effect of	291	

Index Terms

Links

Annealing (*Cont.*)

process annealing	294
spheroidizing	291–293
subcritical annealing	290
supercritical or full annealing	291
temperatures	291
tubular products	303

Annealing, industrial

furnace atmospheres	295–296
furnaces, types of	295
uniformity across load	296–297
uniformity of temperature	296

Annealing, steel forgings

for cold forming	301
for machinability	301
to obtain pearlitic microstructures	301–302
overview	301
for re-forming	301

Annealing, steel sheet and strip

automotive applications	297–301
overview	297
process annealing, use of term	297
subcritical annealing, use of term	297

ANNs. *See* Artificial neural networks (ANNs)

Antigalling properties 651 680 709 710

Antiscuffing 686 687–688

Aqueous carboxymethyl cellulose

solution 257

Aqueous salt (brine) solutions 122–125

Arc lamps 397

Argon

fluidized-bed quenching 241

gas quenching 223

Artificial neural networks (ANNs) 334

ASM Handbook, Volume 4C, Induction

Heating and Heat Treatment

(2014) 438 454

ASM International 16–17 149

Index Terms

Links

Atlas zur Wärmebehandlung der Stähle	313	
Atmosphere-control setpoints	546–547	
Ausferrite	233	
Austempered ductile iron (ADI)	233	
Austempered steel. <i>See also</i> Austempering		
advantages	352	
overview	352	
process	352–353	
Austempering		
advantages	128	
alloying elements, effect of	354	
applications	354–357	
austenitizing temperature	354	
carbon content, effect of	354	
carburizing and	357	
defined	352	
dimensional control	357	
IT diagrams	353	
limitations of	128–129	
modified austempering	357–359	
overview	126	
problems and solutions	359–361	
quenching, selection for	128	
section thickness limitations	354	
selection, of steels	353–354	
steels adaptable to	353–354	
surface austempering	357	
TTT diagrams	353	354
Austenite		
carbon control, evaluation in carburized		
parts	523	
carbon transfusion in	536	
grain growth	314–315	
intercritical annealing	290	
overview	8	
solute concentrations, control of	315–316	
Austenitic nitrocarburizing	657	
Austenitization, defined	309	

Index Terms

Links

Austenitizing

austenite formation, mechanisms and kinetics	311–314	
austenite grain growth	314–315	
austenitizing temperature	309–311	
equipment	377	
full annealing	291	
induction hardening and tempering	446–448	458
introduction	309	
Johnson-Mehl-Avrami-Kolmogorov model	312	
overview	309	
purposes	309	
solute concentrations in austenite, control of	315–316	
time-temperature transformation (TTT) diagrams	312	313
time-temperature-austenitization (TTA) diagrams	313	314

Autocatalytic plating

478

Automotive applications. *See also* Electron beam

hardening (EBH), applications		
cryogenic treatment	384	
low-pressure carburizing (LPC)	586	
TRIP steels	317	

Automotive applications, sheet steels for

bake-hardening steels	299	
commercial-quality	298	
deep-drawing -quality	298	
drawing-quality	298	
dual-phase steels	300	
interstitial-free (IF) steels	298–299	
microalloyed high-strength low-alloy (HSLA) steels	299	
open-coil annealing	301	
overview	297–298	
solution-strengthened steels	299	
tin mill products	300–301	

Index Terms

Links

AWT. *See* German Association for Heat Treatment
and Material Science (AWT)

Axle-shaft forging

284 286

B

Bacon bomb fluid-sampler thief (Bacon bomb)

140

Bainite

heat treated steel, phases of

10

overview

9–10

Bake-hardening steels

299

Beam-deflection technique

464–465

Bending

borided parts

721

carburized components

347

carburizing

505

507

case depth

603

CFC fixtures

230

flame hardening

419

437

hardenability

41

42

50

inverse hardening

213

IQ process

207

residual stresses

275

551

tempering

554

Bending fatigue

carburizing

508

case depth

397

controllable delayed quenching

219

intergranular oxidation

550

inverse hardening

213

tensile strength, relationship between

508

Bending-under-tension test

320

321

Bernoulli's equation

193

Biosolvents

269

Biot number

active heat-transfer boundary

condition

169

170

171

heat-transfer coefficient based on laboratory

tests, calculation of

179

Index Terms

Links

Biot number (*Cont.*)

heat-transfer coefficient calculations	110
IQ-3 process	203
lumped heat-capacity method	179
overview	32
quench severity	100
rewetting	167
thermal field	167

Bismuth

125 126

Bitumen

135–136

Black light

271

Blind holes

abnormal glow region (for nitriding)	694
active-screen plasma nitriding	692–693
cleaning methods	267
injection nozzles	583
low-pressure carburizing (LPC)	586
mechanical masking	399
plasma (ion) nitriding	697
plasma carburizing	591 593 598
salt removal (washing)	575 576
selective carburizing	554
tempering in salt	345
vacuum carburizing	392

Blue brittleness

341

Body-centered cubic (bcc)

3 9

Body-centered tetragonal (bct) crystal

structure

4 336

Boiling

160–161

film boiling	167
forced convective boiling	161
pool boiling	160–161

Boiling heat transfer

160

Boiling liquid expanding vapor explosion

(BLEVE)

234

Boost-diffuse

carburization reactions	510 511 520
-------------------------	-------------

Index Terms

Links

Boost-diffuse (*Cont.*)

carburizing modeling and case depth			
prediction	536		
consecutive cuts, analysis of	523		
gas carburizing	545–546	550	556

Borax

CFC in	730		
electroless salt bath boriding	719		
high-temperature salt bath carbide			
coating	733–734		
liquid boriding	719		
multicomponent boriding	720		
plasma boriding	720		
TRD process	730	740	

Borax salt baths

carbide coating nucleation and growth	727		
high-temperature carbide coating	730		
high-temperature salt bath carbide			
coating	733–734		
TRD coatings	732		
TRD process	726		

Boride layers

advantages	709–711		
disadvantages	711–712		
overview	709		
thermal stability at elevated service			
temperatures	712–713		

Boriding (boronizing)

boride layers, characteristics features of.			
<i>See</i> Boride layers			
chemical vapor deposition (CVD)	722–723		
diffusion coatings	396		
electroless salt bath boriding	719		
electrolytic salt bath boriding	719		
ferrous materials	719		
fluidized-bed boriding	720		
gas boriding	719		
liquid boriding	718–719		

Index Terms

Links

Boriding (boronizing) (Cont.)

multicomponent boriding	720–721			
overview	709			
paste boriding	718			
plasma boriding	719–720			
powder-pack boriding	714–715	716		

Boriding (boronizing), ferrous materials

alloying elements, influence of	716			
dual-phase FeB and Fe ₂ B layers	713–714			
heat treatment after	716			
materials for	715			
overview	713			
pack cementation	714–716			

Boriding (boronizing), multicomponent

boroaluminizing	720			
borochromizing	720			
borochromtitanizing	720			
borochromvanadizing	720–721			
borosiliconizing	720			
borovanadizing	720–721			
overview	720			

Boriding (boronizing), nonferrous

materials	716–717			
------------------	---------	--	--	--

thermochemical. *See* Thermochemical boriding,
application of; Thermochemical boriding
techniques

Boron

boron-based stop-off paints	401	402		
in carburizing steels	46			
DI calculation for	69			
hardenability, effect on	46			
multiplying factors	83	87		

Boron steels

65	69	70	71
----	----	----	----

Boudouard reaction

505	624	625	656
663	667		

Brazing

265	438	577	
-----	-----	-----	--

Brine, defined

122			
-----	--	--	--

Brooks' equation

64	65		
----	----	--	--

Index Terms

Links

Burnout	539			
C				
Carbide-forming elements (CFEs)	725			
Carbides				
annealed structures for machining	295			
annealing	291			
austempering	354	355	360–361	
austenitizing	309	312	314	316
boriding	722			
boriding, nonferrous materials	716			
carburization, as complication in	516–517			
carburized parts, carbon control in	524	526		
carburizing	517			
Caterpillar hardenability calculator (1E0024)	66			
controlled carburizing	625			
controlled nitrocarburizing	625			
cryogenic treatment	383	384		
electron beam surface hardening	467			
gas carburizing	531	532	548	553
hardness and hardenability	36	45	47	48
heat transfer during quenching	158			
high-carbon steels, calculation of hardenability	80–81	84		
high-temperature fluidized-bed carbide coating	735			
induction surface hardening	447	448	460	
induction tempering	349			
intercritical annealing	291			
laser surface hardening (LSH)	484	487		
low-pressure carburizing (LPC)	581	584	586	
low-temperature nitriding and nitrocarburizing	649	650		
nitriding	651	653		
nitriding carbide-containing steels	638–639			
nondestructive case-depth measurement	414			
nonmartensitic structures, tempering	347			
normalizing	282	307		

Index Terms

Links

Carbides (*Cont.*)

overview	517			
pack carburizing	562			
plasma carburizing	594	595		
prior austenite grain boundaries	517			
Q&P steel heat treatment	322	327		
solution nitriding	658			
spheroidizing	292	293		
steel forgings, annealing	302			
steel heat treatment, introduction	15	16	20	
steel sheet and strip, annealing	300			
subcritical annealing	290	305		
supercarburizing	741	742	743	744
	745			
supercritical or full annealing	291			
surface hardening	391	397		
tempering	328	329–330	337	340–341
	343			
TRD	725	726	727	728
	729	733		
TRD, practical applications	738	739		
TRD, properties of coated parts	737			
TRD coating processes	730	731		
two-step batch quenching	244			
Carbo-Austempering	357			
Carbon				
during boriding	716			
effects, on iron	3–4			
hardness, effect on	26			
Carbon content				
gas nitriding	653			
principles of computational hardenability	60			
quenchant selection	124			
steel, quenching of	97–99			
Carbon control, evaluation in carburized parts				
consecutive cuts, analysis of	523			
electromagnetic testing	527			
hardness testing	522			

Index Terms

Links

Carbon control, evaluation in carburized parts (*Cont.*)

microscopic examination	
austenite	523
ferrite	522
martensite	523
overview	522
pearlite	522
overview	522
rolled wire, analysis of	526
shim stock, analysis of	524–527
spectrographic analysis	526–527
surface carbon	523–524

Carbon dioxide

ammonia guidelines	614		
batch furnace atmospheres	608–609		
carbonitriding	600		
carburization	393	510	511
combustion analysis, measuring			
case depth	406		
endothermic carburizing atmospheres	534		
extinguisher, salt bath	367		
extinguishing oil fires	146		
extinguishing salt bath fires	367		
furnace atmospheres	296		
gas nitrocarburizing	663	664	
gas quenching	223–224		
helium-carbon dioxide, HPGQ	223		
HPGQ	223–224		
hydrogen analyzer	666		
infrared analyzers	667		
noncyanide liquid carburizing	579	580	
oil fires, extinguishing	146		
oxygen probe	667		
oxynitriding	655		
pack carburizing	560	562	
plasma nitrocarburizing	701		
safety precautions	674	684	
water-gas reaction	649		

Index Terms

Links

Carbon- fiber-reinforced carbon (CFC) fixture	229–230		
Carbon monoxide (CO)			
carburization	393		
carburizing	505	506	510
cyaniding (liquid carbonitriding)	566		
endothermic carburizing atmospheres	534		
furnace atmospheres	296		
gas carburizing	520	533–534	
infrared analyzers	667		
liquid nitrocarburizing	685		
low-temperature cyanide-type baths	566		
nitriding	651	664	
nitriding processing	660		
nitrocarburizing	664		
noncyanide liquid carburizing	567		
oxygen probe	667		
pack carburizing	519	560	562
safety precautions	674		
surface hardening	393		
water-gas reaction	649		
Carbon steels			
austempering	354		
CCT diagram	18		
flame hardening	436		
iron nitrides in	645–646		
normalizing	282–283		
tempering	334		
Carbon step bars	523–524		
Carbonitriding. <i>See also</i> Carburizing			
ammonia guidelines	614		
applications			
overview	613		
steel selection, examples	613		
transmission gears, pitting			
resistance of	613–614		
carburizing, differences between	520–521		
carburizing, used together	600–601		
case, hardenability of	604–605		

Index Terms

Links

Carbonitriding (*Cont.*)

case composition	601–602	
case composition, example	602–603	
case-depth uniformity	603	
case-depth uniformity, example	603–604	
depth of case	603	
furnace atmospheres	606–609	
hardness gradients	605	
hardness testing	612–613	
introduction	505	
nonmartensitic transformation products (NMTP)	601	
overview	520–521	599–600
powder metallurgy (PM) parts	614	
powder metallurgy (PM) parts, tempering	614	
process description	600–601	
quenching media and practices	610–611	
retained austenite, control of	605–606	
safety	614	
stop-off paints	401	
surface hardening, introduction to	393	
temperature selection	609–610	
temperature selection, examples	610	
tempering	611–612	
void formation	605	

Carbonitriding, furnace atmospheres

control of		
ammonia content	607–608	
contaminants	608	
overview	607	
furnace type, influence of		
batch furnace atmospheres	608–609	
continuous furnace atmospheres	609	
overview	608	
overview	606	

Carbon-transfer mechanism 535–536

Carboxymethyl cellulose (CMC) 257

See also Wire patenting

Index Terms

Links

Carburized hardenability test	36	38
Carburized steels		
carbon content, effect of	390–391	
case depth	391	
intensive quenching	205	
Carburizing		
advantages	512–513	
basic reactions		
boost-diffuse technique	510	520
dewpoint measurement	511	
diffusion and the effects of time and temperature	510–511	
overview	510	
oxidation	511–512	
shim stock test	512	
water-gas reaction	511	
carbonitriding, differences between	520–521	
carburize, how to		
carbon-rich source	509	
container	509	
heat	509	
low-carbon base steel	509	
time	509–510	
carburizing steels	391–392	514
complications		
carbides	517	
decarburization	516–517	
intergranular oxidation	518	
masking	517–518	
disadvantages	513–514	
glow-discharge optical emission spectroscopy (GDOES)	527	
history	505–506	
introduction	505	
overview	390–391	
process description		
beneficial residual-stress profile	506–508	
carbon gradient	506	

Index Terms

Links

Carburizing (*Cont.*)

design considerations	508–509
hardness	508
martensite start temperature	506
overview	506
strength	508
stop-off paints	401
total case depth	506
vacuum carburizing	402

Carburizing, quality assurance

carbon gradient	514
case depth	514–515
case microstructure	515–516
core hardness	514
high-carbon (plate) martensite	515
low-carbon (lath) martensite	515
overview	514
retained austenite	515–516
statistical process control (SPC)	514
surface hardness	514

Carburizing alloys

548 552

Carburizing containers

construction	
conditioning	564
lid construction	563–564
design	563
materials	563

Carburizing cycle development

design of	545–546
process parameters	
carbon potential	544–545
temperature	544
time, effect on case depth	545

Carburizing methods

gas carburizing	506	519–520
liquid carburizing	519	
low-pressure (vacuum) carburizing	520	
overview	392	

Index Terms

Links

Carburizing methods (*Cont.*)

pack carburizing	506	518–519
process characteristics	392–393	
salt bath carburizing	519	
selective carburizing	392–393	

Carburizing modeling and case depth prediction

analytical solutions	537–538	
diffusion modeling	536–537	
numerical approach	538	
overview	536	

Carburizing potential, definition of

624

Carburizing steels

bearings	392	
core hardness	391–392	
gears	392	
low-distortion applications	392	
overview	391	

Carney empirical correlations

35

Case depth

carburized case depth	558	
carburizing modeling and	536–538	

Case depth, measuring

Brinell microscope	409	
chemical method		
combustion analysis	406	
example test procedures	406–407	
overview	406	
spectrographic analysis	406	
introduction	405	
Knoop indenter	407–408	409
measurement specifications		
effective case depth	405	
overview	405	
total case depth	405	
mechanical methods	407–411	
microhardness test	407–411	
nondestructive methods		
eddy-current tests	413–414	

Index Terms

Links

Case depth, measuring (*Cont.*)

magnetic Barkhausen noise phenomenon	414	
overview	413	
ultrasonic techniques	414	
Rockwell hardness conversions	409–411	
Vickers indenter	408	409
visual methods		
macroscopic visual procedures	412	
microscopic visual procedures	412–413	
overview	411–412	

Case hardening

applied energy case hardening	419–494	
carburizing and carbonitriding of steels	503–615	
core cracking	23	
gas nitriding	647–679	
gas nitrocarburizing	647–679	
intergranular oxidation	518	
liquid nitriding	680–689	
plasma (ion) nitriding and nitrocarburization	690–703	
plasma carburizing	595	596
sinter metals	595	
of steels	389–414	
stop-off technologies	399–404	

Case hardening steels

CrNiMo	73	
HPGQ	221	224
Jominy curves, HPGQ	227	
MnCr-alloyed	73	
NiCrMo-alloyed	73	
regression analysis of hardenability in Europe	75	

Case-hardening depth (CHD) 581

Cast iron

flame hardening	436	
valve seats, EBH	473	

Index Terms

Links

Castings

abrasive blast cleaning	268			
cold treating	382			
compressive stresses	382	383		
flame hardening	436			
induction hardening	446			
IQ process	210			
normalizing	280	282	283	287
pickling	272			

Caterpillar hardenability calculator (1E0024)

calculation example, 8645 steel	70–71
ideal critical diameter (DI)	65
Jominy curves	65
Jominy curves, estimation from compositions	69–70
nonboron steels, DI calculation for	66–69
overview	64–66

CCT curves. *See* Continuous cooling transformation

(CCT) curves

CCT diagram. *See* continuous cooling

transformation (CCT) diagrams

Cementite

crystal structure	3
hardness	3
heat treated steel, phases of	12–13
introduction	3
proeutectoid	12–13

Ceramic coatings

554

CFC fixture. *See* Carbon- fiber-reinforced carbon

(CFC) fixture

CFD. *See* Computational fluid dynamics (CFD)

modeling

CFEs. *See* Carbide-forming elements (CFEs)

Chauffage

289 310

CHD. *See* Case-hardening depth (CHD)

Chemical vapor deposition (CVD)

476 707 722–723 725

Index Terms

Links

Chlorine

activation/depasivation	660	
aluminizing	708	
carburizing parts, cleaning before	548	
cleaning, steel	272	
cyanide wastes, disposal of	578–579	684
liquid boriding	718	
pack cementation boriding	717	
safety precautions	674	

Chromium

hardenability, effect on	46	
multiplying factors	83–84	

Chromium-nickel-molybdenum

steels	354	552
---------------	-----	-----

Chromizing

708

CHT. *See* Conventional heat treatment (CHT)

Ck 45 steel, TTA diagram

313

Cleaning

biosolvents	269	
case studies	272–273	
cleaning system	265–266	
cleanliness measurement	271–272	
contaminants	266–267	
degree of cleanliness	272	
Occupational Safety and Health Administration (OSHA)	273–274	
overview	265–266	
parts for carburizing	548	
pollution control	273	
qualitative tests		
black light	271	
magnified visual inspection	271	
overview	271	
transparent tape test	271	
water-break test	271	
white/clean towel test	271	
quantitative tests		
desorption atmospheric pressure chemical		

Index Terms

Links

Cleaning (*Cont.*)

ionization (DAPCI)	272
direct solid probe mass spectrometry	272
dirt catching (wash and filter)	272
Fourier transform infrared (FTIR)	272
gravimetric measurement test	272
laser-induced breakdown spectroscopy	272
overview	272
Raman spectroscopy	272
resource recovery	273
safety	273–274
substrate considerations	267
surface contaminants on heat treated parts	266–267

Cleaning methods

abrasive blast cleaning	268
acid cleaning	270
alkaline cleaning	269–270
alkaline descaling	270–271
electrolytic alkaline cleaning	271
electrolytic pickling	271
emulsion cleaning	269
overview	267
pickling	270
salt bath descaling	270
solvent cleaning	269
supercritical fluid (SCF) cleaning	270
tumbling	268–269
ultrasonic cleaning	270
vapor degreasing	270

Cleaning system 265–266

Climax Molybdenum calculator 48

Closed-loop recycling 273

CMC. *See* Carboxymethyl cellulose (CMC)

Cold drawing process 745–746

Cold treatment of steel

advantages of	383
cold treating versus tempering	382
equipment for	383

Index Terms

Links

Cold treatment of steel (*Cont.*)

hardening and retained martensite	382
hardness testing	382
overview	382
precipitation-hardening steels	382
process	382
process limitations	382
Rockwell C hardness (HRC) readings	382
shrink fits	382
stress relief	382–383
time at temperature	383

Compressed Gas Association

431

Computational fluid dynamics (CFD) modeling

192

Conduction

160

Consecutive cuts method

523–524

Continuous carbide network

517

Continuous cooling transformation (CCT) curves

20

62

96

Continuous cooling transformation (CCT) diagrams

heat transfer, during quenching	162
heat treatment	20–21
principles of computational hardenability	60
quenching, metallurgical aspects	96–97

Continuous EB interaction (CI technique)

465

466

470

472

473

Continuous precipitation (CP) region

632

633

Continuous transformation (CT)

290

Controllable delayed quenching

213

215–218

Convection

160

Conventional heat treatment (CHT)

485–486

Cooling curve test

cooling curve analysis	109–110
cooling curve data acquisition	105–106
cooling curves	105
overview	104–105
the probe	106–109

Copper alloys

277

Copper plating

399–400

554

Index Terms

Links

Corrosion

annealing	300	301		
boriding	710	711	720	722
carburizing	518	540	572	
cleaning, steel	266	267	270	272
cryogenic treatment	383			
flame hardening	428	429		
flame hardening heads	429			
gas nitriding/gas nitrocarburizing	647	648	649	650
	656	657		
laser surface hardening (LSH)	476	478	481	482
	483	484	491	
liquid carburizing and cyaniding	575			
liquid nitriding	680	684	685	
masking	518			
molten metal quenchants	125	148		
nitrided parts	669			
nitriding	620			
nitriding processing	659			
pack cementation processes	707	708		
phase control, nitriding	665			
plasma (ion) nitriding	699	700		
postoxidation	660			
probes	106			
solution nitriding	658			
stress-relief heat treating	275			
surface hardening	389	393	396	
tempering	345			
TRD	733	737		

CP. See Continuous precipitation (CP) region

Cracking

due to hardening	22–23
induction heating	460–461
nitrided surfaces	674
tempering, in processing	346–347

Cryogenic Society of America

383

Index Terms

Links

Cryogenic treatment of steels

equipment for	384–385	
overview	382	383
treatment cycles	383–384	
uses of	384	

Curie temperature

alpha iron	5	
eddy-current distribution	444	
GM Quenchometer test	104	
magnetic properties of steel	441–442	
magnetic-wave characterization	445–446	

Cut-off saw

671

Cyanide

cyanide salts, precautions in use of	577–578	
overview	565	

Cyanide wastes, disposal of

chemical treatment	578	
electrochemical treatment	579–580	
overview	578	
treatment equipment	578–579	

Cyanide-containing liquid carburizing baths

combination treatment	566	
high-temperature cyanide-type baths	566	
light case/deep case, use of terms	565	
low temperature/high temperature, use of terms	565	
low-temperature cyanide-type baths	565–566	
overview	565	

Cyaniding (liquid carbonitriding)

bath composition	567	
cyanided parts, washing	576	
overview	566–567	
process control		
bath composition, control of	571–572	
daily maintenance routines	572	
externally heated salt baths	571	
graphite cover	572	
internally heated salt baths	571	

Index Terms

Links

Cyaniding (liquid carbonitriding) (Cont.)

restarting	572
shutdown	572
time and temperature	571

D

DANTE computer program	199
-------------------------------	-----

Datanit sensor	668
-----------------------	-----

DC. *See* Discontinuously coarsened (DC)

microstructure

Decarburization

austempered steel	354		
carburization, as complication in	516–517		
carburizing	510	512	
case depth, measuring	407		
consecutive cuts method	523	524	
copper plating	399		
cracking and spalling, nitrided surfaces	674		
cracking in processing	346		
electron beam (EB) process	462		
flame hardening	435		
fuel gases	421		
furnace atmospheres	296		
gas carburizing	529	547	551
gas nitriding	649		
hardness testing	522		
induction surface hardening	457		
martempering	371		
noncyanide liquid carburizing	567		
oxynitriding	655		
pack carburizing	561		
polyacrylates	150		
powder metallurgy (PM) parts	459	460	
stop-off paints	400		
surface decarburization	460		
tubular products	286		

Deep cryogenic treatment (DCT). *See* Cryogenic

treatment of steels

Index Terms

Links

Deformation-induced martensitic transformation (DIMIT)	321			
Delayed quenching				
inverse hardening	213	219		
PAG test	213			
Delayed quenching, controllable	213	215–218	219	
Desorption atmospheric pressure chemical ionization (DAPCI)	272			
DET. <i>See</i> Divorced eutectoid transformation (DET)				
Dewpoint measurement	511			
DHCP. <i>See</i> Direct heat-conduction problem (DHCP)				
DI. <i>See</i> Ideal critical diameter (DI)				
Diffusion				
carburizing modeling	536			
plasma carburizing	593–594			
Diffusion coatings				
boriding	396			
introduction	396			
titanium carbide	396			
Diffusion path	619	629	631	
Diffusion zone				
aerated bath nitriding	681			
aerated cyanide-cyanate nitriding	682			
austenitic nitrocarburizing	657			
boriding, ferrous materials	713			
case structure, nitrided steel	698			
classical nitriding	651	652		
controlling	660–661			
gas nitriding	647	648	670	674
high- low-pressure nitriding	653			
liquid nitriding	682			
low-temperature nitriding	649			
nitride coating nucleation and growth	728			
nitrided case	698–699			
nitriding and nitrocarburization	620	629	632	635–641
nitriding process, simulation of	669			
oxynitriding	655			
plasma (ion) nitriding	698–699			
solution nitriding	658			

Index Terms**Links**

Dilatometer method	17			
DIMT. <i>See</i> Deformation-induced martensitic transformation (DIMT)				
Direct convection cooling	198	200	201	203
Direct heat-conduction problem (DHCP)	168	169	172	173
Direct solid probe mass spectrometry	272			
Direct-current plasma nitriding (1970–1980)	690–691			
Discontinuously coarsened (DC) microstructure	632			
Displacement plating	478			
Distortion				
carburization	513			
control, press quenching	255–256			
due to hardening	22–23			
flame hardening	432–433			
gas carburizing	555			
gas nitriding	648			
gas nitrocarburizing	648			
induction heating	460			
IQ process	207			
pack carburizing	560			
Divorced eutectoid transformation (DET)	293			
Doppler effect	193			
Dual-phase FeB and Fe₂B layers	713–714			
Dual-phase steels				
annealing	300			
bake-hardening steels	299			
DP 780, forming	319			
DP 980, dynamic tensile properties	319			
DP 980, forming	319			
DP 980, shear fracture behavior	320			
DP 980, springback behavior	320			
Durofer process	570–571			
Dusinberre numerical method	538			
Dwell time	208	209	210	234

Index Terms

Links

Dynamic gas quenching

idler gears	228–229
internal ring gears	229
overview	228

Dynamic vapor blanket

259	260	261
-----	-----	-----

E

EB hardening. *See* Electron beam hardening (EBH)

EBSD. *See* Electron backscatter diffraction (EBSD)

ECD. *See* Effective-case depth (ECD)

Eddy-current distribution

Curie temperature	444
current cancellation	445
magnetic-wave characterization	445–446
overview	443
reference depth from skin effect	443–445

Eddy-current tests

413–414

Edge effect

active-screen plasma nitriding	692
direct-current plasma nitriding (1970–1980)	691
glow-discharge process	694
hollow-cathode and	694
induction surface hardening	459
low-pressure carburizing (LPC)	585
probes	107
stop-off paints	403

Effective-case depth (ECD)

205

Electroless plating

478

Electromagnetic testing

effectiveness	527
limitations	527
magnetic-comparator testing	527
overview	527
standards	527
test procedures	527

Electron backscatter diffraction (EBSD)

322

Index Terms

Links

Electron beam (EB)

generation	462–463
heat transfer	464
interaction with material	463
overview	462
thermal processes	462

Electron beam (EB) facilities

facilities	470–471
manufacturing systems with integrated EB facility	470 471
overview	469–470

Electron beam (EB), processing techniques

beam-deflection technique	464–465
continuous EB interaction (CI technique)	465
electron beam flash technique	465–466
multifield EB-deflection technique	466
multiprocess technique	466

Electron beam flash technique

465–466

Electron beam hardening (EBH)

advantages	462
characteristics	466
component specifics	469
facilities	470–471
introduction	395–396
manufacturing systems with integrated EB facility	470 471
microstructure	466–467
overview	469–470
surface properties	467–469

Electron beam hardening (EBH), applications

camshafts	472
characteristics	471–472
connecting rods	472
injector boxes	473
pump cams	472
shafts	473
slotted shafts	473
valve seats	473

Index Terms

Links

Electron beam surface hardening. <i>See also</i> Electron beam (EB); Electron beam hardening (EBH); Electron beam hardening (EBH), applications			
laser beam hardening (LBH)	462		
overview	462		
short-cycle heat treatments	462		
Electroplating	476	478	
Embrittlement			
blue brittleness	341		
temper embrittlement (TE)	339–341		
tempered martensite embrittlement (TME)	341–344		
Endothermic carburizing atmospheres	534–535		
Endothermic carrier gas (endogas)			
annealing	296		
carburizing	393		
gas carburizing	520	530	534
nitrocarburizing	663	664	674
Environmental Protection Agency (EPA)	273	569	677
Equilibrium transformations	5		
Erosion			
CVD process	722		
EB generator	470		
flame hardening heads	428	429	
high-temperature fluidized-bed carbide coating	735		
LH	484		
LSH	476	478	
Etchants			
austenitizing	315		
case depth, measuring	409	413	
masking	518		
nitriding	670	672	
Etching			
acid etching	458		
boriding, ferrous alloys	713		
carbon content	523	553	
carburized hardenability test	38		
diffusion zone, nitrided case	698		

Index Terms

Links

Etching (*Cont.*)

hot-walled plasma pulsed-dc furnaces	696	
microscopic visual procedures	412–413	
nitriding	670	673
quenching	99	
SEM, Q&P steel	321	

Eutectoid reaction

austenite formation	312	
bainite	9	
defined	9	
pearlite	9	19
proeutectoid cementite	11	
proeutectoid ferrite	11	
substitutional alloying elements	19–20	

Eutectoid transformation, time-temperature

effects of	17	
-------------------	----	--

Exothermic gas	296	
-----------------------	-----	--

EXPANITE process	660	
-------------------------	-----	--

F

Face-centered (fcc) crystal structure	3	
----------------------------------------------	---	--

Falex testing	687–688	737
----------------------	---------	-----

Falex tests	687	
--------------------	-----	--

Fatigue strength

aerated bath nitriding	681	
austempering	357	
borosiliconizing	720	
carburizing	357	505
contact	613	
cooling curve test	104	
excessive surface decarburization	516	
LPC	586	
LSH, aluminum alloys	493	
nitriding	652	700
shear	509	
transformation hardening	397	
TRD coated parts	738	

FDM. *See* finite-difference method (FDM)

Index Terms

Links

FEA. *See* Finite-element analysis (FEA)

Ferrite

carbon control, evaluation in carburized

parts

522

overview

9

Ferrous alloys

alkaline descaling

271

atomic volumes of

4

boriding

713

719

diffusion zone, nitriding

698–699

hardenability, measuring

62

induction heating

440

Jominy testing

62

laser alloying

482

laser cladding

482

laser glazing

482

LH of

490

491

quenching treatments

146

Ferrous materials

boriding

713–716

electroless salt bath boriding

719

electrolytic salt bath boriding

719

Fick's first law

535

536

626

634

660

Fick's second law

511

536

633

639

640–641

661

Film boiling (FB)

92

Film boiling process

201

207

Finite-difference method (FDM)

187

Finite-element analysis (FEA)

62–63

Finite-volume method (FVM)

187

Fixturing

electrolytic salt bath boriding

719

gas carburizing

555

induction heating coils

454

liquid carburizing

574

martempering

363

380

plasma nitriding furnaces

695

Index Terms

Links

Fixturing (*Cont.*)

restraint fixturing	151
selective tempering	346

Flame annealing 436–437

Flame hardening

advantages	419
air-fuel gas burners	425
burners	423
burners, materials for construction of	425–426
dimensional control	433
disadvantages	419
example: flame hardening versus induction	
hardening	435
flame annealing	436–437
fuel gases	421–423
hardness, depth and pattern of	427–428
high-velocity convection burner	425
introduction	395
martensitic critical cooling velocity	419
overview	419
oxy-fuel gas flame heads	423–424
preheating	427
problems and causes	432–433
process selection	433–435
radiant-type burner	425
related equipment	425
safety precautions	431
surface conditions	433
tempering, flame-hardened parts	
flame tempering	433
overview	433
self-tempering	433

Flame hardening, equipment maintenance

air-gas type burners	429
carbon deposit	428–429
corrosion	429
electrical components	429–430
erosion	429

Index Terms

Links

Flame hardening, equipment maintenance (*Cont.*)

mechanical components	429
oxy-fuel gas type flame heads (nonferrous)	428
piping	431
spindle and movable holding fixtures	430–431

Flame hardening, material selection

alloy steels	436
carbon steels	436
cast iron	436
other materials	436
overview	435–436

Flame hardening, methods

combination progressive-spinning method	421
overview	419–420
progressive method	420
spinning method	420–421
spot (stationary) method	420

Flame hardening, operating procedures and control

coupling distance	426
example: 1045 steel bar	426
examples: flame-hardening procedures	427
flame head, speed of travel of	426
flame velocity	426
gas pressures	426
hardening temperatures	426–427
operating variables	426
overview	426
oxygen-to-fuel ratio	426

Flame hardening, problems and causes

distortion	432–433
excessive depth of hardening	433
excessive scaling	433
hardness below minimum required	432
overheating	432
shallow depth of hardening	433
spotty or uneven hardening	432

Index Terms

Links

Flame hardening, quenching media

forced air	432
immersion quenches	432
overview	432
self-quenching	432

Flame hardening, quenching methods and equipment

overview	431
quenching after progressive heating	431
quenching after spin heating	431–432

Floe process

652

Fluid flow

measurement	
effective pressure	193
heat-based flow measurement	193–194
overview	192
velocity measurement by correlation	
methods	193
velocity measurement, using thermal	
probes	194–195
velocity measurement—means of lasers	193
volumetric measurement	192–193
overview	192
in quenching	192

Fluidization

238

See also fluidized-bed quenching.

Fluidized beds

annealing	303
CFEs/NFEs	732
high-temperature fluidized-bed carbide	
coating	735
martempering	365–366
TRD	726

Fluidized-bed, design of

bed cooling and temperature control	238–239
container	238
gas distributor	238
overview	238
plenum	238

Index Terms

Links

Fluidized-bed boriding	720	
Fluidized-bed quenching		
advantages	242–243	
aluminum oxide (Al ₂ O ₃)	240	
continuous quenching	244	
conventional batch quenching	243–244	
cooling rates	239–240	
fluidization	238	
fluidized-bed, design of	238–239	
heat-transfer coefficients	240	
important features	243	
limitations of	243	
processes	243	
quenching power, factors affecting		
bed pressure	241–242	
bed temperature	241	
fluidization velocity	241	
fluidized particles	240–241	
fluidizing gas	241	
geometry of parts and their configuration	242	
overview	240	
silicon carbide (SiC)	240–241	
two-step batch quenching	244	
Fluid-Quench Sensor	195	
Flux leakage	455	
Fog cooling	259	
Forced convection	160	
Forgings, normalizing		
axle-shaft forging	284	286
furnaces	284	
locomotive-axle forgings	286	
low-carbon steel forgings	286	
multiple normalizing treatments	286	
overview	284	
processing	284	
structural stability	286	
Fourier transform infrared (FTIR)	272	
Fourier's law	160	167

Index Terms

Links

Fourier's second law of heat conduction	31	
Free convection	160	
Full-film boiling. <i>See also</i> Vapor blanket (full-film boiling)		
cooling curve analysis	110	
cooling curves	105	
first heat-transfer mode	94	
Leidenfrost temperature	92	
mathematical models of second heat-transfer mode	111	
probe shape	107	
quench severity	100	
Furnace temperature and atmosphere control, (gas carburizing). <i>See</i> Gas carburizing, furnace temperature and atmosphere control		
Furnaces		
annealing	295–297	
bar and tubular products	286–287	
batch furnaces	538	608–609
batch/integral quench furnaces	676	
bell-type movable furnace	675–676	
box furnaces	563	
box-type movable furnaces	676	
carbonitriding	606–609	
car-bottom furnaces	563	
castings	287	
catenary furnaces	288	
cold-walled plasma furnaces	695–696	
conditioning	540	
continuous batch-type furnaces	676	
continuous furnaces	538	609
conveyor belt furnaces	676	
conveyor-type	287	
direct-current plasma nitriding (1970–1980)	690–691	
drip-type carburizing furnace	745	
dual-chamber box-type gas carburizing furnace	742–743	

Index Terms

Links

Furnaces (*Cont.*)

gas carburizing	538–540		
gas nitriding	674–675		
horizontal retort furnaces	675		
hot-walled plasma pulsed-dc furnaces	696		
internal pressure	538–539		
medium-frequency coreless furnace	745		
nitriding	668	674–676	
nitrocarburizing	674–676		
normalizing, sheet and strip	287		
pack carburizing	562–563		
pit furnaces	538	563	
plasma carburizing	591	595–596	
plasma nitriding furnaces	695–696		
pusher furnaces	676		
salt bath furnaces	345		
sealed-quench furnaces	538		
single-chamber furnaces	222	223	224–225
temperature and atmosphere control	540–544		
tube retorts	676		
vacuum	520		
vacuum furnaces	367–368		
vertical retort furnace	675		

FVM. *See* Finite-volume method (FVM)

G

Galling

boriding	710
carburizing steels	392
dimensional stability	549
TRD coatings	739

Gas boriding

719

Gas carburizing

carbon sources and atmosphere types	
CO level, selection of	533–534
endothermic carburizing	
atmospheres	534–535
overview	532–533

Index Terms

Links

Gas carburizing (*Cont.*)

overview	528
thermodynamics and kinetics	
carbon potential via shim stock, validation of	530–531
equilibrium gas composition, calculation of	528–529
gas carburizing reactions	528
gas carburizing reactions, kinetics of	529
measurement of carbon potential, calculation of	529–530
steel alloy composition, effect of	531–532

Gas carburizing, carbon-transfer mechanism

analytical solutions	537–538
carbon diffusion, in austenite	536
carburizing modeling and case depth prediction	536–538
mass-transfer coefficient	535–536
numerical approach	538
overview	535
preoxidation, effect of	536
surface finish, effect of	536

Gas carburizing, carburizing cycle development

atmosphere-control set-points, selection of	546–547
carburizing cycle, design of	545–546
carburizing process parameters	544–545

Gas carburizing, case depth evaluation

carburized case depth	557–558
case depth measurement	556–557
effective case depth (hardened depth)	557–558
overview	556

Gas carburizing, dimensional control

distortion, factors affecting	555
distortion control, methods for	
fixturing	555
marquenching	555
overview	555

Index Terms

Links

Gas carburizing, dimensional control (*Cont.*)

press quenching	555
straightening	555
overview	555

Gas carburizing, equipment for

batch furnaces	538
burnout	539
continuous furnaces	538
furnace conditioning	540
furnace internal pressure	538–539
overview	538
sooting	539–540

Gas carburizing, furnace temperature and atmosphere control

atmosphere carbon potential control, implementing	542–543
atmosphere introduction and uniformity	541
atmosphere-control system type, selection of	542
control-system features	541–542
gas sampling	543–544
overview	540
quenching uniformity	541
temperature control and uniformity	540–541

Gas carburizing, process planning

alloy selection	551–552
case depth/hardened depth relationship	548
decarburization	551
direct hardening versus reheat hardening	552–553
intergranular oxidation	550–551
overview	547
parts for carburizing	548
quenchants	553
residual stress	551
retained austenite	548–550
selective carburizing	55

Index Terms

Links

Gas carburizing, process planning (*Cont.*)

surface nonmartensitic transformation	
products (NMTP)	551
tempering	553–554

Gas nitriding. *See also* Nitriding

atmosphere control	661–665
inspection	669–670
introduction	647–648
low-temperature nitriding	649–651
measuring errors	669
quality control	669
quenching	648
reasons for	647
rules of thumb	674
safety precautions	674
selective nitriding	673
simulation of process	669
temperature control	668
terminology	648–649

Gas nitriding, common problems

compound layer thicker than permitted	674
cracking and spalling, nitrided surfaces	674
discoloration of parts	673–674
excessive dimensional changes	674
low case depth	673
shallow case depth	673
uneven case depth	673

Gas nitriding, equipment

ammonia supply	677
fixtures	674–676
furnace control system	677
furnaces	674–676
overview	674–675

Gas nitriding, lab equipment and sample control

cut-off saw	671
hardness profile	673
mounting	672–673
overview	670

Index Terms

Links

Gas nitriding, lab equipment and sample control (*Cont.*)

polishing	673
sample, choice of	671
sample location	671
surface hardness measurement	672

Gas nitriding, measuring the potentials

combinations	667–668
hydrogen analyzer	666
infrared analyzers	667
lambda probes	667
overview	665
oxygen probe	667
pressure increase	666–667
water burette (pipette)	665

Gas nitrocarburizing. *See also* Nitriding;

Nitrocarburizing

atmosphere control	661–665
inspection	669–670
introduction	647–648
low-temperature nitrocarburizing	649–651
measuring errors	669
quality control	669
quenching	648
reasons for	647
rules of thumb	674
safety precautions	674
selective nitriding	673
simulation of process	669
temperature control	668
terminology	648–649

Gas nitrocarburizing, common problems

compound layer thicker than permitted	674
cracking and spalling, nitrided surfaces	674
discoloration of parts	673–674
excessive dimensional changes	674
low case depth	673
shallow case depth	673
uneven case depth	673

Index Terms

Links

Gas nitrocarburizing, equipment

ammonia supply	677
fixtures	674–676
furnace control system	677
furnaces	674–676
overview	674–675

Gas nitrocarburizing, measuring the potentials

combinations	667–668
hydrogen analyzer	666
infrared analyzers	667
lambda probes	667
overview	665
oxygen probe	667
pressure increase	666–667
water burette (pipette)	665

Gas quenching. *See* High-pressure gas quenching (HPGQ)

Gas sampling 543–544

Gas-flow reversing 227–228

Geldart group A powders 241–242

Geldart group D powders 241

German Association for Heat Treatment and Material Science (AWT)

659 664

Gibbs energy 622 632 636 637

Gibb's phase rule 629

Global crude steel production (2012) 158

Glow-discharge optical emission spectroscopy (GDOES) 407 527

Glow-discharge plasma 393 591–592 690

Glow-discharge process

edge effect	694
hollow cathode effect	694
mass-transfer mechanisms	695
overview	693
pressure and gas composition	694
voltage current conditions	693–694

GM Quenchometer test 143

Gravimetric measurement 272

Green function method 110

Index Terms

Links

Grinding

boriding	712			
carbonitriding	605			
case depth, measuring	408			
cold treatment of steel	382			
cracks	394			
EBH process	472			
flame hardening	434			
martempering	363	373	380	
nitriding	659			
pack carburizing	561			
pitot tube	118			
quenching	113			
selective carburizing	554			
as source of residual stress	275			
steel, cleaning for heat treatment	265	267		
tempering	612			
tempering, carburized components	347			
void formation	605			
Grinding cracks	382	394	612	
Grinding fluids	266–267	270		
Grossmann charts	35			
Grossmann method	65	86	100–101	103
Grossmann number	30–33			

H

Hardenability, defined	60			
Hardenability, factors affecting	45–46			
alloying elements	45–46			
carbon content, effect of	45			
ferrite stabilizers	45			
synergistic combinations	46			
Hardenability bands	49	50	99–100	392
Hardenability calculation of carbon and low-alloy steels with low or medium carbon				
Caterpillar hardenability calculator (1E0024)	64–71			
introduction	60			

Index Terms

Links

Hardenability calculation of carbon and low-alloy (*Cont.*)

principles of computational hardenability	60–64
regression analysis of hardenability	
in Europe	71–79

Hardenability correlation curves

33–35

Hardenability requirements

depth of hardening	41–43
overview	41
quenching media	43–45

Hardenability tests

air hardenability test	39	
carburized hardenability test	36	38
hot-brine test	39	
Jominy test	35–36	
<i>See also</i> Jominy		
end-quench testing		
low-hardenability steels	39–40	
surface-area-center (SAC) test	39–40	

Hardness and hardenability

air hardenability test	39	
carbon content, effect of	26	
carburized hardenability test	36	38
Carney empirical correlations	35	
hardenability, defined	26	
hardenability, factors affecting	45–46	
hardenability correlation curves	33–35	
hardenability requirements		
depth of hardening	41–43	
overview	41	
quenching media	43–45	
H-steels		
classified by hardness at end-quench		
positions	51–58	
hardenability limits and	50–51	
ideal critical diameter	33	
introduction	26	
Jominy data sets, variability in	46–47	
Jominy end-quench testing	26–30	

Index Terms

Links

Hardness and hardenability (*Cont.*)

Jominy equivalence charts	40–41
Jominy test	35–36
low-hardenability steels	
hot-brine test	39
surface-area-center (SAC) test	39–40
quench severity	30–33
steel hardenability, calculation of	47–48
steel selection for	48–50

Hardness testing

382 522 612–613

HAZ. *See* Heat-affected zone (HAZ)

Heat transfer, during quenching

active heat-transfer boundary condition	167–173
boiling heat transfer	160
CCT diagrams	162
forced convective boiling	161
heat-transfer basics	159–160
liquid quenching heat transfer	162–163
Liscic-Nanmac probe	159
microstructural evolution, heat generated by	162
overview	158–159
physical phenomena during quenching	158–159
pool boiling	160–161
rewetting	164–167
thermal field	167
time-temperature transformation (TTT)	
diagrams	162

Heat treated steel, phases of

bainite	10
cementite	12–13
iron-carbon phase diagram	7–9
martensite	13–16
overview	7
pearlite	9–10
proeutectoid ferrite	10–12

Heat Treating, Volume 4 of ASM Handbook 1991

542

Index Terms

Links

Heat treatment

after boriding	716
continuous cooling transformation (CCT) diagrams	20–21
cracking, due to hardening	22–23
defined	3
distortion due to hardening	22–23
heat treated steel, phases of	7–16
introduction	3–4
iron, constitution of	4–7
isothermal transformation diagrams	16–20
residual stresses	21–23
thermal stresses	21–23
transformation diagrams	16

Heat-affected zone (HAZ)

laser cladding	481	482
laser heat treatment	484	
laser welding	323	
metal active gas (MAG) welding	324	

Heat-conduction equation (HCE), finite-volume

method for

FVM, control volumes for	187
implicit finite-volume method	187–188
implicit iterative computation of temperatures	188
time and space discretizations	187

Heat-extraction dynamics

overview	213
quench analysis	213–214
temperature fields displayed	214–215

Heat-transfer basics

boiling heat transfer	160
conduction	160
convection	160
Fourier's law	160
heat flow	160
heat source/sinks	160
Liscic-Nanmac probe	159
mechanisms of	160

Index Terms

Links

Heat-transfer basics (*Cont.*)

Newton's law of cooling	160
overview	159–160
pool boiling	160–161
radiation, heat exchange by	160
Stefan-Boltzmann equation	160
thermal balance, modifying	160

Heat-transfer coefficient (HTC)

calculation based on laboratory tests	178–179	
calculations	110–113	186–187
cooling intensities of liquid quenchants, database of	184	
fluidized-bed quenching	240	
IQ-3 process	203	
simulation examples	189–191	
smoothing, of measured temperatures	188	

Helium

fluidized-bed quenching	241	244
gas quenching	223	

HER. *See* Hole-expansion ratio (HER)

Heterogeneous water gas reaction

625 663 666 667

High-alloy steels

annealing of forgings for machinability	301	
boriding	716	717
carbide coating nucleation and growth	727	
carburizing	532	
electrolytic salt bath boriding	719	
IQ process	200	
nitride coating nucleation and growth	728	
nitriding	394	
nominal subcritical annealing temperatures	306	
oxynitriding	655	
preheating plus EBH	466	
salt quenching	232	
stress-relief heat treating	277	
tempering	330	346

High-carbon (plate) martensite

515

Index Terms

Links

High-carbon steels, calculation of hardenability

background	80	82–83
multiplying factors (MF)	83–86	
derivation of	83	
limitations of	87	
use of	86	
overview	48	80

High-performance stereo industry

384

High-pressure gas quenching (HPGQ)

368

advantages	221	222	
applications	221		
CFC materials	229–230		
cold chambers	222–223	224	225
cooling curves	224–225		
core hardness, prediction of	225–227		
disadvantages	221		
distortion, control with HPGQ	230		
dynamic gas quenching	228–229		
equipment for	222–223		
fixtures for	229–230		
gas types	223–224		
gas-flow reversing	227–228		
high-nickel-content alloys	229		
introduction	221		
low-pressure carburizing (LPC)	221	230	582
physical principles	221–222		
single-chamber furnaces	222	223	224–225

High-speed steel (HSS)

319

320

384

683

High-strength low-alloy (HSLA) steels

299

315–316

High-strength steels (HSS)

abrasive blast cleaning	268
acid cleaning	548
Q&P steels	317
<i>See also</i> Quenching and partitioning (Q&P) steel	
springback behavior	320
TRD	737

Index Terms

Links

High-temperature fluidized-bed carbide coating	735		
High-temperature processes			
N-quench	657–658		
solution nitriding	658–659		
High-temperature salt bath carbide coating	733–735		
Hole-expansion ratio (HER)	319		
Hollomon-Jaffe equation	349		
Hollomon-Jaffe method	333		
Hot deformation	8–9		
Hot wire test	104	105	143
Hot-wire anemometer	224		
HPGQ. <i>See</i> High-pressure gas quenching (HPGQ)			
HSLA steels. <i>See</i> High-strength low-alloy (HSLA) steels			
H-steels			
carbon content, effect on hardenability	50–51		
classified by hardness at end-quench			
positions	51–58		
example	51	56	
overview	51		
hardenability bands	50	99–100	
hardenability limits and selection for hardenability	50–51		
selection for hardenability	49		
HTCs. <i>See</i> Heat-transfer coefficient (HTC)			
Hydrogen			
fluidized-bed quenching	241	244	
gas quenching	223		
Hydrogen analyzer	666		
Hydrogen cyanide	684		
Hydrogen embrittlement			
abrasive cleaning	268		
alkaline descaling	271		
austempering	352	355	
EB process	462		
HSS, acid cleaning of	548		

Index Terms

Links

Hydrogen embrittlement (*Cont.*)

quenched and tempered steels	339
surface cleaning	265

Hypochlorination 579

Hysteresis

flux concentrators	456	
in heating and cooling	5	
induction heating	395	
iron-carbon phase diagram	7	
magnetic hysteresis	442	
magnetic properties of steel	441	442
transformational diagrams	16	

I

Ideal critical diameter (DI) 33 65 80

Idler gears 228–229

IHCP. *See* Inverse heat-conduction problem (IHCP)

Incoloy 800 707

Inconel 600

probes	106	107	110	137
	160			
salt bath furnaces	684			
thermal properties	112			

Inconel 718 712–713

Incubation time 22 213 215–216 217 628 633–634

INDUCTER-B 63

Induction case hardening 200 457

Induction coils

overview	439
progressive (scanning) coils	440
single-shot coils	439–440

Induction hardening and tempering

austenitizing	446–448
induction tempering	451
overview	446
quenching	
as-quenched hardness	450–451

Index Terms

Links

Induction hardening and tempering (*Cont.*)

methods	448
overview	448
spray quenching, severity of	449–450

Induction heating

advantages	438
eddy-current distribution	443–446
high-temperature electrical properties	440–441
induction coils	439–440
induction hardening and tempering	446–451
introduction	395
magnetic hysteresis	442
magnetic properties	440 441–442
overview	438
principles of	438–439
processes used in	438
thermal properties	440 442–443

Induction heating coils

454

Induction heating, equipment and process factors

frequency selection	452–453
induction heating coils, design of	454
magnetic flux concentrators	454–456
overview	451–452
power density and heating time	453–454

Induction normalizing

307

Induction surface hardening. *See also* Induction

heating

eddy-current distribution	443–446
powder metallurgy (PM) parts	459
rules of thumb	457
surface-hardening parameters	
austenitization, heating times for	458
frequency selection	456–457
heating time, methods to establish	458–459
power selection	457–458

Induction surface hardening, application tips and troubleshooting

cracking	460–461
----------	---------

Index Terms

Links

Induction surface hardening, application tips and (*Cont.*)

distortion	460
parts with complex geometries	459
powder metallurgy parts	459–460
surface decarburization	460

Induction tempering

advantage of	348
application	347–348
equivalent heating for	348–349
frequency, selection of	348
overview	347
power densities, selection of	348

Induction thread softening 307–308

Industrial annealing 295–297

Infrared analyzers 667

IN-PHATRAN 63

Intensive quenching (IQ). *See also* Production

IQ systems

advantages	211
applications	210–211
batch intensive quenching (IQ-2 process)	201–203
benefits of	204–206
carburized steels	205
heat transfer during	
conventional quenching	200–201
IQ-2 process	201
IQ-3 process	201

IQ systems, design of. *See* Production IQ systems

IQ zone	199		
IQ-2 process	198	200	201–203
IQ-3 process	198	200	203
limitations for applying	211		
mechanical properties and cooling rate	198–199		
and other quench methods	199–200		
overview	198		
and part distortion	207		
residual-stress conditions	205–206		

Index Terms

Links

Intensive quenching (IQ) (Cont.)

single-part IQ process. *See* Intensive quenching

(IQ): IQ-3 process

strength and ductility, improvements to

204–205

through-hardening steels

204

Intergranular fractures

proeutectoid cementite

12

temper embrittlement (TE)

340

tempered martensite embrittlement (TME)

343

Intergranular oxidation (IGO)

550–551

582

Intergranular oxide (IGO)

gas carburizing

533

544

545

550–551

552

low-pressure carburizing (LPC)

582

583

Interlamellar spacing

17–18

Internal ring gears

229

International Organization for Standardization

(ISO). *See also* Specifications

isothermal transformation curves

16–17

Interstitial-free (IF) steels

298–299

Inverse hardening

average cooling rates A_1 to 500 °C within

subsurface region

216–218

heat-extraction dynamics

213–215

metallurgical aspects

215–216

overview

213

poly(alkylene glycol) (PAG) copolymer

213

218

properties

fatigue resistance, effects on

219

hardness distribution

218–219

overview

218

quenchants, enabling controllable delayed

quenching

218

Temperature Gradient Quenching Analysis System

(TGQAS)

213

Inverse heat-conduction problem (IHCP)

active heat-transfer boundary

condition

169–170

171

172–173

Index Terms

Links

Inverse heat-conduction problem (IHCP) (*Cont.*)

numerical solution of	184–188
overview	168

Ion carburizing. *See* Plasma carburizing

Ion implantation 396–397 709

Ion plating 476

Iron

alloying elements	7–8
austenite	8
constitution of	4–7
diffusion coefficient of carbon in	6–7
heating and cooling, hysteresis in	5
phase transformation	4–5
pure iron, ferrite and austenite in	5–6

Iron-base alloys 468 633 636 639

Iron-carbon phase diagram

introduction	7–9
lower critical temperature	7
upper critical temperature	7

Iron-nitrogen phase diagram 621–622

Isothermal heating transformation (IHT)

diagram 16–17

Isothermal transformation (IT) curves 62

Isothermal transformation (IT) diagrams

alloying, effects of	18–20
austempering	353
eutectoid transformation, time-temperature	
effects of	17
intercritical annealing	290
interlamellar spacing	17–18
overview	16–17
transformation times	18

IT curves. *See* Isothermal transformation

(IT) curves

Ivanit control approach 666–667

Index Terms

Links

J

Japan. *See also* Specifications

cooling curve standards	177	
high-temperature fluidized-bed carbide		
coating	735	
nitriding/nitrocarburizing	651	
N-quench	657–658	
silver probe	177	
supercarburizing	742	
TRD process	726	738

Jet cooling 248–249

Jet cooling, modeling

global modeling	249	
mechanistic modeling	249–250	

Jet quenching

jet cooling, modeling	249–250	
jet cooling, steady-state		
investigations of	248–249	
nucleate boiling region	246	
overview	248	
transient studies	248	

Johnson-Mehl-Avrami-Kolmogorov model 312 641

Jominy curves

calculation of	48	
Caterpillar hardenability calculator		
(1E0024)	65	69–70
cooling intensities of liquid quenchants,		
database of	184	

Jominy data sets, variability in 46–47

Jominy end-quench test 14–15 101–103

Jominy end-quench testing

CCT diagrams	20	
cooling rates	27	
hardenability correlation curves	33–34	
hardenability of a given steel	159	
hardenability of steels, discerning	27–28	
hardness values, plot of	27	
ideal critical diameter	33	

Index Terms

Links

Jominy end-quench testing (*Cont.*)

inflection point	29–30	
Jominy hardenability to round bar hardness		
transformation—Rushman approach	103	
Lamont transformations	30	
objectionable feature of	30	
overview	14–15	
process	26–27	
quench severity	101–103	
quenchant	28–29	120
regression analysis of hardenability		
in Europe	72	73
test bars	26	
water temperature, effect of	28	

Jominy equivalence charts

equivalent cooling rates	41	
Jominy equivalence, determining	40	
Jominy equivalent hardness method	40–41	
overview	40	
rectangular or hexagonal bars		
and plate	41	
steel, selection for hardenability	49	
tubular parts	41	

Jominy hardenability curve

Caterpillar hardenability calculator		
(1E0024)	65	
HPGQ	226–227	
oil quench system monitoring	144	
overview	226–227	
prediction of hardness distribution	183	
TGS computer program	184	

Jominy test 35–36

Jominy testing

ferrous alloys	62	
Liscic/Petrofer probe	184	

Jominy value 226–227

Index Terms

Links

K

Knoop indenter	407–408	409	557	689
Kocevar hot wire method	194			
Kondratjev form (shape) factors	98	110	111	112–113
	170	202–203		
Kondratjev theory	111			
Kramer factors	48			

L

Lamont transformations	30	35		
Larson-Miller equation	276	277		
Larson-Miller parameter	306	333	334	
Laser annealing	481	482		
Laser beam hardening (LBH)	396	462		
Laser cladding (LC)	481–482			
Laser direct metal deposition (LDMD)	481–482			
Laser glazing	482			
Laser hardening (LH). <i>See also</i> Laser surface hardening (LSH)				
cooling rate, influence of	488			
processing parameters, effect on temperature, microstructure, and case depth				
hardness	488–491			
specified hardness, challenges in obtaining	487–488			
Laser heat treatment	483–484			
Laser scanning technology	480–481			
Laser shot peening (LSP)	483			
Laser surface hardening (LSH)				
absorptivity	479–480			
cooling rate, influence of	488			
laser annealing	481			
laser cladding	481–482			
laser cladding, laser alloying, laser glazing, differences between	482			
laser heat treatment	483–484			
laser scanning technology	480–481			

Index Terms

Links

Laser surface hardening (LSH) (*Cont.*)

laser shot peening (LSP)	483			
laser surface hardening	478–479			
laser technology development, timeline	476	477		
nonferrous alloys	491			
overview	476			
specified hardness, challenges in obtaining	487–488			
techniques	476			
autocatalytic plating	478			
chemical vapor deposition (CVD)	476			
displacement plating	478			
electroless plating	478			
electroplating	476	478		
ion plating	476			
physical vapor deposition (PVD)	476			
sputter deposition	476			
thermokinetic (TK) process	485–487			
Laser surface heat treatment	395	478		
Laser technology development, timeline	476	477		
Laser welding	323–324			
Laser-induced breakdown spectroscopy	272			
LC. <i>See</i> Laser cladding (LC)				
LDMD. <i>See</i> Laser direct metal deposition (LDMD)				
Lead				
baths	257			
as molten metal quenchant	125			
Lead baths				
patenting	261			
tempering	345			
Least-squares (LSQ)	110	168	170	188
	189			
Lehrer diagram	622–623			
Leidenfrost phenomenon	195			
Leidenfrost temperature	164			
Liquid boriding	718–719			

Index Terms

Links

Liquid carbonitriding. *See* Cyaniding (liquid carbonitriding)

Liquid carburizing and cyaniding. *See also* Cyaniding (liquid carbonitriding)

applications

combined carburizing and brazing 577

overview 576–577

selective carburizing 577

stopoffs 577

carbon gradients 571

carbon penetration 571

case depth, control of 572–573

cyanide salts, precautions in use of 577–578

cyanide-containing liquid carburizing

baths 565–566

cyanided parts, washing 576

cyaniding (liquid carbonitriding) 566–567

difference between 565

dimensional control 574

hardness gradients 571

noncyanide liquid carburizing 567–571

overview 565

process control 571–572

quenching media

oil quenching 575

overview 574

quenching baths, maintenance of 575

quenching cyanided parts 575

quenching oils 575

salt bath quenching 575

salt bath quenching, safety caution 575

water and brine 574–575

salt removal (washing) 575–576

Liquid nitriding

aerated bath nitriding 681–682

applications 680

case depth 683

case hardness 683

Index Terms

Links

Liquid nitriding (*Cont.*)

equipment	684	
high-speed steels	683	
liquid pressure nitriding	681	
liquid salt bath nitriding	689	
liquid salt bath nitriding noncyanide baths	688–689	
maintenance schedules	684	685
operating procedures		
bath, aging	684	
bath, starting	683–684	
bath maintenance	684	
overview	683	
prior heat treatment	683	
safety	684	
overview	680	
safety precautions	685	
systems	680–681	
use of term	680	

Liquid nitrocarburizing

compound layer	686	
compound zone produced in salt baths, wear and antiscuffing characteristics of	687–688	
nontoxic salt bath nitrocarburizing treatments	686–687	
overview	685	
process 1: high cyanide without sulfur	685	
process 2: high cyanide with sulfur	685–686	

Liquid pressure nitriding

681

Liquid quenching heat transfer

162–163 164–167

Liquid salt bath nitriding

689

Liquid salt bath nitriding noncyanide

baths

688–689

Lišćić-Nanmac probe

159

Lišćić /Petrofer probe

design of	181	
finite-volume method for HCE	187	
heat-extraction dynamic	181–182	

Index Terms

Links

Lišćić /Petrofer probe (Cont.)

simplified 1-D temperature distribution

 model

185

simulation examples

189–191

wetting kinematics

183

Local equilibrium

626

Low-alloy medium-carbon steels

60–79

271

Low-alloy steels

 austempering

353

354

 nominal subcritical annealing

 temperatures

305–306

 tempering

334

Low-carbon (lath) martensite

515

Low-carbon steels. *See also* Carburizing

 annealing

299

 boriding

717

 boron, effect of

46

 carbonitriding

505

599

605

 cold forming

301

 diffusion treatments, characteristics of

390

 Falex tests

687

 hardenability calculation

60–79

 machining

513

 microstructures

9

 normalizing

282

 N-quench

658–659

 short-time subcritical annealing

302

 siliconizing

708

 spheroidizing

292

 stage I tempering

330

 TME

342–343

 TRD coatings

726

 unalloyed low-carbon steels

716

 Widmanstätten ferrite

12

Low-pressure carburizing (LPC)

221

230

 applications

586–587

 carbon profiles, prediction of

585–586

 carburizing strategies

584–585

Index Terms

Links

Low-pressure carburizing (LPC) (*Cont.*)

equipment for	583–584	
high-pressure gas quenching (HPGQ)	582	583–584
high-temperature LPC	587–589	
intergranular oxidation (IGO)	582–583	
overview	581	
physical principles	582–583	
process	581–582	
production part approval process (PPAP)	587	
quality control, in mass production	587	

Low-pressure vacuum gas

carburizing (LPC)	368	
--------------------------	-----	--

Low-temperature nitriding

application	650	
overview	649–650	
process description	650–651	
thermodynamic background	650	

Low-temperature nitrocarburizing

application	650	
overview	649–650	
process description	650–651	
thermodynamic background	650	

Low-temperature salt bath nitride coating

overview	736	
preparation and maintenance	736	
quality issues	736–737	

LPC. *See* Low-pressure carburizing (LPC);

Low-pressure vacuum gas carburizing (LPC)

LSQ. *See* Least-squares (LSQ)

Lumped heat-capacity method 178–179

LUMPPROB computer code 168

M

Machining, annealed structures for 294–295

MAG. *See* metal active gas (MAG) welding

Magnetic Barkhausen noise phenomenon 414

Magnetic flux concentrators 454–456

Index Terms

Links

Magnetic hysteresis	442		
Magnetic-comparator testing	527		
Manganese			
hardenability, effect on	46	313	
multiplying factors	83–84	86	
steel, selection for hardenability	49		
MAPP. <i>See</i> Methylacetylene propadiene (MAPP), propane			
Marquenching. <i>See also</i> Martempering			
fluidized-bed quenching	243		
gas carburizing	555		
molten salts	232		
oil quenchants	138		
process	224–225		
quenchants	553		
step quenching	233		
temperature considerations	233		
transformation time	233		
two-step batch quenching	244		
use of term	363		
Marquenching oil	138	140	575
Martempering			
advantages	364		
applications	376–377		
austenitizing equipment	377		
bath maintenance	378–380		
equipment	377		
equipment requirements	377–378		
gas carburizing	555		
handling parts	380		
high-pressure gas quenching (HPGQ)	368		
low-pressure vacuum gas carburizing (LPC)	368		
modified martempering	364		
oil system maintenance	379–380		
overview	126	362–364	
precautions. <i>See</i> Martempering, safety precautions			

Index Terms

Links

Martempering (*Cont.*)

process variables, control of	
agitation	372
austenitizing temperature	371
martempering bath, cooling from	372–373
martempering bath temperature	371
martempering bath, time in	371–372
overview	371
salt contamination	371
water additions, to salt	372
quench oil classification	132–133
racking	380
salt system maintenance	378–379
selection of process	128
steel, selection for hardenability	50
steels, suitability for	
borderline grades	370
effect of mass	370–371
low-carbon steels	369–370
medium-carbon steels	369–370
overview	368–369
TTT diagrams	369–370
use of term	363
washing the work	
martempering salts	380
quenching oils	380

Martempering, dimensional control

examples	373–374
forming after martempering	375–376
overview	373
stabilizing after martempering	374

Martempering, safety precautions

hot oil	367–368
nitrate-nitrite salts	367
overview	367

Martempering media

example	366
fluidized beds	365

Index Terms

Links

Martempering media (*Cont.*)

oils	366
oils, advantages/disadvantages	367
overview	364
salt, advantages of	365
salt, composition and cooling power of	364–365
salt, disadvantages of	365

Martensite

as-quenched martensite, hardness of	419
body-centered tetragonal (bct) crystal structure	4
carbon control, evaluation in carburized parts	523
formation of	4
hardenability	14–15
hardness	14
heat treated steel, phases of	13–14
high-carbon (plate) martensite	515
intensive quenching (IQ)	200
introduction	13–16
low-carbon (lath) martensite	515
martensite start temperature	506
tempered martensite	15–16
tempered martensite embrittlement (TME)	341–344
unit cell	4

Martensitic critical cooling velocity 419

Masking

boriding	715
boriding, nonferrous materials	716
carburization, as complication in during heat treatment	517–518 402
ion nitriding	690
liquid carburizing	519
mechanical masking	399
plasma carburizing	595 596
plasma nitriding	695
selective carburizing	393

Index Terms

Links

Masking (*Cont.*)

selective nitriding	673	674		
spraying	404			

MATLAB 63

Mead turbine velocimeter 118

Mechanical masking 399

Melon 687

Metal active gas (MAG) welding 324

Metal dusting 540 625

Metal Progress 47

Metallurgical Society of AIME 16–17

Methylacetylene propadiene (MAPP), propane 421 422 423 426
431

MF. *See* Multiplying factors (MF)

Microalloying 8–9 298 316 318

Microalloying elements, solubility of 316

Microhardness test 407–411

Microhardness testers 409

Microhardness testing 409 522

**Military Specification MIL-S-10699A
(Ordnance)** 345

Minitech 63

Minitech Predictor 63–64

Modified martempering 364

Molten salts. *See also* Salt quenching

environmental and safety considerations 236

overview 232–233

potassium nitrate (KNO₃) 232

sodium nitrate (NaNO₃) 232

sodium nitrite (NaNO₂) 232

Molybdenum

hardenability, effect on 46

multiplying factors 83–84

nitrided steels 394–395

temper embrittlement, effect on 341

Mounting press 670

MPLHT. *See* Multipass laser heat treatment
(MPLHT)

Index Terms

Links

Multicomponent boriding	720–721			
Multifield EB-deflection technique	466			
Multipass laser heat treatment (MPLHT)	484			
Multiplying factors (MF)	80	82	83–86	
Multiprocess technique	466			
Music wire	276	278		
Musical instrument makers	384			
N				
Nakal system	665			
National Aeronautics and Space Administration (NASA)	384			
National Fire Protection Association	431			
Nernst voltage	667			
Neural-Network Modeling in <i>Fundamentals of Modeling for Metals Processing, Volume 22A of ASM Handbook</i>	334			
Newtonian cooling	164			
Newton's law of cooling	160	168		
NFEs. <i>See</i> Nitride-forming elements (NFEs)				
Nickel				
hardenability, effect on	46			
multiplying factors	83–84	86		
Nickel strike	400			
Nitralloy 135M	394	395	697	
Nitrate-nitrite salts	364	367	371	685
Nitrided steels	394–395			
Nitride-forming elements (NFEs)	725			
Nitriding				
advent of	619			
application	651			
carburizing potential	624–625			
case depth, controlling	653			
catalytic nitriding	665			
compound-layer growth, kinetics of	633–635			
controlled carburizing	625			
controlled nitriding	623–624			
diffusion zone. <i>See</i> Diffusion zone				
diffusion-zone growth, kinetics of	639–641			

Index Terms

Links

Nitriding (*Cont.*)

epilogue	641–643	
high- low-pressure nitriding	653–654	
introduction	619	
iron-nitrogen phase diagram	621–622	
Lehrer diagram	622–623	
local equilibria and stationary states		
gas-solid interface	626–628	
solid-solid interface	628	
low-temperature nitriding	649–651	
microstructural development of the compound		
layer	628–629	
microstructural development of the compound		
layer, in the presence of allowing		
elements	632–633	
nitrided steels	394–395	
nitrided/nitrocarburized microstructure	620–621	
nitriding potential	622–623	
nitrogen-diluted atmospheres	654	
overview	393–394	651
oxysulfonitriding	655	
plasma nitriding	402	
porosity, interpretation and		
development of	621–622	
preoxidation	653	
process description	652–653	
process methods	395	
solution nitriding	658–659	
stop-off paints	402	
sulfonitriding	655	
thermodynamic background	651–652	
zero-flow nitriding	665	
Nitriding processing		
activation/depassivation	660	
cleaning	659	
diffusion zone and compound layer,		
controlling	660–661	
nucleation	660	

Index Terms

Links

Nitriding processing (*Cont.*)

postoxidation	660
preoxidation	659–660
safety purge	659

Nitriding steels

699

Nitrocarburizing. *See also* Nitriding

application	656
austenitic	657
compound layer, controlling	657
compound-layer growth, kinetics of	633–635
controlled nitrocarburizing	625–626
diffusion zone. <i>See</i> Diffusion zone	
epilogue	641–643
ferritic	656–657
introduction	619
iron-nitrogen phase diagram	621–622
low-temperature nitrocarburizing	649–651
microstructural development of the compound layer	629–632
overview	656
porosity, interpretation and development of	621–622
process description	656–657
stop-off paints	402
surface hardening	395
thermodynamic background	656

Nitrogen

carbonitriding	505	520
fluidized-bed quenching	241	
gas quenching	223	
immobile	640	641
industrial annealing	296	
mobile	640	
nitrogen-diluted atmospheres	654	

Nitrogen-methanol atmospheres

534–535

NMTP. *See* Nonmartensitic transformation

products (NMTP)

Nonboron steels

66–69 70

Index Terms

Links

Noncyanide liquid carburizing

low-toxicity and regenerable salt bath	
processes	569–571
noncyanide carburizing process	569
noncyanide carburizing salts, safety and	
disposal of	568–569
overview	567

Nondestructive testing

case depth, measuring	413–414
electromagnetic tests	527
low-pressure carburizing (LPC)	589

Nondispersive infrared (NDIR) analyzers

530	535	542	543
544			

Nonferrous alloys

conventional surface-hardening techniques	476–478
laser surface hardening	491
stress-relief heat treating	275

Nonferrous materials

boriding	710	716–717
salt quenching	232	

Nonmartensitic transformation products

(NMTP)	551	601
--------	-----	-----

Non-Newtonian cooling

164

Non-Newtonian fluids

403

Nontoxic salt bath nitrocarburizing treatments

overview	686
process: low cyanide with sulfur	686–687
process: low cyanide without sulfur	686–687

Nonuniform three-dimensional (3-D) heat generation

439

Normalizing

applications, based on steel classification		
alloy steels	283–284	
carbon steels	282–283	
overview	282	
castings	287	
cooling	281	
forgings	284	286
heating	281	

Index Terms

Links

Normalizing (*Cont.*)

induction normalizing	307
introduction	280–281
sheet and strip	287–288
subcritical annealing and normalizing	307
wrought products	281

Normalizing, bar and tubular products

furnace requirements	286–287
overview	286

Normalizing, forgings

axle-shaft forging	284	286
furnaces	284	
low-carbon steel forgings	286	
multiple normalizing treatments	286	
overview	284	
processing	284	
structural stability	286	

N-quench 657–658

Nucleate boiling

aqueous salt (brine) solutions	123	124		
controllable delayed quenching	218			
cooling curve test	105	107	109	110
defined	92			
heat-transfer basics	161			
HTCs	111	112		
intensive quenching	200–201	202	203	
IQ-2 process	198	202		
jet quenching	246			
liquid quenching heat transfer	167			
oil quenchants	129	131	132	135–136
	138			
probes	179	180	183	189
quench oil bath maintenance	143			
quench severity	100			
quenching mechanism	92	93	94	
rewetting	164			
spray quenching	246	247	248	249
	250	449		

Index Terms

Links

Nucleate boiling (*Cont.*)

water- and air-quenching media	122		
wire patenting	258		

Nusselt number	202	239	248
-----------------------	-----	-----	-----

O

Occupational Safety and Health Administration

(OSHA)	273–274	569	
--------	---------	-----	--

Oil fires, extinguishing	146		
---------------------------------	-----	--	--

Oil quench system monitoring

polycyclic aromatic hydrocarbons (PAHs)	144		
quench oil toxicity	144		
for system changes in quench severity	144		

Oil quenchants	129–139		
-----------------------	---------	--	--

animal oils	129		
-------------	-----	--	--

basestocks	130–131		
------------	---------	--	--

bath temperature and agitation, effect of	137–139		
----------------------------------------------	---------	--	--

bright quenching oils	136–137		
-----------------------	---------	--	--

cooling rate acceleration	135–136		
---------------------------	---------	--	--

martempering	132	366–368	
--------------	-----	---------	--

oil fires, extinguishing	146		
--------------------------	-----	--	--

oil quench system monitoring	144		
------------------------------	-----	--	--

overview	129–132		
----------	---------	--	--

oxidative stability	133–135		
---------------------	---------	--	--

petroleum quench oils, safe use of	144–146		
------------------------------------	---------	--	--

quench oil bath maintenance	139–143		
-----------------------------	---------	--	--

quench oil classification	132–133		
---------------------------	---------	--	--

surface pressure, effect of	133		
-----------------------------	-----	--	--

vegetable oils	129		
----------------	-----	--	--

Oil quenching

applied energy case hardening	432		
-------------------------------	-----	--	--

aqueous salt (brine) solutions	124		
--------------------------------	-----	--	--

austempering	126	357	359
--------------	-----	-----	-----

bright quenching oils	136		
-----------------------	-----	--	--

carbonitriding	505	521	599
----------------	-----	-----	-----

carburizing steels	392		
--------------------	-----	--	--

CCT diagrams	97		
--------------	----	--	--

Index Terms

Links

Oil quenching (*Cont.*)

cleaning for heat treatment	265			
continuous furnaces	538			
Fe ₂ B layers	714			
fluidized-bed quenching	242	243		
gas quenching	221			
hardness and hardenability	26			
HPGQ	229	230		
inverse hardening	214			
ion nitriding	700			
IQ process	200	204	207	211
large probes, industrial quenching processes	189			
liquid carburizing and cyaniding	575	576		
low-pressure carburizing (LPC)	582			
maintenance schedule	121			
martempering	364	370	371	373
	377			
powder metallurgy (PM) parts	614			
press quenching	252	254–255		
proeutectoid cementite	12			
propeller agitation	116			
tanks	118	145		
through-hardening steels	204			
versus water quenching	44			
Open-coil annealing	301			
OSHA. <i>See</i> Occupational Safety and Health Administration (OSHA)				
Oxidation				
carburization	511			
intergranular oxidation	518			
Oxy-fuel				
flame hardening	426	435		
gas flame	422			
oxy-fuel gas type flame heads	423–424	425	429	
oxy-fuel gas type flame heads, non-ferrous	428			
Oxynitriding	655			
Oxysulfonitriding	648	655		

Index Terms

Links

P

Pack carburizing

advantages	560	561		
carburizing compounds	561			
carburizing containers	563–564			
carburizing medium	561			
depth of case	560			
disadvantages	560	561		
distortion	560			
furnaces for	562–563			
introduction	560			
packing				
overview	564			
procedure	564			
process-control specimens	564			
work-load density	564			
process control				
carburizing rates	562			
case depth	562			
example	562			
overview	562			
surface carbon content	562			
selective carburizing	560			
steel composition	560			

Pack cementation boriding

717

Pack cementation processes

aluminizing	707–708			
chemical vapor deposition (CVD)	707			
chromizing	708			
overview	707			
siliconizing	708			

PAG. *See* Poly(alkylene glycol) (PAG) copolymer

Paschen curves

592 593 693 694

Pass/fail test

271

Paste boriding

718

Patenting

303 357–358 360

See also Wire patenting

Index Terms

Links

Pearlite

carbon control, evaluation in carburized

parts

522

heat treated steel, phases of

9–10

overview

9–10

Permalloy

716

722

Petroleum quench oils, safe use of

explosions or fire, source of

145

extinguishing oil fires

146

overview

144

quench tanks, types

145

Physical vapor deposition (PVD)

476

700–701

725

Pickling

270

271

Pitot tube

118

Plain carbon steels

aerated bath nitriding

681–682

aerated cyanide-cyanate nitriding

682

annealing

289

298

applied energy methods

395

as-quenched hardness

450

austempering

354

austenitic nitrocarburizing

657

austenitization

446–447

bake-hardening steels

299

blue brittleness

341

boriding

714

716

carbide coating nucleation and growth

727

case depth prediction

536

Curie point

442

flame hardening

435

436

gas carburizing

552

hardenability calculation

60–79

hardness testing

522

induction hardening

457

IQ process

200

liquid nitriding

682

magnetic properties

441

modified austempering

341

Index Terms

Links

Plain carbon steels (*Cont.*)

nominal subcritical annealing			
temperatures	305–306		
normalizing temperatures	282		
plasma (ion) nitriding	699		
quenching, transformation time	233–234		
spheroidizing	302		
steel selection for hardenability	49		
surface hardening	395		
tempering	328	331	336–337

Plasma (ion) nitriding

advantages	690		
applications			
dimensional control, as alternative to			
carbonitriding	700		
duplex processes	700–701		
overview	700		
stainless steels, sputtering and ion			
nitriding of	700		
case structure and formation	698		
diffusion zone, nitrided case	698–699		
furnaces. <i>See</i> Plasma nitriding furnaces			
gas nitriding, difference between	690		
glow-discharge process	693–695		
introduction	402	690	
limitations of	690		
process control			
arc detection and suppression	697		
atmosphere control	697		
overview	696–697		
part temperature	697		
power-supply controls	697		
pressure control	697		
workpiece factors			
hardness profiles	699		
overview	699		
prior microstructure, effect of	699		
white-layer properties	699–700		

Index Terms

Links

Plasma (ion) nitriding, history and developments

active-screen plasma nitriding	692–693
direct-current plasma nitriding (1970–1980)	690–691
pulsed-current plasma nitriding	691–692

Plasma boriding

719–720

Plasma carburizing

advantages	594
application example	596–597
carbon input, influence of pulse length on	595
carburizing reaction in	593–594
diffusion characteristics	593–594
disadvantages	594
furnaces	595–596
loading requirements and limitations	596
mechanical masking	595
overview	591
principles of	
coverage	593
glow-discharge plasma	591–592
glow-discharge plasma, range of	592
limitations of	592
overview	591
voltage levels	592–593
wrap-around effect	593
process parameters	596
atmosphere/gas flow rate, composition of	596
current density	596
pressure	596
pulse—power density	596
surface condition	596
temperature	596
voltage density	596
production equipment	595–596
sinter metals	595
sputter plasma	595
stainless steels	595

Index Terms

Links

Plasma nitriding furnaces

cold-walled plasma furnaces	695–696
hot-walled plasma pulsed-dc furnaces	696
overview	695

Plasma nitrocarburizing

690 701–702

Plate

annealing	303
carburizing, quality assurance	515
Jominy equivalence charts	41

Plenum.

238

Polyacrylates

149–151

Polyalkylene glycol

control measures	149
cooling characteristics	148–149
overview	148

Poly(alkylene glycol) (PAG) copolymer

147 213–214 218

Polycyclic aromatic hydrocarbons (PAHs)

144

Polymer quenchants

overview	146
polyacrylates	149–151
polyalkylene glycol	148–149
polymer primer	146–147
polyvinyl alcohol (PVA)	147
polyvinyl pyrrolidone (PVP)	149
thermal separation/inverse solubility	147

Poly(sodium acrylate) (PSA)

147

Polyvinyl alcohol (PVA)

148

Polyvinyl pyrrolidone (PVP)

149

Pool boiling

160 161

Porosity. *See also* Carbonitriding

carbonitrided case	393
compound layer, controlling	657
compound layer growth, kinetics of	635
controlled nitriding	624
copper plating	399 577
gas boriding	716
iron-nitrogen phase diagram	621–622
laser cladding	482

Index Terms

Links

Porosity (*Cont.*)

liquid carburizing and cyaniding	577			
liquid salt bath nitriding noncyanide				
baths	688	689		
nitrided parts	669	670		
nitriding	628	629	653	
nitrocarburizing	631	656	657	664
	665			
pack carburizing	561			
plasma boriding	719			
powder metallurgy parts	459			
TRD coated parts	737			

Postoxidation

648	654	656	657
660	664		

Potassium nitrate (KNO₃)

232

Powder metallurgy (PM) parts

carbonitriding	614
induction surface hardening	459–460
ion nitrided	699

Prandtl number

239 248

Preoxidation

gas nitriding	674	
horizontal preheat furnace	675	
nitriding	653	659–660
nitrocarburizing	664	
prior to carburizing	536	

Press quenching

distortion control	255–256
equipment	252–255
gas carburizing	555
oil-quenching process	254–255
overview	252
pulse feature	256

Pressure nitriding

654

Prior austenite

austenite grain growth	315
austenitizing	315

Index Terms

Links

Prior austenite (*Cont.*)

normalizing of steel	280
use of term	315

Prior austenite grain boundaries

carbides	517
continuous carbide network	517
intergranular oxidation	550
isothermal transformation (IT) diagrams	19
martensite	13
NMTP	601
TE	340
temper embrittlement (TE)	340
TME	342

Probes

Datanit sensor	668			
Lambda probes	667			
nondispersive infrared (NDIR) analyzers	530	535	542	543
	544			
oxygen probe	667			
QE sensor	668			
salt quenching	235			
thermal	194			
wire patenting	261			
Wolfson probe	106			
zirconia oxygen probe	511–512	530		

Probes, industrial quenching processes

axially symmetrical workpieces, prediction of hardness distribution	183–184
critical heat-flux densities of liquid quenchants	
first critical heat-flux density	179–180
initial heat-flux density	179–180
heat-transfer coefficient, calculation based on laboratory tests	
inverse heat-conduction method	178
lumped heat-capacity method	178–179
IHCP, numerical solution of	
HCE, finite-volume method for the	187–188
heat-transfer coefficient, calculation of	186–187

Index Terms

Links

Probes, industrial quenching processes (*Cont.*)

overview	184–185	
simplified 1-D temperature distribution		
model	185–186	
laboratory tests and characterization of industrial		
quenching processes	179	
for laboratory tests and resultant curves	176–178	
laboratory tests, scope of	178	
Liscic/Petrofer probe	181–183	
simulation examples		
oil quenching	189	
overview	189	
polymer quenching	189–191	
smoothing, measured temperatures	188–189	
temperature gradient method	180	
workshop designed test, requirements for	179	
Production IQ systems		
batch-type systems	208	
continuous-type systems	208–209	
overview	207–208	
single-part-processing systems	209–210	
Production part approval process (PPAP)	587	
Proeutectoid ferrite		
acicular	13	
heat treated steel, phases of	10–12	
isothermal transformation (IT) diagrams	19	
patenting	303	
Q&P steels	318	
wire patenting	258	
Programmable logic controllers (PLCs)	541	
Propeller-driven flow meter	193	
Propellers		
agitation equipment	115	116–118
batch quenching systems	233	
fluid flow measurement	193	
IQ-2 systems	210	
mild steel IQ tank	208	
oil quenching	575	

Index Terms

Links

Pulsed-current plasma nitriding	691–692		
Pure iron			
ferrite and austenite in	5–6		
iron nitrides in	645–646		
Q			
QE sensor	668		
QT. <i>See</i> Quenched and tempered (QT); Quenching temperature (QT)			
Quench aging	9		
Quench cracking			
alloy steels	50		
austempering	352	353	
carburizing	392		
geometric stress	23		
hardenability	43	44	45
induction surface hardening	448	461	
intensive quenching	198		
selective tempering	345		
surface condition	113		
tempering	336	346	
Quench oil bath maintenance			
cooling curve characterization	143		
overview	139		
physical property characterization			
acid number	142		
Bacon bomb fluid-sampler thief (Bacon bomb)	140		
flash point	141–142		
induction-coupled plasma analysis	142–143		
overview	139		
sampling	139–140		
saponification	142		
viscosity	140–141		
water content	141		
Quench process sensors			
Fluid-Quench Sensor	195		
overview	192		
quenching, fluid flow in	192		

Index Terms

Links

Quench severity

Jominy end-quench test	101–103
Jominy hardenability to round bar hardness transformation—Rushman approach	103
molten salt	127
overview	100–101
quenching media	43–44
salt quenching	234–235
steel	120–121

Quench severity, in hardenability evaluation

30–33

Quenchants

bismuth	125
enabling controllable delayed quenching	218
gas carburizing	553
gravity fall	116
hot oil quenchants	126–129
lead	125
liquid, critical heat-flux densities of	179–180
liquid, database of cooling intensities	184
molten metal quenchants	125–126
molten salt quenchants	126–129
oil fires, extinguishing	146
oil quench system monitoring	144
oil quenchants	129–139
petroleum quench oils, safe use of	144–146
polymer quenchants	146–151
quench oil bath maintenance	139–143
selection	120–121
temperature, effect of	94

Quenched and tempered (QT)

327

Quenching

air-quenching media	122
aqueous salt (brine) solutions	122–125
as-quenched hardness	450–451
brine quenching	122
carbonitriding	610–611
cold die quenching	151
delayed. <i>See</i> Delayed quenching	

Index Terms

Links

Quenching (*Cont.*)

empirical methodology	159	
fixtures		
cold die quenching	151	
overview	151	
restraint fixturing	151	
flame hardening	431–432	
fluid flow in. <i>See</i> Fluid flow		
fluidized-bed. <i>See</i> Fluidized-bed quenching		
gas (quenching). <i>See</i> Gas quenching		
gas carburizing	555	
gas nitriding	648	
gas nitrocarburizing	648	
gas quenching	610–611	
goal of	159	
gravity fall	116	
hot oil quenchants	126–129	
ideal quench	61	
induction hardening and tempering	448–451	
intensive. <i>See</i> Intensive quenching (IQ)		
jet. <i>See</i> Jet quenching		
liquid carburizing and cyaniding	574–575	
liquid quenching heat transfer	162–167	
mechanism of	91–93	
media, tests and evaluation of		
cooling-power tests	103–104	
hardening-power tests	103	
overview	103	
metallurgical aspects		
carbon content and hardenability	97–99	
hardenability bands (H-steels)	99–100	
overview	95–97	
molten metal quenchants	125–126	
molten salt quenchants	126–129	
oil fires, extinguishing	146	
oil quench system monitoring	144	
oil quenchants	129–139	
oil quenching	122	189

Index Terms

Links

Quenching (*Cont.*)

overview	91	
petroleum quench oils, safe use of	144–146	
physical phenomena during		
quenching	158–159	
polyacrylate quenchant	150	
polymer quenchant	146–151	
polymer quenching	189	
press(quenching). <i>See</i> Press quenching		
quench cracks	448	
quench oil bath maintenance	139–143	
quench severity	120–121	
Jominy end-quench test	101–103	
Jominy hardenability to round bar		
hardness transformation—Rushman		
approach	103	
overview	100–101	
salt. <i>See</i> Salt quenching		
as source of residual stress	275	
spray (quenching). <i>See</i> Spray quenching		
step quenching	233	
systems	118–122	
Tensi classification of surface-cooling modes		
of heat transfer	93–94	
thermal field	167	
water quenching	122	610
water-quenching media	122	
Quenching, heat-transfer coefficient calculations		
cooling rate calculation	112	
cooling-time calculation	112	
examples	112–113	
general approach of solving inverse-heat		
conduction and mass transfer problems	111	
Green function method	110	
inverse method	110	
mathematical models of second heat-transfer		
mode	111–112	
overview	110	

Index Terms

Links

Quenching, heat-transfer coefficient calculations (*Cont.*)

regular thermal condition theory	111
simplified methods	111–112
statistical regularization method	110
Tikhonov regularization method	110

Quenching, mechanism of

cooling curves	92–93
factors involved	91

Quenching, process variables

agitation	94	114–115
equipment	115–118	
flow velocity, measurement of	118	
mass effects	114	
Mead turbine velocimeter	118	
overview	94	
quenchant temperature	94	
section size effects	114	
surface condition	113–114	
workpiece temperature	94	

Quenching and partitioning (Q&P) steel

annealing process	318
application properties	
hole-expansion ratio (HER)	319
shear fracture behavior	320
springback behavior	320
applications	319
chemical composition	317–318
defined	317
dynamic tensile properties	319
forming	319
mechanical properties	319
microstructure	318
overview	317–318
phase diagram	318
retained austenite	
mechanical properties	320–321
microstructure evolution with strain	321–322

Index Terms

Links

Quenching and partitioning (Q&P) steel (*Cont.*)

transformation	321
thermal profile	318

Quenching and partitioning (Q&P) steel, welding

properties

laser welding	323–324
metal active gas (MAG) welding	324
overview	322
Q&P 980 steel	322
resistance spot welding	322–323
transformation-induced plasticity (TRIP) steel	317

Quenching installations, maintenance of

brine quenching	122
for oil quenching	121–122
for water quenching	122

Quenching media

air-quenching media	122
aqueous salt (brine) solutions	122–125
flame hardening	432
hardenability requirements, determining	43–45
hot oil quenchants	126–129
liquid carburizing and cyaniding	574–575
molten metal quenchants	125–126
molten salt quenchants	126–129
tests and evaluation of	
cooling curve test	104–110
cooling-power tests	103–104
GM Quenchometer test	104
hardening-power tests	103
interval test	103–104
magnetic test	104
overview	103
water-quenching media	122

Quenching methods

direct quenching	91
fog quenching	91
selective quenching	91

Index Terms

Links

Quenching methods (*Cont.*)

spray quenching 449–450
time quenching 91

Quenching systems

overview 118 120
quench severity 120–121
quench selection 120–121

Quenching temperature (QT)

318 327 334 338

R

Radiation, heat exchange by

160

Raman spectroscopy

272

Refroidissement

289 310

Regression analysis of hardenability in Europe

derivation of formulas 73
formulas, assessment of 73–74
formulas, using 74–76
overview 71–73
Steel Institute VDEh 72–73

Residual stresses

carburization 506–508 513
gas carburizing 551 555
intensive quenching 205
introduction 21–23
retained austenite, effect of 549

Resistance spot welding

microhardness 323
microstructure 323
overview 322
spot weld strength 323
weld lobe 322

Retained austenite

aerospace applications 586
annealing 291
austenite 523
austenitizing 309 312
automotive applications 586
carbonitriding 605–606 613

Index Terms

Links

Retained austenite (*Cont.*)

carburized components	347			
carburized hardenability test	38			
carburizing	508	513	514	515–516
cold treatment of steel	382	383		
cryogenic treatment	383	384		
decarburization	516			
and dimensional stability	549–550			
direct hardening versus reheat				
hardening	552–553			
electron beam surface hardening	467			
flame hardening	419			
furnace atmospheres	606			
gas carburizing	532	547	548–550	
gas carburizing, quenchants	553			
gas carburizing, tempering	553–554			
hardening and	382			
hardness testing	522			
heat transfer during quenching	162			
high-carbon (plate) martensite	515			
high-carbon steels	80			
Hollomon- Jaffe method	333			
induction surface hardening	450	461		
laser surface hardening (LSH)	482	487	488	489
	490			
liquid carburizing and cyaniding	566			
low-pressure carburizing (LPC)	581	584	586	
martensite formation	14			
martensite start temperature	506			
mechanical behavior and stability of	320–322			
multiple tempering	345	346		
noncyanide liquid carburizing	568			
performance, effect on	550			
quenching and partitioning (Q&P) steel	317	318	319	
refrigeration	329			
solution nitriding	659			
steel quenching	97	121		
supercarburizing	741	745		

Index Terms

Links

Retained austenite (*Cont.*)

surface hardening	391	393	
surface nonmartensitic transformation			
products (NMTP)	551		
tempered martensite	15	16	
tempered martensite embrittlement (TME)	343		
tempering	327	328	330–332
tempering, cracking in processing	346		
tempering, dimensional change during	336–338		
TRD	732		

Rewetting

active heat-transfer boundary condition	170		
bath agitation	164		
cooling curves	92		
film boiling	167		
hollow/non hollow cylinders	165		
jet quenching	248		
Leidenfrost temperature	164		
Newtonian cooling	164		
non-Newtonian cooling	164		
nonuniform rewetting	165		
orientation, effect on wetting front	166–167		
probe geometry, effect on heat extraction	165		
quenching into a vaporizable fluid without			
the use of additives	91		
quenching into vaporizable liquids	107		
SAE 304 steel rings	165–166		
Tensi classification of surface-cooling			
modes of heat transfer	93	94	
vapor blanket	164		
wetting front kinematics	164–165		
wetting front velocity	164		
wetting kinematics, influence of	183		

Reynolds number	118	239	248
------------------------	-----	-----	-----

Rockwell C hardness (HRC) readings	382		
-------------------------------------------	-----	--	--

Rockwell hardness

carburized hardenability test	38		
case depth, measuring	409–411		

Index Terms

Links

Rockwell hardness (*Cont.*)

Jominy test	36
prediction of hardenability in steels	63

Rolled wire	526
--------------------	-----

Rotating-bending fatigue	360	368	369	508
---------------------------------	-----	-----	-----	-----

Rushman approach	103	235
-------------------------	-----	-----

S

SAE J 406 hardenability predictor	63
------------------------------------------	----

Salt, as martempering media	364–367	371	378–379	380
------------------------------------	---------	-----	---------	-----

Salt baths. *See also* Cyaniding (liquid carbonitriding); Liquid nitriding

electroless salt bath boriding	719
--------------------------------	-----

electrolytic salt bath boriding	719
---------------------------------	-----

high-temperature salt bath carbide

coating	733–735
---------	---------

liquid salt bath nitriding	689
----------------------------	-----

liquid salt bath nitriding noncyanide

baths	688–689
-------	---------

low-temperature salt bath nitride

coating	736–737
---------	---------

nontoxic salt bath nitrocarburizing

treatments	686–687
------------	---------

salt bath descaling	270
---------------------	-----

salt quenching	233–234
----------------	---------

See also Molten salts;

Salt quenching

salt system maintenance	378–379
-------------------------	---------

TRD	730–731
-----	---------

washing the work	380
------------------	-----

wear and antiscuffing characteristics of

the compound zone	687–688
-------------------	---------

Salt quenching

environmental and safety considerations

handling, molten salts	236
------------------------	-----

parts washing	236
---------------	-----

reclamation, salt	236
-------------------	-----

salt disposal	236
---------------	-----

Index Terms

Links

Salt quenching (*Cont.*)

storage, molten salts	236		
equipment for			
batch operation	233		
continuous operation	233		
mass of the quench	233		
step quenching	233		
molten salts	232–233		
overview	232–233		
probes	235		
Rushman approach	235		
systems, critical characteristics for operation of			
agitation and water additions	234–235		
composition of quenchant	234		
contaminants	234		
handling systems	235		
loading systems	235		
preventive maintenance	235		
time and temperature considerations			
nitrite-nitrate quench tanks	233		
quenching temperature range	233		
transformation time	233–234		
water, addition of	234–235		
Salt removal (washing)	575–576		
Saponification	147	270	272
Saybolt universal seconds (SUS)			
agitation equipment	117		
conventional quenching oils	132–133		
kinematic velocity or cSt, converting to	141		
oil quenching installations, maintenance of	122		
quenching oils, washing problems	380		
re-refined paraffinic baseoils	131		
Scanning electron microscope (SEM)	257	258	313
SCC. <i>See</i> Stress-corrosion cracking (SCC)			
Scuffing	687–688	737	
Secondary hardening			
alloy steels capable of	327		
bainitic steels	347		

Index Terms

Links

Secondary hardening (*Cont.*)

defined	16		
gas carburizing	552		
tempering, effect of composition	336		
tempering stages	329	330	
tempering time and temperature	332		
TRD	732		

Selective carburizing

ceramic coatings	554		
copper plating	554		
liquid carburizing and cyaniding	577		
overview	554		
partial immersion	577		
stopoffs	554		

SEM. *See* Scanning electron microscope (SEM)

Shear stress

carburizing	509	513	516
hardenability	50		
stop-off paints	403		
stress relief	382		

Sheet and strip

annealing	297–301		
normalizing	287–288		

Sheet steels, annealing for automotive applications

bake-hardening steels	299		
commercial-quality	298		
deep-drawing-quality	298		
drawing-quality	298		
dual-phase steels	300		
interstitial-free (IF) steels	298–299		
microalloyed high-strength low-alloy (HSLA) steels	299		
open-coil annealing	301		
overview	297–298		
solution-strengthened steels	299		
tin mill products	300–301		

Index Terms

Links

Shim stock

analysis of 524–526
validation of carbon potential via 530–531

Shim stock test

512

Shock-film boiling

92 105 163

Shot/sand blasting

400–401

Shrink fits

382

Silicon

alkaline cleaners 269
austenitizing temperatures 305
boriding 716
carbonitriding 613
carburizing cycle development 536
case depth, measuring 411
Curie point, effect on 441
fluidized-bed boriding 720
gas carburizing 531
hardenability and tempering of steels,
 effect of 46
hardness, effect on 334 336
intergranular oxidation 550
interstitial-free (IF) steels 299
laser hardening (LH) 488
liquid boriding 719
multicomponent boriding 720
multiplying factors (MF) 80 82 83 84
 86
nitriding 651
nominal subcritical annealing temperatures 305
pack cementation boriding 717
pack cementation processes 707
preoxidation 536
Q&P steels 317 318 320
silicone-based defoaming agents 548
solution-strengthened steels 299
spheroidizing 292
stop-off paints 401
supercarburizing 745

Index Terms

Links

Silicon (*Cont.*)

surface nonmartensitic transformation	
products (NMTP)	551
TME, effect on	343
vertical retort furnace	675

Silicon carbide (SiC)	240–241
------------------------------	---------

Siliconizing	708
---------------------	-----

Single-pass heat treatment (SPHT)	484
------------------------------------------	-----

Sinter metals	595
----------------------	-----

Skin effect	443–445
--------------------	---------

Smoothing, of measured temperatures

exponential C^1 splines	188–189
monotone smoothing	188–189
monotone smoothing, of measured	
temperatures	189
ordinary smoothing without constraints	188
overview	188

Snap draw treatment	347
----------------------------	-----

Sodium nitrate (NaNO₃)	232
------------------------------------------	-----

Sodium nitrite (NaNO₂)	232
------------------------------------------	-----

Solution-strengthened steels	299
-------------------------------------	-----

Sooting	539–540
----------------	---------

Spalling

air-gas type burners	429
boriding, ferrous materials	714–715
boriding, nonferrous materials	716
borochromtitanized structural alloy steel	721
dual-phase FeB and Fe ₂ B layers	713
high-temperature fluidized-bed carbide	
coating	735
nitrided surfaces	674
nitriding	394
pack cementation boriding	714–716
	717

Specifications

Aerospace Standard AS 1260	98
AFNOR NFT 60178, silver probe standard	106
AMS 2418, copper plating	399

Index Terms

Links

Specifications (*Cont.*)

AMS 2753, Liquid Salt Bath Ferritic Nitrocarburizing Non-Cyanide Bath	682	
AMS 2755B, aerated cyanide-cyanate nitriding	682	
AMS 2755C, case hardness	682	
ARP1820, Chord Method of Evaluating Surface Microstructural Characteristics	670	
Association of American Railroads Specification M-126, Class F	286	
ASTM 6, grain size	48	
ASTM 6 to 9, hardenability in high-carbon steels	80	
ASTM 7, grain size	48	
ASTM 8, grain size	48	64
ASTM 9, grain size	64	
ASTM 10, grain size	64	
ASTM 11, grain size	64	
ASTM 12, grain size	64	
ASTM A236, Class F, Association of American Railroads Specification M-126, Class F	286	
ASTM A255 Jominy end-quench test	101	
Standard Test Methods for Determining Hardenability of Steel	26	62
ASTM A255-10, Standard Test Methods for Determining Hardenability of Steel	65	
ASTM A370 Standard Test Methods and Definitions for Mechanical Testing of Steel Products Active Standard(Latest Version)	669	
Standard Test Methods and Definitions for Mechanical Testing of Steel Products	669	
ASTM B571, Standard Practice for Qualitative Adhesion Testing of Metallic Coatings	399	

Index Terms

Links

Specifications (*Cont.*)

ASTM B734, Standard Specification for Electrodeposited Copper for Engineering Uses	399
ASTM Code A255-89, Quenching and Cooling, Residual Stress and Distortion Control	47
ASTM D92, Cleveland open-cup procedure	141–142
ASTM D94, Standard Test Methods for Saponification Number of Petroleum Products Active Standard(Latest Version)	142
ASTM D455, method of viscosity determination	140
ASTM D664, acid number test	142
ASTM D2161, Standard Test Method for Saybolt Viscosity	140
ASTM D2270, Standard Guide for Evaluation of Hydrocarbon Heat Transfer Fluids	140
ASTM D3520, GM Quenchometer times	104
ASTM D6200 Standard Test Method for Determination of Cooling Characteristic of Quench Oils by Cooling Curve Analysis	177
Standard Test Method for Determination of Cooling Characteristics of Aqueous Polymer Quenchants by Cooling Curve Analysis with Agitation	110
Standard Test Method for Determination of Cooling Characteristics of Quench Oils by Cooling Curve Analysis	143
Wolfson probe	106
ASTM D6482, Standard Test Method for Determination of Cooling Characteristic of Aqueous Polymer Quenchants by Cooling Curve Analysis with Agitation	110
ASTM D6482-6, Standard Test Method for Determination of Cooling Characteristic of Aqueous Polymer Quenchants by Cooling	

Index Terms

Links

Specifications (*Cont.*)

Curve Analysis with Agitation	177		
ASTM D6549			
Standard Guide for Evaluation of Aqueous Polymer Quenchants	110		
Wolfson probe	106		
ASTM D6549-06, Standard Test Method for Determination of Cooling Characteristic of Quenchants by Cooling Curve Analysis with Agitation	177		
ASTM D6710			
Standard Guide for Evaluation of Hydrocarbon-Based Quench Oil	143		
Standard Guide for Evaluation of Hydrocarbon-Based Quench Oil Active Standard(Latest Version)	142		
ASTM D7646, silver probe standard	106		
ASTM E48, hardness conversion table	338		
ASTM E92, core and surface hardness testing	669		
ASTM E140, Standard Hardness Conversion Tables	669		
ASTM E384			
core and surface hardness testing	669		
Standard Test Method for Knoop and Vickers Hardness of Materials	670		
ASTM E1019-11, Standard Test Methods for Determination of Carbon, Sulfur, Nitrogen, and Oxygen in Steel, Iron, Nickel, and Cobalt Alloys by Various Combustion and Fusion Techniques	524	530	
ASTM E140-07, Standard Test Methods for Rockwell Hardness of Metallic Materials	1	2	557
ASTM E384-11, Standard Test Method for Knoop and Vickers Hardness of Materials	557		
ASTM F1503, Standard Practice for Machine/Process Capability Study			

Index Terms

Links

Specifications (*Cont.*)

Procedure	557			
ASTM International grain size number	315			
DIN 50191, Jominy end-quench test	101			
DIN EN ISO 642, Jominy hardenability curve	226			
EN 746, Industrial Thermo- Processing Equipment	674			
EN 746, Industrial Thermo-Processing Equipment	674			
ISO 642, Hardenability test by end quenching (Jominy test)	26	73		
ISO 642:1999, Hardenability test by end quenching (Jominy test)	101			
ISO 9950 determination of cooling characteristics— Nickel-alloy probe test method	137			
Industrial Quenching Oils—Determination of Cooling Characteristics—Nickel Alloy Probe Test Method	177			
Wolfson probe	106			
ISO 9950-1995, Industrial Quenching Oils—Determination of Cooling Characteristics—Nickel Alloy Probe Test Method	176			
JB/T 7951-2004, Wolfson probe	106			
JIS 2242:2012, silver probe standard	106			
JIS G 0561, Jominy end-quench test	101			
JIS K 2242 heat treating fluids	106			
Heat treating fluids	168			
JIS K 2242:1980, silver probe standard	106			
JIS K 2242-method B, Standards for Cooling Curve Analysis of Quenchants	177			
MIL-C-14550, Military Specification: Copper Plating (Electrodeposited)	399			
National Fire Prevention Association (NFPA)	86	274	659	674
SAE 2707, brake dynamometers	384			

Index Terms

Links

Specifications (*Cont.*)

SAE AMS 2759/10A, Heat Treatment of Steel Parts General Requirements	652			
SAE AMS 2759/12, Automated Gaseous Nitriding Controlled by Nitriding Potential	656	664		
SAE AMS 2759/6, procedure for gas nitriding of lowalloy and tool steels by the use of ammonia and dissociated ammonia	652			
SAE ARP 1820, Chord Method Of Evaluating Surface Microstructural Characteristics	522			
SAE J406 Jominy end-quench test	101			
Methods of Determining Hardenability of Steels	26	38	47	65
SAE J423, Methods of Measuring Case Depth	413	522	556	670
SAE J1268 Hardenability Bands for Carbon and Alloy H Steels	552			
hardness range for standard H-band steels	99			
SAE J1868, Restricted Hardenability Bands for Selected Alloy Steels	552			
SEP1664, Derivation of equations by multiple regression for the calculation of hardenability in the Jominy end quench test on the basis of the chemical composition of steels	73			
SH/T0220-92, silver probe standard	106			

Spheroidizing

291–293

SPHT. *See* Single-pass heat treatment (SPHT)

Spin-off technologies

copper plating	399–400
mechanical masking	399
overview	399
stop-off paints	400–404

Index Terms

Links

Spray quenching

advantage of	245
application of	245
concepts of	245–247
defined	245
introduction	245
water quenching heat transfer	247–250

Spring wire

salt quenching	126	232
stress-relief heat treating	276	278

Springback

320 321 359

Springs, stress relief of

277–279

Sputter cleaning

696

Sputter deposition

476

Sputter plasma

595

Sputtering

case depth, measuring	407
glow-discharge process	695
plasma nitriding	395
stainless steels	700

Stainless steel, specific types

304

aqueous salt (brine) solutions	123–124
pack cementation	707
probes	106

316

active heat-transfer boundary condition	171
nitrocarburizing	651
pack cementation	707

321, cooling behavior experiment

257

410

martempering	368
nominal subcritical annealing temperatures	306
pack cementation	707

631, stress relieving

278

Stainless steels

austenitic	306
ferritic	306

Index Terms

Links

Stainless steels (*Cont.*)

gas nitriding	653
plasma carburizing	595
solution nitriding	658–659
sputtering and ion nitriding of	700

Statistical process control (SPC)	514
------------------------------------------	-----

STECAL	63
---------------	----

Steel, AMS-HY, specific types

AMS 4140, liquid nitriding	683
AMS 4340, liquid nitriding	683
AMS 6475, liquid nitriding	683
HY-100, stress-relief heat treating	276–277

Steel, ASTM, specific types

5130M	229
8625	229

Steel, EN type

EN 40C, nitriding	395
EN-GJS-600, EB hardening	472
EN-GJS-600, EBH	473

Steel, Q&P, specific types

1180, HER	319
980	
forming	319
HER	319
retained austenite, mechanical behavior of	321
shear fracture behavior	320
springback behavior	320
welding properties	322–324

Steel, selection for hardenability

alloy steels	49–50
core hardness	49
example	50
Jominy equivalence charts	49
maximum attainable hardness chart	48–49
overview	48–49

Steel alloys

gas carburizing	531–532
Grossmann method	65

Index Terms

Links

Steel alloys (*Cont.*)

hardenability, defined	64–65
nitriding steels	699
plasma (ion) nitriding	699

Steel hardenability, calculation of

Climax Molybdenum calculator	48
Grossmann factors	47–48
high-carbon steels	48
Jominy curves, calculation of	48
Kramer factors	48

Steel Institute VDEh

72–73

Steel rod test

733 734 735 736

Steels

boron steels, DI calculation for	69
carbide steels, nitriding	638–639
carburizing	391–392 514
interstitial-free (IF) steels	298–299
magnetic properties of steel	441–442
for martempering	368–371
nonboron steels, DI calculation for	66–69

Steels, AISI-SAE, specific types

1008, cold forming	301
1010	
liquid nitriding	687
shim stock	524
shim stock test	512
1016, carburizing	392
1018	
boride layer stability	712–713
carburizing	392
IQ process	205
1019, carburizing	392
1020	
hardness gradients	571
IQ-3 process	203
1034	
austempering	354
martempering	369

Index Terms

Links

Steels, AISI-SAE, specific types (*Cont.*)

1040			
Jominy equivalent hardness method	40		
spheroidizing	292		
1042			
austenitizing	447		
induction-hardening temperature range	458		
1045			
bath temperature and agitation,			
effect of	137–138		
flame hardening	434		
IQ process	199	204	207
IQ-3 process	203		
test on flame-hardening procedures	426		
1050			
active heat-transfer boundary condition	171		
selection for hardenability	49		
1070, annealing	302		
1070 to 1090, polyacrylate solutions,			
quenching	150		
1080			
austempering	353	354	
austenitizing	447		
modified austempering	358–359		
1090			
austempering	354		
martempering	368	369	
1095			
annealed structures for machining	295		
iron-carbon phase diagram	12–13		
martempering	364		
1117			
hardness gradients	571		
noncyanide carburizing process	569		
1141, martempering	368		
1513, cold forming	301		
15B35, annealing	301		
300M, martempering	368		

Index Terms

Links

Steels, AISI-SAE, specific types (*Cont.*)

3310				
gas carburizing	552			
normalizing	283			
press quenching	252			
3311, gas carburizing	548			
3312, martempering	368			
4023				
carburizing	392			
Jominy equivalent hardness method	40			
4037, annealing	302			
4068, prediction of hardenability in steels	63			
4118, carburizing	392			
4122, gas carburizing	549			
4130, martempering	368			
4140				
hardness distribution after quenching,				
predicting	184			
inverse hardening	214	216	218	219
ion nitrided	697			
Jominy data sets	46			
liquid nitriding	683			
martempering	364	368		
nominal subcritical annealing temperatures	305			
self-quenching	432			
surface oxidation	114			
tempered martensite embrittlement				
(TME)	343–344			
wetting kinematics, influence of	183			
4140, bath temperature and agitation,				
effect of	137–138			
4140H				
hardenability band	49			
selection for hardenability	50			
4150				
carburized and austempered	357			
flame hardening	434			
martempering	368			

Index Terms

Links

Steels, AISI-SAE, specific types (*Cont.*)

self-quenching	432	
upper bainite formation	10	
4320		
carburizing	392	
gas carburizing	552	
IQ process	205	
normalizing	283	
4340		
austempering	354	
liquid nitriding	683	
martempering	368	369
nominal subcritical annealing		
temperatures	305–306	
self-quenching	432	
tempered martensite embrittlement		
(TME)	343	
4620		
carburizing	392	
hardness gradients	571	
martempering	368	
4640		
martempering	368	
self-quenching	432	
4815, hardness gradients	571	
4817, carburizing	392	
5120		
carburizing	392	
gas carburizing	552	
IQ process	205	
martempering	368	
5140		
austempering	353–354	
martempering	368	369
5160		
annealing	301	
austempering	354	
52100		

Index Terms

Links

Steels, AISI-SAE, specific types (*Cont.*)

annealed structures for machining	295	
annealing	301	
austenitizing	309	
forced air quenching	432	
IQ process	205	
martempering	368	372
normalizing	283	
press quenching	252	
spheroidizing	301	
6150		
liquid nitriding	683	
martempering	368	
7140, liquid nitriding	683	
8615		
carburized and austempered	357	
hardness gradients	571	
8620		
carburized and austempered	357	
carburizing	392	
case depth, measuring	405	
cold forming	301	
flame hardening	434	
fluidized-bed quenching	244	
gas carburizing	552	
hardness gradients	571	
IQ process	205	
IQ-3 process	203	
Jominy data sets	46	
Jominy equivalent hardness method	40	
press quenching	252	
quench selection	121	
8620H, Minitech computations	64	
8621, martempering	368	
8630		
carbon content, effect on hardenability	51	
martempering	368	

Index Terms

Links

Steels, AISI-SAE, specific types (*Cont.*)

8640H				
depth of hardening	42–43			
martempering	368			
8645, Caterpillar hardenability calculator (1E0024)	70–71			
8650, carbon content, effect on hardenability	51			
8720, cold forming	301			
8740, martempering	368			
8745, martempering	368			
8822, carburized and austempered	357			
9261, austempering	354			
9310				
carburizing	392			
flame hardening	434			
gas carburizing	548	552		
martempering	368			
press quenching	252			
D2, cryogenic treatment cycles	384			
Stefan-Boltzmann equation	160			
Stellite	483	484	728	729
	730			
StopGQ process	368			
Stop-off paints				
application methods				
brushing	403			
dipping/immersion	403			
dispensing	403–404			
overview	403			
spraying	404			
stamping	404			
cleaning in industrial washers	400			
curing/drying	401			
edge effect	403			
general considerations	402–403			
hand cleaning	401			
non-Newtonian fluids	403			
overview	400			

Index Terms

Links

Stop-off paints (*Cont.*)

part cleanliness	400–401
shot/sand blasting	400–401
uses of	
carbonitriding	401
carburizing	401–402
deep case carburizing	401–402
nitriding	402
nitrocarburizing	402
plasma nitriding	402
scale prevention	402
vacuum carburizing	402

Stopoffs

554 577 680

Strain aging

bake-hardening steels	299
defined	9
overview	9
steel, annealing of	297

Stress-corrosion cracking (SCC)

275 277

Stress-relief heat treating

overview	275
post-weld heat treating, difference	
between	275
residual stress, sources of	275
of springs	277–279
stress-corrosion cracking (SCC)	275
thermal stress-relief methods	
alloy considerations	277
overview	275–276
time-temperature factors	276–277

Subcritical annealing and normalizing

induction annealing, time temperature	
relations	306–307
induction thread softening	307–308
normalizing	307
overview	305
subcritical temperatures	305–306

Index Terms

Links

Subcritical annealing and normalizing (*Cont.*)

temperature-time relations 306–307
use of term 305

Sulfonitriding

648 655

Sulfur

685–687

Supercarburizing

with conventional carburizing steel 741–744
equipment 742–743
overview 741
process curves 743
steels for 744–746

Supercritical fluid (SCF) cleaning

270

Surface Engineering, Volume 5 of ASM

Handbook

266 269 273

Surface hardening

applied energy methods 395–396
with arc lamps 397
carbonitriding 390–391 393
carburizing 390–393
diffusion coatings 396
diffusion methods 389–390
electron beam (EB) hardening 395–396
flame hardening 395
heating time, methods to establish 458–459
induction heating 395
ion implantation 396–397
laser surface heat treatment 395
nitriding 393–395
nitrocarburizing 395
overview 389
process selection 397

Surface nonmartensitic transformation products

(NMTP)

551

Surface treatment. *See also* Electron beam surface

hardening; Nitriding; Surface hardening
cleaning 265–274
discoloration of parts 673

Index Terms

Links

Surface treatment (*Cont.*)

laser surface heat treatment	395	
TRD coatings	737	739

Surface-area-center (SAC) test

39–40

SUS. *See* Saybolt universal seconds (SUS)

T

TE. *See* Temper embrittlement (TE)

TEL. *See* Total elongation (TEL)

Temper embrittlement (TE)

339–341

Temperature Gradient Quenching Analysis System (TGQAS)

213

Temperature Gradient System (TGS)

cooling intensities of liquid quenchants,

 database of 184

HTC, calculation of 186

Liscic/Petrofer probe 181

monotone smoothing 188

Tempered martensite

austempering 352–353

carburized case depth 558

carburized cases 413

carburizing 516

carburizing and austempering 357

embrittlement 307 331

See also Tempered

 martensite embrittlement (TME)

gas carburizing 553

IHT diagrams 17

induction annealing 305

induction normalizing 307

induction surface hardening 458

introduction 15–16

inverse hardening 219

IQ-2 process 202

laser surface hardening (LSH) 487

process 158

supercarburizing 745

tempering 327

Index Terms

Links

Tempered martensite embrittlement (TME)	341–344	
Tempering		
artificial neural networks (ANNs)	334	
carbonitriding	611–612	
cold treating versus tempering	382	
composition, effects of		
alloying effects, other	336	
overview	334	336
residual elements	336	
cooling rate	327	
dimensional change during	336–338	
flame-hardened parts		
flame tempering	433	
overview	433	
self-tempering	433	
gas carburizing	553–554	
induction. <i>See</i> Induction tempering		
induction hardening and	446–451	
induction tempering	451	
introduction	327	
powder metallurgy (PM) parts	614	
principle variables	327	
quenched and tempered (QT) alloy steel	327	
tensile properties and hardness		
hardness, variations after tempering	338–339	
overview	338	
toughness and embrittlement		
blue brittleness	341	
overview	339	
temper embrittlement (TE)	339–341	
tempered martensite embrittlement (TME)	341–344	
Tempering, equipment for		
convection furnaces	344	
molten metal baths	345	
oil bath equipment	345	

Index Terms

Links

Tempering, equipment for (*Cont.*)

salt bath furnaces	344–345
selection of	344
temperature control	345

Tempering procedures

cracking in processing	346–347
fixtures, use of	346
multiple tempering	346
overview	345
selective tempering	345–346
snap draw	347

Tempering temperatures and stages

overview	327–330
tempering at 230 to 370 °C (450 to 700 °F)	331
tempering at 370 to 540 °C (700 to 1000 °F)	331
tempering at 540 to 700 °C (1000 to 1300 °F)	331–332
tempering at 95 to 200 °C (200 to 400 °F)	330–331

Tempering time and temperature

estimating an equivalent time-temperature condition for tempering to a similar hardness	333
estimating difference in hardness fro two tempering treatments	333–334
overview	332–333
parametric models, other	334

Tensi classification of surface-cooling modes of

heat transfer	93–94
----------------------	-------

Test-pin section	563	564
-------------------------	-----	-----

TGQAS. *See* Temperature Gradient Quenching
Analysis System (TGQAS)

TGS. *See* Temperature Gradient System (TGS)

Thermal stresses

bath temperature and agitation, effect of	137
carbonitrided parts	700
dynamic gas quenching	228
induction normalizing	307

Index Terms

Links

Thermal stresses (*Cont.*)

induction surface hardening	459
introduction	21–23
Liscic/Petrofer probe	181
normalizing	307
quench process sensors	192
temperature gradient method	180

Thermochemical boriding, applications of

721–722

Thermochemical boriding techniques

fluidized-bed boriding	720
gas boriding	719
liquid boriding	718–719
multicomponent boriding	720–721
pack cementation boriding	717
paste boriding	718
plasma boriding	719–720

Thermocouples (TCs)

active heat-transfer boundary condition	167	171
annealing	296	302
CCT diagrams	96	
CFEs/NFEs	734	735
cooling curves	92	
cyaniding	571	
gas carburizing	540	541
gas quenching	223	
heat-transfer basics	159	
least-squares function	170	
liquid quenching heat transfer	163	
Liscic/Petrofer probe	181	
martempering	367	377 378
near-surface thermocouples	107	
rewetting	165	
selective nitriding	674	
sheathed	108	
silver probes	106	
simplified 1-D temperature distribution		
model	185	186

Index Terms

Links

Thermocouples (TCs) (*Cont.*)

simulation examples	189	
steel heat treating, temperature range	108	
temperature gradient method	189	
Tensi classification of surface-cooling modes of heat transfer	94	
TGQAS	213	214
TRD	732	
type K thermocouples	137	
workshop designed test	179	

Thermokinetic phase transformations 485–487

Thermoreactive deposition and diffusion (TRD)

process

applications	738–739	
carbide coating nucleation and growth	727–728	
carbide-forming elements (CFEs)	725	
chemical vapor deposition (CVD)	725	
coated parts	737–738	
coating mechanisms	726	
coating processes	730	731–732
coating reagent conditions, controlling	732–733	
coating types	726–727	
growth rate, factors controlling	729–730	
high-temperature fluidized-bed carbide coating	735	
high-temperature salt bath carbide coating	733–735	
introduction	725–726	
nitride coating nucleation and growth	728–729	
nitride-forming elements (NFEs)	725	
physical vapor deposition (PVD)	725	

Three-dimensional (3-D) heat transfer 439

Tikhonov regularization method 110

Time-temperature cooling curves 92–93 94

Time-temperature transformation (TTT)

diagrams

austempering	353	
austenite formation	312	313
austenitizing temperature	354	

Index Terms

Links

Time-temperature transformation (TTT) (Cont.)

heat transfer, during quenching	162
martempering	369–370
modified austempering	358–359
quenching steel	95–96

Time-temperature-austenitization (TTA) diagrams

313 314

Tin mill products

300–301

Titanium

boriding	717
boron factors	87

Titanium carbide

390 396 397 707
735

TME. *See* Tempered martensite embrittlement
(TME)

Tool steels

annealing	282	291		
boriding	396	714	717	721
cold treating	382			
conventional batch quenching	243			
flame hardening	436	437		
fluidized-bed quenching	238			
gas nitriding	651	652		
gas nitrocarburizing	656			
hardenability, calculation of	80			
HPGQ	221			
induction annealing	307			
laser transformation hardening	395			
liquid nitriding	680	683		
liquid nitrocarburizing	685			
liquid salt bath nitriding noncyanide baths	688	689		
martempering	367	368		
nominal subcritical annealing temperatures	306			
quenching	127			
quenching oils	133			
salt bath descaling	270			
salt quenching	232			
spheroidizing	292			

Index Terms

Links

Tool steels (*Cont.*)

surface hardening	389	397		
titanium carbide	396			
TRD process	728	731	732	739
two-step batch quenching	244			

Tool steels, specific types

A2, press quenching	252			
AISI 01, martempering	364			
D2, liquid nitriding	683			
D2, nominal subcritical annealing				
temperatures	306			
H11, liquid nitriding	683			
H12, liquid nitriding	683			
H13, marquenching in a fluidized bed	244			
low-carbon H11, liquid nitriding	683			
low-carbon H15, liquid nitriding	683			
M-20, liquid nitriding	683			
M48, nominal subcritical annealing				
temperatures	306			
medium-carbon H11, liquid nitriding	683			

Total case depth, defined 556

Total elongation (TEL) 321

Townsend discharge 694

Toyota

CFEs/NFEs	732–733			
diffusion process	389			
high-temperature fluidized-bed carbide				
coating	735			
TRD process	726			

Toyota diffusion process 389 726

Transformation diagrams

continuous cooling transformation (CCT)				
diagrams	16	20–21		
introduction	16			
isothermal transformation (IT) diagrams	16–20			

Transformation-induced plasticity (TRIP)

steel	317	318	319	320
	321			

Index Terms

Links

Transformer action	438	
Transgranular fractures	13	342–343
TRD. See Thermoreactive deposition and diffusion (TRD) process		
TRIP steels. See Transformation-induced plasticity (TRIP) steel		
TTA diagrams. See Time-temperature-austenitization (TTA) diagrams		
Tube retorts	676	
Tubular products		
annealing	303	
normalizing	286	
Tumbling	268–269	
Two-dimensional (2-D) computer program	183	
U		
Ultimate tensile strength (UTS)	321	
Ultrasonic cleaning	270	
UTS. See Ultimate tensile strength (UTS)		
V		
Vacuum carburizing. See also <i>Low-pressure carburizing (LPC)</i>		
carburizing steels	514	
cleaning methods	267	
intergranular oxidation	518	
liquid carburizing, as replacement for low-pressure vacuum gas carburizing (LPC)	519	
overview	520	
pack carburizing, as replacement for stop-off paints	392	
	518–519	
	400	402
Van der Waals	260	
Vane sensor	193	
Vapor blanket cooling		
aqueous salt (brine) solutions	122	
cooling curves	110	258
Leidenfrost temperature	195	

Index Terms

Links

Vapor blanket cooling (*Cont.*)

quench severity 100
quenching process variables 113

Vapor blanket cooling stage

92 258

Vapor blanket (full-film boiling)

agitation 94
bath temperature and agitation, effect of 137
conventional quenching 201
cooling curve test 104 105 110
cooling curves 92
cooling rate acceleration 136
heat-flux density 180
interval test 104
PAG quenchants 218
pool boiling 161
press quenching 254 255
quenching process variables 113 115 116
rewetting 164 183
spray quenching 246 449
surface nonmartensitic transformation
 products (NMTP) 551
Tensi classification of surface-cooling
 modes of heat transfer 93
velocity measurement, using thermal probes 195
water- and air-quenching media 122 123
wire patenting 258 259 260 261

Vapor degreasing

270

Vickers hardness

case depth 670
hardenability tests 36
Jominy end-quench test 101
surface hardness comparison 710
surface hardness measurement 672
tensile properties and hardness 338

Vickers hardness tester

672

Vickers indenter

408 409 557

Viscosity increasers

736

Void formation

605 607 608

Index Terms

Links

W

Water, additions to salt	372			
Water burette (pipette)	665			
Water quenching	122			
Water quenching heat transfer				
immersion quenching	247			
jet quenching	248–250			
quenching agitation, effect of	247			
spray quenching	247–248			
Water-gas reaction	511			
Water-gas shift reaction	649			
Weld lobe	322			
Welding				
laser welding	323–324			
metal active gas (MAG) welding	324			
Q&P 980 steel	322			
resistance spot welding	322–323			
as source of residual stress	275			
weld lobe	322			
White layer				
defined	394			
direct-current plasma nitriding (1970–1980)	690			
gas nitriding	647	654	661	673
	674	699		
nitrided steels	698			
nitriding	394			
plasma (ion) nitriding	698	699–700		
properties	699–700			
Widmanstätten side plates	19			
Wire				
annealing	302–303			
carburizing and brazing, combined	577			
cleaning with	429			
deep cryogenic treatment (DCT)	384			
fluidized-bed quenching	243			
hot wire test	104	105		
induction heating	289			
laser cladding	481			

Index Terms

Links

Wire (Cont.)

martempering	380			
modified austempering	357–359			
multiple anneals and tempering	286			
music wire	276	278		
noncyanide liquid carburizing bath, analysis of	571			
open-coil annealing	301			
oven stress-relief temperatures and times	276			
patenting	125	150	244	357–359
platinum	194			
pool boiling	160			
process annealing	294			
quench process sensors	194			
rolled, analysis of	526			
salt quenching	232			
Wire industry	294	302–303	357–358	
Wire patenting				
concentration-fog flux effect	260–261			
continuous quenching	244			
controlled fog-cooling patenting with CMC additive	261			
cooling behavior experiment	257			
cooling curves and cooling-rate curves results and analysis				
CMC solutions, measurement in	257–258			
fog cooling, cooling curve	259			
microstructure comparison	258			
polymer additive introduced	259–260			
drawing process	257			
fluidized-bed quenching	238			
processes				
aqueous carboxymethyl cellulose solution	257			
lead baths	257			
overview	257			
polyacrylate solutions	150			
wire patenting beds	238			

Index Terms**Links**

Wire patenting beds	238			
Wire resistance method	535			
Wolfson probe	106			
Work-load density	564			
Wrap-around effect	593			
X				
X-ray diffraction (XRD)	323	548	549	745
Y				
Yttrium-aluminum-garnet (Nd: YAG)	484			
Z				
Zero-flow nitriding	665			
Zero-volume chambers	470			
Zirconium				
as alloying element	45			
boron factors	87			
chemical vapor deposition (CVD)	722			
gas nitriding	667			
gas nitrocarburizing	667			
Lambda probes	667			
liquid induction carburizing	519			
low-temperature salt bath nitride coating	736			
multiplying factors	66	87		
oxygen probes	667			
TRD process	725			